LBNL-5808E

Proceedings of the TOUGH Symposium 2012

September 17–19, 2012

Lawrence Berkeley National Laboratory
Berkeley, California

Editors

Stefan Finsterle, Daniel Hawkes, George Moridis,
Sumit Mukhopadhyay, Curt Oldenburg, Loic Peiffer,
Jonny Rutqvist, Eric Sonnenthal, Nicolas Spycher,
Carol Valladao, and Liange Zheng

Lawrence Berkeley National Laboratory
Earth Sciences Division
1 Cyclotron Road, Mail Stop 74-324
Berkeley, CA 94720

This work was supported by the U.S. Department of Energy under Contract No. DE-AC02-05CH11231.

Foreword

This volume contains more than 100 papers presented at the TOUGH Symposium 2012 in both oral and poster formats. The full papers are also available as pdfs linked from the program posted on the TOUGH Symposium 2012 website at

http://esd.lbl.gov/research/projects/tough/events/symposia/toughsymposium12/program.html

The papers cover a wide range of application areas and generally reflect the continuing trend toward increasing capabilities and broader application of the TOUGH codes to critical problems in Earth sciences and engineering. Nearly one-third of the papers this year are in the area of geologic carbon sequestration, a reflection of the TOUGH development and international research focus on CO_2 problems over the last decade.

The Organizing Committee wishes to thank the session chairs, presenters, key note speakers, and participants for their ongoing interest in the TOUGH codes. The support from various agencies and offices in the U.S. and around the world for the development and application of the TOUGH codes is greatly appreciated. We also are grateful to Thunderhead Engineering, Geofirma Engineering, Shell and Statoil for financial support of the Welcome Reception, Poster Session, Symposium Banquet, Short Courses, and for the Karsten Pruess Student Paper Award.

The papers are grouped by topic, and within a topic order alphabetically by the last name of the first author. The topical sections start at the following pages numbers:

The Organizing Committee

Stefan Finsterle (Chair)
George Moridis
Curt Oldenburg
Jonny Rutqvist
Eric Sonnenthal
Nicolas Spycher
Carol Valladao

Berkeley, September 17, 2012

AGENDA

Sunday, September 16, 2012	
Icebreaker	
6:00 PM	**Welcome Reception, Hotel Shattuck Plaza**
Monday, September 17, 2012, Morning Sessions	
7:30 AM	**Registration, Building 50 Auditorium**
Welcome and Opening Remarks	
8:30	**Welcome** **Horst Simon, Deputy Director, Lawrence Berkeley National Laboratory (LBNL)**
8:40	**Opening Remarks** **Stefan Finsterle, Karsten Pruess**
8:50	**Announcements** **TOUGH Symposium Organizing Committee**
Session I: Carbon Dioxide Storage I	
Session Chairs: Edward Mehnert, Christine Doughty	
9:00	**Migration of Exsolved CO_2 Following Depressurization of Saturated Brines** **Ronald W. Falta,** Lin Zuo, Sally M. Benson
9:20	**Comparison of a 2D TOUGHREACT Model of CO_2 Injection into a Carbonate Reservoir with Chemical Data from a CO_2 Enhanced Oil Recovery Project** **Maurice Shevalier,** Michale Nightingdale, Bernhard Mayer
9:40	**Influence of Geological Parameters on CO_2 Storage Prediction in Deep Saline Aquifer at Industrial Scale** **Sarah Bouquet,** Dominique Bruel, Chantal de Fouquet
10:00	**Impact of Data Uncertainty on Identifying Leakage Pathways in CO_2 Geologic Storage Systems and Estimating their Hydrogeological Properties by Inverse Modeling** **Yoojin Jung**, Quanlin Zhou, Jens T. Birkholzer
10:20	***Break***
10:50	**Modeling CO_2 Injection at Cranfield, Mississippi: Investigation of Methane and Temperature Effects** **Christine Doughty,** Barry Freifeld
11:10	**Expansion and Migration of Gaseous and Dissolved CO_2 in a Site Specific Shallow Aquifer** **Carla E. Wiegers**, Dirk Schäfer, Ralf Köber, Andreas Dahmke

Session I: Carbon Dioxide Storage I (cont.)	
11:30	**Assessing Pre-Injection In Situ Alteration of Wellbore Cement in a Site for CO_2 Geological Storage: A Numerical Approach** **Fabrizio Gherardi,** Pascal Audigane
11:50	*Lunch*
Session II: Numerical Methods	
Session Chairs: Emily Clearwater, Yu-Shu Wu	
1:20	**Adding Geology to the Equation: Towards Integrating Structural Geological Data into Inverse Modeling with iTOUGH2** **J. Florian Wellmann,** Stefan Finsterle, Adrian Croucher
1:40	**Innovative Tools for Continuum Discretization, Better Management of TOUGH2 Input Data and Analysis of the Numerical Simulation Results** **Carlo Cormio**, Paolo Berry, Stefano Bondua, Villiam Bortolotti
2:00	**Thermal-Hydrologic-Mechanical Model for Fracture Propagation, Fluid Flow, and Transport in Porous Rock** **Daisuke Asahina,** Jim Houseworth, Jens Birkholzer
2:20	**Geophysical Data Improve Stability and Convergence of Hydrological Property Estimation: A Synthetic CO_2 Injection Study** **Joseph Doetsch,** Michael B. Kowalsky, Stefan Finsterle, Christine Doughty, Jonathan B. Ajo-Franklin, Thomas M. Daley
2:40	**Optimizing the Modeling Performance for Safety Assessments of Nuclear Waste Repositories by Approximating Two-Phase Flow and Transport by Single-Phase Transport Simulations** **Philipp Schädle,** N. Hubschwerlen, H. Class
3:00	*Break*
3:30	**Geothermal Model Calibration using a Global Minimization Algorithm Based on Finding Saddle Points as Well as Minima of the Objective Function** **Manuel Plasencia Gutierrez,** Andreas Pedersen, Andri Arnaldsson, Hannes Jónsson
3:50	**iTOUGH2 Global Sensitivity Analysis Module: Applications to CO_2 Storage Systems** **Haruko M. Wainwright,** Stefan Finsterle, Yoojin Jung, Quanlin Zhou, Jens T. Birkholzer
4:10	**Reduced Order Models for Subsurface Flow in iTOUGH2** **George Pau,** Yingqi Zhang, Stefan Finsterle
4:30	**What's New in iTOUGH2?** **Stefan Finsterle**

Evening Poster Session and Reception	
Session Chairs: Dorothee Rebscher, Haruko Wainwright, Michael Kowalsky, George Pau	
5:30 – 8:00	*LBNL Cafeteria*
8:00	**Shuttle Bus leaving for Hotel Shattuck Plaza and Downtown Berkeley BART**

Tuesday, September 18, 2012, Morning Sessions

Session III: Geothermal

Session Chairs: Edda Aradottir, Micol Todesco

8:30	**Improving the Treatment of Saline Brines in EWASG for the Simulation of Hydrothermal Systems** **Alfredo Battistelli**
8:50	**The Deep Roots of Geothermal Systems in Volcanic Areas: Boundary Conditions and Heat Sources in Reservoir Modelling** **Gunnar Gunnarsson,** Edda S.P. Aradottir
9:10	**Modeling the Ohaaki Geothermal System** **Emily K. Clearwater,** Michael J. O'Sullivan, K. Brockbank, W. I. Mannington
9:30	**Simulating Microhole-Based Heat Mining from Enhanced Geothermal System** **Yingqi Zhang,** Lehua Pan, Patrick Dobson, Ken Oglesby, Stefan Finsterle
9:50	***Break***
10:20	**Enhanced Heat Transport Via Simmering Phenomena in Geothermal Models** **Tom Brikowski**
10:40	**Towards Cleaner Geothermal Energy Utilization: Capturing and Sequestering CO_2 and H_2S Emissions from Geothermal Power Plants** **Edda S.P. Aradottir,** Ingvi Gunnarsson, Bergur Sigfússon, Gunnar Gunnarsson, Einar Gunnlaugsson, Hólmfríður Sigurðardóttir, Einar Jón Ásbjörnsson, Eric Sonnenthal
11:00	**Numerical Reservoir Model of the Takigami Geothermal Field, Oita, Japan** **Saeid Jalilinasrabady,** Ryuichi Itoi, Hiroki Gotoh, Toshiaki Tanaka
11:20	**Basin-Scale Geothermal Model Calibration using iTOUGH2** **Lynn B. Reid,** J. Florian Wellmann

Awards

11:40	**Award Ceremony** **TOUGH Symposium Organizing Committee**
12:00	***Lunch***

Tuesday, September 18, 2012, Afternoon Sessions

Session IV: Hydrocarbon Recovery and Reservoir Processes

Session Chairs: Alfredo Battistelli, Matthew Reagan

1:00	**Geochemical Reactive Transport Modeling in Oil & Gas Industry—Business Drivers, Challenges and Solutions** **Guoxiang Zhang,** Esra Inan-Villegas
1:20	**Integrated Reactive Transport Modelling: Challenges and Opportunities for Improved Prediction of Diagenetic Impact on Reservoir Quality** **Fiona Whitacker,** Tatjana Gabellone, Graham Griffiths
1:40	**Massively Parallel Simulation of Production from Field-Scale Oceanic Gas Hydrate Deposits** **Matthew T. Reagan,** George J. Moridis, Katie L. Boyle, C. Matthew Freeman, Lehua Pan, Noel D. Keen, Jarle Husebo
2:00	**Development of the T+M Coupled Flow-Geomechanical Simulator to Describe Fracture Propagation and Coupled Flow-Thermal-Geomechanical Processes in Tight/Shale Gas Systems** **Jihoon Kim,** George J. Moridis
2:20	**Modeling of Flow and Transport Induced by Production of Hydrofracture Stimulated Gas Wells Near the Rulison Nuclear Test** **Rex A. Hodges,** Clay Cooper, Ron Falta
2:40	**The RealGas and RealGasH_2O Options of the TOUGH+ Code for the Simulation of Coupled Fluid and Heat Flow in Tight/Shale Gas Systems** **George J. Moridis,** C. Matthew Freeman, Stephen W. Webb, Stefan Finsterle
3:00	***Break***

Session V: Carbon Dioxide Storage II

Session Chair: Ron Falta, Tim Tambach

3:30	**Simulations of Upward Leakage of CO_2 in Long-Column Flow Experiments: Effect of Lateral Boundary Condition** **Curtis M. Oldenburg,** Christine Doughty, Catherine A. Peters, Patrick F. Dobson
3:50	**Comparison of Supercritical and Dissolved CO_2 Injection Schemes** **Catherine M. Ruprecht,** Ronald W. Falta
4:10	**Behaviour of the CO_2 Injection Well and the Near Wellbore During Carbon Dioxide Injection in Saline Aquifers** **Mohamed Azaroual,** Laurent Andre, Yannick Peysson, Jacques Pironon, Daniel Broseta, Fabien Dedecker, Patrick Egermann, Jean Desroches, Joëlle Hy-Billiot

Session V: Carbon Dioxide Storage II (cont.)	
4:30	**Development of an Advanced Thermal-Hydrologic-Mechanical Model for CO_2 Storage in Porous and Fractured Saline Aquifers** **Philip H. Winterfeld,** Yu-Shu Wu, Karsten Pruess, Curtis Oldenburg
Banquet Dinner	
6:00	**Shuttle Bus Pick up at the Guest House and Hotel Shattuck**
6:30	**Banquet, *Caffe Venezia*, 1799 University Avenue, Berkeley**
8:00	**The Science Behind the Taming of the Deepwater Horizon Oil Spill** **Paul Hsieh**
9:00	**Shuttle Bus leaving for the Guest House and Hotel Shattuck**

Wednesday, September 19, 2012, Morning Sessions

Session VI: Nuclear Waste

Session Chair: James Houseworth, Nicolas Hubschwerlen

8:30	**Extension and Tuning of TOUGH2-MP EOS7R for the Assessments of Deep Geological Repositories for Nuclear Waste: Hydrogen, Arbitrarily Long Decay Chains, and Solubility Limits** **Thomas Kaempfer,** Yury Mishin, Jürgen Brommundt, Jean Roger, Eloi Treille, Nicolas Hubschwerle
8:50	**Multiphase Flow and Interaction Dynamics between Bentonite Clay and Fractured Crystalline Rock** **Benoît Dessirier,** Jerker Jarsjö, Andrew Frampton
9:10	**T2GGM – A Coupled Gas Generation Model for Deep Geologic Disposal of Radioactive Waste** **John Avis,** Paul Suckling, Nicola Calder, Robert Walsh
9:30	**Probabilistic Analysis Based on Simulations of the Long-Term Gas Migration at Repository-Scale in a Geological Repository for High and Intermediate Level Radioactive Waste Disposal in a Deep Clay Formation** Eloi Treille, Jacques Wendling, **Laurent Trenty**, Laurent Loth, Guillaume Pepin and Frédéric Plas
9:50	***Break***
10:20	**Development and Application of a Chemical Osmosis Simulator Based on TOUGH2** **Mikio Takeda,** Tsuyoshi Hiratsuka, Kazumasa Ito, Stefan Finsterle
10.40	**3D Modeling of the Long-Term Behaviour of a Geological Repository for HLW and ILW-LL Nuclear Waste, Considering Heat, Gas, and Radionuclide Release and Transport – Optimizations that Allow for Detailed Large-Scale Modeling** **Carl Philipp Enssle,** Jürgen Brommundt, Thomas U. Kaempfer, Gerhard Mayer, Jacques Wendling

Session VII: Tips & Tricks

Session Chair: Karsten Pruess

11:00	**Short Pop-Ups with TOUGH Tips and Tricks** **All Participants – sign up**
12:00	***Lunch***

Wednesday, September 19, 2012, Afternoon Sessions

Session VIII: Environmental Engineering

Session Chairs: Andrea Borgia, Julia Diessl

1:00	**Importance of Overland Flow in Dentrification of Wastewater Applied to Rapid Infiltration Basins** **Maryam Akhavan,** Paul T. Imhoff, Scott Andres
1:20	**Experimental and Numerical Evaluation of Dual Phase Flow During Liquid Injection in a Coarse Sand** **Tryambak Kaushik,** Milind V. Khire
1:40	**Feasibility Analysis of Underground Compressed Air Energy Storage in Lined Rock Caverns using TOUGH-FLAC Simulator** **Hyung-Mok Kim,** Jonny Rutqvist, Byung-Lee Choi
2:00	**EOS7Rn–a New TOUGH2 Module for Simulating Radon Emanation and Transport in the Subsurface** **Zakaria Saâdi,** Didier Gay, Jérôme Guillevic, Roselyne Améon
2:20	**On Parameterizing Heterogeneity and Incorporating Geophysical Measurements in Hydrogeophysical Inverse Modeling** **Michael B. Kowalsky,** Michael Commer, Kennet H. Williams, Stefan Finsterle
2:40	*Break*

Session IX: Carbon Dioxide Storage III

Session Chair: Fabrizio Gherardi, Mohamed Azaroual

3:00	**Modeling the Geochemical Impact of an Injection of CO_2 and Associated Reactive Impurities into a Saline Reservoir** Laurent Andre**, Mohamed Azaroual**, Christian Bernstone, Andrea Wittek
3:20	**Effect of Gas Field Production And CO_2 Injection on Brine Flow and Salt Precipitation** **Tim Tambach**, Daniël Loeve, Cor Hofstee, Willem-Jan Plug, Jos Maas
3:40	**Near-Well Pressure Distribution of CO_2-Injection in a Partially Penetrating Well** **Edward Mehnert,** Roland T. Okwen
4:00	**Simulation of CO_2 Storage in Coal Seams: Coupling of TOUGH2 with the Solver for Mechanics CODE_ASTER®** **Annick Loschetter,** Farid Smai, Sérigne Sy, André Burnol**,** Aurélien Leynet, Stéphane Lafortune, Alain Thoraval

Session X: General	
4:20	**Numerical Modeling of NaCl-H_2O Phase Separation in a Mid-Ocean Ridge Hydrothermal Vent Field** **Benjamin Larson,** Warwick Kissling, Christof Meile
4:40	**To Seep or Not to Seep?** **Some Considerations Regarding Water Infiltration in Volcanic Lakes** **Micol Todesco,** Dmitri Rouwet, Massimo Nespoli, Raul A. Mora-Amador
5:00	**Closing Remarks /Adjourn** **TOUGH Committee**

POSTER SESSION

Monday, September 17th, 5:30–8:00 PM
LBNL Cafeteria

BOARD	Title / Author
Session Chairs: Dorothee Rebscher, Haruko Wainwright, Michael Kowalsky, George Pau	
Carbon Dioxide Storage	
Board 1	**A Fully Coupled Model for Nonisothermal Multiphase Flow, Geomechanics, and Geochemistry during CO_2 Sequestration in Brine Aquifers** **Ronglei Zhang,** Xiaolong Yin, Philips H. Winterfeld, Yu-Shu Wu
Board 2	**A Novel Concept for Long-Term CO_2 Sealing by Intentional Salt Clogging** **Laura J. Wasch,** Jens Wollenweber, Tim J. Tambach
Board 3	**A Preliminary Study on the Applicability of the TOUGHREACT Code to South African Coal Seam CO_2 Storage Operations: A simulation Tool that can Model Potential Regional Groundwater Contamination Risks** **Tshegofatso O.P. Mophatlane**
Board 4	**An improved 2-D Reactive Transport Model of the Fate of CO_2 Injected into a Saline Aquifer in the Wabamun Lake Area (Alberta, Canada)** **Chantsalmaa Dalkhaa**, Maurice Shevalier, Michael Nightingale, Bernhard Mayer
Board 5	**Behavior of Brines Containing Dissolved CO_2 in Abandoned Wellbores** **Kirk M. Ellison,** Ronald Falta, Lawrence Murdoch, Scott Brame
Board 6	**Caprock Integrity Assessment by Reactive Transport Modeling: A Code Intercomparison Approach** **Dimier Alain,** Gherardi Fabrizio
Board 7	**Effects of Groundwater Chemical Compositions in Deep Saline Aquifers on CO_2 Geologic Sequestration** **Hongwu Lei,** Tianfu Xu, Fugang Wang, Yanlin Yang, Hailong Tian, Yan Shi
Board 8	**Efficient Data Assimilation Tool in Conjunction with TOUGH2 for CO_2 Monitoring** **Judith Yue Li**, Sivaram Ambikasaran, Peter K. Kitanidis, Eric Darve
Board 9	**EOS7C-ECBM: Modification of EOS7C to Include Enhanced Coal—Bed Methane and the Dusty Gas Model** **Stephen W. Webb,** Curtis M. Oldenburg
Board 10	**Evaluation of CO2 Storage Potential Focused on CO2 Sealing Efficiency of the Seal Layer at a Feasibility Study Site** **Seiichi Ikeda, Satoshi Tomimori, Masao Ohoka, Mariko Seguchi, Junya Takeshima, Hiroyuki Azuma**

BOARD	Title / Author
Carbon Dioxide Storage (cont.)	
Board 11	**Feasibility of CO_2 Injection in the Deep Saline Aquifers of the Bécancour Region, Québec (Canada)** **Tien Dung Tran Ngoc,** René Lefebvre, Michel Malo, Christine Doughty
Board 12	**Fundamental Analysis of Heterogeneity and Relative Permeability on CO_2 Storage and Plume Migration** **Nathan Moodie,** Brian McPherson, Si-Yong Lee, Prashanth Mandalaparty
Board 13	**Modeling Approaches for Wellbore Boundary Conditions for Simulation of CO_2 Geologic Sequestration in Saline Aquifers** **Keni Zhang,** Lulu Ling, Yang Wang
Board 14	**Modeling CO_2-Driven Cement Alteration at Well-Caprock Interface** Frédéric Wertz, **Fabrizio Gherardi**, Philippe Blanc, Anne-Gaëlle Bader, Antonin Fabbri
Board 15	**Modeling of the CO_2 Geological Storage at the S3 Site (Sim-SEQ Comparative Project)** Christophe Chiaberge, Joachim Tremosa, Anne-Gaëlle Bader, **Pascal Audigane**
Board 16	**Preliminary Model-Comparison Results from the Sim-SEQ Project using TOUGH2, STOMP, ECLIPSE, and VESA Approach** **Sumit Mukhopadhyay,** Christine Doughty, Diana Bacon, Giacomo Bacci, Rajesh Govindan, Ji-Quan Shi, Sarah Gasda, Ramya Ramanathan, Jean-Philippe Nicot, Seyyed Hosseini, Jens T. Birkholzer
Board 17	**Simulation of CO_2 Storage in the Basal Aquifer in the Northern Plains – Prairie Region of North America** **Dorothee Rebscher,** Quanlin Zhou, and Jens T. Birkholzer
Board 18	**The Influence of Capillary Entry-Pressure Representation on the Rate of CO_2 Solubility Trapping** **Boxiao Li,** Hamdi A. Tchelepi, Sally M. Benson
Board 19	**TOUGH2 Simulation of CO_2 Leakage from a Geologic Reservoir through Mixed Sandstone/Siltstone Caprock Formation** **Rodrigo Sebastian Iglesias,** Luciano da Silva Müller, Roberto Heemann, João Marcelo Medina Ketzer
Board 20	**TOUGH2 Simulation of the Pumping Tests at Ketzin Site: Heterogeneity Effects and Model Calibration** **Fei Chen,** Quanlin Zhou, Jens Birkholzer
Board 21	**TOUGHVISUAL: A User-Friendly Pre-Processing and Post-Processing Graphical Interface for TOUGHREACT** **Yanlin Yang,** Tianfu Xu, Fugang Wang, Hongwu Lei, Guangrong Jing, Gaofan Yue

BOARD	Title / Author
Environmental Engineering	
Board 22	**A Least-Cost Strategy for Evaluating a Brownfields Redevelopment Project Subject to Indoor Air Exposure Regulations** **Xiaomin Wang,** André J.A. Unger, Beth L. Parker
Board 23	**Hydro-Geochemical Modeling in the Passo a Campalto Phosphogypsum Dump in the Lagoon of Venezia, Italia** **Andrea Borgia,** M. Calcara, L. Cattaneo, M. Kennard
Board 24	**Simulating Migration of CO_2 and CH_4 Generated from Geothermal Treatment and Biodegradation of Sanitation Waste in the Deep Subsurface** **Julia Diessl,** M. S. Bruno, J.T. Young
Geothermal	
Board 25	**A 20 Year Progress in the TOUGH2 Modeling of the Mutnovsky Geothermal Field, Kamchatka, Russia** **Alexey Kiryukhin,** Olga Miroshnik
Board 26	**A Fully Coupled Flow and Geomechanics Model: Application to Enhanced Geothermal Reservoirs** **Perapon Fakcharoenphol,** Litang Hu, Yu-Shu Wu, Sarinya Charoenwongsa, Hossein Kazemi
Board 27	**A Novel, Fully Coupled Flow and Geomechanics Model in Porous and Fractured Geothermal Reservoirs** **Litang Hu,** Philip H. Winterfeld, Perapon Fakcharoenphol, Yu-Shu Wu, Keni Zhang, Tianfu Xu
Board 28	**A Sequential Implicit Algorithm of Chemo-Thermo-Poro-Mechanics for Fractured Geothermal Reservoirs** **Jihoon Kim,** Eric Sonnenthal, Jonny Rutqvist
Board 29	**Coupled MULTIFLUX-TOUGH2-TOUGHREACT T-H-M-C Model for EGS Studies** **George Danko,** Davood Bahrami, Liange Zheng
Board 30	**Implementation of Anisotropic Flow into the TOUGH2 Code** **Andri Arnaldsson,** Jean-Claude Berthet, Snorri Kjaran, Sven Þ. Sigurðsson
Board 31	**Improved Visualization of Reservoir Simulations: Geological and Fluid Flow Modeling of a High-Temperature Geothermal Field in New Zealand** **Sophie C.P. Pearson,** Angela Prieto
Board 32	**Laboratory and Numerical Studies of Heat Extraction from Hot Porous Media by Means of Supercritical CO2** **Mario Magliocco,** Timothy J. Kneafsey, Karsten Pruess, Steven Glaser

BOARD	Title / Author
Geothermal (cont.)	
Board 33	**Modeling of Calcite Scaling in a Geothermal Well** **Giordano Montegrossi,** Francisco Ernesto Montalvo López
Board 34	**Modeling of Wellbore Flow within Geothermal Reservoir Simulations at Field Scale** **Marica Marcolini,** Alfredo Battistelli
Board 35	**Numerical Modeling of Geothermal Systems: The Effect of Overpressure and Injection Fluid Temperature in Inducing Microearthquakes, with Application to a New Zealand Geothermal Field** **Lauriane Chardot,** Steven Sherburn, Nicolas Fournier
Board 36	**Recent Developments in the AUTOUGH2 Simulator** **Angus Yeh,** Adrian E. Croucher, Michael J. O'Sullivan
Board 37	**Three-Dimensional Modeling of Basin and Range Geothermal Systems using TOUGH2-EOS1SC** **Ann E. Moulding,** Tom Brikowski
Board 38	**TOUGH2 as a Tool for Performance Prediction of the Balcova Geothermal Field, Turkey** **Goker Ertunc,** Mahmut Parlaktuna
Board 39	**TOUGH-FLAC Coupled THM Modeling of Proposed Stimulation at the Newberry Volcano EGS Demonstration** **Antonio Pio Rinaldi,** Jonny Rutqvist, Eric L. Sonnenthal, T.T. Cladouhos
Nuclear Waste	
Board 40	**A Simple Implementation of 1D Hydromechanical Coupling in TOUGH2** Robert Walsh**, Nicola Calder,** John Avis
Board 41	**Development of Geohydrologic Model of the Wildcat Fault Zone** **Kenzi Karasaki,** Christine Doughty, Junichi Goto
Board 42	**The Effect of Stress on Flow and Transport in Fractured Rock Masses Using TOUGH-FLAC and a Modified Crack Tensor Theory** **Zhen Wang,** Jonny Rutqvist, Yuan Wang, Colin Leung, Andrew Hoch, Ying Dai
Board 43	**Two-Phase Flow Modeling with TOUGH2 of a Waste Geological Repository within the FORGE Project** **Manuel Lorenzo Sentís**
Board 44	**Using a Generalized Power Law for Simulating the Feedback Effect of Dissolution/Precipitation on Diffusive Transfer in TOUGHREACT** **André Burnol,** F. Claret

BOARD	Title / Author
Numerical Methods, Pre- and Postprocessors	
Board 45	**A New Library to Improve TOUGH Parallel Development** **Noel Keen,** George Pau, Jeff Johnson, Eric Sonnenthal, Stefan Finsterle
Board 46	**A Simple History-Dependent Nonwetting-Phase Trapping Model for the TOUGH Simulators** **Christopher G. Patterson,** Ronald W. Falta
Board 47	**Advances in Hydrogeophysical Joint Inversion** **Michael Commer,** Michael B. Kowalsky, Stefan Finsterle, Gregory A. Newman
Board 48	**An Approach for Modeling Rock Discontinuous Behavior under Multiphase Fluid Flow Conditions** **Pengzhi Pan,** Jonny Rutqvist, Fei Yan, Xiating Feng
Board 49	**Conceptual Model Tools in the PetraSim Graphical User Interface for the TOUGH2 Suite of Simulators** **Alison Alcott,** Daniel Swenson, Brian Hardeman
Board 50	**Methodology for Assessing Scalability and Optimizing the Usage of TOUGH2-MP on a Cluster – Application Case for a Radioactive Waste Repository** **Nicolas Hubschwerlen,** Keni Zhang, Gerhard Mayer, Jean Roger, Bernard Vialay
Board 51	**Modeling Transport of Water, Ions and Chemical Reactions in Compacted Bentonite – Comparison between TOUGHREACT, Numerrin and COMSOL Multiphysics** **Aku Itälä,** Mika Laitinen, Veli-Matti Pulkkanen, Merja Tanhua-Tyrkkö, Markus Olin
Board 52	**Numerical Simulation of DNAPL Source Zones above and below the Water Table in Fractured Sandstone** **Ken Walton,** Andre Unger, Mario Ioannidis, Beth Parker
Board 53	**Performance Improvement of TOUGH2 Simulation with Graphics Processing Unit** **Yusuke Shimotoku,** Toshiaki Tanaka, Ryuichi Itoi
Board 54	**T2Well—An Integrated Wellbore-Reservoir Simulator** **Lehua Pan,** Curtis M. Oldenburg
Board 55	**mView – A Powerful Pre- and Post-Processor for TOUGH2** **John Avis,** Nicola Calder, Robert Walsh

BOARD	Title / Author
General	
Board 56	**Borehole and Formation Analyses to Support Compressed Air Energy Storage Development in Reservoirs** **Stephen W. Webb**
Board 57	**Surface Deformation Due to Compressed Air Tunneling using TOUGH2 and FLAC3D** **Avirut Chinkulkijniwat**
Board 58	**Initial Investigations of thee Productive Perched Aquifers on the Volcanic Island of Montserrat** **Brioch Hemmings,** Fiona Whitaker, Joachim Gottsmann
Board 59	**Modeling Brine Reflux using the Pitzer Ion-Interaction Model in TOUGHREACT** **Anwar Al-Helai,** Fiona F. Whitaker, Nicolas Spycher, Yitian Xiao
Board 60	**Modeling Gas Transport and Reactions in Polydimethylsiloxane** **Chuanhe Lu,** Yunwei Sun, Stephen J. Harley, Elizabeth A. Glascoe
Board 61	**Simulation of Soil Water with Different Water Table Depths under Drip Irrigation along the Tarim Desert Highway, China** **Xue Li,** Guomin Li, and Zhimin Wang
Board 62	**Understanding Gas Migration in Unsaturated Fractured Porous Media using Field Experiments and Numerical Simulations** **Sophie Guillon,** E. Pili, J-C. Sabroux, T.M. Vu, P.M. Adler

Numerical Methods, Pre- and Postprocessing

CONCEPTUAL MODEL TOOLS IN THE PETRASIM GRAPHICAL USER INTERFACE FOR THE TOUGH2 SUITE OF SIMULATORS

Alison Alcott[1], Daniel Swenson[2], Brian Hardeman[2]

[1]RockWare Inc.
2221 East St. #1
Golden, CO 80401
e-mail: alison@rockware.com

[2]Thunderhead Engineering
403 Poyntz Ave., Suite B
Manhattan, KS, 66502
e-mail: support@thunderheadeng.com

ABSTRACT

PetraSim—an integrated program for model creation, analysis, and results display using the TOUGH2 suite of simulators—has undergone continual development since its first release in August 2002. The latest release (version 5.2) includes a conceptual model Layer Manager which, when used in conjunction with internal boundaries, allows the user to quickly create meshes with varying element shape (rectangular vs. polygonal) thickness, and size. Other new features include: TOUGH2-MP support with automatic execution on multiple core machines; conceptual model wells that can be used to apportion total injection and production rates across elements that intersect the well completion interval; and flux boundary conditions in which the flux rate for individual cells is proportional to the surface area of the element. We will demonstrate these features and discuss the new features being developed for PetraSim version 6.0.

PETRASIM FEATURES

PetraSim provides four key features that help speed and simplify the use of the TOUGH2 family of codes: (1) use of a high level model description based on geometric features of the reservoir, (2) presentation of the required input options grouped in a logical format with appropriate default options activated, (3) automatic writing and execution of the input file, and (4) rapid access to visualization of results. PetraSim is interactive, with immediate visual confirmation of any user actions.

The Conceptual Model

PetraSim allows the user to define layers and regions as high-level geometric entities, independent of the grid. For example, Figure 1 shows a model in which conceptual layers have been defined and can then be used to control material properties, initial conditions, and the spacing of cells in the z direction.

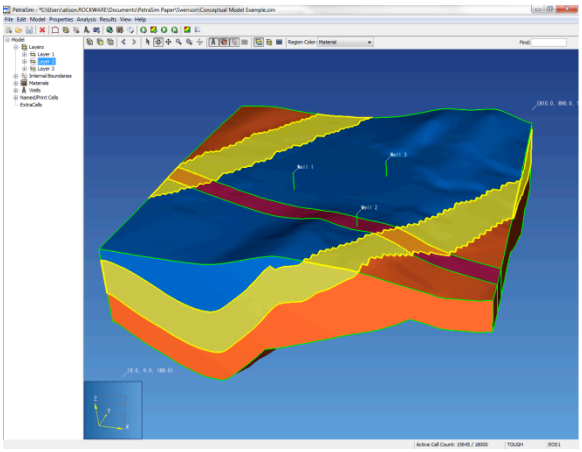

Figure 1. Model with layers and regions defining material boundaries, Layer 2 is highlighted in yellow.

Layers can be broken up into regions using internal boundaries, which are surfaces or planes that typically intersect many layers. Like layers, regions can be used to define material properties and physical and chemical initial conditions. In Figure 1, note that three conceptual layers are intersected by two planar internal boundaries used to represent a crosscutting material change—in this case a fault zone colored red.

Conceptual model layers and regions are independent of the mesh. When the grid is created, the cell properties will inherit the proper material values and initial conditions from the layer or region in which they are located.

Layer boundaries and internal boundaries can be created using xyz ASCII files, DXF files composed of triangular meshes, or through the definition of planar orientation. Conceptual layers are generally used to represent boundaries between stratigraphic formations, while internal boundaries often represent fault zones or other types of structures, but can represent stratigraphic boundaries as well.

Figure 1 also illustrates several options for high-level interaction with the model. On the left of the window is a tree that displays features in the model. Using the tree, the user can select a specific feature. Alternatively, the model can be manipulated in the 3D display and features selected with the mouse. In either case, once a feature is selected, all associated properties can be modified.

Grid Definition

An appropriate grid for an analysis must satisfy several constraints: (1) it must be able to capture the essential features of the reservoir, such as stratigraphic layers with different material properties; (2) it must be sufficiently refined to accurately represent regions of high gradient in the solution; and (3) it must satisfy the requirements of the simulator for proper convergence of the solution. PetraSim supports prismatic (rectangular) 3D grids and non-uniform polygonal (voronio) meshes.

When creating a rectangular grid (Figure 2), the user can simply specify the number of cells to be used along the x and y edges (along with an optional size factor for geometrically increasing cell sizes) or use input similar to the Meshmaker input for TOUGH2 (Pruess et. al., 1999). To specify the Meshmaker input, the user populates a table that defines the direction, number of repeated cells, and the cell sizes.

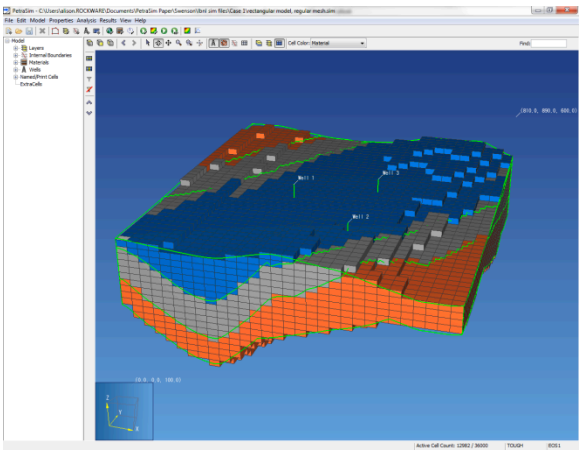

Figure 2. Example of an evenly spaced rectangular grid. Cell color is based on material type.

Input during the creation of a polygonal mesh entails the definition of the maximum cell area, the maximum area of cells adjacent to wells, and the maximum refinement angle, which controls how quickly the cell area near wells disperses to the maximum cell area. Along with providing additional refinement around wells, a polygonal mesh can match an arbitrary model boundary defined during the creation of the conceptual model (Figure 3).

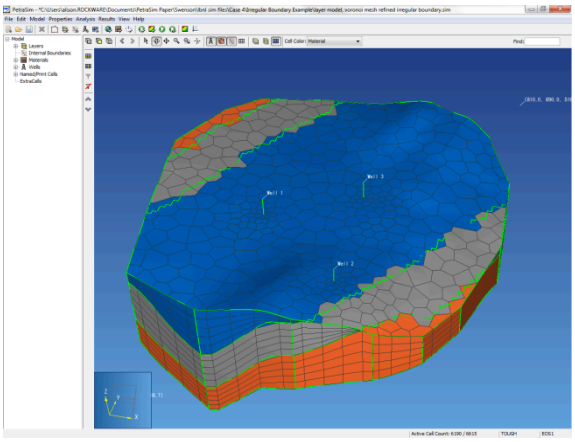

Figure 3. Example of a polygonal mesh that conforms to an irregular model boundary. Cell layer spacing varies with the thickness of the model layer.

Spacing in the z direction is controlled through the Layer Manager. Each model layer is divided into a number of cell layers based on the number of z divisions specified by the user. The thickness of the cell layers vary with the thickness of the model layer (Figure 3). In each

cell column, cell layers can be evenly spaced, or can have variable spacing based on a Dz table. If a Dz table is used, z divisions must be entered such that a fraction of the layer is divided into a specified number of cells.

Editing of Cell Properties

Once a mesh has been created, every cell will be assigned to a region in the conceptual model based on the center of the cell. This allows each cell to inherit the properties of the owning region, such as materials and physical and chemical initial conditions. Cells can be further edited individually or in groups. The user can edit the properties of a cell from the 3D View or Tree View by double-clicking the desired cell, or by selecting the desired cells, right-clicking on one, and selecting Edit Cells… from the context menu. A list of cell IDs and associated material types or PMX values can be imported as an ASCII file to represent complex geology or heterogeneity extracted from more advanced modeling or geostatistical applications.

Model sinks and sources can be added to a single cell or selected group of cells. Input and output rates can be entered in traditional units of kg/s (J/s for heat) or "flux" across the xy area of the cells (kg or J/(s*m^2)). This new flux boundary condition allows users to more easily apply a surface boundary condition such as evapotranspiration or recharge to a group of cells with variable volumes. Both traditional and flux-based sinks/sources can be entered as constant values, or can be entered in a time-based table.

Additionally, conceptual model "wells" can be created to represent well completions through multiple adjacent cells (Figure 4). When wells are used, flow in or out of the model can be evenly apportioned across the cells that intersect the completion interval of the well, or the total flow for the well can be proportionally divided based on the product of the permeability and production length within each cell. Like layers and regions, wells are high-level entities that are independent of the grid. Total flow in or out of the well is apportioned to the appropriate model cells when the simulator input file is written.

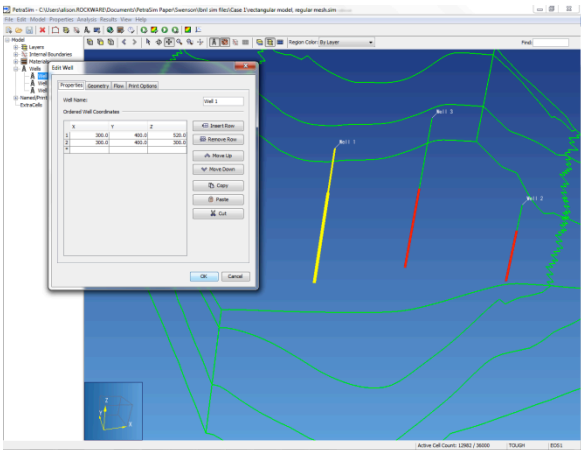

Figure 4. Example of conceptual model wells in PetraSim.

Writing a Simulator Input File

The purpose of a pre-processor is to automatically write the simulator input file in a correct format and without intervention by the user. In PetraSim, this task is performed by a function that accesses the model, the grid, and all other data necessary to write the file.

A portion of an example file is shown in Figure 5. Since the TOUGH2 simulators included with PetraSim have not been modified with respect to input file format, the input file written by PetraSim is in standard TOUGH2 format. Because PetraSim writes the file, there is no need to keep the file small. Each element, connection, and initial condition is written explicitly. It can also be seen that the elements are given sequential numerical names. It is intended that the user never needs to know or examine these names. Any type of data, such as the definition of a source or sink, knows the associated cell and correctly writes the cell name when the simulator input file is written. The resulting input file is correctly formatted and ready for input to TOUGH2.

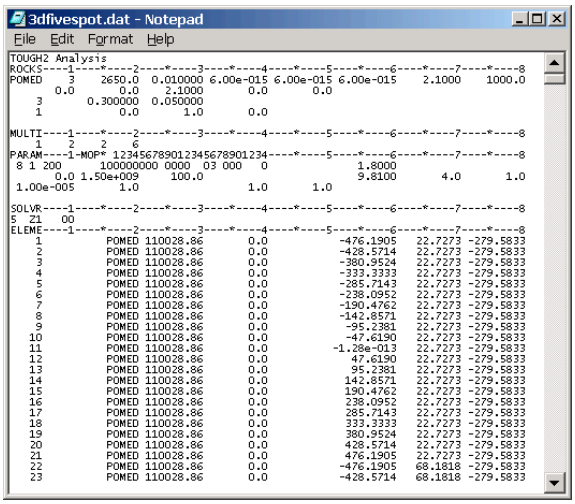

Figure 5. Portion of TOUGH2 input file created by PetraSim

Visualization

After the solution is completed, either 3D or 2D plots of the results can be made. Figure 6 shows an example of an iso-surface plot of temperature. PetraSim uses a common results display component for all simulators. The TOUGH2 simulators included with PetraSim output comma separated value (CSV) files in addition to the normal simulator-specific output. The CSV files provide a consistent format that can be used by both PetraSim and external tools such as MS Excel.

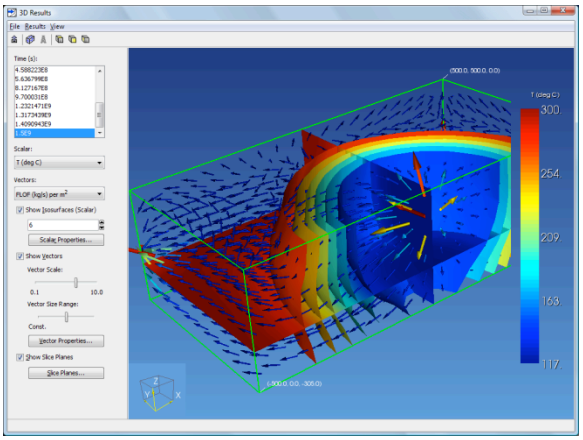

Figure 6. Iso-surface plot of temperatures

As shown in Figure 6, once the data is read, the user can select any available variable and time for plotting. The user can rotate, pan, and zoom the image interactively. Image details, such as the number of iso-surfaces and the data range, can be controlled. Also, cutting planes can be defined on which the results are contoured. Vectors can be used to display items such as fluid flow. Finally, the user can export the data in a simple X, Y, Z, value format for import into other presentation-quality graphics programs, such as TECPLOT. In PetraSim, results are readily accessible to rapidly evaluate the analysis.

In a similar manner, time history plots and line plots of results can be made. For time history plots, which display results over time for individual cells, data from the FOFT file are used (Pruess, 1999). If FOFT data are not available for a cell, then time series information from the general CSV output files is used. Well plots can be used to show time series data for entire wells (Figure 7). Well plots can show liquid and gas flow rate, as well as the total thermal energy moving in and out of the cells that intersect the completion interval of the well.

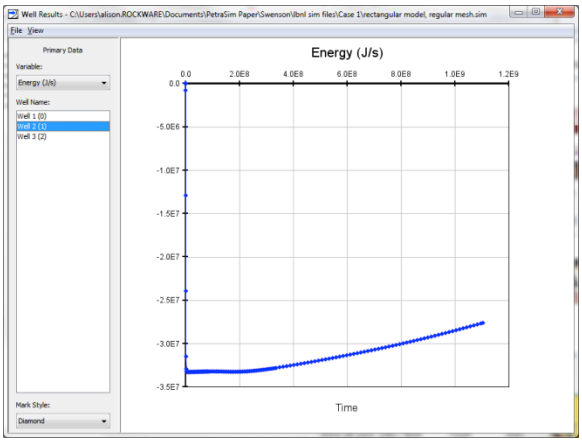

Figure 7. Well Plot showing change in Energy over time.

Line plots are created through the 3D viewer and display an XY plot of a variable along a line. This is useful for viewing the change in a variable, such as temperature or gas saturation along a wellbore over time. Once any plot is made, the data can be exported in a format that can be read in a spreadsheet or other presentation-quality graphics program.

Integrated Solution

Thunderhead Engineering has received a license from the U.S. Department of Energy that allows the integrated distribution of TOUGH2, TMVOC, and TOUGHREACT executables. Therefore, to run the analysis, all the user needs to do is select Analysis->Run TOUGH2 and the analysis will proceed, using the integrated executable. Licensed TOUGH2-MP executables can be purchased with PetraSim and are installed with the software as well.

If the user owns his or her own license for the TOUGH2 source code (can be obtained separately from the US DOE or LBL), PetraSim can be used to write the input file. Then the user can edit the input file to accommodate any specific input changes needed to run their version of TOUGH2.

A QUICK COMPARISON OF LAYERING AND MESH OPTIONS

For comparison purposes, identical material properties, initial conditions and conceptual model wells were applied to four models (Cases 1 through 4). Table 1 describes the various layer and mesh options used in each model.

Table 1. Vertical Division and Mesh Options used in comparison experiment

Case #	Z Divisions	Mesh Type
1	Constant	Rectangular
2	Constant	Polygonal
3	Variable	Rectangular
4	Variable	Polygonal

Cases 1 and 2 were created with a single conceptual layer (with flat boundaries), and internal boundaries defining the extents of three geological formations (Figure 8). Cells were evenly spaced in the z direction, and cells above and below the top and base of these formations were "disabled" in PetraSim. Cases 3 and 4 were created using three conceptual layers, with the thickness of the model layers varying based on the thickness of the conceptual layers.

Case 1

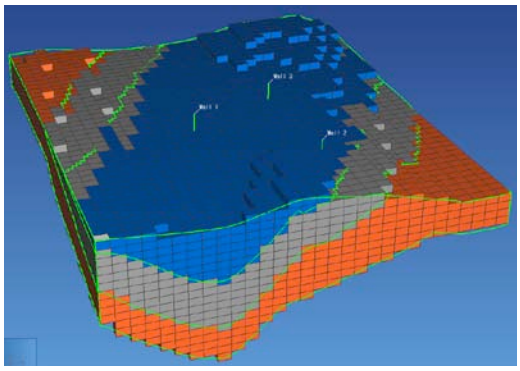

Case 2

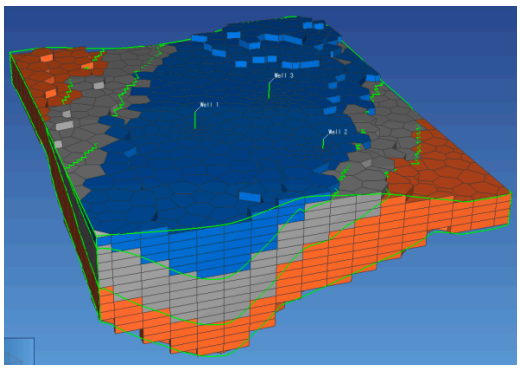

Case 3

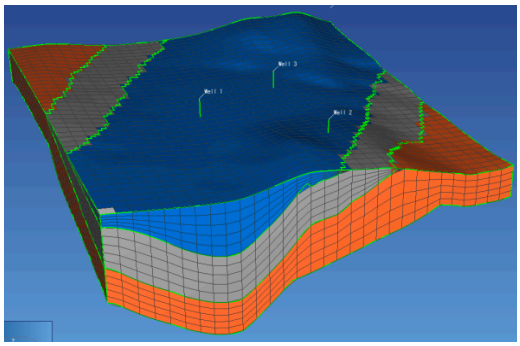

Case 4

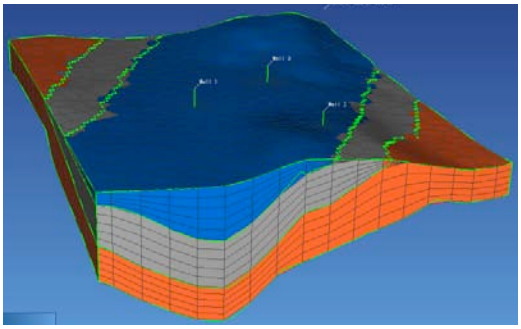

Figure 8. Three-dimensional display of Cases 1 through 4 showing varying mesh and layer geometry

Each model was run to steady-state conditions with closed boundaries to establish linear

pressure and temperature gradients. Results from the steady-state models were loaded as initial conditions into new models to which two production wells (Wells 1 and 2) and one injection well (Well 3) were added. Figure 9 shows the relative locations of Wells 1, 2, and 3.

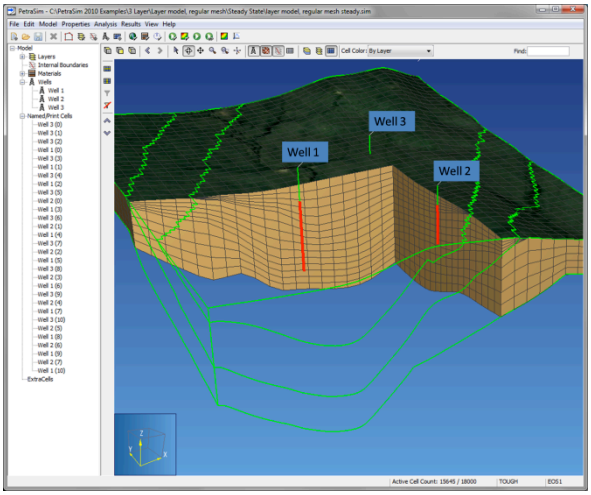

Figure 9. Three-dimensional view of model mesh and labeled well locations

Wells 1 and 2 were production wells using the Well Model option included in TOUGH2. The pressure for each well was determined based on the initial pressure in the center of the top cell that intersected the well completion interval. The productivity index for both wells 1 and 2 was held constant at 2.0E-12 m^3. Water was injected into Well 3 for 35 years at a constant rate of 30 kg/s and an enthalpy of 5e5 J/kg.
All four models show the same general results at 35 years, with a decrease in temperature from 300°C to around 117°C caused by the injection of colder water at Well 3 (Figure 10).

It should be noted that in order to produce a reasonable temperature distribution in the models with polygonal grids, the area of the elements around the wells needed to be decreased to about $1/6^{th}$ the area of the cells in the rectangular grids.

Case 1

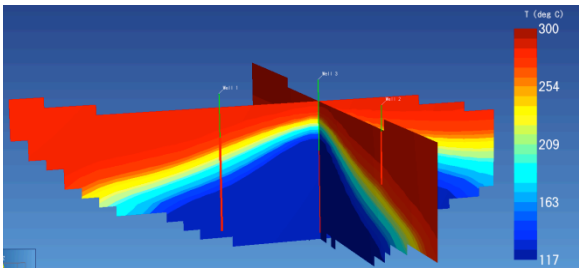

Case 2

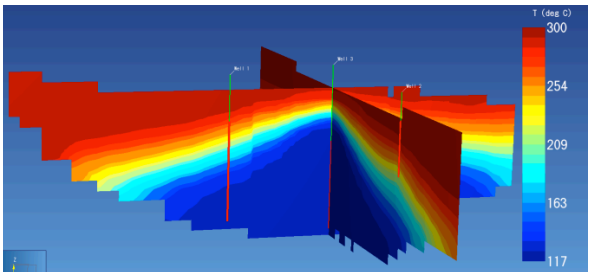

Case 3

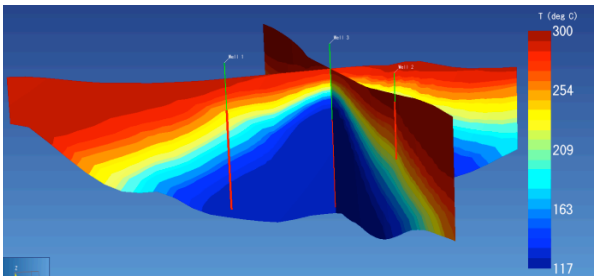

Case 4

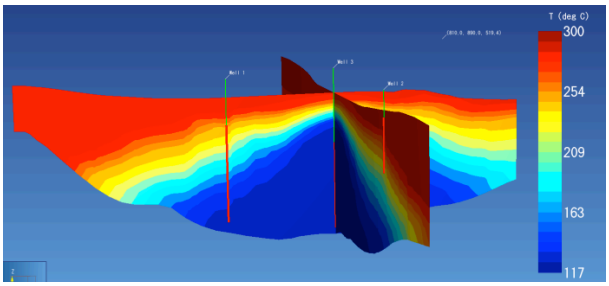

Figure 10. Temperature levels at 35 years in Cases 1 through 4

Even with this increased refinement around wells, the polygonal models had fewer cells and therefore shorter run times than the grid cells with rectangular meshes in the x and y directions (Table 2).

Table 2: Summary of the number of cells, time steps and run times for Cases 1 through 4

Case #	#Cells	#Time Steps	Run Time (s)
1	12,982	160	355
2	6,076	242	255
3	15,645	255	775
4	7,100	248	329

Well plots showing Energy Production and Flow are similar, although not identical (Figure 11).

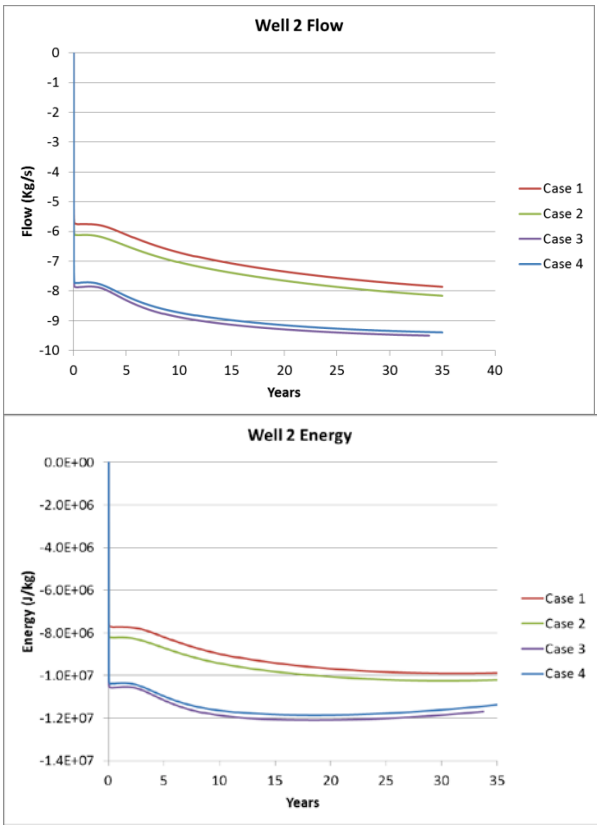

Figure 11. Plots showing Flow and Energy for Well 2 for Cases 1 through 4

Even if the mesh were refined, the type of mesh (i.e., rectangular vs. polygonal) did not affect the flow in and out of the wells. Instead, Well Plot results are grouped based on the use of conceptual model layers. In cases 1 and 2 (uniform horizontal mesh), the flow from Well 1 is greater than cases 3 and 4 (layered mesh in the z direction). Correspondingly, the flow from Well 2 is smaller for cases 1 and 2 and larger for cases 3 and 4. This means that in cases 1 and 2 (with a horizontal Z mesh), it is relatively easier to flow from Well 3 to Well 1 than from Well 3 to Well 2. The converse is true for the layered models (Cases 3 and 4).

As described by Pruess (1991), for a regular rectangular grid, flow can be preferentially oriented along the rectangular directions and more difficult in the diagonal direction. As shown in Figure 12, flow from Well 3 to Well 2 must cross grid diagonals for cases 1 and 2 (uniform horizontal mesh), while the layered mesh does not require as much flow across the diagonals. It is hypothesized that this is the primary reason that Well 2 produces less flow for cases 1 and 2 and more flow in cases 3 and 4.

Case 1

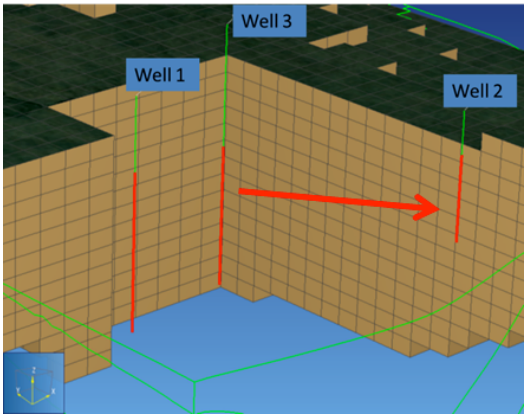

Case 3

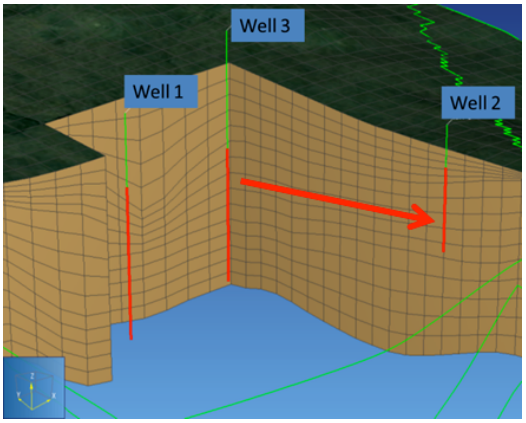

Figure 12. Views showing varying mesh geometry in the z direction for Cases 1 and 3. Red arrows illustrate the intersection of flow vectors from Well 3 to Well 1 with mesh lines.

FEATURES TO BE INCLUDED IN VERSION 6

Development has begun on version 6 of PetraSim. Some of the features to be included are:

- Support for newer TOUGH2 EOS modules, including EO7C and ECO2M
- Support for TOUGH2 v2.1 and TOUGHREACT v2
- Improved support for larger MINC
- Support for the porosity modifier
- Support for more units during model input and result visualization
- More efficient tools for the creation of multiple wells and internal boundaries

OBTAINING PETRASIM

A 30-day trial version of PetraSim can be downloaded at www.petrasim.com. Sales are through RockWare (www.rockware.com). Licenses are available for education (free), research, and commercial use.

ACKNOWLEDGEMENTS

Original development of PetraSim was a joint venture between Thunderhead Engineering and GeothermEx, with primary funding from a Department of Energy Phase II Small Business Innovative Research grant.

REFERENCES

Pruess, K., Grid Orientation Effects in the Simulation of Cold Water Injection into Depleted Vapor Zones, Proceedings, Sixteenth Workshop on Geothermal Reservoir Engineering, Stanford University, Stanford, California, , SGP-TR-134, January 23-25, 1991.

Pruess, K., Oldenburg, C., and Moridis, G., TOUGH2 User's Guide, Version 2. 0, Earth Sciences Division, Lawrence Berkeley National Laboratory, LBNL-43134, November, 1999.

THERMAL-HYDROLOGICAL-MECHANICAL MODEL FOR FRACTURE PROPAGATION, FLUID FLOW, AND TRANSPORT IN POROUS ROCK

Daisuke Asahina, Jim Houseworth, and Jens Birkholzer

Earth Sciences Division
Lawrence Berkeley National Laboratory
Berkeley, CA 94720, USA
e-mail: dasahina@lbl.gov

ABSTRACT

Understanding thermal-hydrologic-mechanical (THM) behavior in geomaterials (e.g., porous rock), including fracture propagation, is key for many engineering underground applications such as high-level radioactive waste disposal, geothermal energy recovery (e.g., enhanced geothermal systems), petroleum recovery (e.g., shale gas and oil extraction), and geologic CO_2 sequestration (cap-rock fracturing and leakage). In this paper, a numerical modeling method for coupled THM processes, including fracture formation and evolution is presented. The method is facilitated by a three-dimensional (3D) Voronoi-based discretization technique, capable of representing discrete fractures and fracture damage development within a permeable rock matrix. This approach is illustrated with examples of hydromechanical coupled processes and fracture formation. Additional computational examples are also given for flow and transport processes in a fractured, permeable rock.

INTRODUCTION

Geomechanical processes are known to play an important role in hydrogeological behavior (Neuzil, 2003). Linkage between mechanics and hydrogeology occurs in two fundamental ways: through feedback between (1) rock strain, the geometry of pores and fractures, and their permeability and porosity; and (2) fluid pressure and rock mechanical stress. Although there have been great strides in the capability to compute problems involving hydromechanical coupling (e.g. Rutqvist et al., 2002), the problem of fracture initiation and propagation, and its impact on fluid flow processes, remains a major difficulty. Such problems are of particular importance for mechanically weak rock types such as clays and shales, because fractures can be relatively transient as a result of fracture self-sealing processes (Bastiaens et al., 2007). Such issues are important, e.g., for geo-environmental issues related to nuclear waste disposal (Bossart et al., 2004) and geologic carbon sequestration (Chiaramonte et al., 2008).

The first part of this paper covers a computational method applicable to 3D discrete fracture networks (DFNs). Fractures are considered as discrete features that interact with a porous rock matrix. Fracture configurations are mapped onto an unstructured, 3D Voronoi grid, which is based on a deterministic or random set of spatial points. DFNs are represented by the connections of the edge of a Voronoi cell. This methodology has the advantage that fractures can be more easily introduced in response to coupled hydro-mechanical processes, and it generally eliminates several potential issues associated with the geometry of DFN and numerical gridding. In this paper, the multiphase fluid-flow simulator, TOUGH2, is used to simulate flow and transport through discrete fractures in porous rock. Fracture cells are introduced at the boundaries of Voronoi cells so that flow and transport through a DFN interacting with a permeable rock matrix can be studied. Analytical solutions of saturated flow and transport through a single fracture are also **developed to verify the numerical results.**

The second part of this paper describes a newly developed coupling between a mechanical-damage model and TOUGH2, which allows us to compute fracture evolution as well as flow and transport through the fractured porous rock, thus accounting for dynamically changing THM conditions. Elastic response and fracture development is modeled by the mechanical-damage model based on the rigid-body-spring

network (RBSN). Spring constants are related to elastic rock mechanical properties, and fracture initiation is determined using a classical brittle approach. Both models share the same geometrical information from a 3D Voronoi grid and associated nodes, where the scalar field quantities (e.g., temperature, pressure, and saturation) and the generalized displacements are obtained by TOUGH2 and RBSN, respectively. Fractures propagate along Voronoi cell boundaries as THM-induced stresses evolve and exceed the material strength. In particular, an example application is presented that addresses the modeling of moisture-driven fracture problems, such as shrinkage cracking.

GRID GENERATION

Voronoi discretization

Voronoi discretization is an effective approach to partition a computational domain into an unstructured grid. The defining characteristic of the Voronoi cell is that all locations within the cell lie closer to the associated nodal point than to any other nodal point. In this study, the procedure of Voronoi discretization starts with nodal point insertion. Nodal points are sequentially placed into the domain by a pseudo-random number generator. The use of a random point set simplifies mesh generation and increases flexibility in the model geometry. Two inputs, the dimensions of the computational domain and a minimum allowable distance l_m between nodes, are prescribed to control the mesh size. The domain is eventually saturated through a set of points with the l_m constraint. By connecting these nodal points, the Delaunay tessellation is generated, after which the dual Voronoi tessellation is constructed. More details about Voronoi discretization techniques can be found in Asahina and Bolander (2011).

Discrete fracture representation

In this study, fractures are considered as discrete features that interact with a porous rock matrix. An irregular Voronoi grid is used to represent the rock matrix as a basic material structure. Existing or newly generated fractures are directly mapped onto such a Voronoi grid. A discrete fracture is represented by a series of Voronoi cell boundaries (i.e., edges of polygon) as shown in Figure 1 for a two-dimensional (2D) case. Fracture geometric data (e.g., fracture orientation, length, width, and shape) can be obtained by field mapping or by computer-generated information based on statistical representation. A single fracture is represented as follows (Fig. 1):

- Discretize rock matrix based on an irregular Voronoi grid.
- Overlay a reference fracture on top of the Voronoi grid.
- Select node-node connections which cross the reference fracture. The Voronoi cell boundaries of such node connections are defined as a part of the discrete fracture.
- Connect all segments of the discrete fracture.

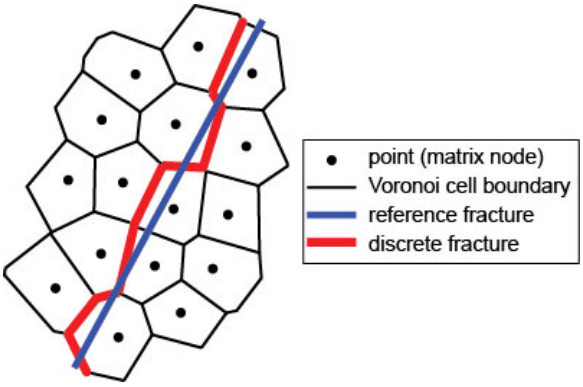

Figure 1. Mapping of a fracture geometry on top of an irregular Voronoi grid.

By repeating this process for a series of fractures, the modeler can generate a network of discrete fractures. The grid size must be carefully selected or scaled to obtain the required accuracy of discrete fracture representations. The advantages of this DFN generation method include: (1) simple activation and connection of new fractures, (2) automated treatment of fracture intersections, (3) capability to control mesh gradation (node density), and (4) straightforward extension to 3D geometry (Fig. 2). These advantages are especially beneficial when simulating fracture damage that develops into fracture networks. By automating the process of the proposed DFN approach, fracture intersections in 3D can be effectively generated. Figure 2a shows a fracture intersection mapped onto an irregular 3D Voronoi grid. The Voronoi cell boundaries tile the discrete fractures. This

facilitates the visualization of DFN, especially for 3D representation.

Alternatively, the Voronoi grid can be controlled by deterministic point selection to generate straight fractures with an intersection as shown in Figure 2b. Such grid generation, however, becomes cumbersome due to greater limitation on the point allocations around straight fractures, especially for fracture intersections in 3D.

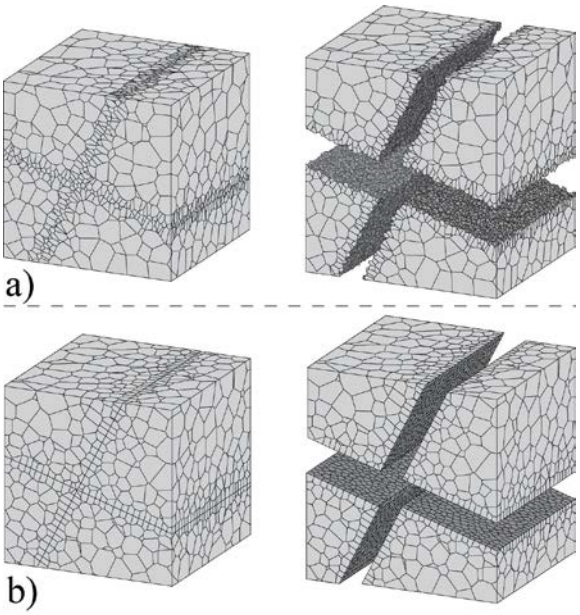

Figure 2. Fracture interface with the representation of DFN in 3D Voronoi grid: (a) irregular fractures, and (b) straight fractures.

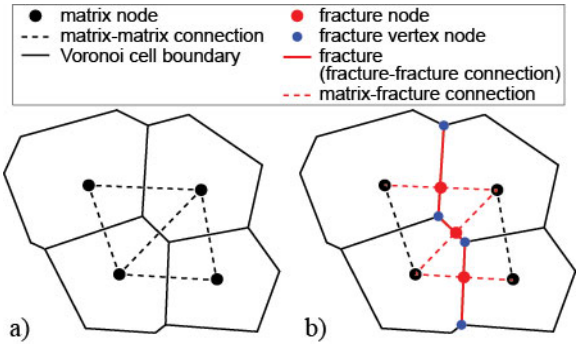

Figure 3. Node and connection in the TOUGH2 simulator: a) ordinary matrix nodes and connections, and b) new fracture nodes and connections.

Fracture nodes and connections in the TOUGH2 simulator

The simulations of flow and mass transport through discrete fractures, presented in a later section, are based on the TOUGH2 EOS7R simulator (Oldenburg and Pruess, 1995). As discussed in the preceding section, the DFN is explicitly represented at the Voronoi cell boundaries in a computational domain. To activate flow pathways along a discrete fracture, the fracture nodes and connections are newly introduced at the Voronoi cell boundary in addition to Voronoi cell nodes and connections for the rock matrix (Fig. 3). A new fracture node is inserted at the intersection of a Voronoi cell boundary and the original matrix-matrix connection. Then, the connection is generated between the fracture node and the adjacent matrix nodes. Also, the fracture vertex node is added to support fracture-fracture connections along the Voronoi cell boundary. These additional nodes and connections in the TOUGH2 simulator permit flow and transport through the DFN. Local fracture permeability and porosity are based on grid geometry and apertures, which can be either assigned as a pre-existing fracture or computed by a mechanical-damage model, as shown below. Performance of the proposed discrete fracture approach was tested against an analytical solution, as described in the following section.

NUMERICAL DISCRETE FRACTURE MODEL

A numerical discrete fracture model for a single fracture in a porous rock matrix is described here. Our current results focus on cases that can be verified with an analytical model, in which the fracture is a single linear feature that connects across the entire domain. The analytical model used here is an extension of the model developed by Houseworth (2006) for flow and transport in a single fracture. The model is capable of representing flow in the fracture, as well as flow in the matrix at an arbitrary oblique angle to the fracture. As for the original model (Houseworth, 2006), all transport mechanisms are represented except for longitudinal diffusion/dispersion.

The linear fracture model is a useful simplification because numerical results can be verified against the analytical model. These results, therefore, provide a reliable baseline for flow and transport behavior in more complex irregular fracture geometries. Two cases are presented below, involving flow parallel to the fracture and flow at an oblique angle to the fracture. The numerical solutions for flow and transport were conducted using TOUGH2 with the EOS7R module (Oldenburg and Pruess, 1995). Flow calculations were performed to establish steady-state flow fields that were used as an initial condition for the tracer-transport problem. For transport, an instantaneous point release of tracer was approximated by including at the beginning of the transport calculation tracer mass in one cell of the fracture. All problems were solved for a two-dimensional rectangular domain.

For parallel flow, the solution is symmetric with respect to the fracture orientation, so one boundary is taken along the fracture centerline. The domain is 10 m long and about 0.4 m in width, with a 0.015 m fracture half-aperture. Flow was computed using constant-pressure boundary conditions at each end of the 10 m long domain, and no-flow boundary conditions for the transverse direction. For the cross-flow case, the domain length is also 10 m, but symmetry is broken; therefore, the fracture is placed in the middle of the domain with a full aperture of 0.03 m and a domain width of about 1 m. For the cross-flow cases, a transverse pressure gradient of about 49,000 Pa/m is established. In all cases, the longitudinal pressure gradient is about 5000 Pa/m.

A uniform grid was used in the longitudinal direction (along the fracture axis). In the base case, a longitudinal grid spacing of 1 cm was used for the parallel flow condition and 2 cm for the cross-flow condition. Grid spacing laterally was 0.002 m near the fracture for these base cases, with coarser grids further from the fracture. There are three sensitivity cases each for parallel-flow and cross-flow conditions. For parallel flow, Sensitivity Case 1 uses a longitudinal grid spacing of 0.06 m, Case 2 a longitudinal grid spacing of 0.1 m, and Case 3 a longitudinal grid spacing of 0.1 m and a minimum lateral grid spacing of 0.01 m. For cross-flow, cases 1 and 3 use a longitudinal grid spacing of 0.1 m. Also, for the cross-flow base case and Case 3, fine gridding in the transverse direction was used for a larger region around the fracture than in the parallel-flow case. Hydrogeologic parameters are given in Table 1.

Table 1. Linear Fracture Simulation –Parameters.

Fracture permeability (m^2)	Matrix permeability (m^2)	Fracture aperture (m)	Fracture porosity	Matrix porosity	Diffusion coefficient (m^2/s)
2.4×10^{-15}	1.0×10^{-18}	0.03	0.087	0.2	1.0×10^{-11}

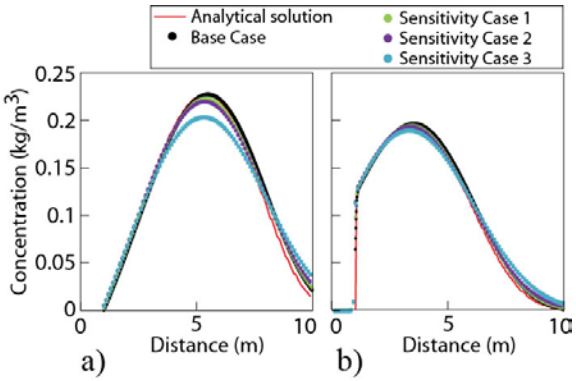

Figure 4. Mass concentration for parallel flow cases: (a) fracture concentration profile; and (b) matrix concentration profile about 2 cm from fracture.

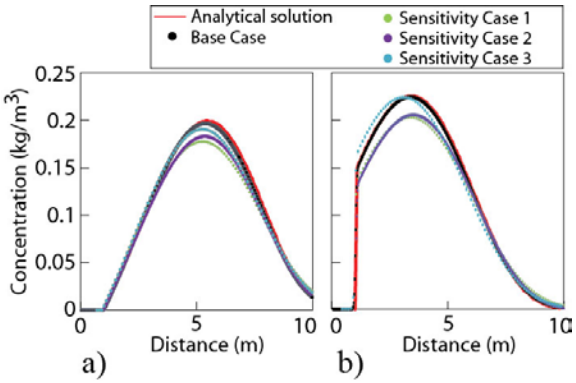

Figure 5. Mass concentration for cross-flow cases: (a) fracture concentration profile; and (b) matrix concentration profile about 2 cm from fracture.

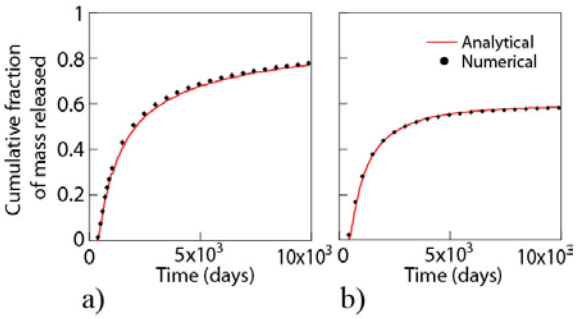

Figure 6. Cumulative mass arrival 4 m from release point: (a) parallel flow base case; and (b) cross-flow base case.

Results for the simulations are compared with analytical solutions in Figure 4 and 5. These figures show that the solution is most sensitive to grid refinement near the fracture and that longitudinal grids may be coarser. Additional transverse grid refinement in the matrix near the fracture appears to be necessary to achieve the same level of accuracy in the numerical model for the cases with cross flow. This appears to be a result of cross flow moving the peak mass concentration from the fracture and into the matrix. Steep concentration gradients are associated with the location of the peak mass concentration. The results also show that with sufficient grid refinement, numerical results can closely match the analytical solution, even though the numerical model includes longitudinal diffusion not represented in the analytical model. The numerical base-case results are compared with analytical results in Figure 6 for cumulative mass arrival at a downstream position 4 m from the release point. Cross flow is seen to slow longitudinal mass transport at later times. Cumulative mass arrival is a convenient metric for comparing results for linear and irregular fracture cases, which will be done in a future report.

MECHANICAL-DAMAGE MODEL

Elastic response and fracture development is modeled by the mechanical-damage model based on the rigid-body-spring concept of Kawai (1978). To provide a basic understanding of this modeling approach, an overview of the element formulation is given here. Geometry of the rigid-body-spring network (RBSN) is defined by the dual Delaunay tessellation of the nodal points. The basic unit of RBSN is a 1D lattice element consisting of a zero-size spring set located at the centroid of the Voronoi boundary (Fig. 7). Each node has six degrees of freedom for the 3D case. The spring set is formed from three axial springs and three rotational springs (referenced to local coordinate axes *n*-*s*-*t*) as shown in Figure 7 (the rotational springs have been omitted for clarity). The local spring coefficients are assigned according to

$$k_s = k_t = \alpha_1 k_n = \alpha_1 \alpha_2 E \frac{A_{ij}}{h_{ij}} \qquad (1)$$

in which E is the elastic modulus and A_{ij} is the area of the Voronoi boundary common to nodes i and j (Fig. 7). By adjusting α_1 and α_2 in accordance with experimental results, macroscopic modeling of both elastic constants (E and Poisson ratio, ν) is possible. The Voronoi scaling of the spring constants, A_{ij}/h_{ij}, , enables the method to be elastically homogeneous under uniform modes of straining. Such Voronoi scaling also serves energy conserving, grid-size-insensitive representations of tensile fracture. Details and indication of model accuracy can be found elsewhere (Bolander and Saito 1998, Asahina et al. 2011).

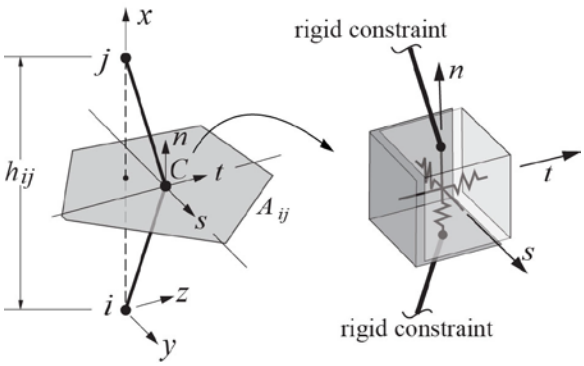

Figure 7. Typical lattice element with a zero-size spring set located at centroid C of facet area A_{ij}. Note that A_{ij} is tha Voronoi cell boundary and i and j is the neighboring Voronoi cell nodes (matrix nodes).

COUPLING OF TOUGH AND RBSN

Basic approach

TOUGH2 is coupled with RBSN to compute fracture damage development, as well as flow and transport through the fractured porous rock, accounting for dynamically changing THM conditions. The general procedure for the two-code coupling (hydraulic and mechanical code)

is similar to the earlier work of Rutqvist et al. (2002) who linked TOUGH2 to a commercial continuum-mechanics simulator, FLAC3D. In this paper, TOUGH2 is used to simulate the hydraulic quantities (e.g., temperature, pressure, and saturation), while RBSN accounts for the mechanical quantities (e.g., stress, strain, displacement, and damage). Such primary variables are coupled through simplified linear relationships or through nonlinear empirical expressions, which could be estimated by laboratory experiments with appropriate calibration. The main advantage of coupling TOUGH2 and RBSN is that both models share the same unstructured, 3D Voronoi grid and the same set of nodes. This greatly simplifies the process of exchanging primary variables between two codes. At the current stage, TOUGH2 and RBSN are linked through an external coupling module, which transfers the relevant variables at each time step. It is assumed that the local changes in hydraulic variables produce strain as follows:

$$\Delta\varepsilon_T = \alpha_T \Delta T \tag{2}$$

$$\Delta\varepsilon_s = \alpha_s \Delta S \tag{3}$$

$$\Delta\sigma = (\Delta\varepsilon_T + \Delta\varepsilon_s)E \tag{4}$$

where ε_T is the thermal strain, ε_s is the shrinkage/swelling strain, ΔT and ΔS is the change in temperature and saturation over the time step in one lattice element, respectively, α_T is the coefficient of thermal expansion, α_s is the moisture swelling coefficient, and σ is the stress. The hydraulic valuables, ΔT and ΔS , are taken as the average of two neighboring nodes *i* and *j*. At this stage of model development, hydro-mechanical coupling is based on one-way coupling, in which flow processes affect mechanical strain but mechanical behavior does not affect flow parameters (e.g., permeability, porosity). Since the flow parameters are constant during the simulations, mechanical stress is computed independent of fluid pressure. Examples in subsequence sections only explore the effect of saturation change on the mechanical response. Future work will include model development for more general approaches, such as two-way coupling and a fully coupled poro-elastic model.

Model validation

The TOUGH-RBSN simulator is validated by comparison with an independent simulation of the same process using TOUGH-FLAC (Rutqvist 2011). Consider a soil sample (20×20×20 mm) wetted at the bottom and fully confined mechanically, as shown in Figure 8. The model is discretized with 19 lattice elements and 20 nodes. Model boundaries are fully confined with mechanical fixed supports, and there is no flow across the boundaries except at the bottom water inlet. Both simulations were calibrated using data from an experiment that was part of the international collaborative model comparison project DECOVALEX III. The experiment was conducted for about 10 days at isothermal conditions (T=25°C). Initial saturation was 65% with elastic modulus of 60 MPa. From this information, the moisture swelling coefficient, α_s (Eq. 3), can be back-calculated to 0.238, as shown in Rutqvist et al. 2011.

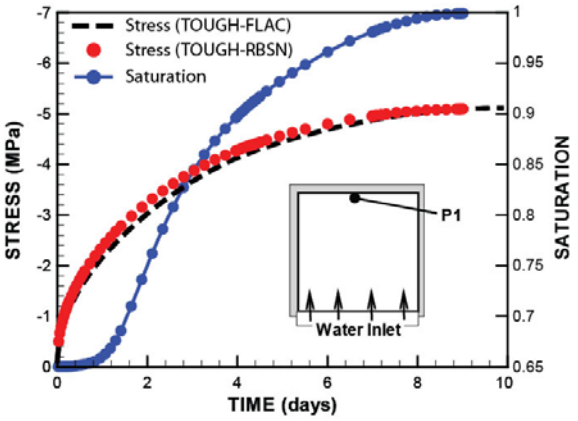

Figure 8. Time evolution of compressive stress and saturation at point P1 for simple swelling model.

Figure 8 shows the simulation results for time evolution of compressive stress and saturation. The hydraulic primary variables are accurately simulated by TOUGH2 as reported in Rutqvist et al. 2011. Stress increments are based on the saturation changes. The final stress is 5.12 MPa, which consists of 5 MPa (calibrated value) on top of the initial atmospheric stress of 0.12 MPa. Good agreement between the results simulated by TOUGH-RBSN and TOUGH-FLAC is achieved.

Simulation of desiccation cracking

Desiccation cracking is demonstrated by the TOUGH-RBSN simulator. Consider a slab subject to drying from the top surface. The initial saturation is set to 80%. The convective boundary condition is implemented by a thin layer of nodes at the top surface with prescribed nodal saturation (30%). Model boundaries are fixed at the bottom surface, whereas the vertical surfaces are only free to move in-plane. The vapor diffusion induced by saturation changes induces changes in strain within the mechanical element. In general, elements closest to the top surface shrink the most due to experiences the largest changes in saturation. The model is parameterized using hydrogeological and mechanical properties characteristic of expansive clay rock. Here, a classical brittle approach is used to break the lattice elements. Desiccation of expansive clay produces predominantly tensile stress fields due to the drying shrinkage. Tensile fracture is based on a measure of tensile stress calculated as $\sigma_R=F_R/A^P_{ij}$, where F_R is the resultant force acting on the element facet and A^P_{ij} is the projected area of the Voronoi cell boundary to the resultant force (Asahina et al. 2011). Simulation is conducted until no more major changes in the crack pattern are observed.

First, the insensitivity of the fracture pattern with respect to mesh size is studied using two different meshes with 2680 nodes and 297 nodes. Figure 9 shows the fracture pattern. The results show about the same number of major crack features, as well as similar spacing between the cracks.

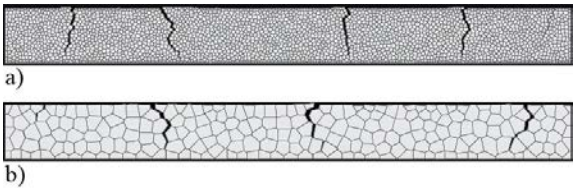

Figure 9. Fracture pattern with various mesh sizes: (a) fine mesh (2680 nodes), and (b) coarse mesh (297 nodes).

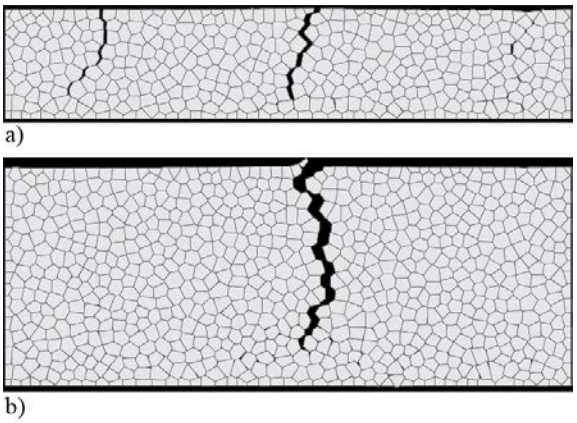

Figure 10. Fracture pattern with various thicknesses: (a) 20 mm, and (b) 40 mm.

Second, the basic aspect of fracture patterns is further studied for various slab thicknesses, as shown in Figure 10. Model thicknesses of 10 mm (Fig. 9b), 20 mm, and 40 mm are simulated. The resulting number of major cracks is about 4, 2, and 1, respectively. This general response, in which the distance between cracks increases with material thickness, has been observed in experiments (Colina and Roux, 2000). Bolander et al. (2007) have conducted a similar study for cement composite materials, where lattice-type models are used to calculate both mechanics and transport (e.g., moisture transport). Future work for desiccation cracking will involve more realistic simulations and quantitative comparisons with experimental data.

CONCLUSION

Computational methods are needed to address fracture initiation and propagation as a hydro-mechanical coupled process. The method reported here uses a finite volume method for flow processes and RBSN modeling for geomechanics. This allows for the coupling to be computed on a common grid using a random Voronoi gridding approach for two or three dimensions. The proposed methodology, in which fractures are placed along Voronoi cell boundaries, eliminates many issues regarding incorporating new fractures into a numerical grid, minimizing computational aspects associated with regridding. This allows for a more practical incorporation of fracture initiation and propagation into numerical models of coupled hydromechanical processes. Examples presented here have shown some of the applications of this computational strategy for modeling

hydrogeological and geomechanical coupled processes.

ACKNOWLEDGMENTS

The authors gratefully acknowledge Dr John E. Bolander at UC Davis for his suggestions and comments. We also thank Peter Persoff at LBNL for his careful review of a draft manuscript. Funding for this work was provided by the Used Fuel Disposition Campaign, Office of Nuclear Energy, of the U.S. Department of Energy under Contract Number DE-AC02-05CH11231 with Berkeley Lab.

REFERENCES

Asahina, D. and Bolander, J.E., Voronoi-based discretizations for fracture analysis of particulate materials, *Powder Technology*, *213*, 92–99, 2011.

Asahina, D., Landis, E.N., and Bolander, J.E., Modeling of phase interfaces during pre-critical crack growth in concrete, *Cement & Concrete Composites*, 33, 966-977, 2011.

Bastiaens W., Bernier, F., and Li, X.L., SELFRAC: Experiments and conclusions on fracturing, self-healing and self-sealing processes in clays, *Physics and Chemistry of the Earth* 32, 600–615, 2007.

Bolander, J.E. and Saito, S., Fracture analyses using spring networks with random geometry. *Eng Fract Mech*, 61, 569–91, 1998.

Bolander, J.E., Li, Z., and Yip, M., Restraint and cracking during non-uniform drying of cement composites, *Proceedings of the Transport Properties and Concrete Quality Workshop - Materials Science of Concrete*, American Ceramic Society, 123-140, 2007.

Bossart, P., Trick, T., Meier, P.M., and Mayor, J.-C., Structural and hydrogeological characterization of the excavation-disturbed zone in the Opalinus Clay (Mont Terri Project, Switzerland), *Applied Clay Science* 26 (2004) 429– 448.

Chiaramonte, L., Zoback, M.D., Friedmann, J., and Stamp, V., Seal integrity and feasibility of CO2 sequestration in the Teapot Dome EOR pilot: geomechanical site characterization, *Environ Geol* (2008) 54:1667–1675.

Colina, H. and Roux, S., Experimental model of cracking induced by drying shrinkage *Eur. Phys. J. E* 1, 189-194, 2000.

Houseworth, J.E., An analytical model for solute transport in unsaturated flow through a single fracture and porous rock matrix. *Water Resources Research*, 42, 2006

Kawai, T., New Discrete Models and their Application to Seismic Response Analysis of Structures, *Nuclear Engineering and Design* 48, 207-229, 1978.

Neuzil, C.E., Hydromechanical coupling in geologic processes, *Hydrogeology Journal* (2003) 11:41–83.

Oldenburg, C.M. and Pruess, K., EOS7R: Radionuclide Transport for TOUGH2, Lawrence Berkeley National Laboratory, LBL-34868, 1995.

Rutqvist, J., Wu, Y.-S., Tsang, C.-F., and Bodvarsson, G., A modeling approach for analysis of coupled multiphase fluid flow, heat transfer, and deformation in fractured porous rock, *International Journal of Rock Mechanics & Mining Sciences*, 39, 429–442, 2002.

Rutqvist, J., Ijiri, Y., and Yamamoto, H., Implementation of the Barcelona Basic Model into TOUGH–FLAC for simulations of the geomechanical behavior of unsaturated soils *Computers & Geosciences* 37, 751–762, 2011.

MVIEW—A POWERFUL PRE- AND POST-PROCESSOR FOR TOUGH2

John Avis, Nicola Calder, and Robert Walsh
Geofirma Engineering
Ottawa, Ontario, K1R 1A2, Canada
javis@geofirma.com, ncalder@geofirma.com, rwalsh@geofirma.com

ABSTRACT

mView is a software tool used to pre- and post-process TOUGH2 models. Originally developed to assist in visualization of model results for the Yucca Mountain Project, mView has evolved into a powerful numeric modeling support system designed to process, analyze, and visualize complex geoscientific data. mView is model independent and supports a number of finite-difference (FD), finite-element (FE) and integral finite-difference (IFD) codes, including TOUGH2.

mView uses a toolkit paradigm for the modelling process. It does not presuppose a workflow, but provides the tools necessary for an analyst to address the specific requirements of their projects. These tools consist of a large number of objects that individually perform simple tasks, but can be linked in a data-flow network to function as complex algorithms. This approach provides extremely flexible capabilities for 2D and 3D gridding, property assignment, results analyses, and preparing complex 2D and 3D visualizations.

mView supports most common versions of TOUGH2 (all EOS) and TOUGH_MP. Rather than create a single monolithic input file, mView creates text files containing one or more TOUGH2 input blocks that can be simply combined with external batch programs. mView objects are available to create PARAM, ELEME, CONNE, ROCKS, GENER, INCON (up to 8 primary variables), FOFT, COFT, GOFT and TIME blocks. Time-varying boundary condition files (timbc.dat) for TOUGH_MP can also be created. For post-processing, mView reads time step (i.e. TIME block specified) gridblock and connection output and FOFT/COFT/GOFT files.

mView is implemented within an object-oriented application framework. Each mView object is an independent testable entity and has been developed under an ISO9001:2008 software quality assurance program.

INTRODUCTION

The TOUGH2 family of codes (Pruess et al., 1999) provides the modeler with extensive capabilities to simulate complex flow processes. However, it can be difficult to fully utilize the codes, since conventional groundwater flow and transport code pre- and post-processors are generally incompatible with TOUGH2 discretization and output. The few pre- and post-processors that are TOUGH2-specific are generally limited to using specific versions of the code in executable form only. Support is not available for all EOS, and user-customized versions of TOUGH2 may be difficult to incorporate into the workflow.

mView was originally created to provide visualization support for the Yucca Mountain Project, with the goal of integrating results from multiple models (TOUGH, FEHM, NUFT) in 3D visualizations (Avis et al. 1998, Avis et al. 2001). This original requirement led to the design choice that mView would be model agnostic—internal data structures were not tied to any particular model implementation (i.e., FD, FE, or IFV), but would rather support all implementations with generic data structures and file formats. This ensured that mView had integrated support for TOUGH2 specific data types. For example, most FE and FD codes provide flow output as vectors associated with elements (FE) or nodes (FD), while TOUGH2 defines flows over connections; all of these approaches are supported within mView.

mView has been built by modelers for use by modelers. At Geofirma, we have been using TOUGH2 for the last 10 years, primarily on radioactive-waste-related projects (Calder et al, 2006; Geofirma and Quintessa, 2011; Avis et al.,

2012). Other investigators have used mView in radioactive waste (Senger et al., 2007, Senger et al., 2009) and energy projects. mView has also been used to support conventional flow and transport modeling with other codes such as MODFLOW and FRAC3DVS. Over this time period, we have added extensive pre-processing capabilities to mView to assist in grid generation and property assignment. Post-processing capabilities have also been augmented as dictated by project requirements. Currently, there are over 400 mView objects available to perform a wide range of pre- and post-processing tasks.

SOFTWARE DESIGN

mView is fundamentally different from other pre- and post-processors. It allows the user to work with multiple models (from the same or different codes) simultaneously. Results from different grids and/or simulations can be loaded and compared or used in defining boundary conditions (i.e., regional model to local model). Each grid is tied to a coordinate system, with a default world coordinate system provided. Additional coordinate systems may be defined to allow grids to be rotated and offset within the world system for calculations and visualization.

The mView user interface (UI) follows a folder-tree paradigm (Figure 1).

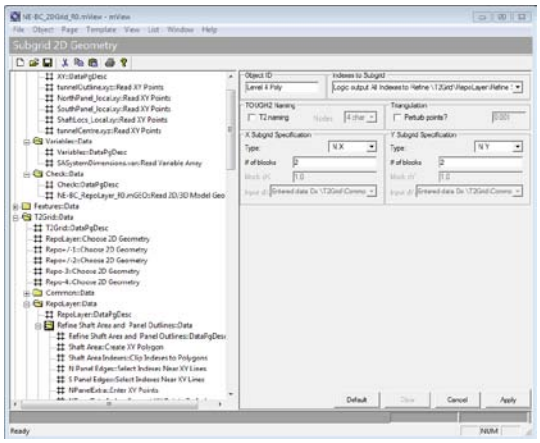

Figure 1. Example mView configuration.

The user creates "pages," which are analogous to folders. Objects are created and added to pages via a drop-down selection. The UI for each object is displayed in the main window adjacent to the tree when the object is first created or subsequently selected. The combination of objects and pages is called a "configuration" and is saved in a specially formatted text file.

mView defines data types that can be communicated between objects. Example data types are: model geometries, model result data sets, scalars (arrays of values associated with a nodes or connections), and single real values.

The data-flow network is established by linking objects, whereby the output(s) from one object becomes input(s) for one or more other objects. Input objects are selected from a drop-down menu displaying all available outputs of the required data type. After an object's output is changed, all downstream objects are recalculated and associated visualizations redrawn. Object linkages are shown on the object tree—icons associated with upstream and downstream objects are highlighted.

Another mView innovation is the use of "data indexes." These are data types that are essentially lists of geometry elements associated with gridblocks (nodes) or connections, which can be derived from model results (e.g., indexes of all nodes with SL < 0.5) or from pre-processing (e.g., all nodes of rock type X, all nodes within a polygon, all connections between specified node data indexes). Data indexes are used extensively in logical operations, property assignment, and in results presentation.

GRIDDING

Grid discretization is usually the first step in creating a model. mView supports 2D and 3D grids. Grid sizes are essentially unlimited. Element identifiers can be specified as 5 to 8 characters in length and are compatible with TOUGH2, iTOUGH (Finsterle, 1999), and TOUGH_MP (Zhang et al., 2003).

There are four options for creating 2D grids: simple FD type regular rectangular, regular radial, irregular Voronoi, and irregular subgridded. Irregular grids are frequently used to minimize grid size by applying reduced discretization only where necessary. Voronoi grids respect the IFD formulation whereby connections are orthogonal to flow areas, but are difficult to create where precisely located property

transitions are required. Subgridding allows the combination and stepwise reduction of regular rectangular and radial grids and allows for easy implementation of local grid refinement that respects property boundaries but violates the orthogonality requirement. Our experience has shown that this leads to only very minor errors in calculated pressures. Figure 2 illustrates the difference between approaches in a portion of a relatively complex grid containing repository features.

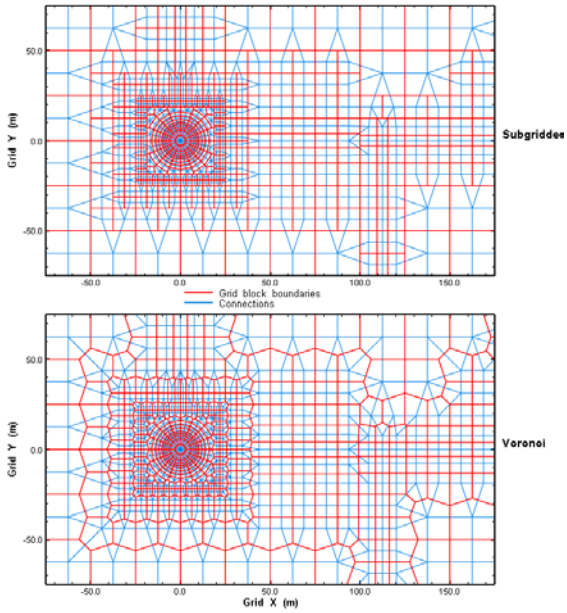

Figure 2. Comparison of subgridded and Voronoi 2D Grids.

3D grids are constructed as multiple layers of 2D grids. Layer orientation is usually in the horizontal (XY) plane, but can be vertical (XZ or YZ) if required. Creating a 3D grid requires definition of layer boundaries. mView can use existing digital elevation model (DEM) grids to specify layering coincident with geology. DEMs can also be created within mView using available kriging objects. Layers can also be defined by elevation or thickness. Each specified layer can be divided into multiple intermediate layers using fixed or adaptive spacing. Figure 3 is a cross section through an example 3D grid for a gas storage reservoir. Layers are specified at formation tops, with each formation subdivided into multiple intermediate layers.

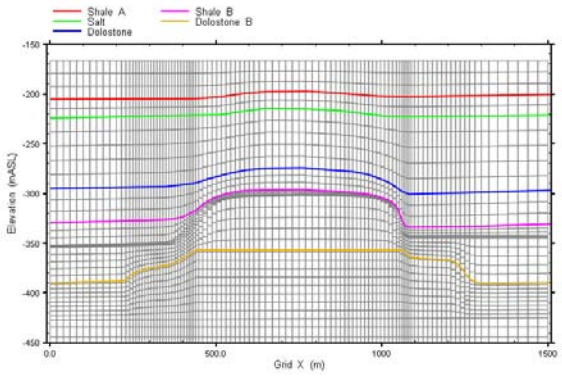

Figure 3. Slice through 3D grid showing layering from geologic surfaces.

3D grids can be combined to allow for variation in discretization by layer.

PROPERTY ASSIGNMENT

Property assignment is similarly flexible. A property set is created for a grid, and rock parameters entered in a spreadsheet format to define property groups. Groups are then assigned to model elements with a variety of objects. Basic objects include properties from DEM elevations, specified layers, constant elevations or within volumes and areas defined by polygons. Objects can be cascaded, for example to set basic layer properties from geology then to modify and add repository features or faults. Figure 4 shows a grid where formation data imported from a VULCAN geology model is used to set properties.

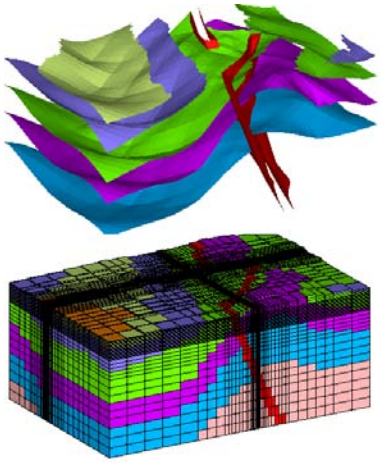

Figure 4. Geologic layers and property assignments.

Figure 5 illustrates property settings from polygons defining repository features. The figure also shows connections selected for COFT output specifications.

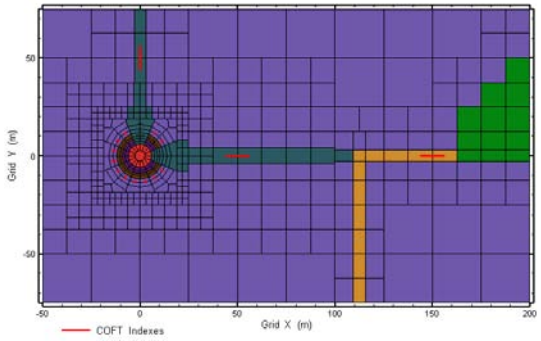

Figure 5. Repository feature property assignments from polygons and COFT connection indexes.

BOUNDARY AND INITIAL CONDITIONS

Fixed pressure/saturation boundary nodes are specified using data indexes. For example, nodes in top and bottom layers can be selected and combined. The data indexes can be used directly as negative volume (-VOLX) gridblocks in the TOUGH grid, or the block volume associated with those gridblocks can be specified to be an extremely large value. Initial conditions can be calculated from grid geometry (e.g., hydrostatic pressure or specified gradient) or specified by property (e.g., SG in repository nodes = 10.999). Results from other simulations, either on the same grid or a larger grid, can also be used. Figure 6 shows results from a previous steady-state flow simulation with repository operating period pressures imposed.

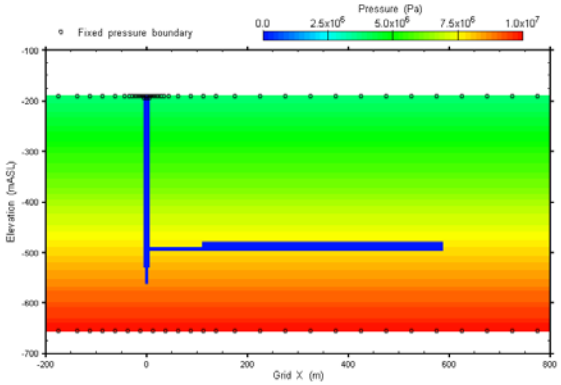

Figure 6. Initial pressure conditions and fixed pressure boundary nodes.

TOUGH2 INPUT FILE CREATION

As mentioned previously, mView objects are used to create text files comprising the major portions of a typical TOUGH2 input file. A brief review of these objects follows:

Create PARAM—provides a UI for most components of the PARAM block including MOP settings.

Create ELEME/CONNE/ROCKS—combines mView geometry and property data. ELEME and CONNE blocks are written to a single mesh file, while ROCKS are written separately. If IRP or ICP properties are defined, two-phase flow parameters are included in the ROCKS file. Default values for element volume and connection interface properties can be overridden. AHTX and PMX scalars can be incorporated. Automatic grid reorganization to incorporate negative volume boundary elements is performed if indicated.

Create INCON—Up to 8 primary variables may be specified. Optional PORX and INDICEE (for TMVOC) values can be used. Restart information from an existing SAVE file can be added.

Create FOFT/COFT/GOFT—creates file of gridblock identifiers from data index object input.

Create GENER—writes constant or time variable GENER for data indexes. Options allow rates to be allocated based on scaling factors. GX, EX and HX can be specified.

Create TIME—writes formatted table of output times from input table.

Create TIMBC—writes timvsp.dat file for TOUGH_MP time varying pressure boundary conditions.

mView-generated text files can be combined with other input files containing required TOUGH2 blocks (e.g., MULTI, START, DIFFU, ENDCY) using a simple batch command.

POST-PROCESSING

After a simulation is executed, mView is used to convert TOUGH2 text file output to an internal binary file format. Binary files require less disk space, can be accessed randomly to extract time step data, and are much faster to load. Versions of TOUGH2 used at Geofirma have been modified to include a binary file output option. File format and implementation details are available upon request.

After data conversion, post-processing objects are used to analyze and visualize model results.

There are over 200 objects that provide various analytic capabilities, from straightforward data extraction (select time step and variable as scalar, modify to include selected properties only), conversion (variable values at nodes/connections to time series tables, connection to node, connection to vector), math (symbolic arithmetic with scalars) and statistics (univariate on scalar, CDF calculation), to more complex processes (upscale results to different grids, stepwise regression). Additional objects are available to extract slices and layers from 3D grids for data analyses and plotting support, and to interpolate results from one grid to another. One of the major impediments to using mView is the plethora of available objects; the initial learning curve can be very steep. In the decade during which we have been using and developing mView, nearly every modeling project we have undertaken has resulted in the addition of one or more objects to perform specific tasks required to meet project goals.

Visual output is available as 2D or 3D plots. Plots can be further categorized as spatial (linear axes with fixed axes scale relationships, usually 1:1) and nonspatial (logarithmic or linear axes, no scale relationship).

The page and object UI paradigm extends to plots. When an mView plot page is created, a new top level window containing the plot appears on the user's desktop. Every object that is added to the plot page will cause a corresponding visual feature to appear on the plot. Plot objects can be categorized as data display (they appear within the axes limits and respect the axes scaling) or annotation objects (labels and legends that can appear anywhere within the plot window). Data display plot objects include contouring, gridblock areas colored by node values or continuous shading over a nodal triangulation, vectors, isovolumes (3D), particle tracks and context information. Annotation plot objects include labels, grid lines, symbol/line legends, color bars, and data values.

Axes can be labeled and grid lines or tics displayed. Alternatively, the appearance of the axes can be suppressed. Figure 7 shows the plot window for a 3D plot with multiple data display plot objects (solid colors for all nodes with SG > 10^{-4}, vertical and horizontal slices with pressures) and annotation objects (two color legends, a label showing selected time step) with no axes plotted.

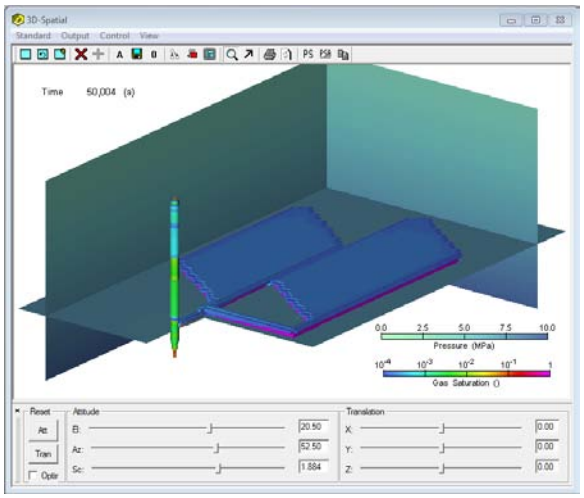

Figure 7. 3D plot window showing gas saturation and pressure.

Slider bars below the graphic window are used to precisely set the viewpoint and scale. The mouse wheel can also be used to rotate, tilt, and zoom. 3D plot objects can be visualized using transparency. This is useful for nested isovolume plots.

A 2D plot window is shown in Figure 8. Data display plot objects have a "layer" setting which governs visibility. All objects on layer 0 are plotted first, followed by layer 1, layer 2, etc. In the figure, gas saturation is plotted on Layer 1, while permeability is plotted on Layer 0. Many data-display objects have a "report" capability that will indicate data identifiers and values under the cursor, also shown in the figure. This

capability is useful for diagnosing simulation problems and analyzing results.

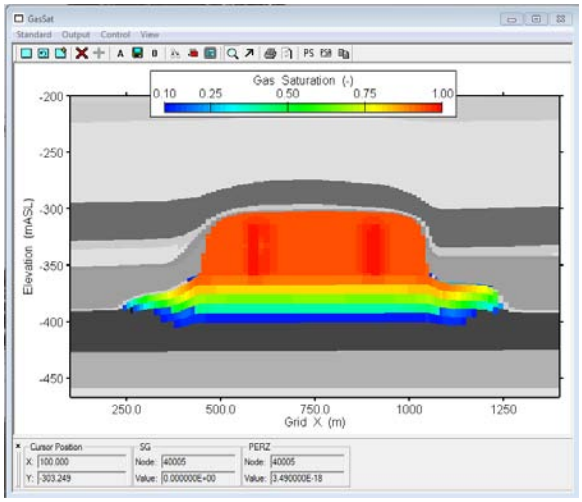

Figure 8. 2D plot window showing gas saturation and vertical permeability.

A final plot-page type is called a "Composite Plot." These plots allow multiple 2D and 3D plot windows to be combined and embedded in a single window using flexible layout specifications, as shown in Figure 9.

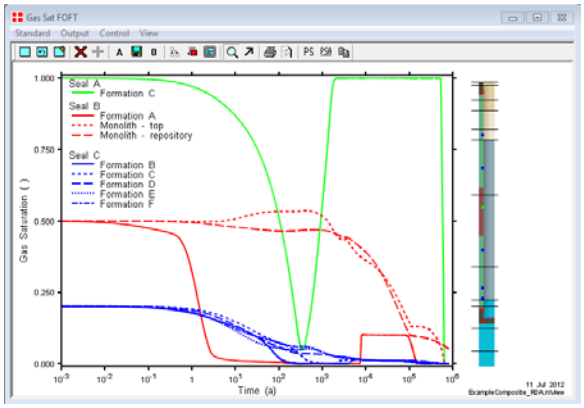

Figure 9. Composite plot with saturation versus time and monitoring point location plots

The graphics content of any plot window can be easily imported into reports using copy/paste or can be saved as jpeg or bitmap files. PostScript output files can be created when higher quality is required, such as on posters or large plots.

mView can be used to create animations. Plot windows can be set to write numerically sequenced bitmap files after each window update. These files can be processed by 3rd party animation software such as VideoMach (www.gromada.com) to create Windows AVI files. Data objects have capabilities to step through sequences (e.g., time steps, grid layers) or to increment values (e.g., data interpolation times, iso-volume concentrations). 3D plot viewpoint parameters can also be varied over prescribed ranges to rotate or zoom in a 3D animation.

QUALITY ASSURANCE

mView was initially developed using C++ on Unix platforms under the Yucca Mountain Project DOE QA regime. Version 4.0 was qualified to these standards in 2004. Subsequently, the code was ported to Windows, which is the current development platform (Windows 7). mView is available in 32-bit and 64-bit versions for Windows XP or later. All code development has been performed under Geofirma Engineering's ISO 9001:2008 quality system, which contains procedures governing all software development activities. The procedures require unit testing and verification for all code. The mView architecture lends itself to testability since each object is independent of all other objects and can be easily verified. mView is currently undergoing qualification to the Canadian Nuclear Waste Management Organization (NWMO) software standards as Nuclear Grade software, used to support safety assessments.

CONCLUSIONS

mView is an powerful pre- and post-processor that provides a high level of support for TOUGH2 applications. It has been developed by modelers to support complex modeling projects and is continuously updated as needs evolve. It should be considered by the TOUGH community as an alternative to existing tools.

REFERENCES

Avis, J.D., J.A. McNeish and S. Gurumurthy, *Scientific Visualization for Radioactive Waste Repository Analyses: mView*. EOS, Transactions American Geophysical Union Vol. 79, No. 45, pg.F24. 1998 Fall Meeting.

Avis, J.D., Greenberg, H.R., and J.A. McNeish , *Visualization of Performance Assessment Process Model Results*. Presented at the American Nuclear Society 9th International High-Level Radioactive Waste Management

Conference (IHLRWM), Las Vegas, Nevada, April 2001.

Avis, J.D., P. Suckling, N. Calder, and R. Walsh, *T2GGM – a Coupled Gas Generation Model For Deep Geologic Disposal Of Radioactive Waste*, Proceedings TOUGH Symposium 2012, Lawrence Berkeley National Laboratory, Berkeley, California, 2012.

Calder, N., J.D. Avis, R. Senger and H. Leung, *Modifying TOUGH2 To Support Modelling Of Gas-Transport Through Saturated Compacted Bentonite As Part Of The Large-Scale Gas Injection Test (LASGIT) In Sweden*. Proceedings TOUGH2 Symposium, Berkeley, California, 2006.

Finsterle, S. *iTOUGH2 Command Reference, Version 4*. Report LBNL-40041, Earth Sciences Division, Lawrence Berkeley National Laboratory. University of California, Berkeley, USA. 1999

Geofirma and Quintessa, *Postclosure Safety Assessment: Gas Modelling*, Geofirma Engineering Ltd. and Quintessa Ltd. report for the Nuclear Waste Management Organization NWMO DGR-TR-2011-31, Toronto, Ontario, 2011.

Senger, R., P. Marschall, and S. Finsterle, *Investigation of Two-Phase Flow Phenomena Associated with Corrosion in an SF/HLW Repository in Opalinus Clay, Switzerland*, Physics and Chemistry of the Earth, vol. 33, p. S317-S326, 2007

Senger, R., J. Ewing, K. Zhang, J.D. Avis, P. Marschall, I. Gaus, *Modeling Approaches For Investigating Gas Migration From A Deep Low/Intermediate Level Waste Repository (Switzerland)*, Proceedings TOUGH Symposium 2009 Lawrence Berkeley National Laboratory, Berkeley, California, 2009

Pruess, K., C. Oldenburg, and G. Moridis, *TOUGH2 User's Guide, Version 2.0*, Report LBNL-43134, Lawrence Berkeley National Laboratory, Berkeley, Calif., 1999.

Zhang, K., Wu, Y.S., Ding, C. & Pruess, K.:*TOUGH2_MP: A parallel version of TOUGH2*.Proceedings TOUGH2 Symposium 2003, Lawrence Berkeley National Laboratory, California, 2003.

GALLERY

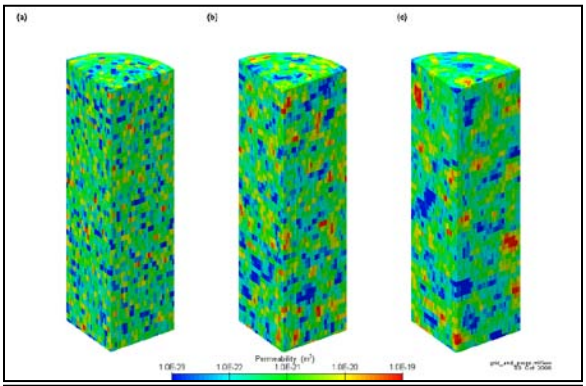

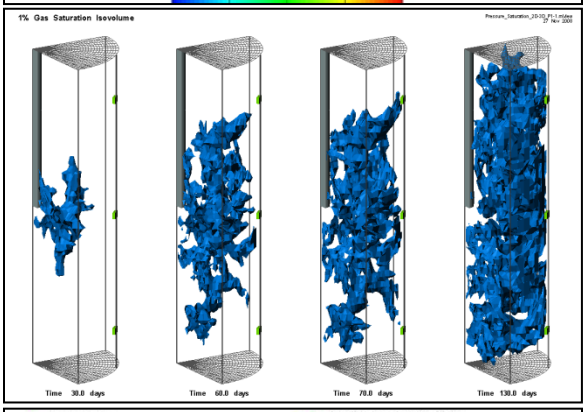

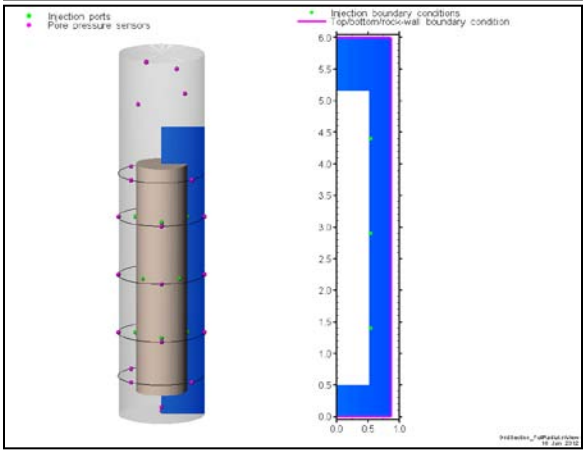

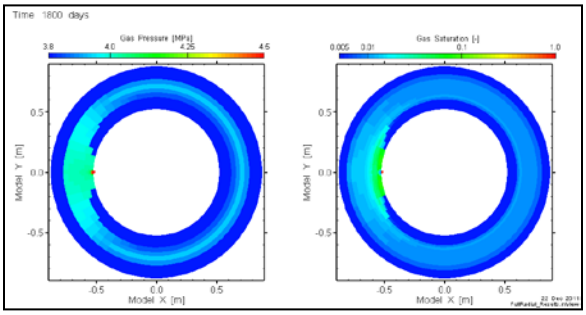

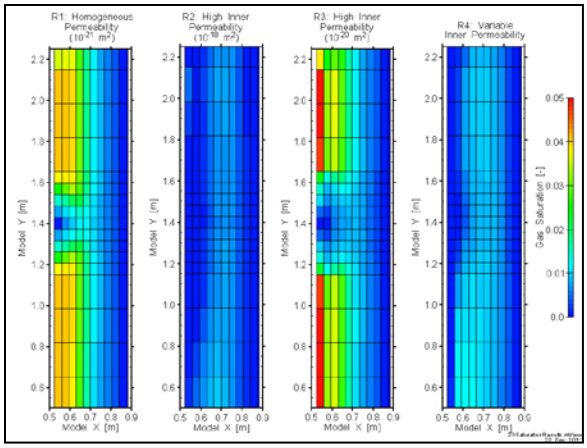
R1: Homogeneous Permeability
R2: High Inner Permeability
R3: High Inner Permeability
R4: Variable Inner Permeability
Model Y [m]
Model X [m]
Gas Saturation [-]

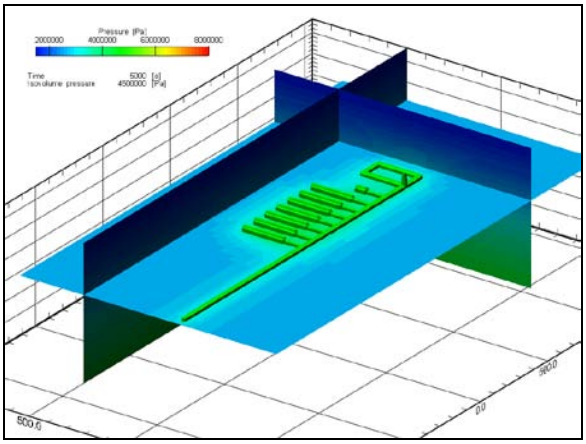
Pressure [Pa]
Time
Isovolume pressure

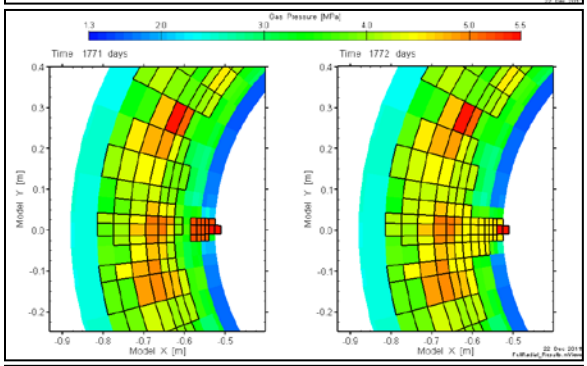
Gas Pressure [MPa]
Time 1771 days
Time 1772 days
Model Y [m]
Model X [m]

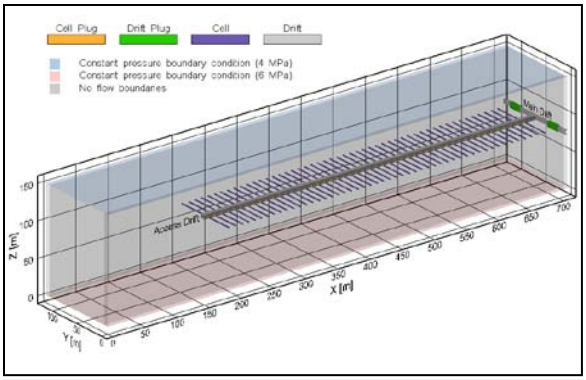
Cell Plug
Drift Plug
Cell
Drift
Constant pressure boundary condition (4 MPa)
Constant pressure boundary condition (6 MPa)
No flow boundaries
Access Drift
Z [m]
X [m]
Y [m]

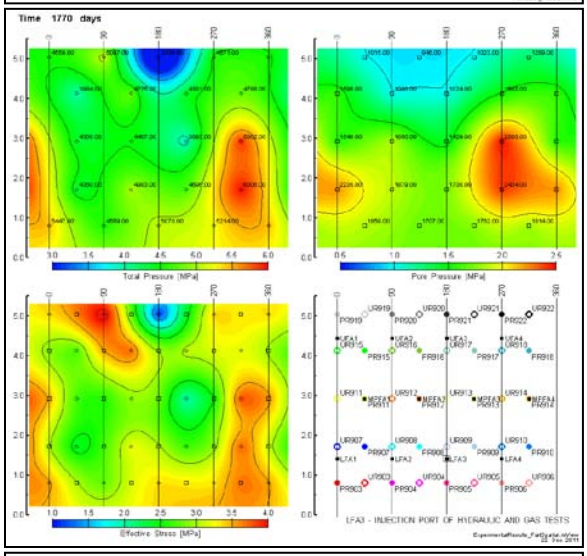
Time 1770 days
Total Pressure [MPa]
Pore Pressure [MPa]
Effective Stress [MPa]
LFA3 - INJECTION PORT OF HYDRAULIC AND GAS TESTS

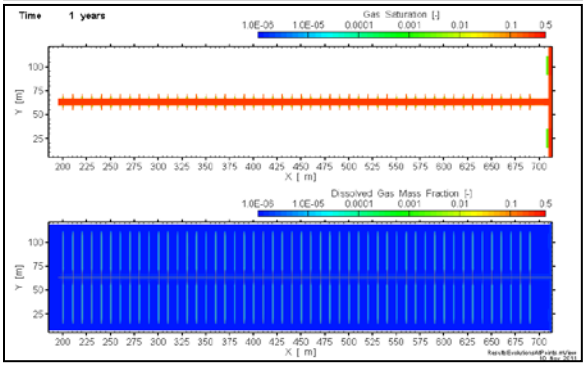
Time 1 years
Gas Saturation [-]
Dissolved Gas Mass Fraction [-]
Y [m]
X [m]

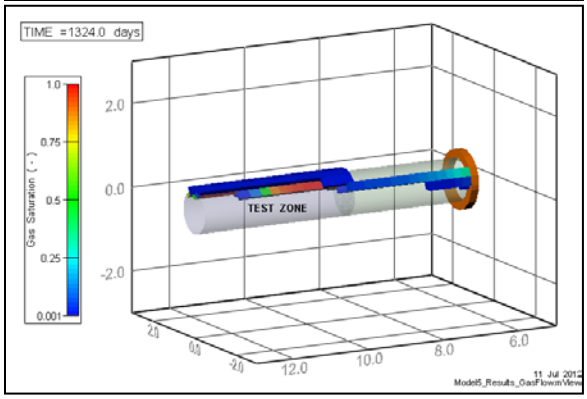
TIME =1324.0 days
Gas Saturation [-]
TEST ZONE

ADVANCES IN HYDROGEOPHYSICAL JOINT INVERSION

Michael Commer, Michael B. Kowalsky, Stefan Finsterle, Gregory A. Newman

Lawrence Berkeley National Laboratory
Earth Sciences Division, 1 Cyclotron Rd.
Berkeley, California, 94720, USA
e-mail: MCommer@lbl.gov

ABSTRACT

The inversion framework iTOUGH2 provides inverse modeling capabilities for TOUGH2, a general-purpose simulator for multiphase, multi-component, nonisothermal flows in multidimensional fractured-porous media. We have developed a parallel version of iTOUGH2, MPiTOUGH2, which realizes a hierarchically parallel architecture using the Message Passing Interface. This architecture allows employing large numbers of parallel processes for running many-parameter inverse problems on large meshes, such as those occurring in pixel-based parameterizations.

We have further combined the parallel hydrological inversion method with a geophysical modeling and inversion framework, called Electromagnetic Geological Mapper (EMGeo). The combined inversion method provides a tool for investigating coupled hydrogeophysical processes in the context of, for example, geologic CO_2 storage, geothermal system characterization, and environmental remediation and monitoring applications. In this work, we focus on the introduction of parallel computing paradigms to iTOUGH2, and carry out basic scalability tests. Further, exploiting the forward simulation capabilities of EMGeo, we present synthetic data inversions, demonstrating the potential model resolution enhancement obtained through joint inversion of hydrological and geophysical measurements.

INTRODUCTION

Joint inversion of hydrological and geophysical data has been recognized as a means of enhancing the typically sparse coverage of hydrological data, and thus achieving enhanced parameter resolution. A number of deterministic and stochastic joint inversion approaches have been reported. We refer the reader to the works of Kowalsky et al. (2004, 2005), and Finsterle and Kowalsky (2008), and related works referenced in those for a comprehensive overview of various methods.

Whenever a significant number of hydrological (and geophysical) simulations are carried out, such as in inverse modeling, computational efficiency becomes paramount. In this work, we advance the inverse modeling capabilities of iTOUGH2 by introducing parallel computing paradigms, using the Message Passing Interface (MPI), both into the underlying (forward) simulator given by TOUGH2, as well as the inverse modeling scheme. We further enhance the joint inversion capabilities by merging the parallel iTOUGH2 framework, called MPiTOUGH2, with the geophysical modeling methods provided by the geophysical simulator EMGeo. EMGeo is a 3D finite-difference scheme for the simulation and inversion of electrical/electromagnetic geophysical data types, including controlled-source electromagnetics, magnetotellurics, electrical resistivity tomography, and (spectral) induced polarization (Newman and Alumbaugh, 1997; Commer and Newman, 2008; Commer et. al., 2011).

In this and an accompanying work, two hydrogeophysical joint inversion approaches are used. The first strategy (presented in the second example of Kowalsky et al., 2012, this issue) involves a two-step approach. Field-scale electrical resistivity distribution maps, which would be obtained by inverting geophysical tomography data, are matched with their counterparts calculated from tracer concentrations. The latter are updated from the parameter estimates obtained during the iterative hydrological inversion procedure. The second approach, on which we focus in this work, involves a direct

joint inversion of hydrological and geophysical data. After each iTOUGH2 model updating step, the subsurface electrical resistivity distribution is updated from the current hydrological parameter state. Geophysical measurements are then simulated by the modeling methods available through EMGeo and matched with field data. We focus on the geophysical resistivity tomography (ERT) method for the geophysical data component, which is sensitive to the subsurface electrical resistivity. Hence, we use Archie's law as the petrophysical model to link hydrological to electrical attributes:

$$\sigma = \sigma_f \Phi^m S^n,$$

where σ is bulk electrical conductivity, σ_f is fluid electrical conductivity, Φ is porosity, S is saturation, and m and n are site-specific parameters. The joint inversion capabilities are demonstrated by carrying out synthetic inversion studies based on experiments performed at the U.S. Department of Energy Integrated Field Research Challenge Site (IFRC) at Rifle, Colorado.

METHODOLGY

The aforementioned geophysical component EMGeo is a geophysical data inversion package by itself, using nonlinear conjugate-gradient based optimization strategies. At the current development stage, we only utilize the inverse modeling capabilities of iTOUGH2, namely the Levenberg-Marquardt modification of the Gauss-Newton algorithm (Finsterle and Kowalsky, 2011). Parallelizing multiple forward simulations is essential in solving parameter estimation problems with many unknowns. iTOUGH2 includes this feature, using the Parallel Virtual Machine (PVM) (Finsterle, 1998). However, limitations are currently imposed by the fact that each forward problem can only be solved serially, i.e., using one process.

Hierarchical Parallel Architecture

The overall parallel architecture of the hydrogeophysical inversion scheme presented here borrows a parallel layout used for the inversion of large-scale electromagnetic data sets (Commer et al., 2008), and combines it with slightly modified techniques used by the parallel simulator TOUGH-MP (Zhang et al., 2008) for the hydrological flow-simulation component. Both the fluid-flow and geophysical *forward* simulators divide their respective simulation domains into a number of subdomains. The geophysical simulator uses proprietary parallel iterative solvers for solving either Maxwell's equations, for simulating frequency-domain EM methods, or the Poisson equation, for potential field simulations (such as electrical resistivity soundings), on large structured Cartesian finite-difference grids. TOUGH-MP uses the parallel linear-equation solver AZTEC (Tuminaro et al., 1999) in conjunction with the TOUGH2 simulation framework to solve the fluid flow problem's mass and energy balance equations (Zhang et al., 2008). The underlying simulator TOUGH2 employs integral finite-differences on structured or unstructured grids for the spatial descretization, while time is discretized using standard first-order backward finite differences.

Here, we outline some new but straightforward aspects of adding another parallel level to the inverse scheme, employing the Message Passing Interface (MPI). In the inverse problem, the sensitivity calculations involved in the parameter estimation steps are by far the most computationally intense. As illustrated in Figure 1, these calculations are distributed among multiple processor groups, also called *model communicators*. Each one is a separate MPI communicator and holds a copy of the simulation domain.

In the Levenberg-Marquardt implementation of iTOUGH2, the parameter sensitivity matrix is calculated by a perturbation approach. In the parallel version MPiTOUGH2, each model communicator is in charge of a subset of the parameter space and the corresponding forward simulations of their perturbations. Note that one parameter makes one column in the sensitivity matrix. The communicators can be scaled up according to the size of the matrix system to be solved in the forward problem, using the aforementioned parallel structures of the geophysical and fluid-flow simulators. Thus, if massively parallel resources are available, inverse problems with both large simulation domains and large parameter numbers can be solved, within reasonable computing times, by adequately increasing the size and number of the model communicators.

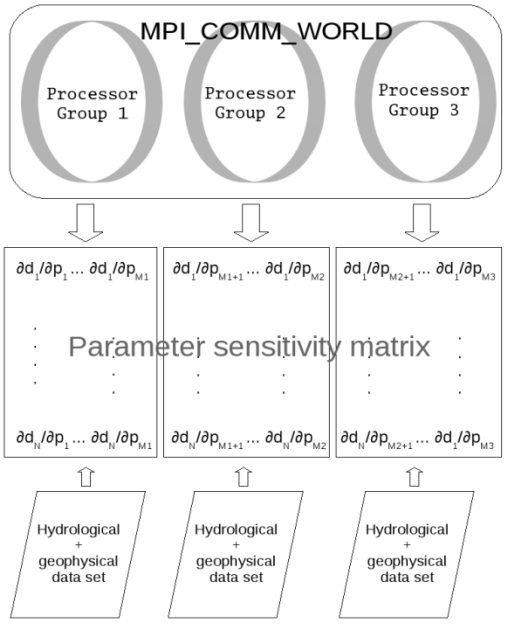

Figure 1. Illustration of the parallel layout used in the parallel inversion scheme MPiTOUGH2. Multiple forward simulations are distributed across multiple processor groups, where each group calculates a part of the parameter sensitivity matrix.

Parallel Scaling Tests

In this work, we use a 3-D TOUGH2 model created for the inversion of tracer data collected during the 2007 "Winchester" surveys (Williams et al., 2011) for some parallel scalability tests. The TOUGH2 grid comprises 52,235 elements and 151,149 connections, and has been used by Kowalsky et al. (2012) for simulating the flow cell of interest in inversions of tracer breakthrough data using a variety of hydraulic permeability parameterizations. We consider a three-parameter setup here, but for brevity, we omit further details about the model and data and refer to the aforementioned publication.

Parallel forward solution scalability test

Figure 2 shows run times for a forward simulation using from one to eight Intel® Xeon 3.20 GHz processors of a desktop computer. The bulk of the computing time is used for the iterative solution of the flow equations, including the AZTEC parallel solver's internal message passing. More (external) message passing of primary thermodynamic variables across subdomain boundaries is involved in the equation-of-state update before each Newton-Raphson iteration. However, it appears that the overhead of this message passing is negligible, owing to communication improvements reported by Zhang et al. (2008). The second-largest computing time fraction is needed for assembling the flow equation's matrix system at each Newton-Raphson iteration, followed by updating the equation-of-state and miscellaneous routines. In this example, because the mesh size is not highly demanding of the computing hardware, we observe a quick flattening of the run times when using more than three parallel tasks. Further increasing the number of parallel tasks would thus not further speed up the simulation time, due to the solver library's internal message passing overhead.

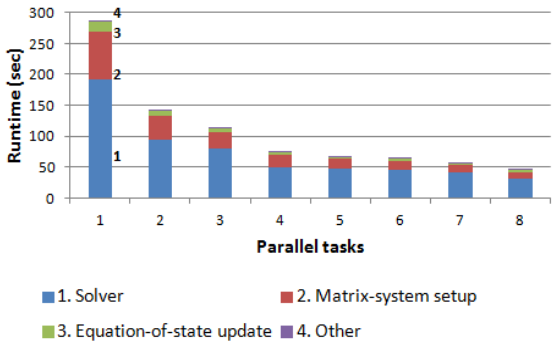

Figure 2. Runtimes for a parallel forward simulation using 1-8 parallel processes on a desktop computer.

Parallel inverse solution scalability test

The same model and computing hardware as used before is now employed in a three-parameter hydrological tracer data inversion, based on studies of optimal permeability model parameterizations (Kowalsky et al., 2012). Since the inversion involves multiple forward simulations, we expect that the behavior of the runtimes behaves similar to Figure 2. This can be observed in general in Figure 3, which depicts the average runtimes per inversion iteration. However, the runtime increases going from two to three parallel tasks. It is common in parallel numerical calculations for the solution accuracy to vary with the number of parallel tasks employed, owing to the round-off error propagation of the floating-point arithmetic (Asserrhine et al., 1995). In this particular example, it could be observed that the differences in the

iterative forward solutions propagate in a way that leads the three-process inverse solution onto a solution path in model space with a lower convergence rate. Figure 4 further illustrates this effect by comparing the data objective functional values between the one- and three-process runs. While we do not elaborate further on details of this observation, we mention that both solutions yielded similar parameter estimates close to the true model. This round-off error effect may need to be taken into account as part of a systematic modeling error, especially in the presence of ill-posed inverse problems, where it is likely to be enhanced. The corresponding parameter-estimation uncertainty may then be quantified by carrying out multiple inversion realizations using different parallel configurations. Note that this can also be emulated if fewer physical processors than parallel processes are available.

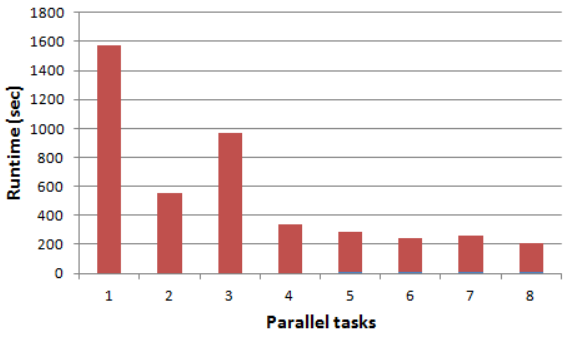

Figure 3. Runtimes for a parallel inverse solution using 1-8 parallel processes on a desktop computer.

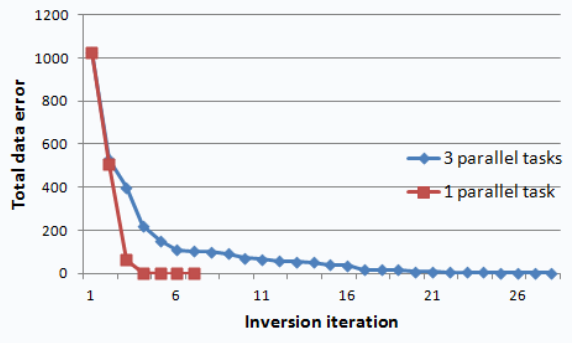

Figure 4. Data fitting error functional convergence for the one- and three-processor inversion runs of the inversion scalability test (Figure 3).

INVERSE MODELING RESULTS

The simulation cases generated for this next study are based on experiments in a shallow aquifer at the IFRC site. The aquifer is 2.5–3 m thick and is located on the floodplain of the Colorado River in alluvium, with the base given by the impermeable Wasatch formation (Williams et al., 2011). One part of the 2011/12 "Best Western" field experiments, on which we base our simulations, involved a conservative bicarbonate tracer injection to study uranium desorption in the absence of biostimulant-dependent uranium immobilization effects. The synthetic data used in the following inversion studies are generated from a subset of the survey geometries and measurement time intervals of this bicarbonate tracer injection experiment. Figure 5 illustrates the spatio-temporal layout of the simulated experiment. We consider an eight-parameter layered model, with vertically varying absolute hydraulic permeabilities as unknowns. As shown in the upper panel, the eight layers cover the aquifer's depth from 3 to 6 m below the surface. The tracer was introduced in the aquifer at the depth range indicated by the white symbols in the left part of the second panel. Groundwater flows along the *x*-axis from left to right, and was simulated for a period of 149 days after injection begin. The principal effect of the tracer is an increased flux of dissolved ions (in this case Na^+ and HCO_3^-) resulting in an electrical conductivity increase, where panels 2–6 show the reciprocal: electrical resistivity in units of Ωm.

The data set comprises a total of 219 average fluid electrical conductivity (EC) samples (given in units of μS/cm) measured in four boreholes, which are indicated by black lines in Figure 5. The EC data span a time period of more than 140 days. The data errors are given by standard deviations of 25. Using this standard deviation, which amounts to roughly 1% of the mean data amplitude, Gaussian noise with zero mean is added to the data. The geophysical data set is given by ERT measurements at 30 days. The ERT borehole array has altogether 30 electrodes distributed over four wells (indicated by red symbols). Inverted data comprise a subset of six source current electrode pairs and a total of 123 receiver electrode pairs, where one receiver electrode pair constitutes one geophysical data

point. Gaussian noise with zero mean and a standard deviation of 1% of the data amplitude is added to the data, in addition to a noise floor. The ERT data are characterized by a much larger dynamic range than the range of the EC data. Thus, the used standard deviation implies a lesser degree of noise distortion than is the case for the EC data set.

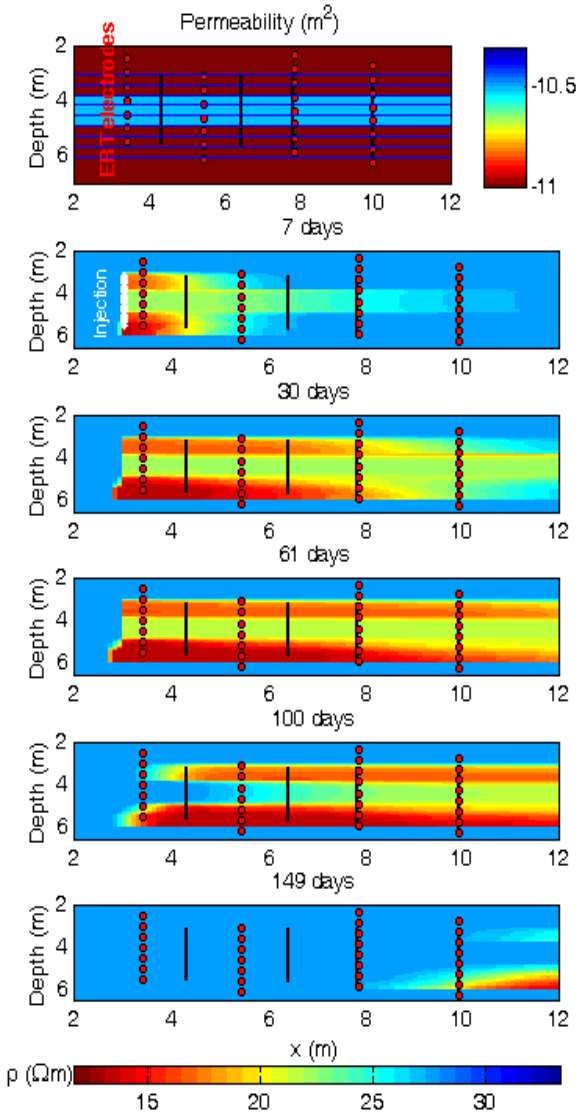

Figure 5. Spatio-temporal setup and plume development of an electrically conductive tracer injection simulated after a bicarbonate injection experiment at the IFRC site. The upper panel shows the true permeability model, where the horizontal lines indicate the boundaries of the eight layer parameters. Panels 2–6 show the change of the aquifer's electrical resistivity over a time period of 149 days after injection.

Regularization of the Inverse Problem

Many-parameter inverse problems, such as pixel-based inverse problems, are typically underdetermined, requiring the introduction of additional stabilization terms into the otherwise ill-posed problem. Two constraint types can be activated in iTOUGH2; these are *prior knowledge* and *smoothness constraints* (Finsterle, 2009). For the eight-parameter inverse problems in this work, we also observed a significant non-uniqueness problem that can be alleviated by introducing additional constraints. We introduce a practical method of automatically defining smoothness constraints in the presence of many parameters. The approach uses the ensemble of interfaces (i.e., the connection block in the TOUGH2 input) between the elements of the simulation domain. From the elements belonging to inversion parameters, all (TOUGH2) connections are determined. If there exists at least one connection between the element ensembles of two given parameters, a regularization term is introduced for this parameter pair. In our case, an element ensemble is given by a layer parameter. This idea implies that the absence of connections between two neighboring parameters would allow for a sharp (unconstrained) contrast of their estimates. The regularization is incorporated into the inverse problem by augmenting the parameter sensitivity matrix by one line per unique parameter connection.

One important aspect of constrained inversions is to properly weight the regularization terms against the information given by the calibration data. Figure 6 demonstrates the influence of the regularization weight, here called β-factor, on some trial inversions for the 8-layer test case. The β-factor is multiplied to the regularization term's objective functional, and thus has the effect of balancing it with the data-fitting component. All inversions used a homogeneous starting model with a negative log (base 10) permeability of -10.75. Each column group in Figure 6 pertains to the results for one layer parameter, where the first (left) column represents the true model, and the second, third, and fourth columns represent, respectively, the result from a regularized inversion with β=1, β=0 (no regularization), and β=10.

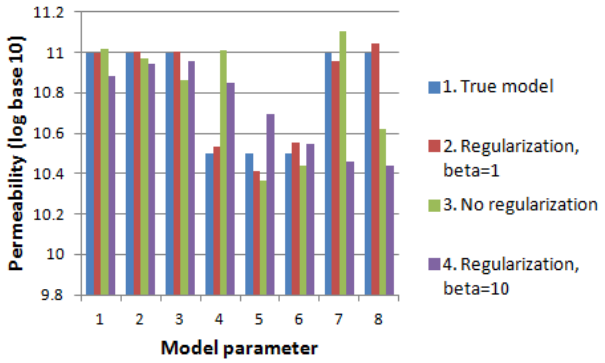

Figure 6. Inversion results with different smoothing regularization settings. Shown are permeability (negative log base 10) estimates for the 8-layer model. For each layer parameter, the results using a β-factor of 1 (red), 0 (green), and 10 (purple) are shown with the true model (blue).

While the EC data of these inversions were not contaminated with noise, their assumed error standard deviation in the inversion was 250. With these error assumptions, a regularization weight of β=1 leads to parameter estimates very close to the true model, with the corresponding data fits shown in Figure 7 (red curves). Neglecting the regularization causes an overestimated parameter 4, compensated for by an underestimated parameter 8. The resulting data fits, shown by green curves in Figure 7, are very similar to the regularized (β=1) result, indicating the non-uniqueness of the unconstrained inverse solution.

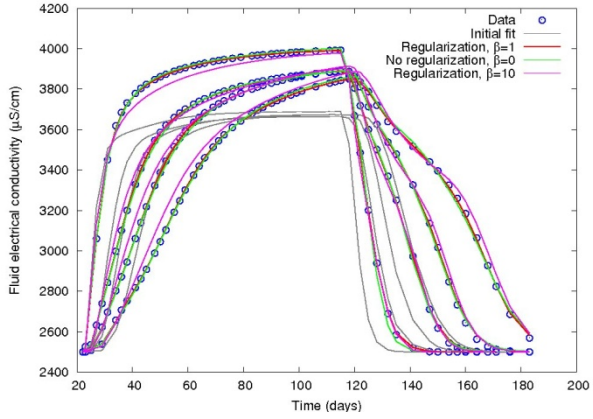

Figure 7. EC data fits calculated from inversion results with different smoothing regularization settings. The corresponding parameter estimates are shown in Figure 6.

Imposing a factor of β=10 also leads to a parameter overshoot of the low-permeability layers, where now the smoothing constraint forces the permeability to gradually decrease for the deeper layers. This happens at the expense of the data fits, as shown by the worsening fits (purple curves in Figure 7).

For all inversion runs carried out in the following, a regularization parameter of β=1 was found to be optimal.

Hydrological Inversion

In the following, all inversions are initiated with the homogeneous permeability model (log permeability of -10.75) as used before. Figure 8 shows the results of an inversion of the EC data set, where the upper part (a) shows original data (black), and initial (blue) and final (red) data fits. The model result in the lower figure (b) was obtained after 10 Levenberg-Marquardt iterations, with the same colors referring to the true, initial, and final models, where the error bars for the final model indicate two standard deviations. A good overall EC data fit is achieved by the final model. However, the noise distortion causes layer parameters 1 and 3 (from top) to deviate beyond the estimated parameter standard deviations. However, the inversion achieves an acceptable data fit, indicating that despite the regularization constraints, the non-uniqueness problem is amplified by the data's noise distortion.

Hydrogeophysical Joint Inversion

Next, we include both the geophysical ERT data and the EC data sets in the inversion. Figures 9a and 9b again show original data, and the initial and final data fits for both the ERT and EC data sets, respectively. A greatly improved model result (c) is achieved by the combined data set. The final model also improves the fit of the EC data – a 13% decrease from the total EC data fitting error in the previous EC data inversion. The total data fitting errors are plotted in Figure 10 against the inversion iterations for both inversion cases. Note that the initial total error of the EC data inversion is identical to the EC component of the joint inversion, since the homogeneous starting model produces no contribution to the error function's regularization term. We observe that the EC data errors have a similar

convergence rate, which indicates that the influence of the EC and ERT components is well balanced in the joint inversion.

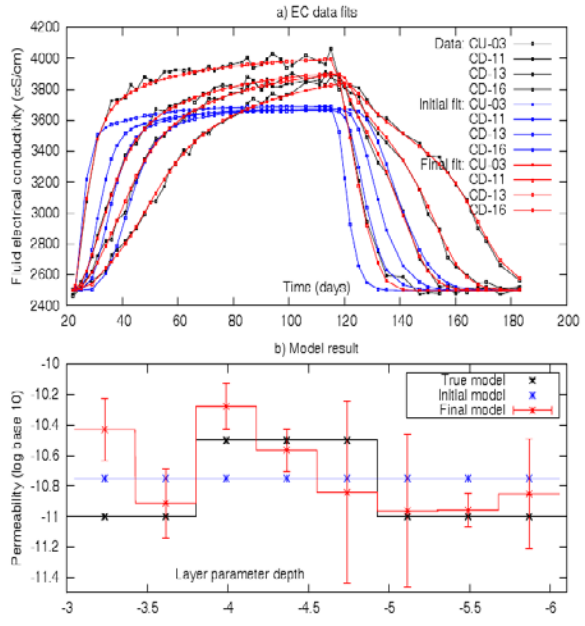

Figure 8. Inversion of the hydrological (EC) data set for the 8-layer parameter model. The boreholes named CU-03, CD-11, CD-13, and CD-16 correspond to the positions shown in Figure 5 (black lines) at x=4.3, x=6.4, x=7.8, and x=10 m, respectively.

CONCLUSIONS

We have developed a parallel framework for the joint inversion of hydrological and geophysical data. The value of geophysical data, usually covering larger survey areas than hydrological data and being cost effective, has been recognized. The development of efficient tools is thus important to fully exploit the potential resolution improvements given by combined hydrogeophysical data sets, and to investigate optimal spatiotemporal survey layouts for field applications.

Inverse modeling in general poses large computing demands. These are addressed by joining different parallelization levels, both over the forward problem, i.e., the simulation domain, and over the inverse problem, i.e., the parameter space.

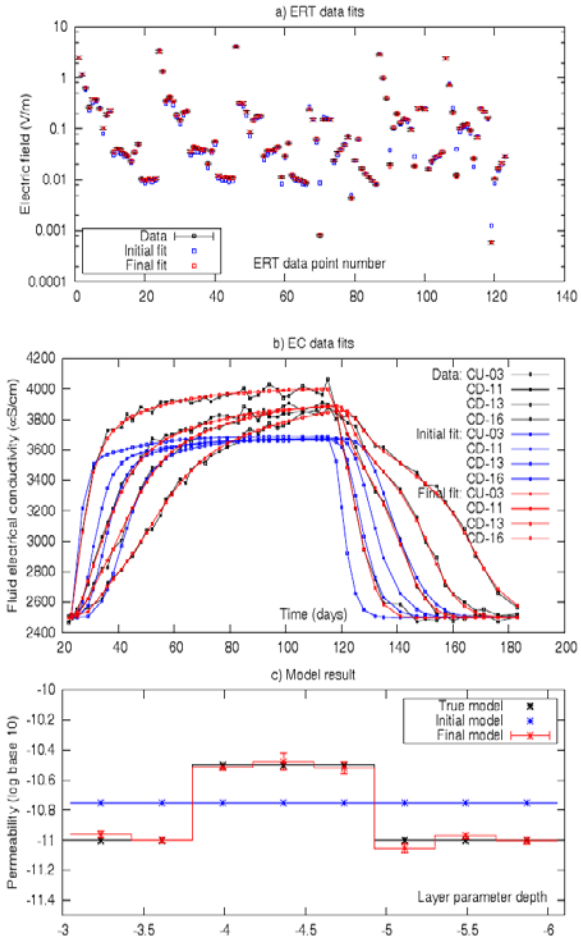

Figure 9. Joint inversion of the hydrological (EC) and geophysical (ERT) data sets for the 8-layer parameter model.

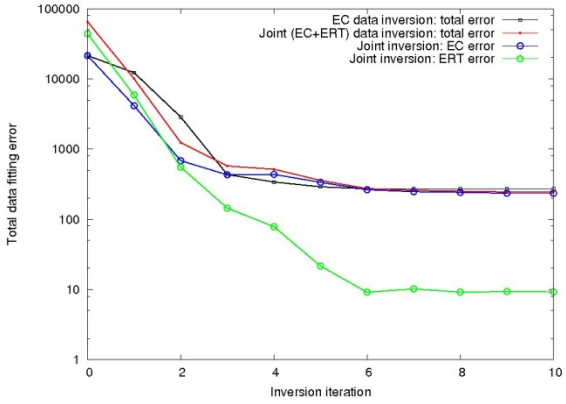

Figure 10. Comparison of total data fitting errors for the EC-data inversion (black) and joint inversion. For the joint inversion, the total (red), and separate EC (blue) and ERT (green) errors are shown

Our parallel hydrogeophysical parameter estimation framework maximizes scalability by allowing the increase of both size and number of communicators sharing the whole inverse modeling problem. The scalability of the hydrological simulator is particularly important for the joint inversion with geophysical data, because of the typical large-scale nature of geophysical inverse problems. Limitations are currently imposed by memory constraints, owing to storage requirements of a potentially large copy of the parameter sensitivity matrix on each parallel process.

The shown examples have demonstrated the potential model-resolution enhancements provided by geophysical data. It has also been shown that a properly chosen regularization parameter is essential for stabilizing the inherently ill-posed geophysical inverse problem. For the presented results, the petrophysical transform was assumed to be known. A next step will evaluate whether uncertainty in the petrophysical model can be accounted for by considering some of its parameters to be estimated in the inverse problem, utilizing the sensitivity of the geophysical data to these unknowns.

ACKNOWLEDGMENT

This work was supported by a LBNL Laboratory Directed Research and Development program granted to the authors.

REFERENCES

Asserrhine, J., J.-M. Chesneaux, and J.-L. Lamotte, Estimation of round-off errors on several computers architectures, *Journal of Universal Computer Science*, 1 (7), 454-468, 1995.

Commer, M., G.A. Newman, New advances in controlled source electromagnetic inversion, *Geophysical Journal International*, 172, 513-535, 2008.

Commer, M., G.A. Newman, J.J. Carazzone, T.A. Dickens, K.E. Green, L.A. Wahrmund, D.E. Willen, and J. Shiu, Massively-parallel electrical-conductivity imaging of hydrocarbons using the Blue Gene/L supercomputer, *IBM Journal of Research and Development*, 52-1/2, 93-103, 2008.

Commer, M., G.A. Newman, K.H. Williams, and S.S. Hubbard, Three-dimensional induced polarization data inversion for complex resistivity, *Geophysics*, 76(3), F157-171, 2011.

Finsterle, S., and M.B. Kowalsky, A truncated Levenberg-Marquardt algorithm for the calibration of highly parameterized nonlinear models, *Computers and Geosciences*, *37*, 731–738, 2011.

Finsterle, S., *Parallelization of iTOUGH2 using PVM*, Report LBNL-42261, Lawrence Berkeley National Laboratory, Berkeley, Calif., Oct. 1998.

Finsterle, S., and M.B. Kowalsky, Joint hydrological-geophysical inversion for soil structure identification, *Vadose Zone J.*, *7*, 287-293, 2008.

Finsterle, S., What's new in iTOUGH2?, Proc. TOUGH Symp., Lawrence Berkeley National Laboratory, Berkeley, Calif., 2009.

Kowalsky, M.B., S. Finsterle, and Y. Rubin, Estimating flow parameter distributions using ground-penetrating radar and hydrological measurements during transient flow in the vadose zone, *Adv. in Water Res.*, 27(6), 583-599, 2004.

Kowalsky, M.B., S. Finsterle, J. Peterson, S. Hubbard, Y. Rubin, E. Majer, A. Ward, and G. Gee, Estimation of field-scale soil hydraulic and dielectric parameters through joint inversion of GPR and hydrological data, *Water Resour. Res.*, 41, W11425, doi:10.1029/2005WR004237, 2005.

Kowalsky, M. B., S.A. Finsterle, K.H. Williams, C.J. Murray, M. Commer, D. Newcomer, A. Englert, C.I. Steefel, and S.S. Hubbard, On parameterization of the inverse problem for

estimating aquifer properties using tracer data, *Water Resour. Res.*, 48, W06535, doi:10.1029/2011WR011203, 2012.

Newman, G.A., and D.L. Alumbaugh, 3-D massively parallel electromagnetic inversion - Part I. Theory, *Geophysical Journal International*, 128, 345-354, 1997.

Tuminaro, R.S., M. Heroux, S.A. Hutchinson, and J.N. Shadid, Official Aztec user's guide - version 2.1, Massively Parallel Computing Research Laboratory, Sandia National Laboratories, Albuquerque, NM, 1999.

Williams, K.H., P.E. Long, J.A. Davis, C.I. Steefel, M.J. Wilkins, A.L. N'Guessan, L. Yang, D. Newcomer, F.A. Spane, L.J. Kerkhof, L. McGuinness, R. Dayvault, and D.R. Lovely, Acetate availability and its influence on sustainable bioremediation of uranium-contaminated groundwater. *Geomicro. J.*, 28(5-6),519-539, 2011.

Zhang, K., Y.-S. Wu, and K. Pruess, *User's Guide for TOUGH-MP – A Massively Parallel Version of the TOUGH2 Code*, Report LBNL-315E, Lawrence Berkeley National Laboratory, Berkeley, Calif., May 2008.

INNOVATIVE TOOLS FOR CONTINUUM DISCRETIZATION, BETTER MANAGEMENT OF TOUGH2 INPUT DATA AND ANALYSIS OF THE NUMERICAL SIMULATION RESULTS

Cormio C., Berry P., Bonduà S., Bortolotti V.

Department of Civil, Environmental and Materials Engineering, University of Bologna
Via Terracini, 28
40131, Bologna, Italy
e-mail: carlo.cormio3@unibo.it, paolo.berry@unibo.it, stefano.bondua@unibo.it, villiam.bortolotti@unibo.it

ABSTRACT

The natural state model and full-field exploitation simulation of geothermal reservoirs usually requires grids with an enormous number of gridblocks, in order to obtain local refinement and to investigate wider domains. This means greater computational and operational costs, in particular when using unstructured (Voronoi) grids to enhance spatial discretization. As well known, TOUGH2 does not have a native pre-processing module for unstructured grid generation and input data management—neither a post-processor nor a graphical visualization tool for output data analysis.

In order to provide effective support to the simulation of high enthalpy geothermal reservoirs, we have developed a pre-processor based upon Geographical Information Systems (GIS) called TOUGH2GIS, as well as a 3D visualization software tool called TOUGH2Viewer. TOUGH2GIS lets the user create locally refined unstructured grids, automatically assign rock types to gridblocks, and create a suitable TOUGH2 MESH file. TOUGH2Viewer enables the display of 3D grid and simulation output, a 3D flow vector of mass and heat, isosurfaces, contour maps, and scatter plots of the simulated thermodynamic variables, providing a simple and intuitive graphical interface. We have tested these two programs, which significantly reduce the time required in pre- and post-processing activities, and reduce user errors, by conducting a history-matching simulation of high enthalpy geothermal reservoirs in Tuscany (Italy).

INTRODUCTION

Attempts at numerically representing geothermal reservoirs in their entirety (full field simulation), unavoidably create huge amounts of data (due to the size of the investigated domain, usually hundreds of square kilometers and a few kilometers in depth). Typically, tens to hundreds of thousands of elementary volume elements can be required, and several thermodynamic variables and petrophysical properties have to be managed for each element and each flow interface. Discretizing the reservoir with a large number of small elements greatly improves the accuracy of the simulation outcomes, but computational time and user errors invariably grow, due to the increase in data volume.

It should also be recognized that any numerical model is a simplified, dynamic representation of the physical system that grows as the reservoir is exploited. In other words, as soon as new data are available for the system being investigated, these should be included in the model.

Spatial discretization

As already mentioned, it is quite obvious that the finer the discretization of the investigated domain, the smaller the approximation error introduced in the transition from the conceptual model to the numerical model. On the other hand, discretization improvement substantially increases the calculation time, also depending on the number of the mathematical model equations to be solved.
The compromise between accuracy and acceptable overall simulation task time usually takes the form of constructing smaller grid elements only in the areas of interest (or where measured values are available) and greater

where there are, for instance, small gradients, and there is no interest to investigate.

Local refinement within structured (telescopic, Townley and Wilson, 1980) grids is quite easy to create and manage (Figure 1) but generates many blocks that are not useful for the aims of the investigation, thus creating an undesirable increase in computational and data management time. In response to this problem, the Integral Finite Differences Method (IFDM, Narasimhan and Witherspoon, 1976) was developed, enabling the modeler to use unstructured grids with local refinement. However, this tool requires that the line joining the nodes of two adjacent blocks of the grid is orthogonal to the interface between blocks.

Creating an efficient spatial discretization can be achieved through Voronoi tessellation (Aurenhammer, 1991), which also satisfies the geometric conditions required by the IFDM and allows the user to generate locally refined grids with irregular polygons (Figure 2). Once the grid has been created, another operation to be performed, which may be a source of errors and time consuming, is properties assignation to gridblocks according to the conceptual model. Making use of maps representing, for instance, the horizons between different hydrogeological layers, the modeler can associate the proper rock type to each node of the grid.

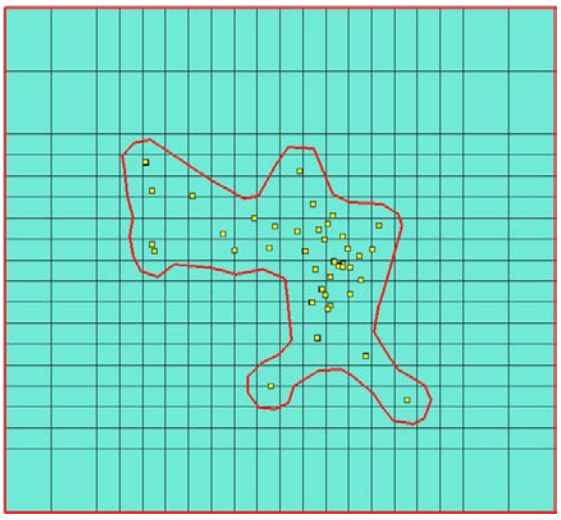

Figure 1. Structured grid with local (telescopic) refinement including an area of inter-est around geothermal wells (yellow boxes within the red boundary line).

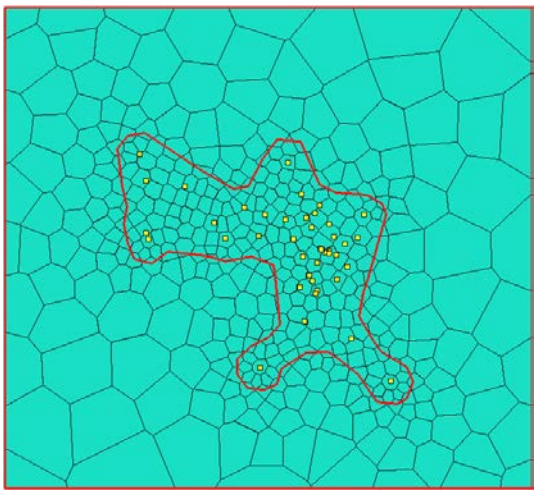

Figure 2. Unstructured grid with local refinement applied within an area of interest (red boundary line) around geothermal wells (yellow boxes).

TOUGH2 pre and post-processing

TOUGH2 does not have a native Graphical User Interface (GUI) tool to easily manage its input and output text files. This is a severe limitation, especially when creating and managing numerical models with locally refined unstructured spatial discretization—and when visualizing and analyzing the large amount of data contained in the output text file coming from a TOUGH2 simulation run. Several software programs have been developed for TOUGH2 input data pre-processing and output data post-processing and visualization, both by software houses and by scientific research groups. Most of them require the grid nodes to be provided as input, usually realized through a different software, but one of the major tasks in 3D numerical-model pre-processing is actually the automatic node generation of a locally refined, unstructured grid.

The need to improve the natural state model and exploitation simulation of high enthalpy geothermal reservoirs has led to the development of some dedicated software tools for TOUGH2 pre- and post-processing. They are: (i) TOUGH2GIS, a suite of BASH scripts that, by means of a GUI, allows a more effective and efficient creation and maintenance of 3D numerical models; (ii) TOUGH2Viewer (Bonduà et al, 2012), a home-made 3D viewer that allows a complete exploration of the

numerical model and simulation results. These new tools take into account the need to minimize operational errors and numerical model preparation time.

We have applied TOUGH2GIS and TOUGH2Viewer in modeling the large high-enthalpy geothermal fields of Tuscany, showing how these software programs significantly reduce pre- and post-processing time and user errors, in particular for full-field reservoir simulations.

TOUGH2GIS

Regardless of its source format, the information used in studying a geothermal reservoir is usually suitable to be used with a Geographical Information System (GIS), making possible a faster formulation of the conceptual model, based on the analysis and processing of a uniform dataset. Once the conceptual model is created, the numerical model can be quickly realized without further file format conversions, using raster and vector maps and database management GIS tools.

The passage from the 3D conceptual model to the corresponding 3D numerical model has been implemented in two main phases (Figure 3). The first phase produces a structured or unstructured 3D grid vertically refined but with default rock types assigned (same rock type for the nodes belonging to the same layer, not necessarily corresponding to hydrogeological rock-type distribution in the conceptual model). The second phase lets the user associate the proper material type to each gridblock using elevation raster maps (representing the bottom surface of each hydrogeological layer defined in the conceptual model).

GRASS GIS (Neteler and Mitasova, 2007) was adopted as the main development environment, in order to: (i) create a homogeneous geodatabase with all the available and required reservoir information; (ii) create exhaustive conceptual models; (iii) generate numerical models discretized through 3D locally refined structured or unstructured grids complying with the constraints imposed by the IFDM; (iii) automatically assign rock types to grid nodes.

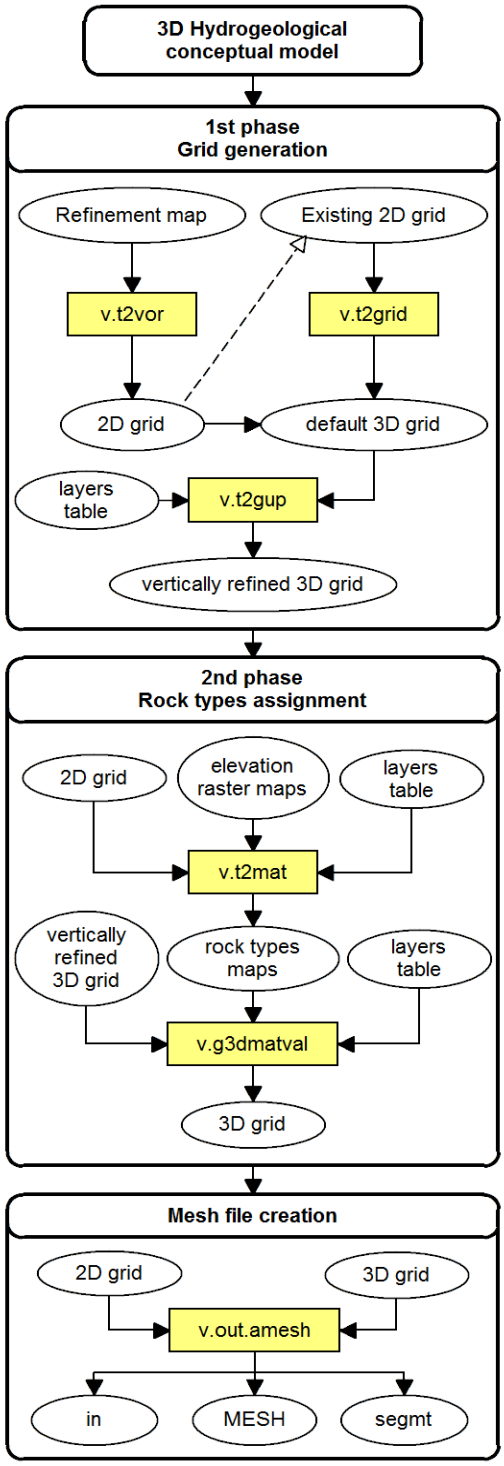

Figure 3. Procedure flow to realize the mesh file from the conceptual model with TOUGH2GIS.

Table 1. TOUGH2GIS tools overview

Tool name	Description
v.g3dmatval	Updates 3D grid attribute table with actual rock types
v.out.amesh	Creates a MESH file ready for TOUGH2
v.t2grid	Creates a "default" 3D grid from an existing 2D grid
v.t2gup	Turns the default 3D grid into a "vertically refined" grid
v.t2mat	Elaborates raster elevation maps over 2D grid producing "rock types raster maps"
v.t2vor	Creates a "default" unstructured 3D grid (all layers with the same thickness)

GRASS GIS, owing to the add-on module "v.trimesh" (Carrera-Hernandez, 2008) which implements the 2D Delaunay triangulation and mesh generator code "Triangle" (Shewchuk, 1996), is able to discretize the spatial domain generating locally refined, conforming Delaunay grids (Bern and Plassman, 2000). Through an appropriate BASH script specifically developed (v.t2vor) for this purpose, it is possible to obtain a 3D numerical model discretized with Voronoi tessellation, made up of a 3D point vector map linked to a set of database tables (specifically created to store model properties, such as geometrical information, boundary conditions, rock types assigned to grid nodes, etc.).

TOUGH2GIS pre-processing tools (Table 1 and Figure 3), enable the user to: (i) efficiently generate a locally refined unstructured 3D grid; (ii) efficiently generate a 3D grid from an existing 2D grid (structured or unstructured); (iii) automatically assign material types to each gridblock from elevation raster maps; (iv) generate a TOUGH2 MESH file; (v) export the grids generated in shapefile format; and (vi) import the simulation results and link them, through appropriate attribute tables, to the numerical model previously created, in order to be used for further model analysis and developments.

Unstructured 3D grid generation procedure

As a first step in the first phase, the user needs to produce a vector map (named "refinement map") which individuates domain boundary and refinement areas (Figure 4). This map can be realized in several ways in the GRASS GIS environment: importing a geo-referenced Computer-Aided Design (CAD) map, manually digitizing areas, automatically creating "buffers" at a given distance from points, lines, or areas of interest)—and each area has to be defined through a boundary and a centroid (a topological object which identifies the interior of the area). The same category value (an integer number that identifies, in the database table linked to the refinement map, the attribute to be associated to map objects) has to be assigned to the centroids of all refinement areas, and a different one to the not refined areas.

The spatial discretization (Figure 5) of the investigated domain is performed using v.t2vor and v.t2gup scripts to create a locally refined unstructured 2D grid and a 3D grid with vertical local refinement. This refinement is created through the parallel replication of 2D grid nodes along the z axis for such times as the number of layers defined in the vertical discretization. The 3D grid is then linked to an attribute table (automatically generated and populated with proper default values through the tools developed) containing all the information related to each gridblock, needed to produce the MESH file. The default data can be updated by the user with standard Structured Query Language (SQL) queries and GIS update tools.

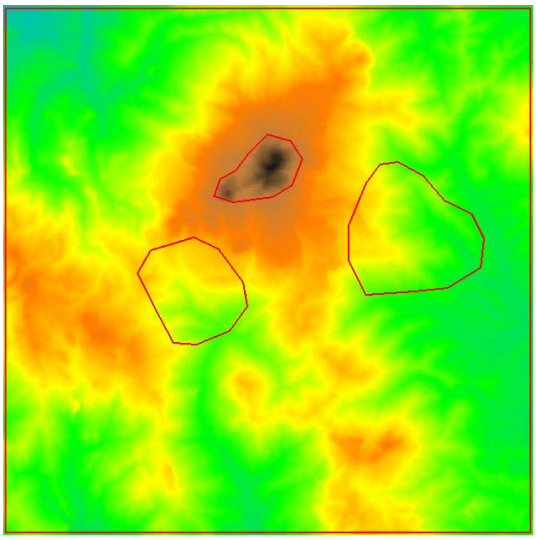

Figure 4. Refinement map overlapped to topography raster map. Red irregular boundary lines individuate refinement areas.

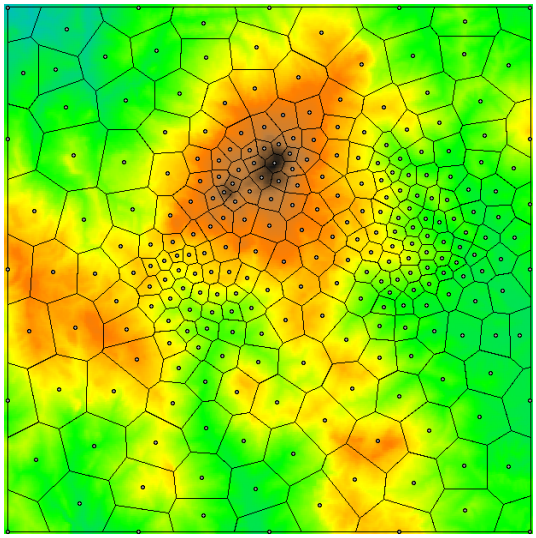

Figure 5. Locally refined unstructured 2D grid used to create the 3D grid.

Rock type assignment

The second phase involves the processing of elevation raster maps—for example, representing the horizons between rocks characterized by different permeability values—in order to automatically assign the appropriate rock material to each volume element of the 3D grid. Each elevation raster map used (topography, hydrogeological layer top/bottom surface, isothermal surface, etc.) is transformed by v.t2mat script into a "mean elevation values" raster map (m.e.v. map). The mean values are calculated within each 2D gridblock. These "graded" surfaces are then analyzed together by v.g3dmatval script, and for each vertical layer, the proper rock types are assigned, comparing node elevation value and m.e.v. maps. The result is a "rock type map" (Figure 6) which reproduces the original conceptual model discretization over the unstructured 3D grid.

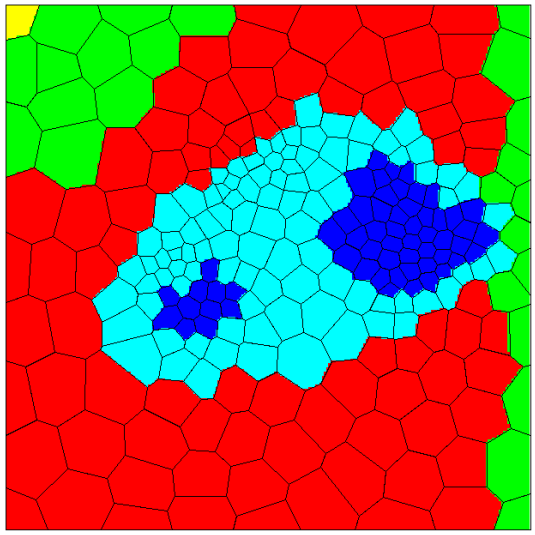

Figure 6. Example of rock types map referred to a specific grid layer. Each color identifies a different rock type.

MESH file creation

Once the attribute table linked to the 3D grid (our numerical model) has been updated with all the values required by the user (rock type, layer thickness, initial and boundary conditions, etc.), according to the conceptual model, the MESH file can be automatically generated, using the v.out.amesh script providing as input the 2D and 3D grid previously generated and updated.

TOUGH2VIEWER

This software can manage 3D locally refined structured grids, such as telescopic refinement grids, cylindrical grids, and unstructured (Voronoi complying) grids. At present, it fully manages output data files coming from the EOS EWASG (Battistelli et al., 1997) and EOS1 (Pruess et al., 1999) modules, and is easily adaptable for other EOS. It implements standard CAD commands such as zoom, rotation, and pan.

Software implementation

The software is written in Java and uses mainly Java3D libraries to display the 3D block model and Scientific Graphics Toolkit (SGT, Denbo, 1999) for contour maps visualization. GeoTools library (http://geotools.org) is used for vector maps reading (ESRI shapefile format), while JFreeChart (Gilbert, 2007) has been adopted for the construction of graphs like histograms and scatter plots and Visad (Hibbard, 1998) for isosurfaces rendering.

Input files

In order to visualize a simulated numerical model discretized with a structured grid, TOUGH2Viewer requires as input the MESH file and the simulation output file. To visualize an unstructured 3D grid, realized, for instance, with TOUGH2GIS, TOUGH2Viewer requires: (i) the "in" file, containing the x, y, z coordinates of the grid nodes, layers thickness and the rock types assigned to gridblocks; (ii) the "segmt" file, containing the coordinates of the segments constituting the boundary of the blocks base; (iii) the simulation output file. The MESH file can be read instead of the "in" file, but the "segmt" file has to be provided as input.

When using TOUGH2GIS, rock-types assignation is carried out using the elevation raster maps describing the horizons between different hydrogeological layers. TOUGH2Viewer allows the display of such surfaces as shape files together with the 3D grid, so as to increase the model visualization details and to enable the user to better check model suitability. A specific dialog box enables reading and importing shape files (which must contain polyline objects representing contour lines of a hydrogeological layer or thermophysical data, with elevation information).

Display features

3D Block Model view

The three-dimensional visualization takes place within a dialog box (Figure 7) made up of a frame window containing a visualization window object and a set of controls. The control elements are pull-down menus and slide bars that allow the user to: (i) select the type of variable to display (i.e., temperature, pressure, etc.); (ii) switch between the simulated time steps; (iii) switch to the visualization of the rock types associated to gridblocks; (iv) access the different visualization modalities. At the bottom of the visualization dialog box, all the information about the selected block (i.e. block name, x, y, z node coordinates, index, material type, displayed variable value) is given by means of the "Block selection" or "Quick Selection" functionalities. Note that it is also possible to produce plots of the variables along both Cartesian directions, usually z, and versus time.

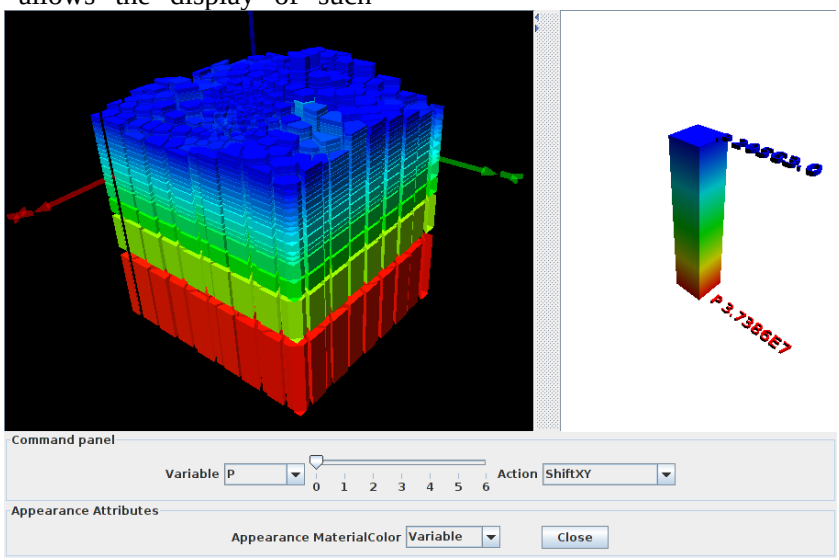

Figure 7. 3D Block model dialog box

3D Flow vector view

The “flow vector” visualization modality gives vector flows that are shown in two different ways—one in which the length of the shown vector is proportional to flow rate intensity, and one in which all vectors have unitary length, and the flow-rate intensity is represented in color scale. To increase readability, each grid node is represented by the vector resulting from the sum of all flows across the interfaces of the block.

Contour plot

This option allows the creation of 2D contour maps (vertical or horizontal sections for a given time step) of the selected variable, making an interpolation of data points. The user can interact with the interpolation process defining the resolution of the estimation grid, and the location and orientation of the sectioning plane (Figure 8). The variable analyzed is shown in false-color scale, and the style of representation can be customized. The user can also create the isolines of the selected variable, and overlap them on the contour map (see Figure 8). In order to work properly with the SGT library, which requires equally spaced data, we have implemented an interpolation processing of the original data, based on the IDW (Inverse Distance Weighting) method.

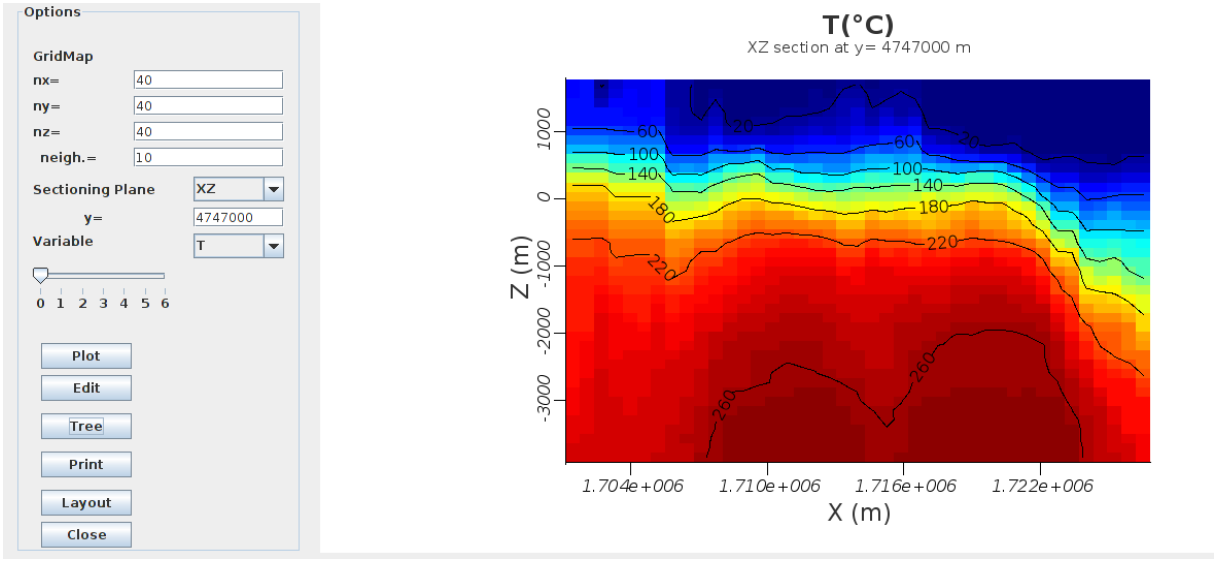

Figure 8. Pressure contour map.

3D isosurface

To better understand the behavior of thermophysical properties, is helpful a representation of a isosurface of the simulated variables (Figure 9). By means of two slide selector, it is possible to change the threshold value and the time step (the graph is updated in real time). This representation is obtained by Visad library (Hibbard, 1998), that requires equally spaced data, so it's been introduced an interpolation processing of the original data based on IDW method.

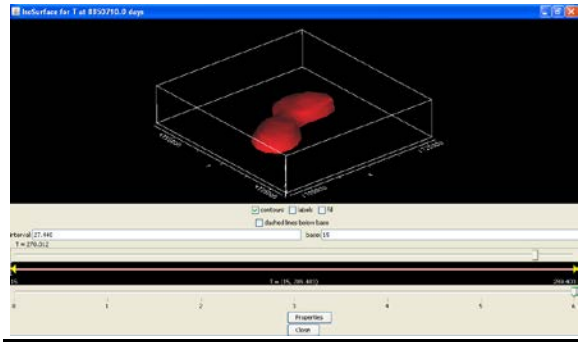

Figure 9. Example of isosurface representation.

CONCLUSIONS

The software tools described in this paper both represent improvements for the TOUGH user related to pre- and post-processing of TOUGH model simulations. The pre-processor TOUGH2GIS is a powerful tool by which the creation phase of numerical modeling for computer codes using the IFDM has been significantly improved. This improvement can be seen both in the simplification of complex 3D numerical model creation and management, and in the reduction of operational errors occurring during the handling of substantial amounts of data. Similarly, TOUGH2Viewer, with its easy-to-use GUI, provides the user with powerful tools by which to display and examine data in 3D graphic mode. It strongly reduces the tasks necessary to understand and interpret simulation outputs. The use of these two software programs greatly increases the efficiency of the overall simulation task.

REFERENCES

Aurenhammer, F., Voronoi diagrams—a survey of a fundamental geometric data structure, *ACM Computing Surveys*, New York, NY, USA, pp. 345-405, 1991.

Bern M., and Plassmann P, *Chapter 6 - Mesh Generation*, In: Sack, J.R., and Urrutia, J., Editor(s), "*Handbook of Computational Geometry*", North-Holland, Amsterdam, pp 291-332, 2000, ISBN 9780444825377, 10.1016/B978-044482537-7/50007-3.

(http://www.sciencedirect.com/science/article/pii/B9780444825377500073)

Bonduá, S., Berry, P., Bortolotti, V., and Cormio, C., TOUGH2Viewer: a post-processing tool for interactive 3D visualization of locally refined unstructured grids for TOUGH2, *Computers & Geosciences*, Available online 25 April 2012, ISSN 0098-3004, 10.1016/j.cageo.2012.04.008.
(http://www.sciencedirect.com/science/article/pii/S0098300412001318?v=s5)

Carrera-Hernandez, J., University of Alberta, Edmonton Canada (2008).

http://www.valledemexico.ambitiouslemon.com/vtrimesh.html.

Denbo, D.W, The Scientific Graphics Toolkit. In: Proceedings of *OCEANS '99 MTS/IEEE*. *Riding the Crest into the 21st Century*, Seattle, Washington, USA, September 13-16, Vol. 1, pp.470-473, 1999.

doi: 10.1109/OCEANS.1999.799789.

Geotools, 2010. Open Source Geospatial Foundation, www.geotools.org, [Accessed November 21,2011]

Gilbert, D., 2007. *The JFreeChart Class Library, Version 1.0.4, Developer Guide*. Object Refinery Limited, Harpenden, Hertfordshire, UK, 642pp.

Hibbard, W., VisAD: Connecting people to computations and people to people, Computer Graphics 32(3), 10-12, 1998.

Narasimhan, T.N. and P.A. Witherspoon, An Integrated Finite Difference Method for Analyzing Fluid Flow in Porous Media, *Water Resour. Res.*, Vol. 12, No. 1, pp. 57 – 64, 1976.

Neteler M., and Mitasova H. *Open Source GIS: A GRASS GIS Approach. Third edition*, Springer, New York, 2007.

Pruess, K., C. Oldenburg, and G. Moridis, *TOUGH2 User's Guide, Version 2.0*, Report LBNL-43134, Lawrence Berkeley National Laboratory, Berkeley, Calif., 1999.

Shewchuk J.R., Triangle: Engineering a 2D Quality Mesh Generator and Delaunay Triangulator, *Applied Computational Geometry towards Geometric Engineering*, Springer-Verlag, Berlin, 1996.

Townley, L.R., Wilson J.L., 1980. *Description of an user's manual for a finite element aquifer flow model*. Report 79-3, AQUIFEM-1: Ralph M. Partson Laboratory Technology Adaptation Program, Cambridge Massachusetts.

GEOPHYSICAL DATA IMPROVE STABILITY AND CONVERGENCE OF HYDROLOGICAL PROPERTY ESTIMATION: A SYNTHETIC CO_2 INJECTION STUDY

J. Doetsch, M.B. Kowalsky, S. Finsterle, C. Doughty, J.B. Ajo-Franklin, and T.M. Daley

Lawrence Berkeley National Laboratory
One Cyclotron Road
Berkeley, CA, 94720, USA
e-mail: jdoetsch@lbl.gov

ABSTRACT

Monitoring and modeling migration of injected CO_2 in the subsurface is critical for assessing the risk of leakage from geologic carbon sequestration sites, but it is also very challenging. Integrating complementary hydrological and geophysical monitoring data in a coupled hydrogeophysical inversion can help to address this challenge. We consider a synthetic CO_2 injection study to analyze the effect of adding cross-borehole electrical resistance and seismic data to inversions of pressure and gas-composition data. The geophysical data are found to significantly improve convergence and stability of the inversions. Parameterizing mean aquifer permeability and differences from this mean value are found to be superior to inverting for the permeability of each layer directly. These results will be the starting basis for analysis of the actual field data.

INTRODUCTION

Geologic sequestration of carbon dioxide (CO_2) is a promising approach for offsetting anthropogenic carbon emissions, and deep saline aquifers have been identified as potential target formations. Several pilot studies are currently under way to demonstrate the feasibility of long-term underground CO_2 storage, to assess risks associated with it, and to improve the overall understanding of CO_2 migration in the subsurface. A key component in these efforts is the integrated analysis of complementary hydrological and geophysical monitoring data. Whereas traditional hydrological measurements are useful for determining the properties immediately surrounding boreholes, geophysical cross-borehole measurements are sensitive to subsurface properties over larger regions, but can have lower spatial or temporal resolution and can be difficult to interpret quantitatively. We combine the advantages of hydrological and geophysical data sets in a fully coupled hydrogeophysical inversion, using iTOUGH2 (Finsterle, 2004).

The fully coupled hydrogeophysical inversion (Kowalsky et al., 2005) calibrates a hydrological flow and transport model simultaneously to the hydrological and geophysical data. Performing this model calibration and setting up an inverse problem involves many steps and decisions (Carrera et al., 2005), some of which are implicit and therefore easily overlooked. The main steps in developing a model can be described as follows (Finsterle and Kowalsky, 2011): (1) data selection, (2) development of a conceptual hydrological model, (3) parameter definition or parameterization, (4) choice of an objective function and optimization algorithm and (5) *a posteriori* assessment of the appropriateness of the choices in steps 1–4, and uncertainty analysis for estimated parameters and model predictions. Each of these points invites extended analysis.

Here, we concentrate on points (1) and (3), analyzing the effect and value of geophysical data for the inversion process and touching upon some aspects of model parameterization. We focus on an application involving the hydrogeophysical monitoring of CO_2 injection in a deep saline aquifer. We present a synthetic study and show some preliminary results after providing a brief overview of a field experiment and corresponding data that motivate the study.

DESCRIPTION OF THE EXPERIMENT

Field site and injection experiment

The synthetic study considered here is based on the general field layout, aquifer properties, and data availability from a large-scale injection experiment at the SECARB-Cranfield CO_2 injection pilot site (Hovorka et al., 2009). The experiment involved the injection of approximately 1 M tonne of CO_2 into a saline aquifer at a depth of ~3200 m. The injection interval is in a segment of the Lower Tuscaloosa Formation referred to as the Tuscaloosa D/E sand; this unit ranges from 15 to 25 m in thickness across the field and consists of relatively permeable fluvial sandstones and conglomerates. Injection began on December 1, 2009, at a rate of 3 kg/s, which was subsequently increased to 7 kg/s.

Borehole logs suggest that the Tuscaloosa unit is separated into two permeable layers of approximately 16 m (top) and 7.5 m (bottom) thickness, with the separating aquitard being laterally continuous. Based on measurements from sidewall cores, the permeability of the aquitard is about 50 times lower than that of the overlying and underlying aquifer layers.

As shown in Figure 1, the aquifer is accessed by three wells, one used as an injection well (F1) and two as monitoring wells (F2 and F3), allowing for the collection of hydrological and geophysical monitoring data. Data availability for our synthetic example is mostly based on that of the field experiment.

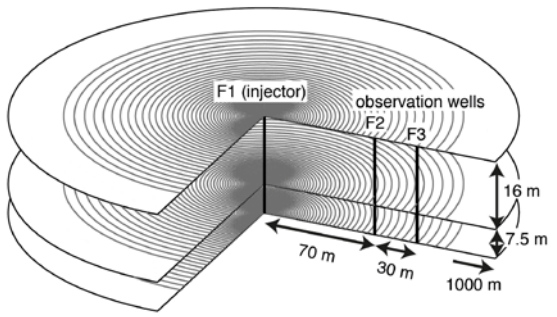

Figure 1. Schematic of the two-layer radial model used for the synthetic example. The model consists of two unconnected layers that are accessed by three wells.

Hydrological data

A variety of hydrological characterization and monitoring data were collected before and during the injection experiment (e.g., core and geophysical logging data, pressure fall-off tests). In this study, we focus mostly on (1) pressure in the injection well (F1), which was measured at a high temporal sampling rate, and (2) U-tube sampling data that provide information on the time-varying gas composition of the fluid in the monitoring wells, using on-site mass spectroscopy (Freifeld et al., 2011). The main gas-phase components that were present include CO_2, CH_4, and the injected tracers SF_6 and Kr.

Geophysical data

Cross-borehole seismic and electrical resistivity tomography (ERT) data were acquired between monitoring wells F2 and F3.

A continuous active-source seismic monitoring system (CASSM, Daley et al., 2011) was installed for the Cranfield experiment, but stopped operating before the start of the CO_2 injection. Therefore, seismic data were only acquired once before the start of the CO_2 injection and once after ~300 days of injection (Ajo-Franklin et al., 2012). For the purpose of this synthetic study, which is intended to examine our parameter estimation methodology, we assume that seismic data were acquired daily as intended.

The time-lapse ERT monitoring began before the CO_2 injection started and continued for ~300 days (Yang et al., 2012). Because directly including thousands of electrical resistance measurements in a coupled hydrological-geophysical inverse modeling procedure (see Kowalsky et al., 2005) is computationally very expensive, we begin by using a reduced form of the data that represents an average response of the aquifer to the CO_2 injection. We calculate an average value of electrical resistivity in the reservoir as a function of time, which can be obtained through traditional tomographic inversion of the ERT data. The output of this pre-processing step is then used as input in the inversion.

Specifically, the reduced form of the ERT data that we incorporate in the inversion procedure is

the average change in the reservoir electrical conductivity (EC) relative to the pre-injection value. We assume that the CO_2 and CH_4 gas phase and the host rock are infinitely resistive, and no gas phase exists at time zero. Under these assumptions, Archie's law (Archie, 1942) can be expressed as

$$EC(t) \big/ EC(0) = S_w^n ,$$

with the brine saturation S_w and Archie's saturation exponent n. Formulating the measurement as the change in electrical conductivity makes it unnecessary to know the electrical conductivity of the brine, the porosity, and the cementation exponent, otherwise required for applying Archie's law. Furthermore, the ERT processing and inversion techniques handling the changes in EC rather than the absolute value of EC are more reliable (e.g., Daily et al., 1992).

APPROACH

Coupled hydrological-geophysical model

The hydrological model used to simulate the CO_2 injection and the corresponding synthetic data consists of a two-layer radial model (Figure 1), with the layers unconnected from each other to represent the high permeability layers of the saline aquifer, as described above. The injection well and monitoring wells are connected to both layers to allow for injection to occur into both layers and for hydrological measurements, which represent an average response over both layers, to be simulated. Each layer consists of 99 cells in the radial direction with a maximum radius of 1000 m. The outermost cells in each layer are given a constant-pressure boundary condition.

Hydrological properties are modeled as homogeneous within each layer. However, to reproduce the double arrivals of CO_2 and CH_4 that are observed in the field data, it was necessary to use different values of absolute permeability for each layer (1.5×10^{-13} m^2 for the top, and 2.2×10^{-13} m^2 for the bottom). The simulations were performed using TOUGH2 EOS7C (Pruess et al., 1999; Oldenburg et al., 2004), and the resulting synthetic data appear consistent with the field data (see Figure 2). Note that our intention was to obtain synthetic data for examining a coupled hydrological-geophysical inverse modeling approach. Rather than aiming to develop a more complex and computationally intensive model that reproduces the field data exactly, for this study we chose to use a simplified representation of the system that reproduces the general characteristics observed in the field data.

In the coupled hydrological-geophysical model, the ERT data, that is, the change in average EC as defined above, is simulated daily as a function of the time-varying properties simulated in TOUGH2 for a given set of hydrological input parameters. The change in EC depends on the average gas saturation in the aquifer layers (as well as on Archie's parameter n, which we assume to be known and equal to 2) and, therefore, becomes a function of the hydrological input parameters (e.g., the permeability).

Similarly, seismic travel times are calculated in the hydrological-geophysical model and are a function of the time-varying CO_2 saturation, among other things (Daley et al., 2011). We simulate seismic data for 11 sources in F2 and 11 receivers in F3, yielding a full data set of 121 travel times at each time step. The number of sources and receivers is varied to look at the optimal setup (see below). The conversion from CO_2 saturation to seismic velocities uses the patchy saturation model described by Daley et al. (2011).

Gaussian noise was added to the synthetic hydrological and geophysical data, based on the error level observed in the field data. Table 1 gives an overview of the available data and the assumed errors. The actual field data are compared with the simulated data (with and without noise) in Figure 2. Observe the double arrival in the CO_2, CH_4, and tracer mass fractions; this feature is explained only by the two layers of differing permeability, which is consistent with the choice of the conceptual model used in this study (i.e., the radial model that assumes two unconnected layers).

The simulation time for a single forward run on a 2.7 GHz single core CPU machine is ~2 minutes, which enables relatively fast

inversions, even when testing many parameter sets.

Inverse modeling approach

We use the inverse modeling capabilities of iTOUGH2 (Finsterle, 2004) for evaluating the objective function for many parameter sets and studying the inversion performance for different combinations of the synthetic data set. Most analysis is based on inversions for the absolute permeability (or log permeability) of the two model layers.

Table 1. Overview of the available data and assumed measurement errors

Data type	*Time [days]*	*Interval [days]*	*Number of data*	*Error (std. dev.)*
F1 Press.	0 – 300	10	31	2.00E+04 Pa
F2 CO_2	11.5 – 30	0.25 / 0.5 / 1	46	0.04
F3 CO_2	14.5 – 30	0.25 / 0.5 / 1	18	0.04
F2 Tracer	11.5 – 30	0.25 / 0.5 / 1	46	2.00E-06
F3 Tracer	14.5 – 30	0.25 / 0.5 / 1	18	2.00E-06
ERT	0 – 300	1	300	0.01
Seismic	0 - 300	2 / 4 / 8 / 16	55	8.00E-06 ms

THE EFFECT OF PARAMETERIZATION CHOICES ON INVERSION STABILITY

The process of deciding which parameters to estimate and how to formulate the inverse problem is critical for successful inverse modeling. Inverting for too many parameters simultaneously (over-parameterization) can lead to a non-unique solution due to the strong correlation between model parameters and a lack of information independently related to each parameter, leading to large uncertainty in the parameter estimates. Over-parameterization can be caused either by attempting to estimate a property with too much geometrical detail (e.g., defining unknown permeability values in too many pixels or spatial regions) or by estimating too many different properties that are not related spatially (without sufficiently sensitive data to support their estimation). Over-parameterization due to high spatial resolution of parameters is regularly encountered in geophysical inversions and is partly overcome through regularization; smoothing and damping techniques stabilize the inversion and reduce ambiguity for large-parameter fields by preventing too much fine-scale detail (Constable et al., 1987). It is potentially more difficult to reduce non-uniqueness between parameters that are not geometrically related.

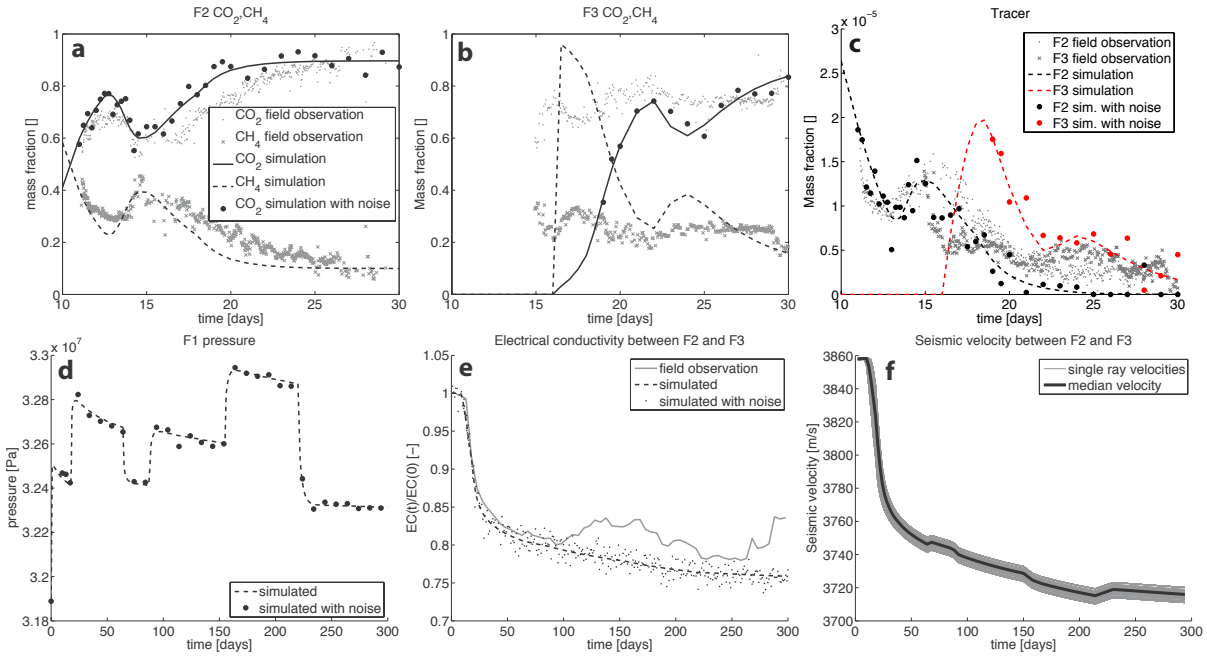

Figure 2. Overview of observed (gray), simulated (lines) and noisy simulated (black and red dots) hydrological and geophysical data. The noisy simulated data is used as input for the inversions.

For the 2-layer radial model example, properties are defined as homogeneous within each layer, but the permeability in each layer is unknown. An obvious choice for estimating the permeability values might be to invert for the permeability (or log permeability) of each layer directly. However, the parameters are highly correlated (>80%) in this example, meaning that changes in the permeability of either layer similarly affect the simulated data, making a unique determination of either parameter difficult. Figure 3a illustrates the objective function with respect to variation of the log permeability of each layer, highlighting the high correlation between the two parameters, the presence of a local minimum, and the poorly defined global minimum for this parameterization.

An alternative way to solve the same problem is to invert for the mean of the log permeability of the two layers, and also for the difference in log permeability between the two layers. This transformation corresponds to a rotation of 45º in parameter space, as is shown in Figure 3b. The transformation—although seemingly equivalent to the previous formulation—reduces the parameter correlation and stabilizes the inversion. The importance of proper parameterization, as shown in this simple two-parameter problem, is amplified when attempting a multi-parameter inversion. Finding independent parameters should be viewed as a priority when defining the parameterization for an inverse problem. It is similarly important to determine what types of data should be collected to maximize parameter independence.

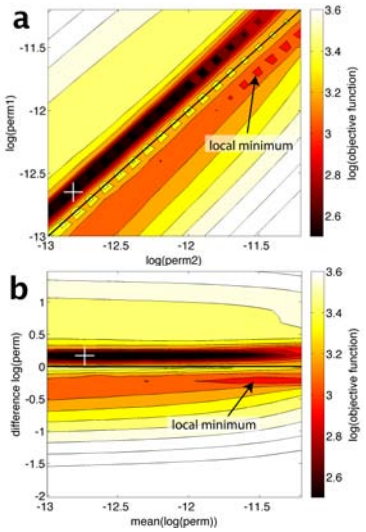

Figure 3. Contour plots of the objective as a function of (a) log permeability in the two layers, and (b) mean log permeability and difference in log permeability between the two layers. The minimum of the objective function is marked by a white '+'.

THE EFFECT OF DIFFERENT DATA TYPES ON INVERSION STABILITY

For successful inversion, the availability of data with sufficient informational content to estimate the parameters of interest is key. Parameters can only be resolved if the data are sensitive to them and, ideally, the correlations between parameters are low. Another factor influencing the performance of inverse modeling is the shape of the objective function. Clearly, the presence of local minima can make finding the global minimum difficult, especially when gradient-based optimization algorithms are used.

In general, large-scale measurements tend to create smoother objective functions, compared to point measurements. We examine how the inclusion of geophysical measurements in a hydrological-geophysical inversion affects the shape of the objective function and overall inversion performance.

Figure 4 shows the objective function for the different data sets as a function of the difference in log permeability between the two model layers. The objective functions for the CO_2 and tracer mass fractions contain local minima and will likely hinder an optimization from global convergence unless the initial guess is close to the global minimum. The objective functions for the geophysical data, on the other hand, gradually decrease towards a single minimum and thus may facilitate easier convergence.

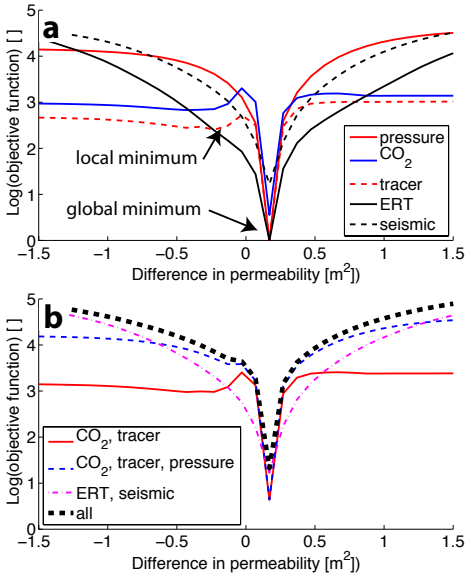

Figure 4. (a) Contributions of each data set to the objective function and (b) objective functions for subsets of the data and for the complete data set containing all hydrological and geophysical data.

When combining hydrological and geophysical data, the geophysical data stabilize the inversion, resulting in better convergence to the true solution. This effect is illustrated in Figure 5, which shows the convergence behavior for inversions performed using the same data subsets shown in Figure 4b with nine different sets of initial guesses for the parameters.

For the cases in which the geophysical data are included (Figure 5c and d), the convex shape of the objective function helps all inversions, each starting from a different initial guess, converge to the correct value. On the contrary, few of the inversions using hydrological data alone converge to the global minimum (Figure 5a and b). Note how the objective function for the combined data sets (Figure 5d) reflects the shape of the contributions from the pressure and geophysical data (Figure 5b and c, respectively), nicely illustrating the link between the choice of data included in a study and the resulting objective function character. It should also be noted that changing the weights and error assumptions of the data sets considered in this study could change the objective function shape and inversion performance.

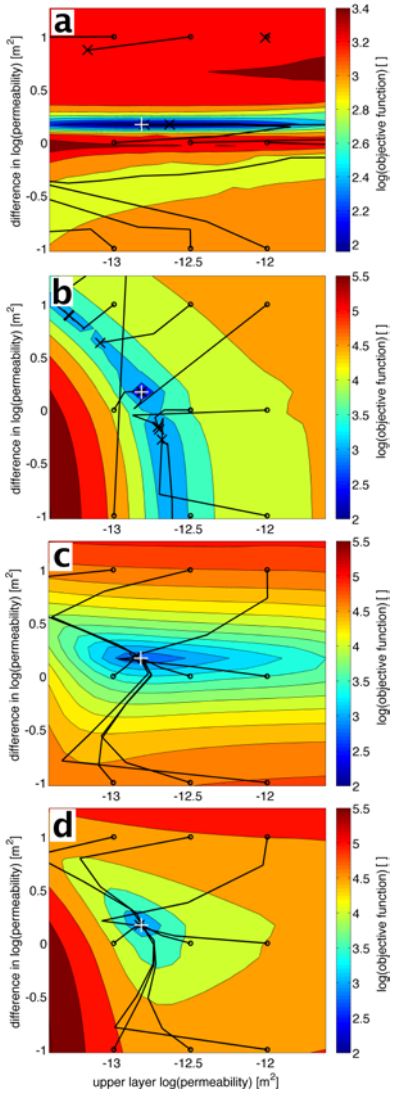

Figure 5. Contour plots of the objective function and example inversion paths (lines) for nine sets of initial values (black dots) using (a) CO_2 and tracer data, (b) CO_2, tracer and pressure data, (c) ERT and seismic data and (d) all available data. Each inversion results is marked with a black "x" and the true value with a white "+".

Due to the high cost and effort of obtaining geophysical data for such a field experiment, optimizing data collection is a worthwhile consideration. For example, the continuous seismic data collection using the CASSM system (Daley et al., 2011) is very promising, but the number of sources is restricted and should be minimized. Analysis of the objective function for the 121 source and receiver combinations shows that it is possible to constrain the global minimum with a single seismic source if the source position is carefully

chosen. Figure 6 shows the contributions of each ray to the objective function (gray lines), as well as two zero-offset (horizontal) rays through each layer. If the source position is chosen close to the layer boundary, the difference between the two layers can be resolved equally well as with the full data set.

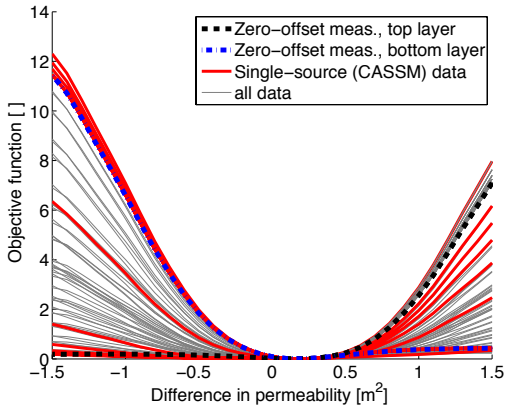

Figure 6. Objective function for different parts of the seismic data. Single-source data can define the global minimum if the source position is well chosen.

DISCUSSION

Parameterization and data selection are critical components for setting up a successful inversion, as they affect the shape of the objective function and the likelihood of obtaining accurate parameter estimates. In order to illustrate the objective function and show the inversion paths (Figures 4 and 5), the above analysis concentrates on two-parameter inversions. When inverting for more than two parameters, the objective function gets more complex and the inversion problem less unique. Choosing a good parameterization and including data with reasonable error assumptions and weighting thus becomes even more critical.

Even in the two-parameter inversion case, our analysis shows how important the geophysical data can be for a successful inversion: only when the ERT and seismic data are included can the inversion converge to the global minimum of the objective function, except when the initial values are very close to the true parameter values.

The results of the particular example discussed here may not be directly applicable to other problems, but certain characteristics are generally valid. For example, geophysical data usually have a larger support volume than measurements in wells, and their inclusion is expected to result in objective functions that are more favorable for inverse modeling.

The integration of geophysical and hydrological data in an inversion can be made difficult by uncertainty or spatial variation in the petrophysical relationships that are needed to translate geophysical parameters into hydrological properties and state variables. Uncertainties in the petrophysical models translate into uncertainties of the geophysical data, and nonlinearity of the petrophysical relationships adds further complications. However, in some cases uncertainty in petrophysical parameters can be accounted for by including their estimation in the inversion process (Kowalsky et al., 2005).

The number of petrophysical parameters and their uncertainty can also be reduced when inverting time-lapse data. For example, in our ERT formulation, dependence on porosity and the cementation exponent was removed, and only the relatively well-known saturation exponent needs to be determined.

CONCLUSIONS

In this study, we analyzed the effect of parameterization and geophysical data on the stability and convergence of coupled hydrogeophysical inversions. The analysis is based on a synthetic study that mimics a CO_2 injection experiment at Cranfield, MS.

We find that:

- Geophysical data (ERT and seismic) greatly stabilize the inversion and improve convergence.
- Parameterizing mean and difference of permeability in different layers rather than the permeability of each layer improves convergence.

- Time-lapse formulation (e.g., for ERT) can reduce the number of uncertain petrophysical parameters.

Although the analysis is specific to this case study, we believe these three points to be generally valid. The presented results will be the starting basis for analysis and inversion of the field data from the CO_2 pilot site at Cranfield, MS.

ACKNOWLEDGEMENTS

The authors would like to thank Susan Hovorka for her leadership and assistance (Texas Bureau of Economic Geology) and Xianjin Yang and Charles R. Carrigan (Lawrence Livermore National Laboratory) for their contributions. This work was supported by the National Risk Assessment Partnership (NRAP) of the US DOE under contract DE-AC02-05CH11231.

REFERENCES

Ajo-Franklin, J.B., J. Peterson, J. Doetsch, and T.M.Daley, High-resolution characterization of a CO_2 plume using crosswell seismic tomography: Cranfield, MS, *Int. J. Greenhouse Gas Control*, under review.

Archie, G. E., The electrical resistivity log as an aid in determining some reservoir characteristics, *Transactions of the American Institute of Mining, Metallurgical and Petroleum Engineers*, *146*, 54-62, 1942.

Carrera, J., A. Alcolea, A. Medina, J. Hidalgo, and L. J. Slooten, Inverse problem in hydrogeology, *Hydrogeology Journal*, *13*(1), 206-222, 2005.

Constable, S. C., R. L. Parker, and C. G. Constable, Occam's inversion: A practical algorithm for generating smooth models from electromagnetic sounding data, *Geophysics*, *52*(3), 289-300, 1987.

Daily, W., A. Ramirez, D. Labrecque, and J. Nitao, Electrical resistivity tomography of vadose water movement, *Water Resour. Res.*, *28*(5), 1429-1442, 1992.

Daley, T. M., J. B. Ajo-Franklin, and C. Doughty, Constraining the reservoir model of an injected CO_2 plume with crosswell CASSM at the Frio-II brine pilot, *Int. J. Greenh. Gas Control*, *5*(4), 1022-1030, 2011.

Finsterle, S., Multiphase Inverse Modeling: Review and iTOUGH2 applications, *Vadose Zone J.*, *3*(3), 747-762, 2004.

Finsterle, S., and M. B. Kowalsky, A truncated Levenberg–Marquardt algorithm for the calibration of highly parameterized nonlinear models, *Computers & Geosciences*, *37*(6), 731-738, 2011.

Freifeld, B., C. Doughty, P. Cook, K. Romanak, J. Lu, and C. Yang, Flow and Geochemical Sampling at SECARB's Phase-III Cranfield Site – Initial Results, *Ann. Conf. Carbon Capture, Utilization & Sequestration, Pittsburgh*, 2011.

Hovorka, S. D., T. A. Meckel, R. H. Treviño et al., *SECARB Phase III – Early Test, Cranfield, MS*, GCCC Digital Publication #09-04, Southern States Energy Board Stakeholders' Meeting, 2009.

Kowalsky, M. B., S. Finsterle, J. Peterson, S. Hubbard, Y. Rubin, E. Majer, A. Ward, and G. Gee, Estimation of field-scale soil hydraulic and dielectric parameters through joint inversion of GPR and hydrological data, *Water Resour. Res.*, *41*(11), W11425, 2005.

Oldenburg, C. M., G. J. Moridis, N. Spycher, and K. Pruess, *EOS7C Version 1.0: TOUGH2 Module for Carbon Dioxide or Nitrogen in Natural Gas (Methane) Reservoirs*, Report LBNL-56589, Lawrence Berkeley National Laboratory, Berkeley, Calif., 2004.

Pruess, K., C. Oldenburg, and G. Moridis, *TOUGH2 User's Guide, Version 2.0*, Report LBNL-43134, Lawrence Berkeley National Laboratory, Berkeley, Calif., 1999.

Yang, X., C. Carrigan, and B. Labrecque, ERT monitoring at the Cranfield CO_2 injection site, *Geophysics*, under review.

WHAT'S NEW IN iTOUGH2?

Stefan Finsterle

Lawrence Berkeley National Laboratory
Earth Sciences Division
One Cyclotron Road, MS-wherever
Berkeley, CA 94720
e-mail: SAFinsterle@lbl.gov

ABSTRACT

iTOUGH2 supports the TOUGH suite of nonisothermal multiphase flow simulators by providing capabilities for sensitivity analyses, automatic parameter estimation, and uncertainty quantification. iTOUGH2 is continuously updated in response to scientific challenges and user needs, with new capabilities added to both the forward simulator and the optimization framework. This article summarizes some of these new iTOUGH2 features.

INTRODUCTION

iTOUGH2 (Finsterle 2007abc) provides inverse modeling capabilities for the TOUGH suite of nonisothermal multiphase flow simulators (Pruess et al., 1999). By running TOUGH simulations multiple times for different input parameter sets, iTOUGH2 can be used for parameter estimation through automatic model calibration, for formalized sensitivity analyses, and for assessing the uncertainty of model predictions. iTOUGH2 updates are driven by scientific challenges and user needs, with new capabilities added to both the forward simulator and the optimization framework.

Recent advances related to the forward simulator include: overland flow and coupling to subsurface flow; semianalytical solution for radial heat exchange between wells and the formation; addition of gravitational potential to enthalpy; and additional time-stepping options.

Recent advances within the inversion framework include: a link from iTOUGH2's optimization and analysis routines to any simulation software that uses text files for input and output; inclusion of global sensitivity analysis methods; calculation of parameter identifiability; model reduction through automatic selection and estimation of superparameters; measuring the relative impact of omitting individual data points; evaluation of the Nash-Sutcliffe and Kling-Gupta efficiency criteria; assigning properties and sinks/sources to regions and estimation of their geometric parameters; reading spatial observation data; tying of parameters; and joint hydrogeophysical inversions.

CODE ENHANCEMENTS

The following subsections describe some of the features recently incorporated into iTOUGH2, starting with additions to the forward operator (i.e., TOUGH2), followed by enhancements of the inverse operator.

Enhancements of TOUGH2 Forward Model

iTOUGH2 is wrapped around standard TOUGH2 (Pruess et al., 1999), calling it to obtain select output evaluated for a given parameter set. However, many modifications to the TOUGH2 simulator have been made. Some of these features are motivated by the fact that—if used within the iTOUGH2 optimization framework—the simulation problem has to be solved in a single run, i.e., it cannot be interrupted, for example, to edit the mesh, or to change boundary conditions. This requirement has led to a number of useful features, such as the ability to connect steady-state and transient simulations; to change geometric mesh information after internal mesh generation; to change element volumes, primary variables, and certain material properties and flags at specified times; and to select additional convergence criteria.

Other enhancements were driven by specific user needs, such as the incorporation of non-Darcy flow based on the Forchheimer equation and choked flow in gas wells; internal genera-

tion of spatially correlated, random property fields using geostatistics (Finsterle and Kowalsky, 2007); time-dependent Dirichlet and free-drainage boundary conditions; more flexible formulations of the van Genuchten and Brooks-Corey relative permeability and capillary pressure functions; Leverett scaling of capillary strength parameter; inclusion of the active fracture concept of Liu et al. (1998); material-related sinks and sources; vapor-pressure reduction to prevent disappearance of the liquid phase; and five- to nine-character element names.

A third group of enhancements includes features that simply increase user convenience, such as the signal handler, which allows a user to request printout or to gently terminate a TOUGH2 run at any point during the simulation; free-format and tabular reading of GENER and TIMES blocks; improved time-stepping and printout control; and intermediate saving of restart files.

Most of these options are described in Finsterle (2007b; Appendix A) or in separate reports. They are useful even if iTOUGH2 is only used to perform forward simulations. The following paragraphs describe capabilities and features that were recently added to the simulator in iTOUGH2.

Coupled overland-subsurface flow

Coupling between overland flow and subsurface flow has been added to iTOUGH2. Overland flow is solved using the non-inertial, diffusion wave form of the Saint-Venant equations, where the momentum and continuity equations are given by:

$$S_{f,i} = -\nabla(z_l + h_s) \tag{1}$$

$$\frac{\partial h_s}{\partial t} + \nabla \cdot (h_s U) = q_s \tag{2}$$

Here, $S_{f,i}$ is the friction slope [-] in the direction i, z_l is land surface elevation [L], h_s is the water depth on the surface, U is the depth-averaged flow velocity [LT^{-1}], and q_s is a source/sink term [LT^{-1}]. The Manning-Strickler formula is used for relating velocity to friction slope:

$$U_i = \frac{h_s^{2/3}}{n_{man}} \sqrt{S_{f,i}} \tag{3}$$

with n_{man} being the Manning roughness coefficient [$L^{-1/3}T$]. The diffusion wave form of the Saint-Venant equation assumes slowly varying flow.

The approach developed by Weill et al. (2009) is followed to couple the surface and subsurface flow equations. A surface layer of thickness e is expected to be present at the top of the numerical model. For liquid flow within the surface layer, Eqs. (1)–(3) are combined into a form that is similar to that describing flow in a porous medium:

$$\frac{\partial h_s}{\partial t} - \nabla \cdot \left(K_s \nabla (z_l + h_s) \right) = q_s \tag{4}$$

Here, the nondiagonal terms of the hydraulic conductivity tensor K_s are zero, and the diagonal components are

$$K_{s,xx} = \frac{h_s^{5/3}}{n_{man} \sqrt{\nabla_x (z_l + h_s)}} \tag{5}$$

$$K_{s,yy} = \frac{h_s^{5/3}}{n_{man} \sqrt{\nabla_y (z_l + h_s)}} \tag{6}$$

$$K_{s,zz} = k_{zz} \frac{k_{rl}}{\mu_l} \tag{7}$$

The horizontal hydraulic conductivities describe surface water flow, while the vertical hydraulic conductivity describes resistance to liquid flow between the surface and subsurface layer, with k_{zz} equal to the vertical permeability of the subsurface layer. The liquid pressure in the surface layer is assumed hydrostatic. Because liquid and gas pressures are continuous across the surface/subsurface boundary, negative water depths occur when there is no runoff. The volumetric liquid content in the surface layer is defined as

$$\theta_l = \begin{cases} 0 & \text{for } h_s < 0 \\ h_s / e & \text{for } h_s \geq 0 \end{cases} \tag{8}$$

For vertical liquid flow, the relative permeability is set to one, unless $h_s/e < 10^{-5}$, at which point it is set to zero. To capture the head due to ponding in the surface layer, a positive capillary pressure is calculated as a function of h_s.

For gas flow within the surface layer and between the surface and subsurface layers, the regular subsurface flow equations are used. If

runoff occurs in the surface layer, i.e., $\theta_l > 0$, then $k_{rg} = 0$ for pressure gradients from the surface to the subsurface layers such that no gas flows into the subsurface (though it is possible for pressurized gas to escape the subsurface and flow to the surface layer), and $k_{rg} = 1$ within the surface layer such that gas flows freely into the atmosphere. If there is no runoff, $\theta_l = 0$, $k_{rg} = 1$ and the intrinsic permeability of the surface layer is assumed isotropic and equal to the vertical intrinsic permeability of the subsurface layer.

Surface water flow is solved simultaneously and fully coupled with subsurface flow using the standard TOUGH2 implicit scheme. Note that time-step size may be governed by the relatively fast flow occurring in the surface-water layer.

The implementation of each component of the coupled surface-subsurface flow model has been tested, and the new capability has been applied for the design of a rapid infiltration basin system, where the interaction of overland flow of treated wastewater and its infiltration into the unsaturated soil impacts groundwater mounding, as well as the conditions determining denitrification rates (Akhavan et al., 2012)

Semi-analytical radial heat exchange

In applications of oil, gas, and geothermal energy production, as well as geological CO_2 storage, injection and production wells serve as a conduit between the ground surface and the subsurface reservoir. The great length of these wellbores results in a very large heat exchange area between the well and the formation. If such a well is used to inject CO_2 for geological carbon sequestration, the heat transfer between the well and the surrounding formation will have a significant effect on the properties of the CO_2 as it flows down the well, and thus on the downhole conditions, potentially affecting injectivity and thereby overall storage efficiency. Similarly, the performance of an injection-production cycle in an engineered geothermal system depends on the temperature and thus phase state, density, and viscosity of the working fluid in the cool injection and hot production wells. An accurate simulation of heat-transfer processes between the formation and fluids in these wells is thus essential for performance evaluation and design of injection and production systems.

The processes to be considered in the low-permeability caprock above the target reservoir mainly include nonisothermal, multiphase fluid flow within the wellbore and conductive heat exchange between the wellbore and the geologic formation. The processes within the well can be modeled using Darcy's law with an effective permeability, or a numerical wellbore simulator, such T2Well, which uses a drift-flux model (Pan et al., 2011). However, numerical modeling of the conductive heat exchange between the cased well and the formation would be computationally costly if the region around the well affected by this heat transfer were fully discretized, especially when the target formation is very deep. Because the only process involved in this transfer is heat conduction (e.g., no fluid exchange), a viable alternative is to solve the heat conduction problem between the wellbore and formation analytically. Avoiding numerical discretization of the formation above the reservoir significantly reduces computational cost.

A semi-analytical solution using a time-convolution approach was implemented into iTOUGH2 for efficiently calculating radial conductive heat exchange between a wellbore and the surrounding formation. The details of the approach can be found in Zhang et al. (2011). The model allows for a nonconstant initial temperature profile, and heterogeneity in thermal properties along the well. The model was used to examine how radial heat exchange affects CO_2 injection into a deplete gas reservoir. The comparison included four conceptual models: (1) the numerical solution of a fully discretized model; (2) the new semi-analytical approach; (3) the analytical solution of Ramey (1962); and (4) the response of a system in which the heat transfer between the wellbore and the formation is ignored.

Figure 1 shows the simulated temperature evolution at the bottom of the wellbore for the four scenarios. Upon initial injection, the bottomhole temperature decreases sharply as the cooler CO_2 arrives at depth. However, after this initial drop, as the pressure in the well increases during this constant-rate injection period, injection temperature also increases due to the large Joule-Thomson coefficient of CO_2, which is dominant so that the temperature in the well

follows the injection rate change. During high-rate periods, conductive heat exchange with the formation is negligible compared to the convective heat transport and Joule-Thomson effects; as a result, the details of the heat-exchange model are irrelevant, and all solutions coincide. However, when the injection rate is low, Joule-Thomson cooling due to decompression of the fluid and the reduced advective downflow of relatively cool CO_2 are insufficient to counter the heating of the wellbore by conduction from the formation. During these transient periods, the choice of the heat-exchange model is significant, with the numerical and proposed semi-analytical solutions yielding consistent results. Ramey's solution, which makes a steady-state heat flow assumption in the wellbore, does not properly react to these changes in wellbore conditions, and overestimates the heat uptake from the formation. Conversely, neglecting any heat exchange between the well and the formation results in a drastic underestimation of injection temperatures, since no warming of the CO_2 occurs as it flows down the well at a relatively slow velocity.

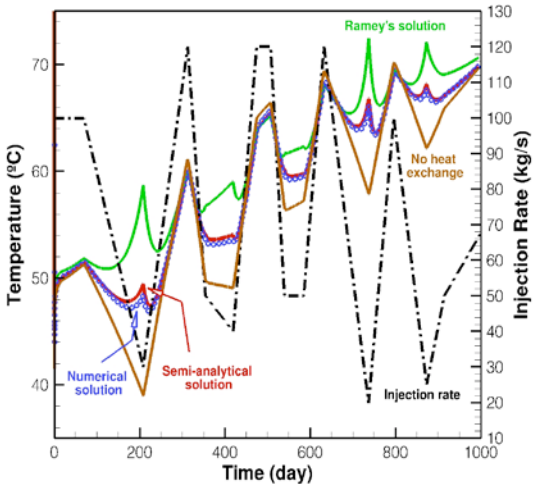

Figure 1. Injection rate and temperature change at the well obtained with four heat-exchange modeling approaches.

This example demonstrates the sensitivity of predicted wellbore and formation temperatures to the choice of the heat-exchange model. Accounting for heat exchange and coupled thermal-hydraulic processes is especially significant for fluids whose properties vary considerably as a function of pressure and temperature, such as CO_2. The comparison between the developed solution and fully discretized numerical solution shows that the proposed semi-analytical solution is a good approximation.

For long vertical wells, the gravitational potential needs to be added to the energy-balance equation (Stauffer et al., 2003). This effect, which is similar in magnitude to the temperature changes caused by the negative Joule-Thomson coefficient of water, is added in iTOUGH2 to avoid an overprediction of the temperature and heat content of the produced fluid.

Regions

Sinks and sources, as well as permeabilities, can be assigned to regions (boxes, ellipsoids, cylinders) that are defined by a few geometrical parameters. These geometrical parameters can be adjusted by iTOUGH2, allowing the user to, for example, examine the impact of the location of a fault, or to estimate the location and extent of a heat upflow zone in a geothermal system.

Enhancements of iTOUGH2 Optimization Framework

The following subsections summarize some of the features added to the iTOUGH2 optimization framework.

Link to external models with PEST protocol

While the original iTOUGH2 code is tightly linked to the TOUGH2 simulator, its optimization routines are general enough to also be applicable to other forward models. The concept of separating the forward model and inversion framework has long been followed by general, model-independent, nonlinear parameter estimation packages, specifically Doherty (2008). The PEST protocol (Banta et al., 2008) defines the interface between the analysis tool and the input and output files of the application software. To make iTOUGH2 capabilities accessible to more application models, the subroutines comprising the PEST protocol have been implemented into iTOUGH2 (Finsterle, 2010).

PEST protocol requires the application model (1) to provide input through one or more ASCII input files (or the keyboard), (2) to return output to one or more ASCII output files (or the screen), (3) to run the model or multiple models using a system command (an executable or

script/batch file), and (4) to run the models to completion without user intervention. For each forward run invoked by iTOUGH2, selected parameters in the application model input files are overwritten with values updated by iTOUGH2, and selected variables in the output files are extracted and returned to iTOUGH2. iTOUGH2's core, its optimization routines and related analysis tools, remains unchanged; only the communication format between input parameters, the application model, and output variables are borrowed from PEST.

The inclusion of the PEST protocol into the iTOUGH2 architecture is shown in Figure 2. The parameter vector **p** (which is updated by iTOUGH2's minimization algorithm or by the sampling procedure used for uncertainty quantification) is transferred to the PEST protocol, which replaces generic parameter names in the so-called template file with the appropriate numerical values, and generates a valid input file. The external model is executed using a system call, which may be the name of an executable code, a command line, or a script file. After completion of the model run, the resulting output files are parsed using directives from the PEST instruction file, and the values of interest are extracted and filled into the observation vector **z**, which is then used by iTOUGH2 to evaluate the objective function or for further analysis.

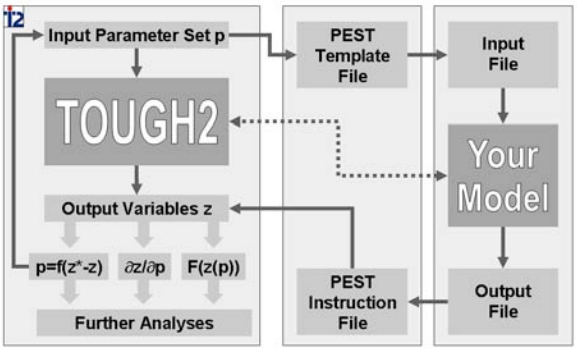

Figure 2. iTOUGH2 optimization and analysis tools evaluate the system response **z** as a function of adjustable input parameters **p**, where the relation between **z** and **p** is either given by the fully integrated TOUGH2 simulator or by an external model through the PEST protocol, which uses text-based template and instruction files for communication with the external model.

The extended code allows the user to invoke optimization of TOUGH2 models, which are fully integrated within iTOUGH2, or any external models, which are loosely linked by the PEST protocol, or a combination thereof. The latter is especially powerful, since it allows the user to include TOUGH2 pre- or postprocessors within the iTOUGH2 optimization framework.

Illustrative applications of the PEST protocol as part of iTOUGH2 are discussed in Finsterle and Zhang (2011) and Wellmann et al. (2012). In particular, this new capability allows users to perform inverse analyses of TOUGH-related models that are not integrated into iTOUGH2, such as TOUGHREACT (Xu et al., 2012), TOUGH2-MP (Zhang et al., 2008), and TOUGH+Hydrate (Moridis et al., 2008).

Global sensitivity analysis

The derivative-based minimization algorithms implemented in iTOUGH2 require the calculation of a Jacobian matrix, whose elements are the partial derivatives of each observable variable z_i with respect to each parameter p_j. This Jacobian matrix provides information for a local sensitivity analysis, supported by iTOUGH2.

Such a sensitivity analysis is local in the sense that it is valid for a specific point in the parameter space. If the model is nonlinear, however, sensitivity coefficients are different for each parameter combination. Global sensitivity-analysis methods address this issue by examining many combinations within the range of acceptable parameter values. Two global sensitivity-analysis methods have been implemented into iTOUGH2. In the Morris one-at-a-time (MOAT) elementary-effects method (Morris, 1991), each axis of the parameter hypercube is subdivided into k-1 intervals for a total of k^n grid points, where n is the number of parameters. A perturbation Δ is then calculated for each parameter i:

$$\Delta_i = \frac{k}{2(k-1)} \cdot (p_{i,\max} - p_{i,\min}) \qquad (9)$$

Next, a random grid point in the parameter space is selected, the model is run, and the performance measure z is evaluated. Then—one at a time and in random order—each parameter p_i is perturbed by Δ_i, the model is run to recalculate z, and the corresponding impact (or

elementary effect, EE_i) on the output is computed as

$$EE_i = \frac{z(p_1,\ldots,p_i+\Delta_i,\ldots,p_n)-z(p_1,\ldots,p_n)}{\Delta_i} \quad (10)$$

The procedure is repeated for multiple, randomly selected starting points of a path in the parameter space that consists of n steps and n+1 simulation runs for the evaluation of the elementary effect in the vicinity of this point. After completion of a number of such paths, the mean and standard deviation of the absolute elementary effects is calculated. The mean assesses the overall influence of the respective parameter on the output; the standard deviation indicates whether the effects are linear and additive or nonlinear, or whether interactions among the parameters are involved. A second, variance-based method (Saltelli et al., 2008) is also implemented. However, it usually requires a large number of model evaluations and is thus less practical for computationally expensive models. Applications of iTOUGH2's global sensitivity-analysis methods are described in Wainwright et al. (2012).

Statistical analyses

iTOUGH2 performs a rather extensive residual and uncertainty analysis (Finsterle and Zhang, 2011), helping the user to decide whether the model is a likely representation of the real system, and to examine the reliability and usefulness of certain observations. This analysis has been expanded to include the Nash-Sutcliffe (NS) and Kling-Gupta (KG) efficiency criteria. The NS index can be interpreted as the relative ability of a model to predict the data, where NS = 0 indicates that the model is not a better predictor than simply obtaining the mean of the observed values. The KG index allows a breakdown of the misfit in contributions from correlation errors, variability, and bias. (See Gupta et al. (2009) for a detailed interpretation.) These indices are goodness-of-fit criteria that can be used for model comparison studies, or directly as objective functions to be minimized by iTOUGH2 (with the estimated error variance as the third, standard alternative). An application is described in Kowalsky et al. (2012a).

As part of the residual analysis, iTOUGH2 now also calculates the relative impact of omitting an individual observation. This measure is useful during the design stage of a project to evaluate "data worth," i.e., the potential benefit of taking a certain measurement for parameter estimation. The measure is calculated based on the D-optimality criterion. If omitting a certain data point from a synthetic inversion leads to a significant increase in the determinant of the covariance matrix of the estimated parameters, then this data point should be collected, because it contributes substantially to obtaining an accurate solution of the inverse problem. Note that the inverse problem needs to be solved only once to obtain the data-worth measure for all observations.

The sensitivity analysis is expanded to include a statistic for evaluating parameter identifiability. Introduced by Doherty and Hunt (2009), parameter identifiability indicates the degree to which a parameter lies within the calibration solution space, which is obtained by truncated singular value decomposition (SVD) of the weighted parameter sensitivity matrix. A similar concept is used to define so-called superparameters (Tonkin and Doherty, 2009), which allow parameter estimation in a subspace of the original parameter hypercube. This implementation is an extension of the approach described in Finsterle and Kowalsky (2011). Note that these approaches are based on linear theory, and additional testing is required to assess their usefulness for highly nonlinear TOUGH2 models.

Hydrogeophysics

The capabilities for jointly inverting hydrological and geophysical data for the estimation of hydrogeological, geophysical, and geostatistical parameters have been extended, as is described in Kowalsky et al. (2012b), Doetsch et al., (2012), and Commer et al. (2012).

Other user features

The following user features have been added to iTOUGH2:

(1) Parameters can be tied to a parent parameter, so that a single value is estimated and then assigned to all tied parameters (potentially with shifts and scaling factors applied). Parameters defined in an iTOUGH2 input file can also be made inactive.

(2) Observations with a relatively large support scale generally refer to lists of elements or connections. Region definitions (boxes, cylinders, and ellipsoids) can now be used to internally generate these lists. Moreover, the geometrical parameters of these regions can be updated or estimated, whereby the contribution of the output at a given location is weighted according to its distance from the center of the region, thus assuring a differentiable result (see Finsterle and Zhang (2011) for an example).

(3) iTOUGH2 mainly supports time-series data, i.e., measurements that are taken at a few points in space and many points in time. For geophysical applications, however, the reverse is often the case, i.e., data of high spatial resolution are taken at only a few points in time. The reading and processing of spatial data is now supported.

(4) iTOUGH2 now supports automatic selection of measurement times as calibration times, with the user having the flexibility to define additional points in time where the measured and calculated system response will be compared.

WHAT'S NEXT?

We will continue to update iTOUGH2 and add new features and analysis methods to both its forward model and inversion framework in response to user requests and to address scientific challenges. Emphasis will be placed on reduced-order modeling and subspace approaches (Pau et al., 2012) and hydrogeophysical applications. We will report on these enhancements in due time.

ACKNOWLEDGMENT

I would like to thank all the developers and users who contributed to the formulation, implementation, and testing of new iTOUGH2 features. This work was supported, in part, by the U.S. Department of Energy under Contract No. DE-AC02-05CH11231.

REFERENCES

Akhavan, M., P.T. Imhoff, S. Finsterle, and S. Andres, Application of a coupled overland flow-vadose zone model to rapid infiltration basin systems, *Vadose Zone J.*, *11*(2), doi:10.2136/vzj2011.0140, 2012.

Banta, E.R., M.C. Hill, E. Poeter, J.E. Doherty, and J. Babendreier, Building model analysis applications with the Joint Universal Parameter IdenTification and Evaluation of Reliability (JUPITER) API, *Computers and Geosciences*, *34*, 310–319, 2008.

Commer, M., M.B. Kowalsky, S. Finsterle, and G.A. Newman, Advances in hydrogeophysical joint inversion, TOUGH Symposium, Sept. 17–19, 2012.

Doetsch, J., M.B. Kowalsky, S. Finsterle, C. Doughty, J.B. Ajo-Franklin, and T.M. Daley, Geophysical data improve stability and convergence of hydrological property estimation: a synthetic CO_2 injection study, TOUGH Symposium, Sept. 17–19, 2012

Doherty, J., *PEST: Model-Independent Parameter Estimation*, Watermark Numerical Computing, Brisbane, Australia, 2008.

Doherty, J., and R.J. Hunt, Two statistics for evaluating parameter identifiability and error reduction, *J. Hydrol.*, *366*, 119–127, 2009.

Finsterle, S., *iTOUGH2 User's Guide,* Report LBNL-40040, Berkeley Lab, Berkeley, Calif., 2007a.

Finsterle, S., *iTOUGH2 Command Reference,* Report LBNL-40041, Berkeley Lab, Berkeley, Calif., 2007b.

Finsterle, S., *iTOUGH2 Sample Problems*, Report LBNL-40042, Berkeley Lab, Berkeley, Calif., 2007c.

Finsterle, S., *iTOUGH2 Universal Optimization Using the PEST Protocol — User's Guide*, Report LBNL-3698E, Berkeley Lab, Berkeley, Calif., July 2010.

Finsterle, S., and M.B. Kowalsky, *iTOUGH2-GSLIB User's Guide*, Report LBNL/PUB-3191, Berkeley Lab, Berkeley, Calif., June 2007.

Finsterle, S., and M.B. Kowalsky, A truncated Levenberg-Marquardt algorithm for the calibration of highly parameterized nonlinear models, *Computers and Geosciences*, *37*, 731–738, 2011.

Finsterle, S., and Y. Zhang, Error handling strategies in multiphase inverse modeling, *Computers and Geosciences*, *37*, 724–730, 2011.

Finsterle, S., and Y. Zhang, Solving iTOUGH2 simulation and optimization problems using the PEST protocol, *Env. Modelling and Software*, *26*, 2011.

Gupta, H. V., H. Kling, K. K. Yilmaz, and G. F. Martineza, Decomposition of the mean squared error and NSE performance criteria: Implications for improving hydrological modeling, *J. Hydrol.*, *377*, 80–91, 2009.

Kowalsky, M.B., S. Finsterle, K.H. Williams, C. Murray, M. Commer, D. Newcomer, A. Englert, C.I. Steefel, and S.S. Hubbard, On parameterization of the inverse problem for estimating aquifer properties using tracer data, *Water Resour. Res.*, 48, W06535, doi:10.1029/2011WR011203, 2012a.

Kowalsky, M.B., M. Commer, K.H. Williams, and S. Finsterle, On parameterizing heterogeneity and incorporating geophysical measurements in hydrogeophysical inverse modeling, TOUGH Symposium, Sept. 17–19, 2012b.

Liu, H.-H., C. Doughty, and G. S. Bodvarsson, An active fracture model for unsaturated flow and transport in fractured rocks, *Water Resour. Res.*, *34*(10), 2633–2646, 1998.

Moridis, G.J., M.B. Kowalsky, and K. Pruess, *TOUGH+HYDRATE v1.0 User's Manual: A Code for the Simulation of System Behavior in Hydrate-Bearing Geologic Media*, Report LBNL-149E, Berkeley Lab, Berkeley, Calif., 2008.

Morris, M.D., Factorial sampling plans for preliminary computational experiments. *Technometrics*, *33*(2), 161–174, 1991.

Pan, L., C.M. Oldenburg, K. Pruess, and Y.S. Wu, Transient CO_2 leakage and injection in wellbore-reservoir systems for geologic carbon sequestration. Greenhouse Gases, *Science and Technology*, *1*(4), 335–350, 2011.

Pau, G., Y. Zhang, and S. Finsterle, Reduced order models for subsurface flow in iTOUGH2, TOUGH Symposium, Sept. 17–19, 2012.

Pruess, K., C. Oldenburg, and G. Moridis, *TOUGH2 User's Guide, Version 2.0*, Report LBNL-43134, Berkeley Lab, Berkeley, Calif., 1999.

Ramey, H. J., Wellbore heat transmission, *J. Petrol. Tech. Trans.*, AIME, *225*, 427–435, 1962.

Saltelli, A., M. Ratto, T. Andres, F. Campolongo, J. Cariboni, D. Gatelli, M. Saisana, and S. Tarantola, *Global Sensitivity Analysis, the Primer,* 292 pp., John Wiley & Sons Ltd., West Sussex, England, 2008.

Stauffer, P.H., J.S. Stein, and B.J. Travis, *The Correct Form of the Energy Balance for Fully Coupled Thermodynamics in Liquid Water*, Report LA-UR-03-1555, Los Alamos National Laboratory, Los Alamos, New Mexico, 2003.

Tonkin, M., and J. Doherty, Calibration-constrained Monte Carlo analysis of highly parameterized models using subspace techniques, *Water Resour. Res.*, *45*, W00B10, doi:10.1029/2007WR006678, 2009.

Weill S., E. Mouche, and J. Patin, A generalized Richards equation for surface/subsurface flow modeling, *J. Hydrol., 366*, 9–20, 2009.

Wainwright, H., S. Finsterle, Y. Jung, and J. Birkholzer, iTOUGH2 global sensitivity analysis module: Applications to CO_2 storage systems, TOUGH Symposium, Sept. 17–19, 2012.

Wellmann, F., A. Croucher, and S. Finsterle, Adding geology to the equation: towards integrating structural geological data into inverse modeling with iTOUGH2. TOUGH Symposium, Sept. 17–19, 2012.

Xu, T., N. Spycher, E. Sonnenthal, L. Zheng, and K. Pruess, *TOUGHREACT User's Guide: A Simulation Program for Non-Isothermal Multiphase Reactive Geochemical Transport in Variably Saturated Geologic Media, Version 2.0*, Report LBNL-DRAFT, Berkeley Lab, Berkeley, Calif., 2012.

Zhang, K., Y.-S. Wu, and K. Pruess, *User's Guide for TOUGH2-MP — A Massively Parallel Version of the TOUGH2 Code*, Report LBNL-315E, Berkeley Lab, Berkeley, Calif., 2008.

Zhang, Y., L. Pan, K. Pruess, and S. Finsterle, A time-convolution approach for modeling heat exchange between a wellbore and surrounding formation, *Geothermics*, *40*(4), 251–266, 2011.

Lewis, R.W., Schrefler, B.A., *The finite element method in the static and dynamic deformation and consolidation of porous media*. Chichester, England: Wiley, ^{2}nd edition. 1998.

Merle, H.A., Kentie, C.J.P., Van Opstal, G.H.C., Schneider, G.M.G., 1976. The Bachaquero Study-a composite analysis of the behavior of a compaction drive/solution gas drive reservoir. *JPT*, 1107–1114.

Pruess, K., and T.N. Narasimhan, A practical method for modeling fluid and heat flow in fractured porous media, *Soc. Pet. Eng. J.*, 25(1), 14-26, 1985.

Pruess, K., C., Oldenburg, and G., Moridis, *TOUGH2 User's Guide, V2.0*, Lawrence Berkeley National Laboratory Report LBNL-43134, Berkeley, CA, 1999.

Rutqvist, J., Tsang, C.F., A study of caprock hydromechanical changes associated with CO_2-injection into a brine formation, *Environmental Geology*, 42, 296–305, 2002.

Settari, A., Walters, D.A., Advances in coupled geomechanical and reservoir modeling with applications to reservoir compaction, *SPE Journal*, 6(3), 334-342, 2001.

Warren, J.E., and P.J., Root, The behavior of naturally fractured reservoirs, *Soc. Pet. Eng. J.*, 245-255, 1963.

Wilson, R.K., Aifantis, E.C., On the theory of consolidation with double porosity, *Int. J. Engng. Sci.*, 20(9), 1009-1035, 1982.

Winterfeld, P.H., Wu, Y.S., Parallel simulation of CO_2 sequestration with rock deformation in saline aquifers, *Society of Petroleum Engineers*, *SPE 141514*, 2011.

Wu, Y. S., H. H. Liu, and G. S. Bodvarsson, A triple-continuum approach for modeling flow and transport processes in fractured rock, *Journal of Contaminant Hydrology*, 73, 145-179, 2004.

METHODOLOGY FOR ASSESSING SCALABILITY AND OPTIMIZING THE USAGE OF TOUGH2-MP ON A CLUSTER – APPLICATION CASE FOR A RADIOACTIVE WASTE REPOSITORY

Nicolas Hubschwerlen[1], Keni Zhang[2], Gerhard Mayer[1], Jean Roger[3], Bernard Vialay[3]

[1]AF-Consult Switzerland Ltd
Täfernstrasse 26, 5405 Baden, Switzerland
e-mail: nicolas.hubschwerlen@afconsult.com

[2]College of Water Sciences, Beijing Normal University
19 Xinjiekouwai St, Beijing, China

[3]Andra, Agence nationale pour la gestion des déchets radioactifs
Parc de la Croix Blanche, 92298 Châtenay-Malabry, France

ABSTRACT

Many numerical simulations are required to assess what impact heat and gas generated in the emplacement areas of a deep geological repository for radioactive waste may have over time on fluid pressure and saturation fields in the repository's drifts, shafts, and host rock. Ever-larger problems are being simulated, due to higher mesh resolutions and the consideration of larger scales (such as the full repository scale). To take advantage of cluster architecture, physical processes can now be simulated with the EOS5 module of the massively parallel multiphase flow and transport simulator TOUGH2-MP. However, the high demand in CPU time that such simulations require still makes optimal use of available computing resources a key issue.

Many TOUGH2-MP users may have little knowledge of, or experience in, how to efficiently set up, within their computational system, the parallel environment parameters of a TOUGH2-MP simulation. We have developed a new methodology whose purpose is to facilitate the efficient resource use of a cluster, by guiding the selection of the domain partitioning settings for the model and the distribution of the computation load among the nodes and cores.

This methodology involves a series of numerical test routines—such as parameter sensitivity analyses—which can be performed easily prior to the realization of production simulations.

The methodology is presented in this article using a simple case study based on the Couplex-Gaz 1b exercise, modeling the resaturation of a disposal cell for intermediate-level long-lived radioactive waste (ILW-LL), from its closure to the end of the gas production phase. The results demonstrate good scalability of TOUGH2-MP under certain conditions, as well as possible good practices for processor load distribution and the selection of the domain partitioning method. Parallel acceleration occurs with as little as (approximately) one thousand unknowns per partition, but optimal efficiency is achieved for larger partitions.

Finally, the methodology was validated successfully by applying it to a larger scale simulation case.

INTRODUCTION

The French National Agency for radioactive waste management (Andra) is currently investigating the feasibility of deep geological disposal of radioactive waste in an argillaceous formation (Andra, 2005). The long-term safety performance of this repository is strongly dependent on the impact that the heat and gas generated in the emplacement areas may have on the evolution of fluid pressure and saturation fields in repository drifts and shafts, as well as in the host rock itself.

In this context, many simulations of nonisothermal, multiphase fluid flow and multi-component transport in porous media are

performed using TOUGH2 and TOUGH2-MP (Pruess et al., 1999; Zhang et al., 2008). These simulations lead to very large computational demands that fully justify the use of the massively parallel TOUGH2-MP on a cluster. Trials on Andra's cluster Azurite showed that optimal use of TOUGH2-MP, which means achieving linear or even supralinear acceleration, is not that easy to predict using simple rules linking number of unknowns and number of parallel processes.

In this paper we present a methodology by which TOUGH2-MP on large clusters such as Azurite may be optimized. It was applied to two models of repository-relevant physical processes, material complexities and dimensions: first, the Couplex-Gaz 1b simulation model (Andra, 2006) and some derivate calculations; and second, a larger 3D model representing an entire ILW-LL emplacement cell.

METHODOLOGY

Performance objective and relevant parameters

In the current context of TOUGH2-MP usage, the objective is to perform many different calculations on a cluster where computational resources are shared and limited. Therefore, the chosen performance measure for optimal use is defined as efficiency in terms of the number of reference calculations performed per time and per utilized node[1]. This performance measure allows some very easy comparisons between different computation strategies, in particular regarding node load and distribution of multiple computations on nodes. Moreover, this measure is very simple to obtain, since it relies exclusively on the measured CPU times provided by standard outputs of TOUGH2-MP and parallel computation parameters.

In the present work, performance dependency on hardware specifics was not considered, since all testing computations were performed on Andra's Azurite cluster. This equipment consists of 128 cores grouped in 16 computation nodes (2 quad-core Intel Xeon 5365 processors, 3GHz, 32GB RAM), for a peak accessible performance of about 1.5 Tflops. Dependency on the type of simulation problem was not studied either; the work was limited to one category of TOUGH2-MP EOS5 application: gas generation.

The study focused on the setup of parallel computations in terms of domain decomposition and repartition of the parallel processes on the cluster. Domain decomposition within TOUGH2-MP is performed using one of the METIS partitioner domain decomposition algorithms (Karypsis and Kummar, 1998, 1999). With respect to the repartition of parallel processes, we studied the influence of the cluster's nodes' loads.

Building a test case

The methodology requires a testing problem that must be as representative as possible of the real simulation cases performed with TOUGH2-MP EOS5 for the phenomenological analysis of a radioactive waste repository. This includes the modeled scenario, the discretization, and the choice of the numerical parameters. The number of unknowns typically ranges from a few thousand to several hundred thousand, and computation times may reach up to several days.

The representativeness of a test problem is ensured by respecting the following conditions:

- The modeled physical processes and parameters must be similar to those of the targeted real case. Some numerical parameters, such as solver parameters whose influence are not studied, are also considered as invariants and chosen as representative of the targeted case's settings.
- The computation must be able to perform several tests in a reasonable time. However, using the CPU time measurements from the TOUGH2-MP outputs requires long enough computation times to make measurement bias negligible.
- The test model must be large enough to profit from the parallel acceleration, i.e., its size must be representative with respect to the targeted problem as well.

[1] For the sake of legibility, and due to the average duration of the considered test runs, it is expressed in "runs performed per 1000 seconds per node".

- To study the scalability, i.e., estimate how well parallel acceleration results of TOUGH2-MP can be scaled to larger problems and numbers of partitions, the number of unknowns must be easy to vary, and this variation must be as neutral as possible on the convergence. A proposed solution is to use a pseudo-2D model and extend it by stacking several layers of it (Hubschwerlen et al., 2012).

One solution for limiting CPU time, while keeping a model large enough for parallel acceleration, is to limit the simulated time to a critical phase of a full simulation. One such phase occurs when saturation and pressure vary most, with very strong capillary pressure variations and variable production kinetics.

Partitioning, job repartition and scalability testing

On the basis of a test model built according to the rules set above, it is possible to test the computing performance behavior of TOUGH2-MP. Tests are performed in two steps. First, the impact of the different partitioning algorithms is investigated. Second, tests concerning the optimal number of parallel processes and node load repartition are conducted.

METIS provides three partitioning algorithms: *Recursive*, *Kway* and *VKway* (Karypsis and Kummar, 1998). The TOUGH2-MP documentation suggests that the optimal METIS algorithm choice depends on the number of domain partitions (Zhang et al., 2008). Therefore, the performed test will consist of comparing, for the three available algorithms, the performance of a TOUGH2-MP calculation when varying the number of subdomains. Moreover, the model must be selected in order to have large-enough subdomains to benefit from parallel acceleration, even with the greatest number of nodes available. The (lower) threshold is estimated to be 1000 equations per parallel process (Hubschwerlen et al. 2012).

Once the optimal partitioning algorithm has been determined, some tests on the node load are performed, by varying the number of parallel processes being simultaneously run on one node of the cluster, from one to the maximal load per node allowed by the cluster resources manager. In the case of Azurite, this maximum was set to 8 processes per nodes, which coincides with the number of cores. This setup is, however, not a general rule.

Varying the node load is achieved under invariant partitioning and invariant node repartition to ensure comparability of the different tests. This is achieved by running calculations with *n* parallel processes, each on a different node of the cluster, and augmenting the node load by raising the number of computations being run simultaneously (Figure 1).

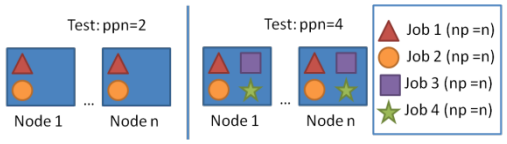

Figure 1. Scheme of node load variation test; *np*= nb. parallel processes per TOUGH2-MP run, *ppn* = nb. of processes per node.

A supplementary test to assess influence of node repartition is made by running simultaneously *n* times the same problem with the same decomposition (*n* subdomains and the same METIS algorithm), at constant node load, with all processes of one single run being dispatched alternatively on one to *n* nodes (Figure 2).

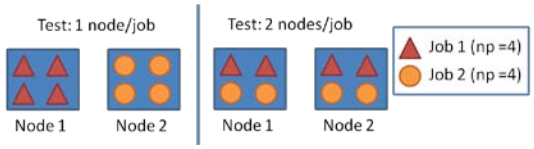

Figure 2. Scheme of node repartition test.

Finally, a scalability test is made by varying the number of unknowns of the test problem, to see if results obtained with a small test problem are representative for larger scale problems.

SCALABILITY TESTS BASED ON THE COUPLEX-GAZ 1B EXAMPLE

Preparation of the Couplex-Gaz 1b case for the tests

The methodology described above was applied on the Couplex-Gaz 1b case, which models the resaturation of a disposal cell for ILW-LL waste from its closure to the end of the gas production phase (Andra, 2006). The goal of the simulation

is to predict the position of the saturation front, the position of the dissolved-hydrogen front, the saturation variation in the different material zones of the repository, and the evolution of the gas and water pressure with time. TOUGH2-MP EOS5 is used with isothermal conditions (two equations per element).

The Couplex-Gaz 1b problem is an ideal candidate for applying the developed methodology, since highly heterogeneous materials and capillary properties make the problem very demanding in terms of computation needs. Moreover, the model layout has only 2480 elements on one layer, which makes it quite suitable as an elementary mesh for scalability testing (Figure 3).

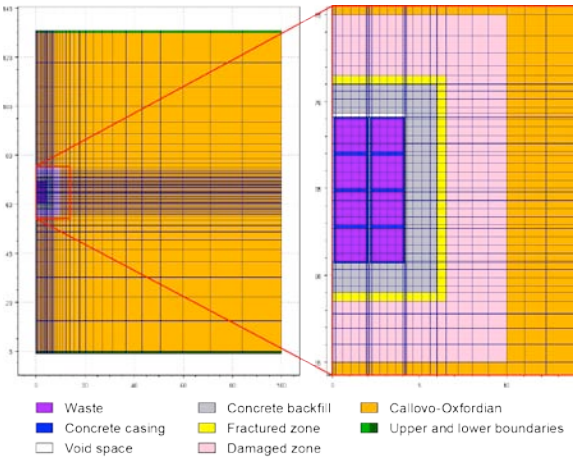

Figure 3. The 'elementary' Couplex-Gaz 1b model.

Preliminary tests (Hubschwerlen et al., 2012) showed a threshold for the parallel acceleration, in this case for as little as around 800 unknowns per parallel process. However, acceleration only became significant and approached linear rates above 2500 unknowns per parallel process. Therefore, and in order to make tests with the widest possible spectrum of parallel processes, the test model was extended to around 300 000 unknowns, which was a priori estimated as sufficient. Indeed, Azurite has 16 nodes with the possibility to run up to 8 processes per node, i.e. a maximum of 128 parallel processes. This was achieved by connecting 64 layers of the reference mesh layout, resulting in a 158,720-element mesh (Figure 4). Some other meshes with intermediate sizes were created for the scalability study upon the same method.

Even with the 2480-element reference mesh, the computation time over the entire simulation period of 50 000 years requires considerable CPU time. After observing the physical behavior of the model, we decided to work with a simulation period of 10 years starting at t=1000 years, corresponding to a critical period in which water pressure rises as hydrogen is produced, inducing nonlinear behavior. This reduction enabled CPU times reduced to a few minutes for the test simulations.

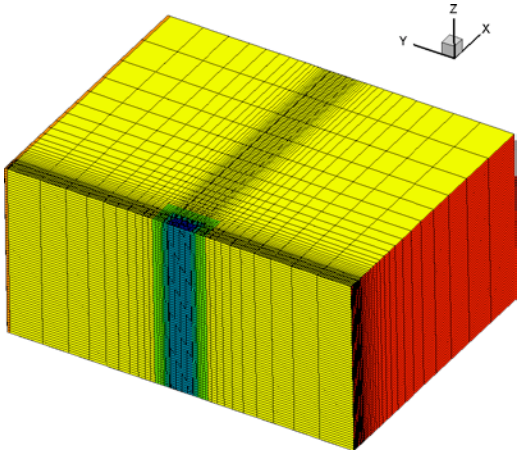

Figure 4. Couplex-Gaz 1b mesh replicated 64 times: 158 720 elements. Stacking is performed in the z dimension.

Couplex-Gaz 1b: Test of the partitioning algorithm

The test of the METIS algorithms was performed as described above. All 16 nodes of the Azurite cluster were used, and the number of tested partitions *np* was varied from 16 to 128. Results showed no clear trend in terms of computation efficiency (Figure 5). For example, for the number of partitions *np* = 96, the results were good, while for *np* = 80 and *np* = 112, they were poor (for all three algorithms). Reasons for this apparent randomness can be found in the total number of solver iterations performed for the different runs (Hubschwerlen et al., 2012) owing to the conditioning of systems resulting from the domain partitioning.

However, from observing cases with good solver convergence, we could see that the best efficiency for a relatively small number of partitions (*np* = 48) was reached by the METIS *Recursive* partitioning, whereas for larger partitions (*np* = 96, 112 and 128), the best efficiency was reached with *Kway*. This

confirmed the recommendations on the METIS algorithm selection found in Zhang et al. (2008). Moreover, *VKway* performed poorly overall. This algorithm minimizes communication between nodes best, but this does not seem to be a bottleneck for such relatively small partitions on the Azurite cluster, which is equipped with a good Infiniband connection.

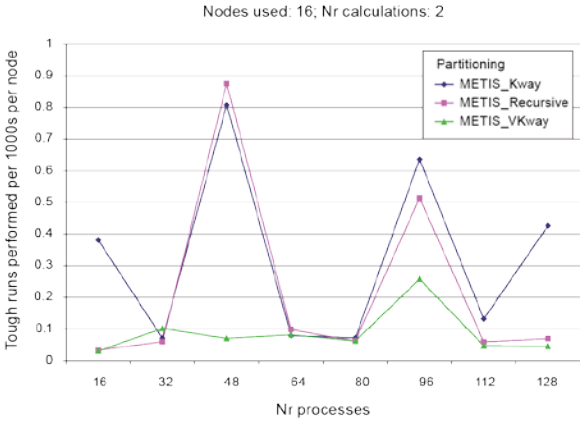

Figure 5. Couplex-Gaz 1b: Efficiency versus number of parallel processes for the test of the METIS partitioning algorithms on Azurite; simulation period 1000-1010 years; 158 720 elements model.

Couplex-Gaz 1b: Search of the optimal parallel process distribution

The search for best distribution of parallel processes on nodes was done via the two described tests: varying the node load on the cluster, and testing the influence of repartitioning the processes of one calculation on the nodes.

Variation of the node load was done according to the methodology. The computation used is a METIS *Recursive* with 8 parallel processes for the 64-layer (158 720 elements) Couplex-Gaz 1b problem. The node load was increased progressively from 1 to 8 processes per node by increasing the number of simultaneously running computations on an 8-node restriction of the Azurite cluster. Under these conditions, the individual run time of a single computation progressively rises with the node load, because each single computation has to share node resources (Table 1). Degradation of performance becomes more important when more than four processes are running simultaneously per node—attributed to saturation of the node's cache memory. This hypothesis was confirmed by a supplementary test under the same conditions with a smaller 8-layer (19,840 elements) Couplex-Gaz 1b problem. This lighter problem showed much less degradation of CPU time for the same node loads, because nodes had to process many fewer unknowns simultaneously.

Table 1. Couplex-Gaz 1b – Degradation of pure performance, measured as % increase in CPU time, when increasing the number of processes per node; comparison for 64-layer and 8-layer models runs on 8 nodes of Azurite.

Node load variation	CPU time increase	
	64-layers Couplex-Gaz 1b case	8-layers Couplex-Gaz 1b case
1 to 2 p. p. node	+20%	+0%
2 to 4 p. p. node	+22%	+0%
4 to 8 p. p. node	+90%	+21%
1 to 4 p. p. node	+46%	+0%
1 to 8 p. p. node	+180%	+22%

For the 64-layer mesh, (Figure 6), with up to four parallel processes running per node, the efficiency increased strongly and almost linearly because of the better capacity utilization of the cores in the nodes. Beyond this threshold, efficiency stagnated, because the nodes's cache memory saturation acted as a bottleneck.

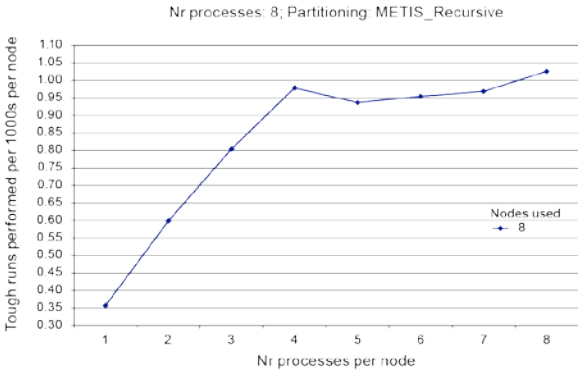

Figure 6. Couplex-Gaz 1b: Efficiency as a function of the number of processes simultaneously assigned to each of the 8 Azurite nodes; 158 720 elements model.

Repartition of the processes for a single calculation on the Azurite cluster nodes had no significant influence, as shown by results in

Figure 7. This means the communication between nodes is not a performance bottleneck for partition domains of this size (average 40 000 unknowns) on this particular cluster.

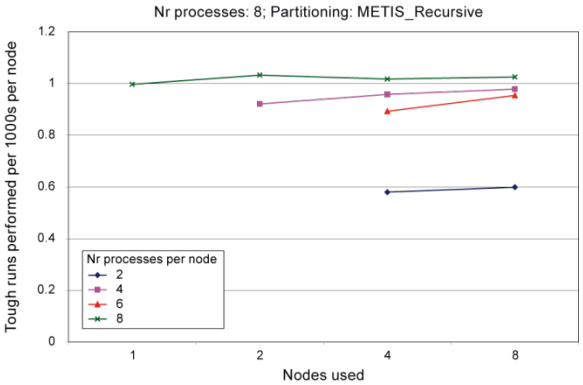

Figure 7. Couplex-Gaz 1b: Efficiency as a function of the number of Azurite nodes involved for the calculation, for different constant node loads; 158 720 elements model.

Couplex-Gaz 1b: Study of scalability

Scalability testing was carried out with the METIS-*Kway* partitioning algorithm, since the behavior of TOUGH2-MP for large numbers of partitions is of most interest. The number of processes was varied from 2 to 128 (i.e., the maximal possible on Azurite), and node load was ensured constant to 8 processes running per node, if necessary by running several identical runs simultaneously (for low numbers of parallel processes). The test was repeated for six different multiplication factors of the reference Couplex-Gaz 1b mesh with 4960 (2 layers) to 158 720 elements (64 layers).

Analysis of the measured efficiencies when increasing the number of parallel processes (Figure 8) shows two phases:

- Increase in the efficiency until a peak, corresponding to supralinear acceleration. This phase is not encountered for the smallest mesh, since partition size is too small.
- Decrease in efficiency. At first, this decrease corresponds to sublinear parallel acceleration when CPU gains on one run do not compensate for the extra usage of cluster resources. Over a certain number of domains, the number of unknowns per parallel process becomes too small to allow any parallel acceleration. Individual CPU times even increase because the supplementary communication overhead between subdomains becomes a bottleneck.

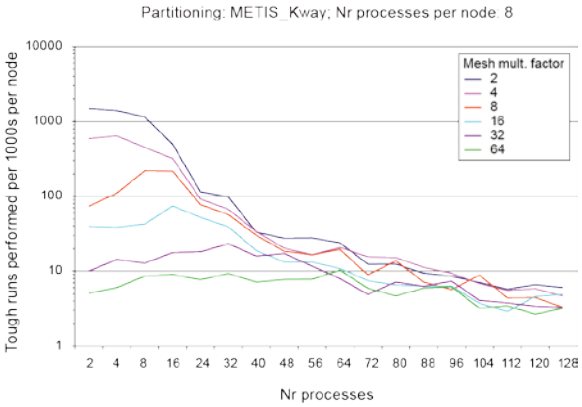

Figure 8. TOUGH2-MP scalability for the Couplex-Gaz 1b: Efficiency on a logarithmic scale as a function of number of parallel processes for various mesh sizes.

The bigger the meshes, the later the optimal efficiency peak and decrease occur. The measured number of domain partitions achieving best efficiency is proportional to the mesh size (Figure 9), resulting in a constant optimal partition size of about 5000 unknowns and showing good scalability of TOUGH2-MP.

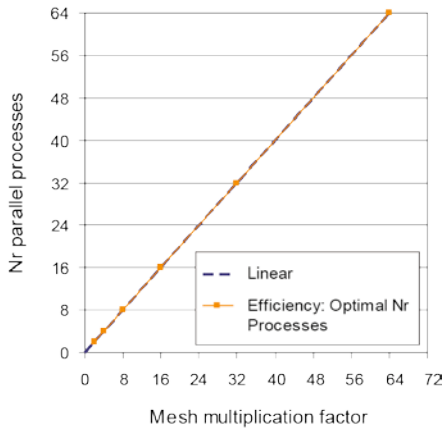

Figure 9. TOUGH2-MP scalability: for each multiplication factor of the Couplex-Gaz 1b mesh (which is proportional to number of unknowns), number of parallel processes reaching peak efficiency.

DIRECT APPLICATION TO A LARGE CASE

The MAVL 3D case

The selected large case is the MAVL 3D model used to calculate the coupled hydrogen production and heat generation arising in a radioactive waste disposal drift containing ILW-LL (Poller et al., 2009). This 55 345 elements 3D mesh (Figure 10) was run with TOUGH2-MP EOS5 with nonisothermal conditions (three equations per element). It leads to a 166 035 equations problem.

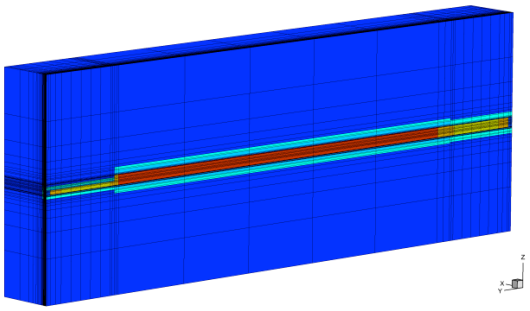

Figure 10. Mesh used for the MAVL 3D case.

To obtain a test case that could be run in a reasonable time, the simulation was reduced to a 0–50 years period, which according to Figure 11, corresponds to a phase in which the strongest variations in pressure, saturation degree, and temperature occur. Accordingly, the CPU time is reduced from several hours to approximately 600 seconds with 8 parallel processes.

Testing of the different partitioning algorithms showed that best efficiency is achieved with *Kway* and 16 processes (Figure 12). The size of one partition is then close to 10,000 unknowns.

Node load performed with 8 processes on 8 nodes showed results comparable to those of the Couplex-Gaz 1b case. Computational efficiency steeply increases until 4 processes per node. Over this threshold, efficiency improvement continues, but is less pronounced. Different process repartitions over several nodes of the cluster have little influence as well (Figure 13).

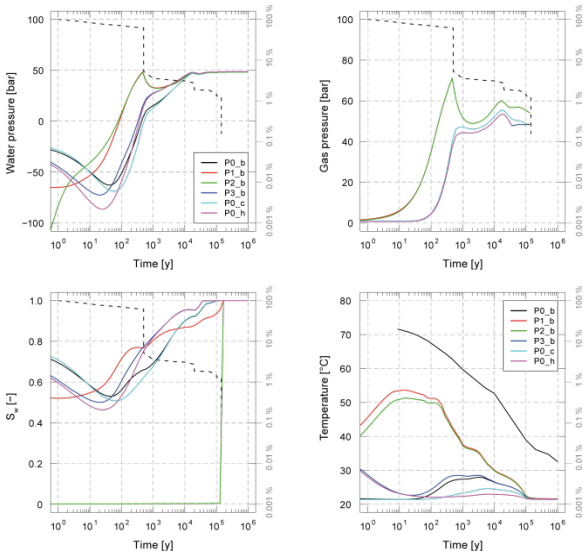

Figure 11. Evolution of pressure, saturation and temperature over time for the reference MAVL 3D computation.

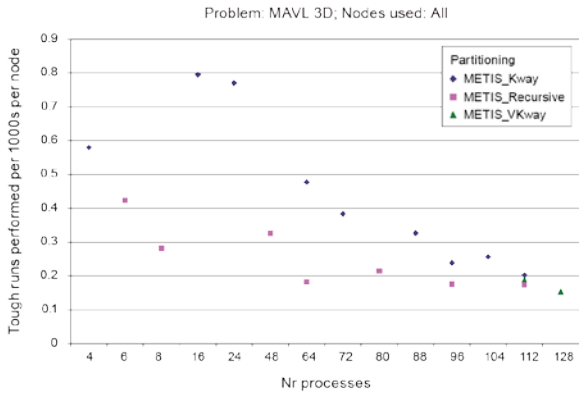

Figure 12. MAVL 3D – Efficiency as a function of the number of parallel processes for the 3 available METIS partitioning algorithms.

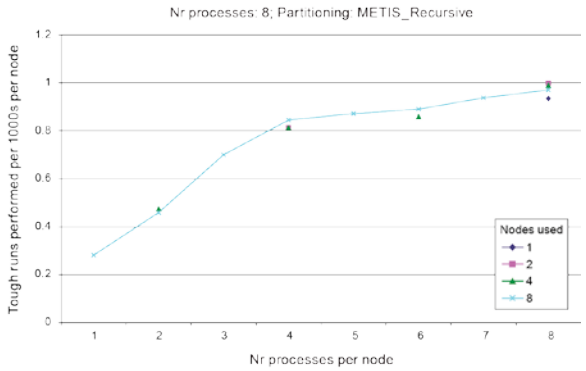

Figure 13. MAVL 3D – Efficiency expressed in terms of performed runs per time per Azurite node as a function of the node load.

Comparison between large scale results

The results obtained with the largest Couplex-Gaz 1b problem (64-layer mesh) and the MAVL 3D case lead to comparable findings regarding the parallel settings used to reach optimal performance. In the Couplex-Gaz 1b case, best efficiency was achieved with $np = 64$, and results with $np = 16$ and $np = 32$ are very good as well. This corresponds to partition sizes with average number of unknowns in the 5000–20,000 range. Best efficiency with the MAVL case is obtained for $np = 16$ (10,000 unknowns per partition) and $np = 24$ (7000 unknowns per partition). Thus, both models are processed optimally with similarly defined partitions.

CONCLUSIONS

In this paper, we presented a methodology to improve the conditions for use of TOUGH2-MP on a cluster. Although predicting with precision the best parallel settings to run a given simulation is impossible—because of the heterogeneous number of solver iterations performed by TOUGH2-MP with different partitions—it *is* possible to derive some good practices from the experience gathered on Azurite. First, the METIS *Recursive* algorithm is preferable for small numbers of partitions, and *Kway* is preferable for larger numbers of partitions. Second, efficiency is optimal when cluster nodes are well loaded, which corresponds for Azurite to at least 4 parallel processes per node with 10,000 unknown partitions. Maximal efficiency seems to be reached for partition domains of about this size, and is not influenced by the way the different parallel processes are distributed on the cluster nodes. Finally, both tests with Couplex-Gaz 1b and MAVL 3D models have demonstrated good scalability with TOUGH2-MP. This scalability allows using the methodology on a small-scale representative model in order to prepare a sensible parallel setup for a large-scale simulation.

REFERENCES

Andra, *Synthesis. Evaluation of the feasibility of a geological repository in an argillaceous formation. Dossier Argile 2005. Collection les Rapports,* Andra, Châtenay-Malabry, France, 2005.

Andra, *Cas test Couplex-Gaz 1 : modélisation 2D d'une alvéole de déchets de moyenne activité à vie longue*. http://www.andra.fr/couplex/Exercice_Couplex_Gaz_1.pdf, 2006. [Accessed 2 July 2012]

Hubschwerlen, N., K.. Zhang, G. Mayer, J. Roger, and B. Vialay, Using TOUGH2-MP on a cluster - optimization methodology and study of scalability, *Computers & Geosciences*, doi:10.1016/j.cageo.2012.03.005, 2012.

Karypsis, G. and V. Kumar, *METIS: A Software Package for Partitioning Unstructured Graphs, Partitioning Meshes, and Computing Fill-Reducing Orderings of Sparse Matrices, V4.0,* Technical Report, Department of Computer Science, University of Minnesota. 1998.

Karypsis, G. and V. Kumar, A Fast and Highly Quality Multilevel Scheme for Partitioning Irregular Graphs. *SIAM Journal on Scientific Computing, Vol. 20, No. 1,* 359-392, 1999

Poller, A., C. P. Enssle, G. Mayer, and J. Wendling, Repository-scale modeling of the long-term hydraulic perturbation induced by gas and heat generation in a geological repository for high and intermediate level radioactive waste— Methodology and results. *TOUGH Symposium 2009, Lawrence Berkeley National Laboratory, Berkeley, California,* 2009.

Pruess, K., C. Oldenburg, and G. Moridis, *TOUGH2 User's Guide, Version 2.0*, Report LBNL-43134, Lawrence Berkeley National Laboratory, Berkeley, Calif., U.S.A., 1999.

Zhang, K., Y. S. Wu, and K. Pruess, *User's guide for TOUGH2-MP – A Massively parallel Version of the TOUGH2 Code –,* Report LBNL-315E, Lawrence Berkeley National Laboratory, Berkeley, Calif., 2008.

MODELLING TRANSPORT OF WATER, IONS AND CHEMICAL REACTION IN COMPACTED BENTONITE – COMPARISON BETWEEEN TOUGHREACT, NUMERRIN AND COMSOL MULTIPHYSICS

Aku Itälä[1], Mika Laitinen[2], Veli-Matti Pulkkanen[1], Merja Tanhua-Tyrkkö[1], Markus Olin[1]

[1] VTT Technical Research Centre of Finland
Espoo, FI-02044 VTT, Finland
[2] Numerola Oy
Jyväskylä, FI-40101, Finland
e-mail: aku.itala@vtt.fi

ABSTRACT

The bentonite barrier is an essential part of a safe spent-fuel repository in granitic bedrock. One of the most important safety functions of the bentonite buffer is to limit groundwater flow so that all mass transport takes place by diffusion. Here, we report on a new mathematical model developed to define the transport of ions inside the bentonite, with the ability to track bound interlayer water, free extra-layer water, and sorption capacity. This model was tested in a specified geometry and calculated by two numerical platforms, Numerrin and COMSOL Multiphysics®, and then compared to the original TOUGHREACT model. The model comparison was not a straightforward task, due to the different approaches in the model setup. Therefore, all associated equations are reported, and the models were parameterized such that they are comparable.

INTRODUCTION

Many phenomena and processes have to be understood when considering engineering barrier system (EBS) safety within a spent-fuel repository. Our main interest is in the bentonite-buffer part of the EBS. Bentonite is a natural composite material with:

- Smectite layers and charge-compensating cations
- Water, part of which is free in large pores and part of which is bound in smectite layers
- Salts and minerals dissolved into pore water and in solid state

A composite material like bentonite can behave in quite a complex and nonlinear way, with interactions among its components occurring at the nanoscale level. A bentonite buffer must survive under changing conditions, and in many cases these conditions may change far into the future, with reactions taking thousands of years to be completed. Thus, modeling is the only option for studying these systems in order to guarantee the proper functioning of such a buffer for the planned period of over a hundred thousand years. Our approach is based on segregation of the following modeling steps to enable more flexibility:

1) Conceptualization, which is at least partially free from any limitations in the code to be applied.
2) Collection of data needed. Creation of a mathematical model, partially limited by the chosen code.
3) Implementation of the model within TOUGH2 (Pruess et al., 1999) and/or TOUGHREACT (Xu et al., 2004), which are specifically designed for earth-sciences applications.
4) Implementation of the model on two other platforms: COMSOL Multiphysics and Numerrin (Itälä et al., 2010), which are not bound to any application area and therefore flexible.
5) Solution of the models by the selected approach.
6) Evaluation of the differences in these approaches: basically, COMSOL and Numerrin should be able to use exactly the same

equations as the TOUGH family of codes, the state of the art in earth-sciences applications.

7) Comparison of the results.

Here we present a new version of our transport and chemical reaction model (RFT, Reactions, Fluxes, Temperature), which will be validated against experimental data to be provided by VTT. The wetting processes are studied by tomographical methods, and models based on those experiments are planned to be implemented onto Numerrin and COMSOL, and (if possible) within the TOUGH family of codes as well.

MODEL FOR CATION EXCHANGE AND DIFFUSION

Definitions

Compacted bentonite consists of dry bentonite (montmorillonite and accessory minerals), water, and air, which together fill all the available space (see Figure 1).

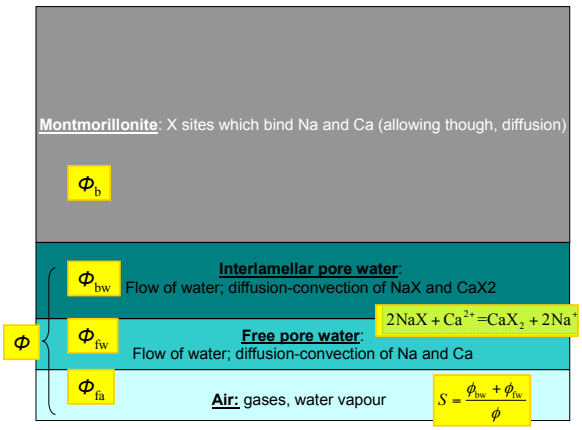

Figure 1. Basic concept

Total mass of bentonite in volume V is therefore

$$\begin{aligned} M &= M_b + M_{bw} + M_{fw} + M_{fa} \\ &= \rho_b \phi_b V + \rho_w \left(\phi_{bw} V + \phi_{fw} V\right) + \rho_a \phi_{fa} V \\ &\cong \left[\rho_b \phi_b + \rho_w \phi_{bw} + \rho_w \frac{\chi}{1-\chi} \phi_{bw}\right] V \end{aligned} \qquad (1)$$

which yields the following for the density of the bentonite:

$$\rho \cong \phi_b \rho_b + \frac{\phi_{bw} \rho_w}{1-\chi} \qquad (2)$$

where

M_i is the mass of dry bentonite (b), water bound on bentonite (bw), free water (fw) or air (fa)

ρ_b is the specific dry density of bentonite (2,760 kg m^{-3})

ρ_w is the density of water; both bound on bentonite and free ($\cong$ 1,000 kg m^{-3}), though bound water may have higher density

ρ_a density of air ($\cong$ 1.3 kg m^{-3})

ϕ_i is the volume fraction of component i: $\sum_{i=b,bw,fw,fa} \phi_i = 1 = \phi_b + \phi$

ϕ is the volume fraction of all fluids: $\phi = \phi_{bw} + \phi_{fw} + \phi_{fa}$

χ is the ratio of volume fractions of free and total water volume: $\chi = \phi_{fw} / \left(\phi_{bw} + \phi_{fw}\right)$

The mass of bentonite per total volume,

$$\rho_d = M_b / V = \left(1 - \phi\right) \rho_b \qquad (3)$$

is called the dry density. Total porosity ϕ, as well as dry and specific densities, are related by

$$\phi = 1 - \rho_d / \rho_b \qquad (4)$$

Cation exchange capacity CEC (eq/kg) is the fixed charge content (negatively charged sites X occupied by cations) of the solid bentonite. Concentration of CEC per bound water volume is given by

$$c_X = \frac{M_{CEC}}{\phi_{bw} V} = \frac{\phi_b}{\phi_{bw}} CEC \cdot \rho_b \qquad (5)$$

Any other quantity given as content (moles per kilogram of bentonite) will be transformed similarly to concentration per bound water. For example,

$$c_{NaX} = \frac{M_{NaX}}{\phi_{bw} V} = \frac{\phi_b}{\phi_{bw}} CEC \cdot \rho_b \beta_{NaX} \qquad (6)$$

Cation exchange reactions

The chemical model is simple: two sodium isotopes (^{s}Na and ^{r}Na), two chloride isotopes (^{s}Cl and ^{r}Cl), and a cation exchange site (X). ^{s}Na and ^{r}Na form complexes ^{s}NaX and ^{r}NaX with X:

$$^{s}\mathrm{NaX} + {}^{r}\mathrm{Na}^{+} \underset{k}{\overset{k}{\rightleftharpoons}} {}^{r}\mathrm{NaX} + {}^{s}\mathrm{Na}^{+} \qquad (6)$$

where k is the kinetic constant, which in this case is the same in both directions. Possible stable (s) and radioactive (r) sodium isotopes are Na-23 and Na-22, respectively; the half-life of beta-active Na-22 is about 2.6 years. Chlorine has two stable isotopes: Cl-35 and Cl-37. The half-life of beta-active Cl-36 is about 300,000 years.

At equilibrium, reaction (7) gives

$$\frac{\beta_{\mathrm{rNa}}}{\beta_{\mathrm{sNa}}} = \frac{c_{\mathrm{rNa}}}{c_{\mathrm{sNa}}} \qquad (6)$$

where c_{iNa} is the concentration (mol/m^3) and β_i is the equivalent fraction of cation isotope i.

For implementation in COMSOL or Numerrin, the cation exchange reaction is reformulated for aqueous concentrations, which are the variables applied in the transport equations instead of equivalent fractions ($\beta_i = z_i c_{\mathrm{Xi}} / c_{\mathrm{X}}$):

$$\beta_{i\mathrm{NaX}} = \frac{\phi_{\mathrm{bw}}}{\phi_{\mathrm{b}}} \frac{1}{CEC \cdot \rho_{\mathrm{b}}} c_{i\mathrm{NaX}} \qquad (6)$$

The equilibrium equation rewritten is then

$$\frac{c_{\mathrm{rNaX}}}{c_{\mathrm{sNaX}}} = \frac{c_{\mathrm{rNa}}}{c_{\mathrm{sNa}}} \qquad (6)$$

The total mass of each element is conserved:

$$\begin{aligned} \overline{c_{\mathrm{sNa}}} &= \phi_{\mathrm{fw}} c_{\mathrm{sNa}} + \phi_{\mathrm{bw}} c_{\mathrm{sNaX}} \\ \overline{c_{\mathrm{rNa}}} &= \phi_{\mathrm{fw}} c_{\mathrm{rNa}} + \phi_{\mathrm{bw}} c_{\mathrm{rNaX}} \\ \overline{c_{\mathrm{sCl}}} &= \phi_{\mathrm{fw}} c_{\mathrm{sCl}} \\ \overline{c_{\mathrm{rCl}}} &= \phi_{\mathrm{fw}} c_{\mathrm{rCl}} \end{aligned} \qquad (6)$$

where $\overline{c_i}$ is the total concentration of element i.

The charge balance must be kept in the bound and free aqueous phase:

$$\begin{aligned} c_{\mathrm{X}} &= c_{\mathrm{sNaX}} + c_{\mathrm{rNaX}} \\ c_{\mathrm{sCl}} + c_{\mathrm{rCl}} &= c_{\mathrm{sNa}} + c_{\mathrm{rNa}} \end{aligned} \qquad (6)$$

2.3 Chemical kinetics

For reaction (8) it is possible to write forward and reverse rates

$$r_{\mathrm{f}} = k \cdot c_{\mathrm{sNaX}} c_{\mathrm{rNa}} \qquad (6)$$

and

$$r_{\mathrm{r}} = k \cdot c_{\mathrm{rNaX}} c_{\mathrm{sNa}} \qquad (6)$$

which gives, for the total reaction rate,

$$r = r_{\mathrm{f}} - r_{\mathrm{r}} = k_{\mathrm{c}} \left(c_{\mathrm{sNaX}} c_{\mathrm{rNa}} - c_{\mathrm{rNaX}} c_{\mathrm{sNa}} \right) \qquad (6)$$

which at equilibrium is zero, giving properly Eq. (9).

2.4 Mass transport by molecular diffusion

The mass-transport problem can be formulated as follows: find $c=c(\boldsymbol{x},t)$ such that

$$\frac{\partial}{\partial t}\left(\phi_j c_i\right) = \nabla \cdot \left(\mathbf{j}_{ij} - \mathbf{u} c_i\right) + R_{ij} \qquad (6)$$

Diffusion in porous media is often described by modified Fickian laws of diffusion. Instead of Fick's first law, the diffusion flux j is given in the form

$$\mathbf{j}_{ij} = -\phi_j G\left(\phi_j, S\right) D_j \nabla c_i \qquad (6)$$

where i denotes the species; j= bw or fw for bound- and free-water species, respectively; G is the geometric factor, which accounts for the longer diffusion path in a porous medium compared to free space and other geometric processes. It may depend both on volume fraction and saturation. Free- and bound-water diffusion constants have traditionally been named pore (D_{p}) and surface diffusion (D_{s} constants, respectively (Rasmuson and Neretnieks, 1983).

It is clarifying to write out the complete set of transport equations:

$$
\begin{aligned}
\partial_t c_{\mathrm{sCl}} &= D_{\mathrm{p}} \nabla^2 c_{\mathrm{sCl}} \\
\partial_t c_{\mathrm{rCl}} &= D_{\mathrm{p}} \nabla^2 c_{\mathrm{rCl}} - \lambda_{\mathrm{Cl}} c_{\mathrm{rCl}} \\
\partial_t c_{\mathrm{sNa}} &= D_{\mathrm{p}} \nabla^2 c_{\mathrm{rNa}} + \phi_{\mathrm{fw}} r \\
\partial_t c_{\mathrm{sNaX}} &= D_{\mathrm{s}} \nabla^2 c_{\mathrm{sNaX}} - \frac{\phi_{\mathrm{fw}}}{\phi_{\mathrm{bw}}} r \\
\partial_t c_{\mathrm{rNa}} &= D_{\mathrm{p}} \nabla^2 c_{\mathrm{rNa}} - r - \lambda_{\mathrm{Na}} c_{\mathrm{rNa}} \\
\partial_t c_{\mathrm{rNaX}} &= D_{\mathrm{s}} \nabla^2 c_{\mathrm{rNaX}} + \frac{\phi_{\mathrm{fw}}}{\phi_{\mathrm{bw}}} \left[r - \lambda_{\mathrm{Na}} c_{\mathrm{rNaX}} \right]
\end{aligned}
\tag{6}
$$

where $\lambda_i \quad (i = \mathrm{Cl,Na})$ is the linear reaction rate, e.g., radioactive decay.

2.4 . With and without surface diffusion

Both Numerrin and COMSOL apply surface diffusion (Section 2.3 above) and exchange kinetics, but TOUGHREACT applies traditional porous media diffusion and assumes exchange equilibrium, so that a K_{d} value is required.

Assuming that equilibrium has already been reached, the effective diffusivity formulae for the two approaches are given by (see, e.g., Olin (1994))

$$
\begin{aligned}
D_{\mathrm{e}}^{\mathrm{t}} &= \phi^{\mathrm{t}} D_{\mathrm{p}}^{\mathrm{t}} \\
D_{\mathrm{e}}^{\mathrm{s}} &= \phi^{s} D_{\mathrm{p}}^{s} + \left(1 - \phi^{s}\right) K_{\mathrm{d}}^{\mathrm{s}} \rho_{\mathrm{d}} D_{\mathrm{s}}
\end{aligned}
\tag{6}
$$

where *t* and *s* stand for traditional and surface diffusion, respectively. Similarly, for apparent diffusivities, we have

$$
\begin{aligned}
D_{\mathrm{a}}^{\mathrm{t}} &= \frac{D_{\mathrm{e}}^{\mathrm{t}}}{\alpha^{\mathrm{t}}} = \frac{\phi^{\mathrm{t}} D_{\mathrm{p}}^{\mathrm{t}}}{\phi^{\mathrm{t}} + \left(1 - \phi^{\mathrm{t}}\right) K_{\mathrm{d}}^{\mathrm{t}} \rho_{\mathrm{d}}} \\
D_{\mathrm{a}}^{\mathrm{s}} &= \frac{D_{\mathrm{e}}^{\mathrm{s}}}{\alpha^{\mathrm{s}}} = \frac{\phi^{s} D_{\mathrm{p}}^{s} + \left(1 - \phi^{s}\right) K_{\mathrm{d}}^{\mathrm{s}} \rho_{\mathrm{d}} D_{\mathrm{s}}}{\phi^{\mathrm{s}} + \left(1 - \phi^{\mathrm{s}}\right) K_{\mathrm{d}}^{\mathrm{s}} \rho_{\mathrm{d}}}
\end{aligned}
\tag{6}
$$

In order to compare the models, the effective and apparent diffusivity should have similar values from one model to the other:

$$
\begin{aligned}
\phi^{\mathrm{t}} D_{\mathrm{p}}^{\mathrm{t}} &= \phi^{s} D_{\mathrm{p}}^{s} + \left(1 - \phi^{s}\right) K_{\mathrm{d}}^{\mathrm{s}} \rho_{\mathrm{d}} D_{\mathrm{s}} \\
\phi^{\mathrm{t}} + \left(1 - \phi^{\mathrm{t}}\right) K_{\mathrm{d}}^{\mathrm{t}} \rho_{\mathrm{d}} &= \phi^{\mathrm{s}} + \left(1 - \phi^{\mathrm{s}}\right) K_{\mathrm{d}}^{\mathrm{s}} \rho_{\mathrm{d}}
\end{aligned}
\tag{6}
$$

where in the latter formula, the equality of effective diffusivity values have been utilized. Finally, the parameter values to be applied in traditional modeling, given by surface diffusion parameters, are:

$$
\begin{aligned}
D_{\mathrm{p}}^{\mathrm{t}} &= \chi D_{\mathrm{p}}^{\mathrm{s}} + \left(\frac{1}{\phi} - \chi \right) K_{\mathrm{d}}^{\mathrm{s}} \rho_{\mathrm{d}} D_{\mathrm{s}} \\
K_{\mathrm{d}}^{\mathrm{t}} &= \frac{(\chi - 1)\phi + (1 - \chi\phi) K_{\mathrm{d}}^{\mathrm{s}} \rho_{\mathrm{d}}}{(1 - \phi) \rho_{\mathrm{d}}}
\end{aligned}
\tag{6}
$$

CASES

In all test cases, a simple 1D geometry of length 0.1 m is applied. The right boundary is closed for mass transport, the left boundary is closed only for bound-water species. However, a concentration boundary condition is applied for free-water species on the left boundary.

The required bentonite parameters are given in Table 1. The initial state is established by assuming that all bound sites are occupied by stable sodium, whereas in free water there is a concentration of 100 mol/m^3 of stable sodium and chloride. The left boundary has the same total concentration, but the fraction of "radioactive" NaCl varies. The goal is to model the evolution of the system, varying kinetics in COMSOL and Numerrin as well.

Table 1. Parameter values for test cases

Symbol	Value
ρ_{d}	1 600 kg/m^3
ϕ	0.4
χ	0.25
$\chi\phi$	0.1
S	1
$D_{\mathrm{p}}^{\mathrm{s}}$	1e-10 m^2/ s
D_{s}	1e-12 m^2/s
$D_{\mathrm{p}}^{\mathrm{t}}$	6.1E-11 m^2/s
$K_{\mathrm{d}}^{\mathrm{s}}$	0.010 m^3/kg
$K_{\mathrm{d}}^{\mathrm{t}}$	0.015 m^3/kg
CEC	1 eq/kg

RESULTS

Results (with fraction of radioactive NaCl 0.001) from comparing the three models (COMSOL, Numerrin, TOUGHREACT) are shown in Figure 2. Due to relatively high kinetical rates, all the approaches give rather similar results.

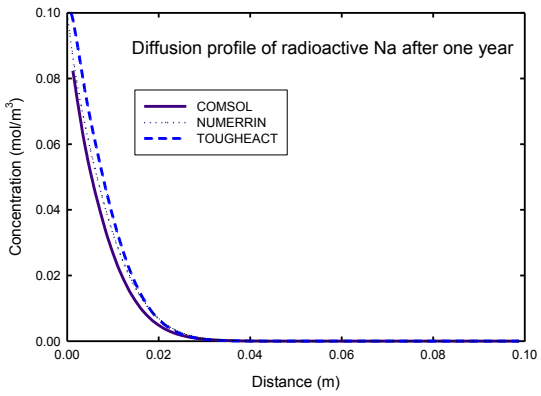

Figure 2. Comparison among the models applied.

CONCLUSIONS

Two of our test models (COMSOL, Numerrin) are more suitable for kinetic surface reactions, while the third one, TOUGHREACT, accepts equilibrium models in a rather straightforward manner. In addition, while the implementation of surface-diffusion submodels is straightforward for the first two models, in TOUGHREACT we applied traditional porous medium diffusion with modified parameter values.

No substantial difference was observed among the chosen models. We are planning to produce more results for the present implementation, and also to extend the model to include sodium-calcium exchange reactions. Adding other important chemical reaction into the COMSOL and Numerrin implementations is planned as well.

REFERENCES

Itälä, A., V. Pulkkanen, M. Tanhua-Tyrkkö and M. Olin, Comsol Multiphysics, TOUGHREACT and Numerrin Comparison in Some Modelling Task of Spent Nuclear Fuel Disposal. Comsol Conference 2010, Paris, France, 2010. www.comsol.com/papers/8807/

Olin, M., Diffusion in Crushed Rock and in Bentonite Clay, VTT Publications 175, VTT Technical Research Centre of Finland, Espoo, Finland, 1994.

Pruess, K., C. Oldenburg and G. Moridis, TOUGH2 User's Guide, Version 2.0, LBNL-43134, Lawrence Berkeley National Laboratory, Berkeley, California, USA, 1999.

Rasmuson, A. and I. Neretnieks, Surface migration in sorption processes, TR 83-87, SKBF/KBS, Stockholm, Sweden, 1983.

Xu, T., E. Sonnenthal, N. Spycher and K. Pruess, TOUGHREACT User's Guide: A Simulation Program for Nonisothermal Multiphase Reactive Geochemical Transport in Variably Saturated Geologic Media, Version 1.2.1, LBNL-55460, Lawrence Berkeley National Laboratory, Berkeley, California, USA, 2004.

A NEW LIBRARY TO IMPROVE TOUGH PARALLEL DEVELOPMENT

Noel Keen, George Pau, Jeff Johnson, Eric Sonnenthal, Stefan Finsterle

Lawrence Berkeley National Laboratory
Earth Sciences Division, MS 74-0120
Berkeley, CA 94720
e-mail: NDKeen@lbl.gov

ABSTRACT

Many users and developers have contributed to the success of the TOUGH suite of codes. However, the wide range of problems the codes can simulate has led to significant modification and fragmentation of the codes, exemplified by the multiple flavors of TOUGH. Maintenance of the codes becomes increasingly difficult, and improvement in one branch of the codes cannot be easily propagated to other branches. In addition, parallel computing resources cannot be uniformly utilized by all the codes, due to the lack of a parallel programming framework that simplifies this task.

We are in the process of re-engineering the TOUGH codes, specifically by developing a library (named *toughlib*), which includes functions that are commonly used by the TOUGH codes, such as the linear solvers. For example, adding a new parallel linear solver package (such as PETSc) to *toughlib* would enable any TOUGH code to use it. We are also writing functions that hide more complex constructs such as parallelism behind an abstraction layer, which will make it easier to combine serial and parallel versions of TOUGH codes. When complete, the *toughlib* library will serve as a working Application Programming Interface (API), so that all TOUGH codes using it will have similar structure. We will demonstrate how these new concepts are used in a combined version of TOUGH2 and TOUGH2-MP.

In addition, we are improving the software engineering processes that are used to develop the TOUGH codes. In particular, we have improved the build process using CMake, which simplifies the installation of external packages on multiple platforms. We also utilize the Bitbucket service, which provides maintenance-free access to the Mercurial version control system, to manage the development of this new library.

INTRODUCTION

The TOUGH suite of simulators (http://esd.lbl.gov/TOUGH) is one of the most complete software packages in the market for numerical modeling of nonisothermal multiphase flow and reactive transport in porous media. Over the past 30 years, the suite has been widely adopted by universities, government organizations, and private industry for applications to nuclear waste disposal, environmental remediation problems, energy production from geothermal, oil, and gas reservoirs as well as gas hydrate deposits, geological carbon sequestration, vadose zone hydrology, and other uses that involve coupled thermal, hydrological, geochemical, and mechanical processes in permeable media.

The suite is continually being updated in response to scientific advancements, technical needs, user requests, and changes in hardware and software architectures. Foremost, code changes are made to provide the user with the capabilities needed to address specific scientific challenges. This requires the development of new equation-of-state (EOS) modules and refined process descriptions. Moreover, the simulators are being used for systems of increasing size and complexity, making high numerical performance a key target for further developments. The system of equations to be solved increases significantly, not only because of increased dimensionality, larger model domains, and higher resolution, which lead to many more gridblocks, but also because of the coupling of hydrological, thermal, mechanical, and biogeochemical processes, which leads to more equations that need to be solved per

gridblock. Finally, improved support tools for model setup, mesh generation, and visualization and analysis of modeling results are essential for making an advanced simulator applicable to complex subsurface flow and transport problems. This paper focuses on developments that are mainly concerned with numerical performance and code maintenance.

PERFORMANCE AND MAINTENANCE

Larger parallel computing resources are becoming economically viable for many TOUGH users. This increased processing power will naturally allow them to tackle problems with greater complexity and at a larger scale. In addition, the need to solve large problems is becoming more acute as numerical models are increasingly used as predictive and regulatory tools. For example, for a geological carbon sequestration problem that is of interest to government and industry alike, scientists and engineers have to use a numerical model that is sufficiently resolved over a large area, thus requiring the model to be solved in parallel. This parallelism is a driving requirement in the work described in this paper.

TOUGH was initially designed to be a serial code. To address the need to solve larger problems and to take advantage of the increased availability of multiprocessor computers, TOUGH2 (Pruess et al., 1999; Zhang et al., 2008) and TOUGH+ (Moridis et al., 2008) were parallelized based on the standard Message Passing Interface (MPI) protocol. iTOUGH2, which uses TOUGH runs to perform parameter estimation, is parallelized based on the Parallel Virtual Machine (PVM) protocol (Finsterle, 1998) and can run several (serial) forward simulations simultaneously.

While these efforts have made available parallel versions of TOUGH, this parallelization is far from comprehensive. First, the parallel versions of these codes are separate software packages with different source code and are not maintained or versioned with the "mainline" TOUGH codes. Second, other codes within the suite have not been parallelized at all. In particular, the reaction-transport code TOUGHREACT V2 is one of the most demanding codes in terms of equations solved and computing time, but it has only recently been partially parallelized for shared memory architectures using OpenMP (Sonnenthal et al., in prep.)

In addition, further work must be done on the existing parallelized codes to allow them to realize their full potential. Presently, these codes cannot perform parallel I/O tasks effectively. This can cause major slowdowns in simulations that write a lot of data. The parallel TOUGH codes are also unable to take advantage of new computing architectures such as heterogeneous multicore systems and GPU systems without significant code modifications.

There are several versions of TOUGH that were developed to solve particular problems (e.g., the TOUGH2 and TOUGH2-MP families, the TOUGH+ and pTOUGH+ families, as well individual codes such as TOUGHREACT, iTOUGH2, TOUGH-FLAC, etc.). While the development of a single inclusive "über-TOUGH" code may not be feasible (or desired), there are significant components of all TOUGH codes that are similar and could leverage a single shared library. There are obvious engineering benefits to having a common code base for the TOUGH applications; debugging and making incremental improvements becomes more practical when it can be done once, at a single location in the source code.

THE *TOUGHLIB* LIBRARY

A library called *toughlib* is being designed to provide an API that has functionalities common to all TOUGH codes. It will focus on two main functionalities: (1) to provide a common interface to all internal and external linear solvers, and (2) to provide a more user-friendly implementation of routines involving parallel communications. We believe the first functionality will have immediate benefits, since all TOUGH codes require solving a large linear system in the nonlinear solver used in codes. The second functionality will significantly reduce the overhead of maintaining (and debugging) a parallel code. It will also lower the barrier for future developers that are not familiar with parallel programming to more easily work with a parallel code.

toughlib consists of several Fortran90 modules. The modules contain data types that are designed in an object-oriented manner. The representation of a type, such as a sparse matrix or a vector, is thus separated from its implementation. Encapsulation of data and logic in a type reduces complexity of the code. *toughlib* also helps distinguish which data arrays are global or local to each processor.

Interface to External Linear Solver Packages

One important component to all TOUGH codes is the sparse linear solver. At present, the parallel versions of TOUGH (TOUGH-MP and pTough+) use AZTEC (Tuminaro et al., 1999) as the main workhorse. However, the development of AZTEC has long ceased, at least in its present form. As such, it does not include some of the latest developments of linear solver technologies. The serial version of the TOUGH codes (TOUGH2, TOUGHREACT and TOUGH+) use a collection of preconditioned iterative solvers implemented in T2SOLV (Moridis and Pruess, 1997), but this code has not been updated for the past 15 years.

To exploit some of the newer linear solver packages, *toughlib* will provide an interface to these packages. One solver that has demonstrated success on large parallel systems is PETSc (Portable, Extensible Toolkit for Scientific Computation; Balay et al., 2012). PETSc allows for the use of several preconditioners (e.g., LU, Block Jacobi, Multigrid) and has many other features.

While developers can work directly with the above packages, *toughlib* aims to provide a solver API that is specific to the TOUGH codes. It enables developers to only learn one interface and have access to all the linear packages that *toughlib* will incorporate. In addition, *toughlib* will also provide an API to the existing AZTEC and T2SOLV routines, allowing developers to easily transition to the new interface of *toughlib*. All the benefits of these additional external linear solvers will then be immediately available to developers, including the ability to choose the appropriate solvers and preconditioners, without recompiling the code.

In addition to the nonlinear solver used to solve the flow and transport phenomena, the geochemistry model in TOUGHREACT (Xu et al., 2011) requires solution of ordinary differential equations. While current in-house approaches appear to be satisfactory for the moment, *toughlib* can provide other alternatives. Under consideration is an interface to an external ODE solver such as the SUNDIALS package (Hindmarsh et al., 2005). This would allow TOUGHREACT users to easily test out different numerical algorithms to improve the efficiency of the code.

Figure 1 schematically shows the interfaces between *toughlib* and the core simulator.

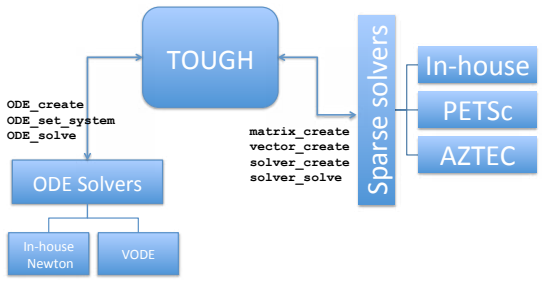

Figure 1. Interfaces are layers that allow interchangeable implementations.

Parallel Framework

High-performance computing is a peculiar branch of science, because its significance is completely determined by its success at performing ever-larger simulations in ever-less time. Thus, the performance of parallel simulations is paramount in any modern scientific code that aims to solve the types of problems that interest TOUGH users.

Improving the parallel performance first requires improving a parallel framework, accomplished by *toughlib*. The parallel versions of the TOUGH codes require several steps that are not needed in a serial version, such as domain decomposition, various functions required by the parallel solver algorithms, and any necessary additional data storage. Additionally, the serial versions can (and typically do) use a different solver than the parallel version. However, there are good reasons to write functions that will allow development of a TOUGH code that will run in serial or parallel (or parallel using only one processor). The functions in *toughlib* are

written such that they can be used in serial or parallel mode. For example, a function for domain decomposition would simply return when only one processor is being used. The advantages of one code that can run in serial or parallel are reduction in the total amount of code, easier maintenance, more robust testing, and easier debugging.

We would also like to make parallel programming with MPI easier for the TOUGH developer. One way to do this is write functions that do most or all of the communication in *toughlib* and provide convenience functions for doing typical operations, such as summing a variable to obtain the global value or interacting with the parallel file system.

There are various ways that *toughlib* can address parallel performance. If most of the code to handle parallel operations and communication are implemented in *toughlib*, then any performance improvements would benefit all TOUGH codes that use it. For example, a common performance improvement is caching and serializing data before sending it to another processor. It is often best to reduce the number of communication calls and increase the buffer sizes.

The field of high performance computation is advancing rapidly, and with each new parallel machine being built comes new hardware and software that may require code changes in the application to compile or effectively use the resources. The *toughlib* library will be portable and strive to be efficient across a wide range problem types and sizes on available platforms. It will focus on relatively uncomplicated data types such as matrices and vectors that are commonly used in existing TOUGH codes. and whose use and characteristics are well understood by developers.

Essential to improving computational performance for any serial or parallel code is the measurement of quantities like wall-clock time, memory use, and floating-point operations. Utility functions can help provide these in a manner that makes sense to TOUGH codes for various machine architectures.

Other *toughlib* Benefits

Toughlib uses CMake, which is a package for managing configuration and building of software applications. CMake is especially useful for building external libraries that *toughlib* or TOUGH codes may depend on. We will use version control software for developing *toughlib*, and it currently exists in a Mercurial repository (distributed source control management tool). The *toughlib* software will be distributed through a Bitbucket account at Lawrence Berkeley National Laboratory. Bitbucket offers secure source-code hosting of repositories, making it easier to manage team software development. CMake, Mercurial, and Bitbucket are freely available. These practices could be extended to the TOUGH codes.

We can include functions that perform routine checks, ensuring valid input to save time tracking down problems. Output functions, such as those for writing VTK-formatted files, could be maintained in *toughlib* as well. The mesh format for TOUGH codes has many features that are similar, and common operations on the mesh can be maintained in *toughlib*. Various physical constants could be defined and maintained in one place.

FUTURE WORK

TOUGHREACT developers are beginning to use threading (via OpenMP) to speed up the calculation of chemical reactions, which are usually the most cpu-intensive component of reactive-transport problems (Sonnenthal et al., in prep). This might prove to be beneficial for other TOUGH codes.

As *toughlib* matures, the TOUGH developers and users will be able to focus more on the science and less on the solvers and parallel concepts.

ACKNOWLEDGMENT

We acknowledge the support of Lawrence Berkeley National Laboratory's Innovation Grant. This work was supported, in part, by the U.S. Dept. of Energy under Contract No. DE-AC02-05CH11231.

REFERENCES

Finsterle, S., *Parallelization of iTOUGH2 Using PVM*, Report LBNL-42261, Lawrence Berkeley National Laboratory, Berkeley, Calif., October 1998.

Moridis, G.J., and K. Pruess, *T2SOLV: An Enhanced Package of Solvers for the TOUGH2 Family of Reservoir Simulation Codes*, Report LBNL-40933, Lawrence Berkeley National Laboratory, Berkeley, Calif., 1997.

Moridis, G.J., M.B. Kowalsky, and K. Pruess, *TOUGH+HYDRATE v1.0 User's Manual: A Code for the Simulation of System Behavior in Hydrate-Bearing Geologic Media*, Report LBNL-149E, Lawrence Berkeley National Laboratory, Berkeley, Calif., 2008.

Pruess, K., C. Oldenburg, and G. Moridis, *TOUGH2 User's Guide, Version 2.0*, Report LBNL-43134, Lawrence Berkeley National Laboratory, Berkeley, Calif., 1999.

Tuminaro, R. S., Heroux, M., Hutchinson, S. A., Shadid, J. N., *Official AZTEC User's Guide: Version 2.1*, December, 1999.

Balay S., Brown J., Buschelman K., Eijkhout V., Gropp W., Kaushik D., Knepley M., McInnes L., Smith B., and Zhang H., *PETSc Users Manual*, ANL-95/11 – Revision 3.3, Argonne National Laboratory, 2012.

Hindmarsh A. C., Brown P. N., Grant K. E., Lee S. L., Serban R., Shumaker D. E., and Woodward C. S., "*SUNDIALS: Suite of Nonlinear and Differential/Algebraic Equation Solvers*," ACM Transactions on Mathematical Software, 31(3), pp. 363-396, 2005.

Xu, T., N. Spycher, E. Sonnenthal, G. Zhang, L. Zheng, & K. Pruess, *TOUGHREACT Version 2.0: A simulator for subsurface reactive transport under non-isothermal multiphase flow conditions*.Computers and Geosciences, 37:763–774, 2011.

Zhang, K., Y.-S. Wu, and K. Pruess, *User's Guide for TOUGH2-MP — A Massively Parallel Version of the TOUGH2 Code*, Report LBNL-315E, Lawrence Berkeley National Laboratory, Berkeley, Calif., 2008.

T2WELL—AN INTEGRATED WELLBORE-RESERVOIR SIMULATOR

Lehua Pan and Curtis M. Oldenburg

Earth Sciences Division 74-316C
Lawrence Berkeley National Laboratory
Berkeley, CA 94720, USA
e-mail: lpan@lbl.gov, cmoldenburg@lbl.gov

ABSTRACT

We have developed T2Well, a numerical simulator for nonisothermal, multiphase, multicomponent flows in integrated wellbore-reservoir systems. The new model extends the existing numerical reservoir simulator TOUGH2 to calculate the flow in both the wellbore and the reservoir simultaneously and efficiently, by introducing a special wellbore subdomain into the numerical grid. For gridblocks in the wellbore subdomain, we solve the 1D momentum equation of the mixture (which may be two-phase) as described by the Drift-Flux Model (DFM). The velocity of the mixture is calculated by solving the momentum equation numerically, while the individual phase velocities are calculated from the mixture velocity and other fluid parameters as defined by the DFM. A novel mixed implicit-explicit scheme is applied to facilitate the solution of the momentum equation within the Newton-Raphson iteration framework of TOUGH2. Specifically, the pressure gradient, gravity component, and time derivative of momentum are treated fully implicitly, whereas the spatial gradient of momentum is treated explicitly. The friction term is calculated with a mixed implicit-explicit scheme. Applications of the new simulator to problems in various fields are presented to demonstrate its capabilities.

INTRODUCTION

At its most basic level, management of subsurface resources involves a system comprising the wellbore and the target reservoir. As discrete pathways through geologic formations, boreholes and wells are critical to the success of many water, energy, and environmental management operations (e.g., geologic carbon sequestration, oil and gas production, compressed air energy storage, geothermal energy production, and subsurface remediation). Simulating nonisothermal, multiphase, and multicomponent flows in both wellbore and reservoir as an integrated system (as it is in reality) remains a challenging, yet important task, required to answer critical questions as to the design and performance of fluid production, injection, and transport systems.

Because of the many water, energy, and environmental applications of wellbore-reservoir systems, many stand-alone simulators have been developed for two-phase flow in wellbores with various levels of coupling to the reservoir, even though the flow processes in wellbores and in reservoirs are often strongly coupled in reality. Lu and Connell (2008) proposed a quasi-steady numerical approach that included two-phase flow of CO_2 and used a productivity index approach to couple the wellbore to the reservoir. Lindeberg (2011) included transient effects of two-phase CO_2 flows in the well without coupling to the reservoir. Remoroza et al. (2011) developed an approach for geothermal applications that coupled the wellbore flow with the reservoir, but assumed steady-state and single-phase flow in the well. Hadgu et al. (1995) developed a similar approach for geothermal applications using dynamic production index methods. Livescu et al. (2009) developed fully coupled wellbore-reservoir flow simulators for oil/gas industry applications, using a simplified correction term to account for the transient flow in the wellbore.

The main difficulties for simulating wellbore-reservoir flow as an integrated system are the following: (1) different governing equations apply to the wellbore and the reservoir that need to be solved efficiently in a uniform framework; (2) the significant contrast in temporal and spatial scale between the wellbore and the reservoir that results in a very challenging set of stiff

partial differential equations, and (3) other complexities (e.g., dryout) that are caused by the interactions between the wellbore and the reservoir.

This paper presents a new approach that we recently developed for simulating non-isothermal, two-phase, multicomponent flow in a wellbore-reservoir system. The new model (T2Well) uses an integrated wellbore-reservoir system in which the wellbore and reservoir are two different subdomains in which flow is controlled by different physics, but solved uniformly within the Newton-Raphson iteration scheme in the TOUGH2 code.

THEORY

We treat the wellbore-reservoir flow problem as an integrated system in which the wellbore and reservoir are two different subdomains, within which flow is controlled by different physics—specifically, viscous flow in the wellbore is governed by the 1D momentum equation, and 3D flow through porous media in the reservoir is governed by a multiphase version of Darcy's law. As a result, the governing equations for the flow processes in a wellbore-reservoir system are an extended set of those used by the standard TOUGH2. As shown in Table 1, the major differences in governing equations between the wellbore and the reservoir are the definitions of energy flow terms and the phase velocities. Because the velocities in the reservoir are usually very small, the kinetic energy can be ignored in the energy balance, and the phase velocities can be calculated by the multiphase Darcy's law.

However, this is not the case in the wellbore, where the kinetic energy cannot be ignored and the phase velocities are governed by two-phase momentum equations. Even though the wellbore flow can be reasonably simplified as 1D, the two-phase momentum equations are still very difficult to solve, mainly because of the complex two-phase flow structure in wellbores. The Drift-Flux-Model (DFM), first developed by Zuber and Findlay (1965) and Wallis (1969), among others, provides a conceptually robust and simpler way to tackle the problem.

Table 1. The mass and energy balance equations solved in T2Well

	Description	Equation
	Conservation of mass and energy	$\frac{d}{dt}\int_{V_n} M^\kappa \, dV_n = \int_{\Gamma_n} \mathbf{F}^\kappa \bullet n \, d\Gamma_n + \int_{V_n} q^\kappa \, dV_n$
	Mass accumulation	$M^\kappa = \phi \sum_\beta S_\beta \rho_\beta X_\beta^\kappa$ for each mass component
	Mass flux	$\mathbf{F}^\kappa = \sum_\beta X_\beta^\kappa \rho_\beta \mathbf{u}_\beta$ for each mass component
Porous media	Energy flux	$\mathbf{F}^\kappa = -\lambda \nabla T + \sum_\beta h_\beta \rho_\beta \mathbf{u}_\beta$
Porous media	Energy accumulation	$M^\kappa = (1-\varphi)\rho_R C_R T + \varphi \sum_\beta \rho_\beta S_\beta U_\beta$
Porous media	Phase velocity	$\mathbf{u}_\beta = -k \frac{k_{r\beta}}{\mu_\beta}\left(\nabla P_\beta - \rho_\beta \mathbf{g}\right)$
Wellbore	Energy flux	$F^\kappa = -\lambda \frac{\partial T}{\partial z} - \frac{1}{A}\sum_\beta \frac{\partial}{\partial z}\left(A \rho_\beta S_\beta u_\beta \left(h_\beta + \frac{u_\beta^2}{2}\right)\right) - \sum_\beta \left(S_\beta \rho_\beta u_\beta \, g \cos\theta\right) - q''$
Wellbore	Energy accumulation	$M^\kappa = \sum_\beta \rho_\beta S_\beta \left(U_\beta + \frac{1}{2}u_\beta^2\right)$
Wellbore	Phase velocity	$u_G = C_0 \frac{\rho_m}{\rho_m^*} u_m + \frac{\rho_L}{\rho_m^*} u_d$ $u_L = \frac{(1-S_G C_0)\rho_m}{(1-S_G)\rho_m^*} u_m - \frac{S_G \rho_G}{(1-S_G)\rho_m^*} u_d$

Although various nomenclatures and forms of equations have been used in the literature over the recent past to describe DFM approach, its the basic idea is to assume that the gas velocity, u_G, can be related to the volumetric flux of the mixture, j, and the drift velocity of gas, u_d, by the empirical constitutive relationship:

$$u_G = C_0 \, j + u_d \qquad (1)$$

where C_0 is the profile parameter to account for the effect of local gas saturation and velocity profiles over the pipe cross-section. The liquid velocity u_L can be solved by considering the definition of the volumetric flux of the mixture

$$u_L = \frac{1 - S_G C_0}{1 - S_G} j - \frac{S_G}{1 - S_G} u_d \qquad (2).$$

where S_G is the gas phase saturation.

With the drift-flux model (1)-(2), the momentum equations of two-phase flow in a wellbore can be simplified into a single equation in terms of the mixture velocity u_m and the drift velocity u_d as follows (Pan et al., 2011a, Appendix A):

$$\frac{\partial}{\partial t}(\rho_m u_m) + \frac{1}{A}\frac{\partial}{\partial z}\left[A\left(\rho_m u_m^2 + \gamma\right)\right] = -\frac{\partial P}{\partial z} - \frac{\Gamma f \rho_m |u_m| u_m}{2A} - \rho_m g \cos\theta \quad (3)$$

where the term $\gamma = \frac{S_G}{1-S_G}\frac{\rho_G \rho_L \rho_m}{\rho_m^{*2}}\left[(C_0 - 1)u_m + u_d\right]^2$ is caused by slip between the two phases. The terms ρ_m, u_m, and ρ_m^* are the mixture density, the mixture velocity (mass centered), and the profile-adjusted average density of the mixture.

Therefore, with the DFM approach, solving the complicated momentum equations of two-phase flow becomes an easier task executed in two steps. First, we obtain the mixture velocity by solving the momentum equation (3) and the drift velocity from empirical relationships (discussed below). Second, we calculate the gas velocity and the liquid velocity as a function of u_m and u_d.

The empirical relationships for the drift velocity and the profile parameter used in T2Well/ECO2N are based on the drift flux model developed by Shi et al. (2005). They proposed functional forms for the profile parameter and drift velocity with a set of optimized parameters obtained from an extensive set of large-scale pipe flow experiments performed by Oddie et al. (2003) for one-, two-, and three-phase flow at various inclinations. These functional forms can be applied continuously for all flow regimes, from bubble flow to film flow. A summary of the mathematical formulations related to the drift velocity proposed by Shi et al. (2005) that are implemented in T2Well can be found in the T2Well/ECO2N manual (Pan et al., 2011c) and a related paper (Pan et al., 2011b).

Because the original equation for drift velocity proposed by Shi et al. (2005) cannot be applied to the mist flow regime, i.e., the special two-phase flow pattern that often occurs at high velocity and high gas mass fraction, X. In the mist flow regime, the gas velocity is so high that the small amount of liquid (i.e., $X \approx 1$) cannot form a film, but instead forms tiny droplets that are uniformly distributed in the gas flow. As a result, the slip between the two phases in the mist flow regime diminishes. Cheng et al. (2008) developed a flow pattern map for CO_2 that suggests that the mist flow regime occurs when mass velocity (i.e., the total mass flow rate per unit cross-sectional area, G) reaches more than 300 kg/m^2/s at higher X. To account for this region, we used a modified equation to calculate the drift velocity as follows:

$$u_d = \frac{(1 - S_G)\, u_c\, K(S_G, K_u)\, m(\theta) f(G, X)}{S_G \sqrt{\rho_G / \rho_L} + 1 - S_G} \quad (4).$$

The adjustment function $f(G, X)$ is a smooth function that quickly approaches zero as the state point in the G-X plane approaches the mist flow regime, whereas it would equal one everywhere else (Pan et al., 2011a, Appendix B). In addition, a cosine-type function K(•) is used in (4) to make a smooth transition of drift velocity between the bubble-rise stage and the film-flooding stage, which is slightly different from the linear interpolation suggested by Shi et al. (2005).

IMPLEMENTATION

The component mass- and energy-balance equations of Table 1 are discretized in space using the conventional integrated finite-difference scheme of TOUGH2 for both the wellbore and the reservoir. Apart from the special treatment of the momentum equation for wellbore (discussed below), time discretization is carried out using a backward, first-order, fully implicit finite-difference scheme. In the framework of TOUGH2, the discretized mass and energy conservation equations are written in residual forms as functions of primary variables, and are solved using Newton-Raphson iteration, during which all elements in the Jacobian matrix are evaluated by numerical differentiation (Pruess et al., 1999).

Unlike in the reservoir, where the phase velocities can simply be obtained using Darcy's Law, the phase velocities in the wellbore are functions of the mixture velocity, which is an unknown variable of the momentum equation. Solving an additional governing equation (i.e., the momentum equation) simultaneously is tedious, because (1) the momentum equation is only needed for a

very small portion of the domain (i.e., the wellbore) and (2) the velocity is naturally defined at the interfaces between grid cells, whereas other primary variables are defined at the grid cells. Our approach is to solve the momentum equation using a hybrid formula at interfaces of the neighboring wellbore cells as

$$u_m^{n+1} = \frac{DR^{n+1} + \frac{1}{\Delta t}\rho_m^n u_m^n - \left(\frac{1}{A}\frac{\partial}{\partial z}\left(A\sum_\beta \rho_\beta S_\beta u_\beta^2\right)\right)^n}{\frac{\rho_m^{n+1}}{\Delta t} + \frac{f^n \Gamma \rho_m^{n+1}\left|u_m^n\right|}{2A}} \quad (5)$$

where, the superscripts n and $n + 1$ indicate the previous and current time levels, respectively; Δt is the time-step size, and DR is the total driving force given by

$$DR = -\frac{\partial P}{\partial z} - \rho_m g \cos\theta \quad (6).$$

Here, the driving force term (pressure gradient and gravity) is treated fully implicitly, whereas the spatial acceleration term is treated explicitly. The friction term is evaluated part explicitly and part implicitly.

The flow terms at the interface between the perforated wellbore sections and the surrounding formations are calculated based on Darcy's law, because they are usually limited by the flow through formations. However, the nodal distance to the interface of the wellbore side is set to zero, which is equivalent to the resistance to flow inside the wellbore being negligible relative to that on the formation side.

The heat exchanges between wellbore and the surrounding formation will either be calculated as the "normal" heat flow terms in standard TOUGH2, if the surrounding formation is explicitly represented in the numerical grid, or they will be calculated (optionally) semi-analytically (Ramey, 1962), if no gridblocks of the surrounding formation exist.

In standard TOUGH2, besides pressure, temperature, and gas saturation (if two phase), the mass fractions of non-water components are usually used as the primary variables. However, this practice could be problematic for a system with multiple gas components (e.g., CO_2, CH_4, and air), especially if one or more of the components disappear at any cells in the domain. This is because physically, the sum of all mass fractions should be one at all gridblocks. As a result, the partial derivative with respect to one mass component could become close to a linear function of the partial derivative with respect to another mass component, especially if one of the three mass components does not exist. Consequently, the Jacobian matrix would become singular or close to singular, resulting in a failure of the Newton-Raphson iteration. To avoid this trouble, a new set of primary variables (for the gas components) is used. Taking the research module EOS7CMA (water, brine, CO_2, CH_4, air) as an example, the new primary variables X3 and X4 are defined as the scaled mass fraction in noncondensable mass components, as follows:

$$X_3 = \frac{2X_{CO2}}{X_{CO2} + X_{nc}} \quad (7a)$$

$$X_4 = \frac{2X_{CH4}}{X_{CH4} + X_{nc}} \quad (7b)$$

$$X_5 = \begin{cases} S_g & if\ two-phase \\ X_{nc} & otherwise \end{cases} \quad (7c)$$

where X_{nc} is the total mass fraction of noncondensable gas components (= X_{CO2} + X_{CH4} + X_{air}). Each mass component can be easily calculated from the primary variables as follows:

$$X_{CO2} = \frac{X_3 X_{nc}}{2 - X_3} \quad (8a)$$

$$X_{CH4} = \frac{X_4 X_{nc}}{2 - X_4} \quad (8b)$$

$$X_{air} = X_{nc} - X_{CO2} - X_{CH4} \quad (8c)$$

In the case of two-phase conditions, X_{nc} is obtained by solving the solubility equation in a similar way as in standard TOUGH2. The new primary variables defined in (7) would never be co-linear. However, numerical differentiation could still lead to negative mass fraction, which could either cause problems in the calculation of fluid properties if not forced to zero, or worsen the condition of the Jarcobian matrix if forced to zero, for the case in which the air component does not exist or only CO_2 or CH_4 exists in any gridblock. In this case, a special formula for

calculating the increments in primary variables (X_3 and X_4) is used to enforce that all mass fractions be in physically reasonable ranges and that Equation (8c) is conserved such that the partial derivatives with respect to each primary variable are not linearly correlated.

VERIFICATION AND APPLICATION EXAMPLES

Verification against an analytical solution of steady-state two-phase flow

To verify the T2Well code, we first compare the numerical model against the analytical solution by Pan et al. (2011a). We consider an idealized problem of steady-state, isothermal, two-phase (air and water) flow through a vertical wellbore of 1000 m length.

The T2Well/EOS3 problem is run as a transient problem with adaptive time steps. The ending simulation time is 7.85×10^{8} seconds (4100 steps), at which the average time-derivative of momentum is about -2.2×10^{-17} (Pa/m), indicating an effective steady state was reached. As shown in Figure 1, the agreement is very good between the numerical solution and the analytical solution (coefficient of determination $R^2 > 0.998$).

Validation with field CO_2 production test data

To demonstrate the adequacy of T2Well to describe wellbore flow in an actual well, we compared T2Well/ECO2N simulation results to the field data of Cronshaw and Bolling (1982). Flow in the wellbore was believed to reach steady-state after half a day during a field production test (Cronshaw and Bolling, 1982), and the pressure and temperature data were measured at that time. In total, four flow rates (2.5, 7.4, 11.2, and 13.7 kg/s) were used in the test. The well had a length of 914.4 m with a incline angle of 26.5°. Its diameter was 0.088 m.

In these simulations, only the lower portion (below the measured depth of 595 m) of the wellbore was simulated, because three-phase (water, liquid CO_2, and gaseous CO_2) conditions may develop in the upper portion of the wellbore, which is beyond the phase handling capability of

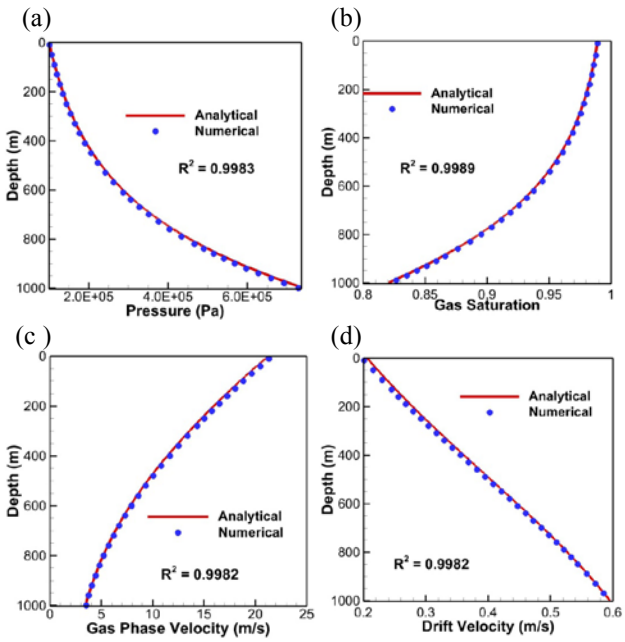

Figure 1. Depth profiles of pressure, gas saturation, gas-phase velocity, and drift velocity under steady-state, isothermal, two-phase (air/water) flow conditions in a vertical wellbore showing excellent agreement between analytical and numerical results. R^2 is the coefficient of determination.

ECO2N. The heat exchange between the wellbore and the surrounding formation is calculated using an analytical approach implemented in the code, and the corresponding heat conductivity is 2.51 (W/m oC). The vertical grid resolution is 1 m.

As shown in Figure 2, the match between the simulated results and the field data is reasonably good, except for the extra-high temperature at the measured depth of 750 m for case R1. Cronshaw and Bolling (1982) did not explain why the measured temperature at that point in Case R1 was higher than the ambient formation temperature and very close to the temperature at 914 m depth. One possibility is that a vertical convective heat-transfer mechanism in the annulus outside the production tube was established prior to the production test, which was able to maintain an almost constant temperature in the well completion fluid up to the depth of 750 m (at least) before production. As a result, the production tube was effectively surrounded by the hot fluid, which enhanced the lateral heat exchange and tended to maintain a higher

temperature in the lower portion of the tube. If this is the case, the density of CO_2 in the production tube would be lower, and thus the gravity-pressure loss would be smaller than that without this additional heating. This temperature difference seems to contribute to the under-predictions of pressure by the model for the lower flow rate cases, because the model does not include this additional heating mechanism. Even when we tried to compensate for this effect by slightly altering the T and P boundary conditions, the predicted pressure profile was still not as steep as the measured ones for cases R1 and R2, mainly because of the overestimation of the density (increasing as temperature decreases) resulting from ignoring such heat exchange effects. Notably, this effect becomes much smaller as the flow rate increases (i.e., the inflow CO_2 becomes more dominant). As a result, the deviations between predictions and the measured data become smaller for the higher flow-rate cases .

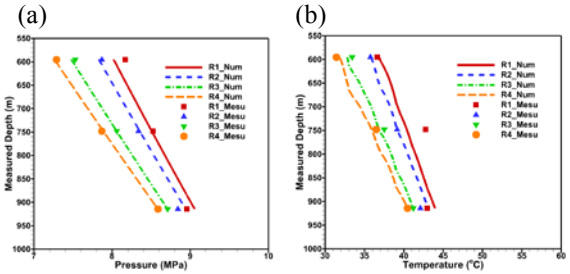

Figure 2. Simulated depth profiles of pressure (a) and temperature (b) after 12 hours of production under different flow rates as compared to the measured data Lines are predictions by T2Well/ECO2n, and symbols are the measured data (red – R1; blue – R2; green – R3; and yellow – R4).

Cronshaw and Bolling (1982) did not report the downhole gas saturation, but mentioned that their model was able to predict the pressure profile correctly only if assuming pure CO_2 production, even though there was 3% water produced in each case. In our simulations, the gas saturation at well bottom was assigned between 0.988 and 0.989, which was obtained from the previous analytical solutions (Pan et al., 2011a). The predicted water fraction in the produced fluid is 3.16%, 3.06%, 2.99%, and 2.99% for cases R1, R2, R3, and R4, respectively, which are pretty close to the reported value of 3%.

Estimation of oil and gas flow-rate for the 2010 BP Macondo Well Blowout

On April 20, 2010, the Macondo well drilled by BP from the Deepwater Horizon floating platform in the Gulf of Mexico suffered a blowout. Eleven people were killed by the explosion and fire on the platform shortly after the blowout. Estimation of the magnitude of the oil and gas discharge into the marine environment became an urgent priority after numerous attempts to stem the flow failed. Such an estimate would be critical for addressing the environmental consequences of the oil and gas release, for developing engineering solutions for a temporary containment cap, and for evaluating the liability of the operating companies for the resulting environmental damage.

T2Well was used with a simplified TOUGH2 EOS for oil to estimate the gas and oil flow rate (Oldenburg et al., 2011). The model was constructed as a single well problem in a simple radial symmetric reservoir. Figure 3 shows the oil and gas flow rates for various lengths of opening of the wellbore in the reservoir. In addition to sensitivity of results to the connectivity of the well and the reservoir, we also observed sensitivity of results to the pressure at the bottom of the blowout preventer. This pressure boundary condition also controls the amount of degassing of the oil during upward flow in the well, which in turn affects oil flow rate (Oldenburg et al., 2011).

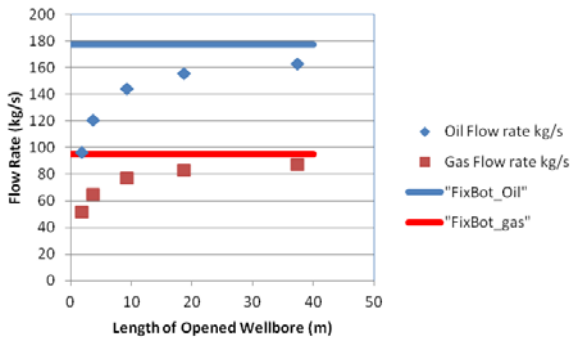

Figure 3. Simulated oil and gas flow rates as response to the length of opened ("broken") wellbore. "FixBot_oil" and "FixBot_gas" are the simulated flow rates as if the wellbore is attached to an infinite pool of oil under reservoir conditions (i.e., the upper limit for the given parameters).

Modeling brine leakage to shallow aquifer through an open well

Potential leakage of brine to a shallower potable aquifer through open wellbores is a common concern for GCS projects, because the area of hydraulic overpressure is usually much larger than the free-phase plume, and many wellbores may be completely plugged only near the land surface. T2Well was used to study such a problem (Hu et al., 2011). A hypothetical system consists of two aquifers separated by a thick aquitard but connected by an open wellbore which is closed at the land surface as well as the aquitard formation, but fully perforated in both aquifers (Figure 4(a)). The system starts at hydrostatic conditions with various salinity conditions and responds to a pressure perturbation at the far end of the lower aquifer as if CO_2 were injected into the lower aquifer at a great distance from the well.

Figure 4(b) shows the simulated brine leakage rates 10 days after the pressure perturbation is applied. As expected, the lower the salinity, the higher the leakage rate under the same pressure perturbation, and the leakage rate increases with the pressure perturbation. However, the widely used EDM (Equivalent Darcy Medium) approach could over- or underestimate the leakage rate, depending on specifc conditions. The critical equivalent permeability for the wellbore used in the EDM approach is not an intrinsic parameter of the wellbore, but rather a function of flow status, simply because the flow in an open wellbore does not in general obey Darcy's law.

CONCLUSION

We have developed a new modeling approach that can simulate nonisothermal, two-phase, multicomponent flow in wellbores connected to reservoirs as an integrated system within the framework of TOUGH2. The new model has been verified against both analytical solutions and field-measured data gathered during a CO_2 production test. As demonstrated in the example applications, the code can be used to analyze many practical problems in various fields with proper EOS modules. In many cases, the integrated wellbore-reservoir modeling approach is necessary for correctly solving problems that could not be solved by wellbore or reservoir simulator alone.

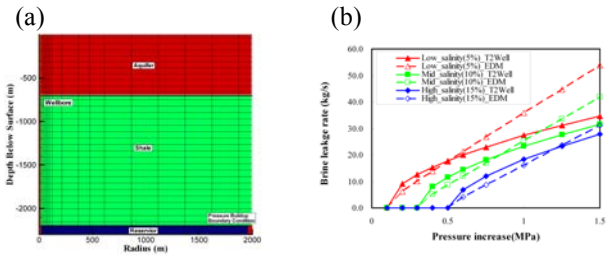

Figure 4. (a) A radial symmetric grid for a two-aquifer, one-aquitard, and one-well system. (b) Simulated leakage rates (after 10 days) as response to the pressure perturbation under the effects of 5%, 10%, and 15% salinity by T2Well and EDM (Equivalent Darcy Medium) approach. The equivalent permeability for the wellbore in the EDM model was obtained by matching the flow rate under the low salinity (5%) case as response to 0.5 MPa pressure perturbation calculated by T2Well.

ACKNOWLEDGEMENT

This work was supported, in part, by the CO_2 Capture Project (CCP) of the Joint Industry Program (JIP), by the National Risk Assessment Partnership (NRAP) through the Assistant Secretary for Fossil Energy, Office of Sequestration, Hydrogen, and Clean Coal Fuels, through the National Energy Technology Laboratory, and by Lawrence Berkeley National Laboratory under U.S. Department of Energy Contract No. DE-AC02-05CH11231.

REFERENCES

Cheng, L., G. Ribatski, J.M. Quiben, J.R. Thome. New prediction methods for CO_2 evaporation inside tubes: Part I – A two-phase flow pattern map and a flow pattern based phenomenological model for two-phase flow frictional pressure drops, *Int. J Heat and Mass Transfer*, 51: 111–124, 2008.

Cronshaw, M.B. and J.D. Bolling. A numerical model of the non-isothermal flow of carbon dioxide in wellbores. In: SPE 10735, SPE California Regional Meeting, San Francisco, May 22-26, 1982.

Hadgu, T., R.W. Zimmerman, and G.S. Bodvarsson. Coupled reservoir-wellbore simulation of geothermal reservoir behavior. *Geothermics* 24(2), 145-166, 1995.

Hu, L., L. Pan, and K. Zhang. Modeling brine leakage to shallow aquifer through an open wellbore using T2WELL/ECO2N. *International J. of Greenhouse Gas Control,* 9 393–401, 2012.

Lindeberg, E. Modelling pressure and temperature profile in a CO_2 injection well, *Energy Procedia*, 4, 3935-3941, 2011.

Livescu, S., L.J. Durlofsky, K. Aziz, and J.C. Ginestra. A fully-coupled thermal multiphase wellbore flow model for use in reservoir simulation. *J. of Petroleum Science and Engineering*, 2009.

Lu, M. and L.D. Connell. Non-isothermal Flow of Carbon Dioxide in Injection Wells during Geological Storage, *Int. J. Greenhouse Gas Control*, 2(2), pp. 248–258, 2008.

Oddie, G., H. Shi, L.J. Durlofsky, K. Aziz, B. Pfeffer, and J.A. Holmes. Experimental study of two and three phase flows in large diameter inclined pipes, *Int. J Multiphase Flow,* 29:527–558, 2003.

Oldenburg, C.M., B.M. Freifeld, K. Pruess, L. Pan, S.A. Finsterle, and G. Moridis. Numerical simulations of the Macondo well blowout reveal strong control of oil flow by reservoir permeability and exsolution of gas, *Proc. National Acad. Sci.*, Early Edition, 2011.

Pan L., S.W. Webb, and C.M. Oldenburg. Analytical solution for two-phase flow in a wellbore using the drift-flux model. *Advances in Water Resources*. 34, 1656–1665, 2011a.

Pan L., C.M. Oldenburg, K. Pruess, and Y.-S. Wu. Transient CO_2 leakage and injection in wellbore-reservoir systems for geologic carbon sequestration. *Greenhouse Gas Sci Technol.* 1:335–350; DOI: 10.1002/ghg, 2011b.

Pan, L., Y.-S. Wu, C.M. Oldenburg, and K. Pruess. T2Well/ECO2N Version 1.0: Multiphase and Non-Isothermal Model for Coupled Wellbore-Reservoir Flow of Carbon Dioxide and Variable Salinity Water. LBNL-4291E, 2011c.

Pruess, K., C.M. Oldenburg, and G.J. Moridis. TOUGH2 User's Guide Version 2. Lawrence Berkeley National Laboratory Report, LBNL-43134, November 1999.

Ramey Jr, H.J. Wellbore heat transmission. *J. of Petroleum Technology*, 225, 427–435, 1962.

Remoroza, A.I., B. Moghtaderi, and E. Doroodchi. Coupled wellbore and 3D reservoir simulation of a CO_2 EGS, Proceedings, SGP-TR-191, Thirty-Sixth Workshop on Geothermal Reservoir Engineering, Stanford University, Stanford, California, Jan 31 - Feb 2, 2011.

Shi, H., J.A. Holmes, L.J. Durlofsky, K. Aziz, L.R. Diaz, B. Alkaya, and G. Oddie. Drift-flux modeling of two-phase flow in wellbores, *Soc. Pet. Eng. J.,* 10(1), 24-33, 2005.

Wallis, G.B. One-dimensional Two-phase Flow, McGraw-Hill Book Company, New York, 1969.

Zuber, N. and J.A. Findlay. Average volumetric concentration in two-phase flow systems, *J. Heat Transfer* ASME, 87(4), 453-468, 1965.

AN APPROACH FOR MODELING ROCK DISCONTINUOUS BEHAVIOR UNDER MULTIPHASE FLUID FLOW CONDITIONS

Peng-Zhi Pan[1,2], Jonny Rutqvist[2], Fei Yan[1], Xiating Feng[1]

[1] State Key Laboratory of Geomechanics and Geotechnical Engineering, Institute of Rock and Soil Mechanics, Chinese Academy of Sciences, Wuhan, 430071, China.
[2] Lawrence Berkeley National Laboratory, Berkeley, CA 94720, USA
e-mail: ppan@lbl.gov

ABSTRACT

In this paper, we report the integration of two computer codes, TOUGH2 and RDCA (Rock Discontinuous Cellular Automaton), for coupled hydromechanical analysis of multiphase fluid flow and discontinuous behavior in heterogeneous rock. The RDCA is a numerical model being developed for simulating the nonlinear and discontinuous behavior of rock. TOUGH2 is a well-established code for geo-hydrological analysis with multiphase, multicomponent fluid flow and heat transport. The integration of these two codes is executed sequentially and linked through external coupling modules. TOUGH2 modeling provides the changes in effective stress as a function of multiphase pore pressure and thermal expansion. RDCA corrects porosity, permeability, and capillary pressure for changes in mechanical behavior. By introducing discontinuous function in RDCA, we can conveniently apply the fluid pressure obtained from TOUGH2 to any discontinuous inner boundaries. As a result, rock nonlinear and discontinuous deformation behavior, such as plastic yielding, crack initiation, propagation and coalescence etc., induced by the change of fluid pressure and thermal expansion, can be simulated in RDCA. RDCA incorporates the discontinuity of a crack independently of the mesh, such that the crack can be arbitrarily located within an element. The method does not require any re-meshing for crack growth, which greatly simplifies the modeling procedure and its integration with TOUGH2. Here, we provide a detailed description of TOUGH-RDCA integration and then present numerical examples to show the combined code's capability to model discontinuous deformation and fracturing of rock masses within a multiphase fluid flow environment.

INTRODUCTION

Rock masses are generally strongly heterogeneous, containing rock matrix and discontinuities. Rock masses may be exposed to complex environments, such as mechanical, hydraulic, and thermal fields and their couplings. The study of coupled thermal-hydro-mechanical (THM) processes is key for understanding the complex physical behavior within rock masses. In the last few decades, a steadily growing interest in coupled THM phenomena in geological media has encouraged development of many computer codes at various levels of sophistication. Based on Biot's theory of consolidation, several simulators such as THAMES (Ohnishi et al., 1996), MOTIF (Guvanasen and Chan, 1995), FRACON (Nguyen, 1996) and ROCMAS (Noorishad et al. 1984) were developed and applied mostly to geological nuclear waste disposal. Other simulators (FEMH (Bower and Zyvoloski, 1997), GeoSys/Rockflow (Wang and Kolditz, 2007), FRACTure (Kohl and Hopkirk, 1995), GEOCRACK (Swenson et al., 1997)) were originally applied to the field of hot-dry-rock geothermal energy, although they have also been applied to other types of coupled problems. Some commercial codes (e.g., ABAQUS (Börgesson, 1996), FLAC (Israelsson, 1996), UDEC (Israelsson, 1996)) have been applied in soil and rock mechanics. In the field of soil mechanics, COMPASS (Thomas and Sansom, 1995) and CODE-BRIGHT (Olivella et al., 1994) were developed to simulate coupled two-phase (gas and liquid) fluid flow and thermo-mechanical responses in partially saturated soil and isothermal multiphase flow of brine and gas in saline media. TOUGH2, developed by Pruess et al. (1999), is a well established numerical model that can simulate non-isothermal, multiphase flow processes. Because TOUGH2 does not include mechanical modules, a practical way

to consider the mechanical effect is to link it with other codes. Rutqvist and Tsang (2002) and Rutqvist et al. (2002) pioneered this approach by linking TOUGH2 (Pruess et al., 1999) and FLAC3D (Itasca Consulting Group, 2000) for modeling multiphase flow, heat transport and geomechanics.

The codes and numerical methods mentioned above are versatile in modeling coupled THM processes, including some of them under multiphase flow conditions. However, the ability to model nonlinear and discontinuous behavior in rock masses, including fracture propagation, under multiphase flow and non-isothermal conditions, still needs to be strengthened. Rock masses are generally heterogeneous, containing different minerals, joints, and fractures. Under such conditions, the rock mass behavior can be nonlinear and discontinuous, with strong coupling between THM processes. Therefore, we require an appropriate numerical model that can adequately consider the heterogeneous and discontinuous behavior of rock and simulate its fracturing process under strongly coupled THM conditions.

The Rock Discontinuous Cellular Automaton (RDCA) (Pan et al., 2012) code, developed to simulate the fracturing process in heterogeneous rock, is effective in considering the nonlinearity and discontinuity of rocks. RDCA contains a thermo-hydro-mechanical module, but is limited to single-phase fluid flow (Pan et al. 2009). This paper describes taking the RDCA approach a step further by linking TOUGH and RDCA for modeling the nonlinear and discontinuous behavior of heterogeneous rock under multiphase flow and nonisothermal conditions. We present coupling functions and a linking approach, and then show numerical examples demonstrating the capability of the coupled TOUGH-RDCA simulator.

NUMERICAL TOOL—A COMBINATION OF TOUGH-RDCA

An Introduction to the Rock Discontinuous Cellular Automaton (RDCA) Code

The Rock Discontinuous Cellular Automaton (RDCA) (Pan et al., 2012) incorporates the following methods and techniques: (1) a special displacement function to represent internal discontinuity; (2) a level set method to track the fracturing path; (3) a partition of unity method to improve the integral precision of fracture surface and fracture tip; (4) a cellular automaton updating rule to calculate the mechanical state; (5) a mixed-mode fracture criterion to determine the fracturing behavior. By doing so, this code incorporates the discontinuity of a crack independently of the mesh, such that the crack can be arbitrarily located within an element. The method does not require any re-meshing for crack growth. These aspects greatly reduce the complexity and improve modeling efficiency.

The previous version of RDCA did not include the function for modeling discontinuous deformation behavior induced by fluid injection. To do that, we discretize the domain to be solved into a system of cell elements in which the discontinuity of a crack is incorporated (Figure 1). To extend this approach to fracturing under internal fluid pressure, we also discretize the crack surface into one-dimensional segments used for applying fluid pressure on the two opposing crack surfaces. Gaussian quadrature points are defined along each of the one-dimensional subelements to numerically integrate the terms on Γ_c (Figure 2). Each Gaussian point coordinate on Γ_c is mapped on global coordinates, which are then mapped within the local coordinate system to cell elements. A Gaussian quadrature is performed by a loop over one-dimensional elements. The nodal forces induced by fluid pressure on crack surfaces and crack tips can be respectively calculated as

$$f_i^a = 2\int_{\Gamma_c} \mathbf{n} \cdot N_i \mathbf{p}\, \mathrm{d}\Gamma \qquad (1)$$

$$f_i^{b\alpha} = 2\int_{\Gamma_c} \mathbf{n}\sqrt{r} \cdot N_i \mathbf{p}\, \mathrm{d}\Gamma \qquad \alpha = 1,2,3,4 \qquad (2)$$

where **p** is the fluid pressure applied on the crack surfaces. **n** is a vector normal to crack surface. r is the radius for integration around the crack tip. N*i* is shape function. To judge whether a crack propagates, we introduce linear-elastic-fracture mechanics and the stress intensity factor concept (SIF) (Knott 1973; Broek 1982; Kanninen and Popelar 1985; Atkinson 1987). For a two-dimensional problem, the stress intensity factor for mixed mode failure is

$$J = \frac{K_I^2}{E^*} + \frac{K_{II}^2}{E^*} \quad (3)$$

For plane stress, $E^* = E$, whereas for plane strain, $E^* = \frac{E}{1-v^2}$.

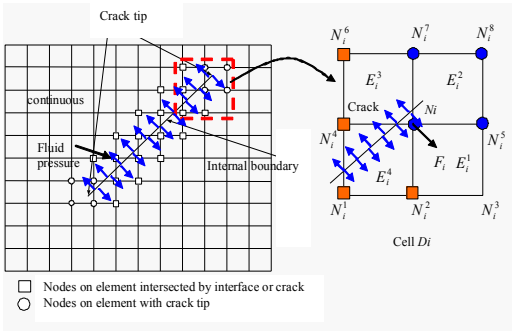

Figure 1. Representation of the discontinuous cellular automaton model

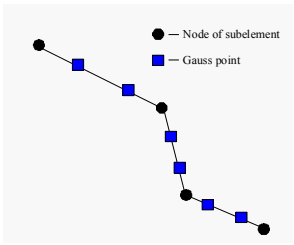

Figure 2. Gauss quadrature points on a crack surface.

Consider two equilibrium states of the body, i.e., State 1 and State 2. State 1 is the actual state of the body; State 2 is an auxiliary state. Field variables associated with the two states are denoted with superscripts 1 and 2. Superposition of the two equilibrium states leads to another equilibrium state denoted by $J^{(1+2)}$.

$$J^{(1+2)} = \int_\Gamma \left[\frac{1}{2}\left(\sigma_{ij}^{(1)} + \sigma_{ij}^{(2)}\right)\left(\varepsilon_{ij}^{(1)} + \varepsilon_{ij}^{(2)}\right)\delta_{1j} - \left(\sigma_{ij}^{(1)} + \sigma_{ij}^{(2)}\right)\frac{\partial\left(u_i^{(1)} + u_i^{(2)}\right)}{\partial x_j} \right] n_j \, d\Gamma \quad (4)$$

We can write a simplified form of the above equation:

$$J^{(1+2)} = J^{(1)} + J^{(2)} + M^{(1,2)} \quad (5)$$

Assuming that the crack surface near the crack tip is straight and is in the integral boundary C_0 shown in Figure 3, the M-integral can be expressed as,

$$M^{(1,2)} = \int_C \left[\sigma_{ij}^{(1)} \frac{\partial u_i^{(2)}}{\partial x_1} + \sigma_{ij}^{(2)} \frac{\partial u_i^{(1)}}{\partial x_1} - W^{(1,2)}\delta_{1j} \right] q m_j \, dC - \quad (6)$$

$$\int_{C_+ + C_-} \left[\sigma_{i2}^{(1)} \frac{\partial u_i^{(2)}}{\partial x_1} + \sigma_{i2}^{(2)} \frac{\partial u_i^{(1)}}{\partial x_1} - W^{(1,2)}\delta_{1j} \right] q m_j \, dC$$

where $C = \Gamma \cup C_+ \cup C_- \cup C_0$, m_j is the outward normal vector to domain and q is the weight function. The second term of the right-hand side in Eq. (6) considers the effect of fluid pressure on crack surface.

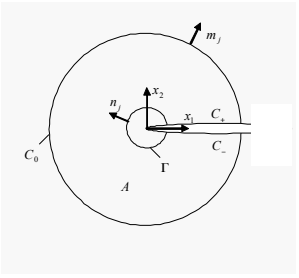

Figure 3. Representation of M-integral at the crack tip

Rock-mass failure can be induced by mixed-mode cracking. In RDCA, several criteria, such as the maximum circumferential stress criterion, maximum tangential stress criterion, and minimum strain energy criterion, are used to determine the cracking conditions. During the simulation, the criterion provides the amount and direction of crack advancement. Take the maximum circumferential stress criterion as an example: an explicit solution for the direction of crack propagation would be:

$$\theta_c = 2\tan^{-1}\left[\frac{1}{4}\left(\frac{K_I}{K_{II}} - \text{sign}\left(K_{II}\right)\sqrt{8 + \left(\frac{K_I}{K_{II}}\right)^2} \right) \right] \quad (7)$$

where θ_c is measured with respect to a local polar coordinate system with its origin at the crack tip, and is aligned in the direction of the existing crack. Once the crack-growth orientation is determined, a propagation increment is added to the existing crack, and the analysis procedure is repeated. Stress intensity factors K_I and K_{II} are calculated using the domain form of the interaction integral.

An Introduction to TOUGH2

TOUGH2 is a well-established numerical simulation program for multidimensional fluid and heat flows of multiphase, multicomponent fluid mixtures in porous and fractured media. It has been widely used in geothermal reservoir engineering, nuclear waste isolation studies, environmental assessment and remediation, and flow and transport in variably saturated media and

aquifers. Detailed description can be found in the work by Pruess et al. (Pruess et al. 1999; Pruess and Garc¨a 2002)

The Combination of TOUGH-RDCA

In this work, the coupled THM analysis is conducted by combining TOUGH2 and RDCA. Figure 4 shows the relation between TOUGH2 and RDCA codes in the THM coupling modeling. A TOUGH-to-RDCA link takes multiphase pressures, saturation and temperature from the TOUGH2 simulation and provides the updated temperature and pore-pressure information to RDCA. In RDCA, the thermal expansion and effective stress is calculated, and then the failure analysis (plasticity or discontinuity) is conducted. An RDCA-to-TOUGH link takes the mechanical variables (stress, plastic strain or fracture opening displacement) from RDCA and updates the corresponding element porosity, permeability, and capillary pressure to be used by TOUGH2.

The combined simulator can model nonisothermal, multiphase flow processes coupled with mechanical behavior changes induced by temperature and fluid pressure. One of the main features of the RDCA mechanical model is the ability to analyze the stress path, nonlinearity, and discontinuity in a rock mass that might be critically stressed, on the verge of failure because of THM effects.

To run a TOUGH-RDCA simulation, the numerical grids for the two codes should be developed with the same geometry and element numbering. In RDCA, the crack geometry (or other internal boundaries) and numerical grid are independent of each other. Using the level-set method, we divide the elements intersected by a crack into several quadrilateral sub-elements based on the *partition of unity* concept (Figure 5). The pressure in each element is determined from the solution of the flow equation over the entire domain. For elements intersected by the crack, the fluid pressure is applied on the crack surface. As seen from Figure 5, the fluid pressure applied on the crack surface can be non-uniform, since different places may have different fluid pressures.

The mechanical response is calculated by the equivalent nodal force induced by fluid pressure. Based on the fluid pressure on each element, the equivalent nodal force can be calculated using the effective stress theory. For a normal element, i.e., with no crack surface or crack tip included, the equivalent nodal forces can be calculated by

$$\{f\}^e = \int_{\Omega^e} [B]^T \{p, p, 0\}^T \, d\Omega \qquad (8)$$

where p is fluid pressure and B is strain-displacement matrix.

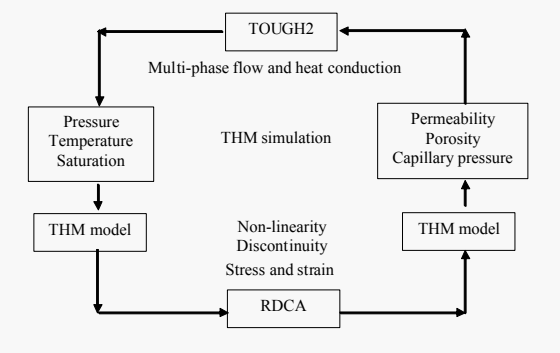

Figure 4. Schematic of linking TOUGH2 and EPCA for coupled thermo-hydro-mechanical (THM) simulations.

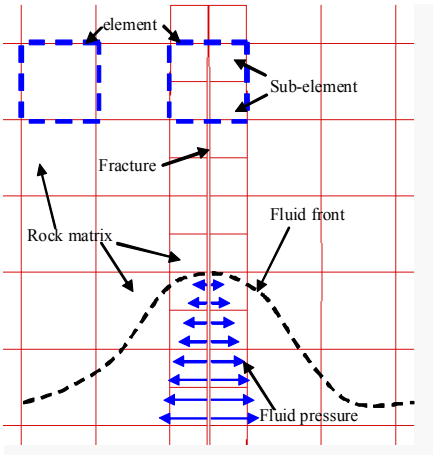

Figure 5. The mechanical state of rock mass induced by fluid flow

For elements that include crack surface or crack tip, the equivalent nodal force includes two parts. One is from the fluid pressure applied to the crack surface, as calculated by Eq. (1) and Eq. (2). The other is from the sub-elements, which are regarded as the rock matrix. Therefore, the contribution of sub-element on element equivalent nodal force can be calculated by Eq. (8), in which the matrix B is different from a normal element and the nodal force involves additional degrees of freedom.

Input parameters for the TOUGH simulation include grain density, porosity, permeability, thermal conductivity, specific heat, relative permeability and water retention curves, as well as hydraulic and thermal boundary conditions (e.g., fixed fluid pressure and temperature). Typical input parameters for the RDCA simulation include bulk density, elastic parameters (Young's modulus, Poisson's ratio), fracture-mechanics parameters (e.g., fracture toughness), as well as mechanical boundary conditions (e.g., fixed displacement or stress). We developed an external routine in which the THM model is included, linking TOUGH2 and RDCA. In this model, porosity, permeability, and capillary pressure are dependent on certain mechanical variables, such as mean stress, volumetric strain, or fracture aperture. For different applications, the THM model may be different.

NUMERICAL EXAMPLE RELATED TO GEOLOGIC CO_2 STORAGE

Problem description

We conducted a numerical simulation of hydromechanical changes during a deep underground injection of supercritical CO_2 in a hypothetical brine aquifer/caprock system, validating our TOUGH-RDCA simulator by comparing it with TOUGH-FLAC (Rutqvist and Tsang 2002) results.

In the modeling, CO_2 is injected at a constant rate over a 10-year period into a permeable injection zone at a depth of 1,300-1,500 m. The injection zone is overlain by a 100 m thick cap rock, located at 1,200-1,300 m, which in one of the studied cases is intersected by a vertical fault (Figure 6). The model description and parameters can be found in the work by Rutqvist and Tsang (2002). For the rock matrix, the constitutive relations of an isotropic linear poroelastic medium can be expressed in terms of the effective stress σ'_{ij} (positive for tension), strain ε_{ij} and temperature change ΔT as (Pan et al. 2009),

$$\sigma'_{ij} = 2G\left(\varepsilon_{ij} + \delta_{ij}\frac{v}{1-2v}\varepsilon_{kk}\right) - K'\alpha\Delta T\delta_{ij} \quad (9)$$

where $\sigma'_{ij} = \sigma_{ij} + \xi\bar{p}\delta_{ij}$ and σ_{ij} is the total stress (positive for tension), δ_{ij} is the Kronecker's delta, $\xi(\le 1)$ is a coefficient that depends on the compressibility of the constituents. Here, $\xi = 1$ is assumed. $\bar{p}$ is an average pore pressure defined as

$$\bar{p} = S_l p_l + (1 - S_l) p_g \quad (10)$$

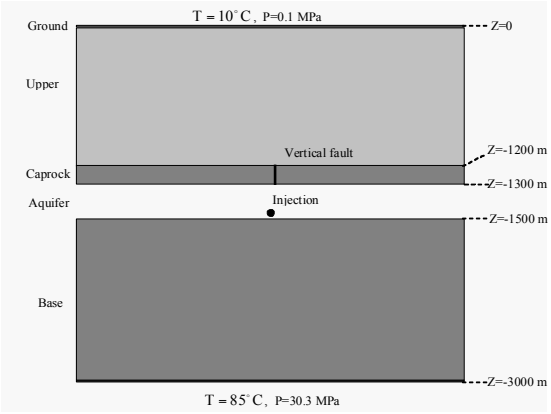

Figure 6. Problem description

For rock fractures, the fluid pressure is applied on a fracture surface normal to the surface. If the shear stress on the fracture surface is not considered, the effective stress is expressed as

$$\sigma'_n = \sigma_n + \xi\bar{p} \quad (11)$$

Isotropic hydromechanical rock properties are represented by porosity-mean stress and permeability-porosity relationships. The porosity, φ, is related to the mean effective stress as (Rutqvist and Tsang 2002)

$$\varphi = (\varphi_0 - \varphi_r)\exp\left(5\times10^{-8}\times\sigma'_M\right) + \varphi_r \quad (12)$$

where ϕ_0 is porosity at zero stress, ϕ_r is residual porosity at high stress and the mean effective stress (in Pa) is defined from the stress components as

$$\sigma'_M = \frac{1}{3}\left(\sigma'_x + \sigma'_y + \sigma'_z\right) \quad (13)$$

Permeability is correlated to porosity according to the following exponential function:

$$k = k_0\exp\left[22.2\left(\varphi/\varphi_0 - 1\right)\right] \quad (14)$$

where k_0 is the zero stress permeability.

Homogeneous case

Figure 7 shows a comparison between different simulators with and without considering hydro-mechancial coupling. It is found that after 10 years' evolution, both TOUGH-FLAC and TOUGH-RDCA injection pressures are lower than that with TOUGH pure (uncoupled) hydraulic modeling. The TOUGH-RDCA modeling of injection pressure evolution has almost exactly the same results as those obtained with TOUGH-FLAC (maximum difference is 0.01 MPa in the 10^{th} year), even though different models, i.e., 2D for RDCA and 3D for FLAC3D, are used.

Figure 8 shows a comparison of displacements at four points: (1) top of well at ground surface, (2) top of cap rock, (3) top of injection zone and (4) bottom of injection zone. The good agreement shows that TOUGH-RDCA displacement evolutions are consistent with that of TOUGH-FLAC. After 10 years of injection, the relative errors for these four points are 2.05%, 0.93%, 1.01% and 2.73%, respectively.

The small discrepancies between these two simulators may be induced by the sub-models used within RDCA and FLAC3D. The current RDCA system is based on a 2D formula that simplifies it to a plane strain problem, in which only σ_x, σ_y and τ_{xy} are independent variables, and σ_z given by $\sigma_z = \nu(\sigma_x + \sigma_y)$, where ν is the Poisson's ratio. But in the FLAC3D model, all three components (σ_x, σ_y and σ_z) are independent variables, i.e., σ_z is not exactly equal to $\nu(\sigma_x + \sigma_y)$. Thus, although there are some differences between these two simulators, the results from TOUGH-RDCA are reasonable and acceptable for homogeneous cases.

The effect of fault in the caprock

We simulate a vertical fault (or fracture) within the cap rock to study its influence on cap-rock THM behavior. In RDCA, the fault is regarded as an internal boundary. By introducing the special displacement function, the discontinuity can be located arbitrarily in an element, which is divided into several sub-elements based on *partition of unity* concept. By doing so, the discontinuous boundary coincides with the edge of the sub-elements. In TOUGH2, the fracture is regarded as a porous medium. Initially, the fault has the same permeability as the cap rock. After fluid injection, it will open up and become more permeable than the surrounding cap rock (Figure 9). For the sake of simplicity, the permeability of a fracture element follows the same evolution rule as a matrix element.

Figure 10 shows the evolution of the CO_2 plume as a result of a constant rate injection. Already after 1 year injection, the CO_2 has penetrated into the fracture, but not yet up into the overlying aquifer. After 10 years' injection, the CO_2 plume has penetrated into the upper aquifer and spread laterally as well as upwards (by buoyancy) about 200 m.

Figure 11 and 12 show the evolution of fracture surface deformation. Figure 11 shows how the fracture opens, with the maximum opening at the center distance between the two crack tips, located just above and below the cap rock. Figure 12 shows the evolution of crack opening displacement (COD) at the inlet (at the bottom of the cap rock) and outlet (at the top of the cap rock). The COD increases more at the inlet because of the higher pressure changes compared to that at the outlet.

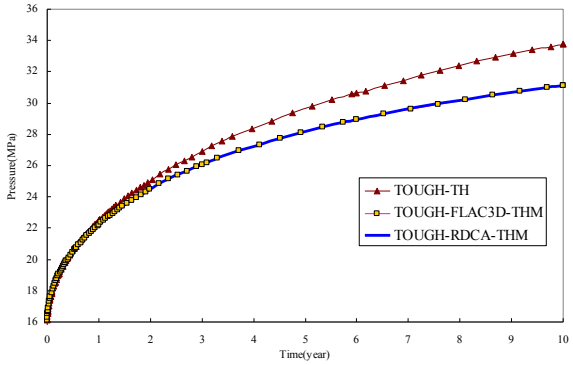

Figure 7. Injection pressure as a function of time with and without considering hydromechanical coupling effects—comparisons between different simulators.

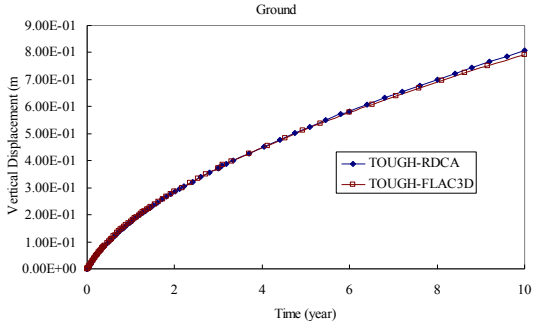

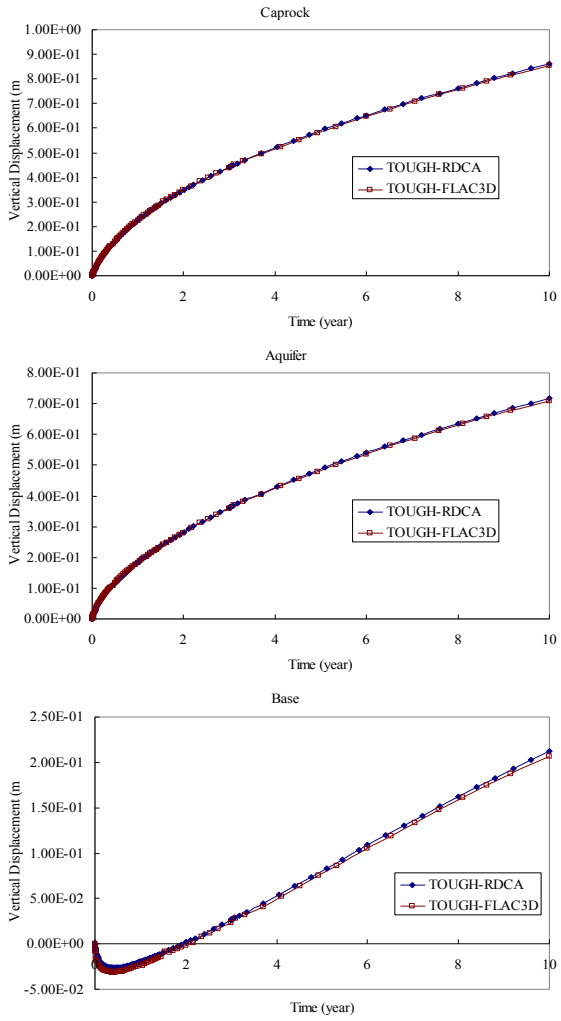

Figure 8. Vertical displacements during 10 years of CO2 injection on four points (i.e. (1) top of well at ground surface, (2) top of caprock, (3) top of injection zone and (4) bottom of injection zone) using different simulators.

Owing to the presence of the vertical fault (or fracture) in the rock mass, some of the reservoir pressure can be released. As a result, after 10 years of injection, the injection pressure decreases about 1.14 MPa compared with the result from homogeneous case (Figure 13).

By using a discontinuous method in RDCA, the detailed mechanical behaviors (e.g., fracture opening, close, or sliding) of fractures can be studied explicitly. This is different from the continuum method, in which the fracture zone is simulated as a porous medium that is more porous than the surrounding caprock and has a much more sensitive HM relationship (Rutqvist and Tsang 2002). One of the disadvantages of this method is that the results are greatly dependent on element size. Higher precision requires a fine grid with small element sizes. RDCA completely overcomes this disadvantage through its special displacement functions to represent discontinuity. These functions include the Heaviside function for the discontinuous field along the length of the crack, and the near-tip function, which guarantees precision even though the numerical grid is relatively sparse.

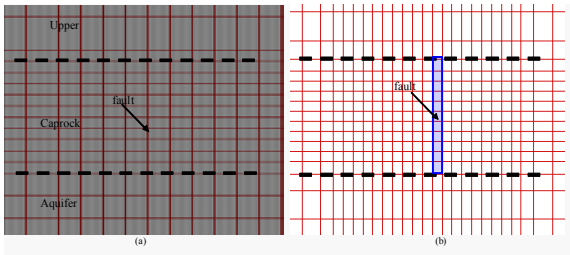

Figure 9. Grids used in (a) RDCA and (b) TOUGH2

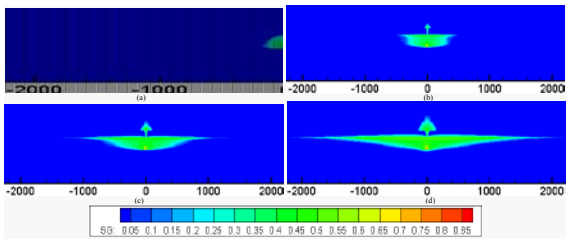

Figure 10. CO_2 saturation during active CO_2 injection at (a) 1 year; (b) 3 years; (c) 6 years, and (d) 10 years

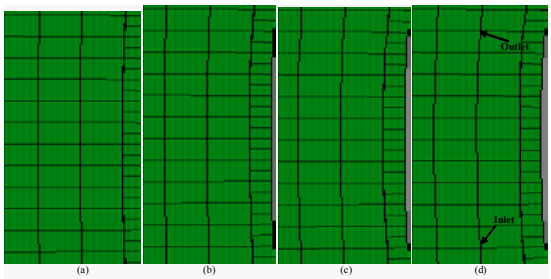

Figure 11. The fracture surface deformation (enlarge 10 times) during the injection of CO2. (a) 1 year; (b) 3 years; (c) 6 years and (d) 10 years.

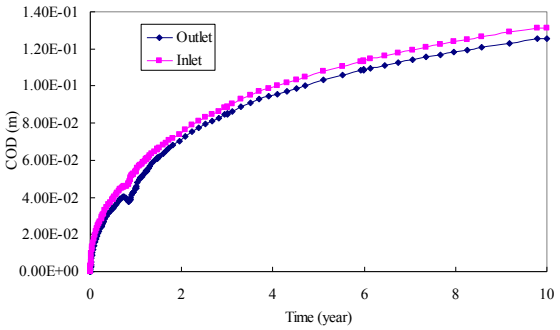

Figure 12. The crack opening displacement evolution at inlet and outlet.

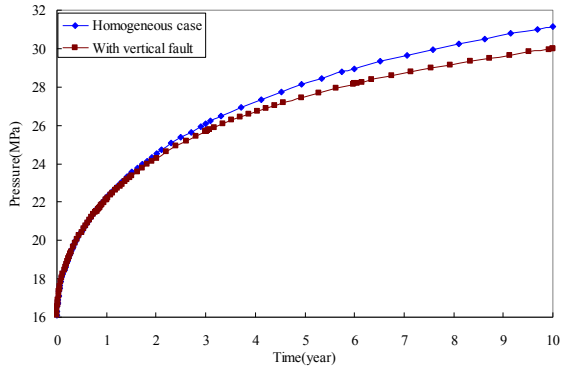

Figure 13. Injection pressure as a function of time with/without considering fault in cap rock.

CONCLUDING REMARKS

This paper demonstrates a numerical method that can simulate the nonlinearity and discontinuity of rock masses involving coupled multiphase nonisothermal fluid flow and geomechanics by linking the numerical codes TOUGH2 and RDCA. The preliminary results from numerical examples show that the TOUGH-RDCA simulator is capable of modeling discontinuous behavior in a rock mass under multiphase fluid flow conditions. More applications based on the developed simulators will be implemented and tested in the future, including fracture propagation.

ACKNOWLEDGMENTS

This work was finically supported by the National Natural Science Foundation of China (Grant Nos. 10972231 and 41272349) and the National Basic Research Program of China under Grant No. 2010CB732006, and in part, supported by the U.S. Dept. of Energy under contract No. DE-AC02-05CH11231.

REFERENCES

Atkinson, B. K. *Fracture mechanics of rocks*, Academic Press Inc., Orlando, FL. 1987.

Börgesson, L. ABAQUS. *Developments in geotechnical engineering* 79, 565-570. 1996.

Bower, K. and G. Zyvoloski A numerical model for thermo-hydro-mechanical coupling in fractured rock. *International Journal of Rock Mechanics and Mining Sciences* 34(8), 1201-1211. 1997.

Broek, D. *Elementary engineering fracture mechanics*, Springer. 1982.

Guvanasen, V. and T. Chan A new three-dimensional finite-element analysis of hysteresis thermohydromechanical deformation of fractured rock mass with dilatance in fractures. 1995.

Israelsson, J. I. Short description of FLAC version 3.2. *Developments in geotechnical engineering* 79, 513-522. 1996.

Israelsson, J. I. Short Descriptions of UDEC and 3DEC. *Developments in geotechnical engineering* 79, 523-528. 1996.

Itasca Consulting Group, I. PFC3D user's guide. *Mineapolis: Itasca Consulting Group Inc*. 2000.

Kanninen, M. F. and C. L. Popelar Advanced fracture mechanics. 1985.

Knott, J. F. Fundamentals of fracture mechanics. 1973.

Kohl, T. and R. Hopkirk The finite element program "FRACTure" for the simulation of Hot Dry Rock reservoir behavior. *Geothermics* 24(3), 345-359. 1995.

Nguyen, T. Description of the computer code FRACON. *Developments in geotechnical engineering* 79, 539-544. 1996.

Noorishad, J., C. Tsang and P. Witherspoon Coupled thermal-hydraulic-mechanical phenomena in saturated fractured porous rocks: numerical approach. *Journal of Geophysical Research* 89(B12), 10365-10310,10373. 1984.

Ohnishi, Y., A. Kobayashi, O. THAMES In Stephansson, L. Jing and C. Tsang Coupled thermo-hydro-mechanical processes of fractured media. *Developments in Geotechnical Engineering, Elsevier* 79, 545-549. 1996.

Olivella, S., J. Carrera, A. Gens and E. Alonso Nonisothermal multiphase flow of brine and gas through saline media. *Transport in Porous Media* 15(3), 271-293. 1994.

Pan, P.-Z., F. Yan and X.-T. Feng Modeling the cracking process of rocks from continuity to discontinuity using a cellular automaton. *Computers & Geosciences* 42(0), 87-99. 2012.

Pan, P. Z., X. T. Feng, X. H. Huang, Q. Cui and H. Zhou Coupled THM processes in EDZ of crystalline rocks using an elasto-plastic cellular automaton. *Environmental Geology* 57(6), 1299-1311. 2009.

Pruess, K. and J. Garc ¨ ª a Multiphase flow dynamics during CO 2 disposal into saline aquifers. *Environmental Geology* 42(2), 282-295. 2002.

Pruess, K., G. Moridis, C. Oldenburg and L. B. N. Laboratory *TOUGH2 user's guide, version 2.0*, Lawrence Berkeley National Laboratory Berkeley, CA. 1999.

Rutqvist, J. and C. F. Tsang A study of caprock hydromechanical changes associated with CO 2-injection into a brine formation. *Environmental Geology* 42(2), 296-305. 2002.

Rutqvist, J., Y. S. Wu, C. F. Tsang and G. Bodvarsson A modeling approach for analysis of coupled multiphase fluid flow, heat transfer, and deformation in fractured porous rock. *International Journal of Rock Mechanics and Mining Sciences* 39(4), 429-442. 2002.

Swenson, D., R. DuTeau and T. Sprecker A coupled model of fluid flow in jointed rock applied to simulation of a hot dry rock reservoir. *Int. J. Rock Mech. Min. Sci. & Geomech. Abstr* 34. 1997.

Thomas, H. R. and M. R. Sansom Fully coupled analysis of heat, moisture, and air transfer in unsaturated soil. *Journal of Engineering Mechanics* 121, 392. 1995.

Wang, W. and O. Kolditz Object ‐ oriented finite element analysis of thermo ‐ hydro ‐ mechanical (THM) problems in porous media. *INTERNATIONAL JOURNAL FOR NUMERICAL METHODS IN ENGINEERING* 69(1), 162-201. 2007.

A SIMPLE HISTORY-DEPENDENT NONWETTING-PHASE TRAPPING MODEL FOR THE TOUGH SIMULATORS

Christopher G. Patterson, Ronald W. Falta

Illinois State Geological Survey
615 E. Peabody Dr.
Champaign, IL, 61820, US
e-mail: patterc@illinois.edu

ABSTRACT

Nonwetting phase trapping by local capillary forces plays a key role in several multiphase flow processes of interest. When LNAPLs or DNAPLs are released into the subsurface, nonwetting-phase trapping causes a significant fraction of the NAPL to become immobilized in the pore space. This trapped fraction is known as the residual saturation, and it is defined as the saturation at which the relative permeability (and capillary pressure) becomes zero. Residual saturations of NAPL typically cannot be removed from the subsurface by pumping; special remediation techniques that enhance the evaporation or dissolution of the NAPL are usually required.

When supercritical CO_2 is injected into deep formations for geologic storage, similar nonwetting-phase trapping takes place, but in this setting, the trapping contributes to the long-term security of CO_2 storage. In either case, the degree to which the nonwetting phase becomes trapped is dependent on the nonwetting-phase saturation history. If the porous medium experiences high nonwetting-phase saturations (high capillary pressures), the resulting residual saturation is also large. However, prior to nonwetting-phase invasion, the nonwetting-phase residual saturation should be zero. The publicly available forward versions of the TOUGH code (e.g. TMVOC, TOUGH2-ECO2N) typically do not account for this nonwetting-phase trapping hysteresis.

The proposed trapping model adds a variable S_{nmax} to the secondary variable list to TMVOC and TOUGH2-ECO2N. S_{nmax} is defined as the maximum historical nonwetting-phase saturation within an element during a simulation. This secondary variable is fully incremented and updated during each Newton-Raphson iteration, and it is used in the relative permeability and capillary pressure subroutines to compute the nonwetting phase residual saturation, using either a linear relationship, or the equation by Land (1968). At the end of each converged time-step, S_{nmax} is stored separately, so that it can be written to the SAVE file for restarting. This approach of adding saturation hysteresis is relatively straightforward to program, it does not increase the number of model parameters in the relative permeability and capillary pressure functions, and it produces continuously differentiable functions that transition smoothly between imbibition and drainage conditions without any interpolation. A feature of the method is that the shape of the main drainage relative permeability and capillary pressure curves that result from this approach are altered from curves that use a static residual saturation.

An assessment of the new model was made by simulating an experiment by Johnston and Adamski (2005) that explored the relationship of residual- and maximum- LNAPL saturations using an undisturbed soil sample. Another assessment was made by comparing the results of the new model to an analysis by Doughty (2007) for injection and migration of a supercritical CO_2 plume in a deep storage formation. The results compare favorably and suggest that the new model can duplicate essential features of more complicated hysteretic models.

INTRODUCTION

Many multiphase flow systems involve significant nonwetting-phase trapping. For example, geologic CO_2 sequestration is a proposed method of reducing anthropogenic emissions of CO_2 by injecting CO_2 into a deep geologic unit, where all or part of the CO_2 is intended to remain. A popular method of geologic carbon

sequestration involves injecting supercritical-phase CO_2 into deep brine reservoirs. In a two-phase CO_2/brine system, the CO_2 is the nonwetting phase, and a certain fraction of the CO_2, known as the residual saturation, becomes locally trapped in the pore space due to capillary forces. This residual trapping is one of the most significant mechanisms for preventing unwanted migration of injected CO_2 (IPCC, 2005, Saadatpoor et al., 2009; Suekane et al., 2009). If the residual saturation of the CO_2 phase is low, then the CO_2 phase will tend to be mobile at low saturations, and can potentially migrate long distances under gravitational and pressure forces. Similarly, if CO_2 residual saturation is high, the CO_2 phase is only mobile at high saturations, and CO_2 phase migration will tend to be smaller due to trapping.

Environmental contaminant transport involving nonaqueous-phase liquids (NAPLs) is another area where nonwetting-phase trapping plays a key role. In a NAPL/water system, the NAPL is usually the nonwetting phase, and the residual saturation has a large effect on the NAPL migration. When NAPLs such as gasoline or chlorinated solvents are released in the environment, they migrate down through the vadose zone to the water table. Light nonaqueous-phase liquids (LNAPLs) tend to depress the water table and spread along its surface, while dense nonaqueous-phase liquids (DNAPLs) can penetrate the water table and migrate downward until a low-permeability unit is reached (Charbeneau 2007).

During supercritical CO_2 injection, or when a NAPL spill reaches the water table, the pressure difference (known as capillary pressure) between the nonwetting phase (CO_2 or NAPL) and the wetting phase (water) will drive the nonwetting phase into the largest pores of the rock first, pushing the wetting phase out of the pores (Mayer et al. 2005, Juanes et al. 2010). Smaller pores can be invaded by the nonwetting phase following increasing differential pressure between wetting and nonwetting phases (increases in capillary pressure). Once the injection stops or the spill subsides, the CO_2 or NAPL continues to migrate due to buoyancy and regional groundwater gradients. At the leading edge of the migrating CO_2 or NAPL plume, the CO_2/NAPL continues to displace the water; at the trailing edge of the plume, the water displaces the CO_2 or NAPL as capillary pressure decreases (Juanes et al., 2006). The water imbibition process leads to snap-off at the pore scale and trapping of the CO_2 or NAPL phase at the residual saturation (Juanes et al. 2010).

Several multiphase flow experiments have demonstrated that the amount of trapped nonwetting phase is dependent on the saturation history—meaning if the porous medium experiences high nonwetting-phase saturations (high capillary pressures), the resulting residual saturation is also large. Kueper et al. (1993) and Johnston and Adamski (2005) performed NAPL displacement experiments showing that the residual NAPL saturation in unconsolidated soils is approximately a linear function of the maximum historical NAPL saturation in the soil. Similarly, Krevor et al. (2011) found that the residual saturation of supercritical CO_2 in a heterogeneous rock core was a function of the maximum CO_2 saturation in the core, although the relationship between the maximum and residual saturation was nonlinear.

The amount of fluid trapped at the pore scale affects the overall mobility of the fluid in the subsurface. Where there exists both imbibition- and drainage processes, e.g., during buoyancy-driven flow of supercritical CO_2, or during NAPL transport through geologic media, the use of hysteretic values for residual saturation is critical to the prediction of fluid movement. Hysteresis has been observed experimentally in problems involving NAPLs (Lenhard and Parker 1987, Lenhard 1992, Kueper et al. 1993, Steffy et al. 1997, Johnston and Adamski 2005), and a number of hysteretic extensions to characteristic curves have been devised for predicting phase saturations in multiphase flow simulations for environmental and petroleum applications (Parker and Lenhard, 1987; Lenhard and Parker, 1987; Niemi and Bodvarsson, 1988; Kaluarachchi and Parker ,1992; Van Geel, 2002; Fagerlund et al., 2008). However, the incorporation of these hysteretic models into multiphase flow codes such as TOUGH2 (Pruess, 1999) can become relatively complex, and typically require more parameters for the hysteretic model than

for the nonhysteretic model (Doughty, 2007, Fagerlund et al., 2008).

It has been common to assume static values for the nonwetting-phase residual saturation in multiphase flow simulations. For example, the NAPL transport and remediation codes T2VOC (Falta et al., 1995) and TMVOC (Pruess and Battistelli, 2002) use a constant NAPL-phase residual saturation in the capillary pressure and relative permeability curves. Similarly, the TOUGH2-ECO2N code (Pruess, 2005; Pruess et al, 1999) used for CO_2 sequestration simulations assumes a constant value for the CO_2-phase residual saturation in the relative permeability and capillary pressure curves.

In this paper, we present a straightforward numerical method for adding hysteretic nonwetting-phase trapping, where the residual saturation in a gridblock is a dynamic function of the maximum nonwetting-phase saturation in the gridblock. This method does not require any more parameters than similar nonhysteretic models, and it produces smooth, reversible, and continuously differentiable relative permeability and capillary pressure curves under all conditions.

CHARACTERISTIC CURVES

Multiphase flow numerical models use characteristic curves to describe the interactions of the separate phases. Characteristic curves are functions describing relative permeability-saturation and capillary pressure-saturation relationships at gridblock scale, and ultimately control multiphase flow. Characteristic curves are dependent upon the properties of the material each gridblock represents.

Relative permeability curves

A relative permeability curve is a function that controls the ease at which fluids may flow in a multiphase model. Relative permeability (k_r) is a scaling factor (0-1), and it is the ratio of the effective β phase permeability, $k_{e\beta}$, to the intrinsic permeability, k.

$$k_{r\beta} = \frac{k_{e\beta}}{k} \quad , \qquad (1)$$

It is used to adapt the single phase flow Darcy equation to multiphase flow;

$$q_\beta = \frac{-k_{r\beta}k}{\mu_\beta}\left(\nabla P_\beta + \rho_\beta g \nabla z\right) \quad , \qquad (2)$$

where q_β is the darcy flux in phase β, μ_β is the viscosity of phase β, ∇P_β is the pressure gradient in phase β, ρ_β is the density of phase β, g is gravitational acceleration, and ∇z is the elevation gradient.

Nonhysteretic relative permeability curves are limited to one value of residual nonwetting-phase saturation (S_{nr}), which represents the saturation at which k_{rn} =0. Figure 1, calculated using Equation (3),

$$k_{rn}\left(S_n\right) = \sqrt{1-\bar{S}_w}\left(1-\bar{S}_w^{\,1/m}\right)^{2m} \quad , \qquad (3)$$

shows two nonhysteretic nonwetting phase relative permeability curves calculated with nonwetting phase residual saturation (S_{nr}) values of 0 and 0.25.

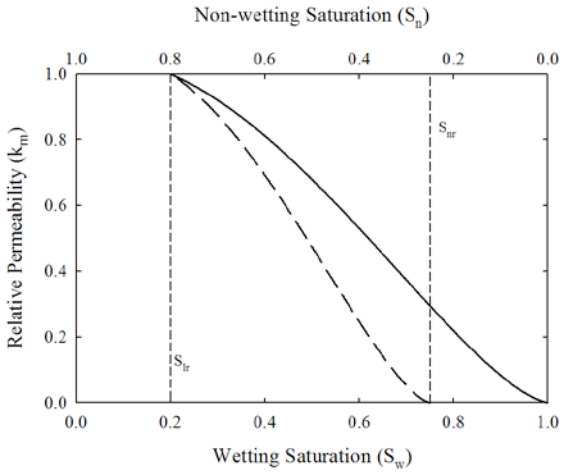

Figure 1. Examples of nonhysteretic relative permeability curves by Mualem (1976). The two curves are calculated using an S_{nr} value of 0 (solid line) and 0.25 (dashed line).

Relative permeability curves not considering hysteresis tend to underpredict the nonwetting-phase relative permeability when the phase first invades a water-filled system, and tend to overpredict the mobility if the nonwetting phase is being displaced by water (Parker and Lenhard, 1987; Lenhard and Parker, 1987; Niemi and Bodvarsson, 1988; Kaluarachchi and Parker, 1992; Fagerlund et al., 2008). If a nonhysteretic

relative permeability curve with a S_{nr} of 0.25 (i.e., dashed line in Figure 1) is used, nonwetting-phase saturation must build to 0.25 before becoming mobile. However, if the nonhysteretic relative permeability curve with an S_{nr} of 0 (i.e., solid line in Figure 1) is used, then no trapping of the nonwetting phase occurs as it leaves the pore system.

Capillary pressure curves

The capillary pressure in a two-phase system is the difference in phase pressure between the nonwetting and wetting phases. In a water-saturated system, the nonwetting phase will not enter the pores until the nonwetting-phase entry pressure (capillary pressure) is exceeded (Mayer et al. 2005). Increases in capillary pressure can drive the nonwetting phase into the smaller pores, expelling the wetting phase. Decreases in capillary pressure reverse the process. As the process is reversed, and the nonwetting phase is displaced from the media, the capillary pressure returns toward zero as the nonwetting phase residual saturation is approached. A model can only follow the capillary pressure curve as far as the residual nonwetting-phase saturation as determined from the relative permeability function, since a relative permeability of 0 deems a phase immobile.

Hysteretic characteristic curves

Nonhysteretic characteristic curves use a static value of S_{nr} and do not have the ability to capture the accurate saturation sequence for a dynamic flow process with variable trapped saturations (Mualem, 1984; Doughty, 2007). A system of pores is complex, and the saturation path upon nonwetting-phase invasion is not the same as when the nonwetting phase leaves the pores (Charbeneau, 2007). For useful estimates of residual nonwetting-phase saturation, the maximum value of nonwetting-phase saturation must be considered (Charbeneau, 2007), because regions that achieve greater nonwetting-phase saturations will retain greater residual nonwetting-phase saturations as nonwetting phase leaves the pores (Lenhard and Parker, 1987; Lenhard, 1992; Kueper et al., 1993; Steffy et al., 1997; Johnston and Adamski, 2005; Charbeneau, 2007). Hysteresis refers to irreversible saturation paths for multiphase flow interactions.

The nonwetting-phase relative permeability curve in Figure 2 is hysteretic, meaning it describes the relative permeability based not only on the current saturation, but also on the history of saturation at the respective location.

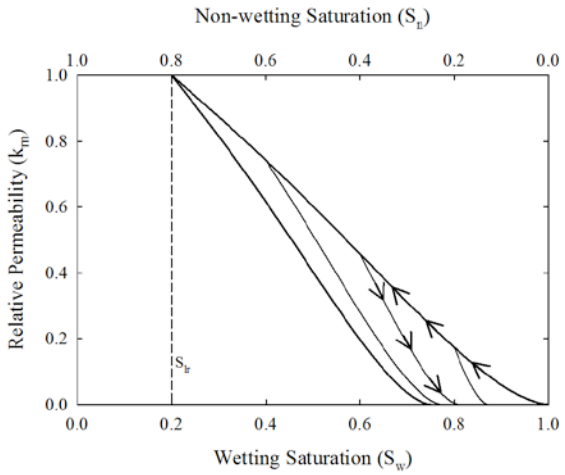

Figure 2. A hysteretic nonwetting phase relative permeability curve from Doughty (2007). The fluid saturation will follow the main drainage branch upward during nonwetting phase invasion, and will follow a secondary scanning curve downward as the nonwetting phase leaves the pore system. The path of the scanning curve depends on the turning-point saturation. This example shows multiple potential turning points each with a separate scanning curve. The value of S_{nr} is represented by $(1\text{-}S_w)$ at $k_{rn} = 0$.

Here, the amount of trapped nonwetting-phase fluid in the pores is dependent on the maximum amount of that fluid that initially entered the pores (Parker and Lenhard, 1987; Lenhard and Parker, 1987; Niemi and Bodvarsson, 1988; Kaluarachchi, 1992; Van Geel, 2002; Fagerlund et al., 2008). Note that there are multiple scanning curves for different turning-point saturations (the saturation value at the point where the nonwetting phase stops invading and starts leaving the pore system). The arrows on the curve represent the direction in which the model follows the curve during nonwetting-phase invasion and subsequent evacuation. Probably the most important aspect of hysteretic characteristic curves is the calculation of S_{nr}, represented as the value of S_n at which a scanning curve has led to a nonwetting-phase relative permeability value of zero. This varies depending on the maximum value of S_n reached during nonwet-

ting-phase invasion. Greater values of S_n reached during nonwetting-phase invasion correspond to greater values of S_{nr}.

NEW HYSTERETIC MODEL

The history-dependent trapping model was applied to the ECO2N (Pruess 2005) and TMVOC (Pruess and Battistelli 2002) codes, both of which are modules of the TOUGH2 (Pruess et at. 1999) numerical simulators developed at the Lawrence Berkeley National Laboratory. These codes are capable of simulating multidimensional fluid and heat flows of multiphase, multicomponent fluid mixtures through porous and fractured media. ECO2N is specifically designed for applications to geologic sequestration of CO_2 in saline reservoirs, capable of modeling isothermal or nonisothermal single-phase or two-phase fluid mixtures of water, CO_2, and NaCl. The chemical reactions modeled by ECO2N include equilibrium phase partitioning of water and carbon dioxide between liquid and gaseous phases, and precipitation and dissolution of solid salt. TMVOC is capable of modeling the nonisothermal flow of water, gas, and multicomponent mixtures of volatile organic chemicals (VOCs) that form a NAPL phase.

New trapping model

The new trapping model adds a variable S_{nmax} to the secondary variable list to TMVOC and TOUGH2-ECO2N. S_{nmax} is defined as the maximum historical nonwetting-phase saturation within an element during a simulation. During each Newton-Raphson iteration, S_{nmax} is updated as the primary variables change, so that the effects of the variable nonwetting trapping are fully incorporated in the Jacobian matrix. At the end of each time step, S_{nmax} is updated accordingly, and stored in a separate array. At the end of a simulation, the value of S_{nmax} in each element is written to the "SAVE" file, so that a simulation may be restarted with the historical saturation values known.

The variable S_{nmax} is used in the relative permeability and capillary pressure subroutines to compute the nonwetting-phase residual saturation. Two methods are used in this project to compute residual saturation: one trapping model is a linear relationship;

$$S_{nr} = f_r(1 - S_{w\min}) = f_r S_{n\max} \qquad (4)$$

where f_r is the slope of the linear relationship between maximum- and residual nonwetting phase saturation. The other trapping model is a popular method of estimating residual nonwetting-phase saturation from an equation by Land (1968):

$$S_{nr} = \frac{S_{n\max}}{1 + R(S_{n\max})}, \qquad (5)$$

where

$$R = \frac{1}{S_{nr\max}} - 1,$$

where $S_{nr\max}$ is the maximum possible nonwetting-phase residual saturation reached following nonwetting-phase evacuation. This is a static parameter used for the characteristic curve, determined by the maximum amount of nonwetting fluid that can be retained by the specific porous medium. S_{nr} is incorporated into the relative permeability and capillary pressure functions through the effective wetting-phase saturation, usually

$$\overline{S}_w = \frac{S_w - S_{lr}}{1 - S_{nr} - S_{lr}} \qquad (6)$$

A significant characteristic of other hysteretic models (Kaluarachchi and Parker, 1992; Doughty, 2007; Fagerlund et al., 2008) is that the derivatives of the relative permeability and the capillary pressure with respect to saturation are discontinuous at the turning points. The discontinuity is caused by an abrupt switch from a value of zero for S_{nr} while nonwetting phase is entering the element to a non-zero value for S_{nr} as nonwetting phase is leaving the element. In codes such as TOUGH2, which are based on a residual minimization method using Newton-Raphson iteration, discontinuous functions can cause a multiphase flow code to take short time steps and run very slowly (Fagerlund et al. 2008). To alleviate the numerical difficulties, the characteristic curves can be artificially smoothed as the turning points are approached (Doughty, 2007; Fagerlund et al., 2008).

Instead, we propose continuously updating the value of S_{nr} based on the S_{nmax} to ensure that the resulting curves are always smooth and continuously differentiable, leading to good numerical performance in numerical codes such as TOUGH2.

The concept of a dynamically updated residual saturation can be applied to any relative permeability or capillary-pressure function that incorporates a residual saturation. Continuously updating the value of residual nonwetting-phase saturation during nonwetting-phase invasion results in an alteration of the shape of the main drainage curve compared to traditional approaches. Therefore, adjustment of the curve parameters is necessary to match the main drainage curve with similar curves that do not incorporate the dynamic S_{nr}. In this paper, we apply our hysteresis effects to relative permeability curves by Mualem (1984) and Charbeneau (2007) and to the capillary pressure curve by van Genuchten (1980).

MODEL APPLICATIONS

NAPL displacement in a core

Johnston and Adamski (2005) measured the relationship between maximum NAPL saturation and residual NAPL saturation using unconsolidated soil cores. For their experiments, the water was the wetting phase while the decane (an LNAPL) was the nonwetting phase.

The experimental setup involved a core barrel that held a core sample with a water reservoir and a decane reservoir connected to either end. The soil core sample measured 47 mm in diameter and 50 mm in length, and was classified as a sand. A hydrophilic ceramic plate separated the core from the water reservoir, while a hydrophobic ceramic plate separated the core from the decane reservoir. The plates were placed to ensure that decane would not leak into the water reservoir and that water did not leak into the decane reservoir. The elevation of the decane reservoir remained constant to provide consistent pressure on the decane end of the cell, while the elevation of the water reservoir was varied to apply and release capillary pressure within the cell. The test cell was subjected to cycles of subsequently increasing water suction to allow decane to flow into the core. The suction was released between cycles to return capillary pressure back to zero and allow the water and decane saturations to equilibrate.
Over a span of about 90 days, six NAPL flooding cycles were performed on the soil core sample. The measurements of residual NAPL saturations showed an approximate linear relationship with the maximum NAPL saturations with a slope (f_r) of 0.394.

A one-dimensional model was set up with the modified TMVOC code to simulate this experiment. The core sample was represented by 10 gridblocks in the center of the model, the ceramic plates were each represented by 2 gridblocks on both ends of the core cells, and the reservoirs were each represented by 1 gridblock on each end of the model. Hydraulic properties of the ceramic plates and intrinsic permeability of the core sample were not measured, so estimated values were used for these parameters in the simulation (Patterson, 2011).

The gridblocks representing the core sample were initially fully saturated with water. The gridblocks representing the water and decane reservoirs were initially fully saturated with water and decane, respectively, and were held at the desired conditions—the decane reservoir gridblock kept at a constant pressure while the pressure of the water reservoir was controlled to match the experimental conditions. Actual times and values of pressure change were obtained through personal communication with Colin Johnston (2010) and were used in the pressure control for the water reservoir gridblock.

Gridblocks representing the hydrophilic plate were given a high nonwetting-phase entry pressure to repel the decane, and gridblocks representing the hydrophobic plate were given a large negative capillary pressure to repel water. The value of f_r measured by Johnston and Adamski (2005) was used to calculate S_{nr} in the hysteretic relative permeability function. The fitted van Genuchten capillary pressure parameters for the sample from Johnston and Adamski (2005) were used for the capillary pressure function (not hysteretic in this simulation), and the n value from the capillary pressure curve was used for the relative permeability curves.

Results and Discussion

The experiment was first simulated with non-hysteretic relative permeability curves to demonstrate the inaccuracy of this approach. Figure 3 shows the result of a nonhysteretic simulation run with S_{nr} value of 0. During intermittent times of applied suction, NAPL saturation returns to 0. Figure 4 shows the result of a nonhysteretic simulation run with S_{nr} value of 0.15. Obviously, the nonhysteretic relative permeability curves are unable to predict the variable trapping occurring in this experiment.

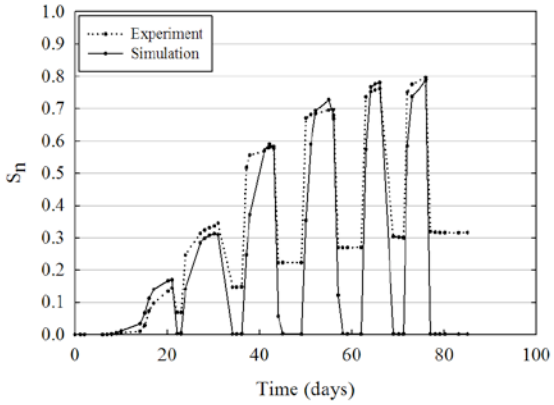

Figure 3. Nonhysteretic simulation of experiment by Johnston and Adamski (2005) using a S_{nr} value of 0.

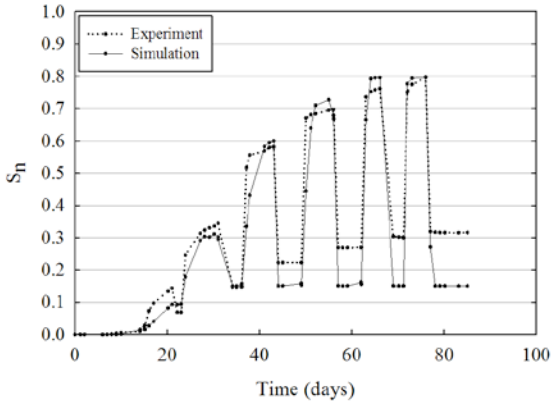

Figure 4. Nonhysteretic simulation of the experiment by Johnston and Adamski (2005) using a S_{nr} value of 0.15.

Results from the simulation using the new hysteretic relative permeability function compare favorably to the experimental results (Figure 5).

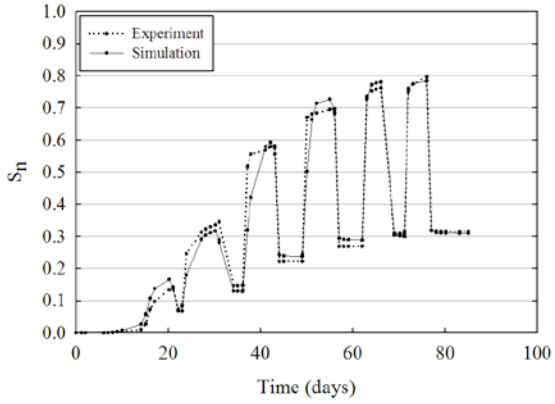

Figure 5. Simulation results for the hysteretic relative permeability model plotted with experimental results from Johnston and Adamski (2005).

Comparison with a more advanced hysteretic k_r-P_c model

The second assessment made with the new hysteretic model was to compare simulation results for a case developed by Doughty (2007) related to geologic sequestration of supercritical CO_2. Doughty's study compared the behavior of CO_2 injection simulations made using hysteretic characteristic curves with typical non-hysteretic characteristic curves.

The model scenario that was compared was a 2D cylindrical model with CO_2 injection into a 100 m thick interval with leakage through a homogeneous zone 1000 m thick. The model extended radially to 40,000 m, and was divided into 61 layers, each with 41radial gridblocks. The layers were 20 m thick except for a few thinner layers near the surface. The gridblocks were 20 m wide extending to 600 m, and then increased steadily to produce an infinite acting model. Both the injection formation and overlying formation were homogeneous, with a vertical permeability of 100 md and horizontal permeability of 200 md. The model was initially fully brine-saturated with a salinity of 100,000 ppm. The model was nonisothermal and followed a fixed geothermal gradient of 30°C/km with the surface and bottom of the model held constant at 15°C and 48°C, respectively. The simulation began by injecting 900,000 tons of CO_2 over a period of 30 days, with redistribution for 1,000 years.

To help ensure an accurate comparison of the behavior of the two hysteretic formulations, we

used the TOUGH2 input files provided by Doughty (Doughty, personal communication, 2010). The published simulations were carried using ECO2, an older version of the TOUGH2 module ECO2N. One small difference between the two modules is that ECO2N includes the density effect that CO_2 has in the aqueous phase once dissolved. This turns out to have a significant effect on the results at late simulation times. Doughty (personal communication, 2010) also provided an updated simulation using ECO2N and shared her new (unpublished) results. The comparison shown here uses these new simulations results.

Doughty (2007) employed extensions to her hysteretic formulations to ensure numerical stability. They include a power-law extension to the van Genuchten capillary pressure function to account for dissolution of trapped CO_2 and a cubic splice in the relative permeability function to smoothly connect the drainage branch to the imbibition branch (Doughty 2007). Mualem (1984) gives expressions for first- and second-order scanning curves that are implemented and expanded to third-order scanning curves by Niemi and Bodvarsson (1988). Doughty (2007) used this interpolation between scanning curves; it is recommended that the reader refer to the literature for detailed discussion on higher-order scanning curves (Niemi and Bodvarrson, 1988).

In addition to running a simulation with the new hysteretic characteristic curves, two nonhysteretic cases were simulated to further illustrate the comparison between the new hysteretic model and the hysteretic model from Doughty (2007). The same input files were used for the simulation to ensure consistency between the hysteretic and nonhysteretic models. One nonhysteretic case used a residual gas-phase saturation (S_{gr}) value of zero; the other case used an S_{gr} value of 0.25. The nonhysteretic simulations here are run with the Charbeneau (2007) relative permeability function and van Genuchten (1980) capillary pressure function. Other than the constant value of S_{gr}, model parameters are kept consistent with that of the hysteretic simulations.

The new hysteretic method used here alters the shape of the primary drainage relative permeability and capillary pressure curves. To account for this, the parameter values in our characteristic curves were adjusted so that the primary wetting-phase drainage curves were similar to those in Doughty's model.

Figures 6 and 7 show the curves fit to Doughty's capillary pressure curve and nonwetting-phase relative permeability curve, respectively. Table 1 shows both the fitted parameters used for our hysteretic capillary pressure curve and the parameters used in Doughty's hysteretic capillary pressure curve. Table 2 shows both the fitted parameters used for our hysteretic nonwetting-phase relative permeability curve and the parameters used in Doughty's hysteretic nonwetting-phase relative permeability curve.

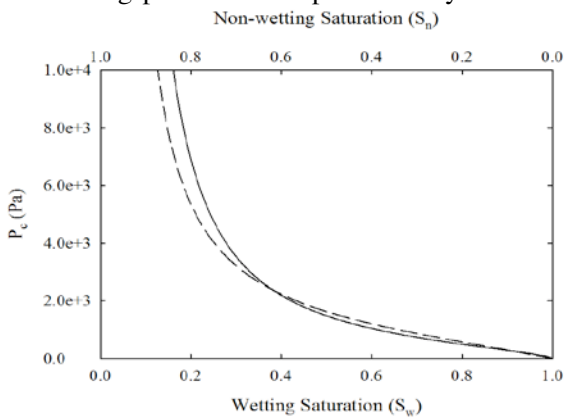

Figure 6. Main wetting-phase drainage capillary pressure curve based on van Genuchten (1980) (dashed line) that best fit the main wetting-phase drainage capillary pressure curve (solid line) from Doughty (2007).

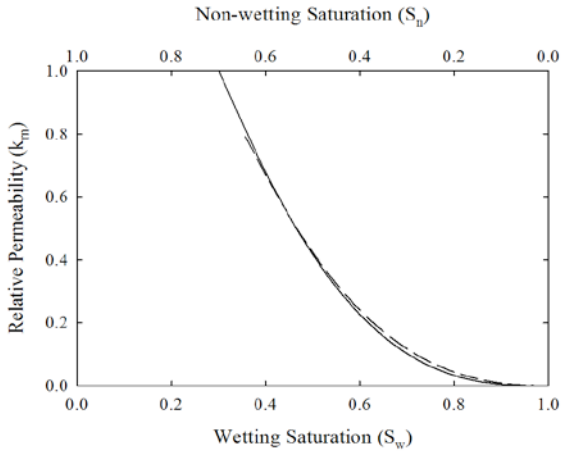

Figure 7. Primary drainage nonwetting-phase relative permeability (dashed) that best fit the relative permeability curve (solid line) from Doughty (2007).

Table 1. Hysteretic capillary-pressure-curve parameters for both the fitted curve and the curve used in Doughty (2007).

Model parameter	Fitted value	Doughty (2007) value
n	2.94	1.7
S_{lr}	0.2	0.03
α	0.53933	0.737293
S_{gr} max	0.25	0.25

Figure 8 shows the results from the nonhysteretic simulations: one case with an S_{gr} value of zero and another case with an S_{gr} value of 0.25. The first case (S_{gr} = 0) predicts a completely mobile CO_2 plume, and by 1,000 years all of the CO_2 has leaked to the surface. The second case (S_{gr} = 0.25) shows a fairly immobile plume; the CO_2 never reaches the surface and remains trapped indefinitely.

Table 2. Hysteretic relative permeability curve parameters for both the fitted curve and the curve used in Doughty (2007).

Model parameter	Fitted value	Doughty (2007) value
n	2.083	12
S_{lr}	0.3	0.3
S_{grmax}	0.25	0.25

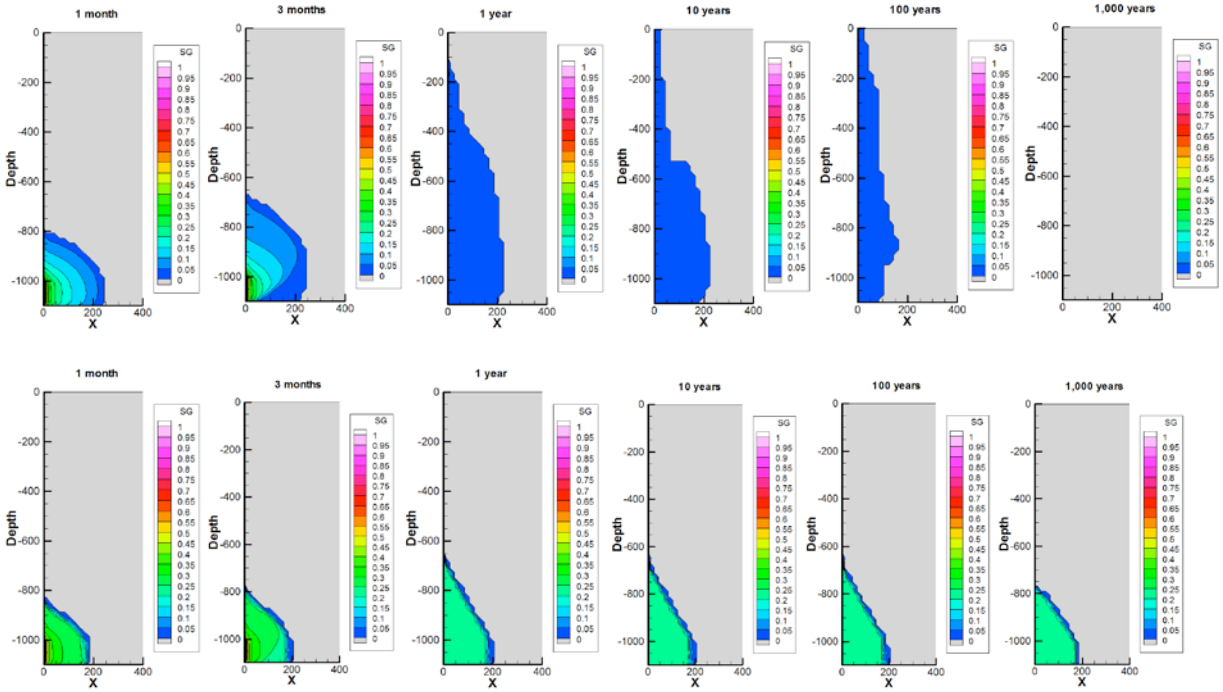

Figure 8. Nonhysteretic simulations with S_{gr} = 0 (on top) and S_{gr} = 0.25 (on bottom).

Figure 9 shows the results of Doughty's simulation and our simulation using hysteretic characteristic curves. Both models predict CO_2 plumes of an intermediate mobility compared to the nonhysteretic simulations. Doughty's model predicts a slightly more mobile CO_2 plume than our model predicts; seen at 10 and 100 years, where the 5% CO_2 saturation contour reaches a depth of about 500 m for Doughty's simulation and a depth of about 600 m for our simulation. The new model predicts a CO_2 plume of similar shape to Doughty's model, and the final snapshot at 1,000 years shows a comparable size of CO_2 plume. The simulation results compare favorably and confirm that the new and simplified hysteretic CO_2 trapping function is able to reproduce the essential features of a more complicated hysteretic model.

The CO_2 saturation for the four simulations is plotted as a function of time at a depth of 700 m on the radial center of the grid (figure 10). The four models predict the highest CO_2 saturations at early simulation time, then variable behavior as simulation time progresses. The nonhysteretic high S_{gr} case retains CO_2 saturation around 25% for most of the simulation, but at 700 m of depth on the radial center, the CO_2 saturation drops to

0 over time due to dissolution of the CO_2 phase. The nonhysteretic low S_{gr} case predicts that CO_2 saturation quickly drops to 0 due to the lack of trapping. The two hysteretic cases show predictions of CO_2 saturation with intermediate behavior, but complete CO_2 dissolution by the 1,000-year simulation time.

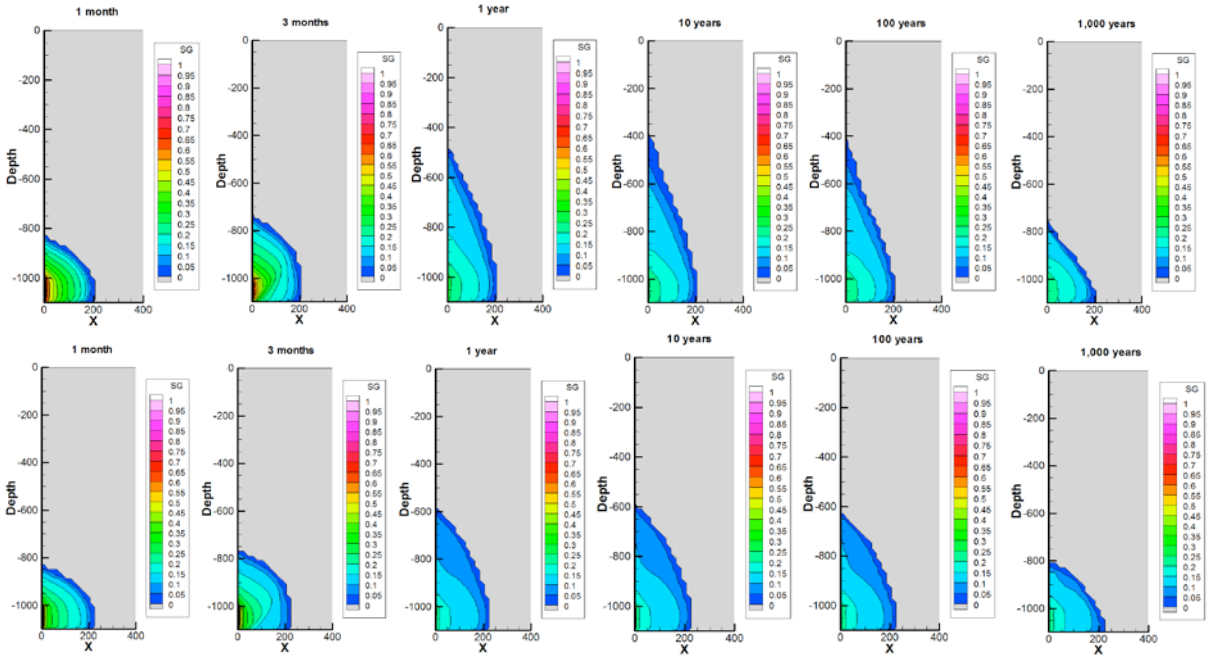

Figure 9. Simulation results from Doughty (2007) on top, and the new hysteretic simulation on bottom.

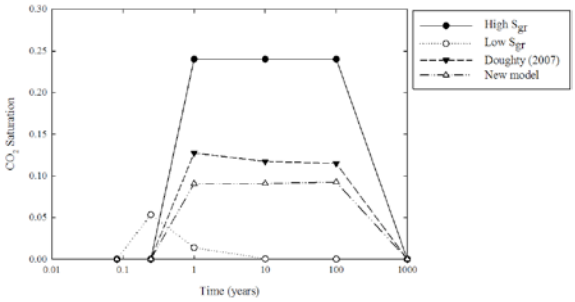

Figure 10. Plot of CO_2 saturation over time at a depth of 700 m at the radial center of the simulation grid.

CONCLUSION

The use of hysteretic characteristic curves greatly impacts the results of numerical simulations of multiphase flow by controlling the mobility of the fluids. For problems with significant nonwetting-phase trapping, the most important part of a hysteretic characteristic curve may be the variable value of residual saturation, which represents the saturation of the nonwetting phase that has become immobilized due to capillary forces.

A new, efficient, and straightforward hysteretic model is described to implement the history-dependent trapping processes during multiphase flow simulations. The numerical nature of the new model ensures continuously differentiable saturation turning points, which eases performance in numerical simulators. An advantage of this new method of tracking hysteresis in the multiphase flow characteristic curves is the fact that there is no need for additional characteristic curve parameters. The new hysteretic model is capable of irreversible saturation paths using the same number of parameters that a simple non-hysteretic model would employ.

The new model was assessed by comparison to experimental results and published simulation results. The results confirm that the new model performs favorably and is capable of reproducing the essential features of more complex hysteretic models used for multiphase modeling.

ACKNOWLEDGEMENTS

We would like to thank Christine Doughty and Colin Johnston for their contributions to this

project. This work was funded by U.S. EPA STAR Grant #834383. Publication authorized by the Director, Illinois State Geological Survey.

REFERENCES

Alley, R., T. Berntsen, N.L. Bindoff, Z. Chen, A. Chidthaisong, P. Friedlingstein, J. Gregory,G. Hegerl, M. Heimann, B. Hewitson, B. Hoskins, F. Joos, J. Jouzel, V. Kattsov, U. Lohmann, M. Manning, T. Matsuno, M. Molina, N. Nicholls, J. Overpeck, D. Qin, G. Raga, V. Ramaswamy, J. Ren, M. Rusticucci, S. Solomon, R. Somerville, T.F. Stocker, P. Stott, R.J. Stouffer, P. Whetton, R.A. Wood, D. Wratt, 2007, Climate change 2007: The physical science basis, Summary for policymakers, IPCC WGI Fourth Assessment Report, Intergovernmental panel on climate change, Cambridge University Press, Cambridge, U.K.

Charbeneau, R., 2007, LNAPL Distribution and Recovery Model (LDRM) Volume 1: Distribution and Recovery of Petroleum Hydrocarbon Liquids in Porous Media, American Petroleum Institute API Publication 4760.

Doughty, C., 2007, Modeling geologic storage of carbon dioxide: comparison of non-hysteretic and hysteretic characteristic curves, Energy Conversion and Management, 48, 1768-1781.

Doughty, C., 2010, personal communication with Christine Doughty.

Fagerlund, F., A. Niemi, and T.H. Illangasekare, 2008, Modeling of nonaqueous phase liquid (NAPL) migration in heterogeneous saturated media: Effects of hysteresis and fluid immobility in constitutive relations, Water Resources Research, 44, W03409.

Falta, R.W., K. Pruess, S. Finsterle, and A. Battistelli, 1995, T2VOC user's guide, Rep. LBL-36400, Lawrence Berkeley National Laboratory, Berkeley, California.

Johnston, C., and M. Adamski, 2005, Relationship between initial and residual LNAPL saturation for different soil types, Proceedings of the 2005 Petroleum Hydrocarbons and Organic Chemicals in Groundwater®: Prevention, Assessment, and Remediation Conference. 17-19 August, Costa Mesa, 29-42.

Johnston, C., 2010, personal communication with Colin Johnston.

Juanes, R., E.J. Spiteri, F.M. Orr Jr., and M.J. Blunt, 2006, Impact of relative permeability hysteresis on geological CO_2 storage, Water Resources Research, 42, W12418.

Juanes, R., C.W. MacMinn, and M.L. Szulczewski, 2010, The footprint of the CO_2 plume during carbon dioxide storage in saline aquifers: storage efficiency for capillary trapping at the basin scale, Transp Porous Med, 82, 19-30.

Kaluarachchi, J.J., and J.C. Parker, 1992, Multiphase flow with a simplified model for oil entrapment, Transport in Porous Media, 7, 1-14.

Krevor, S.C.M., R. Pini, B. Li, and S.M. Benson, 2011, Capillary heterogeneity trapping of CO_2 in a sandstone rock at reservoir conditions, Geophysical Research Letters, 38: L15401.

Kueper, B.H., D. Redman, R.C. Starr, S. Reitsma, and M. Mah, 1993, A field experiment to study the behavior of tetrachloroethylene below the water table: spatial distribution of residual and pooled DNAPL, Ground Water, 31: 5, 756-766.

Land, C. S., 1968, Calculation of imbibition relative permeability for two- and three-phase flow from rock properties, Transactions, 243, 149-156.

Lenhard, R.J., and J.C. Parker, 1987, A model for hysteretic constitutive relations governing multiphase flow: 2. Permeability-saturation relations, Water Resources Research, 23:10, 2197-2206.

Lenhard, R.J., and J.C. Parker, 1987, Measurement and prediction of saturation-pressure relationships in three-phase porous media systems, Journal of Contaminant Hydrology, 1, 407-424.

Lenhard, R.J., 1992, Measurement and modeling of three-phase saturation-pressure hysteresis, Journal of Contaminant Hydrology, 9, 243-269.

Mayer, A.S., and S.M. Hassanizadeh (Eds.) (2005), *Soil and Groundwater Contamination: Nonaqueous Phase Liquids–Principles and Observations*, Water Resour. Monogr. Ser., vol. 17, 216 pp., AGU, Washington, D.C., doi: 10.1029/WM017.

Mualem, Y., 1976, A new model for predicting the hydraulic conductivity of unsaturated porous media, Water Resources Research, 12:6, 513-522.

Mualem, Y., 1984, A modified dependent-domain theory of hysteresis, Soil Science, 137:5, 283-291.

NETL, 2007, Carbon Sequestration Atlas of the United States and Canada, U.S. Department of Energy, National Energy Technology Laboratory. Available from http://www.netl.doe.gov/technologies/carbon_seq/refshelf/atlas/ATLAS.pdf

Niemi, A., and G.S. Bodvarsson, 1988, Preliminary capillary hysteresis simulations in fractured rocks, Yucca Mountain, Nevada, Journal of Contaminant Hydrology, 3, 277-291.

Parker, J.C., and R.J. Lenhard, 1987, A parametric model for constitutive properties governing multiphase flow in porous media, Water Resources Research, 23: 4, 618-624.

Patterson, C.G., 2011, A history-dependent nonwetting phase trapping model for multiphase flow characteristic curves, Master's thesis, Clemson University.

Pruess, K., C. Oldenburg, and G. Moridis, 1999, TOUGH2 user's guide, version 2.0, Rep. LBNL-43134. Berkeley: Lawerence Berkeley National Laboratory.

Pruess, K. and A. Battistelli, 2002, TMVOC, A numerical simulator for three-phase non-isothermal flows of multicomponent hydrocarbon mixtures in saturated-unsaturated heterogeneous media, LBNL-49375, Lawrence Berkeley National Laboratory, Berkeley, CA.

Pruess, K., 2005, ECO2N: A TOUGH2 fluid property module for mixtures of water, NaCL, and CO_2, LBNL-57952, Earth Sciences Division, Lawrence Berkeley National Laboratory, University of California, Berkeley, CA.

Saadatpoor, E., S.L. Bryant, and K. Sepehrnoori, 2009, Effect of capillary heterogeneity on buoyant plumes: a new local trapping mechanism, GHGT-9, Energy Procedia 1, 3299-3306.

Suekane, T., N.H. Thanh, T. Matsumoto, M. Matsuda, M. Kiyota, A. Ousaka, 2009, Direct

measurement of trapped gas bubbles by capillarity on the pore scale, GHGT-9, Energy Procedia 1, 3189-3196.

Steffy, D.A., D.A. Barry, and C.D. Johnston, 1997, Influence of antecedent moisture content on residual LNAL saturation, Soil and Sediment Contamination: An International Journal, 6: 2, 113-147.

Van Geel, P.J., and S.D. Roy, 2002, A proposed model to include a residual NAPL saturation in a hysteretic capillary pressure-saturation relationship, Journal of Contaminant Hydrology, 58, 79-110.

van Genuchten, M.T., 1980, A closed-form equation for predicting the hydraulic conductivity of unsaturated soils, Soil Sci. Soc. Am. J., 44, 892-898.

van Genuchten, M.T. and D.R. Nielsen, 1985, On describing and predicting the hydraulic properties of unsaturated soils, Annales Geophysicae, 3:5, 615-628.

REDUCED ORDER MODELS FOR SUBSURFACE FLOW IN iTOUGH2

George Pau, Yingqi Zhang, Stefan Finsterle

Lawrence Berkeley National Laboratory
1 Cyclotron Road, Mail Stop 74-0120
Berkeley, CA 94720, USA
e-mail: gpau@lbl.gov, yqzhang@lbl.gov, safinsterle@lbl.gov

ABSTRACT

Inverse modeling involves repeated evaluations of the forward simulation, which can be computationally prohibitive for large numerical models. To reduce the overall computational burden of these simulations, we study the use of reduced order models (ROMs) as numerical surrogates. These ROMs usually involve using solutions at different sample points within the parameter space to construct an approximate solution at any point within the parameter space.

This paper examines a black-box relational approach based on Gaussian process regression. We demonstrate how an approximate error bound of the predicted solution can be constructed from the estimated variance of the approximation. We show that these ROMs perform better than look-up tables, particularly when the number of sample points is small. In particular, we show how these sample points can be chosen optimally to minimize computational efforts. Finally, we incorporate these ROMs within the inverse modeling framework of iTOUGH2 and demonstrate how ROMs can be used within that framework.

INTRODUCTION

The need to accurately simulate the multiscale dynamic behavior of multiphysics systems and inclusion of a variety of data has led to increasingly large and complex models in areas of geological CO_2 sequestration, nuclear waste disposal, environmental remediation, as well as the recovery of conventional (geothermal, oil, gas) and unconventional (hydrates, tight gas) energy resources. These simulations of nonisothermal flows of multicomponent, multiphase fluids in three-dimensional porous and fractured media may involve the iterative simultaneous solution of millions of coupled partial differential equations (PDEs) at each time step. While high-fidelity simulations are essential for understanding coupled processes, they may be computationally very expensive. As a result, it is impractical to use these models as the basis for conducting analyses that require many simulation runs (such as inverse modeling, parametric study of state variables, uncertainty analysis, and optimal design). High-fidelity models are needed to capture the physics of the problem with the required accuracy. The development of defensible reduced-order models for inversions and uncertainty quantification may offer a solution, but requires a careful evaluation of errors which we will use to inform our analysis.

Due to the complexity of subsurface simulation, most existing ROMs attempt to approximate the relationship between the parameters and outputs of interest using a response surface approach. In particular, lookup tables in combination with linear or higher-order polynomial interpolation are commonly used. However, polynomial interpolation is generally inaccurate (except for very smooth response surfaces) and not robust in the presence of uncertainties when the problem of interest is stochastic in nature.

In this paper, we consider the use of Gaussian process (GP) regression (Rasmussen and William, 2006) for ROM construction. It is a generalization of the kriging technique commonly used in geostatistics. We will briefly describe the GP regression model and how we can adaptively construct a ROM that minimizes the number of simulations needed to evaluate the outputs. We will then demonstrate its performance in several test problems, comparing it to an adaptive look-up table approach. We will finally describe an example in which this GP-based ROM is used within the iTOUGH2 framework.

METHODOLOGY

Gaussian Process Regression

Let us first give an abstract formulation for the response surface problem. Given a scalar function $f(\mathbf{p})$, where $\mathbf{p}=\{p_1, \ldots, p_n\}$ is a parameter vector of length n, we would like to approximate $f(\mathbf{p})$ by $g(\mathbf{p})$ using only known solutions of $f(\mathbf{p}\ p)$ for $\mathbf{p}$ in a sample set $\boldsymbol{S}_N=\{q_1, \ldots, q_N\}$ of size N.

A Gaussian process regression first assumes the relation between $\mathbf{p}$ and $f(\mathbf{p})$ can be described by a Gaussian process characterized by its mean function, $m(\mathbf{p})$, and covariance function, $k(\mathbf{p}, \mathbf{p}')$ (Rasmussen and William, 2006):

$$m(\mathbf{p}) = E[f(\mathbf{p})] \quad (1)$$

$$k(\mathbf{p},\mathbf{p}') = E[(f(\mathbf{p}) - m(\mathbf{p}))(f(\mathbf{p}') - m(\mathbf{p}'))] \quad (2)$$

Knowing $f(\mathbf{q})$ where $\mathbf{q}\in\boldsymbol{S}_N$, the joint distribution of the $f(\mathbf{q})$ and $g(\mathbf{p})$ based on the above prior is then

$$\begin{bmatrix} f \\ g \end{bmatrix} : N\left(m(q), \begin{bmatrix} K(q,q) & K(q,p) \\ K(p,q) & K(p,p) \end{bmatrix} \right) \quad (3)$$

where $K(\mathbf{q},\mathbf{p})$ is the covariance matrix. The joint posterior distribution of g(p) is then given by

$$g(p)\,|\,q, f(q) \sim N(K(p,q)K(q,q)^{-1} f(q), \\ K(p,p) - K(p,q)K(q,q)^{-1}K(p,q) \quad (4)$$

In other words, for any given p, the GP regression procedure gives the expected value and variance of the approximating function g(p):

$$E[g(p)] = K(p,q)K(q,q)^{-1} f(q) \quad (5)$$

$$\sigma^2[g(p)] = K(p,p) - K(p,q)K(q,q)^{-1}K(p,q) \quad (6)$$

The accuracy of the results then crucially depends on the priors for the mean and covariance functions over the entire parameter space. In this paper, we consider a constant mean function ($m(\mathbf{p}) = c_0$) and examine two different covariance functions.

The first covariance function we use is an isometric squared exponential (isoSE) function given by

$$K(\mathbf{p},\mathbf{p}') = \sigma_f \exp(-(|\mathbf{p}-\mathbf{p}'|/l)^2/2) + \sigma_n \delta_{\mathbf{p},\mathbf{p}'} \quad (7).$$

The hyperparameters σ_f represent the variance at the point, l is the characteristic length, and σ_n represents the variance of the noise. This function depends on parameter distance $|\mathbf{p}-\mathbf{p}'|$ only, and is thus stationary. As a result, this covariance function is appropriate if $f(p)$ varies smoothly in p. Without the noise variance σ_n, the covariance function is equivalent to an infinite linear combination of Gaussian radial basis functions. The resulting GP regression is then equivalent to a radial basis function interpolation. Note, however, that the GP regression is capable of modeling noise within the current formalism.

The second covariance function we considered is a neural network (NN) covariance function (Williams, 1998) given by

$$k(p,p') = \sigma_f \sin^{-1}\left(\frac{2pp'/l^2}{\sqrt{(1+2pp/l^2)(1+2p'p'/l^2)}} \right) + \sigma_n \delta_{p,p'} \quad (8)$$

This is an inhomogeneous covariance that allows abrupt change in $f(\mathbf{p})$ that depends on the sign of $\mathbf{p}$. There are other covariance functions that one can use; a sample list can be found in Rasmussen and William (2006). The two covariance functions we have used here are, however, sufficient to illustrate the importance of choosing the appropriate priors.

In the above definitions, c_0, σ_f, and σ_n are known as the hyperparameters. To determine these hyperparameters, we will solve an optimization problem that maximizes the marginal Gaussian likelihood function, which is equivalent to minimizing the following negative log marginal likelihood (Rasmussen and William, 2006)

$$-\log(P(f|\mathbf{p})) = (1/2)(f^T K f + \log(|K|) + n\log(2\pi)) \quad (9)$$

For this work, we built our ROM based in part on Gaussian Process Regression and Classification (GPML) Toolbox version 3.1, but added additional functionalities, such as the adaptive sampling procedure. The optimization procedure used is based on the conjugate gradient method. Finally, we implemented the algorithms mentioned in this paper within iTOUGH2, allowing us to use the resulting

reduced-order model for uncertainty quantification.

Sampling procedure

Eq. (5) shows that results will largely depend on the samples selected. The question remains, how can we select parameters in S_N? One may use statistical approaches, such as the Latin Hypercube sampling procedure, to determine S_N, but we will still need to determine the number of samples needed. Here, we examine an adaptive approach known as the "greedy algorithm," or (in the context of neural networks) the forward selection algorithm. The greedy algorithm has been proposed in Carr et al. (2001) for radial basis functions and in many other references (e.g., Rozza, 2007) for other ROM approaches.

In the greedy algorithm, we first construct a large search sample set S_S that sufficiently represents the entire parameter space. Starting with a randomly selected parameter point $\mathbf{p}_1 \in S_S$ we compute $f(\mathbf{p}_1)$ and construct our first ROM, $g_1(\mathbf{p})$ based on $S_1=\{\mathbf{p}_1\}$. We then determine $\mathbf{p}_2^* = \arg\max_{\mathbf{p}\in S_S} e_1(\mathbf{p})$ where e_1 is an appropriate error measure of $g(\mathbf{p})$ -$f(\mathbf{p})$. Then, we append $\mathbf{p}_2$* to S_1 to form S_2. We repeat the procedure to construct ROM $g_2(\mathbf{p})$, …, $g_n(\mathbf{p})$ until either $e_{max}= e_n(\mathbf{p}_{n+1}*)$ is below a predetermined error tolerance, or the number of sample points in S_S reaches the maximum allowable number.

In this work, we use σ (from Eq. 6) as our error measure e_n. Thus, we do not need to evaluate $f(\mathbf{p})$, $\forall \mathbf{p} \in S_S$. If our final ROM consists of N sample points, we only perform N full simulations. We will examine how this affects the distribution of points in S_N. We may use other error measures, but the choice will affect the accuracy and efficiency of the ROM. For example, one may choose to use the actual absolute error. Although this may lead to a more accurate model, it requires $f(\mathbf{p})$ to be predetermined for $\forall \mathbf{p} \in S_S$. We intend to examine other error measures that may lead to more accurate and efficient ROM in the future.

The above construction procedure also leads to a series of hierarchical ROMs that are increasingly more accurate. At each iteration n, we build a ROM that perform optimally given S_n and $f(\mathbf{p})$, $\mathbf{p} \in S_n$. For a GP regression model, we thus optimize the hyperparameters in every iteration. We then have at our disposal a series of ROMs that we can use, depending on the accuracy and efficiency needed in our application.

RESULTS

Sample problem

This test problem is based on the iTOUGH2 sample problem 6 (Finsterle, 2007), in which the forward model describes a ventilation experiment conducted at the Grimsel Rock Laboratory, Switzerland. The purpose of this particular test is to quantify the extent of the two-phase region and to study its hydraulic properties. *In situ* measurements of water potential, water content, temperature, and ambient air humidity were performed. Details of the forward model can be found in Finsterle and Pruess (1995).

The three uncertain parameters considered in the inverse problem are the logarithm of the absolute permeability, log(k), and the van Genuchten parameters n and $\log(1/\alpha)$. For our purpose, we select capillary pressure at one point location only as the model output of interest, f(p).

The ranges of log(k), n and $\log(1/\alpha)$ that we have considered are [-19,-14], [2,3] and [5,6]. Figure 1 shows how f(p) varies with log(k) and n for selected values of $\log(1/\alpha)$. There is clearly a sudden change between log(k) = -16 and -14 but for log(k) between [-19,-16], $f(p)$ appears reasonably smooth.

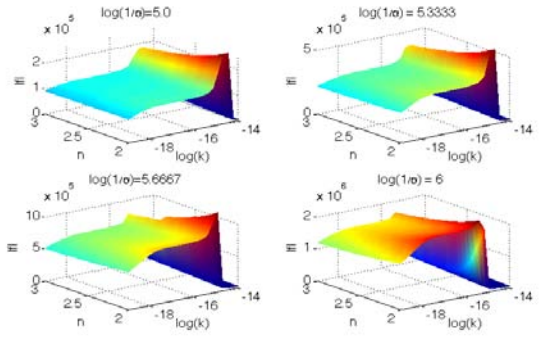

Figure 1. Model output $f(\mathbf{p})$ as a function of three input parameters for the sample problem.

We first consider two cases in which log(k) stays within a smaller range, [-19,-16], and a larger range, [-19,-14]. Ranges for n and log(1/α) are the same for both cases as given earlier. In a second analysis, we will use the constructed ROM to do an uncertainty quantification analysis in iTOUGH2. Note that we normalize the parameters such that they vary between 0 and 1. We set N to be 30. The search sample set, S_S, which we use for our greedy algorithm is 22 points in each direction.

Sample space

We first examine how the parameter points selected from the adaptive procedure are distributed in the sample space. With the isoSE covariance function, the distribution of sample points for the two cases is shown in Figure 2. Since the adaptive algorithm attempts to minimize the variance of the approximation (Eq. 6), which mostly depends on the distance between two points (Eq. 7), the selected samples are distributed almost but not exactly uniformly across the domain, independent of the behavior of f(p).

Based on the above observation, we constructed a ROM based on a uniform distribution of 27 points in the parameter space (each direction is uniformly divided into two intervals). The resulting maximum, mean and standard deviation of the errors are 0.056, 0.019 and 0.013. If we set N=27 and allow the adaptive algorithm to determine the points, these quantities are 0.062, 0.021 and 0.015. The slightly poorer performance is probably due to the initial poor approximation resulting from the small number of parameter points used to construct the ROM, leading to poor initial selection of the points.

Note that the apparent poorer performance of the adaptive algorithm should be put into context. With just 3 additional points, we are able to reach the same performance as uniform grid, as indicated by Table 1. This is obtained without the insights that we concluded from the previous paragraph. Indeed, the adaptive algorithm will work with any error measure for which insights on the optimal layout of sample points are not readily available or obvious. Finally, it is not necessary to start the adaptive algorithm with 1 parameter point. We can then easily start the adaptive algorithm with a larger S_n that incorporates these insights.

Approximation

To quantify the actual error, we use the relative error of the approximation:

$$e_{\text{rel}}(p) = \frac{|f(p) - g(p)|}{|f(p)|} \tag{10}$$

for p within a test sample set (we use the search sample set, S_S), and determine maximum, mean and standard deviation of $e_{\text{rel}}(\mathbf{p})$. To evaluate $e_{\text{rel}}(\mathbf{p})$, we thus need to evaluate $f(\mathbf{p})$ for all $\mathbf{p}$ in S_S.

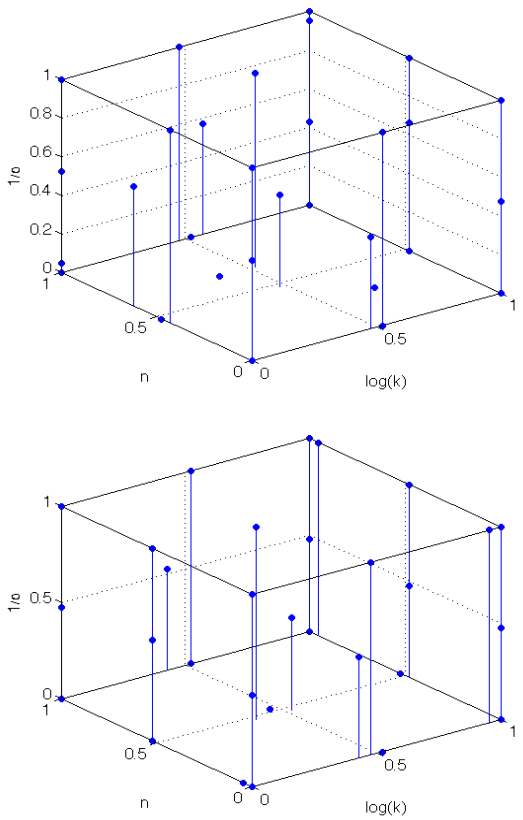

Figure 2. Distribution of sample points for smaller log(k) range (top) and longer log(k) range (bottom).

Table 1 shows the results for two ranges using the isoSE covariance function and the results for the larger range of log(k) using NN. Table 2 shows the results for two ranges using linear interpolation.

Table 1. Maximum, mean and standard deviation of approximation errors of GP regression with N=30.

Range, covariance function	$e_{rel}(p)$		
	maximum	mean	Standard deviation
[-19,-16], isoSE	0.057	0.017	0.012
[-19,-14], isoSE	1.60	0.31	0.26
[-19,-14], NN	2.40	0.26	0.32

Since f(p) is a smooth function for the smaller range of log(k), Table 1 shows that the isoSE covariance function was able to approximate f(p) accurately. The maximum relative error is only 5.7%, and the mean error is 1.7% with only 30 samples. Compared to a linear interpolation procedure, the performance is significantly better for the same number of points.

Table 2. Maximum, mean and standard deviation of approximation errors of linear interpolation, N= 30.

Range	$e_{rel}(p)$		
	maximum	mean	Standard deviation
[-19,-16]	0.096	0.017	0.018
[-19,-14]	4.42	0.28	0.43

For the larger range of [-19,-14], the accuracy of the approximation deteriorates, especially in the region where there is a large jump in the solutions shown in Figure 1. The isoSE covariance function is thus not an appropriate covariance function to use.

The NN covariance function is inhomogeneous and is expected to model the jump more accurately. However, based on Table 1, the resulting errors appear to be comparable to those obtained using the isoSE covariance function. This is because the inhomogeneity being modeled by NN covariance function is incompatible with our data; NN covariance function is suited for data that have abrupt change when **p** changes from positive to negative. However, 50% of the sample points in S_S have errors below 10% when the NN covariance function is used compared to 20% when the isoSE covariance function is used. The optimized hyperparameters of the NN covariance function are l = 0.072 and σ_f = 2.47. This short characteristic length and large variance reflects the attempt of the NN covariance function to model the jump. With the isoSE covariance function, the hyperparameters are l = 4.20e-1 and σ_f = 1.83. Here, the jump is not sufficiently captured since most of f(**p**) is smooth in the parameter space.

It is clear that both covariance functions do not provide the accuracy we need. A more appropriate covariance function is one where the hyperparameters are function of **p** (Plagemann, 2008). However, the expected optimization problem will be arduous, and the resulting covariance function is harder to interpret.

In all of the above approximations, the hyperparameter σ_n is close to zero, because we are approximating the solution obtained through a deterministic simulation. However, the presence of σ_n implies that we could model noise in our solution. This will be explored in the future in the context of flow through heterogeneous formations.

One should note that these hyperparameters are obtained through a local optimization algorithm (steepest descent), and are thus sensitive to the starting position. This could also explain why the previous errors from both the isoSE covariance function and NN are not satisfying. More optimal hyperparameters may be obtained if global optimization algorithm is used, leading to better ROMs. The use of global optimization algorithm will be explored further in the future.

Uncertainty quantification

The purpose of developing such a ROM is to substitute a time-consuming high-fidelity model by a ROM in an inverse analysis or sampling-based uncertainty quantification (UQ) analysis, where many forward model evaluations are needed. We have implemented such capability into iTOUGH2, and performed UQ for the same sample problem (we have considered the smaller range of log(k)).

For comparison purposes, we performed an UQ using the high-fidelity model (HFM). The Monte Carlo simulation is performed with a

sampling size of 100 and 1000 for both the ROM and HFM. The mean and variance of the model output from each Monte Carlo simulation are listed in Table 3.

Table 3. Comparison of UQ results between a HFM and its corresponding ROM

	HFM-1000	ROM-1000	HFM-100	ROM-100
Mean	1.11e6	1.15e6	1.14e6	1.17e6
Standard deviation	2.4e5	2.4e5	2.3e5	2.3e5

The ROM seems to be able to reproduce the standard deviation of the UQ analysis. The error of the mean estimation using the ROM is about 3%. For this particular example, 100 samples seem to be sufficient for uncertainty quantification.

The histogram using 1000 samples are plotted in Figures 3 (a) and (b). The ROM appears to re-produce the histogram of the model output relatively well. In this particular problem, it does not seem necessary to have a large number of samples for an UQ analysis (i.e., 100 samples is sufficient). However, most problems, especially the nonlinear ones with many sensitive and uncertain parameters, may need many forward evaluations, in which case ROM would save time. The ROM construction in this example requires only 30 forward HFM evaluations. Since the evaluation of the ROM during the Monte Carlo sampling has a negligible computational cost compared to running a single simulation with the HFM, the cost savings are proportional to $N_{MC}/30$, where N_{MC} is the number of Monte Carlo simulations.

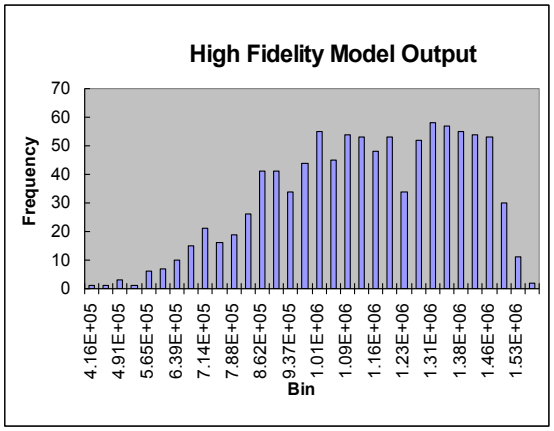

(a)

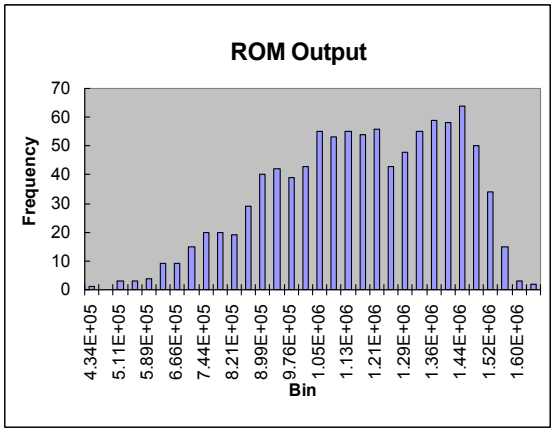

(b)

Figure 3. Histogram of the Model output from the Monte Carlo simulation with 1000 samples, using both (a) HFM and (b) ROM

CONCLUSION

In this work, we examined two types of ROMs to approximate a high-fidelity model for inverse analysis: A Gaussian Process (GP) regression model and neural networks. We provided an error-estimation method for the proposed ROM methods. We improved the performance of GP-based ROM by implementing an adaptive sampling approach, so the ROM can be constructed with a minimum amount of expensive HFM simulations. In the sample problem, the ROMs using both approaches perform significantly better than a linear interpolation approach. However, the performance is not very satisfying when the model output experiences sudden changes. This implies that our prior models for the mean and covariance are inappropriate.

Constructing the ROM requires some CPU time, specifically the estimation of hyperparameters, which in itself is an optimization problem. However, this computational cost is relatively small and just a one-time effort. Once a ROM is constructed, the computational savings are demonstrated by a UQ analysis. The savings can be large for a big problem (i.e., problems with many uncertain parameters, large sample size, and each HFM evaluation taking a long time).

ACKNOWLEDGMENT

This work was conducted as part of Berkeley Lab's National Risk Assessment Partnership (NRAP) effort, supported by the Assistant Secretary for Fossil Energy, Office of Sequestration, Hydrogen, and Clean Coal Fuels, of the U.S. Department of Energy, under Contract No. DE-AC02-05CH11231 and TOUGH2 development grant.

REFERENCES

Carr J.C., R.K. Beatson, J.B. Cherrie, T.J. Mitchell and T.R. Evans, Reconstruction and Representation of 3D Objects with Radial Basis Functions, *ACM SIGGRAPH 2001*, 12-17 August 2001, Los Angeles, CA, USA.

Finsterle, S., and K. Pruess, Solving the estimation-identification problem in two-phase flow modeling, *Water Resour. Res.*, *31* (4), 913–924, 1995.

Finsterle, S., *iTOUGH2 Sample Problems*, Report LBNL-40042, Lawrence Berkeley National Laboratory, Berkeley, Calif., 2007.

Plagemann C., K. Kersting and W. Burgard, Nonstationary Gaussian Process Regression Using Point Estimates of Local Smoothness, In *Machine Learning and Knowledge Discovery in Database, Lecture Notes in Computer Science*, 5212, 204-219, 2008.

Rasmussen, C.E. and C.K.I. Williams, *Gaussian Processes for Machine Learning*, MIT Press, 2006.

Rozza, G., D.B.P. Huynh and A.T. Patera, Reduced Basis Approximation and a Posteriori Error Estimation for Affinely Parametrized Elliptic Coercive Partial Differential Equations: Application to Transport and Continuum Mechanics, *Archives of Computational Methods in Engineering*, 15(3), 229–275, 2007.

Williams, C.K.I., Computation with Infinite Neural Networks, *Neural Computation*, 10(5), 1203–1216, 1998.

GEOTHERMAL MODEL CALIBRATION USING A GLOBAL MINIMIZATION ALGORITHM BASED ON FINDING SADDLE POINTS AS WELL AS MINIMA OF THE OBJECTIVE FUNCTION

Manuel Plasencia[1], Andreas Pedersen[1], Andri Arnaldsson[2] and Hannes Jónsson[1,3]

[1]Science Institute of University of Iceland, VR-III
107 Reykjavík , Iceland
[2]Vatnaskil Consulting Engineers, Sudurlandsbraut 50
108 Reykjavík , Iceland
[3]Faculty of Science, University of Iceland VR-III
107 Reykjavík , Iceland
e-mail: mpg2@hi.is

ABSTRACT

Here we present a specific method for global optimization of parameters within a model for multiphase flow in porous media. This model, which involves a search for first-order saddle points and the minima of an objective function obtained from the iTOUGH2 code, has been implemented within the EON software for distributed and cloud computing. While it can be applied to problems with a large number of parameters, the application presented here is a simple illustrative model of the Laugarnes geothermal area in Reykjavík, Iceland, calibrated in two-dimensional parameter space.

INTRODUCTION

The development of reservoir models often involves inverse modeling, which consists of estimating model parameters from measurements of system response made at discrete points in space and time. The difference between model calculations and the data at calibration points is measured by the objective function. This objective function could, for example, be the sum of the squares of the difference between calculated model output and field-measured data. Estimating model parameters is then formulated as an optimization problem, in which the goal is to find the parameter values that minimize the objective function.

Even for small models with only a few parameters, the objective function can have more than one minimum. This is illustrated in Figure 1, which shows a 1D cut through an objective function for the model described below. Within the interval shown, three local minima appear.

The occurrence of multiple minima is more likely in models with a larger number of parameters. The main task then becomes that of finding the global minimum of a function among the several local minima—a very challenging problem. It is also important to know whether additional local minima, which are insignificantly higher (compared with estimated error bars), are present and could represent equally good parameter sets for practical purposes.

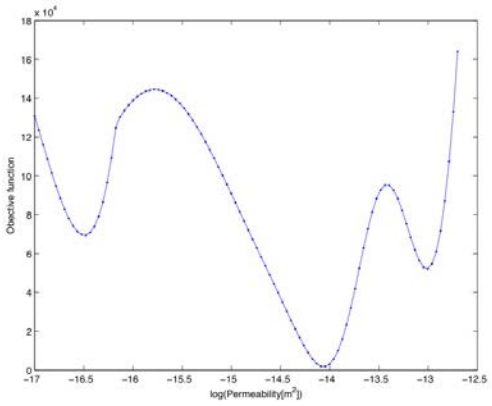

Figure 1. A 1-dimensional cut through the objective function for the model system studied here, illustrating the problem of multiple local minima. The goal is to find the global minimum (vicinity of -14.1) among the local minima.

Global optimization of functions of many variables is often carried out using simulated annealing algorithms that roughly mimic the annealing of materials. The 1983 article by Kirkpatrick, Gelatt and Vecchi (Kirkpatrick 1983) illustrated how such an approach could be applied to circuit design. This article has since been cited exten-

sively, and the authors' method applied to many different optimization problems. There, the objective function is taken to represent an "energy" of the system, and a fictitious temperature is introduced. By applying a Monte Carlo algorithm, we can simulate the annealing process by accepting or rejecting changes in the arguments of the objective function. The reason for introducing temperature is to introduce and control the probability of accepting increases in the objective function, since they may be an essential intermediate step in ultimately reaching lower function values.

A central issue in simulated annealing calculations is the time scale of the "cooling" of the system, from high temperatures to zero temperature. The lower the cooling rate, the more likely the method will find the global minimum. For a given amount of computational effort, a method that can simulate longer time intervals is therefore more likely to reach the global minimum.

One method for long time-scale simulations, known as the adaptive kinetic Monte Carlo (AKMC) algorithm, has recently been developed (Henkelman 2001) in the context of transitions for atomic-scale systems. It can be used for global optimization in a way that is analogous to simulated annealing (Pedersen 2012). The important feature of this approach is the ability to move from one local minimum of the objective function to another, via paths that lie close to first-order saddle points. The saddle points are found using the minimum mode following method (Henkelman 1999). The kinetic Monte Carlo algorithm is used to select between the determined possible paths through different saddle points. Alternatively, the path lying through the lowest saddle point leading to a new local minimum can be chosen, in which case a temperature does not need be defined (Pedersen 2012). The advantage of this algorithm over the original simulated annealing algorithm is that fewer objective-function evaluations are needed to move from one local minimum to another. Also, the objective function only gets evaluated for parameter values for which its value is relatively small, while the regions with excessively high values for the objective function are avoided.

CONCEPTUAL AND NUMERICAL MODEL

Here, we apply this algorithm to a specific geothermal modeling problem. Laugarnes is a low-temperature field in Iceland, which has been described in some detail by Thorsteinsson and Eliasson (1970). This geothermal area is fed by three aquifers: Aquifer A with water of 110–120°C, Aquifer B with water of 135°C and Aquifer C with water of temperature of 146°C. Tuffs and sediments act as aquicludes between the aquifers. The active reservoir underlies an area of 5 km^2 within the city of Reykjavik and has a base temperature about 145°C (Bodvarsson 1978). Prior to exploitation, the hydrostatic pressure at the surface in the geothermal field was 6–7 bars (Einar Gunnlaugsson et al., 2000) and about 10 L/s of 88°C water issued in free flow from the hot spring. (Thorsteinsson and Eliasson 1970).

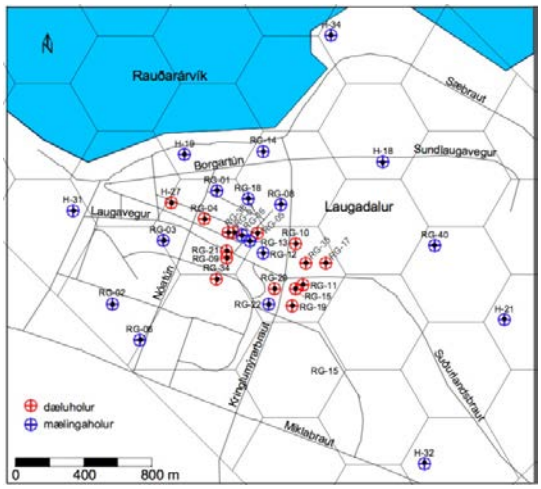

Figure 2. Aerial partial view of Voronoi mesh used to model the area. Red and blue circles production and observation wells respectively.

To build a simplified model for this area, we created a mainly hexagonal Voronoi mesh with 38 volume elements, covering an area of 12 km^2 (Figure 2). The model extends to 2235 m depth in eight layers. There is a single volume element at layer 1 and at layer 8, both of which are inactive and represent the reservoir top and bottom. Layers 3, 5, and 7 represent aquifers A, B and C respectively; layers 2, 4, and 6 represent aquicludes and were assigned lower permeability values (Figure 3).

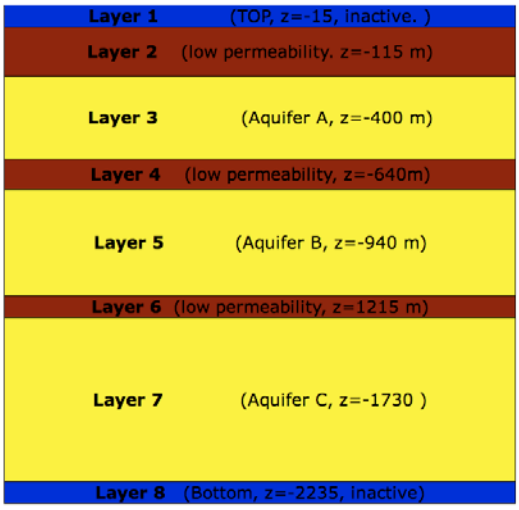

Figure 3. View of layers used in the model. Colors correspond to different material properties.

A 3D representation of the geometry of the model can be seen in Figure 4. The red point at the surface represents the location of an observation well, while the blue point represents the location of a hot spring. Thus, a well on deliverability was defined there acting as a sink.

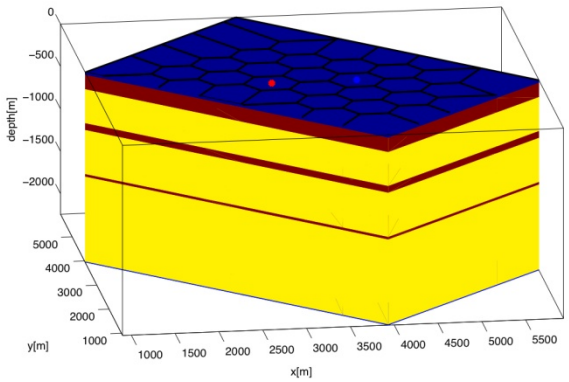

Figure 4. 3D view of the model. Colors correspond to different material properties The blue and red points at the top layer represent the location of hot spring (water sink) and an observation well respectively.

Two types of sources have been included: first, a mass source located at the bottom of the reservoir was positioned in the area where the upflow is thought to be located. Second, heat sources where placed at scattered positions on the bottom (Figure 5).

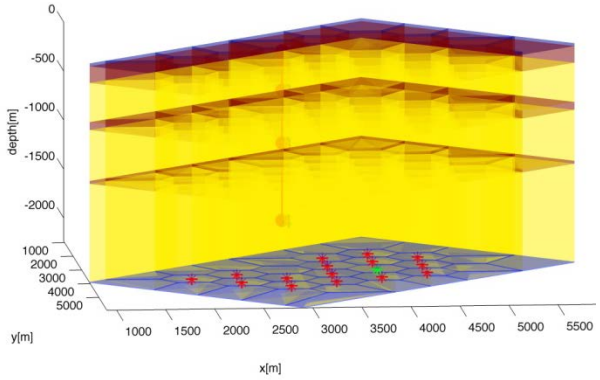

Figure 5. Semi-transparent 3D view of the model. The red starts at the bottom layer represents the heat sources distribution and the green start signifies a water source.

Six calibration points are used (Figure 6). The red line in Figure 6 represents the observation well; it has four calibration points at four different depths. Starting from the top, point 1 represents pressure at the top of reservoir. Points 2, 3 and 4 represent temperatures in aquifer A, B, and C respectively. Points 5 and 6 are in the same location and represent the water flow rate from the hot spring and enthalpy of its water.

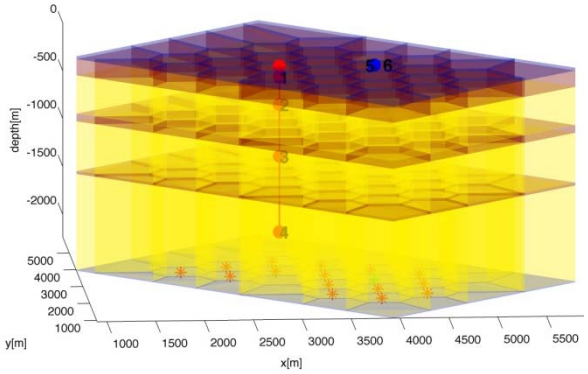

Figure 6. Semi-transparent 3D view of the model. From the top, points from 1 to 4 in red color and 5 to 6 in blue color are calibration points. Points 5 and 6 coincide in the same position.

This model has been constructed to represent a realistic system, but at the same time be simple enough to allow tests and studies of the performance of the optimization algorithm. Focus is mainly on the inverse modeling, so it was decided to generate the data at the calibration points, add some Gaussian noise, and then use this as a representation of the real data for the

natural-state calibration process. Reasonable values were chosen for the fixed parameters in the model, i.e., those that will not change during the optimization, in order to produce a model result close to what already has been reported for this region. Fitting the generated data instead of what is measured has the main advantage that the location of the minimum is known beforehand, which makes the analysis of the optimization algorithm simpler.

OBJECTIVE FUNCTION

The objective function may be close to quadratic or highly nonlinear in nature; it may be continuous, differentiable, and smooth; or discontinuous, not differentiable, and rough. For a nonlinear model, the topography of the objective function away from the minimum becomes intricate, making it difficult for the optimization algorithm to iteratively proceed towards the minimum (Finsterle, 2007).

The two-dimensional optimization problem addressed here originates from the calibration of the simplified model described above. In this case, the objective function is the squared deviation between "observed" and calculated pressure at calibration point 1, temperature at calibration points 2 to 4, and water flow rate and water enthalpy at calibration points 5 and 6 respectively. Figure 7 shows the shape of the objective function in the parameter space defined by the logarithm of mass generation rate (log(q)) and the logarithm of permeability (log(k)) for the aquiclude layers—obtained using the Grid Search Method implemented in iTOUGH2. It should be noticed that within the interval for the permeability between -17.0 and 15.5 the objective function is not smooth. It furthermore shows some point-like discontinuities that probably are caused by numerical instabilities in the forward model. Thus, our focus will mainly be on the smooth regions.

Note that the contour lines in Figure 8 show that the objective function has three minima. The global minimum is known to be located for log(k)=-14.00 and log(q)=1.00, (will be referred as M2), but two local minima also occur, one at log(k)=-16.46 and log(q)=1.10 (M1) and another at log(q)=12.79 and log(q)=1.76 (M3). Between minima M1 and M2, there is a first-order saddle point (SP1), and between M2 and M3, there is another first-order saddle point (SP2).

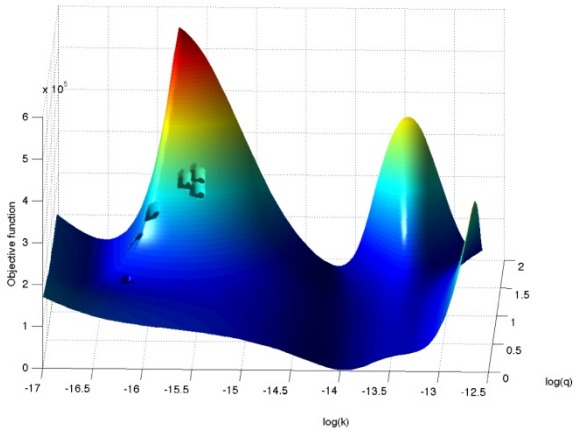

Figure 7. The objective function for the simplified model, as a function of two variables: log(generation rate) on the x-axis and log(permeability) on the y-axis. Between -17.0 and 15.5 it shows some point-like discontinuities that probably are caused by numerical instabilities in the forward model

Both local minima correspond to a significantly higher value of the objective function, but they will attract minimization paths started from nearby regions in parameter space. While it can easily be discounted in this simple two-dimensional problem, this can be a severe problem for models involving many parameters. Furthermore, more complex problems are also likely to have more local minima, several of which can have reasonable values for the parameters.

FINDING THE NEAREST LOCAL MINIMUM

The Levenberg-Marquardt minimization algorithm is found to perform well for most iTOUGH2 applications (Finsterle, 2007). It can be made to converge efficiently by selecting appropriate values for convergence parameters, but as for most other local minimization algorithms, it only strives to converge to the minimum closest to the initial guess of the model parameters. Figure 8 shows the solution paths, for the Levenberg-Marquardt minimization algorithm, starting from four different initial guesses. If the initial guess is in vicinity of the global minimum, the method converges to it. But if the initial guess is not in the proximity of

the global minimum, the method converges to the higher local minima. A region of parameter space leads to convergence to local minima.

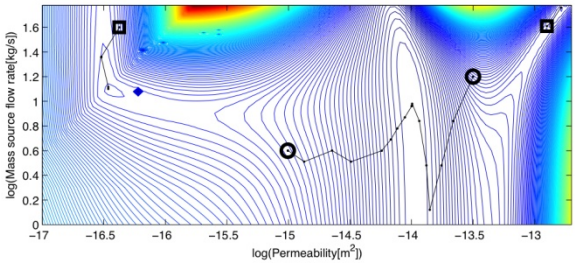

Figure 8: Contour lines of the objective function and solution paths of Levenberg-Marquardt minimization algorithm in the 2D parameter space log (g)-log(k), starting from 4 different points. The squares represent initial guesses that lead to convergence to local minima. The circles represent initial guesses that lead to convergence to the global minimum. This illustrates the possibility that a minimization from an initial guess of the parameter values can lead to convergence to a local minimum with a substantially higher value of the objective function than the global minimum.

This example illustrates the need for exploring the objective-function surface beyond just finding the local minimum nearest to the initial guess. While it is easy to envision setting up enough minimization calculations to cover a fine grid of possible initial guesses for all parameters when the number of parameters is small, this will quickly become unmanageable as the number of parameters increases.

SEARCHING FOR MULTIPLE MINIMA

The task of finding the global minimum of a function with multiple local minima is challenging—the only method that is guaranteed to work is a simulated annealing method requiring an impossibly slow cooling rate and impossibly large computational effort. Therefore, we need a more efficient method for dealing with objective functions with multiple local minima.

The AKMC algorithm can be applied to explore functions with multiple minima. The basic feature of this algorithm is the ability to climb up the objective function surface to focus on regions around first-order saddle points. The algorithm thereby gains the ability to reach new minima adjacent to a known minimum. In a simulated annealing formulation, the new minimum can be accepted or rejected based on the difference in objective-function values and the current value of the temperature (Pedersen 2012). Alternatively, a map of the minima can be generated, with each additional minimum selected based on the height of the first-order saddle point on the path to the minimum.

The AKMC algorithm works by the following principle (for a more detailed description, see Henkelman (2001) and Pedersen (2011)). For a given local minimum, several saddle-point searches are carried out (on the order of 10 to 100), starting from a random change in the model parameters. To initialize each search, we impose a small change in the parameter values at the minimum, generated from a Gaussian random distribution. For each of the perturbed parameter values, the minimum mode following method (Henkelman, 1999) is then used to climb up the objective-function surface and home in on a first-order saddle point. Such searches are continued, using a probabilistic confidence estimate, until additional searches reveal no new low-lying saddle points (Xu 2008).

The most important aspect of the AKMC method is the slow increase in computational effort with the increase in the number of parameters. This method was originally developed to search for transition mechanisms and find stable arrangements of atoms in solids. It has been applied successfully to systems with thousands of parameters (atom coordinates in those cases). It has been implemented in software for both distributed computing and cloud computing (Pedersen 2010), making it possible to use multiple CPUs simultaneously connected by a simple internet connection. Idle time on computer clusters or personal computers can be used to carry out the calculations. The saddle-point searches are farmed out to the various CPUs, and the saddle points and minima found are reported back to the server, which keeps track of them.

We carried out calculations using this algorithm for the simplified test problem, one starting from an initial point close to the global minimum and

another from an initial point close to a local minimum. In either case, both the global and the local minimum are found (to within a chosen tolerance in the gradient).

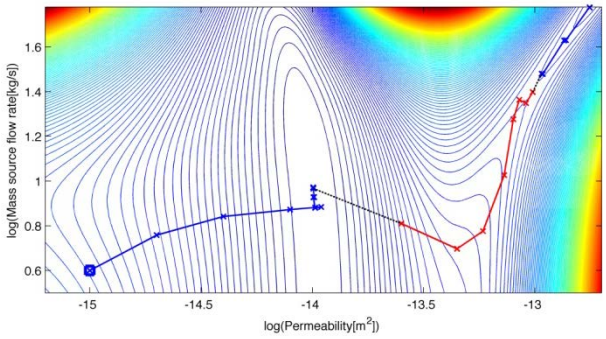

Figure 9. AKMC minimization path from initial guess represented as a blue square. It converges to the global minimum (path in blue), given an initial displacement (black dotted line) it climbs up to converge to the saddle point (path in red), given a displacement from saddle point (black dotted line) it converges also to the local minimum.

Figure 9 shows the minimization path using AKMC. From the initial guess (-15.0, 0.6), represented in the figure as a blue square, the path converges to the global minimum through the blue path. Then, after a small increment in parameter values, it starts a climb up the objective-function surface and converges on a first-order saddle point to a rather loose tolerance. After a displacement along the mode for which the saddle point is a maximum, a minimization converges to the adjacent local minimum.

Similarly, Figure 10 shows the minimization path using a different initial guess (-12.9, 1.61). It converges to a local minimum and, after a displacement, climbs up to converge to a saddle point. Another displacement is given from the saddle point, which then converges to the global minimum.

Both paths go through the vicinity of the first-order saddle point. The tolerance for the convergence onto the saddle point can be large, since the precise value of the objective function there is not important. The fact that the paths taken from one minimum to another go through the vicinity of saddle points means that parameter regions with very large objective-function values are avoided, which can be advantageous, since unphysical parameters can lead to ill-defined values of the objective function, as well as a large computational effort.

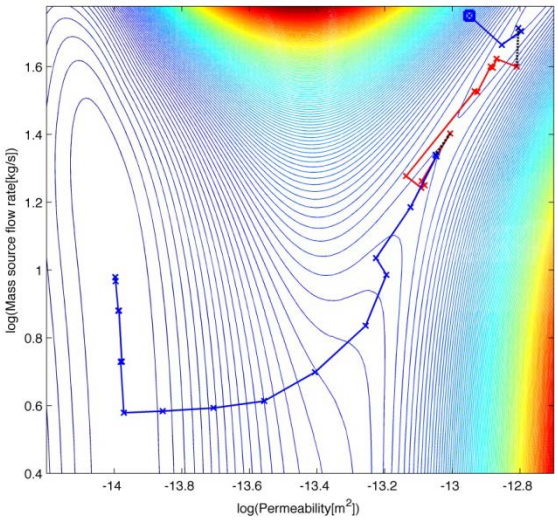

Figure 10. AKMC minimization path from initial guess represented as a blue square. It converges to the local minimum (path in blue), given an initial displacement (black dotted line) it climbs up to converge to the saddle point (path in red), given a displacement from saddle point (black dotted line) it converges also to the global minimum.

DISCUSSION

The problem of finding the global minimum of an objective function that has many local minima is a challenging one—with the only method guaranteed to work being a simulated annealing method with an impossibly slow cooling rate requiring infinite computational effort (Kirkpatrick, 1983). For object functions that are continuous and differentiable, the gradient can be used to navigate on the objective function surface, so as to move from one local minimum to another. This assumes the minima can be associated with basins of significant extent and that the surface is not "rippled." If these conditions are met, the AKMC method with systematic coarse graining (Pedersen 2012) can be used to map out the local minima. Not only will this method provide an estimate of the global minimum (as the lowest minimum

found), but it will also give an estimate for the uniqueness of the solution found, and the most important parts of the objective function.

REFERENCES

Bodvarsson, G., and Elliot Zais. A field example of free surface testing. Report, 1978.

Finsterle, S., "iTOUGH2 User's Guide," *LBNL-40040*, February; "iTOUGH2 Sample Problems," LBNL-40042, February 2007.

Gunnlaugsson, E., G. Gislason, G. Ivarsson, and S. P. Kjaran. Low temperature geothermal fields utilized for district heating in reykjavik, iceland. Proceedings World Geothermal Congress 2000 Kyushu - Tohoku, Japan, May 28 - June 10, 2000.

Henkelman, G., and H. Jónsson, "A Dimer Method for Finding Saddle Points on High Dimensional Potential Surfaces Using Only First Derivatives," *J. Chem. Phys.*, **111**, 7010, 1999.

Henkelman G., and H. Jónsson, Long Time Scale Kinetic Monte Carlo Simulations without Lattice Approximation and Predefined Event Table, *J. Chem. Phys.*, **115**, 9657, 2001.

Kirkpatrick, S., C.D. Gelatt Jr and M.P. Vecchi, "Optimization by Simulated Annealing," *Science*, **220**, 671, 1983.

Pedersen, A., L. Pizzagalli and H. Jónsson. Finding mechanism of transitions in complex systems: Formation and migration of dislocation kinks in a silicon crystal, Journal of Physics: Condensed Matter; 21, 084210, 2009.

Pedersen A., and H. Jónsson. Simulations of Hydrogen Diffusion at Grain Boundaries in Aluminum, Acta Material; 57, 4036-4045, 2009.

Pedersen, A., G. Henkelman, J. Schiøtz and H. Jónsson. Long Time Scale Simulation of a Grain Boundary in Copper, New Journal of Physics; 11, 073034, 2009.

Pedersen, A. and H. Jónsson, "Distributed Implementation of the Adaptive Kinetic Monte Carlo Method," *Mathematics and Computers in Simulation*, **80**, 1487, 2010.

Pedersen, A., S.F. Hafstein and H. Jónsson, "Efficient Sampling of Saddle points with the Minimum Mode Following Method," *SIAM Journal on Computational Science*, **33**, 633, 2011.

Pedersen, A., J-C. Berthet and H. Jónsson, "Simulated Annealing with Coarse Graining and Distributed Computing," Lecture Notes in *Computer Science*, **7134**, 34, 2012.

Thorsteinsson, T., and J. Eliasson. Geohydrology of the Laugarnes hydrothermal system in Reykjavik, Iceland. U.N. Symposium on the Development and Utilization of Geothermal Resources, Pisa. 1970.

Xu L., and G. Henkelman, "Adaptive kinetic Monte Carlo for first-principles accelerated dynamics," J. Chem. Phys., 129, 114104, 2008.

OPTIMIZING THE MODELING PERFORMANCE FOR SAFETY ASSESSMENTS OF NUCLEAR WASTE REPOSITORIES BY APPROXIMATING TWO-PHASE FLOW AND TRANSPORT BY SINGLE-PHASE TRANSPORT SIMULATIONS

P. Schädle[1,2], N. Hubschwerlen[2], H. Class[1]

[1]Universität Stuttgart, Institute for Modelling Hydraulic and Environmental Systems
Pfaffenwaldring 61, 70569 Stuttgart, Germany

[2]AF-Consult Switzerland Ltd
Täfernstrasse 26, 5405 Baden, Switzerland
Email: Philipp.Schadle@afconsult.com

ABSTRACT

The long-term safety performance of a potential deep geological repository for high-level and intermediate-level long-lived nuclear waste can be studied through numerical simulation tools capable of appropriately modeling the phenomenologies of interest in the repository and its environment. Because of the complexity of the modeled layout, the numerous physical processes, and the simulated times (up to 1 million years), computational needs are very high. TOUGH2-MP (Pruess et al. 1999, Zhang et al. 2008) is a suitable tool for modeling the impact that heat and gas generated in the emplacement areas may have on the evolution of fluid pressure and saturation fields in repository drifts and shafts (as well as in the host rock itself). The module EOS7R also enables the computing of coupled radionuclide transfer.

With respect to computational efficiency, it is useful to decouple transport from hydraulic calculations, for three primary reasons: (1) it allows using the hydraulic calculation once for several transport computations of a performance analysis and safety assessment (PA/SA) study, which is expected to lead to a substantial gain in CPU time; (2) it allows for optimizing the discretization separately for both hydraulic and transport calculations; and (3) it also allows for combining the TOUGH2 hydraulic and other codes modeling radionuclide transport. This advantage enables the consideration of phenomenologies not available through TOUGH2.

This work shows how to establish a sequential approach between TOUGH2 and another code. It also presents the conditions of use for such an approach, in terms of performance and the impact of the discretization on the results.

INTRODUCTION

In the course of a performance analysis and safety assessment (PA/SA) of a potential deep geological repository for high-level and intermediate-level long-lived nuclear waste, we must establish ways to simulate hydraulic and gas flow and transport of radionuclides through the repository and the embedding host rock. The PA/SA must consider phenomenologically detailed models, models that describe the flow and transport processes as accurately as possible. This leads to highly nonlinear models, owing to the consideration of such factors as sorption or variable relative permeability. Since the resulting discretized equations have to be solved iteratively, the computational effort is large.

Furthermore, a potential repository is expected to extend over an area of 10 to 20 km^2 and to consist of thousands of emplacement cells, with relevant details at the scale of decimeters. Potential radionuclide release from a repository and transport to the biosphere must be estimated for up to one million years. Consequently, both the spatial and temporal scales represent severe challenges for any numerical modeling approach. Finally, any modern PA/SA includes probabilistic studies to assess uncertainties; for such probabilistic approaches, several hundred or thousand numerical simulations must be performed.

All of the above suggests that fundamental simplifications are required in the course of defining a numerical strategy and solution. One

approach is to simplify the simulations by decoupling the flow and transport computations. The idea is to perform the resource-intensive two-phase flow computation only once, followed by many less demanding single-phase unsaturated transport simulations that reuse the two-phase results. Additionally, the two-phase hydraulic calculation is realized on the coarsest possible discretization in time that would still lead to a reasonable approximation for flow. The discretization for the subsequent transport simulations might be chosen finer, with much less impact on computational time. There are some limitations to this approach, however: The considered nuclides need to be fully soluble in water, and the influence of the nuclides on the flow must be negligible.

The goal of the present work is (1) to implement the aforementioned technique using TOUGH2 for the two-phase flow and the code Traces for the simulation of single-phase unsaturated transport and (2) to study how different discretizations in time for flow and transport simulations impact results. First, we calculate a benchmark two-phase flow and transport and single-phase transport with a very fine discretization. With the discretizations being identical for the two simulations, the decoupling method itself is validated. Subsequently, discretizations are coarsened. The aim of this approach is to meet the benchmark as closely as possible in every calculation using a progressively coarser discretization. This goal is achieved with carefully selected temporal discretizations and interpolation schemes.

The methodology, the construction of a sequential approach, and its application to a simulation case are presented in this paper, followed by a study of the conditions of use for a sequential approach, focused on temporal discretization variation.

METHODOLOGY

The aim of this project is to establish a sequential approach for flow and transport using a hydraulic computation made with TOUGH2-MP with the EOS5 (water and hydrogen) module (hereafter referred to as the T2MP+E5 code). Once this sequential approach is validated by comparison with a reference coupled simulation, the impact of the simplification of the hydraulic data on the transport results is studied.

Decoupling of flow and transport

The first step consists of decoupling the flow component from the transport component of the computation. The computationally intensive two-phase flow field thus needs to be calculated only once and can be used as an input for various transport calculations. For the following decoupled transport calculation, the computational effort is relatively low. This approach can lead to a significant reduction of potentially scarce computational resources when performing the probabilistic studies.

In practice, the decoupled computation is realized in four main steps, as schematized in Figure 1. First, the two-phase hydraulic flow field is calculated. The pore velocity and saturation fields are written as output for every time step by TOUGH2. Then, in order to simulate the transport of the radionuclides, this intermediate output data must be converted into the hydraulic data required by the transport code used in the sequential approach. After this conversion, the unsaturated transport calculation is executed.

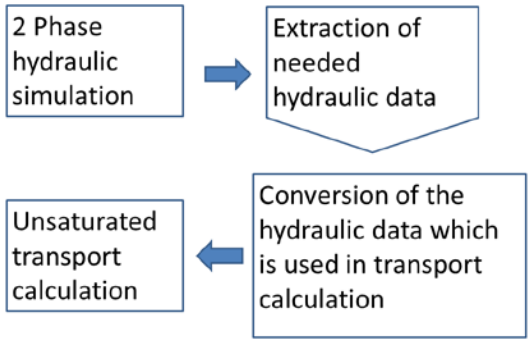

Figure 1. Schematic representation of a decoupled sequential approach for hydraulic and transport simulation.

To validate this method, we perform a coupled two-phase benchmark calculation, and compare the results with those from the sequential approach single-phase transport calculation.

Simplification of the hydraulic data

Once the sequential approach is validated, the hydraulic data required for the transport

computation should be optimized. The work discussed here is a first step towards the separate optimization of the two parts of the sequential approach. This task consists mainly of coarsening the temporal density of the hydraulic data given to the transport computation (Figure 2). Reducing the amount of hydraulic data necessary to run the transport-calculation part is expected to reduce the computation time of the sequence. because processing of flow-field data is minimized.

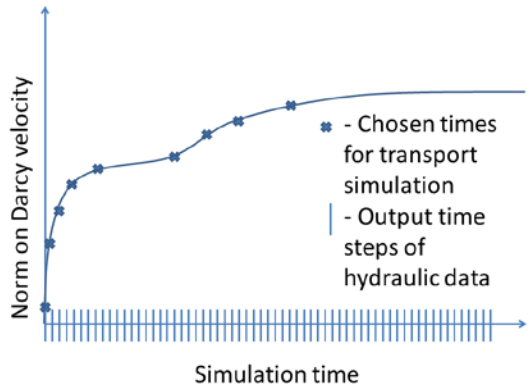

Figure 2. Schematic presentation of the approach to reduce the amount of hydraulic data resulting from the two-phase flow calculation as input for the transport calculation

ESTABLISHMENT OF THE SEQUENTIAL APPROACH

In this section, the setup of a sequential approach is described in detail for simulations modeling the release of radionuclides from an intermediate-level long-lived radioactive (ILW-LL) waste cell, during the resaturation phase occurring after its closure. The gas phase present is hydrogen; hence, T2MP+E5 is used for the flow calculation. For the transport part, we use the one-phase unsaturated transport version of the Traces mixed hybrid finite element (MHFE) code available at Andra.

These results are compared with a coupled reference simulation performed with the TOUGH2-MP EOS75R model, a derivate of EOS7R in which air has been replaced by hydrogen (Kaempfer et al., 2012).

The compatibility between two-phase hydraulics (TOUGH2) and single-phase unsaturated transport (Traces) is monitored carefully, as are the differences between this transport model and the transport model used in EOS7(5)R.

Compatibilities between two-phase hydraulic and unsaturated transport

The mass conservation equation and Darcy's law for the computation of the two-phase flow used in TOUGH2 are described in Pruess et al. (1999). The equation for single-phase unsaturated transport in porous media is formulated according to the Richards model. In the Richards model, the gaseous phase is not modeled, and no exchange between the phases is considered.

Conservation equation for concentration C_i of solute component i per time t – transport equation (Traces):

$$\frac{\partial(R_i\theta_i C_i)}{\partial t} = \nabla\left(\overline{\overline{D_i^*}} \cdot \vec{\nabla} C_i - \boldsymbol{q} C_i\right) + Q_i$$

Here, R_i is the retardation and Q_i the source of component i. To solve the transport problem, the Darcy velocity $\boldsymbol{q}$ and the liquid saturation field are required. The liquid saturation S_l is used to compute the volumetric water content $\theta_i = S_l \cdot \phi$ where ϕ is the porosity. The Darcy velocity is also needed to compute the dispersion present in the diffusion tensor $\overline{\overline{D_i^*}}$. The saturation field is also indirectly used through θ_i to compute the retardation factor R_i, the saturation-dependent dispersion coefficients, and the solubility limits.

The Darcy velocity field in the liquid phase and the liquid saturation field are given by the two-phase hydraulic flow equations. So, physically, there are no inconsistencies between formulating the transport problem either by two-phase flow and transport equations or by a single-phase formulation using hydraulic data from the two-phase simulation—as long as the transport in the gas phase remains negligible. However, inconsistencies may occur because of definition incompatibilities among the variables in the two codes composing the sequential chain.

Creation of two-phase flow data

The results of the two-phase flow calculation are the basic input data for the transport part of the sequential approach, and are therefore generated

for every time step. T2MP+E5 produces the liquid pore velocity (VEL(LIQ)) at the element interfaces and the saturation (SL) of each element in the mesh.

Conversion of hydraulic data

One important step of the sequential approach is to convert the flow data produced by T2MP+E5 into data compatible with transport. In the case of a MHFE code such as Traces, saturation is required at element centers, so the TOUGH2-MP output can be used directly in the transport calculation. The pore velocity, on the other hand, needs to be converted to the Darcy velocity for use by the MHFE transport code. This is done by multiplying the pore velocity by the porosity. The pore velocity is defined at the faces of the element, thus posing the problem of determining the one from among the neighboring elements, the porosity of which is to be used. For two-phase computations, TOUGH2 uses upstream weighting to select the porosity for the computation of the pore velocity from the Darcy velocity. We use the same method.

If mechanical dispersion is considered, Traces also needs the Darcy velocity at the element centers. This is not an issue in this study because we did not consider mechanical dispersion.

Setup of the transport calculation codes

The transport calculation is set up using the generated hydraulic data. Transport-specific parameters must be defined for the Traces code. To be able to compare the results with the EOS75R reference simulation, we must select some equivalent parameters. As a consequence, the differences and incompatibilities between transport in two-phase and single-phase unsaturated (Richards) porous media are studied below.

In terms of processes, TOUGH2-MP EOS75R computes radionuclide transport in the gas phase, which is not possible with the Richards model. However, in the present case, in which we are limited to a radionuclide that remains in solution, transport in the gaseous phase is assumed to be negligible, and this is then not a major incompatibility.

Another limitation of the Richards model described above is the assumption of no temperature dependence of the various properties and parameters. Here we restrict ourselves to an isothermal simulation that serves as a reference. If the influence of temperature on transport is to be accounted for, T2MP+E5 can seamlessly solve the flow problem under non-isothermal conditions. The temperature-dependence of the various transport parameters could be mimicked in Traces by setting up time- and space-dependent parameters that are functions of temperature. EOS75R does not account for precipitation and dissolution of the radionuclides, but this is not an issue in the cases studied here, in which radionuclides with infinite solubility limits are considered.

Other differences stem from the different physical laws employed to model processes and define the parameters:

- Radioactive and decay chains are defined similarly in both models. However, EOS75R is limited to two radionuclides. This limitation is not relevant when tracking the transport of a single radionuclide.
- For retardation, EOS75R considers only the K_d retardation model. The parameters for calculating retardation are defined for every component and material. Other transport codes, such as Traces, also propose other retardation models (Langmuir, Freundlich).
- Diffusion models also have differences. In EOS7(5)R, effective diffusion is defined as $D_{eff} = \phi\tau_0\tau_\beta d_\beta^k$, with d_β^k being molecular diffusion. Three models are proposed (Millington-Quirk, relative permeability, and constant diffusivity) depending on the mode of definition of tortuosity ($\tau_0\tau_\beta$) and d_β^k, whereas in Traces, only constant diffusivity is available. On the other hand, Traces can model dispersion, which is not available in EOS75R. In summary, diffusion models are perfectly compatible between TOUGH2 and Traces as long as the constant diffusivity model is activated in TOUGH2 and there is no dispersion.
- In TOUGH2, porosity is defined by materials in the ROCKS block. Hence it is not possible to define the portion of the porosity

that is accessible by each component, as can be done in Traces. A Traces model equivalent to the TOUGH2 model must be set up accordingly.

- Radionuclide source terms are defined in TOUGH2 EOS7(5)R in kg/s for each element containing a source in the GENER block. Sources can be time dependent. In the particular case of Traces, it is necessary to convert these sources into mol/m^3/s.

Run of the transport simulation

Once all parameters are adequately defined, the Traces model is run, using as input the hydraulic data derived from the T2MP+E5 computation.

APPLICATION OF THE SEQUENTIAL APPROACH

The methodology described above is applied to realize a sequential approach calculation with T2MP+E5 and Traces. Results are compared with a reference coupled calculation performed with TOUGH2-MP EOS75R, which is set up to minimize incompatibilities between the transport parameters, according to the study realized previously.

Benchmark calculation with Couplex-gaz 1b

The benchmark coupled two-phase computation is based on the Couplex-Gaz 1b case (Andra, 2006), which includes simulations of the resaturation period of an emplacement cell of ILW-LL waste. This period starts after backfilling the gallery and lasts till the end of gas production, after 20,000 years. Within the gaseous phase, there are two components, vapor and hydrogen. Hydrogen is transported in the gaseous and the liquid phase. From an extensive geologic analysis it is known that there is an upward-oriented pressure gradient.

The mesh (see Figure 3) uses 2480 elements, among which 80 are boundary elements for the Dirichlet boundary conditions on the bottom and top. The boundaries on the left and right side are no-flow boundaries. The model contains materials with very different hydraulic and capillary properties. For instance, the gap between the concrete and the concrete backfill is modeled as an equivalent porous media material with porosity set to 1.

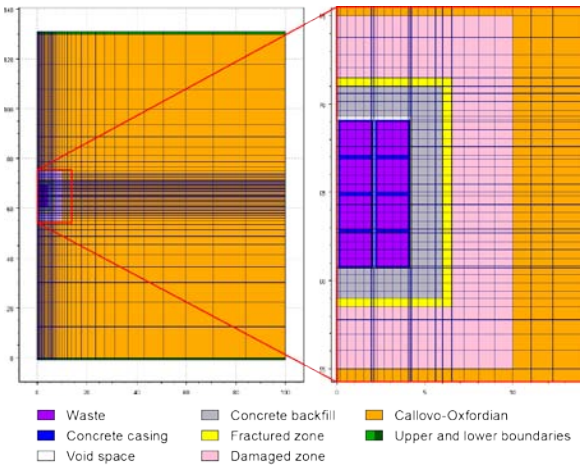

Figure 3. Model domain of Couplex-gaz benchmark case with 2400 elements and 80 boundary elements at top and bottom specified in TOUGH2

A source of I^{129} radionuclide was added in the waste cells with the following production rates:

- $2.5 \cdot 10^{-11}\ kg/s$ from 0 to 500 years.
- $2.0 \cdot 10^{-12} kg/s$ from 500 to 5000 years.

The diffusion model is set to constant diffusivity, in order to be compatible with Traces, and pore diffusion is set to 5×10^{-9} m^2/s.

Performing the sequential approach

The sequential approach is run as described in the previous section. First the two-phase flow transport calculation is run with TOUGH2-MP EOS5. Second, the resulting output data is converted so that finally the transport calculation can be carried out with Traces.

Validation of the sequential approach calculations

The liquid-concentration fields obtained with Traces are compared to the results obtained with the reference TOUGH2-MP EOS75R simulation. TOUGH2 provides these results as a field of mass fraction X_β^k for component k in liquid-phase β, which must first be converted into a concentration field. This is achieved by multiplying the mass fraction by elements volume, density, and porosity, which are also dependent on pressure and temperature by compressibility and expansivity.

Figure 4 shows a comparison of the concentration fields at three different time instants: t= 100 years, t=500 years, i.e., the end of the first phase of I^{129} release, and t=5000 years, i.e., the end of the I^{129} release.

The following observations can be made: First, the concentration fields at all observation times look very similar. There is, however more advancement in the results of the sequential computation, which is particularly visible at t=5000 years. The shape of the concentration plume is very regular, despite the head gradient in the z direction. However, advective transport seems negligible compared to diffusive transport.

To further investigate the differences between the two simulation results, the injected mass and the mobile mass in the model are compared for every output time step. Injected masses in both models are identical, which shows that an adequate conversion of the flow rates was done. However, the mobile mass computed by Traces appears to be slightly high.

Finally, we check that the mobile mass of I^{129} in the gaseous phase within the reference EOS75R calculation is negligible.

We conclude that the quality of the results obtained by the sequential approach is acceptable, taking into account the fact that two very different numerical solutions were used to compute transport.

In terms of CPU time, the reference EOS75R simulation was run in 13,000 seconds on two processors. For the sequential approach, the hydraulic part with T2MP+E5 ran in 2400 seconds on four processors, and Traces in 2450 seconds on one processor. Moreover, the sequential approach required some extra overhead to convert the TOUGH2 hydraulic result into Traces-compatible input files. However, when several transport computations need to be performed with the same hydraulic data, the TOUGH2 simulation and the conversion work necessary for the sequential approach are performed only once. In this case, the Traces transport calculation time is to be compared directly with the CPU times obtained with the coupled TOUGH2-MP EOS75R computation. This illustrates the advantage of the sequential approach in terms of computational speed.

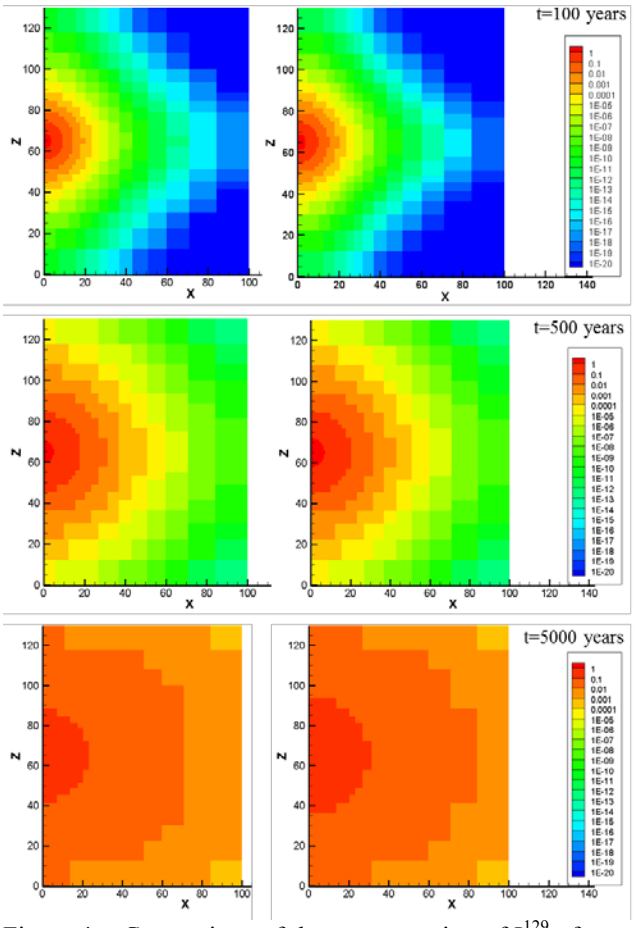

Figure 4. Comparison of the concentration of I^{129} of the reference coupled calculation in TOUGH2 (left) and the sequential approach with Traces (right) for t=100y, t=500y and t=5000y

REDUCTION OF THE HYDRAULIC DATA INPUT FOR SEQUENTIAL APPROACH

In this section, the results of the step involving the simplification of the hydraulic data are presented. As already mentioned, the aim is to reduce the computational effort for one transport calculation by optimizing the amount of necessary hydraulic input data. The process through which appropriate input data are chosen, and the corresponding consequences on the accuracy and the computational performance, are explained in the following paragraphs.

Choice of the time steps from the hydraulic data

The times at which the results of the hydraulic simulation are read into the transport model need to be chosen very carefully. As a criterion for the picking of the relevant time steps, the L_2 norm of the Darcy velocity on all faces of the model domain is calculated for every available time step. This results in a characteristic value for each time step.

The first time step is taken as a reference point. Iteratively, if the relative error, expressed in percentage, of the reference point's norm n_t and the next time step's norm n_{t+1} does not exceed a tolerance threshold tol_{max}, named percentage of tolerance in the following, the latter point n_{t+1} is eliminated. Otherwise, it is selected and becomes the next reference point:

$$\frac{n_{t+1} - n_t}{n_t} < tol_{max} \Rightarrow n_{t+1}\ eliminated$$
$$\frac{n_{t+1} - n_t}{n_t} \geq tol_{max} \Rightarrow n_{t+1}\ selected$$

Only the Darcy velocity and the saturation fields of the selected time instants are used as input for the transport calculations.

Influence of the given input of the hydraulic data on the results of the sequential transport calculations

It must be guaranteed that the accuracy of the results does not suffer from simplifying the time discretization of the hydraulic field data. In order to study the effect of the threshold selection on the percentage of tolerance tol_{max}, the results of the transport of the sequential approach are compared for tol_{max} equal to 1, 2, 4, 8, 16, 32, and 64%. The model is run for these tolerances, and the results are summarized in Table 1 and Figure 5. To compare the results of the simulations, the comparison points are the L-2 norm of the mass fluxes at the top and bottom boundaries of the model domain.

The observation of the results showed that the most significant relative error is found at the top boundary.

Table 1. Time instants, measured computational time and relative error on top boundary of the model for different percentages of tolerance

Number of instants	Percentage of tolerance	Relative error on top boundary	CPU time (s)
2023	0	0.0	2444.8
560	1	3.50E-05	2135.37
364	2	7.74E-05	1971.91
239	4	7.54E-05	1927.43
146	8	1.17E-04	1933.35
91	16	3.20E-04	1550.26
53	32	4.24E-04	1509.49
29	64	1.07E-03	1539.27

The effect of the time discretization on the hydraulic data appears to be very small in this case. This can be explained by the fact that this problem appears to be strongly diffusion-dominated (see Figure 4).

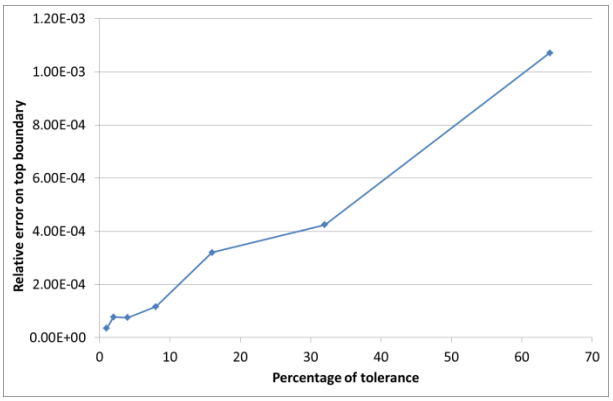

Figure 5. Relative error in fluxes at the top boundary over percentage of tolerance

The computational time is significantly reduced when the hydraulic data provided to the Traces transport code is simplified (see Figure 6). Furthermore, even with a percentage of tolerance on Darcy velocity of 1%, the number of hydraulic times is divided by a factor 4, which is relevant for the production and storage of input and output data.

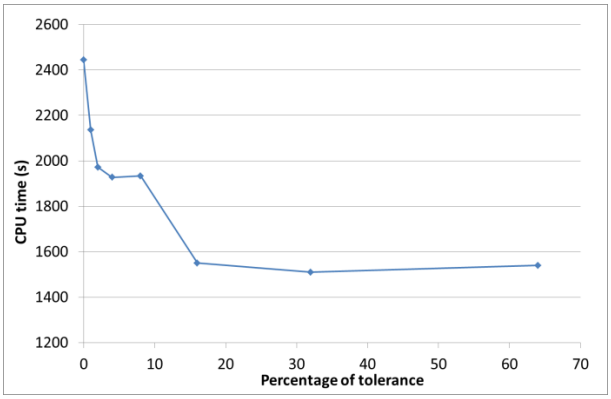

Figure 6. Measured computational time over percentage of tolerance

CONCLUSION

In this work we developed a sequential approach for computing hydraulic and transport in unsaturated porous media and compared it with a coupled two-phase flow coupled hydraulic and transport calculation. In the decoupled calculation, the hydraulic part was computed as a two-phase flow problem solved by the T2MP+E5 code, but for the transport part, the two-phase model was replaced by a single-phase unsaturated transport model (Richards). The study of the two physical models shows that this approach is reasonable under certain conditions, which is confirmed by comparing our results with the coupled and the sequential approach on a Couplex-Gaz 1b based simulation case. The sequential approach has benefits in terms of computation time and also allows the modeler to work around some of the model limitations of the EOS75R model, such as the absence of dispersion or precipitation-dissolution, by using an alternative simulation code for transport.

Gains in terms of CPU time become more significant if the hydraulic data are selected carefully. In practice, the sequential approach will allow modelers to fine-tune the hydraulic and transport simulations separately.

ACKNOWLEDGEMENT

This work was performed in a Diploma study at AF-Consult Switzerland as part of a project funded by Andra. The authors would like to warmly thank Laurent Loth and Jean Roger for providing the reference test case of this study and access to the Traces transport code, as well as numerous advice and kind assistance with Traces issues.

REFERENCES

Andra, *Cas test Couplex-Gaz 1 : modélisation 2D d'une alvéole de déchets de moyenne activité à vie longue*. http://www.andra.fr/couplex/Exercice_Couplex_Gaz_1.pdf, 2006. [Accessed 2 July 2012]

Kaempfer, Th. U., Y. Mishin, J. Brommundt, J,. Roger, E. Treille and N. Hubschwerlen, Extension and tuning of TOUGH2-MP EOS7R for the assessments of deep geological repositories for nuclear waste: Hydrogen, arbitrarily long decay chains, and solubility limits. *TOUGH Symposium 2012, Lawrence Berkeley National Laboratory, Berkeley, California,* 2012.

Pruess, K., C. Oldenburg, and G. Moridis, *TOUGH2 User's Guide, Version 2.0*, Report LBNL-43134, Lawrence Berkeley National Laboratory, Berkeley, Calif., U.S.A., 1999.

Zhang, K., Y. S. Wu, and K. Pruess, *User's guide for TOUGH2-MP – A Massively parallel Version of the TOUGH2 Code –,* Report LBNL-315E, Lawrence Berkeley National Laboratory, Berkeley, Calif., 2008.

PERFORMANCE IMPROVEMENT OF TOUGH2 SIMULATION WITH GRAPHICS PROCESSING UNIT

Yusuke SHIMOTOKU, Toshiaki TANAKA, Ryuichi ITOI

Faculty of Engineering, Kyushu University
Nishi-ku, Fukuoka, JAPAN 819-0395
e-mail: y-shimotoku@mine.kyushu-u.ac.jp

ABSTRACT

We tried to accelerate the computational speed of TOUGH2 simulation by introducing a linear computation routine using a Graphics Processing Unit (GPU). Libraries for GPU computation were introduced, and new solvers for linear equations were developed. Out of those, CLLUSTB, an ILU preconditioned BiCGSTAB solver made with the CULA Sparse, demonstrated good performance both in speed and accuracy. We introduced the new solvers into TOUGH2 to improve its performance and, for a sample problem, conducted a natural-state three-dimensional simulation of a geothermal reservoir. As a result, the routine with GPU was 1.44 times faster in matrix calculation, and 1.34 times faster in simulation, than the computed results with the iterative solver DLUSTB, originally built into TOUGH2.

INTRODUCTION

In the numerical simulation of mass and heat flows in porous media, calculations of linear equations are required, and TOUGH2 spends considerable time on them. TOUGH2 includes direct and iterative solvers, and the user can choose one of them according to the characteristics of the model to be simulated. Moridis (1995) compared computational performances of the matrix computation routines built into TOUGH2 and evaluated each performance. In this study, we developed new routines that we incorporated into TOUGH2 to speed up calculation of linear equations, and tested these new routines in a simulation performance. The entire process described above was conducted using a function of a graphics processing unit (GPU) parallel computing routine.

MATRIX CALCULATION WITH GPU

GPU (Graphics Processing Unit) consists of a semiconductor chip that has multiple cores for parallel computing. GPU has been used for image processing, but we used GPU on which a part of the computation with respect to matrix calculation in TOUGH2 was carried out. For this purpose, we developed an operational code using CUDA, an integrated development environment for GPU in C language.

Numerical Libraries for GPU

We developed routines using three libraries for matrix computation: CUDA SDK, CUSP, and CULA Sparse. These libraries include a variety of iterative calculation methods: BiCG, BiCGSTAB, BiCGSTAB, and GMRES. These methods are described in detail as follows:

BiCG

The BiCG (biconjugate gradient) method is an algorithm to solve a set of linear equations expressed as:

$$\mathbf{Ax} = \mathbf{b}$$

where **A** is the square coefficient matrix, **x** is the solution vector, and **b** is the known vector. This method can solve linear equations even if **A** is not symmetric. However, the solving methods for asymmetric matrices tend to have difficulty with convergence compared to those for positive-definite symmetric matrices (Hasegawa et al., 2004).

BiCGSTAB

The BiCGSTAB (biconjugate gradient stabilized) method was developed an improvement to BiCG. It has faster and smoother convergence capability than the original BiCG and the conjugate gradient squared method (CGS). In general, it has good

performance both in speed and cost, unless the matrix is too large (Nodera, 1993).

BiCGSTAB(l)

BiCGSTAB(*l*) is a generalization of BiCGSTAB, with *l* denoting the degree of minimal residual polynomials. BiCGSTAB fails computation when the imaginary part of eigenvalues of the coefficient matrix is large. On the other hand, BiCGSTAB(*l*) can detect and avoid such situations by changing the value of *l*. The computational cost depends on the size of *l*.

GMRES

GMRES (generalized minimal residual method is a robust Krylov subspace method for ansymmetric square matrices (Hayami, Ito, 2005). Memory usage and computational cost increase as the number of iterations increases. Using this method the calculation restarts after a specified number of iterations, and an approximate solution is given as an initial value for the subsequent iteration.

Preconditioners

In the three libraries above, preconditioners for matrix calculation are available as described below:

Jacobi

The Jacobi preconditioner is a replication of the diagonal of the coefficient matrix. The costs of generation, memory usage, and application are very small. Thus, a user can expect to save calculation time when this preconditioner is suitable for the matrix.

Block Jacobi

The Block Jacobi preconditioner is a replication of a block diagonal (of specified size) of the coefficient matrix. The calculation time per iteration increases when the size of the block becomes large. However, processes of both generation and application are suitable for the GPU.

ILU(0)

ILU(0) is the incomplete LU factorization with zero(0) fill-in. In application, two triangular solvers are used, but these are not well suited for parallel computing on GPU. It may thus take up longer computing time, but may improve convergence significantly for some matrices.

AINV

AINV (Approximate INVerse) approximates the inverse of the coefficient matrix as follows:

$$\mathbf{A}^{-1} \cong \mathbf{Z}\mathbf{D}^{-1}\mathbf{Z}^{t}$$

where $\mathbf{A}^{-1}$ is the inverse matrix of **A**, **Z** is the upper triangular matrix, $\mathbf{Z}^{t}$ is the transposed matrix, and **D** is the diagonal matrix. Using this method, the operation called dropping is carried out to preserve the sparsity of the preconditioner. The dropping operation signifies that the values of non-zero elements generated in the process are less than a specified threshold value, at which point they are regarded as zero. This operation improves computation speed, but has a negative influence on convergence, because the positive definiteness of the preconditioner is lost with this operation (Fujino, 2004).

AMG based on Smoothed Aggregation

The multigrid method is an algorithm by which to solve differential equations by discretization into multiple layers. The algebraic multigrid method (AMG) is a modified version of the multigrid method, and is available as a solver for sparse matrices. AMG based on smoothed aggregation makes some aggregations and defines the interpolation operator. This can be used as a preconditioner by introducing in the algorithm**.**

PERFORMANCE IMPROVEMENT

We developed routines by combining iterative methods and preconditioners, and then compared their performances by simulating sample problems with TOUGH2: We used two models: Model A , a porous type, and Model B, a double porosity type.

Hardware specification

In this study, we used Intel Core i7-980X (12 MBs Cache, 3.33 GHz) as CPU and TeslaC2070 as GPU. This CPU has six cores and supports hyper-threading technology. Thus, it can process twelve threads in parallel. Therefore, we used only one CPU core for evaluating the parallelism of GPU.

Performance comparison on the Model-A

This model has a dimension of 8 km×4.2 km and 3 km depth. It was divided into 26×8 grids for the horizontal plane and 17 layers for the vertical plane. Three rock types were assigned; Rock1, Rock2, and Atmosphere. Their density was 2500 kg/m^3, porosity 0.10, heat conductivity 2.50 W/mºC, and heat capacity 1000 J/kgºC. With respect to the permeability, they have different values. Rock1 has 1.0×10^{-16}m^2, Rock2 has 1.0×10^{-13}m^2, and atmosphere has 1.0×10^{-11} m^2 for all directions.

Figure1 shows a grid system of Model A.

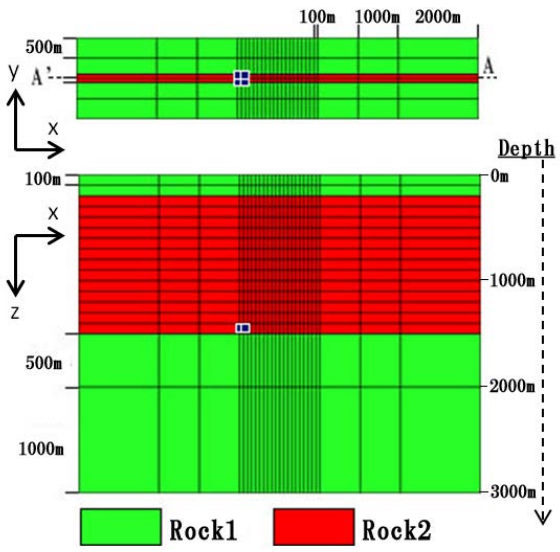

Figure 1. Grid system of Model A

In Figure 1, the top figure represents the plan view at a depth of 200 m; the bottom figure represents the vertical cross section along the A-A' line in the top figure. High temperature fluid of 1.085×10^6 J/kg at 10kg/s was assigned as a source at four grids in the layer of 1400 m to 1500 m depth (blue squared dots in the figure). A hydrostatic condition filled with 15ºC water was given as the initial condition.

Convergence and matrices

First, we solved a matrix equation generated in this simulation using the methods without preconditioners. However, the number of iterations would soon be too large, and failure of calculation was often observed. Then, we checked the magnitude of the value for each element in the matrix to find that characteristics. As a result, we found that the values of element varied over a wide range, from 1.0×10^{-28} to 1.0×10^5. Figure 2 shows the distribution of the number of elements according to their value.

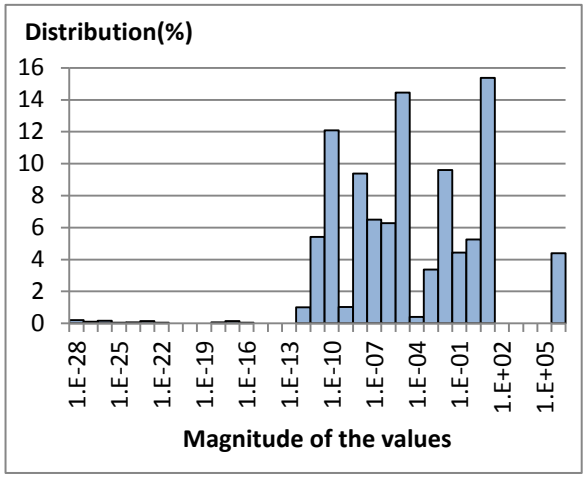

Figure 2. Histogram of the elements of the matrix generated in the simulation of Model A

It is well understood that convergence is difficult to attain when the difference between the absolute value of the maximum and the minimum is large, because this situation leads to loss of precision and reduces calculation accuracy. The Krylov subspace method is likely to be affected significantly by round-off error. Thus, it is difficult for these methods to converge against such matrices. For solving this problem, proper preconditioners needs to be introduced.

Solvers with preconditioners

We subsequently developed routines by combining the solver methods with the preconditioners. The routines we developed are summarized in Table 1.

We incorporated these routines into TOUGH2 and simulated the sample problems. The number of time steps was set to 100. Then, we compared the routines with DLUSTB to evaluate their efficiency. DLUSTB is a built-in function of TOUGH2 and is BiCGSTAB with ILU preconditioner. Five routines, CSJACSTB, CSAINVSTB, CSAINVGM, CSSAGM, and SDKSTB, are excluded from the comparison because of a lack of convergence.

Table 1. Routines developed with GPU

Routine name	Library	Method	Preconditioner
CLLUBCG	CULA sparse	BiCG	ILU
CLJACBCG			Jacobi
CLBJBCG			Block Jacobi
CLLUSTB		BiCG STAB	ILU
CLJACSTB			Jacobi
CLBJSTB			Block Jacobi
CLLUSTBL		BiCG STAB(L)	ILU
CLJACSTBL			Jacobi
CLBJSTBL			Block Jacobi
CLLUGM		GMRES	ILU
CLJACGM			Jacobi
CLBJGM			Block Jacobi
CSJACSTB	Cusp	BiCG STAB	Jacobi
CSAINVSTB			AINV
CSSASTB			AMG based on Smoothed Aggregation
CSJACGM		GMRES	Jacobi
CSAINVGM			AINV
CSSAGM			AMG based on Smoothed Aggregation
SDKSTB	SDK	BiCG STAB	None

Table2 shows the simulation time calculated by each routine. The results indicate that CLLUSTB is the fastest among the developed routines. The execution time required by using the routines with GPU is 4.29 to 42.8 times as long as that with DLSUSTB, as indicated in Table 2. This is partly because overhead occurs during the exchange of the data between PC and GPU. This overhead has no relationship with the size of the data to be exchanged, so we can assume that the performance of the routines with GPU improves as the size of the target matrix increases. Therefore, we computed a sample problem for Model B with a larger sized matrix, and then compared the performances for DLUSTB and CLLUSTB.

Evaluation of accuracy

We found that CLLUSTB performed at relatively faster computation speed compared to the other routines. However, even if the simulation terminates in a short time, the accuracy of computation among the routines needs to be confirmed at the same time. Hence, we compared the time histories of Model A simulation calculated by DLUSTB and CLLUSTB. The gridblock that contains fluid source was checked in terms of pressure and temperature. We found that both routines result in the same values. Therefore, CLLUSTB was confirmed to have equivalent calculation accuracy to DLUSTB.

Table 2. Comparison of execution time

Routine	Execution time (sec)
CLLUBCG	71.878
CLJACBCG	129.99
CLBJBCG	113.08
CLLUSTB	47.018
CLJACSTB	65.005
CLBJSTB	57.456
CLLUSTBL	52.149
CLJACSTBL	51.084
CLBJSTBL	52.683
CLLUGM	331.46
CLJACGM	468.64
CLBJGM	353.27
CSSASTB	422.57
CSJACGM	1146.5
DLUSTB	10.957

Performance comparison on the Model-B

Next, we conducted simulations to test the efficiency of routines with the large-scale Model B, increasing the size of matrix. Figure 3 shows a grid system of the model. Physical properties are the same as those of Model A.

In this evaluation, we used the MINC-method to easily increase the number of elements, and then measured the calculation time. We assumed the same simulation conditions except for the number of elements. In Figure 3, the top part of the figure represents the plan view at a depth of 200 m, and the bottom part represents the vertical cross section along the A-A' line in the top part. The number of time steps was set to 3000, and high temperature fluid of 1.085×10^{6} J/kg at 10 kg/s was assigned as a source. They

are placed at the bottom of the model (blue squared dots in the figure) to avoid any calculation instability caused by the MINC-model.

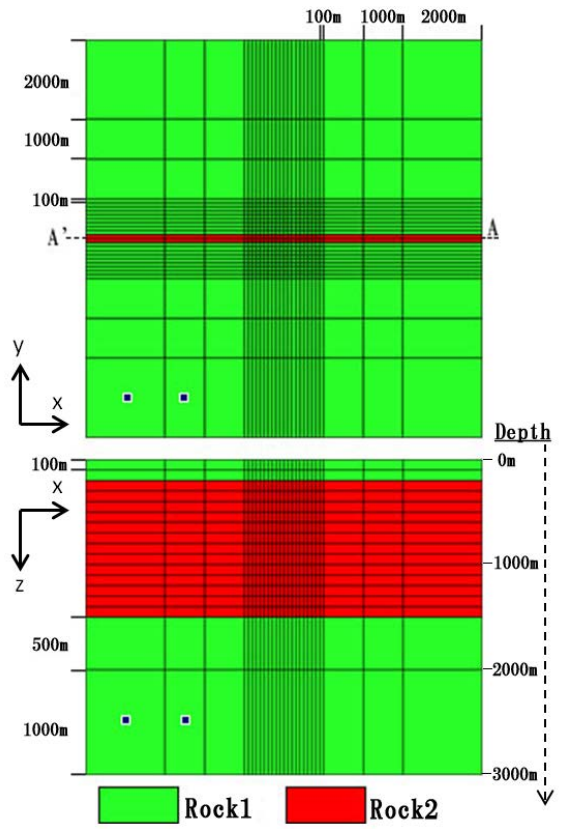

Figure 3 Grid model of Model B

When the elements that contain the fluid source are processed with the MINC-method, the pressure change per unit of time increases, because of the small fracture pore volume. Therefore, time-step size is reduced significantly to ensure numerical stability, and the calculation time becomes long. For this reason, we placed the sources into the blocks that have large volume, allowing a small pressure change with the same time step size.

Using this method, we compared DLUSTB with CLLUSTB by increasing the number of the elements from two to twelve times. The results from comparing the computational times of CLLUSTB and DLUSTB for 3000 time steps are summarized in Tables 3 and 4. Table 3 shows the matrix-calculation times of the routines; Table 4 shows the simulation times of the routines. Figure 4 presents the plot of these results. From this figure, we can see that CLLUSTB performs better than DLUSTB when the size of matrix is greater than about 50,000.

Table 3. Comparison of execution time for matrix calculation with CLLUSTB and DLUSTB

Size of Matrix	Time(sec)	
	CLLUSTB	DLUSTB
45972	39.80	38.33
91944	56.97	67.39
137916	73.79	92.60
183888	87.07	115.1
229860	105.0	137.5
275862	123.1	177.4

Table 4. Comparison of execution time for simulation

Size of Matrix	Time (sec)	
	CLLUSTB	DLUSTB
45972	52.99	52.21
91944	72.10	87.46
137916	92.42	118.3
183888	113.7	146.2
229860	131.7	174.0
275862	165.1	221.2

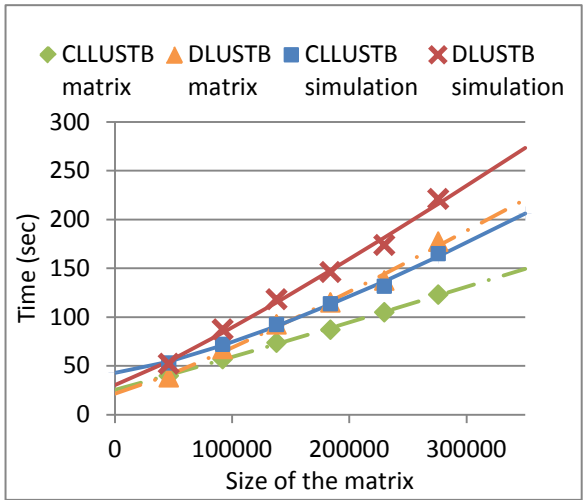

Figure 4. Comparison of the execution time

In addition, we verified the effectiveness of the GPU when the matrix size is large. In general, the larger the size of the matrix, the faster the computational times, regardless of the routines. The results were approximated using the

following equations for DLUSTB and CLLUSTB.

$$\mathrm{DLUSTB}: t = 8.37 \times 10^{-5} N^{1.15} + 21.4$$

$$\mathrm{CLLUSTB}: t = 2.04 \times 10^{-4} N^{1.04} + 25.5$$

where t is the calculation time (sec), and N is the size of the matrix. The third term on the right-hand side is the intercept for the overhead of the transferring matrices. From this result, we can conclude that performance of the routine with GPU improves significantly as the size of the matrix increases.

The routine with GPU achieved 1.44 times faster matrix calculations and 1.34 times faster simulations compared to the computed results with the iterative solver DLUSTB, at the matrix size of 275,862.

CONCLUSIONS

The following conclusions can be drawn:

(1) Matrix computation on TOUGH2 failed when no preconditioners were incorporated.

(2) The ILU preconditioned BiCGSTAB, developed with CULA sparse, performed the best among the three libraries: CUDA SDK, Cusp, and CULA sparse. The routine developed with GPU achieved 1.44 times faster matrix calculation, and 1.34 times faster overall simulation, compared to the computed results with the iterative solver DLUSTB at the matrix size of 275,862.

(3) The computational performance of the routine with GPU improves as the size of the matrix increases.

REFERENCES

Fujino, S., Robustness and Efficiency of Recent Preconditioners of CG Methods, *RIMS Kokyuroku 1362*, 13-21, 2004 (in Japanese)

Hasegawa, H., Sogabe, T., and Ogita, T. CG Method for Symmetric Matrices Generated by Unsymmetric Matrices, *RIMS Kokyuroku 1362*, 6-12, 2004 (in Japanese)

Hayami, K., T. Ito, Solution of Least Squares Problems Using GMRES Methods, *Proceedings of the Institute of Statistical Mathematics Vol. 53*, No. 2, 331-348, 2005 (in Japanese with English abstract)

Moridis, G. J., *A New Set of Direct and Iterative Solvers for the TOUGH2 Family of Codes*, Report LBL-37066, Lawrence Berkeley National Laboratory, Berkeley, Calif., 1999.

Nodera, T., Overview of Solving Method for Sparse Matrices, *RIMS Kokyuroku 832*, 127-136, 1993(in Japanese)

iTOUGH2 GLOBAL SENSITIVITY ANALYSIS MODULE: APPLICATIONS TO CO_2 STORAGE SYSTEMS

Haruko M. Wainwright, Stefan Finsterle, Yoojin Jung, Quanlin Zhou, Jens T. Birkholzer

Lawrence Berkeley National Laboratory
1 Cyclotron Road
Berkeley, CA, 94720, USA
e-mail: hmwainwright@lbl.gov

ABSTRACT

We have implemented a global sensitivity analysis module into iTOUGH2. While a *local* sensitivity analysis perturbs parameters from a single set of reference values and computes the derivative of system responses, a *global* sensitivity analysis explores the entire parameter space, providing more robust sensitivity measures as well as identifying the presence of nonlinearity in system responses and interactions among parameters. The new module includes two global sensitivity methods: the Morris and Saltelli methods.

To demonstrate this new capability, we coupled this module with two forward models related to CO_2 sequestration: (1) a high-resolution reservoir-scale model for a hypothetical CO_2 storage project and (2) an analytical model for computing the transient head change induced by injection/ extraction/ leakage through multiple wells in a multilayered system. Our results illustrate the characteristics of each sensitivity method. The local sensitivity is sufficient to identify dominant parameters and useful for understanding the system. The Morris method can identify nonlinear/interaction effects as well as provide more robust sensitivity measures with relatively small computational cost. The Saltelli method can provide more rigorous and quantitative sensitivity measures in the context of uncertainty quantification, although it comes at a high computational cost.

INTRODUCTION

iTOUGH2 (Finsterle, 2010) has been developed first as an inverse modeling and parameter estimation (PE) tool for hydrogeological applications, which works with the TOUGH2 flow and transport simulators as well as other simulators through the PEST protocol. Various modules have been implemented, such as the uncertainty analysis module for Monte-Carlo simulations, the coupled hydrogeological-geophysical inversion module, and various other tools.

Many studies (e.g., Finsterle et al., in press) have identified essential tools for hydrological modeling under uncertainty, and also for real-world hydrological projects that start from site characterization and lead to prediction. They include parameter estimation, uncertainty analysis (UA), sensitivity analysis (SA), data-worth analysis, and experimental design. With the first two already implemented and tested intensively, we consider iTOUGH2 to be one of the most effective, comprehensive tools for model development and analysis.

The ability to support a formal sensitivity analysis is a key component in such a software tool, since there is a strong interaction between SA and other components of the workflow. Identifying sensitive or important parameters is critical (1) to check whether a given dataset has sufficient information to determine a parameter given the uncertainty of other parameters in PE, (2) to identify the most effective data locations and timing in the experimental design, (3) to determine how to allocate limited resources for estimating each parameter as part of a data-worth analysis, and (4) to reduce the number of parameters to be varied/estimated and hence to reduce the computational burden in PE and UA.

In addition, we believe that the SA tool can be used not only for selecting the important parameters, but also for improving the understanding of the system. For example, identifying the positive or negative effects of each parameter

will be important for determining safety margins in engineering systems. The time profile of sensitivity can identify which parameter influences the model output at which time period. We can also identify interactions among parameters.

In the iTOUGH2 SA module, we have, in addition to the existing local sensitivity method, implemented two global sensitivity methods—that of Morris (Morris, 1991) and Saltelli (Saltelli et al., 2008). These global methods provide more robust sensitivity measures as well as identify the nonlinearity in system responses and interactions among parameters.

The objectives of this study are to (1) introduce the global-sensitivity-analysis methods, (2) compare the three sensitivity methods in terms of interpretation and computational cost. To demonstrate the utility of the iTOUGH2 sensitivity analysis module, we used two hydrological problems related to CO_2 sequestration: a high-resolution basin-scale model for a hypothetical storage project (using TOUGH-MP) and an injection/leakage-induced pressure model (using an analytical solution). Since the latter model is computationally inexpensive, we use it to explore the computational cost of the Morris method in more detail.

METHODOLOGY

In this section, we introduce the global sensitivity methods. Although each method is documented in detail in Morris (1991) and Saltelli et al. (2008), we describe them briefly here for completeness. We denote a set of parameters by $\{x_i|\ i=1,\ldots,k\}$ (the number of parameters is k) and a scalar output of a model by y, which is a function of $\{x_i\}$; $y = f(\{x_i\})$.

Local Sensitivity Method

The local sensitivity is defined as a partial derivative, i.e., the change in an output variable caused by a unit change in each parameter from the reference value. When we have a numerical model, we can compute the derivative by changing each parameter by a small increment Δx_i from the reference parameter values x_i^* and computing the difference in the output. The scaled sensitivity is the derivative scaled by the standard deviation of parameters and measurement errors. The scaled, dimensionless sensitivity is defined as:

$$S_i^{local} = \frac{\sigma_x}{\sigma_y}\left.\frac{\partial y}{\partial x_i}\right|_{x_i^*} = \frac{\sigma_x}{\sigma_y}\frac{f(x_1^*,..,x_i^*+\Delta x_i,..) - f(x_1^*,..,x_i^*,..)}{\Delta x_i}$$

where σ_x is the standard deviation of the parameter, and σ_y is the standard deviation of the model output, reflecting its measurement error or acceptable mean residual in an inversion.

Morris Sensitivity Method

In the Morris one-at-a-time (OAT) method (Morris, 1991), the parameter range— normalized as a uniform distribution in [0, 1]—is partitioned into (p–1) equally sized intervals, so that each parameter takes values from the set {0, 1/(p–1), 2/(p–1), …, 1}. From the reference point of each parameter randomly chosen from the set {0, 1/(p–1), 2/(p–1), …, 1– Δ}, the fixed increment $\Delta = p/\{2(p-1)\}$ is added to each parameter in a random order to compute the elementary effect (EE) of each parameter, which is the difference in output y caused by the change in the respective parameter. k+1 runs are necessary to complete one path, which is to change each parameter once from one set of reference values. By having multiple paths (i.e., multiple sets of reference parameter values and multiple, random orders for changing each parameter), we have an ensemble of EEs for each parameter. We can compute three statistics: the mean of EE, the variance in EEs, and the mean of absolute EEs (mean of |EE|). The mean EE can be regarded as a global sensitivity measure, and is used to identify noninfluential factors. The variance of EEs is used to compute the standard error of mean (SEM) for identifying nonlinear or interaction effects.

Saltelli Sensitivity Method

While the local and Morris sensitivity is difference-based, the Saltelli method is variance-based. Saltelli et al. (2008) defined the sensitivity by $\mathbf{V}[\mathbf{E}[Y|X_i]]/\mathbf{V}[Y]$ for parameter importance, where $\mathbf{E}[\bullet]$ and $\mathbf{V}[\bullet]$ represent mean and variance, respectively. Conceptually, this measure quantifies the contribution of each parameter to the uncertainty of the output. In addition, Saltelli et al. (2008) defined the total sensitivity by $\mathbf{V}[\mathbf{E}[Y|X_{-i}]]/\mathbf{V}[Y]$, where $\mathbf{E}[Y|X_{-i}]$ represents the mean of Y conditioned on all the

parameters but X_i. The total sensitivity is used to identify unimportant parameters. We can compute these two measures–sensitivity and total sensitivity–using the Monte-Carlo integration described in Saltelli (2008).

DEMONSTRATION PROBLEM SETUP

Reservoir-scale CO_2 Migration Problem

The reservoir-scale CO_2 migration model was developed based on a geological study in the Southern San Joaquin Basin, California, using the datasets obtained at many oil fields in that region (Birkholzer et al., 2011; Zhou et al., 2011; Zhou and Birkholzer, 2011). The domain includes 12 discontinuous or continuous formations, extending 84 km in the eastern direction and 112 km in the northern direction. The domain also includes several faults, which are known to be near-impermeable sealing faults at large depth.

The Vedder Formation—considered as the injection formation—dips upward towards a shallow outcrop area located along the eastern model boundary, at an average slope of 7 degree. The overlying Temblor-Freeman Shale (TF Shale) is considered a suitable caprock for stratigraphic containment of the injected super-critical CO_2. We also consider six alternating sand/shale layers—Vedder Sand (V Sand) and Vedder Shale (V Shale)—in the Vedder Formation, based on the datasets. At the injection well, the Vedder Formation is 400 m thick, and its top elevation is -2,751 m. The cap rock (TF Shale) is about 200 m thick. The plan view of the Vedder Formation is shown in Figure 1(a).

We used the massively parallel version of TOUGH2 (Zhang et al., 2008) with the ECO2N module to simulate injection and migration of supercritical CO_2 in the brine system. The simulation time includes an injection period of 50 years with an injection rate of 5 Mt per year, and a post-injection period of 150 years. In this study, the 3D mesh consists of 64,214 elements, the number of which falls in between that of the fine mesh (Zhou et al., 2010; Zhou and Brikholzer (2011) and that of the coarse mesh used in Birkholzer et al. (2011). Figure 1(b) shows the plan view of the numerical mesh.

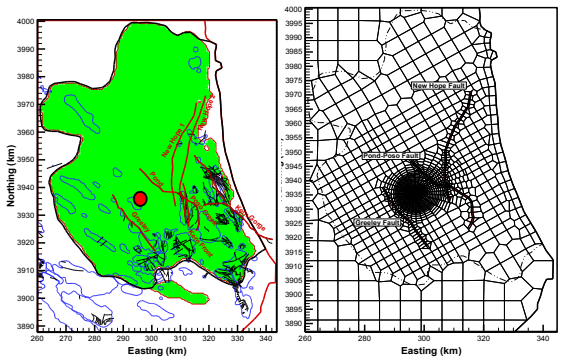

(a) (b)

Figure 1. (a) Plan view of the Vedder formation and the faults, and (b) Plan view of the numerical domain with mesh. The red dot is the injection location.

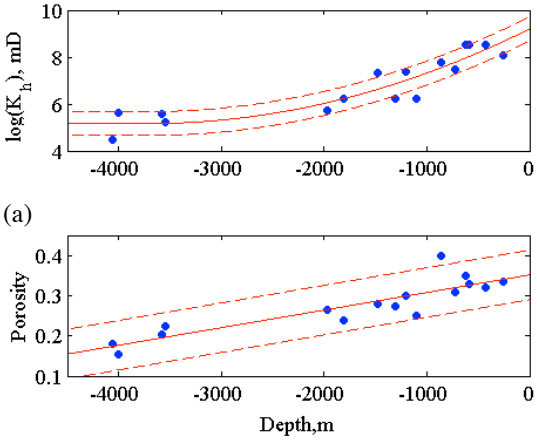

(a)

(b)

Figure 2. Estimated depth-dependent (a) V Sand permeability and (b) V Sand porosity. The blue dots are the data values, the solid red line is the estimated parameter value, and the dotted read lines are the uncertainty bounds (± two standard deviations).

In our SA, we varied five properties (permeability, porosity, pore compressibility, van Genuchten α and m) of three geological units (V Sand, V Shale, TF Shale), so that we have a total of 15 parameters. For the V Sand permeability and porosity, we estimated the depth-dependent parameter values and their uncertainty ranges using the available datasets (Figure 2). For the rest of the parameters, the reference parameter values are shown in Table 1. The range of parameters in this study is one order of magnitude in permeability, a factor of five in pore compressibility, 30% in porosity and van

Genuchten m, and half an order of magnitude in van Genuchten α. As performance measures, we consider various system responses, such as CO_2 saturation and pressure buildup at various locations, and CO_2 plume extent. For demonstration purposes, we chose one performance measure; CO_2 saturation (S_{CO2}) at 1.78 km east from the injection point.

Table 1. Reference parameter values: horizontal permeability k_h, anisotropy ratio k_v/k_h, porosity Φ, pore compressibility β_p, van Genuchten α and m

	TF Shale	V Sand	V Shale
k_h, mD	0.002	*dep-dep.	0.1
k_v/k_h	0.5	0.2	0.5
Φ	0.338	*dep-dep.	0.32
β_p,10^{-10}, Pa^{-1}	14.5	4.9	14.5
α, 10^{-5}, Pa^{-1}	0.42	13	0.42
m	0.457	0.457	0.457

* Depth-dependent values shown in Figure 2.

Leakage-Induced Pressure Problem

A semi-analytical model was developed by Cihan et al. (2011) to describe the transient pressure changes caused by injection or extraction activities in a multilayered aquifer system. It models flow through aquitards (diffusive flow or diffusive leakage) as well as flow through the leaky wells (focused flow or focused leakage). In the CO_2 storage system, this model has been used to predict the pressure disturbance caused by the CO_2 injection. Also, this model has become the basis for developing a system to detect possible CO_2 leakage through wells or faults, since the pressure propagates much faster than the CO_2 plume. (We refer to Cihan et al. (2011) for a more detailed description and a discussion of the assumptions.)

In this study, we consider a three-layered system that consists of the reservoir (injection layer), the aquitard, and an upper aquifer, as shown in Figure 3. Each layer is assumed to be a homogenous and isotropic medium with uniform thickness and infinite extent. We also assume that the leaky well is 2000 m away from the injection point.

In SA, we perturbed the following parameters: hydraulic conductivity K and storativity S for the reservoir, the aquitard and the aquifer, and the hydraulic conductivity of the leaky well. The total number of parameters is seven. Reference parameter values are shown in Table 2. The parameter range is one order of magnitude in hydraulic conductivity, and a factor of five in storativity. As a performance measure, we are interested in the pressure buildup at a fixed point in the overlying aquifer, which corresponds to the leaky well location.

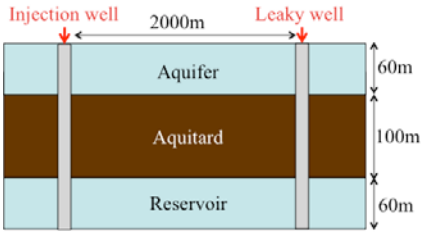

Figure 3. Conceptual model setup for the pressure leakage problem.

Table 2. Reference parameter values: hydraulic conductivity K and storativity S

	Aquifer	Aquitard	Reservoir	Well
K, m/s	2.00E-1	2.00E-6	2.00E-1	2.00E+5
S, 1/m	1.88E-6	1.47E-6	1.88E-6	N/A

RESULTS AND DISCUSSION

Reservoir-scale CO_2 Migration Problem

Local sensitivity

The local sensitivity was computed using 16 simulations. Figure 4(a) shows the time series of local sensitivity for CO_2 saturation (S_{CO2}) at a fixed point. There are three dominant parameters: V Sand permeability, porosity and van Genuchten m. All three curves have two spikes, which correspond to the plume arrival and departure. Higher permeability and m lead to higher plume/brine mobility, which leads to positive sensitivity at the plume arrival (i.e., earlier arrival and higher S_{CO2}) and negative sensitivity at plume departure (i.e., earlier departure and lower S_{CO2}). The large porosity means there is more brine to be displaced at the arrival and more CO_2 at the departure, so that porosity has the opposite effect of permeability and m.

The pore-size distribution index m has a large impact at the arrival but not at the departure. This is attributed to the specific implementation

of the two-phase model in the current version of TOUGH2-MP, which uses the van Genuchten model for relative brine permeability (k_{lr}) and capillary pressure, and the Corey model for relative gas permeability—so that the relative gas permeability does not depend on m (Pruess et al., 1999). Since the derivative of relative brine permeability with respect to m ($\partial k_l/\partial m$) increases in absolute magnitude towards full brine saturation, m is more influential near full brine saturation and hence at plume arrival. This result may change once the full van Genuchten model and the hysteresis model (Doughty, 2007) are implemented in TOUGH2-MP, which makes m dependent on gas relative permeability. The point to address here is that the sensitivity analysis is useful in identifying and understanding an effect that is potentially an artifact of model implementation.

CO_2 saturation at other locations (not shown here) also had similar profiles and showed significant sensitivities to the same three parameters. This result may support the development of simple analytical or semi-analytical solutions, or decoupled reservoir-only CO_2 migration models. For example, we found that the van Genuchten α has a negligible effect on far-field CO_2 saturation, consistent with some of the analytical studies that neglect the capillary pressure (e.g., Nordbotten et al., 2009). We also note that this conclusion is applicable only to the CO_2 saturation; we observed significant sensitivity of pressure buildup to other parameters, such as V Sand pore compressibility and TF Shale permeability.

Morris sensitivity

In the Morris method, the EEs were computed by four partitions and ten paths. The total number of simulations was 160. Figure 4(b) shows the time profile of mean EE from the Morris method. Compared to the local sensitivity in Figure 4(a), the spikes are smoothed out over time, since the plume arrival/departure time is more distributed. In terms of importance ranking and sign of effects, we draw a conclusion similar to the local sensitivity analysis, with the same three parameters being identified as most influential. However, there are some differences from the local sensitivity: the porosity effect is more prominent at early times, and the V Sand permeability becomes dominant in the post-injection period.

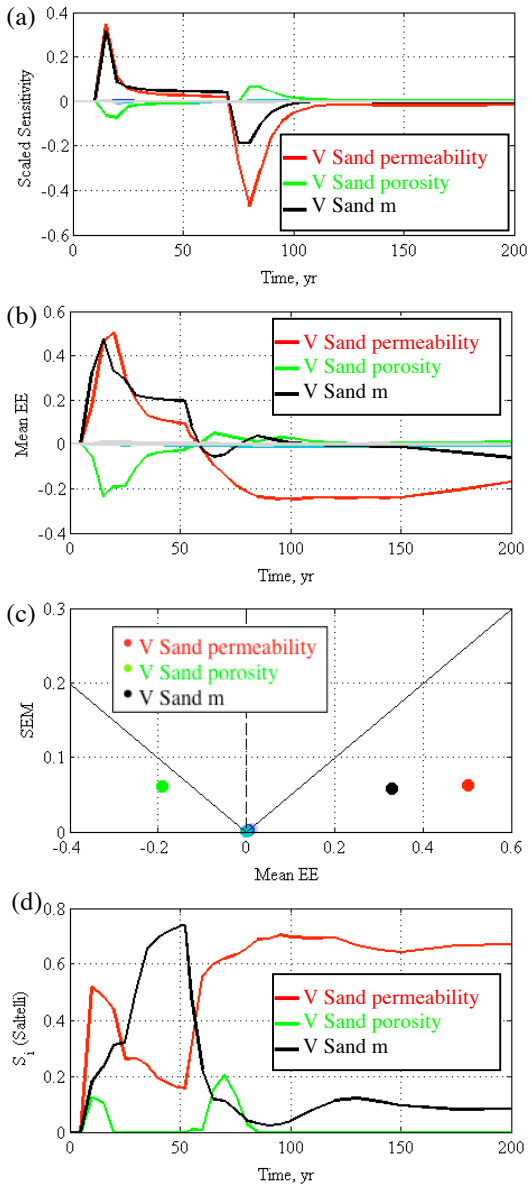

Figure 4. SA results for the reservoir-scale CO_2 migration problem: (a) time profile of the local sensitivity, (b) time profile of the Morris mean EE, (c) crossplot of Mean EE and SEM of S_{CO2} at 20 years from the Morris method, and (d) time profile of Saltelli sensitivity. In (c), the solid black lines correspond to (Mean EE) = ± 2SEM.

Figure 4(c) shows the cross-plot of mean EE and standard error of mean (SEM) at one time (20 years). In this figure, parameters with higher SEM, i.e., those that are closer to the grey solid lines (Mean EE = ±2SEM) exhibit stronger nonlinearity or interaction effects. The reservoir

permeability and *m* have large mean EE and low SEM values; the porosity is close to the black line, indicating nonlinearity or interaction effects. In general, we observe that the parameters with higher SEM have different interpretations or importance rankings between the local and global sensitivity analyses.

Saltelli sensitivity

Based on the Morris method, we chose five parameters for the Saltelli sensitivity (V Sand permeability, porosity, compressibility, *m*, and TF Shale permeability). We computed the Saltelli sensitivity using 840 realizations. Figure 4(d) shows the time profile of Saltelli sensitivity. The sensitivity is normalized by the variance at each time slice, so that there are no peaks such as those that appeared in the Morris sensitivity in Figure 4(b). The sum of the sensitivity of each parameter, however, does not become one, since there exist nonlinear or interaction effects (Saltelli, 2008).

Based on this figure, the V Sand van Genuchten *m* accounts for about 70% of the total variability of the output at time 30–50 years, and the V Sand permeability accounts for about 70% after 100 years (most of the post-injection period). The qualitative interpretation and ranking, however, are the same as the Morris mean EE.

Leakage-Induced Pressure Problem

Local sensitivity

In the same manner as in the reservoir model, the time profile for scaled sensitivity is plotted in Figure 5(a) for 10 years and (b) for 1 year.

In Figure 5(a), we can see that the aquifer and reservoir *K* is influential, while the sensitivity to the aquitard *K* increases as the diffusive leakage reaches the shallow aquifer. The hydraulic conductivity of the leakage pathways—the well *K* and aquitard *K* at later times—have a positive impact, whereas the aquifer and reservoir *K*s have a negative impact; the higher *K* dissipates and reduces the pressure buildup, except for pressures along the leakage pathways.

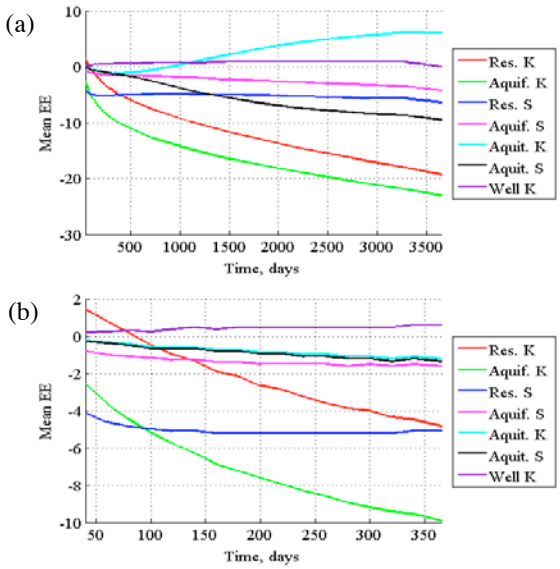

Figure 5. Local sensitivity results for the pressure leakage problem.

In Figure 5(b), however, we can see that the reservoir *K* has a positive effect at the beginning. This is because the reservoir *K* contributes to pressure propagation through the system, and the higher reservoir *K* produces faster arrival of the pressure buildup at this observation point. The reservoir *S* has a relatively large effect at the beginning, since the compressible matrix pores absorb the initial pressure increase.

Morris sensitivity

Figure 6 shows the mean EE from the Morris method. Although the magnitude is different, it gives a fairly consistent interpretation compared to the local sensitivity method, except that (1) the sensitivity to the aquitard *S* becomes smaller relative to the other parameters, and (2) the sensitivity to the reservoir *S* increases at early times. This is considered to be an interaction effect, since hydraulic conductivity and storativity have a nonadditive impact on pressure buildup.

Figure 7 shows the mean EE of the aquitard *K* and reservoir *K* at 10 years as a function of the number of paths with different numbers of partitions *p*. As expected, there are considerable fluctuations in the estimated EE if only a few paths are evaluated. After about 100 paths, the estimate appears stabilized. Note that evaluating 100 paths is generally unfeasible for a computationally expensive simulation model. Running

fewer paths still provides some useful information on the relative importance of a parameter, making the Morris approach a viable tool for global sensitivity analysis.

The number of partitions has little impact on the mean EE in this case. We note that increasing the number of partitions tends to systematically reduce mean EE, an effect that requires further analysis, but that seems likely to be related to the nature of nonlinearity and its evaluation using a decreasing perturbation Δ.

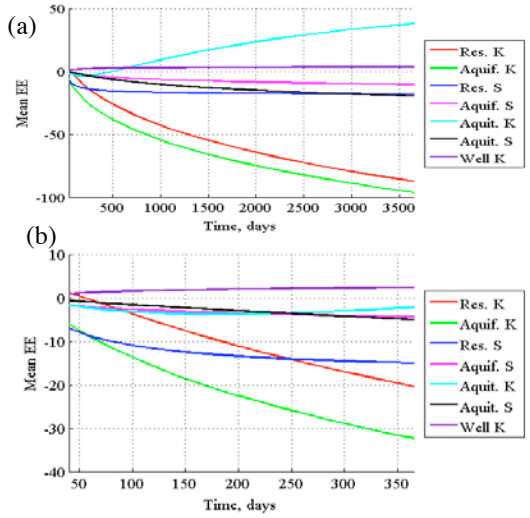

Figure 6. Morris sensitivity results for the pressure leakage problem.

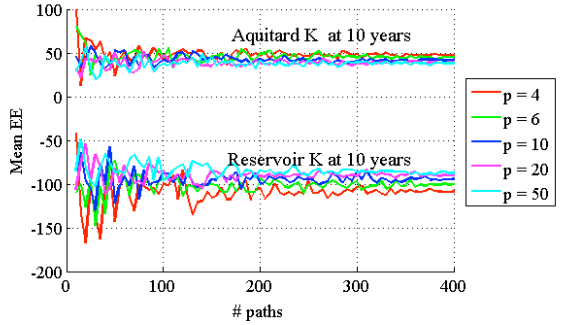

Figure 7. Mean EE of the aquitard *K* and reservoir *K* as a function of the number of paths with different numbers of partitions *p*

Figure 8 shows the crossplot of the mean EE and STD for the reservoir *K*, reservoir *S* and aquitard *K* with different number of paths (*n*). The reservoir *K* has a large effect compared to the reservoir *S* and aquitard *K*. The dots are converged at 200-400 paths, although 10 paths are enough to compare the importance of these three parameters qualitatively; for example, the reservoir *K* has a large mean EE with relatively smaller STD. Since SEM decreases as the number of paths increases, the line for Mean EE = ± 2SEM changes with the number of paths. The effect of aquitard *K*, for example, is not significant with *n*=10 (above the line), but it is significant at *n*=400 (below the line). With the Morris method, we can determine whether the effect is significant or not, with nonlinearity/interaction effects as well as with a limited number of runs.

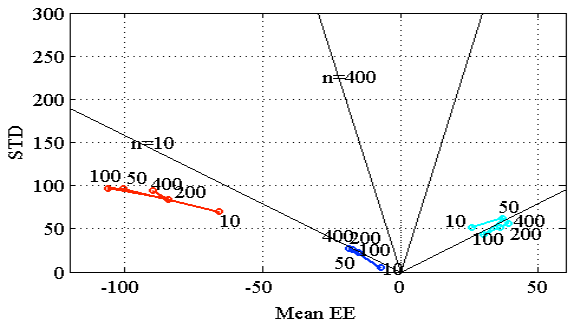

Figure 8. Mean EE vs. STD for the reservoir *K* (red), reservoir *S* (blue) and aquitard *K* (light blue) with different number of paths (10, 50, 100, 200,400). *p* = 20. The black lines correspond to Mean EE = ± 2SEM.

CONCLUSIONS

In this study, we have introduced the new global sensitivity analysis (SA) tool of iTOUGH2. We have shown that the SA tool can be used not only for selecting the important parameters, but also for better understanding systems.

Using the reservoir-scale CO_2 migration model, we compared three SA methods. The results showed that the three sensitivity methods give similar interpretations and importance rankings, except when a parameter has a strong nonlinear effect or interacts with some other parameters—which is the case when a global SA is warranted. We have found that the local sensitivity is sufficient in our cases to identify the influential parameters. Even for cases with nonlinear or interaction effects, the local sensitivity is still useful in improving system understanding (e.g., the high sensitivity of plume arrival/departure to parameters affecting CO_2 mobility) and helps interpret the results from the Morris or Saltelli methods. The Morris sensitivity method provides many uses (e.g., it can identify positive or negative effects, select influential parameters, suggest the presence of nonlinear or interaction effects) with relatively small computational

burden. The Saltelli sensitivity method gives more rigorous/quantitative sensitivity measures, although it is computationally expensive.

With our semi-analytical pressure leakage model, we have explored the computational cost of the Morris method in more detail, in addition to comparing the local and Morris methods. In the Morris method, increasing the number of partitions did not change the mean EE of parameters significantly. Using the crossplot of mean EE and STD, we found that increasing the number of paths has a small effect on the estimation of EE, i.e., the relative importance of a parameter can be evaluated using a relatively small number of simulation runs. The Morris method also allows us to tell the significance of sensitivity measures (e.g., Mean EE) under non-linearity or interactions as well as a limited number of runs. Finally, this study has shown that incorporating global-sensitivity analysis methods into iTOUGH2 strengthens the code's overall value as a model development, experimental design, and data analysis tool.

ACKNOWLEDGMENT

The authors wish to thank to Jeff Wagoner for developing the geologic framework model of the Southern San Joaquin Basin. This work was funded by the Assistant Secretary for Fossil Energy, National Energy Technology Laboratory (NETL), National Risk Assessment Partnership (NRAP), of the U.S. Department of Energy under Contract No. DE-AC02-05CH11231.

REFERENCES

Birkholzer, J.T., Q. Zhou, A. Cortis and S. Finsterle, A sensitivity study on regional pressure buildup from large-scale CO2 storage projects, *Energy Procedia*, 4:4371-4378, 2011

Birkholzer, J.T., A. Cihan, Q. Zhou, Impact-driven pressure management via targeted brine extraction—Conceptual studies of CO_2 storage in saline formations, Int. J. of Greenhouse Gas Control, 7, 168-180, 2012.

Cihan, A., Q. Zhou and J.T. Birkholzer, Analytical solutions for pressure perturbation and fluid leakage through aquitards and wells in multilayered aquifer systems, *Water Resour Res.*, W10504, 2011.

Doughty C. Modeling geologic storage of carbon dioxide: comparison of non-hysteretic and hysteretic characteristic curves, *Energy Conversion and Management*, 48(6), 1768-1781, 2007.

Finsterle, S., *iTOUGH2 User's Guide*, Report LBNL-40040, Lawrence Berkeley National Laboratory, Berkeley, Calif., 2010.

Finsterle, S., M.B. Kowalsky, and K. Pruess, TOUGH: Model Use, Calibration and Validation, *Transaction of the American Society of Agricultural and Biological Engineers*, in press.

Jung, Y., Q. Zhou, and J.T. Birkholzer, Joint inversion of pressure-based observation data for early detection of brine or CO2 leakage through high-permeability pathways, Ground Water, 2012 (in preparation).

Morris, M.D., Factorial Sampling Plans for Preliminary Computational Experiments, *Technometrics*, 33(2):161-174, 1991.

Nordbotten, J. M., D. Kavetski, M. A. Celia, and S. Bachu, Model for CO2 Leakage Including Multiple Geological Layers and Multiple Leaky Wells, *Environ. Sci. and Technol.*, 43 (3), 743-749, 2009

Pruess, K., C. Oldenburg, and G. Moridis, *TOUGH2 User's Guide, Version 2.0*, Report LBNL-43134, Lawrence Berkeley National Laboratory, Berkeley, Calif., 1999.

Saltelli, A., Ratto, M., Andres, T., Campolongo, F., Cariboni, J., Gatelli, D., Saisana, M., Tarantola, S., Global Sensitivity Analysis: The Primer, John Wiley and Sons, 2008

Zhang, K., Wu, Y.S., Pruess, K., 2008. *User's Guide for TOUGH2-MP – A Massively Parallel Version of the TOUGH2 Code*. Report LBNL-315E, Lawrence Berkeley National Laboratory, Berkeley, CA, USA.

Zhou, Q., J.T. Birkholzer, and J.L. Wagoner, Modeling the potential impact of geologic carbon sequestration in the southern San Joaquin basin, California, The Ninth Annual Carbon Capture & Sequestration, Pittsburgh, PA, May 2011.

Zhou, Q., and J.T. Birkholzer, On scale and magnitude of pressure build-up induced by large-scale geologic storage of CO2, Greenhouse Gases: Science and Technology, 1,11-20 2011.

NUMERICAL SIMULATION OF DNAPL SOURCE ZONES ABOVE AND BELOW THE WATER TABLE IN FRACTURED SANDSTONE

Ken Walton[1], Andre Unger, Mario Ioannidis, and Beth Parker

[1]Department of Earth and Environmental Sciences, University of Waterloo
200 University Avenue West
Waterloo, Ontario, N2L3G1, Canada
e-mail: kmwalton@uwaterloo.ca

ABSTRACT

Numerical simulation of flow of two or three mutually interactive phases is a standing challenge for model developers and practitioners. Applying such flow models in the context of fractured rock, an extreme case of heterogeneity, further increases the complexity of the problem. Depending on the rigor of the coupling of flow and transport equations and the geometric description of the fractured-rock domain, problems such as these quickly become at best computationally burdensome, and at worst completely intractable.

In this paper, we describe a mesh generator that spatially discretizes a porous medium and network of discrete, orthogonal fractures and provides influence coefficients for fracture-fracture, matrix-matrix, fracture-matrix, and asperity contact-bridged matrix-matrix flow. We demonstrate an application of this non-uniform spatial mesh in the numerical model *CompFlow Bio* (a multi-component, three-phase flow and transport simulator) in the real-world context of the Santa Susana Field Laboratory site (a site of trichloroethylene (TCE) contamination in fractured sandstone). We provide demonstration simulations of TCE source evolution via a series of three simulations: two smaller-scale (~10 m) air/water/TCE simulations in a near-surface zone; and one larger-scale (~100 m) water/TCE simulation below the water table. The physical processes we consider are capillary barriers to water and TCE flow in the vadose zone, asperity contact bridged flow, and fast preferential flow in the fracture network. All of these processes are parameterized in the model by quantities that could be derived from real site data. Finally, we touch on the computational burden of these various scenarios and contrast meshes of this scheme to conventional finite volume grids.

INTRODUCTION

Numerical modeling of two- and three-phase flow is relevant in fields of carbon sequestration, radionuclide storage, petroleum reservoir production, and (as is our focus) contaminant hydrogeology. These fields seek to predict how distinct fluid phases flow and interact within geologic media. The presence of heterogeneity, be it from differences in rock or soil type, local variations in rock or soil characteristics, or the presence of fractures with varying orientation and aperture, complicate the physical description of the domain of interest and increase the computational burden of numerical simulators, a tool commonly used by practitioners.

These tools, their conceptual design and implementation, unite knowledge from chemistry, fluid mechanics, geology, applied mathematics, and computer science. Here, we omit many relevant details from these fields as we elaborate only on our geometric description of discrete fractures, and show numerical simulations that act as examples of its use in the numerical model *CompFlow Bio* (see e.g., Unger et al., 1995). The ultimate goal of our geometric description is to produce "influence coefficients" (blended spatial and geophysical values that quantify the degree to which adjacent computational entities interact) suitable for a finite volume discretization scheme. Herein, we highlight the major concepts behind our approach, including (1) our motivation to consider fractures as distinct computational entities, (2) our notion of a discrete fracture with asperity contact area, (3) the procedure for addition of fractures into the spatial mesh as control volumes (CVs), and (4) the advantageous step of eliminating small-volume CVs that occur at the intersection of fractures. We then briefly describe some

simulation results and discuss pros and cons of this method.

METHOD

Motivation

First, we examine our choice of the discrete fracture conceptual model: We take the pedagogical assumption that small-scale flow and transport phenomena (when upscaled appropriately) contribute to the overall flow field, and that a statistically generated fracture network based on field measurements represents the actual fracture network sufficiently well. Furthermore, we assume that discrete fractures have three-phase relative permeability-saturation-capillary pressure (k_r-S-P_c) relationships (similar to porous media, as per Reitsma and Kueper, 1994) that are an important aspect of their influence on multiphase flow.

Figure 1 shows a complex pattern of aqueous phase and nonaqueous phase saturation that may arise from fracture-matrix interactions. Capillarity causes fractures to be gas-filled and act as barriers to liquid flow; areas where opposing fracture walls are in contact relieve these barriers.

Discrete Fracture Conceptualization

We consider individual rough fractures, such as in Figure 2(a), to be composed of one or more component CVs, which are distinct computational entities in the simulator. Fracture CVs are much like porous media CVs, except that they have porosity 1.0, they have fewer than three spatial dimensions (i.e. they are planar as in Figure 2(b), or in the case of fracture intersections, are one- or zero-dimensional). Moreover, their intrinsic permeability tensor is limited by the dimensionality of the CV, permeability is calculated according to the cubic law using effective hydraulic aperture, and they hold their own set of k_r-S-P_c relationships.

Fracture CVs may connect to other fractures at their edges and adjacent porous medium (or rock matrix) CVs over their faces. We augment connectivity by allowing direct matrix-to-matrix flow across a fracture plane by asperity contact-bridged flow; we assume the porous media at contact points to be continuous and that regular

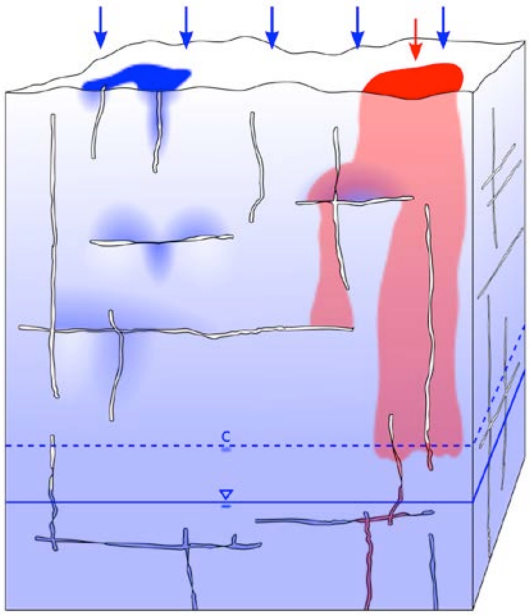

Figure 1. Schematic of how discrete fractures may influence fluid phase saturation in the vadose and shallow saturated zones, given infiltrating aqueous phase (blue), nonaqueous phase contaminant (red), and a resident gas phase (white).

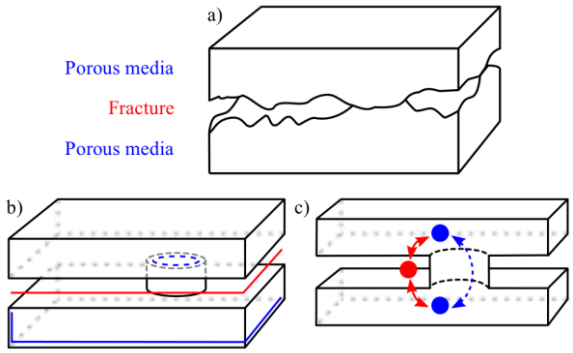

Figure 2. (a) Conceptual diagram of a rough fracture, (b) dimensions of 2D fractures and 3D porous media CVs, and (c) fracture-matrix and matrix-matrix connectivity.

Darcy flow occurs through these areas. Thus, a fraction, $0.0 \leq \alpha \leq 1.0$, of each planar fracture CV's area is allocated for such flow, as depicted conceptually in Figure 2(c).

Spatial Discretization

For the purpose of reducing the overall number of control volumes in the domain, porous media CVs are refined only in areas local to fractures. This is accomplished in a mesh preprocessing step whereby the fractures are added one by one

to an initial grid of porous media CVs. Porous media blocks are bisected in the plane of the fracture, but not necessarily at the edges of the fracture. This is different from a conventional finite volume or finite element discretization, in which the boundaries of fractures or adjacent CVs/elements always coincide. Fractures are subdivided into CVs based on the boundaries of surrounding CVs.

For example, in Figure 3, the porous medium block A is split into A' and A" to accommodate C. B remains unchanged. Connectivity is rees-tablished based on the interfacial areas of CVs in contact with one another.

We note that the resulting mesh lacks the original well-defined grid-like structure. The boundaries of adjacent CVs are often mis-aligned, as Figure 3 indicates. This misalign-ment is an extra source of numerical inaccuracy in the solution of flow and transport equations (Dehotin et al., 2011). We feel that the trade-off of reduced accuracy in order to reduce the overall number of CVs is warranted.

Numerical Formulation

Once the CVs and connectivity relationships have been established, the next step is to quantify those relationships for flow and transport.

To illustrate how to calculate interfacial areas and influence coefficients in an irregular mesh formed by the process above, we present Figure 4. In this situation, typical of relatively large initial porous media CVs bisected by randomly spaced fractures, the boundaries of porous media CVs, *i* and *j*, are disjointed, and the fracture CV,

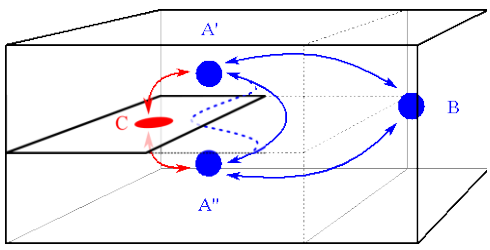

Figure 3. Adjacency relationships of fracture-matrix (red) and matrix-matrix (blue) CVs, including an asperity contact connection between A' and A" (blue, dashed).

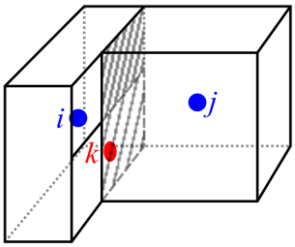

Figure 4. An example of adjacent porous media CVs, *i* and *j*, and fracture CV *k* with disjointed boundaries.

k, lies between them. The dark gray area of direct contact between *i* and *j* plus the light gray area times the asperity contact fraction com-prises the entire interfacial area.

Influence coefficient calculation

Influence coefficients in *CompFlow Bio* are calculated in a typical way for finite volume dis-cretizations. Interfacial area is multiplied by a weighted average of permeabilities, and divided by the distance between the node centroids. For example:

$$\gamma_{ij} \coloneqq A_{ij} \frac{k_{II,i} k_{II,j} \left(\Delta x_{I,i} + \Delta x_{I,j}\right)}{k_{II,j} \Delta x_{I,i} + k_{II,i} \Delta x_{I,j}} \left(\frac{\Delta x_{I,i} + \Delta x_{I,j}}{2}\right)^{-1}$$

where *i* and *j* are CV labels, A_{ij} is the interfacial area between *i* and *j*, $k_{II,i}$ is the intrinsic perme-ability of node *i*, entry *I*-*I* of the 3×3 tensor, and $\Delta x_{I,i}$ is the size (or aperture) of node *i* in direc-tion principle Cartesian direction *I*. (We note that the above formula could be replaced with an equation from the literature to accommodate a permeability tensor that is not aligned with the principle Cartesian vectors. Because our fractures and porous media CV faces are aligned with the axes, this is not necessary.)

Intersection Node Elimination

Although fracture intersections may be important preferential pathways in multiphase flow, we eliminate these CVs from the mesh to ease the numerical burden they impose. (This is a necessary step for "large" simulations; inter-sections can be retained otherwise.) Elimination occurs in a post-processing step, in which new connectivity and influence coefficients are formed. These influence coefficients arise from algebraic manipulation of the steady-state flow

equation at the eliminated node. Thus, some information/effect of the node is retained.

Node elimination occurs in two stages: Point intersections are removed, then line intersections are removed. Influence coefficients are calculated at each iteration, as they are all used in forming subsequent coefficients.

Figure 5 shows the CVs representing the fracture planes and intersections in a situation where three fractures meet in a corner-like configuration.

Influence coefficient calculation for control volume elimination

Taking the *E*-*F* connection in Figure 5 as an example, the influence coefficient, which uses information from former neighbors of *b*, is given by:

$$\gamma''_{EF} := \frac{\gamma_{bE}\gamma_{bF}}{\sum_{j\epsilon\eta_b}\gamma_{bj}}$$

$$= \frac{\gamma_{bE}\gamma_{bF}}{\gamma_{bE}+\gamma_{bF}+\gamma'_{bc}+\gamma'_{bd}}$$

$$= \frac{\gamma_{bE}\gamma_{bF}}{\gamma_{bE}+\gamma_{bF}+\frac{\gamma_{ab}\gamma_{ac}}{\gamma_{ab}+\gamma_{ac}+\gamma_{ad}}+\frac{\gamma_{ab}\gamma_{ad}}{\gamma_{ab}+\gamma_{ac}+\gamma_{ad}}}$$

where η_b is the set of neighbors of node *b*, γ'_{bc} and γ'_{bd} are defined in-place, and other unprimed γs are defined in the previous equation.

APPLICATION

As a demonstration of this mesh creation approach and examples of the scale of the problem it is being employed to tackle, we present the sample meshes and results of three simulations conducted with *CompFlow Bio*.

The simulation scenario is based on subsurface contamination at the Santa Susana Field Laboratory site, located near Los Angeles, California. To investigate dense, nonaqueous phase liquid (DNAPL) source zone architecture, DNAPL is introduced at the ground surface and allowed to infiltrate downward through the vadose zone, capillary fringe, and below the water table. We consider gravity-driven gas, aqueous phase, and NAPL flow, capillarity, equilibrium phase partitioning, and dissolved species transport. Gas exchange and steady recharge occur at the top of the domain, while

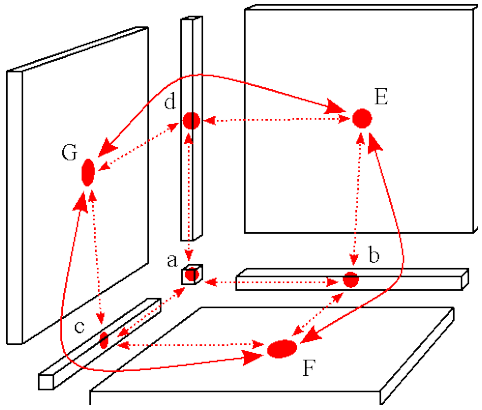

Figure 5. Neighbor relationships between fracture CVs at the intersection of three orthogonal fractures before and after node elimination. CVs are separated spatially for clarity.

hydrostatic, free-flow conditions exist at the bottom. The rock matrix properties, such as permeability and k_r-S-P_c relationships, are homogeneous. Fracture spacing is approximately 3 per meter (or 1 per meter in the 3D, saturated simulation) and fracture aperture varies log-normally with mean aperture 150 μm. Wherever possible, simulation parameters are derived from measurements of the fractured Chatsworth formation sandstone taken from the site. DNAPL loading occurs in a small area at the top of the domain at a steady rate of 7 L/day (or about one 55 gallon drum per month) in each case.

Figures 6, 7, and 8 show transient DNAPL source zones at various points in time. They also demonstrate the density of the fracture network, and complicated architecture that ensues from the contributions of distinct fracture and matrix CVs.

To provide a basic description of the certain computational costs, characteristics of the meshes in the preceding simulations are provided in Table 1. These data are highly implementation- and random-fracture-network-dependent, but nonetheless provide a baseline for comparison to simulations from other platforms. For further comparison, we give values for analogous meshes generated in the conventional fashion: we take the same fracture networks and a priori impose grid lines in the plane of each fracture.

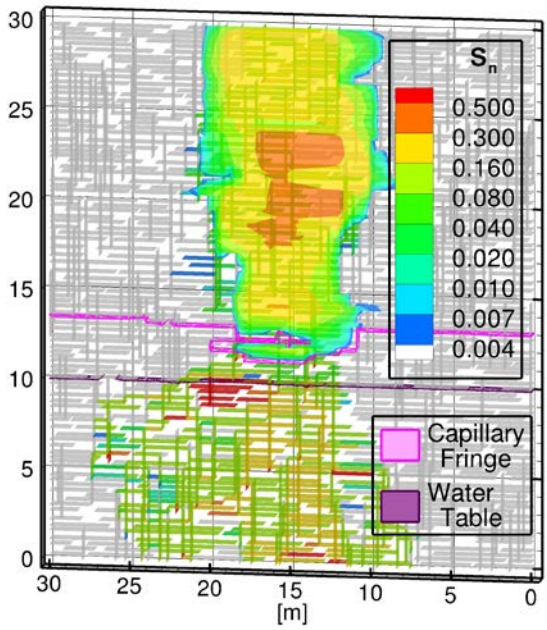

Figure 6. DNAPL saturation after 2 years of contaminant loading in a 30×1×30 m domain.

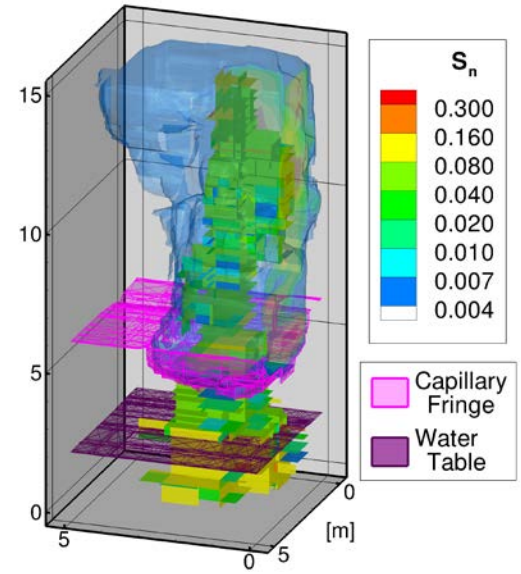

Figure 7. DNAPL saturation after 1 year of contaminant loading in a 5×5×15 m domain. Fracture CVs with low DNAPL saturation omitted.

DISCUSSION

To support the modeling of three-phase flow in fractured media, we have presented a framework for creating a spatial mesh which (1) reduces the number of CVs, and (2) removes numerically troublesome, small-volume CVs. As evidence that the approach is viable, we presented results

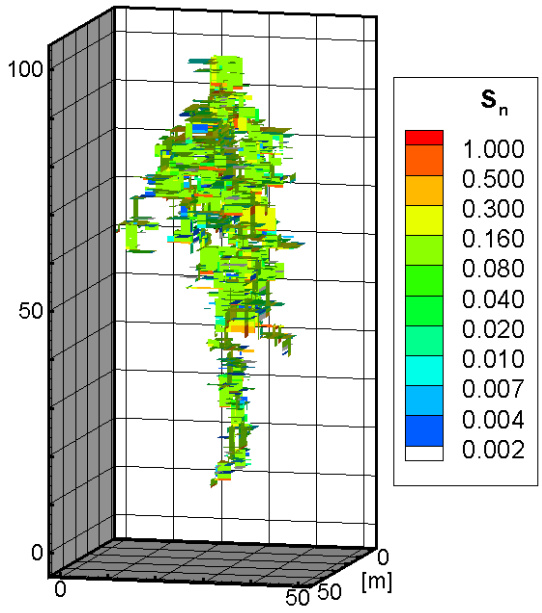

Figure 8. DNAPL saturation after 30 days of contaminant loading in a 50×50×100 m domain in the fracture network. Fracture CVs with low DNAPL saturation omitted.

Table 1. Mesh Data

	2D	3D Unsat.	3D Sat.
Fractures	890	230	7800
Fracture CVs	6900	31,000	200,000
Intersection CVs eliminated	2700	22,000	70,000
Porous Medium CVs	11,000	13,000	120,000
Porous Medium CVs*	23,000	80,000	$15x10^6$

* Count of CVs for a conventional finite volume grid.

of three simulations representing DNAPL loading in the near-surface sandstone of the Santa Susana Field Laboratory site.

The main computational advantage of the unstructured mesh over conventional grids is in the reduction of the size of the problem (i.e., number of CVs) in terms of algorithmic complexity of building and solving the numerical system of equations. Disadvantages include numerical error associated with the irregular CV connections. Many tradeoffs and computational costs regarding other implementation details (e.g., inclusion of a mobile gas phase, coupling of governing equations, field data collection and model

parameterization) are important, but shall not be discussed here.

Finally, although we have presented our CV bisection and elimination process in the context of orthogonal fractures, we believe that it could be generalized; arbitrary fracture orientations could be accommodated by a more robust fracture network generator and appropriate treatment of the permeability tensor.

ACKNOWLEDGMENTS

Funding for this project was provided by Strategic Environmental Research and Development Program, ER-1610, and subsequently by The Boeing Company via the University Consortium for Field-Focused Groundwater Contamination Research and an Industrial Research Chair grant from the Natural Sciences and Engineering Research Council of Canada.

REFERENCES

Dehotin, J., R. F. Vazquez, I. Braud, S. Debionne, and P. Viallet, Modeling of Hydrological Processes using Unstructured and Irregular Grids: 2D Groundwater Application, *J. Hydrol. Eng.*, 16 (2) 108–125, 2011.

Reitsma, S., and B. H. Kueper, Laboratory Measurement of Capillary Pressure-Saturation Relationships in a Rock Fracture, *Water Resour. Res.*, 30 (4) 865–878, 1994.

Unger, A.J.A, E. Sudicky, and P. Forsyth, Mechanisms Controlling Vacuum Extraction Coupled with Air Sparging for Remediation of Heterogeneous Formations Contaminated by Dense Nonaqueous Phase Liquids, *Water Resour. Res.*, 31 (8) 1913–1925, 1995.

ADDING GEOLOGY TO THE EQUATION: TOWARDS INTEGRATING STRUCTURAL GEOLOGICAL DATA INTO INVERSE MODELING WITH iTOUGH2

J. Florian Wellmann[1], Stefan Finsterle[2], Adrian Croucher[3]

[1]CSIRO Earth Science and Resource Engineering, Kensington WA 6151 Australia, florian.wellmann@csiro.au
[2]Earth Sciences Division, Lawrence Berkeley National Laboratory, University of California, Berkeley
[3]Department of Engineering Science, University of Auckland, Private Bag 92019, Auckland, New Zealand

ABSTRACT

The subsurface structural setting, as a part of the conceptual model, can have a strong influence on the outcome of a flow simulation. The structural geological model should therefore be considered in uncertainty studies or parameter estimations. However, in practice, this inclusion is not easily possible, because the generation of an input mesh for a flow simulation, populated with properties according to a geological model, requires at least some manual work. We present here a method that removes this gap between geological data and flow simulation and propose that it will enable insights into the significance of structural uncertainties in the context of inversion modeling that is not yet possible.

Practical applications of the methods are demonstrated with two simple examples: the inversion of the distance to an impermeable boundary in an aquifer, and the significance of uncertainties in the exact position of structural geological observations, in a CO_2 injection scenario with possible leakage over a fault with an uncertain position.

The presented examples show that the integration of geological structures into an inversion framework enables a consideration of structural uncertainties that is not easily possible with the methods available to date. Geological data can be highly uncertain and limited, and our examples emphasize the fact that these uncertainties can strongly influence the outcomes of a flow simulation.

INTRODUCTION

Structural representations of the subsurface, commonly called geological models, are an important part of the conceptual model and therefore a relevant part of most realistic large-scale flow simulations (e.g., Bundschuh and Arriaga, 2010). It is well known that these geological models contain uncertainties for a variety of reasons, and several recent developments address the analysis of these uncertainties (Thore et al., 2002; Turner, 2006; Wellmann et al., 2010; Lindsay et al., 2012). Furthermore, recent studies show that these uncertainties in the geological model can have a significant influence on flow simulations that are based on these models (Nilsson et al., 2007; Refsgaard et al., 2012).

Even though it is widely accepted that geological uncertainties should be considered in flow simulation studies, this is usually not done in most practical applications. An important reason for this neglect is the lack of an integrated workflow that combines all relevant steps, from the initial structural geological data, to the flow simulation and result analysis, into a coherent inversion framework. We propose here a method to overcome this limitation with a completely automated workflow that combines novel geological modeling methods with TOUGH2 flow simulations in an inversion framework with iTOUGH2. As a test of feasibility, we apply the workflow to test the integration of geological data in flow inversion and uncertainty propagation studies, using two synthetic examples.

MATERIALS AND METHODS

Our aim is to combine geological modeling with the multiphase flow simulation code TOUGH2 (Pruess et al., 2011). We apply here a method that combines and automates TOUGH2 preprocessing methods with the inverse and parameter estimation package iTOUGH2. Specifically, we use a recently developed Python module library that efficiently wraps TOUGH2 input files and greatly simplifies the mesh generation (Croucher, 2012). This library is combined with the inverse capabilities of iTOUGH2, making use of the PEST interface

(Finsterle and Zhang, 2011). Furthermore, we combine these methods with an innovative geological modeling approach based on an implicit potential-field method (Lajaunie et al., 1997) to allow the consideration of complex geological structures in the workflow. The most relevant aspects of the workflow are described in the following.

An overview of the workflow is presented in Fig. 1. The method is centered around iTOUGH2. iTOUGH2 itself was developed as a sensitivity analysis, parameter estimation, and uncertainty propagation package for TOUGH2 simulations (Finsterle, 1999). An iTOUGH2 run commonly incorporates the definition of uncertainties for specific input parameters, the forward simulation for a given problem with TOUGH2 for these parameters, and then the output analysis and comparison to actual observations (see Fig. 1 bottom right). For different types of analyses, these steps are repeated a certain number of times, for example to determine an optimal input parameter set, or to test how uncertainties in the input parameters propagate to flow field observations (e.g. Finsterle, 1999).

The capabilities of iTOUGH2 are accessible for other pre- and post-processing methods through an interface defined with template and instruction files (Finsterle and Zhang, 2011). Interface types are based on the widely used parameter estimation package PEST (Doherty, 1994); template files can be used to control parameters with iTOUGH2 that are not parameters of a TOUGH2 simulation itself (see Fig. 1 bottom left). In addition, the PEST interface can be used to include simulation results from external simulations into the iTOUGH2 framework using instruction files. For more details on the interface and its possibilities, see Finsterle and Zhang (2011).

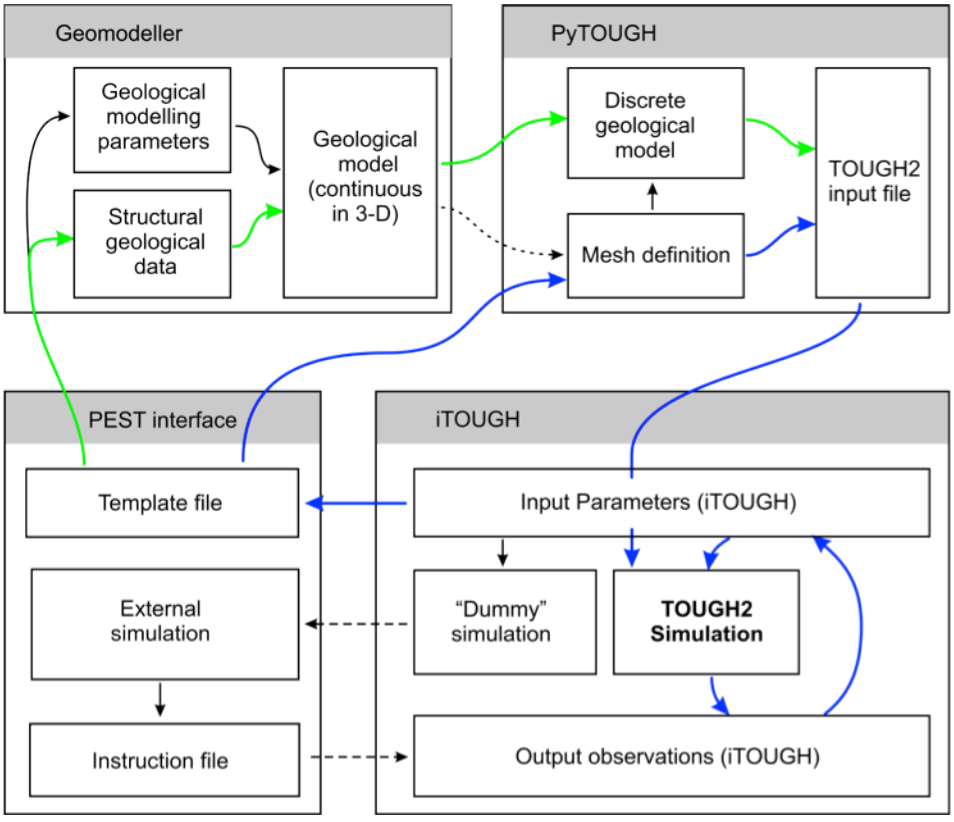

Figure 1. Workflow for the combination of structural geological model construction with iTOUGH2 inversion and model calibration methods

We combine the functionalities of iTOUGH2 here with two external modules: the TOUGH2 preprocessing methods of the Python library PyTOUGH (Croucher, 2012; Wellmann et al., 2011), and the geological modeling methods of a commercial geological modeling package, GeoModeller (Calcagno et al., 2008).

PyTOUGH is a set of modules designed to simplify the input file generation for TOUGH2 simulations, and to provide powerful data analysis and visualization methods (Wellmann et al., 2011). It is written in Python, an open-source interpretative programming language that provides powerful numeric and scientific methods, and data visualization techniques (e.g., Langtangen, 2008). Both PyTOUGH and Python are available at no cost.

We are using here the functionality of PyTOUGH to generate input meshes and input files for TOUGH2 simulations that can be adapted to several structural parameters and considerations (Fig. 1 upper right). The libraries provide several convenient ways that greatly simplify the generation of mesh structures.

We extended the functionality of PyTOUGH with an interface to an innovative geological modeling method (Fig. 1, upper left), implemented in the commercial geological modeling package Geomodeller (www.geomodeller.com). The geological model is constructed through an implicit potential-field interpolation method (Lajaunie et al., 1997). This method enables the interpolation of a full 3-D geological model directly from geological data, implicitly respecting realistic geological constraints (Calcagno et al., 2008). The advantages of this method over standard surface interpolation approaches (e.g., Caumon et al., 2009) are that it enables the automatic reconstruction of a model when the geological input data are changed, and that it is possible to construct realistic 3-D models with a relatively small input data set (e.g., Maxelon and Mancktelow, 2005; Putz et al., 2006; Joly et al., 2008; Calcagno et al., 2012). We consider both aspects as essential for the consideration of structural geological modeling in an inverse simulation context.

The developed workflow can be used in a variety of ways to include different types of pre-processing methods into the inversion frameworks of iTOUGH2. We will use it here along two lines: the automation of mesh and input file generation (indicated by blue arrows in Fig. 1), and the additional combination with the geological modeling module (highlighted with green arrows in Fig. 1). In both scenarios, we will evaluate how the developed workflow enables insight into the relevance of structural geological model uncertainties in the context of flow simulations, and how these uncertainties can be considered.

APPLICATION

Example 1: Inversion for the distance to an impermeable boundary

Pressure drawdown curves, determined during pumping tests in an aquifer, contain important information about hydrogeological properties and the general structure of an aquifer (e.g., Marsily, 1986). It is well known from theory that an impermeable boundary in the vicinity of a pumping well has an influence on the pressure drawdown curves, and analytical methods exist

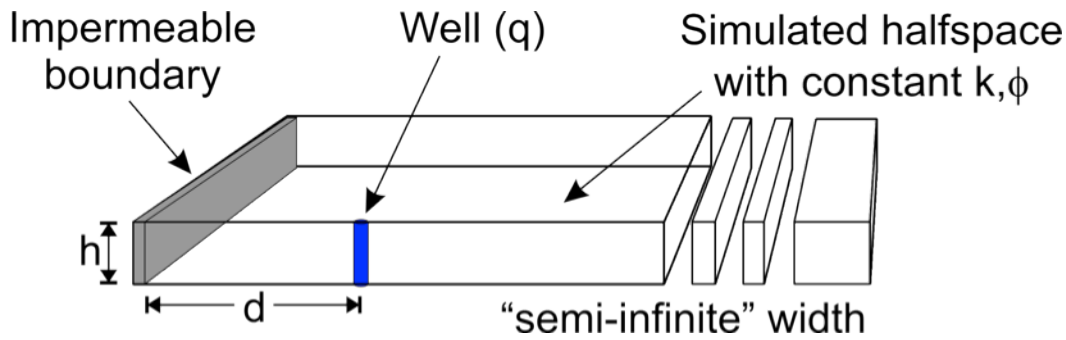

Figure 2. Conceptual model set-up for the pumping half-space model: the simulation is performed in a semi-infinite half-space with an impermeable boundary in an unknown distance d to the well. Additionally, aquifer thickness h and permeability k are considered uncertain.

Table 1. Initial parameters and results determined in different inversion scenarios; results are given with the estimated marginal standard deviation apart from the case of perfect data, where it is negligible.

Parameter	Correct value	Initial Guess	Perfect Data	Noise "1"	Noise "2"	Thickness and Noise
log10(k) [k in m^2]	-12	-11.5	-12	-12 + 0.005	-11.9 + 0.04	-11.9 + 0.026
d [m]	40	100	40	42 + 3.62	34 + 24	36.4 + 3.11
h [m]	20	(25)	(fixed)	(fixed)	(fixed)	17 + 7.84

to determine this influence (Ferris et al., 1962).

In this first example, we apply the developed workflow as a simple method to determine the distance to an impermeable boundary from observed (and potentially noisy) pressure drawdown data.

Model setup

We consider here a simple hydrogeologic setting of a confined aquifer with constant thickness, with an impermeable boundary at one side and a quasi-infinite extension in all other directions. The conceptual model is shown in Fig. 2: the well is placed in a distance d to an impermeable boundary. The aquifer is semi-infinite, with constant permeability k and porosity ϕ, and of constant thickness h. Pumping is performed for two days with a constant rate q.

We use here the part of the workflow that enables an automatic mesh generation and TOUGH2 input file generation with PyTOUGH, with the inversion framework of iTOUGH2, as highlighted by the blue arrows in Fig. 1. The only structural ("geological") input parameter in this case is the distance d to the impermeable boundary. The parameter is updated in every iTOUGH2 iteration, then passed through the PEST interface to adapt a template file that is then used to generate an adapted mesh, before the next TOUGH2 simulation. Two map views for generated meshes with a distance of 30 m, and a distance of 60 m between well and impermeable boundary are shown in Fig. 3, with the simulated pressure distribution in the aquifer after two days of pumping, highlighting the obvious effect of the boundary on the pressure distribution.

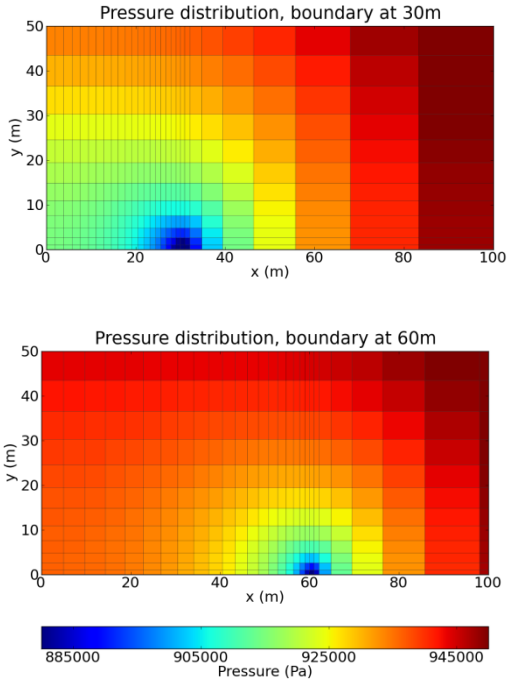

Figure 3. 2-D Map view of pressure distribution in the aquifer after two days of pumping for two different distances between impermeable boundary and pumping well: the different pressure distribution around the well is clearly visible.

An initial synthetic pressure drawdown curve for the following inversion studies is determined for the parameter settings d = 40 m, h = 20 m and k = 1E-12 m^2 (Tab. 1). A total of 192 measurements are simulated over the pumping period of two days (blue curve in Fig. 4). We will now apply the workflow to invert for the aquifer permeability and the distance to the impermeable boundary in several scenarios.

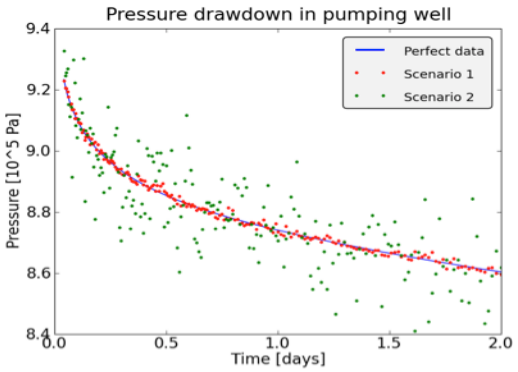

Figure 4. Pressure drawdown curves: initial synthetic drawdown curve (blue line) and measurement scenarios with added random noise (red dots: low noise, green dots: high noise)

Inversion results

In a first step, we test the workflow for a joint inversion for aquifer permeability and the distance to the impermeable boundary for a perfect data set, i.e. we take the generated synthetic pressure drawdown curve as observed data. As a first guess, we assume that we considered the permeability as a bit too high (k = 5E–11 m^2) and that there is no impermeable boundary in the close vicinity of the well (d = 100 m). In this case, the method determines both the position of the impermeable boundary and the aquifer permeability perfectly well (Tab. 1 “Perfect data”).

With some more simple tests, we now evaluated how the inversion performs in the case of noisy data. We generated two data sets with added random noise to the observations to simulate measurement error. In the first scenario, we added small random Gaussian error with a standard deviation of σ = 1000 Pa, and in the second case a higher error with σ = 10,000 Pa.

For both scenarios, the aquifer permeability is determined almost perfectly (Tab. 1). The distance d to the impermeable boundary is overestimated by 2 m in the case of low noise, and underestimated by 6 m in the case of high noise, although the estimated standard deviation is very high.

As a further comparison of the behavior of the objective function in the case of the high-noise scenario, a grid search was performed over a range of 30–50 m for the distance d, and -12.25 to -11.75 for $\log_{10}(k)$ for the logarithm of permeability (Fig. 5). The grid search results show that permeability in this range can be well determined in both cases, a behavior that is reflected in the results presented in Table 1. The distance to the impermeable boundary is more difficult to estimate with high accuracy, and the determination is only very vague in the case of the highly noisy data (Fig. 5b).

In the third scenario, the performance of the inversion scenario is evaluated for an additional uncertain structural geological parameter: the thickness h of the aquifer. The inversion is performed for an initially overestimated aquifer thickness of 25 m. The inversion performed well in determining the permeability and reasonably well in determining the distance to the boundary (although the real value is outside of one standard deviation σ). In this case, the aquifer thickness is not very well determined with the amount of observed data.

Example 2: CO2 injection and potential leakage over

In the second example, we apply the entire workflow, including geological modeling (upper left in Fig. 1, combined along green arrows), to evaluate the sensitivity of a flow simulation directly with respect to structural geological observations in a more complex scenario. The flow simulation considered here is a synthetic example of simulated CO_2 sequestration into an anticlinal structure, with potential leakage over a fault in the vicinity (Fig. 6a).

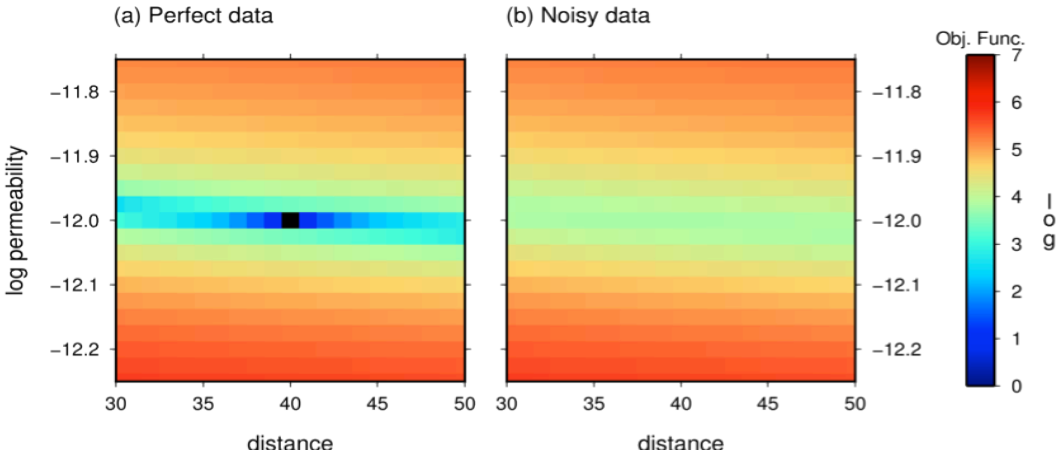

Figure 5. Results for grid search of objective function for the case of (a) perfect data, and (b) a noisy dataset (second scenario with high noise, green dots in Fig.); The grid search results suggest that it is in both cases possible to invert for the permeability, but the determination of the structural uncertainty, the distance to the impermeable boundary, is problematic for high noise.

Model setup

The geological modeling method that we implemented in the workflow is capable of representing complex 3-D geological structures with relatively few input parameters. We use it here to construct a 3-D model of a folded sedimentary pile that is intercepted by a fault (Fig. 6a). The sedimentary pile comprises three layers and is folded, with an anticlinal structure in the center of the model. The sedimentary pile (including the folding) is parameterized by four geological surface contact points ("control points" in Fig. 6a) and the fault by three points. As further geological constraint, the sedimentary layers are defined to be subparallel and offset by the fault (see Calcagno et al., 2008, for more details about geological logic and implementation). With these geological settings, and additional interpolation parameters, the seven contact points are sufficient to describe the entire geological model in full 3-D (Fig. 6b).

The geological model is a continuous representation in 3-D. To use it as a conceptual model for a TOUGH2 simulation, it needs to be discretized. As before, we use PyTOUGH for the mesh generation (Fig. 1). We create here a simple regular mesh with a defined number of elements in each coordinate direction. An extension module for PyTOUGH is then used to determine the size of the geological model to set up the mesh structure. In a next step, for each cell in the mesh, the geological unit (i.e., the "rocktype") is determined from the geological model; in this way, the continuous geological model is mapped onto the discrete mesh structure (Fig. 6c). The mesh information is then combined with a template TOUGH2 input file that contains definitions for rocktypes, the CO_2 source, and other model settings.

The CO_2 injection and subsurface flow are simulated with the TOUGH2 fluid property module for mixtures of water, NaCl, and CO_2: ECO2N (Pruess and Spycher, 2007). Rocktype, source, and modeling parameters are adapted from the second example in the manual (Pruess, 2005), the (radial) flow from a CO_2 injection well (rcc3). We use here the same basic settings, i.e., injection into a reservoir with constant temperature, consideration of salt precipitation without associated permeability reduction. Initial pressure is 120 bar.

The properties of the rock types for the different geological units are adapted from the "sand" and "shale" rocktypes of "Problem No. 4 (rtp7)" of the ECO2N manual (Pruess, 2005). The "shale" properties are assigned to the reservoir cap (see Fig. 6b), and "sand" properties to all other geological units. The permeability of the cap is set to k = 1E-18 m^2 and to 1E-12 m^2 for the other units.

Sensitivity study

An important consideration in any CO_2 injection scenario is the possible leakage of CO_2 to the surface, e.g., over a fault in the vicinity of the injection site. It is a common case in the early stage of a feasibility study that the subsurface structural setting is highly uncertain. In the case of the conceptual model considered here (Fig. 6a), uncertainties are considered directly for the surface contact points (indicated with error bars around the contact points in Fig. 6a). We now use the developed framework combining geological modeling with iTOUGH2 to test which data point uncertainties have the highest influence on potential leakage over the fault, with a sensitivity study.

We consider the change of total mass of CO_2 in the undifferentiated geological unit to the West of the fault as indicator for fault leakage. The parameters included in the analysis are the z-position of the surface contacts point defining the reservoir-seal boundary (points R_W and R_top, in Fig. 6a), and the E-W position of the point defining the fault (point F in Fig. 6a). All values are assigned a normal distribution with a standard deviation of 100 m. Additional parameters could be considered, for example the thickness of the seal, but for simplicity we restrict the analysis to these three parameters as a first test.

The results of this analysis are shown in Fig. 7. The total parameter sensitivity is highest for the structural geological contact point that defines the top of the reservoir, R top (see Fig. 6a). In addition, the data point that defines the western side of the reservoir, R_W, is important for the consideration of fault leakage. However, the data point that defines the actual position of the fault, F, is less relevant in this analysis.

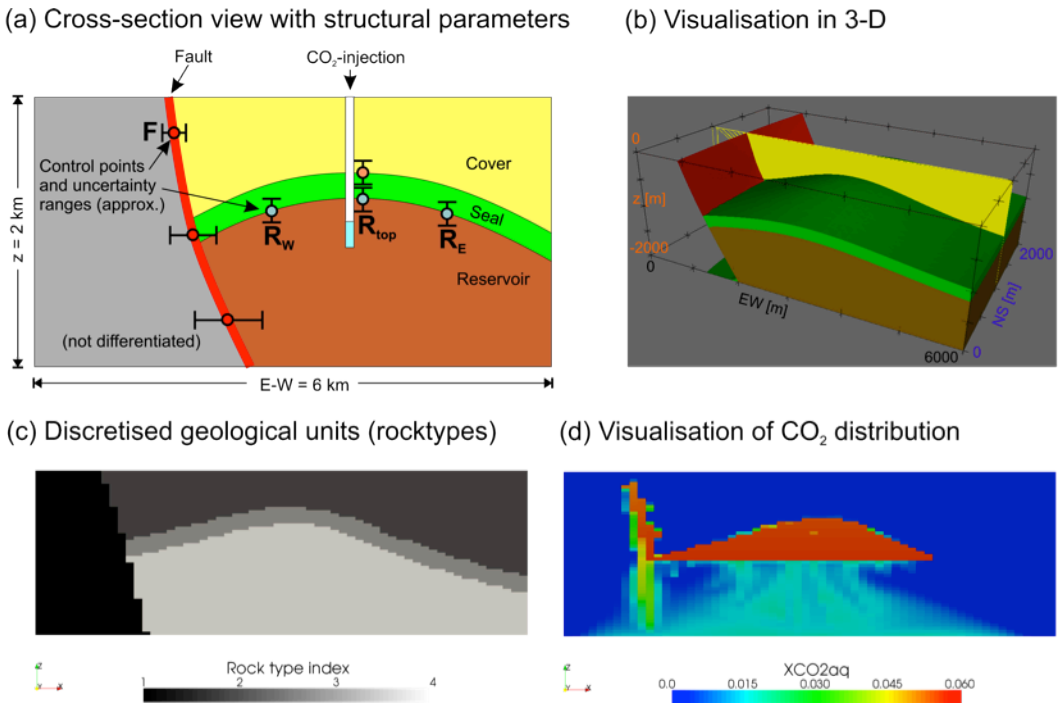

Figure 6. (a) Conceptual model for a CO_2-injection scenario with an uncertain distance to a fault: the figure shows a 2-D section through the model; CO_2 is injected into an anticlinal structure. The points denote contact points between geological units with an uncertain position; (b) full 3-D view of the model; (c) discretized model in a 2-D slice; (d) example of simulated CO_2 distribution with leakage over fault

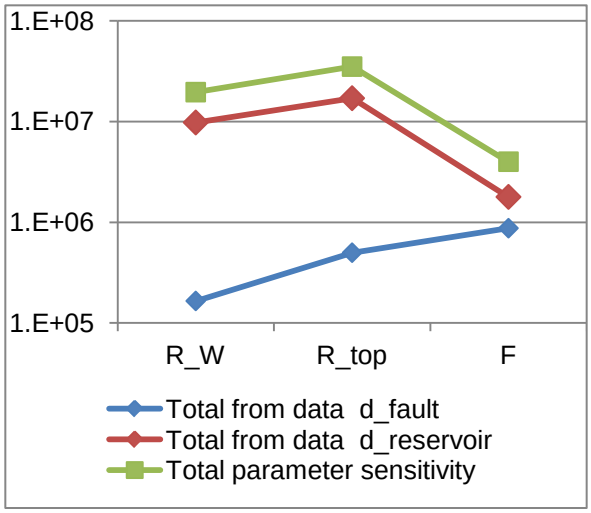

Figure 7. Parameter sensitivity for three geological contact points

DISCUSSION

The geological structure is an important aspect of subsurface uncertainties. Here we presented a method to include it in the framework of multiphase flow simulations with TOUGH2. The most important feature of the geological modeling that we integrated here is that it allows the representation of complex and realistic 3-D structural geological settings with a relatively small parameter set. This feature is an important prerequisite to integrating it into an inverse framework.

As a test of feasibility, we applied the workflow to two synthetic examples: in the first case, we used the methods to invert for the distance from a pumping well to an impermeable boundary in an aquifer, using the pressure drawdown in the well.

In the second example, we addressed the more complex problem of combining geological modeling and multiphase flow simulations: we evaluated how uncertainties in the subsurface structure influence fluid flow predictions. We considered a scenario in which CO_2 was injected into an anticlinal structure, with a possible leakage over a fault in the vicinity. Both examples show that it is possible to consider geological information in an inverse flow simulation framework, as an important step forward for adding geological data into uncertainty estimations of flow simulations.

ACKNOWLEDGMENT

The work was supported by the Western Australian government as the Western Australian Geothermal Centre of Excellence (WAGCOE), a joint partnership between CSIRO, the University of Western Australia, and Curtin University. The work of the second author was supported, in part, by the U.S. Dept. of Energy under Contract No. DE-AC02-05CH11231.

REFERENCES

Bundschuh, J., Arriaga, S., 2010. Introduction to the numerical modeling of groundwater and geothermal systems: Funda- mentals of mass, energy and solute transport in poroelastic rocks. Vol. 2 of Multiphysics Modeling. CRC Press/Balkema, Leiden.

Calcagno, P., Bouchot, V., Thinon, I., Bourgine, B., Mar. 2012. A new 3D fault model of the Bouillante geothermal province combining onshore and offshore structural knowledge (French West Indies). Tectonophysics 526-529 (C), 185–195.

Calcagno, P., Chiles, J.-P., Courrioux, G., Guillen, A., 2008. Geological modelling from field data and geological knowledge: Part I. Modelling method coupling 3D potential-field interpolation and geological rules: Recent Advances in Computational Geodynamics: Theory, Numerics and Applications. Physics of the Earth and Planetary Interiors 171 (1-4), 147–157.

Caumon, G., Collon-Drouaillet, P., Le Carlier de Veslud, C., Viseur, S., Sausse, J., 2009. Surface-Based 3D Modeling of Geological Structures. Mathematical Geosciences 41 (8), 927–945.

Croucher, A., Apr. 2012. PyTOUGH User's Guide, 1–88.

Doherty, J., 1994. PEST: a unique computer program for model-independent parameter optimisation. Water Down Under 94: Groundwater/Surface Hydrology Common Interest Papers; Preprints of Papers, p.551.

Ferris, G. J., Knowles, B. D., Brown, H. R., Stallman, W. R., 1962. Theory of Aquifer Tests: Water Supply Paper 1536-E.

Finsterle, S., 1999. iTOUGH2 user's guide. Tech. rep., Lawrence Berkeley National Laboratory, Berkeley

Finsterle, S., Zhang, Y., 2011. Solving iTOUGH2 simulation and optimization problems using the PEST protocol. Environmental Modelling and Software 26 (7), 959–968.

Florian Wellmann, J., Croucher, A., Regenauer-Lieb, K., 2011. Python scripting libraries for subsurface fluid and heat flow simulations with TOUGH2 and SHEMAT. Computers & Geosciences.

Joly, A., Martelet, G., Chen, Y., Faure, M., 2008. A multidisciplinary study of a syntectonic pluton close to a major lithospheric-scale fault—Relationships between the Montmarault granitic massif and the Sillon Houiller Fault in the Variscan French Massif Central: 2. Gravity, aeromagnetic investigations, and 3-D geologic modeling. Journal of Geophysical Research 113 (B01404).

Lajaunie, C., Courrioux, G., Manuel, L., 1997. Foliation fields and 3D cartography in geology: Principles of a method based on potential interpolation. Mathematical Geology 29 (4), 571–584.

Langtangen, P. H., 2008. Python scripting for computational science. Springer Verlag, New York.
Lindsay, M., Ailleres, L., Jessell, M., de Kemp, E., Betts, P. G., Apr. 2012. Locating and quantifying geological uncertainty in three-dimensional models: Analysis of the Gippsland Basin, southeastern Australia. Tectonophysics, 1–44.

Marsily, G., 1986. Quantitative hydrogeology: groundwater hydrology for engineers. Academic Press, San Diego.

Maxelon, M., Mancktelow, S. N., 2005. Three-dimensional geometry and tectonostratigraphy of the Pennine zone, Central Alps, Switzerland and Northern Italy. Earth-Science Reviews 71 (3-4), 171–227.

Nilsson, B., Højberg, L. A., Refsgaard, C. J., Troldborg, L., 2007. Uncertainty in geological and hydrogeological data. Hydrology and Earth System Sciences 11 (5), 1551–1561.

Pruess, K., 2005. ECO2N: A TOUGH2 fluid property module for mixtures of water, NaCl, and CO2. Lawrence Berkeley National Laboratory.

Pruess, K., Oldenburg, C., Moridis, G., Aug. 2011. TOUGH2 V2.1 Users Guide, Report LBNL-43134, Lawrence Berkeley National Laboratory, Berkeley, Calif., 1–208.

Pruess, K., Spycher, N., 2007. ECO2N-A fluid property module for the TOUGH2 code for studies of CO2 storage in saline aquifers. Energy Conversion and Management 48 (6), 1761–1767.

Putz, M., Stuwe, K., Jessell, M., Calcagno, P., 2006. Three-dimensional model and late stage warping of the Plattengneis Shear Zone in the Eastern Alps. Tectonophysics 412 (1-2), 87–103.

Refsgaard, J. C., Christensen, S., Sonnenborg, T. O., Seifert, D., Højberg, A. L., Troldborg, L., Feb. 2012. Review of strategies for handling geological uncertainty in groundwater flow and transport modeling. Advances in Water Resources 36 (0), 36–50.

Thore, P., Shtuka, A., Lecour, M., Ait-Ettajer, T., Cognot, R., 2002. Structural uncertainties: Determination, management, and applications. Geophysics 67 (3), 840–852.

Turner, A., 2006. Challenges and trends for geological modelling and visualisation. Bulletin of Engineering Geology and the Environment 65 (2), 109–127.

Wellmann, J. F., Horowitz, F. G., Schill, E., Regenauer-Lieb, K., 2010. Towards incorpor-ating uncertainty of structural data in 3D geological inversion. Tectonophysics 490 (3–4), 141–151.

Geothermal

TOWARDS CLEANER GEOTHERMAL ENERGY UTILIZATION: CAPTURING AND SEQUESTERING CO_2 AND H_2S EMISSIONS FROM GEOTHERMAL POWER PLANTS

Edda S.P. Aradóttir[1], Ingvi Gunnarsson[1], Bergur Sigfússon[1], Gunnar Gunnarsson[1], Einar Gunnlaugsson[1], Hólmfríður Sigurðardóttir[1], Einar Jón Ásbjörnsson and Eric Sonnenthal[2]

[1]Reykjavík Energy, Bæjarhálsi 1, 110 Reykjavík, Iceland
[2]Lawrence Berkeley National Laboratory, 1 Cyclotron Rd, Berkeley, CA 94720, USA
e-mail: edda.sif.aradottir@or.is

ABSTRACT

Field-scale reactive transport models of CO_2 and H_2S mineral sequestration are in development, with a focus on Reykjavík Energy's ongoing gas reinjection tests at Hellisheidi geothermal power plant. A new thermodynamic dataset describing the minerals of interest was developed as a part of this study, since widely used thermodynamic databases did not contain the mineral assemblage needed for the simulations.

Simulations predict efficient precipitation of both CO_2 and H_2S into thermodynamically stable minerals, with calcite and pyrrhotite being the favored carbonate and sulfide sequestering minerals, respectively. Despite only being indicative, we conclude from this study that the capture and sequestration of CO_2 and H_2S from geothermal power plants is a viable option for reducing their gas emissions, and that basalts may comprise ideal geological CO_2 and H_2S storage formations.

INTRODUCTION

Geothermal energy is a sustainable and clean energy source. Its utilization is, however, generally associated with emissions of geothermal gases, like carbon dioxide (CO_2) and hydrogen sulfide (H_2S), to the atmosphere. These emissions remain one of the main environmental concerns of geothermal energy utilization.

CO_2 is the most abundantly emitted greenhouse gas, and reduction of its anthropogenic emissions is among the great challenges of this century (e.g., Broecker, 2007; Oelkers and Cole, 2008). CO_2 emissions from geothermal energy are of volcanic origin and, according to the International Energy Agency, IEA, they are only about 5–6% of the CO_2 emissions from a fossil-fuel-burning power plant of a comparable size. It is, nevertheless, important to aim at reducing CO_2 emissions from geothermal power plants, so that geothermal energy utilization continues to be considered environmentally benign and friendly.

H_2S is a colorless, flammable gas with the characteristic odor of rotten eggs at low concentrations, while being toxic at high concentrations. H_2S concentration in geothermal fluids is usually in the range of few ppb to several hundred ppm (Arnórsson, 1995a; 1995b). A new regulation regarding atmospheric H_2S concentration was issued by the Government of Iceland in 2010 and will become valid in 2014. The regulation is significantly stricter than the WHO (World Health Organization) Air Quality Guidelines (WHO, 2000), as is shown in Table 1, and puts high demands on the geothermal industry in Iceland to reduce atmospheric H_2S concentrations in the vicinity of geothermal power plants.

Table 1 Comparison of H_2S in ambient air standards by WHO and the Icelandic Government.

WHO Air quality guidelines, 2nd Edition :	
Averaging period	**Value ($\mu g/m^3$)**
24 hour	150
30 minute*	7[a]
2010 Icelandic Regulation on atmospheric H_2S concentration:	
Averaging period	**Value ($\mu g/m^3$)**
24 hour**	50[b]
1 year	5

[a] Smell nuisance
[b] May be exceeded 5 times annually until July 2014

Reykjavík Energy, the largest geothermal power company in Iceland, is developing innovative methods aimed at capturing the CO_2 and H_2S currently emitted from its power plants and sequestering the gases as minerals in nearby basaltic formations (Aradóttir et al., 2011 and Gunnarsson et al., 2011). Pilot scale capture and injection tests have already commenced at the Hellisheidi geothermal power plant in southwest Iceland, as a first step towards that goal.

The current paper provides an overview of ongoing CO_2 and H_2S sequestration activities at Reykjavík Energy. Reactive transport models that have been developed of pilot sequestration tests are furthermore discussed, along with results from predictive reactive transport simulations.

CARBFIX AND SULFIX

The Hellisheidi geothermal power plant generates 303 MW_e and 133 MW_{th}, and annually emits some 40,000 and 16,000 tons of volcanic CO_2 and H_2S, respectively, as a by-product of the ongoing energy production. Three experimental pilot projects were commissioned in 2007–2009 as a first step towards minimizing these emissions.

Geothermal gas from the Hellisheiði geothermal field consists primarily of CO_2, H_2S, and H_2, and to a lesser degree of N_2, CH_4, and Ar. A pilot gas separation station has been built next to the power plant. The station scrubs less soluble gases (H_2, N_2, CH_4 and Ar) from the more soluble CO_2 and H_2S. Approximately 3% of the total geothermal gas coming from the power station is currently being separated this way. The gas stream coming from the station consists of approximately 75% CO_2, 24% H_2S and 1% H_2. Two pilot injection projects, CarbFix and SulFix, will use the gas stream for studying the feasibility of sequestering CO_2 and H_2S into minerals within the subsurface.

CarbFix (e.g., Aradóttir et al., 2011; Gíslason et al., 2010; and references therein) is a combined industrial/academic research project between Reykjavík Energy, the Institute of Earth Science at the University of Iceland, Earth Institute-Lamont-Doherty Earth Observatory at Columbia University in New York and the Centre National de la Recherche Scientifique/Universite Paul Sabatier in Toulouse, that was developed in order to assess the feasibility of *in situ* CO_2 mineral sequestration in basaltic rocks. The project involves a pilot injection of at least 1200 tons of the gas mixture coming from the pilot gas separation station.

The CarbFix storage formation lies between 400-800 m depth, is 30-80°C in temperature, and consists of relatively fresh basalts (Aradóttir et al. 2011, Alfredsson et al., 2008). Rather than injecting CO_2 directly into geological formations, CarbFix has developed a technology to dissolve CO_2 into formation fluids and well water during injection. Once dissolved, CO_2 is no longer buoyant compared to pore fluids, minimizing considerably the risk from leakage. This solubility-trapping approach also promotes carbonation of the host rock and thus facilitates the safe long-term sequestration of CO_2 in the subsurface. The dominant aquifer in injection well HN-02 is at 500 m depth, so most of the injected carbonated water should enter the storage reservoir at that depth.

The SulFix project aims as assessing the feasibility of *in situ* H_2S mineral sequestration in basaltic rocks by applying similar methods and technology as CarbFix. The main difference between the projects is that in SulFix, dissolved gases are injected back into the high temperature geothermal reservoir (below 800 m depth), whereas in CarbFix, it is being injected above this level. Furthermore, hot geothermal water (90°C) is used for dissolving gases in SulFix, while relatively fresh, 30°C warm groundwater is used in CarbFix. Aquifer temperature in the SulFix storage formation is around 270°C, and the dominant aquifer in injection well HE-08 is at 1350 m depth.

Different reservoir conditions in SulFix and CarbFix are emphasized in Figure 1, which shows well-logs for SulFix injection well HE-08 and CarbFix injection well HN-02.

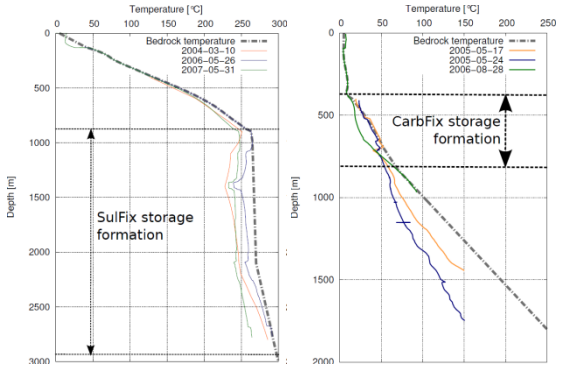

Figure 1. Temperature well logs from SulFix injection well HE-08 (left) and CarbFix injection well HN-02 (right). The SulFix storage formation lies within the Hengill high temperature geothermal system, whereas the CarbFix storage formation lies above it.

Figure 2 shows an aerial map of the CarbFix and SulFix injection sites in Hellisheidi. The well fields shown in Figure 2 comprise ideal conditions for studying the long-term effect of mineral CO_2 and H_2S sequestration in basaltic rocks. Connection to the Hellisheidi power plant provides access to a concentrated source of the gases. Additionally, field data, such as drill cuttings and a calcite cap rock overlying the high-temperature reservoir, suggests mineral CO_2 and H_2S sequestration already playing an important role in the evolution of the Hellisheidi geothermal system (Níelsson, 2010, Gebrehiwot, 2010, and Helgadóttir, 2010). CO_2 sequestration is most intensive from 550 to 800 m depth below surface, while H_2S sequestration is most intensive below 800 m depth. Injecting and precipitating CO_2 and H_2S into nearby formations with the objective of imitating and accelerating natural sequestration processes should therefore be considered an environmentally benign process.

Injection of otherwise emitted CO_2 and H_2S commenced in 2012 and Hellisheidi power plant became consequently one of the very few worldwide power plants that operate a full CCS cycle.

REACTIVE TRANSPORT MODELS

Numerical modeling plays an important role in the CarbFix and SulFix projects, because it provides tools for predicting and optimizing long-term management of injection sites, as well as quantifying the amount of CO_2 and H_2S that can be mineralized. The following subsections describe reactive transport models developed for the CarbFix and SulFix experiments.

CarbFix model

Two and three-dimensional reactive transport models have been developed of the CarbFix pilot injection. Aradóttir et al. (2012a) describe in detail conceptual and numerical models of the CarbFix injection site; a short summary is given below.

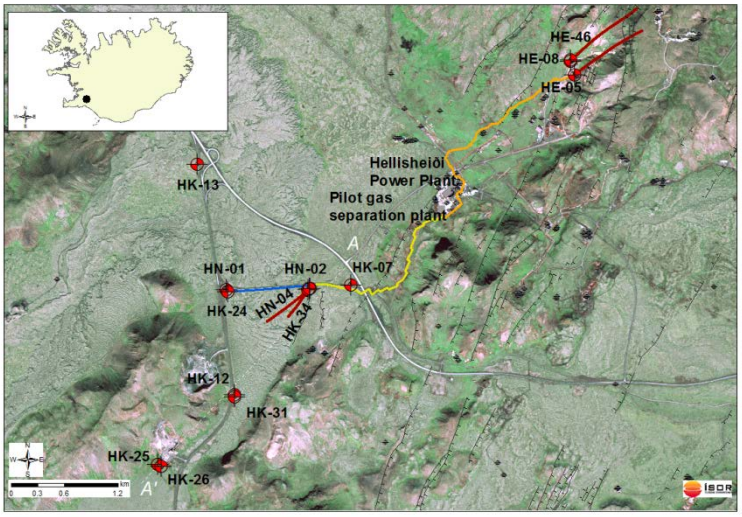

Figure 2. Aerial map of the CarbFix and SulFix injection sites. Gas mixture consisting of 75% CO_2, 24% H_2S and 1% H_2 will be transported in a pipeline towards the CarbFix (yellow line) and SulFix (orange line) injection sites. HN-02 and HE-08 are CarbFix and Sulfix injection wells, respectively. Other wells are observation wells. Fresh groundwater, used for dissolving gases in CarbFix, will be pumped from well HN-01 and transported to well HN-02 (blue line). Separated geothermal water from HE-05 will be used for dissolving gases in SulFix. Well deviation is depicted by red lines. Combed lines represent faults.

Flow setup

Tracer tests that have been ongoing at the CarbFix injection site since 2007 show that most of the storage formation consists of a relatively homogeneous porous media. A low volume and fast breakthrough path channels only about 3% of the tracer flow between injection well HN-02 and observation well HN-04. Fracture flow thus plays a minor role in the storage formation. In view of this, it was decided to develop the CarbFix numerical models as single porosity models representing the dominant matrix flow in the storage formation.

Models were aligned in the direction of regional groundwater flow, from NE-SW. Hydrological properties of the storage formation were calibrated against a large set of field data using iTOUGH2. Resulting principal hydrological properties are lateral and vertical intrinsic permeabilities of 300×10^{-12} m^2 and 1700×10^{-12} m^2, respectively, effective matrix porosity of 8.5% and a 25 m/year estimate for regional groundwater flow.

Geochemical setup

Aradóttir et al. (2011) carried out an extensive literature review of water-basalt interaction at low and elevated CO_2 conditions, with the objective of predicting which minerals are likely to dissolve and precipitate during *in situ* CO_2 mineral sequestration. Widely used thermodynamic databases did not contain the mineral assemblage needed for successfully simulating the alteration processes observed in nature, since important primary and secondary minerals were missing (Aradóttir et al., 2012b). Aradóttir et al. (2012b) thus developed and evaluated a thermodynamic dataset describing 36 mineral reactions of interest for CO_2-water-basalt interaction. All minerals in the database were compiled to the CarbFix numerical models, along with kinetic variables describing their dissolution and precipitation. Four primary minerals and/or glasses were used in CarbFix simulations; Plagioclase, Pyroxene, Olivine and basaltic glass. (See Aradóttir et al., 2012a for more detail and references.)

Simulations

Reactive chemistry was coupled to calibrated hydrological models and predictive mass transport and reactive transport simulations carried out for both a 1200-ton pilot CO_2 injection and a full-scale 400,000-ton CO_2 injection scenario. Pure CO_2 was assumed to be injected in the simulations, and the effects of H_2S and H_2 in the gas mixture that is actually being injected were thus neglected.

SulFix model

Development of reactive transport models for the SulFix project has only recently begun; the models are consequently not as complex as the CarbFix models, and results are preliminary.

Flow setup

A tracer test carried out in 2010 indicates a fast flow path between SulFix injection well HE-08 and observation well HE-46, indicating fracture flow to be dominant in the storage formation (Gunnarsson et al., 2011, and Scott et al., 2011). Fractures are, however, connected to a porous matrix that contains the majority of the reactive surface area in the storage formation.

In view of this, it was decided to use a one-dimensional dual porosity model as a first approach to simulating the SulFix injection. Figure 3 shows a simple schematic of the conceptual model along with an illustrative representation of elements and connections.

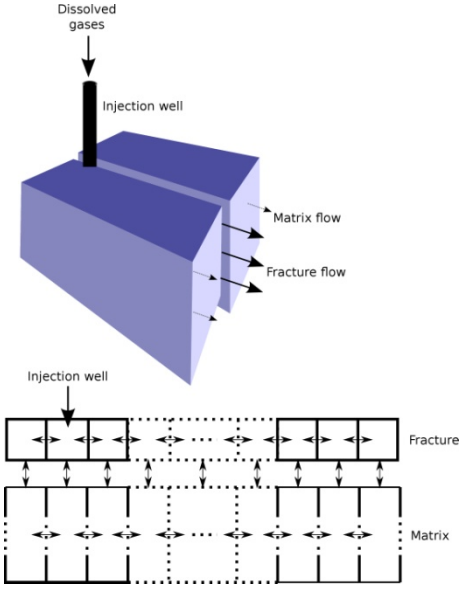

Figure 3. Schematic of the conceptual one-dimensional dual porosity model used for SulFix simulations (top) and illustration of elements and connections in the developed model (bottom).

Fracture permeability was calculated to be 733×10^{-12} m^2, by assuming laminar flow and fracture diameter of 2 mm. Matrix porosity was assumed to be 2.5%, and the assumed matrix permeability of 0.02×10^{-12} m^2 is that of the Hengill reservoir model at a corresponding depth (Gunnarsson et al., 2011).

Geochemical setup

The thermodynamic dataset developed for CarbFix by Aradóttir et al. (2012b) was used as a basis for a thermodynamic database for SulFix simulations. Several minerals needed to be added to the dataset, since the alteration mineralogy associated with the injection is different from that in CarbFix, due to additional H_2S-water-basalt interaction and a considerably higher reservoir temperature.

Minerals added to the database were epidote, goethite, grossular, magnetite, prehnite, pyrite, pyrrhotite, sulfur and wollastonite. $Fe(OH)_4^-$ was furthermore added as a primary species. Data for $Fe(OH)_4^-$ was taken from Diakonov et al. (1999) and SUPCRT92 used for calculating logK values at discrete temperatures. Thermodynamic data for goethite and magnetite was taken from Holland and Powell (1998), and SUPCRT was used for calculating logK values for corresponding dissolution reactions. Equilibrium constants for other minerals were taken from Stefánsson et al. (2009).

Kinetic variables describing dissolution of epidote, goethite, grossular, magnetite, prehnite and wollastonite were taken from Palandri and Kharaka (2004). Mineral precipitation was represented using the same kinetic expression as that for dissolution. Kinetic variables describing dissolution and/or precipitation of sulfur, pyrite, and pyrrhotite at reducing conditions were not found in the literature. These minerals had thus to be assumed to precipitate and dissolve under equilibrium.

Basaltic glass (Oelkers and Gíslason, 2001 and Gíslason and Oelkers, 2003) was the only primary mineral used in SulFix simulations.

Simulations

Predictive simulations were carried out of a 6-month continuous pilot injection. Gas mixture containing 75% CO_2, 24% H_2S, and 1% H_2 was dissolved in 10 kg/s HE-05 water and continuously injected into well HE-08. Simulation of water-rock interaction was then continued for up to 10 years.

RESULTS

CarbFix model

Reactive transport simulations of the 1200 ton pilot injection predict 85% CO_2 mineral capture within 5 years and 100% capture within 10 years. Simulations of the full-scale injection scenario predict 80% CO_2 mineral capture after 100 years. CO_2 sequestration rate is predicted to range between 1200 and 22,000 tons/year in both scenarios, a value in good agreement with the natural sequestration rate of the Hellisheidi geothermal system, which has been estimated to be 4100–23,500 tons/year. Relatively fresh basaltic formations are thus predicted to be promising geological CO_2 storage formations.

Figure 4 shows a cross-sectional view of modeled reservoir HCO_3^- concentration in the pilot injection scenario, as predicted by three-dimensional reactive transport simulations. The figure indicates how injected carbonated water travels downstream as a plume with regional groundwater flow. Carbonate precipitation leads to significant dilution of the plume within five years and its disappearance within 10 years.

Calcite is predominantly the most abundant carbonate to form in reactive transport simulations, which is in agreement with natural basalt alteration in Iceland. Magnesite-siderite solid solution also precipitates, but in significantly lower quantities. Figure 5 shows a cross-sectional reservoir view of calcite precipitation after five years simulation time in the pilot injection scenario. $SiO_{2(am)}$, quartz and antigorite (Gunnarsson et al., 2005) precipitation is associated with calcite precipitation in the simulations, which is in agreement with natural alteration in the vicinity of mineral springs in Iceland.

Ca leached from primary minerals is modeled to preferentially form calcite rather than zeolites, while clay minerals, simple oxides, and oxyhydroxides are predicted to compete with magnesite–siderite solid solution for leached Mg and Fe.

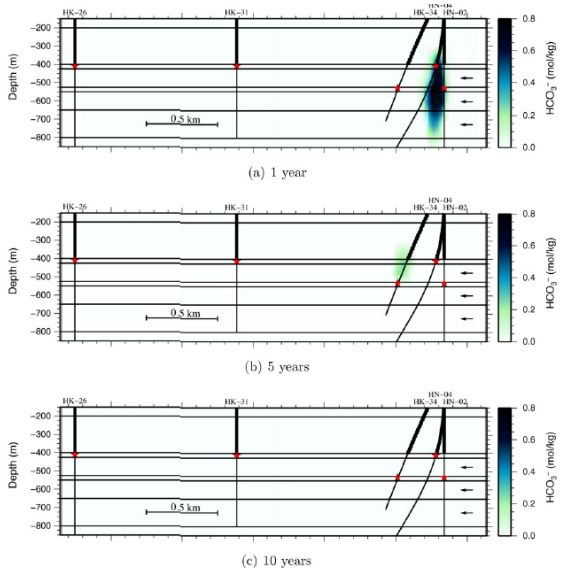

Figure 4: Cross sectional view of modeled reservoir HCO_3^- concentration in the pilot injection scenario after 1, 5 and 10 years, as predicted by three-dimensional reactive transport simulations. Cross sections are drawn along A-A' on figure 2. (Figure from Aradóttir et al, 2012a).

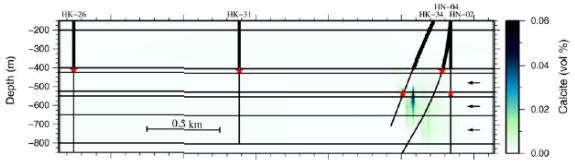

Figure 5: Cross sectional view of modeled calcite precipitation in the pilot injection scenario after 5 years simulation time.The cross section is drawn along A-A' on figure 2. (Figure from Aradóttir et al, 2012a).

SulFix model

Predictive simulations of the pilot SulFix injection show injected H_2S to be sequestered into pyrrhotite. Pyrrhotite is a part of the mineral buffer assemblages believed to control H_2S concentrations in geothermal systems, so, to that extent, simulated results are in agreement with observations from nature (Stefánsson, 2011).

Magnesite-siderite solid solution precipitation provides the primary CO_2 sink in the SulFix reservoir.

Other minerals that form in simulations are quartz, simple oxides and oxyhydroxides, magnetite, wollastonite, and clays.

Clay minerals, magnetite, and siderite appear to be competing with pyrrhotite for Fe leached from the primary basaltic glass. Precipitation of secondary minerals occurs both within the fracture and the matrix continuum.

DISCUSSION

It is interesting to compare simulated CO_2 sinks in CarbFix and SulFix simulations. Calcite is predominantly the most abundant carbonate to form in the CarbFix reservoir, while magnesite-siderite solid solution precipitation provides the primary CO_2 sink in the SulFix reservoir. This is in agreement with well drill cuttings from Hellisheidi, which indicate calcite stability decreasing around 270°C (e.g., Helgadóttir et al., 2010). CarbFix and SulFix simulations were carried out at 25–90°C and 270°C, respectively. Thermodynamic data used for carbonates in the simulations is thus able to capture natural behavior of carbonate minerals.

Various indications point towards it not being feasible to inject large quantities of CO_2 along with H_2S into deep and hot formations, if the objective is to sequester H_2S. On the one hand, more water is needed for dissolving the gas mixture than purer H_2S, as CO_2 is less soluble than H_2S. On the other, calcite is no longer the primary CO_2 sink under such reservoir conditions, but rather magnesite-siderite, a solid solution that competes with pyrrhotite and pyrite for Fe. The competition reduces the efficiency of mineral H_2S sequestration. The above arguments support the separation of CO_2 and H_2S prior to injection.

Concentration of H_2S in aquifer fluids in Hellisheidi appears to be controlled by mineral buffer assemblages. Pyrite, prehnite, pyrrhotite and epidote or pyrite, pyrrhotite and magnetite have been identified as potential governing mineral buffers (Gunnarsson et al., 2011 and Stefánsson et al., 2011). Stefánsson et al. (2011) concluded that H_2S concentrations in Hellisheidi equilibrate to the prehnite-bearing mineral assemblage, because Icelandic geothermal areas are usually low in magnetite, indicating that it is unstable in Icelandic geothermal systems. This is not in agreement with SulFix reactive transport simulations, in which magnetite and

pyrrhotite buffered injected H_2S but not prehnite, epidote, and pyrite. This suggests that the thermodynamic data used for describing the above mineral assemblages should be critically evaluated in future work.

It is furthermore important to acquire data describing the kinetics of H_2S precipitation into minerals, as it is not reasonable to describe it only through thermodynamics. Additional sulfur-bearing minerals such as mackinawite (FeS) and greigite (Fe_3S_4) might also be important in simulating H_2S sequestration in basaltic aquifers: studies have shown these minerals to be stable under anoxic conditions, which persist in Hellisheidi (e.g., Cahill et al., 2000; Benning et al., 2000).

CONCLUSIONS

Reactive transport simulations carried out in this study indicate *in situ* CO_2 and H_2S mineral sequestration in basalts to be a viable option in reducing gas emissions from geothermal power plants, as they predict fast mineralization of injected gases.

ACKNOWLEDGMENT

We would like to thank Einar Örn Þrastarson, Trausti Kristinsson and Magnús Þór Arnarson for their never-ending contribution to CarbFix and SulFix. We are furthermore grateful to all our CarbFix collaborators for a challenging and fruitful cooperation since 2007. This work was funded by Reykjavík Energy, the 7th Framwork Programme of the EC (project no. 283148) and Geothermal Research Group GEORG (09-02-001).

REFERENCES

Alfredsson HA, Hardarson BS, Frnzson H and Gíslason SR, CO2 sequestration in basaltic rock at the Hellisheidi site in SW Iceland: Stratigraphy and chemical composition of the rocks at the injection site, *Mineral Mag 72*; 1-5 (2008).

Aradóttir ESP, Sigurdardóttir H, Sigfússon B and Gunnlaugsson E. CarbFix: a CCS pilot project imitating and accelerating natural CO_2 sequestration, *Greenhouse Gas Sci Technol. 1*: 105-118, 2011.

Aradóttir ESP, Sonnenthal EL, Björnsson G and Jónsson H, Multidimensional reactive transport modeling of CO2 mineral sequestration in basalts at the Hellisheidi geothermal field, Iceland, *Int J Greenhouse Gas Cont 9*: 24-40, 2012a.

Aradóttir ESP, Sonnenthal EL and Jónsson H, Development and evaluation of a thermodynamic dataset for phases of interest in CO2 mineral sequestration in basaltic rocks, *Chemical Geology 304-305*, 26-38, 2012b.

Arnórsson S., Hydrothermal systems in Icelands: Structure and conceptual models. 1. High-temperature areas, *Geothermics 24*, 561-602, 1995a.

Arnórsson S, Hydrothermal systems in Icelands: Structure and conceptual models. 2. Low-temperature areas, *Geothermics 24*, 603-629, 1995b.

Benning LG, Wilkin RT and Barnes HL, Reaction pathways in the Fe-S system below 100°C, *Chem. Geol. 167*: 25-51, 2000.

Broecker WS, Climate change: CO2 arithmetic. *Science 315*: 1371, 2007.

Cahill CL, Benning LG, Barnes HL and Parise JB, In situ time-resolved X-ray diffraction of iron sulfides during hydrothermal pyrite growth, *Chem. Geol. 167*: 53-63, 2000.

Diakonov I, Schott J, Martin F, Harrichourry JC and Escalier J, Iron(III) solubility and speciation in aqueous solutions. Experimental study and modeling: Part 1. Hematite solubility from 60 to 300°C in NaOH-NaCl solutions and thermodynamic properties of $Fe(OH)_4^-(aq)$, *Geochim et Cosmochim Acta 63*, 2247-2261, 1999.

Gebrehiwot K, Koestono H, Franzson H and Mortensen AK, Borehole Geology and Hydrothermal Alteration of Well HE-24, Hellisheidi Geothermal Field, SW-Iceland, *Proeedings World Geothermal Congress*, 2010.

Gíslason SR and Oelkers EH, Mechanisms, rates and consequences of basaltic glass dissolution:

II. An experimental study of the dissolution rates of basaltic glass as a function of temperature, *Geochim. Cosmochim. Acta 67*: 3817-3832, 2003.

Gíslason SR, Wolff-Boenisch D, Stefánsson A, Oelkers EH, Gunnlaugsson E, Sigurdardóttir H et al., Mineral sequestration of carbon dioxide in basalt: A pre-injection overview of the CarbFix project, *Int J Greenhouse Gas Cont 4*: 537-545, 2010.

Gunnarsson G, Arnaldsson A and Oddsdóttir AL, Model Simulations of the Hengill Area, Southwestern Iceland, *Transp Porous Med 90* 3-22, 2011

Gunnarsson I, Arnórsson S and Jakobsson S, Precipitation of poorly crystalline antigorite under hydrothermal conditions, *Geochim Cosmochim Acta 69*, 2813-2828, 2005.

Gunnarsson I, Sigfússon B, Stefánsson A, Arnórsson S, Scott SW and Gunnlaugsson E, Injection of H_2S from Hellisheidi power plant, Iceland, *Proceedings, 36th Workshop on Geothermal Reservoir Engineering*, 2011.

Helgadóttir HM, Snaebjörnsdóttir SO, Níelsson S, Gunnarsdóttir SH, Matthíasdóttir T, Hardarson BS, Egilsson GM et al., Geology and Hydrothermal Alteration in the Reservoir of the Hellisheidi High Tempterature System SW-Iceland, *Proceedings World Geothermal Congress*, 2010.

Holland T and Powell R, An internally consistent thermodynamic data set for phases of petrological interest, *J. Metam. Geol. 16*, 309-343, 1998.

Níelsson S and Franzson H, Geology and Hydrothermal Alteration of the Hverahlíd HT-System, SW-Iceland, *Proceedings World Geothermal Congress*, 2010.

Oelkers EH and Gíslason SR, The mechanisms, rates and consequences of basaltic glass dissolution: I. An experimental study of the dissolution rates of basaltic glass as a function of aqueous Al, Si and oxalic acid concentrations at 25°C and pH = 3 and 11, *Geochim. Cosmochim. Acta 65*: 3671-3681, 2001.

Oelkers EH and Cole DR, Carbon dioxide sequestration: A solution to a global problem. *Elements 4*: 305-310, 2008.

Palandri J and Kharaka Y, *A compilation of rate parameters of water-mineral interaction kinetics for application to geochemical modeling*, Report 2004-1068, USGS, 2004.

Scott S, Gunnarsson I, Arnórsson A and Gunnlaugsson E, Gas Chemistry of the Hellisheidi Geothermal Field, SW-Iceland, *Proceedings, 36th Workshop on Geothermal Reservoir Engineering*, 2011.

Stefánsson A, Arnórsson S, Gunnarsson I, Kaasalainen H and Gunnlaugsson E, The geochemistry and sequestration of H2S into the geothermal system at Hellisheidi, Iceland, *J. Volcanol. Geoth. Res. 202*: 179-188, 2011.

Stefánsson A, Arnórsson S, Gunnarsson I, Kaasalainen H, *H_2S disposal at Hellisheidi Power Plant: A Geochemical Study*, Report RH-14-2009, Science Institute of the University of Iceland, 2009 [in Icelandic].

World Health Organization, Regional Office for Europe, *Air quality guidelines for Europe*, European Series No. 91, Copenhagen, Denmark, 146 pp, 2000.

IMPLEMENTATION OF ANISOTROPIC FLOW INTO THE TOUGH2 CODE

[1]Andri Arnaldsson, [1]Jean-Claude Berthet, [1]Snorri Kjaran, [2]Sven Þ. Sigurðsson

[1]Vatnaskil Consulting Engineers
Suðurlandsbraut 50
108 Reykjavík, Iceland
[2]School of Engineering and Sciences, University of Iceland
Hjarðarhagi 7
107 Reykjavík, Iceland
e-mail: andri@vatnaskil.is

ABSTRACT

Characteristics of groundwater flow in porous media can be heavily influenced by local anisotropy in intrinsic permeability. Therefore, the ability of a numerical model to properly simulate anisotropy is vital in designing a well-calibrated model capable of predicting the response of a system under stress. A new numerical scheme for fully tensorial treatment of anisotropic flow within model layers (2D) has been designed and implemented into the TOUGH family of simulators. Previously, the TOUGH simulators were only able to accurately resolve anisotropic flow in two cases, i.e., when the connections between two gridblocks were either along the principal direction or along a streamline.

A simulation using the new anisotropic scheme is activated by a MOP parameter and the existence of two new data blocks in the TOUGH input file. The first block (ANISO) contains the gridblock name, coordinates, permeability values along the first and second principal axes, and the angle of the principal direction from the local x-axis. The second block (SEGST) lists the gridblocks for each connection needed to calculate the additional flow gradients in the Jacobian matrix, along with a vector along the interface between the neighboring gridblocks.

Testing has shown that the new scheme adds approximately 16% to the execution time of multiphase (water and steam) simulations using the TOUGH2 simulator. In order to account for anisotropy between two gridblocks, flow from neighboring gridblocks must be incorporated into the calculations as well, resulting in more off-diagonal elements in the Jacobian matrix. About 33% of the execution time is used for constructing the Jacobian matrix elements, and another 25% is used for sorting the array containing the matrix elements during each iteration.

The new scheme has been rigorously tested against simple theoretical solutions to Darcy's law, as well as more complicated examples solved by numerical software packages with anisotropic flow capabilities. In all cases, a good agreement with the new scheme has been found.

This work has been performed as a part of a MoU (Memorandum of Understanding) between the Earth Sciences Division of Lawrence Berkeley National Laboratory and Vatnaskil Consulting Engineers.

INTRODUCTION

Here, we present a short description of the numerical scheme that has been implemented into the TOUGH2 simulator. For simplification, the emphasis will be on horizontal two-dimensional flow.

Consider a general mesh as shown in Figure 1. The goal is to calculate the flow through the face *st* connecting elements (gridblocks) O and B by including full permeability anisotropy. The mesh was generated with a Voronoi tessellation (de Berg, 2000) which guarantees that the line connecting the interior "central" points O and B will be perpendicular to the line *st* and will be exactly halved by that line. Note, on the other hand, that the line segment *st* will in general not be halved by the line OB, and the line OB may indeed intersect *st* at a point exterior to the segment *st*.

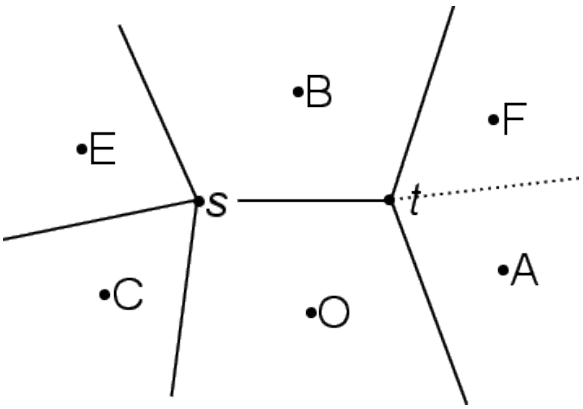

Figure 1. A general Voronoi mesh. The aim is to calculate the flow through the line segment *st* connecting points O and B.

The figure defines the points O, B, C, E, A, F, which are the centers of elements surrounding the edge (interface area) in question. Points *s* and *t* are defined as the vertices of the edge. Elements C and E will always be in contact with edge *st* through vertex *s*, and elements A and F will always be in contact through vertex *t*. Elements A and C will always be the elements sharing an edge with Element O. Elements E and F will always be elements sharing an edge with Element B. When one vertex of the edge *st* is on an outer boundary of the region, it will always be vertex *t*, and thus vertex *s* will be inside the region. Moreover, in such cases, elements A and F will not exist.

Within our implementation, all information pertaining to the elements are stored in arrays in the following order: O, B, C, E, A, F. The inclusion of the additional points, A, C, E, and F, serves to obtain an approximation of the gradient for the pressure along the edge *st*, which in turn allows us to take into account the anisotropy when calculating the flow across the edge. This approximation of the gradient is a linear combination of the approximate gradients in the triangular planes OBE, OBF, BOA, and BOC. Following this setup, the flow through *st* can be compactly represented as (Sigurðsson, 2009)

$$\mathrm{F} = \frac{k_r \rho}{\mu}\left[\alpha_O\ \alpha_B\ \alpha_C\ \alpha_E\ \alpha_A\ \alpha_F\right]\begin{bmatrix} P_O \\ P_B \\ P_C \\ P_E \\ P_A \\ P_F \end{bmatrix} \qquad (1)$$

with k_r, ρ, and μ as the relative permeability, density, and viscosity, respectively. The *P* vector represents pressure at each element center. As an example, an element in the vector α is of the form

$$\alpha_O = \frac{h}{4}\left[s_y - t_y \quad s_x - t_x\right]\begin{bmatrix} k_x & k_{xy} \\ k_{xy} & k_y \end{bmatrix} \left[\begin{array}{l} \frac{1}{2\lvert OCB\rvert}\begin{bmatrix} C_y - B_y \\ B_x - C_x \end{bmatrix} + \frac{1}{2\lvert OAB\rvert}\begin{bmatrix} B_y - A_y \\ A_x - B_x \end{bmatrix} + \\ \frac{1}{2\lvert OEB\rvert}\begin{bmatrix} E_y - B_y \\ B_x - E_x \end{bmatrix} + \frac{1}{2\lvert OFB\rvert}\begin{bmatrix} B_y - F_y \\ F_x - B_x \end{bmatrix} \end{array}\right] \qquad (2)$$

Here, h is the model or layer thickness and k_x, k_y, k_{xy}, the elements of the permeability tensor, are:

$$k_x = k_n \cos^2\theta + k_t \sin^2\theta \qquad (3)$$

$$k_y = k_n \sin^2\theta + k_t \cos^2\theta \qquad (4)$$

$$k_{xy} = (k_n - k_t)\sin\theta\cos\theta \qquad (5)$$

where k_n and k_t (Strack, 1989) are the permeability values along the principal directions and θ is the angle of the first principal direction from the x-axis. At the boundaries, the α values are calculated in a different manner. With vertex *t* being on the boundary (see Figure 1), triangles OAB and OFB are missing. Therefore, the contributions from triangles OCB and OEB are doubled. When the vertices are in contact with only three elements, the C term is equal to E and A is equal to F.

CHANGES TO THE CODE

Subroutine INPUT

Two sections have been added to subroutine INPUT: ANISO (label 3200) and SEGST (label 3300). New common blocks have been added to the program to store the extra data required by the anisotropic method, including the element coordinates, the permeability tensors, and the interface area vectors *st*. When the anisotropy method is used, up to six elements may contribute to the flow along a connection, as opposed to only two elements when the isotropic method is used. New common blocks have been added to subroutine INPUT and to the program to store data for the extra elements. Note that for a connection, the elements in arrays ELEM1, ... and NEX1, ... must correspond, respectively, to elements O, B, C, E, A, F. When close to a boundary, ELEM5 and ELEM6 shall be left

blank, and NEX5 and NEX6 will be set to zero by the program.

Two new sections were added to the subroutine to parse the new input blocks, ANISO and SEGST. The format of the new blocks is discussed later in this article.

Subroutine ANISOTROPY

Subroutine ANISOTROPY is triggered when a block ANISO is detected in the input. It is possible, though, to force the run in either isotropic or anisotropic mode by means of a MOP parameter. The new subroutine is called from subroutine MULTI to supplant the loop over connections implemented there. The loop has been implemented again in the new subroutine, ANISOTROPY, and has a structure similar to that of the original code. It includes a flux loop to calculate the finite differences required to build the Jacobian matrix of the residuals (Pruess, 1999). Including anisotropy introduces additional non-zero elements into the Jacobian matrix. For instance, in the isotropic case, the Jacobian element for the neighboring elements B and C is zero. In the anisotropic case, it is no longer zero, since the flow between elements O and B depends on the pressure in Element C. Note, however, that these additional elements in the Jacobian only depend on physical parameters in the regions surrounding points O and B, since the additional points only serve to obtain an approximation of the gradient of the pressure along the edge *st*. Therefore, no extra finite difference is required to compute the new Jacobian elements, since the flow across segment *st* is a linear function of the pressure in elements C, E, F, A (i.e., in Equation 1, the permeability, viscosity, and density are functions of P_O and P_B but not of P_C, P_E, P_F, and P_A).

ADDITIONAL INPUT

Two extra data blocks are required to run a simulation using anisotropy. Throughout this work, AMESH (Haukwa, 1998) was used to generate the necessary input for TOUGH2. An external program was then used to convert the output data produced by AMESH into input data needed for anisotropy.

Block ANISO

Block ANISO has the following structure:

- element names (columns 1 to 5),
- element *x*, *y,* and *z* coordinates (6 to 20, 21 to 35, 36 to 50),
- permeability along first and second principal axes (51 to 60, 61 to 70),
- angle between first principal axis and axis *x* (71 to 80).

Block ANISO must always come after block ELEME, and the elements must be in the same order.

Block SEGST

Block SEGST has the following input:

- names of elements O, B, C, E, A, F (columns 1 to 30, five characters each),
- *x* and *y* coordinates of vector *st* (31 to 45, 46 to 60).

Block SEGST must come after block CONNE, and the connections must be in the same order. A line with four elements (A and F blank) indicates that the connection is next to a boundary. A line with two elements means that the connection is parallel to the *z* axis, which will always be treated as the vertical (as well as a principal) axis. Note that in such a case, the vector *st* is not used by the program. An interface area vector *st* must never be zero.

Care must be taken that block SEGST is consistent with the data provided in block CONNE. Connections in the *xy* plane must have their ISOT number set to 1 or 2. These connections will be treated anisotropically using the permeability provided in input block ANISO. Connections parallel to *z* must have their ISOT number set to 3. Those connections will be treated isotropically using the permeability provided in input block ROCKS. BETAX, the cosine of the angle between the connection and the gravity axis, must be zero for the *xy* connections (ISOT 1 or 2), and 1 or -1 for the *z* connection (ISOT 3). Parameters PER(1) and PER(2) in block ROCKS are not used in the simulation, since the permeability values for connections in the *xy* plane are defined in the ANISO block.

PROFILING AND PERFORMANCE

A test performed on a hypothetical multiphase system reveals that the anisotropic method is about 16% slower than the original isotropic method. About 25% of the computation time is used in sorting the array containing the Jacobian elements (array CO). Since array CO is always filled in the same disordered manner, computation time could be reduced by implementing a system that memorizes the positions of the elements after sorting. This would require the array to be ordered only once at the beginning of the simulation.

In the original isotropic implementation of TOUGH2, array CO is sorted inside the solver. Our anisotropic implementation requires the array to be sorted earlier. To prevent the solver from attempting to sort the array again, a Boolean parameter SORTED was added to the solver subroutines. The parameter is used to inform the solver that it is unnecessary to sort the array again. This new feature reduces computation time by several percentage points.

About 33% of the computation time is spent in subroutine ANISOTROPY, which contains the essential lines of code needed to implement anisotropy, excluding the sorting algorithm. Averaging of the absolute permeability is performed according to the definitions in MOP(11).

EXAMPLES

Four examples are presented in this section. Each one validates the correct implementation, or re-implementation when necessary, of different sections and/or features of the program. To begin, we shall discuss the comparison with the Theis solution in order to verify our approach.

Comparison with Analytical Theis Solution

The Theis solution gives the drawdown in an infinite homogeneous aquifer under constant pumping (Bear, 1979). It is represented here in the form of pressure change as a function of several parameters that are either TOUGH2 input parameters or parameters generated by the equation of state module (EOS1) in TOUGH2:

$$\Delta P = \frac{Q}{4\pi T\beta} W\left(\frac{S}{4Tt}\left(u_1^2 + \frac{1}{\beta^2}u_2^2\right)\right) \qquad (5)$$

Here, T is the aquifer transmissivity (m^2/s), S is the aquifer storage coefficient, Q is the production rate (kg/s), t is the time (s) and u_1 and u_2 are the coordinates in the principal coordinate system. When the coordinates differ from the canonical x and y system, the coordinates must be rotated according to:

$$u_1 = x\cos\theta + y\sin\theta \qquad (6)$$
$$u_2 = -x\sin\theta + y\cos\theta \qquad (7)$$

with θ as the angle between u_1 and x. The well function, W, is in this case the exponential integral (Abramowitz et al., 1965)

$$W(x) = \int_{-\infty}^{x} \frac{e^t}{t} dt \qquad (8)$$

A test was performed using a simple one-layer square mesh of size 5000×5000 m^2 consisting of elements of size 50×50 m^2. Using a mesh consisting of regular hexagonal elements with 80 m side length provided identical results. A sink was attached to an element close to the center, producing 10 kg/s of water. The model consisted of an anisotropic rock having permeability values along its principal axes of 10^{-14} and 10^{-15} m^2. The angle between the first axis and the x axis was set to 0.2π rad. The porosity was set to 0.1. Initial pressure was set to 50 bar and initial temperature to 220°C for all elements.

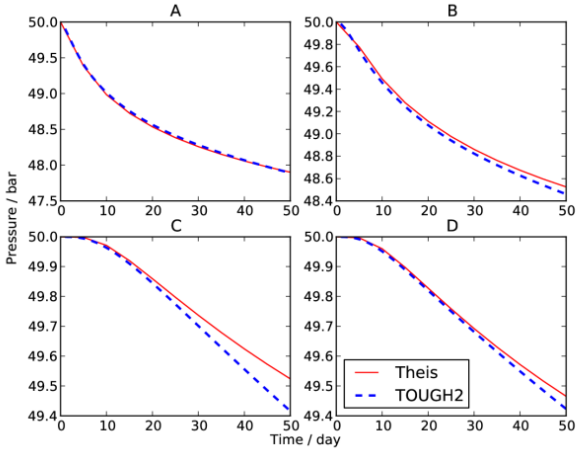

Figure 2. Comparison between TOUGH2 (including anisotropy) and the Theis solution for anisotropic aquifer at four different points.

The pressure was recorded at four different points within the model during a run of 50 days. The results are shown in Figure 2. A contour plot of the simulated pressure across the model area at the end of the 50 days is shown in Figure 3. The location of the four different calibration points is also shown in Figure 3.

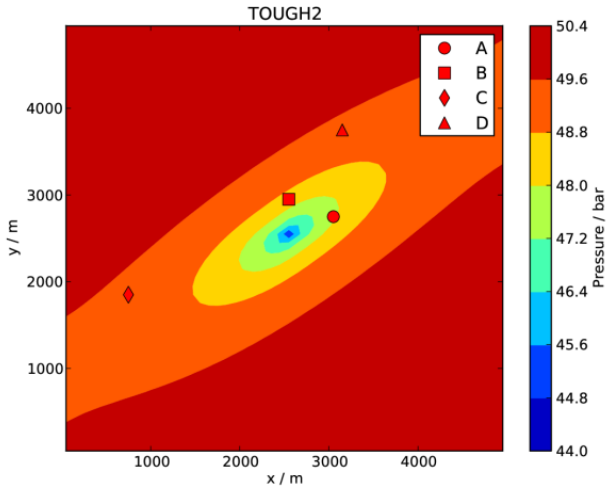

Figure 3. Areal plot of simulated pressure contours generated by TOUGH2 after 50 days. The red symbols show the locations of the four calibration points represented in Figure 2.

The results of the TOUGH2 simulation plotted in Figure 2 show good agreement with the Theis solution. As the simulation time progresses, the curves begin to diverge due to the no-flow boundaries used in the TOUGH2 model. The Theis solution assumes an aquifer of infinite extent. The discrepancy becomes more prominent closer to the boundary as time passes.

The comparison with the Theis solution confirms the correct behavior of the method and implementation presented here.

Immobile Water

In this and all subsequent examples, the calculations were performed on a rectangular mesh grid with 50 m between two adjacent points and a total area of 4750×4750 m^2.

Here, the new implementation is compared to the original TOUGH2 code by setting the permeability values to $k_x = 10^{-13}$ m^2, $k_y = 10^{-11}$ m^2 and rotating the principal axes along x and y axes to allow for direct comparison. The following example represents a two-phase system in which the water phase is immobile due to a low saturation level (below the residual saturation) (Grant, 1982). A producing well located at $(x,y) = (0,0)$ m produced at a constant rate of 30 kg/s. All boundaries are assumed to be impermeable (no flow).

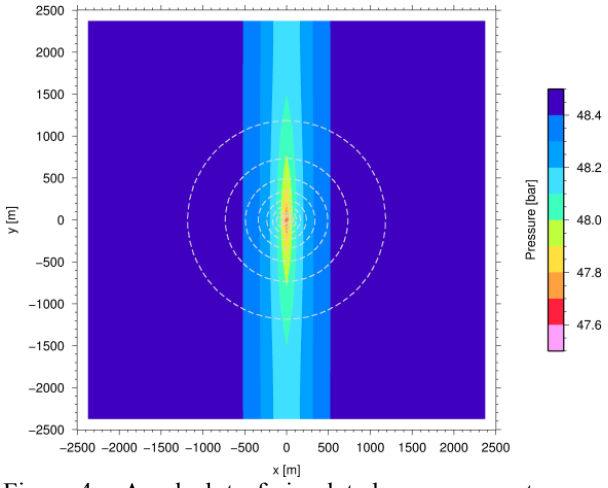

Figure 4. Areal plot of simulated pressure contours generated by TOUGH2 after five days of producing at a constant rate of 30 kg/s. The dotted circles represent the pressure decline cone without anisotropy.

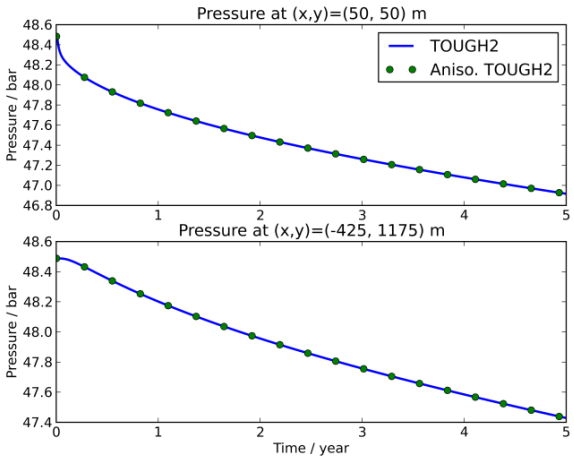

Figure 5. Comparison between the original and anisotropic methods in TOUGH2 for a system containing both liquid water and steam. The principal permeability axes are along x and y and the mesh rectangular to allow comparison between the two different methods.

Figure 4 shows the simulated pressure contours after five days of production. Figure 5 shows the comparison of pressure at two different

calibration points within the mesh. The results produced by the two different methods show that the methods agree to at least three significant digits at all times.

Five Different Regions

The following example compares TOUGH2 with the single-phase flow program Aqua3D (http://www.vatnaskil.is/softwaredevelopment/aqua3d-). Aqua3D is based on a finite element approximation with basis function on a triangular mesh. Aqua3D can properly handle anisotropy. Great care was taken to make the two simulations (TOUGH2 and Aqua3D) as similar as possible. Some discrepancy is to be expected, since the physical properties calculated by the EOS1 module may not exactly correspond to the constant values assumed by Aqua3d at all times.

This example consisted of a model containing five regions, each with different physical rock properties. The mesh was divided into a background region plus four additional rectangular regions (Figure 6). A producing well was located at $(x,y) = (0,0)$ m and produced at a constant rate of 30 kg/s.

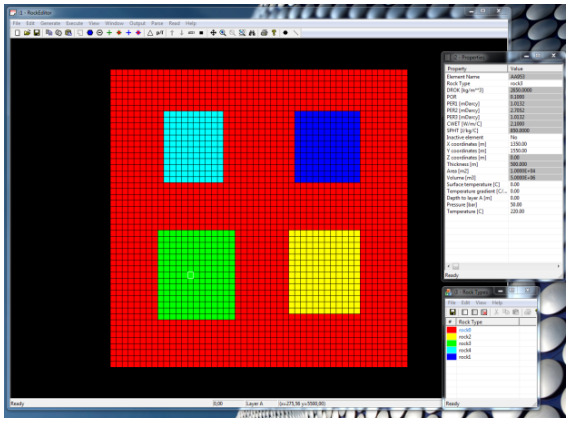

Figure 6. Hypothetical reservoir consisting of five different rock types.

The different rock properties were described by four parameters: porosity, permeability (along the primary principal axis), permeability ratio (between the two principal axes), and angle between the primary axis and the abscissa.

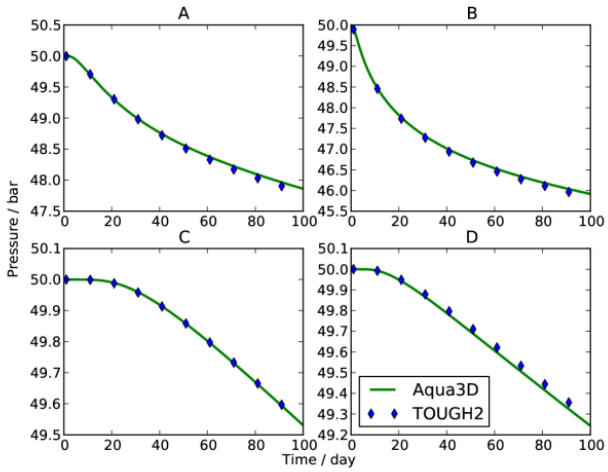

Figure 7. Comparison between TOUGH2 and Aqua3D for a model containing five different regions of anisotropic rock.

In each of the rectangular regions, one parameter differs from the background rock. The results of the simulations are presented in Figure 7 and Figure 8. Figure 7 shows the simulated pressure from TOUGH2 and Aqua3D at the four calibrations points.

Figure 8 shows simulated pressure contours at the end of the TOUGH2 run.

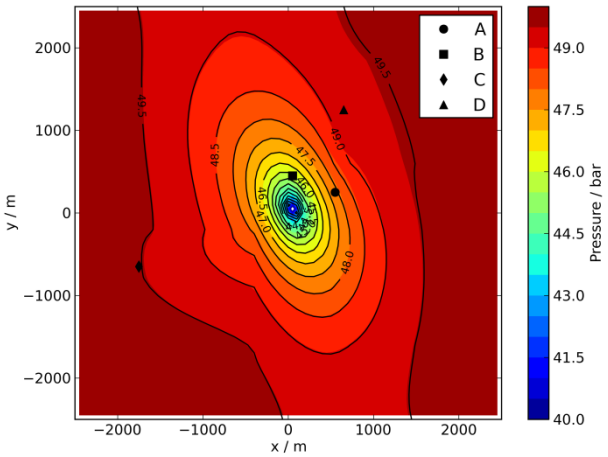

Figure 8. Areal plot of simulated pressure contours generated by TOUGH2 after 100 days. Black contour lines are Aqua3D results. The four symbols show the locations of the calculation points represented in Figure 7.

Although the methods employed in the two programs are different, Aqua3D and TOUGH2 gave similar results. This test validates our

approach in the case of nonhomogeneous anisotropic rock.

Multiple Layers

Previous test examples have all been single-layer systems. The following multilayer example was used to test whether the vertical flow (flow between horizontal layers), which includes the effects of gravity, has been correctly implemented into the new section of code handling anisotropy. As mentioned above, the solution used to implement anisotropy is a two-dimensional solution, and therefore the vertical flow is calculated in exactly the same way as in the original isotropic method. The vertical axis is therefore always a principal axis.

To allow for comparison between the original isotropic and the new anisotropic methods, the test example chosen is anisotropic but its principal axes are along *x*, *y*, and *z*. The same mesh as before was used, but the vertical depth was split into 10 layers of varying thickness (layers A–J). Initially, a run was performed without any sources or sinks to allow the pressures, under the effect of gravity, to reach equilibrium. Then, two sinks and one source were added to the system. The first sink (production rate of 50 kg/s) was added to an element in Layer C (Figure 9).

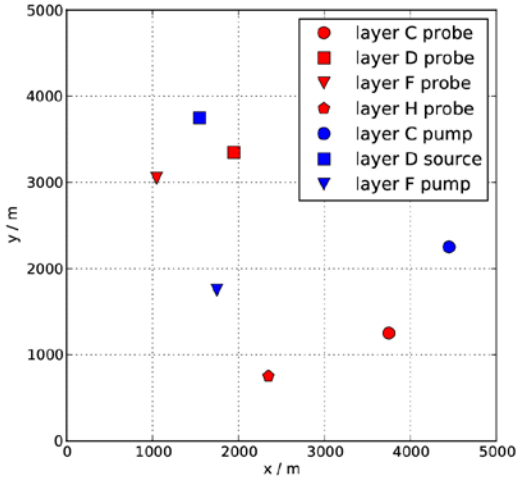

Figure 9. Top view of the multi-layer system showing the horizontal positions of the probes, sinks and source.

The second sink (production rate of 30 kg/s) was added to an element in Layer F. The source (rate of 15 kg/s) was added to an element in Layer D. Four measurement points were chosen to record the simulated pressure at different time intervals and produce a time series. Three of the measurement points were placed in the layers containing the sinks and the source (layers C, F and D), while the fourth probe was placed in layer H. A top view of the multilayer system in Figure 9 shows the horizontal positions of the probes, sinks, and source.

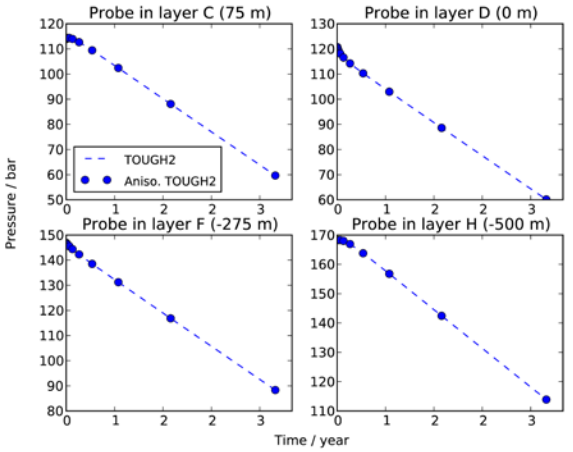

Figure 10. Simulated pressure time-series at each probe within the multi-layer system. Plot titles indicate the depth of the probes.

The simulated pressure time-series are shown in Figure 10 at each measurement point. The similarities in the curves produced by the isotropic and anisotropic methods indicate that the vertical flow between horizontal layers has been correctly implemented.

CONCLUSIONS

The result of this work is a fully functional addition to TOUGH2 and other simulators in the TOUGH family. This new addition includes the capability of defining anisotropic conditions within the model area. The code for the original isotropic method has been preserved, however, and it is therefore still possible to run a simulation using the unaltered version of TOUGH2. A switch was implemented to allow the user the option to change between the original isotropic method and the new anisotropic method. Input without any reference to anisotropy will automatically run using the original isotropic method. The new anisotropic method can only properly handle models where

the anisotropy is defined in a horizontal (*xy*) plane. Vertical flow is modeled using a scheme similar to the one used in the original isotropic method.

The new implementation has thoroughly tested with several examples and the results compared to either analytical solutions or other software packages. On all occasions, the comparison has been favorable.

Although not specifically dealt with in this report, it would be beneficial in the future to have the three new parameters available in iTOUGH2.

ACKNOWLEDGMENT

The authors acknowledge the cooperation with Karsten Pruess and Stefan Finsterle at LBNL.

REFERENCES

Abramowitz, M. and I. Stegun, *Handbook of mathematical functions: with formulas, graphs and mathematical tables*, Dover publications, USA, 1965.

Bear, J., *Hydraulics of groundwater*, McGraw-Hill Book Company, USA, 1979.

de Berg, M., M. van Krefeld, M. Overmans and O. Schwarzkopf, *Computational geometry: Algorithms and applications*, Springer, USA, 2000.

Grant, M., I. Donaldson and P. Bixley, *Geothermal reservoir engineering*, Academic Press Inc., USA, 1982.

Haukwa, C., *AMESH: A mesh creating program for the integral finite difference method: A User's Manual.*, Technical Report LBNL-45284, Lawrence Berkeley National Laboratory, Berkeley, Calif., 1998.

Pruess, K., C. Oldenburg and G. Moridis, *TOUGH2 User's Guide, Version 2.0*, Report LBNL-43134, Lawrence Berkeley National Laboratory, Berkeley, Calif., 1999.

Sigurðsson, S. and Vatnaskil Consulting Engineers , *Unpublished technical report*, 2009.

Strack, O., *Groundwater Mechanics*, Prentice-Hall Inc., New Jersey USA, 1989.

IMPROVING THE TREATMENT OF SALINE BRINES IN EWASG FOR THE SIMULATION OF HYDROTHERMAL SYSTEMS

Alfredo Battistelli

RISAMB Dept., Saipem SpA
Via Toniolo 1, Fano, 61032, Italy
e-mail: alfredo.battistelli@saipem.com

ABSTRACT

The EWASG EOS module was developed within the frame of the TOUGH2 numerical reservoir simulator for the modeling of hydrothermal systems containing salt and a non-condensable gas (NCG). The code version distributed in 1999 suffered, however, from a few notable limitations: brine correlations are derived from different sources, with the potential risk of limited internal coherence; brine correlations do not properly cover the entire P-T-X space of interest; and NCG effects are evaluated with an approach limited to low partial pressures.

Improvements developed so far to overcome some of the above limitations are described in the present work, with regard to the modeling of saline hydrothermal systems. It must be reiterated that the brine treatment employed by EWASG was subsequently inherited by other EOS modules such as ECO2, ECO2N, EOSM, TMVOC V.2.0, and TMGAS. Described improvements can be easily implemented in other TOUGH2 EOS modules dealing with NaCl solutions.

INTRODUCTION

The EWASG EOS module (Battistelli et al., 1993; Battistelli et al., 1997) was developed within the frame of the TOUGH2 (Pruess, 1991) numerical reservoir simulators, and then distributed by LBNL embedded into TOUGH2 V.2 (Pruess et al., 1999). Since then, EWASG was included within the inverse simulation code iTOUGH2 (Finsterle, 2007) and the parallel code version TOUGH-MP (Zhang et al., 2008). It was also used by LBNL as the starting point for ECO2 (Pruess and Garcia, 2002) and then ECO2N (Pruess, 2005), the latter widely used for the modeling of geological sequestration of supercritical CO_2 in saline aquifers. The correlations for NaCl properties are also used in TMVOC V.2.0 (Battistelli, 2008) for environmental applications, TMGAS (Battistelli and Marcolini, 2009) for GHG sequestration and acid gas mixtures injection, and EOSM (Pruess, 2011) for CO_2 sequestration in saline aquifers under sub- and supercritical conditions.

EWASG is used primarily for modeling hydrothermal systems containing dissolved solids and noncondensable gases. The version distributed in 1999 suffered, however, from some key limitations: brine correlations are derived from different sources, with the potential risk of limited internal coherence. Moreover, brine correlations do not cover properly the entire P-T-X space of interest (T=0-350°C; P=0-1000 bar; XS=0-1). In addition, the effects of NCG are evaluated with an approach limited to low partial pressures of the noncondensable gas.

Since the initial delivery of the code, several improvements have been implemented in an attempt to overcome the above limitations and extend the applicability of EWASG to a wider range of thermodynamic conditions (Battistelli et al., 2009). Some of the main improvements included are described in the present work:

- IAPWS-IF97 correlations for pure water and steam (IAPWS, 1997) and a more recent formulation for water and steam viscosity (IAPWS, 2008).
- An internally consistent H_2O-NaCl EOS package derived from the work of Driesner and Heinrich (2007) and Driesner (2007).
- A more consistent approach of vapor pressure lowering (VPL) and water adsorption, including the dependency of capillary pressure on temperature and salt concentration.

IAPWS-IF97 CORRELATIONS

TOUGH2 V.2 uses the IFC67 correlations (IFC, 1967) for computing vapor pressure, density, and the internal energy of liquid water and steam within the following regions of P-T space:

Region 1: liquid water to 350°C and 1000 bar;

Region 2: steam up to 800°C and 1000 bar;

Region 4: vapor pressure up to the critical point of water.

The IAPWS-IF97 formulation (IAPWS, 1997) is made available within TOUGH2 as summarized in Table 1. The relative subroutines were kindly supplied by Michael O'Sullivan (Croucher and O'Sullivan, 2008). A more recent formulation for the dynamic viscosity of water and steam has been coded (IAPWS, 2008) that computes more accurate viscosity values at high temperatures. The new subroutines are included into the T2F.f module and can be invoked in a TOUGH2 simulation run using a flag from the SELEC block in the input file. Even though the correlations are officially limited to 350°C for liquid water, they can be safely used up to 360°C and, with minor errors, up to 370°C.

Table 1. New subroutines for the properties of liquid water and steam.

Subroutine	Region	Property
COWAT97	1	density and internal energy of liquid water
SUPST97	2	density and internal energy of steam
SAT97	4	saturation pressure
TSAT97	4	saturation temperature
VISH2008	1, 2 & 4	water and steam dynamic viscosity

NEW EOS FOR H_2O-NACL MIXTURES

Driesner and Heinrich (2007) (D&H) revised published data on H_2O-NaCl-phase boundaries up to 1000°C and 5000 bar, and for mixtures ranging from pure water to pure salt compositions. Driesner (2007) presented a comprehensive set of correlations for the computation of phase-mixture properties over the above P-T-X space. D&H computed pure water properties using the IAPS-84 formulation as described by Haar et al. (1984). In implementing the D&H approach into the TOUGH2 framework, the IAPWS-IF97 correlations have been used to evaluate pure water properties in Regions 1, 2, and 4. Thus, the H_2O-NaCl EOS implemented into EWASG is limited to temperatures up 350°C, and with minor errors up to 370°C; pressures up 1000 bar and NaCl concentrations from 0 up to saturation.

D&H used the same molecular weight of water implemented into TOUGH2, 18.015 g/mol, but a slightly different molecular weight for the NaCl: 58.443 g/mol against 58.448 g/mol used in EWASG (Battistelli et al., 1997). Thus, the value of 58.443 g/mol is used with the D&H model. As in EWASG, the D&H reference condition for the brine enthalpy is pure liquid water with zero enthalpy at the triple point of water (0.01°C, P=611.73 Pa). (The main equations are restated below; for the whole set of correlations and related coefficients, I refer the reader to the papers by D&H.)

Brine density

The computation is performed according to Driesner (2007) by determining the temperature T_V*, as a function of pressure and salinity, at which the pure water has the same molar volume V_b of the brine at temperature T (°C), pressure P (bar) and salt molar fraction X_{NaCl}, as expressed by Eq. (1).

$$V_b(T,P,X_{NaCl}) = V_{H2O}(T_V^*,P) \tag{1}$$

All related equations are included into the new subroutine DRIESNER, called by COBRI if the D&H model is selected from the input file. The mass density of the brine is computed from that of pure water using the molecular weights as shown in Eq. (2).

$$\rho_b(T,P,X_{NaCl}) = \rho_{H2O}(T_V^*,P)\frac{PM_b}{PM_{H2O}} \tag{2}$$

where the brine molecular weight PM_b is computed from the mass fraction of salt XS in a straightforward way. Driesner (2007) also suggests corrections of Eq. (1) in specific ranges of P-T-X space, which have been also implemented into the DREISNER subroutine.

In Fig. 1, the brine density calculated as a function of salinity using EWASG, D&H and the BRNGAS correlation of Pritchett (1993), already included in TMVOC V.2.0, TMGAS and EWASG, is compared with the density data tabulated by Pitzer et al. (1984) at 800 bar and

300°C. Then BRNGAS correlation starts to underestimate the density at 200°C, while the D&H model reproduces Pitzer's density well at all temperatures.

Brine enthalpy

Following Driesner (2007), a similar approach is used for the brine enthalpy. The temperature T_H*, as a function of pressure and salinity, is the

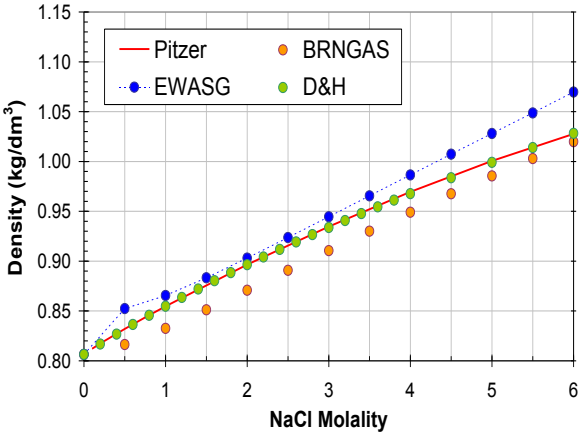

Figure 1. Brine density at 800 bar and 300°C. Comparison among values computed with EWASG, Pritchett (1993) and Driesner (2007) correlations and those published by Pitzer et al. (1984).

temperature at which pure water has the same enthalpy h_b of the brine at temperature T (°C), pressure P (bar), and salt molar fraction XNaCl, as expressed by Eq. (3).

$$h_b(T,P,X_{NaCL}) = h_{H2O}(T_H^*,P) \quad (3)$$

The necessary equations have been coded into subroutine DRIESNER called by COBRI.

Halite density

The density of solid salt (halite) is computed following Driesner (2007) by adding, to the density of halite at zero pressure, a correction proportional to the pressure as shown by:

$$\rho_{halite} = \rho^0_{halite}(T) + l(T)\,P \quad (4)$$

The correlation is included in subroutine DHAL.

Halite solubility

Halite solubility is computed in EWASG as a function of temperature using a correlation due to Potter and quoted by Chou (1987). Dreisner and Heinrich (2007) computed the brine composition at equilibrium with halite as a function of both temperature and pressure, using Eq. (5), where coefficients e_i are functions of pressure P (bar):

$$X^L_{NaCl,sat} = \sum_{i=0}^{5} e_i \left(\frac{T}{T_{hm}}\right)^i \quad (5)$$

T_{hm} is the temperature of halite melting:

$$T_{hm} = T_{triple,NaCl} + a(P - P_{triple,NaCl}) \quad (6)$$

The solubility dependence from pressure becomes remarkable only for temperatures higher than about 450°C and for very high pressures, as shown by Driesner (2007). Within our field of interest, temperatures lower than 400°C, the solubility dependence of pressure up to 1000 bar is negligible. Thus, the above D&H correlation was not included in EWASG, to avoid an increase in computation effort for a negligible increase in accuracy.

Halite solubility at 1 bar up to 100°C and then at the brine-saturation pressure for higher temperatures has been computed using Eq. (5). Computed values are compared in Fig. 2 to the solubility calculated within EWASG and to the values computed according to Palliser and McKibbin (1998) (P&McK).

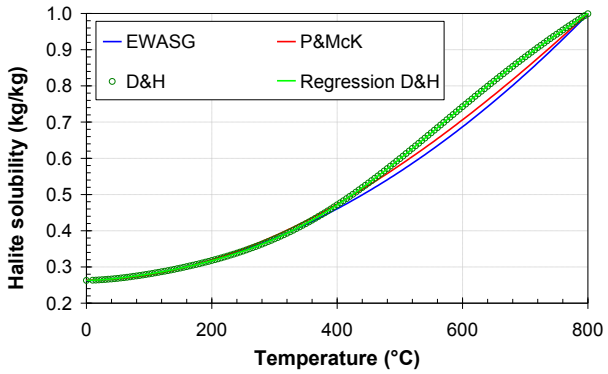

Figure 2. Halite solubility computed using EWASG, Palliser and McKibbin (1998) and Driesner and Heinrich (2007).

The standard EWASG correlation reproduces the D&H values up to 350°C with an error lower than 1%, while the P&McK's correlation has a higher error. Conversely, at high temperature, P&McK's correlation performs slightly better and is closer to D&H values. D&H solubility values have been regressed as a function of

temperature, using a polynomial expression included in subroutine HALITE.

Halite enthalpy

Halite enthalpy in EWASG is computed, as a function of temperature only, by integrating the specific heat given by Silvester and Pitzer (1976). The chosen reference state for halite enthalpy is that of the triple point of water (T=0.01°C, P=611.73 Pa) at which halite enthalpy is set to zero. Driesner (2007) supplies a correlation for the specific heat of halite as a function of both temperature and pressure, as shown by Eq. (7):

$$c_{P,halite} = r_0 + 2r_1(T - T_{triple,NaCl}) + 3r_2(T - T_{triple,NaCl})^2 + r_3 P + r_4 P^2 \qquad (7)$$

Coefficients r_0, r_1, and r_2 are constants, while r_3 and r_4 are polynomials of third degree with respect to temperature. Integrating the specific heat, Driesner considers the triple point of halite as the reference state for halite enthalpy, in order to be consistent with the reference assumed for the enthalpy of pure water. For comparison purposes, the halite enthalpy as been computed as a function of temperature, assuming zero enthalpy at the triple point of water, and at pressure of 1 bar, integrating the specific heat of Eq. (7); using the standard EWASG code; and by integrating the specific heat given by Pitzer et al. (1984). Computed enthalpy is shown in Fig. 3.

The plot shows good agreement as far as the reproduction of enthalpy at low pressure is concerned among the three approaches.

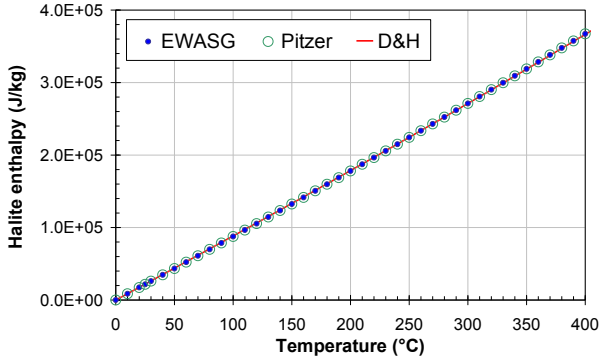

Figure 3. Halite enthalpy computed using EWASG and by integrating the specific heat given by Pitzer et al. (1984) and by Driesner (2007) assuming zero enthalpy at 0.01°C.

The effect of pressure is the increment of halite enthalpy by an amount, proportional to the pressure, which is almost constant in the temperature range of interest for EWASG (T< 400°C). The enthalpy at 1 bar has been computed with a 3rd degree polynomial shown in Eq. (8), while the pressure correction is made using Eq. (9). The error with respect to the enthalpy computed using the SOWAT code (Driesner, 2007) at 400°C and 500 bar is lower than 0.2% and is considered satisfactory for the purposes of EWASG improvement.

$$h_{halite}(T,1bar) = 8.8101E-5\,T^3 + 6.4139E-2\,T^2 + 8.7664E2\,T - 5.6125E5 \qquad (8)$$

$$h_{halite}(T,P) = h_{halite}(T,1bar) + 44.14(P - 1bar) \qquad (9)$$

The new correlation has been included in function HHAL to substitute for the old correlation. In fact, D&H enthalpy reference conditions are different from those assumed in the old EWASG; they are congruent with the computation of water and brine enthalpy, but this was not the case for the old EWASG. Because of that, the calculation of heat effects during precipitation or dissolution of halite are affected by an error in the old EWASG code. This error is insignificant for most applications, but can yield noticeable effects when localized precipitation/dissolution determine large changes in solid salt saturation.

Brine vapor pressure

In EWASG the vapor pressure of sodium chloride brines is computed as a function of temperature and salinity, using a correlation by Haas (1976) calibrated over experimental data covering a temperature range from –11 to 300°C. Driesner and Heinrich (2007) present a new correlation covering a wider field of temperatures and salinities although with a much more complex approach, as shown by Eq. (10).

$$X_{NaCl}^{VL,liq} = X_{crit} + g_0\sqrt{P_{crit} - P} + g_1(P_{crit} - P) + g_2(P_{crit} - P)^2 \qquad (10)$$

In fact, Eq. (10) gives the composition of saturated liquid brine at the vapor pressure P, and as a function of brine critical pressure P_{crit} and composition X_{crit}. Terms g_1 and g_2 are functions of temperature, while g_0 is not explicitly given by D&H and needs to be evaluated with the

constraint that Eq. (10) should deliver the NaCl concentration on the equilibrium surface V+L+H at temperatures lower than the triple point of NaCl (800.7°C).

The SOWAT code has been used to compute the composition of saturated brine as a function of pressure along isotherms from 150 to 350°C. Fig. 4 shows the comparison among these values and those computed using the Haas (1976) correlation implemented in EWASG. Fig. 4 shows negligible differences up to 250°C, which increase at higher temperatures and for salinities greater than 5% by mass. Differences are noticeable at 350°C, because Haas's correlation was calibrated using experimental data at T lower than 300°C.

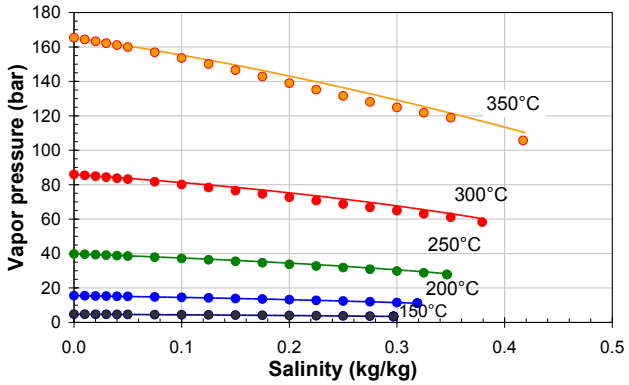

Figure 4. Comparison of saturated brine pressure as function of salinity at different temperatures computed using Haas (1976) (circles) and Driesner and Heinrich (2007) (lines) correlations.

Due to the complexity of the D&H correlation, which would also require an iterative approach, Eq. (10) has not yet been implemented within EWASG. The planned alternative approach is as follows:

- Use the SOWAT code to compute salinity-vapor pressure values for isotherms going from 0.01°C to 400°C;
- Use a new calibration of the coefficients present in the Haas (1976) correlation to reproduce the brine vapor pressure computed by SOWAT.

SUCTION PRESSURE EFFECTS

To model fractured geothermal reservoirs with low matrix permeability and high capillary pressure, it is necessary to account for suction pressure effects. These have already been studied by several authors, who focused either on the processes at low water saturation involving vapor pressure lowering (VPL) effects (O'Sullivan and Pruess, 1995; Battistelli et al., 1998), or on water adsorption processes in vapor-dominated reservoirs (Nghiem and Ramey, 1991; Sta. Maria and Pingol, 1996). VPL has been included in EWASG by using the Kelvin's equation as given by Eq. (11). The vapor partial pressure under two-phase conditions is obtained by multiplying the saturation pressure times the VPL factor given by Eq. 11.

$$f_{VPL} = \exp\left[\frac{W^{H2O} P_{cap}(S_L)}{\rho_L(P_L, T, X_L^{NaCl}) R(T + 273.15)}\right] \quad (11)$$

Phase equilibrium is solved assuming the additivity of partial pressures of water vapor and of the NCG. In EWASG, the aqueous-phase density in Kelvin's equation is computed using the aqueous-phase pressure.

Modeling of vapor adsorption

VPL is described using distinct approaches, even though they are different aspects of the same process: the vapor adsorption on the rock surface, and the capillary condensation of aqueous phase. In both cases, the aqueous phase is present under metastable conditions at a pressure lower than the saturation pressure for local temperature. The presence of two-phase conditions instead of single steam, in a vapor-dominated reservoir, has strong implications for the amount of fluid initially stored in the reservoir. Even small saturations of liquid water can contribute substantially to the mass of fluid stored in the unit reservoir volume.

Adsorption and capillary condensation have usually been described with different modeling approaches. In addition to Kelvin's equation used in the TOUGH2 simulator (Pruess and O'Sullivan, 1992; Pruess et al., 1999), the vapor adsorption is described with adsorption isotherms, as generated by Stanford University researchers, who made prolonged experimental studies on rock samples collected at The Geysers and Larderello steam-dominated geothermal fields. The adsorption isotherms are described with several formulations, among which the classical one is that due to Langmuir (Nghiem

and Ramey, 1991), as expressed by Eq. 12. X^W is the mass fraction of water with respect to rock mass, and A and B are experimental coefficients:

$$X^W = \frac{A\, f_{VPL}}{1 + B\, f_{VPL}} \tag{12}$$

It is useful to model (with a unique formulation) both adsorption and capillary condensation within a reservoir simulator. Sta Maria and Pingol (1996) observed that adsorption isotherms are generally able to describe experimental results for values of VPL coefficients lower than 0.9, while Kelvin's equation has difficulty at low water saturation values, when the capillary pressure becomes extremely high. The adsorption isotherm establishes a relationship between the mass of absorbed water and the VPL coefficient. Assuming that the density of adsorbed water can be estimated with conventional correlations at saturated conditions, from rock porosity and grain density, it is possible to convert the adsorbed mass in an equivalent liquid saturation, assuming also that adsorbed water on grain surfaces occupies a fraction of pore volume. The equivalent liquid saturation is given by Eq. 13 (Sta. Maria and Pingol, 1996):

$$S_{Aq} = \frac{1-\varphi}{\varphi}\frac{\rho_R}{\rho_{Aq}} X^W \tag{13}$$

This saturation can be used to determine the capillary-pressure value, which reproduces the experimental VPL coefficients computed with the Kelvin equation. Adsorption and capillary pressure data can then be combined for a regression on a unique capillary-pressure curve.

Dependency of capillary pressure on surface tension

Both adsorption and capillary-condensation processes are function of temperature. The capillary pressure depends in fact on the surface tension between the two phases at equilibrium. For steamwater two-phase conditions, the surface tension decreases with temperature, to vanish at the water critical temperature. The capillary-pressure values obtained for a given pair of fluids can be normalized using the J-Leverett function (Leverett, 1941):

$$J(S_{Aq}) = \frac{P_c}{\sigma \cos\theta}\sqrt{\frac{k}{\varphi}} \tag{14}$$

where σ is the surface tension (N/m) (IFT), θ is the contact angle, k the absolute permeability (m^2) and φ is rock porosity. Once the J-Leverett function is obtained with a regression on experimental data for a specific rock formation, the capillary pressure can be computed as a function of petro-physical and fluid properties, as follows:

$$P_c = J(S_W)\,\sigma \cos\theta \sqrt{\frac{\varphi}{k}} \tag{15}$$

IFT is a function of fluid phases at equilibrium, of their composition and local temperature. The J-Leverett function is customarily used to evaluate the capillary pressure at reservoir conditions from laboratory measurements performed at different conditions and with different fluid phases. The temperature affects both IFT and the contact angle, the latter changing also with rock type. Assuming the contact angle changes marginally with temperature, the capillary pressure at reservoir conditions is given by Eq. 16:

$$P_{c,res}(T) = P_{c,lab}(T_{ref})\frac{\sigma(T,X,Y)}{\sigma_{ref}(T_{ref},X,Y)} \tag{16}$$

X and Y represent the composition of aqueous and gaseous phases, respectively. In hydrothermal systems, the gaseous phase contains mainly water vapor and a mixture of NCG, among which CO_2 usually predominates. In the aqueous phase, sodium chloride is generally the predominant dissolved solid. The pure-water IFT is computed in TOUGH2 using subroutine SIGMA (module T2F.f), based on the IAPS (1976) formulation. It differs from the more recent IAPWS (1994) release only in its different definition for the critical point of water, 647.096 K instead of 647.15 K.

The water IFT declines rapidly at increasing temperatures, from 72.74E-3 N/m at 20°C to 58.92E-3, 37.68E-3, 14.37E-3, and 3.67E-3 at 100, 200, 300 and 350°C, respectively. The capillary pressure should then become increasingly less important at reservoir temperatures greater than 300°C, common in the deep zones of many geothermal fields. On the other hand, the presence of salt increases the brine critical temperature substantially. For instance, NaCl mass fractions of 3 and 5%, found in some geothermal fields, increase the critical temperature to 403 and 493°C, respectively.
Thus, brine at 300°C has IFT greater than that of pure water at the same temperature, as it is farther than pure water from its critical temperature. For

instance, Ozdemir et al. (2009) reports experimental data indicating a consistent increment of brine IFT with salt content. Assuming the corresponding state principle is applicable to the IFT, then the IFT of brine at a given NaCl concentration is equal to that of pure water at the same reduced temperature.

Fig. 5 shows the critical temperature of brine as a function of NaCl mass fraction computed using the old EWASG correlation, and P&McK and D&H values. Up to a NaCl fraction of 0.3, the critical temperature is comparable. D&H supplied the relationships between salinity and critical temperature up to 1000°C. Thus, a regression on values given by P&McK has been included in EWASG. Fig. 6 shows the computed brine surface tension as function of temperature for salt mass fractions of 5, 10, 20, and 25% in NaCl.

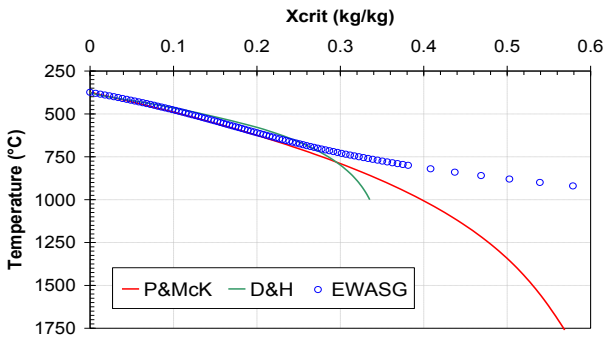

Figure 5. NaCl solubility at critical conditions computed using EWASG, P&McK and D&H.

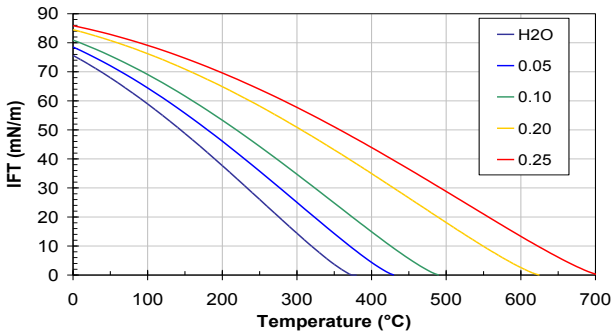

Figure 6. Surface tension of water and NaCl brines as function of temperature assuming the corresponding state principle is applicable.

The computation of capillary pressure in TOUGH2 has been modified, including its dependency on temperature through the brine IFT. The option is invoked giving the reference surface tension (in N/m) to parameter CP(7,nmat) in the ROCKS block of input file. The option is available for the van Genuchten (ICP=7), and Parker (ICP=8) models for water-gas two-phase conditions.

CONCLUSIONS

EWASG allows the modeling of ternary mixtures of water, NaCl, and a NCG within TOUGH2 V.2.0. While developed primarily for hydrothermal systems, the brine correlations have been extensively used in other EOS modules (such as ECO2N, EOSM, TMVOC V.2 and TMGAS) for environmental applications, GHG, and acid gas geological storage. The description of water-NaCl mixtures in EWASG has been improved by implementing correlations recently developed by Driesner and Heinrick (2007) and Driesner (2007). They were able to describe the thermodynamics and calculate phase properties for temperatures from 0 to 1000°C, pressures from 1 to 5000 bar, and NaCl mass fractions from 0 to 1. Pure water properties within EWASG are now computed using the IAPWS-IF97 (1997) and IAPWS (2008) correlations up to 350°C. (They can be used up to 370°C with minor errors.) D&H correlations for brine density and enthalpy are included in a new subroutine DRIESNER, while new correlations for halite density, enthalpy, and solubility have been included in the old EWASG subroutines. The composition of brine at critical conditions is computed using the correlation from Palliser and McKibbin (1998) in closed form.

An approach to describe VPL effects due to both water adsorption and capillary condensation using Kelvin's equation is proposed within TOUGH2, following St. Maria and Pingol (1996). Temperature and salinity effects on capillary pressure at high temperatures are accounted for including IFT effects, following the J-Leverett (1941) normalization.

ACKNOWLEDGMENTS

The management of Saipem SpA is acknowledged for the permission to publish the present work. Thanks are due to Michael O'Sullivan and Adrian Croucher, who kindly supplied the routines for the IAPWS-IF97 correlations.

REFERENCES

Battistelli A., C. Calore, and K. Pruess, *A fluid property module for the TOUGH2 simulator for saline brines with non-condensible gas*. Proc. 18th Work. Geoth. Res. Eng., Stanford Un., CA, 249-259, 1993.

Battistelli A., C. Calore, and K. Pruess K., The simulator TOUGH2/EWASG for modelling geothermal reservoirs with brines and a non-condensible gas. *Geothermics*, 26(4), 437-464, 1997.

Battistelli A., Modeling multiphase organic spills in coastal sites with TMVOC V.2.0. *Vadose Zone Journal*, 7, 316-324, 2008.

Battistelli A., M. Carpita, C. Geloni, and M. Marcolini, *New TOUGH2 EOS modules for the simulation of geothermal reservoirs containing saline brines and non-condensable gases*. GeoTherm Expo, Sept. 23-25, 2009, Ferrara, Italy, 2009.

Croucher A.E., and M.J. O'Sullivan, Application of the computer code TOUGH2 to the simulation of supercritical conditions in geothermal systems. *Geothermics*, 37, 622–634, 2008.

Driesner T., and C.H. Heinrich, The system H_2O–NaCl. Part I: Correlation formulae for phase relations in temperature–pressure–composition space from 0 to 1000°C, 0 to 5000 bar, and 0 to 1 XNaCl. *Geoch. Cosm. Acta*, 71, 4880–4901, 2007.

Driesner T., The system H_2O–NaCl. Part II: Correlations for molar volume, enthalpy, and isobaric heat capacity from 0 to 1000°C, 1 to 5000 bar, and 0 to 1 XNaCl. *Geoc. Cosm. Acta*, 71, 4902–4919, 2007.

Haar L., J.S. Gallagher, and G.S. Kell, *NBS/NRC Steam Tables*. Hemisphere Publ. Corp., 1984.

Haas Jr, J. L. (1976) Physical properties of the coexisting phases and thermochemical properties of the H2O component in boiling NaCI solutions. USGS Bulletin 1421-A.

International Association for the Properties of Water and Steam, *Release on the IAPWS Formulation 2008 for the Viscosity of Ordinary Water Substance*. Berlin, Germany, 2008.

International Association for the Properties of Water and Steam, *Release on the IAPWS Industrial Formulation 1997 for the Thermodynamic Properties of Water and Steam*. Erlangen, Germany, 1997.

International Association for the Properties of Water and Steam,. *Release on Surface Tension of Ordinary Water Substance*, 1994.

International Association for the Properties of Steam, *Release on Surface Tension of water substance*. NBS, Washington, USA, 1976.

International Formulation Committee, *A Formulation of the Thermodynamic Properties of Ordinary Water Substance*, IFC Secretariat, Düsseldorf, Germany, 1967.

Leverett M.C., Capillary Behavior in Porous Solids. *Trans. Soc. Pet. Eng. AIME*, 142, 152-169, 1941.

Ozdemir O., S.I. Karakashev, A.V. Nguyen, and J. Miller, Adsorption and surface tension analysis of concentrated alkali halide brine solutions. *Minerals Eng.* 22(3), 263-271, 2009.

Palliser C., and R. McKibbin, A model for deep geothermal brines. I. T–p–X state–space description. *Transp. Por. Med.*, 33, 65–80, 1998.

Pitzer K.S., Peiper J.C., and Busey R.H. Thermodynamic properties of aqueous sodium chlorides solutions. *J. Phys. Chem. Ref. Data*, 13(1), 1-102, 1984.

Pritchett J. W. *STAR User's manual. Appendix F.1 - The "BRNGAS" equation-of-state*. S-Cubed Report SSS-TR-89-10242, revision A., 1993.

Pruess K., *TOUGH2 A general-purpose numerical simulator for multi-phase fluid and heat flow*. Report LBL-29400, Lawrence Berkeley National Laboratory, Berkeley, Calif., 1991.

Pruess K., C. Oldenburg, and G. Moridis, *TOUGH2 User's Guide, Version 2.0*. Report LBNL-43134. Lawrence Berkeley National Laboratory, Berkeley, Calif., 1999.

Pruess K., and M. O'Sullivan M., *Effects of capillarity and vapor adsorption in the depletion of vapor-dominated geothermal reservoirs*. Proc. 17th Work. Geoth. Res. Eng., Stanford, USA, 165-174, 1992.

Pruess K., and J. Garcia (2002). Multiphase flow dynamics during CO_2 disposal into saline aquifers, *Env. Geology*, 42, 282-295.

Pruess, K., ECO2N : *A TOUGH2 Fluid Property Module Mixtures of Water, NaCl and CO_2*. LBNL Report 57952, Lawrence Berkeley National Laboratory, Berkeley, Calif., 2005.

Silvester L.F., and K.S. Pitzer, *Thermodynamics of geothermal brines I. Thermodynamic properties of vapor-saturated NaCl (aq) solutions from 0-300°C.* Report LBL-4456, Lawrence Berkeley National Laboratory, Berkeley, Calif., 1976.

Sta. Maria R., and A.S. Pingol, *Simulating the effects of adsorption and capillary forces in geothermal reservoirs*. Proc. 21st Work. Geoth. Reservoir Eng., Stanford, CA, SGP-TR-151, 165-173, 1996.

van Genuchten, M.Th., A Closed-Form Equation for Predicting the Hydraulic Conductivity of Unsaturated Soils. *Soil Sci. Soc. Am. J.*, 44, 892 – 898, 1980.

Zhang K., Wu Yu-Shu, and K. Pruess, *User's Guide for TOUGH2-MP - A Massively Parallel Version of the TOUGH2 Code*. Report LBNL-315E, Lawrence Berkeley National Laboratory, Berkeley, Calif., 2008.

ENHANCED HEAT TRANSPORT VIA SIMMERING PHENOMENA IN GEOTHERMAL MODELS

Tom Brikowski

Geosciences Dept., The University of Texas at Dallas
800 W. Campbell Rd.
Richardson, TX, 75080, USA
e-mail: brikowski@utdallas.edu

ABSTRACT

Simmering, or enhanced heat transport via transient vapor bubbles is a persistent state in strongly heated H_2O systems, e.g., in household cooking. Although rarely discussed in geologic settings, simmering should be equally important and persistent in nature. Numerical models are used here to assess simmering in magma-hydrothermal systems using the latest NIST-standard high-temperature/pressure equation of state for H_2O, embedded in the TOUGH2 geothermal simulator. A HYDROTHERM model of the same setting was made for comparison. The TOUGH2 models exhibit persistent simmering, owing to the development of a strong feedback between heat transport rate, fluid pressure, and phase state. In freely convecting systems, this feedback is manifested in upflow zones by oscillatory P-T conditions, creating spiral paths along and to the liquid-stable side of the two-phase boundary, extending to supercritical conditions at depth. P-T vary cyclically at each point in the upflow zone by about ten degrees and tens of bars over a scale of decades as steam "bubbles" develop and buoyantly rise. This simmering develops whenever basal heating in the reservoir significantly exceeds liquid convective heat transport rates. Simmering enhances heat transport by an order of magnitude or more and successfully dissipates the excess heating. This state persists through almost all of prograde heating and much of retrograde cooling, even through external perturbations such as lithocap fracturing or magma re-intrusion.

HYDROTHERM models of an identical system do not exhibit simmering, and instead develop a longer-lived higher-saturation steam zone immediately above the magmatic heat source. Temperatures above this zone are significantly cooler than in the TOUGH2 models. TOUGH2 computational effort is much greater, as time steps decline to month scales when pressure spikes related to steam formation impact cell mass balances. The origin of this marked difference in result between the two codes most likely relates to differences in computation or treatment of fluid-property extrema. These extrema result in highly efficient heat transport (simmering) in TOUGH2, encouraging development of a vertically extensive simmering zone above the pluton. The extrema are not as influential in HYDROTHERM, limiting the vertical extent of boiling. This difference is at least partly related to the mathematical form of the equations of state (EOS), where the NIST EOS is physically based, and the HYDROTHERM EOS is a polynomial fit to tabulated values; however, regardless of EOS formulation, models with boundary inflow held on the two-phase boundary or its supercritical extension can exhibit simmering behavior.

INTRODUCTION

Incipient boiling (simmering) reflects the development of enhanced heat transport through transient phase change. Anyone who has boiled water has experience with this phenomenon; some of the earliest technical investigations of simmering arose from the nuclear power industry (Davis and Anderson, 1966; Tachibana et al., 1968; Takashi and Hirohisa, 1964). More recent research has focused on development of high-flux heat sinks for microcircuitry, utilizing two-phase phenomena to maximize heat dissipation on a microscopic scale (Qu and Mudawar, 2002, 2004). Given the ubiquity of incipient boiling in daily life, it is surprising that simmering is not a more common feature of hydrothermal/geothermal models. Indeed, abundant geological evidence exists for transient, cyclical convection, e.g., fine-scale hydrothermal banded veins and breccia, (Corbett

and Leach, 1997), multidecadal variability of hot springs (Minerva Hot Springs, USNPS, 2012), and pre- and post-development seismicity at geothermal systems (Fialko and Simons, 2000). While these geological features are often attributed to tectonic fracturing or boiling events, the models outlined below demonstrate that periodic hydrothermal features can also be related to flow instability controlled by fluid properties, i.e., simmering. Similar flow instability has been observed and modeled for single-phase supercritical flow—black smoker systems, HYDROTHERM, Coumou et al. (2006); Fontaine and Wilcock (2007); Ingebritsen et al. (2010)—and two-phase subcritical two-phase flow (micro-channel heat sinks with "severe pressure drop oscillation"; Qu and Mudawar, 2003). Oscillatory boiling has also been modeled for a geyser conduit (Ingebritsen and Rojstaczer, 1996, *HYDROTHERM*) assuming extremely high permeability, with inlet conditions fixed on the two-phase boundary. In each of these cases, fluid properties control conditions in the convective outflow zone, and this is the key to development of simmering phenomena.

BACKGROUND

For simplicity, an idealized system was modeled approximating a single plutonic intrusion into uniform host rock with a previously-formed cap rock above the pluton (Figure 1). This is Example 10 of HYDROTHERM (Hayba and Ingebritsen, 1997; Kipp et al., 2008) with cap r ock added. Assigned rock properties are summarized in Table 1.

Results are compared for two hydrothermal simulators, HYDROTHERM (v. 3.1) and TOUGH2 (utilizing supercritical equation of state EOS1sc, Brikowski, 2001b). The fluid equation of state for *HYDROTHERM* uses bicubic interpolation of water properties tabulated in the NIST steam tables. The equation of state EOS1sc implements the physically based water-property computation routines available from NIST (1999). Compared to table lookup, EOS1sc is computationally intensive, but provides important increased accuracy in regions of water property extrema.

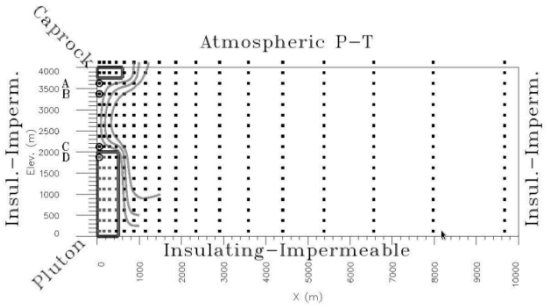

Figure 1. Computational grid and lithologic zones for hypothetical system of caprock, host rock and pluton. Cell centers shown by square symbols, permeability zone boundaries by gray rectangles. Streamlines for 5,000 years shown. Labels A-D show location of monitoring points for P-T profiles (Figure 3-Figure 4) along first column of nodes (at x = 50 m).

Table 1: Rock properties assigned to materials in Figure 1. Pluton permeability is temperature dependent, and increases below 400ºC. All units assigned thermal conductivity 2 W/mºC and heat capacity 1000 J/kgºC. Pluton initially at 900ºC.

Parameter	Cap rock	Host	Pluton
Porosity	0.05	0.1	0.05
Permeability(m^2)	10^{-18}	10^{-15}	10^{-18}

Transport Property Extrema

The effects of fluid-property extrema in hydrothermal systems have been observed in many numerical models (Brikowski, 2001a; Brikowski and Norton, 1989; Fontaine and Wilcock, 2007; Norton and Knight, 1977; Norton and Dutrow, 2001). The extrema provide a feedback mechanism by maximizing buoyancy forces (primarily dependent on horizontal density gradients, which are in turn dependent on fluid expansivity and compressibility) in a region of minimal viscosity (resistance to flow) and maximum heat capacity along the two-phase boundary and critical isochore (Figure 2). Since this feedback operates primarily on the convection rate, it is most visible in the upflow zones where those rates are highest.

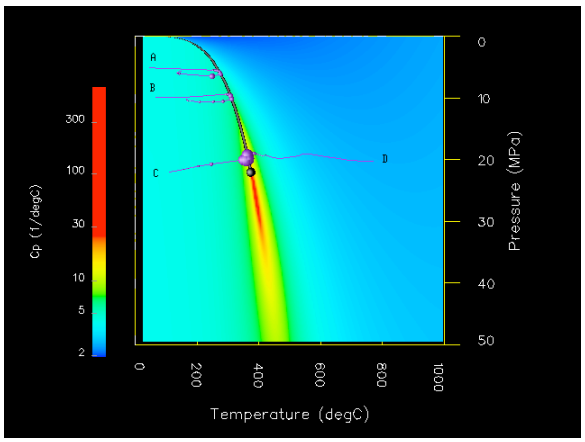

Figure 2. P-T vs. time paths (lines marked with spheres) in the upflow zone of a magma-hydrothermal system (point locations shown in Figure 1), TOUGH2-EOS1sc model. Letters show starting point of each path, points above pluton follow counter-clockwise paths, point "D" lies within pluton, and follows right-to-left path. Velocity magnitude (spheres, size proportional to magnitude) reaches a strong maximum in the vicinity of the two-phase boundary (gray line) and critical isochore (diamond). Shading shows zone of strong fluid property controls, represented here by Cp.

The nature of this feedback process can be illustrated by noting the evolution of fluid/rock P-T conditions and convection rates at fixed points in a magma-hydrothermal system model. Immediately after magma intrusion in such a system (Figure 1), conditions in the heated host rock migrate toward the two-phase boundary or critical isochore from low temperature (points A-C, Figure 2). As conditions enter high-density gradient zones along the two-phase boundary or critical isochore, increasing buoyancy forces cause a sharp increase in velocity (convection). This limits further temperature increase by increasing convective heat removal. Points in the hot pluton cool toward the critical isochore (e.g., point D, Figure 2), with velocity peaking sharply near the isochore, partly because of fluid property extrema, partly because of cooling-related fracture formation (brittle-ductile boundary is crossed).

Portions of the system attempting to depart from this zone of maximum density gradient experience reduced convection. Above the pluton, points depressurizing above the two-phase boundary don't heat as rapidly, and move left on the P-T diagram back into the region of maximum buoyancy. Similarly, pluton points cooling beyond the critical isochore experience reduced convection, and cool more slowly, eventually moving to the right on the P-T diagram back into the region of maximum convection along the critical isochore. Forced convection systems (externally controlled vertical pressure gradient) may show other P-T distributions, but upflow zones in freely convecting systems will strongly tend toward the two-phase boundary/critical isochore, and exhibit boiling-curve P-T profiles (e.g., Figure 4).

RESULTS

Both the TOUGH2 and HYDROTHERM model results are strongly influenced by fluid property extrema. Both experience rapid conductive heat transfer from the pluton into adjacent country rock, forming vigorous early upflow zones at its lateral margin (X=0.8-1 km, Figure 1). Early in both models, boiling begins directly above the pluton at elevation 2 km. In the HYDROTHERM model, this zone persists to about 3000 yrs, reaching up to 35% steam. It then disappears, reappearing during 7000–8000 yrs (i.e., only small depth ranges lie on the two phase boundary—Figure 3). In contrast, the TOUGH2 model develops a vertically extensive incipient boiling zone by 3000 yrs, persisting until around 8000 yrs (Figure 4). In this zone, small regions of minimal steam saturation form at its deeper end, and advect upward, accumulating beneath the lithocap (Figure 7). Pressure spikes related to the formation or condensation of steam affect cell mass balance, and reduce timesteps to less than one year. Individual cells in the simmering zone follow elliptical paths in P-T space, slowly warming during the prograde development of circulation, then cooling (Figure 6). Each transition to two-phase causes a significant pressure spike, and thereby an increase in local heat transfer (Figure 8). It is this phenomenon that is key to modern microchannel heat sinks, and likely drives more efficient hydrothermal heat transport than is generally recognized.

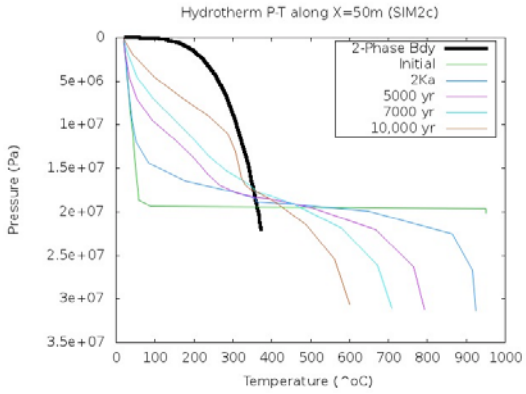

Figure 3. *HYDROTHERM* P vs. T along X=50 m

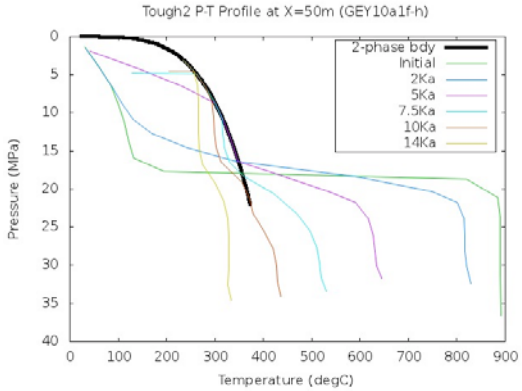

Figure 4. TOUGH2 P vs. T along X=50 m

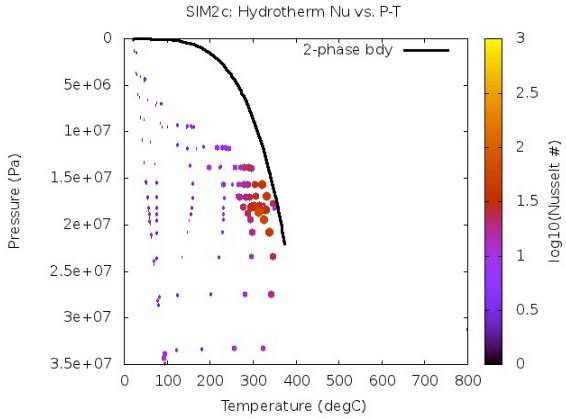

Figure 5. *HYDROTHERM* Nusselt number vs. P-T, 5Ka. An extensive simmering zone (Figure 5) will develop only with extreme permeability (e.g., k = 10^{-8} m^2; Ingebritsen and Rojstaczer, 1996).

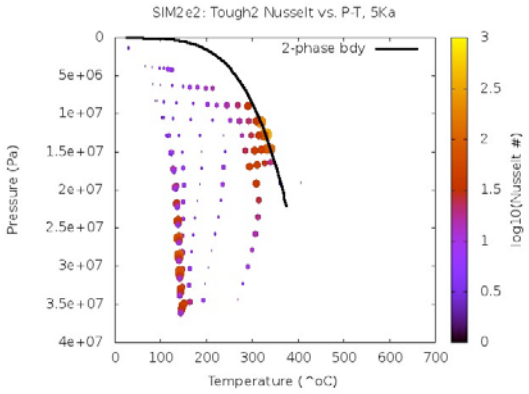

Figure 5. TOUGH2 Nusselt number vs. P-T, 5Ka. Elevated Nu points at lower left represent inflow into convective cell

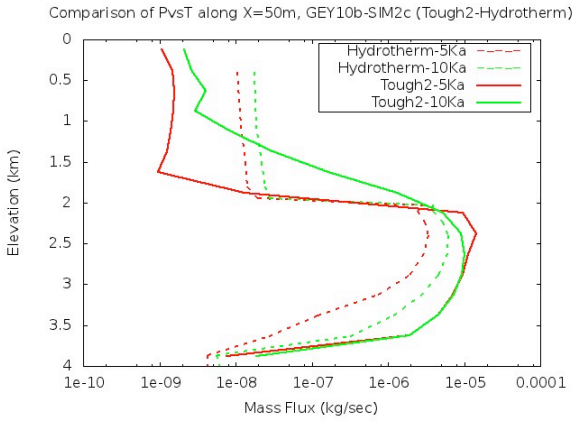

Figure 7. Comparative Mass Flux along X=50 m

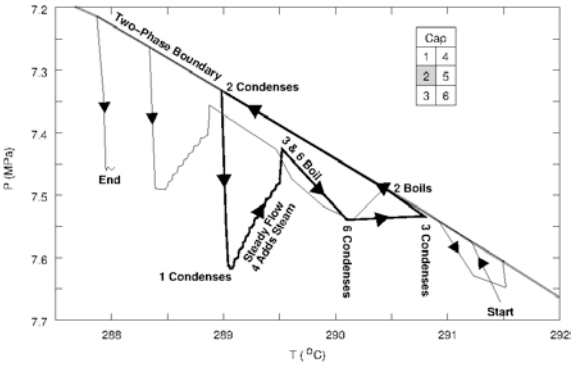

Figure 6. TOUGH2 oscillatory P-T path at point B (Figure 1) for 50 years, labeled as point 2 in this diagram (see inset), at approximately 7000 years in the simulation. Oscillatory P-T conditions produced by advecting steam phase, yielding roughly elliptical counter-clockwise path on P-T diagram. One complete cycle is illustrated by bold line, prior and following cycles shown by thin line. Two-phase boundary shown by gray line.

The effect of fluid transport property extrema is clearest when considering cell Nusselt number (Nu, ratio of convective to conductive heat flow) plotted on a P-T diagram (Figure -Figure 5). Points lying along the two-phase boundary (in the upflow region above the pluton) experience maximum buoyancy forces and heat capacity. This significantly raises Nu, to a much greater extent in TOUGH2 (max. Nu ~400) vs. HYDROTHERM (max Nu ~120), despite similar above-pluton mass fluxes for both models (Figure). The heat-transport feedback represented by this enhanced Nu serves to reinforce the simmering region. Whether driven by differences in formulation of EOS, or averaging of phase properties, relative or thermal permeability formulations, fluid paths move off the two-phase boundary in HYDROTHERM compared to TOUGH2, and computed heat transport is not as efficient. As a result, heating of country rock above the pluton is significantly greater in the TOUGH2 model of this system (compare curves, Figure 3–Figure 4). Interestingly, this produces considerably greater steam saturations immediately above the pluton in the HYDROTHERM model, and lesser but more persistent steam in the TOUGH2 model. Ultimate heat transport from the magma is limited by its conductive rind, so the duration of hydrothermal circulation is similar in both models.

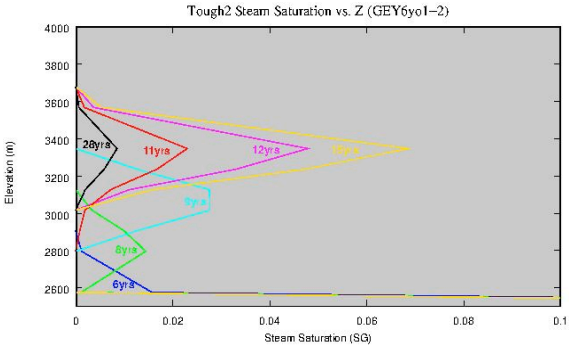

Figure 7. TOUGH2 steam saturation profiles x=50 for sequential times. Shown are years after beginning of the cycle at 5390 system years. The low-density steam phase forms at base of two-phase zone, then migrates upward buoyantly.

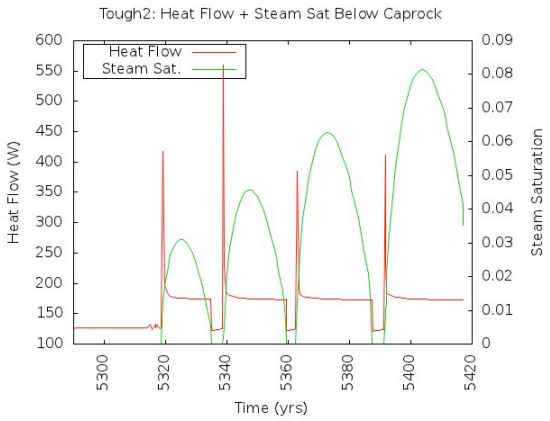

Figure 8. TOUGH2 heat flux and steam saturation vs. time at point "A", Figure 1. See text for detailed explanation. The vertical development of the last cycle in this figure (5375-5425 yrs) is shown in Figure 7.

CONCLUSIONS

Incipient boiling or simmering is a ubiquitous phenomenon in rapidly heated systems, and many of us observe it almost daily. It seems quite reasonable that simmering is common in hydrothermal systems as well, and abundant geological evidence exists for short-term transient thermal behavior in paleo- and modern hydrothermal/geothermal systems. If simmering is common in natural systems, it should also be common in models of those systems, yet it is rarely reported. Since simmering inherently represents a feedback system of enhanced heat transport, it is likely to be most apparent when great attention is paid to accuracy of EOS and heat-transfer formulations. The most accurate will be physically based EOS formulations, but these can be extremely computation intensive. For models concerned with detailed conditions above a heat source, e.g., for prograde geothermal systems or detailed alteration studies, simmering is likely to be a dominant heat transport process.

ACKNOWLEDGMENTS

The original modeling in this study was supported by U. S. Dept. of Energy grant DE-FG07-98ID13677.

REFERENCES

Brikowski, T. H., 2001a, Deep fluid circulation and isotopic alteration in The Geysers geothermal system: Profile models. Geothermics 30(2-3), 333–47.

Brikowski, T. H., 2001b, Modeling Supercritical Systems With Tough2: Preliminary Results Using the EOS1sc Equation of State Module. In: Proceedings: Twenty-Sixth Workshop on Geothermal Reservoir Engineering, Stanford University, Stanford, CA, vol. 26 of SGP-TR-168, p. 8, p. 8.

Brikowski, T. H., Norton, D., 1989, Influence of magma chamber geometry on hydrothermal activity at mid-ocean ridges. Earth Planet. Sci. Lett. 93, 241–255.

Corbett, G. J., Leach, T. M., 1997, Southwest Pacific Rim Gold-Copper Systems: Structure, Alteration and Mineralization. Short course manual, Corbett Geology, Corbett Geological Services, 29 Carr Street, North Sydney NSW 2060, Australia.

Coumou, D., Driesner, T., Geiger, S., Heinrich, C. A., Matthäi, S., 2006, The dynamics of mid-ocean ridge hydrothermal systems: Splitting plumes and fluctuating vent temperatures. Earth and Planetary Science Letters 245(1–2), 218 – 231.

Davis, E. J., Anderson, G. H., 1966, The incipience of nucleate boiling in forced convection flow. AIChE J. 12, 774-780.

Fialko, Y., Simons, M., 2000, Deformation and seismicity in the Coso geothermal area, Inyo County, California: Observations and modeling using satellite radar interferometry. J. Geophys. Res. 105(B9), 21781–21793.

Fontaine, F. J., Wilcock, W. S. D., 2007, Two-dimensional numerical models of open-top hydrothermal convection at high Rayleigh and Nusselt numbers: Implications for mid-ocean ridge hydrothermal circulation. Geochem. Geophys. Geosyst. 8(7), Q07010.

Hayba, D. O., Ingebritsen, S. E., 1997, Multiphase groundwater flow near cooling plutons. J. Geophys. Res. 102(6), 12235–12252.

Ingebritsen, S. E., Geiger, S., Hurwitz, S., Driesner, T., 2010, Numerical simulation of magmatic hydrothermal systems. Rev. Geophys. 48(1), RG1002.

Ingebritsen, S. E., Rojstaczer, S. A., 1996, Geyser periodicity and the response of geysers to deformation. Journal of Geophysical Research 101(B10):21891-21905.

Kipp, Jr., K. L., Hsieh, P. A., Charlton, S. R., 2008, Guide to the Revised Ground-Water Flow and Heat Transport Simulator: HYDROTHERM - Version 3. Techniques and Methods Book 6-A25, U. S. Geol. Survey, Reston, VA.

NIST, 1999, NIST/ASME STEAM PROPERTIES DATABASE: VERSION 2.2. NIST Standard Reference Database 10, U.S. National Institute of Standards and Testing.

Norton, D., Knight, J., 1977, Transport phenomena in hydrothermal systems: Cooling plutons. Am. J. Sci. 277, 937–981.

Norton, D. L., Dutrow, B. L., 2001, Complex behavior of magma-hydrothermal processes; role of supercritical fluid. Geochim. Cosmo. Acta 65(21), 4009–4017, Special Issue: Helgeson Tribute.

Qu, W., Mudawar, I., 2002, Prediction and measurement of incipient boiling heat flux in micro-channel heat sinks. Int. J. Heat Mass Trans. 45(19), 3933 – 3945.

Qu, W., Mudawar, I., 2003, Measurement and prediction of pressure drop in two-phase micro-channel heat sinks. Int. J. Heat Mass Trans. 46(15), 2737 – 2753.

Qu, W., Mudawar, I., 2004, Measurement and correlation of critical heat flux in two-phase micro-channel heat sinks. Int. J. Heat Mass Trans. 47(10–11), 2045 – 2059.

Tachibana, F., Akiyama, M., Kawashima, H., 1968, Incipient boiling on exponentially heated surfaces. Journal of Nuclear Science and Technology 5(3), 133–135.

Takashi, S., Hirohisa, M., 1964, On the Conditions of Incipient Subcooled-Boiling with Forced Convection. Bulletin of JSME 7(26), 392–398.

USNPS, 2012, Yellowstone Hot Springs: Minerva Terrace. website. URL: http://mms.nps.gov/yell/features/mammothtour/minerva.htm

NUMERICAL MODELING OF GEOTHERMAL SYSTEMS: THE EFFECT OF OVERPRESSURE AND INJECTION FLUID TEMPERATURE IN INDUCING MICROEARTHQUAKES, WITH APPLICATION TO A NEW ZEALAND GEOTHERMAL FIELD

Lauriane Chardot[1,2], Steven Sherburn[1], Nicolas Fournier[1]

[1]GNS Science – Wairakei Research Centre
114 Karetoto Road, SH1, Wairakei
Taupo, 3377, New Zealand
e-mail: l.chardot@gns.cri.nz

[2]EOST, Strasbourg, France (now at University of Canterbury, Christchurch, New Zealand and GNS Science)

ABSTRACT

Induced seismicity in active geothermal areas is often thought to be linked to the re-injection of cold fluids into the subsurface hot rock which is close to failure. However, fluid flow processes leading to failure are poorly understood, because they are intrinsically complex and interrelated. Using a numerical modeling approach, this study aims at a better understanding of how overpressure and injection fluid temperature could potentially induce microearthquakes. Multiphase fluid flow in a homogeneous porous medium and the poroelastic and thermal response of this medium were modeled using the TOUGH2/BIOT2 package. The model was based on characteristics representative of a geothermal field located in the Taupo Volcanic Zone, New Zealand, but does not include pre-existing fractures. Stresses were computed over time, with a Mohr-Coulomb failure criterion defined to assess when and where failure (microearthquakes) was most likely to occur. A range of simulations were run to characterize the driving process for failure (poroelastic versus thermal). Finally, a sensitivity analysis to key parameters highlights the paramount importance of injection parameters and of the reservoir *in situ* properties on the occurrence and location of induced seismicity.

INTRODUCTION

Induced seismicity has often been linked to geothermal activity when some fluid is injected into—or extracted from the subsurface hot rock (Majer et al., 2007). Indeed, if some areas are very close to failure, even a small change in the local stress field can lead to fracturing. However, the driving processes for induced seismicity remain poorly understood, because they are often interrelated, and any attempt at modeling them requires multiphysics numerical modeling strategies.

The aim of this study is to model the effect of two possible driving processes for microearthquakes: (1) the overpressure due to the injection of new fluid, and (2) the thermal effect due to the injection of cold fluids into a hot surrounding host rock. What is their respective role in the evolution of the stresses during the injection? Do they act at the same spacio-temporal scale? How do they affect the failure process?

We first describe our model, which is generic, but representative of a New Zealand geothermal field, along with our modeling approach (fluid flow simulation, stress computation and failure definition). We then present some general results about the evolution of stresses through time and the respective contribution of poroelasticity and thermoelasticity, along with their impact on the failure process. Finally, we show the effect of key parameters (cohesion, friction angle, shear modulus, thermal expansivity coefficient, injection rate, temperature of the injected fluid) on our modeling results, and discuss how failure could potentially be minimized.

METHODOLOGY

Model description

The model used in this study aims at being representative of conditions that can be encountered at the Rotokawa Geothermal Field, in the Taupo Volcanic Zone (TVZ), where local induced seismicity has been recorded following the commencement of deep fluid re-injection. Our geothermal field is considered to be quasi-circular in map view with a radius of 5 km. Fluids colder than the surrounding rock are injected through a well having a main feed zone at 2 km depth and situated at the center of the field.

Our representative model is 2D axi-symmetrical having a thickness of 2 km and a radius of 5 km (Figure 1), with its left edge representing the central axis of the geothermal field.

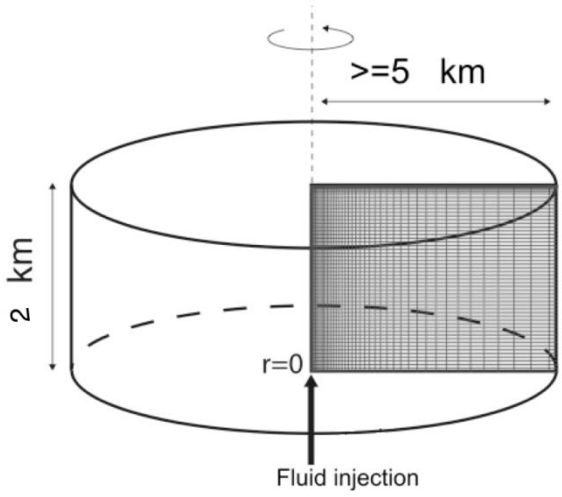

Figure 1. Computational domain for TOUGH2/BIOT2 simulations (adapted from Hutnak et al. (2009)).

The model is based on the work by Hutnak et al. (2009) on caldera-related processes, but modified to better fit the characteristics of the studied geothermal system: we use the same boundary conditions, but our model is smaller and has different input parameters. The host rock is considered to be homogeneous, with permeability and elastic parameters constant over the domain and through time. While our model remains simple, domain and input parameters are based on data from the Rotokawa geothermal field (temperature, porosity, permeability).

Fluids (H_20 and CO_2) at a temperature of 150°C are continuously injected into the host rock from a point source situated at the bottom-left corner of the half-domain, where the medium temperature is 300°C. The temperature of the injected fluids is specified using their respective enthalpy. Medium properties are adjusted to be representative of the Rotokawa Geothermal Field. However, we used a homogeneous permeability representative of the matrix—a mean value of the range of matrix permeabilities presented in Bowyer and Holt (2010), which is a lower limit of this parameter if the geothermal field contains fractures and if the fluid flow is fracture-controlled. The parameters used for our reference geothermal model are summarized in Table 1.

Table 1. Input parameters for TOUGH2/BIOT2 simulations.

Parameter	Simulation values
Rock grain density	2700 kg m^{-2}
Porosity	0.1
Thermal conductivity	2.8 W m-1 $°C^{-1}$
Rock permeability	1.2 mD
Rock grain specific heat	1000 J kg^{-1} $°C^{-1}$
Basal heat flux	400 mW m^{-2}
H_20 injection rate	97 kg s^{-1}
Specific enthalpy of H_20	6.44×10^5 J kg^{-1}
CO_2 injection rate	10^{-12} kg s^{-1}
Specific enthalpy of CO_2	5.23×10^5 J kg^{-1}
Medium shear modulus	8 GPa
Medium Poisson ratio	0.25
Medium thermal expansivity	10^{-5} $°C^{-1}$
Biot-Willis coefficient	1

Fluid flow modeling, stress computation and failure criterion definition

Majer et al. (2007) emphasized that processes leading to induced seismicity are complex and require coupled models. We therefore used the TOUGH2/BIOT2 modeling package—see Hurwitz et al. (2007) for details on the one-way coupling between TOUGH2 (Pruess, 1999) and BIOT2 (Hsieh, 1996)—in order to simulate fluid flow and associated deformation. This modeling package solves the following equation (Equation (1)):

$$G\nabla^2 u + \frac{G}{1-2\nu}\nabla(\nabla.u) - \nabla(p-p_0) - \frac{2G(1+\nu)\alpha}{3(1-2\nu)}\nabla(T-T_0) = 0 \quad (1)$$

where u is the displacement, G the shear modulus, ν the Poisson ratio, p the pore pressure, T the temperature, and α the thermal expansivity coefficient of the porous matrix. The simulation was run for 10 years to study the different time-scale processes. Outputs were extracted at 100 specific times and comprised the radial distance from the center of the domain and depth of each node, as well as the temperature and pressure at the center of each cell (Figure 2).

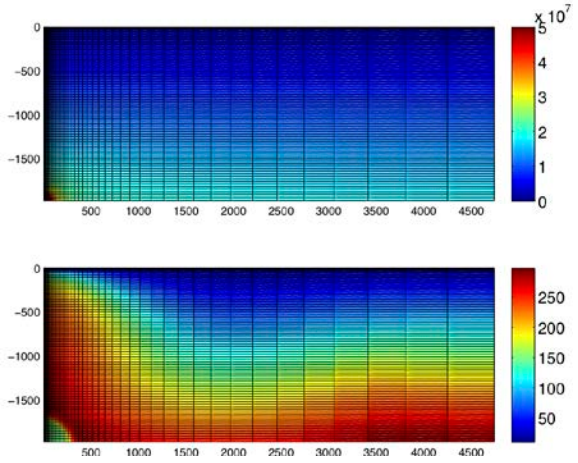

Figure 2. Pressure (Pa) (upper panel) and temperature (℃) within the domain (axes in meters) after 10 years of continuous injection.

We then followed the same procedure as Hsieh (unpublished) to compute strains and effective stresses from the displacement of each cell corner—Equations (2) and (3)—from which principal effective stresses are calculated. Positive normal stress is positive and positive normal strain denotes a shortening of length.

$$\epsilon_{ij} = -\frac{1}{2}\left(u_{i,j} + u_{j,i}\right) \quad (2)$$

$$\sigma_{ij}^{eff} = 2G\epsilon_{ij} + \frac{2\nu G}{1-2\nu}\epsilon\delta_{ij} \quad (3)$$

Finally, to assess when and where failure is most likely to occur during the simulation, we defined a Mohr-Coulomb criterion as in Jaeger et al. (2007) (Equation (4)), which forecasts failure if the condition below is true:

$$|\tau_{max}| \geq S_0 \times cos(\phi) + \sigma_{mean} \times sin(\phi) \quad (4)$$

with $\sigma_{mean} = (\sigma_1 + \sigma_3)/2$, $\tau_{max} = (\sigma_1 + \sigma_3)/2$ (σ_1 and σ_3 the maximum and minimum principal effective stress respectively), S_0 the cohesion of the rock and ϕ the friction angle.

In our model, every point is assumed to be on optimally oriented failure planes in a medium close to failure. Theoretically, in such a medium, even a very small change in the stress state should lead to failure. Hence, the cohesion term (S_0) is set to 0MPa. We chose a value of 30° as a plausible friction angle (ϕ) for the TVZ (Kissling et al., 2009).

Theoretically, in a homogeneous medium, the onset of failure would create a plane of weakness, and subsequent failure would preferentially occur along this plane instead of creating new fractures. However, our simple model doesn't consider pre-existing fractures and fracture propagation. We therefore modeled the failure-initiation front propagation through time to gain insights into the possible occurrence and location of failure at each time step, assuming that it had not occurred previously. To a certain extent, this may better represent a natural system that is not uniformly close to failure: Fluids may flow through a part of the medium which is not close to failure, with the induced stresses hence not causing failure. When fluids reach an area close to failure, the associated stress change may lead to failure.

GENERAL RESULTS

Stress evolution during the injection

We simulated the evolution of the stresses through time for our reference model. During the first 6 weeks after the start of the injection, the main significant change is the development of a tensile zone very close to the injection zone. Then, this tensile zone becomes surrounded by a compressive zone, itself bound outside by another tensile zone (see Figure 3 after 5 years of injection). Through time, the amplitude of the stresses within these zones increases along with the size of the respective zones. However, most of the changes remain localized within 500 m of the injection zone.

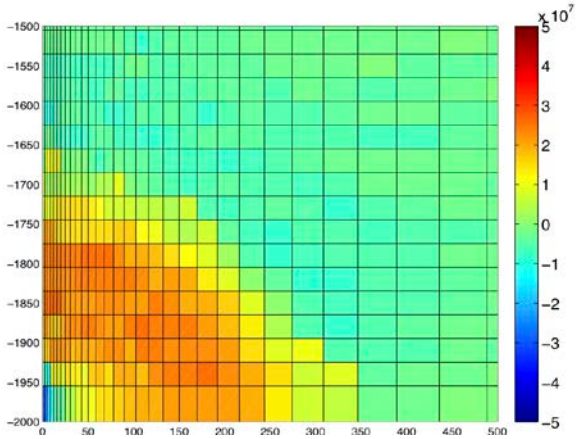

Figure 3. Mean effective stress (Pa) within the domain (axes in meters) after 5 years of injection.

Poroelastic vs. thermal effect through time

When studying surface displacement due to the injection of hot fluids into a colder caldera system, Hurwitz et al. (2007) and Hutnak et al. (2009) mentioned that two main processes drive the observed displacement: (1) the poroelastic response (due to increased fluid pressure) and (2) the thermal effect (due to thermal rock expansion). To assess the relative contribution of overpressure and thermal effect to the effective stresses, we ran a range of additional TOUGH2/BIOT2 simulations.

As in Hurwitz et al. (2007), we first assessed exclusively the poroelastic response by inhibiting the thermal effect using a null thermal expansivity coefficient, while the other parameters remained unchanged. Similarly, we then assessed the thermo-elastic response only, by inhibiting poroelasticity using an unrealistic high shear modulus of 5×10^{11}GPa. Displacement at each node through time was extracted from each of these simulations, with the associated effective stresses computed using Equations (2) and (3) where G and ν used for the reference model.

In the model where poroelasticity is the dominant effect, some tensile effective stresses appear from the very beginning of the injection and are of high magnitude close to the injection zone (Figure 4). These tensile stresses result from the pore-pressure increase due to fluid flow. However, most of the stress changes for this model remain close to the injection zone during the simulation.

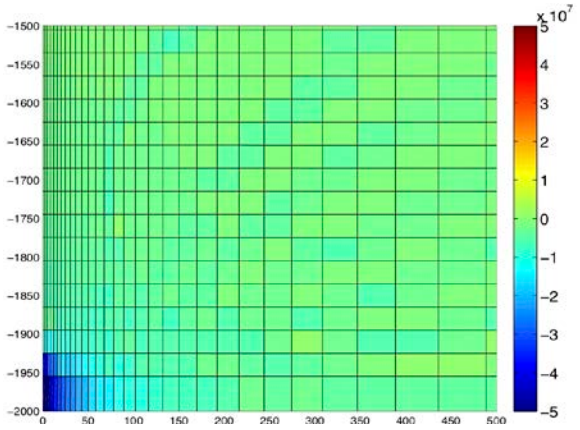

Figure 4. Mean effective stress (Pa) due to poroelastic effect within the domain (axes in meters) after 5 years of injection.

In the model where thermal effect is the main driving process for stress changes, a compressive zone develops close to the injection point, surrounded by a low amplitude tensile zone (Figure 5). These compressive stresses result from the contraction of the rock due to the interaction between cold fluid and hot host rock. Note that these stress changes only become significant after 6 weeks of injection.

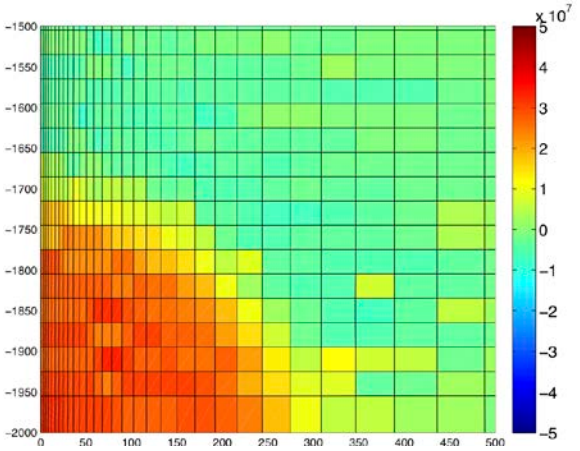

Figure 5. Mean effective stress (Pa) due to thermal effect within the domain (axes in meters) after 5 years of injection.

Then, we compared the results of these simulations with the full poro-thermoelastic reference model to discriminate the main driving process (poroelastic versus thermal) for stress changes through time in the reference model. We observe that the effective stresses for the reference model are the sum of the effective stresses in the poroelastic and thermal models.

Poroelastic effect is then the main process for stress changes at the early stage of the injection. While it remains the main process very close to the injection zone, the thermal effect becomes progressively the dominant effect in the region surrounding this injection zone.

Failure process

Failure location was simulated through time (Figure 6) using the Mohr-Coulomb criterion defined in Equation (4). We observe that failure occurs from the very beginning of the injection (Figure 6a.). This is expected for a medium close to failure, where even a small change in the stress state can lead to failure. The failure zone is mainly localized within 500 m of the injection point.

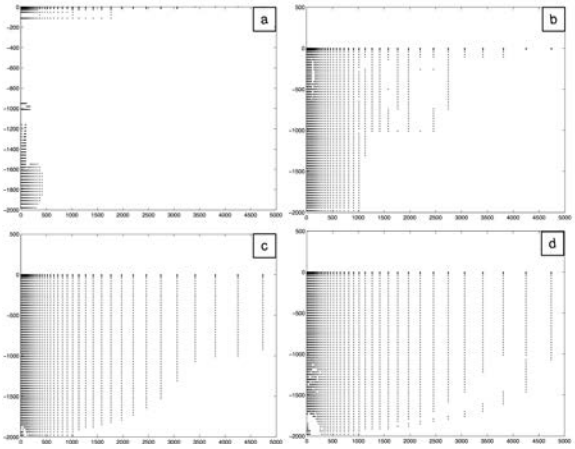

Figure 6. Failure points (black dots) after (a) 1 day (b) 1 month, (c) 1 year, (d) 10 years after the start of the injection (axes in meters).

As mentioned before, if we consider at each time step that there has been no failure at the previous time step, we observe that globally, the size of the potential failure zone increases with time (Figures 6 b., c., d.). Looking more closely at the zone around the injection point, we observe that an aseismic zone develops and becomes wider over time, reaching 300 m radius after 10 years of injection. Moreover, a new seismic zone develops inside this aseismic zone and also increases with time.

We then studied the sign of $|\sigma_{mean\_thermo}| - |\sigma_{mean\_poro}|$ to assess the dominant process for failure over time. A positive value means that the thermal effect is dominant, whereas a negative value indicates that the poroelastic effect is dominant. At the start of injection, Figure 7 shows that the failure zone coincides with the zone where the mean effective stresses are mainly caused by the poroelastic effect. Thermal stresses also act immediately, but are smaller than those due to poroelastic effect.

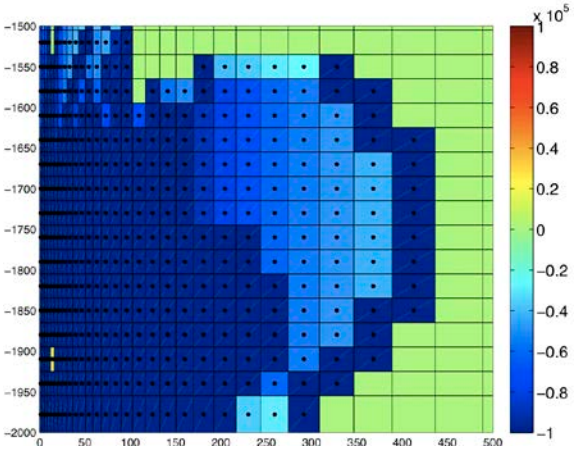

Figure 7. Failure (black dots) and $(|\sigma_{mean\_thermo}| - |\sigma_{mean\_poro}|)$ (colour) after 1 day of injection within the domain (axes in meters).

The aseismic zone developing after a few days of injection clearly coincides with a zone in compression, while the inside seismic zone coincides with a zone in tension (Figure 8). Given these findings, we propose that thermal effect is responsible for the aseismicity while poroelasticity remains the main driver for failure close to the injection zone.

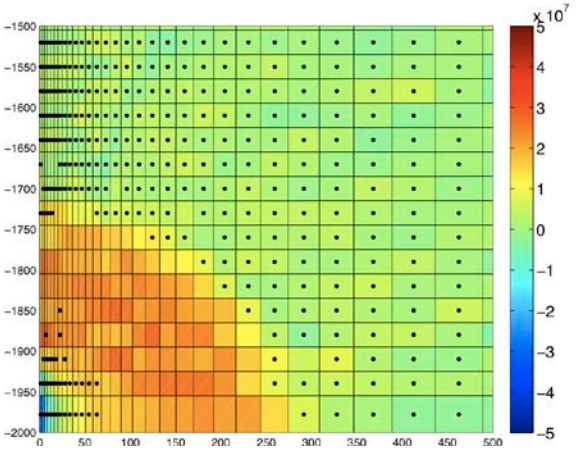

Figure 8. Failure (black dots) and $(|\sigma_{mean\_thermo}| - |\sigma_{mean\_poro}|)$ (colour) after 10 years of injection within the domain (axes in meters).

Finally, the seismic zone around the aseismic zone coincides with a slightly tensile zone, created by both thermal and poroelastic effects.
As a general comment, we note that failure mainly occurs where the stress regime is tensile. This is consistent with the fact that rock is often less resistant in traction than in compression, according to the Griffith criteria, which predicts that the value of the uniaxial compressive strength can be eight or twelve times that of the uniaxial tensile strength (Jaeger et al., 2007).

SENSITIVITY ANALYSIS

We assessed the effect of key parameters on effective stress changes and failure processes by running additional test simulations. We first considered a medium having a cohesion of 1MPa as used by Kissling et al. (2009) when studying the brittle/ductile transition at the TVZ, then a medium having a friction angle of 45° because it can be representative for andesite (Carmichael, 1982), commonly found at TVZ geothermal fields. We also used end-member shear moduli (1 and 20 GPa) to account for uncertainty in the local velocity models, along with a range of thermal expansivity coefficients (10^{-6} to 10^{-4} °C^{-1}). Finally, a range of plausible injection rates and temperatures for the injected fluid were used to define the impact of injection parameters. A summary of the various test parameters is presented in Table 2. Note that the shear modulus, thermal expansivity coefficient, injection rate, and temperature of the injected fluid impact both the stress changes and failure process, whereas rock cohesion and friction angle affect the failure process only.

Table 2. Input parameters for TOUGH2/BIOT2 the simulations used for this study sensitivity analysis.

Parameter	Simulation values
Cohesion (MPa)	0, 1
Friction angle (°)	30, 45
Shear modulus (MPa)	1, 8, 20
Therm. exp. coef. (°C^{-1})	10^{-6}, 10^{-5}, 10^{-4}
Injection rate (t/day)	100, 225, 350, 475
Inj. fluid temp. (°C)	135, 140, 145, 150, 155, 160, 165

We observe the following points:

- Increasing the rock cohesion does not affect failure within 500 m from the injection zone, but leads to less failure further away.
- Increasing the friction angle has no clear effect on the failure process in the models.
- Increasing the shear modulus (i.e., the rigidity of the medium) decreases the poroelastic effect while not affecting the thermal effect (this was the assumption of our modeling strategy, to account exclusively for the thermal effect) and hence, leads to less failure.
- Increasing the coefficient of thermal expansion increases the thermal effect while not affecting the poroelastic effect, and leads to less failure close to the injection zone.
- Increasing the injection rate increases the poroelastic effect (because of a greater pore pressure) and a wider zone of the model is affected by stress changes. This leads to more failure within the domain.
- Increasing the temperature of the injected fluid does not affect the poroelastic effect but decreases the thermal effect, because the fluid temperature becomes closer to the medium one. However, we do not observe any clear effect on the failure process, possibly due to the limited range of tested temperatures.

To summarize, failure can be minimized by selecting host rock with high cohesion, shear modulus, and thermal expansivity coefficient (thus requiring good knowledge of the pre-injection rock properties) and by using a reasonably low injection rate and an injected fluid temperature close to that of the medium.

CONCLUSION

We presented results from numerical modeling of fluid flow due to re-injection and its effect on stress changes and failure, in a domain using parameters encountered at a typical TVZ geothermal field. While our models are simplified and do not include, for instance, either fractures or the regional stress field, they still provide insights into the fundamental processes poten-

tially driving induced seismicity. The computed effective stresses show three distinct main zones across the domain: a tensile zone very close to the injection point (1), surrounded by a compressive zone (2), and an external tensile zone (3). These zones change in magnitude and size through time, but most of the changes remain within 500 m of the injection zone.

The effective stresses were computed independently for various effects: poroelastic only, thermal only, and combined poroelastic and thermal. The results show that the effective stresses due to combined poroelastic and thermal effects represent the sum of the individual poroelastic and thermal-related effective stresses. Moreover, the effective stresses due to poroelasticity are tensile, due to the increase in pore pressure, and localized close to the injection area. Conversely, the effective stresses due to thermal effects are mainly compressive, where the temperature decreases due to cold fluid injected into a hot rock, and tensile at the margins of the compressive zone.

Failure -following a Mohr-Coulomb criterion, occurs at the very beginning of the injection within 500 m of the feed zone and is mainly driven by the poroelastic effect. Through time, assuming that there is no propagation of the pre-existing fractures but failure on new fractures, a small seismic zone remains close to the injection zone (with dominant poroelastic tensile stresses). It becomes surrounded by an aseismic zone with dominant compressive thermal stresses, and, further away, by another seismic zone (resulting from poroelastic and thermal tensile stresses).

A sensitivity analysis was performed to assess how the cohesion of the rock, coefficient of internal friction, shear modulus, thermal expansivity coefficient, injection rate, and temperature of the injected fluid impact the effective stress evolution and the failure process. Results suggest that failure can be mitigated by using low injection rates and a fluid temperature close to that of the host rock—or by selecting a site where the medium has high cohesion, shear modulus and thermal expansivity coefficient.

Further modeling work could include:

- Changing the depth of the injection point source to account for stress changes and potential failure below the injection point.
- Fine-tuning our mesh and time stamps to provide more accuracy with respect to location and timing of the observed changes.
- Introducing sinks that represent the production wells.
- Modeling a shut-in in pressure to see the evolution of the poroelastic and thermal effect when re-injection stops. Indeed, there have been several cases in which induced seismicity occurred after the end of the injection.
- Introducing fractures into the model to be more representative of real cases. Along the same lines, some further testing needs to be carried out to consider the effect of permeability, especially since this model uses a relatively low value compared to what could be observed in geothermal fields where fluid flow is fracture-controlled.
- Accounting for the regional stress field.
- Using the two-way TOUGH/FLAC modeling package (Rutqvist et al., 2002) to better account for coupled thermo-hydrological and mechanical processes.

However, even using a simple model, our work shows the fundamentals of what can cause failure and seismicity in active geothermal areas. This study therefore represents a first step towards a more complete assessment of the relative contribution of poroelasticity and thermal effects on induced seismicity.

ACKNOWLEDGMENT

We are grateful to Shaul Hurwitz and Mike Hutnak (USGS, Menlo Park, USA) for providing us the TOUGH2/BIOT2 simulation codes, and stimulating discussions. We also thank Mighty River Power, particularly Steven Sewell for discussions on the Rotokawa geothermal field. This project was initially funded by Foundation for Research Science and Technology “Geothermal: New Zealand's Energy Solution,” which has (from 1 July, 2011)

been incorporated into the GNS Science CSA (Core Science Area) Geothermal Research. Finally, we thank Patrick Baud and Francois Cornet for early reviews of this work.

REFERENCES

Bowyer D, and R. Holt, Case Study: Development of a numerical model by a multi-disciplinary approach, Rotokawa Geothermal Field, New Zealand, *Proceeding World Geothermal Congress 2010, Bali Indonesia, 25-29 April 2010*, 2010.

Carmichael, R., *Handbook of Physical Properties of Rocks*, CRC Press, 1982.

Hsieh, P.A., Deformation-induced changes in hydraulic head during ground-water withdrawal, *Ground Water, 34*, 1082-1089, 1996.

Hurwitz, S., L. B. Christiansen and P. A. Hsieh, Hydrothermal fluid flow and deformation in large calderas: Inferences from numerical simulation, *J. Geophys. Res., 112*, B02206, doi:10.1029/2006JB004689, 2007.

Hutnak, M., S. Hurwitz, S. E. Ingebritsen, and P. A. Hsieh, Numerical models of caldera deformation: Effects of multiphase and multicomponent hydrothermal fluid flow, *J. Geophys. Res., 114*, B04411, doi:10.1029/2008JB006151, 2009.

Jaeger, J., N. Cook, and R. Zimmerman, *Fundamentals of Rock Mechanics* (4th ed), Blackwell Publishing, 2007.

Kissling, W., S. Ellis, F. Charpentier, and H. Bibby, Convective flowa in a TVZ-like setting with a brittle/ductile transition, *Transport in Porous Media, 77*, 335-355, 2009.

Majer, E., R. Baria, M. Stark, S. Oates, J. Bommer, B. Smith, and H. Asanuma, Induced seismicity associated with enhanced geothermal systems, *Geothermics, 36(3)*, 185-222, 2007.

Pruess, K., C. Oldenburg, and G. Moridis, *TOUGH2 User's Guide, Version 2.0*, Report LBNL-43134, Lawrence Berkeley National Laboratory, Berkeley, Calif., 1999.

Rutqvist, J., Y. S. Wu, C-F Tsang, and G. Bodvarsson, A modeling approach for analysis of coupled multiphase fluid flow, heat transfer, and deformation in fractured porous rock, Int. J. Rock Mech. Min. Sci., 39,429-442, doi:10.1016/j.ijrmms.2007.04.006, 2002.

MODELING THE OHAAKI GEOTHERMAL STSYEM

E.K. Clearwater[1], M.J. O'Sullivan[1], K.Brockbank[2], W. I. Mannington[2]

[1]Department of Engineering Science, The University of Auckland,
Private Bag 92019, Auckland 1142, New Zealand
[2]Wairakei Power Station, Contact Energy, State Highway 1, Private Bag 2001, Taupo 3352, New Zealand
e-mail: ecle011@aucklanduni.ac.nz

ABSTRACT

The Ohaaki geothermal system lies within the Taupo Volcanic Zone (TVZ) in the North Island of New Zealand. Since the early 1980s, a series of numerical models of the Ohaaki geothermal system have been developed at the University of Auckland in collaboration with Contact Energy and its predecessors. The simulator used is AUTOUGH2 (adapted from TOUGH2) and the extra capabilities of this simulator, plus the use of PyTOUGH (a library of Python scripts), have been invaluable.

Natural state simulations are used to compare the model results to the temperature data for the pre-exploitation state of the reservoir. Then production history simulations are carried out, and model results for pressure, temperature, CO_2 flow, and enthalpy are compared to data from the well testing period, the recovery period, and the production period.

Maintenance and improvement of the model is part of an ongoing effort to represent the Ohaaki system more accurately, enabling the model to be utilized as a tool for reservoir management and to predict the future behavior of the resource under various scenarios.

THE OHAAKI SYSTEM

The Ohaaki geothermal system lies on the eastern margin of the Taupo Volcanic Zone (TVZ). The Waikato River bisects the system, dividing it into the West and East Bank areas (see Figure 1). There are two separate upflow zones for each of the East and West Banks. Ohaaki (along with the other systems within the TVZ) is a high-temperature liquid-dominated hydrothermal convective system. The driving force of such a system is convection of water driven by density differences. Heat and mass are transported through the permeable rock of the reservoir by convection of water and steam. Ohaaki has a base temperature in excess of 300ºC and a large gas (CO_2) content. More information on the system can be found in Hedenquist (1990).

The basement of the Ohaaki system is a pre-volcanic greywacke, which down-faults to the north-west. This is overlain by a volcano-clastic sequence interspersed with dacitic and rhyolitic volcanic domes and flows, with complex permeability and porosity distributions. The two main production reservoirs are the Wairoa formation at depths of 400 to 1200 m field wide, and the Tahorakuri formation on the West Bank below depths of 1500 m. Details on the structure and stratigraphy of the field are outlined in Wood et al. (2001) and Rae et al. (2007).

OHAAKI POWER STATION

Drilling commenced at Ohaaki in 1965, with a total of 44 wells drilled between 1966 and 1984. There was an extended period of well testing and recovery up to 1988, when the Ohaaki Geothermal Power station was commissioned [Lee and Bacon (2000), Clotworthy et al. (1995)]. There are now over 65 wells drilled in the area.

The plant commissioned in 1988 was 116 MW_e and during the first 5 years of production, generation was maintained at ~100 MW_e. In 1993, the available steam began to decline. A deep drilling program was undertaken in 1995, which identified high temperatures and permeability in the deep volcanic formations underlying the West Bank [Lee and Bacon (2000)]. This was relatively successful; however, steam supply continued to decline. A second deep drilling program also focused on the West Bank was undertaken in 2005–2007 (Rae et al., 2007), allowing generation output to be maintained at about 60MW_e.

RESERVOIR MODEL

Grid structure

Over time, a deeper understanding of the reservoir has been developed based on data gathered by various geoscience techniques and from deeper drilling. Also over time, computational power has increased, and so it has been possible to make the reservoir model more and more refined. Earlier grid structures for the Ohaaki model have been described in Blakely et al. (1983), Newson and O'Sullivan (2001), Zarrouk et al. (2004), and Zarrouk and O'Sullivan (2006). The reservoir model discussed here is the "2011" model described in Clearwater et al. (2011).

The size of the model grid is chosen to include as much area as is needed for recharge to the system, and as much depth as is feasible in terms of the limitations of the equation of state for H_2O/CO_2 available in TOUGH2. The deepest well drilled at Ohaaki reaches a depth of almost 2.6 km, and the base of the model is set at 3 km depth.

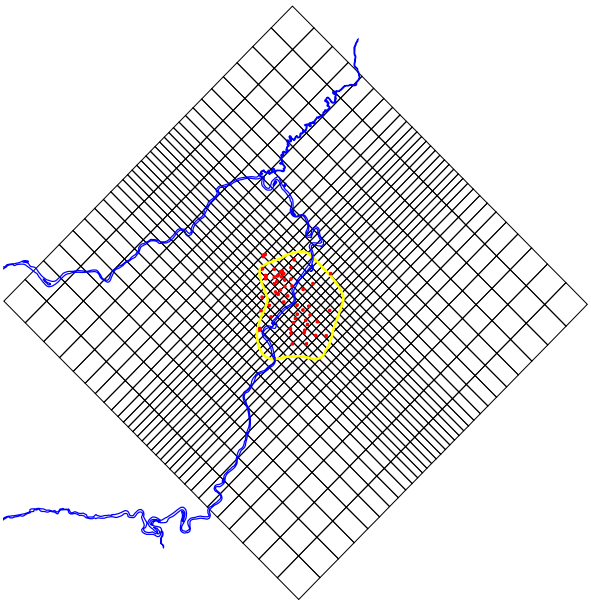

Figure 1. Plan view of the Ohaaki reservoir model grid. The blue line is the Waikato River, the yellow line the resistivity boundary, and the red dots show well-head locations.

The grid has been rotated so that columns align with the dominant faulting direction – NW-SE. The model consists of 23 layers, each with 992 elements, plus one atmosphere block, leading to a total number of elements of 22817. The grid is roughly a square covering 16 km by 15 km. Figure 1 shows a plan view of the model grid.

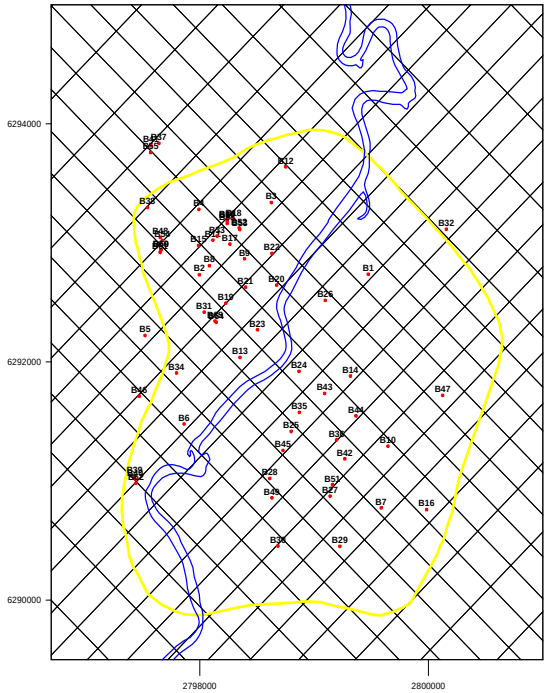

Figure 2. Close up of the model grid. The yellow line is the resistivity boundary, the red dots show well-head locations and the blue line is the Waikato River. The West bank lies on the North-West side of the river, the East bank on the South-East side.

The greatest refinement of the grid occurs within the reservoir resistivity boundary. The aim is to allow each well to be placed in a separate block and to avoid 5-sided blocks or connections that are not orthogonal. The gradual expansion of block size goes from 250 m by 250 m in the central borefield, to 1 km by 1 km at the outer boundary of the model. A close-up view of the grid is shown in Figure 2.

The layer structure of the model is shown in Figure 3. The top four layers are 100 m thick. There is then a refinement down to a layer of 20 m to give a good resolution of the Ohaaki Rhyolite, which acts as a fluid pathway. After that, the layers increase again to a maximum thickness of 250 m.

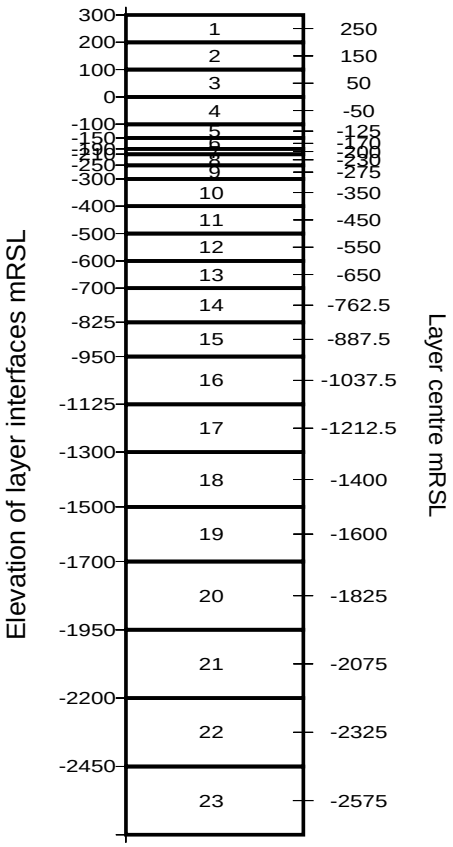

Figure 3. Vertical layer structure and layer names.

Boundary Conditions

Due to the large area of the model (and also from observing pressure changes at the boundary blocks), the model is thought to be large enough to capture all pressure changes created within the borefield and within the whole of the hydrothermal convective regime, and so all side boundaries are treated as closed. This is also a reasonable approximation for Ohaaki, because of the high CO_2 content and large boiling zone. The pressure changes in the reservoir get buffered by the expansion and contraction of the boiling zone, and hence do not spread to the edges of the model.

The top layer of the model follows the surface of the water table. The temperature and pressure of this top layer are fixed at atmospheric conditions – a temperature of 10°C, pressure of 1bar. This is a suitable approximation if the water table does not vary too much during production, and lies at a shallow depth. Over the bottom boundary mass, heat and CO_2 are injected. These are varied as calibration proceeds.

A background conductive heat flux of 120 mW/m² is used— typical of the values found throughout the TVZ. This heat flux is increased in blocks close to the main reservoir, representing the greater heat flow anomaly associated with Ohaaki. The mass inflow at the base of the model represents the upwelling fluid near the base of the convective plume which has not been captured within the model. The CO_2 is injected at an average mass fraction of 2.5%— which is representative of the amounts found in wells at Ohaaki.

A summary of the total heat, mass, and CO_2 injected into the base of the model is shown in Table 1. The total amount of carbon dioxide injected gives an average flowing mass fraction of 2.5%. A total heat input of 119 MW is applied to the model, which is close to the natural heat flow of around 100 MW (Allis, 1980), but as there is large uncertainty around this value, the model is reasonable.

Table 1. Total flow into the base of the model.

	Enthalpy (kJ/kg)	**Temperature (°C)**	**Total**
Mass	1430	314.4	68.32 kg/s
Heat	-	-	39.64 MW
CO_2	1430	310.51	1.7 kg/s

Populating grid blocks

Geoscience data is invaluable in helping to decide what rock properties should be assigned to each element in the model. Recent collaboration with ARANZ and GNS Science and the use of the LEAPFROG geological modeling software has introduced an automated way of extracting the geological model rocktypes and applying them to the elements in our TOUGH2 model. New TOUGH2 simulation input files can be created within the software and results can be visualised (e.g. Newson et al. (2012)).

The LEAPFROG software is a three-dimensional geological mapping package that allows a new integration between modeling and earth science. Reservoir modelers can view a compilation of different geological, geophysical and geochemical data to compare and relate

back to the reservoir model. A MULGRAPH [O'Sullivan and Bullivant (1995)] grid and TOUGH2 input file can be loaded and any rock parameter visualized, and the geological model can be integrated into the reservoir model—geological lithologies can be exported on to TOUGH2 grids.

Simulator

The simulator used for this model is AUTOUGH2. This is a local version of TOUGH2.2 developed at the University of Auckland. Details of the development of this simulator can be found in Yeh et al. (2012). The main improvements compared to TOUGH2.2, in a geothermal reservoir modeling context, are the inclusion of all EOS modules in a single executable, increased allowable numbers of blocks and connections, and the inclusion of new well types for production and future scenario simulations. EOS2 is the fluid property module used, first because Ohaaki is a gas-rich reservoir, and second because no EOS module is available in TOUGH2 for handling the interaction of air, water and CO_2 at the temperatures encountered in the reservoir. The coefficient used for Henry's law is the original version developed by O'Sullivan et al. (1985), and is a slightly different correlation to that used in TOUGH2.

For the steady-state simulation, the GENER types used are those in the original TOUGH2-MASS, HEAT and COM2 (CO_2). However for production and future scenarios, we have had to implement new GENER types in order to represent the complicated production and reinjection requirements.

NATURAL STATE MODELING

Implementation

To get initial conditions for the Ohaaki reservoir model, a natural state simulation must be performed first. This is to try and reproduce the conditions of the reservoir before any production or drilling occurred. The TOUGH2 model is set to run to a large time step, usually 1.0E+15 seconds is deemed to be large enough, until all primary variables have stopped changing and the simulation is in a steady state. Permeability and deep inflows are then adjusted iteratively until the model matches the observed temperature distributions.

Temperature Results

Comparison of the model result with data for a well on the West Bank can be seen in Figure 4. There is a temperature inversion at 0 mRL, which is due to the Ohaaki Rhyolite formation allowing cold groundwater to seep into the main reservoir. Early wells drilled on the West Bank feed from the Intermediate reservoir, about 400–1200 m depth. Newer West Bank wells are feeding from levels between 1600 and 2400 m deep. The model shows a reasonable match to the field temperatures in this area.

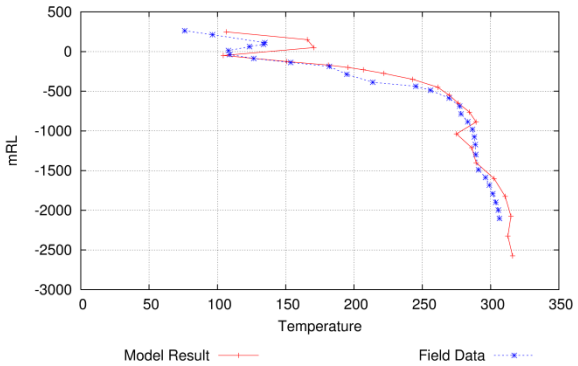

Figure 4. Temperature profile for a typical West Bank well.

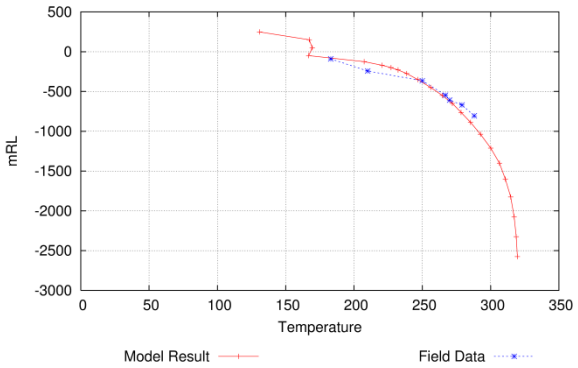

Figure 5. Temperature profile for a typical East Bank well.

Model results for a typical well on the East Bank are shown in Figure 5. East Bank wells all produce from volcanic formations between 500 and 1200 m deep. No significant permeability has been found any deeper, and so most new drilling is focused deep on the West Bank. Field data for the East Bank is more limited than for the West, but the model is showing a good match to the data.

PRODUCTION HISTORY MODELING

Implementation

To simulate the production history, we locate the coordinates within the reservoir model pertaining to each of the feed zones for each well. Each block containing a feed zone location is then assigned a time-dependent mass production rate (using a MASS generator), taken from measured field data. This sounds simple, but there has been considerable difficulty in extracting this field data.

Due to the limitations of accurately measuring two-phase flow at the time of commissioning the power plant, a continuous record of production data from individual wells at Ohaaki is not available. Instead, the total combined mass and total production enthalpy data (for each group of wells connected to each separator) is recorded.

For each well, the operating well-head pressure is recorded regularly, along with the status of the well (whether it is on production, on bleed, closed, reinjecting, etc.). The number of days per week that the well is on production is recorded, and thus the proportion of each week that each well is open is available. Individual wells are output tested every six months, and these tests provide characteristic curves for each well, from which it is possible to derive a flow rate given the measured wellhead pressure. These tests also provide information on the proportion of total flow each well is providing to the separator

From the calculated flow rate and the open times for each well, we can calculate a weekly mass flow, by multiplying the mass flow per week by the proportion of open time. These proportions are used to calculate weekly flows for each well to be used in the model as the time-dependent mass flow rate.

For multi-feed wells, the production is further broken down by assigning a proportion of the total flow rate to each feed.

Neither of these two procedures (obtaining continuous records of well by well production using occasional output test data to assign separator flows to individual wells, and assigning set proportions to multi-feed wells) is entirely satisfactory. The well characteristic curves and proportion of the contribution from each well to the separator vary from one output test to the next, and the enthalpy response of the model is quite sensitive to flow rate. So this approach to creating production rates may lead to incorrect model enthalpies.

Entering the injection data into the model is much simpler and more accurate: continuous injection rates for each injection well are provided. These are implemented as MASS just like production, but with a negative generation rate. One hundred percent of remaining separated geothermal water (SGW) is reinjected at Ohaaki, 30% of the condensate is reinjected, and the rest is lost to the atmosphere through the large natural draft cooling tower.

The period simulated is from 1966 until 2010. This encompasses early well testing, a recovery period, and commencement and continuation of the power station production.

Calibration of the production history is performed by comparing pressure, enthalpy, and CO_2 histories. Porosity, permeability, and adjustment to the boundary upflows is made as required. Pressure data are continually available from monitoring wells throughout the field, and well output tests performed every 6 months provide individual well data for pressure, production enthalpy, and CO_2 flow as a percentage of total flow rate.

At Ohaaki, there are very few significant surface features (vents, hot springs, etc.), and only one of them—the Ohaaki pool—is represented in the reservoir model. The Ohaaki pool at natural state discharged at a constant rate of about 10 kg/s. After early well testing and production, discharge from this pool fluctuated, then ceased. The bottom of the pool has since been cemented, blocking natural fluid flow, and the pool is now filled with runoff from other wells discharge. Because the initial flows were relatively constant, and the flow is still 10 kg/s (although artificial), a MASS generator of 10 kg/s at the depth in the reservoir that the fluid is known to come from is applied for natural state and production simulations.

Contact Energy supply heat to local timber drying companies. Prior to 1997 two-phase flow was supplied for timber drying from a well separate from the production field. The timber drying facility required a specific amount and dryness fraction. This was applied using a POWR generator (a new well type created in AUTOUGH2). In 1998, the well providing the timber plant was hooked up to the production system, and no excess steam was available to the timber drying plant. Instead, some of the SGW, rather than being re-injected, was supplied, so the fluid going to the timber drying no longer needs to be included in the reservoir model.

Results

Pressure

The model pressures during the well testing and production period show a good match to the field data, especially for most new, deeper wells on the West Bank. The model result for block eca11 is shown in Figure 6. Layer 11 in column eca has been allocated as the feed zone for this well, 750 m deep. The model follows the pressure drawdown reasonably, showing the correct trend but a bit too much drawdown.

Drawdown history from deeper-feeding West Bank wells is shown in Figure 7. The model results in this plot are taken from layer 19 (1900 m deep) in column eqe. There are two wells that feed from this block, the first being BR15 during the early well testing and production period until 1995, to which the model shows a good match. The model then shows the correct amount of drawdown until 2007 onwards, when BR60 started producing. The latest drawdown pressure match is reasonable.

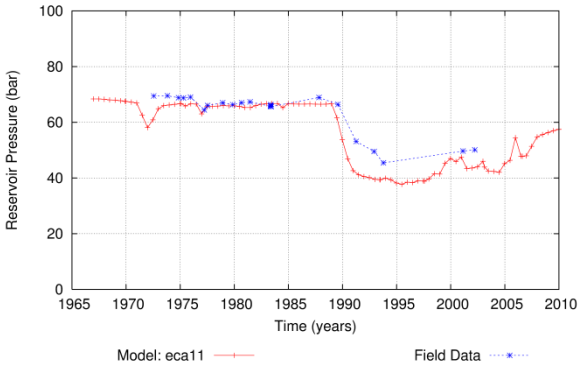

Figure 6. Pressure vs. time for a typical shallow East Bank well.

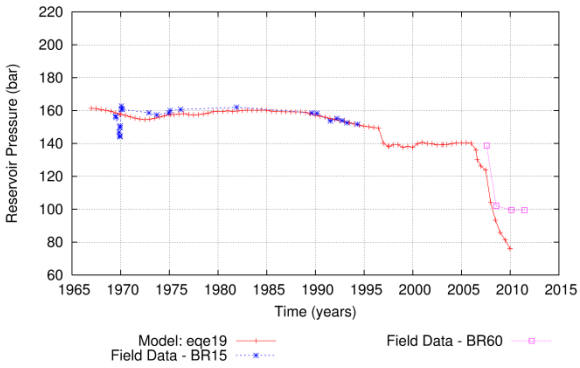

Figure 7. Pressure vs. Time for a typical deep West Bank well.

Enthalpy

The match with field data is quite varied. In general the well-by–well performance of the model match is reasonable. However, further calibration is required for some areas where not enough boiling is occurring—especially over a period over 1990 to 2000, as seen in Figure 8.

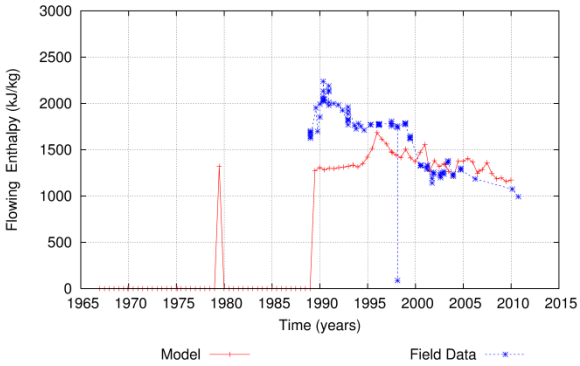

Figure 8. Enthalpy result for a typical East Bank well.

Enthalpy data is quite variable from well to well—the East Bank wells tend to have an initial increase in enthalpy followed by a slow decline, whereas the West Bank wells start out at a lower enthalpy that stays constant or increases over time.

CO_2 percent mass fraction

The model results for carbon dioxide content over time are very mixed in quality. For some wells, the model match is very poor, but often this is associated with a mismatch in enthalpy which can hopefully be improved by further calibration. For other wells, the match is very good, as seen in Figure 9. Overall trends and magnitudes averaged field wide are reasonable.

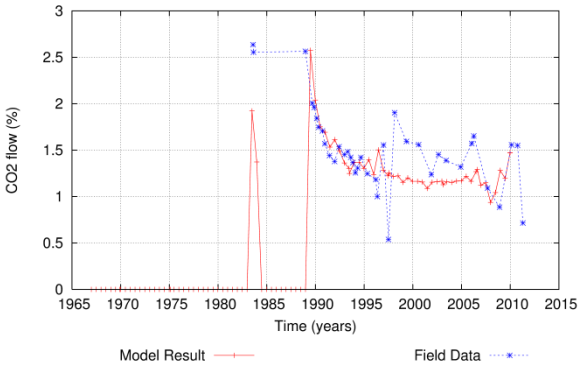

Figure 9. The CO_2 vs. Time for a typical West Bank well.

FUTURE SCENARIO MODELING

The Ohaaki reservoir model is currently being used as a tool for reservoir management. Various drilling/production/injection scenarios are carried out with the model, over both short and long-term time scales, to get an understanding of how the reservoir may behave in the future.

Implementation

The final conditions from the history-matching simulation are used as initial conditions. All boundary conditions remain the same as for production and natural state conditions. Future scenarios for Ohaaki may contain existing wells, new make-up wells, or a combination of the two. The production requirements may be restrictions on steam or mass take or both from different areas of the field. The reinjection requirements can be complex combinations also. Make-up wells are added or removed over time to meet the mass and steam requirements. Wells are run on deliverability, so each well needs a cut off pressure and a productivity index (PI). The PI is easily automatically obtained for existing wells by using DELG, a mass type in AUTOUGH2 (Yeh et al., 2012). PI for make-up wells is determined from similar existing wells PI's. Cut-off pressures are obtained using a well bore simulator.

CALIBRATION

Aside from the field data extraction difficulty outlined earlier in this paper, another particular problem has been found when trying to calibrate the Ohaaki reservoir model. This difficulty appears to be particularly severe for models with a CO_2/water equation of state, but could be due to the interaction of any liquid and gas phases, since it has also been seen on layers near the unsaturated zone when using an air/water model.

In some cases, a small change in the permeability structure resulted in a particular model block needing to change from a two-phase state to compressed hot water. In the Ohaaki model, the high CO_2 content can often make this phase change difficult, and the natural state simulation takes a very large number of time steps to complete. Or, the time step may get so small that the simulation may never reach completion.

Unfortunately, this problem makes it difficult to use the inverse modeling code iTOUGH2 (Finsterle, 1993) to assist with model calibration, and makes it hard to determine the sensitivities of the model to variation in parameter values. This is where PyTOUGH [Croucher (2011)] has been invaluable—Python scripts can be used in conjunction with inverse modeling software, such as PEST (Doherty, 2000), to ensure that only a true steady-state simulation is reached before any parameter changes are made. PyTOUGH also enables automation of the calibration process. A script can be used so that if a block is holding up the simulation, the gas saturation or another property of that block and its neighbors can be checked. Then, depending on what is holding up the simulation, we can push the saturation to either single phase or two-phase in the INCON file, or alter permeability in the TOUGH2 input file. This can all be performed without the user having to intervene.

FUTURE WORK

The current refinement of the shallow layers in the model (100 m thick) is too large to accurately capture shallow pressure transients, and having the top surface as the water table constrains the table level to be unrealistically fixed. Shallow pressure changes can be very important in a geothermal context, to look at any consequences of fluid extraction such as ground deformation. The model is currently being refined in the shallow layers, and the top layer's elevation updated to reflect the surface topography rather than the water table. To

continue having CO_2 in the model will mean having an unsaturated zone filled with CO_2 rather than air.

REFERENCES

Allis, R.G. "Heat Flow." In *Guide to Geophysics of the Volcanic and Geothermal Areas of the North Island, New Zealand.*, Miscellaneous Series 3, 47-48: The Royal Society of New Zealand, 1980.

Blakely, M.R., M. J. O'Sullivan, and G.S. Bodvarsson, A Simple Model of the Ohaaki Geothermal Reservoir, *5th New Zealand Geothermal Workshop,* University of Auckland, pg 11-16, 1983.

Clearwater, E. K, M. J. O'Sullivan, and K. Brockbank, An Update on Modelling the Ohaaki Geothermal System, *33rd New Zealand Geothermal Workshop,* Auckland, 2011.

Clotworthy, A., Lovelock. B., and B. Carey, Operational History of the Ohaaki Geothermal Field, New Zealand., *World Geothermal Congress,* Florence, Italy, pg 1797-1802, 1995.

Croucher, A.E., Pytough: A Python Scripting Library for Automating Tough2 Simulations, *33rd New Zealand Geothermal Workshop,* Auckland, New Zealand, 2011.

Doherty, J. *Pest - Model Independent Parameter Estimation. User Manual: 5th Edition.* Watermark Numerical Computing, Corinda, Australia, 2000.

Finsterle, S. *Itough2 User's Guide Version 2.2*. Lawrence Berkeley Laboratory, University of California, 1993.

Hedenquist, J.W., The Thermal and Geochemical Structure of the Broadlands - Ohaaki Geothermal System, New Zealand., *Geothermics,* 19(2), 151-185, 1990.

Lee, S., and L. Bacon, Operational History of the Ohaaki Geothermal Field, New Zealand, *World Geothermal Congress,* Kyushu-Tohoku, Japan, pg 3211-3216, 2000.

Newson, J.A., W. Mannington, F. Sepulveda, R. Lane, R. Pascoe, E. K Clearwater, and M. J. O'Sullivan, Application of 3d Modelling and Visualization Software to Reservoir Simulation: Leapfrog Geothermal and Tough2, *Thirty-Seventh Workshop on Geothermal Reservoir Engineering,* Stanford University, Stanford, California, 2012.

Newson, J.A., and M. J. O'Sullivan, Modelling the Ohaaki Geothermal System, *26th Workshop on Geothermal Reservoir Engineering,* Stanford University, Stanford, California, pg 186-192, 2001.

O'Sullivan, M. J., G.S. Bodvarsson, K. Pruess, and M.R. Blakely, Fluid and Heat Flow in Gas Rich Geothermal Reservoirs, *Society of Petroleum Engineers Journal,* 25(2), 215-226, 1985.

O'Sullivan, M. J., and D.P. Bullivant, A Graphical Interface for the Tough Family of Flow Simulators, *TOUGH Workshop,* Berkeley, California, pg 90-95, 1995.

Rae, A.J., M.D. Rosenberg, G. Bignall, G.N Kilgour, and S. Milicich, Geological Results of Production Well Drilling in the Western Steamfield, Ohaaki Geothermal System:2005-2007, *(29th) New Zealand Geothermal Workshop*, 2007.

Wood, C.P., R.L. Brathwaite, and M.D. Rosenberg, Basement Structure, Lithology and Permeability at Kawerau and Ohaaki Geothermal Fields, New Zealand, *Geothermics,* 30, 461-481, 2001.

Yeh, A., A.E. Croucher, and M. J. O'Sullivan, Recent Developments in the Autough2 Simulator, *TOUGH Symposium 2012,* Lawrence Berkeley National Laboratory, Berkeley, California, 2012 of Conference.

Zarrouk, S. J., and M. J. O'Sullivan, Recent Computer Modelling of the Ohaaki Geothermal System, *(28th) New Zealand Geothermal Workshop,* University of Auckland, 2006.

Zarrouk, S. J., M. J. O'Sullivan, and J.A. Newson, Computer Modelling of the Ohaaki Geothermal System, *(26th) New Zealand Geothermal Workshop,* University of Auckland, Auckland, pg 114-120, 2004.

COUPLED MULTIFLUX-TOUGH2-TOUGHREACT T-H-M-C MODEL FOR EGS STUDIES

George Danko, University of Nevada, Reno, danko@unr.edu
Davood Bahrami, University of Nevada, Reno, dbahrami@unr.edu
Liange Zheng, Lawrence Berkeley National Laboratory, lzheng@lbl.gov

ABSTRACT

We have developed a coupled numerical model for simulating flows of coolant mass, as well as transport of heat and chemical species, in Enhanced Geothermal System (EGS) reservoirs with discrete fractures. A Computational Fluid Dynamics (CFD) submodel in MULTIFLUX solves for laminar or turbulent flows in any planar-, penny-, or lens-shaped fracture. The CFD submodel includes advective, convective, and diffusive transport of heat and mass in a multicomponent mixture within a fracture. Discrete fractures may form a network of planar fractures and connecting conduits. The fracture aperture of each planar configuration is variable with space and time, due to (a) thermal dilatation of the strata, (b) elastic deformation by hydraulic pressure in the fracture system, and (c) geochemical precipitation and dissolution.

The new concept is used in the formulation of a mechanical model for aperture variation in a self-propped fracture with hydrodynamic pressure and temperature. The CFD submodel is coupled to the submodel for the host geothermal formation, a porous, fractured, and jointed rock mass. Multiphase, multicomponent heat and fluid flow simulations are provided by TOUGH2 and/or TOUGHREACT in the geologic submodel. Coupling of the overlain fracture network system in the CFD model-element to the host geothermal formation involves the Numerical Transport Code Functionalization (NTCF) technique, a modeling accelerator of the iterations in MULTIFLUX.

Our new model can be used to interpret short-term injectivity test results and help in evaluating fracture aperture and planar extension. An industrial application example (and validation) of the model is provided for the Desert Peak EGS site in Nevada, operated by ORMAT. The model is also applicable to long-term thermal drawdown simulations and life-cycle studies.

INTRODUCTION

Advanced numerical models currently applied to thermal-hydrologic-chemical (T-H-C) component transport in a geologic formation assume a porous matrix for the media with equivalent-continuum porosity and permeability, overlain with equivalent-continuum fractures in the geologic media. Such models include TOUGH (Pruess et al., 1999), NUFT (Nitao, 2000), and UDEC (Itasca, 2009). Blackwell and McKenna used TOUGH to demonstrate transient and steady-state heat flow fields for a typical basin over hundreds of thousands of years (McKenna and Blackwell, 2003). However, their model used only a single fault with a rather coarse discretization and with a 10^{-14} m^2 permeability, contrasted with 10^{-20} m^2 in the bedrock. TOUGHREACT (Xu, et al., 2004) with reactive chemistry was utilized (Xu and Pruess, 2001) to model 3-D multiphase fluid flow and reaction of hot brine injection wells. Individual fractures and/or faults represent a challenge for porous-media models. A set of discrete fractures is used by researchers at National Energy Technology Laboratory (NETL) (Brohmal, et. al, 2011) for modeling the flow field in a natural geothermal system at the Brady's Hot Springs site, operated by ORMAT Technologies in Nevada, USA. This model, however, deals only with flows and does not have T-H-M-C capabilities.

What has not been seen in the literature is a numerical model for flow, heat, and mass transport for a single fracture or a system of single fractures, fully coupled to the rock mass with its porous and finely distributed continuum fractures. To serve the needs and overcome the difficulties listed in the foregoing, we have developed a new, fully-coupled T-H-M-C model, using a discrete fracture or fractures with autonomous, planar flow and aperture variation characteristics, as well as connections to the surrounding rock mass.

TIME-DEPENDENT MODEL-ELEMENTS FOR T-H-M-C PROCESSES

Time-Dependent Coolant Loss or Gain

Coolant fluid in the fracture may be lost or gained. The coolant mass flux from or to the rock mass is by Darcy flow (Bird and Stewart, 1960; Welty et al., 1984; Danko, 2011). The coolant fluid mass-flux density, q_{mF}, in $[kg/(m^2 s)]$ units may be written as an advective flux component across a unit wall surface area of the fracture opening:

$$q_{mF} = k/\nu \; \text{grad}(P)|_w \qquad (1)$$

In Eq. (1), k in $[m^2]$ and ν in $[m^2/s]$ are the rock-mass permeability and coolant-fluid kinematic viscosity, respectively. The grad(P) term denotes the gradient (which, in a one-dimensional case, is a simple differential with respect to distance from the wall) of the flow pressure in the rock-mass pores and fractures within close proximity of the fracture wall.

Applying the NTCF model solution to Eq. (1), the time-dependent coolant-fluid flux density, q_{mF}, may be expressed in a matrix-vector equation, as follows (Danko, 2011):

$$[q_{mF}] = [q_{mF}^c] + [[M_P]] [P - P^c] \qquad (2)$$

In Eq. (2), the bracketed variables are vectors composed of the sampled values of the variables taken at pre-selected time instants. Vectors $[q_{mF}^c]$, and $[P^c]$ are "central" values around which the linearized model in Eq. (2) is valid and defined during model identification. Matrix $[[M_P]]$ is a dynamic admittance operator of constant coefficients that are identified by the NTCF procedure.

Time-Dependent Rockmass Heat Flux

The total heat flux density, $[q_h]$ from the rock mass at the fracture wall boundary is the sum of the conduction and advection components. The following boundary equation can be written (Bird and Stewart, 1960; Welty et al., 1984; Danko, 2011):

$$q_h = \rho \; c_p \; a \; \text{grad}(T)|_w + q_{hc}|_w \qquad (3)$$

In Eq. (3), ρ in $[kg/(m^3)]$, c_p in $[J/(kg\ K)]$, a in $[m^2/s]$, and T in $[K]$ are density, specific heat, and thermal diffusivity, respectively. The last term, $q_{hc}|_w$, in $[W/m^2]$ is the advective component of heat-flux density due to convective, Darcy-flow transport of all mass fluxes entering the fracture space from the rock mass. The time-dependent temperature gradient, grad(T), and the pressure-driven, advective Darcy flux components are expressed with analytical matrix-vector equations using a mathematical-numerical technique called Numerical Transport Code Functionalization (NTCF) (Danko 2006). The corresponding NTCF model to Eq. (1) is as follows (Danko, 2011):

$$[q_h] = [q_h^c] + [[H_T]] [T - T^c] + [[H_P]] [P - P^c] \qquad (4)$$

In Eq. (4), the bracketed variables are vectors composed of the sampled values for the temperature, T, and pressure, P, variables taken at pre-selected time instants. Time-dependency of q_h in Eq. (4) is in its vector form as a list of n values taken at n increasing time instants over a time interval. Vectors $[q_h^c]$, $[T^c]$, and $[P^c]$, also n-vectors, are "central" values around which the linearized model in Eq. (4) is defined during model setup. Matrices $[[H_T]]$ and $[[H_P]]$, all nxn in size, are dynamic admittance operators of constant coefficients that are identified by the NTCF procedure. This procedure employs system identification of the heat-transport process from the rock mass using a numerical transport model (i.e., a code such as TOUGH; Pruess, et al., 1999) with a set of pre-determined test boundary conditions as input histories with time.

Eq. (4) may be viewed as the algebraic, general representation of the differential model given in Eq. (3). The gradients, as driving forces of the diffusive and advective flux components, are replaced with finite differences, varying directly with time through the time-series of sampled boundary values given by vectors $[T]$ and $[P]$. The obvious advantage of using Eq. (4) is that the boundary values [T] and [P] can be calculated or modeled from the ventilation air temperature and pressure, and can even be measured for verification. In contrast, the $\text{grad}(T)|_w$ and $q_{hc}|_w$ are unknown and difficult-to-capture variables, dependent on time and the boundary conditions of T and P on the bounding wall.

In Eq.(4), the dynamic admittance matrices $[[H_T]]$, and $[[H_P]]$ may be determined

against model identification runs, using the thermal-hydrologic model of the rock mass, e.g., applying a TOUGH2 model (Pruess, et al., 1999). The advantage of using a rock-mass heat-transport model in the form of Eq. (4) is its accuracy in true time-dependent tasks, as well as its computational efficiency in iterative calculations.

Time-Dependent Chemical Species Flux

Chemical species may escape from the rock mass and flow into the coolant fluid in the fracture. Mass transport may occur by diffusion and advection. The rock mass is formed of porous and fractured geologic deposits and gives off its stored aqueous species by diffusion and advection. Additionally, dissolution or deposition may occur at the surface layer of the fracture wall. According to the basic governing laws introduced by Fick and Darcy (Danko, 2011; Danko, 2006; Pruess et al., 1999), the mass flux density, q_m, in *[kg/(m²s)]* units, may be written as the sum of the diffusive and advective flux components across a unit wall surface area of the fracture opening, and added to the source or sink term, q_{mS}:

$$q_{mC} = \rho\, D_m\, \mathrm{grad}(c)|_w + c\, q_{mF} + q_{mS} \qquad (5)$$

In Eq. (5), ρ in *[kg/(m³)]*, D_m *in [m²/s]*, c in *[kg/kg],* and q_{mF} are the mixture density, species diffusion coefficient, concentration, and coolant-fluid loss or gain to or from the rock mass, respectively. The grad(c) term denotes the gradient (which, in a one-dimensional case, is a simple differential with respect to distance from the wall) of the concentration of aqueous species in the rock-mass pores and fractures in close proximity to the fracture wall.

Applying the NTCF model solution to Eq. (5), the time-dependent species flux density, q_m, may be expressed in a matrix-vector equation as follows (Danko, 2006):

$$[q_{mC}] = [q_{mC}^{c}] + [[M_c]]\,[c - c^{c}] + [(c - c^{c})]\, q_{mF}] + [q_{mS}] \qquad (6)$$

In Eq. (6), the bracketed variables are vectors composed of the sampled values for the variables taken at pre-selected time instants. Vectors *[q_{mC}^{c}],* and *[c^{c}],* are "central" values around which the linearized model in Eq. (6) is valid and defined during model identification. Matrix *[[M_c]]* is a dynamic admittance operator of constant coefficients that are identified by the NTCF procedure. The source or sink term, *[q_{mS}],* may be temperature- and concentration-dependent, requiring modeling. The estimation of *[q_{mC}]* may require another expansion of Eq. (6), with the use of the *[[M_T]]* admittance operator for the temperature effect:

$$[q_{mC}] = [q_{mC}^{c}] + [[M_c]]\,[c - c^{c}] + [(c - c^{o})\, q_{mF}] + [[M_T]]\,[T - T^{c}] \qquad (7)$$

The boundary values, *[c],* and *[T]* can be calculated and/or modeled from the fracture-flow model. The dynamic admittance matrices in Eq. (7) can be determined from pre-selected model runs using (for example) TOUGHREACT for a given rock mass.

A simplified treatment of the temperature-dependent source term, q_{mS}, for a single-component reactive species, such as quartz, is as follows:

$$q_{ms} = A^{*} M / A \left[1 - (Q/K)\right] k_{25} \exp\left[\frac{-E}{R}\left(\frac{1}{T} - \frac{1}{298.15}\right)\right] \qquad (8)$$

Equation (8) is based on the reaction-rate model used in TOUGHREACT(Xu et al., 2006) with some commonly accepted simplification, most notably, the omission of pressure dependency. In Equation (8), the following notations are used:

- r reaction mass flux (also called kinetic rate, of which positive values indicate dissolution, and negative values precipitation), in [kg/(s-m²)]
- A^* total available reactive specific surface area (surface area per mol amount of mineral species), in [m²/mol]
- M molar weight (mass) of the mineral species, in [kg/mol]
- A transport model surface area (bounding surface area per mol amount of mineral species) in [m²/mol]
- Q reaction quotient for the mineral-water reaction at the interface between the mineral-species layer and the solution. The unit of Q depends on the chemical species involved in the reaction. Note that in simple reactions with only one aqueous species, such as with quartz, Q equals the concentration, Q= c in [kg/kg]

K equilibrium constant for the mineral–water reaction. It is a function of temperature, defined by Equation (10). K has the same unit as Q and also depends on the chemical species involved in the reaction.

$k_{25.}$ Reaction-rate constant (mole mass per unit mineral surface area and unit time), taken at 25°C, in [mol/(s-m^2)]

E activation energy for the reaction in [J/mol]

R gas constant in [J/(mol-K)]

T absolute temperature of the surface layer in [K]

The equilibrium constant, K, is as follows for any species

$$\log(K) = C_1 + C_2*\ln(T) + C_3*T + C_4*T^{-1} + C_5*T^{-2} \quad (9)$$

where C_1 ,C_2, C_3, C_4 and C_5 are constants and log(K) is the 10-based logarithm of K. The A^*/A surface ratio in Equation (9) may be viewed as a "projection" of the total reactive surface of a mole amount (or 1 kg amount, for that matter) of mineral crystals to the plane of the mass-transport surface of the rock mass in the reactive transport model.

TIME-DEPENDENT MODEL-ELEMENTS FOR COOLANT FLOW, HEAT, AND CHEMICAL SPECIES TRANSPORT IN A FRACTURE

Time-Dependent Coolant-Flow Model

The *bulk* flow in the fracture is modeled as a discretized fluid network. The flow is governed by the Navier-Stokes equation (Danko, 2008). In its simplified form for flow channels along given grid lines; it reads:

$$\rho\left(\partial v_x / \partial t + \mathbf{v}\cdot\nabla v_x\right) = \rho g_x - \partial Pb/\partial x + F_x \quad (10)$$

$$\rho\left(\partial v_y / \partial t + \mathbf{v}\cdot\nabla v_y\right) = \rho g_y - \partial Pb/\partial y + F_y \quad (11)$$

$$\rho\left(\partial v_z / \partial t + \mathbf{v}\cdot\nabla v_z\right) = \rho g_z - \partial Pb/\partial z + F_z, \quad (12)$$

where v_x, v_y, v_z are velocity components of *vector* v; g_x, g_y, g_z are gravitational forces that include buoyancy in x, y, and z directions, Pb is total mixture pressure and F_x, F_y, F_z are viscous and kinetic dissipation terms. Note that the $\partial v_x / \partial t$, $\partial v_y / \partial t$, and $\partial v_z / \partial t$ terms in Eqs. (10)–(12), accounting for the inertia forces accelerating or stopping coolant flow, may be insignificant and omitted in slow transients.

The viscous dissipation terms are calculated from Moody's friction-resistance coefficient, while the kinetic dissipation terms are evaluated using fitting loss coefficients at network branch connections. The network-solution equation corresponding to Eqs. (10)–(12) for the flow total pressure, Pb, as a function of the bulk branch mass flow rate, qa, is as follows (Danko, 2008):

$$iRSa\cdot Pb = qa + iRSag\cdot Pbg - iRRSa\cdot Z\cdot g + iRRSag\cdot Zg\cdot g \quad (13)$$

Time-Dependent Heat Transport in the Fracture Flow

The heat balance for fracture flow is governed by Fourier's second law, as follows (Welty et al., 1984):

$$\rho c\frac{\partial T}{\partial t} + \rho c_p v_i \frac{\partial T}{\partial x} = \rho c_p a\frac{\partial^2 T}{\partial x^2} + \rho c_p a\frac{\partial^2 T}{\partial y^2} + \rho c_p a\frac{\partial^2 T}{\partial z^2} + q_h \quad (14)$$

where q_h is the heat dissipation in the dx, dy, dz gridblock due to heat exchange on the rock-mass interface as well as viscous dissipation and expansion or compression work. The differential equation may be integrated over a finite element to form an integrated-parameter CFD solution. This approach allows for reducing the number of discretization elements in the computational domain. A mass, energy, and momentum network-solution method is implemented in MULTIFLUX (Danko, 2008). The network-solution equation corresponding to Eq. (14) for the time-dependent temperature field, T, is as follows:

$$iRSh\cdot T = qh + qh_n + qL + qVD + qCE + iRShg\cdot TG + ICgh \quad (15)$$

Time-Dependent Chemical Species Transport in Fracture Flow

The species concentration model in the fracture void space may be described by Fick's second law, as follows (Welt et al., 1984):

$$\rho\frac{\partial c}{\partial t}+\rho v_i\frac{\partial c}{\partial x}=\rho D\frac{\partial^2 c}{\partial x^2}+\rho D\frac{\partial^2 c}{\partial y^2}+\rho D\frac{\partial^2 c}{\partial z^2}+q_{mC} \quad (16)$$

where ρ is density of the bulk flow mixture in the void space; *x, y, z* are Cartesian coordinates; t is time; *c*, D, and q_{mC} are respectively concentration, diffusion coefficient, and mass flux source of a given species; and v_i is the bulk velocity in flow channel *i* in a discretized flow network model. The network solution equation corresponding to Eq. (16) for the time-dependent concentration field *c* is as follows:

$$iRSc * c = qmC + qc_n + iRScg. * c_G + ICgc \quad (17)$$

ROCK MECHANICS MODEL FOR THE ROCK MASS

A new approach is a conceptual fracture-aperture construct with tunable constants for a self-propped fracture model that can be calibrated against either (a) field measurements of injection rate and wellhead pressure, or (b) against a three-dimensional (3-D) rock-mass model, e.g., in 3DEC (Itasca, 2009). Figures 1 and 2 show the self-propped fracture model element of a pixel for an open, planar fracture. The flow channels are assumed to be among "self-propping" islands." The concept is very different from assuming an open planar fracture with a "penny-shaped" or "lens-shaped" cavity with free-hanging walls. The detailed solution for the self-propped fracture model is described in a separate paper (Danko and Bahrami, 2012). The final solution for the aperture of each fracture pixel is as follows:

$$\delta(X)=\delta_0+C^p\left[\overline{Pb}(X)-\overline{Pb_0}(X)\right]+C^T\Delta\overline{L}\left[T(X)-T_0(X)\right] \quad (18)$$

In Eq. (18), $X=(x,y,z,t)|_{\Delta A}$ denotes any point over the planar fracture at a grid of ΔA and at any instant in the simulation time interval. The bars in Eq. (18) indicate grid-averaged values in the (x,y,z) plane at any point over a ΔA surface. Term δ_0 is a small initial aperture that remains open under hydrostatic pressure when $\overline{Pb}(X)=\overline{Pb_0}(X)$. The scale factors, called pressure and thermal aperture coefficients, C^p, and C^T, respectively, are as follows:

$$C^p=\frac{\delta_p}{E_F} \text{ and } C^T=C^p\frac{E_R}{L} \quad (19)$$

Notations:

δ:	Hydrodynamic fracture aperture under load, pressure, flow, and thermal effects
δ_p:	Fracture aperture under hydrostatic (no-flow) pressure
S:	Static deformation of L due to in situ stress
$\Delta L(T)$:	Total, integrated thermal contraction of the rock strata, function of temperature, T
σ :	in situ stress
p:	Hydrodynamic pressure in the fracture
E_F:	Self-popper fracture layer elastic modulus
E_R:	Rock mass elastic modulus

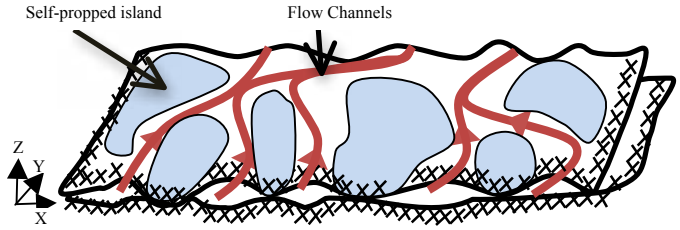

Figure 1. Self-propped fracture with flow channels and support islands.

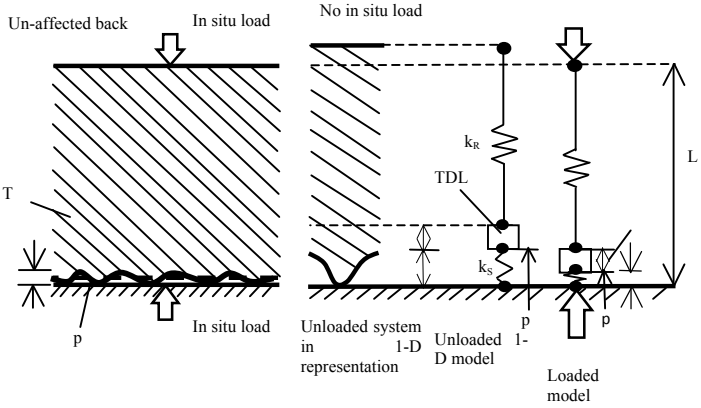

Figure 2. Thermal-hydraulic conceptualization of the fracture aperture change.

COUPLED SOLUTION FOR FLOW AND TRANSPORT PROCESSES BETWEEN THE ROCK MASS AND FRACTURE FLOW

The NTCF model elements for the rock mass and the CFD model elements for the fracture are coupled by an iterative procedure in MULTILUX (Dank, 2008). Figure 3 is a solution flowchart showing the coupling process by the Direct Iteration and Successive Approximation coupler (DISAC) module. DISAC matches temperature (*T*), heat flux (q_h), concentration (*c*), species flux (q_{mC}), and bulk flow flux (q_{mF}) on the boundary

surface node and time instance during simulation. The coupled simulation results are processed and saved by the DISAC module.

Three iteration loops are used in the Internal Balance Iteration (*IBI*) cycle to balance rock mass and airway transport processes, starting from the first innermost loop to the third outermost loop:

- Bulk flow calculation in the discretized fracture network system assuming an initial temperature, pressure, and concentration distribution.
- Heat-flow-balance iteration between the NTCF and airway CFD models for each time division.
- Chemical species mass-flow-balance iteration between the NTCF and fracture CFD models for each time division.

The three iteration loops are executed until no significant change is observed in the results between consecutive iterations. While the CFD model-element is solved within MULTIFLUX, the NTCF model elements are only surrogate models for the rock mass. TOUGH2 may be used as an independent solver for the heat and bulk coolant-transport processes in the rock mass. TOUGHREACT may be used as an independent solver for the chemical species transport. At high-temperature, strongly nonlinear applications, the NTCF model parameters must be refreshed during coupling iterations (Danko, 2006).

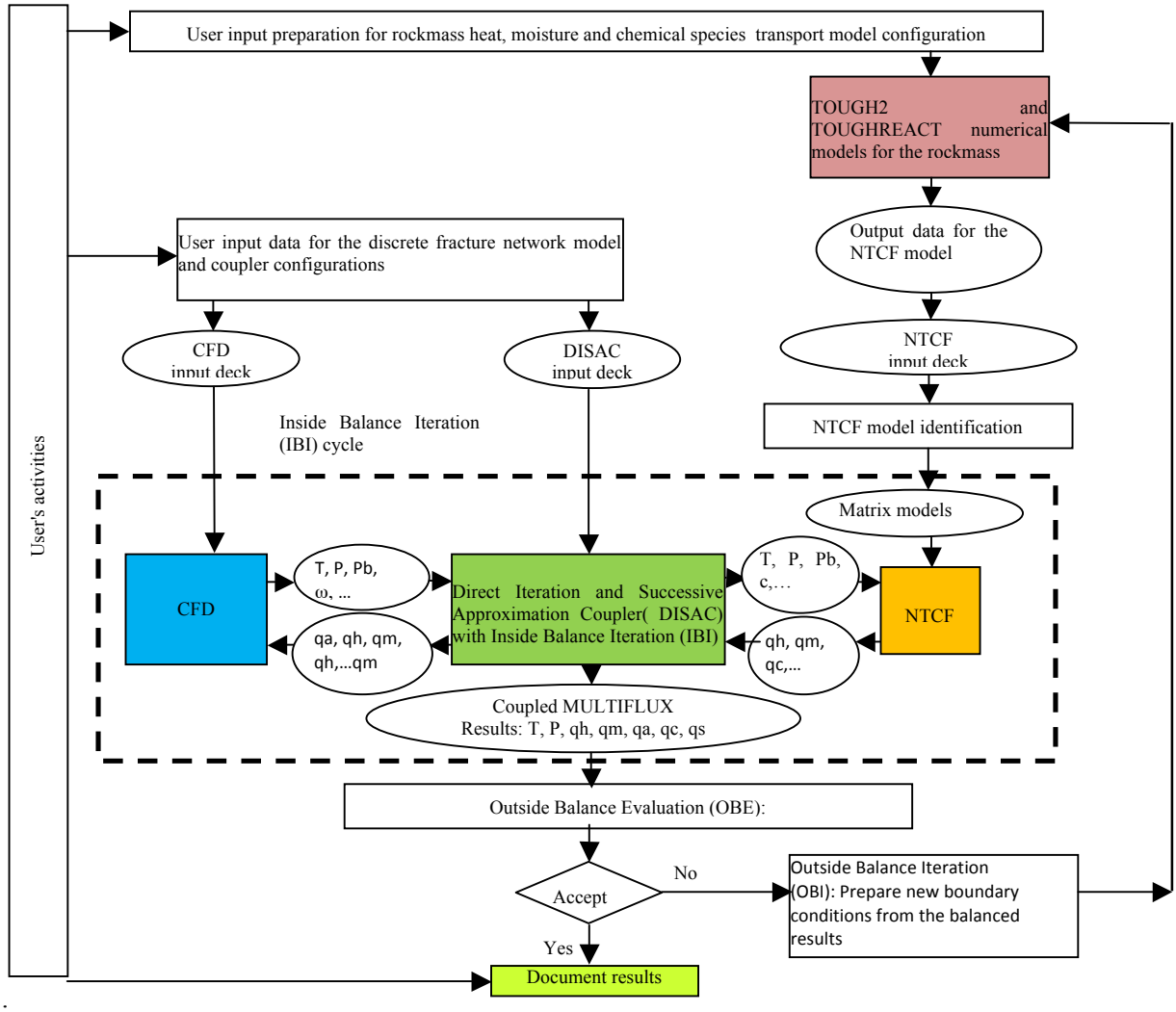

Figure 3. Solution of the coupled flow and transport processes between the rock mass and the discrete fracture.

MODEL APPLICATION EXAMPLE FOR THE DESERT PEAK EGS SITE

Here we use the MULTIFLUX model to characterize the EGS fracture at ORMAT's Desert Peak site in terms of fracture size from a single, short-time pumping test. A Rapid T-H-M process model is configured in MULTIFLUX for the explanation of the measurement results shown in Figure 4.

Application of the T-H-M model to interpret injection test results

The hypothesis of fracture-aperture variation according to Eq. (7) in a self-similar fracture over its entire spatial domain can be tested using the coupled T-H-M model in MULTIFLUX against injection pressure, flow, and thermal drawdown-measurement results.

For short-time, high-pressure-peak injections, it is necessary to use a transient model of fracture flow in the fracture plane surrounded with the porous media, filled with compressible fluid. Even if an EGS fracture were isolated with no connection to a production well or natural fracture and/or faults draw, fluid would flow into the rock mass due to elastic storativity. We modeled this flow process using TOUGH2, and results from TOUGH2 are imported via an NTCF model element. The rapid T-H-M process part of the curve is redrawn and restored by removing the interruption spike for model matching, shown in Figure 5.

The numerical model in MULTIFLUX is configured to deal with the storativity of pores and micro-fractures within the rock mass, and the storativity of the injection fluid in the EGS fracture void, due to the change in the fracture aperture and the extension of the opened fracture area. The changing size of the planar (penny or lens-shaped) EGS fracture in its extent (radius) and surface area is modeled by adjusting the fracture aperture according to Eq. (18)

Determination of the pressure coefficient, C^P, was accomplished using measured data from the short-term pumping test shown in Figure 5. The matching is achieved using 20 points along the curve, also shown in Figure 5. in the first step, the self-propped pressure coefficient is determined as a variable for each pumping time instant, while the thermal coefficient is kept at zero (C^T=0) due to the short time period with negligible thermal penetration and thermal contraction. The variable C^P over time is shown in Figure 6. As depicted, the variation disappears after a few hours, and C^P becomes near-constant.

In the second step, a constant pressure coefficient value of 2.3597e-11 for C^P is used for the entire time period of 10 hours. The wellhead pressure variation from the T-H-M model when using this constant and the self-propped fracture model is shown in Figure 7.

Figures 8 and 9 show the magnitude of the fracture-flow velocity and the hydrodynamic pressure in the EGS fracture according to the self-propped model, respectively. As depicted, the flow field does not completely occupy the available fracture extension to R=700 m, although this size would be available for flow in the fracture plane according to the envelope of the fracture in the model configuration.

Figures 10 and 11 show the hydrodynamic pressure and the self-adjusting fracture aperture profiles, respectively, across one cross section as a function of radius at three selected time instants.

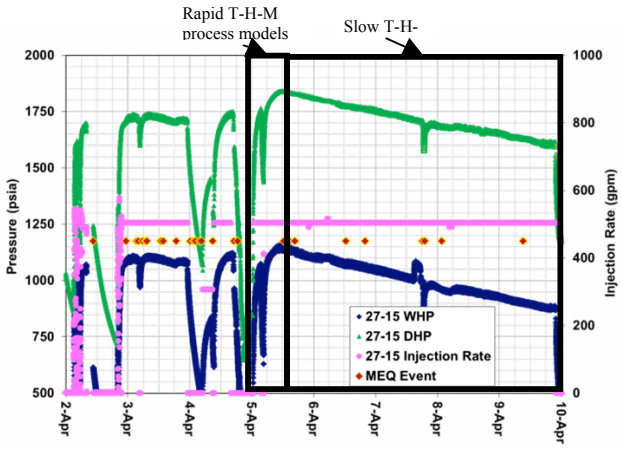

Figure 4. Short-time injection pressure and flow rate data from the pumpability tests at Desert Peak, ORMAT

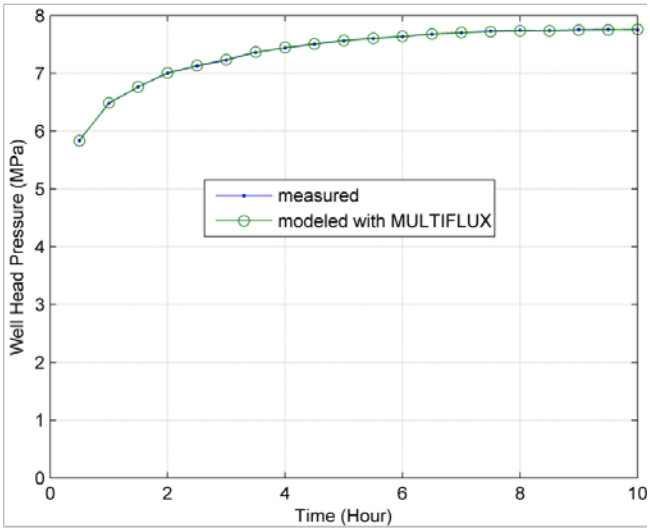

Figure 5. Comparison between measured and modeled results with variable C^P coefficient.

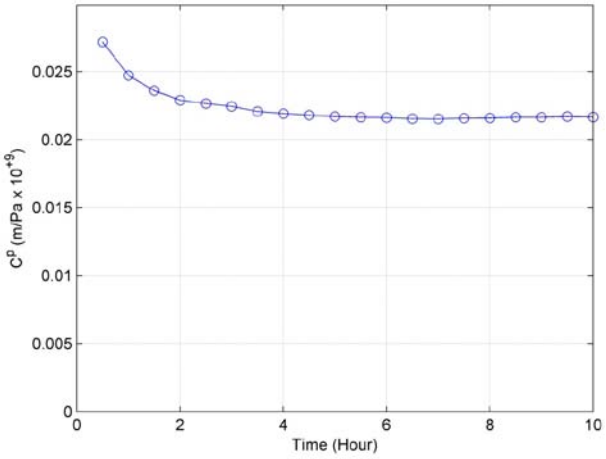

Figure 6. Variation of C^P with time for a perfect match in the wellhead pressure between model and measurement shown in Figure 5.

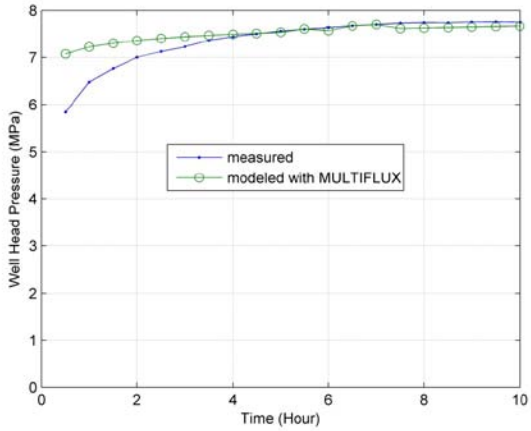

Figure 7. Wellhead pressure match between measurement and model simulation with a constant pressure coefficient of C^P=2.3597e-11.

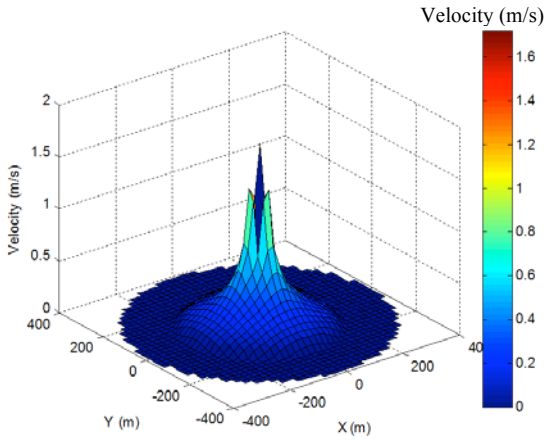

Figure 8. Distribution of the magnitude of the fracture flow velocity at time=10 hr.

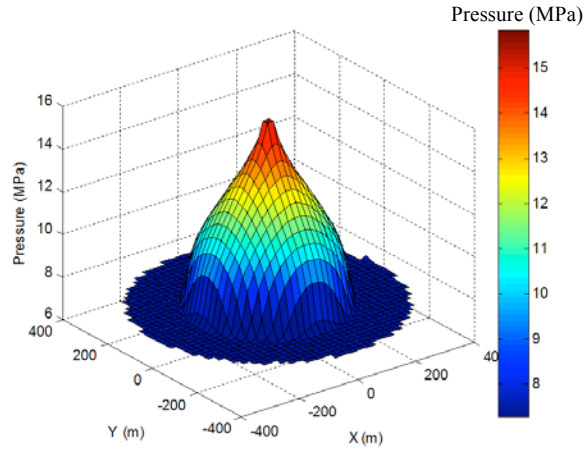

Figure 9. Distribution of the hydrodynamic pressure under flow condition at time=10 hr.

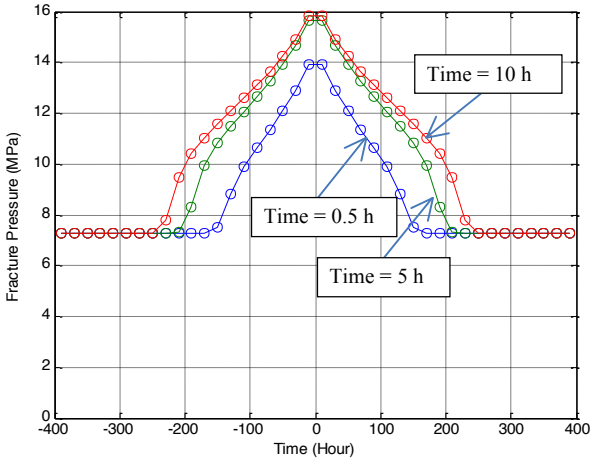

Figure 10. Hydrodynamic pressure profile at three selected time periods during the pumping test.

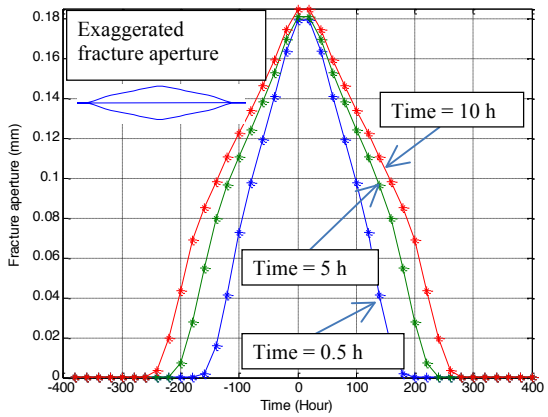

Figure 11. Fracture aperture profile at three selected time periods during the pumping test.

CONCLUSIONS

- We present a new T-H-M-C model for an EGS reservoir.
- The model describes the fracture aperture variation as it evolves under the injection pressure using a self-propped fracture model-element with self-similarity over the entire fracture envelope.
- There is no need to predetermine the extent of the fracture radius along its plane. The outer radius is self-determined by the model, governed by the force and mass balance of the system.
- The fracture-aperture model parameters, such as initial, open aperture as well as pressure and thermal coefficients in Eq. (18), can be uniquely identified from the measurement data of a single injection test.
- The MULTIFLUX model, with its new fracture-aperture model element, matches very well with published results from an EGS well at Desert Peak, operated by ORMAT.

ACKNOWLEDGEMENT

The financial support of DOE under grant number EE0002759 is appreciated. The in-kind support provided by ORMAT, the project's industrial partner, is also appreciated.

REFERENCES

Bird, R. B., Stewart, W. E., and Lightfoot, E. N., (1960), "Transport Phenomena," Wiley and Sons.

Brohmal G., Crandall D., Eastman H., Harbert B., Haljasmaa I., Siriwardane H., Disenhof D., Gill M., Roberts E., Gyovai K. and Soong Y., 2011. "Rock Core Evaluation: Brady's Hot Springs Well BCH-03." National Energy Technology Laboratory, DOE Award Number: DE-PS36-09GO99017.

Danko, G., 2006. "Functional or Operator Representation of Numerical Heat and Mass Transport Models." ASME J. of Heat Transfer, vol. 128, pp. 162-175.

Danko, G., 2008. "MULTIFLUX V5.0 Software Documentation Qualification Documents, Software Tracking Number: 1002-5.0-00, Software Management Office, Berkeley National Laboratory."

Danko, G., 2011. "Ventilation and climate control of deep mines." McGraw-Hill 2011 Yearbook, Mining and Metallurgical Section, pp. 1-4.

Danko, G., and Bahrami, B., 2012. "A New T-H-M-C Model Development for Discrete-Fracture EGS Studies", GRC's 36th Annual Meeting, Reno, Nevada.

McKenna, J. R., and Blackwell, D. D., 2003. "Numerical Modelling of Transient Basin and Range Extensional Geothermal Systems ." Proceedings, TOUGH Symposium, Laurence Berkeley National Laboratory, Berkeley, California.

Welty, J. R., C. E.Wicks, and R. E.Wilson (1984), "Fundamentals of Momentum, Heat, and Mass Transfer," 3rd edition, Wiley and Sons.

Xu, T., Sonnenthal, E., Spycher, N., and Pruess, K., 2004. "TOUGHREACT User's Guide: A Simulation Program for Non-isothermal Multiphase Reactive Geochemical Transport in Variably Saturated Geologic Media." Report LBNL-55460, Lawrence Berkeley National Laboratory, Earth Sciences Division, Berkeley, California.

Xu, T. and Pruess, K. (2001), "Modeling multiphase non-isothermal fluid flow and reactive geochemical transport in variably saturated fractured rocks: 1. Methodology." American Journal of Science, 301, 16-33.

TOUGH2 AS A TOOL FOR PERFORMANCE PREDICTION OF THE BALCOVA GEOTHERMAL FIELD, TURKEY

Goker Ertunc, Mahmut Parlaktuna

Middle East Technical University (METU)
Department of Petroleum and Natural Gas Engineering
Ankara, 06800, TURKEY
e-mail: egoker@metu.edu.tr

ABSTRACT

The Balcova geothermal field, located in the Izmir Bay area of the Aegean coast of Turkey, is the first field utilized in Turkey for direct heat application. Today, the total residential area being heated by the produced water is around 2,470,000 m^2. The produced water with a temperature range of 100–140°C has low dissolved solids and noncondensable gas content. The field has production characteristics of 1800 m^3/hour at peak times of the heating period and about 300 m^3/hour during summer months, when water is needed for balneology. On average, 85% of the produced fluid is re-injected after its energy is taken into heating centers. The field currently has 11 production, 6 re-injection and 4 observation wells.

We recently constructed a three-dimensional numerical simulation model of the field using the TOUGH2 software. A natural-state model was established based on the conceptual model of the field and further calibrated by the available production/injection data, recorded pressure-temperature values from production wells and water level measurements from observation wells for 1996–2012. Future performance of the field was discussed after forecasting runs. Results show that production could be sustained for the next 15 years with the existing production/injection scheme.

INTRODUCTION

Balcova Geothermal Field, the first field utilized in Turkey for direct heat application, is located in the Izmir Bay area of the Aegean coast, 11 km southwest of the city of Izmir (Figure 1).

Figure 1. Location map of the Balcova geothermal field (Aksoy & Filiz, 2001).

The construction of the Balcova district geothermal district heating system was started in 1996; today, the system is the biggest district heating application in Turkey with heating capacity of 159 MW_t heating an area of 2,470,000 m^2. The hot-water production rate of the field is 1800 m^3/hour at peak times of the heating period, and the field has a theoretical production capacity of 2050 m^3/hour, if all the production wells were put into production (Ozdiler & Sayik, 2011).

There has been a continual increase in demand for space-heating applications in the Balcova area. As a result, both produced and injected volumes of geothermal water for heating have been increasing. Large production and injection practices in any geothermal field must be carefully with respect to not harming the reservoir characteristics of the field, such as avoiding a decline in reservoir pressure due to high production without sufficient injection, or avoiding a decline in temperature due to excess injection and early breakthrough.

This study is aimed at constructing a reservoir simulation model for the Balcova Geothermal Field, to help in making performance predictions that could guide us in future field operations.

CONCEPTUAL MODEL

Reservoir simulation starts with the construction of a detailed conceptual model, in which existing field data are evaluated carefully and important physical and chemical processes that influence the system are identified. The conceptual model defines a grid-free representation of all the properties that are used to describe the geothermal system. These are generally flow boundaries, alteration, main geologic features such as faults and layers.

The extensive fracture system that developed in the Balcova area within the Izmir Flysch sequence created a convective hydrothermal system. The geothermal system in Balcova is fed by meteoric water that infiltrates down through faults, joints and fractures (pointing to the NW, N and NE) into the Izmir Flysch, attaining deep levels (at least 2000 m). Deep circulating waters are heated by an unidentified heat source, and then ascend through the Agamemnon Fault. Uprising geothermal fluids change flow laterally to the north through two main highly fractured zones, acting as outflow zones of the geothermal system. These zones are situated at 40 - 100 m and 300 - 1000 m depths. At present, both the hot water in the shallow alluvium, and the hot water in the deeper outflow zone are used (Serpen, 2004). To date, around 50 wells, with depths ranging from 45 m to 1100 m, have been drilled in the Balcova area. Some of these wells have been abandoned because of technical difficulties. The field currently has 11 production, 6 re-injection and 4 observation wells. Figure 2 illustrates the hydrogeological conceptual model and also well locations of the Balcova geothermal field.

DEVELOPMENT OF THE NUMERICAL MODEL

The purpose of developing a numerical model is to match the static and dynamic temperatures and pressures of the system and reproduce all the significant features of the conceptual model. In this study, TOUGH2 (Pruess et al., 1999), a numerical simulation program designed for multi-dimensional fluid and heat flows of multiphase, multi component fluid mixtures in porous and fractured media, was used to develop the numerical model.

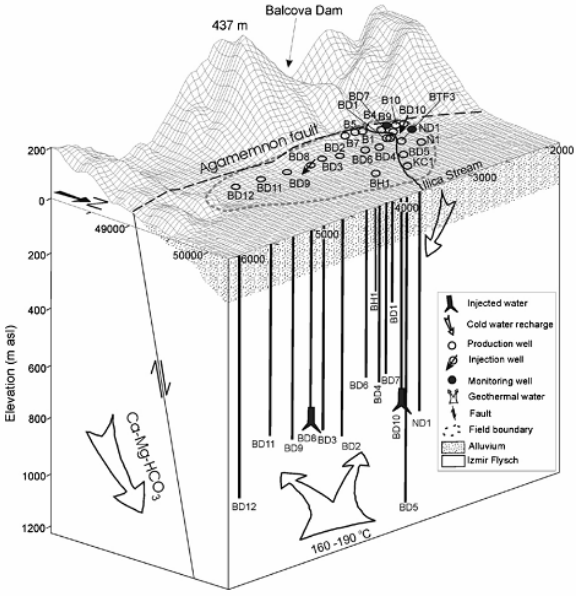

Figure 2. Conceptual model of the Balcova geothermal field (Aksoy et al., 2007).

A total of 45,696 grid blocks were used to define the geothermal system in Balcova; overall dimensions of the model are 3200 m × 1600 m × 2550 m in x, y and z directions, respectively. Thus, total volume is around 13.2 km^3. The model consists of 26 layers, with thicknesses ranging from 5 m to 400 m. By using small thicknesses, it is possible to separate different formations, permeable and impermeable zones at nearly exact depths. Figures 3 and 4 show the top and elevation views of the three-dimensional model constructed.

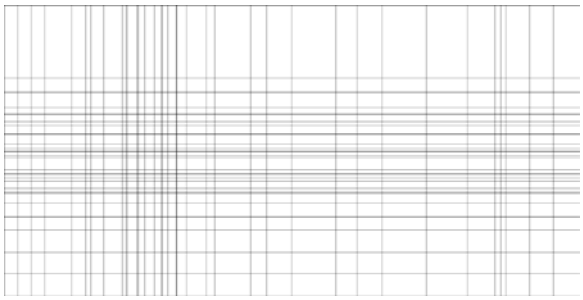

Figure 3. Top view of the three-dimensional model.

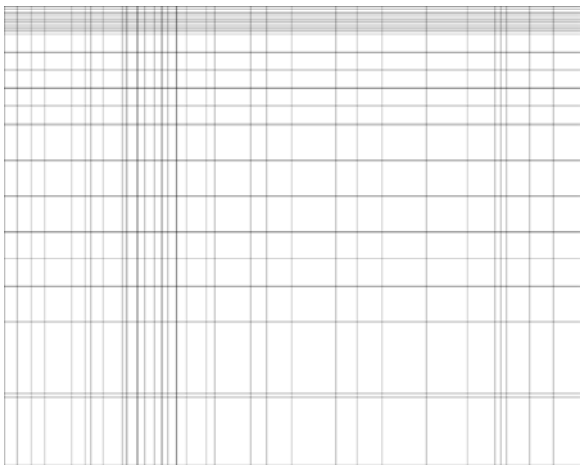

Figure 4. Elevation view of the three-dimensional model.

The numerical model was then calibrated in two stages, first by matching the natural state of the reservoir, and then by matching the production/injection history of the field.

NATURAL-STATE MODELING

Natural-state modeling is the stage of geothermal reservoir modeling in which the state of the field before its exploitation is modeled. It is known that geothermal reservoirs evolve over geological time. The rate of change in thermodynamic properties during geological time is minimal compared to changes resulted from exploitation of the reservoir. Thus, the geothermal reservoirs in their natural state can be considered in pseudo-steady state conditions. It is a common practice in geothermal reservoir simulation studies to run the model without any production/injection conditions to reach the pseudo-steady state (Bodvarsson et al., 1986).

The natural state model was developed using trial and error procedures until the calculated temperatures reasonably matched the measured temperatures. Permeability values were adjusted until a good match was obtained. Also, the natural influx was specified as a rate of 50 kg/s with an enthalpy of 6.6E5 J/kg at the base of the Agamemnon Fault.

Figures 5 and 6 compare the measured and model temperature profiles of shallow B-10 well and deep BD-2 well, respectively. In both wells, the measured and model temperature values are in good agreement.

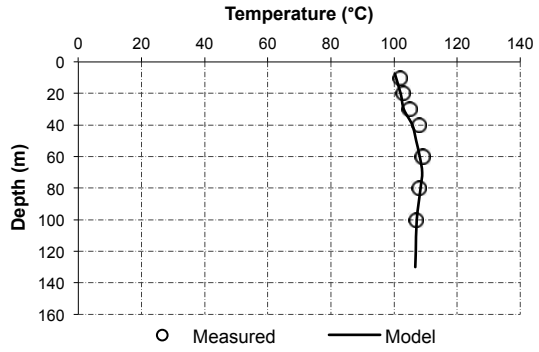

Figure 5. Temperature vs. depth profiles of the shallow B-10 well.

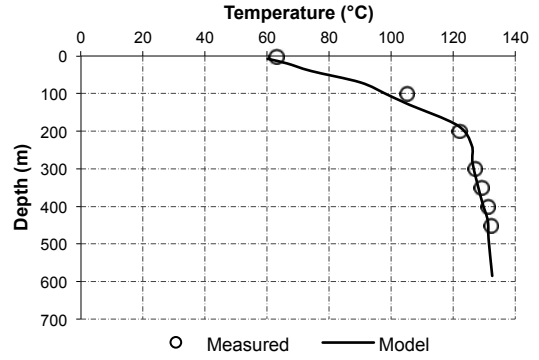

Figure 6. Temperature vs. depth profiles of the deep BD-2 well.

HISTORY MATCHING

A second matching stage of calibration has been carried out for systems having some production history. The history-matching process involves numerous iterations and parameter adjustments until a reasonable agreement is obtained with the time-dependent production history (Bodvarsson, 1988).

Using the temperature and pressure values obtained from the natural state modeling and production/injection data recorded between years 1996 and 2012, we conducted a simulation of the exploitation period for 16 years. After making several adjustments to the model, we arrived at a reasonable match to the measured data.

Bottom-hole temperature values obtained from the simulation study were matched with the values measured during the period 1996–2012. Figures 7 and 8 show the simulated (model) temperature values compared with the measured temperature values for the shallow B-10 well

and deep BD-2 well, respectively. As can be seen in the figure, both data sets are in good agreement.

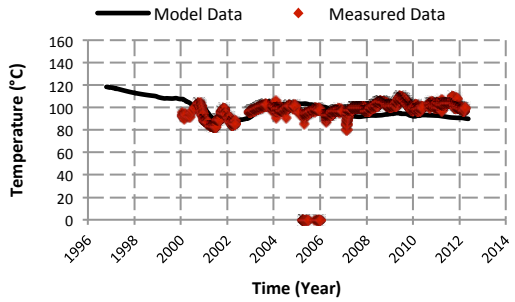

Figure 7. A comparison of simulated (model) and measured temperatures for the shallow B-10 well.

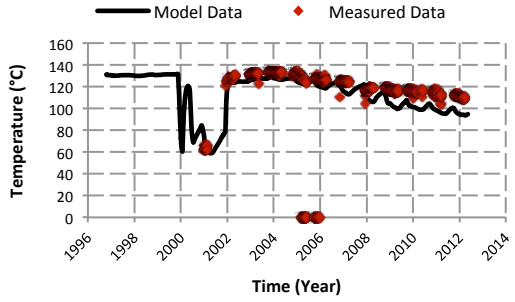

Figure 8. A comparison of simulated (model) and measured temperatures for the deep BD-2 well.

Since there are no recorded bottomhole pressure values for production wells, measured water level data obtained from the observation wells were matched with the simulated pressure values. Again, the model data reasonably matched the measured water level data.

FUTURE PERFORMANCE PREDICTIONS

After successfully calibrating the model by natural-state modeling and history matching, we then used it to predict the future performance of the field. The forecasting run, which covered a period of 15 years, assumed that the production and injection history for the entire field as of January 2012 would be maintained for the next 15 years. For initial conditions, temperature and pressure values obtained at the end of the history matching stage were used.

The results of the forecasting run show that the temperature values could not reach their original values at the end of each year. The decline in simulated bottom-hole temperature values at wells B-10 and BD-2 is illustrated on Figures 9 and 10, respectively.

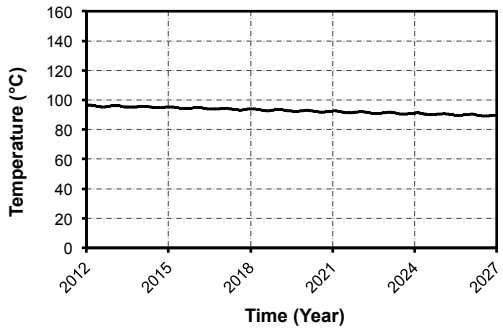

Figure 9. Simulated bottomhole temperature profile of the shallow B-10 well.

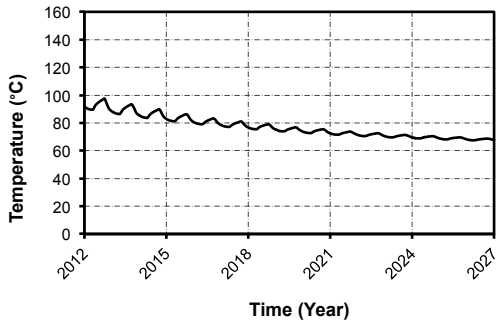

Figure 10. Simulated bottomhole temperature profile of the deep BD-2 well.

On the other hand, as seen in Figure 11, the bottom-hole pressure of the shallow B-10 well declines ~2 MPa in winter (at peak times of the heating period) and recovers to its original value in summer due to natural recharge. The pressure trend in the deep wells is also similar. A pressure drawdown of ~1 MPa is observed from winter to summer months in the deep BD-2 well (Figure 12).

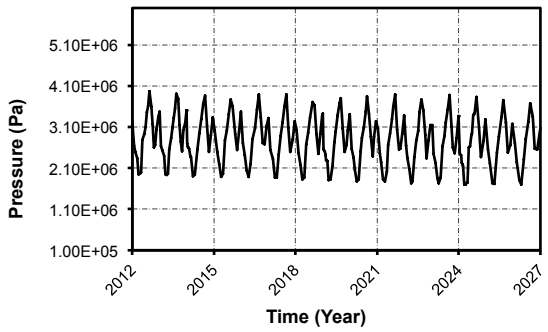

Figure 11. Simulated bottomhole pressure profile of the shallow B-10 well.

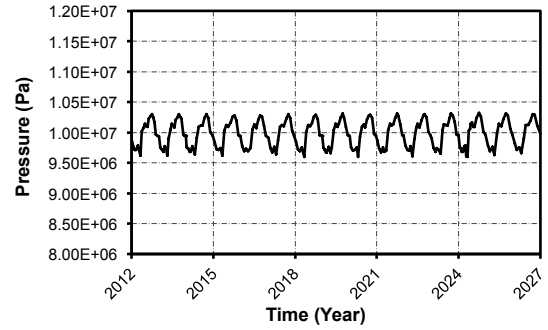

Figure 12. Simulated bottomhole pressure profile of the deep BD-2 well.

CONCLUSIONS

A numerical model of the Balcova geothermal field was constructed. The numerical model was then calibrated in two stages, first by matching the natural state of the reservoir, and then by matching the production history of the field.

The natural state modeling of the field reasonably matched with the available bottomhole temperature and pressure data from existing wells in the field. The model was then calibrated against the available production/injection data with reasonable matches being obtained to the temperature and pressure of the reservoir. Thus, the obtained model provides a good representation of the field, which could be used for predicting the response of the field exploitation.

The results from the forecasting run, which covered a period of 15 years, indicate that the Balcova Geothermal Field is sustainable for the next 15 years with the existing production/injection scheme.

REFERENCES

Bodvarsson, G., Pruess, K., & Lippmann, M. *Modeling of Geothermal Systems*. Journal of Petroleum Technology, 1007-1021, 1986.

Bodvarsson, G., *Numerical modeling of geothermal systems with applications to Krafla, Iceland and Olkaria, Kenya*, Lawrence Berkeley National Laboratory Report 23950, 1988.

Pruess, K., Oldenburg, C., Moridis, G., *TOUGH2 User's Guide, Version 2.0*, Berkeley University Press, California, 1999.

Aksoy, N., Filiz, S., *Investigation of Balcova-Narlıdere Geothermal Field by Isotopes*, Proceedings, 1st Environment and Geology Symposium (ÇEVJEO'2001), Izmir, 21-23 March, 2001.

Serpen, U., *Hydrogeological investigations on Balçova geothermal system in Turkey*. Geothermics , 33, 309-335, 2004.

Aksoy, N., Serpen, U., Filiz, S., *Management of the Balcova-Narlidere geothermal reservoir*, Geothermics, Turkey, 2007.

Ozdiler, U., & Sayik, T., *Balçova - Narlidere Jeotermal Saha İşletmesi*. X. Ulusal Tesisat Mühendisliği Kongresi, 219-240, Izmir, 2011.

A FULLY COUPLED FLOW AND GEOMECHANICS MODEL: APPLICATION TO ENHANCED GEOTHERMAL RESERVOIRS

Perapon Fakcharoenphol, Litang Hu, Yu-Shu Wu, Sarinya Charoenwongsa, and Hossein Kazemi

Colorado School of Mines
1500 Illinois street
Golden, CO, 80401
e-mail: pfakchar@mymail.mines.edu

ABSTRACT

This paper presents a fully coupled, fully implicit geomechanics-flow model for fluid and heat in porous media. The model is built and transferred onto the TOUGH2 (Pruess et al, 1999) infrastructure. A staggered grid is used, with flow-related primary variables (pressure, temperature, and phase saturations) located at the center and geomechanics-related variables (displacement components) on the borders of the matrix block.

The model was verified against analytical solutions: (1) 1D heat conduction in deformable media (Jaeger et al., 2007), (2) 1D consolidation (Terzaghi, 1943), and (3) the Mandel and Cryer problem for transversely isotropic poroelastic media (Abousleiman et al., 1996). The model was also verified against the published numerical results of geothermal reservoir modeling (Rutqvist et al., 2008). To demonstrate the capability of the new model, we present a 5-spot well-pattern example of an enhanced geothermal system.

INTRODUCTION

The growing public concern regarding EGS-induced earthquakes causes delays in (and threatens) EGS development worldwide. At least one commercial EGS project (Deep heat mining Basel in Switzerland), has been abandoned because of felt induced earthquakes (Giardini, 2009). Many other commercial EGS fields (Landau in Germany, Berlin in El Salvador) and a conventional geothermal field (The Geysers) have been reported increasing seismic activities once production and injection started (Majer et al.; 2007, Giardini; 2009). As a result, site selection, including earthquake risk assessment, is vital for the development of geothermal fields, especially for a field located in suburb areas.

Production and injection activities alter pressure, temperature, and stress states within geothermal reservoirs, which can cause rock deformation (and even failure) as well as increased seismicity or micro-earthquake (MEQs) events. For example, many studies have demonstrated that MEQs at The Geysers, one of the largest geothermal fields in the world, are associated with water injection and steam extraction (Oppenheimer, 1986; Stark, 2003; Smith et al., 2000; Mossop, 2001; Majer and Peterson, 2005; Majer et al., 2007). Majer et al. (2007) report the correlation between water injection rate and seismic events for a magnitude lower than 1.5—see Fig. 1. Rutqvist et al. (2006, 2007, and 2008) conducted a comprehensive simulation study to simulate production and injection effects on stress changes at The Geysers. Their results indicate that steam extraction could cause seismic activity at shallow depths above the geothermal reservoir, whereas cold-water injection increased seismic activities and could extend the active slip zone several hundred meters below injection zones. These results are consistent with the observed MEQs data.

Majer et al. (2007) point out that large earthquake risks are associated with a large fault system with significant slip. While geological information is required to evaluate the geothermally induced earthquake risks, a coupled flow-geomechanics model can be used to support the analysis of how cold-water injection, steam, or hot-water production could affect the stress field in geothermal reservoirs in a similar manner to that of Rutqvist et al. (2006, 2007, and 2008).

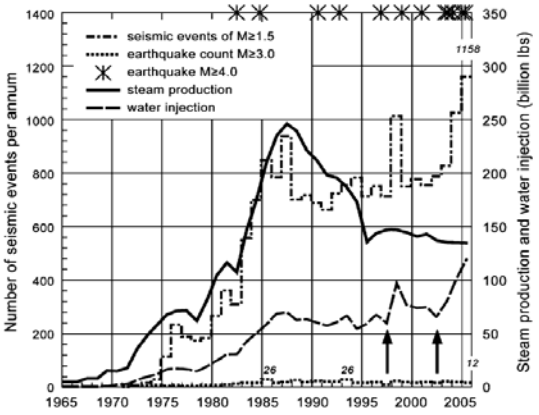

Figure 1. Historical seismicity from 1965 to 2006 at The Geysers: the two arrows indicate the increases in fluid injection in 1997 and 2002 (Majer et al., 2007)

Moreover, change in stress and strain induced by cold-water injection and steam extraction alters hydraulic properties, especially porosity and permeability. Many research efforts (Rutqvist et al., 2002; Davies and Davies, 1999; McKee et al., 1988; Ostensen, 1986) have either experimentally or theoretically investigated the impact of rock deformation on hydraulic properties. As a result, well productivity and injectivity are changed throughout the life of the wells. Thus, to evaluate production from a geothermal field, it is important to include the effect of rock deformation.

In this paper, we present a fully coupled, fully implicit flow-geomechanics model for fluid and heat flow in porous media. Simulated stress and strain can be used to perform shear slip analysis. The developed simulator is built on TOUGH2 (Pruess et al, 1999), a well-established simulator for geo-hydrological-thermal analysis with multiphase, multi-component fluid and heat flow. This simulator is not the first coupled flow-geomechanics model, but it will be among the first fully coupled flow-geomechanics models available in the public domain.

The organization of this paper is as follows. First, we briefly present the mathematical model, similar to TOUGH2. Then, the general concept and numerical treatment of geomechanical formulation are discussed. We compare analytical solutions to numerical results to show the validity of our coupling model. Furthermore, we compare our simulation results of the stress and strain analyses for production-and injection-induced stress changes in The Geysers to Rutqvist et al.'s (2006, 2007, and 2008) simulation results. Finally, we present an application example for 5-spot EGS model.

MATHEMATICAL MODEL

We have developed a fully coupled geomechanics and flow model, based on Charoenwongsa et al. (2010) and Shu (2003). We assume that the boundaries of each simulation grid can move only perpendicularly to its interface as an elastic material, and obeys the generalized Hooke law. Three additional primary variables, namely displacement in x, y, and z direction (u_x, u_y, u_z), are introduced for each grid. Although this numerical scheme is applicable only for a Cartesian grid, it is sufficient to simulate the flow and geomechanical behavior in geothermal reservoirs where geological information (as well as actual subsurface information from drilled wells) is rather sparse and less abundant than that for oil and gas reservoirs.

Reservoir rock is assumed under force equilibrium at all time, and the effect of rock-frame acceleration is ignored. The force equilibrium equations under Newtonian law can be expressed as follows:

$$\nabla \bullet (\Delta\sigma) + \Delta\rho\vec{g} = 0 \tag{1}$$

where $\Delta\sigma$ is the tensor of total stress change from the previous equilibrium condition (here, compression is positive and tension is negative); $\Delta\rho$ is the average bulk-density change from the previous equilibrium condition (typically, this value is very small and dominated by the change in fluid density inside pore space); and $\vec{g}$ is the gravity vector.

In Cartesian coordinates, Eq. (1) can be written as:

$$\begin{bmatrix} \nabla \bullet (\Delta\vec{\sigma}_x) \\ \nabla \bullet (\Delta\vec{\sigma}_y) \\ \nabla \bullet (\Delta\vec{\sigma}_z) + \Delta\rho\vec{g} \end{bmatrix} = \begin{bmatrix} 0 \\ 0 \\ 0 \end{bmatrix} \tag{2}$$

where $\vec{\sigma}_x$ is the stress-component vector acting in the x-direction, composed of normal stress in x-plane (σ_{xx}), shear stress in y-plane (σ_{yx}), and

shear stress in z-plane (σ_{zx}); $\vec{\sigma}_y$ is the stress-component vector acting in the y-direction; and $\vec{\sigma}_z$ is the stress-component vector acting in the z-direction.

Following the numerical framework used in TOUGH2, we can discretize Eq. (2) as follows:

$$\int_{\Gamma_n} \mathbf{F}_j \bullet \mathbf{n} d\Gamma_n + q_j = 0 \tag{3}$$

where $\mathbf{F}_j = \left[\Delta\sigma_{xj} \quad \Delta\sigma_{yj} \quad \Delta\sigma_{zj} + \delta_{zj}\Delta\rho g\right]^T$, $j \in \{x, y, z\}$, and q_j is the external force added to the system.

Stress-Strain Relation

Using the above formulation, we can include different stress-strain relationships. Here, we assume that the rock behaves as a linear poro-thermo-elastic medium with orthotropic material. The stress-strain relationship is given by:

$$\begin{bmatrix} \Delta\sigma_{xx} - \alpha_x\Delta p \\ \Delta\sigma_{yy} - \alpha_y\Delta p \\ \Delta\sigma_{zz} - \alpha_z\Delta p \\ \Delta\sigma_{xy} \\ \Delta\sigma_{yz} \\ \Delta\sigma_{zx} \end{bmatrix} = \begin{bmatrix} \frac{1}{E_x} & -\frac{\nu_{yx}}{E_y} & -\frac{\nu_{zx}}{E_z} & 0 & 0 & 0 \\ -\frac{\nu_{xy}}{E_x} & \frac{1}{E_y} & -\frac{\nu_{zy}}{E_z} & 0 & 0 & 0 \\ -\frac{\nu_{xz}}{E_x} & -\frac{\nu_{yz}}{E_y} & \frac{1}{E_z} & 0 & 0 & 0 \\ 0 & 0 & 0 & 1/G_{xy} & 0 & 0 \\ 0 & 0 & 0 & 0 & 1/G_{yz} & 0 \\ 0 & 0 & 0 & 0 & 0 & 1/G_{zx} \end{bmatrix}^{-1} \begin{bmatrix} \varepsilon_{xx} + \beta_x\Delta T \\ \varepsilon_{yy} + \beta_y\Delta T \\ \varepsilon_{zz} + \beta_z\Delta T \\ 2\varepsilon_{xy} \\ 2\varepsilon_{yz} \\ 2\varepsilon_{zx} \end{bmatrix} \tag{4}$$

where ε_{ij} is normal strain if $i=j$ and shear strain if $i \neq j$, $i, j \in \{x,y,z\}$, E is elastic modulus, ν is passion ratio, G is shear modulus, β is linear thermal expansion, α is Biot coefficient, ΔT is temperature change, and Δp is pressure change.

Also, we assume that the small-strain assumption is adequate for capturing strain in our system. Strain can be calculated from:

$$\varepsilon_{ij} = \frac{1}{2}\left(\frac{\partial u_i}{\partial x_j} + \frac{\partial u_j}{\partial x_i}\right) \qquad i, j \in \{i, j, k\} \tag{5}$$

where, u_x, u_y, and u_z are displacement of the rock frame in x, y, and z-directions, and ε_{ij} is a strain component.

Boundary Treatment

Three types of boundary conditions are discussed here. First, a rigid boundary signifies a stationary rock frame at the reference point. Second, a sliding boundary signifies that the movement of a boundary face occurs exclusively in parallel to the face; no movement in the perpendicular direction to the face is allowed. This type of boundary is commonly used for the outer model boundaries. The last boundary type is a specific stress boundary in which a boundary is subject to a constant stress condition, including normal and shear stresses. Typically, ground surface is modeled by a constant zero-stress boundary. All three boundaries types can be mathematically expressed as follows:

Rigid boundary:

$$u_x = 0, \quad u_y = 0, \quad u_z = 0 \tag{6}$$

Sliding boundary:

$$u_i = 0, \quad \sigma_{ij} = 0 \quad i, j \in \{i, j, k\} \text{ and } i \neq j \tag{7}$$

Specific stress boundary:

$$q_j = \int_s C_{ij} \bullet \vec{n} ds \qquad i, j \in \{i, j, k\} \tag{8}$$

where, C_{ij} is stress component at boundary

Effect of Geomechanics on Mass- and Energy-Balance Equations

Rock deformation affects fluid and heat flow in many ways. The following section explains how we incorporate these effects mathematically.

Permeability and Porosity:

These two quantities, which are among the most important properties for fluid flow, can be significantly affected by rock deformation. Many research efforts (Rutqvist et al., 2002; Davies and Davies, 1999; McKee et al., 1988; Ostensen, 1986) have either experimentally or theoretically investigated the impact of rock deformation on hydraulic properties. A summary of permeability and porosity as functions of stress can be found in Wu et al. (2011). The general mathematical form can be expressed as:

$$k = k(\sigma', \varepsilon) \tag{9}$$

$$\phi = \phi(\sigma', \varepsilon) \tag{10}$$

where k is absolute permeability, ϕ is porosity, σ' is effective stress, and ε is strain.

Mass accumulation:

The total mass within a unit volume of rock may be changed as a result of rock deformation. We account for the mass calculation as:

$$M^{\kappa} = \sum_{\varphi} (1-\varepsilon_v)\phi S_{\varphi}\rho_{\varphi}X_{\varphi}^{\kappa} \tag{11}$$

where, M^{κ} is mass accumulation of component κ, ε_v is volume metric strain, φ is porosity, ρ_{φ} is density of phase φ, S_{φ} is saturation of phase φ, and X_{φ}^{κ} is the mass fraction of component κ in phase φ.

Capillary pressure:

Due to the change in permeability and porosity, Rutqvist et al. (2002) use J-function to correct capillary pressure change.

$$p_c = p_{c,0}\sqrt{\frac{k_0\phi}{k\phi_0}} \tag{12}$$

where, $p_{c,0}$ is nondeformed capillary pressure, k_0, k are initial permeability and deformed permeability, respectively, and φ_0, φ are initial porosity and deformed porosity, respectively,

Fluid mass flow rate:

Not only are intrinsic rock properties altered, but also gridblock surface area is changed due to deformation. Here, we include the effect.

$$q_{\varphi,i} = -F_v\frac{kk_{r\varphi}}{\mu_{\varphi}}\nabla\Phi A_0 \tag{13}$$

where F_v is deformation correction defined as

$$F_{v,i} = \frac{(1-\varepsilon_{jj})(1-\varepsilon_{kk})}{1-\varepsilon_{ii}}$$

and $i,j,k \in \{x,y,z\}$ and $i \neq j \neq k$,

A_0 is initial surface area, k is absolute permeability, $k_{r\varphi}$ is relative permeability of phase φ, and μ is viscosity of phase φ.

MODEL VERIFICATION

Mandel-Cryer Problem for Transversely Isotropic Porous Media

The classical Mandel-Cryer problem involves an infinitely long rectangular specimen, sandwiched at the top and bottom by two rigid frictionless plates; see Fig. 2. The lateral sides are free from normal and shear stresses, as well as pore pressure. At t=0, a force of 2F is applied to the rigid plates. As a result, pore pressure is uniformly increased by the Skempton effect. The pore pressure then dissipates from the side edges.

Abousleiman et al. (1996) extended the classical problem to account for transversely isotropic material. Fig. 2 shows the Mandel-Cryer problem for a transverse isotropic material where (a) case#1 is the axis of material rotational symmetry coinciding with the z-axis, and (b) case#2 is the specimen rotated 90˚.

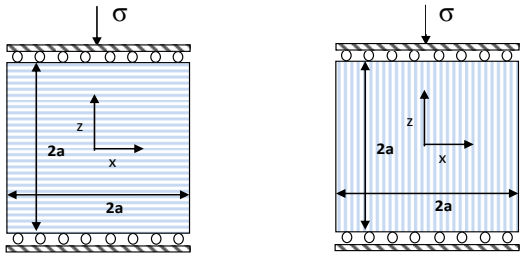

(a) (b)

Figure 2. Problem description (a) Case#1: the axis of material rotational symmetry coincide with z-axis and (b) Case#2: the specimen is rotated by 90˚ from case#1

Table 1. Input parameters for Case#1: Mandel-Cryer problem

Parameters	Value	unit
Young modulus in x and z-direction	20.6, 17.3	GPa
Poisson ratio in xy and xz direction	0.189, 0.246	-
Biot coefficient in x and z-direction	0.733, 0.749	-
Permeability x and z-direction	1.0×10^{-19}, 2.0×10^{-20}	m^2
Porosity	0.1	-
Fluid viscosity	0.001	Pa.s
Pore compressibility	2.0×10^{-10}	1/Pa
Fluid compressibility	4.4×10^{-10}	1/Pa
Applied stress	10	MPa

The simulation results and analytical solution are compared in Fig. 3 and Fig. 4. The figures show good agreement between the two methods, consequently lending credibility to our numerical simulation model.

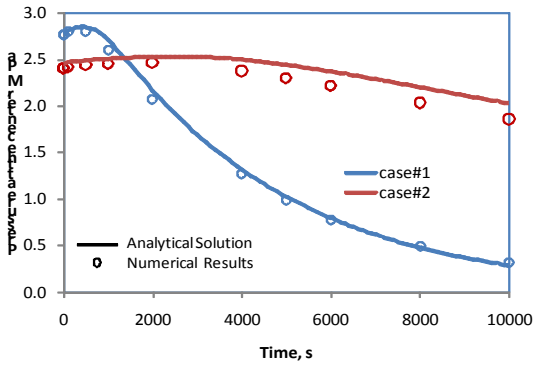

Figure 3. Comparison of pressure solutions between numerical simulation and analytical solution for (1) case#1: material properties according to Table1 and (2) Case#2: the specimen is rotated 90 from Case#1.

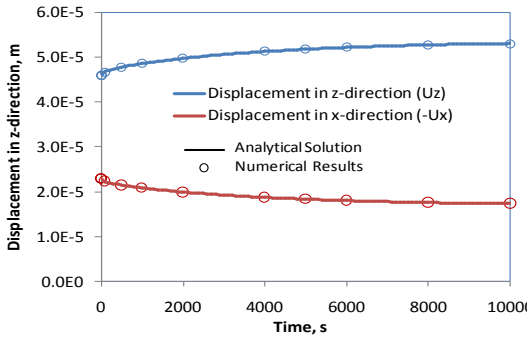

Figure 4. Comparison of displacement in x-direction at the right edge and z-direction at the top of the specimen, between numerical simulation and analytical solution for case#1.

Published Simulation Results: The Geysers Geothermal-Induced Micro-Earthquake Study

In this section, we compare our simulation results (here called 'TOUGH2-EGS') to the published simulation results of The Geysers geothermally induced Micro-Earthquake (MEQs) Study. The study was conducted by Rutqvist et al. (2006, 2007, and 2008), to investigate the effects of steam extraction and water injection in The Geysers.

The Geysers is one of the largest geothermal reservoirs in the world and located in one of the most seismically active regions, Northern California. It is a vapor-dominated geothermal reservoir system, hydraulically confined by low-permeability rock units. Many studies have demonstrated that MEQs at Geysers are associated with water injection and steam extraction (Oppenheimer, 1986; Stark, 2003; Smith et al., 2000; Mossop (2001); Majer and Peterson, 2005; Majer et al., 2007).

Rutqvist et al. (2006, 2007, and 2008) conducted a two-dimensional model simulation representing one-half of a NE-SW cross section of a NW-SE trending of The Geysers geothermal field (Fig. 5). The initial (pre-production) conditions were established through a steady-state multiphase flow simulation. Published data were used to constrain a conceptual Geysers model; detailed model setup can be found in their papers by Rutqvist et al. . (2006, 2007, and 2008). One producer and two injectors are located at the model center (Fig. 6). The steam production and water injection rates over 44 years were scaled to represent the ratio of withdrawal and injection volume to the cross-sectional model.

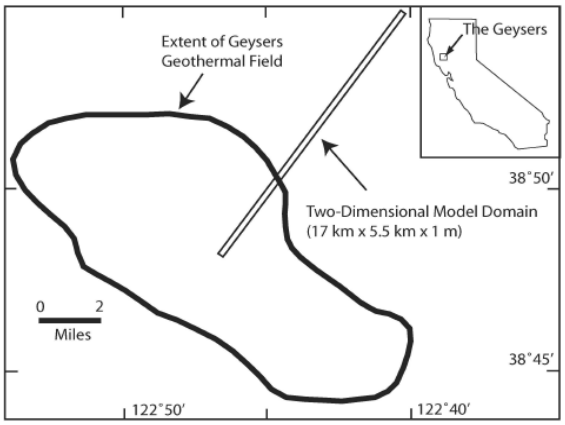

Figure 5. Schematic maps of the study area (Rutqvist and Odenburg, 2008)

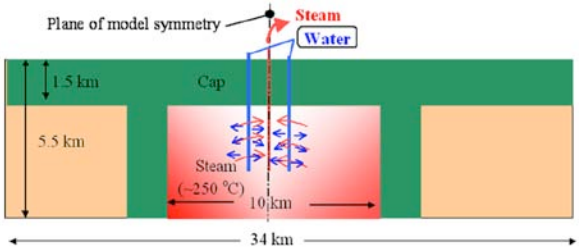

Figure 6. Model schematic: one producer and two injectors (Rutqvist et al. 2008)

The authors employed a coupled flow-geomechanics model using two separated simulators, TOUGH2 (a fluid- and heat-flow simulator) and FLAC (a commercial geomechanics simulator).

TOUGH2 provided pressure and temperature changes to FLAC to calculate stresses changes. Then, stress information from FLAC was returned to TOUGH2 for use in the next time step. This coupling technique is known as "one-way coupling," where pressure and temperature changes influence stresses changes, but stresses changes do not affect the hydraulic properties of current time steps and thus mass- and energy-balance calculations.

The production and injection-rate history of The Geysers was scaled and used to control production and injection rate of the model. This case was set up to investigate both steam-extraction and water-injection effects.

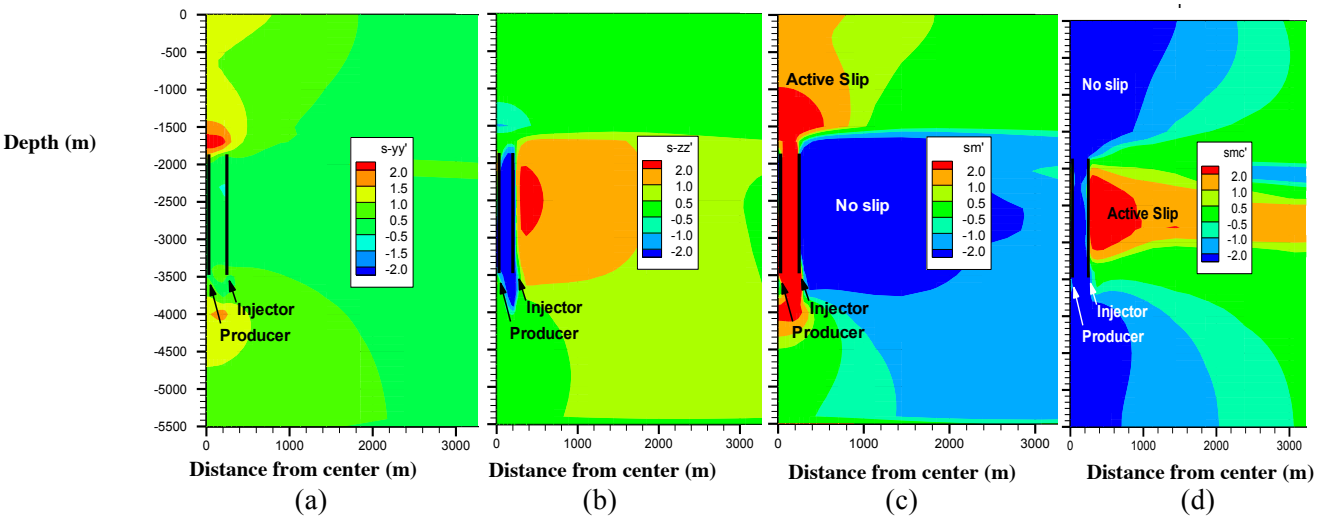

Figure 7. Simulation results using TOUGH2-EGS: (a) change in effective horizontal stress, (b) change in effective vertical stress, (c) $\Delta\sigma'_1$-$\Delta\sigma'_{1c}$ for compressional stress regime ($\sigma'_1 = \sigma'_h$) , where positive value indicates the stress change exceed the critical stress change and can activate MEQs, and (d) $\Delta\sigma'_1$-$\Delta\sigma'_{1c}$ for extensional stress regime ($\sigma'_1 = \sigma'_v$).

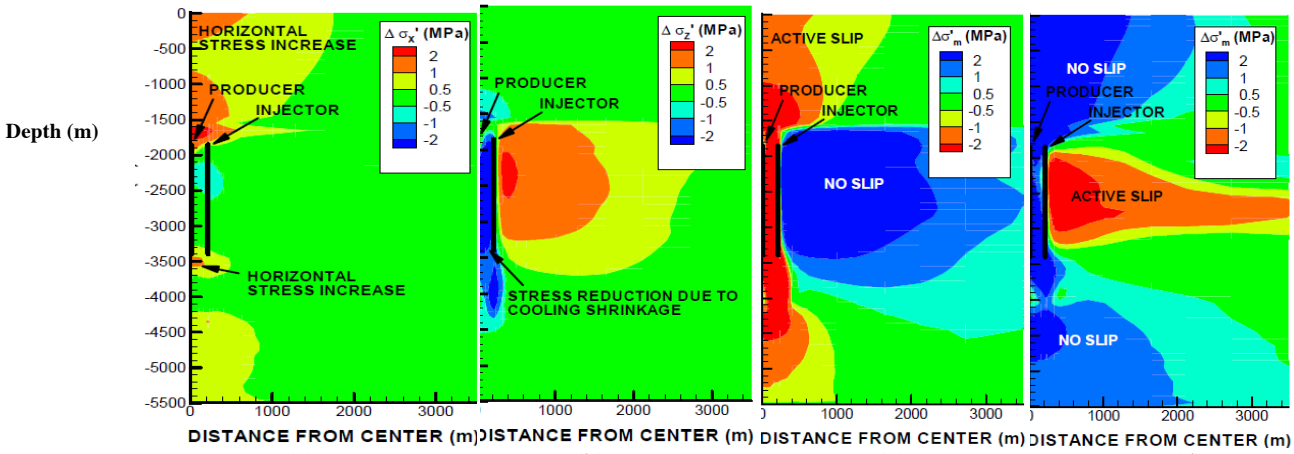

Figure 8. Rutqvist et al. (2007) simulation results: (a) change in effective horizontal stress, (b) change in effective vertical stress, (c) $\Delta\sigma'_1$-$\Delta\sigma'_{1c}$ for compressional stress regime ($\sigma'_1 = \sigma'_h$) , where positive value indicates the stress change exceed the critical stress change and can activate MEQs, and (d) $\Delta\sigma'_1$-$\Delta\sigma'_{1c}$ for extensional stress regime ($\sigma'_1 = \sigma'_v$).

Fig. 7 shows simulation results from TOUGH2-EGS. Fig. 7(a) and Fig. 7(b) depict vertical and horizontal stress changes at the center of the field, respectively. Based on the Mohr-Coulomb

failure criterion, the critical stress change in the maximum principal stress ($\Delta\sigma_{1c}$) is calculated as three times the change in minimum principal stress ($\Delta\sigma_3$) (Rutqvist et al., 2006). Fig. 7(c) and Fig. 7(d) show the indication of active-slip or rock-failure potential, where positive values indicate a failure zone and negative values indicate a stable zone in a compressional stress regime ($\sigma'_1=\sigma'_h$) and an extensional stress regime ($\sigma'_1=\sigma'_v$), respectively. The simulation results indicate that steam extraction yields an active slip regime in shallow depths at the reservoir cap rock for a compressional stress regime, while no slip is expected in the extensional stress regime. These results are consistent with that of published simulation results shown in Fig. 8 (Rutqvist et al., 2006).

APPLICATION EXAMPLE

In geothermal reservoir development, production and injection wells are often drilled in regular geometric patterns. The present problem considers a large well field with wells arranged in a "5-spot" pattern. Because of symmetry, only a quarter of the basic pattern needs to be modeled. Fig. 9 shows a simulation grid in which the grids are refined in the vicinity of injection, while production wells and coarse grids are used elsewhere. The system is initialized as a normal pressure regime where subsurface pressure follows the hydrostatic pressure of the water head, and the temperature gradient is set at 4˚C/km. The reservoir is fully saturated with water. Reservoir rock properties are corresponding to conditions that may typically be encountered in deeper zones of hot and fairly tight geothermal reservoirs.

Continuum Slip Analysis

We employed continuum shear-slip analysis to investigate the extension of potential slip zones, as discussed by Rutqvist et al. (2006). Cold-water injection and steam extraction could cause pressure and temperature changes, as well as alter stress field in reservoirs. To evaluate the potential slip zone, we compared the effective stress to a Mohr-Coulomb failure criterion. In this case, fracture orientations must be known. However, the orientation data may not available. As a precaution, we assumed that preexisting fractures could rotate in any direction. The Mohr-Coulomb failure criterion is given as (Jaeger et al., 2007):

$$\tau_m = S_0 \cos\theta + \sigma_m \sin\theta \qquad (14)$$

where τ_m and σ_m are the two-dimensional maximum shear stress and mean stress in the principal stress plane (σ'_1, σ'_3), defined as:

$$\sigma_m = \frac{1}{2}(\sigma'_1+\sigma'_3), \quad \tau_m = \frac{1}{2}(\sigma'_1-\sigma'_3) \qquad (15)$$

where S_0 and Θ are the coefficient of internal cohesion and angle of internal friction of the fractures, respectively.

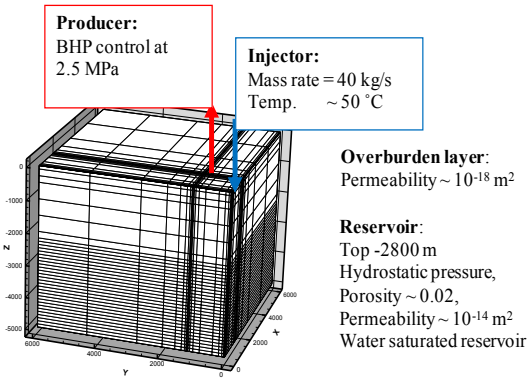

Figure 9. A quarter model for 5-spot pattern

In this example, the potential for shear slip is estimated using zero cohesion ($S_0 = 0$) and a friction angle of 30°, leading to the following criterion for shear slip:

$$\sigma'_1 = 3\sigma'_3 \qquad (16)$$

Thus, shear slip would be induced whenever the maximum principal effective stress exceeds three times the minimum compressive effective stress.

Simulation Results

Fig. 10 and Fig. 11 show simulation results after 6 months of production in the vicinity of the injector and producers, respectively. Around the injector, the temperature is reduced by cooling effects and causes stress reduction, as can be seen from the horizontal stress change following the temperature change pattern—see Fig. 10(a) and (b).

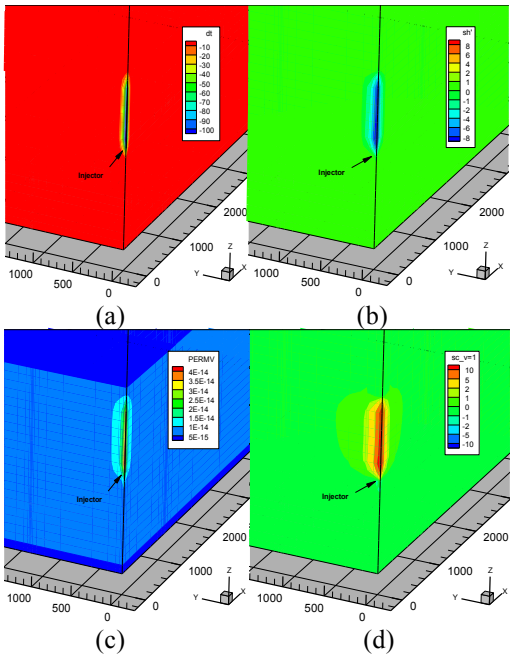

Figure 10. Simulation results at the injector after 6 months: (a) temperature change (b) horizontal stress change, (c) permeability evolution, and, (d) $\Delta\sigma'_v$-$\Delta\sigma_c$ plot for extensional stress regime where positive indicates slip zone.

As a result, permeability is enhanced around the injector, Fig. 11(c). Fig. 11(d) demonstrates active slips zone for the extensional regime (the maximum stress is in the vertical direction). Here, a positive value indicates a failure zone. Clearly, the failure zone evolves around the injector in both cases.

The pressure reduction caused by steam extraction dominates the stress changes around the producer, as the horizontal and vertical stress changes follow the pressure change pattern, Fig. 11 (a) and (b). Consequently, the permeability around the producer declines. Unlike around the injector, Fig. 10 (d) indicates that no active slip zone develops around the producer. As pressure reduction raises the effective normal stress around the producer, the fracture slip potential is reduced. We can see that the active slip zone is developed exclusively around the cold-water injector. Thus, we can study the detailed evolution of the active slip zone around the injector.

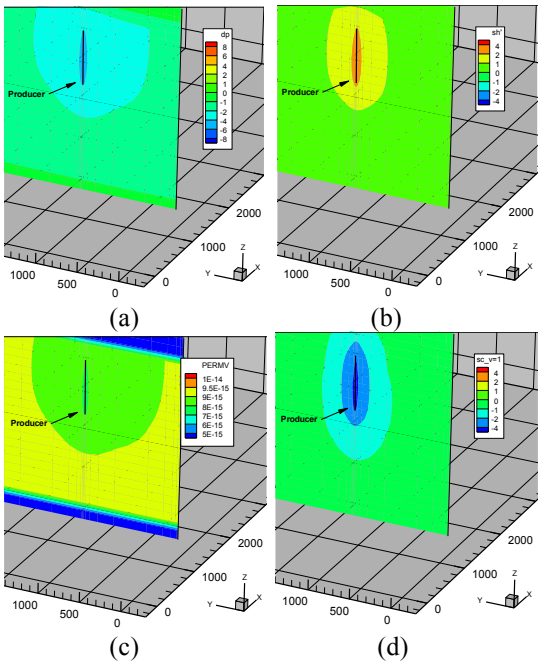

Figure 11. Simulation results at the producer after 6 months: (a) pressure change, (b) vertical stress change, (c) permeability evolution , (d) $\Delta\sigma'_v$-$\Delta\sigma'_c$ plot for extensional stress regime where positive indicates slip zone.

Fig. 12 shows the active-slip-zone evolution around the water injector in both extensional and compressional stress regimes. Under the extensional stress regime, the active slip zone can extend several hundred meters above the injection point during the early production period—Fig. 12(a). Later, the active slip zone extends horizontally only, away from the injector. After five years of production, this zone could extend more than 500 m away from the injector—Fig 12(c). This is because during early production, the pressure drop in the reservoir is insignificant, thus only temperature drop causes stress reduction and dominates the stress field. As temperature change occurs locally, it creates a tension zone in the vertical direction, thus extending the failure zone vertically. However, once the reservoir pressure drop is significant, it raises the effective stress and counteracts the temperature effect. As a result, it diminishes the vertical tension zone and the active slip zone exclusively extends horizontally.

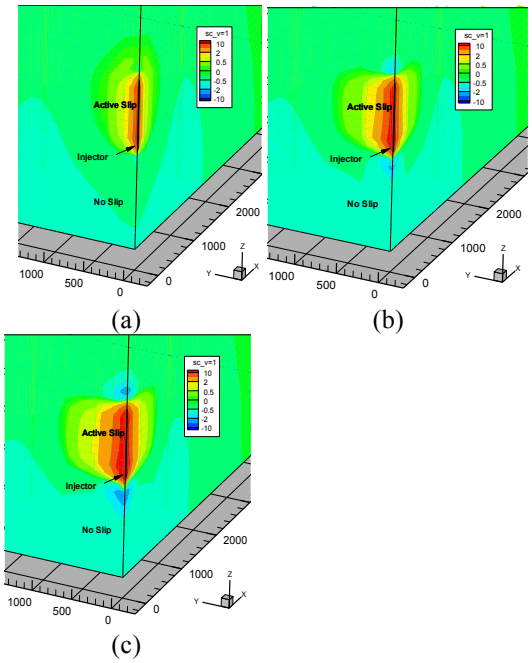

Figure 12. Slip potential plot ($\Delta\sigma'_1$-$\Delta\sigma'_{1c}$) where positive indicates active slip and negative indicates no slip zones for: extensional stress regime (maximum stress is the vertical stress) at (a) 0.5 year, (b) 1.5 year, (c) 5 years.

CONCLUSIONS

In this paper, we describe a fully coupled, fully implicit flow-geomechanics model for fluid and heat flow in porous media. The simulated stress and strain can be used to perform shear slip analysis as well as to analyze the effect of rock deformation on fluid and heat flow in geothermal reservoirs. The developed simulator is built on TOUGH2 (Pruess et al, 1999), a well-established simulator for geo-hydrological-thermal analysis with multiphase, multi-component fluid and heat flow. The developed simulator is not the first coupled flow-geomechanics simulator; however, it will be one of the first fully coupled flow-geomechanics simulators available in the public domain.

We successfully validated our simulator against the analytical solution of Mandel and Cryer problem for transversely isotropic poroelastic media (Abousleiman et al., 1996) and against the published numerical results from a field-application of geothermal reservoir simulation (Rutqvist et al., 2008). In addition, we present an application example for a 5-spot EGS model.

As the public concerns with respect to EGS-induced earthquakes mount, site selection and earthquake risk assessment is vital for EGS development. Our simulator can be used to support the assessment of how cold-water injection and steam or hot-water production could affect the stress field and productivity in geothermal reservoirs—as well as applied to studies of induced seismicity.

ACKOWLEDGMENTS

This work is supported by the U.S. Department of Energy under contract No. DE-EE0002762. Special thanks are due to the Energy Modeling Group (EMG) and Marathon Center of Excellence for reservoir studies (MCERS) at Colorado School of Mines. The authors are also grateful to Jonny Rutqvist at LBNL for the help he provided to this study.

REFERENCES

Aoki, T., C.P. Tan, and W. E. Bamford, Effects of elastic and strength anisotropic on borehole failures in saturated rocks, *Int. J. Rock Mech. Min. Sci.*, **10**, 1031-1034, 1993.

Abousleiman, Y., A. H.-D. Cheng, E. Detournay, L. Cui, and J.-C. Roegiers, Mandel's problem revisited, *Géotechnique,* **46**(2), 187-195, 1996.

Carslaw, H. S., J. C. Jaeger, *Conduction of heat in solids*, second ed. Oxford University Press, USA, 1986.

Charoenwongsa, S., H. Kazemi, J. L. Miskimins, and P. Fakcharoenphol, A fully-coupled geomechanics and flow model for hydraulic fracturing and reservoir engineering applications, *in proceeding of Canadian Unconventional Resources & International Petroleum Conference*, Calgary, Alberta, Canada, 2010.

Davies, J.P., D.K. Davies, Stress-dependent permeability: characterization and modeling, *in proceeding of SPE Annual Technical Conference and Exhibition*, SPE 56813, Houston, Texas, 1999.

Giardini, D, Geothermal Quake Risks Must be Faced, *Nature*, **462**(7275), 848-849, 2009.

Jaeger, J., N.G. Cook, and R. Zimmerman, *Fundamentals of rock mechanics*, forth ed. Wiley-Blackwell, 2007.

Majer, E. L., R. Baria, M. Stark, S. Oates, J. Bommer, B. Smith, and H. Asanuma, Induced Seismicity Associated with Enhanced Geothermal Systems, *Geothermics*, **36**(3), 185-222, 2007.

Majer, E.L., and J.E. Peterson, Application of microearthquake monitoring for evaluating and managing the effects of fluid injection at naturally fractured EGS sites, *Geotherm. Resour. Counc. Trans*, **29**, 103–107, 2005.

McKee, C.R., A.C. Bumb, and R.A. Koenig, Stress-dependent permeability and porosity of coal and other geologic formations, *SPE Formation Evaluation*, **3**(1), 81–91, 1998.

Massachusetts Institute of Technology (MIT), The future of geothermal energy impact of enhanced geothermal systems (EGS) on the United States in the 21st Century, *A report for the U.S. Department of Energy, 2006*.

Mossop, A.P., Seismicity, subsidence and strain at The Geysers geothermal field, *Ph.D. dissertation*, Stanford University, Stanford, CA, 2001.

Ostensen, R.W., The effect of stress-dependent permeability on gas production and well testing, *SPE Formation Evaluation*, **1**(3), pp. 227–235, 1986.

Oppenheimer, D.C., Extensional tectonics at the Geysers geothermal area, California, *J. Geophys. Res.*, **91**, 11463–11476, 1986.

Pruess, K., C. Oldenburg, and G. Moridis, *TOUGH2 user's guide, Version 2.0*, Lawrence Berkeley Laboratory Report LBL-43134, Berkeley, CA, 1999.

Rutqvist, J., J. Birkholzer, F. Cappa,C.M. Odenburg, and C.F. Tsang, Shear-slip analysis in multiphase fluid flow reservoir engineering applications using TOUGH-FLAC, *in proceeding of TOUGH Symposium*, LBNL, Berkeley, California, 2006.

Rutqvist J., and C.M. Odenburg, Technical Report#1: Development of fluid injection strategies for optimizing steam production at The Geysers geothermal field, California, LBNL, Berkeley, California, LBNL-62577, 2007.

Rutqvist, J., and C.M. Odenburg, Analysis of injection-induced micro-earthquakes in a geothermal steam reservoir, The Geysers geothermal field, California, *in proceeding of The 42nd U.S. Rock Mechanics Symposium (USRMS)*, San Francisco, California, 2008.

Rutqvist, J., Y.S. Wu, C.F. Tsang, and G. Bodvarsson, A modeling approach for analysis of coupled multiphase fluid flow, heat transfer, and deformation in fractured porous rock, *Int. J. Rock Mech. Min. Sci.,* **39**, 429–42, 2002.

Smith, J.L.B., J.J. Beall, and M.A. Stark, Induced seismicity in the SE Geysers field, *Geotherm. Resour. Counc. Trans*, **24**, 24–27, 2000.

Stark, M.A, Seismic evidence for a long-lived enhanced geothermal system (EGS) in the Northern Geysers Reservoir, *Geotherm. Resour. Counc. Trans*, **27**, 727-731, 2003.

Shu, T., *Development of Efficient Fully Coupled Geomechanics and Fluid Flow Simulator*, Master Thesis, Stanford University, Stanford, CA, 2003.

Terzaghi, K., *Theoretical Soil Mechanics*, John Wiley and Sons, New York, 1943.

Wu, Y.S., H. Kazemi, T. Xu, K. Zhang, L. Hu, L., X. Zhao, and P. Fakcharoenphol, Quarterly Report 2 of Year 2: Development of Advanced Thermal-Hydrological-Mechanical-Chemical (THMC) Modeling Capabilities for Enhanced Geothermal Systems, *A report for the U.S. Department of Energy, 2011*.

THE DEEP ROOTS OF GEOTHERMAL SYSTEMS IN VOLCANIC AREAS: BOUNDARY CONDITIONS AND HEAT SOURCES IN RESERVOIR MODELLING

Gunnar Gunnarsson and Edda S.P. Aradóttir

OR – Reykjavík Energy
Bæjarhálsi 1
IS-110 Reykjavík, Iceland
e-mail: gunnar.gunnarsson@or.is

ABSTRACT

The energy sources of geothermal systems in volcanic areas are cooling and solidifying intrusions in the crust. The nature of the heat transfer from these hot bodies to the groundwater is not known in detail—it is not known at what depth this interaction takes place, nor is it known at what depth ranges water circulation occurs.

When geothermal modelers construct a model of a production field, this issue is normally avoided. The heat sources are believed to be below the depth range of the model and are accounted for by choosing appropriate boundary conditions in the bottom layer of the model. Another standard practice in geothermal modeling is to drive the model using steady boundary conditions for a long period of time until it reaches a steady state, the so-called natural state, before production is simulated.

This approach to modeling geothermal systems in volcanic areas has worked reasonably well for industrial purposes. However, a model that does not include the entire water circulation is not complete. Recently a well was drilled into magma in the Krafla Geothermal Field in North-Iceland at a depth of 2.1 km (Friðleifsson et al., 2010). This drilling, and an older example of a well in Nesjavellir in the Hengill Area, Southwest Iceland, that was unexpectedly drilled into a very hot formation (> 380°C) in 1986 at a depth of 1800 m (Steingrímsson et al, 1990), has shown that the industry cannot overlook this imperfection in geothermal modeling. These examples from Krafla and Nesjavellir, along with other observations, indicate that the roots of geothermal systems in the volcanic active zone in Iceland are at shallower depths than previously believed. Thus, the structure of existing numerical models has to be reconsidered: Heat sources must be incorporated within the models.

Including heat sources within models also challenges the practice of driving the models into a steady state or natural state, since intrusions in the roots of volcanoes are not steady phenomena. Periods of high intrusion activity are known in volcanic systems in Iceland. In an improved modeling scheme, the heat sources should be included in any model, along with the entire water circulation, and the heat sources should be time dependent.

INTRODUCTION

Numerical modeling of geothermal fluid and heat flow is a valuable tool when operating a geothermal field. It has been used for estimating the production capacity of an operation, its environmental impact, and its sustainability. One of the most commonly used software when constructing and maintaining a numerical model of a geothermal field is the TOUGH2/iTOUGH2 software suite (Pruess et al., 1999). This software has previously been used in simulating the behavior of volcanic geothermal fields under operation in Iceland.

The main operating geothermal power plants in Iceland—Krafla, Nesjavellir, Hellisheiði, Svartsengi, and Reykjanes—are all in active volcanic zones. The energy sources of the systems are cooling and solidifying intrusions in the Earth's crust. How and where the heat transfer between the hot bodies and the groundwater takes place is not known, neither is the depth range of the water circulation. In conceptual models of the geothermal field on which numerical models are based, the heat transfer is assumed to be below the model depth ranges (see, e.g., Björnsson et al., 2003). The deeper roots of the geothermal systems are taken into account by choosing appropriate boundary

conditions for the bottom layer. Heat transfer; i.e., the roots of the geothermal system, is thus avoided. This method has proven to be useful when simulating a geothermal system for practical purposes. A model avoiding the roots of a system is, however, incomplete.

Another useful method when simulating a geothermal production field is to assume that the geothermal system is in equilibrium when production begins. Such a model uses applied boundary conditions and/or steady heat and mass sources until it reaches equilibrium before simulating production. *Equilibrium* in this case means that the system is stable over the period of ~10.000 years. This method is a standard practice in geothermal modeling (O'Sullivan et al., 2001); the main advantage of having a stable system before production is simulated is that all model changes of state are solely due to production. Without artifacts, it is much easier to compare different production scenarios.

The geothermal activity in the volcanic active zones of Iceland is, however, very dynamic making this method questionable. One example of the dynamic nature of geothermal activity is the 1976–1983 rifting period in the Krafla Volcano in Northern Iceland. In a series of events, numerous dykes were formed in the geothermal field of the Krafla Area. Some of these dykes were at relatively shallow depths and did in some cases reach production wells of the Krafla Power Plant. The most dramatic event occurred when a small amount of magma erupted from a well (Einarsson and Brandsdóttir, 1980; Buck et al., 2006).

Another example of the dynamic nature of geothermal systems in Icelandic volcanic zones is the new hot spring area, formed near the village of Hveragerði after an earthquake in May 2008. The Hveragerði village is located in the vicinity of the Hengill Volcano in southwestern Iceland. In this case, higher permeability due to fractures opening was responsible for these changes in the geothermal activity of the area (Hreinsdóttir et al, 2009).

THE ROOTS OF A GEOTHERMAL SYSTEM

Three components are necessary for a geothermal system: a heat source, water, and permeability. These components must be in the correct quantity. Cooling and solidifying intrusions are the energy sources of the geothermal systems in the volcanic zone of Iceland. Water is supplied by precipitation or the ocean, and the movement due to the plate boundary provides the permeability. These components are depicted in Fig. 1. The upper limit of the heat source is d_i, and the water circulation reaches the depth of d_w. Neither of those depths is well known. The heat source is (as said) above a cooling and/or solidifying intrusion. The energy exchange between the intrusion and the groundwater is mainly through thermal conduction, but can also be through degassing of the intrusion.

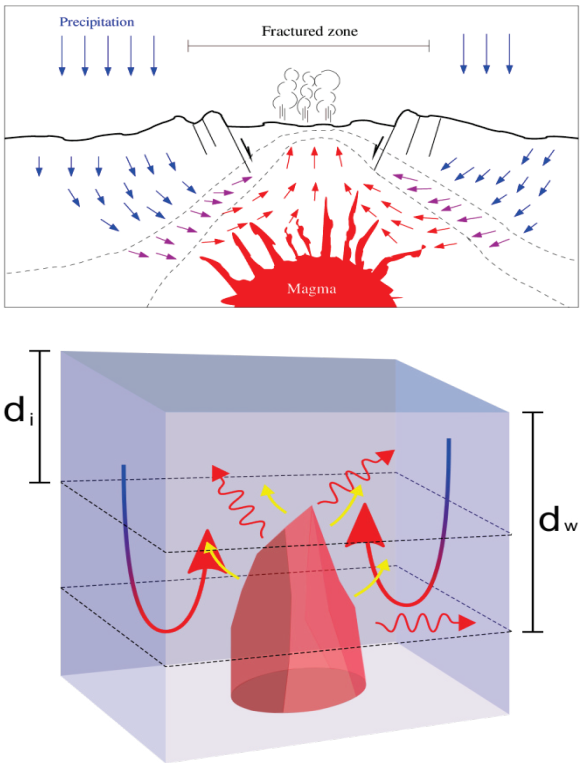

Figure 1. The roots of a geothermal system. The upper part shows the components needed for forming an geothermal system. The lower part shows the depth ranges and the heat transfer. The depth of the source is d_i and the depth range of the ground water circulation is d_w.

The depth of the heat sources are normally taken to be at much greater depths than the depth range of the model The roots are taken into account by choosing appropriate boundary conditions in the bottom layer of the model—a constant temperature and pressure boundary. The disadvantage of such a constant pressure boundary is that production will increase the inflow of hot fluid into the system significantly. A more conservative method is to inject a fixed amount of fluid and heat into the second deepest layer while having very low permeability in the bottom layer and constant temperature and pressure. Both of these methods are depicted in Fig.2.

Determining the depth range of the water circulation and the depth of the intrusions driving the geothermal systems is essential. This can partly be done by studying extinct geothermal systems where erosion has opened them up. One has to bear in mind that such a study does not show the system as it was in its most active phase —it shows the entire history of the system. One must also rely on the data that can be sampled using surface geology and geophysical exploration and downhole data (well logs and analysis of cuttings).

A SIMPLE CONCEPTUAL MODEL

Iceland is located at the plate boundary between the N-America and the Eurasian plate. The plates move from each other at an average speed of 2 cm/year. In the conceptual model used here, we assume that the opening space between the plates is filled with 1300°C hot magma. This is known to happen in abrupt events as in Krafla Volcano in the late 1970s–early 1980s. Dykes having thickness on the order of a few meters are formed every one or two centuries. Repeated dyke formation at shallow depths where groundwater is present loads the area with thermal energy and creates a geothermal field.

Icelandic rock, which can be seen on the surface, consist mainly of basalt in the older parts of the country and hyaloclastites in younger areas. Those formations are intersected by few intrusions, mainly dykes. The concentration of intrusions is relatively low except for some specific areas believed to be extinct volcanoes (see, e.g., Walker, 1963). The concentration of intrusive rocks is also high in wells in geothermal fields. In the Nesjavellir field in the northern part of the Hengill Volcano, the ratio of intrusive rocks is normally above 50% in wells below a depth of 1500 m (Franzson, 1988).

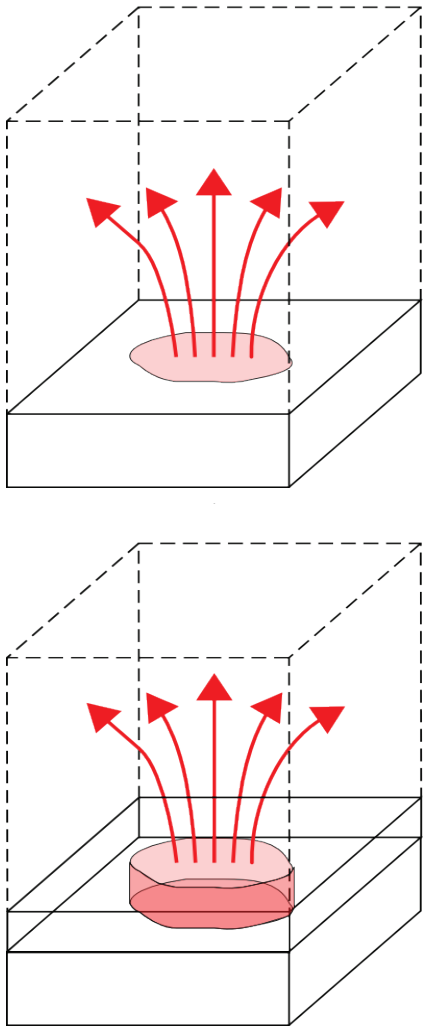

Figure 2. The use of boundary conditions to account for the heat sources of the geothermal systems. The sources are assumed to be below the model's depth range. The upper one shows the constant temperature and pressure boundary and the lower one shows the constant inflow.

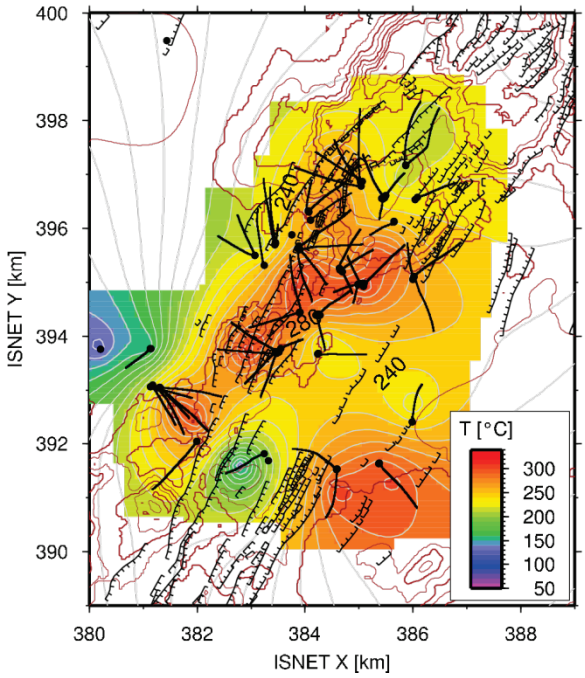

Figure 3. Formation temperature at 1000 m b.s.l in the southern part of the Hengill Area, SW-Iceland.

The abundance of intrusive rocks seen in wells in active geothermal fields supports the hypothesis that dykes and other intrusions at relatively low depths, i.e., within the drilling range, are the fields' energy sources. The depth range of the water circulation is harder to determine. Experience at Krafla, where magma was found at 2.1 km depth (Friðleifsson et.al 2010), and the well data from the Hengill-Area indicate that the water circulation does not reach much deeper that 2–3 km. In the conceptual model used in this study, it is assumed that we have an impermeable bottom at ~2.3 km depth. One can, however, expect that the depth range of the water circulation differs from one field to another in this volcanic zone.

NUMERICAL CALCULATIONS

To test the conceptual model described in the previous section a numerical dummy model was set up. The dummy model is a simplified geothermal field typical of Icelandic volcanic zones. A formation of high permeability housing the geothermal system is surrounded by formations of lower permeability and covered with a cap rock of low permeability. The cap rock separates the geothermal system from the groundwater system above it. It is common to have different water levels in the groundwater system than in the geothermal system. In the Hellisheiði Field, the typical groundwater level of the geothermal system is ~200 m below surface, but the groundwater level of the upper groundwater system is ~20 m below the surface. The core of the system has a slightly higher permeability than the rest of the geothermal system. The heat sources are mainly placed in the core.

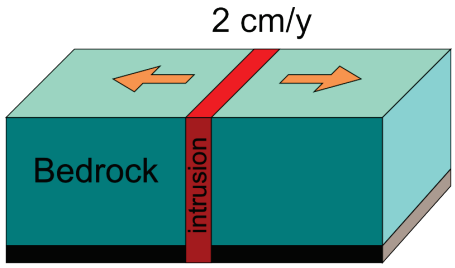

Figure 4. Boundary of two plates moving from each other. The average speed is 2cm/year and magma fills up the gap between the plates forming dykes.

The structure of the numerical model is shown in Fig.5. The energy sources were predefined "dykes" formed every 100 years on an average. The formation of dykes is hard to model in detail. In this work it was assumed that the dykes released their thermal energy into the elements where the dyke was formed. The energy release in each element where the dyke was formed was assumed to obey the relation

$$Q = \frac{E_0}{\tau} e^{-\frac{t}{\tau}} \quad (1)$$

where Q is the energy flow into the element from the dyke, $\tau = 25$ years is the time constant and E_0 is the total energy stored in the magma, i.e., the thermal energy released when a 2 m thick layer of magma within the element cools from 1300°C to the solidification temperature of 1100°C, at which time it solidifies and cools down to the temperature of the geothermal system (here taken as 250°C). There were 14 predefined dykes, i.e., walls of elements from north to south sometimes having small shifts in east-west position. These walls were mainly in

the core of the system and in the four model layers from the depth of 650 m down to 2150 m (see Fig.5). Each of these predefined "dykes" had its own possibility of being formed, but at an average, a dyke was formed every 100 years. Forming of dykes was accounted for by releasing the energy as described in Eq. (1) into the elements of the wall representing the dyke.

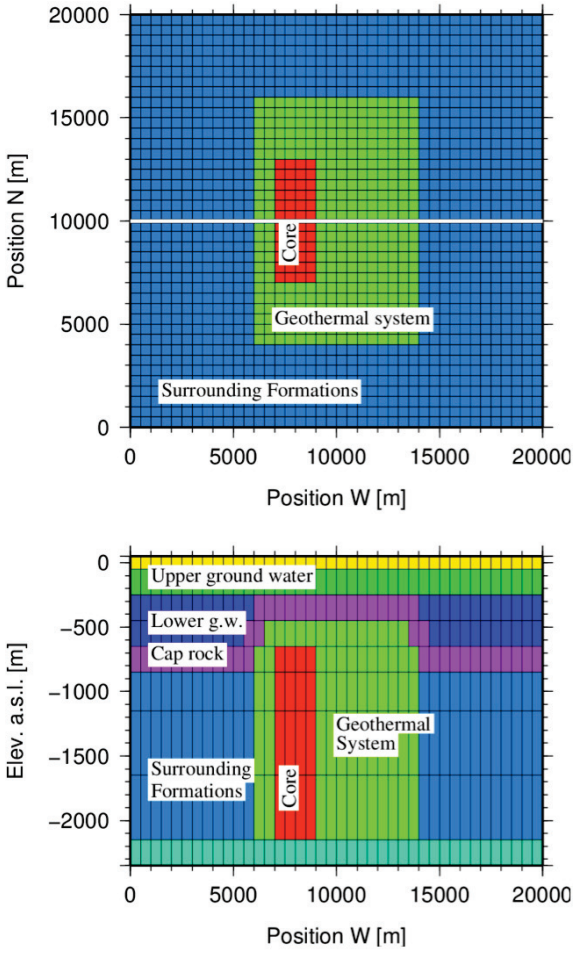

Figure 5. Schematics of the numerical model presented in this work. The upper part shows the model at the depth of 1000 m. The lower part shows the W-E section (marked by the white line the upper part) through the center of the model.

The top layer and the bottom layer of the system had a fixed temperature and pressure, as did the bottom layer. The bottom layer is much thicker, as depicted in Fig. 5, to minimize the effects of the boundary bottom boundary condition, and it was impermeable. In the beginning, the temperature gradient was 100°C/km in the entire model, and the pressure was in hydrostatic equilibrium. The system was driven using randomly formed dykes, as described above, for 100,000 years. That is a significant time span for the lifetime of a volcanic system in the Icelandic rift zone. It is also a significant time span for a TOUGH2 simulation, because in this case 100,000 years means 1,000 intrusion events, each of them necessarily described in the GENER-block of the input file. The total length of the GENER-block was 278,760 lines when it had been processed, to minimize the number of values describing heat inflow.

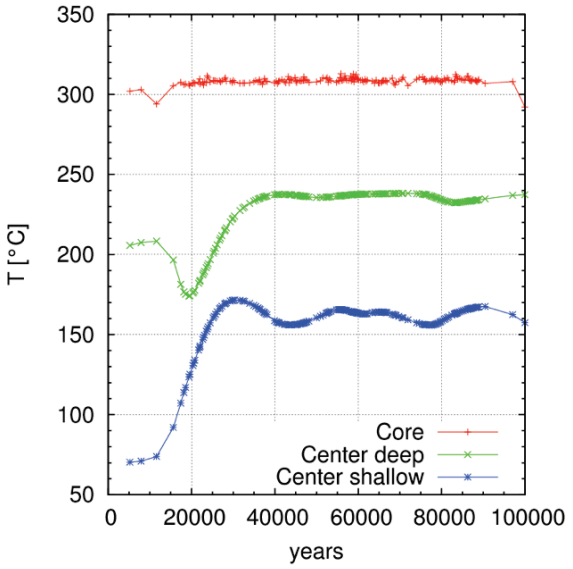

Figure 6. The evolution of temperature at three different locations in the model: In the Core at the depth of 750 m, and at two depths in the center of the geothermal system at of 1850 m (deep) and at 750 m (shallow).

In Fig. 6, the evolution of temperature at three different locations is shown. As can be seen, it takes the system around 30,000 years to reach a metastable equilibrium. The core of the system where the intrusion activity takes place heats up very rapidly, i.e., within the first 2000 years. The outer parts of the geothermal systems take longer to reach equilibrium. In Fig. 7, the temperature at 750 m depth is depicted, as is the temperature in a cross section through the center of the system from west to east. This is the temperature after running the model for 100,000 years. The structure of the temperature is relatively sharp and characterized by a reverse

temperature gradient in the hottest part of the system.

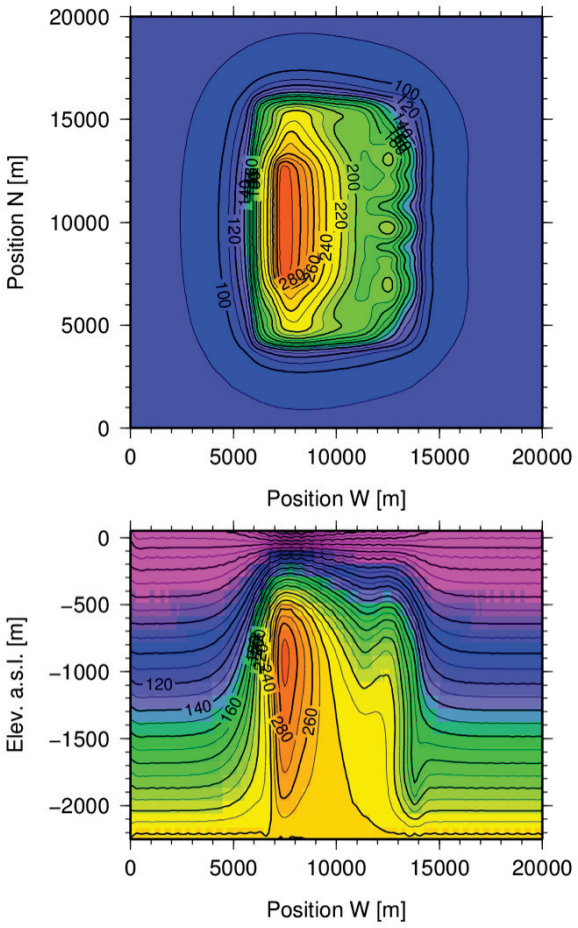

Figure 7. Temperature distribution at the depth of 750 m (above) and in a cross section through the center of the model from west to east (below) as it is calculated by the model. (Same sections as in Fig.5.)

SUMMARY AND CONCLUSION

The standard procedure of building a model for a geothermal system does in many ways avoid the roots of the geothermal system. The energy sources are often accounted for by assuming that they are below the depth range of the model and by choosing appropriate boundary conditions in the bottom layer. This has worked well for practical purposes, as does the assumption that the energy sources are constant in time. However, a model not including the roots of the geothermal system will always be incomplete, and recent cases in which wells were drilled into the heat source of a geothermal system have shown that it has also practical to incorporate the roots into the numerical models.

In this study, a simple conceptual model of a volcanic geothermal system was used in which it assumed that repeated formations of dykes are the driving mechanism of the system. Implementing the conceptual model using the TOUGH2 code (or any other code) can be carried out by making some simplifications to the problem. The dyke formation was simulated by injecting heat into predefined walls of elements, and a 2 m thick dyke was assumed to be formed (on average) every 100 years. (Note that the expansion of the crust due to rifting cannot be simulated using the TOUGH2 code.) The thickness of the dyke is just an indicator of the amount of energy injected into the predefined walls of elements when dyke formation is simulated. The bottom layer of the model is impermeable, so the entire water circulation is simulated.

The model was run for 100,000 years, with the time dependent heat sources driving it. The model reaches a metastable equilibrium within that time length. When the system has been charged up with heat, it is relatively stable, and temperature fluctuations are relatively small. These features are, however, dependent on model parameters, especially permeability. (The effects of different values for permeability have to be studied further; the time length of each run of the model is strongly dependent on permeability values.) It is, however, astonishing how stable the temperatures are after reaching the metastable equilibrium.

The lateral size of the elements of the model used in this study is relatively big—500×500 m. The area in which thermal energy injection due to formations of dykes was simulated was much wider than measured in the geothermal field in the Hengill Area. Formation temperature there has relatively narrow structures (See Fig. 3). There is still a lot of work to be done in trying to reproduce formation temperature structures seen in real geothermal systems. For that purpose, the elements must be smaller and the heat injection more concentrated.

We attempted to construct a complete model of a volcanic geothermal system in this work. The entire water circulation was included in the model, as were the heat sources. The question remains open as to whether we will have enough data for including events such as rifting and formation of intrusions as heat sources for our geothermal models.

ACKNOWLEDGMENT

We would like to thank our colleagues at Reykjavík Energy; Bergur Sigfússon, Einar Gunnlaugsson, Gretar Ívarsson, and Ingvi Gunnarsson, our colleagues at ÍSOR; Sigríður Sif Gylfadóttir and Sæunn Halldórsdóttir, and Andri Arnaldsson at Vatnskil, for fruitful discussions.

REFERENCES

Björnsson, G., A. Hjartarson, G. Bödvarsson, B. Steingrimsson, *Development of a 3-D geothermal reservoir model for the greater Hengill volcano in SW-Iceland*, Proceedings of TOUGH Symposium 2003, Lawrence Berkeley National Laboratory, Berkeley, California, May 12-14, 2003.

Buck, W.R., P. Einarsson, and B. Brandsdóttir: Tectonic stress and magma chamber size as controls on dike propagation: constraints from the 1975–1984 Krafla rifting episode. *J. Geophys. Res.* 111, B12404, 2006.

Einarsson, P. and B. Brandsdóttir, Seismological evidence for lateral magma intrusion during the July 1978 deflation of the Krafla volcano in NE-Iceland. *J. Geophys.* 47, 160–165, 1980.

Franzson, H: Nesjavellir. down hole geology and hydrology of the geothermal reservoir, (in Icelandic), Report OS-88046/JHD-09, 1988

Friðleifsson, G.F., B. Pálsson, B. Stefánsson, A. Albertsson, E. Gunnlaugsson, J. Ketilsson, R. Lamarche, and P.E. Andersen, *Iceland Deep Drilling Project. The first IDDP Drill Hole Drilled and Completed in 2009,* Proc. World Geothermal Congress 2010, Bali Indonesia, paper 3902, 2010.

Gunnarsson, G., A. Arnaldsson, and A.L. Oddsdóttir, Model Simulations of the Hengill Area, Southwestern Iceland, *Transp Porous Med,* 90, 3–22, 2010.

Hreinsdóttir, S., Árnadóttir, T., Decriem, J., Geirsson, H., Tryggvason, A., Bennett, R.A., LaFemina, P.: A complex earthquake sequence captured by the continuous GPS network in SW Iceland. *Geophys. Res Lett.* 36, L12309, 2009.

O'Sullivan, M. J.; Pruess, K. & Lippmann, M. J. State of the art of geothermal reservoir simulation, *Geothermics*, 30, 395-429, 2001.

Pruess, K., C. Oldenburg, and G. Moridis, *TOUGH2 User's Guide, Version 2.0*, Report LBNL-43134, Lawrence Berkeley National Laboratory, Berkeley, Calif., 1999.

Steingrímsson, B., A. Gudmundsson, H. Franzson, and E. Gunnlaugsson, *Evidence og Supercritical Fluid at depth in the Nesjavellir Field*. Proc, Fifteenth Workshop on Geothermal Reservoir Engineering, Stanford University, SGP-TR-130 pp. 81 – 88, 1990.

Walker, G.P.L., The Breiðdalur central volcano, eastern Iceland. *Quart. J. Geol. Soc. London* 119, 29 – 63, 1963.

A NOVEL, FULLY COUPLED FLOW AND GEOMECHANICS MODEL IN POROUS AND FRACTURED GEOTHERMAL RESERVOIRS

Litang Hu[a,b*], Philip H. Winterfeld[b], Perapon Fakcharoenphol[b], Yu-Shu Wu[b], Keni Zhang[c,a], and Tianfu Xu[c,d]

[a] College of Water Sciences, Beijing Normal University, Beijing 100875, PR China
[b] Petroleum Engineering Department, Colorado School of Mines, Golden, CO, USA, 80401
[c] Earth Sciences Division, Lawrence Berkeley National Laboratory, Berkeley, California, 94720, U.S.A
[d] College of Environment and Resources, Jilin University, Changchun, Jilin 130026, PR China
e-mail: litanghu@bnu.edu.cn

ABSTRACT

Numerical simulation of thermal-hydrologic-mechanical (THM) processes in porous and fractured media has become increasingly important and valuable for its role in the understanding of fluid flow, heat transfer, and rock deformation in stress-sensitive geothermal reservoirs. This paper presents a novel, fully coupled fluid-flow and geomechanics simulator (TOUGH2-EGS), in which the fluid flow portion is based on the general-purpose numerical model TOUGH2/EOS3, and the geomechanical portion is developed from the linear elastic theory for a thermo-poro-elastic system using the Navier equation. The multiple interacting continua method is applied to simulate flow in the fracture and fracture-matrix interaction. Porosity and permeability depend on effective stress, and several correlations describing that dependence are incorporated into the simulator. The established model is verified against analytical solutions for the one-dimensional dual-porosity consolidation problem by Wilsion and Aifantis (1982). Two cases—a five-spot injection and production pattern, and the Rutqvist and Tsang (2002) model—are examined for analyzing the effects of changes in pressure on fracture flow and rock deformation. The results demonstrate that our new model can be used for field-scale geothermal reservoir simulation of fluid flow and geomechanical effects in porous and fractured media.

INTRODUCTION

Geomechanical effects within porous and fractured media must be seriously considered with respect to enhanced geothermal systems, particularly in analyzing associated formation subsidence and stress-sensitive fractured reservoirs (Merle et al., 1976; Lewis and Schrefler, 1998; Settari and Walters, 2001; Boutt et al., 2011). Moreover, the coupling of geomechanics with porous-media fluid and heat flow would also be valuable for a variety of other technical problems—e.g., soil shrinkage from water evaporation and soil heaving due to water freezing; formation permeability and porosity changes; rock deformation associated with heavy oil recovery processes such as steam assisted gravity drainage (SAGD) or from cold water injection and steam/hot water production in geothermal fields. Furthermore, most geothermal reservoirs are situated in igneous and metamorphic rocks that have low matrix permeability. Well-connected cracks and fractures provide highly permeable fluid-flow paths through unfractured tight rock matrix. Artificial fractures or hydraulic fractures will be vital in providing additional highly permeable flow paths for underground fluid flow and heat exchange. For all these issues, numerical simulation of thermal-hydrologic-mechanical (THM) processes in porous and fractured media has become increasingly important.

Winterfeld and Wu (2011) have recently presented a fully coupled THM model based on a generalized version of Hooke's law in porous media, and have verified the model using several sample problems. However, how to simulate geomechanical behavior in fractured media remains a question. The first conceptualization of model flow in fractured media is the double-porosity concept, originally developed by Barenblatt et al. (1960), and later developed to classical double-porosity concept for modeling flow in fractured, porous media developed by Warren and Root (1963). The multiple interacting

continua (MINC) numerical approach has been used to simulate fracture and porous-matrix flow and interactions (Pruess and Narasimhan, 1985). The basic concept of MINC is that changes in fluid pressures (due to the presence of recharge or discharge from boundaries of the model domain) will propagate rapidly through the fracture system, while only slowly invading tight matrix blocks. Therefore, changes in matrix conditions will be controlled locally by the distance from the fractures. Fluid flow from the fractures into the matrix blocks or from the matrix blocks into the fractures can then be modeled by means of one-dimensional strings of nested gridblocks (Pruess et al., 1999). Doughty et al. (1999), in thoroughly examining and comparing fractured rock modeling methods for flow and transport processes in the unsaturated zone (UZ) at Yucca Mountain, NV, found that the MINC approach with multi-matrix-gridblocks gives the most accurate infiltration pulse and tracer arrival time among all methods. Wu et al. (2004) introduced the triple continuum concept, consisting of (1) tight rock matrix, (2) small-scale fractures, and (3) large-scale fractures. Each continuum can interact with any other, and global flow takes place in large fractures and rock matrix continua.

This paper will present a novel, fully coupled fluid flow and geomechanical simulator (TOUGH2-EGS) in detail, and then the model will be verified, through a 1D flow-geomechanical case using the dual porosity method for fractured reservoirs, by comparison with analytical solutions. Finally, two cases, one involving a five-spot injection and production pattern, and the other the Rutqvist and Tsang (2002) model, are simulated for analyzing how changes in pressure affect fracture flow and rock deformation.

MATHEMATICAL MODEL

Formulation of fluid and heat flow in porous and fractured media

Our new simulator was developed based on the general framework of mathematical and numerical models, which solve mass- and energy-balance equations describing fluid and heat flow in general multiphase, multicomponent systems (TOUGH2/EOS3). Fluid flow is described using a multiphase extension of Darcy's law. Heat flow is governed by conduction and convection, including sensible as well as latent heat effects. Following Pruess et al. (1999), the mass- and heat-balance equations in each model subdomain or REV of an EGS can be written as in Table 1. The MINC method is used to simulate fracture-fracture flow or fracture-matrix flow.

Table 1. Equations of fluid and heat flow solved in TOUGH2-EGS

Description	Equation
Conservation of mass and energy	$\frac{d}{dt}\int_{V_n} M^\kappa \, dV_n = \int_{\Gamma_n} \mathbf{F}^\kappa \bullet n \, d\Gamma_n + \int_{V_n} q^\kappa \, dV_n$ $\kappa = 1, 2, 3$
Mass accumulation	$M^\kappa = \phi \sum_{\beta w} S_{\beta w} \rho_{\beta w} X^\kappa_{\beta w}$, $\kappa = 1, 2$
Mass flux	$\mathbf{F}^\kappa = \sum_{\beta w} X^\kappa_{\beta w} \rho_{\beta w} \mathbf{u}_{\beta w}$, $\kappa = 1, 2$
Energy flux	$\mathbf{F}^3 = -\lambda_T \nabla T + \sum_{\beta w} h_{\beta w} \rho_{\beta w} \mathbf{u}_{\beta w}$
Energy accumulation	$M^3 = (1-\phi)\rho_R C_R T + \phi \sum_{\beta w} \rho_{\beta w} S_{\beta w} U_{\beta w}$
Phase velocity	$\mathbf{u}_\beta = -k \frac{k_{r\beta w}\rho_{\beta w}}{\mu_{\beta w}} (\nabla P_{\beta w} - \rho_{\beta w} \mathbf{g})$

Formulation of geomechanics in porous and fractured reservoir

The poroelastic version of the Navier equations for matrix (Jaeger et al., 2007) is as Equation 1. The definition of symbols is shown in the Symbol Chapter.

$$G\nabla^2 \bar{u} + (G+\lambda)\nabla(\nabla \cdot \bar{u}) = -\bar{F} - \alpha \nabla P - 3\beta K \nabla T \quad (1)$$

The poroelastic version of the Navier equations for matrix and fractures (Bai and Roegiers, 1994) is

$$G\nabla^2 \bar{u} + (G+\lambda)\nabla(\nabla \cdot \bar{u}) = -\bar{F} - \alpha_f \nabla P_f - \alpha_m \nabla P_m - 3\beta_m K_m \nabla T_m - 3\beta_f K_f \nabla T_f \quad (2)$$

where

$$a_f = 1 - K_f / K_m; \;\; a_m = K_f / K_m (1 - K_m / K_s) \quad (3)$$

Here, K_f is the fracture medium bulk modulus, K_m is the bulk modulus of the matrix, and K_s is the solid bulk modulus.

Strain can be expressed in terms of a displacement vector, u. The displacement vector points from the new position of a volume element to its previous position. The strain tensor is related to the displacement vector by

$$\bar{\bar{\varepsilon}} = \frac{1}{2}[\nabla \bar{u} + (\nabla \bar{u})^T] \quad (4)$$

Hook's law for the normal stress of a thermoporoelastic dual-permeability medium, generalized from Bai et al., 1995, is

$$\tau_{ll} - (\alpha_f p_f + \alpha_m p_m + 3\beta_f (T_f - T_{ref}) + 3\beta_m (T_m - T_{ref})) = 2G\varepsilon_{ll} + \lambda(\varepsilon_{xx} + \varepsilon_{yy} + \varepsilon_{zz}), l = x, y, z \quad (5)$$

The volumetric strain is obtained from summing the normal stress components in the above equation:

$$K\varepsilon_v = \tau_m - (\alpha_f p_f + \alpha_m p_m + 3\beta_f (T_f - T_{ref}) + 3\beta_m (T_m - T_{ref})) \quad (6)$$

The above two equations can be generalized to the MINC formulation by replacing the fracture (f) and matrix (m) terms with a summation over MINC, for example:

$$K\varepsilon_v = \tau_m - \sum_{i=1}^{N} (\alpha_i p_i + 3\beta_i (T_i - T_{ref})) \quad (7)$$

For each set of MINC blocks, there is one mean stress and one volumetric strain. Mean stress is a gridblock primary variable. The mean stress equation of discretation is

$$\frac{3(1-\nu)}{(1+\nu)} \nabla^2 \tau_m = -\nabla \cdot \bar{F} + \frac{2(1-2\nu)}{(1+\nu)} \sum_{i=1}^{N} (\alpha_i \nabla^2 P_i + 3K\beta_i \nabla^2 T_i) \quad (8)$$

Rock property corrections

When the spatial average stress distribution is calculated, permeability and porosity are both dependent on effective stress:

$$k = k(\sigma') \quad (9)$$

$$\phi = \phi(\sigma') \quad (10)$$

These relationships are based on experimental formula and can be input to the model. Since bulk volume is related to porosity, we also allow bulk volume to depend on effective stress and pore pressure

$$V_b = V_b(\sigma', P) \quad (11)$$

Code integration

The mean total stress is added as an additional primary variable. Thus there are four primary variables: pressure, temperature, air mass fraction, and the mean total stress. Secondary variables such as liquid saturation and volumetric strain are calculated from the primary variables. Pressure, temperature, and mean total stress initialization parameters are first input into the model, and the initial stress field is then calculated from them. Finally, pressure, temperature, air mass fraction, and mean total stress are solved iteratively for each Newton iteration. The calculation of fluid and geomechanical variables is fully implicit and fully coupled with fluid and heat flow.

MODEL VERTIFICATION

A 1-D column consisting of a double-porosity medium (which may be fissured rock) is considered by Wilson and Aifantis (1982). The conceptual model is shown in Figure 1.

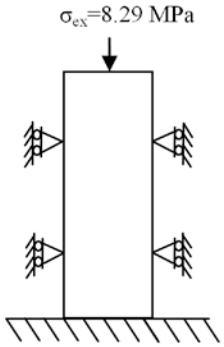

Figure 1. Schematic figure representing a double-porosity model in 1-D fractured reservoirs.

Height of sand column is 50 m. The primary rock properties are basically from Berea sandstone experimental data. The porosity of fracture and matrix is 0.019 and 0.19 respectively. Permeability of fracture and matrix is 1.0×10^{-13} m^2 and 1.0×10^{-17} m^2 respectively. Rock compressibility is 4.40×10^{-10} Pa^{-1}, Poisson ratio is 0.20, Young modulus is 14.40 GPa, and Biot coefficient is 1.0. This actual physical situation occurs in a geothermal reservoir where the initial condition is drained, with zero deformation. When fluid is produced from the reservoir, the rock frame starts to deform. Thus, in our simulation setup, the difference between initial pressure and bottomhole pressure was constructed to be equivalent to pressure change resulting from the top load. Also, the productivity index of the producer is calculated to be equivalent to a constant pressure boundary at the top of reservoir. Analytical and numerical solutions for pressure in fractured media and displacement are shown in Figure 2 and 3. The match is good, adding to the creditability of the model.

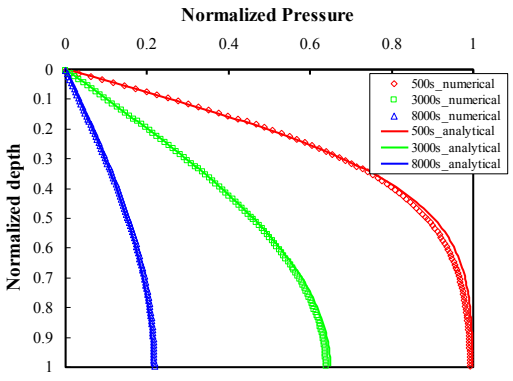

Figure 2. Comparisons of numerical and analytical solutions for pressure in the fracture.

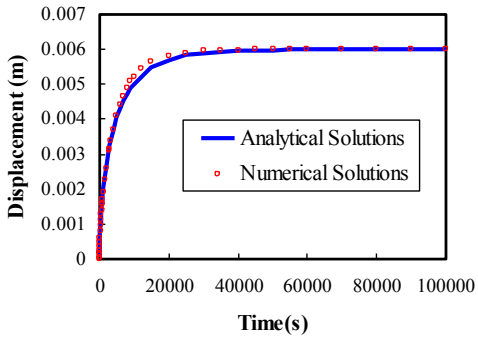

Figure 3. Comparisons of numerical and analytical solutions for normalized displacement at the top of the column.

MODEL APPLICATION

Problem of five-spot injection and production pattern

In geothermal reservoir development, production and injection wells are often sited in regular geometric patterns. In our application, we consider a large well field with wells arranged in a "5-spot" pattern. Because of symmetry, only a quarter of the basic pattern needs to be modeled. Figure 4 shows a simulation in which the fine grids are used near the injection and production wells, whereas coarse grids are used elsewhere. The system is initialized as a normal pressure regime in which subsurface pressure follows the hydrostatic pressure of the water head, and the temperature gradient is set at 4˚C/km. The reservoir is fully saturated with water. Some rock properties are shown in Figure 4.

In this simulation, to analyze the effect of fracturing on pressure and strain distribution, we calculate two scenarios: with and without the consideration of fractures. Figure 5 shows simulation results with consideration of fracturing after 3 years of production near the injector and producers, respectively. Around the injector, the temperature is reduced, as a result of cooling effects, in turn resulting in stress reduction, as can be seen in the pressure and mean normal stress changes following the temperature change pattern (Figure 5(a) and (c)).

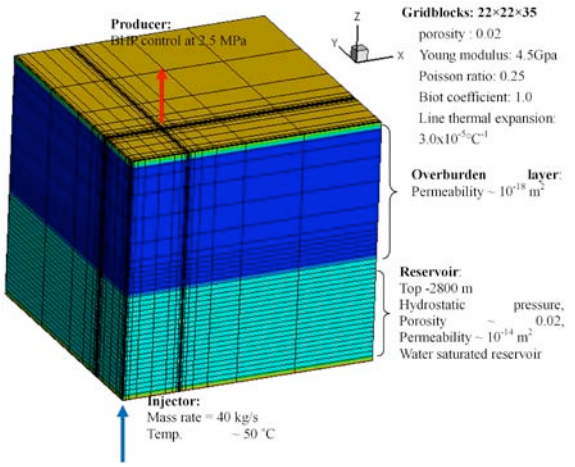

Figure 4. Schematic figure of a quarter model for 5-spot pattern

As shown in Figure 6, the pressure at the injection point in the with-fracture scenario decreases more rapidly than that in the without-fracture scenario; also, volumetric strain is much larger in the with-fracture scenario than in the without-fracture scenario. From Figure 6, the pressure for the with-fracture scenario after 3 years is ~36 MPa, whereas the without-fracture scenario is ~25 MPa. From Figure 7, the total settlement for the with-fault scenario after 3 years is almost 1.50 m, whereas the settlement for the without-fault scenario is less than 0.25 m. The differences in the total settlements demonstrate that the existence of fractures will cause a sharp decline in pressure and large deformation.

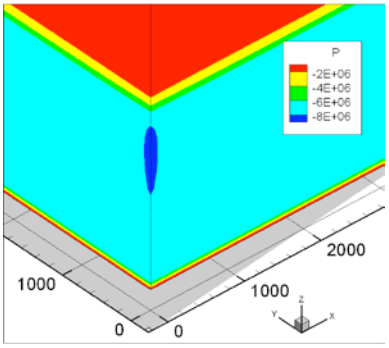

(a) pressure change.

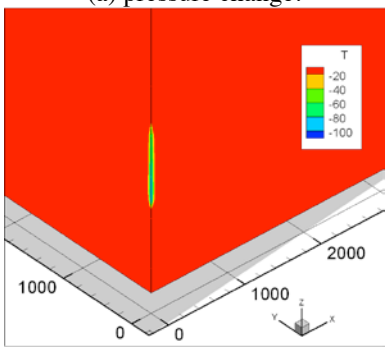

(b) temperature change.

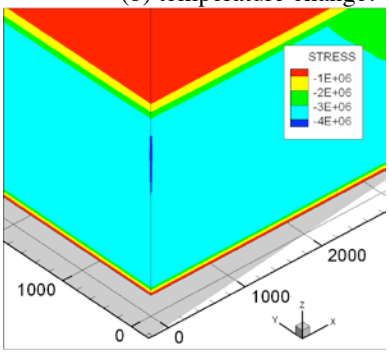

(c) mean normal stress change.

Figure 5. Simulation results with the consideration of fracture at the injector after 3 years.

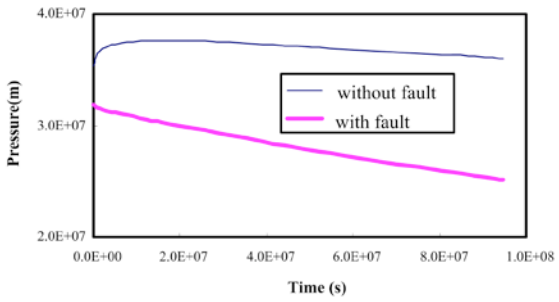

Figure 6. Changes of pressure with time at the injection point

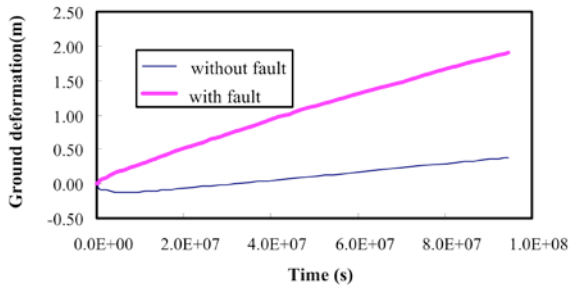

Figure 7. Changes of the total settlement with time at the injection point

The Rutqvist and Tsang CO2 injection model simulation

Rutqvist and Tsang (2002) presented a two-dimensional vertical section model (Figure 8), extended far enough in lateral directions to be considered infinite acting. The injection formation is 200 m thick and bounded by a low permeability basement rock and a 100 m thick cap rock, which in turn is overlain by an upper 1,200 m homogenous formation. The parameters for each formation can be found in Rutqvist and Tsang (2002). Unlike Rutqvist and Tsang (2002) we simulate water injection rather than supercritical CO_2 and focus our study on the effects of the fault. This conducted by comparing the simulation results with and without including the fault into the model simulation.

The functions for porosity and permeability changes are obtained by correlation with laboratory measurements on sandstone (Rutqvist and Tsang, 2002). The porosity, ϕ, is related to the mean effective stress as

$$\phi = (\phi_0 - \phi_r)e^{5\times10^{-8}\cdot\sigma'} + \phi_r \qquad (13)$$

where ϕ_0 is porosity at zero stress, ϕ_r is residual porosity at high stress. Moreover, the permeability is correlated to the porosity according to the following exponential function:

$$k = k_0 e^{22\times(\phi/\phi_r - 1)} \qquad (14)$$

where k_0 is the zero stress permeability.

The simulated pressure, permeability, mean total stress, and volumetric strain profile in the vertical direction for the with-fault scenario after 10 years is shown in Figure 9. Figure 10 shows a comparison of the contour lines of volumetric strain by our model with and without considering faults. In the without-fault scenario, the strain propagates mainly along the bottom of the cap rock, but cannot break through the cap rock. However, in the with-fault scenario, pressure-induced changed in permeability, mean total stress and volumetric strain reach their maximum value around the injection point, and then propagate to the surrounding, and more importantly, changes are found along both the bottom of the cap rock and the fault (Figure 9). When compared with Rutqvist and Tsang's results, the results seem similar and reasonable.

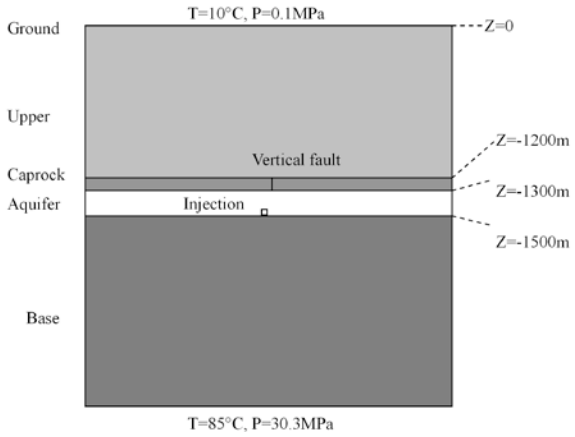

Figure 8. Vertical profile of study area.

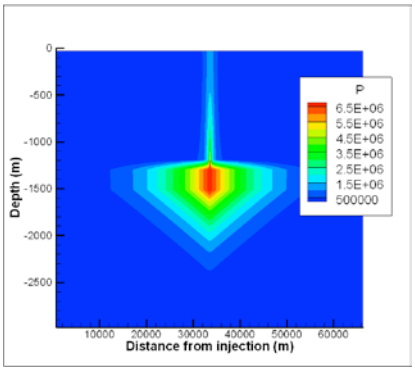

(a) pressure change.

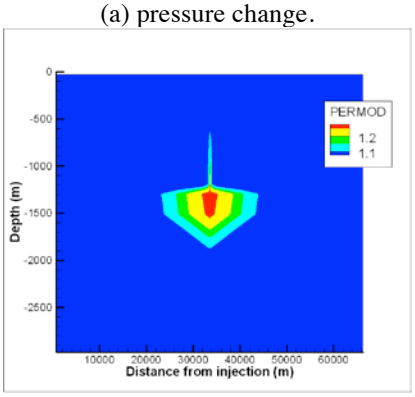

(b) permeability change (K/K_0).

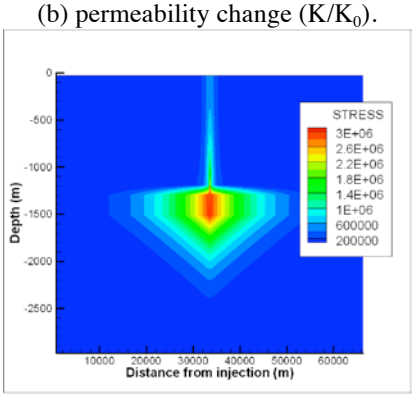

(c) mean normal stress change.

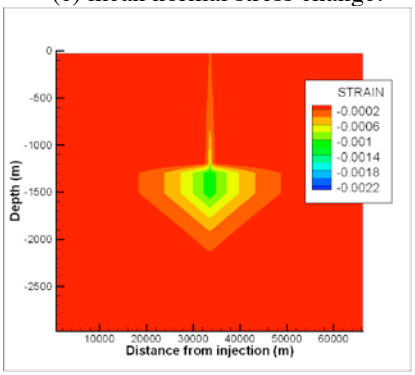

(d) volumetric strain change.

Figure 9. Simulated profile at with-fault scenario after 10 years.

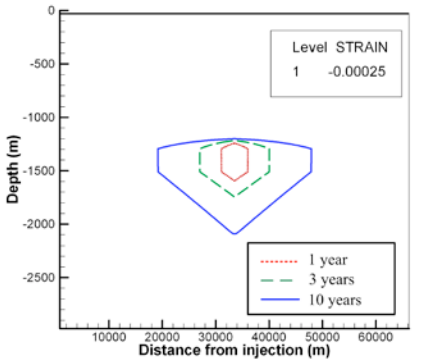

(a) without fault

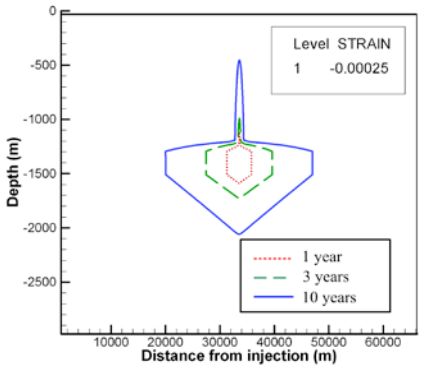

(b) with fault

Figure 10. Simulated contour lines at a value of 0.00025 with-fault and no-fault scenario for 1, 3 and 10 years.

CONCLUSION

We present an efficient, fully coupled fluid flow and geomechanics simulator (TOUGH2-EGS) for simulating multiphase flow, heat transfer, and rock deformation in porous and fractured media. The fluid and heat flow formulation is based on that for TOUGH2/EOS3; the geomechanics formulation is based on the theory of thermo-poroelasticity (the Navier thermo-poroelastic equation). The flow, heat, and stress equations are solved at each Newton-Rapson iteration. The mean total stress is added as an additional primary variable.

Our numerical model is verified for a 1D flow-geomechanics case using a dual porosity method in a fractured reservoir, and is tested by comparison with analytical solutions. In comparing our simulated changes in pressure and strain to analytical model results, we find that our numerical model can produce essentially the same results as analytical models. Two cases—a 5-spot EGS model, and a similar case as posed by Rutqvist and Tsang (2002), are simulated. The results demonstrate that our model can assess how cold water injection and steam or hot water production might affect the stress field in fractured reservoirs—and most importantly, how faults could lead to changes in pressure, stress, and strain.

The presented numerical model only calculates the mean total stress, as opposed to the total stress tensor. Such a simplification may be a shortcoming in our model, since it therefore cannot analyze phenomena dependent on shear stresses, such as rock failure. Also, the model represents instantaneous, undrained responses as well deliverability and changes in the mean normal stress. However, TOUGH2-EGS is rigorous in handling coupled flow and rock deformation and is easily applied to stress-sensible reservoirs for analyzing multiphase fluid, heat flow, and rock deformation in porous and fractured media.

SYMBOLS

Nomenclature

C_R heat conductivity, $W\ K^{-1}\ m^{-1}$.

$\overline{F}$ body force (gravity), Pa m^{-1}.

F^κ the mass or energy transport terms along the borehole due to advective processes, W m^{-1}.

g Gravitational acceleration constant, m s^{-2}.

G shear modulus, Pa.

$h_{\beta w}$ Specific enthalpy in phase βw, J kg^{-1}.

k Absolute permeability, m^2.

K Bulk modulus, Pa.

K_i Bulk modulus, Pa, (i=f, fracture; i=m, matrix)

$k_{r\beta w}$ Relative permeability to phase $\beta\omega$.

M^κ the accumulation terms of the components and energy κ, kg m^{-3}.

$\boldsymbol{n}$ Normal vector on surface element, demensionless.

N the nubers of MINC.

t Time, s.

T Temperature, ˚C or K.

T_i Temperature, ˚C or K, (i=f, fracture; i=m, matrix)

T_{ref} Reference temperature, ˚C or K.

$u_{\beta w}$ the Darcy velocity in phase $\beta\omega$, m s^{-1}.

$U_{\beta w}$ the internal energy of phase β per unit mass, J kg^{-1}

V_b Bulk volume, m^3.

V_n Volume of the n^{th} grid cell, m^3.

P Pressure. Pa.

P_i Pressure of frature. Pa, (i=f, fracture; i=m, matrix)

P_{c0} Reference capillary pressure. Pa.

$P_{\beta w}$ the fluid pressure in phase $\beta\omega$, Pa.

q^{κ} Source/sink terms for mass or energy components, kg $m^{-3}s^{-1}$.

$S_{\beta w}$ Saturation of phase $\beta\omega$, dimensionless.

T Temperature, °C.

$\bar{u}$ Displacement vector, m.

$X^{\kappa}_{\beta w}$ Mass fraction of component κ in fluid phase $\beta\omega$, dimensionless.

Greek Letters

α Biot's coefficient, dimensionless.

α_i Biot's coefficient of fracture, dimensionless, (i=f, fracture; i=m, matrix)

β Linear thermal expansion coefficient, $°C^{-1}$.

β_i Linear thermal expansion coefficient, $°C^{-1}$, (i=f, fracture; i=m, matrix)

β_w fluid phases (=liquid, gas)

$\mu_{\beta w}$ Viscosity, Pa.s

ϕ Porosity, dimensionless.

λ_T Thermal conductivity, $W K^{-1} m^{-1}$

λ Lame's constant, Pa.

ε_{ll} Strain components, l=x,y,z, dimensionless.

ε_v Volumetric strain, dimensionless

$\bar{\bar{\varepsilon}}$ Strain tensor, dimensionless.

ν Poisson's ratio of rock, dimensionless.

σ' Effective stress, Pa.

σ_{ex} External load per area at the top column, Pa.

ρ_R the density of rock grain. kg m^{-3}.

$\rho_{\beta w}$ the density of phase $\beta\omega$, kg m^{-3}.

Γ_n Area of closed surface, m^2.

τ_{kl} k=l for shear stress; k≠l for normal stress, k=x,y,z, l=x,y,z, Pa.

τ_m Mean total stress, Pa.

Subscripts and Superscripts

κ the index for the components, κ = 1 (water), 2 (air), and 3 (energy).

β_w = G for gas; = L for liquid.

ACKNOWLEDGEMENT

This work is supported by the U.S. Department of Energy under Contract No. DE-EE0002762, "Development of Advanced Thermal-Hydrological-Mechanical-Chemical (THMC) Modeling Capabilities for Enhanced Geothermal Systems". This work is also supported by the CMG Foundation and the National Nature Science Foundation of China (Grant Numbers: 41072178 and 40872159).

REFERENCES

Bai, M., Roegiers, J.-C., Fluid flow and heat flow in deformable fractured porous media, *Int. J. Engng Sci.*, 32(10), 1615-1633, 1994.

Bai, M., Roegiers, J.-C., Elsworth, D., Poromechanical response of fractured-porous rock masses, *J. Petroleum Sci. Engng.*, 13, 155-168, 1995.

Barenblatt GI, Zheltov IP, and Kochina IN. Basic concepts in the theory of seepage of homogeneous liquids in fissured rocks. PMM, Sov Appl Math Mech, 24(5):852-864, 1960..

Boutt, D.F., Cook, B.K., Williams, J.R., A coupled fluid-solid model for problems in geomechanics: application to sand production, *International Journal of Numerical and Analytical methods in Geomechanics*, 35, 997-1018, 2011.

Doughty, C., Investigation of conceptual and numerical approaches for evaluating moisture, gas, chemical, and heat transport in fractured unsaturated rock, *J. Cont. Hydro.*, 38, 69-106, 1999.

Jaeger, J. C., N. G. W. Cook, and R. W. Zimmerman, *Fundamentals of rock mechanics.* Blackwell, Forth edition, 2007.

Lewis, R.W., Schrefler, B.A., *The finite element method in the static and dynamic deformation and consolidation of porous media*. Chichester, England: Wiley, ^{2}nd edition. 1998.

Merle, H.A., Kentie, C.J.P., Van Opstal, G.H.C., Schneider, G.M.G., 1976. The Bachaquero Study-a composite analysis of the behavior of a compaction drive/solution gas drive reservoir. *JPT*, 1107–1114.

Pruess, K., and T.N. Narasimhan, A practical method for modeling fluid and heat flow in fractured porous media, *Soc. Pet. Eng. J.*, 25(1), 14-26, 1985.

Pruess, K., C., Oldenburg, and G., Moridis, *TOUGH2 User's Guide, V2.0*, Lawrence Berkeley National Laboratory Report LBNL-43134, Berkeley, CA, 1999.

Rutqvist, J., Tsang, C.F., A study of caprock hydromechanical changes associated with CO_2-injection into a brine formation, *Environmental Geology*, 42, 296–305, 2002.

Settari, A., Walters, D.A., Advances in coupled geomechanical and reservoir modeling with applications to reservoir compaction, *SPE Journal*, 6(3), 334-342, 2001.

Warren, J.E., and P.J., Root, The behavior of naturally fractured reservoirs, *Soc. Pet. Eng. J.*, 245-255, 1963.

Wilson, R.K., Aifantis, E.C., On the theory of consolidation with double porosity, *Int. J. Engng. Sci.*, 20(9), 1009-1035, 1982.

Winterfeld, P.H., Wu, Y.S., Parallel simulation of CO_2 sequestration with rock deformation in saline aquifers, *Society of Petroleum Engineers*, *SPE 141514*, 2011.

Wu, Y. S., H. H. Liu, and G. S. Bodvarsson, A triple-continuum approach for modeling flow and transport processes in fractured rock, *Journal of Contaminant Hydrology*, 73, 145-179, 2004.

NUMERICAL RESERVOIR MODEL OF THE TAKIGAMI GEOTHERMAL FIELD, OITA, JAPAN

Saeid Jalilinasrabady[1], Ryuichi Itoi[1], Hiroki Gotoh[2], Toshiaki Tanaka[1]

[1]Faculty of Engineering, Kyushu University, Fukuoka 819-0395, Japan
[2]Idemitsu Kosan Co. Ltd., Tokyo, Japan
e-mail: jalili@kyudai.jp

ABSTRACT

We developed a conceptual model of the Takigami geothermal field and corresponding numerical models using the TOUGH2 simulator, rock types were assigned to each gridblock in several layers. Initial and boundary conditions were defined according to available data. The model, which covers a square area of 9.6 km by 9.6 km, with 3 km depth below sea level, consists of 12 horizontal layers, with layer thickness varying from 200 m to 800 m. For the optimum model, we estimated the permeability values of the various rock types, mass flow rates, enthalpies and locations of recharge zones. These were based on matching between computed temperatures at the wells and their measured temperature profiles before exploitation. A comparison between observed and calculated temperature profiles confirmed the validity of the conceptual model and provided the first stage of calibration of the 3-D numerical model. The iTOUGH2 simulator was used for the calibration. Our best model could successfully reproduce the initial temperature profiles of 13 wells located mainly in the production area. Overall, history-matching results for enthalpy production from the simulated model show an acceptable match with measurements in four production wells.

INTRODUCTION

The Takigami geothermal field is located in the southwestern part of the Oita prefecture, Kyushu Island, Japan. Central Kyushu is intersected by a volcano-tectonic depression that has developed within a tensile stress field since the Neogene, resulting in Plio-Pleistocene to recent volcanism (Hase et al., 1985). The northeastern part of Central Kyushu, known as the Hohi region, is one of the most active geothermal areas in Japan (Figure 1). Although the Takigami system lies within this very active Hohi geothermal region, there is no surface manifestation in the immediate area: The nearest hot springs are located 1–2 km north and east of the area. (Furuya et al., 2000). Geothermal exploration in the Takigami area began in 1979 with various surveys and drilling.

In and around the Takigami area, gravity and electromagnetic prospecting has been conducted since 1979, while resistivity logging began in 1981 (Aoki, 1988). These surveys confirmed the existence of three main layers in the resistivity structure of the field that extend laterally over the area. The intermediate layer has an extremely low resistivity, while the bottom layer has relatively high resistivity. The second, conductive layer is shallow and thin in the east, and deepens and becomes thicker to the west (Furuya et al., 2000).

A geochemical model of the Takigami area was discussed by Takenaka and Furuya (1991). Relatively low salinity and a low concentration of non-H_2O, non-condensible gas in the produced steam characterize the Takigami geothermal fluids (Furuya et al., 2000). Itoi et al. (1993) obtained fairly good estimates of reservoir parameters by analyzing pressure interference tests using an infinite reservoir model for wells. Also, Gotoh (1990), in another study, stated that, with small decreases in reservoir pressure and temperature in the production zone, a production of 1850 t/h of geothermal fluid should be maintainable for more than 30 years

The Takigami power station, which started operation in November 1996 with a capacity of 25 MW, has increased its power to 27.5 MW as

of June 2010. Five production wells are located in the southwest part of the field; seven to ten reinjection wells are located in the northern part. Idemitsu Oita Geothermal Co., Ltd is in charge of production and reinjection operations, supplying separated steam to the power station, which is operated by Kyushu Electric Power Co., Inc.

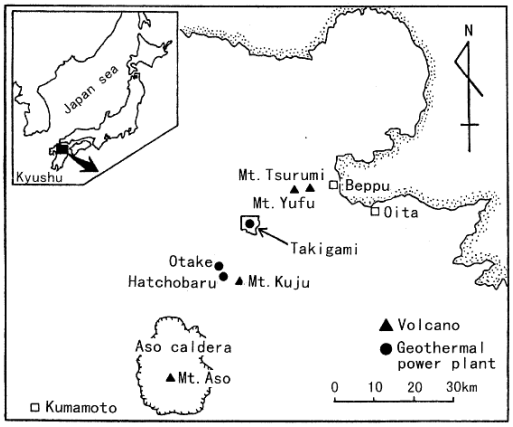

Figure 1. Map of the Hohi geothermal region, northeast Kyushu, showing the location of the Takigami area, the major Quaternary volcanoes and the Otake-Hatchobaru geothermal area (Furuya et al., 2000).

A three-dimensional numerical reservoir model of Takigami was developed by inverse modeling methods, using discharge enthalpies from production wells over ~11 years of the exploitation history (Nakatani et al., 2007). A wellbore flow model was coupled to the numerical reservoir model to improve the description of the physical system (Hozumi, et al., 2009).

We developed a new and improved model for the Takigami geothermal field, which draws from (and is enhanced by) previous experience. We recently conducted a simulation using the TOUGH2 code with the EOS1 module (Pruess, et al., 1999), with the objective of developing of natural state model of the field.

In addition to the numerical model, we also constructed a conceptual model of the field. As part of this effort, rock types were assigned to each block in several layers. Initial and boundary conditions were defined/assigned based on the availability of data, and reasonable assumptions when such data were unavailable.

The objective of this study is to develop a numerical model of Takigami geothermal field by means of inverse modeling (history matching). This was achieved by matching model predictions to measurements of downhole temperatures (Jalilinasrabady et al., 2010). The simulation process required running the models to steady state and comparing the simulated data with the known or interpreted conditions in the system (Noorollahi et al., 2008). This is an iterative process that continues until a good match is obtained and requires changing model properties (such as permeability and inflow/ outflow conditions) to obtain improved matches. With every set of reservoir properties, vertical heat flow and temperature distribution in each layer were also analyzed using Mulgraph (O'Sullivan, 1995). However, developing a reliable numerical reservoir model using this method can be time consuming.

CONCEPTUAL MODEL

The Takigami area is surrounded by the late Pleistocene volcanoes of the Beppu-Shimabara Graben, which traverses middle Kyushu from east to west. This water-dominated field is characterized by the absence of surface geothermal manifestations, such as hot springs and fumaroles. There are a number of E-W, NW-SE, and N-S trending faults and fractures (Figure 2 and Figure 3).

The N-S trending Noine fault is important because it divides the area into eastern and western parts. The E-W trending faults, such as the Teradoko fault, are estimated to have a small vertical displacement. A high-permeability zone and a feed zone for the wells appear along these fault sets (Hayashi et al., 1988).

The geological structure of the Takigami geothermal field is as follows (Hayashi et al., 1988): A thick layer of Quaternary volcanic and associated rocks overlies the Tertiary Mizuwake andesite, which is estimated to overlay the basement. The Quaternary volcanic rocks are classified into four formations from top to bottom: the Noine-dake volcanic rocks, Kusu,

Ajibaru, and Takigami formations. These units consist of andesitic and dacitic volcanic-rocks layers. The Mizuwake andesite is composed mainly of altered andesite lava flows and pyroclastic rocks.

The thermal structure of this field is basically composed of three layers (Furuya et al., 2000). The first layer is isothermal (50°C), the second layer has a steep and constant thermal gradient because of its low permeability, and the third layer is characterized by high temperature that ranges from 160°C (in the northeast) to 250°C (in the southwest).

The layer comprising the geothermal reservoir is used for both production and reinjection, but communication between the production and injection wells is limited because of a low permeability zone in the reservoir (indicated from interference tests conducted using these wells). According to current estimates, the low-permeablility zone is located on the northeastern side of the Noine fault (Figure 2).

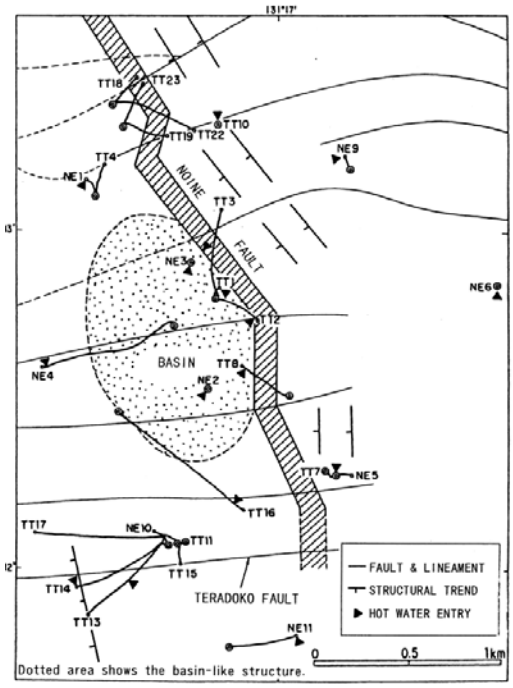

Figure 2. Location of Takigami geothermal field and conceptual geological structure.

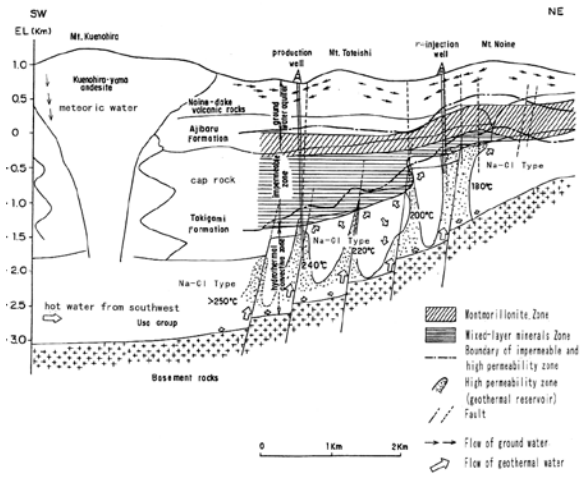

Figure 3. Schematic cross-sectional model of the Takigami geothermal system (modified from Takenaka and Furuya, 1991).

NUMERICAL SIMULATION

iTOUGH2 using inversion techniques and can serve as a calibration tool for numerical models. It is an optimization code that allows estimation of any input parameters of a non-isothermal, multi-phase flow simulator (Finsterle et al., 1997). The iTOUGH2 code allows to the estimation of TOUGH2 input parameters based on any type of observation for which a corresponding simulation output can be calculated. At the same time, iTOUGH2 carries out a residual and error analysis that allows us to choose an optimum model. This simulator systematically modifies the values of a small set of parameters and uses mathematical optimization techniques to improve the match to the field data. The process requires a selection of parameters to be adjusted (i.e., to construct an objective function; Finsterle et al., 1999).

According to the available literature on the Takigami geothermal field, and on the basis of studies of the field's conceptual model, we used iTOUGH2 to develop a three-dimensional numerical model. The model was calibrated using a trial-and-error approach, using available data on the natural-state conditions of the reservoir to obtain a good match between measurements and numerical predictions. Results of this match were used as initial parameters for inverse modeling.

iTOUGH2 allows us to conduct both natural-state and exploitation-history simulations. These simulations are carried out sequentially in a single run of iTOUGH2 (Finsterle, 2000). However, this method may require long computing times to achieve optimum values of parameters. To solve this problem, we first conducted a natural-state simulation. Then, both natural state and exploitation history were simulated sequentially, using the parameters estimated from natural-state simulation as the initial conditions for the exploitation simulations.

Grid system and layers

A grid system was developed for modeling purposes. The grid system covers the square area of 9.6 km by 9.6 km, with 3 km depth below sea level (b.s.l.) (Figure 4). The model consists of 12 horizontal layers, with layer thickness varying from 200 m to 800 m. The coordinates of the system reflected correct surface elevations. Layers bb and cc had thicknesses of 300 m and 200 m, respectively; layers dd, ee, ff, gg, and hh were 200 m thick; layers ii, jj and kk were 400 m thick; and layer ll is the bottom layer, with a thickness of 800 m. Each layer has 414 gridblocks of various (non-uniform) sizes. Finer grids of 200×200 m were assigned to the areas corresponding to wells and power plant locations. The codes Mulgeom and Mulgraph (O'Sullivan et al., 1995) were used as pre-and post-processors.

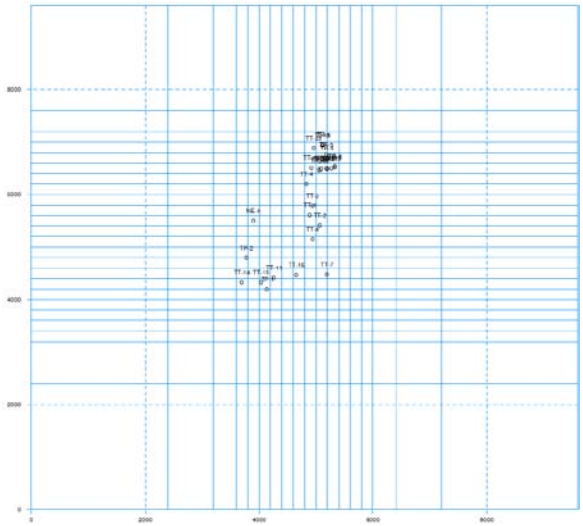

Figure 4. Grid system of the model.

Rock properties

Density, permeability, thermal conductivity, porosity, and specific heat were taken into account as rock properties.

Table 1. Initial rock parameters.

Rock type	Intrinsic Permeability (m^2)		Thermal Conduct. (W/mK)
	K_{XY}	K_Z	
ATM (A_T)	$1.00x10^{-10}$	$1.00x10^{-10}$	3.0
NVR (N)	$1.00x10^{-14}$	$1.00x10^{-12}$	3.9
KLY (K)	$1.00x10^{-14}$	$1.00x10^{-15}$	2.6
LOW (L)	$1.00x10^{-18}$	$1.00x10^{-19}$	2.6
ALY (A)	$1.00x10^{-16}$	$1.00x10^{-17}$	2.5
MED (M)	$1.00x10^{-13}$	$1.00x10^{-14}$	3.6
MED1 (M_1)	$1.30x10^{-12}$	$5.00x10^{-14}$	1.3
MED2 (M_2)	$1.00x10^{-14}$	$1.00x10^{-15}$	1.3
MED3 (M_3)	$7.90x10^{-15}$	$3.20x10^{-15}$	2.1
UTL (U)	$1.00x10^{-15}$	$1.00x10^{-13}$	1.5
LTL (L_T)	$1.00x10^{-13}$	$1.00x10^{-16}$	2.3
MAL (M_A)	$1.00x10^{-14}$	$1.00x10^{-16}$	4.0
UHW (U_H)	$2.00x10^{-12}$	$5.00x10^{-14}$	1.8
UBAS (U_B)	$1.00x10^{-14}$	$1.00x10^{-15}$	2.0
LBAS (L_B)	$1.00x10^{-13}$	$1.00x10^{-15}$	2.7

The model requires estimates of rock properties as input data. These data were provided using the best available information on the geology, reservoir system, and fault characteristics of the system. One of these rock properties, the intrinsic permeability, plays a key role in achieving the most realistic model. Each layer of the grid was further subdivided into zones of different permeability values according to available data. Initial estimates of rock properties were based on the conceptual model and geologic media analogs. We used the locations of the main faults as well as the low- and high-permeability zones, to reproduce the

hydrogeological characteristics of the subsurface formation.

Initially, 18 rock types were assigned for the entire reservoir; Table 1 summarizes these rock types, indicating their permeability values in each direction after simulation. One reason for the large number of rock types was to investigate the system sensitivity to the properties of each layer and each zone, especially in the central part of the model, which covers the power station and all wells. As a result of optimization, some of the rock types in Table 1 that initially had different permeability values ended up with the same permeability values. This inverse modeling and parameter estimation method was very useful for understanding the system's sensitivity to each layer and each zone.

Permeability values vary between 9.20×10^{-21} m^2 and 1.00×10^{-12} m^2. The rock types of MED, MED2 and MED3 represent high permeable zone such as the Noine fault. Table 2 shows the distribution of rock types in different layers. Porosity was specified as 10% for all rock types and a density of 2500 kg/m^3 was assigned to all rock types.

Calibration of the model

The objective of the natural-state simulation is to reproduce the initial temperature and pressure distributions before any exploitation. The corresponding numerical simulations of the model need to cover a very long time, allowing the equilibration of the geothermal system. This involves running the simulation until approximately steady state conditions are reached, which means a simulation period for about 1 million years (Nakatani et al., 2007). The results of natural-state simulation were compared with the measured temperature data from 20 wells. The parameters estimated from the inverse modeling (matching) process were the permeabilities, flow rates, and enthalpies of recharges.

Table 2. Rock types in each layer of the model.

Layers	Rock Types
bb	N, M_1
cc	K, M_1, M_A
dd	A, M_1, M_A
ee	A, U, M_2, M_A, M_1, M
ff	U, L, M_A, M_1, M
gg	L_T, L, M_A, M_1, M
hh	L_T, M_A, U_B, L, M_3, M_1, M
ii	M_A, L, U_B, M_1, M_3, M
jj	M_A, L, M_1, U_B, M_3, M
kk	L_B, U_H

Table 3. Rock parameters in the final model

Rock type	Permeability (m^2)		Thermal Conduct. (W/mK)
	Kxy	Kz	
ATM (A_T)	$1.00x10^{-10}$	$1.00x10^{-10}$	3.0
NVR (N)	$1.50x10^{-14}$	$3.90x10^{-15}$	3.9
KLY (K)	$8.80x10^{-17}$	$3.60x10^{-15}$	2.6
LOW (L)	$9.20x10^{-21}$	$2.70x10^{-20}$	2.6
ALY (A)	$8.50x10^{-16}$	$1.60x10^{-20}$	2.5
MED (M)	$6.10x10^{-14}$	$3.30x10^{-13}$	3.6
MED1 (M_1)	$4.80x10^{-16}$	$1.30x10^{-14}$	1.3
MED2 (M_2)	$5.60x10^{-14}$	$6.80x10^{-13}$	1.3
MED3 (M_3)	$1.80x10^{-15}$	$1.90x10^{-13}$	2.1
UTL (U)	$3.20x10^{-15}$	$8.40x10^{-18}$	1.5
LTL (L_T)	$1.50x10^{-15}$	$1.00x10^{-19}$	2.3
MAL (M_A)	$1.30x10^{-15}$	$1.40x10^{-14}$	4.0
UHW (U_H)	$1.00x10^{-12}$	$3.80x10^{-15}$	1.8
UBAS (U_B)	$1.00x10^{-14}$	$3.60x10^{-16}$	2.0
LBAS (L_B)	$1.20x10^{-15}$	$4.40x10^{-16}$	2.7

As for initial conditions, it was assumed that all gridblocks were saturated with 15ºC water and pressure equilibrated. The cap rock was assigned to the lowest initial permeability of 1.0×10^{-18} m^2, and the maximum initial permeability was set at 2×10^{-12} m^2. Thermal conductivities were in a range from 1.3 to 4.0 W/m^2K.

A constant temperature of 15ºC and pressure of 0.879 bar were applied to the layer above the top layer as a boundary condition. The other outer boundaries of the domain were assumed to be impermeable to mass and adiabatic to heat. The bottom layer (kk) was assigned two recharge zones. A high-temperature fluid recharge (R1) was imposed on the southeast to the finer grids at this part of the domain, and another recharge (R2) was imposed to the west of the finer grids of the model's bottom layer.

History matching was conducted using production and reinjection data covering 10 years of field operation. Estimated parameters of permeability and recharge flow rates with their enthalpies were modified. Table 3 summarizes the estimated permeability values. Fluid recharges are calculated to be 12 kg/s with an enthalpy of 946 kJ/kg for R1, and 15.7 kg/s with enthalpy of 1110 kJ/kg for recharge R2. A heat flux of 80 mW/m^2 was applied to all grids of the bottom layer. Figure 5 shows the initial and estimated values of rock types in the model.

SIMULATION RESULTS

The constructed model was evaluated in an iterative manner, in order to create the initial conditions. Available subsurface data play an important role in constructing a realistic conceptual model. The adequacy of the model was evaluated by the quality of match of the natural-state conditions of the system to the model predictions. As mentioned before, permeability was a key parameter to be adjusted after each run of the model.

According to a suggested conceptual model modified from Takenaka and Furuya (1991), the subsurface fluid probably flows from southwest to northeast, and maintains chemical and thermal equilibrium with alteration minerals. The heat flow pattern was one of the criteria to be taken into account in each run, in order to confirm flow directions.

The temperature distribution in each layer was also taken into account, in parallel with matching of measured temperature from the wells and computed results. The magnitude and locations of recharge zones were also adjusted in order to achieve satisfactory matches.

Appendix I compares the measured and simulated temperature profiles of ten wells. These plots were produced using calculated values of both the optimum and initial models. Relatively good matches were observed for Wells TT-1, TT-2, TT-3, TT-4, TT-8, TT-13, TT-14, TT-16 and NE-4. Well NE-5, located to the east of the Noine fault, also shows a good match, except at the depth of -100 m.b.s.l. In general, the model successfully reproduces the temperature profiles of 13 wells.

Figure 6 compares the enthalpy histories of four production wells at the Takigami geothermal power plant from 1996 to January 2007. The figure shows the measured enthalpy at Well TT-2 gradually decreasing over time, with the simulated values slightly lower than the measured ones for most of the simulated time. The measured enthalpy value of 7 kJ/kg is higher than the computed values at its maximum.

The model achieves good matches after year 2000 for Well TT-2. For Well TT-7, the simulated values are higher than the measured ones for all cases, and the simulated values are higher by 45 kJ/kg than the maxiumm measured values. The prediction of enthalpy at Well TT-13 is lower to that from the measured values; the thus, the measured enthalpy is 14 kJ/kg higher than the maximum simulation estimate. Well TT-14 shows a good match between simulated and measured enthalpies.

Overall, the history matching results based on enthalpy production show an acceptable match between measurements and numerical predictions in four production wells.

CONCLUSIONS

A numerical model of the Takigami geothermal field was constructed using inverse analysis methods. Parameters such as permeabilities, flow rates, and enthalpies of recharges have been estimated. The best model can successfully reproduce the initial temperature profiles of 13 wells with natural-state simulations. Recharges zones were estimated to be 12 kg/s of 946 kJ/kg and 15.7 kg/s of 1110 kJ/kg at two different locations.

ACKNOWLEDGMENT

The authors thank Idemitsu Oita Geothermal Co. for permission to publish their data. Thanks are also extended to the geothermal Institute of the University of Auckland for permission to use MULGRAPH. The paper's first author thanks the Japan Society for Promotion of Science (JSPS) for his scholarship.

REFERENCES

Aoki, M., Geophysical exploration at Takigami geothermal field in Oita Prefecture, Japan, *Abst., Int. Geothermal Symp*., Kumamoto and Beppu, Japan 567-568, 1988.

Finsterle, S., K. Pruess, D.P. Bullivant and M.J. O'Sullivan, Application of inverse modeling to geothermal reservoir simulation. *Proc. Twenty-Second Workshop on Geothermal Reservoir Engineering Stanford University*, California, 309-316, 1997.

Finsterle, S. and K. Pruess, Automatic Calibration of Geothermal Reservoir Models through Parallel Computing on a Workstation Cluster. *Proc. Twenty Forth Workshop on Geothermal Reservoir Engineering Stanford University, California*, 123-130, 1999.

Finsterle, S, *iTOUGH2 User's Guide*, Earth Sciences Division Lawrence Berkeley National Laboratory, 2000.

Furuya S., M. Aoki, H. Gotoh and T. Takenaka, Takigami geothermal system, northeastern Kyushu, Japan, *Geothermics* 29, 191-211, 2000.

Gotoh, H., Reinjection plan in Takigami geothermal field, Oita Prefecture, Japan, *Geothermal Resources Council Trans.* 14 (2), 897-899, 1990.

Hase, H., K. Ogawa and K. Kimbara, Research in the Hohi geothermal area: outline and summary, *Rept. Geol. Survey Japan No. 264*, pp. 13-25 (in Japanese with English abstract), 1985.

Hayashi, J., T. Motomatsu, and M. Kondo, Geothermal resources in the Takigami geothermal area, Kyushu, Japan", *CHINETSU*, Vol.25, No2, 112-137 (in Japanese with English abstract), 1988.

Hozumi, S., R. Itoi, T. Tanaka, and H. Gotoh, Development of Numerical Model of Takigami Geothermal Reservoir, Oita, Jaoan, Incorporated with Wellbore Flow Simulation, *proceedings*, International Symposium on Earth Science and Technology, Fukuoka, Japan, 2009.

Itoi, R., K. Fukuda, K. Jinno, and H. Gotoh, Interference Test Analysis at the Takigami Geothermal Field, Japan, *Proceedings*, Eighteenth Workshop on Geothermal Reservoir Engineering, Stanford University, 1993.

Jalilinasrabady, S., R. Itoi, H. Gotoh, and T. Tanaka, The Natural State Numerical Model of Takigami Geothermal Reservoir, Oita, JAPAN. *Proceeding, Thirty-Fifth Workshop on Geothermal Reservoir Engineering.* Stanford University, Stanford, California, 2010.

Nakatani, A., R. Itoi, H. Gotoh, and T. Tanaka, Development of Numerical Model of Takigami Geothermal Reservoir, Kyushu, Japan, Using iTOUGH2 Simulator, *Proceedings*, 29th NZ Geothermal Workshop, 2007.

Noorollahi, Y. and R. Itoi, Numerical Simulation for Development Scenarios of NW-Sabalan Geothermal Reservoir, IRAN, *Proceedings, Thirty-Third Workshop on Geothermal Reservoir Engineering, Stanford University,* 2008.

O'Sullivan, M.J., and D.P. Bullivant, A Graphical Interface for the TOUGH Family of Flow Simulators, Proceedings of the TOUGH Workshop 1995, Lawrence Berkeley Laboratory *Report LBL-37200*, Berkeley, CA, USA, 90-95, 1995.

Pruess, K., C. Oldenburg, and G. Moridis, *TOUGH2 User's Guide, Version 2.0*, Lawrence Berkeley National Laboratory,

Report LBNL 43134, Berkeley, CA, USA, p. 197, 1999.

Takenaka T. and S. Furuya, Geochemical model of the Takigami geothermal system, northeast Kyushu, Japan, *Geochemical Journal*, Vol.25, pp. 267-281, 1991.

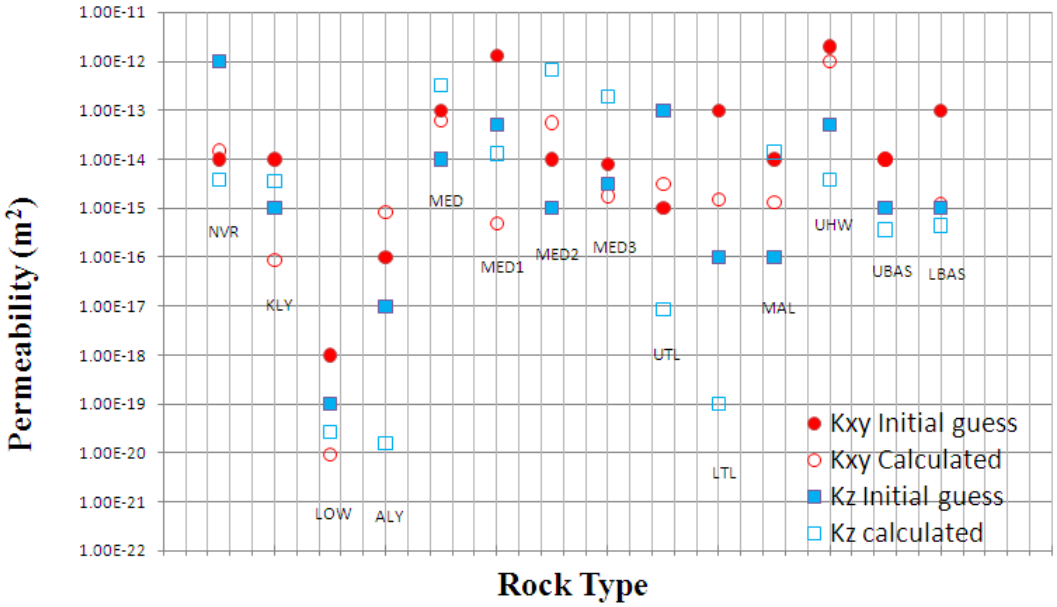

Figure 5. The initial and estimated values of rock types in the model.

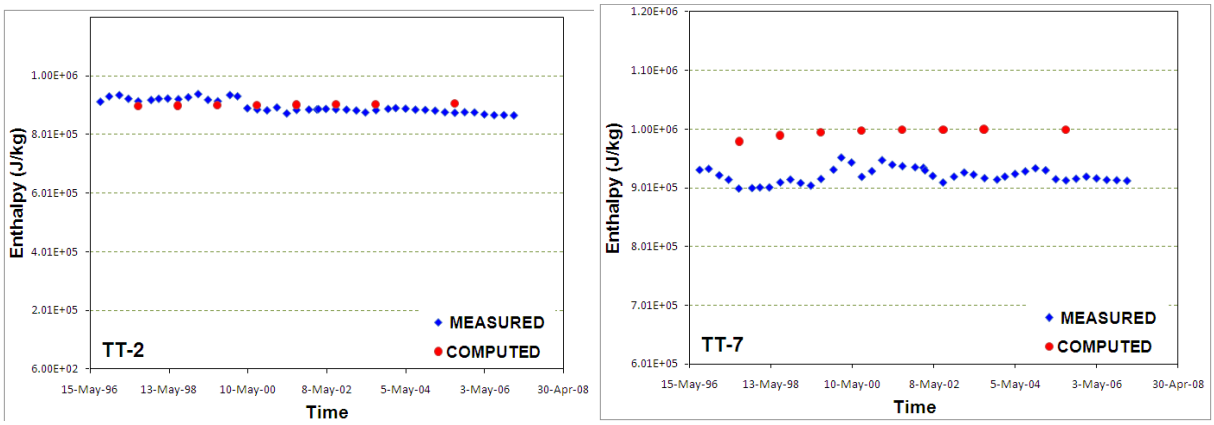

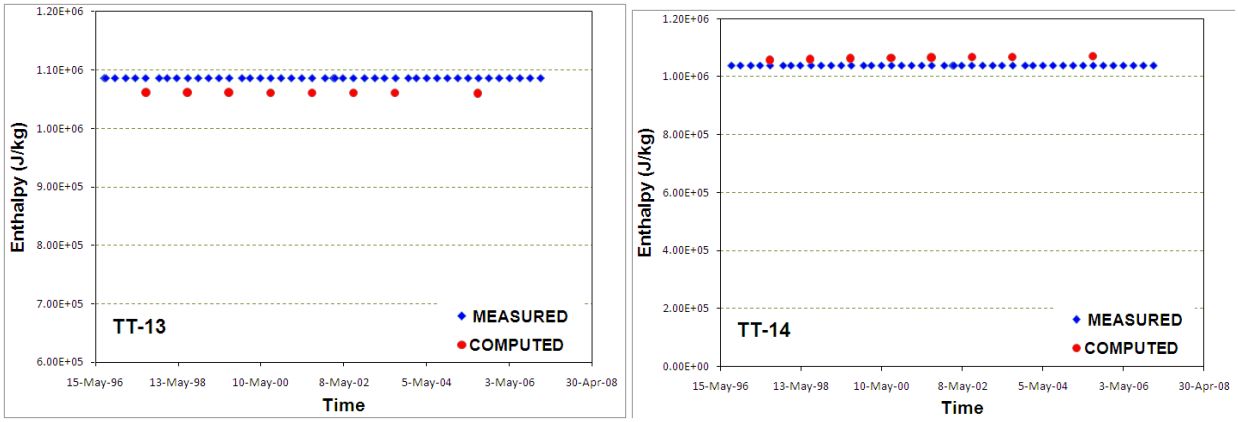

Figure 6. Measured and computed enthalpy of production wells TT-2, TT-7, TT-13 and TT-14.

Appendix I. Comparison between measured and simulated temperature profiles.

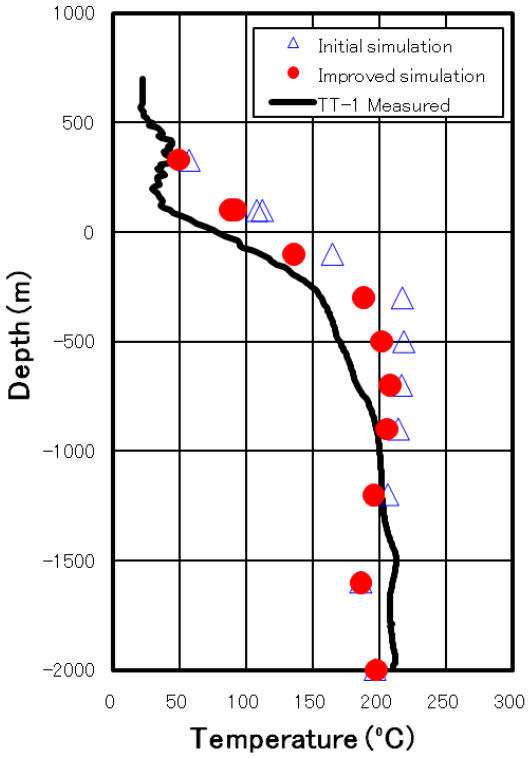

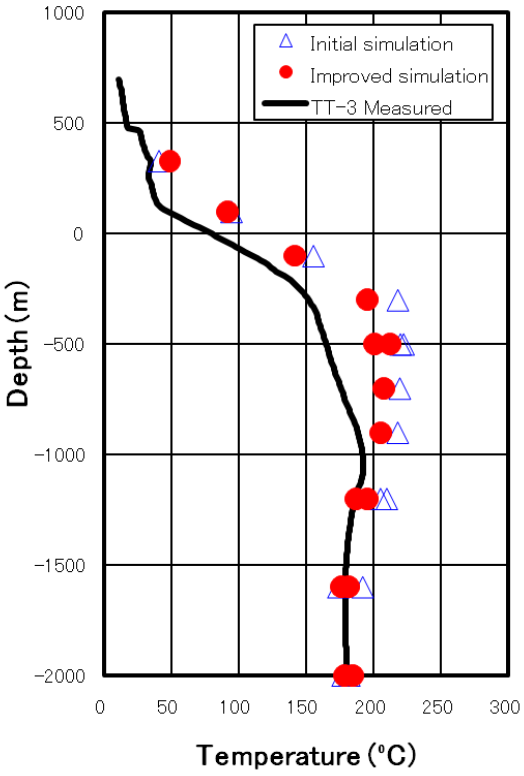

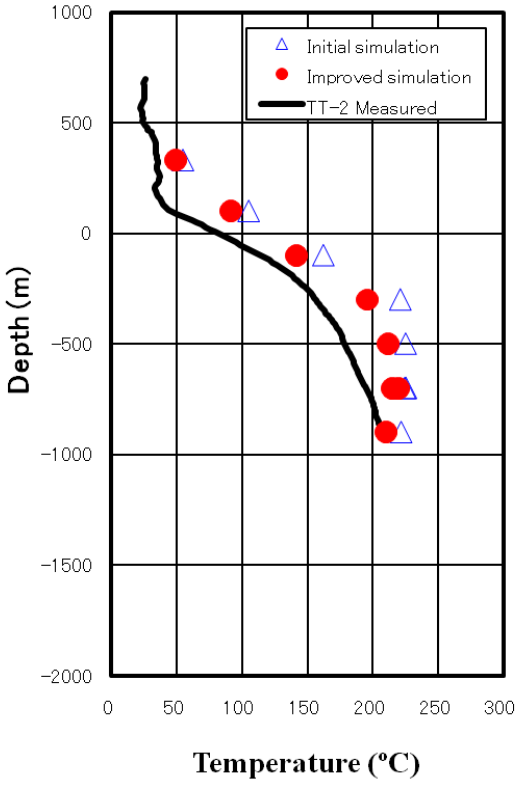

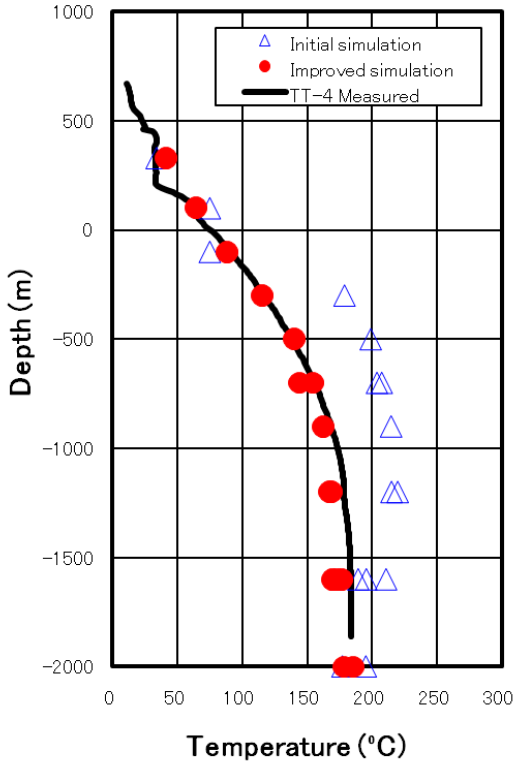

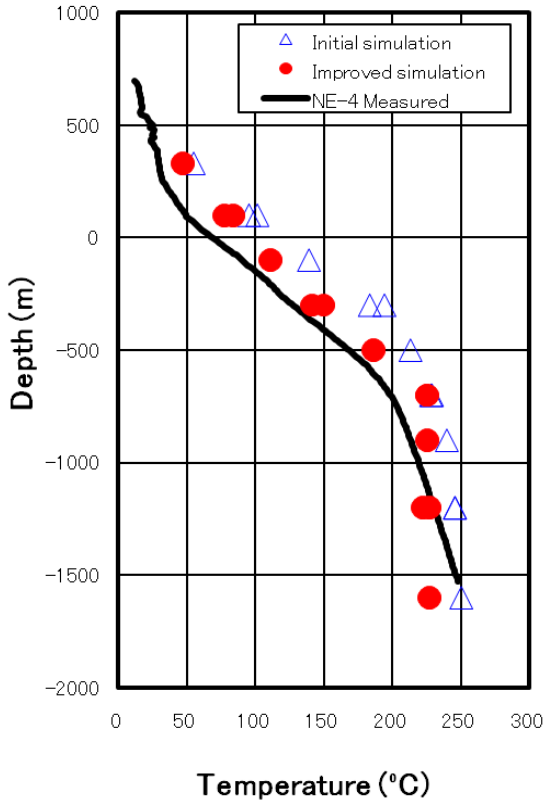
Initial simulation
Improved simulation
NE-4 Measured
Depth (m)
Temperature (°C)
1000
500
0
-500
-1000
-1500
-2000
0
50
100
150
200
250
300

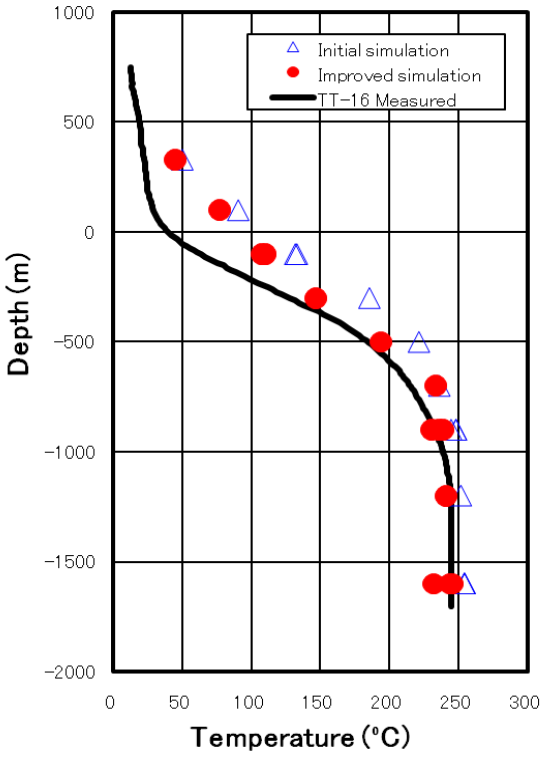
Initial simulation
Improved simulation
TT-16 Measured
Depth (m)
Temperature (°C)
1000
500
0
-500
-1000
-1500
-2000
0
50
100
150
200
250
300

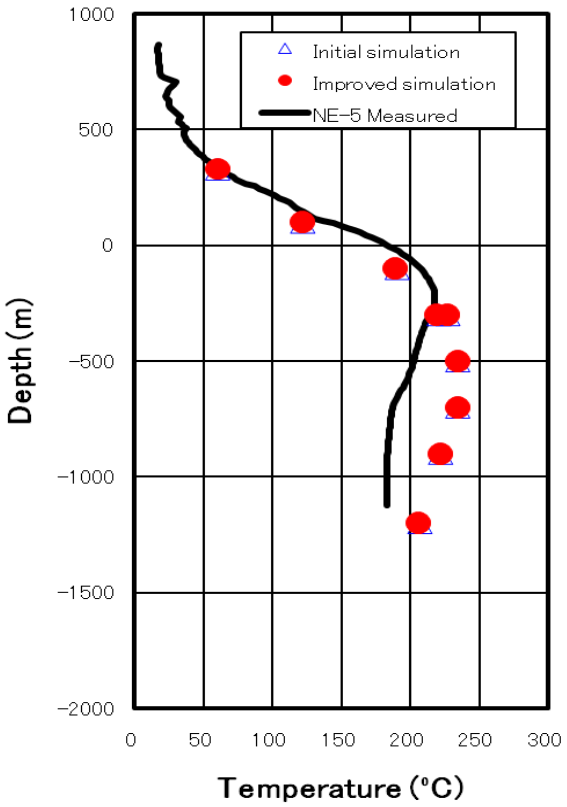
Initial simulation
Improved simulation
NE-5 Measured
Depth (m)
Temperature (°C)
1000
500
0
-500
-1000
-1500
-2000
0
50
100
150
200
250
300

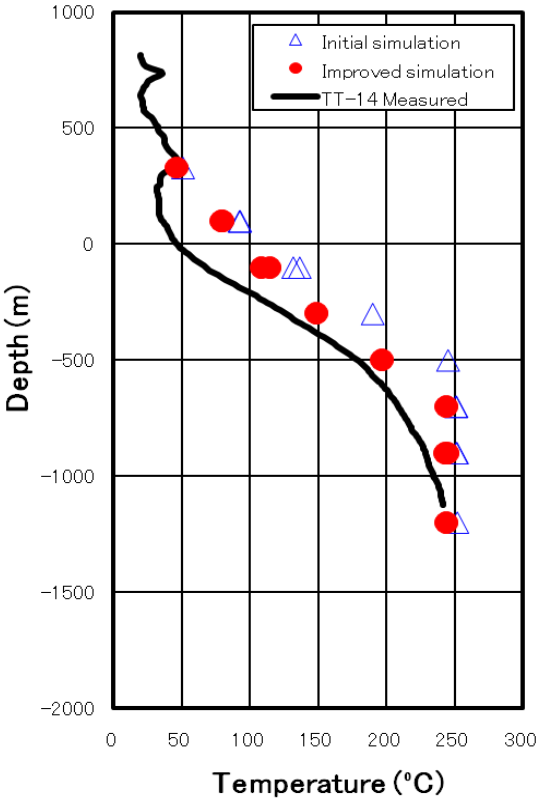
Initial simulation
Improved simulation
TT-14 Measured
Depth (m)
Temperature (°C)
1000
500
0
-500
-1000
-1500
-2000
0
50
100
150
200
250
300

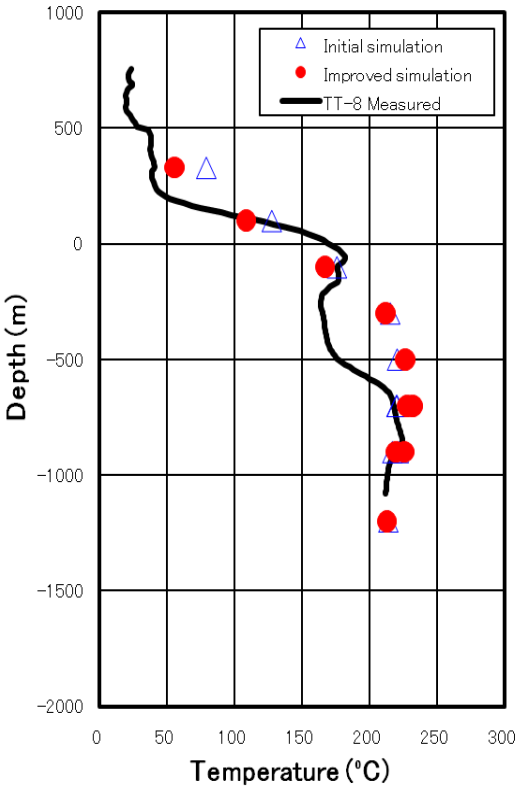
Initial simulation
Improved simulation
TT-8 Measured
Depth (m)
Temperature (°C)
1000
500
0
-500
-1000
-1500
-2000
0
50
100
150
200
250
300

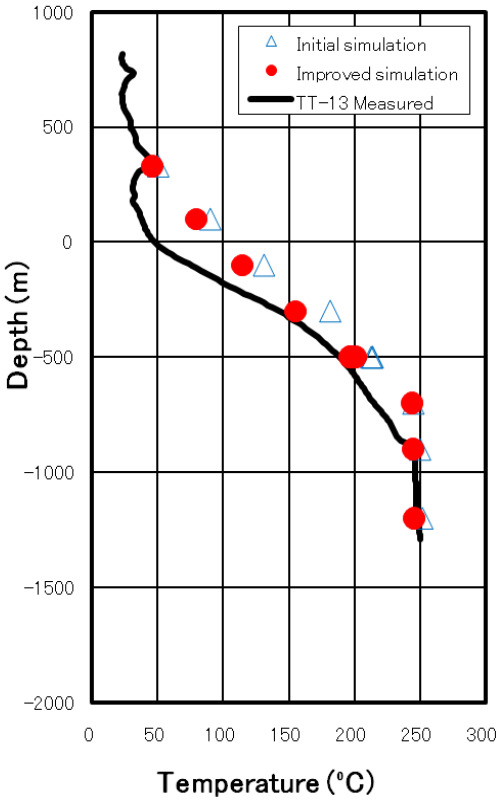
Initial simulation
Improved simulation
TT-13 Measured
Depth (m)
Temperature (°C)
1000
500
0
-500
-1000
-1500
-2000
0
50
100
150
200
250
300

A SEQUENTIAL IMPLICIT ALGORIIHM OF CHEMO-THERMO-PORO-MECHANICS FOR FRACTURED GEOTHERMAL RESERVOIRS

Jihoon Kim, Eric Sonnenthal, Jonny Rutqvist

Lawrence Berkeley National Laboratory
1 Cyclotron Rd.
Berkeley CA, 94720, USA
e-mail: JihoonKim@lbl.gov

ABSTRACT

Here we describe the development of a sequential implicit formulation and algorithm for coupling fluid-heat flow, reactive transport, and geomechanics. We consider changes in pore volume from dissolution and precipitation caused by chemical reactions, in addition to coupled flow and geomechanics. Moreover, we use the constitutive equations for a multiple porosity model for fractured geothermal reservoirs, employing nonlinear permeability and Young's modulus for the fractures and dynamically updating them every time step. For a well-defined simple test problem, we explore the differences in coupled flow and geomechanics with and without reactive transport.

1. INTRODUCTION

Enhanced geothermal reservoirs that exhibit increased permeability resulting from shear stimulation of a fracture volume can provide large heat extraction accompanied by economic flow rates and energy production. Fractures are highly compressible compared with intact rock, so they may affect overall geomechanical responses significantly, even though they occupy a smaller bulk volume. Permeability can be significantly affected by deformation of fractures through the relationship between fracture aperture and permeability. Furthermore, chemical or thermal disequilibrium between injection fluid and the reservoir host rock can result in dissolution and precipitation, changing the porosity. Such changes in pore volume can change fluid pressure, and hence effective stress and strain. Permeability changes through mineral-water reactions and geomechanics affects solute transport which can lead to strong thermal, hydrological, mechanical, and chemical coupling.

The multiple continuum approach is a widely used approach that can represent fracture–rock matrix systems consisting of highly permeable fracture contimuum transporting fluid over the domain, while the matrix store fluid and convey it to the highly permeable fracture continuum (Barenblatt et al., 1960; Berryman, 2002; Sonnenthal et al., 2005; Taron et al., 2009). In geothermal reservoirs, we may introduce more than two continua (e.g., representing fracture and several rock matrix continua) for more accurate modeling of heat flow. Recently, Kim et al. (2012) proposed formulation and sequential numerical algorithms for coupled fluid-heat flow and geomechanics within such a multiple continuum approach.

This study is based on the latter study, and employing nonlinear dynamic strain-dependent permeability and geomechanical moduli in order to capture complex interactions between flow and geomechanics, as applied to shale gas reservoirs (Kim and Moridis, 2012b). Moreover, we consider the changes in pore volume, induced by chemical reaction, when solving for fluid and heat flow.

We have recently implemented these functionalities within ROCMECH (RM for short), an in-house geomechanics simulator, which is coupled to TOUGHREACT (TR), a flow and reactive transport simulator (Kim et al., 2012). We solve fluid and heat flow, geomechanics, and reactive transport problems sequentially, adopting implicit solution schemes for the subproblems (i.e., sequential implicit method). Based on the coupled simulator, TR-RM, flow-geomechanics properties and variables (e.g., porosity, permeability, fluid-phase pressure and saturation, displacement, effective stress, geomechanical moduli, failure

status) are updated dynamically along with the transient coupled simulation.

We performed several verification test cases for TR-RM (e.g., the Terzaghi and Mandel problems), as well as a 1D reactive transport problem. Then, we investigated a 2D geothermal problem, using coupled thermo-poro-mechanics simulations with and without reactive transport, and analyze the differences between them in the results.

2. MATHEMATICAL FORMULATION

We briefly describe the governing equations of geomechanics, fluid and heat flow with reactive solute transport. Then, we introduce constitutive equations for the multiple porosity model, the changes in pore volume from chemical reactions, nonlinear permeability, and Young's modulus.

2.1. Governing Equation

The governing equation for geomechanics is based on the quasi-static assumption, written as

$$\mathbf{Div}\boldsymbol{\sigma} + \rho_b \mathbf{g} = \mathbf{0}, \tag{1}$$

where $\mathbf{Div}$ is the divergence operator, $\boldsymbol{\sigma}$ is the total stress tensor, and ρ_b is the bulk density. An infinitesimal transformation is used to allow the strain tensor, $\boldsymbol{\varepsilon}$, to be the symmetric gradient of the displacement vector, $\mathbf{u}$,

$$\boldsymbol{\varepsilon} = \frac{1}{2}\left(\mathbf{Grad}^T\mathbf{u} + \mathbf{Grad}\,\mathbf{u}\right) \tag{2}$$

where **Grad** is the gradient operator.

The governing equations for fluid and heat flow are derived from the conservation law (Pruess et al., 1999), as follows,

$$\frac{d}{dt}\int_\Omega m^k d\Omega + \int_\Gamma \mathbf{f}^k \cdot \mathbf{n} d\Gamma - = \int_\Omega q^k d\Omega \tag{3}$$

where the superscript k indicates the fluid components or heat. $d(\cdot)/dt$ denotes the time derivative of a physical quantity $(\cdot)$ relative to the motion of the solid skeleton. m^k is the mass of component k or heat. $\mathbf{f}^k$, and q^k are its flux and source terms on the domain Ω with the boundary Γ, respectively, where $\mathbf{n}$ is the normal vector of the boundary.

The flux for multiphase multicomponent flow is supplemented by Darcy's and Fick's laws. The heat flux is obtained by heat conduction and convection laws. The governing equation for solute transport with reactive transport is obtained from mass conservation (Xu et al., 2011), described as

$$\begin{aligned}&\frac{d}{dt}(\Phi C_i) + \mathbf{Div}(\Phi \mathbf{v}_i C_i - \Phi \mathbf{D}_i \mathbf{Grad} C_i) \\ &= -\sum_{m=1}^{n_c} \gamma_{im} r_m + q_i,\end{aligned} \tag{4}$$

where Lagrange's porosity, Φ, is defined as the ratio of the pore volume in the deformed configuration to the bulk volume in the reference (initial) configuration. C_i is the concentration of the ith chemical. $\mathbf{v}_i$ and $\mathbf{D}_i$ are the Darcy velocity vector and diffusion coefficient of the ith chemical, respectively. γ_{im} and r_m are the stoichiometric coefficient of the ith chemical in the mth chemical and the reaction rate of the mth chemical, respectively. n_c is the total number of the chemicals, and q_i is the possible external source of the ith chemical.

2.2. Constitutive relations

We employ the constitutive equations proposed by Kim et al. (2012) for the multiple porosity model, extended from the isothermal double porosity elastic model (Berryman, 2002) to the nonisothermal multiple porosity elastoplastic model, described as

$$\delta\boldsymbol{\sigma} = \overbrace{\mathbf{C}_{up}\delta\boldsymbol{\varepsilon}}^{\delta\boldsymbol{\sigma}'} - \sum_{l,J} b^*_{l,J}\delta p_{l,J}\mathbf{1} - \sum_l \tilde{b}^*_l \delta T_l \mathbf{1}, \tag{5}$$

$$b^*_{l,J} = -K_{dr} b_l S_{l,J}, \tilde{b}^*_l = -K_{dr}\tilde{b}_l,$$

$$\begin{aligned}\delta\xi_{l,J} &= b^*_{l,J}\delta\varepsilon_v + \sum_{m,I} L^{-1}_{l,J,m,I}\delta p_{m,I} \\ &\quad + \sum_{m,I} \overline{D}_{lm}\delta T_{m,}\end{aligned} \tag{6}$$

where the subscript l indicates a material (sub-element) with a gridblock. $\boldsymbol{\sigma}'$, K_{dr}, $\mathbf{C}_{up}$ are the effective stress tensor, upscaled drained bulk

modulus, and upscaled elasticity tensor at the level of the gridblock, respectively. $\delta\xi_{l,J} = \delta m_{l,J} / \rho_{l,J}$. $b_{l,J}^*$ and $\widetilde{b}_l^*$ are the coupling coefficients, where b_l and $\widetilde{b}_l$ are written as

$$b_l = -\frac{\alpha_l \eta_l}{K_l}, \widetilde{b}_l = -3\alpha_{T,l}\eta_l,\ \alpha_l = 1 - \frac{K_l}{K_s}\ , \quad (7)$$

where α_l , $\alpha_{T,l}$, η_l , and K_l are the Biot coefficient, thermal dilation coefficient, volume fraction, and drained bulk modulus for material *l,* respectively. K_s is the intrinsic solid grain bulk modulus. K_{dr}, and $\mathbf{C}_{up}$ are described as

$$K_{dr} = \sum_{l=1}^{n_m} \frac{\eta_l}{K_l},\ \mathbf{C}_{up} = K_{dr} \sum_{l=1}^{n_m} \frac{\eta_l}{K_l} \mathbf{C}_l, \quad (8)$$

where $\mathbf{C}_l$ is the isothermal drained elasticity tensor for material *l*. n_m is the total number of the materials. $L_{l,J,m,I}$ represents a modulus for the multiple porous model, similar to the Biot modulus matrix, and the inverse of its matrix form (i.e., $\mathbf{L}^{-1}$) can be expressed as an example of an vapor-water two-phase system with the fracture-rock matrix double porosity model,

$$\mathbf{L}^{-1} = \begin{bmatrix} \eta_f \mathbf{N}_f & \mathbf{0} \\ \mathbf{0} & \eta_M \mathbf{N}_M \end{bmatrix}, \quad (9)$$

where $\mathbf{N}_f$ and $\mathbf{N}_M$ are the inverse of the Biot modulus matrices, $\mathbf{M}_f$ and $\mathbf{M}_M$, for the fracture and rock matrix, respectively. $\overline{D}_{lm}$ is the coupling coefficient between fluid flow and heat flow.

The effective stress at each subelement *l*, $\boldsymbol{\sigma}_l'$, is obtained as

$$\delta\boldsymbol{\sigma}' = \sum_l \eta_l \delta\boldsymbol{\sigma}_l',\ \delta\boldsymbol{\sigma}_l' = \mathbf{C}_l \delta\boldsymbol{\varepsilon}_l,\ \delta\boldsymbol{\varepsilon}_l = \frac{K_{dr}}{K_l}\delta\boldsymbol{\varepsilon}, \quad (10)$$

where $\boldsymbol{\varepsilon}_l$ is the local total strain at each sub-element *l*. According to Kim et al. (2012), Lagrange's porosity of material *l* without chemical reaction, Φ_l^M, can be written as

$$\delta\Phi_l^M = \left(\frac{\alpha_l^2}{K_l} + \frac{\alpha_l - \Phi_l}{K_s}\right)\delta p_l + 3\alpha_{T,l}\alpha_l \delta T_l - \frac{b_l}{\eta_l}\delta\sigma_v\ , \quad (11)$$

where σ_v is the total volumetric mean stress. Equation 11 is typically known as the porosity change, when reservoir simulation is coupled to geomechanics. The additional change in the porosity due to reactive solute transport can be formulated as (Xu et al., 2006)

$$\delta\Phi_l^C = -\sum_{m=1}^{n_c} \delta\chi_{m,l}\ , \quad (12)$$

where $\chi_{m,l}$ is the m[th] solid volume fraction of material *l*. Then, from Equations (11) and (12), we obtain the total porosity change due to geomechanics and geochemistry, as follows.

$$\begin{aligned}\delta\Phi_l &= \delta\Phi_l^M + \delta\Phi_l^C \\ &= \left(\frac{\alpha_l^2}{K_l} + \frac{\alpha_l - \Phi_l}{K_s}\right)\delta p_l + 3\alpha_{T,l}\alpha_l \delta T_l \\ &\quad - \frac{b_l}{\eta_l}\delta\sigma_v - \sum_{m=1}^{n_c}\delta\chi_{m,l}\end{aligned} \quad (13)$$

For permeability and stiffness of the fractured medium, we employ the strain-dependent permeability and Young's modulus. For an example of 2D plane strain geomechanics coupled to fluid flow, as used in Kim and Moridis (2012b), we use in this study

$$k_{xx}^p = k_{xx,0}^p \left(1 + \varepsilon_{xx}\right)^3,\ k_{zz}^p = k_{zz,0}^p \left(1 + \varepsilon_{zz}\right)^3,$$

$$E_x = E_{x,0}\frac{1}{(1+\varepsilon_{xx})^2},\ E_z = E_{z,0}\frac{1}{(1+\varepsilon_{zz})^2}, \quad (14)$$

where k^p and E are the absolute permeability and Young's modulus. We may use different types of the nonlinear permeability and Young's modulus for specific conditions or reservoirs.

For modeling elastoplastic shear failure, we use the Drucker-Prager and Mohr-Coulomb models, which are widely used to model failure in cohesive frictional materials. The Drucker-Prager model is expressed as

$$f = \beta_f I_1 + \sqrt{J_2} - \kappa_f \le 0,$$
$$g = \beta_g I_1 + \sqrt{J_2} - \kappa_g \le 0, \quad (15)$$

where I_1 is the first invariant of the effective stress and J_2 is the second stress invariant of the effective deviatoric stress. The Mohr-Coulomb model is given as

$$f = \tau'_m - \sigma'_m \sin\Psi_f - c_h \cos\Psi_f \le 0,$$
$$g = \tau'_m - \sigma'_m \sin\Psi_d - c_h \cos\Psi_d \le 0, \quad (16)$$

$$\sigma'_m = \frac{\sigma'_1 + \sigma'_3}{2},\ \tau'_m = \frac{\sigma'_1 - \sigma'_3}{2}, \quad (17)$$

where σ'_1 σ'_2 σ'_3 are the maximum, intermediate, and minimum principal effective stresses. Ψ_f and Ψ_d are the friction and dilation angles, respectively. c_h is the cohesion.

3. NUMERICAL INTEGRATION

For space discretization, we use finite volume and finite element methods for flow and geomechanics, respectively. In time discretization, the backward method is used as typically employed in reservoir simulation. The initial total stress satisfies the geomechanical equilibrium with the boundary conditions. We implement in TR-RM the numerical modeling for the Mohr-Coulomb and Drucker-Prager models with slight modification of the algorithms proposed by Wang et al. (2004), which has been applied to the numerical studies in Kim et al. (2012a). TR-RM thus has the capability to simulate hydro-shearing (shear activation of fractures by hydraulic pressurization) as a continuum shear failure process.

In numerical integration, we use a sequential implicit approach, by which fluid and heat flow, geomechanics, and reactive solute transport are solved sequentially, with each subproblem being solved implicitly. We extend the modified fixed-stress-split method in coupling between fluid and heat flow and geomechanics for the multiple porosity model, to a chemo-thermo-poro-mechanics approach. Specifically, from Equation 13, we can easily implement the extended and modified fixed stress split by using porosity function and correction, as follows.

$$\Delta\Phi_l^n = \left(\frac{\alpha_l^2}{K_l^n} + \frac{\alpha_l - \Phi_l^n}{K_s} + \omega_p^c\right)\Delta p_l^n + \left(3\alpha_{T,l}\alpha_l + \omega_T^c\right)\Delta T_l^n - \frac{b_l}{\eta_l}\Delta\sigma_v^{n-1} - \left(\omega_p^c \Delta p_l^{n-1} + \omega_T^c \Delta T_l^{n-1} - \Delta\Phi_l^{C,n-1}\right), \quad (18)$$

where $\Delta(\cdot)^n = (\cdot)^{n+1} - (\cdot)^n$. ω_p^c and ω_T^c are introduced as relaxation parameters for numerical stabilization due to chemical reaction. Even though the modified fixed stress split for the multiple porosity model is unconditionally stable for thermo-poro-mechanics (Kim et al., 2012), it cannot guarantee unconditional stability of chemo-thermo-poro-mechanics, because thermo-poro-mechanics is a subproblem of chemo-thermo-poro-mechanics. (Determining ω_p^c and ω_T^c is an open question, which will not be discussed in this study.)

For permeability and Young's modulus of the fracture medium, we use the explicit treatment, as follows.

$$k_{xx}^{p,n+1} = k_{xx,0}^{p}\left(1 + \varepsilon_{xx}^n\right)^3,\ k_{zz}^{n+1} = k_{zz,0}^{n+1}\left(1 + \varepsilon_{zz}^n\right)^3$$
$$E_x^{n+1} = E_{x,0}\frac{1}{(1+\varepsilon_{xx}^n)^2},\ E_z^{n+1} = E_{z,0}\frac{1}{(1+\varepsilon_{zz}^n)^2}, \quad (19)$$

4. NUMERICAL EXAMPLES

We first conduct verification tests for TR-RM's chemo-thermo-poro-mechanics approach. To this end, we first introduce the Terzaghi and Mandel problems to verify the simulator in poromechanics. Then we compare TR only with TR-RM in a 1D elastic single-phase flow problem, because the 1D elastic problem can allow the decoupling of flow and geomechanics, using an exact rock compressibility. After verification, we compare the numerical results among chemo-thermo-poro-mechanics, thermo-poro-mechanics without reactive transport, and TR-only with and without reactive transport.

4.1. Terzaghi's and Mandel's problems

Figure 1 shows the domains for the Terzaghi and Mandel problems. For Terzaghi's problem, we have 31 gridblocks, the sizes of which are uniform, 1.0 m. Liquid water is fully saturated, and the initial pressure is 8.3 MPa. We impose a drainage boundary on the left side and no-flow conditions on the right side. The initial total stress is also 8.3 MPa over the domain, and we set 16.6 MPa as the side burden, two times greater than the initial total stress. The Young's modulus and Poisson ratio are 450 MPa and 0.0, respectively. Only horizontal displacement is allowed. The monitoring well is located at the right end.

For Mandel's problem, we have 40×5 gridblocks. The size of the gridblocks in the x direction is uniform, 0.5 m, while the size in the z direction is non-uniform. The medium is fully saturated with water, and the initial pressure is 10.0 MPa. We impose drainage boundaries at the left and right sides, and no-flow conditions on the other sides. Initial total stress is also 10.0 MPa over the domain, and we set 20.0 MPa for the overburden, two times greater than the initial total stress. The Young's modulus and Poisson ratio are 450 MPa and 0.0, respectively. 2D plane strain geomechanics is employed. The monitoring well is located in the middle of the domain, as shown in Figure 1. No gravity is considered for the Terzaghi and Mandel problems. The permeability and porosity are 6.51×10^{-15} m^2, 6.6 mD (1 Darcy=9.87×10^{-13} m^2), and 0.425, respectively for both problems. Biot's coefficient is 1.0.

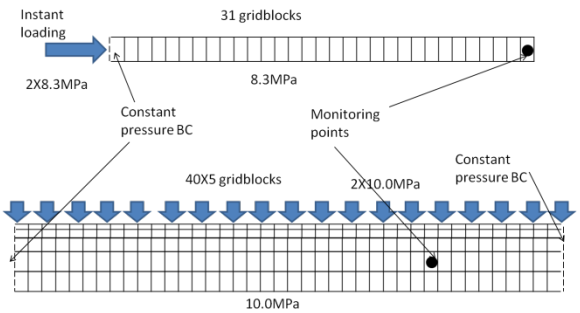

Figure. 1. The domains for Terzaghi's (top) and Mandel's problems (bottom).

Figures 2 and 3 show that the results from TR-RM match the analytical solutions. The numerical results correctly capture the instantaneous pressure buildup for Terzaghi's problem and the Mandel-Cryer effect for Mandel's problem—these could not be captured by a flow-only simulation.

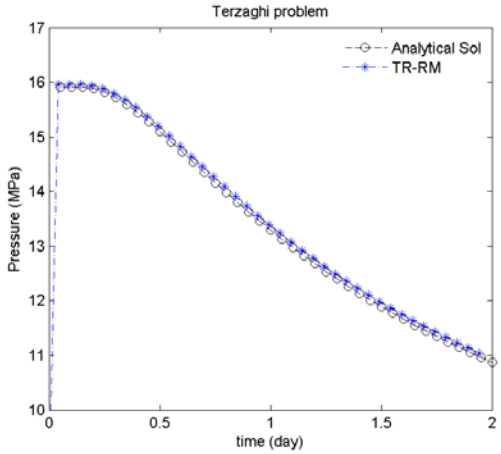

Figure. 2. Comparison between the analytical solution and the result of TR-RM for Terzaghi's problem.

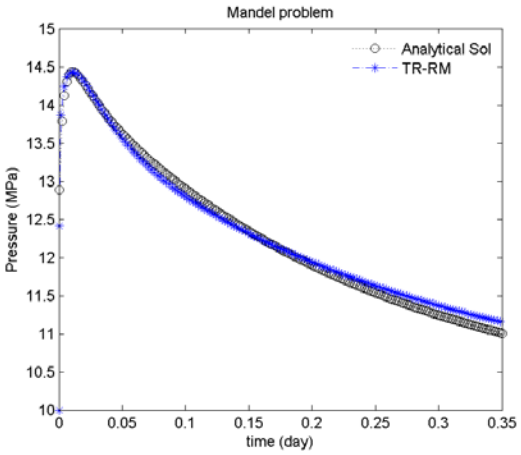

Figure 3. Comparison between the analytical solution and the result of TR-RM for Mandel's problem.

4.2. 1D chemo-poro-mechanics

We reuse the domain, initial conditions, and geomechanics and flow properties of the Terzaghi problem. We have the same side burden of the initial pressure. The monitoring point is located at the third gridblock from the right end. Isothermal single-phase flow is considered. We employ $\omega_p^c = -3.6 \times 10^{-9}$ Pa^{-1} for numerical stability. The production and injection are applied to the left and right end gridblocks,

respectively with the same rate, 1.0×10^{-4} kg/s. Quartz dissolution was assumed to be the only reaction as observed in the experiment described by Johnson et al. (1998), and modeled using a linear kinetic rate law.

From Figure 4, we can see that the result of TR-RM matches the result for TR-only. At initial time, the pressure increases instantaneously due to the injection, and then drops rapidly due to chemical dissolution. Dissolution causes an increase in pore volume, which causes a decrease in pressure based on fluid compressibility. After the initial time, the pressure increases again, reaching steady state.

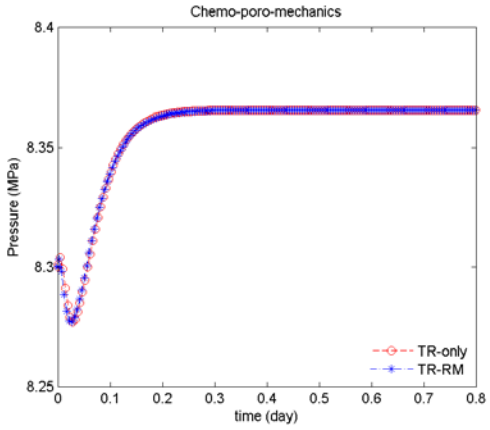

Figure 4. Comparison of the results between TR only and TR-RM for the 1D chemo-poro-mechanics problem.

4.3. 2D chemo-thermo-poro-mechanics

We consider the fractured geothermal problem shown in Figure 5. The geothermal reservoir has a large dimension perpendicular to the fracture plane, i.e., the problem can be reduced to one of multiple porosity 2D plane strain geomechanics, as shown in Figure 6.

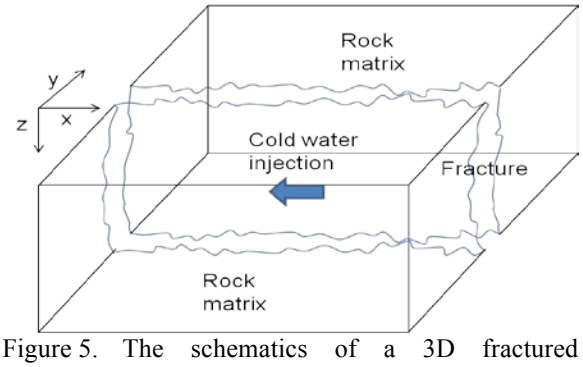

Figure 5. The schematics of a 3D fractured geothermal reservoir

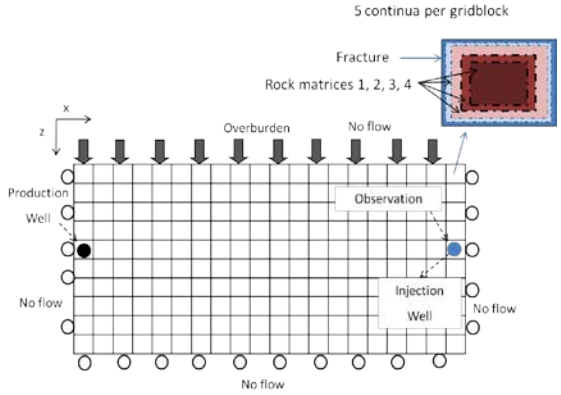

Figure 6. The discretized domain of the fractured geothermal reservoir with the 2D plane strain geomechanics and the multiple porosity model.

For the 2D problem, we have 20×10 gridblocks in the x and z directions, the sizes of which are uniform, 10.0 m. The size of the dimension in the y direction is 500 m, large enough for the constant temperature boundary for heat flow. Each gridblock has five subelements, one fracture and four rock matrix domains, the volume fractions of which are 0.002, 0.098, 0.20, 0.35, and 0.35, respectively. The reservoir is fully water saturated, and the initial pressure and temperature at the top are 19.0 MPa and 146.7°C, respectively, which is much cooler than a producing geothermal system, but which shows qualitatively the same behavior. They are distributed with the hydrostatic pressure gradient, 9806Pa/m, and the geothermal gradient, 25°C/km. The initial permeabilities of the fracture and the rock matrices are 5.9×10^{-13} m^2 and 5.9×10^{-19} m^2, respectively, and their porosities are 0.5 and 0.3, respectively. We impose no-flow boundaries on all sides. Heat conductivities under desaturated and saturated conditions are 0.5 W/m/°C and 3.1 W/m/°C, respectively, for all the materials. Specific heat capacity is 1000 J/kg/ °C for all materials. The monitoring point is the fracture medium at the injection point, as shown in Figure 6.

For geochemistry, we take the same quartz dissolution process used in the previous 1D chemo-poro-mechanics problem. For geomechanics, the initial vertical principal total stress is 19.0 MPa at the top, vertically distributed based on the bulk density, 2200kg/m^3.

The horizontal principal total stress in the x direction is the same as the vertical stress. We have 19.0 MPa overburden, and horizontally constrained boundaries at the sides and no vertical displacement at the bottom. Young's modulus and Poisson's ratio for the fracture are 213.75 MPa and 0.0, respectively. Young's modulus and Poisson's ratio for the rock matrices are 5.586 GPa and 0.0, respectively. We use $\omega_p^c = 0.0\,\mathrm{Pa}^{-1}$ and $\omega_T^c = 0.0\,^{\circ}\mathrm{C}^{-1}$. Biot's coefficients and thermal dilation coefficients are 1.0 and 4.5×10^{-5} $^{\circ}\mathrm{C}^{-1}$ for all materials. The injection and production wells are located on the right and left sides of the domain, as shown in Figure 6. Injection and production rates are 50.0 kg/s, with 20°C water and 50.0 kg/s with water of the reservoir temperature, respectively.

Figure 7 shows the comparison between chemo-thermo-poro-mechanics and thermo-poro-mechanics without reactive transport. Figure 8 also shows the comparison between TR only with and without reactive transport. In Figure 7, unlike with TR only, we observe the increase in pressure with TR-RM, resulting from the complicated interactions between the fracture and rock matrices due to mechanical and thermal contraction or dilation.

Comparing Figure 7 with Figure 8, we find that cold-water injection induces thermal contraction, followed by the support of the reservoir pressure, which can be properly captured by the coupling between flow and geomechanics.

In Figure 8, TR-only with geochemistry shows more pressure drop than TR-only without geochemistry, because the dissolution increases the pore volume, as shown in Figure 9, which causes the pressure drop. However, we observe that the pressure of chemo-thermo-poro-mechanics is slightly higher than the pressure of thermo-poro-mechanics. The monitoring point is affected by the compaction due to dissolution at another location, and undergoes additional compaction and decrease in porosity, unlike thermo-poro-mechanics without the reactive transport shown in Figure 9. Note that the perturbation of geomechanics at a certain location affects the entire domain instantaneously, because of the nature of quasi-static mechanics.

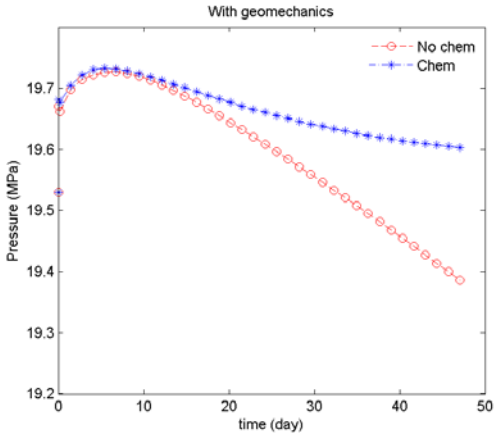

Figure 7. Comparison of the pressure results between chemo-thermo-poro-mechanics, ('Chem'), and thermo-poro-mechanics only, ('No chem').

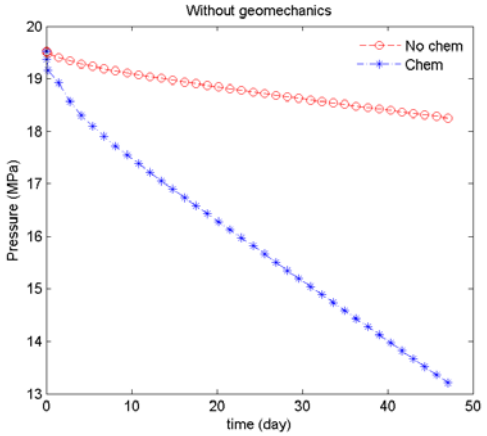

Figure 8. Comparison of the pressure results between with ('Chem') and without ('No chem') reactive transport in TR-only.

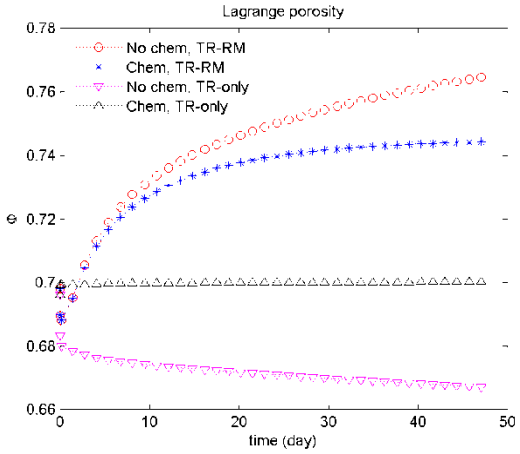

Figure 9. Comparison of Lagrange's porosities among chemo-thermo-poro-mechanics, thermo-poro-mechanics only, and TR only with and without reactive transport.

CONCLUSIONS

We proposed a sequential implicit formulation and algorithm for chemo-thermo-poro-mechanics, and implemented the coupling algorithm within a flow and geomechanics simulator. This simulator can handle the multiple porosity model in fractured geothermal reservoirs and nonlinear permeability and geomechanics, including plasticity. From numerical simulation of the 2D fractured geothermal reservoir, we found that chemo-thermo-poro-mechanics can yield significantly different results from thermo-poro-mechanics, because small pore volume changes can lead to large fluid pressure effects.

ACKNOWLEDGMENT

This work was supported by the American Recovery and Reinvestment Act (ARRA), through the Assistant Secretary for Energy Efficiency and Renewable Energy (EERE), Office of Technology Development, Geothermal Technologies Program, of the U.S. Department of Energy under Contract No. DE-AC02-05CH11231, and by 2011 TOUGH2 development grants in the Earth Sciences Division of Lawrence Berkeley National Laboratory.

REFERENCES

Barenblatt GE, Zheltov IP, Kochina IN. 1960 Basic concepts in the theory of seepage of homogeneous liquids in fissured rocks. *J. Appl. Math.*;24(5):1286 – 1303.

Berryman JG. 2002 Extension of poroelastic analysis to double-porosity materials: New technique in microgeomechanics. *J. Eng. Mech.* ASCE; 128(8):840 – 847.

Johnson J.W., Knauss K.G., Glassley W.E., DeLoach L.D., Tompson A.F.B. 1998. Reactive transport modeling of plug-flow reactor experiments: quartz and tuff dissolution at 240^{o}C. *J. Hydrol* 209:81-111

Kim J., Sonnenthal E., and Rutqvist J. 2012 Formulation and sequential numerical algorithms of coupled fluid/heat flow and geomechanics for multiple porosity materials. *Int. J. Numer. Meth. Engrg.* doi: 10.1002/nme.4340.

Kim J. and Moridis G. M. 2012a Gas flow tightly coupled to elastoplastic geomechanics for tight and shale gas reservoirs: material failure and enhanced permeability. *SPE Uncon. Resour. Conf.*, Pittsburgh, PA, 5-7 Jun.

Kim J. and Moridis G. M. 2012b Numerical Studies for Naturally Fractured Shale Gas Reservoirs: Coupled Flow and Geomechanics in Multiple Porosity/permeability Materials. *46th U.S. Rock Mechanics/Geomechanics Sym.*, Chicago, IL, 24-27 Jun

Pruess, K., C. Oldenburg, and G. Moridis, 1999 TOUGH2 User's Guide, Version 2.0, Report LBNL-43134, Lawrence Berkeley National Laboratory, Berkeley, Calif.

Sonnenthal E, Ito A, Spycher N, Yui M, Apps J, Sugita Y, Conrad M, Kawakami S. 2005 Approaches to modeling coupled thermal, hydrological, and chemical processes in the Drift Scale Heater Test at Yucca Mountain. International *Journal of Rock Mechanics and Mining Sciences* 42:698–719.

Taron J, Elsworth D, Min K. 2009 Numerical simulation of thermo-hydrologic-mechanical-chemical processes in deformable, fractured porous media. *International Journal of Rock Mechanics and Mining Sciences* **46**:842–854.

Wang X. and Wang L.B. and Xu L.M. 2004 Formulation of the return mapping algorithm for elastoplastic soil models. *Comput. Geotech.* **31**:315–338.

Xu T, Sonnenthal E, Spycher N, Pruess K. 2006 TOUGHREACT: A simulation program for non-isothermal multiphase reactive geochemical transport in variably saturated geologic media: Applications to geothermal injectivity and CO2 geological sequestration. *Computers and Geosciences* 32:145–156.

Xu T, Spycher N, Sonnenthal E, Zhang G, Zheng L, Pruess K. 2011 TOUGHREACT Version 2.0: A simulator for subsurface reactive transport under non-isothermal multiphase flow conditions. *Computers and Geosciences* **37**:763–774.

A 20 YEAR PROGRESS IN THE TOUGH2 MODELING OF THE MUTNOVSKY GEOTHERMAL FIELD, KAMCHATKA, RUSSIA

Alexey Kiryukhin and Olga Miroshnik

Institute of Volcanology & Seismology FEB RAS, Piip 9
Petropavlovsk Kamchatsky, Russia, 683006
e-mail: AVKiryukhin2@mail.ru

ABSTRACT

An initial 3D, rectangular, 517-element (partially double-porosity) TOUGH2-EOS1 numerical model of the Mutnovsky geothermal field (Dachny site) was developed in 1992–1993. (Kiryukhin, 1996). This model calibration was performed by trial and error, with six temperature and three pressure data as key calibration points. Visual matches with temperature/pressure distributions maps were conducted for natural-state model calibration, and five wells providing enthalpy transient data were used for exploitation history in calibrating the years from 1984 to 1987. This simple model was used for the Mutnovsky geothermal project feasibility study, followed first by a 12 MWe pilot project started in 1999, and then a full-scale system with a capacity of 62 MWe, in operation since 2002.

The same geometric model has been recently adopted in rebuilding the preprocessor PetraSim v.5.0. Observational data used for model recalibration are as follows: 29 key temperature calibration points for the natural state, 14 production wells with monthly averaged enthalpies (592 values during the time periods 1983–1987 and 2000–2006), and two transient pressure monitoring wells (51 values from 1995 to 2006) for exploitation history match.

The recalibration process (started by hand) reveals necessity to add double porosity in all active permeable elements, increase reservoir permeabilities and improve boundary conditions. Second stage of recalibration using iTOUGH2-EOS1 inversion modeling capabilities, was very useful to remove outliers from calibration data, model parameterization and parameter estimation.

Comparison of the reservoir parameter estimations (which have been recently obtained using iTOUGH2 inversion modeling) with reservoir parameters (which were estimated by TOUGH2 "trial-and–error" method 20 years ago, given in parentheses) are as follows: total upflow recharge rate in natural conditions 80.5 (54.1) kg/s, Main upflow enthalpy 1430 (1390) kJ/kg, reservoir permeabilities based on history match 27-616 (3-90) mD. Inverse modeling was also used to estimate unknown parameters and boundary conditions attributed to exploitation: reinjection rates, meteoric downflow recharge in the central part of the geothermal field and reservoir compressibility, which add upflow component during exploitation.

INTRODUCTION

Exploitation of the Mutnovsky geothermal field (Fig. 1) with installed power plants capacity of 62 MWe is important for Kamchatka renewable energy use. Besides, Mutnovsky experience may be useful in development projects of other large geothermal fields in Kamchatka-Kurile region to understand relationship between volcanic, hydrothermal and seismic activity.

Since the beginning of large-scale exploitation, Mutnovsky field production experienced significant steam fraction decline from 0.46 to 0.27 during the first years (2002 – 2006) of the exploitation (Fig. 2). Some production wells were switched of exploitation (049N, 055, 5E, 4E, 053N, 017N) due to reasons which are not completely understood. There is also some evidence of the local meteoric water inflow in reservoir (Kiryukhin et al, 2010).

In adition, large-scale exploitation started from 2000 year with fluid extraction up to 500 kg/s (600 MW) comparable with the magma energy rates of adjacent active volcanoes: Mutnovsky (8 km, 190 MW) and Gorely (10.5 km, 100 MW).

Mutnovsky field development is synchronized with increased hydrothermal explosion activity of Mutnovsky volcano after 40 years of silence (hydrothermal explosions in crater on March, 17, 2000, April, 2007 and May, 2012) (Gavrilenko, 2008), initialization of fumaroles activity of Gorely volcano in 2010 and drainage of Mutnovsky crater lake (2004) and Gorely crater lake (2012). It is also noted by seismic activity increase (11 earthquakes Ks=4.1-5.4 recorded at depth from 2 to 6 km during the time period from Feb. 2009 to May 2012 (data of KB GS RAS)).

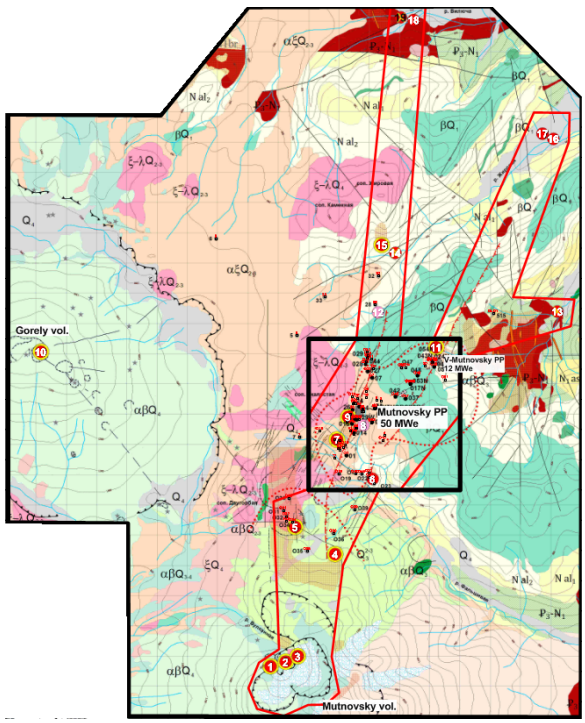

Figure 1. Schematic geological map of the Mutnovsky geothermal area. Black rectangle – defines model limits; circles with numbers - thermal sites (fumaroles or hot springs areas); a dashed line – horizontal projection (at 0 m.a.s.l.) of the Main production zone, hydraulically connecting volcanic and hydrothermal systems; red polygon – boundaries of the North Mutnovsky Volcano-Tectonic Zone; dotted line – temperature contour 230°C at -250 masl. Map grid – 1 km.

Hydrothermal explosions and emerging of new boiling pots (#6) inside the exploitation area, degradation of chloride hot springs in the areas, adjacent to geothermal field are noted (2 bars pressure decline at Viluchinsky Site (#18), disappearance of Voinovsky (#13) and Verkhne-Zhirovsky (#14) hot springs, significant chloride decline at Nizhne-Zhirovskoy hot springs are recorded (Fig. 1).

Hence, the process of the Mutnovsky field exploitation and related events need integrated hydrogeological analysis, including modeling studies targeting at development of the new methods of exploration, geothermal resources and reserves assessment, sustainability of the existing geothermal field and extension of its potential.

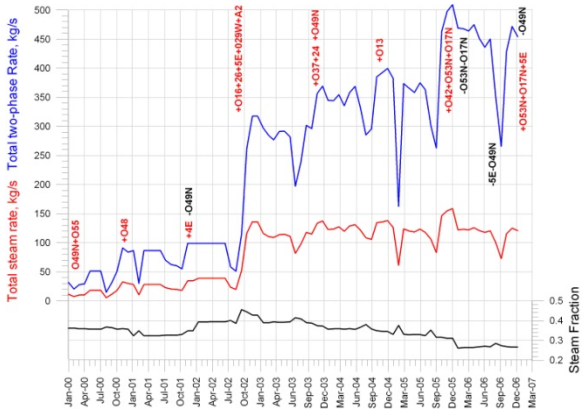

Figure 2. Mutnovsky geothermal field: observed total two-phase production rate (upper graph), observed total steam production rate (middle graph) and corresponding steam fraction (lower graph). Data from Maltseva et al, 2007.

MUTNOVSKY GEOTHERMAL FIELD MODEL SETUP

Model Setup

An "old" 3D rectangular TOUGH2 numerical model of the Mutnovsky geothermal field (Dachny site) was developed at Lawrence Berkeley National Laboratory in 1991 and simulated using the CRAY-X-MP supercomputer. Model calibration was achieved by "trial and error" to the 1984-1987 exploitation history. This model application for different exploitation scenarios was discussed in earlier papers (Kiryukhin, 1996, 2002).

Model development tools have been significantly improved in recent years with effective TOUGH2 pre- and postprocessors and inverse modeling (iTOUGH2) capabilities. Hence, the Mutnovsky 1996 model has been recently rebuilt with preprocessor PetraSim v.5.0

(Figs. 3-6). This model may also be applied to Mutnovsky geothermal field reserves estimation, since this model was designed "as simple as possible" to contain a minimum number of elements (500+) to describe the existing reservoir with production/injection. Such a model is referred to as a "hydraulic type model", which is acceptable by Russian Authorities for high temperature geothermal reservoir reserves estimation.

This model with top at +750 m.a.s.l., covers 5×5×2 km^3, includes 5 horizontal layers and 500 basic grid elements of 500×500×500 $м^3$ each, 21 domains with different petrophysical properties, heat and mass recharge defined at the base layer, and recharge corresponding to known significant hot springs and steam ground areas. In all elements of the base layer of the model a conductive heat flow of 60 mW/m^2 was defined. In selected elements corresponding to upflow zones, mass flows were assigned (Main upflow: 39 kg/s, 1390 kJ/kg and NE upflow: 15 kg/s, 1270 kJ/kg) (Fig. 3).

Discharge conditions were specified in the model elements corresponding to the Dachny (D) and Verkhne-Mutnovsky (VM) steam fields, and integrated hot springs discharge (NZ) (Fig. 4). Integrated hot springs discharge (NZ) represents in the model all existing groups of hot springs in the areas adjacent to Mutnovsky geothermal field (see Fig.1, Nizhne-Zhirovsky, Verkhne-Zhirovsky, Viluchinsky) in a lumped parameter form.

Twenty wells were defined in the model, including 16 production and 4 groups of injection wells (027 (+028+044), 07, 043N, 054N (+024N)) wells (Figs. 4 – 6).

Production wells 016 and 26 are steam-dominated wells fed from the second layer from the top of the model (rhyolitic tuff layer, domain "Tuff2" in the model) (Fig. 4).

Production wells 01, 014, 029W, 24, 055, 048 and injection wells 027 (+028+044), 07 are located in the middle layer of the model, comprising volcanogenic and sedimentary rocks (domain "Sand1" in the model) (Fig.5).

Production wells 1, 4E, 013, 042, 037, 053N, 017N, 049N and injection wells 043N, 054N are located in the forth layer from the top of the model (intrusion contact zone, domain "Cont1" in the model) (Fig. 6).

Production and injection wells were defined in the model with the time-dependent rates and enthalpies (for injection wells) in accordance with the reported data (Maltseva et al., 2007).

Double-porosity was assigned in the old model defined in selected elements containing production wells to reproduce excess enthalpies of the modeling production wells during exploitation. Wells 016, 26, 01, 1, 24 demonstrate enthalpies greater than the enthalpy of liquid water at given temperature, pointed out on local boiling in the underground reservoir. Double porosity assignment in the model was achieved by reducing initial volume of the "fractured" model element and adjoining it to the low permeable "matrix" element with the volume equal to difference between initial volume and "fractured" element volume.

Some Modifications of the Old Mutnovsky Model

Some direct runs of the Mutnovsky model with "old" parameters reveal, that reservoir permeability and fracture volume fractions should be increased to reproduce the long term history of exploitation. Some enthalpy increase in NE upflow up to 1350 kJ/kg was assumed. The enthalpy of upflows is believed to be estimated by maximum values of Na-K geothermometers for Mutnovsky geothermal reservoir (306-310^oC, that corresponds 1390 kJ/kg for water phase). Insignificant shift of NE upflow zone in SW direction was assumed too.

Global definition of the double porosity was assigned in the updated model, to be able to perform iTOUGH inverse modeling calibration, since "domain by domain" double porosity MINC processing is not available in current version of TOUGH2/iTOUGH2.

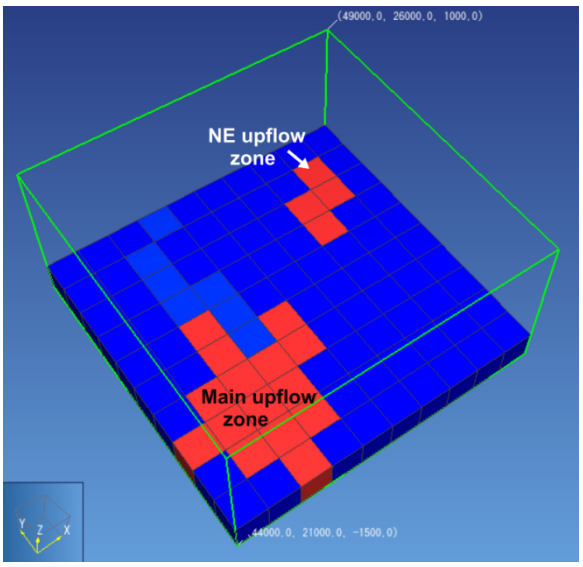

Figure 3. Base layer (-1250 masl) of the Mutnovsky geothermal field model. Upflow zones (Main and North-East (NE)) are shown by red color.

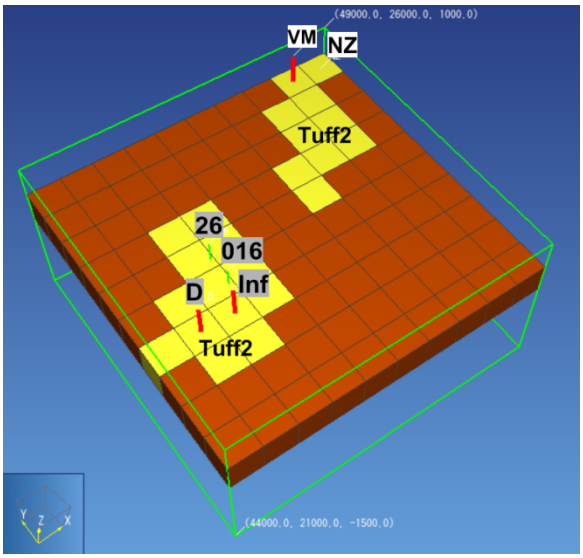

Figure 4. Layer +250 masl (2nd from the top) of the Mutnovsky geothermal field model. Positions of discharge elements of the model: D – Dachny fumaroles field (assigned in the top layer at +750 masl), VM – Verkhne-Mutnovsky fumaroles field (assigned in the top layer at +750 masl), NZ – integrated hot springs discharge area (assigned at +250 masl). Permeable reservoir domain "Tuff2", representing rhyolitic tuffs is shown by yellow color. Production wells 016 and 26 penetrated in this layer are shown by numbers on a grey background.

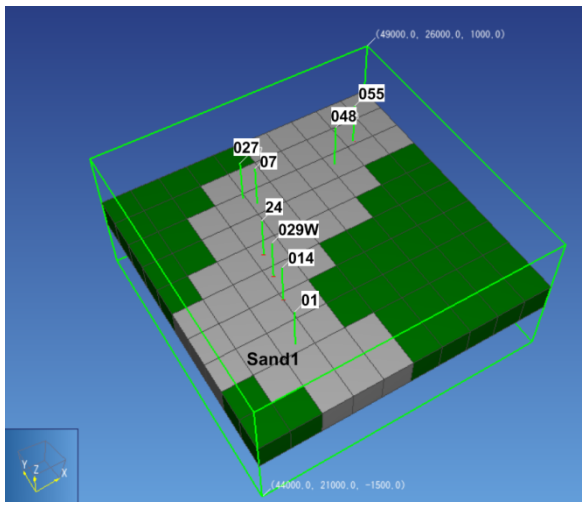

Figure 5. Layer -250 masl (middle) of the Mutnovsky geothermal field model. Permeable reservoir domain "Sand1", representing volcanogenic-sedimentary unit is shown by grey color, production wells penetrated in this layer are shown by numbers on a white background.

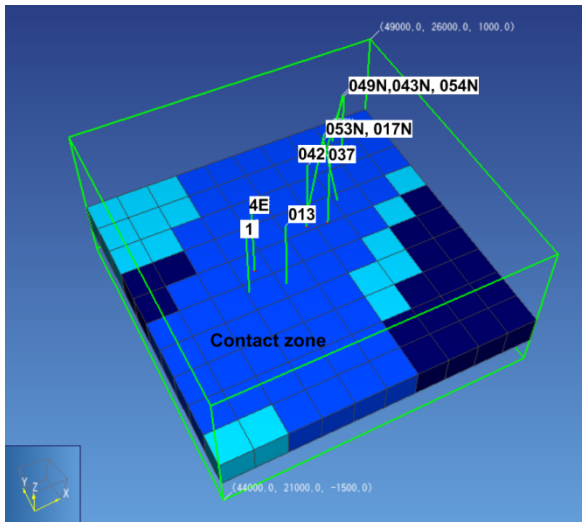

Figure 6. Layer -750 masl (2-nd from the bottom) of the Mutnovsky geothermal field model. Permeable reservoir domain "Cont1", representing intrusion contact zone is shown by blue color, production wells penetrated in this layer are shown by numbers on a white background.

NATURAL STATE + HISTORY EXPLOITATION iTOUGH2-EOS1 INVERSION MODELING

This study is aiming to use all available observational data (natural state temperatures and exploitation history data, including production wells transient enthalpies and

monitoring wells transient pressures) for a single calibration modeling process. In order to do this, inversion modeling was organized so, that at the 1st stage natural state modeling runs from -∞ matching initially observed temperatures, then at the 2-nd stage modeling time is reset to 1985 year starting history match until 2006 year with production wells enthalpies and monitoring wells pressures as calibration data.

Observational data

Eight temperature measurements in wells confirmed by geochemical data (Na-K geothermometer) were selected for model calibration (natural state) and shifted into centers of model elements (Table 1). STD for temperature calibration data were assumed as 3ºC. Pressure data obtained from water column calculations during drilling are not to be used for inverse modeling calibration, since there is no guaranty that water levels are in equilibrium with two phase reservoir pressures due to significant circulation losses or skin effects at those wells.

Table 1. *Natural state temperatures used for model calibration (input data from Kiryukhin, 1996).*

Well	T Na-K, ºC (geothermometer estimate)	T,ºC (measured)	Model elevation, masl	Assumed calibration temperature, ºC
016	Steam well	228	+250	228
26	Steam well	236	+250	236
01	298-310	275	-250	275
1	275-285	276	-250	280
24	276	265	-250	270
013	301-306	305	-750	304
037	282-298	284	-750	290
055	284		-250	284

Two pressure-monitoring wells #30 and #012 were used for exploitation history match. In those wells Pruett capillary tubing systems were deployed and pressure records available during the time period of 1995-2006 years (total number of 51 used pressure values). Capillary tubing chambers are located at -156 masl in well #30 and at -682.5 masl in well 012, hence pressure records were converted at elevations -250 masl and -750 masl to be consistent with the model grid. For these purposes, hydrostatic corrections for water column in well #012 were applied, while these corrections were not applied to well #30 at two phase conditions. STD for pressure calibration data were assumed as 1.0 bars.

14 production wells (016, 26, 01, 1, 24, 048, 042, 029W, 037, 013, 055, 049N, 4E, 017N) with monthly averaged enthalpies (592 values during the time period 1984-1987, 2000-2006 years) were also used for model calibration (Maltseva et al, 2007). It is worth noting, that regular production well testing usually took place just once in a year using a transportable full scale separator device C-100. The rest of the time, flow rates and enthalpies of production wells were defined as a function of WHP, based on annual flow test data. Additional control of the individual well flowrate and enthalpy (wells 016, 26, 01, 1, 24, 042, 029W, 037, 013, 4E, 017N) was achieved at Mutnovsky Power Plant (where total steam and water flow rates are recorded) when such well was closed, while other wells continue to produce. STD for enthalpy measurements data assumed 50 kJ/kg.

Estimated parameters

The list of estimation parameters is shown in Table 2.

Mass high temperature upflow rates.

There are two upflow zones identified in Mutnovsky field, since mass sources in each of these two zones were qualified as estimated parameters. Main Upflow includes 15 model elements, while NE-upflow includes 4 model elements, where mass sources were estimated.

Reinjection rates.

The rates of four groups of injection wells (027 (+028+044), 07, 043N, 054N (+024N)) were assigned as parameters to be estimated. Using the reinjection rates as estimated parameters was necessary due to the impossibility to reproduce enthalpies of the production wells at injected rates reported as 100% of production rate (Maltseva et al, 2007). Moreover, significant waste fluid discharge into the Falshivaya river and Trudny creek was clearly observed all the time of the Mutnovsky geothermal field large scale exploitation. Initial guess – 100%.

Fracturs permeabilities

Fracture permeabilities of the main reservoir geological units include values (from top to bottom) of: rhyolite tuffs (domain Tuff2), sandstones (domain Sand1), intrusion contact

zone (domain Cont1), and diorite intrusion (MagmF). Initial guesses, respectively, are: 24 mD, 100 mD, 500 mD, 0.3 mD.

Natural discharge (productivity indexes)

There are three main discharge areas of the Mutnovsky geothermal field: Dachny (D) (steam), Verkhne-Mutnovsky (VM) (steam) and hot water discharge, represented by several groups of hot springs, but lamped in this model as "Nizhne-Zhirovskoy" (NZ) hot spring discharge (Fig. 2). All of these three discharge features are represented in the model like "wells on deliverability", with production indexes used as estimated parameter. In this case, "bottomhole pressures" were assigned as 15 bars (D, +750 masl), 5 bars (NM, +500 masl), 1 bar (NZ, +250 masl). Initial guesses for PI's are: 6.1E-10, 5.6E-12, 4.5E-12 m^3.

Infiltration rate

There is geochemical evidence of local meteoric water downflow into the production reservoir. The recharge area may coincide with the artificial Utinoe Lake and also some recharge may take place through damaged casings of the numerous old exploration wells, drilled in the Dachny Site Mutnovsky geothermal field in 80-th. Hence, one element of the top layer was assigned with the source of 42 kJ/kg injected water (local meteoric inflow), where mass flow rate was used as an estimated parameter of 154 kg/s (Fig. 3).

Double porosity parameters

Fracture spacing and fracture fraction porosity were used as estimated parameters. The double porosity approach was applied to all active elements of the model, hence these parameters are characterized with reservoir properties as a whole. The initial conceptual model for the double porosity approach is a 3D orthogonal fracture system with fracture fraction (FF) of 0.01 and fracture spacing (FS) of 50 m.

Rock compressibility

In spite of two-phase nature and significant boiling at shallow layers, lower parts of reservoir may contribute to some fluids due to compressibility. Hence, integrated compressibility of sandstones and the contact zone are considered as a model estimated parameter, with an initial guess of 1E-7 Pa^{-1}.

Discussion of the modeling results, estimates and convergence achieved

Table 2 represents five outputs of iTOUGH2-EOS1 modeling (scenarios #12-NS+EX-11, 7, 8, 11A, 12). Scenario 11 estimates reinjection flow rates as 42-85% of reported values at different reinjection sites (62% of total volume). If no reinjection is assumed at all, then objective functions significantly improve (scenarios 7, 8, 11A, 12). The minimum objective function (OF=11390) achieved corresponds to scenario 12.

Nevertheless, significant model standard deviations (STD) of temperatures (6.2^{o}C), pressures (1.9 bars) and enthalpies (179 kJ/kg) have been obtained in this modeling scenario. These modeling STD exceed corresponding measurements STD. Moreover, systematic underestimation of enthalpies (MEAN=71 kJ/kg) and temperatures (MEAN=14.9^{o}C), and systematic overestimation of pressures (MEAN=-0.9 bars) has been observed (Table 2).

This situation has been partially improved by adjusting one of relatively unknown parameters in the model: bottom hole pressure in discharge element D. This parameter is not included in the list of iTOUGH2 estimated parameters, hence we just change this to 25 bars by hand (scenario 12A, Table 2). This results in a significant decrease of the objective function (OF=7968) and systematic deviation of temperatures (7.4^{o}C) have been achieved.

Hence, the following estimations of the reservoir parameters for the best modeling scenario (#12NS-EX-12A) have been obtained (Table 2): Main upflow rate 60.2 kg/s, NE upflow rate 20.3 kg/s, tuffs permeability 27 mD, sandstones permeability 85 mD, contact zone permeability 616 mD, fractures spacing 4.3 m, fracture fraction porosity 0.42, infiltration rate 103 kg/s, thermal discharge area productivity indexes 1.1E-9 m^3, 5.9E-12 m^3, 6.6E-12 m^3 (for NZ, D and VM correspondingly), rock compressibility of sandstones and contact zone 1.3E-7 Pa^{-1}.

Table 2. Output of iTOUGH2-EOS1 inversion modeling (natural state+exploitation history): obtained values of estimated parameters and convergence achieved.

Estimated parameters	Dimension	Run ##12-NS+EX						
		11	7	8	11A	12	12A	6
Mass upflow (Main)	kg/s	3.66 x 15 =54.9	3.73 x 15 =56.0	3.83 x 15 =57.5	3.96 x 15 =59.4	3.76 x 15 =56.4	4.01 x 15 =60.2	
Enthalpy (Main)	kJ/kg							1432
Mass upflow (NE)	kg/s	3.81 x 4 =15.2	3.61 x 4 =14.4	3.44 x 4 =13.8	3.44 x 4 =13.8	3.52 x 4 =14.1	5.07 x 4 =20.3	
Enthalpy (NE)	kJ/kg							1406
Injection 027	%	53						
Injection 07	%	42						
Injection 043N	%	85						
Injection 054N	%	68						
Permeability Tuff2	mD	31	38	33	36	31	27	
Permeability Sand1	mD	114	98	96	89	83	85	
Permeability Contact zone	mD	307	745	750	789	631	616	
Permeability MagmF	mD	1.1	1.1					
Infiltration rate	kg/s	148		159	146	156	103	78
Fracture spacing	m			57	57	50	4.3	4.5
Fracture porosity				0.44	0.42	0.30	0.42	0.36
Prod. index NZ	m^3				2.9E-9	2.5E-9	1.1E-9	
Prod. index D	m^3				5.7E-12	4.3E-12	6.6E-12	
Prod. index VM	m^3				9.8E-12	5.2E-12	6.6E-12	
Compressibility Contact zone + Sand1	Pa^{-1}					4.3E-9	1.4E-7	1.4E-7
Convergence parameters								
Objective Function (OF)		13440	11640	11930	11440	11390	7968	10150
STD Temperature	°C	6.9	6.5	6.3	6.1	6.2	10.0	22.5
Mean Temperature	°C	16.2	16.2	15.6	15.4	14.9	10.5	-7.8
STD Pressure	bars	1.4	1.6	1.7	1.7	1.9	1.3	1.2
Mean Pressure	bars	-1.1	-1.1	-1.4	-1.6	-0.9	-0.9	-0.8
STD Enthalpy	kJ/kg	183	181	181	180	179	172	173
Mean Enthalpy	kJ/kg	80	80	78	76	71	51	45

Model Verification Using Direct Temperature and Water Level Measurements

Temperature logging performed during the exploration stage of Mutnovsky geothermal field during well drilling yielded 72 records of the bottom hole recovered temperatures. 29 of 72 measurements, which were closer than 250 m to the model element centers, were selected as additional calibration points for the natural state.

A direct iTOUGH2 run with parameters (#12NS-EX-12B) shows systematic underestimation of the temperatures (MEAN=7.5°C). This 7.5°C temperature model underestimation may be caused by Na-K geothermometer underestimation used to define the high temperature upflow base temperature (308°C).

Hence additional inversion modeling was performed with enthalpies of upflows used as estimated parameters with upper allowed limit of 1450 kJ/kg (318°C). Inverse modeling run #14-NS-EX-6 (this is 6-parameter run with the rest of parameters assigned accordingly to run #12, Table 2) updated the following estimates: Main upflow enthalpy 1432 kJ/kg (water 314°C), NE upflow enthalpy 1406 kJ/kg (water 311°C), fractures spacing 4.5 m, fracture fraction porosity 0.36, infiltration rate 78 kg/s, rock compressibility of sandstones and contact zone 1.4E-7 Pa^{-1}. Opposite to previous runs, this modeling scenario shows overestimation of temperatures (MEAN=-7.9°C), which is qualified as reasonable, caused by not full recovery of bottomhole temperatures.

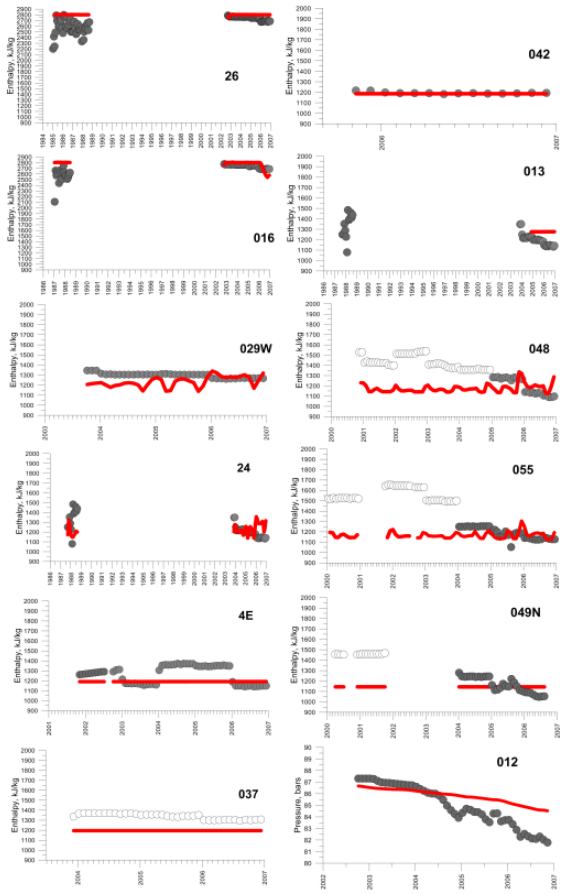

Figure 7. Transient enthalpy and pressure matches: grey circles – observational data, empty circles – potential outliers, red thick lines – modeling results (scenario #12-NS-EX-6).

Fig. 7 shows matches of this modeling scenario to observational data. As seen from Fig. 7, the model matches relatively well production enthalpies of wells from central part of the Mutnovsky geothermal field, including wells 26, 016, 24, 029W, 4E, 013, 042 (connected to Mutnovsky PP, where individual wells input may be confirmed). The largest enthalpy misfit occurs in wells 048, 055, 049N (connected to Verkhne-Mutnovsky PP), which were tested rarely using a transportable separator only. Hence, at this stage it is not clear whether additional model improvement, or data

verification (for NE wells enthalpies) are needed.

Model (scenario #12-NS-EX-6) verification match with pressures calculated from water levels elevations in 11 wells was also performed (direct run). The match shows convergence in mean terms (MEAN= 0.3 bars), assumed to be reasonable taking into account the uncertainty of pressures calculated from water levels under high temperature reservoir conditions.

CONCLUSIONS

A TOUGH2-EOS1 numerical model of the Mutnovsky geothermal field (Kiryukhin, 1996) was re-calibrated using natural state and history exploitation data during the time period 1984-2006. Recalibration process (started by hand) reveals the necessity to add double porosity in all active permeable elements, increase reservoir permeabilities and improve boundary conditions. The second stage of recalibration using iTOUGH2-EOS1 inversion modeling was very useful to remove outliers from calibration data, identify sets of the estimated parameters of the model, and perform estimations.

The following features of Mutnovsky geothermal reservoir based on integrated analysis of natural state and exploitation data are now better understood: 1. Reservoir permeability was found to be one order more compared to the 1996 model, especially the lower part coinciding with the intrusion contact zone (600-800 mD at -750 - -1250 masl); 2. Local meteoric inflow in the central part of the field accounting for more than 80 kg/s since year 2002; 3. Reinjection rates are significantly lower, than officially reported at 100% of total fluid withdrawal (Maltseva et al, 2007); 4. Upflow fluid flows were estimated hotter (314ºC) and the rates are larger (+50%), than assumed before; 5. Global double porosity parameter estimates are: fracture spacing - 5 m, void fraction N 10^{-3}.

"As simple as possible" model yields reasonable convergence with production enthalpies (reflecting volumetric reservoir properties). We understand that the coarse model is not able to describe satisfactorily (with small deviations) point type measurements, such as bottom hole temperature records, etc. Nevertheless, large sets of such calibration data may improve model mean and forecasting properties.

ACKNOWLEDGMENT

Authors appreciate to Y.F. Manukhin and Agency of mineral resources of Kamchatka for providing input data for Mutnovsky modeling. Authors also appreciate S. Finsterle, who provided iTOUGH2-beta version to perform this study. This work was supported by RFBR under project 12-05-00125 and FEB RAS under projects 12-III-A-08-170, 12-I-П27-04.

REFERENCES

Asaulov G.M. et al. *Report on results of the exploration works on Dachny site of the Mutnovsky geothermal field with reserves assessment for 50 MWe power plant.* Thermalny, Kamchatka, 1987.

Gavrilenko G.M., Melnikov D.V. 15 Years in Life of Mutnovsky Volcano. *Priroda,* #2, 2008, p. 54-58 (in Russian).

Maltseva K.I., Pashkevich R.I., Manukhin Y.F., Chernev I.I. Kotelnikova T.K., Kirichenko O.V., Petrova N.S., Shadrin A.V. *Report on reassessment of the Mutnovsky geothermal field reserves by 31.12.2006*. Elizovo, Kamchatka, 2007.

Finsterle, S. *iTOUGH2 User's Guide. Rep.* LBNL-40040, Lawrence Berkeley Natl. Lab., Berkeley, California, 1999.

Kiryukhin A.V. High temperature fluid flows in the Mutnovsky hydrothermal system, Kamchatka // *Geothermics.* 1993. V. 23. # 1. P. 49-64.

Kiryukhin A.V. Modeling Studies: the Dachny Geothermal Reservoir, Kamchatka, Russia // *Geothermics.* 1996. V. 25. # 1. P. 63-90.

Kiryukhin A.V., N.P. Asaulova, A.Y. Polyakov, O.B. Vereina. *Estimated Effect of the Exploitation Induced Infiltration in the Pauzhetsky and Mutnovsky Geothermal Fields, Kamchatka, Russia //* Proceedings World Geothermal Congress 2010 Bali, Indonesia, 25-29 April 2010, 5 p.

Pruess, K., C. Oldenburg, and G. Moridis, *TOUGH2 User's Guide, Version 2.0*, Report LBNL-43134, Lawrence Berkeley National Laboratory, Berkeley, Calif., 1999.

LABORATORY AND NUMERICAL STUDIES OF HEAT EXTRACTION FROM HOT POROUS MEDIA BY MEANS OF SUPERCRITICAL CO_2

Mario Magliocco[1,2], Timothy J. Kneafsey[2], Karsten Pruess[2], and Steven Glaser[1]

[1]Department of Civil and Environmental Engineering
[2]Lawrence Berkeley National Laboratory
University of California
Berkeley, CA, 94720, USA
e-mail: mag@berkeley.edu

ABSTRACT

The use of CO_2 as a heat-transfer fluid has been proposed as an alternative to water in enhanced geothermal systems (EGS). Numerical simulations have shown that under expected EGS operating conditions, CO_2 would achieve more efficient heat extraction performance compared to water. In a set of laboratory experiments, we have investigated heat extraction by flowing dry supercritical CO_2 through a heated porous medium in a laboratory pressure vessel. We have assembled a laboratory apparatus capable of operating at temperatures up to 200°C, pressures up to 340 bar, and flow rates up to 400 ml/min. The experimental system was designed such that measurements and controls at the boundaries could be readily modeled in TOUGH2. We have implemented a model of the experimental system in TOUGH2 and have obtained reasonable agreement between the laboratory measurements and the predictions of the numerical simulation. By continuing to improve both the experimental apparatus and the numerical model, we hope to document the ability of TOUGH2 to make accurate predictions of CO_2 heat extraction performance, with a focus on the application of CO_2 in EGS.

INTRODUCTION

Geothermal energy is a vast resource that, if efficiently utilized, could satisfy the majority of the base load energy demand in the United States (Tester et al., 2006). Current commercial geothermal electricity production is dependent on a number of factors, including an optimized combination of geological conditions such as presence of hydrothermal fluid, high heat flux, high rock permeability and/or high rock porosity. Enhanced (or Engineered) Geothermal Systems (EGS) are an attempt to exploit geothermal energy in locations where these conditions are not optimal (Tester et al., 2006). Most EGS strategies involve reservoir stimulation to overcome the lack of porosity and/or permeability of the rock using various chemical and physical processes, as well as supplying the needed heat transfer process fluid (e.g., water or CO_2) (Majer et al., 2007).

The novel concept of using supercritical CO_2 (SCCO2) as the working fluid in EGS for both reservoir creation and heat extraction was first proposed by Brown (2000). Subsequent work includes numerical simulations of a five-spot well pattern in a hot dry rock (HDR) system, which estimated an approximately 50% greater heat extraction rate using SCCO2 instead of water given the same operating conditions (Pruess, 2006). The advantages of using CO_2 over water as the process fluid in a closed loop HDR system include (1) the much lower viscosity of CO_2, which means that substantially larger mass flow rates can be achieved for a given pressure drop between injection and production points; (2) the much larger density difference between cold fluid in the injection well and hot fluid in the producer, which means increased buoyancy forces for CO_2, which will reduce or even eliminate pumping requirements; (3) the lower mineral reactivity of dry SCCO2, which would reduce equipment fouling, and reduce the possibility of dissolution and precipitation reactions that could negatively impact the reservoir quality; and (4) the hotter reservoirs, which means that reservoirs could be developed without the silica dissolution problems that are present in water-based systems. As an ancillary benefit, practical operation of a SCCO2 system would result in de facto carbon sequestration due to fluid loss to the surrounding

formations (Brown, 2000; Pruess, 2006). In light of the promising results of both thermodynamic and chemical simulations (Pruess and Spycher, 2010; Xu and Pruess, 2010), it is necessary to confirm the theoretical work with practical laboratory and field experiments.

This paper presents the ongoing design, implementation, and results of a laboratory-scale SCCO2-based heat extraction experiment, with the goal of verifying and validating TOUGH2 and the ECO2N module for the tested conditions, and improving the design of an experimental system.

EXPERIMENT DESCRIPTION

Our research consists of two major efforts: the creation of a laboratory-derived data set, and the creation of a well-behaved TOUGH2 model of the physical experiment. Great care has gone into designing the physical experiment, such that the boundary conditions could be accurately implemented in the TOUGH2 model.

Experimental Apparatus

The apparatus consists of a temperature-controlled pressure vessel filled with porous media, through which temperature-controlled fluid could be introduced by means of high-pressure high-flow rate pumps (Figure 1). The fluid flow in the vessel can be operated as either a constant fluid injection rate or in a constant differential pressure mode.

The fluid was delivered by a pair of Quizix C-6000-5K pumps, capable of 5,000psi (345 bar) and 400 ml/min fluid delivery rate. The pumps are capable of precisely controlled continuous and pulse-free flow with a resolution of 27.2 nanoliters. The CO_2 is passed through a chiller before entering the pumps in order to fill the pumps with high-density liquid CO_2. After leaving the pumps, the fluid can be either chilled by a second fluid chiller, or heated, depending on the desired experimental parameters. Before entering the vessel, the CO_2 passes through a Siemens Coriolis style mass flow meter. The meter could also be placed at the outlet and used in conjunction with the pump flow readings to measure fluid accumulation in the vessel.

The pressure vessel is a hollow stainless steel cylinder with an inside diameter of 9.1 cm, outside diameter of 12.7 cm, 50.8 cm distance between the end caps, and a pressure safety rating of 34.5 MPa (345 bar, 5000 psi). Instrumentation access to the interior of the vessel is via three axial passages through one end cap, and one passage through the other. The central passages through the end caps are used as the injection and production ports, and the remaining two passages are used exclusively to pass thermocouples through (see below).

Temperature measurements within the sample were made with 23 stainless-steel clad type-T

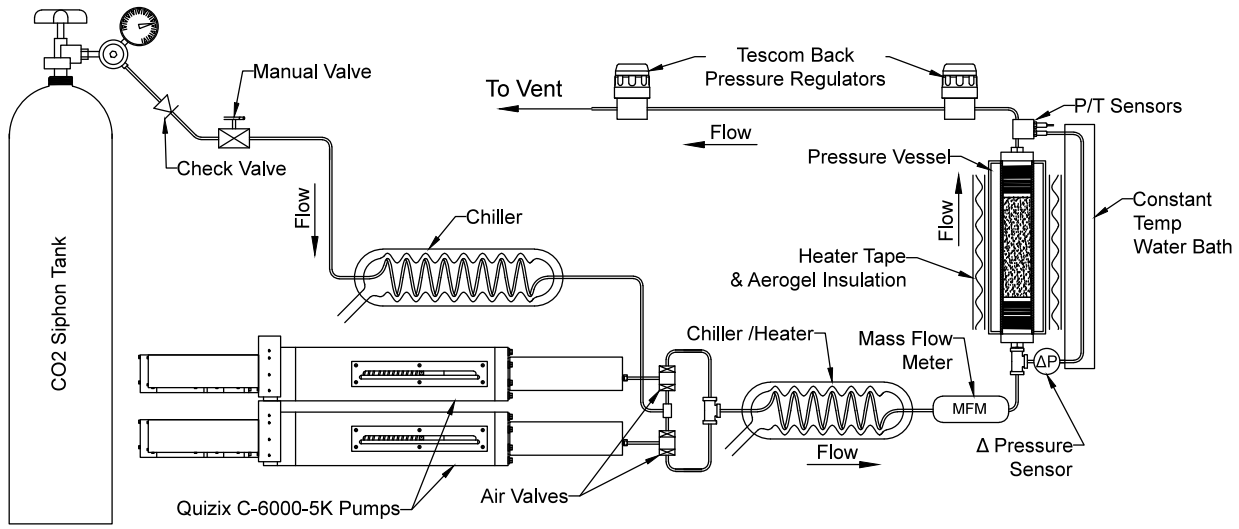

Figure 1. Simplified schematic of the experimental apparatus.

thermocouples, which have a small diameter (0.79 mm) in order to increase the sensor response time and to minimize disturbance to fluid flow. The thermocouples have been arranged at various elevations and radii in the sample, such that each successive vertical level is offset angularly to minimize vertical sensor shadowing (Figure 2).

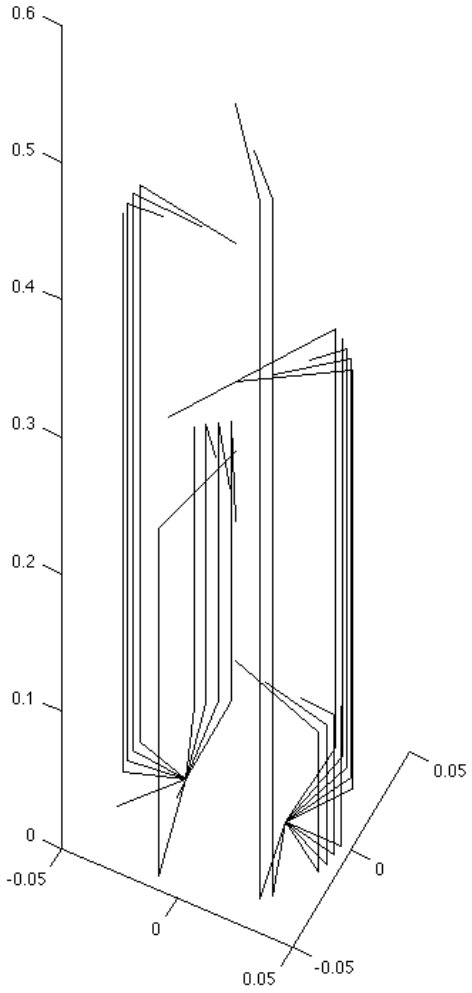

Figure 2. Orthographic diagram of thermocouple placement inside the vessel. Axis units are in meters.

At one elevation in the porous media, two thermocouples were mirrored so that they were both at the same radial distance from the central axis of the vessel. The radially mirrored temperature measurement was designed to test our assumption of radial symmetry in the heat-transfer process.

The injection port of the vessel was lined with a length of nylon tubing through the end cap in order to provide thermal insulation for the injected fluid as it passed through the relatively massive end cap. The injection port was also fitted with a single thermocouple mounted where the injected fluid enters the sample space (not shown in figure).

The sand used in the test sample was prepared from F95 Ottawa silica sand. Sieving and washing resulted in a relatively narrow grain size distribution. The mean grain size falls between 147 and 105 microns with no measurable portion below a grain size of 45 microns. The sand was dry placed in the vessel in multiple lifts, with vibratory compaction between lifts. The vessel was wrapped with heat tape that extended around the exterior of both end caps. Heat-tape thermal output was controlled by either a PID controller using a thermocouple secured on the vessel exterior, or with a pulse-width modulated signal generated by a computer. This allows the vessel boundary to act in either a constant-temperature or a constant-heat-flux mode. Finally, the vessel was wrapped in an aerogel insulation jacket and sealed. The current supplied to the heat tape was monitored using a true RMS current sensor.

The pressure at the outlet of the vessel was controlled by a pair of digital backpressure regulators in series. The fluid exiting the backpressure regulators was vented to the atmosphere. A differential pressure sensor was located at the base of the vessel and connected to the inlet and outlet of the vessel. The tubing that connected the differential pressure sensor to the inlet was encased in a constant-temperature water bath, so that the state of the fluid column in the tube can be determined. It was found in early tests that the small variations in fluid temperature resulted in large variations in fluid density—variations that significantly impacted the differential pressure measurement.

We developed software that incorporates experimental control and data acquisition. All sensor readings were collected by a single Labview-based program that allows for accurate time synchronization of experimental data. The

program is capable of controlling the pumps, vessel heat input, and the backpressure regulators. Combining these functions allows for a tightly integrated experimental setup, faster data processing and experimental turnaround time, and less chance of experimental errors.

Experiment Procedure

The tubing and sand-filled vessel were filled with dry CO_2. After heating the vessel to the desired operating temperature, we added or removed anhydrous fluid CO_2 to achieve the desired operating pressure, and the apparatus was allowed to thermally equilibrate. At this point, the backpressure was set to the desired pressure, and cold CO_2 was injected into the bottom of the vessel at a prescribed volumetric flow rate or injection pressure. When the first injection pump approached the end of its cycle, the second injection pump was activated, allowing the first pump to be refilled from the siphon tank. The injection pumps were cycled in this manner until the experimental run was completed.

TOUGH2 Modeling

A 2-D axisymmetric model of the experimental apparatus, which included porous medium, steel vessel, and inlet and outlet material domains, was implemented in TOUGH2/ECO2N. The majority of the modeling work was executed on a dual core 64-bit x86 processor running Apple OSX operating system software. A suite of Matlab scripts was written to allow for automatic generation of the mesh file, input files, and extracting and plotting of the post simulation data. We found that the simulations with TOUGH2/ECO2N were sensitive to cell size, resulting in runs that would produce errors before completion.

The errors appeared to be a result of the small scale of the model. When cells were too small, differences between variables in adjacent cells became too small compared to the machine epsilon (rounding of floating point operations) resulting in errors. The errors occurred at different times in the simulation on different computers that were using different operating systems and CPU architectures. These errors were also found to be dependent on the simulation parameters such as temperature, pressure, and flow rate. The mesh generation script allowed properly sized models to be produced rapidly with a user-selected quantity of cells in each domain axis. When an error was encountered, the number of cells was reduced until the simulation could run to completion.

For example, a simulation run with parameters of 121 bar back pressure, 150 ml/min injection rate, and 75C initial core temperature would fail when the porous medium was modeled with 45 or more horizontal cell layers (cell size height of 11.3 mm). When the number of horizontal cell layers was decreased to 44 (cell height of 11.5 mm) the simulation would run to completion without errors.

PRELIMINARY RESULTS

The temperature data from 22 thermocouples from a representative experimental run is shown in Figure 3. The thermocouples are numbered primarily in order of increasing radii and secondarily by increasing elevation in the vessel. Thermocouple 1, for example, is located on the central axis at the bottom of the vessel, while Thermocouple 22 is located near the vessel wall, at the top of the vessel.

It can be seen from the plot that there is an initial temperature gradient present in the saturated medium with a lower temperature at the base. This gradient is most likely driven by some heat loss to the environment. The numerical model did not develop a similar gradient until a heat sink was included on the vessel exterior.

The temperature front can be seen in the plot as it passes axially through the sample past the measurement locations. After the initial sharp temperature drop, the temperatures gradually approach equilibrium, and a radial temperature gradient then develops, indicated by the grouped lines spreading out. The exterior locations trend towards a higher temperature than locations that are more central (solid lines).

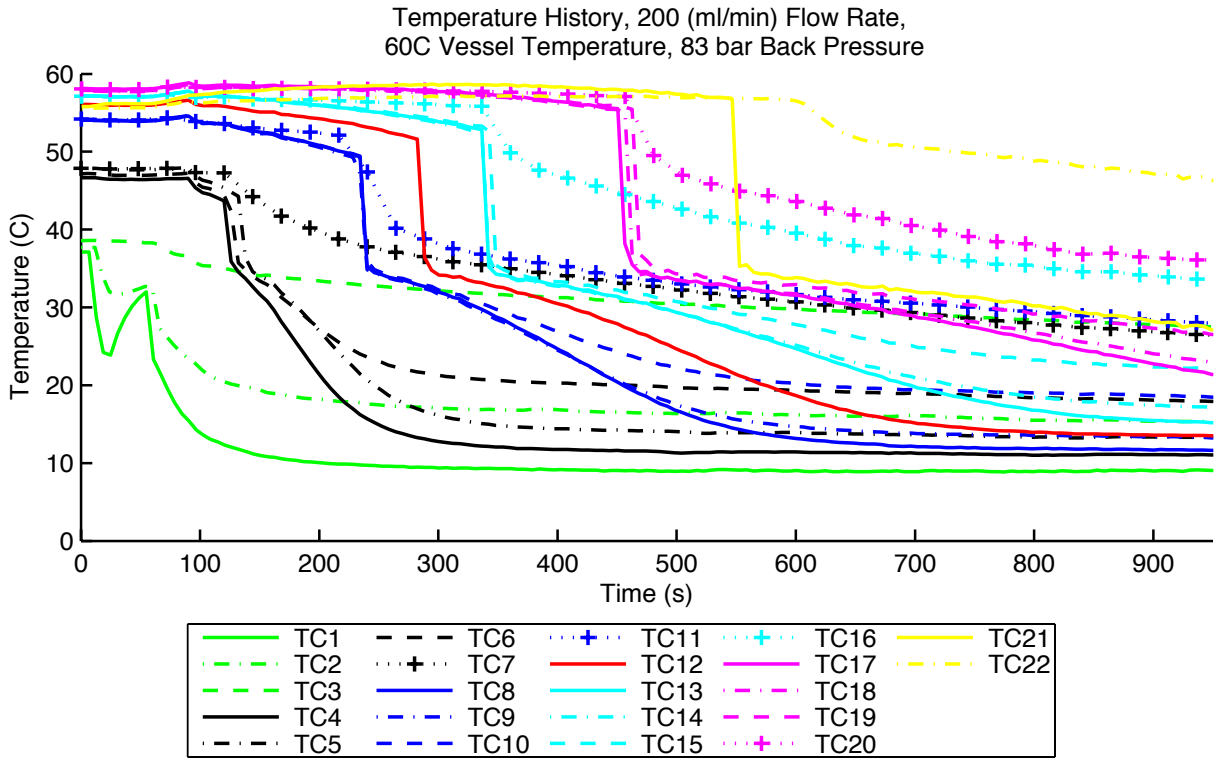

Figure 3. Temperature vs. time data for 22 thermocouples from a representative experimental run.

The interplay between convective and conductive transport can be seen in the shape of the temperature versus time curves. A purely convective process would feature sharp thermal fronts and a near-vertical slope at the time when the cold fluid slug reached the thermocouple. A purely conductive process would generate a gentler slope with smooth transitions. The experimental run shown in Figure 3 was at a relatively high flow rate, and the steep temperature front indicates a convectively dominated behavior. Figure 4 shows temperature data from a lower-flow-rate experimental run that was less convectively dominated (only temperature data from the central axis of the vessel are shown for clarity).

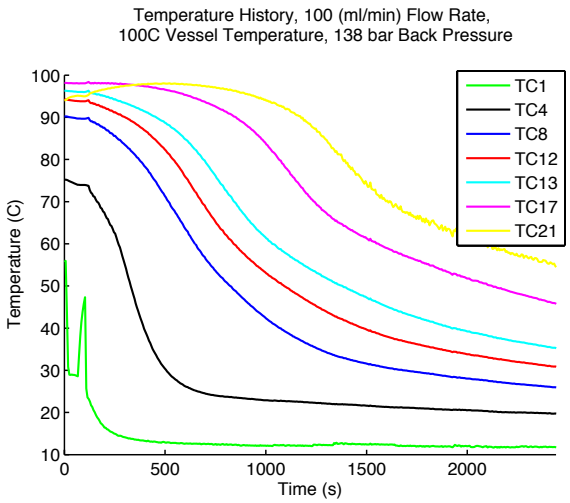

Figure 4. Temperature vs. time from experimental run with a CO_2 flow rate of 100 ml/min.

Modeling results were compared to runs made with an earlier version of the apparatus and generally agreed well (Magliocco et al., 2011). In order to reduce the differences between the modeling results and the experimental results, we made several control and measurement improvements to our apparatus. In our previous experimental setup, we found it difficult to measure the state of the fluid in the fluid delivery pumps, which made it difficult to estimate the mass flow rate of the fluid entering the system. We added a mass flow sensor to our inlet in order to directly measure the mass flow rate regardless of fluid state. We have also added the capability of controlling the exterior of the vessel as a constant heat flux boundary by using pulse-width modulation of the heater current.

Combined with the more efficient insulation provided by the aerogel jacket, the thermal boundary condition at the vessel exterior is much more certain. These hardware improvements will allow us to model the experiment in TOUGH2 more easily and accurately.

FUTURE WORK

We are working on expanding our experimental data set to cover more pressures, temperatures, flow rates, and fluid mixtures (CO_2, water, NaCl brine). Concurrently, we are improving the TOUGH2 model to more accurately reproduce the boundary and initial conditions found in the lab.

REFERENCES

Brown, D.W., A hot dry rock geothermal energy concept utilizing supercritical CO_2 instead of water, *Proceedings of the Twenty-Fifth Workshop on Geothermal Reservoir Engineering*, Stanford University, Stanford, California, January 24-26, 233–238, 2000.

Magliocco, M., T.J. Kneafsey, K. Pruess, and S. Glaser, Laboratory experimental study of heat extraction from porous media by means of CO_2, *Proceedings of the Thirty- Sixth Workshop on Geothermal Reservoir Engineering*, Stanford University, Stanford, California, January 31 - February 2, 2011.

Majer, E.L., R. Baria, M. Stark, S. Oates, J. Bommer, B. Smith, and H. Asanuma, Induced seismicity associated with enhanced geothermal systems, *Geothermics*, *36*(3), 185–222, 2007.

Pruess, K., The TOUGH codes–A family of simulation tools for multiphase flow and transport processes in permeable media, *Vadose Zone J.*, *3*, 738–746, 2004.

Pruess, K., Enhanced Geothermal Systems (EGS) using CO_2 as working fluid–A novel approach for generating renewable energy with simultaneous sequestration of carbon, *Geothermics*, *35*(4), 351–367, 2006.

Pruess, K., Enhanced Geothermal Systems (EGS) comparing water with CO_2 as heat transmission fluids, *Proceedings, New Zealand Geothermal Workshop 2007*, Auckland, New Zealand, November 19-21, 2007.

Pruess K. and N. Spycher, ECO2N–A fluid property module for the TOUGH2 code for studies of CO_2 storage in saline aquifers, *Energy Conv. Mgmt.*, *48*(6), 1761–1767, 2007.

Pruess, K. and N. Spycher, Enhanced Geothermal Systems (EGS) with CO_2 as heat transmission fluid – a scheme for combining recovery of renewable energy with geologic storage of CO_2, *Proceedings, World Geothermal Congress 2010*, Bali/Indonesia, 25-29 April, 2010.

Tester, J.W., B. Anderson, A. Batchelor, D. Blackwell, R. DiPippo, E. Drake, J. Garnish, B. Livesay, M.C. Moore, K. Nichols, S. Petty, N. Toksoz, R. Veatch, C. Augustine, R. Baria, E. Murphy, P. Negraru, and M. Richards, The future of geothermal energy: Impact of enhanced geothermal systems (EGS) on the United States in the 21st century, Massachusetts Inst. Technology, DOE Contract DE-AC07-05ID 14517 Final Rept., 374 p., 2006.

Xu, T., and K. Pruess, Reactive transport modeling to study fluid-rock interactions in enhanced geothermal systems (EGS) with CO_2 as working fluid, *Proceedings*, *World Geothermal Congress 2010*, Bali/Indonesia, April 25-29, 2010.

MODELING OF WELLBORE FLOW WITHIN GEOTHERMAL RESERVOIR SIMULATIONS AT FIELD SCALE

Marica Marcolini and Alfredo Battistelli

Saipem SpA
Via Toniolo 1, Fano, 61032, Italy
e-mail: marica.marcolini@saipem.com; alfredo.battistelli@saipem.com

ABSTRACT

Geothermal field exploitation is achieved by a wellhead control of well discharge to satisfy the constraints imposed by the surface steam-gathering system. Modern simulation approaches consist of coupled fluid dynamic modeling of the reservoir, the wellbores, and the surface steam-gathering system for a comprehensive evaluation of the entire production system. The conventional approach describes the fluid extraction by imposing a suitable bottomhole pressure and using a deliverability model to compute the production rate. While more realistic than previous approaches, new approaches have the disadvantage of coupling different codes, each one with specific modeling issues that may require longer simulation times. An improvement on the conventional approach is presented here, based on a modification of the well on deliverability method in the presence of multiple feed zones. Wellbore flow is solved in a more rigorous way between wellbore nodes, and can be extended up to the surface, allowing for modeling of reservoir exploitation with wells producing at a fixed wellhead pressure. The approach has been developed within the TOUGH2 V.2.0 numerical reservoir simulator and is presently limited to geothermal fluids that may be properly modeled using pure water.

INTRODUCTION

Exploitation of geothermal fields is achieved with the extraction and reinjection of fluids through production and reinjection wells. Thus, the realistic modeling of wellbore flow in geothermal field simulation is very important for obtaining reliable results. Field exploitation is achieved by wellhead control of well production, which needs to satisfy the constraints imposed by the separation pressure, the pressure drops in the surface steam-gathering system, and the turbine inlet pressure. Modern approaches to geothermal reservoir simulation consist of coupled fluid dynamic modeling of the reservoir and wellbores (Murray and Gunn, 1993; Hadgu et al., 1995; Bhat et al., 2005; Pan et al., 2011), including the surface steam-gathering system (Tokita et al., 2005; Butler and Enedy, 2010; Blöcher et al. 2010) for a comprehensive evaluation of the entire production system. On the other hand, the conventional approach handles fluid extraction by imposing a suitable bottomhole pressure and using a deliverability model to compute the production rate. The new approach has the disadvantage of coupling different codes, each one with specific modeling issues, which may require longer simulation times than conventional simulations. The older approach is based on a rough representation of wellbore-reservoir coupling that may significantly alter the description of reservoir behavior under exploitation.

A modification of the conventional approach is here presented, in order to obtain a satisfactory description of a coupled wellbore-reservoir system, preserving a computational speed compatible with simulations of geothermal reservoirs at the field scale and for the exploitation times of interest. The conventional well on deliverability method in the presence of multiple feed zones is modified by solving (in a rigorous way) the flow between wellbore nodes accounting for gravitational, frictional, and acceleration pressure drops in the momentum conservation equation—while potential, kinetics, and heat-transfer contributions are considered in the energy conservation equation. Wellbore flow simulation can be extended up to the surface, allowing the modeler to capture reservoir exploitation with wells producing at fixed wellhead pressure. The approach, which has been developed within the TOUGH2 V.2.0 reservoir

simulator, is presently limited to geothermal fluids that may be properly modeled using pure water.

OPTIONS AVAILABLE IN TOUGH2

TOUGH2 V.2 implements two basic options for the treatment of production wells (Pruess et al., 1999): (i) a wellbore on deliverability approach (DELV), extended to simulating wells producing from multiple feed points; and (ii) the so-called F-type option, in which the bottomhole pressure (BHP) of a wellbore on deliverability is not held constant, as in the conventional DELV option, but is determined by looking at a pre-calculated table of BHP as a function of rate and enthalpy. The table is computed using a wellbore flow simulator for a given well completion and fixed wellhead pressure (WHP).

DELV option

With the DELV option, the production rate of generic phase β is determined as a function of the wellblock mobility and the pressure difference between wellblock (P_β) and wellbore (P_{wb}), proportionally to a productivity index PI (Pruess et al., 1999):

$$q_\beta = \frac{k_{r\beta}}{\mu_\beta} \rho_\beta \, PI(P_\beta - P_{wb}) \qquad (1)$$

When a well is completed over multiple permeable layers, the wellbore pressure depends on the contribution of different feed points and should be computed by solving mass-, momentum-, and energy-balance equations describing the wellbore flow. In TOUGH2, this is accomplished in a simplified way by using an approach based on Coats (1977), originally developed for hydrocarbon wells, in which a gas and an oil phase of low mutual solubility are flowing. The main assumptions made in solving wellbore flow are:

i. The volumetric rate from each feed point is determined assuming the wellbore pressure were zero;

ii. At each node, volumetric rates from wellbore and feed points are added;

iii. The flowing density at each node is computed using phase flowing rates determined as per point (ii), and phase densities equal to those computed at wellblock conditions.

The above procedure provides a reasonable calculation of wellbore pressure profiles under flowing conditions only in the presence of single-phase liquid conditions: the gravitational contribution is predominant over friction and acceleration contributions, which are completely neglected. However, they can be considerable in both two-phase and single-gas flowing conditions, making the calculation of feed point rate unreliable. Moreover, if one wellblock element has single-phase conditions, the density of the nonexisting phase is missing, and the calculation of flowing density at wellbore node is completely erroneous.

F-type option

The so-called F-type option was introduced in TOUGH2 V.2.0 (Pruess et al., 1999) by replicating the approach used by Murray and Gunn (1993) for the TETRAD simulator. Fluid is extracted from a wellblock element in analogy with the DELV option (Eq. 1) in which the wellbore pressure is not held constant along the simulation, but determined at each time step as a function of rate and enthalpy. In practice, wellbore flow for a specific well completion and a fixed WHP is solved using a wellbore simulator. The wellbore pressure needed to have the desired WHP is given through a table as a function of rate and fluid enthalpy. TOUGH2 determines the BHP, rate, and enthalpy using an iterative procedure in which the capillary pressure in the wellblock element is neglected. The main limitation of this option is that it is applicable to a single feed point only, while most geothermal wells produce from multiple distinct feed points.

F-TYPE OPTION EXTENDED TO MULTIPLE FEED POINTS

The first step towards a more realistic simulation of coupled wellbore and reservoir flow within TOUGH2 has been made by coupling the F-type and DELV options. An inactive dummy element is added to the ELEME block for each producing wellbore. An F-type option is activated for each of these dummy elements, in order to read the file containing the tabulated BHP as a function of rate and enthalpy. To couple F-type and DELV, we add the reading of F-type file name in correspondence of the uppermost source of the well on deliverability completed over multi-

ple layers. At the end of a converged time step, subroutine WF is called to determine the BHP as a function of rate and enthalpy at the converged time step. This BHP is then used in subroutine GCOR to calculate the approximate wellbore pressure profile under flowing conditions needed by the DELV option. To avoid oscillations in computed well-production rates and enthalpy, subroutines WF and GCOR are actually called at the end of each completed Newton-Raphson (NR) iteration. The table of BHP values as a function of total rate and mixture enthalpy is computed in one single run using the PROFILI wellbore simulator (Battistelli, 2010). A few checks of flowing pressure profiles computed by TOUGH2 using PROFILI clearly show that neglecting frictional and acceleration pressure drops in the momentum equation and not solving the energy-balance equation lead to unreliable results.

IMPROVEMENT OF SUBROUTINE GCOR

The second step towards a more realistic simulation of coupled wellbore and reservoir flow was the improvement of subroutine GCOR. Within the standard TOUGH2 code (Pruess et al., 1999), GCOR is called once for a completed simulation time step to compute the flowing wellbore pressure profile for each DELV option applied to wells producing from multiple feed points. The pressure profile is then held constant along the NR iterations of the subsequent time step. For a more realistic coupled simulation, subroutine GCOR is called at the beginning of each NR iteration to update the flowing pressure profile used by DELV.

The major change is the complete rewriting of the iteration process used by GCOR to compute the flowing pressure profile, starting from the wellbore pressure assigned for the uppermost wellbore node. This new approach, based on a rigorous solution of wellbore flow, carries the major assumption that wellbore conditions in a field-scale simulation change slowly, so that a steady-state solution can be used within each time step. The approach, starting from the bottom, is as follows:

- Model wellbore flow between two (virtual) well nodes by solving mass-, momentum-, and energy-balance equations.
- Once the wellbore pressure is determined at the upper node, compute the discharge rate and enthalpy from the layer connected to the upper node and then compute new rates, mixture enthalpy, and wellbore temperature after the mixing between well flow and feed point flow. In practice, an isenthalpic flash is solved by knowing total mass, mixture enthalpy, wellbore pressure, and overall composition (for EOSs other than EOS1).
- The above steps are performed starting from the bottom node up to the top node of the wellbore, and they are iteratively repeated until the given wellbore pressure at the top well node is reproduced within a given accuracy.

It must be pointed out that the solution of isenthalpic flash and of wellbore flow is dependent on the EOS module used.

Modeling of wellbore flow

Momentum- and energy-balance equations are written analogously to PROFILI implementation. PROFILI is a steady-state wellbore simulator initially developed (Battistelli et al., 1990) for modeling steady-state flow in geothermal wells producing mixtures of water, NaCl, and a non-condensable gas (NCG), inspired by the work by Barelli et al. (1982). The present PROFILI version uses the EWASG EOS correlations (Battistelli et al., 1997; Battistelli, 2012). Momentum and energy equations are written following approaches for two-phase flow developed for nuclear plant applications by CISE (Lombardi e Ceresa, 1978; Bonfanti et al., 1979) and by CeSNEF (Lombardi e Carsana, 1992). The momentum equation is given by Eq. 2:

$$\frac{dP}{dz} = \tau_{fr} + \tau_{ac} + \tau_{gr} \qquad (2)$$

where τ is the gradient and subscripts *fr*, *ac*, and *gr* stand for friction, acceleration, and gravity, respectively. The energy balance, with respect to the unit mass of fluid, is given by Eq. 3:

$$dh = Q + dE_k + dE_p \qquad (3)$$

where h is the specific enthalpy, Q the heat exchanged with rock formations, and E_k and E_P the kinetic and potential energy, respectively.

With reference to the Barelli et al. (1992) approach, Eq. 2 can be written as follows:

$$\frac{dP}{dz} = \frac{2f\rho u^2}{D} + \frac{d(\rho u^2)}{dz} + \rho g \qquad (4)$$

where f is the Fanning friction factor equal to one fourth of the Darcy-Weisbach (Moody) friction factor, D is wellbore diameter, u is the fluid velocity, g is the acceleration of gravity, and ρ the fluid density.

CeSNEF-2 correlations for two-phase pressure drops are given by Eq. 5, where, f_L and f_G are the Fanning friction factors of liquid and gas phases, determined as if the entire flow rate were liquid or gaseous; f_m is the mixture friction factor; b_L, b_G and b_m are interpolation functions of the mixture dryness fraction x; and A is the well section surface:

$$\frac{dP}{dz} = \frac{2G^2(f_L b_L + f_G b_G + f_m b_m)}{A^2 D \rho_m} + \frac{G^2(1/\rho_m)}{A^2 dz} + \rho_m g \qquad (5)$$

The mixture friction factor is computed using an empirical correlation based on an extensive set of experimental data:

If $L < 30\,C_e$

$$f_m = 0.046 \times 30\, C_e\, L^{-1..25} \qquad (6)$$

else:

$$f_m = 0.046 L^{-0.25} \qquad (7)$$

where the dimensionless parameter C_e is given by:

$$C_e = \frac{\rho_L\, g\,(D - D_0)^2}{\sigma} \frac{\mu_G}{\mu_L} \qquad (8)$$

and:

$$L = \frac{G^2 D}{A^2 \rho_m \sigma} \left(\frac{\mu_G}{\mu_L} \right)^{0.5} \qquad (9)$$

σ and μ are the surface tension and dynamic viscosity, and D_0 = 0.001 m. The interpolation functions in Eq. 5 are given by:

$$b_G = x^{(600\,\rho_G/\rho_L)} \qquad (10)$$

$$b_L = (1-x)^{(2\,\rho_L/\rho_G)} \qquad (11)$$

$$b_m = 1 - b_G - b_L \qquad (12)$$

The Fanning friction factor is computed for both laminar and turbulent regimes, as a function of Reynolds number and well wall roughness, using a correlation from Sze-Foo (1990). Wellbore heat transfer with the surrounding rock formation is computed following Ramey (1975):

$$dq = \frac{2\pi\, k_T\, r_w U}{k_T + r_w U\, f(t_P)} (T_1 - T_e)\, dz \qquad (13)$$

where k_T is the rock thermal conductivity, r_W is the radius of wellbore, U is the overall heat transfer coefficient of well completion computed according to Whillite (1967), T_I and T_e are the fluid and formation temperature, and $f(t_p)$ is a dimensionless function of production time t_p computed according to Chiu and Thakur (1991).

VERIFICATION OF WELLBORE FLOW MODELING WITHIN TOUGH2

For verification of this new approach, we constructed a 3D model with sides of 5 km extending from an elevation of +500 masl down to -3000 m asl, with elements of 500 m side and thickness of 100 m. Atmospheric conditions are assigned on the top surface, while lateral sides are closed. Constant heat flux at the bottom boundary, and rock properties are assigned in order to have a conductive heat flow in the upper 500 m (the cap rock), vapor dominated or liquid dominated conditions from 0 m asl down to the bottom. The 3D model is not intended to replicate any natural geothermal system, but is used merely for verification purposes of the new developed algorithm by comparison with wellbore flow simulated by PROFILI. A well completed on 16 layers, from nodes at -1050 m asl to -2550 m asl, was defined. PI of 4.87E-12 m^3 is used on layers open to flow, while zero values are assigned to all layers from which no flow is desired. Several tests were run by assigning the wellbore pressure at the top of well section at -1050 m asl, or directly at wellhead (+500 m asl), and simulating a single feed point at the well bottom, as well as an additional feed at an upper elevation. Single gas, two-phase, and single-liquid conditions were simulated for the bottom feed to test all possible cases. Some of them are discussed here below.

Single Feed Point

A bottom feed at -2550 m asl under single liquid conditions is simulated, with an assigned wellbore pressure of 20 bara at -1050 m asl. Fig. 1 shows the flowing pressure and temperature

(P&T) computed by TOUGH2 (symbols) and PROFILI (lines), while Fig. 2 shows, in addition to pressure, the dryness fraction as well.

P&T profiles computed by TOUGH2 are well reproduced by PROFILI, even if the latter solves wellbore flow with a much finer discretization. A single feed at -2550 m asl under single-gas conditions is simulated with an assigned wellbore pressure of 18 bara at -1050 m asl.

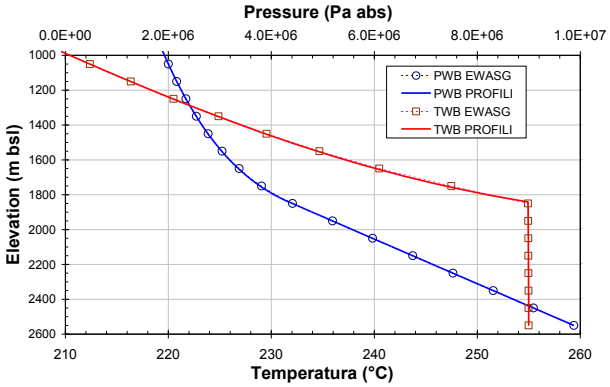

Figure 1. Single liquid feed at -2550 m asl. TOUGH2 P&T (symbols) vs PROFILI (lines) results.

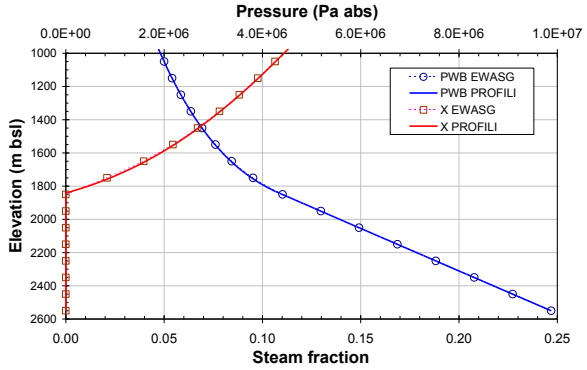

Figure 2. Single liquid feed at -2550 m asl. TOUGH2 P & dryness (symbols) vs PROFILI (lines) results.

Fig. 3 shows the flowing P&T computed by TOUGH2 and PROFILI. To show the effect of energy losses, wellbore flow has been computed in both adiabatic and isenthalpic conditions with both TOUGH2 and EWASG. While the reproduction of TOUGH2 results by PROFILI is good for both simulations, Fig. 3 shows that energy losses have a remarkable effect on the temperature profile of a steam-producing well. Avoiding the solution of the energy-balance equation may result in poor reliability of the computed flow temperatures.

A single feed point at -2550 m asl under single-pahse gas conditions is simulated with an assigned wellbore pressure of 10 bara at well head, at the elevation of 500 m asl. Fig. 4 shows a good reproduction of TOUGH2 results by PROFILI.

The wellbore flow was simulated from a single liquid feed point at -2550 m asl up to wellhead at +500 m asl, by assuming a WHP of 10 bara. Fig. 5 shows a good reproduction by PROFILI of flowing P&T computed by TOUGH2. Fig. 6 shows the good reproduction of dryness fraction.

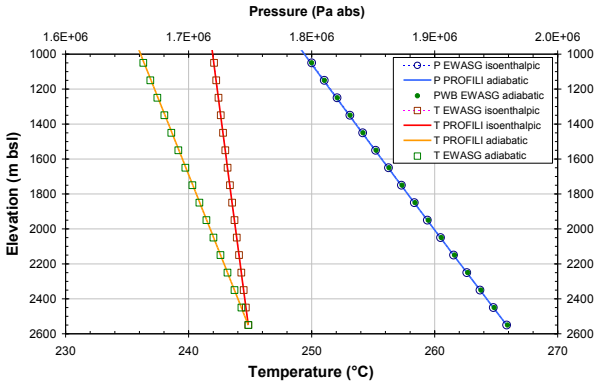

Figure 3. Single gas feed at -2550 m asl. TOUGH2 P&T (symbols) vs PROFILI (lines) results. Adiabatic and isenthalpic simulations are presented.

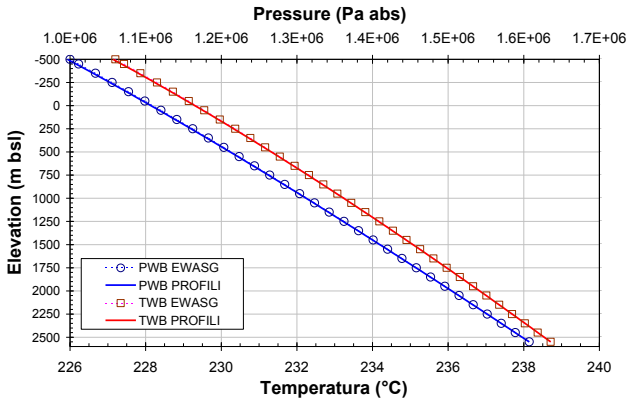

Figure 4. Single gas feed at -2550 m asl. TOUGH2 P&T (symbols) vs PROFILI (lines) results computed up to the well head.

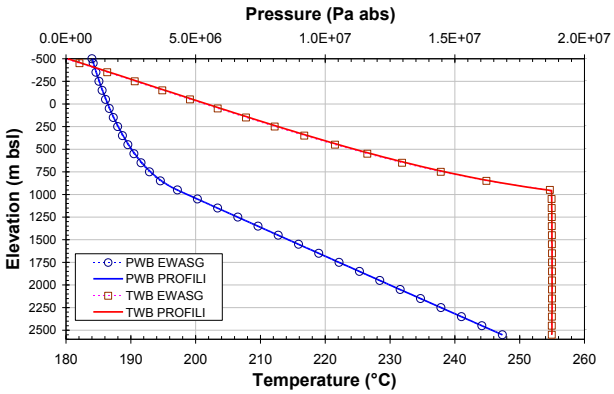

Figure 5. Single liquid feed at -2550 m asl. TOUGH2 P&T (symbols) vs PROFILI (lines) results computed up the wellhead.

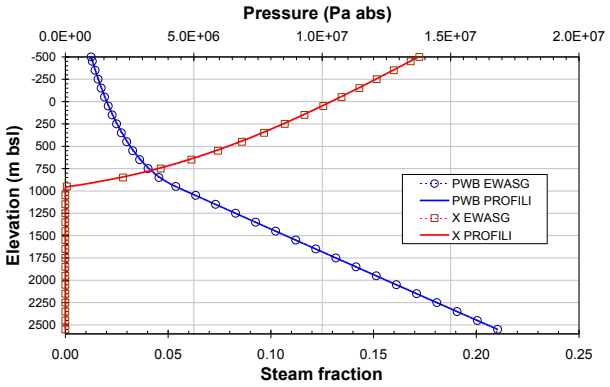

Figure 6. Single liquid feed at -2550 m asl. TOUGH2 P &T dryness (symbols) vs PROFILI (lines) results computed up to the wellhead.

Two Feed Points

Modeling of a single feed enabled us to verify that wellbore flow is properly computed within TOUGH2. Inclusion of an additional upper feed point enabled us to verify that the isenthalpic flash at the mixing between well and reservoir flow is properly solved. In addition to a single-phase liquid feed point at -2550 m asl, an additional feed point of higher enthalpy is added at -1250 m asl. Since PROFILI cannot solve wellbore flow with multiple feeds, the simulation is started from the wellhead considering the total mass discharged. Fig. 6 shows that down to -1250 m asl, PROFILI reproduces both P&T well, while below the upper feed, simulated P&T diverge widely from TOUGH2 results. Fig. 7 suggests how wellbore flow modeling can help in inferring feed zones using flowing P&T logs.

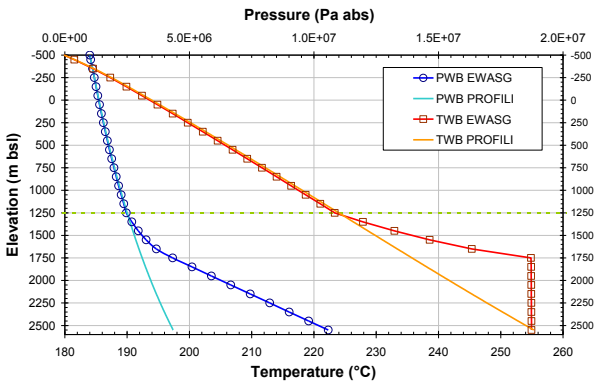

Figure 7. Single liquid feed at -2550 m asl and upper feed at -1250 m asl. TOUGH2 P&T (symbols) vs PROFILI (lines) results computed up to the wellhead.

Fig. 8 shows how PROFILI properly reproduces the flowing enthalpy and dryness fraction down to the upper feed. Note that if two-phase conditions are present where the inflow occurs, the mixing does not have an effect on temperature, because it is constrained by pressure. A change in T gradient is nevertheless visible in Fig. 7. A change in P gradient also occurs, but it is less clear than that of temperature. Dryness fraction and enthalpy are also well reproduced by PROFILI, as shown in Fig. 8.

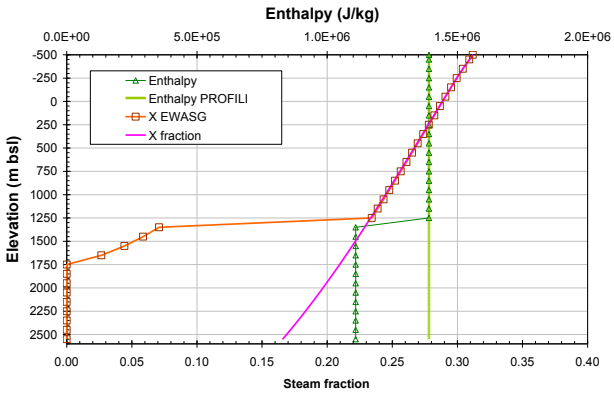

Figure 8. Single liquid feed at -2550 m asl and upper feed at -1250 m asl. TOUGH2 P & dryness (symbols) vs PROFILI (lines) results computed up to the wellhead.

We performed an additional test with a deep feed at -2550 m asl producing two-phase fluid, and an upper feed at -350 m asl producing a higher enthalpy mixture. Wellbore flow is controlled assigning a WHP of 10 bara. Fig. 9 shows TOUGH2 P&T results compared to those

simulated by PROFILI starting from the well-head.

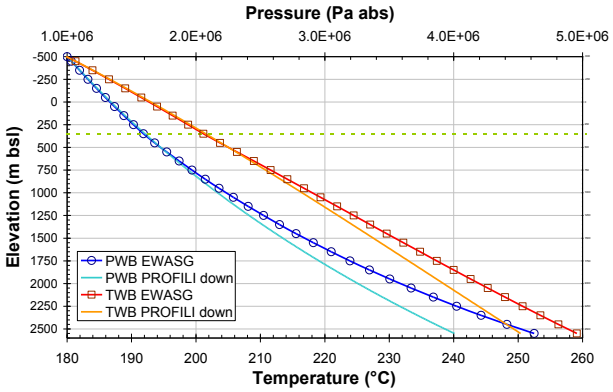

Figure 9. Two-phase feed at -2550 m asl and upper feed at -350 m asl. TOUGH2 P&T (symbols) vs PROFILI (lines) results computed up to the wellhead.

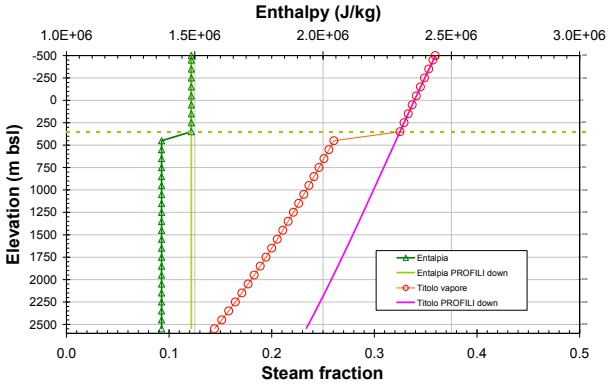

Figure 10. Two-phase feed at -2550 m asl and upper feed at -350 m asl. TOUGH2 P & dryness (symbols) vs PROFILI (lines) results computed up to the wellhead.

P&T are well reproduced down to the upper feed and depart below from TOUGH2 results. Fig. 10 shows the comparison for mixture enthalpy and dryness fraction. This time as well, the upper feed does not produce a step change in flowing temperature, because it is constrained by pressure. Also, P&T gradients are changed marginally by the upper feed and cannot be easily recognized by flowing P&T logs without wellbore flow simulation.

DIRECTIONAL WELLS

Directional wells are being drilled more often in geothermal fields, since they enable the concentration of several wells in clusters, with (1) the reduction of land surface occupation and well pad costs, (2) a reduction in environmental impact, (3) a speeding-up of rig moving operations, (4) a reduction in surface production equipment costs, and (5) an increased chance of intersecting sub-vertical conductive faults. Directional wells can in principle be modeled with the improved GCOR subroutine by providing (within the GENER input block) the cosine value of the angle between the well axis and the vertical direction.

CONTROL OF WELL PRODUCTION BY CHANGING OF WELLHEAD PRESSURE

The developed algorithm allows the user to simulate the coupled wellbore and reservoir flow in wells producing from multiple feeds by assigning the wellhead pressure, if the well description within the DELV option is extended up to the surface. In the present development, the WHP is held constant throughout the simulation. In principle, it could be changed during reservoir exploitation to meet field production constraints. Constant production rate could be allowed, at the beginning of field exploitation, with WHP higher than the minimum required by the surface fluid-gathering system. Further on, when WHP reaches the minimum value required because of reservoir-pressure decline, constant rate production could be switched to constant WHP. The developed algorithm can be used to compute the wellbore flow for a desired total mass rate, by computing (at the same time) the corresponding WHP. Switching to constant WHP can then be performed when the computed WHP drops below the minimum required value. In principle, this approach would make for a more reliable coupled simulation of reservoir and wellbore flow, with more realistic modeling of well production control during the life of a geothermal field.

CONCLUSIONS

The modeling of coupled wellbore-reservoir flow is important for realistic simulation of fluid withdrawal during the exploitation of geothermal reservoirs. Coupled flow must be simulated in directional wells and in the presence of the multiple feed points often encountered in exploited geothermal fields. The DELV and F-type options presently available in TOUGH2 have limitations relative to the realistic handling of wellbore flow

in the presence of multiple feeds. First, TOUGH2 is modified to allow the use of the F-type option, with wellhead control of well production, coupled to the well on deliverability approach (DELV) for wells completed over multiple layers.

Then, subroutine GCOR is modified to allow a more reliable simulation of wellbore flow by solving mass-, momentum- and energy-conservation equations between wellbore nodes under the assumption of steady-state conditions. At each feed point, mass and energy balance equations are solved, accounting for well and reservoir contributions, and new thermodynamic conditions are determined, performing an isoenthalpic flash calculation for given pressure, enthalpy, and composition of the mixture. Flowing P&T profiles for single and two feed points, with different combinations of thermodynamic conditions, have been simulated with the modified TOUGH2 version. Comparison with results computed by the PROFILI wellbore simulator showed consistently good reproduction of TOUGH2 results.

The developed approach can be used to control wellbore production in the presence of multiple feeds by assigning the flowing pressure at the top of production interval, as well as at the surface, thus allowing wellhead control of wellbore flow. Tests performed so far have indicated a marginal incremental increase in computing time in 3D simulations, suggesting that the approach can be safely used in field-scale simulations of geothermal reservoir exploitation.

In future work, the developed approach needs to be extended to fluid mixtures containing dissolved solids and noncondensible gases.

ACKNOWLEDGMENTS

The management of Saipem SpA is acknowledged for their permission to publish the present work.

REFERENCES

Barelli A., Corsi R., Del Pizzo G., Scali C., A two-phase model for geothermal wells in the presence of non-condensable gas. *Geothermics*, 11 (3), 175-191, 1982.

Battistelli A., Rivera R. J., Celati R., Mohamed A.H., *Study of the effect of several wellbore conditions on the output characteristics of wells at the Asal Field, Republic of Djibouti*. Proc. 15th Work. Geoth. Res. Eng. Stanford, 1990.

Battistelli A., C. Calore, and K. Pruess K., The simulator TOUGH2/EWASG for modelling geothermal reservoirs with brines and a non-condensible gas. *Geothermics*, 26(4), 437-464, 1997.

Battistelli A., *PROFILI wellbore flow simulator: from geothermal to GHG injection wells*. GeoTherm Expo, Ferrara, Italy, 2010.

Bhat A., Swenson D., Gosavi S., *Coupling the HOLA wellbore simulator with TOUGH2*. Proc., 30th Work. Geoth. Res. Eng. Stanford Un., SGP-TR-176, 2005.

Blöcher G., Kranz S., Zimmermann G., Frick S., Hassanzadegan A., Moeck I., Brandt W., Saadat A., Huenges E. (2010). *Conceptual Model for Coupling Geothermal Power Plants with Deep Reservoirs.* Proc. World Geoth. Cong. 2010.

Bonfanti F., Ceresa I. and Lombardi C., Two-phase pressure drops in the low flowrate region. *Energia Nucleare*, 26(10), 481-492, 1979.

Butler S.J., Enedy S.L., *Numerical Reservoir-Wellbore-Pipeline Simulation Model of The Geysers Geothermal Field, California, USA*. Proc. World Geoth. Cong. 2010.

Coats K.H. (1977). Geothermal reservoir modelling. *Paper SPE 6892*.

Chiu K., Thakur S.C., Modeling of Wellbore Heat Losses in Directional Wells Under Changing Injection Conditions. *Paper SPE 22870, 1991*.

Hadgu T., Zimmerman R.W., Bodvarsson G.S. (1995). Coupled Reservoir-Wellbore Simulation of Geothermal Reservoir Behavior. *Geothermics*, 24(2), 145-166, 1995.

Lombardi C. and Ceresa I., A generalized pressure drop correlation in two-phase flow. *Energia Nucleare*, 25(4), 181-198, 1978.

Lombardi C., Carsana C.G., A dimensionless pressure drop correlation for two-phase mixtures flowing up in vertical duct covering wide parameter ranges. *Heat & Technology*, 10(1-2), 125-141, 1992.

Murray L., Gunn C., *Toward Integrating Geothermal Reservoir and Wellbore Simulation: TETRAD and WELLSIM*. Proc. 15th New Zealand Geoth. Work., Auckland, 1993.

Pan L., Oldenburg C.M., Wu Yu-Shu, Pruess K., *T2Well/ECO2N Version 1.0: Multiphase and Non-Isothermal Model for Coupled Wellbore-Reservoir Flow of Carbon Dioxide and Variable Salinity Water*. Lawrence Berkeley National Laboratory, report LBNL-4291E, 2011.

Pruess K., C. Oldenburg, and G. Moridis, *TOUGH2 User's Guide, Version 2.0*. Report LBNL-43134. Lawrence Berkeley National Laboratory, Berkeley, Calif., 1999.

Ramey H.J. Jr., Heat losses during flow of steam down a wellbore. *JPT*, pp. 845-851, 1975.

Sze-Foo Chien, Predicting wet-steam flow regime in horizontal pipes. *JPT*, 356-370, 1990.

Tokita H., Lima E., Hashimoto K., *A Middle-Term Power Output Prediction at the Hatchobaru Field by Coupling Multifeed Wellbore Simulator and Fluid-Gathering Pipeline Simulator to Reservoir Simulator*. Proc. World Geoth. Cong. 2005.

Willhite G.P., Over-all heat transfer coefficients in steam and hot water injection wells. *Paper SPE 1449*, 1967.

MODELING OF CALCITE SCALING IN A GEOTHERMAL WELL

Giordano Montegrossi

Consiglio Nazionale delle Ricerche, Istituto di Geoscienze e Georisorse
Via G. La Pira 4
50121 Firenze, Italy
Giordano.Montegrossi@igg.cnr.it

Francisco Ernesto Montalvo López

LaGeo S.A. de C.V.
15 Av. Sur, Col. Utila,
Santa Tecla
EL SALVADOR
fmontalvo@lageo.com.sv

ABSTRACT

In this paper, we describe the construction of a relatively simple well model by means of the TOUGHREACT code. We used a kinetic approach to compute calcite precipitation/ scaling in two producing geothermal wells at the geothermal field of Ahuachapan in El Salvador. The model succeeded in accurately computing the depth of calcite encrustation, and shows a strict correlation between scaling and flashing. For this computation, we used only the major chemical composition of the water, a kinetic model for calcite deposition, and two fixed pressure (infinite-volume gridblocks) boundary conditions for the well-head (fluid extraction) and reservoir.

INTRODUCTION

Rock-fluid interaction studies suggest that mineral dissolution and precipitation effects have a major impact on the long-term performance of a geothermal well. Since it is common to have geothermal wells drilled in carbonate formations, or formations with significant carbonate contents, we decided to investigate the precipitation and dissolution of calcite in geothermal wells. Calcite relates to the carbon dioxide behavior, as governed by boiling, dilution, and condensation processes (Simmons and Christenson, 1994).

Calcite dissolution gradually decreases along the flow path from the recharge inflow of fresh water toward the extraction well, whereas calcite precipitation occurs within the extraction well. The deposition of calcite is mainly related to two effects: (1) evaporation of the brine, which leads to an increase in dissolved calcium and carbonate concentrations, and (2) forced CO_2 exsolution during boiling, which leads to an increase in the saturation index of calcite.

We considered scaling processes in the extraction well from an infinite-extent reservoir, where vaporization of the solution occurs within the well because of fluid extraction at constant pressure. The calcite sealing mechanism, which has been studied by several authors using different approaches, increases the complexity of the sealing model itself. The first approach is a stationary equilibrium model (e.g., Moller et al., 1998) where sealing is obtained by defining the CO_2 exsolution point; another approach (and further improvement) is a reactive transport model (e.g. Xu et al., 2004) used to simulate fluid production and calcite deposition/ dissolution processes from a well located at the center of a 2D radial carbonate reservoir.

In this study, we present a reactive transport model that takes into account the kinetics of dissolution/precipitation of carbonates, with a significant amount of carbonate minerals present in the modeled system. The model is based on data from the geothermal field at Ahuachapan, El Salvador, where calcite makes up ~30% of the entire rock.

The chemical composition of modeled reservoir water was obtained by using a brine with measured NaCl content, and calcium and carbonate concentrations computed assuming CO_2-brine-rock equilibrium in a 2D radial carbonate reservoir. Because initial equilibrium is assumed, the resulting reservoir fluid composition is independent from the amount of carbonates minerals as long as these phases remain present after reaction.

For the well-scaling model, we used an upward linear model, with two infinite-volume grid-blocks simulating the extraction pressure condition (measured in dynamic regime at the well-head) and the reservoir pressure condition (measured in dynamic regime at the well-bottom), and a well discretized with a cell length of 0.5 m up to the total well depth.

The well-scaling model, computed by means of the TOUGHREACT software package, is then calibrated by varying the CO_2 partial pressure in the reservoir in order to match the pH measured at the well-head. After calibration, the depth of the calcite precipitation level is compared with the scale depth measured during well-cleaning operations; unfortunately, it was not possible to compare the predicted amount of precipitated calcite with measured amounts because these data were not available.

This procedure was applied to the geothermal wells AH33A-B and AH35A-B (Fig. 1) in Ahuachapan, El Salvador, which are known to be affected by calcite scaling, mainly in the southern part of the geothermal field, due to the relatively high calcite content in the host rocks.

Increasing the model complexity requires a more complete input thermodynamic database and a more detailed knowledge of the reservoir conditions. In this study, we present a real but simplified case in order to show how a relatively simple model may be able to forecast calcite scaling with reasonable accuracy.

GEOTHERMAL FIELD SETTINGS

The Ahuachapán geothermal field (Fig. 1) is located in the western part of El Salvador, some 20 km from the border with Guatemala, 40 km from the Pacific Ocean, and 120 km from San Salvador, the capital city. The geothermal area is about 100 km^2 and is associated with the andesitic stratovolcano Laguna Verde. The system is located between the southern flank of the central salvadorean graben median trough and the northwestern sector of the Cerro Laguna Verde Volcanic group. This group constitutes a complex extrusive structure developed during the Quaternary near the Pliocene tectonic block of Tacuba-Apaneca, the regional faults of which have controlled (first) the sinking of the graben and (subsequently) the extrusion of volcanic products. This complex structural location favors deep hot fluid ascent through a marginal set of faults and further lateral fluid migration along a NW-SE oriented transversal fault system.

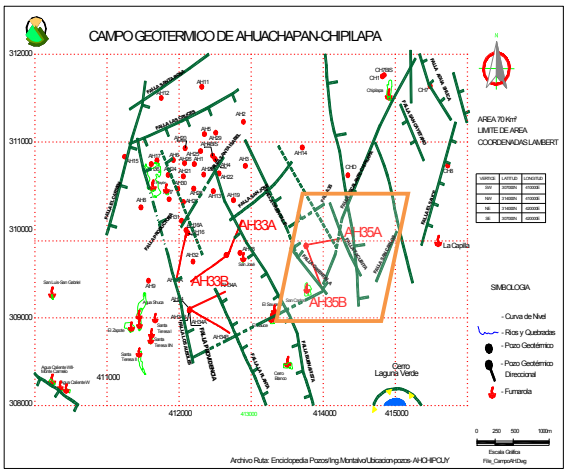

Figure 1. Wells location in the Ahuachapan geothermal field. The current investigation was carried out at AH35A - B and AH33A-B wells (within the rectangle).

At present, the Ahuachapán geothermal field has 16 production wells generating around 79 Mwe (gross), representing 12% of the total electricity consumption in the country. Production wells AH-33B and AH-35A, located in the SSE part of the field, requires a chemical antiscalant dosing system to prevent calcite scaling.

The Ahuachapan waters are medium to high saline waters, similar to those found at many other geothermal fields. Such waters are characterized by near-neutral pH, high calcium concentrations, and relatively low bicarbonate concentrations. The waters sampled in the southern part of the field show different

chemical compositions, and the well-head pH is higher for wells affected by scaling, like AH-35B. This seems to point to an increased pH due to CO_2 exsolution during fluid upraising.

MODEL SETTINGS

The calcite scaling potential is determined by the concentrations of calcium and carbonate species, which dictate the calcite solubility product:

$$CaCO_3 = Ca^{+2} + CO_3^{=} \quad (1)$$

At most geothermal reservoirs calcite is present in the wall-rock, and the waters are at or close to calcite saturation. Waters become supersaturated with respect to calcite when they flow up a well, boil, and lose CO_2, shifting reaction (2) to the right:

$$Ca^{+2} + 2HCO_3^{-} = CaCO_3 + H_2O + CO_2 \quad (2)$$

To model the well flow, which should take into account both the water boiling and the CO_2 exsolution, we must know the reservoir CO_2 partial pressure. Boiling-degassing is not a linear process, involving an irreversible step (i.e., calcite precipitation). We started by constructing an equilibrium model of 1 m^3 at reservoir conditions (10% porosity, 235°C, 66 bar, 23% calcite) and computed the water compositions resulting from equilibration with CO_2 at various P_{CO2} values. The resulting water compositions are used in the infinite-volume griddblock representing the reservoir in the well-scaling model. The well bore is simulated by means of the TOUGHREACT code with equation of state EOS2, using gridblocks (corresponding to a 7-inch liner) with a height of 0.5 m along the well axis. For computation, the effective well depth is used, rather than actual length, in order to preserve a linear pressure gradient with depth. The extraction at the well top is modeled with an infinite-volume gridblock at a constant pressure, i.e., well-head pressure.

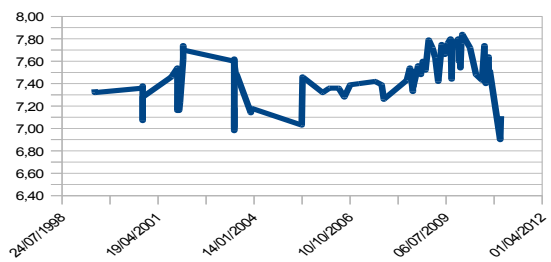

Figure 2. Measured pH time series at the AH35B well

The water salinity is ~0.4 M NaCl; using these data, the P_{CO2} value is adjusted in order to match the 7.2 pH (recent pH average, Fig. 2) at the well head, resulting in a 10 bar P_{CO2} over 66 bar total reservoir pressure.

We use these conditions to set up the reservoir fluid with respect to carbonate species and $CO_{2(g)}$, and to model fluid rising in similar wells, i.e., AH35A-B and AH33A-B.

MODEL VALIDATION

In order to validate the model, we compared the results of the model with the available data. Unfortunately the only available data are the depth of calcite encrustation found during the cleaning of the AH33B and AH35A wells; no quantitative information is available on calcite amounts. The AH33B and AH35A wells have similar well-head pressures, 6.8 and 6.48 bar, respectively. Fig. 3 shows how the encrustation found at 714–797 m depth relates with water flashing (beginning at 842.8 m depth).

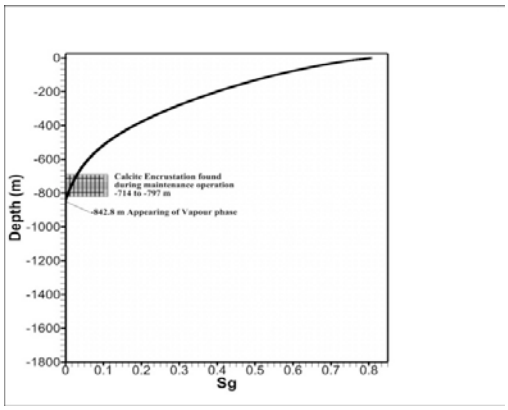

Figure 3. Gas saturation (Sg) vs depth in well AH35A

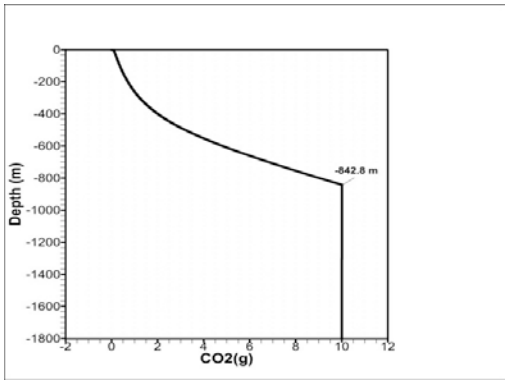

Figure 4. $CO_{2(g)}$ partial pressure (bar) vs depth profile

At the same depth, the CO_2 partial pressure decrease and pH increase begin, as shown in Figs. 4–5.

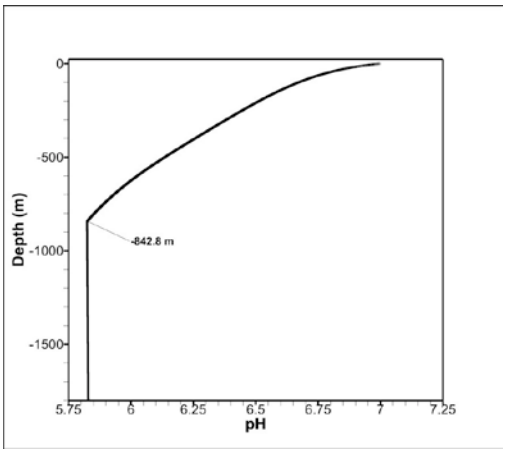

Figure 5. pH vs depth profile

The same modeling procedure was followed for the AH33B well. Fig. 6 shows the location of calcite encrustation (790-841 m depth) with respect to water flashing (beginning at 843.8 m depth). In these cases, there is very good agreement among water flashing and calcite precipitation depth.

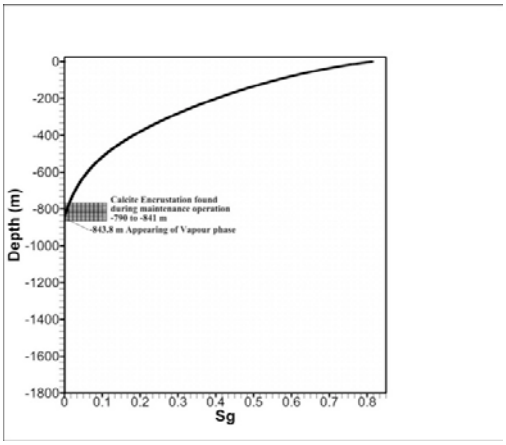

Figure 6. Gas saturation (Sg) vs depth in well AH33B

In this kind of model, the saturation index of calcite starts from zero in the reservoir (due to the imposed equilibrium condition) and maintains a very small value (around or slightly higher than zero) over the entire model. The main role in controlling calcite deposition is played by both $CO_{2(g)}$ exsolution and solution concentration due to boiling, but these two phenomena are superimposed, making it impossible to isolate the effect of either one alone. Since calibrating the amount and geometry of deposited calcite is not possible, we do not have any other comment apart from the fact that we used a "guessed" geometric deposition surface corresponding to a 45-micron crystal size, corresponding to the commercial steel-pipe roughness.

WELL MANAGEMENTS

Given the strict relation of calcite precipitation with water flashing, and knowing that changing the well-head pressure moves the flash point up or down within the well, we constructed a graph of well-head pressure versus flash point depth, while keeping reservoir conditions constant (Figure 7).

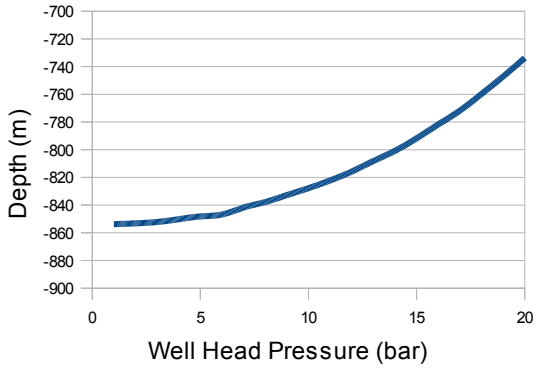

Figure 7. Computed flash point depth vs well-head pressure

Within a reasonable range of well head pressures (2-20 bar), the flash-point depth varies only from 740 to 850 m depth; thus, the effect of "diluting" the encrustation by regulating the well-head pressure (and reducing the cleaning operation frequency) is very limited.

The solution used here was to add an anti-scalant to the well fluid below the flashing point, at a depth around 1000 m in the liquid phase. In the AH35A and AH33B wells, the anti-scalant was injected at -975 and -1050 m, respectively.

It is also useful to evaluate the flash-point variation while keeping constant the extraction pressure and varying the reservoir pressure, to check how the recharge-exploitation of the reservoir affect the flash point (and encrustation) position.

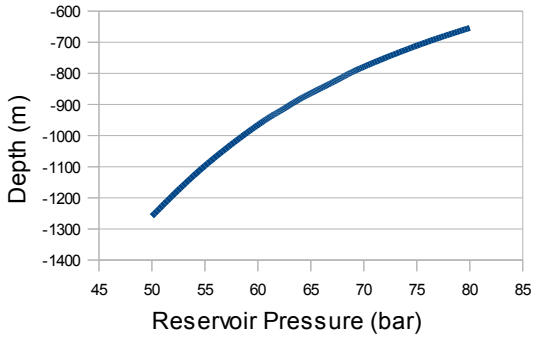

Figure 8. Flash point depth vs reservoir pressure

Fig. 8 shows that the flash-point position is very sensitive to the reservoir pressure, and that if the reservoir pressure decreases too much, the flash point will enter the reservoir, with the risk of sealing it.

CONCLUSIONS

Briefly summarizing our findings, we conclude that (1) calcite scaling can be modeled by using a simple (kinetic) model considering only the carbonate species, (2) we must use the effective well length in order to preserve a linear pressure gradient, (3) flash-point control by means of regulating well-head pressure may not be very effective in mitigating calcite encrustation, and (4) reservoir conditions play a significant role in regulating both flash point and calcite encrustation depth.

ACKNOWLEDGMENT

This work was possible thanks to the material supplied by LaGeo, El Salvador. Special thanks are due to Antonio Caprai, coordinator of the "Geothermal Diploma Course Project at the University of El Salvador," and all the people involved in El Salvador, for their kindness and hospitality.

REFERENCES

Herrera R., Montalvo F., Herrera A., El Salvador Country Update. Proceedings World Geothermal Congress 2010, Bali, Indonesia 25-29 April 2010

Montalvo F., Xu T., Pruess K., TOUGHREACT Code Applications to Problems of Reactive Chemistry in Geothermal Production-injection Wells. First Exploratory Model for Ahuachapán and Berlín Geothermal Fields. Proceedings World Geothermal Congress 2005 Antalya, Turkey, 24-29 April 2005

Simmons, S. F. and Christenson, B. W., 1994, Origins of calcite in a boiling geothermal system: *American Journal of Science*, v. 294, p. 361-400

Moller N., Greenberg J. P., Weare J. H., Computer Modeling for Geothermal Systems: Predicting Carbonate and Silica Scale Formation, CO2 Breakout and H2S Exchange, *Transport in Porous Media* **33:** 173–204, 1998.

Xu T., Rose P., Fayer S.,Pruess K., Numerical simulation study of silica and calcite dissolution around a geothermal well by injecting high pH solutions with chelating agent, Thirty-Fourth Workshop on Geothermal Reservoir Engineering, Stanford University, Stanford, California, February 9-11, 2009, SGP-TR-187

THREE-DIMENSIONAL MODELING OF BASIN AND RANGE GEOTHERMAL SYSTEMS USING TOUGH2-EOS1SC

Ann Moulding and Tom Brikowski

University of Texas at Dallas, Department of Geosciences ROC 21
800 West Campbell Road
Richardson, TX, 75080-3021, United States
e-mail: aem058000@utdallas.edu, brikowski@utdallas.edu

ABSTRACT

The Basin and Range (B&R) province is host to numerous geothermal systems with observed temperatures of 200–280°C at 2–3 km depth. Most of these were blind discoveries and are poorly understood. No known magmatic heat source for these exist; rather deep circulation of meteoric water through structural conduits in the presence of steep conductive geothermal gradients is believed to drive these systems. B&R systems are geologically transient—triggered by recent and ongoing tectonic events.

Using TOUGH2-EOS1sc, we investigated a three dimensional (40×26×12 km) polygonal model of an idealized B&R system. Various combinations of bulk rock and range-front fault permeability were tested with the fault zone extending down to 8 km depth. A basal heat flow of 85 mW/m^2 was used for all models.

Two end-member conceptual models for this setting were considered, both terminating in a narrow tube-like conduit for upflow within the range-front fault plane. Concept 1 supplies fluids into this conduit at depth from a deep, distributed source. Concept 2 adds significant horizontal flow within the fault plane, supplying the bulk of upflowing fluids. A spectrum of combinations for these two end members was also evaluated. TOUGH2 models of these concepts were calibrated to observations at Dixie Valley, NV.

The upflow zone for Concept 1 was modeled as a narrow, vertical conduit (~1 km×200 m) along the fault plane with permeability k = 10^{-14} m^2. Various permeabilities of bulk rock were tested. Models with deep basin (bulk rock) k > 5×10^{-17}m^2 exhibited upflow through the conduit, reaching a thermal peak in 50–300 ka). Deep inflow of cooler water below the basin eventually cools these systems. Models with bulk rock k < 5×10^{-17} m^2 required millions of years to reach maximum thermal outflow, with no apparent falloff of outflow temperature.

Models of Concept 2 maintained the narrow conduit in the fault (10^{-14} m^2), assumed low bulk rock permeability (< 5×10^{-17} m^2), but allowed convection in the entire fault plane (extending 26 km horizontally, k= 10^{-16} m^2). Initial pressure was hydrostatic, with temperature either set by conductive gradient or with the fault plane preheated by earlier circulation of fluids. Results from all of these models show extensive fluid flow along the fault plane to the narrow conduit. Also, cooling of the bulk rock does not occur after a thermal maximum is reached. Models with a preheated fault plane reach higher temperatures much more quickly (100–500 ka).

Concept 1 and Concept 2 models were then tested using k = 10^{-13} m^2 in the fault conduit and 10^{-17} m^2 in the bulk rock. All of these models showed a thermal "pulse" in 500–1500 years. The pre-heated high-permeability conduit model showed significantly higher temperatures than all other models (295°C at 3 km depth).

Bulk rock permeabilities > 5×10^{-17} m^2 at depths >8 km are probably not found in actual B&R systems. B&R geothermal systems also appear transient, reaching temperature maximums in <100 ka, and do not appear to cool the deep basin. Adding the third dimension of fluid flow along a "preheated" fault plane and increasing the permeability of the fault conduit may help to explain the geologic, temporal, and thermal evolutions of these systems.

INTRODUCTION

Non-magmatic B&R geothermal systems present many vexing questions. Most importantly, how does the system achieve very high temperature fluids at relatively shallow depth. Blackwell et al. (2000) reports temperatures in excess of 280°C at 3 km depth in Dixie Valley.

Dating of sinter deposits and springs in Dixie Valley indicate that "episodic" geothermal activity may be temporally related to seismic events (Lutz et al., 2002). These events are relatively recent (<6 ka) with possible associated sinter deposits dating to within a few hundred years of the initiation of these events.

The sources of fluids in these systems is also of interest. Helium isotope studies indicate that a portion (~7.5%) of the helium in these systems is derived from the mantle, and that there is a mixing trend with other meteoric waters (Kennedy and Soest, 2006).

Previous modeling efforts have investigated the effects of topographically driven flow in mountainous terrain (Forster and Smith, 1989), demonstrating that fluid pathways from topographic highs are driven to greater depths than low-relief terrains, with advective heat transport as fluids ascend along fractures. Looking specifically at B&R terrains, McKenna (2004) expanded on this study with a 2D model extending to 8 km depth with upflow along range-bounding faults to look at the effect of rock permeability on transient heating processes. These models reached temperatures close to those observed in Dixie Valley, but required assumptions of bulk rock permeability, and the temporal response of these models are inconsistent with field data. López and Smith (1995, 1996) utilized 3D models (3 km depth) to investigate fluid flow within a fault "plane" in a thermally convective system (as seen in the B&R), demonstrating the effect of anisotropic permeability on flow patterns in the fault plane. Their models did not reach temperatures seen in Dixie Valley geothermal systems.

This study expands on the work done by McKenna, using a 3D model to 12 km depth. The fault geometry contains a narrow vertical "conduit" for fluid flow, along a range-bounding fault "plane." Increasing the permeability along the fault plane is also investigated.

MODEL

A 3D polygonal model consisting of 7740 nodes (and 23,652 connections) was created to represent a typical B&R "block," approximately 40×26×12 km (Fig. 1b). Distribution of litholigies is illustrated in a cross section perpendicular to the fault (Fig. 1a). These lithologies extend the full width of the model along fault strike, except for "fault conduit" and "fault transition."

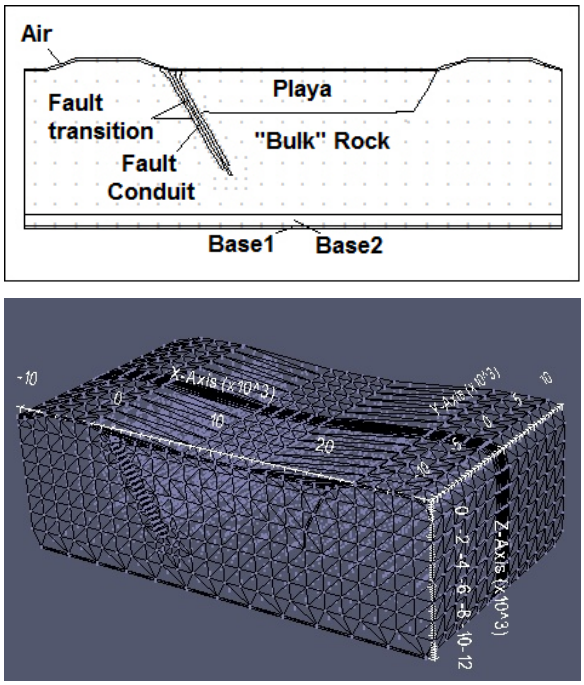

Figure 1. (a) x-z Cross section through the center of the model with rock type blocks noted; (b) 3-dimensional polygonal mesh replicating the x-z section in the y direction.

The fault conduit is 5 cells wide within the fault play, with a single column of cells on either side as a fault transition or "skin" (Figs 2a –b). Rock properties assigned to elements within blocks are shown in Table 1.

Models were run until passing a temperature maximum along the fault conduit. Results for node points located at 3 km depth (equivalent to the deepest observation point at Dixie Valley) and at the bottom of the conduit were monitored for calibration. Fluid transport properties (heat

capacity, expansivity, viscosity) were also monitored to evaluate their role in supporting these surprisingly vigorous B&R geothermal systems.

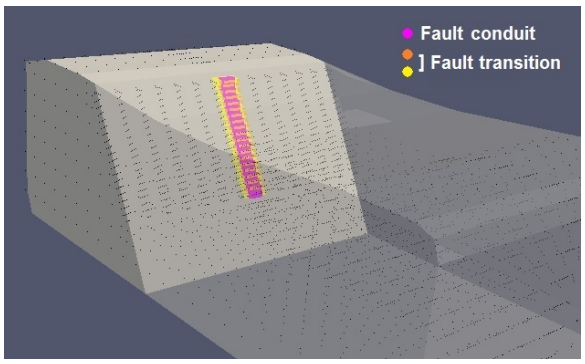

Figure 2a. Fault conduit and transition elements used for Concept 1 models.

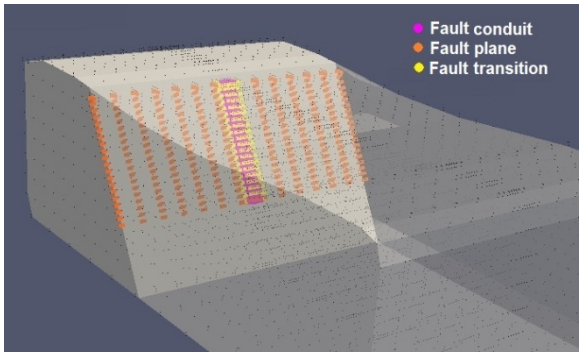

Figure 2b. Fault conduit, transition and fault plane elements used for Concept 2 models.

Table 1. Rock Properties

Block		Permeability	Conductivity ($Wm^{-1}K^{-1}$)
Bulk Rk.	Concept 1	$5 * 10^{-16}$ to $1 * 10^{-17}$ m^2	2.5
	Concept 2	$1 * 10^{-17}$ m^2	2.5
Conduit	Concepts 1 and 2	$1 * 10^{-14}$ m^2 *$1 * 10^{-13}$ m^2*	2.5
Flt. transition		$1 * 10^{-15}$ m^2	2.5
Fault plane (concept 2)		$1 * 10^{-16}$ m^2	2.5
Playa		Horiz.: same as bulk Vert.: $1 * 10^{-19}$ m^2	1.25
Base 1		1 * 10-20 m^2	2.5
Base 2		1 * 10-18 m^2	2.5

RESULTS

Results for Concept 1 models

Figures 3a and 3b are plots of temperatures at 3 km depth and at the bottom of the fault conduit over time for a range of bulk rock permeability.

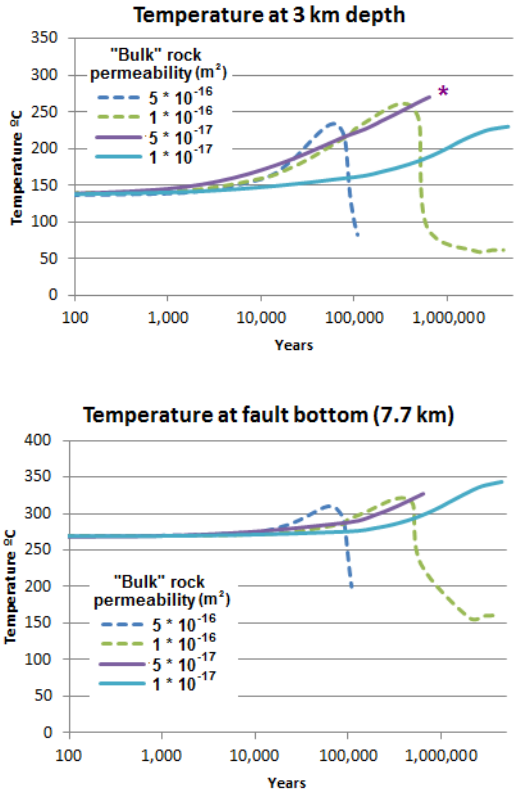

Figures 3a, 3b. Temperatures in fault conduit at (a) 3 km and (b) temperatures at bottom of fault conduit for Concept 1 models. * Flow "bottlenecks" within the fault conduit cause models with bulk rock permeability = $5 * 10^{-17}$ m^2 to slow at ~620 ka.

For bulk permeability of 5×10^{-16} and 1×10^{-16} m^2, a temperature maxima of 234°C and 261°C is reached at 60 ka and 300 ka (respectively) at 3 km depth, after which the entire model block cools due to convection. The progression of this model (Figure 4) is not realistic for actual B&R systems.

Models with bulk permeability 10^{-17} m^2 heat to a temperature "maximum" of 230°C at 4.5 ma (Figure 5), at which point the model reaches steady-state equilibrium and converges. This is also not realistic for B&R systems.

Models with bulk rock permeability of 5×10^{-17} m^2 heat to 270°C in ~620 ka, after which the model computationally slows appreciably because of "bottlenecks" in the flow "into" the fault conduit (from the top of the fault). Because of this, these models were not run past 650 ka.

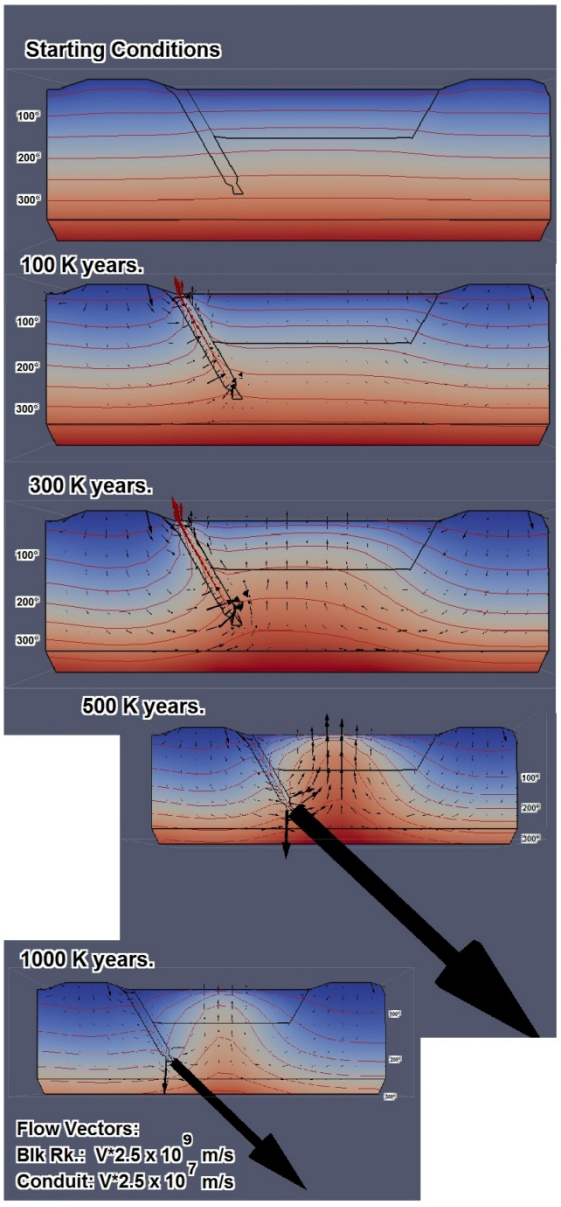

Figure 4. Cross sectional views of Concept 1, 10^{-16} bulk rock permeability model.

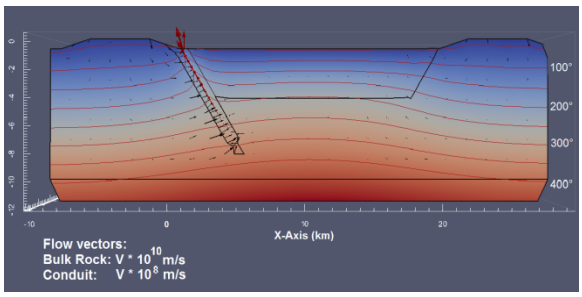

Figure 5. Cross sectional view of Concept 1 - 10^{-17} bulk rock permeability model at 4.5 ma.

In all Concept 1 models, inflow from the top of the conduit becomes a significant source of fluids as the system evolves. (Figure 6 shows this for the bulk rock k = 10^{-17} m^2 model.) While there is little field evidence for such flow, it is a useful indication of the potential importance of inflow along the fault. Concept 2 adds such along-strike inflow to the system.

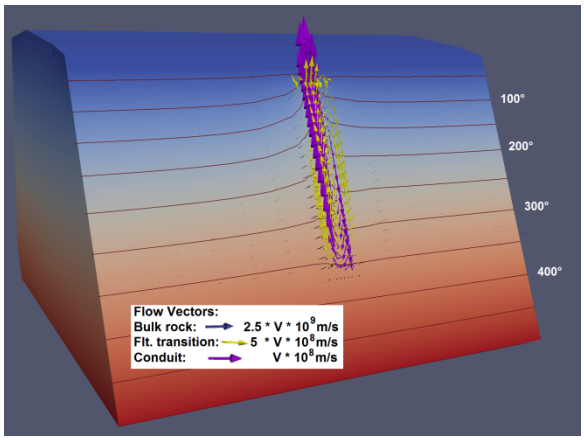

Figure 6. Fault view of Concept 1, 10^{-17} m^2 bulk rock permeability model at 4.5 ma.

Results for Concept 2 models

Figures 7a and 7b are plots of temperatures at 3 km depth and at the bottom of the fault conduit over time for Concept 2 pre-heated and conductive T initial conditions.

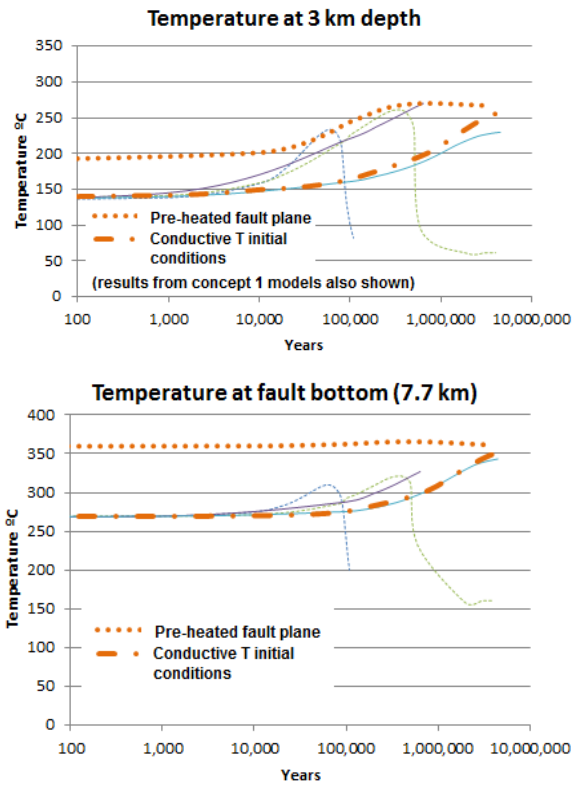

Figures 7a, 7b. a) temperatures in fault conduit at 3 km depth and b) temperatures at bottom of fault conduit for Concept 2 models.

Temperatures at 3 km depth for the pre-heated model approach 270°C after ~400ka (i.e. matching observed temperatures at Dixie Valley). This model was not run beyond 5 ma, but it appears although the fault conduit may cool off over time, the overall system will not.

Temperatures for the non-preheated model may reach similar temperatures as the pre-heated model but take significantly longer than 5ma to do this.

Fault views of Concept 2 models show significant flow from the fault plane to the fault conduit. Over time (too much time for B&R systems), the non-preheated system is very similar to the pre-heated system (Figures 8a, 8b).

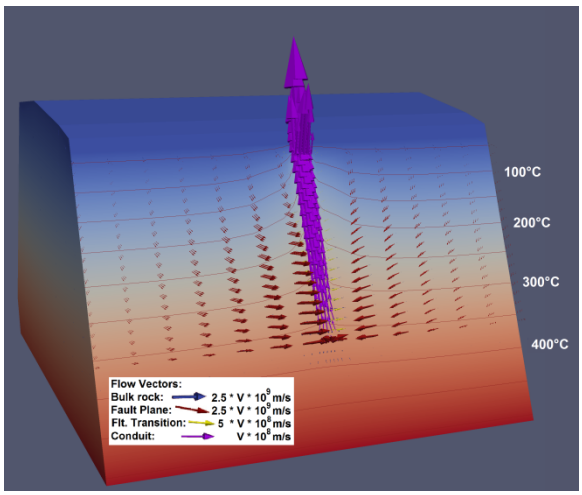

Figure 8a. Fault view of pre-heated concept 2 model at 800 ka.

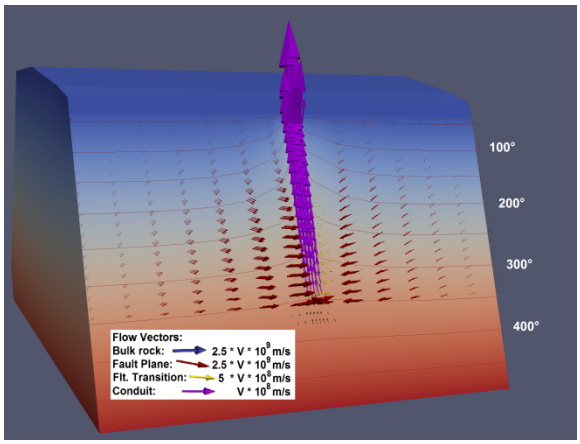

Figure 8b. Fault view of Concept 2 non-preheated (conductive T initial conditions) at 5 ma.

High conduit permeability models.

Figures 9a and 9b are plots of temperatures at 3km depth and at the bottom of the fault conduit over time for a high permeability (k = 10^{-13} m^2) conduit. These models used a bulk rock of k = 10^{-17} m^2. Three models were tested: (1) using Concept 1 configuration (low permeability fault plane outside of conduit); (2) using Concept 2 configuration (w/intermediate k=10^{-16} m^2 fault plane) with conductive T initial conditions; and (3) Concept 2 with pre-heated initial T.

All of these models show a thermal "pulse" by 2 ka (consistent with field evidence from Dixie Valley), but Model 3 results were the most dramatic—reaching a maximum or 295° in 725 years. Figures 10a, 10b, and 10c show the fault view for the maximum temperatures reached by

these models. Note that the flow vectors for the fault conduit (purple) in these views are scaled by 0.1 compared to Figures 6, 8a, and 8b.

.

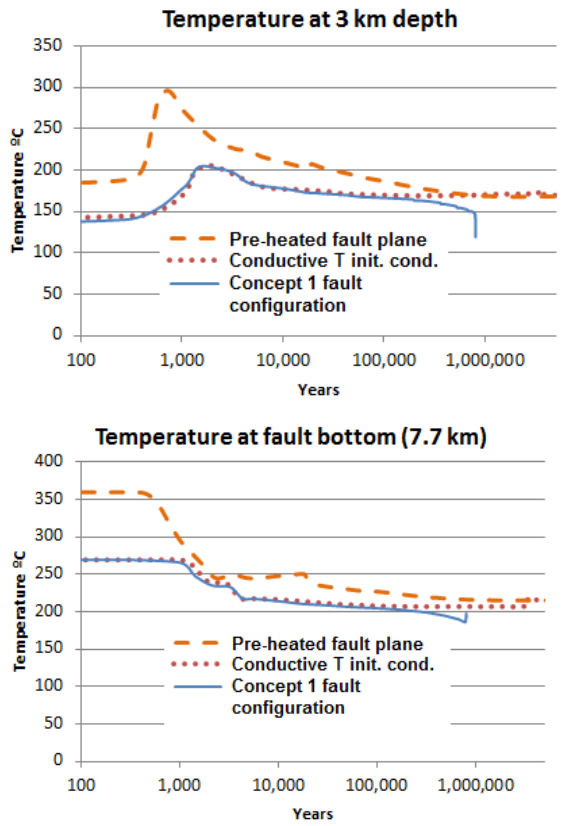

Figures 9. (a) temperatures in fault conduit at 3 km depth; and (b) temperatures at bottom of fault conduit for conduit k=10^{-13}m^2 models.

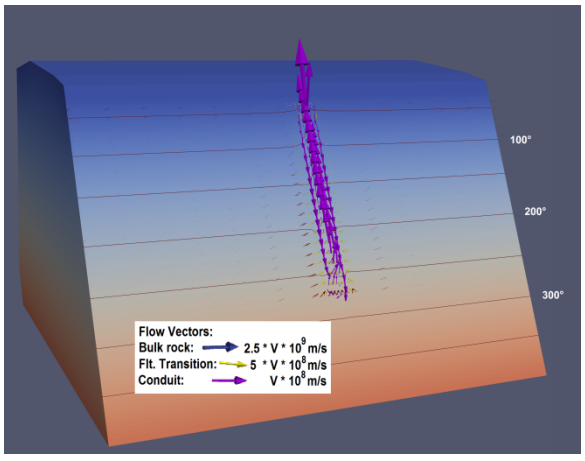

Figure 10a. Fault view of high permeability conduit Model 1 (no intermediate fault plane permeability) at 2 ka.

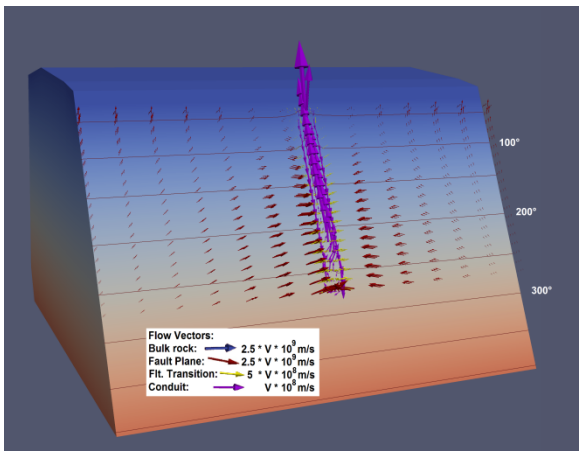

Figure 10b. Fault view of high permeability conduit Model 2 (fault plane k = 10^{-16} m^2, conductive T initial conditions) at 1.5 ka.

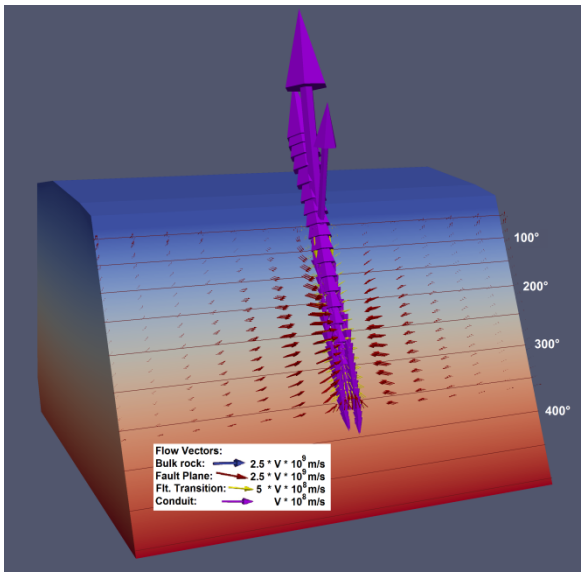

Figure 10c. Fault view of high permeability conduit Model 3 (fault plane k = 10^{-16} m^2, pre-heated initial conditions) at 725 yr.

The extreme thermal pulse seen in Model 3 may be enhanced by fluid properties (e.g., buoyancy and heat capacity) that significantly increase as temperature and pressure approach the "critical" point water. Figures 11a and 11b show the temperature and heat capacity of upflowing fluids in the fault conduit. The equation of state, EOS1sc, used for these models accurately models these properties (Brikowski, 2001).

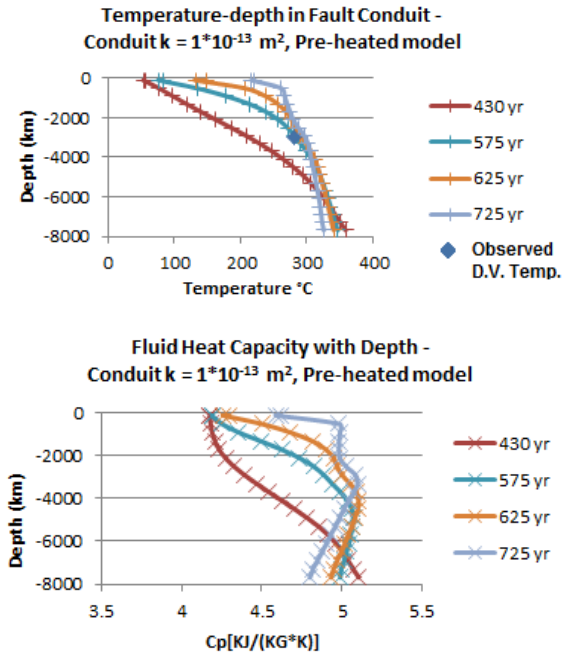

Figures 11a, 11b. Temperature and fluid heat capacity with depth in center of fault conduit for high permeability conduit—Model 3 (pre-heated with intermediate fault plane).

DISCUSSION AND CONCLUSION

Results from Concept 1 models are quite similar to those of McKenna (2004), at least for high permeability (> 5×10^{-17} m^2) models. In these systems, a transient thermal "high" is seen at 50–300 ka, and the entire system eventually cools due to convection (or perhaps due to downflow of cool fluids in the fault conduit). For systems with k < 5×10^{-17} m^2, they reach steady-state thermal equilibrium.

The problem with these models is that deep rock permeability >5×10^{-17} m^2 seems unrealistic, considering lithostatic stress at several-kilometer depths, as does the cooling of the model over time. Systems with k < 5×10^{-17} m^2 did not allow sufficient convective heat flow to match temperatures seen in Dixie Valley.

Results of Concept 2 models are a somewhat better match to observations, and do not require uncomfortably high permeability at depth to do this. In addition, the temporal response (at least for the pre-heated model) may be more realistic.

High permeability (k = 10^{-13} m^2) conduit models with moderate along-strike inflow, particularly when preheated, provide the most satisfactory match with current conditions and geologic evidence (temporal correlation of sinter and seismic events) at Dixie Valley. All of the high permeability conduit models show a thermal "pulse" within 2000 years of opening up the fault conduit. This may help explain the origin of these geothermal features in these systems. Enhanced flow from fluid properties of water approaching the critical point is also beginning to occur in Model 3.

Understanding geothermal systems in the B&R province probably involves a combination of several factors. Quasi-3D flow (diffuse recharge into elongated fault zone), "pre-heating" of the fault zone, and enhanced heat transport under semi-optimal fluid conditions may all play a role in the development of these systems.

REFERENCES

Blackwell DD, B. Golan, and D. Benoit, Temperatures in the Dixie Valley, Nevada geothermal system. Geotherm. Resour. Council Trans. 24, 223-8, 2000.

Brikowski TH., Modeling supercritical systems with TOUGH2; the EOS1sc equation of state module and a Basin and Range example. Geotherm. Resour. Council Trans. 2, 285-9, 2001.

Forster C. and Smith L., The influence of groundwater flow on thermal regimes in mountainous terrain: A model study. J Geophys Res 94:9439-51, 1989.

Kennedy, BM, and M.C. van Soest, A helium isotope perspective on the Dixie Valley, Nevada, hydrothermal system. Geothermics 35(1):26-43, 2006.

Lopez, D.L., L. Smith, Fluid flow in fault zones: analysis of the interplay of convective circulation and topographically driven groundwater flow. Water Resour. Res. 31, 1489-1503, 1995.

Lopez, D.L., L. Smith, Fluid flow in fault zones: influence of hydraulic anisotropy and heterogeneity on the fluid flow and heat transfer regime. Water Resour. Res. 32, 3227-3235, 1996.

Lutz SJ, S.J. Caskey, D.D. Mildenhall, P.R.L. Brown, S.D. Johnson. Dating sinter deposits in northern Dixie Valley, Nevada - the paleoseismic record and implications for the Dixie Valley geothermal system. Proceedings, Twenty-Seventh Workshop on Geothermal Reservoir Engineering, 284-297, 2002.

McKenna JR and Blackwell DD., Numerical modeling of transient Basin and Range extensional geothermal systems. Geothermics 33(4):457-76, 2004.

Pruess, K., C. Oldenburg, and G. Moridis, *TOUGH2 User's Guide, Version 2.0*, Report LBNL-43134, Lawrence Berkeley National Laboratory, Berkeley, Calif., 1999.

IMPROVED VISUALIZATION OF RESERVOIR SIMULATIONS: GEOLOGICAL AND FLUID FLOW MODELING OF A HIGH-TEMPERATURE GEOTHERMAL FIELD IN NEW ZEALAND

Sophie C. P. Pearson and Angela Prieto

GNS Science
Wairakei Research Centre, 114 Karetoto Rd
Taupo 3384, New Zealand
e-mail: s.pearson@gns.cri.nz

ABSTRACT

Geothermal energy has been used for electricity production in New Zealand for decades. Our study area, a high-temperature geothermal field in the center of the North Island of New Zealand, has been developed for electricity for over ten years. Previous models have tried to replicate the field, but some unexplained complexity has remained. By creating a Leapfrog Geothermal geological model and incorporating it into a TOUGH2 reservoir model, a detailed simulation of the system can be created that represents more realistic geology. Outputs from the TOUGH2 model can then be read back into Leapfrog Geothermal, facilitating direct comparison between measured and modeled temperatures, and highlighting regions that need to be better modeled.

The geological model of our study area incorporates 20 volcanic units, interpreted from topographic data, surface feature locations, regional and local geological maps, stratigraphic interpretations from geothermal drill hole data, and regional 3D geological models. There are a number of faults trending N, NE, and NW. Although this level of detail cannot be replicated directly in a TOUGH2 model, or is necessary given the sparsity of data, starting from a more realistic geological model will improve the TOUGH2 model and allow future study of the effects of geology, for example including distinct, discrete rhyolitic domes.

Integrating Leapfrog Geothermal and TOUGH2 software creates a useful tool in reservoir simulation, facilitating model calibration and allowing reservoir models to be more easily disseminated to a much wider audience.

INTRODUCTION

Numerical models of geothermal fields in New Zealand are industry standard for assessing energy potential, constraining upflow zones, and satisfying resource consent requirements (O'Sullivan, Pruess and Lippmann 2001). Numerical simulations using specialized software like TOUGH2 (Pruess 1991) provide significant information, but are limited by a lack of good visualization tools that would make the models easier to understand and disseminate to a wider audience. By combining TOUGH2 software with 3D modeling software like Leapfrog Geothermal, inputs can be more easily visualized, and outputs can be compared with both the original model and any other datasets like well temperature, lithology or surface features. This helps to create more accurate models and to vastly improve the way that model results can be visualized and shared.

Geothermal areas are located throughout New Zealand (Figure 1), providing approximately 13% of electricity generation and up to 19% of total primary energy (Statistics New Zealand 2012). Geothermal fields are, therefore, an important energy source for the country. High temperature fields that produce electricity are concentrated in the Taupo Volcanic Zone (TVZ), which runs up the center of the North Island (Figure 1). Eight of these 29 fields, including our study area (Figure 2), are used for energy production.

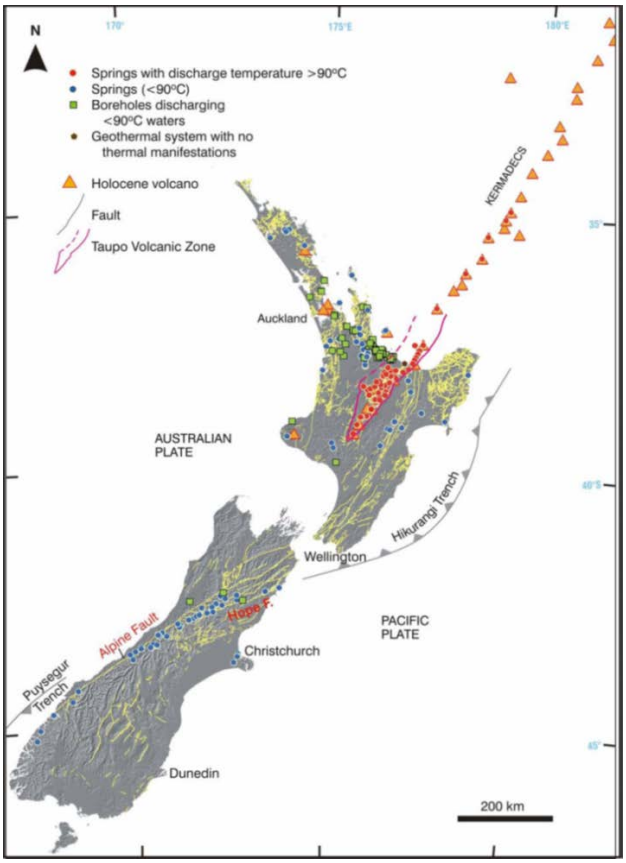

Figure 1. Distribution of geothermal features in New Zealand. High-temperature geothermal fields are concentrated in the Taupo Volcanic Zone.

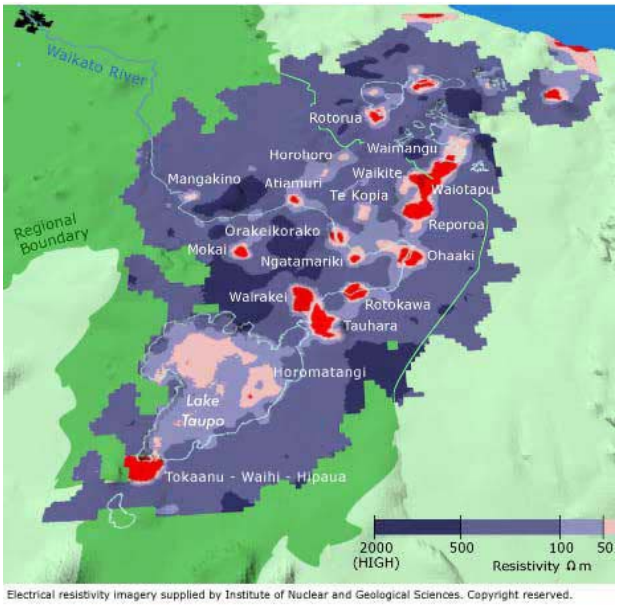

Figure 2. Geothermal fields in the Taupo Volcanic Zone (see Figure 1) as delineated by resistivity. The exact location of the field is not identified for confidentiality reasons.

Our study area is located in the center of the North Island of New Zealand. It was first explored over 20 years ago and has some of the hottest recorded downhole temperatures in the country (New Zealand Geothermal Association 2009). Due to the relatively few scenic areas and the complete lack of unusual, fragile, or unique features, it was deemed fit for development, and a power station has now been operating for several years. There are some complexities to the field that have proved difficult to replicate in numerical models, and geophysical data has also been collected that is not routinely included. In this study, therefore, we create a Leapfrog Geothermal geological model of the field and export this into TOUGH2 to create as accurate a model as possible. We also set up the model so that future work can easily incorporate calibration with traditional data like well temperatures, and other geophysical parameters, like microgravity.

GEOLOGY

Geologic Setting

The Taupo Volcanic Zone (TVZ) is uniquely situated above the oblique subduction of the Pacific plate beneath the Australian plate (Cole and Spinks 2009). Because of the obliquity, the TVZ is extending at about 8 mm/yr to the NW-SE (Darby, Hodgkinson and Blick 2000), with a thin, rifted crust, and is the most active rhyolitic system on Earth (Houghton, et al. 1995). Our field comprises more than 20 volcanic units overlain by some sparse sediments (Figure 3). The volcanic units are primarily Pleistocene and Holocene volcanoclastic rocks. The area is quite strongly faulted, with three dominant trends to the NE, N and NW (Soengkono 2011).

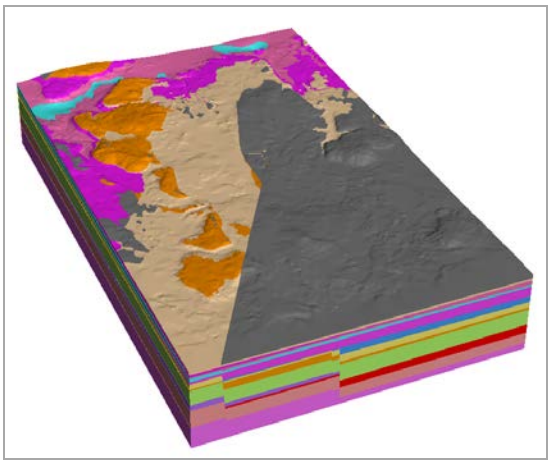

Figure 3. Geological model of our study area. Grey represents sediments, all other colours are volcanic units.

Leapfrog Geothermal

Leapfrog Geothermal is a 3D modeling and visualization software package developed by ARANZ Geo (Christchurch, New Zealand), with input from GNS Science (Wairakei, New Zealand), University of Auckland (Auckland, New Zealand), and Contact Energy Ltd (Wairakei, New Zealand). It is an integrated interface that allows the development of conceptual and quantitative geological models (Alcaraz, et al. 2012). It incorporates lithology, structure, faulting and well data, as well as allowing geophysical and other information to be saved within the well data information.

As well as creating detailed geological models, it allows surfaces to be exported in a number of formats, including x,y,z, so that they can be imported into other software for further calculations like heat and fluid flow models. As data can also be imported directly from TOUGH2 (Newson, et al. 2012) or as x,y,z,T (for example), TOUGH2 model outputs can then be plotted against the geological model, allowing measured well temperatures, isotherms interpreted from the well temperatures, and isotherms from the reservoir model to be compared directly. This not only makes the outputs easier for a non-modeler to understand, but allows much easier and more direct comparisons for improving the fluid flow models.

Geological Model

The 3D geological model of our study area was built incorporating topographic data, surface feature locations, regional and local geological maps, stratigraphic interpretations from geothermal drill-hole data, and regional 3D geological models. It extends to 2600 m depth, the depth of the deepest well. It comprises a number of layers, with thick sections of ignimbrites filling the active basin to the SE, intercalated with rhyolite domes and lavas (Figure 4). There is no local evidence of the deep greywacke basement found in other geothermal fields of the region. The model includes a number of high-angle normal faults dipping to the SE that correspond to the western side of the Taupo Rift (Figure 5).

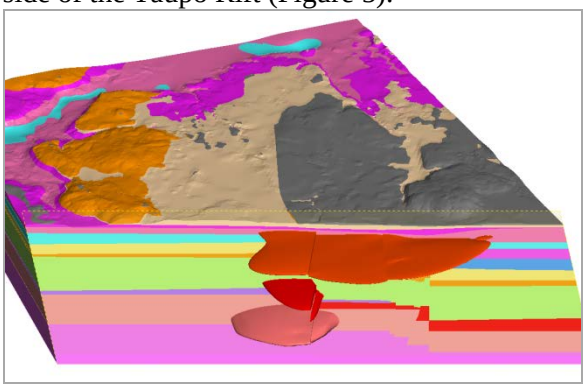

Figure 4. Geological model showing sediments (grey), rhyolitic domes (red) and other volcanic units including ignimbites, breccias and rhyolites (all other colours).

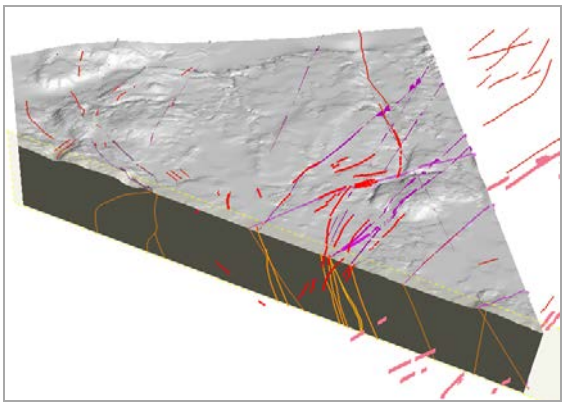

Figure 5. Faults active in the area.

RESERVOIR MODEL

From the geological model and a number of other constraints, a heat and fluid flow model can be created that allows the extent and energy of the system to be determined, as well as the

effects of extracting energy. The Leapfrog Geothermal software and TOUGH2 will be used to create a numerical model of this system.

TOUGH2-Leapfrog Interface

The most recent update to Leapfrog Geothermal interfaces with TOUGH2 files directly to facilitate visualizing inputs and results of the model. It works with traditional TOUGH2 from Lawrence Berkeley National Lab (Pruess 1991) or with AUTOUGH2 from University of Auckland, New Zealand (O'Sullivan 2000). It can also be used to create and populate the grid, and the resulting model is exported to run with TOUGH2. The TOUGH2 output file can then be imported back into Leapfrog to view results and compare them with input data and any relevant local measurements. Leapfrog enables easy visualization of model temperatures or pressures—for example, allowing isotherms to be modeled, cross sections or slices of data to be plotted, and viewing angles to be changed easily (Figure 6). Future discussion may also include time-varying plots.

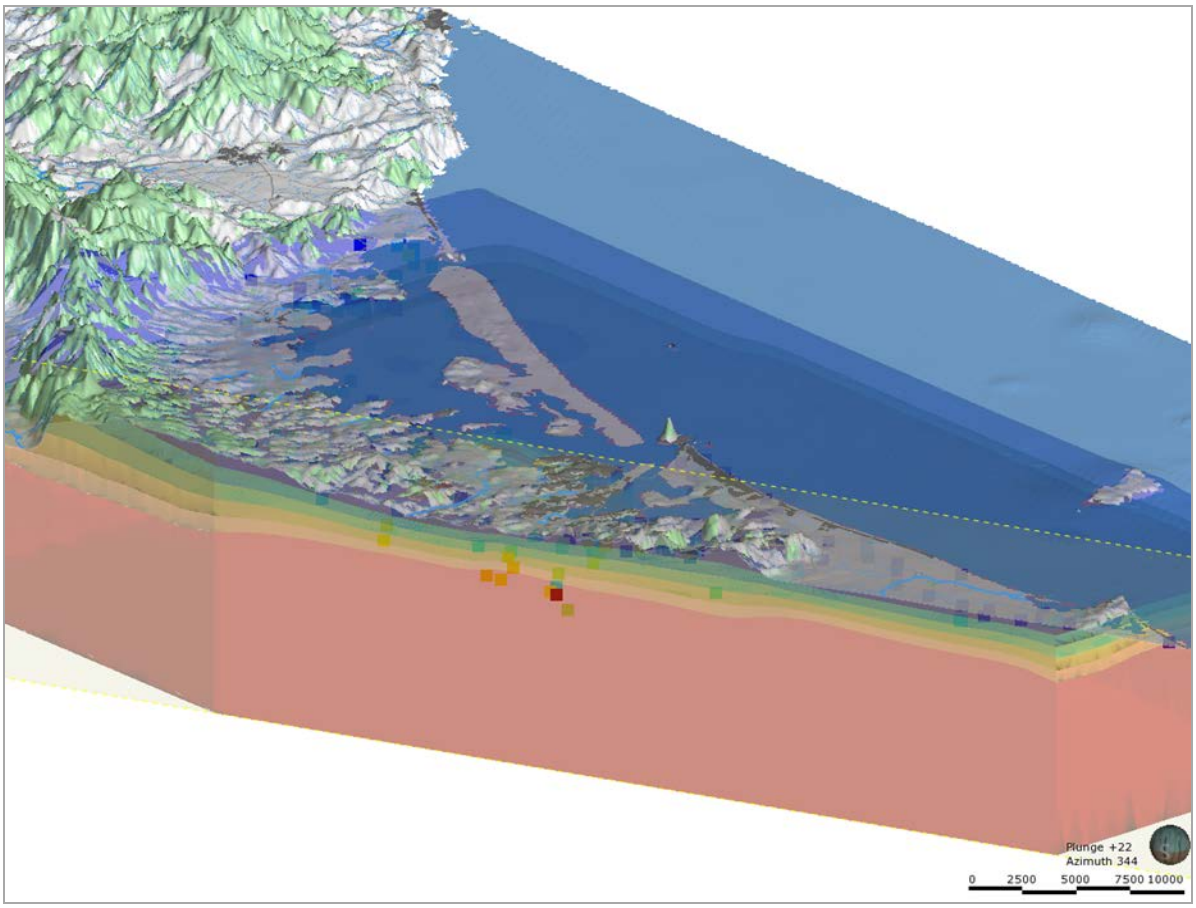

Figure 6. Example of a Leapfrog Geothermal plot of TOUGH2 output temperatures (solid isotherms) compared to measured well temperature data (solid squares) from the Tauranga geothermal field, New Zealand.

FUTURE WORK

Future work will be to create the complete TOUGH2 model from the Leapfrog Geothermal geological model, and to populate it with relevant parameters. The model will be run and calibrated against measured data like well temperatures (both with depth and time). The goal is to use iTOUGH2 to find the best-fit model, and then to further refine it based on microgravity data collected in the region over the last several years.

CONCLUSIONS

Combining Leapfrog Geothermal with a TOUGH2-Petrasim model facilitates the creation of a more realistic model, visualization of model outputs, and comparison of model outputs directly with well data. This not only makes the modeling process easier, but also helps when disseminating TOUGH2 models to a non-specialist audience. Our study area provides a perfect case study, as there are a number of wells with temperature measurements down to kilometers depth collected over a period of years. Microgravity data in the area also provides an ideal opportunity to further calibrate the model, hopefully creating a model that can replicate the available data and provide a realistic simulation of the geothermal field, so that the field can be used sustainably and optimally for the foreseeable future.

REFERENCES

Alcaraz, S. A., S. Rattenbury, S. Soengkono, G. Bignall, and R. Lane. "A 3D multi-disciplinary interpretation of the basement of the Taupo Volcanic Zone." *Proceedings, Thirty-Seventh Workshop on Geothermal Reservoir Engineering, Stanford University.* Stanford, California, 2012.

Cole, J. W., and K. D. Spinks. "Caldera volcanism and rift structure in the Taupo Volcanic Zone, New Zealand." *Geological Society, London, Special Publications* (Geological Society, London, Special Publications), 2009: 9-29.

Darby, D. J., K. M. Hodgkinson, and G. H. Blick. "Geodetic measurement of deformation in the Taupo Volcanic Zone, New Zealand: The north Taupo network revisited." *New Zealand Journal of Geology and Geophysics* 43 (2000): 157-170.

Houghton, B. F., et al. "Chronology and dynamics of a large silicic magmatic system: Central Taupo Volcanic Zone, New Zealand." *Geology* 23, no. 1 (1995): 13-16.

New Zealand Geothermal Association. *New Zealand Geothermal Fields.* 2009. http://www.nzgeothermal.org.nz/nz_geo_fields.html (accessed July 19, 2012).

Newson, J., et al. "Application of 3D modelling and visualization software to reservoir simulation: Leapfrog Geothermal and TOUGH2." *Proceedings, Thirty-Seventh Workshop on Geothermal Reservoir Engineering, Stanford University.* Stanford, California, 2012.

O'Sullivan, M. J. *AUTOUGH2 Notes.* Department of Engineering Science, University of Auckland, 2000.

O'Sullivan, M. J., K. Pruess, and M. J. Lippmann. "State of the art of geothermal reservoir simulation." *Geothermics,* 2001: 395-429.

Pruess, K. *TOUGH2 - A general purpose numerical simulator for multiphase fluid and heat flow.* Berkeley, CA: Lawrence Berkeley Laboratory, 1991.

Soengkono, S. "Deep interpretation of gravity and airborne magnetic data of the central Taupo Volcanic Zone." *Proceedings 33rd New Zealand Geothermal Workshop.* Auckland, New Zealand, 2011.

Statistics New Zealand. *Estimated Subnational Population (TA,AU) by Age and Sex at 30 June 2006–11 (2011 boundaries).* January 12, 2012. http://www.stats.govt.nz/tools_and_services/tools/TableBuilder/intercensal-population-estimates-tables.aspx (accessed January 12, 2012).

BASIN-SCALE GEOTHERMAL MODEL CALIBRATION USING ITOUGH2

Lynn B. Reid[1,2,3], J. Florian Wellmann[2]

[1]NTEC Environmental Technology, Subiaco WA 6008 Australia
[2]CSIRO Earth Science and Resource Engineering, Kensington WA 6151 Australia
[3]School of Environmental System Engineering, Uni. Western Australia, Crawley WA 6009 Australia
lynn.reid@uwa.edu.au

ABSTRACT

We showcase how the application of parameter-estimation and sensitivity-study methods implemented in iTOUGH2 improved model calibration to measured data and provided insight into model uncertainties and data outliers. The methodology was applied to a basin-scale conductive heat model of temperature in the Perth Basin, Western Australia.

MOTIVATION AND INTRODUCTION

Geothermal resource estimations require a trade-off between conceptualizing the complicated geological system with a finite numerical representation, and estimating these model parameters from scarce data. There is often a high degree of uncertainty about the heat flow parameters used in the simulation, especially for large-scale systems with poorly detailed boundary conditions (see, e.g., Kohl, 2003).

A suitable input parameter set may be estimated by first performing a forward simulation of temperatures, and second by comparing simulated to measured values in wells. A common approach is to simply compare values by "eyeballing", for example by plotting simulated next to measured values along a temperature log (Saibi, 2011), or by comparing a sum of simulated mismatch across all data points (Reid et al., 2012a). The input parameters are then adjusted by trial-and-error until a reasonable fit is obtained. Although this method seems to be very "ad-hoc," it is usually possible to obtain acceptable results with a reasonable amount of manual calibration steps. For purely conductive geothermal models, this approach may be adequate, as the forward simulation is approximately linear in its response to the parameters and the sensitivities of the single model parameters can be reasonably well determined.

This simple manual calibration method can be automated with several more sophisticated model calibration methods. The advantages of automatic calibration are a requirement to mathematically define what constitutes a "good" fit, systematic analysis of the sensitivity of the computational model to both the parameters and the calibration data, an indication of the adequacy of the conceptual model, and calibrated parameters which hopefully provide an adequate fit to measurements—of course all at the expense of computational complexity. We do not claim that automatic calibration methods produce a "true" or unique model (Moore and Doherty, 2005), but the approach, when applied carefully, will produce a well-considered model.

In this work we apply the iTOUGH2 program (Finsterle, 1999) to automatically calibrate a complex geothermal model using the PEST protocol (Finsterle and Zhang, 2011). The conductive forward simulations are performed in SHEMAT (Clauser and Bartels, 2003), as multi-phase flow is not considered at this stage. We utilize the stand-alone capabilities of iTOUGH2 to estimate thermal rock parameters and boundary conditions. Our aim is to produce a simplified basin-scale model to act as a basis for future detailed reservoir-scale simulations representing more complex physical heat transport mechanisms, such as convection and groundwater advection.

GEOTHERMAL MODELING PROJECT

We developed three-dimensional models of the geology and the conductive temperature regime of the entire Perth Basin in Western Australia, with an extent of nearly 800 km from north to south and 150 km east to west. The enormous physical scale required many simplifications to integrate the three-dimensional geological model and discrete geothermal simulation.

The geological model is based on an amalgamation of data from petroleum exploration wells, existing geological studies, and new fault interpretations. Full details are provided in Reid et al. (2012a, 2012b). The model covers an area of over 100,000 km^2 and extends to a depth of 120 km. The stratigraphic column includes twelve sedimentary units. Because of the large latitudinal extent of the Basin and computational limitations, the model was developed in three overlapping regions representing the South, Central, and North Perth Basins.

The geological model is discretized into a deep model down to 120 km, below the Mohorovičić discontinuity, and a shallow model down to 16 km [Figure **1**]. The deep model provides the lower boundary condition of vertical heat flux to the shallow model, which has a finer resolution and contains the sedimentary geologic units. Horizontal mesh resolution is 500 × 500 m, and vertical resolution is 25 m at the surface and 1 km at the base, leading to a total of approximately 50 million cells. Mean annual surface temperature determined from remote sensing data (Horowitz, 2009) is applied as an upper boundary condition. Regional studies and local measurements provide initial estimates of thermal properties as detailed below. The steady-state conductive temperature distribution with these properties and boundary conditions was calculated using SHEMAT.

PARAMETER IDENTIFICATION

When building the geologic model, we intentionally kept the number of rock formations as small as possible while still adequately representing the thermal regime at measured depths. Because the Perth Basin has a depth of up to 16 km, the deeper formations are poorly constrained geometrically and petrophysically. However, in the central part of the Basin near the city of Perth, previous research had developed a sophisticated geologic model with considerable detail in the shallow sedimentary layers (Reid et al., 2012b). Geothermal measurements suggest that heat moves in the Perth Basin via simple conduction, but also via nonlinear physical processes such as groundwater advection and density-driven convection (Sheldon et al. 2012b). Nonetheless, our initial modeling efforts focus only on steady-state heat conduction, due to the difficulty in identifying hydrogeologic boundary conditions at the basin scale, and the lack of transient temperature measurements.

For steady-state heat conduction, only three rock properties are relevant: radiogenic heat production, thermal conductivity, and porosity. SHEMAT requires radiogenic heat production rates and thermal conductivity to be expressed as pure rock properties, which can be derived from bulk matrix values by correcting with porosity. Manually calibrated estimates of these rock properties for the 12 stratigraphic units are provided in Table **1**. The values were derived from specific studies within the Perth Basin and Australia, and in some cases from worldwide representative ranges; further discussion is provided in Reid et al. (2012a).

Additional boundary condition parameters to the model were the upward basal heat flux at 55 km in depth. Again, a parsimonious model was assumed, with basal heat flux described by a planar function that varied only in the north-south direction along the basin axis.

CALIBRATION DATA SET

Few meaningful measurements of heat transport properties were available within the range of the basin. However, more than 130 point temperature observations exist in the area. Temperature measurements in the Perth Basin are available from deep petroleum exploration wells, usually from bottomhole temperature (BHT) measurements or from drill stem tests (DST). Observations are acquired shortly after the well is drilled, due to equipment logistics and costs. The well measurements do not exhibit consistent reliability and can often underestimate temperature by 15% (Ricard et al., 2012). Several reliability classifications exist that take into account the type of measurements and reservoir conditions. We selected 135 high reliability temperature measurements from 97 wells across the whole Perth Basin. The spatial coverage of the measurements varies considerably. While 114 high-quality measurements are available in the North Perth Basin, only 5 are available in the South Perth

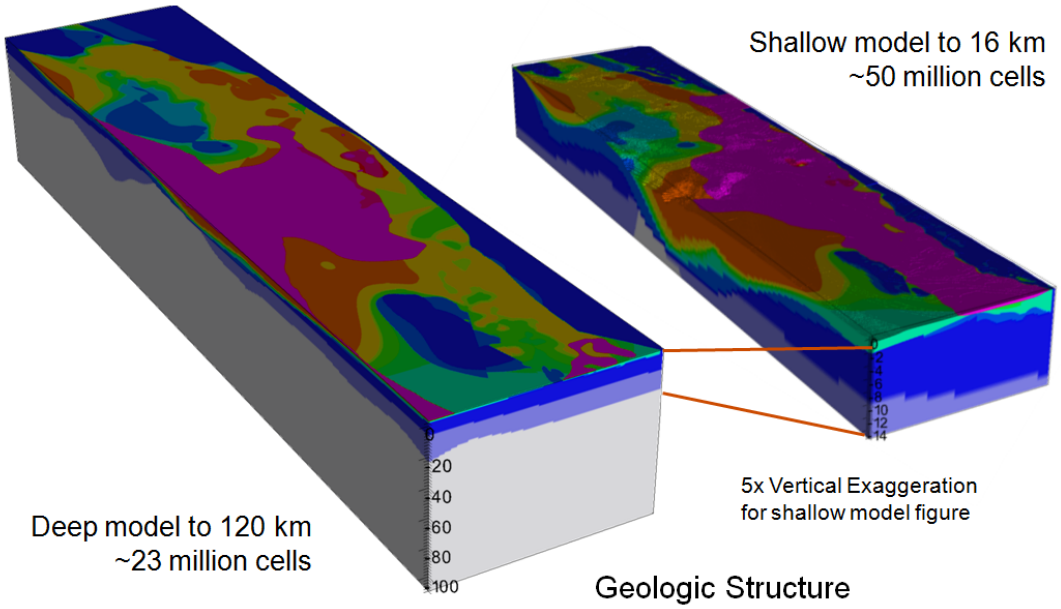

Figure 1. Deep and shallow geologic models, showing extent of formations

Table 1. Initial manual and final automatic calibrated parameter values. The upper crust radiogenic heat production was initially 2.4×10^{-6}; the final calibrated 2.2×10^{-6} μW m^{-3}

Formation	Porosity (-)	Radiogenic heat production (μW m^{-3})	Manual Calibrated Thermal Conductivity (W m^{-1} K^{-1})	Automatic Calibrated Thermal Conductivity (W m^{-1} K^{-1})
Mantle	0.01	0.0	4.0	N/A
Lower Crust	0.01	1.5 x 10^{-7}	3.2	N/A
Upper Crust - Basement	0.01	See legend	2.7	3.0
Sue Group (Permian)	0.05	4.0 x 10^{-7}	3.1	2.6
Kockatea Shale	0.12	1.2 x 10^{-6}	1.5	1.3
Late Triassic Formations	0.05	5.0 x 10^{-7}	4.3	N/A
Lesueur Formation	0.09	5.0 x 10^{-7}	3.8	4.2
Eneabba Formation	0.06	5.0 x 10^{-7}	3.6	3.4
Cattamarra Coal Measures	0.10	4.5 x 10-7	4.1	2.3
Yarragadee Formation	0.20	5.0 x 10^{-7}	4.3	4.9
Parmelia Formation	0.20	5.0 x 10^{-7}	3.1	N/A
Gage Sandstone	0.10	5.0 x 10^{-7}	3.9	N/A
South Perth Shale	0.10	8.0 x 10-7	1.5	N/A
Leederville Formation	0.30	6.0 x 10^{-7}	3.4	N/A
Superficial Formation	0.30	6.0 x 10^{-7}	3.4	N/A

Basin and 16 in the Central Perth Basin. No temperature measurements were available outside the Perth Basin sedimentary rocks, e.g., in the eastern Yilgarn Craton. All the measurements are located at depths less than 4.8 km, with the majority at economic petroleum exploration depths between 1.5 and 3.5 km.

These measurements were corrected to provide true formation temperature estimates, which are always higher than the initial measurements. More importantly, uncertainty on the correction was also calculated, which depended upon the measurement technique, number of samples, and the depth of measurement (Richard et al., 2012). Over the 135 measurements, the average measurement error was 5°C. A full table of the measurements, the corrected true formation temperature, and the standard deviation of the measurement error is provided in Reid et al. (2012a). Our aim in the calibration was to reproduce these temperature measurements by simulation, within the limits of measurement uncertainty.

MANUAL CALIBRATION

The model was calibrated in two stages: first via manual calibration and then by the automatic technique described below. In the initial calibration procedure, thermal conductivity, radiogenic heat production rate (HPR) of the upper crust, and deep basal heat flux were altered to better match the measured temperatures. Porosity and HPR in shallower sediments were fixed at initial estimates, due to their limited effect on the model output. The simulated temperature was obtained at the measurement location through trilinear interpolation from the surrounding model node values. Subtracting the simulated from the measured temperature produced a temperature residual at each well, which is then considered in conjunction with the estimated measurement error. Simulated temperatures were considered "very good" if they fell within one standard deviation of the corrected BHT, and "good" if within two standard deviations. Two additional measures of goodness-of-fit were provided by (1) the average temperature error in the model domain and (2) a squared residual weighted by the measurement error.

The simulated temperature and residual difference from the true formation temperature from the manual calibration are shown in Reid et al. (2012a). Mean residual was -5.3°C, showing that the manual calibration systematically underestimated the temperature. The standard deviation of the residuals was 12.8°C, which also demonstrated that the manual calibration did not reproduce all measurements within a 95% measurement error confidence. Only 24% of simulated measurements were very good and lay within one standard deviation of TFT, and 45% were reproduced within two standard deviations. Initial sensitivity runs during manual calibration suggested that the most important parameters for calibration were the basal heat flux at 120 km and the radiogenic heat production value of the upper crust.

Based on the poor performance of the manual calibration, automatic calibration was begun using iTOUGH2. We used iTOUGH2 as the parameter estimation engine, controlling the SHEMAT simulations through the recently developed PEST interface (Finsterle and Zhang, 2011).

SENSITIVITY OF PARAMETERS

The first step in the calibration was a sensitivity study performed with iTOUGH2, to determine whether all parameters could be identified from the scattered measurements. We performed the study using the least-square goodness-of-fit objective function, where temperature measurements are weighted by the measurement errors derived above. Because of the relatively shallow distribution of measurements, and because conductive heat diffuses upwards, we presumed that identification of the deeper formation properties would be difficult due to auto-correlation. However, the shallow formations do not influence results in the northern and southern sub-basins due to the limited detail in those areas.

Figure **2** confirms our physical intuition: the two major sources of heat in the conductive model (basal heat flux and radiogenic heat production in the upper crust) were among the most sensitive parameters. In addition, the thermal conductivity of the Yarragadee Formation was also quite important to the value of the objective function.

We decided to estimate only those parameters that cumulatively contributed up to 95% of the

total sensitivity of the objective function. We therefore were faced with estimating two parameters for the basal heat flux, the radiogenic heat production rate (HPR) rate of the upper crust, and eight thermal conductivity values. The most sensitive thermal conductivities were found in the deeper sedimentary layers, which had the most volume in the conductive model.

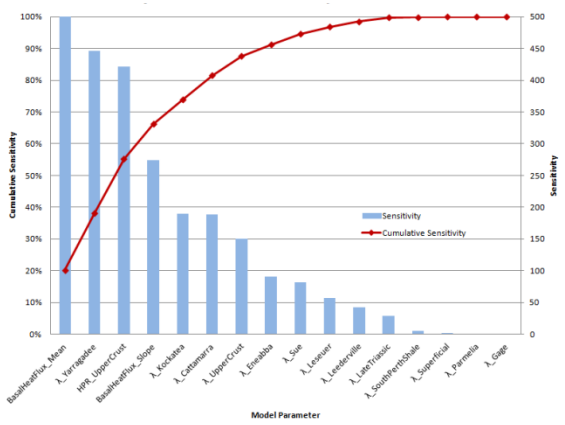

Figure 2. Sensitivity of the least-squares objective function to formation thermal conductivity [λ], radiogenic heat production [HPR] of the upper crust, and basal heat flux mean and slope.

The contribution of individual data points to simulated output is shown in Figure **3**. No evidence of bias to any of the sub-basins is shown, although the iTOUGH2 analysis did show that wells in the north sub-basin were five times as important as those in the central and south. The importance of the basal heat flux and HPR parameters are clear in this chart as well. Because there were only 15 parameters to estimate and 135 data points to provide information, sophisticated analyses such as eigenvalue grouping or singular value decomposition were not utilized in the estimation procedure.

AUTOMATIC CALIBRATION

Basal Heat Flux

Unfortunately, the parameters for the basal heat flux and the HPR of the upper crust were highly correlated to each other. It was impossible to distinguish between the two while performing automatic calibration. Therefore, we took the pragmatic approach of first estimating the basal heat flux of the combined deep and shallow models, while leaving all other parameters fixed at their prior, manual calibration values. Parameter estimation was performed in iTOUGH2 using a least squares Levenberg-Marquardt estimator. The procedure estimated a basal heat flux varying between 20 mW m^{-2} at the southern limit and 32 mW m^{-2} in the northern extent of the model. This decision allowed us to perform future calibrations with only the shallow model: the deep and shallow models are coupled only through the basal heat flux at this stage in the calibration. Forward-simulation running times were reduced by half.

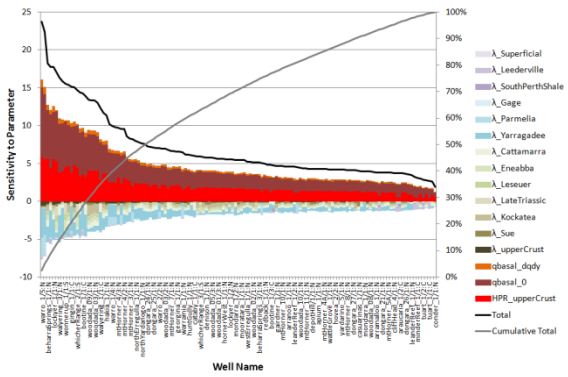

Figure 3. Sensitivity matrix plotted by wells and formation. Sub-basin is appended as a suffix to well name.

Thermal Conductivity and HPR

Least Squares Estimator

Next, we performed parameter estimations of the eight thermal conductivities and the upper crust HPR, again using a least-squares Levenberg-Marquardt estimator. To stabilize the inversion, we used the prior weighting capabilities of iTOUGH2. The manual calibration parameter was treated as a prior value. Upper and lower bounds for the parameters were determined by inspecting detailed core measurements and by comparing analogous formations worldwide (see Reid et al., 2012a, for references). Once the permissible parameter range was fixed, a standard deviation for the parameter was calculated by assuming a normal distribution and using the fixed range as ± 2 standard deviations. Note that the mean of this assumed distribution was generally not equivalent to the prior calibrated value. Moreover, directly measured thermal conductivity values were obtained with two different techniques.

iTOUGH2 calibration decreased the temperature residuals and improved the objective function by 32%. However, analysis of the temperature residuals was still disappointing. As in the manual calibration, only 55% of simulated temperatures at the wells were good. The mean residual was 0.273°C, with standard deviation of 2.8°C; an ideal model would have 0 mean and a standard deviation of 1°C. More sophisticated analysis techniques of iTOUGH2 indicated that the model failed the Fisher Model Test, or equivalently that the residual errors could not be considered to come from a stochastic distribution, and were not randomly distributed.

Least squares estimation assumes that the measurement error is the only source of error in the model system. The system error is presumed to be zero when the forward model exactly describes the physical state of the system. However, in our model, 21% of the residuals were more than 3 standard deviations away from the theoretical mean of zero, and could be considered outliers.

Physically, the conduction model assumes that heat moves in the subsurface only by a diffusive process. It does not assume the movement of heat by advectively moving groundwater, or by density-driven convection. However, there is considerable evidence to show that the aquifers of the Perth Basin do exhibit advective and convective heat transport (Sheldon et al. 2011; 2012a; 2012b). These modes of transport produce temperature profiles horizontally and in depth that are nonlinear and can have considerable deviation from the conductive profile (Rühaak et al., 2010; Sheldon et al. 2012b). Our simulator is, quite frankly, inadequate to describe the processes that produce the subsurface measurements.

Robust Andrew's Estimator

We therefore turned to a more robust estimator for calculating the model parameters (Finsterle and Najita, 1998). The Andrew's estimator discounts residuals that are far from the expected normal behaviour. As we believed that our corrected true formation temperatures had measurement error that was randomly distributed, we applied an Andrew's estimator with a parameter c=2.1. In plots below, this estimator is termed "Robust."

Again an iTOUGH2 estimation was run, but with the changes to the objective function and modifications to the Levenberg-Marquardt stepping scheme to decrease overshoot. The final estimated parameters are shown in Table **1**. After inversion, the objective function decreased by 38%, similar to the least-squares estimator but the large residual outliers are not counted in this calculation. Now, 66% of residuals are good and within 2 standard deviations of the measurement error. The overall mean residual has improved to 0.07°C, with a standard deviation of 0.66°C.

Comparison of Estimators

The residuals are plotted in histogram format in Figure **4**. Neither set of residuals appear normal; both fail the Fisher Model Test. However, the robust estimator has many more residuals within the ±2 standard deviation range.

To see whether the residuals had a trend, several analyses were performed. One example is shown in Figure **5**, where the residuals are plotted against depth. No strong depth-related trend is obvious, although a linear regression through the data shows that simulated temperatures are slightly cooler with depth, but errors are essentially uncorrelated.

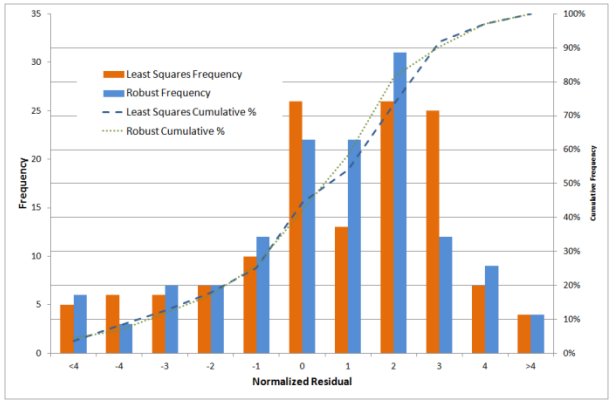

Figure 4. Histogram of temperature residuals for least squares and robust estimators.

Using the robust estimator was particularly helpful in identifying data that did not fulfill the conductive assumption, by pinpointing locations with large absolute normalized residuals. For example, Well Gingin 1 is located in the Central Perth Basin and has two high quality DST temperature measurements at -3874 m AHD and -4453 m AHD. The respective temperature

measurements are 93.3 and 160°C. The local geothermal gradient between these two measurements is 115°C km^{-1}. Assuming no measurement or model error, this gradient is wildly different than the more reasonable average geothermal gradient of 25°C km^{-1} obtained from nearby Gingin 3 and reflected in other Perth Basin wells. This type of statistical analysis could be used to answer fundamental process questions such as posed by Sheldon et al. (2011).

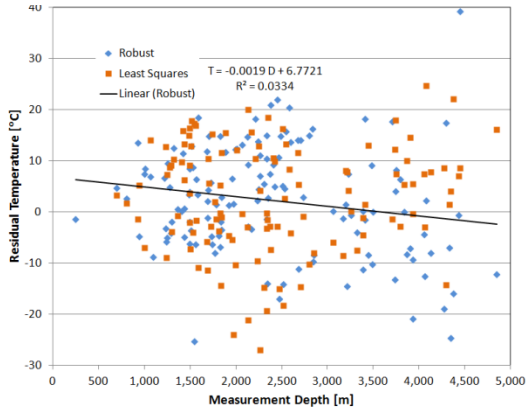

Figure 5. Scatter plot of temperature residuals versus depth.

DISCUSSION

Manual calibration of the model to available temperature data proved to be a complicated task due to the simplified rock formations and different qualities of temperature measurements. Combining the geothermal simulation performed with SHEMAT with the inverse modeling capabilities of iTOUGH2, through the recently developed PEST interface, greatly facilitated estimating model parameters.

However, the automatic estimation procedure is not a panacea for physical analysis. For example, the final results shown in Table **1** have four parameters that are restricted by the reasonable bounds applied as prior information. Additional inversions should be performed removing these bounds, to see if estimated parameters remain physically realistic. The imposed bounds are also influenced by the difference in measurement types, which can produce parameter measurements with different fundamental scales. It is difficult to reconcile these types of system error in the iTOUGH2 inversion process. Alternatively, reaching the parameter bounds in the estimation process can indicate the most fruitful areas for additional direct parameter measurements.

Another consideration raised by the inversion process is whether the highly correlated basal heat flux and radiogenic heat production from deep layers can truly be estimated from relatively shallow measurements. This ill-posed problem should be further investigated mathematically; such has been done with magnetic or seismic estimation of the Mohorovičić discontinuity, to see whether the deep parameters can be determined from near surface data.

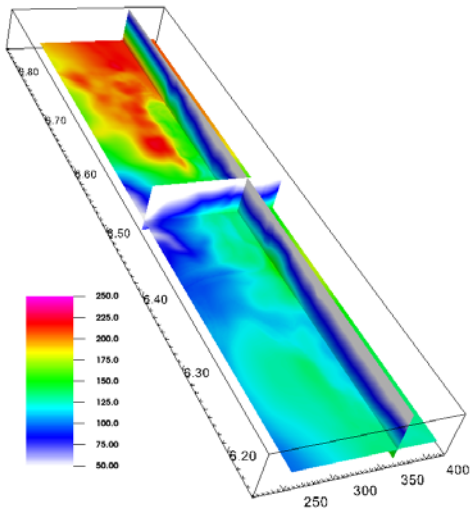

Figure 6. Simulated temperature [°C] at 5000 m depth.

The final simulated temperature field [Figure **6**] provides a picture of large-scale temperature variations in the Perth Basin, which may be used to identify possible locations of attractive geothermal resources. Extending the previously existing large-scale geothermal simulation with iTOUGH2 provided us with a more detailed insight into the sensitive parameters and data in the model, which would clearly not be possible with a simple trial-and-error calibration method. Using the gained knowledge, future work will include more detailed submodel studies on the reservoir scale including hydrogeological and geothermal processes such as advection and convection.

ACKNOWLEDGMENT

Initial work on the geothermal model of the Perth Basin was funded by the Western Australian government as the Western Australian Geothermal Centre of Excellence (WAGCOE), a joint partnership between CSIRO, the University of Western Australia, and Curtin University. WAGCOE members, in particular Soazig Corbel, Heather Sheldon, and Thomas Poulet, were vital members of the team who developed the initial basin-scale model.

REFERENCES

Clauser, C., Bartels, J., *Numerical simulation of reactive flow in hot aquifers: SHEMAT and processing SHEMAT*. Springer, Berlin, 2003.

Finsterle, S., Najita, J. Robust estimation of hydrogeologic model parameters, Water Resources Research 34(11), 2939—2947, 1998.

Finsterle, S., iTOUGH2 user's guide. Tech. rep., Lawrence Berkeley National Laboratory, Berkeley, 1999.

Finsterle, S., Zhang, Y., Solving iTOUGH2 simulation and optimization problems using the PEST protocol. *Environmental Modelling & Software* 26 (7), 959–968, 2011.

Horowitz, F., Regenauer-Lieb, K., Mean annual surface temperature (MAST) and other thermal estimates for Australia and New Zealand from 6 years of remote sensing observations. In: *Proceedings, NZ Geothermal Workshop*. pp. 65–68, 2009.

Kohl, T., Andenmatten, N., Rybach, L., 2003. Geothermal resource mapping–example from northern Switzerland: Selected Papers from the European Geothermal Conference 2003. *Geothermics* **32** (4-6), 721–732.

Moore, C., Doherty, J., The cost of uniqueness in groundwater model calibration, *Advances in Water Resources*, **29**, 605-623, 2006.

Reid, L.B., Corbel, S., Poulet, T., Ricard, L.P., Schilling, O., Sheldon, H.A., Wellmann, J.F., Hydrothermal modelling in the Perth Basin, Western Australia. Final report of Project 3, Perth Basin Assessment Program. CSIRO EP121504, 202 pp., 2012a.

Reid, L.B., Wellmann, J.F., Corbel, S., Sheldon, H.A., Poulet, T., Integrated geological and geothermal 3D models of the Perth Basin, Western Australia, *Western Australian Geothermal Energy Symposium 2012*, Perth, Western Australia, 2012b.

Ricard, L.P., Reid, L.B., Corbel, S., Deep temperature measurements analysis in the onshore Perth Basin, Western Australia. *Western Australian Geothermal Energy Symposium 2012*, Perth, Western Australia, 2012.

Rühaak, W., Rath, V., Clauser, C., Detecting thermal anomalies within the Molasse Basin, southern Germany. *Hydrogeology Journal* **18** (8), 1897–1915, 2010.

Saibi, H., 3D Numerical model of the Obama hydrothermal–geothermal system, Southwestern Japan. *Computational Geosciences* **15** (4), 709–719, 2011.

Sheldon, H.A., Reid, L.B., Florio, B., and Kirkby, A.L., Convection or conduction? Interpreting temperature data from sedimentary basins, *in* Budd, A.R., ed., Proceedings of the 2011 Australian Geothermal Energy Conference, 16-18 November, Melbourne, Volume 2011/43: Geoscience Australia Record: Canberra, Geoscience Australia, p. 233-238, 2011.

Sheldon, H.A., Florio, B., Trefry, M.G., Reid, L.B., Ricard, L.P. and Ghori, A., The potential for convection and implications for geothermal energy in the Perth Basin, Western Australia. *Hydrogeology Journal*, DOI 10.1007/s10040-012-0886-7, 2012a.

Sheldon, H.A. Schilling, O., Reid, L.B., Corbel, S., Convection in the Yarragadee Aquifer: Simulations and implications for geothermal energy in the Perth Metropolitan Area, *Western Australian Geothermal Energy Symposium 2012*, 2012b.

TOUGH-FLAC COUPLED THM MODELING OF PROPOSED STIMULATION AT THE NEWBERRY VOLCANO EGS DEMONSTRATION

A. P. Rinaldi[a], J. Rutqvist[a], E. L. Sonnenthal[a], T. T. Cladouhos[b]

[a]Lawrence Berkeley National Laboratory
1 Cyclotron Road
Berkeley, CA, 94720, USA
e-mail: aprinaldi@lbl.gov, jrutqvist@lbl.gov, elsonnenthal@lbl.gov

[b]AltaRock Energy
7900 E. Green Lake Drive N
Seattle, WA, 98115, USA
e-mail: tcladouhos@altarockenergy.com

ABSTRACT

In this study, we use the TOUGH-FLAC simulator for coupled thermo-hydro-mechanical (THM) modeling of the planned well stimulation for the Newberry EGS (Enhanced Geothermal System) demonstration. We analyze the potential for injection-induced fracturing and reactivation of natural fractures with associated permeability enhancement. More specifically, related to the design of the stimulation, our analysis aims at understanding how far the EGS reservoir may grow. We analyze the extent of the reservoir by studying the extent of the failure zone, using an elasto-plastic model and accounting for permeability changes as a function of the induced stresses.

INTRODUCTION

In 2009 the U.S. Department of Energy's Geothermal Technology Program awarded a grant to AltaRock Energy to demonstrate an Enhanced Geothermal System (EGS) at Newberry Volcano, Oregon. During Phase I of the project, completed in April 2012, pre-stimulation field investigations were performed to understand the tectonic and volcanic setting, characterize the volume around the proposed EGS demonstration area, and plan the stimulation parameters. A preliminary 3-D model of stress and fracture patterns by Davatzes and Hickman (2011) showed that faulting was mainly evident along the caldera rim about 3 km from the designated injection well, with no evidence (from drilling logs) of ring fractures or faults in the injection well (NWG 55-29). Furthermore, Newberry Volcano was found to have a very low seismicity rate; a much-improved seismic network installed in 2011 detected just two events (M 1.0 and 1.5) over approximately 1 year of monitoring (http://www.pnsn.org/volcanoes/newberry#). An analysis of the natural fractures there showed that there are two dominant sets that strike N-S and dip approximately 50˚ to the east and west (Davatzes and Hickman, 2011).

Modeling of the stimulation by Cladouhos et al. (2011) using the AltaStim simulator showed that it was possible to reach the EGS reservoir length goal (greater than 500 m), with the most attractive model reservoirs resulting when the pressures were well into the hydroshearing regime and just below the hydrofracking or tensile failure regime. Here, we compare those results with our alternative TOUGH-FLAC THM analysis and perform a sensitivity analysis of some key parameters, such as the initial state of stress and the frictional angle for shear reactivation.

MODEL SETUP

We conduct a coupled thermo-hydro-mechanical (THM) analysis using the simulator TOUGH-FLAC (Rutqvist et al., 2002), based on the geothermal reservoir simulator TOUGH2 (Pruess et al., 1999), which models multiphase and multicomponent fluids in a porous medium, and the geomechanical code FLAC3D (Itasca, 2009), which models the stress changes induced by pressure and temperature. Following the approach of Rutqvist et al. (2010) for modeling the stimulation injection at the Northwest Geysers EGS Demonstration Project, we study

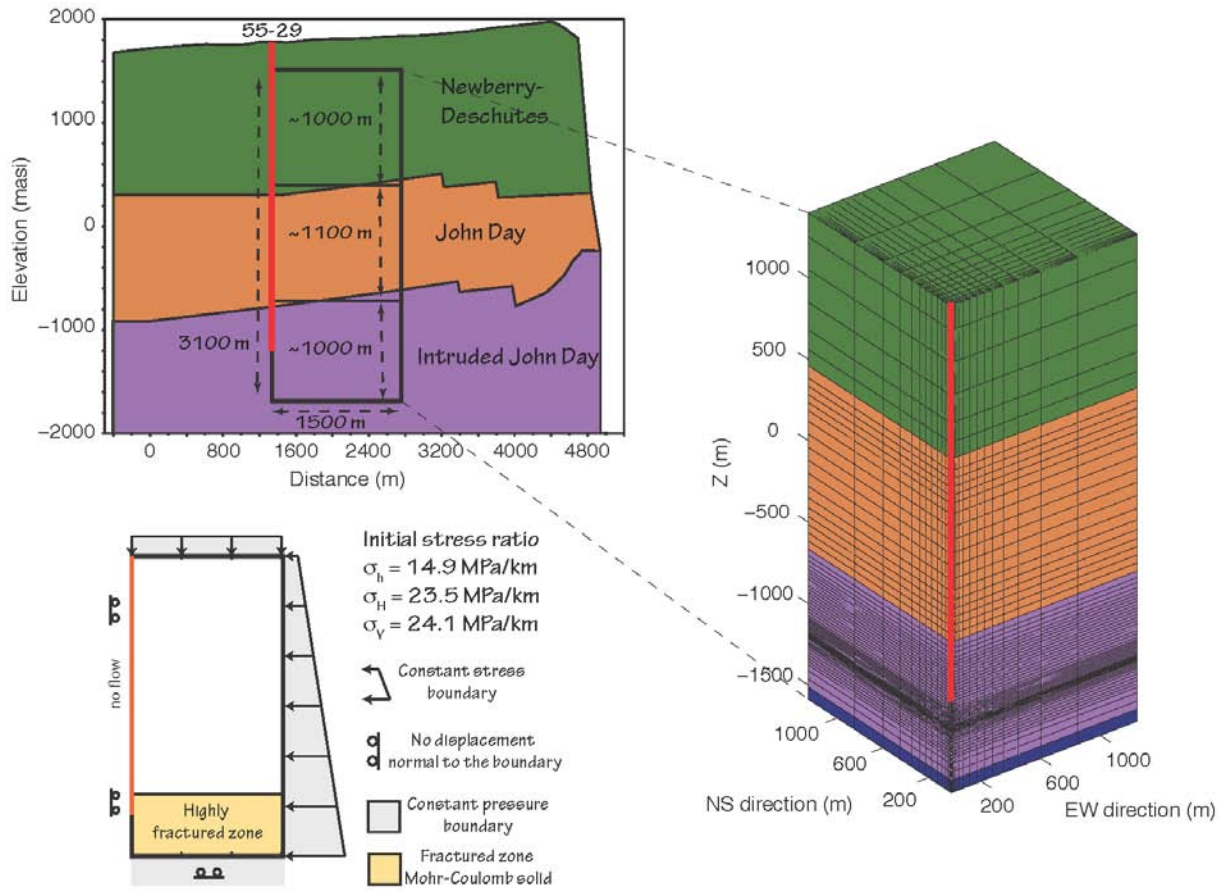

Figure 1. Mesh and boundary conditions for modeling stimulation at the Newberry EGS demonstration.

the stimulation at the Newberry Volcano. We consider a quarter symmetric model with injection well (NWG 55-29) located at one vertical edge (Fig. 1). The model consists of four layers, representing the main geological formations of the Newberry area (Sonnenthal et al., 2012). Hydrological properties are listed in Table 1. We assume a stress-dependent permeability (hence also an anisotropic initial permeability) with maximum permeability in the NS-direction, in order to simulate the highly fractured zone in the Intruded John Day formation at Newberry Volcano.

The injection well is divided into two parts, the first representing a cased well (high vertical permeability and very low horizontal permeability), and the second representing an open well allowing injection of cold water into the highly fractured zone. Pore compressibility (c_p) and thermal conductivity (λ) within the injection well are calibrated to match field data related to an injection test. Initial temperature and pressure distributions are extracted from earlier analyses of the prestimulation steady-state conditions at Newberry Volcano (Sonnenthal et al., 2012). The temperature follows a high gradient of ~100˚C/km, with a maximum temperature of about 315˚C at the bottom of the domain. The pressure is slightly lower than hydrostatic, with a linear gradient of about 8.3 MPa/km. Constant pressure is set at the top and bottom boundaries, whereas the side boundaries are assumed closed for fluid flow.

Mechanical properties follow the results by Li et al. (2012). We chose to simulate a homogeneous model using a Young's modulus E = 15 GPa and Poisson's ratio ν = 0.3. A homogeneous model should be adequate in this case, due to our short-term simulation (~3 weeks), which should affect only the injection zone (EGS reservoir). Geomechanical initial conditions follow those used by Cladouhos et al. (2011) for the AltaStim

Table 1. Hydrological properties. κ_i permeability along i-direction. ϕ porosity. ρ_{rock} rock density. D rock grain specific heat. λ thermal conductivity. c_p pore compressibility

	Newberry-Deschutes	John Day	Intruded John Day	Cased well	Open well
κ_x (m^2)	10^{-17}	$2.6\cdot10^{-16}$	$5\cdot10^{-18}$	10^{-20}	$5\cdot10^{-16}$
κ_y (m^2)	10^{-17}	$2.6\cdot10^{-16}$	$5\cdot10^{-17}$	10^{-20}	$5\cdot10^{-16}$
κ_z (m^2)	10^{-17}	$2.6\cdot10^{-16}$	$5\cdot10^{-18}$	10^{-8}	10^{-8}
ϕ (%)	10	5	3	95	100
ρ_{rock} (kg/m^3)	2400	2400	2400	-	-
D (J/kg ˚C)	1000	1000	1000	800	800
λ (W/m ˚C)	1.80	2.15	2.20	2.20	1.80
c_p (Pa^{-1})	$3.2\cdot10^{-9}$	$3.2\cdot10^{-9}$	$3.2\cdot10^{-9}$	-	-

simulation. We consider a vertical stress gradient of 24.1 MPa/km (σ_V, maximum principal stress on z-axis). The intermediate principal stress is oriented in the NS-direction (σ_H, y-axis), with a gradient of 23.5 MPa/km. Finally, the minimum principal stress is oriented in the EW-direction, with a gradient of 14.9 MPa/km (σ_h, x-axis).

Permeability changes

Changes in hydraulic properties may arise as the state of stress changes. In particular, the medium permeability is related to the fracture aperture b and the effective stress normal to the fracture σ_n, according to the following exponential function (Rutqvist et al., 2008):

$$b = b_i + b_{\max}\left(\exp(\alpha\sigma_n) - \exp(\alpha\sigma_{ni})\right) \qquad (1)$$

where b_i is the initial aperture, $b_{\max}$ is the mechanical aperture corresponding to zero normal stress, α is a parameter related to the curvature of the function, and σ_{ni} is the initial stress normal to the fractures. In our formulation, compressive stresses are considered negative. Because Newberry Volcano features a NS-striking fracture system (i.e. y direction), we can calculate the changes in permeability along the y-direction (κ_y) as a function of the normal stress (σ_x), using the cubic law of parallel-plate flow (Witherspoon at al., 1980) and an approach for scaling the fracture properties with the initial permeability (Liu et al., 2004):

$$\frac{\kappa_y}{\kappa_{yi}} = \left[\frac{R_b + \exp(\alpha\sigma_x)}{R_b + \exp(\alpha\sigma_{xi})}\right]^3 \qquad (2)$$

where the stress aperture function is related to the dimensionless parameter $R_b = b_r/b_{\max}$, where b_r represents the residual aperture. Using R_b, the permeability change factor is independent of initial permeability, and we need to calibrate our model using two parameters only (R_b and α; see following section).

Shear reactivation also enhances permeability changes—it is the main mechanism for generating permanent permeability enhancement within the EGS reservoir. In this work, we assume that permeability would change by a fixed factor if a gridblock is subjected to shear reactivation:

$$\kappa_i = K_{HS} \cdot \kappa_i^{bHS} \qquad (3)$$

for the i-direction. K_{HS} is the constant value (set to 1 or 100 for the base-case analysis), and the index bHS refers to the permeability before the hydroshearing.

Model calibration

Model calibration was conducted by simulating an injection test and comparing the resulting pressure and temperature profiles along the well with data collected at well NWG 55-29 during a field injection test (September–October 2010).

According to Davatzes and Hickman (2011), the injection test was performed in two steps. The injection began for three days with an injection rate of 10 gpm (~0.63 kg/s) and temperature of 10˚C, and a wellhead pressure of about 5 MPa (750 psi), followed by a two-week shut-in. Then the injection restarted for nine days with an injection rate of 22 gpm (~1.4 Kg/s) and temperature of 10˚C, and a wellhead pressure of about 8 MPa (1153 psi).

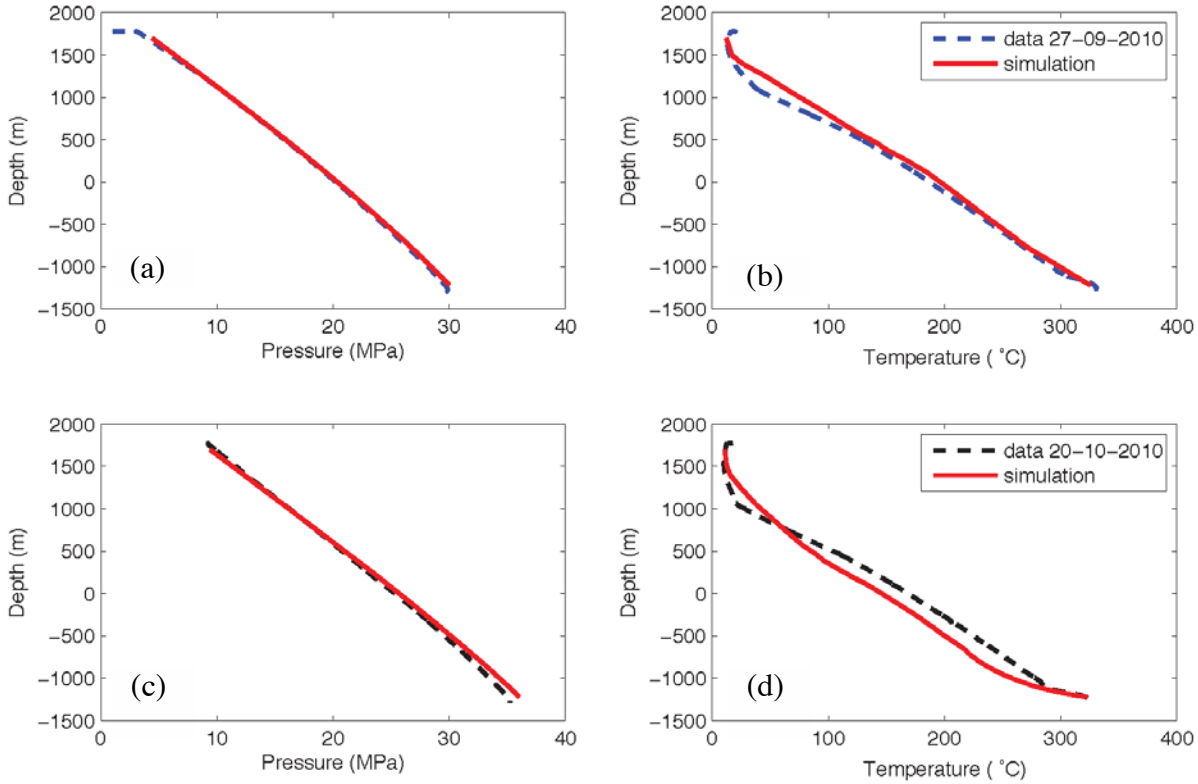

Figure 2. Model calibration. (a) Pressure well log (blue dashed line) and simulated pressure (red line) after 3 days (09/27/2010) of 10 gpm injection rate. (b) Temperature well log (blue dashed line) and simulated temperature (red line) after 3 days (09/27/2010) of 10 gpm injection rate. (c) Pressure well log (black dashed line) and simulated pressure (red line) after 9 days (10/20/2010) of 22 gpm injection rate. (d) Temperature well log (blue dashed line) and simulated temperature (red line) after 9 days (10/22/2010) of 22 gpm injection rate.

In our model, we aim to reproduce the same observed profiles along the well while considering permeability changes that might arise with the evolving stresses. The resulting profiles are shown in Figure 2. The parameters determining permeability changes are set to $R_b = 0.2$ and $\alpha = 0.13$ MPa^{-1} (see Eq. 2). The pore compressibility and thermal conductivity are calibrated as well, to allow a good match between the simulated and measured profiles (Tab. 1). As stated by Davatzes & Hickman (2011), the pressure log after the nine-day 22 gpm injection was made with a lower well-head pressure; hence, the pressure field data in Figure 2d need to be recalibrated to match a wellhead pressure of 8 MPa (1153 psi).

STIMULATION MODELING

In the stimulation of the Newberry EGS system, at most 24 million gallons are expected to be injected into at least three separate zones or depth ranges (Cladouhos et al., 2012). The stimulation is planned for three weeks (21 days) —one week per zone, with a maximum injection rate of 800 gpm (about 50 kg/s) in each zone. However, in our stimulation modeling, we consider a fixed, high wellhead pressure of 16.2 MPa (2350 psi), rather than a constant rate of injection, following the simulation performed by Cladouhos et al. (2011, 2012).

To estimate the extent of the EGS reservoir in this case, we look at the zone where the system is subjected to hydroshearing. This can be done with a Mohr-Coulomb model; assuming a cohesionless solid, a shear reactivation will occur when the following criterion is respected:

$$\sigma'_{1c} = N_\phi \sigma'_3 , \quad N_\phi = \frac{1+\sin(\phi)}{1-\sin(\phi)} \qquad (4)$$

where σ'_{1c} is the critical maximum principal effective stress (σ'_V or σ'_{zz} in our case), and σ'_3 is the minimum principal effective stress (σ'_h or σ'_{xx}). ϕ is the frictional angle (with frictional

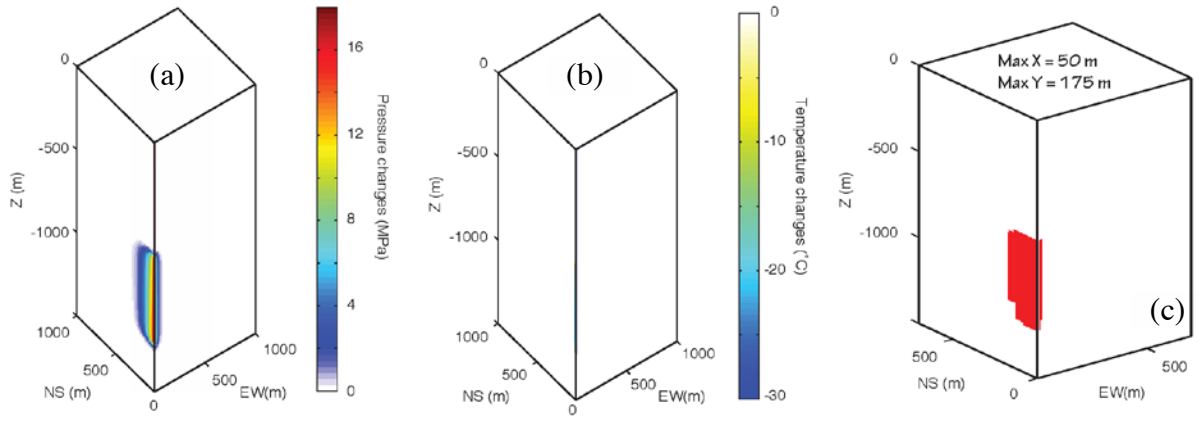

Figure 3. Simulation results for the base case simulation without shear-enhanced permeability after a stimulation 21 days long at constant wellhead pressure (16.2 MPa). (a) Resulting pore pressure changes. (b) Resulting temperature changes. (c) Resulting hydrosheared zone. Without considering shear-enhanced permeability, the shear reactivation occurs up to about 200 m from the injection well in the NS-direction.

coefficient $\mu = \tan\phi$), which is set to 30˚ for the base-case simulation.

Equation 3 corresponds to the case in which the fractured media with fractures of any orientation exist at every location. However, in the case of the anisotropic stress field at Newberry Volcano, east and west dipping, pre-existing fracture planes will most likely hydroshear, resulting in permeability enhancement in the subvertical and NS directions. Using this approach, shear reactivation would be induced whenever the maximum principal stress is N_ϕ times higher than the minimum principal stress.

Base case

The first model we analyze does not take into account permeability changes owing to hydroshearing (i.e., K_{HS} = 1 in Eq. 3). Figures 3a and b show the resulting changes in pressure and temperature, respectively, within the EGS reservoir after 21 days of stimulation. The pressure perturbation spreads out between 300 and 400 m from the injection well in the NS-direction, while it is confined along the EW-direction (spreading less than 100 m). The injection produces pressure changes at the reservoir depth up to about 18 MPa around the well. The temperature variation is mostly confined around the injection well, and extends only a few meters, with changes up to more than 100ºC (scale in Figure 3b is saturated at 30ºC).

Figure 3c shows the resulting extent of the EGS reservoir for this base case. The red zone in the figure represents the region where hydroshear reactivation has occurred. In this case, the hydrosheared zone extends about 200 m in the NS-direction (strike direction of the fracture system). In the EW direction, on the other hand, the EGS system is quite confined, extending only about 50 m. The total water flux calculated after 21 days of stimulation is about 2.5 million gallons. These values are not in agreement with the analysis performed with the AltaStim software, which predicted, with the prescribed wellhead pressure of 16.2 MPa, an EGS length greater than 500 m and a total volume of about 22 million gallons (Cladouhos et al., 2011).

Base case with shear-enhanced permeability

In this section, we assume that hydroshearing will affect permeability by up to two orders of magnitude when shear reactivation takes place. Enhanced permeability allows the pressure perturbation to propagate further into the reservoir. As shown in Figure 4a, the pressure perturbation extends to between 800 and 900 m in the NS-direction and up to 200 m in the EW-direction. In this case, injection produces pressure changes of up to 10 MPa around the well. Although the temperature changes are still mostly confined to the injection well, the enhanced permeability permits the temperature to decrease up to 50 to 100 m from the injection well, with changes up to about 30˚C (Fig. 4b).

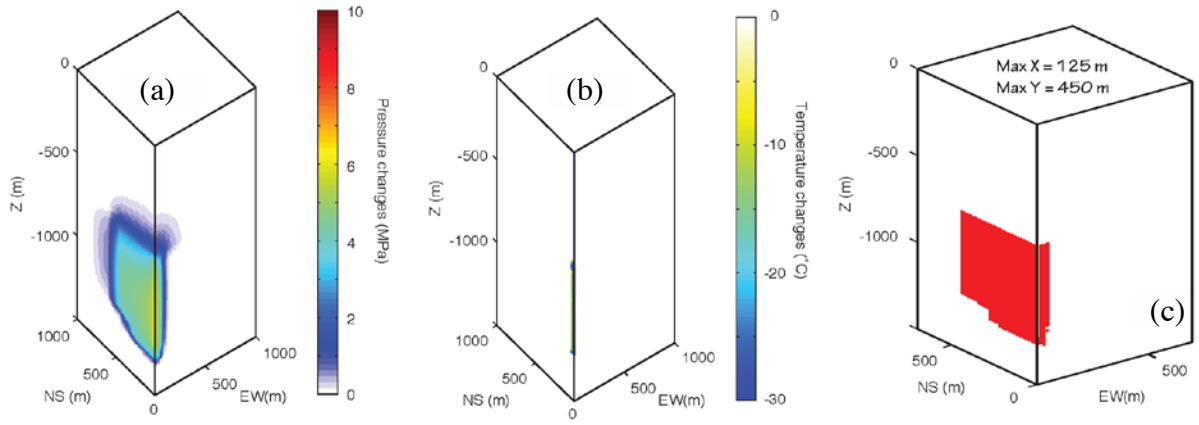

Figure 4. Simulation results for the base-case simulation considering shear-enhanced permeability after a stimulation 21 days long at constant wellhead pressure (16.2 MPa). (a) Resulting pore pressure changes. (b) Resulting temperature changes. (c) Resulting hydrosheared zone, with shear reactivation occuring up to about 500 m from the injection well in the NS-direction and 150 m in the EW-direction.

Figure 4c shows the resulting extent of the EGS reservoir for this case. Hydroshear occurs up to ~500 m from the injection well in the NS-direction, and up to 150 m in the EW-direction. In this case, the EGS reservoir extent is similar to that calculated using AltaStim, whereas the calculated total water injected is about 14 millions gallons, still slightly lower than the value found by Cladouhos et al. (2011).

SENSITIVITY ANALYSIS

In this section, the extent of the hydrosheared zone, and hence the extent of the EGS reservoir, will be analyzed as a function of two key parameters: (1) the factor for shear-enhanced permeability changes (K_{HS} in Eq. 3), and (2) the frictional angle (ϕ in Eq. 4).

Figure 5 shows the zone where shear reactivation occurred for three different values of the shear-permeability enhancing factor. The region subjected to shear reactivation is directly proportional to this factor, i.e., the higher the permeability after hydroshearing, the larger the shear reactivated region. The extent of the EGS reservoir in the NS-direction varies from about 350 m for a factor K_{HS} = 10, to a value of 600 m when that factor is increased by several orders of magnitude (K_{HS} = 10000). The extent of the hydrosheared region in the EW-direction is about 150 m, independent of permeability-enhancing factor for the range considered.

In the base-case simulations, we previously used a very low frictional angle, which results in a friction coefficient of about 0.6, i.e., almost a critical value for the considered initial stress distribution. Assuming a lower value for the frictional angle (ϕ <30˚) would cause shear reactivation of the entire highly fractured zone (Fig. 1) under initial stress conditions (i.e., before the stimulation starts). For this reason, we studied values higher than 30° in our sensitivity analysis of the frictional angle.

Figure 6 shows the resulting EGS reservoir extent as a function of the frictional angle. The extent of the reactivated region in the NS-direction is inversely proportional to the frictional angle, varying from about 500 m in case of low angle (30º with frictional coefficient μ=0.6), to as short as 275 m for the highest considered angle (39º with frictional coefficient μ=0.8). The same inverse correlation is observed for the extent in the EW-direction, with the minimum value (about 30 m) resulting for the highest frictional coefficient.

CONCLUSIONS

In this paper, we report on the THM modeling of the proposed stimulation at the Newberry EGS Demonstration site in Oregon. Starting with previous results from the AltaStim software, and building on experience from the Northwest Geysers EGS demonstration Project,

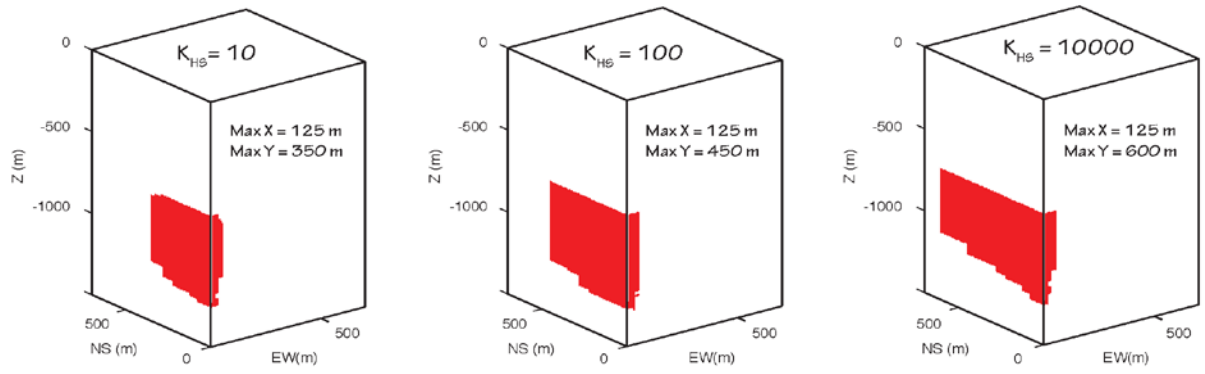

Figure 5. Sensitivity analysis results for the Mohr-Coulomb solid stimulation modeling, with the factor for shear-enhanced permeability given by (a) 10, (b) 100 (base case), and (c) 10,000.

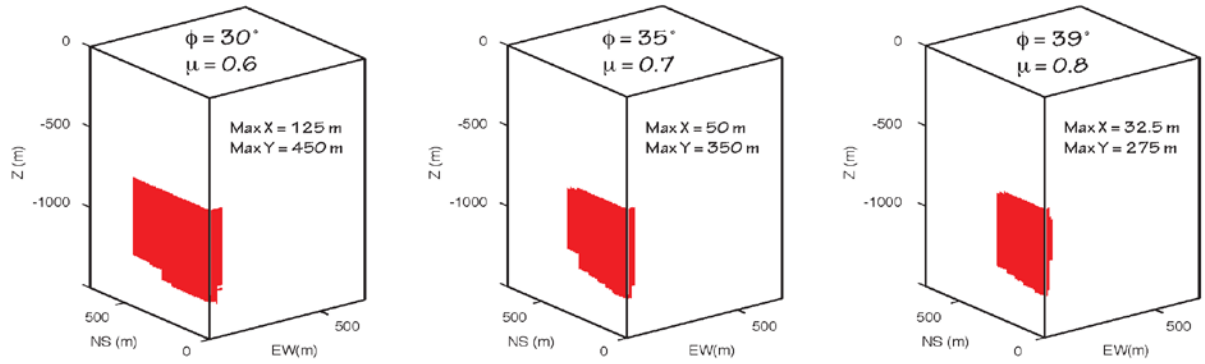

Figure 6. Sensitivity analysis results for the Mohr-Coulomb solid stimulation modeling, with the frictional angle given by (a) 30^{o} (base case), (b) 35^{o}, and (c) 39^{o}.

we modeled the stimulation phase using the coupled TOUGH-FLAC code. Taking into account permeability changes that can result from stimulating a pre-existing NS-striking fracture system, we first calibrated our model by simulating an injection test and comparing the results with field data. Then we simulated a high-rate injection, fixing the wellhead pressure to the same value used previously with the AltaStim simulator.

Results show that shear-enhanced permeability has to be accounted for when hydroshearing occurs in order to reach the 500 m stimulation-zone goal. In all of the TOUGH-FLAC simulation cases, the total volume of injected water is less than that observed in the AltaStim simulation (Cladouhos et al., 2011). However, we did not consider shear-induced changes in porosity. In fact an enhanced porosity would tend to increase the water volume injected.

We also present a sensitivity analysis focusing on the extent of the hydrosheared zone as a function of the shear-enhanced permeability factor, and of the frictional angle. For values of the permeability factor that range over several orders of magnitude (and only for values greater than 10), the stimulated rock extent is very close to the target length of 500 m. Regarding the frictional angle, unless the system is close to a critical state (μ=0.6), the target length of 500 m is unlikely be reached.

ACKNOWLEDGMENTS

This work was supported by the U.S. Department of Energy under Award Number DE-EE0002777 and by the American Recovery and Reinvestment Act (ARRA), through the Assistant Secretary for Energy Efficiency and Renewable Energy (EERE), Office of Technology Development, Geothermal Technologies Program, of the U.S. Department of Energy under Contract No. DE-AC02-05CH11231.

REFERENCES

Cladouhos, T. T., M. Clyne, M. Nichols, S. Petty, W. L. Osborn, L. Nofziger, Newberry Volcano EGS Demonstration Stimulation Modeling, *GRC transactions*, *35*, 2011.

Cladouhos, T. T., W. L. Osborn, S. Petty, D. Bour, J. Iovenitti, O. Callahan, Y. Nordin, D. Perry, P. L. Stern, Newberry Volcano EGS Demonstration–Phase I results, *Proceedings of 37th Workshop on Geothermal Reservoir Engineering*, Stanford, California, January 30 – February 1, 2012.

Davatzes N. C. and S. H. Hickman, Preliminary Analysis of Stress in the Newberry EGS Well NWG 55-29, *GRG transactions*, 35, 323–332, 2011.

Li, Y., J. Wang, W. Jung, A. Ghassemi, Mechanical Properties of Intact Rock and Fractures in Welded Tuff from Newberry Volcano, *Proceedings of 37th Workshop on Geothermal Reservoir Engineering*, Stanford, California, January 30 – February 1, 2012.

Liu, H. H., J. Rutqvist, G. Zhou, G. S. Bodvarsson, Upscaling of normal stress-permeability relationship for fracture network obeying the fractional levy motion. In: Stephansson O., Hudson J. A., Jing L., editors. *Coupled THMC processes in geo-system: fundamentals, modelling, experiments and applications*. Oxford: Elsevier; p.263–268, 2004.

Itasca, *FLAC3D, Fast Lagrangian Analysis of Continua in 3 Dimensions, Version 4.0*, Minneapolis, Minnesota, Itasca Consulting Group, 2009.

Pruess, K., C. Oldenburg, and G. Moridis, *TOUGH2 User's Guide, Version 2.0*, Report LBNL-43134, Lawrence Berkeley National Laboratory, Berkeley, Calif., 1999.

Rutqvist, J., Y.-S. Wu, C.-F. Tsang, G. Bodvarsson, A modeling approach for analysis of coupled multiphase fluid flow, heat transfer, and deformation in fractured porous rock, *Int. J. Rock Mech. Min. Sc.*, 39, 429–442, 2002.

Rutqvist, J., B. Freifeld, K.-B. Min, D. Elsworth, Y. Tsang, Analysis of thermally induced changes in fractured rock permeability during 8 years of heating and cooling at the Yucca Mountain Drift Scale Test, *Int. J. Rock Mech. Min. Sc.*, *45*, 1373–1389, 2008.

Rutqvist, J., C. M. Oldenburg, P. F. Dobson, J. Garcia, M. Walters, Predicting the Spatial Extent of Injection-Induced Zoned of Enhanced Permeability at the Northwest Geysers EGS Demonstration Project, *Proceedings of 44th U.S. Rock Mechanics Symposium and 5th U.S.-Canada Rock Mechanics Symposium*, Salt Lake City, Utah, June 27-30, 2010.

Sonnenthal E., N. Spycher, O. Callahan, T. Cladouhos, and S. Petty, A thermal-hydrological-chemical model for the Enhanced Geothermal System Demonstration Project at Newberry Volcano, Oregon, *Proceedings of the 37th Workshop on Geothermal Reservoir Engineering*, Stanford, California, January 30 - February 1, 2012.

Witherspoon, P. A., J. S. Y. Wang, K. Iwai, J. E. Gale, Validity of cubic law for fluid flow in a deformable rock fracture, *Water Resour. Res.*, 16, 1016–1024, 1980.

RECENT DEVELOPMENTS IN THE AUTOUGH2 SIMULATOR

Angus Yeh, Adrian E. Croucher, and Michael J. O'Sullivan

Department of Engineering Science, University of Auckland
Private Bag 92019
Auckland 1142, New Zealand
e-mail: cyeh015@aucklanduni.ac.nz

ABSTRACT

For over a decade, the geothermal modeling group at the University of Auckland has been improving the capability of AUTOUGH2, a modified version of TOUGH2. This paper describes these additional features and the reasons they were introduced.

One of the main changes with AUTOUGH2 is that all EOS modules are compiled with other subroutines into one executable, and the user specifies appropriate EOS flags in the input file. Several new EOS modules have also been added. The input and output file names are also specified by the user directly at run time.

Many internal data array sizes, such as the number of rock types, have been increased. More recently, dynamic allocation of most of the major arrays has been implemented to improve the efficiency of memory use.

The most important change made in AUTOUGH2, however, has been the addition of many new generator (sink and source) types. For example, a recharge well type was added to ease the implementation of recharge boundary conditions. Another new well type was implemented to allow new production and injection wells to be added automatically to meet a specified steam flow or mass flow target as reservoir conditions change over time. These well types were introduced to aid modeling studies of geothermal power projects conducted at the University of Auckland.

INTRODUCTION

The geothermal modeling group at the University of Auckland started working on the MULKOM code in the early 1980s and this work has continued for more than three decades as the TOUGH and TOUGH2 simulators (Pruess et al., 1999) were introduced. The main aims of this continuing effort were to increase execution speed and introduce additional input/output options and graphical utilities (Bullivant, 1990; O'Sullivan and Bullivant, 1995). This customization has accumulated to form the present-day AUTOUGH2.

One of the earliest changes was the introduction of iterative conjugate gradient linear equation solvers to replace the direct solver (MA28) used in MULKOM (Bullivant et al., 1991). (Subsequently, similar solvers have been added to standard TOUGH2 (Moridis, et al., 1998).) Also, faster and more accurate versions of the thermodynamic routines were implemented pre-1990. The combining of all equation of state (EOS) modules into a single executable was implemented at an early stage in the 1990s, along with minor input/output changes. Many new generator types were coded during this time. More generator types were added, and some old ones were modified during the 2000s as new requirements came up. Changes in array size/memory management have been introduced very recently.

Most changes made to TOUGH2 leading to AUTOUGH2 were also implemented in iTOUGH2 to form AUiTOUGH2. Thus, most of the core code is shared between AUTOUGH2 and AUiTOUGH2.

The aim in the development of AUTOUGH2 has been to improve the ease of use, efficiency, and capability of TOUGH2.

RUNNING AUTOUGH2 – EASE OF USE

One of the most obvious changes from a user's perspective between AUTOUGH2 and TOUGH2 is the handling of different EOS

modules. AUTOUGH2 compiles all the EOS modules together with the rest of the TOUGH2 code into a single executable. The choice of EOS is achieved via an additional SIMULator block in the input file. This allows the user to choose the desired EOS as well as allowing backward compatibility with earlier versions of the code, such as MULKOM, TOUGH and TOUGH2.

Upon execution, the user is allowed to specify names of the model input file, incon file, and save file. This relatively small change made to the original TOUGH2 has proved to be both user-friendly and flexible. It makes it easy to run and maintain a series of model files in a single directory. This is found to be quite useful when lengthy calibration is carried out on a model, and all versions of the model need to be kept and tracked, with no external file/version control system needed.

OUTPUT MODIFICATION

In order to deal with the inclusion of all EOS modules in a single executable, some modifications to the output format for TOUGH2 were required.

Internally, AUTOUGH2 uses a piece of centralized "format control" code to print the simulation results appropriately for each EOS. The locally developed pre-/post-processing software MULgraph (Bullivant et al., 1995; Bullivant and O'Sullivan, 1998; O'Sullivan and Bullivant, 1995) uses the same piece of formatting control code to ensure that results for all EOS modules can be dealt with correctly. The consistency of output formatting across different EOS modules also helps facilitate machine-readability for post-processing.

In MULKOM, the only output options were results at a single element for every time step, or results at all elements every so many time steps. We introduced a SHORT output option so that results can be produced at every time step for a number of nominated elements, connections, or wells. (Later versions of TOUGH2 introduced the FOFT, COFT, and GOFT modules that provide similar functionality, via additional output files.)

FASTER THERMODYNAMICS

A series of changes was made to the original thermodynamics subroutines COWAT and SUPST. These two subroutines included a number of variables raised to integer powers as part of the calculations. We re-implemented these calculations using repeated multiplications, which resulted in a 5–10 fold increase in the speed of calculation of the secondary thermodynamic variables.

SUPERCRITICAL AUTOUGH2

Standard TOUGH2 and AUTOUGH2 both use the IFC-67 formulation (IFC, 1967) for thermodynamic properties of water. However, they both omit the equations dealing with supercritical conditions at high pressures and temperatures, a fluid state that is becoming of more interest as deep geothermal systems are being studied (Fridleifsson and Elders, 2005).

In addition, the 1967 formulation has since been superseded by the IAPWS-97 formulation (Wagner et al, 2000), which is faster, more accurate, more consistent and has a simpler representation around the critical point. This formulation has been implemented in an extended version of AUTOUGH2 with supercritical capability for EOS1, EOS3, and EOS4 (Croucher and O'Sullivan, 2008).

LINEAR SOLVERS

Back in the 1980s, we wished to set up models with more elements than the limit of around 500 imposed by MA28, the linear equation solver in MULKOM, and the memory limitations of the hardware of the day. To overcome this problem, we introduced iterative conjugate gradient solvers (Bullivant et al., 1991), which have been used in AUTOUGH2 ever since. Similar solvers were soon introduced in TOUGH2 (Moridis et al., 1998).

MORE EFFICIENT MEMORY USE

In MULKOM, TOUGH, and TOUGH2, all major arrays are statically allocated to predetermined fixed lengths, a restriction from early versions of the FORTRAN language and compilers. To use memory efficiently, it is necessary to recompile the code with array

dimensions set appropriately for the size of model being used.

In recent years, the size of models has grown, and the restriction of static memory allocation has become an important issue. On many operating systems, static memory allocation has a smaller size limit than memory allocated dynamically at execution time (Yeh et al., 2011).

The AUTOUGH2 code has been restructured to use dynamic memory allocation. At execution, the input file is processed first to determine the problem size. All major arrays are then allocated to their appropriate sizes. If the machine does not have enough free memory, the user is informed. In AUTOUGH2, all main arrays are dynamically allocated if their lengths depend on the numbers of rock types, elements, connections, generators or generation table entries.

NEW GENERATOR TYPES

Perhaps the most important change in AUTOUGH2 is the introduction of many more generator types. Some new generator types are used to deal with boundary conditions, while some are extensions of those provided by the original TOUGH2 code. Many others were designed with the motivation of simulating complicated real world geothermal production, injection, and power generation scenarios.

Table 1. Featured new generator types

Type	*Description*
Deliverability	
DELG	DELV with extended features
Boundary Condition	
HLOS	Heat loss boundary condition
RECH	Recharge boundary condition
Make-up production/injection	
TMAK	Total demand of make-up wells
DMAK	Make-up production wells
FINJ	Fixed injection
PINJ	Fixed portion injection
RINJ	Remained portion injection
IMAK	Pressure controlled injection

The following table provides a list of the main new generator types introduced. There are others not listed here, as they are minor variations of the listed ones or of the original set available with TOUGH2. Details of some of these new generator types are given in the following sections, with examples illustrating their use.

Deliverability Wells

TOUGH2 includes a DELV generator type, which allows the user to represent a geothermal well that may be partly throttled when it is first brought online. The user is allowed to limit the flow by specifying a maximum steam flow rate, which is calculated using a user-specified separator pressure.

One of the early additions to AUTOUGH2 was the DELG generator type, an extension of DELV. DELG allows users to specify a time-dependent productivity index in the form of a standard TOUGH2 well table. Alternatively, the user can specify an enthalpy-dependent bottom-hole pressure. There is also a very useful feature within DELG that automatically calculates the productivity index using the initial model pressure and a user-specified bottomhole pressure. This enables the model to start a simulation with each well at a specified flowrate, and then to vary the flowrate when the pressure changes over time. Thus, DELG can ensure a smooth flow-rate transition from a previous run to a subsequent one. A limit can be set with DELG to restrict mass or steam flowrate.

A typical use of DELG is for production wells in a future scenario. In the production history part of the model, a well may use a MASS generator, with the mass flow rate obtained from the actual production data. The same well can appear in the future scenario model as a DELG well. This allows the well to produce or cease production according to reservoir conditions.

DELG can also be used to simulate certain types of hot springs. Placing DELG at depth, it can simulate a localized direct link between the surface and the reservoir below the cap rock. Enthalpy-dependent bottom-hole pressure can be set to encourage high flow rates when the reservoir's boiling increases.

Boundary Conditions

With the original TOUGH2, modelers often needed to use special techniques to simulate an open boundary, for example by connecting a boundary block to a very large inactive block, to allow flow into or out of the model when the pressure in the boundary blocks changes. The RECH and HLOS generators were introduced into AUTOUGH2 to make this easier to implement.

RECH generators have behavior similar to that of a deliverability well, but can act as a source (inflow) or sink (outflow) depending on changes in reservoir pressure (unless the "no inflow" or "no outflow" options are used). The reference pressure can be specified manually or determined automatically from the initial conditions.

For example, at the bottom boundary of a model where natural hot upflow is represented by standard MASS generators, RECH generators can be added into a production/transient model. If the modeled pressure drawdown reaches the bottom boundary during production, the RECH generator will introduce additional upflow, at a specified enthalpy. In contrast, if brine injection raises the pressure at a boundary block above its initial state, a RECH generator can allow some fluid exit out of the model at a rate depending on how much overpressure exists.

The HLOS generator is similar to RECH, except that heat, instead of mass, is added or taken out.

Make-up Production/Injection Wells

Often geothermal reservoir models are used for investigating various future production/injection scenarios. In such simulations, it is useful to allow future "make-up" wells to be put into production when needed, and taken out when they become unproductive or are no longer needed.

At the core of the group of generators introduced for future scenario modeling are the TMAK and DMAK generators. The user provides a list of make-up wells, labeled with DMAK, in order of priority. This is followed by a TMAK well, which specifies the desired total mass flow and/or total steam flow (with a choice of separator pressure). The DMAK/TMAK option will automatically turn on new make-up wells if the production cannot meet the total mass or steam flow target. Individual DMAK wells have behavior similar to that of the DELG generators described above.

For the disposal of separated geothermal water and steam condensate, the TMAK/DMAK option keeps track of the amount of both separated geothermal water and steam. This can be reinjected via the new generator types FINJ, PINJ, RINJ, and IMAK, which are designed to deal with a wide range of injection configurations. All injection wells can be set to inject either the steam or separated water, and can be listed in any priority order.

FINJ injects a fixed amount. PINJ injects a fixed proportion of the total demand. RINJ injects a proportion of the remaining amount. IMAK behaves much like DMAK, using an injectivity calculation against a specified cut-off pressure, with an option to cap the amount injected.

Combinations of these generator types can be used to simulate the complicated scenarios commonly specified by field operators (O'Sullivan and Yeh, 2011). This is particularly useful for geothermal production in countries like New Zealand, where field operators need to optimize their operations for profitability, while conforming to environmental resource consent restrictions such as mass take limits, pressure constraints, etc.

Scenario Example with Make-up Wells

This is an example taken from a series of modeling studies for Contact Energy's proposed Tauhara II development near Taupo, New Zealand (O'Sullivan and Yeh, 2011). It is modified to demonstrate more clearly the application of make-up production and injection wells, and therefore does not reflect actual operation of the field.

Scenario specification

The specification included total steam demand for the power station, contributions from various parts of the field, and guidelines for disposal of used geothermal water:

TAKE

47,3000 t/day LP steam flow at 2.5 bar absolute, model to calculate total mass take

- 15% North Tauhara
- 40% East Tauhara
- 20% Centre Tauhara
- 25% South Tauhara

DISCHARGE

- 60% of steam flow injected as condensate in shallow East Tauhara Area
- 40% of steam flow lost to atmosphere from cooling tower
- Separated geothermal water (SGW) split equally between North, East, Centre, and South Tauhara

Building the scenario

To construct this scenario run, a list of potential production model blocks was prepared and used to form a series of DMAK generators, grouped into four respective production zones. Each zone of DMAK generators ends with a TMAK with the corresponding steam demand.

Each DMAK generator has its own bottom-hole pressure, depending on the depth of its model block. External wellbore simulation data were used to build the table of enthalpy-dependent bottom-hole pressures. This allows the well to flow with a lower cut-off pressure in two-phase or steam conditions. Note that a single DMAK generator here does not necessarily correspond to a single well in the field. It simply represents a portion of the production reservoir. A suitable productivity index was used and a limit on flow rate was set. A separator pressure of 2.5 bar absolute was set for all DMAKs.

A group of injection generators was inserted after the four DMAK/TMAK groups. The condensate injection uses the fixed portion PINJ generator type. The SGW injection was formed by a long list of IMAK generators. Each IMAK has a pressure limit depending on the location, depth and available overpressure from injection pumps. IMAKs from different zones were sorted so that the flow was split evenly into four zones. If a certain zone had difficulty injecting, the excessive SGW would be redistributed to other zones.

Results

Fig. 1 shows the result steam production from the scenario. All targets were met.

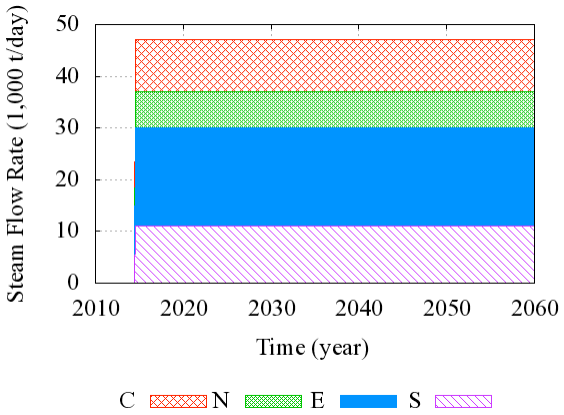

Figure 1. Steam flow rate from different production zones.

For each production zone, enough generators were turned on to maintain the target steam flow rate. With the original implementation of DMAK in AUTOUGH2, a DMAK could only be either completely off or fully open. In this case, if the steam flow only drops a small amount below the demand, a newly opened DMAK may add more than the required amount. This produces “steps” in the resulting mass flow rate, as shown in Fig. 2.

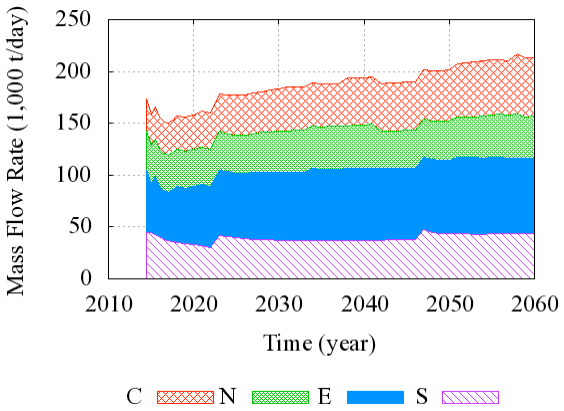

Figure 2. Mass flow rate computed by older code that does not support partial make-up well opening.

In recent years, the DMAK implementation has been modified to allow partial opening in order to meet demand precisely. Fig. 3 shows the result of using the newer code. A smoother increase in mass take can be observed, which was used to produce the precise steam flow rate shown previously in Fig. 1. This is achieved internally by scaling, and the scaling is configurable to be performed on either a single DMAK, or evenly on all opened DMAKs in the same group.

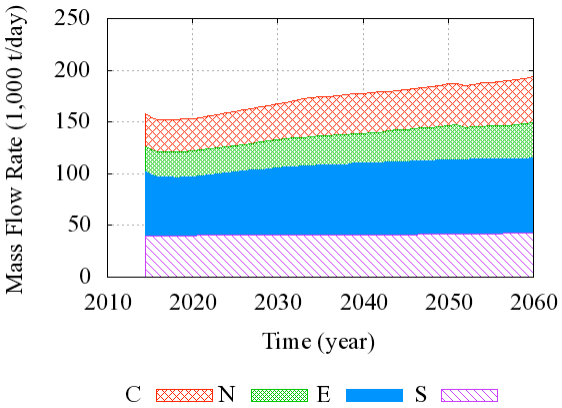

Figure 3. Mass flow rate computed by newer code. It is used for the rest of scenario results presented here. Note it is a lot smoother than Fig. 2.

The result shows some zones having to increase more mass take than others. This is caused by different enthalpy declines in each zone. The average enthalpy is shown in Fig. 4. In this scenario run, the DMAKs were configured to shut down if the enthalpy produced dropped below 850 kJ/kg. Production would then be taken from other DMAKs in the group. Many DMAKs from the North zone were shut down around the year 2050 due to low enthalpy. Production was shifted to other model blocks in the zone automatically. Note that it is possible to have production below target if productive model blocks in a zone are exhausted.

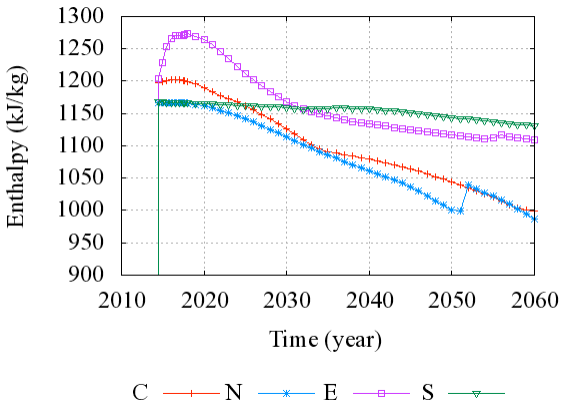

Figure 4. Average enthalpy from each of the production zones.

Fig. 5 shows the limited injection capacity of the South and East zones. Flows had to be redistributed to the Centre and North zones. The relatively small condensate injection is simply a fixed proportion (60%) of the total steam amount, which is not shown here.

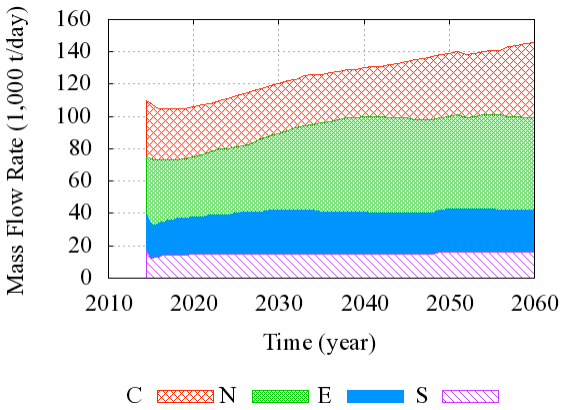

Figure 5. SGW injection rate into each zone. East and South zones are limited in capacity, and excessive SGW was distributed to North and Centre zones.

GRAPHICAL INTERFACE

One of the first software developments we made in association with use of TOUGH2 was the MULgraph graphical interface (Bullivant et al., 1995, Bullivant and O'Sullivan, 1998, O'Sullivan and Bullivant, 1995). We continue to use MULgraph to help with setting up TOUGH2 data files and with visualizing results from simulations, but we have more recently developed the PyTOUGH scripting library (Croucher, 2011; Wellmann et al., 2011) and are using it to assist with model building and visualization. For some of our models, we also use the Leapfrog Geothermal visualization software (Newson, 2012), and have been involved in adding TOUGH2 integration to it, which also makes use of the PyTOUGH library.

The flexibility available with the loose coupling between AUTOUGH2 and MULgraph or PyTOUGH we have found to be essential for carrying out very complex modeling projects, such as our study of the Lihir geothermal system, in which a gold mine is being excavated in the geothermal field. We have used PyTOUGH to run a year-by-year sequence of simulations with a mine pit being excavated at the top of the model (O'Sullivan et al., 2011). This kind of model development would be difficult to achieve with a more tightly coupled graphical interface such as PetraSim (Alcott et al., 2006).

CONCLUSIONS

The changes we have made with AUTOUGH2 have improved the capability of TOUGH2 for geothermal simulation. Some of the most significant changes we have made, such as the introduction of conjugate gradient solvers, were quickly adopted in the LBNL version of TOUGH2.

Many of the modifications we have introduced were aimed at making modeling of real geothermal systems easier, and some of our generator types, such as DMAK/TMAK, are very effective in this regard.

More remains to be done with regard to modeling production histories and future scenarios of geothermal systems. Rather than further modification of generator types, a new "SCENARIO" module is probably required to allow greater flexibility in the specification of a schedule of production and injection wells.

Overall, our experiences with using and modifying TOUGH2 have been very positive. Its longevity is testimony to the skill and judgment of the original developer, Karsten Pruess. There are further improvements we would like to make to AUTOUGH2, some of which we are currently not sure how to achieve. Probably at the top of our priority list is to speed up the approach to steady state in air/water or water/CO_2 models. For example, our models of Ohaaki (Clearwater et al., 2012) and Wairakei-Tauhara (O'Sullivan et al., 2009) both have difficulty reaching a steady state—often the time step will not increase past 1.0E11–1.0E12 seconds, whereas for other models the time step may increase easily up to 1.0E15 seconds.

We have been sharing experiences in using TOUGH2 with colleagues at LBNL for more than 30 years and look forward to continuing this relationship for the next 30 years.

ACKNOWLEDGEMENTS

Thanks are due to all who have contributed to the development of AUTOUGH2, particularly David Bullivant and George Zyvoloski, and many others whose names are hidden deeply in the code.

REFERENCES

Alcott, A., D. Swenson, and B. Hardeman, Using PetraSim to create, execute, and post-process TOUGH2 models, *Proc. TOUGH Symposium 2006*, Lawrence Berkeley National Laboratory, Berkeley, Calif., 2006.

Bullivant, D., Making MULKOM/TOUGH faster and easier to use, *Proc. TOUGH Workshop '90*, Lawrence Berkeley Laboratory, Berkeley, Calif., 1990.

Bullivant, D.P. and M.J. O'Sullivan, Graphics and TOUGH2, *Proc. TOUGH Workshop '98*, Berkeley, Calif., 1998.

Bullivant, D.P., M.J. O'Sullivan, and M.R. Blakeley, A graphical interface for a geothermal reservoir simulator, *Proc. World*

Geothermal Congress, Florence, Italy, p. 2971-2976, 1995.

Bullivant, D.P., M.J. O'Sullivan, and G.A. Zyvoloski, Enhancements of the MULKOM geothermal simulator, *Proc. 13th New Zealand Geothermal Workshop*, 1991.

Clearwater, E.K., M.J. O'Sullivan, K. Brockbank, and W.I. Mannington, Modelling the Ohaaki geothermal system, *Proc. TOUGH Symposium 2012*, Lawrence Berkeley National Laboratory, Berkeley, Calif., 2012.

Croucher, A.E., PyTOUGH: a Python scripting library for automating TOUGH2 simulations, *Proc. 33rd New Zealand Geothermal Workshop*, Auckland, New Zealand, 2011.

Croucher, A.E. and M.J. O'Sullivan, Application of the computer code TOUGH2 to the simulation of supercritical conditions in geothermal systems, *Geothermics*, 37, 622-634, 2008.

Fridleifsson, G.O. and W.A. Elders, The Iceland Deep Drilling Project: A search for deep unconventional geothermal resources, *Geothermics*, 34(3), 269-285, 2005.

IFC, *A formulation of the thermodynamic properties of ordinary water substance,* International Formulation Committee, Düsseldorf, Germany, 1967.

Moridis, G.J. and K. Pruess, T2SOLV: An Enhanced Package of Solvers for the TOUGH2 Family of Reservoir Simulation Codes, *Geothermics,* 27(4), 415 - 444, 1998.

Newson, J.A., W. Mannington, F. Sepulveda, R. Lane, R. Pascoe, E.K. Clearwater, and M.J. O'Sullivan, Application of 3d Modelling and Visualization Software to Reservoir Simulation: Leapfrog Geothermal and TOUGH2, *Proc. Thirty-Seventh Workshop on Geothermal Reservoir Engineering*, Stanford University, Stanford, Calif., 2012.

O'Sullivan, M.J. and D.P. Bullivant, A graphical interface for the TOUGH family of flow simulators, *Proc. TOUGH Workshop '95*, Berkeley, Calif., 1995.

O'Sullivan, M. J., J.P. O'Sullivan, A.E. Croucher, L. Stevens, M. Esberto, Modelling the evolution of a mine pit in a geothermal field at Lihir Island, Papua, New Guinea, *Proc. 33rd New Zealand Geothermal Workshop*, Auckland, New Zealand, 2011.

O'Sullivan, M.J. and A. Yeh, *Wairakei-Tauhara modelling report*, Uniservices and Department of Engineering Science, University of Auckland, 276 pp. (http://www.contactenergy.co.nz/web/pdf/environmental/P4ReservoirModellingReport.pdf), 2010.

O'Sullivan, M.J., A. Yeh and W.I. Mannington, A history of numerical modeling of the Wairakei geothermal field, *Geothermics*, 38, 155-168, 2009.

Pruess, K., C. Oldenburg, and G. Moridis, *TOUGH2 User's Guide, Version 2.0*, Report LBNL-43134, Lawrence Berkeley National Laboratory, Berkeley, Calif., 1999.

Wagner, W., J.R. Cooper, A. Dittman, J. Kijima, H.-J. Kretzschmar, A. Kruse, R. Mareš, K. Oguchi, H. Sato, I. Stöcker, O. Šifner, Y. Takaishi, I. Tanishita, J. Trübenbach, J. and Th. Willkommen, The IAPWS Industrial Formulation 1997 for the Thermodynamic Properties of Water and Steam, *ASME J. Eng. Gas Turbines and Power*, 122, 150-182, 2000.

Wellmann, J.F., Croucher, A.E. and Regenauer-Lieb, K., Python scripting libraries for subsurface fluid and heat flow simulations with TOUGH2 and SHEMAT, *Computers & Geosciences*, 43 (197-206), 2012.

Yeh, A., A. Croucher, and M.J. O'Sullivan, Recent experiences with overcoming TOUGH2 memory and speed limits, *Proc. 33rd New Zealand Geothermal Workshop*, Auckland, New Zealand, 2011.

SIMULATING MICROHOLE-BASED HEAT MINING FROM ENHANCED GEOTHERMAL SYSTEMS

Yingqi Zhang[a] , Lehua Pan[a], Patrick Dobson[a], Ken Oglesby[b], Stefan Finsterle[a]

[a] Lawrence Berkeley National Laboratory
Earth Sciences Division, MS 74-120
Berkeley, CA, 94708
e-mail: YQZhang@lbl.gov

[b] Impact Technologies, LLC
Tulsa, Oklahoma 74153

ABSTRACT

This study investigates the use of microholes as a potential approach to enhancing fluid flow and heat exchange within an engineered geothermal system (EGS), using numerical simulations. The idea behind microholes is that injecting the working fluid into a large number of spatially distributed microholes, rather than a few conventionally drilled wells, is likely to provide access to a larger reservoir volume, with enhanced overall flow distances and increased contact area between flowing fractures and the hot rock matrix. In this paper, we compare heat recovery factors calculated for EGS reservoirs with a conventional well configuration and with microhole arrays. The synthetic reservoir used has properties similar to those of the EGS test site at Soultz-sous-Forêts. The simulations provide preliminary insights into the potential of microholes for improving the efficiency and robustness of heat extraction from an EGS.

INTRODUCTION

In addition to a heat source, extraction of geothermal energy requires fluids that are able to transfer the heat from the hot rock matrix to the surface, and interconnected pore space that allows fluid flow at an appropriate rate between injection and production wells. In the absence of such favorable conditions, the concept of enhanced geothermal systems (EGS) provides a means to create a reservoir by hydraulically or thermally fracturing the rock to generate or increase permeability and inter-well connectivity, allowing injected working fluids to pick up reservoir heat as they flow along the created permeable pathways toward production wells.

Advances in drilling technology are essential for the technical success and economic viability of EGS. Specifically, the development of drilling technology for slimholes or microholes (bores less than 4 inches or 10.2 cm diameter) (Pritchett, 1998; Finger et al., 1999) may offer the flexibility needed to design well configurations that enable optimization of geothermal heat mining using EGS.

The objective of this study is to examine the potential of microholes—used as injection or production wells—to improve the efficiency and sustainability of geothermal energy production, as compared to EGS with a conventional well configuration. We test the supposition that this improved performance is achieved because (1) directionally drilled microholes can be distributed widely (both horizontally and vertically), so they intersect a larger portion of the hot reservoir and its fracture network, thus increasing the rock volume that is accessed by the circulating working fluid; and (2) the distributed nature of flow originating from or converging to spatially separated microholes reduces the risk of creating thermal short circuits.

These premises are examined through numerical modeling of a synthetic EGS reservoir, which is modeled after (but does not represent) the conditions at the European EGS test site at Soultz-sous-Forêts, France (e.g., Gérard and Kappelmeyer, 1987; Sausse et al., 2010). Temperatures and recovery factors are calculated for a conventional well configuration and one based on microhole arrays.

MODEL DEVELOPMENT

Reservoir Model

The reservoir model developed for the comparison of EGS performance using conventional and microhole well configurations has characteristics similar to those encountered at the European EGS demonstration site in Soultz-sous-Forêts, France. However, this is strictly a synthetic modeling study, and no conclusions about the potential performance of microholes at the test site should be drawn from this analysis, as the model is a highly simplified representation of the conditions at Soultz-sous-Forêts.

The model domain consists of a rectangular cuboid of dimensions 2.0 × 3.0 × 1.5 km, positioned at a depth between 3.8 and 5.3 km. The temperatures at the impermeable top and bottom boundaries of the model domain are fixed at 160ºC and 200ºC, respectively. Initial pressures vary hydrostatically from about 3.7 MPa at the top to about 5.1 MPa at the base. Within this block of low-permeability rock lies the EGS reservoir, consisting of a zone of fractures that were created or reactivated by hydraulic stimulation. The shape and size of this zone is based on the cloud of micro-seismic events recorded at Soultz-sous-Forêts (Michelet and Toksöz, 2007); the zone is assumed to be a horizontal, approximately elliptical region with a length and width of about 2.0 km and 1.0 km, respectively, and a thickness of 0.4 km, located at a depth between 4.4 and 4.8 km. The EGS reservoir is represented by a dual-permeability model, where permeable fractures and the essentially impermeable rock matrix are modeled as overlapping interacting continua. We account for global heat flow through the matrix continuum added to global fracture flow and the interaction between the fracture and matrix continua.

Finally, within the fractured EGS reservoir, we added a highly permeable, planar wide-aperture feature as a potential zone for preferential flow between the injection and production wells. We define the slightly inclined plane by the points of highest injectivity observed during hydraulic testing at Soultz-sous-Forêts (Sausse et al., 2010); it is assumed to extend across the entire stimulated reservoir.

The key heat mining process can be described as conductive heat transfer between the hot rock matrix and the working fluid flowing through the fracture network; this sustains the convective transport of heated fluid to the production well. The overall effectiveness of the conductive heat transfer depends on the contact area between the rock and the working fluid, which as a first approximation can be taken as the total fracture surface area. However, flow is likely to be channelized, i.e., the actual contact area available for heat transfer is substantially smaller than the geometric fracture surface area, which is calculated from fracture spacing information for the dual-permeability model. We therefore include a contact area reduction factor and apply it to the dual-permeability regions of our model. Table 1 summarizes some key model parameters.

Table 1. Base-case model parameters and ranges examined in global sensitivity analysis

Parameter	Value
Log_{10}(permeability wide-aperture zone [m^2])	-10.0
Log_{10}(permeability fractures horizontal [m^2])	-13.0
Log_{10}(permeability fractures vertical [m^2])	-13.0
Log_{10}(permeability matrix [m^2])	-18.0
Porosity wide-aperture zone [%]	2.0
Porosity fractures [%]	0.5
Porosity matrix [%]	5.0
Fracture spacing [m]	30.0
Log_{10}(fracture-matrix area reduction [-])	-1.0
Thermal conductivity [W m^{-1} ºC^{-1}]	3.0
Heat capacity [J kg^{-1} ºC^{-1}]	950.0
Injection rate [kg s^{-1}]	80.0
Injection temperature [ºC]	50.0

EGS performance is simulated using the non-isothermal, multiphase, multicomponent flow and transport code TOUGH2 (Pruess et al., 1999; http://esd.lbl.gov/TOUGH), as incorporated into iTOUGH2 (Finsterle, 2004; http://esd.lbl.gov/iTOUGH2).

Well Configurations

We compare EGS heat mining performance using two distinct well configurations (Fig. 1). The first configuration consists of conventionally drilled, large-diameter injection and production wells in an arrangement similar to that used at Soultz-sous-Forêts (Fig. 1a), where three conventional wells, aligned parallel to the maximum principal stress, were drilled from a single well pad, reaching the target formation at a depth between 4.5 and 5.0 km, and having a bottomhole separation distance of about 600 m. Cold water is injected through the central well, and hot water is produced from the two peripheral wells.

In the second configuration (Fig. 1b), 40 microholes of diameter 0.064 m emanate as two arrays from a conventionally drilled well. Thirty-four of the 40 microholes are drilled such that their end points circumscribe the outer edge of the stimulated zone, with the remaining six microholes terminating on the short axis of the elliptical fracture zone (i.e., the pattern of the end points of the microhole arrays resembles the Greek character θ). The kickoff angle of the microholes is 45º from the axis of the central well. While most likely curved in a real application, we assume that they are drilled straight until they reach their final position in the X-Y plane, at which point they become vertical. Each microhole is approximately 1 km long. The first array of 13 microholes kicks off at a depth of 3.8 km; this array comprises the microholes that reach the outermost portion of the EGS reservoir. The second array consists of the remaining 27 microholes, which emanate from the conventional well at a depth of 4.1 km. The microholes are used for injection; two conventional wells are used for production. The conventional wells are the same as those shown in Fig. 1a, except that the central well is shorter, terminating at the lowest microhole kickoff point at a depth of 4.1 km.

The conventional wells and the microholes are explicitly discretized in our numerical model, albeit in a simplified manner. Following the trajectory of the borehole, cylindrical gridblocks are inserted into the existing elements of the basic grid (Fig. 1a shows the basic grid on the faces of the model domain, where the unstructured, elliptical part indicates the location of the EGS reservoir). These well elements are connected to each other in the axial direction and to the elements in which they are embedded. The conventional wells are perforated only within the stimulated reservoir zone; the microholes are uncased and thus connected to the formation over their entire length.

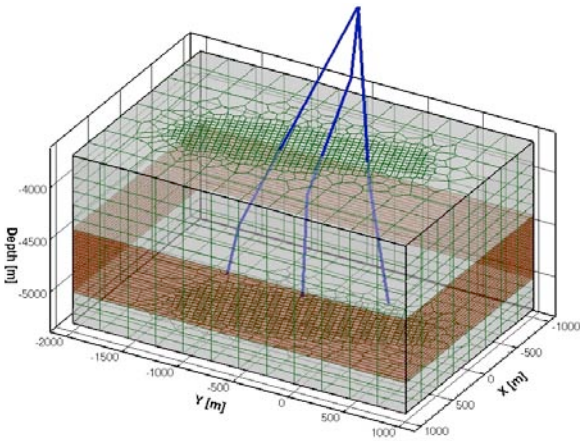

(a)

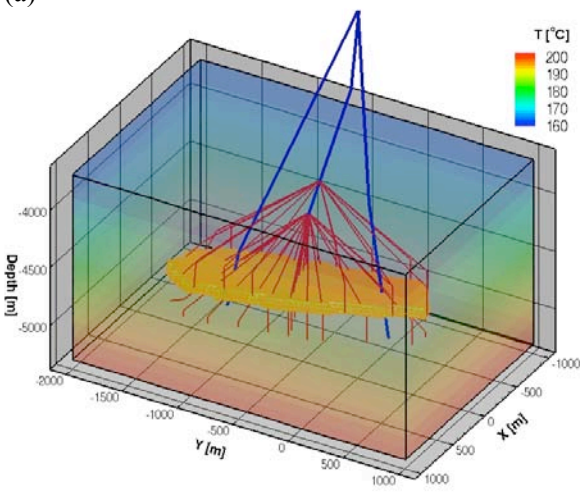

(b)

Figure 1. Simulated borehole configurations: (a) conventional wells, numerical grid on model domain faces, with unstructured portion indicating projection of elliptical EGS reservoir (model layer containing reservoir is highlighted); (b) microhole arrays, initial temperature distribution, and wide-aperture zone

Wellbore flow is calculated using the standard Darcy law with an effective permeability, which was determined for the expected flow velocities using a wellbore simulator that is integrated into the TOUGH2 code, calculating the transient

multiphase nonisothermal wellbore flow using the drift-flux model (Pan et al., 2011). For the wellbore sections above the model domain, i.e., from the land surface to a depth of 3,800 m, a semi-analytical solution for radial heat exchange with the surrounding formation is used (Zhang et al., 2011) to efficiently calculate heating of the injected water and heat losses from the produced water. Given the relatively long vertical flow distance in these wellbore sections, gravitational potential is added to the energy balance equation (Stauffer et al., 2003).

Heat Recovery Factor

The comparison of conventional and microhole-based EGS is made using a simple performance measure, which is the heat recovery factor at the end of a 30-year exploitation period. The heat recovery factor is defined as the cumulative heat recovered at the well head divided by the initial heat in the reservoir, E_0:

$$F = \frac{\int (q_p h_p - q_i h_i)\, dt}{E_0} = \frac{\Delta E}{E_0} \qquad (1)$$

Here, q_p and q_i are the mass production and injection rates, and h_p and h_i are the enthalpies of the produced and injected fluids, respectively. The net energy extracted from the reservoir, ΔE, can be used to assess the electrical potential of the well system. In addition to the heat recovery factor as an integral performance measure, we also monitor the thermal drawdown in the production wells as a function of time.

RESULTS AND DISCUSSION

We first describe the temperature of the produced fluid and the total thermal energy extracted from the two wells for an exploitation period of 30 years. Both configurations—injection through a conventional, central well and injection through an array of microholes—are presented and compared. Fig. 2 shows the temperature evolution of the produced fluid, which is indicative of thermal breakthrough and overall heat mining effectiveness.

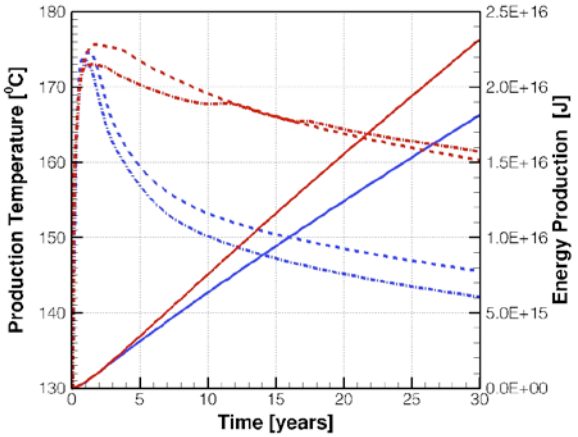

Figure 2. Fluid temperatures at well head of left (dash-dotted lines) and right (dashed lines) production wells for conventional (blue) and microhole (red) configurations. Total produced thermal energy (solid lines).

The temperature of the produced fluid at very early times is essentially equal to the temperature encountered at the depth of the wide-aperture, high-permeability feature, which is the main feed zone. Temperatures at the well head rise as the relatively colder fluid that is initially in the wells is flushed out, and as the formation in the immediate vicinity of the production wells warms up, reducing heat losses in the upper part of the reservoir and in the 4 km long sections from the reservoir to the surface, as calculated using the semi-analytical approach of Zhang et al. (2011).

After this initial temperature increase, colder injection fluid soon reaches the production wells, leading to substantial cooling, especially for the conventional well configuration. The temperatures in the two production wells differ slightly as the feed zones are at different depths due to the inclination of the wide-aperture zone, and due to the fact that their location with respect to the injection well and the geological features are asymmetric. In contrast to the conventional well case, injection through a microhole array distributes the fluid over a wider volume of the stimulated reservoir. Flow velocities in the formation are slower, and a larger fraction of the produced water enters the well through the fracture network of the stimulated rock rather than almost exclusively through the

wide-aperture feed zones, as is the case for the conventional well configuration. As a result, thermal breakthrough is much less pronounced, and the temperature of the produced fluids at the end of the simulated period is substantially higher (approximately 161°C) compared to that obtained with the conventional well configuration (approximately 146°C).

Fig. 2 also shows the cumulative heat extracted from the reservoir, which mirrors the trend of the production temperature as the total flow rate remains essentially constant and (for this system which is essentially closed for fluid flow, but not for heat flow) equal to the injection rate of 80 kg/s. For the base-case scenario, about 27% more energy is produced with the microhole configuration.

Fig. 3 shows the temperature distribution after 30 years of exploitation for both the conventional and microhole configurations. The conventional well configuration results in a large volume of fluid flowing along the wide-aperture zone, limiting heat exchange to a relatively narrow channel. This is clearly visible as an essentially one-dimensional zone of reduced temperature between the injection and production wells. In contrast, injecting the working fluid through a microhole array accesses a larger reservoir volume from which heat can be extracted. The temperature decline in that region, which includes a substantial portion of the fractured reservoir outside the wide-aperture zone, is proportionally less severe; this is reflected in the higher temperature of the produced fluid (see Fig. 2).

These simulations support the concept that distributing the working fluid through microholes leads to more effective heat extraction from a larger rock volume, and is less susceptible to the presence of a wide-aperture feature that promotes preferential flow, reduced contact with the reservoir matrix, and thus early thermal breakthrough. Note that the configuration of the microhole array (the number of microholes, their length, diameter, orientation, and spatial distribution) has not been optimized for maximum heat mining efficiency. It has been designed based on simple criteria assuming some knowledge about the extent of the stimulated reservoir. A formal optimization of microhole configuration parameters to maximize heat recovery factors will be undertaken in a future analysis.

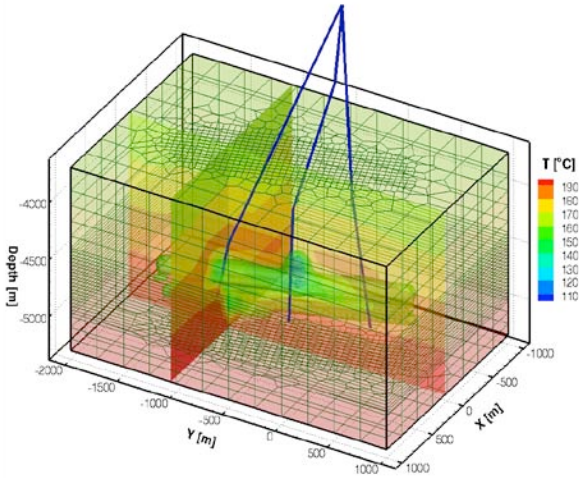

(a)

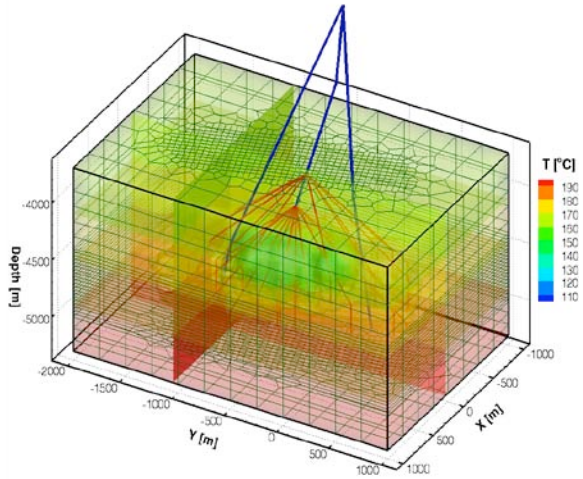

(b)

Figure 3. Simulated temperature distribution after 30 years of exploitation using (a) conventional and (b) microhole configurations.

CONCLUDING REMARKS

The success and sustainability of energy production from enhanced geothermal systems largely depends on the ability of the working fluid to get in contact with a substantial volume of hot reservoir rock. Large-scale stimulation of existing fractures or creation of a new fracture system with sufficient density and connectivity is a prerequisite. However, even if such stimulation is successful, the volume of the heat-storing reservoir accessed by the working fluid may be

very limited for a conventional well configuration, where cold water is injected at discrete locations within a small number of injection wells and produced from a few feed zones in production wells.

The flexibility offered by microhole drilling technology enables installation of a large number of boreholes from a central well, in a configuration that allows for distributed injection (or production) of geothermal working fluids. Such a configuration has the potential to (1) increase the probability of intersecting flowing fractures, (2) increase the fracture surface area contacted by circulating water and thus increase the volume of rock accessible for heat mining, and (3) reduce the risk of flow channeling and early thermal breakthrough.

The generic modeling study presented here indicates that EGS based on microhole arrays could significantly increase heat mining rates and their sustainability over longer time periods.

While the study examined the general concept and showed the potential benefits of microhole-based EGS, its viability strongly depends on the technical feasibility and costs of drilling microhole arrays from a central, conventionally drilled large-diameter well. Great advances have been made in horizontal and directional drilling, opening up opportunities for additional well configurations that support the overall goal of increasing the accessible rock volume. Stimulation of that rock volume is another key issue that may benefit from the flexibility offered by advanced drilling technologies and multiple wells emplaced with an optimized configuration. Some of these issues will be addressed in future research.

ACKNOWLEDGMENT

This work was supported by Lawrence Berkeley National Laboratory under U.S. Department of Energy, Assistant Secretary for Energy Efficiency and Renewable Energy, Geothermal Technologies Program, Contract No. DE-FOA-0000075: Recovery Act: Enhanced Geothermal Systems Component Research and Development/Analysis.

REFERENCES

Finger, J., R. Jacobson, C. Hickox, J. Combs, G. Polk, and C. Goranson, *Slimhole Handbook: Procedures and Recommendations for Slimhole Drilling and Testing in Geothermal Exploration*, Report SAND99-1076, Sandia National Laboratories, Albuquerque, New Mexico, 1999.

Finsterle, S., Multiphase inversion modeling: Review and iTOUGH2 applications, *Vadose Zone Journal*, *3*, 747–762, 2004.

Gérard, A., and O. Kappelmeyer, The Soultz-sous-Forêts project, *Geothermics, 16*(4), 393–399, 1987.

Michelet, S., and M.N. Toksöz, Fracture mapping in the Soultz-sous-Forêts geothermal field using microearthquake locations, *Journal of Geophysical Research*, *112*, B07315, 2007.

Pan, L., C.M. Oldenburg, K. Pruess, and Y.S. Wu, Transient CO_2 leakage and injection in wellbore-reservoir systems for geologic carbon sequestration, *Greenhouse Gases: Science and Technology, 1*(4), 335–350, 2011.

Pritchett, J.W., *Electrical Generating Capacities of Geothermal Slim Holes*, Report MTSD-DFR-98-16223, Maxwell Technologies Systems Division, Inc., San Diego, California, 1998.

Pruess, K., C. Oldenburg, and G. Moridis, *TOUGH2 User's Guide, Version 2.0*, Report LBNL-43134, Lawrence Berkeley National Laboratory, Berkeley, Calif., 1999.

Sausse, J., C. Dezayes, L. Dorbath, A. Genter, and J. Place, 3D model of fracture zones at Soultz-sous-Forêts based on geological data, image logs, induced microseismicity and vertical seismic profiles, *C. R. Geoscience,* 342, 531–545, 2010.

Stauffer, P.H., J.S. Stein, and B.J. Travis, *The Correct Form of the Energy Balance for Fully Coupled Thermodynamics in Liquid Water*, Report LA-UR-03-1555, Los Alamos National Laboratory, Los Alamos, New Mexico, 2003.

Zhang, Y., L. Pan, K. Pruess, and S. Finsterle, A time-convolution approach for modeling heat exchange between a wellbore and surrounding formation, *Geothermics*, *40*(4), 251–266, 2011.

Nuclear Waste Storage

T2GGM—A COUPLED GAS GENERATION MODEL FOR DEEP GEOLOGIC DISPOSAL OF RADIOACTIVE WASTE

John Avis[1], Paul Suckling[2], Nicola Calder[1], and Robert Walsh[1]

[1] Geofirma Engineering
Ottawa, Ontario, K1R 1A2, Canada
javis@geofirma.com, ncalder@geofirma.com,
rwalsh@geofirma.com

[2] Quintessa Limited
Henley-on-Thames
Oxfordshire, RG9 1AT, U.K.
e-mail: paulsuckling@quintessa.org

ABSTRACT

Deep geologic disposal of radioactive waste is being planned in a number of international programs. Within a deep geologic repository (DGR), gases are generated by corrosion of metals and degradation of organic wastes. Reactions, and thus gas generation rates, are dependent upon pressures, temperature, and the availability of water or water vapor within the repository. Furthermore, many reactions consume water. Consumption rates and repository state are not known a priori and are in fact coupled processes.

A numeric model of coupled gas generation and transport has been developed and implemented in a code (T2GGM). The code consists of a gas generation model (GGM), which calculates rates of gas generation and water consumption within the DGR due to corrosion and microbial degradation of the waste packages, integrated with the widely used two-phase flow code TOUGH2 (Pruess et al, 1999), which models the subsequent two-phase transport of the gas through the repository and into the DGR shafts and geosphere.

T2GGM has been applied to the assessment of gas transport from a proposed low- and intermediate-level radioactive waste (L&ILW) DGR and to study the impact of container corrosion in a hypothetical used fuel DGR.

INTRODUCTION

In Canada, Ontario Power Generation, assisted by the Nuclear Waste Management Organization (NWMO), is currently seeking regulatory approval for construction of a DGR for L&ILW at the site of the Bruce Nuclear Power Plant. The plan involves storing wastes in rooms constructed in extremely low-permeability sedimentary formations. The rooms will not be backfilled to allow for a large void space to minimize possible overpressures created by gas generation. Engineered seals will be emplaced in tunnels and shafts.

NWMO is also conducting evaluations of generic sites for disposal of used fuel. In one scenario under investigation, used fuel would be packaged in carbon steel containers, emplaced in disposal tunnels backfilled with bentonite, and sealed.

In both these programs, numeric modeling work has been undertaken to calculate the generation and buildup of gas in the repository, the exchange of gas and groundwater between the repository and the surrounding rock, and between the rock and the surface environment. The results are used to inform the repository design and postclosure safety assessment modeling.

Initial versions of safety assessments used TOUGH2 with the EOS3 equations of state (Pruess et al, 1999) and a standalone version of GGM. Gas generation rates were calculated based on assumptions regarding repository resaturation and repressurization rates and subsequently input to TOUGH2 as time-varying rates. Analysis of modeling results indicated that the actual repository resaturation and repressurization profiles predicted by TOUGH2 varied considerably from those assumed in developing the gas generation rates. T2GGM was developed to eliminate this discrepancy.

The GGM includes four of the key mechanisms for the generation of gas and consumption of water. Reactions are determined independently

in one or more compartments. Each compartment contains a separate inventory, which could range from a panel of disposal rooms, individual rooms, or indeed individual waste containers or portions of waste containers.

Each GGM compartment comprises one or more TOUGH2 elements. At each time step, the integration code calculates compartment average values of pressure, saturation, temperature, and relative humidity, which are passed through to GGM. Gas and water generation rates for the subsequent time step are calculated by GGM and introduced into the TOUGH2 elements as sources. T2GGM data flows are shown in Figure 1.

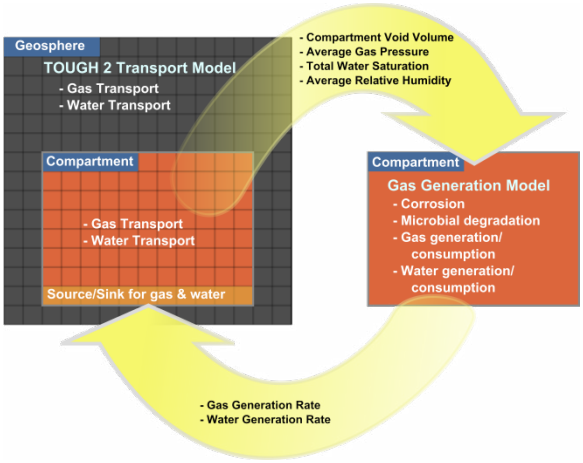

Figure 1. Data flows within the T2GGM code.

GAS GENERATION MODEL

The GGM tracks the production and consumption of the key chemical species (e.g., metals, organic wastes, gases, water) in the repository, and the fluxes of the water and gases into and out of the repository. It is designed to fully conserve Fe, C, and water, and to ensure that reactions are limited by the availability of water. Some elements are conservatively assumed not to be limiting and are not tracked to complete mass balance (e.g., N needed to support microbial reactions).

A simplified version of the complete gas generation model (GGM) is presented here. The full GGM additionally includes: enhanced corrosion of metallic wastes due to high CO_2 partial pressures; oxidation-reduction reactions for the consumption of O_2, NO_3^-, Fe(III), and SO_4^{2-} terminal electron acceptors; and a model for biomass growth, death, and recycling as an additional source of organic waste.

The organic and metallic wastes are classified into a number of waste streams. This allows the degradation/corrosion of each waste stream to be modeled independently and assigned different reaction rates. Organic wastes are classified into three groups: cellulosic wastes, ion-exchange resins, and plastics and rubbers. Metallic wastes are classified into four groups: carbon and galvanised steels, passivated carbon steels, stainless steels and nickel alloys, and zirconium alloys. The GGM includes three key mechanisms for the generation of gas and consumption of water:

- The microbial degradation of organic wastes;
- Methanogenesis via the microbial hydrogen mechanism; and
- The corrosion of metallic wastes.

These processes may occur in either the saturated (water submerged) or vapor phases. Gases are modeled as partitioning between the saturated and vapor phases according to Henry's Law. The relative humidity of the vapor phase is calculated by TOUGH2 and provided as an input to the model. Microbial activity in the vapor phase is dependent on the relative humidity and ceases below a specified threshold (default value of 0.6).

Microbial Degradation of Organic Wastes

Cellulosic wastes are modeled as cellulose that degrades in the presence of water according to the following reaction:

$$C_6H_{10}O_5 + H_2O \rightarrow 3CO_2 + 3CH_4 \qquad (1)$$

The limiting reaction rate is that for cellulose hydrolysis. Ion exchange resins, plastic, and rubber are modeled in a similar fashion.

Methanogenesis via the Microbial Hydrogen Mechanism

Significant amounts of hydrogen may be produced via anaerobic corrosion. This can be consumed anywhere in the system via microbial hydrogen oxidation. During the final methanogenic stage, the relevant reaction is:

$$4H_2 + CO_2 \rightarrow CH_4 + 2H_2O \quad (2)$$

provided that there is sufficient humidity to support microbial processes. The rate for this reaction is modeled as first order with respect to CO_2 concentration, but limited by the availability of hydrogen.

Corrosion of Metallic Wastes

Separate corrosion models are used for L&ILW and used fuel containers (UFC). The L&ILW model assumes isothermal conditions, whereas the UFC model allows for high temperature corrosion of the steel containers.

Corrosion of L&ILW metallic wastes and container materials occurs within the saturated (water submerged) and vapor phases. Corrosion processes in the vapor phase are dependent on the relative humidity, and cease below a threshold of 0.6. Galvanized and carbon steels are treated as a single metallic source, represented by the corrosion of Fe as carbon steel (C-steel). The overall reaction for the anaerobic corrosion of C-steel is given below:

$$3Fe + 4H_2O \rightarrow Fe_3O_4 + 4H_2 \quad (3)$$

The nonisothermal UFC corrosion model includes four phases of corrosion processes, each of which occurs under different conditions (rather than in strict sequence) based on the conceptual model for the corrosion: (1) Dry Air Oxidation, (2) Aerobic Unsaturated Corrosion, (3) Anaerobic Unsaturated Corrosion, and (4) Anaerobic Saturated Corrosion.

Phase 1—Dry Air Oxidation occurs under the initial high temperature, low relative humidity aerobic environment. This is represented by

$$4Fe + 3O_2 \rightarrow 2Fe_2O_3 \quad (4)$$

As the relative humidity increases, Phase 2, Aerobic Unsaturated Corrosion, will start to dominate, which is represented by

$$4Fe + 3O_2 + 2H_2O \rightarrow 4FeOOH \quad (5)$$

Eventually, conditions will become anaerobic, and saturation will remain low in the backfill close to the canister. Phase 3, Anaerobic Unsaturated Corrosion, is represented by Equation (3).

Finally, water may reach the canister. In the presence of water containing carbonates from the surrounding clay, the dominant corrosion mechanism becomes

$$Fe + CO_3^{2-} + 2H_2O \rightarrow FeCO_3 + H_2 + 2OH^- \quad (6)$$

This is referred to as Phase 4, Anaerobic Saturated Corrosion.

Each of these corrosion processes has its own temperature-dependent corrosion-rate expression.

Implementation

GGM consists of first-order coupled differential equations given by the mass-balance equations and nondifferential equations, such as Henry's law. These equations are evolved forward in time using a modified Euler time stepping scheme, and the nondifferential equations are solved for the remaining variables at each time step.

TOUGH2 INTEGRATION

GGM capabilities are invoked by using the GGMIN keyword in the T2GGM input file, typically generated using the mView pre-processor (Avis et al. 2012). Control flags are read and GGM elements and compartment numbers are specified. Connections from GGM compartments to the geosphere are defined, and GGM basic rate constants are specified. Compartment inventories are defined in separate individual input files. A pre-run check confirms consistency of entered data and echoes input to the standard output file.

After each time step is executed, average compartment pressures, saturations, and relative humidity (RH) are calculated. These are passed to GGM, which then calculates gas generation and water consumption for each compartment. Internally, GGM tracks generation and consumption of six gases: H_2, H_2S, CH_4, CO_2, N_2, and O_2. However, TOUGH2/EOS3 uses a single gas, air. Modifications have been made to TOUGH2/EOS3 to use other single gases (currently, H_2, CH_4, CO_2, He, Ne). GGM sums the individual molar generation rates of the six GGM gases to result in a total molar generation rate for each compartment, which is converted to

a mass rate for the equivalent number of moles of the single specified TOUGH2 gas.

Simulations were conducted under two GGM scenarios: (1) non-water-limited (NWL), which assumed that there was always sufficient water available to support reactions and water consumed by reactions was not removed from the repository; and (2) water-limited (WL), which enforced a mass balance of water and limited reaction rates to available water inflow rates.

Total compartment gas generation and water consumption rates (for WL simulations) are then allocated to each element in a compartment using one of several available allocation schemes. The rates are incorporated in the TOUGH2 matrix assembly in subroutine MULTI in a manner similar to TOUGH2 subroutine QU.

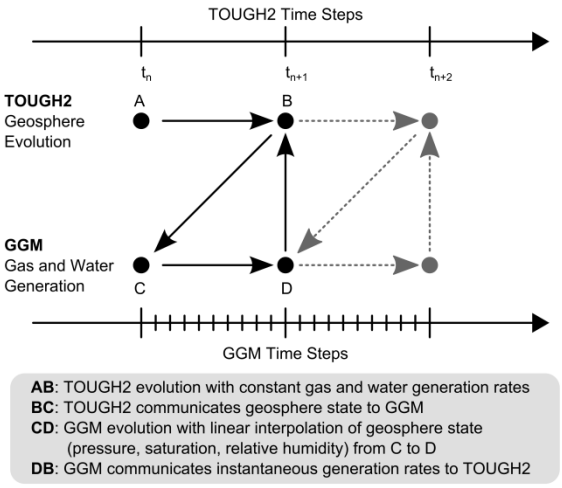

Figure 2. Time-stepping approach

Time stepping for GGM and TOUGH2 are largely decoupled. As shown in Figure 2, GGM will typically take multiple time steps during each TOUGH2 time step. GGM suggests a maximum time step size for TOUGH2 based on rates of change of calculated generation and consumption rates.

APPLICATION TO L&ILW DGR

Detailed gas modeling (Geofirma and Quintessa, 2011) of the proposed DGR was conducted to support regulatory submissions (OPG 2011a, 2011b). The modeling was performed for a number of parameter and conceptual-model sensitivity cases, over a 1 Ma time frame starting at repository closure. All cases were derived from a reference case characterization of the system that assumes a constant present day climate, with no change in boundary conditions during the 1 Ma period.

Data

Most of the data used in the modeling are specific to the DGR system and have been taken from the waste characterization, site characterization, and repository engineering programs. The overall DGR program has been structured such that the safety assessment has been produced in multiple iterations, in synchronization with the inventory, design, and geosciences programs.

The repository is planned to be excavated at a depth of about 680 m in low permeability Ordovician age limestone. Several hundred meters of low permeability shales and limestones separate the repository from the nearest permeable formations above and below. Site characterization results indicate that the Ordovician formations are underpressured and show evidence of the presence of a partial gas phase. Porewater within the host rock is extremely saline, as are groundwaters in the underlying and overlying medium permeability formations.

Capillary pressure and relative permeability data are represented using the modified van Genuchten equations, with parameter values derived from site characterization data for geosphere materials and external sources for shaft-sealing materials. Parameters are adjusted within the excavation damaged zones (EDZ) to reflect increased permeability in these zones.

The inventory of approximately 200,000 m^3 of waste packages includes organic (2.2×10^7 kg) and metallic (6.6×10^7 kg) materials.

Discretization and Property Assignment

The model discretization uses a simplified representation of the repository panels, access tunnels and shaft system. The planned repository will have two shafts (main and ventilation) that are located in close proximity. For modeling purposes, these were combined to form a single

shaft with the effective cross-sectional area equivalent to that of the two designed shafts. Access tunnel layout was also simplified and individual emplacement rooms in each panel combined. The resulting model grid consists of 126,000 nodes and 390,000 connections. Figure 3 is an illustration of the model discretization.

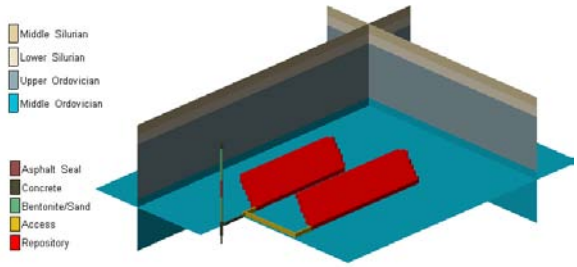

Figure 3. Model discretization showing repository panels, access tunnels, and combined shaft.

The emplacement rooms and repository tunnels are not backfilled, so as to allow void space for expansion of gas. The two waste panels form a single GGM compartment.

Reference Case (NE-RC) Results

The NE-RC case assumes 10% gas saturations within an underpressured Ordovician geosphere, consistent with site characterization results.

The operational phase of the facility was simulated as a 60-year period when shaft and repository pressures were set to atmospheric and gas saturations were set to 100%. At closure, the monolith (emplaced concrete seal within access tunnels and the bottom part of the shafts) and shaft seals are assumed to be placed instantaneously at specified gas saturations.

From this point forward, gas forming from degradation and corrosion reactions starts to pressurize the repository. The first few years involve sustained gas and water consumption due to aerobic degradation. There is a sharp peak in the rate of gas consumption (primarily hydrogen) and water production during the ferric iron and sulphate reduction stages, due to hydrogen oxidation.

The longest sustained period of gas generation occurs during the methanogenic stage up to 4000 years, primarily due to the production of hydrogen through the corrosion of the carbon and galvanized steels. Methane generation via the microbial metabolism of carbon dioxide and hydrogen, and the exhaustion of the metallic wastes, causes a decline in the amount of hydrogen present after this time. The NE-RC case parameters maximize microbial activity and gas generation by assuming that microbes are active if there are organics and water present, regardless of salinity or other factors, and that essentially complete degradation occurs.

Gas generation and water consumption rates both continue to decline as the waste packages become fully degraded. Figure 4 shows predicted rates, while Figure 5 presents the evolution of gas composition within the repository.

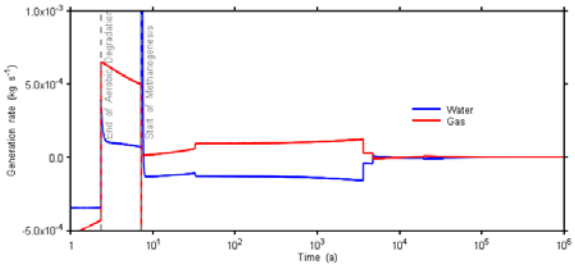

Figure 4. Non-water-limited reference case gas generation and water consumption rates in repository

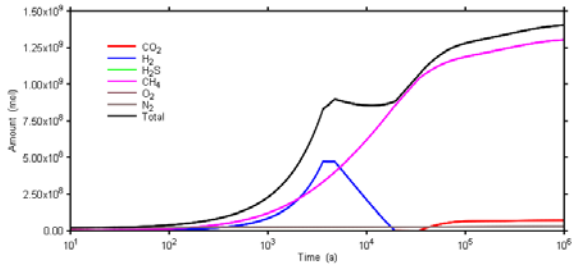

Figure 5. Amounts of gas in the vapor phase within the repository (Non-water-limited reference case)

Pressures rise in the repository as gas is generated. The low permeability of the seal system prevents pressurized gas from traveling up the shaft. The reference case assumes that gas is present in the geosphere, albeit in small amounts due to the low gas saturations (10%) and low porosities of the rock mass. In addition to gas generated within the repository by degrada-

tion/corrosion, formation gas flows into the repository and contributes to the increase in pressure. For the NWL scenario, small amounts of formation liquid enter the repository during the period up to approximately 80 ka when pressure in the repository is lower than the liquid pressure in the surrounding geosphere. In the WL scenario, all water initially present in the repository is consumed within 500 years, after which reactions are limited by inflow rates. In both scenarios, any residual water is expelled as pressures in the repository continue to increase. The evolution of repository pressure and saturation is shown in Figure 6. Repository saturation (the fraction of the repository volume that is filled with liquid) peaks at less than 0.01 or 1%. For the WL scenario, a minimum repository liquid saturation (10^{-4}) is enforced for numeric reasons during the period of liquid inflow. At the end of the 1 Ma simulation period, the repository is essentially dry.

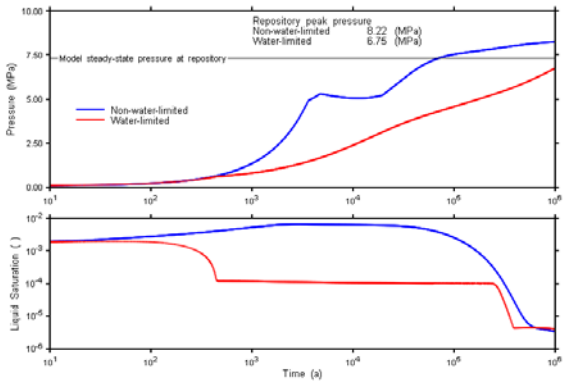

Figure 6. Evolution of reference-case repository pressure and liquid saturation for water-limited and non-water-limited scenarios

Other Cases Results

Figures 7 and 8 present the repository pressure and saturation evolution for all calculation cases for the NWL scenario.

It can be seen that pressures never exceed 10 MPa and are thus well below the estimated lithostatic pressure at the repository horizon (17 MPa). Repository saturations do not exceed 15%, except for cases with no gas generation (NE-NG1 and NE-NG2) and the disruptive event shaft failure cases (SF-BC and SF-ED).

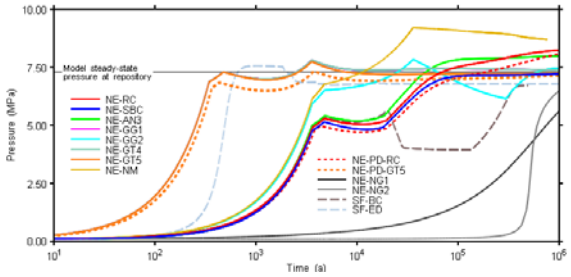

Figure 7. All Cases: Evolution of repository pressure (non-water-limited scenarios)

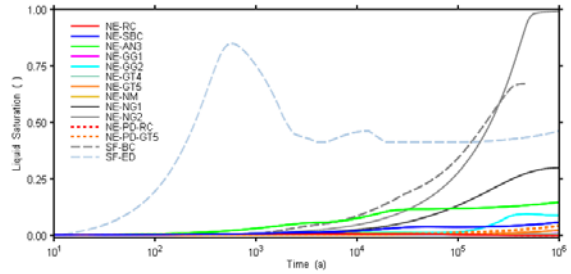

Figure 8. All Cases: Evolution of repository saturation (non-water-limited scenarios)

There are five normal evolution cases where pressures in the repository are sufficient to initiate flow up the shaft. These are high gas generation rate cases (NE-GG1 case or variants NE-GT4, NE-GT5, NE-PD-GT5), or the high gas pressure case (NE-NM). Shaft gas flow for normal evolution cases exits the shaft at the overlying, more permeable formation, with no free gas reaching potable groundwater. Only the shaft seal failure cases have the potential for free gas to directly reach the shallow groundwater.

NWL results were conservative, leading to generally higher repository pressures and saturations. For most WL simulations, the repository remained virtually dry for the majority of the 1 Ma simulation period.

Conclusions

Normal evolution and sensitivity cases indicate that the repository will perform as designed, isolating the waste and generated gases for the 1 Ma performance period.

APPLICATION TO NEAR-FIELD UFC CORROSION

The goal of this ongoing work is to assess room resaturation, gas pressures, and container corrosion for an all-steel UFC in a low-permeability

sedimentary host rock. While copper shell UFCs are the reference design, steel UFCs are being evaluated as a design option consistent with some sedimentary rock DGR concepts in Europe. Unlike a UFC with a copper shell, the steel canister will corrode over time, producing hydrogen gas.

Simulations to date have focused on the scale of the UFC/placement room, assessing the near-field response of the geosphere and engineered sealing materials to steel used-fuel-container corrosion and consequent gas generation. Only water-limited scenarios have been assessed. With focus on a single container, the model accounts for nonisothermal behavior, two-phase flow, variable saturation, and variable corrosion. As a conservative simplification for this work, the placement room is assumed to be fully sealed—continuity of the excavation damaged zone (EDZ) beyond the placement room is not considered.

Discretization and Property Assignment

The near-field geometry of this model, called the quarter-container model, is shown in Figure 9.

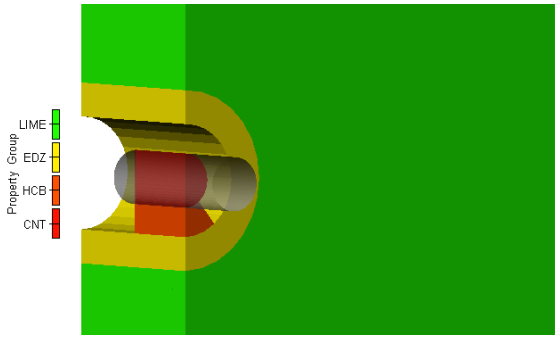

Figure 9. Close-up views of container, EDZ, highly compacted bentonite pedestal, and limestone host rock.

The model extends 500 m above and 1000 m below the repository horizon. Horizontally, the model extends 10 m from the center of the canister, assuming that emplacement drifts are spaced on 20 m centers. The large vertical extents were required to appropriately model heat dissipation over one million years. The reference case assumes that the void space surrounding the canister will be filled with bentonite pellets. A single layer of elements in contact with the container are connected to the GGM, as shown in Figure 10.

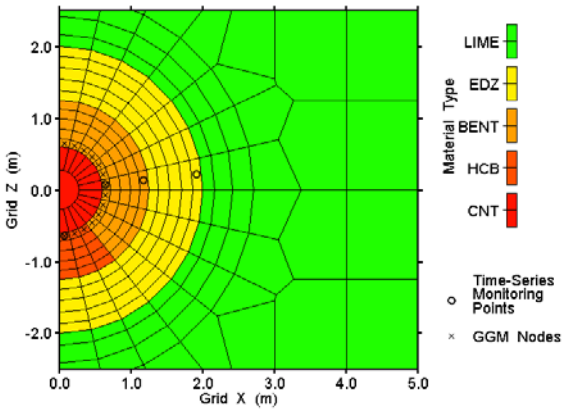

Figure 10. Discretization in container plane.

Preliminary Results

Initial results of the modeling include corrosion, thermal, and saturation response (Figure 11). Although preliminary and conservative, these results provide an example of the value of this coupled approach to modeling long-term degradation of waste canisters in low-permeability sedimentary environments.

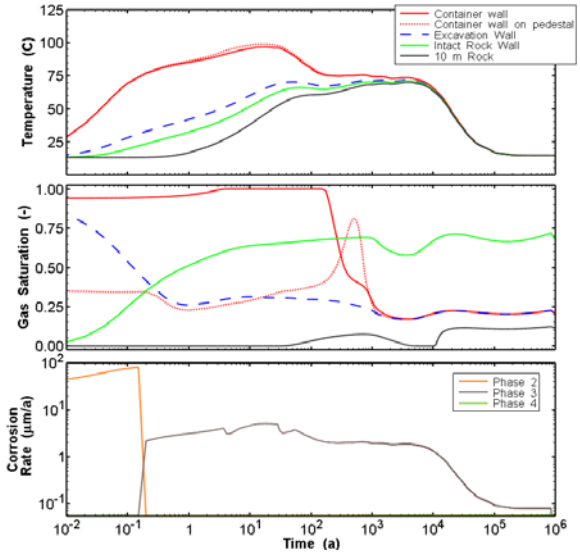

Figure 11. Time series results for temperature, gas saturation, and corrosion rate.

The bentonite pellets adjacent to the container are fully gas saturated at approximately 3 years and begin to resaturate with water at approximately 200 years, as the temperature drops. By 2000 years, gas saturations are approximately 20%, and remain so for the remainder of the simulation. Gas saturations in the EDZ are

higher due to reduced capillary pressures, when compared to the host rock and bentonite.

Corrosion results show that Phase 1 never occurs: repository relative humidity is at 100% from the time of emplacement with 6% liquid in the gap fill and 65% in the pedestal. Phase 2 corrosion occurs for a period of approximately 0.2 years, after which all oxygen is exhausted. Phase 3 corrosion is initiated, and continues under water-limited conditions until the canister is consumed completely at 850 ka. Beyond 2000 years, as the bentonite resaturates and the incoming water flow rate is reduced, the rate of Phase 3 corrosion gradually moderates, reaching a new equilibrium that persists until 850 ka.

CONCLUSIONS

The T2GGM code allows for an assessment of system behavior that couples gas generation processes with repository pressure and saturation states. It has been applied to L&ILW and used fuel DGR assessments in low-permeability media. The water-limited scenario results show the impact of limiting reaction processes to available resources. T2GGM provides a new capability to include important coupled repository processes in TOUGH2 simulations.

ACKNOWLEDGEMENTS

The authors would like to thank the NWMO for continued support, and particularly Helen Leung and Erik Kremer, the project managers for the work described herein. We would also like to thank Richard Little, the Quintessa project manager for the L&ILW DGR Postclosure Safety Assessment project.

REFERENCES

Avis, J., N. Calder, and R. Walsh, *mView – A powerful pre- and post-processor for TOUGH2*, Presented at the TOUGH Symposium 2012, Lawrence Berkeley National Laboratory, Berkeley, Calif., 2012.

Geofirma and Quintessa, *Postclosure Safety Assessment: Gas Modelling*, Geofirma Engineering Ltd. and Quintessa Ltd. report for the Nuclear Waste Management Organization NWMO DGR-TR-2011-31, Toronto, Ontario, 2011.

OPG, *OPG's Deep Geologic Repository for Low and Intermediate Level Waste: Environmental Impact Statement*, Ontario Power Generation Report 00216-REP-07701-00001 R000. Toronto, Ontario, 2011a.

OPG, *OPG's Deep Geologic Repository for Low and Intermediate Level Waste: Preliminary Safety Report*, Ontario Power Generation Report 00216-SR-01320-00001 R000, Toronto, Ontario, 2011b.

Pruess, K., C. Oldenburg, and G. Moridis, *TOUGH2 User's Guide, Version 2.0*, Report LBNL-43134, Lawrence Berkeley National Laboratory, Berkeley, Calif., 1999.

Quintessa and Geofirma, *T2GGM Version 2: Gas Generation and Transport Code*, Quintessa Ltd. and Geofirma Engineering Ltd. report for the Nuclear Waste Management Organization NWMO DGR-TR-2011-33, Toronto, Ontario, 2011.

USING A GENERALIZED POWER LAW FOR SIMULATING THE FEEDBACK EFFECT OF DISSOLUTION/PRECIPITATION ON DIFFUSIVE TRANSFER IN TOUGHREACT

A. Burnol, F. Claret

BRGM (French Geological Survey)
Water, Environment and Ecotechnology Division (D3E)
3 avenue Claude-Guillemin - BP 36009
45060 Orléans - France
e-mail: a.burnol@brgm.fr

ABSTRACT

In the case of variable porosity calculations (due to precipitation/dissolution in a calculation coupled with chemistry), the permeability and diffusion coefficients in different porous media vary with porosity. In the case of nuclear waste storage, solute transport is assumed to be diffusion-controlled, because of the extremely low permeability of surrounding materials, like concrete or clay. Various experiments and also different reactive transport modeling show a possible clogging due to the alkaline perturbation at the concrete/bentonite or concrete/clay interfaces (Gaucher et al., 2004; Burnol et al. 2006; Trotignon et al., 2007; De Windt et al., 2008). The decrease in porosity will therefore impact the extent of diffusion of all chemical elements, including radionuclides, through the engineered and geological barriers. Accounting for the feedback effect of porosity changes due to the chemical reactivity is therefore an important issue in simulating the migration of radionuclides out of the disposal drift. The chemical conditions found in deep nuclear waste storage raise some concern about the migration of radionuclides at the interface between the engineered and geological barriers, where the alkaline perturbation could cause a "clogging" and therefore could impact the diffusion-controlled process itself.

In this paper, we describe and test a new general "power law" which connects the effective diffusion coefficient and the porosity evolution. We conclude that if the version V1.0/V1.2 is used to study the diffusion of radionuclides in the surrounding zone of a waste nuclear disposal, the effective diffusion could be overestimated, even with the Millington Law. A modified version of TOUGHREACT with diffusion harmonic weighting gave the same results as the HYTEC code, both in the case of weak feedback (power=1/3) or strong feedback (power=2) in the new "power law". Note that the power law described in this paper is only verified for the aqueous phase, but the same kind of law has been developed for the gaseous phase in a two-phase system.

STATE OF ART AND THE NEW PROPOSED POWER LAW

The law of Millington and Quirk (1961) is implemented in TOUGHREACT V1.0 (YMP Q V3.1). The user must set a "virtual" null value for the tortuosity parameter in the flow.inp file to introduce a so-called "tortuosity" τ value equal to the porosity power 1/3. Under saturated conditions, the effective diffusion coefficient D_e is written as a product of the porosity ω, the "tortuosity" τ and the free-water diffusion D_0 :

$$D_e = \omega \tau D_0, \qquad \tau = (\omega)^{1/3} \qquad \text{(E1)}$$

Some limits to this specific law are as follows: the porosity power 4/3 is not the experimental cementation factor for cementious materials like the CEM I paste (Trotignon et al., 2007); it is not possible to consider different tortuosities if the feedback effect with the Millington law is taken into account. The effective diffusion coefficient may be very different between materials, e.g., about 2 orders of magnitude for chloride effective diffusion between clay and concrete (Trotignon et al., 2007). To overcome these limitations, and in the absence of better information on the physical characteristics of perturbated CEM I cement, MX80 bentonite, or Callovo-Oxfordian clay, a general power law similar to Archie's law (Archie, 1942), as modified by Winsauer et al. (1952), has been chosen to describe the relation between the

effective diffusion and the porosity evolution (Lagneau, 2002):

$$D_e = \omega \tau D_0, \qquad \tau = \left(\frac{\omega - \omega_{\min}}{\omega_o - \omega_{\min}} \right)^p \tau_0 \quad \text{(E2)}$$

with ω_{min}, the critical porosity under which diffusion is supposed to stop (percolation threshold), and p, the power coefficient (e.g., 0.3 for a nonconsolidated sand, 1.2 for a limestone, and 2 for a cement paste chosen by Trotignon et al. (2007)).

Test-Case I : Verification case for power coefficient p=1/3 (Millington and Quirk)

In test-case I, the objective is not yet to validate the new law but only to verify that the old law (E1) is equivalent to the new law (E2) with a power 1/3 and with a tortuosity parameter in the new law within both media.

Two media with a different porosity in a 2m length 1D geometry were considered. The effective diffusion coefficients are initially very similar in both media, with the small differences only due to the difference in porosity. The physical characteristics of both media are presented in Table 1.

Table 1. Physical parameters of both media.

Parameters	Medium I	Medium II
De (m^2 s^{-1})	2.92×10^{-12}	5×10^{-12}
ω_0 (-)	0.2	0.3
w_{min}	0	0
p	1/3	1/3
τ_0 (-)	0.585	0.669
Length, L (m)	1.05	1.05
Δx (m)	0.05	0.05

Initially, aqueous $SrCl_2$ (10^{-1} mol kgw^{-1}) and a nonreactive tracer (10^{-6} mol kgw^{-1}) were assumed present in Medium I, whereas only SO_4Na_2 (10^{-1} mol kgw^{-1}) without tracer is assumed to be present in Medium II. The chemical parameters used for calculation are summarized in Table 2. Diffusion of the strontium and sulfate ions will lead to the precipitation of celestite ($SrSO_4$) at the interface: $SrSO_4(s) = SO_4^{2-} + Sr^{2+}$ with log K = -6.632. In order to increase the porosity variation, and therefore the feedback effect of celestite precipitation on the diffusion of the tracer, the precipitation is not treated under kinetic constraints, but rather at local equilibrium, and the molar volume of the solid phase is arbitrarily increased (10 L/mol instead of 46.25 cm^3/mol).

Table 2. Chemical parameters of both media.

Parameters	Medium I	Medium II
pH	7	7
tracer (mol kgw^{-1})	10^{-6}	10^{-20}
Sr (mol kgw^{-1})	10^{-1}	10^{-10}
Cl (mol kgw^{-1})	5×10^{-2}	5×10^{-9}
S(6) (mol kgw^{-1})	10^{-10}	10-1
Na (mol kgw^{-1})	5×10^{-9}	5×10^{-2}

The results are presented in Figure 1. As might be expected, (E1) and (E2) are rigorously equivalent if the tortuosity $\tau_0 = (\omega_0)^{1/3}$ is chosen in the new law in both media (Table 1).

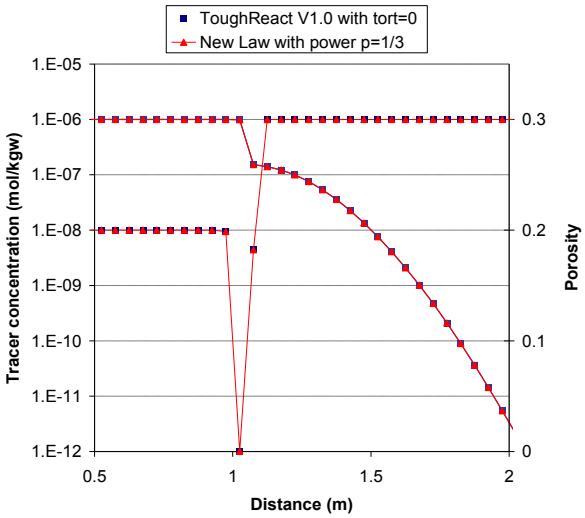

Figure 1. Porosity variation and tracer concentration after 10 years calculated with the old law (E1) and new law (E2).

Test-Case II: Comparison case of TOUGHREACT V1.0 with HYTEC V3.3 for weak (p=1/3) and strong (p=2) feedback

The aim of Test-Case II is to compare the results of two different codes for different values of the power p. The results of V1.0 with the new law are compared with the results given by HYTEC 3.3, a French code (van der Lee et al., 2003) that is also able to simulate reactive transport with variable porosity.

The HYTEC retroaction law is the same as the power law described in Equation (E2). The physical parameters are the same parameters as in Test-Case I, except for the effective diffusion which is different by one order of magnitude at the interface.

For the boundary conditions, the 1D system is assumed closed with both codes, i.e., no mass flux at X=0 m X=2 m.

Table 3. Physical parameters of both media in Test-Case II (see Table 1 for the other parameters).

Parameters	Medium I	Medium II
D_e (m^2 s^{-1})	10^{-12}	10^{-11}
$\tau_0 D_0$ (m^2 s^{-1})	$1/2\times10^{-11}$	$10/3\times10^{-11}$
ω_0 (-)	0.2	0.3
p	1/3, 2	1/3, 2

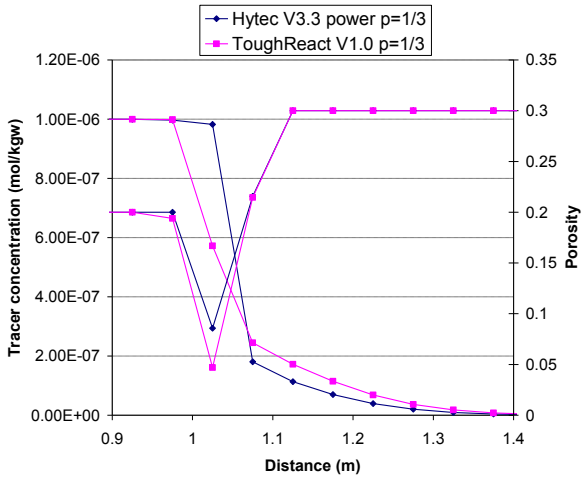

Figure 2. Comparison of tracer concentration and porosity after 10 years between TOUGHREACT V1.0 and HYTEC V3.3 with power p=1/3.

The parameter p is either fixed to 1/3 for a "weak" feedback or to 2 for a "strong" feedback. In both cases, there are significant differences between the results of the two codes (Figures 2 and 3).

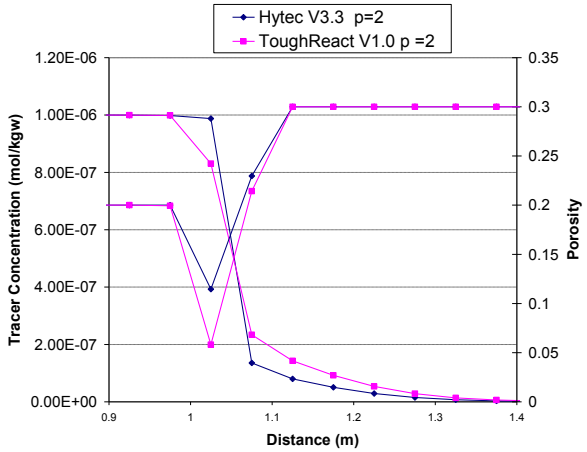

Figure 3. Comparison of tracer concentration and porosity after 10 years between V1.0 and HYTEC V3.3 with power p=2.

It is well known that for single-phase flow, the appropriate interface weighting scheme for the effective diffusion coefficient is a harmonic weighting. In TOUGHREACT V1.0, the effective diffusion at the interface is the product of D_0 with two terms: the first term of (E1), i.e., the porosity ω, is calculated as a harmonic mean at the interface, and the second term, i.e., the tortuosity τ, is a weighted mean (the weights are the nodal distances from the interface).

A new version of TOUGHREACT with harmonic weighting of the effective diffusion coefficient at the interface, gives much better results, as shown in Figure 4.

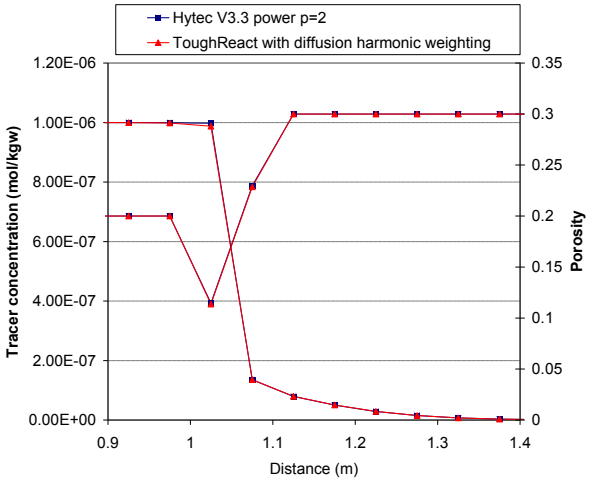

Figure 4. Same as for Figure 3 but with diffusion harmonic weighting (see text).

The interface diffusion coefficient calculation used in TOUGHREACT V1.0 is roughly valid without the feedback effect of porosity variation, departing from true diffusion values as porosity decreases, and the error in case of low or strong feedback could be significant, as shown in Figures 2 and 3.

CONCLUSION

The chemical conditions found in deep nuclear waste storage raise some concern about the migration of radionuclides at the interface between the engineered and geological barriers, where the alkaline perturbation could cause a "clogging" and therefore could impact the diffusion-controlled process itself.

In this study, we describe and test a new general "power law" that connects the effective diffusion coefficient and the porosity evolution. We conclude that if the TOUGHREACT version V1.0 is used to study the diffusion of radionuclides in the surrounding zone of a waste nuclear disposal, the effective diffusion could be overestimated even with the Millington Law. A modified version of TOUGHREACT with diffusion harmonic weighting gave the same results as the HYTEC code, both in the case of weak feedback (power=1/3) and strong feedback (power=2) in the new "power law".

Note that the power law described in this paper is only verified for the aqueous phase, but the same kind of law has also been developed for the gaseous phase in a two-phase system.

ACKNOWLEDGMENT

The Power Law in TOUGHREACT was developed with financial support provided by the French Nuclear Waste Agency (Andra). We thank J. Van Der Lee for the installation of Version 3.3, Release 9, Patch-level 1 of HYTEC developed at the Geosciences Department of Mines ParisTech graduate school.

REFERENCES

Archie, G. E., The electrical resistivity log as an aid to determining some reservoir characteristics. *Transactions of the American institute of mining engineers* 146, 54–61, 1942.

Burnol, A., Blanc, P., Xu, T., Spycher, N., and Gaucher, E. C. Uncertainty in the reactive transport model response to an alkaline perturbation in a clay formation. TOUGH Symposium, 2006.

De Windt, L., Marsal, F., Tinseau, E. and Pellegrini, D., Reactive transport modeling of geochemical interactions at a concrete/argillite interface, Tournemire site (France): 33, S295-S305, 2008.

Gaucher, E. C., Blanc, P., Matray, J. M., Michau, N., Modeling diffusion of an alkaline plume in a clay barrier. *Applied Geochemistry, 19*(10), 1505-1515, 2004.

Lagneau, V., *Influence des processus géochimiques sur le transport en milieu poreux ; Application au colmatage de barrières de confinement potentielles dans un stockage en formation géologique*, Thèse, CEA, 2002.

van der Lee, J., De Windt, L., Lagneau, V. and Goblet, P., Module-oriented modeling of reactive transport with HYTEC: *Comput. Geosci,., 29*, 265-275, 2003.

Trotignon, L., Devallois, V., Peycelon, H., Tiffreau, C., Bourbon, X., Predicting the long term durability of concrete engineered barriers in a geological repository for radioactive waste. *Physics and Chemistry of the Earth 32*, 259–274, 2007.

Winsauer, W. O., Shearin, H. M. J., Masson, P. H., Williams, M., Resistivity of brine saturated sands in relation to pore geometry. *Bulletin of the American association of petroleum geologists, 36*(2), 213–238, 1952.

MULTIPHASE FLOW AND INTERACTION DYNAMICS BETWEEN BENTONITE CLAY AND FRACTURED CRYSTALLINE ROCK

Benoît Dessirier, Jerker Jarsjö, Andrew Frampton

Department of Physical Geography and Quaternary Geology, Stockholm University
Stockholms Universitet
Stockholm, 106 91, Sweden
e-mail: benoit.dessirier@natgeo.su.se

ABSTRACT

Deep geological repositories are commonly considered as suitable environments for final disposal of high-level spent nuclear fuel. In the Swedish and Finnish repository design concept, copper canisters containing spent nuclear fuel are to be placed in deposition holes, as part of a system of deep underground tunnels in sparsely fractured crystalline bedrock, within which each canister is embedded with a bentonite-clay-mixture buffer in the deposition holes.

Bentonite is a porous, expansive clay material with low permeability that develops a relatively high swelling pressure when hydrated. The swelling acts to tightly embed and seal the canister in its deposition hole, minimizing void space and, combined with the low hydraulic conductivity of saturated bentonite, reducing advective water flow in the immediate vicinity of the canister. Also, the retention characteristics of bentonite limit particle dispersion, thereby acting as a formidable transport barrier. However, there are several unresolved issues related to the resaturation dynamics of bentonite in bedrock, in particular when in contact with water-conducting fractures in a strongly heterogeneous and anisotropic sparsely fractured rock environment.

In this study, a set of semi-generic, radially symmetric TOUGH2 simulation experiments are conducted to investigate the resaturation and multiphase dynamics of water and air in a bentonite-rock environment, with a particular focus on the dynamics at the bentonite-rock interface. The main objective is to identify how sensitive resaturation times are to assumed constitutive relationships for relative permeability as a function of saturation, and to the geometry and properties of the rock fractures. A scenario analysis is carried out using the scripting capabilities of the PYTOUGH library for optimum flexibility. This work will be further extended for use in combination with a suite of onsite subsurface tunnel experiments denoted as the Bentonite Rock Interaction Experiments (BRIE), currently being conducted at the Äspö Hard Rock Laboratory in Sweden. The main aims of the BRIE experiments are to identify and quantify interactions of water resaturation of bentonite clay under *in situ* conditions, that is, in a deep geological environment consisting of sparsely fractured rock similar to the candidate site for the final repository in Sweden.

Preliminary results identify fracture geometry as a primary factor affecting the resaturation time. The parameterization of the gas permeability appears as very important for correctly rendering the behavior close to saturation, the domain in which most uncertainties remain.

INTRODUCTION

Management and disposal of high-level spent nuclear fuel is an open question in countries that rely on nuclear power. An envisaged solution is to build final repositories in deep geological formations. The underlying idea is that such underground environments, where transport mechanisms are slow, would act as a natural barrier and delay the release of the decaying waste for a sufficient amount of time in the event of a failure of the engineered containers.

The Swedish repository design concept targets sparsely fractured granite bedrock as the host formation. In deep underground tunnels, vertical deposition holes would be drilled in the tunnel floor to receive copper canisters containing the nuclear waste. The deposition holes would be packed and the tunnels backfilled with a pre-

packed partially wetted bentonite clay mixture (Johannesson et al., 2007). Bentonite is a porous clay material with a complex microstructure depending heavily on its water content—a material that exhibits an overall swelling behavior when it rehydrates. The choice of an expansive clay material is made for several reasons: with its very low permeability and high-retention characteristics, bentonite would keep the advective transport to a minimum. Its high swelling pressure would seal void spaces in the back-fill material and contact points within the deposition hole and tunnel walls, as well as prevent the occurrence of bacterial activity as a possible corrosion enhancer in the canisters.

Despite its many advantageous features, predicting the behavior of a bentonite buffer embedded in fractured crystalline rock is a significant modeling challenge, due to the complex interactions between thermo-hydro-mechanical (THM) processes. The considered large-scale conditions point towards a full resaturation of the system in the long run, but we need to determine at what rate the originally unsaturated clay can take up water at the interface with the neighboring rock.

The fate of the air present in the originally unsaturated zone also has to be determined. Several possibilities could occur, like air entrapment in some regions of the buffer or in rock fractures, or a temporary desaturation of the rock mass in contact with the bentonite due to the very high affinity with water of the latter. The presence of intersecting rock fractures, their respective geometry and transmissivity, as well as the hydromechanical properties of the buffer are expected to play a major part in the above-mentioned features. The ongoing Bentonite Rock Interaction Experiment (BRIE) at the Äspö HRL in Sweden is conducted to achieve a better understanding of the dynamics and to gather modeling experience for such systems.

Several models are available at different levels of complexity. A common simplification is to use Richards' assumptions—that is, to neglect the air mass balance and treat the gas phase as a passive, perfectly mobile bystander. A more rigorous way is to use a two-component multiphase flow model, which accounts for all thermo-hydrological (TH) processes for air and water present in gas and liquid form. Only the latter can help determine whether air entrapment is likely in the selected design, or what the possible extent and duration of system transient behavior might be. Further couplings can integrate the mechanical (M) aspects together with the hydrological dependence of the problem (Rutqvist et al., 2010).

This study investigates the influence of some of the abovementioned factors, namely the intersection of boreholes by fractures at different points, and the effect of different parameterizations of bentonite permeability to air. In this study, we use TOUGH2 with its two-component (air, water) equation-of-state module EOS3 to simulate bentonite resaturation in a simplified, semi-generic fractured rock setting, with an open tunnel and a deposition hole filled with bentonite. Specifically, we investigate the constitutive relationships for gas-phase relative permeability. The main model variables of interest in terms of results are the resaturation and gas pressure fields. These are analyzed in the bentonite and fractured rock regime close to the deposition hole. Results between the various assumed constitutive relationships for gas permeability are then compared.

METHOD

We choose to look primarily at hydrogeological (H) processes under isothermal conditions with help of the TOUGH2 multiphase flow code (Pruess et al., 1999). The underlying assumptions are that both water and air fluxes are described by Darcy's law generalized to multiphase applications. Gases are described by the ideal gas law, and the total gas pressure is taken as the sum of the pressures of all the constituents (perfect mixing). Henry's law drives the dissolution/release of air into/from water. The capillary pressure and the relative permeability to gas and liquid are defined as characteristic curves. Closure relationships on water and air mass fractions and on liquid and gas saturations complete the system.

The water retention curves (capillary pressure as a function of liquid saturation) of the bentonite and the rock follow a van Genuchten curve as defined by the standard input in TOUGH2

(Pruess et al., 1999) using parameter values corresponding, respectively, to the properties of the commercial MX-80 bentonite mixture and to values reported as representative of the bedrock at the Äspö HRL in Sweden.

The mechanical (M) processes are not included directly but introduced instead as an alteration of the water retention curve of the bentonite (Dueck, 2004). A relationship linking the suction of the bentonite, here taken as the capillary pressure $P_{cap,}$ i.e., the difference between the pressure in the gas and the liquid phase, under free swelling ($P_{cap\ free}$) and under confined conditions ($P_{cap\ conf}$), is proposed as follows (Dueck, 2004):

$$P_{cap\ conf}(w,P) = P_{cap\ free}(w) - \alpha \cdot P$$

where P is the mean stress, w is the water content and α has been reported numerically close to 1.0. Estimates of the capillary pressure under confined conditions are available through free capillary pressure data and free swelling data. The modification of the water retention properties of the bentonite due to swelling are integrated by calibrating the set of van Genuchten parameters against $P_{cap\ conf}$.

We undertook a scenario analysis to test the impact of the gas relative permeability on the bentonite (Table 1). The implemented alternative 1 comes from standard TOUGH2 input methods, and alternative 2 is fitted from field data reported in the literature (Alonso et al., 2005).

The first scenario respects the traditional concept of intrinsic permeability being allocated to the gas or liquid phase through varying relative permeability functions, with values ranging between 0 and 1. The second scenario, based on laboratory experiments, abandons this hypothesis and considers much higher permeability values for gas when liquid saturation is smaller than 90%. The corresponding permeability functions are presented in Figure 1. Scenarios 2, 3 and 4 collectively investigate what impact the point-of-intersection location has between the fracture and the deposition hole (Table 1). The last complementary scenarios, 5 and 6, add a new permeability definition (also present in Figure 1) and make use of Richards' equation by running EOS9. They will be key in the discussion below.

A radial geometry is configured according to Figure 2. The tunnel and the deposition hole are placed on the symmetry axis. A horizontal fracture intersects the deposition hole at mid-depth and is assigned effective hydraulic properties typical for Äspö granitic rock. Here, a constant effective hydraulic transmissivity of 5×10^{10} m^2/s is used. The mesh generation is performed with AMESH adopting an unconventional approach: the radial slice is taken as a layer with variable thickness.

Table 1. Description of the implanted scenarios

Scenario	Description
1 (base)	Base scenario: EOS3, relative permeabilities in clay by standard Tough2 input reported from Fatt and Klikoff (1959) as reported in Pruess et al. (1999) (Fig. 1): $k_{rl}=S^3$: $k_{rg}=(1-S)^3$
2 (perm)	EOS3, permeabilities in clay to fit the lab-measured values reported in Alonso et al. (2005): $k_{rl}=S^3$: $k_{rg}=10^8.(1-S)^4$ (Fig. 1)
3 (permtop)	Similar to scenario 2 but fracture intersecting at the top of the deposition hole
4 (permbot)	Similar to scenario 2 but fracture intersecting at the bottom of the deposition hole
5 (perfmob) Qualitative results only	EOS3, permeabilities in clay by standard Tough2 input, with perfectly mobile gas and $k_{rl}=S^3$, $k_{rg}=1.0$ (Fig. 1)
6 (rich) Qualitative results only	EOS9, air is a passive bystander, permeability to liquid in clay by standard Tough2 input, $k_{rl}=S^3$

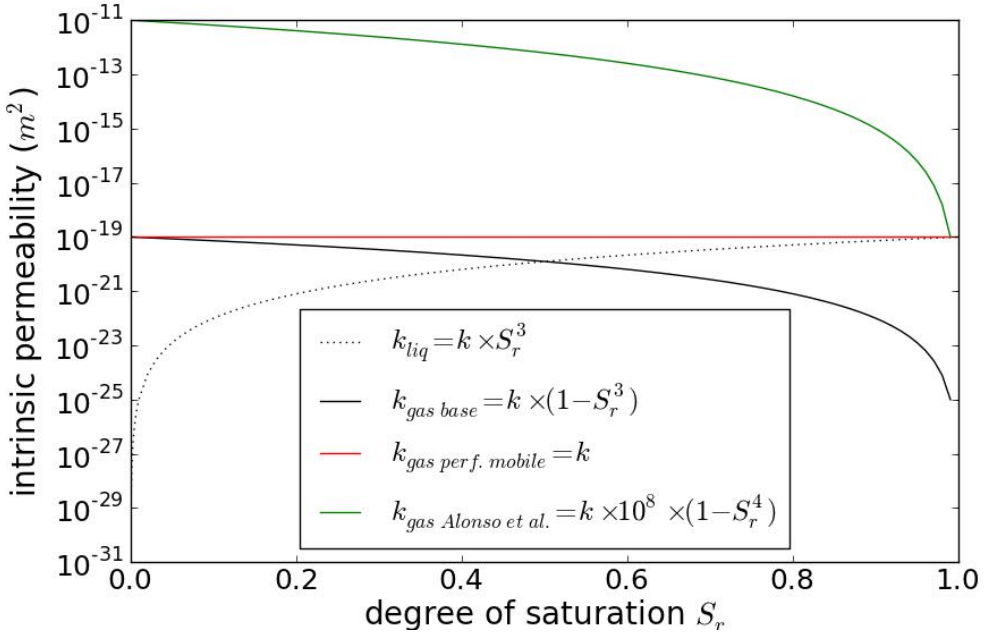

Figure 1. The constitutive relationships used for relative permeability of liquid (black dotted) and gas (solid) as a function of saturation. Scenario 5 adopts a constant relative permeability (red), scenarios 2, 3, and 4 adopt the approach used by Alonso et al. (2005) (green), and scenario 1 adopts a cubic power approach and is used as a reference base case for the simulations (black).

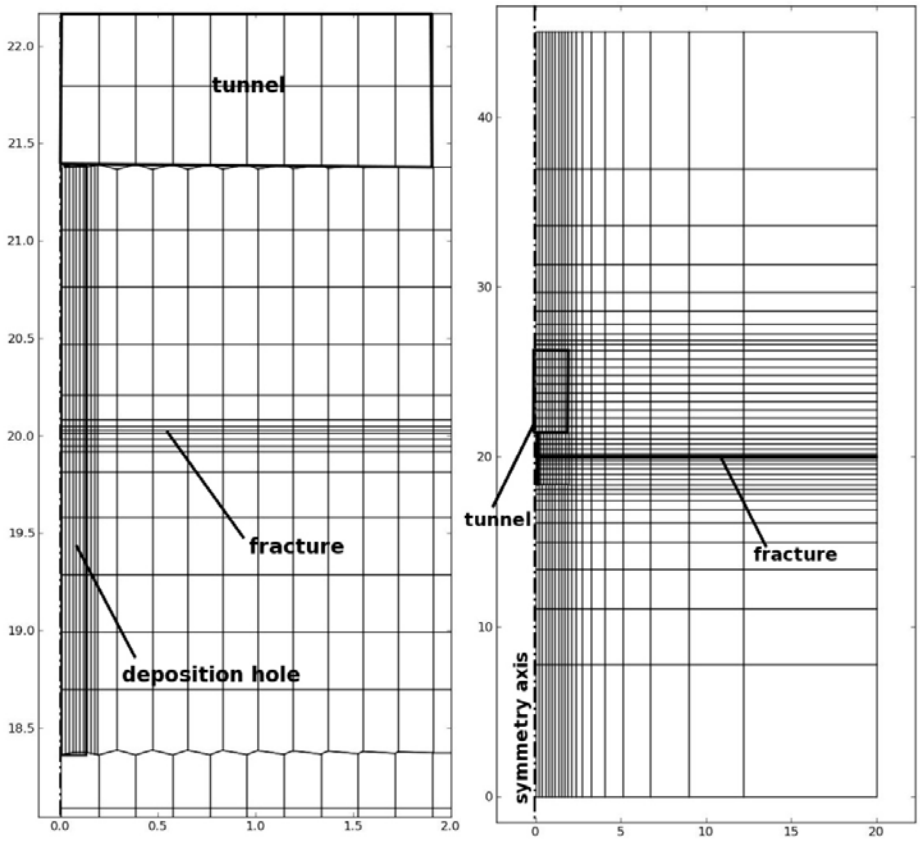

Figure 2. A radially symmetric domain is applied with a tunnel, deposition hole and fracture. The deposition hole consists of bentonite MX-80, the fracture consists of mesh elements with higher hydraulic conductivity K than the background rock matrix. The tunnel is implemented as a boundary condition with atmospheric pressure.

Interface areas are then corrected to approximate radial conditions, and the axes convention is switched back to its usual convention: vertical coordinate z and radial coordinate r.

The application uses the equation of state EOS3, which accounts for air and water present in gas and liquid phases. Fixed boundary conditions are imposed at the borders other than the symmetry axis and in the cells forming the tunnel: water saturation with pressure equal to 2.0 MPa for the outer boundaries and air saturation at atmospheric pressure is assumed in the tunnel.

For more flexibility in generating the different sets of TOUGH input files in the frame of this scenario analysis, the PYTHON programming language and the PYTOUGH library are used.

RESULTS AND ANALYSIS

The resaturation of the clay buffer is represented here by the time saturation S_r takes to reach a certain percentage in every cell in the lower half of the deposition hole. Results obtained for the bounds S_r>50%, S_r>90 % and S_r>99% are presented in Table 2. The simulation output frequency increases from one record per day initially to once every 10 days beyond t=100 days. We observe that the permeability definitions used in scenario 1 and 2 follow very close patterns up to 90% saturation.

The comparison of fracture locations via scenarios 2, 3, and 4 shows that the quickest re-saturation event happens for case 2 (where the fracture intersects the middle of the deposition hole). This can be interpreted as the case when the longest flow path of water from the fracture outlet to any point in the deposition hole is minimal. This observation may indicate that the fracture considered has water-bearing properties on par with the background flow through the rock matrix to globally provide water to the system. This hypothesis could be verified by calculating the accumulated flow values through key vertical cross sections in the model.

Table 2. Time in days until all cells in the lower half of the deposition hole reach certain levels of water saturation

Scenario	$T_{50\%}$	$T_{90\%}$	$T_{99\%}$
1_base	140 d	180 d	>215 d
2_perm (middle)	140 d	180 d	>215 d
3_perm top	260 d	310 d	>330 d
4_perm bottom	240 d	320 d	>706 d

Comparing the differences between inflow from the top or the bottom, several influences come into play: the effect of gravity against capillarity forces, the proximity to the tunnel floor that might drain more water, and the possibility of air entrapment slowing down the full resaturation time. However, the similar outcome from both extremities could indicate that, in the current setup, the presence of a fracture within the studied range of transmissivity is not sensed further than 1.5 m away (half the height of the borehole) from the outlet during the first 300 days of the experiment. Water balance and analyses of the flow field should provide the opportunity to confirm or reject this idea.

The implementation of these scenarios also highlights some peculiar behavior related to the gas pressure in the clay buffer close to saturation. For simulation case 2, the gas pressure distribution after 215 days would indicate that the gas pressure in the deposition hole, then within the last few percent to full re-saturation, is ~3 MPa and hence actually exceeds the 2 MPa pressure imposed at the boundary (Fig. 3). Further investigations are required, since it has not yet been successfully linked to the swelling or to any other known effect related to pressure, such as the Klinkenberg effect or the vapor pressure lowering effect offered by EOS4. However, different assumptions such as a perfectly mobile gas (scenario 5) or simulations based on the Richards equation (scenario 6) did not demonstrate this particular feature. It is thus suspected that the ratio of permeability to

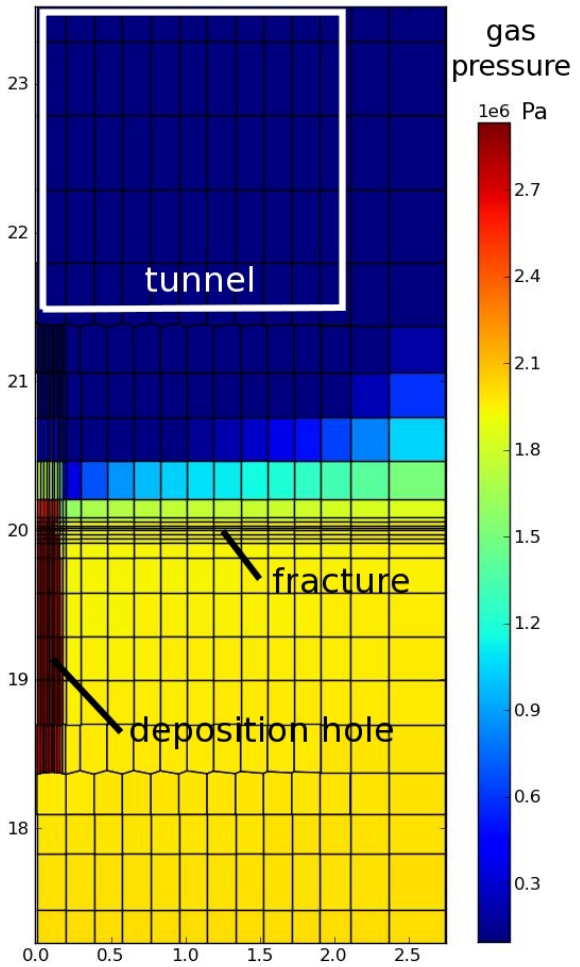

Figure 3. Gas pressure profile in the close field with scenario 2 after 215 days, the gas pressure in the bentonite domain exceeds the far field boundary value of 2 MPa.

gases over permeability to liquids is a key factor close to saturation. Hence, the area where unsaturated conditions approach full saturation is highly sensitive to the assumed constitutive relationship used, and as such, becomes all the more important for determining the risk of air entrapment.

SUMMARY AND CONCLUSIONS

In this initial study, resaturation effects and interactions between bentonite clay and sparsely fractured granitic rock is investigated. The main focus is to study the effects of constitutive relationships for gas permeability as a function of saturation. Three possible constitutive relationships have been investigated. We also analyzed the location of rehydration. The main results of this analysis show that:

- The location of the fractures around the deposition hole significantly influences the total time for resaturation. Interestingly, the central intersection location has the fastest rewetting time. This is attributed to combined gravitational and capillary re-wetting effects, since the flow-path distance to all points of the bentonite domain are minimized. Complementary investigations of fracture-network transmissivity and connectivity are required to deepen the understanding of that factor.
- The choice of permeability functions for gas in the bentonite seems to be determinant for behavior close to saturation. A better conceptual understanding of the processes and their parameterization in that regime is necessary. Modeling, together with the data generated by the BRIE experiments, will be an asset toward reaching this goal.

ACKNOWLEDGEMENTS

This study was supported by the Swedish Nuclear Waste Management Company (SKB).

REFERENCES

Alonso, E.E., J. Alcoverro, F. Coste, L. Malinsky, V. Merrien-Soukatchoff, I. Kadiri, T. Nowak, H. Shao, T.S. Nguyen, A.P.S. Selvadurai, G. Armand, S.R. Sobolik, M. Itamura, C.M. Stone, S.W. Webb, A. Rejeb, M. Tijani, Z. Maouche, A. Kobayashi, H. Kurikami, A. Ito, Y. Sugita, M Chijimatsu, L. Börgesson, J. Hernelind, J. Rutqvist, C.-F. Tsang, P. Jussila, The FEBEX benchmark test: case definition and comparison of modelling approaches, *International Journal of Rock Mechanics and Mining Sciences 42*(5–6) 611-638, 2005

Dueck, A. *Hydro-mechanical properties of a water unsaturated sodium bentonite. Laboratory study and theoretical interpretation*, Doctoral thesis ISBN 91-973723-6-6, Lund University Faculty of Engineering, Lund, Sweden, 2004.

Johannesson, L. E., L. Börgesson, R. Goudarzi, T. Sandén, D. Gunnarsson, C. Svemar, Prototype repository: A full scale experiment at Äspö HRL, *Physics and Chemistry of the Earth 32*, 58-76, 2007

Pruess, K., C. Oldenburg, and G. Moridis, *TOUGH2 User's Guide, Version 2.0*, Report LBNL-43134, Lawrence Berkeley National Laboratory, Berkeley, Calif., 1999.

Rutqvist J., Y. Ijiri, H. Yamamoto, Implementation of the Barcelona Basic Model into TOUGH-FLAC for simulations of the geomechanical behavior of unsaturated soils, *Computers and Geosciences 37*, 751-762, 2011

3D MODELING OF THE LONG-TERM BEHAVIOR OF A LARGE GEOLOGICAL REPOSITORY FOR HLW AND ILW-LL NUCLEAR WASTE, CONSIDERING HEAT, GAS, AND RADIONUCLIDE RELEASE AND TRANSPORT – OPTIMIZATIONS THAT ALLOW FOR DETAILED LARGE-SCALE MODELING

C.P. Enssle[1], J. Brommundt[1], Th.U. Kaempfer[1], G. Mayer[1], J. Wendling[2]

[1]AF-Consult Switzerland Ltd, Dep. Groundwater Protection and Waste Disposal,
Taefernstrasse 26, CH-5405 Baden, Switzerland
e-mail: carl-philipp.enssle@afconsult.com
[2]Andra, Parc de la Croix-Blanche, F-92298 Châtenay-Malabry, France

ABSTRACT

Deep geological repositories for radioactive waste are currently being planned in several countries. France envisages the disposal of high-level and intermediate-level long-lived waste in the low-permeable Callovo-Oxfordian clay rock, with the objective of retarding the radioactive substances from entering the biosphere.

To assess the long-term safety and performance of the repository, we use numerical modeling to incorporate the relevant nonlinear and coupled thermo-hydraulic flow and transport processes, the impact of construction, and parametric uncertainty. However, addressing all these aspects in a single, large numerical model with a sufficient level of detail poses a challenge with respect to computation.

In the study presented here, we developed a model concept for simulations of a large repository with special regard to computational feasibility, using a modified version of TOUGH2-MP EOS7R accounting for hydrogen instead of air. The model concept involves a set of computing-time-reducing optimization measures, such as suitable geometrical simplifications and skilful discretization techniques.

The simulations performed demonstrate the effectiveness of the developed optimization measures, allowing for reasonable computation times and providing novel, comprehensive insight into the long-term comportment of thermo-hydraulic flow and transport processes within the entire repository and host rock.

BACKGROUND & SCOPE

The French national radioactive waste management agency (Andra) plans the disposal of high-level waste (HLW) and intermediate-level long-lived waste (ILW-LL) in a deep geological repository. The construction and operation of the repository will alter the natural conditions and properties of the affected host rock. Moreover, the generation and release of heat and gas by the stored waste, which will continue for several thousand years, will persistently influence the evolution of the physical state inside the repository and potentially decrease the retention capability of the engineered barriers and host rock for the radionuclides released by the waste. The involved processes take place on different spatial scales—from the decimeter scale of a waste package to the kilometer scale of the entire repository—and over the large time scale of several hundred thousand years.

The current repository concept (Andra, 2006) consists of several thousand horizontal tunnels for waste emplacement and additional tunnels and shafts for access, logistics, and ventilation during construction and operation of the repository. The entire repository encompasses a horizontal area of several kilometers in width and length (Figure 1). The repository is designed such that after its closure (i.e., after all waste has been emplaced and all tunnels and shafts have been backfilled and sealed), no human supervision will be required. To evaluate feasibility Andra has conducted many research programs assessing the performance and safety of the envisaged repository concept, aiming at addressing all relevant phenomenological and technical aspects during operation and post-operation.

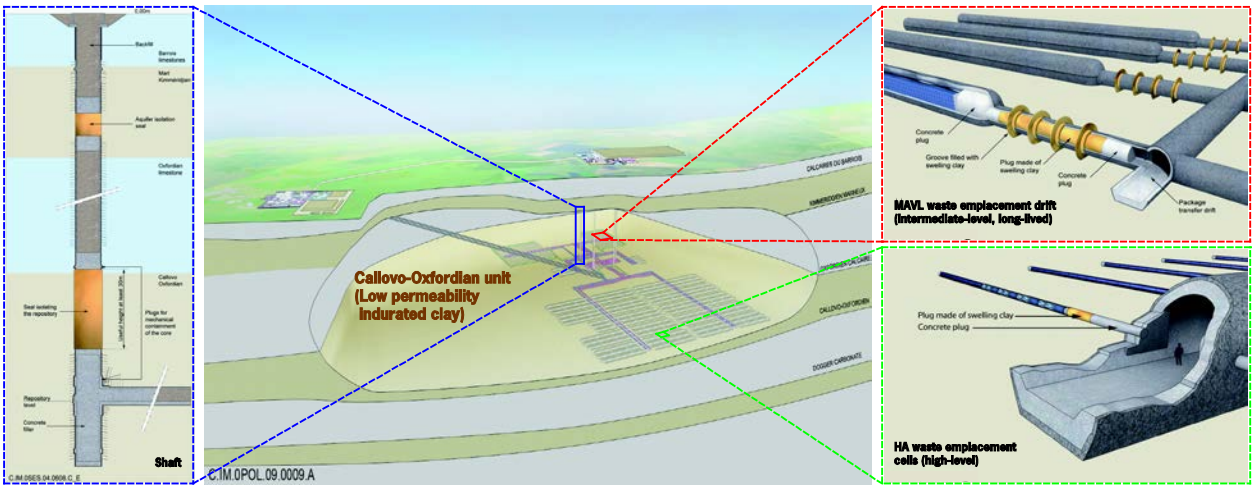

Figure 1. General repository architecture concept with emplacement tunnels for HLW & ILW-LL waste packages, tunnels and shafts for access, logistics, and ventilation, Andra (2006).

In the context of these programs, the objective of the study presented here is to model the thermo-hydraulic behavior inside the entire repository and the ambient host rock, as well as the migration of mobilized radionuclides within a time-frame of 1 million years. The model should represent all relevant details with a single integrated model mesh of the entire repository domain. Important phenomenological aspects to be considered are (i) the depressurisation and desaturation of the excavation damaged zone (EDZ), and the adjacent intact host rock, as a result of tunnel ventilation in the operational phase, with a re-saturation by pore water from the host rock and repressurisation in the post-operational phase; (ii) the appearance, migration, and disappearance of a gas phase due to waste-type-specific release of gaseous substances, mainly hydrogen; (iii) the decay-heat induced temperature increase leading to a pressure increase resulting from heat expansion of fluids and solids; and (iv) the mobilization of the radionuclide species ^{14}C and ^{129}I due to the degradation and corrosion of the waste packages and their migration under advection, diffusion, retardation, and decay.

The modeling requirements are to provide an adequate spatial representation of all repository components, considering the arrangement of the more than 10 different waste types, the waste-type-specific source terms of heat, gas, and radionuclides, respecting cooling times and early canister failure, and the spatial and temporal schedule of tunnel excavation, emplacement, and backfilling during construction and operational phases. Given these complex processes, the huge number of constructional elements, and the large range in scale—from the kilometer scale of the overall repository site to the decimeter scale of a single waste canister—an adequate and still manageable model representation poses a challenging task with respect to setup and its numerical computation on a medium-sized Linux-cluster.

Standard TOUGH2-MP (Pruess et al., 1999, Zhang et al., 2008) enables consideration of the above processes using equation-of-state module EOS7R. For the study presented here, some modifications were implemented: (a) hydrogen instead of air as primary gaseous component; (b) temperature-dependent diffusion of the dissolved components in the liquid phase[1]; (c) a break of the radionuclide decay chain to represent two individual radionuclides; and (d) fully mass conservative source-terms[2].

In a previous study on the maximum pressures and hydrogen transfer in the entire repository, spatial discretization of the entire repository site

[1] Andra heating experiments showed a factor of ~5 in diffusivity increase for dissolved components in fully saturated argillite heated from 22° C to 80°C, Andra (2009).

[2] With the exception of MOP(12)=2 (rigorous step rate) in standard TOUGH2, the implemented routines for transient source terms in the original TOUGH2/-MP source code do not guarantee a numerically exact input of the specified quantities

was implemented using the approach of *Subdivision, Multiplication, and Connection* (Poller et al., 2009, 2011, Enssle et al., 2011) in which symmetrical and repetitive subareas of the repository were discretized using a single mesh with effective properties representing the aggregated area. To form the mesh of the entire repository, several aggregated sub-area meshes were attached to each other. The approach allows for a massive reduction of the mesh size (i.e., the number of gridblocks and connections) and of the corresponding order of the Jacobian matrix solved by TOUGH2-MP, but nevertheless preserves a relatively fine mesh discretization at the locations of interest and does not compromise the robustness of the solution.

The simplifications used there are appropriate when maximum pressures or cumulated fluxes are of interest. However, in the study presented here, a straightforward adoption of this approach is not feasible, since radionuclide transport processes are to be studied in detail and resolved in time. Hence, we develop a new concept of the geometrical model, with special regard to radionuclide transport on a detailed temporal scale over the entire repository site, as well as to the computational feasibility of this approach.

The modeling concept, its parameterization, and the mesh optimization techniques are explained in the following section (Modeling Concept). Examples of physical results, and an assessment of the performance and benefits of the optimized modeling approach, are given in the results section below, followed by our conclusions.

MODELING CONCEPT

Physical & Numerical Model

The numerical TOUGH2-MP model is based on the equation-of-state module EOS7R considering all relevant implemented processes, including abovementioned code modifications (a) to (d), concerning two-phase flow and transport of mass and heat components. We modeled the radionuclide species ^{14}C in the chemical form of methane (and hence highly volatile[3]), and ^{129}I in the chemical form of hydroiodic acid (and hence perfectly soluble, i.e. with virtually no volatile fraction). Decay products and chemical reactions were not considered.

Parameterization

The model domain represents the host rock in its full vertical depth of ~150 m between the cap rock and bed rock, and has a lateral extent extending sufficiently beyond the horizontal dimensions of the repository, in order to minimize the influences of lateral no-flow boundaries. The surface area (footprint) of the domain totals $\sim 3 \times 5\ km^2$. The top and bottom boundaries were time-invariant and fixed at the values corresponding to the naturally occurring conditions of pressure[4], temperature, concentration, and 100% water saturation.

The overall simulation was split into seven phases. The first phase concerned the simulation of the natural conditions for initialization of the model. Phases 2 to 6 concerned the operational phase with excavation, ventilation, waste emplacement, and backfilling/sealing. In total, they lasted 100 years and represented the planned chronogram by Andra. Phase 7 concerned the post-operational phase, lasting between 100 and 1 million years.

Reference material properties were assigned according to Enssle et al. (2011). Selected reference transport properties are given in Table 1.

Table 1. Selected reference transport parameters.

Parameter	H_2	^{14}C	^{129}I
D_{gas} [m^2/s]	9.5E-5	1.3E-4	-
D_{liq} [m^2/s]	6.0E-9	4.9E-11	4.9E-11
Inv. Henry's const. [1/Pa]	1.4E-10	3.0E-10	1E+50
Half life [a]	-	5.7E+3	1.6E+7

$D_{gas/liq}$ = diffusion coefficient in the gas or liquid phase.

Source terms for hydrogen, heat, and radionuclide release were assigned, and accounted for the various expected waste types, as well as for

[3] Dissolution is considered according to Henry's law yet allowing for solute transport of ^{14}C.

[4] At the top boundary pressure decreased linearly by ~3 bar over the entire simulation time of 1 million years reflecting the expected evolution of the regional hydraulic state

the corresponding cooling times, emplacement dates, and the possibility of early canister failure.

Discretisation & Mesh Optimization

From physical and numerical perspectives, the domain discretization must be sufficiently fine to reflect all relevant geometrical features and to ensure a numerically robust solution, minimizing numerical diffusion. Conversely, from the computational point of view, the discretization needs to be sufficiently coarse in order to produce a computable solution within a reasonable execution time and without exceeding memory requirements. The reconciliation of these conflicting requirements is a steady issue in numerical modeling, especially when creating mesh designs.

In view of the given large and spatially heterogeneous repository domain, as well as the physical complexity, (e.g., nonlinear capillarity, relative permeability, sharp contrasts in permeability), model-mesh simplifications and optimizations were inevitable. A set of measures including topological simplifications and a methodology (to which we refer as the *embedded meshing approach*) was developed, exploiting the meshing flexibilities inherent to the finite volume method in TOUGH2/-MP[5].

Topological Simplifications

(S1) All tunnels and shafts, including their concrete lining and EDZs, are represented by squared or rectangular instead of circular cross sections respecting the real cross-sectional area[6]—see Figure 2 for illustration.

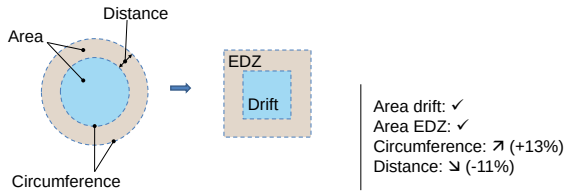

Figure 2. Transition from circular to squared cross-sectional shape of tunnels and shafts.

(S2) Parallel tunnels are represented by a single tunnel with an equivalent cross-sectional area, (Figure 3).

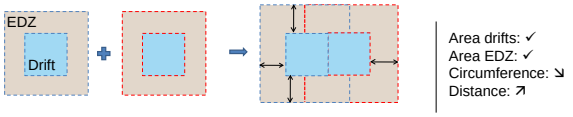

Figure 3. Aggregation of two parallel drifts with adaption of geometrical properties.

(S3) Inclined ramps are represented by horizontal drifts and vertical shafts with combined equivalent lengths.

(S4) The spatial arrangement of the waste emplacement zones and the locations of the shafts and tunnels are slightly shifted in order to gain a higher degree of symmetry.

(S5) Meshing algorithms for regular gridblock meshes such as MESHMAKER (Pruess et al., 1999) extend the cell size of a gridblock over the entire plane of the model mesh. Hence, small gridblock sizes—from the topological perspective needed only at certain locations—lead to a needless fine discretization at distant locations. In the study presented here, such configurations result especially from the discretization of annulus shapes, such as the EDZs. To avoid these, the concerned gridblocks are adapted to have nonrectangular cuboidal shapes, removing the comparatively small corner gridblocks (see Figure 4). These new gridblocks do not strictly satisfy the Voronoi criterion that postulates orthogonality of the connection between the centres of adjacent gridblocks and their common interface.

Further, the definition of the effect of gravity in these connections is ambiguous. The concerned connections occur, however, only at the annular space of the EDZs and thus enter the computation of circular fluxes within these materials

[5] In the finite volume method in TOUGH2 space is discretized by gridblocks and connections between adjacent gridblocks. Normally, the arrangement and properties of the gridblocks and their connections are chosen in a geometrically realistic fashion; however, the user is free to modify the geometrical arrangement and properties such as (for example) to increase the volume of a certain gridblock.

[6] The entailed increase in circumference and reduction of radial distance is less than 13% and 11%, respectively, and was neglected, yet this could be corrected for if sensitive.

only. These fluxes are of negligible magnitude compared to the axial and radial fluxes, where the mesh conforms to the Voronoi criterion as well as to gravity orientation; thus, the impact of the simplification on the simulation results is estimated to be minor.

(S6) Certain small-scale components are upscaled to larger components with equivalent properties. This is, for example, applied to some components within the interior of a waste emplacement tunnel, e.g., the ILW-LL primary waste packages and the waste containers, or the EDZs and the concrete lining of the tunnels and shafts.

Incorporating these simplification measures, we generate the actual mesh of the entire model domain by following the process outlined in the following section.

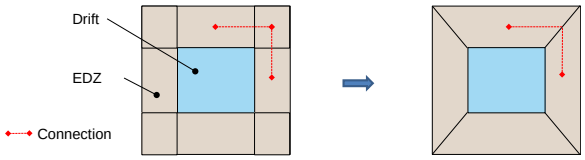

Figure 4 Modification of rectilinear gridblocks. Left: drift cross section discretized with nine rectangular gridblocks. Right: same drift configuration composed of five geometrically adapted gridblocks.

Embedded Meshing Approach

As a starting point, the entire model domain (i.e., the host rock including all waste emplacement zones, as well as the cap rock and bedrock) are discretized in a straightforward way with gridblocks of rectangular cuboidal shape, using MESHMAKER (Pruess et al., 1999). This mesh is referred to as the *global mesh*.

Tunnels and shafts, including their concrete linings and EDZs, are embedded into the global mesh with gridblocks having (a) a non-rectangular cuboidal shape (per the simplification discussed in S5) and (b) a rectangular cross section (cf. S1). This includes all ILW-LL emplacement tunnels.

The representation of the thousands of HLW emplacement cells is implemented by aggregation[7]. This means that several adjacent identical emplacement cells of the same geometry and waste-type are assembled into one aggregated emplacement cell with adapted geometry and properties. The adaptation is performed radially, and the axial length kept constant. The aggregation factor f equals the number of assembled emplacement cells[8].

The consequences for an aggregated HLW emplacement cell are as follows:

- Its extensive quantities (such as the ones listed below) are multiplied by f:
  - volume of gridblocks
  - interface areas
  - source terms
- Its intensive quantities or properties remain unchanged, such as:
  - distances between gridblocks
  - material properties
  - state variables, i.e., pressure, saturation, and temperature

Each aggregated emplacement cell is discretized with an axi-symmetric submesh (MESHMAKER 2D-R-Z grid). This submesh contains the engineered components of the HLW emplacement cell, the EDZ, and the near-field host rock in a radius of ~ 1.2 m (Figures 5 and 6). The outer, surrounding host rock is represented by brick-shaped gridblocks in the global mesh to which the submesh (the aggregated emplacement cell) is connected. The embedding of each of the submeshes into the global mesh is carried out as follows:

(A) Each submesh is connected to the global mesh at its radial average location. The average location is the location of the emplacement cell situated at the center of the set of emplacement cells assembled together (cf. Figure 6, position "(f+1)/2"). The global mesh is constructed such that this location coincides with the centers of several specific gridblocks to which the corresponding sub-mesh gridblocks are connected.

[7] This approach partially adopts the previously developed approach of *Subdivision, Multiplication, and Connection* (Poller et al., 2009).

[8] In the model mesh presented here, the aggregation factor was chosen to be around 10.

(B) The volumes of the global mesh gridblocks that are intersected by the sub-mesh are adjusted by subtracting the volume of the intersecting sub-mesh (see Figure 5).

(C) All gridblocks on the mantle of the sub-mesh are connected to the corresponding (intersecting) gridblocks of the global mesh (see Figure 5). The connection lengths are the distance between the center of the mantle gridblock to the mantle (*d1*) and the distance between the mantle and the center of the corresponding gridblock in the global mesh, i.e., the mantle radius of the submesh (*d2*) (Figure 6).

An illustration of the entire repository mesh created with the embedded meshing approach is given in Figure 7. The complete mesh consists of some 250,000 gridblocks and around 700,000 connections. With "conventional" mesh generation, i.e., without topological simplifications, aggregation of HLW emplacement cells and their representation by axi-symmetric gridblocks, the mesh size would reach some tens of millions of gridblocks and connections, and the corresponding Jacobian matrix would have been correspondingly large and possibly beyond the solution capabilities of practically all but the largest clusters and/or supercomputers.

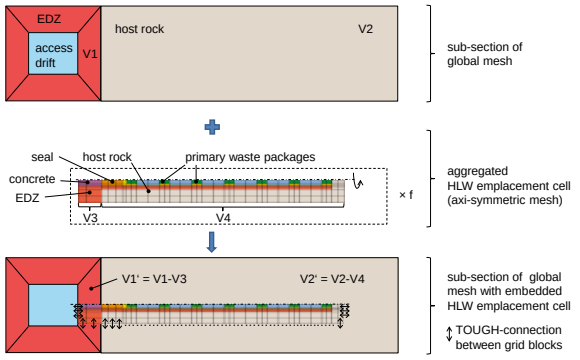

Figure 5. Aggregation and embedding of HLW emplacement cells to global mesh (cross-sectional view along a HLW emplacement cell). Top: gridblocks of the global mesh. Middle: gridblocks of the axi-symmetric submesh. Bottom: gridblocks of the global mesh with embedded axi-symmetric sub-mesh.

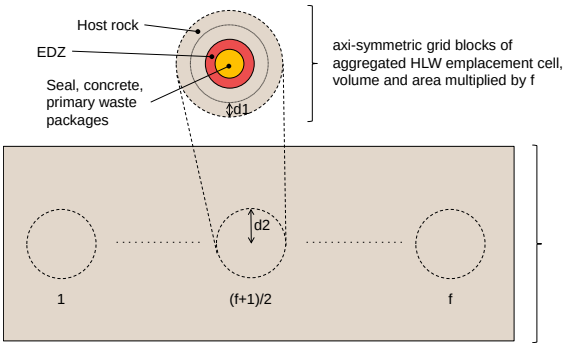

Figure 6. Aggregation and embedding of HLW emplacement cells to global mesh (cross-sectional view along an access drift).

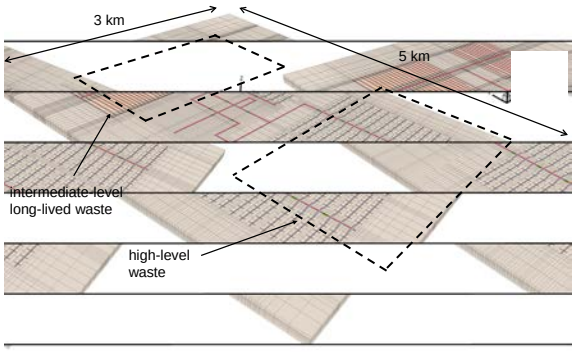

Figure 7. Entire repository mesh representing the planned layout; all gridblocks above the repository level are blanked.

RESULTS

Simulation Results

Approximately 20 simulation cases with and without radionuclides[9] were conducted. We considered two different layouts of the repository, and single- and two-phase flow. We varied important parameters, such as permeability, diffusion coefficients, gas generation-rates, and saturation-dependent gas generation, adopting the approach by Croisé et al. (2011), which considers the impact of water consumption and saturation-dependent corrosion rate on the hydrogen generation.

The simulation results represent a comprehensive and unprecedented pool of information regarding the transient thermo-hydraulic performance of the repository concept, one that particularly enables thorough insight into the

[9] Simulations without radionuclides used TOUGH2-MP EOS5.

coupled effects resulting from the large system heterogeneity in terms of space, time, and processes. As an example, the simulations demonstrate (and confirm) that all factors influencing hydrogen generation, its migration, and thus the distribution of a gas phase are of great importance for the transfer of ^{14}C. Figure 8 illustrates the ^{14}C transport at the repository level for the cases with and without hydrogen generation.

In contrast to the ^{14}C transport, the transport of ^{129}I shows little sensitivity with respect to the number of phases involved (one- vs. two-phase conditions resulting from gas generation), as is shown on Figure 9.

The different migration behavior of the two radionuclide species is attributed to their oppositional thermo-dynamic properties, with ^{14}C (in the chemical form of CH_4) being highly volatile and hence mainly transported in the gas phase (if present), which preferentially follows higher permeability pathways such as the EDZs around the tunnels. In contrast, ^{129}I, in the chemical form of hydroiodic acid, is very soluble and mainly transported by diffusion in the formation water. Regarding the gaseous convective transport of ^{14}C, only a very small fraction of the totally mobilized mass finally reaches the shafts (~10^{-4} % in the reference case).

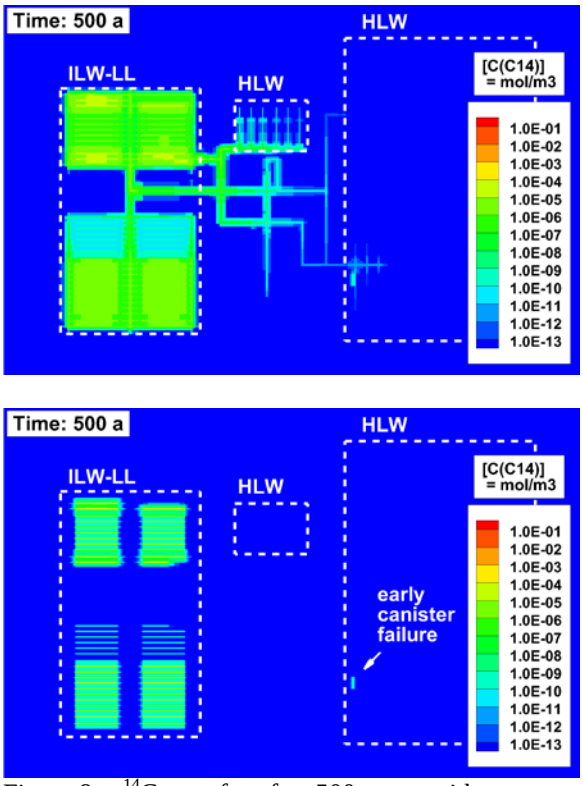

Figure 8. ^{14}C transfer after 500 years with gas generation (top) and without gas generation (bottom)

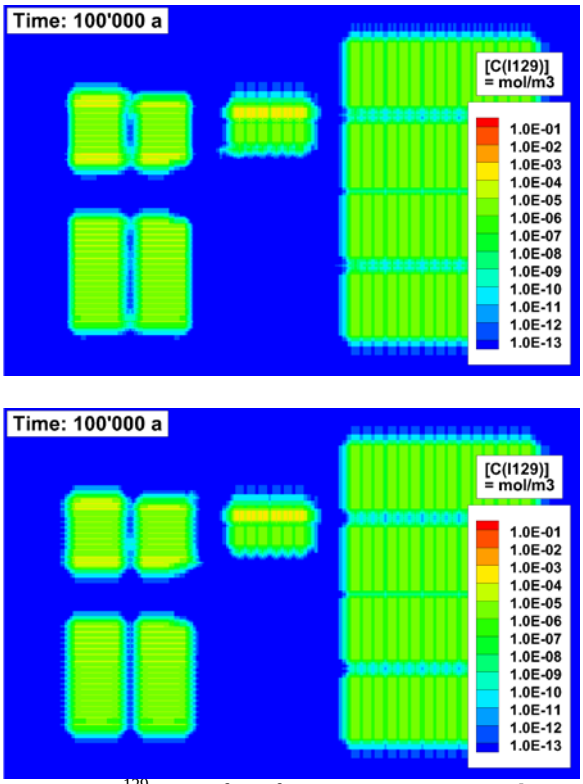

Figure 9. ^{129}I transfer after 100,000 years with gas generation (top) and without gas generation (bottom).

Comprehensive details of the simulation results will be presented in a separate paper (Enssle et al., 2012).

Assessment & Justification of the Approach

Previous large-scale modeling studies using TOUGH2-MP revealed the need for optimization measures to enable computationally feasible two-phase flow and transport simulations. This led to the developments of the embedded meshing approach. Relevant details, such as the corresponding topological simplifications and mesh manipulation measures, were presented above.

The first test simulations in the early stages of this study had extremely large computational demands and led to further mesh optimization measures, such as the upscaling of the HLW components and the EDZs.

The computation times strongly depended on the simulation case and the degree of complexity/nonlinearity of the processes and conditions under study. For single-phase cases, omitting gas generation led to computational times in the range of a few hours, whereas two-phase simulation cases with gas generation exhibited execution times as high as 30 days[10]. These computational times were observed using a parallel system involving six Intel Core2Quad 2.83 GHz machines with eight processors each.

To the extent possible, the results were validated by comparison with previous modeling studies. However, it is important to note that these studies usually involved smaller domains with different assumptions concerning the model boundaries, and often disregarded coupled phenomena.

An assessment of the Péclet numbers corresponding to the major travel paths of the radionuclides suggested that the mesh discretization resulting from the simplified approach described in this paper is sufficiently fine for an accurate computation of the quantities in question.

[10] This computation time was required in a case with reduced hydrogen diffusion in the liquid phase and hence a prolonged presence of the gas phase. With the reference diffusion coefficient, resaturation occurred considerably earlier and a computation time of around 10 days.

CONCLUSION

This study demonstrates the general feasibility of simulating coupled thermo-hydraulic two-phase flow and radionuclide-transfer processes on the scale of an entire repository, while simultaneously accounting for the relevant small-scale details. The simulations revealed that hardware resources are not necessarily the most important factor for successful model simulations. By choosing a suitable model conceptualization, including adequate upscaling, aggregation and mesh embedding techniques, and efficient data handling, we have developed a successful model, that is capable of solving very large problems without the need to resort to very large clusters and/or supercomputers, and which is a good basis for future parametric studies.

The single-phase and two-phase simulations in this study produced a consistent dataset characterizing the repository performance with respect to water, gas, ^{14}C, and ^{129}I transport. We have observed the strong dependency of ^{14}C transport on several parameters, such as permeability, diffusion coefficients, gas generation-rates, and saturation-dependent gas generation. The most important aspect here is the consideration of gas generation, which leads to largely increased transport rates of ^{14}C along the backfilled drifts and shafts by advection in the gas phase. By contrast, the transport of ^{129}I is virtually independent of the gas generation because of its high solubility.

ACKNOWLEDGMENT

This work was funded by Andra, and the modelling presented is based on data provided by Andra. Valuable input was provided by Guillaume Pépin and Jean Croisé. Thanks also to Keni Zhang, who kindly performed test calculations on a supercomputer.

REFERENCES

Andra, *Dossier 2005 Argile – Synthesis – Evaluation of the feasibility of a geological repository in an argillaceous formation,* ISBN: 2-916162-00-3, 2006.

Andra, *Référentiel du Site Meuse/Haute-Marne - Tome* 2, Internal Report C.RP.ADS.09.0007, 2009.

Croisé, J., G. Mayer, J. Talandier, and J. Wendling, *Impact of Water Consumption and Saturation-Dependent Corrosion Rate on Hydrogen Generation and Migration from an Intermediate-Level Radioactive Waste Repository*, Transport in Porous Media, DOI: 10.1007/s11242-011-9803-0, 2011.

Enssle, C.P., J. Croisé, A. Poller, G. Mayer, and J. Wendling, *Full scale 3D-modelling of the coupled gas migration and heat dissipation in a planned repository for radioactive waste in the Callovo-Oxfordian clay*, Physics and Chemistry of the Earth, DOI: 10.1016/j.pce.2011.07.033, 2011.

Enssle, C.P., J. Brommundt, Th. U. Kaempfer, G. Mayer, and J. Wendling, *Full scale 3D modelling of a repository in the Callovo-Oxfordian clay with focus on two-phase transport of ^{14}C and ^{129}I,* submitted to Proceedings of "Clays in Natural & Engineered Barriers for Radioactive Waste Confinement", October 2012, Montpellier, France.

Poller, A., C.P. Enssle, G. Mayer, J. Croisé, and J. Wending, *Repository-Scale Modeling of the Long-Term Hydraulic Perturbation Induced by Gas and Heat Generation in a Geological Repository for High-Level and Intermediate-Level Radioactive Waste: Methodology and Results*, PROCEEDINGS TOUGH Symposium 2009, Lawrence Berkeley National Laboratory, Berkeley, Calif., U.S.A., 2009.

Poller, A., C.P. Enssle, G.Mayer, J. Croisé, and J. Wending, *Repository-Scale Modeling of the Long-Term Hydraulic Perturbation Induced by Gas and Heat Generation in a Geological Repository for High-Level and Intermediate-Level Radioactive Waste: Methodology and Example of Application*, Transport in Porous Media, DOI: 10.1007/s11242-011-9725-x, 2011.

Pruess, K., C. Oldenburg, and G. Moridis, *TOUGH2 User's Guide, Version 2.0*, Report LBNL-43134, Lawrence Berkeley National Laboratory, Berkeley, Calif., U.S.A., 1999.

Zhang, K., Y.-S. Wu, and K. Pruess, *User's Guide for TOUGH2-MP – A Massively Parallel Version of the TOUGH2 Code*, Report LBNL-315E, Lawrence Berkeley National Laboratory, Berkeley, Calif., U.S.A., 2008.

EXTENSION AND TUNING OF TOUGH2-MP EOS7R FOR THE ASSESSMENTS OF DEEP GEOLOGICAL REPOSITORIES FOR NUCLEAR WASTE: HYDROGEN, ARBITRARILY LONG DECAY CHAINS, AND SOLUBILITY LIMITS

Th. U. Kaempfer[1], Y. Mishin[1], J. Brommundt[1], J. Roger[2], E. Treille[2], N. Hubschwerlen[1]

[1]AF-Consult Switzerland Ltd, Groundwater Protection and Waste Disposal
Taefernstrasse 26, 5405 Baden, Switzerland
e-mail: thomas.kaempfer@afconsult.com

[2]Andra, Agence nationale pour la gestion des déchets radioactifs,
Parc de la Croix-Blanche, 92298 Châtenay-Malabry, France

ABSTRACT

Numerical simulation of flow and transport processes forms an important base for the assessment of the performance of deep geological radioactive waste repositories. The TOUGH2-MP simulation code with its EOS7R equation-of-state module is a good starting point for large-scale simulations of the relevant processes, including solute transport of radionuclides, in and around a geological repository.

On this base, we developed the equation-of-state module EOS75Rx that contains optimizations and specific extensions, allowing for a much more efficient treatment of the problem at hand. First, hydrogen, which is formed by corrosion of waste containers and by radiolysis of organic wastes, replaces air as the main component of the gas phase; second, an arbitrary number of arbitrarily long decay chains with branching can be considered; third, solubility limitation and associated precipitation of chemical elements are modeled; finally, a bug fix related to the source terms has been implemented.

The new TOUGH2-MP EOS75Rx module has been validated using unitary tests and benchmark problems for the single- and two-phase flow and transport of radionuclides through porous media and soils. It is currently applied to a large scale 3D simulation of the performance of a generic deep geological repository in clay host rock.

INTRODUCTION

Deep geological repositories for radioactive waste are currently being planned in several countries, including France (Andra, 2006). Among many studies to respond to the specific objectives and requirements of radioactive waste disposal, the French national agency Andra has engaged in a numerical simulation program for its deep geological repository project. The simulation program is an important tool for the conceptualization and phenomenological analysis of the future repository. It requires numerical tools that are capable of modeling appropriately the physical processes of interest in the repository and its environment. The time span of interest lasts from the constructional phase, over the operational phase with waste disposal, to the end of the post-operational phase roughly one million years later. Physical phenomena of main interest are (i) de- and re-saturation of engineered components and porous rocks, (ii) gas production due to e.g., corrosion of engineered components and subsequent migration by advection and diffusion, and (iii) release of energy and radionuclides from the waste and their transport through the engineered system, the host rock, and the embedding geological formations up to the biosphere. Furthermore, accurate models of radionuclide transport must include retardation phenomena, such as sorption or solubility limitations, and must consider radioactive decay.

From the computational point of view, the numerical tools must be highly efficient in order to allow for the simulation of very large systems as well in space as in time. For example, the

current French repository concept (Andra, 2006) consists of several thousand horizontal tunnels for the emplacement of the waste and additional tunnels and shafts for access, logistics, and ventilation during construction and operation of the repository. It encompasses a horizontal area of several kilometers in width and length, for a vertical extension of about 500 m. Moreover, the necessary phenomenological understanding and performance assessment of the repository spans over a period of up to one million years.

For the problem at hand, the parallelized program TOUGH2-MP (Pruess et al., 1999, Zhang et al., 2008) is well suited and has been used extensively in the past (e.g., Enssle et al., 2011, 2012). Within its EOS7R equation-of-state module, many of the relevant features are implemented and are ready to be used, namely the modeling of nonisothermal two-phase flow of a mixture of water, brine, air, and a two-radionuclide decay chain.

There is, however, a particular need to model arbitrarily long decay chains and consider radionuclide retardation by precipitation-dissolution, both features not available in EOS7R. Moreover, the dominant component of interest in the gas phase is often hydrogen rather than air. These requirements led us to the development of the EOS75Rx equation-of-state module.

TOUGH2-MP EOS75Rx

The TOUGH2-MP EOS75Rx module is based on the standard TOUGH2-MP EOS7R module (Pruess et al., 1999), but features (i) thermophysical properties of the water-hydrogen system instead of water-air, similar to the EOS5R module (Pruess et al., 1999), (ii) the treatment of arbitrarily long radionuclide decay chains, and (iii) retardation due to solubility limitations with precipitation-dissolution of the radionuclide components. The latter is implemented following the approach used for precipitation-dissolution of brine in the module EWASG (Battistelli et al., 1997). Moreover, the new EOS75Rx module contains a bug fix in the source-term implementation.

Hydrogen

Within a deep geological repository, the main gas of interest is often hydrogen that is formed by corrosion of waste containers and radiolysis of organic wastes. We have thus adapted the EOS7R module to consider the thermodynamic properties of the water-hydrogen system rather than that of water-air, resulting in the EOS75R module.

The adaptation required the following four properties of air being replaced by those of hydrogen: (i) molar mass, (ii) heat capacity, (iii) the viscosity model of the gas phase, and (iv) the solubility model defined by the description of Henry's constant. While the first three properties can be taken in a straightforward manner from the implementation within module EOS5, the solubility model requires some closer attention. In fact, Henry's constant is temperature dependent in EOS5 but, for the water-air system, salinity dependent in EOS7R. A detailed analysis of the new system, based on the survey study regarding solubility of gases in water and brine by Cygan (1991), showed a clear dominance of the salinity dependence in the water-hydrogen system, with the solubility model thus following the approach of EOS7R. Solubility is interpolated as a function of salinity between given values in pure water and 5N brine and independent of temperature.

Arbitrarily long decay chains

A considerable restriction of module EOS7(5)R is its mandatory consideration of exactly two radionuclides representing one parent decaying to its daughter. At least one TOUGH2 module, namely EOS9nT, can model longer decay chains (Moridis et al., 1999). However, this functionality had to be implemented from scratch within the TOUGH2-MP framework, resulting in module EOS75Rx.

The new module can treat arbitrarily long decay chains, several independent chains at the same time, and allows for branching, i.e., the decay of one parent radionuclide into several daughters.

From an implementation point of view, the extension implied the replacement of any two variables that were associated with the two radionuclides by arrays as e.g., XRN1, XRN2 by

XRN(NRN), where NRN denotes the number of radionuclides. Formulae involving explicit sums of such variables have been replaced by using implicit summation functions available in Fortran 90.

To decouple decay chains and allow for branching, two additional variables were associated to each radionuclide: an index variable specifying its parent—if existent—and a fraction of mass increase specifying the proportion of the parent decaying into the radionuclide in question (Figure 1). This approach of associating the parent to the daughter rather than the opposite was chosen to facilitate the implementation of radioactive decay.

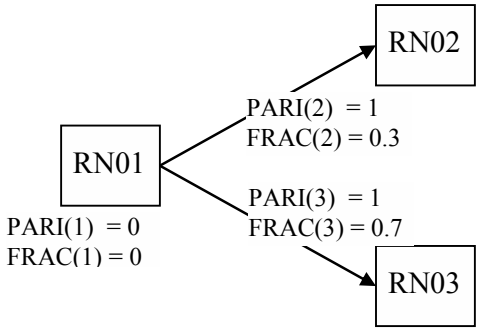

Figure 1. A parent index PARI and decay mass fraction variable FRAC per radionuclide allow for an efficient implementation of radioactive decay, including branching.

The decay chain extension also implied changes to the input functionalities of TOUGH2-MP, particularly:

- In the MULTI block, the last variable NKIN has been replaced by NRN.
- Radionuclides are numbered starting from one and labeled as RN01, RN02, … compared to their old indices 3 and 4 and labeled COM3, COM4; the hydrogen component is labeled as HYDR instead of COM5.
- The SELEC block is extended in a straightforward manner.
- Material specific distribution coefficients are defined in a new block named SORPT.

The output was intuitively adapted and includes the relevant data for all the radionuclides.

Solubility limit and precipitation-dissolution

An important retardation effect during the transport of radionuclides can be solubility limitations that result in precipitation. Given the time scales of relevance here, kinetic effects can safely be neglected and precipitation-dissolution be modeled using the so-called C_{sat} approach: Whenever, at a given location, the concentration of a radionuclide in the liquid phase would start to exceed its solubility limit C_{sat}, the radionuclide starts to precipitate and the liquid concentration remains fixed at the solubility limit. The liquid concentration is allowed to drop below the solubility limit only after all the solid phase has been dissolved again.

In some circumstances, precipitates might influence porosity and thus have a feedback on fluid flow; this is, however, neglected here. Moreover, precipitates are supposed to be immobile.

In the TOUGH2(-MP) EWASG module (Battistelli et al., 1997), solubility limitation is implemented for the brine component. This formed the basis for our implementation with respect to radionuclides in EOS75Rx. For the EWASG approach to be feasible, solubility limits are defined per radionuclide and must be independent of each other. Finally, we postulate that precipitates can exist only with a liquid phase also being present. In this case, the phase concentrations of a radionuclide are assumed to respect (i) Henry's law between the liquid and (potential) gas phase and (ii) the solubility limit between the liquid and solid phase.

With these assumptions, precipitation-dissolution can be implemented using the standard TOUGH2 approach for phase changes, namely by switching primary variables. It is implemented analogous to EWASG, as follows.

Precipitation of a radionuclide K occurs as soon as its liquid concentration C_l^K (mass per volume in the liquid phase) exceeds its user-defined solubility limit C_{sat}^K:

$$C_l^K = \frac{V_{por} S_l \rho_l X_l^K}{V_{por} S_l} = \rho_l X_l^K \; > \; C_{\mathrm{sat}}^K,$$

where $V_{por} = \phi V$ is the pore volume in an element with volume V and porosity ϕ, and

S_l, ρ_l, X_l^K are the liquid fraction, liquid density, and mass fraction of radionuclide K in the liquid phase within the element, respectively. Expressed as a condition for X_l^K, this gives

$$X_l^K \; > \; \frac{C_{\text{sat}}^K}{\rho_l}.$$

As soon as the solubility limit is reached, X_l^K is fixed and the primary variable for the radionuclide will be changed from X_l^K to the quotient between precipitated mass m_s^K and pore volume:

$$X_l^K \; = \; \frac{C_{\text{sat}}^K}{\rho_l} \;\; , \;\; X_l^K \rightarrow \; Z_s^K = \frac{m_s^K}{V_{por}}.$$

If variable Z_s^K decreases to zero, the precipitated phase disappears, Z_s^K is set to zero, and the primary variable switched back:

$$Z_s^K \; = \; 0 \;\; , \;\; Z_s^K \rightarrow \; X_l^K.$$

When phase change occurs, the new primary variable is initialized in the TOUGH2 manner using the small parameter ZERO, which is by default set to 10^{-6}. This initialization approach reduces numerical oscillation, but is not necessarily mass conservative.

As TOUGH2-MP uses the Newton-Raphson method to solve the nonlinear system of equations, checks for phase-change and associated switches of primary variables can be implemented "on the fly" using the set of secondary parameters and without changing the matrix assembling functionality of the code.

Supposing that precipitates neither modify porosity nor saturation with respect to liquid and gas phases and do not contribute to internal energy, the mass- and energy-balance equations solved by TOUGH2-MP (Pruess et al., 1999) require only minor adaptations to account for the additional solid phase. For example, the mass accumulation term for radionuclide K, which is implemented as a sum over phase contributions

$$M^K = \phi \sum_{\beta} S_\beta \, \rho_\beta X_\beta^K,$$

with $\beta \in \{l, g, s\}$ the phase index and S, ρ, X the saturation degree, density, and mass fraction, respectively, can be written as

$$M^K = \phi \left(S_g \rho_g X_g^K + S_l \rho_l X_l^K + Z_s^K \right).$$

Precipitation-dissolution capability necessitated extending the TOUGH2-MP input functionalities, particularly as follows:

- Solubility limits are input using a new block called SOLUL that is repeated for each material that has solubility limitation for at least one radionuclide.
- For initial conditions and the SAVE format, the potential presence of precipitates is specified using flags. For each element, after the usual set of initial conditions for the primary variables, a line with a list of logical flags ('T' for True and 'F' for False) of length NRN is added (e.g., 'TFFTF' for five radionuclides with the first and fourth one present in solid form).

The output was intuitively adapted and includes all the relevant data of the potential three phases per radionuclide.

Mass conserving source terms

In standard TOUGH2(-MP), transient source terms are not necessarily interpreted in a mass and energy conserving way, depending on the choice of the interpolation scheme with MOP(12). This has been corrected for in EOS75Rx with new options MOP(12) = 3,4,5 corresponding to mass conservative implementations of the interpolation schemes MOP(12) = 0,1,2.

CODE VALIDATION

Hydrogen

The EOS75R module with the water-hydrogen system has been validated by comparison with module EOS5 for single-phase liquid, single-phase gas, and two-phase conditions. For appropriate choices of temperature that short-circuit dependencies in EOS5, the results must be and are identical up to rounding errors between the two modules. To test salinity dependence of solubilities in two-phase conditions, we have successfully compared simulated fractions of dissolved hydrogen for brines with different molarities to the fractions expected from the conceptual model.

Solubility limit and long decay chains

The new EOS75Rx module has, for all functionalities already available in EOS75R, been thoroughly tested, using an extensive non-regression test series available at AF-Consult Switzerland Ltd. The new features of precipitation-dissolution and arbitrarily long decay chains were evaluated first using several unitary tests and second on a more complicated physico-numerical test case (see next section).

A simple unitary test, consisting of four Finite Volumes, external no-flow boundary conditions for all components, and a radionuclide source that is first positive, then negative at constant rates in all elements, demonstrates the precipitation-dissolution feature (Figure 2). The liquid concentration increases from the start at a constant rate. As soon as the solubility limit is reached, the liquid concentration remains fixed and the solid concentration increases at the same rate as the liquid concentration did before. The inverse behavior occurs in the second half of the test, when the source is negative. Total mass balances have been successfully compared between a case with and one without solubility limit.

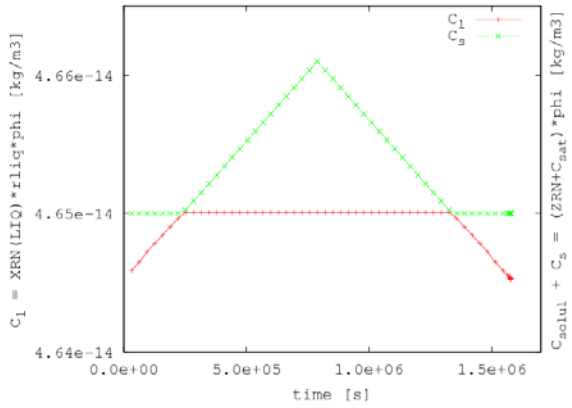

Figure 2. Evolution of radionuclide concentration (liquid in red left, solid in green right) in the very simple four-element test case. The concentrations have been calculated from 'liquid mass fraction XRN(LIQ)', 'liquid density rliq', 'solid mass per pore volume ZRN', and 'porosity phi' and the solid concentration was shifted by the solubility limit.

As a more complex test case, we designed a vertical "one-dimensional" column of saturated Callovo-Oxfordian clay with dimension 1×1×50 m that was discretized by 250 Finite Volumes. Fixed pressures of 5×10^6 Pa and 6×10^6 Pa at the top and bottom of the column, respectively, induced a pressure gradient and slight upward flow. The column was either fully saturated or had an initial saturation of 0.9 and was allowed to resaturate from the top. We considered the simple decay chain $^{245}Cm\rightarrow^{241}Pu$ and defined a source with a release rate of 10^{-13} kg·s^{-1} for the parent radionuclide in the bottom-most Finite Volume and over the whole simulation period of 2 000 years. However, in order to test a precipitation-dissolution process that is decoupled from the release rate, and in order to trigger precipitation after a relatively short simulation time, we modified the radionuclide properties such that ^{245}Cm had no solubility limit and a short half-life, while ^{241}Pu did decay only very slowly. This led to a situation where the solubility limit of the daughter radionuclide was reached after around 500 years.

We compared qualitatively the concentrations (Figures 3 and 4) and quantitatively the mass balances of the two radionuclides between a simulation without and one with solubility limit of the daughter radionuclide.

a) no solubility limit b) with solubility limit

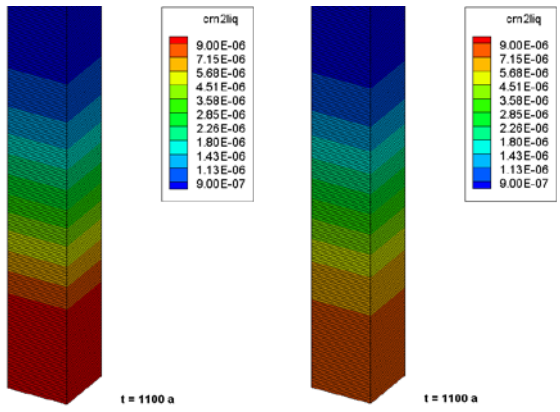

Figure 3. Liquid concentration (in kg per m^3 overall volume) of the daughter radionuclide for the fully saturated situation without (left) and with (right) solubility limit.

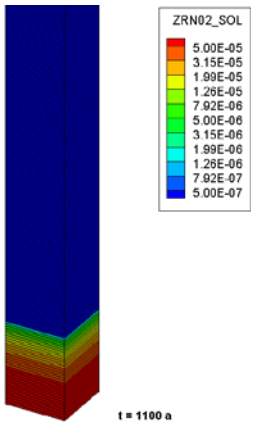

Figure 4. Solid concentration (in kg per m^3 pore volume) of the precipitating daughter radionuclide for the fully saturated case.

PHYSICO-NUMERICAL TEST-CASE

We considered the two-dimensional transport of radionuclides from a schematic representation of half of an emplacement cell for radioactive waste embedded in Callovo-Oxfordian clay (Figure 5). At time zero, the emplacement cell is partially desaturated and it resaturates over time from the host rock inwards. We considered the 4N+1 radionuclide decay chain

$$^{245}Cm \rightarrow ^{241}Pu \rightarrow ^{241}Am \rightarrow ^{237}Np \rightarrow ^{233}U \rightarrow ^{229}Th,$$

where ^{245}Cm is released at a constant rate for the first 100 years.

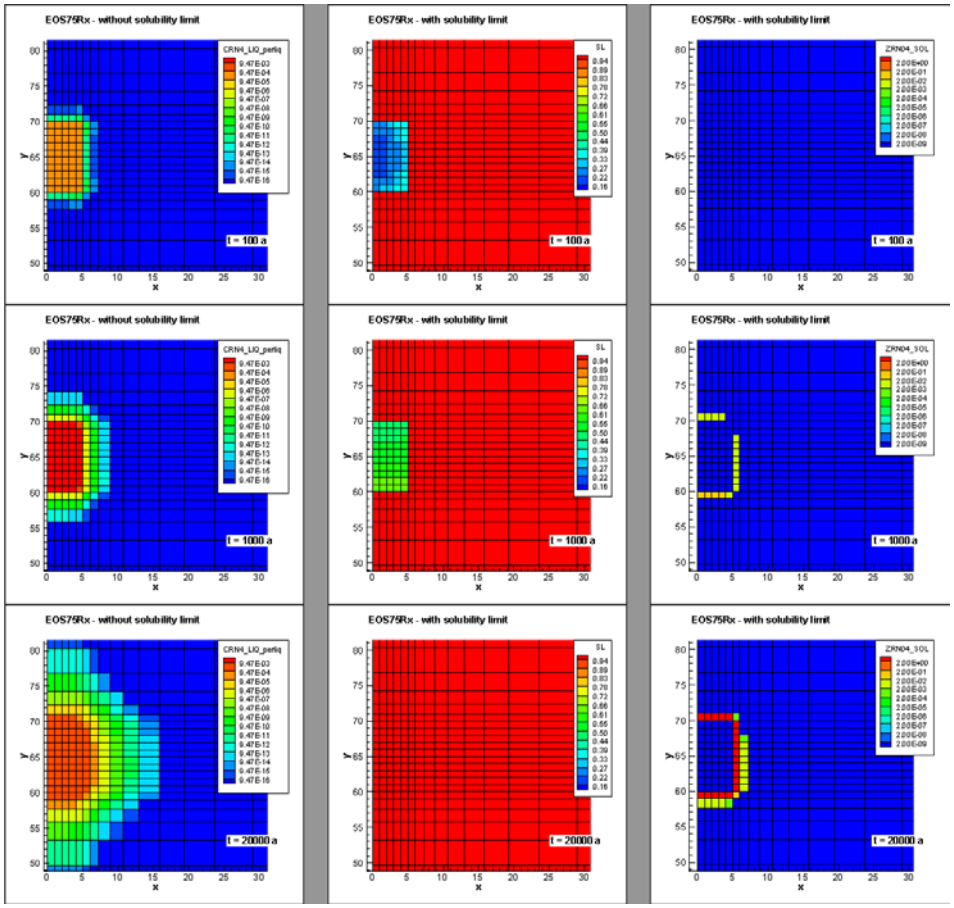

Figure 5. Evolution of the liquid concentration of ^{237}Np (in kg per m^3 liquid volume, left), the liquid saturation (middle), and the solid concentration of ^{237}Np (in kg per m^3 pore volume, right) for the physico-numerical test-case with solubility limitations in an area close to the emplacement cell.

We performed two simulations up to 20,000 years, one without solubility limitation and one for which the radionuclide solubility limits were set to their reference values in Callovo-Oxfordian clay. In particular, for ^{237}Np a solubility limit of 4×10^{-6} mol·l^{-1} was imposed.

For the case with solubility limitation, the evolution of the liquid concentration of ^{237}Np, the saturation level, and the mass of precipitates is shown in Figure 5. As can be seen, the solubility limit of ^{237}Np is reached in the host rock in Finite Volumes close to the emplacement cell.

In the present test-case, only the solubility limit of ^{237}Np is reached. The radionuclide concentrations are thus identical between the two simulations for the first three radionuclides in the decay chain. The retardation effect due to precipitation is best seen for ^{237}Np (Figures 6 and 7), but prevails also for the further decay products ^{233}U and ^{229}Th.

In summary, the present physico-numerical test case demonstrates the capability of TOUGH2-MP EOS75Rx for treating long decay chains with retardation by precipitation.

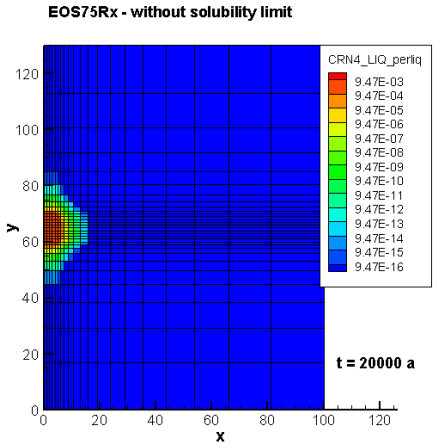

Figure 6. Distribution of the liquid concentration of ^{237}Np (in kg per m^3 liquid volume) at the final simulation time for the physico-numerical test-case without solubility limit. Shown for the full computational domain.

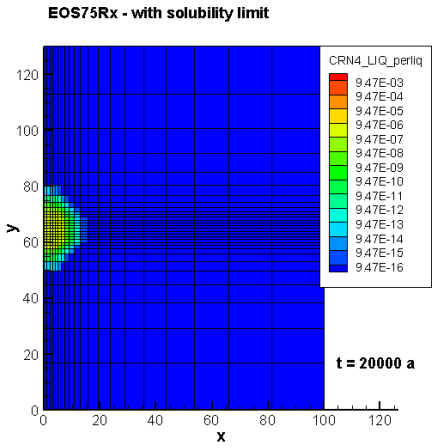

Figure 7. Distribution of the liquid concentration of ^{237}Np (in kg per m^3 liquid volume) at the final simulation time for the physico-numerical test-case with solubility limit. Shown for the full computational domain.

PERFORMANCE

The implementation within the EOS75Rx module, when compared to the EOS7(5)R module, uses array variables associated with the radionuclides instead of two individual variables for radionuclide one and two. Moreover, many computational formulae have been rewritten using intrinsic summation functions of Fortran 90.

Solving the physico-numerical test-case described above for a decay chain of two radionuclides, we consistently observe an improvement in performance from module EOS7(5)R to EOS75Rx of approximately 10%. Similar performance increases are seen for more advanced benchmark problems. In the case of computations with only one radionuclide, performance is further increased, since in this case the EOS75Rx module indeed considers just one radionuclide, while the original TOUGH2-MP EOS7R module always builds up a system that includes two radionuclides.

CONCLUSION

We built a new TOUGH2-MP equation-of-state module, called EOS75Rx, based on the EOS7R module, but which considers hydrogen as the primary gas phase instead of air. This allows for arbitrarily long radionuclide decay chains to be considered, has retardation by precipitation-

dissolution implemented, and contains a bug fix within the source term implementation. The module has been thoroughly tested using an extensive set of nonregression and unitary tests, and its capabilities have further been demonstrated using a two-dimensional physico-numerical test case. A performance increase of approximately 10% has been observed in our new module compared to module EOS7(5)R.

The module is currently applied to large-scale simulations of radionuclide release for the French deep geological repository concept.

ACKNOWLEDGMENT

The developments of the EOS75Rx module and part of this publication have been funded by Andra. Valuable input was provided by Carl-Philipp Enssle. Thanks to Keni Zhang who kindly responded to questions regarding TOUGH2-MP.

REFERENCES

Andra, *Dossier 2005 Argile – Synthesis – Evaluation of the feasibility of a geological repository in an argillaceous formation,* ISBN: 2-916162-00-3, 2006.

Battistelli, A., C. Calore, and K. Pruess, *The simulator TOUGH2/EWASG for modelling geothermal reservoirs with brines and non-condensible gas,* Geothermics, Vol. 26, No. 4, pp. 437-464, 1997.

Cygan, R. T., *The solubility of gases in NaCl brine and a critical evaluation of available data,* Report SAND90-2848, Sandia National Laboratories, Albuquerque, New Mexico, 1991.

Enssle, C.P., J. Croisé, A. Poller, G. Mayer, and J. Wendling, *Full scale 3D-modelling of the coupled gas migration and heat dissipation in a planned repository for radioactive waste in the Callovo-Oxfordian clay*, Physics and Chemistry of the Earth, DOI: 10.1016/j.pce.2011.07.033, 2011.

Enssle, C.P., J. Brommundt, Th. U. Kaempfer, G. Mayer, and J. Wendling, *Full scale 3D modelling of a repository in the Callovo-Oxfordian clay with focus on two-phase transport of ^{14}C and ^{129}I,* submitted to Proceedings of 'Clays in Natural & Engineered Barriers for Radioactive Waste Confinement', October 2012, Montpellier, France, 2012.

Moridis, G. J., Y.-S. Wu, and K. Pruess, *EOS9nT: A TOUGH2 module for the simulation of water flow and solute/colloid transport in the subsurface,* Report LBNL-42351, Lawrence Berkeley National Laboratory, Berkeley, California, 1999.

Pruess, K., C. Oldenburg, and G. Moridis, *TOUGH2 user's guide, version 2.0*, Report LBNL-43134, Lawrence Berkeley National Laboratory, Berkeley, California, 1999.

Zhang, K., Y.-S. Wu, and K. Pruess, *User's Guide for TOUGH2-MP – A massively parallel version of the TOUGH2 code*, Report LBNL-315E, Lawrence Berkeley National Laboratory, Berkeley, California, 2008.

DEVELOPMENT OF GEOHYDROLOGIC MODEL OF THE WILDCAT FAULT ZONE

Kenzi Karasaki[1], Christine Doughty[1], and Junichi Goto[2]

[1]Lawrence Berkeley National Laboratory
Berkeley, California, 94720, USA
e-mail: kkarasaki@lbl.gov, CADoughty@lbl.gov

[2]Nuclear Waste Management Organization of Japan
Tokyo, Japan
e-mail: jgoto.numo.or.jp

ABSTRACT

We have conducted field investigations of the Wildcat Fault starting with a literature survey, an aero-photo-based geomorphological study, geologic mapping, geophysical surveys, trenching, and borehole drilling and hydraulic testing in the LBNL area. A geologic model was constructed, which became the basis of the hydrologic model. Here, we outline the effort of constructing the geohydrologic model of Strawberry Canyon, the area on which our study focuses. We also created an East Canyon submodel, which is part of Strawberry Canyon.

The models were constructed by using PetraSim commercial software, which is a pre- and post-processor for TOUGH2. One of our goals is to understand the role of the Wildcat Fault in controlling the natural-state groundwater flow. With limited data in numbers and areal extent, we hope to build a model that is valid for a scale larger than the observation area. We performed both manual and automated inversion analysis and produced reasonable matches between the observed head data and model predictions. By varying the structure of the Wildcat Fault, we found that the base-case representation, which includes a high-permeability damage zone and a low-permeability fault core, best matches the observed head data. Using the submodel, we conducted a two-phase nonisothermal simulation utilizing the pressure and temperature data from the boreholes. We also used the information obtained from pump tests, including permeability anisotropy of the fault plane.

After parameter searches, we were able to match the head and temperature profiles along boreholes relatively well. We then used the best matching models to predict the rate of head decline during a dry period, and found that an anisotropic fault zone with 5% porosity predicts the rate of decline reasonably well. There is the potential that the rate of decline may be useful in estimating the permeability downstream, where there are no boreholes for observation/testing.

INTRODUCTION

The primary objective of the Fault Zone Hydrology Project is to develop an effective and reliable methodology for fault-zone characterization. To this end, we have conducted field investigations of the Wildcat Fault (WF) starting with a literature survey, an aero-photo-based geomorphological study, geologic mapping, geophysical surveys, trenching, borehole drilling, and hydraulic testing in the LBNL area. According to the systematized investigation flow proposed in Karasaki et al. (2009, 2010) and Kiho et al. (2012), a geologic model would be constructed as information and data gathered by the field investigation started to come in. Then, the geologic model would become the basis of a hydrologic model that honors hydraulic data obtained by passive and active hydrologic tests. The hydrologic model would then be used to make predictions of the outcome of the next stage of investigations, and to identify data holes (if any). Thus, the field investigation, geologic model, and hydrologic model would compose a circular feedback loop.

In the present paper, we outline the effort of constructing the geohydrologic model of the Strawberry Canyon (Berkeley, California), the basin within which our current study area is concentrated. We also created a smaller subregion model of the East Canyon. One of our

goals is to understand the role of the Wildcat Fault in controlling natural-state groundwater flow, and one means to assist in developing this understanding is to develop a numerical model of groundwater flow in the basin containing the fault. Our flow-modeling strategy was to calculate the natural-state flow field and also to investigate the transient inter-well response to drilling, well tests, long-term pumping, and seasonal fluctuations.

DATA AVAILABLE

A great deal of site characterization data is available from which to construct the model, including:

- Geologic map (Graymer, 2000; Karasaki et al., 2009, 2010, 2011; Kiho et al., 2012)
- Digital elevation model (up to 3 m resolution)
- Surface fault location in trenches (TR-1~5)
- Three vertical wells with geophysical log information and permanent pressure and temperature sensors at 5 depths (WF-1–WF-3)
- Two diagonal wells crossing the fault (WF-4 and WF-5)
- Two deep wells with water-level and pumping rate data (SSL-1 and 2)
- Flow rates for three existing wells/hydraugers (Lennert, BG-1, Quarry)
- Many shallow wells with water-level data and permeability estimates (often from slug tests) from the Site Environmental Remediation Project
- Precipitation record
- Air temperature record.

NUMERICAL SIMULATOR

The TOUGH2 code, a general purpose numerical simulator for fluid flow and heat transport in geological media (Pruess et al., 1999), is used for the numerical simulations. TOUGH2 preliminary simulations use the equation of state module EOS9, which considers single-phase liquid water or a unsaturated system in which the air is a passive spectator (a common soil-physics approximation) and temperature does not change. Results of TOUGH2/EOS9 simulations include steady-state and transient hydraulic head distributions, infiltration rates, and flow rates from various outlets in the model (creeks, springs, hydraugers). We also use equation-of-state module EOS3 (which is non-isothermal and includes an active gas phase), for the East Canyon submodel. Temperature profiles in boreholes can provide up-flow or down-flow signatures of groundwater.

MODEL DOMAIN

Figure 1 shows a 3 m resolution digital elevation map (DEM) of the Berkeley Hills area. The map is shaded to show the topographic relief, so that basins are easily identified. Note that our study area is in a well-defined basin, Strawberry Canyon. We chose the model area to coincide with the basin, which covers the Strawberry Creek watershed east of the Hayward Fault. The model is roughly diamond-shaped, with diagonal lengths 3 km in the E-W direction and 2.4 km in the N-S direction. Boundaries to the northwest, northeast, and southeast were determined by following ridgelines on the DEM.

The surface trace of the Hayward Fault forms the southwest boundary of the model. It follows a strong break in slope between the hilly terrain of the model and the much gentler slope that extends to San Francisco Bay. The elevation along this boundary is gently undulating, with several creeks running NE-SW crossing the fault. The rectangular area is the University of California, Berkeley Campus. Note that there are several creeks running EW, which are the continuation of Strawberry Creek displaced by the Hayward Fault.

In the vertical direction, the model extends from the ground surface, which ranges from about 120 masl to 540 masl, to an elevation of -400 masl. No wells extend any deeper than 0 masl, but the large vertical extent is provided so that the model horizontal-to-vertical aspect ratio is near one, in order to not artificially constrain natural groundwater flow lines.

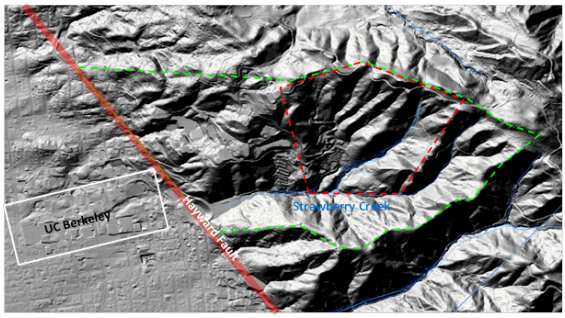

Figure 1. Shaded DEM map of the Berkeley Hills. The Strawberry Canyon model area is outlined in green. The red dashed line is the East Canyon Submodel area.

GEOLOGIC MODEL

The current geologic model used in the hydrologic simulation can be seen in Figure 2, based on available geologic maps and core analysis from five boreholes, WF-1 through WF-5. (Graymer, 2000; Karasaki et al., 2009, 2010, 2011, 2012; Kiho et al., 2012).

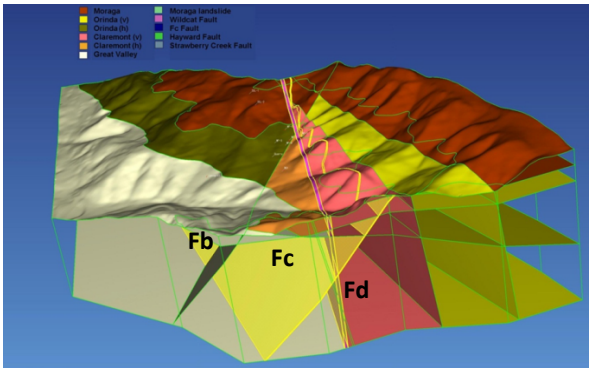

Figure 2. Perspective view of the geologic model showing faults and contacts between formations. Three faults are highlighted: the vertical Wildcat Fault (Fd), the sloping Fc and Fb structure.

Our geologic model essentially incorporates the Fb, Fc, and Fd structures proposed by Kiho et al. (2012), except our model assumes that Kiho et al.'s Fd-branch is the main Wildcat Fault. Fb is modeled as the geologic boundary between the Orinda Formation/San Pablo Group and Claremont Formation, without any thickness or independent permeability. Fc is modeled as a permeable structure, while Fd is modeled as a dual structure, with low permeability perpendicular to the fault and high permeability parallel to the fault. All the features are treated as a plane. We assume that hydrologically there are two types of Orinda Formation and Claremont Formation The Orinda Formation observed in WF-2, WF-3, and WF-4 appears to be subhorizontal, whereas the same formation on the east of the Wildcat Fault is reported to be subvertical, as is the Claremont Formation on the east side of the Wildcat Fault (Geomatrix, 2008). In general, a sedimentary layer is anisotropic, with a lower vertical permeability than horizontal when it is in the original depositional state. Therefore, we expect a lower permeability in the vertical direction of the Orinda Formation in the west, and vice versa on the east of the fault. As for the Claremont Formation, we assumed that the Claremont on the west is of a different material than on the east of the fault.

GRID

Strawberry Canyon Model

The preliminary numerical grid is constructed of 23 layers, each with the same lateral discretization. Lateral discretization is done with Voronoi tessellation and is variable, with finest resolution near the wells and Wildcat Fault, and a gradually coarsening grid beyond that (Figure 3). Each layer has 4295 gridblocks, and the total number of active gridblocks for the model is 101,024 (the top layer, representing the constant atmospheric boundary, is inactive).

Three features present in the numerical model are not shown in the original geologic model: the Hayward Fault, the Strawberry Creek Fault, and the Moraga landslide. The top of the model is defined by the DEM, and layer thickness gradually adjusts to conform to it. The top three layers are thinner, to better represent surface changes in topography. Permeabilities for all the materials are given in Table 1.

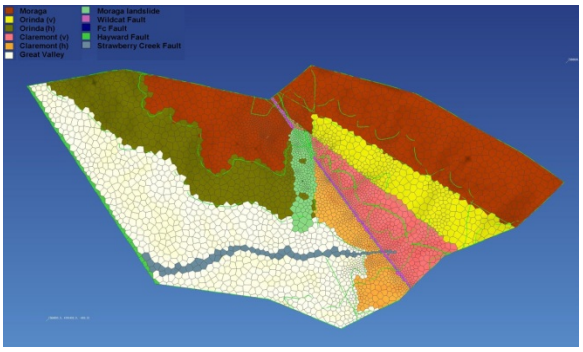

Figure 3. Plan view of the computational grid. Area around boreholes and along the Wildcat Fault is highly discretized.

Table 1. Permeability values used for the Strawberry Canyon model.

	Orinda		Claremont		Moraga	Great Valley	Fault Core	Fault Damage
	To_H	To_V	Tc_H	Tc_V				
Kx	8×10^{-16}	4×10^{-16}	1×10^{-14}	1×10^{-15}	7×10^{-15}	7×10^{-15}	2.6×10^{-16}	1.3×10^{-13}
Ky	8×10^{-16}	4×10^{-16}						
Kz	1×10^{-16}	8×10^{-16}						

East Canyon Sub-Model

The Strawberry Canyon model we have discussed above is based on a topography that clearly defines a closed basin, as shown in Figure 1. Using the hydraulic test results and pressure monitoring data, we estimated the permeability structure of the fault and the surrounding rocks. However, the parameters we obtained are, strictly speaking, only valid within the extent of the tests. We did find that long-term monitoring of seasonal changes in pressure may be useful in estimating the parameters of a larger volume outside of the well field. In particular, we found that the rate of decline in pressure during a dry season may be used to further calibrate or to verify the model. We used a Voronoi tessellation for the Strawberry Canyon model to keep the number of elements to a manageable size and still have fine discretization near a borehole. However, for the purpose of matching the static pressure and temperature profiles in boreholes and seasonal fluctuations due to rainfalls, no discretization is necessary in the vicinity of boreholes. Rather, a uniform grid with the finest affordable resolution is better for accuracy and manageability. For these reasons, we created a submodel, which we call the East Canyon Submodel, with regular discretization, whose boundary is shown with the red broken line in Figure 1. As can be seen from the figure, the submodel captures a smaller but less well-defined basin. Figure 4 shows the numerical mesh of the East Canyon submodel. Table 2 shows the permeability values for the model.

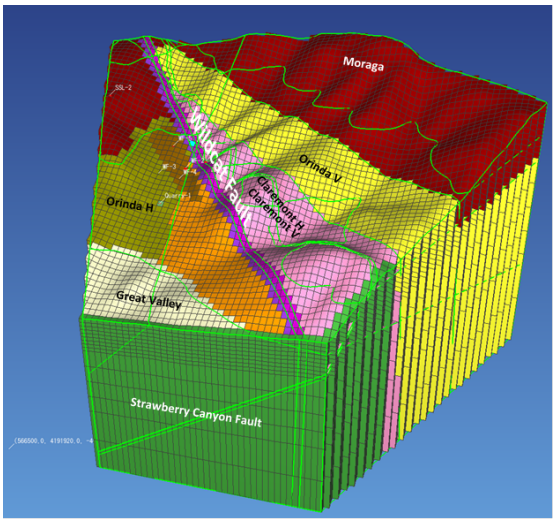

Figure 4. The numerical mesh of the east Canyon submodel. The Wildcat is modeled by two planes of low (purple) and high permeability (dark pink). The brown colored cells are the landslide material.

Table 2. Permeability values used for the East Canyon submodel. The anisotropic values for the fault reflect the pumping test results. The rest of the values are optimized values to match the observation data.

	Orinda		Claremont		Moraga	Great Valley	Landslide Material	Surface deposits	Fc	Fault Core	Fault Damage
	To_H	To_V	Tc_H	Tc_V							
K_x	1e-17	1E-17	1e-16	5e-17	3e-15	1.5e-16	5e-16	2e-11	1e-13	1e-17	1e-13
K_y	1e-17	1e-17	1e-16	5e-17				2e-11		1e-17	1e-13
K_z	1e-17	1e-17	5e-17	1e-16				5e-12		5e-18	1e-14

In the Strawberry Canyon model, we represented the duality of the Wildcat, i.e., high permeability along the fault and low permeability across it, by using a customized anisotropic permeability assignment. This is done by assigning high permeability between the cells of the same material but low permeability between different materials, specifically between the fault material and Orinda or Claremont Formations. In the East Canyon model, we represented the Wildcat with two side-by-side planar features—one represent-

ing the high permeability damaged zone and the other the low permeability core, as can be seen in Figure 4. We assigned a 10-to-1 ratio of anisotropy to the fault damage zone, based on interference tests. The recharge rate was determined by calibrating to the observed head data. The temperature profile data from WF boreholes indicate that the geothermal gradient is ~4°C/100 m, which is relatively high. This is the result of the balance between cold rain recharging form the surface and the heat flux from the deeper subsurface. The bottom heat flux boundary condition was set at a constant rate of 85 mW/m^2. Karasaki et al. (2011b) followed a similar approach by utilizing the temperature profile from boreholes to reduce the uncertainties of a geohydrologic model.

Simulation Results for Strawberry Canyon Model

Figure 5 compares hydraulic head values observed at the WF and SSL wells with model values for the simulation, with the best match between the two. The impact of the Wildcat Fault is apparent as a small jump in pressure. Several simulations were run with varying amounts of infiltration, including 50%–100% of the average annual precipitation rate of 1,000 mm/yr. Here, infiltration is specified as 67% of precipitation. If precipitation is too low, well SSL-1 cannot sustain the observed pumping rate. Although the modeled heads are somewhat large for all the wells, the field-observed separation between wells WF-1 and WF-2 is captured by the model.

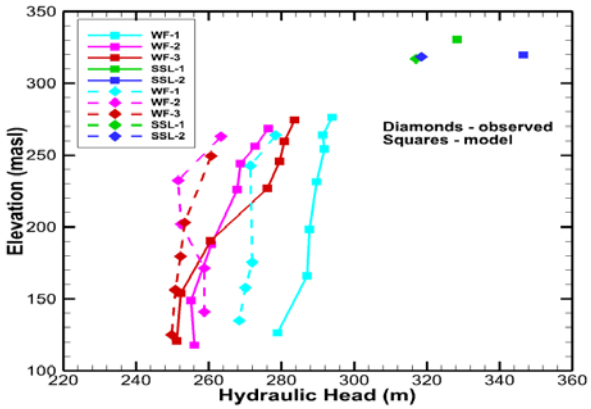

Figure 5. Comparison of modeled and observed hydraulic head measurements of the best case.

Simulation Results for East Canyon Sub-Model

Figure 6 shows the comparison between the observed head data in WF-1–WF-3 boreholes to one of the best simulation results. Note that the simulation reproduces the decreasing head distribution along the depth of the boreholes, the separation of heads between WF-1 and WF-2, and the low head anomaly in WF-2, which is likely caused by the permeable Fc feature that drains water to lower elevation. Figure 7 shows the simulated and observed temperature distributions along the WF boreholes. The solid and broken lines denote the observed and simulation results, respectively. As can be seen from the figure, the simulation reproduces the temperature profiles relatively well. The observed head data are represented by vertical line segments and the temperature data are continuous lines, because the head within an observation interval is assumed constant along the entire length as it is packed with coarse sand—whereas the temperature is thought to be linearly varying within an interval.

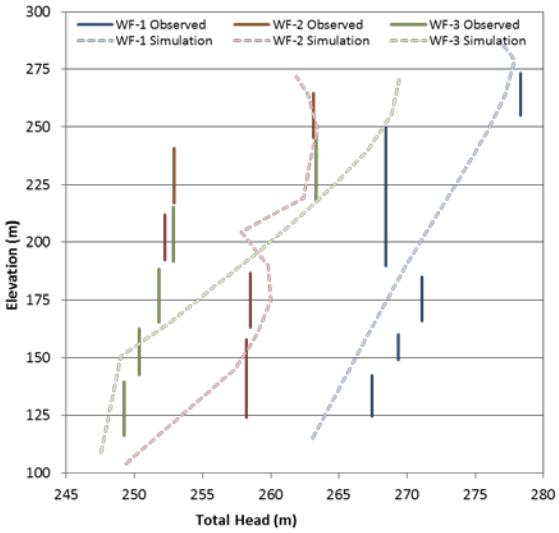

Figure 6. Comparison of simulation results with the observed head data of WF-1–WF-3. Note that the model reproduces the deceasing head with depth very well, as well as the low head anomaly in WF-1 possibly caused by the Fc fault.

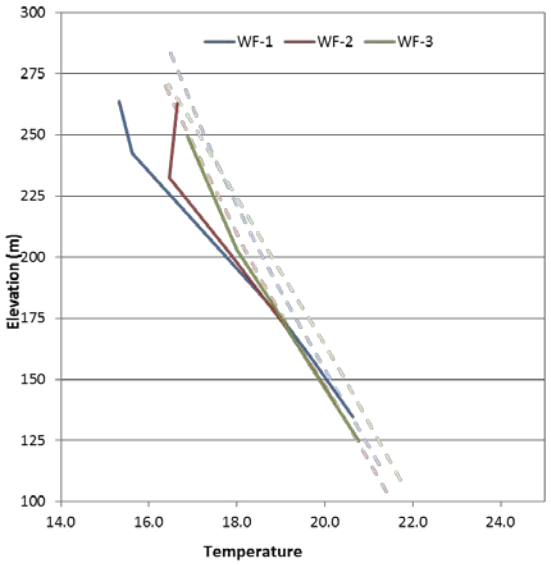

Figure 7. Comparison of simulation results with the observed temperature data of WF-1–WF-3. Note that the model reproduces the increasing temperature with depth very well below elevations of about 200 m.

This raises the question of the soundness of the traditional approach, in which observation intervals are very long and isolated by short packers. (In our case, grout was used in place of packers.)

Model Verification

Now we have an East Canyon submodel that reasonably reproduces the key aspects of head and temperature distribution observed in WF holes. In fact, several combinations of permeability produce similar goodness of fit. The next question is, how good are these models in predicting phenomena that were not used in the model calibration. The rate of head decline in WF-1 is ~2 m per half year during a dry period. We now try to see if the models predict a similar rate of decline by imposing a boundary condition simulating a wet and dry season. In developing the East Canyon model, we imposed a constant mass-flow-rate boundary condition (2.2×10^{-6} kg/m^{2}s, equivalent to 7% of the annual average rainfall) on the surface and ran the simulation until steady state was reached, which is typically over 100,000 years of simulation time. We then use the steady-state condition produced by models that match the borehole head profiles as the initial condition to simulate rainfall during a rainy season, followed by a dry season, for one year. Although we could use the actual daily rainfall data from the previous year as the boundary condition, we simplified the recharge event to a constant flux at 1×10^{-5} kg/m^{2}s for 80 days for the rainy period and zero rainfall thereafter for one year.

Figure 8 shows the head transients at WF-1#3 from January 2011 through the end of February 2012, compared to the simulation results. The negative spikes in the observed data are due to pumping tests, which were not simulated. Both red and green lines have the same permeability structure that produces the match shown in Figure 6 and Figure 7. Specifically, they have a 10:1 anisotropy ratio in the fault zone. The only difference between the two curves is the porosity: the red line represents the case in which the fault zone rock has 10% porosity and the green, 5%. As can be expected, the larger porosity value shows a smaller head increase during the rainy period and slower head decrease during the dry period. Also shown is a modeled case with 10% porosity and an isotropic Fd feature (the pink curve), which matched the head profiles just as well as the previous two cases, but did not match the interference-test data as well. During the dry period from June and thereafter, the green curve declines in parallel with that of the observed data. The red line declines too slowly, while the pink declines too fast.

It is possible that having a constant recharge for 80 days represent the rainy period is too much of a simplification. The rate of decline during the dry period is controlled by the overall throughflow permeability from the area around the boreholes and to the discharge location, as well as by the porosity. Out of the three models, the 5% porosity model with 10:1 anisotropy ratio is the best model thus far. Note that porosity was not directly used in the calibration when we tried to match the head profiles along WF boreholes, since steady-state flow fields do not depend on porosity. Consequently, choosing the 5% porosity over 10% is actually a secondary calibration. It should be noted that a crude porosity estimate of 1.5% in the Moraga Formation, based on the level observation in SSL-1, is not reflected in the model. Although both numbers are at least in the ballpark, and the porosity variation in the Moraga Formation is expected to have little

impact on the borehole area because it is rather far away, the model run with the 1.5% porosity should be examined.

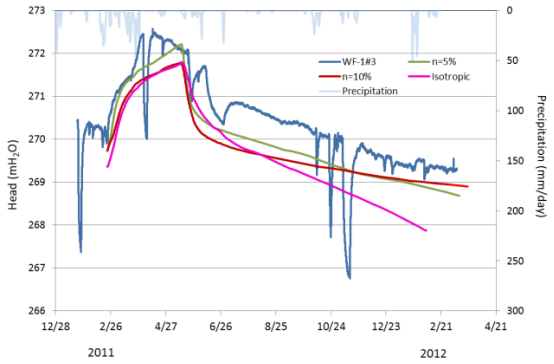

Figure 8. Comparison of simulation and observed head transients at WF-1#3 (blue) in response to seasonal rainfall using the best East Canyon submodel with 10% (red) and 5% (green) porosity, and isotropic Fd zone The daily precipitation (light blue) is plotted against the right axis. Negative spikes in head in data are caused by pump tests, which were not modeled. Note that the head decline rate during the dry period is reproduced better assuming 5% average porosity.

CONCLUSIONS

We developed hydrologeologic models of the Wildcat Fault Zone that incorporates most of the geologic features at two different scales: the Strawberry Canyon basin model and the East Canyon submodel. We performed both manual and automated inversion analysis and produced reasonable matches between the observed head data and model predictions. We varied the infiltration rate and found that specifying infiltration as 67% of precipitation produced the best match to observed head data. This 67% rate is rather high and could possibly be an artifact of the way we handled recharge; actual recharge into the model may be much less. By varying the structure of the WF, we find that the representation that includes a high-permeability damage zone and a low-permeability fault core best matches the observed head data. It is possible to obtain better matches to the observed heads with a mesh refinement and local adjustments of parameter values. However, our objective here is to develop a methodology by which to understand the role of faults at a bigger scale though numerical modeling. If a better match is obtained by local refinements, it is probably not very important at a larger scale, unless the refinement itself is some culmination of a larger scale property.

We constructed a submodel with uniform horizontal gridding and carried out a two-phase non-isothermal simulation utilizing the steady-state pressure and temperature data from the boreholes. For this submodel, we found that a recharge rate of 7% of the annual rainfall produces a best match, which is somewhat contradictory to the finding using the larger Strawberry Canyon model. Future studies will be directed at determining the source of this discrepancy.

We also obtained information by calibrating the model to interference well tests, such as the anisotropic permeability in the fault zone. After parameter searches, we were able to match the static head and temperature profiles along boreholes relatively well. We then used the best matching models to predict the rate of head decline during a dry period, and found that an anisotropic fault zone with 5% porosity predicts the rate of decline reasonably well. Further optimization may be possible by using more realistic boundary conditions. Thus, we used static and dynamic data to calibrate the submodel.

In theory, the larger the degree of freedom in the model, the easier it is to match the observed data. However, the goal here is not to simply match the observed data. Typically, data are limited in numbers and areal extent. We would like to build a model that is valid for a scale larger than the observation area. There is the potential that the rate of decline may be used to estimate the permeability downstream of the borehole complex, although more study is necessary to verify this claim.

It should be noted that because of the sloping nature of the model layers the gridding used in the model, in a strict sense, violates the conditions for the finite difference model approximation, where the line that connects adjacent element centers should be perpendicular to the element boundary. Although we don't expect a significant error, it should be examined.

REFERENCES

Geomatrix, Preliminary Geologic Section Along Proposed Fourth Bore Alignment, Caldecott Tunnel Improvement Project, Alameda and Contra Costa Counties, California, 2008.

Graymer, R.W., 2000, Geologic map and map database of the Oakland metropolitan area, Alameda, Contra Costa and San Francisco Counties, California. USGS Miscellaneous Field Studies MF3242g Version 1.0.

Karasaki, K., Onishi, C.T., Doughty, C., Gasperikova, E., Peterson, P., Conrad, M., and Cook, P., 2011, Development of Hydrologic Characterization on Technology of Fault Zones – Phase II 2nd Report–, NUMO-LBNL-CRIEPI Collaboration Research Project.

Karasaki, K., Onishi, C.T. and Zimmer, V., 2010, Development of Hydrologic Characterization on Technology of Fault Zones – Phase II Interim Report-, NUMO-LBNL-CRIEPI Collaboration Research Project.

Karasaki, K., C.T. Onishi, and Y.S. Wu, 2009, Development of Characterization Technology for Fault Zones, LBNL-1635E, pp 157.

Karasaki, K., K. Ito, Y.S. Wu, M. Shimo, A. Sawada, K. Maekawa, K. Hatanaka, 2011b, Uncertainty reduction of hydrologic models using data from surface-based investigation, doi: 10.1016/j.jhydrol.2011.03.039, Journal of Hydrology, 403 (1-2), pp49-57.

Kiho, K., Ueta, K., Miyakawa, T., Hasegawa, T., Ito, H., Hamada, M., Nakada, H., Tanaka, S., and Tsukuda, K, 2012, CRIEPI Technical Report, Survey and Analysis related to Development of Hydrologic Characterization Technology of Fault Zones IV.

Pruess, K., Oldenburg, C., and Moridis, G., TOUGH2 User's Guide, Version 2.0, Rep. LBNL-43134, Lawrence Berkeley National Laboratory, Berkeley, CA, 1999.

TWO-PHASE FLOW MODELING WITH TOUGH2 OF A WASTE GEOLOGICAL REPOSITORY WITHIN THE FORGE PROJECT

Manuel Lorenzo Sentís

Swiss Federal Nuclear Safety Inspectorate (ENSI)
CH-5200 Brugg, Switzerland
e-mail: manuel.sentis@ensi.ch

ABSTRACT

FORGE (Fate Of Repository Gases), a four-year (2009–2013) international research project supported by funding under the European Commission FP7 Euratom programme, is dedicated to the understanding of gas generation and migration as part of the quantitative assessment of a waste geological repository. Within the FORGE project, Work Package 1 is dedicated to the numerical modeling of a two-phase flow system (gas, mainly hydrogen as a result of corrosion and groundwater) in a radioactive waste geological repository. Several exercises were proposed that cover the modeling of a waste geological repository from the disposal cell scale to the repository scale with different codes. Special emphasis was placed (during the definition of the exercises) on the role of the EDZ and of the interfaces between materials, which could act as a conduit for preferential flow. During the calculations of the cell-scale benchmark, some convergence problems were encountered and will be described here. Some changes were made in the TOUGH2 code (Pruess, Oldenburg et al. 1999) to make implementing the prescribed conditions and parameters of the benchmark possible. The results of the calculations performed with different codes show that TOUGH2 obtains comparable results under the numerically challenging conditions defined in the exercise. This paper shows the results of the cell-scale benchmark obtained by ENSI with TOUGH2.

INTRODUCTION

Several benchmark exercises have been defined within the first work package of the FORGE project. The starting point for the definition of the exercises was a general agreement that the reference exercises will be as generic as possible and more aimed at studying how the system reacts rather than an intercomparison of codes. A second agreement was that the first exercise should be rather simple and at cell scale, aiming at a stepwise approach at a repository scale. The proposed calculation domain for the first exercise is shown in Figure 1 (Wendling, Yu et al. 2010).

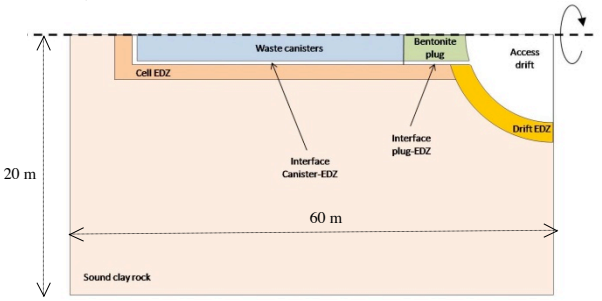

Figure 1. Domain of the model proposed for the first exercise.

The calculation domain is axisymmetric around the waste canister, with the effect of gravity in the vertical direction not considered. A gas production term provided for the disposal cell is imposed on an external surface of a cylinder representing the canister (blue domain in Figure 1). The canister material is considered impermeable to both water and gas, and therefore it is not explicitly represented in the model. The materials to be taken into account in the simulation include the EDZ of both the cell and the access drift, the cell plug, the backfill of the access drift, and the geological medium. The interfaces around the EDZ are considered in the model, with the material properties different for the interface facing the canister and for the interface facing the bentonite.

The objective of this benchmark is to better understand numerically the mechanisms of gas transport at the cell scale, and in particular to analyze the effect of the presence of different materials and interfaces on such mechanisms.

PARAMETERS: INITIAL AND BOUNDARY CONDITIONS

Important parameters prescribed for the benchmark at a reference temperature of 20°C are listed in Table 1 and Table 2.

Table 1 Material parameters for the interfaces and drift.

Parameter (at 20°C)	Materials		
	Interface facing plug	Interface facing canister	Backfill (access drift)
K_v [m^2]	$5.0\ 10^{-18}$	$1.0\ 10^{-12}$	$5.0\ 10^{-17}$
K_h [m^2]	$1.0\ 10^{-17}$	Kv=Kh	
Porosity [%]	30	100	40
Specific storage coefficient [m^{-1}]	$4.6\ 10^{-06}$	$4.6\ 10^{-06}$	$1.0\ 10^{-05}$
Two-phase flow parameters			
S_{gr} [%]	0	0	0
S_{wr} [%]	0	0	0
Van Genuchten parameters			
n [-]	4	4	1.5
P_r [Pa]	10^4	10^4	$2\ 10^6$
τ (Tortuosity)	1	1	2

One of the objectives of this benchmark is to study the effect of interfaces as preferential paths for the gas. For example, the interface facing the canister has a thickness of 1 cm and an intrinsic permeability of 10^{-12} m^2. The interface facing the bentonite has the same thickness and intrinsic permeability of 10^{-17} m^2.

The following expressions of the relative permeability for water and gas were proposed to be used in this benchmark:

$$k_r^w = \sqrt{S_{we}}\left[1-\left(1-S_{we}^{1/m}\right)^m\right]^2 \quad \textbf{[1]}$$

$$k_r^g = \sqrt{1-S_{we}}\left[1-S_{we}^{1/m}\right]^{2m} \quad \textbf{[2]}$$

Over the first 10,000 years, we imposed a constant production term for gaseous hydrogen of 0.2 kg/a as source term.

Table 2. Material parameters for bentonite, EDZ, and host rock.

Parameter (at 20°C)	Materials		
	Bentonite plug	EDZ	Geological Medium
K_v [m^2]	$1.0\ 10^{-20}$	$5.0\ 10^{-18}$	$5.0\ 10^{-21}$
K_h [m^2]	Kv=Kh	$1.0\ 10^{-17}$	$1.0\ 10^{-20}$
Porosity [%]	35	15	15
Specific storage coefficient [m^{-1}]	$4.4\ 10^{-06}$	$2.3\ 10^{-06}$	$2.3\ 10^{-06}$
Two-phase flow parameters			
S_{gr} [%]	0	0	0
S_{wr} [%]	0	0	0
Van Genuchten parameters			
n [-]	1.6	1.5	1.5
P_r [Pa]	$1.6\ 10^7$	$1.5\ 10^6$	$1.5\ 10^7$
τ (Tortuosity)	4.5	2	2

The initial saturation of the rock and of the EDZ is 100%, and the initial water pressure is 5 MPa. Initial saturation for the interface is 5%, and for the drift and bentonite 70%. The gas pressure for partially saturated materials is 1 atm; water pressure is obtained according with van Genuchten models.

As indicated in Figure 2, time-dependent boundary conditions are prescribed on the drift for the water pressure and water saturation. The rest of the boundary conditions are shown in the next figure.

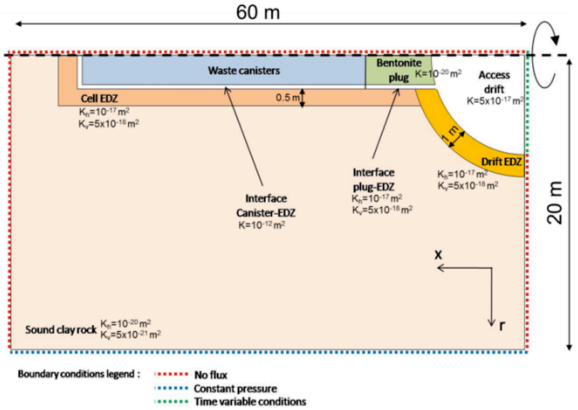

Figure 2. Representation of the model together with important parameters and boundary conditions.

IMPLEMENTATION OF THE MODEL WITH TOUGH2/TOUGH2-MP

To reduce the differences between the results of the different teams using the different codes, ENSI attempted to implement the parameters and models as prescribed in the exercise. Some of them, like the thin interfaces and the time-dependent boundary conditions, were difficult to implement in TOUGH2. The simulations were initially performed with TOUGH2 but some difficulties were found, such as the implementation of time-dependent boundary conditions and (above all) the long computational times. To reduce (as much as possible) these limitations, we decided to use the code TOUGH2-MP (Zhang, Wu et al. 2008), which is the parallel version of TOUGH2 developed also by Lawrence Berkeley National Laboratory. Our computer cluster consists of IBM AIX machines; this computer architecture was not included among the systems in which the program was tested. Therefore, the compiling options had to be adapted to our system, and additional features had to be installed in it. The code also requires the external libraries AZTEC and METIS. Compilation of these libraries was also system dependent, and besides, no compiling options were specified for our system.

After the installation of TOUGH2-MP, some tests were performed with inputs included in the distribution. The existing input for TOUGH2 was adapted to the code TOUGH2-MP, although in fact there are some slight differences between the input definitions of the two codes. After an extensive check of the code, we noticed that some lines had to be implemented in the code in order to be able to use TOUGH2-MP with our computer architecture.

Compared to the same simulations performed with TOUGH2, we observed that the code TOUGH2-MP ran faster at the beginning, but after some hundred years of simulation time, the codes start slowing down. In a first approach to the benchmark, the interface layer was modeled using three layers of nodes. Due to the small dimensions of the node elements in the interface, the code was very slow after some hundred years. It was therefore decided to use only one layer of nodes at the interface, which reduced the computation time.

The prescribed model for the gas relative permeability given by the van Genuchten-Mualem relation (γ=0.5) in Equation (2) is not available either in TOUGH2 or in TOUGH2-MP. The code was modified to allow this expression for the gas relative permeability; however, this option causes a slowdown of and instabilities within the code. Moreover, for a few calculations cases, we experienced a crash of the simulation after 10,000 years' time.

Some differences were also observed between the diffusion coefficients of hydrogen in the gas and liquid phase. Changes were made in the code TOUGH2/TOUGH2-MP to adapt it to the specifications. The diffusion coefficients of dissolved hydrogen in the binary hydrogen/water vapor mixture of the porous medium was specified in the benchmark as:

$$D^{g}_{H_2/vap} = (1 - S_w)\left(\frac{\phi}{\tau^2}\right) D_0 \left(\frac{P_0}{P}\right)\left(\frac{T}{T_0}\right)^{1.75} \qquad \textbf{[3]}$$

whereas in TOUGH2/TOUGH2-MP, the equivalent expression is given by:

$$D^{g}_{H_2/vap} = \phi\tau_0\tau_\beta \left(\frac{1}{\tau^2}\right) D_0 \left(\frac{P_0}{P}\right)\left(\frac{T}{T_0}\right)^{1.75} \qquad \textbf{[4]}$$

Equivalently the expression for the diffusion coefficient of dissolved hydrogen in the waster of the porous medium is given by:

$$D^{w}_{H_2} = S_w \left(\frac{\phi}{\tau^2}\right) \times 1.5710^{-14} \frac{T}{\mu_{water}(T)} \qquad \textbf{[5]}$$

In TOUGH2/TOUGH2-MP, the equivalent expression is given by:

$$D^{w}_{H_2} = \phi\tau_0\tau_\beta \left(\frac{1}{\tau^2}\right) \times 1.5710^{-14} \frac{T}{\mu_{water}(T)} \qquad \textbf{[6]}$$

Also, the expression for Henry's law proposed in the FORGE project is somewhat different from the one used in the TOUGH2/TOUGH2-MP code. Specifically, the expression proposed in FORGE contains the concentration of hydrogen in mol/m^3, whereas the expression in TOUGH2 uses the mol fraction of hydrogen. A conversion factor was implemented in the TOUGH2/TOUGH2-MP code to adapt it to the prescribed expression.

The influence of the initial conditions on the behavior of the system was studied with numerical simulations. We found that the numerical convergence of the simulations were improved if the initial conditions through the different nodes in the interface, EDZ and host rock changed smoothly. The best convergence was obtained when the initial conditions of the EDZ and the interface are the same. The results of ENSI and other teams confirm that, assuming the prescribed initial conditions, an initial transient of pressure occurs during the first thousandth of a year, as shown in Figure 3. This is explained by the different initial saturations of the interface (5%) and the EDZ (100%).

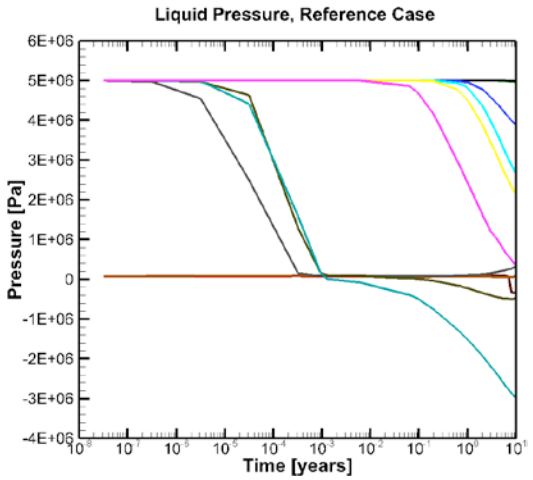

Figure 3. Values of the liquid pressure during the first ten years in different points of the model.

Initially, TOUGH2 was used to perform the simulations for this exercise. Also initially, the prescribed variations in pressure and saturation were implemented with a time-dependent source term. In this way, a variable mass of gas was introduced into the system, the effect of which required analysis. To avoid possible correlations with the inserted gas, another strategy was followed. The code TOUGH2-MP, unlike TOUGH2, includes the capability of implementing time-dependent boundary conditions for the pressure. As in the exercise, not only time-dependent boundary conditions for pressure but also for saturation were prescribed: the code had to be modified to allow the implementation of time-dependent saturation values as boundary conditions. The time-dependent boundary conditions caused the code to slow down, because it was realized after comparing calculations with and without time-dependent boundary conditions.

Since the model is axisymmetric around the axis of the cell, each element of the grid includes all elements generated by rotating each planar element around this axis. Therefore, intrinsic horizontal permeabilities are implemented in the input as prescribed, but intrinsic vertical permeabilities for the rotated elements can take values limited by the values of the horizontal and vertical permeabilities. Therefore an averaged value around the rotation axis was taken for the vertical intrinsic permeabilities.

The table below shows the calculation cases defined for this benchmark. Gas flux and dissolved hydrogen values through the defined surfaces are required, as well as values for water and gas pressure and saturation at different points and along the vertical and horizontal lines defined on the model. The considered points and an example of a vertical line are indicated in Figure 4.

Table 3. Calculation cases for the cell-scale benchmark

Reference Case	Parameter and conditions as specified before
Sensitivity analysis 1	EDZ intrinsic permeability equal to the one of the undisturbed rock (reduction of EDZ intrinsic permeability)
Sensitivity analysis 2	Power law for EDZ and host rock intrinsic permeability
Sensitivity analysis 3	Increase of diffusion coefficient of dissolved hydrogen
Sensitivity analysis 4a/4b	Delay of gas production of 1 year/ 2 years
Sensitivity analysis 5a/5b	Intrinsic permeability interface = 10^{-15}m^2/ Intrinsic permeability of the interface equal to the one of the EDZ
Sensitivity analysis 6	Mesh refinement

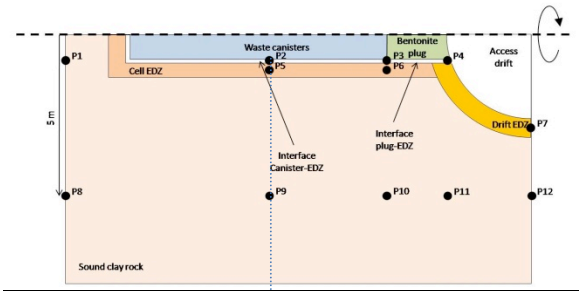

Figure 4. Schematic representation of the points as well as a vertical line where results are provided.

SOME RESULTS FOR THE REFERENCE CASE

In this section we present a selection of results for the reference case. The saturation close to the interface remains practically 100% until approximately 10,000 years, when it decreases but no less than 80%—as shown in Figure 5, which represents the variation of the saturation along a vertical line starting at the interface as shown in Figure 4.

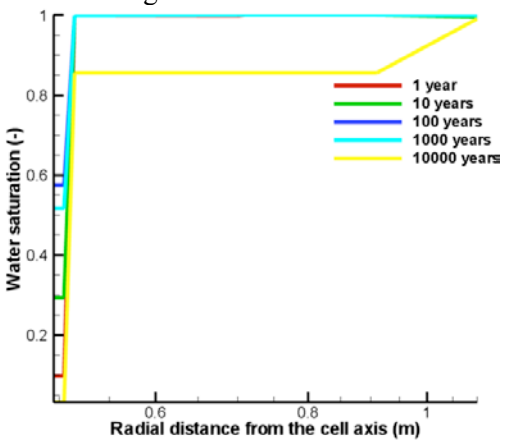

Figure 5. Variations in the saturation along a vertical line starting in the interface as shown in Figure 4.

The values of the saturation around the repository are shown in Figure 6. A detailed view of the interface facing the bentonite plug is also shown at the top.

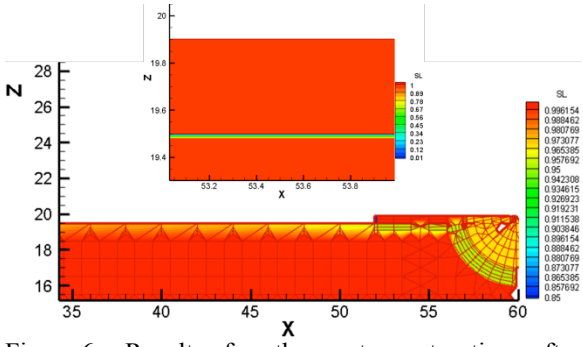

Figure 6. Results for the water saturation after 10000 years for the reference case. On the top a detail of the interface facing the bentonite plug is shown.

It can be observed in Figure 6 that, because of the very small permeability of the argillites and its high capillary entry pressure, desaturation occurs primarily inside the cell and up to the radial end of the EDZ, but the undisturbed argillites are not significantly desaturated. A tiny desaturation of the host rock close to the EDZ occurs. The interface is initially highly desaturated, but then partial resaturation occurs rapidly (10 years) before a general desaturation dominates the remaining years (Figure 5).

The evolution of gas pressure for the points where a gas phase exists is shown in Figure 7. Maximal pressure is 5.2 MPa, obtained shortly before 10,000 years. Other teams participating in the benchmark obtained similar results, with the highest pressures oscillating between 5 and 5.5 MPa. The equivalent values for liquid pressure are shown in Figure 8.

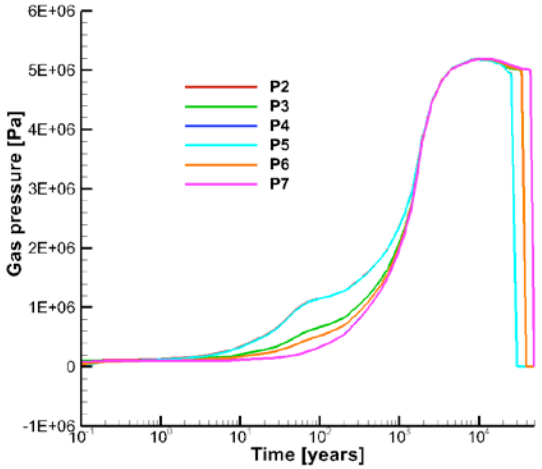

Figure 7. Values of the gas pressure at different points.

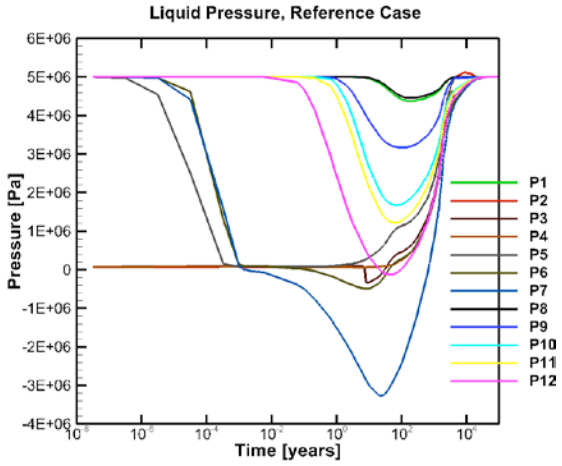

Figure 8. Values of the liquid pressure at different points.

Figure 9 shows values of the flux of gas and liquid through the drift and through the EDZ. A maximal flux of around 0.15 kg/a is obtained after 200 years. Afterwards, the flux decreases slowly up to the end of the gas generation period at 10,000 years. Comparing these values with

the values of the liquid flux, we conclude that most of the hydrogen is being transported in a gas phase, with only a small part transported and dissolved in a liquid phase. Based on this figure we further conclude that most of the gas flux **migrates** first along the interface and then, when the peak of flux through the drift is reached, the flux through the EDZ starts increasing to reach a maximum at 10,000 years.

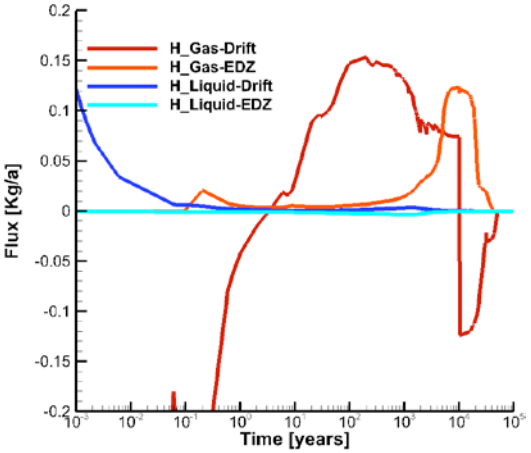

Figure 9. Flux of hydrogen in gas form and dissolved through the EDZ and through the drift for the reference case.

INFLUENCE OF THE MESH REFINEMENT

Figure 11 shows a detail of the grid with 2,500 nodes used for the reference case, generated with the program WinGridder (Pan 2001).

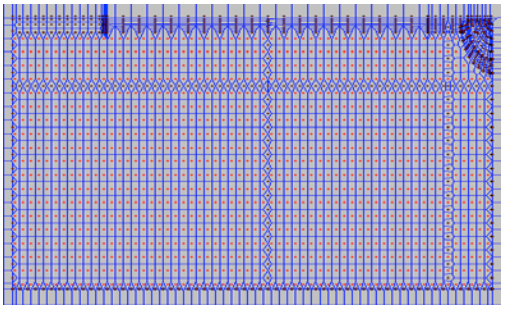

Figure 10. Mesh with 2500 nodes used for the calculations shown in this report.

The effect of mesh refinement was analyzed as prescribed in sensitivity analysis 6 (Table 3). Three different meshes were used, as shown in Table *4*; we concluded that the results of the calculations with the different meshes are similar. One difference, however, is that much more computation time is consumed than in the simulations, as shown in Table *4*. All the meshes considered have one layer of nodes in the interface.

Table 4. Different meshes used for sensitivity analysis 6.

	Computation time
Mesh 1: 2500 nodes	1-3 days
Mesh 2: 6300 nodes	2-7 days
Mesh 3: 1200 nodes	6-14 days

A detail of the mesh with 6200 nodes is shown in the next figure.

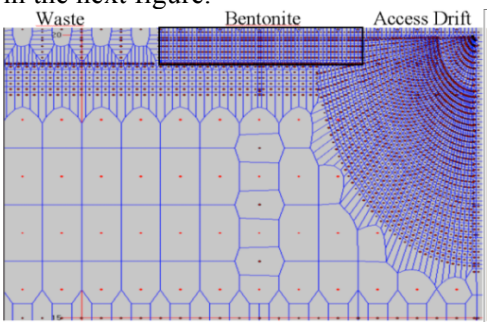

Figure 11. Detail of the nonconformal Voronoi mesh used to solve this exercise.

SOME RESULTS OF THE SENSITIVITY ANALYSES

In sensitivity analysis 1, only the intrinsic permeability of the EDZ for both drift and cell is changed to the same value as in the undisturbed rock. The resistance to the gas transport along the EDZ pathway is now higher; we expect (as shown in Figure 12) an increase in gas pressure close to the EDZ, compared to the reference scenario in Figure 7.

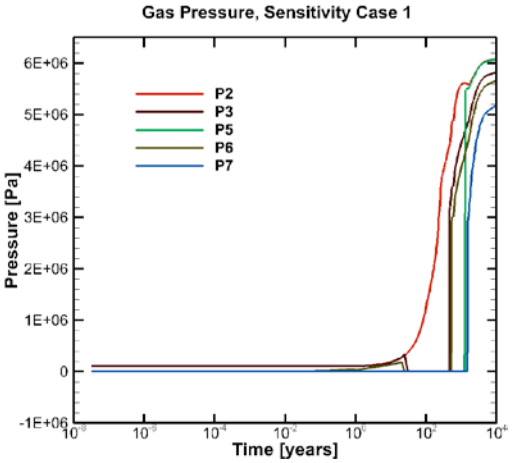

Figure 12. Values of the gas pressure at different points for sensitivity analysis 1.

As also expected, the liquid pressure decreases slower than in the reference case, and the minimal values of the pressure are higher than in the reference case—compare Figure 13 with Figure 8.

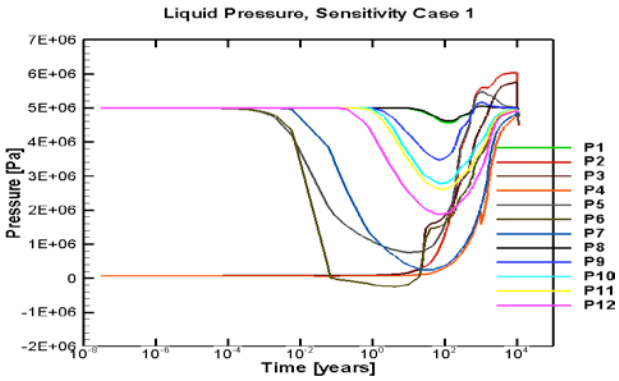

Figure 13. Values of the liquid pressure at different points for sensitivity analysis 1.

In sensitivity analysis 2 the permeability curve for EDZ water and gas, and of the undisturbed rock, follows a power law:

$$K_r^w = S_w^3 \qquad K_r^g = S_g^3 = (1 - S_w)^3 \qquad [7]$$

The influence of inserting expression (7) for the relative permeability can be seen when comparing Figure 14 with Figure 8. In fact, the minimal values of the water pressure are higher than in the reference case (see Figure 8). On the other hand, the values of the gas flux through the drift are the same as in the reference case. As the relative permeability function for the interface is not changed in this sensitivity analysis, this result confirms that the pathway through the interface is very important for gas transport.

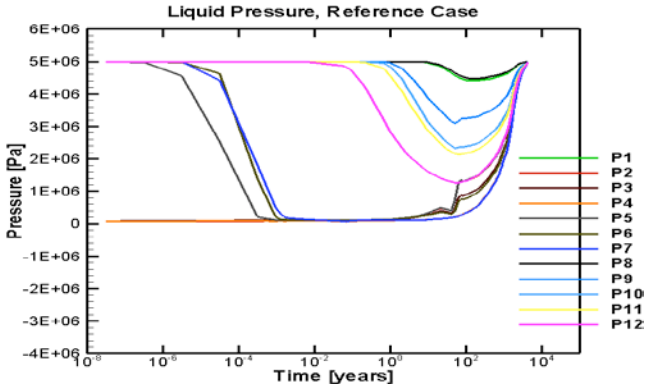

Figure 14. Values of the liquid pressure at different points for sensitivity analysis 2.

In sensitivity analysis 3 the diffusion coefficient of dissolved hydrogen under water-saturated conditions is incremented by a factor of 10 (Table 1 and Table *2*) for all materials in the model.

In Figure 15, the gas flux for this sensitivity analysis is compared with the results from the reference scenario and from sensitivity analysis 1. In the case of sensitivity analysis 1, the gas flux through the drift increases mainly along the interface as the permeability of the EDZ increased. In the same figure, we can see that the increase of the diffusion coefficient of dissolved hydrogen has a significant impact on the total gas flow through the drift. For sensitivity analyses 2, 4a, 4b, 5a, 5b and 6 (see Table 3), the results of the flux through the drift are close to the ones of the reference case.

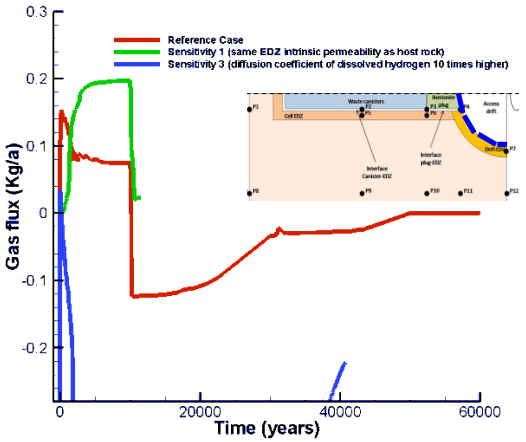

Figure 15. Comparison of gas flux through the drift for the reference case and sensitivity cases 1 and 3. The considered surface for the drift flux is indicated in the model.

In sensitivity analysis 4, the effect of a delay at the beginning of gas production of 1 year and of 2 years was simulated. These variations cause negligible differences in the results, as can be seen in Figure 16.

In sensitivity analysis 5, the permeability of the interface facing the canister was changed from 1.0×10^{-12} m^2 to 1.0×10^{-15} m^2 in sensitivity case 5a and to 1.0×10^{-18} m^2, the same value as in the EDZ, in sensitivity case 5b. The results of this sensitivity analysis show that the gas keeps being transported along the same pathway— that is to say, the EDZ and the interface are main pathways around the drift.

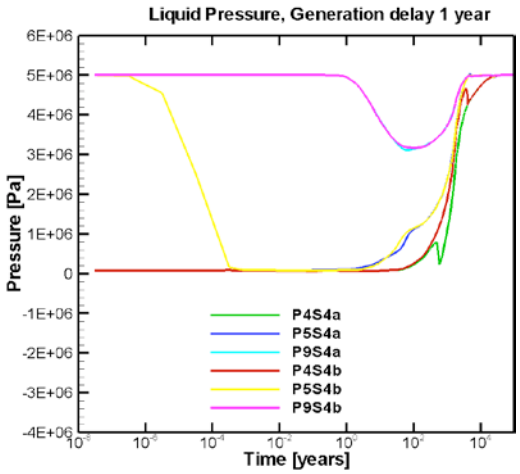

Figure 16. Values of the liquid pressure at different points for sensitivity analysis 4.

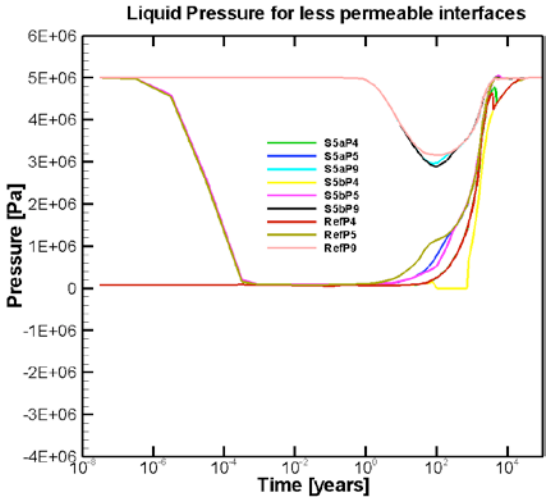

Figure 17. Values of the liquid pressure at different points for sensitivity analysis 5.

CONCLUSIONS

As result of this benchmark test, the following conclusions can be drawn:

- In order to represent the model and parameters as prescribed in the exercise, modifications of the codes TOUGH2/ TOUGH2-MP had to be made.
- The implementation of a interface in the model caused many numerical difficulties (convergence, increase in computation time).
- The interface and the EDZ represent the main pathway for migration of the hydrogen from the drift. The hydrogen is transported mainly in gas form and through the interface and EDZ.
- Implementing the expression for relative permeability as specified in the exercise caused many convergence problems; these problems disappeared using the original expression used in the TOUGH2/TOUGH2-MP code.
- Calculation time increases with the refinement of the mesh (Table 2), whereas the simulation results did not change significantly.
- The flux toward the drift increases with a low-permeable EDZ (sensitivity 1). Increasing the diffusion coefficient by a factor of 10 (sensitivity 3) decreases the flux toward the drift (Fig. 10, right).
- The results of the different teams are similar and within the same order of magnitude. Differences could be explained as resulting from the various approaches and simplifications to the model. Some differences were found in the values of the fluxes.

ACKNOWLEDGMENT

The research leading to these results has received funding from the European Atomic Energy Community's Seventh Framework Programme (FP7/2007-2011) under Grant Agreement no230357, the FORGE project.

REFERENCES

FORGE: http://www.bgs.ac.uk/forge/

Pan, L. (2001). Users Manual for WinGridder V2.0, Lawrence Berkeley national laboratory.

Pruess, K., C. Oldenburg, et al. (1999). TOUGH2 USER'S GUIDE, VERSION 2.0. Berkeley, California, Lawrence Berkeley National Laboratory.

Wendling, J., L. Yu, et al. (2010). Progress report on benchmark studies on repository-scale numerical simulations of gas migration. Euratom 7th Framework project: FORGE 2010.

Zhang, K., Y. Wu, et al. (2008). User's Guide for TOUGH2-MP, A massively Parallel Version of the TOUGH2 Code, Lawrence Berkeley National Laboratory.

DEVELOPMENT AND APPLICATION OF A CHEMICAL OSMOSIS SIMULATOR BASED ON TOUGH2

M. Takeda[1*], T. Hiratsuka[1], K. Ito[1], S. Finsterle[2]

[1] National Institute of Advanced Industrial Science and Technology (AIST)
Higashi 1-1-1, Central 7
Tsukuba, Ibaraki 305-8567, Japan
e-mail: mikio-takeda@aist.go.jp

[2] Lawrence Berkeley National Laboratory, Earth Sciences Division
1 Cyclotron Rd., MS 74-0120
Berkeley, CA 94720, United States
e-mail: safinsterle@lbl.gov

ABSTRACT

One of the key issues for radioactive waste disposal in clayey formations is uncertainty with respect to fluid pressure anomalies, which could be caused by chemical osmosis. For the examination of chemical osmosis in groundwater systems, a 3D, site-scale simulator with chemical osmosis simulation capabilities is needed. In this study, the TOUGH2 code with the EWASG module (hereafter referred to as the T2+EWASG code) was modified to simulate chemical osmosis in clayey geologic media. In the modified code, chemical osmosis is treated as a diffusion of water rather than the advective flux of a solution (consisting of water and salt), which has been the conventional approach in chemical osmosis modeling. The modified code was tested against a semi-analytical solution and a laboratory experiment of chemical osmosis. The simulation results agree well with both the experimental data and the semi-analytical solution, and attest to the practical effectiveness of the chemical osmosis simulation capabilities in the modified T2+EWASG code.

INTRODUCTION

Clayey rocks are potential host rocks for the geological disposal of radioactive wastes, due to their low hydraulic conductivities and efficient retention properties. For the long-term stable isolation of radioactive wastes, the processes relevant to the migration of radionuclides through groundwater need to be identified and incorporated into the radionuclide transport model for safety assessment. Interactions between different processes, such as coupled thermal, hydrological, mechanical, and chemical (T-H-M-C) processes, have been one of the main research subjects in geological disposal projects. However, a different type of H-C coupled phenomenon caused by the membrane property of clayey rock has recently received attention in the context of geological disposal of radioactive waste (e.g., Soler, 2001; Gonçalvès et al., 2004; Garavito et al., 2007; Horseman et al., 2007; Cruchaudet et al., 2008; Rousseau-Gueutin et al., 2009).

The membrane property of clay works to partially restrict the passage of ions while allowing water to migrate into the clayey materials (Fritz, 1986). This causes a coupled flow phenomenon, termed chemical osmosis, in which the gradient of solute concentration causes water migration. Strictly speaking, chemical osmosis is water migration through a semi-permeable membrane driven by the difference in the chemical potential of water across the membrane (Mitchell and Soga, 2005). The net migration of water continues until the difference in potential energy is compensated by the other potential differences, such as the pressure difference. Accordingly, if geologic media can act as semi-permeable membranes, and if the salt concentration is not uniform in the formation, localized, erratic fluid pressures may be generated by chemical osmosis (Neuzil, 2000). Ignoring osmotically induced pressures may lead to erroneous predictions of groundwater flow direction (Marine and Fritz, 1981). Therefore, a numerical code capable of simulating chemical osmosis must be developed. Simulation codes for chemical osmosis have so far been developed for the interpretation of

chemical osmosis experiments in the laboratory and the field; however, these codes are mostly based on 1D linear or radial models (Gonçalvès et al., 2004; Bader and Kooi, 2005; Garavito et al., 2006, 2007; Gueutin et al., 2007; Horseman et al., 2007; Gonçalvès, 2008; Cruchaudet et al., 2008; Rousseau-Gueutin et al., 2008, 2009). In order to develop a chemical osmosis simulator capable of using 3D, site-scale models based on the T2+EWASG code, we revisit the function of clay as a selective permeable membrane in mass transport through clayey geologic media and the conventional mathematical formulation of the coupled flow phenomenon caused by the membrane effect. We then describe the mathematical formulation of the coupled flow phenomenon for the modification of the T2+EWASG code. The modified simulation code is then tested against a laboratory experiment of chemical osmosis through a mudstone rock sample, and verified against a semi-analytical solution derived from a conventional mathematical formulation.

MATHEMATICAL FORMULATION OF CHEMICAL OSMOSIS

Membrane Effect on Mass Transport

The membrane property of clay causes two major processes in mass transport through pore spaces. One process is chemical osmosis, which is the diffusion of water through pores driven by the gradient of the chemical potential of water. The other process is the filtration of solutes at the pore entrance, by which the advective and diffusive solute migrations are partially restricted (Ingebritsen, 2006).

These clay membrane effects arise from the existence of electrical diffuse layers (EDLs) formed between pore spaces with negative charges on the surfaces, as shown in Figure 1 (e.g., Appelo and Postma, 2005). The negative electrical potentials formed between pore spaces generate an electrical repulsive force on anions at the pore entrance. The migration of cations is also hindered at the pore entrance since the solution must remain electrically neutral at the entrance. Consequently, neutral components, such as water molecules and uncharged species, can migrate through pore spaces without electrical restrictions. Because of this process, clays behave like selectively permeable membranes. However, the clayey media also contain large pores and minerals without surface charges, in which the EDLs do not overlap or do not exist, resulting in the preferential migration of charged ions through large pores with less electrical repulsion force. Accordingly, the clayey media act as imperfect membranes.

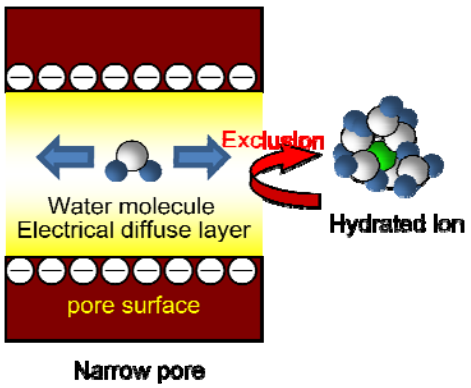

Figure 1. Membrane effects of clayey minerals on mass transport in pore spaces.

The membrane's ability to retard the transport of solutes relative to water is represented by a reflection coefficient or osmotic efficiency (e.g., Neuzil and Provost, 2009). The relationship between the reflection coefficient and the solute selective passage through a semi-permeable membrane is expressed as (Katchalsky and Curran, 1965):

$$\left.\frac{v_s}{v_w}\right|_{\Delta\pi=0} = 1-\sigma \qquad (1)$$

where v_s and v_w are the velocities of solute and water, respectively, $\Delta\pi$ represents the difference in water osmotic pressures between solutions sandwiching the membrane, and σ is the reflection coefficient, which ranges in value between 0, indicating no retardation, and 1, indicating a perfect semi-permeable membrane. For an ideal membrane of σ=1, v_s becomes zero, meaning the solute is completely repelled by the membrane. As mentioned above, the extent of EDL overlap determines the filtration effect in the clayey media, and hence, the reflection coefficient σ depends on both the geological medium and solution properties (e.g., Bresler, 1973).

Conventional Mathematical Formulation

Chemical osmosis is essentially the diffusion of water molecules through a semi-permeable membrane. Chemical osmosis has been conventionally described as an advective flux of a solution consisting of water and salt (e.g., Bader and Kooi, 2005):

$$\mathbf{q} = -\frac{k}{\mu}\cdot\left(\nabla P + \rho\cdot g\cdot\nabla z + \sigma\cdot\nabla\pi\right) \tag{2}$$

where **q** is the volumetric flux of the solution, k is the intrinsic permeability, μ is the dynamic viscosity of solution, P and ρ are the pressure and density of the solution, g is the gravitational acceleration, and z is the elevation. In Equation (2), chemical osmosis is expressed as if it were driven by the gradient of osmotic pressure; however, the gradient of osmotic pressure is a measure of the gradient of the chemical potential in water (e.g., Spiegler and Kedem, 1966):

$$\nabla\pi = -\frac{1}{\overline{V}_w}\cdot\nabla\mu_w \tag{3}$$

where $\overline{V}_w$ is the molar volume of water and μ_w is the chemical potential of water. Conventionally, the gradient of osmotic pressure given by Equation (3) is approximated using the concentration or the mass fraction of salt (e.g., Fritz, 1986; Gonçalvès et al., 2004; Bader and Kooi, 2005):

$$\nabla\pi \approx \upsilon\cdot R\cdot T\cdot\nabla C \text{ or } \nabla\pi \approx \upsilon\cdot R\cdot T\cdot\frac{\rho}{M_s}\cdot\nabla X \tag{4}$$

where υ is the number of constituent ions of the dissociating salt, R is the universal gas constant, T is the temperature, C is the salt concentration, M_s is the molar mass of salt, and X is the mass fraction of salt. Using Equation (2), the mass-balance equation for solution is generally expressed as (e.g., Bader and Kooi, 2005):

$$\frac{\partial}{\partial t}\left(\varphi\cdot\rho\right) + \nabla\left(\rho\cdot\mathbf{q}\right) = 0 \tag{5}$$

where t is the time and ϕ is the porosity. The third term on the right-hand side of Equation (2) corresponds to the volumetric solution flux due to chemical osmosis, and the second term on the left-hand side of Equation (5) represents the solution mass transport, which implicitly describes the salt as also transported along with water by chemical osmosis.

The filtration effect on the advective mass flux of salt, $\mathbf{F}|_{adv}$, is expressed as:

$$\mathbf{F}\big|_{adv} = \left(1-\sigma\right)\cdot\rho\cdot X\cdot\mathbf{q} \tag{6}$$

Similarly, the diffusive mass flux of salt, $\mathbf{F}|_{dif}$, under the influence of the filtration effect, can be expressed as:

$$\mathbf{F}\big|_{dif} = -\left(1-\sigma\right)\cdot\rho\cdot D\cdot\nabla X \tag{7}$$

where D is the diffusion coefficient of salt. The salt mass-balance equation is expressed as (e.g., Bader and Kooi, 2005):

$$\frac{\partial}{\partial t}\left(\phi\cdot\rho\cdot X\right) + \nabla\mathbf{F} = 0 \tag{8}$$

where **F** is the mass flux of salt and is given by:

$$\mathbf{F} = \mathbf{F}\big|_{adv} + \mathbf{F}\big|_{dif} \tag{9}$$

In the modeling of chemical osmosis, the medium and solution parameters, such as k, μ, ϕ, and D, are usually treated as constants. The reflection coefficient σ is also treated as a constant parameter (Soler, 2001; Gonçalvès et al., 2004; Bader and Kooi, 2005; Horseman et al., 2007; Gonçalvès, 2008), or as a function of properties of the medium and solution (Garavito et al., 2006, 2007; Cruchaudet et al., 2008; Gueutin et al., 2007; Rousseau-Gueutin et al., 2008, 2009). In the latter case, the reflection coefficient σ is often represented by Bresler's (1973) model, in which σ is obtained based on a graphical approximation of Bresler's curve of σ, as described by Neuzil and Provost (2008).

Governing Equations in TOUGH2

The balance equations solved by TOUGH2 can be written in the following general form (Pruess, 1991):

$$\frac{d}{dt}\int_{V_n} M^\kappa dV_n = \int_{\Gamma_n}\mathbf{F}^\kappa\bullet\mathbf{n}d\Gamma_n + \int_{V_n} Q^\kappa dV_n \tag{10}$$

The quantity M on the left-hand side represents mass or energy per volume, with κ=1, …, NK corresponding to the mass components, and κ=NK+1 denoting heat. **F** denotes mass or heat flux, and Q denotes sinks and sources. **n** is a normal vector on surface element $d\Gamma_n$, pointing inward into V_n. The total mass, mass flux, and sink/source of component κ are obtained by

summing over fluid phases β=1, …, NPH. In the EWASG module formulation, NK=3, NPH=3, and κ=1, 2, 3, 4 indicates water, NaCl, a non-condensible gas (NCG) and heat, respectively, and β=1, 2, 3 indicates the gas, liquid, and solid salt phases, respectively (Battistelli et al., 1997). The flux of component κ is expressed as

$$\mathbf{F}^{\kappa} = \mathbf{F}^{\kappa}\Big|_{\text{adv}} + \mathbf{F}^{\kappa}\Big|_{\text{dis}} \tag{11}$$

where $\mathbf{F}^{\kappa}|_{adv}$ is the advective mass flux and $\mathbf{F}^{\kappa}|_{dis}$ is the dispersive and/or diffusive mass flux.

In the governing equations of the T2+EWASG code, water and salt are treated as components. This enables explicit description of chemical osmosis as a diffusion process of water in the mass flux equation. The general forms of advective and diffusive mass fluxes of component κ can now be given as:

$$\mathbf{F}^{\kappa}\Big|_{\text{adv}} = \sum_{\beta}\left(1-\sigma^{\kappa}\right)\cdot X_{\beta}^{\kappa}\cdot\mathbf{F}_{\beta} \tag{12}$$

$$\mathbf{F}^{\kappa}\Big|_{\text{dis}} = -\sum_{\beta}\left(1-\sigma^{\kappa}\right)\cdot\rho_{\beta}\cdot\mathbf{D}_{\beta}^{\kappa}\cdot\nabla X_{\beta}^{\kappa} \tag{13}$$

where σ^{κ} is the reflection coefficient of component κ, and ρ_{β} is the density of phase β. The advective mass flux of phase β is given by:

$$\mathbf{F}_{\beta} = -k\cdot\frac{k_{r\beta}\cdot\rho_{\beta}}{\mu_{\beta}}\cdot\left(\nabla P_{\beta}-\rho_{\beta}\cdot g\right) \tag{14}$$

where $k_{r\beta}$ is the relative permeability to phase β, μ_{β} is viscosity, and P_{β} is the fluid pressure in phase β. Equations (12) and (13) are the generalized forms of mass fluxes, and hence, σ^{κ} of water needs to be assigned as zero in the numerical computation.

In the T2+EWASG code, the fluid density and viscosity, ρ_{β} and μ_{β}, are calculated based on the equation of state, and the reflection coefficient σ is assigned as a constant, or is represented by a graphical approximation of Bresler's (1973) model.

APPLICATION TO A CHEMICAL OSMOSIS EXPERIMENT

Coupled Processes in the Chemical Osmosis Experiment

Figure 2 shows a schematic of coupled processes in the chemical osmosis experiment. In the experiment, solutions of different NaCl concentrations are separated by a rock sample. The concentration difference between solutions induces chemical osmosis through the rock sample, from the low-concentration solution to the high-concentration solution. The migration of water increases the pressure of the high-concentration solution. The pressure difference evolving between the two solutions causes an advective flow of the solutions that counter chemical osmosis. The solute also diffuses through the rock sample toward the low-concentration solution. Although the solute migration due to advection and diffusion is partially hindered by the filtration effect of the rock sample, the solute concentration eventually becomes uniform throughout the system. The pressure difference evolving between solutions dissipates as the concentration becomes uniform. In the actual experiment, the pressure of the low-concentration solution was kept constant, and the pressure of the high-concentration solution was allowed to change.

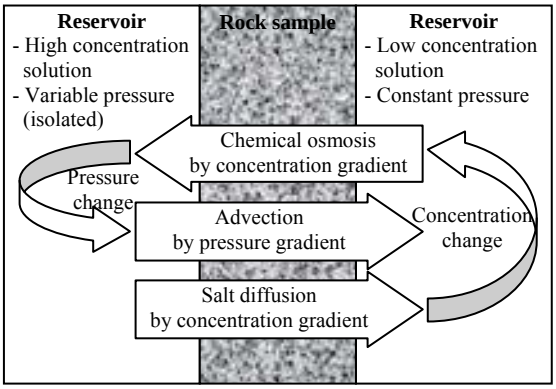

Figure 2. Diagram of the chemical osmosis experiment using a closed system.

Experiment

A chemical osmosis experiment was performed on a siliceous mudstone, taken at a depth of 982 m from the Wakkanai formation in the Horonobe research area of Japan, where the Japan Atomic Energy Agency (JAEA) has been operating an Underground Research Laboratory

(URL) for research and development related to the geological disposal of high-level radioactive waste (Matsui et al., 2007). A disc-shaped sample with a diameter of 5 cm and length of 1 cm was taken from the drill core, then immersed in 0.1 mol/L (M) NaCl solution and vacuumed to remove the air in the pore space.

Figure 3 shows the schematic of the experimental system developed for performing permeability and chemical osmosis experiments. The system mainly consisted of a stainless-steel pressure vessel, a syringe pump for imposing confining pressures, two solution reservoirs, pressure-control equipment for reservoir solutions, a data acquisition system, and a temperature controlled incubator accommodating the reservoirs and pressure vessel. The solution reservoirs were symmetrical, and each reservoir contained a magnetic gear pump for the circulation of reservoir solution, a pressure transducer, an electric conductivity sensor for concentration measurement, a porous stone, valves, and a pressure buffer tank. The stainless-steel pressure vessel supported hydrostatic pressures of up to 40 MPa, and accommodates a disc-shaped specimen with a diameter of 5 cm and lengths ranging from 1 to 2.5 cm. The maximum allowable back pressure for the reservoirs is 0.7 MPa. The electric conductivity was calibrated against NaCl solutions of 0.05 to 0.8 M.

The prepared rock sample was first installed in the pressure vessel, and a confining pressure of 15 MPa was applied to the sample. Each reservoir was filled with 100 mL of 0.1 M NaCl solution. To remove the entrapped air in the reservoir tubing, a vacuum was applied to each reservoir while the magnetic gear pumps circulated the reservoir solutions. After the release of air entrapped in the reservoir tubing, a back pressure of 100 kPa was applied to each reservoir. In order to obtain the intrinsic permeability and pore compressibility of the rock sample, we performed a permeability experiment before the chemical osmosis experiment. After the permeability experiment, a back pressure of 200 kPa was applied to the rock sample and reservoirs.

The chemical osmosis experiment was initiated by replacing the bottom reservoir solution with a 0.6 M NaCl solution using the magnetic gear pump embedded in the bottom reservoir. After the solution replacement, the cross-over valve of the bottom reservoir was closed, and the increasing solution pressure in the bottom reservoir was monitored. The NaCl concentrations of reservoir solutions were also measured. Both the permeability and chemical osmosis experiments were conducted at temperature of 313K.

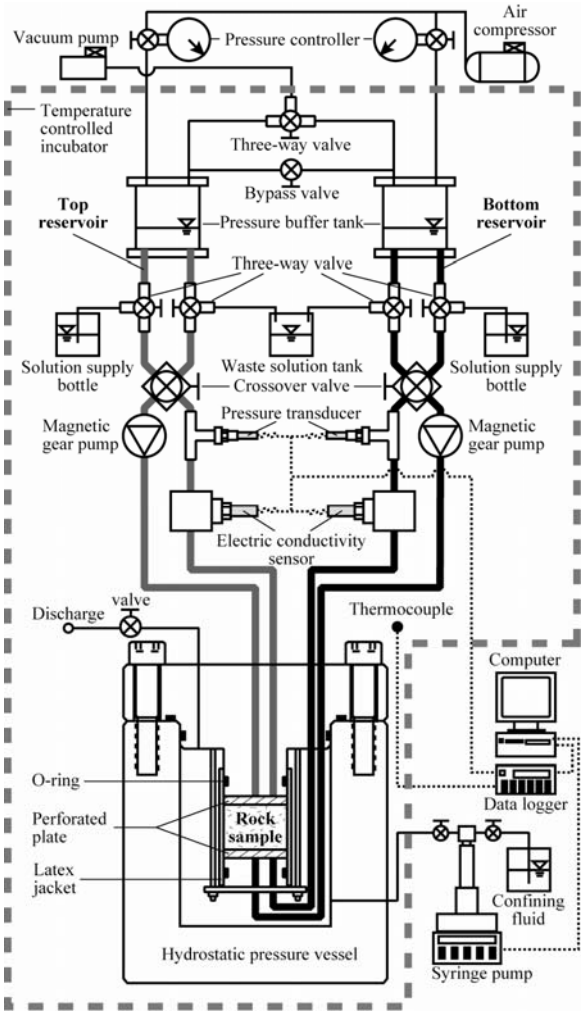

Figure 3. Schematic of experimental setup for the chemical osmosis experiment.

Modeling and Results

Figure 4 shows the 1D geometrical model and the zones representing the reservoirs and rock sample in the chemical osmosis experiment. The elements RSVR1 and RSVR2 represent the bottom and top reservoirs, respectively. The rock sample is discretized into 190 elements. The left side of the rock sample is discretized by 100 elements with an element length of 10^{-5} m, and the right side of the rock sample is represented by 90 elements with an element length of

10^{-4} m. The nodal points of the reservoir elements are located at the interfaces between the reservoir and rock sample. The nodal points of rock sample elements are located at the center of each element.

The physical properties and simulation parameters assigned to the reservoir and rock sample elements are summarized in Table 1. The intrinsic permeability and pore compressibility of the rock sample were determined from the permeability experiment performed before the chemical osmosis experiment, using iTOUGH2 (Finsterle, 2007). The compressible storage of the bottom reservoir was also determined by the permeability experiment and is represented by the pore compressibility of RSVR1. In the top reservoir, the fluid pressure was kept constant in the chemical osmosis experiment. In order to keep the fluid pressure constant in the numerical computation, the pore compressibility of RSVR2 is assigned a large value. The physical properties of water and NaCl are summarized in Table 2. The diffusion coefficient of water is the self-diffusion coefficient at 313 K. The diffusion coefficient and the reflection coefficient of NaCl were selected so that the numerically calculated pressures and concentrations fit the experimentally obtained pressures and concentrations in the reservoirs.

Figure 5 shows the pressures and NaCl concentrations obtained from the experiment and the numerical computation using the modified TOUGH2 EWASG code. The reservoir pressures and concentrations were also simulated by the semi-analytical solution derived from the conventional mathematical formulation defined by Equations (2)–(9) (Takeda et al., 2009), using the same parameters shown in Tables 1 and 2. The pressures and concentrations simulated by the T2+EWASG code generally agreed well with both the experimental data and the simulated curves calculated by the semi-analytical solution. The simulated bottom reservoir concentrations are slightly higher than the experimental data because the initial concentration of RSVR1 was selected to match the simulated curves with the late part of the experimental data. The bottom reservoir concentrations simulated by the T2+EWASG code is slightly lower than those calculated by the semi-analytical solution at later time. This may be because the diffusion of water is accounted for in the T2+EWASG code, resulting in a dilution effect in the bottom reservoir caused by water diffusion.

The pressure and NaCl concentration profiles in the rock sample were also simulated, as shown in Figure 6. For $t \leq 10^4$ s, negative pressures (i.e., pressures less than the initial pressure of 3.01×10^5 Pa) evolved in the rock sample. This can be interpreted as indicating that the gradients of NaCl concentration in the rock sample are so large at early times that they induce a water flux due to chemical osmosis that is larger than the advection-fueled water flux from the top reservoir. After the NaCl concentration profile evolved across the rock sample, i.e., at $t \leq 10^5$ s, the solution pressures become positive. At $t = 10^7$ s (about 116 days), the osmotically induced pressures dissipate, as the NaCl concentration gradient becomes almost uniform in the rock sample.

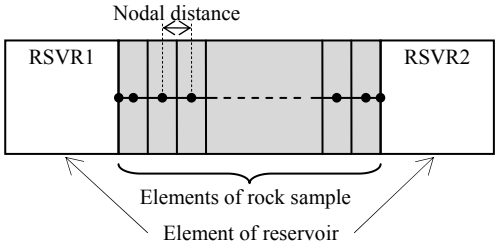

Figure 4. Element array and connections in the TOUGH2 EWASG model.

Table 1. Physical properties and simulation parameters for 1D chemical osmosis experiment.

Parameter	Value		
	RSVR1	Rock	RSVR2
Intrinsic permeability (m^2)	1.00×10^{-13}	1.55×10^{-19}	1.00×10^{-13}
Pore compressibility (Pa^{-1})	3.00×10^{-8}	1.88×10^{-8}	1.00×10^{50}
Porosity (-)	1.00	0.28	1.00
Tortuosity (-)	1.00	1.00	1.00
Interface area (m^2)	1.96×10^{-3}	1.96×10^{-3}	1.96×10^{-3}
Volume (m^3)	2.1×10^{-5}	1.96×10^{-5}	1.00×10^{-4}
Initial pressure (Pa)	3.01×10^5	3.01×10^5	3.01×10^5
Initial NaCl concentration (mol/L)	0.55	0.10	0.10

Table 2. Physical properties of water and NaCl.

Parameter	Value	
	water	NaCl
Diffusion coefficient (m^2/s)	3.21×10^{-9}	1.01×10^{-10}
Reflection coefficient (-)	0.00	4.23×10^{-2}

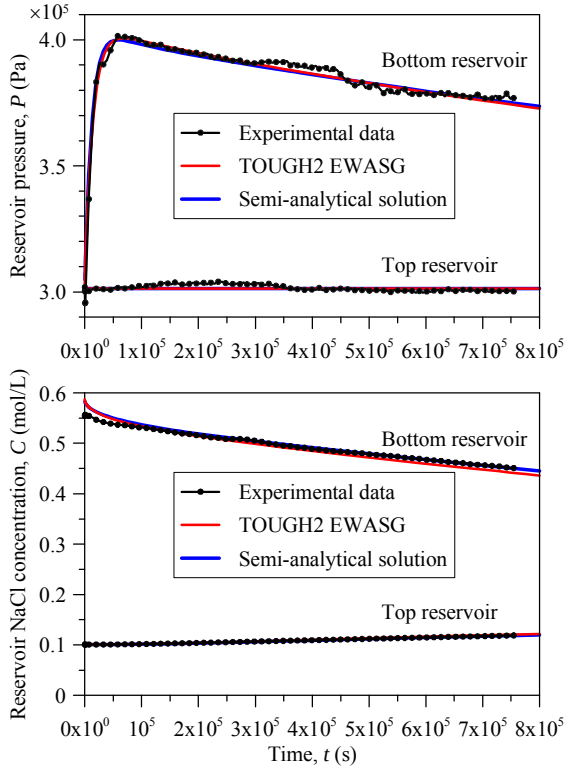

Figure 5. Simulated pressures and NaCl concentrations in reservoirs *vs* experimental data.

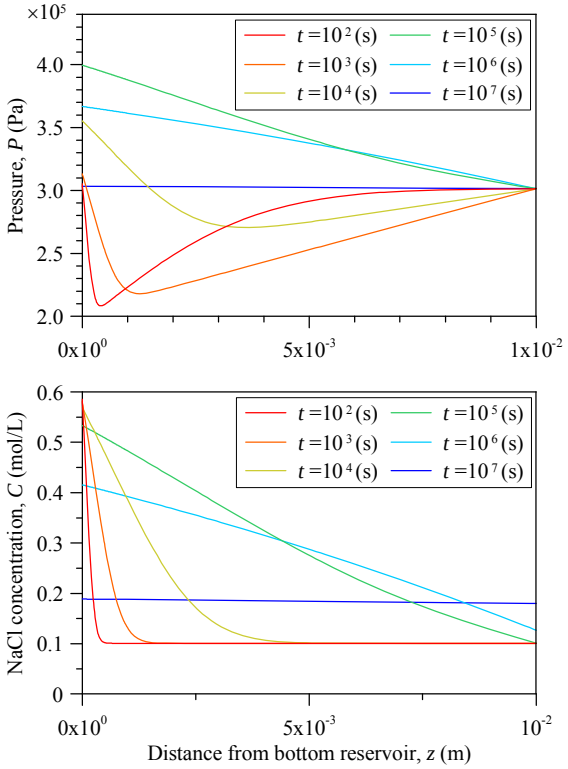

Figure 6. Simulated pressure and NaCl concentration profiles in the rock sample.

CONCLUSION

In order to implement the computational capability for simulating chemical osmosis, this study outlined the membrane effect of clay and described the mathematical formulation necessary for the modification of the T2+EWASG code. Chemical osmosis is incorporated as the diffusion of water in the water mass flux term, rather than the advective flux of solution consisting of water and salt, which has been conventionally adopted in chemical osmosis modeling.

The modified T2+EWASG code was tested against a laboratory chemical osmosis experiment and was compared with a semi-analytical solution derived from the conventional mathematical formulation. The simulation results agreed well with both the results calculated by the semi-analytical solution and the experimental data. This agreement verifies the correct implementation of the equations governing chemical osmosis and provides confidence that the relevant processes are captured. It confirms the chemical osmosis simulation capabilities of the modified T2+EWASG code.

In simulating the chemical osmosis experiment, we selected the physical parameters of both the rock sample and the solution to match the experimental data. The interpretation of the experiment may be further improved by the use of iTOUGH2, which can also provide parameter uncertainties necessary for the field-scale examination of the chemical osmosis effect. The implementation of the chemical osmosis simulation capabilities into iTOUGH2 is currently being conducted.

In the modified code, the reflection coefficient can be assigned as a constant value or can be treated as a function graphically approximated from Bresler's curve of σ, as described by Neuzil and Provost (2008). However, the reflection coefficient can be directly calculated from Bresler's model or other models, which enables the chemical osmosis simulation under nonisothermal conditions. The physicochemical model accounting for the dependency of the membrane effect on geological and solution properties will be incorporated into the modified T2+EWASG code for further study.

ACKNOWLEDGMENT

The authors wish to thank Masashi Nakayama and JAEA for providing the mudstone samples. This study is regulatory support research funded by the Nuclear and Industrial Safety Agency, Ministry of Economy, Trade and Industry, Japan. The last co-author was supported, in part, by the U.S. Department of Energy under Contract No. DE-AC02-05CH11231.

REFERENCES

Appelo, C.A.J., and D. Postma, *Geochemistry, groundwater and pollution. 2nd edn*., A.A. Balkema Publishers, Leiden, 2006.

Bader, S., and H. Kooi, Modelling of solute and water transport in semi-permeable clay membranes: Comparison with experiments, *Advances in Water Resources*, *28*, 203–214, 2005.

Battistelli, A., C. Calore, and K. Pruess, The simulator TOUGH2/EWASG for modelling geothermal reservoirs with brines and noncondensible gas, *Geothermics*, *26*, 437–464, 1997.

Bresler, E., Anion exclusion and coupling effects in nonsteady transport through unsaturated soils: I. Theory, *Proceedings - Soil Science Society of America*, *37*, 663–669, 1973.

Cruchaudet, M., J. Croisé, and J. M. Lavanchy, In situ osmotic experiment in the Callovo-Oxfordian argillaceous formation at the Meuse/Haute-Marne URL (France): Data and analysis, *Physics and Chemistry of the Earth*, Parts A/B/C, 33, S114–S124, 2008.

Finsterle, S., *iTOUGH2 User's Guide*, Report LBNL-40040, Lawrence Berkeley National Laboratory, Berkeley, Calif., 2007.

Fritz, S.J., Ideality of clay membranes in osmotic processes; a review, *Clays and Clay Minerals*, *34*, 214–232, 1986.

Garavito, A.M., H. Kooi, and C.E. Neuzil, Numerical modeling of a long-term in situ chemical osmosis experiment in the Pierre Shale, South Dakota, *Advances in Water Resources*, *29*, 481–492, 2006.

Garavito, A.M., P.De Cannière, and H. Kooi, In situ chemical osmosis experiment in the Boom Clay at the Mol underground research laboratory, *Physics and Chemistry of the Earth*, Parts A/B/C, *32*, 421–433, 2007.

Goncalvès, J., S. Violette, and J. Wendling, Analytical and numerical solutions for alternative overpressuring processes: Application to the Callovo-Oxfordian sedimentary in the Paris basin, France, *Journal of Geophysical Research*, *109*: B02110, doi: 10.1029/2002JB002278, 2004.

Gonçalvès, J., A slug test to assess the osmotic and hydraulic properties of argillaceous formations, *Water Resources Research*, *44*, W07501, doi:10.1029/2007WR006547, 2008.

Gueutin, P., S. Altmann, J. Gonçalvès, P. Cosenza, and S. Violette, Osmotic interpretation of overpressures from monovalent based triple layer model, in the Callovo-Oxfordian at the Bure site, *Physics and Chemistry of the Earth*, Parts A/B/C, *32*, 434–440, 2007.

Horseman, S.T., J.F. Harrington, and D.J. Noy, Swelling and osmotic flow in a potential host rock, *Physics and Chemistry of the Earth*, Parts A/B/C, *32*, 408–420, 2007.

Ingebritsen, S.E., W.E. Sanford, and C.E. Neuzil, *Groundwater in Geologic Processes, 2nd edn*., Cambridge University Press, Cambridge, 2006.

Katchalsky, A., and P.F. Curran, *Nonequilibrium Thermodynamics in Biophysics*, Harvard University Press, Cambridge, 1965.

Matsui, H., H. Kurikami, T. Kunimaru, H. Morioka, and K. Hatanaka, Horonobe URL project—present status and future plans, In: Eberhardt, E., Stead, D., Morrison, T. (Eds.), *Rock Mechanics: Meeting Society's Challenges and Demands*. Taylor & Francis Group, London, 2007.

Marine, I.W., and S.J. Fritz, Osmotic model to explain anomalous hydraulic heads, *Water Resources Research*, *17*, 73–82, 1981.

Mitchell, J.K., and K. Soga, *Fundamentals of Soil Behavior, 3rd edn.*, John Wiley & Sons, Hoboken, 2005.

Neuzil, C.E., Osmotic generation of 'anomalous' fluid pressures in geological environments, *Nature*, *403*, 182-184, 2000.

Neuzil, C.E., and A.M. Provost, Recent experimental data may point to a greater role for osmotic pressures in the subsurface, *Water Resources Research*, *45*, W03410, doi:10.1029/2007WR006450, 2009.

Pruess, K., C. Oldenburg, and G. Moridis, *TOUGH2 User's Guide, Version 2.0*, Report LBNL-43134, Lawrence Berkeley National Laboratory, Berkeley, Calif., 1999.

Rousseau-Gueutin, P., J. Gonçalvès, and S. Violette, Osmotic efficiency in Callovo-Oxfordian argillites: Experimental vs. theoretical models, *Physics and Chemistry of the Earth*, Parts A/B/C, *33*, S106–S113, 2008.

Rousseau-Gueutin, P., V. de Greef, J. Gonçalvès, S. Violette, and S. Chanchole, Experimental device for chemical osmosis measurement on natural clay-rock samples maintained at in situ conditions: Implications for formation pressure interpretations, *Journal of Colloid and Interface Science*, *337*, 106–116, 2009.

Spiegler, K., and O. Kedem, Thermodynamics of hyperfiltration (reverse osmosis): criteria for efficient membranes, *Desalination*, *1*, 311–326, 1966.

Soler, J.M., The effect of coupled transport phenomena in the Opalinus Clay and implications for radionuclide transport, *Journal of Contaminant Hydrology*, *53*, 63–84, 2007.

Takeda, M., T. Hiratsuka, and K. Ito, Laboratory characterization of chemico-osmotic, hydraulic and diffusion properties of rocks: Apparatus development, *Proceedings of Waste Management 2009*, Phoenix, Arizona, 2009.

PROBABILISTIC ANALYSIS BASED ON SIMULATIONS OF THE LONG-TERM GAS MIGRATION AT REPOSITORY-SCALE IN A GEOLOGICAL REPOSITORY FOR HIGH AND INTERMEDIATE LEVEL RADIOACTIVE WASTE DISPOSAL IN A DEEP CLAY FORMATION

Eloi Treille, Jacques Wendling, Laurent Trenty, Laurent Loth, Guillaume Pepin and Frédéric Plas

ANDRA, Scientific Division
Parc de la Croix Blanche, Châtenay-Malabry, France
e-mail: eloi.treille@andra.fr, jacques.wendling@andra.fr, laurent.trenty@andra.fr, laurent.loth@andra.fr, guillaume.pepin@andra.fr, frederic.plas@andra.fr

ABSTRACT

The current design for a deep geological repository for high- and intermediate-level radioactive waste in France consists of a complex system of different underground structures. In such a disposal system, some uncertainties related to physical parameters could arise from various origins. In the frame of the long-term performance assessment, probabilistic analysis must then be conducted to determine the physical parameters of the model, the uncertainty over which has a decisive influence on the general uncertainty concerning the long-term hydraulic evolution of the entire repository.

In that context, we conducted numerical simulations (using TOUGH2-MP) of an entire repository region, over a long-term period (up to 1 million years). However, such a detailed numerical model of the entire repository system requires a tremendous computational effort and poses a laborious task with respect to the operation of the model. To handle these difficulties, an innovative method for efficient numerical modeling of a complete repository system and its geologic environment has been applied (developed by AF-C for Andra and presented in the 2009 TOUGH Symposium). This method allows for a massive reduction in overall finite volume elements, while at the same time provides an adequate representation of the small-sized structures in the repository.

Using this method, probabilistic density functions (PDF) are defined for 10 physical parameters—including intrinsic permeabilities, capillary-pressure relationship parameters, porosities, diffusion coefficients, and corrosion rates. These distributions are then used to select 120 simulations using the Latin Hypercube Sampling (LHS) method. We then perform a statistical analysis, using relevant output results. This analysis consists of an uncertainty analysis (computation of quantiles, moments, distributions) and a sensitivity analysis (statistical-indicator calculations) whose objective is to rank the input parameters with respect to their importance to the hydraulic and gas transfer, and how they affect the output indicators. We thus identify those parameters that require better and more precise characterization.

INTRODUCTION

The French National Radioactive Waste Management Agency (Andra) have established the feasibility of a deep geological disposal of high-level and long-lived radioactivity waste in an argillaceous formation (Andra, 2005). The repository would be built within an indurated clay formation at around 500 m depth, and have a horizontal extension of roughly 3 km × 5 km. Questions related to the performance of this repository integrate concerns regarding the impact of the (mainly) hydrogen gas generated by anoxic corrosion of metallic components and radioactive waste. Of particular interest is the potential for overpressure in the near field of the repository, because this could affect the mechanical integrity of geotechnical and geologic barriers.

Achieving a good understanding of the hydraulic system behavior of the repository requires numerical, nonisothermal, two-phase flow and transport simulations. However, a detailed 3D modeling of the repository, accounting for both detailed structures at the local scale and the global geometry of the drift network, would

require a tremendous computational effort, even when using a high-performance code like TOUGH2-MP (Zhang et al., 2008). To handle these difficulties, we developed an innovative method for the efficient numerical modeling of a complete repository system and its geologic environment (developed by AF-C for Andra and presented at the 2009 TOUGH Symposium). This method allows for a massive reduction in overall finite volume elements, while at the same time providing an adequate representation of the small-sized structures in the repository.

In such a disposal system, some uncertainties related to physical parameters could arise from various origins. In the frame of the long-term performance assessment, we must then conduct a probabilistic analysis.

This article describes a probabilistic study using hundreds of TOUGH2-MP simulations at global repository scale, in an attempt to determine the physical parameters of the model, the uncertainty over which has the greatest influence on the overall uncertainty of the entire repository's long-term hydraulic evolution.

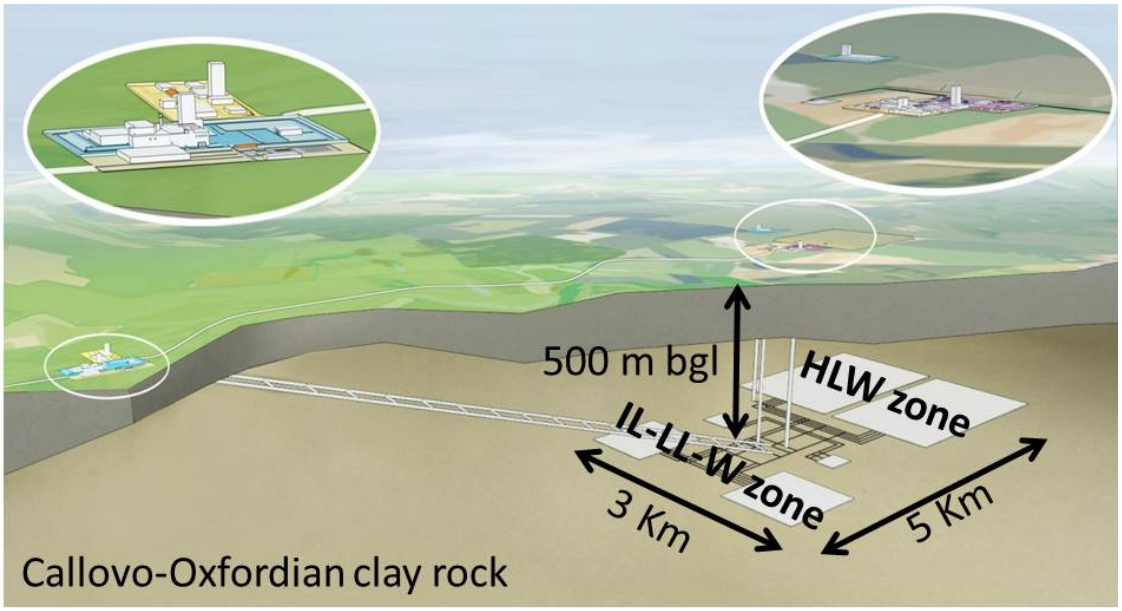

Figure 1. General architecture of the repository with emplacement of the HLW and ILW-LL zones

SYSTEM DESCRIPTION

The general layout of the repository is presented in **Figure 1**. The repository architecture is subdivided into three major zones: a large zone for high-level radioactive waste (HLW zone), a zone for long-lived intermediate-level radioactive waste (ILW-LL), and a zone for infrastructure facilities and access shafts in between. Inside the HLW zone, waste canisters are emplaced in several thousands of horizontal tunnels (0.75 m in diameter, 40 m long). In the ILW-LL zone, the waste canisters are emplaced in several tens of horizontal vaults (10 m in diameter, 400 m long). Individual wastes zones are connected through access and ventilation drifts. The horizontal extent of the complete repository is several kilometers in width and length; the thickness of the very-low-permeable host rock (Callovo-Oxfordian Clay) is around 150 m. The repository is located in the vertical mid-region of the host rock unit, around 500 m below ground level.

During the operational period of the repository (about 100 years), the complex network of drifts and disposal cells is ventilated under conditions of low relative humidity, leading to a drawdown of hydraulic pressure in the near field of the repository, as well as to a slight desaturation of the host rock in the vicinity of the drifts and caverns. At the end of the operational period, all repository structures are backfilled with

specifically designed geomaterials. A set of hydraulic barriers (seals) is foreseen at the end of the emplacement drifts, at specific locations within and between the major zones, as well as in the upper part of the access shafts, to hinder the transport of potentially contaminated water or gas along the backfilled drifts and shafts.

During the post-operational period, the waste containers (in particular those with high-level waste) emit considerable amounts of heat, generated as a consequence of radioactive decay. Moreover, the corrosion and degradation of some waste components produce large amounts of gases (mostly hydrogen). Both processes have a strong impact on the resaturation of the repository and the geologic environment. The expected time scales of the major transient thermal and hydraulic phenomena is around 100,000 years

PHYSICAL PROCESSES

During the operational phase of the repository, the disposal and access drifts, as well as the access and ventilation shafts, are ventilated, and the low-permeable clay host rock is progressively depressurized and even desaturated in the vicinity of the drifts. The gas-water flow is modeled as two-phase flow using the generalized Darcy's law and the relative permeability/capillary pressure concept.

As soon as the drifts are backfilled and sealed, the post-operational period begins, and the principal processes modeled are:

- Thermal dissipation into the host rock, mainly by conduction, and an induced porewater pressure increase by thermal expansion of the water[1].
- Resaturation of the backfill materials, due to the drainage towards the drifts and the capillary suction of the backfill materials (at early times)
- Hydrogen-gas generation and gas-pressure buildup in the backfilled repository[1].
- Displacement of water into the host rock due to the gas-pressure buildup[1].**Error! Reference source not found.Error! Reference source not found.Error! Reference source not found.**
- Dissolution of hydrogen into the pore water and transport by diffusion/advection[1].
- Advection and diffusion in the gas phase (in partially saturated backfill materials and host rock) and in the liquid (water) phase[1].

Because hydrogen is the dominant gas species, the TOUGH2-MP module EOS5 (water/hydrogen) is used for our computations (Pruess et al., 1999; Zhang et al., 2008). The impact of disregarding the true initial composition of the gas phase, e.g., air during the ventilation phase, is small on the scale of the entire repository and over the long term. Further, module EOS5 does not account for vapor-pressure lowering due to capillary and phase-adsorption effects. However, during the ventilation phase, the relative humidity prescribed at the surface of the drift walls is computed according to the vapor-pressure-lowering factor given by Kelvin's equation (cf. Pruess et al., 1999). Thus, the ventilation-driven desaturation of the porous waste containments, drift walls, and host rock is represented realistically. No geomechanical coupling is considered.

SPATIAL REPRESENTATION

A detailed numerical model of the entire repository system would require a tremendous computational effort and pose a laborious task with respect to the operation of the model. To offset this difficulty, an innovative method for the efficient numerical modeling of a complete repository system and its geologic environment has been applied (developed by AF-C for Andra and presented in the 2009 TOUGH symposium, Poller and al., 2009)—a method that allows for a massive reduction in overall finite volume elements, while at the same time providing an adequate representation of the small-sized structures in the repository.

This embedded modeling approach exploits the fact that, in the finite volume scheme, discretization does not necessarily need to respect spatially realistic geometries of the domain to be

[1] This process begins as soon as the waste packages are inserted into the emplacement drifts.

modeled. At first glance, this circumstance may seem irritating, but in view of the scale of the problem at hand, it offers the possibility for tackling the technical limitations inherent in the computation of large numerical models, and hence—important for this study—it paves the way for computation of the entire repository system with one single fully coupled model, including a physically and numerically appropriate representation of all spatial scales. This method enables us to keep the number of gridblocks for the designated model within a 100,000 magnitude (instead of a 10 million magnitude) for a complete repository representation. Schematically, and synthetically, the methodology considers three phases (Figure 2):

- Subdivision of the repository plane into a large number of "sectors" based on the position of seals and on geometrical considerations (e.g., different drift types or dimensions, symmetries). Each sector represents a 3D block of the geological pile (host rock and adjacent aquifers) and the repository components, such as access drifts, sealed drifts, and emplacement cells.
- A "multiplying concept" is used specifically for the approximation of symmetric[2] and repetitive structures, such as a series of emplacement cells along access drifts, as well as a series of waste emplacement areas. Thus, the number of gridblocks to be computed is reduced, while simultaneously the details of the geometrical fine-scale structures are accounted for. Several sectors are grouped to form a "zone" (e.g., a unit of high-level waste or a unit of intermediate level waste) by hydraulic connections at the drift interfaces.
- Interconnection of all zones at drift interfaces to form a model of the entire repository.

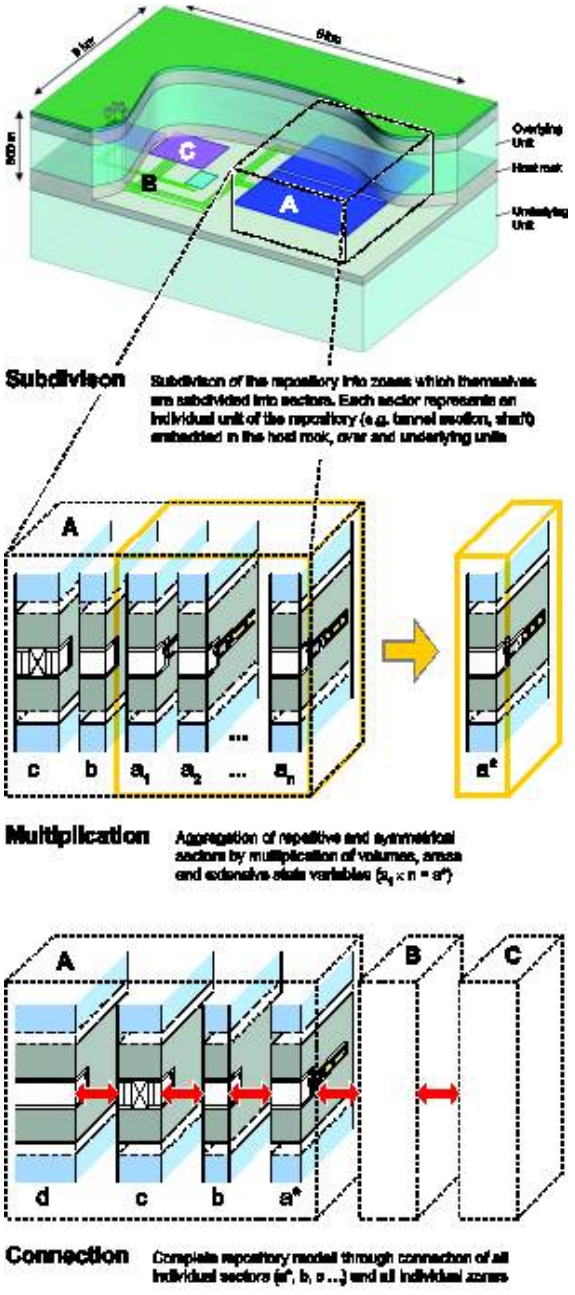

Figure 2. Schematic representation of the methodology used to develop the meshing

PARAMETERS

All parameter values were chosen to represent the available data. For some parameters however, the uncertainty is important, and the

[2] In this context symmetric conditions prevail if a spatially defined section of the repository (e.g. an emplacement cell with its surrounding host rock) appears in a repetitive manner, each section bearing identical conditions concerning its geometry, its hydraulic properties (materials, initial state, boundary conditions, sinks and sources). In other words, in every individual symmetric section, all conditions and processes influencing the thermo-hydraulics are identical in space and time.

presupposed influence on the simulation results is high. Simulations were done using a probabilistic approach for 10 of these parameters. Table 1 describes the way they were represented.

Table 1. Probabilistic Distribution Functions (PDF) for each parameter

	Type of PDF	Mean/SD	Min/Max
Host rock permeability (m/s)	Log Normal	$2\ 10^{-13}$ 10^{-13}	$10^{-14}/10^{-12}$
EDZ permeability (m/s)	Log Normal	10^{-9} $5\ 10^{-8}$	$10^{-11}/10^{-8}$
Bentonite permeability (m/s)	Log Uniform	-	$10^{-12}/10^{-10}$
Backfill porosity (%)	Uniform	-	20/50
Dissolved H2 molecular diffusion (m2/s)	Normal	$5\ 10^{-9}$ $2\ 10^{-9}$	$2\ 10^{-8}/10^{-9}$
VG-M n for EDZ (-)	Uniform	-	1.2/1.8
VG-M Pr for EDZ (MPa)	Uniform	-	0.5/10
VG-M n for bentonite (-)	Uniform	-	1.2/1.8
VG-M Pr for bentonite (MPa)	Uniform	-	1/15
Corrotion rate (micron/year)	Uniform	-	1/15

For permeability, Callovo-Oxfordian argilites and EDZ log-normal probabilistic functions were used, based on data for the mean, standard deviation, and minimum/maximum truncation values. For bentonite permeability, which can be conceptually designed, we assumed a uniform probabilistic function between acceptable values. Backfill porosity can also be designed, so the representation is the same as for bentonite permeability.

For dissolved H2 molecular diffusion literature **[?]** extreme values were chosen for minimum and maximum values, and normal probabilistic function assumed.

For van Genuchten/Mualem parameters (VG-M in the first column of **Table 1**) describing the unsaturated behavior of a porous media, we chose extreme values from partially available data and assumed uniform probabilistic distribution, owing to a lack of data regarding a more realistic distribution. For corrosion rate, extreme values were drawn from available data (on samples and *in situ* in the URL), and uniform distribution is assumed, again because of a lack of data regarding a more realistic distribution.

Figure 3 shows how the theoretical distributions are related by the actual 120 values chosen for dissolved H_2 molecular diffusion, corrosion rate, and EDZ permeability. All other parameters have been assigned values in line with the phenomenological knowledge concerning the process, mainly mean of available data for natural porous media and optimal designed values for engineered components.

These distributions are then used to construct 120 simulations via the LHS method. All these simulations were performed with TOUGH-MP software on highly parallel cluster Jade (more than 4 000 cores, property of the French CNRS organization). A total of 128 cores were used for each simulation, leading to a computation time of ~8 hours to one day to compute a 100,000 years two-phase flow period.

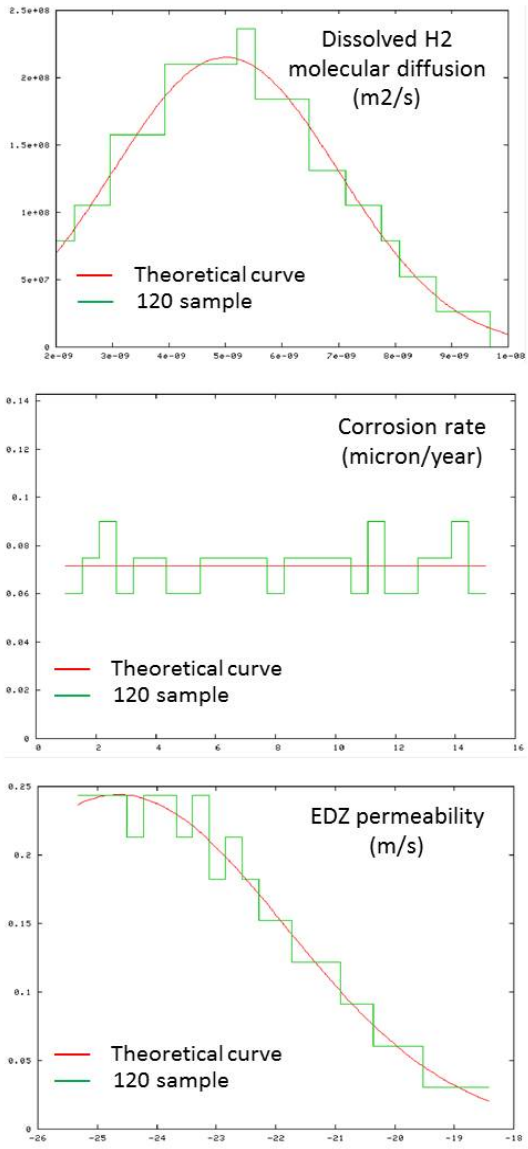

Figure 3. Theoretical and constructed PDF for selected parameters

MODELING RESULTS

The results presented here focus on one specific Andra concern, the eventual high gas pressures in the ILW-LL cells. figure 4 and figure 5 show several results for this state variable. The maximum is never higher than 5.5 MPa.

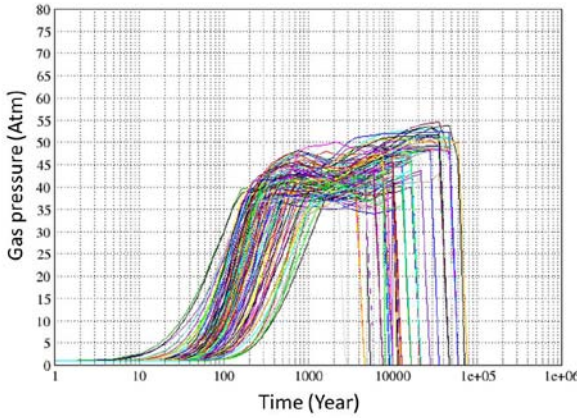

Figure 4. Calculated pressure in an ILW-LL vault for 120 simulations

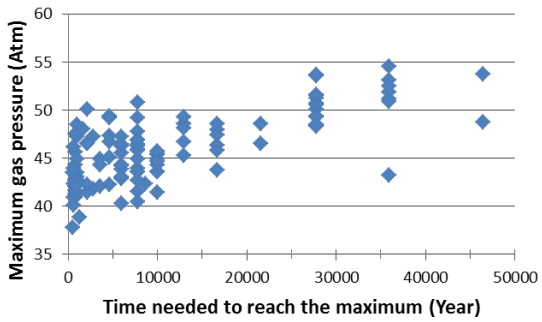

Figure 5. Maximum gas pressure for each simulation represented versus the time at which it appears

Depending on the simulation, this maximum occurs between several hundred years and several tens of thousands years. When occurring later, the maximum seems to be higher. This pressure is not a concern for the repository, since the hydrostatic water pressure is ~4.5 MPa, while the minimum mechanical stress at this depth is ~12 MPa.

The evolution of the maximum gas pressure as a function of the uncertain parameters allows us to define the first trend. We can see, in **figure 6**, a reasonable correlation between the solute molecular diffusion coefficient and the maximum gas pressure in the ILW-LL cells. Less significantly, corrosion rate and horizontal host-rock COX permeability seems to be correlated as well.

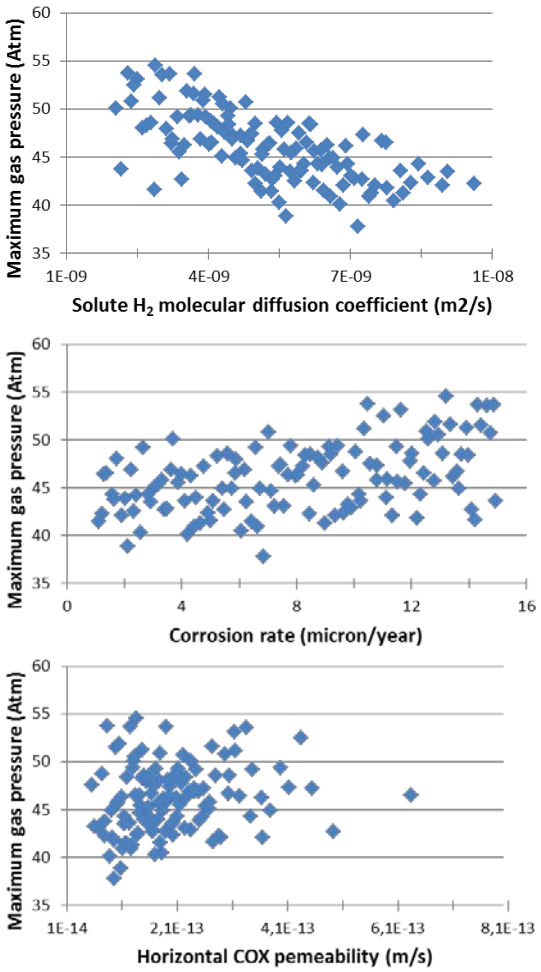

Figure 6. Maximum gas pressure for each simulation represented versus some chosen parameters values

To perform further statistical analyses we constructed a response surface based on a neural network, using URANY (Gaudier, 2008) and ROOT (Brun et al.) codes, combined with the 120 simulations described above. The determination coefficient between TOUGH results and response surface approximation shows a value greater than 0.95 (see figure 7), which represents a first rough validation of this surface. To validate this surface more thoroughly, we generated several sets of entry (stochastic) parameters by the LHS method, including 1000, 2000, 5000, 10,000, 20,000, and 50,000 vectors and surface-based approximations for all these sets. Several statistical quantities (5% quintiles, 95% quintiles, mean, and median) were computed (see figure 8) showing a regularity of the surface when increasing the number of simulations in the set.

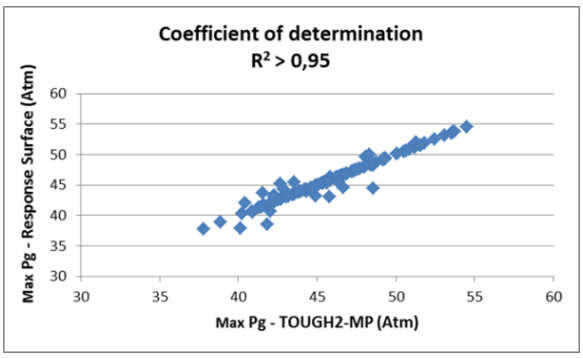

Figure 7. TOUGH vs. response surface results

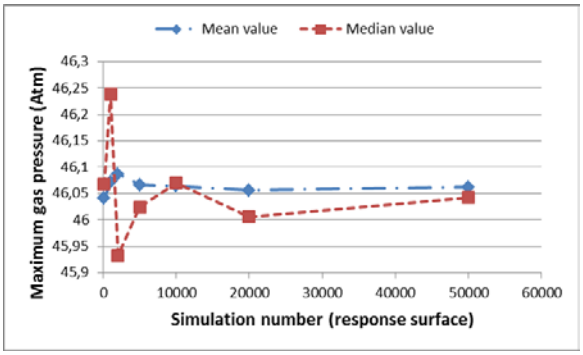

Figure 8. Evolution of maximum gas pressure mean and median values as a function of response-surface simulation results

Having shown that the surface is valid, we performed a sensitivity analysis to confirm the first correlation trend (figure 9).

The results show a consistency between several sensitivity estimators (PCC, Spearman, etc.) and also between the different simulation sets, from the initial 120-simulation set to the 50,000-simulation set.

The most influential parameter is the dissolved diffusion coefficient (on average, more than 50% of the gas dissolves inside the IL-LLW vaults); the second-most decisive parameter is the corrosion rate (the bigger the corrosion rate, the higher the gas pressure) and the third most decisive parameter is host-rock (COX) permeability (the higher the permeability, the higher the pressure). These findings highlight the fact that the water resaturating flux (which increases with this permeability) is an important variable controlling the gas pressure.

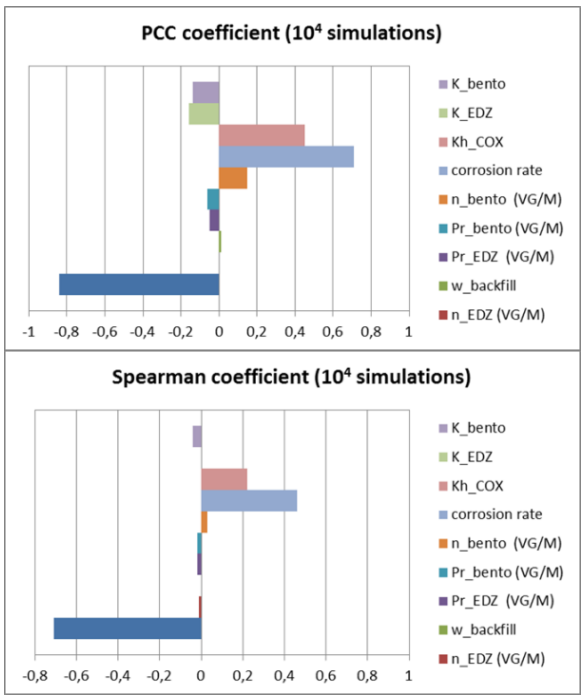

Figure 9. Sensitivity analysis results

FUTURE DIRECTIONS OF WORK

Our next step will be to add even more surface-response estimations, to reach a set large enough (at least 100,000 values) to perform a SOBOL analysis (sensitivity analysis on the variance, second-order statistical estimator) and to confirm the sensitivity analysis conducted up to now on the mean (first-order statistical estimator). Once this first methodological step is completed, we intend to do the same type of exercise on different criteria, including HLW maximum pressure, time of total resaturation of the repository, and maximum gas flux at the shafts.

Some parameters showing no impact on maximum pressure variance will be dropped from the stochastic analysis and replaced by others, like the Millington-Quirk exponent for saturation (linked to dissolved gas diffusion) or Henry's coefficient (linked to dissolution processes).

CONCLUSIONS

This first trial using TOUGH2-MP to generate hundreds of results at repository scale for the hydraulic-gas transient in a French nuclear repository, to define a surface response and statistical analysis, shows that this task is workable and the methodology well adapted. The "maximum pressure in ILW-LL vaults" criteria chosen for this first test shows that, for our concept, gas pressure is not an issue for this type of waste. The main parameters influencing this maximum gas pressure are the dissolved gas-diffusion coefficient, the corrosion rate, and the host-rock permeability.

Complementary work will be focused on more complex analysis like SOBOL estimators, use of new criteria (time of total resaturation, maximum gas flux through the shafts, etc.), and introducing new parameters in the statistical process.

ACKNOWLEDGMENT

K. Pruess (Lawrence Berkeley National Laboratory) is gratefully acknowledged for his help and for his insightful remarks in using TOUGH2. AF-C is acknowledged for its work done on the development of the embedded modeling approach and the generation of the entire process for launching a repository-scale simulation. CEA is acknowledged for granting the opportunity to use the URANY and ROOT codes to compute surface response and sensitivity analysis.

REFERENCES

Andra (2005) Dossier Argile 2005. Agence Nationale pour la Gestion des Déchets Radioactifs, Châtenay-Malabry, France.

Pruess, K., Oldenburg C., and Moridis G., *TOUGH2 User's Guide, Version 2.0*, Report LBNL-43134, Lawrence Berkeley National Laboratory, Berkeley, Calif., 1999.

Zhang, K., Wu Yu-Shu, Pruess K.. User's guide for TOUGH2-MP – A Massively Parallel Version of the TOUGH2 Code, Report LBNL-315E, Lawrence Berkeley National Laboratory, Berkeley, Calif., 2008.

Poller A., Enssle C. Ph., Mayer Gerhard, Croise Jean, Wendling Jacques. Repository-scale modeling of the long-term hydraulic perturbation induced by gas and heat generation in a geological repository for high and intermediate level radioactive waste – Methodology and example of application. TOUGH2009 Symposium proceedings,

Lawrence Berkeley National Laboratory, Berkeley, Calif., 2009.

Gaudier F;. Manuel utilisateur d'Uranie SFME/LGLS/RT/08/003/A CEA Saclay 91191 Gif-sur-Yvette, France, 2008.

Brun René (CERN), Rademakers Fons (CERN), Canal Philippe (FNAL), Antcheva Ilka (CERN), Buskulic Damir (LAPP) The ROOT Users Guide : ftp://root.cern.ch/root/doc/Users_Guide_5_20.pdf.

A SIMPLE IMPLEMENTATION OF 1D HYDROMECHANICAL COUPLING IN TOUGH2

Robert Walsh, Nicola Calder, and John Avis

Geofirma Engineering Limited
1 Raymond St., Suite 200
Ottawa, ON, K1A 1R2, Canada
e-mail: ncalder@geofirma.com, rwalsh@geofirma.com, javis@geofirma.com

ABSTRACT

In recent years, there has been increasing interest in hydromechanical coupling in two-phase flow systems. Modelling systems such as TOUGH-FLAC have been developed, but can be very demanding to use, both computationally and in terms of human effort. This paper describes a simplified one-dimensional hydromechanical coupling model implemented directly in TOUGH2. This is appropriate for modelling the effects of relatively uniform changes in mechanical loading over a large area, such as occurs during continental glaciations or laterally extensive erosion/deposition events. In these situations, the assumption of purely vertical strain is applied. The approach used was inspired by the methods described for pure vertical strain and single phase flow in Wang (2000) and Neuzil (2003).

Traditionally, single phase flow codes model mechanical expansion and contraction of the porous medium as a source/sink type of term, such that a pore pressure increase causes water to leave the system, and a pore pressure decrease has the opposite effect. However, TOUGH2 models this phenomenon directly, by changing the volume of the pores and the density of fluids as a function of pore pressure. This meant that when implementing the uniaxial strain hydromechanical coupling model in TOUGH2, a very careful consideration of the poroelastic equations was necessary. We were able to simplify the complex equations of poroelasticity down to a very manageable form. We also noted some limitations inherent in the current set of assumptions built into the TOUGH2 equations.

The model has been verified for single phase systems against an analytical solution described in Lemieux et al. (2008), and other simple analytical systems. The hydromechanical effect of gas in such simplified systems is shown. The effects of partial gas saturation on the development of the fluid pressure profile during glacial advance and retreat over a horizontally bedded sedimentary sequence are examined.

INTRODUCTION

In recent years, there has been increasing interest in hydromechanical coupling in two-phase flow systems. The effect of future glaciation on groundwater and gas transport in the formations surrounding a deep geologic repository for radioactive waste is an important issue. In a sedimentary setting, the units providing geological confinement can have small but significant gas saturations. The presence of gas in formations is expected to greatly reduce the magnitude of hydromechanical coupling. Modelling systems such as TOUGH-FLAC (Rutqvist and Tsang, 2003) combine the two-phase flow capability of TOUGH2 with mechanical simulators, but these simulators are demanding to use, in terms of computational and human effort, and may require some approximation in accounting for the markedly increased fluid compressibility in a gas-water system.

To avoid these limitations, a simple one-dimensional (1D) hydromechanical coupling algorithm was implemented directly in TOUGH2. The algorithm relies on the simplifying assumptions of horizontally bedded formations and uni-axial strain. These limitations do not preclude modelling the effects of relatively uniform changes in mechanical loading over a large area, such as occurs during continental glaciations or laterally extensive erosion/deposition events.

METHODS

External stresses arising from transient ice-sheet mechanical loading and elevated sub-glacial hydraulic head can potentially influence groundwater system dynamics and solute migration. The potential influence of such perturbations is explored by modifying TOUGH2 to include an approximate solution to coupled hydro-mechanical processes as described by Neuzil (2003). This approach is similar to that implemented in FRAC3DVS_OPG (Therrien et al. 2010) but has been extended to two-phase flow systems.

In TOUGH2, the mass balance equation can be written as follows (Pruess et al. 1999):

$$\frac{d}{dt}\int_{V_n} M^\kappa dV_n = \int_{\Gamma_n} F^\kappa \cdot \boldsymbol{n} d\Gamma_n + \int_{V_n} q^\kappa dV_n \qquad (1)$$

This expression integrates over the subdomain V_n, which is bounded by the surface Γ_n, with $\boldsymbol{n}$ being an inward pointing vector, normal to the surface element $d\Gamma_n$. The symbol κ represents the mass component (i.e., water, air, methane). Hydromechanical coupling under a homogeneous and laterally extensive load is implemented within the mass accumulation term, which has the following general form (Pruess et al. 1999):

$$M^\kappa = \phi \sum_\psi S_\psi \rho_\psi X_\psi^\kappa \qquad (2)$$

Where

ϕ = porosity (-);
S_ψ = saturation of phase ψ (-);
ρ_ψ = density of phase ψ (kg/m^3), a function of pressure and phase compressibility;
X_ψ^κ = mass fraction of component kappa in phase ψ (-).

Unlike single phase codes, porosity (ϕ) in TOUGH2 is not constant, but is updated at the end of each iteration to account for changes in pressure. The change in porosity as a function of the pressure is analogous to the addition or subtraction of water from storage in single-phase codes. The expression for the updated porosity for the current timestep (ϕ_t), including hydromechanical effects, is:

$$\phi_t = \phi_{t-1} + \phi_{t-1} C_{pore} dp + S_{S-1D} \zeta d\sigma_{zz} \qquad (3)$$

Where

ϕ_{t-1} = porosity of previous timestep(-);
C_{pore} = pore compressibility (Pa^{-1}), COM in the ROCKS record;
dp = change in pressure during timestep $t-1$ (Pa);
S_{S-1D} = specific storage (Pa^{-1});
ζ = 1-dimensional loading efficiency (-);
$d\sigma_{zz}$ = change in vertical load during timestep $t-1$ (Pa).

The third term in equation (3), namely $\phi_{t-1} C_{pore} dp$, represents the change in porosity due to the change in pore pressure during timestep $t-1$. This expression has always been in TOUGH2, and is analogous to the storage term in single-phase flow mass balance equations. The fourth term in equation (3), ($S_{S-1D} \zeta d\sigma_{zz}$) is the new hydromechanical term, and represents the change in porosity due to the change in vertical load during timestep $t-1$. The terms of equation (3) which are unique to the hydromechanical formulation are the one dimensional loading efficiency (ζ), the change in vertical load ($d\sigma_{zz}$), and the one-dimensional (uniaxial) specific storage (S_{S-1D}).

The hydro-mechanical capability requires the one-dimensional loading efficiency to be defined for each material type. This parameter is used to determine what percentage of the applied vertical stress is borne by the pore-fluids. The equation used to calculate one-dimensional loading efficiency (ζ) is (Neuzil 2003):

$$\zeta = \frac{\beta(1+\nu)}{3(1-\nu) - 2\alpha\beta(1-2\nu)} \qquad (4)$$

Where

β = Skempton's coefficient (-)
α = Biot-Willis coefficient (-)
ν = Poisson's Ratio (-)

In the newly developed hydromechanical module for TOUGH2, ζ is read as an input parameter. Strictly speaking S_{S-1D} should be calculated according to equations (5) through (9) (Wang, 2000; Neuzil, 2003):

$$S_{S-1D} = \left(\frac{1}{K} - \frac{1}{K_S}\right)(1-\lambda) + \phi\left(\frac{1}{K_f} - \frac{1}{K_\phi}\right) \quad (5)$$

$$\frac{1}{K_S} = \frac{1-\alpha}{K} \quad (6)$$

$$\lambda = \frac{2\alpha(1-2\nu)}{3(1-\nu)} \quad (7)$$

$$\frac{1}{K_f} = \frac{S_w}{K_w} + \frac{S_g}{K_g} \quad (8)$$

$$\frac{1}{K_\phi} = -\frac{1}{\phi}\left[\left(\frac{1}{K} - \frac{1}{K_S}\right)\left(\frac{1}{\beta} - 1\right) - \frac{\phi}{K_f}\right] \quad (9)$$

Where

K = Drained bulk modulus (Pa), ($1/K = \phi C_{pore}$);
K_S= Unjacketed bulk modulus, often denoted solid phase bulk modulus (Pa);
K_f= Effective fluid bulk modulus (Pa);
S_w= Water saturation (-);
S_g= Gas saturation (-);
K_w= Water bulk modulus, calculated by TOUGH2 (Pa);
K_g= Gas bulk modulus, calculated by TOUGH2 (Pa);
K_ϕ= Unjacketed pore compressibility (Pa).

However, although the storage coefficient is not used directly, the implementation of pore compressibility in TOUGH2 is equivalent to a storage coefficient defined as follows:

$$S_S = \frac{1}{K} + \frac{\phi}{K_f} \quad (10)$$

This equation is a simplified version of equation (5), which implicitly assumes incompressible grains ($\alpha = 1$). In order for the pressure effects of externally applied loads and changes in pore pressure to be expressed in a consistent fashion, it is necessary to use this simplified form of the storage coefficient equation. Ultimately, the ideal solution to this problem would be to alter the internal calculation of pore deformation in response to pressure change to make it consistent with the 1D hydromechanical formulation.

At first glance, it appears that the 1D hydromechanical term is a function of fluid compressibility, and thereby gas saturation; however, the term $S_{S-1D}\,\zeta$ (see equation (3)) reduces to:

$$S_{S-1D}\,\zeta = \frac{\left(\frac{1}{K} - \frac{1}{K_S}\right)(1+\nu)}{3(1-\nu)} \quad (11)$$

Thus, this formulation is a function of material parameters which we assume (in a linear poroelastic model), do not change significantly (i.e. $S_{S-1D}\,\zeta$ is a constant). A judicious choice of the input parameters ζ and C_{pore} allows us to use a simplified expression to calculate $S_{S-1D}\,\zeta$, which is also consistent with the definition of the storage coefficient in TOUGH2:

$$S_{S-1D}\,\zeta = \phi\left(C_{pore} + \frac{1}{K_{water}}\right)\zeta \quad (12)$$

This approach (using equation 12) is a good estimate of the effect of hydromechanical coupling on in-situ pore pressures. The input value C_{pore} should be corrected to account for uniaxial versus triaxial mechanical constraints.

MODEL VERIFICATION

Two analytical verification cases are described. The two cases are similar in that they are both one-dimensional problems in which a load is applied at the upper surface causing increased pore pressures, which subsequently drain. Both verification cases are for water saturated systems, as analytical solutions for partially gas saturated systems do not exist.

1D Consolidation after Terzaghi (1943)

For this case, model results are compared with the analytical solution for one-dimensional consolidation by Terzaghi (1943). In this problem, a layer of water-saturated rock is subjected to an instantaneously applied vertical load at the upper surface. The rock layer has a specified thickness (h), and water is allowed to drain at the surface, where pressure is maintained constant. Hydraulic boundaries on all other sides are set as zero-flow. Mechanical boundary conditions on the vertical sides are roller boundaries, allowing only vertical

movement. The analytical solution for pore pressure (P_p) is as follows (Jaeger et al. 2007):

$$P_p(z,t) = \frac{\alpha M \sigma_{zz}}{(\lambda + 2G + \alpha^2 M)} * \sum_{i=1,3,\ldots}^{\infty} \frac{4}{i\pi} \sin\left(\frac{i\pi z}{2h}\right) \exp\left(\frac{-i^2\pi^2 kt}{4\mu S h^2}\right) \quad (13)$$

Where

α= Biot-Willlis coefficient (-);
t= time (s);
z= depth (m);
M= Biot modulus (Pa);
σ_{zz}= instantaneous vertical load (Pa);
λ = drained Lame's modulus (Pa);
G= Shear modulus (Pa);
h= maximum depth (or thickness) of rock layer (m);
k= permeability (m^2);
μ= dynamic viscosity (kg $m^{-1}s^{-1}$);
S= uniaxial storage coefficient (Pa^{-1}).

A TOUGH2 model of a similar system was developed. As TOUGH2 applies load as a rate, it was not possible to obtain an instantaneous application of load. Instead, load was applied at such a rate that maximum loading was achieved within 0.1 years, which was short (i.e., nearly instantaneous) when compared to the total runtime of approximately 100 years. A second minor divergence between the numerical model and the analytical model is that TOUGH2 does not assume constant water density and compressibility, but calculates these as a function of temperature and pressure. However, over the pressure range examined here, the impact on results was minor. Model properties are shown in Table 1. For comparison's sake, the mechanical parameters used are equivalent to those used for a similar verification exercise by Nasir et al. (2011), namely Young's modulus (E) of $4x10^7$ and Poisson's ratio (ν) of 0.3. The TOUGH2 model used a porosity of 0.1.

A comparison of analytical and numerical model results is shown in Figure 1. For this run the applied load (σ_{zz}) was 3.0 MPa. The time axis is plotted as dimensionless time, defined as $kt/\mu Sh^2$. The agreement between numerical and analytical solutions is good, although the TOUGH2 model does seem to drain faster at greater depths and times.

Table 1: Model Properties for the First Verification Case

Analytical		**TOUGH2**	
Property	Value	Property	Value
k (m^2)	2.04 x 10^{-15}	k (m^2)	2.04 x 10^{-15}
S (Pa^{-1})	1.86 x 10^{-8}	C_{pore} (Pa^{-1})	1.86 x 10^{-7}
α	varies	ζ	varies
h (m)	1000	*h (m)*	1000

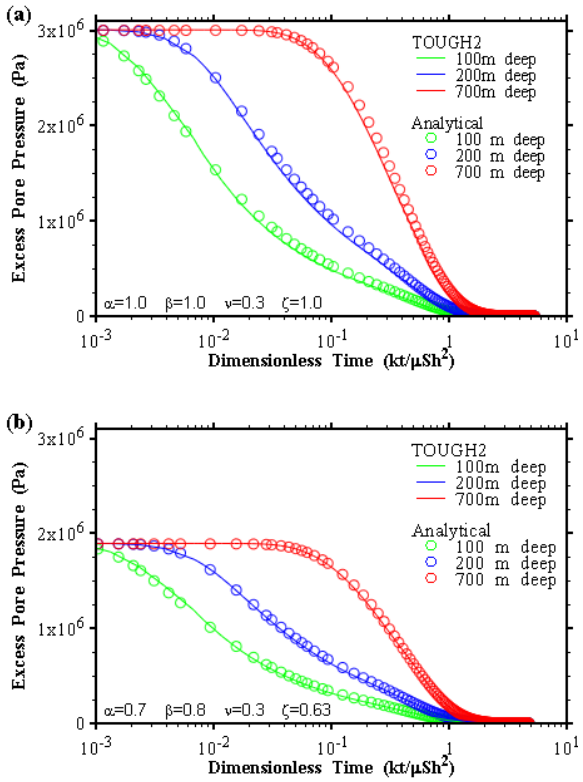

Figure 1: Analytical and TOUGH2 pressure time-series, various depths, (a) ζ =1, (b) ζ =0.63.

1D Hydromechanical Coupling in a Semi-infinite Column with Gradual Loading

For the second case verifying the implementation of the hydromechanical model in TOUGH2, the analytical solution described in Lemieux et al. (2008) was used. This is an analytical solution for one-dimensional hydromechanical coupling in a semi-infinite column. In this model, the applied stress is

continually increased as a linear function of time. The top of the column is drained (hydraulic head is held constant at zero) and the base of the column is at an infinite distance. The analytical solution to this problem is as follows:

$$h(z,t) = \frac{\zeta}{\rho g}\frac{d\sigma_{zz}}{dt}\left[t - \left(t + \frac{z}{2D}\right) erfc\left(\frac{z}{2\sqrt{Dt}}\right) + z\sqrt{\frac{t}{\pi D}} exp\left(-\frac{z^2}{4Dt}\right)\right] \quad (14)$$

Where

ζ = one dimensional loading efficiency (-);
ρ = fluid density (kg/m^3);
g = gravity (m/s^2);
$d\sigma_{zz}/dt$ = stress application rate (Pa/s), a constant as discussed above;
t = time (s);
z = depth (m);
D = hydraulic diffusivity (m^2/s), hydraulic conductivity divided by specific storage.

Note that there is a slight difference between equation (14) and the solution shown in Lemieux et al. (2008), which has a typographical error.

A similar system was modelled using TOUGH2. Model properties are shown in Table 2. The primary difference between the numerical model and the analytical model was the total vertical depth of 7000 m for the numerical model. The analytical model is semi-infinite, but a greater depth in the numerical model would have led to pore pressures in excess of 100 MPa, which is a hard-coded cut-off beyond which the TOUGH2 EOS3 module does not function. The TOUGH2 model had a constant specified pressure of 100 kPa (~1 atm) at the top, a no-flow boundary at the base, and was water saturated throughout. As with the previous case, TOUGH2 does not assume constant water density and compressibility as does the analytical model, which has a minor impact on results over the pressure range examined here .

The TOUGH2 pressure results were converted to hydraulic head, and compared against the analytical solution, as shown in Figure 2. Despite the slightly different assumptions between the two models, the TOUGH2 results are a good match with the analytical solution.

The impact of changing the loading efficiency was also assessed, in both the analytical and the TOUGH2 models (see Figure 3). Once again, the numerical and analytical models correspond very well. As expected, reducing the loading efficiency reduces the mechanically-induced pressure rise in the 1D column.

Table 2: Model Properties for the Second Verification Case

Analytical		**TOUGH2**	
Property	Value	Property	Value
K_{zz} (m/a)	1.0 x 10^{-3}	k_{zz} (m^2)	3.23 x 10^{-18}
S_s (m^{-1})	1.0 x 10^{-6}	C_{pore} (Pa^{-1})	5.70 x 10^{-10}
ζ	varies	ζ	varies

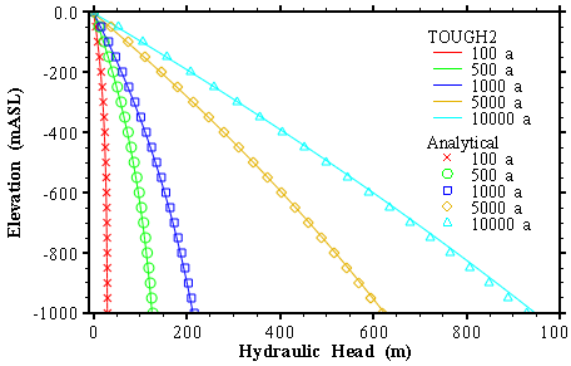

Figure 2: Analytical and TOUGH2 calculated hydraulic head versus depth at different times.

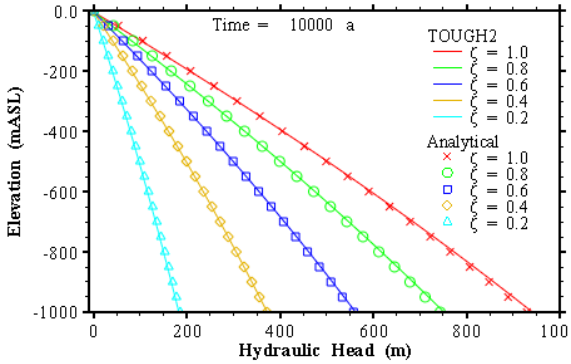

Figure 3: Analytical and TOUGH2 calculated hydraulic head versus depth at 10 000 years, for different loading efficiencies (ζ).

MODEL APPLICATION

In this section the 1D hydromechanical model is applied to a simple uniform column model and subsequently to another test case representing a layered sedimentary sequence containing rocks of different compressibilities. Both examples include partial gas saturations. The second test cases explores the possibility of developing anomalous pressures through geomechanical processes in a partially gas saturated sequence.

A Simple Two-phase Test Case

In this section, a homogeneous, one-dimensional model is used to examine the effects of gas in a hydromechanical system. The example is simplified and artificial, but nevertheless allows us to focus on the effects of gas without the complexity inherent in most natural systems. This homogeneous system is loaded (as shown in Figure 4), and the change in water pressure (expressed in m H_2O) under various conditions is assessed. The permeability is rather low to remove drainage effects, and a generic capillary pressure curve, typical of such low permeability rock, was used. Water pressure was initialized at hydrostatic, gas pressure was initialized in equilibrium with the water pressure as a function of the capillary pressure curve. Loading efficiency was set to 0.7.

Figure 4 shows how the initial gas saturation affects the hydromechanical (HM) process: as gas saturation increases, the degree of HM coupling drops Low gas saturations can still have a profound effect on the HM response. Also interesting to note, for the models with very low gas saturations, the changing shape of the curve indicates a transition from two-phase to fully saturated behavior as the increased pressure causes the gas in the system to dissolve.

Figure 5 shows the effect of compressibility. As the compressibility increases, more of the load is passed to the fluid in the system, despite the fact that the loading efficiency (valid for saturated systems) remains constant. The pink line in the plot, for pore compressibility of 5E-8, is clearly an unphysical result. Some caution is necessary when selecting a consistent set of poroelastic parameters for unsaturated HM coupling. In this case, such a high compressibility is incompatible with the loading efficiency of 0.7, and the model prediction should not be relied upon.

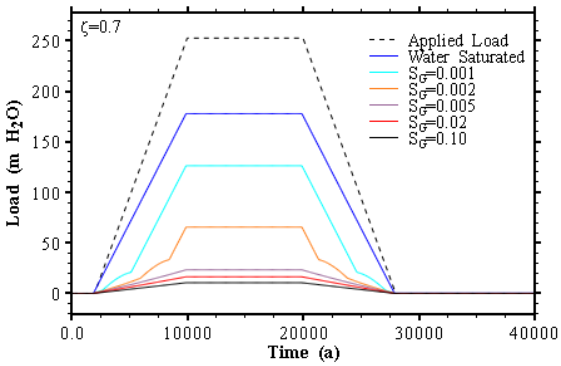

Figure 4: Effect of gas saturation.

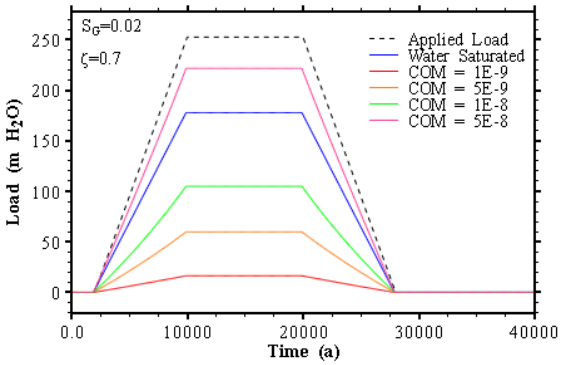

Figure 5: Effect of pore compressibility.

Figure 6 shows the effect of depth on the hydromechanical response. Depth is a proxy for gas compressibility which decreases with increasing pressure. As gas compressibility drops at greater depth, the two-phase curve approaches the fully saturated curve.

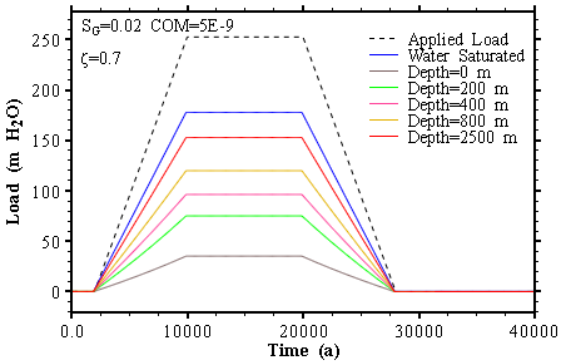

Figure 6: Effect of depth (gas compressibility).

Figure 7 shows the effect of capillary pressure on the hydromechanical response. As the capillary pressure at a given saturation increases

from zero, to a very high capillary pressure, the HM response increases. Similar to the effect of depth, increased capillary pressure increases the gas pressure, and thus reduces the gas compressibility. Because the capillary pressure curve is presumed to remain constant, even as the pores deform, and the gas deforms much more than the water, external loading can significantly change the gas saturation, and thereby the capillary pressure. The dashed pink line shows the magnitude of this effect. This model was altered to reverse the effect of pore deformation when calculating the capillary pressure.

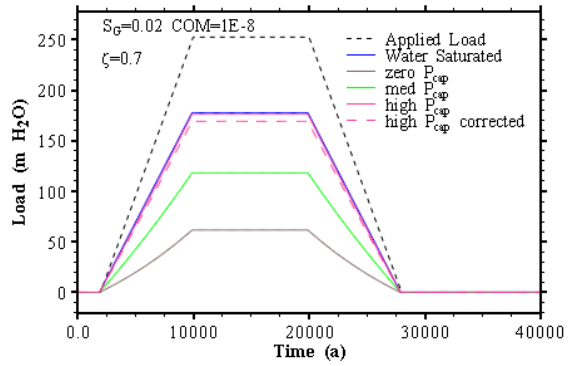

Figure 7: Effect of capillary pressure.

Figure 8 brings together the previous discussion, showing the hydraulic head profiles at different gas saturations under the maximum load (at 10000 years). The impact of depth dependent gas compressibility is evident.

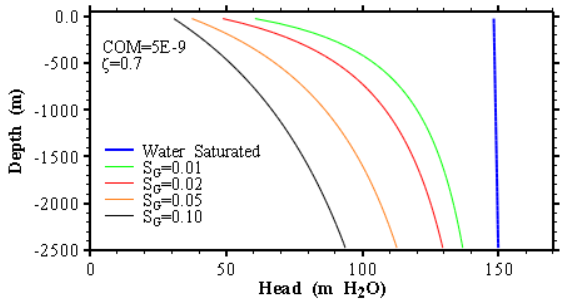

Figure 8: Pressure profiles, effect of gas saturation.

HM Coupling in a Layered Sequence

This is an example of a simple layered sequence, with a relatively compressible unit sandwiched between two stiff units. The properties are summarized in Table 3.

Table 3: Model Properties

Name	ϕ	k (m^2)	C_{pore} (Pa^{-1})	ζ
LowC	0.02	1E-20	1E-9	0.5
HighC	0.05	1E-20	1E-8	1.0

The loading curve is identical to the previous test case (see Figure 4), except that loading rates are 10x higher. Three scenarios are simulated: (1) water saturated, (2) gas saturation of 10% everywhere, (3) gas saturation of 10% only in the high compressibility zone. The model results are shown in Figure 9.

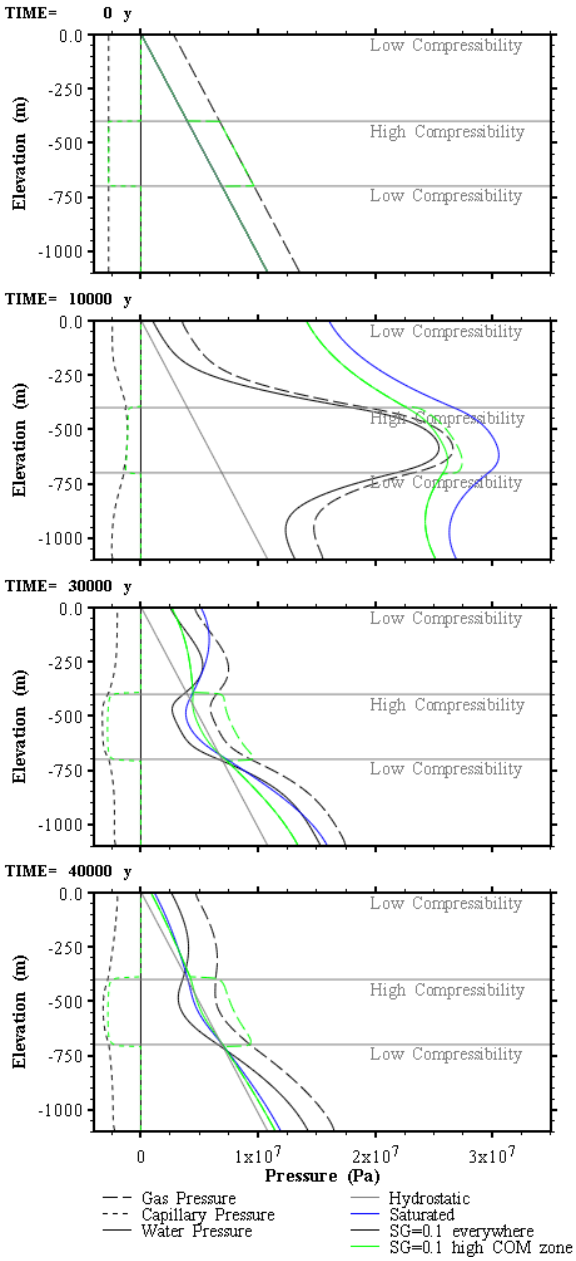

Figure 9: Pressure profiles, layered sequence example.

Every geological system is different, so one cannot generalize these results to develop widely applicable rules concerning gas saturation and HM coupling. In this example it is interesting that although the pressurization of the model with partial gas saturation in all layers (black line in Figure 9) is less than the water saturated model, after unloading the two phase model has a much greater underpressure, which persists 10000 years after the load has been withdrawn completely. The reason for this is clear: partial gas saturations cause a greater reduction in HM coupling in the stiffer rock than they do in the softer rock. As a result, when load is applied hydraulic gradients are much higher in the two phase model (see Figure 9, 10000 y).

When gas saturations are only applied to the central, compressible layer (green line in Figure 9), the reverse occurs. Vertical hydraulic gradients under maximum loading are moderated, as is the degree of under- and over-pressure post-unloading.

CONCLUSION

A model for one-dimensional hydromechanical coupling has been implemented in TOUGH2. The application of this model is limited, relying on the simplifying assumptions of horizontally bedded formations and uni-axial strain. However, these limitations do not preclude modelling the effects of relatively uniform changes in mechanical loading over a large area, such as occurs during continental glaciations or laterally extensive erosion/deposition events.

Within this scope, the observed model results are interesting. The examples presented here show that the presence of partial gas saturations in a formation can have a large effect on the hydromechanical behavior of the system. When assessing the response of a geological formation to applied load at the surface, even rather small amounts of gas in the system may greatly moderate the hydromechanical effect. In layered systems with variable properties, the effects of partial gas saturation can be counterintuitive, showing that it is necessary to account for site specific properties and conditions when examining the genesis of under- and over-pressurized zones in contemporary formations, or predicting the effect of future events (such as glaciation) on hydrogeological systems.

ACKNOWLEDGMENT

The authors would like to thank the Nuclear Waste Management Organization (NWMO) for continued support.

REFERENCES

Jaeger, J., N. Cook and R. Zimmerman. *Fundamentals of Rock Mechanics, Fourth Edition*. Blackwell Publishing, Malden, MA, USA, 2007.

Lemieux, J-M, E. Sudicky, W. Peltier, L. Tarasov, Simulating the impact of glaciations on continental groundwater flow systems: 1. Relevant processes and model formulation, *Journal of Geophysical Research*, doi:10.1029/2007JF000928, 11pp, 2008.

Nasir, O., M. Fall, T.S. Nguyen and E. Evgin. Modelling of the hydro-mechanical response of sedimentary rocks of southern Ontario to past glaciations. *Engineering Geology*, 123, 271-287, 2011

Neuzil, C., Hydromechancial coupling in geological processes. *Hydrogeology Journal*, 11, 41-83, 2003.

Pruess, K., C. Oldenburg, and G. Moridis, *TOUGH2 User's Guide, Version 2.0*, Report LBNL-43134, Lawrence Berkeley National Laboratory, Berkeley, Calif., 1999.

Rutqvist, J., and Tsang, C.F. TOUGH-FLAC: A numerical simulator for Analysis of Coupled Thermal-Hydrologic-Mechancial Processes in Fractured and Porous Geological Media under Multi-phase flow Conditions. *Proccedings, TOUGH2 Symposium 2003*, Berkeley, California, 2003.

Terzaghi, K. 1943. *Theoretical Soil Mechanics*. John Wiley and Sons, New York, USA.

Therrien, R., R.G. McLaren, E.A. Sudicky, S.M. Panday and V. Guvanasen, *FRAC3DVS-OPG: A Three Dimensional Numeric Model Describing Subsurface Flow and Solute Transport. User's Guide*, Groundwater Simulations Group, Waterloo, Canada, 2010.

Wang, H., *Theory of Linear Poroelasticity with Application to Geomechanics and Hydrology*. Princeton University Press, Princeton, USA, 2000.

THE EFFECT OF STRESS ON FLOW AND TRANSPORT IN FRACTURED ROCK MASSES USING TOUGH-FLAC AND A MODIFIED CRACK TENSOR THEORY

Zhen Wang[1, 2], Jonny Rutqvist[1], Yuan Wang[1, 3], Colin Leung[4], Andrew Hoch[5], Ying Dai[2]

[1]Earth Science Division, Lawrence Berkeley National Laboratory (LBNL), Berkeley, CA 94720 USA
[2]School of Aerospace Engineering and Applied Mechanics, Tongji University, Shanghai 200092, China
[3]Hohai University, Nanjing, China
[4]Imperial College, London, UK
[5]Serco Energy, Didcot, UK
e-mail: wangzhen@lbl.gov

ABSTRACT

We used a slightly modified version of Oda's crack tensor theory for developing and applying a modeling approach (that we characterize as a discrete continuum) to upscale the hydraulic and mechanical properties of fractured rock masses. The modified crack tensor theory was used to calculate the stress-dependent permeability tensor and compliance tensor for the individual gridblock. By doing this, we transformed a discrete fracture network model into a grid-based continuum model. The methodology was applied to a benchmark test related to fluid flow and transport through a 20 × 20 m model domain of heavily fractured media. This benchmark test is part of the international DECOVALEX project, thus providing us with the opportunity to compare our results with the results of independent models. We conducted the hydro-mechanical analysis with TOUGH-FLAC, a simulator based on the TOUGH2 multiphase flow code and FLAC3D geomechanical code, using a multiple interacting continua (MINC) method to simulate the flow and transport of fractured rock. The results of our simulations were consistent with the results of the other independent modeling approaches.

INTRODUCTION

Coupled hydromechanical effects, such as the effect of stress on permeability, could have a significant impact on flow and transport in fractured rock (Rutqvist and Stephansson 2003). These are complex processes that can be studied using numerical modeling, although not without encountering difficulties related to upscaling and deriving representative values for both mechanical and hydrological parameters. In this study, our modeling approach is to use a modified version of the crack tensor theory (Oda 1986) to upscale the hydraulic and mechanical properties determined from a discrete-fracture-network model—and then calculate the stress-dependent permeability (Leung et al. 2009). Using this modeling approach, the discrete fracture network was transformed into a grid-based continuum model. We implemented this modeling approach into the framework of TOUGH-FLAC (Rutqvist et al. 2002), a simulator that links the TOUGH2 (Pruess 1999) multiphase fluid flow code with the FLAC3D (Itasca 2006) geomechanical code.

We applied this methodology to a 2D Bench Mark Test (BMT) problem denoted as Task C in the international DECOVALEX project. The BMT consists of a 20×20 m model domain with a 2D fracture-network model (Figure 1) composed of 7797 individual fractures with correlated aperture length. The effects of stress and hydraulic pressure gradients are considered through various boundary conditions (Figure 2).

For the mechanical boundary conditions, we specify a constant vertical stress of 5 MPa at the top and bottom surfaces, whereas a varying horizontal stress is specified for the right- and left-hand side boundaries to capture different fracture shear behaviors inside the model (Figure 2). We apply the horizontal stress with increasing magnitude, corresponding to the stress ratio (K) of horizontal/vertical stress, varying from 1,2,3,5, to progressively induce shear failure along fractures within the model.

At each set of the stress boundary conditions (after the model is in an equilibrium state), fluid flow and transport through the model is simulated by the specific hydraulic boundary conditions representing a hydraulic gradient P1-P2 (Figure 2). For such hydraulic boundary conditions, a constant pressure gradient of 1.0×10^4 Pa/m and 10 Pa/m is simulated.

The mechanical properties of the rock matrix and fractures are listed in Table 1. For simplicity, mechanical and hydraulic apertures are assumed to be equal.

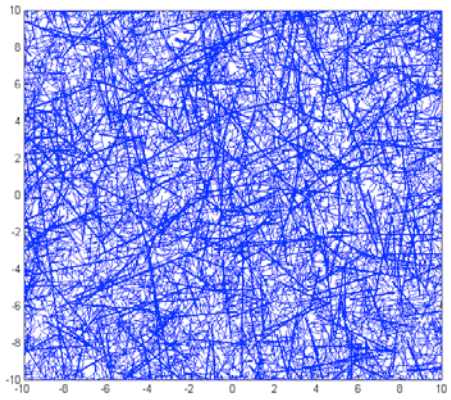

Figure 1. 2D BMT fracture network

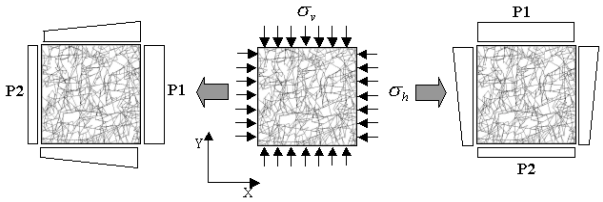

Figure 2. Mechanical and hydraulic boundary conditions

METHODOLOGY

Modified Crack Tensor Theory

According to the BMT definition, the normal stiffness of a single fracture is linked to the normal stress and initial fracture aperture by (Baghbanan and Jing 2008)

$$K_n = \frac{(10\sigma_n + \sigma_{nc})^2}{9\sigma_{nc} b_0} \qquad (1)$$

where σ_n is normal stress across the fracture, b_0 is the initial aperture, and σ_{nc} is critical normal stress defined as σ_{nc}[MPa]=0.487×b_0[μm]+2.51. A constant shear stiffness of K_s=434 (GPa) is used for simplicity (Table 1).

Table 1. Model properties of intact rock and fractures

	Properties	Value
Intact rock	Elastic modulus, E (GPa)	84.6
	Poisson's ratio, υ	0.24
Fractures	Shear stiffness, K_s (GPa/m)	434
	Friction angle, ϕ (°)	24.9
	Dilation angle, d (°)	5
	Cohesion, c (MPa)	0
	Critical shear displacement for dilation, U_{cs} (mm)	3
	Minimum aperture value, a_{res} (μm)	1
	Maximum aperture value, a_{max} (μm)	200

The anisotropy for the permeability and elastic stiffness was obtained using Oda's crack tensor theory, using the theory to formulate a discrete summation of contributions from each fracture that intersect an element volume. We could apply this discrete summation approach because the description of fractures given by the Task C BMT definition is explicit: each fracture is known by its position, its geometric properties-length orientation, and aperture. The basic quantities of the crack tensor for each crack in an element are as follows:

$$F_{ij} = \frac{1}{V_e}\frac{\pi}{4} D^3 n_i n_j \qquad (2)$$

$$F_{ijkl} = \frac{1}{V_e}\frac{\pi}{4} D^3 n_i n_j n_k n_l \qquad (3)$$

$$P_{ij} = \frac{1}{V_e}\frac{\pi}{4} D^2 b^3 n_i n_j \qquad (4)$$

where F_{ij}, F_{ijkl}, P_{ij} are basic crack tensors, V_e is the element volume, D is the diameter of the crack, b is the aperture of the crack, and **n** is the unit vector of normal orientation for each crack with the component n_i (i=1,2,3).

By using the basic crack-tensor quantities defined in Equations (2), (3) and (4) and the mechanical properties for each fracture, we calculate the anisotropic compliance tensor C_{ijkl} and permeability tensor k_{ij} using

$$C_{ijkl} = \sum^{NCR} [(\frac{1}{K_n D} - \frac{1}{K_s D})F_{ijkl} + \frac{1}{4K_s D}(\delta_{ik}F_{jl} + \delta_{jk}F_{il} + \delta_{il}F_{jk} + \delta_{jl}F_{ik})] \quad (5)$$

$$k_{ij} = \sum^{NCR} \frac{1}{12}(P_{kk}\delta_{ij} - P_{ij}) \quad (6)$$

where NCR is number of cracks in an element and δ_{ij} is Kronecker's delta. So the total elastic compliance tensor can be formulated as

$$T_{ijkl} = C_{ijkl} + M_{ijkl} \quad (7)$$

$$M_{ijkl} = (1/E)[(1+\nu)\delta_{ik}\delta_{jl} - \nu\delta_{ij}\delta_{kl}] \quad (8)$$

where M_{ijkl} is the elastic compliance tensor of the intact rock.

Stress/Aperture Coupling Considering Shear Dilation

The stress effect on the permeability tensor was evaluated for each element, considering stress-induced aperture changes for each fracture intersection of the element. Stress-induced aperture change is expressed as follows:

$$b = b_0 - \delta + \Delta b_{dil} \quad (9)$$

$$\delta = \frac{9\sigma_n b_0}{\sigma_{nc} + 10\sigma_n} \quad (10)$$

where δ is normal closure caused by an increase in normal stress, and Δb_{dil} is dilatational normal displacement. Eq. (10) displays the typical nonlinear normal stress/aperture relationship for rock fractures (Baghbanan and Jing 2008).

The approach for modeling shear dilation is shown in Figure 3. If the shear stress τ on a fracture is below the critical shear stress τ_{sc} (Region 1), no normal displacement resulting from shear occurs. When the shear stress is larger than the critical shear stress (Region 2), slip occurs, and the fracture shear stiffness in Region 2 is calculated using Eq.(11):

$$K_{s2} = \eta\frac{G}{r} \quad (11)$$

where G is the shear modulus of the intact rock, r is the radius of the fracture, and η is a factor with a value that depends upon the geometry of the slip patch. In our case, we may consider a circular crack in which η=7π/24. Thus, the dilatational normal displacement can be calculated using

$$\Delta b_{dil} = \frac{\tau - \tau_{sc}}{K_{s2}} \times \tan(d) \quad (12)$$

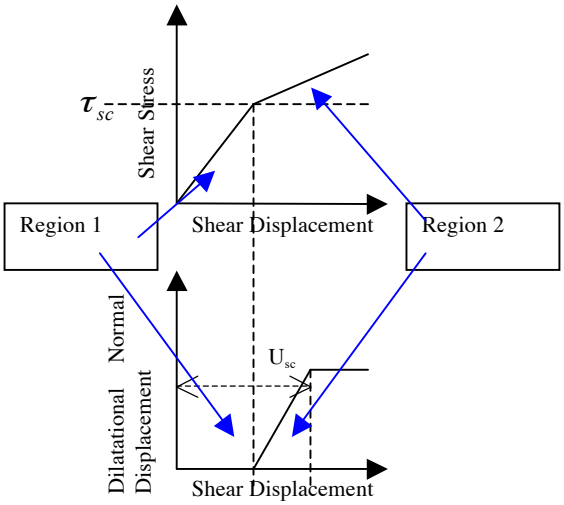

Figure 3. Strategy for modeling shear dilation

Calculation Procedure

When the stress ratio K=0, we can use the fracture-geometry information and mechanical information to calculate the initial total elastic compliance tensor and permeability tensor. When the stress ratio K=1, we first assign initial total elastic compliance tensor fields to each element in the FLAC3D model (employing a user-defined elastic anisotropic constitutive model) and calculate the new stress state. Note that because of the heterogeneous compliance within the model, with different compliance tensors for each element, the new stress state will be heterogeneous, somewhat different from the stress applied at boundaries. Then, we use the new stress fields to calculate the stress-induced fracture change and update the permeability tensor and compliance tensor fields. With the permeability tensor defined in each element, we use TOUGH2 to simulate the flow and transport through the model. The same procedures are used for stress ratios K=2, 3, and 5. Consequently, the elastic stiffness and permeability tensors are updated anisotropically and heterogeneously, depending on the stress state when stress ratio K increases from 0 to 5.

RESULTS AND DISCUSSION

We used a "multiple interacting continua" (MINC) method (Pruess and Narasimhan 1985) in TOUGH2 to perform the flow and transport simulation, which characterizes the rock-matrix-diffusion process in the solute transport simulation. One fracture continuum and three matrix continua were used in the MINC model. In the simulations presented in this paper, we divided the model domain into 40×40 elements of side length 0.5 m. TOUGH-FLAC results (denoted as LBNL) were compared with three other teams with different approaches. The IC team used a discrete fracture network (DFN) model with computer program NAPSAC, whereas KTH used the 2D discrete element code UDEC, and TUL used the combined DFN and EC (equivalent continuum) flow and solute transport simulation code FLOW123D. The approaches and results of other teams are described in Zhao et al (2012).

Figure 4 shows the resulting equivalent-modeling-domain permeability changes at different stress ratios. Permeability tensor fields under different stress ratios from K=0 to K=5 are shown in Figure 5. When the stress ratio K increases, the permeability of Kx and Kz within the modeling domain decreases correspondingly. We used the flow rate at a downstream outlet to inversely calculate the equivalent permeability. The results in Figure 4 are consistent with Figure 5 and are sensible. For example, assuming an increasing horizontal stress while keeping a constant vertical stress, it would be expected that the equivalent vertical permeability decreases much more than the equivalent horizontal permeability.

For the transport calculation, we used a solute transport approach, which can be described as follows: (1) zero initial concentration over the entire model; (2) a short interval of constant concentration at the inlet boundary; (3) thereafter, zero concentration inflow along all the boundaries, including the lateral sides parallel to the macroscopic flow direction.

Under the high hydraulic pressure gradient of 10^4 Pa/m, advection is the main "driving force" of solute transport. As shown in 6, under a high hydraulic gradient, a negligible amount of solute diffuses into the rock matrix no matter what kind of stress state exists. The simulation results for the case of horizontal flow along a relatively high horizontal gradient are compared in terms of breakthrough curves in Figure 7. When K=0 (Figure 7a), the breakthrough curves given by the four teams are quite similar. When considering the stress effects (Figure 7b-d)), the four teams predicted a general shift in breakthrough curves in the longer time direction with increasing stress ratios.

The rock-matrix diffusion has an important influence on transport behavior under low hydraulic gradients (10 Pa/m) (Figure 8). The general trend of breakthrough curves shifting with increasing stress ratios was consistent with the high hydraulic gradient case. The much longer tails for breakthrough curves assuming matrix diffusion indicate that a portion of solute could stay in the matrix micropores for a long time before diffusing back to the fractures. Under a low hydraulic gradient, rock-matrix diffusion will retard solute transport. As shown in Figure 9, when the stress ratio increases, more solute will diffuse into the matrix, and as a result, solute transport will be strongly retarded.

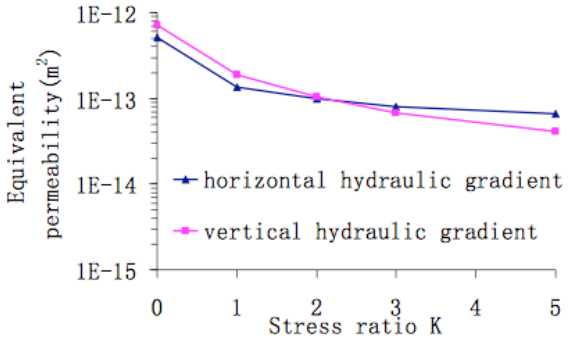

Figure 4. Equivalent permeability for horizontal and vertical flow at different stress ratios

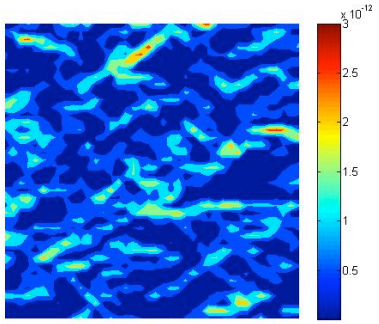

(a) K=0 Kx

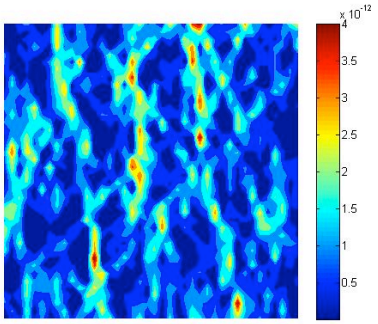

(b) K=0 Kz

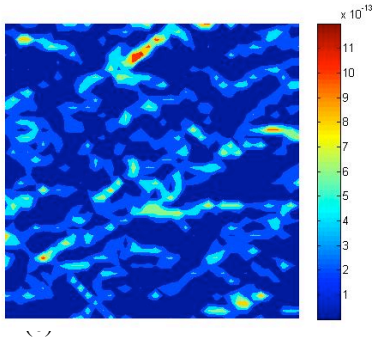

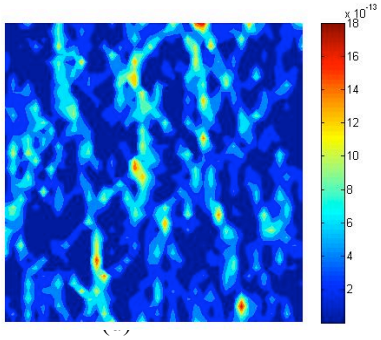

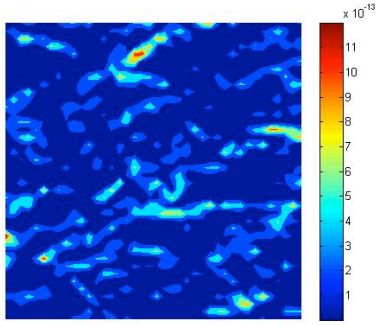

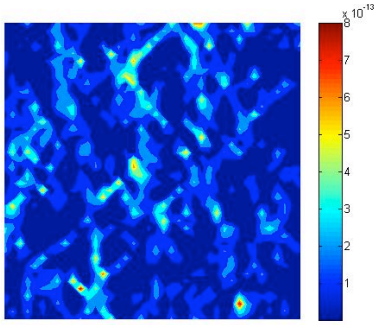

(h) K=3 Kz

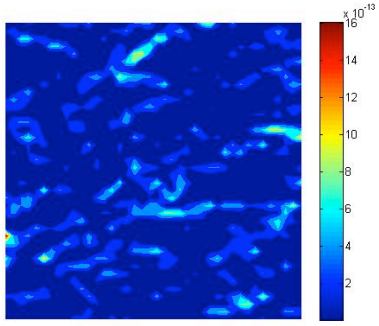

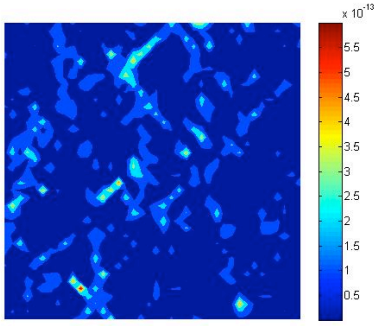

Figure 5. Permeability tensor fields with increasing stress ratio from K=0 to K=5

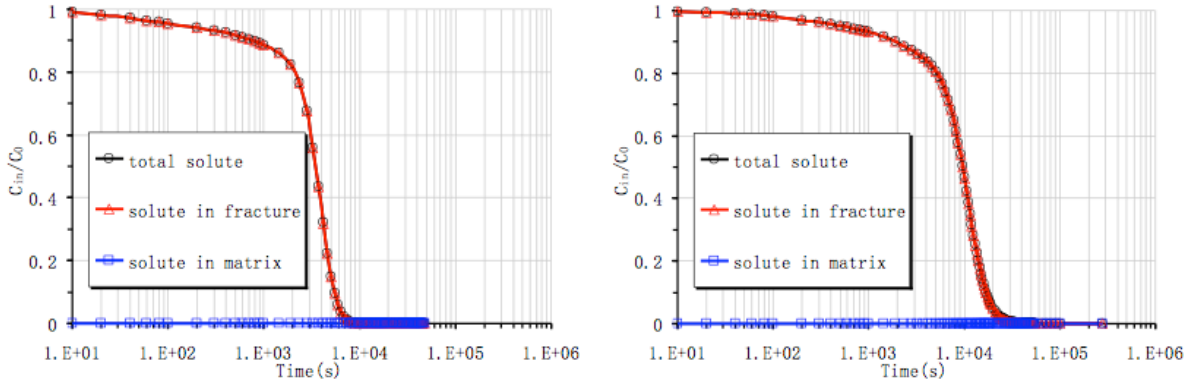

(a) K=0 (b) K=5

Figure 6. Solute concentration variation in fractures and rock matrix when K=0, 5 under a horizontal hydraulic gradient of 10^4 Pa

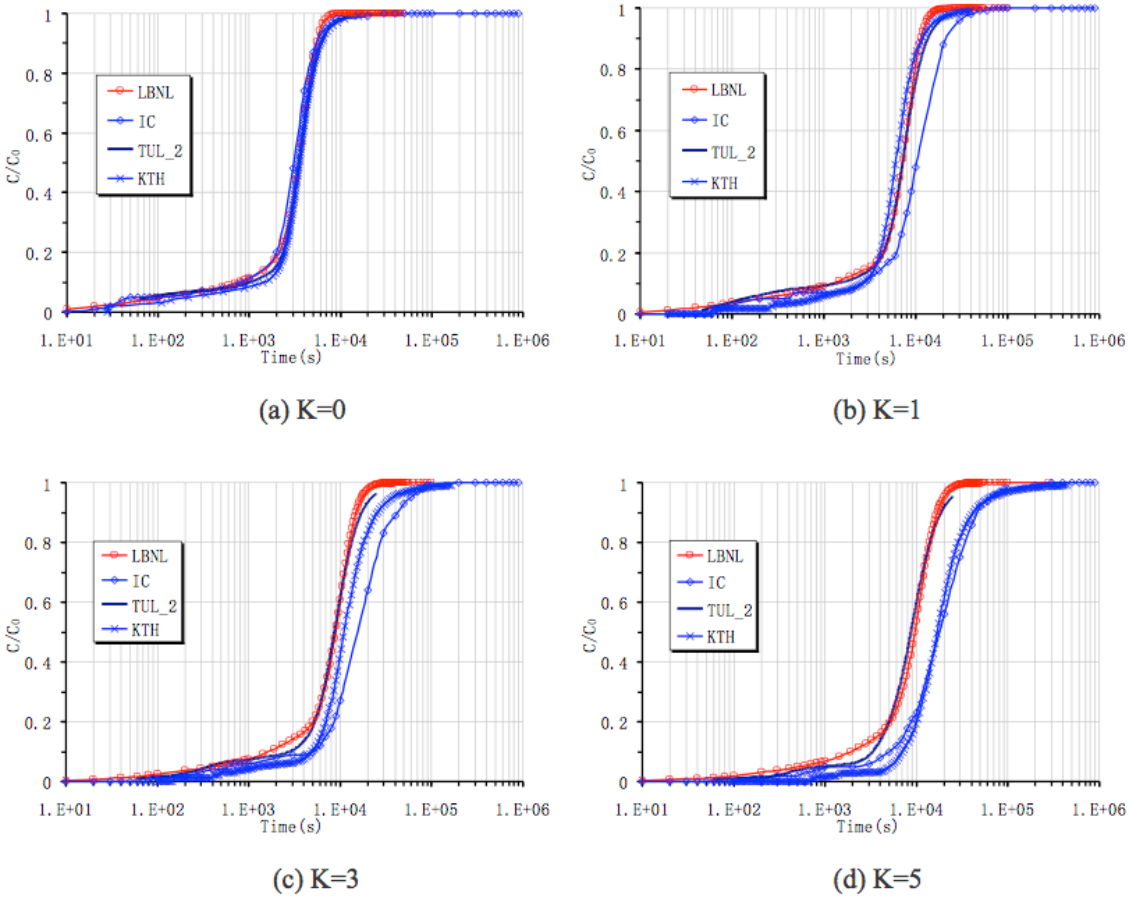

(a) K=0 (b) K=1

(c) K=3 (d) K=5

Figure 7. Comparison of breakthrough curves for conservative tracers exiting from all the three outlet boundaries with increasing stress ratio, under a horizontal hydraulic gradient of 10^4 Pa/m

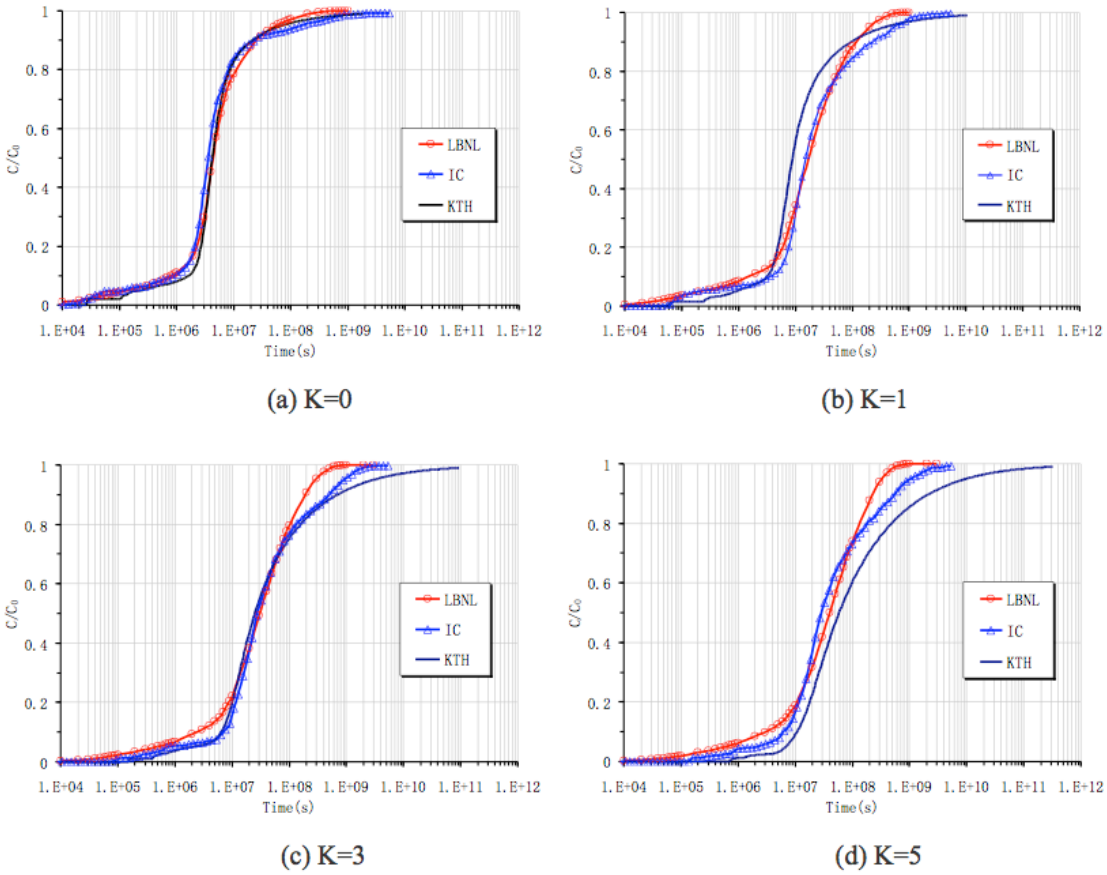

Figure 8. Comparison of breakthrough curves for interacting tracers exiting from all the three outlet boundaries with increasing stress ratio, under a horizontal hydraulic gradient of 10 Pa/m

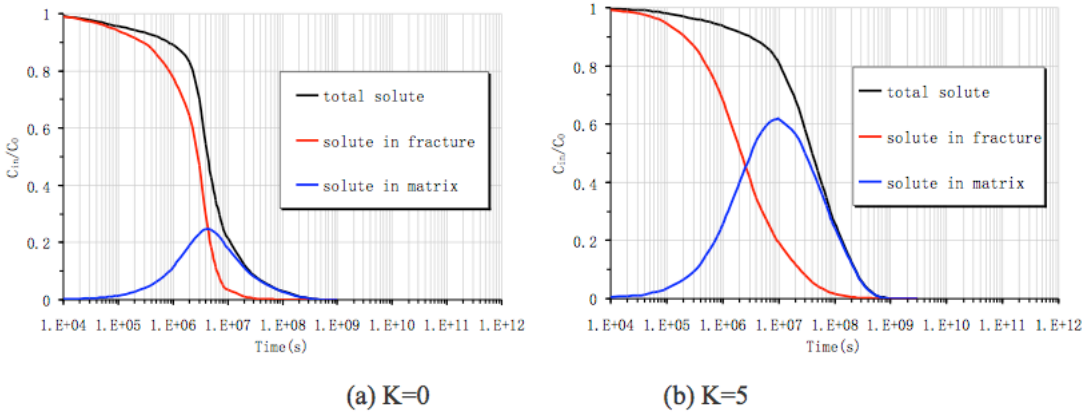

Figure 9. Solute concentration variation in fractures and rock matrix when K=0, 5 under a horizontal hydraulic gradient of 10 Pa/m

CONCLUDING REMARKS

In this paper, the stress effect on fluid flow and transport in fractured rock masses is investigated through a discrete continuum model derived from a modified crack tensor theory. We applied this methodology to a 2D benchmark test denoted as Task C in the DECOVALEX-2011 project. Results were compared with other independent model simulation results, including discrete fracture models, and the result comparisons show good agreement. Some conclusions can also be drawn:

1. When the stress ratio increases, fractures aperture close, resulting in a reduction of permeability and porosity, and solute is significantly retarded as a result of the permeability reduction.

2. When the model is under a low hydraulic gradient, rock-matrix diffusion in addition to advection will play a very important part in solute transport, retarding the solute transport substantially.

In this paper, we applied a one-way coupled hydromechanical model, in which we considered the effects of stress-dependent permeability on the fluid flow, but not pore-pressure effects on fracture deformation**.** The one-way coupled approach is justifiable in this case, because the fluid pressure is very small compared to the applied stress. However, our approach can be readily extended and applied for two-way coupled problems, and this possibility will be the subject of future studies.

ACKNOWLEDGMENT

The first author would like to acknowledge the financial support from the National Basic Research Program of China (973 Program: 2011CB013800) and China Scholarship Council (CSC). Financial support was also provided by the UK Nuclear Decommissioning Authority (NDA) to the Lawrence Berkeley National Laboratory through the National Energy Technology Laboratory, under U.S. Department of Energy Contract No. DE-AC02-05CH11231. Editorial review by Dan Hawkes at Berkeley Lab is greatly appreciated.

REFERENCES

Baghbanan, A. and L. Jing, Stress effects on permeability in a fractured rock mass with correlated fracture length and aperture, *International Journal of Rock Mechanics and Mining Sciences* 45(8): 1320-1334, 2008.

Itasca Consulting Group, *FLAC3D, Lagrangian Analysis of Continua in 3 Dimensions. Version 3.1*. MInneapolis, MInnnesota, 2006.

Leung, C., J. Rutqvist, et al., The use of TOUGH-FLAC for coupled hydro-mechanical modeling of fractured rock masses, *Proceedings of the Tough2 symposium 2003 Lawrence Berkeley National Laboratory, Berkeley, September 14-16*, 2009.

Oda, M., An Equivalent Continuum Model for Coupled Stress and Fluid-Flow Analysis in Jointed Rock Masses, *Water Resources Research* 22(13): 1845-1856, 1986.

Pruess, K. and T. N. Narasimhan, A Practical Method for Modeling Fluid and Heat-Flow in Fractured Porous-Media, *Society of Petroleum Engineers Journal* 25(1): 14-26, 1985.

Pruess, K., C. Oldenburg, and G. Moridis, *TOUGH2 User's Guide, Version 2.0*, Report LBNL-43134, Lawrence Berkeley National Laboratory, Berkeley, Calif., 1999.

Rutqvist, J. and O. Stephansson, The role of hydromechanical coupling in fractured rock engineering, *Hydrogeology Journal* 11(1): 7-40, 2003.

Rutqvist, J., Y. S. Wu, et al., A modeling approach for analysis of coupled multiphase fluid flow, heat transfer, and deformation in fractured porous rock, *International Journal of Rock Mechanics and Mining Sciences* 39(4): 429-442, 2002.

Zhao, Z., J. Rutqvist, C. Leung, M. Hokr, I. Neretnieks, A. Hoch, J. Havlíček, Y. Wang, Z. Wang, R. Zimmerman, Stress effects on solute transport in fractured rocks: A comparison study, *International Journal of Rock Mechanics and Geotechnical Engineering* (Submitted March 2012).

Environmental Engineering

IMPORTANCE OF OVERLAND FLOW IN DENITRIFICATION OF WASTEWATER APPLIED TO RAPID INFILTRATION BASINS

Maryam Akhavan[1], Paul T. Imhoff[1], Scott Andres[2], Stefan Finsterle[3]

[1]Department of Civil and Environmental Engineering, University of Delaware
Newark, DE 19716, USA
e-mail: makhavan@udel.edu

[1] Delaware Geological Survey
Newark, DE 19716, USA

[3]Earth Sciences Division, Lawrence Berkeley National Laboratory
Berkeley, CA 94720, USA

ABSTRACT

Rapid Infiltration Basin Systems use the controlled application of treated wastewater to soil to remove constituents in the wastewater before recharging groundwater. Effluent from most new wastewater treatment plants is enriched in NO_3^-, so denitrification (DNF) is the main reaction for N removal. The absence of molecular oxygen and an adequate supply of carbon to serve as a substrate for heterotrophic bacteria are the required conditions for DNF.

During RIBS operation, wastewater is applied to open basins cyclically, usually with a flooding period followed by days or weeks of drying. Key operational parameters impacting DNF include the ratio of wetting to drying time and the hydraulic loading rate, which affect water saturation and air content in the vadose zone and residence time of contaminants. To investigate the effects of complex surface and subsurface flow patterns caused by non-uniform flooding on system performance, we applied a coupled overland flow-vadose zone model previously implemented in iTOUGH2 to TOUGHREACT. The flow portion of the coupled code was previously tested with published laboratory and field data. This modified TOUGHREACT was then used to investigate effects of operating conditions on the fate and transport of N.

Simulations with the coupled overland flow-vadose zone model predict uneven water distribution over the basins, a condition that significantly affects DNF. Smaller ratios of wetting to drying time, i.e., shorter but more intense flooding periods, result in greater water saturations, shorter residence times, and lower oxygen concentrations in the vadose zone, ultimately resulting in greater DNF. For the same reasons, higher loading rates also result in greater DNF, because of favored growth of microbial communities at deeper depths. Using a coupled surface-subsurface model is critical for predicting DNF when the hydraulic loading rate is not sufficiently large to quickly spread the wastewater over the whole basin.

INTRODUCTION

Rapid infiltration basin systems (RIBS) are one of the major land-treatment techniques for disposal and treatment of reclaimed wastewater (US EPA, Office of Water, 2003). In these systems, treated wastewater using primary, secondary, or advanced treatment techniques is disposed into shallow basins constructed in permeable soils such as sand. Effluents from wastewater treatment systems potentially contain a number of contaminants, and nitrogen (N) compounds are of particular concern.

During RIBS operations, wastewater is applied intermittently in a cycle of a flooding period–wastewater application—followed by days or weeks of drying (NRMRL, 2006; US EPA, 1984). The drying period is required for restoration of the infiltration capacity and allows renewal of the biological and chemical treatment capability of the soil. As a result, the ratio of flooding to drying time (referred to here as the application cycle) is critical to the successful operation of RIBS and varies with the quality of

applied wastewater and soil type. This ratio is recommended to be between 0.5 to 1.0 when N removal is the main objective of RIBS operations and the wastewater is not completely nitrified (NRMRL, 2006; US EPA, 1984). In this case, the effluent must first be nitrified and then denitrified. Therefore, oxic conditions in the vadose zone are required for nitrification. However, in most new sequenced batch reactor wastewater treatment plants, a fully nitrified wastewater is applied and DNF is the primary reaction for removing N from subsurface water. In this case, anoxic conditions and an adequate supply of organic C are critical for DNF. There are no EPA recommendations for the ratio of flooding to drying time for such systems.

Another design parameter is the hydraulic loading rate within each application cycle, which affects O_2 availability, pore-water velocity, and thus retention time. Because of the fixed total amount of wastewater discharged on a basin, the loading rate and application cycle are interdependent. For example, achieving a low loading rate may require a high ratio of flooding to drying time.

In previous modeling and experimental studies of RIBS, the basin was always assumed to be flooded completely and instantaneously during the flooding period (Gungor and Kahraman, 2005; Kopchynski et al., 1996). However, the use of a low applied loading rate and overdesign of the required infiltration area in many RIBS will cause nonhomogeneous distribution of wastewater (Mottier et al., 2000), and the conditions under which water reaches areas farthest from the discharge valves by overland flow after the infiltration capacity of areas nearest discharge valves is exceeded.

The objective of this work was to apply a coupled surface–subsurface flow model in TOUGHREACT to elucidate the utility of existing approaches for estimating DNF under RIBS when wastewater is applied non-uniformly due to overland flow, and to study effects of operating conditions and wastewater quality on N fate and transport. The flow portion of the coupled code was previously tested with published laboratory and field data (Akhavan et al., 2012).

MODEL DEVELOPMENT

Numerical simulations were performed using TOUGHREACT v1.1 (Xu et al., 2006; Xu, 2008). Modifications previously implemented in iTOUGH2 that coupled overland flow with subsurface transport were added to TOUGHREACT v1.1, and the flow portion of the coupled code was retested.

Surface and Subsurface Flow Equations

The Saint-Venant equations were used to model surface-water flow, where the diffusion wave (non-inertial wave) form was chosen for the momentum equation. The surface-water flow equations were coupled with the two-phase flow equations for water and air (EOS3). A surface layer of thickness *e* was assumed superimposed on the topsoil layer in the numerical model. Liquid flow within the surface layer was presented in a similar form that describes flow in a porous medium:

$$\frac{\partial h_s}{\partial t} - \nabla \cdot \left(K_s \nabla (z_l + h_s) \right) = q_s$$

where h_s is the water depth on the surface [L], K_s is the hydraulic conductivity tensor [LT^{-1}], z_l is land surface elevation [L], and q_s is a source/sink term [LT^{-1}]. The nondiagonal terms of the hydraulic conductivity tensor K_s are zero and the diagonal components are

$$K_{s,xx} = \frac{h_s^{5/3}}{n_{man} \sqrt{\nabla_x (z_l + h_s)}}$$

$$K_{s,yy} = \frac{h_s^{5/3}}{n_{man} \sqrt{\nabla_y (z_l + h_s)}}$$

$$K_{s,zz} = k_{zz} \frac{k_{rl}}{\mu_l}$$

The horizontal hydraulic conductivities describe surface water flow, while the vertical hydraulic conductivity describes resistance to liquid flow between the surface and subsurface layer, with k_{zz} equal to the vertical permeability of the subsurface layer, and n_{man} the Manning roughness coefficient [$L^{-1/3}T$]. More details of the coupling approach are given in Akhavan et al. (2012).

Solute Transport and Biogeochemical Reactions

The macroscopic equations governing aqueous and gaseous advective–diffusive transport in a variably saturated porous medium were used for solving transport of chemical species. The multiple Monod expression was used for describing kinetic reactions among primary species (Xu, 2008)

$$r_i = \hat{k}_i X_m F(X_m)\left[\frac{C_{i,k}}{C_{i,k} + \hat{K}_{Mi,k}}\right]\left[\frac{\hat{K}_{i,p}}{C_{i,p} + \hat{K}_{i,p}}\right] f(pH)$$

where r_i is the reaction rate of the ith reaction, $\hat{k}_i$ is the maximum specific consumption rate, X_m is the biomass of the population m responsible for the reaction, $F(X_m)$ is the biomass growth inhibition term (MacQuarrie and Sudicky, 2001), $C_{i,k}$ is the concentration of the kth Monod species, $C_{i,p}$ is the concentration of the pth inhibiting factors, $\hat{K}_{Mi,k}$ and $\hat{K}_{i,p}$ are the kth Monod half-saturation constant of the ith species and the pth inhibition constant, and $f(pH)$ is the piecewise linear function accounting for microbial acidity stress (Maggi et al., 2008):

$$f(pH) = \begin{cases} \min\left[\frac{1}{4}pH - \frac{3}{4}, -\frac{1}{4}pH + \frac{11}{4}\right] & 3 < pH < 11 \\ 0 & Otherwise \end{cases}$$

In order to account for rate limitations as a result of excessive biomass accumulation, a biomass growth inhibition term was incorporated in the Monod expression (Kindred and Celia, 1989)

$$F(X_m) = \frac{\hat{K}_{b,m}}{\hat{K}_{b,m} + X_m}$$

where $\hat{K}_{b,m}$ is an empirical inhibition constant. As discussed by Kindred and Celia (1989), when the biomass of the population m becomes much larger than $\hat{K}_{b,m}$, the reaction rate formula is similar to the basic Michaelis-Menton expression except that the biomass is replaced by the constant $\hat{K}_{b,m}$. The effect of microbial volume augmentation on soil porosity and its effect on water flow were neglected.

Biodegradation reactions

The carbon oxidation and DNF reactions were

$$CH_2O + O_2 \xrightarrow{X_1} CO_2 + H_2O$$

$$CH_2O + \frac{4}{5}NO_3^- \xrightarrow{X_1} \frac{2}{5}N_2 + \frac{2}{5}H_2O + \frac{1}{5}H^+ + HCO_3^-$$

and were modeled using the multiple Monod expression. It was assumed that the same bacteria population, X_1, was responsible for both reactions. Production of intermediate N compounds such as NO and N_2O were not included in the formulation because the focus of this study was on NO_3 removal. A kinetic dissolution model presented by Jardine et al. (1992) was used for modeling adsorption and dissolution of dissolved organic carbon

$$\frac{d\,\overline{DOC}}{dt} = \alpha_d (K_d \times DOC - \overline{DOC})$$

where DOC is the dissolved organic carbon concentration [ML^{-1}], $\overline{DOC}$ is the mass of solid organic carbon per mass of solid [MM^{-1}], α_d is a first-order mass-transfer coefficient [T^{-1}], and K_d is a linear distribution coefficient [L^3M^{-1}]. K_d=50 L kg^{-1} and $\alpha_d = 4.21\times10^{-7}\,S^{-1}$ were used for these simulations. Monod parameters are given in Table 1.

Table 1. Monod parameters used for simulations

Parameter	Value
Death rate of bacteria (d^{-1})	0.05
Max. carbon oxidation rate (d^{-1})	4.9
Max. DNF rate (d^{-1})	4.9
Half saturation constant NO_3 (mg L^{-1})	0.5
Half saturation constant *DOC* (mg L^{-1})	7.41
Half saturation constant O_2 (mg L^{-1})	0.2
O_2 Inhibition constant (mg L^{-1})	0.2
Microbial yield coefficient (-)	0.63

RAPID INFILTRATION BASIN SIMULATIONS

To study the effects of a spatially non-uniform distribution of wastewater, hydraulic loading rate, and application cycle on DNF in RIBS, we simulated different scenarios using the coupled surface–subsurface code that accounts for overland flow. Initial and boundary conditions and other RIBS properties were selected to represent a common scenario in RIBS operation.

A number of simulations were conducted with a specified flux boundary at the basin surface to reproduce the approach used in conventional modeling studies.

We developed a two-dimensional, vertical model 55.5 m long and 26.1 m in depth, which represented one-half of the physical domain. The horizontal grid size ranged from 0.05 to 1 m, with a refined grid beneath the basin area, and the vertical grid size ranged from 0.02 to 1 m, with a refined grid in the unsaturated zone. The infiltration basin in the model was 5 m wide and positioned at the top left-hand boundary, with wastewater distribution represented as a line source on the left edge of the basin. This line source represented a distribution pipe. A schematic of the model domain is shown in Figure 1. The thickness of the surface layer for overland flow was defined as 1 m.

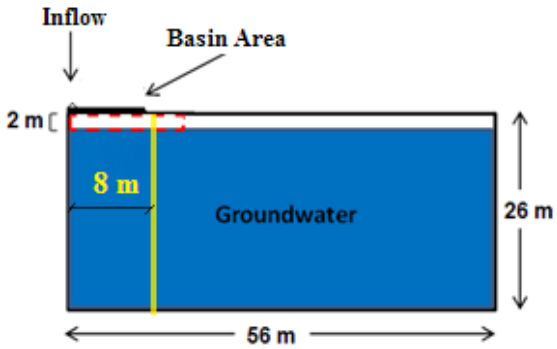

Figure 1. Schematic of model domain. The denitrification reduction factor, F_s, was calculated in the dashed red rectangle. Vertical yellow line is the compliance boundary where NO_3 concentrations were monitored in groundwater.

Sand—USDA textural class—was used for simulations, and the ROSETTA pedotransfer function model was used to estimate the parameters of the van Genuchten–Mualem model for this soil, using the textural class option (Radcliffe and West, 2009) (Table 2). A homogeneous medium with an anisotropy ratio of $k_{xx}/k_{zz} = 10$ was assumed for all simulations.

Table 2. Hydraulic parameters used for modeling

$K_{s,z}$ (cm d^{-1})	n	α (cm^{-1})	θ_r	θ_s
645	3.18	0.0353	0.053	0.375

Initial conditions were defined by an equilibrium head distribution, with the water table located at a depth of 2.05 m below the basin floor. No-flow boundary conditions were defined for the bottom and left boundary of the model, while at the right boundary, a constant-head boundary condition was specified, sufficiently far from the basin to minimize its effect on simulation results. Initial conditions and wastewater source properties for selected aqueous species are listed in Table 3. The RIBS were simulated with three alternative hydraulic loading rates and two application cycles. The three hydraulic loading rates were 0.5, 0.75, and 1 m wk^{-1} (L2–L4), while the application cycle was either 0.5 flooding days followed by 6.5 drying days (C1), or three flooding days followed by four drying days (C2). The total amount of wastewater discharged in the basin in each 7 d cycle was identical for a particular hydraulic loading rate. The three hydraulic loading rates tested are equivalent to annual loading rates of 13 to 52 m yr^{-1}.

Table 3. Initial conditions and wastewater source properties for selected aqueous species

Aqueous species	Initial Value	Source Value
NO_3 (mole L^{-1}-N)	0.0	10.0
DOC (mg L^{-1})	0.0	25.0
$\overline{DOC}$ (mg mg^{-1})	0.0	0.0
O_2* (mole L^{-1})	0-8m: 2.3×10^{-4} 8-10m: 1.3×10^{-4} 10-26m: 3×10^{-5}	2.3×10^{-4}
pH	6.9	6.0
HCO_3 (mole L^{-1})	1.7×10^{-5}	3.9×10^{-5}
N_2 (mole L^{-1})	0.0	0.0
X_1 (mg L^{-1})	0.47	0.0

*O_2 is given in different depths.

Simulations were run for 8 weeks until quasi-steady-state conditions were achieved, where the change in percent removal of NO_3 and DOC (described below) between consecutive cycles was <2%. The right boundary was specified sufficiently far enough from the discharge valve that the wastewater plume did not reach this boundary in 8 weeks.

The results of the three hydraulic loading rates and two application cycles were compared using two performance measures. The first was the percent removal of NO_3 and *DOC*, which was computed by subtracting the current NO_3 (*DOC*) in the domain from the total added NO_3 (*DOC*), normalized by the total mass added. The second performance measure was the maximum NO_3 concentration in a vertical cross section (compliance plane) located 8 m from the discharge valve (see Figure 1).

The effect of operating conditions on DNF was also studied using a simplified approach that accounts for the impact of pore water saturation on DNF. In this approach, a variable, F_s, was introduced, which is a measure of the reduction in DNF because liquid saturation conditions were not ideal. Liquid saturation is an important parameter that controls O_2 diffusion from the atmosphere and affects local O_2 concentrations in pore water. Anoxic conditions are one requirement for DNF, but modeling O_2 dynamics in the subsurface is complicated. Therefore, liquid saturation was used as a surrogate variable to evaluate O_2 limitations in the pore water in previous work (Heinen, 2006; Vereecken et al., 1991). F_s, the reduction factor due to water saturation, was defined as

$$F_s = \begin{cases} 0 & S_l < S_t \\ \left(\dfrac{S_l - S_t}{S_m - S_t} \right)^w & S_t \le S_l \le S_m \\ 1 & S_m < S_l \end{cases}$$

where S_l is liquid saturation, S_m is a threshold liquid saturation above which $F_s = 1$, and S_t is a value below which $F_s = 0$. We selected $S_m = 1$, $S_t = 0.62$, and $w = 1.74$. In our simulations, F_s was computed in a rectangular region beneath the infiltration basin, as shown in Figure 1. It was evaluated at each location in the rectangular region and then averaged across space. More details are presented in Akhavan et al. (2012).

Two values for $\hat{K}_{b,m}$ were tested: 1 and 10 mgL^{-1}. These values were selected such that biomass growth did not reduce initial porosity more than 20%, and as a result would not significantly affect hydraulic conductivity. The fraction of pore space occupied by biomass, $n_{X'_m}$, was estimated from Brovelli et al. (2009); Kildsgaard and Engesgaard (2001); and Lee et al., (2009):

$$n_{X'_m} = \frac{X'_m \rho_b}{\rho_{X'_m}}$$

where ρ_b is the bulk density [ML^{-3}], $\rho_{X'_m}$ is the density of solid biomass [ML^{-3}], and X'_m is solid biomass concentration [MM^{-1}]. $\rho_{X'_m}$ was considered to be in the range of 2500–6000 mgL^{-1} (Kildsgaard and Engesgaard, 2001). Using $\hat{K}_{b,1}$=1 and 10 mgL^{-1} limited maximum biomass concentration to less than 600 mgL^{-1}. $\hat{K}_{b,1}$= 0.5 and 1 mgL^{-1} were used in previous numerical studies (Lee et al., 2006; MacQuarrie and Sudicky, 2001)

MODELNG RESULTS

Removal Process

To illustrate NO_3 removal and system dynamics, we present results after 8 weeks of wastewater flooding. Figure 2 shows water saturation, NO_3, biomass, and O_2 (aq) biomass contours for loading rate 4, application cycle 1 (L4C1), and loading rate 4, application cycle 2 (L4C2) after flooding in week 8. $\hat{K}_{b,1}$=1 mg L^{-1} was used in these two simulations. Contours are shown for a 30 m wide and 15 m deep portion of the domain beneath the basin. Because of the higher instantaneous hydraulic loading rate in cycle 1 versus cycle 2 (loading over 0.5 versus 3 days), the area below the RIBS has higher water saturation for L4C1. However, NO_3 contours indicate that in both application cycles, DNF occurs primarily beneath the water table. O_2 contours show that although soil under the basin is more saturated for L4C1 than L4C2, an anoxic zone in both cycles only forms beneath the water table.

Because of the lower instantaneous hydraulic loading rate in L4C2 than L4C1, higher biomass concentrations developed for L4C2 in the vadose zone beneath the basin (see Figure 2). For example, the maximum biomass concentration in this region was 66 and 41 mg L^{-1} for L4C2 and L4C1, respectively. Although the total biomass produced for L4C2 and L4C2 was nearly the same, the higher loading rate for L4C1 resulted in lower biomass growth under

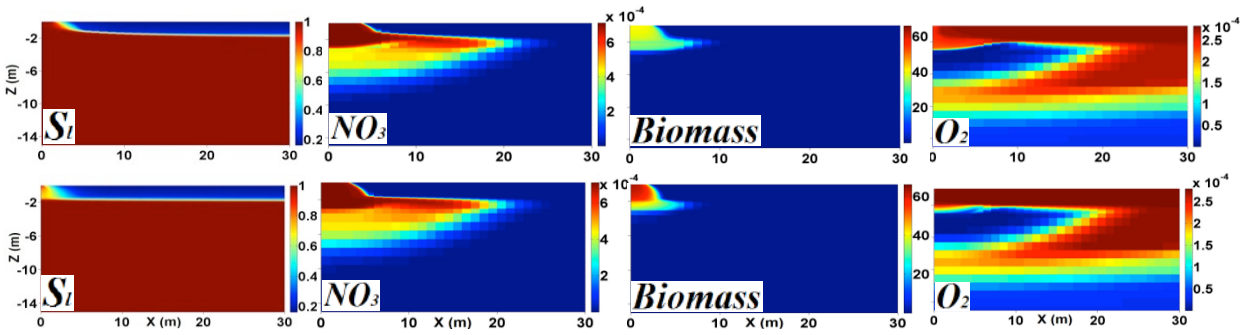

Figure 2. Water saturation, S_l (-); NO_3(mole L^{-1}); biomass(mg L^{-1}); and O_2(aq) (mole L^{-1}) contours for L4C1 (top) and L4C2 (bottom)

the basin but a more extensive region of biological growth laterally, due to the greater lateral movement of water and substrate. Thus, shorter but more intense flooding periods distribute biomass over a larger area, and in some cases to greater depths (e.g., for $\hat{K}_{b,1}$=10 mg L^{-1} simulations not shown here), which could improve DNF when the biomass growth is extended to the anoxic zone under the water table.

The first moment of biomass and *DOC* were computed in the Z direction in a 5 m long and 6 m deep region beneath the infiltration basin after flooding in week 8. The total mass of *DOC* was also computed in this region. These results for $\hat{K}_{b,1}$=1 mg L^{-1} are shown in Figure 3.

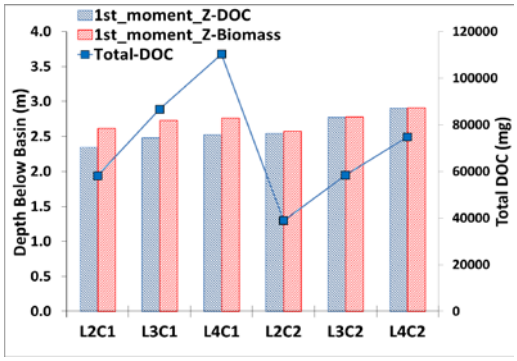

Figure 3. First moment and total mass of *DOC* beneath the basin for $\hat{K}_{b,1}$= 1 mg L^{-1} for different loading rates and application cycles.

As the hydraulic loading rate increased from L2 to L4 (0.5 to 1.0 m per week) for both cycles (C1 and C2), the residence time in the vadose zone decreased, and more substrate (*DOC*) and biomass were transmitted downward, resulting in larger first moments. The results are similar for $\hat{K}_{b,1}$=10 mg L^{-1}. As will be shown below, application of larger loading rates improves DNF, because it develops biomass at greater depths and preserves more carbon for DNF under the water table (see the first moment of biomass and total *DOC* plotted in Figure 3). For the same loading rates, application of shorter flooding periods (cycle 1 versus cycle 2) improves DNF as well, because the residence time of *DOC* in the vadose zone is reduced, resulting in less *DOC* oxidation. For these cases, more of the *DOC* is transported below the water table where it supports DNF.

To evaluate where DNF occurred, concentrations of NO_3 and a conservative tracer with the same loading as NO_3 were examined at different depths to compute the cumulative percent NO_3 removal at the end of the flooding period in week 8. Figure 4 shows cumulative NO_3 removal versus depth for $\hat{K}_{b,1}$=1 mg L^{-1}.

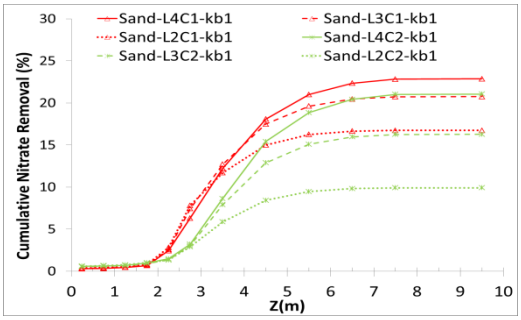

Figure 4. Cumulative NO_3 percent removal over depth

DNF occurred almost entirely beneath the water table at depths of 2–7 m for both cycles. In both

cycles, cumulative DNF was larger for higher loading rates, ranging from 16 to 23% for cycle 1 and from 10 to 21% for cycle 2. The DNF zone extended to greater depths as loading rate increased. For the same loading rate, DNF was also larger in cycle 1 (shorter flooding period), than cycle 2, where the higher DNF occurred at the depth of 2–3 m.

While results presented above were for $\hat{K}_{b,1}$=1 mg L^{-1}, similar trends and conclusions regarding the impact of hydraulic loading rate and application cycle on DNF were drawn from simulations with $\hat{K}_{b,1}$=10 mg L^{-1}.

Microbial Growth Model vs. Simplified Process Model

Figure 5 shows NO_3 removal for alternative loading rates and application cycles predicted with the microbial growth model and the simplified process model, where an average NO_3 reduction factor was calculated (F_s). Water saturations used in the calculation of F_s and shown in this figure were averaged over a 5 m long and 2 m deep region beneath the infiltration basin. The simplified process model evaluates DNF by only accounting for water saturation and predicts much larger DNF than the microbial growth model. However, the simplified process model and microbial growth model both show increasing DNF with loading rate for a given cycle, and higher DNF for cycle 1 than cycle 2. The final cumulative NO_3 removed shown in Figure 4 for the vertical region beneath the basin were in good agreement with NO_3 removal computed for the entire domain in Figure 5.

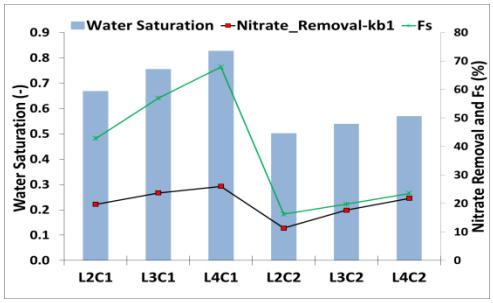

Figure 5. NO_3 removal for alternative loading rates and application cycles computed with the microbial growth model and F_s from the simplified process model

To evaluate the effect of different operating conditions on reducing NO_3 concentrations in the groundwater, NO_3 concentrations were computed in a vertical cross section located 8 m from the discharge valve (see Figure 1). Although percent NO_3 removed increased by applying higher loading rates and using shorter but more intense flooding periods (see Figure 5), the maximum NO_3 concentration along the compliance boundary did not differ significantly for alternative operating conditions: the maximum NO_3 concentration was reduced by 1.7–4.5% from that in the discharged wastewater, which is negligible.

The primary limitation on DNF was the lack of sufficient *DOC* in the effluent for NO_3 removal. In a well well-mixed system and assuming no *DOC* is consumed by the carbon oxidation reaction, 10.7 mgL^{-1} *DOC* is required for DNF of 10 mgL^{-1} NO_3. However, because of oxic conditions in the vadose zone, even the 25 mgL^{-1} *DOC* applied here was insufficient for complete DNF of the 10 mgL^{-1} NO_3. Instead, DNF ranged from 11 to 26%, depending on operating conditions (see Figure 5).

Overland Flow Top Boundary Condition vs. Specified Flux

For the simulations where a specified flux was assumed across the top boundary, the same loading rates used in the overland flow simulations were applied, except that each loading rate was spread evenly across the total basin area. Figure 6 shows NO_3 removal predicted with the overland flow boundary was higher than removal predicted using a specified flux boundary condition for both $\hat{K}_{b,1}$. Thus, the error in neglecting overland flow on NO_3 removal is significant and can exceed 300%.

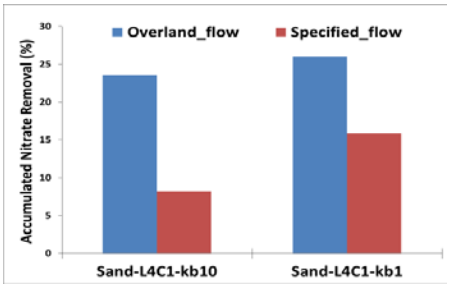

Figure 6. NO_3 removal using overland flow and specified flux boundary conditions

CONCLUSIONS

Rapid infiltration basin-system operations are guided by requirements to reduce NO_3 to maximum acceptable groundwater concentrations. Anoxic conditions and an adequate supply of carbon are required for DNF. In the absence of other electron donors, carbon is consumed by microbial oxidation. Percent NO_3 removed was found to be sensitive to the basin boundary condition—either overland flow or a specified flux boundary—the hydraulic loading rate, and the flooding/drying period ratio. However, because of insufficient *DOC*, maximum NO_3 removal was <30% for all operating conditions. The most significant DNF occurred for high loading rates and small flooding/drying ratios. Here, the residence time of *DOC* in the vadose zone was reduced, allowing more to reach the anoxic zone under the water table where it was available for DNF.

In this study, the commonly assumed specified flux boundary condition resulted in underpredictions of DNF by as much as 300%.

ACKNOWLEDGMENTS

The authors thank Dr. Chuanhui Gu and Dr. Federico Maggi for their help with TOUGHREACT. Financial support for this study was provided by the Delaware Water Resources Center.

REFERENCES

Akhavan M., Imhoff P.T., Finsterle S. and Andres A.S. 2012. Application of a coupled overland Flow–Vadose zone model to rapid infiltration basin systems. Vadose Zone Journal 11.

Brovelli A., Malaguerra F. and Barry D.A. 2009. Bioclogging in porous media: Model development and sensitivity to initial conditions. Environmental Modelling & Software 24:611-626.

Gungor K. and Kahraman U. 2005. Nitrite and nitrate removal efficiencies of soil aquifer treatment. Turkish J.Eng.Env.Sci 29:159-170.

Heinen M. 2006. Simplified denitrification models: Overview and properties. Geoderma 133:444-463.

Jardine P.M., Dunnivant F.M., Selim H.M. and Mccarthy J.F. 1992. Comparison of models for describing the transport of dissolved organic-carbon in aquifer columns. Soil Sci. Soc. Am. J. 56:393-401.

Kildsgaard J. and Engesgaard P. 2001. Numerical analysis of biological clogging in two-dimensional sand box experiments. J. Contam. Hydrol. 50:261-285.

Kindred J.S. and Celia M.A. 1989. Contaminant transport and biodegradation .2. conceptual-model and test simulations. Water Resour. Res. 25:1149-1159.

Kopchynski T., Fox P., Alsmadi B. and Berner M. 1996. The effects of soil type and effluent pre-treatment on soil aquifer treatment. Water Sci. Technol. 34:235-242.

Lee E.J., Kim M., Kim Y. and Lee K. 2009. Numerical and field investigation of enhanced in situ denitrification in a shallow-zone well-to-well recirculation system. Ecol. Model. 220:2441-2449.

Lee M.S., Lee K.K., Hyun Y.J., Clement T.P. and Hamilton D. 2006. Nitrogen transformation and transport modeling in groundwater aquifers. Ecol. Model. 192:143-159.

MacQuarrie K.T.B. and Sudicky E.A. 2001. Multicomponent simulation of wastewater-derived nitrogen and carbon in shallow unconfined aquifers I. model formulation and performance. J. Contam. Hydrol. 47:53-84.

Maggi F., Gu C., Riley W.J., Hornberger G.M., Venterea R.T., Xu T., Spycher N., Steefel C., Miller N.L. and Oldenburg C.M. 2008. A mechanistic treatment of the dominant soil nitrogen cycling processes: Model development, testing, and application. Journal of Geophysical Research-Biogeosciences 113:G02016.

Mottier V., Brissaud F., Nieto P. and Alamy Z. 2000. Wastewater treatment by infiltration percolation: A case study. Water Sci. Technol. 41:77-84.

NRMRL. 2006. Process design manual; land treatment of municipal wastewater effluents. U.S. Environmental Protection Agency, National Risk Management Research Laboratory, Office of Research and Development, Land Remediation and Pollution Control Division, Cincinnati, OH.

Radcliffe D.E. and West L.T. 2009. Design hydraulic loading rates for onsite wastewater systems. Vadose Zone J. 8:64-74.

US EPA. 1984. Process design manual for land treatment of municipal wastewater, supplement on rapid infiltration and over-land flow. Rep. EPA 625/1-81-013a. U.S. Environmental Protection Agency, Cincinnati, OH.

US EPA, Office of Water. 2003. Wastewater technology fact sheet: Rapid infiltration land treatment. Rep. EPA 832-F-03-025.

Vereecken H., Vanclooster M., Swert M. and Diels J. 1991. Simulating water and nitrogen behavior in soils cropped with winter-wheat. Fertilizer Research 27:233-243.

Xu T.F., Sonnenthal E., Spycher N. and Pruess K. 2006. TOUGHREACT - A simulation program for non-isothermal multiphase reactive geochemical transport in variably saturated geologic media: Applications to geothermal injectivity and CO2 geological sequestration. Comput. Geosci. 32:145-165.

Xu T. 2008. Incorporating aqueous reaction kinetics and biodegradation into TOUGHREACT: Applying a multiregion model to hydrobiogeochemical transport of denitrification and sulfate reduction. Vadose Zone Journal 7:305-315.

HYDRO-GEOCHEMICAL MODELLING IN THE PASSO A CAMPALTO PHOSPHOGYPSUM DUMP IN THE LAGOON OF VENEZIA, ITALIA

Borgia A.[1,2], Calcara M.[3], Cattaneo L.[2,4], Kennard M.[5]

1. *Lawrence Berkeley National Laboratory, Berkeley, CA 94720, USA*
2. *EDRA, 00134 Roma, Italia*
3. *Istituto Nazionale di Geofisica e Vulcanologia, 00143 Roma, Italia*
4. *Università degli Studi di Milano, 20133 Milano, Italia*
5. *Aquaveo, Provo, Utah 84604*

Corresponding author:
Borgia Andrea
LBNL
1 Cyclotron rd., Berkeley, CA 94720, USA
e-mail: aborgia@lbl.gov

ABSTRACT

We have developed a hydrogeochemical transport model for a phosphogypsum dump located on the intertidal deposits of the Venetian Lagoon. To produce this model, we first constructed a complex conceptual and geologic model from field data, using the Groundwater Modelling System GMS™ graphical user interface. Second, we mapped the numerical MODFLOW grid onto the geological model. Third, using a FORTRAN90 code, we translated this grid into the MESH and INCON blocks that are the input files for the TOUGH2 series of codes. Finally, we ran TOUGH-REACT to model flow and reactive transport in the dump and the sediments below it. The model includes three different dump materials (phosphogypsum, bituminous, and hazardous wastes) with the pores saturated by specific **[=different?]** fluids. The sediments below the dump are formed by an intertidal sequence of calcareous sands and silts, in addition to clays and organic deposits, all of which are saturated with lagoon salty waters. The fluids in the dump react with the solid matrix, while the recharge from rainwater dilutes them. In turn, the percolates from the dump react with the underlying sediments and lagoon waters. In spite of the simplicity of our model, we were able to show how the pH becomes neutral at a short distance below the dump, a fact observed during water monitoring. Dissolution reactions in the dump and mineral precipitation in the sediments below suggest that the sediments tend to contain the transport of contaminants.

INTRODUCTION

The Passo a Campalto dump is located in the Venetian Lagoon (Italy; Fig. 1 and 2). The dump is divided into two areas: the phosphogypsum section in the East and the toxic-waste section in the West.

Since the year 2000, to inhibit leaching of pollutants and infiltration in the underlying aquifers, the dump has been covered and laterally isolated by two engineered barriers, each 0.25–0.50 m thick that extend down to -10 m bsl. The internal of these two barriers, constituted by calcareous sand, was made to control the pH of percolates; the external barrier, made of clay, inhibits their outward flow. Underneath the dump, down to the depth of -10 m bls, the sequence of discontinuous interdigitated layers of clay, silty clay, silt, silty sand can be considered the lower natural barrier: as soon as the polluted water reaches larger depths, the system is assumed to be leaking. We stress that while the two engineered lateral barriers are thin and continuous, the lower barrier, while discontinuous, is more than one order of magnitude thicker than the higher.

To verify the potential reactions of the dump percolates with the lateral barriers, and those of

the underlying sediments with their formation aqueous phases, we have simulated a scenario for the geochemical evolution of this system, using the TOUGH-REACT code (Xu et al., 2005).

Figure 1. The Passo a Campalto dump. a) Google™ view of the Venezia Lagoon. Red box is the studied area. b) To the east are phosphogypsum (red colored), and to the west is toxic wastes (green colored).

THE DUMP

The phosphogypsum in the dump is a byproduct of the industrial processes that produce phosphates from phosphorites (Rutheford et. al., 1994):

$$Ca_{10}(PO_4)_6F_2 + 10H_2SO_4 + 20H_2O = 10CaSO_4.2H_20 + 6H_3PO_4 + 2HF$$

Impurities in the apatites, from which phosphogypsum is derived and which become concentrated in it, are: SiO_2 (0.1–14%), F (1.3–4.1%), CO_2 (0.2–7.3%), SO_3 (0.0–3.3%), Al_2O_3 (0.2–1.8%), Fe_2O_3 (0.1– 2.6%), MgO (0.0–2.2%), and Na_2O (0.2–1.5%). Mineral impurities are quartz 10%, illite and muscovite 5%, organic matter 2%, with traces of dolomite, calcite, iron oxides, fluorite, zircon, tormaline, montmorillonite, caolinite, and pirite. The phosphogypsum itself also contains trace amounts of the anions PO_4, OH, F, Cl, Br, and radionuclei of the ^{238}U and ^{235}Th series.

The toxic-waste dump is less well characterized, and has a few hydrocarbon waste pools both on top of it and within it.

CONCEPTUAL MODEL

Our geologic model is based on Borgia et al. (2010). Fig. 2 shows the two parts of the dump with the complex digitation of intertidal sediments underneath. In our conceptual model (Fig. 3), the fresh recharge-water mixes with the fluids originally contained in the dump materials and percolates downward, displacing the saline fluids contained in the intertidal deposits underneath the dump. We account for reactions among the fluid phases and solid phases of the rock matrix. Although probably present, we do not include density or permeability changes that are a consequence of these reactions.

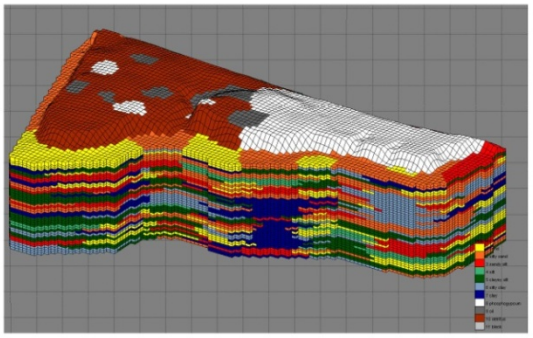

a)

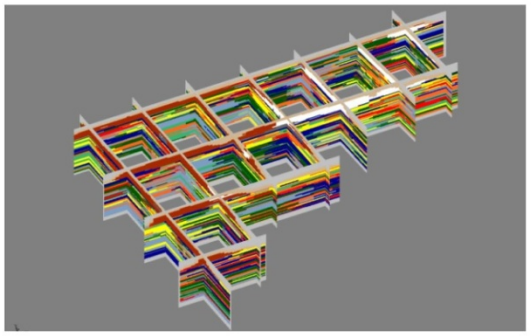

b)

Figure 2. The geologic model after Borgia et al. (2010). Note the complex relations among hydrogeologic units that are reflected in the model. a) 3D view of the modeled dump and underlying barena deposits: white is phosphogypsum, brown is toxic-waste, gray are hydrocarbons. b) Box cross-section of the model.

There are a total of five different fluid compositions to consider (Table 1), in addition to the various mineral phases (Table 2). Since we have not done any laboratory experimental study of the behavior of the system, the goal of our modeling is to investigate possible reaction scenarios among the various fluids and rock phases during downward percolation that could inhibit or enhance the downward migration of pollutants.

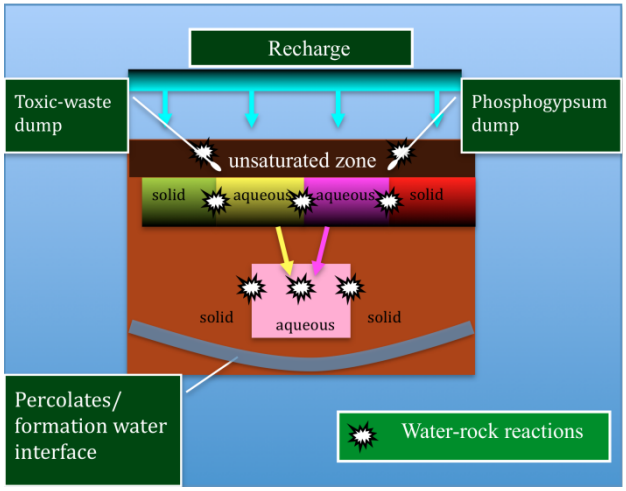

Figure 3. Conceptual model for the reactions occurring in the Passo a Campalto dump system. There are five different water components in addition to the various mineral phases.

TMT2-CODE

To represent the complex topological relationships among the various lithological units of the intertidal deposits of the Venetian Lagoon, we used GMS™ (GMS, 2005) as the geologic graphical user interface to construct (from a conceptual model) a numerical model based on a MODFLOW (MODFLOW, 1996) grid. We then translated this grid to a TOUGH2 grid (Pruess et al., 1999), to be used in TOUGH-REACT (Xu et al., 2005), using the TMT2 code (Borgia et al., 2010; TMT2, 2012). The output files are either read back into GMS or read into other plotting software such as SURFER™ or TECHPLOT™.

MODFLOW specifically requires a rectangular structured grid made of columns, rows, and layers of cells, which are only in part active. In contrast, TOUGH2 and TOUGH-REACT have cells organized in a vector, with active cells only. Each cell in the vector contains the identification code, the volume, the cells to which it is connected and the interface areas, the distances to this area, and angles with the gravity acceleration of the connections. MODFLOW's constant head cells are translated into TOUGH2 as unchanging cells with "infinite" volume. MODFLOW recharge is translated into water-generation cells.

Table 1. The five water types used in the TOUGHREACT model

Chemical species	Phosphogypsum process water	Toxic-waste water	Hydrocarbon-contaminated water	Sediments water	Rain water
H2O	1.000 E+00	1.000 E+00	1.000 E+00	1.000 E+00	1.000 E+00
H+	1.000 E-02	1.000 E-06	0.900 E-06	1.000 E-08	1.000 E-06
Na+	1.400 E-01	1.400 E-04	1.400 E-04	5.760d-1	1.400 E-04
K+	2.623 E-03	1.900 E-05	1.900 E-05	1.260d-2	1.900 E-05
Mg++	7.660 E-03	0.900 E-04	0.900 E-04	6.170d-2	0.900 E-04
Ca++	4.225 E-02	7.700 E-05	7.700 E-05	1.220d-2	7.700 E-05
Al+++	2.200 E-05	1.200 E-07	1.200 E-07	5.570d-6	1.200 E-12
Fe++	2.100 E-05	2.100 E-05	2.100 E-06	8.460d-10	2.100 E-20
Fe+++	9.400 E-07	9.400 E-07	9.400 E-08	9.400d-7	9.400 E-13
SiO2(aq)	4.400 E-02	9.400 E-12	9.400 E-12	9.400d-6	9.400 E-12
Cl-	4.389 E-02	2.818 E-04	2.818 E-04	6.848d-1	2.818 E-04
F-	3.000 E-02	0.500 E-12	0.500 E-12	8.220d-5	0.500 E-12
HS-	1.430 E-09	1.430 E-07	1.430 E-07	1.430d-40	1.430 E-40
SO4--	6.010 E-02	2.200 E-05	2.200 E-05	1.107d-2	2.200 E-05
HPO4--	5.000 E-02	5.000 E-12	5.000 E-12	7.430d-7	5.000 E-12
HCO3-	1.500 E-03	1.500 E-04	1.500 E-04	1.670d-3	1.500 E-04
H2AsO4-	1.184 E-10	1.184 E-10	1.184 E-10	2.420d-16	1.000 E-28
Cr+++	1.572 E-07	1.200 E-07	1.200 E-07	5.576d-13	1.200 E-26
Methane(aq)	1.600 E-40	1.600 E-40	1.600 E-03	1.600d-40	1.600d-03
Benzene(aq)	4.800 E-40	4.800 E-40	4.800 E-06	4.800d-40	4.800d-06

Table 2. The various mineral phases used in the TOUGH-REACT model.

mineral (vol.frac.)	sand	silty sand	sandy silt	silt	clayey silt	silty clay	clay	phospho-gypsum	toxic waste
Calcite	0.5	0.5	0.45	0.3	0.3	0.3			0.9
Dolomite	0.3	0.3	0.25	0.2	0.2	0.2			
Quartz	0.1	0.1	0.05	0.05	0.05	0.05			
Illite	0	0	0.05	0.15	0.15	0.15	0.3		
Smectite-low-Fe-Mg	0	0	0.1	0.2	0.2	0.2	0.6		
Gypsum								0.7	
Fluorapatite								0.05	
Hydroxylapatite								0.2	

In addition to the parameters used in MODFLOW, we provide the parameters that are specific to TOUGH2 (density, thermal conductivity and heat capacity of rock matrix) and to TOGUH-REACT (mineralogy of solid phases, chemistry of liquid phases etc.).

TOUGH-REACT SIMULATIONS

We run TOUGH-REACT with the EOS3 module. This module provides the thermophysical properties of air and pure water (Pruess et al., 1999). We ignore heat fluxes, considering the system isothermal at 25°C, because recorded temperatures vary only a few degrees seasonally. Our choice of temperature is slightly higher than the maximum recorded temperature (which is 18°C): at higher temperature, chemical reactions tend to occur faster, while there are larger hydraulic

conductivities; the two processes probably tend to compensate for each other.

We set constant head boundaries at sea level in all cells around the model, which reflect the presence of the lagoon all around the dump. Also, the bottom-layer cells are set at the same constant head. When possible, we verified input parameters and results with other numerical codes: MODFLOW for the hydrogeologic transport and PHREEQ (Parkhurst and Appelo, 1999) for the chemical reactions.

We compute our starting condition for the TOUGH2 simulation by letting the model equilibrate at sea level with no recharge. Then, we introduce a recharge of 70 (mm/a), which is calibrated against a recorded piezometric head, and let the model run for many hundreds of years to achieve steady state. The following reactive-transport runs have a maximum time-step interval of 1 day. Results where obtained at 1, 3.16, 10, 31.6, and 100 years from the creation of the dump. The last two output times approximately correspond to the time at which the barriers were built to isolate the dump from its surroundings and to a future forecast at 70 years.

The pH remains practically at the original seawater value at all times below the dump, suggesting that the sediments are very effective at neutralizing the dump percolates.

RESULTS

Our 3D model shows the downward percolation (over time) of the recharge fluids which dilute the toxic-waste and phosphogypsum-dump aqueous phases. As time passes, these percolates downwardly displace the salty seawater that, at the beginning of the simulation, fills the porous medium from sea level downward. The presence of more impermeable layers at depths of 7–10 m on the toxic-waste side of the model tend to inhibit percolation, while the percolates from the phospogypsum section of the dump do not have such a continuous clayey layer, thus potentially becoming a threat to the superficial groundwater.

Here, we account for some of the relevant results of the reactive transport simulations, showing the evolution of pH and the hydroxyapatite mineral phase. The pH in the phosphgypsum dump slowly becomes neutralized by the recharge water, from the dump's original pH of 2 (Fig. 4). In keeping with field evidence, it is still below 5 after 31.6 years, and it takes many decades to reach values closer to neutral.

As the pH increases above a value of 4.5, hydroxiapatite precipitates in the phosphogypsum of the dump and remains stable during the whole run of the numerical experiment (Fig. 5). Hydroxyapatite continues to precipitate during our numerical experiment in the sediments underneath the dump (Fig. 5) only down to a

Table 3. Hydrodynamic parameters used for the TOUGH2 model.

	Horizontal Hydraulic Conductivity (m/s)	Vertical Hydraulic Conductivity (m/s)	Porosity	Source
Sand	$5,0 * 10^{-6}$	$5,0 * 10^{-6}$	0,3	Lefranc Experimental Tests
Silty Sand	$1,0 * 10^{-6}$	$0,5 * 10^{-6}$	0,3	Lefranc Experimental Tests
Sandy Silt	$5,0 * 10^{-7}$	$2,5 * 10^{-7}$	0,3	Extrapolated
Silt	$1,0* 10^{-7}$	$3,3 * 10^{-8}$	0,3	Extrapolated
Clayey Silt	$5,0 * 10^{-8}$	$1,67 * 10^{-8}$	0,3	Extrapolated
Silty Clay	$1,0 * 10^{-8}$	$2,0 * 10^{-9}$	0,3	Extrapolated
Clay	$5,0 * 10^{-9}$	$5,0 * 10^{-10}$	0,3	Laboratory Tests
Phosphogypsum	$1,0 * 10^{-6}$	$0,5 * 10^{-6}$	0,3	C.V.N. Technical Report
Wastes Detritus, Bitumes	$5,0 * 10^{-6}$	$2,5 * 10^{-6}$	0,3	Extrapolated

maximum depth of less than 5 m bsl, even after 100 years. These results indicate that the sediments and the formation seawater are effective in inhibiting the downward transport of at least some of the pollutant species present in the dump. However, some metal ions, such as Fe, Mg, and As, tend to be more mobile and can percolate downward to -10 m bsl in less than 100 years.

CONCLUSIONS

Using the GMS™ conceptual-model-oriented graphic user interface (used for the USGS MODFLOW **code),** we made a 3D model of the highly complex geologic environment that characterizes the intertidal deposits underneath the dump of Passo a Campalto (Venezia). We translated the MODFLOW grid into a TOUGH2 input file, using the TMT2 code. For visualization purposes, the results can be easily translated back to GMS™ or plotted with any adequate graphical software package.

We ran the TOUGH-REACT with the EOS3 equation of state in isothermal mode and attempted to calibrate the simulations using water-table and chemical-monitoring data.

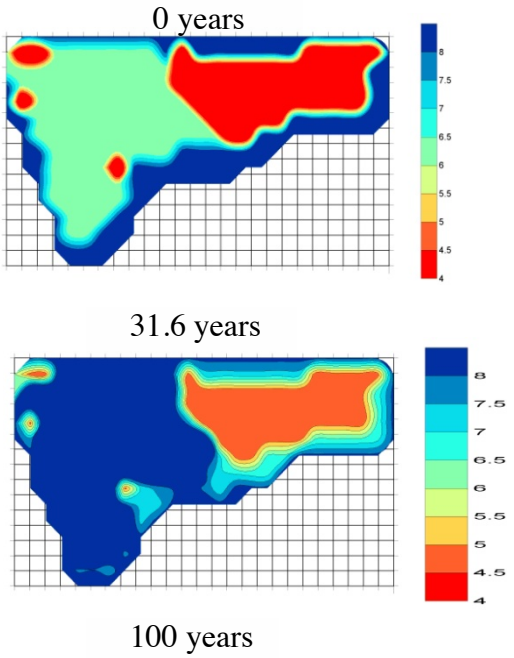

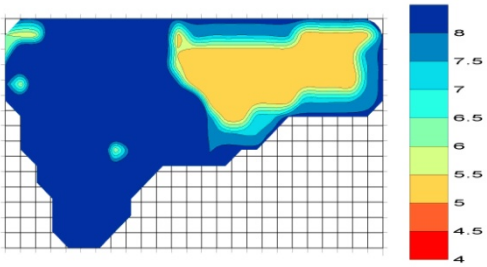

Fig. 4. Evolution of pH in time. Note how the pH of the phosphogypsum dump becomes neutralized by recharge water in more than 100 years.

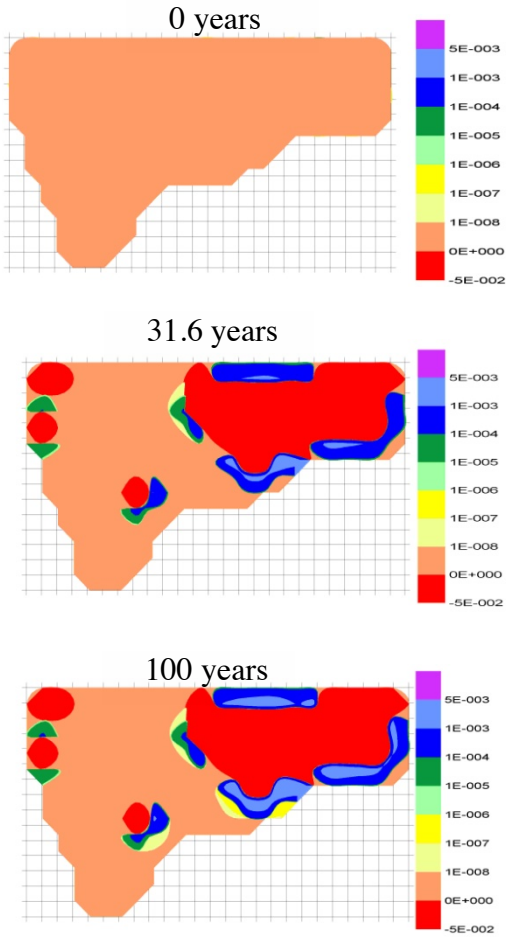

Fig. 5. Evolution of hydroxyapatite mineral phase in time. Note how as the pH of the phosphogypsum dump becomes neutralized the apatite precipitates, becoming immobile, inside the dump.

The results show that while some pollutants are effectively trapped within the dump and the underlying sediments, others have a higher

mobility, leaching downward and potentially polluting the aquifers.

Our simple TMT2 program allows the use of a set of geological graphic user interfaces, available "off the shelf" for MODFLOW with the TOUGH2 series of codes, providing at the same time the freedom to work directly with the TOUGH2 input file.

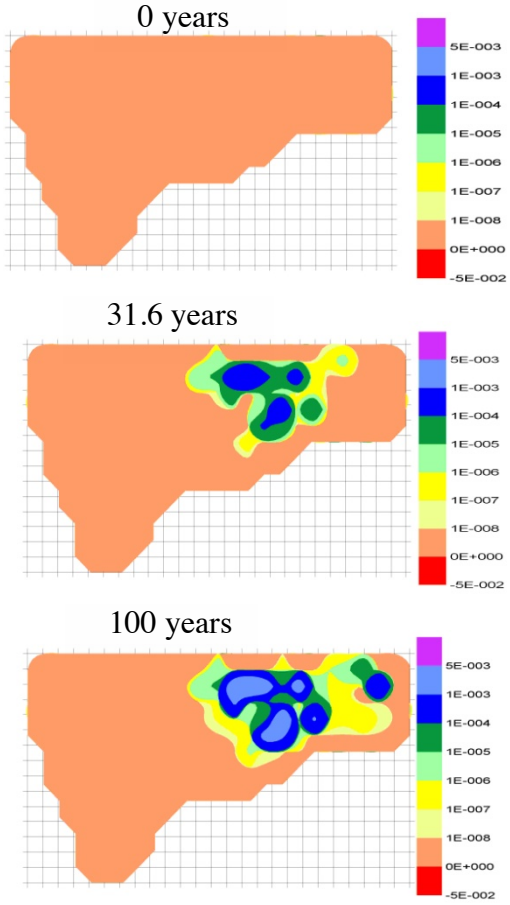

Fig. 6. Evolution of the Hydroxiapatite mineral phase in time at -2 m bsl. Note how, this phase precipitates in the sedimentary layers underneath the dump.

We hope that this effort may enable hydrogeologists concentrating on modeling complex geology (before actually solving the fractured-porous-media flow problem) to use the powerful capabilities inherent in the TOUGH2 codes.

ACKNOWLEDGMENTS

This project received financial support by EDRA, the Magistrato delle Acque di Venezia, the U.S. Dept. of Energy under Contract No. DE-AC02-05CH11231, and LBNL TOUGH2-Development Grant, 2011.

REFERENCES

Borgia A., Cattaneo L., Marcono D., Rossi E.L., Amoroso C.G., Lo Re F., Tozzato E., 2010. Using a MODFLOW grid, generated with GMS, to solve transport problems with TOUGH2 in complex geological environments: the intertidal deposits of the Venetian Lagoon. TOUGH 2009. Computer & Geosciences, doi 10.1016/j.cageo.2010.11.007.

GMS™ , 2005. Groundwater Modeling System Version 6. Environmental Modelig Research Laboratory, volume I, pp. 134, volume II, pp. 207, volume III, pp. 113, volume IV, pp. 167.

MODFLOW, 1996. Programmer's Documentation for Modflow-96, an update to the U.S. Geological Survey Modular Finite-Difference Ground-Water Flow Model. U.S. Geological Survey, volume I, pp 56, volume II, pp. 220.

Parkhurst, D.L. and Appelo, C.A.J., 1999. User's guide to PHREEQC (Version2)—A computer program for speciation, batch-reaction, one-dimensional transport, and inverse geochemical calculations: U.S.Geological Survey Water-Resources Investigations Report 99-4259, 310 p.

Pruess K., Oldenburg C., and Moridis G., 1999. TOUGH2 USER'S GUIDE, VERSION 2.0. Laurence Berkeley National Laboratory – 43134. pp. 198.

Rutherford P.M., Dudas M.J., and Samek R.A., 1994. Environmental impacts of phosphogypsum. The Science of the Total Environment 149, 1-38.

Scheidegger A.E., 1961. The Physics of Flow Through Porous Media. University of Toronto Press, Canada.

Xu T., Sonnenthal E., Spycher N., Pruess K., 2005. TOUGH-REACT User's Guide: A Simulation Program for Nonisothermal Multiphase Reactive Geochemical Transport in Variably Saturated Geologic Media. Ernest Orlando Lawrence Berkeley National Laboratory, Berkeley, (LBNL-55460) pp. 197.

TMT2,2012.http://esd.lbl.gov/research/projects/tough/licensing/free.html#TMT2.

SIMULATING MIGRATION OF CO_2 AND CH_4 GENERATED FROM GEOTHERMAL TREATMENT AND BIODEGRADATION OF SANITATION WASTE IN THE DEEP SUBSURFACE

J. Diessl, M. S. Bruno, and J.T. Young

GeoMechanics Technologies
103 E. Lemon Ave.
Monrovia, California, 91016, USA
e-mail: juliad@geomechanicstech.com

ABSTRACT

The Terminal Island Renewable Energy (TIRE) Project is the nation's first full-scale application of deep-well injection technology to treat and convert sanitation plant residuals (biosolids or wetcake) into a renewable energy source (high purity methane) while simultaneously sequestering greenhouse gases. During the past four years, a slurry mixture composed of digested sludge, trucked wetcake, and reverse-osmosis-treated brine has been injected into sandstone formations more than 1500 m beneath the City of Los Angeles Terminal Island Wastewater Treatment Plant. At that depth, the earth's natural high temperature biodegrades the organic mass into methane and carbon dioxide. The carbon dioxide dissolves in the aqueous phase, leaving relatively pure methane in the gas phase. The EOS7C module of TOUGH2 is used to model migration of these components in the target formation. Temperature and pressure are continuously monitored at the injection well and at two offset monitoring wells. Fluid and gas samples have been collected at the offset monitoring wells, for comparison and calibration of the 3D simulation results. We present herein simulation results and field monitoring observations.

INTRODUCTION

Millions of tons of sewage sludge (biosolids) are generated each year by municipal sanitation agencies around the world. In the United States and elsewhere, most biosolids are currently trucked long distances and applied to the land surface. But the ratio of rural land to urban development is decreasing, while the volume and costs associated with biosolid trucking and disposal are steadily increasing. With increasing urban development and population growth, environmentally sustainable alternatives are desperately needed.

GeoEnvironment Technologies has developed and successfully demonstrated an innovative new technology to manage municipal sludge with significant environmental benefits. Through appropriate geological formation selection, well design, and advanced geophysical monitoring, the biomass can be injected into soft, porous, sand formations in the deep subsurface (on the order of 1500 m or more).

Deep underground, the earth's natural geothermal heat pasteurizes the biomass quickly (within 24 hours), and then through continuing anaerobic biodegradation, converts the organic mass to methane and carbon dioxide (CO_2). The CO_2 is preferentially absorbed by formation waters (due to its high solubility in water) while relatively pure methane gas collects and may be stored long term, or eventually produced for beneficial use. (Bruno et al., 2012; 2005). As compared to landfill or land application, deep-well injection provides greater protection for shallow groundwater, significantly reduced pollution and greenhouse gas emissions, and provides large urban areas a local management solution without imposing on rural areas.

About 150 tons per day of biosolids have been injected at the City of Los Angeles Terminal Island Wastewater Treatment Plant since July 2008. Injection cycles last about 12 hours per day, five days per week, with extended shut/in over each weekend. Injection rates vary from 10 to 24 L/s (4 to 9 bpm).

The local surface-infrastructure footprint for the TIRE project is only 1,600 m^2; thus, the project could easily be embedded in an existing treatment plant. The system is shown in Figure 1. An image of the biosolids material that is being injected is shown in Figure 2.

1) Wetcake & sludge blending pit
2) Screen
3) Mixing tank
4) Electric Pumps
5) Injection well
6) Monitoring well
7) Office

Figure 1. TIRE project site

Figure 2. Biosolids in the blending pit

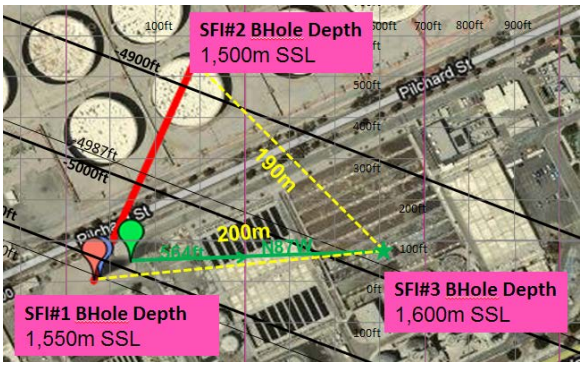

Figure 3. Well paths of monitoring wells

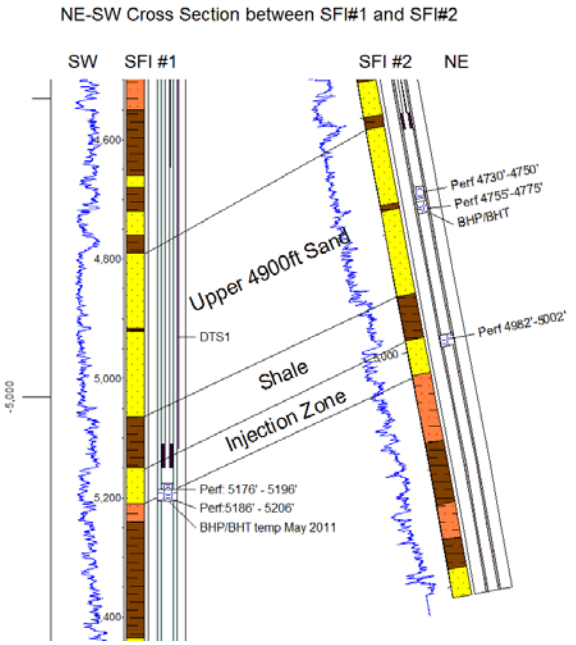

Figure 4. Gamma ray log data and lithology of SFI1 and SFI2 (numbers in ft)

SUBSURFACE GEOLOGY

The subsurface at the project site includes interbedded sands and shales to a depth of about 2,500 m. One injection well and two monitoring wells are drilled to a depth of about 1,500 m (5200 ft). The bottom-hole locations of the monitoring wells are located about 160 m north and west of the injection well—see Figure 3. The geologic setting and cross section between well SFI1 (injection well) and well SFI2 (monitoring well to the north) is illustrated in Figure 4.

TOUGH2 MODEL CONCEPT

A 3D simulation model for the subsurface has been defined using TOUGH2/EOS7C software. We take into account the dipping formation and directional fracturing observed during the initial phase of the project. A symmetry plane is applied in direction of the dip. Figure 5 shows a visualization of the model domain.

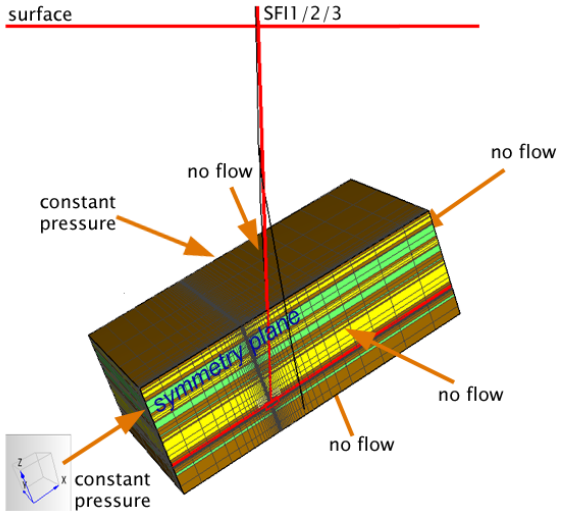

Figure 5. Reservoir simulation model grid covers 1500 m × 750 m × 500 m discretized into 47,200 cells

Material properties

Geological analysis of injection and monitoring wells identified a 16 m thick target formation (lower sand) shown in close up in Figure 6. Four different material types are defined (Table 1).

Table 1. Material properties

Material name	density [kg/m³]	porosity [-]	x permeability [mD]	y permeability [mD]	z permeability [mD]	pore compressibility [1/Pa]
SAND	2660	0.25	60	60	30	1.50E-09
FSAND	2660	0.25	500	500	500	1.5E-09
SHALE	2600	0.05	1	1	1	1.39E-09
SILT	2600	0.25	15	15	7	1.39E-09

	rel. Permeability				capillar pressure				
Material name	λ	S_{lr}	S_{ls}	S_{gr}	λ	S_{lr}	$1/P_0$ (PSI)	P_{max} (PSI)	S_{ls}
SAND	0.9167	0.1	1	0.01	0.4118	0.03	0.51849	1363	1
FSAND	0.9167	0.1	1	0.01	0.4118	0.03	0.51849	1363	1
SHALE	0.9167	0.2	1	0.02	0.4118	0.03	0.11583	1363	1
SILT	0.9167	0.15	1	0.015	0.4118	0.03	0.34474	1363	1

FSAND is a material with 10 times higher permeability than surrounding SAND. This represents the fracture opened during the initial phase of the project. For relative permeability and capillary pressure functions, the van Genuchten model is assumed.

Grid setup

The coordinate system is rotated to consider dipping formation layers. An average 20° up-dip angle is estimated. Vertical refinement is based on sand, shale, and silt layers from geological interpretation of well logs. Injection and cap rock zones are further refined in vertical direction. Horizontal (in dip direction) refinement starts with a smallest cell size of 0.006 m^3 at injection point and gradually increases with distance.

In the y-direction (away from the symmetry plane), we install a 3 cm thin cell layer. Thus we can apply the high permeability FSAND material to an area of 120×60 m around the injection point representing the assumed fracture plane. An extra source cell is connected to six perforated cells to facilitate injection of water in the target zone.

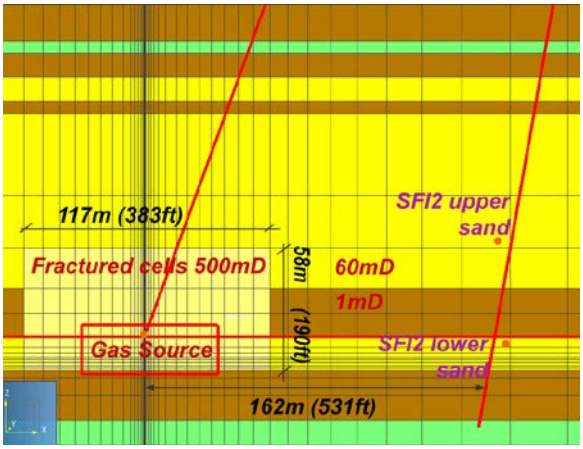

Figure 6. Closeup of injection well, assumed fracture, and gas source area

Initial conditions

Based on the analysis of an *in situ* pressurized sample taken prior to any injection of biosolids, salinity of 28,300 ppm (= 11% brine fraction for EOS7C input (Pruess et al., 2011)) is applied throughout the modeled area. Temperature and pressure gradient as measured in SFI1 are applied. Thus, we start with 14.2 MPa and 74°C at the point of water injection. Initial CO_2 and CH_4 mass fractions measured are not taken into account for *in situ* conditions, but shall be considered when estimating changes in concentration.

Dirichlet boundary conditions

The Thums Huntington Beach fault northeast of the modeling area is represented by a no-flow boundary condition. Bottom, top, and symmetry plane are also set to no flow. All other edges are set to constant pressure boundary. The modeling is done for isothermal conditions.

Neumann boundary conditions

Gas generation assumption

Lab experiments completed prior to start of injection give us an idea about gas-generation amounts under prevailing pressure and temperature conditions. Based on Bruno et al. (2005), we assume 900 L gas with a ratio of 70:30 for CH_4:CO_2 are generated per kilogram of volatile solids decomposed. It has therein also been observed that after 90 days, about 20% of volatile solids have been biodegraded. Assuming a linear degradation rate, material injected on Day 1 shall be fully biodegraded on Day 450. Until Day 450, gas generation is linearly increasing up to a stabilized daily gas-generation rate of 5,000 m^3. This amount is estimated based on average daily injection rates of 5,500 kg volatile solids.

Water injection rate

Biosolids have an average water content of 72%. Thus, we make the simplified assumption of pure water injection to simulate the injected volumes into the target formation. Field injection rates are applied, and a maximum time step of two hours is used to allow simulating the injection cycles.

FIELD MEASUREMENTS

Pressurized samples

Pressurized fluid samples have been taken at the injection well (SFI1) and the monitoring wells (SFI2 & SFI3). Monitoring wells hit the target formation at a distance of 160 m away from the injection point. Table 2 lists the mass fraction results from the pressurized samples.

Table 2. Mass fraction CO_2 and CH_4 (average of two sample analyses for each date)

Well	CO_2 (-)	CH_4 (-)
SFI1(*in situ*)	2.84E-06	5.30E-04
SFI2(518 days)	1.56E-05	6.77E-04
SFI3(889 days)	4.50E-06	5.81E-04
SFI3(1,383 days)	2.96E-05	9.63E-04

Starting from the first sampling in SFI2 monitoring well (Day 518 of injection), we found that the biosolids have reached a distance of 160 m away from the injection well.

Gas samples from monitoring wells

Starting November 2010, gas samples have been collected at the well head of the two monitoring wells (SFI2 and SFI3). Figure 7 shows steadily increasing methane concentration and steadily decreasing nitrogen content in Well SFI2. Note that at the end of 2011, the well was opened to atmosphere for a workover, allowing air (primarily nitrogen) to fill the well. After shut/in and starting in March 2012, the methane content again started to rise and the nitrogen content again started to decline. Well SFI3, which was sampled later in time than Well SFI2, showed consistently high methane content until late April 2012, when it was also opened to the atmosphere. After shut/in and starting in May 2012, methane also started to increase again in SFI3—see Figure 8. CO_2 amounts are below 0.1% volume in the head space gas for all of the samples analyzed.

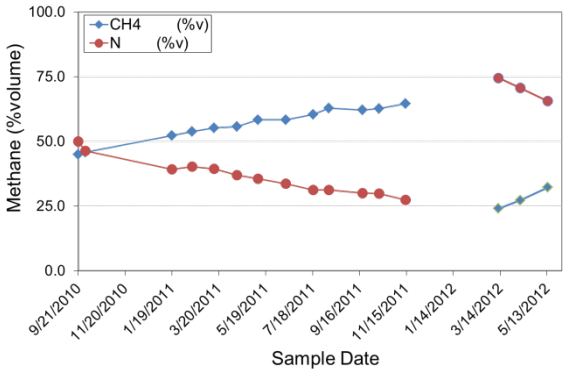

Figure 7. SFI2: methane concentration

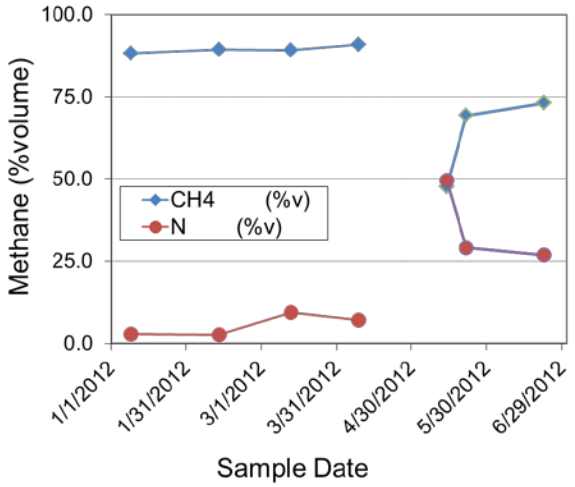

Figure 8. SFI3: methane concentration

RESULTS AND DISCUSSION

To date, we have been able to model one year of real-time simulation using the EOS7C module of TOUGH2. This module can simulate components CO_2 and CH_4 simultaneously at the subsurface conditions prevailing in our system (see Oldenburg et al., 2004).

Pressure

Initial calibrations focused on the pressure match during injection in the injection well (SFI1) and one of the two monitoring wells (SFI2). Good match has been found for an injection rate of 15 L/s (6 bpm) which is the average injection rate in the initial phase of the project.

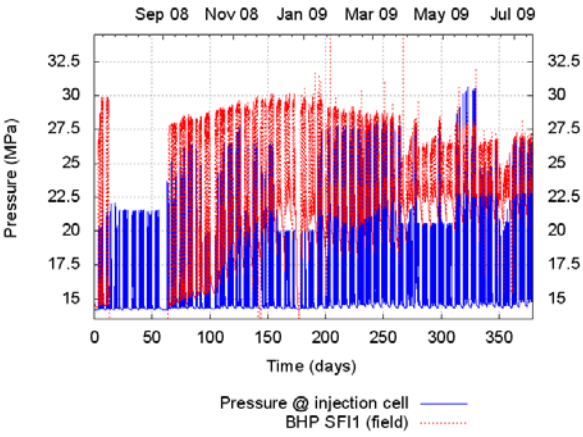

Figure 9. Measured (red) and simulated (blue) bottom-hole pressure of injection well SFI1

Fluid migration

As we inject pure water as a proxy for carrier fluid, we use the decrease in initial salinity as an indicator for injected fluid migration. Figure 10 shows that injected water has reached out to a radius of 100 m on top of target sand. Moreover, salinity at monitoring well SFI2 has started to decline after 362 days of injection. Changes are below 0.5% of initial salinity.

We cannot directly compare this result with our field measurement, because the project also injects high salinity brine with the biosolids. Salinity stays fairly stable over time in the field.

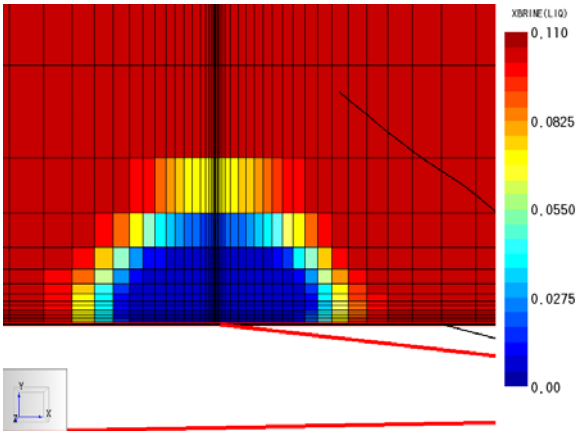

Figure 10. Brine distribution top of target zone—Day 362

CO_2 and CH_4 migration

After 362 days, a maximum gas saturation of 22% is observed in the model. An oxygenated activated (OA) log performed in June 2009 (about a year after injection start) did not detect any free gas phase in the injection well. Detection limits for OA logs are about 30% free gas. Thus, we have a reasonable qualitative match regarding free gas.

Distribution of gas phase (= inverse of liquid saturation) in the symmetry plane and top of the target zone sand is shown in Figure 11 and 12. Maximum extent of the gas plume into the model (= perpendicular to the symmetry plane) is 25 m. The gas plume migrates 75 m vertically and 90 m horizontally in the symmetry plane. Initial preferred migration of gas in the horizontal and vertical directions occurs due to the fracture plane.

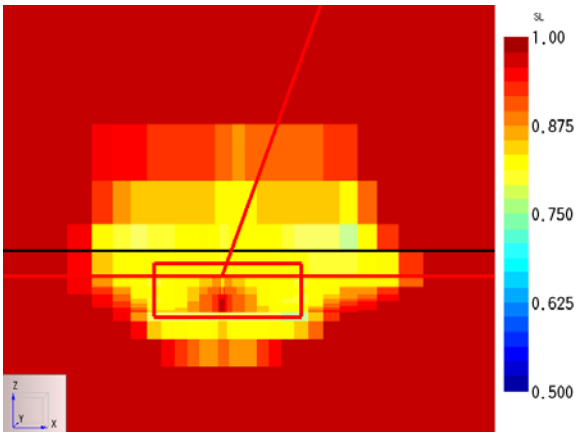

Figure 11. Liquid saturation in symmetry plane—Day 362

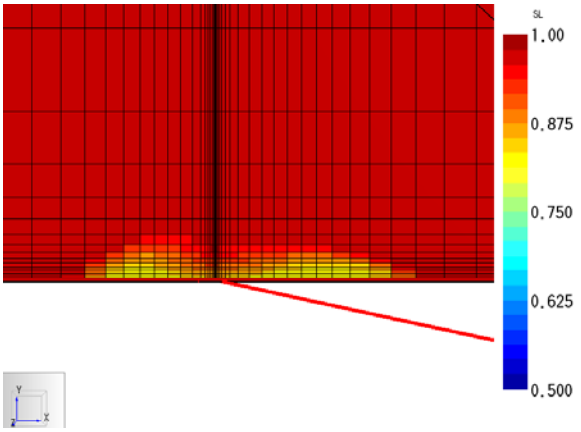

Figure 12. Liquid saturation at top of target zone—Day 362

Figure 13 and 14 show the mass fractions of CH_4 and CO_2 in liquid phase at the top of the target zone.

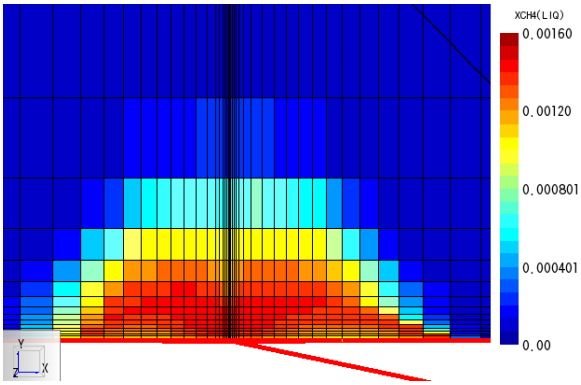

Figure 13. CH_4 mass fraction in liquid phase at top of target zone—Day 362

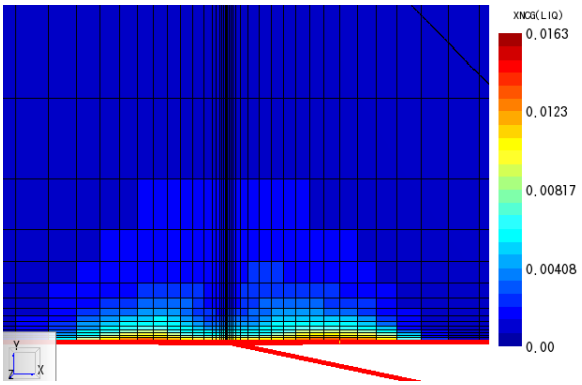

Figure 14. CO_2 mass fraction in liquid phase at top of target zone—Day 362

About Day 360, CH_4 appears in monitoring cell SFI2—see Figure 15.Slightly increased methane content has been measured at SFI2 on Day 518.

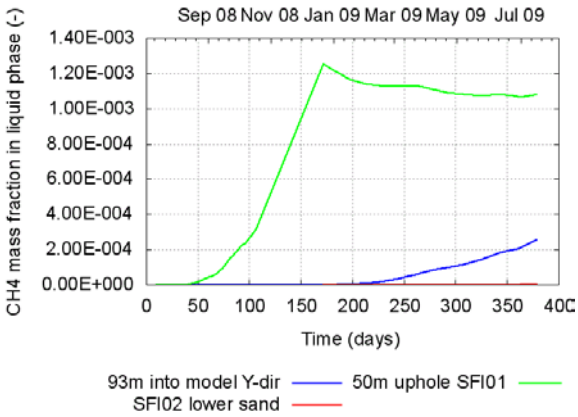

Figure 15. CH_4 mass fraction at different monitoring points

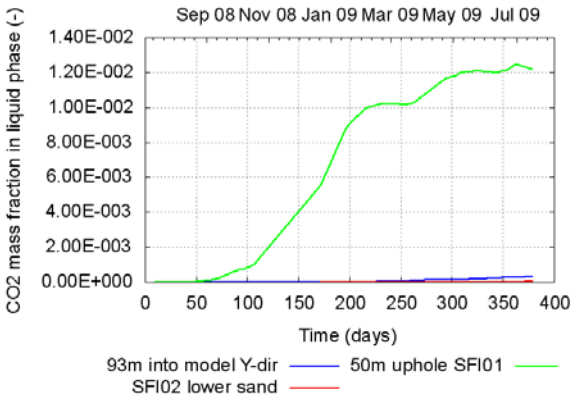

Figure 16. CO_2 mass fraction at different monitoring points

Liquid at prevailing conditions can hold CO_2 up to a mass fraction of about 1.60E-02 in liquid phase—see Figure 14. Field and simulation results at monitoring points are at least an order of magnitude lower. That is consistent with observations of no free CO_2 in the head space gas sampling. Up to 1.60E-03 mass fraction of CH_4 in liquid phase is observed on top of the target zone—see Figure 13.

Figure 15 and 16 show us that CO_2 and CH_4 components started reaching monitoring point SFI2, but at concentrations still significantly lower than saturation limits.

In order to make more detailed qualitative comparison between field and modeling measurements, we need to continue simulating for a minimum of 4 years. Currently, it takes us about 1 month of computer time to simulate one year.

CONCLUSIONS

More than 100 million gallons of slurry containing biosolids have been successfully injected at the Terminal Island Treatment Plant since mid-2008. The process is being monitored by a variety of techniques, including downhole pressure sensors, downhole temperature sensors, microseismic sensors, and offset well fluid and gas sampling. We have developed a 3D flow simulation model to simulate the process of *in situ* biodegradation of the organic mass into CO_2 and CH_4, with subsequent fluid and gas migration. The model currently provides a reasonable match to observed pressure behavior. Both simulation results and field measurements indicate that CH_4 and CO_2 have reached the monitoring wells. Initial simulations show reasonable qualitative results, but longer real-time simulation is still required and is continuing.

ACKNOWLEDGMENT

The authors would like to thank cooperation partners of TIRE project: City of Los Angeles, GeoEnvironment Technologies and Environmental Protection Agency (EPA). Appreciation goes to Curt Oldenburg for technical support with EOS7C.

REFERENCES

Bruno, M.S., Couture, J., Moghaddam, O., *Extreme Cost Savings at Extreme Depth: Geothermal Treatment of Biosolids Through Deep Well injection,* Proc. WaterEnvironment Federation Residuals and Biosolids Conference, Raleigh, N.C. March 25-28, 2012

Bruno, M.S., Young, J.T., Moghaddam, O., Wong, H., and Apps, J.A., *Chapter 46: Thermal Treatment, Carbon Sequestration, and Methane Generation Through Deep-Well Injection of Biosolids, Underground Injection Science and Technology,* C.F. Tang and J. Apps, ed., Elsevier, Amsterdam, 2005.

Oldenburg, C.M., Moridis G.J., Spycher N., and K. Pruess, *EOS7C Version 1.0: TOUGH2 Module for Carbon Dioxide or Nitrogen in Natural Gas (Methane) Reservoirs,* Report LBNL-56589, Lawrence Berkeley National Laboratory, Berkeley, Calif., 2004.

Pruess, K., Oldenburg C.M., and Moridis G., *TOUGH2 User's Guide,* Version 2.1, Report LBNL-43134 (revised), Lawrence Berkeley National Laboratory, Berkeley, Calif., 2011

Rebscher, D., Oldenburg C.M., *Sequestration of Carbon Dioxide with Enhanced Gas Recovery-Case Study Altmark, North German Basin,* Lawrence Berkeley National Laboratory, 2005.

EXPERIMENTAL AND NUMERICAL EVALUATION OF DUAL PHASE FLOW DURING LIQUID INJECTION IN A COARSE SAND

Tryambak Kaushik and Milind V. Khire

Department of Civil and Environmental Engineering, Michigan State University, Engineering Building, 428 S. Shaw Lane, East Lansing, MI 48824, USA
e-mails: kaushikt@egr.msu.edu and khire@egr.msu.edu

ABSTRACT

Leachate recirculation in municipal solid waste (MSW) landfills is a relatively common operational method for managing leachate and to accelerate the biodegradation of MSW for enhanced gas production (and energy recovery). However, one of the key concerns related to the addition of leachate in landfills is the increase in liquid and gas pressures if the gas extraction system cannot keep up with the enhanced gas generation. Slope stability of the landfill can be jeopardized if the fluid pressures are excessive. Dual phase models are required to evaluate the fluid pressures in a landfill subjected to leachate or liquid injection and to design a gas extraction system that couples the effects of leachate recirculation. However, there is lack of validated dual phase models for such applications. Hence, we designed and fabricated a large-scale lab model, 86 cm long × 30 cm wide × 56 cm high and made of plexiglass, to simulate the hydraulics of subsurface liquid injection. This physical scale model was filled with poorly graded coarse Ottawa sand. The saturated and unsaturated hydraulic properties of the sand were fully characterized. De-ionized (DI) water, injected in a horizontal perforated pipe installed in the sand, operated at constant flux using a high precision miniature gear pump. A 3.8 cm thick drainage layer made up of pea gravel was placed at the lower boundary of the model to create a free drainage boundary. The sand was instrumented with pressure transducers to measure pressure heads and time-domain reflectometry (TDR) sensors to monitor water contents. The numerical model Transport of Unsaturated Groundwater and Heat (TOUGH) was used to predict the fluid pressures. TOUGH was able to predict the magnitude of the air pressure buildup as a result of liquid injection However, TOUGH was not able to accurately predict the duration of air-pressure dissipation.

INTRODUCTION

In 1976, EPA enforced RCRA subtitle D for MSW landfills in order to decrease groundwater contamination and minimize human health hazards. Consequently, to reduce environmental pollution and meet EPA compliance criterion, MSW landfill operators have adopted an innovative technology of leachate recirculation to manage landfill leachate (Benson et al., 2007). Vertical wells, horizontal trenches, and permeable blankets are popular subsurface leachate-recirculation technologies to manage leachate by operating landfills as “bioreactors” (Reinhart, 1996; Haydar and Khire, 2005; Khire and Mukherjee, 2007). Bioreactor technology offers financial gain for landfill operators in the form of reduced offsite leachate treatment cost. Recently, significant research has focused on the design of these subsurface liquid-injection systems for landfills operated as a bioreactor. The underlying assumption in all these studies had been a fully vented porous medium with the gas component as a passive phase (McCreanor and Reinhart, 2000; Haydar and Khire, 2005; Khire and Mukherjee, 2007; Jain et al., 2010)—which may not be valid in real-life conditions.

Under static conditions, the liquid within the solid-waste pores is in hydraulic equilibrium with the atmosphere. Waste produces methane, carbon dioxide, and xeno-biotic gases within the landfill (Barlaz et al., 2002). These continuously generated gases are unable to fully escape the solid-waste matrix unless the gas extraction system has an efficiency of 100%, contributing to a buildup of pressure within the landfill. For example, Dona Juana landfill failure (Merry et

al., 2005) was attributed to undissipated excessive pore-gas pressures within the landfill. Thus, geo-environmental designs that are unsafe due to ignoring the effect of gas components have resulted in unprecedented loss of human lives and public property. Scant literature is available on the design and operation of bioreactor landfills as a multicomponent, multiphase porous media. Hence, to study the pore-water pressure and gas-pressure distribution within a bioreactor landfill, we custom-built a large-scale landfill model to represent a leachate recirculation system. The model consisted of an 86 cm long × 30 cm wide × 56 cm high plexiglass box (Figure 1). The box consisted of an injection pipe at the top and two exit outlet pipes at the bottom. The pipes were perforated for free flow of water. The bottom of the box was sloped at 3% to exit pipes. Additionally, piezometer tubes were installed at the exit pipes to measure the pressure head buildup in the leachate collection system (LCS). The water in the tubes always remained at zero level during the experiment, verifying a fully vented condition. Additional details of the laboratory model are presented in Mukherjee and Khire (2012).

ELECTRONIC SENSORS

Automated electronic sensors were installed to measure the pressure head and volumetric water content of porous media during the experiment. The electronic sensors consisted of (1) a liquid flow sensor, (2) pressure transducers with built-in thermistors; and (3) time domain reflectometry (TDR-based) water-content sensors. Datalogger and multiplexer were programmed to automatically record data from the sensors at a constant time interval of 60 s. A detailed description of the sensors is presented in Mukherjee and Khire (2012).

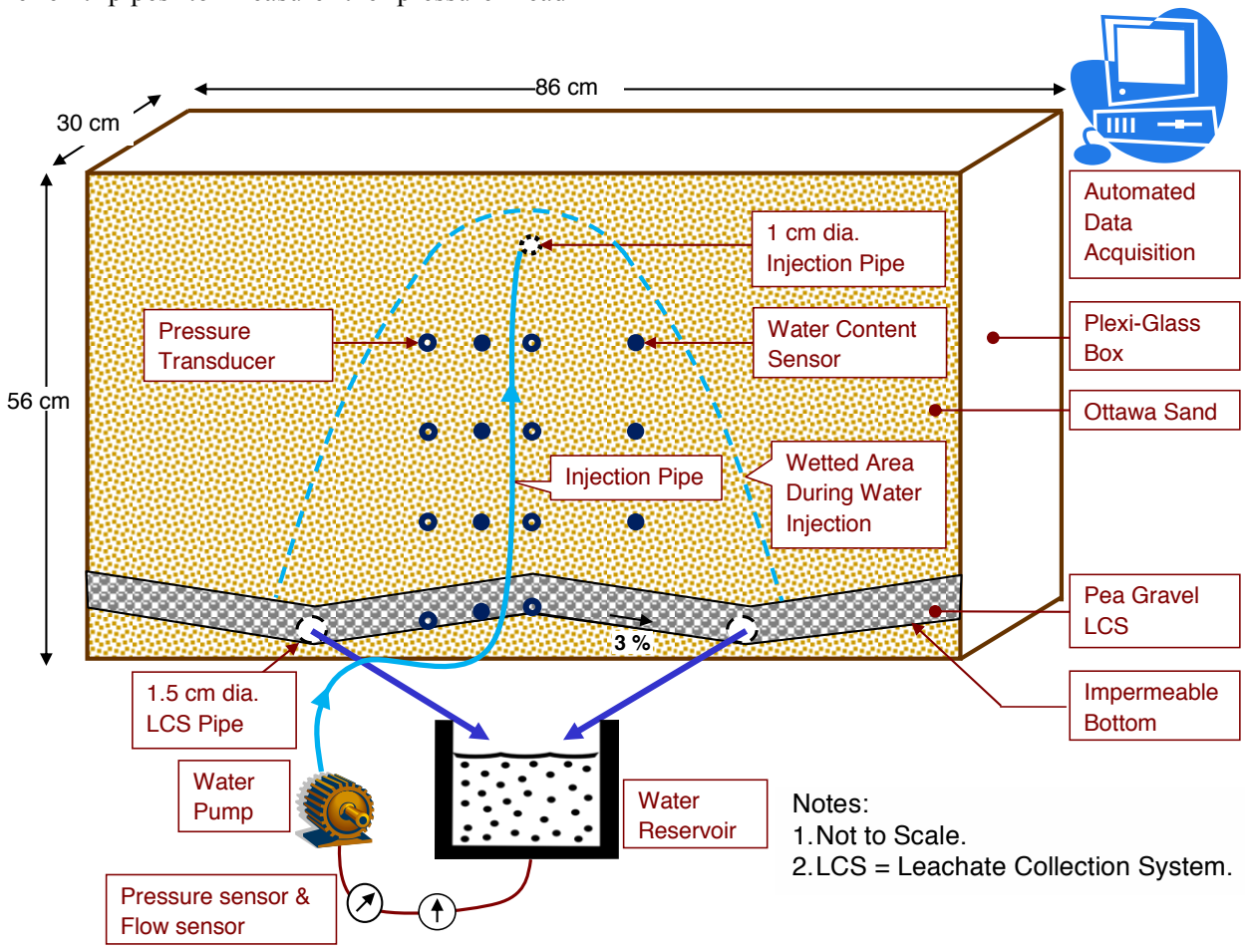

Figure 1. Large-scale leachate recirculation tank

Table 1. Properties of soils used in the physical model (Mukherjee and Khire, 2012)

Soil Type	Grain Size Distribution				Saturated and Unsaturated Hydraulic Properties				
	D_{50} (mm)	C_u	C_c	ρ_d (g/cm^3)	K (cm/s)	θ_s	θ_r	α (1/cm)	n
Ottawa Sand	0.35	2.04	1.4	1.60	3.5×10^{-2}	0.4	0.03	0.023	4.5
Pea Gravel	2.84	1.68	0.96	1.55	2.0	0.43	0.01	0.45	3.3

Note: D_{50} = diameter at 50% finer; C_u = co-efficient of uniformity;
C_c = co-efficient of curvature; ρ_d = dry density; K = saturated hydraulic conductivity

LABORATORY EXPERIMENT

Materials

To ensure homogeneity and isotropy of the test domain for the numerical model validation, uniformly graded Ottawa sand and washed Pea gravel were used in the experiment to simulate MSW and LCS, respectively. van Genuchten-Maulem (van Genuchten, 1980) curve fitting parameters were used to characterize the unsaturated hydraulic properties of the sand and gravel as per the following equations.

$$\theta = \theta_r + \frac{\theta_s - \theta_r}{\left(1 + |\alpha h|^n\right)^m} \quad (1)$$

$$k_l = \frac{\left\{1 - (\alpha h)^{nm}[1 + (\alpha h)^n]^{-m}\right\}^2}{[1 + (\alpha h)^n]^{m/2}} \quad (2)$$

$$k_l = 1 - k_g \quad (3)$$

where θ = volumetric water content; θ_r = residual volumetric water content; θ_s = saturated volumetric water content; h= matric suction; α, n, and m are curve fitting parameters; k_l (k_g) = relative unsaturated hydraulic conductivity of liquid (gas) phase. The grain-size parameters and hydraulic characteristics of soils are presented in Table 1.

Experimental Parameters

Pea gravel simulating LCS was 3.8 cm thick. It was overlain by 46 cm of Ottawa sand. A 0.2 cm thick nonwoven geo-textile fabric separated the sand from the pea gravel underneath. The fabric prevented sand washing into gravel pores. The hydraulic conductivity of the fabric was 0.3 cm/s (ASTM D 4491). Eight pressure transducers were embedded in two vertical rows in the sand and gravel. Similarly, seven water content sensors were embedded in two vertical rows as shown in Figure 1. Note that the water content and pressure sensors were placed along the same horizontal plane. A small piece of geotextile, wrapped around the tip of each pressure sensor, prevented sand particles from falling onto the sensor diaphragm. The PVC injection pipe ran parallel to the width of the model, ensuring a uniform wetting front in the horizontal plane and a two-dimensional water injection event. De-ionized (DI) water was pumped through the injection pipe with the help of a small DC pump. The voltage of the DC pump was adjusted to control the flow of water to a constant injection flux of about 5.3 L/min. Water exiting the landfill model through bottom pipes was collected in a reservoir tank and re-injected into the sand layer.

NUMERICAL MODELING USING TOUGH

The TOUGH code developed by Pruess et al. (1999) was used to simulate the two-phase hydraulics of the water-recirculation experiment. The landfill model was conceptualized as a two-dimensional rectangular domain in TOUGH. Injection flux measured by the flow sensor was used as the time-varying source term at injection pipe. The bottom boundary was kept at constant

atmospheric pressure and at a fixed liquid saturation of 0.999. The bottom boundary with two perforated pipes (with the rest of the boundary being impermeable) could not be simulated in the version of TOUGH we used. The top boundary was defined as air permeable, maintained at a constant atmospheric pressure, and also water impermeable. All other boundaries were assigned as no-flow boundaries. Atmospheric pressure was assumed as the reference pressure. Isothermal conditions at 20°C were assumed.

RESULTS AND DISCUSSION

DI water was injected into the model at a constant flux of about 5.3 L/min. Electronic pressure transducers and TDRs were used to monitor the water pressures and water contents.

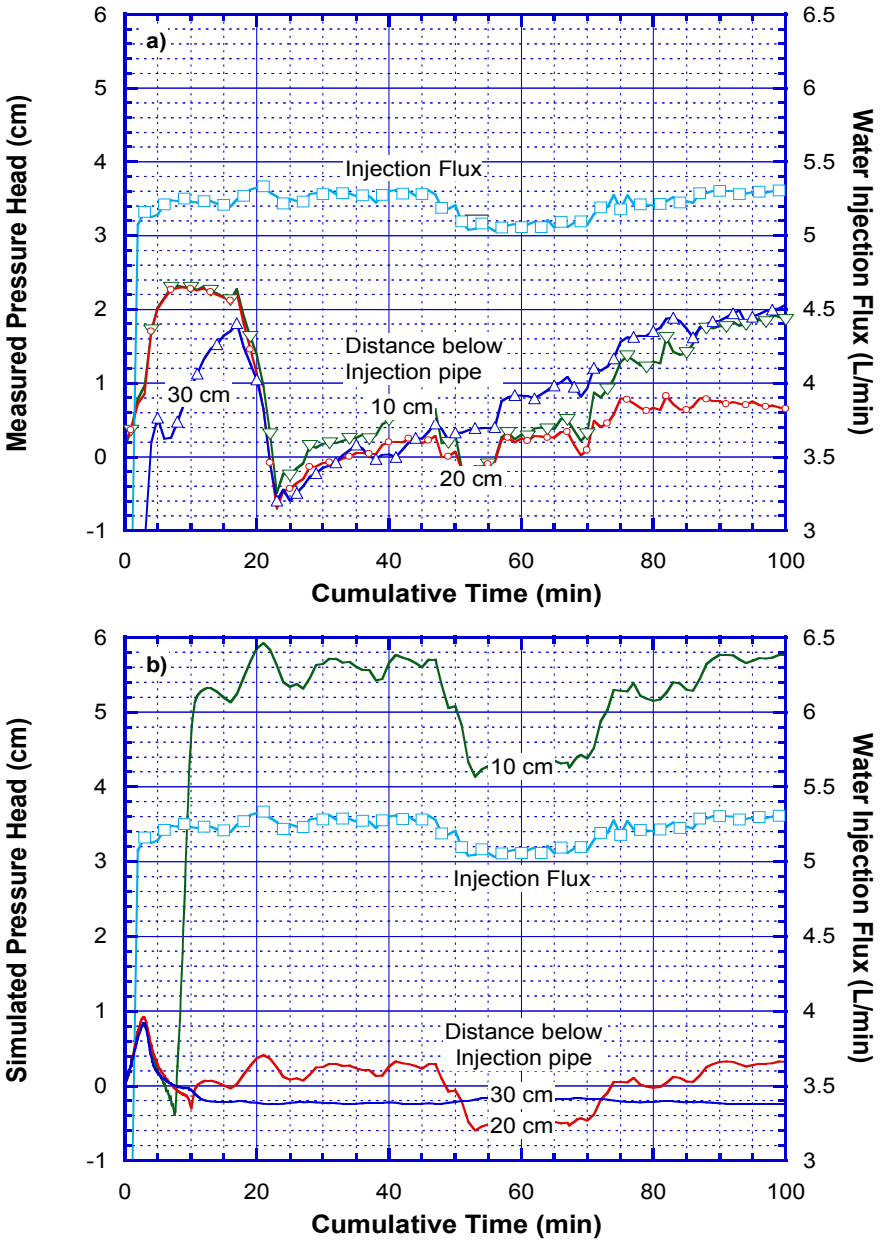

Figure 2. Measured (a); and simulated (b) pressure heads in recirculation experiment

Water Recirculation Lab Experiment

The water-injection experiment lasted a total of two weeks. Immediately after the injection started, an increase in pressure was recorded by pressure transducers at all depths below the injection pipe as shown in Figure 2(a). For brevity, only pressure sensors located vertically below the injection pipe are discussed here. The water pressures at 10 cm and 20 cm below the injection pipe reached a maximum value of 2.5 cm within 7 min. The pressures started to dissipate after 17 min and rose again gradually. Lower pressure was recorded at a depth of 30 cm, with a maximum value of only 1.8 cm. Sensors at lower depths were closer to the bottom drainage boundary of the box and hence offered less resistance to entrapped air trying to escape the sand pores. Consequently, the lower sensor recorded lower pressures than the sensors near the injection pipe.

The water-content sensors located at various depths reached a steady-state value after about 11.5 days. The sensors located at 10 and 20 cm depths reached a maximum saturation of about 90%, while the deepest sensor (40 cm) reached about 100% saturation in 11.5 days (Khire and Kaushik, 2012).

The pressure heads did not completely dissipate till about 11.5 days after injection started (not shown in Figure 2). Mukherjee and Khire (2012) reported similar time frames for dissipation of air pressures for an experiment carried out using the same physical model. Wang et al. (1998) also reported an increase in air pressure and subsequent pressure drop to a minimal value for an air-confining infiltration experiment. The reason for such an air-pressure buildup has been attributed to the unconnected pores of the media and restricted hydraulic boundaries for an unrestricted exit of entrapped air in the sand.

Numerical Modeling Results

The EOS3 module in TOUGH considers air and water as active gas and liquid phase components, respectively. Hence, it was used to simulate the experiment. Figure 2(b) presents simulated pressure heads. TOUGH was able to capture the initial increase in pressure due to entrapped air, at all depths below the injection pipe. The simulated pressures increased to 0.8 cm at 3 min and dropped to zero within 10 min. The simulated pressures, while lower, are still within the same order of magnitude as the measured pressures at the corresponding depths. TOUGH predicted an early dissipation of air pressure, whereas it took about 17 min to 11.5 days for the air pressures to fully dissipate in the experiment (Khire and Kaushik, 2012). The reason for such a difference could be that dead-end pores within the sand made the time to remove trapped air longer, resulting in higher air pressures for an extended period of time. In addition, with respect to TOUGH input, the lower boundary could not be simulated as the physical setup—it consisted of two free-flowing perforated pipes, which is more restrictive for air flow than what was input into the model.

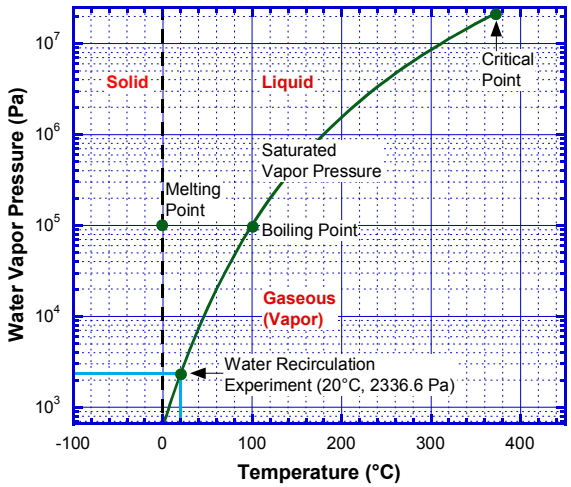

Figure 3. Water-phase diagram

TOUGH considers air and water as two components present in both liquid and gas phase. The total gas-phase pressure is calculated following Dalton's law of partial pressures:

$$P_g^{tot} = P_g^a + P_g^w \tag{4}$$

where, P_g^a = pressure in the gas phase due to air and P_g^w = water vapor pressure. For unsaturated element volume, i.e., $0 < S_l < 1$ (S_l = liquid saturation) where both liquid and gas phase co-

exist, P_g^w is equal to saturated vapor pressure (2336.6 Pa at 20°C temperature) as per the water-phase diagram (Figure 3).

The air pressure in gas phase (P_g^a) is calculated by Henry's law:

$$P_g^a = K_H \times X_l^a \quad (5)$$

where K_H is Henry's constant (assumed to be 10^{10} Pa/mole at all temperatures, for air-gas interface in TOUGH). X_l^a is air mass fraction of the liquid phase defined by M_l^a / M_l (M_l^a is mass of air in liquid phase and M_l is total liquid mass) and is computed from mass-balance equations in TOUGH.

As the water-injection event began, the air mass fraction in the liquid phase increased from 1.5912E-5 to a maximum 1.5927E-5 at 3 min for all depths (Figure 4). X_l^a eventually decreased to a relatively low value below the initial condition of 1.5912E-5 at all depths, which resulted in below-atmospheric gas-phase pressures.

With the onset of saturation at 7.5 min and 10 min, the air mass fraction in liquid phase dropped steeply for nodes at 10 cm and 20 cm below the injection pipe, respectively (Figures 4 and 5). On the contrary, X_l^a at 30 cm depth dropped to a constant value of 1.5908E-5, indicating a two-phase unsaturated condition. As calculated by TOUGH2, the value at 1 bar pressure and 20°C temperature is ~1.6×10^{-5}. The unsaturated conditions at 30 cm depth and saturated conditions at 10 cm and 20 cm depth are also validated by the liquid saturation plot (Figure 4). Under saturated conditions, Darcy's law was used to evaluate pressures from liquid discharge (mass), while for unsaturated conditions, X_l^a calculated at different depths was used by TOUGH to evaluate air pressure and total gas-phase pressures.

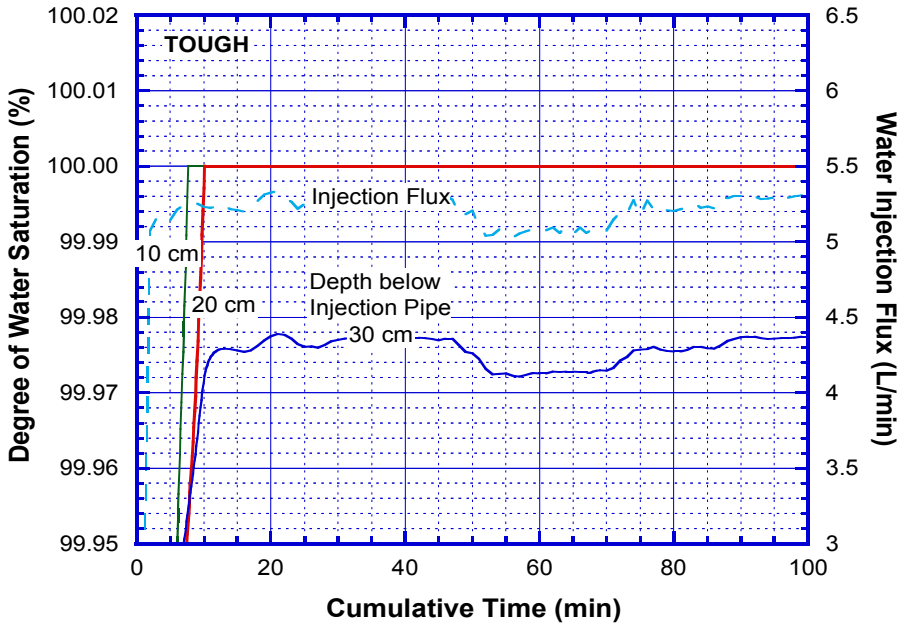

Figure 4. TOUGH simulated water saturation

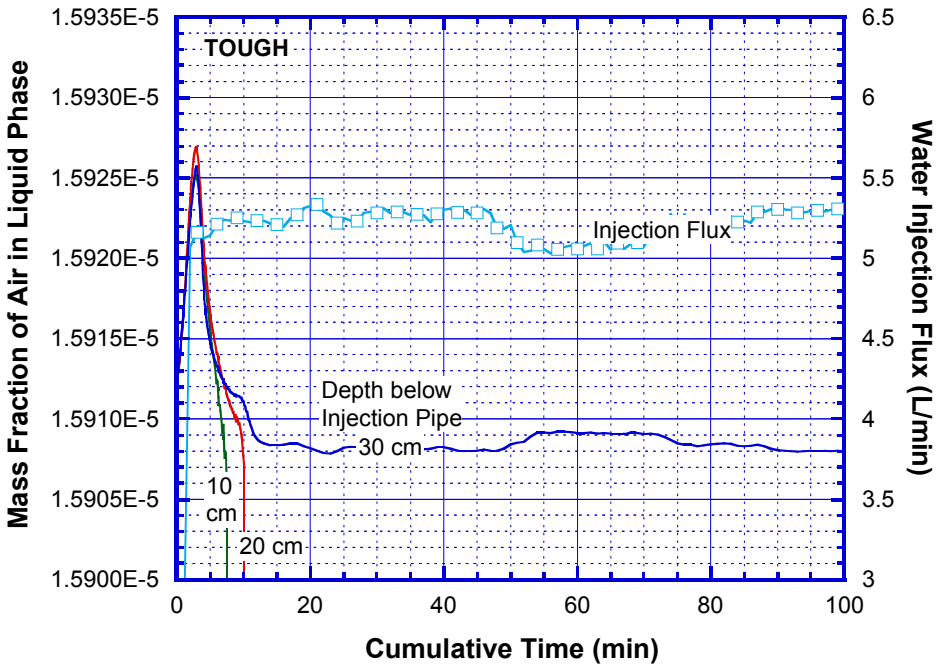

Figure 5. TOUGH simulated mass fraction of air in liquid phase

SUMMARY

Single-phase and single-component models have been commonly used to design subsurface liquid injection systems in bioreactor landfills. The underlying assumption of a passive gas phase in such models results in underestimation of fluid pressures. To assess the suitability of two-phase models such as TOUGH, a large-scale recirculation experiment was conducted using a horizontal perforated pipe, with the experiment simulated by the TOUGH code. This study resulted in the following observations:

1) TOUGH is able to simulate air-pressure increases in dry sand due to pressurized injection of water. TOUGH predicted air pressures relatively accurately.

2) TOUGH is unable to model dead end pores and the vented-perforated-pipe lower boundary in the physical model. Hence, TOUGH was not able to accurately predict the duration of air dissipation observed in the experiment.

Additional simulations using WinGridder are planned to simulate the lower boundary accurately.

ACKNOWLEDGEMENT

This project was partially funded by National Science Foundation Grant No. CMS-0510091.

REFERENCES

ASTM Standard D4491, Standard Test Methods for Water Permeability of Geotextiles by Permittivity, Book of ASTM Standards, 4(13), ASTM International, West Conshohocken, PA, 2009.

Barlaz, M. A., A. P. Rooker, P. Kjeldsen, M. A. Gabr, and R. C. Borden, Critical evaluation of factors required to terminate the post-closure monitoring period at solid waste landfills, *Envir. Sci. and Tech.*, 36 (16), 3457-3464, 2002.

Benson, C. H., M. A. Barlaz, D. T. Lane, and J. M. Rawe, Practice review of five bioreactor/recirculation landfills, *Waste Manage.*, 27, 13-29, 2007.

Haydar, M., and M. V. Khire, Leachate Recirculation Using Horizontal Trenches in Bioreactor Landfills, *J. Geotech. Geoenviron. Eng.*, 131(7), 837-847, 2005.

Jain, P., T. G. Townsend, and T. M. Tolaymat, Steady-state design of vertical wells for

liquids addition at bioreactor landfills, *Waste Manage.,* 30, 2022-2029, 2010.

Khire, M. V., and M. Mukherjee, Leachate injection using vertical wells in bioreactor landfills, *Waste Manage.*, 27, 1233-1247, 2007.

Khire, M. V., and T. Kaushik, Experimental and Numerical Evaluation of Liquid Injection using Horizontal Trench System for Bioreactor Landfills, GeoCongress 2012, *ASCE Geotechnical Special Publication No. 225*, Geotechnical Engineering State of the Art and Practice, Oakland, CA, 27-29, March, 2012.

McCreanor, P. T., and D. R. Reinhart, Mathematical Modeling of Leachate Routing in a Leachate Recirculating Landfill, *Water Resour.*, 34(4), 1285-1295, 2000.

Merry, S. M., E. Kavazanjian Jr., and W. U. Fritz, Reconnaissance of the July 10, 2000, Payatas Landfill Failure, *Journal of Performance of Constructed Facilities*, 19(2), 100-107, 2005.

Mukherjee, M., and M. V. Khire, Instrumented large scale subsurface liquid injection model for bioreactor landfills, *Geo. Test. Jour.*, 35(1), 1-10, 2012.

Pruess, K., C. Oldenburg, and G. Moridis, *TOUGH2 User's Guide, Version 2.0,* Report LBNL-43134, Lawrence Berkeley National Laboratory, Berkeley, Calif., 1999.

Reinhart, D. R., Full-scale experiences with leachate recirculating landfills: case studies, *Waste Manage. And Res. (ISWA)*, 14: 347-365, 1996.

van Genuchten, M. Th., A Closed-form Equation for Predicting the Hydraulic Conductivity of Unsaturated Soils, *Soil Sci. Soc. Am. J.*, 44(5), 892-898, 1980.

Wang, Z., J. Feyen, M. T. van Genuchten, and D. R. Nielsen, Air entrapment effects on infiltration rate and flow instability, *Water Resources Res.*, 34(2), 213-222, 1998.

FEASIBILITY ANALYSIS OF UNDERGROUND COMPRESSED AIR ENERGY STORAGE IN LINED ROCK CAVERNS USING THE TOUGH-FLAC SIMULATOR

Hyung-Mok Kim[1)], Jonny Rutqvist[2)], Byung-Hee Choi[3)]

[1)] Energy and Mineral Resources Engineering, Sejong University
98 Gunja-Dong, Gwangjin-Gu, Seoul 143-747 Korea
e-mail: hmkim@sejong.ac.kr (H.M. Kim)
[2)] Lawrence Berkeley National Laboratory (LBNL)
1 Cyclotron Rd. Berkeley, CA94720 USA
e-mail: jrutqvist@lbl.gov (J. Rutqvist)
[3)] Korea Institute of Geoscience and Mineral Resources (KIGAM)
124 Gwahang-no, Yuseong-gu, Daejeon 305-350 Korea,
e-mail: bhchoi@kigam.re.kr (B.H. Choi)

ABSTRACT

In this paper, we describe the use of the TOUGH-FLAC simulator for feasibility analysis of underground compressed air energy storage (CAES) within lined rock caverns (LRC). We investigated complex thermodynamic processes involved in the CAES operation, such as heat transfer during the compression and decompression of air, groundwater flow and potential leaked-air migration, and mechanical deformation induced by pressurized air in the storage cavern. For this feasibility study, we conducted a 2-D model simulation of a vertical cross section within an LRC for compressed air storage (up to 8 MPa) at the relatively shallow depth of 100 m. In the model, vital components of the CAES system were incorporated, including the cavern, surrounding rock, an excavation damaged zone (EDZ), a concrete lining, and a thin, impermeable, inner synthetic lining. The simulation results demonstrate that underground CAES in LRCs, even at a shallow depth, can be technically feasible with respect to air tightness, energy efficiency, and geomechanical stability. This model approach will be validated through a planned pilot-scale test in Korea where the proposed underground CAES concept will be studied *in situ*.

INTRODUCTION TO UNDERGROUND CAES IN LINED ROCK CAVERNS

Large-scale energy storage systems (ESS) are becoming more important for load leveling, especially in connection with increasing interest in renewable energy. Wind and solar power are promising energy sources, but they are intermittent, which means that they cannot provide electricity steadily and stably, owing to changing weather conditions. They are also often located at remote distances from the energy demand.

Along with pumped hydroelectric storage, underground compressed air energy storage (CAES) is considered to be one of the most promising large-scale electric-energy-storage technologies. In CAES, excess electric energy is used to compress air, which is then injected into underground caverns, large cavities (in salt deposits or mines) or porous reservoirs (aquifers or depleted hydrocarbon reservoirs). When power demand exceeds supply, compressed air is produced from the cavern or reservoir, and fed into a gas turbine that produces electricity that is provided to the grid (Figure 1).

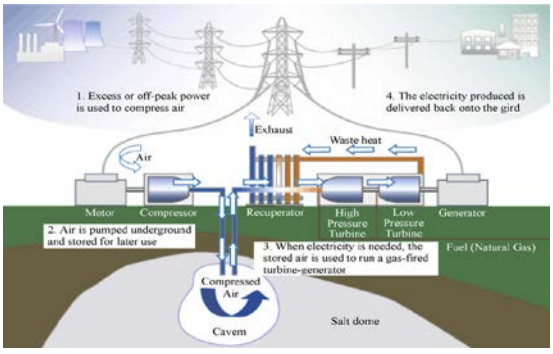

Figure 1. Sketch of an underground CAES reservoir http://www.scotland.gov.uk/, accessed 2012.7).

Excavated underground rock caverns for CAES may be more expensive to develop than solution-mined salt cavities and naturally occurring reservoirs. However, excavation of rock caverns provides more possibilities for site selection closer to energy sources (wind and solar power). Including the transmission-line cost from energy source to demand, the overall costs of energy storage can be reduced by the use of well-located excavated rock caverns. Moreover, CAES in rock caverns lined and reinforced by concrete and steel can be located at shallow depths, independent of surrounding geological conditions, thus significantly reducing construction costs and enabling even greater flexibility in site selection.

THERMODYNAMIC AND GEOMECHANICAL PROCESSES ASSOCIATED WITH UNDERGROUND CAES

General requirements for underground rock caverns for CAES include stability, air tightness, acceptable surface uplift, and eventual environmentally safe decommissioning and abandonment. These general requirements are influenced by thermodynamic and geomechanical design parameters, such as cavern geometry and volume, cavern depth, operation pressure and temperature inside the cavern, distance between the caverns (in case of multiple storage caverns), allowable convergence of the excavated cavern, and operation patterns—in addition to the strength and permeability of concrete linings and surrounding rock mass. Groundwater table level and degrees of saturation in both concrete linings and rock are key in maximizing storage pressure while minimizing air leakage.

Significant temperature changes are expected during the compression and decompression cycles. As a result of such temperature changes and heat transfer to the concrete lining and surrounding rock mass, thermal stresses could be induced that could influence the mechanical stability of a storage cavern. In addition, highly pressurized air may significantly reduce effective stress, which in turn may impact mechanical stability and air leakage.

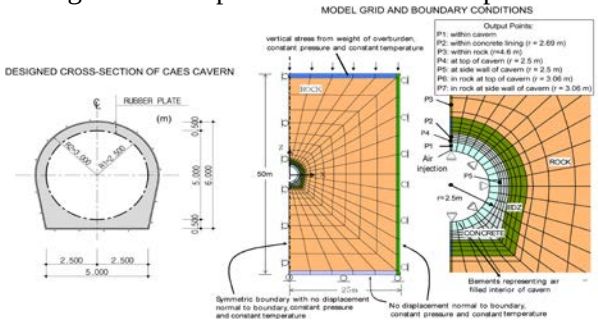

Figure 2. Preliminary design of a cross section of a rock cavern for CAES with concrete lining and model grid with boundary conditions.

ANALYSIS MODEL AND CONDITIONS

We conducted numerical modeling of coupled thermodynamic, multiphase fluid flow, and heat transport associated with underground CAES in lined rock caverns using the TOUGH-FLAC simulator (Rutqvist, 2011). The principles of TOUGH-FLAC coupled analysis are not discussed in detail in this paper. In short, the simulator is based on linking two established codes, TOUGH2 (Pruess et al., 1999) for multiphase flow and heat transfer, and FLAC3D (Itasca, 2009) for geomechanical analysis using sequential coupling and data transfer.

For this study, we carry out a 2-D model simulation for a vertical cross section of an underground CAES system, based on a preliminary design for a pilot test in Korea. The numerical grid shown in Figure 2 contains the vital components of the CAES system, including the cavern, rock, concrete lining, and an excavation disturbed zone (EDZ) that could have different material properties from the surrounding undisturbed host rock. As an option, we could also simulate a thin, impermeable synthetic seal at the inner surface of the concrete lining. In our model, the optional inner-surface synthetic seal is so thin that it has no load-bearing capacity, meaning that the air pressure within the cavern is directly transferred as stress normal to the inner surface of the concrete lining

In the model, the interior of the air-filled cavern is explicitly represented as a medium of high porosity (1.0), high permeability (1.0×10^{-9} m^2), and mechanical softness (E = 3.5 MPa, v = 0.3). The exact values used for the permeability and

deformation modulus of the cavern interior are not important, as long as the values are much less than the values for the concrete lining and surrounding rock. This approach was verified to be useful in simulating air pressure, temperature, and even stress exerted from the air pressure on the inner surface of the lining (Rutqvist el al., 2012). A set of base-case material properties for our analysis is listed in Table 1.

Table 1. Material properties used as a base case for modeling of CAES in a lined rock cavern.

Property	Material		
	Rock mass	EDZ	Concrete lining
Young's modulus, E (GPa)	35	35	35
Poisson's ratio, ν (-)	0.3	0.3	0.3
Thermal expansion coefficient ($°C^{-1}$)	1×10^{-5}	1×10^{-5}	1×10^{-5}
Effective porosity, ϕ (-)	0.01	0.01	0.1
Permeability, k, (m^2)	1×10^{-17}	1×10^{-17}	1×10^{-20}
Residual gas saturation (-)	0.0	0.0	0.0
Residual liquid saturation(-)	0.01	0.01	0.01
van Genuchten, P_0 (MPa)	1.47	1.47	1.47
van Genuchten, m (-)	0.595	0.595	0.595
Thermal conductivity λ (J/s/m K)	3	3	3
Specific heat (J/kg K)	900	900	900

When modeling coupled thermodynamic and geomechanical behavior, we must capture the entire construction and operation sequence. The system therefore was initialized by the following steps:

Step 1: Initial simulation to achieve steady-state vertical gradients of pore pressure, temperature, and stress in the rock mass as initial conditions before excavation.

Step 2: Excavating the cavern and keeping it open for 1 week at atmospheric pressure within the open cavern, to allow the cavern to converge mechanically and to achieve new distributions of pressure, temperature, and stress in the rock mass.

Step 3: Installing the concrete lining at a specific initial saturation (e.g., 70%), atmospheric air pressure, and near-zero effective stress, to keep atmospheric air pressure in the cavern.

After Step 3, proper initial conditions for the start of the CAES operation are achieved. This includes atmospheric cavern pressure, a concrete lining with an initial saturation of 70% and zero stress, a fully saturated surrounding rock mass with excavation induced gradients of pressure, and stress concentrations around the cavern.

After this initialization, the simulated CAES operation was started by injecting and withdrawing air from the cavern for various modeling cases. Analysis conditions are summarized in Table 2.

Table 2. Analysis conditions for initialization and operation simulations.

Initialization
· Cavern depth: 100m
· Rock mass specific weight: 2,700 kg/m^3
· Ground surface temperature: 10 °C
· Vertical gradient of temperature: 0.03 °C/m
· Groundwater table is close to ground surface
· Isotropic stress field (vertical stress equals to overburden rock mass)
Operation
· Operation pressure range: 5 to 8 MPa
· Daily cycle: constant rate injection (8h) - shut in (4h) - constant rate production (4h) - shut in (8h)
· Constant injection rate: 2.2×10^{-2} kg/s
· Constant production rate: 4.2×10^{-2} kg/s
· Injection temperature: 21.5 °C

RESULTS AND DISCUSSION

Base case simulation

We first present an initial model simulation for one daily compression and decompression cycle, which will show the general thermodynamic and mechanical deformation response of the system. Figure 3 shows the calculated evolution of pressure and temperature at three points (P1, within the cavern; P2, within the concrete lining; and P3, within the rock), with their locations shown in Figure 2. Figure 3 also shows the radial displacements of the inner surface of the concrete lining and stress evolution at a point (P2) located in the concrete lining (positive values signify tension). The results show pressure evolution induced by a pre-designed daily cycle of compression and decompression. Some changes in gas pressure and temperature occur in the concrete lining, whereas pressure and temperature do not change significantly in the rock a few meters from the excavation. Figure 3(c) shows that the air-filled cavern expands and contracts with a maximum magnitude of 0.3 mm (radius change). This is a very

small displacement, leading to a volume change of about 5×10^{-3} m^3—negligible compared to the total cavern volume of 19.63 m^3. In Figure 3(d), it is shown that the maximum and minimum compressive effective stresses (taking into account gas pressure evolution) are synchronized with the pressure evolution during the daily cycle.

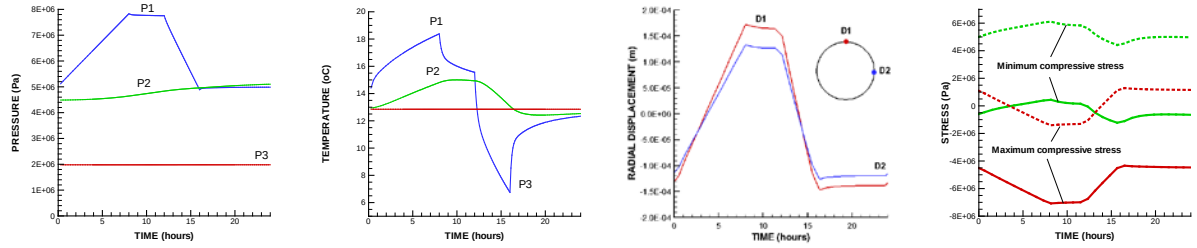

(a) (b) (c) (d)

Figure 3. Calculated evolution of (a) pressure (b) temperature (c) radial displacement of the inner surface of the concrete lining (d) stress in the concrete lining (P2) (green lines are maximum compressive stress, red lines minimum compressive stress; dashed lines are effective stresses and solid lines total stresses)

Air tightness performance

The total mass stored in a storage cavern at a certain pressure and temperature can be estimated from the ideal gas law. During compression and decompression cycles, pressure and temperature within the cavern vary nonlinearly with time, and with the air mass lost from the cavern; a leakage rate can be determined using Eq. (1) according to.

$$\Delta m = m_1 - m_2 = \frac{V_{cavern}}{R_{air}}\left(\frac{P_1}{T_1} - \frac{P_2}{T_2}\right) \quad (1)$$

where m is mass of gas (kg), P is absolute pressure (Pa) within the cavern, V_{cavern} is cavern volume (m^3), R_{air} is the specific gas constant for air (=286.9 J/kg K), and T is absolute temperature (K). Total volume of the open cavern inside the concrete lining is assumed constant during compression and decompression cycles. Subscripts 1 and 2 indicate initial and later states, respectively.

Figure 4 presents the evolution of leakage rate and daily leakage percentage for various combinations of lining and rock permeability. The results show that leakage of less than 1% would be achieved if permeability of the concrete lining were less than 1×10^{-18} m^2, even if the permeability of the rock were as high as 1×10^{-15} m^2. A less than 1% leakage rate is also achieved if the rock mass permeability were less than 1×10^{-17} m^2, even with a comparatively permeable concrete lining.

Figure 5 presents the leakage rate and daily leakage percentage as a function of gas saturation in the lining, when the lining intrinsic permeability is 1×10^{-16} m^2, i.e. a relatively high value. The leakage rate increases with increasing gas saturation (decreasing water saturation) in the concrete lining, indicating that the saturation in the concrete has a significant impact on the CAES system air tightness. We calculated a daily leakage of 12% when the gas saturation in the concrete lining was 74%, while the leakage rate decreased to 0.8% when the gas saturation was 29%. Our simulations indicate that a daily leakage of 12% would be achieved as the lining dries out after 3 years of continuous operation. Thus, unless the gas saturation of the lining can be kept low, a lining permeability of 1×10^{-16} m^2 does not provide sufficient air-tightness for an efficient CAES system.

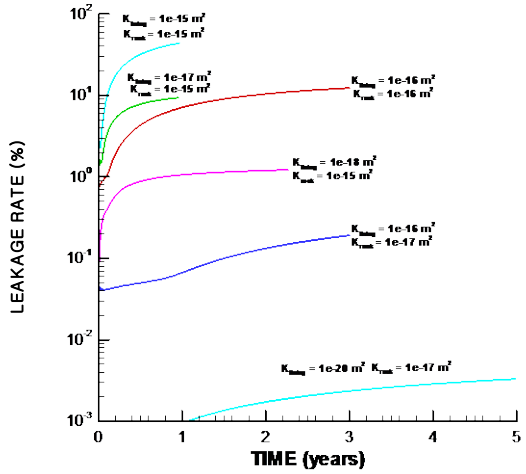

Figure 4. Calculated evolution of daily leakage percentage for different combinations of concrete lining and rock permeability

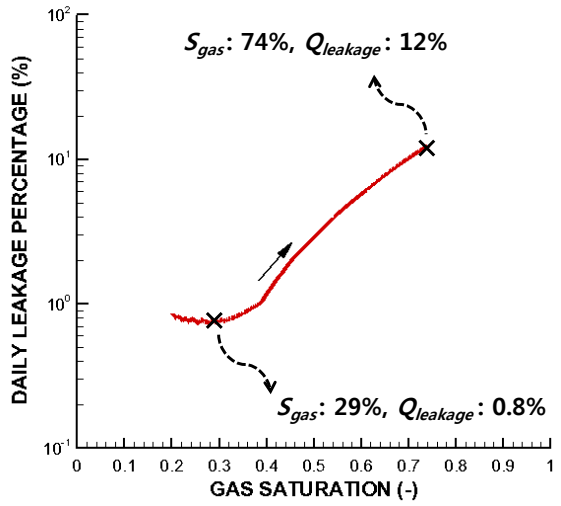

Figure 5. Calculated daily leakage percentage versus saturation in the concrete lining for a lining intrinsic permeability 1×10^{-16} m^2.

Thermodynamic energy efficiency

The energy balance equation for the CAES system can be written as follows (Kim et al., 2012):

$$C_{air}T_s\Delta m_s = \frac{C_{air}}{R}V_s\frac{\partial P_s}{\partial t} = (C_{air}+R_{air})T_m\Delta m_m - (C_{air}+R_{air})T_l\Delta m_l + (\Delta Q_c + \Delta Q_a) \quad (2)$$

where Δm_s is the rate of change of stored air mass, m_m and m_l are the mass flows (kg/s) by air movement due to injection and production as well as air leakage, and air is assumed to be an ideal gas. T_s, T_m, and T_l are the temperatures (K) of stored air, injected/produced, and leaking air, respectively. Here, V_s is the volume of stored air, equal to cavern volume. T_m is equal both to the injection temperature (21° C = 294.15 K) during compression and to cavern temperature, i.e., the temperature of stored air T_s during decompression. The temperature of leaking air (T_l) is taken to be equal to the temperature of stored air (T_s). C_{air} is the specific heat of air at constant volume (1,006 J/(kg K)), and R_{air} is the specific gas constant for air (286.9 J/(kg K).

Eq. (2) indicates that the change in total energy stored in the CAES underground cavern can be expressed as the summation of the internal energy change, the work done by injected compressed air, and the sum of outflows from production, air leakage, and heat transfer. From the TOUGH2 simulation, each term of the above energy balance equation was evaluated.

Figure 6 demonstrates the energy loss and gain for a tight and leaky case including both air leakage and heat transfer, with a negative energy rate indicating an energy gain. The shaded area in Figure 6(b) represents the energy loss solely by air leakage; air leakage and consequent energy loss are clearly more significant in leaky lining cases with higher permeability of concrete linings.

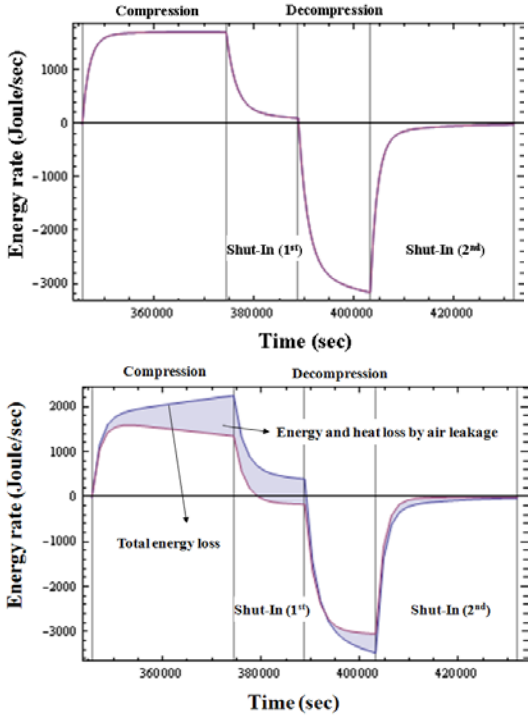

Figure 6. Energy balance analysis for (a) tight lining case with concrete lining permeability of 1.0 x 10^{-18} m^2, (b) leaky lining case with concrete lining permeability of 1.0 x 10^{-16} m^2

For a more quantitative energy-balance analysis, we calculated the time-integrated values for each term in Eq.(2). In the tight-lining case, the energy loss through heat conduction was greater than that through air leakage by two orders of magnitude, constituting as much as 28% of the total injected energy during compression. Energy gain—the energy recovered through heat conduction from the concrete lining to the stored air during the decompression phase— was as much as 24% of total injected energy. Thus, 4% of injected energy was lost during the cycle. In the leaky lining case, total energy loss during the compression phase was as much as 36% of total injected energy, and ultimately 10% of the total injected energy was lost due to air leakage.

We also investigated the influence of injection temperature and the thermal conductivity of the concrete lining on energy balance. We found that the energy loss from heat conduction can be minimized by keeping the air-injection temperature closer to the ambient temperature of the storage cavern. (The thermal conductivity of the concrete linings was insignificant.)

Geomechanical stability

Coupled modeling to study the geomechanical stability of the underground CAES system was conducted in several steps to simulate the sequence of excavation, installation of concrete lining, and subsequent air compression from an initial atmospheric pressure to CAES operation pressure. In this simulation, we assumed that the concrete lining is installed several months after excavation. The initial pressure in the cavern is atmospheric and the initial stress in the concrete lining is zero. The initial water saturation within the concrete lining is 70%, and the rock mass outside the concrete lining is fully saturated.

Figure 7 presents the results of pressure and stress in the concrete lining during a simulation over 100 daily cycles. Figure 7(a) shows the results for a simulation case assuming that the concrete lining serves as a primary seal with a relatively low permeability of 1.0 × 10^{-20} m^2. On the other hand, Figure 7(b) shows the simulation results for a case in which a perfect synthetic air-tight seal (e.g. welded steel lining or rubber sheet) is installed inside the concrete lining.

In Figure 7, we also show, in more detail, the results for the first 7 cycles (first week) as well as one cycle at the end of the 100-day simulation (cycle#100). For the case of concrete lining as a primary seal, the pore pressure in the concrete lining (P2 in Figure 7(a)) increases slowly with time and reaches about 6 MPa by the end of the 100th cycle. This pressure increase has implications for the mechanical stability of the CAES system, since it leads to changes in the effective stress in the concrete lining. Figure 7 further shows the evolution of maximum and minimum principal stresses. Red lines are total stresses; green lines are effective stresses. Most importantly, the minimum principal stress is in tension (positive sign), and the tension increases over time in concert with the increase in gas pressure within the lining. In Figure 7(a), at the 100th day, the minimum effective principal stress fluctuates between 5 to 7 MPa (tensile stress), which may initiate radial fractures and air leakage through the fractures.

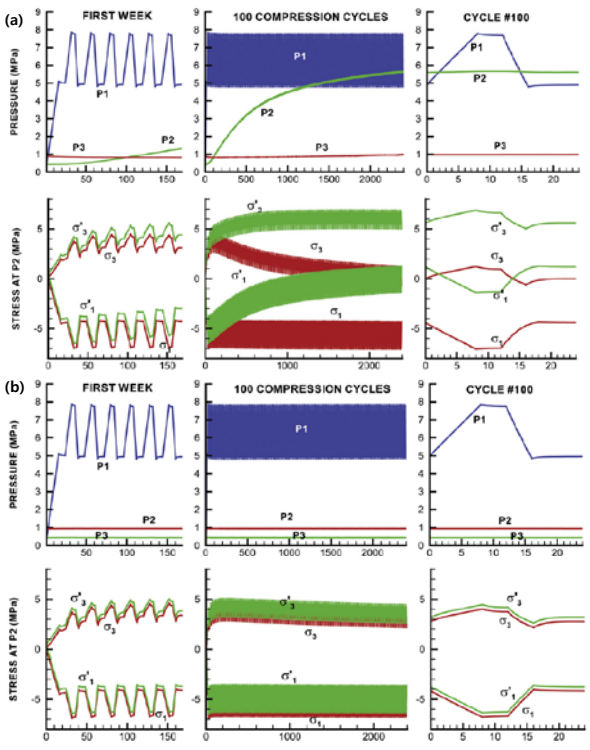

Figure 7. Calculated pressure and stress in the concrete linings during the 100 cycles, (a)

when only the concrete lining was installed, (b) when the air-tight inner seal was installed inside the concrete lining.

The main difference between the case with the impermeable internal seal (Figure 7(b)) and the case without internal seal (Figure 7(a)), is that in the former, the fluid pressure within the concrete lining remains constant and equal to the initial pressure. As a result, the minimum effective principal stress does not exceed 5 MPa in tension over the entire 100-day simulation time. This shows that an impermeable synthetic seal can help to reduce effective tensile stress, and reduce the potential for fracturing in the concrete lining.

The potential impact of permeability changes in the concrete lining as a result of straining and potential fracturing was investigated. Laboratory data showed that cracked concrete is several orders of magnitude more permeable than intact, uncracked concrete (Hoseini et al., 2009). Laboratory results have also indicated a threshold in the crack-opening displacement (COD), below which there is no significant change in permeability. In this study, we estimated COD from the tangential strain, assuming that when tensile failure occurs, the tangential strain is localized to opening of one fracture intersecting the element. We related the COD (equivalent to aperture) to permeability using the cubic law for fracture flow, and then calculated the change in equivalent permeability resulting from crack opening, as if it were superimposed on the initial rock permeability (Figure 8).

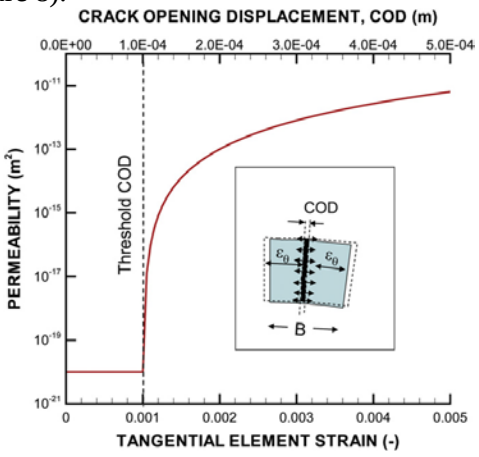

Figure 8. Element strain (and implicit crack opening displacement) versus element permeability model for simulating permeability changes caused by cracking of concrete lining (Rutqvist et al., 2012).

Figures 9 and 10 show how pressurization of a cavern leads to tensile failure and localized permeability increases, and a breakthrough, with air leakage out of the cavern. The modeling results showed that larger strains are localized at the top of the cavern and at one location at the side of the cavern after 24 hours. At this instant, the air pressure quickly propagates through the concrete lining and leads to an increase in pressure within the rock mass outside the lining. However, despite an abrupt pressure change in the lining and in the surrounding rock mass, the average pressure within the cavern remains nearly constant during 10 cycles of simulation, indicating that fracturing within the concrete lining has no significant impact on the pressure evolution within the cavern. We also investigated the influence of the excavation damaged zone (EDZ) on the geomechanical performance of CAES in lined rock caverns.

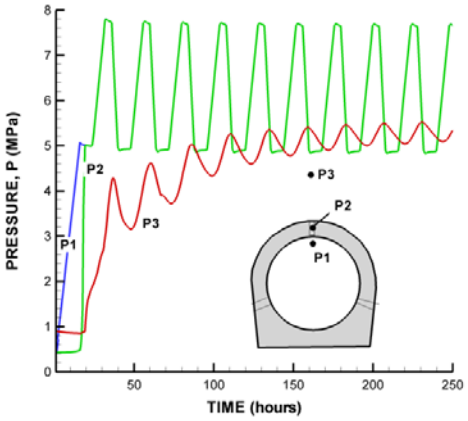

Figure 9. Calculated evolution of pressure through a tensile crack in concrete linings during 10 pressure cycles using the element strain versus permeability function.

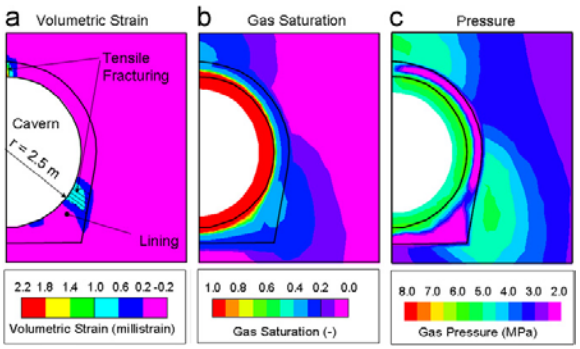

Figure 10. Calculated distribution of (a) volumetric strain, (b) saturation, and (c) pressure after 10 pressure cycles when cracking has occurred in the concrete lining.

Figure 11 compares the calculated evolution of stress within the concrete lining and the radial displacement of the inner surface of the concrete lining under more or less compliant EDZ conditions. Here, the compliance of the EDZ was defined as EDZ thickness multiplied by EDZ compressibility. In Figure 11, the increased compliance of the lining-EDZ-rock system results in an increase of tangential stress from 2.4 to 5.26 MPa, and radial displacement from 0.46 to 0.66 mm. From our further simulations, aiming at more precisely investigating the relative effect of the EDZ on the concrete lining, we found that the most favorable design for reducing tensile tangential stress in the lining would be a relatively compliant lining and relatively stiff (uncompliant) rock that is not significantly softened in the EDZ.

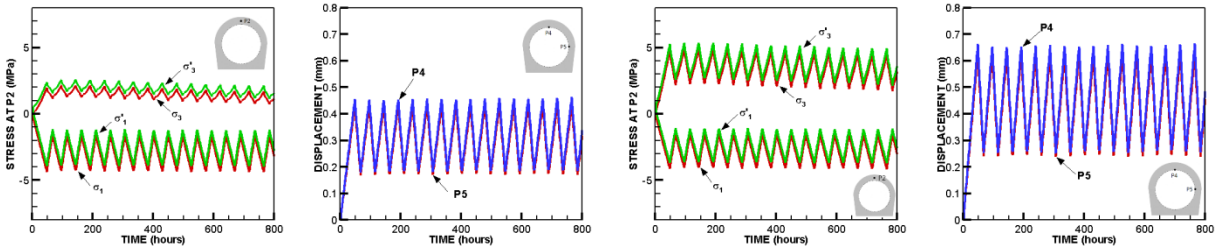

(a) (b) (c) (d)

Figure 11. Calculated evolution of (a) stress and (b) displacement of concrete lining in less compliant EDZ condition, and (c) stress and (d) displacement of concrete lining in more compliant EDZ condition.

SUMMARY AND CONCLUSIONS

We carried out numerical modeling of coupled thermodynamic, multiphase fluid flow and geomechanical processes associated with underground CAES in a lined rock cavern. Specifically, we investigated air tightness, energy efficiency, and the geomechanical stability.

Our air-mass balance analysis showed that the key parameters for assuring the long-term air tightness of the CAES system were (1) the permeability of both the concrete lining and the surrounding rock and (2) the gas (and water) saturation of the lining. The analysis shows that the concrete lining would dry out over time, leading to increased leakage, unless the concrete can be kept moist at a relatively high liquid saturation. Nevertheless, a concrete lining with a permeability of less than 1×10^{-18} m^2 would result in an acceptable air-leakage rate even if completely dry. Subsequent energy-balance analyses demonstrated that the energy loss for a daily compression and decompression cycle depends on the air-pressure loss, as well as on energy loss resulting from heat conduction to the concrete lining and surrounding rock. In our geomechanical analysis, investigating the potential failure from tensile stress in concrete linings, we found that the air leakage out of a cavern did not increase to unacceptable levels even after a significant pressure increase in the surrounding rock—as long as the rock is sufficiently impermeable or the inner impermeable lining remains robust.

From these results, we conclude that underground CAES in rock caverns with concrete linings at the comparatively shallow depth of 100 m is technically feasible. These findings will be further verified through ongoing pilot tests in Korea.

ACKNOWLEDGMENT

This research was supported by the Basic Research Project of the Korea Institute of Geosci-

ence and Mineral Resources (KIGAM, GP2012-001) funded by the Ministry of Knowledge and Economy of Korea. Funding from KIGAM for Dr. Jonny Rutqvist and Berkeley Lab was provided through the U.S. Department of Energy Contract No. DE-AC02-05CH11231.

REFERENCES

Hoseini M., V. Bindiganavile, N. Banthia, The effect of mechanical stress on permeability of concrete: A review. *Cement & Concrete Composites*, 31, 213–220, 2009.

Itasca, *FLAC3D, Fast Lagrangian Analysis of Continua in 3 Dimensions, Ver. 4.0* Minneapolis, Minnesota, 2009.

Kim, H.M., J. Rutqvist, D.W. Ryu, B.H. Choi, C. Sunwoo, W.K. Song, Exploring the concept of compressed air energy storage (CAES) in lined rock caverns at shallow depth: A modeling study of air tightness and energy balance, *Applied Energy*, 92, 653-667, 2012.

Pruess, K., C. Oldenburg, and G. Moridis, *TOUGH2 User's Guide, Version 2.0*, Report LBNL-43134, Lawrence Berkeley National Laboratory, Berkeley, Calif., 1999.

Rutqvist, J., Status of the TOUGH-FLAC simulator and recent applications related to coupled fluid flow and crustal deformations, *Comp. Geosci.*, 37(6), 739-750, 2011.

Rutqvist, J., H.M. Kim, D.W. Ryu, J.H. Synn, W.K. Song, Modeling of coupled thermodynamic and geomechanical performance of underground compressed air energy storage in lined rock caverns, *Int. J. Rock Mech. Min. Sci.*, 52, 71-81, 2012.

ON PARAMETERIZING HETEROGENEITY AND INCORPORATING GEOPHYSICAL MEASUREMENTS IN HYDROGEOPHYSICAL INVERSE MODELING

Michael B. Kowalsky, Michael Commer, Kenneth H. Williams, and Stefan Finsterle

Lawrence Berkeley National Laboratory
Berkeley, California, 94720, U.S.A.
e-mail: mbkowalsky@lbl.gov

ABSTRACT

We consider the estimation of hydrological parameters through inverse modeling of hydrological (tracer) data and/or geophysical (electrical resistivity) data associated with experiments from the shallow unconfined uranium-contaminated aquifer at the DOE Integrated Field Research Challenge (IFRC) site at Rifle, Colorado. The purpose of this study, which draws on examples from recent and ongoing research, is to highlight the degree to which certain modeling decisions impact inversion results. Through synthetic examples based on field experiments with real-world complexities, we focus on decisions related to (1) how heterogeneity and other hydrological features are parameterized, and (2) how geophysical monitoring data are incorporated.

INTRODUCTION

Obtaining estimates of hydrological properties through inverse modeling requires decisions of great consequence to be made on how to parameterize heterogeneity (i.e., how to represent a heterogeneous distribution using a limited number of parameters that are amenable to estimation) and how to include different types of measurements in a model. Inadequate parameterization of heterogeneity or other hydrological features leads to errors in the model structure that are partly compensated for by biased property estimates, which may allow for an improved fit to the calibration data but lead to incorrect interpretations of hydrological phenomena and reduce the ability of the model to make reliable predictions. The manner in which observations are integrated in inverse modeling is similarly important. If the procedure for simulating measurements is not consistent with the true measurement process, then the resulting property estimates may be biased.

The purpose of this study is to highlight the degree to which certain modeling decisions can affect inverse modeling results. Through synthetic examples based on field experiments with real-world complexities, we focus on two areas in particular: (1) how heterogeneity and other hydrological features are parameterized, and (2) how geophysical monitoring data are incorporated.

An overview of the methodology and the field experiments that provide motivation for the study are given, followed by some examples and conclusions.

METHODOLOGY

The inverse modeling approach, as described by Kowalsky et al. (2012), consists of three main parts: a forward model, parameterization of heterogeneity and hydrological features, and an inverse modeling framework that integrates different types of data. In this study, TOUGH2 (Pruess et al., 1999) provides the forward model used to simulate the flow and transport phenomena in the experiment and the corresponding measurements for a given set of input parameters.

Simplifying assumptions made in the parameterization of heterogeneity must be carefully considered to insure they are adequate for a given application and consistent with site conditions (e.g., Moore and Doherty, 2006). A variety of approaches are available. A pixel-based approach divides the model into discrete regions, often in a regularly spaced grid or layers, allowing for values at each pixel to be estimated through inversion. In the related zonation approach, uniform properties are assigned to model regions based on practical considerations or based on spatial information related to the geology that is available from

characterization data (e.g., geophysical data or core descriptions) to a varying degree of spatial coverage and accuracy. A geostatistical parameterization treats the heterogeneous property as a spatially correlated random field that is a function of the semivariogram and conditioning values at so-called pilot point locations estimated during inversion. Various aspects of these parameterization approaches or combinations thereof are considered in the examples given below.

The inverse modeling framework used here is iTOUGH2 (Finsterle, 2004). It provides capabilities for parameter estimation, error analysis and uncertainty propagation for TOUGH2 and other linked forward models, including geophysical models. Suitable geophysical measurements are made a function of properties that are simulated in the TOUGH2 forward model and, therefore, a function of the hydrological input parameters. In other words, iTOUGH2 allows for coupled inversion of hydrological and geophysical data (or hydrogeophysical inversion). A variety of geophysical measurements have been integrated into iTOUGH inversions, including time-lapse ground-penetrating radar, electrical resistivity, and seismic (Kowalsky et al., 2004, 2005, 2008, 2010, 2011).

Geophysical monitoring data can be included in hydrological inversions in different ways (e.g., Hinnell et al., 2010). In one approach, the geophysical observations are directly simulated based on TOUGH2 state variables at a given time and compared to the measured values as part of the calibration procedure. A petrophysical model converts the TOUGH2 state variables to the input needed for the geophysical simulation. For example, Archie's law (1942) relates porosity, saturation, and fluid electrical conductivity—which itself is a function of the concentration of dissolved mass components—to bulk electrical resistivity, the input property needed for an electrical resistivity simulation. Commer et al. (2012) present an example, which is also related to this study, using this approach.

In a second approach, traditional geophysical tomography is performed as a pre-processing step. The resulting tomogram of the relevant geophysical property is then used as spatially distributed calibration data in the inversion, typically also requiring a petrophysical model to relate the simulated hydrological response to the geophysical tomogram. While the sequential application of geophysical tomography and hydrological inversion is a straightforward means for incorporating geophysical data, errors that are commonly introduced in the tomography procedure (such as smoothing or streaks in the image) may cause the hydrological parameter estimates to be biased, as is demonstrated in an example below.

OVERVIEW OF FIELD EXPERIMENTS

The examples in this study were motivated by experiments at the U.S. Department of Energy (DOE) Integrated Field Research Challenge Site (IFRC) at Rifle, Colorado in a shallow unconfined aquifer that was contaminated from uranium mill tailings. The aquifer is 2.5 to 3 m thick, and is located on the floodplain of the Colorado River in alluvium situated above an impermeable bedrock formation. A main objective at the IFRC site has been to perform biostimulation experiments for uranium remediation through the injection of acetate. Nonreactive (i.e., conservative) tracers are typically also injected into the groundwater to aid in characterization of the transport processes and properties of the subsurface. Detailed descriptions of the IFRC site and related field experiments are given elsewhere (Anderson et al., 2003; Vrionis et al., 2005; Yabusaki et al., 2007; Williams et al., 2011). In the examples given below, we consider the "Winchester" experiment of 2007 (Williams et al., 2011), and the "Best Western" experiment of 2011.

Understanding subsurface heterogeneity is key to analyzing complex biogeochemical reactions such as those occurring in these field experiments. Heterogeneity is expected to have a large impact on the efficacy of biostimulation. Thus, developing, testing, and analyzing techniques for estimating heterogeneous properties based on limited characterization data, such as tracer concentrations, core data, and geophysical data, continues to be a critical research topic in hydrogeology.

EXAMPLE 1. PARAMETERIZING HETEROGENEITY

A recent study by Kowalsky et al. (2012) on inverse modeling of synthetic and actual field data from the Winchester experiment highlights some issues related to parameterization, and forms the basis for discussion in this example. The experiment involved the injection of groundwater amended with acetate, to induce biostimulation, and sodium bromide, to act as a conservative tracer and allow for investigation of hydrological properties at the site. The amended groundwater was injected into 10 wells (shown with triangles in Figure 1) situated perpendicularly to the direction of groundwater flow, and the time-varying concentrations were measured in 12 down-gradient monitoring wells (shown with circles in Figure 1).

To investigate how various choices related to the parameterization of heterogeneity in such a system can affect inverse modeling results, a hydrological model was developed to simulate the experiment and the measurements. Based on a permeability distribution generated in GSLIB (Deutsch and Journel, 1992) using Gaussian sequential simulation (SGSIM), synthetic bromide concentration data were simulated for different sampling intervals and noise levels. Figure 2 shows a best-case scenario data set with high temporal sampling and no added noise. The permeability distribution, as shown in Figure 1a, represents the true model for the synthetic study. Snapshots of the concentration at several times are shown in Figure 3.

When characterization data related to the spatial distribution of geological properties or facies are available (e.g., from geophysical data, well logging data or core descriptions), it is naturally of interest to incorporate this information into a hydrological model. For this purpose, a zonation parameterization may be used in which each zone or facies is modeled with uniform properties that are measured somehow or estimated through inversion. To explore some aspects of this approach, several facies "data sets" were derived from the true permeability distribution—with varying resolution, coverage, and accuracy—and used for inversion.

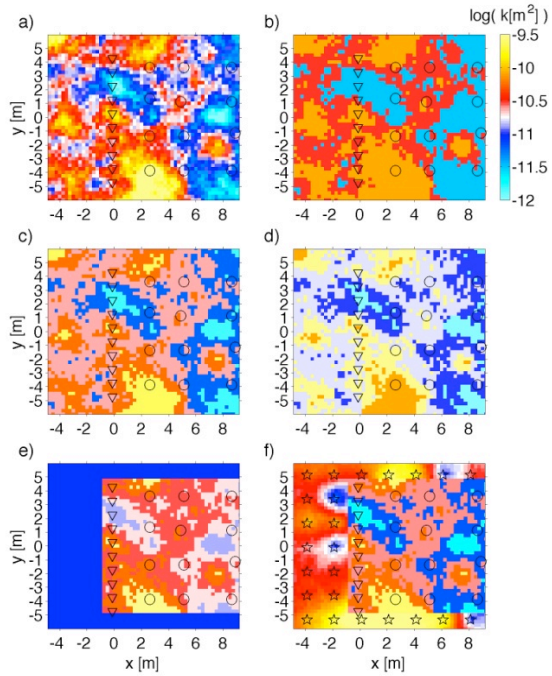

Figure 1. Inversion of synthetic data with zones or "facies" information of varying accuracy and completeness. (a) True permeability. Inversion with the geometry of (b) three zones known perfectly, (c) five zones known perfectly, (d) slightly inaccurately, and (e) perfectly but only for the well region with core data. (f) Inversion with geometry of five zones known in the well region, and pilot points used elsewhere.

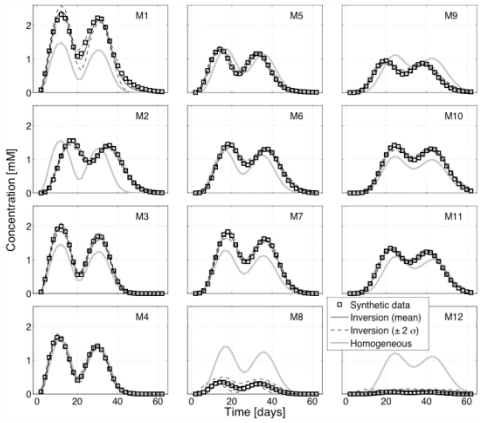

Figure 2. Noise-free bromide concentrations used as synthetic data (symbols), fit by inversion with a homogeneous model (solid gray line) and by inversion with a geostatistical parameterization (black lines show mean with +/- 2 standard deviations).

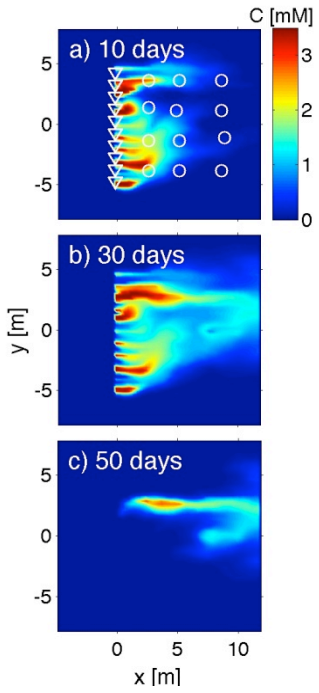

Figure 3. Bromide concentration at several times.

For the case in which facies data comprise 3 zones (permeability ranges), the inversion is not able to obtain a good fit between the simulated and measured (synthetic) data, and the resulting parameter estimates are inaccurate (Figure 1b), revealing an inadequate parameterization. On the other hand, when the facies data comprise 5 zones, inversion provides a nearly perfect data fit and accurate parameter estimates (Figure 1c). Introducing a small amount of error in the facies geometry, by introducing 50 cm shifts in the geometry in 2 m by 2 m regions, considerably worsens the parameter estimates (Figure 1d). When the facies data are without error but limited to the region near the wells where core data are available, then the parameter estimates are again poor (Figure 1e). However, combining the facies data from the limited region with a geostatistical parameterization, in which pilot point values are also estimated in the inversion, allows for accurate parameter estimates (Figure 1f). Thus, accounting for errors in the zonal geometry and properly parameterizing regions where no information is available (e.g., up-gradient of the injection wells) is clearly important for accurate inverse modeling results.

Implementing pilot points in a geostatistical parameterization must also be done with care. Rather than placing pilot points throughout the entire model domain, a practitioner might choose to reduce the number of unknowns by modeling the region up-gradient (to the left) of the wells using a uniform zone with a single unknown parameter. However, the estimated permeability distribution is then inaccurate (Figure 4a) and does not allow for an adequate fit to the data. When the region is modeled with unconditional heterogeneity (i.e., reflecting the correct spatial correlation structure but not controlled by pilot points), the data fit and the parameter estimates are similarly not optimal (Figure 4c). The best inversion results are achieved by also including pilot points in the up-gradient region (Figure 4e).

Kowalsky et al. (2012) provide metrics to further quantify improvement between cases. Deteriorating experiment conditions, variable porosity, and errors in the semivariogram and gradient direction are also considered, as is application to the field data and a 3D model.

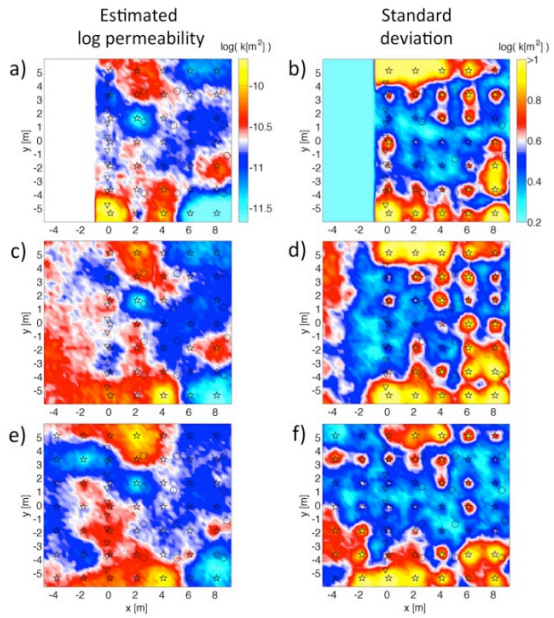

Figure 4. Sensitivity of geostatistical inversion to the parameterization in the region up-gradient (to the left) of the injection and monitoring wells. The region is parameterized with (a) one zone of uniform permeability, (b) unconditional heterogeneity (no pilot points), and (c) two columns of pilot points. Figure 1a shows the true permeability model.

EXAMPLE 2. INCORPORATING GEOPHYSICAL MONITORING DATA

This second example is motivated by the Best Western experiment which sought to study, among other things, the impact of prolonged bicarbonate injection on metal oxyanion (U, As, V, Se, Mo) mobility. In one portion of the area used for this experiment (plot C at the IFRC site), sodium bicarbonate was injected into the groundwater, having the added benefit of serving as an electrically conductive tracer (while not strictly conservative, it can be considered as a tracer to a first approximation). Electrical conductivity (EC) measurements were regularly made on fluid samples from the monitoring wells. In addition, crosshole electrical resistance tomography (ERT) data were collected at a number of times.

A hydrological model, representing a 2D vertical plane aligned with the direction of groundwater flow, was constructed for the vicinity of the bicarbonate injection (Figure 5). The model includes the vadose zone in the upper 3 meters and a saturated zone in the lower 3 meters (only the saturated zone is depicted). The top boundary is given by constant atmospheric pressure, while the bottom is a no-flow boundary. A gradient is added to the constant hydrostatic pressure specified on the side boundaries to induce lateral groundwater flow. The amended groundwater is injected into a high-permeability well at x = 3 m.

A hypothetical model is considered with simple layered heterogeneity given by a zone of higher log permeability (-10.5) between 4.2 and 5.3 m depth and a moderately lower log permeability (-11) elsewhere. Figure 5 shows the simulated fraction of bicarbonate in the groundwater, and the locations of monitoring wells M1–M4. Note the fast path causing lower concentrations and faster breakthrough at ~4.5 m depth. The density of the injected fluid is higher than the resident groundwater, as seen with the higher fraction sinking toward the bottom of the model.

Fluid EC measurements were simulated in the monitoring wells (Figure 6). As the monitoring wells are screened in the saturated zone, each simulated measurement represents the average EC value in the saturated zone.

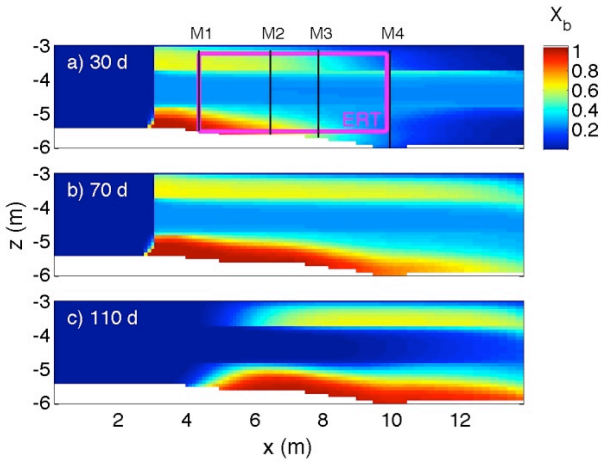

Figure 5. Fraction of injected fluid at (a) 30, (b) 70 and (c) 110 days after the start of injection. The locations of monitoring wells (M1 to M4) and the region corresponding to the idealized ERT data (magenta line) are shown in (a).

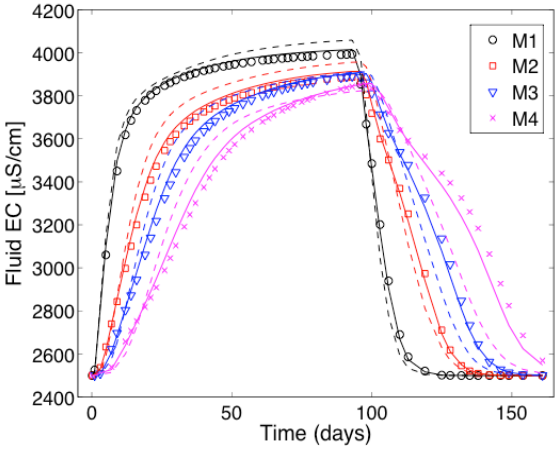

Figure 6. Fluid EC data at monitoring wells M1 to M4. The (synthetic) data are shown with symbols while inversion results are shown with solid and dashed lines for the inversion cases with EC and ERT data smoothed at 0.5 m and 1.1 m, respectively.

Intentionally idealized time-lapse ERT data were "simulated" for cases with increasing distortion to mimic the smoothing that is expected in ERT tomography (Figure 5 shows the region that is considered to contain ERT data). The images in the left column of Figure 7 represent the most ideal case in which ERT tomography images perfectly reflect the spatial variations in electrical conductivity resulting from the injected fluid.

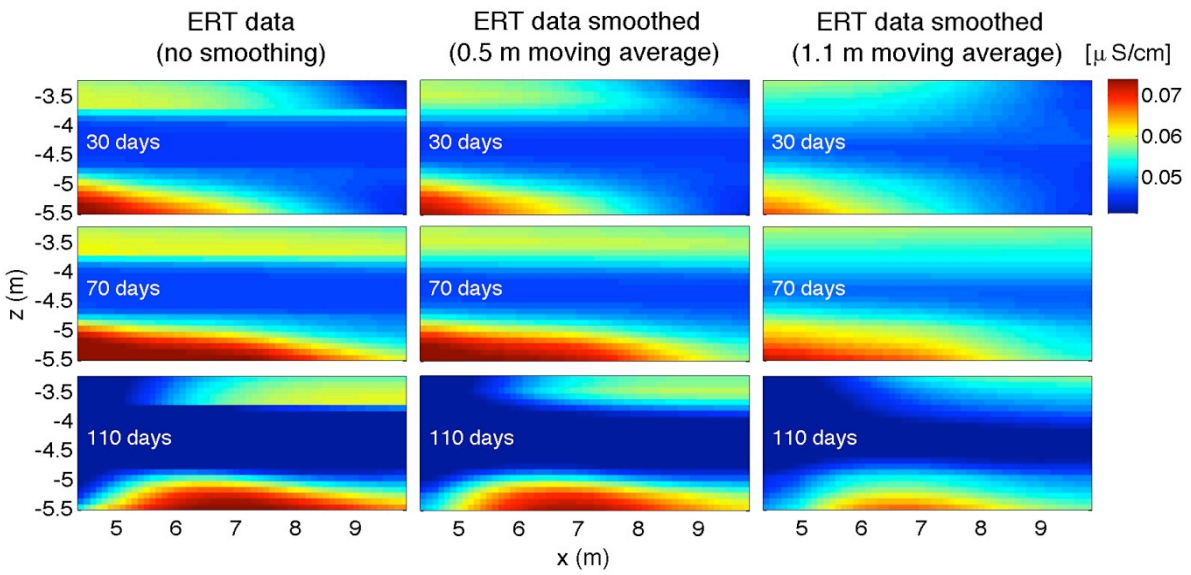

Figure 7. Intentionally idealized (synthetic) time-lapse ERT data. The images in the left column represent the most ideal case, the true distribution (i.e., the ERT tomography images perfectly reflect the spatial variations in electrical conductivity resulting from the injected fluid) at three times. The middle and right columns are increasingly smoothed versions of the true distribution obtained with a moving average of 0.5 m (middle column) and 1.1 m (right column), respectively; they are also considered idealized in the sense that real ERT tomography results would undoubtedly be more corrupted with imaging artifacts and affected by measurement noise. The quantity shown is the electrical conductivity [μS/cm], defined as the inverse of electrical resistivity.

The middle and right columns are increasingly smoothed versions of the true distribution obtained with a moving average of 0.5 m (middle column) and 1.1 m (right column), respectively. While they represent tomograms with error having been introduced in the tomography procedure, in actuality, these cases are still considered idealized in the sense that real ERT tomography results would undoubtedly be more corrupted with imaging artifacts and affected by measurement noise.

Figure 8 shows results for hydrogeophysical inversion using the EC data (Figure 6) and the idealized ERT data (Figure 7) together. With a pixel-based (or layered) parameterization, a total of 9 unknown parameters are estimated, including 8 log permeability values for different depth ranges and also a parameter from the petrophysical model (the cementation exponent *m* of Archie's law). With the most ideal case in which the ERT map perfectly represents the true distribution of the electrically conductive tracer, the parameter estimates are correct. But when including the ERT data with a small amount of error (middle column of Figure 7), whether starting the inversion with the unknown parameters set to the true values or set to initial guesses of -10.75, the parameter estimates are biased (see Figures 8a and 8b, respectively), having moved away from the true values. When more significant smoothing is present in the ERT data (right column in Figure 7), the parameter estimates become even more inaccurate (see Figure 8).

These results highlight the importance of choosing a proper method for including geophysical data in a hydrogeophysical inversion. When implementing tomograms directly as calibration data, even for idealistic cases, errors inherent to geophysical tomography can introduce bias or inaccuracy into the hydrological parameter estimates. However, as has been demonstrated (Commer et al., 2012), when using the approach in which the geophysical measurements themselves are simulated directly in the inversion, such bias is overcome and improved results are obtained.

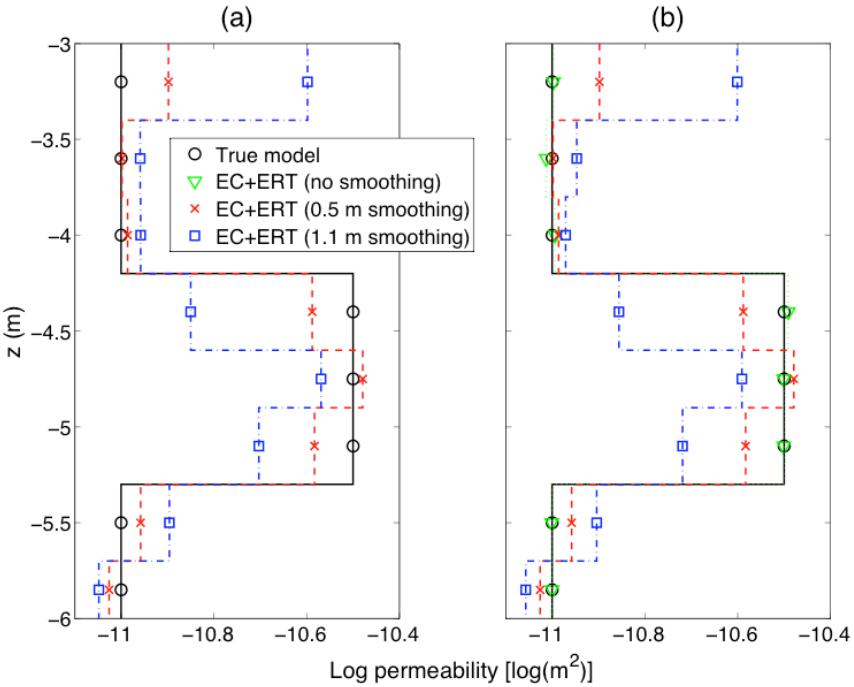

Figure 8. True and estimated log permeability values when starting with the initial guesses (a) set to the true values and (b) set uniformly to -10.75. The *m* value of Archie's law was also estimated.

CONCLUSIONS

One of the main difficulties in building biogeochemical models for complex field experiments continues to stem from uncertainty in the basic heterogeneous hydrological properties, such as permeability and porosity. Thus, testing, improving, and refining techniques for estimating such properties remains an essential research topic in hydrogeology.

We presented examples intended to highlight the importance of decisions made in the process of parameterizing heterogeneity and incorporating data into a hydrogeophysical inversion. Some observations of interest are as follows: When incorporating spatial data, like geometry inferred from core descriptions or geophysical data, uncertainty in such data must be accounted for, and parameterization in regions without data coverage must be done carefully, otherwise biased estimates of hydrological parameters may result. In a geostatistical parameterization, a variety of considerations are necessary, such as the coverage and spacing of pilot points.

Incorporating time-lapse geophysical monitoring data has long been viewed as a promising way to supplement limited hydrological measurements with more spatially extensive and cost effect information. But the manner in which geophysical data are introduced into an inverse modeling framework determines whether they will in fact improve hydrological parameter estimates or introduce bias. Calibrating a hydrological model with a geophysical image that contains errors from tomography (smoothing and streaks) may be less effective than directly simulating the geophysical measurements in a coupled fashion within the inversion, as has been demonstrated here and by others (Hinnell et al., 2010; Commer et al., 2012).

ACKNOWLEDGMENT

This material is based on work supported by the Subsurface Science Scientific Focus Area funded by the U.S. Department of Energy, Office of Science, Office of Biological and Environmental Research, under award DE-AC02-05CH11231.

REFERENCES

Anderson, R.T., et al. (2003), Stimulating the in situ activity of Geobacter species to remove uranium from the groundwater of a uranium-contaminated aquifer, *Appl. Environ. Microbiol.*, *69*(10), 5884–5891.

Archie G.E. (1942), The electrical resistivity log as an aid in determining some reservoir characteristics, Trans. Am. Inst. Min. Metall. Pet. Eng., 146, 54–62.

Commer, M., M.B. Kowalsky, S. Finsterle, and G.A. Newman (2012), Advances in hydrogeophysical joint inversion, TOUGH Symposium, Sept. 17–19.

Deutsch, C.V., and A.G. Journel (1992), GSLIB: Geostatistical Software Library and User's Guide, Oxford Univ. Press, New York.

Finsterle, S. (2004), Multiphase inverse modeling: Review and iTOUGH2 applications, *Vadose Zone J.*, *3*, 747–762.

Hinnell, A.C., T.P.A. Ferré, J. A. Vrugt, J.A. Huisman, S. Moysey, J. Rings, and M.B. Kowalsky (2010), Improved extraction of hydrologic information from geophysical data through coupled hydrogeophysical inversion, *Water Resour. Res.*, 46, W00D40, doi:10.1029/2008WR007060.

Kowalsky, M.B., S. Finsterle, and Y. Rubin (2004), Estimating flow parameter distributions using ground-penetrating radar and hydrological measurements during transient flow in the vadose zone, *Adv. Water Resour.*, *27*(6), 583–599.

Kowalsky, M.B., S. Finsterle, J. Peterson, S. Hubbard, Y. Rubin, E. Majer, A. Ward, and G. Gee (2005), Estimation of field-scale soil hydraulic and dielectric parameters through joint inversion of GPR and hydrological data, *Water Resour. Res.*, 41, W11425, doi:10.1029/2005WR004237.

Kowalsky, M.B., J. Birkholzer, J. Peterson, S. Finsterle, S. Mukhopadhyay, and Y. Tsang (2008), Sensitivity analysis for joint inversion of GPR and thermal-hydrological data from a large-scale underground heater test, *Nuclear Technology*, *164*(2), 196-206.

Kowalsky, M.B., S. Nakagawa, and G.J. Moridis (2010), Feasibility of monitoring gas hydrate production with time-lapse vertical seismic profiling, *SPE J.*, 15(3), 634-645. SPE-132508-PA, doi: 10.2118/132508-PA.

Kowalsky, M.B., E. Gasperikova, S. Finsterle, D. Watson, G. Baker, and S.S. Hubbard (2011), Coupled modeling of hydrogeochemical and electrical resistivity data for exploring the impact of recharge on subsurface contamination, *Water Resour. Res.*, *47*, W02509, doi:10.1029/2009WR008947.

Kowalsky, M.B., S. Finsterle, K.H. Williams, C. Murray, M. Commer, D. Newcomer, A. Englert, C.I. Steefel, and S.S. Hubbard (2012), On parameterization of the inverse problem for estimating aquifer properties using tracer data, *Water Resour. Res.*, *48*, W06535, doi:10.1029/2011WR011203.

Moore, C., and J. Doherty (2006), The cost of uniqueness in groundwater model calibration, *Adv. Water Resour.*, *29*(4), 605–623.

Pruess, K., C. Oldenburg, and G. Moridis, *TOUGH2 User's Guide, Version 2.0*, Report LBNL-43134, Lawrence Berkeley National Laboratory, Berkeley, Calif., 1999.

Vrionis H.A., R.T. Anderson, I. Ortiz-Bernad, K.R. O'Neill, C.T. Resch, A.D. Peacock, Dayvault, D.C. White, P.E. Long, D.R. Lovley (2005), Microbiological and geochemical heterogeneity in an in situ uranium bioremediation field site, *Appl. Environ. Microbiol,* 71:6308–6318.

Williams, K.H., et al. (2011), Acetate availability and its influence on sustainable bioremediation of uranium-contaminated groundwater, *Geomicrobiol. J.*, *28*(5–6), 519–539, doi:10.1080/01490451.2010.520074:2011.

Yabusaki, S. B., et al. (2007), Uranium removal from groundwater via in situ biostimulation: Field-scale modeling of transport and biological processes, *J. Contam. Hydrol.*, 93, 216–235.

EOS7RN—A NEW TOUGH2 MODULE FOR SIMULATING RADON EMANATION AND TRANSPORT IN THE SUBSURFACE

Zakaria Saâdi[1], Didier Gay[1], Jérôme Guillevic[1] and Roselyne Améon[2]

Institut de Radioprotection et de Sûreté Nucléaire (IRSN)
[1]PRP-DGE/SEDRAN/BRN, 31 Avenue de la Division Leclerc
Fontenay-aux-Roses, 92262, France
[2]PRP-ENV/STEM/LEI, 31 rue de l'Ecluse
Le Vésinet, 78116, France
e-mail: zakaria.saadi@irsn.fr, didier.gay@irsn.fr, jerome.guillevic@irsn.fr, roselyne.ameon@irsn.fr

ABSTRACT

A new fluid property module, EOSRn, was developed for TOUGH2 to simulate the transport of the radon gas (^{222}Rn) in saturated-unsaturated soils. It is an enhanced version of the EOS7R module for radionuclide transport, with a source term added in the transport equation to model radon generation by emanation from radioactive decay of the soil radium (^{226}Ra) content. We implemented physical properties of this gas component in two-phase (liquid-gas) porous media, as a function of soil moisture and/or soil temperature, such as those of the diffusion coefficient, the emanation factor, the adsorption coefficient and Henry's law coefficient. To ensure that temporal and spatial numerical discretization of this nonlinear source term is effective and has been well implemented in TOUGH2, we performed comparative studies between EOS7Rn and an exact analytical solution at steady-state isothermal unsaturated conditions for many numerical experiments of one-dimensional radon transport in homogeneous and layered soil columns.

We found that the radon activity concentration profiles and flux densities calculated by EOS7Rn were in good agreement with the analytical solution for all the studied numerical experiments. Consequently, relative errors for calculated TOUGH2's radon mass balance and flux densities were very negligible. Like most other sister modules, EOSRn can simulate nonisothermal multiphase flow and fully coupled three-dimensional transport in fractured porous media. It will help in predicting the radon exhalation from highly radium-contaminated soils and underground cavities to outdoor and indoor environments.

INTRODUCTION

Radon (^{222}Rn), a naturally occurring radioactive gas, with a half-life of 3.8 days, is produced by the radioactive decay of radium ^{226}Ra, which is in turn a decay product of the radioactive decay series of uranium ^{238}U. It occurs naturally in small concentrations in all soils, but in higher concentrations in granite, shale, and phosphates, which have higher concentrations of uranium. Being a rare gas, it usually migrates freely through faults and fractured soils, and may sink into groundwater or caves, or rise into the atmosphere.

Radon accounts for the largest proportion of our annual average radiation dose. Its greatest impact occurs when it becomes trapped and breaks down inside of buildings or caves. In caves or aerated mines, or ill-aerated houses, radon activity concentration can achieve many kilo-becquerels per m^3 of air, but can be much higher in mining contexts (1 $MBq.m^{-3}$). Studies concerning occupationally radon-exposed miners and direct observation of individuals exposed to radon in their homes provide firm scientific evidence that radon is a major environmental carcinogen. Radon exposure increases the risk of lung cancer—it is linked to approximately 5 to 12% of lung cancer deaths in France every year, according to the French Institute for Public Health Surveillance.

The important mechanisms that affect multiphase radon transport in the subsurface are advection, diffusion, radioactive decay, dissolu-

tion or phase partitioning, adsorption on soil solid grains, and emanation from materials with radium sources (Rogers and Nielson, 1991a,b). The release mechanism of radon from mineral grain to pore space is called emanation. This mechanism is described by the emanation coefficient, E, dimensionless, which is the ratio of the radon produced in the grain of the material to the radon in the pore space of that material. Its value varies between 0 and 1, and basically depends on soil grain size-distribution, porosity, and water content (Nielson et al., 1982; Sasaki et al., 2004). It is also temperature dependent.

Emanation and transport mechanisms depend to a large extent on soil moisture content. Thus, radon flux exhalation at the soil surface is strongly affected by weather conditions (Ferry et al., 2002). The adsorption effect significantly reduces radon migration fluxes in dry soils, since vapor adsorption in these cases takes place directly on the grain surfaces (Schery et al., 1989). Radon dissolution depends on temperature (Clever, 1979) and salinity (brine) as well.

Both radon diffusion and dissolution can be strongly temperature and pressure dependent in the context of geothermal reservoirs (Shan and Pruess, 2004). Modeling of radon transport in the subsurface, involving more complex phenomena occurring near the land surface or in deeper unsaturated zones, requires accurate description of hydrogeological features, physical processes, and thermodynamic properties. While few numerical simulators can study radon transport—in the context of nonisothermal flows of multiphase, multicomponent fluids in permeable (fractured and porous) media, by accounting for such mechanisms—the TOUGH numerical simulators, based on their underlying conceptualizations and methodologies, are well suited for the solution of like vadose-zone flow and transport problems (Finsterle et al., 2008).

The fluid property module, EOS7R (Oldenburg and Pruess, 1995; Pruess et al., 1999), is one among many TOUGH2 modules that can simulate two-phase, five-component flow and transport problems. The two phases are water and gas, and the five components are water, brine, air, and two radionuclides. Unger et al. (2004) studied the transport of radon into a tunnel at Yucca Mountain using TOUGH2/EOS7R. Their study considered radon transport in a fractured tuff, but only as a radioactive tracer without a source term of radon from the tuff. Their study was limited to estimating the large-scale hydraulic properties of the fractured tuff and its implications for the operation of the ventilation system of the tunnel.

In the context of soil/rock with radium sources, the TOUGH2/EOS7R module can be suitable for modeling radon transport in the subsurface. However, the module must be enhanced to account for the soil radon emanation process and all radon-related physical properties with their dependency on soil hydrodynamic and thermodynamic properties (water saturation, salinity, temperature and pressure). For this purpose, a new TOUGH2 module, EOS7Rn, has been developed. As an alternative to the physically based Millington and Quirk (1961) (MQ) formulation for binary diffusion of gas components in each phase of an unsaturated soil, which is already implemented in TOUGH2, the empirical formulation of Rogers and Nielson (1991a) (RN), developed specifically for radon gas diffusion, has been implemented in EOS7Rn**.**

In addition, four new subroutines have been implemented to account for the physical properties of radon: RnHEN for calculating the water temperature and/or salinity dependent Henry's law coefficient, RnDIF0 for calculating temperature and/or pressure-dependent diffusivities in free gas and liquid phases, RnEMAN for calculating water saturation and/or temperature-dependent emanation coefficient, and RnADS for calculating water saturation and/or temperature-dependent adsorption coefficient between gas and solid phase. Within each of these four subroutines there is the possibility of choosing between different functions or adding user-specified ones if needed.

In this study, we verify the numerical discretization of the nonlinear source term of radon emanation in the transport equation and its implementation in TOUGH2/EOS7Rn. We will focus on comparative studies between this module and an exact one-dimensional analytical solution for steady-state radon transport in homogeneous and layered unsaturated soil

columns. (Note that the temperature effect on radon transport in the subsurface will be addressed in future work.)

MODULE DESCRIPTION

First, we assume that the two radionuclides are ^{222}Rn and ^{218}Po, with the latter a stable tracer component with infinite half-life value. For each gridblock element i with a given volume V_i in the flow domain, the general space-discretized form of the mass conserving equations of each component κ, using the Integral Finite Difference Method (IFDM), is given by (Oldenburg and Pruess, 1995):

$$\frac{dM_i^{(\kappa)}}{dt} = \frac{1}{V_i}\sum_j A_{ij}F_{ij}^{(\kappa)} + q_i^{(\kappa)} \qquad \kappa = 1, \ldots, NK \quad (1)$$

where NK = 5, which is the number of components; j labels the gridblocks connected to i through the surface area A_{ij} (m^2); t is time (s); $q^{(\kappa)}$ is a sink/source term (kg.m^{-3}.s^{-1}); $M^{(\kappa)}$ is the mass accumulation term (kg.m^{-3}); and $\boldsymbol{F}^{(\kappa)}$ is the total flux term (kg.m^{-2}.s^{-1}). The latter results from advection and diffusion and is given, according to Darcy's and Fick's laws, by:

$$\boldsymbol{F}^{(\kappa)} = \sum_{\beta=g,l}\left(X_\beta^{(\kappa)}\rho_\beta \boldsymbol{v}_\beta - \phi S_\beta \rho_\beta \tau_0 \tau_\beta d_\beta^{(\kappa)} \boldsymbol{\nabla} X_\beta^{(\kappa)}\right) \quad (2)$$

where ϕ is porosity; $\tau_0\tau_\beta$ is the tortuosity that includes a porous medium dependent factor τ_0 and a coefficient τ_β that depends on saturation of phase β (gas and liquid), S_β; ρ_β is density (kg.m^{-3}); $d_\beta^{(\kappa)}$ is the diffusion coefficient of component κ in free fluid phase β (m^2.s^{-1}); $\boldsymbol{v}_\beta$ is the Darcy flow velocity or flux density of the fluid phase β (m.s^{-1}); and $X_\beta^{(\kappa)}$ is the mass fraction of component κ in phase β (-). For radon component (κ = 3 = Rn), the terms $M^{(\kappa)}$ and $q^{(\kappa)}$ are given by:

$$M^{(\kappa)} = \phi \sum_{\beta=g,l} S_\beta \rho_\beta X_\beta^{(\kappa)} + \rho_d \rho_g K d_g^{(\kappa)} X_g^{(\kappa)} \quad (3)$$

$$q^{(\kappa)} = -\lambda_\kappa M^{(\kappa)} + u_\kappa E(S_l) \quad (4)$$

$$u_\kappa = C_s^{^{226}Ra}\rho_d\left(\frac{M_{Rn}}{N_{Av}}\right)\times 10^{-3} \quad (5)$$

where ρ_d is the rock dry bulk density (kg.m^{-3}), equal to $(1-\phi)\rho_R$, with ρ_R is the rock solid grain density (kg.m^{-3}); λ_κ is the radioactive decay constant of radon (2.1×10^{-6} s^{-1}); $C_s^{^{226}Ra}$ is the rock radium activity mass content (Bq.kg^{-1}); M_{Rn} is the molecular weight of radon (222 g.mol^{-1}); N_{Av} is Avogadro's number (6.022×10^{23} mol^{-1}); and E is the emanation coefficient (-). In (3), we use the gaseous phase (g) as a reference to describe the adsorption isotherm for radon, unlike in the Oldenburg and Pruess (1995) approach. Hence, radon gas-component partitions only between the gas phase and soil solid grains. As in TOUGH2, we assume a partition phase of radon according to Henry's law:

$$P_{Rn} = K_H x_l^{Rn} \quad (6)$$

where P_{Rn} is the partial pressure of Rn (Pa); x_l^{Rn} is the mole fraction of the dissolved Rn (-); and K_H is the Henry's law coefficient (Pa).

We use the same approach of Oldenburg and Pruess (1995) for time discretization of (1), by using two variable time-weighting parameters for decay and emanation terms. This helps to alternate between Crank-Nicolson and a fully implicit scheme for both terms.

Emanation Coefficient

RnEMAN calculates the radon emanation coefficient E in (4) as a function of the soil water saturation S_l, using the widely used linear model of Nielson et al. (1982):

$$E = \begin{cases} E_w S_l/S^* + E_a(1 - S_l/S^*) & if\ S_l \le S^* \\ E_w & elsewhere \end{cases} \quad (7)$$

where E_w and E_a are the emanation coefficients at saturation and at dryness (-), and S^* is the minimum water saturation on the plateau of an emanation–water saturation curve. Equation (7) has been shown to be very accurate for describing radon-emanation laboratory data in soils with different soil textures.

Adsorption Coefficient

RnADS calculates the adsorption or distribution coefficient Kd_g in (3) according to the empirical relationship of Rogers and Nielson (1991b):

$$Kd_g = Kd_g^0 e^{-bS_l} \quad (8)$$

where Kd_g^0 is the distribution coefficient at dryness ($m^3.kg^{-1}$) and b is a correlation constant, generally lying between 10 and 15 but can be significantly higher. Equation (8) assumes that Kd_g generally decreases rapidly with increasing water saturation and that adsorption on wet surfaces is negligible. Rogers and Nielson (1991b) showed that (8) can best fit the Kd_g data of Schery et al. (1989) measured at the ambient temperature for different soil textures.

Henry's Law Coefficient

The temperature-dependent Henry's law coefficient of radon is computed by RnHEN using the Crovetto et al. (1982) (CRO82) model:

$$K_H = 10^9 \cdot e^{a_0 + a_1/x + a_2/x^2 + a_3/x^3} \qquad (9)$$

where $x = 10^{-3}T$, with T is temperature (K). No K_H-data for radon are available above 100°C. However, the four regression coefficients in (9) (Table 1) were obtained by fitting the Clever (1979) data for Rn to (9), for temperatures below 100°C (Figure 1).

Table 1. Best fit regression coefficients to CRO82 model for Rn K_H Clever79-data

	a_0	a_1	a_2	a_3
Rn	-23.5229	20.5167	-5.32751	0.374797

Figure 1 shows a comparison between CRO82 and the empirical model of Yaws et al. (1999) (Yaws99). Both models give satisfactory results for noble gases for temperatures below 100°C. As expected, the decrease in Henry's law coefficient with the increased molecular weight of noble gases is fulfilled, regardless of the model used.

Diffusion Coefficient in Soil Fluid Phase

Tortuosity factor

The unsaturated soil tortuosity factor ($\tau_0\tau_\beta$ in (2)), is modeled by the well-known formulation of Rogers and Nielson (1991a):

$$\tau_0\tau_g = \phi e^{-6\phi S_l - 6(S_l)^{14\phi}} \qquad (10)$$

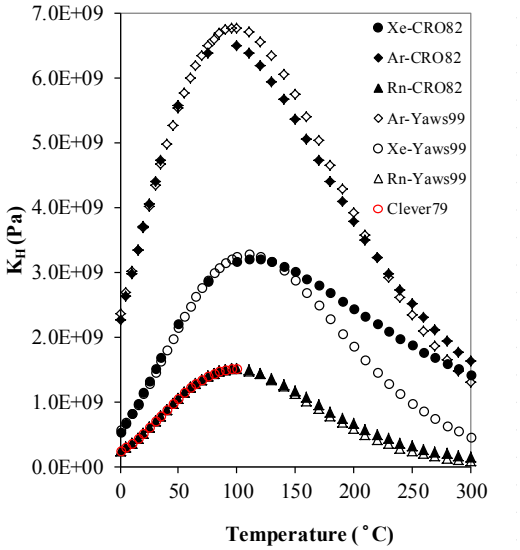

Figure 1. Best fit for Clever (1979) radon data to the CRO82 model and comparison with Yaws99 model.

where τ_0 is assumed equal to the soil porosity. Radon diffusion in soil liquid is assumed negligible in that case. Equation (10) is an empirical case obtained through the best fit to $\tau_0\tau_g d_g^{(Rn)}$ for 1073 experimental data points of diffusion coefficients measured on natural soils. As reported by Rogers and Nielson (1991a), MQ-formulation cannot be suitable for radon diffusion through earthen materials, since it considers diffusion through the pore air only, and ignores pore air-water interactions. Figure 2 shows the diffusion coefficient of radon as a function of water saturation at ambient temperature for soil with porosity $\phi = 0.4$, using both formulations, MQ and RN. The MQ-formulation is more diffusive than the RN-one with decreasing soil water saturation.

Gas phase

We use the same theoretical approach applied by Shan and Pruess (2004) for noble gases to calculate the radon diffusion coefficient in pure air and saturated water vapor ($d_\beta^{(\kappa)}$ in (2)). This approach is based on the Chapman-Enskog theory of diffusion with Lennard-Jones (LJ) intermolecular potential for binary gas mixture. Table 2 shows values of molecular weights M_{AB} and values of LJ-parameters ε_{AB} and σ_{AB} used for binary gas mixtures Rn-air (i.e., A=Rn, B=air) and Rn-H_2O, with H_2O being the

saturated water vapor. The latter have been calculated using values ε_{Rn} = 283 K and σ_{Rn} = 4.36 Å for Rn, as taken from Gopal (1962). Also shown in Table 2 are parameter values for diffusion of air and two nobles gases (Ar, Xe) in H_2O (Shan and Pruess, 2004). The LJ-parameters of Rn-H_2O mixture are in reasonable agreement with the findings of these authors. Indeed, the values of ε_{AB} and σ_{AB} increase with increasing noble gas weight (Table 2), and inversely for radon diffusion in H_2O (Figure 3).

For groundwater flow and transport problems, temperature generally fluctuates around the ambient temperature, with air the dominant component in gas phase. Thus, it is advised to use LJ-parameters for the Rn-air mixture (Table 2).

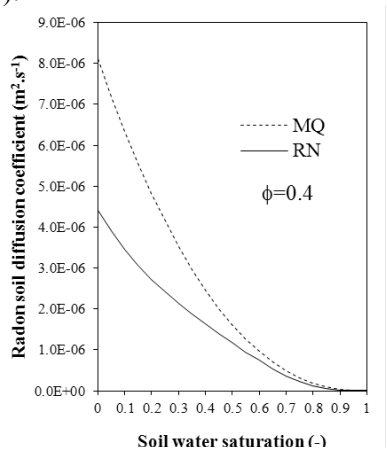

Figure 2. Radon diffusion coefficient in an unsaturated soil with porosity ϕ = 0.4, using MQ and RN formulations.

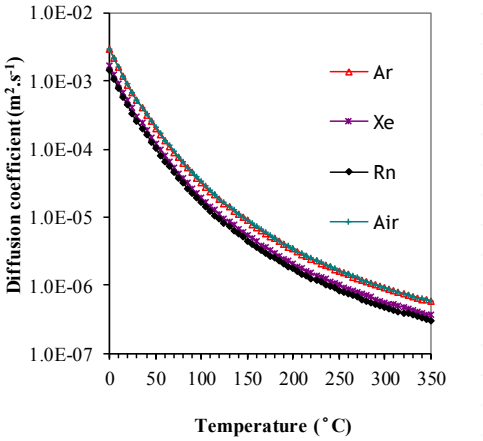

Figure 3. Diffusivity of air, Ar, Xe, and Rn in saturated water vapor.

Table 2. LJ-parameters for binary gas mixtures.

A-B	M_{AB}	σ_{AB}	ε_{AB}/k
Ar-H_2O	0.28859	3.0915	274.7527
Xe-H_2O	0.251242	3.344	432.3218
Rn-H_2O	0.244971	3.5005	478.5136
Rn-Air	0.197556	4.0355	149.1436
Air-H_2O	0.30005	3.176	252.181

Liquid phase

Two mathematical formulations are proposed for estimating the radon diffusion in free water as a function of temperature. The first alternative is the default empirical model of Hayduk and Minhas (1982) (HM82); the second alternative is the Wilk and Chang (1955) (WC55) theoretical model. Figure 4 shows Broecker and Peng (1974) measured data of Rn diffusivities in free water, against the two proposed models. Both models overestimate measured data with increasing temperature. The HM82 model is more accurate than the WC55, but discrepancies between them are very small compared to measurements uncertainties.

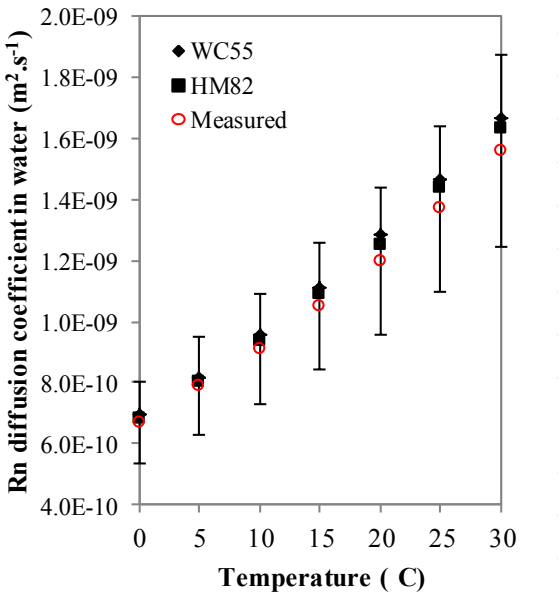

Figure 4. Comparison between WC55 and HM82 models and measured data of Broecker and Peng (1974).

MODULE VERIFICATION

Numerical Experiments

Results from the TOUGH2's numerical solution are compared with the analytical solution of Guérin (1991) (GU91) developed for one-dimensional steady-state transport in layered soil columns, with Dirichlet boundary conditions. Isothermal conditions were assumed at 25°C. K_H = 6.06844× 10^8 Pa, from (11), and the diffusion coefficient in free air and water are taken to 1.1× 10^{-5} and 1.4 ×10^{-9} $m^2.s^{-1}$, respectively.

The column is 10 m in height with the three soil configurations generally observed in a landfill of uranium mill tailings (UMT) (1) homogeneous UMT soil, (2) two-layered soil in the sequence of a cover material (CM) over UMT (CM/UMT), and (3) five-layered soil in the sequence CM/UMT/CM/UMT/CM (CM/UMT_5L). The studied CM and UMT soils are those from the Lavaugrasse (France) landfill, which have been characterized as loamy sand and sandy silt soils, respectively (Ferry et al., 2002). Table 3 summarizes parameter values for the numerical experiments carried out on these three soil column configurations to study radon transport in single-phase gas and unsaturated conditions.

The gas pressure difference between column boundaries (ΔP_g) is chosen so as to produce an upward advective transport. The steady state v_g, used as an input parameter in GU91 solution, can directly be calculated from Darcy's law for the UMT# experiments. However, for the layered case, its value is obtained from TOUGH2's numerical solution of the two-phase flow problem. For all these experiments, calculations were performed with MQ and RN-formulations. The soil profile has been assumed initially free of radon and zero, or constant radon concentration was imposed at the column boundaries (z = 0, 10 m).

Table 3. Parameter values for numerical experiments of the three soil configurations.

Soil	Experiment #	S_g (-) CM	S_g (-) UMT	Δ_z (m)	Δ_{P_g} (Pa)
UMT (H-UMT=10 m) and CM/UMT (H-CM=4 m, H-UMT=6 m) and CM/UMT_5L (H-CM=2 m, H-UMT=2 m)	#1	1	1	0.1	0
	#2			0.1	1000
	#3	0.5	0.5	0.02, 0.1, 0.1*	0
	#4			0.02	1000
	#5	0.75	0.25	0.02, 0.1, 0.1	0
	#6			0.02	300$
	#7			0.005, 0.02, 0.01	1000
	#8	0.25	0.75	0.02, 0.1, 0.1	0
	#9			0.02, 0.01, 0.01	300$
	#10			0.02, 0.01, 0.01	1000

*Different values Δz for the three soil column configurations

$Not used for the UMT soil column

The Crank-Nicholson time discretization scheme has been used for both decay and emanation terms. The TOUGH2 numerical solution corresponds to the one achieved at steady state after solving the transient two-phase flow and transport problems. Numerical calculations are performed with regular grid spacing: Δz=0.1, 0.02, 0.01, 0.005 m, so as to have a Peclet number less than 2, avoiding numerical dispersion. Two values of the upstream weighting factor (WUP) for mobilities at interfaces are chosen: 0.5, 1.0. The maximum time step is 1/100 of the half-life time of radon.

Comparison between TOUGH2/EOS7Rn and GU91 analytical solution

Transport in homogeneous soil columns

Figure 5 shows a simulation example with comparison between numerical (TOUGH2: T2) and analytical (GU91) radon concentration profiles in the soil gas of an unsaturated UMT-soil column (S_g=0.75), without radon adsorption. Good agreement is found between the two solutions. We obtain the same radon-concentration-profile shapes using both RN and MQ formulations, but with radon concentration higher for RN than MQ, which is in accordance with Figure 2.

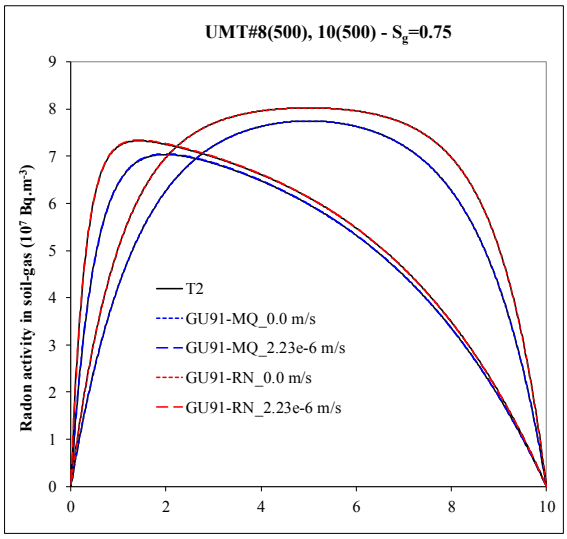

Figure 5. Numerical and analytical profiles of radon activity in the soil-gas without adsorption. Experiments UMT#8, 10 (MQ and RN).

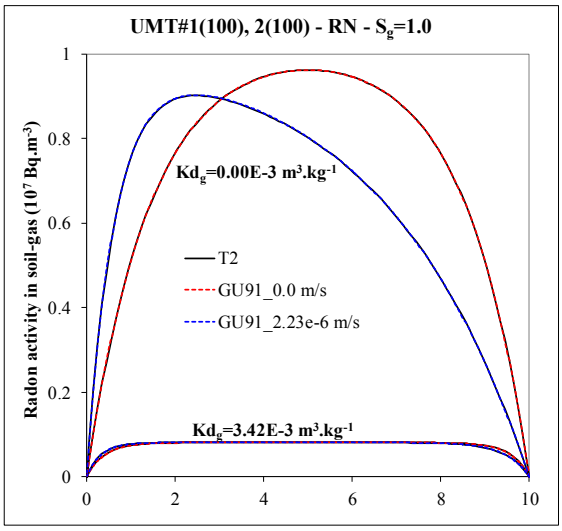

Figure 6. Numerical and analytical profiles of radon activity concentration in the soil-gas with and without adsorption. UMT#1-2 (RN).

By introducing the adsorption effect, concentration profiles are highly reduced, especially for single-phase gas conditions (Figure 6, UMT#1-2). The maximum percentage reduction of the total radon flux exhalation is 77.6% (UMT#2). For gas saturation less than 0.5, the reduction is unimportant. The radon flux at column boundaries, calculated by TOUGH2, can best fit the 1:1 curve (Figure 7), predicting that calculated by GU91. Relative errors in TOUGH2's flux density and mass balance were less than 0.8%.

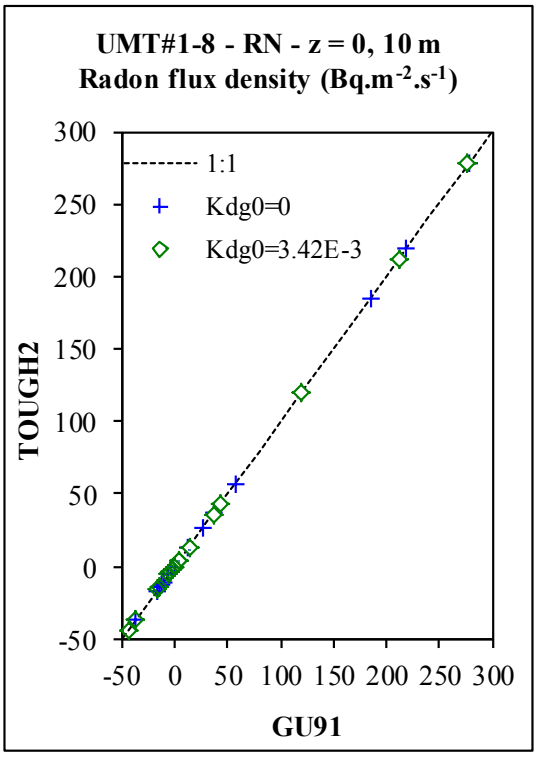

Figure 7. Numerical (TOUGH2) and analytical (GU91) radon flux densities (UMT#1-5, 7-8, 10).

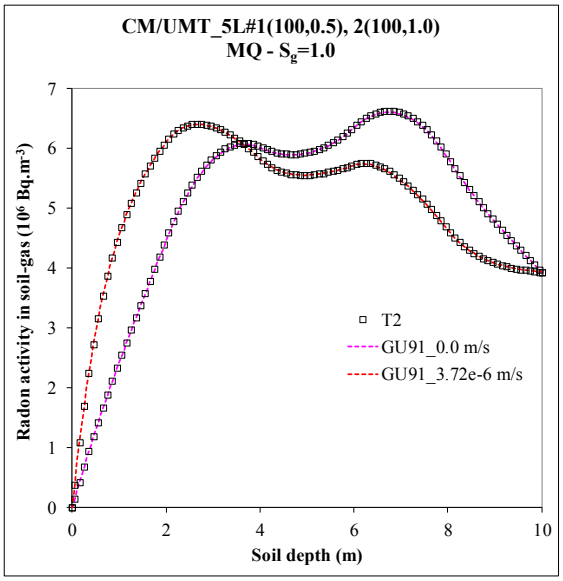

Figure 8. Numerical (T2) and analytical (GU91) profiles of radon activity in the soil-gas (CM/UMT_5L#1-2).

Transport in layered soil columns

Figures 8 and 9 show two simulation examples of radon concentration profiles calculated by TOUGH2 and GU91 for single-phase gas and unsaturated experiments CM/UMT_5L#1-2 and CM/UMT_5L#5-7, respectively. There is good agreement between the two solutions, whatever the number of soil column layers. For all experiments, the radon flux calculated by TOUGH2 at different depths is well predicted by the GU91 solution (e.g., Figure 10), regardless of the WUP-value used. However, because of the non-uniform TOUGH2's gas velocity profile, the relative error in flux density was higher for small diffusive fluxes at z=10 m. It exceeds 10% for CM/UMT_5L#4,9 with WUP = 1.0, but was less than 5% for WUP = 0.5. Mass-balance relative errors were less than 3.0% regardless of the WUP-value. Layering did not greatly increase the errors compared to those of the UMT# experiments, showing the mass conservation of the TOUGH2's numerical scheme IFDM.

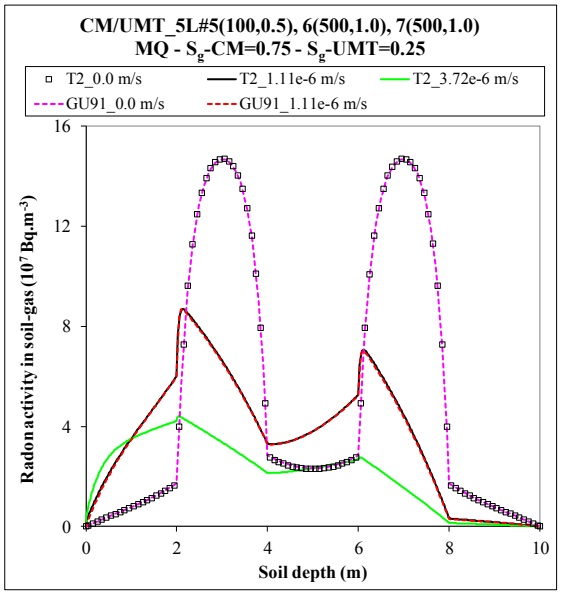

Figure 9. Numerical (T2) and analytical (GU91) profiles of radon activity in the soil-gas (CM/UMT_5L#5-7).

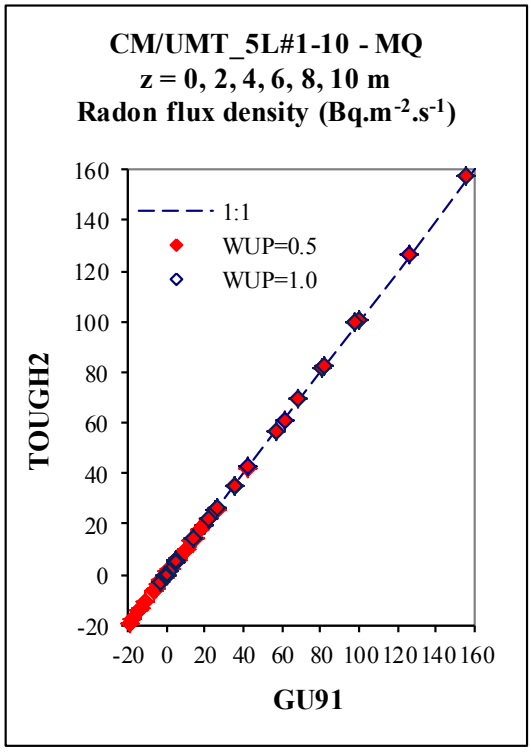

Figure 10. Numerical (TOUGH2) and analytical (GU91) radon flux densities at different depths (CM/UMT_5L#1-10).

CONCLUSION

The newly developed EOS7Rn module can now simulate radon generation by emanation, and its transport within the subsurface by accounting for all its physical properties and their eventual dependency on hydrodynamic and thermodynamic soil properties. The EOS7Rn module can be applied to groundwater and geothermal reservoir processes as well. The next task will be the *in situ* validation of EOS7Rn for radon exhalation to indoor and outdoor environments.

ACKNOWLEDGMENT

We are very grateful to Dr. Karsten Pruess and the National Energy Agency (NEA) for providing us the TOUGH2 software by which to develop the new module EOS7Rn.

REFERENCES

Broecker, W. S., and T.-H. Peng, Gas exchange rates between air and sea, *Tellus*, 26, 21–35, 1974.

Clever, H. L., *Krypton, Xenon and Radon - Gas Solubilities*, International Union of Pure and Applied Chemistry Solubility Data Series, Pergamon Press, New York, 1979.

Crovetto, R., R. Fernandez-Prini, and M. L. Japas, Solubilities of inert gases and methane in H2O and in D2O in the temperature range of 300 to 600 K, *J. Chem. Phys.*, 76(2), 1077-1086, 1982.

Ferry, C., P. Richon, A. Beneito, and M.-C. Robé, Evaluation of the effect of a cover layer on radon exhalation from uranium mill tailings: transient radon flux analysis, *J. Environ. Radioactiv.*, 63, 49–64, 2002.

Finsterle, S., C. Doughty, M. B. Kowalsky, G. J. Moridis, L. Pan, T. Xu, Y. Zhang, and K. Pruess, Advanced vadose zone simulations using TOUGH, *Vadose Zone J.*, 7(2), 601-609, 2008.

Gopal, R., On intermolecular Lennard-Jones potential energy parameters for radon. *Journal of the Indian Chemical Society, Absorbed Indian J. Appl. Chem.*, 39, 791-792, 1962.

Guérin, F., *Production et mécanismes de migration du radon-222 dans les milieux fissurés: application à la recherche des discontinuités perméables du socle cristallin*, PhD Thesis, Pierre et Marie Curie University - Paris 6, Hydrogeology – Water Sciences, 1991.

Hayduk, W., and B. S. Minhas, Correlations for prediction of molecular diffusivities in liquids, *Can. J. Chem. Eng.*, 60, 295-299, 1982.

Millington, R. J., and J. M. Quirk, Permeability of porous solids, *Faraday Soc. Trans.*, 57 (7):1200-1207, 1961.

Nielson, K. K., V. C. Rogers, M. L. Mauch, J. N. Hartley, and H. D. Freeman, *Radon emanation characteristics of uranium mill tailings*, In Uranium mill tailings management-V. Colorado State Univ., Fort Collins, p. 335-368, 1982.

Oldenburg, C., and K. Pruess, *EOS7R: Radionuclide Transport for TOUGH2*, Lawrence Berkeley National Laboratory Report LBL-34868, Berkeley, CA, November 1995.

Pruess, K., C. Oldenburg, and G. Moridis, *TOUGH2 User's Guide, Version 2.0*, Report LBNL-43134, Lawrence Berkeley National Laboratory, Berkeley, Calif., 1999.

Rogers, V. C., and K. K. Nielson, Correlations for predicting air permeabilities and ^{222}Rn diffusion coefficients of soils, *Health Phys.*, 61(2), 225-230, 1991a.

Rogers, V. C., and K. K. Nielson, Multiphase radon generation and transport in porous materials, *Health Phys.*, 60(6), 807-815, 1991b.

Sasaki, T., Y. Gunji, and T. Okuda, Mathematical modeling of radon emanation, *J. Nucl. Sci. Technol.*, 41(2), 142–151, 2004.

Schery, S. D., and S. Whittleston, Desorption of radon at Earth's surface, *J. Geophys. Res.*, 94, 18297-18303, 1989.

Shan, C., and K. Pruess, EOSN - A New TOUGH2 Module for Simulating Transport of Noble Gases in the Subsurface, *Geothermics*, 33(4), 521-529, 2004.

Unger, A. J. A., S. Finsterle, and G.S. Bodvarsson, Transport of radon gas into a tunnel at Yucca Mountain-Estimating large-scale fractured tuff hydraulic properties and implications for the operation of the ventilation system, *J. Contam. Hydrol.*, 70(3-4), 151-299, 2004.

Wilke, C. R., and P. Chang, Correlation of diffusion coefficients in dilute solutions, *AIChE Journal*, 1, 264–270, 1955.

Yaws, C. L., J. R. Hopper, X. Wang, A. K. Rathinsamy, and R. W. Pike, Calculating solubility and Henry's Law constants for gases in water, *Chem. Eng. J.*, 102-105, 1999.

A LEAST-COST STRATEGY FOR EVALUATING A BROWNFIELDS REDEVELOPMENT PROJECT SUBJECT TO INDOOR AIR EXPOSURE REGULATIONS

Xiaomin Wang[1], André J.A. Unger[1], and Beth L. Parker[2]

[1]Department of Earth and Environmental Sciences, University of Waterloo, 200 University Avenue West, Waterloo, Ontario, N2L3G1, Canada
[2]School of Engineering, University of Guelph, 50 Stone Road East, Guelph, Ontario, N1G 2W1, Canada
e-mail: xm4wang@uwaterloo.ca

ABSTRACT

This paper presents a framework for alleviating the risk of exposure during brownfields redevelopment projects by improving the prediction of contaminated indoor air concentrations, and by searching for the optimal balance between increasing site characterization budgets and decreasing contingency measures to cover the risk exposure (and also to quantify and manage the risk). A three-dimensional model *CompFlow Bio* is used to anticipate the intrusion pathways of TCE from a residual source zone into buildings. The result indicates that the geological condition of the site and the heterogeneity in each stratigraphic unit have the most compelling impact on the indoor air concentration of TCE. We develop a methodology by which to price the risk associated with the number of sampling data available from site characterization and long-term monitoring, incorporating hydrogeological as well as financial uncertainties into an insurance premium. As a result, the trade-off between increasing site-investigation budgets and overall cost reductions is optimized.

INTRODUCTION

Brownfields are defined by the U.S. Environmental Protection Agency (US EPA) as "abandoned, idled, or under-used industrial and commercial facilities where expansion or redevelopment is complicated by real or perceived environmental contamination." Brownfields are usually unintended by-products of industrial practices of the last several decades, in which measures were not taken to ensure that industrial operations did not harm the natural environment. In brownfields, there exist known and potential contaminants, such as volatile organic compounds (VOCs) or semi-volatile organic compounds (SVOCs) which over time, may be exposed to the air, potentially threaten public health, and have negative impacts on ecological systems. Redevelopment of such brownfields is beneficial for the environment as well as for communities. It is an efficient, effective, and environmentally friendly way to encourage development using existing infrastructures, services, and resources. Redeveloping brownfields can also generate great economic benefits if appropriate and reasonable methodologies are designed. There are strong environmental, social, and economic grounds to redevelop and utilize brownfields (US EPA, 1999; NRTEE, 2003; UK Environment Agency, 2003).

Since the 1980s, North America and Europe have made moves to foster sustainable redevelopment of brownfields. The United States of America enacted the Liability Act Superfund to reclaim 1,410 heavily contaminated sites, and the National Brownfields Association has estimated that 600,000 brownfield sites exist across the nation (Mueller, 2005). Canada also has paid a great deal of attention to brownfield redevelopment projects (aboutRemediation™, 2012). Policy makers and developers have focused their efforts on transforming brownfields into industrial areas, commercial areas, and residential areas, depending on the characteristics of the community and the site itself. At the same time, brownfield redevelopment projects also harbor great risks, which can impede the decision-making process. Major risks faced during brownfield redevelopment associated with costs include possible cost overruns in cleanup operations (the technologies for remediation of brownfields are summarized by Reddy et al., (1999)), possible liability claims from accidents or contaminant exposure from past spills or spills during the cleanup, and

uncertainty about future community acceptance (Wade VanLandingham et al., 2002). All of these risks mainly arise from imperfect knowledge of the complexity of brownfield sites. Complications include complex geological formations and physical properties of the subsurface, the uncertainty of the source zone, the number and features of existing and potential contaminants, and the unreliability of detecting and contouring of the contaminant plume. As a result, a better understanding of the physics of contaminated soil vapor transport and developing a methodology to evaluate the associated risks are crucial.

Soil vapor VOC intrusion pathways into buildings have been commonly studied using analytical models, numerical modeling, and field studies. A discrepancy between field measurements and analytical solutions is often seen. The influence of the geometry of houses on the soil vapor distribution is often ignored. Yu et al. (2009) simulated the TCE soil vapor intrusion into a single house using *CompFlow Bio* in two dimensions. They examined the roles that a number of uncertainties—heterogeneity, the pressure difference between indoor and outdoor, source-zone location, aperture of the crack in the foundation slab, depth of the foundation slab, capillary fringe thickness, and infiltration rate—might play in determining the indoor air concentration of TCE. The largest remaining uncertainties result from the inherent complexity of the geology, heterogeneity, which was responsible for deflecting the groundwater plume upward towards the capillary fringe, diffusing across the capillary fringe, and then migrating into the basement. This work intends to use the three-dimensional *CompFlow Bio* model to simulate the fate and transport of soil vapor into multiple residential houses. We focus more on the significance of the geological conditions, the geometry of house locations, and the heterogeneity influencing the indoor air concentration distribution of TCE. Attenuation factors in different scenarios are calculated in contrast with those using the model by Johnson and Ettinger (1991).

Developers want to keep project overhead as low as possible, but characterizing site geology and probing for contaminants are necessary and costly. What is the most cost-effective way to conduct site characterization? To answer this question, different concentration and permeability sampling schemes are set up. The heterogeneous permeability fields are constructed using a conditional stochastic approach, generating a high-resolution aquifer analog based on permeability measurements. The geostatistical program *S-GEMS* (Stanford geostatistical earth modeling software) is utilized for this purpose. Once we have concentration measurements, an optimal estimator Kalman filter can be used to deduce a minimum error estimate to improve model prediction. Zhang and Pinder (2005) applied this algorithm to determine the least-cost design of groundwater quality monitoring networks.

How can one optimize the trade-off between increasing site-investigation budgets and overall cost reductions? First of all, the cost of risks, combining both hydrogeological and financial risks, is defined using a modified actuarial approach. The risk-cost-benefit analysis is then conducted according to the Massmann and Freeze (1987) strategy, of which the objective function is the sum of the project risk, cost, and benefit, to maximize profits by adjusting the number of data. The financial factors, which in most cases follow a Geometric Brownian Motion, (e.g., the discount rate, U.S. house price index), are estimated using financial models, and their importance is weighed compared with the hydrogeological factors (mentioned above) contributing to uncertainties in the decision-making process.

SIMULATING THE FATE AND TRANSPORT OF SOIL VAPOUR TCE

The numerical simulator *CompFlow Bio* is applied to the soil-vapor-intrusion problem in this case. It is a fully coupled, multiphase, multicomponent model capable of simulating groundwater flow and solute transport with variable water saturation in the subsurface. It involves advective and diffusive transport of TCE in water, oil, and gas phases under scenarios with different geological and hydrogeological conditions, (e.g., heterogeneity, the capillary fringe thickness, the existence of low permeable

soil and the distance of houses offsetting the TCE plume).

Conceptual Model

The hypothesis of this model is that a brownfield site has been remediated and residential buildings have been built, but a residual TCE source exists below the water table in the subsurface. The problem is as illustrated in Figure 1. The source of TCE, which is located upstream of residential houses, can either dissolve into the ambient groundwater or volatilize into the ambient soil gas. It continues to migrate along with groundwater flow, diffuse across the capillary fringe, and is subsequently transported towards the foundation slab of a structure located below grade, due to the vacuum pressure in the basement.

The computational model domain for the base scenario is depicted in Figure 2 and Figure 3 without the clay layer. Six houses are constructed on the domain with seven monitoring wells in the front, and the central houses are aligned with the source zone. The houses are depressurized, with the pressure difference from the ambient atmosphere pressure 10 *Pa*. The aquifer is heterogeneous. The permeability field is created stochastically with the same statistics (mean, variance and correlation lengths) as the Borden field site (see Figure 4). Five scenarios are set up for investigating the sensitivities of the different influential factors.

1) Base scenario;
2) Base scenario under recharge condition with recharge rate of 20 cm/yr;
3) Base scenario with a layer of clay permeability 10^{-15} m^2 and the thickness 2 m situated beneath the houses;
4) The same as case (3) but under recharge conditions;
5) The vadose zone is 7 m thicker than the one in the base scenario.

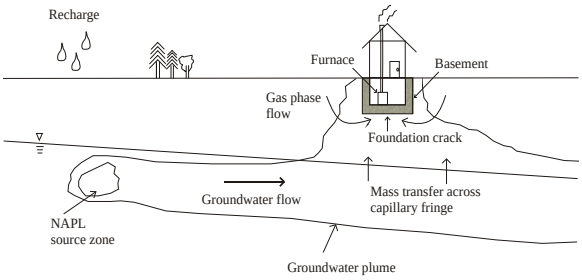

Figure 1. Conceptual model

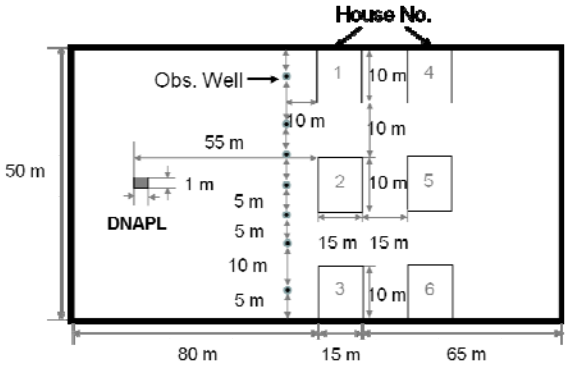

Figure 2. The plan view of the model domain for the base scenario

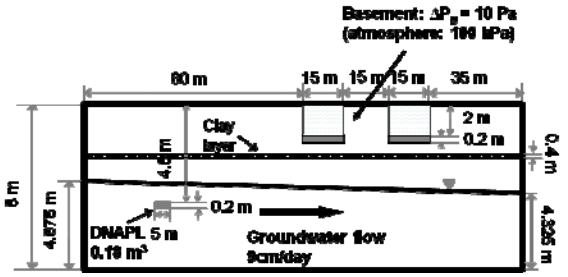

Figure 3. A 2D cross-sectional view of the model domain for Scenario 3 with a clay layer

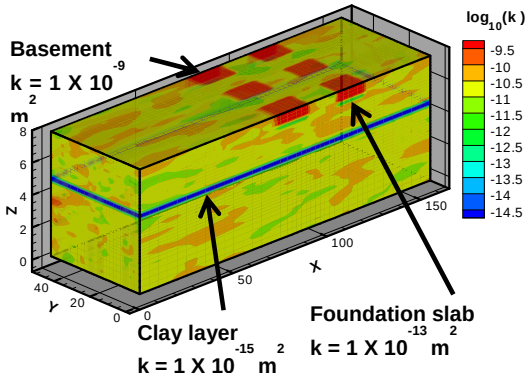

Figure 4. 3D plot of the heterogeneous permeability field with a clay layer

Model Results

The results in Figure 5 for Scenarios 1, 2, and 5 show that the TCE plume travels longitudinally along the groundwater flow direction for some distance, and then transfers across the capillary fringe into the vadose zone. The plume is quite narrow because the transverse migration of the plume is primarily driven by the concentration gradient and heterogeneity. When the vacuum pressure is applied, the central houses directly above the groundwater plume have the highest indoor air concentration of TCE. The TCE concentrations in the lateral houses vary, which results from heterogeneity, i.e., the structure of the permeability field. If a low-permeability soil layer is located below the foundation slab, when it is saturated with water, it behaves as a barrier and prevents the soil vapor from migrating upwards into the basement. The thicker vadose zone alters the offset between the source zone and center of the foundation slab, allowing more mass transfer of vapor TCE into the houses. The indoor air concentration of TCE calculated for the five scenarios is illustrated in Figure 6. It indicates that the geological clay unit and the recharge condition play important roles in vapor TCE transport.

Additionally, the comparison of the five different scenarios is conducted in terms of the attenuation coefficient (defined as the ratio of the contaminant vapor concentration in buildings to the vapor concentration at the source of contamination) with respect to the Johnson and Ettinger (1991) (J&E) model. The attenuation coefficients calculated by the *CompFlow Bio* are far smaller compared to those under the same conditions using the J&E model (see Table 1).

Since heterogeneity is a primary driving factor in determining soil gas exposure pathways, the Monte Carlo method is adopted, using permeability as the primary uncertainty for the model input, to address this issue. Figure 7 shows the concentration results for different permeability realizations. The differences in indoor air concentration of TCE can reach up to four orders of magnitude in one single house.

Table 1. The attenuation coefficients calculated using both J&E and *CompFlow Bio* (CFB) models

	Scenario	J&E attenuation coefficient $\alpha_{J\&E}$ (x10^{-6}) House No.						CFB attenuation coefficient α_{CFB} (x10^{-6}) House No.					
		1	2	3	4	5	6	1	2	3	4	5	6
1)	Base scenario	3.3	3.4	3.3	2.2	2.3	2.2	0x10^{-1}	0.116	2x10^{-2}	1x10^{-2}	0.167	4x10^{-2}
2)	Infiltration = 20 cm/yr	3.3	3.4	3.3	2.3	2.3	2.2	5x10^{-2}	6x10^{-3}	2x10^{-3}	3x10^{-3}	0.023	8x10^{-3}
3)	Clay – no recharge	3.3	3.4	3.3	2.2	2.3	2.2	1x10^{-4}	0.011	4x10^{-4}	8x10^{-4}	0.031	2x10^{-3}
4)	Clay – with recharge	3.3	3.4	3.3	2.2	2.3	2.2	3x10^{-5}	6x10^{-7}	1x10^{-7}	2x10^{-5}	1x10^{-6}	2x10^{-7}
5)	Thicker vadose zone	3.3	3.4	3.2	2.2	2.3	2.2	3x10^{-7}	0.090	6x10^{-3}	0.010	0.171	0.017

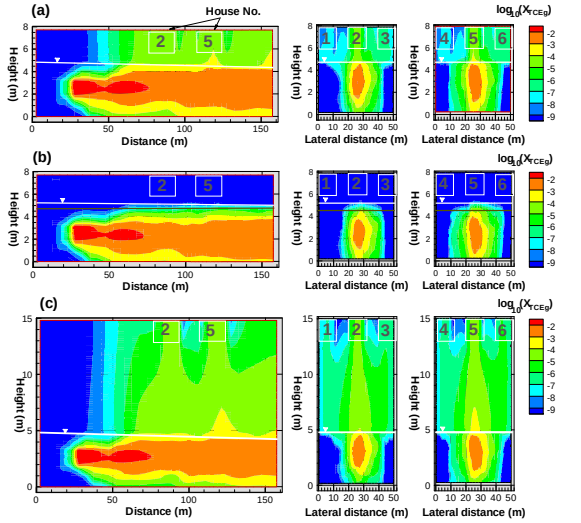

Figure 5. 2D cross-section plots along x- axis and y-axis of mole fraction of TCE in gas phase 1800 days after TCE was injected into the aquifer: (a) Scenario 1, (b) Scenario 4, and (c) Scenario 5

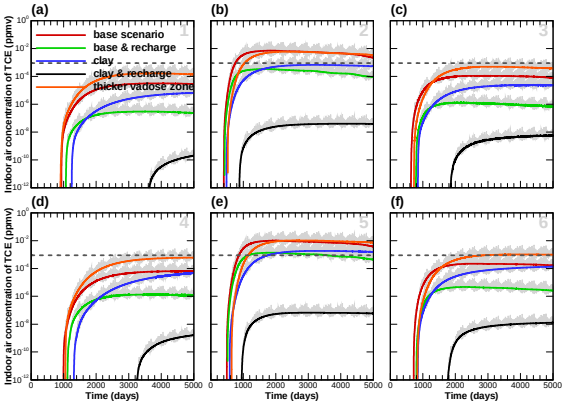

Figure 6. Indoor air concentration of TCE in logarithmic scale with transient air exchange rate limited to wind speed for the five scenarios: (a) house no. 1, (b) house no. 2, (c) house no. 3, (d) house no. 4, (e) house no. 5, and (f) house no. 6
Note: The numbers 1–6 represent the house number from Figure 2. The dashed line represents the regulatory limit for TCE

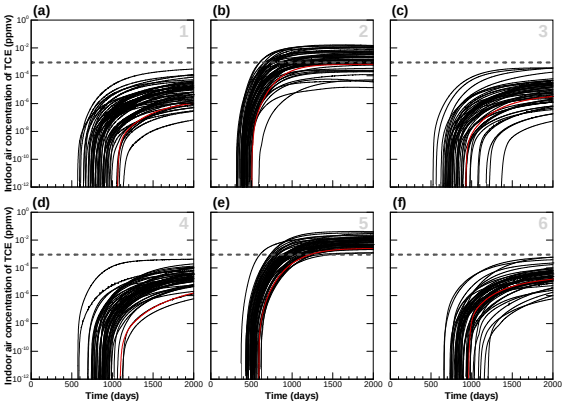

Figure 7. Indoor air concentration of TCE in logarithmic scale with the air exchange rate 0.5/hr for 50 unconditioned random permeability realizations: (a) house no. 1, (b) house no. 2, (c) house no. 3, (d) house no. 4, (e) house no. 5, and (f) house no. 6
Note: The numbers 1–6 represent the house numbers from Figure 2. The dashed line represents the regulatory limit. The red line represents the hypothetical real world result

DATA-WORTH ASSESSMENT

Kalman filtering (KF) is a technique to describe how a system would respond after processing measurements to achieve an optimal estimation. It is, in essence, a recursive solution to a least-squares problem. In this work, KF is applied to estimate and predict the indoor air concentration in multiple houses, with prior knowledge and statistical information on state variables obtained from the *CompFlow Bio* model.

Methodology

The strategy to assess the data-worth issue here is to choose one of the randomly generated permeability realizations to be reality, and to extract the permeability data from 1 to 7 boreholes in front of the houses as the sampling data. The next step is to use the statistics and the correlation of the sampling data, to apply the kriging technique to reconstruct the permeability field of the entire domain, and then to employ a sequential Gaussian simulation to create multiple realizations (shown in Figure 8). 1, 3, 5, and 7 boreholes of data (labelled as 1K, 3K, 5K, and 7K) are taken respectively for the inspection, and an extreme case with 80 boreholes of data (80 K) is also considered. Every permeability realization is used as a numerical model input to estimate the indoor air concentration of TCE at six houses and five observation wells at 100-day intervals over 2000 days. Sequentially, the space-time TCE concentration covariance matrix is constructed for the 11 locations. Concentration samples are taken from 2, 4, and 7 locations (taken as 2C, 4C, and 7C) out of 11, and then KF is used to update the concentration estimation by minimizing the error covariance matrix. The concentration sample in house no. 2 is always included.

The purpose of this method is not only to examine the data-worth issue for this application, but also to use sparse data to infer whether one of the houses located adjacent to house no. 2 has indoor air problems subject to the condition that house no. 2 is monitored and has problems; adjacent houses are not monitored, but developers assume liability if a problem occurs. After filtering, the expected value and the standard deviation of the TCE concentration in adjacent houses can be calculated.

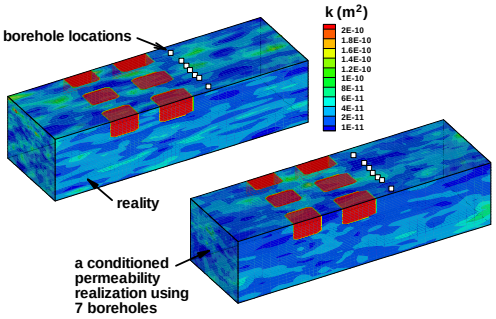

Figure 8. An example of a randomly generated permeability field realization conditioned on the 7 boreholes data

KF Results

Combinations of different numbers of permeability data and concentration data are made in order to get a good estimation of reality. The representative four cases (1K, 2C; 1K, 4C; 7K, 4C; and 7K, 7C) are chosen for illustration in Figure 9.

Increasing the number of permeability samples can give a better estimation of the expected value of the TCE concentration in comparison with reality; increasing the number of concen-

tration samples may reduce the variance in the TCE concentration, so that the uncertainty in prediction may be reduced.

The probability of failure is the likelihood that indoor air concentration of TCE exceeds a regulatory level. It is defined as the total number of Monte Carlo realizations in which the failure occurs, divided by the total number of realizations. The probability is calculated for house no. 1, 3, 4, 5, and 6 at each monitoring interval; the result is shown in Figure 10.

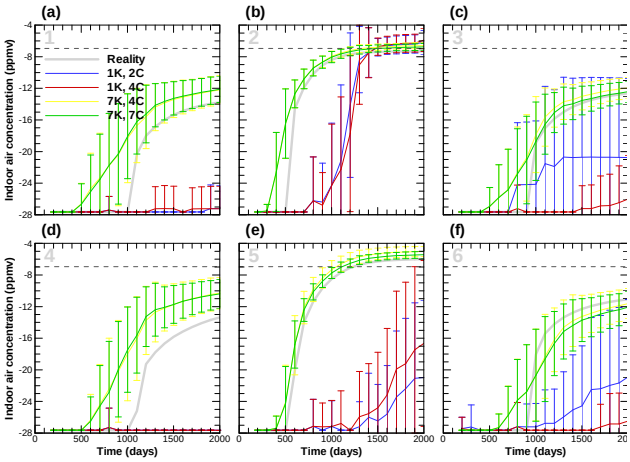

Figure 9. Updated indoor concentration of TCE in logarithmic scale using a Kalman filter: a) house no. 1, b) house no. 2, c) house no. 3, d) house no. 4, e) house no. 5, and f) house no. 6
Note: The number 1 – 6 represents the house number from Figure 2. The dash line represents the regulatory limit. The red line represents the hypothetical real world result

.

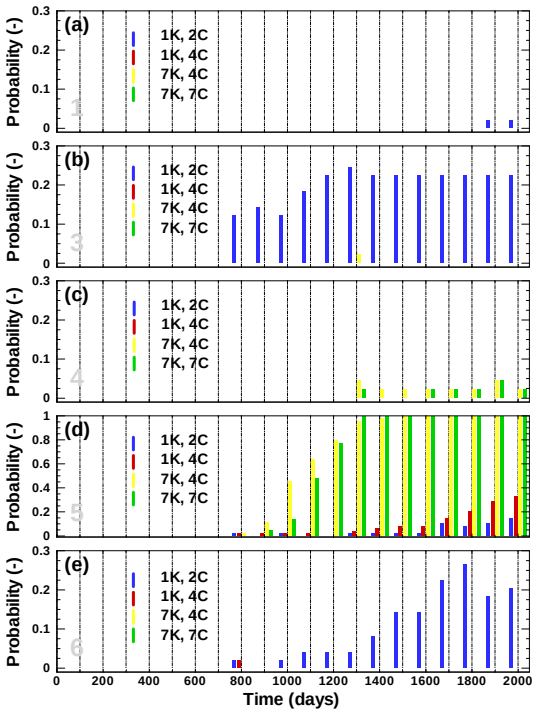

Figure 10. The probability of failure at each 100 days monitoring intervals for four cases: (a) house no. 1, (b) house no. 3, (c) house no. 4, (d) house no. 5, and (e) house no. 6
Note: The numbers 1–6 represent the house number from Figure 2

LEAST-COST OPTIMIZATION

As mentioned above, after the brownfield site is cleaned up, there is still a chance that the residential houses will be affected unexpectedly by contaminated soil vapor. If it happens, the cost is essentially described as the probability of failure times the cost of failure, with an additional safety loading term to compensate against the associated hydrological and financial uncertainties. The probability of failure can be obtained from the last section (above), and the cost of failure is contributed by the house price as well as the uncertainty of the financial market. The safety loading term reflects the level of risk aversion and is usually defined as the variance or standard deviation in the cost of risk. The total cost concerned for the redevelopment is the sum of the cost of risk and the cost of data. In order to determine the least cost among the numerous cases listed earlier, the objective function is herein proposed in Equation 1 and 2.

$$Obj = E[H] + A[H] + \sum_{i=1}^{N} (n_C w_C + n_K w_K) \exp\left\{\int_{t_0}^{t_i} \pi_t \, dt\right\} \exp\{-d_i t_i\}\} \quad (1)$$

and $H(t_0) = \sum_{i=1}^{m} H_i(t_0)$ (2)

where H is the present value of the sum of the basic risk capital in each future period $(t_{i-1}, t_i]$; $E[H]$ is the expected value of losses from repossessing houses in each future period $(t_{i-1}, t_i]$; $A[H]$ is the uncertainty in predicting future repossession expenditures due to imperfect knowledge of hydrogeology and financial market; n_C is the number of sample locations for soil gas concentration; n_K is the number of wells extracting permeability; w_C is the unit cost for each sample concentration, w_K is the cost of taking one borehole permeability measurement, π_t is the inflation rate at time t and d_i is the discount rate at time t_i.

Suppose that every house is sold at $200,000, and that the central two houses have been repurchased since a potential soil vapor TCE exposure risk is considered. If the indoor air concentration of TCE in lateral houses exceeds the regulatory limit, it assumes that developers have the liability for repurchasing the house, and when the house is resold, it will lose 20% of its original value. For developers, the maximum liability would be when all the lateral houses are repossessed and they can never sell them again, which is $800,000. The expected value of H, the safety loading term, the cost of data and the total cost-risk are shown in Figure 11, with numerous permeability and concentration sampling schemes.

If more permeability data are available prior to the model prediction and more concentration data are applied for data assimilation, there is a lower expected value of risk, due to the fact that the lateral houses in reality have no risk of exceeding the regulatory limit. Such a situtation also means a lower safety loading reserve for contingency. The cases with 5 and 7 wells of permeability data show this pattern, while the case with only 1 well of permeability data shows some oscillations and therefore should not be used for this demonstration. On the other hand, with more data, the operational cost increases. Consequently, there must be an optimal solution in which the cost-effectiveness is achieved. In Figure 11(d), seven wells of permeability data with four of concentration data gives us the minimum cost; seven wells of permeability data with seven of concentration data can be an alternative solution.

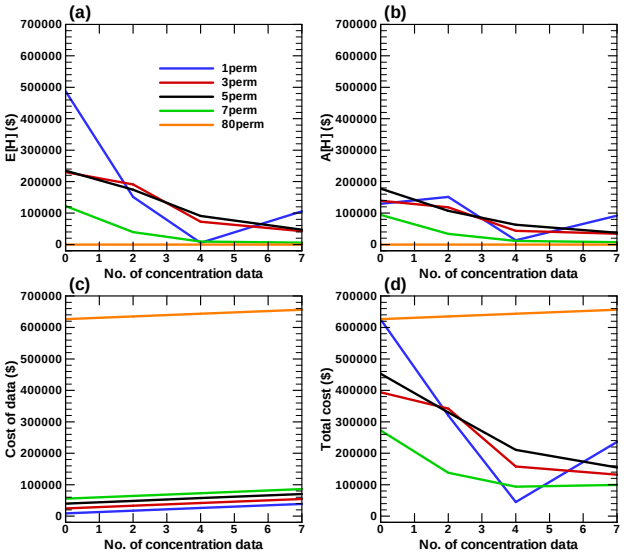

Figure 11. The variability of the related costs with different number of permeability and concentration data: (a) the expected value of the cost of risk, (b) the safety loading term on the cost of risk, (c) the cost of data, and (d) the overall cost

CONCLUSIONS

On the basis of the above results, the following conclusions may be drawn:

- First, the geological condition of an aquifer is one of the most important factors controlling the fate and transport of TCE from a source zone below the water table into houses. When a low-permeability layer saturated with water is located beneath the foundation slab, it prevents the soil gas TCE pathways from moving upwards. If a thicker vadose zone exists, it makes the mass

transfer across the capillary fringe more difficult, and the soil gas is more likely to diffuse away from the houses.

- Heterogeneity in the permeability of the aquifer causes the TCE plume to be deflected upward towards the houses. The impact of heterogeneous porosity will be investigated in future research.
- By using the spatial and temporal sampling data, and dynamically updating the sampling strategy, the model result is greatly improved. The more data that the Kalman filter utilizes for assembling the concentration correlation, the more accurate the estimations are.
- The cost of risk is defined in the same way that actuaries calculate the insurance premium, with an additional term —a safety loading term—to compensate for hydrogeological and financial uncertainties.
- An optimal solution, with the minimum cost of a brownfield redevelopment project for different numbers of permeability data and concentration data, can be obtained by a risk-cost-benefit analysis.

ACKNOWLEDGMENT

Funding for this work is provided by the University Consortium for Field-focused Groundwater Contamination Research Program.

REFERENCES

aboutRemediation™, Brownfields redevelopment toolbox™. Available at http://www.aboutremediation.com/Toolbox/Introduction.asp (accessed April 2012).

Johnson, P.C. and Ettinger, R.A., Heuristic model for prediction the intrusion rate of contaminant vapors into buildings, *Environ. Sci. Technol.*, 25: 1445-1452, 1991.

Massmann, J. and Freeze, R.A., Groundwater contamination from water management sites: The interaction between risk-based engineering design and regulatory policy: 1. Methodology, *Water Resources Research*, 23(2): 351-367, 1987.

Mueller, G. R., Brownfields capital - unlocking value in environmental redevelopment, *Journal of Real Estate Portfolio Management, 11*(1), 81-92, 2005.

National Round Table on the Environment and the Economy (NRTEE) Canada, Cleaning up the Past, Building the Future: A National Brownfield Redevelopment Strategy for Canada, 2003. Available at http://nrtee-trnee.ca/wp-content/uploads/2011/06/brownfield-redevelopment-strategy-eng.pdf (accessed February 2012).

Reddy, K. R., Adams, J. A. and Richardson, C., Potential technologies for remediation of brownfields, *Practice Periodical of Hazardous, Toxic, and Radioactive Waste Management*, *3*(2), 19821, 1999.

UK Environment Agency, Brownfield Land Redevelopment: Position Statement. May 2003. Available at http://www.environment-Agency.gov.uk/static/documents/Research/brownfield_land_908146.pdf (accessed February 2012).

United States Environmental Protection Agency (US EPA), A sustainable brownfields model framework. January 1999. Publication Number: EPA-500-R-99-001.

Wade VanLandingham, H., The stormstown group and Meyer, P. B., Public strategies for cost-effective community brownfield redevelopment. Southeast Regional Environmental Finance Center, EPA Region 4, University of Louisville, 2002. Available at http://cepm.louisville.edu/Pubs_WPapers/practiceguides/PG1.pdf.

Yu, S., Unger, A.J.A. and Parker, B., Simulating the fate and transport of TCE from groundwater to indoor air, *Journal of Contaminant Hydrology*, 107(3-4): 140-161, 2009.

Zhang, Y. and Pinder, G.F., Least cost design of groundwater quality monitoring networks, *Water Resources Research*, 41: W08412, doi:10.1029/2005WR003936, 2005.

Hydrocarbon Recovery

MODELING OF FLOW AND TRANSPORT INDUCED BY PRODUCTION OF HYDROFRACTURE STIMULATED GAS WELLS NEAR THE RULISON NUCLEAR TEST

Rex A. Hodges; Clay Cooper, Desert Research Institute; Ronald Falta, Clemson University

S.M. Stoller Corporation
2597 Legacy Way
Grand Junction, CO, 81503, U.S.
e-mail: rex.hodges@lm.doe.gov

ABSTRACT

The Project Rulison test in western Colorado, the second natural gas stimulation experiment in the Plowshare Program, was conducted in 1969 to determine if a nuclear device could be used to fracture low-permeability, gas-bearing rock to enhance natural gas production. Testing on the reentry well produced gas at rates significantly greater than those of conventional wells of the time; however, the presence of radionuclides (specifically tritium) in the produced gas persisted above acceptable levels, and the test was abandoned. Recent advances in hydrofracturing technology have made it feasible to extract natural gas from low-permeability reservoirs and have led to a significant increase of drilling in the area. However, drilling activity near the Rulison site has raised concerns that remnant radioactivity in the detonation zone could migrate to nearby producing wells and enter the natural gas distribution system.

The potential for tritium migration at Rulison was modeled with TOUGH2-EOS7R in 2007. The model has been revised to improve model defensibility and to reduce uncertainty by addressing reviewer suggestions and incorporating geologic and production data from the gas industry. Tritium is present as tritiated water, and since the gas permeability of the native formation is several orders of magnitude higher than the liquid permeability, any significant migration occurs with the gas phase. Tritium is introduced into the model as a fraction of the liquid mass in the detonation zone and partitions between the aqueous and vapor phases in relation to the Henry's law constant. The Henry's constant for tritiated water vapor is simply the water vapor pressure. The code was modified to calculate a temperature-dependent Henry's law constant based on the vapor pressure. The code was also modified to substitute methane for air. Historical production and pressure data from the reentry well were used to calibrate model flow properties. The original and subsequent modeling with TOUGH2-EOS7R simulated the effects of production from an interval at the same depth as the detonation zone in a well positioned in the most vulnerable location (as near to the institutional control boundary as would be allowed, inline with the direction of highest formation permeability). More recently, the Rulison model domain has been expanded to include gas production wells installed in 2010 0.75 mile from the site. With over 1,000,000 elements, simulations required the use of the massively parallel version TOUGH2_MP-EOS7R. The new domain allows the simulation of production from the entire targeted gas-bearing section by multiple wells, each with multiple hydrofractured intervals. The model was calibrated to both the historical reentry well data and to data from the nearby gas wells. The large domain model has been used to simulate the effects of future wells that could potentially be installed nearer the Rulison site.

INTRODUCTION

The Piceance Basin in western Colorado contains significant reserves of natural gas in poorly connected, low-permeability (tight) sandstone lenses of the Mesaverde Group. The ability to enhance the production of natural gas in this area has long been a goal of the oil and gas industry. The U.S. Atomic Energy Commission, predecessor agency to the U.S. Department of Energy (DOE) and the U.S. Nuclear Regulatory Commission, participated in three tests using nuclear detonations to fracture tight formations in an effort to enhance gas production. The tests were conducted under

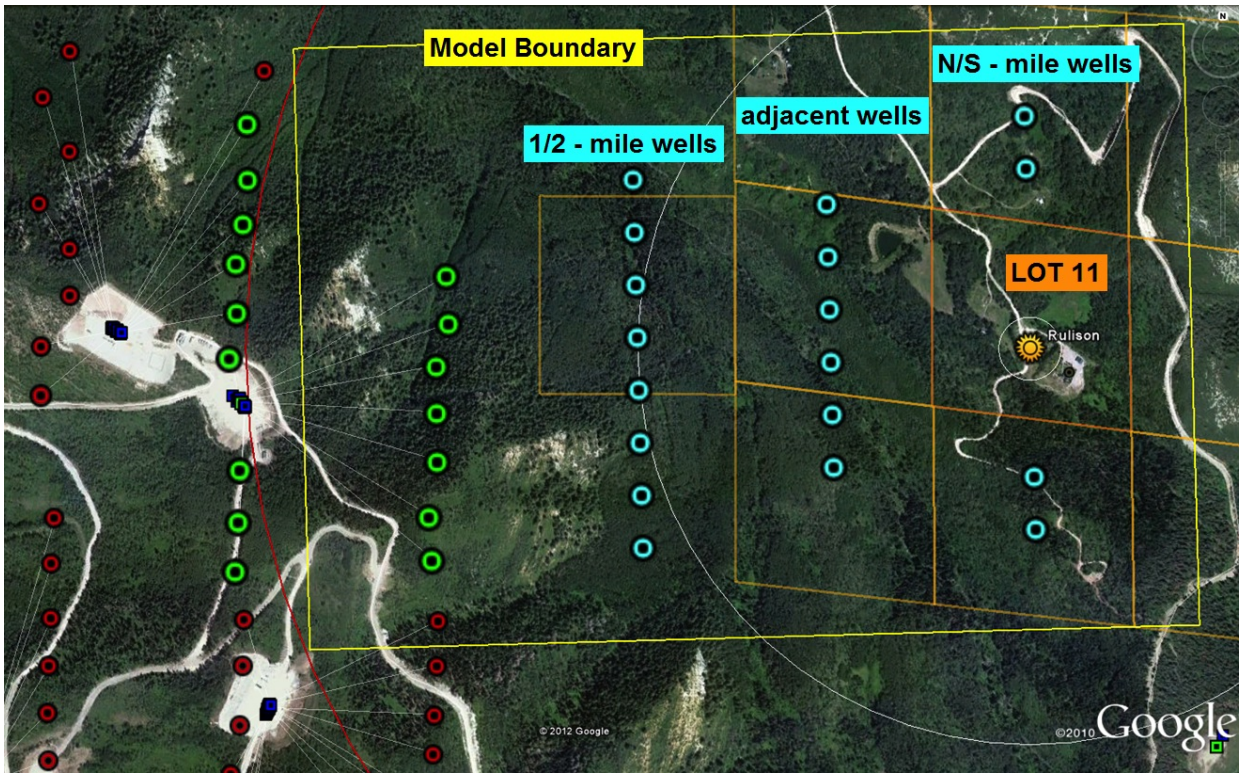

Figure 1. Model outline, institutional control (Lot 11), existing wells (red and green [sampled]), modeled future wells (blue).

Project Plowshare, a program designed to identify peaceful, beneficial uses for nuclear devices. The first, Project Gasbuggy, was conducted in 1967 in the San Juan Basin of New Mexico. The two subsequent tests, Project Rulison in 1969 and Project Rio Blanco in 1973, were in the Piceance Basin.

The ability to enhance natural gas production from tight sands has become practical through advances in hydrofracturing technology. This technology has led to an increase in drilling activity near the Rulison site, raising concerns that contamination currently contained in the subsurface could be released through a gas well drilled too close to the site. As wells are drilled nearer the site, the DOE Office of Legacy Management has taken the approach outlined in the June 2010 Rulison Path Forward document (DOE 2009), which recommends that drillers adopt a conservative, staged approach to gas development. They are encouraged to drill wells in areas with a low likelihood of encountering contamination (both distance and direction from the detonation zone are factors) and to collect data from these wells prior to drilling nearer the site's 40-acre institutional control boundary (Lot 11). Modeling results indicate that contamination has been contained within Lot 11 (Figure 1). The Path Forward document couples the model predictions with the monitoring of gas and produced water from the gas wells and the monitoring of shallow groundwater near the site.

Geologic Setting and Conceptual Model

Natural gas reserves in the Tertiary and Cretaceous strata of the Piceance Basin are estimated at 300 trillion cubic feet (http://oilshalegas.com/piceancebasin.html). The Williams Fork Formation, in which the Rulison blast occurred, is the primary producing interval near the Rulison site. It is composed of discontinuous, interbedded fluviodeltaic, low-permeability sandstones and shales (on the order of microdarcys for the sandstones and even less for the shales). The sandstones in the lower two-thirds of the Williams Fork can be stimulated by hydrofracturing to enhance production. Sandstones in the upper one-third of the Williams Fork are not production targets due to their higher water content, which lowers the relative permeability of the gas phase and causes

water production to be excessive compared to the amount of gas that can be extracted.

Wells near Rulison typically drain an area of roughly 1,200 ft by 300 ft (10 acres), with the long axis oriented east-west, along the natural fracture trend in the Williams Fork. In practice, this requires four wells per quarter-quarter section (centered east-west and aligned north-south) to drain each 40-acre parcel. The typical drainage pattern and area has been confirmed by over a hundred wells drilled near the Rulison site. Each well is expected to produce about a billion cubic feet (BCF) or more of gas on average over a 20- to 25-year life. It is evident that wells east and west of the detonation zone would be in the most susceptible transport direction, due to the increased permeability in that direction and the tendency of fractures to propagate in that direction.

The extremely high temperatures associated with a nuclear detonation vaporize a volume of rock and produce a roughly spherical cavity surrounding the blast point. A high-pressure shock wave spreads from the blast, fracturing the rock beyond the cavity wall. Within minutes to hours after the detonation, the fractured rock above the cavity collapses, forming a rubble-filled chimney. The Rulison detonation was at a depth of 8,425 ft below ground surface, and the top of the chimney was interpreted to be where the reentry well lost circulation 275 ft above the detonation.

Source and Potential Migration Pathway

Radionuclides that can exist in the gas phase, have a relatively long half-life, and were created in significant amounts by the detonations are of primary concern, because of their persistence in the subsurface and their potential mobility. The relative permeability of the gas phase is orders of magnitude greater than that of liquids in the natural-gas-producing reservoirs of the Williams Fork. Gas-phase radionuclides produced by the Rulison detonation (Reynolds 1971) in estimated order of abundance were tritium (approximately 10,000 curies), krypton-85, and minor amounts of argon isotopes and carbon-14.

A reentry well was drilled into the Rulison chimney and tested to determine the success of the detonation at improving gas production. The well produced 455 million cubic feet (MMCF) of gas in 107 days of testing that took place from October 1970 through April 1971 in four separate flow tests. The produced gas was flared to the atmosphere, and samples of the produced gas and produced water were collected and analyzed to determine the degree to which radioactivity levels changed as testing progressed. Radioactivity levels decreased throughout the testing as gas from the chimney region was produced, burned, and replenished by uncontaminated gas from the surrounding formation. Approximately 3,000 of the original 10,000 curies of tritium were removed by the production testing, leaving 7,000 curies of tritium that would have decayed to 600 curies by 2012. Radionuclides other than tritium were largely removed by production testing and radioactive decay. The depletion of tritiated methane by the production testing leaves tritiated water as the primary contaminant source for the Rulison site.

Modeling Objectives

A major limitation of the previous Rulison models was the computational constraints on the number of elements that nonisothermal EOS7R models could accommodate. With the advent of a massively parallel version of the modeling code (TOUGH2_MP), problems requiring several million elements can now be simulated. The modeling effort has been continued with an extended model domain that includes current gas production wells to the west and spans the entire productive interval. This new Rulison model was calibrated to not only the historical reentry well data, but also to production data from current producing wells. The extended domain made it possible to simulate the effects of the enactment of the Rulison Path Forward.

MODEL CONSTRUCTION

The model uses an equivalent porous media approach even though flow is predominantly through a fractured system. The approach is justified in that the fractures through which flow occurs are assumed to be frequent with limited extents. The mechanical forces that create the nuclear fractured and hydrofractured regions rubblize the formation to increase permeability.

Model Domain and Discretization

The horizontal and lateral extents of the Rulison model domain were designed to include existing gas production wells 0.75 mile west of the site (Figure 1) and to include the entire gas-productive lower two-thirds of the Williams Fork Formation. The horizontal extent is 6,000 ft in the east-west direction and 4,000 ft in the north-south direction. The vertical extent of the model domain is 2,200 ft—the 2,000 ft thick lower two-thirds of the Williams Fork Formation and an additional 200 ft into the non-producing upper third of the Williams Fork. This allows data from the recently installed (2010) producing wells to be incorporated into the model to support historical data from the emplacement well and the re-entry well. The three-dimensional model is discretized into elements that are 50 ft (15.24 m) in the horizontal x and y directions and 20 ft (6.1 m) in the vertical z direction, for a total of 1,056,000 cells (120x, 80y, 110z).

Material Types

Geophysical and lithologic logs from the exploratory and emplacement wells, and gas wells in the domain, were used with published statistics on sand body sizes and correlation lengths to generate the sand-shale distributions. Data from Noble Energy, the primary operator in the area, indicate that about 42.5 percent of the targeted Williams Fork section near Rulison can be considered producing sandstones. The remaining 57.5 percent is considered shale for the purposes of the model. Figure 2 shows a vertical slice through a sandstone (yellow)-shale (olive) realization with the detonation zone (chimney [red], nuclear fractures [white]) and hydrofracture zones (red). Separate ROCK types were assigned to lower Williams Fork sandstones (LWFsd), upper Williams Fork sandstones (UWFsd), and shales.

The nuclear fractured region was defined as a truncated (at depth) ellipsoid with a longer east-west axis. Elements within the nuclear fracture and chimney ellipsoids were changed to ROCK types NFrac, chimn, or glass to allow for their own specified set of parameters. The melt glass provides a constant heat source at the base of the chimney.

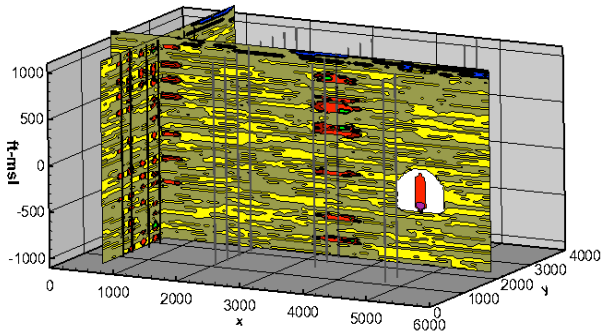

Figure 2. Sandstone/shale distribution.

Hydrofractured formation

At gas well locations, sandstones within the lower Williams Fork Formation that were 40 ft or more in thickness (model layers are 20 ft thick) were hydrofractured. Like an actual well, no information about how laterally extensive the sandstone was away from the wellbore was used to decide which interval would be hydrofractured. And, like an actual well, the horizontal distance that hydrofracturing extended from the wellbore was to a degree controlled by the lithology surrounding the wellbore. Hydrofractures were assumed to extend farther in sandstones than in shales, and it was assumed that hydrofracturing would be more effective in the sandstones. Figure 2 shows hydrofractures elongated in the east-west direction.

Model Parameters

Capillary pressure and relative permeability curves for each ROCK type were based on published information about the Mesaverde in Byrnes and Cluff (2009). The capillary pressure curves were based on the TRUST capillary function (Narasimhan et al. 1978), and the relative permeability curves were based on Corey (1954). A reasonable range of permeability and porosity values for the various ROCK types were determined by calibrating the Rulison model to production and pressure data from the reentry well and to gas wells within the domain.

Boundary Conditions

The size of the model domain in combination with the very low native permeabilities of the formations allows for no-flow boundaries on all sides without significantly altering the flow

field, even for wells near boundaries. The majority of flow within the model domain is from regions that have been fractured to allow flow, the nuclear fractured region, or hydraulically fractured regions surrounding gas wells. These regions are separated from boundaries by the very low permeability formation, and any significant interaction with boundaries over the time frame of the simulations would in itself indicate that the model is not calibrated to observed real-world conditions.

Initial Concentration and Partitioning of Tritiated Water (THO)

The Henry's law constant is used to describe the partitioning of a compound between the gas and aqueous phases. This partitioning provides a method to calculate the mass fraction of THO in the gas phase using the vapor pressure of water, assuming that THO is in molecular equilibrium with the gas and liquid phases. The Henry's law constant used to calculate the partitioning of THO between the two phases is simply the water vapor pressure. The water vapor pressure is directly related to temperature (Figure 3), and the code was modified to calculate a spatially variable temperature-dependent Henry's law constant based on the vapor pressure. The inverse pressure form of the Henry's law constant is developed below and was used to reproduce published values (Smiles et al. 1995) for confirmation.

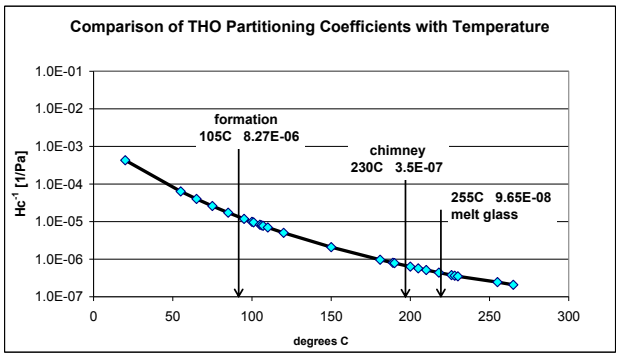

Figure 3. Inverse vapor pressure of water relative to temperature

The initial concentration was assigned to chimney elements (1.0×10^{-9} for Rulison) as a mass fraction of THO in the aqueous phase (a primary variable). The gas-phase mass fraction of THO (a secondary variable) is calculated (partitioned) with the first time step of the simulations based on the initial thermophysical properties for the chimney elements. The code was also modified to replace air (not in the gas reservoirs) with methane. This was necessary to get the initial partitioning correct, because the molecular weight of air (29 g/mol) is greater than that of methane (16 g/mol). The mass fraction of THO in the gas phase will be higher if it partitions into a less-dense gas phase (methane rather than air).

Inverse Henry's Law constant (*HCRN1*):

$$HCRN1 = \frac{\chi_l^{THO}}{P_g^{THO}}$$

Gas and aqueous phases should have same ratio of molecules:

$$\frac{P_g^{THO}}{P_g^{H_2O}} = \chi_g^{THO} = \chi_l^{THO}$$

Substitute to get HCRN1, same pressure units (pascals [Pa]) as TOUGH2 EOS7R (1/Pa)

$$HCRN1 = \frac{\chi_l^{THO}}{P_g^{THO}} = \frac{\frac{P_g^{THO}}{P_g^{H_2O}}}{P_g^{THO}} = \frac{1}{P_g^{H_2O}}$$

where:

χ_l^{THO} = mole fraction of tritiated water in the aqueous phase

P_g^{THO} = partial pressure of tritiated water vapor in the gas phase

Initial Conditions

The initial pressures ranged of 19.7 to 22 MPa (about 2,850 to 3,190 psi) from the top to the bottom of the domain. Shut-in pressures through the productive interval from drill-stem tests in the pre-shot exploratory well ranged from 2,250 to 3,050 psi (Nork and Fenske 1970). Water saturations are about 0.5 in the sandstones and about 0.65 in the shales, with the variation due to the capillary pressure curve used for each and some variation with depth. Formation temperatures were initialized to 105°C (220°F) (from Montan, 1971). The temperature of the chimney was assigned an initial value of 230°C (445°F) (from DeGolyer and MacNaughton 1971). The melt glass elements at the base of the chimney were assigned a temperature of 255°C to act as a constant heat source.

Well Treatment

Production from the reentry well was simulated using a MASS extraction (Pruess et al. 1999) of combined gas and water based on the historical data that recorded both the amount of gas and water extracted over time and the resulting pressure decline. A total of 455 MMCF of gas (430 MMCF dry gas) was produced along with 20,244 barrels of water during the testing.

Production from current and future gas wells was simulated as production against a specified wellbore pressure (well on deliverability, Pruess et al. 1999). An estimated down-hole pressure of 600 psi (based on discussions with operators of gas wells within the model domain) was assigned to perforated well elements using the DELV option in the model (pressure differential of about 2,300 psi; 2,900–600). The resulting production rate declined over time as fluids were depleted. The simulated production rate was compared to the actual production rate from existing producing wells within the model domain to determine how well the model simulated actual production.

MODEL CALIBRATION

Reentry Well Calibration

The primary calibration of the model was based on the historical reentry well data. Parameters adjusted during the calibration process were the permeability and porosity of the chimney, nuclear fractured region, and the lower Williams Fork sandstone. The fit parameters are given in Table 1, and the best fit is shown in Figure 4. The permeability of the lower Williams Fork sandstone in the horizontal direction of the natural fracture trend (kx) was assumed to be 10 times that of the permeability normal to the trend (ky) and that of the vertical permeability (kz). This anisotropy ratio was constant for all simulations.

Table 1. Reentry well calibrated parameters.

ROCK	kx [m^2]	Porosity
chimn	0.4×10^{-11}	0.33
NFrac	0.6×10^{-15}	0.06
LWFsd	0.5×10^{-17}	0.05
shale	0.1×10^{-19}	0.06

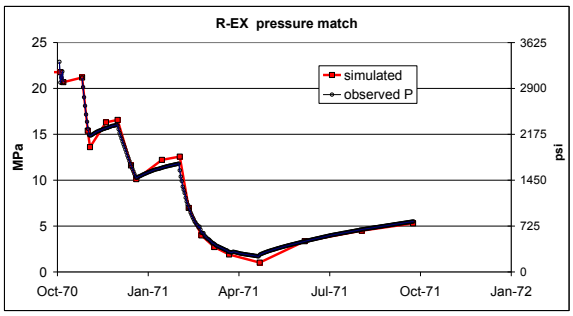

Figure 4. Observed and simulated pressures

Gas Well Calibration

Parameters adjusted during the calibration process were the permeability and porosity of the LWFsd, the hydrofractured sandstone near the well (HFnsd), the hydrofractured sandstone far from the well (HFfsd), and the hydrofractured shale near the well (HFshl). Three wells, two with many sand layers perforated (26-33B, 26-34C) and one with few sand layers perforated (26-34D), were chosen for the calibration. The best fit (solid lines) plus two other simulation results are shown on Figure 5. The best fit parameters are given in Table 2.

Table 2. Gas well calibrated parameters.

ROCK	kx [m^2]	k increase [a]	Porosity
LWFsd	0.4×10^{-11}		0.06
HFnsd	0.6×10^{-15}	40	0.06
HFfsd	0.8×10^{-17}	4	0.06
HFshl	0.1×10^{-19}	4 (800x shale)	0.06

[a] k increase is permeability multiplier over LWFsd

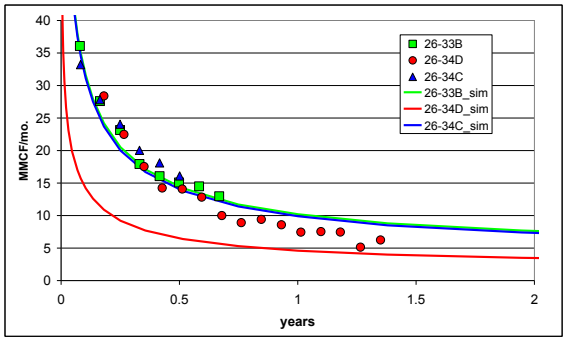

Figure 5. Observed and simulated production.

Because of the limited production history, a better method than matching simulated and actual production rates for these wells is to compare the simulated and industry-expected total production over the life of a well. With a simulated production life of 25 years, wells 26-33B and 26-34C would produce about 1.44 and 1.34 BCF, respectively, given the parameters of the calibrated model. The low simulated-production rate well 26-34D would produce about 0.66 BCF.

MODEL RESULTS

The first step after model construction was to simulate the post-detonation events up until the gas wells in the model domain were installed (2010). The second step simulated production from the existing gas wells and staged additions of future gas wells for 25 years as suggested in the Rulison Path Forward document.

Post-detonation to 2010 Simulations

The post-detonation simulations show conditions after the detonation through the reentry well testing to just before recent gas development in the area. Figure 6 and Figure 7 show the conditions after the fourth and last production test. The low pressures caused by the production testing enhanced the evolution of THO from the aqueous phase into the gas phase, increasing the concentration in the gas phase in the lower chimney. The pressure drop in the chimney extended through the nuclear fractured region into adjacent sandstones. Diffusion of THO did not extend much beyond the nuclear fractured region, and the pressure in the chimney recovered to near pre-detonation levels.

Path Forward Simulations

The Rulison Path Forward recommends that wells encroaching on the site be drilled in a staged approach to minimize the risk of encountering contamination. The path forward simulations begin with the onset of production from wells installed in 2010. The plots of simulated results in 2015 show the pressure drop extending from the existing wells and the remnant pressure effect from the reentry well (Figure 8), and the unaffected concentration distribution (Figure 9). Production from the 0.5-mile wells begins at this time.

Figure 10 shows the pressure distribution in 2030, 5 years after the closest simulated wells (adjacent) started producing.

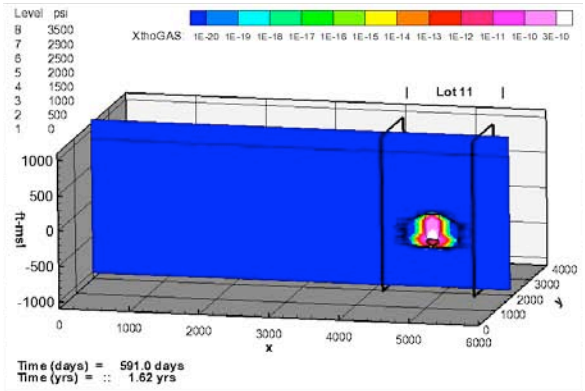

Figure 6. Concentration distribution after testing.

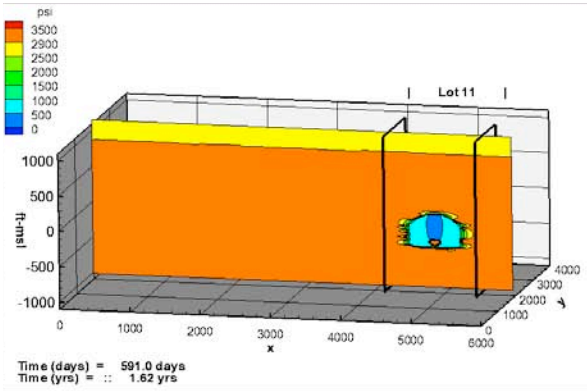

Figure 7. Pressure distribution after testing.

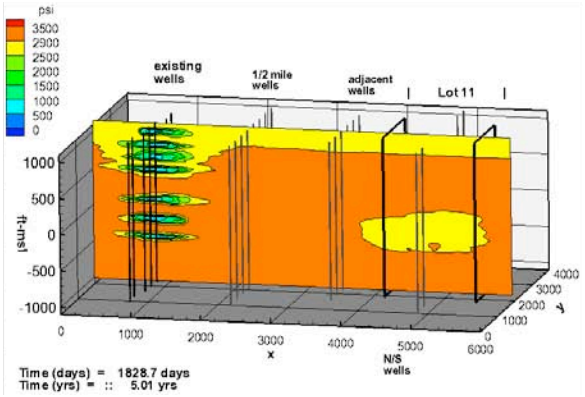

Figure 8. Simulated pressure distribution in 2015.

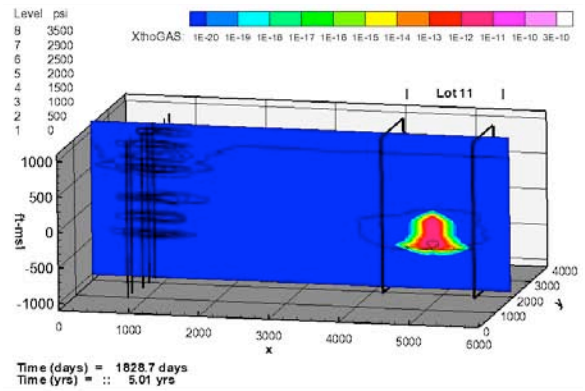

Figure 9. Simulated THO distribution in 2015.

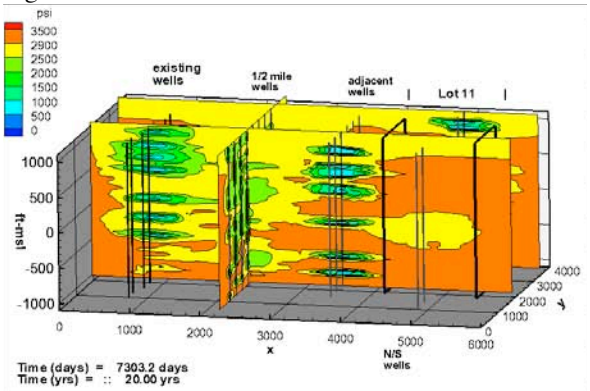

Figure 10. Simulated pressure distribution in 2030.

Figure 11 shows the pressure distribution in 2045, at the end of the adjacent wells' production life. An additional contour (2875 psi) was added to see the pressure effects extending into the chimney region. Note that this pressure gradient is insufficient to induce migration of THO from the detonation zone (Figure 12).

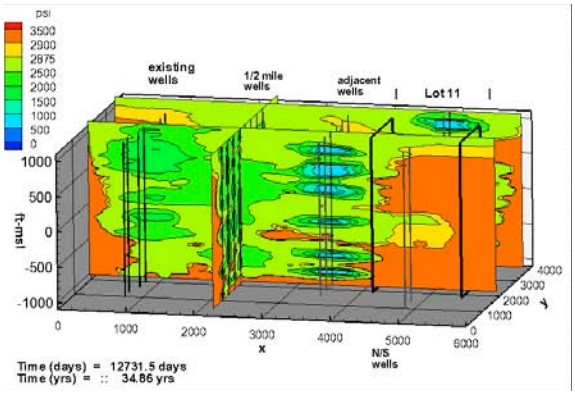

Figure 11. Simulated pressure distribution in 2045.

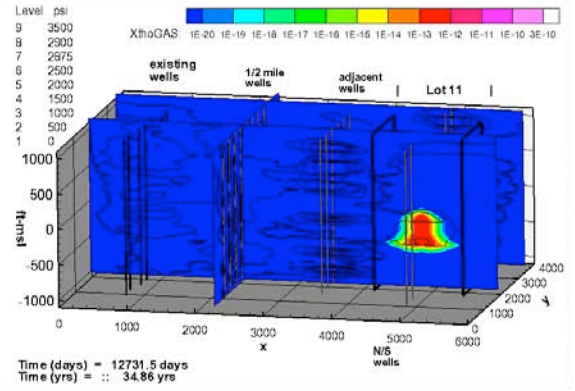

Figure 12. Simulated THO distribution in 2045.

CONCLUSIONS

The finding that THO did not migrate from the detonation zone was fully expected, considering the retarding effects of THO vapor coming into contact with liquid water. In addition, the possibility that production from nearby gas wells could reduce pressure in the formation enough to make a connection with the detonation zone was demonstrated for a few perforated intervals in a simulated well in the most vulnerable location. However, the induced pressure gradient was less than observed natural pressure variations in different sandstones in the same well and was not sufficient to induce contaminant migration.

REFERENCES

Byrnes, A.P., and R.M. Cluff, *Analysis of Critical Permeability, Capillary Pressure and Electrical Properties for Mesaverde Tight Gas Sandstones from Western U.S. Basins*, U.S. DOE Contract Number: DE-PS26-04NT42072, 2009.

Corey, A.T., The interrelation between gas and oil relative permeabilities, *Producers Monthly*, 38–41, November, 1954.

DeGolyer and MacNaughton Co. *Report on Interpretation of Test Data for Project Rulison in the Rulison Field, Garfield County, Colorado*. Prepared for Austral Oil Company, Inc., 1971.

DOE, *Rulison Path Forward Document 2009*, http://www.lm.doe.gov/Rulison/Documents.aspx

Montan, D.N., Project Rulison Gas Flow Analysis, *Nuclear Explosives Technology*, 1971.

Narasimhan, T.N., P.A. Witherspoon, and A.L. Edwards, Numerical model for saturated-unsaturated flow in deformable porous media, Part 2: The algorithm," *Water Resour. Res.*, 14(2), 255–261, 1978.

Nork, W.E., and P.R. Fenske, *Radioactivity in Water—Project Rulison*, NVO-1229-131, 1970.

Pruess, K., C. Oldenburg, and G. Moridis, *TOUGH2 User's Guide, Version 2.0*, Report LBNL-43134, Lawrence Berkeley National Laboratory, Berkeley, Calif., 1999.

Reynolds, M., 1971. *Project Rulison—Summary of Results and Analyses*, presented at the American Nuclear Society winter meeting, Miami, Florida.

Smiles, D.E., W.R. Gardner, and R.K. Shulz, Diffusion of tritium in arid disposal sites, *Water Resour. Res.*, 31(6), 1483–1488, 1995.

DEVELOPMENT OF THE T+M COUPLED FLOW-GEOMECHANICAL SIMULATOR TO DESCRIBE FRACTURE PROPAGATION AND COUPLED FLOW-THERMAL-GEOMECHANICAL PROCESSES IN TIGHT/SHALE GAS SYSTEMS

Jihoon Kim, George J. Moridis
Lawrence Berkeley National Laboratory
1 Cyclotron Rd.
Berkeley, CA, 94706, USA
e-mail: JihoonKim@lbl.gov

ABSTRACT

We developed a T+M hydraulic fracturing simulator by coupling a flow simulator with a geomechanics code. Modeling of the vertical fracture development involves continuous updating of the boundary conditions and of the connectivity data. This T+M simulator can model the initial fracture development during hydraulic fracturing operations, after which the domain description changes from single continuum to double or multiple continua, in order to rigorously model both flow and geomechanics. The T+H simulator allows explicit description of nonlinear permeability and geomechanical moduli, provides two-way coupling between fluid and heat flow and geomechanics, and continuously tracks changes in the fracture(s) and in the pore volume, and fully accounts for leak-off in all directions during hydraulic fracturing.

1. INTRODUCTION

Hydraulic fracturing is widely used in reservoir engineering applications to increase production by enhancing permeability. In particular, gas production in shale/tight gas reservoirs typically hinges on hydraulic fracturing because of the extremely low permeability of such reservoirs.

Several studies to develop algorithms for coupled simulation have been made in reservoir engineering. Ji et al. (2009) developed a numerical model for hydraulic fracturing, considering coupled flow and geomechanics, in which the algorithm is based on a dynamic update of the boundary condition along the fracture plane, fundamentally motivated by node splitting. In addition, Nassir et al. (2012) incorporated shear failure into a hydraulic fracturing model. Dean and Schmidt (2008) employed the same fracturing algorithm as Ji et al. (2009), while using different criteria for tensile failure. Fu et al. (2011) used the node-splitting method when material undergoes tensile failure. The method by Ji et al. (2009) exclusively considers vertical fracturing, but allows the fracturing algorithm to be implemented easily to the finite element method, changing the boundary conditions and data connectivity. Furthermore, it can easily couple flow and geomechanics, accounting for leak-off of the proppants to the reservoirs. On the other hand, Fu et al. (2011) developed a method that is not restricted to vertical fracturing, but using this method for 3D fracturing problems causes considerable complexity in code development, and modification of the data connectivity is also challenging compared to Ji et al.'s (2009) algorithm. Moreover, the Fu et al. (2011) method only allows flow along gridblocks, so the leak-off of proppants to gridblocks cannot properly be considered.

For the aforementioned issues related to hydraulic fracturing, we have developed an algorithm similar to that of Ji et al. (2009). We address shear failure by implementing the Drucker-Prager and Mohr-Coulomb models, considering coupled flow and geomechanics affecting pore volume and permeability for the multiple porosity model.

2. MATHEMATICAL FORMULATION

2.1. Governing Equation

Hydraulic fracturing requires the combined modeling of coupled fluid and heat flow and geomechanics. The governing equation for fluid flow is as follows.

$$\frac{d}{dt}\int_\Omega m^k d\Omega + \int_\Gamma \mathbf{f}^k \cdot \mathbf{n} d\Gamma = \int_\Omega q^k d\Omega \qquad , (1)$$

where superscript k indicates the fluid component. $d(\cdot)/dt$ refers to the time derivative of a physical quantity $(\cdot)$ relative to the motion of

the solid skeleton. m^k is the mass of component k. $\mathbf{f}^k$, and q^k are its flux and source terms on the domain Ω with boundary Γ, where $\mathbf{n}$ is the normal vector of the boundary.

The mass of component k is written as

$$m^k = \sum_J \phi S_J \rho_J X_J^k \ , \qquad (2)$$

where subscript *J* indicates fluid phases. ϕ is the true porosity, defined as the ratio of the pore volume to the bulk volume in the deformed configuration. S_J, ρ_J, and X_J^k are saturation and density of phase *J*, and the mass fraction of component k in phase *J*.

The mass flux term is obtained from

$$\mathbf{f}^k = \sum_J (\mathbf{w}_J^k + \mathbf{J}_J^k) \ , \qquad (3)$$

where $\mathbf{w}_J^k$ and $\mathbf{f}_J^k$ are the convective and diffusive mass flows of component *k* in phase *J*, respectively. For the liquid phase, *J*=*L*, $\mathbf{w}_J^k$ can be given by Darcy's law as

$$\mathbf{w}_J^k = X_J^k \mathbf{w}_J,$$
$$\mathbf{w}_J = -\frac{\rho_J k_{rJ}}{\mu_J}\mathbf{k}\left(\mathbf{Grad} p_J - \rho_J \mathbf{g}\right), \qquad (4)$$

where $\mathbf{k}$ is the absolute (intrinsic) permeability tensor. The terms μ_J, k_{rJ}, p_J are the viscosity, relative permeability, and pressure of the fluid phase *J*, respectively. $\mathbf{g}$ is the gravity vector, and $\mathbf{Grad}$ is the gradient operator. Note that, depending on the circumstances, other, more flow equations may be appropriate, such as the Forchheimer equation (Forchheimer, 1901) that incorporates laminar, inertial and turbulent effects.

For the gaseous phase, *J*=*G*, $\mathbf{w}_G^k$ is given by

$$\mathbf{w}_G^k = X_G^k \mathbf{w}_G$$
$$\mathbf{w}_G = -\left(1 + \frac{k_K}{P_G}\right)\frac{\rho_G k_{rG}}{\mu_G}\mathbf{k}\left(\mathbf{Grad} p_G - \rho_G \mathbf{g}\right) \qquad (5)$$

where k_K is the Klinkenberg factor. The diffusive flow can be written as

$$J_J^k = -\phi S_J \tau_G \rho_J \mathbf{D}_J^k \mathbf{Grad} X_J^k \ , \qquad (6)$$

where $\mathbf{D}_J^k$ and τ_G are the hydrodynamic dispersion tensor and gas tortuosity, respectively.

The governing equation for heat flow comes from heat balance, as

$$\frac{d}{dt}\int_\Omega m^H d\Omega + \int_\Gamma \mathbf{f}^H \cdot \mathbf{n} d\Gamma = \int_\Omega q^H d\Omega \ , \qquad (7)$$

where the superscript H indicates the heat component. m^H, $\mathbf{f}^H$, and q^H are heat, its flux, and source terms, respectively. The term m^H is the heat accumulation term, and is expressed as

$$m^H = (1-\phi)\int_{T_0}^T \rho_R C_R dT + \sum_J \phi S_J \rho_J e_J \ , \qquad (8)$$

where ρ_R, C_R, T, and T_0 are the density and heat capacity of the porous medium, temperature, and reference temperature, respectively. The heat flux is written as

$$\mathbf{f}^H = -\mathbf{K}_H \mathbf{Grad} T + \sum_J h_J \mathbf{w}_J \ , \qquad (9)$$

where $\mathbf{K}_H$ is the composite thermal conductivity tensor of the porous media. The specific internal energy, e_J, and enthalpy, h_J, of components *k* in phase *J* become, respectively

$$e_J = \sum_k X_J^k e_J^k \ , \ h_J = \sum_k X_J^k h_J^k \qquad (10)$$

The governing equation for geomechanics is based on the quasi-static assumption (Coussy 1995), written as

$$\mathbf{Div}\boldsymbol{\sigma} + \rho_b \mathbf{g} = \mathbf{0}, \qquad (11)$$

where $\mathbf{Div}$ is the divergence operator, $\boldsymbol{\sigma}$ is the total stress tensor, and ρ_b is the bulk density. The infinitesimal transformation is used to allow the strain tensor, $\boldsymbol{\varepsilon}$, to be the symmetric gradient of the displacement vector, $\mathbf{u}$,

$$\boldsymbol{\varepsilon} = \frac{1}{2}\left(\mathbf{Grad}^T \mathbf{u} + \mathbf{Grad}\,\mathbf{u}\right) \qquad (12)$$

where $\mathbf{Grad}$ is the gradient operator. The boundary conditions for the geomechanical problems are as follows; $\mathbf{u} = \bar{\mathbf{u}}$, given displacement, on a boundary Γ_u, and $\boldsymbol{\sigma}\cdot\mathbf{n} = \bar{\mathbf{t}}$, traction on a boundary Γ_t, where $\Gamma_u \bigcup \Gamma_t = \partial\Omega$, the

boundary over the domain, and $\Gamma_u \bigcap \Gamma_t = \emptyset$. The initial total stress satisfies the mechanical equilibrium with the boundary conditions. We may take a larger domain than a reservoir in order to determine geomechanics and heat transport more accurately.

Remark 1. Note that the boundary conditions for a given mathematical model in hydraulic fracturing are not prescribed but rather dependent on geomechanical solutions (i.e., nonlinearity). Conventional plastic mechanics, such as Mohr-Coulomb failure, results in material nonlinearity, while the boundary conditions are still prescribed (Simo and Hughes, 1998; Wang et al., 2004). On the other hand, the geomechanics of hydraulic tensile fracturing in this study does not yield material nonlinearity while nonlinearity lies in the boundary condition (Ji et al., 2009).

2.2. Constitutive relations

Gas flow within homogeneous rock can be modeled using single porosity poromechanics, extended from Biot's theory (Coussy, 1995). However, when failure occurs and fractures are created, we have local heterogeneity because fractures and rock matrix coexist. In this case, we use double or multiple porosity models, which allow local heterogeneity. In particular, for single phase flow, the constitutive equations are written as follows (Berryman, 2002, Kim et al., 2012).

$$\delta\boldsymbol{\sigma} = \overbrace{\mathbf{C}_{up}\delta\boldsymbol{\varepsilon}}^{\delta\boldsymbol{\sigma}'} - \sum_l b_l^* \delta p_l \mathbf{1} - \sum_l \widetilde{b}_l^* \delta T_l \mathbf{1}, \qquad (13)$$

$$b_l^* = -K_{dr} b_l,\ \widetilde{b}_l^* = -K_{dr}\widetilde{b}_l,$$

$$\delta\zeta_l = b_l^* \delta\varepsilon_v + \sum_m L_{l,m}^{-1}\delta p_m + \sum_m \overline{D}_{l,m}\delta T_m, \qquad (14)$$

where the subscript l indicates a material (subelement) within a gridblock. The terms K_{dr} and $\mathbf{C}_{up}$ are the upscaled elastoplastic drained bulk and tangent moduli at the level of the gridblock, respectively, and b_l^* and $\widetilde{b}_l^*$ are the coupling coefficients. b_l , $\widetilde{b}_l$, K_{dr}, $L_{l,m}^{-1}$ are written as

$$b_l = -\frac{\alpha_l \eta_l}{K_l},\ \widetilde{b}_l = -3\alpha_{T,l}\eta_l,$$

$$K_{dr} = \sum_l \frac{\eta_l}{K_l},\ \mathbf{L}^{-1} = \begin{bmatrix} \eta_f N_f & 0 \\ 0 & \eta_M N_M \end{bmatrix}, \qquad (15)$$

where α_l , $\alpha_{T,l}$, η_l , and K_l are the Biot coefficient, thermal dilation coefficient, volume fraction, and drained bulk modulus for material *l,* respectively. The term $L_{l,m}(\equiv \mathbf{L})$ represents the Biot modulus matrix of the double porosity model (e.g., the fracture-rock matrix system), where N_f and N_M are the inverse of the Biot moduli, M_f and M_M, for the fracture and rock matrix media, respectively, (i.e., $N_f = 1/M_f$ and $N_M = 1/M_M$). The subscripts f and M indicate the fracture and rock matrix. $\overline{D}_{l,m}$ is the coupling coefficient between fluid flow and heat flow.

For naturally fractured reservoirs, the double porosity model is used initially, while, in this study, we change the single porosity model into a double porosity during simulation when a material fails. Thus, for the naturally fractured reservoirs, $\mathbf{C}_{up}$ and K_{dr} on the level of a gridblock are obtained from an upscaling of given fracture and rock matrix material properties. The return mapping for elastoplasticity is performed at all the subelements (Kim et al., 2012).

On the other hand, in this study, $\mathbf{C}_{up}$ and K_{dr} are directly obtained from the elastoplastic tangent moduli at a gridblock (global) level, not the subelements, while we need to determine the drained bulk moduli of fracture and rock matrix materials for the double porosity model, followed by the coupling coefficients. To this end, we assume that the rock matrix has the same drained bulk modulus as that of the single porosity material before plasticity (i.e., elasticity), because the rock matrix is undamaged (Kim and Moridis, 2012a). Then, from Eq. 15_3, the drained bulk modulus of the fracture can be determined by

$$K_f = \eta_f \frac{K_{dr} K_M}{K_M - K_{dr}(1-\eta_f)}. \qquad (16)$$

Considering K_{dr} and K_f to be positive for well-posedness, the volume fraction of the fracture, η_f, has the constraint as

$$\eta_f > 1 - \frac{K_M}{K_{dr}}. \tag{17}$$

2.3. Failure and Fracturing

We consider two types of failure in geomaterials: tensile and shear failure.

2.3.1. Tensile failure

We use the tensile failure condition for large-scale fracture propagation, as follows.

$$\sigma'_n \geq T_c \ , \tag{18}$$

where σ'_n is the effective stress normal to the plane of a potential fracture, and T_c is the tensile strength of a material. The tensile strength is determined from a tension test such as the Brazilian test. For a given geomechanical loading, the boundary condition for geomechanics is modified when the tensile effective stress reaches the tensile failure condition. In other words, the internal natural (Neumann) boundary conditions are introduced at the areas where the tensile effective stress satisfies the condition of the tensile failure (Eq. 18).

Remark 2. The geomechanics status at early time when tensile fracturing occurs is assumed to exist in undrained condition, with the exception of adding surface loads at the boundary conditions (i.e., traction due to fracturing). The traction normal to the fracture surface, $\bar{t}_f$, can be determined as $\bar{t}_f = \bar{p}_f$. Here, at the early time, we set $\bar{p}_f$ to be the initial reservoir pressure, which implies that the pressure at the fracture is locally equilibrated with the surroundings. On the other hand, after the early time, $\bar{p}_f$ changes due to flow of the proppants.

2.3.2. Shear failure

For shear failure, we use the Drucker-Prager and Mohr-Coulomb models, which are widely used to model the failure of cohesive frictional materials. The Drucker-Prager model of this study is expressed as

$$\begin{aligned} f &= \beta_f I_1 + \sqrt{J_2} - \kappa_f \leq 0, \\ g &= \beta_g I_1 + \sqrt{J_2} - \kappa_g \leq 0, \end{aligned} \tag{19}$$

where I_1 is the first invariant of the effective stress and J_2 is the second invariant of the effective deviatoric stress. f and g are the yield and plastic potential functions, respectively. The Mohr-Coulomb model is given as

$$\begin{aligned} f &= \tau'_m - \sigma'_m \sin\Psi_f - c_h \cos\Psi_f \leq 0, \\ g &= \tau'_m - \sigma'_m \sin\Psi_d - c_h \cos\Psi_d \leq 0, \end{aligned} \tag{20}$$

$$\sigma'_m = \frac{\sigma'_1 + \sigma'_3}{2}, \ \tau'_m = \frac{\sigma'_1 - \sigma'_3}{2} \tag{21}$$

where $\sigma_1', \sigma_2', \sigma_3'$ are, respectively, the maximum, intermediate, and minimum principal effective stresses, where tensile stress is positive. Ψ_f and Ψ_d are the friction and dilation angles, respectively. c_h is the cohesion.

3. NUMERICAL MODELING

We developed the T+M hydraulic fracturing simulator by coupling the LBNL in-house simulator **T**OUGH+RealGasH2O (for the description of nonisothermal flow of water and real gas mixture through porous/fractured media) with the ROC**M**ECH in-house geomechanics simulator. Below, we describe the numerical algorithms and characteristics of the coupled simulator.

3.1. Discretization

Space discretization is based on the integral finite difference method (a finite volume technique) in the simulation of flow and heat flow (TOUGH+RealGasH2O code), and the finite element method in the geomechanical component of the coupled simulations (ROCMECH code). Time discretization in both constituent components of T+M is based on the standard backward method that is typically employed in reservoir simulations.

3.2. Failure Modeling

3.2.1. Tensile failure and node splitting

We introduce the new internal Neumann boundaries by splitting nodes, and assign the traction from the fluid pressure inside the fractures.

Node splitting is performed based on the physical tensile strength. In this study, the focus is on vertical tensile fracturing. Because of symmetry, we extend the numerical simulation capabilities to 3D domains. Then, the fracture plane is located at the outside boundary (Ji et al., 2009).

3.2.2. Shear failure and elastoplasticity

We use classical elastoplastic return-mapping algorithms for the Mohr-Coulomb and Drucker-Prager models (Simo and Hughes, 1998). Unlike for tensile fracturing, we account for shear failure with no assumption of a certain fracturing direction. The Drucker-Prager model provides a simple closed analytical formulation for return mapping because it is associated only with I_1 and J_2. However, the Mohr-Coulomb model also takes J_3, and thus the return mapping is not straightforward, as it is in the Drucker-Prager model.

For the Mohr-Coulomb model, we employ the two-stage return mapping algorithm proposed by Wang et al. (2004) after slight modifications. In the return mapping of the Mohr-Coulomb model at the edges of the failure envelope, we also employ the Drucker-Prager model with explicit treatment of J_3 to avoid numerical instability. According to Kim and Moridis (2012a), the adjusted Drucker-Prager model for the Mohr-Coulomb model (i.e., explicit treatment of J_3) can also simulate the Mohr-Coulomb failure accurately.

3.3. Sequential Implicit Approach

There are two typical methods for solving coupled problems: fully coupled and sequential implicit. The fully coupled method usually provides unconditional and convergent numerical solutions for mathematically well-posed problems. The price for these important advantages is that it requires a unified flow-geomechanics simulation, which results in enormous software development effort and large computational costs.

On the other hand, the sequential implicit method uses existing simulators for the solution of the constituent subproblems. For example, the problem of nonisothermal flow, or of geomechanics, is solved implicitly, fixing certain geomechanical (or flow) variables, and then geomechanics (or flow) is solved implicitly from the flow/geomechanics variables obtained from the previous step. According to Kim et al. (2011), the fixed stress sequential scheme provides unconditional stability and numerical convergence with high accuracy. Using the fixed-stress split method, we can solve the flow problem, fixing the total stress field. This scheme can easily be implemented in flow simulators by using the Lagrange's porosity function and correction term, as follows.

$$\Delta\Phi_l^n = \left(\frac{\alpha_l^2}{K_l^n} + \frac{\alpha_l - \Phi_l^n}{K_s}\right) p_l^n + 3\alpha_{T,l}\alpha_l \Delta T_l^n - \frac{b_l}{\eta_l}\Delta\sigma_v^{n-1} \tag{22}$$

where $\Delta(\cdot)^n = (\cdot)^{n+1} - (\cdot)^n$. σ_v is the total volumetric mean stress. Φ is defined as the ratio of the pore volume in the deformed configuration to the bulk volume in the reference (initial) configuration. The porosity correction term, $b_l / \eta_l \Delta\sigma_v^{n-1}$, is calculated from geomechanics, which corrects the porosity estimated from the pore compressibility.

For permeability of the fracture, we use the following nonlinear permeability motivated by the cubic law.

$$k_{p,f} = k_{p,f}^0 \left(\frac{\omega}{\omega_0}\right)^{n_p}, \tag{23}$$

where $k_{p,f}$ and ω are the fracture permeability and its width, respectively. $k_{p,f}^0$ is a reference fracture permeability for a reference width ω_0. n_p characterizes the nonlinear fracture permeability. When $n_p = 3.0$, Eq. 23 is identical to the cubic law.

For Young's modulus of the fracture, we use a much low value, compared with the rock matrix, when tensile fracturing occurs. For shear failure, the return mapping algorithm automatically determines geomechanical properties such as Eq. 16.

4. NUMERICAL EXAMPLES

Here we first show a verification test, and then discuss a numerical example of hydraulic fracturing induced in a shale gas reservoir. A detailed discussion of this problem can be found in Kim and Moridis (2012b).

4.1. Verification

We use an analytical solution proposed by Sneddon and Lowengrud (1969) that can calculate the width of a fracture in 2D plane stain mechanics (Figure 1), written as

$$w = \frac{l}{E'}\int_0^1 p(sl,t)G_p(\frac{x}{l},s)ds,$$

$$G_p(\xi,s) = -\frac{4}{\pi}\ln\left|\frac{\sqrt{1-\xi^2}+\sqrt{1-s^2}}{\sqrt{1-\xi^2}-\sqrt{1-s^2}}\right|,$$

$$E' = \frac{E}{1-\nu^2}, \qquad (24)$$

where $p = p_f - \sigma_o$. E, and ν are Young's modulus and Poisson's ratio, respectively, p_f and σ_o are fluid pressure within the fracture and total stress normal to the fracture plane, respectively. x/l is the normalized distance from the reference point within the fracture, as shown in Figure 2. Figure 2 shows that the numerical solution matches the analytical solution, validating the simulator.

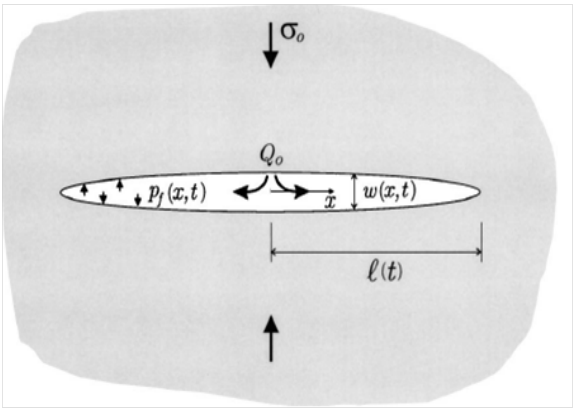

Figure 1. Schematics of a fracture in the 2D plane stain mechanics (Detournay, 2004)

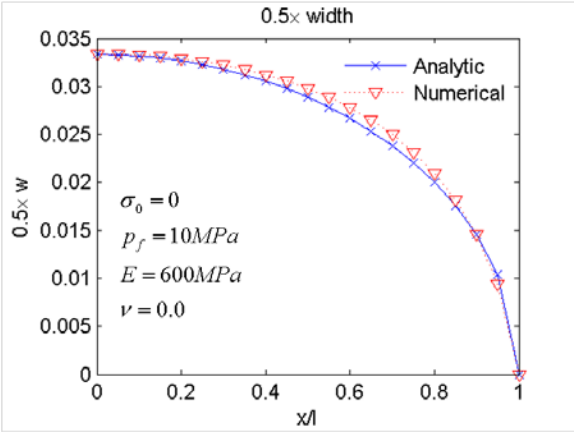

Figure 2. Comparison between the analytical and numerical solutions. The numerical solution matched the analytical solution.

4.2. 3D vertical fracture propagation

We assume the fracturing fluid to be water. We consider 3D coupled flow and geomechanical problems with constant injection rate. The geomechanical domain has 50, 5, 50 gridblocks in the x, y and z directions, respectively, with the x-z plane normal to the minimum compressive principal total stress. Gridblock sizes are uniform, i.e., Δx = Δz = 3 m in the x and z directions, respectively. The size of the gridblocks in the y direction is non-uniform; 0.1 m, 0.5 m 3.0 m, 10.0 m, 20.0 m.

Young's modulus and Poisson's ratio are 6 GPa and 0.3, respectively. The tensile strength of material for the reference case is 4.0 MPa. Initial fluid pressure is 17.10 MPa at 1350 m in depth with the 12.44 kPa/m gradient. Initial temperature is 58.75 ^{o}C at 1350 m in depth with the 0.025 ^{o}C/m gradient. Initial total principal stresses are -26.21 MPa, and -23.30 MPa, and -29.12 MPa at 1350 m depth in x, y, z directions, respectively, where the corresponding stress gradients are -19.42 kPa/m, -17.59 kPa/m, and -21.57 kPa/m, respectively. We set gravity based on a bulk density of 2200 kg/m^3, with no horizontal displacement boundary conditions at the sides (except at the fracture nodes), and no displacement boundary at the bottom.

For flow, we have, respectively, 50, 6, and 50 gridblocks in x, y, and z directions, where one more layer for the fracture plane is introduced for flow within the fracture. The initial permea-

bility and porosity of the shale reservoir are $8.648\times10^{-19}m^2 = 8.76\times10^{-7}$ Darcy, and 0.1. For tensile failure, the fracture permeability is determined from Eq. 23, where $k^0_{p,f} = 5.9\times10^{-11}m^2$ (60 Darcy), $\omega_0 = 1.0\times10^3 m$, and $n_p = 3.0$. For shear failure, we use a constant permeability, $5.9\times10^{-14}m^2$ (60 mD). Once failure occurs, we change the single porosity to the double porosity model where fracture and rock matrix volume fractions are 0.1 and 0.9. The reference fracture porosity is 0.9, when the fracture is created, and the porosity varies after the creation due to poromechanical effects. Biot's coefficient is 1.0. We specify a constant injection rate of 8.0kg/s at x=25 m, z=-1440 m.

Figure 3 shows the fracture propagation during hydraulic fracturing. At the initial time, we have small fracturing. After the initial fracturing, the fracture propagates and becomes larger because of proppant injection within the fracture, which induces additional geomechanical loading to the fracture surface, followed by fracturing.

We then perform another numerical test, in which $\Psi_f = \Psi_d = 28.6^0$ and $c_h = 2.0$ MPa, for shear failure as well as tensile failure. From Figure 4 (and comparing it to Figure 3), we find that shear failure limits the fracture propagation in vertical direction. Shear failure propagates horizontally, and the overall failure occurs not only vertically but also horizontally. Flow of the proppants to the horizontal direction is substantial, compared to the case without shear failure, because shear failure also increases permeability considerably.

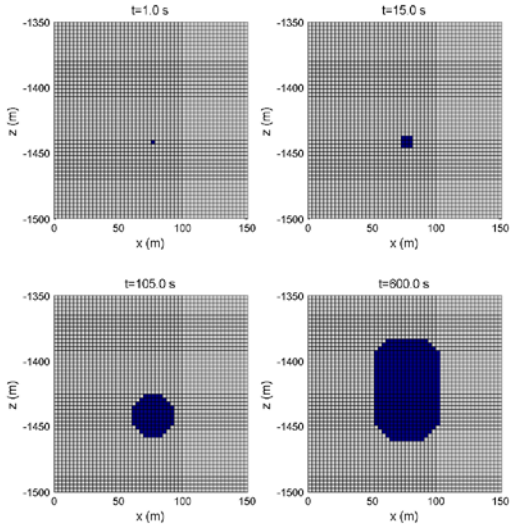

Figure. 3. Fracture propagation from tensile failure with of the constant injection rate of 8.0kg/s at x=25 m, z=-1440 m. The fracture propagation is stable and can be controlled by injection time.

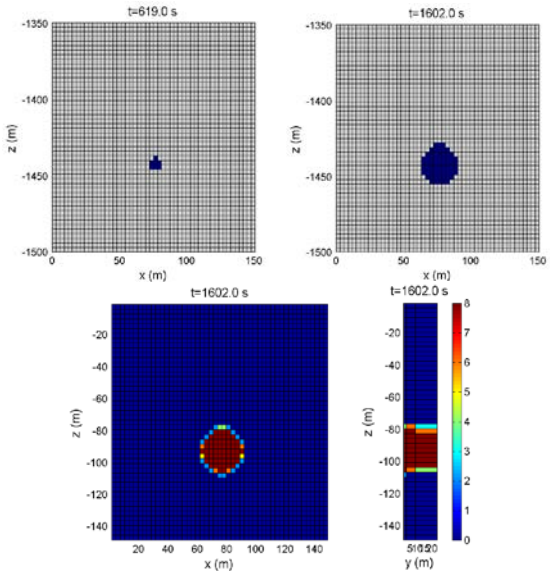

Figure. 4. Fracture propagation with $\Psi_f = \Psi_d = 28.6^0$ and $c_h = 2.0$ MPa. Top: the vertical fracture propagation due to tensile failure. Bottom: the areas of shear failure, where the number indicates failed Gauss points. Shear failure proceeds more horizontally, limiting the vertical fracture propagation.

SUMMARY

We developed the T+M hydraulic fracturing simulator by coupling the TOUGH+RealGasH2O flow simulator with the

ROCMECH geomechanics code. T+M has the following characteristics: (1) vertical fracturing is mainly modeled by updating the boundary conditions and the corresponding data structure; (2) shear failure can also be modeled during the fracturing; (3) a double- or multiple-porosity approach is employed after the initiation of fracturing in order to rigorously model flow and geomechanics; (4) nonlinear models for permeability and geomechanical properties can be easily implemented; (5) leak-off in all directions during hydraulic fracturing is fully considered; and (6) the code provides two-way coupling between fluid-heat flow and geomechanics, rigorously describing changes in the fractures, pore volumes, and permeabilities.

ACKNOWLEDGMENT

The research described in this article has been funded by the U.S. Environmental Protection Agency through Interagency Agreement (DW-89-92235901-C) to the Lawrence Berkeley National Laboratory, and by the Research Partnership to Secure Energy for America (RPSEA - Contract No. 08122-45) through the Ultra-Deepwater and Unconventional Natural Gas and Other Petroleum Resources Research and Development Program as authorized by the US Energy Policy Act (EPAct) of 2005. The views expressed in this article are those of the author(s) and do not necessarily reflect the views or policies of the EPA.

REFERENCES

Berryman JG. 2002. Extension of poroelastic analysis to double-porosity materials: New technique in microgeomechanics. *J. Eng. Mech. ASCE*; 128(8):840 – 847.

Coussy O. 1995. *Mechanics of porous continua*. Chichester, England: John Wiley and Sons.

Dean, R.H. and Schmidt, J.H., 2008 Hydraulic fracture predictions with a fully coupled geomechanical reservoir simulation. *SPE Annual Technical Conference and Exhibition*, Denver, Colorado, 21 – 24 Sep.

Detournay E. 2004. Propagation regimes of fluid-driven fractures in impermeable rocks *Int. J. Geomech*. 4(1) 35-45.

Forchheimer, P. 1901 Wasserbewegung durch Bode, *ZVDI*(1901), 45.

Fu P., and Johnson S.M., and Hao Y., and Carrigan C.R. 2011. Fully coupled geomechanics and discrete flow network modeling of hydraulic fracturing for geothermal applications. *6th workshop Geoth. Res. Eng.* 31 Jan.-2 Feb., Stanford, CA.

Ji, L., Settari A., Sullivan, R.B. 2009. A novel hydraulic fracturing model fully coupled with geomechanics and reservoir simulation. *Soc. Pet. Eng. J.*423-430.

Kim J., Tchelepi H.A., and Juanes R. 2011. Stability and convergence of sequential methods for coupled flow and geomechanics: Fixed-stress and fixed-strain splits. *Comput. Methods Appl. Mech. Engrg.* 200: 1591–1606.

Kim J., Sonnenthal E., and Rutqvist J. 2012. Formulation and sequential numerical algorithms of coupled fluid/heat flow and geomechanics for multiple porosity materials. *Int. J. Numer. Meth. Engrg.* In press, doi: 10.1002/nme.4340.

Kim J. and Moridis G. M. 2012a. Gas flow tightly coupled to elastoplastic geomechanics for tight and shale gas reservoirs: material failure and enhanced permeability. *SPE Uncon. Resour. Conf.*, Pittsburgh, PA, 5-7 Jun.

Kim J. and Moridis G. M. 2012b. Analysis of Fracture Propagation During Hydraulic Fracturing Operations in Tight/Shale Gas Systems, in prep.

Nassir M. and Settari A. and Wan R. 2012. Prediction and optimization of fracturing in tight gas and shale using a coupled geomechancial model of combined tensile and shear fracturing. *Hydr. Frac. Tech. Conf.* The woodland, TX, 6 – 8 Feb.

Simo, J.C. and Hughes, T.J.R. 1998. *Computational Inelasticity*. Heidelberg, Germany: Springer.

Sneddon, I., and Lowengrub, M. 1969. *Crack problems in the classical theory of elasticity*, Wiley, New York.

Wang X. and Wang L.B. and Xu L.M. 2004. Formulation of the return mapping algorithm for elastoplastic soil models. *Comput. Geotech.* **31**:315–338.

THE REALGAS AND REALGASH2O OPTIONS OF THE TOUGH+ CODE FOR THE SIMULATION OF COUPLED FLUID AND HEAT FLOW IN TIGHT/SHALE GAS SYSTEMS

George J. Moridis, C. Matthew Freeman, Stephen Webb and Stefan Finsterle

Lawrence Berkeley National Laboratory
1 Cyclotron Rd.
Berkeley, CA, 94706, USA
e-mail: GJMoridis@lbl.gov

ABSTRACT

We developed two new EOS additions to the TOUGH+ family of codes, the RealGasH2O and RealGas. The RealGasH2O EOS option describes the non-isothermal two-phase flow of water and a real gas mixture in a gas reservoir (including a tight/shale gas one). The gas mixture is treated as either a single-pseudo-component having a fixed composition, or as a multicomponent system composed of up to 9 individual real gases. The RealGas option has the same general capabilities, but does not include water, thus describing a single-phase, dry-gas system. The capabilities of two codes include: coupled flow and thermal effects in porous and/or fractured media, real gas behavior, inertial (Klinkenberg) effects, full micro-flow treatment, Darcy and non-Darcy flow through the matrix and fractures of fractured media, gas sorption onto the grains of the porous media, etc.

The codes are verified against available analytical and semi-analytical solutions. Their capabilities are demonstrated in a series of problems of increasing complexity, ranging from isothermal flow in simpler 1D and 2D conventional gas reservoirs, to non-isothermal gas flow in 3D fractured shale gas reservoirs involving 4 types of fractures, micro-flow, non-Darcy flow and gas composition changes during production.

INTRODUCTION

Background

TOUGH+ is a family of codes developed at the Lawrence Berkeley National Laboratory (Moridis et al., 2008) that are a successor to the TOUGH2 (Pruess et al., 1991) family of codes for multi-component, multiphase fluid and heat flow. It is written in standard FORTRAN 95/2003 to take advantage of all the object-oriented capabilities and the enhanced computational features of that language. It employs dynamic memory allocation, follows the tenets of Object-Oriented Programming (OOP), and involves entirely new data structures and derived data types that describe the objects upon which the code is based. The TOUGH+ code is based on a modular structure that is designed for maximum traceability and ease of expansion.

Objective

The main objective of this study was to develop numerical capabilities allowing the description of a wide range of processes involved in the non-isothermal flow through the spectrum of natural gas reservoirs in geologic systems, including tight-gas and shale-gas reservoirs with natural and/or induced fractures. To that end, we developed two new EOS additions to the TOUGH+ family of codes: the RealGasH2O and RealGas options for the description of two-phase (aqueous and gas) and single-phase (dry-gas) flow through complex geologic media, respectively. Although the new capabilities can provide solutions to the problem of prediction of gas production from the entire spectrum of gas-bearing reservoirs, of particular interest are applications to tight-sand and shale reservoirs, the numerical simulation of which may involve extremely fine domain discretization, complex fracture-matrix interactions in several subdomains of the producing system, and coupled thermophysical phenomena and processes.

CODE DESCRIPTION

The ensuing discussion focuses on the description of the TOUGH+RealGasH2O code (hereafter referred to as T+GW) describing the two-phase flow problem of an aqueous and a gas phase flow through a geologic system. The TOUGH+RealGas code (hereafter referred to as T+G) is entirely analogous, differing only in the

omission of water as a mass component, thus solving the much simpler problem of single-phase, dry-gas flow and production.

Fundamental Equations of Mass and Energy Balance

A non-isothermal fractured tight-gas or shale-gas system can be fully described by the appropriate mass balance equations and an energy balance equation. The following components κ, corresponding to the number of equations, are considered: $\kappa = g^i$, i.e., the various gaseous components (compounds) i constituting the natural gas ($i = 1, \ldots, N_G$, $N_G \geq 1$); water (w), and heat (θ), treated as a pseudo-component. Note that in T+GW it is possible to treat a real gas mixture of constant composition (i.e., with non-variant mole fractions Y^i) as a *single pseudo-component*, the properties of which vary with the pressure P and temperature T.

Following Pruess et al. (1999), mass and heat balance considerations in every subdomain (gridblock) into which the simulation domain is been subdivided by the integral finite difference method in TOUGH+ dictates that

$$\frac{d}{dt}\int_{V_n} M^\kappa dV = \int_{\Gamma_n} \mathbf{F}^\kappa \cdot \mathbf{n}\, dt + \int_{V_n} q^\kappa dV \quad \text{..... (1)}$$

where V, V_n are the volume and volume of subdomain n [m^3]; M^κ is the mass accumulation term of component κ [kg m^{-3}]; A, Γ_n are the surface area and surface of subdomain n [m^2], respectively; $\mathbf{F}^\kappa$ is the flow vector of component κ [kg $m^{-2}s^{-1}$]; $\mathbf{n}$ is the inward unit normal vector; q^κ is the source/sink term of component κ [kg $m^{-3}s^{-1}$]; and t is the time [s].

Mass accumulation terms

Under the two-phase (aqueous and gas) flow conditions described by T+GW, the mass accumulation terms M^κ for the mass components κ in equation (1) are given by

$$\sum_{\beta=A,G} \phi\, S_\beta \rho_\beta X_\beta^\kappa + \delta_\Psi (1-\phi)\rho_R \Psi^i \quad \text{..... (2)}$$

where $\kappa \equiv w, g^i,\ i = 1, \ldots, N_G$; ϕ is the porosity [*dimensionless*]; ρ_β is the density of phase β [kg m^{-3}]; S_β is the saturation of phase β [*dimensionless*]; X_β^κ is the mass fraction of component in phase β [kg/kg]; ρ_R is the rock density [kg m^{-3}]; Ψ^i is the mass of sorbed component g^i per unit mass of rock [kg/kg]; and $\delta_S = 0$ for non-sorbing media (including tight-gas systems) that are usually devoid of substantial organic carbon, while $\delta_S = 1$ in gas-sorbing media such as shales.

The first term in equation (2) describes fluid mass stored in the pores, and the second the mass of gaseous components sorbed onto the organic carbon (mainly kerogen) content of the matrix of the porous medium. The latter is quite common in shales. Although gas desorption from kerogen has been studied extensively in coalbed CH_4 reservoirs, and several analytic/semi-analytic models have been developed for such reservoirs (Clarkson and Bustin, 1999), the sorptive properties of shale are not necessarily analogous to coal (Schettler and Parmely, 1991).

Gas sorption terms

The most commonly used empirical model describing sorption onto organic carbon in shales is analogous to that used in coalbed methane and follows the Langmuir isotherm that, for a single-component gas, is described by

$$\begin{cases} \Psi^i = \dfrac{p_{dG} m_L}{p_{dG} + p_L} & \text{for ELaS} \\ \dfrac{d\Psi^i}{dt} = k_L \left(\dfrac{p_{dG} m_L}{p_{dG} + p_L} - \Psi^i \right) & \text{for KLaS} \end{cases} \quad \text{..... (3)}$$

where p_{dG} is the dry gas pressure, ELaS indicates Equilibrium Langmuir Sorption, and KLaS denotes Kinetic Langmuir Sorption. The m_L term in equation (3) describes the total mass storage of component g^i at infinite pressure (kg of gas/kg of matrix material), p_L is the pressure at which half of this mass is stored (Pa), and k_L is a kinetic constant of the Langmuir sorption (1/s). In most studies applications, an *instantaneous equilibrium* is assumed to exist between the sorbed and the free gas, i.e., there is no transient lag between pressure changes and the corresponding sorption/desorption responses and the equilibrium model of Langmuir sorption is assumed to be valid (Figure 6). Although this appears to be a good approximation in shales (Gao et al., 1994) because of the very low permeability of the matrix (onto which the various gas components are sorbed), the subject has not been fully investigated. For multi-component gas, equation (3) becomes

$$\begin{cases} \Psi^i = \dfrac{p_{dG} B^i m_L^i \Upsilon^i}{1 + p_{dG} \sum_i B^i \Upsilon^i} & \text{for ELaS} \\ \dfrac{d\Psi^i}{dt} = k_L^i \left(\dfrac{p_{dG} B^i m_L^i \Upsilon^i}{1 + p_{dG} \sum_i B^i \Upsilon^i} - \Psi^i \right) & \text{for KLaS} \end{cases} \quad (4)$$

where B^i is the Langmuir constant of component g^i in 1/Pa (Pan et al., 2008), and Y^i is the dimensionless mole fraction of the gas component i in the water-free gas phase. Note that the T+GW and T+G codes offer the additional options of linear and Freundlich sorption isotherms (equilibrium and kinetic). These are described by the following equations:

$$\begin{cases} \Psi^i = K_l^i \, p^i & \text{for ELiS} \\ \dfrac{d\Psi^i}{dt} = k_l^i \left(K_l^i \, p^i - \Psi^i \right) & \text{for KLiS} \end{cases} \quad (5)$$

$$\begin{cases} \Psi^i = K_F^i \, \left(p^i \right)^c & \text{for EFS} \\ \dfrac{d\Psi^i}{dt} = k_F^i \left[K_F^i \, \left(p^i \right)^c - \Psi^i \right] & \text{for KFS} \end{cases} \quad (6)$$

where ELiS and KLiS denote equilibrium and kinetic linear sorption, respectively; EFS and KFS denote equilibrium and kinetic Freundlich sorption, respectively; K^i_l and K^i_F are the distribution coefficients of the ELiS and EFS sorption isotherms of gas component i, respectively; p^i is the partial pressure of i; k^i_l and k^i_F are the kinetic coefficients of the ELiS and EFS sorption isotherms of i, respectively; and c is the exponent of the Freundlich sorption isotherm.

Heat accumulation terms

The heat accumulation term includes contributions from the rock matrix and all the phases, and is given by the equation

$$M^\theta = \begin{cases} (1-\phi)\rho_R \int_{T_0}^{T} C_R(T)\, dT + \\ \sum_{\beta=A,G} \phi S_\beta \rho_\beta U_\beta + \delta_\Psi (1-\phi)\rho_R \sum_{i=1}^{N_G} u^i Y^i \end{cases} \quad (7)$$

where $C_R = C_R(T)$ is the heat capacity of the dry rock [J kg^{-1} K^{-1}]; U_β is the specific internal energy of phase β [J kg^{-1}]; u^i is the specific internal energy of sorbed gas component i [J kg^{-1}]; T is the temperature [K]; and T_0 is a reference temperature [K]. The specific internal energy of the gaseous phase is a very strong function of composition, is related to the specific enthalpy of the gas phase H_G, and is given by

$$U_G = \sum_{\kappa=w,g^i(i=1,N_G)} X_G^\kappa \, u^\kappa + U_{dep} \quad \left(= H_G - \frac{P}{\rho_G} \right) \quad (8)$$

where u^κ is the specific internal energy of component κ in the gaseous phase, and U_{dep} is the specific internal energy departure of the gas mixture [J kg^{-1}]. The internal energy of the aqueous phase accounts for the effects of gas and inhibitor solution, and is estimated from

$$U_A = X_A^w u^w + \sum_{i=1}^{N_G} X_A^{g^i} \left(u^i + U^i_{sol} \right) \quad (9)$$

where u^w and u^i are the specific internal energies of H_2O and of natural gas component i at the P and T conditions of the aqueous phase, respectively, and U^i_{sol} are the specific internal energies of dissolution of the gas component i in H_2O.

Fluid flow terms

The mass fluxes of water and of the gaseous components include contributions from the aqueous and gaseous phases, i.e.,

$$\mathbf{F}^\kappa = \sum_{\beta=A,G} \mathbf{F}^\kappa_\beta, \; \kappa \equiv w, g^i, \; i = 1,...,N_G \quad (10)$$

For phase β, $\mathbf{F}^\kappa_\beta = X^\kappa_\beta \, \mathbf{F}_\beta$. In T+GW and T+G, there are three options to describe the phase flux $\mathbf{F}_\beta$. The first is the standard Darcy's law, i.e.,

$$\mathbf{F}_\beta = \rho_\beta \left[-\frac{k \, k_{r\beta}}{\mu_\beta} \nabla \Phi_\beta \right] = \rho_\beta \mathbf{v}_\beta, \;\; \nabla \Phi_\beta = \nabla P_\beta - \rho_\beta \mathbf{g}, \quad (11)$$

where k is the rock intrinsic permeability [m^2]; $k_{r\beta}$ is the relative permeability of phase β [dimensionless]; μ_β is the viscosity of phase β [Pa s]; P_β is the pressure of the aqueous phase [Pa]; and $\mathbf{g}$ is the gravitational acceleration vector [m s^{-2}]. In T+GW, the relationship between the aqueous and the gas pressures, P_A and P_G, respectively, is given by $P_A = P_G + P_{cGA}$, where P_{cGA} is the gas-water capillary pressure [Pa]. The P_{cGA} options are the standard ones available in the TOUGH2 and TOUGH+ family of codes (Pruess et al., 1999; Moridis et al., 2008).

The mass flux of component κ in the gas phase incorporates advection and diffusion contributions, and is given by

$$\mathbf{F}^\kappa_G = \left(1 + \frac{b}{P_G} \right) \rho_G \mathbf{v}_G X^\kappa_G - \underbrace{\phi S_G \tau_G D^\kappa_G \rho_G \nabla X^\kappa_G}_{-\mathbf{J}^\kappa_G}, \quad (12)$$

where b is the *Klinkenberg* (1941) b-factor accounting for gas slippage effects [Pa], the term $\boldsymbol{J}^k_G$ is the diffusive mass flux of component κ in the gas phase [kg m^{-2} s^{-1}], D^k_G is the multicomponent molecular diffusion coefficient of component k in the gas phase in the absence of a porous medium [m^2 s^{-1}], and τ_G is the gas tortuosity [dimensionless]. There are several methods to compute τ_G in the T+GW and T+G codes, including the Millington and Quirk [1961] model. The diffusive mass fluxes of the water vapor and the natural gas components are related through the relationship of Bird et al. (2007)

$$\mathbf{J}^w_G + \sum_{i=1}^{N_G} \mathbf{J}^{g^i}_G = 0, \quad (13)$$

which ensures that the total diffusive mass flux of the gas phase is zero with respect to the mass average velocity when summed over the components. Then the total mass flux of the gas phase is the product of its velocity and density.

If the flow is non-Darcian, then the equation $\mathbf{F}_\beta = \rho_\beta \mathbf{v}_\beta$ still applies, but $\mathbf{v}_\beta$ is now computed from the solution of the quadratic equation

$$\nabla\Phi_\beta = -\left(\frac{\mu_\beta}{k\, k_{r\beta}} \mathbf{v}_\beta + \beta_\beta \rho_\beta \mathbf{v}_\beta \left| \mathbf{v}_\beta \right| \right), \quad (14)$$

in which β_β is the "turbulence correction factor" (Katz et al., 1959). The quadratic equation in (14) is the general momentum-balance *Forcheimer equation* (Forchheimer, 1901; Wattenbarger and Ramey, 1968), and incorporates laminar, inertial and turbulent effects. This is the second option. The solution then is

$$\mathbf{v}_\beta = \frac{2\nabla\Phi_\beta}{\dfrac{\mu_\beta}{k\, k_{r\beta}} + \sqrt{\left(\dfrac{\mu_\beta}{k\, k_{r\beta}} \right)^2 + 4\beta_\beta \rho \left| \nabla\Phi_\beta \right|}}, \quad (15)$$

and $\mathbf{v}_\beta$ from equation (15) is then used in the equations of flow (11) and (12). T+GW and T+G offer 13 options to compute β_β, several of which are listed in Finsterle (2001). The third option follows the approach of Barree and Conway (2007), as described by Wu et al. (2011), which involves a different formulation of $\nabla\Phi_\beta$.

The Klinkenberg b-factor is either provided as input, or is computed using the relationship proposed by Jones (1972) as

$$\frac{b}{b_0} = \left(\frac{k}{k_0} \right)^{-0.36}, \quad (16)$$

where the subscript 0 denotes a reference medium with a known b-factor and k, such as those listed by Wu et al. (1998).

Micro-flow: Knudsen diffusion and Dusty Gas model

For ultra-low permeability media (such as tight sands and shales) and the resulting micro-flow processes, the Klinkenberg b-factor for a single-component or pseudo-component gas in T+GW and T+G is computed by the method of Florence et al. (2007) and Freeman et al. (2011) as

$$\frac{b}{P_G} = \left(1 + \alpha K_n\right)\left(1 + \frac{4K_n}{1 + K_n}\right) - 1, \quad (17)$$

where K_n is the Knudsen diffusion number (dimensionless), which characterizes the deviation from continuum flow, accounts for the effects of the mean free path of gas molecules being on the same order as the pore dimensions of the porous media, and is computed from (Freeman et al., 2011) as

$$K_n = \frac{\bar{\lambda}}{r_{pore}} = \frac{\mu_G}{2.81708 P_G} \sqrt{\frac{\pi RT}{2M}} \frac{\phi}{k}, \quad (18)$$

with M being the molecular weight and T the temperature (°K). The term α is determined from Karniadakis and Beskok (2001) as

$$\alpha = \frac{128}{15\pi^2} \tan^{-1}\left(4K_n^{0.4}\right), \quad (19)$$

For simplicity, we have omitted the i superscript in equations (16) to (19). The Knudsen diffusion can be very important in porous media with very small pores (on the order of a few micrometers or smaller) and at low pressures. For a single gas pseudo-component, the properties in (16) are obtained from an appropriate equation of state for a real-gas mixture of constant composition Y^i. The Knudsen diffusivity D_K [m^2/s] can be computed as (Civan, 2008; Freeman et al., 2011)

$$D_K = \frac{4\sqrt{k\phi}}{2.81708} \sqrt{\frac{\pi RT}{2M}} \quad \text{or} \quad D_K = \frac{kb}{\mu_G} \quad (20)$$

For a multicomponent gas mixture that is not treated as a single pseudo-component, ordinary Fickian diffusion must be taken into account as well as Knudsen diffusion**.** Use of the advective–diffusive flow model (Fick's law) should be restricted to media with $k \geq 10^{-12}$ m^2; the dusty-gas model (DGM) is more accurate at lower k

(Webb and Pruess, 2003). Additionally, DGM accounts for molecular interactions with the pore walls in the form of Knudsen diffusion. Shales may exhibit k as low as 10^{-21} m^2, so the DGM described below is more appropriate than the Fickian model (Webb and Pruess, 2003; Doronin and Larkin 2004; Freeman et al., 2011):

$$\sum_{j=1,j\neq i}^{N_G} \frac{Y^i N_D^j - Y^j N_D^i}{D_e^{ij}} - \frac{N_D^i}{D_K^i} = \left\{ \frac{p^i \nabla Y^i}{ZRT} + \left(1 + \frac{kp}{\mu_G D_K^i}\right) \frac{Y^i \nabla p^i}{ZRT} \right\}, \quad (21)$$

where N^i_D is the molar flux of component i in mole/m^2/s, D_e^{ij} is the effective gas (binary) diffusivity of species i in species j, D_K^i is the Knudsen diffusivity of species i.

Gas solubility

There are two options for estimating the solubility of a gas i into the aqueous phase in T+GW. The first (and simpler one) is based on Henry's Law, described by the relationship

$$p^i = H^i X_A^i, \quad (22)$$

where H^i [Pa] is referred to as Henry's factor and is a T-dependent, species-specific factor (thus, it cannot be called Henry's *constant*). T+GW includes a library of fast parametric relationships of $H^i = H^i(\mathrm{T})$, and this is the preferred option if a single gas component or pseudo-component is involved. The second option is based on the equality of fugacities in the aqueous and the gas phase, and involves the chemical potentials of the various species in solution.

Heat flux

The heat flux accounts for conduction, advection and radiative heat transfer, and is given by

$$\mathbf{F}^\theta = -\bar{k}_\theta \nabla T + f_\sigma \sigma_0 \nabla T^4 + \sum_{\beta \equiv A,G} h_\beta \mathbf{F}_\beta, \quad (23)$$

where $\bar{k}_\theta$ is a representative thermal conductivity of the fluid-impregnated rock [W m^{-1} K^{-1}]; h_b is a specific enthalpy of phase β [J kg^{-1}]; f_σ is the radiance emittance factor [dimensionless]; σ_0 is the Stefan-Boltzmann constant [5.6687×10^{-8} J m^{-2} K^{-4}]. The specific enthalpy of the gas phase is computed as

$$H_G = \sum_{\kappa \equiv w, g_i} X_G^\kappa h_G^\kappa + H_{dep}, \quad (24)$$

where h_G^κ is the specific enthalpy of component k in the gaseous phase, and H_{dep} is the specific enthalpy departure of the gas mixture [J kg^{-1}]. The specific enthalpy of the aqueous phase is estimated from

$$H_A = X_A^w h_A^w + \sum_i X_A^{g^i} \left(h_A^{g^i} + H_{sol}^{g^i} \right), \quad (25)$$

where h_A^w and $h_A^{g^i}$ are the specific enthalpies of H_2O and of the natural gas components in the aqueous phase, respectively, and $H_{sol}^{g^i}$ is the specific enthalpy of dissolution [J kg^{-1}] of gas component g^i in the aqueous phase.

Source and sink terms. In sinks with specified mass production rate, withdrawal of the mass component k is described by

$$\hat{q}^\kappa = \sum_{\kappa \equiv A,G} X_\beta^\kappa q_\beta, \quad \kappa = \mathrm{w}, g^i \ (i = 1, ..., N_G), \quad (26)$$

where q_β is the production rate of the phase b [kg m^{-3}]. For a prescribed production rate, the phase flow rate q_β is determined from the phase mobility at the location of the sink. For source terms (well injection), the addition of a mass component k occurs at desired rates.

Thermophysical properties

The water properties in the T+GW code are obtained from steam table equations (Pruess et al., 1999; Moridis et al., 2008). All the real gas properties in T+G and T+GW are computed from one of the three available options of cubic equations of state that were first developed for TOUGH+HYDRATE (Moridis et al., 2008).

Solution approach

The fully implicit discretized nonlinear balance equations are expressed in residual form, are then linearized by the Newton-Raphson method, and the resulting Jacobian is solved in the standard approach used in all TOUGH applications (Pruess et al., 1999). In T+G, the primary variables that constitute the solution vector are p, Y^i (i = 1,…, N_G), and T; in T+GW, the primary variables are the same for single-phase gas; p, X^i_A and T for single-phase aqueous conditions, and S_A, Y^i and T for two-phase conditions.

VALIDATION EXAMPLES

Problem V1: Real gas flow in a cylindrical reservoir

Using the concept of pseudo-pressure, Fraim and Wattenbarger (1986) developed a solution to the

problem of transient flow in a finite cylindrical real-gas reservoir with a producing well at its center, described as:

$$p_D = \frac{1}{2} E_i\left(\frac{r_D^2}{4t_D}\right), \quad (27)$$

where E_i denotes the exponential integral,

$$p_D = \frac{kh}{q_V B\mu}(\psi_0 - \psi),\ r_D = \frac{r}{r_w},\ t_D = \frac{k}{\phi\mu c_t r_w^2}t,\ \psi = 2\int_{p_r}^{p}\frac{p}{\mu z}dp,$$

ψ is the pseudo-pressure, r is the radius, r_w is the well radius [m], p_r is a reference pressure [Pa], c_t is the total compressibility [Pa^{-1}], q_V is the volumetric production rate [ST m^3/s], B is the formation volume factor, h is the reservoir thickness, and the subscript 0 indicates the initial conditions. The data used in the simulation of this validation problem appear in Table 1. The domain discretization involved logarithmically increasing Δr's. Figure 1 shows an excellent agreement of the analytical and the T+GW numerical solutions at various sampling times. The T+G code yields an identical solution.

Table 1. Properties and conditions in Problem V1.

Data Type	Values
Matrix permeability k	3.04x10^{-14} m^2 (30.4 mD)
Reservoir thickness h	10 m
Well radius r_w	0.059 m
Reservoir radius r_e	100 m
Reservoir pressure p	10 MPa
Reservoir temperature T	60 °C
Reservoir porosity ϕ	0.30
Rock compressibility	2x10^{-10} 1/Pa
Gas composition	100% CH_4
Gas EOS	Peng-Robinson

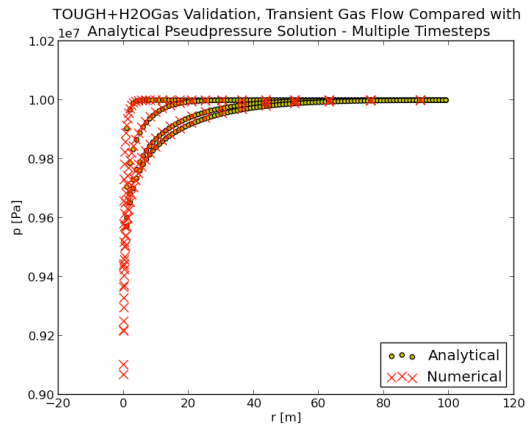

Figure 1. Comparison of the analytical and the T+GW solutions in problem V1.

Problem V2: Water flow in a cylindrical reservoir

Blasingame (1993) developed an analytical solution of pseudo-steady state flow in a circular reservoir with a producing well at its center and impermeable boundaries at $r=r_e$. Using the data listed in Table 2, the T+GW solution in Figure 2 (based on a grid with logarithmically increasing Δr's) practically coincides with the analytical solution, increasing confidence in the code.

Table 2. Properties and conditions in Problem V2.

Data Type	Values
Matrix permeability k	3.04x10^{-14} m^2 (30.4 mD)
Reservoir thickness h	10 m
Well radius r_w	0.059 m
Reservoir radius r_e	100 m
Reservoir pressure p	10 MPa
Reservoir temperature T	30 °C
Reservoir porosity ϕ	0.30
Total compressibility c_t	4.88x10^{-10} 1/Pa
Gas EOS	Peng-Robinson

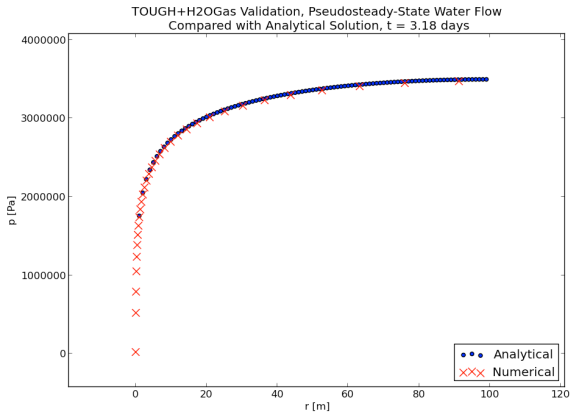

Figure 2. Problem V2: Comparison of the analytical and the T+GW solutions at t = 3.18 days.

Problem V3: Gas flow in a tight gas reservoir with vertical well intersecting a vertical fracture plane

Cinco-Ley et al. (1978) proposed an analytical solution to the problem of a gas flow in a low-permeability 'slab' of a gas reservoir (i.e., with infinite-acting boundaries), in which a vertical well intersects the middle axis of a vertical planar fracture. Treating the "slab" reservoir as a single layer, we solved the same problem numerically using a 2D domain with sufficiently long dimensions to satisfy the infinite-acting

boundary conditions during the simulation period. From the data in Table 3, this is an ultra-tight fractured reservoir with no gas sorption.

The numerical solutions from the T+G and T+GW codes are identical. The point pressure results in Figure 3 identify the element centers and shows the very fine discretization (beginning from mm-scale) in the vicinity of the fracture. The contour plot of the pressure distribution at t = 2.13 years (Figure 4) clearly shows the effect of the fracture and the resulting flow pattern. The log-log plot of production rate vs. time in Figure 5 includes the fully coinciding analytical and numerical solutions, and exhibits the typical -½ slope of vertically fractured reservoirs under production.

Table 3. Properties and conditions in Problem V1.

Data Type	Values
Matrix permeability k	3.08×10^{-19} m^2 (30.8 nD)
Fracture permeability k_f	6.68×10^{-14} m^2 (0.668 D)
Fracture half-length	20 m
Reservoir thickness h	10 m
Well radius r_w	0.05 m
Well pressure p_w	5 MPa
Reservoir pressure p	10 MPa
Reservoir temperature T	60 °C
Reservoir porosity ϕ	0.10
Rock compressibility	2×10^{-10} 1/Pa
Gas composition	100% CH_4
Gas EOS	Peng-Robinson

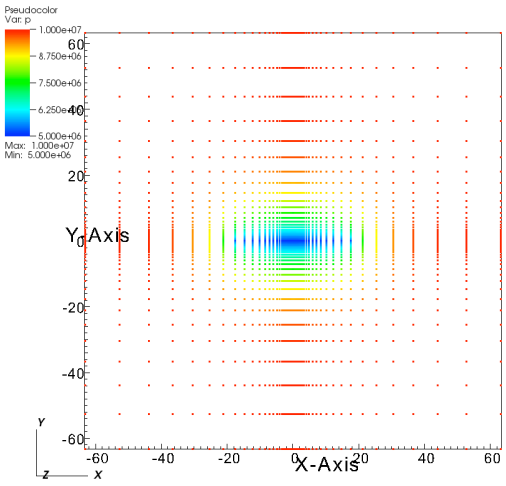

Figure 3. Point cloud of pressure distribution at t = 2.13 years in problem V3, indicating discretization.

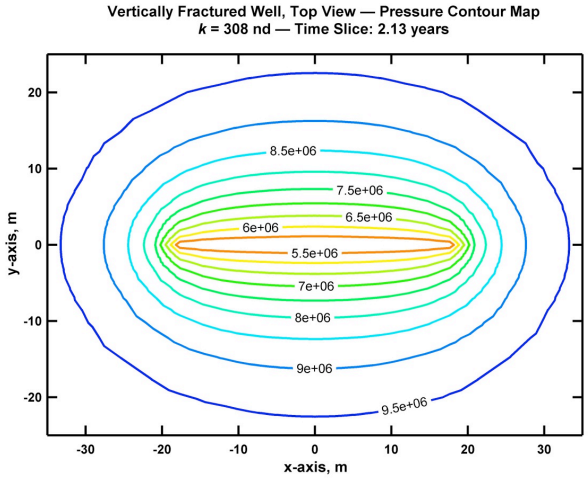

Figure 4. Pressure dustribution in the tight gas reservoir in Problem V3 (T+G and T+GW solutions).

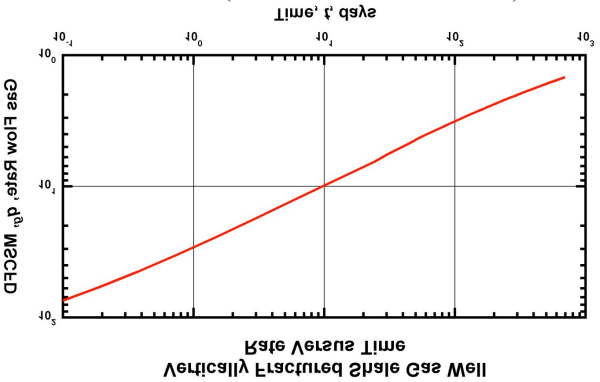

Figure 5. Gas production rate at the well in Problem V3 (coinciding analytical, T+G and T+GW solutions).

APPLICATION EXAMPLES

Problem A1: Gas production from a shale gas reservoir using a horizontal well

This T+G study focuses on a Cartesian 3D stencil of a horizontal well section that is typical of a Type I shale gas system (Figure 6), as defined and investigated by Freeman (2010) and Moridis et al. (2010). Such systems involve the (usually hydraulically) induced primary fractures (PF), the undisturbed matrix, and the stress release fractures around the well. The data used in this simulation were as in Freeman (2010). The surface area of the Cartesian system at the well was corrected to reflect its cylindrical geometry. The discretization involved subdivisions as small as mm-scale near the fracture face, and resulted in about 800,000 gridblocks. The gas was 100% CH_4. The predicted production rate when the well is operated at a constant bottomhole pres-

sure P_w is shown in Figure 7, which also lists some of the data used in the simulation. Note that here, and in Problem A2, dimensioneless variables are used, which are defined as:

$$t_D = 0.0002637 \frac{k}{\phi \mu c_t x_f^2} \frac{1}{[1+(0.00525)V_L]} t \quad \text{(28)}$$

$$q_D = 141.2 \frac{B\mu}{kh(p_i - p_{wf})} q \quad \text{(29)}$$

The T+GW results were identical.

Problem A2: Gas production from a shale gas reservoir with a complex fracture system using a horizontal well

Problem A2 is a sensitivity analysis study that aims to determine the effects of more complex fracture regimes. These are represented by Types II, III and IV (Figure 8), which include secondary planar fractures (perpendicular to the primary fractures), natural fractures, and all types of fractures, respectively. Type IV is the most complex system to describe, simulate and analyze. The data in these simulations were as in Freeman (2010). The natural fractures were described by a dual-porosity model using the MINC concept, and the secondary fractures were represented as individual sub-domains.

The T+G and T+GW results in Figure 9 (which include the Type I predictions for reference) confirm the importance of the additional fractures on production. Type IV exhibits the highest early production because of its maximum surface area and the largest number of flow pathways to the well, but also among the fastest production declines because of exhaustion of the gas and its slow replenishment from sorption. The other types exhibit intermediate behavior.

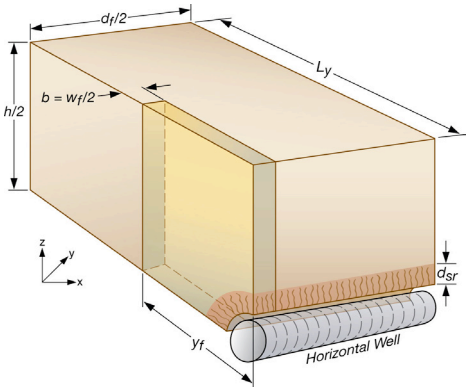

Figure 6. Stencil of a Type I system involving a horizontal well in a tight- or shale-gas reservoir (Moridis et al., 2010).

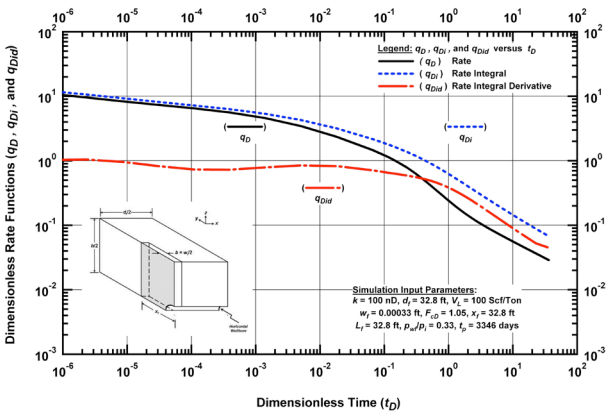

Figure 7. Prediction of gas production in Problem A1 (Freeman et al., 2010).

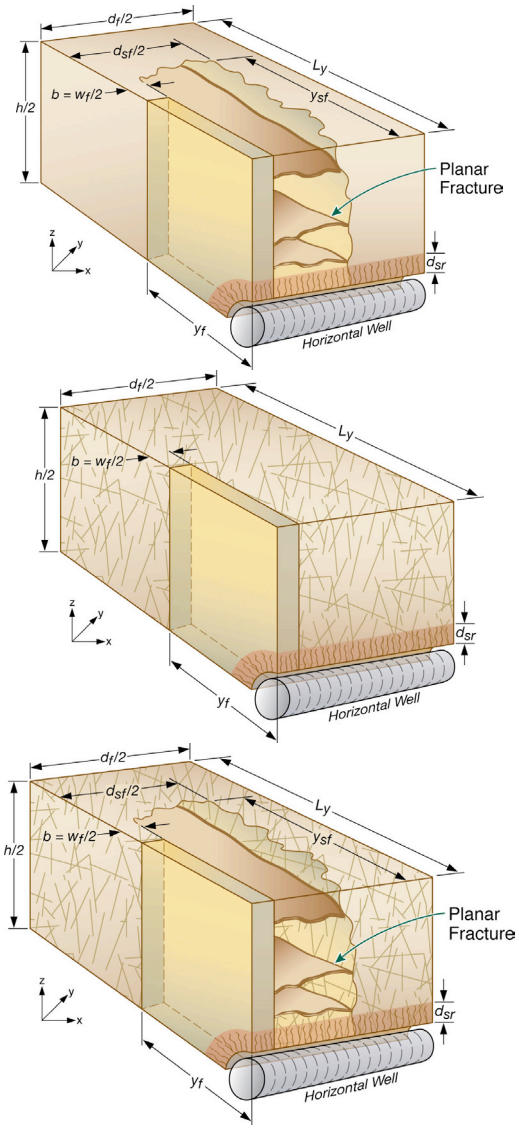

Figure 8. Stencils of Type II, III and IV systems involving a horizontal well in a tight- or shale-gas reservoir (Moridis et al., 2010).

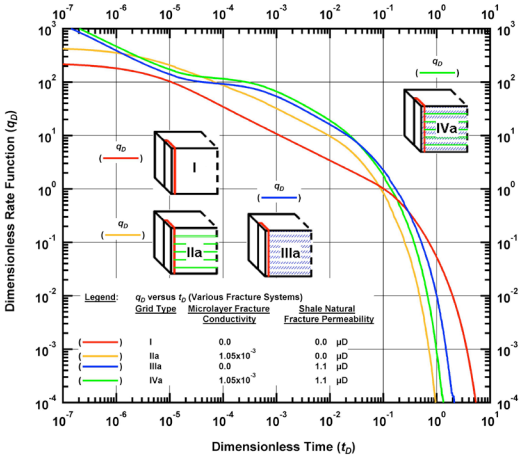

Figure 9. Effect of fracture regime on gas production in Problem A2 (Freeman et al., 2010).

Problem A3: Flowing gas composition changes in shale gas wells

Here we investigate compositional changes over time in gas produced from a shale reservoir. The initial gas composition was: Y = 80% CH_4, 7% C_2H_6, 5% C_3H_8, 5% C_4H_{10}, 2% C_5H_{12} and 1% C_6H_{16}. A Type I system was assumed. The system characteristics, properties and conditions are as described in Freeman et al. (2012). Gas was produced by maintaining the well at a constant bottomhole pressure.

The identical T+G and T+GW results in Figure 10 include both (a) the flow rate, which shows the slope of -½ typical of fractured shale reservoirs, and (b) the compositional deviation of the produced gas over time, which clearly shows inflection points correlating perfectly with the times at which significant changes occur in the gas flow regime in the shale.

SUMMARY

We discuss the T+G and T+GW additions to the TOUGH+ family of codes. T+GW describes the non-isothermal two-phase flow of water and a real gas mixture of up to 9 components in a gas reservoir (including a tight/shale gas one), and accounts for coupled flow and thermal effects in porous and/or fractured media, real gas behavior, inertial (Klinkenberg) effects, full microflow treatment, Darcy and non-Darcy flow through the matrix and fractures of fractured media, gas sorption onto the grains of the porous media, etc. T+G has the same general capabilities, but does not include water, thus describing a single-phase, dry-gas system.

We validate the codes against available analytical and semi-analytical solutions. We show the code capabilities in a series of problems of increasing complexity, ranging from isothermal flow in simpler 1D and 2D conventional gas reservoirs, to non-isothermal gas flow in 3D fractured shale gas reservoirs involving multiple types of fractures, micro-flow, non-Darcy flow and gas composition changes during production.

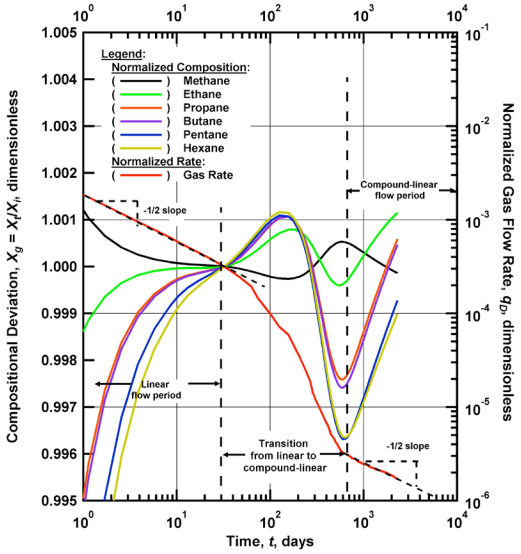

Figure 10. Prediction of gas production and compositional changes in Problem A3 (Freeman et al., 2012).

ACKNOWLEDGMENT

The research described in this article has been funded by the U.S. Environmental Protection Agency through Interagency Agreement (DW-89-92235901-C) to the Lawrence Berkeley National Laboratory, and by the Research Partnership to Secure Energy for America (RPSEA - Contract No. 08122-45) through the Ultra-Deepwater and Unconventional Natural Gas and Other Petroleum Resources Research and Development Program as authorized by the US Energy Policy Act (EPAct) of 2005. The views expressed in this article are those of the author(s) and do not necessarily reflect the views or policies of the EPA.

REFERENCES

Barree R.D., and M.W. Conway, Multuiphase non-Darcy flow in proppant packs, Paper SPE 109561, 2007 Annual Technical Conference and Exhibition, Anaheim, CA, 11–14 Nov 2007.

Bird, R.B., W.E. Stewart, and E.N. Lightfoot, *Transport Phenomena*. New York: John Wiley & Sons, Inc., 2007.

Blasingame, T.A., Semi-Analytical Solutions for a Bounded Circular Reservoir – No Flow and Constant Pressure Outer Boundary Conditions: Unfractured Well Case, Paper SPE 25479, SPE Production Operations Symposium, Oklahoma City, Oklahoma, 21-23 March 1993.

Cinco-Ley, H., F. Samaniego, and N. Dominguez, Transient pressure behavior for a well with a finite-conductivity vertical fracture, *SPE Journal* 18 (4): 253-264. SPE 6014-PA. http://dx.doi.org/10.2118/6014-PA

Civan, F., Effective Correlation of Apparent Gas Permeability in Tight Porous Media. *Transp. in Porous Med*., 2008., DOI: 10.1007/s11242-009-9432-z

Clarkson, C.R. and R.M. Bustin, Binary gas adsorption/desorption isotherms: effect of moister and coal composition upon carbon dioxide selectivity over methane. *International Journal of Coal Geology*, 42, 241-271, 1999.

Doronin, G.G. and N.A. Larkin, On dusty gas model governed by the Kuramoto-Sivashinsky equation. *Computational and Applied Mathematics, 23*(1), 67-80, 2004

Finsterle, S., Implementation of the Forchheimer Equation in iTOUGH2, Project Report, Lawrence Berkeley National Laboratory, Berkeley, Calif., 2001.

Fraim, M.L., and R.A. Wattenbarger, Gas Reservoir Decline Curve Analysis Using Type Curves with Real Gas Pseudopressure and Pseudotime, *SPEFE*, 671-682, 1987.

Freeman, C.M., Study of flow regimes in multiply-fractured horizontal wells in tight gas and shale gas reservoir systems, M.Sc. Thesis, Petroleum Engineering Department, Texas A&M University, 2010.

Freeman, C.M., G.J. Moridis, and T.A. Blasingame, A Numerical Study of Microscale Flow Behavior in Tight Gas and Shale Gas Reservoir Systems. *Transp. in Porous Med., 90*(1): 253-268, 2011, doi:10.1007/s11242-011-9761-6

Freeman, C.M., G.J. Moridis, E. Michael, and T.A. Blasingame, Measurement, Modeling, and Diagnostics of Flowing Gas Composition Changes in Shale Gas Wells, Paper SPE 153391, SPE Latin American and Caribbean Petroleum Engineering Conference, Mexico City, Mexico, 16-18 April, 2012.

Forchheimer, P., Wasserbewewegung durch Boden, *ZVDI* 45, 1781, 1901.

Gao, C., J.W. Lee, J.P. Spivey, and M.E. Semmelbeck, Modeling multilayer gas reservoirs including sorption effects, SPE paper 29173, SPE Eastern Regional Conference & Exhibition, Charleston, West Virginia, 8-10 November, 1994.

Jones, S. C., A rapid accurate unsteady-state Klinkenberg parameter, *SPE Journal* 383–397, 1972.

Katz, D. L. et al., *Handbook of Natural Gas Engineering*, McGraw-Hill, New York, 1959.

Klinkenberg, L.J., The Permeability of Porous Media to Liquid and Gases, Proceedings, *API Drilling and Production Practice*, 200-213, 1941.

Millington, R.J., and J.P. Quirk, Permeability of porous solids. *Trans. Faraday Soc*. 57, 1200-1207, 1961.

Moridis, G.J., M. Kowalsky and K. Pruess. TOUGH+HYDRATE v1.0 User's Manual. LBNL-161E, Lawrence Berkeley National Laborotory, Berkeley, Calif., 2008.

G.J. Moridis, T.A. Blasingame, and C.M. Freeman, Analysis of Mechanisms of Flow in Fractured Tight-Gas and Shale-Gas Reservoirs, Paper SPE 139250, SPE Latin American & Caribbean Petroleum Engineering Conference, Lima, Peru, 1–3 December 2010.

Pruess, K., C. Oldenburg, and G. Moridis, *TOUGH2 User's Guide, Version 2.0*, Report LBNL-43134, Lawrence Berkeley National Laboratory, Berkeley, Calif., 1999.

Schettler, P.D., and C.R. Parmely, Contributions to total storage capacity in devonian shales, SPE paper 23422, SPE Eastern Regional Meeting, Lexington, Kentucky, 22-25 October, 1991.

Wattenbarger, R.A. and H.J. Ramey, Gas well testing with turbulence, damage and wellbore storage, SPE 1835, *J. Pet. Tech.*, 877-884, 1968.

Webb, S.W. and K. Pruess, The Use of Fick's Law for Modeling Trace Gas Diffusion in Porous Media. *Transport in Porous Media, 51,* 327-341, 2003.

Wu, Y.S., B. Lai, J.L. Miskimins, P. Fakcharoenphol and Y. Di, Analysis of Multiphase Non-Darcy Flow in Porous Media, Transport in Porous Media, (2011) 88, 205–223, 2011,DOI 10.1007/s11242-011-9735-8

MASSIVELY PARALLEL SIMULATION OF PRODUCTION FROM FIELD-SCALE OCEANIC GAS HYDRATE DEPOSITS

Matthew T. Reagan, George J. Moridis, Katie L. Boyle, Craig M. Freeman,
Lehua Pan, Noel D. Keen, Jarle Husebo

Lawrence Berkeley National Laboratory
1 Cyclotron Rd.
Berkeley, CA 94720, USA
e-mail: mtreagan@lbl.gov

ABSTRACT

The quantity of hydrocarbon gases trapped in natural hydrate accumulations is enormous, leading to significant interest in the evaluation of their potential as an energy source. It has been shown that large volumes of gas can be readily produced at high rates for long times from some types of methane hydrate accumulations, by means of depressurization-induced dissociation, and by using conventional horizontal or vertical well configurations. However, these resources are currently assessed using simplified or reduced-scale 3D or 2D production simulations. In this study, we use the massively parallel TOUGH+HYDRATE code (pT+H) to assess the production potential of a large, deep-ocean hydrate reservoir and develop strategies for effective production. The simulations model a full 3D system of over a 38 km^2 extent, exploring the productivity of vertical and horizontal wells, single or multiple wells, and the variations in reservoir properties. Meshes involving up to 2.5M gridblocks, running on thousands of supercomputing nodes, are required to simulate such large systems at the highest level of detail. The simulations reveal the challenges inherent in producing from deep, relatively cold systems with extensive water-bearing channels and connectivity to large aquifers—mainly the difficulty of achieving depressurization and the problem of enormous water production. Also highlighted are new frontiers in large-scale reservoir simulation of coupled flow, transport, thermodynamics, and phase behavior, including the construction of large meshes and the computational scaling of larger systems.

INTRODUCTION

Gas hydrates are solid crystalline compounds in which gas molecules occupy the lattices of ice-like crystal structures called hosts (Sloan and Koh, 2008). They may occur in two distinctly different geographic settings, in the permafrost and in deep ocean sediments, where the necessary conditions of low T and high P exist for their formation and stability. The majority of these naturally occurring hydrates contain CH_4 in overwhelming abundance. Interest in hydrates is enhanced by ever-increasing global energy demand and the environmental desirability of natural gas. Although there has been limited work mapping and evaluating this resource on a global scale (Moridis et al., 2009), current estimates of in-place volumes vary widely (ranging between 10^{15} to 10^{17} ST m^3), but the consensus is that the worldwide quantity of hydrocarbon gas hydrates is vast (Milkov, 2004; Klauda and Sandler, 2005; Burwicz et al., 2011). Even if only a small fraction of the most conservative estimate is recoverable, the sheer size of the resource is so large that it demands evaluation as a potential energy source.

However, not all hydrates are desirable targets for production (Moridis et al., 2011). Of the three possible methods of hydrate dissociation (Makogon, 1997) for gas production— depressurization, thermal stimulation, and use of inhibitors—depressurization appears to be the most efficient (Moridis et al., 2009). Recent studies (Moridis and Reagan, 2007a; b) have indicated that, under certain conditions, gas can be produced from natural hydrate deposits at high rates over long periods using conventional technology. Earlier work focused on production from vertical wells, but more recent studies (Moridis et al., 2008) show that horizontal wells

are more productive, and easier to manage, than vertical wells, if the technology is available.

The objective of this study is to simulate a realistic, 3D gas hydrate reservoir, using real geophysical data at the field scale. Previous studies (Moridis et al., 2009; 2011) have tended to focus on simple 2D modeling, 2D modeling with limited heterogeneity, or extremely simplified 3D modeling. Through a collaboration with Statoil, we were able to access real data on the geometry and geology of a known oceanic hydrate system that has been considered for commercial exploitation. Due to confidentiality agreements, the location of this deposit cannot be published, but the knowledge gained from this simulation work can be generally applied, and used to evaluate any kind of oceanic deposit. The deposit, illustrated in Figure 1, is an oceanic, layered system, approximately 7 km×5.5 km×350 m thickness. The hydrate is arranged in high-permeability "channels" bounded by slightly lower-permeability "levees." The system is likely impermeable at the top and bottom boundaries, but may connect to an aquifer along the *x*-*z* face. Note, via the slicing plane, the layering of the hydrate-bearing channels.

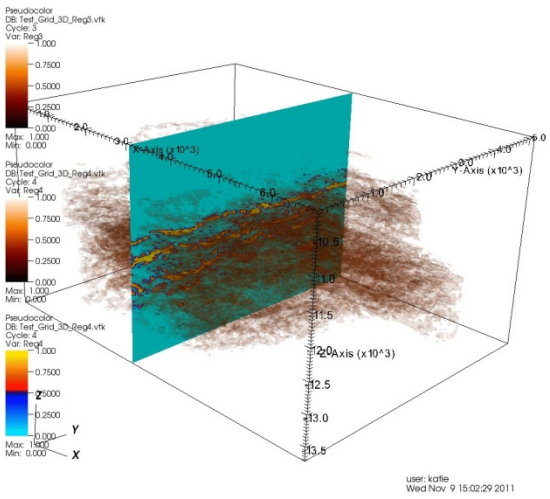

Figure 1. Illustration of the location of hydrate layers within the reservoir domain.

METHODOLOGY

Simulators

Due to the computational challenges of simulating a field-scale system, we use the MPI-parallel TOUGH+HYDRATE code (pT+H) (Zhang et al., 2008). pT+H contains the same coupled thermal-hydrological-chemical capabilities of serial TOUGH+HYDRATE v1.1 (Moridis et al., 2008), but can be executed on shared- or distributed-memory clusters using standard OpenMPI libraries (*http://www.open-mpi.org/*).

Mesh Generation

The construction of 3D volume meshes for systems of this scale is well beyond the means of the standard TOUGH+ MeshMaker routine. Therefore, we deploy advanced tools.

For vertical-well scenarios, the grid was generated using WinGridder (Pan, 2008), an interactive application developed for the Yucca Mountain project. The initial vertical well configuration involves a roughly rectilinear, layer-by-layer mesh of the reservoir, as taken directly from the Statoil dataset, with the discretization matching that of the geophysical data. A cylindrical mesh, with a center at the well, was placed through the region of greatest hydrate accumulation, with the two meshes interpolated at the boundary to conform to TOUGH element-connection rules. The vertical-well mesh is illustrated in Figure 2.

Note in the figure that the domain has been trimmed, with regions of the mesh that do not represent permeable reservoir rocks removed to promote computational efficiency. All subsequent meshing begins with this "reduced" mesh, which contains 1,663,900 elements.

WinGridder does not have the ability to interpolate a horizontal near-well zone into a roughly rectilinear mesh. Therefore, to build the horizontal-well system, a combination of custom tools for manipulating the raw list of element centroids and creating new mesh-element configurations (i.e., cylinders) is combined with the meshing toolkit Voro++ (Rycroft, 2009). Voro++ is a C++ library capable of generating a fully-3D Voronoi mesh for any valid configura-

tion of cell centers. The Voro++ library keeps track of all relevant cell and interface properties and makes them available for manipulation. This allows the creation of highly flexible and dynamically refined meshes.

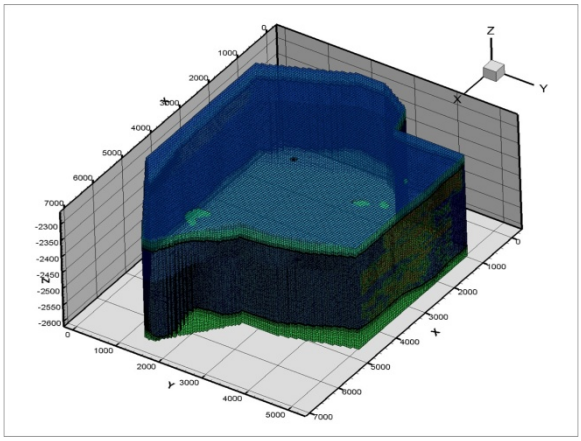

Figure 2. Illustration of the 3D finite-volume mesh, with trimmed boundaries, for the single vertical well scenario. The intersection of the cylindrical well-zone mesh with the top boundary can be seen in the center of the top surface.

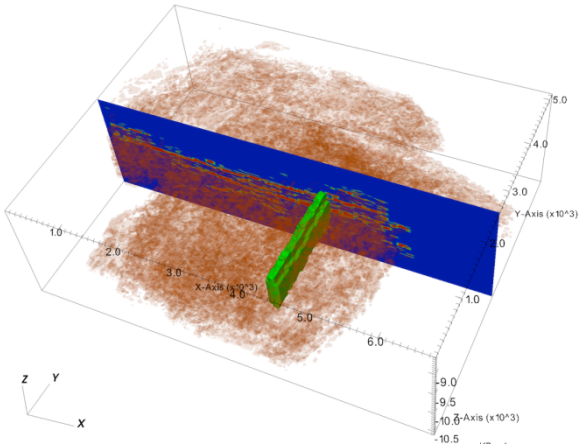

Figure 3. Diagram of the placement of the horizontal well and surrounding cylindrical mesh. Hydrate-bearing sediments are plotted as brown volumes.

For the horizontal well, the geophysical data was analyzed to locate the longest continuous horizontal layers of hydrate more than 60 m thick. A region of roughly 65 m thickness was located near the core of the system, accommodating a horizontal well 1,900 m in length, with no intersection with non-hydrate bearing channels or levees. A cylindrical mesh was constructed around the well to a radius of 250 m, and this radial mesh was inserted into the rectilinear mesh derived from the geophysical data (Figure 3). Element properties (i.e., hydrate saturation) were interpolated from the rectilinear data onto the new mixed mesh. The resulting mesh contains 2,264,000 elements, requiring the simultaneous solution of over 9,000,000 equations, making this the largest TOUGH simulation ever attempted.

Not surprisingly, meshes of this size are challenging to manipulate. Perl and python-based scripts were developed to edit the MESH files after generation (because they are too large for most fully graphical text editors). The system was brought first to hydrostatic equilibrium at the known depth (proprietary) and then to thermal equilibrium using the known geothermal gradient. Due to the size and extent of the system, this consumed significant computing time. Hydrate was added to the system according to the distribution derived from the geophysical data. The system was then allowed to reach full thermal, hydrological, and chemical equilibrium at stated conditions before any simulations were performed.

Reservoir Properties

Although full details of the system may not be disclosed, the initial set of reservoir properties is shown in Table 1.

Table 1. Reservoir parameters.

Region	k (mD)	ϕ	S_H	S_W
0. Bound	0	0.0	0.0	1.0
1. Levee 1	100	0.2	0.0	1.0
2. Levee 2	100	0.21	0.0	1.0
3. Levee 3	100	0.22	0.7	0.3
4. Channel 1	10000	0.33	0.7	0.3
5. Channel 2	10000	0.34	0.0	1.0
6. Channel 3	10000	0.35	0.0	1.0

Regions 3 and 4 are the hydrate-bearing media seen in Figures 1 and 3. Geophysical data suggested the presence of free gas in the reservoir, but TOUGH+HYDRATE pre-run thermo-

dynamic consistency checks ruled this as impossible under the stated conditions. Therefore, the gas was removed from the model.

For additional parameters, we used data from one of the few well-characterized reservoir-grade oceanic hydrate deposits, the Tigershark deposit (Moridis and Reagan, 2007a,b). Relative permeability exponents were estimated by fitting to Statoil effective permeability data. The pressure specified at the well was selected to be 3.0 MPa to prevent ice formation in the wellbore. Other details about Tigershark, the configuration of the simulated wellbore, and examples of production from such a system, can be found in Moridis and Reagan (2007a;b). Key simulation parameters are provided in Table 2.

Table 2. Other simulation parameters.

Water salinity (mass fraction)	0.035
Grain density r_R (all formations)	2750 kg/m^3
Constant pressure at the well P_w	3.0 x 10^6 Pa
Dry thermal conductivity k_{QRD} (all formations)	0.5 W/m/K
Wet thermal conductivity k_{QRW} (all formations)	3.1 W/m/K
Composite thermal conductivity model (Moridis et al., 2008)	$k_{QC} = k_{QRD} + (S_A^{1/2}+S_H^{1/2})\,(k_{QRW} - k_{QRD}) + f\,S_I\,k_{QI}$
Capillary pressure model (van-Genuchten, 1980; Moridis et al., 2008)	$P_{cap} = -P_0\left[\left(S^*\right)^{-1/\lambda}-1\right]^{-\lambda}$ $S^* = \frac{(S_A - S_{irA})}{(S_{mxA} - S_{irA})}$
S_{irA}	1
λ	0.77
P_{max}	10^6 Pa
Relative permeability Model (Moridis et al., 2008)	$k_{rA} = (S_A^*)^n$ $k_{rG} = (S_G^*)^n$ $S_A^*=(S_A-S_{irA})/(1-S_{irA})$ $S_G^*=(S_G-S_{irG})/(1-S_{irA})$ OPM model
n (fitted from data)	4.4292
S_{irG}	0.02
S_{irA}	0.20

RESULTS AND DISCUSSION

Production from a Vertical Well

Initial simulation work by Statoil, using the CMG-STARS with gas hydrate add-ons, suggested that the system could be productive if vertical wells were drilled into the lower part of the formation near areas of high hydrate saturation. However, these simulations used a 2D slice of the full system and assumed significant free gas in the initial configuration of the reservoir. In contrast, here we begin by simulating production from the 3D, single vertical well shown in Figure 2.

We simulate three well configurations: (1) a well perforated throughout the entire hydrate-bearing zone ("Long"), (2) a well perforated only within the topmost hydrate layer ("Short"), and (3) a well perforated within the topmost layer, with the impermeable system boundaries brought inward to simulate the well as part of 500 m well spacing pattern (no-flow boundaries 250 m from the well). We also estimate sensitivity to system permeability by performing four additional simulations in the 500 m pattern case: reducing the permeability of the non-hydrate-bearing levees to 100 mD, 10 mD, 1 mD, and 0.01 mD. For each case, we simulate up to three years of constant-pressure production, using 200–220 processors with pT+H on a departmental computing cluster.

Comparison of Vertical Well Configurations

Figures 4 and 5 track the evolution of production for the seven cases. In Figure 4, we see the hydrate dissociation ("release") begins immediately for the long-interval case, but quickly subsides. Producing from a small interval within the top layer of hydrate ("short"), results in far less dissociation, and no sign of strong methane release. However, if this short-interval well is producing as part of a 500 m pattern, we see strong dissociation/methane release after 1.5 years of depressurization for all subsequent scenarios, with lower-permeability levees surrounding the hydrate, resulting in earlier dissociation of hydrate.

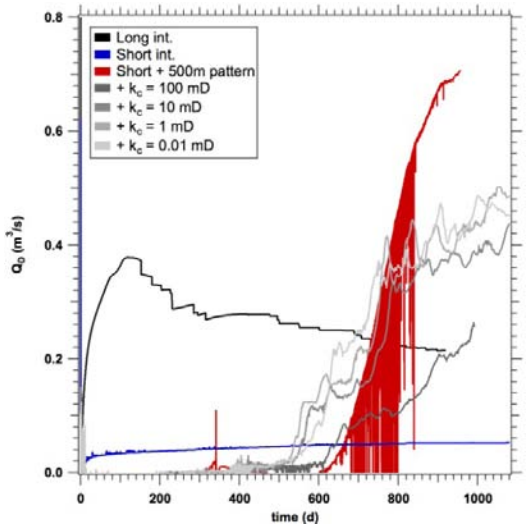

Figure 4. Rate of hydrate dissociation, Q_D, for the reservoir as a whole, for the vertical well scenarios.

Figure 5 shows the resulting methane production at the well for the various scenarios. The full interval generates the highest rates of methane production (unsurprising at first, due to the much greater extent and penetration of the perforated interval), with other configurations lagging significantly. However, production via the long interval levels off quickly, and does not achieve commercially viable rates within 3 yr. Among the other methods, wells in a 500 m pattern with low-permeability levees show some gains in production rate after 2.5 yr, but the viability of these methods are questionable.

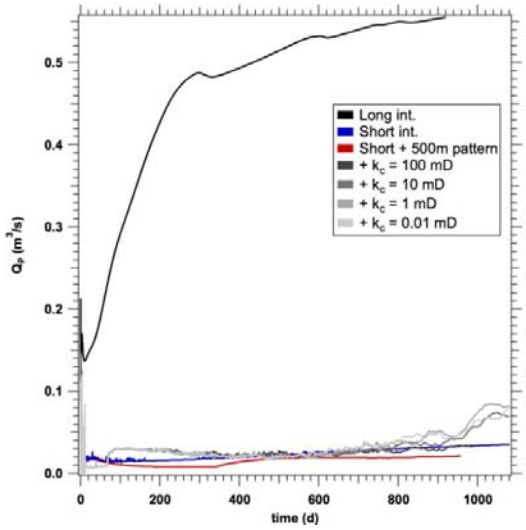

Figure 5. Rate of methane production at the well, Q_P, for the vertical well scenarios.

The nature of the problem is worse than initially suspected, however, for reasons shown by Figure 6, which shows the amount of water removed per m^3 of methane produced, reported as cumulative quantities vs. time. In each case, we see that massive amounts of water are moved to achieve small rates of dissociation and production, even for cases where the communicating water-filled levees have extremely reduced permeability. In absolute quantities, the "best case" scenario produces 4×10^8 kg of water over 3 yr, and the full interval would require the removal of a colossal 10^{11} kg of water in 2.5 yr—nearly one tonne per second.

At best, we also see that 200 kg of water is removed per m^3 of methane after 3 yr, a value that is suspiciously close to the solubility of methane in water under reservoir conditions. This suggests that mobile free gas is not being produced in significant quantities via depressurization, and that the bulk of produced methane results from dissolution of methane directly from solid hydrate and transport to the well via the aqueous phase.

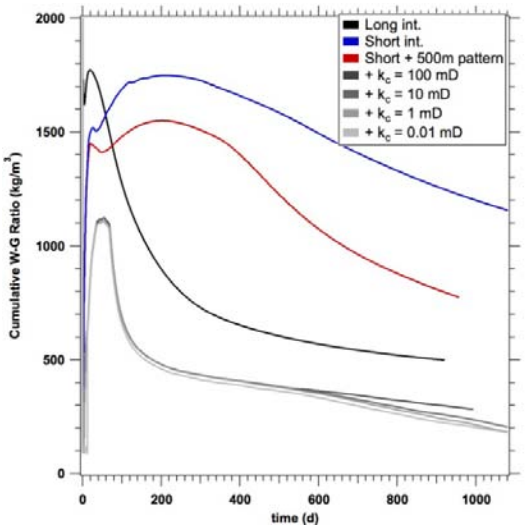

Figure 6. Ratio of total water production to total methane production (cumulative at time t) for the vertical well scenarios.

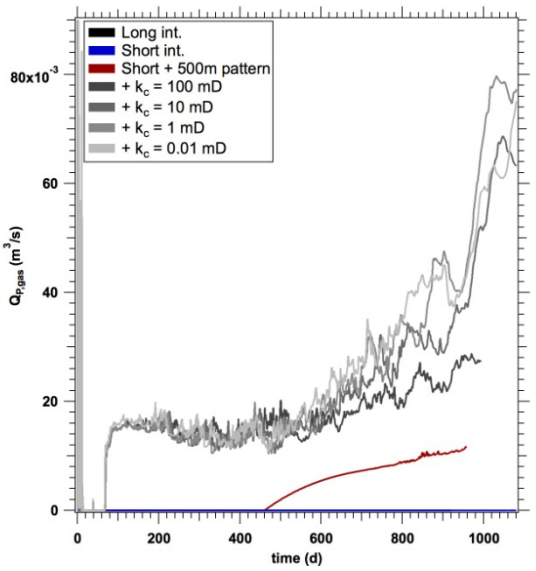

Figure 7. Rate of methane production at the well in the gas phase, $Q_{P,gas}$, for the vertical well scenarios.

Figure 7, showing only production of methane in the gas phase excluding aqueous transport, confirms this problem. Only wells in a 500 m pattern produce any gas at all, and even in those cases, the production of free gas is orders of magnitude less than gas transport in the aqueous phase. It is clear that the presence of large amounts of water in this hydrate reservoir hampers effective depressurization and dissociation. This effect has been seen clearly before, where simulations of Class 2 systems strongly suggest that impermeable boundaries are crucial (Moridis et al., 2009).

Production from a Horizontal Well

For Class 2 and Class 3 hydrate deposits, it has been demonstrated that horizontal wells, properly located, are a far more effective production strategy (Moridis et al., 2008). Therefore, we simulate production from the horizontal well shown in Figure 3, with all simulation and reservoir parameters otherwise unchanged from the vertical-well cases. However, due to the larger mesh (2.46M vs. 1.66M gridblocks) and the nature of the Voronoi grid (on average, more connections per element), the computational requirements for this simulation are approximately an order of magnitude greater. Initial equilibration was performed using our 220-processor in-house cluster, but production was scaled up to the "Hopper" supercomputer, part of NERSC, for multi-day runs using 960 and 1,920 processors. To date, we have been able to simulate 135 days of production time, with simulations ongoing.

Evolution of the rate of hydrate dissociation/methane release (Q_R) and the rate of methane production at the well (Q_P) are provided in Figure 8. Unlike the vertical well examples, here we see that release exceeds production from the beginning, which is necessary to generate free gas in the reservoir for later production (Moridis and Reagan, 2007a;b). Water production (Q_W) is large but steady, and comparable to the best-case vertical well scenario (with greater access to the reservoir via a single well). However, after less than 5 months of production, we see that both release and production are ceasing to increase with time, while water production remains roughly constant. This suggests that once again, effective depressurization is being hindered by the inflow of large quantities of water from the surrounding formation. As economically viable production rates for offshore wells need to reach orders of millions of cubic feet per day (10^4–10^5 m^3/day), this system does not appear to be a desirable production target.

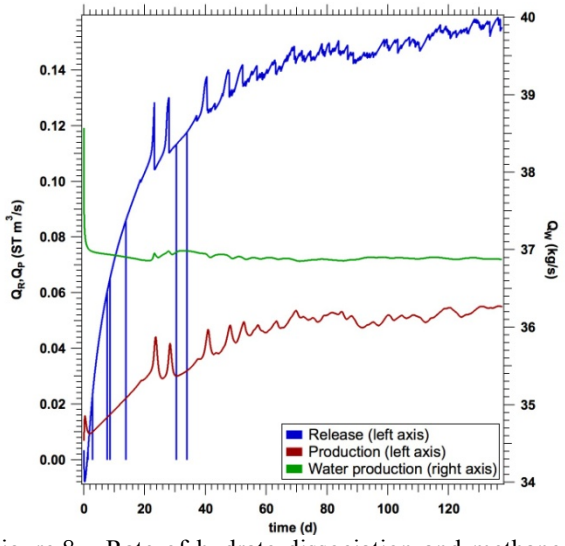

Figure 8. Rate of hydrate dissociation and methane release (Q_R), rate of methane production at the well (Q_P), and rate of water production at the well (Q_W, right axis) for the horizontal well scenario.

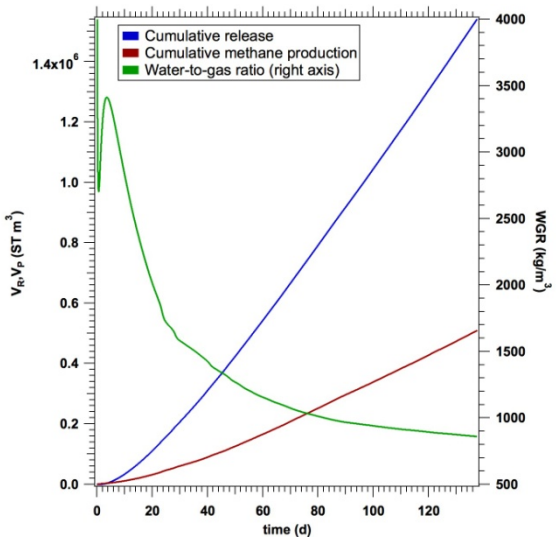

Figure 9. Cumulative methane release (V_R), cumulative methane production (V_P), and ratio of total water production to total methane production (V_W, right axis), for the horizontal well scenario.

Cumulative quantities of methane, released and produced, are shown in Figure 9. More significant, however, is the water-to-gas ratio, shown in green. While this ratio drops rapidly as production proceeds, the curve is heading toward asymptotic behavior at values of 700 to 800 kg per m^3, which suggests again that transport of methane is entirely in the aqueous phase, and even then, that the quantity of water produced greatly exceeds that quantity of water needed to dissolve and transport the methane seen at the well. It is therefore likely that the hydrate zone around the well has been perforated by dissociation, connecting the well to the gigantic reservoir of mobile water surrounding the hydrate layers and hindering depressurization after over a few months of production.

CONCLUSIONS

This study has been the first 3D simulation, at this scale, of production in a real, field-scale oceanic hydrate reservoir. While the simulations use the most extensive, realistic, and data-based model to date, the insights found here strongly relate to earlier studies on the productivity and non-productivity of various configurations of hydrates.

Earlier work has strongly suggested that impermeable boundaries (i.e., sufficiently impermeable to allow strong depressurization of the reservoir through conventional technology) are the key to efficient and economical production (Moridis and Reagan, 2007a;b; Moridis et al., 2009;2011). While this reservoir (as modeled) is indeed bounded on a large scale, the layers of high-saturation hydrate are adjacent to, and effectively surrounded by, levees and channels of high-permeability, water-saturated media. Even when those levees are reduced in permeability, creating bounded, Class 2 systems, the sheer quantity of available water makes depressurization difficult on a reservoir scale or even on a local scale, assuming a pattern of wells and short perforation intervals.

Previous work determined that a horizontal well, properly placed, can mitigate some of these problems as long as the horizontal well stays within the hydrate layer and does not connect to surrounding water-filled media. Our early results for this configuration show that large quantities of water are able to reach the well early in the depressurization process, reducing depressurization effectiveness. Whether this is due to rapid dissociation and breakthough, or other effects (for example, the greatly reduced but still finite effective permeability of hydrate-bearing media) remains to be proven—ongoing simulations will produce detailed 3D images of system evolution to evaluate this hypothesis. As a result, it is becoming clear that systems with large quantities of water in communication with the hydrate reservoir, even if not connection to aquifers beyond reservoir boundaries, are particularly challenging production targets. Permeability of the bounding media, as well as distance from the hydrate stability boundary and configuration of the hydrate into large contiguous masses, needs to be considered in reservoir evaluation.

It is somewhat disappointing that simulations of this size and scale result in “lackluster” results—in terms of active hydrate dissociation, gas formation, and the coupled thermodynamic and transport processes seen in more active and productive systems. However, it is important to note that these are the largest TOUGH simulations to date, with the simultaneous solution of 9,000,000 equations at each step, plus fully

described multiphase thermodynamics. The simulations show that mesh complexity becomes critical for large systems, as the "layered" and mainly rectilinear vertical well mesh (1.66M elements) can be realistically run on a small departmental cluster, while the more complex Voronoi grid used in the horizontal well simulations (2.46M elements) may require over a million processor-hours of time to complete the assessment. The development of user-friendly meshing tools and perhaps active mesh refinement and de-refinement may be needed to move TOUGH simulations fully into the massively parallel universe, as the standard ASCII TOUGH+ hydrate MESH, INCON, and SAVE files quickly become too large to manipulate via hand-editing. Finally, the traditional TOUGH-family visualization methods, mainly via standard outputs or ASCII-based, Tecplot-formatted files, are insufficient to handle datasets of this size. Preliminary real-time visualization of pT+H using Visit (*https://wci.llnl.gov/codes/visit/*) has been successful, although the generation of publication-grade images has not yet been achieved. Key hurdles include finding and implementing modern data formats, and converting the nonstandard TOUGH finite-volume meshes into forms more compatible with high-performance visualization software. These problems must be solved through enhancements and modernization of the pT+H code base.

ACKNOWLEDGMENTS

This research was funded by Statoil Inc. This research used resources of the National Energy Research Scientific Computing Center, which is supported by the Office of Science of the U.S. Department of Energy under Contract No. DE-AC02-05CH11231. The authors would like to thank Shiv K. Pande for assistance with data visualization.

REFERENCES

Burwicz, E.B., Rupke, L.H., Wallmann, K., Estimation of the global amount of submarine gas hydrates formed via microbial methane formation based on numerical reaction-transport modeling and a novel parameterization of Holocene sedimentation. *Geochimica et Cosmochimica Acta*, 75, 16, 4562-4576, 2011.

Klauda, J.B., Sandler, S.I., Global distribution of methane hydrate in ocean sediment. *Energy and Fuels*, 19, 459, 2005.

Makogon, Y.F. *Hydrates of Hydrocarbons.* Tulsa, OK: Penn Well Publishing Co., 1997.

Milkov, A.V. Global estimates of hydrate-bound gas in marine sediments: how much is really out there? *Earth Science Reviews*, 66, 183, 2004.

Moridis, G.J., Reagan, M.T. Gas Production From Oceanic Class 2 Hydrate Accumulations, OTC 18866, *Proc.* 2007 Offshore Technology Conference, Houston, Texas, U.S.A., 30 April–3 May 2007a.

Moridis, G.J., Reagan, M.T. Strategies for Gas Production From Oceanic Class 3 Hydrate Accumulations, OTC 18865, *Proc.* 2007 Offshore Technology Conference, Houston, Texas, 30 April – 3 May 2007b.

Moridis, G.J., M.B. Kowalsky, Pruess, K. TOUGH+HYDRATE v1.0 User's Manual: A Code for the Simulation of System Behavior in Hydrate-Bearing Geologic Media, Report LBNL-0149E, Lawrence Berkeley National Laboratory, Berkeley, CA, 2008.

Moridis, G.J., Reagan, M.T., Zhang, K. The Use of Horizontal Wells in Gas Production from Hydrate Accumulations, *Proc.* 6th International Conference on Gas Hydrates, Vancouver, BC, July 6-10, 2008.

Moridis, G.J., Collett, T.S., Boswell, R., Kurihara, M., Reagan, M.T., Koh, C., Sloan, E.D. Toward Production From Gas Hydrates: Current Status, Assessment of Resources, and Simulation-Based Evaluation of Technology and Potential. SPE 114163, *SPE Journal*, 12(5), 745-771,2009.

Moridis, G.J., Collett, T.S., Pooladi-Darwish, M., Hancock, S., Santamarina, C., Boswell, R., Kneafsey, T., Rutqvist, J., Kowalsky, M.J., Reagan, M.T., Sloan, E.D., Sum, A.K., and Koh, C., Challenges, Uncertainties and Issues Facing Gas Production From Hydrate Deposits in Geologic Systems, LBNL-4254E, *SPE Res. Eval. & Eng*, 14(1), 76-112, 2011.

Pan, L., *User's Information for WinGridder V3.0*., LBNL Report 273E, Lawrence Berkeley National Laboratory, Berkeley, CA, 2008.

Rycroft, C.H., Voro++: A three-dimensional Voronoi cell library in C++, *Chaos*, 19, 041111 (2009).

Sloan, E.D., and C. Koh, *Clathrate Hydrates of Natural Gases. 3rd Edition*, Taylor and Francis, Inc., Boca Raton, FL, 2008.

van Genuchten. A Closed-Form Equation for Predicting the Hydraulic Conductivity of Unsaturated Soils. *Soil Sci. Soc*., 44, 892, 1980.

Zhang, K., Moridis, G.J., Wu, Y.S., Pruess, K. A domain decomposition approach for large-scale simulations of flow processes in hydrate-bearing geologic media. Proc. 6th International Conference on Gas Hydrates, Vancouver, BC, July 6-10, 2008.

INTEGRATED REACTIVE TRANSPORT MODELLING: CHALLENGES AND OPPORTUNITIES FOR IMPROVED PREDICTION OF DIAGENETIC IMPACT ON RESERVOIR QUALITY

F. Whitaker, A. Al-Helal, T. Gabellone, and G. Griffiths

Department of Earth Sciences,
University of Bristol,
Bristol BS8 1RJ, England
Email: Fiona.Whitaker@bristol.ac.uk

ABSTRACT

Process-based numerical modeling offers the potential to improve our predictive concepts for diagenetic modification of reservoir quality, and to better understand drives for fluid flow and resulting reaction patterns. We explore challenges to improve the accuracy of predictions of diagenesis, including specification of more realistic initial distribution of permeability and effective reactive surface area, and diagenetic changes in this distribution. Additional challenges relate to the need to model at length and time scales appropriate to capture key elements of the system, and to better understand controls on solute transport and reactions. Notwithstanding these constraints, we could make more effective use of existing models, for example by extracting information to characterize simulated diagenetic products and developing more general rules about reactions under given flow systems. Finally, simulations of diagenesis in well-constrained modern and ancient systems are needed in order to demonstrate the utility of process-based modeling to reduce risk in prediction of reservoir quality.

INTRODUCTION

Reactive transport models (RTMs) can improve the predictability of carbonate diagenesis and its effect on reservoir quality by:

1. Integrating experimental, observational, and theoretical knowledge about fluid flow and reactions with data from wells and outcrop analogues;
2. Providing quantitative estimates of rates and distribution of diagenesis and its impact on reservoir quality;
3. Describing diagenetic geobodies and trends which can be used to populate geologic models for reservoir simulation;
4. Providing a platform for developing better conceptual models and hypotheses; and
5. Framing new research questions.

Here, we illustrate the potential offered by RTMs using examples drawn from our recent work on dolomitization, driven by brine reflux and geothermal convection. We then consider a number of challenges that are key to developing more meaningful simulations. These challenges range from more realistic specification of initial rock properties and their alteration by diagenesis, to simulating flow and solute transport in highly heterogeneous media, modeling at appropriate length and time scales with meaningful boundary conditions, and finally improving utility and building confidence in model predictions.

OPPORTUNITIES

RTM simulations can provide insight into the dynamics of diagenesis and the operation of both intrinsic and extrinsic controls. A specific focus of our work is the replacement of limestone by dolomite. Dolomites typically have pore systems and reservoir characteristics that differ fundamentally from those of nearby precursor limestones. In some cases, dolomitization can create excellent reservoir potential, but in others it be responsible for destroying it. In addition to the effect of an increase in porosity due to differences in mineral density, permeability can be radically altered by changes in pore structure, and is also impacted by the effects on compaction and fracturing resulting from the increase in mechanical strength. However, reservoir quality

can also be significantly altered by associated diagenetic reactions, ranging from precipitation of pore-occluding dolomite and anhydrite cements by refluxing brines, to calcite dissolution by hydrothermal fluids.

RTMs can provide new insights into the interactions between dolomitization and associated diagenetic reactions, as illustrated by simulations of reflux diagenesis. Carbonate platforms tend to build to sea level, often resulting in an extensive shallow body of sea-water with restricted circulation. Here, evaporative concentration can increase fluid density, generating brines that sink downwards and flow laterally to discharge into adjacent ocean basins. This fluid flow system, termed "reflux," drives replacement of calcite by dolomite, and the Ca^{2+} released by dolomitization reacts with the high SO_4^{2-} brines, resulting in precipitation of $CaSO_4$ (here assumed to be anhydrite) downstream of the zone of dolomitization (Figure 1, Al-Helal et al., 2012a). This occludes porosity and reduces permeability, focusing fluid flow at increasingly shallow depth. However, once all the calcite has been dolomitized, further reflux dissolves the diagenetic $CaSO_4$ creating a more porous dolomite at shallow depth. It is notable that simulations predict only minor volumes of dolomite cement, in contrast to observations in sequences where "over-dolomitization" has been related to reflux diagenesis (Choquette and Hiatt, 2008).

RTMs also allow us to evaluate the effects of individual controls on a given diagenetic system and target gaps in our knowledge that can provide a focus for future research. These controls can be grouped into factors extrinsic to the system under investigation, such as climate and relative sea-level, and intrinsic controls, such as sediment permeability and reactivity.

A key extrinsic control on reflux diagenesis is climate, which can be constrained for ancient carbonate sequences using paleogeographic reconstructions and paleoclimate models. Solar insolation drives evaporative generation of brines, and also controls the temperature of the platform top. For 85‰ brines, the predicted rate of reflux dolomitization increases with platform top temperature up to 40°C (Figure 2). However, the effect on associated $CaSO_4$ precipitation is even more marked, and at temperatures >40°C, the resulting porosity reduction can limit the vertical extent of dolomitization. This effect is separate from the increase in both fluid density-driven fluid flux and the Mg^{2+}/Ca^{2+} of the brine, which also result from higher rates of evaporation (Al-Helal et al., 2012b).

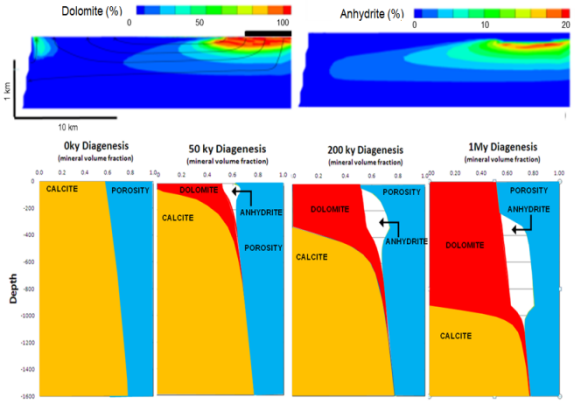

Figure 1. Dolomitization and anhydrite precipitation driven by reflux of 85‰ brines from a 5 km wide pool (black bar) in the center of a broad grain-dominated packstone platform, showing 2D distribution after 1 My of reflux, and 1D evolution over time for a synthetic well in the center of the brine pool.

Intrinsic controls of permeability and effective reactive surface area also play a key role in determining the distribution of diagenetic product formed under a given fluid flow system. The rate of diagenesis increases with both fluid flux and sediment reactivity, but these properties are generally inversely correlated. Fluid flux will be higher in more permeable sediments, which are often the grainier parts of the system, where the reactive surface area may be lower. In contrast, muddier sediments may be less permeable but generally have a much higher reactive surface area. In both cases, differences span several orders of magnitude.

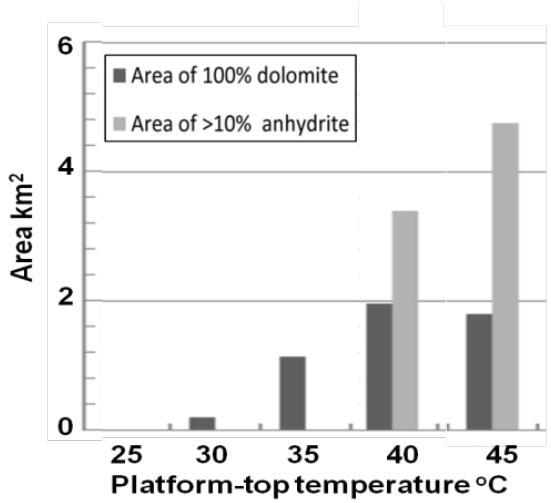

Figure 2. Sensitivity of dolomite and anhydrite abundance formed by reflux of 85‰ brines over 1 My to changing platform top temperature from 40°C of base-case simulation presented in Figure 1.

The relative importance of these two competing intrinsic controls depends upon the Damköhler number (the ratio of the chemical reaction rate to the mass transfer rate). Natural systems will usually comprise a mixture of grainer and muddier sedimentary units. In flow systems where reaction rate limits diagenesis (i.e., high Damköhler number), muddier sediments with higher effective reactive surface area will be altered more rapidly. However, where flow rates are the limiting factor (i.e., low Damköhler number), diagenesis will be more rapid in more permeable, though less reactive, grainier sediments.

This is exemplified by a pair of simulations of dolomitization driven by geothermal convection in the absence of any brine reflux (Figure 3). In contrast to the complex lateral and vertical variations in sediment texture in natural systems, we specify very crude layering. Fifty-meter-thick horizontal beds of either grainstone or mudstone are specified at 200 m depth intervals within the standard grain-dominated packstone platform. Platform groundwater, warmed by geothermal heating, rise buoyantly to discharge at the platform top, and this draws in colder waters from the adjacent ocean basin. Muddy layers within a grain-dominate packstone platform restrict geothermal convection, allowing conduction to warm the interior of the platform. Reactions are flux limited, and dolomitization occurs preferentially in the coarser units near to the platform margin. In contrast, grainstone layers allow convection of cold ocean waters into the platform interior. As a result, reaction rate rather than fluid flux limits dolomitization, which occurs across the whole platform top but is much slower within the grainstone layers.

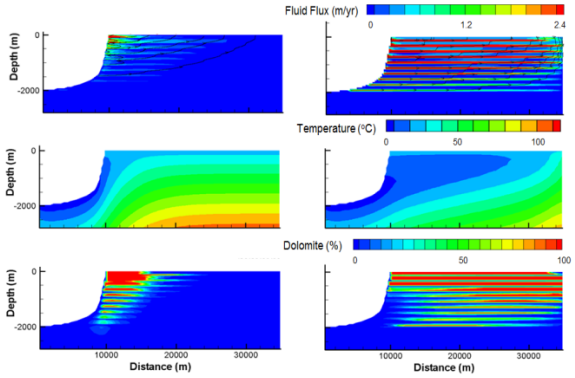

Figure 3. 2D distribution of fluid flux, temperature and dolomitization resulting from geothermal convection in a grain-dominated packstone platform with layers of mudstone (left) and grainstone (right). From Whitaker and Xiao (2010).

CHALLENGES

To better model inherently heterogeneous permeability systems

More realistic representation of spatially variable matrix properties is limited largely by the availability of data describing their distribution in two or three dimensions. Geologic models developed as inputs to reservoir simulation models, and/or forward sediment models, both provide sources of this data. However, appropriate property data may require back-stripping to remove the effect of burial and/or diagenesis post-dating the diagenetic episode of interest. Incorporating more realistic complexity in the initial permeability field results in sharper gradients in diagenetic products reflecting, for example, contrasts in depositional texture. Diagenetic rates are sensitive to the initial mineralogy and the effective reactive surface, which should reflect the nature of the carbonate grains rather than simply their grain size.

RTMs such as TOUGHREACT (Xu et al., 2006) explicitly simulate changes in porosity, and then infer resulting changes in matrix permeability. However simple relationships may fail to represent changes in permeability that can result from textural alteration during diagenesis. For example, the impact of calcite dolomitization on the porosity-permeability relationship is highly variable, dependent upon the type of dolomite. Thus, the Carmen-Kozeny relationship may be adequate for mimetic dolomitization, where grain morphologies are largely unaltered, but poorly represents changes resulting from growth of sucrosic dolomite crystals within a muddy matrix.

Furthermore, the nature and abundance of any associated cements needs careful consideration. A minor amount of vadose cementation at pore throats can give a more significant reduction in permeability than a larger volume of pore-lining phreatic cements. Laboratory measurements and pore-scale numerical experiments allow direct quantification of these effects, and development of more sophisticated algorithms to account for textural changes. In association with this, there is a need to develop our understanding of how dissolution, recrystalization, and cementation affect reactive surface area. Both these effects, operating at scales from the mineral-fluid interface to linked pores, need then to be incorporated into RTMs.

Incorporation of fracture systems and their effect on flow, transport, and reaction remains a major challenge. Neither discrete fracture models or dual permeability models correctly represent fracture-matrix interactions. Geologically more realistic simulations of fracture-matrix interactions (discrete fracture matrix models) are possible (e.g., Belayneh et al., 2006), but at present are more challenging to construct and parameterize.

<u>To model at length and time scales appropriate to capture key elements of the system</u>

Model dimensions need to be appropriate, and only some 3D systems can be meaningfully reduced to 2D. For example 2D simulations of interactions between a discrete fracture and the surrounding matrix will fail to capture the effects of geothermal convection along the plane of the fault (Lopez & Smith, 1995). Coupled with this, discretization of the model domain needs to be at a sufficiently high resolution that the physical processes can be correctly represented (e.g., Yamamoto and Doughty, 2009).

Specification of appropriate boundary conditions is critical for meaningful simulations. One solution is to adopt an embedded approach, in which a larger-scale model is used to condition smaller-scale, but computationally more intensive, simulations. Where reactions of interest occur at relatively shallow depth, they will likely be influenced by boundary conditions that change significantly over the period of diagenesis. The first challenge is then to identify the timescale which controls the system. Thus, for example, in simulating shallow meteoric diagenesis, simple use of a mean annual recharge rate is misleading. In reality, it may be the seasonality of climate, with a switch from net recharge during the wet season to intervening periods of net evapotranspiration, which drives cycling between periods of porosity generation and occlusion (Figure 4). The resulting reorganization of the pore space cannot be derived simply from the total porosity.

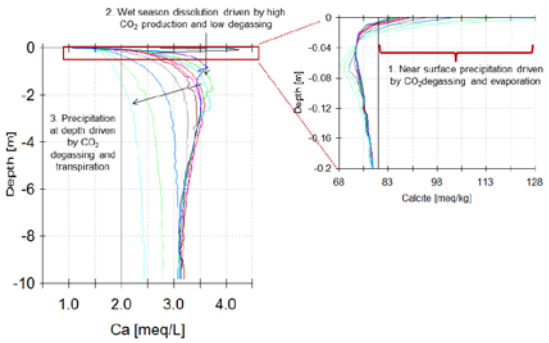

Figure 4. Temporal evolution of calcite dissolution in sands colonised by semi-arid vegetation driven by storms of 100 mm/d recurring at 4-day intervals, followed by 3 dry months of 2 mm/d transpiration (Whitaker and Smart, unpublished research), predicted using HYDRUS (Šimůnek et al., 2008)

More problematic is the simulation of diagenetic processes in areas of rapid sedimentation, which really require explicit coupling between sediment accumulation and changes in boundary

conditions governing flow and reactions. While computational limitations currently challenge direct coupling of forward sediment and RTMs, for some problems temporal evolution can be approximated by stepwise addition of active cells and changes in boundary conditions. An alternative approach is to derive simplified rules to predict diagenesis from RTM simulations and build these into forward sediment models, such as CARB3D^{+}, to predict early diagenesis (Figure 5).

Any significant alteration of depositional texture by early diagenesis, is likely to influence the nature and rates of subsequent diagenesis. To fully understand diagenetic evolution, it is therefore necessary to model diagenetic processes from the cradle (early marine mineral stabilization, dissolution, and cementation) to the grave (which in reservoir rocks may be associated with hydrocarbon emplacement). It is a general truism that in moving from the syn-depositional environment to a burial regime, the rates of fluid flow and diagenetic alteration decrease, while the boundary conditions generally become more stable. However, processes such as sedimentary and tectonic compaction can continue into the burial regime and may require deformation of the grid and/or changes in the boundary conditions (Frazer et al., 2012). Again, analysis of the evolution of the sedimentary system through time will require coupling of models, in this case enabling interactions between geomechanics and reactive transport to be simulated.

To better understand controls on solute transport and reactions

RTM predictions are only as good as the understanding of the thermodynamics and kinetics of the fluid-rock system of interest derived from laboratory studies. For many minerals, the controls on reactions in porous media are still far from well understood. In the case of dolomitization, we use a rate constant derived from experiments of Arvidson and Mackenzie (1999) at temperatures >115–196°C, and there is considerable uncertainty in extrapolating this to temperatures <100°C. Reaction rates are often accelerated in the laboratory by increasing the ratio of mineral surface area to reactor volume and/or running experiments far from equilibrium. In contrast, waters in natural systems tend toward equilibrium where uncertainties in rate constants are greatest (Bethke, 2008). Furthermore, whereas most experiments are abiotic, reactions such as dolomite precipitation can be significantly microbially mediated, at least under some circumstances.

We also face a fundamental problem in the degree to which we can predict solute transport. Pore-scale flow models can be used to define effective properties for flow, at least for single-phase fluid. However, dependent upon the degree of fluid-flow channelling, much of the solute can remain trapped in virtually stagnant regions of the pore space, and transport is limited by very slow diffusion (Blunt et al., 2012). A more realistic determination of averaged reaction rates requires consideration of the local fluctuations in concentration and flow path.

To improve utility and build confidence in RTM predictions of diagenesis

There are undoubtedly a number of challenges ahead in generating more meaningful RTMs. Notwithstanding, current RTM technologies offer significant opportunities for improved understanding of diagenesis. One way forward to optimize these opportunities is to generate output that is more directly comparable with observational data and/or more useful in generating reservoir models. For example, in addition to predicting changes in mineral volumes, we can retain information relating to temperature at which diagenetic products are formed and the composition of their parent fluids. Model output can also be interrogated to extract statistics describing diagenetic trends or the geometry and spacing of diagenetic geobodies and their key petrophysical properties, which can be used to populate geological models.

Finally, it is important to develop RTM simulations of well-constrained field examples. For example, we are using a case study of the Mississippian Madison Formation of Wyoming, to investigate interactions between different episodes of early reflux dolomitization and later high-temperature fracture-guided dolomitization, focusing on questions relating to Mg^{2+} mass-

balance requirements, both in terms of plumbing and fluid chemistry. This will both allow us to test the limits of this technology and demonstrate the potential for improving prediction of diagenetic controls on reservoir quality.

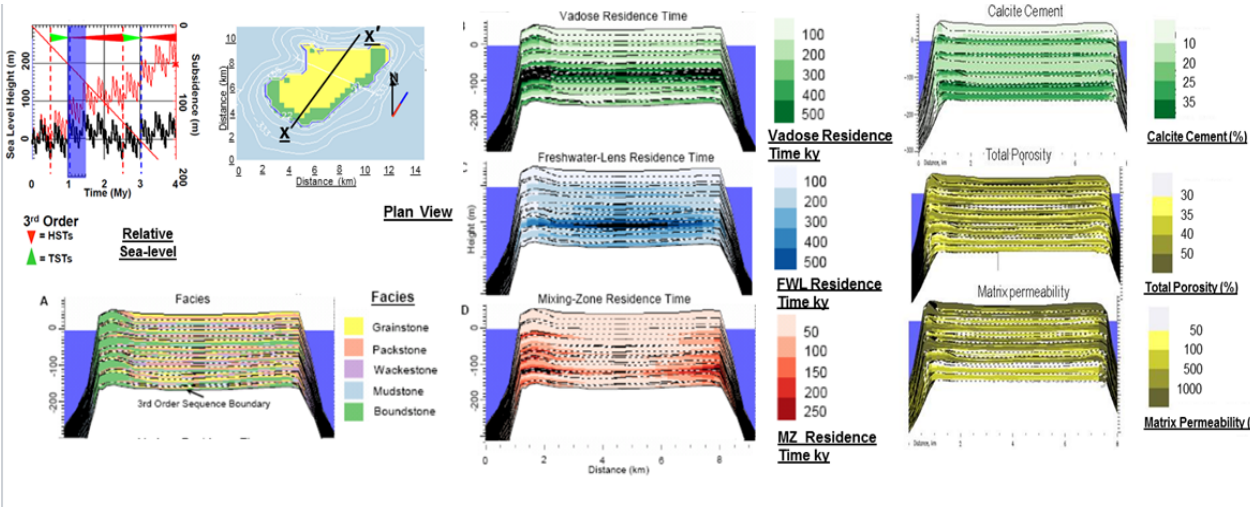

Figure 5. Coupled simulation of architecture, sediment texture, residence time in hydrologically-controlled diagenetic zones (hydrozones) and early diagenesis (calcite cement, porosity and permeability evolution) in a subsiding isolated carbonate platform subject to high-frequency variations in relative sea-level (from study of Paterson et al. (2008) using CARB3D^{+}). Simple diagenetic rules derived from more detailed but essentially static RTM models are used to specify the distribution of diagenesis within these hydrozones.

CONCLUSION

RTMs have the potential to provide a comprehensive, quantitative, and ultimately predictive treatment of diagenetic processes, and their effect on flow behavior and recovery in carbonate reservoirs. They allow simultaneous integration of the major regulatory processes responsible for fluid-rock interaction across a wide range of time and space scales, and can bridge the gap between fundamental, process-oriented research and applied research. However, challenges remain in representation of solute transport and reaction processes, key boundary conditions, and the scale-dependence of key rock properties. While exacerbated by the strong scale dependence in the flow and solute transport of many carbonates, many of these issues also apply to other systems of interest.

ACKNOWLEDGMENT

This research has been supported by sponsors of the Bristol Carbonates Research Group including BG-Group, BHP Billiton, Chevron, ConocoPhillips, ENI, ExxonMobil, Petrobras, SaudiAramco and Wintershall. It has also benefitted from stimulating discussions with many colleagues, including Gareth Jones, Peter Smart and Yitian Xiao.

REFERENCES

Al-Helal, A.B., Whitaker, F.F., Xiao, Y. Reactive transport modelling of brine reflux: dolomitization, anhydrite precipitation, and porosity evolution. *Journal of Sedimentary Research*, 82, 196–215, 2012a.

Al-Helal, A.B., Whitaker, F.F., Spycher, N. Modelling reflux of hypersaline brines using Pitzer ion-interaction model in TOUGHREACT. *Proceedings TOUGH Symposium 2012*, LBNL, Berkeley, California, Sept 17-19, 2012b.

Arvidson, R. S. and Mackenzie, F. T. The dolomite problem: Control of precipitation kinetics by temperature and saturation state. *American Journal of Science*, 299, 257–288, 1999.

Belayneh, M.W. Geiger, S., and Matthäi, S.K. Numerical simulation of water injection into layered fractured carbonate reservoir analogs. *American Association of Petroleum Geologists Bulletin*, 90, 1473-1493, 2006.

Bethke, C.M. *Geochemical and Biogeochemical Reaction Modeling*. Cambridge University Press, 547 pp, 2008.

Blunt, M.J., Branko, B., Gharbi, O. and Mostaghimi, P. From pore structure to mixing and relative permeability in carbonates. *AAPG/SPE/SEG Hedberg Research Conference Fundamental Controls on Flow in Carbonates,* Provence, France, July 8-13, 2012.

Choquette, P.W. and Hiatt, E.E. Shallow-burial dolomite cement: A major component of many ancient sucrosic dolomites. *Sedimentology*, 55, 423-460, 2008.

Frazer, M., Whitaker, F.F., and Hollis, C. Reconstructing Burial Diagenesis in a Post-Rift Regime: The Derbyshire Platform, Northern England. *Proceedings TOUGH Symposium 2012*, LBNL, Berkeley, California, Sept 17-19, 2012.

Lopez D.L. and Smith, L. Fluid Flow in Fault Zones: Analysis of the Interplay of Convective Circulation and Topographically Driven Groundwater Flow. *Water Resources Research*, 31, 1489-1503, 1995.

Paterson, R.J., Whitaker, F.F., Smart, P.L., Jones, G.D. and Oldham, D. Controls on early diagenetic overprinting in icehouse carbonates: Insights from modeling hydrological zone residence times using CARB3D: *Journal of Sedimentary Research*, 78, 258-281, 2008.

GEOCHEMICAL REACTIVE TRANSPORT MODELING IN OIL & GAS INDUSTRY— BUSINESS DRIVERS, CHALLENGES AND SOLUTIONS

Guoxiang Zhang and Esra Inan Villegas

Royal Dutch Shell Exploration & Production Inc.
200 N. Dairy Ashford Rd.
Houston, TX 77079, USA
e-mail: zhang.guoxiang@shell.com

ABSTRACT

Geochemical reactive transport modeling (RTM) offers an integrated approach to understanding the dynamics of physical and chemical processes in the subsurface. It has been considered the most "realistic" approach to investigate coupled physical and chemical processes, such as fluid flow in porous media, phase behavior, and water-rock (WR) interaction through space and time.

Originally developed for environmental studies, early RTM applications inherently focused on thermo-hydro-geochemical (THGC) systems at low temperature and low pressure conditions. In contrast, the oil and gas industry deals with deep, high temperature/pressure/salinity THGC systems (i.e., reservoirs, source rocks and migration paths) to explore and extract hydrocarbons (HC) as well as to dispose of greenhouse gas and waste water. Water, steam, gas (e.g., N_2 and CO_2) or chemicals are commonly injected during HC production, especially for Enhanced Oil Recovery (EOR). Geochemical processes induced by these injections can lead to risks such as injectivity impairment and productivity decline by scaling (mineral precipitation) and/or clay/anhydrite swelling, fluid leakage, and wellbore instability by corrosion (dissolution of minerals) and reservoir souring. RTM is a unique tool that can be used to understand these processes and assess related risks during HC production.

A number of challenges remain for RTM application in the oil and gas industry: (1) pressure and temperature ranges in many fields exceed the range of available thermodynamic data; (2) the presence of hyper-saline reservoir brines requires modeling with dedicated simulators and thermodynamic data; (3) HC has to be considered not only as an additional phase but as a geochemical entity.

Dedicated experimental work and improvement to numerical simulators are needed to overcome these challenges. In the meantime, currently available simulators and thermodynamic data can be used with caution to gain valuable insight. This paper will discuss the business drivers, evaluate the challenges, and propose solutions for applications of RTM technology in the oil and gas industry, using real examples such as water injection, CO_2 injection (CCS or EOR), and water-alternate gas injection (WAG).

BUSINESS DRIVERS

The oil and gas industry typically deals with deep THGC systems at high temperature, high pressure, and high salinity conditions. A broad range of geochemical processes can take place in such systems, including organic processes, i.e., kerogen cracking (KC) and HC transformation, and inorganic processes, i.e., WR interactions. There are also interactions between the organic and inorganic systems: KC and HC transformation are affected by the inorganic system that provides the organic processes necessary conditions such as pH, Eh, salinity and catalytic effects from ionic and mineral compounds (Tannenbaum and Kaplan 1985, and Wei, et al, 2006); On the other hand, products from kerogen cracking can dissolve in water/brine, leading to changes in water/brine chemical composition. HC can coat the mineral surface, impacting mineral dissolution/ precipitation kinetics. During waterflood and enhanced HC recovery (EOR and EGR), water, gases (e.g., N_2 or CO_2), and other chemicals are injected into the reservoir. This fluid injection can lead to property changes in reservoir fluids, mineral dissolution/precipitation, and swelling/ shrinking

of clay and other minerals e.g., anhydrite. These processes can lead to changes in formation porosity and permeability, which can be favorable or unfavorable for HC recovery. Understanding such processes in the THGC systems is very important for evaluation of HC reserves, exploration, and production.

KC and HC transformation are normally simulated using "basin modeling" (BM) technology, which deals with the formation and evolution of sedimentary basins, including burial and thermal histories of the basin, the maturity progression of the source rocks, and the expulsion, migration, and trapping of hydrocarbons. However, processes taking place between kerogen cracking (including HC transformation) and WR interactions have traditionally not been thoroughly and rigorously considered in basin modeling exercises. These processes remain a challenge for basin modeling, in addition to the challenge of complex kinetics within the KC processes.

Normally, BM is conducted in a decoupled sequential manner, i.e., a simulation time step is started from burial calculation, accounting for subsidence and compaction, to simulate pressure distribution, followed by a thermal calculations of given boundary conditions to calculate temperature distribution. The pressure and temperature are then used as given conditions to calculate KC and expulsion with or without consideration of the diffusion process within the source rock. The generated HC is then assumed to migrate through possible pathways "directly" (i.e., no fluid dynamic controls considered) into targeted reservoirs when traps are present, or otherwise lost. BM is presently very comprehensive and robust in dealing with organic geochemical processes of large scale (basin scale) and long elapsed time (geologic time). It is very useful for evaluation of HC resources and helpful in exploration (sweetspotting). However, compared to RTM, it is limited in accuracy and precision, because deterministic principles and mechanisms are omitted to facilitate simulation with restricted computational power.

Reservoir simulation (RS) accounts for the multiphase fluid dynamics in HC reservoirs under isothermal or nonisothermal conditions. Geochemical processes are found, in many cases, as key controls during waterflood and EOR. Modeling the geochemical processes within the reservoir simulation is highly desired. Existing reservoir simulators, however, cannot practically handle the geochemical processes, because most of them have no such capability, while few of them can deal with geochemical systems with a limited number of unknowns, due to the numerical scheme normally deployed (i.e., fully implicit coupling). So far, there are only very limited successful reservoir simulations reported that truly incorporate geochemical reactions.

Reactive transport modeling tracks WR interactions under nonisothermal fluid dynamic conditions. Numerically, thermal, fluid dynamics, and geochemical reactions are all coupled in RTM using a direct substitution approach (DSA, fully implicit), a sequential iteration approach (SIA, implicit), or a sequential non-iteration approach (SNIA, explicitly). Most RTM simulators use SIA and thus can deal with large number of geochemical unknowns—essential for modeling "real" geochemical systems. In addition to WR interactions, KC and HC transformation is also considered in some RTM simulators, although not commonly handled in RTM practice. Geochemical reactions are handled in RTM using deterministic principles, i.e., the first (conservation of mass and energy) and second (mass action) law of thermodynamics. Compared to BM, RTM delivers results with higher accuracy and precision—however, to date, only for problems of a limited scale and time duration, due to restrictions in computational power. Parallel computing technology and the enormous, growing computational power of RTM will eventually bring RTM into problems of sufficient large scale, with reasonable detail in space and time.

Processes in hydrocarbon systems, including KC to generate HC in source rock, expulsion from the source rock, migration in flow paths, trapping in reservoirs and well production—can all be considered appropriate for RTM. Deployment of RTM technology in RS is ongoing. Geochemical processes will likely be well taken into account in future RS practices. Existing RTM simulators, e.g., TOUGHREACT, is still the first choice for modeling geochemical reactive transport of HC systems. Transplanta-

tion of RTM technology into BM, such as fluid-dynamics controls in HC migration, effects of WR interaction on KC, and the effects of KC on WR interaction, would be a great step forward for BM.

Theoretically, RTM can be conducted for systems of different scales (from basin, reservoir, well, core, to pore scale) and different time durations (from geologic to fractions of seconds), over a wide range of temperatures (nominally, up to 330°C or higher) and pressure (theoretically up to 5,000 bars or higher) depending on the availability of the required thermodynamic data of the T&P range. Data from oil and gas exploration, such as seismic, well logs, core analysis/measurements, fluid samples, and production logs, can all be utilized to construct an RTM. Appropriately designed RTMs can describe the interactions of competing processes at a range of spatial and time scales, and hence are critical for connecting the advancing capabilities for material characterization at the atomic scale, with the macroscopic behavior of complex earth systems (Steefel et al., 2005).

RTM numerical simulators have been developed over the last 20 years and have gradually been adopted by the oil and gas industry, through technology transfer or development inside the industry. TOUGHREACT (Xu et al., 2006; 2011) has been transferred to many organizations globally, including a number of major or independent oil companies. Applications with TOUGHREACT are rapidly increasing, and the user community has grown, leading to significant contributions in the oil and gas industry in multiple ways, such as reservoir characterization (Xiao and Jones, 2006), enhanced oil recovery (Zhang and Taberner, 2009) and disposal of greenhouse gas (Xu et al., 2005; Pruess and Muller 2009 and Zhang et al., 2010).

In the oil and gas industry, the development of an RTM simulator has been carried out by normally, adding a geochemical solver into an existing reservoir simulator. Examples are CMG-GEM, Shell's MoReS-PHREEQC and GPRS (Fan, 2012) among a few others. This type of simulator will become mature if more applications can be successfully performed with it.

Limitations to RTM remain when dealing with a complex THGC system of large scale and long time duration, such as the proper treatment of coupled HC and WR system. Consideration of increasing complexity (coupling organic and inorganic systems) in RTM will require finer spatial resolution (more gridblocks), handling large numbers and different mechanisms of reactions over a long time period, i.e., geological time (thousands to millions of years) and thermodynamic database expansion. Numerical simulators accounting for such a coupled HC and WR system have not yet been achieved; their development is of great interest to the oil & gas industry. Temperature and pressure ranges of hydrocarbon systems are normally wider than that of other systems e.g., shallow groundwater systems. Thus, modeling coupled HC and WR systems requires sufficient data to cover wider T&P ranges. Currently available thermodynamic data do not cover these ranges. Dedicated experiments to this end are desired, and some are ongoing.

In the present paper, RTM challenges and possible solutions are discussed using some real examples, in addition to the business drivers discussed above.

CHALLENGES AND SOLUTIONS

Effects of high temperature, high pressure, high salinity and HC phases on geochemical processes

The pressure in typical HC reservoirs ranges from 100 to 30,000 psi (7–2070 bar). Temperature ranges between 10°C and 260°C (500 F) although most oil reservoirs are below 150°C and gas reservoirs below 250°C. Nevertheless, reservoirs can be heated up to 350°C or higher during *in situ* upgrading processes (IUP), *in situ* combustion processes (ICP) and thermal EOR. Water, steam, and/or gases are typically injected during EOR processes. Geochemical reactions induced at high temperature can have significant effects, such as souring due to H_2S generation from thermochemical reduction of sulfates (TSR) (Zhang et al., 2007), CO_2 generation from thermal decomposition of carbonates, scaling from enhanced precipitation of minerals under high temperature, and deformation from swelling/shrinking of clay and anhydrite. RTMs that can track these effects are highly desired, to

help understand these processes and evaluate the relevant risks. Effects of high pressure and high temperature on geochemical reactions must be considered when RTM is performed to properly characterize reservoir properties and evaluation of HC generation, migration, trapping and production.

HC coexists in reservoirs with high salinity water (brine). Salinity of reservoir brines, normally quantified using total dissolved solids (TDS), ranges from 10,000 ppm, translated to about 0.15 molal (*m*) of NaCl-equivalent ionic strength (*I*) up to 280,000 ppm (~1–6 m) or higher. A Na-Mg-Ca-Cl brine (Brine-1 in Table 1) was found from a Middle East carbonate reservoir having a salinity of about 382 g/L (*I* >10 *m*), and halite-saturated. A Na-Mg-Cl brine (Brine-2) was found in a reservoir hundreds of kilometers away from Brine-1, at about 375g/L and halite-saturated. Na-Mg-Ca-Cl or Na-Mg-Cl brine at halite saturation are frequently found in Middle East reservoirs, while halite-saturated Na-Cl type brines are common in HC reservoir and deep saline aquifers (e.g. Brine-3) in the North America basins such as the Gulf of Mexico and Alberta, Canada.

Table 1. Hypersaline brines found from HC reservoirs and saline aquifers (concentration in molality)

Component	Brine-1	Brine-2	Brine-3
Formation	dolostone	carbonate	sandstone
T (°C)	80	127	64
Density (kg/l)	1.28 at 33°C	1.22	1.19
TDS(g/l)	382	375	338
PH	3.8	5.6	5.9
Na^{+}	2.81	4.71	5.54
Ca^{+2}	1.18	1.7	0.056
Mg^{+2}	1.34	0.24	0.043
Fe^{+2}	9.0E-06	N.D.	5.88E-05
Ba^{+2}	N.D.	N.D.	4.08E-06
Sr^{+2}	N.D.	N.D.	4.98E-04
K^{+}	N.D.	0.135	3.46E-02
Cl^{-}	7.64	7.20	6.28
SO_4^{-2}	0.11	0.11	2.19E-02
HCO_3^{-}	N.D.	4.72E-06	1.38E-03
CO_3^{-2}	N.D.	N.D.	N.D.

N.D.: not detected or very low concentration

The origins of these brines have not been thoroughly investigated, although they are believed to be related to the adjacent salt deposition. Enrichment in Ca and/or Mg indicates that the brines or the related salt/evaporites must have been gone through an extreme evaporation as modeled in Zhang et al., (2009).

Simulations involving such hypersaline brines are required to deal with the short-distance ionic interactions using dedicated ionic activity models. Pitzer ion-interaction model (Pitzer, 1979; 1991 and Harvie et al., 1984) is normally used with proper ion–interaction parameters available for the P&T range, consistent with the thermodynamic equilibrium constants (K and usually given in form of log i.e. logK) used. The challenge is that the required ion–interaction parameters are not fully available for these P&T ranges. Compromise must be made, and thus uncertainties remain before appropriate data become available. Careful evaluation is highly recommended when using the current thermodynamic data under high-pressure, high-temperature and high-salinity conditions.

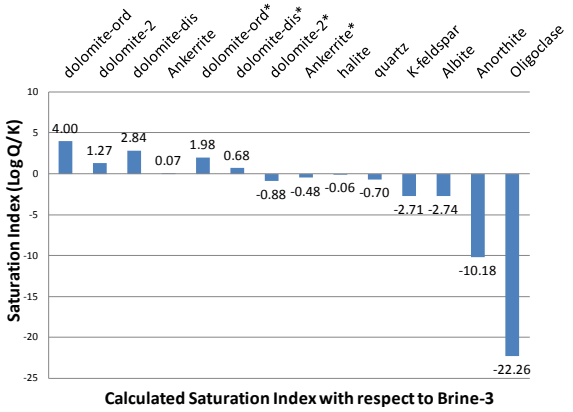

Figure 1. Calculated saturation indices of dolomite minerals with respect to brine-3 on Table 1, using logK data from the TOUGHREACT database *TherAkin8.dat* and Pitzer ion interaction parameters from EQ3/6 Pitzer database *data0.ypf R2*.

As an evaluation example, calculated saturation indices (SI) of dolomite and other minerals with respect to brine-3 using different sets of thermodynamic equilibrium constants are compared in Figure 1. Different sets of thermodynamic equilibrium constants are represented by the name of "*dolomite-ord*" (ordered dolomite), "*dolomite-dis*" (disordered dolomite), and "*dolomite-2*" (representing a validated LogK value data set using measured data, Birkholzer et al., 2008; and Zheng et al., 2009), respectively. Along with these three sets of LogK's, Pitzer

ion–interaction parameters from Alai et al. (2005) have been used (*data0.ypf.r2*). Calculated saturation indices with most of these data are far higher than zero, which is not realistic because there is no dolomite detected in that formation (SEM and XRD measurements). Instead, an iron-rich dolomite, ankerite is present and the calculated SI of ankerite is just about zero, indicating this mineral is in equilibrium with respect to the brine. Based on the same logic, calculated SI of other dolomite members should be negative or close to zero, because of the absence of this mineral from the formation. In fact, only one set of logK data—the data represented by the name of *dolomite-2** assuming the brine is in equilibrium with respect to all major aluminosilicate phases of the formation—can derive a realistic SI, i.e., negative value (see column under caption *dolomite-2** in Figure 1). This test verifies that the logK data set represented by *dolomite-2* in the TOUGHREACT database *TherAkin8.dat* is the best data for dolomite under the high-salinity conditions of this case.

Calculated SI of halite is just about zero, representing reality. The SI of quartz is slightly below zero—still believed realistic because as the dominant mineral, quartz undergoes very slow dissolution. SI's of major aluminosilicate phases in the formation are all negative, because the measured aluminum concentration is not realistic and assumptions of equilibrium or realistic thermodynamic status on one or more major aluminosilicate phases must be made to better simulate the brine-rock system.

The calculated SI of dolomite with respect to brine-1 in Table 1 stays negative (< -5) under the measured reservoir CO_2 partial pressure, no matter which set of the data is used. This situation implies uncertainties in the thermodynamic equilibrium constants ion–interaction parameters, the consistencies of logK and ion–interaction parameters, T- and P- dependence of all parameters at the hypersaline condition, and of course, possible uncertainties in measurements.

The temperature dependence of logK is commonly incorporated into most geochemical simulators. The temperature range of the thermodynamic database of PHREEQC (Parkhurst, and Appelo, 1999) is 0–60°C and that of EQ3/6 (Wolery and Daveler, 1992) is 0-300°C. Most of others lie between. Uncertainties in the temperature dependence of logK have been evaluated (André, et al., 2006); they are believed to be the most significant source of uncertainty in most thermodynamic databases. Similar evaluations have been done on the ion-interaction parameters from Alai et al. (2005) (Zhang and Sturmer, 2011). Uncertainties in the T-dependence significantly impact model results.

Pressure-dependence of logK is generally less than the T-dependence. For pressure variation less than 10 bars, logK can be assumed to be P-independent. For example, Sawamura (2007) studied halite solubility and found that for constant temperatures 37°C, solubility increases from 6.13 *m* at 1 bar, to 6.38 *m* at 500 bar, 6.41 *m* at 1000 bar, 6.61 *m* at 2,000 bar and 6.69 *m* at 3,000 bar. In addition, Morse and MacKenzie (1990), in studying the pressure dependence of CO_2 solubility, found that the equilibrium constant of CO_2 dissolution in pure water changes 0.31 log units, near-linearly, when pressure increases from 1 bar up to 600 bar at constant temperature. However, this value changes 0.27 log units, from 0°C to 25°C, at constant pressure.

These examples illustrate the strong dependence of logK on temperature and weak dependence on pressure. Temperature dependence in an HC system can never be ignored, while pressure dependence can be omitted if pressure variation is not very large and the logK's are calibrated for that pressure range.

Handling high-salinity brines requires not only an appropriate ionic activity model, but also considering the effects on other reactions, such as cation exchange and sorption. Simulation of the geochemical steady-state condition of a high salinity WR interaction system of an Eocene formation (smectite-dominated clay and quartz sandstone interlayer at I ~3 m) requires calibrating the cation exchange selectivity coefficients to the high-salinity conditions. The calibrated values deviate from the normal ranges of literature values used in Zheng et al. (2009) (Table 2) although the mechanism causing the salinity dependence of the selectivity coefficient has not been thoroughly investigated. A new constitutive cation exchange model is needed to account for the salinity effects on cation exchange.

Table 2. Calibrated selectivity coefficients (Gaines-Thomas convention) to high salinity condition and literature value available to low salinity condition (typically $I < 0.1$ m)

Cation	Value calibrated to high salinity	Value available to low salinity
Master	H^+	Na^+
H^+	1.00	1.00
Na^+	0.24	1.00
Ca^{+2}	0.76	0.40
Mg^{+2}	0.88	0.45
K^+	0.27	0.20
Ba^{+2}	0.46	0.35
Sr^{+2}	0.45	n/a

Generally speaking, an RTM involved in problems of high-salinity brine under high P and high T conditions needs to carefully select an ionic activity model and evaluate the thermodynamic data including ion-interaction parameters, as well as the consistency of the parameter sets. Calibration is strongly recommended to reduce the uncertainties.

High-salinity conditions may also be encountered in other situations in an HC system, such as cement corrosion leading to wellbore degradation, especially when CO_2 is injected for the purpose of geological sequestration and/or EOR. RTM of cement corrosion has not been much studied, but still ought to attract attention from both experimental and modeling aspects.

Effects of HC phase on geochemical reactions

As discussed above, HC affects WR systems through dissolution of HC components, such as organic acids. Geochemical modeling of these reactions is not challenging from a numerical perspective; however, not many examples exist. In addition, the HC phase can act as a barrier to WR interaction by coating the solid surface. This effect reduces the effective surface area of minerals for dissolution and precipitation, and can impose a saturation window (Xu et al., 2006). For example, calibrated effective specific surface area of minerals in the same Eocene formation (I ~3 m and oil saturation 40–80%) is 3 to 5 orders of magnitudes lower than the normal ranges of literature values (Table 3).

Table 3. Calibrated effective surface area (cm^2/g) of minerals (along with kinetic rates from Palandri & Kharaka, 2004) to account for the effects of HC coating in dissolution and precipitation and compared to literature values

Mineral	Calibrated to account for the HC effect	Initial Estimate based on SEM	Ranges of literature value*
Quartz	0.255	1.132	$10\text{-}10^4$
K-feldspar	0.185	1.0	$10^2\text{-}10^3$
Albite	0.185	1.2	$10^2\text{-}10^3$
Smectite	55.23	1008	$10^5\text{-}10^7$
Illite	10.22	431	$10^5\text{-}2x10^6$
Muscovite	32.25	1000	$10^4\text{-}3x10^4$
Kaolinite	8.03	560	$10^4\text{-}10^5$
Chlorite	18.1	1000	$10^3\text{-}10^5$
Pyrite	1.992	1.1	$10^3\text{-}10^4$

*Literature values are from Yuang and Shen (2005), Xu et al. (2009), Hamilton et al. (2000), Gaines (1957), Zhou and Gunter (1992), Aylmore et al. (1970), Chirita (2003), and Wolfe et al. (2007), and some of the reference therein.

The coating effects of HC in WR interaction, also characterized as "wettability" in the industry, are complex, and normally a function of phase saturation. There is so far no appropriate relationship useable in the RTM. Developing such a model to actually simulate HC wettability effects on mineral dissolution and precipitation remains a challenge.

Effects of geochemical processes on injectivity and productivity

Charged by injection or extraction of fluid and heat, the near-wellbore region experiences more significant geochemical processes. The major drivers are (1) changes in temperature and pressure, (2) mutual solubility of fluid phases, e.g., injected CO_2 evaporates into formation water, and (3) incompatibility of injection fluid and formation fluids, e.g., contrasts in pH and/or Eh between the injected water and the formation water during waterflood and hydraulic fracturing. Results of associated geochemical reactions are (1) drastic changes in water chemical composition, leading possibly to fluid dynamic property changes, corrosion potential to wellbore, and clay swelling; and (2) changes in porosity and permeability due to dissolution and/or precipitation of minerals/salts and clay swelling/shrinking. Effects of these geochemical

reactions become key issues in risk assessment for HC extraction and CCS projects.

Injection of large amounts of water or gas (mainly CO_2) into an HC reservoir for water-flood or enhanced oil/gas recovery will induce precipitation of minerals, mainly calcite, if the injected water (normally seawater with pH >8.0) is geochemically "incompatible" with the formation water (normally hypersaline with pH ~6 or lower). Precipitation of other minerals (e.g., barite) also contributes to scaling. Scaling is normally modeled using batch geochemical simulators in the industry, such as "Geochemist Workbench" (Bethke and Yeakel, 2012) and Oli "ScaleChem" (2011). Batch calculations cannot give results with spatial variation; nevertheless, the spatial variation is very important for evaluation of scaling potential.

RTM is the right tool to predict mineral dissolution and precipitation in a given time- and space-domain. Variation in time and space are well tracked in RTM simulations. The strong capability of RTM becomes better recognized in the production geology and production technology communities.

TOUGHREACT RTM results show that, during a 20-year waterflood of a hypersaline reservoir using untreated seawater, precipitated calcite will accumulate at the wellbore in significant amounts, causing a volume-averaged porosity reduction in the near-wellbore region, about 2 porosity units (0.02) at the end of the injection, while barite will precipitate at the moving front of the injected seawater and will not be accumulated at a single location.

Injection of CO_2 into a saline aquifer for CCS or saline reservoir for EOR can induce precipitation of halite within a dryout zone near the wellbore, due to the solubility of water in CO_2. The precipitated salt will be accumulated at the moving dryout front, while dissolved salt is supplied by imbibition flow of formation brine from an outer brine-CO_2 mixing zone. This type of process has been simulated using TOUGHREACT-Pitzer (Zhang et al., 2006) for several applications (Zhang et al., 2011). A recent such model effort has been carried out on a sandstone aquifer of halite-saturated brine (brine-3 in Table 1) at 64°C and 2100 m deep. Model-predicted salt precipitation accumulates at the dryout front, up to 70 kg/m^3, higher than the salt contained in the in-place brine, because the imbibition brings salt back toward the dryout front where salt precipitates. Salt has been observed precipitating at the inlet of a similar sandstone core with similar brine while injecting supercritical CO_2 in a lab experiment (Wang et al., 2010). This observation is consistent with the effects of imbibition on salt precipitation observed from the RTM results.

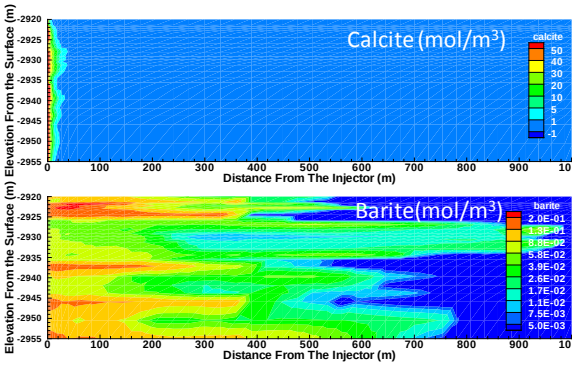

Figure 2. TOUGHREACT RTM predicted accumulative precipitation (mol/m^3 rock) of calcite and barite during 20-years injection of seawater into a hypersaline oil reservoir for secondary oil recovery. Note that the injector is on the left on the figure.

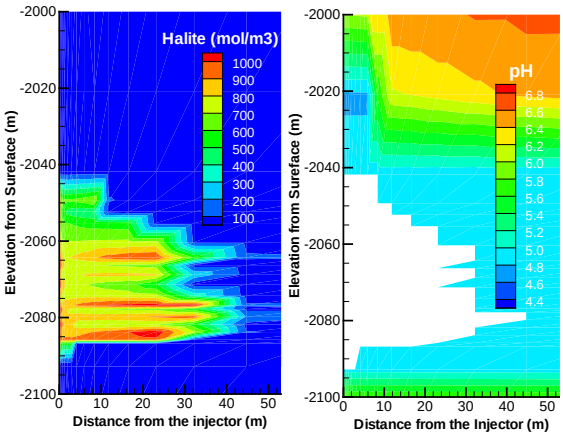

Figure 3. TOUGHREACT RTM predicted halite precipitation and pH at the end of a 25-year injection of CO_2 into a sandstone formation for storage. Blank area represents the near-wellbore dryout zone. Note that the injector is on the left of the figure.

Such a large amount of salt precipitation will likely clog pores, leading to injectivity impairment. Model results indicate that salt will

preferably precipitate in high-permeability layers (Figure 3), tending to even out the permeability over the dryout zone. This phenomenon can be verified by some experimental observations, i.e., during a coreflood experiment, salt first precipitates within the fracture or pore space (Wang et al., 2010) although the hypothesis of salt preferably precipitating at the pore throat has also been accepted by some investigators. However, it is a complicated situation, because in reality, the distribution of salt can also be affected by the injection rate, i.e., CO_2 flux. But, the mechanism that the CO_2 velocity affects the salt distribution is not known. Permeability changes as a function of porosity change adds another challenge, although various models have been suggested and implemented (Pruess et al., 1999). Still, much more efforts in pore or nanoscale research are very much welcomed.

Injectivity/productivity issues can also arise when clay swells during the injection of low-salinity water into a high-salinity formation. Clay swelling can be accounted for in TOUGHREACT, but in a pragmatic way, calculating the porosity change due to clay swelling as an empirical function of salinity. The Gouy-Chapman diffuse-double-layer theory (Wayllace, 2008 and Zheng et al., 2011) considers the chemical controls of water activity and the hydration process of clay interlayer, and calculates the excess pressure (called swelling pressure) caused by the hydration of the interlayer. If coupled with a geomechanical simulator, clay swelling can be better simulated in support of evaluation of well injectivity, productivity, and stability. We hope that this model can be available soon in TOUGHREACT.

A Scheuerman diagram (Scheuerman and Bergersen, 1990) is often used to evaluate the swelling potential of a given clay mineral in contact with a water of known chemical composition. The swelling potential of the given clay mineral is evaluated in a two-dimensional Cartesian domain defined by concentration of total cations (as the Y-axis) and the fraction of divalent cations over total cations (as the X-axis). Giving the chemical composition, water can be mapped on a diagram of a given clay; therefore, the combination of water and clay can be qualitatively evaluated as Zone A, "compatible," meaning no risk of swelling; Zone B, "impairing," meaning a risk of definite swelling, Zone C, "acceptable," meaning slight swelling but not a showstopper, and Zone D, "need more data," meaning the swelling potential cannot be evaluated using this diagram, and more data and more studies are needed, i.e., the swelling risk can no longer be simply viewed as a function of salinity and the ion ratio of the water.

One example is given in Figure 4 for evaluating a clay swelling risk using the Scheuerman diagram, for a case of injecting low-salinity water (I <0.04 m) into a high-salinity reservoir (I ~3 m). Water chemical composition was predicted using a TOUGHREACT RTM, considering the injection of the low-salinity water, mixing with the high-salinity formation brine, dissolution and precipitations of relevant minerals, and, most importantly, cation exchange.

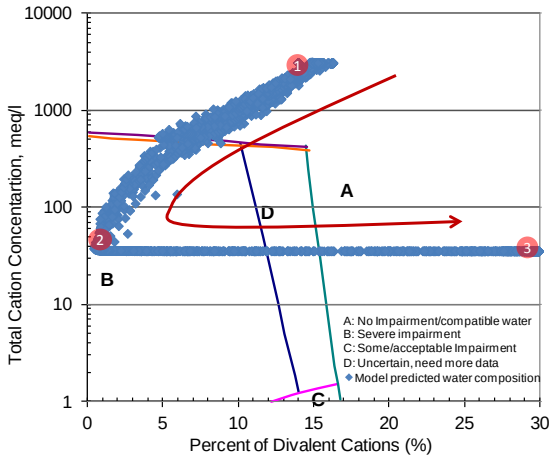

Figure 4. Mapping TOUGHREACT RTM predicted water composition of the whole domain and duration of injection of a low salinity water into a high salinity reservoir on Scheuerman diagram for evaluation of smectite swelling potential.

Both injected low-salinity water and the high-salinity formation brine are located within Zone A (1 and 3), no swelling. However, water composition at a given location through which the injected low salinity water will pass evolves from the initial composition of formation brine into a final composition defined by the equilibrium between the injection water and the formation rock. In between, water composition is transient (e.g., 2) and characterized by

coupled mixing, cation exchange, and mineral dissolution/precipitation under the injection conditions. However, water 2 falls within Zone B, where there is high potential of swelling. The transient water moves away from the injector wellbore. Swelling in the formation can enhance productivity by pressurizing the reservoir, if sufficient effective permeability can still be maintained and the swelling does not take place at or very close to the wellbore. Results of this study can be used to optimize well placement towards maximum productivity.

The coupling between the swelling and flow had to be omitted in the RTM because there is no such capability in the current version of TOUGHREACT. In some other cases, challenges have also arisen because clay is found to swell when CO_2 is involved. The mechanism has not been outlined; it deserves attention from a scientific perspective.

Effects of geochemical processes on wellbore stability

Wellbore instability can be caused by corrosion of wellbore (casing and cement) and near-wellbore rock. Injection of CO_2, other acid gas, or waste waters for geological storage or EOR can significantly acidify the near-wellbore region and lead to corrosion.

In the case of CO_2 injection, a dryout zone can form at the near-wellbore region as long as the CO_2 under injection is dry, as discussed above. Theoretically, a dryout zone around the wellbore can prevent the acid fluid from reaching the wellbore, protecting it from corrosion. However, in reality, the dryout zone barrier cannot be as effective as expected because: (1) residual brine is present in pore spaces after the "dry" CO_2 equilibrates the chemical potential of water with the water chemical potential (i.e., water activity) in the residual brine; and (2) low-permeable layers hold water much longer because of their high capillarity. Even if the adjacent high-permeable layer is dried out, CO_2 from the adjacent 'dryout' layers acidify the low-permeable layers. In particular, the top and bottom seals that are contacting the wellbore always stay wet (see right plot on Figure 3), resulting in a high risk of corrosion. Wellbore cement can be quickly corroded at the contacts of low-permeable layers.

Strong dissolution of near wellbore formation rock can lead to a cavity loosing up the well-bore. This type of incident has in the past taken place in carbonate reservoirs, especially when CO_2 or other acid gases are injected.

RTM is useful in predicting corrosion of the wellbore and dissolution of near-wellbore rock. In addition to the challenge of high-T, high-P and high salinity, RTM must account for cement-concrete. An RTM that incorporates formation rock and wellbore cement will be an ideal model. Successful examples of such models have not been reported for the oil and gas industry, although some RTM development holds promise in this regard (Huet et al., 2010).

A water-alternate-gas (WAG) injection in a carbonate (chalk) reservoir as an EOR scheme was modeled using TOUGHREACT-Pitzer (Figure 5). The WAG involves injection cycles of seawater and CO_2, alternatively, starting with a 15-year injection of seawater, followed by a 2-year injection of CO_2 and then a 2-year injection of seawater. Alternate injection of seawater (again for 2 years) and CO_2 (again for 2 years) continues until the end of field life.

During the 15-year injection of seawater, the seawater displaces 30–40% of the oil at the near-wellbore (injector) region (a zone extending from the injector wellbore to ~100 m away from the injector, top part of Figure 5), especially, within the high-permeable layers. The subsequent 2-year CO_2 injection acidifies the previously injected seawater, leading to calcite dissolution. The dissolution is strongly enhanced when the subsequent 2-year seawater injection is followed, because (1) more water is available and (2) dissolved carbonates are transported away from the near-wellbore region. The largest dissolution of calcite takes place during the 2-year seawater injection following the 2-year CO_2 injection, leading to increased porosity in the near-wellbore zone of about 4 units (i.e., 4% of the total rock volume).

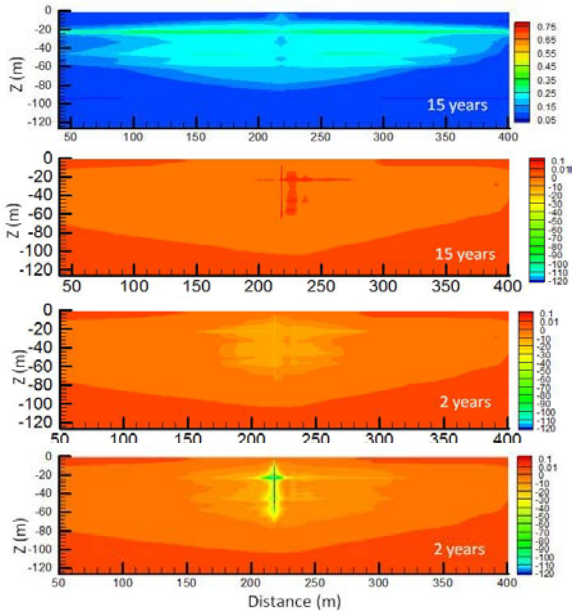

Figure 5. TOUGHREACT RTM predicted swap efficiency (shown as water occupied porosity in the top figure) and change of calcite abundance on the second figure from the top (in mol/m^3 of rock, positive for precipitation) at the end of a 15-year seawater injection, and the change in calcite abundance after the subsequent 2-year CO_2 injection (third) and after the following 2-year seawater injection (bottom), respectively. Injector is located in the middle, producer is at the right, and the left boundary is open.

CONCLUDING REMARKS

Geochemical RTM can contribute significantly to the understanding of HC systems, from exploration to production. Challenges for RTM application in the oil and gas industry are mainly from high-T, high-P and high-salinity conditions, and involvement of HC as both fluid phases and chemical components. Dedicated experimental work and improvement of numerical simulators are needed. Currently available simulators and thermodynamic data should be used with caution, and model calibration is strongly recommended.

ACKNOWLEDGMENT

Our colleagues, Dr. Conxita Taberner, Dr. Cor Kuijvenhoven, Dr. Lee Morgenthaler, and Dr. Mario Winkler are acknowledged for their involvement and support in the work presented here. We also thank Dr. Yaqing Fan, Dr. Klaus Leischner, and Dr. Paul Taylor for Shell internal review.

REFERENCES

Alai, M., M. Sutton, and S., Carroll, Evaporative evolution of a Na-Cl-NO_3-K-Ca-SO_4-Mg-Si brine at 95°C: experiments and modeling relevant to Yucca Mountain, Nevada: Geochemical Transactions, vol.6:31-45, 2005.

Aylmore, L., I. Sills and J. QUIRK, surface area of homoionic illite and montmorillonite clay minerals as measured by the sporption of nitrogen and carbon dioxide, *Clays and Clay Minerals*, 1970, vol. 18: 91-96, 1970.

Bethke C. and S. Yeakel, The geochemist Workbench, release 9.0, Reference Manual, Aqueous Solutions LLC, Champaign, IL 61820 USA, 2012.

Chirita, P., Kinetics of aqueous pyrite oxidation by potassium dichromate - an experimental study, *Turk J Chem*., vol 27:111–118, 2003.

Dubois, I., S. Holgersson and S. Allard, Correlation between particle size and surface area for chlorite and K-feldspar, in Water-Rock Interaction – Birkle & Torres-Alvarado (eds) 2010 Taylor & Francis Group, London, ISBN 978-0-415-60426-0, 2010.

Fan, Y., Durlofsky, L.J., Tchelepi, H., "A fully-coupled flow-reactive-transport formulation based on element conservation, with application to CO_2 storage simulations." *Advances in Water Resources*, vol42:47-61, 2012.

Gaines, G. The ion-exchange properties of muscovite mica, *J. Phys. Chem.*, vol *61* (10): 1408–1413, DOI: 10.1021/j150556a033, 1957.

Hamilton, J., C. Pantano, and S. Brantley, Dissolution of albite glass and crystal, *Geochimica et Cosmochimica Acta*, vol. 64(15): 2603–2615, 2000.

Harvie, C., N. Møller, and J. Weare, The prediction of mineral solubilities in natural waters: the Na-K-Mg-Ca-H-Cl-SO4-OH-HCO_3-CO_3-CO_2-H_2O system to high ionic strengths at 25°C. *Geochim. Cosmochim. Acta*, vol. 48:723-751, 1984.

Huet, B. J. Prevost, G. Scherer, Quantitative reactive transport modeling of Portland

cement in CO_2-saturated water, *International Journal of Greenhouse Gas Control*, vol. 4:561-574, 2010.

Morse J., F. MacKenzie, "Geochemistry of Sedimentary Carbonates", Elsevier, New York, pp. 707, 2002.

Oli, Oli ScaleChem, Version 4.1, Oli System, Inc., Morris Plains, New Jersey 07950 USA, 2011.

Palandri, J., and Y. Kharaka, A compilation of rate parameters of water-mineral interaction kinetics for application to geochemical modeling, USGS, open report, 2004-1068, 2004.

Parkhurst, D. L., and Appelo, C. A. J., User's guide to PHREEQC (Version 2)- a computer program for speciation, batch-reaction, one-dimensional transport, and inverse geochemical calculations. U.S. Geological Survey, Water-Resources Investigations Report 99-4259, Denver, Colorado, 1999.

Pitzer, K. S., Thermodynamics of electrolytes, 1, Theoretical basis and general equations, *J. Phys. Chem.*, vol.77: 268. 1973.

Pitzer, K., Ion interaction approach: Theory and data correlation. *In Activity Coefficients in Electrolytes Solutions*, edited by K. Pitzer, 2nd ed., CRC Press, vol.75, 1991.

Pruess, K., C. Oldenburg, and G. Moridis, TOUGH2 User's Guide, Version 2.0, Report LBNL-43134, Lawrence Berkeley National Laboratory, Berkeley, Calif., 1999.

Pruess, K. and N. Müller, Formation Dry-Out from CO2 Injection into Saline Aquifers: 1. Effects of Solids Precipitation and their Mitigation, *Water Resour. Res.*,vol.45, W03402, doi:10.1029/2008WR007101, 2009.

Scheuerman, R., B. Bergersen, Injection-Water Salinity, Formation Pretreatment, and Well-Operations Fluid-Selection Guidelines, *SPE 18461*, 1990.

Steefel, C., D. DePaolo, P. Lichtner, Reactive transport modeling: An essential tool and a new research approach for the Earth sciences, *Earth and Planetary Science Letters*, vol. 240:539–558, 2005.

Tannenbaum, E, and I. Kaplan, Role of minerals in the thermal alteration of organic matter--I: generation of gases and condensates under dry condition. *Geochim Cosmochim Acta.*, vol. 49:2589-604, 1985.

Wang, Y., T. Luce, C. I. Ishizawa, M. Shuck, K. Smith, H. Ott, and M. Appel, Halite Precipitation and Permeability Assessment during Supercritical CO_2 Core Flood, *SCA 2010 International Symposium Proceeding*, paper SCA 2010-18, Halifax, Canada, 2010.

Wayllace, A., Volume change and swelling pressure of expansive clay in the crystalline swelling regime, PhD dissertation, University of Missouri, 2008.

Wei, Z., J. Moldowan, J. Dahl, T. Goldstein, D. Jarvie, The catalytic effects of minerals on the formation of diamondoids from kerogen acromolecules, *Organic Geochemistry*, vol. 37:1421-1436, 2006.

Wolery, T., and Daveler, S., EQ6, A computer program for reaction path modeling of aqueous geochemical systems: theoretical manual, user's guide, and related documentation (version 7.0): *Lawrence Livermore National Laboratory*, report no. UCRL-MA-110662 PT IV, 1992.

Wolfe, A., R. Liu, B. Stewart, R. Capo1 and D. Dzombak, A method for generating uniform size-segregated pyrite particle fractions, *Geochemical Transactions*, vol. 8:9 doi:10.1186/ 1467-4866-8-9, 2007.

Xiao, Y. and G. Jones, Reactive Transport Modeling of carbonate and siliciclastic diagenesis and reservoir quality prediction, *SPE*, ISBN 978-1-55563-173-4, DOI: 10.2118/ 101669-MS, 2006.

Xu, B., C. Wingate and P. Smith, The effect of surface area on the modelling of quartz dissolution under conditions relevant to the Bayer process, *Hydrometallurgy*, vol. 98 (1–2): 108–115, 2009.

Xu, T., J. Apps, and K. Pruess, Mineral sequestration of carbon dioxide in a sandstone-shale system, *Chemical Geology*, vol. 217(3-4): 295-318, 2005.

Xu, T., Sonnenthal, E., Spycher, N., and Pruess, K., TOUGHREACT—A Simulation Program for Non-Isothermal Multiphase Reactive Geochemical Transport in Variably Saturated Geologic Media: Applications to Geothermal Injectivity and CO_2 Geological Sequestration. *Computers & Geosciences*, vol. 32(2):145–165.doi:10.1016/j.cageo.2005.06.014, 2006.

Xu, T., N. Spycher, E. Sonnenthal, G. Zhang, L. Zheng and K. Pruess, TOUGHREACT

Version 2.0: A simulator for subsurface reactive transport under non-isothermal multiphase flow conditions. *Computers & Geoscience*, vol. 37 (2011): 763–774, 2011.

Yuang, P-C., Y-H. Shen, Determination of the surface area of smectite in water by ethylene oxide chain adsorption, *Journal of Colloid and Interface Science*, vol. 285: 443–447, 2005.

Zhang, G., Spycher, N., Xu, T., Sonnenthal, E., and Steefel, C., Reactive geochemical transport modeling of concentrated aqueous solutions: supplement to TOUGHREACT user's guide for the Pitzer ion-interaction model: Lawrence Berkeley National Laboratory report, LBNL-62718, Berkeley, California, 42 p, 2006.

Zhang, G. and C. Taberner, Reactive Transport Modeling Study of a WAG Cycle in the Dan-Half Dan Danish Chalk Reservoir, Shell, EP 2009-5514, 2009.

Zhang G., N. Spycher, E. Sonnenthal and C. Steefel, Modeling acid-gas generation from boiling chloride brines, *Geochemical Transactions* 2009, vol. 10:11, doi:10.1186/1467-4866-10-11, 2009.

Zhang, G. and D. Sturmer, Development of a Shell in-house geochemical database for reactive transport modeling in CO_2 storage and oil recovery applications -Phase I Report, *Shell*, SR.11.10146, 2011.

Zhang, G., C. Taberner, L. Cartwright and T. Xu, Injection of Supercritical CO_2 Into Deep Saline Carbonate Formations: Predictions From Geochemical Modeling, *SPE Journal*, Vol. 16, No: 4, pp 959-967, 2011.

Zhang, T., G. Ellis, K. Wang, C. Walters, S. Kelemen, B. Gillaizeau, and Y. Tang, Effect of hydrocarbon type on thermochemical sulfate reduction, Organic Geochemistry, vol.38(6): 897–910, 2007.

Zheng, L., H.H. Liu, J. Houseworth, J. Birkholzer, Evaluating the geochemically induced swelling/shrinkage of the near-field host clay rock using a THC model and the Gouy-Chapman diffuse double layer theory, NE/NW Program Meeting, July 6, 2011.

Zheng, L. J. Apps, Y. Zhang, T. Xu, J. Birkholzer. On mobilization of lead and arsenic in groundwater in response to CO2 leakage from deep geological storage. *Chemical geology*, doi:10.1016/j.chemgeo.2009.09.007, vol.268 (3-4):281-297, 2009.

Zhou, Z. and W. Gunter, The nature of the surface charge of kaolinite, *Clays and Clay Minerals*, Vol. 40 (3):365-368, 1992.

Geologic Carbon Sequestration

MODELING THE GEOCHEMICAL IMPACT OF AN INJECTION OF CO_2 AND ASSOCIATED REACTIVE IMPURITIES INTO A SALINE RESERVOIR

Laurent ANDRE[1], Mohamed AZAROUAL[1], Christian BERNSTONE[2], Andrea WITTEK[2]

[1]BRGM - Water, Environment and Ecotechnology Direction,
Avenue Claude Guillemin, BP 36009, F-45060 ORLEANS Cedex 2 - France
[2] VATTENFALL, Research and Development AB, Puschkinallee 52, 12435 BERLIN – Germany
e-mail : l.andre@brgm.fr; m.azaroual@brgm.fr; christian.bernstone@vattenfall.com; andrea.wittek@vattenfall.de

ABSTRACT

Numerical simulations performed with the TOUGHREACT code focus on the chemical reactivity of deep reservoir rock impacted by an injection of CO_2 and associated reactive impurities (mainly SO_2 and O_2). A simplified two-dimensional radial geo-model representing the near wellbore domain of a saline reservoir enabled us to capture the global geochemical behaviour of this underground zone. Two ratios CO_2/SO_2 are investigated. The results of the numerical simulations highlight the high reactivity of the near-well zone in the case where ancillary gases (SO_2 and O_2) are injected with CO_2 with dissolution of carbonates and precipitation of sulfate minerals. Major reactions occur in the reservoir formation, whereas clays of the caprock are only slightly affected by the injection of CO_2 and associated reactive impurities.

INTRODUCTION

Numerical simulations using coupled hydrogeological, thermal, and geochemical codes as TOUGHREACT (Xu and Pruess, 2001) serve as adequate tools to explore different evolution scenarios of gas injection in deep geological structures, and to determine the behavior of the near-wellbore region of the targeted reservoir. Previous numerical studies have demonstrated that massive and continuous injection of pure CO_2 involves a disequilibrium of the physical characteristics (temperature, gas saturation, pressure, capillary pressure…) and geochemical characteristics (dissolution of supercritical CO_2 into the brine, pH variations, dissolution/ precipitation reactions of the porous rock minerals) of the host reservoir (André et al., 2007, 2010).

However, the presence of impurities in the CO_2 gas stream may impair the engineering processes of capture, transport, and injection: some associated reactive gases, i.e., chemical species other than CO_2 in the injected stream—namely SOx, NOx, H_2S, or O_2—may require different adaptations for injection and disposal than if the stream were pure CO_2. Moreover, the presence of associated gases in the CO_2 stream in relatively high proportions can affect the compressibility of the injected gas and reduce the CO_2 storage capacity of the reservoir. This is because of the space taken up by these gases and the unfavorable volume balance of induced geochemical reactions. Additionally, depending on the type of geological storage, the presence of ancillary gases may have some other specific effects, such as trapping performances. In the case of CO_2 storage in deep saline formations, the presence of gas impurities affects the gas solubility in the aqueous phase, as well as the rate and amount of CO_2 stored through mineral dissolution and precipitation.

Hence, we need numerical estimations to forecast how the gas composition might impact the geochemical reactivity inside the host reservoir, potentially modifying the porosity and permeability of the medium and influencing the long-term well injectivity. Two numerical simulations are performed to study the impact of CO_2, SO_2 and O_2 mixtures on the main physico-chemical characteristics of a deep saline aquifer.

NUMERICAL APPROACH

Calculation code

The TOUGHREACT simulator (Xu and Pruess, 2001) is used for all simulations in this study. This code, which issued from TOUGH2 V2 (Pruess et al., 1999), couples thermal, hydraulic and chemical (THC) processes and is applicable to one-, two-, or three-dimensional geologic systems with physical and chemical heterogeneity. TOUGHREACT is coupled with

ECO2n (Pruess, 2005), a fluid property module developed specifically to deal with geologic sequestration of CO_2 in saline aquifers. It can be used to model isothermal or nonisothermal multiphase flow in water/brine/CO_2 systems.

TOUGHREACT simulates the chemical reactivity of systems based on an extended thermodynamic database. In this study, we use the database released with the program, i.e., a modified version of the EQ3/6 database (Wolery, 1992).

Thermodynamic equilibrium between the gas phase and the aqueous phase is assumed for CO_2 dissolution. An extension of Henry's law, including salting-out effect, is used to estimate the solubility of CO_2 in the aqueous phase at high pressure and high salinity.

For this work, the dissolution and precipitation reactions of minerals proceed under kinetic constraints. The general form of the rate law proposed by Lasaga (1984) is applied for both dissolution and precipitation of minerals:

$$r_n = \pm k_n A_n \left| 1 - \Omega_n^{\theta} \right|^{\eta}$$

Positive values for r_n correspond to the dissolution of the mineral n (negative for precipitation), k_n represents the rate constant (mol m^{-2} s^{-1}), A_n is the specific reactive surface area per kg_{H2O}, Ω_n represents the saturation index of the mineral n ($\Omega_n = Q_n/K_n$), and θ *a*nd η are empirical parameters determined from experiments, usually taken as 1.

The dependence of the rate constant k_n with temperature is calculated by means of the Arrhenius equation:

$$k_n = k_{25} \exp\left[\frac{-E_a}{R}\left(\frac{1}{T} - \frac{1}{298.15}\right)\right]$$

where E_a is the activation energy (J mol^{-1}), k_{25} the rate constant at 25°C, R is the gas constant (J mol^{-1} K^{-1}) and T the temperature in Kelvin.

For some minerals, specifically alumino-silicates and salts, the dissolution and precipitation also depend on H^+ (acid mechanism) and OH^- (alkaline mechanism) concentrations, in addition to the neutral mechanism. In this case, k_n is calculated using the following expression:

$$k_n = k_{25}^{nu} \exp\left[\frac{-E_a^{nu}}{R}\left(\frac{1}{T} - \frac{1}{298.15}\right)\right] + k_{25}^{H} \exp\left[\frac{-E_a^{H}}{R}\left(\frac{1}{T} - \frac{1}{298.15}\right)\right] a_H^{n_H} + k_{25}^{OH} \exp\left[\frac{-E_a^{OH}}{R}\left(\frac{1}{T} - \frac{1}{298.15}\right)\right] a_H^{n_{OH}}$$

Superscripts and subscripts *nu*, *H*, and *OH* indicate neutral, acid, and alkaline mechanisms, respectively, and *a* is the activity of the species.

For carbonate minerals, dissolution/precipitation mechanisms are catalyzed by HCO_3^-, and reaction rates depend on the activity of aqueous CO_2. k_n is calculated according to:

$$k_n = k_{25}^{nu} \exp\left[\frac{-E_a^{nu}}{R}\left(\frac{1}{T} - \frac{1}{298.15}\right)\right] + k_{25}^{H} \exp\left[\frac{-E_a^{H}}{R}\left(\frac{1}{T} - \frac{1}{298.15}\right)\right] a_H^{n_H} + k_{25}^{CO_2} \exp\left[\frac{-E_a^{CO_2}}{R}\left(\frac{1}{T} - \frac{1}{298.15}\right)\right] a_{CO_2,aq}^{nCO_2}$$

The kinetic parameters used for the last two equations are from Palandri and Kharaka (2004).

Mineral dissolution and precipitation reactions involve temporal changes in reservoir porosity. Indeed, variations in the mineral volume fraction owing to chemical reactions allow computing the resulting porosity. Permeability variations are calculated from porosity changes using the "tube-in-series" model (Verma and Pruess, 1988), which allows reaching nil permeability even if porosity is not nil.

Geometrical Model

The saline aquifer is schematically represented by a 2D-radial model including the reservoir and caprock units (Figure 1).

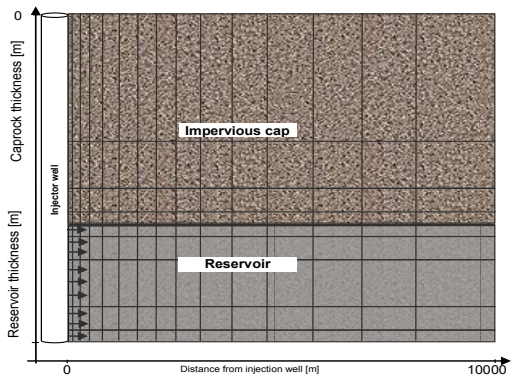

Figure 1. Scheme of the geometrical 2-D radial model (vertical cross-section).

This conceptual model is able to evaluate the evolution of the geochemical reactivity induced by gas injection, both in time and in space. The 200 m thick reservoir is centered on a vertical injection well with a radius of 0.2 m. Maximum radial extent is 100 km. The investigated system is represented by 800 gridblocks comprising the model mesh. Along the radius axis, 29 grid cells are considered between 0.2 m and 1 km, 50 grid cells between 1 km and 10 km, and 20 grid cells between 10 and 100 km. In each interval, the width of the radial elements follows a logarithmic scale. Vertical discretization is achieved by dividing the reservoir into 5 layers (from bottom to top, 20, 40, 80, 40, and 20 m), and the caprock into 3 layers (5, 10, and 25 m).

Reservoir Characteristics

The investigated saline aquifer is a sandstone reservoir of about 200 m thickness. The effective pressure and temperature before any injection are 150 bar and 50°C, respectively.

Since the reservoir rock's porosity ranges between 13 and 18%, an average value of 15% is selected for the calculations. The porosity of the caprock is estimated to be 40%.

The caprock level presents a mean permeability of 0.003 mD, whereas the permeability of the saline reservoir is about 300 mD.

Due to the injection of a gas phase within the deep system, the relative permeability and the capillary pressure characteristics of the medium must be defined to accurately describe the relative flow of gas with respect to the aqueous solution. Since we lacked petrophysical data for the targeted reservoir, we conducted a bibliographic review to define the representative curves and to implement them into the numerical code. Bachu and Bennion (2007) listed data concerning sandstones. Owing to the characteristics of the investigated reservoir (k_{mean} # 300 mD; Φ # 15%; $P_{reservoir}$ = 150 bars; T = 50°C), we found an analogy with the Cardium sandstone and chose it as the reference sandstone (Figure 2). The same characteristic curves for relative permeability and capillary pressure are used for the reservoir and the caprock layer.

For the numerical simulations, the minerals present in the caprock and in the reservoir are selected in conjunction with the mineralogical assemblage determined from core analysis. But some adjustments were made, according to the database used by TOUGHREACT.

The caprock is essentially composed of illite and quartz (77 wt%) while the reservoir rock essentially contains quartz and K-feldspar (91 wt%). Since a plagioclases series (solid solution) is not included in the database, the end-member albite ($NaAlSi_3O_8$) was chosen as a substitute.

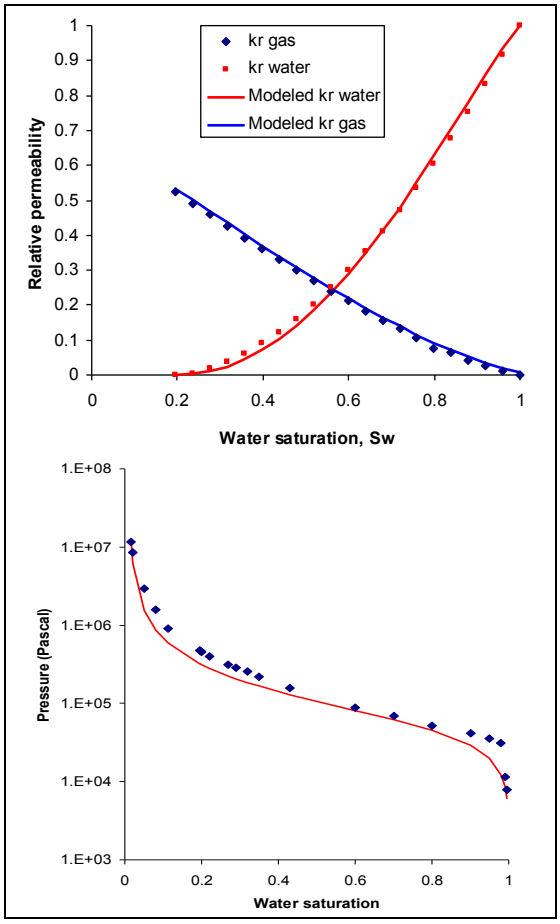

Figure 2. Relative permeability (upper figure) and capillary pressure (lower figure) curves for Cardmium sandstone (symbols are from Bennion and Bachu, 2005). Fitted curves are implemented in TOUGHREACT code.

Chlorite (chloritoïd series) is not in the database, so the clinochlore-7A ($Mg_5Al_2Si_3O_{10}(OH)_8$) was chosen as a chlorite analogue (Gaus et al., 2005). Magnesite ($MgCO_3$) is used instead of siderite ($FeCO_3$), as it is more stable in the initial system at thermodynamic equilibrium. This substitution is acceptable, since magnesite is also a carbonate

that acts as a pH buffer as well as siderite. Rutile and anatase are common detrital minerals. Anatase, which comes from Ti-bearing minerals, is chosen for this study (Table 1).

Table 1. Selected mineralogical composition of the caprock and the reservoir rocks.

	Minerals	Wt%
Caprock	Illite	60
	Quartz	17
	Albite	6
	Clinochlore-7A	5
	K-Feldspar	4
	Hematite	4
	Magnesite	3
	Anatase	1
Reservoir	Quartz	81
	K-Feldspar	10
	Albite	5
	Calcite	3.6
	Anhydrite	0.4

Chemical composition of water

Detailed physico-chemical characteristics of the formation water are provided in Table 2. The chemical analyses are performed in the laboratory at ambient conditions (1 bar, 25°C).

Table 2. Chemical composition of the aquifer water.

Element	Concentration (mg L^{-1})
Na (as Na^+)	90283
K (as K^+)	624
Ca (as Ca^{2+})	13652
Mg (as Mg^{2+})	2206
N (as NH_4^+)	11
Fe (as Fe^{2+})	127
Cl (as Cl^-)	171449
Br (as Br^-)	1162
I (as I^-)	7.4
S (as SO_4^{2-})	566.2
Total Dissolved Salt	280 000

The water composition for *in situ* conditions (150 bars, 50°C) is evaluated based on some relevant hypothesis and the thermodynamic calculations relevant for highly saline aqueous systems using the SCALE2000 code (Azaroual et al., 2004). The pH and bicarbonate concentration of this brine are recalculated for the reservoir pressure and temperature conditions, assuming that the brine is in thermodynamic equilibrium with respect to calcite. This resulted in a bicarbonate concentration of 103 mg L^{-1}. Under these conditions, the brine remains slightly under-saturated with respect to the evaporitic minerals (halite, sylvite and anhydrite), but is slightly supersaturated with respect to dolomite and pyrrhotite (iron sulfide).

NUMERICAL SIMULATIONS

Initial Conditions and Injection Procedure

The assumptions for numerical modeling are as follows:

- *Hydrostatic equilibrium*: no regional flow is considered, and a hydrostatic pressure is imposed in the outermost column of the mesh.
- *Thermal equilibrium*: before starting gas injection, reservoir and caprock are at the same temperature, i.e., 50°C. The numerical simulations are performed in isothermal mode.
- *Geochemical equilibrium*: the aqueous solutions initially present within the reservoir and caprock are in equilibrium with their respective mineral assemblages at the temperature of the system.
- *Injection rates* of *supercritical CO_2 and SO_2-O_2 dissolved in brine*: these are respectively 30 kg s^{-1} and 15 kg s^{-1}. The mass ratio of 2 has been arbitrary chosen for these simulations. Gas and brine are injected over the total thickness of the reservoir during an assumed exploitation period of 30 years.

A mixture of supercritical CO_2 and reservoir brine containing SO_2 and O_2 (namely "SO_2-O_2 brine") are co-injected into the reservoir, because the TOUGHREACT does not handle CO_2-SO_2-O_2-H_2O gas mixtures, only CO_2-H_2O mixtures (specificity of the ECO2n module). Two gas streams mixtures are investigated:

- "Low SO_2-O_2 brine" containing CO_2 (91.61 vol%) and 9.71 vol% of impurities, including a negligible SO_2 (0.08 vol%) and 1.6 vol% of O_2.
- "High SO_2-O_2 brine" containing 90.28 vol% of CO_2, 1.53 vol% of SO_2, and 1.6 vol% of O_2.

The chemical composition of the SO_2-O_2-acidified brine is handled in different steps:

- The injected brine is first equilibrated with the minerals of the reservoir.
- SO_2 and O_2 gases are then dissolved within the brine. Given the chosen mass ratio of 2 between the injected mass of supercritical CO_2

and the mass of SO_2-O_2 brine, the SO_2 and O_2 concentrations within the solution are defined to ensure consistency with the gas composition of an oxy-combustion capture process (given by data from the industry). Such preliminary simulations are performed with the batch option of the PHREEQC code (Parkhurst and Appelo, 1992). The hypothesis that SO_2 is fully dissolved within the SO_2-O_2 brine is acceptable, since its solubility is very high at such temperatures.

➢ The activity model used in the batch simulations is the Davies model. The TOUGHREACT code uses an extended Debye-Hückel model, although admittedly those models are not adapted for highly saline solutions such as in the targeted reservoir (Table 2). For this reason, and for more reliable results, the elemental concentrations of each species of the acidified water are divided by a factor of 10, in order to decrease the ionic strength of the solution (Table 3). This artificial dilution does not drastically modify the simulation results (e.g., reaction paths, dissolution/precipitation magnitudes of minerals) even if it significantly changes the initial saturation state of waters with respect to rock minerals.

Table 3. Chemical characteristics of the fluids used for numerical calculations.

	Reservoir brine	Low SO_2-O_2 brine	High SO_2-O_2 brine
pH	7.9	1.5	0.2
pe	-3.9	17.7	19.0
TDS (g/kg_{H2O})	38.6	~38.6	~38.6
$[SO_4^{-2}]$(mol/L)	1.7e-02	5.0e-02	7.2e-01

The "SO_2-O_2 brines" are very acid, with oxidative and sulfate concentrations higher than in the reservoir brines. These brines are expected to be highly reactive with reservoir minerals.

Results

Case 1: Injection of "a low SO_2-O_2 brine"

The gas and water injection within the reservoir drive changes of physical parameters (gas saturation, pressure, and so forth) and geochemical properties at different scales, with a major impact on the near-wellbore zone.

First, due to the injection of the gas/solution mixture, the gas saturation changes around the injection well. Because the supercritical CO_2 density is lower than that of the formation brine, CO_2 reaches preferentially the top of the aquifer and expands along it (Figure 3). The caprock is less permeable than the reservoir, but considering the selected permeability, the supercritical CO_2 can penetrate it to a certain extent. The pressure around the injector increases to reach 167 bars during the injection period. (Initially, the pressure ranged between 143 and 160 bars between the top and the bottom of the reservoir.)

The pH of the formation water is controlled by water-rock interactions. Initially, the formation water is in equilibrium with the mineral assemblage of the reservoir: the pH is close to 7.9 (Table 3). Co-injection of supercritical CO_2 and SO_2-O_2 brine then modifies this equilibrium: the evolution of pH follows the evolution of the gas saturation within the reservoir, with the impacted zone extending up to 3000 m from the injector after an injection period of 30 years (Figure 3). Consequently, the formation water around the injector acidifies, becomes under-saturated with respect to all minerals, and dissolves them (preferentially the carbonates). As long as reactive carbonates are present, the aqueous solution is in equilibrium with them and the pH is buffered. However, with extended injection, some minerals are exhausted: all carbonates are consumed around the injector and the buffering effect stops. pH is not controlled and decreases to very low values. Near the well, the mineral assemblage is drastically modified, and the pH decreases to a minimum value of 1.4, close to the value of the injected fluid (Table 3). Further within the impacted zone of the reservoir, the pH is buffered to a value ranging between 4 and 6, since not all the carbonates are consumed. The pH is unchanged in the non-impacted zone.

Calcite is the mineral most affected by injection of the acid solution; it dissolves near the injection well (50 m around it), but it is little impacted elsewhere in the reservoir (Figure 3). The other mineral affected by gas and water injection is anhydrite. The behavior of anhydrite differs in time and space: at first, anhydrite precipitates near the injection well, because the injected fluid contains sulfur, oxidized to sulfate by oxygen. Calcite is dissolved by the acidified injected water, releasing Ca^{2+} in solution. With

SO_4^{2-} present in the injected water, these ions combine to form anhydrite.

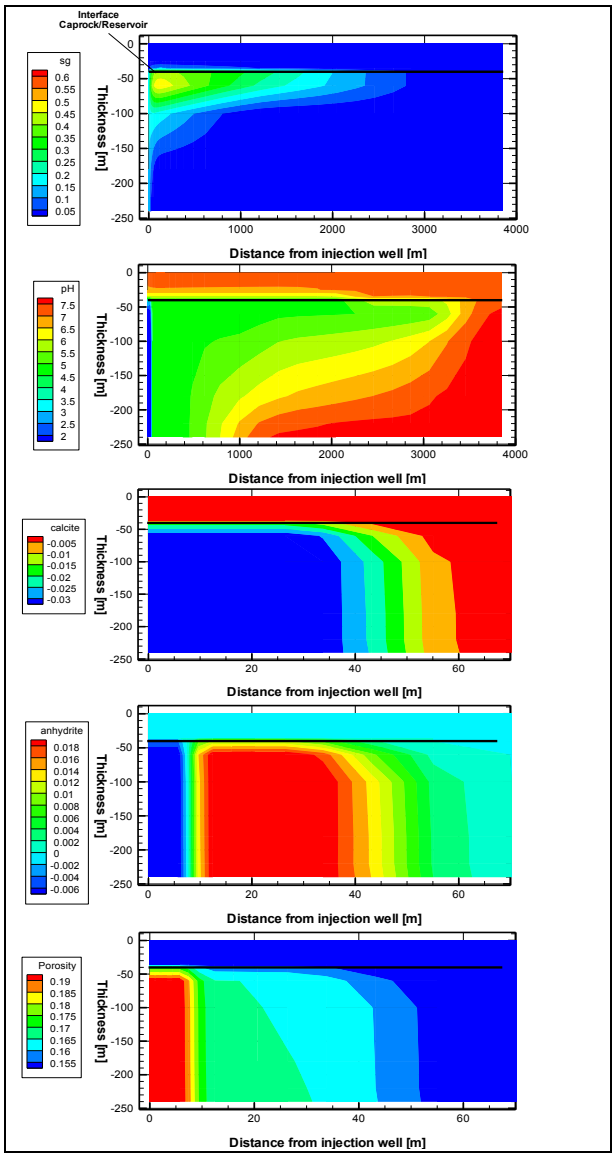

Figure 3. State of the reservoir and caprock after an injection period of 30 years. From top to bottom: gas saturation (Sg), pH with x-axis up to 4000 m, volumic fraction of calcite, volumic fraction of anhydrite and porosity with x-axis up to 400 m.

However, when all the calcite is consumed, the Ca^{2+} source disappears, and anhydrite precipitation stops. Because the injected solution is undersaturated with respect to anhydrite, the secondary precipitated anhydrite and the original anhydrite (initially present within reservoir) dissolve. This is why some zones present a deficit of anhydrite, whereas others present a positive balance of anhydrite compared to its initial amount (Figure 3).

As a consequence of calcite and anhydrite reactivity, porosity increases near the injector (Figure 3). After an injection period of 30 years, at 10 m from the injection well, a porosity of about 19% is estimated (due to calcite and anhydrite dissolution). This value is probably overestimated: in a real injection, a CO_2/SO_2 gas mixture would be injected, preventing the dissolution of primary and secondary anhydrite. Consequently, if anhydrite did not dissolve, the expected porosity would range between 16.5 and 17% (values deduced from the porosity variations between 10 and 40 m from injector). In any case, these values need to be considered as indicative (qualitative) and not effectively quantitative, because of some limiting working hypotheses (dilution of the initial brine, limitations of kinetic parameters, etc.).

All other minerals react but in fewer proportions than calcite and anhydrite (2 to 5 orders of magnitude lower), and their impact on porosity is negligible. Because of the assumptions made regarding caprock permeability, supercritical CO_2 is able to slightly penetrate within it. But the CO_2 amounts are too low and the impact on chemical reactivity and porosity variations are too limited to be seen in the graphical representations of the numerical simulations. Moreover, additional data are needed to better define the hydraulic properties of the caprock and improve the quality of these simulations.

Case 2: Injection of a "high SO_2-O_2 brine"

The same simulation as in the case 1 was performed. At the temperature of the reservoir (i.e. 50°C), the "high-SO_2 brine" is slightly over-saturated with respect to anhydrite. Consequently, after an injection period of 12 years, the anhydrite precipitation fully clogs the porosity around the injection well, indicating the end of the injection if no measures were taken to keep the injectivity stable.

To analyze anhydrite precipitation conditions, we conducted another simulation with a new injected solution. In this last case, the original reservoir brine, still 10-times diluted, was not initially equilibrated with the mineralogical assemblage of the reservoir before adding SO_2

and O_2. In this case, the injected solution was undersaturated with respect to anhydrite.

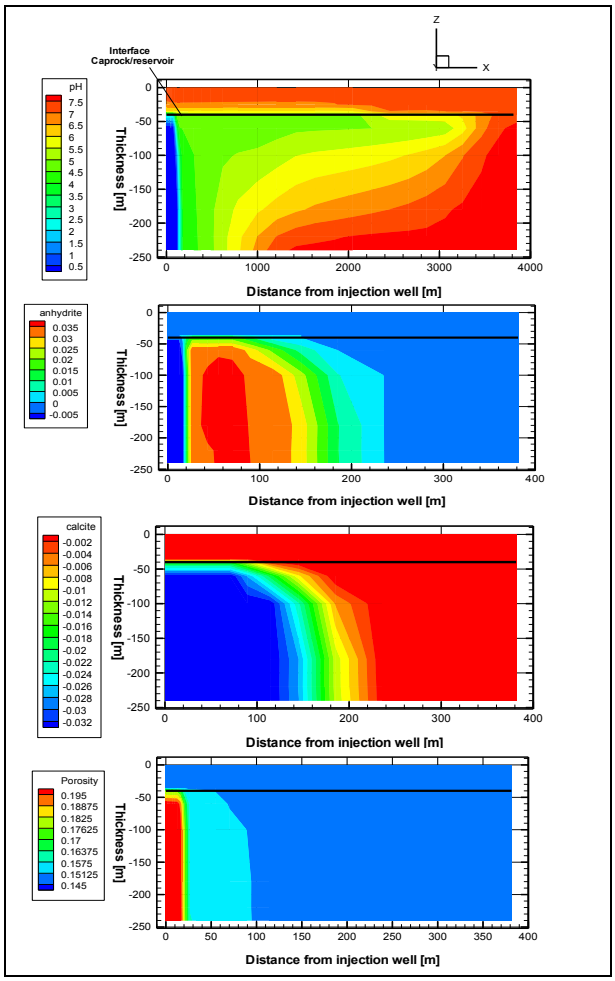

Figure 4. State of the reservoir and caprock after an injection period of 30 years. From top to bottom: pH with x-axis up to 4000 m, volumic fraction of anhydrite, volumic fraction of calcite and porosity with x-axis up to 400 m.

The resulting impact of the co-injection of supercritical CO_2 and acidified brine is a decrease in pH around the injection well and a co-dissolution of both carbonates and anhydrite (since the solution is under-saturated with respect to anhydrite) (Figure 4). Since the acidity is higher than for the "low SO_2-O_2 brine" (Table 3), the impacted zone is also more extended than in the first case (about 50 m in case 1 compared to 200 m in case 2).

The other minerals of the assemblage were also impacted by this strong acidification. They were relatively less impacted than carbonates or anhydrite, but the dissolution of some of them (K-feldspar) and precipitation of others (quartz, kaolinite) must be carefully tracked.

In this last case, the higher acidity of the injected fluid is neutralized to a lesser extent by reactions with minerals: less important variations in porosity are observed in the near-well domain, whereas the impacted zone is extended by the dissolution and precipitation reactions.

CONCLUSIONS

The objectives of this paper were to present the results from numerical simulations of the co-injection of acid gases within a deep saline aquifer. Since the TOUGHREACT code cannot represent the co-injection of these components in a gaseous (nonwetting phase) mixture, some limiting hypotheses were done: CO_2 injection was simulated as in a supercritical form, whereas SO_2 and O_2 injections were simulated as in dissolved species within an aqueous solution. After an injection period of 30 years, simulation results indicate:

- The injected supercritical CO_2 dissolves in solution, increasing its ability to dissolve carbonates. Since calcite is one of the components of the mineralogical assemblage, it dissolves around the injection well and therewith increases porosity. But because of the negligible calcite in the mineralogical assemblage, the impact on pore volume is quite limited.
- SO_2 reacts rapidly around the injection well, forming sulfates because of the traces of oxygen in the injected gas. Through the recombining of Ca^{2+} (coming from calcite) and SO_4^{2-} (issued from SO_2 and O_2), anhydrite precipitates. The SO_2 concentration (low or high) determines the extent of the anhydrite deposition occurring in a radius around the injection well.
- The higher the SO_2 concentration in the injected stream, the larger the radius of anhydrite deposition around the well. However, the SO_2 concentration seems to have no influence on the geochemical mechanisms in terms of (for instance) reaction paths.
- Calcite and anhydrite are the most reactive minerals. All the other initial minerals are also affected by the injection of acid solution, but in less proportion and with a minor impact on porosity and permeability.

➢ When calcite and anhydrite present opposite behaviors, numerical simulations forecast that calcite dissolution will have a more important impact on porosity than anhydrite precipitation. Consequently, increasing porosity is expected around the injection well, supposing an increase in well injectivity and a potential long-term injection period.

However, we must consider these results as qualitative, highlighting only the global trends of the investigated system. Indeed, the real impact (quantitative estimation) is still very difficult to predict. For example, how the dissolution/precipitation of a particular mineral will affect rock porosity will depend on the characteristics of the rock (e.g., micro/macroporosity, connected porosity). Thus, our results must be interpreted cautiously.

ACKNOWLEDGMENT

This work is part of the OXYGAS (phase II) project funded by VATTENFALL. The authors acknowledge the VATTENFALL Directorate and BRGM Research Directorate for allowing publication of these results at the Symposium.

REFERENCES

André L., P. Audigane, M. Azaroual, and A. Menjoz, Numerical modeling of fluid-rock chemical interactions at the supercritical CO_2-liquid interface during supercritical carbon dioxide injection into a carbonated reservoir, the Dogger aquifer (Paris Basin, France). *Energ. Conv. Manage.,* 48, 1782-1797, 2007.

André L., M. Azaroual, and A. Menjoz, Numerical Simulations of the Thermal Impact of Supercritical CO_2 Injection on Chemical Reactivity in a Carbonate Saline Reservoir. *Transp. Porous Med.*, 82, 247-274, 2010.

Azaroual M., C. Kervévan, P. Durst, and M.-V. Durance, SCALE2000 (V3.1) : Logiciel de calculs thermodynamiques et cinétiques ; application aux saumures pétrolières, hydrothermales et industrielles. Manuel d'utilisation; BRGM Editions, ISBN2-7159-0939-X. 70 p., 2004.

Bachu S., and B. Bennion, Effects of in-situ conditions on relative permeability characteristics of CO_2-brine systems, *Environ. Geol.*, 54, 1707–1722, 2007.

Bennion B., and S. Bachu, Relative permeability characteristics for CO_2 displacing water in a variety of potential sequestration zones in the Western Canada Sedimentary Basin. *SPE Paper 95547*, 15 p., 2005.

Gaus I., M. Azaroual, and I. Czernichowski-Lauriol, Reactive transport modelling of the impact of CO_2 injection on the clayey caprock at Sleipner (North Sea). *Chem. Geol*., 217, 319-337, 2005.

Lasaga A.C., Chemical kinetics of water-rock interactions, *J. Geophys. Res.,* 89, 4009-4025, 1984.

Palandri J., and Y.K. Kharaka, A compilation of rate parameters of water-mineral interaction kinetics for application to geochemical modelling. *US Geol. Surv. Open File Report 2004-1068*, 64 p., 2004.

Parkhurst D.L., and C.A.J. Appelo, User's guide to PHREEQC (Version 2) - A computer program for speciation, batch-reaction, one-dimensional transport, and inverse geochemical calculations. *Water-Resources Investigations Report 99-4259*, *US Geol. Surv.*, 1999.

Pruess K., C.M. Oldenburg, and G.J. Moridis, TOUGH2 User's Guide, Version 2.0. Lawrence *Berkeley National Laboratory Report LBNL-43134*, Berkeley, CA (USA), 1999.

Pruess K., ECO2n: a TOUGH2 fluid property module for mixtures of water, NaCl and CO_2. *Lawrence Berkeley National Laboratory Report LBNL-57952*, Berkeley, CA (USA), 2005.

Verma A., and K. Pruess, Thermohydrologic conditions and silica redistribution near high-level nuclear wastes emplaced in saturated geological formations, *J. Geophys. Res*., 93(B2), 1159–1173, 1988.

Wolery T., EQ3/6: Software package for geochemical modeling of aqueous systems: Package overview and installation guide (version 7.0). *Report UCRL-MA-210662*, Lawrence Livermore National Laboratory, CA (USA), 1992.

Xu T., and K. Pruess, Modeling multiphase non-isothermal fluid flow and reactive geochemical transport in variably saturated fractured rocks: 1. Methodology, *Am. J. Sci.*, 301, 16-33, 2001.

BEHAVIOR OF THE CO_2 INJECTION WELL AND THE NEAR WELLBORE DURING CARBON DIOXIDE INJECTION IN SALINE AQUIFERS

Mohamed AZAROUAL[1], Laurent ANDRE[1], Yannick PEYSSON[2], Jacques PIRONON[3], Daniel BROSETA[4], Fabien DEDECKER[5], Patrick EGERMANN[6], Jean DESROCHES[7], Joëlle HY-BILLIOT[8]

[1] BRGM, Water Division, 3 Avenue Claude Guillemin, BP 36009, F-45060 ORLEANS Cedex 2 France
[2] IFP Energies nouvelles, 1-4 avenue de Bois Préau, 92852 Rueil-Malmaison Cedex - France
[3] Université de Lorraine, CNRS, G2R laboratory, BP 70239, 54506 Vandœuvre-lès-Nancy, France
[4] UMR 5150, LFCR, Université de Pau & Pays Adour, BP 1155, 64013 PAU Cedex, France
[5] ITASCA Consultants, S.A.S., 64 Chemin des Mouilles, 69130 ECULLY, France
[6] GDF SUEZ, STORENGY, 12 rue Raoul Nordling, 92270 Bois Colombes, France
[7] SCHLUMBERGER, Etudes et Productions Schlumberger, SRPC, 1 rue Henri Becquerel, 92142 Clamart, France
[8] TOTAL E&P, DGEP/SCR/RD/MGR, Avenue Larribau, 64018 PAU CEDEX, France

e-mail: m.azaroual@brgm.fr; l.andre@brgm.fr; yannick.peysson@ifpen.fr ; jacques.pironon@univ-lorraine.fr; daniel.broseta@univ-pau.fr; f.dedecker@itasca.fr; patrick.egermann@storengy.com; JDesroches1@slb.com; Joelle.HY-BILLIOT@total.com.

ABSTRACT

The project "*ProchePuits*" ("Near Wellbore"), co-funded by the French National Agency for Research (ANR), started in December 2007 and ended in May 2011. The project consortium included three companies (TOTAL, Schlumberger, and GDF-Suez), two applied research centers (BRGM and IFP Energies Nouvelles), two academic research laboratories (CNRS and Université de Lorraine) and a SME (ITASCA). The main processes studied were: (i) physical behavior of flowing fluids in the well and their impacts on the bottomhole T-P conditions, (ii) thermo-kinetic effects on the petrophysical and physico-chemical processes, (iii) dryout of the near-wellbore porous media and reactivity of highly evaporated residual brines retained by capillary and osmotic forces in the pores, and (iv) petrophysical and geomechanical impacts of coupled processes.

The understanding of these phenomena, based on laboratory experiments and numerical modelling, enabled a better interpretation of the coupled processes involved and the development of advanced concepts for CO_2 storage in saline aquifers. The project demonstrates, that injection of large quantity of CO_2 in deep saline aquifers will lead to a strong water desaturation of the near wellbore because of drying. In this context, drying can precipitate the salt in the aquifer water, leading to injectivity alteration due to permeability decrease.

Numerical modeling that couples hydraulic and thermal processes was shown to be able to simulate the observed evolution of liquid and gas saturations, and to estimate the salt depositions. Our numerical-simulation approaches were validated against laboratory experiments in controlled conditions, allowing the determination of the most important parameters for injectivity design (porosity, relative permeability and capillary pressure curves, etc.). The experimental observations, conducted at the centimeter scale, were up-scaled in order to, first extrapolate the results at the near wellbore scale, and then to forecast the impact of CO_2 injection on the petrophysical properties of the host rock.

Finally, our results allow making recommendations and risk analyses with respect to the injectivity for CO_2 for geological storage in an aquifer. The injection flow rates, as well as optimum pressure and temperature in wells, can then be determined to avoid damage in the near wellbore zone and maintain injectivity during the operational life of the well.

INTRODUCTION

The "*Near Wellbore*" project was focused on the study of key physical, physicochemical, and thermo-kinetic phenomena occurring in the well and the near-wellbore domain. The understanding of these phenomena, based on scientific and technical knowledge, will reduce uncertainties related to injectivity and numerical-simulation

predictions regarding the sustainability and security of CO_2 storage. This knowledge will also identify ranges for CO_2 storage-capacity estimates within saline aquifers.

Indeed, it is now established that the amount and quality of injected CO_2 play a key role in the preservation of reservoir injectivity, and on the number and type of required injection wells. On the other hand, depth, location, temperature and pressure conditions, and petrophysical characteristics of the targeted reservoir—as well as the quality of the cap rock—are parameters that must be characterized because of their influence on the required number of wells, on the evolution of injectivity, and on the technical management of pressure conditions at the wellhead and at the bottom of the well. Additionally, the multiphase area that develops nearing the vicinity of the well is a very sensitive, highly reactive zone, where numerous coupled processes have been identified, including hysteretic behaviors. This region may also play a key role during the CO_2 injection phase, which can include repeated injection cessations and restarts.

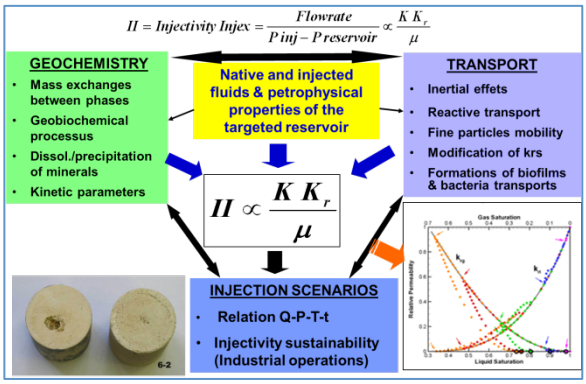

Figure 1. Key coupled processes to integrate in numerical tools for studying injection scenarios, based on controlling relative permeabilities and interfacial mechanisms of mass and heat transfer between phases.

In summary, the integration of the empirical macroscopic parameter defined as the *injectivity index, II*, (Figure 1) is the key condition of success for a Geological Carbon Sequestration (GCS) operation. This parameter expresses the behavior of the reservoir under imposed P-T-Q-t conditions, i.e., injection pressure (P), temperature (T), flow (Q) and their time evolution (t). As illustrated in Figure 1, *II* primarily depends on the evolution of the relationship between water saturation (S_w) and relative permeability (K_r). This relationship depends, in turn, on the properties of the injected fluids and on the characteristics of the target reservoir rock (biochemical and geochemical reactivity, initial petrographic and hydrodynamic properties, etc.).

MULTIPHASE REACTIVE TRANSPORT AND NEARWELLBORE BEHAVIOR

Based on recent numerical and experimental simulations, the near-well injection zone is identified to be particularly impacted by supercritical CO_2 injection, and is the most sensitive area. This area (André et al., 2007; 2010), is where chemical (e.g., mineral dissolution/precipitation) and physical (e.g., temperature, pressure and gravity) phenomena have a major impact on porosity and permeability, and thus, in the end, on well injectivity.

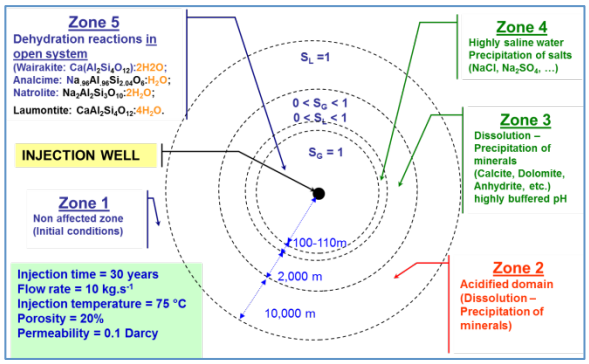

Figure 2. Typical fictive radii of the processes occurring in the near well region after a continuous injection of CO_2 over 30 years with a flow rate of 1 Mm^3/y (André et al., 2007; Gaus et al., 2008).

Figure 2 represents the simulation result from two-phase reactive transport (CO_2—initially porous carbonate rock saturated with water) using TOUGHREACT (Xu et al., 2004), showing the individualization and succession of five major zones of specific physical and physico-chemical properties around the injection well. These zones have the following characteristics:

- Zone 1 (initial unperturbed state): the porous medium contains only the initial aqueous solution. The pores are saturated with water (initial state) under conditions of thermody-

namic equilibrium between minerals of the rock matrix and pore water.

- Zone 2 (monophasic acidified zone): pH decreases due to dissolution of CO_2 (forming carbonic acid H_2CO_3) in the aqueous phase. The porous medium is still saturated with water. This is a more acidic front before the arrival of the supercritical CO_2 phase. This solution at lower pH is aggressive for most of the porous matrix minerals, including carbonates and to a lesser degree aluminosilicates.
- Zone 3 (multiphase zone): the pores of the porous medium contain two phases, namely the aqueous phase and supercritical CO_2. The pH and composition of the aqueous phase and slight change in water saturation continues, with a drying trend of the rock, creating conditions for capillarity.
- Zone 4 (dried zone): pH and ionic strength increase sharply due to the drying. This produces a strong tendency in the system toward reactive mass exchange processes between major phases (residual water–supercritical CO_2–minerals). Pore solutions become highly saline, with ionic-strength values of about 7 to 7.5 (equivalent mol / kg H_2O) although the initial aqueous solution was only at 0.1 (Zone 1).
- Zone 5 (extreme conditions of capillarity and dehydration reactions): the aqueous phase is removed and the porous medium contains only supercritical CO_2, along with a small quantity of metastable and capillary water in the fine pores and microcracks.

The various physical and physicochemical phenomena that predominated in each zone were analyzed separately in the framework of the "*Near Wellbore*" project, by implementing new measurement techniques and some new theoretical approaches. The integration of results from different disciplines helps us understand multiphase reactive transport inducing heat and mass transfer between phases.

The CO_2 injection well behavior: a "Pseudo" steady-state calculation example

This test case, jointly run by Total and Schlumberger, consists of a single-cased off-shore well, located in a shallow water zone (300 m depth). The well is vertical, and its total depth is 1000 m. Boundary conditions (pressure, temperature, and volumetric flow rate) are set at the wellhead. The injection temperature is set at 5°C, while the injection pressure is set at 100 bars. Several volumetric flow rates are considered: 500 t/day, 1000 t/day, 2000 t/day, and 2750 t/day. The far-field temperature in the formation varies linearly from 5°C at wellhead (0 m) to 21°C at 1000 m. The geological formation was made of limestone and sandstone, but since the thermal properties were not available, we chose the same parameters for both layers, assuming that this approach would not change the results significantly.

This example was tested using PipeSIM (developed by Schlumberger) and PROSPER (developed by Total). Each software involves different theoretical approaches and practical assumptions. PipeSIM performs steady-state calculations exclusively, in contrast to PROSPER, which produces results at t = 10 days, 100 days, and 1000 days from the beginning of injection. The longer times arefairly large, and probably sufficiently close to steady state to allow a meaningful comparison of the results of the two simulators. The codes yielded different results. Note that the pressure-versus-temperature curve along the well calculated with PipeSIM looks unconvincing (Figure 3): a substantial change in the slope occurs when the pressure exceeds a value ranging between 72 and 76 bars for the cases investigated (depending on the volumetric flow rate and the equation of state (EOS) considered for CO_2).

The simulations carried out with PROSPER use the Peng-Robinson EOS (Peng-Robinson, 1976) to model the behavior of CO_2. The simulator described here (NEW SIMULATOR) uses the Span-Wagner EOS (Span-Wagner, 1996). PipeSIM calculations are run alternatively using these two equations of state.

In earlier simulations, the convective heat transfer coefficient between tubing and the fluid inside it was considered constant (11 $W.m^{-2}.K^{-1}$) all along the well. This is not the case under realistic conditions: the heat transfer coefficient is usually dependent on numerous parameters evolving with depth and time (e.g., the fluid velocity, density, viscosity). The heat exchange between the fluid and the pipe is often expressed by means of a correlation relating the Reynolds,

Prandtl, and Nusselt numbers of the flow. In the current version of this new simulator, the correlation implemented is that of Gnielinski (Incropera, 2001).

The temperature vs. pressure curves associated with each case are presented in Figure 3. The numbers in the caption are the flow-rate values (in ton/day), while the two-letter acronyms 'SW' and 'PR' denote respectively 'Span-Wagner' and 'Peng-Robinson' (the equations of state of CO_2 used for the current case).

The present simulator is denoted 'NEWSIM' in the caption ('PipeSIM' and 'PROSPER' are self-explanatory). Figure 3 shows that the NEWSIM results are much closer to those from PROSPER than those from PipeSIM. In particular, the associated curves do not exhibit the unexplainable change in slope mentioned above, which tends to suggest a lack of coherence in the PipeSIM results. NEWSIM predicts a temperature 10 to 13% lower than PROSPER, and a pressure 4 to 5% higher.

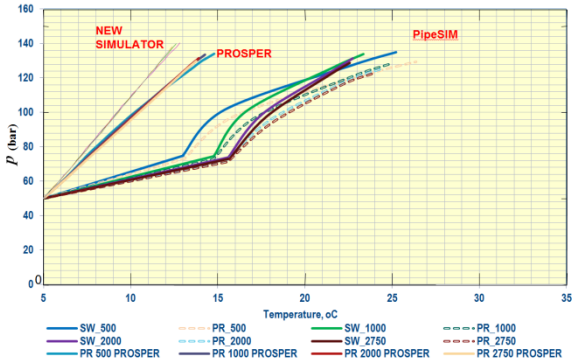

Figure 3. Pressure vs. temperature curves obtained with the three simulators, considering four flow rates and two different equations of states.

To summarize, these discrepancies can be explained by one or a combination of the following reasons:

- The use of the Span-Wagner (1996) EOS instead of the Peng-Robinson (1976) EOS. This trend is similar to that observed in the PipeSIM results when one switches from one EOS to the other: the bottom-hole temperature sustains a 4% to 5% relative decrease, while the bottom-hole pressure increases 4 to 5%.
- The use of a variable CO_2/tubing heat transfer coefficient—described by the Gnielinski's correlation; see Incropera (2001)—instead of a constant one.

The near wellbore dynamics

As shown in Figure 2, the desiccation of the porous medium appears to be a major phenomenon with various consequences, such as salt precipitation (Peysson et al., 2010), the consequent modification of the local geomechanical constraints, modification of internal forces, and the impact of injected fluids on interfacial tensions, including capillary/osmotic phenomena. Desiccation of porous media submitted to gas injections is a well-known process in laboratory studies (Mahadevan, 2005; Mahadevan et al., 2007) and field (Kleinitz et al., 2003) scales. This process began being taken into account only recently in the modeling of CO_2 storage in deep saline aquifers (André et al., 2007; Zeidouni et al., 2009).

First, the massive and continuous injection of CO_2 in a saturated porous medium involves water displacement and evaporation: mobile water is removed by the injected dehydrated supercritical CO_2, enabling a two-phase flow system (brine–CO_2). Finally, the immobile residual water entrapped in pores or distributed on grain surface as a thin film comes into contact with the flowing dry CO_2 (i.e., with very low water vapor pressure). Consequently, a continuous and extensive evaporation process leads to both a drying front moving into the medium and the precipitation of salts and possibly secondary minerals occurring in residual brines.

This study investigated the consequences for permeability degradation of a porous medium potentially influenced by desiccation through the petrophysical properties of different subsystems. Experimental evaluations of brine drying are conducted (at the laboratory scale) on centimeter plugs of different materials. These experiments were then interpreted using a numerical modeling approach coupling hydraulic and thermal processes able to simulate the evolution of liquid and gas saturations in space and time. A very fine discretization of the plugs allowed capturing the continuous evolution of water and gas profiles in the porous medium and estimating the

liquid saturation and permeability evolution during the drying process.

Gas-injection experiments were performed on two materials:

- a low-permeability sandstone ("Grès de Môlière" Φ=14.0 % and K_0=8 µD) in order to have better experimental control of the pressure, to limit the gas flow rate, and to increase the capillary effects that play a key role in drying processes,
- a high-permeability sandstone ("Grès des Vosges" Φ=21.8 % and K_0=60 mD) in order to study a rock with properties close to the ones found in targeted reservoirs for CO_2 storage.

Sandstones samples 6 cm in length, initially saturated with brine (salinity of 160 g L^{-1}), were placed in storage conditions (80°C–120°C–50 bars) and in a cell transparent to x-rays. Dry gas (nitrogen) was injected into the fully saturated core plugs (Figure 4). Four long pressure stages were imposed to progressively desaturate the rock plug. The local water saturation in the sample iwas measured with x-ray attenuation techniques. Pressure differences and outlet gas flow rates were monitored during the experiment. The system evolved until complete drying occurs. The experiments were performed at 90 and 120°C with the "Grès de Môlière" samples, and at 90°C with the "Grès des Vosges" core.

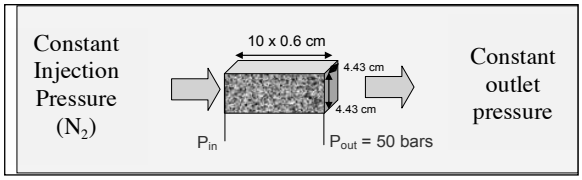

Figure 4. Experimental procedure to investigate the drying out of the core under a continuous flux of nitrogen.

Numerical simulation of multiphase flow and dryout (lab scale)

The TOUGH2 simulator (Pruess et al., 1999) with the EOS7C module (Oldenburdg et al., 2004) was used for all simulations in this study (core experiments and field scale). This code couples thermal and hydraulic processes and is applicable to one-, two-, or three-dimensional geologic systems with physical heterogeneity. The EOS7C is a fluid-property module developed specifically to deal with mixtures of non-condensable gases (like CO_2 or N_2) and methane. It can be used to model isothermal or non-isothermal multiphase flow in water/brine/CH_4/(CO_2 or N_2) systems.

Our modeling approach consisted of simulating the injection of nitrogen into a plug fully saturated with water. This problem of two-phase Darcy flow is solved using relative permeability and capillary pressure curves. Thermodynamic equilibrium between concomitant phases (brine–N_2) is calculated at each time step to evaluate the water vapor fraction in the gas and the dissolved gas in the brine.

A 1D column model 6 cm long was used as a conceptual framework for determining the evolution of the water content induced by the injection of N_2, in both time and space. The column was represented by 10 gridblocks composing the model mesh. The thickness of each grid cell was constant (0.6 cm). The matrix rock was assumed inert with respect to N_2, i.e., without chemical reactivity. The dependence of relative permeability and capillary pressure on the water saturation are given in Figure 5. The relative permeability of the aqueous (k_{rl}) and gaseous (k_{rg}) phases, and the capillary pressure (P_{cap}) are described by the relevant van Genuchten (1980) equations.

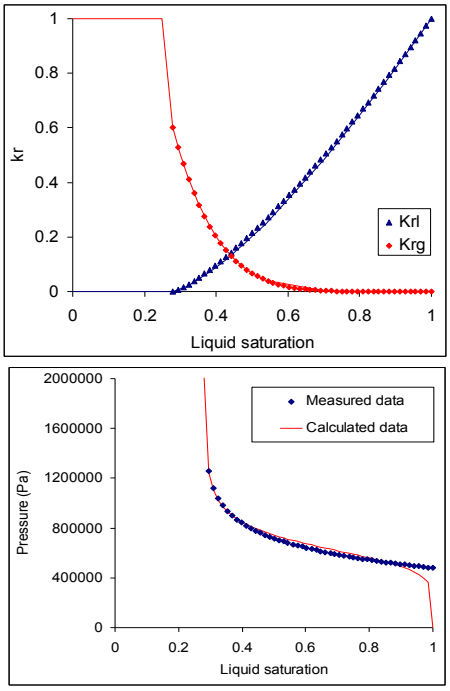

Figure 5. Relative permeability and capillary pressure curve according to water saturation (S_l).

Due to the low permeability of the medium, the model predictions are very sensitive to the relative permeability and capillary pressure characteristics, in particular to the entry pressure. As shown by Figure 5, the van Genuchten (1980) model does not fit the measured data adequately when the liquid saturation is close to 1. This very weak shift has an impact on the breakthrough time.

For the "Grès de Môlière" rock, high-pressure mercury injection and standard centrifugation were used to measure the capillary pressure curve. The model parameters are: S_{lr} = 0.22, S_{gr} = 0.05, P_0 = 645161 Pa and m = 0.95. When these parameters are correctly defined, the code can reproduce, with good agreement, the first three stages of the experiment, including the mean water saturation and the outlet gas flow rate (Figure 5).

These three first stages correspond to the desaturation of the porous medium according to a classical piston effect. The desaturation state is proportional to the pressure gradient applied to the core, whereas the evaporation process is negligible: at the end of stage 3, the water content is close to the residual liquid saturation.

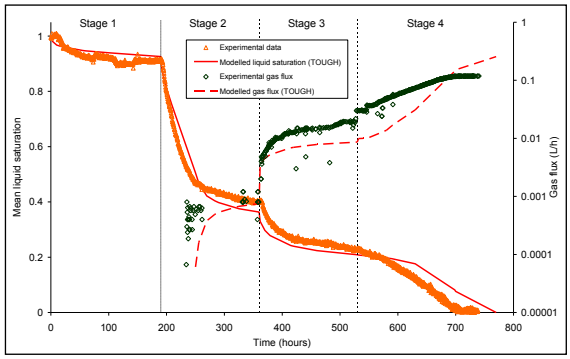

Figure 6. Results of dryout experiments with gaseous N_2 at laboratory scale (Peysson et al., 2010) compared with results from the numerical modeling performed with the TOUGH2 code (André et al. 2010).

During the first three stages, the calculated average water saturation in the core fits the measured data well. Some discrepancies are observed close to the inlet and outlet of the column, resulting mainly from the choice of parameters describing the boundary conditions imposed on the numerical model.

The last stage (stage 4) corresponds to the desiccation of the medium. Even if the global tendency is roughly reproduced, this stage presented some difficulties in reproducing correctly the measured data.

The only way to adequately fit both gas flow rate and desiccation time was to increase the gas permeability when liquid saturation was lower than the residual liquid saturation. By increasing the relative gas permeability, the outlet gas flow rate grows; the evaporation process goes faster and the time needed to totally desiccate the core decreases. These numerical simulations of laboratory experiments at 90°C not only served to check the relevance of the model, but they also helped in determining the parameters of the integrated approaches with the highest sensitivity (i.e., the optimized relative permeability and capillary pressure curves). The good agreement between measured and calculated data is very encouraging. We also demonstrated that the petrophysical parameters established at 90°C are applicable at 120°C without any adjustment for the same rock (André et al., 2010).

Extrapolation at field scale (2D-radial approach)

Because of gravity forces and the supercritical CO_2 density (lower than that of the brine), the reservoir desaturates faster at the top when extrapolated to the near-wellbore field. Figure 7 clearly shows that the porous medium has dried to a radius of about 12 m at the reservoir top, whereas at the bottom, only the first meter around the well is totally desiccated. Inside the drying zone, solid salt (i.e., halite) precipitates. If salt is present anywhere in the entire desaturated zone, the spatial repartition of salt deposits varies, according to the resultant prevalent transport forces (advection, diffusion, capillary, evaporation, etc.) inside the reservoir: the amounts are higher at the bottom of the reservoir, and lower at the top, for the simulation conditions and the specific chararacteristics of the reservoir in this study. The pattern of solid saturation (= solid volume/pore volume) distribution indicates that 40% of the porosity is occupied by salt at the bottom, whereas only 10% at the top is filled. The porosity and, consequently, the permeability are more impacted at the bottom of the reservoir (Figure 8). The permeability decrease is represented by the empirical function k_red (= k/k0). This function clearly shows that largest permeability reductions are

expected close to the well (the skin effect in the first cell next to the well) and at the lower part of the reservoir (in the first meter above the base of the reservoir).

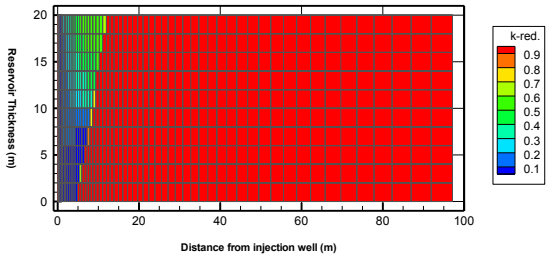

Figure 7. Permeability reduction, k_red (=k/k0) inside a 100 m radius around the injector well after ten years of CO_2 injection.

Finally, we specifically investigated the influence of downtime during the storage phase of well injectivity. Numerical simulations were performed considering the case of CO_2 injection into an aquifer open with a nominal flow of 1MMm^3/y and several short shutdown periods. Pc-Kr models were built to be fully representative of rock types with permeabilities of 10 and 100 mD for an integrated approach ensuring consistency between original K, Kr, and Pc. So far, the results show little effect related to reimbibition layers. The temporary shutdown of the wells does not seem to pose a major problem with respect to injectivity in the homogeneous model even when including hysteretic effects.

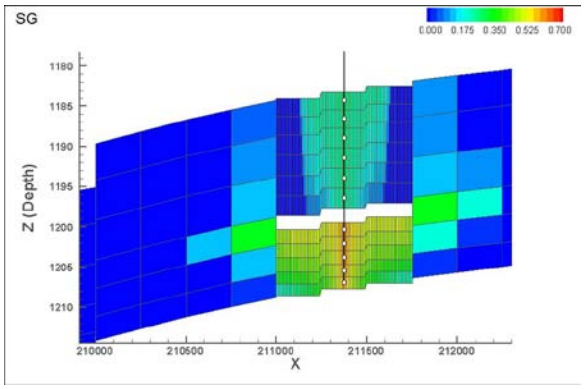

Figure 8. Vertical section illustrating the saturation tank of gas around the injection well for a mid-horizontal permeability 100 mD (RT1) in the deep layers and 10 mD (RT2) in the upper layers. This saturation state is the last day of the injection history, after six years of injections interrupted by two years of rest.

CONCLUSIONS

For the flows in the wells, the numerical simulation results show trends highlighting the problem of an "injectivity gap," showing an inability to maintain a controllable pressure range at the bottom of the injection well because of phase changes in that well. The involvement of industry (i.e., Schlumberger, GDF Suez, and Total) in the project contributes validated injection scenarios.

Most of our efforts to study the mechanisms at the interfaces of geochemical phases (CO_2sc-brines) were focused on CO_2 solubility in capillary water. Detailed speciation of carbonic acid is well established for the range of relative humidity and drying conditions studied in the project. A comprehensive approach for estimating the interfacial tension of a brine-CO_2sc system based on the theory of electrolytic systems was developed (Leroy et al., 2010).

We investigated the drying processes through laboratory experiments and numerical simulations to evaluate the dynamic of the water-saturation decrease in sandstones and the consequences of induced salt depositions on injectivity. We demonstrate that in low-permeability porous media, the relative permeability of the gas phase significantly increases when water saturation is lower than the irreducible water saturation. When this parameter is adjusted, the numerical code is able to reproduce the drying time and the outlet gas flow rate measured at laboratory scale on cores, using a two-phase Darcy flow and thermodynamic equilibrium between phases.

At field scale, the rock characteristics defined at laboratory scale are used to predict the behaviour of the near-well zone according to the injection gas flow rate. We demonstrated that the precipitation process and the amount of salt deposits are related to different parameters:

- The salinity of the initial brine: The more concentrated the brine, the more massive the salt deposit.
- The irreducible water content: water entrapped in pores is evaporated by gas injec-

tion. The higher this content, the more important the amount of precipitated salt.

- The gas injection flow rate and the capillary forces within the system.

Finally, all these parameters have to be known (and defined) in order to improve the management of the long-term injection of CO_2 into saline aquifers. According to reservoir simulations already conducted, several important results can be noted:

1. For high permeabilities (>100 mD), aquifer rewetting is more extensive, but no impact is observed in terms of injectivity because of the high permeability;
2. For low permeabilities (<100 mD), re-imbibition is less extensive and may have an adverse impact on well injectivity after restart;
3. Heterogeneities do not appear to play a major role in these findings
4. The key parameter is the curve of relative permeability to water. It is therefore recommended to measure this parameter accurately during the design phase.

ACKNOWLEDGMENT

This work is carried out within the framework of the "*Proche Puits*" project, co-funded by the French National Agency for Research (ANR). The authors are grateful to all project partners (TOTAL, GDF Suez, Schlumberger, Itasca, CNRS, University of Lorraine, and University of Pau) for allowing the publication of this work.

REFERENCES

André L., P. Audigane, M. Azaroual, and A. Menjoz, Numerical modeling of fluid-rock chemical interactions at the supercritical CO_2-liquid interface during supercritical carbon dioxide injection into a carbonated reservoir, the Dogger aquifer (Paris Basin, France). *Energ. Conv. Manage.,* 48, 1782-1797, 2007.

André, L., M. Azaroual, and A. Menjoz, Numerical Simulations of the Thermal Impact of Supercritical CO_2 Injection on Chemical Reactivity in a Carbonate Saline Reservoir. *Transp. Porous Med.*, 82, 247-274, 2010.

Gaus I., M. Azaroual, and I. Czernichowski-Lauriol, Reactive transport modelling of the impact of CO_2 injection on the clayey caprock at Sleipner (North Sea). *Chem. Geol*., 217, 319-337, 2005.

Incropera F.P., De Witt D.P., (2001) Fundamentals of heat & mass transfer (5th edition), John Wiley and Sons, 980p.

Leroy, P., Lassin, A., Azaroual, M., and André, L., (2010). Predicting the surface tension of aqueous 1:1 electrolyte solutions at high salinity. *Geochimica et Cosmochimica Acta* 74, 5427-5442.

Oldenburg C.M., Moridis G.J., Spycher N., Pruess K., 2004. EOS7C Version 1.0: TOUGH2 Module for Carbon Dioxide or Nitrogen in Natural Gas (Methane) Reservoirs. *Lawrence Berkeley National Laboratory Report* LBNL-56589, Berkeley, CA (USA).

Pruess K., C.M. Oldenburg, and G.J. Moridis, TOUGH2 User's Guide, Version 2.0. Lawrence *Berkeley National Laboratory Report LBNL-43134*, Berkeley, CA (USA), 1999.

Verma A., and K. Pruess, Thermohydrologic conditions and silica redistribution near high-level nuclear wastes emplaced in saturated geological formations, *J. Geophys. Res*., 93(B2), 1159–1173, 1988.

Xu T., and K. Pruess, Modeling multiphase non-isothermal fluid flow and reactive geochemical transport in variably saturated fractured rocks: 1. Methodology, *Am. J. Sci.*, 301, 16-33, 2001.

Peysson Y., Bazin B., Magnier C., Kohler E., Youssef S., 2010. Permeability alteration die to salt precipitation driven by drying in the context of CO_2 injection. International Conference on Greenhouse Gas Technologies (GHGT-10), Amsterdam, 19-23 September 2010.

Mahadevan J., 2005. Flow-through drying of porous media. *PhD Dissertation*. The University of Texas at Austin.

Mahadevan J., Sharma M.M., Yortsos Y.C., 2007. Water removal from porous media by gas injection: experiments and simulation. *Transport in Porous Media*, 66, p. 287-309.

Kleinitz W., Dietzsch G., Köhler M., 2003. Halite scale formation in gas producing wells. Chemical Engineering Research and Design 81 (PartA).

Zeidouni M., Pooladi-Darvish M., Keith D., 2009. Analytical solution to evaluate salt precipitation during CO2 injection in saline aquifers, *International Journal of Greenhouse Gas Control*, 3, p. 600–611

INFLUENCE OF GEOLOGICAL PARAMETERS ON CO_2 STORAGE PREDICTION IN DEEP SALINE AQUIFER AT INDUSTRIAL SCALE

Sarah Bouquet, Dominique Bruel, and Chantal de Fouquet

Mines ParisTech, Geosciences Centre
35, rue Saint Honoré
Fontainebleau, 77305 Cedex France
e-mail: sarah.bouquet@mines-paristech.fr

ABSTRACT

Here we examine the consequences of uncertainty with respect to geological parameters, using large-scale 2D models. We also investigate ways to reduce prediction uncertainty, either by showing how a parameter's influence is negligible for a given project design, or by showing for which parameters additional data will significantly increase the quality of prediction. TOUGH2/ECO2N is used to simulate the injection of millions of tonnes of CO_2 for the specific case of the Dogger Aquifer (a carbonate aquifer in the Paris Basin), which has substantial lateral and vertical heterogeneities and few associated data. The parameters of interest are spatial variability and correlation length of permeability, absolute permeability, pore compressibility, cap rock permeability, and relative permeability curves. Several numerical models of permeability are constructed: two uniform cases (two values of permeability) and 200 geostatistical initial realizations, which are modified according to the studied parameters. Results are compared in terms of propagation of pressure perturbations, injectivity (pressure in the vicinity of the well), and gas migration and dissolution. The results indicate that:

(1) The pore compressibility, and the absolute value and spatial variability of permeability have the strongest influence on pressure propagation and injectivity. Relative permeability curves and correlation lengths have a weaker influence at the peak of pressure, but tend to increase the variations in maximum/minimum cases.

(2) Relative permeability curves and heterogeneities have a significant impact on prediction of gas dissolution and migration.

Finally, we also investigate the possibility of reducing the number of simulations.

INTRODUCTION

In terms of available volume, deep saline aquifers seem suitable for CO_2 storage projects at industrial scale, yet the perturbations resulting from the injection of millions of tonnes of CO_2 will constrain the storage capacity of these aquifers. The extent and intensity of these perturbations, as well as CO_2 plume migration, will depend on the geological characteristics of the reservoir. However, the scarcity of data related to these aquifers leads to uncertain predictions of realistic injectivity and storage capacity.

At the regional scale, several storage projects may be involved in the same groundwater system. Therefore the quality of predictions in large-scale studies is critical to insure the feasibility of these projects.

Several studies at basin scale, such as Nicot (2008), Birkholzer at al. (2009), Zhou et al. (2010), Person et al. (2010), have shown that pressure buildup due to massive injection may extend far from the injection point, causing issues in terms of capacity (e.g., pressure interferences between neighboring sites) and posing risks for natural groundwater resources. Some of these studies have also described the influence of pore compressibility, reservoir permeability, and cap rock permeability on pressure-perturbation results at large scale. Depending on the specific study and model used—especially for homogeneous or layered models—boundary conditions (open/closed systems), permeability, and pore compressibility will have a decisive impact on pressure perturbations, especially compared to other parameters such as porosity, temperature, residual gas saturation, anisotropy, or cap rock permeability—as indicated by Buscheck et al. (2012), Schäfer et al. (2011), Chadwick et al. (2010), Flett et al. (2005).

The purpose of this study is to compare the consequences of uncertainty prediction for these influential parameters, as well as to evaluate the consequences of uncertainties in less-studied geological parameters, such as spatial variability of permeability and relative permeability curves. The spatial variability of permeability is much more likely than an assumption of a homogeneous reservoir, but its description is highly uncertain, and injectivity will be strongly affected by such variability as shown by Heath et al. (2012). By determining fluid mobility, relative permeability curves may constrain injectivity and, in turn, predictions of capacity.

METHODOLOGY

Modeling approach

Our models are representations of the Dogger Aquifer (Paris Basin, France), which is a highly heterogeneous carbonate reservoir and therefore relevant for studying the influence of heterogeneity uncertainties. Numerical simulations are performed with TOUGH2/ ECO2N code (Pruess et al., 1999). Outputs from numerical simulations are analyzed via the R software.

Geometrical configuration

The 2D domains of the simulated system, describing a large-scale system of about 140 km in length, represent a vertical section (154 m) of a horizontal well. Thus, the flow is assumed to be linear and perpendicular to the well. The flow depends on the well length and the reservoir properties (Kawecki, 2000). In order to maintain a realistic well setting, the studied injection period is limited to 1 year.

The injection point, corresponding to a limited section of the horizontal well, is located 21 m above the bottom of the reservoir. The injection rate of the section is equal to 0.185 kg/s. Assuming that the well is several kilometres long, it can be estimated that the total injection rate would be equivalent to several million tonnes a year.

The mesh of the models is irregular, with fine discretization around the well (7×7×7 m gridblocks in the vicinity of the injection point, 14×7×7 m for about 8 km on each side of the well). The length of blocks along the x-direction increases with increasing distance from the well. The size of blocks in the y- and z-directions remains the same over the entire domain (7×7 m).

Boundary and initial conditions

The simulated domain has closed boundaries. However, the size of the domain is chosen such that the lateral boundaries do not affect the results and therefore are infinite-acting. The domain is considered isothermal (65°C) and initially under hydrostatic conditions (166 bars at the top of the reservoir at 1550 m). The initial salinity is 25 g/L.

Generation of stochastic heterogeneous models

We first generate random, independent, normally distributed variables on a fine, isotropic mesh (cells size: 7×7×7 m). Then, we apply the moving average method to correlate variables according to a circular variogram with a geometrical anisotropy. For the base case, correlation length in X is 600 m, in Z 20 m. The correlated variables have a Gaussian distribution and are transformed to obtain a log-normal distribution of the permeability values. Finally, for flow simulation, upscaling techiques are applied to the properties in the X direction by using the geometric mean to get the irregular mesh previously described.

Two hundred equi-probable heterogeneous models are built, plus two homogeneous models (two different values of absolute permeability).
For all these models, permeability is isotropic (Kv/Kh=1). Simulations are conducted using all these representations with the different parameter values.

Geological parameters setting and variations intervals

The spatial variability of permeability is as described above, with a mean at 100 mD, median at 32.4 mD, and standard deviation of $\log_{10}$K equal to 1.5. The range of 99% of permeability values is [0.31mD – 3.16D] which is relevant for Dogger aquifers. Lateral correlation lengths variations are 300 m, 600 m (base case) and 1200 m. Figure 1 illustrates an example of spatial variability representation (heterogeneous models) with different correlation lengths.

In the homogeneous models, the permeability is either equal to the mean of the heterogeneous models (100 mD—mean values are often used to represent the permeability when scarce data are available) or the median value (32.46 mD), which is also the geometric mean, and may represent an equivalent permeability for the entire domain. Porosity is assumed to be uniform in the reservoir and set at 12%.

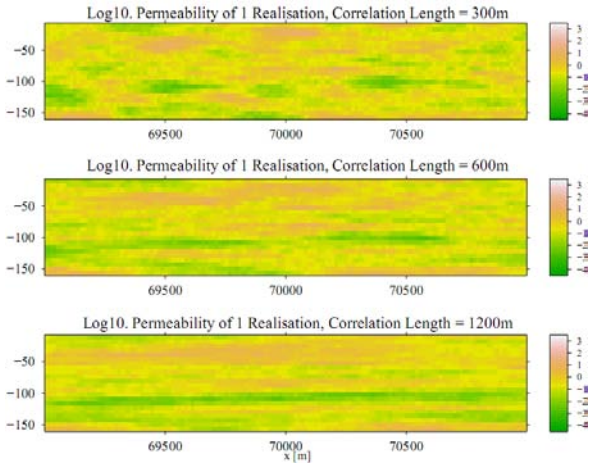

Figure 1. Permeability multipliers (log_{10} scale) for one model realization with different correlation lengths. Pictures are zoomed in around the well (at x=70000 m).

Instead of applying a widely used default value, 4.5E-10Pa^{-1}, we calculate pore compressibility either by correlation between porosity and pore compressibility for carbonates, or by correlation based on the compressibility measurement function for stress conditions and carbonate rock types (16.99E-10Pa^{-1}).

For the relative permeability curves, we use either the Van Genuchten-Mualem and Brooks-Corey methods, or measured data from the Dogger Aquifer (base case, André et al., 2007) or measured data from another carbonate aquifer, the Nisku aquifer (Bennion and Bachu, 2005). For capillary pressure, the same van Genuchten function is used for all scenarios with an entry capillary pressure equal to 5,4E+04 Pa. In the case of heterogeneous models, Leverett scaling is directly applied via the simulator according to the permeability multiplier.

To study cap rock permeability effects, we focus on three possible cases: (1) impermeable cap rock (base case, cap rock not represented, and top reservoir boundary closed), (2) a cap-rock permeability of 1E-19m² or (3**)** a cap-rock permeability 1E-17 m². The thickness of the cap rock is 158 m, and it subdivided into six layers (2 x 7 m and 4 x 36 m in height). The cap rock porosity and pore compressibility are 10.5% and 3.48E-10 Pa^{-1}, respectively. The gas entry pressure is set at 1.5E+07Pa. Because only a short injection period is considered, diffusion and hysteresis are neglected.

RESULTS AND DISCUSSION

Influence of each parameter in homogeneous and heterogeneous cases on prediction uncertainties

Homogeneous Permeability and Spatial Variability

If permeability increases, the maximum pressure at the well decreases, but the propagation of the pressure-induced disturbance extends further (Figure 2). Nevertheless, heterogeneous cases show higher dispersed results than homogeneous ones. The interval between minimum and maximum behavior of heterogeneous models exhibit homogeneous behavior.

Geological uncertainties in terms of permeability cannot be accounted for through the use of homogeneous models. This realization is even more obvious if we consider the extent of the gas migration in the saturation distributions (Figure 6) obtained from the heterogeneous models. The maximum and mean lateral extents of the CO_2 plume estimated from the 200 heterogeneous realizations are longer than the estimates from both the homogeneous models. This is true even if, for homogeneous models, an increase in permeability implies a longer reach of the plume at the interface between the cap rock and the reservoir.

Correlation length of permeability spatial variability

Pressure perturbations at the well tend to increase with a reduction of the correlation length (Figure 3). On the other hand, variations in the extent of the perturbation increase with the increase in correlation length (the standard

deviation decreases with decreasing correlation length).

However, mean results are close for all correlation lengths, and so the variations in predictions resulting from changes in correlation lengths will mainly affect minimum/maximum cases. Uncertainty with respect to correlation lengths will affect the reach of the CO_2 plume, with greater lateral extent associated with longer correlation lengths because the preferential pathways would be elongated (Figure 4). As for pressure, the different scenarios yield similar results in terms of the mean extent of CO_2 plume.

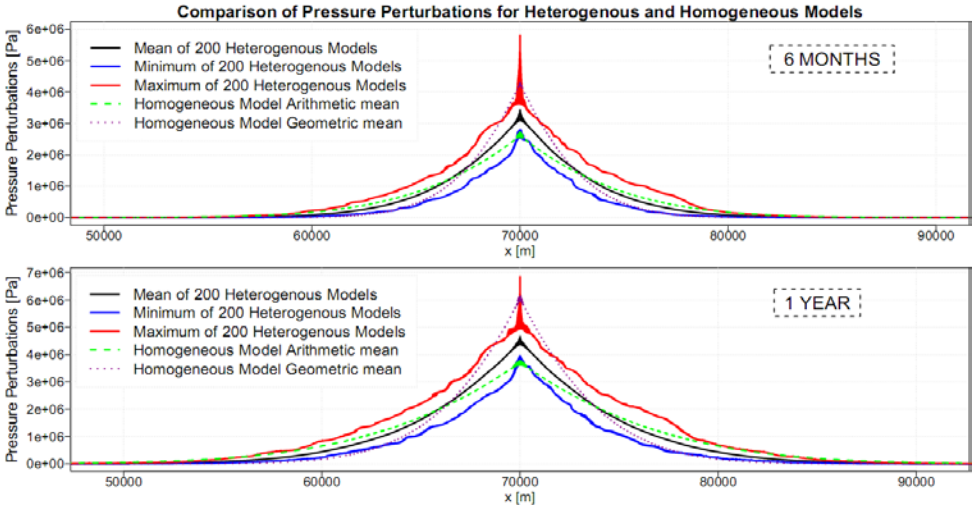

Figure 2. Pressure perturbations results for 200 heterogeneous models (base case, solid lines) and 2 homogeneous models (green and dashed lines: 100mD, purple and dotted lines: 32.4mD).

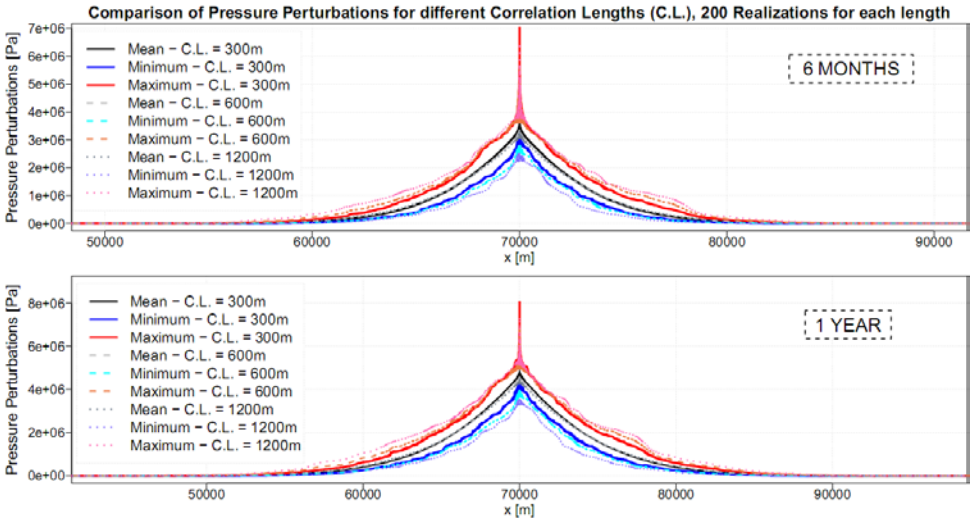

Figure 3. Pressure perturbations results for 200 heterogeneous models with different correlations lengths: 300m, 600m (base case) and 1200m.

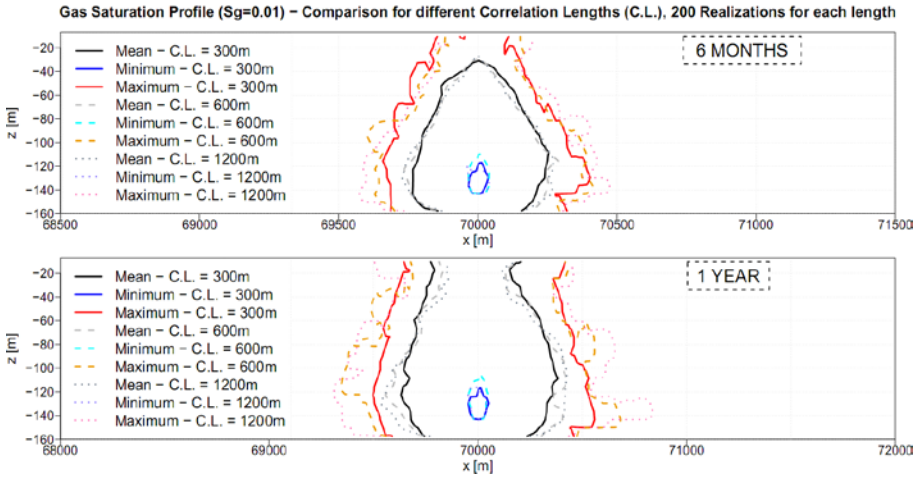

Figure 4. Gas Saturation extension for 200 heterogeneous models with different correlations lengths: 300m, 600m (base case) and 1200m.

Pore Compressibility

Ghaderi et al. (2009) and Schäfer et al. (2011) found that higher pore compressibility increases the injectivity (i.e., decreases the maximum pressure in the well) and slows down the pressure propagation (Figure 5). Therefore, as indicated by the diffusivity equation, pressure propagation would be faster when permeability increases and pore compressibility decreases (Figure 5, right side).

Variations in pore compressibility lead to significant uncertainty in predicting pressure perturbations. For heterogeneous cases (Figure 5, left side), the minimum pressure for the lower pore compressibility is higher than the maximum pressure for the higher pore compressibility. Uncertainty regarding pore compressibility may impact pressure predictions more strongly than heterogeneity uncertainties. Pore compressibility appears to have no influence on gas migration (Figure 6) and dissolution.

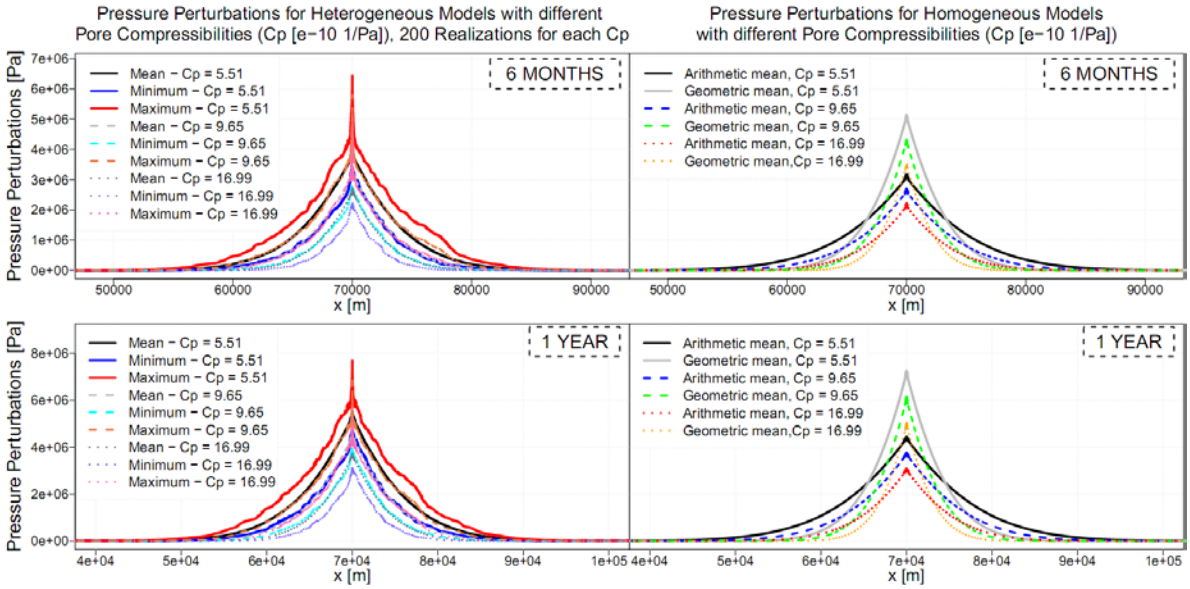

Figure 5. Pressure perturbations for 200 heterogeneous models and 2 homogeneous models with different pore compressibility (solid lines: 5.51E-10Pa^{-1}, dashed lines: 9.65E-10Pa^{-1} and dotted lines: 16.99E-10Pa^{-1}).

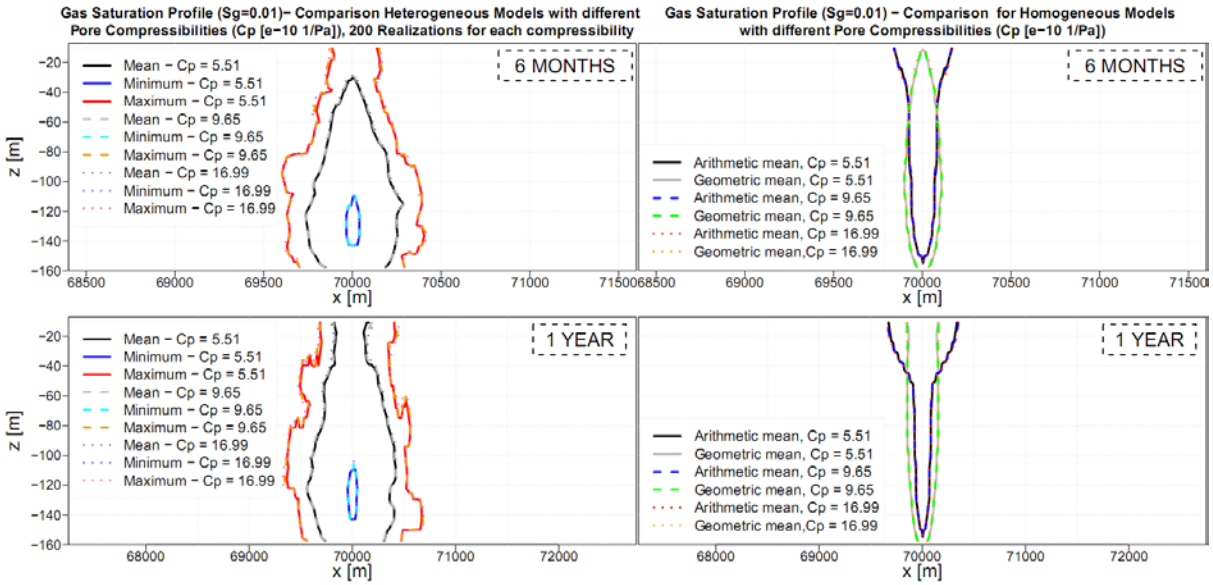

Figure 6. Gas Saturation extension for 200 heterogeneous models and 2 homogeneous models with different pore compressibility (solid lines: 5.51E-10Pa^{-1}, dashed lines: 9.65E-10Pa^{-1} and dotted lines: 16.99E-10Pa^{-1}).

Cap-rock Permeability

The pressure-perturbation differences between the cases involving impermeable cap rock and low-permeability cap rock (1E-19m^2) are negligible (Figure 7). However, when the cap-rock permeability is increased to 1E-17m^2, pressure dissipation through the cap rock becomes more significant, and the extent and amplitude of pressure perturbations in the reservoir decrease. Moreover, changes in cap-rock permeability do not affect the reach of the gas saturation front (the simulation results are identical) and supercritical CO_2 does not escape through the cap rock. This is not only because of the low permeability of the cap rock, but also because of its high gas entry pressure. Additionally, the cap rock permeability does not appear to significantly influence the dissolution rate.

With higher cap-rock permeability, more CO_2 could have dissolved at the interface between the top of the reservoir and the cap rock, where supercritical CO_2, and freshwater in the cap rock coexist. However, the variations in permeability of the impermeable cap rock are lower than 1% and therefore negligible.

Relative permeability curves

Uncertainty over relative permeability curves does not significantly influence pressure- propagation results. However, in maximum cases, because of the decrease in mobility, variations in the relative permeability may exacerbate the maximum peak-pressure behavior in heterogeneous models. The main influence of the relative permeability curves are on the CO_2 plume migration (Figure 8) and dissolution rate.

Comparison of the consequences on predictions from geological uncertainties.

Among all the parameters that have been studied, uncertainty in the pore compressibility has the most significant impact on predictions of pressure perturbation propagation. For a perturbation of 10 bars (Figure 9), estimated propagation differences can reach almost 4 km and have critically important consequences for the injectivity of surrounding wells and for storage capacity predictions. Stochastic dispersion from heterogeneous models can lead to similar uncertainties in the predictions. The differences may even be greater if the correlation length increases. Standard deviation increases with increasing correlation length and with decreasing pore compressibility and cap-rock permeability are associated with the most uncertain predictions.

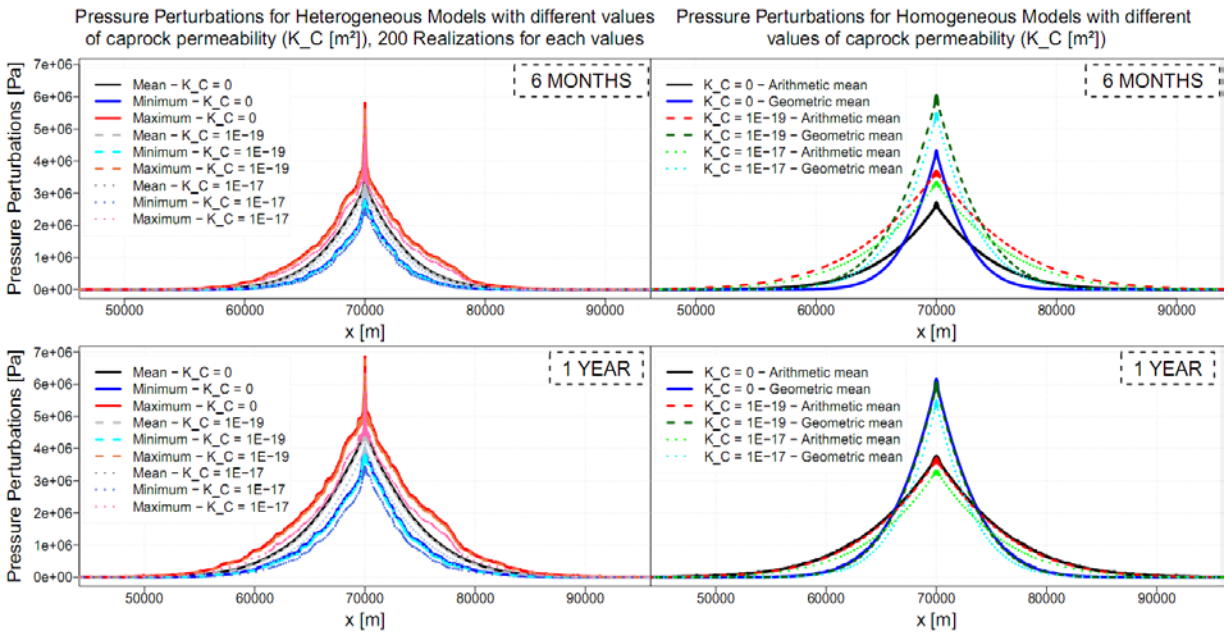

Figure 7. Pressure perturbations results from 200 heterogeneous and 2 homogeneous realizations with different cap-rock permeability (solid lines: Impermeable cap rock, dashed lines: cap-rock permeability = 1E-19 m² and dotted lines: cap-rock permeability = 1E-17 m²).

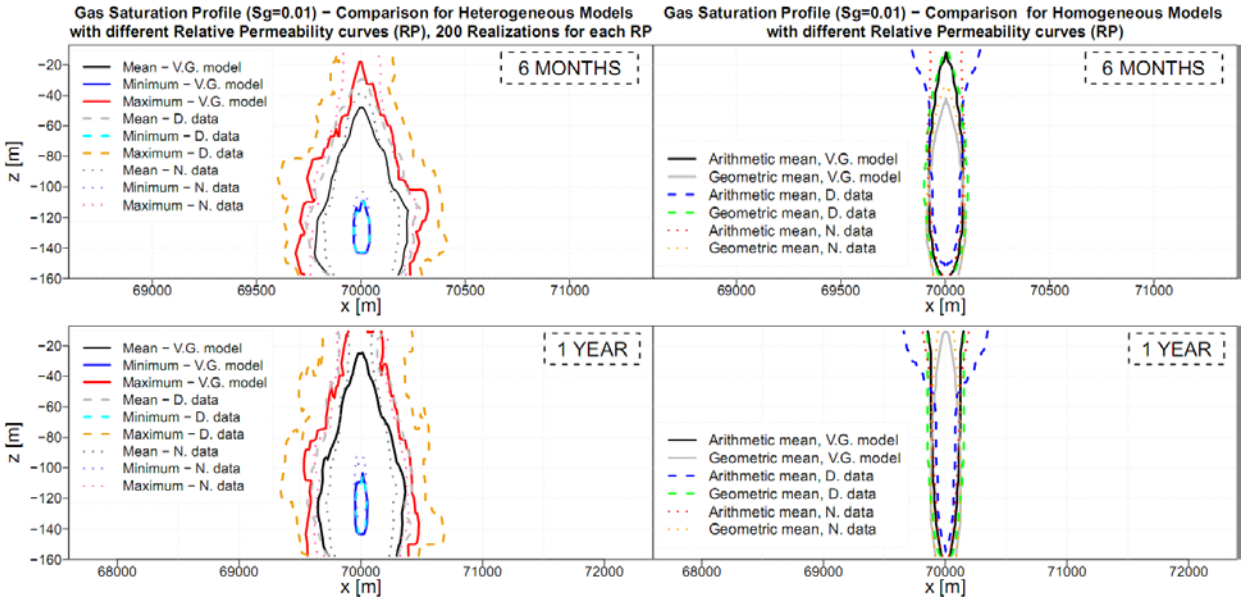

Figure 8. Gas Saturation extension from 200 heterogeneous and 2 homogeneous realizations with different relative permeability curves (solid lines: Van Genuchten-Mualem Model, dashed lines: Dogger aquifer data and dotted lines: Nisku aquifer data).

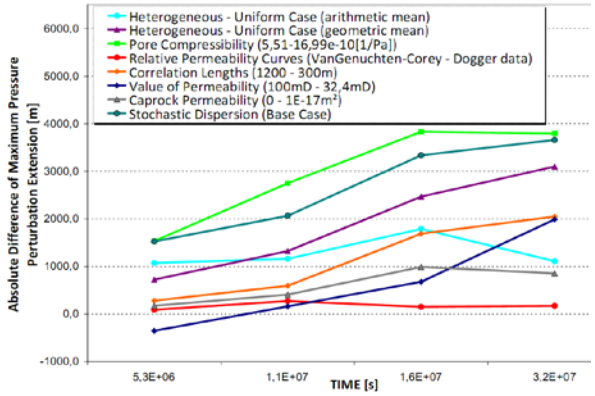

Figure 9. Differences of maximum pressure perturbations (1 MPa) extensions.

Injectivity predictions (i.e., maximum pressure) are less dependent on pore compressibility than on pressure propagation. The absolute values of permeability and heterogeneities uncertainties are the main influences on such predictions. The differences are ~28 bars for base-case stochastic dispersion, and ~24 bars for homogeneous models after one year of injection. Injectivity predictions are also influenced by CO_2 mobility: while differences in results between relative-permeability-curve scenarios are usually not as high as those from heterogeneity scenarios, the injectivity can be greatly reduced in some heterogeneous cases because of lower CO_2 mobility.

Dissolution rates (Figure 10) and CO_2 plume migration depend mainly on heterogeneities and the relative-permeability-curve scenarios. The influences of correlation lengths is weaker, and the influence of pore compressibility and caprock permeability are negligible.

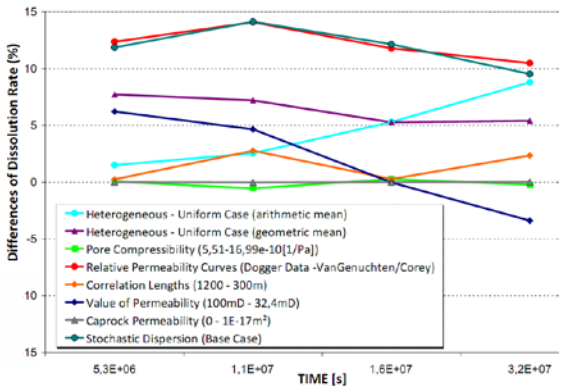

Figure 10. Differences of maximum dissolution rates.

SELECTION OF REALIZATIONS

Based on the pressure results from 200 base-case realizations, we select, at 6 months, the most representative realizations of mean, minimum, and maximum behavior to obtain the same behavior with fewer realizations. This selection (51 realizations) gives equivalent results to those with 200 (Figure 11). Thus, it seems possible to reduce the number of runs for each parameter by a factor of 4. Only 51 realizations need to be run only once, and only up to 6 months, to select a relevant set of realizations for this study.

CONCLUSION

For the large-scale problems and the values of the parameters considered here, uncertainties in pore compressibility and heterogeneities in the permeability appear to have the most effect on the predictions of the extent of the propagation of the pressure. For risk assessment of leakage (i.e., migration of the plume through fault or abandoned wells) or for the amount of CO_2 trapped, heterogeneities in the permeability of the formation and the cap rock and uncertainties in the relative permeability curves have the most influence on predictions.

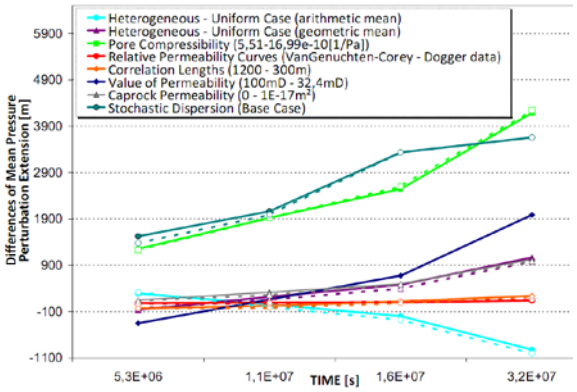

Figure 11. Differences of mean pressure perturbations (1 MPa) extensions (solid lines: 200 realizations, dotted lines with white-filled points: 51 selected realizations).

REFERENCES

Andre, L., Audigane, P., Azaroual, M. & Menjoz, A., Numerical modeling of fluid-rock chemical interactions at the supercritical CO_2-liquid interface during CO_2 injection into a carbonate reservoir, the Dogger aquifer (Paris Basin, France), *Energy Conversion and Management*, 48, 1782-1797, 2007.

Bennion, B., Bachu, S., Relative Permeability Characteristics for Supercritical CO2 Displacing Water in a Variety of Potential Sequestration Zones in the Western Canada Sedimentary Basin, Paper SPE 95547, presented at the 2005 SPE Annual Technical Conference and Exhibition, Dallas, TX, USA, October 9-12, 2005.

Birkholzer, J.T., Zhou, Q. and Tsang, C.-F., Large-scale impact of CO_2 storage in deep saline aquifers: A sensitivity study on pressure response in stratified systems, *International Journal of Greenhouse Gas Control,* 3, 181-194, 2009.

Buscheck, T., *et al.*, Active CO_2 reservoir management for carbon storage: Analysis of operational strategies to relieve pressure buildup and improve injectivity, *International Journal of Greenhouse Gas Control,* 6, 230-245, 2012.

Chadwick, R.A., Noy, D.J. & Holloway, S., Flow processes and pressure evolution in aquifers during the injection of supercritical CO2 as a greenhouse gas mitigation measure. *Petroleum Geoscience,* 15, 59-73, 2009.

Flett, M.A., Gurton, R.M. and Taggart, I.J., Heterogeneous saline formations: Long--term benefits for geo-sequestration of greenhouse gases. *Proc 7th Intl Conf on Greenhouse Gas Control Technologies September 2004 Vancouver Canada,* I, 501-509, 2005.

Heath, J.E., Kobos, P.H., Roach, J.D., Dewers, T.A. & Mckenna, S.A., Geologic Heterogeneity and Economic Uncertainty of Subsurface Carbon Dioxide Storage. *SPE Economics & Management*, 4, 32-41, 2012.

Horne, R.N., *Modern Well Test Analysis: A Computer-Aided Approach*, Petroway Inc, Palo Alto, CA, 1990.

Jalalh, A.A., Compressibility of porous rocks: Part II. New relationships. *Acta Geophysica,* 54, 399-412, 2006.

Kawecki, M.W., Transient Flow to a Horizontal Water Well, *Ground water,* 38, 842-850, 2000.

Nicot, J.-P., Evaluation of large-scale CO_2 storage on fresh-water sections of aquifers: An example from the Texas Gulf Coast Basin, *International Journal of Greenhouse Gas Control,* 2, 582-593, 2008.

Person, M. *et al.,* Assessment of basin-scale hydrologic impacts of CO_2 sequestration, Illinois basin, *International Journal of Greenhouse Gas Control*, 4, 840-854, 2010.

Pruess, K., C. Oldenburg, and G. Moridis, *TOUGH2 User's Guide, Version 2.0*, Report LBNL-43134, Lawrence Berkeley National Laboratory, Berkeley, Calif., 1999.

Schäfer, F., Walter, L., Class, H. & Müller, C., The regional pressure impact of CO_2 storage: a showcase study from the North German Basin, *Environmental Earth Sciences,* 65, 2037-2049 2011.

Zhou, Q., Birkholzer, J.T., Mehnert, E., Lin, Y.-F. & Zhang, K, Modeling basin- and plume-scale processes of CO2 storage for full-scale deployment, *Ground water,* 48, 494-514, 2010.

TOUGH2 SIMULATION OF THE PUMPING TESTS AT KETZIN SITE: HETEROGENEITY EFFECTS AND MODEL CALIBRATION

Fei Chen, Quanlin Zhou, Jens Birkholzer

Lawrence Berkeley National Laboratory
One Cyclotron Road
Berkeley, CA, 94720, USA
e-mail: fei.chen@lbl.gov

ABSTRACT

The Stuttgart formation used for ongoing CO_2 injection at the Ketzin pilot test site in Germany is highly heterogeneous in nature. The characterization data, including 3D seismic amplitude image, the regional geology data, and the core measurements and geophysical logs of the wells, show the formation is primarily composed of permeable sandstone channels of varying thickness and length embedded in less-permeable mudstones. Most of the sandstone channels are located in the upper 20 m of the formation, with only a few sparsely distributed sandstone channels in the bottom 60 m layer. The spatial pattern of these channels can be ascertained from 3D amplitude imaging. Heterogeneity was found to have a substantial effect on the pressure propagation measured during a suite of pumping tests conducted in 2007-2008, and also found to strongly impact the CO_2 arrival times observed during the ongoing CO_2 injection experiment.

To understand the varying effects of heterogeneity at the Ketzin site and calibrate the spatial variability of permeability and porosity using the field monitoring data, we developed a TOUGH2 model for modeling the hydraulic pumping tests. The geological model used in the simulation, provided to us by the German project partner conducting the pilot test (Geoforschungszentrum Potsdam, GFZ), was calibrated against CO_2 arrival times. Our modeling results showed that the simulated pressure responses to the pumping tests were significantly different in magnitude from the measured data. A systematically increase or decrease in the permeability failed to improve the matches to the pressure data in all the observation wells. Further work is needed on the calibration of the geological model against the pumping test results, using inverse modeling approaches.

INTRODUCTION

The Ketzin site is the first pilot test site for onshore CO_2 injection into a natural saline aquifer in Europe. It is located in the eastern part of a double anticline (Ketzin-Roskow anticline) in Northern Germany. Food-grade supercritical CO_2 has been injected into the Upper Triassic Stuttgart formation situated between 630 and 710 m below the ground surface. The Stuttgart formation is highly heterogeneous in nature; site characterization shows the formation to be composed of highly permeable sandy channels of varying width and length, alternating with the facies of low-permeability mudstone (Forster et al., 2006). The width of the channel belts ranges from several tens to hundreds of meters involving stacked subchannels (Forster et al., 2006). The spatial distribution of the permeable channels is difficult to predict (Frykman et al., 2006). Limited wellbore logging data show that the majority of the permeable channels are located in the top 20 m of the formation, with only a few sparsely distributed in the bottom 60 m layer (Norden et al., 2010). Above the Stuttgart formation are layers of claystone, silty claystone and anhydrite. They have an average thickness of about 210 m and provide an excellent seal for the saline aquifer (Forster et al., 2006).

Subsurface heterogeneity has a large effect on pressure propagation and fluid flow. The data gathered from the CO_2 injection and hydraulic tests can provide us information for better understanding of the heterogeneous site. The CO_2 injection test at the Ketzin site shows that CO_2 arrived at one of the observation wells

(Ktzi200) that is 50 m apart from the injection well (Ktzi201) after 21.7 days - whereas it took 271 days to reach the other observation well (Ktzi202), which is 112 m away from the injection well (Kempka et al., 2010). Recent work includes calibration of the geological model against the CO_2 arrival times (Kempka et al., 2010). The model was in good agreement with the first arrival time but failed to capture the later one.

A suite of hydraulic pumping tests were conducted in the three wells between September 2007 and January 2008. Due to the multiple other objectives to be served by the tests, the pumping events were not optimized for the hydraulic tests (Wiese et al., 2010). For example, with the intention of removing all fluids from the borehole, packers were not used in the pumping tests. The pumping test was conducted by pumping fluid from one of the wells and monitoring the pressure in the other two observation wells and the pumping well itself. The pumping rates were adjusted between 1.1 m^3/h and 1.8 m^3/h, based on the allowable drawdown (Wiese et al., 2010). Pressure in the pumping well was measured at locations close to the pump and the bottom-hole screen, while the pressures in the observation wells were measured about 5-15 m below the water table. The pumping test results were interpreted using analytical solutions by Wiese et al (2010). They found that the effective permeability of the 20 m permeable zone is about one order of magnitude lower than the mean permeability of the core samples, a phenomenon that is not frequently seen in the field (Wiese et al., 2010). Despite the importance of the hydraulic test data, we have not seen any simulation of the pumping tests that attempt to calibrate the geological model with these data.

To understand the varying effects of heterogeneity at the Ketzin site and calibrate the spatial variability of permeability and porosity using the field monitoring data, we developed a TOUGH2 model for the hydraulic pumping tests. The geological model used in the simulation, provided to us by the German project partner (GFZ) conducting the pilot test, was calibrated against the CO_2 arrival times. We then compared the simulation results with the measurement data.

MODEL DEVELOPMENT

We created a three-dimensional grid (Figure 1)

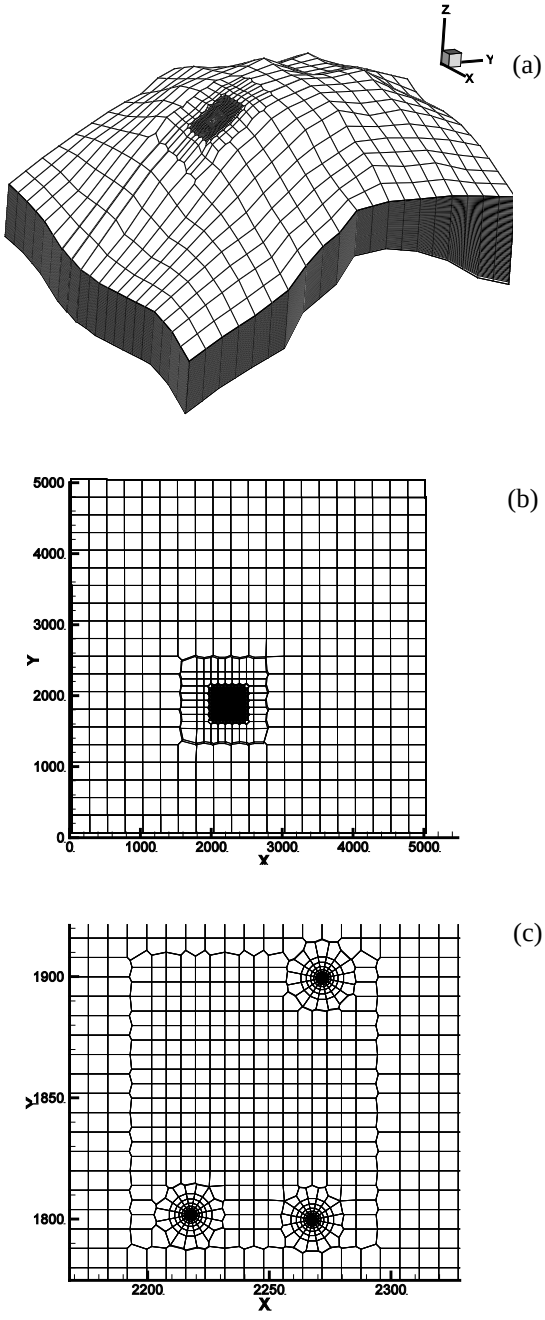

Figure 1 Generated mesh for the 5 km× 5 km model domain (a) in 3D view, (b) in plane view, (c) near the wells

using WinGridder (Pan, 2007). The mesh covers an area of 5000 m × 5000 m with the elevation

of layers and thickness varying to represent the anticline structure of the Stuttgart formation. The area away from the wells is discretized by relatively coarse and regularly spaced meshes (250 m ×250 m). The mesh sizes gradually decrease to 4 m × 4 m as it gets close to the wells. Radially symmetric meshes are used to represent the well geometry (Figure 1c). The formation is uniformly discretized in the vertical direction by 74 layers, with the thickness of each layer proportional to the varying thickness of the formation.

The geological model was generated using a geostatistical approach, based on a collection of measurement data including seismic profiles, stratigraphic and lithological information from boreholes, and CO_2 arrival time (Forster et al., 2006; Kempka et al., 2010). The permeability and porosity distributions used for our model are interpolated from the geological model using the inverse-distance approach.

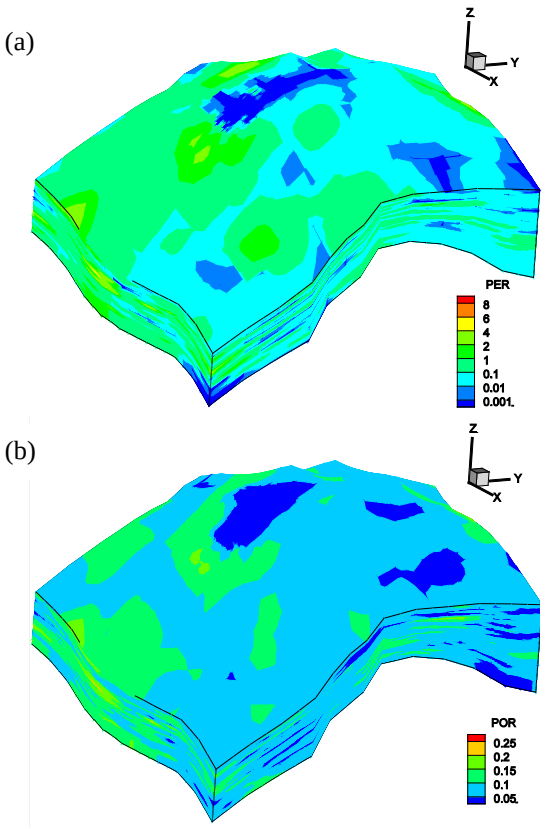

Figure 2 Permeability (a) and porosity (b) distributions used in the model (3D view)

We use the parallel version of the TOUGH2 code (TOUGH2-MP) (Zhang et al., 2008) with the fluid property module ECO2N (Pruess, 2005) to run the simulation. To simulate the vertical well, the permeability of the well elements is assigned with 4.98×10^{-8} m^2, which is equivalent to the permeability of a pipe with a diameter of 0.12 m. Time-dependent pumping rates are parameterized to fit the actual rates in the operation (Figure 3). No-flow boundary conditions are applied to the top and bottom of the model domain, and the lateral boundaries are in fixed condition. The fluid is initially in equilibrium with the hydrostatic pressure. The salt concentration is 0.22 (wt/wt) and the temperature is 34 °C. We do not consider the CO_2 component in the pumping test simulation.

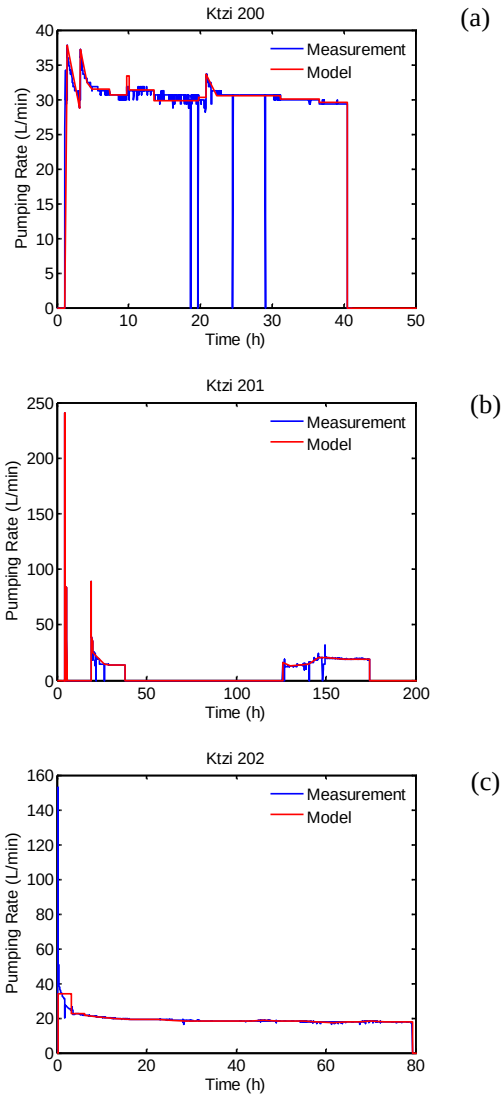

Figure 3 Pumping rates at the wells (a) Ktzi200, (b) Ktzi201, (c) Ktzi202.

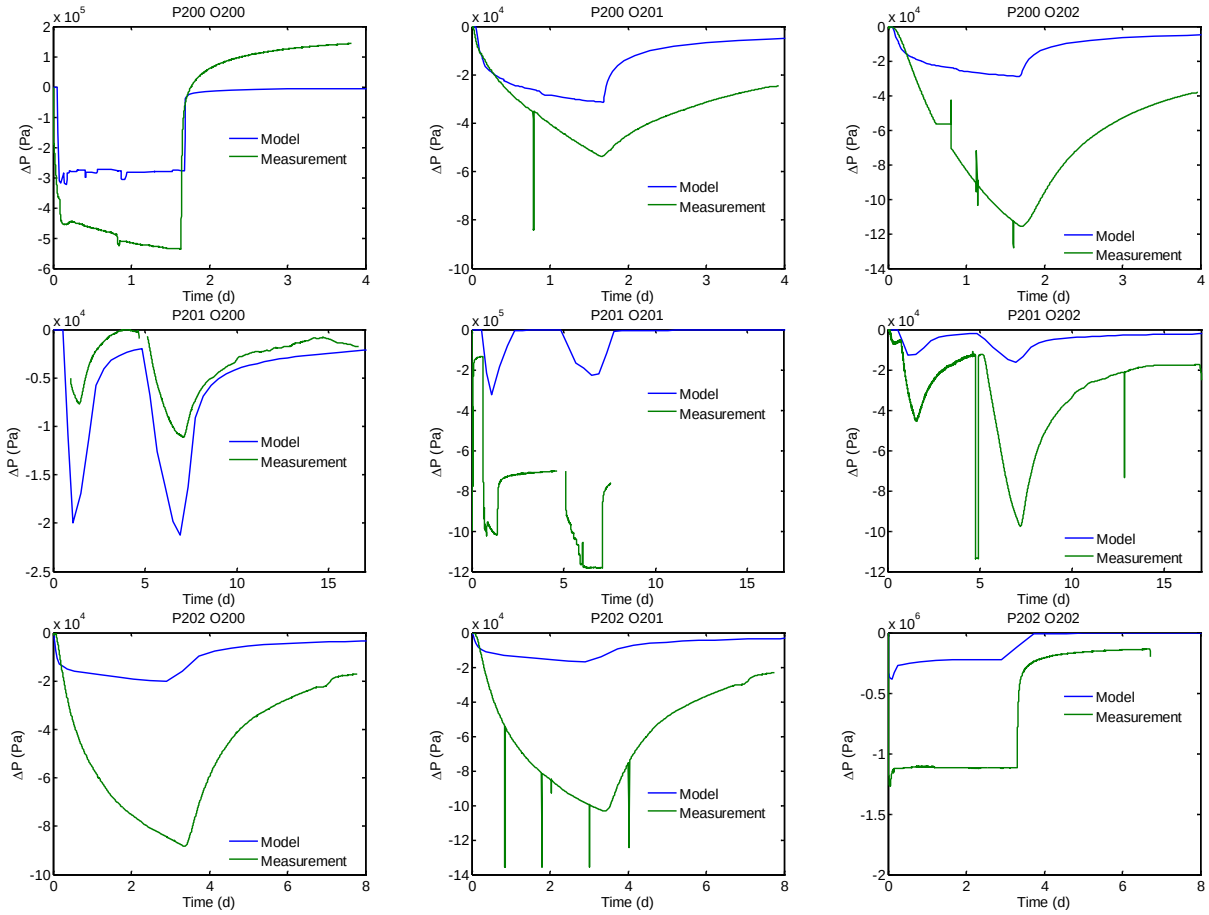

Figure 4 Pressure responses over time based on the geological model provided by GFZ. Here, P stands for pumping well and O observation well.

RESULTS

The simulated pressure changes are compared to the measured data (Figure 4). The pressure simulated with the model shows a similar pattern as a response to the pumping, though mismatch exists in the magnitude of pressure responses. There is no systematical trend on the differences between the model and the measurement data. When water is pumped in Ktzi200 and Ktzi202, the simulated pressure changes in the corresponding observation wells are less than the measured ones. When pumping in Ktzi201, the model overestimates the response at Ktzi200 but underestimates at Ktzi202. The drawdown caused by a pumping event is affected by the spatial distribution of the hydraulic properties (e.g. permeability). For the well pairs having less pressure changes than the measured data, it is likely the permeability between these wells is overestimated in the geological model. On the contrary, for those having larger pressure responses, it is likely the permeability around the region is underestimated (see Figure 5).

The pressure data in the pumping wells are difficult to interpret because many factors contribute to the final results. One of these factors is the density difference between brine and the fluid in the borehole. When water is pumped from the pumping wells, the fluid in the borehole is replaced by the brine from the saline aquifer. This density effect can be large. For a 400 m well, if we assume the well is initially filled with freshwater, the maximum pressure difference caused by the density effects can reach up to about 0.8 MPa. As we mentioned before, the pumping tests serve multiple goals and were not optimized for hydraulic tests. It was reported that a fluid that has a density close to freshwater was injected into the wellbore before the pumping tests (Wiese et al., 2010).

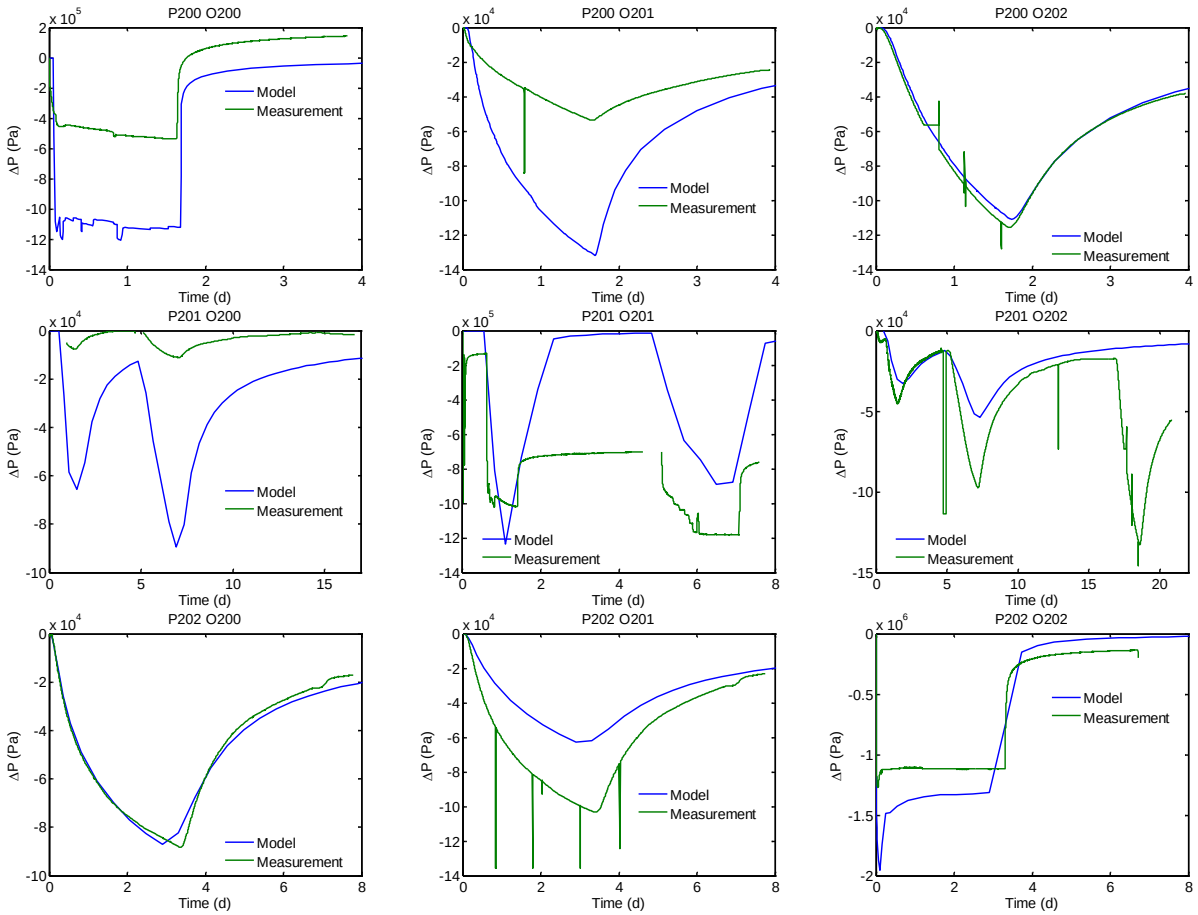

Figure 5 Pressure responses over time with decreased permeability

We do not correct the effects caused by brine replacement in this study, but data corrections are under way to better interpreting of the pressure data in the pumping wells.

Further simulation was conducted by decreasing the permeability of the system by a factor of 10. It appears that such a systematical decrease in permeability improves the match in pressure in Ktzi202/Pumping at Ktzi200, Ktzi 202/Pumping at Ktzi201, and Ktzi200 and Ktzi 201/Pumping at Ktzi 202. However, the decrease of permeability causes mismatches in other wells such as Ktzi200/Pumping at Ktzi201 and Ktzi201/Pumping at Ktzi200.

CONCLUSIONS

We developed a numerical model to simulate a suite of pumping tests conducted at the Ketzin CO_2 storage pilot test site, using the geological model provided by the German project partners conducting the pilot tests. Compared to the measured data, the model shows similar patterns but different magnitude of pressure changes as a response to the pumping regime. Systemically increasing (not shown in this paper) or decreasing the permeability fails to improve the match for all observation wells, suggesting that the permeability and porosity distributions in the geological model do not accurately represent the local heterogeneity near the wells. Further work is required to calibrate the geological model against the pumping tests data using inverse modeling approaches.

ACKNOWLEDGMENT

We acknowledge our German project partners from GFZ: Thomas Kempka, Ben Norden, Christopher Otto, Bernd Wiese, and Michael Kühn for providing geological model and field data.

REFERENCES

Forster, A.; Norden, B.; Zinck-Jorgensen, K.; Frykman, P.; Kulenkampff, J.; Spangenberg, E.; Erzinger, J.; Zimmer, M.; Kopp, J.;

Borm, G.; Juhlin, C.; Cosma, C.; Hurter, S. Baseline characterization of the CO2SINK geological storage site at Ketzin, Germany. *Environmental Geosciences, 13* (3), 145-161, 2006.

Frykman, P.; Zink-Jørgensen, K.; Bech, N.; Norden, B.; Förster, A.; Larsen, M. Site characterization of fluvial, incised-valley deposits. In Proceedings, *CO2SC Symposium*, Lawrence Berkeley National Laboratory, Berkeley, CA, March 20-22, 2006.

Kempka, T.; Kühn, M.; Class, H.; Frykman, P.; Kopp, A.; Nielsen, C.M.; Probst, P. Modelling of CO_2 arrival time at Ketzin – Part I. I*nternational Journal of Greenhouse Gas Control, 4* (6), 1007-1015, 2010.

Norden, B.; Förster, A.; Vu-Hoang, D.; Marcelis, F.; Springer, N.; Le Nir, I. Lithological and Petrophysical Core-Log Interpretation in CO2SINK, the European CO_2 Onshore Research Storage and Verification Project. *SPE Res Eval & Eng, 13* (2), 179-192, 2010.

.

Pan, L. *User information document for: WINGRIDDER version 3.0*; 10024-UID-3.0-00; Lawrence Berkeley National Laboratory: Berkeley, CA, 2007.

Pruess, K. *ECO2N: A TOUGH2 Fluid Property Module for Mixtures of Water, NaCl, and CO_2*; LBNL-57952; Lawrence Berkeley National Laboratory: Berkeley, CA, 2005.

Wiese, B.; Böhner, J.; Enachescu, C.; Würdemann, H.; Zimmermann, G. Hydraulic characterisation of the Stuttgart formation at the pilot test site for CO_2 storage, Ketzin, Germany. *International Journal of Greenhouse Gas Control, 4* (6), 960-971, 2010.

Zhang, K.; Wu, Y.; Pruess, K. *User's Guide for TOUGH2-MP - A Massively Parallel Version of the TOUGH2 Code*; LBNL-315E; Lawrence Berkeley National Laboratory: Berkeley, CA, 2008

MODELING OF THE CO_2 GEOLOGICAL STORAGE AT THE S3 SITE (SIM-SEQ COMPARATIVE PROJECT)

Christophe Chiaberge, Joachim Tremosa, Anne-Gaëlle Bader, and Pascal Audigane

BRGM, French Geological Survey, Orléans, Loiret, France
e-mail: c.chiaberge@brgm.fr

ABSTRACT

The Sim-SEQ project coordinated by the Lawrence Berkeley National Laboratory (LBNL) aims at providing a comparative study of different conceptual models with respect to predicting the behavior of CO_2 geological storage operations conducted on a reservoir formation, while using the same database for site characterization. The S-3 site has been selected for conducting such a comparative study. All site characterization and operational data for the S-3 site are supplied by the Bureau of Economic Geology (BEG) at the University of Texas at Austin. The site is a depleted oil and gas field, located in the Mississippi Gulf Coast (United States), at which CO_2 injection started in November 2009.

Being one of the participating modeling teams, BRGM proposed to provide a complete assessment of the field by generating a 3D static earth geological model using the Petrel reservoir geomodeler, and by using an in-house toolbox to convert the 3D mesh of the static model into TOUGH2 and TOUGHREACT formats, before generating a multiphase flow simulation of the CO_2 injection. The geological model is constructed based on information provided by several well log data. Horizon surface is rebuilt, and fluvial sandstone-shale facies distribution is generated. Reservoir petrophysical properties are associated to each facies in agreement with the provided data (absolute and relative permeability and capillary pressure), as well as temperature and salinity. Hydrostatic pressure and temperature gradient is recalculated before the simulation of the CO_2 injection. Calibration of the model is performed by comparing results from the simulated scenario with observation-well data provided in the project.

The geochemistry of the water and the mineralogy description of the rock will serve as perspectives in evaluating the fluid-rock-interaction evolution of the system for the tens-of-years injection and post-injection period. This paper provides details on the methodology and preliminary results regarding the static geological model and dynamic flow simulation.

INTRODUCTION

The aim of the Sim-SEQ project is to compare modeling prediction studies from different teams, using data based on the observations made during the CO_2 geological storage performed at the S-3 site, a site modeled from a depleted oil and gas field located in the Mississippi Gulf Coast (United States)—see Mukhopadhyay et al. (2012). All data are supplied by the Bureau of Economic Geology.

In this paper, we present the development of a 3D static geological model of the S3 site using the Petrel geomodeler (©Schlumberger) and a multiphase flow modeling of CO_2 injection using TOUGH2-MP (©LBNL) and the previous 3D model.

GEOLOGICAL MODELING

A structural 3D model of the S3 site was developed with Petrel software (© Schlumberger). The modeling process consists of creating surfaces, creating horizons and zones, upscaling well data, and layering, in order to generate a 2000×2000×80 ft grid with 200×200×8 cells as defined in the Sim-SEQ project.

Construction of the structural 3D model

The data used to construct the 3D model is provided by LBNL (Sim-SEQ website at https://gs3.pnl.gov/simseq/wiki/index.php/Sim-SEQ_Home) and consist of one ASCII file with coordinates in XYZ format describing the top of the reservoir as well as the three wells (SS31F1, SS31F2 and SS31F3) information (wellhead

location and well tops), available well logs and core analysis.

The first step is to compute surfaces using the XYZ points. A convergent interpolation algorithm is used with an X/Y increment of 50 ft in order to fit (as close as possible) with input data. This "top reservoir" surface is used to construct the "base reservoir" surface by shifting the top reservoir 80 ft deeper. After analysis of gamma ray (GR) curves at wells SS31F2 and SS31F3, the well tops Top/L Tusc. D Sand are moved slightly, and the top reservoir surface is re-interpolated with the make/edit surface process of Petrel, including a well adjustment in order to fit with the well tops. The same process is applied to the base reservoir surface (Fig. 1).

Based on a GR curve analysis, we identify (within the reservoir) two main sand bodies of 11–12 m delimited by a 1 m thick shaly layer. The well tops corresponding to the top and base of each sand body are chosen, and the corresponding surfaces are interpolated using the top reservoir surface shifted and fitted to the well tops (Figure 1).

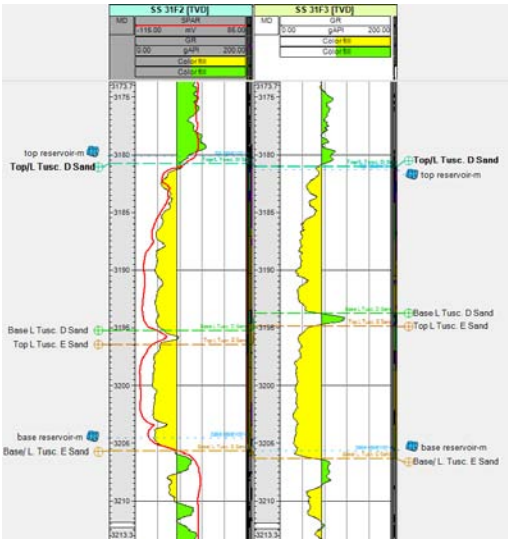

Figure 1. GR curve (green when GR>75 API and yellow when GR<75 API) of wells SS31F2 and SS31F3 used to locate well tops Top D Sand (corresponding to the top reservoir), Base D Sand, Top E Sand and base E sand (base of the reservoir). Red line on SS31F2 well correspond to the sonic curve.

A simple grid is generated with the geometry defined by the Sim-SEQ project. As four surfaces are incorporated in the model and transformed into horizons, three zones are automatically created between these horizons (Figure 2). The zones are in turn divided into layers as follows: D sand (zone 1) with four layers, Shaly bed (zone 2) with one layer and E sand (zone 3) with three layers (Figure 2).

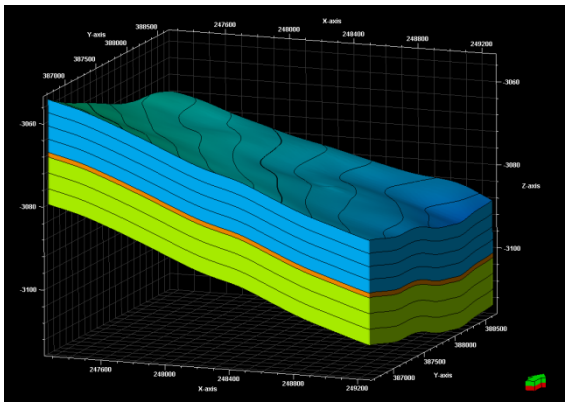

Figure 2. Model zones and layers of GS3 reservoir D Sand is blue, shaly layer, orange and E Sand, green.

Petrophysical modeling

Log data are upscaled so that each cell that is penetrated by the well will give a single value for the property. The arithmetic mean is used on the SPHI curve for porosity and permeability is calculated from the KSDR curve using the neighboring cell method.

Given that the permeability log value is available on SS31F2 only, the data plug analysis on SS31F2 and F3 is also used for permeability evaluation. After the upscaling process, the petrophysical modeling process is used to propagate the property values in the model. Since the data exist exclusively at the three wells located at the center of the model, it is not possible to use interpolation methods such as kriging or Gaussian simulation. We use instead the moving average method for both porosity and permeability distribution (Figures 4 and 5). The 3D petrophysical model obtained corresponds thus to a 200×200×8 cells grid with porosity values between 16% and 25%, and permeability values between 0.7 mD in the shaly layer and 260 mD at the base of the sand bodies.

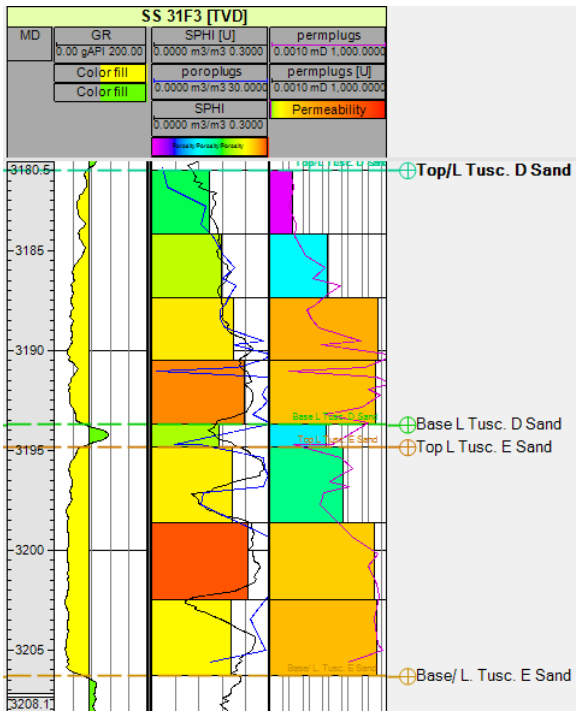

Figure 3. Example of porosity and permeability upscaling on SS31F3 well

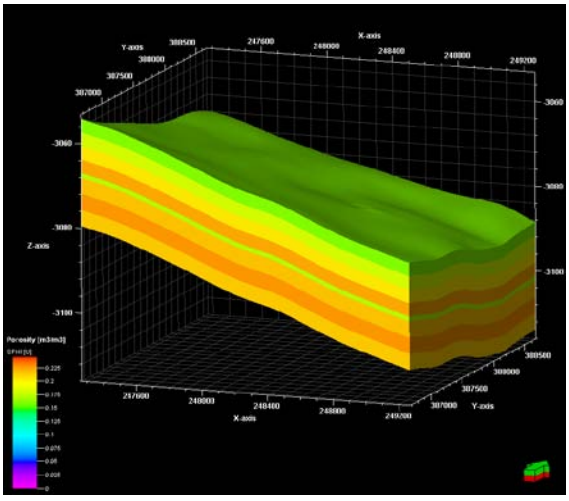

Figure 4. Porosity model of the S3 site

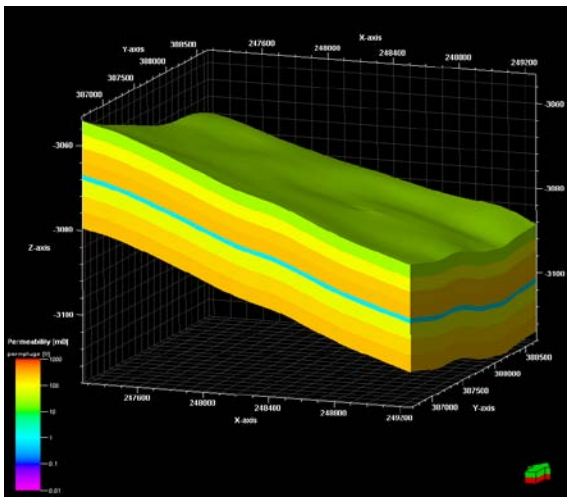

Figure 5. Permeability model of the S3 site.

MULTIPHASE FLOW SIMULATION USING 3D STATIC MODEL

To perform the multiphase flow simulation of CO_2 injection with the 3D static geological model described in the previous section, we first proceed to convert the Petrel model to a TOUGH2 format.

Conversion of geological model

We use an in-house toolbox (Audigane et al., 2011) to convert the 3D static geological model into the TOUGH2 mesh format. In this model, no faults have been accounted for. Some adaptation of the mesh geometry is also required to respect the integral finite-difference scheme used in TOUGH2. From the Petrel grid, we calculate the exact volume and the exact center point of each grid cell, and we calculate approximate values for the interface area and the distances of a connection between two cell centers as required by TOUGH2. Indeed, the grid cells exported from Petrel in the Eclipse format (.grdecl) can generate non-plane faces (with four nodes of the surface not aligned in a plane). Therefore, we calculate a new median plane between the four nodes and use the orthogonal projection of the nodes on this plane to calculate the new interface area. We then use the point of intersection between the line joining the two centers of the two neighbor cells and this plane to calculate the connection distances.

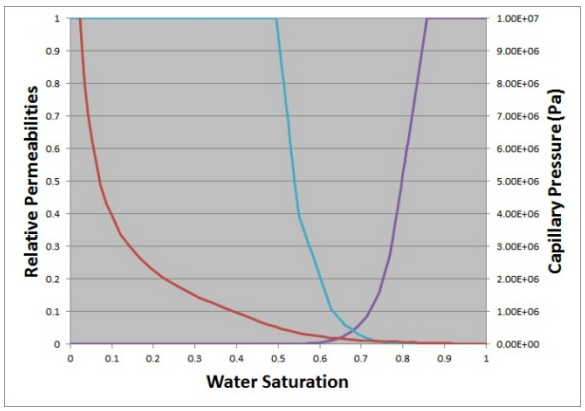

Figure 6. Relative permeabilities and capillary pressure curves used for the simulation of CO_2 injection

Simulation of CO_2 injection

The injection well SS31F1 is at the center of the model, and the two observation wells SS31F2 and SS31F3 are at distances of 223 and 364 ft, respectively, from the injection well.

Initialization and parameters

Initial hydrostatic pressure is calculated with an average value of about 3.25×10^7Pa, the temperature is fixed at 103°C, and a salinity of 15.7% weight is applied. Capillary pressure and relative permeability curves have been fitted to the data obtained by the samples tests (Fig. 6). The flow rate for the CO_2 injection was taken at 5.8 kg m^{-3} during 1 year.

Simulation of CO_2 injection

We use the massive parallel version of TOUGH2-MP (Zhang et al., 2008) with the ECO2N module to overcome CPU-time and memory constraints arising from the large number of gridblocks. Simulated arrival times at the observation wells are about 11 days and 34 days for the SS31F2 and SS31F3 wells, respectively. Figure 7 shows the evolution of gas saturation along the first and second observation wells. Figure 8 shows the extension of the plume of gaseous CO_2 in the aquifer just before the arrival at the 2^d observation well.

Differences between the model predictions and the well observation can be explained by several factors, like the presence of methane in the real reservoir (neglected in this study), the large level of uncertainty regarding the permeability distribution, capillary pressure, and relative permeability curves. For instance, gaseous CO_2 in Figure 7 can easily flow through the shale layer in our model, which is very questionable.

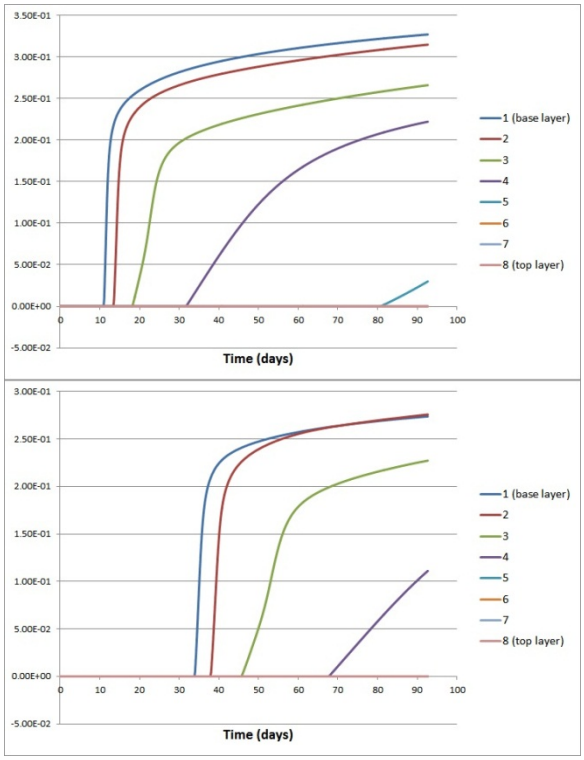

Figure 7. CO_2 gas saturation along the SS31F2 (top) and SS31F3 (bottom) wells, CO_2 arrives first in the bottom of the aquifer

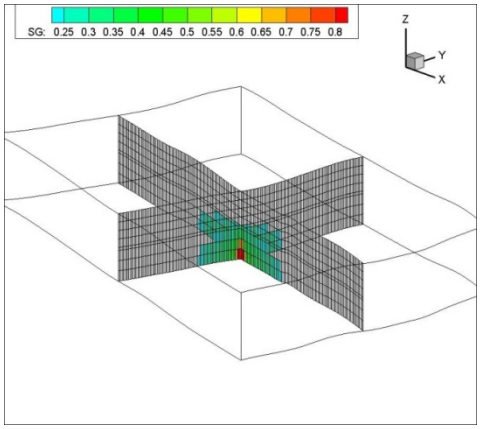

Figure 8. CO_2 gas saturation in the aquifer at 33 days

CONCLUSION

As part of the comparative study project Sim-SEQ conducted by LBNL, BRGM proposes to predict the hydrochemical behavior of a CO_2 injection conducted at the S-3 site, an anticline

sandstone formation originally used for methane production. After we built a 3D model of the geological formation with the geomodeler Petrel, our predictions of arrival time for the CO2 plume at the observations wells were found to be at variance with field data, with discrepancies associated with the high level of uncertainty regarding reservoir properties.

ACKNOWLEDGEMENT

BRGM would like to thank the Bureau of Economic Geology and The University of Texas for supplying the data for this study.

REFERENCES

Audigane, P., Chiaberge, C., Mathurin, F., Lions, J., Picot-Colbeaux, G., A workflow for handling heterogeneous 3D models with the TOUGH2 family of codes: Applications to numerical modeling of CO2 geological storage*, Computers* & Geosciences, 37, 610-620, 2011.

Mukhopadhyay, S., Doughty, C., Bacon, D., Bacci, G., Govindan, R., Shi, J-Q., Gasda, S., Ramanathan, R., Nicot, J-P., Hosseini, S., Birkholzer, J., *Preliminary Model-Comparison Results from the Sim-SEQ Project using TOUGH2, STOMP, ECLIPSE, and VESA Approach*, TOUGH2 Symposium PROCEEDINGS, this issue, 2012.

Pruess, K., *ECO2N: a TOUGH2 fluid property module for mixtures of water, NaCl and CO2*, Report LBNL-57952, Lawrence Berkeley National Laboratory, Berkeley, Calif., 2005.

Xu, T., E. Sonnenthal, N. Spycher and K. Pruess, *TOUGHREACT user's guide: a simulation program for non-isothermal multiphase reactive transport in variable saturated geologic media*, Report LBNL-55460, Lawrence Berkeley National Laboratory, Berkeley, Calif., 2004.

Zhang, K., Y.S. Wu, and K. Pruess, User's Guide for TOUGH2-MP -. A Massively Parallel Version of the TOUGH2 Code, LBNL-315E, Lawrence Berkeley National Laboratory Report, 2008.

AN IMPROVED 2-D REACTIVE TRANSPORT MODEL OF THE FATE OF CO_2 INJECTED INTO A SALINE AQUIFER IN THE WABAMUN LAKE AREA (ALBERTA, CANADA)

Chantsalmaa Dalkhaa[1], Maurice Shevalier[1], Michael Nightingale[1] and Bernhard Mayer[1]
(1) Applied Geochemistry Group, Department of Geoscience, University of Calgary, Calgary, Alberta, Canada T2N 1N4

e-mail: cdalkhaa@ucalgary.ca

ABSTRACT

The Wabamun Area CO_2 Sequestration project (WASP) examined the feasibility of storing 20 million tons (Mt) of CO_2 per year over 50 years in a deep saline aquifer in central Alberta, Canada. In the WASP project, the Devonian Nisku saline aquifer was selected as the primary target for CO_2 injection. The reactive transport code TOUGHREACT was used to investigate CO_2-brine-rock interactions induced by the injection of supercritical CO_2 into the Nisku aquifer. Previously, 1-D and 2-D modeling studies of CO_2 storage in the Nisku Aquifer were performed. Here, we present an extended 2-D modeling study by considering five zones including the Nisku aquifer's three different flow units, the overlying shaly caprock (Calmar) and the underlying shale (Ireton) to obtain more accurate predictions of the fate of injected CO_2. The CO_2 was injected into the bottom 10 m of the Middle Nisku zone at a rate of 1 Mt/year for 50 years. The simulation results revealed that after 1 year, the buoyancy effect resulted in injected CO_2 rising from the Middle Nisku up to the Calmar shale and then expanding as a plume of supercritical CO_2 beneath this cap rock. The injected CO_2 plume spread out radially up to 3.5 km after 50 years of injection, and to 5 km after 1000 years post-injection. Due to dissolution of minerals (mainly dolomite), minor increases in porosity (0.2%) and permeability (2.5 md) of the Middle Nisku aquifer were observed within 3.5 km of the injection well during the 1000 years post-injection period.

The mineral-trapping capacity of injected CO_2 in the Nisku aquifer (mainly composed of carbonate rock) was found to be 0.18 Mt or <0.5% of the 50 Mt of injected supercritical CO_2. This indicates that the carbonate Nisku aquifer does not have a large mineral trapping capacity for CO_2 and that the majority of the injected CO_2 is sequestered by hydrodynamic and solubility trapping mechanisms. The Calmar formation proved to be an excellent caprock for the CO_2 injected into the Nisku aquifer.

2-D simulation results also revealed that density driven flow resulted in CO_2 migrating down from the storage Nisku aquifer to the underlying Ireton formation. The Ireton shale is rich in aluminosilicates such as k-feldspar, albite and chlorite. After 1000 years, it was observed that this shale has a large capacity for mineral trapping of injected CO_2 of up to 20 kg of injected CO_2 per m^3 rock in immobile forms such as ankerite and dolomite.

The results from this 2-D modeling study suggest that the Nisku aquifer is a suitable formation for CO_2 storage in the Western Sedimentary Basin in Canada (WSBC) in terms of geochemistry, injectivity, storage capacity and cap rock integrity. Also, the underlying shale has the potential to sequester CO_2 in mineral (carbonate) form.

INTRODUCTION

Carbon Capture and Storage (CCS) has been considered for a long time as an option to mitigate increasing human-induced greenhouse gas emission to the atmosphere and meet future emission goals. Before CCS becomes fully operational at commercial scale, its long-term impacts and risks associated with human and environmental safety must be assessed. Numerical modeling of CO_2 storage plays an important role in making predictions of short- and long-term behavior of injected CO_2 in geological formations and to help to give insights into its long-term fate via different physical and chemical trapping mechanisms over time.

The WSBC has been the subject of many studies evaluating the potential for CO_2 storage and investigating its hydrogeology, geochemistry, CO_2 storage capacity and CO_2 trapping mechanisms (Bachu et al., 1994, Gunter et al., 1993, 1996). The Wabamun Area CO_2 Sequestration project (WASP) examined the feasibility of storing 20 Mton-CO_2/year over 50 years in central Alberta, Canada (Lavoie and Keith, 2010). In the WASP project, the Devonian Nisku aquifer was selected as the primary target for CO_2 sequestration. Previously, a 1-D modeling study of the fate of injected CO_2 in the Nisku Aquifer was performed to assess the effect of presence of H_2S on CO_2 storage. It was found that H_2S appeared to have little effect on the modeled CO_2-brine-rock reactions in the Nisku aquifer (Shevalier et al., 2011). For the present study, the objective was to develop a 2-D model with three different flow units in the Nisku formation that were observed in petro-physical analyses. The goal was to increase the accuracy of predicting the behavior of the injected CO_2 in the formation and to predict hydrodynamic, solubility, and mineral trapping mechanisms over the simulation time.

THE STUDY AREA

The Devonian Nisku formation in Central Alberta was identified as a potential aquifer for CO_2 injection in the WASP project. It is located in the southwest of Edmonton, Alberta with a total areal extent of approximately 5034 km^2 (Figure 1). The Nisku aquifer was selected because of its depth, good reservoir qualities and lack of oil and gas activities in the area of interest. It was also well suited regarding the delicate balance between the availability of data (number of penetrating wells) and the risk of leakage through wells. No fault through which the injected CO_2 could release back to surface was detected in the seismic survey and interpretations. A number of large stationary CO_2 sources are located in central Alberta with total CO_2 emission of 30Mt/year including four coal-fired power generation plants with more than 4000 MW/year total generating capacity in the Wabamun Lake area. The estimated CO_2 emission from these four power plants is 3-6 Mt/year.

NUMERICAL TOOL

All of the simulations were performed using TOUGHREACT v. 1.2 (Xu and Pruess, 2001). The code was based on the existing multi-phase fluid and heat flow code, TOUGH2 v. 2 (Pruess, 1991) and the geochemical reactive transport code was added. The integral finite difference method for space discretization (Narasimham and Witherspoon, 1976) is the basis for the numerical method for simulation of fluid flow. The coupling between the geochemical reactions and the fluid transport is a sequential iterative approach (Yeh and Tripathi, 1991). The fluid property module ECO2N was used in the modeling.

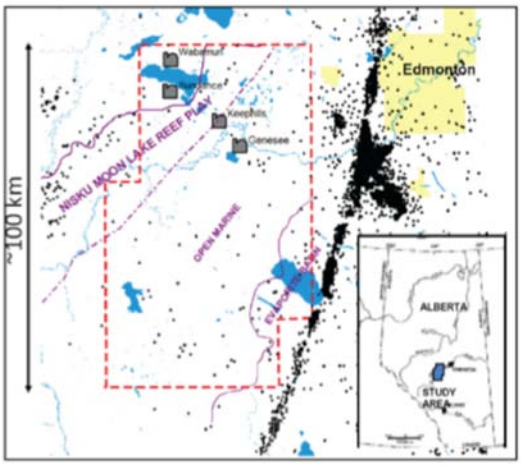

Figure 1. The study area (dashed line) in central Alberta (Canada) with the location of four large power plants. Black circles show well that penetrate the Nisku Formation (Shevalier et al., 2011).

MODEL SETUP

A 2-D radially symmetric model was created in TOUGHREACT/Petrasim for a CO_2 injection into the Devonian Nisku saline aquifer (Figure 2). Three different zones of the Nisku aquifer (the Upper, Middle and Lower Nisku) were introduced into the 2-D model. These different flow regimes in the Nisku formation were identified by petrophysical analyses during the WASP project. The overlying (Calmar shale) cap rock and underlying (Ireton shale) formation were also considered in the model. The model is 90 m thick and 20 km wide in radial distance. The first upper 10 m represents the Calmar cap rock, the next 15 m is the Upper Nisku, and the

following 20 m is the Middle Nisku. The Lower Nisku is 35 m thick, and the remaining 10 m represents the Ireton shale. CO_2 was injected into the bottom 10 m of the Middle Nisku (between 35–45 m in the model), which is the most permeable and porous zone in the Nisku formation.

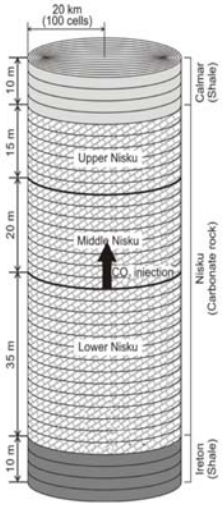

Figure 2. 2D-Model representation formation.

INITIAL GEOCHEMICAL CONDITIONS

Hydrogeological parameters of the Calmar, the Upper, Middle and Lower Nisku and Ireton formations defined in the model are given in Table 1. The Middle Nisku is the most porous and permeable zone, with a porosity of 21.9% and a permeability of 91 md. The overlying Calmar shale is impermeable with a permeability value of 2.9×10^{-6} md, suggesting that it is an excellent cap rock. The van Genuchten (1980) model was used to calculate the capillary pressure and relative permeability curves for each zone in the model.

Table 2 summarizes the measured water composition of brine obtained from a water-producing well located in the Nisku formation (Shevalier and Mayer, 2009). The Nisku brine is "sour," containing a considerable amount of H_2S gas. Within the scope of this modeling work, the content of H_2S was not considered. Shevalier et al. (2011) previously revealed that H_2S appears to have little impact on the fate of the injected CO_2 in the Nisku aquifer.

The initial mineral compositions of a representative sample from the Calmar, Nisku, and Ireton formations used in the modeling are shown in Table 3 (Nightingale et al., 2009). The Calmar is composed of mainly quartz (48.16%), illite (29.28%), k-feldspar (17.31%) and minor amounts of low-albite, pyrite and calcite. The Nisku is a carbonate formation, consisting of mostly dolomite (over 80% in all its three zones). The Ireton is composed of illite (around 40%), calcite (27.36%), quartz (9.82%), k-feldspar (8.42%) and minor amounts of dolomite, chlorite, low-albite and pyrite.

The interaction between the reactive or more acidic fluids caused by CO_2 injection and storage rock minerals is a complex interplay between thermodynamic stabilities, reaction kinetics, and fluid flow. Table 4 provides the parameters for dissolution and precipitation kinetics for the minerals used in the models (Palandri and Kharaka, 2004). Calcite was used as an equilibrium mineral in the simulations: its kinetics are comparably fast. Mineral disequilibria induced by CO_2 injection results in dissolution of primary minerals and precipitation of new, secondary minerals stable at elevated CO_2 pressure. Table 2 shows the secondary minerals considered in the 2-D model.

Table 1. Hydrogeological parameters for the Calmar, Nisku and Ireton formations

	Calmar	Upper Nisku	Middle Nisku	Lower Nisku	Ireton
Porosity(%)	3.9	2.9	20.9	5.1	5.0
Permeability(m2)	2.9×10^{-21}	2.03×10^{-15}	9.1×10^{-14}	1.93×10^{-14}	1.0×10^{-16}
Temperature	70				
Pore Compressibility(Pa-1)	1.07×10^{-7}				
Diffusivity(m2/s)	1.0×10^{-9}				
Torousity	0.3				

Table 2. Initial chemical species concentrations of saline aquifer water used in the ToughReact simulations.

Species	Concentration (mol/kg)	Species	Concentration (mol/kg)
pH	6.1	$SiO_{2(aq)}$	4.56×10^{-4}
Ca^{2+}	0.41	HCO_3^-	2.01×10^{-2}
Mg^{2+}	9.33×10^{-2}	SO_4^{2-}	5.21×10^{-3}
Na^+	2.56	Cl^-	3.44
K^+	0.1	AlO_2^-	1.36×10^{-7}
Sr^{2+}	1.08×10^{-2}	$O_{2(aq)}$	4.88×10^{-70}
Fe^{2+}	9.35×10^{-6}		

Table 3. Mineralogical compositions of the Calmar, Nisku, and Ireton formations

Primary Minerals	Calmar (%)	Upper Nisku(%)	Middle Nisku(%)	Lower Nisku(%)	Ireton(%)
Dolomite		89.2	81.2	91.6	5.7
Calcite	0.5	6.2	15.5	4.7	27.4
Illite	29.3	2.0	1.9	0.5	40.0
K-feldspar	17.3	0.2	0.9	0.4	8.4
Quartz	48.2	2.0			9.8
Low-Albite	3.7		0.6		3.7
Pyrite	1.1				0.7
Chlorite					4.4
Secondary Minerals					
Kaolinite	Ankerite	Ca-smectite	Anhydrite	Aragonite	
Na-smectite	Magnesite	Dawsonite	Siderite		

Table 4. Parameters for calculating kinetic rate constants of minerals considered in the simulations (Palandri & Kharaka, 2004)

Mineral	S. Area (cm^2/g)	Parameters for kinetic rate law							
		Neutral mechanism		Acid mechanism			Base mechanism		
		k_{25} (mol/m2/s)	E_a (kJ/mol)	k_{25} (mol/m2/s)	E_a (kJ/mol)	$n(H^+)$	k_{25} (mol/m2/s)	E_a (kJ/mol)	$n(H^+)$
Dolomite	9.8	2.951×10^{-8}	52.2	6.457×10^{-4}	36.1	0.5			
Illite	151.6	1.660×10^{-13}	35	1.047×10^{-11}	23.6	0.34	3.02×10^{-17}	58.9	-0.4
K-feldspar	9.8	3.891×10^{-13}	38	8.710×10^{-11}	51.7	0.5	6.310×10^{-22}	94.1	-0.82
Low-albite	9.8	2.754×10^{-13}	69.8	6.918×10^{-11}	65	0.457	2.512×10^{-16}	71	-0.57
Kaolinite	108.7	6.918×10^{-14}	22.2	4.898×10^{-12}	65.9	0.777	8.913×10^{-18}	17.9	-0.47
Na-smectite	108.7	1.660×10^{-13}	35	1.047×10^{-11}	23.6	0.34	3.02×10^{-17}	58.9	-0.4
Ca-smectite	108.7	1.660×10^{-13}	35	1.047×10^{-11}	23.6	0.34	3.02×10^{-17}	58.9	-0.4
Dawsonite	9.8	1.260×10^{-9}	62.76	6.457×10^{-4}	36.1	0.5			
Aragonite	9.8	4.571×10^{-10}	23.5	4.169×10^{-7}	14.4	1			
Siderite	9.8	1.260×10^{-9}	62.76	6.457×10^{-4}	36.1	0.5			
Ankerite	9.8	1.260×10^{-9}	62.76	6.457×10^{-4}	36.1	0.5			
Magnesite	9.8	4.571×10^{-10}	23.5	4.169×10^{-7}	14.4	1			
Quartz	9.8	1.023×10^{-14}	87.7						
Chlorite	9.8	3.02×10^{-13}	88	7.762×10^{-12}	88				
Pyrite	12.87	2.818×10^{-5}	56.9 $n(O_{2(aq)})=0.5$	3.202×10^{-8}	56.9	$n(H^+)=-0.5$ $n(Fe^{3+})=-0.5$			

THE CO_2 INJECTION AND POST INJECTION SIMULATIONS

Simulations were performed using the reactive transport code TOUGHREACT. Injection of supercritical CO_2 was simulated into the bottom 10 m of the Middle Nisku formation at a rate of 1 Mton/year (31.69 kg/sec) for 50 years. Following the 50-year injection simulation, a simulation of 1000 years of post-injection was conducted to understand the long-term behavior of the injected CO_2 in the reservoir.

RESULTS AND DISCUSSION

The simulation results are presented in 2-D graphical plots as a function of depth and radial distance at discrete time intervals of 1 and 50 years for the CO_2 injection and 100 and 1000 years for the post injection.

CO_2 Injection Phase

Since supercritical CO_2 is less dense than the formation brine, the injected CO_2 migrated up from the injection point toward the Calmar cap rock. Due to the rapid upward migration of the supercritical CO_2, a plume started to form beneath the cap rock 1 year after commencement of CO_2 injection, spreading radially up to 3.5 km after 50 years of injection (Figure 3). During the 1st year of injection, the CO_2 plume remained within the Nisku formation; however, at the end of the 50-year injection period, it was observed that some supercritical CO_2 entered the underlying Ireton shale, which has a considerably permeability. In contrast, the CO_2 did not diffuse into the Calmar cap rock over the simulation time, suggesting that the Calmar is an excellent cap rock. A dehydrated region with a radial distance of 100 m was observed forming due to complete brine displacement by the supercritical CO_2 injected at a high rate of 31.69 kg/sec. In Figure 3, CO_2 saturations of up to 1.0 were observed in this region. Figure 4 shows that the pH of brines in the Nisku aquifer decreased to a value of ~5.0 in areas affected by the injection as the supercritical CO_2 dissolved in the brine. The acidic brine subsequently dissolved dolomite, which is the main mineral in the Middle Nisku (Figure 5), resulting in increased Mg^{2+} ion concentrations in the reservoir brine (Figure 6). No increase in Ca^{2+} concentration in the brine was observed, which was explained by the precipitation of calcite that took up the Ca^{2+} released by dolomite dissolution (not plotted).

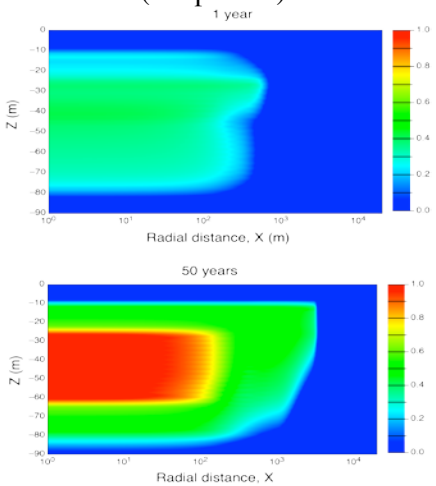

Figure 3. Spatial distribution of CO_2 plume after 1 and 50 years of injection

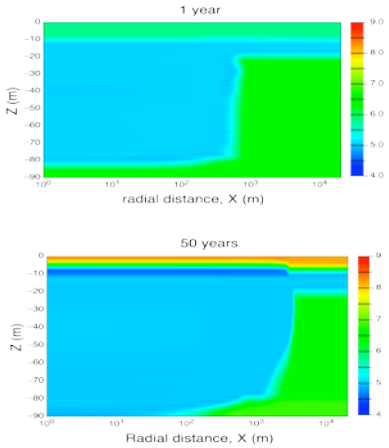

Figure 4. Spatial distribution of pH after 1 and 50 years of injection

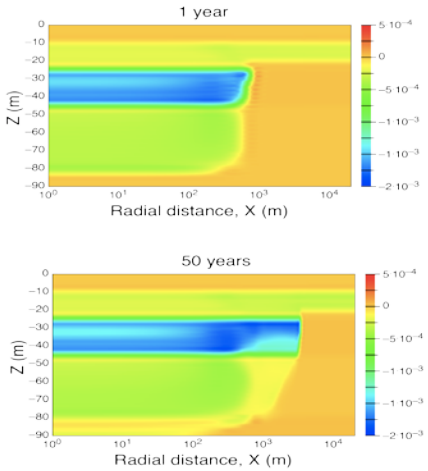

Figure 5. Change in volume fraction of dolomite after 1 and 50 years of injection

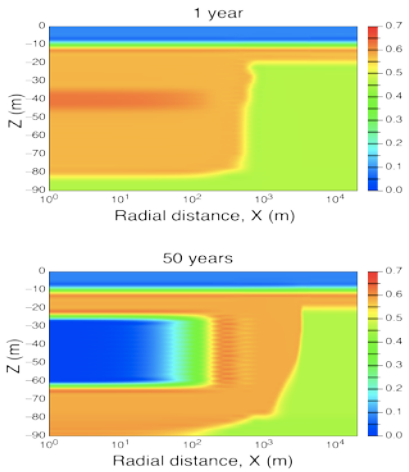

Figure 6. Mg^{2+} ion concentration after 1 and 50 years of injection

Post Injection Phase

Following the CO_2 injection simulation, a post-injection of 1000 years was simulated to evaluate the long-term fate of CO_2 injected into the Nisku aquifer. Also, the effect of geochemical reactions on formation porosity and permeability due to the CO_2 injection was investigated. The simulation result showed that after 1000 years of post injection, the injected supercritical CO_2 did not completely dissolve in the brine, with CO_2 saturations of up to 0.60 in parts of the Nisku aquifer. The plume was extended radially up to 5 km by capillary force, although the injection ceased after 50 years. It was observed that the CO_2 that migrated down into the Ireton shale during the injection was completely dissolved in its brine (Figure 7).

At the base of the Lower Nisku, it was observed that CO_2 was residually trapped after 1000 years. Dolomite dissolution was still ongoing in the Middle Nisku (Figure 8). Dissolution of calcite and chlorite in the Ireton shale (not shown) liberated divalent ions such as Ca^{2+}, Mg^{2+} and Fe^{2+}. Subsequently, dolomite (Figure 8, the bottom 10 m) and ankerite (Figure 9) were forming in the shale. Due to precipitation of these secondary minerals, the CO_2 mineral-trapping capacity was calculated as ~20 kg of CO_2/m^3 rock in the Ireton formation (Figure 10). Dolomite dissolution in the Middle Nisku caused minor increases in porosity (by 0.2%) and permeability (by 2.5 md) (Figure 11).

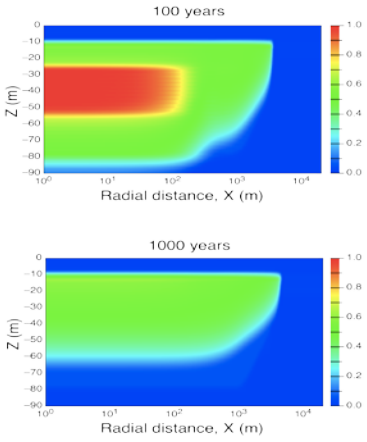

Figure 7. Spatial distribution of CO_2 plume after 100 and 1000 years of post injection

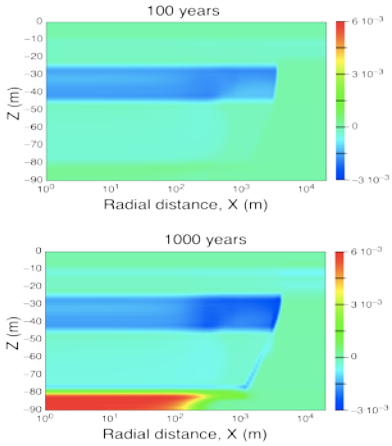

Figure 8. Change in volume fraction of dolomite after 100 and 1000 years of post injection

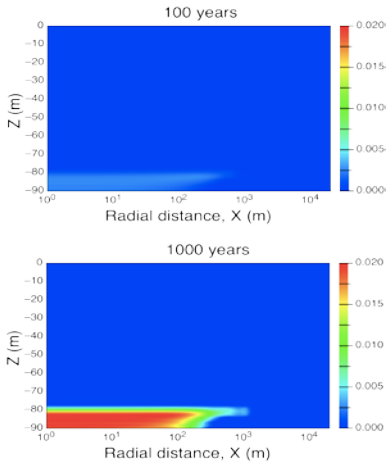

Figure 9. Change in volume fraction of ankerite after 100 and 1000 years of post injection

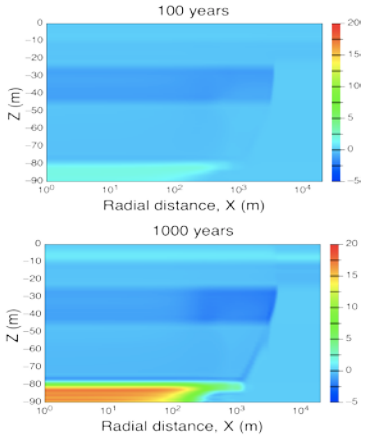

Figure 10. CO_2 mineral trapping after 100 and 1000 years of post injection

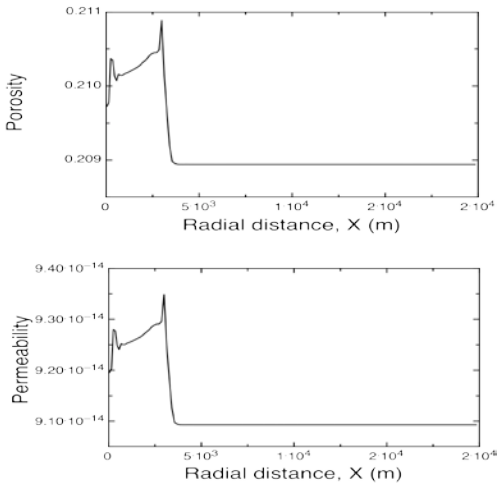

Figure 11. Change in the porosity and permeability of the Nisku aquifer

CONCLUSION

Storage of CO_2 in the Devonian Nisku aquifer in the WSBC was simulated using the multiphase, multicomponent and nonisothermal reactive transport TOUGHREACT code. The 2-D radially symmetric model developed in this work included the three different zones of the Nisku storage aquifer, along with its overlying cap rock and underlying shale. CO_2 injection caused acidification of the reservoir brine and some dissolution of dolomite in the Middle Nisku zone. This resulted in minor increases in the porosity and permeability of the Middle Nisku, although calcite was precipitating in this area. Since the Nisku formation is composed of carbonates, CO_2 mineral trapping was not a major sequestration process over the simulation period. Only 0.18 M tons of CO_2 were trapped as calcite mineral in the Nisku aquifer after 1000 years. The majority of injected CO_2 was trapped in free phase and as dissolved inorganic carbon in the brine. However, some injected CO_2 had also entered the underlying Ireton shale and dissolved in the brine, causing dissolution of calcite and chlorite. These mineral dissolution reactions liberated divalent cations into the brine, and dolomite and ankerite precipitated. The CO_2 mineral trapping capacity of the Ireton formation was calculated as up to 20 kg of CO_2 per m^3 of rock. The impermeable Calmar shale proved to be an excellent cap rock for the CO_2 injected into the Nisku aquifer. This simulation study helped to make better predictions on the interactions of the reactive fluids and minerals of the caprock, the storage reservoir, and the underlying formation induced by CO_2 injection.

REFERENCES

Bachu, S., Gunter, W.D., and Perkins, E.H., 1994, Aquifer disposal of CO_2: hydrodynamic and mineral trapping, *Energy Conversion Management*, 35 (4), 269-279

Gunter, W.D., Perkins, E.H., and McCann T.J., 1993. Aquifer disposal of CO_2-rich greenhouse gases: reaction design for added capacity, *Energy Conversion Management*, 34, 941-948

Gunter, W.D., Bachu, S., law, D.H., Marwaha, V., Drysdale, D.L., Macdonald, D.E., and Mccann, T.J., 1996. Technical and economic feasibility of CO2 Disposal in Aquifers within the Alberta Sedimentary Basin, Canada, *Energy Conversion Management*, 37 (6-8), 1135-1142

Lavoie, R. and Keith, D., 2010. Wabamun Area CO_2 Sequestration Project (WASP)- Executive Summary Report. http://www.ucalgary.ca/wasp/Executive%20Summary.pdf

Narasimhan, T.N., Witherspoon, P.A., An integrated finite dfference method for analyzing fluid flow in porous media, *Water Resour. Res.,* 12, 57–64, 1976.

Palandri, J., Kharaka, Y.K., 2004. A Compilation of rate parameters of water-mineral interaction kinetics for geochemical modeling. *US Geol. Surv*. Open File report 2004-1068.64.

Pruess, K., TOUGH2: A General Numerical Simulator for Multiphase Fluid and Heat Flow, Lawrence Berkeley Laboratory Report LBL-29400, Berkeley, California, 1991.

Shevalier, M., Mayer, B., Wabamun Area Sequestration Project: Baseline Geochemistry and Preliminary Geochemical Modelling, Wabamun Area CO_2 Sequestration Project (WASP) Internal Report, University of Calgary, 2009

Shevalier, M., Nightingale, M., Mayer, B., and Hutcheon, I., 2011, Toughreact modeling of the fate of CO_2 injected into a H_2S containing saline aquifer: example of the Wabamun Area Sequestration project (WASP), *Energy Procedia*, 4, 4403-4410

Van Genuchten, M.Th., A closed-form equation for predicting the hydraulic conductivity of

unsaturated soils. *Soil Sci. Soc. Am. J.,* 44, 892–898,

1980Xu, T., Pruess, K., On fluid flow and mineral alteration in fractured caprock of magmatic hydrothermal systems, *J. Geophys. Res.,* 106, 2121–2138, 2001.

Yeh, G.T., Tripathi, V.S., A model for simulating transport of reactive multispecies components: model development and demonstration, *Water Resour. Res.,* 27, 3075–3094, 1991.

CAPROCK INTEGRITY ASSESSMENT BY REACTIVE TRANSPORT MODELING: A CODE INTERCOMPARISON APPROACH

Dimier Alain [(1)], Gherardi Fabrizio [(2) (3)]

[(1)] KIT Karlsruhe, EIFER Institute – Karlsruhe, Germany
[(2)] BRGM - Orléans, France
[(3)] LE STUDIUM, Loire Valley Institute for Advanced Studies - Orléans & Tours, France
e-mail: Alain.Dimier@eifer.uni-karlsruhe.de

ABSTRACT

In the framework of the recently launched ULTimate-CO_2 Project, funded by the European Commission (FP7 Program), we have conducted reactive transport simulations to assess the containment properties of an idealized clay-rich, impermeable rock. The caprock formation considered for the simulations has a mineralogical composition similar to clays of the Charmotte area, Paris Basin, France. Idealized geometries have been employed to explore likely mineralogical processes expected after prolonged exposure of the cap rock to CO_2-rich fluids. We have investigated the effects of both advection- and diffusion-dominated mass-transport conditions, and have performed numerical simulations in parallel, using TOUGHREACT and the Elmer/PhreeqC simulator. A comparison between the outputs of the two codes indicates that minor mineralogical transformations are expected in the Charmotte claystone over a time span of 100–200 years.

INTRODUCTION

The deep geological storage of CO_2 is currently considered a promising technology for reducing CO_2 emissions in the atmosphere. The assessment of leakage risk from such storage is a primary prerequisite for site approval, public acceptance, and the awarding of credits for stored CO_2 quantities. Numerical simulations are usually employed to demonstrate that a geological reservoir offers the confinement properties required for safe and durable geological storage of CO_2. Among the so-called containment issues is the potential impact on cap-rock-mineral integrity resulting from prolonged exposure to CO_2-rich fluids—an issue of some concern with respect to the long-term effectiveness of CO_2 storage in geological formations.

In the framework of the recently launched ULTimate-CO_2 Project, funded by the European Commission (FP7 Program), exploratory numerical simulations have been performed to predict major mineralogical patterns in selected areas of potential interest for CO_2 geological storage in France. The caprock formation considered for this study has a mineralogical composition similar to the clays of the Charmotte area, France (Bildstein et al., 2010).

The present study has two main objectives. First, we want to set up a reactive transport model for evaluating the mineralogical transformations induced in the caprock of a candidate site for CO_2 geological storage in France—a model that could simulate the propagation of a CO_2-rich aqueous solution likely migrating from the injection target reservoir. Secondly, we want to make an intercomparison between the reactive transport simulator Elmer/PhreeqC and one of the most proven, widely used reactive transport simulators, TOUGHREACT (Xu and Pruess, 1998).

MODEL SETUP

For the sake of simplification and interpretation of results, we considered an idealized homogenous rock medium having fixed initial porosity (0.15) and absolute permeability (10^{-18} m^2). With TOUGHREACT, we simulated a vertical column of 20 m, discretized in 100 cells for the two codes and with uniform spacing of 0.2 m and an interface area of 0.01 m^2. Based on field evidence, we assumed isothermal (T = 80°C) and aqueous saturated conditions (S_l = 1.0). The maximum simulation time considered is 200 years.

Two mass transport conditions have been explored: (1) a pure diffusion case (labeled “D”

in the figures), with dissolved species migrating according to a single average effective diffusion coefficient of 10^{-11} m^2/s; and (2) a mixed case (labeled "A"), i.e., advection-controlled conditions, with an average Darcy velocity of 8.4×10^{-9} m/s.

Table 1. Caprock mineralogical composition and kinetic parameters of minerals considered in the simulations (k_{25} is the kinetic dissolution/precipitation rate at 25°C; E_a the activation energy in kJ/mol; SSA the reactive surface area in cm^2/g-mineral; V_f being the initial volume fraction)

Mineral	k_{25}	E_a	SSA	V_f
Anhydrite	*equilibrium*	-	-	0.047
Calcite	1.6×10^{-6}	23.5	10	0.482
Dolomite	3.0×10^{-12}	52.2	10	0.024
Siderite	1.3×10^{-9}	62.8	10	0.012
Magnesite	4.5×10^{-10}	63.0	10	0
Pyrite	4.0×10^{-11}	62.8	10	0.024
Dawsonite	1.3×10^{-9}	62.8	10	0
Ankerite	1.3×10^{-9}	62.8	10	0
Kaolinite	6.9×10^{-14}	22.2	50	0.106
Illite	8.8×10^{-16}	14.0	50	0.129
Montmor.	3.9×10^{-15}	48.0	50	0.024
Quartz	1.0×10^{-14}	87.7	10	0.106

Table 2. Chemical formulas and thermodynamic constants of minerals considered in the simulations (log K values are calculated at 80°C)

Mineral	Formula	Log K
Anhydrite	$CaSO_4$	-5.20
Calcite	$CaCO_3$	1.06
Dolomite	$CaMg(CO_3)_2$	1.58
Siderite	$FeCO_3$	-1.30
Magnesite	$MgCO_3$	0.97
Pyrite	FeS_2	-90.90
Dawsonite	$NaAlCO_3(OH)_2$	-15.87
Ankerite	$CaFe_{0.7}Mg_{0.3}(CO_3)_2$	0.40
Kaolinite	$Al_2Si_2O_5(OH)_4$	-34.24
Illite	$K_{0.85}Mg_{0.25}Al_{2.35}Si_{3.4}O_{10}(OH)_2$	-38.38
Montmor.	$Na_{0.33}Mg_{0.33}Al_{1.67}Si_4O_{10}(OH)_2$	-31.20
Quartz	SiO_2	-3.17

The mineralogical system is described in terms of nine primary phases (Table 1). Dissolution and precipitation rates for the minerals are calculated with a general kinetic formulation based on the Theory of the Transition State (Aagaard and Helgeson, 1982; Lasaga, 1981, 1984). Kinetic parameters are taken from the compilation of Palandri and Kharaka (2004). Initial mineralogical composition and the kinetic parameters employed in the simulations are listed in Table 1.

Thermodynamic data are mostly from the Thermoddem database (thermoddem.brgm.fr), an internally consistent and thoroughly revised compilation of thermodynamic data prepared at the French Geological Survey (BRGM). Log K values for relevant minerals are listed in Table 2. The initial chemical composition of cap rock and acidic reservoir pore waters has been taken from Bildstein et al. (2010). Clay-rock pore waters have been slightly modified by iterative batch modeling in order to achieve near-steady-state conditions with the mineralogical assemblage of Table 1. These chemical compositions are listed in Table 3.

Table 3. Elemental chemical composition of reservoir and caprock porewaters. Total concentrations are in mol/kgw. Chemical components (or basis species) are in brackets.

Parameter	Caprock	Reservoir
pH	6.08	4.65
redox (as $H_{2(aq)}$)	3.95×10^{-24}	8.15×10^{-8}
Ca (as Ca^{+2})	2.08×10^{-2}	5.93×10^{-2}
Mg (as Mg^{+2})	6.48×10^{-3}	1.67×10^{-2}
Na (as Na^{+})	2.46×10^{-1}	2.50×10^{-1}
K (as K^{+})	2.97×10^{-3}	4.52×10^{-3}
Fe (as Fe^{+2})	9.53×10^{-5}	9.36×10^{-6}
Si (as $SiO_{2(aq)}$)	6.95×10^{-4}	2.48×10^{-4}
Al (as $AlO_2)^{-}$	2.78×10^{-8}	1.21×10^{-8}
Cl (as Cl^{-})	2.68×10^{-1}	3.44×10^{-1}
C (as HCO_3^{-})	8.73×10^{-3}	$1.02 \times 10^{+0}$
S (as SO_4^{-2})	1.61×10^{-2}	1.06×10^{-2}

CODE COMPARISON

The intercomparison study we conducted relied on the resolution of the geochemical-transport equation:

$$\frac{\partial \omega C_i}{\partial t} = -\nabla(\omega v C_i) + \nabla.(\omega D \nabla C_i) - \frac{\partial q_i}{\partial t},$$

the source term $\frac{\partial q_i}{\partial t}$ being determined by the geochemical equilibrium.

The ELMER/PHREEQC environment is based on the operator splitting approach described in Strang (1968). Elmer is a multiphysics software code that can account for flow, ion transport, temperature, and mechanics; it was developed by the CSC-IT (http://www.csc.fi/english), a Finnish institute. This software is based on finite element technologies; while written mainly in fortran90, it also uses C and C++. In its 6.2 version, Elmer is distributed under the GNU license (GPL 2.). The use of Elmer gives access to up-to-date algebraic solvers. For direct methods, Lapack or Umfpack libraries are made accessible; for iterative methods, preconditioned Krylov subspace or multilevel methods can be accessed. The code can also be run parallel using MPI tools, using domain decomposition to distribute the load to multiple processes that are being run either on different cores or CPUs. Here, mesh partitioning can be made using Metis (http://glaros.dtc.umn.edu). In association with Elmer, we use PhreeqC (Parkhurst & Appelo 1999) as geochemical batch solver, here in its 2.17.5 version.

The coupling is carried out in Python for a NI or a CC algorithm, Elmer and phreeqC being shared objects within the environment with memory access to code structure to reach an efficient coupling of the tools. Validation of the coupling algorithm is achieved with ~50 standard geophysical tests. Chemical equilibrium can be distributed on a node-by-node basis over system CPUs to shorten simulation times.

TOUGHREACT (Xu and Pruess, 1998) was developed by introducing reactive chemistry into the framework of the existing multiphase fluid and heat flow code TOUGH2 (Pruess, 1991). Spatial discretization in TOUGHREACT is achieved by means of integral finite differencing (Narasimhan and Witherspoon, 1976). An implicit time-weighting scheme is used to solve equations for flow, transport, and geochemical reactions.

Simulations were performed following a sequential noniterative approach similar for the two tools. After solution of the flow equations, we used the fluid velocities and phase saturations for aqueous-chemical transport simulation, which is solved on a species-component basis. The resulting aqueous concentrations calculated from the transport simulation are substituted into the chemical reaction model. Then the system of chemical reaction equations is solved on a gridblock basis by the Newton-Raphson method.

BENCHMARKING EXERCISE

For this exercise, we used TOUGHREACT version 1.2; for phreeqC, we used version 2.17.5 coupled to Elmer 6.2. The goal of the comparison was to construct a geochemical model to be used with confidence using either of the two simulators, before dealing with unsaturated media.

MODEL RESULTS

Despite two quite similar initial chemical systems, we have not yet been able to reach the same spatial geochemical evolution of the system on the two codes. Figure 1 shows the extension of a tracer within the system (see Figure 1 to relate to porosity variations). Small variations in the pH are noted (Figure 2), but with respect to precipitation/dissolution phenomena, we find differences that induce further differences in the simulated porosity evolution (Figure 3). The porosity evolution rate for Elmer/phreeqC is about two times that calculated with TOUGHREACT. As an example, for the geochemical simulation using phreeqC, no dissolution of the quartz occurs, in contrast with what is determined with the TOUGHREACT solver. In addition, for minerals like calcite or Mg-Na-montmorillonite, dissolution rates are quite different. Parameters such as time integration were studied, but they did not explain the noted differences. Further investigations will be conducted not only on model parameters (such as activity) but also on numerical parameters such as differential integration.

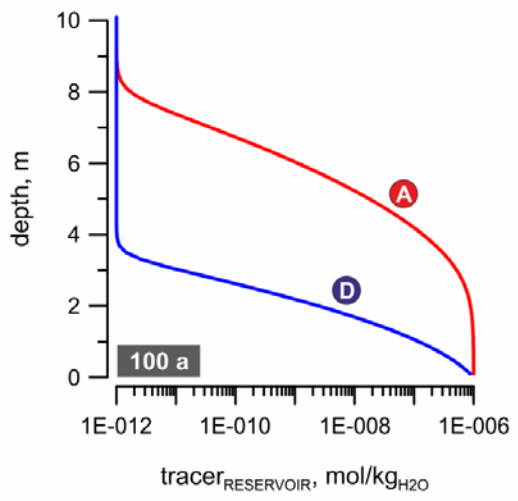

Figure 1. Spatial variation of aqueous tracer concentration in the caprock (10m vertical column) after 100 years. The red and blue curves labeled "A" and "D" are representative of calculations under advection- and diffusion-controlled mass transport conditions, respectively (results from TOUGHREACT simulation).

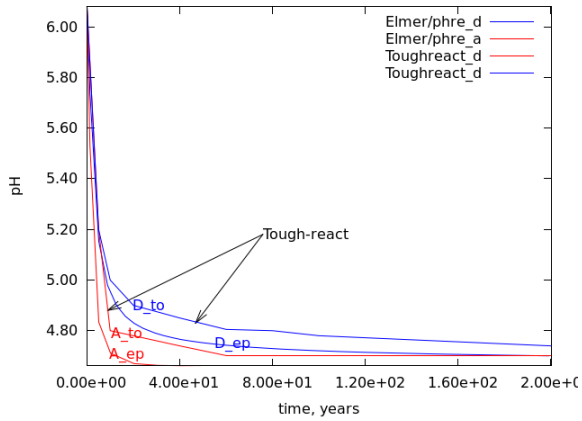

Figure 2. Temporal (0 to 200 years) variation of pH in the first cell of the caprock.

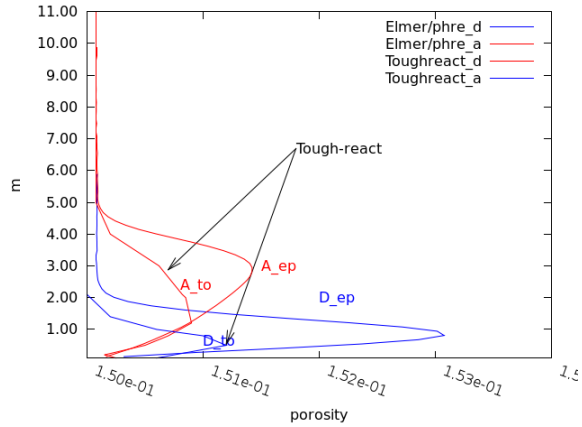

Figure 3. Spatial variation of the porosity after 200 years for TOUGHREACT and Elmer/phreeqC coupling

With respect to numerical integration, the TOUGHREACT solver is about four times faster than Elmer/PhreeqC. For Elmer/PhreeqC, about 95% of the CPU time is dedicated to the numerical integration of the differential equations. That integration is made through the cvode solver, whose numerical parameters have been optimized in terms of CPU time.

CONCLUSIONS

Within the frame of the exercise, we were not able to reach the same evolution for the geochemical system using the two tools. Our time span was too short to make a thorough analysis of all elements potentially explaining the discrepancies. Nevertheless, the two tools

delivered results that can be identified as similar in terms of safety.

Considering CPU times, without making use of any parallel distribution of the chemistry equilibrium states over the CPU architecture, we find that TOUGHREACT is about 4 times faster than the Elmer/phreeqC coupling, with the cvode solver (used within phreeqC for kinetically driven precipitation/dissolution minerals) the primary cause of that difference.

The comparison between the codes will be pursued over the next few months, as we try to match one code's evolution of cap-rock chemistry with the other, in order to get definitive elements of comparison in terms of performance.

ACKNOWLEDGMENTS

We want especially to thank David Parkhurst from the USGS for sharing ideas about geochemical modeling within the phreeqC frame.

REFERENCES

Lasaga, A.C., *Rate laws in chemical reactions*, In: Lasaga, A.C., Kirkpatrick, R.J., (Eds.), Kinetics of Geochemical Processes. Reviews in Mineralogy 8, 135–169, 1981.

Palandri, J.L., and Y.K. Kharaka, *A compilation of rate parameters of water-mineral interaction kinetics for application to geochemical modeling*, U.S. Geological Survey Open File Report 2004-1068. 64 pp., 2004.

Pruess, K., *TOUGH2: A general numerical simulator for multiphase fluid and heat flow*, Rep. LBL-29400, 37 pp., Lawrence Berkeley Natl. Lab., Berkeley, Calif., 1991.

Xu, T., and K. Pruess, *Coupled modeling of non-isothermal multiphase flow, solute transport and reactive chemistry in porous and fractured media, 1, Model development and validation*, Rep. LBNL-42050, 38 pp., Lawrence Berkeley Natl. Lab., Berkeley, Calif., 1998.

Aagaard, P. and H.C. Helgeson, Thermodynamic and kinetic constraints on reaction rates among minerals and aqueous solutions. I. Theoretical considerations. *Am. J. Sci. 282*, 237–285, 1982.

Bildstein O., C. Kérvévan, V. Lagneau, P. Delaplace, A. Crédoz, P. Audigane, E. Perfetti, N. Jacquemet and M. Jullien, Integrative modeling of caprock integrity in the context of CO_2 storage: evolution of transport and geochemical properties and impact on performance and safety assessment, *Oil and Gas Science and Technology 65(3)*, 485-502, 2010.

Lasaga, A. C., Chemical kinetics of water-rock interactions, *J. Geophys. Res., 89*, 4009–4025, 1984.

Narasimhan, T. N., and P. A. Witherspoon, An integrated finite difference method for analyzing fluid flow in porous media, *Water Resour. Res., 12*, 57–64, 1976.

ParkHurst, David L. and C.A.J. Appelo, User's Guide to PHREEQC, *Report 99-4259*

Strang G., 1968: On the construction and comparison of different splitting schemes. 87 SIAM J. Numer. Anal., 5., 506-517.

P. Råback, Elmer—An open source finite element software for multiphysical problems May 2008.

MODELING CO_2 INJECTION AT CRANFIELD, MISSISSIPPI: INVESTIGATION OF METHANE AND TEMPERATURE EFFECTS

Christine Doughty and Barry Freifeld

Lawrence Berkeley National Laboratory
#1 Cyclotron Rd.
Berkeley, California, USA, 94720
e-mail: cadoughty@lbl.gov; bmfreifeld@lbl.gov

ABSTRACT

A large-scale carbon dioxide (CO_2) injection pilot is ongoing at Cranfield, Mississippi, in a saline aquifer where the brine has high dissolved methane (CH_4) content. The pilot site includes one injection well and two observation wells, all with extensive monitoring. The breakthrough of CH_4 and CO_2 at the observation wells provides important insights into phase partitioning and the multipath nature of flow through the storage formation. Injected CO_2 is cooler than the ambient formation temperature, making temperature a potentially important observation as well.

Simulations of the first year of CO_2 injection were conducted using an axisymmetric (RZ) model, with layering based on well logs obtained from the injection well. The equation of state module EOS7C was used, which, unlike the more commonly used module ECO2N, allows temperatures as high as the ambient temperature at Cranfield, about 126–128°C. EOS7C treats CO_2, CH_4, and water, but does not include salt or a salinity dependence on CO_2 solubility. Although the simplification of an RZ model precludes study of those aspects of the pilot test relating to formation dip or lateral heterogeneity, its simple structure enables us to focus on physical processes involving the phase partitioning of CH_4 and CO_2, and temperature effects. Key observations that the model should reproduce include the arrival of a bank of free-phase CH_4 ahead of the main CO_2 plume at each observation well, and nonmonotonic changes in CH_4 and CO_2 mass fraction as a function of time at the observations wells, suggesting that multiple distinct flow paths exist between the injection well and the observation wells, each with its own bank of free-phase CH_4 leading the CO_2. Another interesting feature is the action of buoyancy flow to segregate the much less dense gaseous CH_4 from the supercritical CO_2. Thermal effects that would occur even if the injected CO_2 were at the same temperature as the formation include Joule-Thomson cooling, cooling accompanying water evaporation into the CO2-rich phase, and heating accompanying CO_2 dissolution into the aqueous phase. The bulk cooling arising from the relatively cool (~95°C) CO_2 itself can also provide insight into CO_2 behavior. As the cool CO_2 moves through the formation, it is heated by the existing brine and rock that it passes through; thus, the thermal front lags far behind the actual extent of the CO_2. Examining this lag quantitatively may provide information on the nature of the flow paths through the formation.

INTRODUCTION

A large-scale CO_2 injection pilot is currently under way at Cranfield, Mississippi, in a brine-saturated formation adjacent to an oil field where CO_2 injection is being used for enhanced oil recovery (EOR), operated by Denbury Onshore LLC (Figure 1). CO_2 injection into a 25 m thick saline aquifer known as the Tuscaloosa Formation, at ~3.2 km depth, started in December 2009. The initial injection rate was 3 kg/s, which was subsequently increased to 5 and then 9 kg/s. Two monitoring boreholes were installed approximately 72 m and 98 m from the injector. The gas composition, consisting mainly of CO_2, CH_4, and injected tracers (SF_6 and Kr), was measured frequently in the monitoring boreholes via U-tube (Freifeld et al., 2005) sampling with on-site mass spectroscopy. The pressure in the injection borehole was also monitored at a high temporal rate. In addition, the distribution of gas saturation with depth was measured via well logging before and twice during the injection, using a pulsed neutron reservoir saturation tool (RST). The geophysical datasets included elec-

trical resistance measurements (ERT) and a pair of traditional time-lapse crosswell seismic surveys (Hovorka et al., 2011). Other researchers have made detailed models of the site (e.g., Hoesseni et al., 2012; Doetsch et al., 2012) in order to match various observation datasets. Here a simplified axisymmetric model is used, to enable focus on the physical processes involving CO_2, CH_4, and heat transfer.

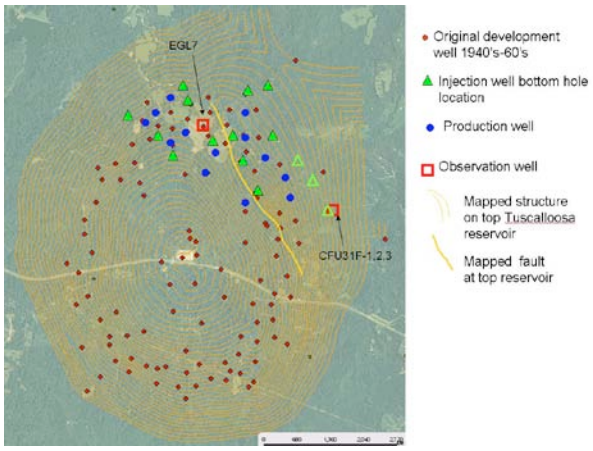

Figure 1. Plan view of Denbury's Cranfield EOR operation. Contours show the elevation of the top of the storage formation. The CO_2 injection pilot well field is identified by the red box labeled CFU31F-1,2,3.

NUMERICAL SIMULATOR AND EQUATION OF STATE

The results shown here are obtained from the numerical simulator TOUGH2 (Pruess et al., 1999; Pruess, 2004) and the equation-of-state module EOS7C (Oldenburg et al., 2004). TOUGH2 is a numerical simulation program for nonisothermal flows of multiphase, multicomponent fluids in permeable (porous or fractured) media. Fluid flow is modeled with Darcy's law extended for two-phase flow via relative permeability and capillary functions. TOUGH2 employs the integral-finite-difference method for spatial (Narasimhan and Witherspoon, 1976) discretization. For regular geometries, this method is equivalent to a simple finite-difference method, whereas for complicated geometries, it has all the flexibility of a finite-element method. TOUGH2 solves fully coupled fluid-flow and heat-flow equations, using implicit time-stepping. The resulting discrete nonlinear algebraic equations for mass and energy conservation are written in a residual form and solved using Newton/Raphson iteration.

EOS7C is a fluid-property module for the TOUGH2 simulator (Version 2.0) that was developed for applications involving geologic storage of CO_2 in formations containing water and methane. It includes a comprehensive description of the thermodynamics and thermophysical properties of H_2O-CO_2-CH_4 mixtures that reproduces fluid properties largely within experimental error for the temperature and pressure conditions of interest. In particular, CO_2 and CH_4 can exist in a gas-like phase (CO_2 is actually supercritical if pressure and temperature are above the critical point (72 bars, 31°C) or dissolved in the aqueous phase, and water can evaporate into the gas-like phase. Due to its numerical formulation, some CH_4 must be present in every gridblock, but the presence of dissolved CH_4 in saline aquifers associated with hydrocarbon production is reasonable. EOS7C also allows a tracer to partition between the aqueous and gas phase. In its present form, EOS7C does not consider salt, although such a capability is currently under development (C. Oldenburg, personal communication, 2012). Additionally, EOS7C does not account for the heat of dissolution of CO_2, but simulations (Han et al., 2012) using ECO2N have shown that this effect is much smaller than other thermal effects (Joule-Thomson cooling and the cooling that accompanies the evaporation of water) occurring when CO_2 is injected into a saline aquifer.

Many simulations of GCS use equation of state module ECO2N (H_2O-CO_2-NaCl; Spycher and Pruess, 2005; Pruess and Spycher, 2007) and are thus limited to temperatures below about 110°C, but EOS7C allows temperatures as high as the ambient temperature at Cranfield, about 126–128°C. Additionally, the inclusion of CH_4 in EOS7C is important, because initial conditions at Cranfield are CH_4-saturated brine and, as will be seen in the results section below, the breakthrough of CH_4 and CO_2 at the observation wells provides important insights into the multipath nature of flow through the storage formation.

MODEL DEVELOPMENT

Figure 2 shows the permeability profiles inferred from well-logs of the injection well. Vertical discretization of the model was chosen to

capture all the important variability in the permeability profile, which results in 20 model layers, each 1.2 m thick, for a 24 m thick storage formation. Because log information is given with 0.5 foot (0.15 m) resolution, averaging must be done to assign model properties. Horizontal permeability for the model is obtained by arithmetic averaging of the well-log permeabilities, and vertical permeability is obtained by harmonic averaging of the well-log permeabilities. The notable minimum in permeability at 3093-3094 m depth is inferred to be caused by a shale baffle.

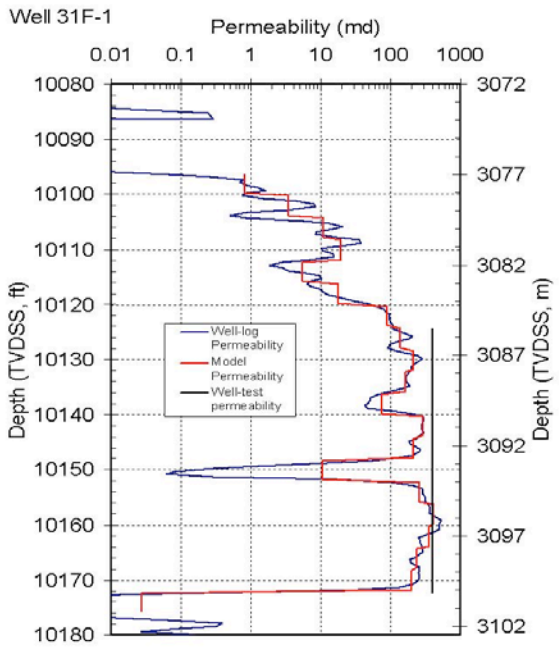

Figure 2. Permeability inferred from well log (blue symbols) and average values used for model (red lines). The black bar shows the perforated interval and the formation-average permeability inferred from a well test. Depths are true vertical depth subsea (TVDSS).

The fact that the well test yielded an average permeability for the storage formation consistent with the higher well-log permeabilities suggests that the high-permeability channels between shale baffles, if not individually continuous, are at least well-connected.

The well logs actually just provide information on porosity, so permeability is inferred by examining the permeability-porosity relationship obtained from sidewell core, as shown in Figure 3. Note that sidewell core samples do not provide information for samples with porosity greater than about 0.25, as these samples are not well recovered by the sidewall coring process. For the model, a curve fit is made to the sidewall core porosity-permeability relationship for porosities up to 0.25, and is then extrapolated to the larger porosity values (up to about 0.35) observed in the well logs.

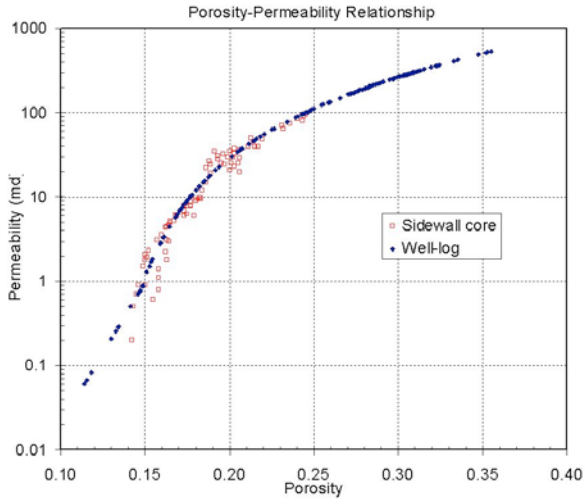

Figure 3. Permeability and porosity measured in sidewall core (red) and the curve fit used to assign permeability for the well-log porosities (blue).

No site-specific information is used for characteristic curves. Instead, functional forms and parameters for capillary pressure and relative permeability are taken from literature values for other Gulf Coast geologic settings (Holtz, 2005; Doughty et al., 2008). Liquid relative permeability uses the van Genuchten (1980) model with $m = 0.65$, and gas relative permeability is quasi-linear (Figure 4). Residual liquid saturation S_{lr} decreases as permeability increases, according to $S_{lr} = 0.2464 - 0.0945 \log(k)$, where k is permeability in millidarcies (M. Holtz, personal communication, 2003), with a minimum value of 0.05. Capillary pressure uses the van Genuchten model with $n = 1.4$, and strength P_{c0} inversely proportional to the square root of permeability, with $P_{c0} = 0.188$ bars for $k = 100$ md. Hysteresis is included in the characteristic curves (IRP = ICP =12, Doughty, 2007, 2009), but since only the injection period is modeled, and injection rate is modeled as monotonically increasing, imbibition is not significant.

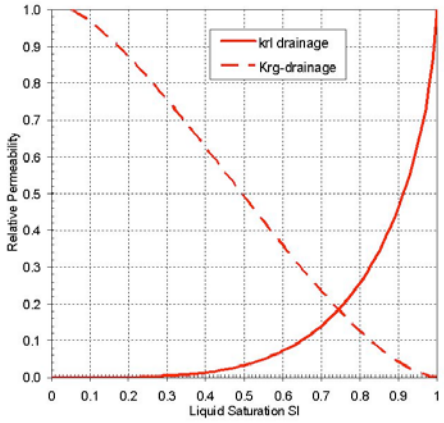

Figure 4. Relative permeability curves for the smallest value of S_{lr} used. For larger values of S_{lr}, the curves are shifted to the right, but the general shape remains the same.

Formation dip is small enough (1–2 degrees) to make an axisymmetric model reasonable for the injection period. This geometry would not be so good for modeling a post-injection rest period, since significant up-dip migration would be expected for the high-permeability sands, even for a slightly dipping storage formation.

Radial grid spacing starts fine at the well and gradually increases to 4 km, where a constant-property boundary is imposed (Figure 5).

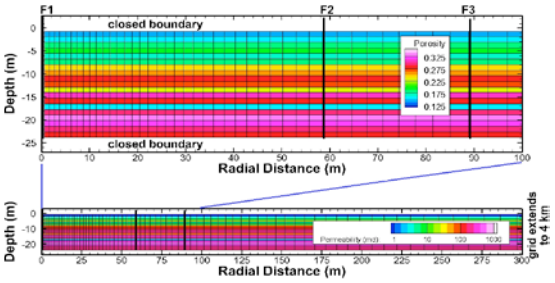

Figure 5. Axisymmetric grid used for the simulations.

The top and bottom boundaries of the model are closed. This is a good approximation for the fluid-flow boundary condition, since cap and bedrock permeabilities are very low. It is not so good for heat flow, however, because heat transfer between the confining layers and formation may be significant, especially for longer times. Future simulations will consider this process by adding the semi-analytical solution by Vinsome and Westerveld (1980) embodied in the Qloss subroutine in TOUGH2, invoked with MOP(15).

Initial conditions for CO_2 injection consist of a water-saturated formation at constant temperature (126°C) and hydrostatic pressure (about 300 bars). The water is saturated with dissolved CH_4 (X_{CH4L} = 0.00285). The hydrostatic pressure distribution is created by temporarily closing the outer radial boundary of the model and running the simulation with no sources or sinks until a steady pressure distribution develops.

The step-wise constant-injection-rate schedule used for the model (Figure 6) corresponds to the first six months of the actual injection at Cranfield, which is extrapolated for the rest of the year. Overall, the amount of CO_2 injected is about right compared to the actual amount. Throughout the injection period, injection consists of 98.5% mass fraction CO_2 and 1.5% mass fraction CH_4. This amount of CH_4 is sufficient to enable the code to run smoothly, is comparable to what was measured at Cranfield, and is typical of with natural CO_2 sources that may not be highly pure. The injection temperature is held fixed at 96°C (by specifying a large heat capacity), which is accurate for the early part of the injection period, but somewhat high for later times when the injection rate increased. Tracer slugs were added to the injected CO_2 at three times (Figure 6).

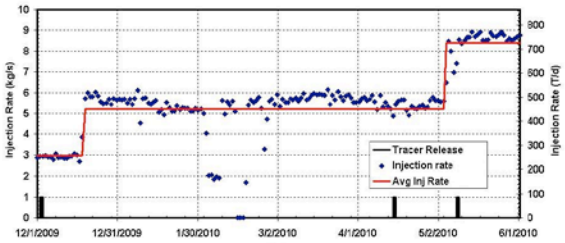

Figure 6. Cranfield injection rate and step-wise approximation used for model. The times of three tracer releases are also shown.

Injection is modeled with a mass source in each model layer, with the fraction of fluid going into each layer proportional to the permeability of that layer. It would be more correct to inject all the CO_2 in the top layer and assign high vertical permeability to all gridblocks representing the well to enable injection of CO_2 throughout the formation according to the pressure difference

between the well and the formation at each layer. This procedure usually works well for isothermal problems; however, it can cause numerical instabilities when the heat flow equation is also solved, so it was not done for the present simulations. Because the column of CO_2 in the well has lower density (~800 kg/m^3) than a column of water in the formation (~1000 kg/m^3), the static pressure profiles in the two columns differ, but the injection interval is only about 14 m thick here, so the pressure difference will be only about 0.3 bars—small compared to the pressure increase accompanying injection (~55 bars), so the error introduced is small.

SIMULATION RESULTS

Time-Series at Observation Wells

Figure 7 shows the modeled gas saturation, and CO_2, CH_4, and SF_6 mass fractions in the gas phase for the two observation wells F2 and F3, during the first 50 days of CO_2 injection, obtained by averaging over the model layers 3-19, which represent the open interval in the observation wells. The model predicts the arrival of a bank of gaseous CH_4 ahead of the super-critical CO_2. This phenomenon has been predicted before (Oldenburg and Doughty, 2011) and reflects the fact that although under ambient conditions, all the CH_4 can be dissolved in the water, as soon as a gas phase is present, much of the CH_4 evaporates into it. The SF_6 tracer also preferentially partitions into the gas phase, and arrives nearly coincidentally with the CH_4.

The corresponding U-tube data is also shown in Figure 7. The U-tubes in both wells became clogged shortly after injection began, and did not operate until the arrival of CO_2 (which proved to be an excellent solvent for cleaning the U-tubes) at about 11 and 15 days in Wells F2 and F3, respectively. Thus the first arrival of CH_4 and SF_6 was not monitored, but the fact that the first CH_4 and SF_6 measurements show a decreasing trend while the first CO_2 measurements show an increasing trend supports the model result for the arrival of a bank of free-phase CH_4 ahead of the CO_2. The model arrival time is just a few days late for Well F2, but is about 15 days late for the more distant Well F3, suggesting that the actual flow field is not well approximated by the radial symmetry of the model, but that CO_2 is travelling in more linear preferential paths.

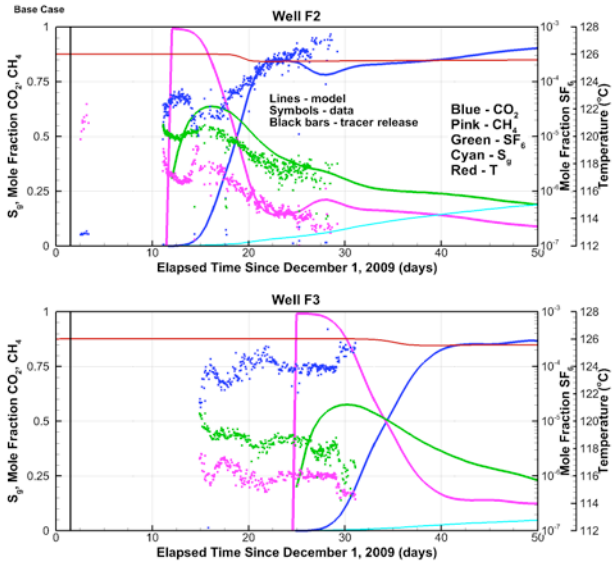

Figure 7. Modeled temperature (T), gas saturation (S_g), and CO_2, CH_4, and SF_6 mass fractions in the gas phase for the two observation wells F2 and F3 for the first 50 days of CO_2 injection. Note that SF_6 is plotted on a log scale.

Both the model and U-tube data show CH_4 and CO_2 mass fractions that oscillate in time. We interpret this as the arrival at different times of injected CO_2 travelling through distinct flow paths. For the RZ model, the only distinct flow paths are those above and below the shale baffle (see Figure 2), but for the field, there could be multiple flow paths in all three dimensions.

Figure 7 also shows modeled temperature at layer 17, which is the layer with the highest permeability, and the first layer to show a temperature response. There is a small temperature drop (~0.5°C) coincident with the arrival of the gas phase at each well, which is interpreted as Joule-Thompson cooling accompanying expansion of CO_2 as it moves away from the injection well (i.e., from higher to lower pressure) and cooling resulting from the evaporation of water into the CO_2-rich phase . Both of these effects would occur even if the injected CO_2 had the same temperature as the formation. The large temperature decrease corresponding to the low temperature of the injected CO_2 (30°C lower than the formation temperature), begins to be

felt at Well F2 at about 160 days (Figure 8), far behind the saturation-front arrival at 12 days. This delay occurs because the CO_2 thermally equilibrates with the brine and formation rock it comes in contact with as it moves away from the injection well. The heat capacity of these components is significant enough that the model predicts the thermal front has not even reached Well F3 within the first year.

Given the late arrival of CO_2 predicted for Well F3 (28 days versus the actual 15 days), the thermal prediction for Well F3 is not expected to be accurate. Based on geological understanding and the quick CO_2 arrival at Well F3, actual CO_2 flow paths are inferred to be localized laterally in contrast to the radial symmetry of the current model. In fact, comparing model and actual temperature arrivals may provide additional information about the nature of the CO_2 flow paths. Many small flow paths would be retarded by the thermal equilibration with their surroundings much more than a few large flow paths, and hence their thermal signature could be well-predicted by the axisymmetric model, even if the arrival of the CO_2 itself were not. In contrast, for a few large flow paths, neither the CO_2 arrival nor the thermal arrival would be well-predicted by an axisymmetric model. Unfortunately, the temperature gauges in Wells F2 and F3 did not function properly, so direct comparison with field measure temperatures has not been possible.

Figure 8 also enables comparison of the SF_6 peaks for all three tracer releases. The first peak, for tracer released just after CO_2 injection began, is much sharper than the latter two peaks, which is consistent with the widely accepted notion that a two-phase plume growing in a single-phase region develops a self-sharpening front. The model matches all peak heights and arrival times for Well F2 reasonably well, but for F3 the model arrivals are not only too late (as expected based on the late CO_2 arrival), but the latter peak is also too low and wide, not even resolving the individual peaks of the latter two tracer releases. This is consistent with the hypothesis that the flow occurs through limited preferential flow paths, rather than spreading radially as in the model.

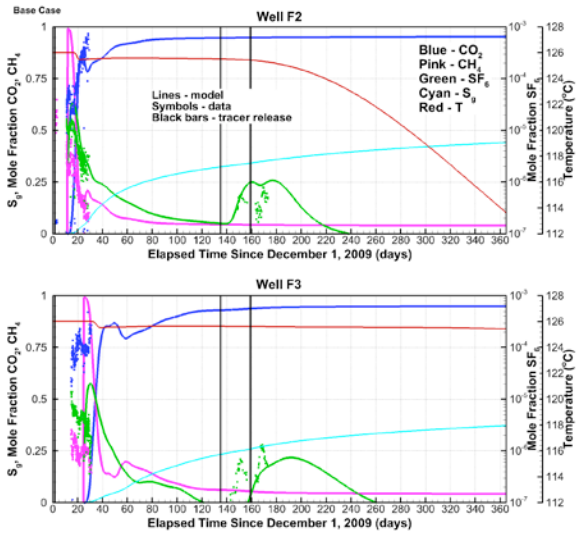

Figure 8. Modeled temperature (T), gas saturation (S_g), and CO_2 and CH_4 mass fractions in the gas phase for the two observation wells F2 and F3 for the entire year of CO_2 injection. Note that SF_6 is plotted on a log scale.

Spatial Distributions

Spatial distributions (r-z cross sections through the axisymmetric model) at 10, 60, and 365 days are shown in Figures 9, 10, and 11 and provide further insights into the physical processes occurring as supercritical CO_2 is injected into a CH_4-saturated brine. The uppermost frame in each figure shows the model porosity distribution. Because permeability increases as porosity increases, this distribution identifies the highest permeability regions in yellow and orange, and the saturation distribution (second frame) indicates that the CO_2 is moving preferentially into the upper portion of these regions. In particular, the low-permeability shale baffle at $z \sim -16$ m ($z = 0$ is the top of the model) divides the CO_2 plume into two parts. Pressure changes are relatively small for this high-permeability formation, but pressure changes extend far beyond the CO_2 plume itself. Note that the temperature scale is non-uniform: most of the range (96°C–125°C) is shown in colors from blue to yellow—this identifies the cooling attributed to the cool temperature of the injected CO_2. From 125°C to 126°C (orange to red), the scale is greatly expanded, to show the small temperature decreases attributed to Joule-Thompson cooling and the evaporation of water.

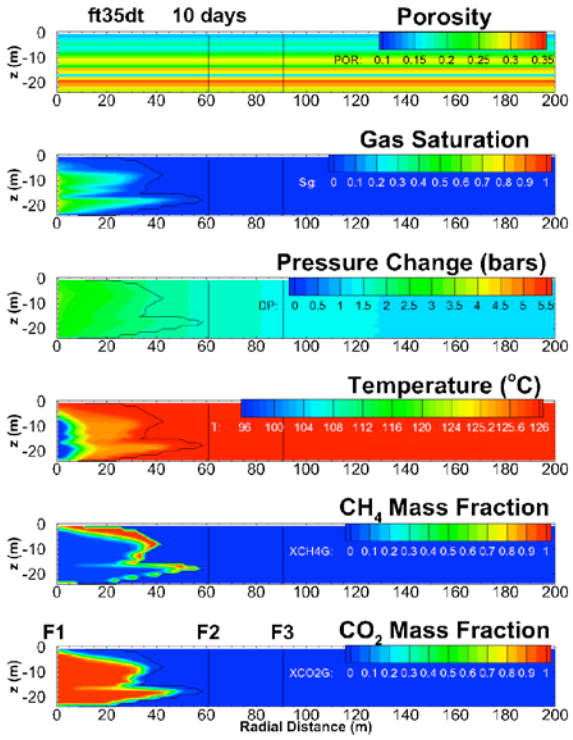

Figure 9. Model results after 10 days of CO_2 injection. In each frame the black contour line shows $S_g = 0$.

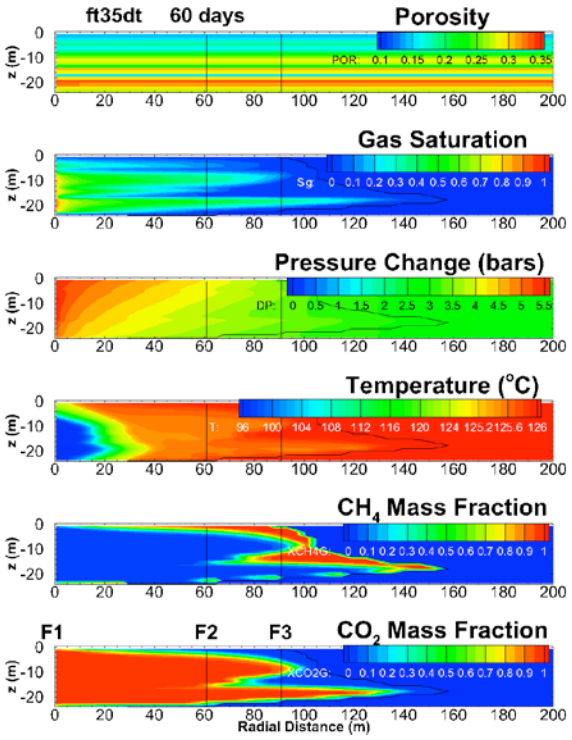

Figure 10. Model results after 60 days of CO_2 injection. In each frame the black contour line shows $S_g = 0$.

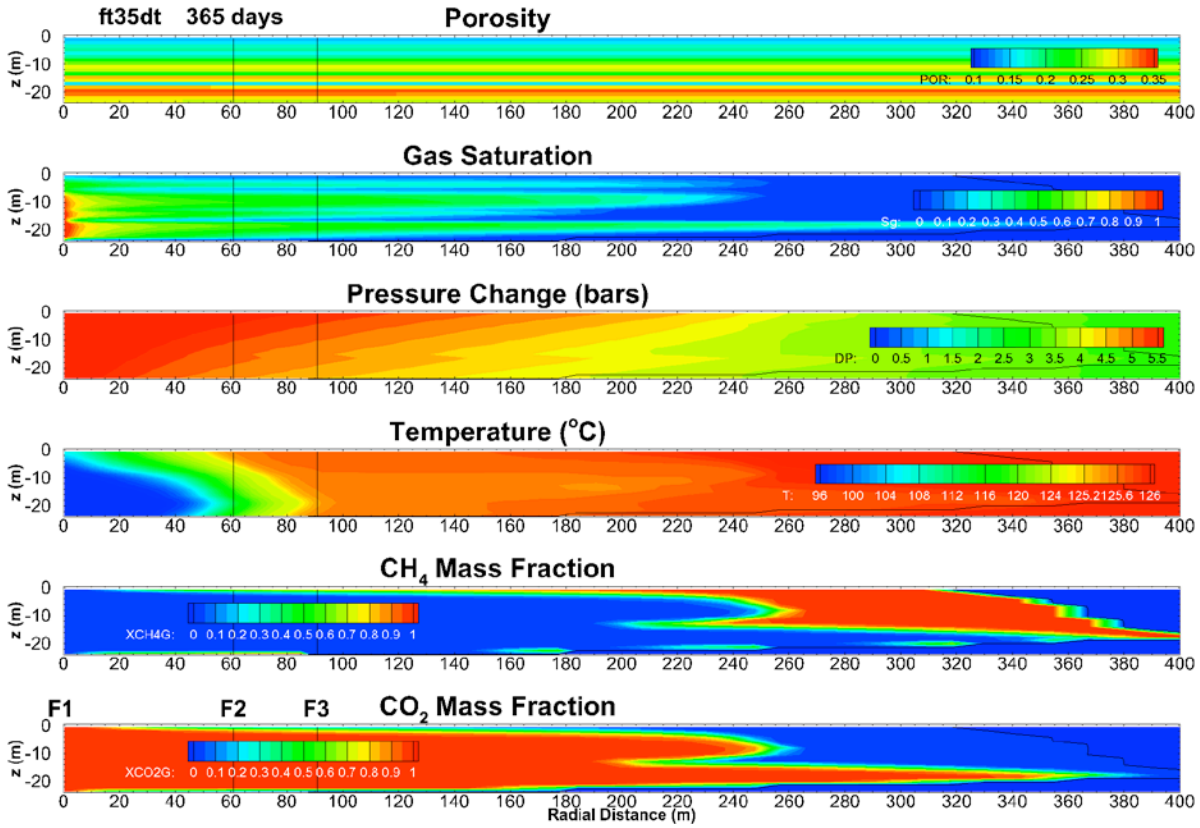

Figure 11. Model results after 365 days of CO_2 injection. In each frame, the black contour line shows $S_g = 0$.

The CH_4 and CO_2 mass fraction plots illustrate how the initially dissolved CH_4 evaporates when the CO_2 arrives and is pushed ahead of the main CO_2 plume. Since the CH_4 has very low density, it is strongly buoyant, and by 365 days it has all moved to the upper portion of the formation.

CONCLUSIONS AND FUTURE WORK

This simplified modeling of the Cranfield CO_2 injection pilot has proved to be an extremely valuable exercise for gaining insight into the physical processes accompanying CO_2 injection into CH_4-saturated brine. The interplay of multiphase flow effects and formation heterogeneity creates distinct signatures of multiple flow paths, something rarely directly observed in the field. Current extensions of this work include a 3D model with lateral heterogeneity, and incorporation of more realistic relative permeability functions, derived from laboratory experiments with Tuscaloosa Formation core samples.

ACKNOWLEDGMENT

We acknowledge Denbury for hosting the CO_2 injection pilot and Sue Hovorka of Texas Bureau of Economic Geology for guiding the project. Funding is through SECARB (Southeast Carbon Sequestration Partnership), provided by the National Energy Research Laboratory, US Department of Energy, Office of Fossil Energy. LBNL is funded under DOE Contract Number DE-AC02-05CH11231.

REFERENCES

Doetsch, J., M.B. Kowalsky, C. Doughty, S. Finsterle, J.B. Ajo- Franklin, X. Yang, C.R. Carrigan, and T.M. Daley, *Towards fully coupled hydrogeophysical inversion of CO2 migration data in a deep saline aquifer*, SEG-AGU Hydrogeophysics workshop, Boise, ID, July 2012.

Doughty, C., Modeling geologic storage of carbon dioxide: comparison of hysteretic and non-hysteretic curves, *Energy Conversion and Management*, 48(6), 1768-1781, 2007.

Doughty, C., *User's Guide for Hysteretic Capillary Pressure and Relative Permeability Functions in iTOUGH2*, Rep. LBNL-2483E, Lawrence Berkeley National Laboratory, Berkeley, CA, 2009.

Doughty, C., B.M. Freifeld, and R.C. Trautz, Site characterization for CO2 geologic storage and vice versa – the Frio brine pilot, Texas, USA as a case study, *Environmental Geology*, 54(8), 1635-1656, 2008.

Freifeld, B.M R.C. Trautz, Y.K. Kharaka, T.J. Phelps, L.R. Myer, S.D. Hovorka, and D.J. Collins, The U-tube: A novel system for acquiring borehole fluid samples from a deep geologic CO2 sequestration experiment, *Journal of Geophysical Research*, 110, B10203, 2005.

Han, W.S., K.-Y. Kim, E. Park, B.J. McPherson, S.-Y. Lee, M.-H. Park, Modeling of spatiotemporal thermal response to CO_2 injection in saline formations: Interpretation for monitoring, *Transport in Porous Media,* 93, 381–399, 2012.

Hosseini, S.A., H. Lashgarib , J.W. Choi, J.-P. Nicot, J. Lua, and S.D. Hovorka, *Static and Dynamic Reservoir Modeling for Geological CO2 Sequestration at Cranfield, Mississippi, U.S.A,* Texas Bureau of Economic Geology, Austin, TX, 2012.

Holtz, M.H., *Reservoir characterization applying residual gas saturation modeling, example from the Starfak T1 reservoir, middle Miocene Gulf of Mexico*, MS thesis, Department of Petroleum and Geosystems Engineering, University of Texas at Austin, Austin, Texas, 2005.

Hovorka, S.D., et al., Monitoring a large volume CO2 injection: Year two results from SECARB project at Denbury's Cranfield, Mississippi, USA, *Energy Procedia*, 4, 3478–3485, 2011.

Narasimhan, T.N. and P.A. Witherspoon, An integrated finite difference method for analyzing fluid flow in porous media, *Water Resources Research*, 12(1), 57-64, 1976.

Oldenburg, C.M. and C. Doughty, Injection, Flow, and Mixing of CO2 in Porous Media with Residual Gas, *Transport in Porous Media*, 90, 201–218, 2011.

Oldenburg, C.M., G.J. Moridis, N. Spycher, and K.Pruess, *EOS7C Version 1.0: TOUGH2 Module for Carbon Dioxide or Nitrogen in Natural Gas (Methane) Reservoirs*, Rep.

LBNL-56589, Lawrence Berkeley National Laboratory, Berkeley, CA, 2004.

Pruess, K., The TOUGH codes - A family of simulation tools for multiphase flow and transport processes in permeable media, *Vadose Zone Journal*, 3(3),738-746, 2004.

Pruess, K., C. Oldenburg, G. Moridis, *TOUGH2 users guide, Ver. 2.0*, Rep. LBNL-43134, Lawrence Berkeley National Laboratory, Berkeley, CA, 1999.

Pruess, K. and N. Spycher, ECO2N—A fluid property module for the TOUGH2 code for studies of CO2 storage in saline aquifers, *Energy Conversion and Management*, 48(6), 1761–1767, 2007.

Spycher, N. and K. Pruess, CO2-H2O mixtures in the geological sequestration of CO2: II Partitioning in chloride brines at 12 − 100◦C and up to 600 bars, *Geochim. Cosmochim. Ac.*, 69(13), 3309–3320, 2005.

van Genuchten MTh, A closed-form equation for predicting the hydraulic conductivity of unsaturated soils, *Soil Sci. Soc. America Journal*, 44(5), 892–898, 1980.

Vinsome, P.K.W., and J. Westerveld. A simple method for predicting cap and base rock heat losses in thermal reservoir simulators, *J. Canadian Petroleum Technology*, 87-90, July-September, 1980.

BEHAVIOR OF BRINES CONTAINING DISSOLVED CO_2 IN ABANDONED WELLBORES

Kirk Ellison[1]; Ronald Falta; Lawrence Murdoch; Scott Brame

Clemson University; 340 Brackett Hall; Clemson, SC 29634

[1]Corresponding Author; present address: Southern Company; 600 N 18th St/14N-8195; Birmingham, AL 35291-8195; kmelliso@southernco.com

ABSTRACT

In order to ensure safe long-term storage of carbon dioxide in geologic formations, the risks posed by improperly abandoned wells must be understood and controlled. Under specific circumstances with formation overpressure or overlying aquifer drawdown, CO_2 that is dissolved in brine can flow up improperly abandoned wells, where it can potentially enter and contaminate USDW. The possibility that depressurization in the wellbore may cause CO_2 exsolution from brine to form a separate buoyant gas phase is of primary concern. Numerical models are used to evaluate these effects in wellbores and to examine the effects of system parameters on CO_2 and brine leakage rates through wellbores.

Up to 20% of the dissolved CO_2 is found to exsolve in simulations of brine transport up a wellbore. The degree of leakage is constrained by the properties of the well, with the permeability of the well being of chief importance. However, at high well permeabilities, the geologic formations provide more resistance to flow than the well and constrain leakage rates. It is found that the presence of stratified permeable layers limit the possibility of upward migration of dissolved CO_2.

INTRODUCTION

During carbon capture and storage (CCS), it is expected that injected supercritical CO_2 will eventually dissolve into the storage formation brines over time scales of hundreds to thousands of years (McPherson and Cole, 2000; Ennis-King and Paterson, 2003). Moreover, some researchers have proposed injecting CO_2 as a dissolved phase (Burton and Bryant, 2007; Leonenko and Keith, 2008; Burton and Bryant, 2009). Once CO_2 is dissolved into storage formation brines, a buoyant CO_2 phase no longer exists. Upon dissolution, the brine becomes about 1% denser (Enick and Klara, 1990; Bachu and Adams, 2003); therefore, it will have a tendency to sink slowly to the bottom of the formation.

While it is less likely that dissolved CO_2 will leak up abandoned wellbores, there is still a potential danger. If the storage formation is overpressured, or if an overlying aquifer is drawn down due to pumping, the pressure differential could induce the brine containing the dissolved CO_2 to flow upward through permeable pathways such as abandoned wells. As pressure decreases, and the leaked brine moves upward, CO_2 solubility decreases, causing gas exsolution (Pruess, 2008). This evolved gas phase has the potential to accumulate in underground sources of drinking water (USDW) or potentially migrate to the surface due to its buoyancy.

The focus of this research is to examine the properties in an abandoned wellbore that control the overall flow rate for leakage of brine containing dissolved CO_2. In addition, gaseous CO_2 exsolution effects and leakage plumes are evaluated. This work builds on studies such as that by Birkholzer et al. (2011), whose focus is brine leakage through wellbores near the area of review boundary. Unlike that study, the present work is specifically directed toward wellbore leakage of CO_2-laden brine. Investigation of how this dissolved-phase CO_2 could leak up wellbores and contaminate overlying USDW is of primary concern. Wellbore leakage of dissolved CO_2-laden brine due not only to stor-

age formation overpressure, but also to overlying aquifer drawdown, are examined.

In the present study, changes in flow due to system parameters are examined in detail. Flow effects when multiple permeable formations are present along the wellbore are considered.

DIRECT LEAKAGE MODEL FROM STORAGE FORMATION TO USDW

In order to perform a detailed analysis of CO_2-laden brine leakage into USDW through abandoned wells, we must consider effects that cannot be accounted for in analytical solutions. Important flow effects may be caused by pressure and temperature gradients, phase changes, salinity, depressurization, and multiphase flow phenomena.

Our numerical model is constructed using the TOUGH2-ECO2N multiphase flow simulator (Pruess, 2007) with the PetraSim GUI (Swenson, D. 2003). The TOUGH2-ECO2N simulator allows for modeling the development of dissolved and gaseous CO_2 plumes in the USDW due to overpressurization of the storage formation or USDW drawdown.

A radially symmetric numerical grid design is used for the simulations, which is similar to numerical grids used in other studies (Birkholzer et al., 2011). In Figure 1, the model design can be seen. This model represents an endpoint case in which a dissolved CO_2 storage formation is directly connected to a USDW through a wellbore. This allows for an evaluation of flow effects with simple, but representative geometry.

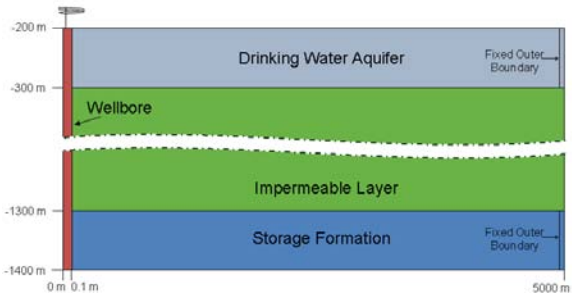

Figure 1. Base-case numerical model setup. The storage formation and USDW are separated by a 1000 m thick impermeable layer. All formations are penetrated by a well in the central radial element.

The outer radius of the model is set to 5,000 m. This radius is sufficiently large to minimalize numerical end effects. The model is given an overall vertical thickness of 1,200 m. Both the storage formation and the drinking water aquifer are 100 m thick. Between the two formations is a 1000 m thick impermeable layer. The impermeable layer between the formations represents a case in which only flow between the storage formation and the USDW are considered. The layer does not transmit fluids, but it does allow for thermal conduction of heat from the warmer storage formation brine as it rises through the wellbore. Finally, the top of the model is set at a depth of 200 m below the ground surface, which is a representative depth for a large regional USDW. Hydrostatic pressure is used to generate the pressure gradient, such that the pressure at the top of the upper formation is 2.0×10^6 Pa, and at the bottom of the lower formation it is 1.4×10^7 Pa. A geothermal gradient of 30°C/km with a surface temperature of 15°C is used. This gradient is typical of the western United States and has been used in other numerical models (Pruess, 2008). Finally, CO_2 exists just below its solubility in the storage formation in order to simulate CO_2-laden brine.

The wellbore is modeled as the central radial element in the model, and it is given a different permeability from the surrounding elements. As in previous studies (Nordbotten et al., 2005; Ebigbo et al., 2007; Nordbotten et al., 2009; Birkholzer et al., 2011), it is assumed that Darcy's law applies to flow in the well.

However, when well permeabilities above 1×10^{-7} m^2 are used in the numerical simulations, it is assumed that they are representative of open pipe flow. We acknowledge that the numerical assumption of laminar flow according to Darcy's law in the wellbore may not fully capture flow effects for the case of turbulent flow or for different multiphase flow regimes in an open wellbore.

The model is discretized by using 87 elements in the radial dimension. The radial gridblocks are refined around the well with each successive

ring increasing in thickness to maximum of 95 m. The outermost ring is used to impose a fixed state boundary on the model. The fixed state conditions (constant pressure, temperature, salt concentration, CO_2 saturation) in this ring allow for flow into the storage formation as well as flow out of the USDW. Similar to Birkholzer et al. (2011), the pressure in the outer ring can be increased to overpressurize the storage formation or lowered to induce drawdown in the USDW.

In the vertical z dimension, 70 elements are used. The storage formation uses ten 10 m thick model layers, whereas the USDW is refined using twenty 5 m thick model layers. The impermeable layer consists of forty 25 m thick model layers (these mainly conduct heat from the wellbore). This discretization results in a total of 6090 gridblocks for the entire model.

Relative permeabilities and capillary pressures for the CO_2 and brine are calculated using modified versions of the van Genuchten equations, and are the same as those used in simulations in Doughty, (2007). Capillary pressure is zero in the well, and, the well porosity is set to 0.98. Other relevant model properties can be seen in Table 1.

Table 1. Material properties

Property	Value
Entire Model	
Thermal Conductivity (W/m·°C)	2.51
Heat Capacity (J/Kg·°C)	920
Rock Density (Kg/m^3)	2600
Drinking Water Aquifer	
Permeability (m^2)	$1x10^{-12}$
Porosity	0.25
Salinity (mg/l)	0
Impermeable Layer	
Permeability (m^2)	$1x10^{-20}$
Porosity	$1x10^{-4}$
Storage Formation	
Permeability (m^2)	$1x10^{-13}$
Porosity	0.25
Salinity (mg/l)	20,000
CO_2 Mass Fraction	0.044
Wellbore	
Permeability, (m^2)	$1x10^{-5}$– $1x10^{-12}$
Porosity	0.98
Well Diameter (m)	0.2 (8 inch)

Simulations can be run with different values of the well's permeability over a range of system overpressures and drawdowns ranging between 10 and 30 bar.

Wellbore Permeability Effects on Leakage

Knowing the apparent permeability of an improperly abandoned well is difficult, since so little is known about the spatial distribution and properties of these wells (Ide et al., 2006). Other researchers have dealt with leaky wellbore permeability by using a range of permeability values (Celia et al., 2004; Birkholzer et al., 2011), and that approach is used here.

This numerical model uses an 8-inch (0.2 m) diameter well, and the storage formation is overpressurized 20 bar to induce flow up the wellbore. This overpressure is consistent with predicted long-term overpressures seen in other studies (Zhou et al., 2010).

In the wellbore, a significant fraction of the CO_2 exsolves to form a separate supercritical or gas phase as the brine is depressurized during upward migration due to storage formation overpressure. For leakage simulations at high well permeabilities, the gas fraction that accumulates in the USDW is higher than for leakage with lower well permeability. Higher gas fractions at high well permeabilities are due to a larger increase in temperature in and around the wellbore. Because flow rates are largest at high permeabilities, more warm brine leaks, which heats up the system and reduces CO_2 solubility.

However, re-dissolution of the exsolving CO_2 as it contacts resident USDW fluid during leakage reduces the gas phase in the USDW. At lower well permeabilities, and thus flow rates, this effect becomes dominant. When the flow rates are very low due to low well permeability, all of the exsolving gas becomes redissolved in the aquifer during leakage (Figure 2).

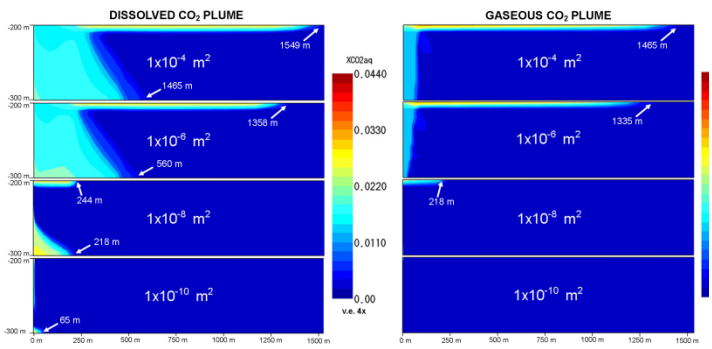

Figure 2. Dissolved and gaseous CO_2 plume in the drinking water aquifer at various well permeabilities at 50 years. Plume formation is not significant at well permeabilities below 1×10^{-10} m^2.

After 50 years of wellbore leakage into the USDW, CO_2 leakage plumes have significantly different magnitudes for cases of different wellbore permeabilities. For well permeabilities below 1×10^{-8} m^2, the CO_2 plume mass decreases linearly with decreasing well permeability. However, in simulations with well permeabilities above 1×10^{-7} m^2, leakage plumes do not continue to increase in magnitude significantly. In addition, examination of leakage velocities into the USDW show a linear increase in velocity with increasing permeability up to 1×10^{-7} m^2, suggesting that the permeability of the wellbore controls the leakage rate. However, at high well permeabilities, the leakage rate remains nearly constant, suggesting that the permeability of the well no longer controls the flow, but rather the permeability of the geologic formations is the liming factor.

The USDW leakage plumes tend to have two separate regions. Along the top of the USDW, a gaseous plume occurs which increases in size with increasing well permeability. Secondly, there is a wedge shaped dissolved plume that extends downward to the base of the USDW. It also increases with increasing well permeability.

The exsolved gaseous plume spreads along the top of the aquifer due to being highly upwardly buoyant compared to the surrounding water. The wedge-shaped dissolved plume migrates downward in the USDW because the CO_2-laden brine that is leaking has a higher density than surrounding waters.

The total CO_2 mass flow rate (dissolved and gaseous) in the well at the base of the USDW over 50 years for well permeabilities ranging between 1×10^{-4} to 1×10^{-12} m^2 show that at higher well permeabilities (1×10^{-4} to 1×10^{-6} m^2), the flow rates are fully established within 3 months. However, as well permeability decreases, the time scale for fully established flow is increased indicating that it takes longer for leaked brine to flow upward at lower permeabilities.

At well permeabilities above 1×10^{-7} m^2, the flow rate never reaches steady state but instead exhibits small oscillations as well as a gradual decline over time. This is due to thermal effects similar to those shown by Oldenburg and Rinaldi, (2010), where warm brine cools upon entry into the USDW and moves downward due to an increase in density. Additional cooling occurs due to gas exsolution. As wellbore permeabilities below 1×10^{-7} m^2, leakage rates of CO_2 reach a steady state once fully established.

Despite these limitations, it is reasonable to surmise that at open wellbore conditions, the well will provide far less resistance to flow than the geologic formations, indicating minimal control over the system. This suggest that even accounting for resistance due to turbulent flow, the geologic formations will provide an upper limit to the leakage rates of CO_2 laden brine.

In order to evaluate the mass of CO_2 that leaks into the USDW as a function of well permeability and storage formation overpressure, many leakage simulations are performed over a matrix of pressure and well permeability values (Figure 3).

After 25 years, the mass of leaked CO_2 ranges from zero at low permeabilities and overpressures to as much as 0.5 Mt for permeabilities meant to represent leakage through an open wellbore, with large formation overpressure.

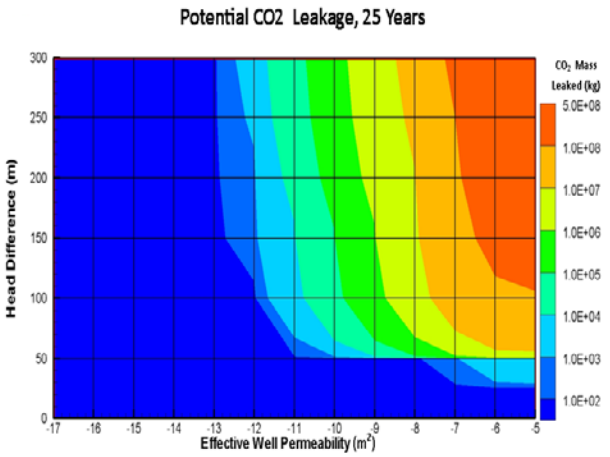

Figure 3. Simulation results showing the simulated mass of CO_2 leakage plumes in the DWA as a function of well permeability and formation overpressure.

Although a large mass of CO_2 leaks for the open-well cases, this represents a worst-case scenario. Leaky well permeability ranges that are probably more realistic for abandoned wells, such as 1×10^{-10} to 1×10^{-14} m^2, have been used in other studies of wellbore leakage (Celia, M.A. 2004; Nordbotten, J.M. 2005; Nordbotten, J.M. 2009). For this permeability range, the mass of CO_2 leaked is at least three orders of magnitude lower than for open wellbore flow leakage. Therefore, leaky wells with some degree of blockage likely pose a far lower leakage risk than for leakage through an open wellbore.

Leakage Plume Behavior Post Injection

Once overpressure or drawdown has been established such that CO_2-laden brine is flowing in a wellbore, there is a concern that as CO_2 exsolves, it might generate a self-enhancing system whereby exsolution causes a gas drive that persists beyond the overpressure or drawdown event. In order to examine these effects as well as leakage plume behavior, the model is overpressured by 20 bar and the simulation is run for 100 years of overpressure.

The dissolved CO_2 leakage plume in the USDW extends out 315 m after 100 years of leakage. In addition, gaseous CO_2 has developed and accumulated along the top of the USDW with a radial extent of 300 m. At the end of the 100-year injection, the outer radial ring pressure in the storage formation is returned to hydrostatic conditions. Within 60 days, the reduction in overpressure reaches the wellbore. As soon as this occurs, the upward flow of CO_2 laden brine ceases.

No solution-gas-drive effects are observed in the simulated system. Because the dissolved CO_2 in the storage formation is only a small fraction of the total fluid mass (4.4%), with less than 20% of that coming out of solution in the wellbore and USDW, the overall flow rate is dominated by the brine and is not controlled by exsolving CO_2. Therefore, for the simulated scenario, in the absence of an external pressure disturbance, the exsolving CO_2 is unable to establish upward gas drive.

Once overpressure ceases, water and CO_2 in the USDW begin flow back down the wellbore and eventually reach a steady downward flow rate of 0.19 kg/s (~3 gal/min) for the water. Due to CO_2 flow back down the wellbore, after 25 years, 7% of the total leaked CO_2 has been flushed down the wellbore while 15.8% has been flushed at 100 years. However, the gaseous plume is diminished much faster than the dissolved CO_2 plume. After 25 years, 29% has left the USDW while 54.5% is removed after 100 years (Figure 4).

Initially, when the overpressure is removed, the leaked CO_2-laden brine in the USDW flows down the well due to its density and the lack of a continued pressure head for inducing upward flow. However, once this initial effect ceases, the fluid around the wellbore in the USDW remains denser than the fluid below it due to its lower temperature, allowing for downward migration. As water in the USDW contacts the gaseous CO_2 plume, the CO_2 is stripped into the dissolved phase in the water, increasing its density. This fluid then drains down the wellbore, allowing more unsaturated water to contact the gaseous plume. Therefore, the bottom of the gaseous CO_2 plume along the top of the aquifer is constantly being contacted by unsaturated water moving past it. The reduction in the gase-

ous and dissolved CO_2 plume in the USDW can be seen in Figure 4.

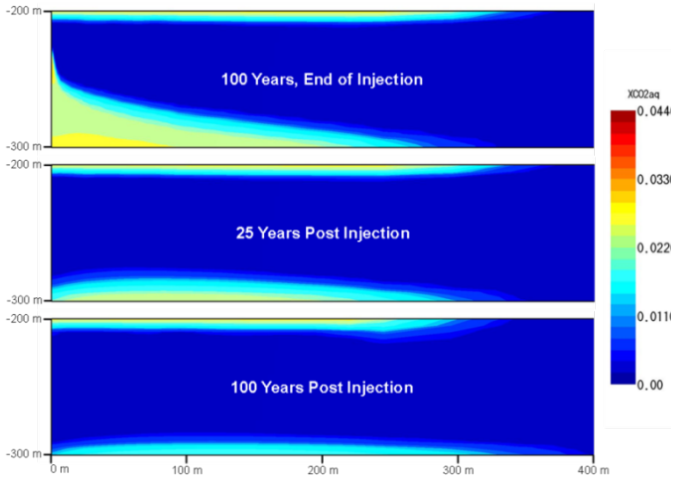

Figure 4. Dissolved CO_2 plume migration in the entire system and in the USDW after 100 years of leakage due to overpressure.

In addition to reducing the plume in the USDW, the area around the wellbore in the dissolved CO_2 storage formation is being diluted with respect to CO_2 content. This is due to the downward migration of water from the USDW. For this simulated case, the downward migration of fluid post injection further reduces the leakage risks posed by dissolved CO_2. However, we note that this backflow phenomena may not occur if the storage formation brine has a high density, due to a higher salinity.

STRATIFIED WELLBORE LEAKAGE MODEL

For this case, the region containing the impermeable layer is modified so that effects due to interbedded stratigraphy can be examined. A formation with the same properties as the USDW is assigned to four 100 m thick zones along the height of the model with top elevations of 350, 550, 750, and 950 m below the ground surface respectively. All formations are penetrated by the 8-inch diameter 1×10^{-8} m^2 permeability well, and the wellbore is open to each formation.

Overpressure with Dissolved CO_2

The stratified model is run for fifty years with an overpressure of 20 bar. After 50 years, no CO_2, dissolved or gaseous, has reached the drinking water aquifer. The four interbedded aquifers provide significant leakage for the CO_2 laden brine as it moves up the wellbore. Because the majority of the CO_2 is dissolved in the leaking brine, the effects of capillary entry pressure and relative permeability are minimal. Therefore, the majority of the dissolved CO_2 is transported into interbedded layers as a part of the single aqueous phase brine. Furthermore, the largest amount of leaked brine migrates directly into the closest overlying formation. Some gaseous CO_2 leaks into the stratified layers as well. CO_2 exsolution occurs within the wellbore during upward migration. However, instead of continuing to migrate upward, the gaseous CO_2 enters into the interbedded stratigraphy. Both the dissolved and gaseous CO_2 plumes in the stratified system can be seen in Figure 5.

In the system modeled, the presence of interbedded stratigraphy reduces the leakage risk for CO_2 into a USDW. Further simulations are run with overpressures as high as 50 bar. Even at this high overpressure, the CO_2 never moves into the drinking water aquifer, but instead has a greater degree of accumulation in the interbedded aquifers between the storage formation and the USDW.

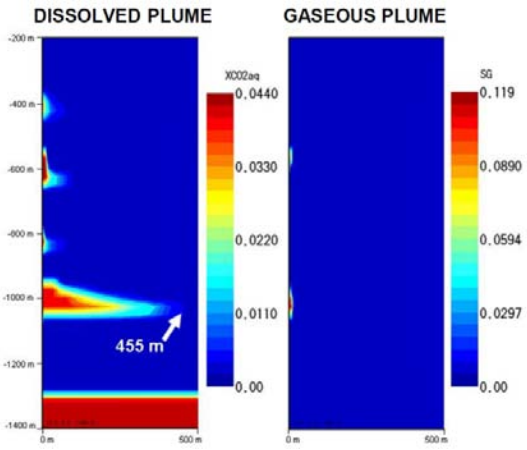

Figure 5. Dissolved and gaseous leakage plumes at 50 years for the stratified simulation at 50 years of leakage.

Effects of USDW Drawdown

The stratified model is used to simulate leakage effects due to USDW drawdown when permeable stratified layers are present. In order to examine a worst-case scenario, the wellbore is made highly permeable (1×10^{-5} m^2) to maximize the possible amount of upward flow due to drawdown. The USDW is then drawn down 20 bar (~200 m head).

Simulations show that as fluid flows into the upper aquifer, it is being pulled directly from the interbedded aquifers below. In this scenario, only a small amount of CO_2-laden brine is drawn out of the storage formation, but it is never pulled up the well far enough to enter overlying permeable layers. Upward flow of fluid from each formation is reduced with depth as each successive permeable layer below the USDW contributes less to overall flow rate. Whenever interbedded permeable layers exist between a formation being drawn down and a dissolved CO_2 storage formation, the possibility of dissolved CO_2 leakage is greatly reduced by the interbedded permeable layers.

SUMMARY

Simulations have been performed to evaluate leakage of CO_2-laden brine through poorly sealed or improperly abandoned wellbores. Through numerical models, it has been found that the overriding controls of wellbore leakage of brines containing dissolved CO_2 are storage formation overpressure and well permeability

In most leakage scenarios where the wellbore is not an open wellbore but instead is blocked in some fashion, well permeability controls the leakage rate of CO_2-laden brine into permeable formations. However, if the endpoint case of leakage through a completely open well occurs, the permeabilities of the geologic formations will provide more resistance to fluid flow. As a result, there is a probable upper limit to the leakage flow of brine, even with an open well.

For the endpoint case where no permeable layers are present between the storage formation and the USDW, significant amounts of gas can exsolve during leakage to form a separate gas phase in the USDW. However, in a more realistic case where interbedded permeable layers are present, simulation results show that while gas phase exsolution does occur, large gaseous plumes are not observed in the USDW.

In the simulations performed, CO_2-laden brine leakage due to drawdown of overlying USDW poses minimal risks if stratified permeable layers are present. During drawdown, fluid is preferentially drawn out of formations directly underneath the formation being pumped. Thus, in a typical stratified system, it is possible that a deep CO_2 storage formation will not be affected by drawdown in an overlying USDW.

After overpressure has ceased, leakage of CO_2 laden brine does not continue. No solution gas drive effects are observed in the simulations. Furthermore, after injection has ceased, significant amounts of the leaked CO_2, especially the gaseous plume, may be flushed back down the wellbore due to a depth decreasing density gradient in the system. This serves as a natural mechanism for CO_2 leakage mitigation.

Numerical simulations are unable to capture the exact behavior of dissolved CO_2 leakage for an open wellbore. Although effects due to turbulent friction as well as multiphase flow regimes are not considered, the high-permeability model results still provide valuable insights into the behavior of dissolved CO_2 leakage.

REFERENCES

Bachu, S. and J. J. Adams, 2003, Sequestration of CO2 in geological media in response to climate change: capacity of deep saline aquifers to sequester CO2 in solution, Energy Conversion and Management, vol. 44, no. 20, p. 3151-3175.

Birkholzer, J. T., J. P. Nicot, C. M. Oldenburg, Q. Zhou, S. Kraemer, and K. Bandilla, 2011, Brine flow up a well caused by pressure perturbation from geologic carbon sequestration: Static and dynamic evaluations, International journal of greenhouse gas control.

Burton, M. M. and S. Bryant, 2007, Eliminating Buoyant Migration of Sequestered CO2 through Surface Dissolution: Implementation Costs and Technical Challenges, SPE 110650, Proceedings, 2007 SPE Ann. Tech. Conf. Exhib., Anaheim, CA, 11-14 November, 2007.

Burton, M. M. and S. L. Bryant, 2009, Surface dissolution: Minimizing groundwater impact and leakage risk simultaneously, Energy Procedia, vol. 1, no. 1, p. 3707-3714.

Celia, M. A., S. Bachu, J. M. Nordbotten, S. E. Gasda, and H. K. Dahle, 2004, Quantitative estimation of CO2 leakage from geological storage: Analytical models, numerical models and data needs, Proceedings of the 7th International Conference on Greenhouse Gas Control Technologies (GHGT-7), September 5-9, 2004, Vancouver, Canada, v.I, 663-672.

Doughty, C., 2007, Modeling geologic storage of carbon dioxide: Comparison of non-hysteretic and hysteretic characteristic curves, Energy Conversion and Management, vol. 48, no. 6, p. 1768-1781.

Ebigbo, A., H. Class, and R. Helmig, 2007, CO 2 leakage through an abandoned well: Problem-oriented benchmarks, Computational Geosciences, vol. 11, no. 2, p. 103-115.

Enick, R. M. and S. M. Klara, 1990, CO 2 solubility in water and brine under reservoir conditions, Chemical Engineering Communications, vol. 90, no. 1, p. 23-33.

Ennis-King, J. and L. Paterson, 2003, Rate of dissolution due to convective mixing in the underground storage of carbon dioxide, Sixth International Conference on Greenhouse Gas Control Technologies, Kyoto, vol. I, Pergamon, Amsterdam, pp. 507–510.

Gasda, S. E., S. Bachu, and M. A. Celia, 2004, The potential for CO2 leakage from storage sites in geological media: analysis of well distribution in mature sedimentary basins, Environmental Geology, vol. 46, no. 6-7, p. 707–720.

Ide, S. T., S. J. Friedmann, and H. J. Herzog, 2006, CO2 leakage through existing wells: current technology and regulations, 8th International Conference on Greenhouse Gas Control Technologies, Trondheim, Norway, June 2006.

Leonenko, Y. and D. W. Keith, 2008, Reservoir engineering to accelerate the dissolution of CO2 stored in aquifers, Environ. Sci. Technol, vol. 42, no. 8, p. 2742-2747.

McPherson, B. and B. S. Cole, 2000, Multiphase CO2 flow, transport and sequestration in the Powder River basin, Wyoming, USA, Journal of Geochemical Exploration, vol. 69, p. 65-69.

Nordbotten, J. M., M. A. Celia, S. Bachu, and H. K. Dahle, 2005, Semianalytical solution for CO2 leakage through an abandoned well, Environmental science & technology, vol. 39, no. 2, p. 602-611.

Nordbotten, J. M., D. Kavetski, M. A. Celia, and S. Bachu, 2009, Model for CO2 leakage including multiple geological layers and multiple leaky wells, Environ.Sci.Technol, vol. 43, no. 3, p. 743-749.

Oldenburg, C. M. and A. P. Rinaldi, 2010, Buoyancy Effects on Upward Brine Displacement Caused by CO2 Injection, Transport in Porous Media, vol. 87, no. 2, p. 525-540.

Pruess, K., 2008, On CO 2 fluid flow and heat transfer behavior in the subsurface, following leakage from a geologic storage reservoir, Environmental Geology, vol. 54, no. 8, p. 1677-1686.

Pruess, K., 2007, ECO2N-A fluid property module for the TOUGH2 code for studies of CO2 storage in saline aquifers, Energy conversion and management, vol. 48, no. 6.

Swenson, D., B. Hardeman, C. Persson, and C. Thornton. 2003. Using PetraSim to create, execute, and post-process TOUGH2 models. In Proceedings of TOUGH Symposium 2003. Berkeley, California: LBNL http://www.esd.lbl.gov/TOUGHsymposium/TOUGHsymposium03/program.html.

Zhou, Q., J. T. Birkholzer, E. Mehnert, Y. F. Lin, and K. Zhang, 2010, Modeling basin- and plume-scale processes of CO2 storage for full-scale deployment, Ground Water, vol. 48, no. 4, p. 494-514.

MIGRATION OF EXSOLVED CO_2 FOLLOWING DEPRESSURIZATION OF SATURATED BRINES

Ronald W. Falta[1], Lin Zuo[2] and Sally M. Benson[2]

[1]Department of Environmental Engineering and Earth Sciences, Clemson University, Clemson, SC, 29634, USA
[2]Department of Energy Resource Engineering, Stanford University, CA 94305, USA

Email: faltar@clemson.edu

ABSTRACT

Geologic disposal of supercritical carbon dioxide in saline aquifers and depleted oil and gas fields will cause large volumes of brine to become saturated with dissolved CO_2 at concentrations of 50 g/L or more. As CO_2 dissolves in brine, the brine density increases slightly. This property favors the long-term storage security of the CO_2, because the denser brine is less likely to move upwards towards shallower depths. While dissolved-phase CO_2 poses less of a threat to the security of shallower drinking water supplies, the risk is not zero. There are plausible mechanisms by which the CO_2-laden brine could be transported to a shallower depth, where the CO_2 would come out of solution (exsolve), forming a mobile CO_2 gas phase.

Recent laboratory experiments of the exsolution process show that the exsolved gas-phase relative permeability is much lower than relative permeabilities measured during CO_2 core floods. Numerical simulations of upward brine migration through an open fault were performed using TOUGH2-ECO2N with the two types of relative permeability functions. When traditional coreflood relative permeabilities are used, upward flow of a CO_2 saturated brine leads to exsolution and the development of a highly mobile CO_2 gas phase. When exsolution relative permeabilities are used, the tendency for the exsolved CO_2 to migrate as a separate phase is greatly reduced, though not eliminated.

INTRODUCTION

Reduction of greenhouse gas emissions to levels required to stabilize the global climate will require an unprecedented societal effort. It is widely agreed that multiple methods will be needed to achieve these emissions reductions. The Intergovernmental Panel on Climate Change (IPCC) has identified carbon dioxide capture and storage (CCS) as one of several key approaches that could substantially contribute to greenhouse gas emissions reductions. CCS focuses on reducing the CO_2 emissions from large stationary sources, typically fossil-fueled electrical power plants. Several methods of CO_2 storage have been proposed, including deep ocean storage, mineral carbonation, and geologic sequestration. Of these three methods, geologic sequestration appears to be the most practical option, and there do not appear to be any insurmountable technical barriers to its widespread adoption (Benson and Cook et al., 2005).

Each of the CCS technologies will have three main components. First, the CO_2 must be separated from other gases (primarily nitrogen) in the combustion gas waste stream. This is currently done using a solvent extraction process, but other methods may become feasible in the future. The low-pressure CO_2 gas from the separation process is then usually compressed into a liquid or supercritical fluid for subsequent transport to a storage site. With geological sequestration, the captured CO_2 is injected into a specific geologic formation with the expectation that it will remain there for thousands of years and longer. Recent estimates of the storage capacity for geologic sequestration in the U.S. are on the order of several hundred times the current U.S. annual CO_2 emissions (NETL, 2007). Most of this capacity exists as deep saline (brine) formations.

CO_2 PROPERTIES

CO_2 has several unique properties that must be considered in the design of a geologic storage project. Key among these are its low critical pressure and temperature. CO_2 becomes a supercritical fluid at a pressure of 73.82 bar and a temperature of 31.04°C. Below this pressure and temperature, CO_2 exists as a gas, liquid, or solid, depending on pressure and temperature. At normal atmospheric temperatures and pressures, CO_2 is always found as a gas, and its density can be calculated from the ideal gas law. For example, at room temperature, pure CO_2 gas has a density of 1.8 g/L. This is about 1.5 times the density of air.

As CO_2 gas is compressed, its density increases almost linearly, following roughly ideal gas behavior. However, as the critical pressure is approached, the gas becomes much more compressible, and density rapidly increases with increasing pressure. At this point, CO_2 gas is nearly 4 times more compressible than an ideal gas, and it is several times more compressible than other common gases such as methane, nitrogen, or oxygen. As the critical pressure is exceeded, the supercritical CO_2 phase density continues to rapidly increase until a pressure of roughly 90 bar is reached. Beyond this pressure, the increase in CO_2-phase density is moderate.

Current strategies for geologic storage take advantage of the high density (and low viscosity) of supercritical CO_2, injecting the CO_2 at depths where the hydrostatic pressure is somewhat above the critical pressure (Figure 1). Depending on the subsurface temperature, the depth where high CO_2-phase density is achieved is around 800–900 m (~2600–2950 ft). Beyond this depth, little is gained in terms of storage efficiency, although storage security may increase.

The CO_2-phase density at typical target injection depths ranges from about 600 to 800 g/L. While this represents a roughly 400-fold increase in density over atmospheric pressure conditions, the phase density is still much lower than that of water or brine. This causes a strong upward buoyancy force that can allow the supercritical (or gas phase) CO_2 to move upward towards the ground surface. This type of uncontrolled vertical migration of a pure CO_2 phase has been the subject of numerous studies (Bachu et al., 1994; Pruess and Garcia, 2002; Pruess, 2005b; Doughty, 2007; Nordbotten et al., 2008). Most strategies for the injection of supercritical CO_2 require a cap rock or stratigraphic trap to prevent the vertical movement. Similarly, most CO_2 escape routes from storage formations consist of defects or penetrations in the confining layer.

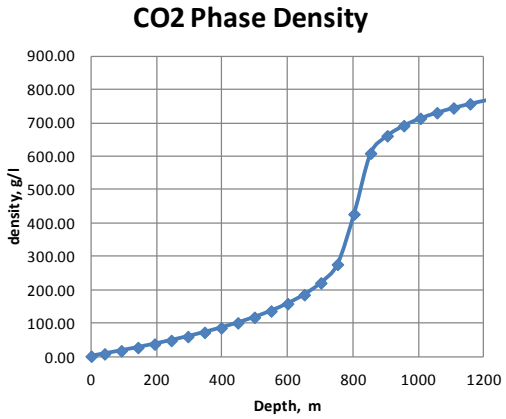

Figure 1. Variation in CO_2 density with depth at a temperature of 35°C (calculated using the TOUGH2-ECO2N equation of state package (Pruess, 2005a)).

Another important property of CO_2 is its high solubility in water and brines, especially at high pressure and low-to-moderate temperature. Starting at atmospheric pressure and 35°C, pure CO_2 gas has an aqueous solubility of about 1 g/l in a brine containing 10,000 mg/l NaCl. As the CO_2 pressure increases, the solubility rises nearly linearly, following Henry's Law (Figure 2). As supercritical pressure is approached, the rate of solubility increase flattens, and the solubility becomes a much weaker function of increasing pressure. At typical injection depths greater than 800 m (~2600 ft), CO_2 solubility can exceed 50 g/l, depending on the salinity and temperature.

The high solubility of CO_2 is significant in terms of geologic trapping. Consider a storage formation that is 900 m (2950 ft) deep in a formation at 35°C with salinity of 10,000 PPM. Under these conditions, the supercritical CO_2-phase density is around 670 g/L, and the solubility in the brine is about 52 g/L. When the CO_2 phase occupies 7% of the pore space, an

equal mass of CO_2 is present in the formation dissolved in the pore water.

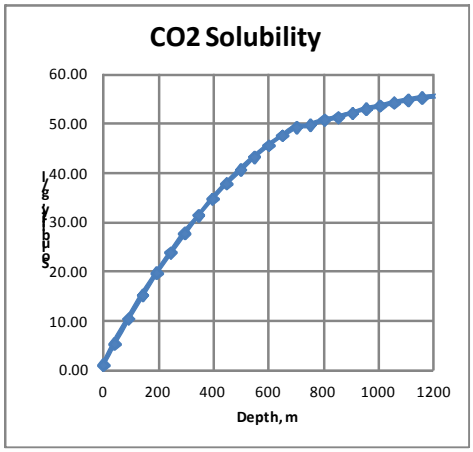

Figure 2. Variation in CO_2 solubility in a 10,000 mg/l NaCl brine at 35°C (calculated using the TOUGH2-ECO2N EOS)

As CO_2 dissolves in water or brine, the aqueous-phase density increases slightly. Over a pressure range from 1 to 155 bar at 35°C, a 10,000 mg/L brine will increase in density from about 1001 g/L to about 1006 g/L due to compression. If CO_2 is dissolved in the brine to its maximum solubility, the density increases with increasing depth. At hydrostatic pressures greater than roughly 60 bar (about 600 m or 2000 ft), the brine containing dissolved CO_2 is around 1% denser than the resident brine. This is a substantial contrast, and it is capable of driving buoyancy flows downward in the aqueous phase. The resulting natural convection flow is of significant interest because it tends to move the dissolved CO_2 down and away from the injected CO_2 phase (Ennis-King and Paterson, 2005; Farajzadeh et al., 2007; Hassanzadeh et al., 2007; Lindberg and Wessel-Berg, 1997). In general, this dissolved-phase CO_2 is believed to be more securely stored than separate-phase CO_2 due to the elimination of the upward buoyancy forces (Benson and Cook et al., 2005, Leonenko and Keith, 2008).

CO_2 EXSOLUTON

The higher security of dissolved CO_2 compared to supercritical CO_2 has led some researchers to propose alternative injection schemes. For example, Leonenko and Keith (2008) and Burton and Bryant (2007, 2008) make a compelling case for injecting the CO_2 dissolved in brine to prevent unwanted buoyancy flows of separate-phase CO_2. Their feasibility studies suggest that dissolved CO_2 injection could compete with supercritical injection, although the capital and operating costs are somewhat higher due to the larger number of injection wells required. Leonenko and Keith (2008) also propose a promising alternative scheme in which a short period of CO_2 injection is followed by a long period of brine injection, to maximize the dissolution process.

Whether by design, or as a consequence of natural processes, it is clear that a significant fraction of the CO_2 that is geologically stored will eventually exist as a dissolved phase in the reservoir brine. While dissolved CO_2 presents a much lower release risk compared to free phase CO_2, the risk is not zero. If a CO_2-saturated brine is depressurized, the CO_2 will come out of solution (exsolve) and become a separate phase. The exsolved CO_2 is then free to migrate subject to large upward buoyancy forces. Consequently, CO_2 could move towards the ground surface and potentially contaminate shallower drinking waters supplies, as well as causing health, safety, and environmental hazards.

The most likely scenario for CO_2 exsolution from brine occurs when the CO_2-saturated brine is transported towards the ground surface. Assuming that some type of high permeability pathway exists (such as a fault or abandoned well), only a moderate upward gradient is needed to mobilize brine. This upward gradient might be caused by groundwater pumping from an overlying aquifer, by high injection pressures in the storage formation, or it could exist naturally.

The necessary gradient for upward mobilization of a CO_2-saturated brine can be calculated from Darcy's law. Following *Falta et al. [1989]*, the buoyancy velocity of a fluid of density $\bar{\rho}$ through an ambient fluid of density ρ_∞ is:

$$V = -\frac{k}{\mu}(\bar{\rho} - \rho_\infty)g \qquad (1)$$

where k is the intrinsic permeability, μ is the fluid dynamic viscosity, and g is the magnitude

of gravitational acceleration. The standard form of Darcy's law for a fluid of uniform density is

$$V = -K\frac{\partial h}{\partial z} \qquad (2)$$

where K is the hydraulic conductivity, h is the hydraulic head, and z is elevation. The hydraulic conductivity is a function of both the porous media and fluid properties:

$$K = \frac{k\rho_\infty g}{\mu} \qquad (3)$$

Substituting Equation (3) into (2), and equating the two forms of Darcy's law, the critical upward hydraulic gradient for mobilizing a dense fluid is:

$$\left|\frac{\partial h}{\partial z}\right| = \frac{(\bar{\rho} - \rho_\infty)}{\rho_\infty} \qquad (4)$$

Recalling that the brine density increase due to dissolved CO_2 is around 1%, Equation (4) indicates that any upward gradient greater than 1% would be capable of mobilizing the CO_2 saturated brine in the upward direction.

RELATIVE PERMEABILITIES

Two-phase CO_2/water relative permeabilities are normally measured by flooding a core with the two fluids. Figure 3 shows a typical set of relative permeability primary drainage data measured by core flooding a Mount Simon sandstone *[Zuo et al., 2012]*. In this test, the CO_2 phase was mobile at a saturation of 3% or less, and the relative permeability increases to a value of 0.38 at a CO_2 saturation of 33%.

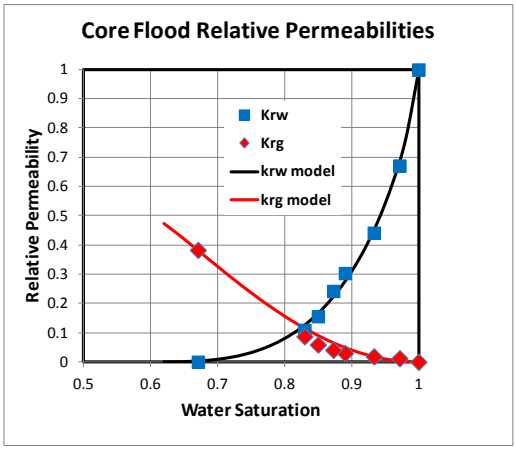

Figure 3. Relative permeabilities for a CO_2/water system measured during a core flooding experiment *[Zuo et al., 2012]*. The solid lines are best fits with Equations (5) and (6).

Zuo et al. (2012) performed exsolution experiments on cores that were initially filled with water saturated in dissolved CO_2. These experiments observed the evolution of the exsolved CO_2 phase as the core confining pressure was dropped from 124.1 bar to 27.6 bar. During this depressurization, the CO_2-phase saturation increased from zero to a maximum value of about 40%. Mobilization of the CO_2 phase occurred between 11.7 and 15.5% saturation, but the measured CO_2-phase relative permeability is extremely low. Figures 4 and 5 show a set of relative permeability curves measured on a Mount Simon sandstone using methods similar to those described by Zuo et al. (2012).

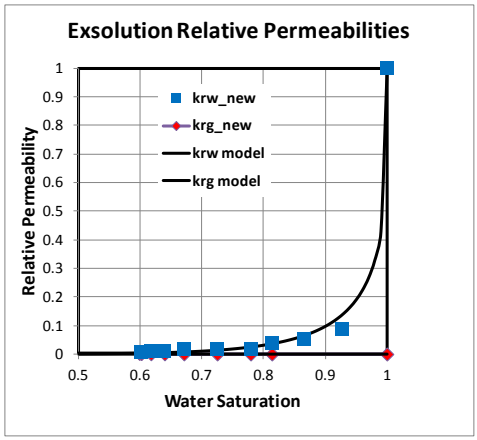

Figure 4. Relative permeabilities for a CO_2/water system measured during exsolution. The solid lines are best fits with Equations (5) and (6).

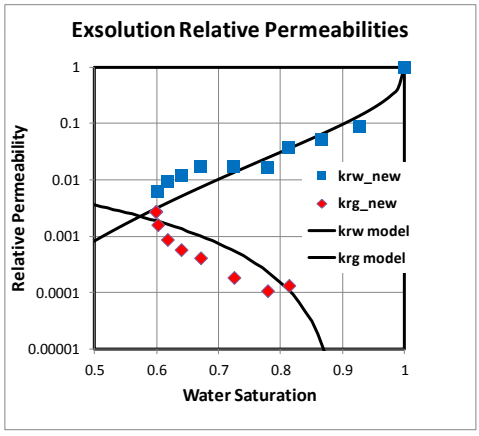

Figure 5. Relative permeabilities for a CO_2/water system measured during exsolution (log scale).

The exsolution relative-permeability values for the CO_2 phase are extremely low (Figure 5), with a maximum measured value of 0.003 at a CO_2 saturation of 40%.

NUMERICAL SIMULATIONS

A series of simplified 2-D multiphase flow numerical simulations were performed to illustrate how a CO_2-saturated brine could escape and result in uncontrolled vertical CO_2 migration to a shallow aquifer. These simulations were performed using the TOUGH2-ECO2N simulator (Pruess, 2005a; Pruess and Spycher, 2007). The scenario consists of a site with a surface elevation of 200 m above mean sea level (MSL). A 100 m thick saline aquifer is located at a depth of 900 m (an elevation of 700 m MSL). This aquifer has a salinity of 10,000 mg/l **[L?]** NaCl, and a temperature of 35°C. The formation has a vertical permeability of 10^{-12} m^2 (a conductivity of 10^{-3} cm/s), a horizontal permeability of 10^{-11} m^2 and it is confined by a low permeability formation 600 m thick. A freshwater aquifer with the same permeability extends from a depth of 200 m to a depth of 300 m (elevations of 0 to -100 m MSL). The freshwater aquifer is hydraulically connected to the saltwater aquifer by a permeable fault zone (k= 10^{-11} m^2) that is 50 m wide (Figure 6). The brine aquifer is assumed to contain 50.7 g/l **[L?]** of dissolved CO_2, which is just below the CO_2 solubility under these conditions. The saline aquifer is assumed to be large in extent and is maintained at a constant (hydrostatic) pressure over time.

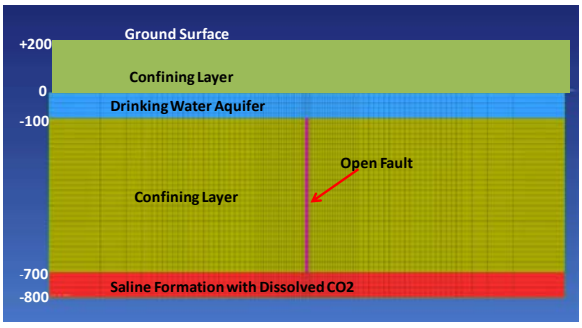

Figure 6. 2D cross sectional model of a saline formation containing dissolved CO_2 that is connected to a confined fresh drinking water aquifer by a high permeability fault zone

The relative permeability data in Figures 3 and 4 were fit using a modified version of the van Genuchten-Mualem *model [Mualem, 1976; van Genuchten, 1980; Charbeneau, 2007]*:

$$k_{rw} = \sqrt{S_w^*}\left\{1-\left(1-S_w^{*1/m}\right)^m\right\}^2 \qquad (5)$$

and

$$k_{rg} = k_{rg\max}\sqrt{1-\hat{S}_w}\left(1-\hat{S}_w^{1/m}\right)^{2m} \qquad (6)$$

where

$$S_w^* = \frac{S_w - S_{wr}}{1-S_{wr}}$$

and

$$\hat{S}_w = \frac{S_w - S_{wr}}{1-S_{wr}-S_{gr}}$$

The factor k_{rgmax} is a scaling factor needed to match the relative permeability data. The model fits to the data are shown in Figures 3–5.

The system is initially in static equilibrium with a water table near the ground surface, and the CO_2 remains confined indefinitely in the deeper brine aquifer despite the presence of the open fault connecting the two aquifers. The hydrogeologic system is then perturbed by simulating groundwater pumping from the top of the confined fresh water aquifer. The hydraulic head at the top outer edges of the aquifer is reduced by 30 m (100 ft). This magnitude of hydraulic head decline is commonly observed in confined aquifers that are pumped for water supply or irrigation.

The drop in head in the aquifer is sufficient to mobilize the CO_2-saturated brine upward through the fault zone, and into the freshwater aquifer. Figure 7 shows the CO_2 gas-phase saturations 30 years after the freshwater aquifer has been depressurized. Here, the CO_2-laden saltwater is pulled upward through the fault and into the freshwater aquifer by the upward hydraulic gradient that was created by pumping the upper aquifer. As the brine moves up the fault, the pressure is lower, and the dissolved CO_2 partial pressure begins to exceed the water pressure. At this point, the CO_2 starts to exsolve, forming a separate gas phase. This simulation used the core-flood relative permeability

function (Figure 3). As the CO_2 comes out of solution, the evolving gas phase becomes mobile as its volumetric saturation increases. The mobility tends to further increase as the gas moves upward because of the large degree of expansion that occurs with depressurization (Figure 1).

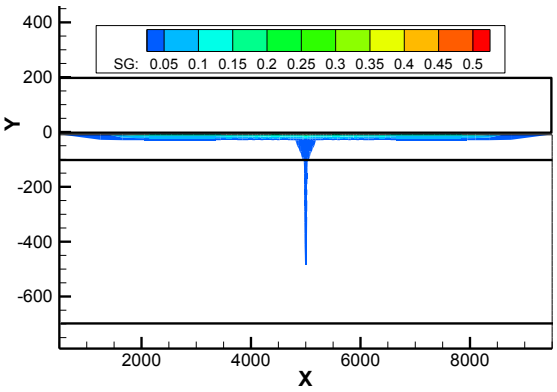

Figure 7. Simulated CO_2 gas saturations 30 years after the freshwater aquifer was depressurized, using the core-flood relative permeabilities. Vertical exaggeration is 5x.

When the brine first reaches the freshwater, it still contains a relatively large amount of dissolved CO_2 (see Figure 2). This dissolved CO_2, along with the dissolved salt, causes the brine to be denser than the fresh water, and the fluid tends to flow along the base of the aquifer (Figures 8 and 9).

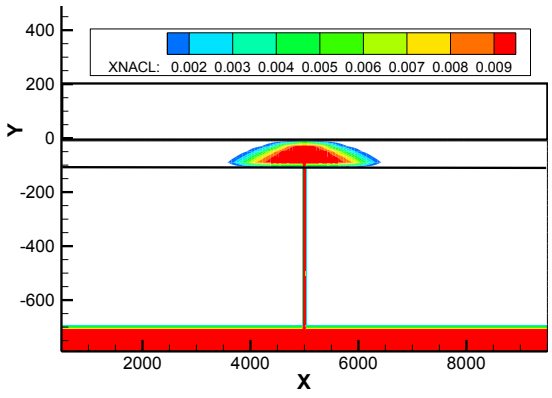

Figure 8. Simulated aqueous salt mass fractions 30 years after the fresh water aquifer was depressurized, using the core flood relative permeabilities.

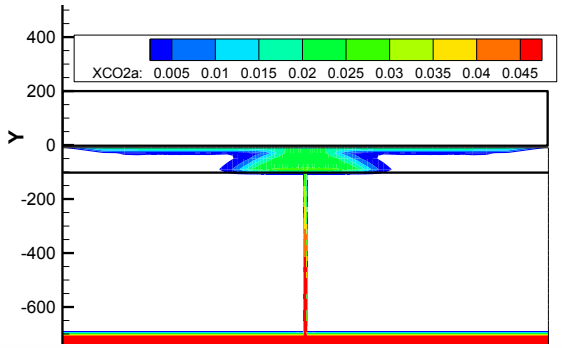

Figure 9. Simulated dissolved CO_2 mass fractions 30 years after the fresh water aquifer was depressurized, using the core flood relative permeabilities.

The mobile gas phase, however, moves upward through the freshwater aquifer, eventually accumulating along the base of the upper confining layer. At 30 years, the CO_2 gas phase extends to the edges of the model, 5000 m away from the fault zone. This accumulated CO_2 could acidify the groundwater, and if the CO_2 plume is intercepted by a shallow well, it could discharge directly to the surface. In the absence of an upper confining layer, the CO_2 gas could easily reach the vadose zone and eventually be discharged at the ground surface.

The simulation was repeated using the exsolution relative permeabilities (Figures 4 and 5). In this case, the extent of the CO_2 gas phase in the drinking water aquifer is much smaller (Figure 10).

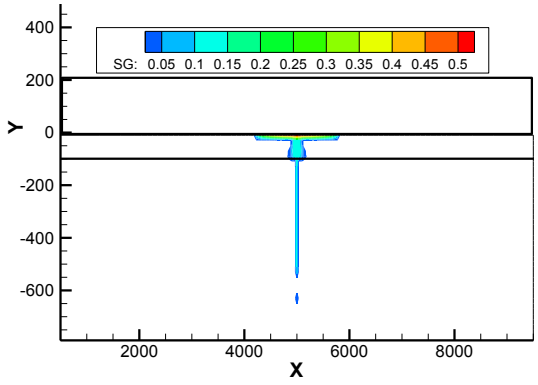

Figure 10. Simulated CO2 gas saturations 30 years after the fresh water aquifer was depressurized, using the exsolution relative permeabilities.

The smaller extent of the gas phase is due mainly to the lower mobility of the exsolved gas phase. In addition, the aqueous-phase plumes of dissolved salt (Figure 11) and CO_2 (Figure 12) are also substantially smaller in this case. This is due in part to the lower aqueous-phase relative permeability observed during exsolution. It is also due to the accumulation of immobile or low mobility gas phase in the fault zone. These combined effects reduce the brine flow up the fault.

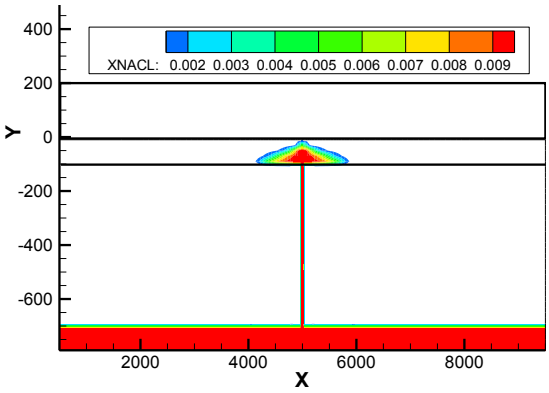

Figure 11. Simulated aqueous phase salt mass fractions 30 years after the fresh water aquifer was depressurized, using the exsolution relative permeabilities.

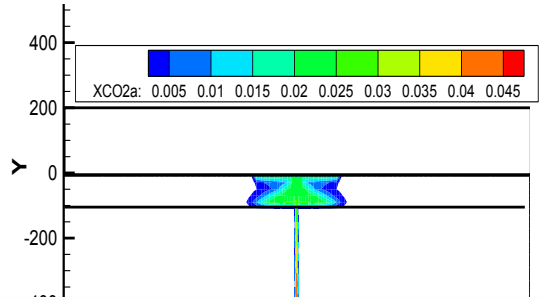

Figure 12. Simulated aqueous phase CO_2 mass fractions 30 years after the fresh water aquifer was depressurized, using the exsolution relative permeabilities.

SUMMARY

Brine containing dissolved CO_2 can be mobilized upward due to modest hydraulic gradients. As the brine becomes depressurized, the CO_2 comes out of solution, forming a gas phase (at subcritical pressures). Recent experiments have shown that the relative permeability of the exsolved gas phase is very low. This low relative permeability limits the mobility of the exsolved gas phase compared to a traditional relative permeability function. However, in high permeability systems, the exsolved gas phase may still exhibit some mobility, especially at shallow depths, where the density contrast between the water and gas phases is very large. In this case, the high buoyancy force allows some migration despite the very low gas-phase relative permeability.

ACKNOWLEDGMENT

This work was supported by the US EPA through STAR Grant #834383.

REFERENCES

Bachu, S., W.D. Gunter and E.H. Perkins,1994, Aquifer disposal of CO_2: hydrodynamic and mineral trapping, Energy Conversion and Management, 35(4), 269-279.

Benson, S.M. and P. Cook, Coordinating Lead Authors., 2005, "Underground Geological Storage," IPCC Special Report on Carbon Dioxide Capture and Storage, Chapter 5. Intergovernmental Panel on Climate Change, Cambridge University Press, Cambridge, U.K

Burton, M. and S. Bryant, Eliminating buoyant migration of sequestered CO_2 through surface dissolution: implementation costs and technical challenges, SPE 110650, Proceedings, 2007 SPE Ann. Tech. Conf. Exhib., Anaheim, CA, 11-14 November, 2007.

Burton, M. and S.L. Bryant, 2008, Surface dissolution: minimizing groundwater impact and leakage risk simultaneously, presented at the 9th International Conference on Greenhouse Gas Control Technologies (GHGT-9), 16-20 November, 2008, Washington, DC.

Campbell, B., 2008, Development and Application of a Ground-Water Flow and Management Model of the Chesterfield County Region in South Carolina. Clemson

Hydrogeology Symposium, Clemson University.

Charbeneau, R., 2007, LNAPL Distribution and Recovery Model (LDRM) Volume 1: Distribuion and Recovery of Petroleum Hydrocarbon Liquids in Porous Media, American Petroleum Institute API Publication 4760.

Doughty, C., 2007, Modeling geologic storage of carbon dioxide: comparison of non-hysteretic and hysteretic characteristic curves, Energy Conversion and Management, 48, 1768-1781.

Ennis-King, J.P., and L. Paterson, 2005, Role of convective mixing in the long-term storage of carbon dioxide in deep saline formations, SPE J 10(3):349-356.

Falta, R.W., I. Javandel, K. Pruess, and P.A. Witherspoon, 1989, Density-Driven Flow of Gas in the Unsaturated Zone Due to the Evaporation of Volatile Organic Compounds, Water Resources Research, Vol. 25, No. 10.

Farajzadeh, R., H. Salimi, and P.La.H.B. Zitha, 2007, Numerical simulation of density driven natural convection in porous media with applications for CO_2 injection projects, Int J Heat Mass Transfer 50(25-26):5054-5064.

Hassanzadeh, H., M. Pooladi-Darvish, and D.W. Keith, 2007, Scaling behaviour of convective mixing with application to geological storage of CO_2, AIChE J 52:1121-1131.

Leonenko, Y. and D.W. Keith, 2008, Reservoir engineering to accelerate the dissolution of CO_2 stored in aquifers, Environ. Sci. Technol. 42, 2742-2747.

Lindeberg, E. and D. Wessel-Berg, 1997, Vertical convection in an aquifer column under a gas cap of CO2, Energy Conversion and Management, 38(Suppl.):S229-S234.

Mualem, Y., 1984, A modified dependent-domain theory of hysteresis, Soil Science, 137:5, 283-291.

NETL, 2007, Carbon Sequestration Atlas of the United States and Canada, U.S. Department of Energy, National Energy Technology Laboratory. Available from http://www.netl.doe.gov/technologies/carbon_seq/refshelf/atlas/ATLAS.pdf

Nordbotten J.M., D. Kavetski, M.A. Celia, and S. Bachu, 2008, A semi-analytical model estimating leakage associated with CO2 storage in large-scale multi-layered geological systems with multiple leaky wells, Environmental Science & Technology, doi:10.1021/es801135v.

Pruess, K., 2005a, ECO2N: A TOUGH2 Fluid Property Module for Mixtures of Water, NaCl, and CO_2, Lawrence Berkeley National Laboratory Report LBNL-57952.

Pruess, K., 2005b, Numerical Studies of Fluid Leakage from a Geologic Disposal Reservoir for CO_2 Show Self-Limiting Feedback between Fluid Flow and Heat Transfer, Geophys. Res. Lett., Vol. 32, No. 14, L14404, doi:10.1029/2005GL023250, July 2005. (LBNL-57362).

Pruess, K. and J. Garcia, 2002, Multiphase flow dynamics during CO_2 disposal into saline aquifers, Environmental Geology, 42:282-295

Pruess, K., and N. Spycher, 2007, ECO2N – A fluid property module for the TOUGH2 code for studies of CO_2 storage in saline aquifers, Energy Conversion and Management, 48, 1761-1767.

van Genuchten, M.T., 1980, A closed-form equation for predicting the hydraulic conductivity of unsaturated soils, Soil Sci. Soc. Am. J., 44, 892-898.

Zuo, L., S. Krevor, R.W. Falta, and S.M. Benson, 2012, An Experimental Study of CO_2 Exsolution and Relative Permeability Measurements during CO_2 Saturated Water Depressurization, *Transport in Porous Media, Vol. 91, Issue 2, p. 459-478.*

ASSESSING PRE-INJECTION IN SITU ALTERATION OF WELLBORE CEMENT IN A SITE FOR CO_2 GEOLOGICAL STORAGE: A NUMERICAL APPROACH

Gherardi Fabrizio [(1) (2)], Audigane Pascal [(1)]

[(1)] BRGM – 3, av. C. Guillemin, F-45060 - Orléans, France
[(2)] LE STUDIUM, Loire Valley Institute for Advanced Studies – 3D, av. de la Recherche Scientifique, F-45071 – Orléans, France
e-mail: F.Gherardi@brgm.fr

ABSTRACT

We present numerical simulations of isothermal reactive flow that might be induced by fluid migration at the caprock-cement interface of an idealized abandoned well, in an area being considered as a site for geological sequestration of carbon dioxide in the Paris Basin, France.

Field evidence, experimental data, and previous numerical simulations have been used to constrain the initial geochemical conditions and the hydraulic parameters of the numerical model. The calculations are aimed at identifying the mineralogical transformations likely occurring in the media before CO_2 injection, during operations and after the closure of the wells present in the area. Major mineralogical transformations in the cement (mainly portlandite dissolution), and moderate modifications of the initial clay-rock mineralogical assemblage (montmorillonite dissolution, and precipitation of zeolite and cement-like phases) are predicted. As a consequence of these reactions, porosity is expected to decrease in the caprock and to increase in the cement.

INTRODUCTION

Site performance prediction is crucial for successful geological storage of CO_2. The geological setting must be properly selected in order to guarantee that caprock formations overlying the storage reservoir will provide an effective seal, and that abandoned or active wells will not compromise the integrity of the seal.

CO_2 must be prevented from leaking in order to avoid hazards for humans, ecosystems, and groundwater. Injection-well failures or leakage through abandoned wells is of major concern in risk assessments of CO_2 geological storage sites (IPCC, 2005). In particular, cement around the casing of existing wells may be deeply altered by interaction with CO_2-rich fluids, compromising the efficiency of the seal over time (e.g. Celia and Bachu, 2003).

Unfortunately, the cement of abandoned wells is usually not accessible for direct inspection. Given this limitation, numerical modeling serves as a powerful means for predicting the mineralogical evolution of cement plugs during their *in situ* working life, and for assessing well integrity and leakage risk for the confining system before CO_2 injection.

Several research projects have been conducted and many others are still ongoing in France to investigate the potential of the Paris Basin aquifers for carbon dioxide geological storage purposes. In this framework, the assessment of sealing efficiency of storage sites emerges as a key factor in evaluating site performance, and ensuring public confidence regarding CO_2 storage (e.g., Fleury et al., 2007; Bildstein et al., 2009; and many others).

This paper presents some results from reactive transport simulations carried out to evaluate the mineralogical transformations likely affecting the sealing efficiency of cement plugs in a generic, abandoned wellbore within the Paris Basin. The objective of these numerical exercises is to identify the key geochemical processes controlling reactivity at the caprock-cement interface, and to verify if the isolation properties of the materials can be compromised during their pre-CO_2 injection lifetimes, i.e.., *in situ* aging.

MODEL SETUP

Conceptual and geometrical model

Based on field data, we performed simulations under isothermal (75 °C), isobaric (15 MPa) and aqueous saturated conditions (Sl = 1.0). Maximum simulation times have been fixed at 80 years to encompass the entire spectrum of ages for wells in the Paris Basin.

Reactive transport across the caprock-cement interface is simulated with a 1D-radial model. Both cement and caprock are assumed homogeneous. This simplification does not consider non-uniform sweep that may occur due to formation heterogeneities. Justification for a 1-D approach stems from the stagnant nature of the investigated system; preliminary flow simulations with 2D-radial geometries demonstrated that the low absolute permeability (κ) values of the two media (κ values determined in the lab between 10^{-20} to 10^{-18} m^2) impedes gravity-driven advection from developing in the system over the maximum considered simulation time of 80 years. In our model, solutes are then subjected to a purely diffusive transport regime, as commonly accepted for the modeling of interactions between concrete barriers and undisturbed clay rock.

In our model, the treatment of diffusion is based on Fick's First Law. A single, average tracer diffusion coefficient has been applied to all dissolved species. The effects of tortuosity and porosity on diffusivity are lumped together in a so-called effective diffusion coefficient, which in our model has an initial value of 5×10^{-11} m^2 s^{-1} at the caprock-cement interface.

The mesh consists of 26 gridblocks with fixed thickness of 0.1 m, and has a radial extent of 2.5 m. The first 20 elements monitored for aqueous chemistry and mineralogy have internodal distances roughly between 2 and 15×10^{-2} m, progressively increasing along the radial direction.

Materials

The initial porosity (φ) and absolute permeability (κ) of cement and caprock materials have been fixed at average values measured on laboratory specimens (Table 1). The cement has been simulated by a homogeneous porous medium having the composition of a hydrated ordinary class G cement paste. The primary mineralogical assemblage consists of predominant poorly crystalline calcium silicate hydrate phases (CSH:1.6), large amounts of portlandite and ettringite, relatively minor amounts of hydrogarnets (katoite-Si and Fe-katoite, C_3FH_6) and hydrotalcite, and traces of calcite (Table 2). Aggregates are not taken into consideration.

The mineralogical composition of the clay rock considered in this study (COx formation) has been thoroughly investigated by experimental methods and numerical simulations (e.g., among many others, Gaucher et al., 2004). The COx argillite is a complex mineral assemblage predominantly composed of phyllosilicates, silicates, carbonates, and S-bearing minerals. An average composition taken from the literature (Marty et al., 2009) has been used in the calculations (Table 2).

Table 1. Cement and caprock transport properties explored in the simulations (absolute permeability is in m^2; values used in the "reference case simulation" are listed in the column "Ref")

Cement	Range	Ref
φ, porosity	0.18 – 0.40	0.30
κ, abs. permeab.	10^{-18} to 10^{-20}	10^{-18}
τ, tortuosity	0.001 to 0.1	0.01

Caprock	Range	Ref
φ, porosity	0.12 – 0.16	0.144
κ, abs. permeab.	10^{-18} to 10^{-20}	10^{-18}
τ, tortuosity	0.001 to 0.1	0.01

Table 2. Cement and caprock mineralogical composition (V_f is the initial solid volume fraction)

Cement	V_f	Caprock	V_f
Calcite	0.006	Calcite	0.140
Ettringite	0.138	Illite-Mg	0.423
CSH:1.6	0.381	Montm-Mg-Na	0.060
Katoite-Si	0.105	Daphnite	0.010
Hydrotalcite	0.054	Quartz	0.240
C_3FH_6	0.055	Pyrite	0.010
Portlandite	0.261	Celestite	0.007

Pore waters chemical composition

It is almost impossible to obtain representative pore-water samples for chemical analysis from both cement and caprock, because of their low hydraulic conductivity (Gaucher et al., 2009). The chemical composition of these pore waters was thus calculated by batch modeling (Table 3), following the same procedure outlined by Gherardi et al. (2012). Cement pore waters are markedly alkaline (pH around 11) and have relatively high total concentrations of dissolved Na, Ca, S, Si and Al. Caprock pore waters have a neutral pH (6.34), and, except for Al, higher total concentration of dissolved species compared to cement. This is mirrored by higher values of ionic strength (0.22 instead of 0.176 mol kg_{H2O}^{-1}), and higher CO_2 fugacities ($\log f_{CO2}$ = -1.08 instead of -10.3).

Table 3. Elemental chemical composition of cement and caprock pore waters used for the reference case simulation (isothermal at 75 °C). Total concentrations and Ionic Strength (IS) are in mol/kg_{H2O}. Chemical components (or basis species) are in brackets.

Parameter	Cement	Caprock
pH	10.99	6.34
IS	0.176	0.224
log a_{O2} (as $O_{2(aq)}$)	-60.0	-58.3
Ca (as Ca^{+2})	1.79×10^{-2}	2.55×10^{-2}
Mg (as Mg^{+2})	4.45×10^{-8}	1.65×10^{-3}
Na (as Na^{+})	3.64×10^{-2}	1.48×10^{-1}
K (as K^{+})	3.80×10^{-3}	6.43×10^{-3}
Fe (as Fe^{+2})	1.34×10^{-9}	1.00×10^{-4}
Si (as $SiO_{2(aq)}$)	1.51×10^{-5}	6.22×10^{-4}
Al (as $AlO_2)^{-}$	2.71×10^{-5}	6.12×10^{-9}
Cl (as Cl^{-})	3.91×10^{-2}	1.90×10^{-1}
C (as HCO_3^{-})	8.53×10^{-6}	2.92×10^{-3}
S (as SO_4^{-2})	2.83×10^{-3}	9.22×10^{-3}

Thermodynamic and kinetic data

The thermodynamic database used in this work includes log K values for aqueous and gaseous species and minerals listed in a recent version of Thermoddem (http://thermoddem.brgm.fr/), a thermodynamic database compiled at the French Geological Survey (BRGM). The primary source for equilibrium constants for aqueous species and minerals is the Slop98.dat database (Shock, 1998), with major improvements concerning cement minerals (Blanc et al., 2010). Kinetic rates and reactive surface areas are highly uncertain, and a coherent and complete kinetic database for all pertinent minerals is still far from being available to date. To circumvent this intrinsic limitation, we followed the same simplified approach outlined by Gherardi et al. (2012), using kinetic rates from Palandri and Kharaka (2004) and Wertz et al (2012).

Numerical simulator

Simulations have been performed with the modular simulator TOUGHREACT (Xu et al., 2004). The modeling is based on space discretization by means of integral finite differences. Flow and reaction/transport equations are solved sequentially and non-iteratively. The chemical transport is solved on a component basis, and the resulting concentrations are substituted into the chemical reaction model. The system of chemical equations is solved on a gridblock basis by Newton-Raphson iteration. Full details on code capabilities and numerical methods are given in Xu and Pruess (2001) and Xu et al. (2006).

RESULTS AND DISCUSSION

Concentration gradients in the chemical composition of cement and caprock pore waters (Table 3) represent the driving force for the mineralogical transformations predicted by TOUGHREACT.

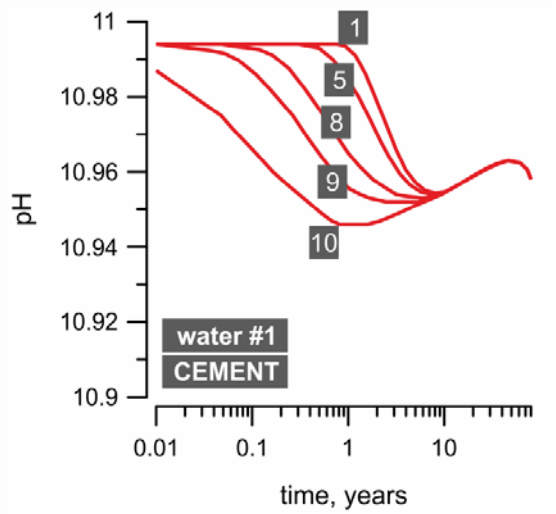

Figure 1. Temporal variation of pH for selected cells in the cement. Cement cells are labeled with numbers increasing along the radial direction, i.e. cell#1 and cell#10 are in center of the well and at the external boundary of the cement domain (i.e. at the interface with the caprock), respectively.

Most of the geochemical processes predicted by the code can be recast in terms of the competing effect between an alkaline, Al-rich plume diffusing from the cement in the caprock, and a slightly acidic, C-rich plume diffusing from the caprock in the cement. A first analysis of reaction paths is performed on the basis of pH patterns. In particular, we observe that the high buffer capacity of the cement minerals + cement pore-water system is able to maintain pH values at relatively high levels, close to the initial value of 10.99, all over the cement domain (Figure 1).

In contrast, major pH variations are predicted in the caprock. The penetration of the alkaline plume in the COx argillite is efficiently traced by a quick rise of pH values between 9 and 10.5 in the first three gridblocks of the caprock domain, and by values above 7 in the 5th cell of the caprock, at 0.4 m from the well axis, after about 38 years simulation time (Figure 2).

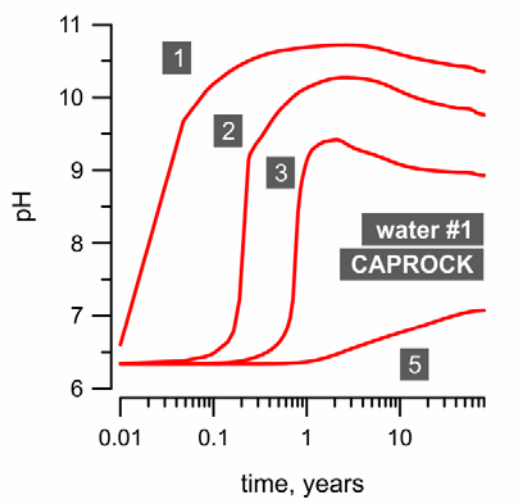

Figure 2. Temporal variation of pH for selected cells in the caprock. Caprock cells are labeled with numbers increasing along the radial direction, i.e. cell#1 is at the internal boundary of the caprock domain (i.e., at the interface with the cement).

Mineralogical transformations in the cement

As widely documented in the literature, most of the pH buffering predicted in the cement domain is obtained at the expenses of portlandite dissolution. Portlandite dissolves in the outermost cell of the domain, and, though at a lower extent, also in all the remaining gridblocks (Figure 3). Portlandite dissolution is an efficient marker of cement degradation, because unreacted portlandite is expected only in defect-free, unaltered cements (e.g., Glasser, 1993). The precipitation of amorphous Ca-Si gel (CSH:1.6) is another major mineralogical transformation predicted by the code (Figure 4).

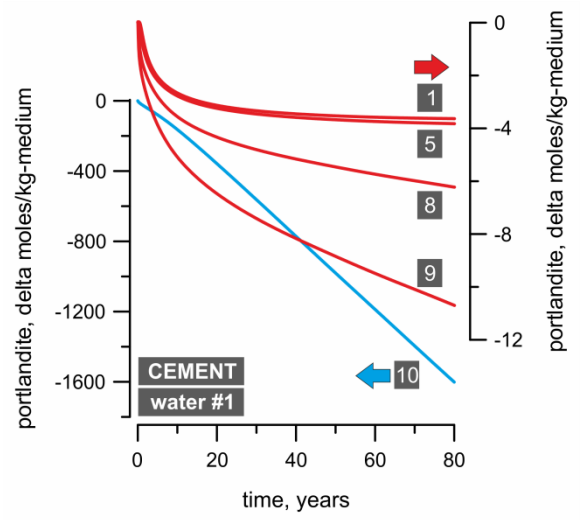

Figure 3. Temporal variation of portlandite abundance in selected cells in the cement. Labels are as in Figure 1.

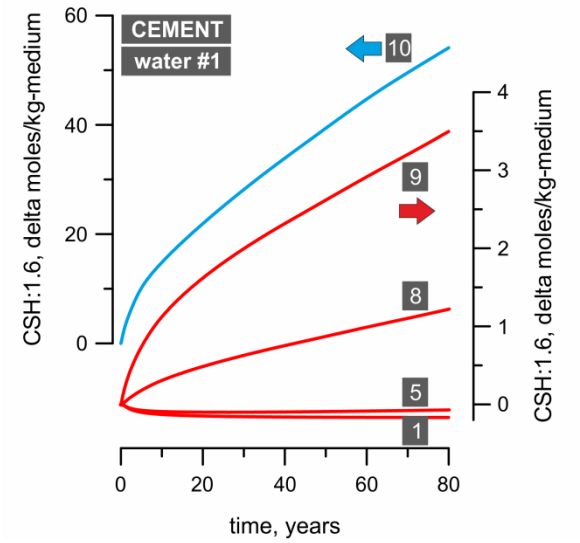

Figure 4. Temporal variation of CSH:1.6 abundance in selected cells in the cement. Labels are as in Figure 1.

The formation of secondary CSH:1.6 is accompanied by the occurrence of newly formed ettringite and hydrotalcite (first cell only). These patterns are consistent with alteration patterns commonly observed at cement-caprock interface (e.g., Gaucher and Blanc, 2006). Together with some minor calcite precipitation (secondary calcite forms in very low amounts solely in the outermost cell of the domain, close to caprock interface), these features reflect the effective buffering of total dissolved inorganic carbon concentrations in the cement (TDIC, 1.5×10^{-5} mol kg_{H2O}^{-1}) at lower than initial caprock concentrations (caprock TDIC = 2.92×10^{-3} mol kg_{H2O}^{-1}). Low TDIC concentrations are the limiting factor controlling the level of cement carbonation.

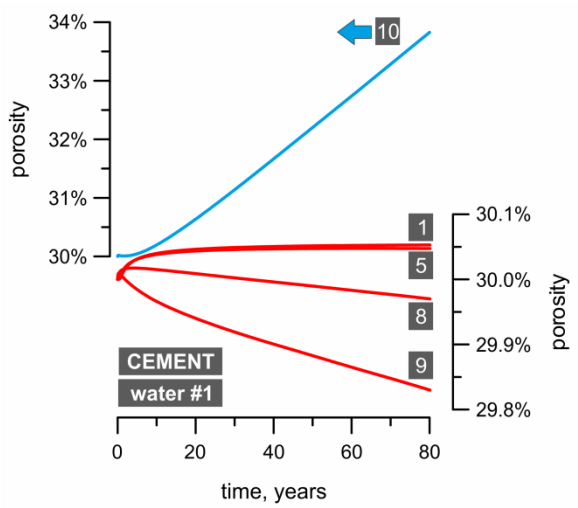

Figure 5. Temporal variation of porosity abundance in selected cells in the cement. Labels are as in Figure 1.

The massive dissolution of calcium hydroxide (portlandite) and the concomitant lack of significant carbonation has the deleterious effect of increasing the porosity in the outermost layer of the cement (about +3.8%; Figure 5), and possibly causing some loss in mechanical strength (e.g., Heukamp et al., 2001).

Mineralogical transformations in the caprock

The overall reactivity of the caprock+cement system is controlled by the geochemical evolution of the caprock volume adjacent to cement interface. In fact, due to the mineralogical transformations occurring in this gridblock, Ca_{TOT} and TDIC concentrations steadily decrease in time (with TDIC buffered at less than 2×10^{-5} mol kg_{H2O}^{-1} after 0.04 years), and virtually do not diffuse in the adjacent cement gridblocks. The mineralogical transformations predicted in the caprock are consistent with the effects of typical alkaline disturbance in clay media (e.g., Gaucher and Blanc, 2006).

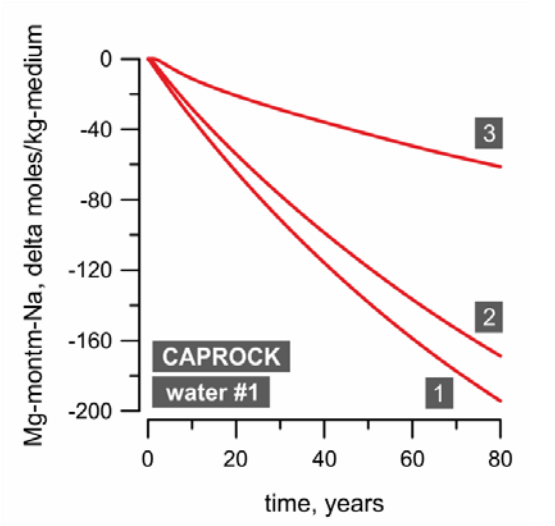

Figure 6. Temporal variation of Mg-Na-montmorillonite abundance in selected cells in the caprock. Labels are as in Figure 2.

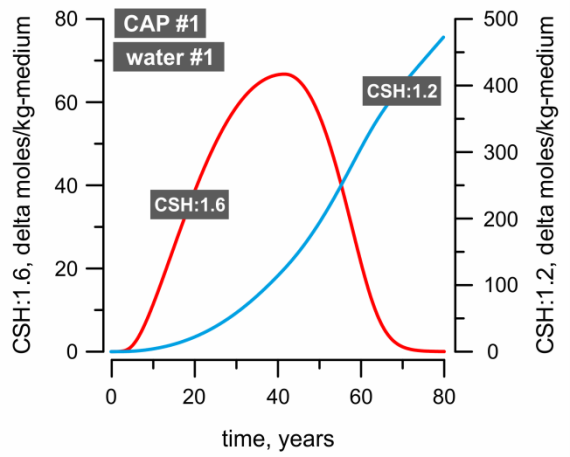

Figure 7. Temporal variation of CSH:1.6 and CSH:1.2 abundances in the first cell of the caprock domain (CAP#1), adjacent to cement interface.

The first noticeable mechanism is represented by montmorillonite destabilization (Figure 6), a process that releases important amounts of Al, Si, Mg, and Na in the aqueous solution. Other major mineralogical transformations include: precipitation of secondary illite, formation of purely cement phases (katoite, CSH:1.6, CSH:1.2; Figure 7), zeolites (K- and Ca-phillipsite; Figure 8), carbonates (calcite and hydrotalcite), chlorites, and sulfates (ettringite), dissolution of primary quartz and celestite.

Due to these reactions, porosity decreases by 3.2% in the first caprock cell adjacent to the cement interface.

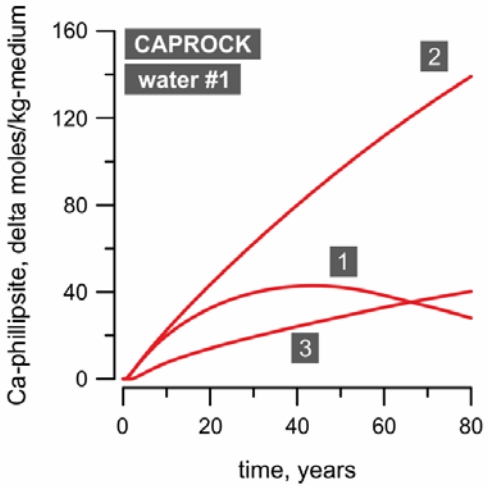

Figure 8. Temporal variation of Ca-phillipsite abundance in selected cells in the caprock. Labels are as in Figure 2.

Sensitivity analysis

We explored the sensitivity of numerical outputs with respect to variable (i) initial chemical compositions of caprock pore waters and (ii) grid specifications.

Different chemical compositions for the COx pore waters can be used in the model, because of the uncertainty in the equilibrium f_{CO2} values for the argillite formation (Gaucher et al., 2009). A second water composition (water #2; Figure 9), was then computed and incorporated into the calculations to explore the effects of low-f_{CO2} initial conditions (log f_{CO2} = -2) on the overall reactivity of the system. Figure 9 indicates that this water has a greater capacity to lower the pH of the cement domain. Compared to the reference-case simulation with water#1, more hydrotalcite and less calcite precipitation are now predicted in the cement, together with comparable portlandite and C_3FH_6 dissolution rates, and ettringite precipitation rates. This behavior can be explained in terms of complex and nonlinear variations of geochemical parameters in the adjacent caprock element (less effective katoite, CSH:1.6 and CSH:1.2 precipitation, more effective calcite precipitation). Overall, the same porosity patterns of the reference-case simulation are predicted, with a

3.8% increase in the outermost cell of the cement domain (CEM#10), and a 3% decrease in the adjacent caprock gridblock (first caprock cell, CAP#1).

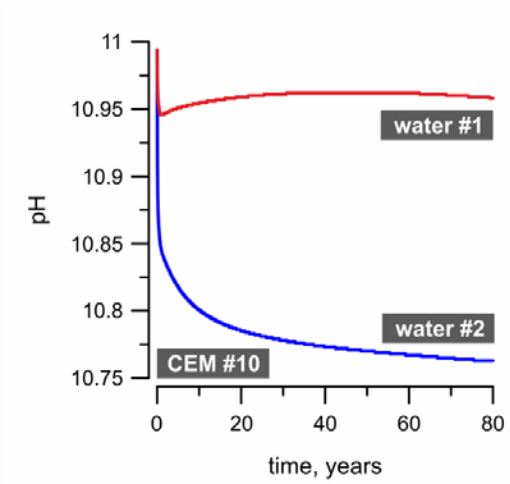

Figure 9. Temporal variation of pH in the external cell of the cement domain (CEM#10) for two different initial chemical composition of caprock pore waters.

In order to explore the effects of some hypothetically enhanced clay-rock pore-water impact on cement geochemistry, a different grid has been used with a large caprock volume set in direct contact with cement elements ("large-CAP" model). The enhanced reactivity of the cement materials now predicted by the code is mirrored by lower pH values (down to 10.88), and large variations in the mineralogical composition (Figure 10) of the outermost cell of the cement domain (CEM#10).

After 80 years simulation time, portlandite, katoite, and C_3FH_6 are predicted to decrease from 26.1% to 12.3%, from 10.5% to 6.1%, and from 5.5% to 5.2% of the solid fraction of cell CEM#10, respectively. In parallel, CSH:1.6, ettringite, hydrotalcite and calcite modal abundances are predicted to increase from 38.1% to 39.5%, from 13.8 to 28.8%, from 5.4 to 6.8%, and from 0.6% to 1.3%, respectively. A major effect of this enhanced reactivity is a reverse trend in porosity compared to the reference-case simulation. Porosity clogging is in fact now predicted also in the cement, near the caprock interface, with calculated negative variations on the order of 3% after 60 years simulation time (Figure 11).

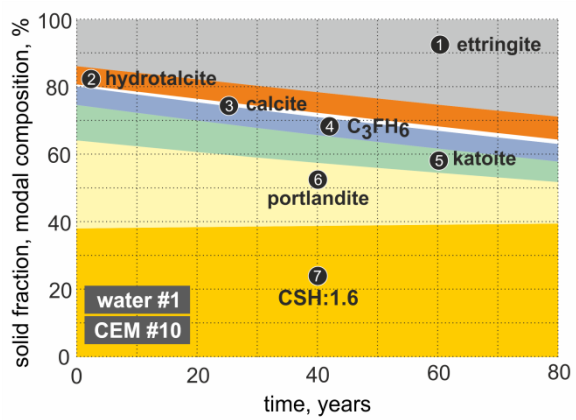

Figure 10. Mineralogical composition of the external cell of cement domain (CEM#10). Features refer to the "large CAP model."

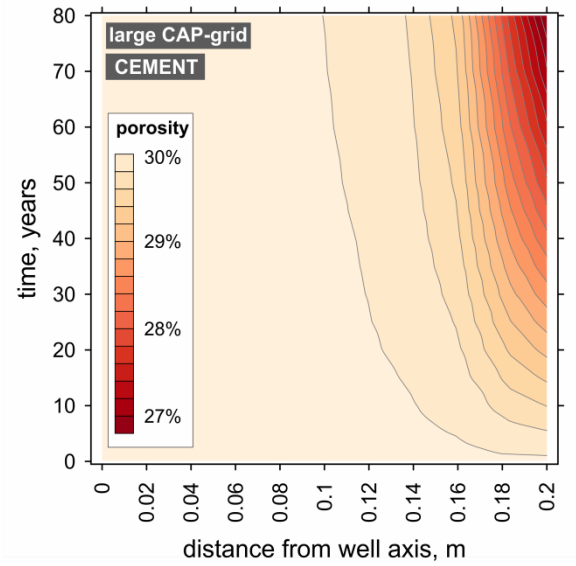

Figure 11. Contour plot showing porosity variations in the cement over 80-year simulation time. Calculations refer to the "single-large-caprock-gridblock" model.

CONCLUSIONS

The class G cement considered in our study is subject to major degradation at pH and temperature conditions typically recognized in the Paris Basin. Together with CSH and ettringite secondary precipitation, portlandite dissolution is the main mineralogical transformation predicted in the cement. Due to the lack of significant carbonation processes, this leads to some undesired porosity enhancement near the caprock interface over the short-term simulation time (80 years) of our calculations. Based on the assumed reaction and diffusion rates, the

penetration of this alteration front is limited to the first few centimeters from caprock interface.

The rate of cement alteration is directly controlled by the geochemical transformations predicted in the adjacent caprock. In fact, due to the precipitation/dissolution processes occurring in this domain, TDIC concentrations are buffered at very low levels near the interface, preventing significant cement carbonation from occurring.

A sensitivity analysis was performed to identify the most important factors controlling the reactivity in the investigated system. Apart from the intrinsic uncertainty in the kinetic parameters and the thermodynamic characterization of field-specific mineralogical phases, the size of the caprock volume containing the infiltrating water, and the chemical composition of this water, emerged as key factors of the model. Variations in these parameters control the efficiency of calcium hydrate carbonation and porosity behavior in the cement, close to the caprock interface. Cement clogging is predicted solely under conditions of enhanced caprock pore-water penetration in the cement.

The model is an oversimplification of the processes expected under field conditions. Predictions of porosity enhancement or clogging also strongly depend on the assumption of a homogeneous distribution of hydraulic and geochemical properties in the media. More heterogeneous distributions than those numerically predicted in this work are then likely expected in reality.

REFERENCES

Bildstein, O., M. Jullien, A. Crédoz., and J. Garnier, Integrated modeling and experimental approach for caprock integrity, risk analysis, and long term safety assessment. *Energy Proc. 1*, 3237-3244, 2009.

Blanc, P., X. Bourbon, A. Lassin, and E.C. Gaucher, Chemical model for cement based materials: temperature dependence of thermodynamic functions for nanocrystalline and crystalline C-S-H phases. *Cem. Concr. Res. 40*, 851–866, 2010.

Celia, M.A., and S. Bachu, Geological sequestration of CO_2: Is leakage avoidable and acceptable? *Proc 6th Int. Conf. Greenhouse Gas Control Techn.s (GHGT-6)*, Gale, J., and Y. Kaya (Eds.), Kyoto Japan, Pergamon, vol. 1, pp. 477–482, 2003.

Fleury, M., The GeoCarbone-Integrity program: evaluating sealing efficiency of caprocks for CO_2 storage, GEOTECHNOLOGIEN "Science Report" No. 9: 1st French-German Symposium on Geological Storage of CO_2, Abstracts from the CO_2-Symposium in Potsdam, June 21-22 2007, Koordinierungsbüro Geotechnologien, p. 72, 2007.

Gaucher E.C., and P. Blanc, Cement/clay interactions—A review: Experiments, natural analogues, and modeling. *Waste Manag. 26*, 776-788, 2006.

Gaucher E.C., C. Tournassat, F.J. Pearson, P. Blanc, C. Crouzet, C. Lerouge, and S. Altmann, A robust model for pore-water chemistry of clayrock. *Geoch. Cosmoch. Acta 73*, 6470-6487, 2009.

Gaucher, E.C., C. Robelin, J.M. Matray, G. Négrel, Y. Gros, J.F. Heitz, A. Vinsot, H. Rebours, A. Cassagnabère, and A. Bouchet, ANDRA underground research laboratory: interpretation of the mineralogical and geochemical data acquired in the Callovian-Oxfordian formation by investigative drilling. *Phys. Chem. Earth 29*, 55-77, 2004.

Gherardi, F., Audigane P., and E.C. Gaucher, Predicting long-term geochemical alteration of wellbore cement in a generic geological CO_2 confinement site: Tackling a difficult reactive transport modeling challenge. *J. Hydrol. 420-421*, 340-359, 2012.

Glasser, F., *Chemistry of cement solidified waste forms*, In: Chemistry and microstructure of solidified waste forms, Spence R. (ed.), Oak Ridge National Laboratory, pp. 1-39, 1993.

Heukamp F.H., F.J. Ulm, and J.T. Germaine, Mechanical properties of calcium-leached cement pastes: triaxial stress states and the influence of pore pressures. *Cem. Concr. Res. 31*, 767–784, 2001.

IPCC, *Carbon Dioxide Capture and Storage,* Metz B., O. Davidson, H. de Coninck, M. Loos, and L. Meyer Eds, Report prepared by the Working Group III of the Intergovern-

mental Panel on Climate Change, Cambridge University Press, 431 pp., 2005.

Marty, N.C.M., C. Tournassat, A. Burnol, E. Giffaut, and E.C. Gaucher, Influence of reaction kinetics and mesh refinement on the numerical modelling of concrete/clay interactions. *J. Hydrol. 364*, 58-72, 2009.

Palandri, J.L., and Y.K. Kharaka, *A compilation of rate parameters of water-mineral interaction kinetics for application to geochemical modeling*, US Geological Survey Open File Report 2004-1068, 64 pp.., 2004.

Wertz, F., F. Gherardi, P. Blanc, A.G. Bader, and A. Fabbri, Modeling CO_2-driven cement alteration at well-caprock interface. Submitted to TOUGH Symposium 2012 Proceedings.

Xu, T., E.L. Sonnenthal, N. Spycher, and K. Pruess, TOUGHREACT - A simulation program for non-isothermal multiphase reactive geochemical transport in variably saturated geologic media: Applications to geothermal injectivity and CO_2 geological sequestration. *Comp. & Geosc. 32*, 145–165, 2006.

Xu, T., E. Sonnenthal, N. Spycher, and K. Pruess. *TOUGHREACT User's Guide: A Simulation Program for Non-isothermal Multiphase Reactive Geochemical Transport in Variably Saturated Geologic Media*, Report LBNL-55460, Lawrence Berkeley National Laboratory, Berkeley, Calif., 2004.

Xu, T., and K. Pruess, Modeling multiphase non-isothermal fluid flow and reactive geochemical transport in variably saturated fractured rocks: 1. Methodology. *Am. J. Sci. 301*, 16-33, 2001.

TOUGH2 SIMULATION OF CO_2 LEAKAGE FROM A GEOLOGIC RESERVOIR THROUGH MIXED SANDSTONE/SILTSONE CAPROCK FORMATION

Rodrigo Sebastian Iglesias, Luciano da Silva Müller, Roberto Heemann, João Marcelo Medina Ketzer

Center of Excellence in Research and Innovation in Petroleum, Mineral Resources and Carbon Storage (CEPAC) / Pontifical Catholic University of Rio Grande do Sul (PUCRS)
Av. Ipiranga 6681, Building 96J
Porto Alegre, Rio Grande do Sul, 90619-900, Brazil

ABSTRACT

Carbon capture and geological storage has been shown to be a viable solution for long-term disposal of CO_2, to avoid increasing greenhouse gas emissions to the atmosphere. For effective and safe storage, a suitable caprock formation is necessary, with sufficiently low permeability to avoid the upward migration of injected carbon dioxide. Here, we report the results of our TOUGH2 numerical simulation of CO_2 and water flow through a caprock formation within the Rio Bonito Formation, in the Charqueadas Coal Field (south of Brazil). At the injection site, the caprock consists of sandstone (5 m) in the base, followed by a siltstone layer (25 m). The sandstone and siltsone have vertical permeabilities of 1.2×10^{-13} and 2.4×10^{-16} D, respectively. The model was built with a radial grid (1 km radius) with 20 horizontal × 30 vertical cells. Initial temperature and pressure of the formation were set to 30°C and 1.2×10^{7} Pa, respectively. We conducted simulations while varying injection rates (from 1 to 10 kg/s), over a period of 30 days. Preliminary results show that the CO_2 plume reaches the siltstone layer before the injection stops, even at the lower rate. Migration is then reduced by the siltstone, with very low saturation in the first 5 m after one year of simulation.

INTRODUCTION

Increasing fossil fuel consumption by mankind since the Industrial Revolution is causing significant changes in greenhouse gas (GHG) concentrations in the atmosphere, especially CO_2, which may reach levels up to 790 ppm by the end of the 21st century. This will intensify the greenhouse effect, which may significantly raise the Earth's average temperature, enough to cause severe and irreversible climatic change (IPCC, 2007).

Geological storage of CO_2 is among several alternatives and solutions that have been proposed to reduce and stabilize greenhouse gas emissions (Ketzer, 2011).

Carbon capture and geological storage

CO_2 capture and geological storage (CCGS, or simply CCS) is the integrated process in which carbon dioxide is captured and separated at stationary sources, transported to an adequate storage site, and injected into the porous space of deep underground rock formations, such as saline aquifers, oil fields, and coal seams.

CO_2 stored under typical geological conditions is likely to occur in a gas or supercritical phase, with density lower than that of water (~600–800 kg/m^3); thus it will tend to move upward in the reservoir and into the overburden sequence until it seeps to the surface. To ensure that the CO_2 will be retained after the first few years of injection, we must seal the reservoir with an overlying impermeable caprock (permeability typically <0.1 mD).

While being mostly immiscible in water and oil phases, a fraction of the CO_2 will gradually dissolve in the formation water, forming carbonate and lowering the pH of the aqueous phase. This may trigger chemical changes in the rock matrix that can either improve injectivity around the well, or damage the reservoir and/or caprock by affecting the porosity and permeability of the medium. Eventually, dissolved CO_2 may form mineral carbonates, trapping CO_2 permanently in a solid phase in the reservoir; however, this process is likely to proceed very slowly, over thousands of years after injection (Iglesias, Bressan et al., 2009).

These trapping mechanisms of CO_2 in the reservoir are interdependent and may change significantly over space and time, on a geological scale. This is why numerical simulation is a powerful tool, one that is systematically employed, in studies of CO_2 geological storage—helping investigators understand the partition among the trapping mechanisms, predicting the displacement of the free CO_2 phase in the reservoir, and detecting chemical alterations in the rock matrix. The TOUGH2 family of codes is a valuable tool for this application because it is capable of simulating multiphase flow and multi-component transport within porous media, in up to three dimensions (Pruess, 1999).

OBJECTIVES

This work aims to study the containment capacity of a moderately porous siltstone and sandstone caprock overlying a coal seam in the Charqueadas Coalfield, southern Brazil, using a numerical model. Both caprock layers belong to the Rio Bonito Formation, from the Parana sedimentary Basin. The study involves simulating CO_2 migration through the caprock, using TOUGH2 and the ECO2N module (Pruess, 2005).

MATERIALS AND METHODS

This study models the flow of CO_2 injected into an interval of the Rio Bonito Formation, a stratigraphic unit belonging to the Parana Basin. At the point of injection, in the Charqueadas coalfield (state of Rio Grande do Sul, southern Brazil) the formation contains a coal seam of ~10 m in thickness, with intercalating sandstone layers, and is overlain by several meters of mixed sandstone/siltstone layers.

For the simulation, we constructed a non-reactive isothermal flow and transport model using TOUGH2 and the ECO2N module, with water and CO_2 as the mobile phases. The PetraSim graphical interface from Thunderhead Eng. was used to facilitate the model grid construction and input of parameters.

Model

A radial model of 1 km diameter and 30 m height was defined (20×30 cells), where the lower 5 m constituted of sandstone and the top 25 m of a porous siltstone. A 1:1 size-increasing factor was applied in the radial direction for increased refinement near the injection point. Pressure and temperature of the reservoir were set at 120 bar and 30°C, respectively. Figure 1 below presents a simplified scheme of the model.

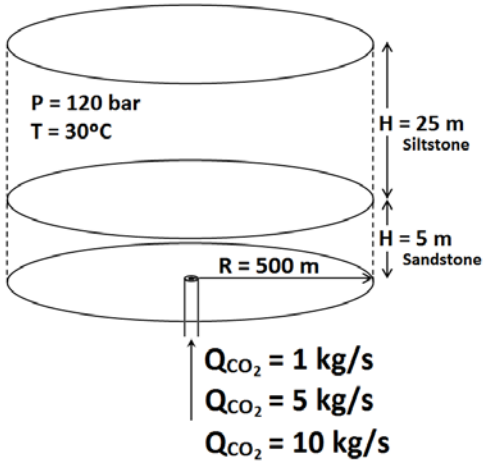

Figure 1. Model scheme

Table 1 below presents the rock properties that were introduced in the model.

Table 1. Rock properties

Property	Siltstone	Sandstone
Density	2520 $kg.m^{-3}$	2650 $kg.m^{-3}$
Porosity	0,158	0,280
Permeabilty	$2{,}4x10^{-16}$ m^2	$1{,}2x10^{-13}$ m^2

As a variable for analysis, three different CO_2 leakage rates were tested for comparison: 1 kg/s, 5 kg/s, and 10 kg/s. CO_2 enters the model at a single point through the lower central part of the grid, for a period of 30 days, which is the time of injection at the site.

Table 2. Summary of variables of simulation

Simulation	Time	CO_2 injection rate
S1	30 days	1 $kg.s^{-1}$
S2		5 $kg.s^{-1}$
S3		10 $kg.s^{-1}$

RESULTS

The main objective of this work was to verify the containment capability of the porous sandstone/siltstone layers with respect to the upward migration of the CO_2 plume after permeation through the coal seam. Figure 2 shows the CO_2 gas saturation after 30 days (end of injection) with the different injection rates. The figure shows that the plume migrates rapidly through the sandstone layer, reaching the bottom of the siltstone in all cases. For the higher injection rates (Figures 2b and 2c), the plume starts to spread below the siltstone layer (because the permeability is lower), containing the migration. This confinement is not very effective, however, because the siltstone is moderately porous and permeable. For high injection rates (Figure 2c), the central, lower part of the siltstone layer has a significant gas saturation after 30 days of simulation.

The same trend in the results is observed for the solubilized CO_2 fraction (Figure 3a-c). The plume spreads in the sandstone ~100 m horizontally from the center. (Note that the figures are not to-scale.)

Figure 4 shows the resulting CO_2 saturation one year after the beginning of injection (which lasted 30 days). As expected, the horizontal spread is more pronounced, reaching ~200 m from the center. However, a rather significant amount of CO_2 still penetrates ~5 m into the siltstone layer.

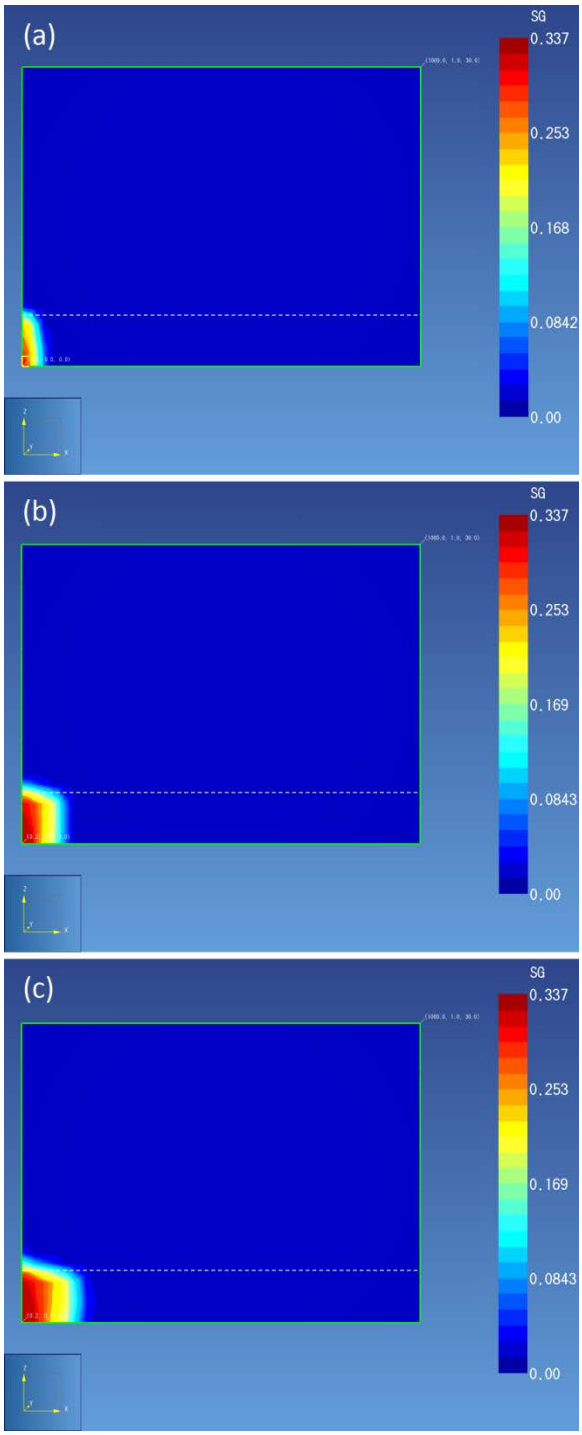

Figure 2. CO_2 saturation at (a) 1 $kg.s^{-1}$, (b) 5 $kg.s^{-1}$ and (c) 10 $kg.s^{-1}$ injection rates after 30 days (Not to scale. Dashed line shows separation between sandstone and siltsone.)

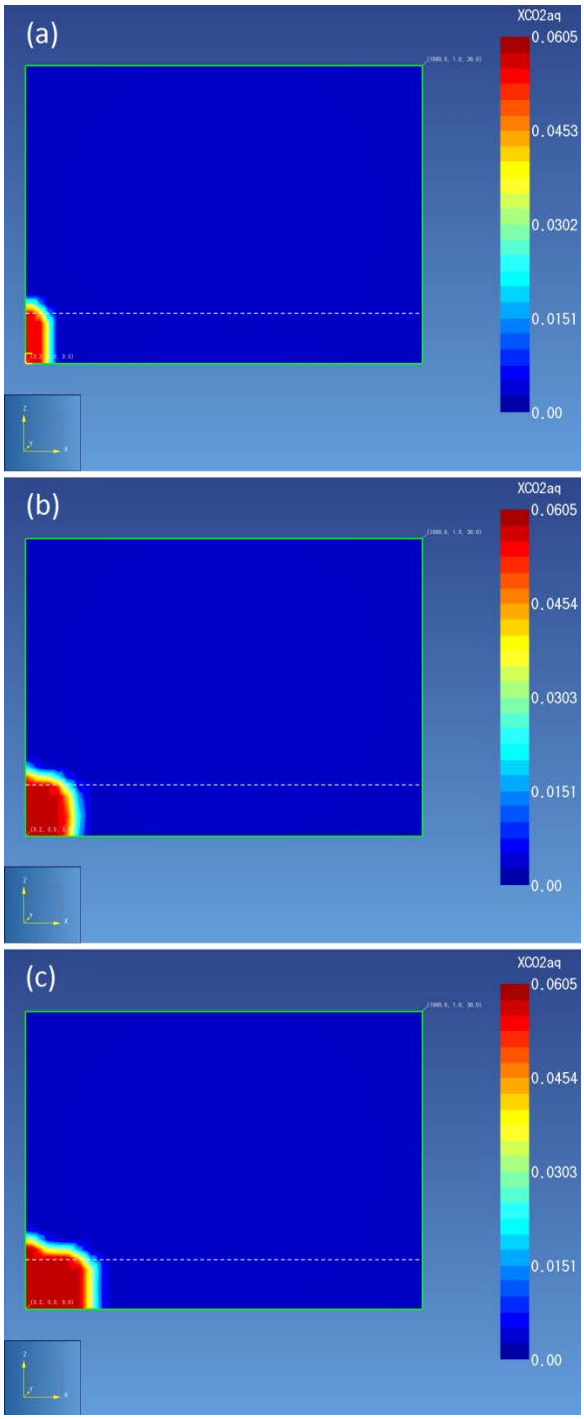

Figure 3. Aqueous CO_2 molar fraction at (a) 1 $kg.s^{-1}$, (b) 5 $kg.s^{-1}$ and (c) 10 $kg.s^{-1}$ injection rates after 30 days (Not to scale. Dashed line shows separation between sandstone and siltsone.)

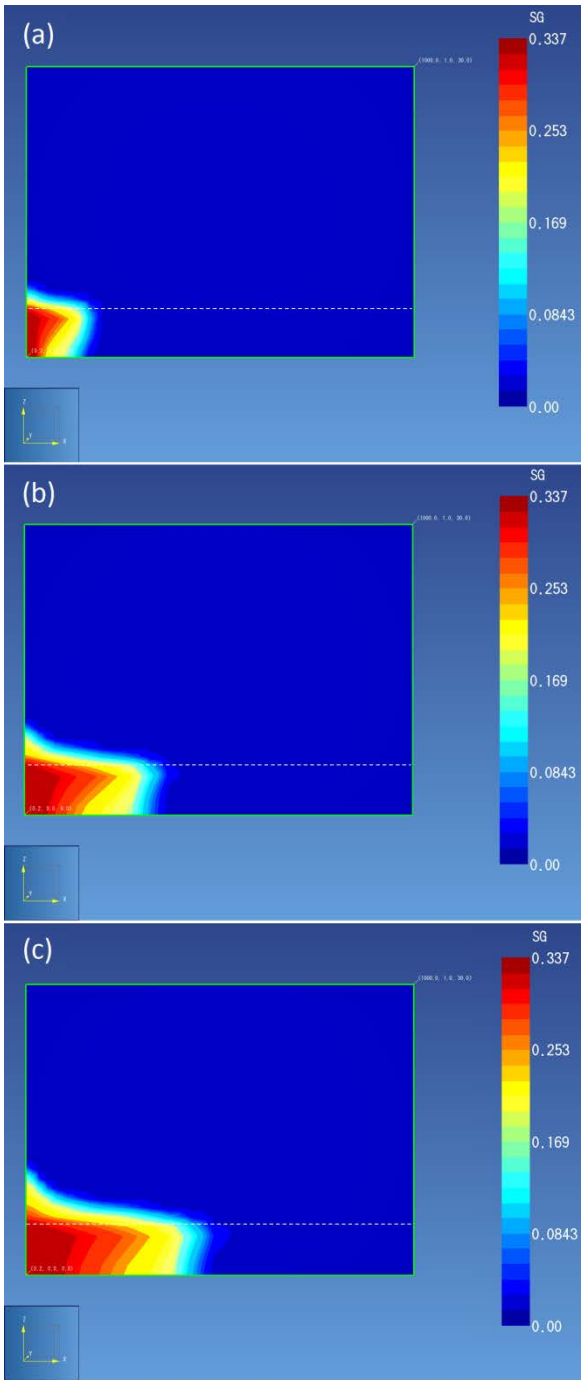

Figure 4. CO_2 saturation at (a) 1 $kg.s^{-1}$, (b) 5 $kg.s^{-1}$ and (c) 10 $kg.s^{-1}$ injection rates after 1 year (injection stops at 30 days). (Not to scale. Dashed line shows separation between sandstone and siltsone.)

CONCLUSIONS

Using numerical simulations of non-reactive flow of CO_2 and water in a geological system composed of sandstone with a siltstone caprock, we analyzed the performance of that system in terms of its ability to contain the upward flow of a CO_2 plume. As expected, given its low porosity and permeability, the sandstone layer is unable to contain the flow: it allows the plume to reach its top during the injection period. The siltstone layer, being less permeable, is able to partially contain this flow, causing the plume to spread through the sandstone layer. However, the siltstone is still sufficiently permeable, allowing a steady migration of CO_2 through this layer and indicating the incomplete containment characteristics of such an overburden.

Further studies, including reactive transport (using TOUGHREACT) are being carried out, as well as different model constructs (finer grids, longer simulation times), which will allow a better comprehension of this caprock capacity for containment of injected CO_2.

ACKNOWLEDGEMENTS

The authors would like to thank PETROBRAS for sample data and research funds.

REFERENCES

IGLESIAS, R. S., L.W. Bressan, J.M. Ketzer. *Armazenamento geológico de carbono em aqüíferos salinos e campos de petróleo: geoquímica do sistema CO2-água-rocha através de experimentos e modelagem numérica.* In: ZILIOTTO, M. A. (Ed.). Mudanças Climáticas, Sequestro e Mercado de Carbono no Brasil. Curitiba, 2009. p. 203-217.

IPCC. *Climate Change 2007: The Physical Science Basis. Contribution of Working Group I to the Fourth Assessment Report of the Intergovernmental Panel on Climate Change.* Cambridge (UK). 2007

KETZER, J. M., R.S. Iglesias and S. Einloft. *Reducing Greenhouse Gas Emissions with CO_2 Capture and Geological Storage.* In: W.-Y. Chen, T. Suzuki and M. Lackner (Eds.) Handbook of Climate Change Mitigation, 2011. Springer Science+Business Media, LLC.

PRUESS, K., Oldenburg, Curt and Moridis, George. *TOUGH2 User's Guide, Version 2.0.* Berkeley, CA, USA : Earth Sciences Division, Lawrence Berkeley National Laboratory, November 1999. LBNL-43134.

PRUESS, K. *ECO2N: A TOUGH2 Fluid Property Module for Mixtures of Water, NaCl, and CO_2.* August, 2005. Earth Sciences Division, Lawrence Berkeley National Laboratory. Berkeley CA USA . LBNL-57952. 2005.

EVALUATION OF CO_2 STORAGE POTENTIAL FOCUSED ON CO_2 SEALING EFFICIENCY OF THE SEAL LAYER AT A FEASIBILITY STUDY SITE

Seiichi Ikeda, Satoshi Tomimori, Masao Ohoka, Mariko Seguchi
Junya Takeshima, Hiroyuki Azuma

OYO Corporation, 1-66-2 Miyahara-cho Kita-ku, Saitama, 331-0812, Japan
e-mail: ikeda-seiichi@oyonet.oyo.co.jp

ABSTRACT

This paper describes our evaluation of CO_2 storage potential, with a focus on CO_2 sealing efficiency, through numerical analysis using TOUGH2/ECO2N applied to a feasibility study site (which we call "Site D"). To create an axisymmetric model, we simplified the geological situations at the injection point at Site D, and using this model, we examined the relationships between integrity of the seal layer and storage volumes of CO_2. We chose some parameters to carry out a sensitivity analysis for understanding the uncertainty included in the analysis. The sensitivity analysis revealed that permeability, capillary pressure, layer thickness, and modeling of the alternating layers will greatly affect our results. Through this numerical analysis focused on sealing efficiency, we estimate the maximum amount of injectable CO_2 in Site D at 1 million tons per well.

INTRODUCTION

This study is a part of the feasibility study project for Zero-emission Coal Gasification Power Generation with CCS, which was funded by the New Energy and Industrial Technology Development Organization of Japan (NEDO).In this study, evaluation of the quantity of CO_2 that can be confined in a storage layer over a long period at a given site is an important consideration. At this feasibility study stage, when sufficient geological survey data have not yet been gathered, it is also important to understand the uncertainty inherent in the numerical-analysis results.

We collected previous geological survey data and created a geological model for the feasibility-study sites. The number of required injection wells and their locations were determined and, using TOUGH2/ECO2N, we simulated CO_2 migration at a single hypothetical site (Site D).

In this paper, we explore Site D storage potential as estimated by the analysis, paying special attention to CO_2 sealing efficiency and the degree of uncertainty in the analysis results, caused by rock properties and other simulation parameters.

MODEL

Geology

The sedimentary basin in Site D mainly consists of sediments from the Neocene to Paleocene periods, with a thickness of 4,000 meter and an area of 1,500 km^2. This sedimentary basin has a vast amount of previous geological survey data. A refraction seismic survey was conducted through 124 survey lines (a total of 4,162 km in length), and four boreholes were drilled during the survey. These areas are located approximately ten kilometers offshore, with the depth of sea water 150 m. The thickness of the massive sandstone layer chosen as the storage reservoir is ~400 m thick, distributed from 1100 to 1500 m below the seabed. The alternating layers of mudstones (predominant) and sandstones are proposed as seal layers, with thickness of ~200 m, distributed from 900 to 1100 m below the seabed.

Numerical Model

A simplified axisymmetric model was created to represent the geological situation at the selected area. Figure 1 shows a schematic of the model geometry. The radius of the model has sufficient length (100 km) to avoid the effect of a side boundary condition on CO_2 migration behavior. Figure 2 shows the numerical axisymmetric model. Table 1 shows the properties of the reservoir and seal layer as a standard case.

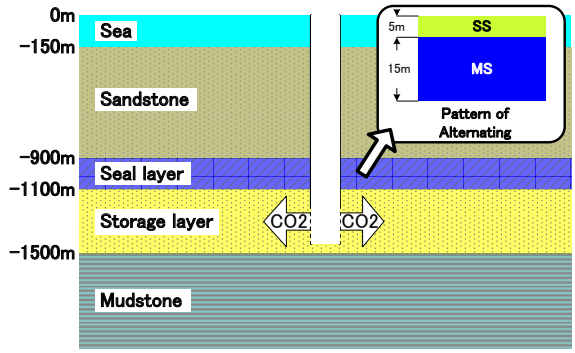

Figure 1. Schematic of model geometry, with simplified geological situation at the injection point.

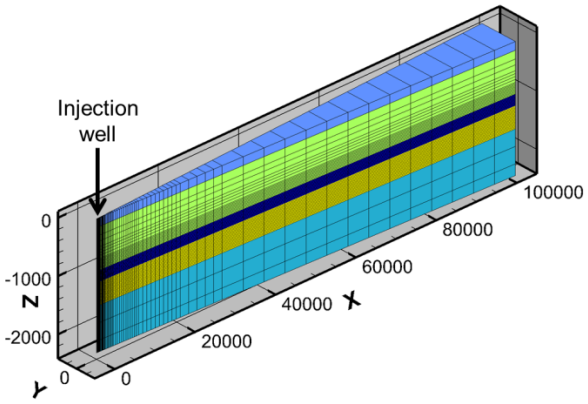

Figure 2. The numerical axisymmetric model.

Conditions of CO_2 Injection

The injection point of CO_2 was selected as through a single vertical well in the middle of the storage layer, at depths from 1250 to 1350 m below the seabed. The rate of CO_2 injection was determined as 1 million tons of CO_2 per year, with a 20-year injection cycle.

SENSITIVITY ANALYSIS

In order to evaluate the quantity/volumes of CO_2 that can be confined in the storage layer over a long period of time, our sensitivity analyses focused on the parameters of the seal layer. The sensitivity of results to (1) the approach to modeling of the alternating layers, (2) permeability, (3) porosity, (4) irreducible water saturation, and (5) capillary pressure of the seal was determined. The ranges of parameters for sensitivity analysis (the maximum and the minimum values) were estimated based on literature data.

Table 1 shows the properties of the standard case; Table 2 shows the variable parameters for the seal layer.

Table 1. Properties of the standard case

Property	Seal layer		Strage layer
	MS	SS	
Porosity (%)	32	32	30
Permeability (vertical)	0.8	36	3.1
Permeability (horizontal)	0.8	36	18
Relative Permeability			
function	VG[1)]	VG[1)]	VG[1)]
λ	0.4	0.4	0.4
Slr	0.8	0.54	0.6
Sls	0.95	0.95	0.95
Sgr	0.05	0.05	0.05
Capillary Pressure			
function	VG[2)]	-	-
λ	0.4	-	-
Slr	0.8	-	-
P_0(Pa)	$3x10^5$	-	-
P_{max}(Pa)	$1x10^6$	-	-
Sls	1	-	-

1) Liquid:van Genuchten(1980) ; Gas:Corey(1954)
2) van Genuchten(1980)

Table 2. Variable parameters of the seal layer.

Item	Standard model	Value of a variable	Case
Modeling	Alternation model	Alternation model	Case1-1
		Equivalent permeability model	Case1-2
Injection rate	1 milion ton-CO2/year	1.5 milion ton-CO2/year	Case2-1
		0.5 milion ton-CO2/year	Case2-2
Permeability	0.8 md	4 md	Case3-1
		0.08 md	Case3-2
Porosity	32%	44%	Case4-1
		20%	Case4-2
Capillary pressure	P_0 = 300 kPa	P_0 = 600 kPa	Case5-1
		P_0 = 30 kPa	Case5-2
	λ = 0.4	λ = 0.8	Case6-1
		λ = 0.2	Case6-2
Irreducible water saturation	Swir = 0.8	Swir = 0.9	Case7-1
		Swir = 0.7	Case7-2
Permeability and Capillary pressure	K = 0.8 md P_0 = 300 kPa	K=4 md, P_0=200kPa	Case8-1
		K=0.08md, P_0=510kPa	Case8-2

Figure 3 shows numerical results that illustrate the difference between Case (a), modeling the alternating mudstones/sandstones, and Case (b),

using an equivalent coefficient of permeability. In the case of the alternating layer model, the CO_2 migration front is in the 4th alternate layer, 80 m above the bottom of the seal layer. In the case of the equivalent permeability model, the CO_2 migration front extends just past the top of the seal layer. These results show that dissipation of CO_2 pressure through the sandstone parts of the seal layer influences CO_2 migration. Table 3 shows the results of sensitivity analysis using the alternating-layer model. If one parameter is changed, the difference in the CO_2 migration front is from 40 to 60 m, in many cases. But changes in two parameters show higher sensitivity with respect to CO_2 migration: these are capillary pressure (p_0, λ) and injection rate. Porosity is not sensitive with respect to CO_2 migration through the seal layer.

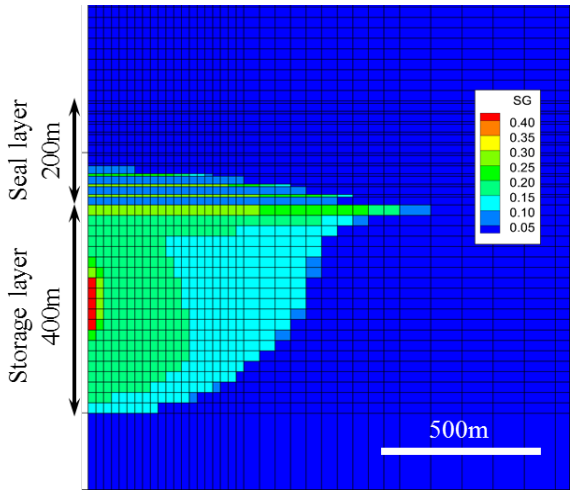

(a) Alternating layer model

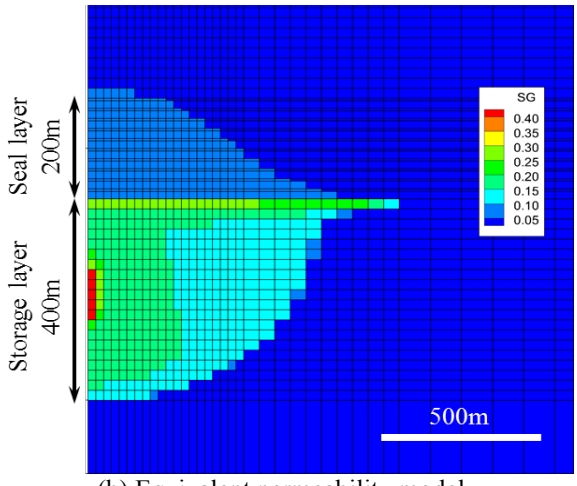

(b) Equivalent permeability model

Figure 3. Simulated CO_2 saturations at t=400years.

Table 3. The results of sensitivity.

Item	Case	CO2 Front Position[1)] (m)	Difference (m)	Sensitivity
Modeling	Case1-1	80	>120	High
	Case1-2	>200		
Injection rate	Case2-1	100	60	Medium
	Case2-2	40		
Permeability	Case3-1	80	40	Low
	Case3-2	40		
Porosity	Case4-1	80	0	very Low
	Case4-2	80		
Capillary pressure	Case5-1	40	>160	High
	Case5-2	>200		
	Case6-1	100	60	Medium
	Case6-2	40		
Irreducible water saturation	Case7-1	40	40	Low
	Case7-2	80		
Permeability and Capillary pressure	Case8-1	80	40	Low
	Case8-2	40		

1) From bottom of seal layer

CONCLUSION

Based on the sensitivity analysis, there are no cases in which CO_2 leaks through the seal layer, except when there are unrealistic parameter conditions. Consequently, even allowing for a degree of uncertainty (in rock properties), we believe that an injection rate of 1 million t-CO_2 is feasible at Site D. However, further investigation is required for the situation of alternating seal layers and the characteristics of the capillary pressure in the seal layer.

In this project at Site D, two different types of injection quantities are considered:

(1) Commercial project level of 31 million tons-CO_2 in total (1.54 million tons-CO_2 per year, 20-year injection cycle)

(2) Large-scale CO_2 storage, assumed to be 200 million tons in total (10 million tons-CO_2 per year, 20-year injection cycle).

The number of required injection wells is two for the commercial project and ten for large-scale CO_2 storage. We think that further research is in order, to reproduce more detailed geological conditions within a numerical model.

ACKNOWLEDGMENT

This study is part of the feasibility study project for Zero-emission Coal Gasification Power Generation with CCS, funded by the New Energy and Industrial Technology Development Organization of Japan (NEDO).

REFERENCES

Pruess, K., C. Oldenburg, and G. Moridis, *TOUGH2 User's Guide, Version 2.0*, Report LBNL-43134, Lawrence Berkeley National Laboratory, Berkeley, Calif., 1999.

Pruess, K., *ECO2N : A TOUGH2 Fluid Property Module for Mixtures of Water , NaCl , and CO_2*, Report LBNL-57952, Lawrence Berkeley National Laboratory, Berkeley, Calif., 2005.

van Genuchten, M. Th., 1980. A closed-form equation for predicting the hydraulic conductivity of unsaturated soils. Soil Sci. Am. J. 44, 892-898.

IMPACT OF DATA UNCERTAINTY ON IDENTIFYING LEAKAGE PATHWAYS IN CO_2 GEOLOGIC STORAGE SYSTEMS AND ESTIMATING THEIR HYDROGEOLOGICAL PROPERTIES BY INVERSE MODELING

Yoojin Jung, Quanlin Zhou, and Jens T. Birkholzer

Earth Sciences Division, Lawrence Berkeley National Laboratory
One Cyclotron, MS 74R316C
Berkeley, CA 94720, USA
e-mail: yoojinjung@lbl.gov

ABSTRACT

For successful risk management of large-scale geologic carbon storage (GCS), it is crucial to detect leakage of brine and/or CO_2 from a storage reservoir through unknown leakage pathways (e.g., abandoned wells and faults) as early as possible, and to determine the leak's impact on the environment. We are currently developing a monitoring and inverse modeling framework for early leakage detection, which uses anomalies in monitoring data on pressure-driven processes—such as pressure measurements from monitoring wells within and above the storage reservoir, as well as surface-deformation InSAR data—as early signals of brine and/or CO_2 leakage through unknown leakage pathways. In a study of idealized GCS scenarios, we have demonstrated the strong sensitivity of pressure and deformation anomalies (i.e., the differences between leakage and no-leakage scenarios) to the location and permeability of potential leakage pathways, and we have successfully detected leakage pathways and calibrated their permeabilities using the approach of modeling and jointly inverting pressure and surface deformation data. However, noise in monitoring data (large random errors or non-normal errors) and drift in pressure transducers (systematic errors) may lower detectability (due to the increased uncertainty they cause), and even lead to failure of leakage detection and parameter estimation. In addition, uncertainties in measured or presumably known hydrogeological properties of the storage system may also increase the difficulty of identifying leakage pathways.

Here, we use iTOUGH2 to examine the effect of various data uncertainties on the accuracy of detection and estimation, and discuss strategies for enhancing detectability and reducing the impact of those uncertainties.

INTRODUCTION

For geologic carbon sequestration (GCS) to have a sizable effect on mitigating climate change, large volumes of CO_2 must be injected into subsurface reservoirs (Benson and Cole, 2008). However, large-scale CO_2 injection may result in a substantial increase in pressure within the storage formation and heighten the potential risks of GCS (Zhou et al., 2010). Brine or CO_2 may leak through unknown high-permeability leakage pathways (e.g., abandoned wells and faults) within the area of influence. In addition, increased pore pressure in the storage reservoir could induce geomechanical alteration of the reservoir and its surroundings, e.g., creating new fractures or reactivating larger faults (Rutqvist, 2012). If these changes occur in the cap rock or overburden, they could become new leakage pathways for brine or CO_2, potentially resulting in localized deformation (in addition to injection-induced deformation). If such leakage events cannot be properly assessed, GCS might cause undesirable environmental and safety consequences, and these events might ultimately prevent future deployment of GCS. Therefore, it is essential to the success of GCS for us to have the ability to detect brine or CO_2 leakage from the storage reservoir through high-permeability pathways, predict potential risk profiles, and manage the risks as early as possible.

We are currently developing a monitoring and inverse modeling framework for early leakage detection, using multiple complementary data sources, such as pressure buildups in monitoring

wells within and above the storage reservoir and surface-deformation data (e.g., Interferometric Synthetic Aperture Radar, InSAR). Within this framework, potential leakage pathways are identified and located as early as possible by inverse modeling of anomalies in monitoring data, and the time-dependent likelihoods of CO_2 leakage through the identified pathways are predicted using calibrated models. Unlike existing leakage-detection techniques, this framework will help with early detection and thereby allow time for risk mitigation and management in advance of actual CO_2 leakage.

In a recent study of idealized GCS scenarios (Jung et al., 2012), we demonstrated the strong sensitivity of pressure and deformation anomalies (i.e., the differences between leakage and no-leakage scenarios) to the location and permeability of potential leakage pathways, and we have successfully detected model leakage pathways and calibrated their permeabilities using the approach of modeling and jointly inverting pressure and surface deformation data. However, the monitoring data available in practical applications may not always be ideal, and such data will likely contain errors that may not automatically be accounted for in the calibrated model. For instance, noise in monitoring data (large random errors or non-normal errors) and instrument drift in pressure transducers (systematic errors) may increase uncertainties in parameter estimation and even lead to failure of leakage detection. In addition, hydrogeological properties obtained from other tests or sources and considered as known parameters may not be error-free, and these uncertainties in the hydrogeological properties of the storage system can increase the difficulty of identifying leakage pathways. Therefore, it is important to assess the impact of data uncertainty on identifying leakage pathways in GCS systems and estimating their hydrogeological properties by inverse modeling.

In this paper, we briefly introduce the concept of early leakage detection, discuss the sensitivity of pressure monitoring for leakage detection, and demonstrate the feasibility of identifying and estimating leakage pathways (and their hydrogeological properties) by inverse modeling in an idealized monitoring scenario. Then, we examine the effect of various data uncertainties on the accuracy of detection and estimation. For simplicity here, we limit our discussion to using only pressure data from monitoring wells.

PRESSURE-BASED EARLY DETECTION FRAMEWORK FOR CO_2 LEAKAGE FROM STORAGE RESERVOIRS

Our early leakage detection framework for GCS is based on the idea of (1) using the signals of fast-traveling pressure-buildup waves (caused by CO_2 injection into the storage reservoir) and pressure-induced surface deformation, and their signal anomalies associated with seal imperfections (e.g., leaky faults, fractures, abandoned wells) to locate, identify, and quantify these seal imperfections; (2) predicting the fronts of slower-migrating CO_2 plumes by flow modeling, with the locations and hydrologic properties of the detected seal imperfections accounted for; and (3) comparing the two time-evolving inverse- and forward-modeling processes to predict the time-dependent likelihood of CO_2 leakage through these features, and to guide mitigation measures to prevent leakage from happening if such likelihood exists.

The core of this approach is to jointly utilize fast-propagating pressure data and high-spatial-resolution surface deformation data to improve the detectability of leakage signals and reduce the uncertainties in locating leakage pathways. Time-dependent pressure buildups caused by CO_2 injection propagate much faster than the CO_2 plume migrates, and therefore the anomalies in observed pressure buildups, which are induced by brine leakage through leakage pathways, may also be revealed quickly. However, only a few monitoring wells may be available (if any), and they may not always be conveniently located close to leakage pathways, such that they could sensitively detect anomalies in pressure buildups. Therefore, surface deformation InSAR data, which can measure ground displacement on the order of centimeters or millimeters and provide dense spatial information on the scale of kilometers, might be able to add useful complementary information for detecting leakage pathways.

METHODOLOGY

Model Setup and Parameters

We consider a simplified conceptual model, which represents a storage system consisting of a target storage formation, a cap rock, and an overlying monitoring formation, as shown in Figure 1. The injection well (IW) is located at the center of the model domain [0 km, 0 km], and the leaky well (LW) is located 2 km away from the injection well [2 km, 0 km]. Resident brine is injected into the storage reservoir at a constant rate, Q =5700 m^3 day^{-1}, and pressure perturbations arising from fluid injection and brine leakage are observed at monitoring wells. The radius of the injection, the leaky well, and the monitoring wells is 0.15 m. The effective permeability of the leaky well is k_L = 10^{-10} m^2. The following properties are used as the formation parameters of the storage system: aquifer (storage and overlying formation) thickness of B = 60 m, aquifer permeability of k = 10^{-13} m^2, aquifer pore compressibility of β_p = 4.5 × 10^{-10} Pa^{-1}, aquitard (caprock formation) thickness of B' = 100 m, aquitard permeability of k' = 10^{-18} m^2, aquitard pore compressibility of β'_p = 9.0 × 10^{-10} Pa^{-1}, and water compressibility of β_w = 3.5 × 10^{-10} Pa^{-1}. Accordingly, the hydraulic conductivities of the aquifers and the aquitard are 0.20 m day^{-1} and 0.20 × 10^{-5} m day^{-1}, respectively, assuming brine density of ρ = 1200 kg m^{-3}, gravity acceleration of g = 9.8 m s^{-2}, and water viscosity of μ = 0.5×10^{-3} Pa s. The specific storativity of the aquifers is calculated using $S_s = \phi\rho g(\beta_w + \beta_p)$ =1.88 × 10^{-6} m^{-1}, where the aquifer's porosity is ϕ = 0.2. The specific storativity of the aquitard is calculated using $S'_s = \phi'\rho g(\beta_w + \beta'_p)$ = 1.47×10^{-6} m^{-1}, where the aquitard porosity is ϕ' = 0.1. These formation parameters are based on previous studies on large-scale injection of CO_2 (Birkholzer et al., 2009) and water (Zhou et al., 2009).

Computational Methods

To calculate pressure buildups in the storage system, we use an efficient semi-analytical solution (Cihan et al., 2011), assuming single-phase water flow. This solution can calculate pressure perturbation and fluid flow that are induced by large-scale fluid injection in multilayer systems (e.g., multiple aquifers and alternating aquitards), combining the effect of diffuse leakage through aquitards and/or focused leakage through leaky wells. The fluid flow in the system is described by coupled one-dimensional horizontal flow in aquifers, vertical flow in aquitards, and Darcy-type vertical flow in leaky wells. Further details on this analytical solution can be found in Cihan et al. (2011).

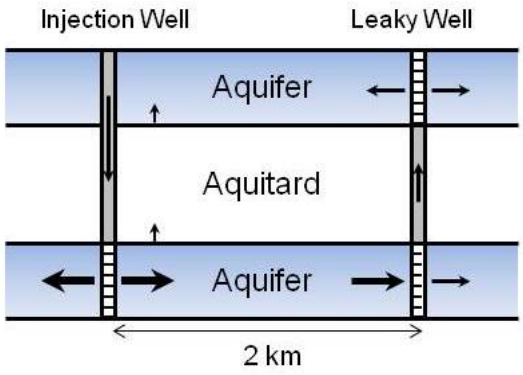

Figure 1. Schematics of a simplified storage system of a target storage reservoir, a caprock, and an overlying aquifer, with an injection well and a leaky well (2 km away).

For inverse modeling, we use iTOUGH2-PEST (Finsterle, 2011). iTOUGH2-PEST is an extended version of iTOUGH2, a computer program for parameter estimation, sensitivity analysis, and uncertainty propagation analysis (Finsterle, 2007), and uses the PEST protocol (Doherty, 2007, 2008) as a way to communicate between application models and iTOUGH2. iTOUGH2 was originally developed for use with the TOUGH2 forward simulator (Pruess, 1999). However, with the iTOUGH2-PEST module, iTOUGH2 can be used as a universal optimization code for non-TOUGH2 models.

DETECTION OF PRESSURE ANOMALIES

Large volumes of CO_2 injection into the storage formation may induce significant pressure buildups. Hydraulic communication between the storage and the overlying formation via diffuse leakage through the cap rock may also influence pressures in both formations. Such pressure perturbations in GCS systems can be simulated using appropriate models, e.g., Cihan et al. (2011). Therefore, for an idealized system with homogenous aquifers and aquitards, the difference between the measured pressures at

monitoring wells and the calculated values based on known hydrogeological properties of the storage system can be attributed to the leakage through unknown leakage pathways. The detectability of this leakage signal greatly depends on various formation parameters, as well as the effective permeability of the leakage pathways.

To determine how sensitively the pressure at monitoring wells changes in response to brine leakage through a leaky well, we compute the absolute difference of pressures measured with and without the presence of the leaky well (= $|h_w - h_{wo}| = \Delta h_{w-wo}$). While the sensitivity of the calculated Δh_{w-wo} to the parameters varied with time and space, the most influential parameter on the whole was found to be the permeability of the cap rock (Jung et al., 2012). We therefore present the result for three different values of aquitard permeability ($k' = 10^{-19}$, 10^{-18}, and 10^{-17} m^2).

Figure 2 shows the time-dependent contour lines of (a) $\Delta h_{w-wo} = 1$ m and (b) $\Delta h_{w-wo} = 0.1$ m in the overlying aquifer. Here, the Δh_{w-wo} values might be assumed to be the minimum pressure buildup to be considered as anomalies induced by high-permeability leakage pathways in different conditions. For instance, $\Delta h_{w-wo} = 1$ m may be used as the detection limit when noises in monitoring data are rather large, and $\Delta h_{w-wo} = 0.1$ m when noises are small. In both cases, the contour lines are centered around the leaky well located at [2 km, 0 km]. In other words, Δh_{w-wo} in Figs. 2a and 2b is higher than 1 m and 0.1 m, respectively, inside the contour line at each time. This means that the detectability of pressure anomalies at monitoring wells would be highly dependent on the location of a monitoring well relative to a leaky well.

Similarly, the time-dependent contour lines of $\Delta h_{w-wo} = 0.1$ m in the overlying formation are shown in Fig. 3 for the case of $k' = 10^{-17}$ m^2. The area in which the anomalies can be detected increases with time, but the area is significantly smaller for the higher-permeability case ($k' = 10^{-17}$ m^2, Fig. 3) than that in the base case ($k' = 10^{-18}$ m^2, Fig. 2b), particularly for late times. An important implication of this result is that early leakage detection is especially critical if the sealing layer has a relatively high permeability. Unless leakage is detected early enough at monitoring wells, it might be difficult to discern leakage signals induced by the presence of high-permeability conduits, such as faults and abandoned boreholes from those by a slow, diffuse process. That is, the accuracy of hydrogeologic parameters (e.g., the cap-rock permeability), which is usually determined by other survey techniques and assumed to be known, might have a large impact on parameter estimation using inverse modeling. (This effect is discussed later.) The difference between the lower-permeability case ($k' = 10^{-19}$ m^2) and the base case ($k' = 10^{-18}$ m^2) was relatively minor, implying diffuse leakage through the caprock is not substantial for the aquitard permeability of up to $k' = 10^{-18}$ m^2.

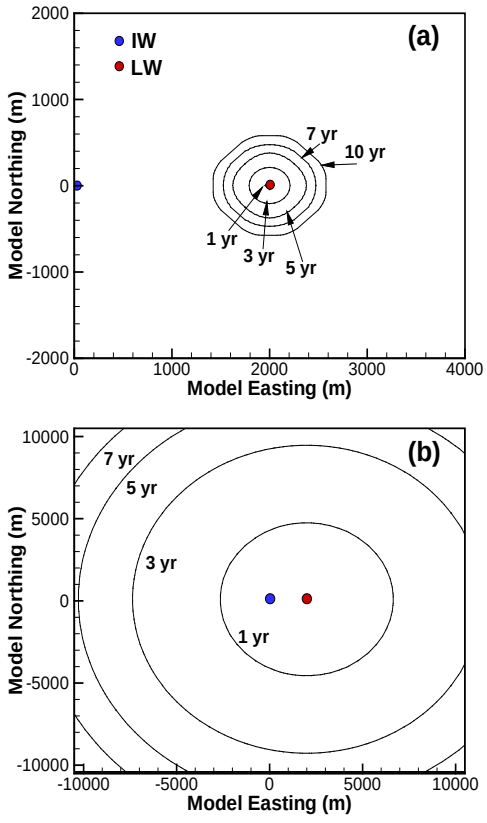

Figure 2. Time-dependent contour lines of (1) $\Delta h_{w-wo} = 1$ m and (b) $\Delta h_{w-wo} = 0.1$ m in the overlying formation for the base case of $k' = 10^{-18}$ m^2.

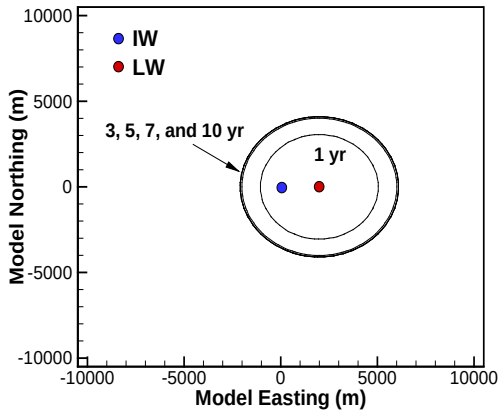

Figure 3. Time-dependent contour lines of Δh_{w-wo} = 0.1 m in the overlying formation for the higher-permeability case of $k' = 10^{-17}$ m^2.

PARAMETER ESTIMATION: IDEALIZED MONITORING SCENARIO

This section presents an idealized monitoring scenario and examines the ability of identifying/locating a leaky well using inverse modeling against pressure data, and calibrating the effective permeability. In addition to the injection well, two monitoring wells (MW1 and MW2) are available for pressure observation in both the storage and the overlying formation, and they are located at [1.5 km, 1.5 km] and [-1.5 km, 1.5 km], respectively. The pressure data collected from these monitoring wells contain only small amount of instrument measurement noise (zero-mean Gaussian noises with standard deviation of 0.0014 bar, which is twice that of the instrument resolution). Here, we assume that any natural background fluctuations due to atmospheric-pressure changes, earth tides, and ocean tides can be filtered out from the data. We use the pressure data measured at the monitoring wells in the storage and the overlying formation and at the injection well in the overlying formation, and test four different initial guesses of the leaky well location at [±1 km, ±1 km] for estimating the leaky well location and permeability.

The match between the computed and the measured pressure buildups was excellent, and all the residuals appeared random (see Fig. 4). The location and effective permeability of the leaky well were also successfully estimated using iTOUGH2-PEST, regardless of the initial guesses away from the actual location. Since the inversion accuracy could be affected by the configuration of available monitoring wells (Jung et al., 2012), we use the same setup in the following section to explore the effect of noise in data and model structure.

PARAMETER ESTIMATION: EFFECT OF RANDOM AND SYSTEMATIC ERRORS

Various errors are introduced into the model and synthetic data (see Table 1) to examine their impact on parameter estimation: (1) the cap-rock permeability derived from other hydraulic tests is overestimated by 20% ($k' = 1.2 \times 10^{-18}$ m^2), (2) the drift in the pressure transducer at MW1 in the overlying formation linearly increases over time (drift rate = 0.001 m d^{-1}), and (3) the pressure measured in the storage formation exhibits pressure-dependent random fluctuations (zero-mean random noises with heterogeneous standard deviation, which increases up to 0.14 bar).

To enhance the fit between the measured and calculated pressures, we incrementally increased the number of parameters considered. At first, similar to the idealized monitoring case, only the location and permeability of the leaky well were estimated. In our second attempt, the permeability of the sealing caprock was included as one of the parameters to be estimated. In the third calibration, the drift rate of the pressure sensor at MW1 in the overlying formation was also parameterized and estimated along with the other parameters. Finally, heteroscedasticity in the monitoring data was also considered in the calibration.

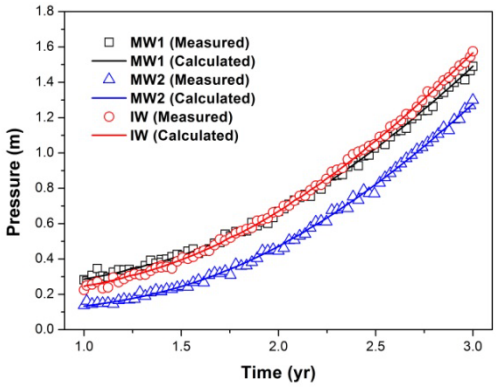

Figure 4. Comparison between the measured and calculated pressures in the overlying formation.

Table 1. Various random and systematic errors introduced into the model and the data.

Error Description	Error Type
• Wrong caprock permeability	Systematic modeling error
• Drift in MW1 pressure transducer in the overlying formation	Systematic measurement error
• Pressure-dependent measurement errors in the storage formation	Heteroscedastic random error

Figure 5 shows the measured against calculated pressures in the storage (SF) and the overlying formation (OF). The estimated parameters in each inversion are summarized in Table 2. As shown in Fig. 5a, when simply the location and permeability of the leaky well are calibrated, the residuals (the deviations from the unit-slope line) at MW2 and IW in the overlying formation are significantly large, indicating that the model failed to account for the true system, and that some systematic errors influenced the inversion results. The observation that the deviations were greater when the distance between the monitoring point and the leaky well was larger suggests that the initial value used for the aquitard permeability was erroneous.

In the second trial, the permeability of the cap rock was parameterized and the fit was then significantly improved (see Fig. 5b). The standard deviation of the estimated parameters also largely decreased. However, even if the degree of deviation was a lot smaller than that in Fig. 5a, all the pressures calculated in the overlying formation still show systematic deviations, suggesting that a more refined model is required. Another interesting observation here is that the estimated leaky well location is almost identical with the location of MW1. If the errors in the model are not carefully analyzed, this erroneous estimate may result in biased conclusions (e.g., a leak in MW1 itself).

In the third inversion, the drift of pressure sensor in MW1 was included as one of the parameters estimated. The residuals of all the pressures measured in the overlying formation appeared random (see Fig. 5c), and the estimated parameters were reasonably acceptable (see Table 2).

Based on the residual analysis, the residuals of the pressures measured in the storage formation also appeared random, but the deviations increased with pressure. In the final inversion, the effect of these heteroscedastic random errors on the parameter estimation was further assessed. To stabilize the errors and make the data more normal distribution-like, the Box-Cox transformation (Box and Cox, 1964), which is a family of power transformations and alleviates heteroscedasticity in the error, was applied to the measured and simulated data.

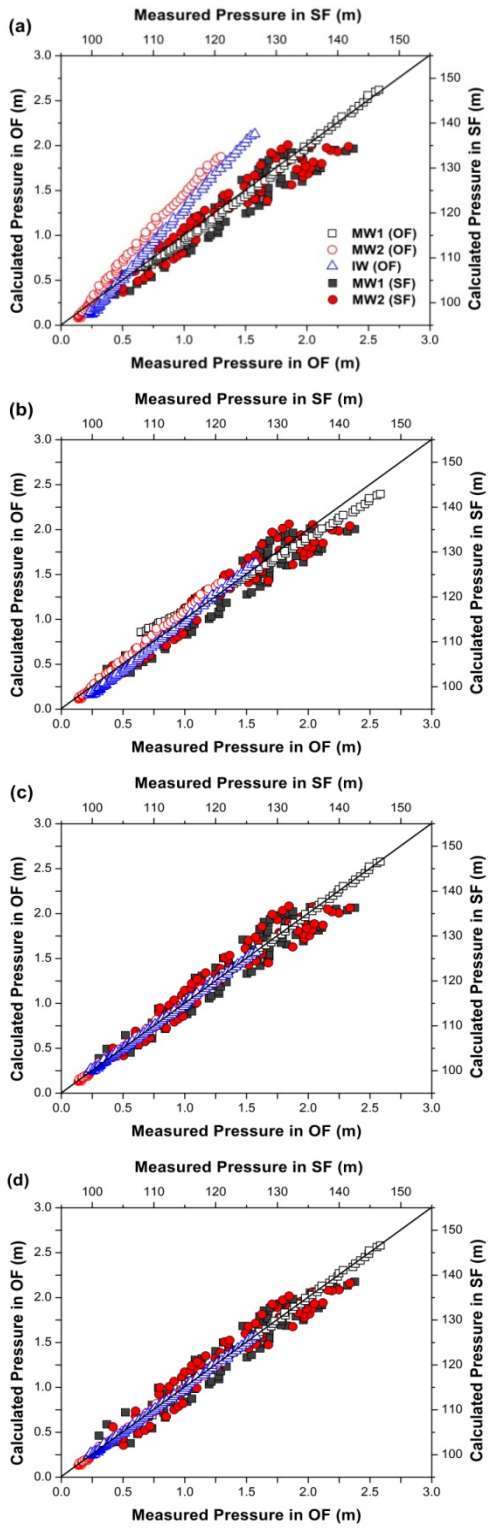

Figure 5. Measured vs. calculated pressures in the cases where (b) *k´*, (c) drift, and (d) Box-Cox parameter are incrementally included in the parameters calibrated, in addition to (a) the case with only the location and permeability of the leaky well calibrated. The solid line is the unit-slope line.

The heterogeneity in the Box-Cox transformed residuals was significantly alleviated (see Fig. 5d), but in this monitoring scenario, this attempt did not necessarily improve the accuracy of the parameter estimation.

CONCLUDING REMARKS

Detection of CO_2 or brine leakage depends on the sensitivity of system responses (monitoring data) to leakage pathways. Our study shows that pressure-based monitoring data are sensitive to leakage pathway properties and change with time and space, therefore allowing parameter estimation through inversion. While large random or systematic errors commonly occur in both the model and the data which can lead to biased parameter estimates, the parameterization of some of these errors in the inverse model greatly helps in mitigating the misfit between the observed and calculated system responses, and improves the estimation process.

In contrast to modeling with the simplified geometric conditions in our model, finding the sources of systematic or non-Gaussian errors may not always be possible for most practical cases. However, a detailed residual analysis on multiple complementary data might enable the modeler to identify such errors. More details on the error-handling strategies and capabilities for mitigating the impact of systematic or non-Gaussian random errors, particularly using iTOUGH2, can be found in Finsterle and Zhang (2011).

ACKNOWLEDGMENT

This NRAP-ARRA work was funded by the Assistant Secretary for Fossil Energy, Office of Sequestration, Hydrogen, and Clean Coal Fuels, National Energy Technology Laboratory, of the U.S. Department of Energy, under Contract No. DE-AC02-05CH11231.

Table 2. Estimated parameters for inversion with different error handling.

Inversion 4	2206 (± 256)	-30 (± 109)	-9.94 (± 0.08)	-18.01 (± 0.002)	9.85E-4 (± 1.67E-5)	-2.4 (±7.37E-1)

Parameter	True	Inversion 1	Inversion 2	Inversion 3
X [m]	2000	1499 (±1031)*	1507 (±201)	2212 (± 209)
Y [m]	0	1501 (± 969)	1504 (± 222)	-11 (± 49)
log (k_L [m^2])	-10.0	-10.41 (± 0.08)	-10.18 (± 0.03)	-9.94 (± 0.06)
log (k' [m^2])	-18.0	n/a	-17.98 (± 0.003)	-18.01 (± 0.002)
Drift [m d^{-1}]	0.001	n/a	n/a	9.82E-4 (± 1.76E-5)
Box-Cox [-]	n/a	n/a	n/a	n/a

* Values in parentheses are the marginal standard deviation of the estimated parameter.

REFERENCES

Benson, S.M. and D.R. Cole, CO_2 sequestration in deep sedimentary formations. *Elements*, 4, 325-331, 2008.

Birkholzer, J.T., Q. Zhou, and C.-F. Tsang, Large-scale impact of CO_2 storage in deep saline aquifers: A sensitivity study on the pressure response in stratified systems, *Int. J. Greenh. Gas Con.*, 3 (2), 181-194, 2009.

Cihan, A., Q. Zhou, and J.T. Birkholzer, Analytical solutions for pressure perturbation and fluid leakage through aquitards and wells in multilayered aquifer systems, *Water Resour. Res.*, doi:10.1029/2011WR010721, W10504, 2011.

Doherty, J., *FORTRAN 90 Modules for Implementation of Parallelised, Model-Independent, Model-Based Processing*, Watermark Numerical Computing, Australia, 2007.

Doherty, J., *PEST: Model-Independent Parameter Estimation*, Watermark Numerical Computing, Brisbane, Australia, 2008.

Finsterle, S., *iTOUGH2 User's Guide,* Report LBNL-40040, Lawrence Berkeley National Laboratory, Berkeley, Calif., 2007.

Finsterle, S., *iTOUGH2 Universal Optimization Using the PEST Protocol*, Report LBNL-3698E, Lawrence Berkeley National Laboratory, Berkeley, Calif., 2011.

Finsterle, S. and Y. Zhang, Error handling strategies in multiphase inverse modeling, *Comput. Geosci.*, 37, 724-730, 2011.

Jung, Y., Q. Zhou, and J.T. Birkholzer, Early detection of brine or CO_2 leakage through high-permeability pathways using pressure-based observation data, Poster session presented at the eleventh annual Carbon Capture, Utilization & Sequestration Conference, Pittsburgh, PA, 2012.

Pruess, K., C. Oldenburg, and G. Moridis, *TOUGH2 User's Guide, Version 2.0*, Report LBNL-43134, Lawrence Berkeley National Laboratory, Berkeley, Calif., 1999.

Rutqvist, J., The geomechanics of CO_2 storage in deep sedimentary formations. *Geotech. Geol. Eng.*, doi:10.1007/s10706-011-9491-0, 2012.

Zhou, Q., J.T. Birkholzer, and C.-F. Tasng, A semi-analytical solution for large-scale injection-induced pressure perturbation and leakage in a laterally bounded aquifer-aquitard system. *Transp. Porous. Med.*, 78, 127-148, doi:10.1007/s11242-008-9290-0, 2009.

Zhou, Q., J. T. Birkholzer, E. Mehnert,Y.-F. Lin, and K. Zhang, Modeling basin- and plume-scale processes of CO_2 storage for full-scale deployment, Ground Water, 48(4), 494-514, 2010.

EFFECTS OF GROUNDWATER CHEMICAL COMPOSITIONS IN DEEP SALINE AQUIFERS ON CO_2 GEOLOGICAL SEQUESTRATION

Hongwu Lei[1], Tianfu Xu[1,2], Fugang Wang[1], Yanlin Yang[1], Hailong Tian[1], Yan Shi[1]

[1]Key Laboratory of Groundwater Resources and Environment, Ministry of Education, Jilin University, Changchun, 130021, China
[2]Earth Sciences Division, Lawrence Berkeley National Laboratory, Berkeley, California 94720

[+]E-mail: hongwulei2008@yahoo.cn

ABSTRACT

Groundwater chemical composition exerts a strong effect on the dissolution of carbon dioxide, in turn affecting the evaluation and prediction of carbon dioxide (CO_2) geological sequestration (CGS). Based on Duan's CO_2 solubility model (2003, 2006), which considered the effects of ions, this paper analyzes the effects of five factors: (1) the equivalent mole fraction of (Na^++K^+) in cations, (2) the equivalent mole fraction of Cl^- in anions, (3) salinity, (4) pressures and (5) temperatures on CO_2 solubility. We then incorporate this model into TOUGH2/ECO2N code as an option for CO_2 solubility calculation. We conclude by considering two typical problems, radial flow from a CO_2 injection well and convective mixing, to study the effects of groundwater chemical compositions on CGS. The results indicate that under different temperatures, pressures, and salinity, the dissolved CO_2 increases with the increase in equivalent mole fraction of (Na^++K^+) compared to (Ca^{2+}+Mg^{2+}) and decreases with the increase in equivalent mole fraction of Cl^- compared to SO_4^{2-}. Low temperatures, high pressures, and low salinity contribute to an increase in the dissolved CO_2. The difference in dissolved CO_2 between cations in low salinity and anions in high salinity become small. Simulations of the two typical problems showed that groundwater chemical compositions have a significant effect on dissolved CO_2 in the two-phase region, but this effect is not obvious on the distribution of pressure and saturation, owing to the scale of the problem. The NaCl groundwater benefited from convective mixing and enhanced solubility trapping more than $CaCl_2$.

1. INTRODUCTION

In recent years, the recognition of climate change as a major global problem has increased. Several special reports from the Intergovernmental Panel on Climate Change (IPCC) suggest that the large emissions of greenhouse gases is one of the main factors in climate change, especially emissions of CO_2 (IPCC, 2005; IPCC, 2007). Researchers around the world now generally hold the view that reducing the emissions of greenhouse gas is very important for the mitigation of global climate change. Given the large amounts of groundwater with high total dissolved solids (TDS) (often >10,000mg/L), which cannot be used as sources of drinking water, and enough porous space, deep saline aquifers are being considered as possible sites for long-term, high-volume CO_2 storage..

Injecting supercritical CO_2 (called "gas" here for simplicity) into a deep saline aquifer will induce a series of complicated physical and chemical processes, including multiphase fluid and heat flow, water-rock reactions, geomechanical changes, and so on. The methods for knowing these processes primarily come down to experiments and numerical simulations. Numerical simulation, a relatively low-cost method for studying complex geological conditions within deep formations, is widely used to study CGS in deep saline aquifers. The TOUGH family of codes has often been used for this purpose (e.g., Pruess and Garcı´a, 2002; Pruess, 2003; Xu et al., 2004).

Injecting CO_2 into saline aquifers displaces the formation water and results in an increase in pressure. Some CO_2 dissolves in formation water as solubility trapping. The acidity of the formation water increases because of the dissolved CO_2 and enhances water-rock interaction, which transforms

CO_2 into carbonate minerals as mineral trapping. The difference in density between CO_2 and water drives the upward migration of CO_2 and large amounts of CO_2 accumulate beneath the low permeability rocks as hydrodynamic trapping. These coupled processes are affected by the geological and hydrogeological conditions, structure, temperature, pressure and so on, which makes the migration and transformation of CO_2 extremely complex. Accurate prediction of these processes thus requires a model that can reliably track and account for this complexity.

For various evaluations and predictions regarding CGS in deep saline formations, CO_2 dissolution is an important process, one which directly affects late mineral trapping and feeds back to early hydrodynamic trapping. The calculation of CO_2 solubility in TOUGH2/ECO2N is similar to (but not the same as) Spycher's mutual solubilities model, based on the equilibrium between gas and aqueous phases, and considers the effect of salinity (Spycher, et al., 2003; Spycher and Pruess 2005; Pruess, 2005). Although the groundwater chemical components of deep formations are mainly dominated by the ions of Na^+ and Cl^-, they also contain other ions such as Ca^{2+}, Mg^{2+}, K^+ and SO_4^{2-}. Therefore, the method in TOUGH2 ECO2N module that only considers the effect of Na^+ and Cl^- on CO_2 solubility is not broad enough. Based on Duan's CO_2 solubility model (Duan et al., 1992; Duan and Sun, 2003; Duan and Sun 2006) which considers different ionic effects, this paper incorporated Duan's model into the ECO2N module as an option for CO_2 solubility calculation, and then, using this modified code, analyzed the effects of groundwater chemical components on CGS in deep saline aquifers.

2. GOVERNING EQUATIONS AND NUMERICAL PROCEDURE

2.1. Mass and Energy Balance Equations

Based on mass and energy conservation, the characterization for CO_2-water-salt system can be expressed as (Pruess et al., 1999):

$$\frac{d}{dt}\int_{V_n} M^\kappa dV = \int_{\Gamma_n} \mathbf{F}^\kappa \bullet \mathbf{n} d\Gamma + \int_{V_n} q^\kappa dV \qquad (1)$$

The left accumulation term of mass and energy is given by (Pruess et al., 1999):

$$M^\kappa = \sum_{\beta=A,G} \phi S_\beta \rho_\beta X_\beta^\kappa, \quad \kappa = w, i, g \qquad (2)$$

$$M^{\kappa+1} = (1-\phi)\rho_R C_R T + \sum_{\beta=A,G} \phi S_\beta \rho_\beta u_\beta \qquad (3)$$

The right flux term of mass and energy follows Darcy's law and Fick's law such as (Pruess et al., 1999):

$$\mathbf{F}_\beta^\kappa = -k\frac{k_{r\beta}\rho_A}{\mu_\beta} X_\beta^\kappa (\nabla P_\beta - \rho_\beta \mathbf{g}) + \mathbf{J}_\beta^\kappa, \quad \kappa = w, i, g \qquad (4)$$

$$\mathbf{F}_\beta^{\kappa+1} = -\lambda \nabla T + \sum_\beta h_\beta F_\beta \qquad (5)$$

where M is mass or energy accumulation; $\mathbf{F}$ is flux of mass or energy; V is volume; Γ and n are surface and normal vector.; $\kappa = w, i, g$ are water, salt, and gas, respectively; $\kappa + 1$ is energy; ϕ is porosity; S is saturation; ρ is density; X is mass fraction; u is internal energy; C is specific heat; k and k_r are, respectively, permeability and relative permeability; P is pressure; T and t are temperature and time, respectively; $\mathbf{J}$ is the diffusion term; λ is thermal conductivity; h is specific enthalpy; and q is sink/source.

2.2. Space and Time Discretization

The discretization in space uses the integral finite difference (IFD) method. The discretization in time is implicit. Equation (1) can be discretized as (Pruess et al., 1999):

$$R_n^{\kappa,k+1} = M_n^{\kappa,k+1} - M_n^{\kappa,k} - \frac{\Delta t}{V_n}\left\{\sum_m A_{nm} F_{nm}^{\kappa,k+1} + V_n q_{nm}^{\kappa,k+1}\right\} = 0 \qquad (6)$$

where R and A are residuals and area, respectively. The nonlinearity of Equation (6) results in difficulty to be solved directly. Therefore, the Newton-Rapson iteration is employed. Jacobian matrixes are evaluated by numerical differentiation. The linear equations are solved by sparse direct matrix methods or iteratively by means of preconditioned conjugate gradients.

3. MUTUAL SOLUBILITIES MODEL OF CO_2 AND GROUNDWATER

3.1. TOUGH2/ECO2N's Mutual Solubilities Model

TOUGH2/ECO2N is based on Spycher's mutual solubilities model, which in turn is based on equilibrium between the aqueous and gas phases (Spycher, et al., 2003):

$$H_2O_{(l)} \Leftrightarrow H_2O_{(g)} \quad K_{H2O} = f_{H2O(g)}/a_{H2O(l)} \tag{7}$$

$$CO_{2(aq)} \Leftrightarrow CO_{2(g)} \quad K_{CO2(g)} = f_{CO2(g)}/a_{CO2(aq)} \tag{8}$$

Considering the effect of pressure and temperature on equilibrium constants, the mole fraction of gas and water in the different phases can be calculated as (Spycher, et al., 2003):

$$y_{H20} = \frac{K^0_{H20}(1 - x_{CO2})}{\phi_{H2O} P_{tot}} \exp\left(\frac{(P - P^0)\overline{V}_{H20}}{RT}\right) \tag{9}$$

$$x_{CO2} = \frac{\phi_{CO2}(1 - y_{H20})P_{tot}}{55.508 K^0_{CO2(g)}} \exp\left(-\frac{(P - P^0)\overline{V}_{CO2}}{RT}\right) \tag{10}$$

where K, f, and a are equilibrium constants, fugacities of the gas components, and the activity of components in the aqueous phase, respectively. y_{H20} and x_{CO2} are H_2O mole fraction in the gas and CO_2 mole fraction in the aqueous phase, respectively; ϕ is the fugacity coefficient. P_{tot} and P are total pressure and partial pressure. R is the gas constant, and T is temperature. The above model is extended to take into account the effect of salinity (including monovalent and divalent cations, Cl^- and SO_4^{2-}) by using activity coefficients (on a mole fraction scale) (Spycher and Pruess, 2005). However, in TOUGH2/ECO2N for CO_2 solubility calculation there exists some difference from Spycher's model because TOUGH2/ECO2N doesn't use the same equation of state for PVT property and only considers the effect of Na^+ and Cl^-.

3.2. Duan's CO_2 Solubility Model

The chemical potential of CO_2 in both the gas and liquid phase can be expressed, respectively, as (Duan and Sun, 2003):

$$\mu^{v}_{CO2}(T,P,y) = \mu^{v(0)}_{CO2}(T) + RT\ln(y_{CO2}P) + RT\ln\varphi_{CO2}(T,P,y) \tag{11}$$

$$\mu^{l}_{CO2}(T,P,m) = \mu^{l(0)}_{CO2}(T,P) + RT\ln m_{CO2} + RT\ln\gamma_{CO2}(T,P,m) \tag{12}$$

At equilibrium, $\mu^{v}_{CO2} = \mu^{l}_{CO2}$. According to these equations and applying a Pitzer-type model for calculating the activity of CO_2 in the liquid phase, the CO_2 solubility in aqueous solutions can be derived as follows (Duan and Sun, 2003):

$$\ln m_{CO2} = \ln(y_{CO2}P) - \frac{u^{l(0)}_{CO2}}{RT} + \ln\varphi_{CO2} - \sum_c 2\lambda_{CO2\text{-}c} m_c - \sum_a 2\lambda_{CO2\text{-}a} m_a - \sum_c\sum_a \varsigma_{CO2-c-a} m_c m_a \tag{13}$$

For certain groundwater components, CO_2 solubility can be expressed as (Duan and Sun, 2003):

$$\ln m_{CO2} = \ln(y_{CO2}P) - \frac{u^{l(0)}_{CO2}}{RT} + \ln\varphi_{CO2} - 2\lambda_{CO2-Na}(m_{Na} + m_k + 2m_{ca} + 2m_{Mg}) - \varsigma_{CO2-Na-Cl} m_{Cl}(m_{Na} + m_k + m_{ca} + m_{Mg}) + 0.07 m_{SO4} \tag{14}$$

The mole fraction of water in the gas phase is (Duan and Sun, 2003):

$$y_{CO2} = (P - P_{H2O})/P \tag{15}$$

where μ^{v}_{CO2} and μ^{l}_{CO2} are the chemical potential of CO_2 in the gas and liquid phases, respectively; $\mu^{v(0)}_{CO2}$ and $\mu^{l(0)}_{CO2}$ are chemical potentials of vapor and liquid CO_2, respectively; and y_{CO2} and m_{CO2} are mole fractions of CO_2 in the gas phase and molality of CO_2 in the liquid phase, respectively. φ and γ are fugacity and activity coefficients, respectively; P is total pressure and P_{H2O} is the vapor pressure of pure H_2O; λ and ς are Pitzer parameters, and m denotes the molality of the ion.

4. ANALYSIS OF CO_2 SOLUBILITY FOR DIFFERENT GROUNDWATER CHEMICAL COMPOSITIONS

The groundwater chemical components in deep saline aquifers are dominated by sodium chloride. However, in carbonate formations, the long-term dissolved carbonate minerals induce an increase of Ca^{2+} in groundwater, which typically makes the

water become of the Ca-Na-Cl type. Also, it contains some SO_4^{2-} due to dissolution of gypsum. Consequently, this paper uses two types of water, Na-Cl type and Ca-Na-Cl type, containing some SO_4^{2-}, to analyze the effects of different ions on the solubility of CO_2.

The effects that ions with the same charges (i.e. Na^+ and K^+) have on the solubility of CO_2 are difficult to evaluate. With this in mind, we consider the five factors to study such effects: the equivalent mole fraction of $(Na^+ + K^+)$ in cations, the equivalent mole fraction of Cl^- in anions , salinity, pressures and temperatures.

Differences between the original ECO2N's and Duan's models are evaluated at two sodium chloride concentrations: 0.0 M (molality) and 3.0 M. The results show that the difference in CO_2 solubility between the two models can be neglected when the temperature is high, but there is a difference when temperature is low (See Figure 1a and 1b). However, the prediction of mole fraction of H_2O in the gas phase shows significant differences (see Figure 1c and 1d) because Duan's model does not account for salt and other non-ideal mixing effects in the partitioning of water into CO_2.

Figure 2 and Figure 3 show that under the different temperatures, pressures, and salinity the dissolved CO_2 increases with the increase in equivalent mole fraction of $(Na^+ + K^+)$ compared to $(Ca^{2+} + Mg^{2+})$ and decreases with the increase in equivalent mole fraction of Cl^- compared to SO_4^{2-}. Low temperatures, high pressures, and low salinity contribute to an increase in the dissolved CO_2. However, the difference in dissolved CO_2 between cations in the low salinity and that between anions in the high salinity become small. (See Figure 2c and Figure 3c). The effects of Cl^- in the high salinity is different from that in the low salinity, with a slight increase as the equivalent mole fraction of Cl^- increases (See Figure 3c).

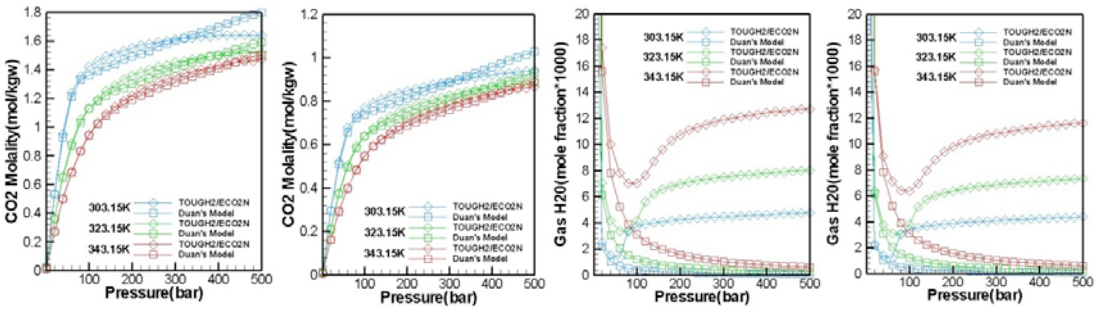

(a) CO_2 molality(0M NaCl) (b) CO_2 molality(3M NaCl) (c) H_2O mass fraction in the gas phase(0M) (d) H_2O mass fraction in the gas phase(3M)

Figure 1. Comparing Duan's model to the original ECO2N's model on CO_2-H_2O mutual solubility

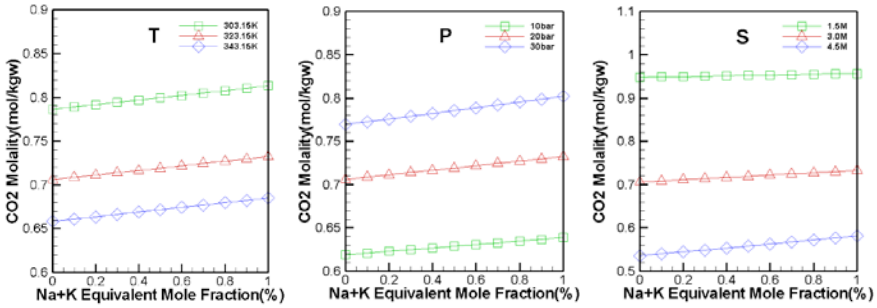

(a) Temperature (b) Pressure (c) Salinity

Figure 2. Effects of temperature, pressure and salinity at different Na^+ equivalent mole fraction on CO_2 solubility (Note that Na+K equivalent mole fraction is: $\frac{m(Na+K)}{m(Na+K)+2m(Ca+Mg)}$,(a) is at the pressure of 200bar and salinity of 1.5M (b) is at the temperature of 323.15K and salinity of 1.5M (c) is at the pressure of 200bar and temperature of 323.15K)

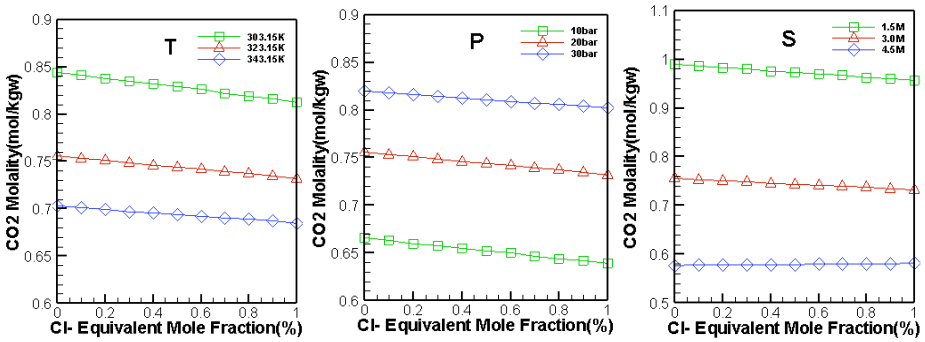

(a) Temperature (b) Pressure (c) Salinity

Figure 3. Effects of temperature, pressure and salinity at different Cl^- equivalent mole fraction on CO_2 solubility (Note that Cl^- equivalent mole fraction is: $\frac{m(Cl)}{m(Cl)+2mSO_4}$ (a),(b) and (c) are at the same conditions as Figure 2)

5. EFFECTS OF GROUNDWATER CHEMICAL COMPOSITIONS ON CGS

The effects of groundwater components are first demonstrated by solubility trapping. Two simple problems, including radial flow from a CO_2 injection well and convective mixing, are employed to investigate these effects.

5.1. Problem 1: Radial Flow from a CO_2 injection Well

The model used in this paper is similar to that of Pruess (Pruess, 2003), with a 100 m domain thickness aquifers at a depth of 1.2 km. Radial length is extended to the greater distance of 100 km. The number of gridblocks is 6000, with 1000 gridblocks for the first 1 km and 5000 gridblocks further away. The upper and lower boundaries of this model are assumed to be impermeable cap rock and bedrock, respectively, and the lateral boundary is constant. Table 1 lists the setup of groundwater components for this model. A CO_2 injection well fully penetrates the aquifer, under conditions of 120 bar pressure, 45°C temperature, and a salinity of 15% by weight. CO_2 is injected at a constant rate of 50 kg/s. The fluid flow is run for a period of 10,000 days (27.38 years).

Table 1. Setup for formation water chemical components (mol/kgw)

Case NO.	Na^++K^+	Ca^{2+}+Mg^{2+}	Cl^-	SO_4^{2-}
Base1	3.0	0.0	3.0	0.0
1	1.0	1.0	3.0	0.0
2	0.0	1.5	3.0	0.0
3	3.0	0.0	2.6	0.2

Note :because there is little CO_3^{2-} and HCO_3^-, this paper neglects them for this model.

Figures 4a, 4b, 5a, and 5b show that the impact of aqueous components on pressure and gas saturation is minimal. This is because the small differences in CO_2 solubility due to aqueous components at the large-field scale do not affect the time evolution and spatial distributions of pressure and gas saturation. However, the amount of dissolved CO_2 in the aqueous phase is affected by the aqueous components (See Figure 4c and 5c). It's obvious that Na^++K^+, SO_4^{2-} under this condition, are more helpful than Ca^{2+}+Mg^{2+} and Cl^- for solubility trapping, respectively. We also see that there is some difference between the TOUGH2 original ECO2N's and Duan's CO_2 solubility models.

5.2. Problem 2: Convective Mixing

When CO_2 is injected into a saline formation, most of the CO_2 accumulates beneath the impermeable cap rock. In the two-phase region, the density of the aqueous phase increases due to the dissolved CO_2, which can result in gravitational instability. The aqueous phase saturated with CO_2 will then migrate downward due to gravity, accompanied by an upward movement

of unsaturated water, giving rise to "convective mixing." A three-dimensional high-resolution model is used to study this phenomenon (Zhang et al., 2007). The density-driven convection can increase the transformation rate of CO_2 from gas phase to the other phase and is favored as the long-term fate of the gas in saline aquifers. Zhang et al. (2007, 2011) have investigated the effects of convective mixing on long-term CO_2 geological storage, considering brine salinity, initial CO_2 gas saturation, the molecular diffusivity of dissolved CO_2, mineralogical compositions, and geochemical reactions. We use the same 2-D model as Zhang et al. (2011) with 50 m height and 50 m width, to study the effects of water composition on convective mixing. The grids, initial and boundary condition are also the same as the study from Zhang et al. (2011). The other parameters are from Zhang et al. (2009). The water composition of the formation is the same as the Problem 1.

The density of aqueous with different components is calculated by converting to salt weight fraction for input into TOUGH2/ECO2N. Figure 6a, b, and c show that the effects of anions on spatial distribution of aqueous phase density. The comparative results indicate that Ca^{2+} and Mg^{2+} slow down the process of convective mixing because of the reduction in the dissolved CO_2, which induces the decrease in the difference of gravity. This finally results in a decrease in CO_2 dissolution rate (See Figure 7). Comparing Base Case 1 to Case 3 (see Figure 6a and d), we find that although the dissolved CO_2 in Case 3 is more than that in Base Case 1, the quantity of total dissolution trapping in Base Case 1 is higher than that in Case 3. This is because the initial density of aqueous in Case 3 is greater than that in Case 1. The increase in the percent of density in Case 3 is smaller than that in Base Case 1, which makes the convective mixing slow.

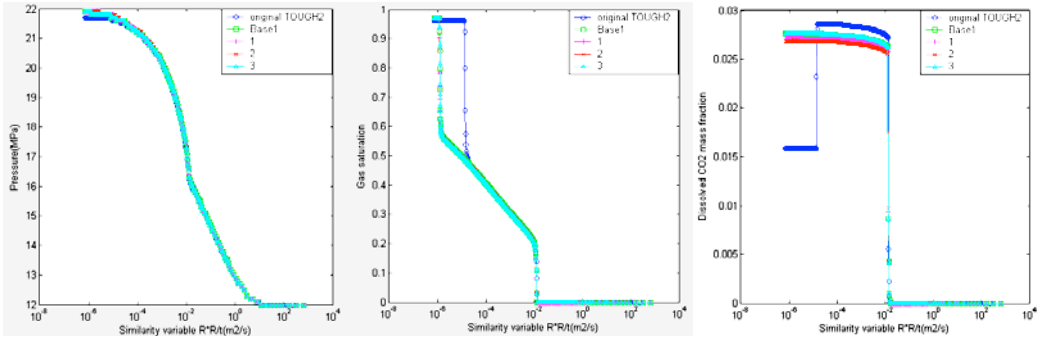

(a) Effects on pressure (b) Effects on gas saturation (c) Effects on dissolved CO_2

Figure 4. Time evolution for effects of groundwater aqueous components on pressure, gas saturation and dissolved CO_2 (x=25.25m)

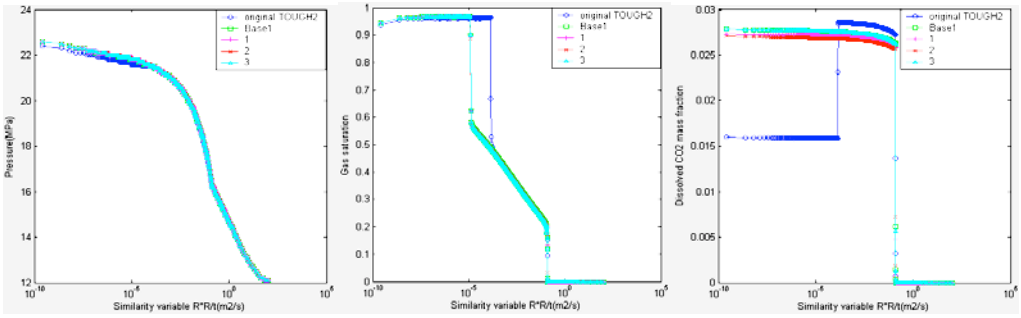

(a) Effects on pressure (b) Effects on gas saturation (c) Effects on dissolved CO_2

Figure 5. Spatial distribution for effects of groundwater aqueous components on pressure, gas saturation and dissolved CO_2 (t=27.38years)

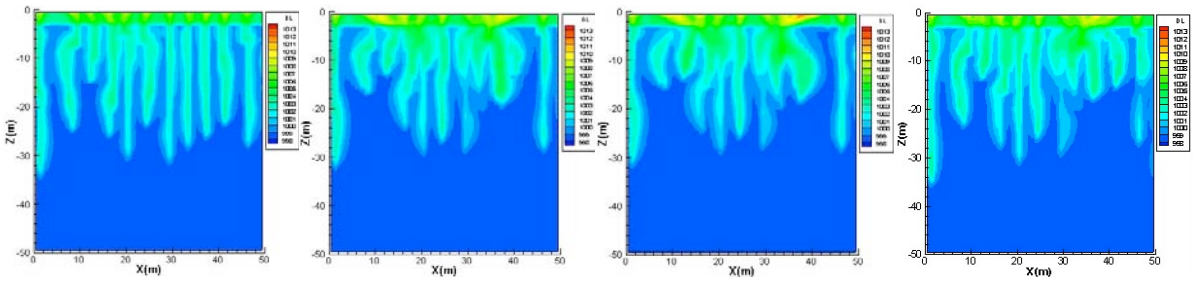

(a) Base1 (b) 1 (c) 2 (d) 3

Figure 6. Spatial distribution of aqueous phase density (unit is kg/L) after 150 years

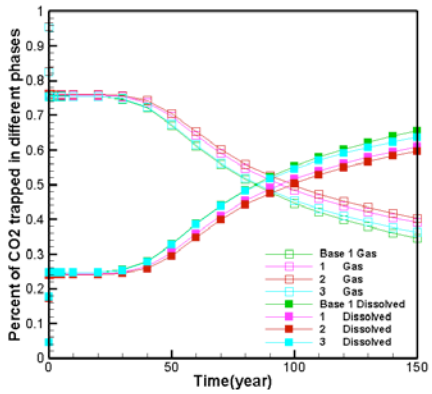

Figure 7. Time evolution of CO_2 trapped in gas and aqueous phases

6. CONCLUDING REMARKS

In comparing the two solubility models (Duan's and original TOUGH2/ECO2N's) using two example problems, we find that:

(1) The effects of different ions on CO_2 solubility are not the same, and we incorporate Duan's solubility model into TOUGH2/ECO2N as an option to consider the difference.

(2) An increase in salinity, the equivalent mole fraction of Ca^{2+}+Mg^{2+} compared to Na^{+}/K^{+}, and that of Cl^{-} compared to SO_4^{2-} under the low salinity, results in a decrease in CO_2 solubility. High pressures and low temperatures are helpful for CO_2 solubility.

(3) According to the two sample problems, the effects of groundwater composition on CO_2 geologic sequestration are mainly demonstrated by the dissolved CO_2. The pressure and gas saturation have no obvious response to differences in groundwater aqueous composition.

Our comparative study and simulation results are specific to the conditions and parameters considered. However, our study has also provided further detail on how groundwater composition affects CGS. Water-rock interaction plays an important role in CO_2 storage, and mineral dissolution could produce more ions affecting CO_2 solubility. This paper does not consider all these processes, making them a possible subject of future work.

ACKNOWLEDGMENT

This work was mainly supported by China Geological Survey project (Grant No. 1212011120048), public welfare industry special funds for scientific research from Ministry of Land and Resources of China (Grant No. 201211063), doctoral interdisciplinary scientific research project of Jilin University (No. 2012DC014), and graduate innovation fund of Jilin University (No. 20121069). This paper was also accomplished in collaboration with Lawrence Berkeley National Laboratory, which is supported by the zero emission research and technology project (ZERT), of the U.S. Department of Energy under Contract No. DE-AC02-05CH11231.

REFERENCES

Duan, Z.H., Moller, N., Greenberg, J., Weare, J.H., The prediction of methane solubility in natural waters to high ionic strength from 0 to 25°C and from 0 to 1600 bar, Geochim. Cosmochim. Acta, 56, 1451-1460, 1992.

Duan, Z.H., Sun, R., An improved model calculating CO_2 solubility in pure water and

aqueous NaCl solutions from 273 to 533K and from 0 to 2000 bar, Chemical Geology, 193, 257-271, 2003.

Duan, Z.H., Sun, R., An improved model for the calculation of CO_2 solubility in aqueous solutions containing Na^+, K^+, Ca^{2+}, Mg^{2+}, Cl^-, and SO_4^{2-}, Marine Chemistry , 98(2-4), 131-139, 2006.

IPCC, Carbon Dioxide Capture and Storage[R], Cambridge University Press, 2005.

IPCC (Intergovernmental Panel on Climate Change), Climate change 2007[R]: The physical science basis. Fourth assessment report, IPCC, Secretariat, Geneva, Switzerland, 2007.

Pruess, K., Curt, O., and George, M., TOUGH2 USER'S GUIDE, VERSION 2.0, Earth Science Division, Lawrence Berkeley National Laboratory, University of California, Berkeley, 1999.

Pruess, K. and Garcı´a, J., Multiphase flow dynamics during CO_2 disposal into saline aquifers, Environmental Geology, 42(2-3), 282-295, 2002.

Pruess, K., The TOUGH codes-A family of simulation tools for multiphase flow and transport processes in permeable media, Vadose Zone Journal, 3(3), 738-746, 2003.

Pruess, K., ECO2N: A TOUGH2 Fluid Property Module for Mixtures of Water, NaCl, and CO_2, Earth Science Division, Lawrence Berkeley National Laboratory, University of California, Berkeley, 2005.

Spycher, N., Pruess. K., and Ennis-King, J. , CO_2-H_20 mixtures in the geological sequestration for CO_2 Ⅰ.Assessment and calculation of mutual solubilities from 12 to 100 ℃ and up to 600 bar, Geochim.Cosmochim. Acta, 67(16), 3015-3031, 2003.

Spycher, N., Pruess, K., CO_2-H_20 mixtures in the geological sequestration for CO_2 Ⅱ .Partitioning in chloride brines at 12-100℃ and up to 600 bar, Geochim. Cosmochim. Acta, 69(13), 3309-3320, 2005.

Xu, T.F., Apps, J.A., and Pruess, K., Numerical simulation of CO_2 disposal by mineral trapping in deep aquifers, Applied Geochemistry, 19(6), 917-936, 2004.

Zhang, K.N., Doughty, C., Wu, Y.S., Pruess, K., Efficient parallel simulation of CO_2 geological sequestration in saline aquifers, In: SPE reservoir simulation symposium, SPE 106026, Houston, TX, 26-28 February, 2007.

Zhang, W., Li, Y.L., Omambia, A.N., Reactive transport modeling of effects of convective mixing on long-term CO_2 geological storage in deep saline formations, International Journal of Greenhouse Gas Control , 5, 241-256, 2011.

Zhang, W., Li, Y.L., Xu, T..F, Cheng, H., Zheng, Y., Xiong, P., Long-term variations of trapped in different mechanisms in deep saline formations: a case study of Songliao Basin, China, International Journal of Greenhouse Gas Control, 3, 161-180, 2009.

THE INFLUENCE OF CAPILLARY ENTRY-PRESSURE REPRESENTATION ON THE RATE OF CO_2 SOLUBILITY TRAPPING

Boxiao Li, Hamdi A. Tchelepi, and Sally M. Benson

Department of Energy Resources Engineering, Stanford University
367 Panama St, Rm 65, Stanford, CA, 94305, USA
e-mail: boxiaoli@stanford.edu

ABSTRACT

The typical shape of a capillary pressure (P_c) curve is either convex (e.g., Brooks-Corey model) or S-shaped (e.g., van Genuchten model). The Brooks-Corey-type (BC-type) model uses a plateau that ends with a nonzero capillary entry pressure, while the van Genuchten-type (VG-type) model uses a steep slope that connects the end-point (usually zero) to the plateau region. If the slope is steep enough, the two models yield similar simulation results when CO_2 dissolution is not modeled. However, we show that the VG-type model accelerates CO_2 solubility trapping significantly, even when the slope is steep. For long times, the amount of dissolved CO_2 when a VG-type model is used can be twice as large as that obtained when a BC-type model is used.

INTRODUCTION

The dissolution of the CO_2 in the formation water, also known as CO_2 solubility trapping, is an important CO_2 trapping mechanism in the post-injection period of CO_2 sequestration (CCS) in deep aquifers. Modeling solubility trapping requires accurate description of CO_2 plume migration and saturation distribution. Capillary pressure (P_c) is one of the major driving forces of fluid migration in CCS, especially during the post-injection period. Therefore, an accurate representation of the P_c is crucial for modeling solubility trapping, and hence long-term CCS.

Usually, a P_c curve is either S-shaped (e.g., van Genuchten model) or convex (e.g., Brooks-Corey model), as illustrated in Figures 1(a) and (b) (Brooks and Corey, 1964; van Genuchten, 1980). The two models represent the entry of the nonwetting phase into the porous medium differently. While the Brooks-Corey model uses a plateau that ends with a nonzero capillary entry pressure, the van Genuchten model uses a steep slope that connects the end-point (usually zero) to the plateau region. We name the region around the end-point in VG-type models the "entry slope" region. The height of this region is the pressure difference between the plateau and the end-point, and its width is given bya "threshold" nonwetting-phase saturation, S_{nt}, as illustrated in Figure 1(a). We refer to the entry-pressure representation in Figure 1(a) as a "van-Genuchten-type" (VG-type), and that in Figure 1(b) as a "Brooks-Corey-type" (BC-type). Note that in the VG-type model, the $P_c(S_w = 1)$ can be zero as in Figure 1(a), or nonzero.

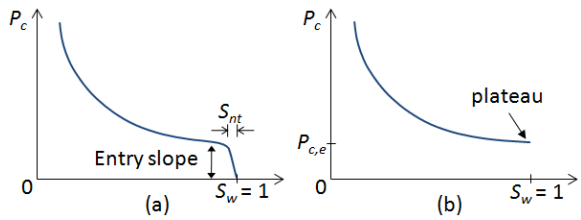

Figure 1. Capillary entry-pressure representations: (a) van-Genuchten-type (VG-type) representation; (b) Brooks-Corey-type (BC-type) representation.

The capillary pressure curves measured in the laboratory using mercury porosimetry usually have an "entry slope" region similar to Figure 1(a), though $P_c(S_w = 1)$ is usually nonzero. There has been wide discussion in the literature on the physical meaning and importance of the entry slope (Schowalter, 1979; Katz and Thompson, 1986; Nabawy et al., 2009). A consensus, however, has not been reached about whether the entry slope should be ignored or honored when interpreting the measurement results. Ignoring the entry slope amounts to applying a BC-type representation, while preserving it amounts to a VG-type representation.

We will show in this work that the representation of the capillary entry pressure can

affect the rate of CO_2 solubility trapping significantly, even when the S_{nt} is very small. Many authors have simulated CCS and performed sensitivity analysis (Ennis-King and Paterson, 2002; Doughty and Pruess, 2004; Pruess and Nordbotten, 2011; Class et al., 2009; Kumar et al., 2005). To our knowledge, the sensitivity of solubility trapping to the representation of the entry pressure (i.e., VG-type versus BC-type curves) has not been investigated. We note that the van Genuchten model has been almost exclusively used in the simulations performed by TOUGH2, a simulator widely used in modeling CCS (Pruess et al. 1999), although several capillary pressure options are available therein. Analytical approaches and high-resolution simulations have been used to model the density-driven convective mixing, which is an important process in solubility trapping (Ennis-King and Paterson, 2005; Riaz et al., 2006; Pruess and Zhang, 2008; Pau et al., 2010; Neufeld et al., 2010). To our knowledge, in most of these and related works, P_c is neglected. Here, we study the impact of the capillary pressure on solubility trapping, with particular emphasis on the representation of the entry-pressure region.

SIMULATION MODEL DESCRIPTION

The aquifer model used in this study is a 2D vertical cross section (x and z directions) of the model proposed by Dahle et al. (2009), which is used as a benchmark for long-term CCS simulations. The 2D model is illustrated in Figure 2, where the size of the aquifer and the location of the injection well are also marked. The aquifer has a dip of 1%, and is deep enough such that the injected CO_2 is in supercritical phase, which is immiscible with the resident water. The top and bottom boundaries are no-flow boundaries. The initial *in situ* pressures at the left and right boundaries are held constant throughout the entire simulation period. Grid size is shown in Table 1. The drainage relative permeability (k_{ri}, $i = w, n$) and P_c curves provided in the benchmark model are used here:

$$k_{rw} = (S_w^*)^4,\ k_{rn} = 0.4[1-(\hat{S}_w)^2](1-\hat{S}_w)^2, \quad (1a)$$

$$S_w^* = (S_w - S_{wi})/(1-S_{wi}),\ S_{wi} = 0.2, \quad (1b)$$

$$\hat{S}_w = (S_w - S_{wi})/(1-S_{wi}-S_{nc}),\ S_{nc} = 0. \quad (1c)$$

$$P_c = P_{c,e}(S_w^*)^{-0.5},\ P_{c,e} = 0.2 \text{ bar}. \quad (2)$$

Subscripts w and n denote the wetting (water) and nonwetting (CO_2) phases, respectively. The capillary pressure curve is BC-type, with irreducible water saturation (S_{wi}) as 0.2 and capillary entry pressure ($P_{c,e}$) 0.2 bar. Notice that the critical gas saturation (S_{nc}) in the relative permeability curves is assumed to be zero. Rock properties, salinity, and the depth of the injection well are the same as those in the benchmark model, which are summarized in Table 1.

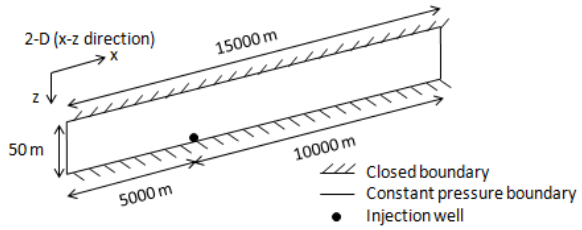

Figure 2. Sketch of the aquifer model.

Table 1: Properties of the aquifer model.

Name	Value
Grid number	$N_x = 150$, $N_y = 1$, $N_z = 40$
Gridblock size	$d_x = d_y = 100$ m, $d_z = 1.25$ m
Permeability	$k_x = k_y = k_z = 100$ md
Porosity	$\phi = 0.15$
Depth at the well	3025 m
Temperature	84.4 ℃
Salinity	0

The aquifer is initially fully saturated with water under hydrostatic equilibrium. Pure CO_2 is injected from the well at a rate of 9000 metric tons per year. The injection lasts for 20 years before the well is shut. The simulated time period is 5000 years. All the simulations in this study were performed using an Equation of State (EOS) based compositional simulator, namely, the Stanford General Purpose Research Simulator (GPRS) (Cao, 2002; Jiang, 2007). We did not use TOUGH2 due to difficulties in using different entry-pressure representations for the capillary pressure curves. Detailed EOS tuning parameters for CO_2-water system can be found in Kumar (2004). The Fully Implicit Method (FIM) was used in all the simulations. All the simulations shown here do not account for hysteresis in either capillary pressure or relative permeability curves. We have performed simulations accounting for hysteresis, and have confirmed that our conclusions will not be altered.

SIMULATION RESULTS

Base Case

The base-case simulation uses the VG-type representation (Figure 1a) to modify the P_c curve (Equation 2). Thus, the Brooks-Corey curve is turned into an S-shape curve with $P_c(S_w = 1)$ of zero. The S_{nt} is set as 0.005.

Figure 3 illustrates the distributions of the CO_2 saturation (S_n) and the mole fraction of CO_2 in the aqueous phase (x_{CO2}) over time. Because it is lighter than water, the injected supercritical CO_2 rises to the top of the aquifer and migrates upward and to the right (the dip is not shown in the figure). As CO_2 dissolves into the water, the plume gets thinner and completely disappears, eventually. The density of the brine increases as more CO_2 dissolves in it. This ultimately leads to the heavier water sinking downward and displacing the lighter CO_2-free water. Such displacement is unstable, which results in the fingering distribution of the x_{CO2}.

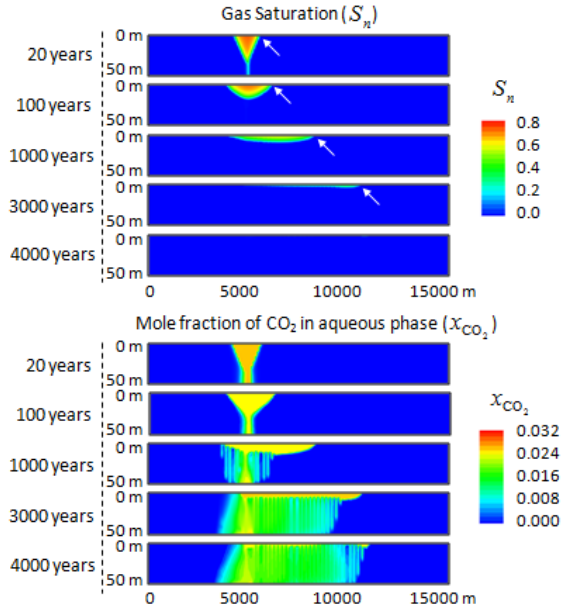

Figure 3. Base-case simulation results: S_n and x_{CO2} distributions over time. The white arrows indicate the locations of the plume tip. Hysteresis is not simulated for simplicity.

Different Entry-Pressure Representations

Keeping all other parameters unchanged, we conduct simulations using different representations of the capillary entry pressure, as shown in Figure 4. The curve labeled 'BC-type' is the original Equation 2. The curves 'S_{nt} = 0.005' and 'S_{nt} = 0.0005' apply the 'VG-type representation' based on Equation 2 with their corresponding S_{nt} values. The "Silin" curve is a P_c model from Equation A.1 of Silin et al. (2009), where the fitting parameters $A = B = 0.2$ bar, $\lambda_1 = 0.5$, and $\lambda_2 = 9$. This model is similar to the van Genuchten model, but it has a steeper "entry slope." All four curves in Figure 4 are similar, except for the small difference near $S_w = 1$. We have also confirmed that the capillary "diffusion" terms for the four cases, defined as

$$D = \frac{\lambda_w \lambda_n}{\lambda_w + \lambda_n} \left| \frac{dP_c}{dS_w} \right|$$

(the phase mobility $\lambda_i = k_{ri} / \mu_i$, $i = w, n$), are bounded. Severe numerical difficulties would occur if D were not bounded.

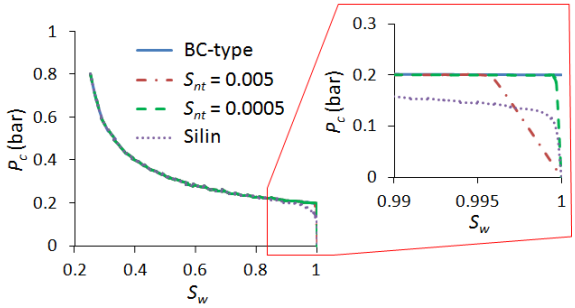

Figure 4. Different representations of the capillary entry pressure.

These apparently small differences in the P_c curves lead to very large differences in the long-term predictions. Figures 5(a) and (b) plot the travel distance of the plume tip and the plume volume for different times. While the "S_{nt} = 0.005" case suggests complete dissolution of the CO_2 plume occurring at about 4000 years, only half of the injected CO_2 has dissolved for the "BC-type" case. In addition, the simulation results are sensitive to the steepness of the 'entry slope'. The plume disappearance is fastest for the Silin case, and slowest for the BC-type case. Such strong sensitivity of the long-term simulation results to the capillary entry-pressure representation is also observed using other industrial reservoir simulators. We note that the sensitivity is not obvious during the injection period, but will intensify and become quite important in the long-term post-injection period.

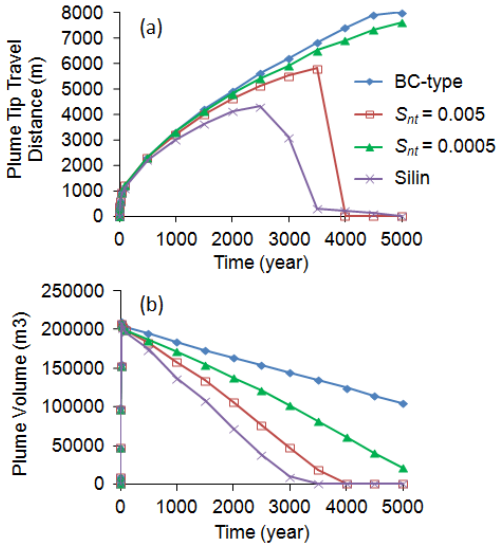

Figure 5. The sensitivity of simulation results to different entry-pressure representations: (a) Distance that plume tip traveled vs. time; (b) Plume volume vs. time.

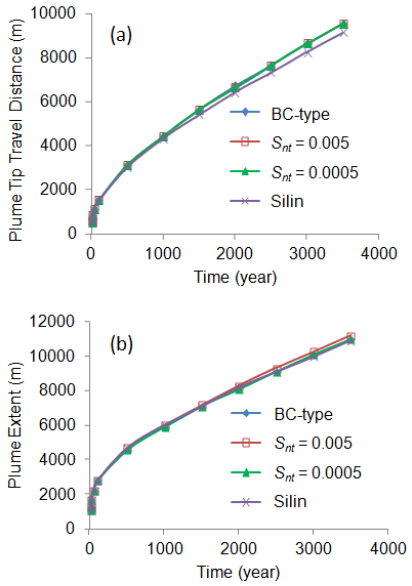

Figure 6. Simulation results for different capillary entry-pressure representations when dissolution is not modeled: (a) Distance that plume tip traveled vs. time; (b) Plume extent vs. time.

Note that although differences in the fluid pressure due to using different capillary entry-pressure representations are present, such differences (0.2 bar at most) are negligible compared with the overall fluid pressure level (about 300 bar), and they are very unlikely to affect the thermodynamic properties of the CO_2 and water, including CO_2 solubility in water.

Note that such sensitivity to the entry-pressure representation is not observed when dissolution is not modeled. Figures 6(a) and (b) show the travel distance and the extent (measured from tail to tip) of the CO_2 plume, if CO_2 is not allowed to dissolve in water. The simulation is terminated when the CO_2 plume reaches the right boundary. As illustrated by the figures, the capillary entry-pressure representation has almost no impact on the results when dissolution is not modeled.

DISCUSSION

Gravity-Capillary-Equilibrium

Due to buoyancy, the injected CO_2 flows towards the top of the porous formation, and accumulates beneath the impermeable cap rock. The column height of the CO_2 plume and the saturation within the plume depend on the interaction between buoyancy and capillary forces. The pressures of the CO_2 and water and P_c can be written as:

$$P_w(z) = P_w|_{z=h_c} - \rho_w g(h_c - z), \quad (3a)$$

$$P_n(z) = P_n|_{z=h_c} - \rho_n g(h_c - z), \quad (3b)$$

$$P_c(z) = P_n(z) - P_w(z), \quad (3c)$$

where z is the depth measured positive downward from the top of the storage formation, and h_c is the column height. Knowing $P_c(z)$ from Equation 3 and the capillary-pressure-saturation relationship, we can compute the CO_2 saturation distribution in the plume column under gravity-capillary-equilibrium analytically as a function of depth, if the total amount of CO_2 in the plume column, $V = \int_0^{h_c} S_n(z)\mathrm{d}z$, is given.

Analytical results and high-resolution numerical simulations were performed using different representations of the capillary entry pressure. Two P_c curves, namely, the 'S_{nt} = 0.005' and the 'BC-type' cases in Figure 4, are compared. The CO_2 and water densities are ρ_n = 727 kg/m^3 and ρ_w = 982 kg/m^3, and the viscosities are μ_n = 0.070 cP and μ_w = 0.342 cP, respectively, all evaluated at the formation pressure and temperature described earlier. The total amount of CO_2 in the plume column, V, is fixed as 0.64 m. The simulation domain is a 1D vertical column of 50 m, with each gridclock being 5

mm in size, for which numerical diffusion effects are negligible. The permeability k_z is 100 md, the porosity is 0.15, and the relative permeability curves are defined in Equation 1. The top boundary is impermeable, and the initial *in situ* pressure at the bottom boundary is held constant throughout the simulation. Initially, the CO_2 saturation at the top 0.8 m of the domain is $S_n = 1 - S_{wi} = 0.8$ (such that $V = 0.64$ m), below which $S_n = 0$. This corresponds to the sharp-interface assumption that ignores capillary pressure. Since P_c is considered here, the CO_2 column height is expected to expand from the initial condition. The simulation stops when gravity-capillary-equilibrium is reached.

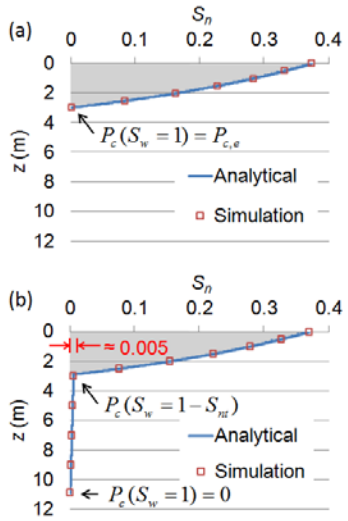

Figure 7. CO_2 saturation distribution within the plume column under gravity-capillary-equilibrium: (a) 'BC-type' case; (b) 'S_{nt} = 0.005' case. The shaded area is the major body of the CO_2 plume.

The CO_2 saturation distributions under gravity-capillary-equilibrium for the two entry-pressure representations are shown in Figure 7. The analytical and numerical solutions agree perfectly (dissolution is not considered here). While the column height of the BC-type case is 2.96 m, the column height of the 'S_{nt} = 0.005' case is 10.91 m. The additional column height is composed of very little CO_2 saturation, because S_{nt} is only 0.005. For simplicity, hereafter we refer to such additional and low-CO_2-saturation column height as a "saturation tail." This tail only occurs when the P_c curve applies the VG-type representation. When S_{nt} is small, the length of the saturation tail can be approximated by:

$$h_c^{VG} - h_c^{BC} \approx [P_c^{BC}|_{S_w=1} - P_c^{VG}|_{S_w=1}]/[(\rho_w - \rho_n)g], \quad (4)$$

where the superscripts BC denotes BC-type representation, and VG denotes VG-type representation. If $P_c(S_w = 1)$ for the VG-type representation is zero, which is the case in previous examples, the right hand side of Equation 4 becomes $P_c^{BC}|_{S_w=1}/[(\rho_w - \rho_n)g]$.

As long as the major CO_2 body has enough CO_2 to supply the saturation tail, the length of the tail is not influenced by the thickness of the major body. Because the tail is composed of very little saturation, it can form even if the major body of the CO_2 plume is thin. The tail is longer when the density contrast between water and supercritical CO_2 is low, which is usually the case in deep storage formations. The influence of the tail becomes increasingly evident as the CO_2 plume migrates under the cap rock and becomes stretched and thinner with time. We reiterate that the saturation tail is not an artifact of numerical diffusion—it is corroborated by analytical calculation and fine-grid simulation. Although the total column heights for the two cases are dramatically different, the CO_2 saturation in the saturation tail is so small that it almost makes no impact in simulations that do not account for dissolution, and it does not affect the extent and the migration speed of the CO_2 plume. Figure 6 illustrates this point.

However, for long-term CCS simulations, where CO_2 dissolution is included, the CO_2 delivered to the long saturation tail will quickly dissolve in water. The tendency toward gravity-capillary-equilibrium keeps delivering CO_2 to sustain the tail, until the water surrounding the tail is fully saturated by the dissolved CO_2. Figure 8 illustrates the evolution of the CO_2 column height subject to dissolution. The CO_2 solubility (expressed as mole fraction, x_{CO2}) is 0.0254. All other properties, model grid, and the boundary conditions are unchanged. The initial condition is the same sharp-interface condition as earlier, where the water in the initial two-phase region is fully saturated with dissolved CO_2. The amount of the dissolved CO_2 is characterized by the parameter $X = \int_0^{h_c} x_{CO_2}(z)\mathrm{d}z$. As indicated in Figure 8, the growth of the saturation tail is hindered by CO_2 dissolution, but the tendency is

to keep transferring CO_2 from the major CO_2 body to the underlying water, causing more CO_2 to be dissolved. Eventually, the amounts of dissolved CO_2 for the two cases become significantly different. So far, all of the simulations covered in this section have been in 1D, where the convective mixing of CO_2 and water—a multidimensional process—is suppressed. Discussion on convective mixing is covered in the next subsection.

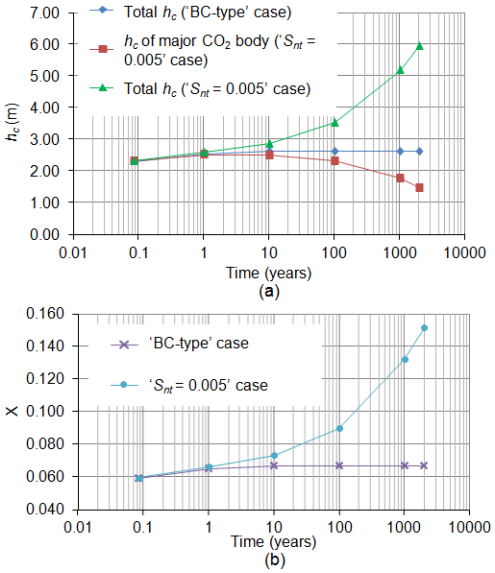

Figure 8. Development of the capillary transition zone for different entry-pressure representations (dissolution is modeled): (a) column height (h_c); (b) amount of dissolved CO_2 (X).

The saturation tail is essentially part of the capillary transition zone. The characteristic time scale for the development of the transition zone can be derived as (Nordbotten and Dahle, 2008):

$$t^* = \frac{\phi}{k_z(\Delta\rho g)^2}\left(\frac{1}{\lambda_w}+\frac{1}{\lambda_n}\right)^*\left(\frac{\mathrm{d}P_c}{\mathrm{d}S_w}\right)^*, \qquad (5)$$

where the superscript * denotes characteristic values. As indicated by Equation 5, the lower the density contrast between water and CO_2, the longer the time for the transition zone, and hence the saturation tail, to develop—but eventually the tail length will be larger (also see Equation 4). In addition, large vertical permeability of the storage formation and large CO_2 mobility facilitate the development of the 'saturation tail'. An important element in the CO_2 relative permeability curve is the critical CO_2 saturation (S_{nc}, see Equation 1). It is defined as the minimum CO_2 saturation that allows the CO_2 to flow in the porous medium for a drainage process. The CO_2 is mobile only if its saturation is above S_{nc}. If S_{nc} is larger than S_{nt} (width of the 'entry slope', see Figure 1a), the saturation tail will not form, due to zero mobility of the CO_2. However, laboratory measurements of CO_2-water drainage relative permeability curves suggest that S_{nc} can be close to zero (Bennion and Bachu, 2006; Perrin and Benson, 2008). It is difficult, in practice, to measure the S_{nc} in a typical core flood experiment accurately. More importantly, the CO_2 relative permeability at $S_n = S_{nt} = 0.005$ is only $O(10^{-7})$ (as calculated from Equation 1) in the simulations described above, where $S_{nc} = 0$. However, even with very low CO_2 mobility, the saturation tail can still grow and influence long-term simulation results dramatically. Therefore, when the VG-type representation is applied to the P_c curve, the simulation result is very sensitive to the value of S_{nc}.

Density-Driven Convection

In multiple dimensions, convective mixing of the heavier CO_2-rich and the lighter CO_2-free water is expected to take place, and the mixing behavior can be influenced by the presence or absence of a saturation tail.

Although many authors have analyzed and modeled the convective mixing problem (Ennis-King and Paterson, 2005; Riaz et al., 2006; Pruess and Zhang, 2008; Pau et al., 2010; Neufeld et al., 2010), to our knowledge, P_c is neglected in most of these and related works. This simplification allows one to analyze or simulate only the single-phase (CO_2-rich and CO_2 free water) region. However, in many cases, the capillary transition zone cannot be ignored, and the two-phase behavior must be carefully studied.

Here, fine-grid, 2D, two-phase numerical simulations were performed to investigate the effect of the entry-pressure representation. The porous medium is 10 m × 50 m in the x and z directions, and each gridblock is 0.1 m × 0.2 m. All the properties, initial conditions, and top and bottom boundary conditions are the same as the simulations that produce Figure 8. The left and right boundaries are periodic, which amounts to

rolling up the domain about a vertical axis and connecting the left boundary to the right. Different entry-pressure representations are employed based on Equation 2. The simulation results are compared in Figure 9, which shows the development of convective fingers after 10 years. The VG-type representation clearly yields more CO_2 dissolution than the BC-type representation. Figure 9 is produced using a first-order two-phase simulator, and it provides merely a rough qualitative comparison. However, this is adequate to demonstrate the importance of the entry-pressure representation on convective mixing. In addition, results from many other such simulations we have performed support our observations. Performing high-order multiphase simulations is exceptionally challenging, and to our knowledge, all of the high-order simulations in the literature that model the convective mixing are for miscible single-phase flow.

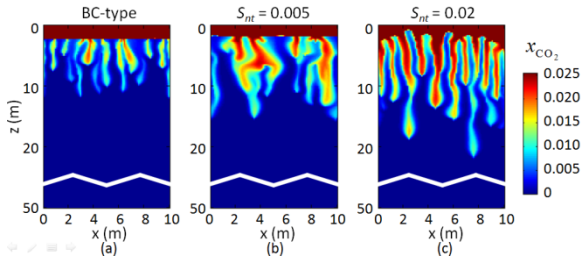

Figure 9. Impact of different entry-pressure representations: (a) BC-type representation; (b) VG-type representation, S_{nt} = 0.005; (c) VG-type representation, S_{nt} = 0.02.

CONCLUDING REMARKS

The typical shape of a capillary pressure curve is either convex (e.g., Brooks-Corey model) or S-shaped (e.g., van Genuchten model). Both models are widely used in simulating long-term CCS. The Brooks-Corey-type (BC-type) model uses a plateau to represent the nonwetting-phase entry into the porous medium, while the van-Genuchten-type (VG-type) model uses an entry slope, which connects the end-point to the plateau region. In this paper, we simulate long-term CCS using these two representations of the capillary entry pressure, and we assign a steep entry slope to the VG-type model to reduce the difference between the two representations. Although the two entry-pressure representations produce similar results when CO_2 dissolution is ignored, the simulation results are dramatically different in the long-term post-injection period if dissolution is modeled. The entry slope of the VG-type capillary pressure curve tends to create a longer CO_2 column height due to the interactions of gravity and capillary forces. High-resolution simulations have confirmed that this is not a numerical artifact. The additional column height consists of very small CO_2 saturation, which can dissolve quickly into the surrounding water. The tendency toward gravity-capillary-equilibrium keeps transferring more CO_2 from the major CO_2 plume body to the underlying water through this additional column height. Density-driven convection then carries the CO_2-rich water away and brings CO_2-free water close by, causing more CO_2 to dissolve. This vertical mass-transfer mechanism introduced by the VG-type representation causes faster CO_2 dissolution compared with the BC-type representation. This is especially the case in deep storage formations where the density contrast between water and CO_2 is low, and in formations that have large vertical permeabilities and small critical CO_2 saturation (S_{nc}) values.

Capillary pressure curves measured in the laboratory tend to have an entry slope region. Consensus has not been reached regarding the importance of this entry slope region. Careful measurements, preferably on core or larger scale, are needed to study this issue. Note that the intention of this work is not to argue whether such entry slope is real in natural systems. The intention is, rather, to point out that the VG-type capillary pressure model, which is widely used in modeling long-term CCS, will cause accelerated CO_2 dissolution, compared with the BC-type model. This has not been reported in the literature. We should also note that the VG-type representation brings several challenges in modeling long-term CCS. First, the simulation results are more sensitive to the steepness of the entry slope and to the S_{nc} value. The S_{nc} can be very small for a CO_2-water system and can be difficult to measure accurately from experiments. Second, the steepness and the curvature introduced by the entry slope challenge the nonlinear solver of the simulator, making the computation highly inefficient. Using a convex capillary pressure model such as a Brooks-Corey model, is computationally

straightforward, and leads to conservative estimates for the amount of CO_2 solubility trapping.

ACKNOWLEDGMENT

The authors acknowledge Dr. Gary Li and Dr. Yaqing Fan for their helpful discussions.

REFERENCES

[1] Brooks, R.H. and A.T. Corey, *Hydraulic Properties of Porous Media*, Colorado State University, Fort Collins, Colo., 1964.

[2] van Genuchten, M.T., A Closed-form Equation for Predicting the Hydraulic Conductivity of Unsaturated Soils, *Soil Sci. Soc. Am. J.*, *44*(5), 892-898, 1980.

[3] Schowalter, T.T., Mechanics of Secondary Hydrocarbon Migration and Entrapment, *AAPG Bulletin*, *63*(5), 1979.

[4] Katz, A.J. and A.H. Thompson, Quantitative Prediction of Permeability in Porous Rock, *Phys. Rev. B*, *34*(11): 8179-8181, 1986.

[5] Nabawy, B.S., et al., Pore-Throat Characterization in Highly Porous and Permeable Sandstones." *AAPG Bulletin*, *93*(6): 719-739, 2009.

[6] Ennis-King, J. and L. Paterson, Engineering Aspects of Geological Sequestration of Carbon Dioxide, SPE Asia Pacific Oil and Gas Conference and Exhibition, Melbourne, Australia, 2002.

[7] Doughty, C. and K. Pruess, Modeling Supercritical Carbon Dioxide Injection in Heterogeneous Porous Media, *Vadose Zone J.*, *3*(3), 837-847, 2004.

[8] Pruess, K. and J. Nordbotten, Numerical Simulation Studies of the Long-term Evolution of a CO_2 Plume in a Saline Aquifer with a Sloping Caprock, *Transp. Porous Med.*, *90*(1), 135-151, 2011.

[9] Class, H., et al., A benchmark study on problems related to CO_2 storage in geologic formations. *Comput. Geosci.*, *13*(4), 409-434, 2009.

[10] Kumar, A., et al., Reservoir Simulation of CO_2 Storage in Deep Saline Aquifers. *SPE J.*, *10*(3), 336-348, 2005.

[11] Pruess, K., C. Oldenburg, and G. Moridis, *TOUGH2 User's Guide, Version 2.0*, Report LBNL-43134, Lawrence Berkeley National Laboratory, Berkeley, Calif., 1999.

[12] Ennis-King, J. and L. Paterson, Role of Convective Mixing in the Long-Term Storage of Carbon Dioxide in Deep Saline Formations, *SPE J.*, *10*(3): 349-356, 2005.

[13] Riaz, A., et al., Onset of Convection in a Gravitationally Unstable Diffusive Boundary Layer in Porous Media, *J. Fluid Mech.*, 548, 87-111, 2006.

[14] Pruess, K. and K. Zhang, Numerical Modeling Studies of the Dissolution-Diffusion-Convection Process During CO_2 Storage in Saline Aquifers, Lawrence Berkeley National Laboratory Report, 2008.

[15] Pau, G.S.H., et al., High-Resolution Simulation and Characterization of Density-Driven Flow in CO_2 Storage in Saline Aquifers, *Adv. Water Resour.*, *33*(4), 443-455, 2010.

[16] Neufeld, J.A., et al., Convective Dissolution of Carbon Dioxide in Saline Aquifers, *Geophys. Res. Lett.*, *37*(22), L22404, 2010.

[17] Dahle, H.K., et al. A Model-Oriented Benchmark Problem for CO_2 Storage, 2009; http://org.uib.no/cipr/Workshop/2009/CO2/benchmark_definition.pdf.

[18] Cao, H., *Development of Techniques for General Purpose Simulators*, Ph.D. Thesis, Stanford University, 2002.

[19] Jiang Y., *Techniques for Modeling Complex Reservoirs and Advanced Wells*, Ph.D. Thesis, Stanford University, 2007.

[20] Kumar, A., *A Simulation Study of Carbon Sequestration in Deep Saline Aquifers*, M.S. Thesis, University of Texas at Austin, 2004.

[21] Nordbotten, J. M. and H.K. Dahle, Impact of the Capillary Fringe in Vertically Integrated Models for CO_2 Storage, *Water Resour. Res.*, *47*(2), W02537, 2011.

[22] Bennion, D.B. and S. Bachu, Dependence on Temperature, Pressure, and Salinity of the IFT and Relative Permeability Displacement Characteristics of CO_2 Injected in Deep Saline Aquifers. SPE Annual Technical Conference and Exhibition. San Antonio, Texas, USA, 2006.

[23] Perrin J.C. and S.M. Benson, Relative Permeability Explorer, Benson Lab, Stanford University, 2008. http://pangea.stanford.edu/research/bensonlab/relperm/index.html.

SIMULATION OF CO_2 STORAGE IN COAL SEAMS: COUPLING OF TOUGH2 WITH THE SOLVER FOR MECHANICS CODE_ASTER®

A. Loschetter[1], F. Smai[1], S. Sy[1], A.Burnol[1], A. Leynet[1], S. Lafortune[2] and A. Thoraval[2]
[1]French Geological Survey (BRGM)
BP 6009 45060 Orléans, France
e-mail: a.loschetter@brgm.fr
[2]French National Institute for Industrial Environment and Risks (INERIS)
BP 2, 60550 Verneuil-en-Halatte, France

ABSTRACT

Amongst the various geological storage options currently under consideration, CO_2 storage in coal formations presents the most economic potential for middle-term spreading but also the most uncertainties and technical difficulties. Indeed, the profit from methane recovery could cover part of the costs, but little testing for this technique has been conducted in European coal deposits. Therefore, there is a need for an in situ injection study at an intermediate scale between a laboratory and an industrial pilot. This is the aim of the CARBOLAB project.

This study investigates coupled flow and mechanical processes that will take place around the injection point at the bottom of the Montsacro mine in Asturias, Spain. Reservoir simulators, such as TOUGH2, have been used for CO_2 storage in saline aquifers and oil and gas reservoirs (Oldenburg et al., 2004; Xu and Pruess, 2001). However, until now, this tool did not represent the adsorption process, a key point for explaining the gas storage and gas migration through coal seams. Moreover, CO_2 sorption and exchange with adsorbed CH_4 are associated with mechanical processes like swelling/shrinkage. In order to quantify the strain and stress fields due to changes in the fluid pressure field and to account for stress/sorption dependent porosity/ permeability effects, an efficient coupling between TOUGH2/EOS7C, a special module with an Extended Langmuir Sorption model, and the solver for mechanics CODE_ASTER® has been developed by BRGM. This new tool will be first verified by intercomparison with the COMSOL-based tool developed by INERIS and, afterwards, validated with in situ data acquired during the ongoing injection at the Montsacro mine.

INTRODUCTION

The injection of CO_2 in deep unmineable coal seams is one way of reducing greenhouse gas emissions, whilst at the same time it enables recovering a high value gas — methane. The potential feasibility and economic interest of this option depend essentially on the coal permeability and the quantity of recoverable methane. This option for CO_2 storage is the one that presents the more uncertainties and technical difficulties. Understanding thermo-hydrological as well as mechanical processes is a serious prerequisite to demonstrate the feasibility of injecting CO_2 in coal seams and is a major handicap for identifying the reliability and safety of this sequestration option. Little testing for this technique has been conducted on European coal deposits. Therefore, there is a need for an in situ injection study at an intermediate scale between a laboratory and an industrial pilot.

The CARBOLAB project intends to advance in this specific target, by performing underground tests of CO_2 injection and Coal Bed Methane (CBM) production in a specially conditioned panel of a coal mine in Spain, and also by developing adequate modeling tools. These developments are necessary for sizing the experiments through preliminary simulations; then the experimental results will be compared to simulations of experimental data in order to validate and improve the models. Modeling developments aim at providing a thermo-hydro-mechanical reservoir simulator taking into account the adsorption process, the mechanical processes like swelling/shrinkage, and stress/ sorption dependent porosity/permeability effects. These effects may indeed play a significant role for simulating CO_2 injection in coal formations.

We first present the implementation of the thermo-hydro-mechanical simulator into a sequential coupling of CODE_ASTER® for mechanics and TOUGH2 for multiphase flow. Then the simulation scenarios are introduced and the results are discussed.

MODEL DESCRIPTION

The modeling of CO_2 injection in a coal seam copes with significant issues which are linked with the specificity of coal characteristics: the adsorption of CO_2 and CH_4 is a predominant phenomenon; effective stresses are significantly impacted by adsorption processes; porosity and permeability depend on stress and adsorption features. In order to consistently model these processes, we propose to couple TOUGH2 including a modified version of module EOS7C with an Extended Langmuir Sorption model, and the solver for mechanics CODE_ASTER®.

Thermo-Hydrological Processes

For modeling the thermo-hydrological processes, the multiphase non-isothermal transport code TOUGH/EOS7C provides a reliable and efficient base. However, until now, this tool did not represent the adsorption process. The developments in this code thus focused on introducing adsorption processes in the module "EOS7CS" based on module "EOS7C". The conservation equation was modified by introducing a new term that corresponds to the subtraction of adsorbed quantities to the free flow:

$$\partial_t \left((1-\Phi)\rho_m M^i Q^i_{sorb} + \sum_\alpha \Phi S_\alpha \rho^i_\alpha \right) - \mathrm{div}\left(\sum_\alpha \rho^i_\alpha q_\alpha + d^i_\alpha \right) = 0$$

with Φ the porosity, ρ_m the matrix density (kg/m^3), M^i the molar mass of component i (kg/mol), S_α the saturation of phase α, Q^i_{sorb} the molar adsorbed quantity of component i (mol/kg), ρ^i_α the density of component i in phase α (kg/m^3), d^i_α the diffusion flux of component i in phase α (kg/m²/s), q_α the flow velocity of phase α (m/s). d^i_α is obtained by the Fick law: $d^i_\alpha = \rho_\alpha D^i_{\alpha,\mathrm{eff}} \nabla x^i_\alpha$ with x^i_α the mass fraction of component i in phase α and $D^i_{\alpha,\mathrm{eff}} = \tau\phi D^i_\alpha$ the effective diffusion coefficient of component i in phase α (m²/s), that includes tortuosity coefficient τ, porosity and the diffusion coefficient D^i_α (m²/s). The Darcy law is used for computing $q_\alpha = \lambda_\alpha k \nabla \mathrm{p}_\alpha$, with p_α the total pressure of phase α, λ_α the mobility of phase α (that depends on saturation in phase α), and k the permeability.

This conservation equation requires implementing a relation that links Q^i_{sorb} with the parameters that control adsorption. A literature review shows that the adsorption is mainly controlled by the values of partial pressures of the components:

$$Q^i_{\mathrm{sorb}}(p^1_{\mathrm{g}}, p^2_{\mathrm{g}}, \dots)$$

with p^i_{g} the partial pressure of component *i* in the gas phase (Pa). A first relation (between the adsorbed quantity and the partial pressure for each component) was implemented with a Langmuir Sorption model. However, this model is not consistent for representing a competitive sorption between different gas species onto the coal surface sites. Therefore an Extended Langmuir Sorption model was implemented and the adsorbed quantity for CO_2 is computed as (and symmetrically for CH_4):

$$Q^{CO_2}_{\mathrm{sorb}} = Q^{CO_2}_{\max} \times \frac{\alpha^{CO_2} p^{CO_2}_{\mathrm{g}}}{1 + \alpha^{CO_2} p^{CO_2}_{\mathrm{g}} + \alpha^{CH_4} p^{CH_4}_{\mathrm{g}}}$$

with $Q^{CO_2}_{\max}$ the constant of maximal adsorbed quantity for CO_2 and α^i the parameters of the Extended Langmuir Sorption Model. In addition to the integration of sorption process, the variation of permeability depending on porosity was also implemented in the new module. The relation currently used is a cubic relation:

$$\frac{k}{k_0} = \left(\frac{\Phi}{\Phi_0}\right)^3$$

with k the permeability, k_0 the reference permeability, Φ the porosity, Φ_0 the reference porosity.

Mechanical Processes

For modeling the mechanical processes, the open CODE_ASTER® (provided by EDF) was

used. CODE_ASTER® offers a full range of multiphysical analyses and modeling methods and enables to model geomaterials. The aim is to simulate with CODE_ASTER® the significant impact of adsorption processes on effective stresses.

The equilibrium equation is written as:

$$\mathrm{div}(\sigma_{ij}) + f_i = 0$$

with σ_{ij} the component of the total strain tensor and f_i the component of the body force. The coal is considered as a homogeneous and elastic continuum, and the system is isothermal, so that the strain-displacement relation can be expressed as:

$$\varepsilon_{ij} = \frac{1}{2}\left(\nabla u_i + \nabla u_j\right)$$

with ε_{ij} the component of the strain tensor and u_i the component of the displacement. The effects of gas-sorption on the strain can be introduced analogously as a thermal contraction in the stress-strain relationship (Shi and Durucan, 2004):

$$\varepsilon_{ij} = \frac{1}{2G}\sigma_{ij} - \left(\frac{1}{6G} - \frac{1}{9K}\right)\sigma_{kk}\delta_{ij} + \frac{b}{3K}p_{\mathrm{pores}}\delta_{ij} + \frac{\varepsilon_{\mathrm{sorb}}}{3}\delta_{ij}$$

with G the shear modulus of coal, K the bulk modulus of coal matrixes, b the Biot's coefficient, p_{pores} the gas pressure in the pores, $\varepsilon_{\mathrm{sorb}}$ the sorption-induced strain and δ_{ij} the Kronecker delta. Combining these equations yields:

$$G\nabla^2(u_i) + \frac{G}{1-2\nu}\nabla(\varepsilon_v) - b\nabla(p_{\mathrm{pores}}) - K\nabla(\varepsilon_{\mathrm{sorb}}) + f_i = 0$$

with ν the Poisson's ratio of the coal-fracture assemblage, ε_v the volumetric strain. Owing to pore pressure and sorption induced strain, the term $\left(bp_{\mathrm{pores}} - K\varepsilon_{\mathrm{sorb}}\right)$ is implemented in our model as a load, because of the chaining strategy chosen as "fixed strain split" (Settari and Mourits, 1998).

Coupling between TOUGH2/EOS7CS and CODE_ASTER®

In order to couple both codes, a supervisor was elaborated in python language. This supervisor manages the launch of both codes and ensures the computing of input parameters for each code. As illustrated on Figure 1, the dialogue between the mechanic and thermo-hydrodynamic codes requires the implementation of three main relations:

i. for updating porosity that depends on stress and adsorption features (permeability is updated within TOUGH2 through the relation porosity-permeability);

ii. for computing the gas pressure in pores;

iii. for computing the sorption-induced strain.

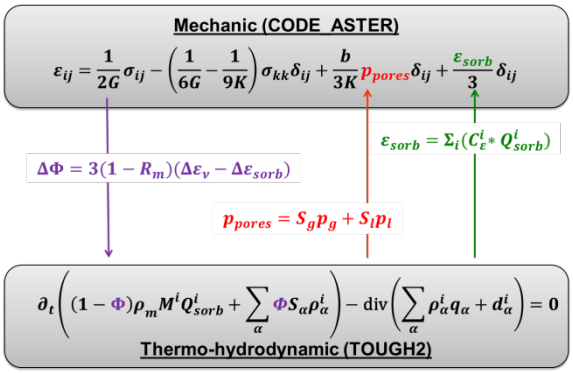

Figure 1. Illustration of relations that enable coupling mechanic with thermo-hydrodynamic equations

For the first point (i), coal matrix porosity (and permeability) changes are controlled by the mechanical effective stress change (Liu et al., 2010):

$$\Delta\Phi = 3(1 - R_m)(\Delta\varepsilon_v - \Delta\varepsilon_{\mathrm{sorb}})$$

with $R_m = \frac{E}{E_m}$ the elastic modulus reduction ratio, E the equivalent Young's modulus of the coal-fracture assemblage and E_m the Young's modulus of the coal matrix. In this relation, the change in porosity and permeability due to coal matrix is neglected, only the change from the coal fractures is considered. The porosity changes are computed from the outputs of CODE_ASTER® and are integrated in the inputs of TOUGH2.

Concerning (ii), p_{pores} is the average pore pressure and is calculated as follows:

$$p_{\text{pores}} = S_{\text{g}} p_{\text{g}} + S_{\text{l}} p_{\text{l}}$$

with S_{g} the gas saturation, p_{g} the total gas pressure, S_{l} the liquid saturation, p_{l} the total liquid pressure. Liquid pressure and gas pressure are extracted from the outputs of the hydraulic module TOUGH2 and used in CODE_ASTER® for determining the pore pressure.

Concerning (iii), the gas sorption-induced strain $\varepsilon_{\text{sorb}}$ is presumed to result in volumetric strain only. According to Chen et al. (2010), experimental evidence supports the use of the extended Langmuir isotherm equation for representing the adsorption of gas mixtures:

$$\varepsilon_{\text{sorb}} = \Sigma_i (C_\varepsilon^i Q_{\text{sorb}}^i)$$

where C_ε^i is the gas volumetric strain of component i at infinite pressure. The adsorbed quantities are extracted from the outputs of TOUGH2 and used in CODE_ASTER® for determining the gas-sorption induced strain.

For efficient coupling the supervisor works with a parallel algorithm, which means that at time n, TOUGH2 calculates the total pressure and adsorbed quantities for time $n+1$ while CODE_ASTER® calculates the induced porosity changes that enable updating the porosity and permeability for time $n+1$.

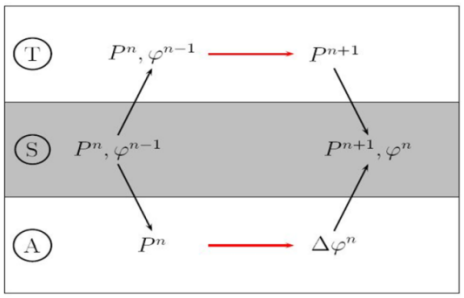

Figure 2. Illustration of the parallel algorithm between TOUGH2 (T), CODE_ASTER® (A) and the supervisor (S).

SIMULATION SCENARIOS

The simulations presented in this paper aim at testing the thermo-hydro-mechanical simulator presented above. The parameters are chosen in order to represent realistic values, but the modeled scenario is purely imaginative. It is planned to perform a second set of simulations that will be based on the experimental scenario. The following choices (for input parameters as well as for boundary and initial conditions) have been made consensually by all attendees using data obtained in the CARBOLAB research projects and other research projects (especially the CHARCO project), data from scientific literature (especially Defossez, 2011) and expert opinion if necessary.

Data and input parameters used

The properties that are used for the coal seam and the shale are presented in Table 1.

Table 1. Properties of rocks

Properties	Coal	Shale
Density ρ (kg/m^3)	1 400	2 300
Porosity Φ	0.086	0.042
Young modulus E (GPa) of the coal-fracture system	2	5.6
Poisson coefficient ν	0.3	0.26
Biot coefficient b	0.9	0.8
Permeability k (m²)	1.8 10^{-16}	8.1 10^{-18}
Gas diffusion (cm^2/s)	1.6 10^{-6}	1.6 10^{-6}

Shi and Durucan (2003) reported CO_2 diffusion coefficient values, estimated by fitting effluent composition data for pulverized coals, of 5×10^{-8} to 5×10^{-6} cm^2/s for micropores and 2×10^{-5} to 7×10^{-4} cm^2/s for macropores. It has been found experimentally that the matrix of the coals from the Montsacro Mine is composed of approximately 29% micropores and 68% macropores (P. Defossez, personal communication), so a representative value was used (1.6×10^{-6} cm^2/s). For simplicity (and lack of data) the coefficients were made the same for CO_2 and CH_4.

The bulk modulus K is obtained by:

$$K = \frac{E}{3\times(1-2\nu)}$$

For obtaining the Young modulus of the coal matrix E_m, we use the formula:

$$K_m = \frac{K}{1-b}$$

By assuming that the Poisson coefficient for the coal matrix is the same as for the coal-fracture assemblage, we obtain:

$$E_m = 3K_m \times (1 - 2\nu) = \frac{3K \times (1 - 2\nu)}{1 - b}$$

The thermo-hydrodynamic model requires noticing the van Genuchten parameters (cf. Table 2) for relative permeability and capillary pressure functions.

Table 2. can Genuchten properties

Properties	Coal	Shale
van Genuchten P_0 (Pa)	$1x10^5$	$1x10^6$
van Genuchten P_{max} (Pa)	$1x10^7$	$1x10^7$
van Genuchten m	0.5	0.5
S_{lr}	0.003	0.003
S_{gr}	0.	0.
S_{ls}	1.	1.

For the dissolution of CO_2, the coefficient of the Henry law is set to $1.53\ 10^8$ Pa at 25°C. The chosen parameters for the extended Langmuir Sorption model are presented in Table 3:

Table 3. Extended Langmuir Sorption Model parameters

Properties	CO_2	CH_4
$Q^i_{\max}$ (mol/kg)	$1.69\ 10^{-3}$	$8.1\ 10^{-4}$
α^i (Pa^{-1})	$1.12\ 10^{-6}$	$1.57\ 10^{-6}$

Concerning the gas volumetric strains $C_\varepsilon^{CO_2}$ and $C_\varepsilon^{CH_4}$, the references are very scarce. Consequently, it was chosen to perform a sensitivity analysis on these parameters.

Reference Case

A first simplified base case has been elaborated to test the developed simulator. It consists in injecting CO_2 in a non-saturated porous coal seam with a pressure controlled injection of 4.5 MPa, during 24 hours, and then in relaxing during 96 hours (total simulated duration is therefore 120 hours. In addition to the coal layer, two surrounding rocks (shale) are considered in the model. We consider a 2D-axisymetric model whose geometry is represented on Figure 3. The model length is 25 m.

The boundary conditions for mechanics are represented on Figure 3: a no-displacement condition is imposed on the upper horizontal boundary and on the injection axis; the stress field is imposed on the lower horizontal boundary (set to 18.5 MPa) and on the lateral boundary for x = 25 m (set to 12.25 MPa).

The boundary conditions for thermo-hydrodynamics are also represented on Figure 3: a no-flow condition is imposed on the upper and lower horizontal bounds; the gas composition and pressure are imposed on the lateral bound at x = 25 m (equal to the initial composition and pressure); the injection axis corresponds to a no-flow condition, except in the coal. The initial conditions are presented in Table 4.

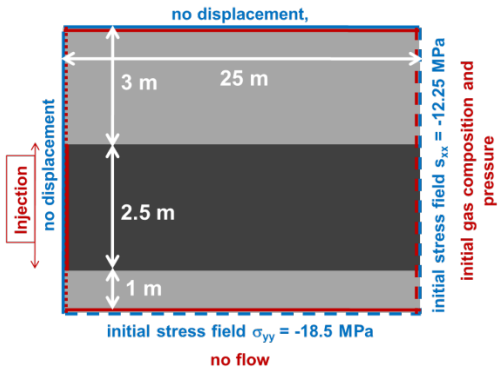

Figure 3. Geometry and boundary conditions (color red: hydrodynamic boundary conditions; color blue: mechanical boundary conditions)

Table 4. Initial conditions

Properties	
Initial water saturation	0.046
Initial gas saturation	0.954
Initial CH_4 pressure (MPa)	1.4955
Initial CO_2 pressure (MPa)	0.0045

In the reference case, the gas volumetric strains $C_\varepsilon^{CO_2}$ and $C_\varepsilon^{CH_4}$ are given in the Table 5.

A first set of simulations has been performed in order to test the influence of the mesh on results. To obtain a satisfying convergence, it is necessary to refine the mesh in the first meter (mesh length of 0.02 m) and to keep mesh not distorted, which imposes using the same order of

magnitude for the mesh height as for the mesh length. For computing time reasons and since the results were significantly the same with and without surrounding rocks (shale), it was chosen to keep only the coal layer in the modeling. The number of cells in the reference case is 7000 (20 for height, 350 for length).

Sensitivity Analysis

The gas volumetric strains $C_\varepsilon^{CO_2}$ and $C_\varepsilon^{CH_4}$ are unknown (because of lack of data) and may have a strong impact on results. Therefore, it was decided to perform a sensitivity analysis on a large range of values for these parameters. This wide range of values may have a physical sense since it is admitted that the swelling behavior of a coal depends highly on its composition. The values of the different test cases are presented in Table 5.

Table 5. Sensitivity analysis parameters

Gas volumetric strains	CO_2	CH_4
Case A	0	0
Case B	$2{,}13\ 10^{-1}$	$5{,}85\ 10^{-1}$
Case C (Reference case)	2,13	5,85
Case D	10,65	29,25
Case E	21,3	58,5

All other parameters and modeling choices are kept identical to the reference case.

RESULTS AND DISCUSSION

The output variables of interest include the pressure, the CO_2 flux, the CO_2 fraction, the porosity, the permeability, the adsorbed quantity of CO_2 and CH_4. These variables may be observed on time-dependent or space-dependent scales. In this section, the results obtained for these variables are presented and discussed for the different simulation cases. The computing time is also an interested observable value to assess the efficiency of the simulator. It was about the same for all the simulations, around 6 hours.

Reference Case

The pressure-controlled injection followed by relaxation is visible on Figure 4. It can be observed that the pressure increase exceeds 0.5 MPa only in the first meters.

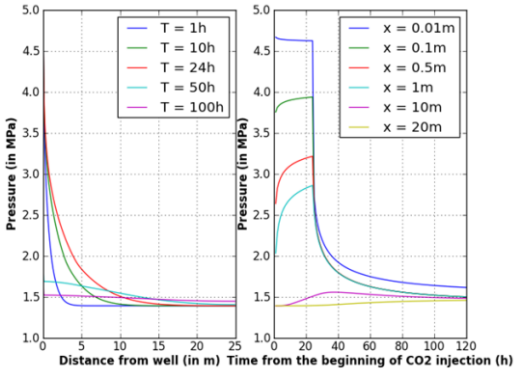

Figure 4. Evolution of pressure, function of space (on left) and function of time (on right)

The porosity varies in a narrow range: it decreases up to 0.085 and increases up to 0.08755 during the injection period, as illustrated on Figure 5. The porosity changes are indeed controlled by two competitive phenomena: the pressure increase tends to increase the porosity while the swelling of coal due to adsorption tends to decrease it.

The analysis of permeability evolution (not shown here) drives to the same conclusions, since permeability is supposed to be connected to porosity by a cubic relation.

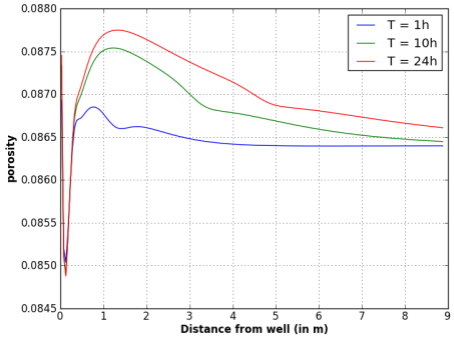

Figure 5. Evolution of porosity depending on space

The flux of CO_2 is maximal at the beginning of injection because the pressure gradient is maximal. The order of magnitude of the flux is 0.008 kg/s, i.e. 691 kg during the 24 hours of injection.

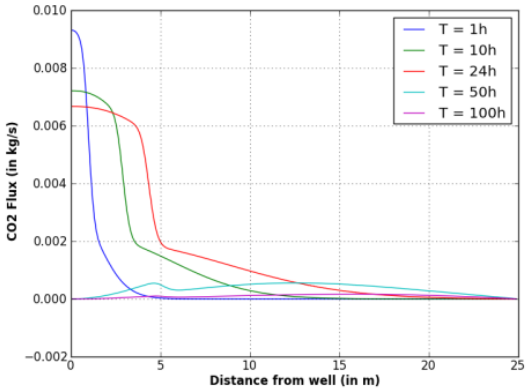

Figure 6. Evolution of CO_2 flux depending on space

The adsorbed quantities of CO_2 and CH_4 are represented on Figures 7 and 8. The orders of magnitude represent the fact that a very large quantity of CO_2 can be stored in coal compared to CH_4. The local quantity of adsorbed CH_4 first increases due to the pressure increase, and then strongly decreases after the arrival of CO_2 due to the competition for the coal sorption sites.

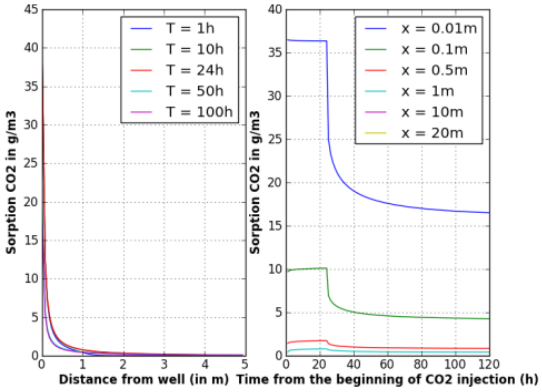

Figure 7. Evolution of CO_2 adsorbed, function of space (on left) and of time (on right)

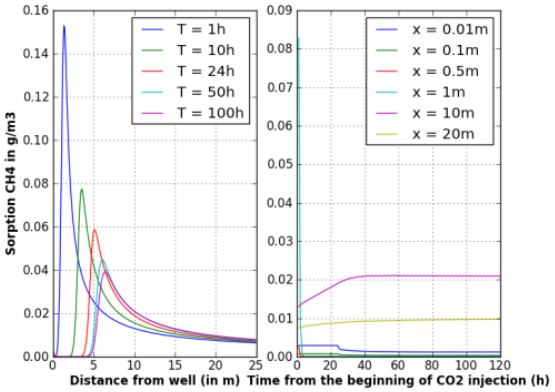

Figure 8. Evolution of CH_4 adsorbed, function of space (on left) and of time (on right)

Sensitivity Analysis

The results of the sensitivity analysis on the gas volumetric strains are presented below (Figure 9 and Figure 10) for the two more influenced outputs: porosity and CO_2 flux. It is noticeable that the gas volumetric strains impact the evolution of porosity. For low-swelling coals, the porosity increases, while for high-swelling coal, the porosity may locally decrease significantly. The CO_2 flux is impacted by the porosity changes: for case C, the flux decreases only slightly (compared to case A) but for case E the flux decreases significantly. This simulation result could be an explanation of the clogging in some specific coals (RECOPOL project in Poland) and not in other projects.

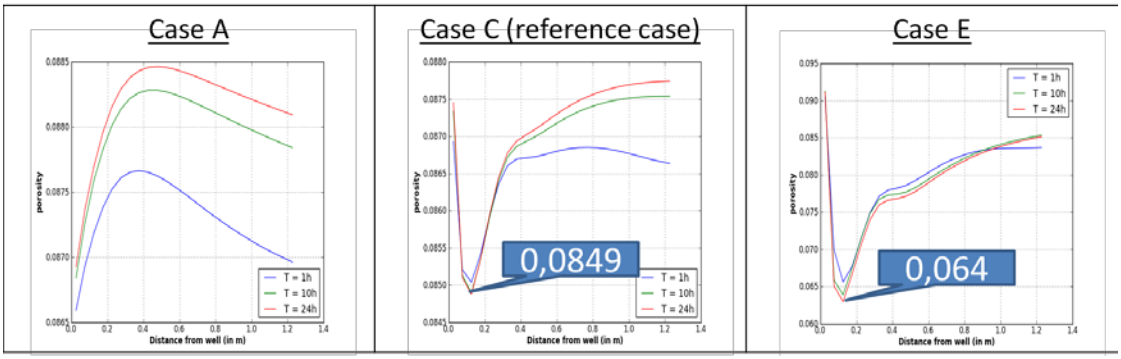

Figure 9. Sensitivity of the porosity to gas volumetric strain (cases A, C and E)

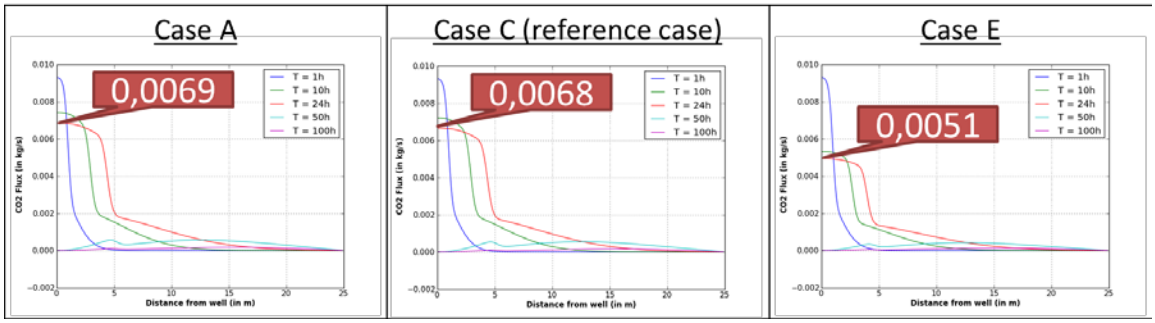

Figure 10. Sensitivity of the CO_2 flux to gas volumetric strain (cases A, C and E)

CONCLUSION

The first stage of numerical developments is achieved and has provided a thermo-hydro-mechanical simulator taking into account the adsorption process, mechanical processes like swelling/shrinkage, and stress/sorption dependent porosity/permeability effects.

Experimental surveys should be launched in next months, and will enable to validate and improve the models by comparison between experimental measures and simulations of experiments. The simulator will also be confronted with the COMSOL-based tool developed by INERIS.

The results of simulations presented in this paper aim at testing the supervisor and should be considered cautiously. Nevertheless, these simulations highlight the utility of such a simulator. It could be used to understand better the very complex behavior of coals. The detailed impact of different parameter perturbations, both individually and simultaneously, in this highly coupled problem will be the subject of further research. The simulator could also be used for monitoring design, for injection scenario studies and for future project sizing.

ACKNOWLEDGMENT

CARBOLAB is a project supported by the European Fund for Coal and Steel involving HUNOSA, owner of the mine, AITEMIN from Spain, BRGM, INERIS and TOTAL from France, GIG from Poland.

REFERENCES

Chen, Z., J. Liu, D. Elsworth, L.D. Connell, Z. Pan, Impact of CO_2 injection and differential deformation on CO_2 injectivity under in-situ stress conditions, *International Journal of Coal Geology, 81* 97–108, 2010.

Defossez, P., *Caractérisations de charbons en vue de leur utilisation pour le stockage géologique de CO_2, (in French)*, PhD thesis, May 2011

EDF, Analysis of Structures and Thermomechanics for Studies & Research, *www.code-aster.org*.

Liu, J., Z. Chen, D. Elsworth, X. Miao, X. Mao, Linking gas-sorption induced changes in coal permeability to directional strains through a modulus reduction ratio, *International Journal of Coal Geology, 83*, 21–30, 2010.

Oldenburg, C.M., G.J. Moridis, N. Spycher, and K. Pruess, *EOS7C Version 1.0: TOUGH2 Module for Carbon Dioxide or Nitrogen in Natural Gas (Methane) Reservoirs*, LBNL Report LBNL-56589, March 2004.

Settari, A. and F.M. Mourits, A coupled reservoir and geomechanical simulation system, *SPE Journal*, 219–226, 1998.

Shi, J.Q., S. Durucan, Drawdown induced changes in permeability of coalbeds: a new interpretation of the reservoir response to primary recovery. *Transport in porous media, 56*, 1–16, 2004.

Shi, J.Q., S. Durucan, A bidisperse pore diffusion model for methane displacement desorption in coal by CO_2 injection, *Fuel, 82,* 1219–1229, 2003.

Xu, T., and K. Pruess, Modeling multiphase non-isothermal fluid flow and reactive geochemical transport in variably saturated fractured rocks: 1. Methodology, *American Journal of Science, 301*, 16-33, 2001.

NEAR-WELL PRESSURE DISTRIBUTION OF CO_2 INJECTION IN A PARTIALLY PENETRATING WELL

Edward Mehnert and Roland T. Okwen

University of Illinois at Urbana-Champaign, Prairie Research Institute, Illinois State Geological Survey
615 East Peabody Drive, Champaign, IL, 61820 USA
emehnert@illinois.edu and rokwen@illinois.edu

ABSTRACT

To mitigate global climate change, the atmospheric concentrations of greenhouse gases such as carbon dioxide, carbon monoxide, methane, and nitrous oxide must be reduced. Carbon dioxide (CO_2) can be captured and injected into subsurface reservoirs in a process known as geologic carbon sequestration (GCS). Geologic carbon sequestration in saline reservoirs offers the greatest storage capacity in the United States and worldwide. Numerical modeling offers planners a useful tool to evaluate the feasibility of GCS in saline and other reservoirs. With its database of CO_2 properties, TOUGH2 and its ECO2N module is an excellent simulator for evaluating the CO_2 movement in the subsurface.

Radial simulations (along the r-z axis) of brine injected into a thick saline reservoir show a smooth exponential increase in pressure over time near the injection well. However, CO_2 injected into a thick saline reservoir does not show the same smooth pressure increase. After some time, the pressure near the injection well levels off, remains steady, and then decreases slightly. The maximum pressure increase at the well is lower for CO_2 injection than for brine injection because brine is more viscous. In addition, the maximum pressure increase occurs before the end of the CO_2 injection period. Okwen et al. (2011) demonstrated this effect for fully penetrating wells and attributed this pressure response to the contrast in fluid density (native brine versus CO_2) and permeability anisotropy (horizontal to vertical permeability). In this paper, we seek to demonstrate that the effect is also observed in partially penetrating wells. Partially penetrating wells are important because they offer a well design that can maximize the storage volume of the buoyant CO_2 in thick reservoirs.

We used TOUGH2 and the ECO2N module to conduct numerical experiments to evaluate the pressure response of injecting CO_2 and brine into saline reservoirs. Preliminary results confirm the results of Okwen et al. (2011) for partially penetrating wells. For a well perforated in the bottom of an anisotropic injection formation, CO_2 injection leads to lower pressures near the injection well perforations but higher injection pressures near the top of the injection formation. Apparently, vertical transport is more significant with CO_2 injection than brine injection, and it alters the pressure profile near the injection well. These results could inform how partially penetrating wells are completed.

INTRODUCTION

Geologic carbon sequestration (GCS) in saline reservoirs offers the greatest storage capacity for greenhouse gases in the United States and worldwide (IPCC, 2005). Numerical modeling offers planners a useful tool to evaluate the feasibility of GCS in saline and other reservoirs. However, numerical simulation of two-phase flow for large geographic areas such as geologic basins can be computationally demanding (thus expensive) and technically demanding. In an attempt to simplify the task of basin-scale modeling, researchers (e.g., Nicot 2008) have suggested that basin-scale simulations could be simplified by injecting brine instead of CO_2. This approach is considered to be adequate if one is interested in studying the far field effects of GCS. Motivated by this concept, we conducted numerical simulations to help define "far field" and "near field" in this context.

Okwen et al. (2011) conducted numerical experiments to study temporal variations in the near-wellbore pressures for a fully penetrating well. They found that temporal variations in pressure near the wellbore depend strongly on the density contrast between the injected and native fluids and vertical anisotropy of the injection formation. Because partially penetrating wells offer a technology to fully utilize the reservoir pore space at GCS sites, we have conducted numerical experiments to explore these temporal variations for partially penetrating wells.

APPROACH

To compare the effects of injecting CO_2 and brine into a deep saline reservoir, a number of simulations were conducted. The simulations were set up using two-dimensional radial grids. The reservoir was assumed to be 50 to 100 m thick and to extend 100,000 m, and have an infinite volume element at this distant boundary. In each case, 1 million tonnes of fluid were injected per year for 10 years. Each modeling scenario evaluated 10 years of fluid injection followed by 40 years of post-injection. The horizontal permeability was set at 4.94×10^{-12} m^2 while the vertical permeability varied (4.94×10^{-14} m^2 to 4.94×10^{-13} m^2). The reservoir thickness and perforated thickness were varied as shown in Table 1. Fluid was injected at the bottom of a deep saline reservoir for the reservoir conditions defined in Table 2. To evaluate the effect that fluid properties have on the pressure response in the injection zone, we conducted a number of simulations using CO_2, high-density CO_2, water, and brine. The density and dynamic viscosity of these fluids at formation pressure and temperature are given in Table 3. As introduced by Okwen et al. (2011), high-density CO_2 is a hypothetical fluid with density equal to that of water and viscosity equal to that of CO_2 which allows us to evaluate the effect of viscosity.

Table 1. Scenarios investigated

Reservoir thickness (m)	Perforated thickness (m)		
	10	25	50
50	RS9a	RS9b	
100	RS9c		RS9d

With its database of CO_2 properties, TOUGH2 (Pruess et al., 1999) and its ECO2N module (Pruess, 2005) is an excellent simulator for evaluating the CO_2 movement in the subsurface. A numerical grid with 50 layers and 53 columns was used, which has 2,650 elements. The grid spacing in the radial direction increased logarithmically from the injection well to the distant boundary. The reservoir was assumed to have a single rock type and was bounded by no-flow boundaries at the top and bottom.

Table 2. Reservoir conditions and TOUGH2 input

Parameter	Value
Dimensions (r x Z, m)	100,000 x 50 or 100
Gridblocks (r x Z)	53 × 50
Horizontal permeability (m^2)	4.94×10^{-12}
Vertical permeability (m^2)	4.94×10^{-13} to 4.94×10^{-14}
Porosity (%)	16
Pore compressibility (Pa^{-1})	3.71×10^{-10}
Temperature (°C)	49.2
Salt mass fraction	0.20
Dissolved CO_2	0
Relative permeability function	
Residual liquid saturation	0.30
Residual gas saturation	0.25
Exponent (λ)	0.40
Capillary pressure function	
Exponent (λ)	0.40
Residual liquid saturation	0.00
Strength coefficient (Pa^{-1})	5.0×10^{-5}
Maximum capillary pressure (Pa)	5.0×10^{5}

Table 3. Properties of injected fluids at formation pressure and temperature (19.6 MPa and 49.2°C)

Fluid	Density (kg/m^3)	Viscosity (Pa sec)
Brine	1140.4	7.8×10^{-4}
CO_2	786.8	6.9×10^{-5}
High-density CO_2	996.5	6.9×10^{-5}
Water	996.0	5.6×10^{-4}

Note: CO_2 viscosity data from Fenghour et al. (1998)

Relative permeability was defined using the van Genuchten (1980)-Mualem (1976) function for liquids and Corey (1954) for gas. Capillary pressure was defined using the van Genuchten (1980) function with the parameters defined in Table 2.

RESULTS

First, the TOUGH2 simulation results regarding the pressure response in the injection zone will be discussed, demonstrating the effect of the injected fluid, formation thickness and perfora-

tion ratio. Next, more detail will be provided for a single scenario where four types of fluid were injected to demonstrate the significance of fluid density and viscosity on the predicted pressure changes.

Effect of Perforation Ratio

In Scenario 9a, the injection zone is 20% perforated, with the lowermost 10 m of the 50 m injection zone accepting the injected fluid (Table 1). In Figure 1a, the pressure at the top of the injection zone (index= 1) is shown for two simulations—when brine is injected and when CO_2 is injected. In addition, the gas saturation curve shows the movement of CO_2 to the top of the injection zone over time. The gas rises quickly through this thin reservoir but does not reach maximum saturation until after the injection period ends (t = 3652.5 days). Pressure at the top of the injection zone is predicted to be higher during the injection period when CO_2 is injected than when brine is injected. Also, at this location, the time to reach maximum pressure is significantly different for the two fluids. During the post-injection period, CO_2 injection leads to higher pressures than those predicted for brine injection. An inverse pattern is observed at the bottom of the injection zone (index = 50) (Figure 1b). Here, we see that brine injection leads to higher pressures during the injection period. During the post-injection period, the formation pressure is higher for CO_2 injection than brine injection, but the difference is much smaller.

When the perforated thickness is increased to 50% in Scenario 9b (25 m of 50 m reservoir is perforated), the predicted pressures at the top of the injection zone are similar to Scenario 9a, but the pressures are lower at the bottom of the reservoir (Figures 2a and 2b). The maximum gas saturation at the top of the injection zone in Scenario 9b exceeds that predicted in 9a.

Another way to evaluate the TOUGH2 output is to examine the normalized pressure difference which is defined as:

$$\Delta P_{norm} = \left(P_{CO_2} - P_{brine}\right) \Big/ P_{brine}(t = 0) \qquad (1)$$

The normalized pressure differences for four scenarios are shown in Figure 3. The graphs show the pressure difference at the top (index 1), middle (index 25) and bottom (index 50) of the injection zone. The fourth location is generally near the middle of the perforated zone (index 45). The pressure difference tends to be positive for the two higher locations and negative for both lower locations. The magnitude of the negative values generally exceeds the magnitude of the positive values.

Effect of Fluid Density and Viscosity

Using Scenario 9a, four different fluids were injected. The normalized pressure differences versus time are shown in Figure 4. Figure 4a shows the pressure difference for the CO_2 and brine simulations. Figure 4b shows the pressure difference for the high-density CO_2 and brine simulations. Figure 4c shows the pressure difference for the water and brine simulations. The pressure differences have the greatest magnitude for CO_2 and brine, while the pressure difference has the smallest magnitude for the water and brine. The differences are greatest early in the injection period for the higher locations, and toward the end of the injection period for the lower locations.

DISCUSSION

The TOUGH2 results shown in Figure 1 demonstrate that injecting CO_2 (rather than injecting brine) via a partially penetrating well leads to higher pressures in the upper portion of the injection zone, but lower pressures in the lower portion of the injection zone due to buoyancy of CO_2. The highest pressures in the upper portion of the injection zone occur early in the injection period, while highest pressures in the lower portion of the injection zone occur at the end of the injection period. The magnitude of the pressure differences, especially those predicted for the lower portion of the injection zone, appears to be a function of the injection zone thickness (compare 9b and 9d), perforation ratio (compare 9a vs 9b and 9c vs 9d), and the anisotropy ratio (data not shown).

The difference in pressures predicted by TOUGH2 (Figure 4) are due to differences in fluid viscosity and density. Water has a lower density and similar viscosity to the brine, while

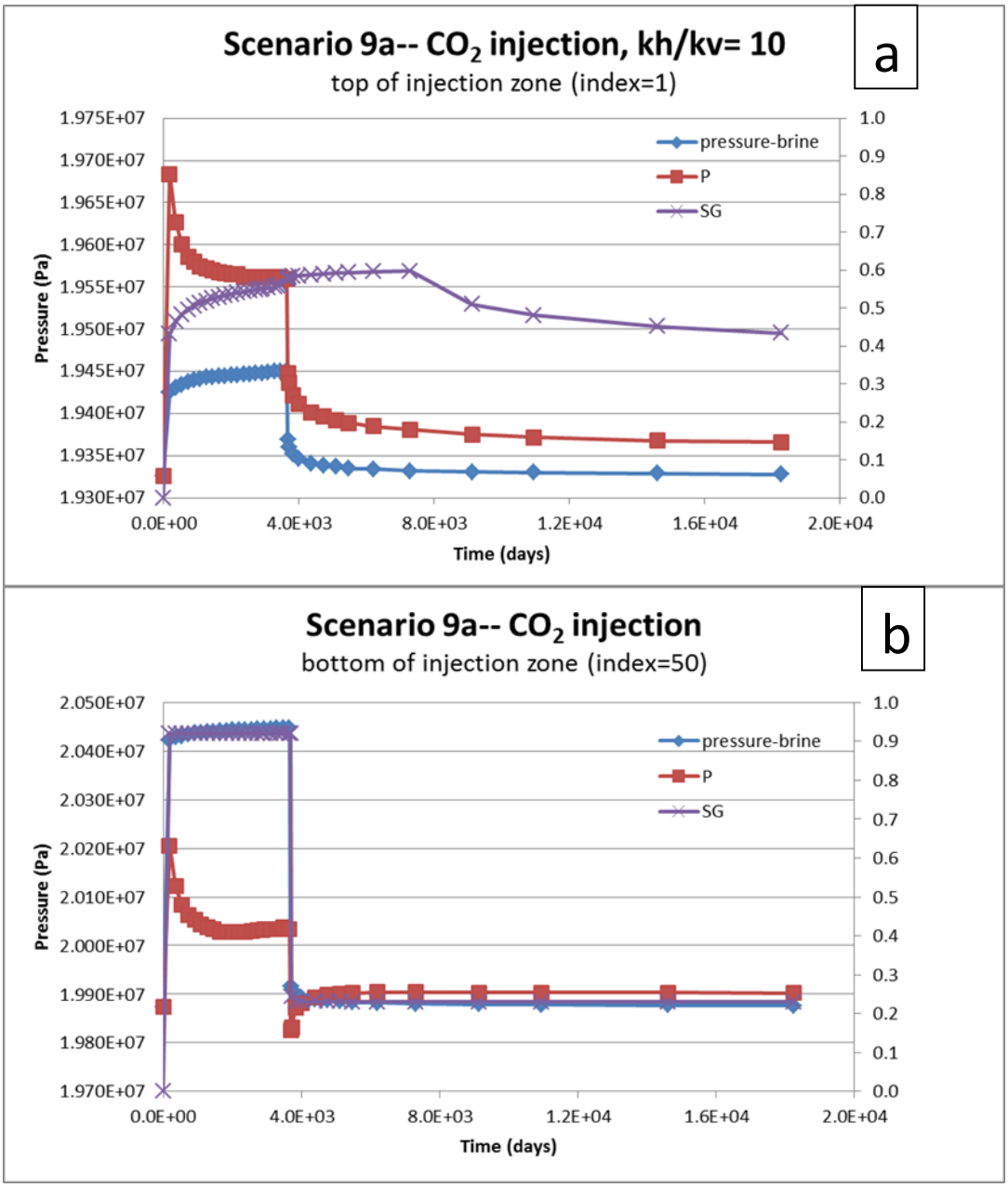

Figure 1. Results for modeling Scenario 9a (perforation thickness = 10 m, reservoir thickness = 50 m). Results are shown for the top of the injection zone (1a) and the base of the injection zone (1b). Fluid is injected from 0 to 3,652.5 days. Figure abbreviations: P = pressure resulting from CO_2 injection & SG = gas or CO_2 saturation which can vary from 0 to 1.0.

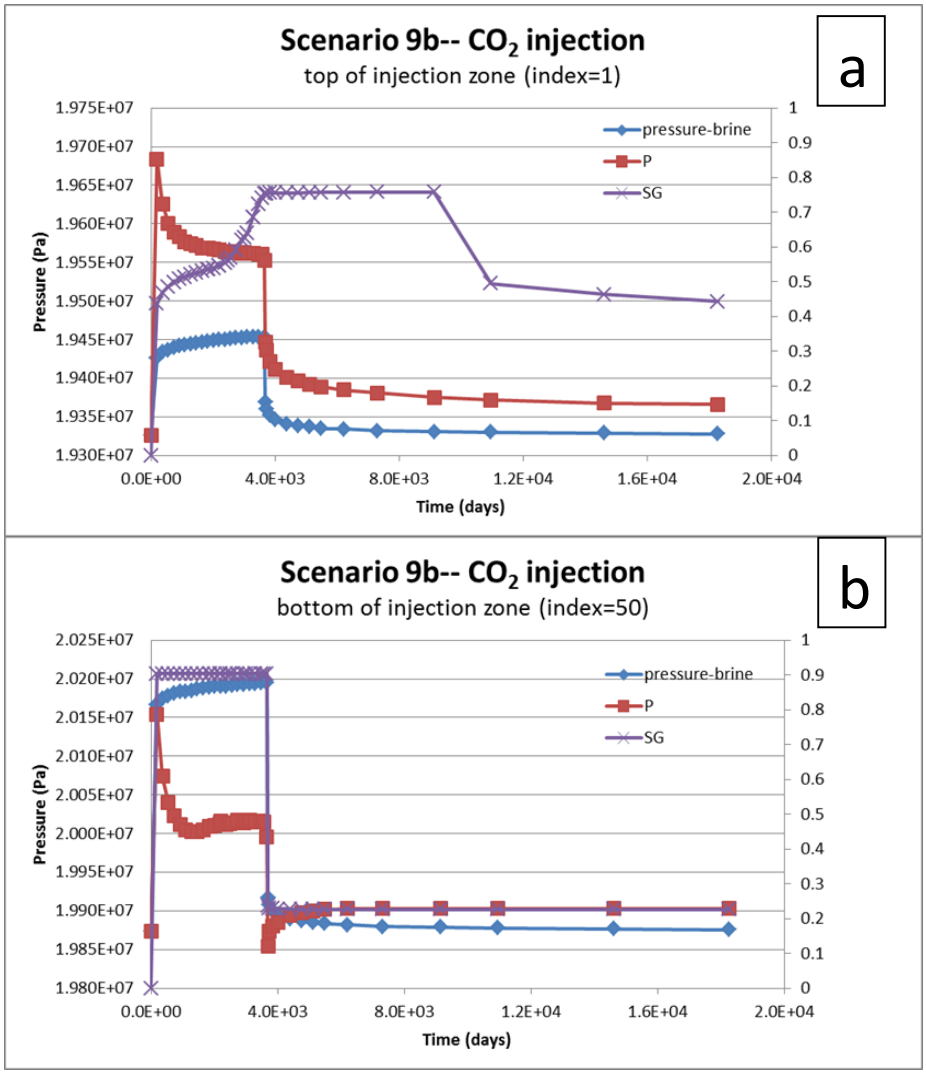

Figure 2. Results for modeling Scenario 9b (perforation thickness = 25 m, reservoir thickness = 50 m). Results are shown for the top of the injection zone (2a) and the base of the injection zone (2b). Fluid is injected from 0 to 3,652.5 days.

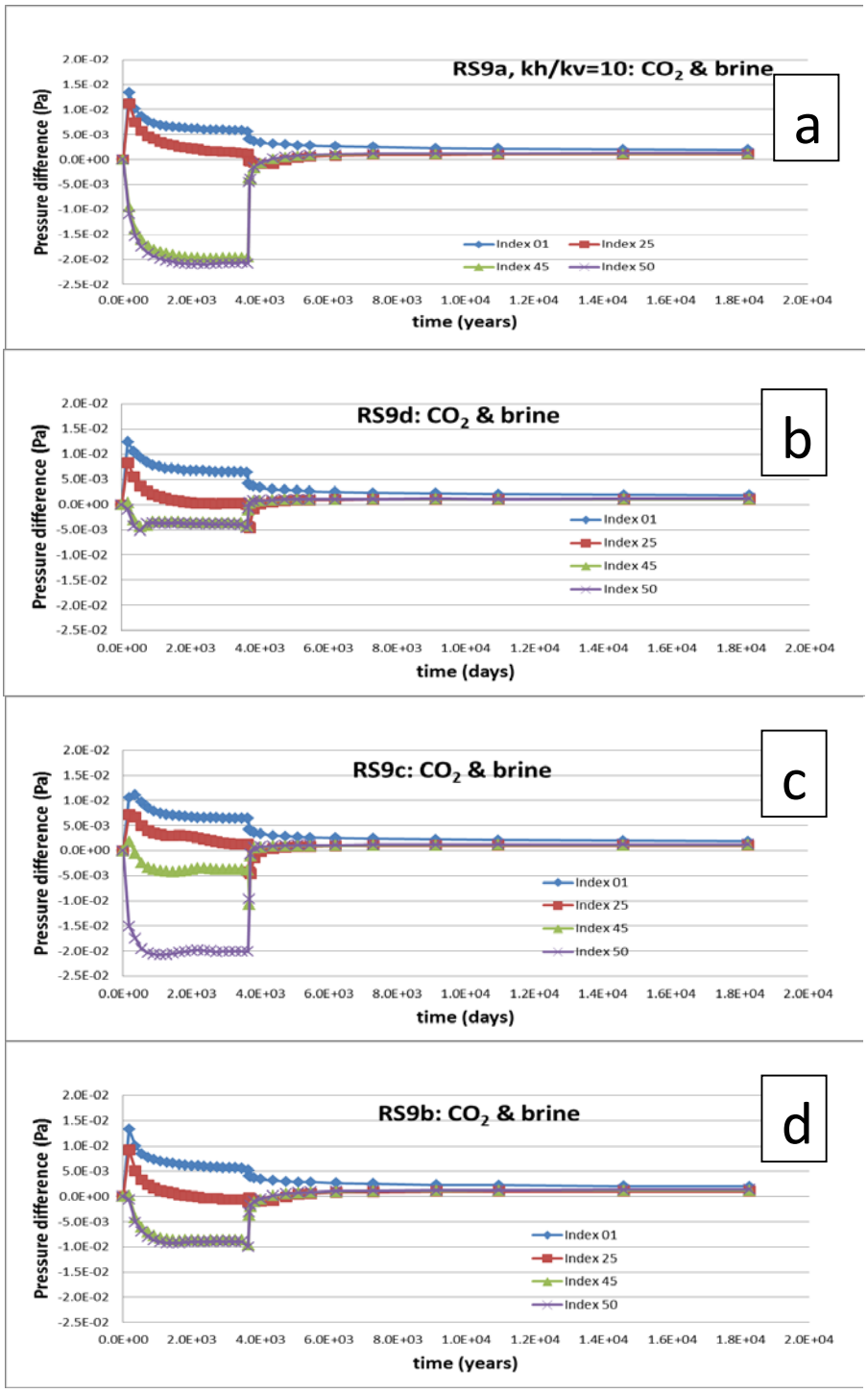

Figure 3. Normalized pressure difference for four scenarios, which shows the difference in the pressure when CO_2 and brine are injected. Data are provided at the top (index 1), middle (index 25) and bottom (index 50) of the injection zone and near the middle of the perforated zone (index 45).

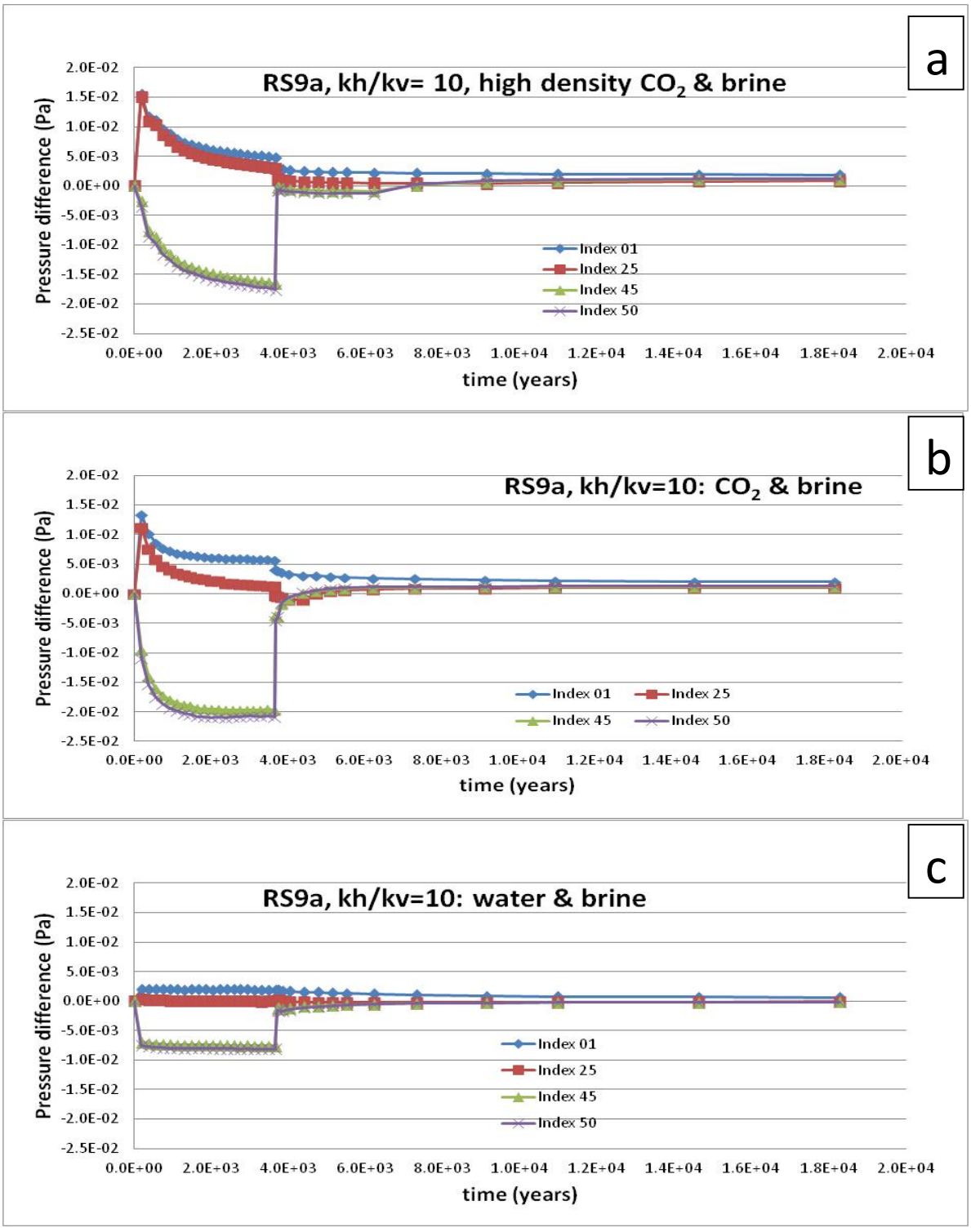

Figure 4. Normalized pressure difference for three fluids (CO_2, high-density CO_2 and water) compared to brine injection.

CO_2 has a lower density and viscosity. Figure 4c demonstrates the effect of fluid density on pressure. Injecting a denser fluid (brine) causes higher pressure in the lower portion of the injection zone, but very little effect on pressure in the upper portion of the injection zone. In addition, the density difference leads to a steady change in pressure in the lower portion of the injection zone. Comparing Figures 4b and 4c demonstrates the effect of fluid viscosity. The magnitude of the pressure difference changes in the upper and lower portion of the injection zone and its effects change over time. The combined effect of fluid density and viscosity can be observed in Figure 4a.

For the scenarios modeled, differences in near-well pressure profiles were observed when brine and CO_2 were injected via partially penetrating wells. The pressure profile near the well depends on fluid viscosity, fluid density, injection zone thickness, and other parameters such as formation permeability. The maximum pressure difference predicted in the upper portion of the injection zone seems small (<2% of the initial formation pressure), but it might be significant in terms of cap-rock integrity. The pressure increase is likely a function of formation permeability and should be investigated further for scenarios with more realistic permeability values (4.9×10^{-15} to 4.9×10^{-13} m^2 or 5 to 500 md).

ACKNOWLEDGMENTS

Publication authorized by the Director, Illinois State Geological Survey.

REFERENCES

Corey, A.T., The interrelation between gas and oil relative permeabilities, *Producers Monthly 19*(1): 38-41, 1954.

Fenghour, A., W.A. Wakeham and V. Vesovic, The viscosity of carbon dioxide. *Journal of Physical and Chemical Reference Data 27*(1): 31-44, 1998.

Intergovernmental Panel on Climate Change (IPCC), *IPCC Special Report on Carbon Dioxide Capture and Storage*. New York: Cambridge University Press, 2005.

Mualem, Y., New model for predicting hydraulic conductivity of unsaturated porous media, *Water Resources Research 12*(3): 513-522, 1976

Nicot, J.-P., Evaluation of large-scale CO_2 storage on fresh-water sections of aquifers: An example from the Texas Gulf Coast Basin. *International Journal of Greenhouse Gas Control 2*(4): 582-593, 2008.

Okwen, R.T., M.T. Stewart and J.A. Cunningham, Temporal variations in near-wellbore pressures during CO_2 injection in saline aquifers, *International Journal of Greenhouse Gas Control 5*(5): 1140-1148, 2011.

Pruess, K., C. Oldenburg, and G. Moridis, *TOUGH2 User's Guide, Version 2.0*, Report LBNL-43134, Lawrence Berkeley National Laboratory, Berkeley, Calif., 1999.

Pruess, K., *ECO2N: A TOUGH2 fluid property module for mixtures of water, NaCl, and CO_2*, Earth Sciences Division, Lawrence Berkeley National Laboratory, Report LBNL-57952, 2005.

van Genuchten, M.T., A closed-form equation for predicting the hydraulic conductivity of unsaturated soils. *Soil Science Society of America Journal 44*(5): 892-898, 1980.

FUNDAMENTAL ANALYSIS OF HETEROGENEITY AND RELATIVE PERMEABILITY ON CO_2 STORAGE AND PLUME MIGRATION

Nathan Moodie, Brian McPherson, Si-Yong Lee, Prashanth Mandalaparty

University of Utah
201 Presidents Circle Room 201
Salt Lake City, Utah 84112
Nathan.moodie@m.cc.utah.edu

ABSTRACT

Relative permeability is a critical flow parameter for accurate forecasting of long-term behavior of CO_2 in the subsurface. In particular, for clastic formations, small-scale (cm) bedding planes can have a significant impact on multiphase CO_2-brine fluid flow, depending on the relative permeability relationship assumed. Such small-scale differences in permeability attributable to individual bedding planes may also have a substantial impact on predicted CO_2 storage capacity and long-term plume migration behavior.

Relative permeability model calibration in this study was accomplished using laboratory-scale measurements of the relative permeability of Berea sandstone, as measured by Krevor et al. (2011). A core-scale model of the flow test was created in TOUGHREACT to elucidate the best-fit relative permeability formulation that matched experimental data. Among several functions evaluated, best-fit matches between TOUGHREACT flow results and experimental observations were achieved with a calibrated van Genuchten-Mualem formulation.

Using best-fit relative permeability formulations, a model of a small-scale Navajo Sandstone reservoir was developed, implemented in TOUGHREACT with the ECO2h module. The model was one cubic meter in size, with eight individual lithofacies of differing permeability, instigated to mimic small-scale bedding planes. The model assumes that each lithofacies has a random permeability field, resulting in a model with heterogeneous lithofacies. Three different relative permeability functions were then evaluated for their impact on flow results for each model, with all other parameters maintained constant. Results of this analysis suggest that CO_2 plume movement and behavior are directly dependent on the specific relative permeability formulation assigned, including the assumed irreducible saturation values of CO_2 and brine. Model results also illustrate that, all other aspects held constant, different relative permeability formulations translate to significant contrasts in CO_2 plume behavior.

INTRODUCTION

Data for the relative permeability of CO_2 and water/brine for most reservoir rocks is lacking in the current literature. Relative permeabilities of the Navajo sandstone in particular have not been measured, or at least are not published. One of our research goals was to investigate the validity of using experimentally derived relative permeability functions for a well-known formation, in this case the Berea sandstone, to calibrate a relative permeability function effective for modeling CO_2 behavior in Navajo sandstone. Ideally, core flood experiments need to be set up for Navajo sandstone and the relative permeability measured, and we just began such experiments. Upon completion of the testing, we will evaluate the measured curves and compare to the relative permeability values measured by Krevor et al. (2011). Because our relative permeability testing just began, the focus of this study was to use TOUGHREACT modeling to investigate the effects of relative permeability on CO_2 plume movement and determine how well different relative permeability curves compare, in this context, to the experimental data measured by Krevor et al. (2011).

Initially, a numerical model of a Berea sandstone core and a Navajo sandstone core were

created to model the relative permeability core flood experiment done by Krevor et al. (2011). The relative permeability curves used in the numerical models were varied, and the response of the CO_2 plume was studied. Next, a small-scale reservoir model was created of the Navajo Sandstone, with the idea of mimicking the layering observed at the Devil's Canyon site in southern Utah. To analyze how CO_2 behaves as it reaches lithofacies with varying permeability, a model was created that has four different lithofacies types, each with its own permeability values, or range of values in the case of the heterogeneous model. The model has Dirichlet boundary conditions on the top and bottom, and Neumann boundaries on the sides. A higher pressure was specified at the bottom to induce a pressure-driven upward flow across the model. This was done to study the effect that relative permeability has on CO_2 movement through lithofacies of different permeability.

LITERATURE SURVEY

Compared to intrinsic permeability, CO_2-brine and CO_2-brine-oil relative permeability data are scarce, and especially so for candidate CO_2 sequestration formations. Krevor et al. (2011) constructed relative permeability laboratory experiments on Berea sandstone. The experimental data were fit to the Brooks-Corey relative permeability function that was modified from the original formula put forth by Brooks and Corey in 1964. Krevor et al. (2011) cites this formula outlined by Dullien (1992) as the best fit for their experimental data. We compared Brooks and Corey's original formula to Dullien's formula and discovered an error in Dullien's equation with respect to the Brooks-Corey relative permeability function. The formula 5.2.21b in Dullien doesn't match the formula developed by Brooks and Corey in their 1964 paper, equation 15. The following two equations are Equation 1 from Dullien's book and Equation 2 from Brooks and Corey (1964); note that the equation from Dullien's book expresses the exponent $(2+\lambda)/\lambda$ on the outside of the parentheses of the third term, but in the original formula developed by Brooks and Corey, this expression $(2+\lambda)/\lambda$ is on the inside of the parentheses, thus modifying S_{eff} directly.

Equation 1. Dullien (1992)

$$k_{rnw} = \left(1 - S_{eff}\right)^2 \left(1 - S_{eff}\right)^{(2+\lambda)/\lambda}$$

Equation 2. Brooks and Corey (1962)

$$k_{rnw} = (1 - S_e)^2 \left(1 - S_e^{\frac{2+\lambda}{\lambda}}\right)$$

Bennion et al. (2007) produced laboratory measurements of potential seal rocks in the Alberta Basin, Canada and evaluated the relative permeability and capillary pressure curves for shale and anhydrites. They concluded that under normal injection pressures and reservoir conditions these formations act as seals over geologic time. Bennion et al. (2006) performed identical relative permeability and capillary pressure experiments on reservoir rock, sandstone, and carbonate formations from the same area in Alberta, Canada. They expressed the importance of relative permeability and residual gas trapping in the pore spaces as important factors affecting injectivity and CO_2/acid gas mobility in a brine reservoir. The authors state the importance of knowing the capillary pressure curves for the seal rock, so that injection pressures can be kept below that threshold and CO_2 is not forced into the seal rock. What is not discussed in these papers is the importance of using appropriate relative permeability curves and parameters for specific rocks under study when evaluating flow with numerical simulations. The numerical models developed by our team suggest that the choice of relative permeability function and parameters may have a significant impact on CO_2 movement and phase behavior, even causing layers to act as a barrier to CO_2 flow under certain conditions.

CONCEPTUAL FRAMEWORK

A critical needs for future CO_2 storage efforts in the western U.S. are robust relative permeability functions for simulating multiphase CO_2 flow in the Navajo sandstone. A goal of this project was to analyze the CO_2 plume response to different relative permeability curves and compare the results to existing experimental curves for Berea sandstone. Specifically, we quantified the disparity of flow fields among results of simulations that used different relative permeability functions.

For this study, the modeling effort was approached in two phases. The first step was to recreate the Krevor et al. (2011) core flood experiments using TOUGHREACT. Then, we applied the same relative permeability curves to a small-scale reservoir model of the Navajo sandstone. The objective was to quantify the magnitude of difference between the mass flux of CO_2 that each relative permeability curve predicts. For the core-model simulations specified, H_2O/CO_2 mixtures were injected into the core at a total flow rate of 15 mL/min to determine the fluid response to different relative permeability curves. Table 1 has the injection rates used in the model. Then the same relative permeability curves were used for a small-scale reservoir simulation of the Navajo sandstone, and the results were compared to the core models to determine the validity of using the Krevor's parameters as a proxy for the unknown Navajo sandstone parameters—or if either of the other two curves yielded better results.

To determine what function would be a fair representation of the experimental relative permeability data for Berea sandstone, we created a single cell "batch" model, assigned specific CO_2 mass fractions, and plotted the relative permeability data against the Berea sandstone experimental data. The experimental relative permeability curve for the Berea sandstone was digitized from Krevor et al. (2011). Using these experimental data points (water saturation values), we calculated the corresponding individual relative permeability values for the Brooks-Corey formula presented by Krevor et al. (2011), the van Genuchten-Mualem function, and a simple linear function. A fundamental regression analysis determined the best-fitting parameters for each of the curves used in the subsequent models. The root mean square error (RMSE) value was then calculated for each function and compared to the experimental data, and the best "fit" was chosen to represent the experimental curve. The RMSE for the fitted van Genuchten-Mualem function was 0.007 for the wetting phase and 0.015 for the nonwetting phase; for the Brooks-Corey curves it was 0.016 for the wetting phase and 0.003 for the nonwetting phase. The difference in RMSE is close enough that the fitted van Genuchten function will work for the core simulations of this study. The other two curves used were not fitted to the Berea sandstone data. Charts 1 and 2 present the regression analysis done to justify using the van Genuchten-Mualem function.

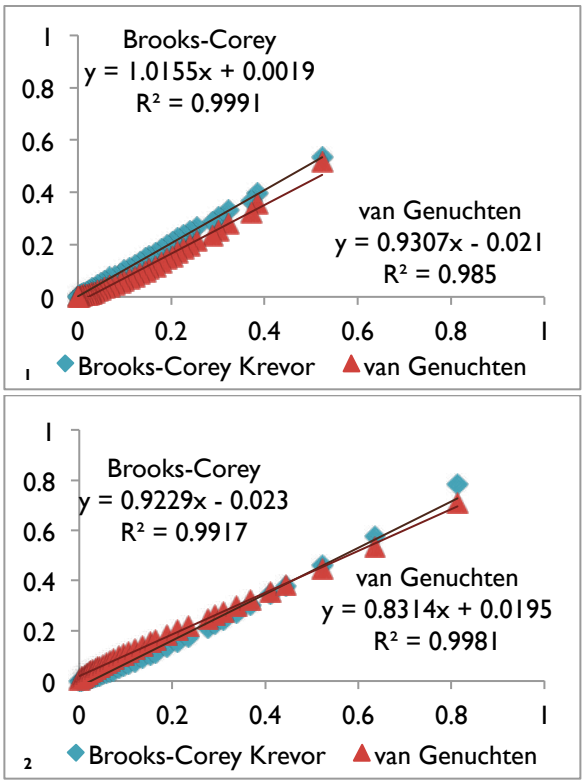

Chart 1, 2. Relative permeability of gas (Chart 1) and water, Chart 2, predicted by the Brooks-Corey and van Genuchten-Mualem functions compared to measured Berea Sandstone data. The x-axis is the fitted experimental relative permeability data and the y-axis is the predicted relative permeability data from the functions listed.

The r^2 values of .985 for the nonwetting phase and 0.998 for the wetting phase were very close to the experimental values, giving confidence in using the van Genuchten-Mualem function to represent the Berea sandstone relative permeability curve from Krevor's experimental data.

Core-scale experiment

To model the Krevor et al. (2011) core-flood experiment, we simulated eleven specific H_2O/CO_2 mixtures for each of the relative permeability curves studied. Each simulation had a

specific ratio of H_2O to CO_2, with a total flow rate of 15 mL/min. This was accomplished by injection of both H_2O and CO_2 at specified mass flow rates along the injection face of the core. Each model had an initial simulation run with 100% H_2O to set up the initial pressure and temperature profile, which was then used as the initial conditions for the subsequent ten simulations. Table 1 shows the H_2O/CO_2 mixtures and mass flow rates used in the simulations.

Table 1. Fractional flows and the associated mass flow numbers used in each injection cell of the core flood models.

Fractional flow		Mass flow per cell (Kg/s)	
		COM1	COM3
H_2O	CO_2	H_2O	CO_2
1	0	1.28E-06	0.00E+00
0.95	0.05	1.22E-06	1.81E-08
0.9	0.1	1.16E-06	3.63E-08
0.8	0.2	1.03E-06	7.25E-08
0.7	0.3	8.99E-07	1.09E-07
0.5	0.5	6.42E-07	1.81E-07
0.3	0.7	3.85E-07	2.54E-07
0.2	0.8	2.57E-07	2.90E-07
0.1	0.9	1.28E-07	3.26E-07
0.05	0.95	6.42E-08	3.45E-07
0	1	0.00E+00	3.63E-07

In each case, three different relative permeability/capillary pressure curves were used. They were derived from the linear relative permeability and capillary pressure function and the van Genuchten-Mualem relative permeability and capillary pressure function that are in TOUGHREACT. Two curves used the van Genuchten-Mualem function—one with the values from Pruess et al. (2004) and the other curve fitted to the data from Krevor et al. (2011)—and one curve used the linear function. The linear function and the van Genuchten-Mualem function with the Pruess parameters have been commonly used by our group to evaluate the storage potential of CO_2 in the Navajo sandstone. Table 2 has the parameters used for each of the functions.

A fourth relative permeability curve was evaluated using the Brooks-Corey function presented in Brooks and Corey (1964) and the parameters from Krevor et al. (2011). It showed a very good fit between the Krevor experimental curve and the curve from the Brooks-Corey function. This was expected, as it is the one cited in the Krevor et al. (2011) paper used to fit their data. But when coded into TOUGHREACT, the function would not work properly, for reasons yet to be determined. This research track was abandoned until more time could be put into determining what was causing the problems.

A numerical model of a 2 inch × 4 inch sandstone core was then built (see Figure 1). The model was created horizontally to match the experimental setup outlined in Krevor et al. (2011). The model contains 193 injection cells on the right face and an infinite-volume boundary on the left face, with no-flow boundaries everywhere else. The fluid mixture was injected at the right side of the model. The model domain has a total of 6,692 cells (see Figure 1 for the Berea and Navajo core models). The pressure and temperature were set to 9MPa and 50°C, respectively. Pure water and CO_2 are the two working fluids used in the simulations. All of the core simulations were run for a simulation period of four hours. The Berea sandstone core was a homogeneous model with a set permeability of 300 mD, to match the Berea core used by Krevor et al. (2011) in their study. This core model was homogeneous and had no bedding planes or other internal structures. The Navajo model has 13 individual zones modeled that are of four different lithofacies types, with each lithofacies being homogeneous. The four distinct lithofacies modeled were the grain flow (GF00x), wind ripple lamina (WRL0x), course lag (CL00x), and wind ripple lamina/grain flow (WRLGx). Table 3 has the permeability values for each of the lithofacies used in the model.

Table 2. Relative permeability parameters used by TIOUGHREACT.

Relative Permeability Parameters			
	Linear	van Genuchten[1]	van Genuchten – fitted[2]
Lambda - λ	n/a	0.457	0.670
Water i-sat. (S_{lr})	0.2	0.3	0.20
Gas i-sat.	0.0	n/a	n/a
Water Sat. (S_{ls})	1	1	1
CO2 i-sat. (S_{gr})	1	0.05	0.05

1 Pruess et al. (2004)

2 Values are modified to match the Berea sandstone as measured by Krevor et al. (2011)

Table 3. Measured permeability data from the Devil's Canyon field site. The standard deviation illustrates that there is large variability in the permeability measurements, highlighting the limitations of the TinyPERM II™ in isolating single layers in the rock matrix.

Layer Data for Navajo Models					
Layer Name	TOUGH code	Permeability		Standard deviation	
		mD	m^2	mD	m^2
Wind ripple lamina	WRL0x	280	2.76E-13	119	1.17E-13
Wind ripple lamina/Grain flow	WRLGx	388	3.83E-13	171	1.69E-13
Grain flow	GF00x	560	5.53E-13	311	3.06E-13
Course lag	CL00x	5346	5.28E-12	2329	2.30E-12

These four lithofacies represent the small-scale heterogeneities in the Navajo sandstone outcrops that were studied at Devil's Canyon, Utah during field research in the summer of 2011 (Allen et al., 2011). This site is an aboveground analog of what the Navajo sandstone is believed to be like at Gordon Creek, Utah. The permeabilities used in each layer were an average of the measured permeabilities for each layer, as measured by Allen et al. (2011). Permeabilities for each layer were measured *in situ* using the TinyPERM II™ air permeameter.

It must be noted here that the permeability values used for each of the individual layers in the Navajo model are averages of the measured values. There was large variability in the values measured for each layer in the field, due to the relatively large diameter, about 9 mm, of the TinyPERM II™ compared to the millimeter scale of the individual lithofacies observed in the outcrop. Also, there were more than the four lithofacies that are used in the model present in the outcrop; the four lithofacies used in the model represent the most common types seen in the outcrop. With such a wide variability in the measured data, the permeability values used in the model can only be thought of as an estimation of the common lithofacies seen in the outcrop. Many factors could make these values to be inaccurate, such as the effects of weathering on the permeability of the rock at the surface, or the difference in scale between the TinyPERM II™ orifice and the individual lithofacies.

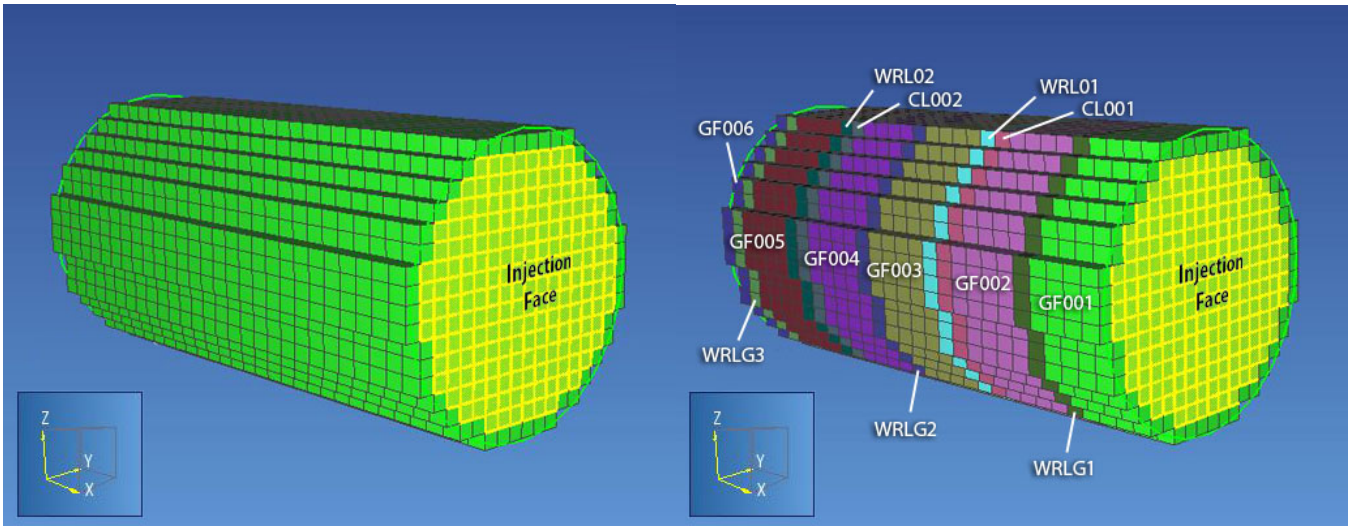

Figure 1. Berea core model on the left and the Navajo core model on the right.

Bedform-scale experiment

The small-scale Navajo model was built to represent an approximate one meter cube of the aeolian Navajo sandstone that is observed in the Gordon Creek area near Price, Utah. The Navajo sandstone at this location is at a depth of 2560 m below the surface, and accordingly, we assigned a hydrostatic initial condition of 25.7 MPa. The temperature is estimated to be 67.8°C at this depth, using an extrapolated linear temperature gradient based on measured values within the White Rim formation yielding a temperature gradient of 22.5°C/km (Chidsey and Chamberlain, 1996). The brine has a salt concentration of 0.36% NaCl, which is typical for the Navajo sandstone in the area surrounding Gordon Creek (Hood and Patterson, 1984).

Using this information, we built a centimeter-scale three-dimensional reservoir model, using TOUGHREACT and the ECO2h module to model multiphase flow of CO_2 in brine. The reservoir model consists of the same aeolian Navajo sandstone rock properties as the core model. The plan was to flow CO_2 through this model under a vertical pressure gradient, while varying the relative permeability curves used, to study the model's response. This model uses the same three relative permeability curves used in the core models and described above. Table 2 has the relative permeability parameters used in this analysis. The specific relative permeability equations are given in the TOUGH2 Users Manual (Pruess et al., 1999).

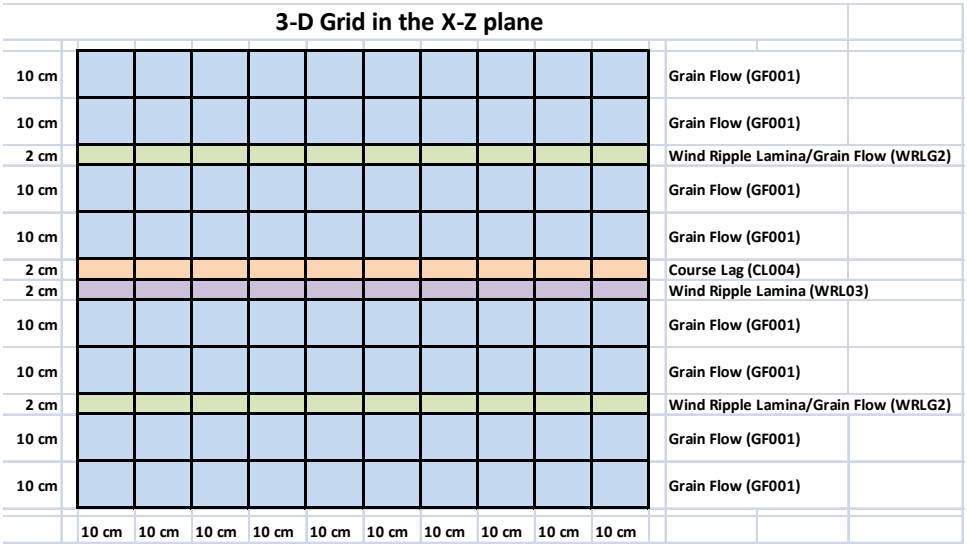

Figure 2. X-Z slice of the mesh grid used in this model.

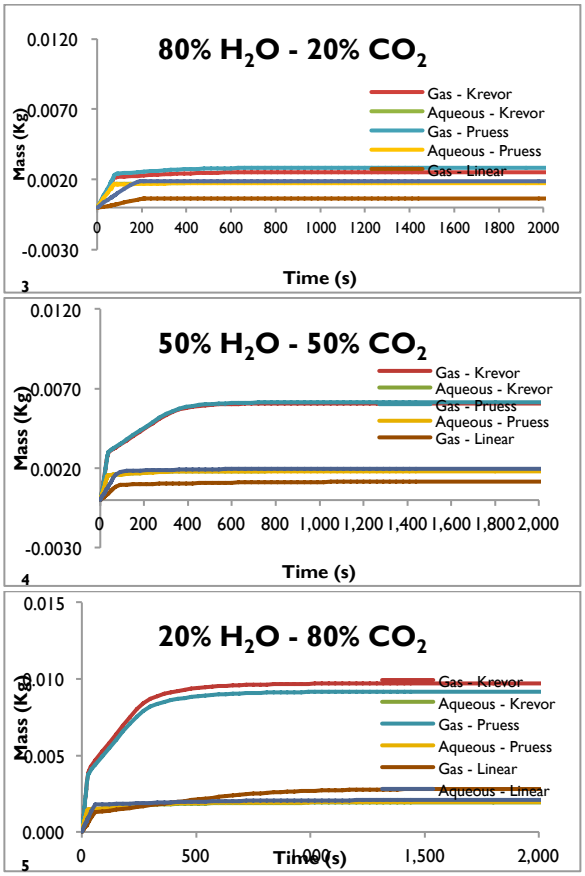

Charts 3, 4, 5. Results of the Berea sandstone simulations showing predicted mass of CO_2 in place for each relative permeability curve used.

The Navajo reservoir model domain is 100 cm × 100 cm × 88 cm in the x, y, z directions; Figure 2 shows the mesh in the x-z plane. It consists of four different layer types patterned after the observed sandstone layers at Devil's Canyon Navajo. A "dummy" bottom layer was added to the bottom of the model with an "infinite volume," a CO_2 concentration of 0.50 mass fraction, and a pressure that was 10 kPa higher than the rest of the model. This created a pressure gradient of 10 kPa to simulate a pressure-driven flow without taking the amount of CO_2 present in this dummy layer into the calculations. The top layer also has an "infinite volume," allowing the CO_2 to flow out of the top of the model while still tracking the amount of CO_2 flowing through the model. This allowed the CO_2 to migrate upwards through the reservoir as if being forced upwards by the high pressure of an injection plume, without having to model the actual injection blocks. The four sides were assigned no-flow boundaries. The dummy layer at the bottom is not used in any of the calculations; consequently, the present amounts of CO_2 and phases represent what has moved through or is in place in the model. A simulation time of three hours was determined to be sufficient for the analysis planned. A 1000-year simulation was run to determine the optimal simulation time. The results indicated that the model reaches near steady state after about one hour. In the interest of saving computational time, a three-hour simulation time was used.

RESULTS

For the Berea core model simulations, the Krevor et al. (2011) parameters were used as the "standard," and the results of that simulation were used as the basis of comparison. The same philosophy was used for the Navajo core model. This was done with the knowledge that the relative permeability curve for Berea sandstone was not going to be the same as one for Navajo sandstone. But even with not having an experimental curve, we still wanted to see what type of variation there was in predicted CO_2 using the Berea curve with Navajo sandstone rock properties.

The Berea core model simulations showed some interesting results for the predicted amount of supercritical CO_2 present as the relative permeability curve was varied. When between 20% and 80% CO_2 is flowed through the model, the Pruess curve predicts the most supercritical CO_2 and the linear curve the least. As the fractional flow of CO_2 is increased, the curve using the Pruess parameters predicts an ever-decreasing amount of CO_2 compared to the Krevor curve. The Pruess curve goes from overpredicting (by about 12%) to under predicting (by about 5%) the mass of supercritical CO_2 in place as the fractional flow increases above 50%. At 50% Pruess overpredicts supercritical CO_2 by only 1.1%. The linear curve consistently underpredicts the amount of CO_2 in place by 70–80%. This trend is illustrated in Charts 3-5. As can be seen by these charts, there is almost no difference in the predicted amount of dissolved CO_2 between the different relative permeability curves. This indicates that the choice of relative

permeability curves does not have an appreciable impact on predicted amounts of dissolved CO_2 in the same way it does for the supercritical phase.

The Navajo core-model simulations show a very different response to the relative permeability curves used then the Berea model did. With the Krevor curve as the "standard," the Pruess curve consistently overpredicts the mass of supercritical CO_2 in place by more than 50%. The linear curve is within a couple of percent of the Krevor curve predictions for most of the simulations. It only overpredicts supercritical CO_2 by 20% for the lower CO_2 fractional flows, 20% and lower. The dissolved CO_2 predicted by the linear and Pruess curves is within a few percent of that predicted by the Krevor curve, indicating again that the relative permeability curve chosen has little impact on the predicted mass of dissolved CO_2. Charts 6-8 clearly show this trend in the supercritical and dissolved CO_2.

When these same relative permeability curves were applied to the small-scale Navajo sandstone model, the results were quite different from the core model simulations. Again, using the Krevor curve as the standard, the Pruess curve overpredicts the mass of supercritical CO_2 in place by almost 40% and the dissolved CO_2 by 6%. The linear curve preformed even worse, overpredicting the total mass in place of supercritical CO_2 by 144% and underpredicting the dissolved CO_2 by 22%.

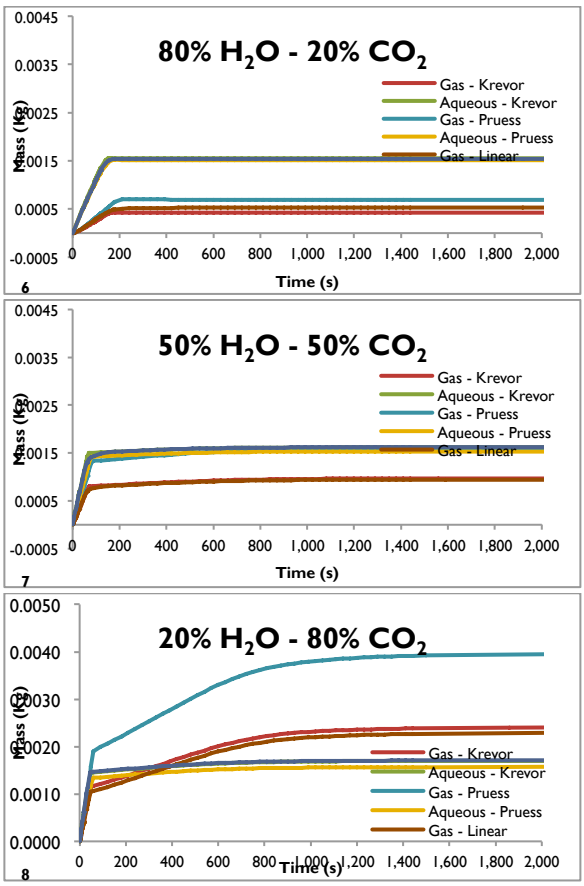

Charts 6, 7, 8. Results of the Navajo sandstone core simulations showing the predicted mass of CO_2 in place for each of the relative permeability curves used.

The really interesting result from this simulation was that both the van Genuchten-Mualem function with the Krevor parameters and the linear function indicated that both phases of CO_2 moved completely through the model. The van Genuchten-Mualem function with the Pruess parameters indicated that both the supercritical and dissolved CO_2 phases got trapped by the lower permeability WRL lithofacies. It indicated that only a small amount of aqueous CO_2 moved into the upper GF lithofacies, and no supercritical CO_2 was present at all in the WRL, CL, and upper GF lithofacies. Chart 9 shows the mass of CO_2 predicted for these simulations, and the trend with the Pruess curve can be seen clearly.

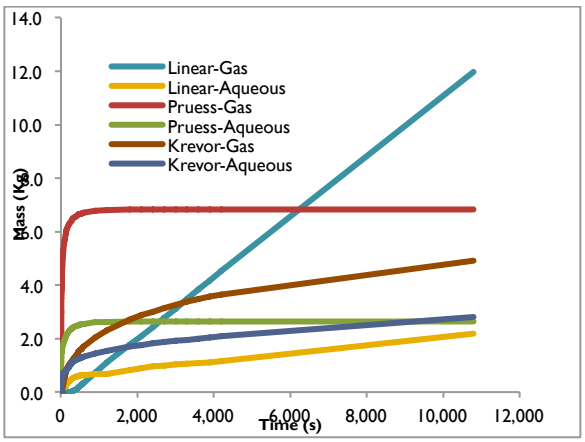

Chart 9. Results of the small scale Navajo sandstone model. The chart highlights the difference in mass of CO_2 that each relative permeability curve predicts.

CONCLUSION

The results of this analysis has shown that the choice of relative permeability function and the parameters used in that function can have a huge impact on predicted CO_2 plume migrations, phase behavior, and storage capacity. It was clear that having experimentally derived relative permeability curves for the target reservoir is essential for getting accurate predictions of the amount of CO_2 and phase behavior. Our study has indicated that the dissolved CO_2 phase is not very sensitive to the relative permeability curve used, but the supercritical phase is. Accurate relative permeability curves for the material being studied are essential for good predictions of CO_2 storage capacity and plume movement. Another important finding was that using an experimentally derived curve for one material, Berea sandstone in our case, as a proxy for a different material, Navajo sandstone, yields completely different CO_2 plume behavior and predicted mass in place. This gives weight to the idea that unless there are good measured relative permeability curves for the particular formation being studied, using a general curve such as the linear relative permeability curve will yield conservative predictions of CO_2 mass and plume behavior.

One finding that was somewhat surprising was that lower permeability lithofacies within what is normally thought of as a homogeneous medium, as the Navajo sandstone is, can act as an effective seal against the movement of CO_2 under certain relative permeability curves. This phenomenon was only observed in the small-scale Navajo simulation and not in either of the core flood simulations. It highlights the finding that using the wrong function or parameters can lead to erroneous predictions of CO_2 behavior. In the case of the small-scale Navajo simulations using the Pruess curve traps the CO_2 below a lithofacies with a lower permeability. This study has shown how critical it is to understand the relative permeability of the reservoir rock in question. Having a relative permeability curve derived from experimental data on the rock unit under study will greatly increase the accuracy of the model's predictions of CO_2 phase behavior and plume movement.

To summarize the important findings of our study:

1. Choice of relative permeability function and parameters can have a significant impact on predicted CO_2 plume migration, phase behavior, and storage capacity.
2. Using an experimentally derived relative permeability function and parameters from one material as a proxy for a different material can yield results worse than if a generic function and parameters were used.
3. Under certain conditions, the relative permeability parameters used can cause lower permeability lithofacies to act as effective seals to CO_2 movement.

REFERENCES

Allen, J., S.-Y. Lee, and S. Potter, *Construction of a 3D Geologic Model of the Aeolian Jurassic Navajo Sandstone in Central Utah for the Evaluation of CO2 Sequestration*, 2011, Utah Geological Survey.

Bennion, D.B. and S. Bachu, *Permeability and Relative Permeability Measurements at Reservoir Conditions for CO2-Water Systems in Ultra Low Permeability Confining Caprocks.* SPE International, 2007 (SPE Paper # 106995).

Bennion, D.B. and S. Bachu, *Supercritical CO2 and H2S - Brine Drainage and Imbibition Relative Permeability Relationships for Intergranular Sandstone and Carbonate Formations*. SPE International, 2006. SPE Paper#: 99326.

Brooks, R.H. and A.T. Corey, *Hydraulic Properties of Porous Media*, in *Hydrology Papers,* 1964: Colorado State University.

Chidsey, T.C. and L. Chamberlain, *Gordon Creek*, Utah Geological Survey: Salt Lake City, 1996.

Dullien, F.A.L., *Porous Media: Fluid Transport and Pore Structure*. Second ed, 1992, San Diego, CA: Academic Press, Inc.

Hood, J.W. and D.J. Patterson, *Bedrock Aquifers in the Northern San Rafael Swell Area, Utah, with Special Emphasis on the Navajo Sandstone*, in *Technical Publication No. 78,* 1984, United States Geological Survey: Salt Lake City.

Krevor, S.C.M., et al., *Relative permeability and trapping of CO2 and water in sandstone rocks at reservoir conditions*. Water Resources Research, 2012. 48(W02532).

Pruess, K., C. Oldenburg, and G. Moridis, *TOUGH2 User's Guide, Version 2.0*, 1999, Earth Sciencees Division, Lawrence Berkeley National Laboratory: University of California, Berkeley.

Pruess, K., et al., *Intercomparison of simulation models for CO2 disposal in underground storage reservoirs*, 2004, Lawrence Berkeley National Laboritory: Berkeley.

A PRELIMINARY STUDY ON THE APPLICABILITY OF THE TOUGHREACT CODE TO SOUTH AFRICAN COAL SEAM CO_2 STORAGE OPERATIONS: A SIMULATION TOOL THAT CAN MODEL POTENTIAL REGIONAL GROUNDWATER CONTAMINATION RISKS

Tshegofatso. O. P. Mophatlane

Wits University, Johannesburg, South Africa
Tshegofatso.Mophatlane@students.wits.ac.za

ABSTRACT

Carbon dioxide capture and storage (CCS) and underground coal gasification (UCG) are both clean development mechanism (CDM) technologies that have been considered, by the global leadership community, to collectively reflect a significant component of the global transition process towards a renewable energy economy. The hybrid technology has the potential to produce energy from gas, particularly for Integrated Combined Cycle Gasification (ICCG) plants, with lower GHG emissions as well as sequester the CO_2 by-product into the coal and remaining ash underground by injection. South Africa is currently the greatest emitter of the region. One of the hybrid technology's major challenges may be the significant threat that both technologies (CCS and UCG) pose to regional groundwater resources. The aim of this study is to determine the degree of applicability of the TOUGHREACT simulation code to South African coal seam CO_2 sequestration operations. Specific objectives include outlining the possible contamination risks that may threaten regional groundwater-resources quality. The methodology is that of a simple desktop study comparing this project's problem setup with the problem setup in the work of Xu et al. (2006). The Springbok Flats Basin Coalfield in South Africa is used as the case study. The research problem setup involves a shallow aquifer system overlying the coal seam storage site. The results show that, in the event of major CO_2 leakages, the aquifer would be at the risk of hexavalent chromium mobilization and contamination, which may also give rise to precipitation of various mineral phases, depending on the groundwater geochemistry and type of other precipitating mineral phases.

INTRODUCTION

There is an urgent need for catalyzed global carbon emission reduction, as global climate-change effects become more evident with passing time. The exact nature of the contribution of increasing atmospheric CO_2 to long-term effects on global climate is unclear and is still being investigated; however, it is generally accepted that the anthropogenic emission of CO_2 and other greenhouse gases (GHG's) may be the primary cause for the current trend of global climate change (Bryant, 1997; Surridge and Cloete, 2009; Cloete, 2010; Viljoen et al., 2010).

The current trend of global climate change has resulted in gradual increased increase worldwide in Carbon Capture and Storage (CCS) and Underground Coal Gasification (UCG) technology, making them a critical option in the portfolio of clean development mechanism (CDM) solutions for combating climate change (Ashworth et al., 2008; Surridge and Cloete, 2009; Beck et al., 2011).

These technologies have been considered by the global leadership community to collectively reflect a significant component of the global transition process towards a renewable energy economy. The hybrid technology has the potential to produce energy from gas, particularly for Integrated Combined Cycle Gasification (ICCG) plants, with lower GHG emissions, while capturing the CO_2 by-product from the synfuel and storing it in the remaining ash residue underground by means of injection (Shu-quin et al., 2007).

The two CDM technologies are important potential solutions, particularly for developing countries that have significant coal resources, (such as the countries of Southern Africa),

because emissions are expected to increase drastically in such regions (Chandler et al., 2002). The South African economy is currently the greatest GHG emitting economy of the region (Chandler et al., 2002), and its government has committed itself to the goal of being the leader in reducing emissions among the developing-countries community—provided there is adequate financial and research support from the developed-countries community.

One of the hybrid technology's major challenges may be the significant threat that both technologies (CCS and UCG) pose to regional groundwater resources, as illustrated by Figure 1. Previous work by Pruess (2010) and Tsang et al. (2008) has shown that CO_2 storage has the potential to contaminate overlying shallow potable groundwater resources. Carbon dioxide will tend to migrate upwards whenever preferential pathways are available; such as fault zones, bedding planes, joint network or improperly abandoned wells. Migration of CO_2 from storage can also be influenced by cap-rock failure (Rutqvist et al., 2008).

Minimal amounts of CO_2 do not pose a direct threat to potable groundwater (Wang and Jaffe, 2004). More attention should be directed towards evaluating the environmental impacts caused by the secondary effects of CO_2 leakage, namely the geochemical changes caused by the increased CO_2 dissolution in these systems; such as hazardous-trace-metal mobilization (Wang and Jaffe, 2004).

Enabling sustainable development and GHG emissions reduction involves adequate legislature which must be based on a rational, process-based understanding of CO_2 behaviour in the subsurface (Tsang et al., 2002, 2008) and likewise for UCG.

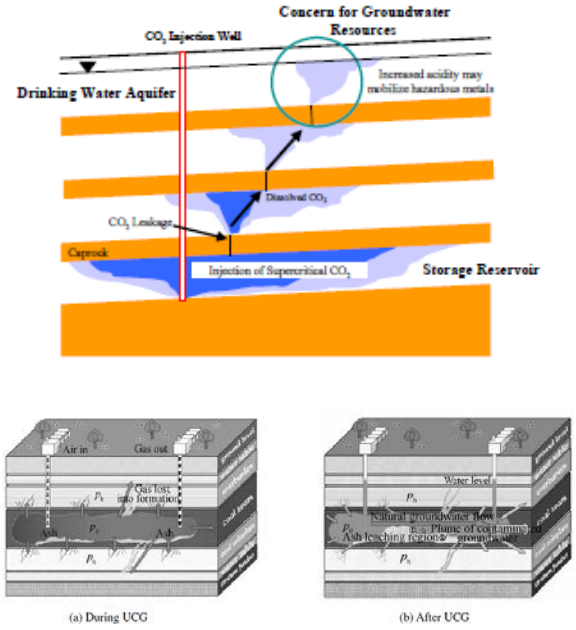

Figure 1. Conceptual model illustrating the possible groundwater contamination risks of CO_2 geological sequestration (Xu et al., 2006) and UCG contamination.

The aim of this investigation is to establish a qualitative rating for the applicability of the TOUGHREACT code to possible future South African coal-seam CO_2 sequestration operations. Specific objectives include outlining the possible hazardous metals that may threaten the groundwater resources of a regional aquifer system

The methodology involved a simple desktop study, which compared this project's problem setup with the problem setup in the work of Xu et al. (2006). The problem setup used in Xu et al. (2006) was modeled on U.S. Gulf Coast sandstone and Ohio carbonate-sandstone.

This research has used the Springbok Flats basin coalfield (Figures 2 -4) and the regional hydro-geological environment as a case study.

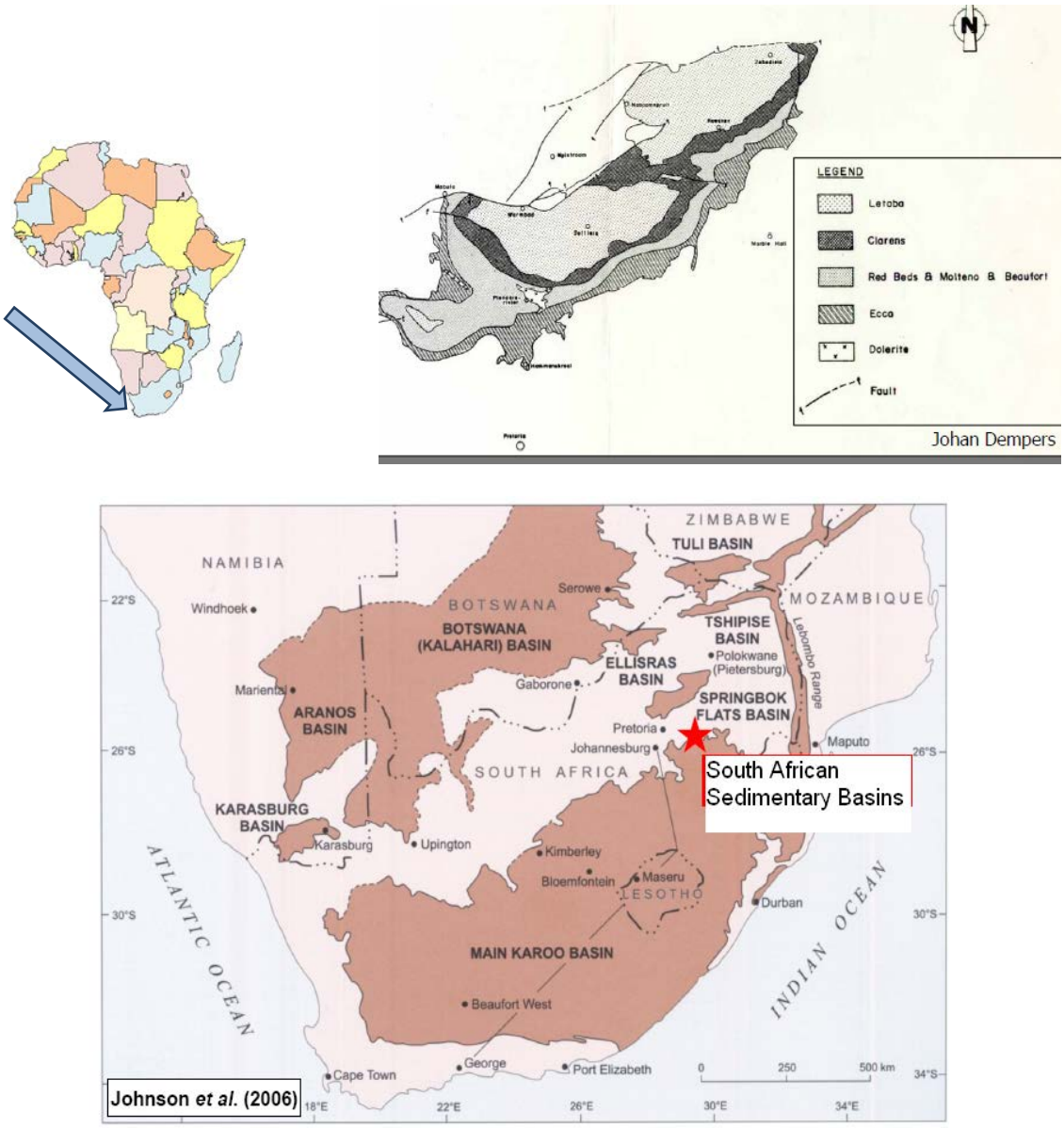

Figure 2. Locality Map of the Springbok Flats basin on the African continent, relative to the other Karoo age basins, illustrating the study area and a geological map of the basin. The geological map illustrates the 3 primary basalt provinces of the Springbok Flats basin

THE STUDY AREA

The problem setup of this paper involves a shallow weathered-zone aquifer system formed by the Clarens Formation Sandstone and Letaba Formation Basalt contact zone, (Figure 3). The coal zone is located within the Hamanskraal Formation and is located ~200 m below the aquifer system (Viljoen et al., 2010).

Topography and Climate

The southern Springbok Flats basin occurs within a relatively flat area with hills at places having elevations between 900 m and 1500 m above mean sea level. The region has a semi-arid climate of hot summers and cold winters and rainfall occurs between October to March receiving 400 mm–800 mm of rain per annum (Rambau, 2011).

Regional Hydrogeology

The primary aquifer of the Springbok Flats is the Karoo Supergroup rocks. The Springbok Flats Basin exists in what has been described as a weathered and fractured aquifer system, and within this aquifer system, groundwater flows through intergranular pores and fractures, in what is regarded as a double porosity system (Rambau, 2011).

The Springbok Flats aquifer system is considered to have high to moderate yielding boreholes, with yields ranging from 3*l*/s to 10 *l*/s making the aquifer system a very significant water source and thus of great importance to the regional communities and municipalities (Rambau, 2011).

The annual recharge of the aquifer system in this region was determined to be 78.10 × 10^6 m^3/a, with the main source of recharge being rainfall that infiltrates the aquifer in the highland areas such as the Waterberg Mountain (Rambau, 2011). The harvest potential of the aquifer has been given as 25 000 and 50 000m^3/km^2/a, as classified by the map of groundwater harvest potential that was published by the Department of Water Affairs (DWAF, 1998).

The Springbok Flats groundwater has been found to contain high concentrations of fluoride and nitrate, with nitrate particularly abundant in the basalt region, which exists primarily within the northern and central regions of the basin, with minor concentrations in the southern portion (Figure 2). In the northern and central regions, concentrations of nitrate regularly exceed 50 mg/*l* ($N0_x$-N).

Fluoride concentrations have been recorded up to 14 mg/*l*, while total dissolved solides (TDS) of up to 8000 mg/*l* have been measured, but is generally constricted between 200 mg/*l* and 1000 mg/*l* (Hobbs, 1996).

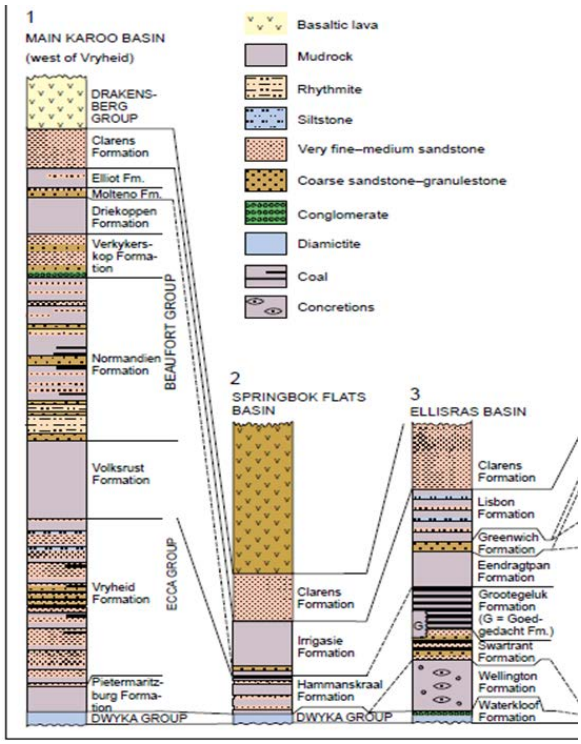

Figure 3. Stratigraphy of the Springbok Flats basin and its correlation with the main Karoo Supergroup in the northeastern part.

Coal Geology

The coalfield has been subdivided based on rank that occurs within the two sub-basins; the shallower northeastern section contains bright, higher-rank coal, while the deeper southwestern section contains raw coal of lower rank. The maximum thickness of Karoo sediments is 1000 m (Viljoen, 2010).

Previous work conducted in the Springbok Flats Basin with respect to CO_2 geo-sequestration has been carried out by Viljoen et al. (2010), who suggest that the possible sites that can accommodate CO_2 geo-sequestration within the basin can only be within the southwestern basin, due to depths there that are greater than 700 m. One of the proposed ideal geological mediums within the sub-basin is the coal zone of the Hamanskraal Formation (Viljoen et al., 2010).

The criteria used to classify the coal zone as a possible site is the potential for coal bed methane (CBM) recovery, the depths of the coal, the 65 m mudrock that has the potential to act as a cap rock, the lateral extent of the coal zone,

and regional dolerite intrusions that could influence CO_2 containment. (Cloete 2010; Viljoen et al., 2010).

There are no mining operations to date within the Springbok Flats coalfield, as this resource has been previously viewed as an unmineable field due to the depth, quality, and high uranium content of the resources (Christie, 1989; Jeffery, 2006; Cloete 2010; Viljoen et al., 2010).

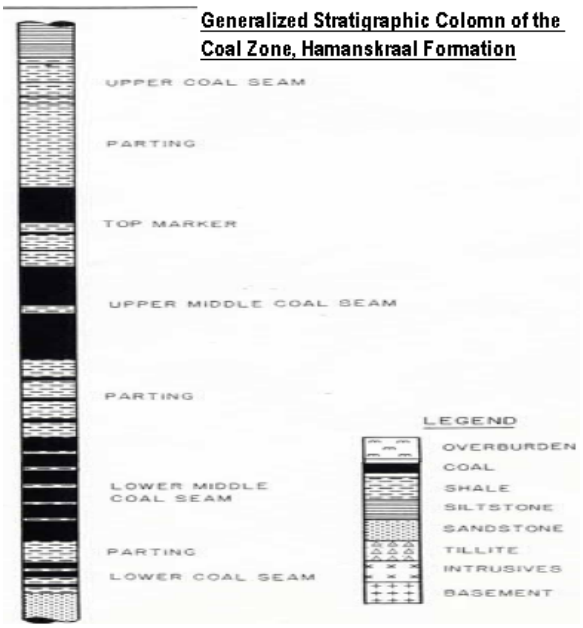

Figure 4. Generalized stratigraphy of the coal zone.

METHODS

Desktop Study

A simple desktop study of the area was undertaken in order to establish the boundaries of the aquifer system, as well as the hydrochemistry and the geochemistry of the aquifer material.

Modeling Approach

This research will only consider conceptual modeling, which will be used as a tool to rate the applicability of the TOUGHREACT code to potential SA CCS operations. The research problem setup is compared to that of Xu et al. (2006), which used the Texas Gulf Coast sandstones and shales as a case study.

A series of chemical kinetics is investigated in order to establish possible dissolution/ precipitation reactions that may take place within the aquifer due to the introduction of $CO_{2..}$ Since the aquifer system is composed of igneous and sedimentary sediments, it is expected to have a wide range of possible trace metal species that may be dissolved by the carbonated groundwater. Thus, for simplicity, this research has only considered the mobilization of Cr species and the possible oxidation of Cr (III) to Cr (IV), as illustrated below in Figure 6.

The provenance of the sandstone is an important aspect to consider when determining the risk associated with trace-metal mobilization by CO_2 contaminant plumes, particularly for hydrogeological modelling (Xu and Pruess, 2005; Wang and Jaffe, 2003; Xu et al., 2006; Little M. and Jackson R., 2010).

Basalts are formed from fractionated magmas and therefore will usually reflect trace-element variation. The Karoo Igneous Province lavas have been found to be layered, with a high Ti-Zr (low Fe) basalt at the base of the lava flow and a high Fe basalt towards the top of the sequence (Sweeny et al., 1994). The rocks have various compositions of Ti, P, Zr, Nb, Y, La, Ce, Nd, K, Rb, Ba, and Sr.

Table 1 lists the geochemical properties of a basalt province occurring in a sub-basin that has been correlated with the Springbok Flats Basin, the Ellisras (Waterberg) Basin, which lies north of the Springbok Flats Basin (Figure 2 and 3; Kalahari basin) (Barker et al., 2006). There is limited literature on the Springbok Flats basin basalts; however, the Ellisras basin basalts are sufficient for estimating the geochemical properties of the Springbok Flats basalt.

Once CO_2 has entered the aquifer, the pH of the system will drop, and a series of Cr reactions may occur, depending on the groundwater quality and geochemistry of the aquifer material (Wang and Jaffe, 2004).

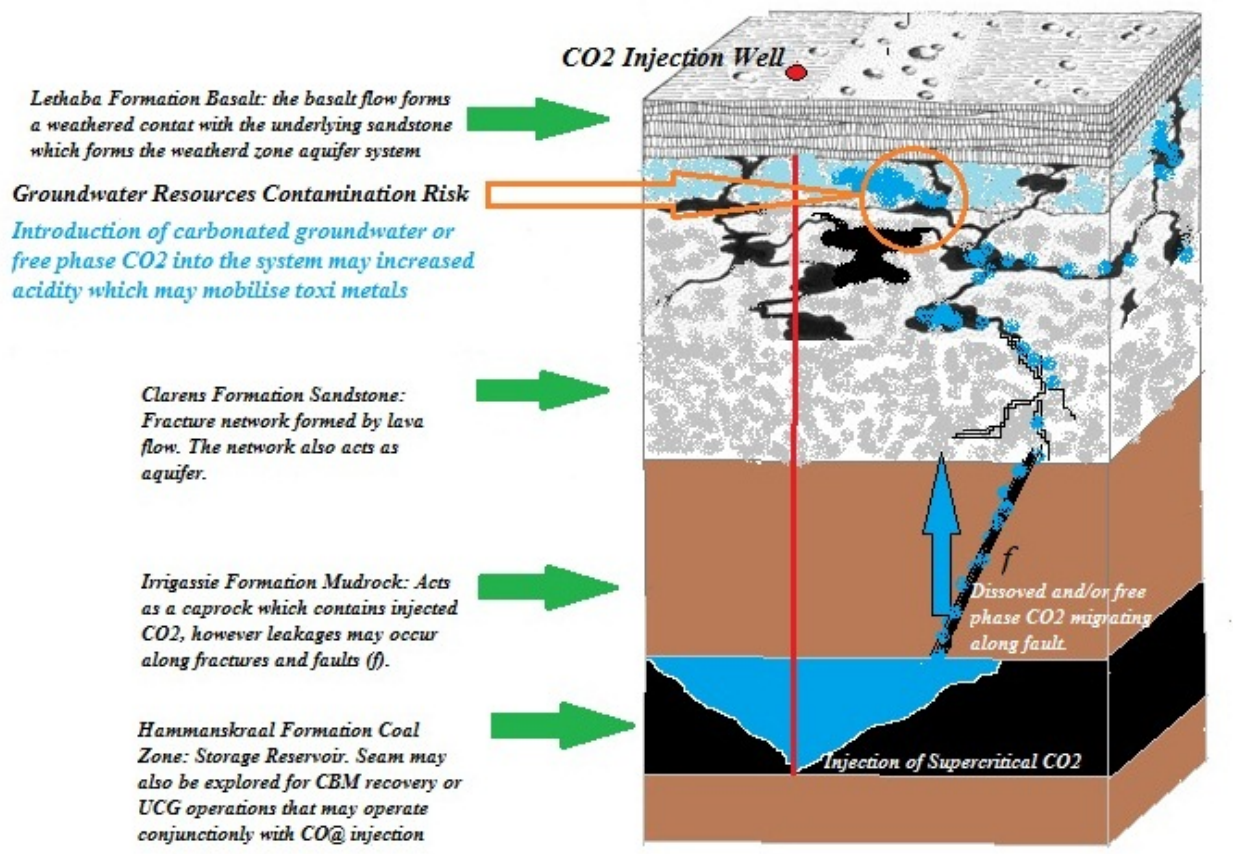

Figure 5. Simplified conceptual model of contamination risks that threaten the weathered-zone aquifer overlying the storage reservoir coal seam. The aquifer sits approximately 200 m above the coal seam

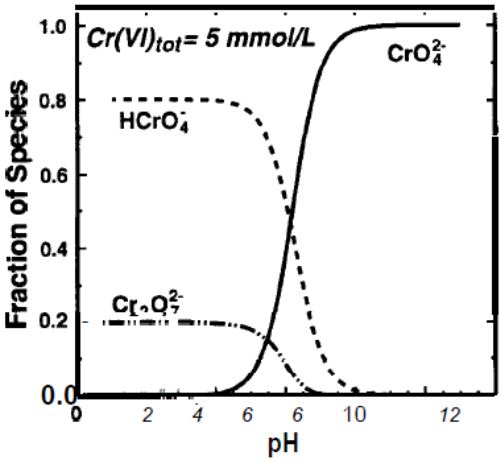

Figure 6. Distribution of Cr (VI) species as a function of pH (Palmer and Puls, 1994).

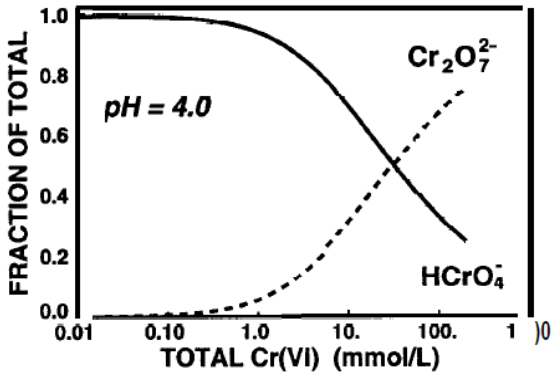

Figure 7. Fraction of bichromate ($HCrO_4^-$) and bichromate ($Cr2O^{2-}{}_7$) at pH 4 as a function of the total Cr (VI) concentration (Palmer and Puls, 1994.

Table 1. Major and minor geochemistry of a basalt lava flow occurring within the Ellisras basin. The boreholes were drilled in the Ellisras basin, Grootgelukke Mine. Major ions (above table) are reported in weight % oxides, while the trace metals are reported in ppm (Reid et al., 1997).

	ELB-4	ELB-15	ELB-20
SiO_2	48.70	50.53	50.43
TiO_2	0.77	0.85	0.87
Al_2O_3	15.22	14.65	14.84
Fe_2O_3	10.21	10.51	9.76
MnO	0.16	0.20	0.20
MgO	7.80	7.42	6.64
CaO	10.35	9.19	10.49
Na_2O	2.19	3.18	1.94
K_2O	0.52	0.67	0.39
P_2O_5	0.11	0.14	0.14
H_2O^-	1.87	1.12	2.15
LOI	1.26	1.96	1.80
TOTAL	99.15	100.42	99.65
Mo	1.4	<0.6	0.7
Nb	4.2	3.8	4.4
Zr	62	63	67
Y	21	22	22
Sr	171	273	192
U	<1.7	<1.6	1.6
Rb	10	11	5
Th	<2.3	<2.3	<2.3
Pb	<2.7	<2.7	2.8
Ba	125	167	126
Sc	30	30	34
Co	48	47	47
Mn	1219	1573	1524
Cr	313	330	335
V	191	210	268
Zn	75	68	77
Cu	41	38	77
Ni	96	83	75
La	12	12	10
Ce	15	14	14
Nd	10	8	9

Hexavalent chromium exists in aqueous state as monomeric ions H_2CrO_4, $HCrO_4^-$ (bichromate), and $CrO^{2-}{}_4$ (chromate), or as the dimeric ion $Cr2O^{2-}{}_7$ (bichromate) (Palmer and Wittbrodt, 1991). The monomeric chromate species are related through a series of acid dissociation reactions:

$$H_2CrO_4^0 \rightleftarrows HCrO_4^- + H^+ \quad ; K, \qquad 1$$

$$HCrO_4^- \rightleftarrows CrO_4^{2-} + H^+ \quad ; K_2 \qquad 2$$

The pK values are -0.86 and 6.51, respectively (Alison et al., 1990). Bichromate is the result of polymerization of the monomeric bichromate ions to form the dimer $Cr2O^{2-}{}_7$, where pK_d is -1.54 (Allison et al., 1990). The relative concentration of each of these species depends on both the pH of the contaminated water (Figure 6) and the total concentrations of Cr(VI) (Figure 7).

$$HCrO_4^- + HCrO_4^- \rightleftarrows Cr_2O_7^{2-} + \& O \quad ; K_d \qquad 3$$

In the Cr(lll)-H_20 system, Cr(lll) exists predominantly as Cr^{3+} below pH 3.5. With increasing pH, hydrolysis of Cr^{3+} yields $CrOH^{2+}$, $Cr(OH)_2^+$, $Cr(OH)_3$;, and $Cr(OH)_4^-$ (Rai, et al., 1987). In the presence of Fe(lll), trivalent chromium can precipitate as a solid solution. If the pH within the contaminant plume is between 5 and 12, the aqueous concentration of Cr(lll) should be less than 1 µmole/L (<.05 mg/L) (Figure 8).

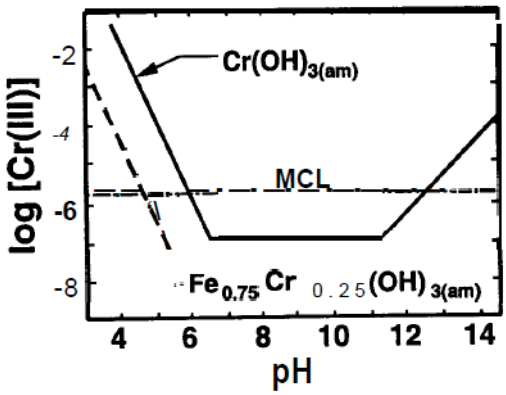

Figure 8. Cr (III) concentration in equilibrium with Cr $(OH)_{3(am)}$ and $Fe_{0.75}Cr_{0.25}(OH)_3$, based on data from Rai et al., (1987) and Sass and Rai (1987), respectively.

Oxidation of Cr (III) to the Toxic Hexavalent Chromium (Cr(VI)) in Groundwater

There are only a few chemical mechanisms for the oxidation of Cr(III) (Bartlett and James, 1979). Only two constituents in the environment

are known to oxidize Cr(III) to Cr(IV): oxygen and manganese dioxides (MnO_2) (Earl and Rai, 1987). Previous work by Schroeder and Lee (1975), and Eary and Rai (1987), has shown that the transformation of Cr(III) by dissolved oxygen is not likely to be a significant mechanism for the oxidation of Cr (III), particularly in groundwater systems.

The other component, MnO_2, has been observed by Bartlett and James (1979); Earl and Rai, (1987); Fendorf and Zasoski (1992) and Risser and Bailey (1992) to have a more significant correlation with Cr (III) oxidation in soils. They found that there is an increase in the rate and amount of Cr (III) oxidation as pH decreases. Experimental results indicate that the oxidation follows Reaction 4:

$$CrOH^{2+} + 1.5\ \delta\text{-}MnO_2 \rightarrow HCrO_4^- + 1.5Mn2+ \quad 4$$

Cr (VI) can be reduced to Cr (III) by a range of various constituents in the environment, such as ferrous (Fe (II)) ion minerals, such as pyrite, reduced sulphur, and soil organic matter (Palmer and Puls, 1994). An example of a Cr (VI) reducing to Cr(III) is given by Reaction 5:

$$HCrO_4^- + 31\%^{2+} + 7H^+ + Cr^{3+} + 3Fe^{3+} + 4H_2O \quad 5$$

The reduction of hexavalent chromium can be limited by a range of compounds such as high sulphate concentrations in groundwater (>2000 mg/L), oxic conditions in the unsaturated zone, high-nitrate concentrations (> 200 mg/L as N). A hydrogeological regime that has high nitrate concentrations will have Cr (VI) plumes persistent in both the unsaturated and saturated zones (Izbicki et al., 2008).

There are several chemical dynamics that involve the reduction of Cr (VI) to Cr (III), also referred to as Cr (VI) attenuation. However, this paper focuses exclusively on the mechanisms that may increase the concentration of Cr (VI) in groundwater, with respect to sequestrated CO_2 leaking into the aquifer.

DISCUSSION AND CONCLUSION

Geological sequestration of CO2 has the potential to mitigate GHG emissions more than any other clean development mechanism (CDM) technology (Ashworth et al., 2008; Surridge and Cloete, 2009; Cloete, 2010; Viljoen et al., 2010; Beck et al., 2011), especially if considered together with coal bed methane recovery and/or underground coal gasification. This technology will therefore represent a significant option for developing countries, particularly South Africa (Beck et al., 2011).

The weathered-zone aquifer of the Springbok Flats basin is a significant shallow aquifer that is extensively used throughout the basin (Heaton, 1985, Rambau, 2011) and represents a resource that would be directly at risk to CO_2 contamination upon commencement of operations. The groundwater resource lies 200m above the coal zone.

The basalt/sandstone sediment aquifer is expected to have a significant Cr content, as illustrated by the Ellisras basalts (Reid et al., 1997), which opens the window to Cr (VI) mobilization and contamination. The probability of Cr (VI) contamination is increased by a decrease in pH (which would be caused by introducing CO_2), the high Mn content of the basalts (Table 1), which bind with oxygen to form MnO_2, which in turn acts as a powerful oxidant to Cr (III), transforming it to the toxic Cr (VI).

The observed high concentrations of nitrate in the Springbok Flats basalt aquifer (Heaton, 1985, Rambau, 2011) is also a major contributor to Cr (VI) contamination (Izbicki et al., 2008).

Such contamination risks should be thoroughly considered and researched in order for adequate site characterization, selection, and policy development, as hexavalent chromium species are extremely toxic—a parameter that should be carefully considered as well as monitored during CO_2 sequestration operations by all stakeholders.

The problem setup of this paper has illustrated that the TOUGHREACT software package has the potential to model contamination risks of CO_2 coal sequestration operations; and thus holds the potential to greatly assist the South African CCS industry in developing a preliminary legislative framework that may be utilized for test injections.

REFERENCES

Abbasi, S.A. and R. Soni, 1984. *Teratogenic Effects of Chromium(VI) in the Environment as Evidenced by the Impact of Larvae of Amphibian **Rand** tigrina: Implications in the Environmental Management of Chromium*. Int. J. Environmental Studies, 23: 131-137.

Allison, J. D., D.S. Brown, K.J. Novo-Gradac, 1990. *MlNTEQA2/PRODEFA2, A Geochemical Assessment Model for Environmental Systems: Version 3*.0. U.S. Environmental Protection Agency, Athens, GA.

Ashworth P, Pisarski A, and Thambimuthu K. 2008; *Public acceptance of carbon dioxide capture and storage in a proposed demonstration area*; Journal of Power and Energy, v223. Part A

Barker O.B., Brand G., Callaghan C.C., Eriksson P.G., van der Neut M., 2006. *The Soutpansberg and Watersberg Groups and the Blouberg Formation.* In: MR Johnson. CR Anhaeusser, RJ Thomas (eds): *The Geology of South Africa.* Geological Society of South Africa, Johannesburg and Council for Geoscience, Pretoria, pg 301 – 318

Bartlett, R.J. and B.R. James, 1979. *Behavior of Chromium in Soils:* Ill. Oxidation. J. Environmental Quality, 8(1):31-35.

Beck B., Surridge T., Liebenberg J., Gilder A., 2011. *The Current Status of CCS development in South Africa.* Journ. of Energy Procedia 4, pp 6157 – 6162

Bryant E. *Climate process and changes*. Cambridge: Cambridge University Press; 1997.

Christie, A.D.M., 1989 *Demonstrated coal resources of the Springbok Flats*

Coalfield. Internal Report No. 1989–0069, Geological Survey.

Chandler W., Secrest T.J. and Logan J., 2002. *Climate change mitigation in developing countries. Brazil, China, India, Mexico, South Africa and Turkey.* Pew Centre on Global Climate Change, Arlington (USA),

Cloete M., 2010, *Atlas on geological storage of carbon dioxide in South Africa*, Council for Geosciences

Department of Water Affairs and Forestry (DWAF) 1998. *The Groundwater Harvest Potential Map of the Republic of South Africa*. Technical Report Gh 3917. Directorate Geohydrology, Department of Water Affairs and Forestry, Pretoria

Eary, L.E. and D. Rai, 1987. *Kinetics of Chromium(lll) Oxidation to Chromium(VI) by Reaction with Manganese Dioxides*. Environmental Science and Technology, 21 (12):1 187-1193

Fendorf, S.E. and R.J. Zasoski, 1992. *Chromium (Ill) Oxidation by 13-MnOz. 1. Characterization*. Environmental Science and Technology, 26: 79-85.

Heaton T.H.E., 1985. *Isotopic and chemical aspects of nitrate in the groundwater of the Springbok Flat.* Journal of Water SA. 11:4, pp 199

Hobbs, P.J., 1996: JICA study - *Situation report on the geology, soils and hydrogeology of the Magalies Water extended supply area*; Report prepared for EVN Consulting Engineers by VSA GeoConsultants, Pretoria

Izbicki J., Kulp T,. Bullemn T,. Ball J.W., And O'Leary D., 2008. *Chromium mobilization from the unsaturated zone*. Abstract for Goldschmisdt Conference, 13 -18 June, Tennessee, USA

Jeffrey L.S., 2006; *Characterization of the coal resources of South Africa*, The Journal of The South African Institute of Mining and Metallurgy, pp95-102

Little M. and Jackson R., 2010; *Potential Impacts of Leakage from Deep CO2 Geosequestration on Overlying Freshwater Aquifers;* Environmental Science Technology, v44, p. 9225 -9232

Mancuso, T.F. and W.C. Heuper, 1951. *Occupational Cancer and Other Health Hazards in a Chrome Plant.* A Medical Appraisal. L Lung Cancers in Chromate Workers. Ind. Med.Surg., 20: 358-363.

Nxumalo. V. *Stratigraphy and Basin Modelling of the Gemsbok Sub-basin (Karoo Supergroup) of Botswana and Namibia,* MSc Dissertation, University of the Witwatersrand

One, B.-L, 1988. *Genetic Approaches in the Study of Chromium Toxicity and Resistance in Yeast and Bacteria. IN: Chromium in the Natural and Human Environments*, Vol. 20 (J.O. Nriagu and E. Nieboer, editors). John Wiley& Sons, New York: 351-368.

Palmer, C.D. and P.R. Wittbrodt, 1991. *Processes Affecting the Remediation of*

Chromium-Contaminated Sites. Environmental Health Perspectives, 92: 25-40.

Palmer C.D. and Puls R.W., 1994 *Natural Attenuation of Hexavalent Chromium in Groundwater and Soils*. EPA Groundwater Issue, US Environmental Protection Agency, EPA/540/5-94/505.

Pruess, K., 2010. *Mathematical models as tools for probing long-term safety of CO2 storage. Lawrence Berkeley National Laboratory LBNL-1587E, University of California.*

Rai, D., B.M. Sass, and D.A. Moore, 1987. *Chromium(lll) Hydrolysis Constants and Volubility of Chromium(lll)* Hydroxide Inorg. 26(3): 345-249.

Rambau E., 2011., *Hydrogeological desktop study for determining the groundwater balance for the proposed Bela Bela Agri Lifestyle Village***.** Geo Pollution Technologies, Report prepared for ENVASS, Pretoria

Reid, D.L. Rex D.C. and Brandl G., 1997.*Karoo basalts in the Ellisras sub-basin, Northern Province* S. Afr. J. Geol, 100: 2pp 151-156

Riser, J.A. and G.W. Bailey, 1992. *Spectroscopic Study of Surface Redox Reactions with Manganese Oxides.* Soil Science Society of America Journal, 56: 82-88.

Rutqvist, J., J. Birkholzer and C.F. Tsang. *Coupled Reservoir-geomechanical Analysis of the Potential for Tensile and Shear Failure Associated with CO2 Injection in Multilayered Reservoir-caprock Systems*, *Int. J. Rock Mech. Mining Sci.*, Vol. 45, No. 2, pp. 132–143, February 2008.

Sass, B.M. and D. Rai, 1987. *Volubility of Amorphous Chromium(lll)-lron(ill) Hydroxide Solid Solutions. Inorg.* Chem., 26(14): 2228-2232.

Schroeder D.C. and G.F. Lee, 1975. *Potential Transformations of Chromium in Natural Waters. Water, Air, Soil Pollution*, 4: 355-365.

Shu-qin L., Jing-gang L.I., MEI M., Dong-lin D., 2007. *Groundwater Pollution from Underground Coal Gasification.* J. of China University of Mining & Technology. V17:4. pp 0467 -0472.

Surridge A. and Cloete M., 2009., *Carbon Capture and Storage in South Africa*. Joun. of Energy Procedia 1, pp2747-2744

Sweeny R. J., Duncan A.R., and Erlank A.J., 1994. *Geochemistry and Petrogenesis of Central Lebombo Basalts of the Karoo Igneous Province*. J. of Petrology, 35:1, pp 95-125

Tsang, C.F., S.M. Benson, B. Kobelski and R.E. Smith. *Scientific Considerations Related to Regulation Development for CO2 Sequestration in Brine Formations*, Environmental Geology, Vol. 42, pp. 275–281, 2002.

Tsang, C.F., J. Birkholzer and J. Rutqvist. *A Comparative Review of Hydrologic Issues Involved in Geologic Storage of CO2 and Injection Disposal of Liquid Waste*, Env. Geol., Vol. 54, No. 8, pp. 1723–1737, DOI 10.1007/s00254-007-0949-6, June 2008

Wang S. and Jaffe P.R., 2004. *Dissolution of a mineral phase in potable aquifers due to CO_2 releases from deep formations; effect of dissolution kinetics*. Journ. Of Energy Conversion and Management. 45, p 2833 - 2848

van Weerelt, M., W.C. Pfeiffer, and M. Fiszman, 1984. *Uptake and Release of 5'Cr(Vl) and 51 Cr(lll) by Barnacles.* Mar. Environ. Res. 11 :201-211.

Viljoen J.H.A., Stapelberg F.D.J. and Cloete M., 2010. *Technical Report on the Geological Storage of Carbon Dioxide in South Africa*. Council for Geosciences. ISBN 978-1-9202266-25-1

Xu, T., E.L. Sonnenthal, N. Spycher, and K. Pruess 2006.*TOUGHREACT – A simulation program for non-isothermal multiphase reactive geochemical transport in variably saturated geologic media: Applications to geothermal injectivity and CO2 geological sequestration*, Computer & Geoscience, v. 32 p. 145-165

Xu, T., J.A. Apps and K. Pruess. 2005. *Mineral Sequestration of Carbon Dioxide in a Sandstone-Shale System*, J. Chemical Geology, Vol. 217, pp. 295–318.

PRELIMINARY MODEL-COMPARISON RESULTS FROM THE SIM-SEQ PROJECT USING TOUGH2, STOMP, ECLIPSE, AND VESA APPROACH

Sumit Mukhopadhyay[1], Christine Doughty[1], Diana Bacon[2], Giacomo Bacci[3], Rajesh Govindan[3], Ji-Quan Shi[3], Sarah Gasda[4], Ramya Ramanathan[2], Jean-Philippe Nicot[5], Seyyed Hosseini[5], and Jens T. Birkholzer[1]

(1) Earth Sciences Division, Lawrence Berkeley National Laboratory (LBNL), One Cyclotron Road, Berkeley, CA 94720, USA
(2) Pacific Northwest National Laboratory (PNNL), Richland, WA 99352
(3) Imperial College London (ICL), South Kensington Campus, London SW7 2AZ, UK
(4) Centre for Integrated Petroleum Research, Uni Research, 5020 Bergen, Norway
(5) Bureau of Economic Geology (BEG), University of Texas at Austin, Austin, TX 78713, USA

e-mail: SMukhopadhyay@lbl.gov

ABSTRACT

Sim-SEQ is an international initiative on model comparison for geologic carbon sequestration (GCS), with an objective to understand and, if possible, quantify model uncertainties. Model comparison efforts in Sim-SEQ are initially limited to one specific field test site, hereafter referred to as the Sim-SEQ Study site (or S-3 site). Within Sim-SEQ, different modeling teams are developing conceptual models of CO_2 injection at the S-3 site. One of the conceptual models, developed by the LBNL team, is based on TOUGH2/EOS7C. In this paper, we present some preliminary model predictions of the S-3 site using the TOUGH2/EOS7C simulator. We also compare the predictions of the TOUGH2 simulator with three other conceptual models, developed by three different organizations, of the S-3 site.

INTRODUCTION

Because of the complexities of subsurface flow and transport processes, choices made while developing conceptual and numerical models for GCS applications may result in a wide range of model predictions, even with each of these models considering the same injection scenario at the same GCS site.

To identify the sources of model uncertainty and, if possible, quantify these uncertainties, we must perform a model comparison study involving both model-to-data and model-to-model comparisons at one or more selected GCS field sites. To accomplish this goal, the United States Department of Energy (USDOE) has initiated a model comparison study, named Sim-SEQ, for GCS.

The objectives of Sim-SEQ, its scope, and its present status can be found in Mukhopadhyay et al. (2012). Briefly, the Sim-SEQ project intends to objectively evaluate the modeling efforts of different groups as they are applied to CO_2 injection field tests. Sim-SEQ began in April 2011 with four modeling teams (all from the United States), but has since then rapidly developed into an international collaboration project with 15 modeling teams from eight countries. A list of the organizations/institutes participating in Sim-SEQ, and the software/modeling approaches that these teams are using, is provided in Mukhopadhyay et al. (2012).

The primary focus of the model comparison effort in the Sim-SEQ project is to correctly predict the behavior of the injected CO_2 plume at the S-3 site. The target formation for injection at the S-3 site comprises fluvial deposits of considerable heterogeneity and is located in the water leg of an active CO_2-EOR field with a strong water drive (Hovorka et al., 2011). These features add significant complexity when approximating the natural system, and challenges arise in dealing with boundary conditions. In addition, the presence of methane has been confirmed in the brine, which can potentially exsolve and impact pressure buildup history and CO_2 plume extent.

The TOUGH2 numerical code (Pruess et al., 1999) has an established reputation for reliably simulating flow and transport behavior in complex subsurface systems. The first objective of this paper is to present a conceptual model of the CO_2 injection scenario at the S-3 site based on the EOS7C module (Oldenburg et al., 2004) of the TOUGH2 simulator, and to illustrate its usefulness in simulating a complex geological system comprised of water, supercritical CO_2, and CH_4. Our second objective is to compare the TOUGH2 predictions against results from other conceptual models based on different simulators. For this purpose, we have selected results from three other groups within the Sim-SEQ project.

We begin the paper by briefly introducing the S-3 site. We then describe the conceptual representation of the S-3 site based on TOUGH2 and the other three conceptual models. Next, we present the results based on TOUGH2 and compare them against the other three models. The paper concludes by summarizing the findings from this preliminary model comparison study, and by making recommendations for future extensions of the Sim-SEQ project.

THE S-3 SITE

The S-3 site is patterned after the Southeast Regional Carbon Sequestration Partnership (SECARB) Phase III Early Test in the southwestern part of Mississippi (USA). A description of the geology of the site can be found in Hovorka et al. (2011). The target formation for injection at the S-3 site is comprised of fluvial sandstones of the Cretaceous lower Tuscaloosa Formation at depths of 3300 m, which form a 4-way anticline cut by a northwest-trending fault (Figure 1). The complex geological features of the site present an opportunity for studying how well the sedimentary architecture controls fluid flow.

Denbury Onshore LLC (hereafter referred to as Denbury) has hosted the SECARB Phase II and Phase III tests in a depleted oil and gas reservoir under CO_2 flood since 2007. The tests are managed by the Bureau of Economic Geology (BEG) at the University of Texas, Austin. The Phase III Early Test started in April 2009 with CO_2 injection in the eastern block of the northwest-trending fault, in an area commonly known as the High Volume Injection Test (HiVIT) area, as shown in Figure 1. The Sim-SEQ project focuses on one part of the HiVIT, referred to as the Detailed Area Study (DAS), located in the water leg of the reservoir, outside of but close to the reservoir under CO_2 flood.

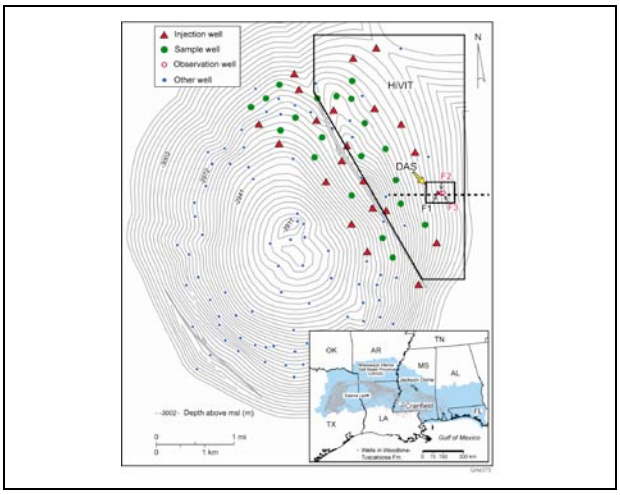

Figure 1. Location map of the S-3 site including the HiVIT and DAS

The DAS area has been designed to collect dense time-lapse data from an array of three closely spaced wells (i.e., F-1, F-2, and F-3), with injection occurring through well F-1 and the other two serving as observation wells, located downdip of F-1. The surface locations of the three wells are aligned approximately in an east-west direction, with F-2 positioned 70 m of F-1 to the west and 30 m of F-3 to the east. Injection in the DAS area (through well F-1) started in December 2009. The observed injection rate and the bottomhole temperature at the injection well are shown in Figure 2.

CONCEPTUAL MODELS

Here, we focus on four different conceptual models of the S-3 site. These models are the LBNL Model (developed by Lawrence Berkeley National Laboratory), the PNNL Model (developed by the Pacific Northwest National Laboratory), the ICL Model (developed by Imperial College, London) and the Vertical Equilibrium Sub-scale Analytical or VESA Model (developed by Center for Integrated Petroleum Research, Uni Research, Norway). We first present the essential features of these four conceptual models.

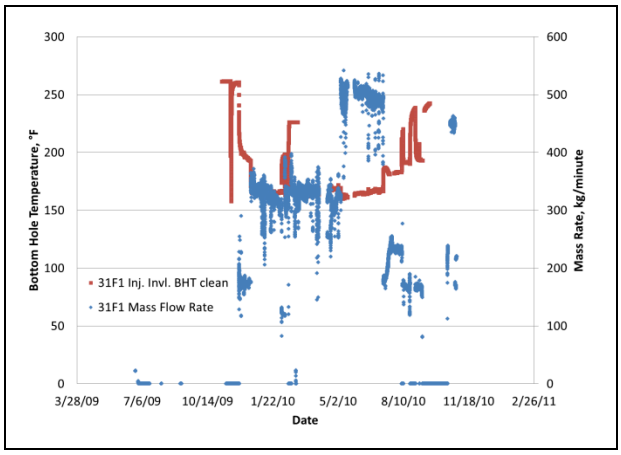

Figure 2. Observed injection rate and bottom-hole temperature at injection well F-1

LBNL Model

Modeling Software

The LBNL Model is based on the numerical simulator TOUGH2 (Pruess et al., 1999) and the equation-of-state module EOS7C (Oldenburg et al., 2004). The EOS7C module is suitable for simulating storage of CO_2 in formations containing water and methane. There is no single TOUGH2 fluid property module presently available that can handle all the features of the S-3 site. EOS7C is used for the present studies, which means that methane can be included but salinity effects on solubility cannot be considered. The temperature range in TOUGH2-EOS7C is wide enough such that the actual formation temperature (~127°C) can be represented.

Model domain and numerical grid

Figure 3 shows the boundaries (thick black lines) of the model domain (4,000 m × 5,200 m) and the numerical grid, which are superimposed on the contour map of the structural dome at the S-3 site. The model covers just one flank of the dome, and for simplicity is modeled as a tilted plane. The plane of the model is tilted two degrees down from the fault (shown in yellow). Voronoi tessellation is used rather than a rectangular grid to allow for local grid refinement and to eliminate grid orientation effects. The red box shows the fine-grid region in which the CO_2 plume is expected to remain. There are 621 gridblocks per layer, and 8 layers, for a total of 4,968 gridblocks.

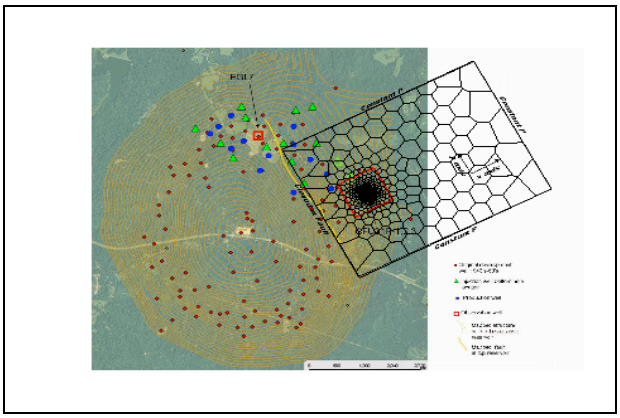

Figure 3. Plan view of the model domain and the numerical grid for the LBNL Model

Rock properties

Permeabilities were inferred from well logs at the injection well (F-1). The first step for assigning model permeabilities was to scale the well-log permeabilities, so that their depth-averaged values over the open interval equaled the permeability values inferred from the well test. Horizontal permeability for the model was obtained by arithmetic averaging of the well-log permeabilities. Vertical permeability was obtained by harmonic averaging of the well-log permeabilities. To reduce vertical permeability relative to horizontal permeability, we also applied an anisotropy factor (0.5).

No lateral property variation in the formation is included. A well test at the injection well indicates a large skin value. This is approximately included in the model by decreasing the permeability in the column of gridblocks representing the injection well, such that the modeled pressure at the injection well matches the observed pressure. No site-specific information is used for characteristic curves. Liquid relative permeability is Corey-like, and gas relative permeability has a similar form. Gas residual saturation is assumed to be zero (i.e., residual-phase trapping is not considered), which is considered reasonable only for the injection period. Capillary pressure strength is inversely proportional to the square root of permeability.

Initial and boundary conditions

Initial conditions for CO_2 injection consist of a water-saturated formation at constant temperature (127°C) and hydrostatic pressure (about 32.0 MPa). The formation water is saturated

with dissolved CH_4. The left boundary of the model is closed to fluid flow, since it coincides with a fault believed to be sealing. The other model boundaries in the horizontal plane (see Figure 3) are constant-pressure boundaries. Top and bottom boundaries are no-flow boundaries.

Injection consists of 92% CO_2 and 8% CH_4 (mole %). A variable injection rate was used in these simulations—see more discussion on this below. Injection was first modeled with a mass source in each model layer corresponding to the open well interval, with the fraction of fluid going into each layer proportional to the permeability-thickness product of that layer. As an alternative, injection was introduced at the top model layer representing the open well interval, with a high vertical permeability assigned to the gridblocks representing the open interval. The second option was finally selected, because it provided more accurate distribution of the CO_2 (i.e., because it accounted for the density difference between water and CO_2).

PNNL MODEL

Modeling software

The PNNL Model is based on the STOMP-WCSE simulator (White and Oostrom, 2006), which can model nonisothermal systems consisting of water, CO_2, and salt. However, it does not include CH_4. This is in contrast to the LBNL Model, which includes CH_4 but ignores the presence of salt.

Model domain and numerical grid

The PNNL Model covers an area of 3,200 m × 3,200 m in the horizontal plane centered on the injection well (F-1), and has 16 layers in the vertical direction. The model domain is bounded on the left-hand side by the sealing fault. A boundary-fitted grid was developed using the surface provided for the top of the lower Tuscaloosa formation. Irregular grid spacing was used to better capture the breakthrough times at the observation wells. There are in total 53×53×16 gridblocks in the numerical grid (Figure 4).

Rock properties

Porosity and permeability values used in the PNNL Model are based on cores obtained from the two observation wells (F-2 and F-3). The measured porosity values have a range of 1.29–31.44% with a mean of 21.76%. Measured permeability values were spread over almost five orders of magnitude (0.01–1890 mD), with a geometric mean of 2.91 mD. From the well logs, a total of 14 facies were identified. For simplicity, these were recombined into three facies: Facies 1 (consisting of sandstone), with porosity of 27% and mean permeability of 360 mD; Facies 2 (consisting of sandstone and limestone), with porosity of 26% and mean permeability of 44 mD; and Facies 3 (all other materials), with porosity of 16% and mean permeability of 9 mD.

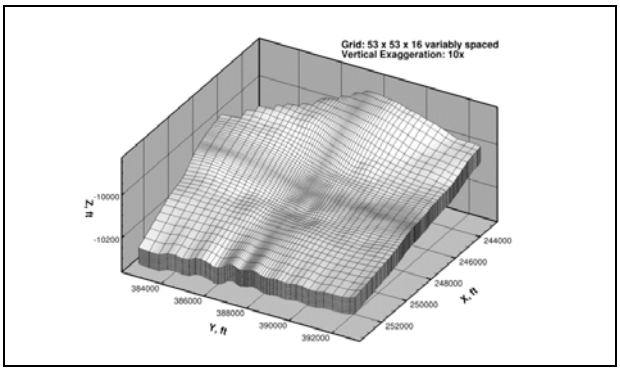

Figure 4. Numerical grid used in the PNNL Model

The program TPROGS (Carle and Fogg, 1997) was used to generate three transition probability-based facies models assuming a fluvial depositional environment. Permeability and porosity were assumed constant within each facies, and different values were assigned to each facies corresponding to the mean values mentioned above. Three additional realizations were generated, where porosity and permeability within each facies followed a uniform random distribution. Finally, three more realizations were generated where porosity and permeability followed a Gaussian random distribution. Overall, nine realizations of the porosity-permeability field were generated.

The thermal properties of the formation were taken from typical values for sand, with a thermal conductivity of 0.582 W/m K and a specific heat capacity of 700 J/kg K. A Brooks-Corey saturation function was fitted to laboratory measurements, using parameters scaling with intrinsic permeability, with an assumed residual saturation of 1%. A Burdine porosity distribu-

tion model was assumed for the calculation of relative permeability. The maximum entrapped gas saturation was assumed to be 20%.

Initial and boundary conditions

The model domain was assigned an initial pressure of 32.3 MPa, a temperature of 128°C, and a dissolved salt mass fraction of 0.157. The initial pressure and temperature were taken from the observed pre-injection values in the injection well. The dissolved salt mass fraction was calculated from the geochemical analysis provided for Lower Tuscaloosa brine. Fluid pressures were allowed to reach hydrostatic equilibrium before the start of CO_2 injection. The four lateral boundaries were held at their initial hydrostatic values, while the corner boundary corresponding to the fault was assumed no-flow. Top and bottom boundaries were also assumed closed to flow.

A well model in STOMP-WCSE was used to simulate CO_2 injection. A well model is defined as a type of source term that extends over multiple grid cells, where the well diameter is smaller than the grid cell. The CO_2 injection rate is proportional to the pressure gradient between the well and the surrounding formation in each grid cell. A bottomhole pressure is calculated iteratively until either maximum borehole pressure or the desired injection rate is reached.

ICL Model

The ICL Model of the S-3 site is based on the E300 module of the ECLIPSE compositional reservoir simulator (http://www.slb.com/services/software/reseng/compositional.aspx). In the E300 module the CO2STORE option was used. This option can handle three phases, which are a CO_2-rich phase, an H_2O-rich phase, and a solid phase. The CO_2-rich phase is labelled the gas phase, while the H_2O-rich phase is labelled the water phase (liquid phase). The mutual solubilities of CO_2 and H_2O are calculated to match experimental data for CO_2-H_2O systems under typical CO_2 storage conditions: 12–100°C and up to 600 bar.

The ICL Model spans a distance of 2000 ft in both the *x* and *y* directions. In the vertical (*z*) direction, the grid is 80 ft thick and centered on the injection well (F-1). Figure 5 shows a schematic diagram of the model domain. Different values of pore volume multipliers were used on each of the four sides of the model to represent the larger size of the site. The grid has 8 layers in the vertical direction. Gridblocks within each layer have the same porosity and permeability values, though they are different from one layer to another. Porosity and permeability values are estimated from core plugs. It is assumed that only water and CO_2 are present in the system. The ICL model uses the actual observed injection rate (Figure 2).

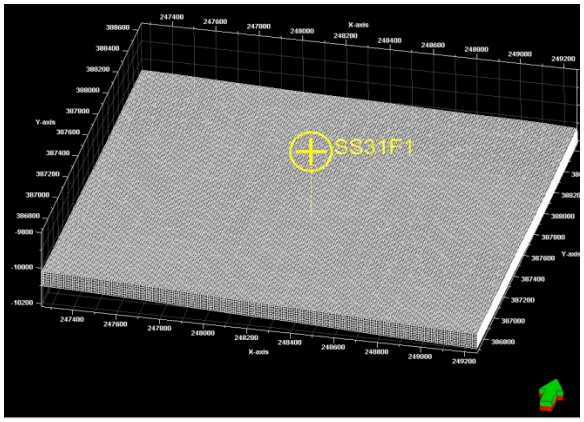

Figure 5. Numerical grid used in the simulations using the ICL Model

VESA Model

The VESA approach (Gasda et al., 2009) is derived through vertical integration of the three-dimensional governing equations for two-phase flow under the assumptions of vertical equilibrium, complete gravity segregation, and capillary equilibrium between CO_2 and brine (Gasda et al., 2009). The resulting model is a two-dimensional model for flow in the lateral directions. The vertically upscaled equations account for fluid and matrix compressibility, as well as hysteresis in the relative permeability function. Solubility of CO_2 in brine is also considered in the upscaled model, which is comprised of equilibrium partitioning into the regions containing residual brine and residual CO_2. No convective mixing is considered in these simulations.

The two-dimensional upscaled equations were discretized on a 201×201 grid using a standard finite difference approximation. The grid has a constant spacing of about 10 ft. For this system,

fluid properties are assumed to be incompressible and constant in space and time. Brooks-Corey-type relative permeability functions are used. The capillary pressure-saturation relation is assumed to be a van Genuchten type. Rock properties are assumed to be homogeneous and isotropic. CO_2 was injected at a constant rate of 4.6 kg/s for a period of 1 year.

RESULTS

Modelers have built their models based on their own interpretation of the site-characterization data provided to them. Caution thus needs to be exercised when comparing the results from one model to another. Note also that the results presented here are obtained through predictive simulations, i.e., the model results are not calibrated to any observation data from the S-3 site except the pressures in the injection well.

LBNL Model

Figure 6 shows the simulated evolution of pressure and gas saturation in the injection (F-1) and two observation wells (F-2 and F-3). It also shows the observed pressure (symbols) at F-1. The predicted pressure at F-1 captures the observed trends in pressure buildup. Note that these predictive simulations were performed using a skin factor of 200. Reducing the skin factor (say, to 100) resulted in a smaller buildup of pressure at F-1. However, changing the skin factor did not have any impact on either the pressure or the saturation response away from the injection well.

Figure 7 shows contours of gas saturation in the layer with the largest permeability at end of injection (1 year). Note that the plume moves only about a few hundred meters away from the injection well at the end of injection. Note also that the plume is mostly radial, with a small preferential movement in the up-dip direction. According to this model, at end of injection (1 year), ~79% of the injected CO_2 remains in the gas phase and the rest is dissolved in water.

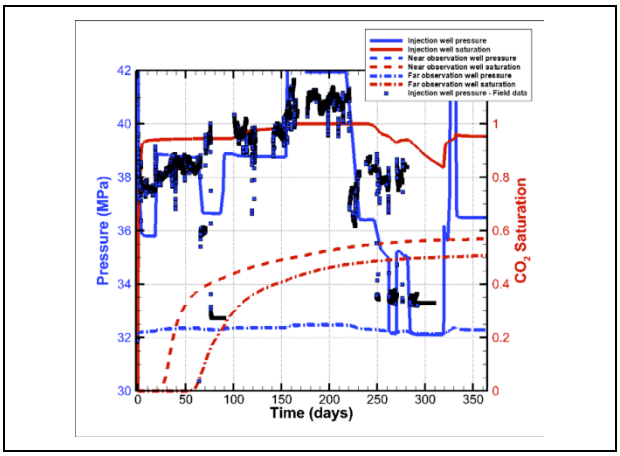

Figure 6. Observed pressure at F-1, and predicted pressure and gas saturation at F-1, F-2, and F-3 using the LBNL Model

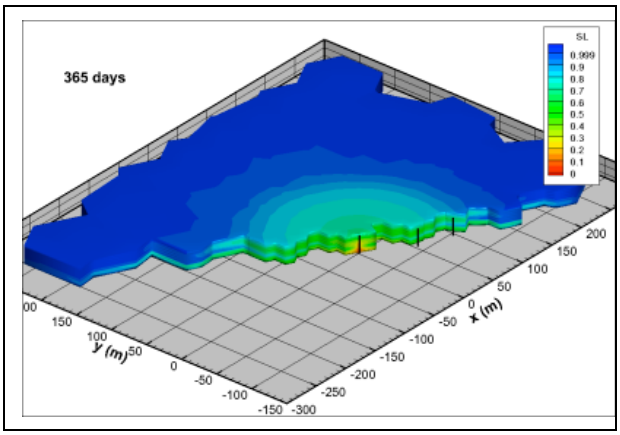

Figure 7. Contours of gas saturation at end of injection. Up-dip direction is towards the right side of the figure

PNNL Model

Analysis of the simulated plume extent using different realizations of the permeability and porosity distributions show that facies orientation, and the distribution of hydraulic properties within each facies, has a significant effect on predictions of supercritical CO_2 saturation and pressure distribution in the formation. As examples, simulated contours of gas-phase saturation at 1 year for Realization #5 (where the property distribution within each facies is uniformly random) and Realization #8 (where the property values within each facies follow a normal distribution) are shown in Figures 8a and 8b, respectively. Preliminary results suggest that realizations with uniform random hydraulic property distribution within each facies match the pressure response at F-1 most closely. The PNNL

Model predicts that about 84% of the injected CO_2 will remain in gas-phase and 16% will undergo dissolution at end of injection.

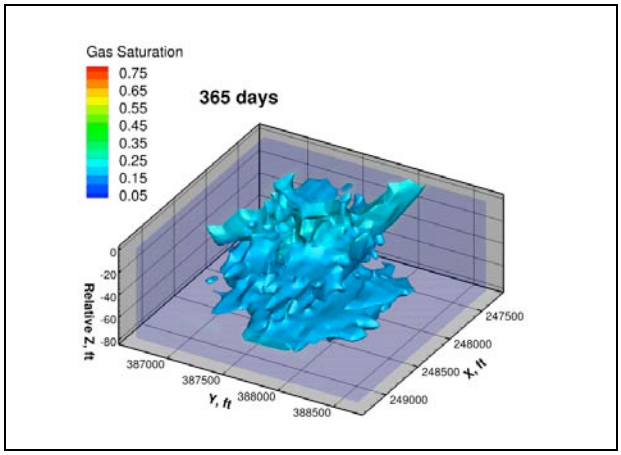

Figure 8a. Contours of CO_2 saturation at 1 year with Realization #5 of the PNNL Model

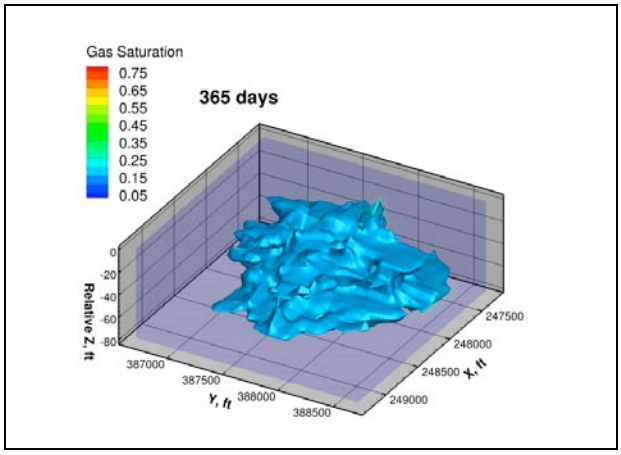

Figure 8b. Contours of CO_2 saturation at 1 year with Realization #8 of the PNNL Model

ICL Model

Simulated contours of the CO_2 saturation at the end of injection (1 year) are shown in Figure 9. The ICL Model predicts that about 86% of the injected CO_2 remains in the gas phase, which is about the same as predicted by the PNNL Model.

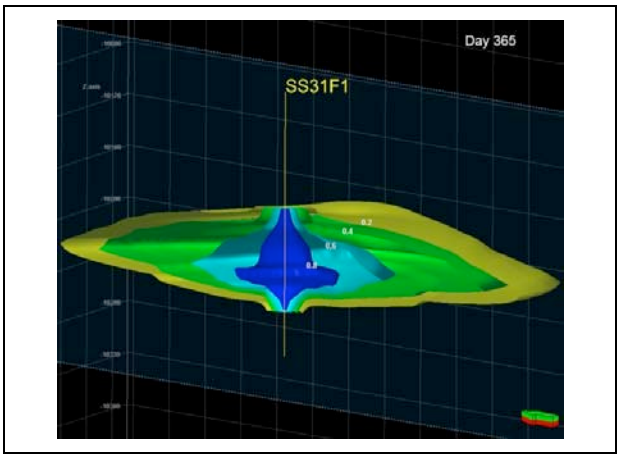

Figure 9. CO_2 contours at 1 year (ICL Model)

VESA Model

Figure 10 shows contours of integrated CO_2 plume thickness at 1 year. In this model, at end of injection, ~95% of the injected CO_2 stays in the gas phase and the rest in brine phase The VESA Model predicts arrival times of 27 days at F-2 and 65 days at F-3.

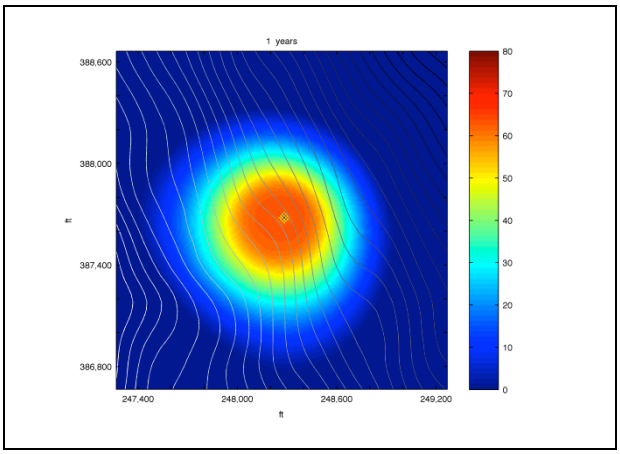

Figure 10. Contours of integrated CO_2 plume thickness in feet at 1 year (VESA Model)

QUALITATIVE MODEL COMPARISON

Even with only four conceptual models, it is clear that model conceptualization varies widely. The differences in conceptualization are reflected in the predictions from these four models. For example, the LBNL Model predicts that CO_2 breakthrough occurs at 19 and 53 days at F-2 and F-3, respectively. Over the nine realizations simulated by the PNNL Model, breakthrough times at F-2 ranged from 8 to 14 days, whereas the same for F-3 was 19 to 53 days (realizations with uniform random property

distribution predict longer breakthrough times). The ICL Model predicts CO_2 arrival times of 36 and 94 days, and the VESA Model predicts breakthrough at 27 and 65 days at wells F-2 and F-3, respectively. If we bracket the range of breakthrough predictions, we have between 8 and 36 days for F-2 and between 19 and 94 days for F-3. This gives an indication of the possible range of uncertainty caused by conceptual model choices, even for a simplified GCS injection scenario. The challenge for modelers is to attempt to reduce this range of uncertainty.

Similarly, if we bracket the fraction of CO_2 in the gas phase after injection ends, we get a minimum of 79% (LBNL) and a maximum of 95% (VESA). One possible reason for this large spread can be how the relative permeability and capillary pressure curves are implemented in each model. For example, the TOUGH2 simulations were performed with nonhysteric characteristic functions and without including residual-phase trapping, resulting in a more spread-out plume, which might have led to more dissolution (and less gas-phase saturation) than would be expected. Clearly, differences in conceptual model choices and numerical implementation cause significant differences in model predictions.

SUMMARY AND CONCLUSIONS

In this paper, we present preliminary predictions made by the TOUGH2 simulator while simulating the CO_2 injection scenario at the S-3 site, whose complex geology poses significant challenges for modelers. These TOUGH2 predictions are compared with those using STOMP, Eclipse, and VESA approaches. From a preliminary comparison of the four models, it is clear that differences in model conceptualization result in a large range of predictions. For example, if we bracket the predicted time for CO_2 arrival at the two observation wells, we have a range of 8–36 days for Well F-2, and 19–94 days at Well F-3. Further, predicted gas-phase saturation at the end of the injection period varies from 79–95%.

The range of prediction uncertainties, of course, will decrease when the models are calibrated to observed data from the S-3 site. Model predictions can be further improved by using more site-specific data, such as the characteristics curves, and by incorporating spatial heterogeneities in key reservoir properties.

ACKNOWLEDGMENT

The authors thank Mark Rockhold (PNNL), Curt Oldenburg (LBNL), and Dan Hawkes (LBNL) for their constructive reviews of the draft manuscript. LBNL's efforts in coordinating Sim-SEQ are supported through funds provided by the U.S. Department of Energy and managed by the National Energy Technology Laboratory. Funds were provided to Berkeley Lab through the U.S. Department of Energy Contract No. DE-AC02-05CH11231.

REFERENCES

Carle, S. F. and G.E. Fogg,. *Mathematical Geology,* 28**,** 453-476, 1997.

Gasda, S.E., J.M. Nordbotten, and M.A. Celia, *Computational Geosciences*, 13(4), 469-481, 2009.

Hovorka, S.D. et al., *Energy Procedia*, 4:3478-3485, doi: 10.1016/j.egypro.2011.02.274, 2011.

Mukhopadhyay, S., J.T. Birkholzer, J.P. Nicot, and S.A. Hosseini, *Environmental Earth Sciences*, doi: 10.1007/s12665-012-1668-1, 2012.

Oldenburg, C.M., G.J. Moridis, N. Spycher, and K. Pruess, Rep. LBNL-56589, Lawrence Berkeley National Laboratory, Berkeley, Calif., 2004.

Pruess, K., C. Oldenburg, and G. Moridis, Rep. LBNL-43134, Lawrence Berkeley National Laboratory, Berkeley, Calif., 1999.

White, M. D. and M. Oostrom, Rep. PNNL-15782, Pacific Northwest National Laboratory, Richland, Washington, 2006.

SIMULATIONS OF UPWARD LEAKAGE OF CO_2 IN LONG-COLUMN FLOW EXPERIMENTS: EFFECT OF LATERAL BOUNDARY CONDITION

Curtis M. Oldenburg[1], Christine Doughty[1], Catherine A. Peters[2], and Patrick F. Dobson[1]

[1]Earth Sciences Division
Lawrence Berkeley National Laboratory 74-316C
Berkeley, CA 94720 USA
e-mail: cmoldenburg@lbl.gov

[2]Department of Civil and Environmental Engineering
Princeton University
Princeton, NJ 08544 USA

ABSTRACT

We are using TOUGH2/ECO2M to simulate CO_2 and brine flow in high-pressure long-column pressure vessels (LCPVs) that could someday be housed in an underground laboratory. The simulations are aimed at designing experiments to understand upward leakage of CO_2 from deep geologic storage, including the transition of CO_2 from super-critical to gaseous and liquid conditions. The LCPV would consist of a vertical steel pipe a few hundred meters in length and one meter in diameter with a centralized vertical pipe analogous to a well for inserting monitoring equipment. The annular region between the inner pipe and the outer wall will be filled with porous materials saturated with brine. The LCPVs would be suspended in a long vertical shaft with thermal control on the outer wall boundary. With TOUGH2/ECO2M, we are able to model all possible phase combinations of CO_2, NaCl, and water. Results for radial 2-D simulations of upward flow in the 500 m high by 1 m in diameter column are very sensitive to the choice of outer thermal boundary conditions. For the case of constant geothermal-gradient temperature on the outer wall, representing flow up a narrow flow channel such as a well, there is very little liquid CO_2 formed, as heat from the sidewall counteracts expansion cooling and the CO_2 generally remains either supercritical or gaseous. For the case of an insulated-sidewall, by which the column represents the center of a large upwelling plume, upward migration of CO_2 and related expansion cooling leads to three-phase conditions through the formation of liquid CO_2 in equilibrium with gaseous CO_2 and brine. The lack of knowledge regarding three-phase relative permeability behavior underlines the need for large-scale flow experiments to understand multiphase CO_2 leakage.

INTRODUCTION

Concern about CO_2 leakage and associated environmental impacts from Geologic Carbon Sequestration (GCS) sites motivates research to elucidate and quantify processes governing upward flow and transport of CO_2. With only a handful of demonstration and industrial projects available, a large amount of research into the performance of GCS is carried out by numerical simulation. Beyond the well-accepted process models such as Darcy's Law for fluid flow, Fick's Law for molecular diffusion, and Fourier's Law for conductive heat transfer, there are numerous multiphase, multicomponent, and process couplings that are not as well understood and whose prediction depends to a large degree on empiricism. Progress in the understanding of hypothetical GCS processes therefore requires encoding into simulators defensible physical and chemical process models, which are often developed through laboratory experimentation.

One limitation of laboratory experiments is the length scale, which is generally restricted to bench scale with a maximum length on the order of one meter. This limitation restricts the aspects of GCS that can be tested in the laboratory. For example, large-scale upward CO_2 migration and associated depressurization would be accompanied by a large expansion as CO_2 transitions from the supercritical or liquid conditions of the storage formation to gaseous conditions at shal-

lower depths. In order to study and understand such processes and related changes in flow velocity, temperature (e.g., by expansion cooling), and trapping in the porous medium, experiments need to be conducted over long vertical length scales.

At least one CO_2-related experiment has been carried out in a long tube suspended in the stairwell of a tall building (de la Reguera et al., 2010). Slim-tube approaches used in the oil and gas industry (e.g., Maloney and Briceno, 2008) provide another method of representing a long flow path, but because slim tubes are normally deployed as tight coils, e.g., for convenience in placing them within ovens for temperature control, they do not provide a hydrostatic pressure gradient. Underground laboratories provide another opportunity for developing pressure-controlled long vertical flow columns, an approach our team has conceptualized for the "Laboratory for Underground CO_2 Investigations" (LUCI) (Peters et al., 2010).

The experiments being considered for LUCI will focus on questions such as:

- What is the extent of cooling due to decompression expansion?
- In addition to the supercritical to gas transition, can liquid CO_2 form?
- How much CO_2 becomes trapped by residual phase trapping during upward flow of CO_2?

The long-column pressure vessels (LCPVs) filled with sand and brine conceived for LUCI will be designed to represent 500 m vertical sections of the subsurface over a depth range controllable by specification of bottom and top pressure and temperature conditions. As an effectively one-dimensional system, the LCPV would formally represent either an actual one-dimensional flow path such as a leaky well (e.g., Gasda et al., 2004), or a small region in the middle of a vast upward-rising plume as sketched in Figure 1. We can control which of these scenarios we want to test through the application of different thermal boundary conditions on the outer wall of the LCPV—constant geothermal gradient temperature for the one-dimensional flow path, and insulated for the middle of a vast plume.

With an understanding developed from numerical simulations of how flow might occur in the LCPV system, precise specifications of the system can be made and used to design and build the LUCI facility. The purpose of this paper is to present simulations of experiments that could be carried out in a specific LCPV and to demonstrate the sensitivity of the formation of liquid CO_2 as supercritical CO_2 flows upwards to the choice of boundary conditions. We emphasize that this paper is not about modeling upward CO_2 and brine flow in natural systems, but rather about simulating flow and transport in a potential future LCPV. As such, the parameters and properties of the system are chosen to be those of the engineered LCPV system, not those of any natural system.

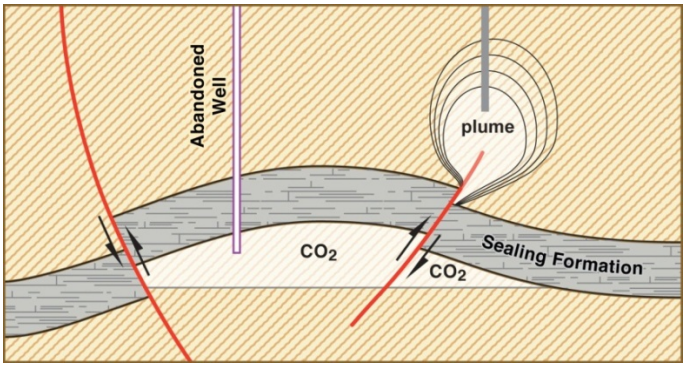

Figure 1. Conceptual models of fault and abandoned-well leakage pathways for CO_2. The one-dimensional nature of the leakage pathway is implicit in the abandoned well; for the CO_2 plume, the one-dimensional flow conceptualization is shown by the light gray bar which represents upward flow in the center of a large upwelling region.

METHODS

We carried out numerical simulations of CO_2 and brine flow in the LCPVs using TOUGH2/ECO2M (Pruess et al., 1999; Pruess, 2011). ECO2M is an equation of state module that describes the pure-component and mixture properties of water, NaCl, and CO_2. ECO2M can model the full range of phase conditions in the system H_2O-NaCl-CO_2, including P-T conditions on the liquid-gas phase boundary (saturation line) with the potential for three-phase conditions (aqueous, liquid CO_2, and gaseous CO_2). Because of its complete description of possible phase conditions, ECO2M is capable of simulating any scenario of upward CO_2 and brine flow, including the formation of liquid CO_2.

Some authors have pointed out the importance of considering the change in gravitational potential in the calculation of the enthalpy of rising fluids (e.g., Stauffer et al., 2003), a term not included in standard TOUGH2. Comparing the enthalpy change caused by pressure change from top to bottom to the gravitational potential change in the system studied here reveals that the change in gravitational potential over 500 m is insignificant relative to the pressure-volume term for the CO_2 rise scenario considered. Therefore, we can neglect the gravitational potential in the energy-balance equations.

A sketch of the long-column pressure vessel with large horizontal exaggeration is shown in Figure 2, along with the radially symmetric domain used for the simulations. The left-hand side (LHS) boundary is placed at the wall of the inner access well, which will be used for monitoring the annular flow region using various down-hole geophysical monitoring tools. This access well is currently specified to be made out of fiberglass and filled with brine under hydrostatic conditions to avoid large pressure gradients that could burst the inner wall. We assume a closed boundary (no-flow and insulated) for the inner-wall (LHS) for all of the simulations. The bottom of the LCPV is also closed and insulated, but includes flow ports such that CO_2 can be injected at a controlled rate. The top of the column is held at constant P-T conditions of 3.43 MPa and 23.75°C. These conditions correspond roughly to a depth of about 350 m in a typical sedimentary basin. Under these conditions and with NaCl brine of 100,000 ppm concentration, the P-T at the bottom of the 500 m long LCPV are 8.67 MPa and 36.25°C. We note finally that the critical pressure and temperature for CO_2 are located at approximately -380 m and -295 m as measured downward within the LCPV, respectively.

The fixed geothermal gradient boundary condition is implemented by setting the thermal heat energy contained in the gridblocks at the boundary to an effectively infinite value (by setting either gridblock volume, rock heat capacity, or rock density to a very large value)

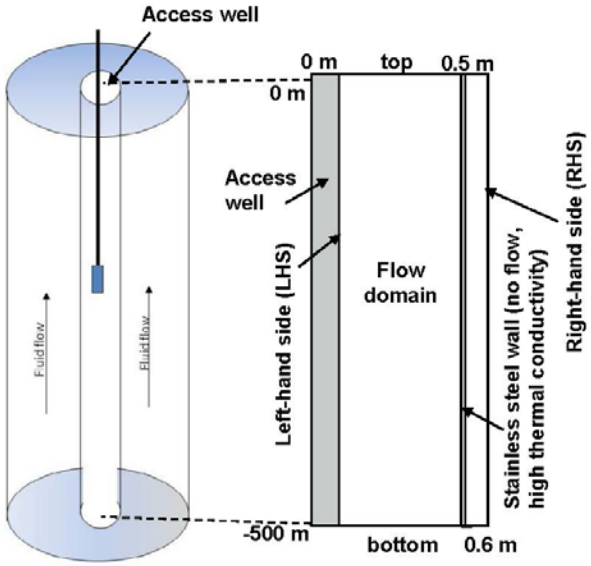

Figure 2. Sketch of annular flow region in long-column flow vessel, which includes an inner column for deployment of monitoring equipment. On the right-hand side is the two-dimensional radial numerical simulation domain with named boundaries (LHS = left-hand side (inner wall), RHS = right-hand side (outer wall)).

so that, regardless of how much heat flows into or out of the gridblock, its temperature remains the same. These fixed-temperature gridblocks are made closed to flow by setting their permeability to zero and using harmonic weighting of permeability at interfaces between gridblocks. The open boundary conditions are implemented by giving the boundary gridblocks non-zero permeability and effectively infinite volume, such that their pressures and temperatures remain constant regardless of how much fluid and heat flows in or out. The closed-to-flow and

thermally insulated boundary conditions are implemented simply by using finite-volume gridblocks with normal flow and thermal properties at the boundaries of the domain.

The model LCPV flow domain is assumed to be filled with unconsolidated sand such as one would emplace by slurry or tremie methods in the actual LCPV. The homogeneous coarse sand was chosen to allow fluid flow in the column over practical experimental time scales rather than to represent any particular sedimentary basin or reservoir system. Specific properties of the unconsolidated sand were estimated using the Rosetta Database (Schaap, 2000) which resulted in porosity, permeability, and capillary and relative permeability parameters shown in Table 1. For cases in which liquid- and gas-phase CO_2 co-exist along with aqueous-phase brine, the three-phase capillary pressure and relative permeability formulations of Parker et al. (1987) are used. The values of capillary pressure for supercritical, gaseous, and liquid CO_2 for a given aqueous-phase saturation are assumed to be the same (i.e., we assume no interfacial tension between the various phases of CO_2). The porous sand is assumed to be unreactive and immobile during all flow processes, i.e., reactive geochemistry and geomechanical stresses and deformation are neglected. We also neglect molecular diffusion because we have observed in test simulations (not presented here) its negligible effect in this high-permeability system.

Hysteretic capillary pressure and relative permeability functions are generally needed when drainage (drying) and imbibition (wetting) occur simultaneously in different parts of the flow domain. Hysteretic functions were not specified for the constant-injection case shown here because the system was expected to always remain on the drainage branch, i.e., CO_2 is injected constantly, resulting in monotonic drying processes. The fact that the constant-injection case is essentially monotonically drying is convenient, because we are not aware of the existence of a three-phase hysteretic model for CO_2-water systems.

For injection into the domain at the bottom, we assume a constant injection rate distributed in the radial direction to produce a uniform mass flux over the bottom boundary. The total mass injection rate at the bottom of the LCPV is 1.58×10^{-2} kg/s (1.36 tonnes/d). This flow rate was derived from preliminary simulations that implemented a constant hydrostatic pressure bottom boundary, with CO_2 saturation at the boundary equal to one, so that only pure CO_2 phase would enter the brine-saturated column. We augmented this injection rate by a factor of two above the pure buoyant rate to make a flow system that would evolve on a relatively short time scale convenient for the experimentalists who would be operating LUCI. The CO_2 injected at the bottom is into a row of gridblocks with infinite heat capacity, which implements a constant-temperature injection.

Table 1. Properties of the of the LUCI system.

Property	Value
Porosity (ϕ)	0.40
Permeability (k)	1.7×10^{-11} m^2
Capillary Pressure (P_{cap}) and Relative Permeability (k_r) *Terminology:* λ = m = 1-1/n = power in expressions for P_{cap} and k_r $S_{ar} = S_m$ = aqueous-phase residual saturation S_{lr} = CO_2 liquid-phase residual saturation S_{gr}= CO_2 gas-phase residual saturation $P_{c0} = \alpha^{-1}$ = capillary pressure between aqueous and non-aqueous phases P_{cmax} = maximum possible value of P_{cap}	van Genuchten[1] two-phase and Parker[2] three-phase $\lambda = 0.774$ $S_{ar} = 0.127$ for P_{cap}, 0.130 for k_r $S_{lr} = 0$ $S_{gr} = 0.01$ $P_{c0} = 2875$ Pa $P_{cmax} = 1\text{x}10^6$ Pa P_{cap} between CO_2 gas, liquid, and supercritical phases is assumed to be zero.
Thermal conductivity of sand and brine mixture[4]	2.5 W/(m K)
Thermal conductivity of 5 cm-thick stainless steel (304) on RHS boundary	14.6 W/(m K)
Density of stainless steel	7920 kg/m^3
Heat capacity (C_P) of stainless steel	502.1 J/(kg K)

[1]van Genuchten (1980), as in Doughty (2007)
[2]Parker et al. (1987) as in Pruess (2011), simplifies to van Genuchten when only two phases present

RESULTS

Fixed geothermal gradient boundary

In this scenario, CO_2 is injected at a constant rate and temperature into the bottom of the LCPV, which is initially filled with a brine with 100,000 ppm NaCl at hydrostatic pressure and temperature equal to the selected geothermal gradient. Temperature at the outer wall or RHS boundary is held fixed at this geothermal gradient profile. Figure 3 shows results at t = 5 d following the start of injection. As shown, the CO_2 front has moved upwards approximately 260 m, creating a region of two-phase gaseous and super-critical CO_2 ($scCO_2$)-brine mixture. The pressure in the system increases due to this injection process. Isotherms are generally lifted upwards as the brine is displaced upwards and the injected CO_2 is at the relatively warmer temperature of the bottom boundary. The injected CO_2 decompresses as it rises upward through the hydrostatic pressure of the brine column and may exchange heat with the outer wall of the column. Overall, the simulation shows some minor two-dimensional effects arising from the fixed geothermal gradient boundary condition.

The nearly one-dimensional nature of the flow problem allows us to plot results as vertical profiles through the system. Figure 4 shows values of P, T, S_{CO2}, and ρ_{CO2} for vertical profiles along the LHS of the LCPV at four times to explicitly show the vertical variations in temperature and phase conditions in the system—for example, the clear indication of the phase front. Note also that we include the liquid-gas phase boundary in the temperature plot. This curve represents the locus of points along which gas and liquid CO_2 are in equilibrium at the given pressure of the system. At t = 5 d, the CO_2 is supercritical below approximately -320 m and gaseous above. The effects of expansion cooling at t = 5 d can be seen clearly on the vertical profile plots of Figure 4 by the deflection toward lower temperatures at around z = -350 m and near-intersection with the liquid-gas phase boundary. The increased T relative to initial condition between z = -250 m and -350 m is likely due to advection of warmer fluid upward.

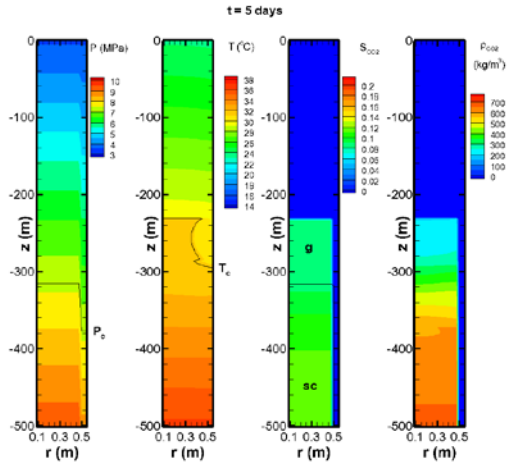

Figure 3. Results at t = 5 d showing P, T, S_{CO2}, and ρ_{CO2} for the case of the fixed geothermal gradient boundary condition on the RHS. The critical pressure (P_c) and temperature (T_c) are indicated by the light solid curves on the P and T plots.

Insulated boundary

To understand the effect of the outer wall (RHS) thermal boundary condition, we consider next a case identical to the above except the RHS (outer wall) is perfectly insulated. Results at t = 5 d are shown in Figure 5 for comparison to Figure 3. The first observation is that the system behaves essentially like a one-dimensional system in terms of fluid (P) and heat (T) flow with no lateral variation whatsoever. Second, with no heat entering or leaving through the RHS boundary, the intrinsic thermal effects are more obvious, because they are controlled solely by advection, conduction, expansion, and phase change effects.

Vertical profiles of results for t = 5 d, 10 d, 20 d, and 30 d are shown in Figure 6. As shown, interesting oscillations in temperature occur at various times, resulting in liquid CO_2 conditions alternating with $scCO_2$ and gaseous CO_2. The occurrence of liquid CO_2 causes phase interference that impedes upward flow and introduces a negative feedback to the expected expansion cooling, resulting in oscillations in density and temperature.

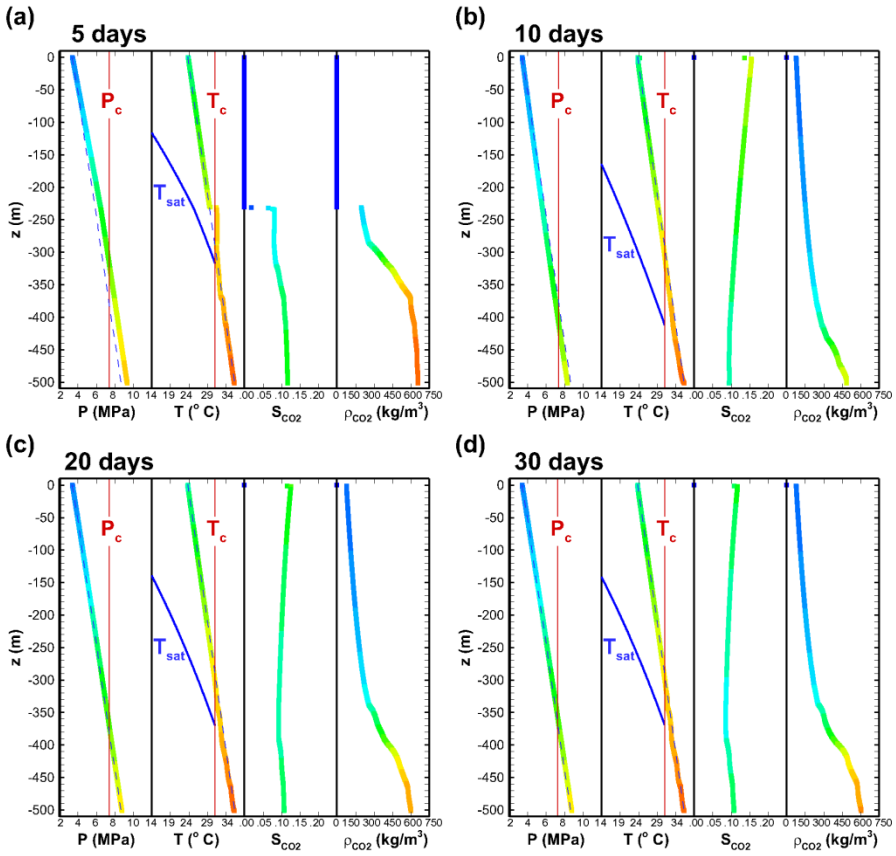

Figure 4. Vertical profiles along the inner radius of the domain at (a) t = 5 d, (b) t = 10 d, (c) t = 20 d, and (d) t = 30 d for the fixed geothermal gradient boundary condition on the RHS. The color of the lines represents the value of the variable being plotted against depth, for visual emphasis. Initial conditions for P and T are shown by the dashed lines. The liquid-gas phase boundary is shown in the temperature frame by the line labeled T_{sat}.

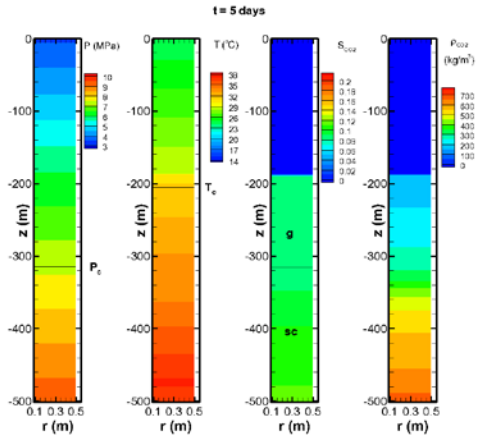

Figure 5. Results for the case with an insulated boundary condition on the RHS. Note that there is no variation in the lateral (r) direction (i.e., the fields are one-dimensional)

At t = 30 d, liquid CO_2 is present from z = -200 m to -370 m. The large region of liquid CO_2 points to the importance of expansion cooling in large-scale buoyant CO_2 rise, at least for systems with high porosity and permeability. At the liquid-gas phase boundary, there are two CO_2 phases (liquid and gas) in equilibrium with an aqueous phase. In this situation, three-phase relative permeability and capillary pressure functions are needed. The migration of the system to the liquid-gas phase boundary seems to be a fundamental behavior of the system observed for all reasonable combinations of relative permeability tested so far. To see alternative graphical and animated representations of these simulation results, please see animated time plots in the Supplementary Material of our *Greenhouse Gases: Science and Technology* paper (Oldenburg et al., 2011).

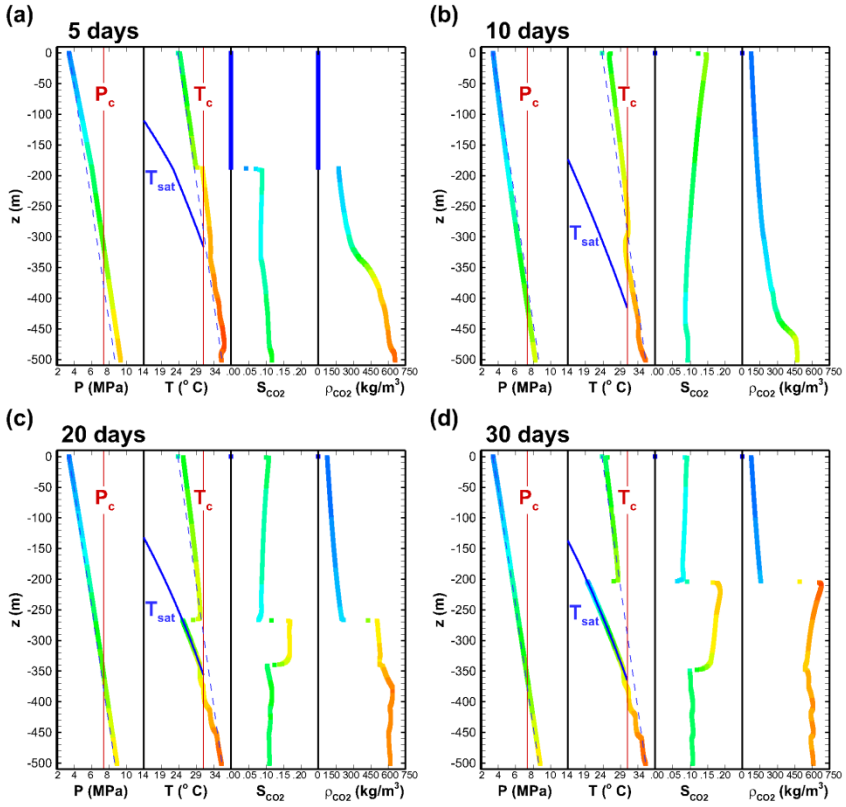

Figure 6. Vertical profiles along the inner radius of the domain at (a) t = 5 d, (b) t = 10 d, (c) t = 20 d, and (d) t = 30 d for the case with insulated boundary condition on the RHS.

CONCLUSIONS

Numerical simulations using TOUGH2/ECO2M for the preliminary design of long-column flow experiments such as those proposed for LUCI have been carried out. The fixed geothermal gradient boundary condition is representative of the case of CO_2 flow up a narrow conduit such as the annulus of an abandoned well or a fault zone. The insulated boundary condition is representative of the upward flow of CO_2 in the middle of a much larger CO_2 plume. Simulation results for scenarios involving constant injection of CO_2 in an initially brine-filled sand column are sensitive to the outer wall thermal boundary condition. Radial gradients in temperature occur for the fixed geothermal gradient case, showing that the outer wall temperature controls the temperature in the system, whereas in the insulated case, heat transfer and temperature are controlled by vertical advection and conduction, expansion, and phase-change processes.

Liquid CO_2 forms in flow simulations using either boundary condition, but much more liquid forms in the insulated outer wall case, because expansion cooling is stronger when the outer wall boundary does not supply heat to the system. When two-phase liquid-gas conditions occur, the system becomes locked onto the liquid-gas phase boundary. The prevalence of liquid CO_2 in these upward-leakage simulations and the lack of knowledge about modeling three-phase relative permeability motivate the development of a large-scale experimental facility with LCPVs, in which controlled flow experiments can be carried out. An experimental facility would provide the opportunity for researchers to investigate outstanding research questions, such as the role of phase interference in multiphase CO_2 systems along with much more realistic and complex systems—for example, by layering different materials into the column, and including reactive transport and other physical and chemical processes. In all likelihood, a large-scale experiment would reveal additional unpredicted behaviors, the study of which could allow increased understanding of large-scale flow and phase change phenomena in CO_2 systems.

ACKNOWLEDGMENT

This work was supported by the National Science Foundation under Grant Numbers CMMI-0965552 (to LBNL) & CMMI-0919140 (to Princeton University), and by Lawrence Berkeley National Laboratory under Department of Energy Contract No. DE-AC02-05CH11231.

REFERENCES

De la Reguera D, Stute M, Matter JM. Laboratory experiments on CO_2 dissolution in water for carbon sequestration. Proceedings of the American Geophysical Union EOS, 2010 Dec 13-17, San Francisco, CA (2010).

Doughty C. Modeling geologic storage of carbon dioxide: Comparison of non-hysteretic and hysteretic characteristic curves. *Energy Conversion and Management* 48(6): 1768–1781 (2007).

Gasda SE, Bachu S, Celia MA. Spatial characterization of the location of potentially leaky wells penetrating a deep saline aquifer in a mature sedimentary basin. *J Environ Geol* 46(6-7): 707-720 (2004).

Maloney DR, Briceno M. Experimental investigation of cooling effects resulting from injecting high pressure liquid or supercritical CO_2 into a low pressure gas reservoir. Proceedings of the International Symposium of the Society of Core Analysts held in Abu Dhabi, UAE, 29 October-2 November 2008.

Oldenburg, C.M., C. Doughty, C.A. Peters, and P.F. Dobson, Simulations of long-column flow experiments related to geologic carbon sequestration: effects of outer wall boundary condition on upward flow and formation of liquid CO_2, *Greenhouse Gases: Science and Technology*, in press.

Parker JC, Lenhard RJ, Kuppusamy T. A parametric model for constitutive properties governing multiphase flow in porous media. *Water Resources Research* **23(4):** 618- 624 (1987).

Peters CA, Dobson PF, Oldenburg CM, Wang JSY, Onstott TC, Scherer GW, et al. LUCI: A facility at DUSEL for large-scale experimental study of geologic carbon sequestration. *Energy Procedia*, 2, Elsevier, GHGT-10, Sept. 19–23, 2010, Amsterdam, The Netherlands (2010).

Pruess K. On CO_2 fluid flow and heat transfer behavior in the subsurface, following leakage from a geologic storage reservoir. *J Environ Geol* 54: 1677-1686 (2007).

Pruess K. Integrated modeling of CO_2 storage and leakage scenarios including transitions between super- and subcritical conditions, and phase change between liquid and gaseous CO_2. *Greenhouse Gases: Science and Technology* 1(3): 237–247 (2011).

Pruess K. ECO_2M: A TOUGH2 fluid property module for mixtures of water, NaCl, and CO_2, including super- and sub-critical conditions, and phase change between liquid and gaseous CO_2. May 2011, Lawrence Berkeley National Laboratory Report LBNL-4590E (2011).

Pruess K, Oldenburg CM, Moridis GJ. TOUGH2 User's Guide Version 2. November 1999, Lawrence Berkeley National Laboratory Report LBNL-43134 (1999).

Schaap MG. Rosetta Version 1.2. U.S Salinity Laboratory ARS-USDA (2000).

Stauffer P, Stein J, Travis B. The correct form of the energy balance for fully coupled thermodynamics in water. Los Alamos National Laboratory Report LA-UR-03-1555, 9 pp (2003).

van Genuchten M Th. A closed-form equation for predicting the hydraulic conductivity of unsaturated soils. *Soil Science Society of America J* 44(5): 892–898 (1980).

SIMULATION OF CO_2 STORAGE IN THE BASAL AQUIFER IN THE NORTHERN PLAINS–PRAIRIE REGION OF NORTH AMERICA

Dorothee Rebscher, Quanlin Zhou, and Jens T. Birkholzer

Lawrence Berkeley National Laboratory
Earth Sciences Division 90-1116
Berkeley, CA, 94720, USA
e-mail: drebscher@lbl.gov

ABSTRACT

The static storage capacity in the Basal Aquifer in the Northern Plains–Prairie Region of North America has been estimated to be more than 10^5 GT (billion metric tonnes) CO_2. This large capacity can be attributed to: (1) the aquifer's area of ~1,500,000 km^2 covering the Alberta Basin and the Williston Basin in Alberta, Saskatchewan, and Manitoba in Canada, and Montana, North Dakota, and South Dakota in the U.S.; and (2) a porosity range from 1% to 25%, a permeability range from 10 to 10^3 mD, and an aquifer thickness up to 300 m. However, the static storage capacity does not consider the effect of pressure buildup induced by CO_2 injection, by which overpressurization might fracture the cap rock, drive brine/CO_2 leakage, and cause induced seismicity. During storage operation, pressure buildup will be controlled under maximum injection pressure to avoid the above negative impacts, leading to a more realistic, dynamic storage capacity. That capacity can be estimated through numerical modeling of CO_2 injection and storage.

We have developed a TOUGH2-MP/ECO2N model for the Basal Aquifer to simulate pressure buildup and dynamic storage capacity, as well as the distribution, migration, and long-term fate of CO_2 plumes in response to CO_2 injection at multiple storage sites. This model development is based on a detailed geologic model, as well as hydrogeological properties and their spatial distributions, and the *in situ* conditions of pressure, temperature and salinity—all of which were provided by our partners. Eleven storage sites, with a cluster of injection wells for each one, are selected through the mapping between CO_2 emissions and sinks (for storage) for the Canadian portion of the aquifer. The number of injection wells at each site is determined using screening modeling, with special attention to pressure buildup. We generated an unstructured 3D grid using WinGridder to account for local 3D mesh refinement around each storage site to capture the evolution of CO_2 plumes, and also generated a single reservoir model layer out of CO_2 plumes to capture the single-phase pressure propagation. The current TOUGH2 model covers the Basal Aquifer, the cap rock, and the basement rock, without consideration of CO_2/brine leakage through abandoned wells. Simulation results indicate that (1) the dynamic storage capacity of the extensive saline aquifer is smaller than the estimated static storage capacity because of localized pressure-buildup constraints, and (2) the degree of the constraints varies over the entire aquifer as a result of (i) the large range in permeability, (ii) the pressure interference between different storage sites and injection wells, and (iii) the realistic CO_2 source-sink mapping for locating and designing storage sites.

INTRODUCTION

The Northern Plains–Prairie Basal Aquifer System is considered an important potential site for the sequestration of carbon dioxide in geological media (e.g., Bachu and Stewart, 2002). The saline aquifer extends over about 1,500,000 km^2 in the southwestern Canadian states and northern prairie states on the U.S. side. This paper focuses on the Canadian portion of the Basal Aquifer in Alberta, Saskatchewan, and Manitoba, covering 811,000 km^2. The model area is marked by the thin white line in the Google map in Fig. 1. Also shown are the locations of the CO_2 injection sites, indicated by red dots. Numerical modeling of the Basal Aquifer over its huge areal extent poses a great challenge, in comparison to other smaller sedimentary basins targeted for potential storage. In such efforts, both high-resolution modeling of the CO_2 plume around each

injection well and low-resolution modeling of the pressure buildup out of the CO_2 plumes at the basin scale are required for reasonable modeling accuracy. A comparable study on basin- and plume-scale modeling of CO_2 sequestration was conducted for the Illinois Basin by Birkholzer and Zhou (2009) and Zhou et al. (2010).

BACKGROUND

All the data for aquifer characterization, including aquifer geometry, rock properties (porosity, permeability, and pore compressibility), capillary pressure, and relative permeability, were provided by our project partner Alberta Innovates–Technology Futures (AITF) (Bachu et al., 2012).

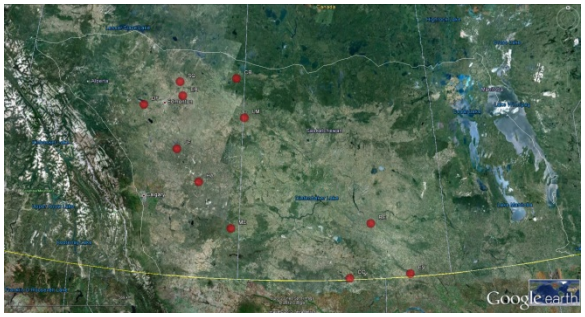

Figure 1. The areal extent (811,000 km^2) of the Basal Aquifer in Alberta, Saskatchewan, and Manitoba in Canada, with its boundary marked by a thin white line and a yellow border line. Eleven storage sites are marked by red dots.

Geology

The Basal Aquifer covers part of the Alberta Basin and the Williston Basin. It consists of several distinctive stratigraphic units: (1) the Basal Cambrian Sandstone unit, (2) a combination of the Basal Cambrian Sandstone unit and Black Island Member of the Winnipeg Formation, (3) the Black Island Member of the Winnipeg Formation, and (4) a combination of the Black Island Member and the Icebox Member of the Winnipeg Formation, which are in hydraulic communication. Its vertical upper border is mainly defined through the first significant overlying cap rock. The Basal Aquifer varies significantly in depth, reaching 5 km near the Rocky Mountains in the west and cropping out towards the east, where the environmental impact of CO_2 storage on freshwater resources may be a concern (Bachu et al., 2012).

Hydrogeological Parameters

Within the Basal Aquifer, hydrogeological properties vary significantly in the vertical and horizontal directions. Porosities range from 1% to 25%, and permeabilities from about 10 mD to 10^3 mD. For example, Table 1 shows the representative values of porosity and permeability at the 11 storage sites. The maximum thickness of the saline aquifer usable for CO_2 sequestration is 300 m.

CO_2 Injection Scenario

The area of interest comprises a significant number of large stationary CO_2 sources, whose total CO_2 emissions amounts to more than 10% of Canada's total greenhouse gas emissions. Eleven storage sites were chosen by AITF on the Canadian side with different amounts of CO_2 to be stored. Their emission ranges from 1.2 to 23 Mt CO_2/year, summing up to a total of 75.1 Mt CO_2/year (see Table 1), corresponding to 86% of the total emissions of large point sources, with more than 1 Mt CO_2/year in the area. Due to the high amount of CO_2 emissions at some of the sites, we determined well arrays, where each well is considered to sequester about 1.5 Mt CO_2 per year, leading to 50 boreholes for the entire saline aquifer in Canada.

Table 1. The 11 injection sites in Alberta and Saskatchewan and their amount of CO_2 to be sequestered and their hydrogeological properties, (from AITF and Geological Survey of Saskatchewan.)

location	CO_2 Mt/y	no. of wells	depth [m]	thickness [m]	porosity [%]	permeability [mD]
Cold Lake - Bonnyville, AB	8.3	6	1259	80	18	1000
Shell Quest Radway, AB	1.2	1	2013	42	14.5	500
Edmonton - Redwater, AB	9.7	6	2055	77	13	500
Duffield, AB	23	15	2964	36	7	100
Lloydminster, SK	2.1	1	1578	109	22	500
Joffre - Forestburg AB	7.1	5	2673	67	7.5	35
Hanna, AB	4.4	3	2427	48	10	50
Regina, SK	1.7	1	2235	48	14	1000
Medicine Hat - Empress, AB	5.2	3	2010	142	8	750
Estevan, SK	8.6	6	2719	59	6	50
Coronach, SK	3.8	3	2667	75	5.5	50
total	75.1	50	-	-	-	-

SCREENING MODELING WITH ANALYTICAL SOLUTION

For the CO_2 source-sink mapping, we used a four-layer model, with alternating aquifers/aquitards for each of the 11 storage sites listed in Table 1. The subsurface systems consist of a top aquifer, the cap rock, the Basal Aquifer, and the Precambrian basement, which were assumed to be homogeneous and isotropic in the horizontal direction. The hydrogeological parameters were derived from the extensive confidential dataset provided by AITF. Model input parameters (layer thickness, hydraulic conductivity, specific storativity) were calculated. Injection rates and number of wells are listed in Table 1. The locations of the storage sites and the spatial distribution of injection wells at each site are kept unchanged for both the screening modeling and the TOUGH2 simulations. The pressure buildup in the four layer systems were calculated using the analytical solution (Cihan et al., 2011). Injection of an equivalent volume of brine was simulated as the single-phase model is accurate in the far-field away from the CO_2 plumes. The injection period is 50 years.

Figure 2 shows the pressure buildup at the end of the 50-year injection at the Regina site with one injection well. The injection of equivalent volume is 4,257 m^3/d and the permeability 1,000 mD, leading to a maximum pressure buildup of 7.5 bar at a radius of 250 m from the injection well at 50 years. Figure 3 shows the pressure buildup at the Duffield site with 15 wells at 5 different time steps as examples. The spatial distribution of the pressure buildup for these two sites is illustrated in Figures 4 and 5, respectively. They show that Regina might not be an issue because of the high permeability there—see Table 1.

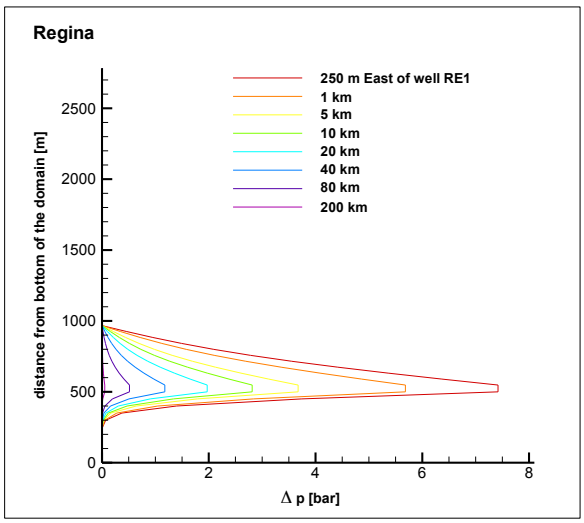

Figure 2. Pressure buildup in the top aquifer, the cap rock, the Basal Aquifer, and Precambrian basement at different radial distances after the injection of equivalent volume of 4,257 m^3 /d for 50 years at the Regina site

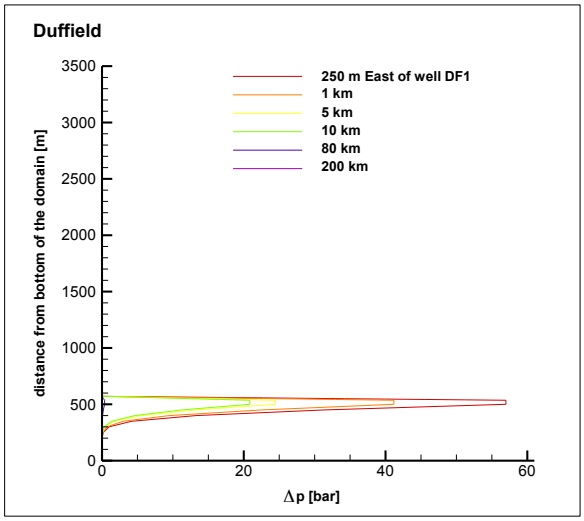

Figure 3. Pressure buildup in the top aquifer, the cap rock, the Basal Aquifer, and the Precambrian basement at different horizontal distances along the easting after the injection of equivalent volume of 3,617 m^3/d for 50 years at the Duffield site

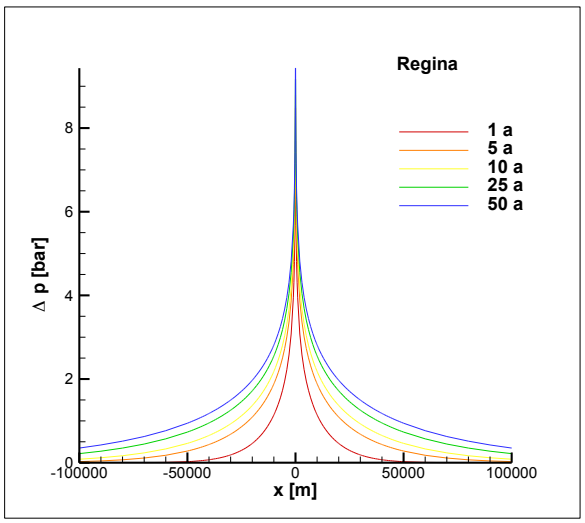

Figure 4. Pressure buildup in the Basal Aquifer at different times during the injection period at the Regina site. The cross section is located at the Easting-axis.

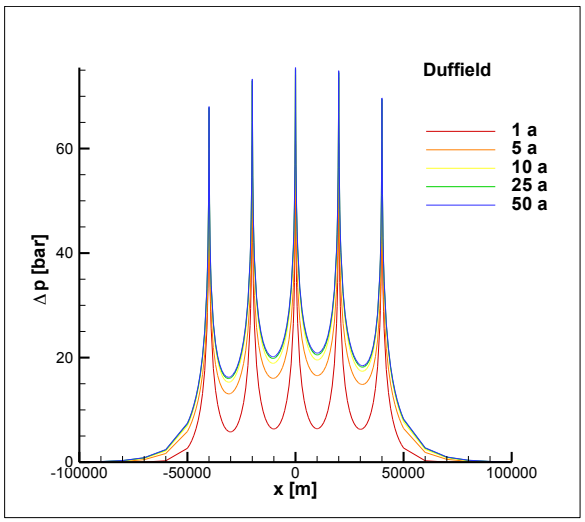

Figure 5. Pressure buildup in the Basal Aquifer at different times during the injection of 4257 m^3 CO_2/d into each of 15 wells for 50 years at the Duffield site. The cross section goes through the five wells located on the easting-axis, centered around DF1, see Figure 7.

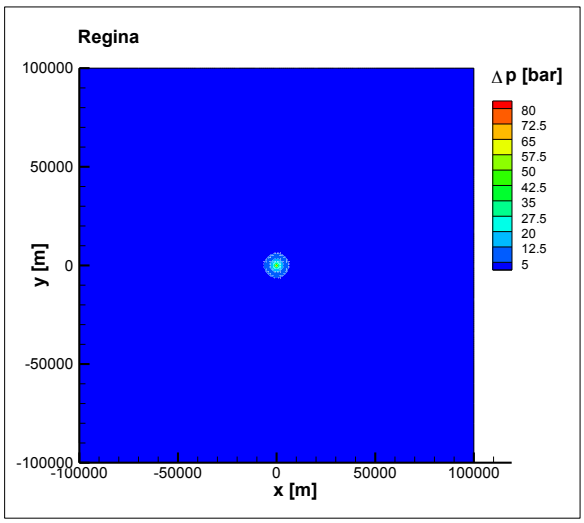

Figure 6. The spatial distribution of the pressure buildup in the Basal Aquifer at the Regina site.

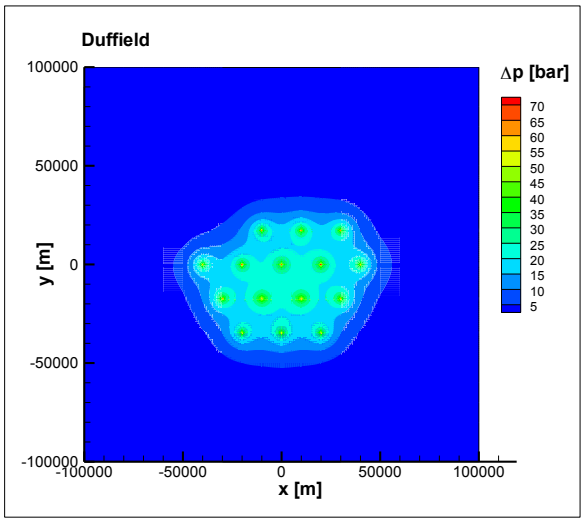

Figure 7. The spatial distribution of the pressure buildup in the Basal Aquifer at the Duffield site.

TOUGH2 MODEL DEVELOPMENT

Map Projection

To develop the basin-scale numerical model, we determined the model domain based on the dataset provided by AITF for the Canadian side of the Basal Aquifer Region. The modified Universal Transverse Mercator (UTM) projection was used as a map projection, consistent with the projection used by Princeton University for model comparison. The coordinates for the entire model domain were calculated using the reference of the -111°

meridian, the central meridian for UTM zone 12, the zone for East Alberta and West Saskatchewan, where many injection clusters are located. The error in area is less than 1% for a neighboring UTM zone, and less than 2% for other relevant UTM zones.

The Unstructured 2D Mesh

The well locations are arranged along a hexagonal spiral, were the center represents the actual site of the emission centers (see Table 1), starting in the spiral center with no. 1, clockwise ascending. An exception was made for the two most-southern sites in Saskatchewan, Estevan and Coronach, as otherwise some of the boreholes would have been situated in the U.S., outside of the domain boundary. Their centers were shifted 40 km to the north. In order to minimize interference between neighboring injection sites (the minimal areal distance between two injection centers is 42 km, equal to that between SQ and ER). Given the expense in pipeline infrastructure on the one hand and the need to minimize interference from CO_2 plumes within one array on the other, we chose a distance of 20 km between wells within one array.

A numerical grid was generated for our basin-scale model. Different grid resolutions were used over the entire domain (see Figs. 8 through 11). For each cluster, a 200 km×200 km subdomain centered at the cluster center was used with a mesh resolution of 10 km×10 km. For these cluster subdomains, we used a mesh resolution of 20 km×20 km. Within these subdomains, a 100 km × 100 km near-field region was defined, with a resolution of 3 km×3 km. Within each near-field, the well locations were arranged along a hexagonal spiral, with the center representing the actual cluster center, starting in the spiral center with number 1, then clockwise ascending. To resolve the time-dependent evolution of the CO_2 plume, we used an unstructured 2D subgrid for each injection well, with a progressive decrease in mesh resolution away from the injection well. Thirty-two concentric circular rings (with 16 nodes for each ring) were used to cover the CO_2 plume; the radial discretization ranged from 50 m to 500 m, with a total radius of 7 km for each plume. A total of 36,000 2D grids were generated using WinGridder (Pan et al., 2001). In the vertical direction, the Basal Aquifer (with a maximum thickness of 400 m) was divided into 25 model layers, covering a thickness of 50 m to 150 m at the injection clusters. The minimum thickness of the model layers was 1 m. For the near field, four model layers were used for the subdomains, with a mesh resolution of 10 km×10 km, while only one model layer was used for the regions with a mesh resolution of 20 km×20 km. In these coarsened-mesh regions, only pressure buildup is of interest to simulations, and pressure buildup in response to CO_2 injection equilibrates quickly in the vertical direction. The generated 3D mesh consists of ~750,000 gridblocks for the entire Canadian part of the Basal Aquifer.

In this model, it is assumed that the difference between hydrogeological parameters of the Basal Aquifer, compared to those of the cap rock and underlying aquitard, is sufficient for CO_2 leakage into or through the aquitards to be neglected. In the vertical direction, the hydrogeological layer of the Basal Aquifer was divided into 25 model layers, covering the thickness of the Basal Aquifer to a maximum of 400 m within the domain, but having a thickness of only 50 m to 150 m at the injection sites. The minimum thickness of the model layers was 1 m.

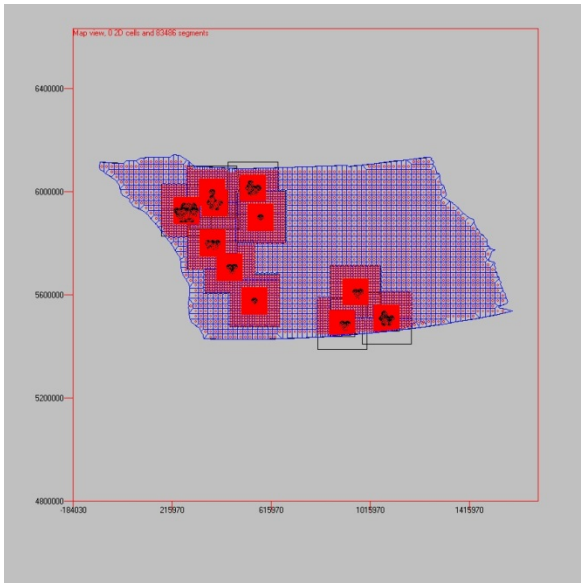

Figure 8. The model domain is subdivided into several grids with varying resolutions.

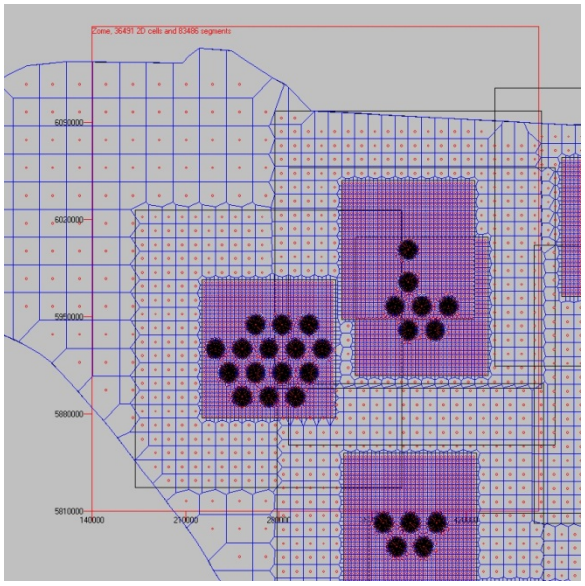

Figure 9. Square plan form gridblocks with sides of 200 km have the next highest resolution with 10 km x 10 km. This excerpt shows the North western part of the domain with the clusters Shell Quest (1 well, in the North), Duffield (15 wells, in the West), Edmonton - Redwater (6 wells, south of Shell Quest), and Joffe (5 wells, in the South).

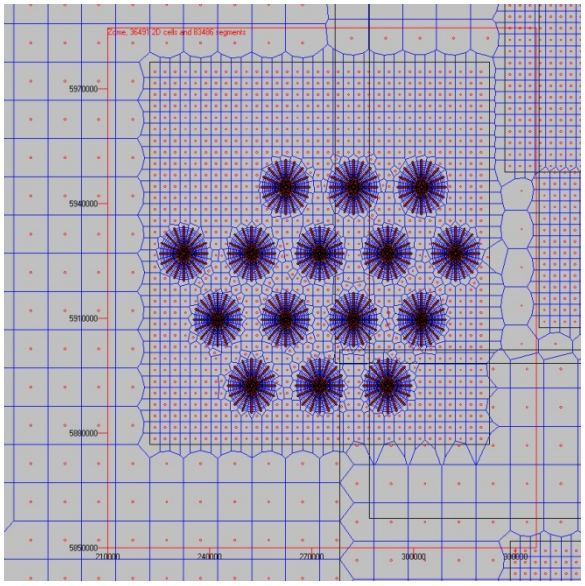

Figure 10. The wells are surrounded by a rectangular grid with sides of 100 km and resolutions of 3 km x 3 km. The Duffield array with 15 wells has the highest number of boreholes.

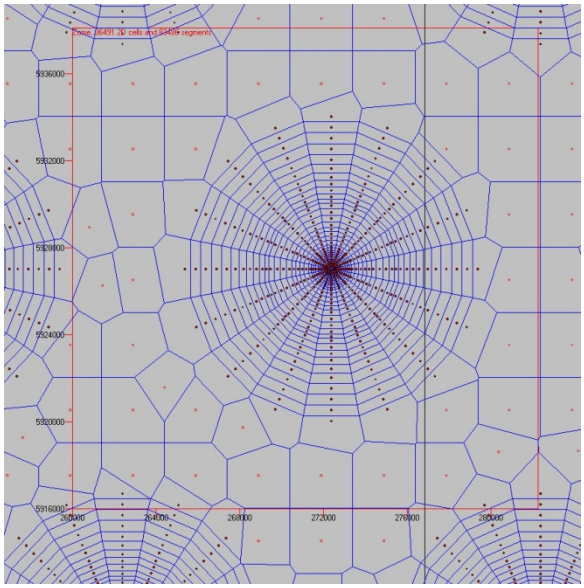

Figure 11. Each well consists of 32 concentric rings with radii from 50 m to 7 km, each formed by 32 points - here the central well in the Duffield borehole array DF1.

SIMULATION

Total annual injection rate is 75.1 Mt CO_2 (Bachu, 2012) over 50 years, distributed to 50 injection wells at 11 injection sites independent of the local emissions of CO_2; see Table 1. Calculations will be performed using the general-purpose numerical simulation program TOUGH2 (Pruess et al., 1999), with the equation of state module ECO2N (Pruess, 2005).

RESULTS AND DISCUSSION

Discussion of the simulations at the Symposium will emphasize basin and plume scale results. The time-dependent development of the CO_2 plume will be analyzed. One focus will be on pressure buildup, which governs the cap-rock integrity. Last but not least, special attention will be given to the dynamic storage capacity.

SUMMARY AND CONCLUSION

Combining the fact that prominent stationary CO_2 emitters are distributed unevenly over the area of interest—with varying spatial distributions of porosity, permeability, and aquifer thickness—the predictive simulations show large regional differences in the dynamic storage capacity of this extensive saline system.

FUTURE WORK

Key future activities include: (1) extending the domain to the south, i.e., including the U.S. part (in North Dakota and Montana) of the aquifer, based on data that will be provided by the Energy & Environmental Research Center (EERC), University of North Dakota; (2) comparison with simulations currently under way by Princeton University.

ACKNOWLEDGMENT

The authors wish to thank Stefan Bachu and other partners from Alberta Innovates–Technology Futures, and the Saskatchewan Geological Survey for their detailed aquifer characterization (and for kindly providing all the data for our simulations). This work is part of the Consolidated Sequestration Research Project (CSRP). It was funded by the U.S. Department of Energy and Lawrence Berkeley National Laboratory under Contract No FWP ESD 09-056.

REFERENCES

Bachu, S, J. Bachu, S, J. Faltinson, T. Hauck, A. Melnik, E. Perkins, J. Peterson, S. Talman, and G. Jensen (2012): The Basal Aquifer in the Prairie Region of Canada: Characterization for CO_2 Storage, Alberta Innovates – Technology Futures and Saskatchewan Geological Survey, Final Report for Stage I (Phases 1 and 2), pp432, 2012.

Bachu, S., and S. Stewart, Geological Sequestration of Anthropogenic Carbon Dioxide in the Western Canada Sedimentary Basin: Suitability Analysis, *Journal of Canadian Petroleum Technology*, 41, No.2, pp99, 2002.

Birkholzer, J. T., Zhou, Q., Basin-scale Hydrological Impacts of Multiple-site CO2 Storage in the Illinois Basin: Regulatory and Capacity Implications, Abstract in Proceedings 8th Annual Conference on Carbon Capture and Sequestration, Pittsburgh, PA, May 4-7, 2009.

Cihan, A., J. Birkholzer, and Q. Zhou, User Guide for an Analytical Solution of Hydraulic Head Changes, Focused and Diffuse Leakage in Multilayered Aquifers: A FORTRAN Program,Lawrence Berkeley National Laboratory, Berkeley, Calif., 2011

Pan, L., J. Hinds, C. Haukwa, Y.-S. Wu, and G. Bodvarsson, *WinGridder - An Interactive grid generator for TOUGH Version 1.0 (User's Manual)*, Report LBNL-42957, Lawrence Berkeley National Laboratory, Berkeley, Calif., 2001.

Pruess, K., C. Oldenburg, and G. Moridis, *TOUGH2 User's Guide, Version 2.0*, Report LBNL-43134, Lawrence Berkeley National Laboratory, Berkeley, Calif., 1999.

Pruess, K., ECO2N: *A TOUGH2 Fluid Property Module for Mixtures of Water, NaCl, and CO_2*, Report LBNL-57952, Lawrence Berkeley National Laboratory, Berkeley, Calif., 2005.

Zhou, Q., Birkholzer J.T., Mehnert E., Lin Y.F., Zhang K., Modeling basin- and plume-scale processes of CO_2 storage for full-scale deployment. *Ground Water*, 48:494–514, 10.1111/j.1745-6584.2009.00657.x, 2010.

COMPARISON OF SUPERCRITICAL AND DISSOLVED CO_2 INJECTION SCHEMES

Catherine Ruprecht and Ronald Falta

Clemson University, Department of Environmental Engineering and Earth Sciences, Brackett Hall 340C, Clemson, SC 29634-0919, USA
e-mail: cruprec@clemson.edu; faltar@clemson.edu

ABSTRACT

The distribution of CO_2 in a storage formation following injection is highly relevant to the risk to drinking water aquifers potentially posed by geological carbon sequestration. Understanding where the injected CO_2 is likely to migrate in the storage formation helps anticipate possible failure modes for the injected fluids. Supercritical CO_2 injection and CO_2 saturated- brine injection have been chosen for investigation in the current work.

Results show that the areal footprint of supercritical CO_2 is initially close to half the size of the dissolved CO_2, independent of formation heterogeneity. Following injection, supercritical CO_2 remains highly mobile, buoyantly flowing upward and significantly extending outwards along the sealing layer; whereas dissolved CO_2 slowly sinks, essentially immobilized following injection. Additionally, dissolved CO_2 distributes more uniformly throughout the storage formation in cases of simple and complex formation heterogeneity. These results indicate that dissolved CO_2 injection may reduce the potential for unwanted release from storage.

INTRODUCTION

There are several proposed methods for CO_2 injection into saline aquifers. The CO_2 may be injected as a supercritical phase (Ennis-King and Paterson, 2002), as CO_2 saturated water (Eke, 2009), as brine alternating CO_2 cycles (Eke et al., 2009), as brine and CO_2 co-injection (Qi, 2007; Qi, 2008), or as a CO_2 saturated brine (Lake, 1989, Burton and Bryant, 2007; Eke et al., 2009, Fang et al., 2010, Jain and Bryant, 2011). These methods seek to immobilize stored CO_2 via structural, residual, or dissolved phase trapping mechanisms (Tao and Bryant, 2012).

In this paper, supercritical and brine-saturated injection strategies are compared in order to determine effects on migration and immobilization of CO_2. Comparisons are made between areal extents of the CO_2 plumes and how the storage volume is utilized, in simulation cases of increasing formation heterogeneity. Plume mobilities are compared during a monitoring period following injection, as are the pressure elevations of the different injection strategies.

BACKGROUND

The prevailing technique for CO_2 injection is in the supercritical phase. This method optimizes the mass of CO_2 injected by volume. In this phase, there is a density difference near 300 kg/m^3 between the CO_2 and resident brine. This density difference drives a buoyant migration of CO_2 upward toward the sealing layer (Bachu, 2002; Eke et al., 2009; Benson et al., 2005). Ideally, the seal would have low permeability and high capillary entry pressure. These properties would then act as a barrier and cause the CO_2 to migrate laterally. Due to lower density and viscosity compared to brine, this buoyant, supercritical CO_2 has a tendency to produce viscous and gravitational instabilities upon injection (Garcia and Pruess, 2003; Yamamoto and Doughty, 2011). These hydrodynamic instabilities may lead to pore space bypassing and reduced sweep efficiency (Garcia, 2003). Previous simulation studies have implied that only 2% of the available pore volume will contain CO_2 if it is injected alone (Fang et al., 2010).

Ex situ dissolution is achieved through surface mixing of CO_2 and brine within a pipeline operating at the storage formation's pressure (Leonenko, 2007). This brine is retrieved from the formation via production wells and re-injected once saturated with CO_2. Surface dissolution of the CO_2 in brine changes the mechanics of flow in the subsurface upon injection. Complications associated with saturation fronts, mobility contrasts, viscous fingering, and

reduced phase permeabilities are eliminated (Burton and Bryant, 2007). This single-phase flow leads to a more uniform sweep of the reservoir (Eke et al., 2009; Fang et al., 2010). The solution will tend to sink as a result of slight density differences with the native brine, removing the need for a perfect seal and allowing safe injection at shallower depths (Fang et al., 2010). Additionally, brine production wells may be used to mitigate pressure elevations during injection and regulate the direction of plume flow and displacement of native brine (Leonenko, 2007; Jain and Bryant, 2011; Tao and Bryant, 2012).

SIMULATION METHODS

Regional-scale multiphase flow models are created using Lawrence Berkeley National Lab's TOUGH2-ECO2N to simulate both supercritical and dissolved CO_2 injection into deep saline aquifers. The first set of models represents a homogeneous formation. The second set of models depicts a stratified heterogeneous formation. The third set of models incorporates heterogeneous, random, spatially correlated permeability fields generated from Lawrence Berkeley National Lab's iTOUGH2-GSLIB. The resultant storage formation is highly heterogeneous in all directions, representing a more realistic permeability distribution. A simple history-dependent nonwetting phase trapping model is incorporated into relative permeability and capillary pressure subroutines of TOUGH2-ECO2N.

Model parameters and hydrogeologic characteristics are held constant between comparisons. The same mass of CO_2 is injected in each case; therefore, a much greater total mass (brine plus CO_2) is injected for the dissolved CO_2 case. To accommodate for the resulting pressure increase, injection schemes are designed so as not to exceed the fracture pressure of the formations.

HOMOGENEOUS FORMATION

A preliminary understanding of supercritical and dissolved CO_2 injection strategies is achieved through comparison of storage in a homogeneous formation.

Model Setup

In initial models, a 200 m thick homogenous storage formation is represented using a radial grid refined around the injection well and extending out 200 km. Pressure and temperature gradients are established between the bottom of the storage formation at 20 MPa and 42ºC and the top at 18 MPa and 40.2ºC. All models are run isothermally. The formation is uniformly given a salinity of 50,000 mg/L. The van Genuchten-Mualem Model is chosen to represent the relative permeability of the liquid phase. A scaled cubic function incorporating a simple history-dependent nonwetting phase trapping model is chosen for the gas phase. The van Genuchten function is used for capillary pressure curves, again incorporating a history-dependent nonwetting phase-trapping model.

Relevant hydrogeologic properties of the storage formation and saturation curve parameters are given in Table 1. Parameter values are determined from Birkholzer et al. (2008), Barnes et al. (2009), and Zhou et al. (2010). These values are characteristic of the deep saline aquifers under consideration for carbon capture and storage activities.

Table 1. Hydrogeologic properties of the homogenous storage formation.

Property		
Porosity	ϕ	0.17
Horizontal permeability	k_r	100 md
Vertical permeability	k_z	10 md
Pore compressibility	β_p	3.71 Pa^{-1}
Relative permeability parameters		
Residual brine saturation	S_{lr}	0.3
Van Genuchten parameter	m	0.41
Max. residual CO_2 saturation	S_{gr}	0.25
Capillary pressure parameters		
Capillary entry pressure	α^{-1}	$4x10^3$ Pa
van Genuchten parameter	m	0.41

Injection is conducted for a 20-year period at approximately 160 Mt/yr of CO_2. The rate of CO_2 injected was chosen so pressure elevations due to injection from any one well would not exceed the fracture pressure of the storage formation, set at 3.17 MPa above hydrostatic pressure. In the case of CO_2 dissolved in brine, the brine is assumed to have the same composition as the resident fluid. At the given pressures

and temperatures, a volume of brine approximately 20 times that of the CO_2 is needed for full dissolution. In order to consider long-term storage security, mobility of both phases is compared during a 25-year monitoring period following injection.

Results

Figure 1 shows the CO_2 fronts at the end of 20-year injection periods. Considering a CO_2 mass fraction of 0.005 as the cutoff, the farthest the supercritical CO_2 travels from the well is 415 m along the caprock. The dissolved CO_2 travels more uniformly, flushing the aquifer 920 m from injection.

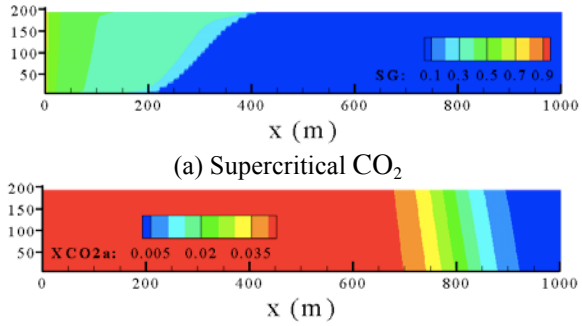

(a) Supercritical CO_2

(b) Dissolved CO_2

Figure 1. The top cross section shows the radial distribution of supercritical CO_2 saturation after 20 years of injection. The bottom cross section shows distribution of the mass fraction of CO_2 in the aqueous phase.

Maximum pressures are achieved at the end of injection in gridblocks along the top of the storage formation closest to the well. These pressures are determined without considering brine production wells elsewhere in the target region. In the supercritical case, the largest pressure increase is 0.60 MPa and in the dissolved case it is at 7.27 MPa. Extents of pressure effects are determined with pressure increase cutoff at 10.0 kPa, or the equivalent of 1 m hydraulic head rise. An elevation in pressure is calculated 24 km from injection in the supercritical CO_2 case and 83 km from injection in the dissolved CO_2 injection case.

Figure 2 shows the distribution of CO_2 80 years after the end of the injection period. Buoyancy and viscous forces drive the supercritical CO_2 to the top of the formation and 550 m from the well. This behavior is an example of gravity override (Yamamoto and Doughty, 2011), which enables CO_2 mobility after injection has stopped. The dissolved CO_2 travels 930 m from the injection well, sinking due to a higher density compared to the resident brine.

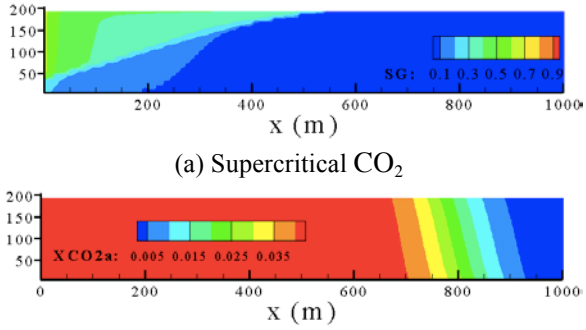

(a) Supercritical CO_2

(b) Dissolved CO_2

Figure 2. The top cross section shows the radial distribution of supercritical CO_2 saturation after 20 years of injection. The bottom cross section shows distribution of the mass fraction of CO_2 in the aqueous phase.

Notably, the dissolved CO_2 sinks to the bottom of the aquifer more slowly than the supercritical CO_2 rises to the top. In the years following injection, it can be seen from these simple models that supercritical CO_2 increases its areal footprint on the cap rock significantly, reducing storage efficiency. Dissolved CO_2 is essentially immobile during this time.

STACKED FORMATION

CO_2 injection into a geology characterized by alternating, laterally extensive layers of higher and lower permeability is anticipated to increase storage security.

Model Setup

In order to simulate this type of geology, a 2 km thick, 200 km radial model is developed. At the base of the model is a storage formation that contains 8 layers of alternating aquifer material. From the storage formation to surface, a stacked system of 12 aquifers and confining units is modeled. Figure 3 shows an image of the model setup.

Pressure and temperature gradients are established between the bottom of the storage formation at 20 MPa and 42ºC to atmospheric

pressure and temperatures. All models are run isothermally. The formation is uniformly given a salinity of 50,000 mg/L. Materials are given as "Aquifer I", "Aquifer II", and "Seal" in Table 2. Parameter values are determined from Birkholzer et al. (2008), Barnes et al. (2009), and Zhou et al. (2011) and are characteristic of the regional geology surrounding target storage formations. Injection rates match those of the homogeneous case at 160 Mt/yr of CO_2. Monitoring time is extended to an 80-year period following injection.

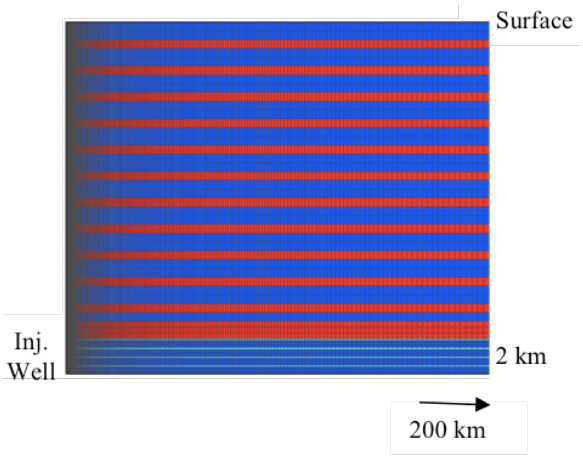

Figure 3. Setup of the stacked formation radial model. "Aquifer I" is given in dark blue, "Aquifer II" in light blue, and confining layers in red. Not to scale.

Results

Figure 4 shows the CO_2 front at the end of a 20-year injection period. The farthest the supercritical CO_2 travels from the well is 400 m. The plume is divided between the four layers of more permeable aquifer material, enhancing the pore volume utilized from the homogeneous case. The dissolved CO_2 travels 1,150 m.

Maximum pressures are achieved at the end of injection in gridblocks along the top of the storage formation closest to the well. These pressures are determined without considering brine production wells elsewhere in the target region. In the supercritical case, the largest pressure increase is 0.86 MPa; in the dissolved case, it is at 10.1 MPa.

Extents of pressure effects are again determined with a cutoff at 10.0 kPa in the vertical and horizontal directions. In the supercritical case, relevant pressure elevations are observed up to 50 m above the storage formation. Laterally, pressure elevations are observed up to 39.5 km from the injection well. In the dissolved case, pressure elevations are observed up to 125 m above the storage formation and up to 84 km radially from the injection well.

Table 2. Hydrogeologic properties of the stacked formation.

Property	Aquifer I	Aquifer II	Confining layers
Porosity	0.17	0.17	0.15
Horizontal permeability	100.0 md	1.0 md	1.0 x10^{-3} md
Vertical permeability	10.0 md	0.1 md	1.0 x10^{-4} md
Pore compressibility	3.71 Pa^{-1}	3.71 Pa^{-1}	7.42 Pa^{-1}
Relative permeability parameters			
Residual brine saturation	0.3	0.3	0.4
Van Genuchten parameter	0.41	0.41	0.41
Max. residual CO_2 saturation	0.25	0.25	0.3
Capillary pressure parameters			
Capillary entry pressure	4x10^3 Pa	4x10^3 Pa	5x10^6 Pa
van Genuchten parameter	0.41	0.41	0.41

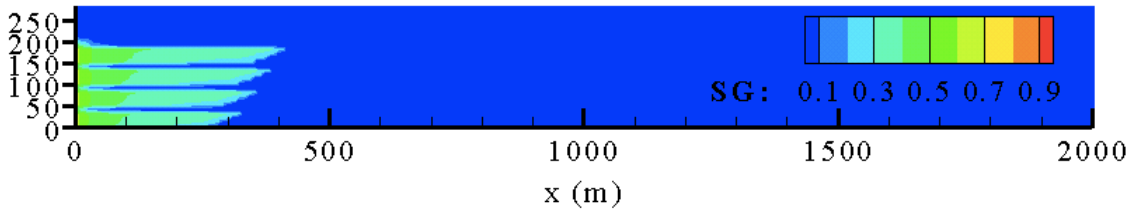

(a) Supercritical CO_2

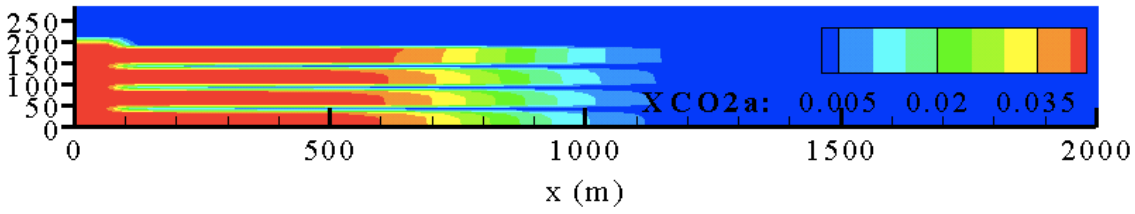

(b) Dissolved CO_2

Figure 4. The top cross section shows the radial distribution of supercritical CO_2 saturation after 20 years of injection. The bottom cross section shows distribution of the mass fraction of CO_2 after 20 years of injection in a dissolved phase.

Figure 5 shows the mobility of CO_2 after 80 years from the end of injection. The supercritical CO_2 travels along the borders of less permeable layers up to 500 m from the well. The less permeable "Aquifer II" layers within the storage aquifer act as barriers to the sinking dissolved CO_2. In 80 years, the dissolved CO_2 does not appreciably migrate.

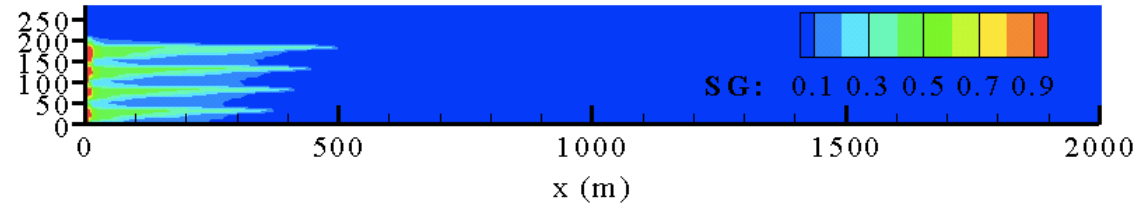

(a) Supercritical CO_2

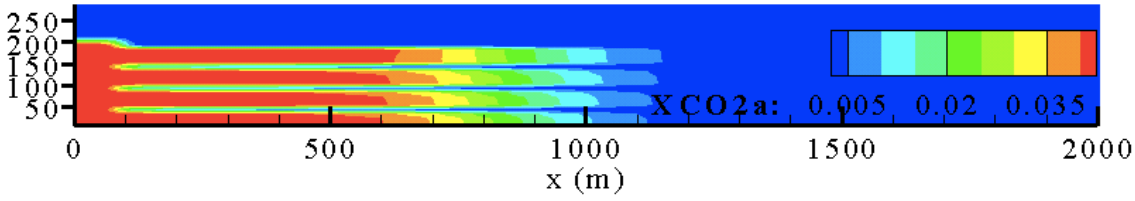

(a) Dissolved CO_2

Figure 5. The top cross section shows the radial distribution of supercritical CO_2 saturation 80 years after CO_2 injection stops. The bottom shows distribution of the mass fraction of CO_2 injected in a dissolved phase.

HETEROGENEOUS FORMATION

A heterogeneous permeability distribution within a storage formation reduces sweep efficiency in both supercritical and dissolved CO_2 injection schemes and may lower storage security (Tao and Bryant, 2012).

Model Setup

A regional scale model is constructed using a 200 km square, 2 km thick Voronoi grid. Within the 200 m thick storage formation, at the base of the model, is a zone surrounding the injection well containing heterogeneous, random, spatially correlated permeability fields. This zone is 10 km in radial extent from the well and is designed to encompass the CO_2 plume in either phase.

Lawrence Berkeley National Lab's iTOUGH2-GSLIB is used to generate these heterogeneous permeability fields. Using parameters similar to Barnes et al. (2009), the intrinsic permeability is given a log-normal distribution with a variance of 2.0 about an average permeability of 100 md. Sequential Gaussian Simulation is used to create a spherical variogram model with a vertical range of 1 m for log permeability. A long horizontal-to-vertical ratio of 10,000:1 is assumed for the variogram length.

Outside of the highly heterogeneous region, the storage formation is homogeneous. Above the storage formation, the model is set up as in the stacked case, alternating aquifers and confining units. Material properties match "Aquifer I" and "Confining layers" given in Table 2. Pressure and temperature gradients are established between the bottom of the storage formation at 20 MPa and 42ºC to atmospheric pressure and temperatures. All models are run isothermally. The formation is uniformly given a salinity of 50,000 mg/L. Injection rates and monitoring periods match those of the stacked cases.

Results

Figure 6 shows areal contours of the CO_2 plumes along the top of the storage formation and isosurface contours within the formation at the end of a 20-year injection period. The farthest the supercritical CO_2 travels from the well is 800 m. The farthest extent of the dissolved phase CO_2 is 1,750 m. The plume shape is largely determined by the permeability distribution, as is seen from the isosurface plots.

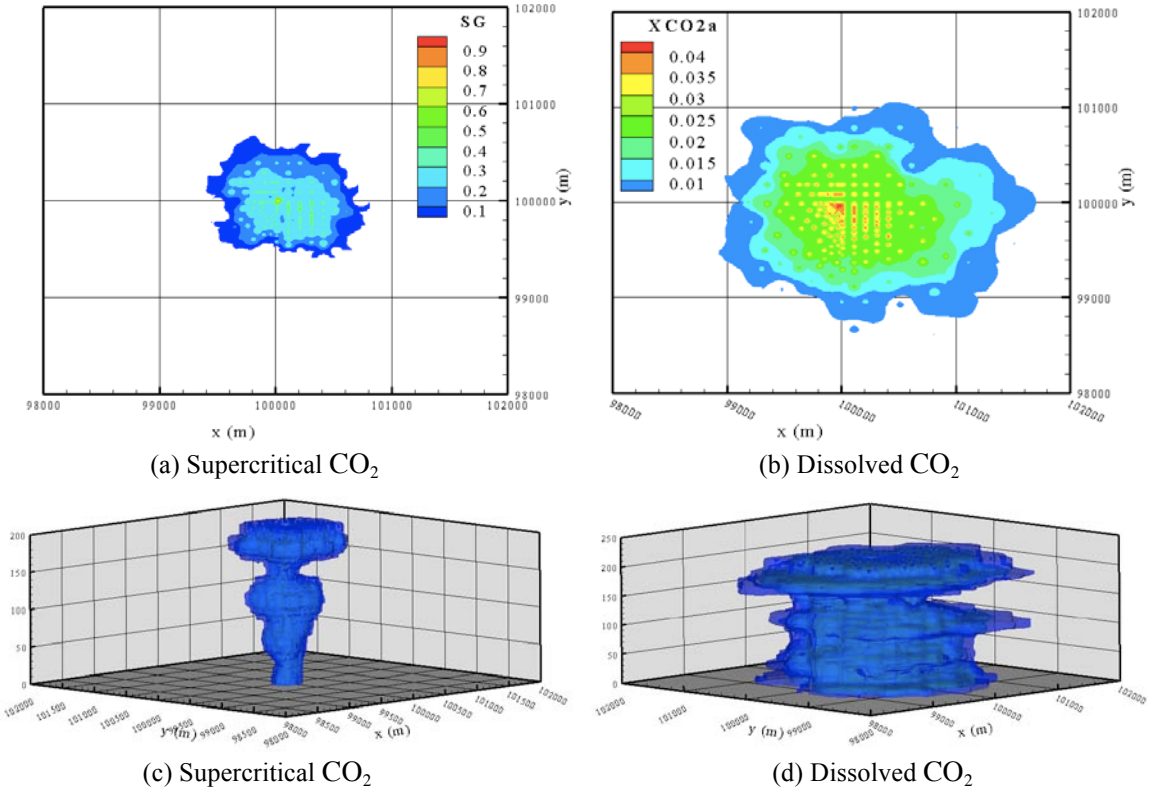

(a) Supercritical CO_2 (b) Dissolved CO_2

(c) Supercritical CO_2 (d) Dissolved CO_2

Figure 6. CO_2 distribution in the heterogeneous region of the storage formation after 20 years of injection (a) Areal cross section of supercritical CO_2 saturation. (b) Areal cross section of the mass fraction of dissolved CO_2. (c) 3-D isosurface of supercritical CO_2 saturation. (d) 3-D isosurface of the mass fraction of CO_2 in the aqueous phase.

Maximum pressures are achieved at the end of injection in gridblocks along the top of the storage formation closest to the well. These pressures are determined without considering brine production wells elsewhere in the target region. In the supercritical case, the largest pressure increase is 0.44 MPa; in the dissolved case, it is 72.3 MPa.

Extents of pressure effects are determined with pressure increase cutoff at 10.0 kPa in the vertical and horizontal directions. In the supercritical case, relevant pressure elevations are observed up to 50 m above the storage formation. Laterally, pressure elevations are observed up to 38.5 km from the injection well. In the dissolved case, relevant pressure elevations are observed up to 125 m above the storage formation. Laterally, pressure elevations are observed up to 89 km from injection well.

Figure 7 shows the mobility of CO_2 80 years from the end of the injection. The supercritical CO_2 remains highly mobile, traveling through high permeability lenses up and along the cap rock out to 1,000 m. The less permeable lenses within the storage aquifer act to immobilize dissolved CO_2. In 80 years, the dissolved CO_2 does not increase in maximum areal extent.

CONCLUSIONS

In this study, comparisons of migration and immobilization of CO_2 were made between supercritical CO_2 and CO_2-saturated brine injection strategies. Results show the initial areal footprint of supercritical CO_2 is less than half the size of the dissolved CO_2 in any formation heterogeneity. Following injection, supercritical CO_2 remains highly mobile, buoyantly flowing upward and extending outwards along the seal at least 20% radially. Dissolved CO_2 slowly sinks, essentially immobilized following injection. Additionally, dissolved CO_2 distributes more uniformly throughout the storage formation in cases of simple and complex formation heterogeneities.

Maximum pressure elevations are calculated without relief from production wells and are shown to be an order of magnitude greater for the dissolved CO_2 strategy in all cases. Vertical and horizontal pressure elevations due to dissolved CO_2 injection are observed to be between 2 and 2.5 times greater than supercritical pressure elevations.

These results indicate dissolved CO_2 injection enhances CO_2 trapping following injection and reduces the potential for unwanted release from storage. A larger volume is utilized for storage based on the properties of flow and total mass injected, requiring appropriate management of pressure elevations in targeted regions.

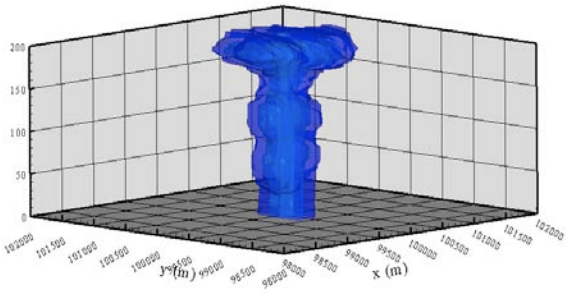

(a) Supercritical CO_2

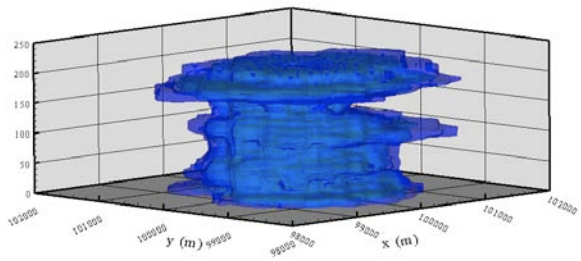

(b) Dissolved CO_2

Figure 7. CO_2 distribution in the heterogeneous region of the storage formation 80 years after injection ends (a) 3-D isosurface of supercritical CO_2 saturation. (b) 3-D isosurface of the mass fraction of CO_2 in the aqueous phase.

ACKNOWLEDGMENT

This research has been funded under U.S. EPA-STAR Grant #834383.

REFERENCES

Bachu, S., Sequestration of CO_2 in Geological Media in Response to Climate Change: Road Map for Site Selection using the Transform of the Geological Space into the CO_2 Phase Space, *Energy Conversion Management, 43*, 87 , 2002.

Barnes, D., D. Bacon, and S. Kelley., Geological Sequestration of Carbon Dioxide in the Cambrian Mount Simon Sandstone: Regional Storage Capacity, Site Characterization, and Large-Scale Injection Feasibility, *Environmental Geoscience,s 16*(3), 163, 2009.

Benson, S., et al. Underground Geologic Storage, *Intergovenmental Panel on Climate Change* Cambridge, U.K.: Cambridge University Press, 2005.

Birkholzer, J. T., and Z. Quanlin, Basin-Scale Hydrogeologic Impacts of CO_2 Storage: Capacity and Regulatory Implications, *International Journal of Greenhouse Gas Control*, *3*(6), 745-756, 2005.

Burton, M., and S. Bryant, Eliminating Buoyant Migration of Sequestered CO_2 through Surface Dissolution: Implementation Costs and Technical Challenges, SPE 110650, *2007 SPE Ann. Tech. Conf. Exhib.* Anaheim, CA. 2007.

Eke, P., M. Naylor, S. Haszeldine, A. Curtis, CO_2 -Brine Surface Dissolution and Injection: CO_2 Storage Enhancement, Publication SPE 124711, *Proceedings of the 2009 SPE Offshore Europe Oil & Gas Conference & Exhibition.* Aberdeen, UK. 2009.

Ennis-King, J. and L. Paterson, Engineering Aspects of Geological Sequestration of Carbon Dioxide, Publication SPE 77809, *Asia Pacific Oil and Gas Conference and Exhibition.* Melbourne, Australia. 2002.

Fang, Y., B. Baojun, T. Dazhen, S. Dunn-Norman, D. Wronkiewicz, Characteristics of CO_2 Sequestration in Saline Aquifers, *Pet. Sci., 7*, 83, 2010.

Garcia, J., K. Pruess, Flow Instabilities during Injection of CO_2 into Saline Aquifers, *TOUGH Symposium 2003,* Berkeley, California. 2003.

Hagoort, J., Fundamentals of Gas Reservoir Engineering, *Elsevier Science Publ.,* 23, 1988.

Jain, L. and S. L. Bryant, Optimal Design of injection/extraction wells for surface dissolution CO_2 storage strategy, *Energy Procedia,* 4, 4299-4306, 2011.

Lake, L. W., *Enhanced Oil Recovery*. NJ: Prentice Hall, 1989.

Leonenko, Y., D. Keith, Reservoir Engineering to Accelerate the Dissolution of CO_2 Stored in Aquifers, *Environ. Sci. Technol.* 42, 4742, 2007.

Tao, Q. and S. L. Bryant, Optimal Control of Injection/Extraction Wells for the Surface Dissolution CO_2 Storage Strategy, Carbon Management Technology Conference, 2012.

Yamamoto, H. and C. Doughty, Investigation of gridding effects for numerical simulation of CO_2 geologic sequestrations, *Int. Journal of Greenhouse Gas Control*, 2011.

Zhou, Q., J.T. Birkholzer, E. Mehnert, Y. Lin, K. Zhang, Modeling Basin- and Plume-Scale Processes of CO_2 Storage for Full-Scale Deployment, *Ground Water, 48*(4), 494-514, 2010.

COMPARISON OF A 2D TOUGHREACT MODEL OF CO_2 INJECTION INTO A CARBONATE RESERVOIR WITH CHEMICAL DATA FROM A CO_2 ENHANCED OIL RECOVERY PROJECT

Maurice Shevalier*, Michael Nightingale and Bernhard Mayer

University of Calgary
Applied Geochemistry Group, Department of Geoscience
Calgary, AB T2N 1N4 Canada

*e-mail: maurice@earth.geo.ucalgary.ca

ABSTRACT

This paper presents a numerical modeling study of CO_2 injection in an Enhanced Oil Recovery Projects (EOR) in central Alberta. Chemical and isotopic monitoring of a small EOR project in Alberta has been under way since March 2008. One objective of this project is to compare measured geochemical parameters obtained from a producing well located ~800 m from the CO_2 injection well, with modeling results obtained by using the geochemical reactive-transport model TOUGHREACT.

A two-dimensional radial symmetrical model was used for the model and was assumed to be a uniform carbonate formation. The model consisted of three carbonate layers, the Lower Ireton Cap rock, the Leduc Fore Reef storage aquifer, and the Leduc Back Reef bottom rock. CO_2 is injected into the bottom 1 m of the Leduc Fore Reef at a rate of 78 kT/y (2.6 kg/s). The integrity of the cap rock is compromised due to injected CO_2 migrated into it, owing to its permeability, 0.1 MD, resulting in carbonate dissolution.

The primary CO_2 sequestration method is solubility trapping. This is evident in the plume region where low pH and high HCO_3 concentrations were observed. The secondary trapping mechanism is ionic trapping, evident by high Mg and Ca concentrations.

A comparison of modeled values with a producing well in the Leduc Fore reef found that the arrival time of injected CO_2 was similar, ~700 days. Further, the concentrations of HCO_3, both modeled and measured were very similar in values, but after the arrival of injected CO_2, the modeled value was three times larger. The pH and Mg concentrations for the modeled and measured values both followed similar trends. With CO_2 arrival, the pH decreased and Mg concentrations increased at similar times. The modeled pH was 0.5 to 1.5 pH units higher than the calculated downhole pH. The Mg modeled concentration was three times higher than the measured concentrations from the wells.

The results show that the modeled and measured values for different species follow the same trend. The difference is probably due to the kinetic parameters, which are measured on ideal samples—and the minerals present in an oil field are not ideal. Also, the inclusion of 16 months of data which has been collected post-injection, is currently under way.

BACKGROUND

CO_2 injection into saline aquifers is considered a promising option for sequestering large amounts of CO_2 captured from point source emitters such as coal-burning power plants. Although Enhanced Oil Recovery Projects (EOR) are not true Carbon Capture and Storage projects, it is nevertheless feasible to assess the fate of injected CO_2 used in the EOR process by modeling and monitoring.

The CO_2 injection area was into the Leduc Fore Reef; the Reef Complex is subdivided into the Lower, Middle, and Upper Leduc members. The pilot area is confined to the upper northeast perimeter of the Upper Leduc member. The Leduc Formation is overlain by the tight calcitic Ireton Formation; the underlying formation is the Leduc Back Reef. Detailed mineralogical studies were conducted on all members of the formation to determine their composition. CO_2 was injected into an up-sloping pinnacle reef.

Pre-injection brine and gas samples were collected on three separate occasions. Syn-injection brine and gas samples are collected on a semi-regular basis for 30 months; post-injection samples have been collected for the past 16 months and is still ongoing. The brine and gas are analyzed for major anions, cations, and gas composition, as well as nine isotopic parameters.

NUMERICAL METHOD

All of the simulations were performed using TOUGHREACT v. 1.2 (Xu et al, 2006). The code was developed by using the existing multiphase fluid and heat flow code, TOUGH2 v.2 (Pruess, 1991) and adding in the geochemical reactive transport code. The integral finite difference method for space discretization (Narasimham and Witherspoon, 1976) is the basis of the numerical method for simulation of fluid flow. Coupling between the geochemical reactions and fluid transport involves a sequential iterative approach (Yeh and Tripathi, 1991). The fluid property module ECO2N was used in the modeling.

SETUP OF THE MODEL

Geometry

A three-layer uniform model is used: the Lower Ireton calcitic cap rock is 3 m in thickness; the Leduc Fore Reef, a mixed calcite/dolomite, is 11 m in thickness; and the Leduc Back Reef, a calcitic bottom rock, is 3 m in thickness. The formations are assumed to be uniform throughout, extend 3 km in the horizontal direction, and have a radial symmetrical with non-uniform spacing. The cap rock and bottom rock have a layer thickness of 0.5 m, with the Leduc having 0.25 m thickness. CO_2 injection occurs in the bottom 2 m of the Leduc.

The simplifications in the model geometry result in a number of shortcomings, and hence we were not able to consider non-uniform sweeps, buoyancy forces, convective mixing, etc. One justification for these simplifications are that the slow reaction rates and the long time scales for geological changes will, in the long run, make the CO_2 distribution more or less uniform over time (Xu et al., 2007).

Initial and boundary conditions

Hydrogeological parameters used in the simulations are shown in Table 1. The Leduc Fore reef is the most porous and permeable zone, with a porosity of 17.5% and a permeability of 750 md. The overlying Ireton is relatively impermeable, with a permeability value of 0.1 md and porosity of 5.0%, suggesting that it is a very good cap rock. The Van Genunchten (1980) model was used to calculate the capillary pressure and relative permeability curves for each layer in the model.

Table 1. Hydrogeological parameters for the Lower Ireton, Leduc Fore Reef and Leduc Backreef formations

	Lower Ireton	Leduc Fore Reef	Leduc Back Reef
Porosity (%)	5.0	17.5	5.0
Perm. (m^2)	0.1	750	2.0
Temperature (°C)		40	
Pressure (MPa)		8.0	
Pore Comp. (Pa^{-1})		$1\ 10^{-8}$	
Diffusivity(m2/s)		$1\ 10^{-9}$	
Torousity		0.3	

Table 2 summarizes the measured water composition of brine obtained during the pre-injection portion of the study. The water composition given in Table 2 is representative for brines measured at surface conditions, i.e., after the sample degassed while moving from depth to surface. The water used in the simulation was re-equilibrated with degassing H_2S, CH_4, and CO_2 using SOLMINEQ88 (Kharaka et al., 1988) as shown in Table 2. The waters were then equilibrated with the three-layered reservoir for 10 years using the static mode of TOUGHREACT. Two species shown in Table 1 were not measured: AlO_2^- and $O_{2(aq)}$. A small amount of each was added, since the first would probably be present due to the presence of silicate minerals, and the $O_{2(aq)}$ was necessary for redox reactions to occur.

The initial mineral compositions of the Lower Ireton, Leduc Fore Reef, and Leduc Back Reef formations used in the modeling are shown in Table 3. The Lower Ireton is composed of mainly calcite (95.51%), dolomite (3.20%), and minor amounts of quartz, k-feldspar, and pyrite.

The Leduc Fore Reef consists of mostly calcite (47.67%) and dolomite (52.01%) with a trace of quartz. The Leduc Back Reef consists primarily of calcite (98.94%) and minor amounts of dolomite.

Table 2. Initial chemical species concentrations of the brine used in the TOUGHREACT simulations

Species	Measured Concentration (mol/kg)	Equilibrium Concentration (mol/kg)
pH	6.82	7.72
Ca^{2+}	0.118	2.170×10^{-2}
Mg^{2+}	.006	0.1745
Na^{+}	1.325	1.267
K^{+}	.0073	6.970×10^{-3}
Sr^{2+}	.0017	1.637×10^{-3}
Fe^{2+}	2.15×10^{-5}	1.940×10^{-5}
$SiO_{2(aq)}$	3.79×10^{-4}	3.623×10^{-4}
HCO_3^-	7.97×10^{-3}	8.320×10^{-3}
SO_4^{2-}	.0175	0.0168
Cl^-	1.672	1.670
AlO_2^-	-	1.36×10^{-7}
$O_{2(aq)}$	-	4.88×10^{-70}
$H_2S_{(aq)}$	3.93×10^{-3}	3.97×10^{-2}

Table 3: Initial mineral volume fractions and secondary minerals used in TOUGHREACT simulations

Primary Minerals	Lower Ireton (%)	Leduc Fore Reef (%)	Leduc Back Reef (%)
Calcite	95.51	47.67	98.94
Dolomite	3.20	52.01	0.86
Quartz	0.74	0.32	0.21
K-feldspar	0.22	0.00	0.00
Pyrite	0.33	0.00	0.00
Secondary Minerals			
Albite-low	Anhydrite	Ankerite	Aragonite
Chlorite	Dawsonite	Illite	Kaolinite
Magnesite	Siderite	Ca-Smectite	Na-Smectite

Table 4 provides parameters for the kinetics of dissolution and precipitation by the minerals, primary and secondary, used in the models (Palandri and Kharaka, 2004). Calcite was used as an equilibrium mineral in the simulations due to its relatively fast kinetics. The secondary minerals considered in the 2-D model are given in Table 3. Specific details about the kinetics used in the simulations can be found in Xu et al. (2007).

Table 4. Parameters for calculating kinetic rate constants of minerals used (Palandri and Kharaka, 2004).

Mineral	A (cm^2/g)	Parameters for kinetic rate law							
		Neutral Mechanism		Acid Mechanism			Base Mechanism		
		k^{25} ($mol/m^2/s$)	E (kJ/mol)	k^{25}	E	$n(H^+)$	k^{25}	E	$n(H^+)$
Dolomite	9.1	$2.9512\ 10^{-8}$	52.2	$6.4565\ 10^{-04}$	36.1	0.500			
Illite	108.7	$1.6596\ 10^{-13}$	35.0	$1.0471\ 10^{-11}$	23.6	0.340	$3.02\ 10^{-17}$	58.9	-0.400
K-feldspar	9.1	$3.8905\ 10^{-13}$	38.0	$8.7096\ 10^{-11}$	51.7	0.500	$6.3096\ 10^{-22}$	94.1	-0.823
Low-Albite	9.1	$2.7542\ 10^{-13}$	69.8	$6.9183\ 10^{-11}$	65.0	0.457	$2.5119\ 10^{-16}$	71.0	-0.572
Kaolinite	108.7	$6.9183\ 10^{-14}$	22.2	$4.8978\ 10^{-12}$	65.9	0.777	$8.9125\ 10^{-18}$	17.9	-0.472
Na-smectite	108.7	$1.6596\ 10^{-13}$	35.0	$1.0471\ 10^{-11}$	23.6	0.340	$3.0200\ 10^{-17}$	58.9	-0.400
Ca-smectite	108.7	$1.6596\ 10^{-13}$	35.0	$1.0471\ 10^{-11}$	23.6	0.340	$3.0200\ 10^{-17}$	58.9	-0.400
Dawsonite	9.1	$1.2598\ 10^{-09}$	62.76	$6.4565\ 10^{-04}$	36.1	0.500			
Aragonite	9.1	$4.5709\ 10^{-10}$	23.5	$4.1687\ 10^{-07}$	14.4	1.000			
Siderite	9.1	$1.2598\ 10^{-09}$	62.76	$6.4565\ 10^{-04}$	36.1	0.500			
Ankerite	9.1	$1.2598\ 10^{-09}$	62.76	$6.4565\ 10^{-04}$	36.1	0.500			
Magnesite	9.1	$4.5709\ 10^{-10}$	23.5	$4.1687\ 10^{-07}$	14.4	1.000			
Chlorite	9.8	$3.02\ 10^{-13}$	88.0	$7.762\ 10^{-12}$	88.0				
Anhydrite	9.1	$6.457\ 10^{-04}$	14.3						
Pyrite	12.87	$2.8184\ 10^{-05}$	56.9 $n(O_{2(aq)})=0.5$	$3.2022\ 10^{-08}$	56.9 $n(H^+) = -0.5$, $n(Fe^{3+})=0.5$				

Notes: (1) all rate constants are for dissolution
(2) A is specific area, k^{25} is kinetic rate constant at 25 ºC, E is activation energy, n is power term (Eq. (3), Xu et al., 2007)
(3) power terms n for both acid and base mechanism are with respect to H^+
(4) for pyrite, the neutral mechanism has n with respect to $O_{2(aq)}$, the acid mechanism has two species involved: one n with respect to H^+ and another n with respect to Fe^{3+} (Eq. (3), Xu et al., 2007)

GEOCHEMICAL REACTIONS

The dissolution of CO_2 in water forms carbonic acid via Reaction 1, also known as solubility trapping, resulting in a decrease in the pH. If there are any reactant minerals present, such as calcite, then mineral dissolution occurs (Reaction 2) resulting in a free cation and a bicarbonate ion, causing both the pH and the cation concentration to increase.

$$CO_2 + H_2O \rightleftharpoons H_2CO_3$$
$$H_2CO_3 \rightleftharpoons H^+ + HCO_3^- \quad \text{Solubility Trapping (1)}$$

$$CaCO_3 + H^+ \rightharpoonup Ca^{2+} + HCO_3^-$$
Mineral Dissolution (2)

Thus, the net reaction between injected CO_2 and calcite is as follows, also known as ionic trapping:

$$CO_2 + H_2O + CaCO_3 \rightharpoonup Ca^{2+} + 2HCO_3^-$$
Ionic Trapping (3)

SIMULATION RESULTS

The simulations conducted for this study considered the fate of injected CO_2 in the reservoir—through geochemical interactions with the brine and comparing the simulation results with data collected from a well ~800 m from the injector. The simulation results are presented in 2-D graphical plots as a function of depth and radial distance at discrete time intervals of 0.33 and 2.5 years for the CO_2 injection. While the simulation covered a radial distance of 3 km, only the first 1 km is shown, since that is where the main reactions are occurring. Specific data are also presented in graphical form as a function of depth at discrete time intervals, 0.09, 0.33, 0.59, 1.0, 1.5, 2.0, and 2.5 years, at a distance of 817 m from the injector. The modeled injection rate of CO_2 into the Leduc Fore Reef was 78 kT/y or 2.6 kg/s.

Spatial Distibution

Supercritical CO_2 is injected into the formation and, having a density less than that of the brine (~ 10 kg/m^3), migrates from the injection region upwards to the Lower Ireton cap rock. Even at the low injection rate, 2.6 kg/s, there is enough injected CO_2 in 0.33 years to see an injection plume (Figure 1). The plume had radially dispersed ~300 m under the cap rock and appears to have migrated slightly into the lower Ireton cap rock. After 2.5 years of injection, the plume had expanded radially to ~700 m. The migration of CO_2 into the Lower Ireton cap rock is evident with a maximum Sg ~0.3 at the Ireton-Leduc interfacial region nearest the injector region. This would indicate that the Lower Ireton is not an impervious cap rock. Also, CO_2 migration has occurred in the bottom rock, the Leduc Back Reef, the bottom rock. It extends out to ~250 m in the bottom rock with a maximum S_g of~0.6 in the region nearest to the injector.

The spatial distribution of HCO_3 within the study region is shown in Figure 2. The HCO_3 has a similar plume shape and size as that of the free-phase CO_2. The concentration in the Leduc Fore reef region is quite high, >1.8 mol/kg after only 0.33 years injection. The susceptibility of the cap rock and bottom rock to CO_2 is evident in both time slices for HCO_3. In the cap rock region, the concentration is ~1.6 mol/kg at the Ireton-Leduc interfacial region. After 2.5 years, both the bottom rock and cap rock region show significant HCO_3 concentration >1.8 mol/kg, indicating poor cap rock and bottom rock integrity.

pH spatial distribution in the Leduc Fore Reef aquifer is shown in Figure 3. The initial pH of the brine is 7.5; after 0.33 years of injection, this decreases to ~5.5. The pH in the cap rock and bottom rock regions also drops to ~5.0 within 0.33 years. The low pH of ~5.5 extends out to ~775 m after 2.5 years. In the bottom and cap rock, the pH ~5.0 region extends out to ~675 and ~775 m respectively.

Figure 4 shows the spatial distribution of Mg. The background concentration of Mg is ~0.18 mol/kg. After 0.3 years of CO_2 injection, the Mg concentration has increased to ~0.52 in the plume region. The significant increase in the concentration of Mg, Ca (not shown), and HCO_3 indicates that ionic trapping, Reaction 3, is an important reaction occurring with the reservoir.

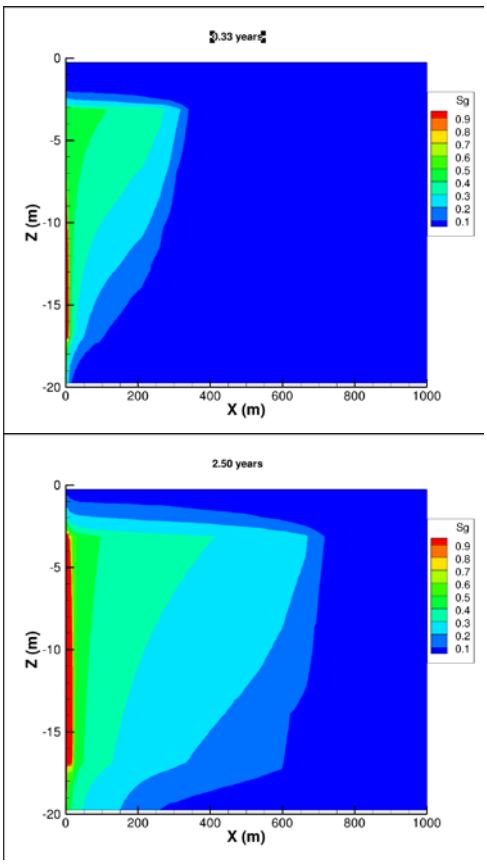

Figure 1. Spatial distribution of CO_2 gas saturation after 0.33 and 2.5 years of injection.

However, that there is no increase in the pH of the system in regions with high Mg concentration indicates that solubility trapping, Reaction 1, is the dominant reaction. This is to be expected, since the Leduc Fore Reef is calcite and dolomite (Table 3). The high Mg also occurs both within the cap rock and bottom rock region. Since there is dolomite present, albeit in smaller amounts, there are sufficient enough amounts to cause a significant increase in Mg concentration. By 2.5 years, the increased Mg occurs throughout the storage reservoir. However, the regions of highest concentration, >0.6 mol/kg, occur in the bottom rock and to a lesser extent in the cap rock. This, along with the high HCO_3 concentration, indicates that a significant amount of ionic trapping is occurring in the bottom rock. The highest concentrations in the bottom rock can be explained by the permeability. At 2.0 mD, it allows CO_2 to easily enter the region, but the formation is tight enough to impede its transport, allowing for significant dolomite dissolution to occur. The reservoir storage region has a lesser amount of dissolution due to its high permeability, 750 mD, more readily allowing the transport of CO_2, resulting in smaller amounts of dissolution but over a wider area.

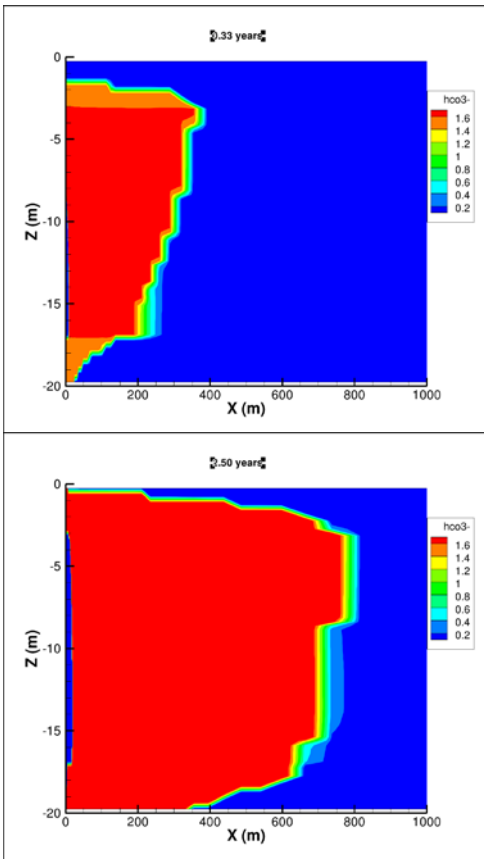

Figure 2. Spatial distribution of HCO_3 after 0.33 and 2.5 years of injection. The units of concentration are mol/kg.

Concentration vs Depth Profile at 817 m

Concentration profiles were isolated from the 2D surface plots at a distance of 817 m from the injector well. This was done to compare the species from the model with results from a producing well located ~800 m from the injector. (This comparison between model and producing well is done in the next section.) Figure 5 shows a depth profile for the concentration of HCO_3 as a function of time. There is no significant change in HCO_3 until after 2 years. The change in concentration varied radially with decreasing depth: as the depth decreased, the concentration of HCO_3 increased, reaching the maximum, twice the initial

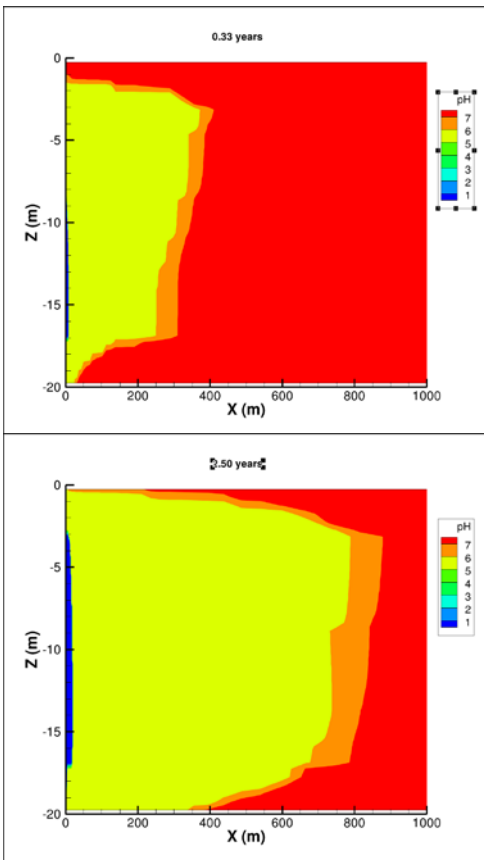

Figure 3. Spatial distribution of pH after 0.33 and 2.5 years of injection.

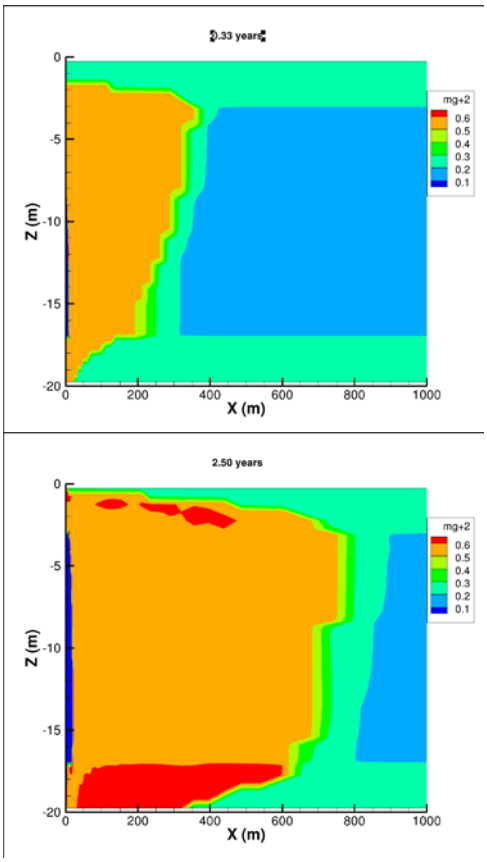

Figure 4. Spatial distribution of Mg after 0.33 and 2.5 years of injection. The units of concentration are mol/kg.

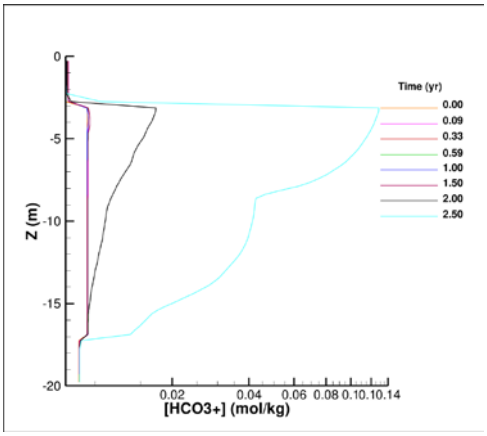

Figure 5. HCO_3 concentration profile as a function of depth.

concentration, at the interface between the Ireton caprock and Leduc storage aquifer. After 2.5 years, the plume dispersion is evident by the concentration profile. The concentration is largest at the Ireton-Leduc interface and has a profile similar to that for plume dispersion. The time/depth profile for the pH is identical to the HCO_3 profile, except that the pH is decreasing over time. There was no change in the pH until after 2 years of CO_2 injection. At 2 years, the pH decreases slightly, from ~7.5 to 7.2, at the Ireton-Leduc interface. As depth increases, the pH increases to its background value at the bottom rock interface. The pH trend after 2.5 years is very similar to the HCO_3 trend but with decreasing pH. The Mg concentration follows that of the HCO_3; after 2 years, there is a very slight increase in Mg at the Ireton-Leduc interfacial region. After 2.5 years, the change in concentration varied radially with decreasing depth; as the depth decreased, the concentration of Mg increased, reaching the maximum at the storage-cap rock interface.

The lack of significant increase in Mg after 2 years, while pH decreased and HCO_3 increased, indicates that solubility trapping is the primary sequestration method. After that, the continuing decrease in pH but increase in Mg and HCO_3

indicated that both ionic and solubility trapping are occurring, with solubility trapping being more dominant.

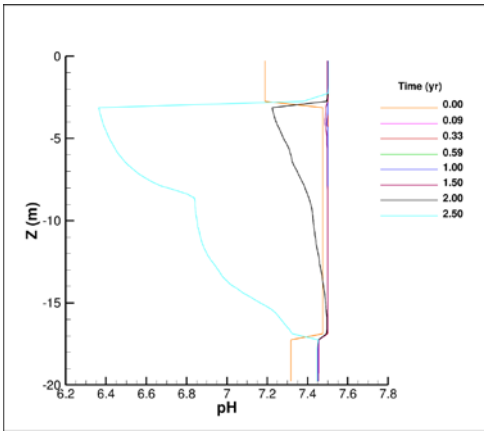

Figure 6. pH profile as a function of depth.

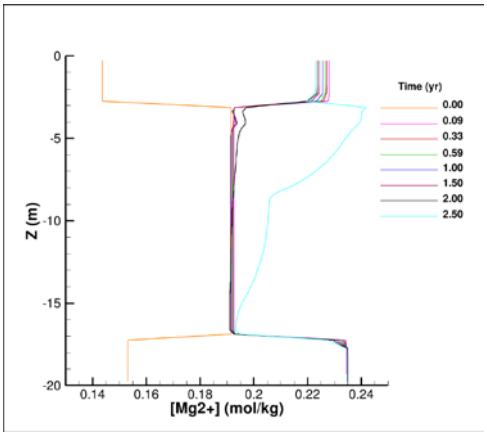

Figure 7. Mg concentration profile as a function of depth.

COMPARISON OF MODEL RESULTS AND MEASURED PARAMETERS

The exact depth of fluid production for a well producing in the Leduc Fore reef is not known. Thus, it is difficult to compare the production concentrations and the modeled concentrations. To accomplish this, the average value for the species of interest in the Leduc Fore Reef was compared with the measured value from the production well.

Figure 8 shows the HCO_3 concentrations modeled using TOUGHREACT compared to measurements from fluid samples from the production well. The observed trends are initially very similar, showing little change in concentration up to ~700 days. After ~700 days after the commencement of CO_2 injection, both modeled and measured bicarbonate concentrations increased, though at different rates.

Figure 9 shows a comparison between the downhole pH modeled with TOUGHREACT and the downhole pH based on measured results and adjusted using SOLMINEQ88 (Kharaka et al. 1988) for the producing well. SOLMINEQ88 allows for a reversal of degassing, which occurred when the sample was brought from depth to the surface, affecting the chemistry of the fluid. While the two pH values deviate by up to 1.5 pH units, the observed and modeled trends are very similar, remaining initially rather constant followed by a marked pH decrease. Also shown in Figure 9 are two linear fits of the measured and corrected downhole pH. The first linear fit is for the sampling times where the pH slowly decreased; the second fit is for the period of rapid pH decrease. The onset of the rapid decrease in the pH of the brine occurs in both the model and the measured data for samples from the well at approximately the same time, ~700 days, as shown by the blue dotted line in Figure 9. This indicates that solubility trapping of injected CO_2 has started to occur, as indicated in Reaction (1).

Figure 10 shows the changes in the calcium and magnesium concentrations obtained through measurements on fluids recovered from the production well. The modeled Mg concentration is constant at ~5000 mg/L for ~700 days, then shows a slight increase in concentration after this to 5520 mg/L. The measured concentrations have a relatively constant value of ~1650 mg/L, but it cannot be determined if there is an increase. The reason for the modeled Mg concentrations being 3 times the measured values has yet to be determined—it may be due to the kinetic parameters for dolomite requiring adjusting. The model kinetic parameters are based on measurements of kinetics for pure mineral phases. The minerals present are far from ideal in terms of surface areas, etc. These kinetic values have to be re-examined to account for real world events, e.g., water flooding corroding the ideal mineral surface areas.

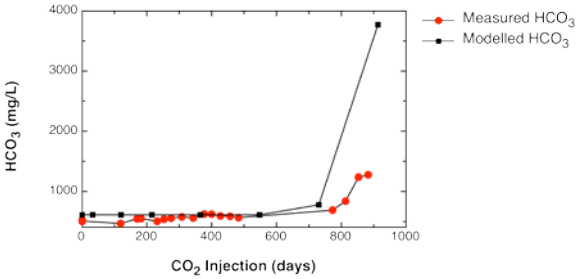

Figure 8. Measured and modeled HCO_3 versus CO_2 injection time.

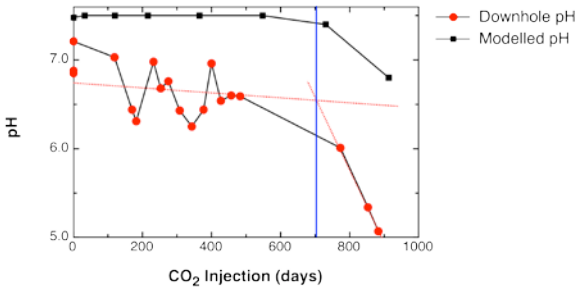

Figure 9. Measured and modeled pH versus CO_2 injection time.

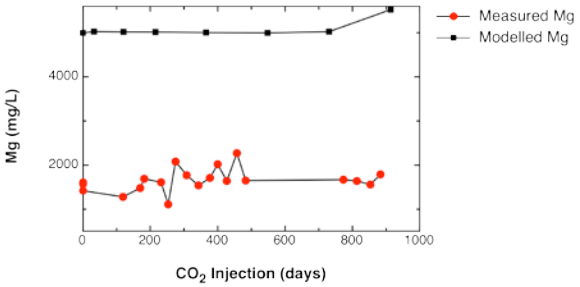

Figure 10. Measured and Modeled Mg versus CO_2 injection time.

CONCLUSIONS

For the TOUGHREACT model, the following has been determined:

1. Solubility trapping, Reaction 1, appears to be the significant method of sequestration.
2. Ionic trapping, Reaction 2, occurs very early on in the injection phase, as early as 30 days after the start of injection.
3. The Lower Ireton and Leduc Back reef are very poor seals. CO_2 infiltration occurred very early on and, in the case of the Leduc Back Reef, significant dolomite dissolution also occurred, shown by the large increase in Mg and HCO_3 concentrations and high CO_2 gas saturation values.
4. Plume dispersion occurred very quickly, evident as early as 30 days, due to the high permeability of the storage aquifer, the Leduc Fore Reef.

For the modeled well at 817 m from the injector, when compared to a well producing in the Leduc Fore Reef ~800 m from the injection well, the following was observed:

5. The arrival time of injected CO_2 was very similar, ~700 days after the onset of injection.
6. The modeled and measured concentrations of HCO_3 are nearly identical until the arrival of CO_2. Then, the modeled concentration increased significantly when compared to the measured value, three times larger.
7. The trends in the pH values are similar, but the modeled pH is 0.5–1.5 higher than the calculated downhole pH.
8. The modeled and measured trends for Mg concentration are similar, but the modeled values are 3 times the measured values.

Future work on this will include examining the kinetic parameters to see the effects on pH and cation concentrations, and adding 16 months of data that has been collected post-injection.

REFERENCES

Corey, A.T., The interrelation between gas and oil relative permeabilities. *Prod. Mon.* 38–41, 1954.

Kharaka, Y. K., Gunter, W., Aggarwal, P. K., Perkins, E. H. and De Braal, J. D., *SOLMINEQ88: a computer programme for geochemical modelling of water-rock reactions.* USGS Water Resources Investigation Report, 88-4227, 1988.

Narasimhan, T.N., Witherspoon, P.A., An integrated finite dfference method for analyzing fluid flow in porous media, *Water Resour. Res.*, 12, 57–64, 1976.

Palandri, J., Kharaka, Y.K., *A compilation of rate parameters of water–mineral interaction kinetics for application to geochemical modeling.* US Geol. Surv. Open File Report 2004-1068.64, 2004.

Pruess, K., *TOUGH2: A General Numerical Simulator for Multiphase Fluid and Heat Flow*, Lawrence Berkeley Laboratory Report LBL-29400, Berkeley, California, 1991.

Van Genuchten, M.Th., A closed-form equation for predicting the hydraulic conductivity of unsaturated soils. *Soil Sci. Soc. Am. J.*, 44, 892–898, 1980.

Xu T, Sonnenthal E, Spycher N, Pruess K. 2006 TOUGHREACT: A simulation program for non-isothermal multiphase reactive geochemical transport in variably saturated geologic media: Applications to geothermal injectivity and CO2 geological sequestration. *Computers and Geosciences* 32:145–156.

Xu, T., Apps, J., Pruess, K., Yamamoto, H., Numerical modeling of injection and mineral trapping of CO_2 with H_2S and SO_2 in a sandstone formation, *Chem. Geol.*, 242, 319-346, 2007.

Yeh, G.T., Tripathi, V.S., A model for simulating transport of reactive multispecies components: model development and demonstration, *Water Resour. Res.*, 27, 3075–3094, 1991.

EFFECT OF GAS FIELD PRODUCTION AND CO_2 INJECTION ON BRINE FLOW AND SALT PRECIPITATION

Tim Tambach[*], Daniël Loeve[*], Cor Hofstee[*], Willem-Jan Plug[**], and Jos Maas[*]

[*]TNO Geological Survey of the Netherlands, P.O. Box 80015, 3508 TA Utrecht, The Netherlands
[**]TAQA Energy B.V., P.O. Box 11550, 2502 AN, Den Haag, The Netherlands

e-mail: tim.tambach@tno.nl

ABSTRACT

This paper reports modeling of gas field production and CO_2 injection from a theoretical reservoir based on characteristics of the P18 gas field in the Dutch offshore, which consists of four geological deposits with different petrophysical properties. We especially focus on the brine flow during and after exploitation of the reservoir, which affects salt precipitation and dissolution in the near-well area. We first computed the water saturation (S_w) with depth, in static equilibrium with a free water level (FWL) at the bottom of the reservoir. We then computed production of the gas field, predicting a very low brine production and mobility, without salt precipitation. Subsequently, injection of dry CO_2 leads to dry-out and salt precipitation in the near well zone and a maximum permeability reduction of 24%. After abandonment, brine flows towards the well, resulting in redissolution of precipitated salt, leading to salt saturated brine in the near-well bore area. After 1,000 years, it is predicted that supersaturated brine is concentrated in the lower part of the reservoir, where solid salt still remains. The computed long-term effects of brine mobility could influence predictions of well-cement degradation and well-abandonment strategies like intentional clogging.

INTRODUCTION

Depleted gas reservoirs are potential sinks for CO_2 in The Netherlands, thereby reducing atmospheric CO_2 (Benson and Cook, 2005). The offshore P18 gas field in the North Sea is a very good candidate for future CO_2 injection, because of its location (close to CO_2 point sources), infrastructure, and reservoir maturity (Arts et al., accepted). Sufficiently high CO_2 injection rates are required for making Carbon Capture, Utilization, and Storage (CCUS) economically attractive for oil and gas operators, while long-term integrity of the whole storage complex is important for license applications. It is therefore important to understand the behavior of the reservoir during and after CO_2 injection.

It is known that salt precipitation can hamper the productivity in gas producing fields (Kleinitz et al., 2003) or the injectivity in natural gas storage aquifers (Lorenz and Müller, 2003). It is also predicted that salt precipitation could reduce the permeability when injecting supercritical CO_2 (SC-CO_2) in saline aquifers (e.g. Pruess and Müller, 2009; Müller et al., 2009; Alkan et al., 2010; André et al., 2007) and depleted gas fields (Giorgis et al., 2007). The physical mechanisms affecting dryout and salt precipitation in saline aquifers are described by Pruess and Müller (2009). Most of these mechanisms also hold for depleted gas fields, although brine displacement by SC-CO_2 away from the well is expected to be less dominant in depleted gas fields due to the (lower) brine relative permeability.

Salt precipitation due to water evaporation into injected dry SC-CO_2, followed by capillary backflow, is demonstrated both in core plug experiments (Ott et al., 2011) and in several modeling studies (e.g., Pruess and Müller, 2009; Müller et al., 2009; Alkan et al., 2010; André et al., 2007; Giorgis et al., 2007; Ott et al., 2011). It was found that brine capillary backflow will have a larger impact when the CO_2 injection rate is lower (Pruess and Müller, 2009), and thus the injection rate should be high enough to avoid injectivity problems (Giorgis et al., 2007). It was also concluded that the saturation gradient and local salt precipitation are determined by water evaporation kinetics. These kinetics are currently not taken into account in TOUGH2

(and other simulators), as discussed by Ott et al. (2011). Thus, modeling the precise impact of capillary backflow during CO_2 injection carries uncertainties.

The initial water saturation (S_w) as a function of reservoir depth also has uncertainties. The S_w is commonly measured during drilling of a well using a logging tool (Rider, 2006), and depends on the various petrophysical properties of all (sandstone) layers and the height above the free water level. The heterogenic character of reservoirs usually makes an accurate description of the petrohysical properties and S_w very difficult, but these properties determine the brine mobility in the reservoir. This mobility is important for CO_2 injection, as demonstrated by Giorgis et al. (2007) showing two cases: mobile and immobile brine. Long-term brine mobility has received much less attention than short-term brine mobility. However, long-term effects could influence well-cement degradation and intentional clogging after well-abandonment (Wasch et al., 2012).

The aim of this work is to simulate effects in the near-well zone of a theoretical reservoir, based on characteristics of the P18 gas field in the Dutch offshore. We focus on the effect of gas production and CO_2 injection on brine flow and salt precipitation.

METHODS

Model setup

The model consists of four geological layers with varying petrophysical properties, as determined from well logs (Table 1). In addition, the salt mass fraction (X_{NaCl}) is 0.1, the reservoir temperature (T) is 90ºC, and the initial (average) gas pressure ($P_{gas,i}$) is 375 bar. Figure 1 shows a 2D window of the radial model setup.

In the horizontal direction, 50 grid cells are imposed per layer with grid refinement (factor of 1.05) in the vicinity of the well. The model has a radius of 1,000 m. In the vertical direction, 80 grid cells are imposed with grid refinement (factor of 1.2) at the upper and lower boundaries of each deposit. Gas production and CO_2 injection were not considered for the VP Formation (Fm) due to its tight properties (Table 1), although it was taken into account for computing the equilibrium brine and gas distribution. The FWL is located at the bottom of the VP Fm, but is not considered an active aquifer. This means that the depth of the FWL does not change upon production and injection.

Table 1. Petrophysical characteristics of the geological deposits in the model: thickness (Δz), porosity (φ), and permeability (k). The number of vertical cells per deposit is also given.

Geological deposit	Δz (m)	φ (-)	k (mD)	cells (-)
Hardegsen (HD) Fm	26	11	154	10
Upper Dethfurt (UD) Mb	50	9	38.5	20
Lower Dethfurt (LD) Mb	22	7	30.6	10
Volpriehausen (VP) Fm	113	3	0.21	40

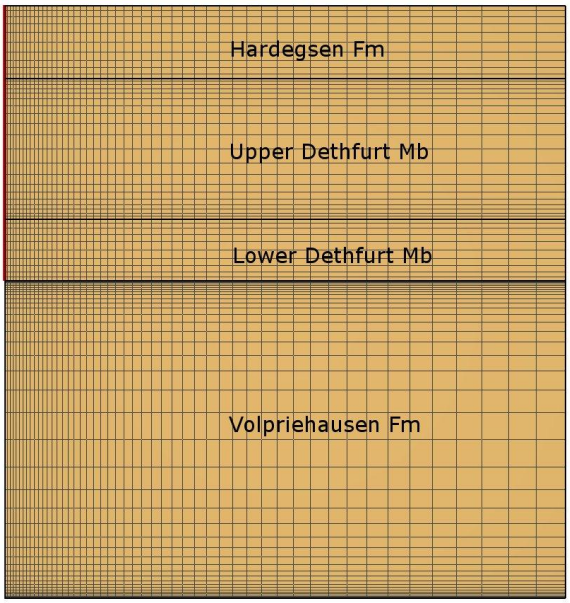

Figure 1. 2D window of the radial model with four geological layers (Petrasim interface). The injection well is located at the left side and does not penetrate the VP Fm.

Capillary pressure and relative permeability

For the capillary pressure and relative permeability curves, a correlation was used with the porosity and height above the FWL ($\Delta h = h - h_{FWL}$) as main parameters. The van Genuchten equations are used to parameterize these curves, as shown in Figure 2 and Figure 3, respectively. The parameters used in these equations are derived from a best fit to the curves used in other work (Arts et al., accepted).

The relative permeability depends on the rock, fluids, and thermodynamic conditions (Krevor et al., 2012). It is commonly believed that the relative permeability is determined by the wettability of the sandstone. Here it is assumed that the wettability and therefore relative permeability of CH_4 and CO_2 is similar. Hysteresis effects were not taken into account in this study.

For a two-phase system, the standard output of the TOUGH2 simulator reports the gas pressure (P_{gas}) and the capillary pressure (P_{cap}). The brine pressure (P_{brine}) can be computed using:

$$P_{brine} = P_{gas} - |P_{cap}|.$$

The formula given above shows the absolute value of P_{cap}, because its definition depends on the simulator (in TOUGH2, P_{cap} is defined negative for drainage). In case of static equilibrium, P_{cap} can also be computed using the difference in brine density (ρ_{brine}) and gas density (ρ_{gas}), the gravitational constant (g), and Δh:

$$P_{cap}(S_w) = (\rho_{brine} - \rho_{gas}) g \Delta h.$$

P_{cap} as a function of S_w depends on the type of gas that is present. Scaling of P_{cap} can be done using the dimensionless Leverett J-function (Leverett, 1941), which is commonly used in the oil and gas industry:

$$J(S_w) = \frac{P_{cap}(S_w)\sqrt{\left(\frac{k}{\varphi}\right)}}{\sigma \cos\theta}.$$

Both J and P_{cap} are given as a function of S_w, σ is the interfacial tension and θ is the contact angle. If we assume that θ is similar for CO_2 and CH_4, we can approximate $P_{cap,CO2}$ using $P_{cap,CH4}$ by

$$P_{cap,CO2}(S_w) = \frac{\sigma_{b,CO2}}{\sigma_{b,CH4}} P_{cap,CH4}(S_w),$$

where $\sigma_{b,CO2}$ and $\sigma_{b,CH4}$ are the brine-CO_2 and brine-CH_4 interfacial tensions, respectively. At high pressure, $\sigma_{b,CO2}$ is smaller than $\sigma_{b,CH4}$ because of the larger affinity of CO_2 to water (Fleury et al., 2010). Reported values of $\sigma_{b,CO2}$ are on the order of 30 mN/m (Fleury et al., 2010; Chalbaud et al., 2010; Saeedi and Rezaee, 2012), while $\sigma_{b,CH4}$ is on the order of 45 mN/m (Saeedi and Rezaee, 2012). For this reason, the curves in Figure 3 are scaled with a factor of 0.667 for CO_2. In this study, it is assumed that σ and θ are independent of pressure.

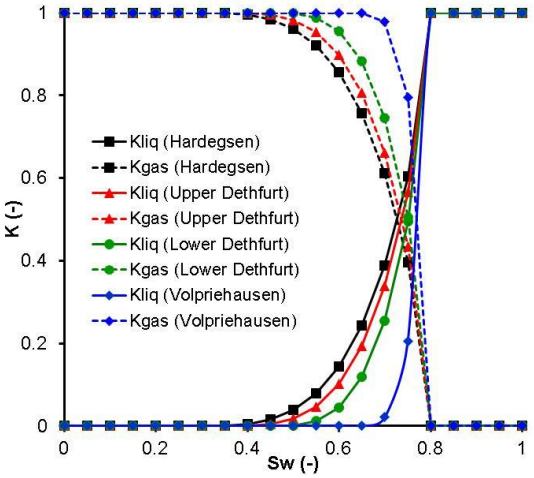

Figure 2. Relative permeability (K) of gas (K_{gas}) and liquid (K_{liq}) for the four geological deposits, used for both CH_4-brine and CO_2-brine.

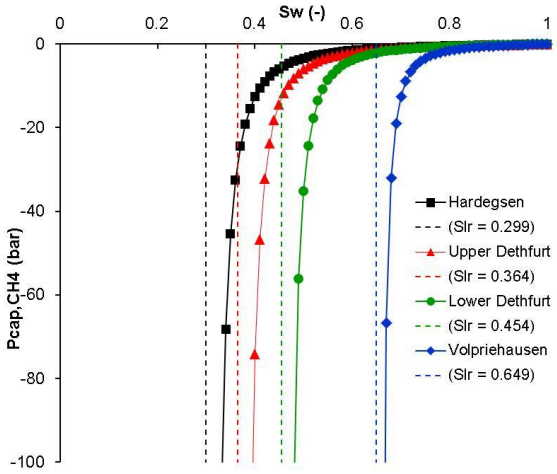

Figure 3. Capillary pressure ($P_{cap,CH4}$) as a function of the water saturation (S_w) for the four geological deposits. $P_{cap,CO2}$ is derived by scaling $P_{cap,CH4}$ with a factor of 0.667. The residual water (S_{lr}) asymptote is also given. $P_{cap,max}$ is 100 bar.

Equilibrium gas and brine saturation

On a geological time scale, upward gas migration into permeable sandstone layers led to brine drainage and lowering of the FWL. The brine that was left behind, due to capillary forces, is the current water saturation and is usually measured with a logging tool (Rider, 2006). The mobility through the VP Fm is relatively low due to its tight properties. In general, other impermeable (shale) layers in the more permeable deposits could also have retarded the brine mobility.

In this study it is assumed that S_w is in hydrostatic equilibrium with the FWL. Below, we describe the workflow how to compute S_w as a function of depth, using the estimated capillary pressure (drainage) curves (Figure 3) and TOUGH2-EWASG (see gas production). The relative permeability of gas and brine were set to perfectly mobile brine (K_{liq}=1 and K_{gas}=1), for speeding up the calculations. A dummy layer on top of the HD Fm is included and serves as a gas inlet (see below). The dummy layer has a thickness of 1.0 cm, which is relatively small compared to the reservoir thickness. In this way it has a negligible effect on the (computed) hydrostatic pressure. The capillary pressure of the dummy layer is set to zero. The three-step workflow is as follows:

1) Hydrostatic equilibrium: The model given in Figure 1 is fully gas-saturated with gas and the average pressure (P_{gas}=375 bar) is assigned. Accordingly, the hydrostatic pressure is computed by TOUGH2, showing a linear relation as a function of depth.

2) Brine and gas distribution: The computed pressure from the previous step is initialized using the SAVE file. All cells in the layers are now assigned fully water-saturated, except the dummy layer. The dummy layer and the bottom layer are assigned as fixed (infinitely large volume), the latter to represent the FWL. Using these constraints, water can flow out at the bottom of the reservoir and gas can flow in from the top of the reservoir. In this way the initial and final hydrostatic pressure is maintained.

3) Equilibrium check: The final conditions of the previous step are initialized using the SAVE file. The dummy layer is removed and the bottom (FWL) layer is unfixed, to check whether the conditions are in equilibrium without constraints.

The results define the equilibrium brine and gas saturation before production.

Salt precipitation

Both gas production and CO_2 injection were simulated using TOUGH2 modules that can handle precipitation of solid salt and permeability reduction (see below). We used a tubes-in-series porosity-permeability model (Verma and Pruess, 1988) with a fractional length of pore bodies (Γ=0.8) and a fraction of original porosity (φ_r=0.8) for which k=0. In practice this means that a salt occupancy of 20% pore volume completely clogs the formations.

Gas production (TOUGH2-EWASG)

We computed the brine mobility during gas production to study whether the computed initial S_w would change. We modeled production from the upper three geological deposits with TOUGH2-EWASG (Battistelli et al., 1997), which was developed for geothermal applications. It can handle a three-phase mixture of water, NaCl, and several non-condensable gases (including CH_4). One disadvantage is that real gas properties are not properly modeled. Gas dissolution is described by Henry's law, with coefficients that depend on the temperature and salinity. EWASG also has an enthalpy limitation (Lorenz and Müller, 2003), but isothermal conditions are imposed in this study.
A constant rate of 0.12 Mton/year is used with a production time of 23.9 years, implying a total production of 2.88 Mton and a depletion pressure (P_{depl}) of 26.6 bar. As mentioned above, the relative permeability (Figure 2) and capillary pressure (Figure 3) are both used.

CO_2 injection (TOUGH2-ECO2N)

After gas production, CO_2 is injected at fixed T (i.e., 90°C) with a constant rate of 1.01 Mton/year for 11.3 years and thus a total CO_2 amount of 11.4 Mton. At a final (average) pressure of 375 bar, the average density of CO_2

(770 kg/m^3) is approximately four times higher than the (ideal) density of CH_4 (200 kg/m^3), which explains why the injected amount of CO_2 is four times larger than the produced amount of CH_4 for returning to the initial pressure.

Injection of CO_2 is carried out with TOUGH2-ECO2N, which describes two-phase flow in the H_2O-salt-CO_2 system. Dissolution of CO_2 in brine and water evaporation in CO_2 is described using equations of state (EOS). ECO2N does not take into account CH_4 and it is assumed that all initial gas consists of CO_2. Hence, the distribution of CO_2 and CH_4 in the reservoir is not modeled. For example, this can be done with TOUGH2-EOS7c (Oldenburg et al., 2001; Audigane et al., 2008) and is of special interest when modeling enhanced gas recovery (EGR). Modeling of salt precipitation cannot be done with TOUGH2-EOS7c.

The final conditions after gas production were initialized using the SAVE file, thereby replacing all CH_4 gas into CO_2. The properties of both gases are different at the given conditions (T=90ºC, P_{depl}=26.6 bar, X_{NaCl}=0.1). However, the differences we computed are less than 1%, e.g., CH_4 and CO_2 solubility in brine and water vapor in gas. Modeling the impact of capillary backflow during CO_2 injection involves uncertainties (see introduction). We therefore assumed immobile brine (K_{liq}=0 and K_{gas}=1) during continuous CO_2 injection, thereby preventing capillary backflow and enhanced salt precipitation.

Table 2. Overview of computed produced amounts of gas and liquid

component	water		methane	
phase	gas	liquid	gas	diss.
initial (Mton)	0.01	11.79	3.07	0.04
final (Mton)	0.01	11.77	0.21	<0.01
produced (Mton)	<0.01	0.02	2.86	0.03
produced (%)	0.8	0.2	93.1	93.1

Long-term effects

After closing the injection well, the simulations are continued up to 1,000 years. The long-term effects of brine flow (including capillary flow) on precipitated salt are computed. Molecular diffusion was neglected in this study, although this could influence salt gradients.

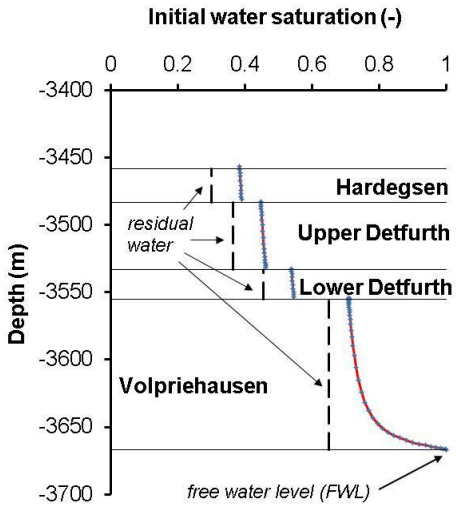

Figure 4. Water saturation (S_w) in the gas field before production. Dashed lines indicate the residual water (S_{lr}), as used in the Van Genuchten relative permeability (Figure 2) and capillary pressure (Figure 3).

RESULTS

Equilibrium water saturation

We followed the scheme mentioned above to compute P_{gas} and P_{cap} as a function of depth using TOUGH2. $|P_{cap}|$ is 0 at the FWL and increases with increasing height above the FWL, up to 17.5 bar at the top of the HD Fm. The computed P_{cap} is directly translated by TOUGH2 into an equilibrium S_w using the curves given in Figure 3. The S_w as a function of depth is given in Figure 4. The S_w in the VP Fm is relatively large, because the deposit has a low porosity and the FWL is located at the bottom. The S_{lr} and initial S_w decrease with increasing porosity in the upper parts of the reservoir up to 11% for the HD Fm (Table 1). As mentioned in the methods section, the S_{lr} is assumed to be similar for both CH_4 and CO_2.

Gas production

Table 2 shows the amounts of water (0.02 Mton) and methane (2.86 Mton) that are produced during 24 year of gas production, which correspond to 0.8% and 93.1% of the initial amounts present. This means that relatively small amounts of water are produced, and the mobility of water is low, owing to the relative

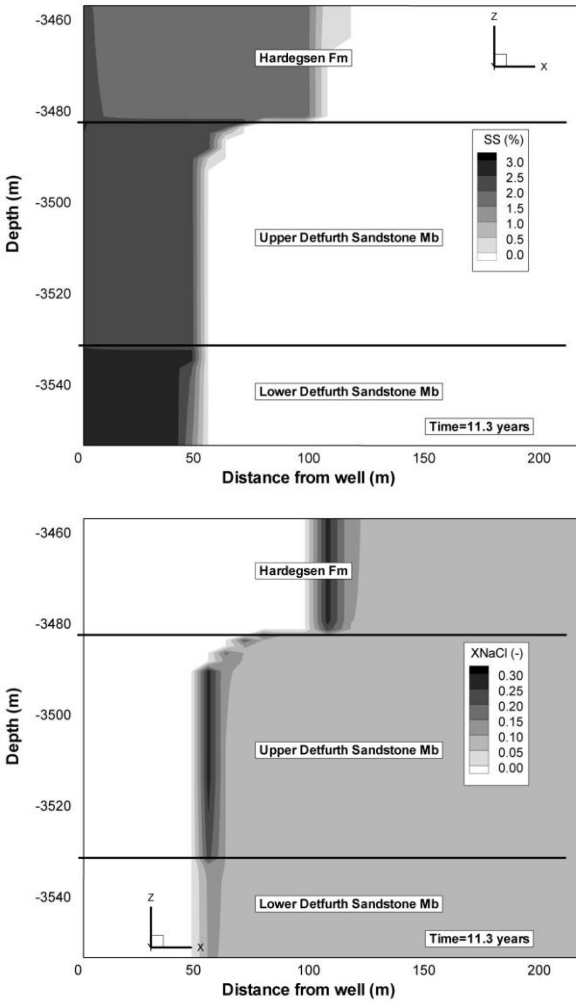

Figure 5. Pore volume percentage (SS) occupied by solid salt (top) and X_{NaCl} (bottom) in the near-well area, after closing the injection well.

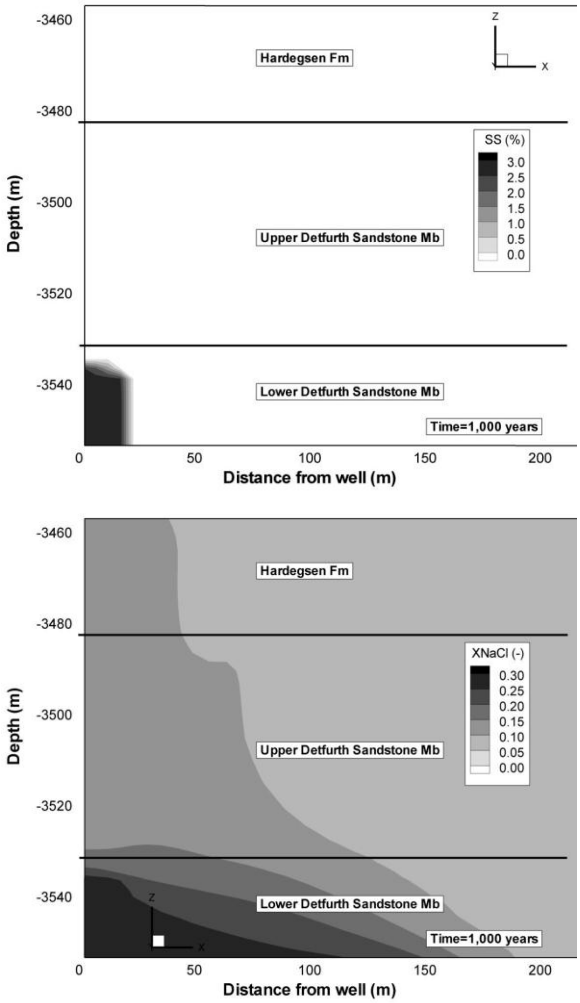

Figure 6. Pore volume percentage (SS) occupied by solid salt (top) and X_{NaCl} (bottom) in the near-well area, 1,000 years after closing the injection well.

permeability. Computed water saturations are 0.05 to 0.1 higher than the residual water saturation (Figure 4), but the corresponding water mobility is low (K_{liq}<0.015; Figure 2). In addition, the maximum computed pressure drawdown is only a few bars. Generally, the drawdown depends on operational constraints, including economics.

Under standard temperature and pressure (NTP) conditions (i.e., T=15.6°C and P=1 bar) the densities of CH_4 and brine are ~0.717 kg/m^3 and 1066 kg/m^3, respectively. The corresponding produced volumes are 0.022 Mm^3 of water and 4330 Mm^3 of gas, indicating that a very small water volume is produced compared to gas volume. Salt precipitation was not observed, most probably due to a relatively low salinity as compared to other studies involving CH_4 (Lorenz and Müller, 2003).

CO_2 injection

Water evaporation in the near-well area was modeled during CO_2 injection, with salt precipitation as a result (Figure 5). The results show that the dryout radius ranges from 53 m (LD Mb) to 113 m (HD Fm). Salt precipitation is modeled from to 2.2% (HD Fm) up to 2.8% (LD Mb) of the pore volume, corresponding to *k*-reductions with 19% and 24%, respectively. These values depend on the characteristics of the tubes-in-series model and uncertainties exists. At the front of the dryout zone, a small zone with increased salinity up to salt-saturation

(X_{NaCl}=0.272) is predicted. The assumption of immobile brine prevented imbibition into the dry-out zone during injection (see Methods).

Long-term effects

After closing the injection well, brine mobility in the reservoir was modeled, resulting in brine flow into the dryout zone (Figure 6). After 1,000 years, most of the precipitated salt dissolved, except for 21 m around the well in the LD Mb at the bottom of the reservoir. In addition, the salinity in the whole near-well bore area increased, but is salt saturated in the LD Mb. These differences are potentially caused by two effects. First, the solid salt in the LD Mb is more concentrated, the dryout zone is smaller, and dissolution is expected to take more time. The brine flow rate into the LD Mb should also be considered. Second, the brine density increases with increasing salinity, resulting in a gravitational flow. Salt undersaturated brine is flowing laterally into the near-well bore area in the upper region of the reservoir (especially in the HD Fm). Then it becomes heavier and migrates into the lower parts of the reservoir, where it starts migration away from the near-well area along the boundary with the VP Fm. These mechanisms retard the solid salt dissolution in the LD Mb, compared to other (more shallow) deposits.

Hysteresis in the capillary pressure was not taken into account, and hence only drainage curves were used (Figure 3). Wetting of the dryout zone should have been considered with an imbibition parameterization. At similar capillary pressure in reservoir rock, imbibition usually corresponds to lower S_w as compared to drainage (Leverett, 1941). For the current study, this would result in a lower S_w of the dryout zone and less faster salt dissolution.

CONCLUSIONS

This paper discusses the effect of gas production and CO_2 injection on brine flow and salt precipitation, using characteristics based on the P18 field in the offshore part of The Netherlands. We computed the initial S_w, assuming equilibrium on a geological time scale, showing mobile water. However, the amounts of production water are relatively small when gas is produced from the field. No salt precipitation was observed.

We assumed immobile brine during CO_2 injection. The results show dryout and salt precipitation in the near-well area and larger amounts of salt in the lower part of the reservoir, compared to the upper part of the reservoir. Permeability reductions up to 24% are expected in the reservoir during CO_2 injection. Capillary backflow of brine was allowed after the closing the well, showing redissolution of salt and induced gravitational flow in the near-well area. Occurrence of solid salt is still predicted in the lower part of the reservoir after 1,000 years, as well as saturated brine. These effects could influence predictions of well-cement degradation and well-abandonment strategies like intentional clogging.

ACKNOWLEDGMENT

This work was carried out in the framework of the Dutch CATO-2 program. The authors are grateful to the Dutch Ministry of Economic Affairs and sponsoring companies for funding. We thank Laura Wasch, Kees Geel, Saskia Roels, and Alfredo Battistelli for helpful discussions.

CITATIONS

Alkan, H., Y. Cinar, and E.B. Ülker, Impact of Capillary Pressure, Salinity and In situ Conditions on CO2 Injection into Saline Aquifers, Transp. Porous Media, 84(3), 799-819, 2010.

André, L., P. Audigane, M. Azaroual, and A. Menjoz, Numerical modeling of fluid-rock chemical interactions at the supercritical CO2-liquid interface during CO2 injection into a carbonate reservoir, the Dogger aquifer (Paris Basin, France), Energy Convers. Manage., 48(6), 1782-1797, 2007.

Arts, R.J., C. Hofstee, V.P. Vandeweijer, M.P. Pluymaekers, D. Loeve, and A. Kopp, CO2 storage in the depleted P18-4 gas field offshore the Netherlands (the ROAD project), Int. J. Greenhouse Gas Control, accepted.

Audigane, P., J. Lions, I. Gaus, C. Robelin, P. Durst, C.M. Oldenburg, T. Xu, B.v.d. Meer, and K. Geel, Geochemical modeling of CO2 injection into a methane gas reservoir at the K12-B field, North Sea, In: Carbon dioxide sequestration in geological media - State of

the science, Eds. M. Grobe, J.C. Pashin and R.L. Dodge. AAPG Studies 59, 1-20, 2008.

Battistelli, A., C. Calore, and K. Pruess, The simulator TOUGH2/EWASG for modelling geothermal reservoirs with brines and non-condensible gas, Geothermics, 26(4), 437-464, 1997.

Benson, S. and P. Cook, Underground geological storage, In: IPCC Special report on carbon dioxide capture and storage, Chapter 5. Intergovernmental Panel on Climate Change, Eds. B. Metz, O. Davidson, H. De Coninck, M. Loos and L. Meyer. Cambridge University Press, 431, 2005.

Chalbaud, C., M. Robin, J.-. Lombard, H. Bertin, and P. Egermann, Brine/CO2 interfacial properties and effects on CO2 storage in deep saline aquifers, Oil Gas Sci. Technol., 65(4), 541-555, 2010.

Fleury, M., J. Pironon, Y.M. le Nindre, O. Bildstein, P. Berne, V. Lagneau, D. Broseta, T. Pichery, S. Fillacier, M. Lescanne, and O. Vidal, Evaluating sealing efficiency of caprocks for CO2 storage: An overview of the geocarbone-integrity program and results, Oil Gas Sci. Technol., 65(3), 435-444, 2010.

Giorgis, T., M. Carpita, and A. Battistelli, 2D modeling of salt precipitation during the injection of dry CO2 in a depleted gas reservoir, Energy Convers. Manage., 48(6), 1816-1826, 2007.

Kleinitz, W., G. Dietzsch, and M. Köhler, Halite scale formation in gas-producing wells, Chem. Eng. Res. Des., 81(3), 352-358, 2003.

Krevor, S.C.M., R. Pini, L. Zuo, and S.M. Benson, Relative permeability and trapping of CO_2 and water in sandstone rocks at reservoir conditions, Water Resour. Res., 48(2), 2012.

Leverett, M.C., Capillary behaviour in porous solids, Transactions of the AIME, 142, 159-172, 1941.

Lorenz, S. and W. Müller, Modelling of halite formation in natural gas storage aquifers. Proceedings TOUGH Symposium 2003, Lawrence Berkeley National Laboratory, Berkeley, California, May 12–14, 2003.

Müller, N., R. Qi, E. Mackie, K. Pruess, and M.J. Blunt, CO2 injection impairment due to halite precipitation, Energy Procedia, 1(1)9th International Conference on Greenhouse Gas Control Technologies, GHGT-9, Washington DC, 3507-3514, 2009.

Oldenburg, C.M., K. Pruess, and S.M. Benson, Process modeling of CO2 injection into natural gas reservoirs for carbon sequestration and enhanced gas recovery, Energy Fuels, 15(2), 293-298, 2001.

Ott, H., K.D. De Kloe, F. Marcelis, and A. Makurat, Injection of supercritical CO2 in brine saturated sandstone: Pattern formation during salt precipitation, Energy Procedia, 410th International Conference on Greenhouse Gas Control Technologies, Amsterdam, 4425-4432, 2011.

Pruess, K. and N. Müller, Formation dry-out from CO_2 injection into saline aquifers: 1. effects of solids precipitation and their mitigation, Water Resour. Res., 45(3), 2009.

Rider, M.H., The Geological Interpretation of Well Logs. 2nd edition, Progress Press Co Ltd., Malta, 2006.

Saeedi, A. and R. Rezaee, Effect of residual natural gas saturation on multiphase flow behaviour during CO 2 geo-sequestration in depleted natural gas reservoirs, J Pet Sci Eng, 82-83, 17-26, 2012.

Verma, A. and K. Pruess, Thermohydrological conditions and silica redistribution near high-level nuclear wastes emplaced in saturated geological formations, J. Geophys. Res., 93(B2), 1159-1173, 1988.

Wasch, L.J., J. Wollenweber, and T.J. Tambach, A novel concept for long-term CO_2 sealing by intentional salt clogging, Proceedings TOUGH Symposium 2012, Lawrence Berkeley National Laboratory, Berkeley, California, September 17-19, 2012.

FEASIBILITY OF CO_2 INJECTION IN THE DEEP SALINE AQUIFERS OF THE BÉCANCOUR REGION, QUÉBEC (CANADA)

Tien Dung Tran Ngoc [(1)], René Lefebvre [(1)], Michel Malo [(1)] and Christine Doughty [(2)]

[(1)] Institut national de la recherche scientifique (INRS), Centre Eau Terre Environnement
490 rue de la Couronne, Québec, QC, G1K 9A9, CANADA
[(2)] Earth Sciences Division, E.O. Lawrence Berkeley National Laboratory
Berkeley, CA 94720, U.S.A.
E-mail: tien_dung.tran_ngoc@ete.inrs.ca

ABSTRACT

The feasibility of CO_2 injection in a reservoir of the Bécancour region was investigated using 2D radial numerical simulations with TOUGH2/ECO2N. To optimize the CO_2 injection rate and the duration of injection, we carried out sensitivity analyses considering different values of completion interval for the single injection well, rock compressibility, and the ratio of vertical and horizontal permeabilities. Simulations took into account Bécancour reservoir conditions, in which injection pressure was limited below the fracturing threshold, and sensitivity analyses provided indications of potential injection scenarios.

To remain below fracturing pressure, we propose intermittent 5-year injection periods, with a mass injection rate up to 20 kg/s, alternating with half-year periods without injection. This scenario may provide maximum CO_2 storage in the aquifer. We also calculated CO_2 storage capacities in different phases versus time. The effective apparent capacity and injection capacity estimated by the dynamic method, as well as effective storage capacity factors, were rigorously redefined on a mass and volume basis. For comparison purposes, CO_2 storage capacity was also estimated using volumetric and compressibility static methods. The storage efficiency factor obtained from the TOUGH2 dynamic method is about 1.5%, but it ranges between 2.2% and 3.3% for the static methods.

This study shows that the northeastern reservoir block of the Bécancour region could host ~10 Mt CO_2, which represents 15% to 50% of regional yearly CO_2 emissions over a few decades (depending on the injectivity scenario). Finally, this modeling study will also be the basis for the design of a pilot CO_2 injection test.

INTRODUCTION

According to a basin-scale assessment for different onshore and offshore basins in Southern Québec, Canada (Malo and Bédard, 2012)., the St. Lawrence Platform has the best potential for CO_2 storage in Quebec. Within the St. Lawrence basin**,** the Bécancour region, located between Montréal and Québec City along the St. Lawrence River, was selected for a site-scale study, because of data availability inherited from hydrocarbon exploration, as well as significant CO_2 production in the area (of about 1 Mt per year) from a cluster of stationary emitters. Deep saline aquifers in this region were characterized in terms of hydrogeology and petrophysics to assess their potential use for CO_2 sequestration. The brine-bearing sandstones of the Potsdam Group were recognized as the most favorable unit for a CO_2 injection (Tran Ngoc et al., 2011). The output of this characterization is summarized in this paper.

Based on a framework for the feasibility assessment of storage capacity, injectivity and integrity of specific sites, this paper presents the feasibility of supercritical CO_2 injection into the northeast reservoir block of the Bécancour region, using a series of 2D radial numerical simulations of multiphase flow and transport of H_2O-NaCl-CO_2 components. The parameterization analysis of hydrogeological properties controlling pressure buildup and CO_2 plume migration during and after injection (Doughty, 2010) is used with a dual purpose. On one hand, this sensitivity study offers an insight into the uncertainty related to our present knowledge of reservoir properties. On the other hand, the

relative advantages and disadvantages of conditions and properties at the Bécancour site as they relate to CO_2 storage are displayed by our simulation results and thus can now be compared to conditions and properties at other sites worldwide. Simulations provide estimated values for storage capacity, indicate potential storage injection scenarios (i.e., CO_2 distribution versus time) and feasible injection rates. This study also provides a comparison between CO_2 storage capacities estimated from several approaches.

SITE CHARACTERISTICS

The saline aquifers of the Bécancour region are part of the Paleozoic sedimentary succession of the St. Lawrence Platform, at depths ranging from 800 to 2400 m. Their lithostratigraphy, identified by well-log correlation and seismic line interpretation (Claprood et al., 2012), consists mainly of the following units: Potsdam Group (Covey Hill and Cairnside sandstones), Beekmantown Group (Theresa and Beauharnois dolostones) and Trenton Group (Chazy, Black-River and Trenton limestones). These saline aquifers are overlain by a cap rock of > 800 m thick shales and siltstones of the Utica Shale and Lorraine Group. The regional reservoir is separated by the SW-NE Yamaska normal fault into two faulted blocks found at different depths. In the present paper, we study CO_2 injection into the upper northeastern block of the fault.

All rock units are subhorizontal strata with excellent lateral continuity and small thickness variation. The units of the Potsdam Group, i.e., Covey Hill (CH) and Cairnside (CA) Formations, are the most porous, most permeable and thickest units of the sedimentary succession. Hydrogeological and petrophysical properties of these units are reported in Table 1. The fracturing pressure of Bécancour reservoir units was derived from minimal horizontal stress calculated in the St. Lawrence Platform basin (Konstantinovskaya et al., 2012). The compressibilities of Potsdam porous rock were determined from core measurements of porosity and net overburden pressures, and compared to literature values (Figure 1).

Capillary properties of Potsdam sandstones were based on measurements made on core samples using both mercury injection and capillary centrifuge tests. The van Genuchten (1980) model for capillary pressure (CP) and the Genuchten-Mualem (VGTM)/Corey model (Corey, 1954) for relative permeability (RP) was fitted to laboratory measurements (Table 2).

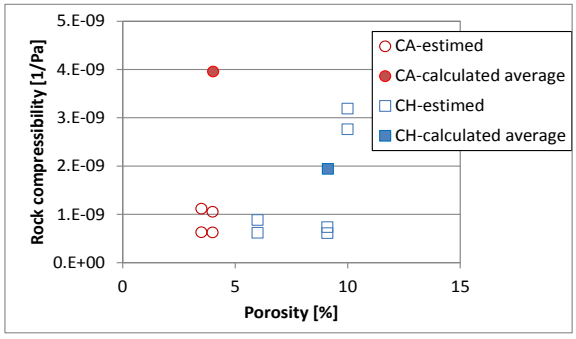

Figure 1. Correlation of rock compressibility with porosity for Covey Hill and Cairnside Fm. (values from empirical estimates and calculated from core measurements of porosity and net confining stress).

Table 1. Main representative properties of Covey Hill and Cairnside Fm.

Property	CH	CA
Porosity φ [%]	6.0	3.5
Horiz. permeability k_r [mD]	0.89	8.9
Vert. permeability k_z [mD]	0.12	0.06
Global permeability k [mD]	4.17/100[a]	
Pressure gradient ΔP_h [MPa/km]	12.17	
Min horiz. stress ΔS_{hmin} [MPa/km]	20.5	
Surface temperature $T_{surface}$ (°C)	8	
Temperature gradient ΔT [°C/km]	23.5	
Salinity *TDS* [g/l]	109	242
Rock compressibility c_r [1/Pa]	2×10^{-9}	4×10^{-9}

[a]: determined from drill stem tests for CA with 4.17 = geometric average and 100 = arithmetic average; 1 mD = 1×10^{-15} m^2.

Capillary properties for the CO_2-brine fluid system were obtained based on conversions from air-mercury and air-brine systems, using the experimental correlation of interfacial tension between CO_2 and brine proposed by Bachu and Bennion (2009). Figs 2 and 3 depict the capillary pressure and relative permeability

curves, respectively. Note that the residual liquid saturation S_{lr} [-] was estimated from sets of measured and deduced saturation values.

The residual gas saturation S_{gr} [-] was determined from Land's equation (Land, 1969), when assuming the liquid saturation at the drainage-to-imbibition turning point is equal to $S_{lcentral}$, the central saturation of the drainage branch, and S_{grmax} is the maximum saturation difference between the drainage and imbibition branches of capillary pressure curves.

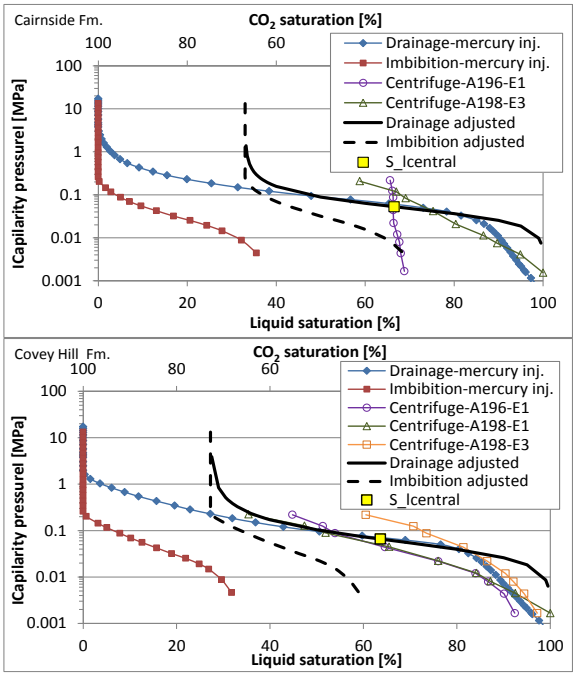

Figure 2. Capillary pressure as a function of fluid saturation for Covey Hill (lower) and Cairnside (upper) Fms.

Table 2. Capillary parameters of Covey Hill and Cairnside Fm. for the van Genuchten capillary model (drainage) and VGTM/Corey relative permeability model.

Capillary properties	CH	CA
Saturated liquid saturation S_{ls} [-]	1	1
Residual liquid saturation S_{lr} [-]	0.27	0.33
Residual gas saturation S_{gr} [-]	0.26	0.21
Exponent m [-]	0.558	0.621
Entry pressure P_{0cap} [Pa]	4.4×10^4	4.0×10^4

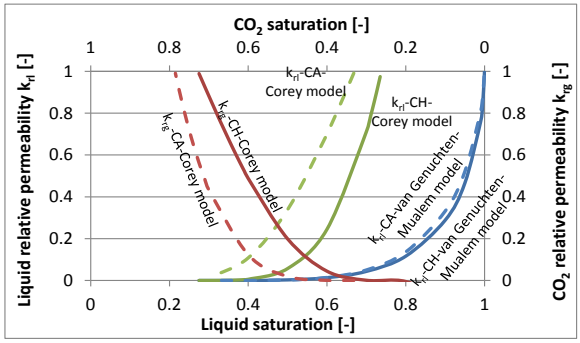

Figure 3. Relative permeability as a function of fluid saturation for CH (solid lines) and CA (dashed lines) Fm. according to the VGTM and Corey model.

NUMERICAL MODEL

The mathematical model of supercritical CO_2 injected and stored in deep saline aquifers was numerically implemented in TOUGH2/ECO2N (Pruess, 2005). We used this code for numerical simulations that were carried out in isothermal and non-hysteretic mode, considering transport only by convection from CO_2 injection and gravity. Certain processes were disabled, such as molecular diffusion, hydrodynamic dispersion, and permeability changes from salt precipitation, rock dissolution, or mineral carbonation.

Conceptual and numerical model

The area of the northeastern reservoir block targeted for CO_2 injection is referred as A [L^2], which is 7 by 5 km, equivalent to the circular surface with a radius of 3.3 km used in the model. The model consists of the Potsdam sandstones found at 1102–1503 m TVD with a thickness h [L] of 288 m for the Covey Hill Fm. and 113 m for the Cairnside Fm.

A two-dimensional (2-D) radial grid model was used to represent a cylindrical volume with central symmetry for the CO_2 storage site. Two homogeneous strata of Covey Hill and Cairnside sandstones are represented in the model, in which a vertical injection well is centered with an open-hole interval completed over the entire thickness of the Covey Hill Fm. A representative inner casing diameter of 0.15 m of other Bécancour boreholes was assumed for the injection well. Radial layers were discretized into 100 gridblocks, with finer meshing in the vicinity of the well using a logarithmic factor of ~1.085,

which allows us to create the radius of the first gridblock size equal to one of the injection wells. The vertical computational domain has a grid resolution of 25 layers (the Covey Hill Fm.) and 10 layers (the Cairnside Fm). All vertical cells are about 11 m thick.

Initial and boundary conditions

Table 3 summarizes the model initial conditions, based on site characterization data. All reservoirs above the Potsdam sandstones, together with cap rocks and the Grenville basement, are considered as sealing units. Therefore, the top and bottom of the model are impervious boundaries. Finally, CO_2 injection was presumed to be made into a closed volume system (Zhou et al., 2008).

Table 3. Initial and boundary conditions used for the Bécancour numerical model.

Initial conditions	CH	CA
Hydrostatic pressure P_{topCA} [MPa]	-	13.41
Temperature at top T_{top} [°C]	36.6	33.9
Salt mass fraction X [-]	0.098	0.195
CO_2 saturation [-]	0	0
CO_2 solubility in brine [g/l]	42.32	28.15
NaCl brine density [kg/m^3]	1140	1059
CO_2 density [kg/m^3]	801	803
NaCl brine viscosity [Pa.s]	1.2×10^{-3}	8.3×10^{-4}
CO_2 viscosity [Pa.s]	7.2×10^{-5}	7.3×10^{-5}
Boundary conditions		
Top z = - 1102 m:	no-flow	
Bottom z = - 1503 m:	no-flow	
Lateral r = 0:	mass injection	
Lateral r = 3300 m	no-flow	

Note: fluid properties correspond to the unit top

SENSITIVITY SIMULATION RESULTS

Simulations took into account Bécancour reservoir conditions in which injection pressure was limited below the fracturing pressure. This pressure is determined from thresholds for fracturing all rocks and displacing native caprock fluid by CO_2 (i.e. capillary pressure strength of caprocks) (Rutqvist et al., 2007). Here, the maximum sustainable injection pressure P_{max} stemmed from only S_{hmin} with a factor of 0.9 according to regulatory agencies, due to a lack of data on caprock units. The simulation base case used parameters from Table 1 and Table 2 with the Corey model for the relative permeability curves. Sensitivity analyses were carried out by varying only the Covey Hill parameters. Simulations considered injection periods of 5 to 50 years and a few hundred years thereafter, following stoppage of injection. We used the Petrasim interface for TOUGH2 simulations (Thunderhead-Engineering, 2010).

Hydrodynamic parameter effects

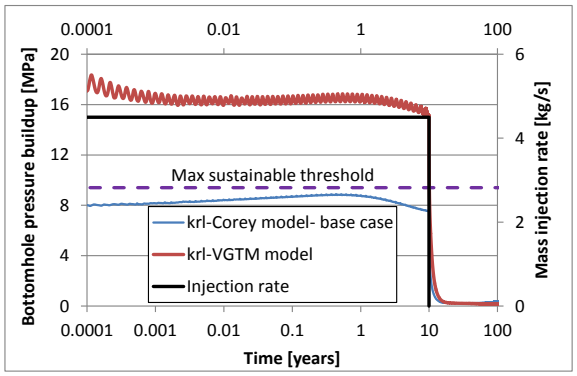

Figure 4. Pressure buildups versus time in the two cases using k_{rl} from the Corey model (base case) and VGTM model.

A mass injection rate of 4.5 kg/s for 10 years was applied at the injector for the base case without fracturing reservoir rocks. The pressure buildup would be double the maximum sustainable threshold ($0.9S_{hmin}$) if simulations used the k_{rl} of CH Fm. from the VGTM model (Figure 4). The overpressure of the base case (Corey k_{rl}) is smaller than the one for the case using VGTM k_{rl}, because the larger Corey k_{rl} (Figure 3) facilitates the displacement of injected brine by CO_2. The pressure transient for the case with VGTM k_{rl} has large oscillations, whereas it is very smooth for the case of Corey k_{rl}. This problem is not only attributed to discretization effects, but also to utilization of a hydrodynamic model. These oscillations occur due to density differences between phases whenever the CO_2 moves from one gridblock to the next in the radial direction. The oscillation effect may be attenuated with simulations using a 3D heterogeneous model.

The pressure buildup increases with a decrease of S_{gr} (not shown here), owing to the RP Corey model, in which k_{rl} decreases, i.e., overpressure increases, as S_{gr} decreases. The difference in the

overpressure is about 0.7 MPa between the two cases of $S_{gr} = 0$ and $S_{grmax} = 0.4$.

Petrophysical parameter effects

Injectivity is always proportional to reservoir permeability. Figure 5 shows the maximal injection rates with an injection period of 10 years as a logarithm function of the horizontal permeabilities k_r that are in the possible range for the target Covey Hill Fm. The maximal injection rate increases faster when $k_r < 5$ mD than $k_r > 5$ mD.

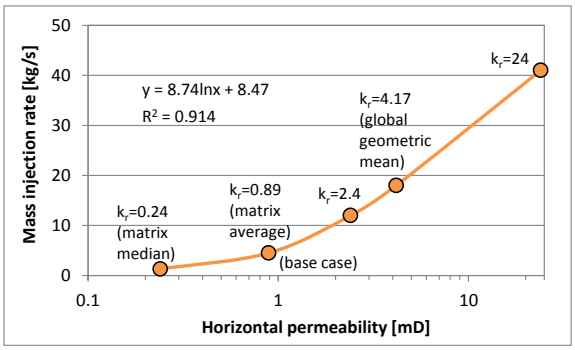

Figure 5. Injection rates used for 10 years as a function of horizontal permeability k_r of Covey Hill Fm.

For the vertical permeability k_z, well injectivity is not considerably changed due to bottomhole pressure buildup (not shown here) for k_z in the range from 0.012 to 1.2 mD. While k_z is not significant for the injection rate, its range of 0.01–0.1 mD being much less than k_r ($k_r/k_z = O(10^2)$) plays a role in delaying CO_2 buoyancy (not shown here). Thus, the storage formations themselves also contribute to secure sequestration of CO_2 by preventing upward migration.

Overpressures changed slightly in simulations (Figure 6) when estimated compressibility varied from 1×10^{-9} to 3×10^{-9} Pa^{-1}, comparable to the range of measured values (Figure 1). While the injection rate had only to be slightly decreased to 4 kg/s (from 4.5 kg/s for base case) to meet the sustainable threshold for the overpressure in the case using a Covey Hill compressibility of 2×10^{-10} Pa^{-1}, it could be increased to about 7 kg/s (factor of 1.5) for the case of 2×10^{-8} Pa^{-1}, and still not exceed the threshold (Figure 6).

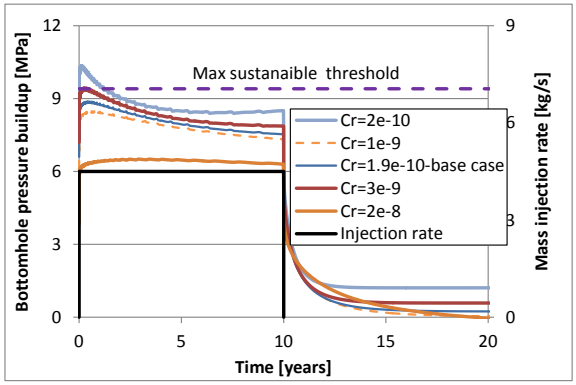

Figure 6. Pressure buildups versus time in the cases of Covey Hill Fm.'s different compressibility coefficients.

STORAGE SCENARIOS

Scenario description

The sensitivity analysis in the previous section shows that the base-case model parameters involve a certain robustness in the injection characteristics of the site. So, from the base case, scenarios of CO_2 injection are proposed that aim to assess reservoir storage capacity.

To use the maximum storage capacity of reservoirs, we tested the strategy of intermittent CO_2 injections. The injection rates and durations were estimated such that the induced aquifer pressures would not only be limited to the maximum sustainable pressure threshold of $0.9S_{hmin}$ within the injection periods, but also they would not exceed 1.3 P_h in the post-injection phase. Two proposed injection scenarios correspond to two cases of Covey Hill horizontal permeability, $k_r = 0.89$ mD and $k_r = 4.17$ mD. The latter belongs to the Cairnside Fm., but was used in simulations. While the small injection rates and a series of injection periods (~total 65 years) are applied in the case with $k_r = 0.89$ mD, the injection rates are large with only 3 injection periods in the case with $k_r = 4.17$ mD (~total 16.5 years) (Figure 7). The relaxation time between two intermittent injection periods is 0.5 years in both cases. It is not surprising that the cumulative injected CO_2 mass are at in the same order of magnitude regardless of the injection scenarios, considering the intrinsic storage capacity of the reservoir.

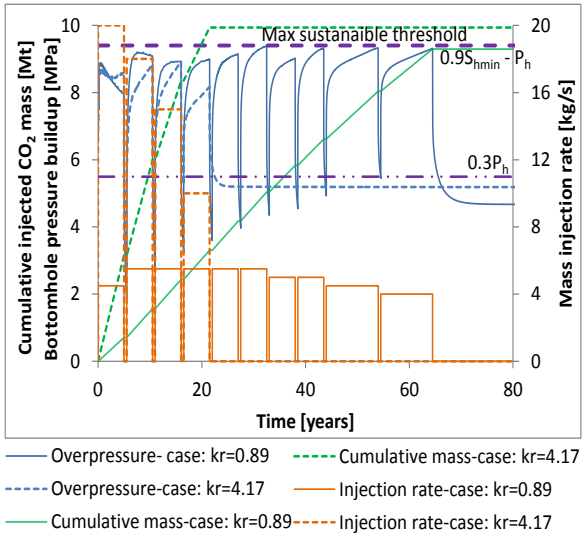

Figure 7. Overpressures at well bottom, injection rates and cumulative injected CO_2 mass versus time in two storage scenarios corresponding to the case with k_r = 0.89 and 4.17 mD respectively.

CO_2 plume migration

The spatial distribution of the supercritical CO_2 plume at t = 100 yrs for the two injection scenarios is presented in Figure 8. After the end of injection, the CO_2 plume migrates far from the injection point with only natural convection generated from the density difference between CO_2 and formation brine. In the scenario with k_r corresponding to the base case, the CO_2 front shows almost no advance in the Covey Hill Fm. beyond its extent at the end of injection, but there is continuous upward CO_2 migration in the Cairnside Fm. (Figure 9). CO_2 leaves the injection formation due to the permeability contrast between the two formations. This observation may be less visual in the scenario with CH k_r = 4.17 mD (Figure 8). Three hundred years after the onset of injection, injected supercritical CO_2 was detected at ~570 and 1130 m of radius of the cylindrically spreading plume in the Covey Hill and Cairnside Fm., respectively, for the case with CH k_r = 0.89 mD and ~680 and 950 m for the case with CH k_r = 4.17 mD.

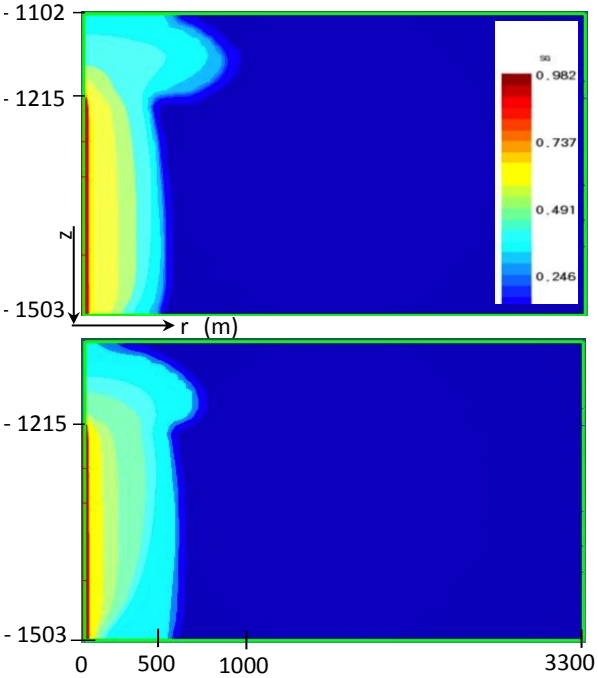

Figure 8. S_g CO_2 saturation at t = 100 years (after ~35 years of injection) in the injection scenarios with Covey Hill Fm. k_r = 0.89 mD (upper) and k_r = 4.17 mD (lower) (5 times vertical exaggeration).

ESTIMATIONS OF STORAGE CAPACITY

The CO_2 storage effective capacity for a potential site can be estimated by different methods using numerical simulations (dynamic methods) or analytic calculations (static methods). Consequently, the storage efficiency factor can vary considerably from one method to another. This section presents a number of estimates of storage capacity derived from various methods. For the purpose of comparison, the same input parameters were used for all methods as much as possible.

Definitions for dynamic method

The effective injection capacity M_{tot} [M] and apparent capacity V_{tot} [L^3] are defined on a mass and volume basis, respectively:

$$M_{tot} = M_{immisc} + M_{aq} = (S_g\,\rho_g)(\phi)\,V\; + + \;(S_l\,X_l^{CO_2}\rho_l)(\phi)\,V \quad (1)$$

$$V_{tot} = V_{immisc} + V_{aq} = (S_g)(\phi)\,V + \,n\,V_{partial} \quad (2)$$

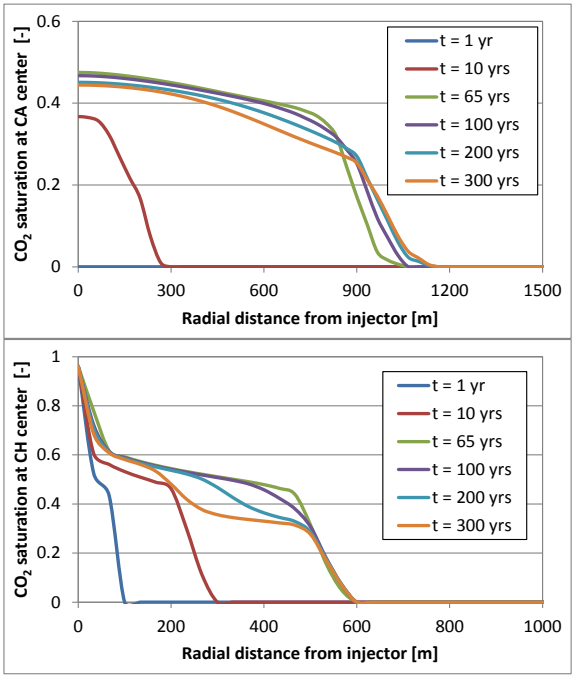

Figure 9. CO_2 saturation profiles at CA (upper) and CH (lower) central depth at different times in the injection scenario with k_r of the base case.

where M_{tot}/V_{tot} are the CO_2 total mass/volume that can be stored into the aquifers, M_{immisc}/V_{mmisc} are the mass/volume of immiscible CO_2 (gas-like phase) made up of the mobile CO_2 plume (M_{mob}/V_{mob}) and residual CO_2 trapped in pores (M_{immob}/V_{immob}) and M_{aq}/V_{aq} are the mass/volume of CO_2 dissolved in the aqueous phase. The sign < > stands for volume average over all domain (thus the "global" qualification used) taking into account the effect of formation geometry and heterogeneity. $V = A \times h$ [L^3] is the volume of aquifer (bulk volume). Note that V_{aq} is deduced from the apparent partial molar volume of CO_2 dissolved $V_{partial}$ [L^3 per mole], which only depends on the reservoir temperature (Pruess, 2005). n [mole] is the number of moles of CO_2 dissolved in the aqueous phase:

$$n = \frac{\langle S_l \, X_l^{CO_2} \rho_l \rangle \langle \phi \rangle \, V}{m_{CO_2}} \tag{3}$$

where m_{CO2} [M/mol] is the CO_2 molecular mass. TOUGH2/ECO2N simulations provides the variables used in Eqs. (1-2) and thus allow estimations of M_{tot}/V_{tot}, M_{immisc}/V_{mmisc}, and M_{aq}/V_{aq}.

From Doughty et al. (2001), the global storage efficient capacity factor C_{dyn} [-] is revisited as follows:

$$C_{dyn-\frac{mass}{vol}} = C_{g-\frac{mass}{vol}} + C_{l-\frac{mass}{vol}} \tag{4}$$

where $C_{g-\frac{mass}{vol}}$ (including C_{gmob} and C_{gimmob}) and $C_{l-\frac{mass}{vol}}$ [-] are efficiency factors of gas- and liquid-phase components. These factors can be defined on a mass or volume basis, assuming that the theoretical mass of CO_2 M_{theory} stored in the entire pore space saturated with a gas-like CO_2 phase corresponds to $C = 1$:

$$C_{g-mass} = \frac{M_{immisc}}{M_{theory}} = \langle S_g \rangle \tag{5}$$

$$C_{l-mass} = \frac{M_{aq}}{M_{theory}} = \langle S_l \, X_l^{CO_2} \frac{\rho_l}{\rho_g} \rangle \tag{6}$$

On a volume basis,

$$C_{g-vol} = \frac{V_{immisc}}{V_{pore}} = \langle S_g \rangle \tag{7}$$

$$C_{l-vol} = \frac{V_{aq}}{V_{pore}} = \frac{V_{partial}}{M_{CO_2}} \langle \rho_g \rangle \langle S_l \, X_l^{CO_2} \frac{\rho_l}{\rho_g} \rangle \tag{8}$$

where $V_{pore} = \langle \phi \rangle V$ [L^3] is the total pore volume of aquifer.

For the static methods, the US-DOE's (in Goodman et al, 2012) methodology is usually used to estimate the CO_2 storage capacity based on the volumetric or compressibility approaches. It is noteworthy that the volumetric approach only applies to an open-system, whereas the compressibility approach applies to a closed-system. In these methods, the pressure buildup is assumed spatially uniform (Zhou et al., 2008).

Results and comparison

From the TOUGH2 results obtained for the two injection scenarios (Figure 8), the evolutions with time of different forms of CO_2 are shown in Figure 10: dissolved CO_2 in liquid-phase, mobile and immobile CO_2 in gas-like phase of stored CO_2 mass. The storage capacity (290 kg per m^2) of the scenario with k_r = 4.17 mD is greater than that of the scenario with k_r base case (270 kg per

m^2) according to the contribution of all CO_2 forms in place within the injection time. Nonetheless, only the immobile CO_2 quantity (M_{immob}) is greater in the case with k_r = 4.17 mD than in the case with k_r of the base case after the end of injection, because the larger permeability allowed CO_2 to travel within a large zone in which much CO_2 was trapped as residual saturation. Dissolved CO_2 (M_{aq}) is almost the same in both scenarios and mobile CO_2 (M_{mob}) is slightly smaller in the case of k_r = 4.17 mD than in the case of k_r for the base case. Finally, the apparent capacity of the scenarios was expressed by ~1.1×10^7 m^3 of stored supercritical CO_2 or ~0.32 m^3 per m^2 of site surface (not shown).

Figure 11 presents the evolution of the storage efficiency factors versus time obtained on a mass and volume basis. As expected, the capacity factor of liquid phase is greater for the mass basis than in the volume basis, while the capacity factors of gas-phase remain the same for both approaches. Consequently, the global capacity factor is larger (but not by much) on a mass basis than for the volume basis. It can be seen that the increase in the capacity factors of dissolved and trapped CO_2, and the decrease in the capacity factor of free CO_2 with time, enhances the storage security of the site.

The storage capacity was also calculated by static methods after estimating efficiency factors (not shown here). The factors from the hydrodynamic contribution were estimated by using their relations to non-dimensional numbers such as the mobility ratio and capillary number proposed in the oil-gas engineering literature. The site storage capacity factor was obtained by using the mass basis. It is 3.3%, which falls within the range (0.51%–5.4% for clastic lithology) determined by the Monte Carlo probability (Goodman et al., 2011). Note that in the compressibility method, we estimated the efficiency factor (2.19%) when calculating the maximum pressure buildup at the center of formations, corresponding to $0.9S_{hmin}$.

The storage capacities of the northeastern reservoir block of the Bécancour region corresponding to the efficiency factors of all the estimates are shown in Figure 12. The stored CO_2 mass obtained from the TOUGH2 dynamic method is smaller than the one of the static methods. The difference is ~30% between the TOUGH and compressibility method and ~50%

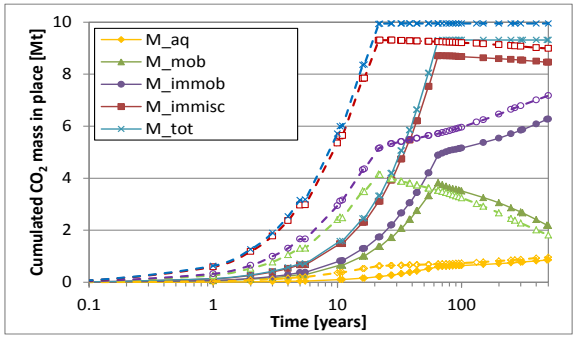

Figure 10. Evolution of different forms of cumulated CO_2 stored in place with time from the injection mass (solid lines for the injection scenario with k_r of the base case and dashed lines for k_r = 4.17).

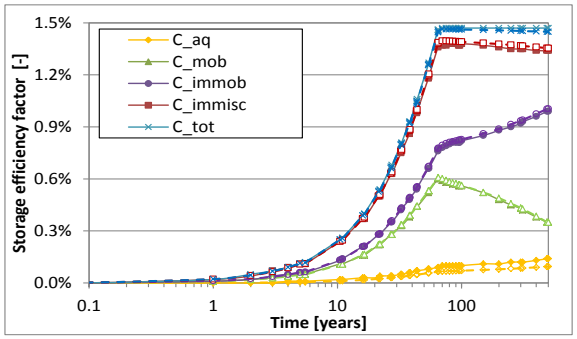

Figure 11. Capacity factors as a function of time for the scenario with k_r of the base case (solid lines for the mass basis and dashed lines for the volume basis).

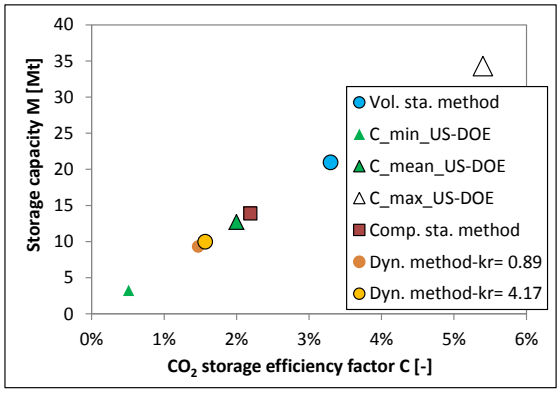

Figure 12. Storage capacity as a function of storage efficiency factors. Comparison between different estimation sources.

between the TOUGH and volumetric method. M_{tot} and $C_{dyn\text{-}mass}$ pairs of the dynamic method are linearly related between the storage capacity and efficiency factor. That reflects the fact that the theoretical mass of CO_2 stored in all the pore space M_{theory} is almost the same in all the methods, because the average CO_2 density over the entire reservoir domain by the TOUGH2 simulations is not much different from the estimated values in the static methods.

DISCUSSION AND CONCLUSIONS

The numerical sensitivity analysis documented in this paper highlights the influence of site properties, pressure constraints, and injection regime on the injection characteristics and thus the storage capacity. Permeability has the most direct impact on injectivity relative to other parameters (such as well diameter, thickness and depth of host formations, degree of CO_2 dissolution, compressibility, and permeability anisotropy), whereas capillary parameters have a global impact. In fact, simulation results for CO_2 injection could depend significantly on the capillary model used, at least for this study. The permeability contrast in the site favors preferential horizontal flow and impedes the upward migration of CO_2. From the point of view of security relative to CO_2 leakage risk, a compromise is needed between the completion interval and the injection rate in relation to vertical permeability. It is clear that greater rock compressibility plays a more important role for the aquifer pressure response. In this study, we did not investigate the sensitivity for the CA parameter, particularly for its permeability, for instance, CA k_r > CH k_r; this contrast could not force out the CO_2 plume remaining in the CH Fm. after the end of injections.

The injection strategy with intermittent and step-rates was applied in two proposed injection scenarios representing two cases: (1) $k_r < 1$ with long injection duration, and 2) $k_r > 1$ mD with short injection duration. The radial plume of injected CO_2 extended less than 1.2 km around the injection well. The total amount of CO_2 injection was on the order of 10 Mt for the two scenarios, which could be equivalent to regional emissions for ten years. Thus, the present geological sequestration option might consume 15%–50% of regional yearly CO_2 emissions in the few first decades from the start of injection. This annual emission of Bécancour would be all hosted in its deep saline aquifers by using vertical and/or horizontal multi-injectors.

The storage capacity estimated by the TOUGH2 simulations is smaller than the one obtained from static methods, because simulations take into account hydrodynamic multiphase processes that are not considered by static methods. It is also difficult to compare with the static volumetric method because of different hydraulic regimes. To compare with the static compressibility method, we modeled the aquifers as closed-system, which is suitable for Bécancour aquifers because no regional flow is observed and because it has small permeability. The efficiency capacity factors defined herein by the dynamic method are a function of time, but the global factor does not decrease after the end of injection. This is contrary to the efficiency capacity factor estimated for the reservoir with lateral spill points in Doughty et al. (2001). However, the local capacity factors, if calculated over a local domain (Doughty et al., 2002) in the closed aquifers, would increase or decrease with time. The application domain was defined for the storage capacity estimates and efficiency capacity factors of the TOUGH dynamic method.

The feasibility assessment of CO_2 injection in the deep saline aquifers of the Bécancour area (Québec) was carried out using TOUGH2 2D radial simulations, in which the injectivity and storage capacity estimates were investigated by the sensitivity study and the injection scenarios. A more detailed analysis will be presented in the forthcoming journal paper. These are the first numerical simulations showing the supercritical CO_2 behavior once the CO_2 is injected into the St Lawrence Lowlands salty sediment. This study is also a useful base for assessing seismicity induced by injection and leakage risk. A heterogeneous hydrodynamic model for the Bécancour reservoir will be developed on the basis of new data, especially the hydrogeology and petrophysical properties of cap rocks. The injection characteristics will be better mastered with the *in situ* permeability of the CH Fm. that will be established from field measurements. Finally, other processes involved in multiphase

flow and transport not yet taken into account in this study, such as capillary hysteresis, permeability modification, and diffusion-dispersion, are planned for future research.

ACKNOWLEDGMENT

We wish to acknowledge the Ministère du Développement durable, de l'Environnement et des Parcs du Québec (MDDEP) who financially supported this research.

REFERENCES

Bachu, S., and D. B. Bennion, Interfacial Tension between CO_2, Freshwater, and Brine in the Range of Pressure from (2 to 27) MPa, Temperature from (20 to 125) degrees C, and Water Salinity from (0 to 334 000) mg/L, *J Chem Eng Data*, *54*(3), 765-775, 2009.

Claprood, M., E. Gloaguen, B. Giroux, M. J. Duchesne, E. Konstantinovskaya, and M. Malo, Workflow using sparse vintage data for building a first geological and reservoir model for CO_2 storage in deep saline aquifer. A case study in the St. Lawrence Platform, Canada, *Greenhouse Gases: Science and Technology*, 2012.

Corey, A. T., The interrelation between gas and oil relative permeabilities, *Producers Monthly*, 38-41, 1954.

Doughty, C., Investigation of CO_2 plume behavior for a large-scale pilot test of geologic carbon storage in a saline formation, *Transport Porous Med*, *82*(1), 49-76, 2010.

Doughty, C., S. M. Benson, and K. Pruess, Capacity investigation of brine-bearing sands for geologic sequestration of CO_2, in *GHGT-6 Conference*, Kyoto, Japan, 2002.

Doughty, C., K. Pruess, S. M. Benson, S. D. Hovorka, P. R. Knox, and C. T. Green, Capacity investigation of brine-bearing sands of the Frio formation for geologic sequestration of CO_2, U.S. Department of Energy, National Energy Technology Laboratory, 2001.

Goodman, A., et al., US DOE methodology for the development of geologic storage potential for carbon dioxide at the national and regional scale, *Int J Greenh Gas Con*, *5*(4), 952-965, 2011.

Konstantinovskaya, E., M. Malo, and D. A. Castillo, Present-day stress analysis of the St. Lawrence Lowlands sedimentary basin (Canada) and implications for caprock integrity during CO_2 injection operations, *Tectonophysics*, *518*, 119-137, 2012.

Land, C. S., Calculation of imbibition relative permeability for two- and three-phase flow from rock properties, *SPE Journal*, *9*, 149-156, 1969.

Malo, M., and K. Bédard, Basin-scale assessment for CO_2 storage prospectivity in the Province of Québec, Canada, *Energy Procedia*, *in press*, 2012.

Pruess, K., *ECO2N: A TOUGH2 fluid property module for mixtures of water, NaCl, and CO_2*, LBNL-57952, 66 pp, Lawrence Berkeley National Laboratory, Berkeley, Calif., 2005.

Rutqvist, J., J. Birkholzer, F. Cappa, and C. F. Tsang, Estimating maximum sustainable injection pressure during geological sequestration of CO_2 using coupled fluid flow and geomechanical fault-slip analysis, *Energ Convers Manage*, *48*(6), 1798-1807, 2007.

Thunderhead-Engineering, *Petrasim user manual*, 124 pp, 2010.

Tran Ngoc, T. D., E. Konstantinovskaya, R. Lefebvre, M. Malo, and L. Massé, Geotechnical characterization of deep saline aquifers for CO_2 geological storage in the Bécancour region, Québec, Canada *Geotechnics for Sustainable Development-Geotec Ha Noi*, Construction Publishing House, Ha Noi, Viet Nam, pp. 623–632, 2011.

van Genuchten, M. T., A closed-form equation for predicting the hydraulic conductivity of unsaturated soils, *Soil Sci Soc Am J*, *44*(5), 892-898, 1980.

Zhou, Q. L., J. T. Birkholzer, C. F. Tsang, and J. Rutqvist, A method for quick assessment of CO2 storage capacity in closed and semi-closed saline formations, *Int J Greenh Gas Con*, *2*(4), 626-639, 2008.

A NOVEL CONCEPT FOR LONG-TERM CO_2 SEALING BY INTENTIONAL SALT CLOGGING

Laura J. Wasch, Jens Wollenweber, Tim J. Tambach
TNO
Princetonlaan 6
3508 TA, Utrecht, The Netherlands
e-mail: laura.wasch@tno.nl

ABSTRACT

Well abandonment after CO_2 storage demands a mitigation strategy for CO_2 leakage along the wellbore. We propose forming a salt seal around the wellbore after CO_2 has been injected into a depleted gas field, preventing possible CO_2 transport to the surface. The placed salt plug will protect the wellbore material from contact with supercritical CO_2 and acid brine. We propose the concept of brine-alternating CO_2 injection for intentional salt clogging of the reservoir. Injection of CO_2 will evaporate water from previously injected brine, causing salt precipitation. The formation of a dryout zone is a known process occurring during CO_2 injection in saline aquifers or depleted gas fields that leads to unintentional clogging and possibly injectivity issues.

Modeling is performed with TOUGH2, simulating injection of brine and subsequently CO_2. Our model is based on the K12-B depleted gas field, using the elevated pressure conditions of a CO_2-filled storage reservoir. The model results indicate that injecting multiple cycles of brine and CO_2 could be used for controlled precipitation of salt in the reservoir. The injection procedure results in a 40 cm thick salt bank around the well, with the precipitated salt reducing the porosity from 10 to 8% at the location of maximum salt precipitation. This porosity decrease causes complete permeability impairment. We conclude that brine-alternating CO_2 injection could pose an effective method for intentional salt-clogging of the near-wellbore area.

INTRODUCTION

Carbon capture and storage (CCS) has great potential for reducing CO_2 emissions into the atmosphere and mitigating climate change (IPCC, 2005). Geological storage reservoirs are commonly pierced by multiple wells, especially reservoirs previously used for oil and gas production. Wells are potential CO_2 leakage pathways to the surface. Hence, reservoirs for CO_2 storage require a long-term wellbore seal to prevent CO_2 leakage to the surface (Bachu, 2003).

A major concern is leakage along the wellbore after extended time intervals caused by mechanical loads and/or chemical degradation of well-cement. CO_2 partially dissolves in the formation water, resulting in acid conditions in the storage reservoir. Wellbore materials react under acid conditions (e.g., Kutchko et al., 2007), possibly affecting its containment properties. Techniques previously suggested to ensure well integrity in CO_2 storage environment include, among others: improvement of cement design (Benge, 2009) and clogging of the reservoir by polymers (Hou et al., 2011) or by biomineralization (Cunningham et al., 2011). We propose salt for sealing the reservoir section of the well, since salt has proven sealing capacities with respect to gas and may "naturally" precipitate during gas storage or production.

Salt clogging of the reservoir or wellbore is generally regarded as a possible problem in gas and oil production (e.g., Kleinitz et al., 2003), CO_2 storage in saline aquifers (e.g., André et al., 2007), and depleted gas fields (e.g., Giorgis et al., 2007, Tambach et al., 2011 and Tambach et al., 2012). Gas production and injection may lead to salt precipitation by the evaporation of water from the brine into the gas phase. Salt precipitation in the pore space reduces flow, negatively affecting gas injectivity or productivity. We propose to reverse this problem using this phenomenon for *intentional* salt clogging (Figure 1). Simulations are performed to investigate controlled salt precipitation by

brine-alternating CO_2 injection. A practical injection strategy must be designed to facilitate the formation of an effective wellbore salt-seal while keeping operational time as short as possible.

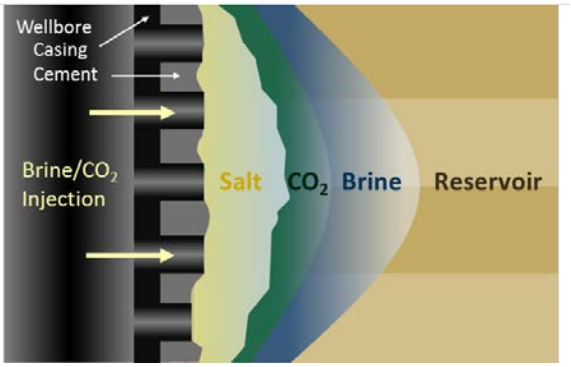

Figure 1. Illustration of the brine alternating CO_2 injection concept forming a salt seal around the wellbore.

SIMULATION DETAILS

Simulations are performed with the flow simulator TOUGH2, using its ECO2N module for CO_2 and brine mass transfer (Pruess and Spycher, 2007). Permeability changes are modeled with a tubes-in-series porosity-permeability model, assuming 20% porosity clogging to result in complete permeability impairment (Verma and Pruess, 1988). Precipitation is studied by the pore-space fraction occupied by salt, the "salt pore volume fraction." Chemical rock-fluid, capillary pressure, permeability hysteresis and nonisothermal effects are neglected.

A simplified one layer model is built after the K12-B depleted gas field (Audigane et al., 2007), a Dutch CO_2 storage demonstration site. The model assumes a homogeneous sandstone reservoir of fluvial facies. The sandstone is characterized by a porosity of 0.11 and a permeability of 22.4 mD. A 1D radial reservoir model is used, described by 59 grid cells with grid refinement towards the well interface. The 20 m near-well model extends from 3640 to 3780 m depth. Ambient conditions applied are a 90°C reservoir temperature and 300 bar pressure after CO_2 storage. The reservoir is assumed dried out after CO_2 injection (no brine) and CO_2 filled (no methane). No initial salt due to previous gas production or storage (e.g. Kleinitz et al., 2003) is assumed for the base-case model.

Injection details are shown in Table 1. The injection strategy is designed with a brine/CO_2 ratio allowing complete evaporation of injected water into CO_2 at reservoir conditions. Note that over 200 times more CO_2 than brine is injected in order to evaporate the injected brine. The injection rates versus times are chosen arbitrarily while respecting the brine/CO_2 ratio. A 0.1 NaCl mass fraction brine (XNaCl) is used.

Table 1. One cycle of brine-alternating CO_2 injection.

Phase	Time (hr.)	Injection rate (kg/s)	Injected mass (kg)
Brine	0.2	1.4	945
CO_2	82.5	0.7	207347

RESULTS

Brine alternating CO_2 injection

Two cycles of brine-CO_2 injection are modeled to assess the effect of repeated injection cycles on salt precipitation. Simulations results are shown in Figure 2 and 3. The injection cycle starts with brine injection. At the end of the cycle, brine has moved 0.23 m into the reservoir. Subsequent CO_2 injection displaces the brine ~0.1 m further into the reservoir. While pushing the brine forward, CO_2 evaporates water from the brine at the CO_2-brine contact. Precipitation occurs in one cell at each time step when dissolved salt reaches the solubility limit.. This precipitation front moves the reservoir inward with time as more CO_2 is injected, leaving a salt bank behind. Salt precipitation progresses from the well, forming a 0.37 m thick salt bank at the end of the cycle (Figure 2, 82.7 hr.).

The second injection cycle starts again with brine injection. Since the brine is NaCl undersaturated, the salt bank formed in the first cycle is redissolved (Figure 2, 82.9 hr.). Brine salinity increases with flow through the reservoir as salt is progressively dissolved. This results in a higher salt mass fraction at the brine injection front (Figure 3, 82.9 hr.). Upon CO_2 injection, the brine is pushed forwards and dissolves the

final part of the salt bank (~0.1 m). In addition, CO_2 evaporates brine at the CO_2-brine contact. This results in a high salinity peak at both the CO_2 and brine injection front (Figure 3, 120 hr.). CO_2 injection evaporates the brine starting from the well reservoir inwards, again forming a continuous salt bank. Furthermore, since the brine at the brine injection front has a higher salt content, a salt peak is formed (Figure 2, 165.4 hr.). This salt peak is located at 0.3 m distance to the injection well, has a thickness of 0.2 m, and clogs up to 3.0% of the original pore volume.

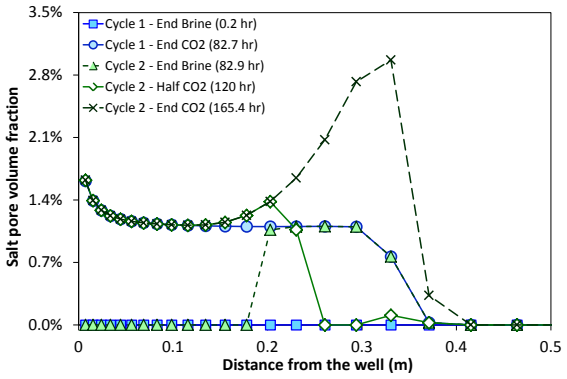

Figure 2. The fraction of pore space occupied by salt with distance from the well. The salt content is illustrated for different times, showing the built up of a salt bank (cycle 1) and dissolution followed by re-precipitation of the salt bank, now forming a salt peak (cycle 2).

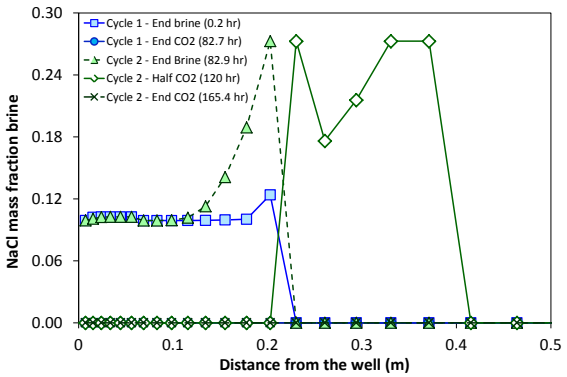

Figure 3. The NaCl mass fraction of brine during cycle 1 and 2. The NaCl mass fraction is close to the initial value of 0.1 in cycle 1. Brine injection in cycle 2 shows an increase of salinity at the front. During CO_2 injection the NaCl mass fraction shows the movement of brine and evaporation from the back increasing the value.

Intentional clogging of the near-well area

Modeling of two cycles of brine alternating CO_2 injection indicated increased pore clogging within the second cycle. To increase the effectiveness of clogging multiple injection cycles are modeled and more salt is added to the system with every brine-CO_2 injection cycle. The modeling will help assess the amount of cycles required for effective clogging.

The model results for the salt content at the end of a cycle are shown in Figure 4. They indicate that the salt peak grows with every cycle while salt clogging near well remains constant. Furthermore, the width of the peak and extent of the salt bank into the reservoir are equal after each subsequent cycle. The salt content near-well remains constant since this salt precipitated out of newly injected brine with constant salinity every cycle. Only the first part of the injected brine dissolves salt, yielding more salt precipitation with each cycle. Because the same amount of brine is injected each cycle, the salt bank reaches an equal distance from the well following drying out at the end of every cycle.

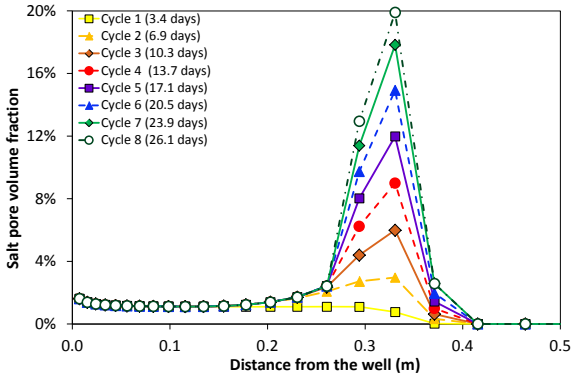

Figure 4. The fraction of pore space occupied by salt with distance in the reservoir. The salt content for eight subsequent Brine-CO_2 injection cycles is illustrated. With every subsequent cycle, salt is added to the salt peak while the near-well part of the salt bank remains constant.

Following the porosity-permeability relationship of Verma & Pruess (1988), the permeability is effectively impaired after a 20% reduction in pore space. Modeling predicts that eight cycles of brine-CO_2 injection are required to reduce the porosity from 10% to 8% and effectively clog the reservoir (Figure 5). The porosity is roughly gradually decreased with subsequent cycles (as

also shown in Figure 4). In contrast, permeability slightly decreases at first but reduces significantly when approaching 20% clogging. Note that the TOUGH2 simulation stops before reaching zero permeability, since the pressure increases to the limit upon complete clogging.

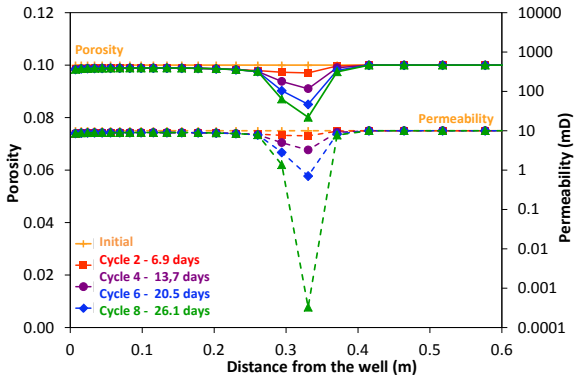

Figure 5. Porosity and permeability development with subsequent cycles of brine and CO_2 injection. Note that the permeability scale is logarithmic. Permeability calculated after the implemented porosity-permeability relationship (Verma and Pruess, 1988).

Sensitivity of the number of cycles

Brine-alternating CO_2 injection is used to increase salt precipitation around the wellbore with every cycle. The number of cycles required for clogging depends on the amount of salt added per cycle (brine salinity and injection rate/time), the amount of salt initially in the reservoir (solid salt or brine), and the spatial distribution of the injected salt. To assess the sensitivity of the predicted clogging towards these factors, two scenarios are run with a higher NaCl mass fraction of 0.2 and with initial salt present (salt mass fraction 0.0125).

The results are compared with the base-case model results. The first cycle already shows clear differences (Figure 6). A higher NaCl mass-fraction brine yields a salt bank with a higher percentage pore clogging (2.5% vs. 1.7%). Initial salt gives a similar salt bank near well, since the injected brine salinity and hence resulting salt is equal. However, this model already forms a salt peak in the first cycle because salt is initially present that is dissolved and re-precipitated further in the reservoir. For initial salt in the reservoir, the shape of the salt peak remains equal to the base case for subsequent stages (Figure 6, cycle 4). Conversely, a higher salinity brine increases the width of peak and enhances clogging in the near-well area. Both scenarios yield faster clogging than the base-case model and require seven instead of eight cycles for effective clogging (Figure 7).

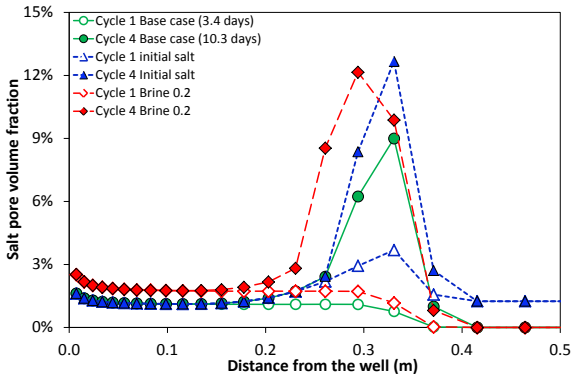

Figure 6. The fraction of pore space occupied by salt with distance from the well, presented for cycle 1 and 4. The salt content is shown for the base case and two scenarios with higher salinity and initial salt in the reservoir.

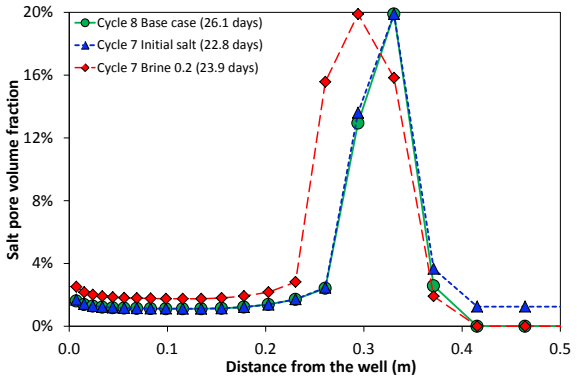

Figure 7. The fraction of pore space occupied by salt with distance from the well, presented for the final cycles yielding 20% salt clogging. The salt content is shown for the base case and two scenarios with higher salinity and initial salt in the reservoir.

DISCUSSION

The model results indicate that controlled CO_2 injection into a brine-containing reservoir (after brine injection) can result in intentional salt clogging. Furthermore, the salt precipitation induces significant permeability impairment. This is in agreement with studies on CO_2-induced salt precipitation. Muller et al. (2009)

report permeability reductions of up to 60% for 16% salt clogging. Experimental work by Bacci et al. (2011) showed an 86% permeability decrease for a ~30% porosity reduction. Although significant permeability reduction is observed, complete clogging could require more (or less) precipitation than the 20% salt saturation assumed. Knowing the amount of precipitation required for effective clogging is crucial for modeling and designing a clogging strategy. Consequently, accurate porosity-permeability relations are required (Bacci et al., 2011).

Modeling predicts that the salt bank has a lateral extent of 0.4 m into the reservoir at the end of a brine-CO_2 injection cycle. A broader salt bank could be formed for longer intervals of brine and subsequent CO_2 injection or higher injection rates. Special care must be taken to design a practical and economic strategy of injection rates and times. Further research is required to study the desired width of the salt bank. This width will depend on the mechanical and chemical stability of the salt bank.

The model predicts the presence of a lower-salt-content zone around the well, while complete clogging is modeled further in the reservoir at the salt peak. Clogging the reservoir up to the well-reservoir interface provides higher safety in terms of leakage prevention along the wellbore and well-material protection. Salt precipitation can be enhanced near the well by increasing the salinity of the injected brine. For example, injecting saturated brine prevents redissolution of the salt bank with a subsequent injection cycle. This allows the buildup of a salt bank from the wellbore interface. Although increased salinity is favorable for clogging up to the wellbore-reservoir interface, high salinity brines can also lead to unintended salt precipitation, which can clog the well before a proper salt plug has been placed. Alternatively, the remaining open pore space around the well could be sealed by injection of a synthetic polymer (Hou et al., 2011).

The current model consists of a homogenous reservoir. However, heterogeneities do exist in the reservoir (vertical and lateral) such as changes in lithology and fractures. Heterogeneities influence the flow of CO_2 and the porosity-permeability relationship and consequently the location of salt precipitation (Pruess and Müller, 2009). Hence, heterogeneities should be considered to insure effective clogging around the entire wellbore in future work.

Currently, capillary-pressure effects are ignored. However, capillary pressure can affect salt precipitation and already precipitated salt by inducing backflow of brine towards the evaporation front (Pruess and Müller, 2009, Alkan et al., 2010, Ott et al., 2011, Zeidouni et al., 2009). Brine backflow enhances precipitation by adding salt to the system. On the other hand, backflow could lead to dissolution of the salt bank after its emplacement. Intentional salt clogging appears therefore particularly suitable for application to depleted gas fields that have low water content and accordingly little chance of salt seal redissolution by the backflowing water. Future modeling work is required regarding the long-term stability of the salt bank and its resistivity to redissolution. This process will eventually define the size of the salt bank required for effective long-term sealing of CO_2 injection wells.

CONCLUSIONS

Intentional salt clogging is proposed to protect wellbore cement against corrosive CO_2 and to mitigate leakage of stored CO_2 to the surface. Brine-alternating CO_2 injection has been found to be effective for intentional clogging of the near-well area. TOUGH2 modeling predicts that multiple cycles of brine-CO_2 injection are required for effective clogging and permeability impairment of the reservoir. For the presented injection strategy and model characteristics, the formed salt bank extends 0.4 m into the reservoir. The salt bank clogs 3% of the original reservoir porosity near the well, whereas the salt peak is responsible for 20% porosity clogging further in the reservoir.

The current injection strategy requires eight cycles of brine-alternating CO_2 injection for complete permeability impairment. However, the number of cycles required for effective clogging depends on the brine salinity and amount of injected brine. Additionally, initial salt or brine present in the reservoir reduces the amount of salt that has to be introduced to the reservoir for clogging. Moreover, when changing the porosity-permeability relationship, more or fewer

stages are required as more or less salt clogging is required.

The presented injection strategy predicts effective clogging in relatively short time periods. Nevertheless, experimental or field case tests are required to assess if intentional salt clogging can be practically applied without, for example, clogging the wellbore. In conclusion, intentional salt clogging potentially provides a practical solution for protecting the wellbore against corrosive CO_2 attack, as well as blocking the flow of CO_2 along the wellbore and mitigating leakage to the surface.

ACKNOWLEDGMENT

We thank Pascal Audigane for providing the K12-B TOUGH2 model. The work was performed within the EU FP7 project "CO2CARE–CO_2 Site Closure Assessment Research" (Grant Agreement no. 256625).

REFERENCES

Alkan, H., Cinar, Y., Ülker, E.B., Impact of Capillary Pressure, Salinity and In situ Conditions on CO_2 Injection into Saline Aquifers, *Transp.Porous Media, 84*(3), 799-819, 2010.

André, L., Audigane, P., Azaroual, M., Menjoz, A., Numerical modeling of fluid-rock chemical interactions at the supercritical CO_2-liquid interface during CO_2 injection into a carbonate reservoir, the Dogger aquifer (Paris Basin, France), *Energy Convers.Manage., 48*(6), 1782-1797, 2007.

Audigane, P., J. Lions, I. Gaus, C. Robelin, P. Durst, B. Van der Meer, K. Geel, C. Oldenburg, and T.Xu, 2009, *Geochemical modeling of CO_2 injection into a methane gas reservoir at the K12-B field, North Sea*, in M. Grobe, J. C. Pashin, and R. L. Dodge, eds., Carbon dioxide sequestration in geological media—State of the science: AAPG Studies in Geology 59, p. 499– 519.

Bacci, G., Korre, A., Durucan, S., Experimental investigation into salt precipitation during CO_2 injection in saline aquifers. *Energy Procedia. 4*, 4450-4456, 2011.

Bachu, S., Screening and ranking of sedimentary basins for sequestration of CO_2 in geological media in response to climate change, *Environ.Geol., 44*(3), 277-289, 2003.

Benge, G., Improving Wellbore Seal Integrity in CO_2 Injection Wells. 2009.

Cunningham, A.B., Gerlach, R., Spangler, L., Mitchell, A.C., Parks, S., Phillips, A., Reducing the risk of well bore leakage of CO_2 using engineered biomineralization barriers. *Energy Procedia. 4*, 5178-5185, 2011.

Giorgis, T., Carpita, M., Battistelli, A., 2D modeling of salt precipitation during the injection of dry CO_2 in a depleted gas reservoir, *Energy Convers.Manage., 48*(6), 1816-1826, 2007.

Hou, M.Z., Wundram, L., Wendel, H., Meyer, R., Schmidt, M., Kretzschmar, H.J., Schmitz, S., Franz, O., Developing, modeling and in-situ-testing a long-term wellbore seal in the framework of the CO_2. *Energy Procedia. 4*, 5291-5298, 2011.

IPCC, 2005. IPCC Special Report on carbon dioxide capture and storage. Prepared by Working Group III of the Intergovernmental Panel on Climate Change [Metz, B., Davidson, O., de Coninck, H.C., Loos, M., Meyer, L.A. (Eds.)]. Cambridge University Press, Cambridge, United Kingdom/New York, NY, USA, 442 pp.

Kleinitz, W., Dietzsch, G., Köhler, M., Halite scale formation in gas-producing wells, *Chem.Eng.Res.Des., 81*(3), 352-358, 2003.

Kutchko, B.G., Strazisar, B.R., Dzombak, D.A., Lowry, G.V., Thauiow, N., Degradation of well cement by CO_2 under geologic sequestration conditions, *Environ.Sci.Technol., 41*(13), 4787-4792, 2007.

Ott, H., De Kloe, K.D., Marcelis, F., Makurat, A., Injection of supercritical CO_2 in brine saturated sandstone: Pattern formation during salt precipitation. *Energy Procedia. 4*, 4425-4432, 2011.

Pruess, K. and Müller , N., Formation dry-out from CO_2 injection into saline aquifers: 1. effects of solids precipitation and their mitigation, *Water Resour.Res., 45*(3), 2009.

Pruess, K. and Spycher, N., ECO2N - A fluid property module for the TOUGH2 code for studies of CO_2 storage in saline aquifers, *Energy Convers.Manage., 48*(6), 1761-1767, 2007.

Tambach, T., Koenen, M., Van Bergen, F., Geochemical evaluation of CO_2 injection into storage reservoirs based on case-studies in The Netherlands. *Energy Procedia. 4*, 4747-4753, 2011.

Tambach, T.J., D. Loeve, C. Hofstee, W.-. Plug, and J.G. Maas, Effect of gas field production and CO_2 injection on brine flow and salt precipitation, Proceedings TOUGH Symposium 2012, Lawrence Berkeley National Laboratory, Berkeley, California, September 17-19, 2012.

Verma, A. and Pruess, K., Thermohydrological conditions and silica redistribution near high-level nuclear wastes emplaced in saturated geological formations, *J.GEOPHYS.RES.*, *93*(B2), 1159-1173, 1988.

Zeidouni, M.,Pooladi-Darvish, M., Keith, D., Analytical solution to evaluate salt precipitation during CO2 injection in saline aquifers, *Int.J.Greenh.Gas Control*, *3*(5), 600-611, 2009.

EOS7C-ECBM: MODIFICATION OF EOS7C TO INCLUDE ENHANCED COAL-BED METHANE AND THE DUSTY GAS MODEL

Stephen W. Webb[1] and Curtis M. Oldenburg[2]

[1]Canyon Ridge Consulting LLC
10 Canyon Ridge Dr.
Sandia Park, NM, USA, 87047
e-mail: Stephen.Webb.CRC@gmail.com

[2]Lawrence Berkeley National Laboratory
Earth Sciences Division 74-316C
Berkeley, CA, USA, 94720
email: cmoldenburg@lbl.gov

ABSTRACT

EOS7C is an equation of state module for the TOUGH2 program for CO_2 or N_2 in Methane (CH_4) Reservoirs. Additions have been made to the EOS7C Version 1.0 module to include Enhanced Coal Bed Methane (ECBM) modifications and the Dusty Gas Model for gas-phase diffusion.

The ECBM modifications to the EOS7C equation of state incorporate the extended Langmuir isotherm for sorbing gases, including the change in porosity associated with the sorbed gas mass. Comparison to hand calculations for pure gas and binary mixtures shows very good agreement. Application to a CO_2 well injection problem given by Law et al. (2002) shows reasonable agreement.

The Dusty Gas Model (DGM) modifications add options to calculate gas diffusion using the Dusty-Gas Model, including separate and coupled approaches. The DGM is recommended for use in lower permeability reservoirs (10^{-15} m^2 or less) (Oldenburg et al., 2004a). Comparison to low-permeability pure gas diffusion data shows excellent agreement. The results from the DGM are compared to the Fick's law behavior for diffusion across a capillary fringe. The differences between the models are small, due to the relatively high permeability (10^{-11} m^2).

INTRODUCTION

EOS7C is an equation-of-state module for TOUGH2 for CO_2 or N_2 in methane (CH_4) reservoirs. The TOUGH2 EOS7C Version 1.0 module for CO_2 (Oldenburg et al., 2004b) has been enhanced to include Enhanced Coal Bed Methane (ECBM) modifications. In addition, the Dusty Gas Model for gas-phase diffusion (Webb, 1998) has been included. Each modification will be discussed separately. Additional details are given in Webb (2011).

Enhanced Coal Bed Modifications

In Enhanced Coal Bed Methane, CO_2 is pumped into methane-rich coal beds. Due to adsorption processes, the CO_2 is sorbed onto the coal, which displaces previously sorbed methane.

The gas storage capacity for a single gas species is given by the Langmuir relationship (Law et al., 2002)

$$G_s = G_{sL}\left[1-\left(w_a + w_{we}\right)\right]\frac{P}{P+P_L} \tag{1}$$

where

G_s	gas storage capacity (sm^3/kg-coal)
G_{sL}	dry, ash-free Langmuir storage capacity (sm^3/kg-coal)
w_a	ash weight fraction
w_{we}	equilibrium moisture weight fraction
P	pressure (Pa)
P_L	Langmuir pressure (Pa)

The individual Langmuir parameters from Equation (1) are used to model multiple gas species through the extended Langmuir isotherm

$$G_{si} = G_{sLi}\left[1-\left(w_a + w_{we}\right)\right]\frac{\frac{P\,y_i}{P_{Li}}}{1+P\sum_{j=1}^{nc}\frac{y_j}{P_{Lj}}} \tag{2}$$

where

y	mole fraction of component i in the gas phase
i	component i
nc	number of components

Gas sorption is added to the basic mass balance equation in TOUGH2 as follows:

$$M_{gas}^{\kappa} = \phi \sum_{gas} S_{gas}\, \rho_{gas} X_{gas}^{\kappa} + (1-\phi)\rho_{coal}\, G_{si}\, \rho_{gas,STP} \quad (3)$$

where M_{gas}^{κ} is the mass of component κ in the gas phase per unit volume and ϕ is total fluid volume fraction including the sorbed gases similar to the Zarrouk and Moore (2009) modifications. The sorbed gases lead to coal-bed volume changes.

In order to include coal-bed shrinking and swelling, the sorbed gases change the local porosity as determined by the sorbed gas density and the amount of gas sorbed. Two porosities or volumes are defined: (1) the total fluid porosity (volume), which includes any sorbed gas volume; and (2) the net fluid porosity (volume), which is the net value available for fluids. These terms are shown schematically in Figure 1.

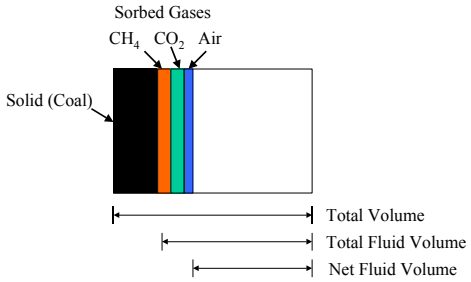

Figure 1. Volume nomenclature

Dusty Gas Model

The general form of the Dusty Gas Model for the gas diffusion of component *i* is given by (Thorstenson and Pollack, 1989)

$$\sum_{j=1, j\neq i}^{n} \frac{y_i N_j^D - y_j N_i^D}{D_{ij}^*} - \frac{N_i^D}{D_i^{K*}} = \frac{\left(\nabla P_i - \rho_g g\right)}{RT} \quad (4)$$

where N^D is the molar diffusive flux, y is the gas-phase mole fraction, D_{ij}^* is the effective binary diffusion coefficient, D^{K*} is the effective Knudsen diffusion coefficient, P is the pressure, R is the gas constant, and T is the temperature. The summation for component j is over all components in the system except I, such that the diffusion of all gas components is coupled.

For a three-component system and ignoring gravity for simplicity in this presentation, the set of equations becomes

$$\begin{aligned}
&-\left[\frac{1}{D_1^{K*}} + \frac{y_2}{D_{12}^*} + \frac{y_3}{D_{13}^*}\right] N_1^{D,g} + \frac{y_1}{D_{12}^*} N_2^{D,g} + \frac{y_1}{D_{13}^*} N_3^{D,g} = \frac{\nabla P_1}{RT} = \frac{P\nabla y_1}{RT} + \frac{y_1 \nabla P}{RT} \\
&\frac{y_2}{D_{21}^*} N_1^{D,g} - \left[\frac{y_1}{D_{21}^*} + \frac{1}{D_2^{K*}} + \frac{y_3}{D_{23}^*}\right] N_2^{D,g} + \frac{y_{21}}{D_{23}^*} N_3^{D,g} = \frac{\nabla P_2}{RT} = \frac{P\nabla y_2}{RT} + \frac{y_2 \nabla P}{RT} \\
&\frac{y_3}{D_{31}^*} N_1^{D,g} + \frac{y_3}{D_{32}^*} N_2^{D,g} - \left[\frac{y_1}{D_{31}^*} + \frac{y_2}{D_{32}^*} + \frac{1}{D_3^{K*}}\right] N_3^{D,g} = \frac{\nabla P_3}{RT} = \frac{P\nabla y_3}{RT} + \frac{y_3 \nabla P}{RT}
\end{aligned} \quad (5)$$

where the two terms on the right-hand side represent ordinary and Knudsen diffusion driving forces, respectively. Note that self diffusion, D_{11}^*, is not explicitly included in the equation set.

For a single component, the DGM equation reduces to

$$N_1^{D,g} = -D_1^{K^*} \frac{\nabla P_1}{RT} \quad (6)$$

where the Knudsen diffusion coefficient models the "slip" of the gas, or the Klinkenberg effect.

As can be seen from Equation (5), the diffusion of any single component may be strongly coupled with the diffusion of the other components. Therefore, in general, a single equation for the diffusion of a given component cannot be developed. Two exceptions are binary gas diffusion, where equations can be developed as given by Thorstenson and Pollock (1989), and

trace gas diffusion, where an effective tortuosity can be defined for use with Fick's law (Webb and Pruess, 2003) that will give the same results as the DGM.

For diffusion of dissolved components in the liquid phase, a simple Fick's law model has been used. The model is different from that of Pruess et al. (1999), however, in that Fick's law is based on mole fractions rather than mass fractions. The present model gives equimolar diffusive fluxes in the liquid, while the model used by Pruess et al. (1999) gives equal and opposite mass fluxes. The diffusive fluxes for each dissolved component (including water) are given by

$$N_i^{D,\ell} = -D^*_{1i,\ell} c_\ell \nabla x_i \tag{7}$$

where i applies to all the components including water.

2.2.1 Coupling of Diffusive Fluxes

The above equations predict gas and liquid diffusion for uniform properties under single-phase conditions. For non-uniform properties and multiphase conditions, the solution of the above equations becomes much more complicated. Pruess and Webb (1999) developed a multiphase diffusion scheme by invoking conservation of total flux across the interface, which leads to harmonic weighting of the strength coefficient. However, their diffusion equations were based on Fick's law, such that coupling between components in a given phase was not included. Only the coupling of gas and liquid diffusion was considered.

The general concept of a weighting scheme for diffusion is that the fluxes to and from an "interface" condition are equal. This "interface" condition is defined by the equality of fluxes. For simple cases, harmonic weighting is the appropriate weighting scheme as discussed by Tsang and Pruess (1990). The same principle of conservation of mass flux, or diffusive flux, will be used in this case, based on the combined gas and liquid diffusive fluxes.

As discussed by Pruess and Webb (1999), the weighting scheme must consider the combined fluxes rather than each one individually. For example, the DGM equation for component 1 can be written in terms of the unspecified interface conditions (mole fraction and pressure) as follows

$$-\left[\frac{1}{D_1^{K*}} + \frac{y_2}{D_{12}^*} + \frac{y_3}{D_{13}^*}\right] N_1^{D,g} + \frac{y_1}{D_{12}^*} N_2^{D,g} + \frac{y_1}{D_{13}^*} N_3^{D,g} = \frac{P}{RT}\frac{y_{1,i} - y_{1,u}}{d_u} + \frac{y_1}{RT}\frac{P_i - P_u}{d_u} \tag{8}$$

where subscript i denotes the interface condition, and d_u is the distance from gridblock 1 to the interface, or the upstream length. Naturally, the properties of gridblock 1 are used for the coefficients. Similarly, the downstream equation is

$$-\left[\frac{1}{D_1^{K*}} + \frac{y_2}{D_{12}^*} + \frac{y_3}{D_{13}^*}\right] N_1^{D,g} + \frac{y_1}{D_{12}^*} N_2^{D,g} + \frac{y_1}{D_{13}^*} N_3^{D,g} = \frac{P}{RT}\frac{y_{1,d} - y_{1,i}}{d_d} + \frac{y_1}{RT}\frac{P_d - P_i}{d_d} \tag{9}$$

and the properties of gridblock 2 are used. Similar sets of equations can be written for each gas-phase component and each liquid-phase component.

The gas equations specify the interfacial mole fraction in terms of the gas mole fraction, while the liquid equations use the liquid mole fraction for the interface. The difference between the mole fractions is resolved by defining an effective value of Henry's constant, which is defined as

$$K_{H,i,eff} = K_{H,i}\frac{c_\ell}{c_g} = \frac{y_{g,i}}{x_{\ell,i}} \tag{10}$$

so the liquid interfacial mole fractions can be converted to gas interfacial mole fractions.

$K_{H,i,eff}$ for the interface is calculated from the upstream and downstream gridblocks based on the element mole fractions. Only gridblocks with gas and liquid in them are considered. The value at the interface is estimated by harmonic weighting of the gridblock values.

The values of the interfacial mole fractions and total interfacial pressure are calculated by invoking equal upstream and downstream total molar fluxes (gas plus liquid) to and from the interface for each component, as well as the requirement that the mole fractions sum to 1.0.

Therefore, for a three-component system, there are 16 equations and 16 unknowns. For a five-component system such as in EOS7C, there are 26 equations and 26 unknowns for the fully coupled solution.

Verification of Modifications

ECBM

Verification of the modifications to TOUGH2 for the ECBM is provided through comparison of the output from the code to literature results. The first verification exercise compares the results from extended Langmuir isotherm calculations with the results presented by Arri et al. (1992). These results are for pure gas and binary gas sorption, where the extended Langmuir parameters are specified by Arri et al. (1992). The second verification exercise is for a sample problem presented by Law et al. (2002), which has been used for comparison of various ECBM simulators.

Isotherms

Arri et al. (1992) present the results of isotherm calculations for pure gas and binary gas conditions for CH_4, CO_2, and N_2. The results from the present calculation are presented in the same English units used in the original reference for ease of comparison. Figure 2 shows the pure gas isotherm results; the extended Langmuir values are summarized in Table 1. The solid line is the isotherm given earlier by Equation (1) with zero ash and moisture weight fractions, while the symbols are the results from the modified TOUGH2 code. The agreement is excellent.

Table 1. Langmuir Parameters (Arri et al., 1992)

Gas	G_{SL}(SCF/ton)	p_L (psia)
CO_2	1128	204.5
CH_4	759	362.3
N_2	616	1458.

Figure 3 presents results for binary gas adsorption using the extended Langmuir isotherm constants given in Table 1. The plot shows the CH_4-N_2 binary gas sorption isotherms at 500 psia given by Equation (2) and the results calculated with the modified TOUGH2 program given by the symbols. The agreement is excellent.

The species splits in the gas phase and the sorbed phase are shown in Figure 4 for the mixture given above. These curves are independent of pressure because pressure is completely defined by the pure gas Langmuir isotherms, as discussed by Arri et al. (1992). The separation factor, α, is given by

$$\alpha_i = \frac{\left(x/y\right)_i}{\left(x/y\right)_j} \tag{11}$$

where x is the sorbed phase mole fraction and y is the gas phase mole fraction, and i and j are the two gases. The value of the separation factor can be calculated from (Arri, et al., 1992)

$$\alpha_i = \frac{\left(G_{sL}/p_L\right)_i}{\left(G_{sL}/p_L\right)_j} \tag{12}$$

which is not a function of pressure. For a binary gas mixture, equation (11) can be rearranged to give the gas phase mole fraction of component i as

$$y_i = \left(1+\alpha_i \frac{1-x_i}{x_i}\right)^{-1} \tag{13}$$

which is the solid line in the figures. Again, the agreement between the results from the modified TOUGH2 code and the above equation is excellent.

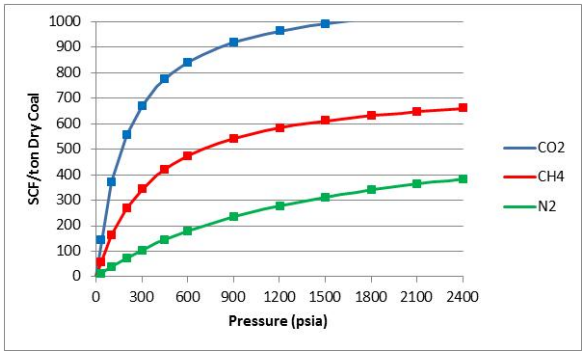

Figure 2. Pure gas isotherms

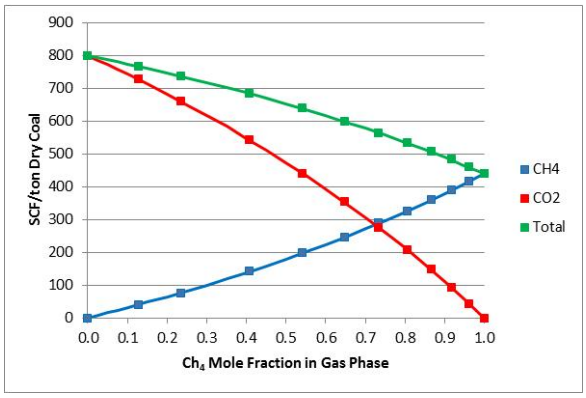

Figure 3. CH_4-CO_2 sorption at 500 psia

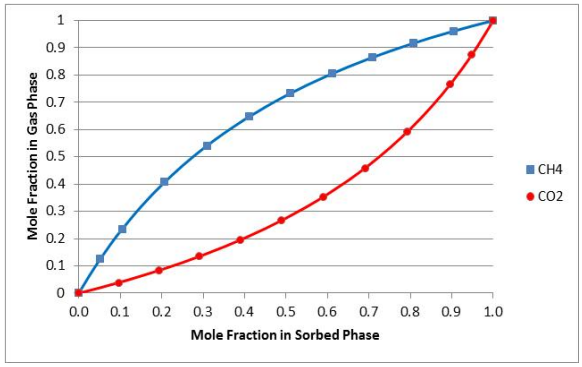

Figure 4. CH_4-CO_2 splits at 500 psia

Law et al. (2002) Problem

Law et al. (2002) have presented a comparison of ECBM simulators for two simplified problem sets. The first problem is a single-well CO_2 injection test, while the second problem is a five-spot CO_2-ECBM recovery process. The geometry and relative permeability functions are explicitly defined by Law et al. (2002); note that there is no capillary pressure. The first problem (single-well CO_2 injection) will be analyzed with the modified TOUGH2 code in this section.

The problem involves injecting pure CO_2 into a coal seam. Flow occurs in natural fractures that have a small natural porosity of 0.001 and a permeability of 3.65 millidarcies. The initial conditions of the reservoir are 7650 kPa, 45°C, and a gas saturation of 0.408 of pure CH_4. Coal matrix swelling/shrinkage is neglected. The problem chronology is an initial 15 days of CO_2 injection followed by a 45-day shut-in period, a 60-day production period, and a 62.5-day shut-in period. As mentioned above, no coal swelling or shrinking is included in the problem definition. This behavior is modeled by specifying the sorbed gas density as artificially high (10^{10} kg/m^3) in order to effectively disable the effect of sorbed gases on the porosity.

One of the parameters from the various codes that is compared in Law et al. (2002) is the initial gas-in-place for the CH_4. The values for the five codes range from 6.0315×10^7 to 6.1681×10^7 sm^3. The present code predicts 6.146×10^7 sm^3.

The predicted bottom-hole pressure as a function of time is shown in Figure 5. The general behavior compares well to the results presented by Law et al. (2002) except that the borehole pressure during CO_2 injection is slightly low. This difference may be due to the treatment of the borehole, which was treated explicitly in the present simulations, or due to differences in CO_2 properties.

Figure 6 gives the gas production rate results. The flow rates of CH_4 and CO_2 are initially in agreement with the results given in Law et al. (2002). At about 64 days, however, the gas production predicted by the present code drops significantly when a gridblock near the borehole changes from pure gas to two-phase conditions and the gas relative permeability decreases from 1.0 to 0.49. This decrease in gas production rate is not seen in the results presented by Law et al. (2002). Overall, the agreement is reasonable.

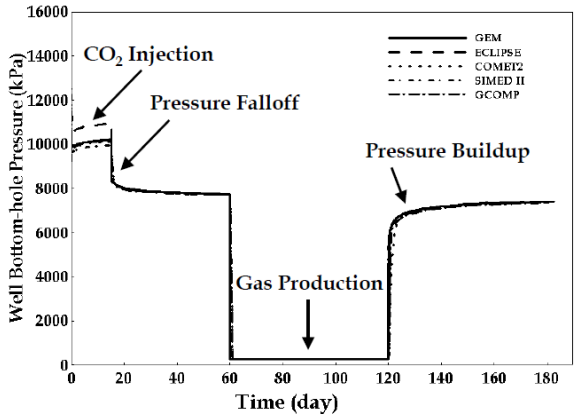

Figure 5a. Law et al. (2002) Borehole pressure results

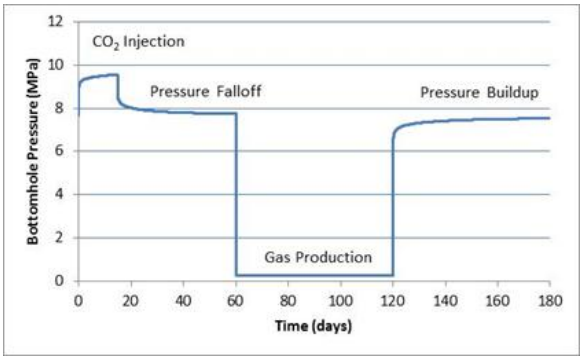

Figure 5b. Modified TOUGH2 borehole pressure results

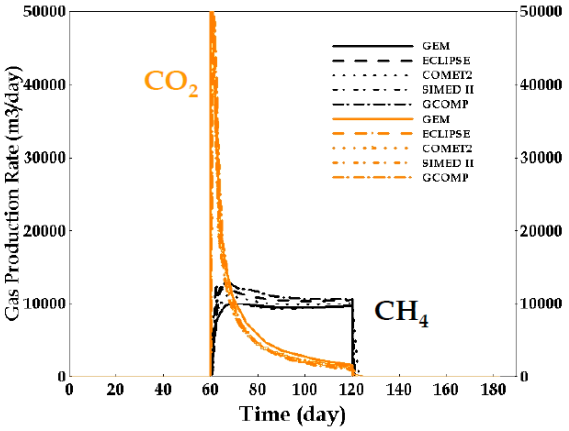

Figure 6a. Law et al. (2002) gas production rate results

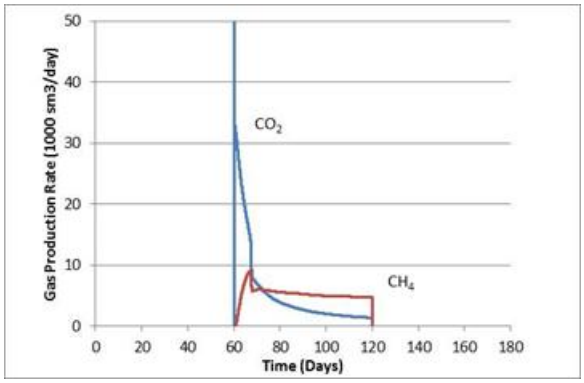

Figure 6b. Modified TOUGH2 gas production rate results

DGM

In this section, the DGM is compared to the experimental data of Evans et al. (1962, 1963) for a low-permeability (2.13×10^{-18} m^2) graphite. The experimental data are for Argon and Helium under combined advection and diffusion conditions. Webb (1998) showed that the DGM compares well to the data, while Fick's law does not.

For this case, Mason et al. (1967) performed an integration of the DGM assuming a linear variation for the mole fraction as above. Iteration is required to obtain the desired fluxes. The experimental data compare very well to the integrated equation. Explicit equations describing the various curves were not presented, so the curves were extracted from the original figures of Mason and Malinauskas (1983). Comparison of the present modified version of TOUGH2 to these curves is given in Figure 7. The predictions compare very well to the original curves. Because the curves assume a linear mole fraction variation in their derivation, the agreement is not expected to be perfect.

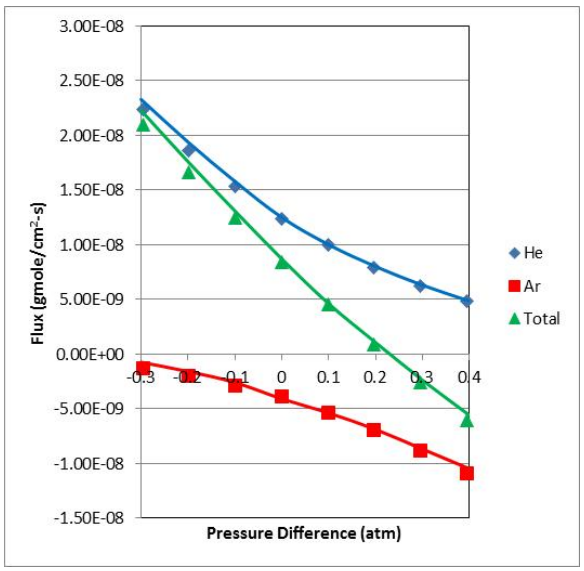

Figure 7. DGM data-model comparison for combined He-Ar advection and diffusion across low-permeability graphite

Diffusion Across a Capillary Fringe

Pruess et al. (1999) presented a sample problem involving TCE and PCE diffusion across a capillary fringe. The problem consists of TCE and PCE in the gas phase at the solubility limits above the water table, which diffuses through the capillary fringe into the water table below. The original TOUGH2 results in Pruess et al. (1999) show considerable differences between the separate and coupled diffusion models. The calculation has been redone with the modified code using the Fick's law model in TOUGH2 as well as the DGM.

Figures 8 and 9 show the results for the original Fick's law approach and for the DGM. The differences between the results are minimal. As discussed by Webb (1998) and Webb and Pruess (2003), differences between Fick's law and the DGM are minimal at higher permeabilities ($> 10^{-13}$ m^2) but they may increase to be orders of magnitude at lower values ($\sim 10^{-18}$ m^2). Therefore, the present problem is not a definitive test of the possible differences between Fick's law and the DGM.

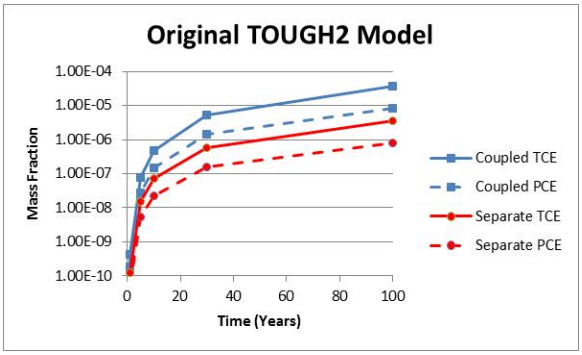

Figure 8. Separate and coupled diffusion across capillary fringe using Fick's law

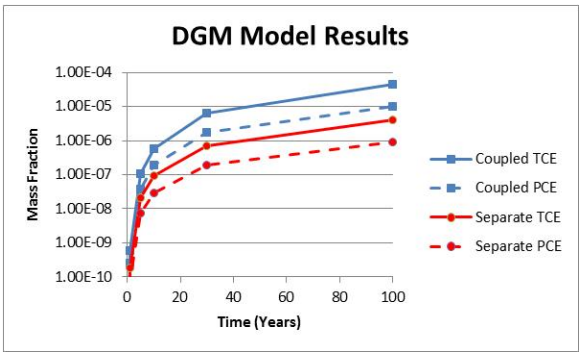

Figure 9. Separate and coupled diffusion across capillary fringe using DGM

SUMMARY AND DISCUSSION

ECBM code modifications have been successfully made to the TOUGH2-EOS7C code as demonstrated by the successful simulation of the Law et al. (2002) problem set 1. While the behavior is qualitatively similar to the behavior seen in Law et al. (2002), there are some quantitative differences, so the overall agreement is only reasonable. Further investigation of the cause for these differences is needed.

The present version of the code includes the porosity change from ECBM. Additional modifications should be made to change the permeability and connection flow area based on the change in porosity. Changes to the connection flow area could be simply related to the porosity change based on an assumed flow geometry.

Implementation of the DGM compares very well to existing gas-phase diffusion data. The use of the DGM may be limited because the computer

time increases significantly compared to the default Fick's law approach. For the Law et al. (2002) problem, the computer time increased by about a factor of three when the DGM model was used compared to the Fick's law approach. The simulation results for the DGM and Fick's law approach are not significantly different, because the permeability (3.65 millidarcies) is not that low. Improving the computational efficiency may be necessary before the DGM is used for large-scale problems.

ACKNOWLEDGMENT

This work was carried out through Lawrence Berkeley National Laboratory as part of the ZERT project, funded by the Assistant Secretary for Fossil Energy, Office of Sequestration, Hydrogen, and Clean Coal Fuels, National Energy Technology Laboratory, of the U.S. Department of Energy under Contract No. DE-AC02-05CH11231.

REFERENCES

Arri, L.E., D. Yee, W.D. Morgan, and M.W. Jeansonne, 1992, "Modeling Coalbed Methane Production With Binary Gas Sorption," SPE 24363, SPE Rocky Mountain Regional meeting, Casper, Wyoming, May 18-21, 1992.

Evans, R.B., III, G.M. Watson, and J. Truitt, 1962, "Interdiffusion of gases in a low permeability graphite at uniform pressure," *J. Appl. Phys*., 33:2682-2688.

Evans, R.B., III, G.M. Watson, and J. Truitt, 1963, "Interdiffusion of gases in a low permeability graphite. II. Influence of pressure gradients," *J. Appl. Phys*., 34:2020-2026.

Law, D. H.-S., L.G.H. van der Meer, and W.D. Gunter, 2002, "Numerical Simulator Comparison Study for Enhanced Coalbed Methane Recovert Processes, Part 1: Pure Carbon Dioxide Injection, SPE 75669, SPE Gas Technology Symposium, Calgary, Alberta, 30 April – 2 May 2002.

Mason, E.A., and A.P. Malinauskas, 1983, Gas transport in porous media: the dusty-gas model, Chem. Eng. Monograph 17, Elsevier, New York.

Mason, E.A., A.P. Malinauskas, and R.B. Evans, III, 1967, "Flow and Diffusion of Gases in Porous Media," *J. Chemical. Physics*, 46:3199-3216.

Oldenburg, C.M., S.W. Webb, K. Pruess, and G.J. Moridis, 2004a, "Mixing of Stably Stratified Gases in Subsurface Reservoirs: A Comparison of Diffusion Models," *Transport in Porous Media*, 54:323-334.

Oldenburg, C.M., G.J. Moridis, N. Spycher, and K. Pruess, 2004b, "EOS7C Version 1.0: TOUGH2 Module for Carbon Dioxide or Nitrogen in Natural Gas (Methane) Reservoirs," LBNL-56589, Lawrence Berkeley National Laboratory, Berkeley, CA.

Pruess, K., C.M. Oldenburg, and G. Moridis, 1999, "TOUGH2 User's Guide, Version 2.0," LBNL-43134, Lawrence Berkeley National Laboratory, Berkeley, CA.

Pruess, K., and S.W. Webb, 1999, "On Finite Difference Modeling of Diffusion of Phase-Partitioning Species under Multiphase Conditions," AGU Fall Meeting, Supplement to Eos, Transactions, AGU Volume 8, Number 46, pg. F385.

Thorstenson, D.D., and D.W. Pollock, 1989, "Gas transport in unsaturated zones: multi-component systems and the adequacy of Fick's laws," *Water Resour. Res*., 25:477-507.

Tsang, Y.W., and K. Pruess, 1990, "Further Modeling Studies of Gas Movement and Moisture Migration at Yucca Mountain, Nevada," LBL-29127, Lawrence Berkeley Laboratory, Berkeley, CA.

Webb, S.W., 1998, "Gas-Phase Diffusion in Porous Media – Evaluation of an Advective-Dispersive Formulation and the Dusty-Gas Model for Binary Mixtures," *J. Porous Media*, 1:187-199.

Webb, S.W., and K. Pruess, 2003, "The use of Fick's Law for modeling trace gas diffusion in porous media," *Transport in Porous Media*, 51:327-341.

Webb, S.W., 2011, "EOS7C-ECBM Version 1.0: Additions for Enhanced Coal Bed Methane Including the Dusty Gas Model," Canyon Ridge Consulting Report CRC2011-0002, December 6, 2011.

Zarrouk, S.J., and T.A. Moore, 2009, "Preliminary reservoir model of enhanced coalbed methane (ECBM) in a subbituminous coal seam, Huntly Coalfield, New Zealand. Int. J. of Coal Geology, 77:153-161.

MODELING CO_2-DRIVEN CEMENT ALTERATION AT WELL-CAPROCK INTERFACE

Frederic Wertz[a]*, Fabrizio Gherardi[a,b], Philippe Blanc[a], Anne-Gaëlle Bader[a], Antonin Fabbri[a,c]

[a] BRGM, 3 Avenue Guillemin, F-45060 Orléans, Cedex 2, France
[b] LE STUDIUM, Loire Valley Institute for Advanced Studies, Orléans & Tours, France
[c] DGCB, ENTPE, 3 Rue Maurice Audin, F- 69518 Vaulx-en-Velin Cedex, France
e-mail: f.wertz@brgm.fr

ABSTRACT

In this paper, we report on the development of a geochemical model for wellbore cement-caprock–reservoir interfaces. This model predicts the mechanisms of cement chemical alteration due to its interaction with acid brine after the injection of supercritical CO_2 within reservoir rock. Numerical outputs indicate that at the well-reservoir interface, the intrusion into the cement paste of acid brine accompanied by aqueous CO_2 transforms portlandite and CSH into calcite and hydrated Si-gel quasi-instantaneously, leading to a slight but moderate porosity decrease. Conversely, at the well-caprock interface, portlandite dissolves, and its released Ca^{2+} ions migrate towards the caprock, where they eventually combine with slowly diffusing aqueous CO_2 to form calcite until the porosity collapses at the interface. This can significantly affect the behavior of the storage reservoir sealing. Finally, we develop a time-space characterization of the system, enhancing the main chemical mechanisms, with a future export to a geomechanical model in mind.

INTRODUCTION

The long-term safety of CO_2 geological storage (CCS) depends on the stability of the reservoir and on a proper assessment of CO_2 leakage and fluid displacement. Particular attention must be paid to the injection wellbore as a human-made discontinuity of the geological medium, especially the caprock. In addition, the chemical and mechanical integrity of the well-reservoir-caprock cement sealing must be ensured for the entire lifetime of the CCS project.

CO_2 geological storage has been quite intensively investigated in the past few years, using experimental, analytical or numerical approaches. For example, within the SACROC unit in Texas, Carey et al. (2007) studied Portland cement cores of a 55-year-old oil well exposed to CO_2 flow for ~30 years. They found that, although the integrity and the structure of the cement survived, casing-cement and cement-shale interfaces were heavily carbonated, and even the caprock showed a disturbed zone called "shale-fragment-zone" (SFZ). These are evidence of high reactivity at the cement edges, where decalcification of the C-S-H phases occurs, calcite precipitates, and even amorphous silica may be mobilized into the SFZ.

In addition, Kutchko et al. (2007) conducted lab-experiments of well cement degradation by CO_2-rich brine under geological (P, T) conditions. They proposed a degradation mechanism for portlandite. Indeed CO_2-rich acid brine dissolves portlandite $Ca(OH)_2$ and precipitates calcite $CaCO_3$. The fully carbonated zone is eventually dissolved by the unbuffered brine (pH~2.9), leading to a very porous silica material. Huet et al. (2010) confirmed these mechanisms by a benchmarked model of class-H-cement in CO_2-saturated water (pH~3.7). However, they identified the need of a better porosity-diffusivity coupling law. Recently, Gherardi et al. (2012) modeled the long-term (1000-year) geochemical evolution of cement from an idealized abandoned well in the Paris Basin, accounting for mutual interactions with adjacent caprock and reservoir domain. Because of the involved timescale, crystallized phases were predominantly involved in their calculations.

The present work aims to establish the main degradation mechanisms at the very thin interface between well and caprock for short space and time scales. To this end, we performed numerical simulations to simulate the short-term degradation of a newly built class-G-cement injection well, by CO_2-acidified brine, at the well-reservoir and well-caprock interfaces. Indeed, we aim at modeling the upward propa-

gation of the CO_2-disturbed cement zone from the reservoir to the caprock interface.

The idea is to reproduce and scale up (on a 3D well geometry) the cement degradation processes observed by Jobard et al. (2012) in laboratory experiments. Indeed, batch reactions of cement-surrounded shales in CO_2 solution over 30 and 60 days showed a highly carbonated interface between cement and shales. Cement even cracks sometimes, due to the shale volume increase. Diffusion is the only transport process considered here.

We also conducted a sensitivity analysis related to the influence of this particular factor with respect to kinetics rates, since these two processes are competing to drive the cement degradation propagation. Mineral dissolution and precipitation, as well as pH propagation, are carefully checked in order to characterize the main cement-alteration mechanisms. Porosity evolution has been paid special attention, since it can be used as a state variable for a further mechanical study on well cement failure risk (Fabbri et al., 2009).

The present work begins with a description of the system (well-reservoir-caprock). Then, the modeling scenarios are presented, including the different hypotheses concerning the effective diffusion in the cement. Presented results support a vertical and lateral scheme for cement-degradation propagation, which we discuss in light of the undertaken sensitivity analysis.

GEOCHEMICAL BACKGROUND

In this paper, we consider a newly built CO_2 injection well that starts operation within a carbonated reservoir, capped by shales, similar to the Dogger and Callovo-Oxfordian formations of the Paris Basin (Rojas et al., 1989). According to previously reported work, the injected supercritical CO_2 will partially dissolve and acidify the brine. Before the well surroundings are totally dried up, CO_2-rich brine will have already reacted with hydrated cement minerals and modified the well-reservoir interface. This degradation scheme then propagates along the well-caprock interface. The present work reports some year-long 3D-centimeter-scale simulations that aim at parameterizing the chemical intensity and spatial propagation of the cement degradation, with respect to the cement diffusivity parameters—based on laboratory experiments undertaken by Jobard et al. (2012)—and illustrates some upscaling effects.

Solutions composition

The geochemical calculations are performed in the chemical system SiO_2-Al_2O_3-Fe_2O_3-FeO-MgO-CaO-K_2O-Na_2O-SrO-CO_2-SO_4-H_2O. It includes minerals phases, aqueous phases, and gases. Different initial conditions are retained, depending on the geochemical domains. The pore solution of the caprock is assumed to be in equilibrium with its constituting minerals (illite, quartz, calcite, montmorillonite, chamosite, dolomite, celestite), following the approach of Gaucher et al. (2009). Similarly, the Dogger Reservoir pore-solution composition has been generated by assuming it to be in equilibrium with illite, montmorillonite, kaolinite, quartz, calcite, dolomite, magnesite, according to mineralogical analyses provided by André et al., (2007).

Table 1. Water initial compositions before speciation

Basis species	Cement (mol/kg)	Caprock (mol/kg)	Reservoir (mol/kg)
pH	11	7	5.1
Ca^{2+}	0.27E-01	0.54E-01	0.10E+01
Mg^{2+}	0.57E-07	0.18E-01	0.10E-01
Na^{+}	0.40E+00	0.10E+00	0.38E-02
K^{+}	0.29E-01	0.80E-03	0.15E+00
Fe^{2+}	0.19E-07	0.90E-06	0.18E-01
H_4SiO_4(aq)	0.32E-04	0.19E-03	0.11E-03
Al^{3+}	0.36E-04	0.41E-06	0.29E-02
Cl^{-}	0.43E+00	0.24E+00	0.35E-08
HCO_3^{-}	0.35E-04	0.23E-03	0.23E+00
SO_4^{2-}	0.90E-02	0.45E-02	0.11E+01
Sr^{2+}	1.00E-10	0.14E-02	0.30E-05

The solution was then acidified with gaseous CO_2 at 180 bar pressure, but still buffered by carbonates. After an initial time period to reach geochemical equilibrium, the respective values of pH are 7 for the caprock and 5.1 for the initially CO_2-acidified reservoir solutions. The cement initial pore solution is eventually calculated by assuming the equilibrium with the minerals portlandite, CSH, katoite, ettringite,

C3FH6, hydrotalcite, and calcite, leading to an initial geochemical equilibrium with pH 11. The resulting solution compositions are reported in Table 1.

Cement Material

Class-G cement involves different mineral phases bearing various elements (Ca, Si, Al, S, Mg, Fe, C, Na, K). Its mineral composition is described by Marty et al. (2009).

Table 2. Cement mineral composition

Cement	Formula	% Vol
CSH1.6	$Ca_{1.6}SiO_{3.6}$:2.58H_2O	38.1
Portlandite	$Ca(OH)_2$	26.1
Ettringite	$Ca_6Al_2(SO_4)_3(OH)_{12}$:26$H_2O$	13.8
Katoite-Si	$Ca_3Al_2SiO_4(OH)_8$	10.5
C3FH6	$Ca_3Fe_2(OH)_{12}$	5.5
Hydrotalcite	$Mg_4Al_2O_7$:10H_2O	5.4
Calcite	$CaCO_3$	0.6

Reservoir and caprock assemblages

Similarly to Gherardi et al. (2012), the reservoir and caprock mineral compositions and proportions are based on the Paris Basin example: Dogger and Callovo-Oxfordian formations, with minerals given by Gaucher et al., (2009). Table 3 gives the mineral composition assumed in these simulations, before and after the CO_2 acidification stage.

Table 3. Cement mineral composition

Mineral	Acidified Dogger (%Vol)	Shales (% Vol)
Calcite	77.5%	14.0%
Dolomite	10.2%	11.0%
Illite-Mg	0.1%	42.3%
Quartz	-	24.0%
Mg-Montm-Na	5.8%	6.0%
Siderite	4.1%	-
Kaolinite	2.0%	-
Magnesite	0.3%	-
Pyrite	-	1.0%
Chamosite	-	1.0%
Celestite	-	0.7%

MODELING APPROACH

Geochemical and physical parameters

To simulate the interactions occurring at the well-reservoir-caprock interface, we developed a simplified conceptual model that assumes the absence of advective flow between the storage reservoir, the caprock, and the well-cement. Aqueous conditions are then assumed to predominate over the entire simulated period, together with transport of dissolved species by molecular diffusion. During the simulations, temperature and pressure were held constant at 75°C and 180 bar, according to the present-day reservoir conditions (André et al., 2007). Since the focus of our modeling exercise was to investigate the very-short-term geochemical behavior of the injection wellbore cement, maximum simulation times were fixed at 365 days, in order to extrapolate from the 30-day experiment undertaken by Jobard et al., (2012). Local equilibrium is based on the thermodynamic database "Thermoddem" (Blanc et al., 2012) developed at the BRGM. The interactions occurring at the reservoir-caprock-cement interface were simulated with the TOUGHREACT simulator (Xu et al., 2004). A kinetic law based on Transition State Theory (Lasaga, 1981) is implemented in the code. Table 4 summarizes different kinetic coefficients used in the simulations.

Table 4. Kinetic coefficients

k25 is the kinetic constant at 25°C, EA the activation energy, n the degree of the additional mechanism (H^+ or HCO_3^-), S the reactive surface of the material.

Mineral	k25 mol/m^2/s	EA kJ/mol	n	S m^2/g
Portlandite[1]	2.18E-08	74.9		0.154
acid mech	8.04E-04	74.9	0.6	
CSH 1.6[2,3]	1.6E-18			2.0
acid mech	5.94E-08		0.275	
Katoite[2,3]	1.6E-18			0.057
acid mech	5.94E-08		0.275	
Hydrotalcite[2,3]	1.6E-18			0.1
acid mech	5.94E-08		0.275	
Ettringite[3]	1.14E-12			0.098
Calcite[4]	1.55E-06	23.5		0.026
acid mech	5.0E-01	14.4	1	
carb mech	6.58E-03	56.1	1.982	
Magnesite[4]	4.47E-10	63		0.026
acid mech	4.37E-05	19	1	

[1] Gali et al. 2001, [2] Schweizer 1999, [3] Baur et al. 2004, [4] Palandri and Kharaka 2004

The porosity Φ is initially 28% in the cement, 20% in the reservoir, 14.4% in the caprock. The diffusion coefficient D is set to that in water for the HCO_3^- ion, whose mobility has been intensively investigated. In our case, we have retained

the value provided by Tamini et al. (1994), where D_{HCO3-} = 6.58×10^{-9} m^2/s at 75°C. A constant Deff=10^{-10} m^2 is assumed from the carbonation experiments reported in Fabbri et al. (2009), by considering $\Phi = \Phi_0$ and $\tau_{cement} = 0.05$. For caprock and reservoir zones, we have considered a faster diffusion process by imposing:

$\tau_{shales} = 10x\ \tau_{cement}$, and $\tau_{reservoir} = 1.6x\ \tau_{shales}$.

Grid and Geometry

A simplified 3D axisymmetric radial model (Figure 1) was designed. The Mesh is 2 m high (1 m caprock, 1 m reservoir) and 1 m wide. Cement occupies the space between R = 0.05 m and R = 0.1 m. The model comprises of 2752 (43×64) cells sized from $2\times2mm^2$ at the interface up to $50\times50mm^2$. This spatial discretization responds to the need for properly solving steep chemical gradients near the interfaces and ensuring an adequate numerical accuracy. Numerical stability has been achieved by reducing the time step down to 8.66 s. Simulation time is about 50 days on a 2.66 GHz CPU. Boundary fixed conditions, are located 0.9 m away in radius from the cement interface, 1 m up and 1 m down from the caprock-reservoir interface. Elsewhere, no-flux conditions were set.

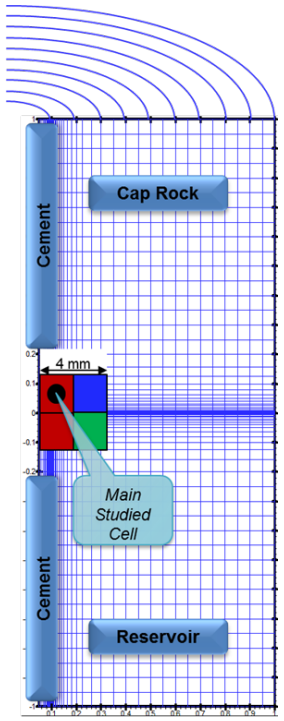

Figure 1. Geometry, Mesh and domains

RESULTS AND DISCUSSION

Identified alteration mechanisms

The first alteration mechanism was observed at the triple well-reservoir-caprock interface, related to cement acidification. Numerical outputs indicate that the pH of cement pore waters decreases with time as the CO_2-rich brines propagate from the reservoir and the caprock (Figure 2). In particular, portlandite, CSH and katoite dissolve following this order, with a decrease in pH from ~11 (near the cement material) to ~6. New phases precipitate in the cement and even at the interface with the caprock, where released ions have migrated. The final (meta)stable assemblage comprises essentially calcite, Si-Gel (hydrated silica), Al-Gel (boehmite), while the considered timescale (1 year) and kinetic rates prevented C3FH6 and ettringite from dissolving. Globally, the affected cement porosity decreases as the alteration proceeds, and is strongly dependent on the alteration stage and location.

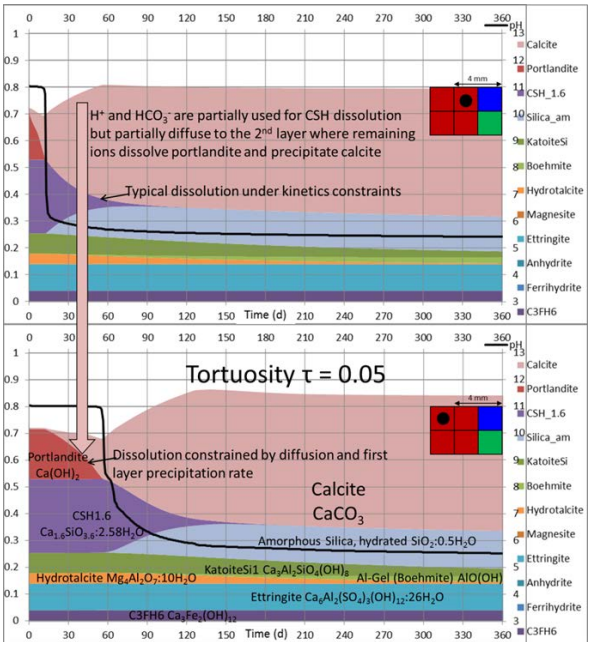

Figure 2. first and second cement layers mineral evolution over time at the interface

Concerning the Ca-bearing phases, we first notice a constant precipitation of calcite (Figure 2) due to portlandite dissolution. The controlling mechanism could be diffusion of carbonates ions. Indeed, all carbonates are trapped in the first cement numerical layer until

portlandite disappears, before calcite could precipitate in the second cement layer. This confirms that portlandite dissolution and calcite precipitation can occur in a very thin layer (less than 2 mm thickness), in spite of the ionic diffusion competition. Conversely, with respect to the Si-bearing phases, dissolution kinetics are quite slow, so that dissolving CSH does not entirely absorb the H^+ and HCO_3^- flux (by precipitating calcite). H^+ and HCO_3^- can then migrate until the second cement layer and interact with the portlandite there. Ionic mobility promotes calcite precipitation far from the location where portlandite and CSH are dissolving. Katoite (bearing Al) and hydrotalcite (bearing Mg) dissolution processes are even slower and contribute to the formation of an Al-gel (boehmite) and magnesite. Ettringite (bearing S) and C3FH6 (bearing Fe) do not dissolve during the considered timescale (1 year).

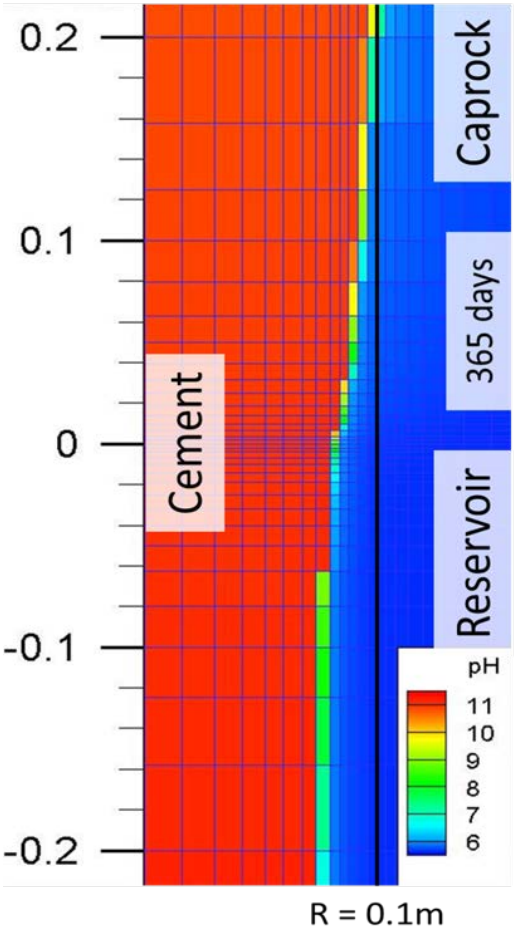

Figure 3. pH after 1 year

The second alteration mechanism concerns the upper well cement–caprock interface (Figure 3), where cement is not directly in contact with the acid brine. Ions must first diffuse vertically in the caprock. This leads to a similar degradation scheme for the cement but delayed in time. The main difference is in the creation of a porous zone (Figure 4) in the cement with a porosity-collapse counterpart in the caprock. Indeed, porosity decreases at the cement-caprock interface, starting from the triple well-reservoir-caprock interface and affecting the upper well-caprock interface by increasing the reaction time. This is due to the dissolution of portlandite and CSH while carbonates are not yet precipitating in the cement domain. Eventually, Ca^{2+} ions migrate sideways in the caprock, where they can precipitate as calcite. Experiments by Jobard et al. (2012) confirmed the highly calcified cement-shale interface.

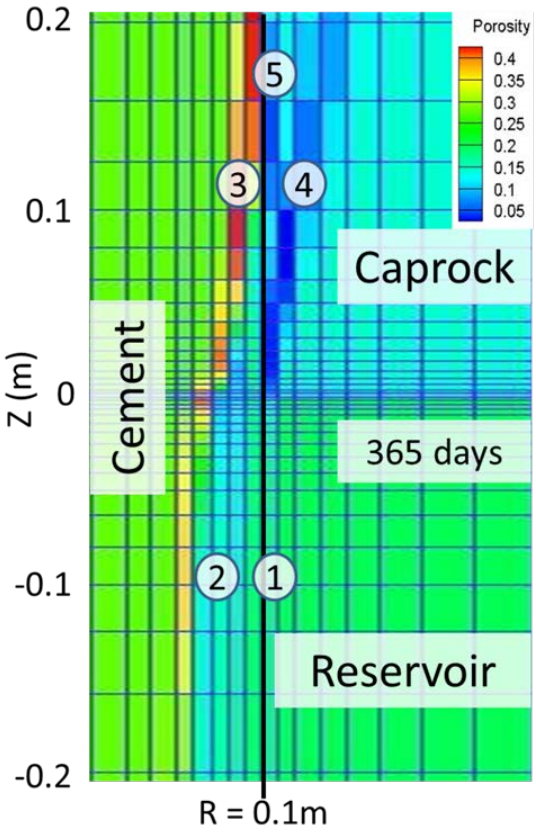

Figure 4. Porosity after 1 year

As displayed on Figure 4, the degradation and propagation mechanism follows different steps in different zones:

- Zone 1: At the well-reservoir interface, immediate dissolution of Portlandite leads to a very fast precipitation of a thin layer of calcite at the reservoir-side. This zone does not evolve further with time.
- Zone 2: Portlandite dissolution leads to a calcite precipitation front propagating radially towards the cement zone with time. This is followed by a slower rate of CSH decalcification over the entire zone, no longer buffered by portlandite. Decalcified CSH is replaced by an amorphous and hydrated silica phase. The final assemblage of silica gel and calcite implies an increase in the molar volume with respect to the portlandite + CSH association; thus, the final porosity is decreased. With time and helped by a higher diffusion rate, some Al-Gel (modeled here by an equivalent of boehmite) and magnesite can eventually precipitate near the interface.
- Zone 3: At the well-caprock interface, the neutral pH of the caprock first destabilizes portlandite. This leads to a substantial increase in porosity, while Ca^{2+} ions migrate in all directions. The thickness of this zone increases with the cement diffusion coefficient.
- Zone 4: Carbonates from the reservoir precipitate as calcite mainly on the caprock side, forming a thicker crust than at the well-reservoir interface. The thickness of this zone increases with the cement diffusion coefficient
- Zone 5: The slower dissolution of CSH delays the diffusion of silica that precipitates as an amorphous hydrated silica phase, even on the caprock side.

CONCLUSION

These simulations offer a clear representation of the different processes and mechanisms involved in cement degradation under well-geometry conditions. As in previous studies, geochemical simulation of the interface between the CO_2-injection well and the acidified reservoir shows cement mineral dissolution, accompanied by calcite precipitation in the cement porosity, as well as in the reservoir side of the interface. The degraded cement thickness reaches ~1 cm after 1 year. Portlandite is the first mineral to dissolve, with a high enough kinetic rate so that pH remains buffered. Then, CSH dissolves as soon as pH decreases, and eventually other cement minerals (katoite, hydrotalcite) also dissolve.

At the well-reservoir interface, the cement effective-diffusion parameter has an impact on the front propagation speed. Higher up, at the well-caprock interface, the degradation scheme is more complex. As the cement starts to leach due to neutral shale-water interactions before acid brines reach it, the main cement mineral portlandite start to dissolve before carbonates are supplied for calcite precipitation. Thus, the degraded zone is divided into highly porous cement and highly carbonated shales near the interface. In that region, the higher cement effective-diffusion parameter has a different impact: rather than accelerating the degradation propagation inside the well, it enlarges the cement porous zone and the carbonated shale zone.

The porosity changes in the interface model will be extracted from this study and applied to a geomechanical code that will help us deduce cement constraints and interpret interface geo-mechanical resilience.

ACKNOWLEDGMENT

This work has been supported by the French Research National Agency (ANR) through CO2 program (project INTERFACE, n° ANR-08-PCO2-006), as well as by the French Environment and Energy Management Agency (ADEME, project France Nord, Lot 7). We also would like to thank Eric Gaucher for is support and constructive review of the article during its elaboration.

REFERENCES

André, L., Audigane, P., Azaroual, M., Menjoz, A., 2007 Numerical modeling of fluid–rock chemical interactions at the supercritical CO2–liquid interface during CO2 injection into a carbonate reservoir, the Dogger aquifer (Paris Basin, France), Energy Conversion and Management 48, 1782-1797

Baur, I., Keller, P., Mavrocordatos, D., Wehrli, B., Johnson, C.A. 2004. Dissolution–precipitation behaviour of ettringite, mono-

sulfate, and calcium silicate hydrate. Cement and Concrete Research 34 (2), 341–348

Blanc, P., Lassin, A., Piantone, P., Azaroual, M., Jacquemet, N., Fabbri, A., Gaucher, E.C. 2012. Thermoddem: A geochemical database focused on low temperature water/rock interactions and waste materials. Applied Geochemistry, in press.

Carey J. W., Wigand M., Chipera S. J., Woldegabriel G., Pawar R., Lichtner P. C., Wehner S. C., Raines M. A., Guthrie Jr G. D. 2007. Analysis and performance of oil well cement with 30 years of CO2 exposure from the SACROC Unit, West Texas, USA. International Journal of Greenhouse Gas Control 1, 75 –85

Fabbri A., Corvisier J., Schubnel A., Brunet F., Goffé B., Rimmelé G., Barlet-Gouédard V. 2009. Effect of carbonation on the hydro-mechanical properties of Portland cements, Cement and Concrete Research 39, 1156–1163.

Fabbri A., Jacquemet N., Seyedi D.M. 2012 A chemo-mechanical model of oilwell cement carbonation under CO2 geological storage conditions, Cement and Concrete Research 42, 8-19

Galí S., Ayora C., Alfonso P., Tauler E., Labrador M. 2001. Kinetics of dolomite–portlandite reaction: Application to portland cement concrete. Cement and Concrete Research, 31 (6), 933-939

Gaucher, E.C., Tournassat, C., Pearson, F.J., Blanc, P., Crouzet, C., Lerouge, C., Altmann, S. 2009. A robust model for pore-water chemistry of clayrock. Geochemica et Cosmochimica Acta 73, 6470-6487.

Gherardi F., Audigane P., Gaucher E.C. 2012. Predicting long-term geochemical alteration of wellbore cement in a generic geological CO2 confinement site: Tackling a difficult reactive transport modeling challenge. Journal of Hydrology 420–421, 340–359

Huet B. M., Prevost J. H., Scherer G.W. 2010. Quantitative reactive transport modeling of Portland cement in CO2-saturated water, International Journal of Greenhouse Gas Control 4, 561–574

Jobard E., Sterpenich, J., Pironon J., Corvisier J., Randi A. 2012: Experimental modelling of the caprock/cement interface behaviour at high temperature and in presence of high pressure of CO2: The "Sandwich" experiment. To be submitted at the International Journal of Greenhouse Gas Control

Kutchko B.G., Strazisar B.R., Dzombak D.A., Lowry G.W., Thaulow N. 2007. Degradation of Well Cement by CO2 under Geologic Sequestration Conditions. Environmental Science and Technology 41, 4787-4792

Lasaga, A.C. 1981. Rate laws in chemical reactions. In: Lasaga, A.C., Kirkpatrick, R.J., (Eds.), Kinetics of Geochemical Processes. Reviews in Mineralogy 8, 135–169

Palandri J.L. and Kharaka Y.K. 2004. A compilation of rate parameters of water-mineral interaction kinetics for application to geochemical modelling. U.S. Geological Survey Report 2004-1068

Rojas, J., Giot, D., Le Nindre, Y.M., Criaud, A., Fouillac, C., Brach, M., Menjoz, A., Martin, J.-C., Lambert, M., 1989. Caractérisation et modélisation du réservoir géothermique du Dogger, Bassin Parisien, France. Rapport final CCE, EN 3G-0046-F(CD), BRGM R 30 IRG SGN 89.

Schweizer Ch. R. 1999. Calciumsilikathydrat-Mineralien. Lösungskinetik und ihr Einfluss auf das Auswaschverhalten von Substanzen aus einer Ablagerung mit Rückständen aus Müllverbrennungsanlagen. PhD thesis, dipl. Chem. Universität Basel, Zürich und Dübendorf

Tamini A., Rinker E.B., Sandall O.C., 1994. Diffusion Coefficients for Hydrogen Sulfide, Carbon Dioxide, and Nitrous Oxide in Water over the Temperature Range 293-368 K. Journal of Chemical Engineering Data 39, 330-332

Xu H., Sonnenthal E. L., Spycher N., Pruess K. 2004. TOUGHREACT user's guide: a simulation program for nonisothermal multiphase reactive geochemical transport in variably saturated geologic media, Lawrence Berkeley National Laboratory, Berkeley, California, Report LBNL-55460.

EXPANSION AND MIGRATION OF GASEOUS AND DISSOLVED CO_2 IN A SITE SPECIFIC SHALLOW AQUIFER

Carla E. Wiegers, Dirk Schäfer, Ralf Köber, and Andreas Dahmke

Christian-Albrechts-University of Kiel
Ludewig-Meyn-Str. 10
24108 Kiel, Germany
e-mail: cw@gpi.uni-kiel.de

ABSTRACT

TOUGHREACT EOS2 was used to quantify the influence of aquifer parameters (e.g., formation pressure, permeability, and effective porosity), the CO_2 leakage rate, the groundwater flow velocity, and the aquifer topography on the extent and migration of CO_2 gas-phase plumes in shallow aquifers. Aquifer pressure and leakage rate are the parameters with greatest impact on the extent of the gas-phase plume. Groundwater flow stretches the gas phase plume in groundwater flow direction and influences the dissolution of CO_2 in the water. The dip of the aquifer controls the migration direction of the gaseous CO_2 along the steepest gradient at the top of the aquifer.

Site-specific impact scenarios show that the gaseous CO_2 migrates preferentially into the highest anticlinal structure at the site. The total impact area due to CO_2 leakage is the combination of the width of the gas-phase body perpendicular to the groundwater flow direction and the transport length of the dissolved CO_2.

Using field site data, we have developed a site-specific scenario simulation to simulate CO_2 leakage impact scenarios and to develop a database for site-specific risk-assessment methods using numerical simulations.

INTRODUCTION

One possibility for reducing the anthropogenic emissions of CO_2 into the atmosphere is carbon capture and storage (CCS). Using this method, however, there is the risk that CO_2 could leak into the subsurface and intrude into freshwater aquifers (Celina et al., 2009). If the CO_2 enters freshwater aquifers, it can reduce groundwater quality, due to the dissolution of minerals and the release of inorganic components like lead or arsenic (Wang and Jaffe, 2004; Zheng et al., 2009; Fahrner et al., 2012). Therefore governmental organizations like the European Union (EU) and the U.S. Environmental Protection Agency (EPA) have proposed regulations for the geological storage of CO_2 (EU Directive, 2009, EPA, 2010), including impact assessment and monitoring for shallow freshwater aquifers. The processes taking place during CO_2 leakage into a shallow aquifer can be identified in laboratory or pilot experiments. Such experiments also demonstrate which geochemical parameters can be used to detect CO_2 leakage and which detection methods are effective (Peter et al., 2012; Oldenburg et al., 2011; Fahrner et al., 2012). These experiments should not be performed at a CCS site, in order to prevent changes to the natural baseline. Onsite scaling additionally would require a site-specific monitoring strategy and risk assessment, but experiments on this scale are extensive and not feasible.

Given these site or field restrictions, numerical scenario simulations are particularly useful in developing suitable and cost-efficient risk assessments or monitoring strategies. They can be used to calculate many impact scenarios and prognosticate the development of CO_2 migration at potential leakage scenarios at large scales and over long time scales.

We expect that the migration of leaking CO_2 is influenced by the leakage geometry (point, line, or diffuse leakage), the leakage rate, hydrogeological parameters, groundwater flow, and geological structures such as aquifer topography. Large-scale numerical simulations are required to investigate the potential spreading of CO_2 with unknown leakage positions at the site-scale.

The migration of gaseous CO_2 has already been part of quantitative scenario simulations of deep reservoir conditions (Bauer et al., 2012; Carroll et al., 2009; Celina and Nordbotten, 2009; Kühn et al., 2012; Oldenburg and Lewicki, 2006; Oldenburg et al., 2010). For protected, shallow aquifers, only a few scenarios have been simulated (e.g., Esposito and Benson, 2012; Carroll et al., 2009; Celina and Nordbotten, 2009), and most of them have not been performed for specific site conditions.

The first aim of this work is to quantify the impact of various potentially influential factors (leakage rate, initial aquifer pressure, water temperature, permeability, effective porosity, and the van Genuchten parameters *m* and alpha) on the spreading of a CO_2 gas-phase plume. The second aim is to investigate the spreading of a gas phase below the top of a confined aquifer and the evolution of a dissolved CO_2 plume at site scale. These site-specific simulations of worst-case leakage are steps toward a database for developing a suitable and convenient CO_2-sequestration monitoring concept, as well as a basis for risk assessment.

METHODS

The modeling code TOUGHREACT EOS 2 (Xu et al., 2004) was used to evaluate the migration of gaseous and dissolved CO_2 after a possible CO_2 leakage. A radially symmetric sensitivity analysis was conducted to quantify the influence of aquifer and hydraulic parameters on the extent of a CO_2 gas-phase body after CO_2 leakage within a shallow groundwater aquifer. To quantify the impact of groundwater flow velocity and the dip of the top of the aquifer, we ran different scenarios in a simplified 3D simulation, using data from a real field site with real topography, Groundwater flow conditions were also developed to simulate impact scenarios for this field site.

Geological Settings

3D virtual shallow aquifer scenarios with data from the joint research project CLEAN were used to perform site-specific numerical simulations, employing realistic geological data on groundwater flow velocity and aquifer topography. The extent of the chosen area is nearly 14 km^2, with thickness varying between 30 m and 50 m. The geological structural model has four geological layers of quaternary sediments (Fig.1).

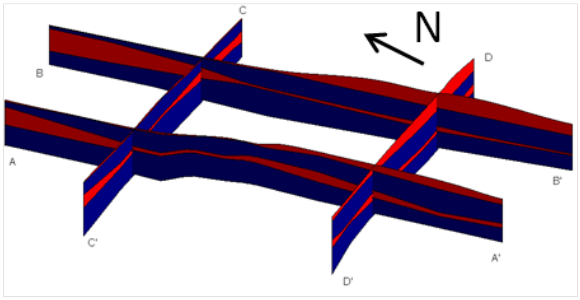

Figure 1. Geological structure model of the CLEAN site (Schäfer et al. in press). Blue: sandy aquifers, red: impermeable till layer

The base of this structural model is a tertiary impermeable clay layer. The lowest layer is a sandy aquifer from the Elster and Saale glacier (L4). The overlaying aquitard is a base moraine from the Saale 1 glacier and defined as a low-permeable till (L3). The till layer is overlain by another aquifer with sandy material. These deposits are from the Saale and Weichsel glaciers (L2). At the top of this aquifer system is yet another till layer, the base moraine of which comes from the Saale glacial and limnic Holocene deposits. This layer is defined as an aquitard (L1)—a detailed description can be found in Kühn (2012).

Conceptual Model

For the 3D multiphase flow scenario simulation, only layer L4 was considered. The interpolated topography for the top and bottom of this aquifer are implemented as input data from the site sampling. Because of the till sediments in layer L3 and the clay deposits at the model base, the top and the bottom of layer L4 are defined as impermeable, with the thickness of layer L4 varying between 5 m and 20 m. The sandy aquifer in the multiphase flow model is simplified as a homogeneous aquifer with a horizontal permeability of $4.2\times10^{-11}m^2$; the permeability in the z-direction is $4.2\times10^{-12}m^2$. The effective porosity is set to n_e= 20% approximated from literature data for the sampled sediment. Relative permeability and capillary pressure are described as a function of saturation using the van Genuchten - Mualem model (van Genuchten, 1980, Mualem, 1976). The parameters for these functions are

approximated from literature from similar sandy sediments (Esposito and Benson, 2011).

Table 1. Assumed parameter for capillary pressure and relative permeability

Capillary Pressure (P_c)	van Genuchten
Van Genuchten parameter	$\lambda = 0.457$
Residual liquid saturation	$S_{lr} = 0.10$
Van Genuchten parameter	$\alpha = 1.48E\text{-}04\ Pa^{-1}$
Max. Pressure	$P_{max} = 5E5$ Pa
Max. liquid saturation	$S_{ls} = 1$
Relative Permeability (k_r)	van Genuchten
Residual liquid saturation	$S_{lr} = 0.15$
Residual gas saturation	$S_{gr} = 0.05$

We implemented a point source as a CO_2 source, which simulates a gas-migration pathway along a borehole into the shallow groundwater (Nordbotton, 2009). Because there has been no observed CO_2 leakage from geological storage sites, assessing a possible leakage rate is not possible. Therefore, we used a range of leakage rates from natural analogues to define leakage rates for our scenarios. Leakage rates at natural analogues have a wide range, 1×10^{-8}kg/s up to 1×10^{-1}kg/s.

Numerical Model Setup

Three different types of 3D multiphase flow simulations have been performed with TOUGH 2 ECO2 to evaluate the expansion of CO_2 gas-phase bodies below the impermeable aquifer top. To evaluate the influence of various geological parameters—permeability (K), effective porosity (n_e), initial aquifer pressure (P), aquifer temperature (T) (aquifer pressure and temperature are defined by the depth of the geological formation), the leakage rate (L), and the van Genuchten parameters alpha and P_{max}—we used a radial symmetrical model setup. Constant CO_2 leakage is established in the center of the cylindrical model domain at the bottom of the aquifer. The thickness of the aquifer is 10 m and the radius is 500 m. For discretization, 1 m×1 m cells are chosen. A finer discretization of 0.5 m×0.5 m is chosen over a width of 2 m within the model domain, where the CO_2 migrates upwards from the leakage to the top of the aquifer, and 2 m below the top of the aquifer, where the CO_2 spreads radially. The parameters for the sensitivity analysis are approximate, due to the uncertainty of site parameters. The applied parameters can be found in Table 2. To quantify the results and to choose parameters for the 3D models, we define a base case (BC), as described in Table 2.

Within a simplified 3D simulation with a horizontal planar aquifer geometry, we varied leakage rates and groundwater flow velocity to evaluate their influence on the migration and extent of the CO_2 gas-phase body and the dissolved CO_2. For the model domain, we defined an area 100 m × 100 m. The thickness of the aquifer is only 2 m, because the area of interest for the migration and extension of CO_2 gas phase bodies is that region directly below the top of the aquifer. From some pretests, we learned that the thickness of the gaseous CO_2 body would not be more than 0.5 m. The horizontal discretization is 1 m × 1 m in the inner zone, 15 m around the leakage location, and 1.5 m × 1.5 m outside that zone. Three grid layers are used for the aquifer depth. At the bottom of the aquifer model domain, we set a layer of 1 m thickness; at the top of the model domain, we set two layers with 0.5 m thickness. The applied input parameters are the same as used in the Base Case scenario from the cylindrical simulations (Table 1 and Table 2).

Table 2. Parameters used for the scenario simulations, m and alpha are van Genuchten parameters. The base case is used to compare the effects of the parameters and for the site scenarios (except for the leakage rate)

Variables	Base Case	Sensitivity analysis
Leakage rate [kg/s]	$1*10^{-4}$	$1*10^{-2}$-$1*10^{-9}$
Initial aquifer pressure [m]	10	0 – 500
Temperature [C°]	11	11 -30
Permeability [m^2]	$4.2*10^{-11}$	$4.2*10^{-9}$ $4.2*10^{-13}$
Eff. Porosity [%]	20	10 -40
m[-]	0.457	0.2 – 0.8
Alpha [m^{-1}]	$5.1*10^{-4}$	$2*10^{-4}$-$8*10^{-4}$

Scenario leakage rates are 1.16×10^{-5}kg/s; groundwater pore velocities are 0.01 m/d, 0.05 m/d, and 0.07 m/d, respectively. In a second simulation series with a pore velocity of 0 m/d, we varied the dip of the aquifer, using dip angles of 1°, 2°, and 3°. Water can leave the model domain to all sides of the model using a constant pressure boundary condition.

For the 3D field-site-scenario simulation, we used the relief data from the CLEAN site structural model for aquifer top and the bottom (Fig. 2). For the aquifer thickness, we used a discretization of five layers. The thickness of these layers varied due to the variation in the aquifer thickness. In the X- and Y- directions, 100 and 50 cells are used, respectively. To evaluate the influence of the groundwater flow velocity, we set pore velocities to 0 m/d, 0.1 m/d, and 0.6 m, respectively, which are approximated to the measured groundwater flow velocities at the CLEAN site.

The hydraulic parameters are the same as in the scenarios described before (Tables 1 and 2). A leakage rate of 1.16×10^{-2}kg/s is chosen. The assumed positions of the leakages are shown in Figure 7.

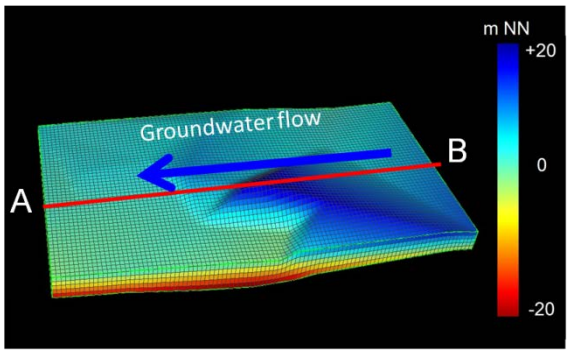

Figure 2. Topography of the layer 4 of the CLEAN site model domain (cf. fig. 1).

RESULTS

Radial symmetric simulations

If CO_2 leaks into the aquifer, it migrates upwards, buoyancy driven, and spreads radially below the impermeable top of the aquifer. The gas phase created is only a thin layer. The radius of the gas-phase body ranges from 10 m to 450 m after a one-year simulation time, depending mainly on the leakage rate and therefore on the volume of inflowing CO_2. The variation in the initial aquifer pressure causes a radius ranging from 8 to 51 m. This is an effect of the gaseous CO_2 solution in the groundwater. Increasing the pressure increases the solubility as well (Duan, 2006). The second reason is the compression of the gas volume, which can be described by the ideal gas law. The pressure contributes only 3% to the decrease in the gas-phase body.

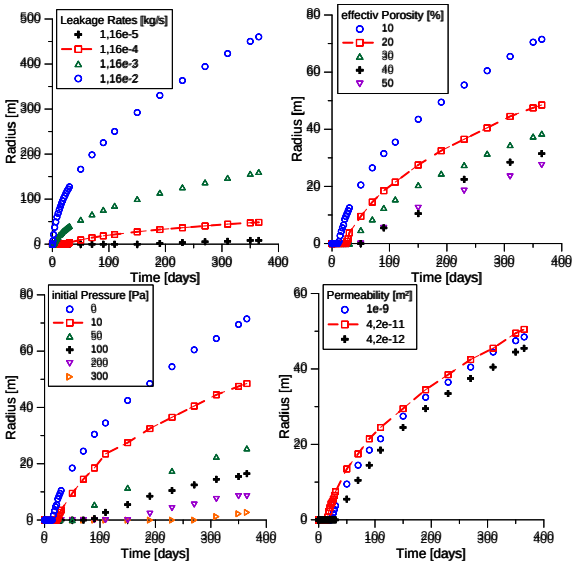

Figure 3. Development of the radius of the gas-phase body under the top of the aquifer over time, due to variation in aquifer parameters.

The variation in porosity results in the radius ranging from 31 m to 48 m. If the pore volume increases, more gas can be stored per volume unit in the aquifer and therefore the extension of the gaseous CO_2 under the impermeable layer becomes smaller. Note that in our simulations, the changes in permeability have no significant effect on the extension of the gas-phase body (Fig.3).

Influence of groundwater flow velocity and aquifer dip

Simplified 3D scenarios considering groundwater flow showed the distinct influence of groundwater flow on the shape of the gas-phase body. Whereas the CO_2 gas-phase body is nearly circular at low groundwater flow velocities, the CO_2 gas-phase body stretches in the flow direction under heavy groundwater flow velocities, and consequently the area of the

gas-phase body decreases (fig 4). In our scenarios, the area of the gas-phase body, with a groundwater flow velocity of 0.01 m/d, after a one-year simulation time, is 772 m², with a flow velocity of 0.07 m/d, it is 15m^2 (Fig. 4).

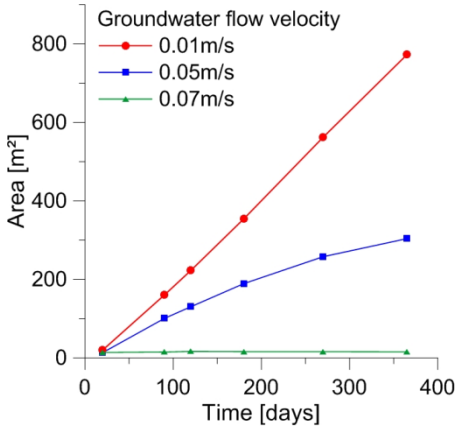

Figure 4. Development of the area of the CO_2 gas-phase body below the impermeable layer of the aquifer top.

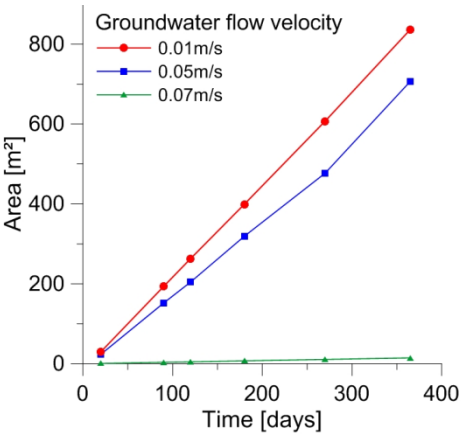

Figure 5. Development of the area of the dissolved CO_2 body below the impermeable layer of the aquifer top.

The gas-phase body gets smaller, because more groundwater saturated with CO_2 is transported downstream with increasing groundwater flow velocity, uncharged water flows from upstream to the phase body, and more gaseous CO_2 dissolves (fig. 5).

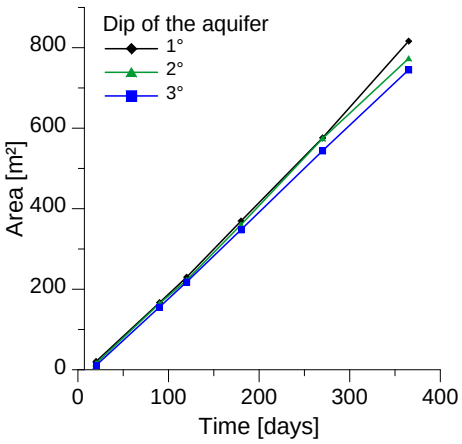

Figure 6. Development of the area of the CO_2 gas-phase body due to the angle of the aquifer dip.

In an aquifer with a dip, the gaseous CO_2 migrates upwards under the top of the aquifer along the steepest gradient. With increasing dip, the CO_2 migrates faster, and the gas-phase body is stretched in the dip direction. With increasing dip, the stretching effect increases. Due to this stretching, the transverse width of the gas-phase body decreases. The area of the gas-phase body does not change significantly (Fig. 6); the difference in area is only 40 m².

3D site scale simulations with a natural relief of the upper aquifer boundary

When the CO_2 enters the model aquifer, it migrates upwards (Fig. 7), and the gas-phase body in the water column is tilted in the flow direction (due to groundwater flow) before it reaches the top of the aquifer. After reaching the impermeable layer, the CO_2 migrates along the steepest gradient of the aquifer topography accumulates in the anticlinal structures (Fig.7).

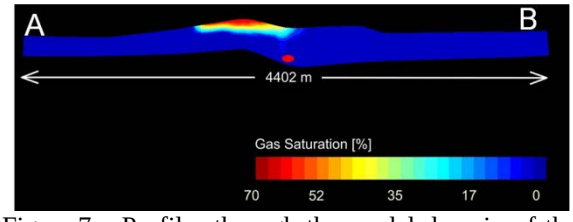

Figure 7. Profiles through the model domain of the site scenario (see Fig. 2). At the bottom of the aquifer is a CO_2 leakage (red point).

After a one-year simulation time, a groundwater flow velocity of 0.1 m/d, and a leakage rate of $1{,}16\times10^{-2}$kg/s below the impermeable top of the

aquifer, the gas-phase body has an area of 3000 m² (Fig. 8). The extent of the gas-phase body is controlled largely by the topography of the aquifer top, and to a lesser extent by the groundwater flow velocity. The groundwater flow influences the dissolution of the CO_2 into the groundwater (see 3D simplified simulations) and the transport of the dissolved CO_2 (Fig. 9).

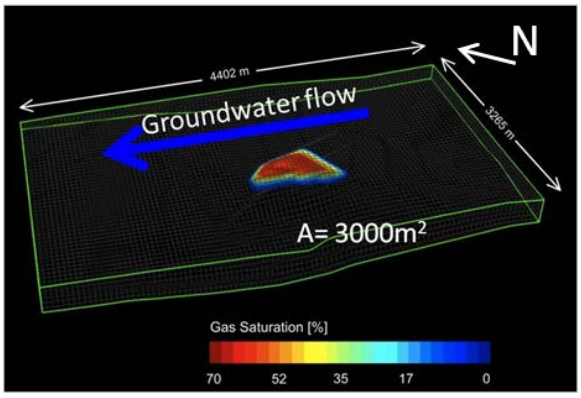

Figure 8. Extent of gaseous CO_2 at the site specific scenario.

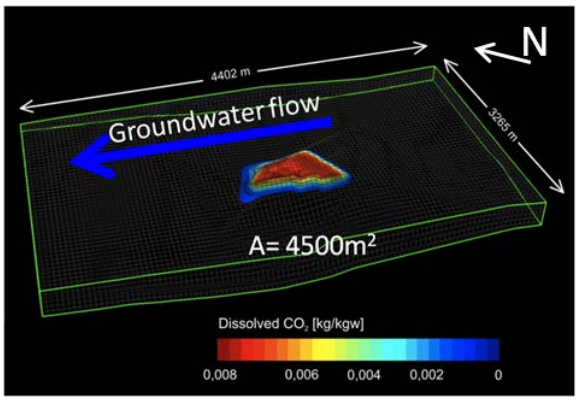

Figure 9. Extent of dissolved CO_2 at the site specific scenario.

The area influenced by dissolved CO_2 is 4500 m². Therefore, the total affected area as a result of CO_2 leakage in an aquifer is controlled by the width of the gas-phase body diagonally to the groundwater flow direction, and the length of the transport of the dissolved CO_2 along the groundwater flow direction.

Figure 10 shows the position of four arbitrarily chosen leakage positions (left) and the results after 10 years simulation time for the saturation of gaseous CO_2 (right). We can see that the gaseous CO_2 migrates from the different leakage positions by following the relief of the aquifer. A comparison between the pathway of the CO_2 migration and the topography of the aquifer top (Fig. 2 and Fig. 6) shows that the gaseous CO_2 migrates along the steepest gradient in the aquifer topography. The main migration direction for leakage A is to the northwest, for leakage B to the north, for leakage C to the northwest, and for leakage D first to the west, into the anticlinal structure and in the anticlinal structure.

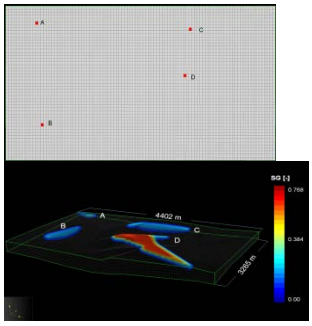

Figure 10. Position of four arbitrarily chosen leakage position (left). Extent of the CO_2 gas phase bodies after 10 years leakage time.

The differences in the extent of gas-phase body leakage depend on the different depths of the aquifer locations and (therefore) on the solubility of the CO_2. This effect can also be seen in the maximum gas saturations. At leakage scenarios A, B, and C, we see the maximum gas saturation of 30%, and in leakage scenario D, we see the maximum gas saturation of 80%. These values result from the accumulation in the fold structure. We showed, in the radial simulations, that the extent of the gas-phase body decreases due to increasing aquifer pressure. In this simulation, the CO_2 first fills the anticlinal structure in the relief, before it migrates in a horizontal direction. The second reason for the higher CO_2 gas saturation of leakage D is the minor dissolution of the gas phase into the aquifer.

CONCLUSION

The simulation scenarios demonstrate that the most important parameters for the extent of the gas-phase body are the leakage rate, the effective porosity, and the hydrostatic pressure of the target aquifer. The volume of the gas-phase body and the gas saturation depend on the pressure and therefore on the aquifer depth, and on

the groundwater velocity, which influences the dissolution of gaseous CO_2 in water as well.
The topography of the aquifer top defines the migration pathway of the gaseous CO_2 along the steepest gradient into anticlinal structures, where the gas accumulates. Heterogeneous permeability distributions may have an influence similar to topography, and can control the migration pathway, but this has not been simulated.

The gas-phase-body shape is controlled by aquifer topography and groundwater flow. Because the gas-phase body is the source of the dissolved CO_2, its width perpendicular to the groundwater flow defines the width of the impact area, while the length of the impact is determined by the pore velocity of groundwater flow. Hence, the area where geochemical reactions are expected is a combination of the extent of the gas-phase body and the extent of the dissolved CO_2.

In a worst-case leakage accident, in which the CO_2 has already leaked into a protected potable aquifer, impact scenario simulations can be used to develop high-resolution monitoring methods at the impacted area. Furthermore, the impact scenarios can be used for the conceptual design of remediation strategies.

The simulations allow some initial conclusions regarding risk assessment at the CLEAN site: For the investigated aquifer, the highest risk for an impact due to a CO_2 leakage is in the vicinity of the anticlinal structure. Hence, this area should be monitored more intensively. A possible remediation measure, e.g., that proposed by Esposito and Benson (2012), could be installed at the highest point of the anticlinal structure. Similar simulations should be performed for deeper potable aquifers.

In general, sensitivity analyses for the leakage rates and locations should be done as part of site-specific scenarios. If there is no obvious leakage pathway due to geological structures, like faults, or anthropogenic pathways, like bore holes (Nordbotten, 2009), the probability of a CO_2 leakage location would be the same for the entire model domain. For risk assessment, numerous scenarios of a site with different leakage locations and rates should be simulated.

Combining the results of the numerous leakage scenarios shows the areas with the highest probability for gas-phase-body accumulation. Accounting for the transport of dissolved CO_2 would indicate the area of highest risk for CO_2 leakage in the target aquifer.

Further work needs to be done on site-specific numerical simulations to transfer the results to real field sites, such as:

- General research geared toward evaluating the influence of hydraulic heterogeneities on gas-phase-body migration.
- Investigation into heterogeneities at large field sites.
- The influence of geochemical reactions on the migration behavior of gaseous CO_2: the coupling of geochemical reactions and multiphase flow in a site-scale simulation.
- Investigation of how to handle geochemical heterogeneities at large scales.

ACKNOWLEDGMENT

A part of this work was developed in a joint research project that was part of the geoscientific research and development program "GEOTECHNOLOGIEN," funded by the German Federal Ministry for Education and Research (BMBF).

REFERENCES

Bauer, S.; H. Class, M. Ebert, V.Feeser, H. Götze, A. Holzheid, O. Kolditz, S. Rosenbaum, W. Rabbel, D. Schäfer, A. Dahmke Modeling, parameterization and evaluation of monitoring methods for CO_2 storage in deep saline formations: the CO_2-MoPa project. Environ Earth Sci. Published online 16 May 2012.

Carroll, S., Y. Hao, R. Aines Transport and detection of carbon dioxide in dilute aquifers, Energy Procedia, 1, 2111-2118, 2009.

Celina, M.A., J.M. Nordbotten, S. Bachu, M. Dobossy and B. Court, Risk of Leakage versus Depth of Injection in Geological Storage, Energy Procedia 1, 2573-2580, 2009.

Celina, M.A., J.M. Nordbotten, Practical Modeling Approaches for Geological Storage of Carbon Dioxide, Groundwater 47(5), 627-638, 2009.

Duan, Z., R. Sun, C. Zhu, I-M. Chou, An improved model for the calculation of CO2 solubility in aqueous solutions containing Na^+, K^+, Ca^{2+}, Mg^{2+}, Cl^-, and SO_4^{2-}. Marine Chemistry, 98, 131-139, 2006.

Esposito, A.; S.M. Benson Evaluation and development of options for remediation of CO_2 leakage into groundwater aquifers from geologic carbon storage. International Journal of Greenhouse Gas Control 7, 62-73, 2012.

Environmental Protection Agency, 2010. Federal requirements under the underground injection control (UIC) program for carbon dioxide (CO_2) geo- logic sequestration (GS) wells. Federal Register 75 (December 10 (237)), 77230:77303.

EU Directive, 2009/31/EC, OJ L 140/114, 5.6.2009. On the geological storage of carbon dioxide and amending Council Directive 85/337/EEC, European Parliament and Council Directives 2000/60/EC, 2001/80/EC, 2004/35/EC, 2006/12/EC, 2008/1/EC and Regulation (EC) No. 1013/200.

Fahrner, S., D. Schäfer, F. Dethlefsen, A. Dahmke, Reactive modeling of CO_2 intrusion into freshwater aquifers: current requirements, approaches and limitations to account from temperature and pressure effects, Environ Earth Sci, DOI:10.1007/s12665-012-1673-4, Online 2012

Kühn, M., M. Tesmer, P. Pilz. R. Mayer, K. Reinicke, A. Förster, O. Kolditz, D. Schäfer, CLEAN Patners CLEAN: projekt overvew on CO_2 large-scale enhanced gas recovery in the Altmark natural gas field (Germany) Environ Earth Sci, Published online 29 June 2012.

Mualem, Y., A new model for predicting the hydraulic conductivity of unsaturated porous media, Water Resources Research, 12(3), 513-522, 1976.

Nordbotten, Jan, M.; D. Kavetski, M.C. Celia and S. Bachu, Model for CO_2 leakage including multiple geological layers and multiple leaky wells. Environ. Sci. Technol. 43, 743-749, 2009.

Oldenburg, C.M. J.L. Lewicki, L. Dobeck, L. Spangler Modeling gas transport in the shallow subsurface during the ZERT CO_2 release test. Transp Porous Med, 82, 77-92, 2010.

Oldenburg, C.M., J.L. Lewicki On leakage and seepage of CO_2 from geologic storage sites into surface water. Environ Geol, 50, 691-705, 2006.

Peter, A., H. Lamert, M. Beyer, G. Hornbruch, B. Heinrich, A. Schulz, H. Geistlinger, B. Schreiber, P. Dietrich, U. Werban, C. Vogt, H-H. Richnow, J. Großmann, A. Dahmke Investigation of the geochemical impact of CO_2 on shallow groundwater: design and implementation of a CO_2 injection test in Northeast Germany. Environ Earth Sci. Special Issue 2012, in press

Sakamoto, Y., A. Tanaka, N. Tenma, T. Komai, Numerical study on flow behavior of CO_2 in an aquifer for risk assessment of carbon capture and storage, Energy Procedia, 4, 4170-4177, 2010.

Van Genuchten, M. Th., A closed-form equation for predicting the hydraulic conductivity of unsaturated soils. Soil Sci. Am J., 44, 892-898, 1980.

Wang, S., P.R. Jaffe, Dissolution of a mineral phase in portable aquifers due to CO_2 releases from deep formations; effect of dissolutions kinetics, Energy Convers 45(18-19), 2833-2848, 2004.

Xu, T., E. Sonnenthal, N. Spycher, and K. Pruess, TOUGHREACT User's Guide: a simulation program for non-isothermal multiphase reactive geochemical transport in variably saturated geologic media. Technical Report, Lawrence Berkeley National Laboratory, Berkeley, Calif., 2004.

Zheng, L., J. Apps, Y. Zhang, T. Xu, J. Birkholzer, On mobilization of lead and arsenic in groundwater response to CO_2 leakage from deep geological storage. Chem Geol 268, 281-297, 2009.

DEVELOPMENT OF AN ADVANCED THERMAL-HYDROLOGICAL-MECHANICAL MODEL FOR CO_2 STORAGE IN POROUS AND FRACTURED SALINE AQUIFERS

by P. H. Winterfeld[*], Y.-S. Wu[*], K. Pruess[†], and C. Oldenburg[†]

[*]Colorado School of Mines
Department of Petroleum Engineering
1613 Illinois St., Golden, CO 80401
pwinterf@mines.edu

[†]Lawrence Berkeley National Laboratory
1 Cyclotron Road
Berkeley CA 94720

ABSTRACT

We developed a fully coupled simulator for modeling thermal-hydrologic-mechanical (THM) effects in fractured and porous media saline aquifers. The multiphase and heat flow formulation is that for TOUGH2-MP, the starting point for our simulator. The geomechanical equations relating stresses and displacements are combined to yield an equation for mean stress as a function of pressure and temperature that is added to the formulation. In addition, theories of poroelasticity and experimental studies have correlated porosity and permeability to effective stress, and we incorporate those dependencies into our simulator as well.

We also developed an advanced physical property module, ECO2M, designed for CO_2 sequestration in saline aquifers. It includes the relevant properties of H_2O–NaCl–CO_2 mixtures for the temperature, pressure, and salinity conditions of interest. Three fluid phases may be present: (1) an aqueous phase that could contain some dissolved CO_2, (2) a liquid CO_2-rich phase that could contain dissolved water, and (3) a gaseous CO_2-rich phase that could also contain dissolved water. Salt may be present in the aqueous phase or as a solid precipitate.

The simulator formulation and numerical implementation are verified using analytical solutions and an example problem from the literature.

MEAN STRESS EQUATION

Our simulator is a modification of TOUGH2-MP (Zhang et al., 2008), which solves mass and energy balances over the simulation domain using the integral finite difference method on an unstructured grid. We extend its formulation to a fully coupled THM one by adding a governing equation for mean stress to the mass and energy balances. The mean stress equation is derived in this section.

The stress-strain relationship for an elastic fluid-filled porous media under nonisothermal conditions is (McTigue, 1986)

$$\bar{\bar{\tau}} - \left(\alpha P + 3\beta K(T - T_{ref})\right)\bar{\bar{I}} = 2G\bar{\bar{\epsilon}} + \lambda(tr\bar{\bar{\epsilon}})\bar{\bar{I}} \quad (1)$$

where T_{ref} is reference temperature, β is linear thermal expansion coefficient, K is bulk modulus, G is shear modulus, λ is the Lamé parameter, and α is the Biot coefficient. Two terms are subtracted from the normal stress tensor components in this thermo-poroelastic extension of Hooke's law. The first is the pressure term from poroelasticity theory, and the second is the temperature term from thermo-elasticity theory. We obtain the multi-porosity generalization of Equation 1 from Bai et al. (1993) while retaining the temperature term

$$\bar{\bar{\tau}} - \left(\sum \alpha_k P_k + 3\beta K(T_k - T_{ref})\right)\bar{\bar{I}} = 2G\bar{\bar{\epsilon}} + \lambda(tr\bar{\bar{\epsilon}})\bar{\bar{I}} \quad (2)$$

where subscript k refers to the porous continuum (fracture or matrix for double-porosity systems). Expressions for the generalized Biot coefficients α_k for a double-porosity medium have been presented by Wilson and Aifantis (1982)

$$\alpha_1 = 1 - \frac{K}{K_*};\ \alpha_2 = \frac{K}{K_*}\left(1 - \frac{K_*}{K_s}\right) \quad (3)$$

where K_s is the solid modulus, K_* is the modulus of the porous medium without the fractures, subscript 1 refers to the fractures, and subscript 2 to the matrix.

We obtain a relationship between volumetric strain, ϵ_v, and mean stress, τ_m, by taking the trace of Equation 2:

$$K\epsilon_v = \tau_m - \sum \alpha_k P_k - 3\beta K(T_k - T_{ref}) \quad (4)$$

The strain tensor and the displacement vector $\bar{u}$ are related by

$$\bar{\bar{\epsilon}} = \frac{1}{2}(\nabla\bar{u} + \nabla\bar{u}^t) \quad (5)$$

and the static equilibrium equation is

$$\nabla \cdot \bar{\bar{\tau}} + \bar{\bar{F}} = 0 \quad (6)$$

where $\bar{\bar{F}}$ is the body force. We combine Equations 2, 5, and 6 to obtain the thermo-poroelastic Navier equations for a multi-porosity medium

$$\nabla(\sum \alpha_k P_k + 3\beta K T_k) + (\lambda + G)\nabla(\nabla \cdot \bar{u}) + G\nabla^2\bar{u} + \bar{\bar{F}} = 0 \quad (7)$$

Taking the divergence of Equation 7, noting the divergence of the displacement vector is the volumetric strain, and combining with Equation 4 yields the governing equation for mean stress:

$$\frac{3(1-\nu)}{1+\nu}\nabla^2\tau_m + \nabla \cdot \bar{\bar{F}} - \frac{2(1-2\nu)}{1+\nu}\nabla^2(\sum \alpha_k P_k + 3\beta K T_k) = 0 \quad (8)$$

where ν is Poisson's ratio.

ROCK PROPERTY CORRELATIONS

Correlations have been developed for porosity as a function of effective stress and permeability as a function of porosity. A theory of hydrostatic poroelasticity (Zimmerman et al., 1986) has been proposed that accounts for the coupling of rock deformation with fluid flow inside the porous rock. Porosity as a function of effective stress is derived from this theory

$$d\phi = -\left[\frac{1}{K}(1-\phi) - C_r\right]d\tau' \quad (9)$$

where τ' is effective stress and C_r is rock grain compressibility.

Porosity is the ratio of fluid to bulk (solid plus fluid) volume. Bulk volume, V, is related to volumetric strain by

$$V = V_0(1-\epsilon_v) = V_i\frac{(1-\epsilon_v)}{(1-\epsilon_{v,i})} \quad (10)$$

where V_0 is zero strain volume and subscript i refers to reference conditions.Gutierrez et al. (2001) presented expressions for solid volume change with pressure and effective stress, which when combined with the above yield the following expression for porosity

$$\phi = 1 - \frac{(1-\phi_i)V_i + \frac{(1-\phi_i)}{K_S}(P-P_i) - \frac{1}{K_S}(\tau'-\tau_i')}{V_i\frac{(1-\epsilon_V)}{(1-\epsilon_{v,i})}} \quad (11)$$

Rutqvist et al. (2002) presented the following function for porosity, obtained from laboratory experiments on sedimentary rock (Davies and Davies, 1999)

$$\phi = \phi_r + (\phi_0 - \phi_r)e^{-a\tau'} \quad (12)$$

where ϕ_0 is zero effective stress porosity, ϕ_r is high effective stress porosity, and the exponent "a" is a parameter. They also presented an associated function for permeability in terms of porosity:

$$k = k_0 e^{c\left(\frac{\phi}{\phi_0}-1\right)} \quad (13)$$

Ostensen (1986) studied the relationship between effective stress and permeability for tight gas sands and approximated permeability as

$$k^n = D\ln\frac{\tau'^{,*}}{\tau'} \quad (14)$$

where exponent n is 0.5, "D" is a parameter, and $\tau'^{,*}$ is effective stress for zero permeability, obtained by extrapolating permeability versus effective stress on a semi-log plot.

Verma and Pruess (1988) presented a power law expression relating permeability to porosity

$$\frac{k-k_c}{k_0-k_c} = \left(\frac{\phi-\phi_c}{\phi_0-\phi_c}\right)^n \quad (15)$$

where k_c and ϕ_c are asymptotic values of permeability and porosity, respectively, and exponent n is a parameter.

The above correlations for porosity and permeability have been incorporated into our simulator.

ECO2M FLUID PROPERTY MODULE

We developed an advanced fluid property module called ECO2M (Pruess, 2011). ECO2M was designed for CO_2 sequestration in saline aquifers. It includes a description of the relevant properties of H_2O–NaCl–CO_2 mixtures that is highly accurate for the temperature, pressure, and salinity conditions of interest (between 10 and 110°C, pressure less than 600 bar, and salinity up to full halite saturation). Three fluid phases may be present: an aqueous phase that could contain some dissolved CO_2, a liquid CO_2-rich phase that could contain dissolved water, and a gaseous CO_2-rich phase that could also contain dissolved water. The partitioning of H_2O and CO_2 between the phases is modeled as a function of temperature, pressure, and salinity, using a slightly modified version of the correlations of Spycher and Pruess (2005).

The ECO2M fluid property correlations are identical to those of the earlier, less advanced ECO2N fluid property module (Pruess and Spycher, 2007). Properties correlated include density, viscosity, and specific enthalpy of the fluid phases as functions of temperature, pressure, and composition. Water properties are calculated from the International Formulation Committee (1967) steam table equations. Properties of pure CO_2 are obtained in tabular form from correlations developed by Altunin et al. (1975).

We neglect effects of dissolved water on the density and viscosity of the CO_2-rich phases. Brine density is calculated from the correlations of Haas (1976) and Andersen et al. (1992). The aqueous-phase density is calculated assuming additive volumes of brine and dissolved CO_2. Brine viscosity is obtained from a correlation by Phillips et al. (1981). Aqueous-phase viscosity does not depend on dissolved CO_2 concentration.

Brine specific enthalpy is calculated from the correlations developed by Lorenz et al. (2000). Aqueous-phase specific enthalpy is obtained by adding the enthalpies of the CO_2 and brine, and accounting for the enthalpy of dissolution of CO_2. The specific enthalpy of water dissolved in the CO_2-rich phases is identical to the enthalpy of saturated water vapor at the same temperature, and heat-of-dissolution effects are neglected. Specific enthalpy of the CO_2-rich phases is calculated by adding the specific enthalpies of the CO_2 and water components.

EXAMPLE SIMULATIONS AND DISCUSSION

We describe three simulations to provide model verification and an application example. The first two, a one-dimensional consolidation problem and a simulation exhibiting the Mandel-Cryer effect, are compared to analytical solutions. The last, pressure response and surface uplift occurring during a CO_2 sequestration project, shows a match of published results.

One-Dimensional Consolidation of a Double Porosity Medium

In the one-dimensional consolidation problem, a z-direction stress is applied to the top of a fluid-filled double porosity (fracture and matrix) porous rock column, instantaneously inducing a deformation and a pressure increase. Afterwards, fluid is allowed to drain out of the column top and the pressure dissipates. An analytical solution to this problem was presented by Wilson and Aifantis (1982). In their analysis, strain is uniaxial and z-direction stress is constant throughout the process.

We first simulate the load application to produce the pressure increase. We start from an unstrained state where pressure and mean stress are both equal, impose a greater mean stress at the system top to induce a pressure increase in the column, and let the system equilibrate. For

uniaxial deformation, mean stress, z-direction stress, and pressure are related by

$$\tau_m = \frac{1}{3}\frac{(1+\nu)}{(1-\nu)}(\tau_{zz} - \alpha P) + \alpha P \qquad (16)$$

and the constant z-direction stress is calculated from the imposed mean stress and the equilibrium pressure. Next, we simulate fluid drainage. The system is initially at the above equilibrated state. We set the pressure at the system top to the initial pressure. The mean stress at the system top is set as well, calculated from Equation 16 using the constant z-direction stress and the initial pressure. Fluid then drains out of the system top as the pressure returns to the initial value. We simulated this for a 400 m long column that contained 800 gridblocks (half fracture, half matrix). Initial pressure and mean stress were 5.0 MPa, and the imposed mean stress was 8.0 MPa. The resulting equilibrium pressure was 6.2 MPa, and the calculated z-direction stress was 9.8 MPa. We ran the drainage portion of the simulation for 4000 seconds with one-second time steps. Comparison of simulated fracture pressure with the analytical solution is shown in Figure 1, with excellent agreement.

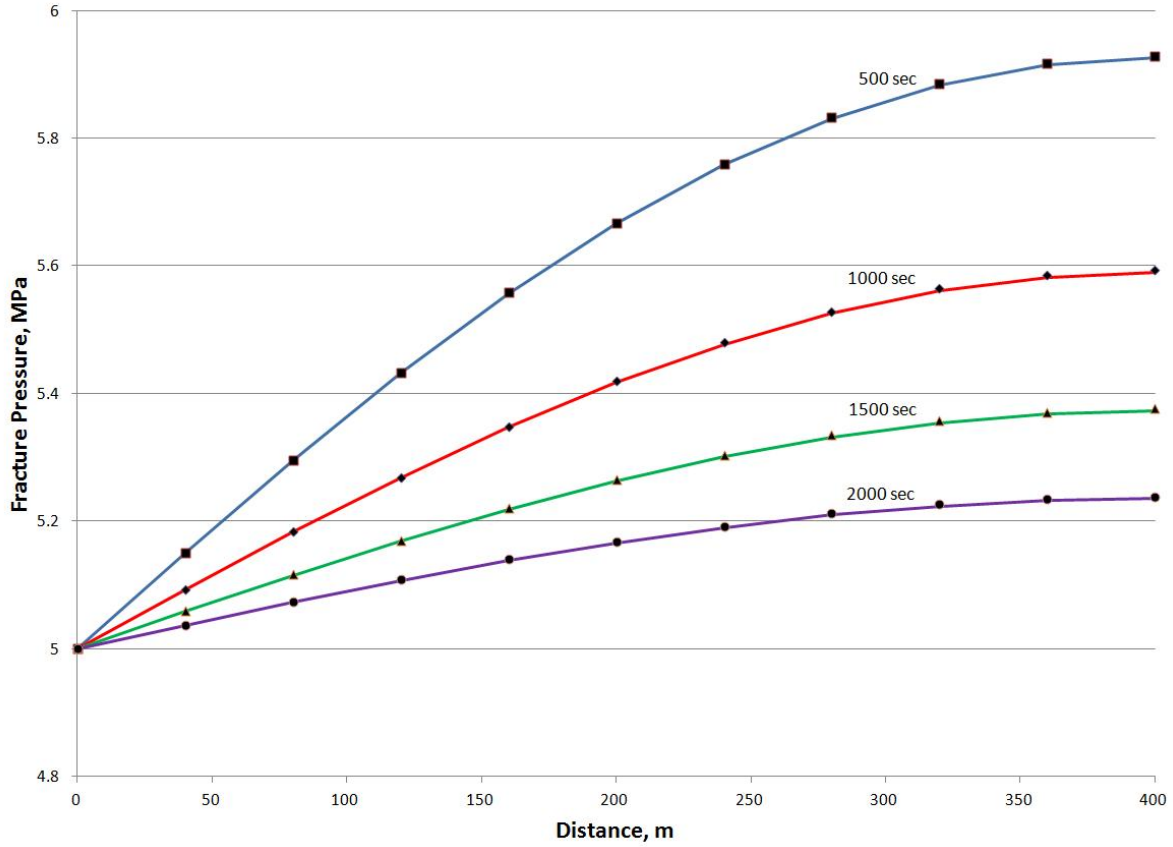

Figure 1. Comparison of analytical solution (solid lines) to simulation (points) for one-dimensional consolidation.

Mandel-Cryer Effect

Consider a poroelastic material that is allowed to drain laterally after a constant compressive force is applied to the top and bottom. Initially, a uniform pressure increase results from the undrained compression of the porous material. Because the pressure near the edges must decrease due to drainage, the material there becomes less stiff, and there is a load transfer to the center, resulting in a further increase in center pressure that reaches a maximum and soon declines due to fluid drainage. This pressure behavior is called the Mandel-Cryer effect (Mandel, 1953), and Abousleiman and Cheng (1996) present an analytical solution to the above process to which we compare our simulated results.

We first simulate the load application to produce the pressure increase. We start from an unstrained state where pressure and mean stress are both equal, impose a greater mean stress at the top and bottom to produce a pressure increase, and let the system equilibrate. Uniaxial stress is assumed in the analytical solution derivation, so mean stress and z-direction stress are related by

$$\tau_m = \frac{\tau_{zz}}{3} \tag{17}$$

Next, we simulate fluid drainage. The system is initially at the above equilibrated state, and we impose the initial pressure on the lateral boundaries to allow for drainage. We simulated this for a square with 1000 m sides that is subdivided into a 200×200 grid. The initial pressure and mean stress were 0.1 MPa, the applied z-direction stress was 3 MPa, and the equilibrium pressure was 2.18 MPa. The system drained for 50,000 seconds. We compare centerline pressure at the top with the analytical solution, shown in Figure 2. The simulated results exhibit the pressure maximum characteristic of the Mandel-Cryer effect and lie close to the analytical solution. The analytical solution and simulator formulation differ in that the analytical solution assumes that pressure varies only laterally; this could account for the difference in pressure peak heights.

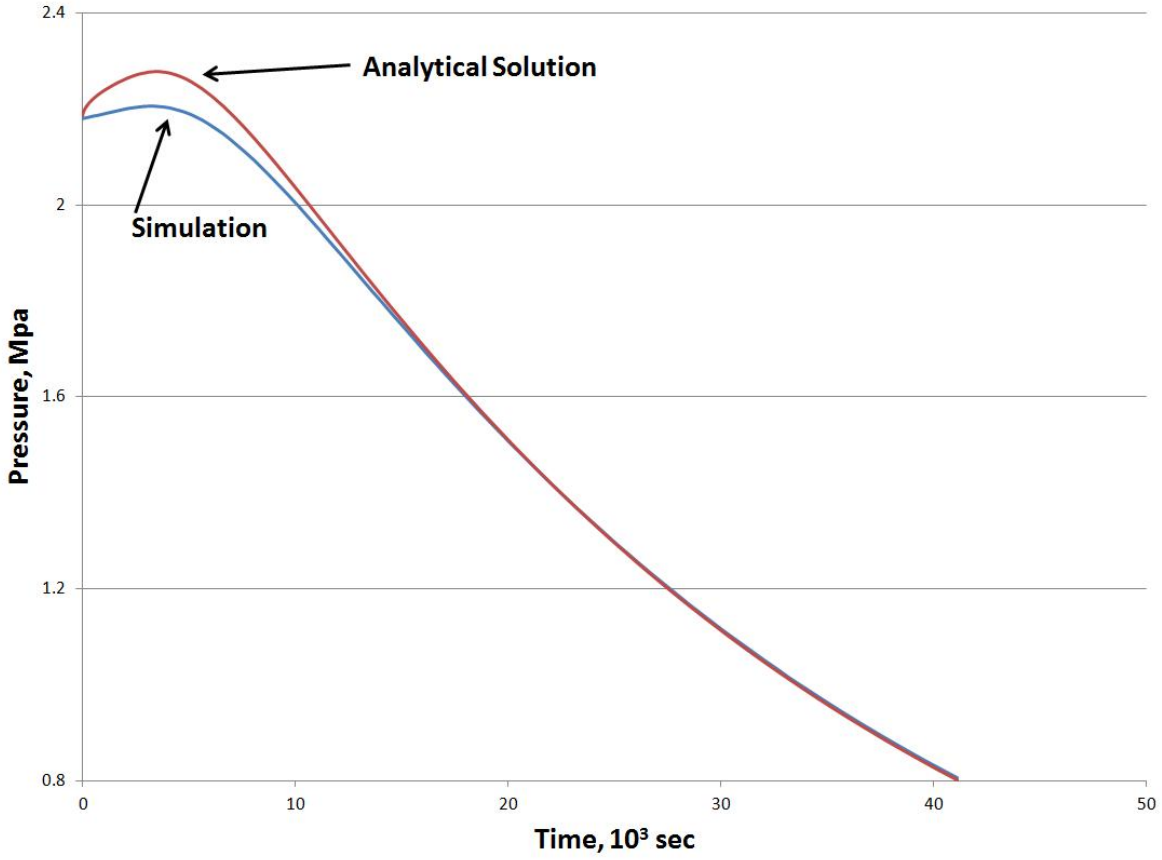

Figure 2. Comparison of analytical solution to simulation for Mandel-Cryer effect.

In Salah Project Simulation

The In Salah Gas Project, located in central Algeria, is a CO_2 storage project. Natural gas produced nearby is high in CO_2, and this CO_2 is injected back into the water leg of a depleting gas field for geological storage. Surface uplift from CO_2 injection has been measured by satellite-based inferrometry; Rutqvist et al. (2010) did a reservoir-geomechanical analysis of In Salah CO_2 injection and surface uplift using the TOUGH2-FLAC numerical simulator to determine if this uplift can be explained by pressure changes and deformation in the injection zone only. We reran their analysis on our code and used a cluster computer to demonstrate our parallel code's ability to simulate larger problems. Our cluster computer contains 16 nodes; each node has 24 GB of memory and two Intel® 5620 2.4GHZ 4-core processors.

The simulated domain was 10×10×4 km with one 1.5 km horizontal injection well at 1810 m depth and in the domain center. The domain consisted of four geological layers—Shallow Overburden, Caprock, Injection Zone, and Base—all with constant properties. CO_2 was injected for three years at 13.6 kg/sec. We simulated a 5×5×4 km quarter symmetry element of their system with a 1000×1000×60 grid (60 million grid-blocks). Figure 3 shows surface uplift, calculated by assuming strain isotropy, after three years of CO_2 injection, and Figure 4 is a comparison of surface uplift at the well's center versus depth to that of the reference.

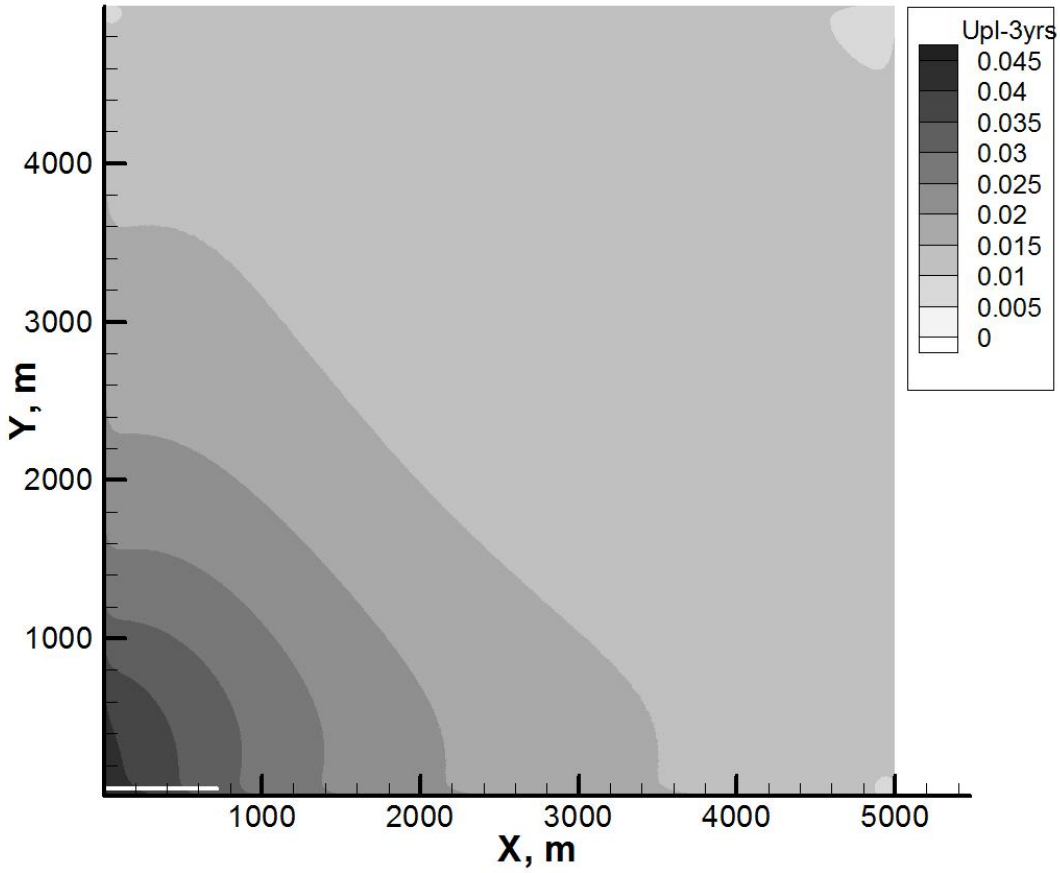

Figure 3. Surface uplift for quarter symmetry element; injection well shown by thick horizontal line at origin.

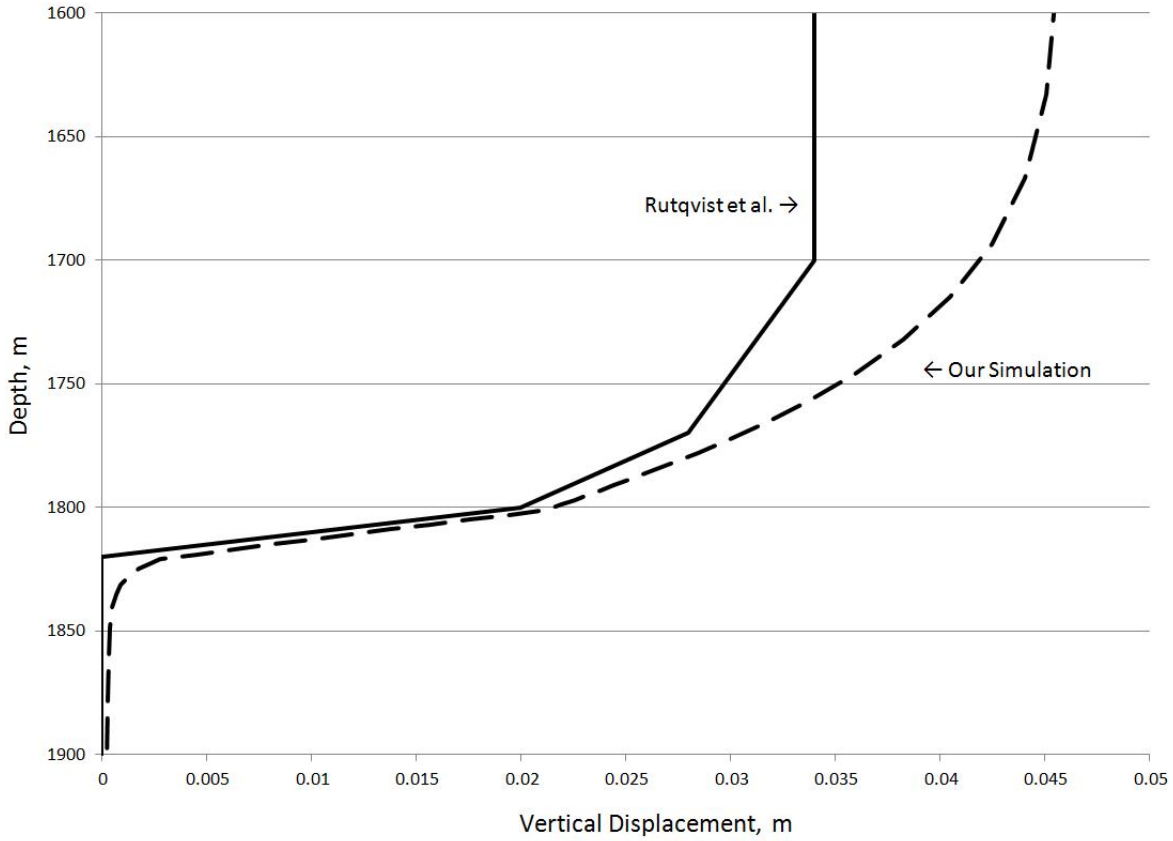

Figure 4. Comparison of surface uplift versus depth at well center.

CONCLUSIONS

We developed a massively parallel reservoir simulator for modeling THM processes in fractured and porous media saline aquifers. From the fundamental equations describing deformation of porous and fractured elastic media, we derived a conservation equation relating mean stress, pressure, and temperature, and incorporated it alongside the mass- and energy-conservation equations of TOUGH2-MP, the starting point for the simulator. In addition, rock properties, namely permeability and porosity, are functions of pressure and effective stress that are obtained from the literature.

We also developed an advanced fluid property module, ECO2M, which was designed for CO_2 sequestration in saline aquifers. It includes a description of the relevant properties of H_2O–NaCl–CO_2 mixtures that is highly accurate for the temperature, pressure, and salinity conditions of interest. Its fluid property correlations are identical to those of an earlier, less advanced fluid property module, but it allows liquid and gaseous CO_2-rich phases to be present, whereas the other does not distinguish between the two.

We verified the simulator formulation and numerical implementation, using analytical solutions and an example problem from the literature. For the former, we matched a one-dimensional consolidation problem and a two-dimensional simulation of the Mandel-Cryer effect. For the latter, we compared our results to those from two coupled computer codes, one that simulates fluid flow and heat transport, and another that simulates rock deformation. We obtained a good match of surface uplift after three years of CO_2 injection into the water leg of a depleting gas field. This agreement indicates that our formulation is able to capture THM effects modeled by a coupled simulation with a more detailed handling of rock mechanics.

ACKNOWLEDGMENT

This work was supported by the CMG Foundation and by the Assistant Secretary for Fossil Energy, Office of Coal and Power R&D through the National Energy Technology Laboratory under U.S. DOE Contract Number DE-FC26-09FE0000988.

REFERENCES

Abousleiman Y., A. H. D. Cheng, L. Cui, E. Detournay, J. C. Roegiers, Mandel's problem revisited, *Géotechnique*, 46**,** 187–95, 1996.

Altunin, V.V, *Thermophysical Properties of Carbon Dioxide,* Publishing House of Standards, 551 pp., Moscow, 1975 (in Russian).

Andersen, G., A. Probst, L. Murray, S. Butler, An Accurate PVT Model for Geothermal Fluids as Represented by H_2O-NaCl-CO_2 Mixtures, *Proc. 17th Workshop on Geothermal Res. Eng.,* 239 - 248, Stanford, CA, 1992.

Bai M., D. Elsworth, J.-C. Roegeirs, Modeling of naturally fractured reservoirs using deformation dependent flow mechanism, *Int. J. Rock Mech. Min. Sci. and Geomech. Abstr.,* 30(7), 1185-1191, 1993.

Davies J. P., D. K. Davies, Stress-dependent permeability characterization and modeling, *SPE 56813, pres. at ATCE*, Houston, TX, Oct. 1999.

Gutierrez M., R. W. Lewis, Petroleum reservoir simulation coupling fluid flow and geomechanics, *SPE Reservoir Evaluation & Engineering*, 164-72, June 2001.

Haas, J.L. Jr., Physical Properties of the Coexisting Phases and Thermochemical Properties of the H_2O Component in Boiling NaCl solutions, *USGS Bulletin 1421-A,* Washington, DC, 73 pp., 1976.

International Formulation Committee, *A Formulation of the Thermodynamic Properties of Ordinary Water Substance,* IFC Secretariat, Düsseldorf, Germany, 1967.

Mandel J., Consolidation des sols (etude mathematique), *Geotechnique,* 3287–99, 1953.

McTigue D. F., Thermoelastic response of fluid-saturated porous rock. *Journal of Geophysical Research*, 91(9), 9533-42, 1986.

Ostensen R. W., The effect of stress-dependent permeability on gas production and well testing, *SPE Form Eval*, 227–35, June 1986.

Phillips, S.L., A. Igbene, J.A. Fair, H. Ozbek and M. Tavana, A Technical Databook for Geothermal Energy Utilization, *Lawrence Berkeley National Laboratory Report LBL-12810*, Berkeley, CA, 46 pp., 1981.

Pruess K, *ECO2M: A TOUGH2 Fluid Property Module for Mixtures of Water, NaCl, and CO_2, Including Super- and Sub-Critical Conditions, and Phase Change Between Liquid and Gaseous CO_2,* Lawrence Berkeley National Laboratory Report LBL-4590E, 2011.

Pruess K. and N. Spycher, ECO2N – A Fluid Property Module for the TOUGH2 Code for Studies of CO2 Storage in Saline Aquifers, *Energy Conversion and Management,* 48(6), 1761–1767, 2007.

Rutqvist J., C.-F. Tsang, A study of caprock hydromechanical changes associated with CO_2-injection into a brine formation, *Environmental Geology* 42, 296–305, 2002.

Rutqvist J., D. W. Vasco, L. Myer, Coupled reservoir-geomechanical analysis of CO_2 injection and ground deformations at In Salah Algeria, *Int. J. of Greenhouse Gas Control*, 4, 225–30, 2010.

Spycher, N., K. Pruess, CO_2-H_2O Mixtures in the Geological Sequestration of CO_2. II. Partitioning in Chloride Brines at 12–100 °C and up to 600 bar, *Geochim. Cosmochim. Acta,* 69(13), 3309–3320, 2005.

Verma A., K. Pruess, Thermohydrological conditions and silica redistribution near high-level nuclear wastes emplaced in saturated geological formations, *J Geophys Res*, 93, 1159-73, 1988.

Wilson R. K., E. C. Aifantis, On the theory of consolidation with double porosity, *Int. J. Eng. Sci,*. 20(9), 1009-35, 1982.

Zhang K., Y.-S. Wu, K. Pruess, *User's guide for TOUGH2-MP - a massively parallel version of the TOUGH2 code,* Lawrence Berkeley National Laboratory Report LBNL-315E, 2008.

Zimmerman R. W., W. H. Somerton, M. S. King, Compressibility of porous rocks, *J Geophys Res,* 91(12), 765–77, 1986.

TOUGHVISUAL: A USER-FRIENDLY PRE-PROCESSING AND POST-PROCESSING GRAPHICAL INTERFACE FOR TOUGHREACT

Yanlin Yang[1,2], Tianfu Xu[1,2], Fugang Wang[1,2], Hongwu. Lei[1,2], Guangrong Jing[1,2] and Gaofan Yue[1,2]

[1]Key Laboratory of Groundwater Resources and Environment, Ministry of Education, Jilin University, Changchun, 130021, China
[2]College of Environment and Resources, Jilin University, Changchun, 130021, China
E-mail: yangyanlinjida@gmail.com

ABSTRACT

TOUGHVISUAL is a complete Windows-based graphical user interface for the TOUGHREACT program, which is a general multiphase multicomponent reactive transport simulator, developed by introducing geochemistry into the existing multiphase fluid and heat flow code TOUGH2. The complexity of the input files (such as flow.inp, solute.inp and chemical.inp) required by TOURHREACT makes manual construction of its input files tedious and error-prone, especially for problems with a large number of elements and complex geological structures. TOUGHVISUAL streamlines the creation of the input files and helps reduce errors, so one can spend more time interpreting and analyzing the modeling results. TOUGHVISUAL builds on the experiences of previous relatively mature interface software such as PetraSim, Tougher, and Winggridder, and is presented here as an improved pre- and post-processing TOUGHREACT graphical interface. TOUGHVISUAL's advantages are as follows:

(1) It is written in the object-oriented language C++, which is convenient for management and future update.

(2) It generates regular or irregular editable and convertible MESH files, such as rectangular, triangular, quadrilateral, thiessen polygon to meet user's needs.

(3) It makes full use of existing geological data. For example, all kinds of attribute data, likes porosity, could be represented as three-dimensional scatter points, then assigned as properties to elements via three-dimensional interpolation.

(4) It translates domain properties into element properties if one builds property domains.

(5) It imports attribute data from other software and exports various common file formats to other software, so that TOUGHVISUAL shares information with other software.

(6) It displays the results of various state variables as temporal evolution curves for single or many elements, space iso-surfaces, or the contours of a cross-sectional map. This can be very helpful for users who want to display results during running time.

1. INTRODUCTION

TOUGHREACT is a general multiphase multicomponent reactive transport simulator (Xu et al., 2006) developed by introducing geochemistry into the existing multiphase fluid and heat flow code TOUGH2 (Pruess et al., 1999). Although TOUGHREACT, as initially developed, is a powerful research tool, its input files are difficult to create and error-prone, requiring using a text-based editor and assigning properties to grid elements. It is especially inconvenient if your study area is irregular or is a heterogeneous porous media. There are a few commercial programs, such as PetraSim, Wingridder, GeoCAD, and Tougher (Alcott et al., 2006; Yamamoto, 2008; Pan, 2003; Burnell et al., 2003; You Li et al., 2011), making graphical interfaces for TOUGH, but they have proved neither very flexible nor convenient.

For these reasons, our research group at Jilin University, considering the shortage of existing interfaces, attempted to develop a better interface software for TOUGHREACT, making it more user-friendly and convenient. While at present TOUGHVISUAL only supports the ECO2N module, additional modules could be easily incorporated in future versions.

2 .DESIGN OVERVIEW

This paper will briefly describe the graphical interface TOUGHVISUAL, which can be used to create input files, edit input data files, and plot TOUGHREACT simulation results. We used the Microsoft Visual Studio 2005 development tool, while utilizing OpenGL to render the model and visualize the result. This tool adapts the methods of modularization architecture. Its portion structure is shown in Figure.1.

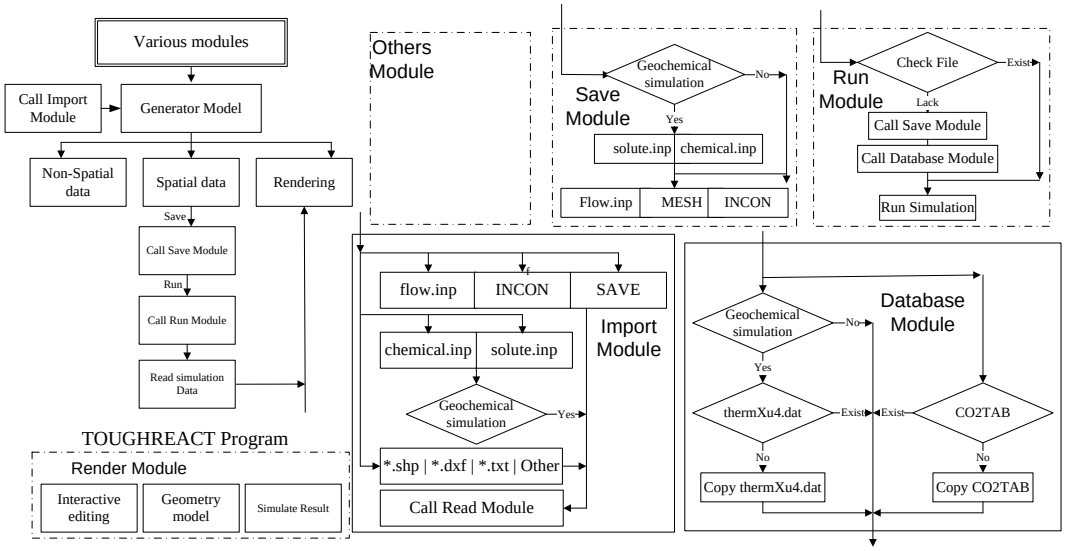

Fig. 1. Portion Structure chart in TOUGHVISUAL

3. TOUGHVISUAL INTERFACE

The TOUGHVISUAL interface software includes a pre-processor and post-processor, each consisting of different components.

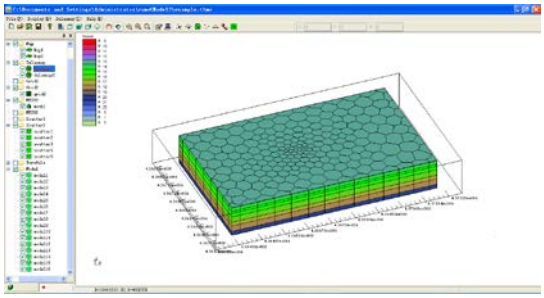

Fig. 2. Main window of TOUGHVISUAL interface

3.1. Pre-processor

TOUGH simulator's input files data are divided into many individual keyword data blocks. Different Keyword data blocks provide different information, such as ROCKS, GENER, INCON. A brief description of the processing methods is given below.

3.1.1. Geometrical Model

The geometrical model generator is one of the most important and critical steps of the interface software. One can use the mouse to draw the simulation domain boundary, and one can of course also specify the boundaries through study area coordinates. Then, the computing grid will be automatically generated by clicking the related menus. Grid shapes may be rectangular or irregular. The number of layers is unrestricted. One can use different methods for generating a geometrical model—for example, one can generate a 3-D geometrical model directly, or initially create a 2-D geometry, then carry out a simple processing step to generate a 3-D model. Three examples of geometrical models are displayed in Figures 3, 4, and 5.

Figure 3(a) shows a regular geometrical model. Note that the element size can be edited interactively in order to meet the user's needs, When the user wants to create a 3-D model, as shown in Figure 3(b), he or she needs to assign each layer's elevation. The user can of course also change the elevation within 3-D models.

Figure 4(a) displays an irregular geometrical model. The green points are the center point of the elements. The element size could be smaller in the key study or fault areas. Figure 4(b) is the corresponding 3-D model.

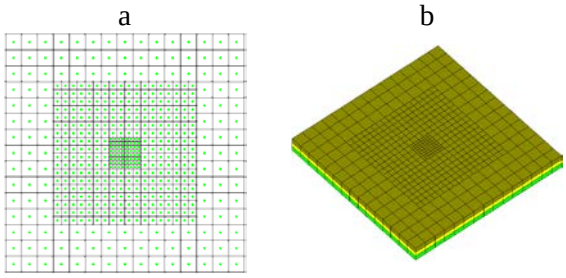

Fig. 3. Typical regular grid model. (a) Layout of a layer . (b) A 3-D model after editing.

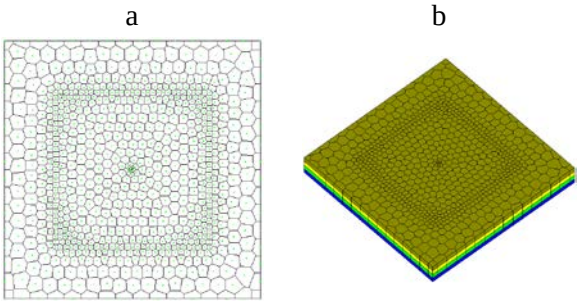

Fig. 4. Typical irregular grid model. (a) Layout of one layer. (b) Irregular geometry model displays in 3-D

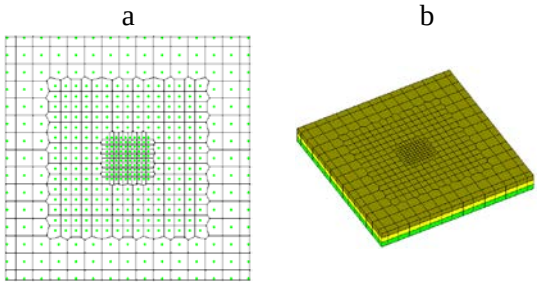

Fig. 5. Regular/irregular grid model. (a) Layout of a layer. (b) 3-D view of the model

In this process, calculating the interface area between two connected elements and element's volume is very important. TOUGHVISUAL mostly uses two methods for achieving this. One can use Equation (1) (Gelder, 1995) to compute the area of an interface of any polygon with N vertices P_i (i=1..N). This formula for computing area is very effective for any polygon in 2-D or 3-D. Moreover, the volume of a polyhedron R, with N vertices and m faces (F1,F2,…Fm), is given in Equation (2). The user can change a complex polygon into a simple polygon first, then compute its area and volume. Finally, using ELEME and CONNE data, the MESH file can be generated. Element properties will inherit the default value, which one can change if needed.

$$A = \frac{1}{2}\sum_{i=1}^{N} P_i \times P_{i+1} \qquad (1)$$

$$V = \frac{1}{3}\sum_{j=1}^{m} F_j \bullet A_j \qquad (2)$$

3.1.2. ROCKS

This keyword data block mainly introduces material (rock) properties, which can be set by the material tab. In default, all blocks will be assigned to the first rock type. The user can then modify the block's material according to the study area's geological conditions. There are three methods to finish this data block: Figures 6 and 7 show two methods; the third method is reserved for use with other modules. When you save this model, these values will be written into the flow.inp file according to the original TOUGH fixed format. When changing a block's material zone, one must select the blocks—see Figures 6 and 7.

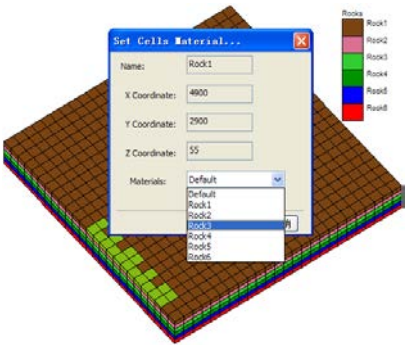

Fig. 6. Modification of gridblocks's material zone.

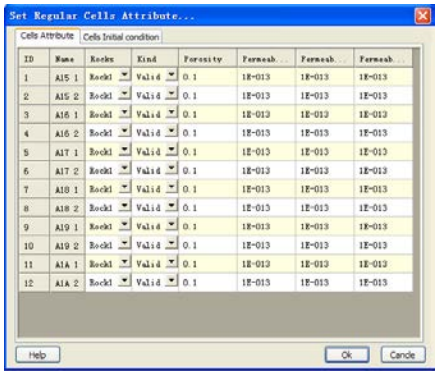

Fig. 7. The second method for modifying the grid-block's material zone.

3.1.3. GENER

Similar to assigning gridblocks to ROCKS data, the user can select a sink or source block to inject/product mass or heat. The associated parameter values to be set are shown in Figure 8.

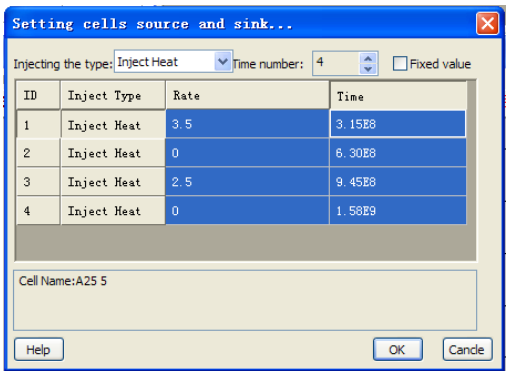

Fig. 8. Defining sinks or sources for a block

3.1.4. Boundary condition

Two basic boundary types can be specified. For the Dirichlet condition, the user can assign large volumes, so that their thermodynamic conditions or state variables, such as pressure and temperature, do not change during the simulation time—see Figure 7 (the fourth column of the cell attribute's tab). Boundary conditions can also be handled by introducing sinks or sources of appropriate rates into the elements, specified in the GENER data block.

3.1.5. Initial condition

All gridblocks are assigned the default initial conditions. The temperature is calculated according to geothermal gradient, and the pressure is calculated according to hydrostatic pressure. The defaults can be overwritten using a simple mouse operation. In addition, the user can import or connect to the existing initial condition, such as the SAVE file.

Figure 9 shows how a user can modify the block's initial condition after selecting the target blocks. The selected blocks will then have the same initial conditions. If one wants to define different initial values for different blocks, one should adopt another method (Figure 10).

Figure 11 show how a user can restart a model by connecting the save/savechem file, generated in a previous run. Then the program will take the corresponding processing for the initialization.

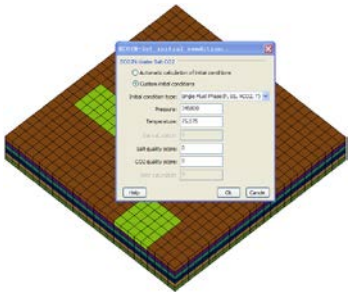

Fig. 9. One method to modify the block's initial conditions

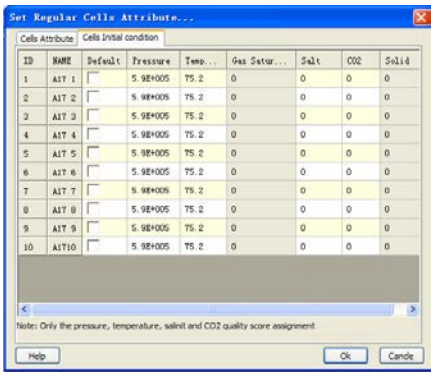

Fig. 10. Another method to modify the block's initial conditions.

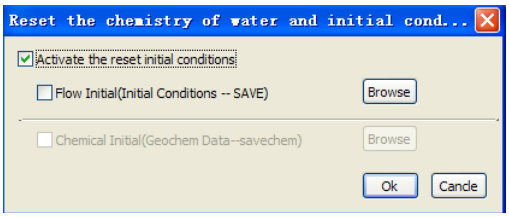

Fig. 11. Connection to a existing initial condition file.

3.1.5. PARA, MULTI, TIMES and SOLVR Keywords

According to the menu operation, the user can also finish the parameters assigned for PARA, MULTI, TIMES, and SOLVER data blocks.

3.1.6. Solute.inp file

This solute.inp file in the original TOUGH-REACT program contains various flags and input parameters for calculations of reactive transport (Xu et al., 2006), such as diffusion coefficients, tolerance limits, and output control. Parameters in this file are organized in various displayed menus, as shown on Figure 12.

a

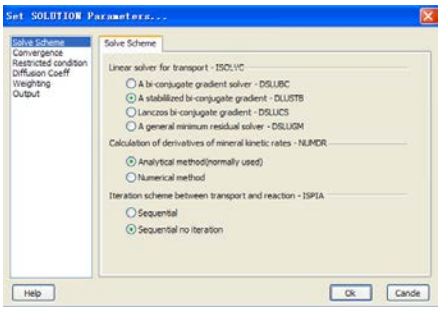

b

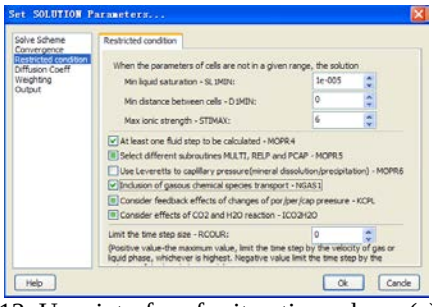

Fig. 12. User interface for iteration scheme(a) and run constraints(b)

3.1.7. Chemical.inp file

This file is used to define the geochemical system (number of aqueous component species, minerals, gases, and sorbed species considered in the simulation). The file also includes the initial composition of water, minerals, and gases for different zones that are assigned to gridblocks. With this interface, the user can readily define the geochemical parameters and properties to be associated to gridblocks.

a

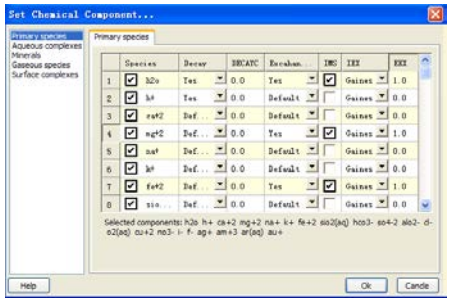

b

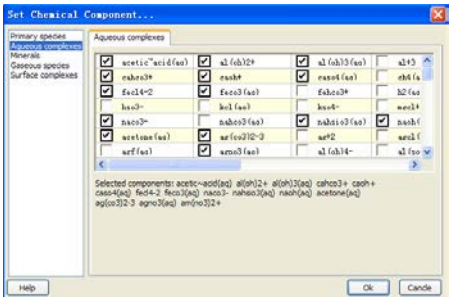

c

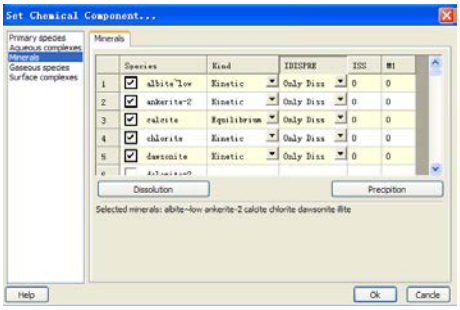

d

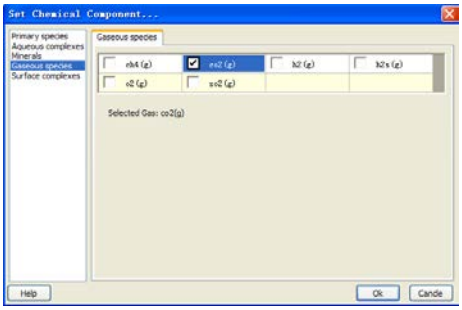

Fig. 13. Interface for primary species (a), aqueous component species (b), mineral phases (c), and gaseous species (d).

a

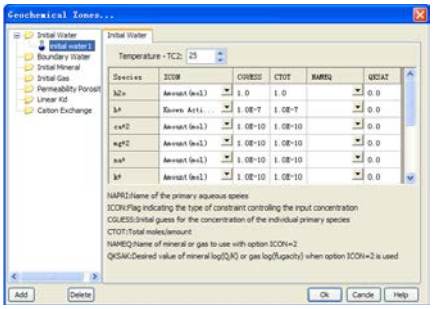

b

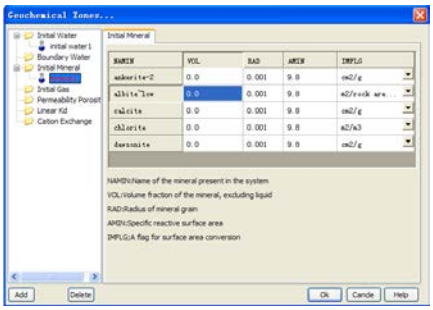

Fig. 14. Initial composition of water (a) and mineral phases (b)

3.2. Running the model

Before running the model, one should make sure that all data are saved. Then, the user selects "Run" on the menu, and the Run model dialog box will appear. Use the combox to select the graph type within which progress data will be displayed, as shown in Figure 15.

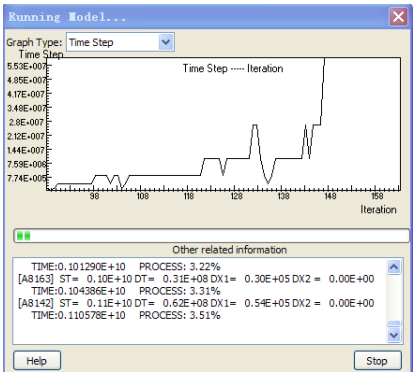

Fig. 15. Simulation progress and time step size.

There are three graph types: Time step versus number of iterations, Error versus number of iterations, and simulation-time progress versus number of iterations. For different graph types, the user will receive different information.

3.3. Post-Processor

The fast visualization of modeling results is very important, so that dynamic analysis can be conducted with minimum delay. For this purpose, post-processing has been developed for modeling results, 3-D iso-surfaces, contour maps, cross sections, piper plots, and temporal evolution plots. In addition, modeling results can be animated.

Using the presented modules, one can create all sorts of figures, such as color-filled contour figures, which may be saved in several formats, including *.shp, *.dxf, *grd, *csv and *.bmp. The data from different modules can be converted to one another. One can import all kinds of popular file formats, likes *.shp, *.dxf, *.grd , *.csv, and so on. These modules also provide some suitable interpolation algorithms. Making full use of these functions, the user will find that they are very useful and convenient.

4. EXAMPLES

Here we present two examples to illustrate the advantages and usefulness of TOUGHVISUAL. Through simple mouse clicking, one can complete the pre-processing of input files for TOUGH2/TOUGHREACT. Analyses of numerical simulations are readily accessible to rapidly evaluate model results.

4.1. Regular Grid Model

The geometry of a model for a CO_2 injection problem is shown in Figure 16(a). This model contains 3750 elements, with 10,325 connections among them. Each layer is color-coded, and the properties of each layer can be varied, especially the mineralogical and hydraulic properties. CO_2 is injected into the center of the sixth layer at a constant pressure.

a b

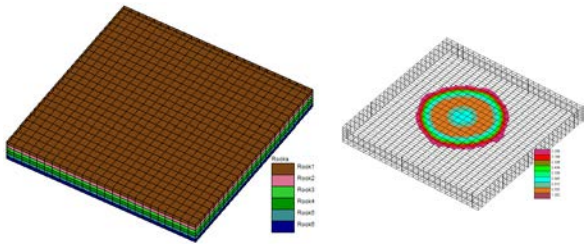

Fig. 16. Regular grid model (a). Result of the model displayed after 30 years (b).

By setting the iso-surface options, the iso-surface maps of P, T, and other state variables will be produced. Figure 16(b) shows the simulated results after 30 years. Image details can be controlled—for instance, the number of iso-surfaces and the data range. If only one time step is selected, the contour map will overlay the finite-difference grid. If more than one time step is selected, then the selected contour maps will be dynamically shown.

a b

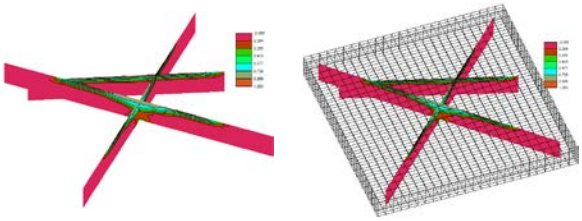

Fig. 17. Cross-sectional contour

To get a cross-sectional contour, the user should first draw the cross-hatching with the help of a mouse, then select the available state variables and plot time. The user can rotate, pan, and zoom the image interactively. By selecting the animation display, one could view the change in the simulated result over time. Finally, the user can export the image. In a similar manner, for one or more elements, the user can plot resulting variables in terms of temporal evolution—see Figures 18.

a

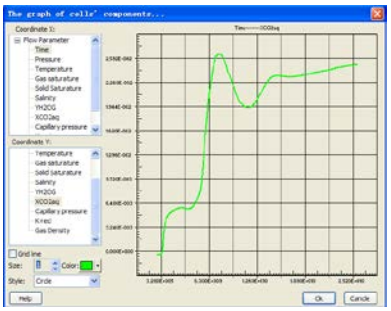

b

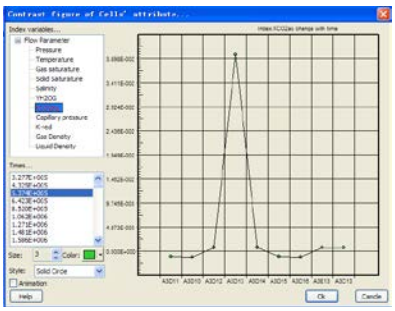

Fig. 18. Temporal evolution for one element (a). Attributed plot for multiple elements (b)

In many cases, it is very useful to display the distribution of each component in the system. Different times would have different distribution—see Figure 19.

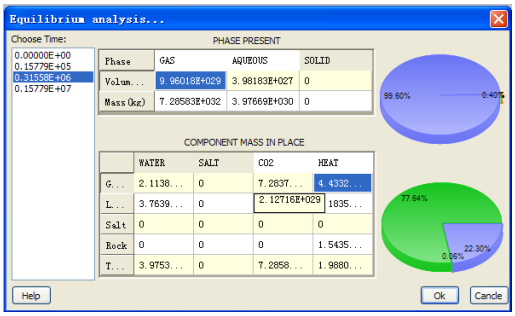

Fig. 19. Component distribution plot

4.2 Building Grid Model from a Geological Model

The second case involves geologic complexity; therefore, we need first to create an adequate geologic model. Once that is done, we can determine the modeling domain area, because in this case the geologic model is very large, about 18 km^2. The geologic model was directly built from 494 available boreholes with minimal user intervention (Figure 20). We must identify the scope of the study, covering an area of 800×500 m^2. Figure 21 displays the numerical grid. This model contains 1912 elements with 7049 connections. Finally, we transfer the properties of the geologic model into the modeling grid (Figure 22a).

a b

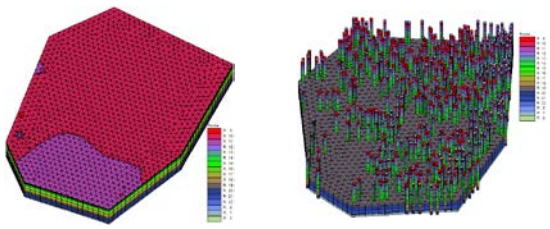

Fig. 20. Generation of a geologic model from borehole data. (a) 3D view of the geologic model. (b) Geologic model with boreholes

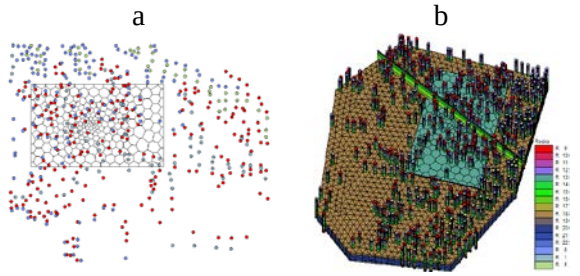

Fig. 21. Determination of the study area. (a) Plan view. (b) 3D view

Figure 21(a) shows the study area using either the black line diagram (a), or the sea-green area in (b).

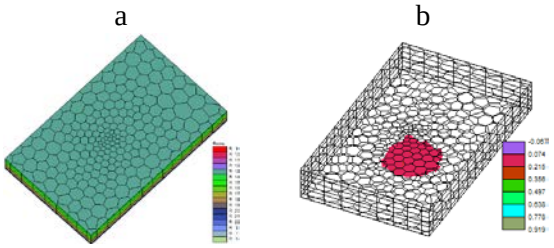

Fig. 22. Grid model (a), Result of the model (b).

Figure 22(a) shows the grid model in 3-D view. As illustrated in Figure 22(b), the user can select any time and available variables (Sl, Sg., etc.) for plotting.

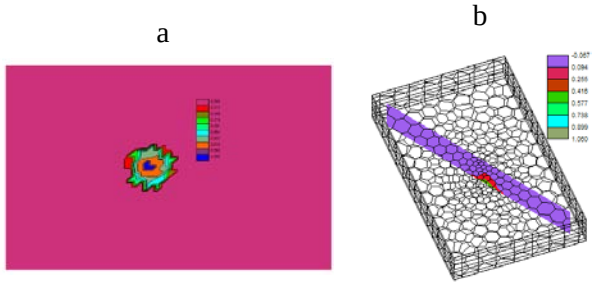

Fig. 23. Sg contours (a) and cross-sectional contour (b)

ACKNOWLEDGMENT

This work was jointly supported by the China Geological Survey project (Grant No.121201112 0048), public welfare industry special funds for scientific research from Ministry of Land and Re sources of China (Grant No.201211063), the doctoral interdisciplinary scientific research proj -ect of Jilin University (No.2012DC014) and the Graduate Innovation Fund of Jilin University (N o.20121069).

REFERENCES

Alcott, A., Swenson, D., Hardeman, B., Using pertrsim to create, execute, and post-process TOUGH2 models. In: Proceedings of the TOUGH Symposium, Lawrence Berkeley National Laboratory, Berkeley, California, p. 8, http://esd.lbl.gov/TOUGHsymposium/pdf/Alcott_PetraSim.pdf, 2006.

Bullivant, D.P., M.J. O'Sullivan, Graphics and TOUGH2, Proceedings of TOUGH Workshop, Lawrence Berkeley National Laboratory, Berkeley, California, May 4-6, 1998.<http://esd.lbl.gov/FILES/research/projects/tough/documentation/proceedings/1998-BullivantOSullivan.pdf >, 1998.

Burnell,J.G., White, S., P., Osato, K., Sato, T., GeoCad, a pre- and postprocessor for TOUGH2. In: Proceedings of the TOUGH Symposium, Lawrence Berkeley National Laboratory, Berkeley, California, < http://esd.lbl.gov/TOUGHsymposium/TOUGHsymposium03/pdfs/BurnellWhiteOsatoSato.pdf>.

Gelder, A. V., 1995. Efficient Computation of Polygon Area and Polyhedron. Graphics Gem, 4th edition. Academic Press.

Pruess, K., C. Oldenburg, and G. Moridis, *TOUGH2 User's Guide, Version 2.0*, Report LBNL-43134, Lawrence Berkeley National Laboratory, Berkeley, Calif., 1999.

Sato, T., K. Ohsato, T. Shiga, G-Star-Base (G*Base)—A data base system for underground information and post-processing for TOUGH2, Proceedings of TOUGH Symposium 2003, Lawrence Berkeley National Laboratory, Berkeley, California, May 12-14, 2003.< http://esd.lbl.gov/FILES/research/projects/tough/documentation/proceedings/2003-SatoOhsatoShiga.pdf >.

Xu, T., Sonnenthal, E.L., Spycher, N., Pruess, K., TOUGHREACT: a simulation program for non-thermal, multiphase reactive geochemical transport in variably saturated geologic media. Computers and Geosciences 32, 14-165, 2006.

Yamamoto, H., PertraSim: a Grapical User Interface for the TOUGH2 family of multiphase flow and transport code. Ground Water 46(4), 525-528, 2008.

Pan, L., WINGRIDDER-an interactive grid generator for TOUGH. In: Proceedings of

the TOUGH Symposium, Lawrence Berkeley National Laboratory, Berkeley, California,http://esd.lbl.gov/TOUGHsymposium/TOUGHsymposium03/pdfs/Pan.pdf, 2003.

EFFICIENT DATA ASSIMILATION TOOL IN CONJUNCTION WITH TOUGH2 FOR CO_2 MONITORING

Judith Yue Li, Sivaram Ambikasaran, Peter K. Kitanidis, Eric Darve

Stanford University
161 Y2E2, 473 Via Ortega,
Stanford, CA, 94305, Santa Clara
e-mail: yuel@stanford.edu

ABSTRACT

We address the problem of monitoring CO_2 in real time to provide early warning of possible leakage. The new data assimilation approach we develop takes advantage of the temporal resolution of continuously acquired seismic survey data, and has been tested on a TOUGH2 synthetic CO2 injection model. This Kalman Filter (KF) based method is sufficiently fast for online data processing and provides risk-based estimates. We also discuss the validity of describing the unknown system dynamics using a random walk model in the context of CO_2 monitoring.

INTRODUCTION

Subsurface monitoring is essential for risk management during many field operations, such as CO_2 injection during Carbon Capture and Sequestration (CCS) and Enhanced Oil Recovery (EOR), hydraulic fracturing. The key challenge in subsurface monitoring is the data assimilation (DA)/ filtering problem of reconstructing an unobservable dynamic process (such as CO_2 plume) using both static data (well-log, seismic data) and dynamic data (such as 4-D seismic data, or well production data).

Time-lapse seismic surveys have been widely adopted for monitoring subsurface fluid flow (Lumley 2001). Recent developments in 4D seismic and continuous active-source seismic monitoring (CASSM) has increased the data output frequency to the order of minutes (Daley et al. 2007). Thus, there is a growing need for a fast data assimilation solution that can update the parameter based on the most recently acquired observations, i.e. real-time monitoring.

On the other hand, practical implementation of data assimilation methods for subsurface monitoring must also address the challenge of limited memory and processing time. Solving the spatio-temporal process jointly incorporating all data sets is time-consuming, whereas sequential filtering only requires storing solutions from the last step and processing the measurement from the current step, which makes the problem tractable for real-time subsurface monitoring purposes.

The general starting point for sequential data assimilation is the Bayesian framework, which finds the posterior pdf of the parameters and model state, i.e., observation-conditioned parameter estimates at each time instance, given a set of measurements and a dynamical model with uncertainties. The dynamic model is assumed to be a Markov model, which holds that state variables at one time-instant are dependent only on the states of the previous time-instant. This condition is normally satisfied for most dynamic models, such as flow simulators. Another assumption is that measurement errors are uncorrelated in time. These two assumptions allow the Bayesian theorem to be written in a recursive fashion. The resulting sequential Bayesian filter obviates the need for reprocessing previous data, while still preserving the influence from measurements at all previous time steps during model updating.

Several Bayesian filters have been applied to subsurface dynamic imaging problems. For linear dynamic problems, the Kalman Filter gives a linear, unbiased, and minimal error-variance estimate of the unknown state (Kalman 1960). The Extended Kalman Filter (EKF), an adaptation of the Kalman Filter for solving nonlinear problems through linearization (Anderson and

Moore 1979), has been applied to field environmental monitoring (Nenna, Pidlisecky and Knight 2011). However, there are two major drawbacks associated with both KF and EKF: (1) advancing a covariance matrix in time is computationally expensive when the number of unknowns is large, and (2) linearization of nonlinear equations by removing high-order terms results in the evolution of the approximation error (Evensen 2003).

The Ensemble Kalman Filter (EnKF), developed by Evensen (1994) provides an alternative solution for data assimilation of large-scale nonlinear problems. A Monte Carlo version of KF, EnKF uses a group of random samples (ensemble) to represent the distribution of the unknown states. For a linear dynamical model, EnKF will converge exactly to KF with larger ensemble size. Another sequential Monte Carlo (SMC) based filter similar to EnKF is the particle filter. However, the particle filter (Doucet, De Freitas and Gordon 2001) requires a large number of realizations to converge, which makes it computationally unrealistic for applications to geophysical problems.

In this paper, we form the monitoring problem as a linear dynamical problem, and compare the performance and computational cost of the Basic Kalman Filter, Fast Kalman Filter, and EnKF. We propose an algorithm that can incorporate fast linear algebra methods to accelerate the statistical filter, in order to cope with real-time high-dimensional problems in subsurface monitoring. We also provide a numerical example of its application to CO_2 monitoring.

DATA ASSIMILATION THEORY

Linear State-Space Model and Random Walk Transition Model

When observations are collected in rapid succession, we can exploit "continuity over time" to combine measurements from different time steps. The intrinsic state s being monitored is a dynamic process governed by a physical model f. We can define a state space model (SSM) that consists of two time series, an unobservable intrinsic state x_k , $k \geq 1$ and an observable intrinsic state $y_k, k \geq 1$ —their relationship is described by $y_i = h(s_i, v_i)$. In the CO_2 monitoring example, we are interested in tracking the CO_2 plume location, so the intrinsic state to be estimated is CO_2 saturation, and the observation is seismic survey data. As CO_2 pushes its way into the pore space, CO_2 saturation changes with time, and the seismic data we record changes accordingly.

We first consider a linear dynamical system governed by the Linear Gauss-Markov model:

$$s_i = Fs_{i-1} + u_i$$
$$y_i = Hs_i + v_i$$

where $F \in R^{m \times m}$ is the state transition matrix; it represents our knowledge about the temporal behavior of s (change in s after one time step); the current state depends only on the previous state. The vector u_i is the zero-mean Gaussian process noise, with $u_i \sim N(0, Q)$, Q is the model error covariance matrix. The measurements (given data) are denoted d_i,,,,,,,, , and are related to x_i through linear operator H; the measurement noise is modeled as white noise $v_i \sim N(0, R)$, where R is a diagonal matrix.

Assuming that the state s_k is a random variable, whose first two moments, mean $\hat{s}_k$ and error covariance P_k, are known, then the mean and covariance propagate as follows:

$$\bar{s}_k = \bar{s}_{k-1}$$
$$P_k = P_{k-1} + Q_k$$

For Gaussian random variables, the probability distribution of s is completely characterized by its first two moments. Without any observations, the linearized forward model can predict the next state with large uncertainty. Extra information can be extracted from online measurements to improve our knowledge of the states and reduce the uncertainty in the system. For a linear state-space model, KF will give LMMSE estimates of the state given observations.

One common state transition model, the random walk model, is usually adopted when data is acquired rapidly, at a rate faster than discernible change in the system, in the absence of a valid physical model for state evolution (Nenna et al. 2011). This random-walk-model assumption

allows us to write the forecast step in a simple linear form, as follows,

$$s_{k+1} = s_k + u_i$$

Given that the dynamics of a complex system (e.g. subsurface fluid flow) often depends on prior knowledge of parameters with high uncertainties, the random walk model is useful in the absence of a reliable physical dynamical model. Moreover, the computational cost of Kalman Filtering can be greatly reduced given this simple model.

Basic Kalman Filter

The KF provides Linear Minimum Mean Square Error (LMMSE**)** estimates for the linear state-space model above. The Kalman filter algorithm enables predicting the most likely state s_i compatible with the probabilistic model for the evolution model (state transition matrix F) and the measurements (matrix H). There are two steps in this algorithm: (1) Forecast Step: projecting forward the current state and error covariance to obtain an a priori estimate for the next time step; (2) Analysis Step: incorporating the new measurements into the a priori estimate to obtain an improved a posteriori estimate. The Kalman gain K tells you how much weight to put on measurements versus the temporal prediction.

Forecast Step

$$s_f^k = Fs_a^{k-1}$$
$$P_f^k = FP_a^kF^T + Q$$

Analysis Step

$$K = P_fH^T\left(HP_fH^T + R\right)^{-1}$$
$$s_a = s_f + K(y - Hs_f)$$
$$P_a = (I - KH)P_f$$

k: time step index f: forecast, a: analysis
s: state to be estimated , F: state transition matrix, P: state error covariance matrix, Q: forecast error covariance matrix, R: measurement error covariance matrix

For numerical implementations, a more efficient algorithm for the analysis step, in which the covariance update is at the cost of $O(m^2)$, is as follows:

$$P_{yy} = HP^fH^T\ ,\ P_{xy} = P^fH^T$$
$$\left(P_{yy} + R\right)B = y - Hs_f$$
$$s_k^a = s_k^f + MB$$
$$P^a\ = P^f - P_{xy}(C + R)^{-1}P_{xy}\ ^T$$

Ensemble Kalman Filter (EnKF)

The EnKF is a Monte Carlo approximation of the KF developed to approximate the LMMSE estimates when the state dimension is too large for KF to propagate the state error covariance in a reasonable amount of time, or the linearization of the forecast model is not possible.

Consider an ensemble matrix

$$X = [x_1, x_2, \dots, x_N], \in R^{m\times N},$$

where each ensemble member x_i is a realization of a known vector. The ensemble mean denoted with a bar is given by

$$\bar{x} = \frac{1}{N}\sum_1^N x_i\ ,$$

and the ensemble covariance matrix is given by

$$P_e = \frac{1}{N-1}\sum_1^N(x_i - \bar{x})(x_i - \bar{x})^T,$$

The ensemble perturbation matrix is $X^{'} = X - \bar{X}$, thus

$$P_e = X^{'}X^{'T}/(N-1).$$

Generating an initial state ensemble S and integrating each ensemble member s_i forward in time according to a dynamical model, we have:

$$s_i^f = As_i + u_i\ \text{ or }\ s_i^f = G(s_i, u_i)$$

Given N realizations of the state vector s and observation vector y to form the state perturbation matrix $S' \in R^{m\times N}$ and observation perturbation matrix $Y' \in R^{n\times N}$, we have:

$$P_e^f = S'^f\left(S'^f\right)^T/(N-1)$$
$$R_e = Y'^f\left(Y'^f\right)^T/(N-1)$$

Rewriting the analysis equation in ensemble form:

$$K_e = P_e^fH^T\left(HP_f^eH^T + R_e\right)^{-1}$$
$$S^a = S^f + K_e(Y - HS^f)$$

With the perturbation form of the EnKF update, the error covariance P^f does not need to be constructed explictly, only the low rank approximation $P_e^f = S'S'^T$ is used. The ensemble approximated Kalman Gain thus can be computed at the cost of $O(m)$, which makes EnKF suitable for high-dimensional geophysical problems. The perturbation of observation is necessary for the EnKF to maintain a sufficient spread in the ensemble and prevent filter divergence (Houtekamer and Mitchell 1998).

Fast Kalman Filter

The Kalman Filter requires recursively updating the state and error covariance. If we denote the state dimension using m, then the computational cost of state update is $O(m)$, while the cost of covariance update, according to the Riccati equation, is $O(m^2)$. In geophysical problems, state dimension N is typically $\sim 10^4 - 10^8$, which makes updating and storing the state error covariance matrix of size N^2 at every time step computationally intractable. An alternative idea is to compute and store only the covariance matrix for measurement prediction $P_{yy} = HP_fH^T \in R^{n\times n}$ and cross covariance $P_{xy} = P^fH^T \in R^{m\times n}$. Under the random walk forecast model assumption (and state transition matrix F is an identity matrix), we show that it is possible to circumvent the state error covariance update, thus reducing the computational cost from $O(m^2)$ to $O(m)$.

This new algorithm consists of two parts: initialization and update. As a first step, we initialize the cross covariance as QH^T, which is the product of model error covariance Q and the transpose of the linear measurement operator. Normally, the cost of computing this product is $O(m^2,)$; however, because Q and H have unique structures, we can use fast linear algebra methods such as the Fast Multipole Method (FMM) hierarchical matrix solver as a blackbox to compute the cross covariance at the cost of $O(m)$.

During the update step, we recursively update the cross covariance at the cost of $O(m)$. Then Kalman Gain is computed as a function of cross covariance, which is then used to update the state at the cost of $O(m)$. The overall cost of the Kalman Filter is now $O(m)$, which means that the computational cost grows linearly instead of quadratically with the state dimension.

Reduce sampling error in EnKF with covariance tapering

From the Monte Carlo theory, the convergence rate is $1/\sqrt{N}$ regardless of the state dimension m. Without any approach for reducing the sampling error, the EnKF is both costly and inaccurate compared to KF. However, covariance tapering or localization can improve the covariance estimates using small sample sizes. It reduces the variance in the estimator, but it does introduce a bias to the solution. We can choose a covariance taper C with a similar structure as P_f so that $P_f^e = C \circ P_f^e$. C can be selected as an identity matrix or a distance-based covariance matrix. $C = \theta \exp\left(\frac{\|x\|}{l}\right)$.

Because we need to run the forward model for each ensemble member at every time step, (which is costly), we want to reduce the size of the ensemble as much as possible. However, a small ensemble size may yield spurious correlations that, when used in the Kalman Gain, can cause changes in the state variables over which the data has no real influence. Also, in the standard EnKF, the posterior ensemble is the linear combination of the prior ensemble, whose rank is less than or equal to N_e, yielding a rank-deficiency problem. To reduce both the sampling error and rank-deficiency problem, we can introduce a distance-dependent localization (Houtekamer and Mitchell 2001). The localized covariance matrix is the Schur product of the correlation function ρ and the original sample covariance, $\rho \circ C_{ss}$. The small error covariances associated with remote observation are removed (Aanonsen et al. 2009) and the new EnKF update step is given by

$$K_e = \left[(\rho H^T) \circ (A_s A_y^T)\right]\left[(H\rho H)^T \circ (A_y A_y^T) + A_d A_d^T\right]^{-1}$$

We use the ray operator H to project the correlation function ρ from $R^{N_s \times N_s}$ to $R^{N_s \times N_d}$. After applying localization, the posterior ensemble is

not restricted to the subspace spanned by the prior ensemble. If the sample covariance is positive semi-definite, with positive values on the diagonal, and the localization matrix is positive definite, then from the Schur product theorem, the resulting localized covariance matrix is guaranteed to be of full rank and positive definite.

Covariance localization reduces the variance of the estimator, yet introduces a bias to the solution. Ideally, the covariance taper C should have a structure similar to the P_f, so that $P_f^e \approx C \circ P_f^e$.

NUMERICAL EXPERIMENTS

The purpose of these numerical experiments is to demonstrate the performance of KF and EnKF in reconstructing the dynamic 2-D object (such as a CO_2 plume) from tomographic measurement (seismic travel time) when no deterministic model for the state evolution is given (transition matrix $F = I$).

We use, as data, synthetic results produced by TOUGH2 (Pruess, Oldenburg and Moridis 1999). This model was implemented to reconstruct the CO_2 injection process at the FRIO II site using real field parameters as constraints (Daley, Ajo-Franklin and Doughty 2011). In the FRIO pilot project, investigators injected, at a depth of 1657 m, about 380 tons of CO_2 at a rate of 76T/day into a 17 m thick blue sand brine aquifer, with a dip of 18 degrees, about 30% porosity, and permeability of 1 to over 4 darcy. The breakthrough time for CO_2 at the observation wells (~30 m apart) was around 2 days. Based on well logs and core measurements, a realistic model was constructed with layered permeability and porosity distribution.

Introducing a petrophysical relationship between CO_2 saturation and seismic properties, we can obtain a time-varying map of seismic velocity and attenuation, and then simulate the CASSM response—which can then be compared with the CASSM field measurement. As previously observed, CO_2 is heterogeneously distributed in brine water, so that the relation between CO_2 saturation and the change in the seismic velocity can be described with a patchy petrophysical model better than with the more classic Gassmann model. The change in velocity and attenuation as a function of CO_2 is shown in Figure 3 of the previously cited work. The change in velocity is captured by CASSM. Field CASSM is equipped with one piezotube source located at 1657 m depth generating 1 kHz seismic signals, and 13 receivers located at varying depths. Travel-time measurements are acquired every 15 minutes beginning 2 hours after injection (Daley et al. 2007). The effects of buoyancy are particularly pronounced. Simulation and data suggest that CO_2 flow is straight up near the injection point until it hits the cap rock; then, it continues upwards along the dip of the cap rock.

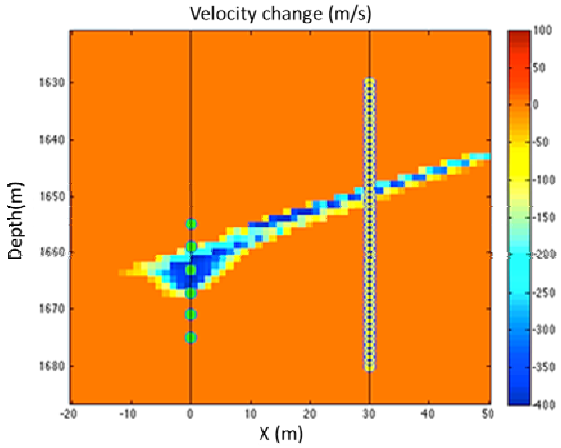

Figure 1. Illustration of general seismic crosswell setup; a transmitter array is installed at the injection well (here: at X-location 0 m) and a receiver array is installed at a nearby monitoring well (here: at X-location 30 m). The CO_2 plume shows up as a decrease in velocity.

The synthetic CASSM survey design is shown in Figure 1. Six sources and 48 receivers are deployed and remain the same over the course of CO_2 monitoring. The background velocity has been removed; only changes in velocity after CO_2 injection are demonstrated in the graph. White Gaussian noise has been added to each measurement, resulting in a 65 dB signal-to-noise ratio (SNR) defined as

$$\mathrm{SNR} = 10 \log_{10} \frac{\|\mathrm{Hs}\|_2^2}{\|\mathrm{v}\|_2^2}$$

Before injection begins, we assume the CO_2 induced velocity perturbation is zero, so it is reasonable to assume $s_0 = 0$ and $P_0 = 0$, true model and inversion results from KF and EnKF are shown in Figure 2. Pre-injection change in velocity is zero. Three hours after injection, a low-velocity zone began to form around the injection point. Another low velocity zone formed below the cap rock and extended laterally over time, which is predicted well by the KF result. The time interval between adjacent pictures is 30 hours. Here, our target domain to be imaged is between the monitoring wells; thus in the figure, only relevant parts are shown. EnKF gives a larger relative estimation error than the fast KF.

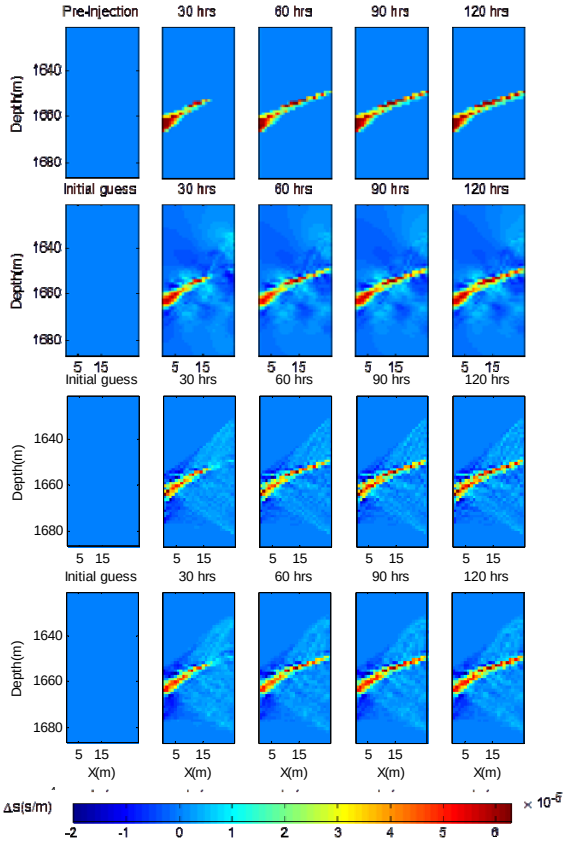

Figure 2. Reconstruct CO_2 induced velocity perturbation (slowness in 10^{-5} s/m) on a 55×59 grid. Only the inversion result between the well is shown in the graph. Case I: True slowness change; Case II: slowness change given by KF; Case III: slowness change given by EnKF with linear covariance tapering; Case VI: slowness change given by EnKF with exponential covariance tapering.

Computational and storage cost is summarized in Table 1. Generally, initialization of cross covariance exhibits quadratic growth with state dimension. However, the Fast Multipole Method (FMM) can reduce the cost to $O(N)$. The cost of state update in 41 time frames also grows linear with state dimension, as well as the storage cost. Thus, we dramatically reduce the computational cost by updating covariance directly with $O(N^2)$ to $O(N)$.

Table 1. Computational and storage cost of fast KF

State Dimension	Initialize QH^T	Initialize QH^T with FMM	State update (41 frames)	Storage Cost
3245 (55x59)	26.37s	31.37s	1.91s	7.5MB
12753 (117x109)	400.9s	91.76s	5.84s	29.4MB
50778 (237x217)	6360.96s	280.07s	21.76s	117MB
250000 (500x500)	N/A	1157.6s	N/A	576MB

CONCLUSIONS

This paper addresses the problem of subsurface monitoring by formulating the problem using a linear state-space model. We showed that the Kalman Filter-based data assimilation tool can reconstruct dynamic objects recursively with good quality and computational efficiency. This is ideal for real-time monitoring applications in which data are collected at a rate faster than a discernible change in state. Fast KF with FMM significantly reduces the computational cost of the Kalman Filter update, from $O(m^2)$ to $O(m)$. Localized EnKF also reduces the computational cost to $O(m)$, yet introduces a bias into the estimation.

ACKNOWLEDGMENT

We want to acknowledge Stanford GCEP for funding this project. The synthetic TOUGH2 results were obtained through the courtesy of Dr. Jonathan Ajo-Franklin at LBNL and his colleagues. We want to thank their general support of this project.

REFERENCE

Aanonsen, S. I., G. Naevdal, D. S. Oliver, A. C. Reynolds & B. Valles (2009) The Ensemble Kalman Filter in Reservoir Engineering-a Review. *Spe Journal,* 14**,** 393-412.

Anderson, B. D. O. & J. B. Moore. 1979. *Optimal filtering*. Prentice-hall Englewood Cliffs, NJ.

Daley, T. M., J. B. Ajo-Franklin & C. Doughty (2011) Constraining the reservoir model of an injected CO2 plume with crosswell CASSM at the Frio-II brine pilot. *International Journal of Greenhouse Gas Control,* 5**,** 1022-1030.

Daley, T. M., R. D. Solbau, J. B. Ajo-Franklin & S. M. Benson (2007) Continuous active-source seismic monitoring of injection in a brine aquifer. *Geophysics,* 72**,** A57-A61.

Doucet, A., N. De Freitas & N. Gordon. 2001. *Sequential Monte Carlo methods in practice*. Springer Verlag.

Evensen, G. (2003) The ensemble Kalman filter: Theoretical formulation and practical implementation. *Ocean dynamics,* 53**,** 343-367.

Houtekamer, P. L. & H. L. Mitchell (1998) Data Assimilation Using an Ensemble Kalman Filter Technique. *Monthly Weather Review,* 126**,** 796-811.

--- (2001) A Sequential Ensemble Kalman Filter for Atmospheric Data Assimilation. *Monthly Weather Review,* 129**,** 123-137.

Kalman, R. E. (1960) A New Approach to Linear Filtering and Prediction Problems. *Transactions of the ASME – Journal of Basic Engineering***,** 35-45.

Lumley, D. E. (2001) Time-lapse seismic reservoir monitoring. *Geophysics,* 66**,** 50-53.

Nenna, V., A. Pidlisecky & R. Knight (2011) Application of an extended Kalman filter approach to inversion of time-lapse electrical resistivity imaging data for monitoring recharge. *Water Resour. Res.,* 47**,** W10525.

Pruess, K., C. Oldenburg & G. Moridis. 1999. TOUGH2 user's guide, version 2.0. Report LBNL-43134, Lawrence Berkeley National Laboratory, Berkeley, Calif.

MODELING APPROACHES FOR WELLBORE BOUNDARY CONDITIONS FOR SIMULATION OF CO_2 GEOLOGIC SEQUESTRATION IN SALINE AQUIFERS

Keni Zhang[1,2] Lulu Ling[2], and Yang Wang[2]

[1] Earth Sciences Division, Lawrence Berkeley National Laboratory, Berkeley, California
[2] College of Water Sciences, Beijing Normal University, Beijing 100875, China
e-mail: kzhang@lbl.gov

ABSTRACT

Numerical simulations have been widely used for CO_2 storage site characterization. The performance of CO_2 injection into saline aquifers can be evaluated by use of site-scale numerical models. Within such models, the treatment of well boundary conditions is one of the most challenging tasks. The difficulty arises because the maximum changes in primary variables and occurrences of maximum mass/heat fluxes occur at wells or in nearby gridblocks. Consequently, these gridblocks may have relatively bad computational convergence. Most simulations use a sink/source term to represent the injection, and directly apply the injection flux to well gridblocks. In a real CO_2 sequestration project, a long well screen may be needed to guarantee sufficient injectivity, regardless of well orientation (vertical, deviated, or horizontal). In modeling, the injected flux allocation along the well screen must typically be determined.

In this paper, three modeling approaches for simulation of long-screen injection wells are proposed. These approaches intend to accurately distribute injection fluxes by a potential or mobility allocation scheme for a multilayered well or a horizontal well. The three approaches include "fixed screen top pressure," "distributed pressure," and "virtual block" methods. Here, implementations of these approaches are discussed, and the advantages and disadvantages of the different approaches are investigated.

INTRODUCTION

CO_2 is the most important greenhouse gas because of its large global emission rate and longevity in the atmosphere. Finding suitable locations for permanently sequestering captured CO_2 is crucially important for reducing net CO_2 emissions. Deep saline formations are thought to be good candidates for CO_2 sequestration, due to their large potential capacity. Numerical simulations play an important role in CO_2 storage site characterization. The performance of CO_2 injection into saline aquifers can be evaluated through numerical modeling studies. Treatment of well boundary conditions is one of the most challenging tasks for numerical simulations because the maximum changes in primary variables and occurrence of maximum mass/heat fluxes occur at wells or in nearby gridblocks. Most site-scale simulations reported in the literature (Yamamoto, et al., 2009; Zhou, et al., 2010) use a sink/source term to represent injection and directly apply the injection flux to well gridblocks. However, actual field injections often use multilayered wells, which must distribute injection to multiple layers. In many cases, efficient and rigorous treatment of well conditions is critical for successfully modeling large-scale CO_2 storage. Fully coupled wellbore-reservoir simulation, with an accurate accounting of well conditions, could be a sensible approach for handling flow from wells to aquifers. Simulation of the fast non-Darcy flow in the wellbore, coupled with slow multiphase Darcy flow in the reservoir, limits convergence rates (Pan, et al.

2011) which may make this coupled approach unsuitable for site-scale reservoir simulations.

Strictly speaking, a well boundary condition in multiphase modeling is a "constraint condition" rather than a rigorous "boundary condition" as used in the mathematical sense for solving partial differential equations [Wu et al., 1996]. Yet accurately allocating (as part of a simulation) injected CO_2 to multi-layer system is a challenging task. The conventional method of well treatment in groundwater, geothermal, and oil reservoir simulations for multiphase flow involves (for a multi-layered well) using a sink/source term approach and distributing flow rates by a potential or mobility allocation scheme [Aziz and Settari, 1979]. This approach is good for most well boundary simulations when modeling CO_2 sequestration: it can estimate correct total fluid injection/production rates as long as the maximum and minimum pressure constraints are not violated. Backflow, however, may occur in multilayered wells within a thick, heterogeneous formation or a long horizontal well. The mobility allocation method, however, distributes grid-layer fluxes along a well based on a mobility ratio and without considering the effects of pressure or potential gradients. This method is easy to implement, but may result in physically incorrect solutions and poor numerical performance [Wu et al., 1996]. In response to this problem, Wu (2000) proposed a "virtual node" approach for treatment of well boundary conditions which allows for backflow.

In this paper, we propose three approaches for injection-fluid allocation along long-screened wells. The three approaches are "fixed screen top pressure," "distributed pressure," and "virtual block." The "fixed screen top pressure" approach applies a constant pressure or constant injection rate at the top-well-screen gridblock. Flux migrates down to the well bottom or to the storage aquifers of the top-well-screen gridblock. Allocation of CO_2 fluxes to different layers proceeds according to pressure differences and flux mobilities in the corresponding formations. The "distributed pressure" approach uses a constant pressure along the well screen for CO_2 injection. Pressure gradient along the well screen is determined from gravity equilibration. The "virtual block" approach simulates a well bore either as a single gridblock or several computational gridblocks screened and connected to many neighboring gridblocks within a multilayered well. In this approach, the wellbore can be vertical, inclined, or horizontal, and the well borehole gridblock is treated in the same way as any other non-well gridblocks for flow calculations. This approach can handle the backflow problem that might occur in a multilayered well within a heterogeneous formation. The proposed approaches have been applied to site-scale CO_2 injection simulations as part of China's first full-process CO_2 sequestration project, the Shenhua Ordos CO_2 sequestration demonstration project.

METHODOLOGY

It is generally understood that a well is screened in multiple layers by means of regions of perforations in the well casing. Injected flux moves downward through the wellbore and then enters into aquifers through these perforated regions. Figure 1 provides a schematic illustration of flow in the wellbore. Such flow is usually not expected to obey Darcy's law. The Equivalent Darcy's Media (EDM) approach has been widely used to simulate wellbore flow as a convenient approximation, especially if the wellbore flow simulation is coupled to reservoir simulation (Birkholzer et al., 2011). Equivalent parameters must be determined for the EDM approach: While researchers often choose a high permeability for

the wellbore, it is hard to know how large it should be for any given problem. Hu et al. (2012) demonstrated that for their problem, an equivalent permeability of 3.16×10^{-6} m^2 can produce a good match between a fully coupled wellbore-reservoir simulation and the EDM approach. We use the EDM approach with high permeability for the wellbore boundary conditions.

The "fixed screen top pressure" approach treats the screen's top gridblock (see Figure 1) as a first-type boundary. This approach can be used for constant pressure or constant rate injection. Pressure at that gridblock is determined by the injection pressure at the top of the well using a wellbore simulator. We use T2WELL (Pan et al. 2011) for the calculation, which simulates flow moving downward within the wellbore. Very high permeability is selected for the EDM guaranteeing vertical flow in the borehole. Total injection rate equals the downward flow rate in the wellbore from the screen-top gridblock, which can be determined by the reservoir simulator at each time step. An alternative approach for constant-rate injection is to apply a constant injection rate at the screen-top gridblock. The injected CO_2 moves downward through the high-permeability EDM and migrates into the storage aquifers. Distribution of CO_2 among storage layers is determined by the pressure gradient and mobility of the layers.

The "distributed pressure" approach is also used for simulating constant-pressure injection. In this approach, the pressures along the well screen are known. Pressures at different elevations are determined through wellbore simulation or estimated using fluid density under the reservoir temperature and pressure conditions. CO_2 migrates into the formation layers from the well gridblocks with a fixed pressure. Total CO_2 injection rate is the sum of the flow rate from well gridblocks into storage aquifers.

The "virtual block" method handles a wellbore as a single gridblock or as several gridblocks (Wu, 2000). Figure 1 illustrates a virtual gridblock representation of a well and its association with formation layers and model grids in a multilayered, vertical wellbore. In this approach, the mass balance and discrete equations are still applicable to well gridblocks. However, the coefficients for flow terms are evaluated differently. In this case, an injectivity index is used for wellbore–formation flow, while wellbore mobility and transmissivity are used for wellbore–wellbore flow.

In TOUGH2 simulation, mobility (λ_β) and transmissivity (γ_{ij}) of flow terms are defined as (Pruess, et al. 1999),

$$\lambda_\beta = k_{r\beta} / \mu_\beta \qquad (1)$$

$$\gamma_{ij} = \frac{A_{ij} k_{ij}}{d_i + d_j} \qquad (2)$$

where $k_{r\beta}$ is the relative permeability of phase β, μ_β is the fluid viscosity in phase β, A_{ij} is the common interface area between connected gridblocks i and j, d_i is the distance from the center of gridblock i to the interface between gridblocks I, and j, k_{ij} is the permeability for the connection between gridblocks i and j, which can be determined using different weighting schemes from the permeability of gridblocks i and j.

Flow between wellbore gridblocks is simulated using the EDM approach. Mobility and transmissivity of the EDM are used for the calculations. The injectivity index needed for wellbore–formation flow calculation can be calculated using many different methods (e.g., Thomas,

1982; Fung et al., 1991). The well index formulation by Thomas (1982) is:

$$II_{ij} = \frac{2\pi k \Delta z_j}{\ln(\frac{r_e}{r_w}) + s - 1/2} \qquad (3)$$

where Δz_j is the thickness of layer j, r_e and r_w are an equivalent radius of gridblock j and the well bore radius, respectively, and s is the skin factor. Through selecting appropriate d_i and A_{ij} for the connection of well gridblock to the neighboring formation gridblocks, we can determine a transmissivity equivalent to the effect of the well injectivity index. By this approach, the well gridblocks can be treated in the same way as regular formation gridblocks, except using equivalent parameters of d_i and A_{ij}.

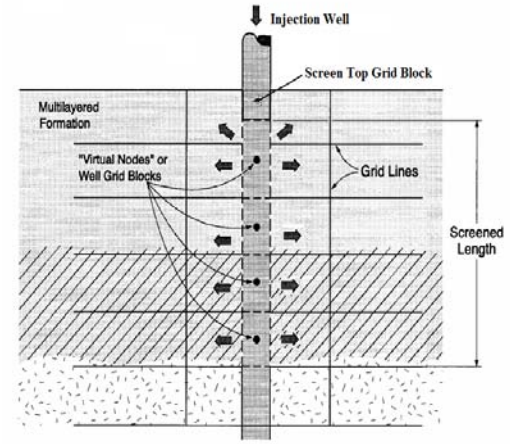

Figure 1. Schematic illustration of wellbore boundary conditions (Modified from Wu, 2000)

EXAMPLES

CO_2 storage in saline aquifers was simulated to observe the CO_2 flow and injectivity by using different wellbore boundary conditons based on the Shehua CCS Project, China's first fully integrated CCS demonstration project. The proposed three approaches, "fixed screen top pressure," "distributed pressure," and "virtual block," are applied in describing the wellbore boundary conditions. The "fixed screen top pressure" approach applies a constant pressure or injectivity at the top gridblock of the wellbore screen for CO_2 injection. Two models—modeling constant injectivity according to actual injection, and modeling constant pressure injection at a pressure of 1.3 times the initial formation pressure—are present for demonstration of this approach. The "distributed pressure" approach simulates constant pressure along the wellbore based on gravity equilibration. A constant pressure of 1.3 times initial equilibrium presssure is applied to the well screen for CO_2 injection. The "virtual block" method uses a single gridblock connected to all wellbore gridblocks for the simulation.

The Shenhua CCS project calls for injecting 100,000 Ton/Yr CO_2 into low-permeability sandy aquifers, within the Ordos Basin in Inner Mongolia. The injection well was drilled to a depth of around 2500 m. Storage aquifers are distributed between the depths of 1690–2400 m, which are interlayered by clay formations. Injection screens are opened to multiple aquifers, represented by 21 model layers. The aquifers have a thickness of several meters with permeability of several millidarcy. Storage layers are numbered as INJ01 to INJ21 from top to bottm. Hydraulic fracturing was conducted at INJ05, INJ06 and INJ15-INJ21 for improving injectivity. A three-dimensional numerical model was developed for simulating CO_2 injection in the site using TOUGH2-MP (Zhang et al., 2008).

Numerical experiments indicate that a model domain of 10 km×10 km is sufficient for treating the four sides as first-type boundaries. Vertically, the model covers the depth from 1680 to 2400 m, including all storage aquifers and clay interlayers (Figure 2). The injection well is located at the

center of the model domain. The 10 km×10 km model domain was discretized into 7481 gridblocks for each model layer, with five levels of refinement around the injection well (see Figure 3). In the vertical direction, the domain was discretized into 59 model layers. At the center of the mesh, a special area with 90 m length and 1 m width along 5 degrees east to north represents hydraulic fracturing zones (Figure 3), and a permeability of 100 mD is assigned to these fracturing zones. Four sides of the domain are treated as first-type boundaries, whereas the top and bottom of the model are non-flow boundaries. The well boundary condition is treated by the three different approaches, as discussed above. Intial contitions of the model are determined based on measured geothermal gradient, gravity equilibrium pressure distribution, and a constant 3% salt mass fraction. Model parameters were provided by core measurements and tests.

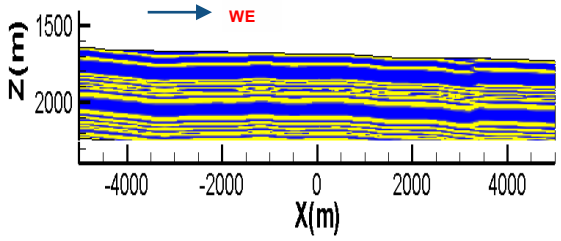

Figure 2. Eest-West cross-section the the model domain (yellow: storage formations, blue: clay layers)

Figure 4 shows the simulated percentage of flux distribution among several key storage layers for the cases with specified injection rate at the top well-screen gridblock (TOP_Q), constant pressure at the top well-screen gridblock (TOP_P_1.3P0), distributed pressure (Dis_P_1.3P0), and virtual block approaches, respectively. All cases show that a high percentage of CO_2 flows into the hydraulic fracturing zone (FRACT) at the beginning. The fluxes reach a peak amount in a couple of months and then drop dramatically afterwards. All these cases show higher percentage fluxes flowing into storage layers INJ01 and INJ06. Both layers have relatively high permeability. Hydraulic fracturing was conducted at INJ06 which may help to improve the storage capacity at the layer. This indicates that the flux migrating into each layer is governed by phase mobility in the formation, no matter how the injection occurred. Among the four cases, TOP_P_1.3P0 and Virtual_block have higher percentages than the TOP_Q and Dis_P_1.3P0 cases for the two layers. INJ01 and INJ06 layers receive similar percentage fluxes (~11%–13%). Every other layer receives less than 10% of the total flux. In distributed pressure schemes, flux discrepency among different layers is relatively small. Most layers receive lower than 10% fluxes. The two cases for "fixed screen top pressure" (TOP_Q and TOP_P_1.3P0) have similar pressure gradient from top to bottom layers. This is comfirmed by the fact that the sequence of flux percentage for the storage layers is almost identical.

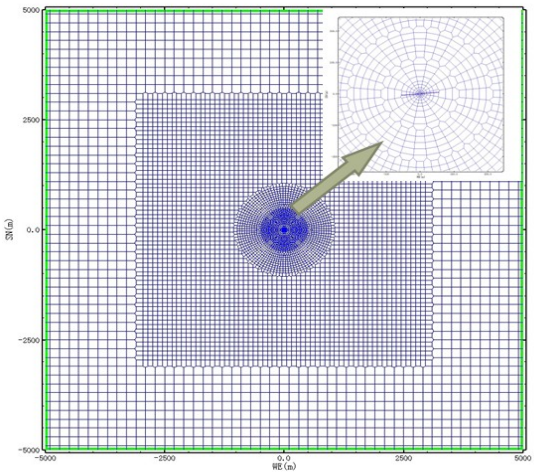

Figure 3. Plane view of the three-dimensional mesh

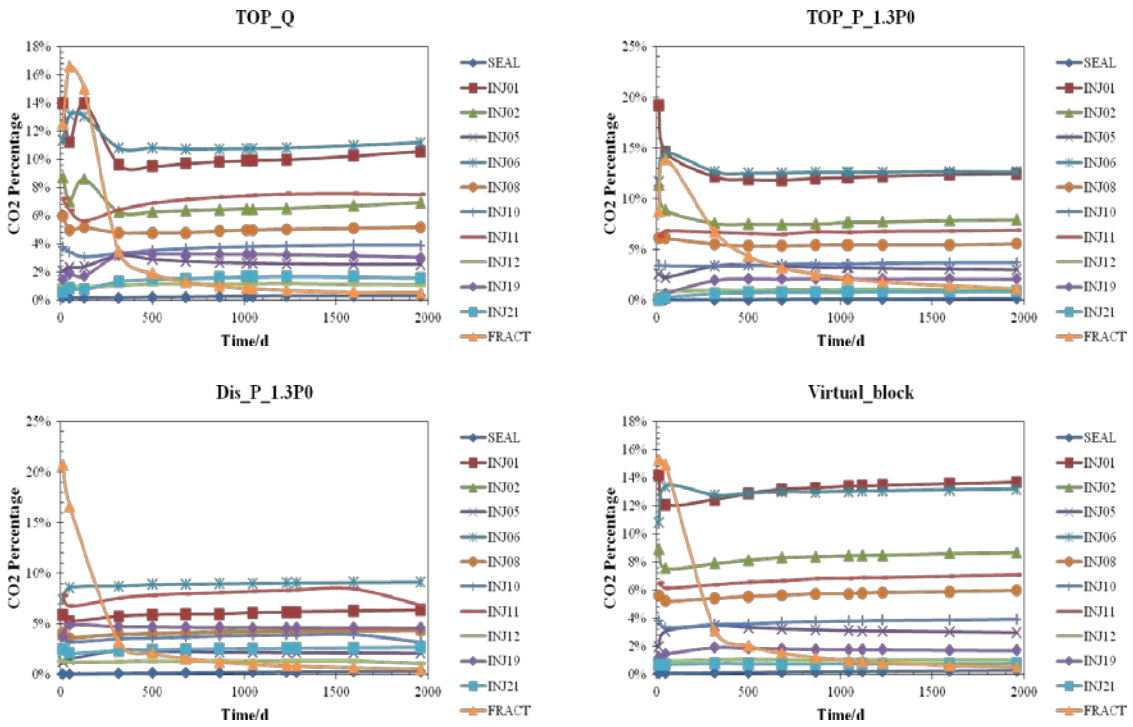

Figure 4. Simulated flux distribution at different layers using (a) fixed rate at the top screen gridblocks , (b) fixed pressure at the top screen gridblocks, (c) the "distributed pressure" approach, (d) the "virtual block" approach

Figure 5 shows the supercritical gas-saturation distribution at the layer INJ06 for the TOP_Q approach, after a 10-day injection. Other approaches produce similar gas saturation distributions. It is clear that the gas distribution is mainly controlled by the hydraulic fracturing zone; gas flow is faster along the fracturing region than in the formation. That may indicate hydraulic fracturing can effectively improve CO_2 injectivity.

The vertical profile of CO_2 gas saturation after a 5.36-year injection for different wellbore boundary condition approaches are shown in Figure 6. The TOP_Q, TOP_P_1.3P0 and Virtual_block cases demonstrate more significant injection at the top layers than the Dis_P_1.3P0 case. This is because the three approaches may have relatively larger pressure gradients between the wellbore and formations at the top layers. It is also the reason why the CO_2 plumes in INJ01 and INJ02 are quite different between the Virtual block scheme and other schemes. Clearly, the pressure gradient between wellbore and storage formations is still one of the key factors controlling flux distribution in the storage layers.

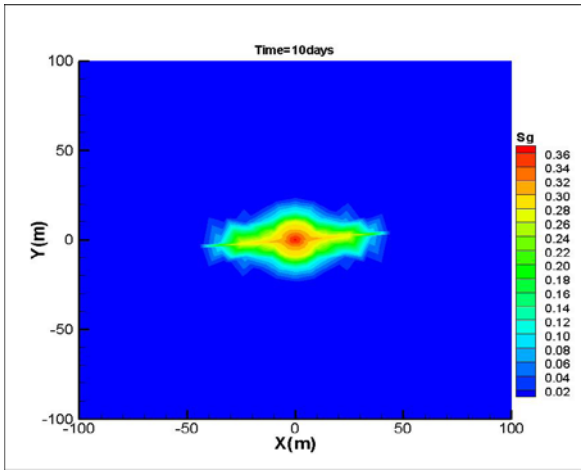

Figure 5. Plane view of CO_2 gas saturation distribution in layer INJ06

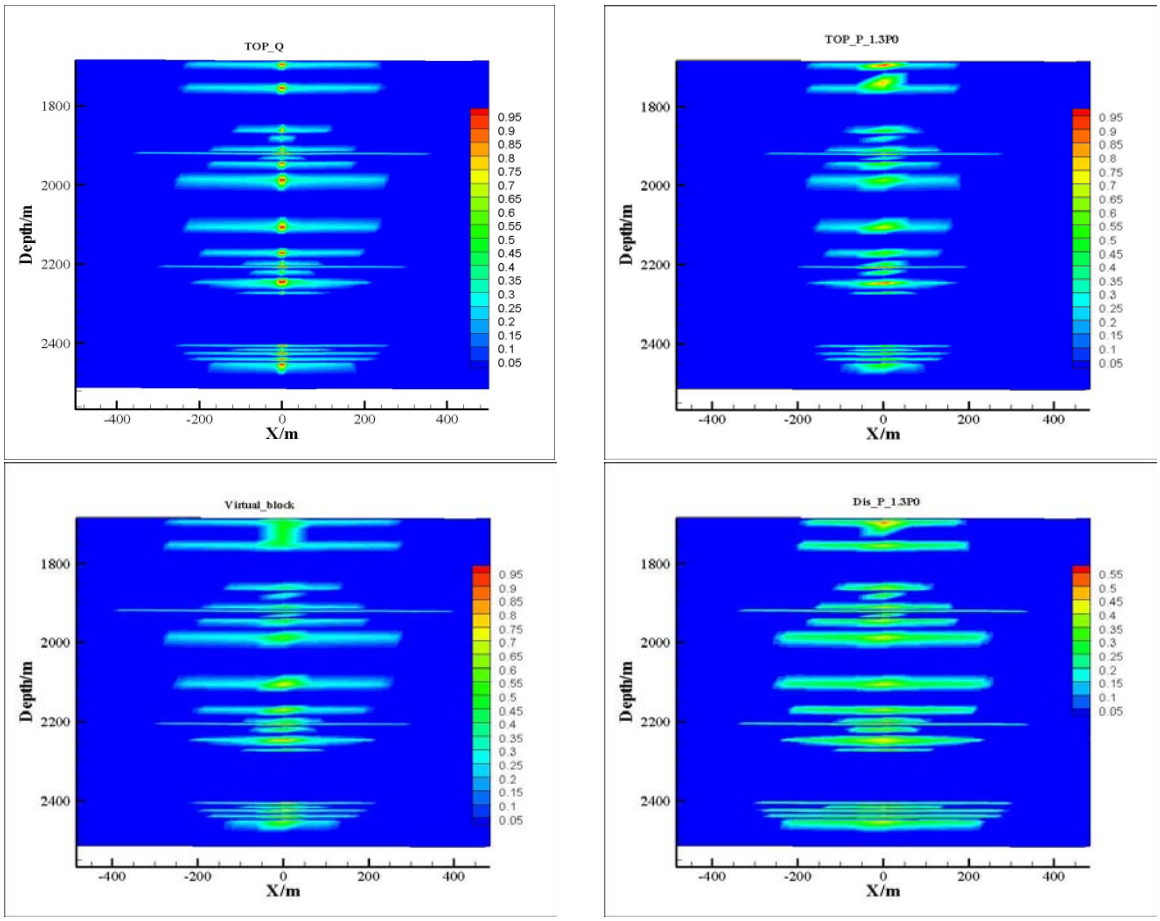

Figure 6. The vertical profile of gas saturation using different wellbore boundary condition approaches: (a) fixed rate at the top screen gridblocks, (b) fixed pressure at the top screen gridblocks, (c) the "distributed pressure" approach, (d) the "virtual block" approach

Simulation results indicate that the different wellbore-boundary-condition approaches may produce quite different results. In most cases, CO_2 injection with a specified rate or pressure at the well head is used. This type of operation can be simulated using the "fixed screen top pressure" approach. If pressure along the wellbore screen does not show a significant gradient, the "virtual block" approach may be selected for the simulation. The "distributed pressure" approach may be used for simulating wells with detailed information about injection pressure along the wellbore screen.

CONCLUSIONS

We propose three approaches—"fixed screen top pressure," "distributed pressure," and "virtual block,"—for treatment of wellbore boundary conditions. These three approaches provide different schemes for injection-fluid allocation along long-screened wells. The "fixed screen top pressure" approach applies a constant pressure or constant injection rate at the top gridblock of the well screen. This approach may be suitable for simulating CO_2 injection with a specified rate or pressure. The "distributed pressure" approach uses a constant pressure along the well screen for CO_2 injection. This approach can be used in simulations with detailed information on injection pressure along the wellbore screen. The "virtual block"

approach simulates a wellbore (in a multilayered well) either as a single gridblock or several gridblocks screened and connected to many neighboring gridblocks. The "virtual block" approach is suitable for simulation of wells without a significant pressure gradient along the wellbore screen.

The proposed approaches were applied to the site-scale CO_2 injection simulations within China's first fully integrated CO_2 sequestration demonstration project. They can effectively simulate CO_2 injection processes and obtain reasonable CO_2 flux distribution among different layers. Note that simulation results show different approaches may produce quite different results. In real injection simulations, an approach best representing field operations must be selected.

ACKNOWLEDGMENT

This work was sponsored by the National Nature Science Foundation of China (Grant Number: 41072178) and supported by the U.S. Department of Energy under Contract No. DE-EE0002762.

REFERENCES

Aziz, K., and A. Settari, Petroleum Reservoir Simulation, *Appl. Sci.*, London, 1979.

Birkholzer J.T., Nicot J.P., Oldenburg C.M., Zhou Q.L., Kraemer S., Bandilla K., Brine flow up a well caused by pressure perturbation from geologic carbon sequestration: static and dynamic evaluations. *International Journal of Greenhouse Gas Control* 5, 850-861, 2011.

Fung, L., A. Hiebert, and L. Nghiem, Reservoir simulation with a control-volume finite-element method, paper SPE-21224 presented at 11th SPE Symposium on Reservoir Simulation, *Soc. of Pet. Eng.*, Anaheim, Calif., Feb, 1991.

Pan, L., Oldenburg C.M., Wu, Y.S., Pruess, K., Wellbore flow model for carbon dioxide and brine. *Energy Procedia, GHGT9 conference*, Washington DC. LBNL-1416E, 2008.

Pan, L., Oldenburg C.M., Wu, Y.S., Pruess, K., *T2WELL/ECO2N Version 1.0: Multiphase and non-isothermal model for coupled wellbore reservoir flow of carbon dioxide and variable salinity water.*, LBNL-4291E,Berkeley, CA, 2011.

Pruess, K., C. Oldenburg, and G. Moridis, *TOUGH2 user's guide*. Report LBNL-43134, Lawrence Berkeley National Laboratory, Berkeley, CA, USA, 1999.

Wu, Y. S., P. A. Forsyth, and H. Jiang, A consistent approach for applying numerical boundary conditions for multiphase subsurface flow, *J. Contam. Hydrol.*, 23, 157–184, 1996.

Wu, Y.S., A virtual node method for handling well bore boundary conditions in modeling multiphase flow in porous and fractured media, *Water Resource Research*, 36(3), 807–814, 2000.

Thomas, G. W., Principles of Hydrocarbon Reservoir Simulation, *Int. Human Resour. Dev.*, Boston, Mass., 1982.

Yamamoto, H., K. Zhang, K., Karasaki, A. Marui, and N. Nishikawa, Numerical investigation concerning the impact of CO_2 geologic storage on regional groundwater flow. *International Journal of Greenhouse Gas Control*, 3(5), 586–599, 2009.

Zhang, K., Y.S. Wu and K. Pruess, *User's Guide for TOUGH2-MP - A Massively Parallel Version of the TOUGH2 Code*, LBNL-315E, CA,2008.

Zhou Q, Birkholzer JT, Mehnert E, Lin YF, Zhang K., Modeling basin- and plume-scale processes of CO_2 storage for full-scale deployment, *Ground Water*, 48(4):494-514,2010.

A FULLY COUPLED MODEL OF NONISOTHERMAL MULTIPHASE FLOW, GEOMECHANICS, AND CHEMISTRY DURING CO_2 SEQUESTRATION IN BRINE AQUIFERS

Ronglei Zhang, Xiaolong Yin, Philips H. Winterfeld, and Yu-Shu Wu

Colorado School of Mines, Golden, CO, 80401, United Sates
e-mail: rozhang@mines.edu

ABSTRACT

The significance of thermal-hydrologic-mechanical-chemical (THMC) processes has been well recognized in the operation of CO_2 geosequestration and geothermal resource development. Geomechanical and geochemical effects may significantly change aqueous-phase composition, porosity, and permeability of the formation, as well as flow and transport. The TOUGHREACT simulator (Xu et al., 2004b) has the capability to quantitatively simulate the fluid flow, solute transport and geochemical reactions of these processes using sequential coupling. Using a mean stress formulation, we have simulated the stresses, displacements, and rock deformation due to fluid injection via the recently developed TOUGH2_CSM (Winterfeld and Wu, 2011) for modeling geomechanical effects in CO_2 flow and transport in brine aquifers. Based on these previously developed numerical simulators—ECO2N (Pruess, 2005), TOUGH2_MP (Zhang et al., 2008), TOUGHREACT, and TOUGH2_CSM—we present a fully coupled computational framework model to simulate reactive transport of CO_2 in porous and fractured media with complex chemical reactions that occur in gaseous, liquid, and solid phases. The framework is designed to keep a unified computational structure for different THMC processes. This fully coupled simulator focuses on: (1) fluid and heat flow, and aqueous-phase solute transport within a three-phase mixture; (2) the stresses and displacements related to the mean stress; (3) the nonisothermal effect on fluid properties and reaction processes, and (4) the equilibrium and kinetics of fluid-rock and gas-rock interactions. A system of partial differential equations is formed to represent the physical, mechanical, and chemical processes of reactive solute transport associated with CO_2 in aquifers. The fully coupled model is verified againt the TOUGHREACT simulator, and we present analytical solutions as well as a few practical examples related to CO_2 sequestration.

INTRODUCTION

Coupled THMC processes have been of increasing interest to researchers studying CO_2 geosequestration, which is regarded as a possible effective solution in preventing CO_2 generated from burning fossil fuels from entering the atmosphere. Saline aquifers have the largest capacity among the many options for long-term geological sequestration. They are large underground formations saturated with brine that are often rich in dissolved minerals. CO_2 is injected into these formations as a supercritical fluid with a liquid-like density and a gas-like viscosity. It is believed that the geomechanical effects during and after CO_2 injection, and the geochemical reactions between CO_2 and rock minerals, are very important for the safe injection and long-term fate of CO_2.

In this paper, we present a fully coupled model—to simulate fluid and heat flow, rock deformation due to fluid injection, and water-rock-gas interaction under chemical equilibrium and/or kinetic conditions—developed for CO_2 geosequestration. The development of this model is based on the algorithms of ECO2N (Puress, 2005), TOUGHREACT (Xu et l., 2004b), TOUGH_MP (Zhang et al., 2008), and TOUGH_CSM (Winterfeld and Wu, 2011). The mean stress and geochemical reaction equations are fully coupled with fluid flow, heat flow, and mass transport equations. In this model, all the governing equations to describe the THMC process are solved simultaneously by Newton-Raphson iteration, which allows a larger time step to be applied. This fully coupled simulator has the following features: (1) the fluid and heat flow, aqueous-phase solute transport within a three-phase mixture, (2) the stresses and displacements related to the mean stress, (3) the

nonisothermal effect on fluid properties and reaction processes, and (4) the equilibrium and kinetics of fluid-rock and gas-rock interactions. The mathematical descriptions and implementation of the fully coupled model are addressed in detail.

To verify and validate the capabilities of the fully coupled simulator, we compare the simulation results with analytical solutions for the mineral dissolution under local equilibrium and chemical kinetics. Furthermore, a batch geochemical system, considering the chemical interaction of gas-liquid-mineral under the equilibrium state, is presented to verify the geochemical capability in the absence of flow and stress. Then, a 1D geochemical reaction system, subjected to the environment of supercritical CO_2 injection, is designed to validate coupled fluid flow and geochemistry. Finally, a complex batch system with both chemical equilibrium and kinetics is simulated to demonstrate the capability of the fully coupled model.

MATHEMATICAL DESCRIPTION

Governing Equations

The governing equations include mass conservation, energy conservation, momentum conservation, and chemical reaction equations. Table 1 provides a brief mathematical description and numerical implementation of the fully coupled THMC model. The fluid and heat flow equations are based on that of the ECO2N module of TOUGH2 (Pruess, 2005), which is a numerical simulator of multicomponent, multiphase fluid and heat flow in porous media and is designed for applications related to geologic sequestration of CO_2 in saline aquifers. Fluid advection is described with a multiphase extension of Darcy's law, and diffusive mass transport is included for all phases. Heat flow occurs by conduction and convection. Furthermore, the equations representing the geomechanical effect during CO_2 injection are based on that of TOUGH_CSM (Winterfeld and Wu, 2011), which is a modified version of TOUGH_MP (Zhang et al., 2008), to incorporate the geomechanical effects in the equation system through effective stress. The detailed derivation of the momentum conservation equation is given by Winterfeld et al. (2011). The derived governing equation of mean stress is shown in Table 1. Equations describing the geochemistry are based on the TOUGHREACT simulator (Xu et al., 2004b), which employs a sequential coupling approach to solve reactive-solute-transport problems in subsurface porous media. The equations for chemical equilibrium and kinetics are now incorporated into the existing phase-behavior equation system to control the local combined phase-chemical equilibrium and kinetics. The mass gain/loss of each component and the associated energy change are then added as source/sink terms into the mass/energy-balance equations.

Time Discretization and Solution Method

By employing the fully coupled approach, the mathematical equations for fluid and heat flow, geomechanics and geochemical reactions are solved simultaneously. Based on the discretization at each grid cell, the entire governing equation system for the multicomponent reactive solute transport can be expressed as residual forms R and F. R's are for the residual forms of mass, energy, and momentum conservation equations; F's are for the residual forms of saturation index for minerals and gases. For each grid cell, there are N equations, including mass balance, energy balance, momentum balance, and chemical constraints for minerals and gases at equilibrium, so a fully coupled reactive solute transport system with NL gridblocks represents a total of $NL \times N$ coupled nonlinear equations. The unknowns are the $NL \times N$ independent primary variables, which completely define the state of the whole THMC system at time level t^{k+1}. These equations are solved by Newton-Raphson iteration. The Taylor series expansion of residual equation for each primary variable is shown in Table 1. By keeping only the terms up to first order, we obtain a set of $NL \times N$ linear equations for the increments. The entire set of linear equations for coupled processes is solved simultaneously until the prescribed convergence criteria are satisfied.

Table 1. Mathematical description for the fully coupled model of fluid and heat flow, Geomechanics, and chemical reactions.

Mass conservation

$$\frac{\mathrm{d}}{\mathrm{d}t}\int_{V_n} M^\kappa \mathrm{d}V_n = \int_{\Gamma_n} \bar{F}^\kappa \cdot \hat{n}\mathrm{d}\Gamma_n + \int_{V_n} q^\kappa \mathrm{d}V_n + \int_{V_n} R^\kappa_{\mathrm{req}}\mathrm{d}V_n + \int_{V_n} R^\kappa_{\mathrm{r}}\mathrm{d}V_n$$

Energy conservation

$$\frac{\mathrm{d}}{\mathrm{d}t}\int_{V_n} U\mathrm{d}V_n = \int_{\Gamma_n} \bar{F}\cdot\hat{n}\mathrm{d}\Gamma_n + \int_{V_n} q_{\mathrm{h}}\mathrm{d}V_n$$

Momentum conservation

$$\frac{3(1-v)}{1+v}\nabla^2\tau_m + \nabla\cdot\bar{F} - \frac{2(1-2v)}{1+v}\left(\alpha\nabla^2 p + 3\beta K\nabla^2 T\right) = 0$$

Chemical equilibrium for mineral

$$F_m = \log\Omega_m = \log\left[X_m^{-1}\lambda_m^{-1}K_m^{-1}\prod_{j=1}^{N_c} c_j^{v_{mj}}\gamma_j^{v_{mj}}\right] = 0$$

Chemical equilibrium for CO_2 gas

$$F_g = \log\Omega_g = \log\left[\Gamma_g^{-1}p_g^{-1}K_g^{-1}\prod_{j=1}^{N_c} c_j^{v_{gj}}\gamma_j^{v_{gj}}\right] = 0$$

Time Discretization and Solution Method

$$\sum_{j=1}^{N_C+N_p+N_g}\left.\frac{\partial R_n^{\kappa,k+1}}{\partial c_j}\right|_p \left(c_{j,p+1}-c_{j,p}\right) = -R_n^{\kappa,k+1}\left(c_{j,p}\right)$$

$$\sum_{j=1}^{N_C+N_p+N_g}\left.\frac{\partial F_m^{k+1}}{\partial c_j}\right|_p \left(c_{j,p+1}-c_{j,p}\right) = -F_m^{k+1}\left(c_{j,p}\right)$$

$$\sum_{j=1}^{N_C+N_p+N_g}\left.\frac{\partial F_g^{k+1}}{\partial c_j}\right|_p \left(c_{j,p+1}-c_{j,p}\right) = -F_g^{k+1}\left(c_{j,p}\right)$$

Supplemental equations for mass conservation

$$M^\kappa = \phi\sum_\beta S_\beta\rho_\beta x_\beta^\kappa$$

$$F^\kappa = F^\kappa_{\mathrm{adv}} + F^\kappa_{\mathrm{dis}} \quad F^\kappa_{\mathrm{adv}} = \sum_\beta x_\beta^\kappa F_\beta \quad F^\kappa_{\mathrm{dis}} = \sum_\beta \rho_\beta \bar{D}_\beta^\kappa \nabla x_\beta^\kappa$$

Supplemental Equations for energy conservation

$$U = (1-\phi)\rho_R C_R T + \phi\sum_\beta S_\beta\rho_\beta h_\beta \qquad F = -\lambda\nabla T + \sum_\beta h_\beta F_\beta$$

Total mass fraction of primary chemical species

$$x^\kappa = \frac{C^\kappa M^\kappa}{\rho_l} \qquad C_j = c_j + \sum_{k=1}^{N_x} v_{kj}c_k \qquad j = 1,\ldots,N_c$$

Aqueous complex

$$c_k = K_k^{-1}\gamma_k^{-1}\prod_{j=1}^{N_c} c_j^{v_{kj}}\gamma_j^{v_{kj}}$$

Kinetic rate for mineral dissolution/precipitation

$$r_n = f\left(c_1, c_2, \ldots, c_{N_c}\right) = \pm k_n A_n\left|1-\Omega_n^\theta\right|^\eta \quad n = 1,\ldots,N_q$$

Convergence Criteria

$$\frac{\left|\Delta c_{j,p+1}^{k+1}\right|}{c_{j,p}^{k+1}} \le \tau \qquad j = 1,2,\mathrm{L}\ ,N_c+N_p+N_g$$

Convergence Criteria

Referring to the TOUGHREACT simulator (Xu et al., 2004b), convergence is achieved when the absolute value of the ratio between the relative increment of concentration and the concentration of primary components or species is less than a given convergence tolerance. The mathematical expression of the convergence criteria is given in Table 1. The default value of the convergence criterion is $\tau = 10^{-4}$. In this fully coupled THMC simulator, we still use this convergence criterion to evaluate the convergence. The convergence is achieved when the absolute value of the ratio between the relative increment of primary variables and primary variables is less than a given convergence tolerance.

CODE STRUCTURE

In this fully coupled simulator, the code structure of the original TOUGH code is kept for consistency. The numerical scheme for solving fluid and heat flow, geomechanics, and geochemistry is a fully coupled solving procedure. The mass-balance equation for each primary component or chemical species, energy-balance equation, momentum-balance equation and chemical constraint equations are constructed simultaneously. These equations are highly nonlinear algebraic equations when taking the geochemical reaction into account. They are solved by the Newton-Raphson iteration method, and the Jacobin matrix coefficients are calculated by the numerical approach. The multi-module (subroutine multi) within the TOUGH family code are rewritten as a result of the increased number of governing equations, with the number of equations in the

equation system possibly being three to six times larger than that in the original equation system. The conjugate gradient solver will be used once to solve the fluid and heat flow, solute transport, geomechanical, and chemical reactions. In addition, for phase behavior and fluid-property calculation, the EOS module is also rebuilt to couple the phase equilibrium, geomechanics, and geochemistry.

Verification and validation

In this paper, we present only the verification of the geochemistry capability within the fully coupled simulator. A verification of mineral dissolution under the conditions of local equilibrium and kinetics is presented against analytical solutions. In addition, we present a batch reaction model and a 1D reactive solute transport model coupled with geochemical reactions under equilibrium conditions, to validate the fully coupled simulator.

Analytical Solution

The TOUGHREACT simulator was verified against analytical solutions (Xu and Pruess, 1998; Xu et al., 1999). These analytical solutions are employed here again to verify the geochemistry calculations of the fully coupled simulator. The initial conditions, boundary conditions, and the derivations of the analytical solutions are given by Xu (1996). The model is a semi-infinite fluid-saturated porous medium under a steady-state uniform velocity flow regime, in which mineral dissolution is considered under the local equilibrium and kinetics. The solution corresponds to 1D transport of two hypothetical species A and B, which originate from the dissolution of a mineral phase AB(s): (1) AB(s) ↔ A + B in local equilibrium, (2) AB(s) → A + B in kinetics. Fig. 1 shows the verification of 1D solute transport under local equilibrium, and Fig. 2 shows the verification of 1D solute transport under chemical kinetics. The numerical results for both conditions agree well with the analytical solutions.

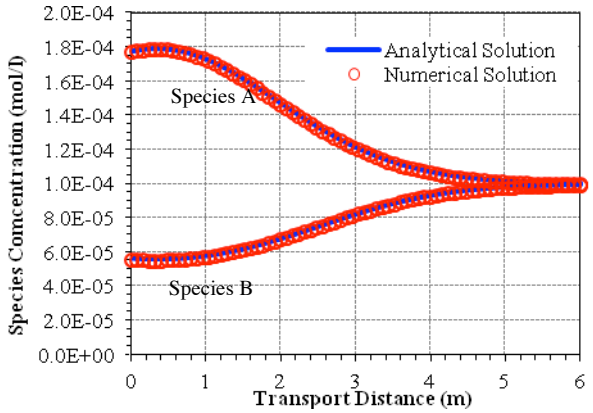

Figure 1. Concentration profiles for two species A and B in a problem involving dissolution of a mineral $AB_{(S)}$ under conditions of local equilibrium

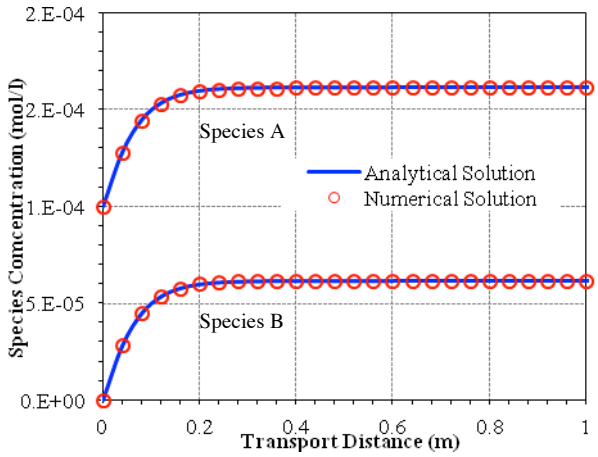

Figure 2. Concentration profiles for two species A and B in a problem involving dissolution of a mineral $AB_{(S)}$ under conditions of kinetics.

Numerical Solution

Batch reaction system with local equilibrium

The batch reaction system includes saline water, CO_2(g) and $CaCO_3$(s). Based on the geochemical and thermodynamic database used in TOUGHREACT simulator, i.e., EQ3/6 (Wolery, 1992), the potential geochemical reactions in the batch reaction system includes twelve aqueous chemical reactions, one calcite dissolution, and one CO_2 gas dissolution. The chemical equations involved in the batch reaction system are listed in Table 2. All the chemical reactions are set in equilibrium. Three phases (aqueous, gaseous, and solid) are taken into account, i.e., the gaseous phase contains CO_2 and vaporized H_2O; the aqueous phase includes aqueous chemical species; the mineral

species includes reactive calcite and nonreactive minerals exclusively. These chemical reactions are controlled by the chemical equilibrium constants, which can be calculated from the EQ3/6 database, and shown in Table 2.

Table 2. Equilibrium constants for chemical reactions in the batch system.

Chemical Reactions	log *K*eq at 75 ^{o}C
Aqueous complex	
$OH^- \text{ É } H_2O - H^+$	12.706522
$CaCl^+ \text{ É } Ca^{2+} + Cl^-$	0.5081909
$CaCl_2(aq) \text{ É } Ca^{2+} + 2Cl^-$	0.5497973
$NaCl(aq) \text{ É } Na^+ + Cl^-$	0.5826229
$NaHCO_3(aq) \text{ É } Na^+ + HCO_3^-$	0.2380571
$CaHCO_3^+ \text{ É } Ca^{2+} + HCO_3^-$	-1.2478107
$CO_2(aq) \text{ É } H^+ + HCO_3^- - H_2O$	-6.2960791
$CO_3^{2-} \text{ É } HCO_3^- - H^+$	10.098570
$CaCO_3(aq) \text{ É } Ca^{2+} + HCO_3^- - H^+$	6.2485457
$Ca(OH)^+ \text{ É } Ca^{2+} + H_2O - H^+$	11.218291
$Na(OH)(aq) \text{ É } Na + H_2O - H^+$	12.881724
$NaCO_3^- \text{ É } Na^+ + HCO_3^- - H^+$	10.262679
Calcite mineral dissolution	
$CaCO_3(S) \text{ É } Ca^{2+} + HCO_3^- - H^+$	1.1147844
Gaseous CO_2 dissolution	
$CO_2(g) \text{ É } H^+ + HCO_3^- - H_2O$	-8.168289

The selected primary components or species are CO_2(g), H_2O, H^+, Na^+, Ca^{2+}, Cl^- and HCO_3^-. All the other twelve aqueous complexes are defined as secondary species. The concentrations of the secondary species can be represented by the primary species. The total concentrations of the primary species can represent the compositions of the batch reaction system.

The geochemical reactions between aqueous and mineral phases result in mass generation, i.e., CO_2(g) dissolution and calcite dissolution. The source or sink terms in the mass-balance equation can be calculated from the dissolved concentration of calcite ($C_{CaCO3(s)}$) and the dissolved concentration of CO_2 ($C_{CO2(g)}$). The algebraic relationships between them are shown by the chemical reaction equations in Table 2. The geochemical reaction between mineral and saline solution is dominated by the equilibrium constant. The chemical reaction between CO_2 (g) and aqueous phase is CO_2 dissolution. It is set to be under equilibrium conditions, and dominated by the partial pressure of CO_2 and the equilibrium constant. Therefore, nine governing equations are solved by Newton-Raphson iteration. Nine primary variables are selected in the batch reaction model, i.e., $P_{CO2(g)}$, C_{H+}, C_{Ca2+}, C_{Na+}, C_{HCO3-}, C_{Cl-}, S_g, $C_{CaCO3(s)}$ and $C_{CO2(g)}$.

The geochemical reaction system is in equilibrium, so the system reaches equilibrium conditions once CO_2 comes into contact with the aqueous phase. The initial input data for the batch reaction model are given in Table 3; the initial concentrations of aqueous species are given in the second column of Table 4. The simulation results by the fully coupled simulator and TOUGHREACT are given in the third and fourth columns of Table 4. We can see that the concentrations of CO_2(aq) and Ca^{2+} have dramatically increased, owing to the dissolutions of CO_2(g) and $CaCO_3$(s), which dominate the entire batch reaction system. By comparing the results from the two bunches, we see that the error is within 4%; we can then conclude that the simulation results from the two simulators agree well.

Table 3. Initial parameters of the batch system.

Parameter	Values
Gas Saturation	0.5
Initial Pressure	200 bar
Temperature	75 ^{o}C
Porosity	0.3
Volume fraction of calcite	0.5
Volume fraction of non-reactive	0.5

Table 4. Result comparison between the fully coupled simulator and TOUGHREACT.

Species	Initial data	Fully-coupled	TOUGHREAC	Errors (%)
H^+	3.0865518E-05	2.385574E-05	2.3200153E-05	2.82580
Ca^{2+}	4.4801997E-03	3.789724E-02	3.7248307E-02	1.74217
Na^+	0.9000024	0.8910427	0.8911388	0.01078
HCO_3^-	1.9974637E-03	6.469279E-02	6.3385779E-02	2.06199
Cl^-	0.9106334	0.9125819	0.9124661	0.01269
OH-	1.4343495E-08	1.892241E-08	1.9503686E-08	2.98034
$CaCl^+$	1.7247709E-04	1.393002E-03	1.3709958E-03	1.60509
$CaCl_2$(aq)	5.9203653E-05	4.642690E-04	4.5762974E-04	1.45079
NaCl(aq)	8.9297867E-02	8.604993E-02	8.6185575E-02	0.15739
$NaHCO_3$(aq)	4.2996252E-04	1.336103E-02	1.3114010E-02	1.88363
$CaHCO_3^+$	2.1416910E-05	5.513980E-03	5.3798849E-03	2.49252
CO_2(aq)	4.3136821E-02	1.012978	0.98246	3.10628
CO_3^{2-}	3.7063587E-08	1.625055E-06	1.6483202E-06	1.41144
$CaCO_3$(aq)	2.1937727E-08	7.349152E-06	7.3491650E-06	0.00018
$CaOH^+$	2.7707266E-10	2.960948E-09	3.0037454E-09	1.42481
NaOH(aq)	3.6957495E-09	4.702559E-09	4.8647524E-09	3.33405
$NaCO_3^-$	3.1457201E-09	1.297723E-07	1.3184608E-07	1.57285
$CaCO_3$(s)	0.0	4.186248E-02	4.0960340E-02	2.20246
CO_2(g)	0.0	1.022362	1.009385	1.28559
P_{co2}(bar)	197.71524	173.2262	168.49643	2.80704

1D Reactive-solute-transport model under chemical equilibrium

A 1D reactive-solute-transport model under local chemical equilibrium is presented to verify the fully coupled simulator against the TOUGHREACT simulator. Sample Problem 5 in the TOUGHREACT manual (Xu et al., 2004b) is the reference for setting up the verification model. We assume that there is CO_2 gas saturated initially in the model (S_g=0.2), and that there are no chemical reactions in the system. The geochemical equilibrium is reached simultaneously at the beginning of CO_2 injection. The hydrogeological parameters for this model are in Table 5. (All the geochemical reactions involved in the model are shown in Table 2, above.) The model corresponds to a 1D reactive-solute-transport problem, and the calculation of nonisothermal and geomechanical effects are deactivated to verify the geochemical reaction calculation of the fully coupled simulator. This model is used to validate the effects of fluid flow mechanics on geochemistry.

Table 5. Parameters for the 1D transport problem.

Parameters	Value
Aquifer thickness	100 m
Permeability	10^{-13} m^2
Porosity	0.3
Compressibility	4.5×10^{-10}
Temperature	75 ^oC
Pressure	200 bar
CO_2 injection rate	5 kg/s
Injection time	365days
Original CO_2 satu-	0.2
Number of grids	22
Aquifer length	500m

To validate the fluid flow, the model is run four times by TOUGH_CSM geomechanics, TOUGHREACT, the fully couple simulator, and the fully coupled simulator without geochemical reaction. Figures 4 and 5 show the saturation profiles and gas pressure profiles after one year's injection of CO_2 gas. In Figure 3, the saturation profiles are very close for TOUGH_CSM, TOUGHREACT, and the fully

coupled simulator without geochemical reactions. In the TOUGHREACT simulator, the fluid flow, solute transport, and geochemistry is treated in three separate systems, with the fluid flow part having no interaction with the other two parts. However, the saturation profile obtained by the fully coupled simulator is lower than the other simulations. The problem is the treatment of CO_2 dissolution. In TOUGH_CSM and TOUGHREACT, the dissolution of CO_2 gas in the aqueous phase is calculated by phase behavior, but in the fully coupled simulator, it is treated as a geochemical reaction involving the mass loss of CO_2 gas. The model instantly becomes equilibrated by geochemical reactions at the beginning of CO_2 injection, and the gas saturation decreases because of the dissolution reactions, shown by the green line in Fig. 3.

Fig. 4 indicates that the gas-pressure profiles obtained by TOUGH_CSM, TOUGHREACT, and the fully coupled simulator without geochemical reactions are close to each other. The pressure obtained by the fully coupled simulator is much lower than the others. The fully coupled procedure in the fully coupled simulator tracks the changes in gas pressure and related fluid flow due to the dissolution of gaseous reactants. However, the assumption is that chemical reactions and accompanying changes in partial pressures do not affect overall gas and liquid flow in TOUGREACT (Xu et al., 2001). This might be a good approximation under some circumstances, but for the supercritical CO_2 geosequestration, this might not reflect the real conditions when fluid flow interacts with geochemical reactions.

Fig. 5 shows the gas partial-pressure evolution in the injection grid cell during one year's CO_2 injection by TOUGHREACT and the fully coupled simulator: the CO_2 gas partial pressure obtained by the fully coupled simulator is much lower than that obtained by TOUGHREACT. As we know, the CO_2 partial pressure is proportional to the quantity of CO_2 dissolved into the aqueous phase. The partial pressure of CO_2 gas dominates the geochemical reaction path of the entire system. CO_2 dissolution decreases the partial pressure, which is quantitatively simulated by the fully coupled simulator. Figures 6–8 show the pH value, the accumulative $CaCO_3$(s) dissolved concentration, and the accumulated CO_2 (g) dissolved concentration after one year's CO_2 injection. The larger partial pressure results in a lower pH value, higher dissolved concentrations of $CaCO_3$(s), and CO_2(gas) simulated by TOUGHREACT.

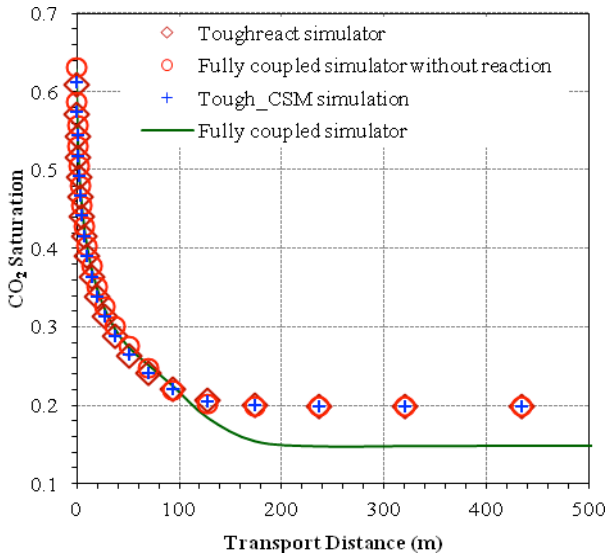

Figure 3. CO_2 saturation profiles after one year's injection simulated by different simulator.

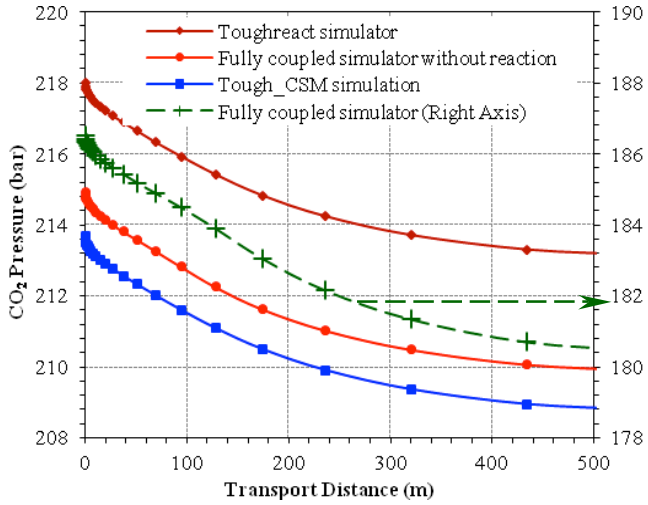

Figure 4. CO_2 pressure profiles after one year's injection simulated by different simulator.

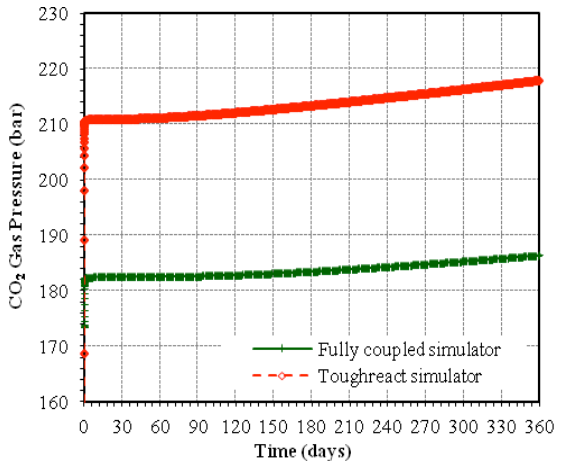

Figure 5. CO_2(g) partial pressure evolution profiles at the CO_2 injection grid cell.

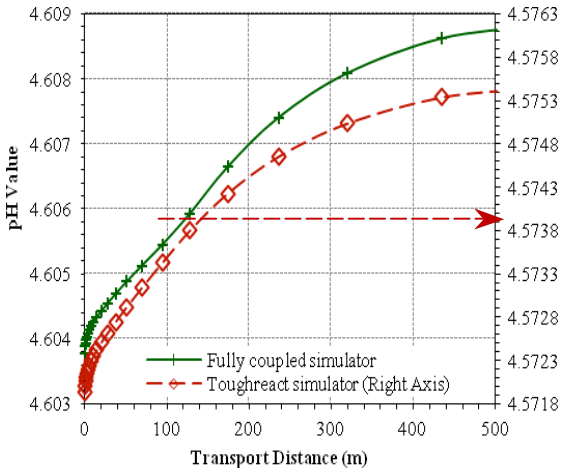

Figure 6. pH value profiles simulated by the fully coupled simulator and TOUGHREACT simulator.

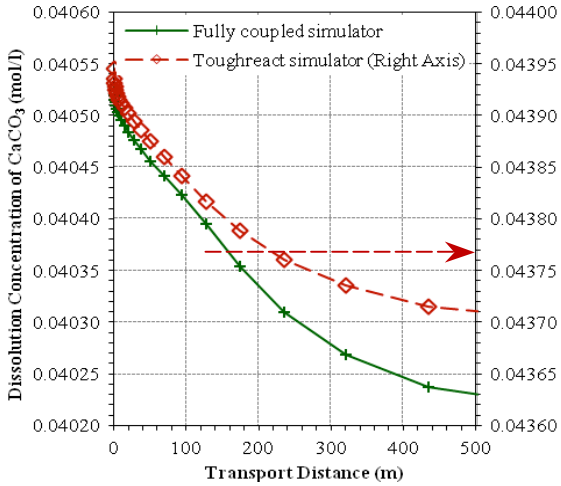

Figure 7. Dissolved concentration of $CaCO_3$(s) by the fully coupled simulator and TOUGHREACT simulator.

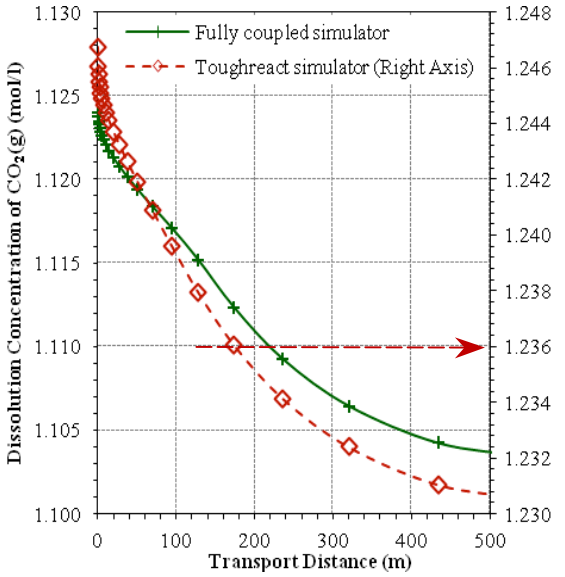

Figure 8. Dissolved concentration of CO_2(g) by the fully coupled simulator and TOUGHREACT simulator.

APPLICATION: BATCH REACTION SYSTEM OF COMPLEX CHEMICAL KINETICS

The fully coupled simulator can be applied to simulate a system that considers the equilibrium and kinetic minerals simultaneously. The initial mineral abundances used in the current batch reaction system are refined from the geochemical modeling study by Xu et al. (2004a) and geochemical reaction modeling Example 5 in the TOUGHREAT manual (Xu et al., 2004b). The initial conditions for this batch are the same as with the previous batch system under equilibrium conditions, as shown in Table 3. The reactive minerals are redefined here, with the initial mineral volume fraction and the distribution of the original mineral shown in Fig. 9. The mineralogy in this problem is similar to that commonly encountered in sedimentary basins (e. g., Gulf Coast sediments).

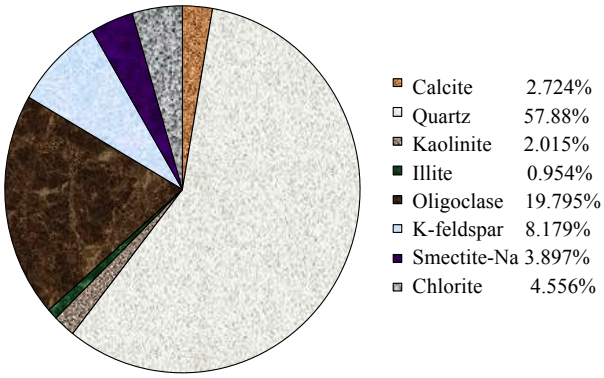

Figure 9. The original rock mineral compositions.

In this complex geochemical reaction system, calcite was assumed to react with aqueous species at local equilibrium, because its reaction rate is typically quite rapid. Dissolution and precipitation of other minerals are kinetically controlled. The equilibrium constants and kinetic-rate constants are again those from the study by Xu et al. (2004a and 2004b). There are four kinds of geochemical reactions, i.e., aqueous equilibrium reactions, kinetic mineral dissolution and precipitation, equilibrium gas dissolution, and equilibrium mineral dissolution. Twelve chemical species are selected as primary species. Thirty aqueous equilibrium chemical reactions form thirty secondary aqueous chemical species, which can be represented by the primary chemical species selected. Fourteen chemical reactions for kinetic mineral dissolution and precipitation are controlled by kinetic reaction rates. All the chemical reaction parameters are from the database of EQ3/6.

From the simulation results, we find that the majority of the CO_2 gas is dissolved into aqueous phase after 3,680 years. During the dissolution of the acid CO_2 gas, the pH value continues to buffer from 4.6 to 7.6, which is shown in Fig. 10. The majority of the calcite is dissolved into aqueous phase, as shown in Fig. 11. Among the original mineral compositions, the oligoclase has an almost 50% volume fraction change, while the Na-smectite and illite have minor precipitations, as shown in Fig. 12. Fig. 13 shows the potential precipitated minerals: significant ankerite and albite-low precipitate due to CO_2 injection and dissolution of aluminosilicate minerals. Minor smectite-Ca and very slight dawsonite precipitation occurs. No dolomite precipitation is observed in the simulation. The redistribution of volume fractions for the rock minerals after 3,680 years' reaction with CO_2 is shown in Fig. 14, with the area enclosed by the red lines representing the newly precipitated minerals after long-term geo-sequestration of CO_2.

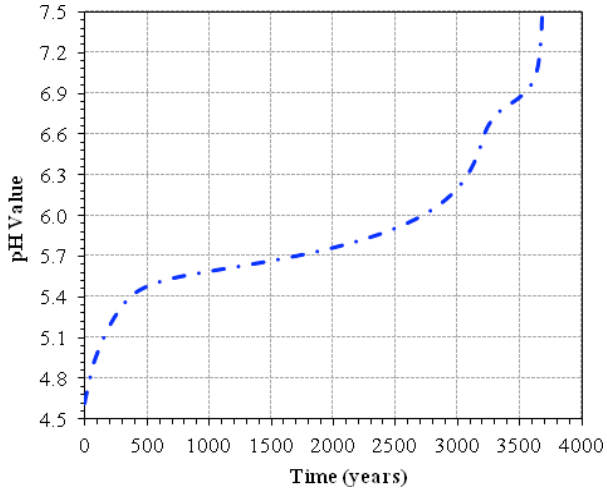

Figure 10. The evolution of pH value during CO_2 geo-sequestration.

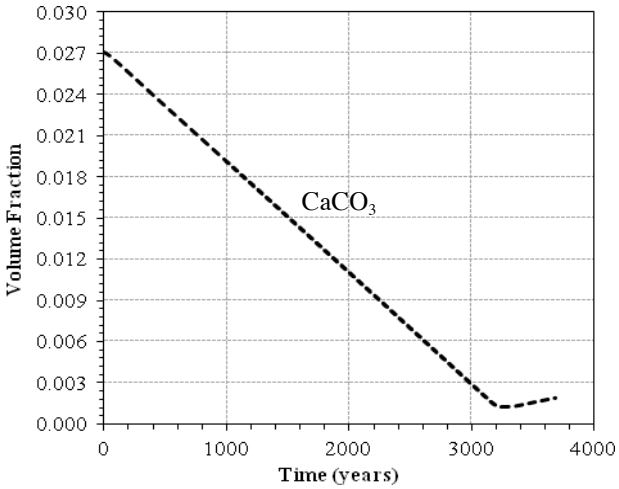

Figure 11. The volume fraction change of $CaCO_3$ in the rock matrix.

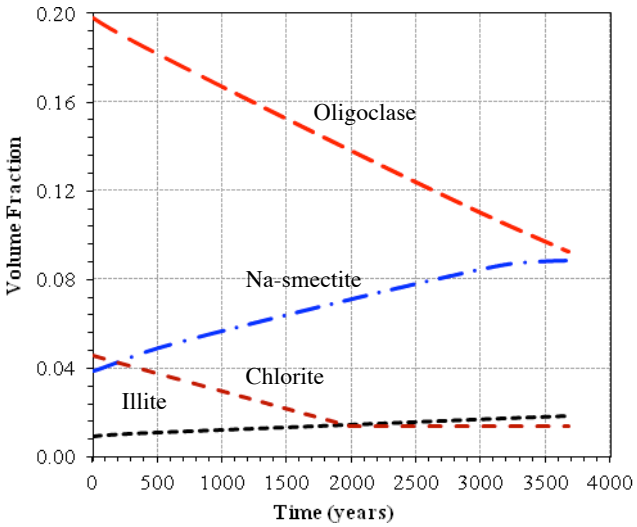

Figure 12. The volume fraction change of rock minerals in the rock matrix.

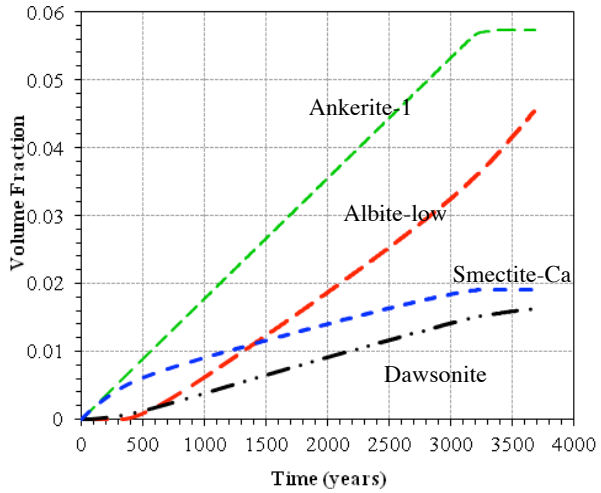

Figure 13. The volume fraction change of precipitated minerals in the rock matrix.

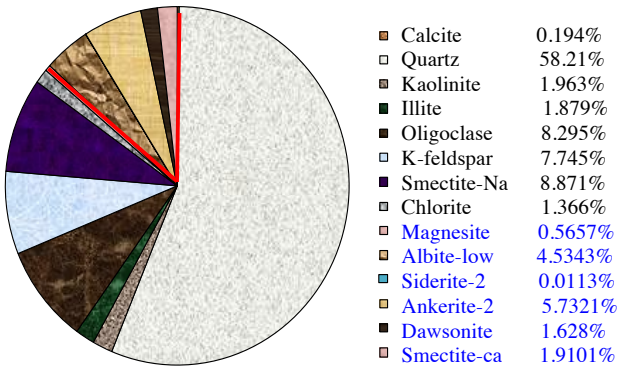

Figure 14. The mineral compositions after CO_2 sequestration.

CONCLUDING REMARKS

The transport phenomena subjected to CO_2 geological sequestration is a THMC process, one that includes fluid and heat flow, rock deformation, a mix of equilibrium and kinetic reactions, as well as an enormous range of aqueous concentrations. This poses great challenges for numerical simulation. Based on TOUGH family simulators, we have developed an efficient fully coupled model, in which the geochemical reactions are quantitatively embedded into the fluid- and heat-flow equations, while pore pressure and temperature are directly related to the rock deformation equation. We presented the fundamental equations describing mean stress, various gas-water-rock interactions in porous media, chemical equilibrium constraint equations relating chemical species' concentration, partial pressure, and temperature—and incorporated them together with the mass and energy conservation equations of primary chemical components or species, which are already embedded in the fully coupled code.

The model was verified against analytical solutions for mineral dissolution under local equilibrium and chemical kinetics. Then a batch system (CO_2, H_2O, NaCl, and $CaCO_3$) under chemical equilibrium was taken as the second validation to compare with the TOUGHREACT simulator. We obtained good matches for the two validations. Furthermore, a 1D transport model with chemical equilibrium was performed as the third validation to simulate the mutual interaction between fluid flow and geochemical reaction. It was indicated that the gas partial pressure dominates the whole THMC process. This pressure directly corresponds to the dissolution quantity of CO_2 gas in aqueous phase, further affecting the chemical reaction path and long-term fate of CO_2 in the saline aquifer. The fully coupled approach has an improved estimate of the CO_2 partial pressure and the geochemistry system. Finally, a complex geochemical batch reaction system, considering the chemical equilibrium and kinetics simultaneously, was simulated to demonstrate its handling capability for complex geochemical reactions in the fully coupled simulator.

ACKNOWLEDGMENT

This work was supported by the CMG Foundation and by the Assistant Secretary for Fossil Energy, Office of Coal and Power R&D through the National Energy Technology Laboratory under U.S. Department of Energy Contract Number DE-FC26-09FE0000988. In addition, the authors thank Tianfu Xu of LBNL for his help of the work.

REFERENCES

Pruess, K., *ECO2N: A TOUGH2 Fluid Property Module for Mixtures of Water, NaCl, and CO_2,* Report LBNL-57952, Lawrence Berkeley National Laboratory, Berkeley, Calif., 2005.

Winterfeld, P. H., and Y. S., Wu, Parallel simulation of CO_2 sequestration with rock deformation in saline aquifers, SPE Reservoir Simulation Symposium held in The Woodlands, Texas, USA, 21–23 February 2011.

Wolery, T.J., *EQ3/6, a software package for geochemical modeling of aqueous systems: package overview and installation guide (version 8.0)*. Lawrence Livermore Laboratory Report UCRL-MA-110662 PT I, livermore, CA, USA, 246 pp, 1992.

Xu, T., Modeling nonisothermal multicomponent reactive solute transport through variably saturated porous media. Ph.D. dissertation, University of La Coruña, La Coruña, Spain, 310 pp, 1996.

Xu, T., and K., Pruess, *Coupled Modeling of Non-isothermal Multi-phase Flow, Solute Transport and Reactive Chemistry in Porous and Fractured Media: 1. Model Development and Validation,* Report LBNL-42050, Lawrence Berkeley National Laboratory, Berkeley, Calif., 1998.

Xu, T., K., Pruess, and G. Brimhallb, An improved equilibrium-kinetics speciation algorithm for redox reactions in variably saturated subsurface flow systems, *Computers & Geosciences, 25,* 655-666, 1999.

Xu, T., and K. Pruess, Modeling multiphase non-isothermal fluid flow and reactive geochemical transport in variably saturated fractured rocks: 1. methodology, *American Journal of Science*, 301, 16-33, 2001.

Xu, T., J. A. Apps, K. Pruess, Numerical simulation of CO_2 disposal by mineral trapping in deep aquifers, *Applied Geochemistry, 19*, 917-936, 2004a.

Xu, T., E. Sonnenthal, N. Spycher, and K. Pruess, *TOUGHREACT users guide: a simulation program for non-isothermal multiphase reactive geochemical transport in variably saturated geologic media,* Earth Sciences Division, Lawrence Berkeley National Laboratory, University of California, Berkeley, CA, 2004b.

Zhang, K., Y.S., Wu, and K., Pruess, *User's Guide for TOUGH2-MP - A Massively Parallel Version of the TOUGH2 Code,* Report LBNL-315E, Earth Sciences Division, Lawrence Berkeley National Laboratory, May, 2008.

Modeling Applications

MODELING BRINE REFLUX USING THE PITZER ION-INTERACTION MODEL IN TOUGHREACT

Anwar Al-Helal[1], Fiona F. Whitaker[1], Nicolas Spycher[2], Yitian Xiao[3]

[1]Department of Earth Sciences, University of Bristol,
Bristol BS8 1RJ, England,
[2]Lawrence Berkeley National Laboratory,
Earth Sciences Division, Berkeley, CA 94720, USA
[3]ExxonMobil Exploration Company, PO Box 2189, Houston TX 77027, USA
An.Alhelal@bristol.ac.uk

ABSTRACT

Reflux of a penesaline (186‰) brine and resulting water-rock interactions were simulated using a modification of TOUGHREACT that incorporates the Pitzer ion-interaction theory. The brine is sourced from a 5 km wide brine pool in the interior of a 25 km wide platform and flows basinward through a 3 km thick sequence of grain-dominated packstone sediments. Ion interactions reduce dolomite supersaturation and anhydrite undersaturation predicted using the Pitzer approach compared with the Debye-Hückel approach, but increase calcite undersaturation. This increased undersaturation, combined with enhanced fluid flow above a shallower zone of anhydrite precipitation, results in more rapid dolomitization despite the lower initial dolomite saturation.

The penesaline brines reflux at up to 7 my^{-1}, three times the maximum flow rate in identical simulations involving a mesohaline (85‰) brine, in direct proportion to the difference in the density gradient. However, dolomitization is an order of magnitude faster for the penesaline brine, with replacement of all limestone to a depth of 43 m within 50 ky. Even after 1 My of penesaline-brine reflux, alteration is largely limited to sediments underlying the brine pool. In contrast, the penesaline brine forms a tabular dolomite body extending some 20 km to the platform margin. The upper 200 m of porous dolomite, lacking significant primary dolomite cements, overlies a thick (>700 m) zone where anhydrite cements plug up to 25% of the porosity. Penesaline brine reflux forms less anhydrite cement, due both to slower anhydrite precipitation (driven by slower upstream dolomitization), and to more .rapid anhydrite dissolution once dolomitization is complete.

INTRODUCTION

Dolomites are a common component of the carbonate rock record, and many were inferred to have formed by reflux of brines through carbonate platforms during early burial. Previous reactive transport modeling (RTM) simulations using TOUGHREACT have demonstrated the diagenetic potential of penesaline brine reflux, and the importance of coupled simulation of solute and heat flux (Al-Helal et al., 2012). We also evaluated sensitivity to the degree of evaporative concentration of the source seawater, via controls on both density-dependent fluid flow rate and chemical composition of reactive fluids. However, the standard version of TOUGHREACT uses the HKF model, based on the Debye-Hückel approach, limiting simulations, which is not reliable for high ionic strength brines.

This study uses a modification of TOUGHREACT that incorporates the Pitzer ion-interaction theory to simulate the reflux of penesaline brines, and compares this with mesohaline reflux, in a large-scale isolated carbonate platform over the timescale of up to one million years (1My). The code incorporates two alternative means of calculating the activity coefficient with respect to pre-estimating the ionic strength: the Helgeson-Kirkham-Flowers (HKF) model (Xu et al., 2004) and the Harvie-Møller-Weare (HMW) model (Zhang et al., 2006a,b).

The standard HKF model, based on the Debye-Hückel approach, is applicable only for dilute to moderately saline waters (<3 molal or 130 ‰) where NaCl is the dominant electrolyte. This approximates the upper range of salinity for mesahaline brines (35-140‰, Warren 1999). For higher ionic strength, solutions with many sepa-

rate ion pairs (secondary species), the Newton–Raphson method employed may converge slowly and to inaccurate results, or may fail to converge. However, when using the HMW model, which considers ion pairing directly through ion-interaction coefficients, simulations typically converge in fewer iterations and produce a more accurate representation of ionic activity. This tends to reduce the overestimation of ionic activity for high solutions with high total molality (Boyd, 1981; Table.1).

METHODS

Flow was simulated in a high-resolution 2D flow domain, using linear (Cartesian) coordinates. The flat-topped shelf measures 25 km from the margin to the interior, with a steep margin sloping down into a 2 km deep basin. The grid system comprises 2964 active blocks of non-uniformly specified node spacing, with reduction in cell width from 1250 m to 250 m and height from 100 m to 1 m (Figure 1). This could represent half of a symmetrical 50 km wide isolated carbonate platform, where brines are formed by evaporation of seawater, or a 25 km wide attached shelf, with no additional component of groundwater discharge from continental source to the right of the modeled domain except to the brine pool.

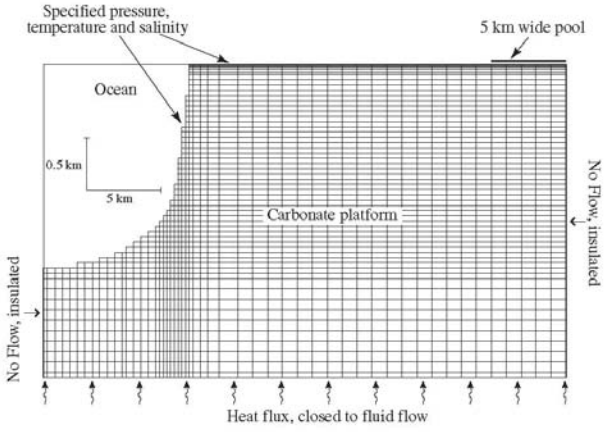

Figure 1. 2D RTM simulation grid and boundary conditions for the current study

Right and left boundaries are no-flow boundaries, while the lower boundary is closed to flow and solute transport but open to heat transport, with a specified heat flux of 60 mW/m^2, representative of a passive margin setting. The upper boundary is a fluid-pressure boundary, allowing the recharge or discharge of fluids at the platform top and slope. The platform top temperature is specified as 40°C and the ocean temperature declines exponentially with depth after Sanford et al. (1998).

The initial porosity declines exponentially with depth based on core data for the Cenozoic and Mesozoic Florida carbonates (Schmoker and Halley, 1982). Permeability was derived from porosity based on grain-size-dependent relations of Lucia (1995). Permeability anisotropy was specified as 10^3 (horizontal to vertical), after flow-based scaled-up simulations (Jones 2000). Diagenetic changes in permeability were calculated from changes in porosity using the Carman-Kozeny relation, ignoring changes in grain size, tortuosity, and specific surface area.

The initial temperature and pressure reflects advective heat transport by geothermal convection. The fluids surrounding the platform are seawater evolved to equilibrium with respect to calcite. The brine pool temperature was set as 40°C, and two alternative brine compositions were specified; a penesaline brine (186‰ or 5.3×seawater) and a mesohaline brine (85‰ or 2.5×seawater). The brine compositions were derived from published analyses of Ralph Sink and Ibis Pond respectively, from the Lake MacLeod evaporite basin (Logan, 1987; Table.1).

Simulations incorporated three solid phases (calcite, dolomite, and anhydrite), with initial mineralogy specified to be 99% calcite and 1% "seed" dolomite. Dolomite is assumed to react under kinetic constraints, using the rate equation of Arvidson and Mackenzie (1999). Calcite and anhydrite, which react much faster, are considered to react locally at equilibrium. Reactive surface area (RSA) was set as 10^3 cm^2/g, based on the average grain size of a grain-dominated packstone sediment (Lucia, 1995) and/or medium crystalline mud-dominated dolostone (Lucia, 2004). Mineral abundance is reported as percentage of total mineral volume.

RESULTS

Comparison of HKF and HMW models for penesaline brines.

A number of key indicators were used to compare calculations of the potential of penesaline brines (186‰) from the HKF and the HMW models:

(1) The number of iterations required to calculate the ionic activity: The HMW model calculates the ionic activity using only four Newton–Ralphson iterations, half the number required by the HKF model.

(2)The difference between the stoichiometric and the true ionic strength: As would be expected, the HMW model yields a true ionic strength that is essentially identical to the stoichiometric ionic strength, because this model does not take into account the formation of separate (secondary) aqueous species to account for ion pairing. In contrast, using the HKF model, which includes secondary species, the two estimates of ionic strength differ for all waters considered, and this difference becomes really substantial for the penesaline brine, with the true ionic strength being about 69% of the stoichiometric ionic strength (Table 1).

Table 1. Chemical composition of initial and boundary fluids for the major ions (mol L^{-1}) from Logan (1987), saturation indices (SI) and ionic strength calculated at 40°C and atmospheric P_{CO2} using the HFK model and the HMW model.

Component	Seawater	Mesohaline Brine (Ibis Pond)	Penesaline Brine (Ralph Sink)
Salinity‰	35	85	186
pH	8.22	7.70	7.10
Na^+	$4.85e^{-1}$	$1.26e^{0}$	$3.18e^{0}$
Mg^{2+}	$5.51e^{-2}$	$1.37e^{-1}$	$3.39e^{-1}$
Ca^{2+}	$1.07e^{-2}$	$2.44e^{-2}$	$2.22e^{-2}$
K^+	$1.06e^{-2}$	$2.56e^{-2}$	$6.56e^{-2}$
Cl^-	$5.66e^{-1}$	$1.46e^{0}$	$3.69e^{0}$
SO_4^{-2}	$2.93e^{-2}$	$7.78e^{-2}$	$1.37e^{-1}$
HCO_3^-	$2.41e^{-3}$	$1.54e^{-3}$	$1.83e^{-3}$
Mg/Ca	5.1	5.6	15.3
Calculated saturation index using the HKF model			
SI calcite	0.89	0.34	-0.45
SI dolomite	3.70	2.63	1.52
SI anhydrite	-0.86	-0.42	-0.53
Ionic Strength			
Stoichiometric	0.72	1.85	4.47
True	0.64	1.50	3.07
Calculated saturation index using the HMW method			
SI calcite	0.60	*	-0.85
SI dolomite	3.54	*	1.41
SI anhydrite	-1.00	*	-0.40
Ionic Strength			
Stoichiometric	0.72	*	4.47
True	0.72	*	4.47

* not computed for this case.

(3) The calculated saturation indices of diagenetic minerals of interest (calcite, dolomite, and anhydrite): Results displayed in Table 1 and Figure 2 show that the application of the HMW model predicts brines have a greater potential to dissolve calcite compared with the HKF model, and a reduced anhydrite undersaturation. In addition, the HMW model significantly overestimates the extent of dolomite supersaturation in the initial penesaline brine solution. The differences in saturation indices result in a difference in computed mineral abundances using the two models. The interplay between kinetically controlled dolomitization and geologically instantaneous dissolution or precipitation of calcite and anhydrite are apparent from the 2D simulations discussed later.

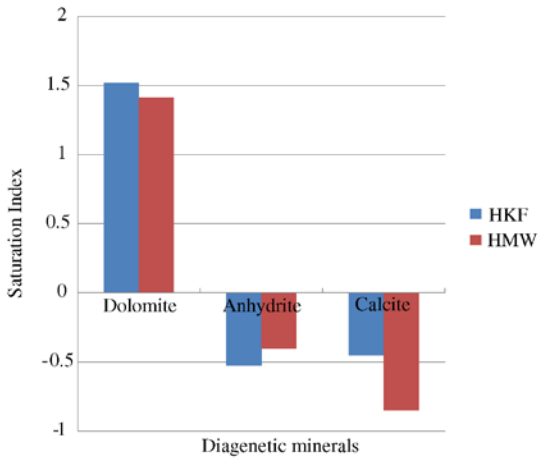

Figure 2. Comparison of the saturation indices for the penesaline brine (186‰) calculated using the HKF model (blue) and the HMW model (red).

(4) Predicted diagenesis: Calcite is dissolved and replaced by dolomite, consuming Mg^{2+} from solution and releasing Ca^{2+}, which then combines with the SO_4^{2-} to form calcium sulfate (modeled as anhydrite). The predicted change in abundance of dolomite and anhydrite, expressed in terms of total cross-sectional area after 1 My, indicates significant differences between the results of simulations using the MMW and HFK models (Figure 3).

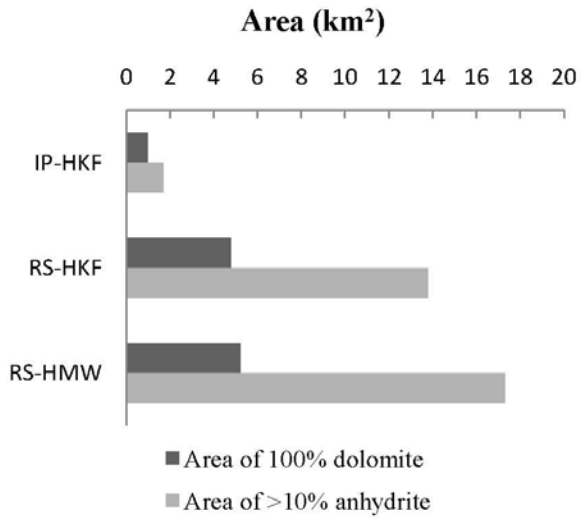

Figure 3. Comparison of reflux diagenesis in a grain-dominated packstone platform expressed in terms of total cross-sectional area exceeding 100% dolomite (dark bars) and 10% anhydrite (light bars) after 1 My for reflux of mesohaline (85‰) brines from Ibis Pond (IP) and penesaline (186 ‰) brines from Ralph Sink (RS) using both the HKF activity coefficient model and the HMW model.

Although the HMW predicts slightly lower dolomite supersaturation than the HKF model, the size of the completely dolomitized body was 9% greater due to more rapid calcite dissolution. The consequent enhanced release for Ca^{2+} into solution also promotes anhydrite precipitation downstream of the zone of dolomitization, with a 25% larger area of >10% anhydrite compared to the HKF model.

Subtle but important differences between predictions of the spatial distribution of diagenetic products using the two models after 1My are shown in Figure 4. For the HKF simulation, rapid fluid flux (>6 my^{-1}) occurs

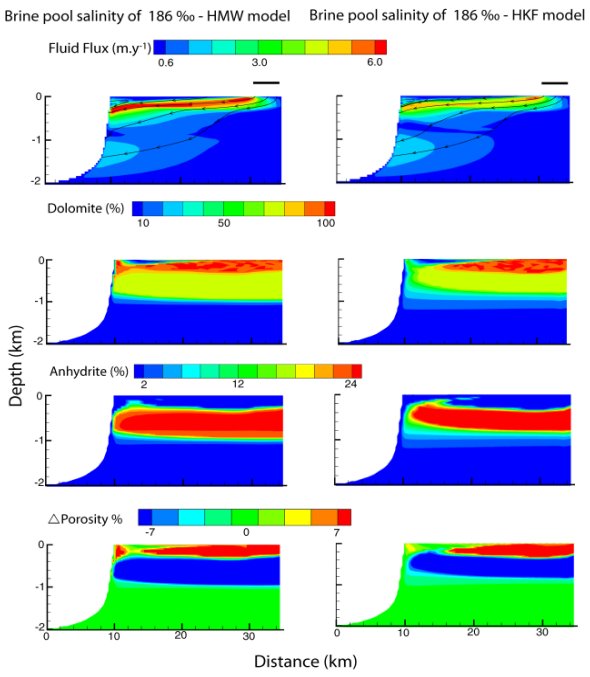

Figure 4. Simulations of fluid flux (with representative streamlines), dolomite and anhydrite abundance and change from initial porosity after 1 My of reflux of penesaline (186‰) brines using the HMW model (left) and the HKF activity coefficient model (right). The solid bar represents the 5 km wide brine pool.

only in a limited zone where the density gradient is highest, underlying the interface between the brine pool and the normal-salinity platform top fluids. In contrast these high rates of fluid flow extend across much of the platform in the HMW simulation, reflecting greater diagenetic enhancement of porosity and permeability at shallow depth, and pore-filling anhydrite precipitation beneath this.

Despite the higher calculated dolomite supersaturation for the penesaline brine, the HKF simulation underestimates the rate of dolomitization. This arises because the replacement reaction is driven in part by the dissolution of calcite, and the HKF model predicts a lesser degree of calcite undersaturation. Accordingly, the zone of complete dolomitization extends laterally some 20 km from the brine pool within 1 My in the HMW simulation, almost twice the extent of the dolomite body in the HKF simulation.

As a result of this, the HKF model underestimates both the depth of the anhydrite body and the area beneath the brine pool affected by dissolution of this secondary anhydrite. More rapid dolomitization increases the onset of downstream anhydrite precipitation. However, once dolomitization is complete, there is no release of Ca^{2+} to buffer the anhydrite undersaturation in the refluxing brines, and thus anhydrite dissolution occurs behind the dolomitization front. With more complete shallow dolomitization, the HMW simulation shows how the brine plume can supply Mg^{2+}-rich fluids to the platform margin, enhancing rates of dolomitization in the zone affected by geothermal convection, where waters are too cold to precipitate anhydrite.

Comparison between diagenesis driven by reflux of mesohaline and penesaline brines

Comparison was made between the penesaline 186‰ brines simulated using the HMW model and the mesohaline 85‰ brines simulated using the HKF model (Table 1) with stoichiometric ionic strengths of 4.47 and 1.85 respectively.

Table 1 highlights the distinct chemical differences between the two brines. The salinity of 186‰ brines is more than twice that of the 85‰ brines. The associated density difference between the penesaline brine and seawater is thus three times greater than that between the mesohaline brine and seawater.In parallel, the Mg/Ca molar ratio of the penesaline brine is almost 3 times higher than that of the mesohaline brine, which has a Mg/Ca only 1.1x that of seawater. The lower pH for the more concentrated brines is consistent with the general decrease in the pH with increasing chlorinity, described by Hanor (2001). In parallel, the measured bicarbonate alkalinity was higher in the high salinity brines.

At 1 My, the simulations showed that all diagenetic reactions were significantly more rapid in the penesaline-brine simulation and affect a larger area of the platform (Figure 5). There is a significant lateral extension of the dolomite body formed from the penesaline brine towards the margin, and dolomitization reaches ~1 km depth. In comparison, dolomitization by the

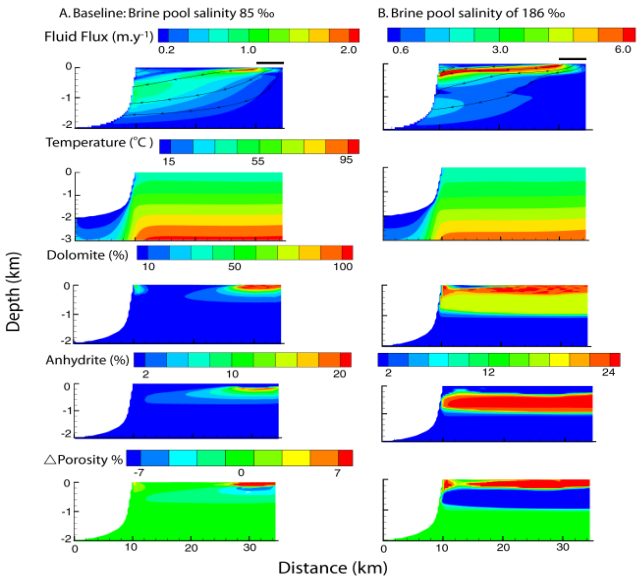

Figure 5. Simulations of fluid flux (with representative streamlines), temperature, dolomite and anhydrite abundance and change in initial porosity after 1 My of reflux of mesohaline (85‰) brines using the HKF model and penesaline (186‰) brines using the HMW model.

mesohaline brine remains focused beneath and immediately downstream of the brine pool.

The resulting enhanced formation of pore-occluding anhydrite in the penesaline reflux simulation provides a barrier preventing significant volumes of brines from circulating through the platform at depth. Rather, the majority of fluid flux, and diagenetic alteration, occurs in the upper 200 m, with lateral transfer and discharging into the ocean at the platform margin; beneath this, there is a broader zone of partial dolomitization.

The increased density contrast between the higher-salinity platform top brines and the ocean waters results in reflux at rates up to 2.5 times those in the mesohaline simulation (7 my^{-1} and 2.8 my^{-1} respectively). One consequence of the high fluid flux is advective cooling of the platform, by some 2.5°C at 500 m depth below the center of the brine pool, and twice this at 2.5 km depth (Figure 5).

The first very shallow occurrence of complete dolomitization is predicted to occur 135 ky earlier in the penesaline-brine simulation,

compared with 335 ky in the mesohaline simulation. The predicted spatial distribution of the penesaline reflux dolomite at 300 ky (plot not shown) is quite similar to that of the mesohaline reflux dolomite at 1 My (Figure 5).

One My of penesaline brine reflux produces a dolomite body with a cross-sectional area five times that of the mesohaline dolomite body, and the cross-sectional area of rock with anhydrite in excess of 10% is 10 times greater than the mesohaline simulation (Figure 3). The tabular-shaped body of penesaline-reflux dolomite extends laterally to join with the geothermal dolomite body. Reflux consequently feeds the geothermal convection cell with Mg^{2+}-rich fluids that increase the dolomitization rate in that area effected by geothermal convection, driving it to complete dolomitization within 1 My.

The mesohaline dolomites are largely restricted to a smaller area that extends <3 km laterally from the brine pool. The penesaline reflux results in a broad zone of complete dolomitization extending across much of the platform. Penesaline dolomites extend to a depth of ~900 m by 1 My, almost 5 times thicker than the dolomite zone predicted in the mesohaline simulation. Associated with the thicker body of dolomite, the underlying zone of partial dolomitization becomes thinner (a sharper "dolomite front").

Significant (≥20%) diagenetic anhydrite developed only after 1 My simulation of the mesohaline brines. Hence, the penesaline brine reflux results in a porosity reduction of 11%, more than double that of the mesohaline brines (5%). From this porosity reduction, the model predicts a permeability reduction of up to 3 darcy and 2 darcy respectively for the penesaline and mesohaline brine simulations .

In addition, the 1 My comparative simulations illustrate that, despite the marginally higher temperatures for mesohaline brine reflux, the predicted preservation of anhydrite cements behind the advancing dolomite front is some 5.6% lower than that of the penesaline case, reflecting the greater fraction of anhydrite formed during penesaline reflux. Figure (5) illustrates a much greater spatial overlap between the zone where porosity increases due to dolomitization and that of porosity reduction by anhydrite cementation. As a result, significant net porosity change is limited to a more limited zone at shallow depth beneath the mesasaline brine pool.

CONCLUSION

The main objective of this study was to highlight the importance of using an appropriate activity coefficient model for RTM simulations. Implementing the Pitzer approach via the HMW model in TOUGHREACT enabled us to simulate the diagenetic potential of penesaline brine reflux. The comparison between the simulated results of hyperaline brines of 186‰ salinity (4.47 ionic strength), using both the HKF and the HMW models, demonstrated that the results of the HKF model underestimates the diagenetic potential of refluxing brines compared to the HMW model, which is expected to be more accurate than the HKF model at high salinities.

Comparison of penesaline and mesohaline brine reflux quantified differences in the rate and distribution of dolomitization and anhydrite precipitation and dissolution. The diagenetic system proved to be critically sensitive to the salinity of the brines, via effects on both fluid flux and reaction rate.

ACKNOWLEDGMENTS

Funding for this study was provided by the public authority for applied education and training "Kuwait." ABA and FFW thank LBNL for supporting stimulating academic exchange visits between LBNL and Bristol.

REFERENCES

Al-Helal, A. B., Whitaker, F. F. and Xiao, Y. Reactive transport modeling of brine reflux: dolomitization, anhydrite precipitation, and porosity evolution. *J. Sediment. Res.,* 82(3), 196-215, 2012.

Arvidson, R. S., and Mackenzie, F. T., The dolomite problem - Control of precipitation kinetics by temperature and saturation state: *Am. J. Sci.*, 299, 257–288, 1999.

Boyd, C. E. Effects of ion-pairing on calculations of ionic activities of major ions in freshwater. *Hydrobiologia,* 80 (1), 91-93,1981.

Hanor, J. S. Reactive transport involving rock-buffered fluids of varying salinity, *Geochim. Cosmochim. Acta,* 65 (21)**,** 3721-3732, 2001.

Jones, G. D. *Numerical modeling of saline groundwater circulation in carbonate platforms*. Earth Sciences. UK, University of Bristol, 2000.

Logan, B. W. The MacLeod evaporite basin, Western Australia. *AAPG Mem.,* 44, 1987.

Lucia, F. J. Origin and petrophysics of dolostone pore space. In Braithwaite, C.J, Rizzi G., and Darke, G. (eds). *The geometry and petrogenesis of dolomite hydrocarbon reservoir*. Geol. Soc. Lond. Spec. Publ., 235, 141-155, 2004.

Lucia, F. J. Rock-fabric petrophysical classification of carbonate pore-space for reservoir characterization. *AAPG Bull.,* 79 (9)**,** 1275-1300, 1995.

Sanford, W. E., Whitaker, F. F., Smart, P. L. and Jones, G. D. Numerical analysis of seawater circulation in carbonate platforms: 1. Geothermal convection. *Am. J.. Sci.,* 298 (10), 801-828,1998.

Schmoker, J. W. and Halley, R. B. Carbonate porosity versus depth - A predictable relation for South Florida. *AAPG Bull.,* 66 (12)**,** 2561-2570, 1982.

Warren, J.K. *Evaporites: their Evolution and Economics.* Wiley Blackwell, 1999.

Xu, T., Sonnenthal, E., Spycher, N. and Pruess, K. *TOUGHREACT User's Guide: A Simulation Program for Non-isothermal Multiphase Reactive Geochemical Transport in Variably Saturated Geologic Media*, Report LBNL-55460, Lawrence Berkeley National Laboratory, Berkeley Calif., 2004.

Zhang, G., Spycher, N., Xu, T., Sonnenthal, E. & Steefel, C. *Reactive Geochemical Transport Modeling of Concentrated Aqueous Solutions: Supplement to TOUGHREACT User's Guide for the Pitzer Ion-Interaction Model*, Report LBNL-62718, 2006a.

Zhang, G., Spycher, N., Sonnenthal, E., Steefel, C. And Xu, T. Modeling Reactive Multiphase Flow and Transport of Concentrated Solutions Using A Pitzer Activity Approach with TOUGHREACT, *J. Nucl. Technol.*, 164(2), 180 – 195, 2006b.

SURFACE DEFORMATION DUE TO COMPRESSED AIR TUNNELING USING TOUGH2 AND FLAC3D

Avirut Chinkulkijniwat

School of Civil Engineering
Suranaree University of Technology
Nakhon-Ratchasima 30000
THAILAND
e-mail: avirut@sut.ac.th

ABSTRACT

In this study, TOUGH2-FLAC3D coupling is employed to simulate flow and deformation due to two-phase flow induced by the application of air pressure into the subsurface. Linear elastic behavior is assumed. To verify the TOUGH2-FLAC3D simulation, I use test results from an *in situ* air flow test in Essen, Germany. Comparison between calculation results and the corresponding test results showed good agreement, I carried out a simulation of compressed air tunneling, which accurately captured surface heaving in front of the tunnel face.

INTRODUCTION

The "new Australian tunneling method" (NATM) is often used in urban tunneling (in combination with compressed air) to prevent groundwater inflow at a tunnel face. Owing to the greater magnitude of air pressure as opposed to groundwater pressure in the surrounding soil, upward air flow can predominate in the tunnel vicinity. This upward air flow can influence surface displacements during tunnel advancement.

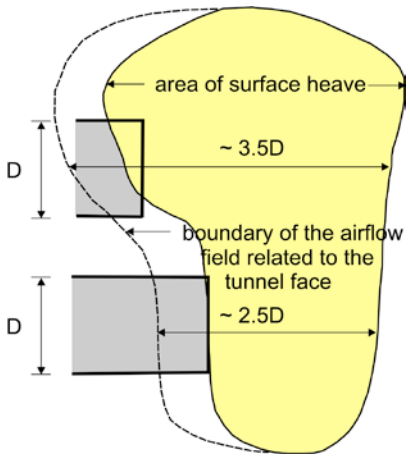

Figure 1. Inverse modeling procedures

Field observations have shown reduction in surface settlements at the tunnel tail, as well as the upward heaves at the surface ahead of the tunnel face in compressed air tunneling—e.g., Schumacher et al. (1987), Weber (1987), and Soos and Weber (1995). Figure 1 shows a surface heaving zone observed during the subway construction in Essen, Germany (Schumacher et al., 1987). As indicated by the figure, a zone of surface heaving is created in front of the tunnel face.

Here, I focus first on the TOUGH2-FLAC3D coupling as introduced by Rutqvist et al. (2002). Then, I examine whether a loose coupling between the two codes can capture the features of flow and deformation caused by introducing air pressure into the subsoil. The results of the German field test as interpreted by Kramer & Semprich (1989) are used in this paper for this purpose. Thereafter, I conduct a simulation of compressed air tunneling, with the principal aim of checking whether the pattern of surface displacements observed in the field can be captured by considering effects of the tunnel excavation and the fluid flow. In this way, the case study is simplified by assuming a homogeneous, isotropic, and linear elastic soil domain.

TOUGH2-FLAC3D COUPLING

The TOUGH2-FLAC3D coupling is conducted following Rutqvist et al. (2002), i.e., sequential execution and data transfer via a set of external ASCII files. TOUGH2 has been developed to handle nonisothermal, multiphase, multicomponent fluid flows in 3-dimensional porous and fracture media. However, mechanical simulation is not possible in a stand-alone TOUGH2 simulation. FLAC3D has been developed to perform mechanical simulation in soils and rocks. Although FLAC3D can also handle fluid-mechanical interactions for single-phase fluid flow, a simulation of two-phase fluid flow is not possible with a stand-alone FLAC3D simulation. Using a sequential coupling of two codes is more time consuming than using a single code. However, the big advantage of coupling TOUGH2 and FLAC3D is that both of them are used worldwide and are well tested in their respective fields. Additionally, source code is available for TOUGH2, and thus modification

of the code as well as implementation of the constitutive transport equations is possible. Moreover, n FLAC3D, an embedded programming language, the so-called FISH language, enables the user to define any new variables and functions. FLAC3D can communicate with TOUGH2 via this feature.

In order for FLAC3D and TOUGH2 to communicate with each other, knowledge of their corresponding meshes (and how the data structure is stored in the meshes) must be established. A finite difference mesh in FLAC3D generated by the user consists of elements and nodal points. An element is the smallest geometric domain within which the change in a phenomenon (e.g., stress versus strain) is evaluated. Nodal points are points at the corners of the corresponding element. In FLAC3D, state variables that are the vector quantities are stored at the nodal points, and state variables that are the scalar and tensor quantities are stored at the element centroids. However, the input variables can be submitted into the FLAC3D mesh only through the FLAC3D nodal points. The TOUGH2 mesh does not use nodal points, but rather elements. Therefore, all the state variables in TOUGH2 are stored at the element centroids.

The effective stress at each FLAC3D element is calculated from the degree of liquid saturation *Sl*, the pressure of liquid phase *pl*, and the pressure of gas phase *pg*.\ which are calculated in TOUGH2.

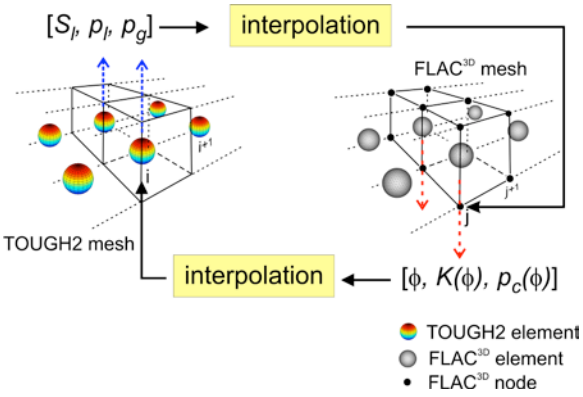

Figure 1. Communication between TOUGH2 and FLAC3D

An increment in porosity is calculated from a volumetric strain. In this paper, the volumetric strain is calculated based on an assumption of linear elastic deformation. The volumetric strain increment is stored at a FLAC3D element centroid, with an updated porosity representing the corresponding element centroid. After the FLAC3D simulation run, that updated porosity is then sent to a corresponding TOUGH2 element. Figure 1 is schematic diagram showing how information from the TOUGH2 mesh is sent to the jth FLAC3D node and how the information from the FLAC3D mesh is sent to the ith TOUGH2 element.

The TOUGH2-FLAC3D coupling is initiated with a TOUGH2 simulation run. TOUGH2 is executed between t0 and t1 until convergence is reached. At each TOUGH2 element, porosity is assumed constant during this time step. Then, FLAC3D is executed for mechanical simulation for the same time step. The effective stress at each FLAC3D element is calculated. At the end of each time step, an increment in porosity is calculated from a volumetric strain as written in Equation 3. TOUGH2 is then executed for the next time step. The updated porosity after the FLAC3D simulation run is then sent to a corresponding TOUGH2 element. TOUGH2 is again executed between t1 and t2 until convergence is reached. These procedures are repeated until the simulation time reaches a time specified by the user. Fig. 1 shows the numerical procedures for coupling TOUGH2 and FLAC3D.

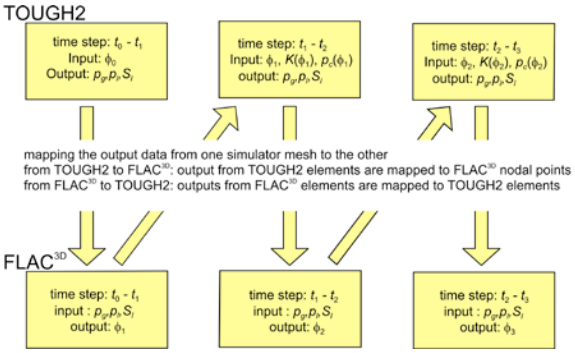

Figure 2. TOUGH2-FLAC3D coupling procedures

Between fluid flow and mechanical simulations in Figure 2, interpolation is required to map inputs and outputs from one mesh to the other—this is because the variables are submitted into FLAC3D mesh through its nodal points, while TOUGH2 mesh uses only elements. Moreover, even the outputs from FLAC3D are at FLAC3D elements. In a loose coupling of the two codes, the computational grid mesh used in each is not necessary, and therefore the same interpolation is required. In this study, a weighted distant interpolation is used for interpolation inside the domain. At the boundaries of the model, the closest point is searched and assigned to the destination, point by point.

SIMULATION RESULTS OF AIR FLOW TEST

The *in situ* air flow test in Essen carried out by the German contractor Bilfinger + Berger Bauaktien-

gesellschaft (Kramer & Semprich 1989) is chosen to test the coupled simulation. This air-flow test was carried out—simultaneously with a tunneling construction project in Essen, Germany—to investigate the fluid conductivity of the gas phase and the deformations due to two-phase flow induced by introducing compressed air into the subsurface. Figure 3 shows a schematic diagram of the experimental setup. Details of the experiment are elaborately discussed in English in Chinkulkijniwat et al. (2006).

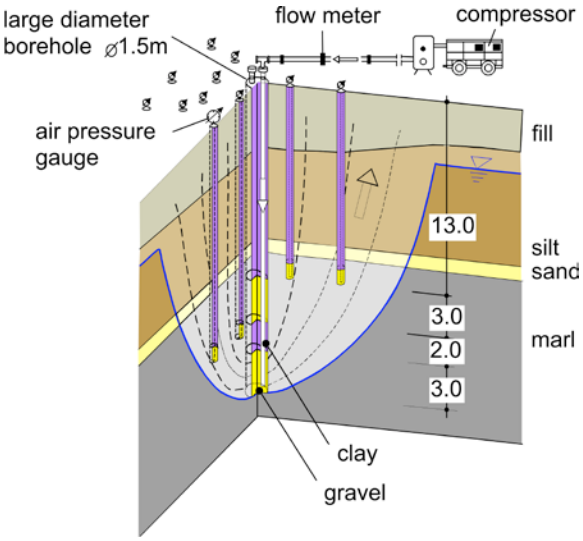

Figure 3. In situ air flow test in Essen (Kramer & Semprich, 1989)

Figure 4 shows the calculated pore pressure and gas saturation after 27 hours of air pressure injection (pa = 160 kN/m^2) into the borehole. The distribution of pore pressure after 27 hours of applying that air pressure is shown in Figure 6a. The pore pressure increases significantly in the vicinity of the borehole, but retains its level of hydrostatic pressure at a certain distance apart from the borehole. The levels of pore pressure measured from 4 piezometers are also shown in Figure 4a. As can be seen in Figure 4a, good agreement between the measured and calculated pore pressures is achieved. The distribution of gas saturation after 27 hours of applying the 160 kN/m^2 of air pressure into the borehole is shown in Figure 4b, with the desaturation zone in the marl layer taking on a bulb-like shape. In this marl layer, a high degree of gas saturation can be found in the vicinity of the air injection zone, but only a small area of the marl layer is desaturated. Within the sand layer, because of its relatively high fluid-conductivity value, the desaturation zone spreads over the entire layer. However, in the silt layer, the desaturation zone does not exist, due to its low fluid conductivity value and high air-entry-pressure value.

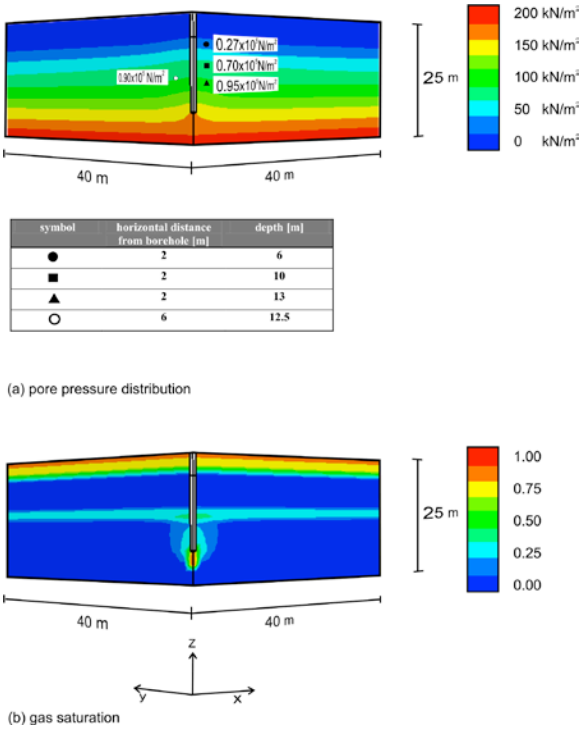

Figure 4. Pore-pressure distribution and gas saturation

Figure 5 shows a comparison between the surface displacement measured from the experiment and that calculated from the loose-coupling simulation at 27 hours, after introducing 160 kN/m^2 of air pressure into the borehole. The blue diamonds are experimental results. Keeping in mind that each soil layer is assumed homogeneous and isotropic, we note the good agreement between the experimental results and the numerical results, even with the level of surface displacement in the numerical simulation being somewhat higher that that found in the experiment.

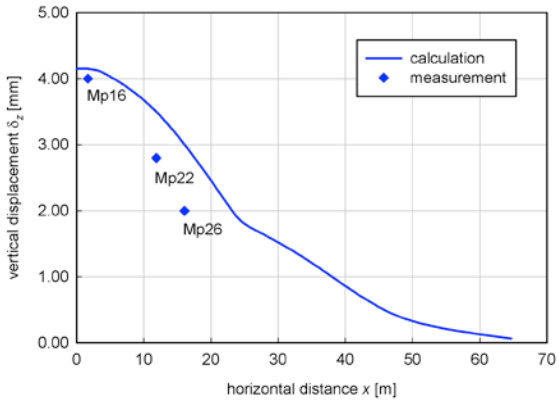

Figure 5. Surface displacement due to the first air pressure level in the test

SIMULATION RESULTS OF COMPRESSED AIR TUNNELING

To simulate the compressed air tunneling, I assumed a silty sand layer, 20 m thick, with a bulk density of 2000 kg/m^3, which converts to a dry density of 1.62 g/cm^3. The silty sand layer is underlined by a thick layer of impervious bedrock, and the groundwater table is at the ground surface. A 6 m diameter circular-shaped tunnel is being excavated within these ground conditions by means of NATM using compressed air. A tunnel base is located at 15 m below the groundwater table. (Figure 6 shows these ground conditions.) According to the location of the tunnel base, air pressure in this example is about 150 kN/m^2. The rate of tunnel advance is assumed to be v = 4 m/day. Physical, mechanical, and fluid properties of the silty sand are summarized in Table 1 and Table 2.

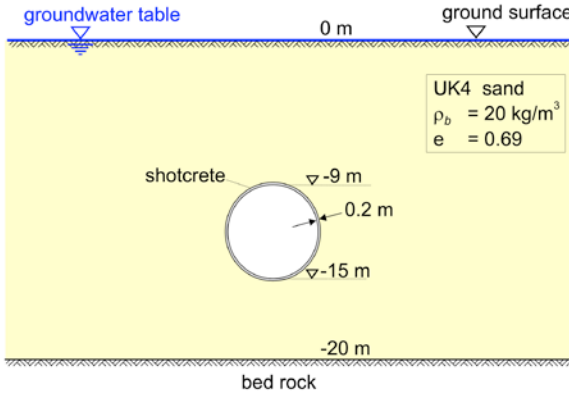

Figure 6. Ground conditions and geometry of the tunnel

Table 1. Properties of the silty sand

			Unit
Grain density	ρ_s	2.74	[g/cm^3]
Dry density	ρ_d	1.62	[g/cm^3]
Young modulus	E	45	[MN/m^2]
Poisson's ratio	ν	0.3	[-]

Table 2. Fluid related properties of silty sand

Parameter		Unit
$\boldsymbol{K}$	$1.50\times10^{-9}\,\phi^{6.4}$	[m^2]
S_{ls}	0.98	[-]
n	3.55	[-]
S_{lr}	0	[-]
p_o	6.80	[kN/m^2]$^{-1}$
τ	2.76	[-]

Parameters in Table 2 follow the constitutive flow equations written in Equations 1 to 3, where p_o is the air entry pressure, k_{rl} is the relative permeability of the liquid phase, k_{rg} is the relative permeability of the gas phase, τ is the tortuosity-related parameter representing how long the liquid-flow component increases as the liquid saturation decreases, n is the pore-size distribution-related parameter, S_l is liquid saturation, S_{lr} is residual liquid saturation, S_{ls} is maximum liquid saturation, and ϕ is porosity.

$$p_c = p_o((S_e)^{-n/n-1} - 1)^{1/n} \tag{1}$$

$$k_{rl} = (S_e)^{\iota}\left[1 + (1 - (S_e)^{n/n-1})^{1-1/n}\right]^2 \tag{2a}$$

$$k_{rg} = (1 - S_e)^{\iota}\left[1 - (S_e)^{n/n-1}\right]^{2(1-1/n)} \tag{2b}$$

$$S_c = \frac{S_l - S_{lr}}{S_{ls} - S_{lr}} \tag{3}$$

Figure 7 shows simulation results of the surface deformation for the tunnel face position y = 40 m. When the tunnel face is at y = 40 m, cross sections of surface displacements at y = 10 m, y = 30 m, y = 40 m, and y = 50 m are shown in Fig. 7. A combination of the settlements due to excavation and the upward heaves due to seepage flow is exhibited. The most pronounced zone of upward heaves is shown within a certain distance in front of the tunnel especially along the centre line of the tunnel.

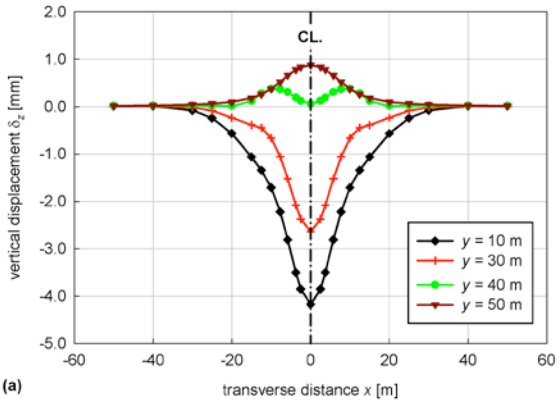

Figure 7. Surface displacements for the tunnel face at y = 40 m

CONCLUSION

The results from the TOUGH2-FLAC3D coupling simulation show good agreement with the corresponding test results, indicating that the TOUGH2-FLAC3D coupling can capture flow and deformation features resulting from air pressure introduced into the subsoil. The next step is to implement an elasto-plastic model for unsaturated soils into FLAC3D and extend the simulation to explain surface settlement due to compressed air tunneling construction.

REFERENCES

Chinkulkijniwat, A., Semprich, S. (2006). Flow-Deformation due to Two-Phase Flow A Loose Coupling Simulation. Proc. 6th European Conf. Numerical Methods in Geotechnical Engineering, Graz, Austria, September 6-8, 2006, 693-698.

ITASCA Consulting Group Inc. (2002). Fast Lagrangian Analysis of Continua in 3 Dimensions Version 2.10, User's Manual. ITASCA Consulting Group Inc, Minnesota.

Kramer, J., Semprich, S. (1989). Erfahrungen über Druckluftverbrauch bei der Spritzbetonbauweise. Taschenbuch für den Tunnelbau. 13. Jahrg, Verlag Glückauf GmbH, Essen, 91-153.

Pruess, K., Oldenburg, C., Moridis, G. (1999). TOUGH2 User's Guide, Version 2.0. Earth Science Division, Ernest Orlando Lawrence Berkeley National Laboratory.

Rutqvist, J., Wu, Y. –S., Tsang, C.F., Bodvarsson, G. (2002). A modeling approach for analysis of coupled multiphase fluid flow, heat transfer, and deformation in fractured porous rock. Int. J. of Rock Mechanic & Mining Sciences, Vol. 39, 429-442.

Schumacher, G., Haardt, H., Kalthoff, D. (1987). U-Bahn Bau in Essen, Baulos 30, Spritzbetonbauweise unter Druckluft – Baukonzept und Bauarwickling. Forschung und Praxis, Vol. 32, 184-192.

Soos, P.v., Weber,J. (1995). Druckluftvortriebe im Münchner U-Bahn-Bau. Schriftenreihe Lehrstuhl und Prüfamt für Grundbau. Bodenmechanik und Felsmechanik der TU München, Germany, Heft 21, 261-279.

Weber, J (1983). Erfahrungen mit Druck-luftvortrieben in Sprizbetonbauweise beim Müchener U-Bahn-Bau, STUVA Tagung 1983 in Nürnberg. Forschung und Praxis, Vol. 32, 184-192.

MODELING GAS TRANSPORT AND REACTIONS IN POLYDIMETHYSILOXANE

Chuanhe Lu, Yunwei Sun, Stephen J. Harley, Elizabeth A. Glascoe

Physical and Life Sciences Directorate, Lawrence Livermore National Laboratory
7000 East Avenue,
Livermore, CA, 94550, USA
E-mail: lu25@llnl.gov

ABSTRACT

Polydimethylsiloxane (PDMS) is the most widely used polymer because it is nontoxic, relatively inert, easy to fabricate, and optically clear. For example, due to its hydrophobic nature relative to other materials, it is often used as a moisture barrier in photovoltaic cells and as a fluid channel in microfluidic devices. In spite of its hydrophobic nature, sorption and diffusion of water vapor through PDMS are still a concern for industry. Water intrusion through the PDMS layer and into an electronic device may result in corrosion, shorting, and other types of electronic failure. Moisture released from neighboring materials may intrude into and react with PDMS to produce copious amounts of hydrogen, which could also result in harmful consequences. Both diffusion and reaction processes occur in a single gas phase at a millimeter-scale. As suggested by experimental results, the diffusion coefficients of gas components depend not only on their molecular weight, but also on sorbent properties. The total gas sorption of water vapor is the sum of Henry's, Langmuir, and pooling processes.

The current version of TOUGHREACT is limited to liquid-phase reactions without considering gas-phase sorption. Here, we report on extending TOUGHREACT's capability for handling reactive-transport applications in material science and chemical engineering, specifically by modifying TOUGHREACT to model gas-phase reactions. This extended TOUGHREACT capability is demonstrated by simulating and interpreting pure gas diffusion and sorption through PDMS. The modified code is then calibrated by results from dynamic water vapor sorption experiments.

INTRODUCTION

PDMS-based materials are used in a wide range of applications because they are nontoxic, relatively insert, easy to fabricate, and have favorable optical and mechanical properties. PDMS materials are considered hydrophobic and are used both as moisture barriers in photovoltaic cells and as fluid channels in microfluidic devices. However, in spite of PDMS's hydrophobic nature, water vapor still can sorb and diffuse through PDMS, albeit at an attenuated rate. Over time, water intrusion through the PDMS layer and into an electronic device can result in compatibility issues and even undesirable effects on electronic components. As such, accurate knowledge of dynamic water-vapor sorption processes and diffusion may lead to a better determination of aging and or failure predictions for devices (Harley et al., 2012).

Gas flow through microporous zeolites (Hassan and Way, 1996) and other nanoporous materials (Tzoulaki et al., 2009) has been studied extensively. The accurate modeling of gas diffusion in porous media is a challenging problem that applies to a variety of engineering domains, including catalysis, fuel cells, batteries, and membrane technology. The microscopic features of a porous medium, and (more specifically) the geometry of its pore phase, affect gas diffusion significantly (Berson et al., 2011). In order to model diffusion through a porous medium at the macroscale without solving the microscopic physics, we must define an effective gas diffusivity that accounts for both the effects of the microstructure geometry and the pore confinement. The use of an effective diffusion coefficient allows for looking at the combined effect of the different diffusion mechanisms that could take place in a porous

media (Ayala et al., 2006; Beygi and Rashidi, 2011).

The effective diffusivity of water vapor in PDMS systems has been studied for a long time (Barrie and Platt, 1963; Favre et al., 1994; Watson and Baron, 1996). Harley et al. (2012) quantified the sorption and diffusion of moisture through Sylgard-184, a commercially available PDMS material that is widely used and particularly popular as a protection layer in photovoltaic cells.

Based on experimental data and the latest version of TOUGHREACT (Xu, et al., 2011), we implemented a new diffusion-property setup to simulate water outgassing from zeolite and diffusion through Sylgard-184 with kinetic reactions within a jar of N_2 gas. We investigated the diffusion pattern in both the zeolite and the Sylgard-184 and evaluated the sensitivities of of water and H_2 concentrations in the headspace above Sylgard-184. Our new calibrated model, as well as our sensitivity analysis, can be used to evaluate and optimize the performance and design of experiments and estimate device lifetime in a moist environment.

CONCEPTUAL MODEL

To design laboratory experiments, we constructed a two-dimensional radial symmetric model as shown in Fig. 1. Zeolite is selected as the water-bearing material and implemented as a cylinder, with a radius of 18 mm and height of 55 cm, at the center of a jar with radius of 22 mm and height of 80 mm. Sylgard-184 seals the zeolite with a thickness of 5 mm above and 4 mm on the sides of the zeolite. The zeolite is fully saturated with water at the beginning, and the headspace is initially saturated with nitrogen gas. There are initially 6.7×10^{-5} mol/g Si-H bonds in Sylgard-184. The water vapor released from zeolite intrudes into Sylgard-184, reacts with Si-H bonds, and produces H_2 gas (Eqn. 1). The volume ratio between zeolite and Sylgard-184 is set up to make sure there is sufficient water in the zeolite, which can exhaust all the Si-H bounds in Sylgard-184. The total system is under constant temperature (50°C) and pressure (1 atm).

$$H_2O + \text{Si-H} \rightarrow \text{Si-OH} + H_2 \qquad (1)$$

The irreversible kinetic reaction is expressed Eqn. 2.

$$r = k\, exp(-E_a/RT) \qquad (2)$$

where k is the rate constant (10^{13} 1/s), E_a is the activation energy (25 kcal/mol), R is the gas constant (1.9858775 cal/mol/K) and T is the absolute temperature (K).

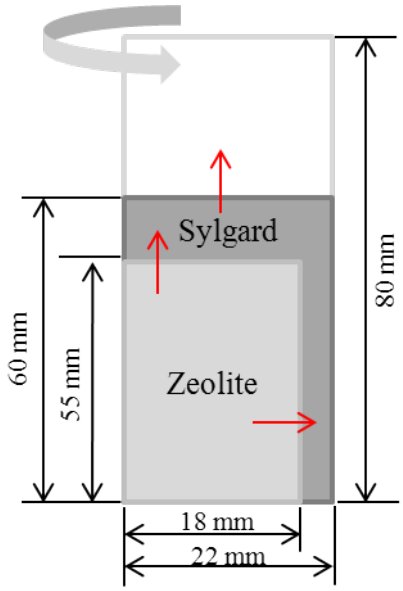

Figure 1. Two-dimensional conceptual model for water sorption and diffusion. Note that the horizontal scale is exaggerated.

The general gas diffusion coefficient in TOUGHREACT is molecular-mass specific. The effective diffusion coefficient depends on the molecular weight of the gas component, the tortuosity of the porous medium, and gas saturation and porosity (at a given pressure and temperature). Experimentally, the measurement of gas concentrations depends entirely on the effective diffusion coefficients. For this reason, a computer model of gas transport in a porous medium should reflect the fact that the measured diffusion is both component and medium dependent (Table 1, Michaels and Bixler, 1961; Crank, 1968; Deas et al., 1972; Eloy-Giorni et al., 1996; Merkel et al., 2000; Steve et al., 2012). Therefore, the diffusive flux of gas in the polymer is modeled with Fick's law:

$$F_{ij} = -De_{ij}\, \Delta C_i \qquad (3)$$

where F_{ij} is the diffusive flux of gas i in material j, De_{ij} is the effective diffusivity of gas i in material j, C_i is the concentration of gas i.

Table 1.Effective diffusion of gases in HDPE and Sylgard-184 (cm^2/s).

Gas	Zeolite	Sylgard-184
Water vapor	3×10^{-8}	5×10^{-6}
H_2	2.3×10^{-6}	1.4×10^{-4}
N_2	9.3×10^{-8}	3.4×10^{-5}

METHODOLOGY

TOUGHREACT is a numerical simulator for modeling chemically reactive nonisothermal flows of multiphase fluid in porous and fractured media (Xu and Pruess, 2001; Spycher et al., 2003; Sonnenthal et al., 2005; Xu et al., 2006; Xu, 2008; Zhang et al., 2008; Zheng et al., 2009). We modified TOUGHREACT and added a new capability to simulate pure gas diffusion in a small-scale polymer, considering effective diffusion coefficients for different gas species in various materials.

PSUADE is a software package developed at Lawrence Livermore National Laboratory for various uncertainty quantification (UQ) activities, such as uncertainty assessment, global sensitivity analysis, response-surface analysis, risk analysis, design optimization, system calibration, and parameter identification (Tong, 2005; 2010). It employs a nonintrusive (sampling-based) approach to UQ that does not require simulation codes to be modified, enabling it to be easily integrated with a variety of application simulators. PSUADE is equipped with many response-surface generation and validation techniques. These techniques can be coupled with other UQ techniques, such as numerical optimization and Markov Chain Monte Carlo methods, for calibration and parameter estimation (Tong, 2010; Sun et al., 2012). We conducted global sensitivity analyses of water vapor and H_2 concentrations in the headspace, in terms of all uncertain parameters.

The models for sensitivity analysis are simulated using NUFT (Nonisothermal Unsaturated-saturated Flow and Transport) code. NUFT is a flexible multipurpose computer code for modeling multiphase, multicomponent heat and mass flow and reactive transport in unsaturated and saturated porous media. It solves the continuum equations for the conservation of mass and energy with an integrated finite-difference spatial discretization.

The code has been widely used for numerical modeling of subsurface multiphase flow and reactive transport processes. Applications include geological disposal of nuclear waste (Buscheck et al., 2003; Sun et al., 2010), geological carbon sequestration (Johnson et al., 2004; Carroll et al., 2009), groundwater monitoring and remediation (Carrigan and Nitao, 2000), and subsurface hydrocarbon production (Sahni et al., 2000).

SENSITIVITY ANALYSIS

For the purpose of guiding experiment design, we conducted a sensitivity analysis to screen system parameters that affect the gas concentration at the headspace. Four parameters are considered in sensitivity analysis, diffusivities of water vapor, hydrogen, and nitrogen in Sylgard-184, and the thickness of Sylgard-184 (the size of HDPE is fixed). The uncertainty ranges are shown in Table 2. The Latin Hypercube (McKay et al., 1979) method is used to generate 1000 sample points in the parametric space of the four selected parameters.

Table 2. Ranges of uncertainty in the parameters used during UQ analysis.

Parameters	Ranges
D_e of H_2O in Sylgard-184 (cm^2/s)	5×10^{-6}~3.5×10^{-5}
D_e of H_2 in Sylgard-184 (cm^2/s)	1×10^{-5}~1×10^{-3}
D_e of N_2 in Sylgard-184 (cm^2/s)	1×10^{-6}~1×10^{-4}
Thickness of Sylgard-184 (mm)	20~50

Considering 100 ppb as a detectable limit, the sensitivity of H_2 arrival time at the headspace is shown in Fig. 2. It illustrates that there is a strong relationship between the H_2 arrival time and the D_e of H_2 in Sylgard-184. H_2 arrives at the headspace earlier when the effective diffusion coefficient of H_2 in Sylgard-184 is

larger. The thickness of Sylgard-184 also effects the H_2 arrival time. A thicker Sylgard-184 layer makes the arrival time of H_2 longer. The global Sobol sensitivity analysis with PSUADE demonstrates that the effective diffusion coefficient of H_2 in Sylgard-184 is the most relevant parameter for H_2 arrival time, with the thickness of Sylgard-184 the secondary sensitive factor (Fig. 3).

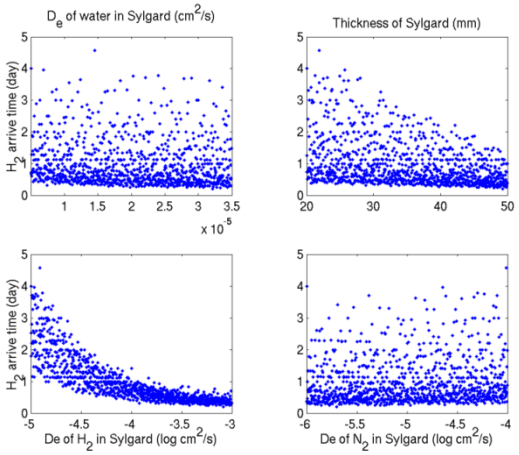

Figure 2. Scatter plots of H_2 arrival time (day) as a function of uncertainty parameters.

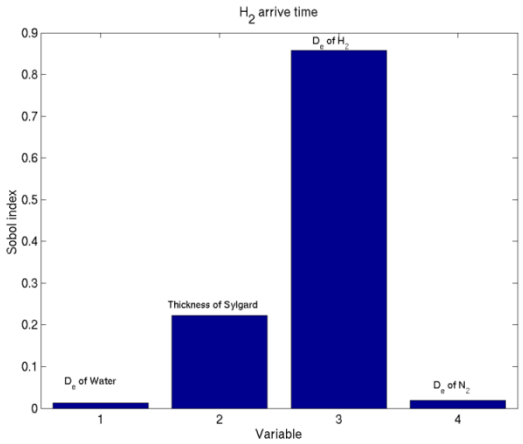

Figure 3. Sobol sensitivity index for the H_2 arrival time at the headspace.

Since the headspace is initially saturated with N_2, its concentration in headspace is mainly affected by the effective diffusion coefficient of N_2 in Sylgard-184 (Fig. 4). The thickness of Sylgard-184 is also sensitive to the N_2 concentration in the headspace because it affects the total N_2 mass in the headspace. The thickness of Sylgard-184 also influences the transport time of water, which, in turn, affects the N_2 concentration in the headspace. Similarly to N_2, the effective diffusion coefficient of N_2 in Sylgard-184 is the most sensitive factor for water vapor concentration in the headspace, as shown in Fig. 5. Because of the small amount of water vapor in the headspace relative to N_2 mass, the migration of N_2 out of the headspace influences the water vapor concentration. The H_2 concentration in the headspace is initially controlled by the effective diffusion coefficient of H_2 in Sylgard-184. After 10 days, it is mainly dominated by the thickness of the Sylgard-184 (Fig. 6). Effective diffusion coefficient of N_2 in Sylgard-184 becomes the secondary sensitive factor.

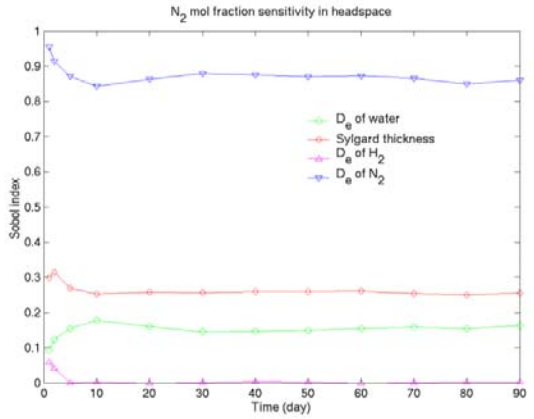

Figure 4. Sobol sensitivity index for the N_2 concentration in the headspace at different times.

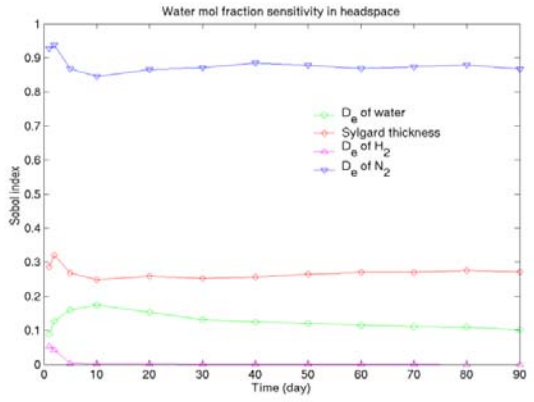

Figure 5. Sobol sensitivity index for the water vapor concentration in the headspace as a function of times.

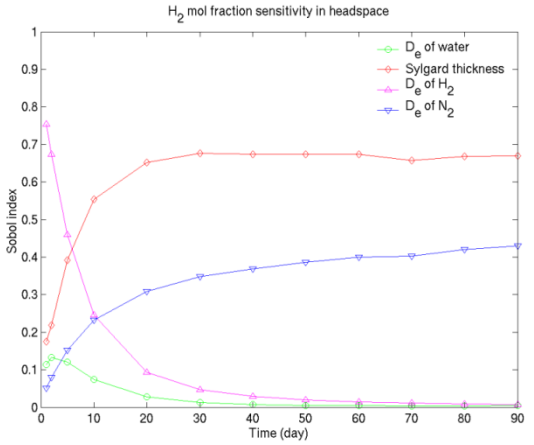

Figure 6. Sobol sensitivity index for the H_2 concentration in the headspace at different times.

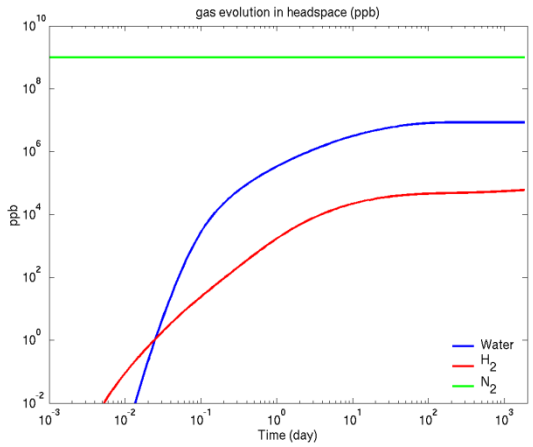

Figure 7. Evolution of the gas concentrations at headspace.

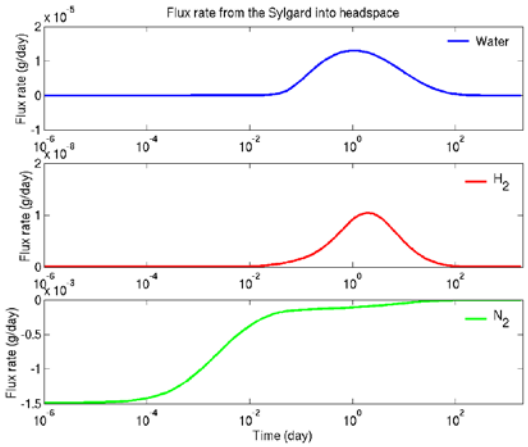

Figure 8. Evolution of gas flux rates from Sylgard-184 into headspace.

DIFFUSION SCENARIO

The pure-gas diffusion simulation with the updated TOUGHREACT is still an ongoing project. A modified version of TOUGHREACT (instead of NUFT) will be used to add a new gas sorption/desorption capability based on experiments.

The water vapor released from zeolite intrudes into Sylgard-184 and reacts with Si-H to produce H_2. H_2 diffuses through the Sylgard-184 and reaches the headspace first (Fig. 7). In contrast with water vapor, which mainly diffuses from zeolite into the headspace through the Sylgard-184, H_2 diffuses into both the headspace and zeolite. Therefore, the accumulation of H_2 in the headspace is slower than that of water vapor. It takes about 100 days for the system to reach steady state. Finally, the concentration of N_2 is two magnitudes higher than that in water vapor, while the concentration of H_2 is much lower (almost two magnitudes lower) than that in water vapor.

H_2 crosses the surface of Sylgard-184 first (Fig. 8), but the water flux rate into headspaces achieves peak value first. The flux rate of N_2 continues decreasing until steady state is reached after 100 days.

CONCLUSIONS

The water vapor released from the zeolite is transported through Sylgard-184, reacting with Si-H to produce H_2. Water vapor and H_2 both diffuse through Sylgard-184 and accumulate at the headspace. The understanding of gas reaction and diffusion phenomena in Sylgard-184 is very important, because such understanding leads to better determination of aging within the devices that use Sylgard-184 as a protection barrier. TOUGHREACT was modified to consider the variable effective-gas-diffusion coefficient, which depends on both components and porous media.

The arrival time of produced H_2 at the headspace is dominated by the effective diffusion coeffi-

cient of H_2 in Sylgard_184, as well as the thickness of Sylgard-184. Since N_2 is the dominant gas in the system, the concentrations of N_2 and water vapor in the headspace are all considerably influenced by the effective diffusion coefficient of N_2 in Sylgard-184. These sensitivity analyses will be perfromed to prepare samples and design experiments.

Although H_2 arrives at the headspace first, the flux rate of water vapor across the Sylgard-184 surface is generally larger than other gas components and approaches the peak earlier. When the system reaches steady state, the concentration of water vapor is two magnitudes higher than that of H_2. A large flux rate of N_2 crosses the surface of Sylgard-184 and finally transports back into the zeolite.

Except for the kinetic reaction of water vapor with Si-OH bonds, the dynamic sorption/desorption of water vapor with silica-filled polymer will be considered to match experimental data. The updated TOUGHREACT will be validated by experimental data and can be used as a predictive tool to evaluate device compatibility.

ACKNOWLEDGMENT

This research was supported by the LLNL LDRD project: "Predicting weapon headspace gas atmosphere: age aware predictive models of weapon component compatibility." The work was performed under the auspices of the U.S. Department of Energy by Lawrence Livermore National Laboratory under Contract No. DE-AC52-07NA27344. This paper is released by LLNL with the release number LLNL-CONF-565272.

REFERENCES

Ayala, H.L.F., T. Ertekin and M. Adewumi, Compositional modeling of retrograde gas-condensate reservoirs in multi-mechanistic flow domains, *SPE Paper 94856. SPE. J,* 11(4), 480–487, 2006.

Barrie, J.A. and B. Platt, The diffusion and clustering of water vapor in polymers, *Polymer*, 4(3), 303–313, 1963.

Berson, A., H. Choi, and J.G. Pharoah, Determination of the effective of a porous composite medium from the three-dimensional reconstruction of its microstructure, *Phys. Rev. E*, 83, 026310, 2011.

Beygi, M.E. and F. Rashidi, Analytical solutions to gas flow problems in low permeability porous media, *Transp. Porous. Med.*, 87, 421–436, 2011.

Buscheck, T.A., L.G. Glascoe, K.H. Lee, J. Gansemer, Y. Sun and K. Mansoor, Validation of the multiscale thermohydrologic model used for analysis of a proposed repository at Yucca Mountain, *Journal of Contaminant Hydrology*, 62(3), 421–440, 2003.

Carrigan, C.R. and J.J. Nitao, Predictive and diagnostic simulation of in situ electrical heating in contaminated, low-permeability soils, *Environmental Science and Technology*, 34(22), 4835–4841, 2000.

Carroll, S., Y. Hao and R. Aines, Geochemical detection of carbon dioxide in dilute aquifers, *Geochemical Transactions*, 10:4, 2009. doi:10.1186/1467-4866-10-4.

Crank, J. and S.P. Geoffrey, *Diffusion in polymers*, Academic Press, 1968.

Deas, T.M., H.H. Hofer and M. Dole, Solubility of hydrogen in polyethylene by a semimicro method, Macromolecules, 5, 223–226, 1972.

Eloy-Giorni, C., T. Pelte, P. Pierson and R. Margrita, Water diffusion through geomembranes under hydraulic pressure, Geosynthetics International, 3(6), 741–769, 1996.

Favre, E., P. Schaetzel, Q.T. Nguygen, R. Clement and J. Neel, Sorption, diffusion and vapor permeation of various penetrants through dense poly(dimethylsiloxane) membranes – a transport analysis, *J. Membrane Sci.*, 92(2), 169–184, 1994.

Glassley, W.E., J.J. Nitao and C.W. Grant, The impact of climate change on the chemical composition of deep vadose zone waters, *Vadose Zone Journal*, 1, 3–13, 2002.

Glassley, W.E., J.J. Nitao and C.W. Grant, Three-dimensional spatial variability of chemical properties around a monitored waste emplacement tunnel, *Journal of Contaminant Hydrology*, 62(63), 495–507, 2003a.

Glassley, W.E., J.J. Nitao, C.W. Grant, J.W. Johnson, C.I. Steefel and J.R. Kercher, The impact of climate change on vadose zone pore waters and its implication for long-term monitoring. *Computers and Geosciences*, 29, 399–411, 2003b.

Harley, S.J., E.A. Glascoe and R.S. Maxwell, Thermodynamic study on dynamic water vapor sorption in Sylgard-184, *Manuscript in Review*, 2012.

Hassan, M.H.M. and D. Way, Gas transport in microporous silica membrane. *SPE paper 36226 presented at the SPE Abu Dhabi international petroleum exhibition and conference*, Abu Dhabi, U.A.E., 13-16 October, 1996.

Johnson, J.W., J.J. Nitao and K.G. Knauss, Reactive transport modeling of CO_2 storage in saline aquifer to elucidate fundamental processes, trapping mechanisms and sequestration partitioning, *Geological Storage of Carbon Dioxide*, Editors: Baines, S.J. and Worden, R.H., Geological Society, London, Special Publications 223, 107–128, 2004.

Mckay, M.D., R.J. Beckman and W.J. Conover, A comparison of three methods for selecting values of input variables in the analysis of output from a computer code, *Technometrics*, 21(2), 239—245, 1979. doi:10.2307/1268522.

Merkel, T.C., V.I. Bondar, K. Nagai, B.D. Freeman and I. Pinnau, Gas sorption, diffusion, and permeation in poly(dimethylsiloxane), *J. Polym. Sci. B: Polym. Phys.*, 38(3), 425–434, 2000.

Michaels, A.S. and H.J. Bixler, Flow of gases through polyethylene, *J. Polym. Sci.*, 50(154), 413–439, 1961.

Sahni, A., M. Kumar and R.B. Knapp, Electromagnetic heating methods for heavy oil reservoirs, *SPE/AAPG Western Regional Meeting*, Long Beach, California, June 19-22, 2000.

Sonnenthal, E., A. Ito, N. Spycher, M. Yui, J. Apps, Y. Sugita, M. Conrad and S. Kawakami.Approaches to modeling coupled thermal, hydrological, and chemical processes in the Drift Scale Heater Test at Yucca Mountain, *Int. J. Rock Mech. Min. Sci.*, 42, 6987–6719, 2005.

Spycher, N., K. Pruess and J. Ennis-King, 2003. CO_2-H_2O mixtures in the geological sequestration of CO_2. I. Assessment and calculation of mutual solubilities from 12 to 100°C and up to 600 bar, *Geochimica et Cosmochimica Acta*, 67(16), 3015–3031, 2003.

Sun , Y., C. Tong, T.A. Buscheck AND J.A. Blink, Combining simulation and emulation for calibrating sequentially reactive transport systems. *Transport in Porous Media*. doi:10.1007/s11242-011-9917-4, 2012.

Tong, C., *PSUADE User's Manual*, Lawrence Livermore National Laboratory, LLNL-SM-407882, 2005.

Tong, C., *PSUADE reference manual (Version 1.3.0)*, Lawrence Livermore National Laboratory, May, 2010.

Tzoulaki, L., D. Heinke, H. Lim, J. Li, D. Olson, J. Caro, R. Krishna, C. Chmelik and J. Karger, Assessing surface permeabilities from transient guest profiles in nanoporous host materials, *Angew. Chem. Int. Ed.*, 48, 3525–3528, 2009.

Watson, J.M. and M.G. Baron, The behavior of water in poly(dimethylsiloxane), *J. Membrane Sci.*, 110(1), 47–57, 1996.

Xu, T., N. Spycher, E. Sonnenthal, G. Zhang, L. Zheng and K. Pruess, TOUGHREACT Version 2.0: A simulator for subsurface reactive transport under non-isothermal multiphase flow conditions, *Computers & Geosciences*, 37(6), 763–774, 2011.

Xu, T. and K. Pruess, Modeling multiphase non-isothermal fluid flow and reactive geochemical transport in variably saturated fractured rocks: 1 Methodology, *Am. J. Sci.*, 301, 16–33, 2001.

Xu, T. and K. Pruess, Numerical studies on enhanced CO_2 dissolution and mineral trapping due to formation of aqueous complexes. *Computational Methods in Water Resources*. San Francisco, California, 2008.

Xu, T., E. Sonnenthal, N. Spycher and K. Pruess, TOUGHREACT: A simulation program for nonisothermal multiphase reactive geochemical transport in variably saturated geologic media, *Computers and Geosciences*, 32, 145–165, 2006.

Zhang G., Spycher N., Sonnenthal E., Steefel C., and Xu T., Modeling reactive multiphase flow and transport of concentrated aqueous solutions, *Nuclear Technology*, 164, 180–195, 2008.

Zheng, L., J. A. Apps, Y. Zhang, T. Xu and J. T. Birkholzer, On mobilization of lead and arsenic in groundwater in response to CO_2 leakage from deep geological storage, *Chemical geology*, 268(3-4), 281–297, 2009.

UNDERSTANDING GAS MIGRATION IN UNSATURATED FRACTURED POROUS MEDIA USING FIELD EXPERIMENTS AND NUMERICAL SIMULATIONS

S. GUILLON[1,2*], E. PILI[1,2], J-C. SABROUX[3], T.M. VU[4], P.M. ADLER[4]

[1]CEA, DAM, DIF, F-91297 Arpajon, France
[2]Institut de Physique du Globe de Paris, 1 rue Jussieu, F-75005 Paris, France, sguillon@ipgp.fr (* presenting author)
[3]Institut de Radioprotection et de Sûreté Nucléaire, Centre de Saclay, F-91192 Gif-sur-Yvette Cedex, France
[4]UPMC Sisyphe. Boîte 105, 4 place Jussieu, F-75252 Paris Cedex 05, France

ABSTRACT

Understanding the transfer mechanisms of gases in unsaturated fractured rocks is essential for the safety of CO_2 sequestration projects and many other applications. In order to develop our understanding and our modeling capacities, we recently compared field experiments with numerical simulations using several codes, including TOUGH2.

At the Roselend Natural Laboratory underground research facility in the French Alps, a tunnel provides access to the center of an unsaturated fractured crystalline rock formation at 55 m below ground surface. This underground research facility enables the study of gas transfer between a 60 m^3 chamber, isolated at the dead-end of the tunnel, and the surface. Pneumatic injection tests are conducted in the chamber.

We conducted numerical simulations to understand flow and transport processes during the field experiments, taking into account the actual boundary conditions and 3D geometry of the tunnel and chamber. Simulations with air flow (single-phase) reproduce the experimental data and yield values of permeability and porosity that compare well with previous estimates made from hydrogeological tracer experiments and stereological determinations. Simulations with an equivalent homogeneous medium satisfactorily model flow in the pneumatic injection tests. Two-phase flow and tracer transport simulations with TOUGH2 /EOS7R help to investigate the influence of water saturation on gas migration in the unsaturated zone.

INTRODUCTION

The Roselend Natural Laboratory is dedicated to the study of water and gas migration at the field scale under natural conditions. Here, joint experimental and numerical approaches are used to help our understanding of gas flow and transport in the unsaturated zone, at a 50 m scale. Pneumatic injection tests are conducted and numerical simulations of gas flow (single-phase) in a porous medium are performed to estimate both the permeability and the porosity. Gas tracer experiments were carried out using SF_6, noble gases and CO_2. Preliminary simulations of two-phase flow and SF_6 transport in the unsaturated fractured medium using the TOUGH2 code give insights into the influence of water flow on gas migration. The simulations also confirm which parameters and computational features that are necessary for simulating the processes with TOUGH2 in this context.

THE ROSELEND NATURAL LABORATORY

The Roselend Natural Laboratory, in the Western Alps (Provost et al., 2004), is composed of a dead-end horizontal tunnel at an altitude of 1576 m, located below an abandoned quarry (Figure 1). The tunnel is 128 m long and ~ 2.4 m in diameter. It is hosted in fractured gneiss and micaschists, and capped by the same rocks with an increasing thickness of 7 m at the entrance to 55 m at its closed end. The tunnel is located nearby the artificial Roselend Lake at slightly higher elevation than the lake. Head measurements at two piezometers located between the tunnel and the lake indicate that the water table level is ~20 m below the tunnel.

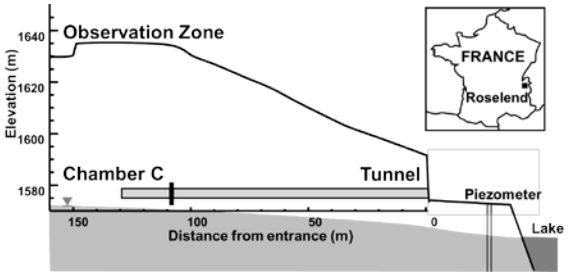

Figure 1. The Roselend Natural Laboratory, with the isolated Chamber C at the end of the tunnel, used for gas tracer injections observed at the surface.

At the end of the tunnel, a chamber (whose length and volume are 20 m and 60 m^3, respectively) is isolated by a wall and a door designed to be air-tight (Figure 1). It is referred to as Chamber C.

EXPERIMENTAL METHODS

Similarly to the work done by Wassermann et al. (2011) to determine the extent of the Excavation Damaged Zone in the Roselend tunnel, we recently conducted pneumatic injection tests in Chamber C (Guillon et al., in prep). Following air injection, a constant overpressure of ca. 200 mbar was reached and maintained for a 100 h period (Figure 2). The injection was then stopped, and the pressure decrease was monitored. Such pneumatic injection tests were repeated several times, under various water saturations.

A gas tracer test with SF_6 was carried out by first injecting the tracer in Chamber C to reach the target concentration, and then injecting fresh air to reach the target 200 mbar overpressure.

NUMERICAL SIMULATIONS

3D numerical simulations of single-phase air flow were conducted in a homogeneous porous medium, using a finite difference code developed at Paris 6 University (Vu, 2012). Water was considered immobile, and water saturation was taken into account by reduction of the apparent porosity and/or permeability. The real 3D geometry of the Roselend site was also taken into account. This numerical model was used to interpret pneumatic injection tests (Guillon et al., in prep). Permeability was estimated from the pressure and flow rate at steady state, while the porosity is obtained by fitting the calculated and experimental pressure decrease (Figure 2).

In the present study, two-dimensional numerical simulations in a homogeneous porous medium were conducted using TOUGH2/EOS7R (water, radionuclide 1, air), in order to investigate the influence of water saturation on gas flow in the unsaturated zone. Simulations were carried out in a 2D vertical cross section perpendicular to the Chamber C axis. Here we consider SF_6 as the gaseous tracer, with a negligible solubility and a diffusion coefficient in air of 10^{-5} m^2/s. The initial concentration of SF_6 in Chamber C was set at 1000 ppm, and a constant injection of air (without tracer) was imposed in the chamber, with a 24 L/min flow rate, identical to the experimental determination (Figure 2).

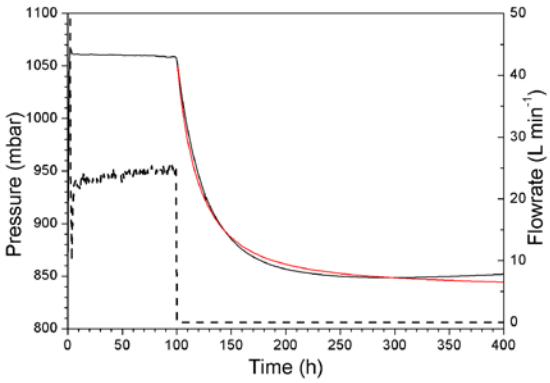

Figure 2. Pressure variation (black solid) and air injection flow-rate (dashed) measured during a pneumatic injection test in Chamber C. The pressure decrease after the end of the injection is reproduced by numerical simulation (red), using the permeability deduced from the steady-state phase of the experiment (Guillon et al., in prep).

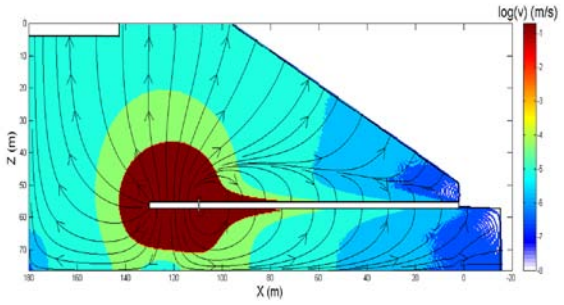

Figure 3. Air velocity and streamlines at steady-state during air injection at 200 mbar overpressure in Chamber C, obtained from 3D numerical simulation of single-phase air flow (modified from Vu, 2012).

RESULTS AND DISCUSSION

Permeability and Porosity in Chamber C

From the repeated pneumatic injection tests, the computed permeabilities and porosities estimated in Chamber C are within a narrow range, from 5×10^{-15} to 8×10^{-15} m² and 4.5% to 4.7%, respectively. Permeability was 1 to 2 orders of magnitude smaller than that obtained for the fully saturated medium by Patriarche et al. (2007) from stereological analysis.

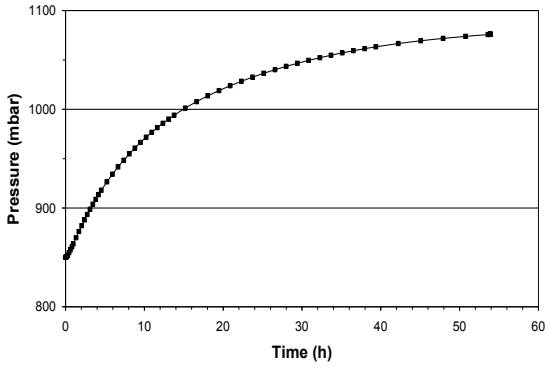

Figure 4. Pressure in Chamber C during air injection at a constant flow-rate of 24 L/min, obtained from numerical simulation with TOUGH2/EOS7R.

Figure 3 shows the steady-state air velocity field and the corresponding streamlines around the tunnel during a pneumatic injection test with an overpressure of 200 mbar in Chamber C. Twenty meters away from Chamber C, air velocity drops and becomes very small. Air injected into the chamber flows towards the atmosphere, but also around the air-tight wall into the tunnel.

The pressure evolution in Chamber C obtained from numerical simulation with TOUGH2 is shown in Figure 4. The values of permeability and porosity necessary to obtain a steady-state pressure in Chamber C consistent with experimental data (Figure 2) are 3×10^{-14} m² and 1% respectively. They are very close to those obtained by Patriarche et al. (2007).

Role of water saturation

Two-phase flow simulations with TOUGH2/EOS7R help to further understand the variations in water saturation during gas migration and the possible effects on both permeability and porosity. Numerical simulations with both air and water flow often led to computational problems and premature stoppages. With an initial water saturation of 20%, water flow is almost nonexistent—but with a higher initial saturation of 80%, the tracer migrates more rapidly towards the surface, and the pressure increases in the chamber. The computed pressure was high compared to experimental data, which suggests that water saturation is lower or that dry fractures are acting as preferential flow paths.

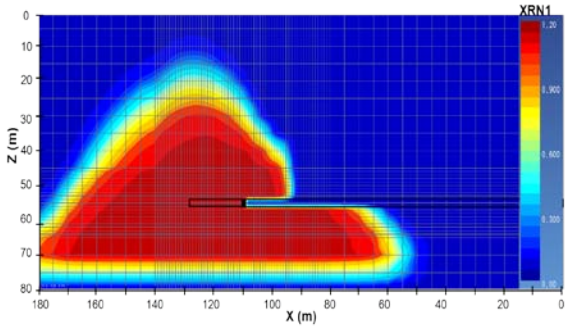

Figure 5. Fraction of the tracer (SF_6) in the gas phase after 60 h of air injection at 24 L/min in Chamber C obtained from numerical simulation with TOUGH2 /EOS7R.

CONCLUSION

An efficient and thorough determination of permeability in the field requires the acquisition of substantial data and interpretation of that data via numerical simulations. In the Roselend Natural Laboratory, permeability was investigated at the field scale, intermediate between borehole and regional scales. Preliminary simulations of two-phase flow confirmed that water saturation strongly influences gas migration in the unsaturated zone.

Further simulations using TOUGH2 will be conducted to improve our understanding of gas flow and transport between Chamber C and the surface. These simulations will also help in preparing and interpreting gas tracer experiments at Roselend.

We aim at modeling an atmospheric pressure boundary condition that would be variable over time. Pressure fluctuations in Chamber C, in response to barometric pressure fluctuations obtained from numerical simulations, could be compared to experimental data to give another estimation of permeability and porosity.

Future work includes introducing heterogeneity and fractures within the porous medium in order to investigate the effects of barometric pumping (Nilson et al., 1991) on gas migration in double porosity media.

ACKNOWLEDGMENT

We thank André Burnol from BRGM for introducing Sophie Guillon to numerical simulation with TOUGH2. The technical help of Patrick Carrera and Marc Perrier in the field is greatly appreciated. Thanks also to the city of Beaufort for granting access to the Roselend Natural Laboratory.

REFERENCES

Guillon S, Vu M.T., Pili E. and Adler P.M. Field and numerical determinations of air permeability of unsaturated fractured porous rocks on various scales. (in prep. for Water Resources Research)

Nilson, R. H., Peterson E. W., Lie K. H., Burkhard N. R. and Hearst J. R. Atmospheric pumping: a mechanism causing vertical transport of contaminated gases through fractured permeable media. *Journal of. Geophysical Research*, 96, 21933-21848, 1991.

Patriarche, D., Pili, E., Adler, P.M. and Thovert, J.-F. Stereological analysis of fractures in the Roselend tunnel and permeability determination. *Water Resources Research*, 43: 09421-09421, 2007.

Provost A.-S., Richon P., Pili E., Perrier, F., Bureau S., Fractured porous media under influence: the Roselend Experiment, *EOS Transactions, American Geophysical Union*, 85(12), 113-124, 2004.

Vu M.T., Applications of the level functions method in hydrogeology. Ph.D dissertation. Université Pierre et Marie Curie (Paris, France), 2012.

Wassermann J., Sabroux J. C., Pontreau S., Bondiguel S., Guillon S., Richon P., and Pili E. Characterization and monitoring of the excavation damaged zone in fractured gneisses of the Roselend tunnel, French Alps. *Tectonophysics* 503, 155-164, 2011.

INITIAL INVESTIGATIONS OF THE PRODUCTIVE PERCHED AQUIFERS ON THE VOLCANIC ISLAND OF MONTSERRAT

Brioch Hemmings, Fiona Whitaker, Joachim Gottsmann

School of Earth Science
University of Bristol
Bristol, BS81RJ, UK
e-mail: brioch.hemmings@bristol.ac.uk

ABSTRACT

An understanding of hydrological processes on volcanic islands is vital for both resource and hazard management. The hydrological system can modify the volcanic hazard and react to volcanic perturbations. Understanding this interaction is essential for the development of a truly multi-parameter hazard-monitoring dataset. The Caribbean island of Montserrat provides a unique environment to study such interactions, since it has both active volcanic and hydrological systems. We aim to gain a more complete understanding of the fundamental hydrology in active volcanic island arc settings by using TOUGH2 models to explore the natural productive springs on the flanks of the extinct volcanic center, adjacent to the active Soufrière Hills Volcano.

INTRODUCTION

A quantitative understanding of hydrology is important for resource management in all island settings. On volcanic islands, such an understanding is also crucial for assessing the interaction between groundwater and volcanic processes. For example, pressurization of pore waters due to magmatic heating can lower effective stresses and cause catastrophic flank collapse (Reid, 2004). The transfer of magmatic heat to circulating groundwater can generate explosive phreatic eruptions (Germanovich and Lowell, 1995) and direct interaction between groundwater and rising magma can produce violent phreatomagmatic explosions. Such events have been observed to precede the onset of major eruptive phases (e.g., the 1995 Soufrière Hills Volcano eruption (Young et al., 1998)) and are also capable of generating large volumes of ash, which can significantly extend the spatial extent of disruption associated with even a minor eruption (e.g. Eyjafjallajökull 2010 (Sigmundsson et al., 2010)).

Hydrological and volcanic interactions play a significant role in the development of valuable mineral deposits, as meteoric and magmatic fluids interact and circulate, driven by large geothermal gradients (Hedenquist and Lowenstern, 1994). The presence of high geothermal gradients and hydrological aquifers also make volcanic islands favorable locations for geothermal energy development (e.g., Nisyros, Greece (Koutroupis, 1992) and Basse-Terre, Guadeloupe (Brombach et al., 2000)). Geothermal energy generation is currently being actively investigated on the volcanic island of Montserrat (Younger, 2010).

Hydrological systems have also been observed to respond to volcanic perturbations (Hurwitz and Johnston, 2003). It is therefore possible that the hydrological system may hold valuable information about the state of a restless volcano prior to eruption. Hautmann et al. (2010) proposed that groundwater migration, in response to changes in volcanic activity, may be responsible for residual gravity anomalies recorded on Montserrat between 2006 and 2008. The potential for groundwater fluxing to represent an eruption precursor and to disrupt the geophysical monitoring of an active volcano demonstrates that understanding the hydrological system in volcanic settings is essential for the development of a truly multi-parameter hazard-monitoring dataset.

The Caribbean island of Montserrat, in the Lesser Antilles volcanic island arc (Figure 1). hosts a number of productive perched springs as well as confined aquifers. The presence of both active volcanic and hydrological systems, as

well as the progressive ages and maturity of the geology, means that Montserrat provides a unique environment to study interactions between hydrological and volcanic systems.

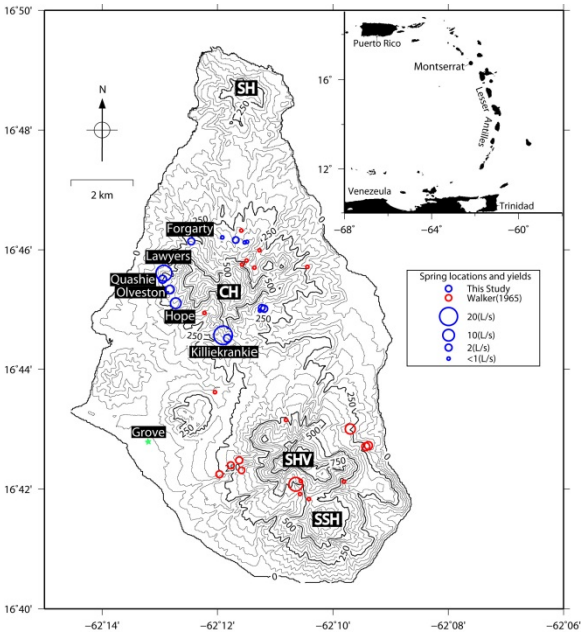

Figure 1. The location of Montserrat's springs and the island's context in the Lesser Antilles. The major springs and the four major volcanic centers are labeled: Silver Hills (SH), Centre Hills (CH), Soufrière Hills Volcano (SHV) and South Soufrière Hills (SSH). Grove rain gauge is also displayed

In this paper, we present the preliminary results from TOUGH2 simulations (Pruess, 1991) that investigate a conceptual understanding of the fundamental hydrogeology of the extinct Centre Hills (CH) complex (0.5–1 Ma), by exploring seasonal spring discharge fluctuations. Ultimately, TOUGH2 models will be developed to explore fluctuating spring production behavior and temperature anomalies that are potentially associated with volcanic activity.

MONTSERRAT

Montserrat is composed of four major volcanic centers. The oldest center, Silver Hills (SH) at the northern tip of the island, is estimated to have been active between 2.6 and 1.2 Ma before present (Harford et al., 2002). Activity on the currently erupting Soufrière Hills Volcano (SHV), in the south of the island, dates back to 170 Ka. The central portion of the island is dominated by the dome complex and eruptive deposits of the extinct Centre Hills volcano (CH), active from 1 to 0.5 Ma (Harford et al., 2002). With the exception of the slightly anomalous South Soufrière Hills (SSH), which erupted between two major eruptive phases of SHV, the style of eruption among the island's volcanoes is thought to be very similar. This apparent consistency in eruptive style means that the island's centers provide a unique insight into the evolution of a system, from the building of a complex volcanic edifice (SHV), to the eventual erosion back to the central core and most proximal deposits of an extinct volcano (SH).

After an initial period of phreatic explosions, in 1995, the ongoing eruption at SHV has been characterized by periods of dome growth and subsequent collapse. The domes grow by extrusion of highly viscous andesitic spines that break off to form blocky and often unstable, talus slopes (Watts et al., 2002). As the domes grow, they can become gravitationally unstable or undermined by slope weakening associated with hydrothermal activity. Dome collapses generate volcaniclastic deposits, including clay-rich debris avalanches, pyroclastic flows, surges, and lahars. Collapse events have also been triggered by violent vulcanian explosions that produce pumice-rich flows, surges, and lahars, as well as significant volumes of ash. Dome collapse events have also been correlated with periods of intense rainfall (Matthews et al., 2002; Barclay et al., 2006).

Montserrat has a subtropical maritime climate and experiences both local, convective storms and heavy rainfall associated with larger tropical weather systems. While rainfall occurs throughout the year, there is a clear seasonality (Figure 2). The wet season extends from July to November, decreasing through December and January into a dry season, which begins in February and ends abruptly in May.

Throughout the year, brief (minute–hour) but intense convective storms provide the majority of the baseline precipitation, while large tropical depressions and hurricanes contribute much of the wet season precipitation. For example, the passing of Hurricane Earl in August 2010, 150 km off the east coast of Montserrat, delivered

almost 10% of the recorded annual rainfall in just a few hours. There is also significant spatial rainfall variation, with strong orographic control; the peaks of CH and SHV (~750 and 900 m elevation respectively) receive ~2500 mm/yr, compared with ~1200 mm/yr and ~ 1800 mm/yr closer to sea level on the windward (east) and leeward coasts.

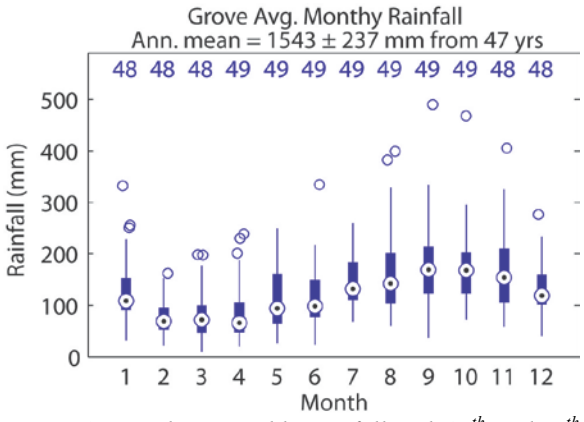

Figure 2. Median monthly rainfall with 25th and 75th percentiles and data limits from Grove rain gauge between 1905 and 1965.The number of years contributing to the medium for each month is give at the top of the plot. Data provided by Montserrat Utilities Ltd (MUL).

Despite relatively high precipitation, there is very little surface water on the island. The steep flanks are drained by a radial system of deeply incised valleys, known locally as ghauts. These ghauts are generally ephemeral, only discharging to the sea during intense or prolonged rainfall events. Whereas springs on SHV have been buried by the ongoing eruption, on CH the loosing streams are sourced from perched springs at elevations between 250 and 450 m (Figure 3). There are a few broader drainage channels, such as the Belham and Farm River valleys, between CH and SHV, which receive contributions from a number of ghauts, as well as inundation with lahars from SHV. The channels in these broader valleys are also ephemeral, with rapid infiltration into the reworked channel and lahar deposits.

Water supply for the population of Montserrat (~5,000 in 2011) is entirely reliant on spring systems on the slopes of CH. Six of the first- and second-order springs (labeled in Figure 1) are trapped for supply, providing, on average, 35 L/s of potable water.

Seasonal variations in rainfall are reflected in spring discharge fluctuations with lag times on the order of 3 to 9 months. Chemical analysis shows no obvious volcanic signature in CH spring waters (Chiodini et al., 1996; Jones et al., 2010). However, our data shows spring temperature variations, suggesting that the Centre Hill hydrological system may not be totally decoupled from the volcanic system to the south (Figure 3).

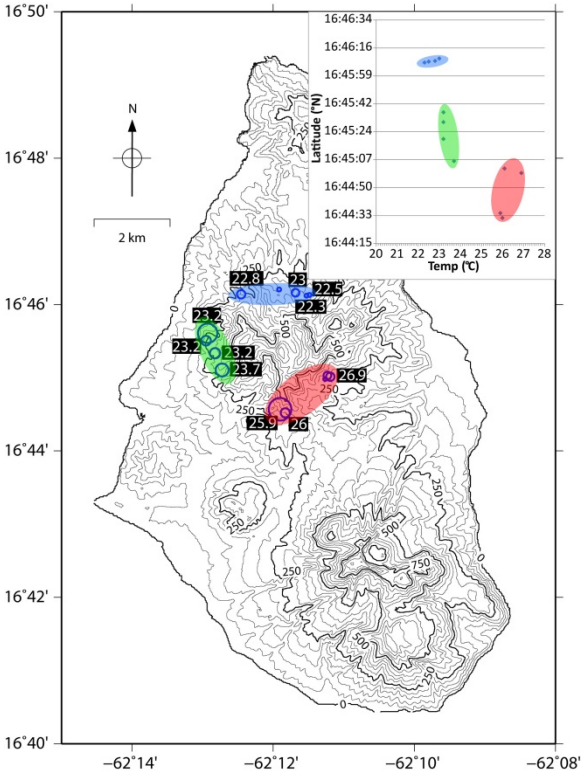

Figure 3. Temperature of the CH springs in °C. Springs on the southern flank, closest to the active SHV, are noticeably warmer than those to the west and north.

The productivity of springs on Centre Hills and pre-eruptions on SHV have been documented to fluctuate "appreciably" in response to seismic and volcanic unrest (Ramdin and George, 1995). However, this is difficult to validate, since spring yield data was not recorded in the aftermath of Hurricane Hugo in 1989 or for over five years after the onset of Phase 1 of volcanic activity in 1995 (Phase 1) (Figure 4). Data are available for the period between 1991 and 1995, when precursor seismicity was intensifying, and

during dome growth phases 2–5 (2001–present). However, the poor temporal resolution of the spring discharge record (monthly) and the complex interplay between recharge and spring discharge obscures any definitive relationship with volcanic activity

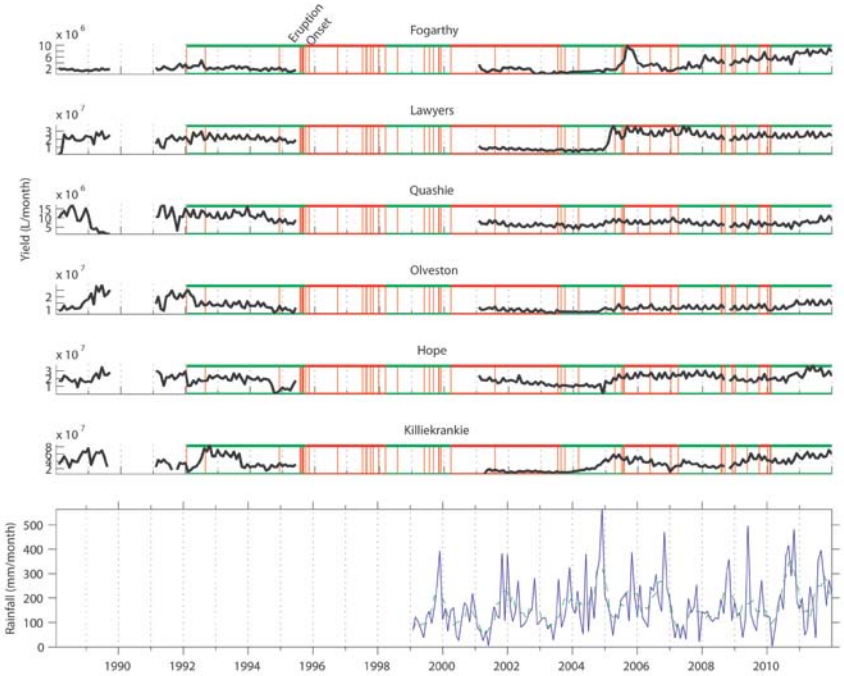

Figure 4. Monthly spring discharge data for the six CH springs used for supply. The onset of the eruption in July 1995 is marked. Red horizontal bars show periods of lava extrusion; green represents pauses where no extrusion occurs. Vertical red lines are timings of distinct events, including seismic swarms, explosions (phreatic and vulcanian) and dome collapse events. Available monthly rainfall data is shown below for a rain gauge at Hope (see Figure 1). Gaps in the spring data are due to disruption caused by Hurricane Hugo in 1989 and the onset of eruption in 1995. Data provided by MUL.

In addition to multiple perched aquifers on the flanks of the Montserratian volcanoes, there are a number of water-bearing aquifers in the more distal, reworked deposits of the major drainage valleys of Belham and Farm, in the west and east respectively, and Carr's and Little Bay, in the north. Three wells in the Belham Valley tap a confined aquifer in reworked gravels and alluvial deposits 20 m below mean sea level. The water level in the wells rose between 2005 and 2006 (Figure 5), a period that included a switch from pause to extrusion at the end of July 2006, and a number of explosion events. The water level in all three wells dropped abruptly a week after a major dome collapse in May 2006, before continuing its general upward trend. In 2011, well MBV2 became flowing artesian; in November 2011 it was flowing at a rate of 3.2 L/s.

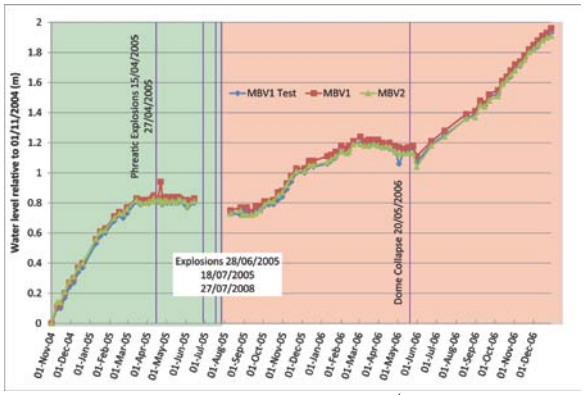

Figure 5. Water level relative to 1st November 2004 in artesian wells in the Belham Valley. Green zone denotes period of no growth; red represents period when lava extrusion is taking place. Vertical purple lines highlight dates of explosive activity or collapse events. Data provided by MUL

THE CONCEPTUAL MODEL

Both the presence of perched springs on the flanks of the younger volcanic centers of Montserrat, and the confined aquifers within the larger drainage valleys which extend below sea level, suggest that substantial low-permeability units are present among the generally high permeability volcaniclastic stratigraphy. The work here concentrates on exploring the nature of these spring systems.

There exist a number of conceptual models that may be applicable to the spring systems on Montserrat. Bramble and Barragne-Bigot (1988) envisaged aquifers of "faulted and jointed volcanic cores" overlying aquicludes of "clayey and unsorted pyroclastic deposits". In contrast, Davies and Peart (2003) proposed spring zones occurring at "the junction between permeable coarse-grained pyroclastic deposits that surround the central volcanic rock core and the impermeable fine-grained pyroclastic flow deposits". Elsewhere in the Lesser Antilles, clay-rich, bulge landslide deposits are postulated to be capable of ponding groundwater on the flanks of Mount Pelée, Martinique (Zlotnicki et al., 1998). Finally, based on observations at nearby Basse-Terre, Guadeloupe, Charlier et al. (2011) indicate that weathered volcanic breccia forms a lower permeability zone, underlying relatively permeable pyroclastic and lava formations at spring sites.

MODELING

This study uses TOUGH2 to explore alternative conceptual models for CH springs. Here, we present results from initial simulations, based on the observations of Charlier et al. (2011) from Basse-Terre. We simulate a perched aquifer developed on a low-permeability layer in an otherwise permeable, but unsaturated, subsurface, and evaluate the fluid flux from a spring draining this perched aquifer.

Geometry

The model space represents a 2D linear cross section through CH with representative surface topography. The model extends from -250 to 750 m in z and 0 to 4000 m in x. The width in y is defined as one unit cell thick. The model is discretized in into 300 regular 13.3 m wide columns (Figure 6). Porosity and isotropic permeability are specified as 35% and 1e-12 m^2 throughout the model, with the exception of a 10 m thick layer between 225 and 235 m elevation, which represents the aquiclude. Porosity and isotropic permeability of the aquiclude is 10% 1e-16 m^2, respectively. Cell thickness is defined as 25 m throughout the model, except in the aquiclude and the lower 120 m of the layer above, where the cell thickness is refined to 2 m and 5 m respectively. The top and bottom layers of cells in the model are set at infinite volume, to allow open boundaries for liquid and gas flow.

Initial conditions define the top of the saturated zone at z=0 m. Relative permeability and capillary pressure are defined by the van Genuchten-Mualem model and van Genuchten function, respectively (van Genuchten, 1980) using parameters from values for volcanic sands given by Fischer and Celia (1999) (Table 1).

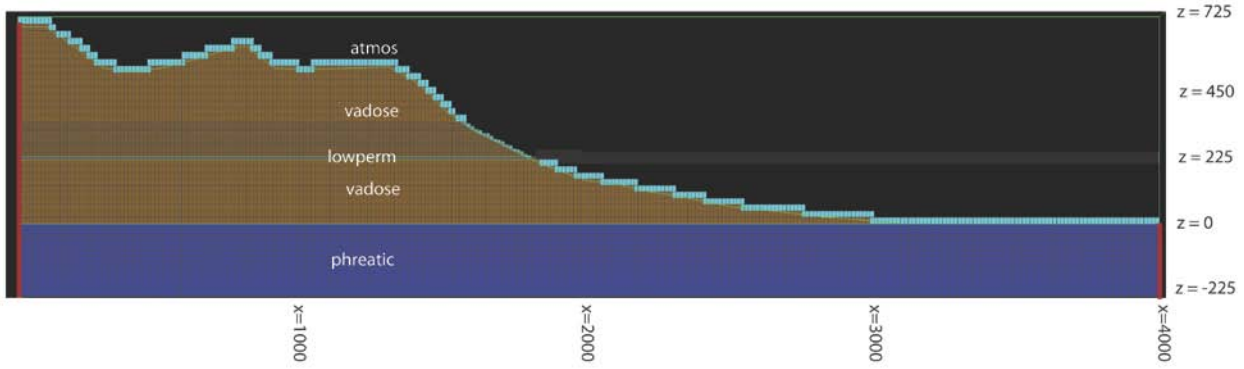

Figure 6. Geometrical setup of model. X limit boundaries are closed to flow (red bars).Top and bottom cell layers have infinite volume and are open to flow.

Table 1. Relative permeability and capillary pressure parameters used for unsaturated zone models. Based on values for volcanic sands from Fischer and Celia (1999). S_r^l is the irreducible liquid saturation; S_s^l is the maximum liquid saturation; S_r^g is the irreducible gas saturation and m and α are the van Genuchten parameters.

	Relative Permeability.	Capillary Pressure
Function	van Genuchten-Mualem	van Genuchten
m	0.85	0.85
S_r^l	0.16	0.16
S_s^l	1.0	1.0
S_r^g	0.0	
α (m^{-1})		45

The models are run in two stages. For Stage 1, the unsaturated zone is initially set to uniform gas saturation (S_g) of 0.84 ($S_s^l - S_r^l$) and atmospheric pressure. Initial conditions for the saturated zone are $S_g = 0$ with a hydrostatic pressure gradient. The model is run to equilibrium with a constant input flux defined in the top cells of the vadose zone. The input is equivalent to 2.1 m/yr, which is equal to the mean annual rainfall recorded at the Hope rain gauge on the western flanks of CH (2006 and 2011). During Stage 1, a perched aquifer develops above the low-permeability layer. Discharge from the cells at the base of this aquifer increases rapidly as the perched aquifer develops, reaching steady state after some 50 years (Figure 7). At this time, ~18% of recharge water percolates through the perched aquifer.

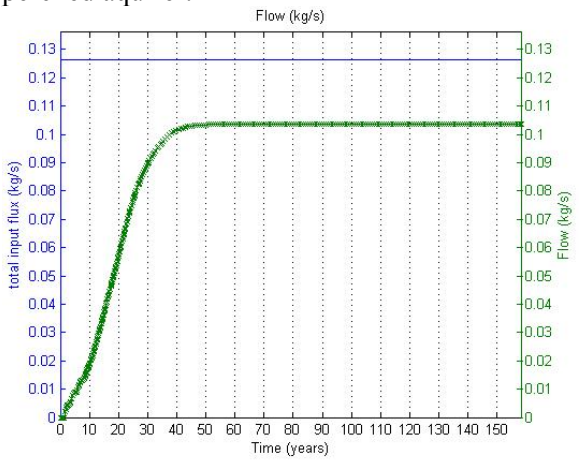

Figure 7. Recharge flux and associated modeled spring discharge (kg/s) for Stage 1 run.

Stage 2 tests the discharge response of the modeled spring to a weekly fluctuating recharge input. Initial conditions for Stage 2 are prescribed by the final conditions of Stage 1 (Figure 8). Recharge rate now varies through time for 6 years, before returning to the mean value used in Stage 1 for a further 6 years. The variable recharge rate is based on the recorded weekly rainfall time series (2006–2011 incl.) at Hope.

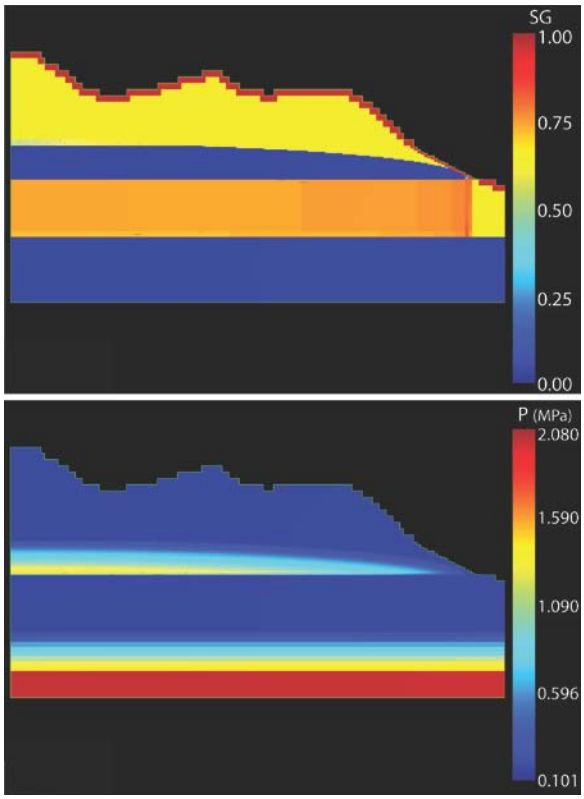

Figure 8. Gas saturation (top) and pressure (bottom) conditions for Stage 2.

INITIAL RESULTS

Initial simulation results from Stage 2 show a very rapid response of the modeled spring discharge to fluctuations in recharge (Figure 9). This does not reflect known temporal variations in spring discharge, where seasonal lag is observed to be on the order of 3 to 9 months. The region immediately above the spring sites on CH is generally characterized by very steep slopes. On such steep slopes, runoff often dominates over infiltration and groundwater recharge is limited. Removing recharge from cells that define the slope in the 120 m above the

aquiclude has a dramatic effect on the modeled discharge response (Figure 10).

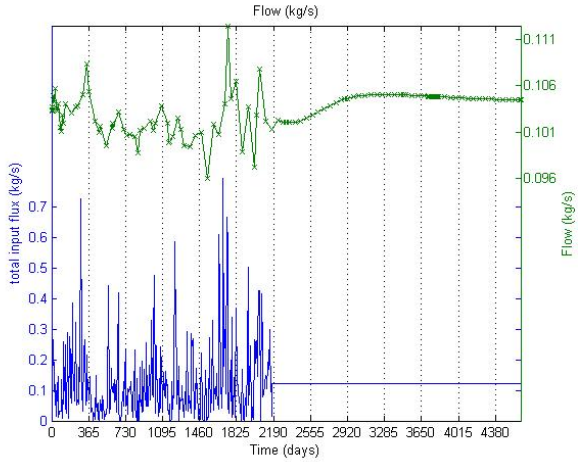

Figure 9. Modeled spring response to fluctuating recharge event.

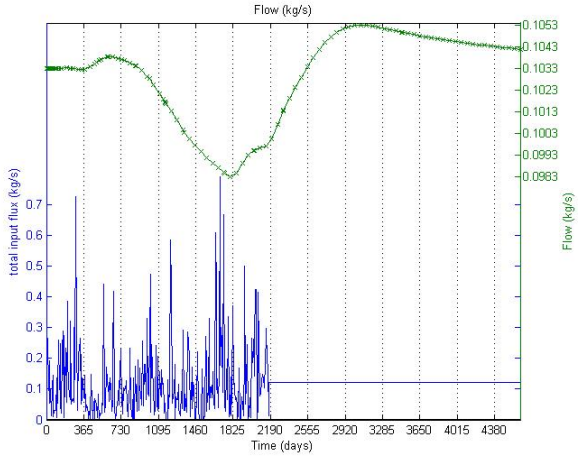

Figure 10. Modeled spring response to fluctuating recharge event, with recharge cells restricted.

DISCUSSION AND FUTURE WORK

The results demonstrate the sensitivity of the models to defined recharge locations. Modifying the specified recharge input with respect to slope angle should account for runoff dominating on steep slopes. Evapotranspiration (ET) would lower recharge further, suggesting that the input fluxes used in these simulations may be excessive. ET of 30% may be typical for the Lesser Antilles (Rad et al., 2007). Incorporation of ET and runoff could reduce net recharge significantly; however, markedly higher rainfall in the recharge area, above the springs, compared with levels recorded at the lower elevation rain gauge on the western flank, could offset this effect.

Further refinement of the method presented here is required, to allow a more quantitative investigation of seasonal fluctuations in spring discharge. Further TOUGH2 simulations can then explore the conceptual models and ultimately help provide an insight into hydrological interactions on active volcanic islands.

ACKNOWLEDGMENT

We are grateful to Montserrat Utilities Ltd (MUL) for providing access to their rainfall and spring data, as well as commercial reports from their archives. MUL also provided invaluable field support and access to the spring sites. Additional valuable field assistance was provided by Mr. Bill Tonge, James 'Scriber' Daly, and the staff at Montserrat Volcano Observatory. Valuable help with initial vadose zone modeling came from Katherine Cooper, also of the School of Earth Science, University of Bristol.

REFERENCES

Barclay, J., Johnstone, J. E., and Matthews, A. J., Meteorological monitoring of an active volcano: Implications for eruption prediction, *Journal of Volcanology and Geothermal Research*, *150*(4), 339-358, 2006.

Bramble, B. L., and Barragne-Bigot, P., Hydrogeological Map of Montserrat, Explanatory Note, *United Nations Department of technical Co-operation for Development, UN Project RLA 82/023*, 1988.

Brombach, T., Marini, L., and Hunziker, J. C., Geochemistry of the thermal springs and fumaroles of Basse-Terre Island, Guadeloupe, Lesser Antilles, *Bulletin of Volcanology*, *61*(7), 477-490, 2000.

Charlier, J.-B., Lachassagne, P., Ladouche, B., Cattan, P., Moussa, R., and Voltz, M., Structure and hydrogeological functioning of an insular tropical humid andesitic volcanic watershed: A multi-disciplinary experimental approach, *Journal of Hydrology*, *398*(3-4), 155-170, 2011.

Chiodini, G., Cioni, R., Frullani, A., Guidi, M., Marini, L., Prati, F., and Raco, B., Fluid

geochemistry of Montserrat Island, West Indies, *Bulletin of Volcanology*, *58*(5), 380-392 ST - Fluid geochemistry of Montserrat Isl, 1996.

Davies, J., and Peart, R., A review of the groundwater resources of central and northern Montserrat, *British Geological Survey Commissioned Report CR/03/257C. BGS, Keyworth. 87pp*, 2003.

Fischer, U., and Celia, M. a., Prediction of relative and absolute permeabilities for gas and water from soil water retention curves using a pore-scale network model, *Water Resources Research*, *35*(4), 1089-1100, 1999.

van Genuchten, M., A closed-form equation for predicting the hydraulic conductivity of unsaturated soils, *Soil Science Society of America Journal*, *8*, 892-898, 1980.

Germanovich, L. N., and Lowell, R. P., The mechanism of phreatic eruptions, *Journal of Geophysical Research-Solid Earth*, *100*, 8417-8434, 1995.

Harford, C. L., Pringle, M. S., Sparks, R. S. J., and Young, S. R., The volcanic evolution of Montserrat using 40Ar/39Ar geochronology, *Geological Society, London, Memoirs*, *21*(1), 93-113, 2002.

Hautmann, S., Gottsmann, J., Camacho, A. G., Fournier, N., Sacks, I. S., and Sparks, R. S. J., Mass variations in response to magmatic stress changes at Soufrière Hills Volcano, Montserrat (W.I.): Insights from 4-D gravity data, *Earth and Planetary Science Letters*, *290*(1-2), 83-89, 2010.

Hedenquist, J. W., and Lowenstern, J. B., The role of magmas in the formation of hydrothermal ore deposits, *Nature*, *370*(6490), 519–527, 1994.

Hurwitz, S., and Johnston, M. J. S., Groundwater level changes in a deep well in response to a magma intrusion event on Kilauea Volcano, Hawai'i, *Geophysical Research Letters*, *30*(22), 2003.

Jones, M. T., Hembury, D. J., Palmer, M. R., Tonge, B., Darling, W. G., and Loughlin, S. C., The weathering and element fluxes from active volcanoes to the oceans: a Montserrat case study, *Bulletin of Volcanology*, 2010.

Koutroupis, N., Update of geothermal energy development in Greece, *Geothermics*, *21*(5), 881-890, 1992.

Matthews, A. J., Barclay, J., Carn, S., Thompson, G., Alexander, J., Herd, R., and Williams, C., Rainfall-induced volcanic activity on Montserrat, *Geophysical Research Letters*, *29*(13), 1644, 2002.

Pruess, K., *TOUGH2: A general-purpose numerical simulator for multiphase fluid and heat flow*.

Rad, S., Allegre, C., and Louvat, P., Hidden erosion on volcanic islands, *Earth and Planetary Science Letters*, *262*(1-2), 109-124, 2007.

Ramdin, R., and George, H., *Investigation on the Decline of Spring Production in Montserrat W.I.*

Reid, M. E., Massive collapse of volcano edifices triggered by hydrothermal pressurization, *Geology*, 373-376, 2004.

Sigmundsson, F. et al., Intrusion triggering of the 2010 Eyjafjallajökull explosive eruption., *Nature*, *468*(7322), 426-30, 2010.

Watts, R. B., Herd, R. a., Sparks, R. S. J., and Young, S. R., Growth patterns and emplacement of the andesitic lava dome at Soufriere Hills Volcano, Montserrat, *Geological Society, London, Memoirs*, *21*(1), 115-152, 2002.

Young, S. R., Sparks, R. S. J., Aspinall, W. P., Lynch, L. L., Miller, A. D., Robertson, R. E. A., and Shepherd, J. B., Overview of the eruption of Soufriere Hills Volcano, Montserrat, 18 July 1995 to December 1997, *Geophysical Research Letters*, *25*(18), 3389–3392, 1998.

Younger, P. L., Reconnaissance assessment of the prospects for development of high-enthalpy geothermal energy resources, Montserrat, *Quarterly Journal of Engineering Geology and Hydrogeology*, *43*(1), 11-22, 2010.

Zlotnicki, J., Boudon, G., Viode, J., Delarue, J., Mille, A., and Bruere, F., Hydrothermal circulation beneath Mount Pelee ´ inferred by self potential surveying . Structural and tectonic implications, *Journal of volcanology*, *84*, 73-91, 1998.

NUMERICAL MODELING OF NACL-H2O PHASE SEPARATION IN A MID-OCEAN RIDGE HYDROTHERMAL VENT FIELD

Benjamin Larson[*1], Warwick Kissling[2], Christof Meile[1]

[1]Department of Marine Sciences, University of Georgia, Athens, GA 30605 USA
[2]Industrial Research Limited, PO Box 31310, Lower Hutt, New Zealand
*e-mail: blarson@uga.edu

ABSTRACT

Mid-Ocean Ridge (MOR) hydrothermal systems host a wide array of unique metabolic strategies and play an important role in cycling of numerous elements. However, the spatial distribution of (bio-) geochemical transformations is poorly constrained, and the impact of multiphase flow on community productivity and chemical flux has not been rigorously determined. Here we report on recent efforts to incorporate an equation of state (EOS) module for the NaCl-H_2O system into TOUGHREACT to study how phase separation of chloride-laden hydrothermal fluid (and pressure-temperature changes therein) impacts the chemical milieu that ultimately supports chemosynthetic hydrothermal communities in the shallow subsurface.

Phase separation of pure water in subaerial geothermal systems has long been recognized as a controlling process of heat and mass transport, but the analogous process in deep-sea hydrothermal systems, where pressures can be in excess of 400 bars, has become widely accepted only in the last few decades. The numerical treatment of phase separation in marine hydrothermal systems has been complicated by the high concentration of salt in seawater, the dominant fluid medium from which hydrothermal fluid is created by high temperature reaction with basaltic rock. The presence of salt (predominantly NaCl) in the fluid matrix adds significant complexity to the phase relations compared to pure water, and this complexity must be accurately represented in the equation of state to correctly calculate fluid transport.

To that purpose, we incorporate a NaCl-H_2O EOS (Kissling, 2005) into TOUGHREACT version 1.2 (Xu et al., 2006), thereby enabling this code to accurately model heat and mass transport in chloride-rich hydrothermal systems. The code is validated through comparison to a simulation performed with the transport code NaCl-TOUGH2, and applied to a hydrothermal upflow zone to assess the role of phase separation in this part of the system.

INTRODUCTION

High temperature hydrothermal vent fields dotting mid-ocean ridges (MOR) play a significant role in heat and mass transfer from the Earth's interior to the overlying ocean. Seawater percolates downward, reacts with hot mafic rock at high temperature and pressure, and then buoyantly ascends to the surface as hydrothermal fluid, transporting the chemical cargo acquired at the base of the system to the upper reaches of ocean crust (Butterfield et al., 2003). In addition to its role as a transport medium, reducing hydrothermal fluid also serves to support a potentially vast subsurface ecosystem of chemosynthetic organisms that capitalize on steep chemical and temperature gradients within subsurface zones of mixing between seawater and hydrothermal fluid (Shock et al., 2004).

Intermingled with the chemical changes wrought by water-rock reactions are the physical changes driven by the process of phase separation, whereby a single homogeneous fluid is transformed into multiple phases, each with properties different than the parent fluid. Phase separation plays a crucial role in determining the distribution and composition of MOR hydrothermal fluids (Comou et al., 2009; Ingebritsen et al., 2010; Butterfield et al., 1994), and so must be rigorously considered in any hydrologic model that seeks to simulate MOR subsurface environments and the biological communities therein.

The TOUGH family of codes offers a well-established platform for modeling thermal-chemical-hydrologic multiphase flow in porous media at high temperatures, so it is conducive to simulating MOR hydrothermal systems. However, publicly available versions of this platform impose temperature limits that exclude important portions of ocean crust and prevent the proper accounting of salt portioning in the vapor phase, a crucial aspect of transport in seawater-based hydrothermal systems where venting of fluids depleted in salt relative to seawater is widespread and ongoing (Butterfield et al., 1994, Lilley et al., 2003, Von Damm, 2004). A precise treatment of this phenomenon is made difficult by the fact that salt (predominantly NaCl) substantially complicates phase relations compared with pure water (Johnson and Norton, 1991, Palliser and McKibbin, 1998a, 1998b, 1998; Driesner & Heinrich, 2007; Driesner, 2007). On the other hand, because the phase relations of the NaCl-H_2O system are well known for MOR pressure and temperature (PT) conditions, chloride—a nonreactive species that can be measured by existing *in situ* chloride sensors (Larson et al., 2007)—is not only a confounding factor, but also a convenient metric for diagnosing subsurface PT conditions that govern the phase separation process.

Here, we report efforts to integrate an equation of state module for the NaCl-H_2O system, established for the transport-only code TOUGH2 (Kissling, 2005) and applicable for P < 1000 bars and T = 10-620 °C, into TOUGHREACT. In so doing, we establish a framework for comprehensive reactive transport modeling of deep-sea MOR hydrothermal systems. We also report preliminary results for a 1D application of the platform to a generic hydrothermal discharge zone.

METHODS

The NaCl-H_2O equation of state module of Kissling (2005) (below referred to as EOS12) is built on mathematical formulations for NaCl-H_2O phase relations and fluid properties that have been studied and refined extensively (e.g., Bischoff and Pitzer, 1989; Palliser and McKibbin 1998a; Driesner & Heinrich, 2007). The module, described in detail in Kissling (2005) and Kissling (2004), considers 6 different system states and the transitions between them using the relations of Palliser and McKibbin (1998a, 1998b, 1998c) and the primary variables pressure, temperature, chloride mass fraction and phase saturation. Compared to the version applicable to transport-only TOUGH2, some important modifications were required for both EOS12 and TOUGHREACT. They can be grouped into the following four types:

1. Adjustment of variable definitions in EOS12 to match TOUGHREACT conventions.
2. Expansion of EOS12 to accommodate TOUGHREACT-specific requirements.
3. Identification and replacement or removal of code fragments containing equations of state in TOUGHREACT not valid at higher temperature.
4. Addition of supporting code in TOUGHREACT subroutines that handle time stepping, mass and flux computation, and post-convergence variable updates.

The result of these changes, a beta version of NaCl-TOUGHREACT, was tested with a benchmark example (Kissling, 2004) to assess the veracity of its implementation in TOUGHREACT before using the platform to simulate a 1D vertical flow scenario.

RESULTS AND DISCUSSION

Benchmark: Test of phase transitions

A simple box model, described in detail in Kissling (2004), was set up to assess NaCl-TOUGHREACT's ability to handle phase transitions between 4 of the 6 states. Mass was withdrawn at a constant rate of 1 kg/s from a 10^9 m^3 grid block with a porosity of 0.1, a heat capacity of 1000 J/kg/K, a density of 2650 kg/m^3, and an initial temperature of 350°C. Figure 1 shows the evolution of the phase distribution in the box as mass is withdrawn and pressure and temperature drop. The results from the modified code are in good agreement with results from NaCl-TOUGH2 (also shown in Figure 1), indicating that the necessary modifications are correctly implemented.

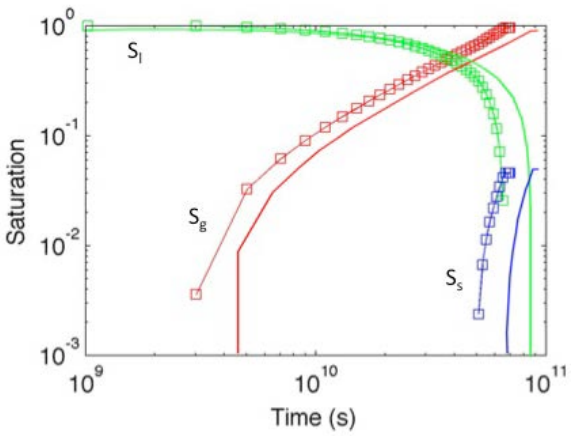

Figure 1. Benchmark example results of phase saturation as a function time. Red, green, and blue are saturation of gas, liquid and solid, respectively. Solid lines with no markers are reprinted with permission from Kissling (2004) Model A. Solid lines with open square markers represent output for the same model from NaCl-TOUGHREACT. As the pressure is decreased at 350°C, the fluid changes from pure liquid to two-phase (liquid + gas) to three-phase (liquid + gas + solid), and finally to two-phase (gas + solid). Results of NaCl-TOUGHREACT are in reasonably good agreement with results from NaCl-TOUGH2.

Application: 1D Vertical Flow Scenario

Subsurface brines in hydrothermal systems have long been postulated (Bischoff and Rosenbauer, 1989), and more recently models of brine movement and storage have been published (Fontaine and Wilcock, 2006; Fontaine et al., 2007). Moreover, brine venting has been observed at multiple sites (Fox, 1990; Von Damm, 1997). To better understand how brines (and their conjugate vapors) apportion during ascent to the surface, our current beta version of NaCl-TOUGHREACT was used to simulate the rising fluid in a hydrothermal vent system (Figure 2). In this simple 1D vertical flow scenario hot brine is injected at the base of a 1500 m column until a steady state is reached in which the modeled vent temperature matches the upper end of observed black-smoker temperatures (Von Damm, 2004).

The column is divided into 60 gridblocks, each 25 m high with a cross sectional area of 100 m^2. We use a 9% NaCl solution, which is in the range of brine chloride concentrations from other studies (Fontaine and Wilcock, 2006; Larson et al., 2009), and assign an enthalpy of 2×10^6 J/kg to achieve an injection fluid temperature >400 °C, which is comparable to root zone conditions derived from a chloride-adjusted silica geobarometer (Foustoukos and Seyfried, 2007). The injection rate was adjusted to achieve a pressure at the bottom of the column that was both within the pressure limits of EOS12 and consistent with inferred hydrothermal reaction zone pressures. Following the example of Fontaine et al. (2007), the flow domain was split into a 400 m 'extrusive' layer with permeability set to an order of magnitude higher (10x) than the lower 1100 m 'intrusive' layer.

Results from this simulation are shown in Figure 3. The modeled temperature in the uppermost block of the flow domain is ~396°C, which is very close to temperatures observed at 9°N latitude on the East Pacific Rise (Von Damm, 2004). Modeled chloride mass fraction of the gas phase (thought to be the dominant constituent in black smoker fluids) is 1×10^{-3} at the surface, about $1/10^{th}$ the typical chloride observed at most black smokers, though transient chloride values in this range have been observed (Lilley, 2003; Von Damm et al., 1997). Also, this simulation does not address the potential for lateral inputs in the shallow subsurface, which may elevate chloride concentrations prior to venting. The phase saturation profile suggests two-phase conditions from ~700 m depth to the surface. This is consistent with measurements reported in Von Damm, (2004) showing the venting of fluids with lower-than-seawater chloride over many years, which suggests two-phase conditions in the upper crust are ubiquitous and long-lived.

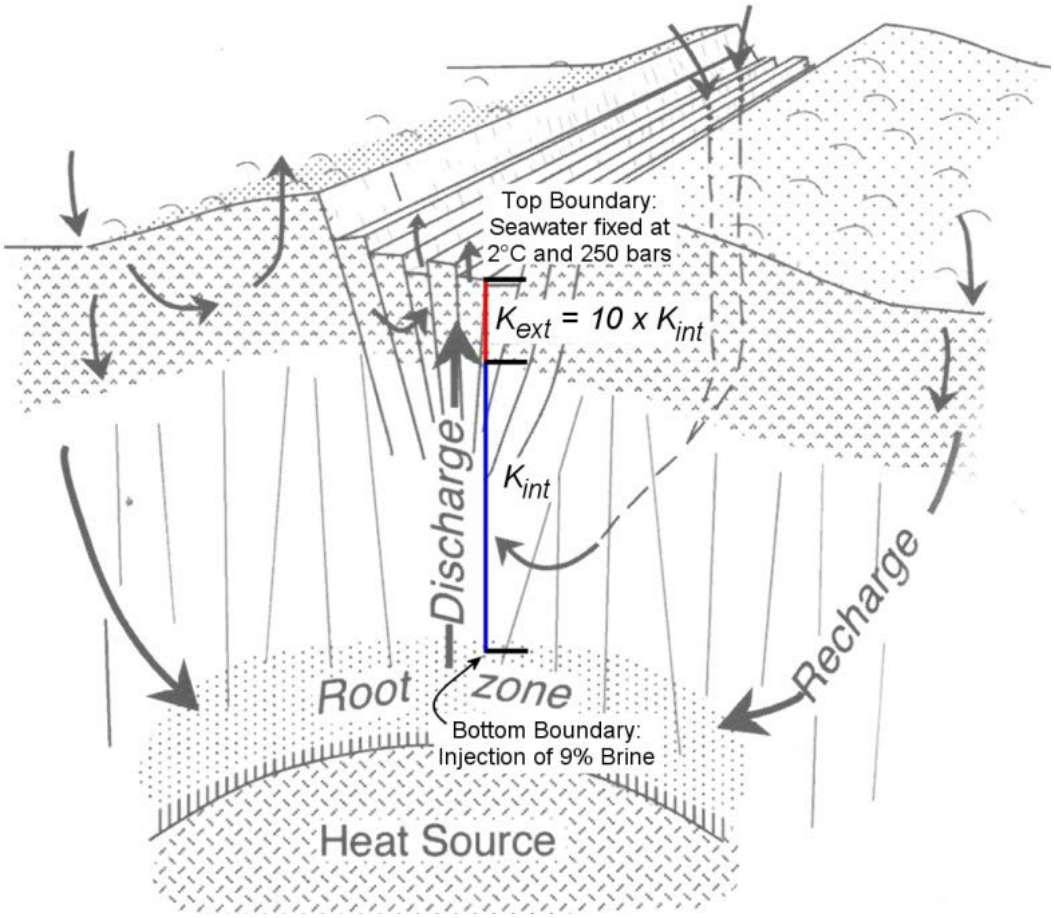

Figure 2. Cross-sectional schematic of convection cell oriented perpendicular to the spreading axis, modified from Alt (1995). The 1D exampled herein approximates the discharge zone, shown here in blue and red for the lower permeability intrusive layer and higher permeability extrusive layer respectively. Upper and lower boundary conditions are shown on the schematic at the top and bottom of the flow domain.

CONCLUSION

We have produced a beta version of NaCl-TOUGHREACT, capable of modeling fluid transport in NaCl-H_2O systems at temperatures up to 620°C and pressures up to 1000 bars. This constitutes an important step towards applying TOUGHREACT's chemical modeling capabilities to seawater-based MOR hydrothermal flow. The new platform has been benchmarked with a box model simulation that highlights the code's ability to handle phase transitions. As a first application, we simulate simple 1D vertical flow that roughly approximates an MOR hydrothermal upflow zone. The preliminary results show a steady state two-phase region in the upper 700 m of the crust, which is consistent with observations over many years of vent fluid depleted in chloride relative to seawater.

This work provides a stepping stone to combine high temperature and pressure multiphase transport simulations in NaCl-H_2O systems with the chemical modeling capabilities of TOUGHREACT. It allows an assessment of feedbacks between chemical reactions and fluid transport associated with precipitation/ dissolution processes driven by compositional and thermal gradients. Additionally, the structure is in place to integrate recent improvements in the formulation of NaCl-H_2O phase relations (Driesner and Heinrich, 2007; Driesner, 2007). These efforts will help establish a more comprehensive picture of the physical and chemical conditions in convection cells that drive flow at MOR vent fields.

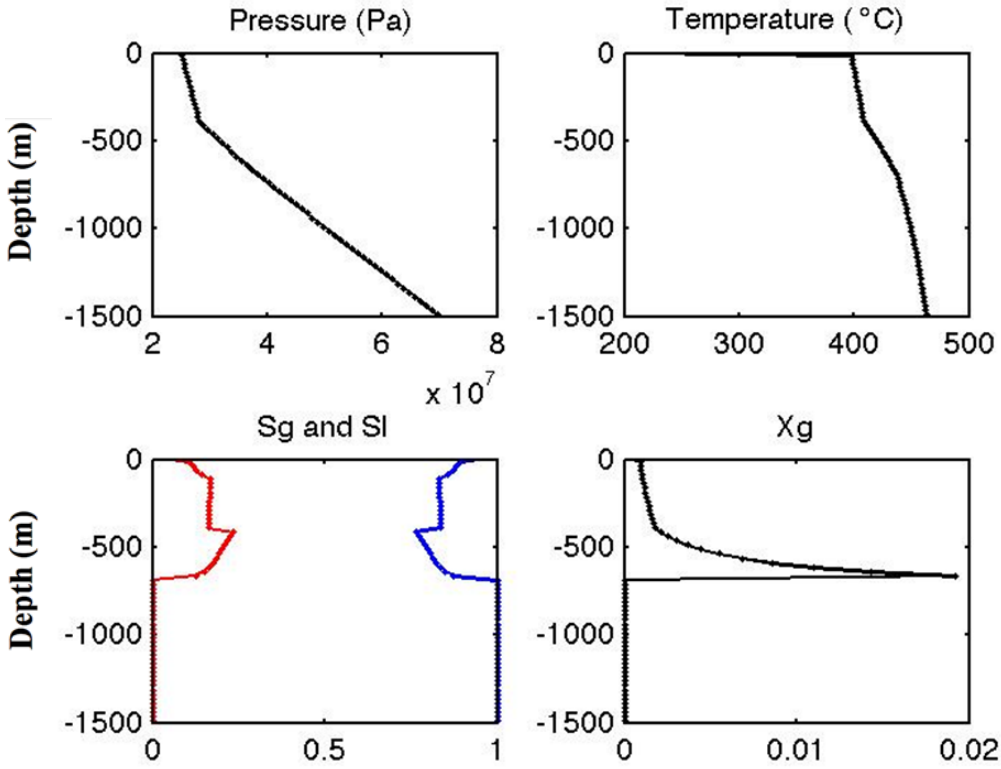

Figure 3. Results from 1D vertical flow simulation showing pressure, temperature, saturation of gas (red) and liquid (blue), and mass fraction of chloride in the vapor phase. The model results show a 700 meter long two-phase zone in the upper portion of the flow domain, which is consistent with the observed venting of chloride depleted fluids (relative to seawater) at MOR sites such as 9ºN latitude on the East Pacific Rise (EPR). Temperatures at the surface in excess of 390°C are also in good agreement with EPR observations.

REFERENCES

Alt J.C. Subseafloor processes in mid-ocean ridge hydrothermal systems, In *Mid-ocean ridges; hydrothermal interactions between the lithosphere and oceans*, AGU Monograph 148 (eds. C.R. German, J. Lin, L.M. Parson), 243-266, 1995.

Bischoff J.L., Pitzer K.S. Liquid-Vapor Relations for the System NaCl-H_2O: Summary of the P-T-x Surface from 300 to 500°C, *Am. J. Sci. 289*, 217–248, 1989.

Bischoff J.L., Rosenbauer R.J., Salinity variations in submarine hydrothermal systems by layered double-diffusive convection, *J. Geol. 97*, 613–623, 1989.

Butterfield D.A., McDuff R.E., Mottl M.J., Lilley M.D., Lupton J.E., Massoth G.J. Gradients in the composition of hydrothermal fluids from the Endeavour segment vent field: Phase separation and brine loss, *J. Geophys. Res.-Solid Earth 99*, 9561-9583, 1994.

Butterfield D.A., Seyfried, Jr. W.E., Lilley M.D. Composition and Evolution of Hydrothermal Fluids, In *Energy and Mass Transfer in Marine Hydrothermal Systems* (eds. P. E. Halbach, V. Tunnicliffe and J. R. Hein), 123-161. Dahlem University Press, 2003.

Coumou D., Driesner T., Weis P., Heinrich C.A. Phase separation, brine formation, and salinity variation at Black Smoker hydrothermal systems, *J. Geophys. Res. 114*, B03212, 2009.

Driesner T., Heinrich C.A., The system H_2O–NaCl. Part I: Correlation formulae for phase relations in temperature–pressure–composition space from 0 to 1000 C, 0 to 5000 bar, and 0 to 1 X_{NaCl}, *Geochim. Cosmochim. Acta 71*, 4880-4901, 2007.

Driesner T., The system H_2O–NaCl. Part II: Correlations for molar volume, enthalpy,

and isobaric heat capacity from 0 to 1000°C, 1 to 5000 bar, and 0 to 1 X_{NaCl}, *Geochim. Cosmochim. Acta 71*, 4902-4919, 2007.

Fontaine F.J., and Wilcock W.S.D. Dynamics and storage of brine in mid-ocean ridge hydrothermal systems, *J. Geophys. Res.* 111, B06102, 2006.

Fontaine F.J., Wilcock W.S.D., Butterfield D.A., Physical controls on the salinity of mid-ocean ridge hydrothermal vent fluids, *Earth Planet. Sci. Lett. 257*, 132–145, 2007.

Foustoukos D.I., Seyfried Jr. W.E. Quartz solubility in the two-phase and critical region of the NaCl–KCl–H_2O system: Implications for submarine hydrothermal vent systems at 9°50'N East Pacific Rise, *Geochim. Cosmochim. Acta 71*, 186-201. 2007

Fox C., Consequences of phase separation on the distribution of hydrothermal fluids at ASHES vent field, Axial Volcano, Juan de Fuca Ridge, *J. Geophys. Res. 95*, 12,923-12,926, 1990.

Ingebritsen S. E., Geiger S., Hurwitz S., Driesner T. Numerical simulation of magmatic hydrothermal systems, *Rev. Geophys. 48*, RG1002, doi:10.1029/2009RG000287, 2010.

Johnson J.W., Norton D. Critical phenomena in hydrothermal systems: state, thermodynamic, electrostatic and transport properties of H_2O in the critical region, *American Journal of Science 291*, 541-648, 1991.

Kissling W.M. Transport of Three-Phase Hyper-Saline Brines in Porous Media: Theory and Code Implementation, *Transport in Porous Media 61*, 25-44, 2005.

Kissling W.M. *Deep Hydrology of the Geothermal Systems in the Taupo Volcanic Zone, New Zealand*, Thesis, University of Auckland, 2004.

Larson, B.I., Lilley M.D., Olson E.J. Parameters of subsurface brines and hydrothermal processes 12–15 months after the 1999 magmatic event at the Main Endeavor Field as inferred from in situ time series measurements of chloride and temperature, *J. Geophys. Res. 114*, B01207, 2009.

Larson, B.I., Olson E.J., Lilley M.D. In situ measurement of dissolved chloride in high temperature hydrothermal fluids, *Geochim. Cosmochim. Acta 71*, 2510–2523, 2007.

Lilley M.D., Butterfield D.A., Lupton J.E., Olson E.J. Magmatic events can produce rapid changes in hydrothermal vent chemistry, *Nature 422*, 878-881, 2003.

Palliser C. and McKibbin R. A Model for Deep Geothermal Brines, I: *T-p-X* State-Space Description, *Transport in Porous Media 33*, 65-80, 1998a.

Palliser C. and McKibbin R. A Model for Deep Geothermal Brines, II – Density, *Transport in Porous Media 33*, 129-154, 1998b.

Palliser C. and McKibbin R. A Model for Deep Geothermal Brines, III: – Enthalpy and Viscosity, *Transport in Porous Media 33*, 155-171, 1998c.

Shock E. L. and Holland M. E. Geochemical Energy Sources that Support the Subsurface Biosphere, In *The Subseafloor Biosphere at Mid-Ocean Ridges*, AGU Monograph 144 (eds. W.S.D. Wilcock, E.F. DeLong, D.S. Kelley, J.A. Baross, S.C. Cary), 153-165, 2004.

Von Damm, K.L. Evolution of the hydrothermal system at East Pacific Rise 9°50'N; geochemical evidence for changes in the upper oceanic crust, In *Mid-ocean ridges; hydrothermal interactions between the lithosphere and oceans*, AGU Monograph 148 (eds. C.R. German, J. Lin, L.M. Parson), 243-266, 2004.

Von Damm K.L., Buttermore L.G., Oosting S.E., Bray A.M., Fornari D.J., Lilley M.D., and Shanks III W.C. Direct observation of the evolution of a seafloor 'black smoker' from vapor to brine, *Earth Planet. Sci. Lett. 149*, 101-111, 1997.

Xu T, Sonnenthal E, Spycher N, Pruess K. TOUGHREACT: A simulation program for non-isothermal multiphase reactive geochemical transport in variably saturated geologic media: Applications to geothermal injectivity and CO_2 geological sequestration. *Computers and Geosciences* 32:145–156, 2006.

SIMULATION OF SOIL WATER WITH DIFFERENT WATER TABLE DEPTHS UNDER DRIP IRRIGATION ALONG THE TARIM DESERT HIGHWAY, CHINA

Xue Li, Guomin Li, and Zhimin Wang

Institute of Geology and Geophysics, Chinese Academy of Sciences
No. 19, Beitucheng Western Road, Chaoyang District
Beijing, 100029, China
e-mail: lixue@mail.iggcas.ac.cn

ABSTRACT

The Tarim Desert Highway is the main transportation artery in China for oil and gas exploration and development, and is in fact the first and longest graded highway (across the Taklimakan Desert) in the world. It suffers from continual sandstorms, and shelterbelts have been built along the road to ensure the smooth, uninterrupted operation of the highway. Recent research on the distribution of soil water under drip irrigation in the shelterbelts has great significance for the robust performance of these shelterbelts. To study the role of water table depth in the soil water distribution of the shelterbelts, we established a 2-D saturated-unsaturated flow model, using the software PetraSim, based on TOUGH2. The model was calibrated by sampling data from where the water table depth was 3 m (under drip irrigation conditions) in the center of the Taklimakan Desert. In addition, several scenarios were simulated using different water table depths. By analyzing the simulation results, some useful conclusions were reached.

Our findings showed that soil water distribution is influenced by the irrigation water and groundwater in the shelterbelts along the Tarim Desert highway. Furthermore, the soil-water content with depth takes the form of the letter ‘‘C”; that is, the water content first decreases and then increases in descending from the surface to the water table. The study emphasizes the profound effect of water table depth on the distribution of moisture in the vadose zone, and thus supplies important reference data and provides useful guidelines for research into building an effective irrigation system.

INTRODUCTION

The Tarim Basin, located in northwest China, is very rich in oil and gas resources (Lu et al., 2004). A large part of the basin is occupied by the Taklimakan Desert, which is the largest active desert in China and the second largest in the world (Zhu et al., 1980). With the enlargement of oil exploration, transportation problems severely constricted the development of the resource (Xia et al., 1995); consequently, the Tarim Desert Highway came into being, extending across the center of the desert. The Tarim Desert Highway starts from north of Lunnan, about 35 km to the Tarim River, and extends south to connect with the 315 National Road, 15 km east of Minfeng, for a total length of 519 km (Han et al., 2004). However, the highway is facing serious sand-drift encroachment problems, caused by its 447 km long passage of sand—including crescent dunes, barchan chains, compound transverse dune ridges, and complex megadunes (Han et al., 2003). Shelterbelts, green corridors 436 km in length on both sides of the highway, were constructed to control the windblown sand and ensure the long-term - uninterrupted operation of the highway (Li et al., 2008; Zhu et al., 2010). Shelterbelt plants, such as Tamarix taklamakanensis, Haloxylon ammodendron and Calligonum caput-medusae, which are strong stress-resistant shrubs with excellent windbreak and sand-fixation properties, were irrigated with saline groundwater bumped from local wells (Han et al., 2012).

Over the past 40 years, many researchers around the world have investigated drip irrigation using analytical solutions (Raats, 1971; Warrick, 1974) and numerical solutions (Bresler et al., 1971; Brandt et al., 1971). Moreover, many studies in the Taklimakan Desert have been carried out on soil-water distribution and dynamics (Zhou et al.,

2000; Wang et al., 2008), the laws of soil-water movement (Huang et al., 2003; Zhou et al., 2010), and the mechanisms of water-salt regulation (Li, 2010) in the Taklimakan desert. There has been little research, however, on how water table depth affects soil-water distribution. In this paper, we describe a numerical model based on the software PetraSim and demonstrate its ability to capture the distribution of soil water for different water table depths, thus providing useful guidelines for building effective irrigation systems in the future.

MATERIALS AND METHODS

Field description

The study area lies in the remote reaches of the Taklimakan Desert, which has an extremely dry continental climate. The average temperature is 12.4℃, with a high temperature of 45.6℃ and a low temperature of -22. The annual precipitation is 11.05 mm; annual rainfall is characterized by an uneven distribution, concentrated between May and August. Average annual relative humidity is 29.4%. Evaporation per year is 3638.6 mm, with a maximum of 563.2 mm in June and a minimum of 34.4 mm in November. With respect to vegetation, types are poor, community structure is simple, and the coverage is extremely low.

Large, mobile, composite sand dunes are the typical landscape in the area. Soil characteristics change with the geomorphology, with the predominant drift sand soil having a salt content of ~1.26–1.63 g/kg. Clay can occasionally be found in the lower layer of sand soil, with a thickness of ~20–60 cm (Zhou et al., 2002).

The peripheral mountain area is the formation region of the Tarim Basin water resources. The alluvial plain and the flood plain in front of the mountains are the phreatic recharge and discharge areas. The desert in the middle is the phreatic runoff discharge area, and the Lop Nor Lake Basin in the east is the phreatic confluence hub (Wang et al., 2004). Within the desert area, the phreatic flow is basically from south to north, turning east at the Tarim alluvial plain. The groundwater is Quaternary loose pore water. The rivers close to the desert highway include the Tarim River (north of the highway), the Niya River, the Yatonggusi River, and the Andiel River (south of the highway). The three rivers south of the highway are the few rivers that flow into the desert (Fan et al., 2008).

The shrubs Tamarix, Haloxylon, and Calligonum are the preferred tree species, considering the harsh desert environmental conditions (Huang, 2002). The configurations can be described as mixed planting between rows with spacing. Groundwater with total dissolved solids of ~3–30 g/L are extracted for drip irrigation at intervals of ~8–12 days, and the irrigation volume is 300 m^3/ha over 8 hours.

Field sampling

Sampling sites shown in Figure 1 were located at the K359 km mark on the desert highway in October 2009. In order to fully consider the influence of irrigation water, sampling took place just after irrigation. The horizontal spacing was 2 m every two sampling points in an east-west direction, and every sampling point was placed next to the emitter and the plant. The vertical spacing between sampling points was 20 cm from the surface to the saturated zone. There were 6 sampling points labeled pm01-06 in the field, and 15 soil samples at each sampling point where the water table depth was at 3 m. All of the samples were sealed in aluminum boxes and weighed on the spot.

Figure 1. Geographic location of sampling sites

Measurement and calculation methods

Measurement of the water content was conducted in November 2009 by means of oven-drying method, which involved drying the samples in a vacuum oven to a constant weight under 65℃. Volumetric water content was then calculated by Equation (1)

$$\theta_V = \frac{\rho_b}{\rho_w}\theta_m = \frac{\rho_b}{\rho_w}\frac{M - M_s}{M_s} \times 100\% \qquad (1)$$

where θ_V is the volumetric water content (%); ρ_b is the soil bulk density (g/cm^3), with a value of 1.5 in the related literature (Huang, 2002); ρ_w is the density of pure water (g/cm^3), with a value of 1; θ_m is the mass water content (%); M is the mass of wet soil (g); and M_s is the mass of dry soil (g).

NUMERICAL MODELING

EOS9 in the PetraSim software package (Thunderhead Engineering, 2007) based on the well-known simulator TOUGH2 (Pruess et al., 1999) was used to simulate the vertical variation in soil water content after drip irrigation under different water table depths (set at 1 m, 3 m, and 5 m).

Concept and mathematical model

The soil-water flow is axially symmetric in the irrigation period, so that it is treated as a 2-D (vertical plane) water flow process (Skaggs et al., 2004). The vertical plane is determined by x and z axes. TOUGH2 is used to simulate the water flow in the unsaturated-saturated zone, with the water flow under isothermal conditions described by Equation (2), which represents a generalization of the Richards' equation (3).

$$\frac{\partial}{\partial t}\varphi S\rho = div[k\frac{k_r}{\mu}\rho\nabla\left(P + \rho g z\right)] \qquad (2)$$

where ϕ is porosity; S is water saturation; ρ is water density; k is the absolute permeability; k_r is the relative permeability to water, varying between 0 and 1; μ is the viscosity; P is the fluid pressure in water (the sum of the reference gas pressure and capillary pressure); g is the vector of gravitational acceleration; and z is the defined positive upward.

$$\frac{\partial\theta}{\partial t} = div[K\nabla h] \qquad (3)$$

where $\theta = \varphi S$ is the specific volumetric water content, $K = kk_r\rho g/\mu$ is the hydraulic conductivity, and $h = z + P/\rho g$ is the hydraulic head.

Boundary and initial conditions

The simulated flow domain is shown in Figure 2. The horizontal range of the flow domain is 1.0 m, i.e., half of the space between two irrigation tubes, and the vertical range is 5.0 m. The drip tubing can be represented as a small circle with a 0.01 m radius placed at the top boundary on the plane of symmetry between two plant rows.

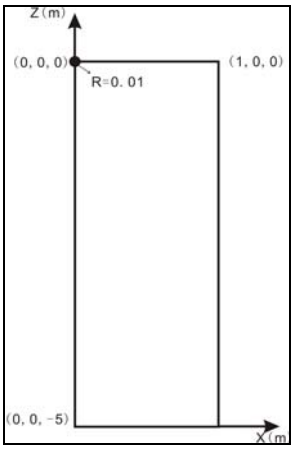

Figure 2. The 2-D model region

The upper boundary is divided into two parts. In the range of the point source (the radius of the point source is 0.01 m), the flux q is constant and calculated by the total irrigation volume divided by the irrigation period—in the modeling, the value is 2.83×10^{-3}kg/s. Outside the irrigation source of the upper boundary, a no-flow boundary condition is employed, i.e., evapotranspiration is ignored.

The lower boundary is set as a free drainage condition, while the lateral boundaries are set to be zero-flux boundary conditions. The pressures at the lower boundary change with water table depth as follows:

$P_l(x, 0, z) = 1.013\times10^5 + 10^3\times9.81\times4 = 1.4054\times10^5$Pa $\quad 0\leqslant x\leqslant 1.0$, $z=-5.0$,
the water table is 1 m below the surface;

$P_l(x, 0, z) = 1.013\times10^5 + 10^3\times9.81\times2 = 1.209\times10^5$ Pa $\quad 0\leqslant x\leqslant 1.0$, $z=-5.0$,
the water table is 3 m below the surface;

$P_l(x, 0, z) = 1.013\times10^5$Pa $\quad 0\leqslant x\leqslant 1.0$, $z=-5.0$,
the water table is 5 m below the surface.

The initial condition of the drip simulation is obtained by running the model to steady state.

Soil hydraulic properties

Soil hydraulic properties could be described with the nonlinear functions (4)–(6) of van Genuchten (1980):

$$k_r = S_e^{1/2}\left[1-\left(1-S_e^{1/m}\right)^m\right]^2 \quad (4)$$

$$P_c = -\alpha^{-1}\left(S_e^{-1/m}-1\right)^{1/n} \quad (5)$$

$$S_e = \frac{S-S_r}{S_s-S_r} \quad (6)$$

where S_e is the effective saturation; n is the pore-size distribution characteristic parameter, m=1-1/n; α^{-1} is the entry pressure; and S_r and S_s denote the residual and saturated water saturation, respectively.

The soil parameters S_r, S_s are taken from measurements, whereas n and α are based on the neural network estimates for sand. The values are listed in Table 1.

Table 1. Soil parameters.

φ	k /m^2	n	α/pa	S_r	S_s
0.37	5×10^{-10}	3.62	2.2×10^{-4}	0.0016	1

RESULTS AND DISCUSSION

Comparing simulated with observed water content

Comparison between simulated data and observed data at the trickle (x=0, z=0) after irrigation (8h) is shown in Figure 3, when the saturation depth is 3 m below the surface. The observed data are mean values of sampling points pm01–06 for the error reduction. Figure 3 shows that the observed and simulated water content match well. Volumetric content decreased from the surface to a depth of about 1.2 m, then increased until it reaches the water table at a depth of 3 m. The water saturation distribution for different times after the beginning of irrigation is shown in Figure 4. Soil water mainly moves downward around the emitter, and the water content has increased over the irrigation period.

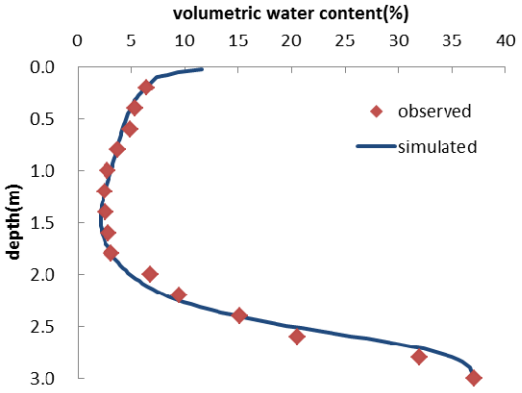

Figure 3. Comparison of simulated and observed soil water content along the depth

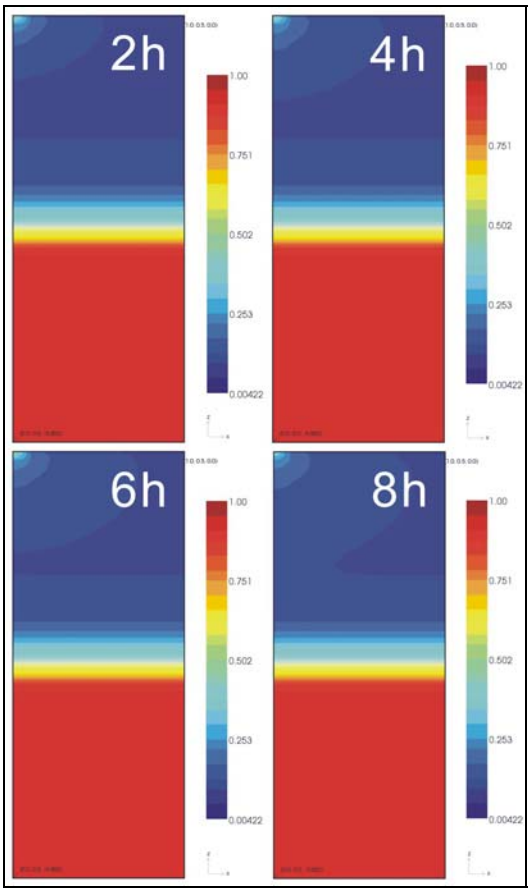

Figure 4. Water saturation distribution for different times of the profile XZ

Scenario simulations

Considering the different locations of the water table along the Tarim Desert Highway, we simulated another two scenarios. Soil-water saturations were calculated by changing the assumed water table depth to 1 m and 5 m. Figures 5 and 6 show variations in volumetric content along the depth at the trickle, as well as

water saturation of the profile XZ under different water table depths.

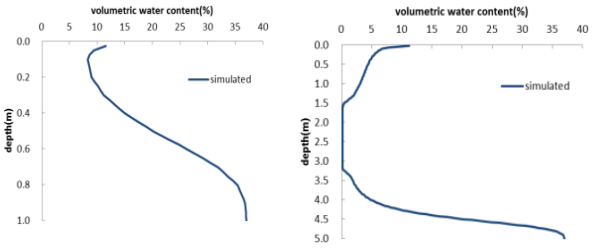

Figure 5. Simulated soil water content along the depth when the water tale depths are 1 m and 5 m

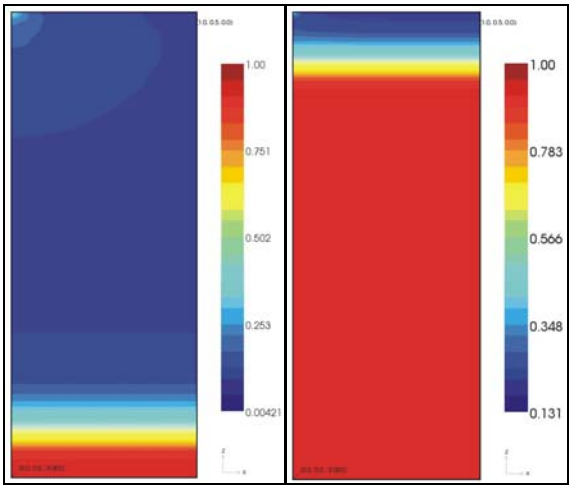

Figure 6. Water saturation distribution of the profile XZ when the water tale depths are 1 m and 5 m

From Figures 5 and 6, it can be seen that at different water table depths, soil moisture first decreases, then increases. The distribution of water soil is affected by the groundwater and irrigation. Water content decreases descending from the surface, mainly because of the effect of irrigation water, and increases again as the top of the capillary fringe zone is reached. Water moves upward from the water table, so that water content becomes greater closer to the saturated zone.

CONCLUSIONS

To study the water table under the Tarim Desert Highway, we established a 2-D unsaturated-saturated model, based on the well-known simulator TOUGH2. By making the simulated soil-water content match the measured data, soil parameters were identified so that the model could be used to simulate the variation in soil water content after drip irrigation under different water table depths (set as 1 m, 3 m and 5 m). The modeling results show that the distribution of soil water is affected by the irrigation water and groundwater in the shelterbelts along the Tarim Desert Highway, with the water content first decreasing and then increasing from the surface to the water table.

REFERENCES

Bresler, E., J. Heller, N. Diner, I. Ben-Asher, A. Brandt, and D. Goldberg, Infiltration from a trickle source. II. Experimental data and theoretical predictions. *Soil Science Society of America Journal*, 35(5): 683-689, 1971.

Brandt, A., E. Bresler, N. Diner, I. Ben-Asher, J. Heller, and D. Goldberg, Infiltration from a trickle source. I. Mathematical models, *Soil Science Society of America Journal*, 35(5): 675-682, 1971.

Fan, J.L., X.W. Xu, J.Q. Lei, J.F. Zhao, S.Y. Li, H.F. Wang, J.G. Zhang, and H.W. Zhou, The temporal and spatial fluctuation of the groundwater level along the Tarim Desert Highway, *Chinese Science Bulletin*, 53(Supp. II), 53-62, 2008.

Han, Z.W., Z.B. Dong, T. Wang, G.T. Chen, C.Z. Yan, and Z.Y. Yao, Observations of several characteristics of aeolian sand movement in the Taklimakan Desert, *Science in China Ser. D Earth Sciences*, 47(1), 86-96, 2004.

Han, Z.W.,W. Tao, Q.W. Sun, Z.B. Dong, and X.M. Wang, Sand harm in Taklimakan desert highway and sand control, *Journal of Geographical Sciences*, 13(1), 45-53, 2003.

Han, W., L. Cao, H. Yimit, X.W. Xu, and J.G. Zhang, Optimization of the saline groundwater irrigation system along the Tarim Desert Highway Ecological Shelterbelt Project in China, *Ecological Engineering*, 40, 108-112, 2012.

Huang, Q., S.X. Li, and Y.D. Song, The movement of water and salt in sandy land after irrigated with saline water, *Acta Pedologica Sinica*, 40(4), 547-553, 2003 (in Chinese).

Huang, Q., Water and salt movement in soil of Taklimakan Desert irrigated with saline water, *Northwest Sci-tech University of Agriculture and Forestry*, 2002 (in Chinese).

Lu, X.X., Z.J. Jin, L.F. Liu, S.L. Xu, X.Y. Zhou, X.J. Pi, and H.J. Yang, Oil and gas accumulations in the Ordovician carbonates in the Tazhong Uplift of Tarim Basin, west China, *Journal of Petroleum Science and Engineering*, 41(1-3), 109-121, 2004.

Li, B.W., X.W. Xu, J.Q. Lei, Y.Z. Qiu, B. Xu, H.W. Zhou, Q. Wang, B. Wang, and W. Su, Site type classification for the shelter-forest ecological project along the Tarim Desert Highway, *Chinese Science Bulletin*, 53(Supp. II), 31-40, 2008.

Li, B.W., Mechanism of water-salt regulation for the shelterbelts with saline water irrigation along the Tarim Desert Highway, Beijing: *Beijing Forestry University*, 2010 (in Chinese).

Pruess, K., C. Oldenburg, and G. Moridis, *TOUGH2 User's Guide, Version 2.0*, Report LBNL-43134, Lawrence Berkeley National Laboratory, Berkeley, Calif., 1999.

Raats, P.A.C., Steady infiltration from point sources, cavities, and basins, *Soil Science Society of America Journal*, 35(5): 689-694, 1971.

Skaggs, T. H., T. J. Trout, J. Šimůnek, and P. J. Shouse, Comparison of HYDRUS-2D simulations of drip irrigation with experimental observations, *Journal of Irrigation and Drainage Engineering*, 130(4), 304-310, 2004.

Thunderhead Engineering, *PetraSim User Manual, Version 4.2*, Manhattan, New York, 2007.

van Genuchten, M. Th., A Closed-form Equation for Predicting the Hydraulic Conductivity of Unsaturated Soils, *Soil Science Society of America Journal*, 44(5), 892-898, 1980.

Warrick, A.W., Time-dependent linearized infiltration. I. Point sources, *Soil Science Society of America Journal*, 38(3): 383-386, 1974.

Wang, Z.H., T.D. Chen, D.S. Yu, and F.J. Song,Division of groundwater system of Tarim basin, *Xinjiang Geology*, 22(3), 262-264, 2004 (in Chinese).

Wang, Y.D., X.W. Xu, J.Q. Lei, S.Y. Li, Z.B. Zhou, Q. Chang, L.H. Wang, F. Gu, Y.Z. Qiu, and B. Xu, The dynamics variation of soil moisture of shelterbelts along the Tarim Desert Highway, *Chinese Science Bulletin*, 53(Supp. II), 102-108, 2008.

Xia, X.C., and G.T. Chen, Study on the engineering technique of oil transporting highway in Tarim desert, *Journal of Desert Research*, 15(1), 1-9, 1995 (in Chinese).

Zhu, Z.D., Z. Wu, S. Liu, et al, *The General Introduction to Chinese Desert*, Science Press, Beijing, China, 1980 (in Chinese).

Zhu, H.L., Y.S. Dong, F.H. Yin, and Y.N. Chen, Historical evolution and the effects of ecological management in Tarim Basin, China, *Chinese Science Bulletin*, 55(36), 4097-4103, 2010.

Zhou, Z.B., X.W. Xu, and B.W. Li, Study on trends of water and salt of artificial greenbelt in hinterland of Taklimakan Desert, *Arid Zone Research*, 17(1), 21-26, 2000 (in Chinese).

Zhou, Z.B., X.W. Xu, J.Q. Lei, and S.Y. Li, Water balance and movement of Tarim Desert Highway Shelterbelt irrigated by saline water, *Arid Land Geography*, 33(6), 904-908, 2010 (in Chinese).

Zhou, Z.B., P.J. Li, X.W. Xu, and B.R. Pan, Effect of artificial greenbelt on salt distribution in sand land in hinterland of Taklimakan Desert, *Journal of Soil and Water Conservation*, 16(2), 16-19, 2002 (in Chinese).

TO SEEP OR NOT TO SEEP?
SOME CONSIDERATIONS REGARDING WATER INFILTRATION IN VOLCANIC LAKES

Micol Todesco (1), Dmitri Rouwet (1), Massimo Nespoli (1,2), Raul A. Mora-Amador (3)

(1) INGV - Sezione di Bologna, via D. Creti 12 40128 Bologna, Italy
e-mail: micol.todesco@bo.ingv.it
(2) Università di Bologna, Bologna, Italy
(3) Red Sismológica Nacional, Universidad de Costa Rica, San José, Costa Rica

ABSTRACT

Volcanic lakes occasionally form as rainwater fills inactive craters. Their existence and survival requires a delicate balance between meteoric recharge, evaporation, and water loss by infiltration within the volcanic edifice, commonly referred to as seepage. Temperature and composition of lake waters often testify to the presence of a deep-seated, volcanic component that may participate to a varying extent in the lake's evolution. In this work, we investigate the interaction between hot volcanic gases, provided by a magmatic source at depth, and the shallow lake water, fed by meteoric recharge. We focus on the conceptual model developed for Poás Volcano (Costa Rica), where a shallow magma intrusion drives the hydrothermal activity underneath and around a crater lake. The computational domain describes the upper portion of the volcanic edifice where the crater lake is located. Along its base, the domain connects to a reservoir of hot, pressurized water vapor, representing the contribution of deep-seated volcanic fluids. Numerical simulations assess the role of relevant system properties, including the conditions of the hydrothermal reservoir, the water level in the lake, and rock permeability. Preliminary results suggest that very shallow features can be responsible for the dynamics around the lake and ultimately control its evolution.

INTRODUCTION

Crater lakes on active volcanoes are very special geological features. Their evolution through time reflects not only changes in the hydrological cycle, but also changes in the magmatic-hydrothermal system that feeds the lake both heat and fluids. Volcanic surveillance programs commonly highlight significant changes in lake water level, temperature, and composition (Rowe et al., 1992; Rouwet et al., 2004; Terada et al., 2012). The interpretation of these changes, however, is not straightforward, and the information provided by the evolution of the lake is difficult to exploit completely. The presence of shallow liquid water may act as a buffer and hinder signs arising from the magmatic system at depth. Some relevant quantities, such as water loss (or seepage) through lake boundaries, are difficult to measure directly. In this work, we focus on the interactions between the hot rising volcanic fluids and the lake waters. We consider the upper portion of a volcanic edifice hosting a lake and perform numerical simulation of heat and fluid propagation from a shallow, pressurized hydrothermal reservoir through an unsaturated volcanic edifice, toward the surface. We define the computational domain and boundary conditions based on data available for Poás Volcano, Costa Rica. Our simulations, however, are not aimed at reproducing any specific feature of this particular volcanic lake, but rather at investigating some general aspects related to the interaction between hydrothermal fluids and volcanic lakes.

THE POÁS VOLCANIC LAKE

Poás Volcano belongs to the Central Volcanic Cordillera of Costa Rica and is one of its most active volcanoes. The summit of this large basaltic-andesite stratovolcano hosts three cones and two lakes. The active crater, 800 m wide and 2300 m asl, contains an active hydrothermal system, a hot, acidic crater lake, Laguna Caliente, 300 m in diameter, and a dome that extruded during the last phreato-magmatic event in 1953–1955. Volcanic activity has been ongoing almost continuously during the last two centuries, involving hydrothermal and fumarolic

activity, phreatic explosions (1980–1990s, 2006-present) and phreato-magmatic eruptions (1834, 1910, 1953-55) (Casertano et al., 1983; Rowe et al., 1992; 1995; Martínez et al., 2000; Mora-Amador, 2010). Geophysical surveys highlighted the presence of a very shallow magma reservoir, which provides both heat and fluids to the system. Shallower and cooler magmatic intrusions are inferred to exist above the magma reservoir (Brown et al., 1989; Rymer et al., 2000; 2009; Fournier et al., 2004). Fumaroles may form (or disappear) on the dome, and their temperatures range from less than 100 to about 1000°C during periods of volcanic unrest (Brown et al., 1989; Vaselli et al., 2003). Hot, acidic springs are located along the northwest flank of the volcano, at ~ 3 km from the active crater. These springs formed along a (lava-lahar) stratigraphic contact that represents a preferential hydraulic pathway driving the hot hydrothermal brines from the crater region down on the volcano's flank (Rowe et al., 1992; 1995). The Laguna Caliente lake was formed on the active crater. The water level has been highly variable, from 50 m to 0 m (Rowe et al., 1992). Steady evaporation dominates during periods of high lake water temperature (as high as 80°C), which are directly related to enhanced magmatic activity at Poás. The decline of the water level, and occasionally the complete lake's desiccation, preceded the onset of phreato-magmatic and magmatic eruptions in 1910 and 1953. During quiescent periods, lower water temperatures (as low as 20°C) are associated with higher lake levels. Water level and properties (temperature, composition) also depend on meteoric recharge. Precipitation in the summit area at Poás ranges from 120 mm/month in the dry season (December-April) to as much as 420 mm/month (May-November). Considering a catchment area corresponding to the crater surface (7.1×10^5 m^2), these values correspond to an average meteoric recharge ranging from 34 to 114 kg/s.

NUMERICAL MODELING

In this work, we focus on the interplay between the lake water infiltrating through the volcanic edifice and the hydrothermal system. In particular, we consider a quiet period, when neither the water level nor the lake temperature is expected to change significantly, as occurred from 1995 to 2005 (Rymer et al., 2009). We describe a small region of the volcanic edifice, 250 m deep and 1000 m wide, located between the shallow hydrothermal reservoir formed above the magma body and the crater lake (Figure 1). We consider a simple 2D, axisymmetric domain, composed by 2288 elements with a constant thickness of 5 m and a radial dimension ranging from 5 to 100 m. Numerical simulations are performed with TOUGH2/EOS3, to describe the propagation of hot volcanic vapor and of lake water into an initially unsaturated volcanic edifice.

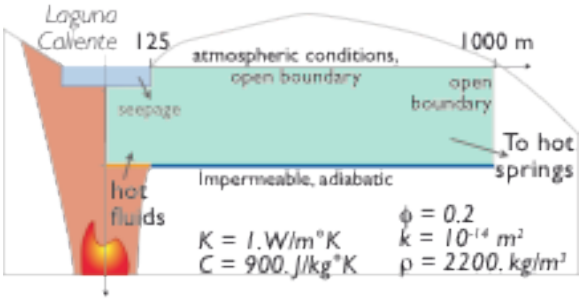

Figure 1. Computational domain, rock properties, and boundary conditions applied for the numerical simulation of the Poás hydrothermal system.

The presence of the lake is simulated as a boundary condition, with fixed pressure, temperature, and water saturation prescribed along the lake bottom and vertical border: pore pressure is fixed at the hydrostatic value for the corresponding lake depth; the pores are fully saturated with water whose temperature is set at 25°C. Lake-water evaporation at this temperature (Fournier et al., 2009) is about one order of magnitude smaller than the average meteoric recharge, and therefore we neglect this effect. With the imposition of a steady water level and a constant water temperature, we assume that the meteoric precipitation and the inflow of hydrothermal condensates perfectly balance the water loss through the lake boundaries. At this time, we also assume that precipitation mostly feeds the lake, while we consider the slopes of the volcano steep enough to prevent infiltration elsewhere in the domain.

In this simple model, the hydrothermal circulation is fed by a hot and pressurized, dry-gas reservoir, located at shallow depth right below the lake. Where not otherwise specified, the reservoir is set at 350°C and 2.4 MPa. These

values were selected considering the temperature proposed for the magmatic intrusion (Rowe et al., 1995) and the hydrostatic pressure at that depth. The outer portion of the bottom boundary is closed to heat and fluid flow, and represents the presence of an impervious layer that drives fluids outward to feed the springs along the volcano slopes. The lateral boundary is open, unsaturated, and at fixed atmospheric conditions (0.1MPa and 15°C). At the beginning of the simulation, the entire volcanic edifice is considered fully saturated by air at atmospheric conditions. Where not otherwise specified, the physical properties of the rock are homogeneous and set as shown in Figure 1. Based on this simple conceptual model, we investigated the role of selected system parameters, such as the conditions of the hydrothermal reservoir feeding the system, permeability of the volcanic rock, and lake water level.

THE REFERENCE CASE

At the beginning of the simulation, the lake water begins to infiltrate into the volcanic rock, while the hot, pressurized vapor in the hydrothermal reservoir propagates upward, heating the lower portion of the domain. A small fraction of this vapor condenses, forming a small rim of warm, liquid water around the edges of the rising plume. After 3 years of simulation, the cold water seeping downward and the hot, ascending fluids merge at a depth of about 150 m (Figure 2a). From this time on, the downward motion of the water is diverted by the uprising fluids. The cold lake water and the hydrothermal condensate, reach the bottom of the domain at some 250 m from the symmetry axis (Figure 2b). As the simulation continues, the interface between the cold water and the hot rising vapor keeps changing. After 40 years, the hot plume reaches the bottom of the lake (Figure 2c) and starts to increase both the temperature and pore pressure along its base. As a consequence, the water seepage through the bottom of the lake is progressively hindered and, at the end of the simulation, the water leaves the lake mostly through its vertical border (Figure 2d). The water that accumulates along the impervious base of the domain is slightly heated (50°C) and tends to propagate outward. At the end of the simulation (100 yr), it has reached as far as 900 m from the symmetry axis (not shown). The entire simulation is shown here for completeness, but when the hot plume reaches the bottom of the lake, water vapor is expected to enter the lake, altering its level and temperature. As a result, our assumption of steady lake conditions would not be realistic anymore. Numerical results allow us to quantify the seepage under the simulated conditions.

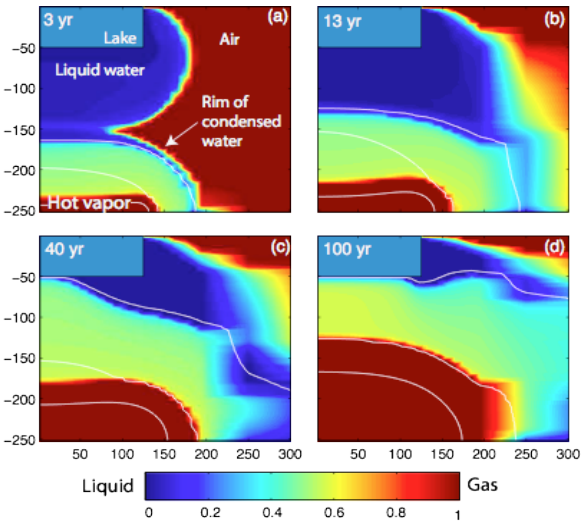

Figure 2. Volumetric gas fraction in the lake region, at different times (reference simulation). The three white contours correspond to temperature of 100°, 200°, and 300°C.

Figure 3 shows the amount of water that leaves the lake through the bottom and the vertical borders, as a function of time. The overall trend is negative, indicating that water loss tends to diminish through time. Water seepage is driven by gravity and by the pressure gradient across the lake boundaries. The liquid water of the lake is denser than the air that initially fills the rock pores, and its hydrostatic pressure is everywhere greater than the atmospheric value that is initially set within the unsaturated volcanic edifice. As liquid water begins to infiltrate, both the density contrast and the pressure gradient across the lake boundaries tend to vanish, and the seepage correspondingly declines through time. This trend, however, is not linear, and the initial quick drop of the seepage rate is followed by a more gentle, steady decline that lasts to the end of the simulation. This abrupt change occurs after about 7 years, when the rock around the lake becomes entirely saturated by liquid water or by a two-phase mixture of hot vapor and water, and the pressure profile around the lake

becomes more stable. The vertical seepage (green in Fig. 3) is initially larger than the horizontal component, but it undergoes a faster decline, and eventually vanishes, as the rising fluids counteract the hydrostatic pressure along the bottom of the lake. After 4 years of simulation, the seepage becomes dominated by the horizontal component, which maintains a rather constant value over time. Figure 3 also shows the time at which the total amount of water lost by seepage equals the amount of water initially present within the lake (cyan dot). Under the conditions considered here, and in absence of meteoric recharge, the lake would drain completely in 12 years. Given that the yearly average precipitation is higher than the simulated seepage rate, the meteoric recharge would easily counteract the effects of seepage in this case.

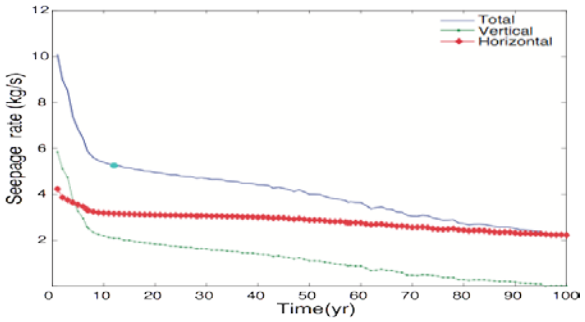

Figure 3. Rate of seepage through the lake bottom (green line) and vertical wall (red line). The cyan dot on the total seepage curve (blue line) indicates the time at which the seepage would completely drain the lake, in absence of meteoric recharge.

THE HYDROTHERMAL RESERVOIR

The evolution of seepage is influenced by the conditions assigned to the reservoir of volcanic fluids. To investigate the effect of these conditions we performed two sets of simulations: the first one explores different reservoir temperatures (from 50° to 300°C) at a fixed pressure (2.4 MPa), whereas the second set describes the role of different reservoir pressures (from 0.7 to 2.8 MPa) at fixed temperature (350°C). All simulations were run for 100 years, and results are compared with those achieved in the reference case.

The reservoir conditions control the phase of the fluid entering the system. For a reservoir pressure of 2.4 MPa, as in the reference case, the saturation temperature is about 220°C. Simulations run with reservoir temperatures up to 200°C therefore describe a system fed by hot liquid water that saturates the domain up to a depth of 150 m, and then mostly propagates outwards, slightly affecting the temperature near the surface (Figure 4a). Higher reservoir temperatures cause the inflow of hot vapor that rises toward the surface and heats the system more efficiently (Figure 4b,c).

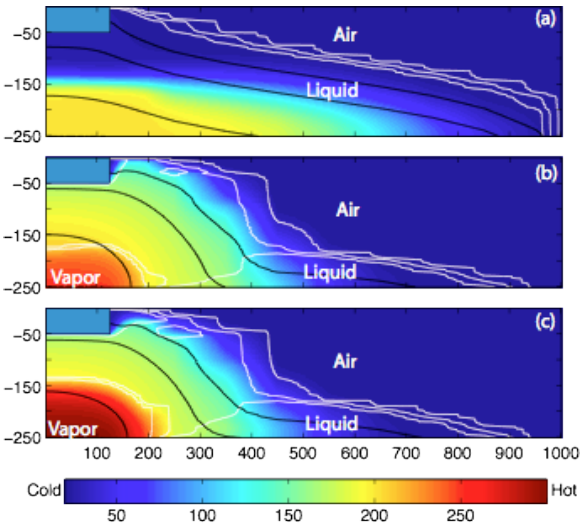

Figure 4. Distribution of temperature (color), pressure (black contours) and volumetric gas fraction (white contours) after 100 yr of simulation. Reservoir temperatures of 200°C (a), 250°C (b) and 300°C (c). Pressure values: 0.4, 0.8, 1.6, 2.4 MPa; gas fraction: 0.3, 0.6, 0.9.

Note that near-surface temperatures do not necessarily reflect the reservoir temperature, since the isotherms around the lake are controlled by complex, small-scale patterns of circulation (Figure 4b,c).

The pressure assigned to the hydrothermal reservoir also affects system evolution. As we set the reservoir temperature at 350°C, the reservoir fluid is always steam at all the considered reservoir pressures. However, values below 2 MPa do not sustain the ascent of the reservoir fluid against the downward motion of the lake water (Figure 5a). In this case, the presence of the hydrothermal reservoir does not

affect the lake, while the lake water saturates the domain and eventually enters the reservoir. Above this pressure value, the ascent of hydrothermal fluids, and the associated heating, are granted (Figure 5b,c). Higher pressures favor a faster evolution: the steam from the reservoir reaches the bottom of the lake in 95 years, when the reservoir pressure is 2.1 MPa, only 23 years after the maximum pressure is assigned. Pressure and temperature of the reservoir influence the seepage process (Figure 6).

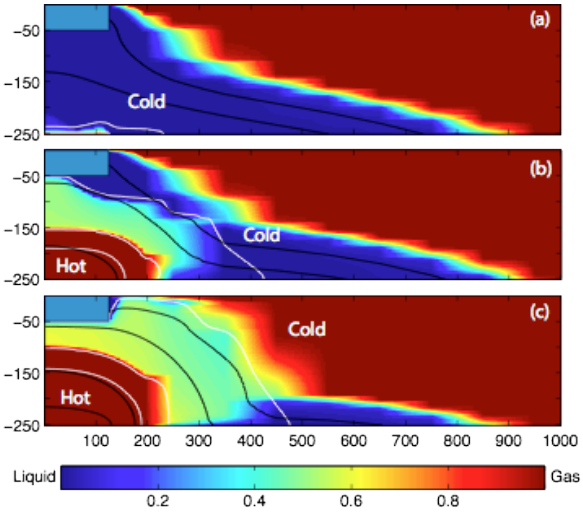

Figure 5. Distribution of gas fraction (color), pressure (black) and temperature (white) after 100 yr of simulation for reservoir pressures of 1.4 MPa (a), 2.1 MPa (b) and 2.8 MPa (c). Pressure contours:0.4, 0.8, 1.6, 2.4 MPa; temperature contours: 100°, 200°, 300°C.

While the general pattern is maintained, with a quick drop in seepage rate followed by a more gentle decline, the absolute values and the details of its temporal evolution depend on the reservoir conditions.

Differences associated with the reservoir temperature increase with time, and become relevant only after a few tens of years (Figure 6a). Note that the effect of reservoir temperature depends on the phase of the fluid within the reservoir: when the source discharges liquid water, the long-term seepage tends to a steady value, maintained throughout the simulation, that is slightly higher for lower reservoir temperature. On the other hand, if the source at depth discharges water vapor, the seepage keeps declining through time, and the reservoir temperature has the opposite effect, with higher temperatures corresponding to higher seepage rates.

Reservoir pressure affects both the initial drop in seepage rate, and its long-term value (Figure 6b). Low reservoir pressures correspond to a small initial decline and to higher and rather constant long-term seepage rates. When the reservoir pressure exceeds 2 MPa, the ascent of hot vapor effectively counteracts the downward motion of liquid water (Figure 5c). Higher reservoir pressures correspond to larger initial drop, and to an overall declining trend throughout the simulation.

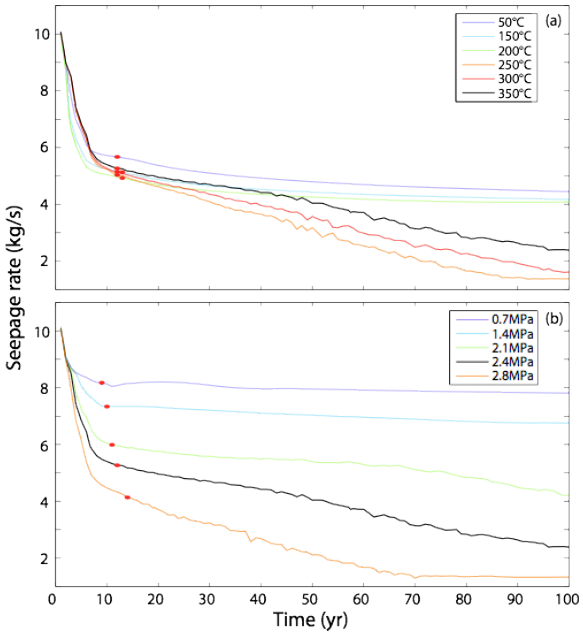

Figure 6. Total seepage rate through time at different reservoir temperatures (a) and pressures (b). The black line refers to the reference simulation. Red dots indicate the time at which the seepage would drain the lake in absence of meteoric recharge.

THE WATER LAKE LEVEL

In all our simulations, the lake has been considered a steady boundary condition. In reality, we know that there are periods during which the lake level changes significantly, modifying the pressure distribution along the lake boundaries. To assess the importance of such a change, we performed a further set of simulations, changing the lake level from 50 to 10 m. As in previous cases, we assume that the

assigned water level is maintained by meteoric recharge and does not change during the simulation. Higher water levels imply a higher hydrostatic pressure at the bottom of the lake and a larger portion of the vertical wall being fully saturated with liquid water. Initially, these differences do not affect the evolution of the system. The interaction of lake waters with the hot, rising vapor takes place in a similar way, and the overall temperature distribution is comparable, whatever the lake thickness is (Figure 7a,b). However, the conditions set along the vertical boundary of the lake affect the amount of water that permeates the surrounding region, and modify the local pattern of circulation. Over the long term, this slightly modifies both the phase distribution and the system temperature (Figure 7c,d).

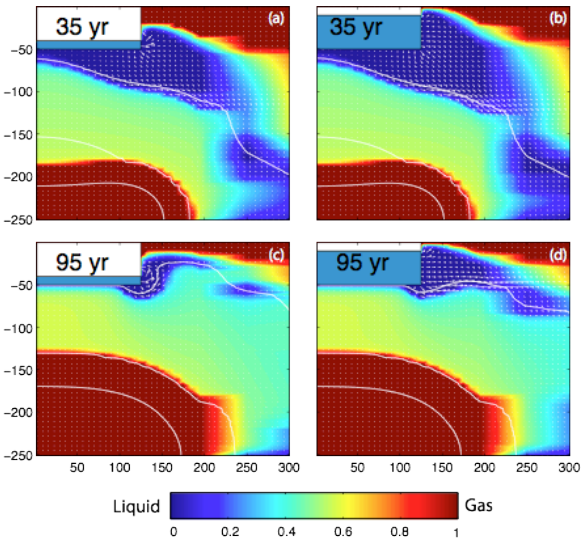

Figure 7. Volumetric gas fraction at different times for a lake level of 10 (a,c) and 40 m (b,d). The three white contours correspond to temperature (100°, 200°, and 300°C). White arrows show the liquid flow pattern.

When the lake level is only 10 m, a large portion of the vertical boundary of the lake is unsaturated and at atmospheric pressure. Under these conditions, the fluids within the volcanic edifice can enter the lake: when the hot vapor reaches the bottom of the lake, pushing the liquid water upwards, some fraction of it flows back into the lake, as shown in Figure 7c.

The different lake levels also affect the total seepage from the lake. While the vertical outflow of water through the bottom of the lake does not change significantly with respect to the reference case (green line, Figure 3), the horizontal seepage is affected by the water level, being reduced from an average value of ~ 3 kg/s, for the maximum lake depth (50 m) to about 1 kg/s, when lake level is only 10 m. As a result, the total seepage changes with lake level, as shown in Figure 8. Lower water levels correspond to lower seepage rates, at any time.

ROCK PERMEABILITY

The interaction between hydrothermal fluids and lake waters also depends on the hydraulic properties of the shallow volcanic rocks.

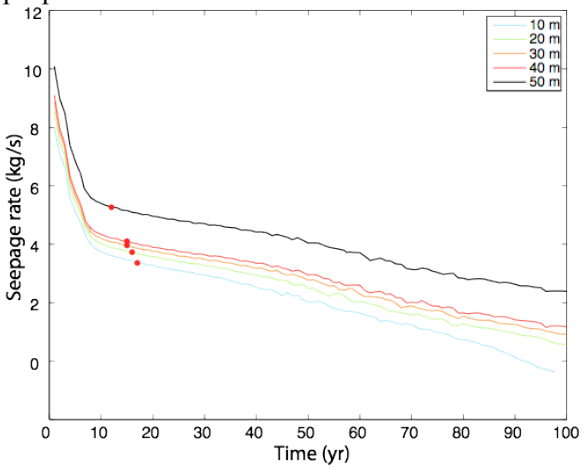

Figure 8. Total seepage rate through time for different water levels. The black line refers to the reference simulation. Red dots indicate the time at which the seepage would drain the lake in absence of meteoric recharge.

Permeability, in particular, affects the rate at which the system conditions evolve through time. Simulations performed with different permeability values (10^{-12} to 10^{-16} m^2) confirm that lower permeabilities cause slower evolution, with similar distribution of temperature and fluid phases achieved at later times in less permeable systems.

The seepage rate also changes, with its order of magnitude increasing with the order of magnitude for permeability. The maximum seepage rates, at the beginning of each simulation, range from 500 to less than 0.4 kg/s

over the considered permeability range. The temporal evolution of the seepage also changes with permeability: a permeable system allows for a quick ascent of hot vapor, which in turn leads to a faster decline of the seepage rate. Less permeable systems are characterized by lower but rather constant seepage rates, which are maintained with small changes to the end of the simulation. All these considerations hold for homogeneous systems. However, active crater lakes are often hosted in stratovolcanoes, where heterogeneous rock properties can be expected. Here we focus on the permeability of the lake boundaries. The permeability of the lake borders controls the amount of liquid water that permeates through the volcanic edifice and the interaction with hydrothermal fluids. Figure 9 and 10 show the phase distribution achieved imposing a very low permeability (10^{-21} m^2) to either the vertical wall of the lake (a), the lake bottom (b), or both (c).

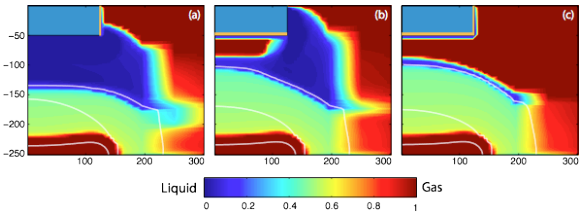

Figure 9. Volumetric gas fraction after 10 years with low permeability (10^{-21} m^2, yellow line) assigned to the lake vertical wall (a), bottom (b) or both (c). The white contours correspond to temperature of 100°, 200°, and 300°C.

When only the lake bottom is permeable (Fig. 9a), the seepage clearly hinders the ascent of hydrothermal vapor. Where the water infiltration only takes place through the vertical wall, or is totally prevented, near surface-heating is more efficient (Fig. 9b,c). After 100 yr of simulation, the overall system conditions are similar, although not identical (Figure 10). When the lake bottom is permeable, the pressure and temperature underneath the lake are slightly lower than in the other cases, and the gas fraction is correspondingly higher (Fig. 10a).

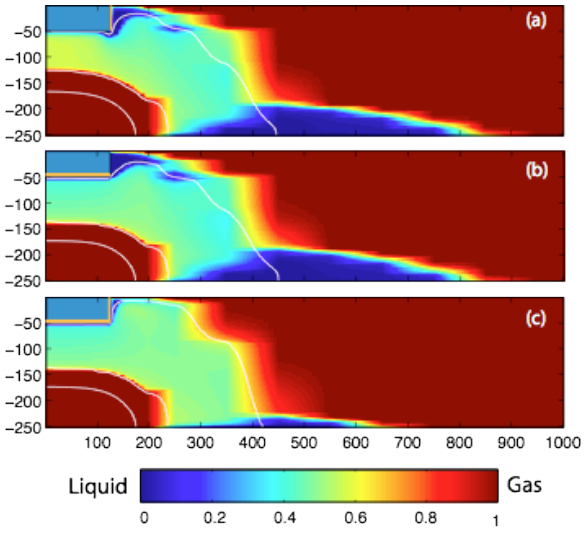

Figure 10. Volumetric gas fraction after 100 years with low permeability (10^{-21} m^2, yellow line) assigned to the lake bottom (a), wall (b) or both (c). The white contours correspond to 100°, 200°, and 300°C.

When any of the lake boundaries is permeable, a larger amount of liquid water permeates the region surrounding the lake, and eventually accumulates along the bottom boundary (Figure 10a,b). Hydrothermal condensate also accumulates along the bottom boundary, so that some liquid water is present along the bottom boundary even when the lake is completely sealed (Fig. 10c). Hydrothermal-vapor condensation takes place in all simulations, but its relative proportion changes, depending on how much water can permeate the system.

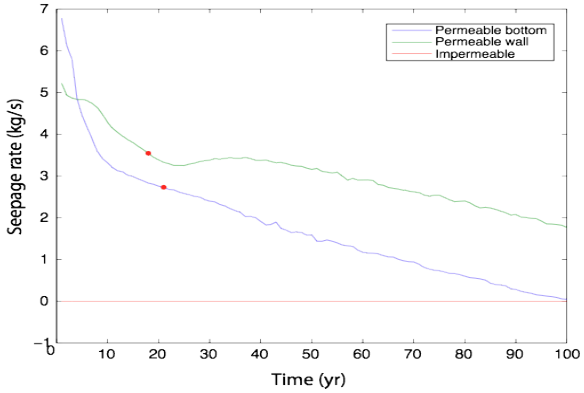

Figure 11. Total seepage rate through time for different permeabilities of the lake boundaries. Red dots indicate the time at which the seepage would drain the lake in absence of meteoric recharge.

The permeability of lake borders also affects the seepage rate (Figure 11). In particular, if only the bottom of the lake is permeable, the seepage rate undergoes the largest variation, and eventually vanishes, hindered by the ascent of the hydrothermal fluids. The seepage through the vertical wall of the lake is affected to a lesser extent by the rising vapor, and turns out to be more effective in draining the lake water.

CONCLUSIONS

We focused on the interaction between a crater lake and the hydrothermal circulation. Numerical simulations were carried out to estimate the infiltration of lake waters (or seepage) at Poás Volcano, under the assumption of steady lake conditions. Our results show that the conditions of the hydrothermal reservoir, the lake water level, and rock permeability may all affect system evolution and the corresponding seepage rate. The infiltration of lake water is effectively hindered by the presence of an active hydrothermal reservoir. Long-term seepage is reduced or totally hindered when the reservoir discharges hot vapor at high pressure. Its ascent effectively reduces the vertical infiltration, limiting the water seepage through the bottom of the lake. Conversely, the horizontal flow through the vertical border of the lake is never completely hindered by the rising fluids. For this reason, the total seepage, and its temporal evolution, are sensitive to conditions set along the vertical boundary of the lake, namely to its water saturation (lake's water level) and to its permeability. Shallow heating and fumarolic activity only develop when water seepage is limited, i.e., when reservoir pressure is high, the water level in the lake is low, or the permeability around the lake is limited. When seepage occurs, liquid water can accumulate along impervious layers, mix with hydrothermal condensates, and eventually propagate to feed hot springs. The hydrothermal component in spring waters is therefore expected to increase when seepage is limited, i.e., when reservoir pressure is high, lake level is low, or the permeability around the lake is reduced. Seepage is difficult to quantify in the field, but is a key parameter in assessing the evolution of the crater lake, and in estimating the volcanic hazard. Further research will be carried out on the feedback between lake conditions and hydrothermal circulation.

REFERENCES

Brown, G., H. Rymer, J. Dowden, P. Kapadia, D. Stevenson, J. Barquero, and L.D. Morales, Energy budget analysis for Poás Crater lake: implications for predicting volcanic activity, *Nature, 339*, 370-373, 1989.

Casertano, L., A. Borgia, and C. Cigolini, El Volcán Poás, Costa Rica: Cronología y características de actividad, *Geofís. Int., 22*, 215-236, 1983.

Fournier, N., H. Rymer, G. Williams-Jones, and J. Brenes, High-resolution gravity survey: Investigation of subsurface structures at Poás volcano, Costa Rica, *Geophys. Res. Lett., 31*, L15602.doi:10.1029/2004GL020563, 2004.

Fournier, N., F. Witham, M. Moreau-Fournier, and L. Bardou, Boiling Lake of Dominica, West Indies: High-temperature volcanic crater lake dynamics, *J. Geophys. Res., 114*, B02203.doi:10.1029/2008JB005773, 2009.

Martínez, M., E. Fernández, J. Valdés, V. Barboza, R. Van der Laat, E. Duarte, E. Malavassi, L. Sandoval, J. Barquero, and T. Marino, Chemical evolution and activity of the active crater lake of Poás volcano, Costa Rica, 1993-1997, *J. Volcanol. Geotherm. Res., 97*, 127-141, 2000.

Mora-Amador, R.A., Peligrosidad volcánica del Poás (Costa Rica), basado en las principales erupciones históricas de 1834, 1910 y 1953-1955, *MSc Thesis, Universidad de Costa Rica*, pp. 115, 2010.

Rouwet, D., Y. Taran, and N.R. Varley, Dynamics and mass balance of El Chichón crater lake, Mexico, *Geofís. Int., 43*, 427-434, 2004.

Rowe, G.L., S.L. Brantley, M. Fernández, J.F. Fernández, A. Borgia, and J. Barquero, Fluid-volcano interaction in an active stratovolcano: the Crater Lake system of Poás Volcano, Costa Rica, *J. Volcanol. Geotherm. Res., 64*, 233-267, 1992.

Rowe, G.L., S.L. Brantley, J.F. Fernández, and A. Borgia, The chemical and hydrologic structure of Poás Volcano, Costa Rica, *J. Volcanol. Geotherm. Res., 64*, 233-267, 1995.

Rymer, H., J. Cassidy, C.A. Locke, M.V. Barboza, J. Barquero, J. Brenes, and R. van der Laat, Geophysical studies of the recent 15-year eruption cycle at Poás Volcano, Costa Rica, *J. Volcanol. Geotherm. Res., 97*,425-442, 2000.

Rymer, H., C.A. Locke, A. Borgi, M. Martínez, J. Brenes, R. Van der Laat, and G. Williams-Jones, Long-term fluctuations in volcanic activity: implications for future environmental impact, *Terra Nova, 21*, 304-309, 2009.

Terada, A., T. Hashimoto, and T. Kagiyama, Water flow model of active crater lake at Aso Volcano, Japan: Fluctuations of magmatic gas and groundwater fluxes from underlying hydrothermal system, *Bull. Volcanol., 74*, 641-655, 2012.

Vaselli, O., F. Tassi, A. Minissale, G. Montegrossi, E. Duarte, E. Fernández, and F. Bergamaschi, Fumarole migration and fluid geochemistry at Poás Volcano (Costa Rica) from 1998 to February 2001, Mem. Geological Society of London, Special Issue on: "Volcanic degassing", C., Oppenheimer, D.M., Pyle & Barclay, J. (Eds.), 213: 247-262. DOI: 10.1017/S0016756805290787, 2003.

BOREHOLE AND FORMATION ANALYSES TO SUPPORT COMPRESSED AIR ENERGY STORAGE DEVELOPMENT IN RESERVOIRS

Stephen W. Webb

Sandia National Laboratories[1]
Albuquerque, NM, USA
e-mail: Stephen.Webb.CRC@gmail.com

ABSTRACT

A 2-D borehole/formation model was developed for Compressed Air Energy Storage (CAES) applications to evaluate the performance of the system under various conditions including two-phase flow. The optimum formation radius, which is directly related to borehole spacing, was determined for given sets of formation parameters, borehole diameter, and CAES operating assumptions based on minimum and maximum formation pressure values. The effect of two formation parameters, permeability and porosity, on the operational parameters was assessed using this model.

INTRODUCTION

Compressed air energy storage (CAES) in reservoirs relies on air flow through boreholes between the above-ground power plant and the underground reservoir. The efficiency of the underground portion of the CAES system depends in part on the porosity and permeability of the formation and on the details of the borehole array. The economic feasibility of a CAES facility may hinge on accessible air volume and/or air mass flow rate. When sufficient air volume and mass flow rates are available, optimal design of the borehole array, including borehole diameter and spacing, will determine the efficiency of the system.

In this study, formation (porosity, permeability, degree of saturation) and borehole parameters (diameter, length, and spacing) were evaluated to determine appropriate ranges for successful CAES application. The flow in the boreholes can be used to determine a minimum number of boreholes of a given diameter to minimize pressure losses while maintaining adequate air flow. In the formation, the flow to these boreholes depends on the formation porosity, permeability, pressure, and degree of saturation (water or gas filled) as well as the borehole diameter and borehole layout. For example, if the boreholes are spaced too close to each other, the flow rate per borehole is less than optimal and the borehole layout is inefficient because fewer boreholes could be used. Similarly, if the boreholes are spaced too far apart, the number of boreholes for the CAES formation will be less than optimal, so the plant capacity will also be less than optimal.

Problem Idealization

In a reservoir CAES facility, air is injected and withdrawn from the underground formation through a number of boreholes. For this study emphasis was placed on understanding the processes that occur for a unit borehole (i.e., one of the boreholes in the array). An idealized plan view of a unit borehole is shown in Figure 1. Each circle represents the flow distance to the nearest adjacent boreholes.

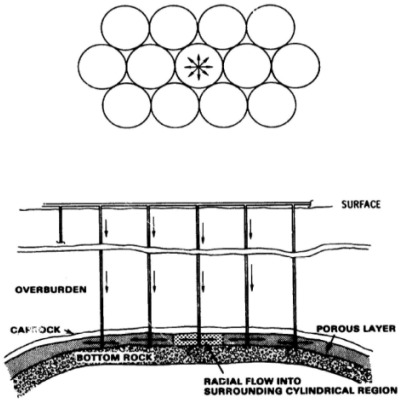

Figure 1. CAES borehole schematic plan and elevation view (Smith and Wiles, 1979).

[1] Presently at Canyon Ridge Consulting LLC
Sandia Park, NM, USA, 87047

Simulations were performed using the TOUGH2 code (Pruess et al., 1999.) modified for CAES operations. TOUGH2 assumes Darcy (laminar) flow in the formulation. Turbulent flow near boreholes is often postulated in CAES operation (Smith and Wiles, 1979, pg. 330 and Katz and Lady, 1976, pg. 65 and elsewhere). However, turbulence is not a significant factor for CAES according to Pittsfield data (EPRI GS-6688, 1990, pg. 4-38), and turbulent flow in the formation was not included in the present simulations.

The simulations in this study modeled processes in a possible CAES formation, including the formation of the initial air bubble and the weekly cycling of air injection and withdrawal for a given formation radius. The resulting borehole/formation pressures were compared to pressure limits to evaluate the given formation radius.

Formation Details

The simulation model shown in Figure 2 consists of a single borehole in a formation with uniform properties (permeability, porosity, rock type); formation properties were varied in this study. The formation height is assumed to be 100 ft (30.5 m); gas flow is restricted to this height. The top boundary is impermeable cap rock. The outer radial boundaries are no-flow because other boreholes are assumed to surround this unit borehole. The bottom boundary is at hydrostatic pressure for the assumed depth. Water may flow into and out of this lower boundary to maintain hydrostatic pressure as well as any capillary fringe. Air may not flow across this boundary. The nominal completion position of the borehole is midway into the formation (50 ft; 15.2 m) to minimize water inflow during air withdrawal from water coning. The depth to the top of the formation is 2000 ft (610 m).

The radial dimension of the formation was varied to reflect CAES operating conditions and pressure limits. Based on this radial dimension, the initial air bubble is formed over a specified number of days. An equilibration time is specified before the weekly CAES injection/withdrawal cycles begin. The parameters are summarized in Table 1.

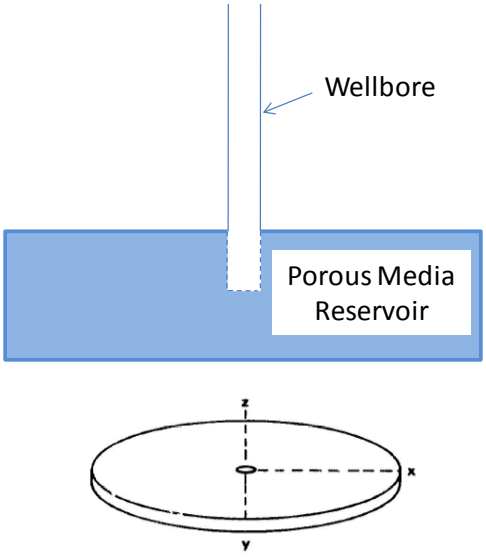

Figure 2. Borehole and formation geometry.

Table 1. Simulation parameters

Reservoir Depth (Top)	2000 ft (610 m)
Reservoir Height	100 ft (30.5 m)
Reservoir Pressure (Top)	880 psig (6.07 MPa)
Reservoir Temperature	25 °C
Borehole Diameters	7 inches (17.8 cm) 12 inches (30.5 cm) 20 inches (50.8 cm)
Porosity	Base Case: 0.2 Range: 0.1, 0.2, 0.3
Permeability	Base Case: 500 mD Range: 100, 500, 1000, 2000 mD
Capillary Pressure and Relative Permeability	Based on Zhou et al. (2010)
Air Bubble Parameters	
Development Time	60 days
Final Gas Saturation	0.5
Equilibration Time	40 days
Weekly CAES Cycle Parameters	
Injection/Withdrawal Rate	Variable
Injection Composition	Dry Air
Injection Temperature	25 °C
Weekly Cycled Air Mass	10%
Weekend Injection	40%
Borehole/Formation Pressure Limits	725 psia (5.0 MPa) 1220 psia (8.4 MPa)

The maximum borehole/formation pressure used in this study is 0.6 times lithostatic pressure, or 1220 psia (8.4 MPa). The minimum borehole/formation pressure is based on a turbine inlet pressure of about 650 psia (4.5 MPa) (Succar and Williams, 2008) and an approximate 75 psi (0.5 MPa) pressure drop from the formation to the surface based on gas-only flow up the borehole, or a minimum borehole/formation pressure of 725 psia (5.0 MPa).

The injection and withdrawal cycle used in these simulations is based on the scheme of Smith and Wiles (1979) as shown in Figure 3. Their weekly cycle consists of alternating 10-hour withdrawal and injection cycles, with 2-hour transition periods during the week and an additional injection on the weekend. The injection and withdrawal rates are based on a user-specified fraction cycled and fraction of mass injected during the weekend. The original cycle proposed by Smith and Wiles based the injection and withdrawal rates on the maximum mass in the air bubble. The present implementation modifies this scheme slightly; the injection and withdrawal rates are based on the initial bubble mass after bubble formation, because the initial bubble mass is known.

The injection and withdrawal rates (1/sec) are given by the following relationships for the assumed cycle

$$\dot{m}_{withdrawal}(1/sec) = \frac{1}{3600}\frac{\lambda}{50\,\psi}\,M_{bubble,initial}$$

$$\dot{m}_{injection}(1/sec) = (1-\psi)\frac{1}{3600}\frac{\lambda}{40\,\psi}\,M_{bubble,initial}$$

where λ is the cycling fraction (0.1) and ψ is the fraction of mass (0.4) injected on the weekend (including Friday evening). There are a total of 50 hours of withdrawal and 40 hours of injection during the week. Air is injected for 26 hours and 40 minutes over the weekend; 10 hours Friday and 16 hours 40 minutes Sunday.

The injected air is assumed to be dry and at 25°C, the same temperature as the reservoir. These assumed conditions necessitate the use of compressors with intercoolers and an aftercooler to compress, cool, and dehumidify the air being injected into the reservoir (Succar and Williams, 2008).

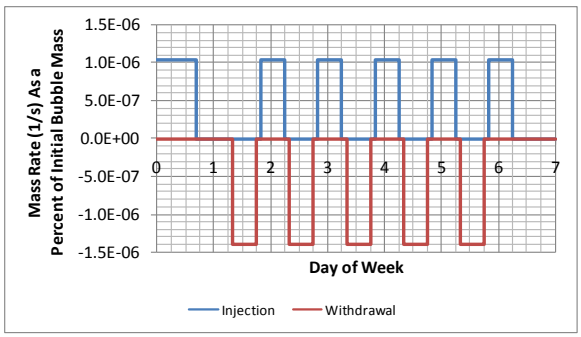

Figure 3. Injection and withdrawal mass flow rates

Two-phase Characteristic Curves

The formation is assumed to be sandstone with isotropic properties. Two-phase characteristic curves (van Genuchten (1980) and Corey (1954)) are based on the work of Zhou et al. (2010). The capillary pressure is scaled using the Leverett J-function (Leverett, 1941).

Borehole Model

The borehole is modeled as a porous medium with a porosity of 1.0 and a permeability of 10^{-7} m^2. Zero capillary pressure was specified. Due to the flow of liquid into and out of the borehole during CAES cycling, linear relative permeability was specified for the liquid and gas phases. The relative permeability for each phase increased over the range 0.01 to 1.0, although the lower limit was sometimes varied to promote convergence. The borehole volume is that of the actual borehole all the way to the surface.

Mesh

The simulations use an R-Z axisymmetric mesh assuming zero dip. The first radial mesh point is the borehole radius, which for the 7-inch diameter borehole is 0.292 ft (0.0889 m). The maximum radial dimension is 1000 ft (305.1 m) with logarithmic mesh spacing between these two points and 44 radial increments. The axial mesh spacing is a uniform 10 ft (3.048 m). The maximum axial value is 100 ft (30.48 m), which is the top of the formation. The minimum axial value is -20 ft (6.096 m). The part of the mesh below the bottom of the formation is a constant head boundary condition to maintain hydrostatic conditions in the formation. Air may not flow into the bottom 20 ft of the mesh while water may flow out to maintain hydrostatic pressure.

RESULTS

Simulation Procedure

The formation is assumed to be initially water saturated at hydrostatic conditions. An air bubble is formed in the formation by injecting air into the formation for 60 days at a constant rate based on the desired initial air bubble mass, which is a function of the formation radius and porosity (pore volume) and the desired final formation gas saturation value. The formation then "rests" for 40 days (no injection or withdrawal to simulate an equilibration period) before CAES injection and withdrawal begins. CAES injection and withdrawal is based on the initial air bubble mass and continues for 70 days (10 weekly cycles). The minimum and maximum pressure at the borehole/formation interface for the last CAES weekly cycle are evaluated and compared to the minimum and maximum limits. The formation radius is iteratively adjusted until either the desired minimum or maximum pressure is reached.

Example Simulation Results

Base-case results are shown in Figure 4 for a borehole diameter of 7 inches (17.8 cm) with a formation permeability of 500 mD, a porosity of 0.2, and a formation radius of 378 ft (115.3 m). Figure 4a shows the pressure variation of the formation with time as the gas bubble forms, which occurs for the first 60 days with a desired 50% gas saturation, followed by 40 days of zero injection. The initial bubble mass is 2.06×10^7 lbm (9.33×10^6 kg). Based on this initial bubble mass and the CAES cycle, the mass rate is 21.5 lbm/s (9.72 kg/s) during injection and 28.6 lbm/s (12.96 kg/s) during withdrawal. The pressure during cycling is shown in Figure 4b. Time zero occurs when the cycling starts at 100 days; cycling continues for 10 weeks. The minimum and maximum pressures during the last cycle are 708 psia (4.88 MPa) and 1043 psia (7.19 MPa). The formation pressure reaches consistent values from cycle to cycle after about five weekly cycles.

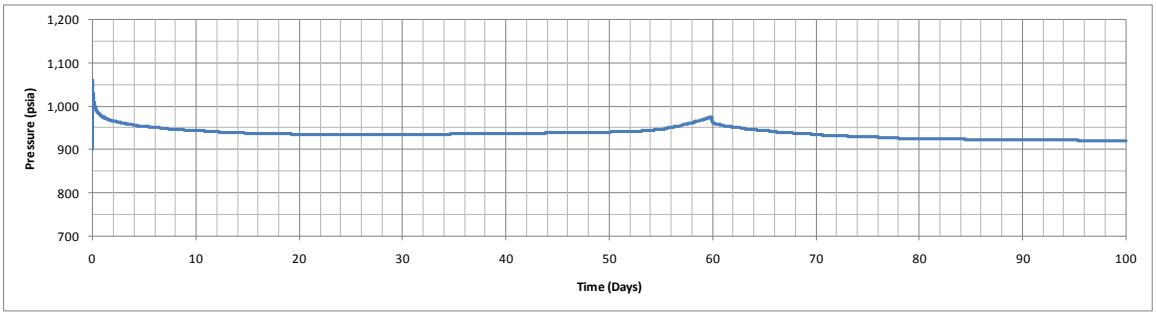

Figure 4a. Formation pressure during air bubble development and rest period

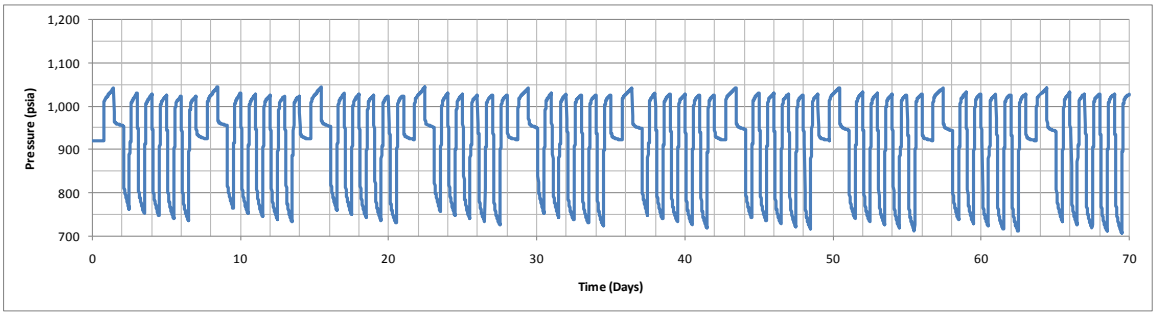

Figure 4a. Formation pressure during air cycling

Formation Radius Results

The base-case simulation results given above are for a given formation radius. The calculated response depends on the formation radius, which is varied by discrete values using the original mesh. Varying the formation radius changes the initial air bubble mass, which, in turn, changes the mass injection and withdrawal rates, which then affect the minimum and maximum pressure at the borehole/formation interface.

Figure 5 shows the CAES borehole withdrawal rate as a function of formation radius for a borehole diameter of 7 inches (17.8 cm), a formation permeability of 500 mD, and a porosity of 0.2. As the formation radius increases, initial air bubble mass/volume increases, as does the injection and withdrawal rate. Figure 6 plots the maximum and minimum borehole/formation pressure at formation depth for different formation radii. The dashed lines are maximum and minimum pressure limits.

The formation radius where the calculated pressure (either minimum or maximum) first crosses a limit is the optimal formation radius for a specific set of formation parameters and depth. The optimal radius is obviously a function of the air-bubble formation parameters, such as the desired gas saturation and the CAES weekly cycle details.

For the base-case formation parameters, the optimum formation radius is about 365 ft (111 m), or slightly less than the value used in the example simulation given above. As can be seen by those results, the minimum pressure shown in Figure 4 (bottom) is slightly below the minimum pressure of 725 psia (5.0 MPa). Consequently, the optimal radius, as well as the corresponding mass injection and withdrawal rates, will be slightly lower than those given in the example.

Note that the mass withdrawal rate influences the minimum pressure, while the mass injection rate results in the maximum pressure. In this case, the pressure limit is due to the mass withdrawal rate.

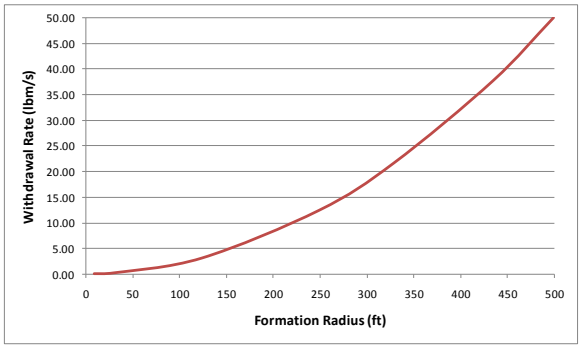

Figure 5. Borehole withdrawal rate vs. formation radius.

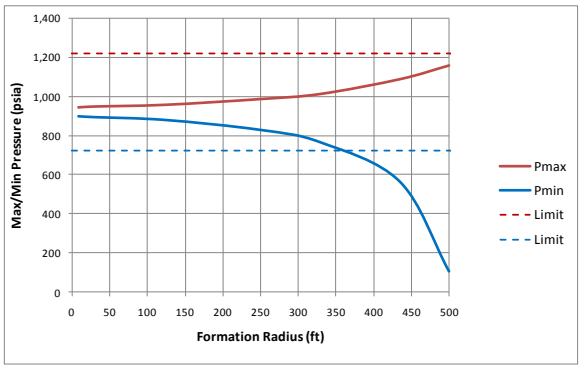

Figure 6. Max/min pressure vs. formation radius.

The results presented above used a permeability of 500 mD and a porosity of 0.2. Sensitivity studies were performed to assess how varying these parameters affected the viability of different formations. The permeability was varied between 100 mD and 2000 mD, while the porosity range was from 0.1 to 0.3. The borehole diameter was also varied from 7 inches to 20 inches. The pressure limit reached in the majority of the cases is the minimum pressure.

Figure 7 summarizes the results. The effect of the borehole diameter is minimal because of the low frictional pressure drop in the borehole. The effect of permeability is larger than porosity. An increase in permeability increases the borehole spacing, while an increase in porosity decreases the borehole spacing.

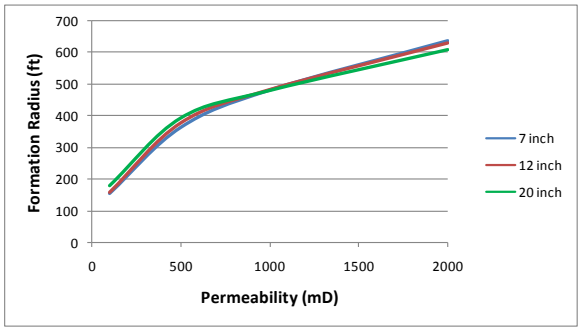

Figure 7a. Effect of permeability and borehole diameter on the formation radius

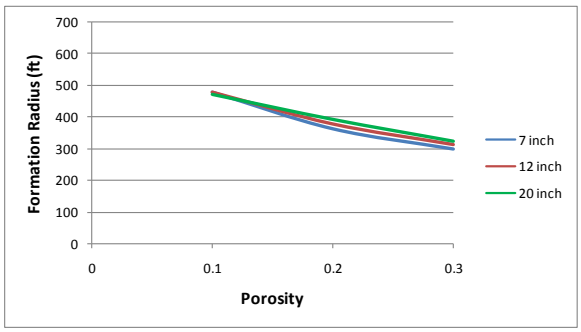

Figure 7b. Effect of porosity and borehole diameter on the formation radius

The formation radius increases with permeability because more of the formation is accessible to the air for a given pressure difference. For porosity, an increase in porosity reduces the formation radius but increases the accessible volume for the air, even for a reduced formation radius.

The results can be further extrapolated to examine MW per borehole and the footprint for a given power plant. Based on Succar and Williams (2008), the power per borehole is approximately 0.335 MW/lbm/s (0.74 MW/kg/s). The approximate MW per borehole is shown in Figures 8a and 8b as a function of permeability and porosity.

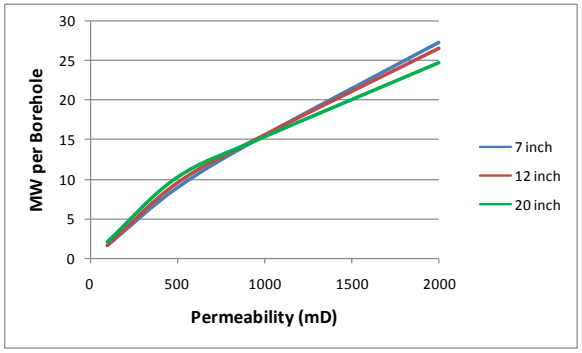

Figure 8a. Effect of permeability and borehole diameter on the MW per borehole

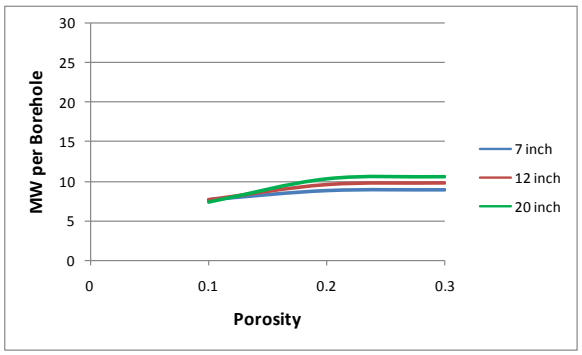

Figure 8b. Effect of permeability and borehole diameter on the MW per borehole

ADDITIONAL STUDIES

The above results are summarized in Webb (2011). Pan et al. (2009, 2011a,b) developed an open borehole model for CO_2 applications. More recently, Pan (2012) extended the open borehole model to the water-air equation of state. Additional studies have been conducted for the present problem using this new model. The current results with the porous medium borehole model assumed a 75 psi (0.5 MPa) pressure drop from the formation to the surface. Using the Pan et al. (2012) borehole model, the pressure drop from the formation to the surface for the base case varied between 45 and 80 psi (0.31–0.55 MPa) with an average value of about 60 psi (0.41 MPa), supporting the previous pressure drop assumption.

Additional studies have also been performed for the simulation model boundary condition. The current results assumed that the bottom of the formation sets the hydrostatic pressure of the formation. In more recent studies, the bottom boundary has been made impermeable, and the outer radius boundary condition establishes hydrostatic conditions for the formation. In this revised case, the formation pressure during air-bubble formation is significantly higher by about 180 psi (1.2 MPa) than the original boundary condition. However, the maximum and minimum cycling pressures are essentially the same as they cycle around the local hydrostatic pressure. Neither set of boundary conditions is correct, but one has to impose hydrostatic conditions somewhere to constrain the results.

SUMMARY AND CONCLUSIONS

A 2-D borehole/formation model was developed for CAES applications to evaluate the performance of the system under various conditions, including two-phase flow. Based on minimum and maximum formation pressure values, the optimal formation radius, which is directly related to borehole spacing, was determined for given sets of formation parameters, borehole diameters, and CAES operating assumptions.

For the conditions addressed in this report, the borehole diameter had a minor influence on all the parameters including the borehole spacing and the power per borehole. These differences are not considered significant due to the uncertainties in the model.

The effect of two formation parameters, permeability and porosity, on the operational parameters was assessed using this model. Changes in formation permeability had a much more dramatic effect than changes in porosity.

These results should help guide the selection of formations for CAES applications by evaluating the influence of different formation parameters. The information on borehole diameter and spacing, and the dependence on formation parameters, can be used to help assess the feasibility of a CAES facility in a reservoir.

ACKNOWLEDGMENT

This work was sponsored by the DOE Energy Storage Systems Program under contract to Sandia National Laboratories. Sandia National Laboratories is a multi-program laboratory managed and operated by Sandia Corporation, a wholly owned subsidiary of Lockheed Martin Corporation, for the U.S. Department of Energy's National Nuclear Security Administration under Contract DE-AC04-94AL85000.

REFERENCES

Corey, A.T., 1954, "The Interrelation Between Gas and Oil Relative Permeabilities," Producers Monthly, pp.38-41, November.

EPRI GS-6688, 1990, Compressed-Air Energy Storage: Pittsfield Aquifer Field Test. Test Data: Engineering Analysis and Evaluation, Final Report.

Katz, D.L. and E.R. Lady, 1976, Compressed Air Storage for Electric Power Generation, Reprinted as an EPRI Report EPRI GS-6784, February 1990.

Leverett, M.C., 1941, "Capillary Behavior in Porous Solids," Trans. Soc. Pet. Eng. AIME, 142, pg 152-169

Pan, L., C.M. Oldenburg, Y.-S. Wu, and K. Pruess, 2009, "Wellbore flow model for carbon dioxide and brine," Energy Procedia, 1(1), 71-78, Proceedings of GHGT9, Nov. 16-20, 2008, Washington DC.

Pan, L., C.M. Oldenburg, Y.-S. Wu, and K. Pruess, 2011a, T2Well/ECO2N Version 1.0: Multiphase and Non-Isothermal Model for Coupled Wellbore-Reservoir Flow of Carbon Dioxide and Variable Salinity Water, LBNL-4291E, Ernest Orlando Lawrence Berkeley National Laboratory, March 11, 2011.

Pan, L., S.W. Webb, and C.M. Oldenburg, 2011b, "Analytical solution for two-phase flow in a wellbore using the drift-flux model," *Advances in Water Resources*, 34:1656-1665.

Pan, L., personal communication, March 16, 2012.

Pruess, K., C. Oldenburg, and G. Moridis, 1999, TOUGH2 User's Guide, Version 2.0,

LBNL-43134, Ernest Orlando Lawrence Berkeley National Laboratory.

Smith, G. C., and L. E. Wiles. 1979. "Analysis of Underground Porous Reservoirs for Compressed Air Energy Storage," In 1978 Compressed Air Energy Storage Symposium Proceedings, pp. 327-367.

Succar, S., and R.H. Williams, 2008, Compressed Air Energy Storage: Theory, Resources, And Applications For Wind Power, Princeton Environmental Institute, Princeton University.

Webb, S.W., 2011a, Borehole and Formation Analyses to Support CAES Development in Reservoirs, SAND2011-2145, Sandia National Laboratories.

van Genuchten, M.Th., 1980, “A Closed-Form Equation for Predicting the Hydraulic Conductivity of Unsaturated Soils,” Soil Sci. Soc., 44:892-898.

Zhou, Q., J.T. Birkholzer, E. Mehnert, Y.-F. Lin, and K. Zhang, 2010, “Modeling Basin- and Plume-Scale Processes of CO_2 Storage for Full-Scale Deployment,” Ground Water, 48:494-514.